AD-A055 654 PENNSYLVANIA STATE UNIV UNIVERSITY PARK DEPT OF MECH--ETC F/G 20/4
SYMPOSIUM ON TURBULENT SHEAR FLOWS HELD AT THE PENNSYLVANIA STA--ETC(U)
APR 77 N00014-77-C-0176

UNCLASSIFIED NL

1 OF 9
ADA
055654

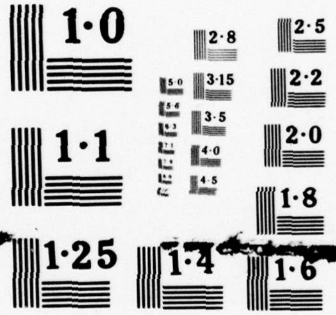

NATIONAL BUREAU OF STANDARDS
MICROCOPY RESOLUTION TEST CHART

AD A055654

DDC FILE COPY

FOR FURTHER TRAN

①

SYMPOSIUM ON

turbulent shear flows

April 18-20, 1977
University Park, Pennsylvania

DDC
RECEIVED
JUN 28 1978
B

Volume I

78 06 08 023

DISTRIBUTION STATEMENT A
Approved for public release;
Distribution Unlimited

DISCLAIMER NOTICE

THIS DOCUMENT IS BEST QUALITY PRACTICABLE. THE COPY FURNISHED TO DDC CONTAINED A SIGNIFICANT NUMBER OF PAGES WHICH DO NOT REPRODUCE LEGIBLY.

DDC
RECEIVED
JUN 23 1978
B

6

Symposium on Turbulent Shear Flows

~~April 18-20, 1977~~

Held at The Pennsylvania State University, University Park, Pennsylvania on April 18-20, 1977.
Volume I.

15 N00014-77-C-0176

11 Apr 1977

12 805p.

Improvements to understanding of the mixing processes associated with turbulent flows have been the aim of investigations over many years and they are increasingly important as technological processes approach and pass limits of available knowledge. Recently, the development of numerical procedures for the solution of conservation equations in discretised form, has provided a means of correlating experimental data and offers the possibilty of predictive capabilities of relevance to engineering flows. Since the time-dependent equations cannot be represented in sufficient detail by the storage of available computers, their time-average forms are usually solved and involve the "closure problem" and the need for turbulence models. Thus, improvements to understanding of turbulent flows are again required but perhaps within a particular framework.

The Symposium on Turbulent Shear Flows was organised with the purpose of advancing the understanding of physical phenomena and existing capabilities for calculating turbulent shear flows. It was arranged to allow the presentation of the latest developments in the calculation of flow and heat-transfer properties of turbulent shear flows and, since the improvement of physical understanding and related measurements were considered essential to this purpose, appropriate emphasis was placed on both topics. Heat transfer and combustion processes involve closure problems similar to those of turbulence models and were included within the scope of the Symposium together with applications of numerical schemes and models to the calculation of properties in problems of engineering significance.

The present Volume contains the papers which were accepted for presentation at the various Sessions and reflects both the intentions of the Organizing Committee and current research emphasis. It is hoped that it will be of value to researchers and engineers and, in particular, that it will provide stimulus for research which will lead to further knowledge of turbulent-flow processes and an even better ability to calculate related properties.

The Organizing Committee wish to acknowledge the financial support of The Pennsylvania State University, the U. S. Army Research office and the U. S. Navy Research office; the cooperation of the American Society of Mechanical Engineers' Heat Transfer and Fluid Engineering Division; the considerable practical assistance of the Department of Mechanical Engineering and Continuing Education of The Pennsylvania State University and in particular the symposium coordinator Ron Avillion; and the essential contributions of their own secretaries.

The many papers submitted to the Symposium were reviewed by members of the Advisory Committee, many of whom also gave of their time and expertise to act as Session Chairmen. The Organizing Committee is glad to acknowledge the considerable assistance of the Advisory Committee as well as the essential contributions of authors and participants.

F. Durst
V. W. Goldschmidt
B. E. Launder
F. W. Schmidt
J. H. Whitelaw

Dr. F. Durst
Sonderforschungsbereich 80
University of Karlsruhe
75 Karlsruhe 1
West Germany

Professor V. W. Goldschmidt
School of Mechanical Engineering
Purdue University
West Lafayette, Indiana 47907, U. S. A.

Dr. B. E. Launder
Department of Mechanical Engineering
University of California - Davis
Davis, California 95616, U. S. A.

Professor F. W. Schmidt
Department of Mechanical Engineering
The Pennsylvania State University
University Park, Pennsylvania 16802, U. S. A.

Professor J. H. Whitelaw
Department of Mechanical Engineering
Imperial College
London SW7 2BX, England

DISTRIBUTION STATEMENT A
Approved for public release;
Distribution Unlimited

78 06 08 023

401929

JOB

SESSION 1

Contents: FREE SHEAR FLOWS-~~1~~I, → to page 3

Chairman: I. Gartshore
Department of Mechanical Engineering
University of British Columbia
Vancouver, Canada

ACCESSION for
NTIS White Section ☑
DDC Buff Section ☐
UNANNOUNCED ☐
JUSTIFICATION
PER LETTER
BY
DISTRIBUTION/AVAILABILITY CODES
Dist. AVAIL. and/or SPECIAL
A 23

SESSION 2

FREE SHEAR FLOWS-2

Chairman: W. Rodi
Sonderforschungsbereich 80
University of Karlsruhe
Karlsruhe, Federal Republic of Germany

SESSION 3

→ IMPINGING JETS; → to page 4

Chairman: A. K. Runchal
Dames and Moore
Los Angeles, California 90017
U.S.A.

SESSION 4

SECOND AND HIGHER ORDER CLOSURES,

→ to page 5

Chairman: W. C. Reynolds
Stanford University
Stanford, California 94305
U.S.A.

SESSION 5

NUMERICAL METHODS

→ to page 6

Chairman: H. McDonald
Scientific Research Associates, Inc.
Glastonburg, Connecticut 06033
U.S.A.

SESSION 6

PLANETARY BOUNDARY LAYERS AND BUOYANT FLOWS

→ to page 7

Co-chairmen:

C. duP. Donaldson
ARAP
Princeton, New Jersey 08540
U.S.A.

J. C. Lumley
Department of Mechanical Engineering
The Pennsylvania State University
University Park, Pennsylvania 16802
U.S.A.

SESSION 7

REACTING FLOWS; → next page

Chairman: H. A. Becker
Queen's University
Kingston, Ontario
Canada

SESSION 8

WALL FLOWS-~~1~~, to page 11

Chairman: T. J. Hanratty
University of Illinois
Urbana, Illinois 61801
U.S.A.

SESSION 9

WALL FLOW-2

Chairman: J. C. Rotta
Institut für Aerodynamik
Güttingen
Federal Republic of Germany

SESSION 10

WALL FLOWS-3

Chairman: J. Mathieu
Ecole Centrale de Lyonnaise
Ecully, France

SESSION 11

LARGE SCALE STRUCTURE → to page 13

Chairman: L. Bradbury
Department of Mechanical Engineering
University of Surrey
Guildford, Surrey
United Kingdom

SESSION 12

GENERAL SESSION-1

Co-chairmen: L. H. Back
J. P. L.
Pasadena, California 91103
U.S.A.

J. J. D. Domingos
Instituto Superio Technico
Lisbon 1, Portugal

SESSION 13

RECIRCULATING FLOW - 1e, → next page

Chairman: K. Owen
NASA Ames Research Center
Moffet Field, California
U.S.A.

SESSION 14

SUB-GRID SCALE MODELLING; and → next page

Chairman: J. Herring
NCAR
Boulder, Colorado 80303
U.S.A.

SESSION 15

PASSIVE SCALAR TRANSPORT

Chairman: P. A. Libby
University of California, San Diego
La Jolla, California
U.S.A.

SESSION 16

OPEN FORUM

5 Minute Presentations

SESSION 17

GENERAL SESSION-2

Chairman: W. P. Jones
Department of Chemical Engineering
Imperial College
London SW7 2BX
United Kingdom

SESSION 18

RECIRCULATING FLOWS-2

Chairman: A. D. Gosman
Department of Mechanical Engineering
Imperial College
London SW7 2BX
United Kingdom

SESSION 1

FREE SHEAR FLOWS-1

Chairman: I. Gartshore
Department of Mechanical Engineering
University of British Columbia
Vancouver, Canada

INTERMITTENCY IN FREE TURBULENT SHEAR FLOWS

Cesar Dopazo
Department of Applied Science
Brookhaven National Laboratory
Upton, New York 11973

Edward E. O'Brien
Department of Mechanical Engineering
State University of New York
Stony Brook, New York 11794

ABSTRACT

A formalism previously used in the context of deformable porous media and turbulent/nonturbulent intermittent flows is restated here. The behavior of the intermittency function derivatives at the interface gives rise to surface integrals over the latter. The conditioned equations of continuity, momentum, energy, vorticity and conservation of a scalar are derived for the turbulent and irrotational zones. Surface integrals with a precise physical meaning enter the conditioned equations. They can be interpreted as entrainment of mass, momentum, energy and scalar, and as direct interactions between the turbulent and irrotational regions. Use is made of the experimental conditioned measurements for: (i) the plane wake behind a heated flat plate, and (ii) the heated turbulent round jet; the profiles of entrainment of mass, and the combination of direct interactive force and entrainment of momentum are calculated. These derived profiles are compared with models proposed by previous investigators.

NOMENCLATURE

C - molecular flux of scalar through the interface, Eq. (41).
D - orifice diameter for the jet
dS - interface surface infinitesimal element
E - entrainment of mass per unit mass, Eq. (17).
$\underset{\sim}{F}$ - mean force per unit mass of turbulent on irrotational zones
f_1, f_2, f_3, f_4 - self-preserving functions defined by Eqs. (51)-(64).
f_γ - interface crossing rate
g, h^2 - self-preserving functions defined by Eqs. (54) and (63)
I - intermittency function
K - entrainment of total kinetic energy, Eq. (30)
$\ell(x)$ - half-width of the wake based on velocity defect
$\underset{\sim}{M}$ - average entrainment of momentum, Eq. (21)
$\underset{\sim}{n}$ - normal to the interface, pointing towards the turbulent zone
P, Q - any fluid mechanical variables
p - pressure
$\underset{\sim}{q}$ - molecular scalar flux vector
r - radial coordinate for the jet
$r_{\frac{1}{2}}$ - half-radius of the jet based on velocity
$S(\underset{\sim}{x}, t)$ - surface of the turbulent/nonturbulent interface
T - scalar
T_m - maximum value of T at a section of the jet
t - time
U_J - jet exit velocity
U_m - maximum value of the mean velocity at a section of the jet
U_o - free stream velocity for the wake
U_s - velocity defect at the centerplane of the wake
$\underset{\sim}{u}$ - velocity vector
$\underset{\sim}{u}^s$ - interface velocity
u, v - x and y (or r) velocity components
V - elementary control volume
v^e - modulus of the velocity of advance of the interface relative to a fluid element at the same point
W - mechanical work done by the turbulent fluid upon the irrotational fluid
w - tangential velocity component for the jet
$\underset{\sim}{x}$ - position vector
x, y - streamwise and normal coordinates
γ - intermittency factor
δ_m - momentum thickness of the boundary layer at the trailing edge of the plate
δ_{ij} - Kronecker delta
η - similarity variable
Θ - mean entrainment of scalar T
μ - viscosity of the fluid
ν - kinematic viscosity of the fluid
ρ - density of the fluid
σ_{ij} - viscous stress tensor
ϕ - $\frac{\sigma_{ij}}{\rho}\frac{\partial u_i}{\partial x_j}$ in the kinetic energy equations
ω_i - vorticity component

Subscripts

$1, 0$ - relative to turbulent and irrotational zone variables
i - vector component
r - axial component of a vector
x, y - streamwise and normal components of a vector

Special Symbols

∇ - gradient operator
∇^2 - laplacian operator
$\sim$ - vector variable
$\overline{}$ - average
$'$ - fluctuating variable or function derivative

INTRODUCTION

Since the discovery of intermittency in free turbulent shear flows by Corrsin (2) and its exploration in subsequent studies by Townsend (10) and Corrsin and Kistler (3), the concept of an intermittency function has been widely used in experimental investigations. The intermittency function allows one to identify separately the turbulent and nonturbulent regions coexisting in an intermittent flow. A more adequate description of velocity and scalar fields can then be provided. The conditional sampling technique (1,6,12,13) multiplies the random variable to be averaged by a generated signal which is unity in the turbulent and zero in the nonturbulent regions, i.e. an intermittency function. The same device has not received much attention in theoretical studies of turbulent shear flows. Quite recently, Libby (7,8) initiated the first theoretical use of the intermittency concept to condition the conservation equations of fluid mechanics for both turbulent and nonturbulent variables; central to Libby's methodology is the postulate of a conservation equation for the intermittency function with an unknown source term, described as a creation of turbulent fluid. Another crucial point is his definition of conditioned fluctuations in terms of the unconditioned variables. They then have no simply physical meaning. With the assumption of a knowledge of the unconditioned velocity components, a subsequent computation of the unconditioned Reynolds stress and with certain additional modeling assumptions he was able to predict conditioned variables and the intermittency factor for mixing layers, boundary layers and wakes. Tutu (12) made use of Libby's concepts but defined fluctuations in turbulent zone variables as fluctuations about the conditioned mean. He obtained the conditioned equations and proposed modeling approximations for the unknown functions which appear. The meanings ascribed by Libby and Tutu to the source term differ one from the other, and, being highly intuitive, are not entirely clear. Analogous to this conditioning problem is that of obtaining the equations governing the flow through deformable porous media (5). The ideas in (5) were extended to the present problem in (4). Dopazo (4) avoided the postulate of a conservation equation for the intermittency function by examining the spatial and temporal derivatives of the intermittency function at the turbulent/nonturbulent interface; rigorous fundamental formulae were derived and used to obtain the conditioned equations. The main advantage of the latter method over that of Libby is that every unknown entering the zone average equations has a clearly defined physical meaning. One expects this direct connection with physics be of help in constructing modeling approximations for these unknown terms.

In the present paper the fundamental formulae used by Dopazo (4) are restated. The zone average equations of continuity, momentum, kinetic energy and conservation of a scalar are then presented. The physical meaning of the surface integrals in the conditioned equations is explained; special emphasis is put on these terms since they are the ones which directly couple the motions in the turbulent and nonturbulent regions. The remaining terms in the equations can readily be interpreted as conditioned production, dissipation, convection, diffusion and pressure transport. Such notions as entrainment of mass, momentum, kinetic energy and scalar content clearly appear in the context of this formalism.

The experimental results for the two-dimensional wake behind a heated flat plate (1) and the axisymmetric turbulent heated jet (12) are utilized to evaluate semi-quantitatively the profiles of the unknown terms. Due to the lack of complete experimental data self-preservation of the turbulence (9,11) has been assumed. Our evaluated profiles for entrainment of mass and momentum are compared to those proposed by Tutu (12) and Libby (7,8). The actual profiles and a better physical understanding of the phenomenon should be helpful in constructing convincing modeling assumptions, namely, the expression of entrainment of mass and momentum in terms of the intermittency, mean conditioned velocity, conditioned Reynolds stress and crossing frequency.

The usefulness of this methodology is discussed and its possible application to reacting and nonreacting transport of scalars in turbulent flows, e.g. the plume of a point source is mentioned.

METHODOLOGY

Fundamental Formulae

Let $I(\underline{x},t)$ be the intermittency function defined as

$$I(\underline{x},t) = \begin{cases} 1 \text{ if } (\underline{x},t) \text{ is in the turbulent zone} \\ 0 \text{ if } (\underline{x},t) \text{ is in the nonturbulent zone.} \end{cases}$$

Let $Q(\underline{x},t)$ be any fluid mechanical property. The following formulae are presented in Dopazo (4) and their derivation is explained therein.

$$\overline{I\nabla Q} = \nabla\overline{QI} - \lim_{V\to 0} \overline{\frac{1}{V}\int_{S(\underline{x},t)} Q\,\underline{n}\,dS} \tag{1}$$

$$\overline{I\frac{\partial Q}{\partial t}} = \frac{\partial}{\partial t}\overline{QI} + \lim_{V\to 0} \overline{\frac{1}{V}\int_{S(\underline{x},t)} Q\,\underline{u}^s\cdot\underline{n}\,dS} \tag{2}$$

The last terms in equations (1) and (2) arise due to the discontinuities of $I(\underline{x},t)$ at the interface $S(\underline{x},t) = 0$; ∇I and $\partial I/\partial t$ are Dirac δ-functions at the interface location and at the time of crossing of the interface respectively. V is an elementary control volume, $\underline{n}$ is the normal to the turbulent/nonturbulent interface pointing towards the turbulent region and $\underline{u}^s$ is the velocity of the interface relation to a fixed observer. Note that the interface, $S(x,t) = 0$, is not a material surface and its velocity $\underline{u}^s$ can be written as

$$\underline{u}^s = \underline{u} - v^e\underline{n} \tag{3}$$

where $\underline{u}$ is the instantaneous velocity of the fluid element at $S(\underline{x},t) = 0$ and $-v^e\underline{n}$ is the velocity of advance of an element of the surface relative to the fluid element at the same point (4).

Decomposition of Averages

Let P and Q be two intermittent signals for two fluid mechanical variables. Let their unconditioned averages be $\bar{P}$ and $\bar{Q}$ and their conditioned averages be defined by

$$\bar{P}_1 = \frac{\overline{IP}}{\gamma} \tag{4}$$

$$\bar{Q}_1 = \frac{\overline{IQ}}{\gamma} \tag{5}$$

$$\bar{P}_0 = \frac{\overline{(1-I)P}}{1-\gamma} \tag{6}$$

$$\bar{Q}_0 = \frac{\overline{(1-I)Q}}{1-\gamma} \tag{7}$$

where the subscripts 1 and 0 refer to the turbulent and nonturbulent zone variables respectively and the intermittency, γ, is defined as

$$\gamma = \bar{I}\,. \tag{8}$$

Let P_1', Q_1', P_0' and Q_0' be the fluctuations in the turbulent and irrotational regions relative to the zone averages of P and Q. Then

$$\overline{IPQ} = \gamma \bar{P}_1 \bar{Q}_1 + \gamma \overline{P_1'Q_1'} \tag{9}$$

$$\overline{(1-I)PQ} = (1-\gamma)\bar{P}_0\bar{Q}_0 + (1-\gamma)\overline{P_0'Q_0'} \tag{10}$$

Note that variables with subscript 1 are only defined in the turbulent region while those with 0 are defined in the irrotational zone. The averages of 1 or 0 variables or their products are therefore only over the corresponding domains of definition. The decomposition in (9) and (10) are different from Libby's (7) as was already remarked (4).

Intermittency Variations

Let Q ≡ 1 in equations (1) and (2). Then (4)

$$\nabla\gamma = \lim_{V\to 0} \frac{1}{V}\int_{S(\underset{\sim}{x},t)} \underset{\sim}{n}\, dS \tag{11}$$

$$\frac{\partial\gamma}{\partial t} = \lim_{V\to 0} \overline{\frac{1}{V}\int_{S(\underset{\sim}{x},t)} \underset{\sim}{u}^s \cdot \underset{\sim}{n}\, dS} \tag{12}$$

A detailed knowledge of the interface dynamics is needed to evaluate the right side of equations (11) and (12). If the flow is statistically stationary identical positive and negative values of $\underset{\sim}{u}^s \cdot \underset{\sim}{n}$ are equally probable.

FUNDAMENTAL EQUATIONS

The equations governing the motion of a fluid in a turbulent/nonturbulent flow are

$$\frac{\partial u_i}{\partial x_i} = 0 \tag{13}$$

$$\frac{\partial u_i}{\partial t} = \frac{\partial u_i u_j}{\partial x_j} = -\frac{1}{\rho}\frac{\partial p}{\partial x_i} + \frac{1}{\rho}\frac{\partial \sigma_{ij}}{\partial x_j} \tag{14}$$

$$\sigma_{ij} = \mu\left(\frac{\partial u_i}{\partial x_j} + \frac{\partial u_j}{\partial x_i}\right) \tag{15}$$

where $\underset{\sim}{u}$ is the velocity, ρ the density, p the pressure, σ_{ij} the viscous stress tensor and μ the viscosity.

To condition the conservation equations one should multiply them by I or (1-I), average them and use equations (1) and (2). This method was utilized to obtain the mean conservation equations in reference (4).

Turbulent Zone Continuity

$$\frac{\partial\gamma}{\partial t} + \frac{\partial\gamma\overline{(u_1)_i}}{\partial x_i} = E \tag{16}$$

where $\underset{\sim}{u}_1$ is the turbulent zone velocity signal and

$$E = \lim_{V\to 0} \overline{\frac{1}{V}\int_S v^e dS} \tag{17}$$

is the volumetric entrainment per unit volume, or the massic entrainment per unit mass.

Irrotational Zone Continuity

$$\frac{\partial(1-\gamma)}{\partial t} + \frac{\partial(1-\gamma)\overline{(u_0)_i}}{\partial x_i} = -E \tag{18}$$

where $\underset{\sim}{u}_0$ is the irrotational zone velocity signal.

Unconditioned Continuity

Adding equations (16) and (18) and taking into account that $\bar{u}_i = \gamma\overline{(u_1)_i} + (1-\gamma)\overline{(u_0)_i}$ one gets

$$\frac{\partial\bar{u}_i}{\partial x_i} = 0 \tag{19}$$

which is the conventional mean continuity equation. While $\bar{u}_i$ is solenoidal, $\overline{(u_1)_i}$ and $\overline{(u_0)_i}$ are not.

Turbulent Zone Momentum

$$\frac{\partial\gamma\overline{(u_1)_i}}{\partial t} + \frac{\partial\gamma\overline{(u_1)_i}\,\overline{(u_1)_j}}{\partial x_j} + \frac{\partial}{\partial x_j}\gamma\overline{(u_1')_i(u_1')_j} = -\frac{1}{\rho}\frac{\partial\gamma\bar{P}_1}{\partial x_i}$$
$$+ \nu\nabla^2[\gamma\overline{(u_1)_i}] + M_i - F_i \tag{20}$$

where $\underset{\sim}{u}_1'$ is the turbulent zone velocity fluctuation, $\bar{p}_1$ is the turbulent zone mean pressure and

$$M_i = \lim_{V\to 0} \overline{\frac{1}{V}\int_S \rho u_i v^e dS} \tag{21}$$

$$F_i = \frac{1}{\rho}\lim_{V\to 0} \overline{\frac{1}{V}\int_S (-p\delta_{ij} + \sigma_{ij})n_j dS}$$
$$+ \nu\frac{\partial}{\partial x_j}\lim_{V\to 0} \overline{\frac{1}{V}\int_S (u_i n_j + u_j n_i) dS} \tag{22}$$

$\underset{\sim}{M}$ is the average entrainment of momentum, i.e. the momentum flux through the interface. $\underset{\sim}{F}$ is the mean force per unit mass that the turbulent fluid exerts upon the irrotational fluid. The meaning of the last term is indicated in reference (4). $\overline{(u_1')_i(u_1')_j}$ is the conditional Reynolds stresses.

Irrotational Zone Momentum

$$\frac{\partial(1-\gamma)\overline{(u_0)_i}}{\partial t} + \frac{\partial(1-\gamma)\overline{(u_0)_i}\,\overline{(u_0)_j}}{\partial x_j} + \frac{\partial}{\partial x_j}(1-\gamma)(u_0')_i(u_0')_j$$
$$= -\frac{1}{\rho}\frac{\partial(1-\gamma)\bar{p}_0}{\partial x_i} + \nu\nabla^2[(1-\gamma)\overline{(u_0)_i}] - M_i + F_i \tag{23}$$

where u_0' is the irrotational zone velocity fluctuations and $\bar{p}_0$ is the irrotational zone mean pressure. Note that the entrainmentof momentum $\underset{\sim}{M}$ and the mean force $\underset{\sim}{F}$ have opposite signs in equations (20) and (23), i.e. fluid is entrained into the turbulent region at the expense of the irrotational zone, and the action $\underset{\sim}{F}$ of the turbulent on the irrotational zones has opposite sign to the reaction-$\underset{\sim}{F}$ of the irrotational upon the turbulent regions.

Unconditioned Momentum

Adding (20) and (23) and taking into account that

$$\overline{u_i}\,\overline{u_j} + \overline{u_i'u_j'} = \gamma\overline{(u_1)_i}\,\overline{(u_1)_j} + (1-\gamma)\overline{(u_0)_i}\,\overline{(u_0)_j}$$
$$+ (1-\gamma)\overline{(u_1')_i}\,\overline{(u_1')_j} + (1-\gamma)\overline{(u_0')_i}\,\overline{(u_0')_j} \tag{24}$$

and $\bar{p} = \gamma\bar{p}_1 + (1-\gamma)\bar{p}_0$ (25)

one obtains

$$\frac{\partial\bar{u}_i}{\partial t} + \frac{\partial u_i u_j}{\partial x_j} + \frac{\partial u_i' u_j'}{\partial x_j} = -\frac{1}{\rho}\frac{\partial\bar{p}}{\partial x_i} + \nu\nabla^2\bar{u}_i \tag{26}$$

which is the conventional mean momentum equation.

Unconditioned Kinetic Energy

If equation (14) is multiplied by u_i one readily obtains

$$\frac{\partial \tfrac{1}{2}u_iu_i}{\partial t} + \frac{\partial u_j\tfrac{1}{2}u_iu_i}{\partial x_j} = -\frac{1}{\rho}\frac{\partial pu_i}{\partial x_i} + \frac{\partial}{\partial x_j}u_i\sigma_{ij} - \frac{1}{\rho}\sigma_{ij}\frac{\partial u_i}{\partial x_j} \tag{27}$$

Ensemble averaging of equation (27) yields

$$\frac{\partial}{\partial t}\frac{1}{2}\overline{u_iu_i} + \frac{\partial}{\partial x_j}u_j\frac{1}{2}\overline{u_iu_i} + \frac{\partial}{\partial x_j}\overline{u_j'\tfrac{1}{2}u_iu_i} = -\frac{1}{\rho}\frac{\partial\overline{pu_i}}{\partial x_i}$$
$$+\frac{1}{\rho}\frac{\partial}{\partial x_j}\overline{u_i\sigma_{ij}} - \frac{1}{\rho}\overline{\sigma_{ij}\frac{\partial u_i}{\partial x_j}} \tag{28}$$

which is the unconditioned total kinetic energy equation. Multiplication of equation (27) by I and (1-I), averaging and use of formulae (1) and (2) yield the:

Turbulent Zone Total Kinetic Energy

$$\frac{\partial}{\partial t}\overline{I\tfrac{1}{2}u_iu_i} + \frac{\partial}{\partial x_j}\overline{Iu_j\tfrac{1}{2}u_iu_i} = -\frac{1}{\rho}\frac{\partial\overline{Ipu_i}}{\partial x_i} + \nu\nabla^2\overline{I\tfrac{1}{2}u_iu_i} - \overline{I\phi}$$
$$+ K - W \tag{29}$$

where

$$\overline{I\phi} = \frac{1}{\rho}\overline{I\sigma_{ij}\frac{\partial u_i}{\partial x_j}}$$

is the conditioned energy dissipation in the turbulent region and

$$K = \lim_{V\to 0}\overline{\frac{1}{V}\int_S \tfrac{1}{2}u_iu_iv^e dS} \tag{30}$$

$$W = \frac{1}{\rho}\lim_{V\to 0}\overline{\frac{1}{V}\int_S(-p\delta_{ij}+\sigma_{ij})u_in_jdS}$$
$$-\nu\frac{\partial}{\partial x_j}\lim_{V\to 0}\overline{\frac{1}{V}\int_S(\tfrac{1}{2}u_in_j+u_jn_i)u_idS} \tag{31}$$

K is the entrainment of total kinetic energy into the turbulent zone and W is the mechanical work done by the turbulent fluid upon the nonturbulent.

Irrotational Zone Total Kinetic Energy

$$\frac{\partial}{\partial t}\overline{(1-I)\tfrac{1}{2}u_iu_i} + \frac{\partial}{\partial x_j}\overline{(1-I)u_j\tfrac{1}{2}u_iu_j} = -\frac{1}{\rho}\frac{\partial\overline{(1-I)pu_i}}{\partial x_j}$$
$$+\nu\nabla^2\overline{(1-I)\tfrac{1}{2}u_iu_i} - \overline{(1-I)\phi} - K + W \tag{32}$$

Equation (28) can be recovered by adding equations (29) and (32).

Equations for the unconditioned, turbulent zone and irrotational zone fluctuating kinetic energies can easily be obtained following the traditional method (9,11). The actual equations will not be presented here. One important remark in connection with the energy balance is that previous investigators [e.g., Wygnanski and Fiedler (13)] do forget K and W in the energy balance. Therefore, the turbulent zone energy balance must necessarily be in error, and the pressure transport computed from the measured convection, diffusion, production and dissipation may not be reliable.

Turbulent Zone Vorticity

Since $(1-I)\omega_i \equiv 0$, $\omega_i \equiv I\omega_i$ and the equation for the conditioned vorticity is the same as that for the unconditioned vorticity. This equation is

$$\frac{\partial\overline{I\omega_i}}{\partial t} + \frac{\partial\overline{I\omega_i\omega_j}}{\partial x_j} = \overline{\omega_j\frac{\partial Iu_i}{\partial x_j}} + \nu\nabla^2\overline{I\omega_i} \tag{33}$$

this implies a balance between "entrainment of vorticity", "vortex line stretching" and "vorticity viscous propagation terms" at the interface, namely,

$$\lim_{V\to 0}\overline{\frac{1}{V}\int_S\omega_iv^edS} - \lim_{V\to 0}\overline{\frac{1}{V}\int_S u_i\omega_jn_jdS}$$
$$-\nu\left(\frac{\partial}{\partial x_j}\lim_{V\to 0}\overline{\frac{1}{V}\int_S\omega_in_jdS} + \lim_{V\to 0}\overline{\frac{1}{V}\int_S\frac{\partial\omega_i}{\partial x_j}n_jdS}\right) = 0 \tag{34}$$

Generalized Corrsin-Kistler equation

The following identity is always true (7)

$$(1-I)\omega_i \equiv 0 \tag{35}$$

Use of equation (35) multiplied by u_j and averaged yields (4)

$$\frac{\partial}{\partial x_j}(1-\gamma)\overline{(u_0)}_i\overline{(u_0)}_j - \frac{1}{2}\frac{\partial}{\partial x_i}(1-\gamma)\overline{(u_0)}_j\overline{(u_0)}_j$$
$$+\frac{\partial}{\partial x_j}(1-\gamma)\overline{(u_0')_i(u_0')_j} - \frac{1}{2}\frac{\partial}{\partial x_i}(1-\gamma)\overline{(u_0')_j(u_0')_j}$$
$$+\lim_{V\to 0}\overline{\frac{1}{V}\int_S(u_iu_jn_j - \tfrac{1}{2}u_ju_jn_i)dS} = 0 \tag{36}$$

The last term in equation (36) is associated with momentum fluxes through the interface.

Corrsin-Kistler equation (3) relating Reynolds stresses and turbulent kinetic energy in the irrotational zone can be recovered from equation (36) in the limit $\gamma\to 0$ and $\overline{\underline{u}_0}\to$ constant vector; in that limit since there are no interface crossings the last term in (36) tends to zero and one recovers (4)

$$\frac{\partial}{\partial x_j}\overline{(u_0')_i(u_0')_j} = \frac{1}{2}\frac{\partial}{\partial x_i}\overline{(u_0')_j(u_0')_j} \tag{37}$$

Turbulent Zone Scalar

Let T be a scalar (e.g. the temperature field in a turbulent heated jet) satisfying the equation

$$\frac{\partial T}{\partial t} + \frac{\partial u_jT}{\partial x_j} = -\frac{\partial q_j}{\partial x_j} \tag{38}$$

where q is the "scalar flux vector" due to molecular agitation. Multiplication by I, averaging and use of equations (1) and (2) yields

$$\frac{\partial\gamma\overline{T_1}}{\partial t} + \frac{\partial\gamma\overline{(u_1)}_j\overline{T_1}}{\partial x_j} + \frac{\partial}{\partial x_j}\gamma\overline{(u_1')_jT_1'} = -\frac{\partial\gamma\overline{(q_1)}_j}{\partial x_j}\quad\Theta + C \tag{39}$$

where T_1 is the turbulent zone scalar signal, T_1' are the turbulent zone scalar fluctuations about $\overline{T_1}$ and $\overline{q_1}$ is the turbulent zone mean "scalar flux vector" due to molecular effects and

$$\Theta = \lim_{V\to 0}\overline{\frac{1}{V}\int_S Tv^edS} \tag{40}$$

$$C = \lim_{V\to 0}\overline{\frac{1}{V}\int_S q_jn_jdS} \tag{41}$$

Θ is the mean entrainment of scalar T into the turbulent region and C is the molecular flux of scalar through the interface.

Irrotational Zone Scalar

$$\frac{\partial(1-\gamma)\bar{T}_0}{\partial t} + \frac{\partial}{\partial x_j}(1-\gamma)\overline{(u_0)_j}\bar{T}_0 + \frac{\partial}{\partial x_j}(1-\gamma)\overline{(u_0')_j T_0'}$$

$$= -\frac{\partial(1-\gamma)\overline{(q_0)_j}}{\partial x_j} - \Theta - C \qquad (41)$$

$\bar{T}_0$, T_0' and $\bar{q}_0$ are the counterpart of $\bar{T}_1$, T_1' and $\bar{q}_1$ in the irrotational region.

Unconditioned Scalar

Addition of (39) and (41) yields

$$\frac{\partial\bar{T}}{\partial t} + \frac{\partial}{\partial x_j}\bar{u}_j\bar{T} + \frac{\partial}{\partial x_j}\overline{u_j'T'} = -\frac{\partial\bar{q}_j}{\partial x_j}$$

which can also be obtained by directly averaging (38). Recall that $\bar{T} = \gamma\bar{T}_1 + (1-\gamma)\bar{T}_0$ and $\bar{\underset{\sim}{q}} = \gamma\bar{\underset{\sim}{q}}_1 + (1-\gamma)\bar{\underset{\sim}{q}}_0$.

ENTRAINMENT PROFILES

The above equations have been particularized for the following two cases:

1. The plane wake behind a heated flat plate (1). A thin aluminum plate was mounted in a low speed wind tunnel, with the plate horizontal and parallel to the mean flow direction. The upper and lower side boundary layers formed were tripped near the leading edge of the plate. The plane turbulent wake behind the trailing edge was studied. A thermal wake was also generated by heating the plate, but only the velocity measurements are utilized here.

2. The heated turbulent round jet (12). An axisymmetric horizontal heated jet emerges into a room. The exit diameter is D = 9 in. A set of screens and a honeycomb were introduced to reduce the exit turbulence intensity level to a minimum. The diffuser was insulated with fiber glass and a collar heater was provided at the end of the contraction.

The statistically stationary equations to be considered are the following:

Plane Wake Turbulent Zone

$$\frac{\partial\gamma\bar{u}_1}{\partial x} + \frac{\partial\gamma\bar{v}_1}{\partial y} = E \qquad (42)$$

$$\gamma\bar{u}_1\frac{\partial\bar{u}_1}{\partial x} + \gamma\bar{v}_1\frac{\partial\bar{u}_1}{\partial y} + \frac{\partial}{\partial x}\gamma\overline{u_1'^2} + \frac{\partial}{\partial y}\gamma\overline{u_1'v_1'}$$

$$= -\frac{1}{\rho}\frac{\partial\gamma\bar{p}_1}{\partial x} + \nu\nabla^2\gamma\bar{u}_1 - F_x + M_x - \bar{u}_1E \qquad (43)$$

$$\gamma\bar{u}_1\frac{\partial\bar{v}_1}{\partial x} + \gamma\bar{v}_1\frac{\partial\bar{v}_1}{\partial y} + \frac{\partial}{\partial x}\gamma\overline{u_1'v_1'} + \frac{\partial}{\partial y}\gamma\overline{v_1'^2}$$

$$= -\frac{1}{\rho}\frac{\partial\gamma\bar{p}_1}{\partial y} + \nu\nabla^2\gamma\bar{v}_1 - F_y + M_y - \bar{v}_1E \qquad (44)$$

where x is the streamwise coordinate and y is perpendicular to x and the flat plate, $\bar{u}_1$ and $\bar{v}_1$ are the x and y mean turbulent zone velocities, respectively, u_1' and v_1' are the zone fluctuating velocities along x and y, respectively.

Heated Turbulent Round Jet

$$\frac{\partial\gamma\bar{u}_1}{\partial x} + \frac{1}{r}\frac{\partial}{\partial r}(r\gamma\bar{v}_1) = E \qquad (45)$$

$$\gamma\bar{u}_1\frac{\partial\bar{u}_1}{\partial x} + \gamma\bar{v}_1\frac{\partial\bar{u}_1}{\partial r} + \frac{\partial}{\partial x}\gamma\overline{u_1'^2} + \frac{1}{r}\frac{\partial}{\partial r}r\gamma\overline{u_1'v_1'}$$

$$= -\frac{1}{\rho}\frac{\partial\gamma\bar{p}_1}{\partial x} + \nu\nabla^2\gamma\bar{u}_1 - F_x + M_x - \bar{u}_1E \qquad (46)$$

$$\gamma u_1\frac{\partial\bar{v}_1}{\partial x} + \gamma\bar{v}_1\frac{\partial\bar{v}_1}{\partial y} + \frac{\partial}{\partial x}\gamma\overline{u_1'v_1'} + \frac{1}{r}\frac{\partial}{\partial r}r\gamma\overline{v_1'^2} - \frac{\gamma}{r}\overline{w_1'^2}$$

$$= -\frac{1}{\rho}\frac{\partial\gamma\bar{p}_1}{\partial r} + \nu\left(\nabla^2\gamma\bar{v}_1 - \frac{\gamma\bar{v}_1}{r^2}\right) - F_r + M_r - \bar{v}_1E \qquad (47)$$

$$\gamma\bar{u}_1\frac{\partial\bar{T}_1}{\partial x} + \gamma\bar{v}_1\frac{\partial\bar{T}_1}{\partial r} + \frac{\partial}{\partial x}\gamma\overline{u_1'T_1'} + \frac{1}{r}\frac{\partial}{\partial r}r\gamma\overline{v_1'T_1'}$$

$$= -\frac{\partial\gamma\overline{(q_1)_x}}{\partial x} - \frac{1}{r}\frac{\partial}{\partial r}r\gamma\overline{(q_1)}_r + C + \Theta - \bar{T}_1E \qquad (48)$$

The equations are in cylindrical coordinates x being the streamwise and r theradial directions, w_1' is the fluctuating velocity in the angular direction and $\overline{(q_1)_x}$ and $\overline{(q_1)_r}$ are the x and r components of the "mean scalar molecular zone flux".

Assumptions

Extensive data are available for conditioned and unconditioned variables forthe heated turbulent jet at a single downstream location x/D = 15. The same is true for the plane wake at several downstream locations x/δ_m = 200 and 345. D and δ_m are, respectively, the jet exit diameter and themomentum thickness of the boundary layers at the trailing edge of the plate. Although self-preservation has almost surely not been achieved at the measuring stations, in the absence of experimental data to computethe x and y (or x and r) derivatives self-preservation for the jet and wake has been assumed. Direct measurements of the x-derivatives in the heated jet facility will hopefully soon be available and one will then be able to make a decision on the effect of the assumption of self-preservation. The traditional boundary layer approximation (9,11) were used to simplify equations (42) through (48). Moreover, we assumedthat $\overline{p_1}$ and $\overline{v_1'^2}$ satisfy the unconditioned cross-stream momentum equation, i.e.

$$\frac{\partial\overline{v_1'^2}}{\partial y} = -\frac{1}{\rho}\frac{\partial\bar{p}_1}{\partial y} \qquad (49)$$

$$\frac{1}{r}\frac{\partial}{\partial r}(r\overline{v_1'^2}) - \frac{\overline{w_1'^2}}{r} = -\frac{1}{\rho}\frac{\partial\bar{p}_1}{\partial r} \qquad (50)$$

and that $(-F_y + M_y - \bar{v}_1E)$ and $(-F_r + M_r - \bar{v}_1E)$ depend only weakly on x. E and theright sides of (43) and (44) and (46)-(48) were then computed by calculating the remaining terms in the equations from the experimental data.

Plane Wake

The following definitions were used

$$\gamma = f_1(\eta) \qquad (51)$$

$$\frac{U_0-\bar{u}_1}{U_s(x)} = f_2(\eta) \qquad (52)$$

$$-\overline{u_1'v_1'} = U_s^2(x)g(\eta) \qquad (53)$$

$$\overline{v_1'^2} = U_s^2(x)h^2(\eta) \qquad (54)$$

$$\eta = \frac{y}{\ell(x)} \qquad (55)$$

$$\frac{U_s(x)}{U_0} = 1.58\frac{\delta_m^{1/2}}{x^{1/2}} \qquad (56)$$

$$\ell(x) = .252\,\delta_m^{1/2}x^{1/2} \qquad (57)$$

where U_o is the free-stream velocity, U_s is the velocity defect at the centerplane, $\ell(x)$ is the half-width of the wake based on velocity defect, δ_m is the momentum thickness of the boundary layer at the trailing edge of the plate. Equations (56) and (57) were taken from Tennekes and Lumley (9). The equations used are the following:

$$f_1'(\eta)h^2(\eta) = -\frac{F_y}{(U_s{}^2/\ell)} + \frac{M_y - \bar{v}_1 E}{(U_s{}^2/\ell)} - \left(\frac{\bar{p}_1}{\rho U_s{}^2}\right) f'(\eta) = \text{MOM} - \text{Y} \tag{58}$$

$$f_1(\eta)\{.0797[f_2(\eta) + f_2'(\eta)] - g'(\eta)\} - f_1'(\eta)g(\eta)$$
$$= \frac{F_x}{(U_s{}^2/\ell)} + \frac{M_x - \bar{u}_1 E}{(U_s{}^2/\ell)} = \text{MOM} - \text{X} \tag{59}$$

The left sides of (58) and (59) were computed from Ali's measurements and the results are plotted in Figures 1 and 2. In Fig. 1 (MOM-X) stands for the right hand side of (59) as a function of η; pressure and viscous forces as well as average entrainment of x-momentum minus the momentum entrained by the mean velocity $\bar{u}_1$ are included in (MOM-X). The abnormal "bumps" at $\eta_1 = 1.125$ and $\eta_2 = 1.375$ are almost certainly due to error in the differentiation process. Using Tutu's modeling (12) for the right side of (59) with $C_{1u} \approx 1$ yields

$$\text{R.H.S. of (59)} \approx 8.95\left(\frac{f_Y \ell}{U_o}\right) f_2(\eta) .$$

The values of the latter are between one and two orders of magnitude higher than those computed from (59). In Fig. 2 (MOM-Y) stands for the right side of (58). All the values obtained for the sum of mean y-force, average entrainment of y-momentum minus the momentum entrained by $\bar{v}_1$ and the pressure force $\bar{p}_1 \frac{\partial \gamma}{\partial \eta}$ are negative. This may be due to the predominance of the net entrainment of y-momentum with the mean vertical velocity $\bar{v}_1$ which has a negative sign.

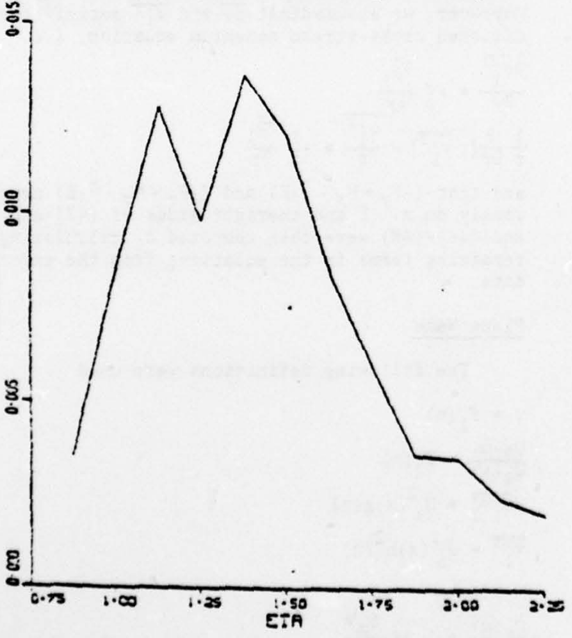

Fig. 1. Average entrainment of x-momentum plus direct force for the heated wake as a function of the similarity variable η.

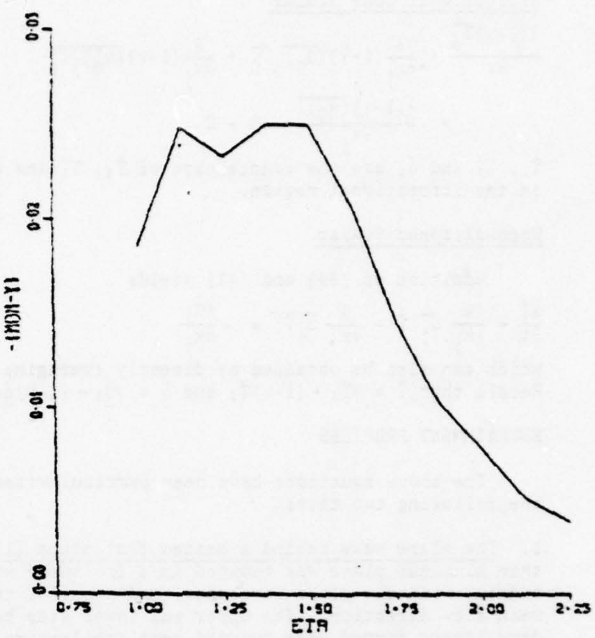

Fig. 2. Average entrainment of y-momentum plus direct force for the heated wake as a function of the similarity variable η.

Libby's modeling of the entrainment of x-momentum has the form

$$\overline{\dot{w}\,u'} \propto \frac{|\overline{u'v'}|}{U_s{}^2}(1-\gamma)\eta\,\frac{\bar{u}\,U_s}{\Lambda}$$

The latter expression with a proportionality constant of .188 is compared with the results obtained here in Table 1.

Table 1. Libby's modeling of x-momentum entrainment and results from equation (59).

η	1.0	1.25	1.5	1.75	2.0
$\frac{\overline{\dot{w}\,u'}}{(U_s{}^2/\Lambda)}$	.00201	.00763	.01209	.00972	.00020
MOM-X (59)	.00839	.00981	.01209	.00600	.00356

Round Jet

The following definitions were used

$$\gamma = f_1(\eta) \tag{60}$$

$$\bar{u}_1 = U_m(x)f_2(\eta) \tag{61}$$

$$\bar{v}_1 = U_m(x)f_3(\eta) \tag{62}$$

$$-\overline{u_1'v_1'} = U_m^2(x)g(\eta) \tag{63}$$

$$\bar{T}_1 = T_m(x)f_4(\eta) \tag{64}$$

$$\overline{v_1'\theta_1'} = U_m(x)T_m(x)h(\eta) \tag{65}$$

$$\eta = \frac{r}{r_{\frac{1}{2}}(x)} \tag{66}$$

$$U_m \propto 1/x \qquad (67)$$

$$T_m \propto 1/x \qquad (67')$$

$$r_{1/2}(x) = .067\, x \qquad (68)$$

where U_m is the maximum mean velocity at a given section and T_m is the maximum mean temp rature, $r_{1/2}$ is the half-radius of the jet, i.e. r for which $\bar{u}/U_m = .5$, and relations (67) and (68) were taken from Tennikes and Lumley (9).

The equations obtained by applying the previous assumptions to the conditioned equations for the turbulent fluid in a jet are

$$f_1'(\eta)[-.067\,\eta f_2(\eta) + f_3(\eta)] + f_1(\eta)\Big\{-.067[f_2(\eta) + \eta f_2'(\eta)] + f_3'(\eta) + \frac{f_3(\eta)}{\eta} = \frac{E}{U_m/r_{1/2}} \qquad (69)$$

$$-.067\, f_1(\eta)f_2(\eta)[f_2(\eta)+\eta f_2'(\eta)] + f_1\Big\{f_2'(\eta)f_3(\eta) - g'(\eta) - \frac{g(\eta)}{\eta}\Big\} - g(\eta)f_1'(\eta) = -\frac{F_x}{(U_m{}^2/r_{1/2})} + \frac{M_x - \bar{u}_1 E}{(U_m{}^2/r_{1/2})} = \text{MOM-X} \qquad (70)$$

$$\frac{r_{1/2}}{T_m}\frac{dT_m}{dx} f_1(\eta)f_2(\eta)f_4(\eta) - \frac{dr_{1/2}}{dx} f_1(\eta)f_2(\eta)\eta f_4'(\eta) + f_1(\eta)f_3(\eta)f_4'(\eta) + h(\eta)f_1'(\eta) + f_1(\eta)h'(\eta) + \frac{f_1(\eta)h(\eta)}{\eta} = \frac{C}{(U_m T_m/r_{1/2})} + \frac{\Theta - \bar{T}_1 E}{(U_m T_m/r_{1/2})} = \text{HEAT} \qquad (71)$$

The left sides of (69)-(71) can be computed from Tutu's experimental data and the results appear on Figures 3-6. In Fig. 3 the dimensionless entrainment from (69) is compared with modeling in Reference (12) of that term. A significant difference in the location of the maxima as well as in the values of these maxima is observed. This may be due to an oversimplification of the actual physical phenomenon in the above reference. Libby's modeling while possibly more realistic includes unconditioned variables and do not serve for predictive purposes here. In Fig. 4 the marked difference between the computed right side of (70) and the modeling in (12) is more noticeable. The latter completely misses a negative region for $\eta \le 1.00$. We ascribe the existence of this negative region to the large positive values of $\bar{u}_1E$ which are plotted in dimensionless form in Fig. 5. While the total entrainment of x-momentum

$$\rho M_x = \lim_{V\to 0} \overline{\frac{1}{V}\int_{S(\underset{\sim}{x},t)} \rho u v^e dS}$$

is positive, the difference

$$M_x - \bar{u}_1 E = \lim_{V\to 0} \overline{\frac{1}{V}\int_{S(\underset{\sim}{x},t)} (u-\bar{u}_1)v^e dS}$$

may well be negative.

Fig. 6 is a plot of the right side of (71) versus η. Tutu's model multiplied by a factor of 10^{-1} is plotted for comparison. The agreement is better than for momentum entrainment.

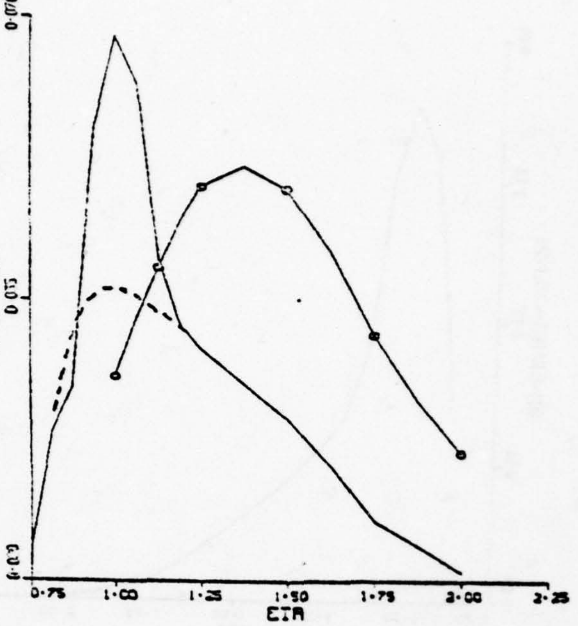

Fig. 3. Mass entrainment per unit mass for the heated jet. The dashed line is the result of taking for $\bar{v}_1/U_m$ the smooth curve in Reference (12). —o— Tutu's modeling, i.e.,

$$\frac{2f\gamma}{(U_m/r_{1/2})}.$$

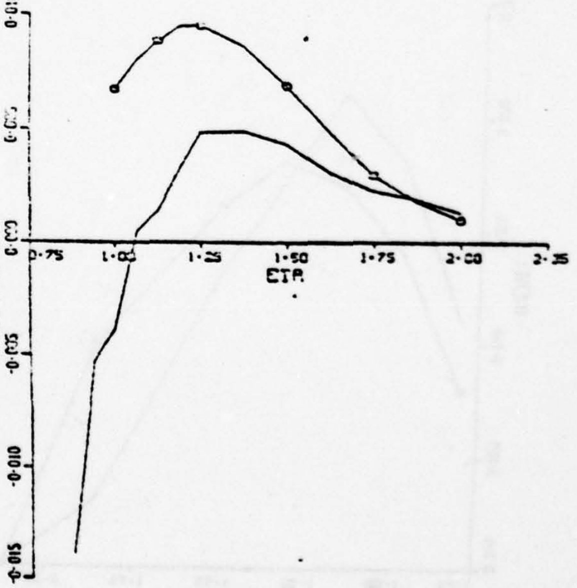

Fig. 4. Average entrainment of x-momentum for the heated jet. —o— Tutu's modeling, i.e.

$$\frac{f\gamma\bar{u}_1}{(U_m{}^2/r_{1/2})}.$$

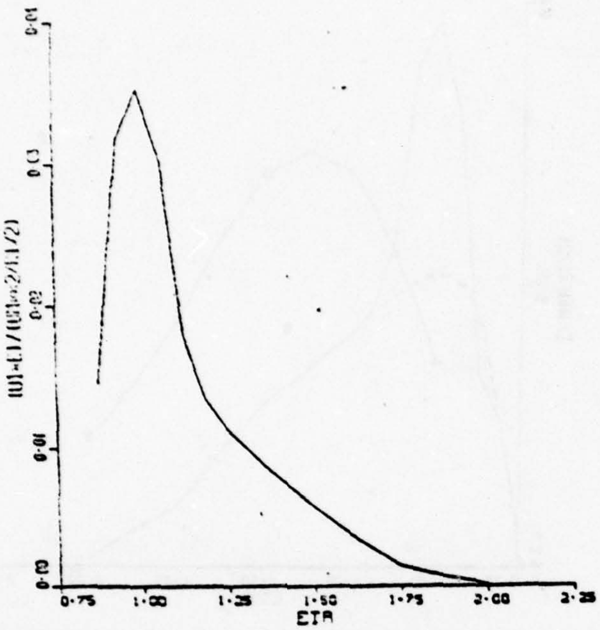

Fig. 5. x-momentum entrained by the mean mass entrainment with the mean velocity for the heated jet.

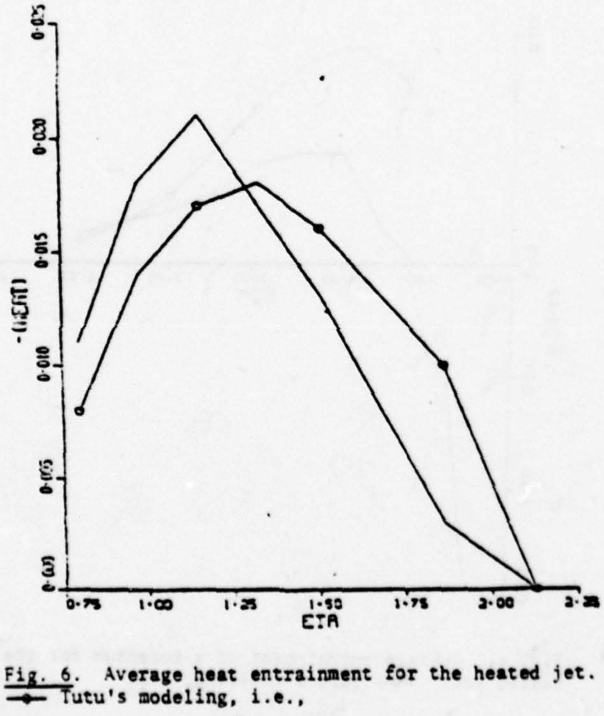

Fig. 6. Average heat entrainment for the heated jet.
—◆— Tutu's modeling, i.e.,

$$\frac{f\gamma\hat{T}_1}{\eta(U_m T_m/r_{\frac{1}{2}})}$$

multiplied by 10^{-1}.

ACKNOWLEDGMENTS

The present research was performed under the auspices of the U. S. Energy Research and Development Administration Contract No. EY-76-C-02-0016. We would like to thank Joyce Tichlerfor her patient generation of the computer plots in this paper.

REFERENCES

1. Ali, S. F., "Structure of the Turbulence in the Plane Wake behind a Heated Flat Plate", Ph.D. Dissertation, The Johns Hopkins University, Baltimore, Md., 1975.

2. Corrsin, S., "Investigation of Flow in an Axially Symmetric Heated Jet of Air", NACA W-94, 1943.

3. Corrsin, S. and Kistler, A. "Free Stream Boundaries of TurbulentFlows", NACA Report 1244, 1955.

4. Dopazo, C., "On Conditioned Averages for Intermittent Turbulent Flows", accepted for publication in the Journal of Fluid Mechanics, 1977.

5. Dopazo, C. andCorrsin, S., "A Statistical *Derivation of the Averaged Equations for Fluid Flows* through Deformable Porous Media", in preparation.

6. Kovasznay, L. S. G., Kibens, V. and Blackwelder, R. F., "Large Scale Motion in the Intermittent Region of a Turbulent Boundary Layer", Journal of Fluid Mechanics, Vol. 41, Part 2, 1970, pp. 283-325.

7. Libby, P. A., "On the Prediction of Intermittent Turbulent Flows", Journal *of* Fluid Mechanics, Vol. 68, Part 2, 1975, pp. 273-295.

8. Libby, P. A., "Prediction of the Intermittent Turbulent Wake of a Heated Cylinder", The Physics of Fluids, Vol. 19, No. 4, April 1976, pp. 494-501.

9. Tennekes, H. and Lumley, J. L., "A First Course in Turbulence", MIT Press, Cambridge, Mass. *and London, England, 1972, pp. 104-135.*

10. Townsend, A. A., "The Fully Developed Turbulent Wake of a Circular Cylinder", Australian Journal Sci. Res., A, Vol. 2, 1949, pp. 451-468.

11. Townsend, A. A., "The Structure of Turbulent Shear Flow", 2nd ed., Cambridge University Press, 1976, pp. 188-255.

12. Tutu, N. K., "An Experimental Investigation of a Heated Turbulent Round Jet", Ph.D. Dissertation, State University of New York at Stony Brook, Stony Brook, N.Y., 1976.

13. Wygnanski, I. and Fiedler, H. E., "The Two-dimensional Mixing Region", Journal of Fluid Mechanics, Vol. 41, Part 2, 1970, pp. 327-361.

THE INTERACTION OF TWO PARALLEL FREE SHEAR LAYERS

A.D. Weir and P. Bradshaw

DEPARTMENT OF AERONAUTICS
IMPERIAL COLLEGE, LONDON.

ABSTRACT

Conditionally-sampled fluctuation measurements in two merging mixing layers, one of which was marked by slight heating, show that the turbulence structure of each layer is significantly altered by interaction with the other. This is in contrast to the case of merging boundary layers in a duct, where the turbulence structure is so little altered that the flow can be predicted by superposition of the two turbulence fields, which are supposed to communicate only via the mean velocity profile. Turbulence intensities are much higher in the mixing layer than in the boundary layer, so that larger structural changes are to be expected. However, it appears possible to correlate these changes in terms of a simple interaction parameter.

NOMENCLATURE

b	breadth of jet nozzle
h	height of jet nozzle
$\overline{q^2}$	$\overline{u^2} + \overline{v^2} + \overline{w^2}$
U	x-component mean velocity
u, v, w	velocity fluctuations in x, y, z directions
V_τ, V_q	turbulent transport velocities, eqs (2) and (3)
x, y	coordinates: x axial, y vertical; origin at start of "hot" mixing layer
γ	temperature intermittency factor
η	similarity ordinate, y/x
τ	shear stress, $-\rho\,\overline{uv}$

Subscripts

C	cold-zone value
H	hot-zone value

INTRODUCTION

Isolated, text-book, turbulent shear layers are rare in engineering practice. A complication that frequently occurs is that two parallel simple shear layers (for example boundary layers on opposite sides of a two dimensional duct) merge and interact as they go downstream. Bradshaw, Dean and McEligot (1) demonstrated that in this case the interaction could be easily incorporated into existing calculation methods by assuming that the shear stress profiles from the individual layers superposed to give the total shear stress. That is, the shear layers are assumed to interact only via their shared mean velocity profile, with no direct interaction of the turbulent eddies. Strictly, the process is "time-sharing" rather than superposition: large eddies erupt across the centre line more-or-less alternately from each layer and the region of overlap of the shear-stress profiles is rather smaller than the intermittent region of an isolated shear layer. The advantage of considering the interaction explicitly is that the thickness of the two shear layers are still identifiable and available for use as eddy length scales as in isolated shear layers. Length-scale transport equations being at present highly controversial, this is a welcome simplification.

Morel and Torda (2) extended the idea of superposition to free shear layers, in which the turbulence levels are much higher than in boundary layers, but found, not unexpectedly, that simple superposition of the individual shear-stress profiles did not give a good fit to the experimental data for the growth of a two-dimensional jet; a strong interaction occurred which changed the structure of the turbulence in the individual layers. Though they were still able to calculate the flow by incorporating "interaction parameters" into their basic calculation method, that of Bradshaw, Ferriss and Atwell (3), a more detailed understanding of the failure of the simple superposition hypothesis in highly turbulent flows is desirable.

Here we report preliminary results of an experiment which uses conditional sampling techniques to study how the eddies of two merging mixing layers change their structure from that of two isolated plane mixing layers into that of a self-preserving two-dimensional jet.

EXPERIMENTAL SET-UP

Figure 1 shows a schematic diagram of the flow. Air passes smoothly through a standard wind-tunnel contraction, fed by a centrifugal blower, and emerges from a slit nozzle into the nominally still air of the laboratory. The boundary layers with nozzle walls are laminar, but two (turbulent) mixing layers form at the exit. These grow as separate self-preserving mixing layers until about x/h = 6, when the potential core between them is absorbed (Fig. 2). Thereafter the jet continues to entrain fluid from the surrounding still air, and spreads out as it goes downstream. By about x/h = 20 (the limit of the present experiment) the mean velocity profile is that of a self-preserving jet, though the turbulence structure has not quite reached that limit (see also Gutmark and Wygnanski (4)). The rig used had the specifications: slot height h = 12.7 cm, slot width b = 76.2 cm, nozzle speed U_j = 15 m/s, giving a Reynolds number $U_j h/\nu \sim 1.3 \times 10^5$.

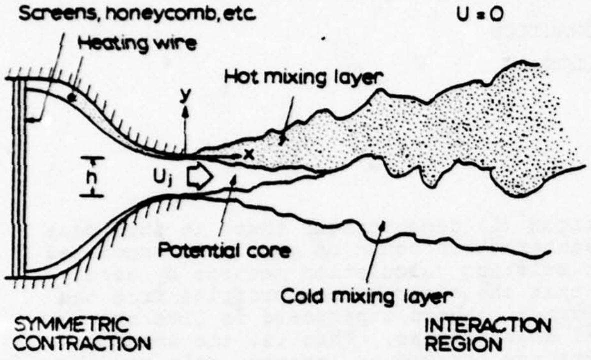

Fig 1 Test rig and coordinate system (not to scale)

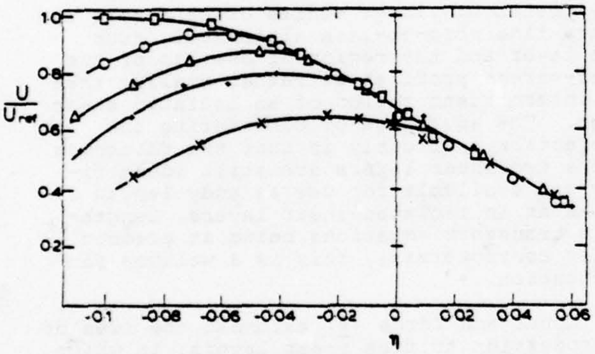

Fig 2 Mean velocity profiles in hot-layer similarity coordinates.
□, x = 4 h: ○, x = 8 h: △, x = 10 h: +, x = 12 h: ×, x = 18 h

In this experiment, one of the boundary layers inside the contraction is heated slightly using Nichrome wires stretched across it. Fluid which has come from this boundary layer, or which has been intimately mixed with such fluid, will remain hotter than its surroundings as it does downstream, and therefore eddies originating in the hot mixing layer can be distinguished by their temperature. Thus, in the region of interaction, the individual contributions of the two original mixing layers to the shear stress and other turbulence quantities can be analysed by simultaneous measurements of the temperature and velocity of the passing fluid. The velocity is measured by a X-probe using two DISA constant-temperature anemometers and the temperature by a 1μm cold wire probe (run at a constant current of about 1mA) attached to the X-probe: the wire lengths are about 1 mm and the distance between them slightly less. The signals from the three wires are recorded on magnetic tape, digitised, and analysed later by a specially written computer program. To ensure that buoyancy forces were negligible the amount of heating was limited so that the temperature difference between the heated and unheated fluid was always less than 6 deg. C.

The main difficulty encountered was, as expected, the inevitable small temperature difference between the jet core air (which was heated by its passage through the blower) and the air entrained from the room. Thus even the "cold" mixing layer contained significant temperature fluctuations, at a level which remained roughly constant downstream while the temperature fluctuation level in the heated mixing layer decreased roughly as 1/x. The deterioration in the accuracy of hot/cold discrimination at large x/h is, however, mainly attributable to the inevitable fine-grained mixing of - say - "hot" fluid into the "cold" layer. After a "hot" large eddy erupts across the centre line into a region of reversed mean shear, its intensity decays fairly rapidly - this is what limits the interaction - and its fluid is entrained into the cold layer so that further large-eddy eruptions from the cold side are in fact slightly hot. Eventually the distinction between hot and cold fluid is lost: both in this experiment and in the duct measurements (10) the downstream limit of reliable discrimination is about twice the value of x at which the shear layers meet. If "hot" layer were heated at this point instead of at its origin, the large-eddy discrimination process could begin again and would show the same time-sharing mechanism. (An indirect proof of this assertion is the success of the calculation method of Ref (1), based on time-sharing, in fully-developed duct flow). A proof that the heat does label the large eddies is given by the behaviour of the typical hot burst frequency. Although this frequency is an artefact of the particular discrimination process it is useful for checking. Our results show that the frequency decreases towards the centre line and that the dimensionless frequency collapses quite accurately when plotted against $\eta \equiv y/x$ for $4\,h < x < 12\,h$. If the interaction between the two layers took place mainly by fine-grained mixing we would expect the burst frequency in the interaction region to increase.

RESULTS

The measurements at x = 4 h (before the two mixing layers meet) agree well with the data of Castro and Bradshaw (5) for a single mixing layer: Rodi (see (6)) regards the latter data, obtained in the same rig, as representative. Other measurements in this rig (7) have shown that the turbulence becomes fully three-dimensional shortly after transition occurs, with no trace of the persistence of two-dimensional large structure found by Brown and Roshko (8). The mean flow is of course two-dimensional. The large eddies in fully-three-dimensional turbulence in mixing layers are still very distinctive, as shown as long ago as 1964 (9).

The intermittency profiles (Fig. 3) show that the "hot" layer continues to spread nearly linearly as x increases, even well after the layers have met. The results are plotted against η = y/x, which is the similarity co-ordinate for a mixing layer. The profiles for x < 12 h collapses onto that at x = 4 h though at x = 12 h the hot fluid has penetrated to the maximum-intensity region of the "cold" mixing layer at y =-h. At x = 18 h the temperature intermittency has started to rise at large negative y (i.e. y < -h, in the outer intermittent region of the cold mixing layer).

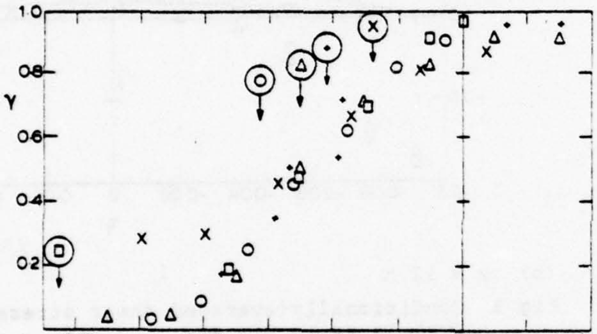

Fig 3 Temperature-intermittency factor in hot layer similarity coordinates. Symbols as in Fig 2. Vertical arrows indicate jet centre-line at that x.

Fig 4 shows the $\overline{u^2}$ and $\overline{v^2}$ intensities at x = 8 h and x = 12 h (w fluctuation data were not taken in this experiment) with curves through the data at x = 4 h for comparison. Results for x = 10 h are intermediate between those for x = 8 h and 12 h. The "hot" and "cold" values plotted here are the "hot" and "cold" contributions to the conventional-average intensity all fluctuations being measured with respect to the conventional mean velocity. If the average value of $\overline{u^2}$ over the "hot" zones is $\overline{u^2}_H$ and the average value over the "cold" zones is $\overline{u^2}_C$ then the quantities plotted in Fig 4 are $\gamma \overline{u^2}_H$ and $(1-\gamma)\overline{u^2}_C$: they add to give the

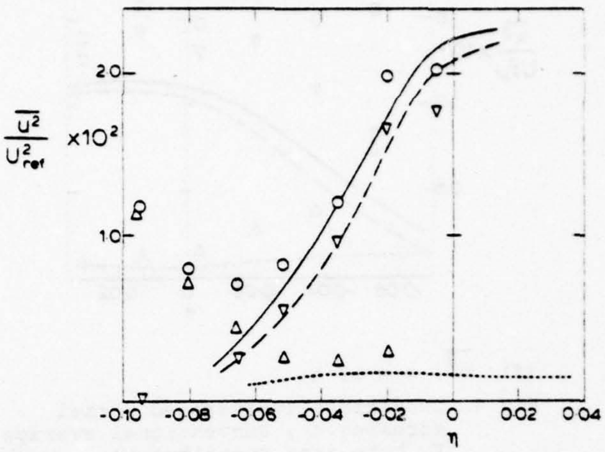

(a) $\overline{u^2}$, x = 8 h

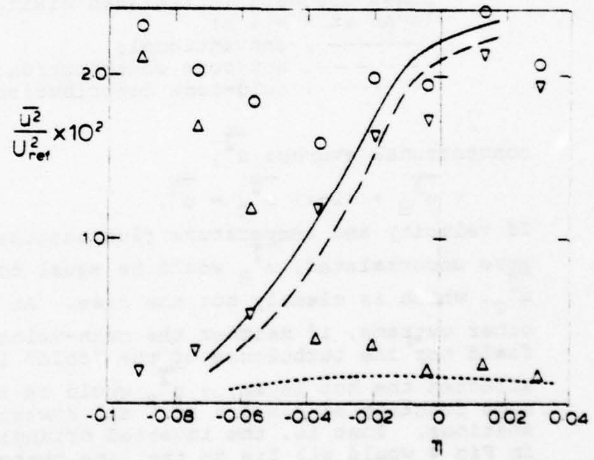

(b) $\overline{u^2}$, x = 12 h

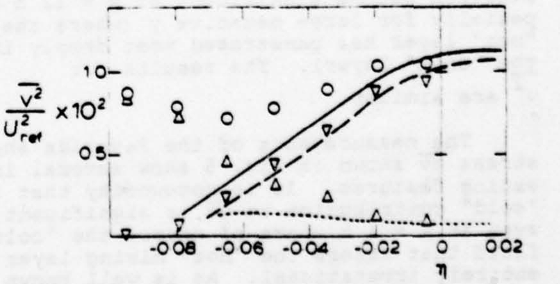

(c) $\overline{v^2}$, x = 8 h

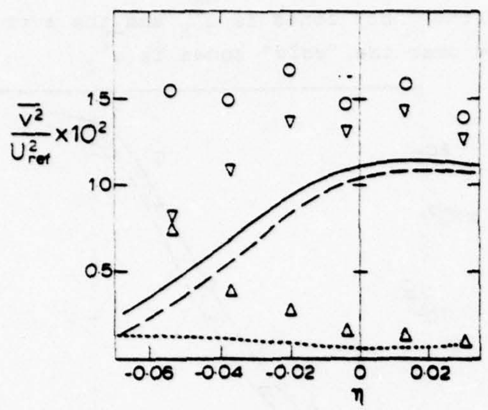

(d) $\overline{v^2}$, x = 12 h

Fig 4 Conditionally-averaged normal stresses. ○ , conventional average: ▽, hot- zone contribution, γ x (hot-zone average); △ , cold zone contribution, (1-γ)x(cold-zone average). Lines are data in isolated mixing layer at x = 4 h:
———— , conventional;
– – – – –, hot-zone contribution;
·········, cold-zone contribution.

conventional average $\overline{u^2}$,

$$\gamma\, \overline{u^2}_H + (1-\gamma)\, \overline{u^2}_C = \overline{u^2}.$$

If velocity and temperature fluctuations were uncorrelated, $\overline{u^2}_H$ would be equal to $\overline{u^2}_C$, which is clearly not the case. At the other extreme, if neither the mean-velocity field nor the turbulence of the "cold" layer affected the hot layer, $\gamma\, \overline{u^2}_H$ would be the same function of y/x ≡ η at all downstream stations. That is, the inverted triangles in Fig 4 would all lie on the line representing the hot-zone contributions at x = 4 h. In fact, departures from this self-preserving function become significant at x = 12 h especially for large negative y (where the "hot" layer has penetrated most deeply into the "cold" layer). The results for $\overline{v^2}$ are similar.

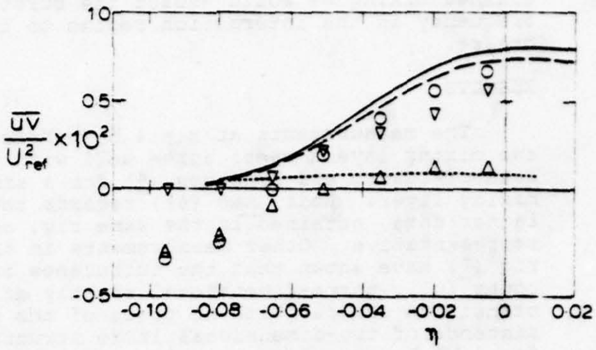

(a) x = 8 h

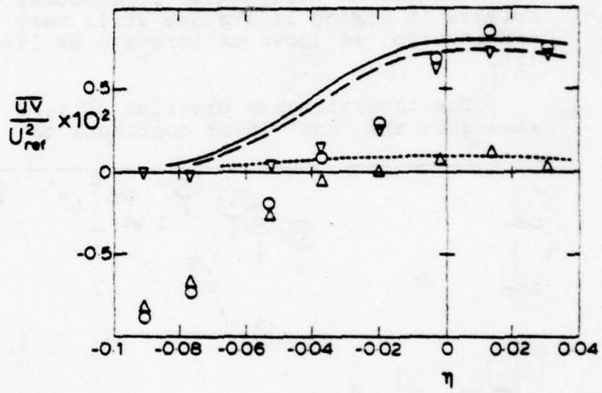

(b) x = 12 h

Fig 5 Conditionally-averaged shear stress. Symbols as in Fig 4.

The measurements of the Reynolds shear stress $\overline{uv}$ shown in Fig. 5 show several interesting features. It is noteworthy that the "cold" contribution to $\overline{uv}$ is significant even at x = 4 h, where of course the "cold" fluid that enters the "hot" mixing layer is entirely irrotational. As is well known (4,5), the intermittency never quite reaches unity and irrotational entrained fluid can evidently acquire uv by the action of pressure fluctuations before acquiring vorticity or temperature by molecular diffusion. The maximum positive value of (1-γ) $\overline{uv}_C$ at x = 4 h is about 0.1 of the maximum value of conventional-average $\overline{uv}$, and it does not appear to change consistently with distance downstream. The recorded value depends on the measurement of (1-γ) and is therefore rather erratic when γ is near unity: in general an underestimate of γ will give spuriously high $\overline{uv}_C$. In the duct (10) γ reaches unity and the "cold" contribution then vanishes. The simplest measure of the strength of the interaction is the difference between $\overline{uv}_H$ and $\overline{uv}_C$ on the centre line (η=-x/(0.5 h)), which is plotted against x/h in Fig 6. The difference at x = 6 h, where the layers have only just met, is not clear from the measurements but is almost zero. As in the duct, the shear-stress profiles are attenuated more rapidly than the intensity profiles by the negative velocity gradient on the far side of the centre line, and at x = 8 h the difference has almost reached its maximum value. The alternative way of defining the strength of the interaction is by the width of overlap of the "hot" and "cold" regions, but because the conditioned averages change signs, as just discussed, this width cannot be defined precisely: the distance between the two crossover points, in η units, is also plotted in Fig 6 and, like the alternative definition of interaction strength grows rapidly at first and then much more slowly. These results suggest that the interaction has almost reached its maximum strength by x = 12 h so that fur-

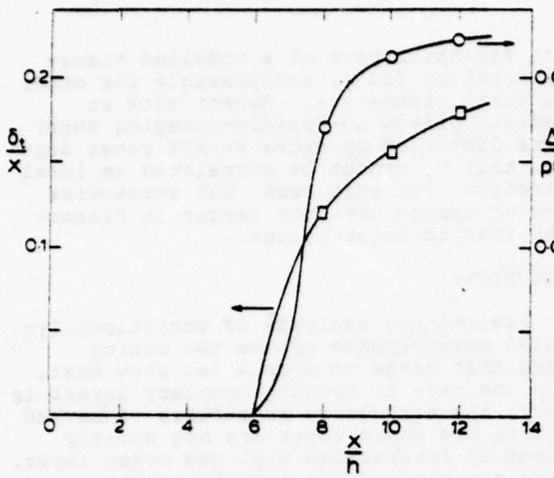

Fig 6 Interaction parameters. ○ : difference between $\gamma\phi\overline{uv}_H$ and $(1-\gamma)\phi\overline{uv}_C$ on centre line, normalized by ρU_j^2; □ δ_t distance between zeroes of $\overline{uv}_H$ and $\overline{uv}_C$, normalized by x.

ther changes in turbulence structure should be fairly small. It is important to note that the behaviour of the interaction and shear stress, considered separately, do not provide evidence for or against superposition because some changes from the isolated mixing layer are bound to be caused by the mean velocity gradient imposed by the second mixing layer. Superposition must be tested by inspection of the structural parameters (whose values are connected with the values of the empirical constants in transport equation calculation methods). Fig 7 shows $\overline{uv}_H/(\overline{u^2}_H + \overline{v^2}_H)$, which is about 1.5 times the hot-zone value of $\overline{uv}/\overline{q^2}$. Unfortunately the results at x = 12 h are rather scattered but there is no doubt that this stress ratio is strongly affected by the interaction and that it is still decreasing with increasing x even at x = 12 h. The results suggest a fairly large change between x = 4 h and x = 8 h, with a slower variation thereafter; this implies that the variation could be correlated empirically as a family of curves with one of the quantities plotted in Fig 6 as a parameter.

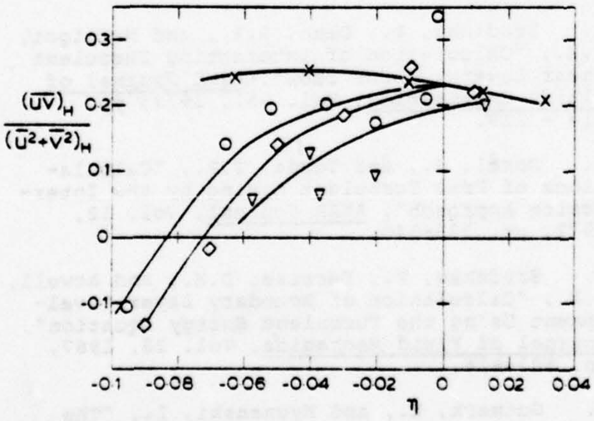

Fig 7 Stress ratio $\overline{uv}_H/(\overline{u^2}_H + \overline{v^2}_H)$. X, x = 4 h: ○, x = 8 h: ◇, x = 10 h: ▽, x = 12 h.

Since any departure from superposition are likely to show up first as changes in the transport of turbulent energy or shear stress in the y direction by the turbulence itself, close study of the triple velocity products that effect this turbulent transport is informative. Transport of $\overline{uv}$ is effected by the gradient of $\overline{uv^2}$ and transport of turbulent energy by the gradient of $(\overline{u^2v}+\overline{v^3}+\overline{vw^2})/2$. It is clear from Fig 8 that the triple pro-

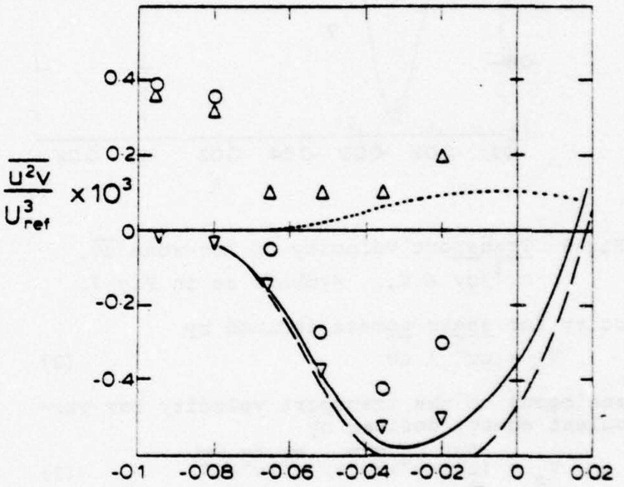

(a) $\overline{u^2v}$ at x = 8 h

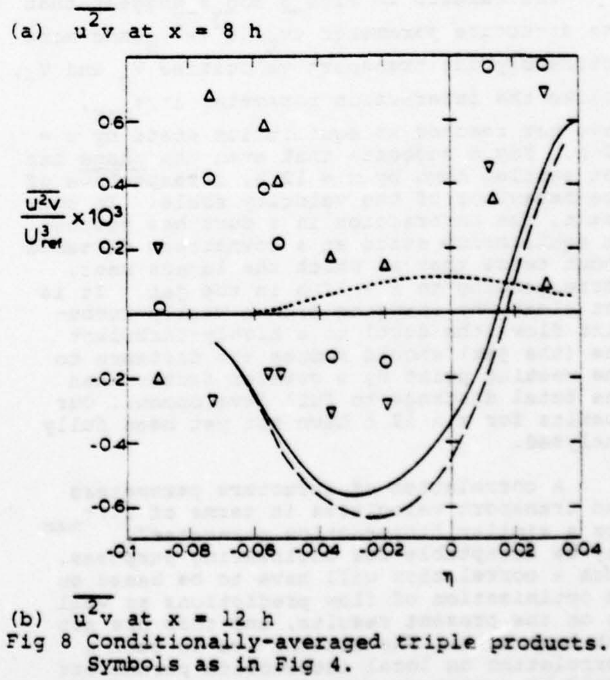

(b) $\overline{u^2v}$ at x = 12 h

Fig 8 Conditionally-averaged triple products. Symbols as in Fig 4.

ducts exemplified by $\overline{u^2v}$ are affected significantly by the interaction and Fig 9 shows that the same is true of the transport velocity for shear stress defined by

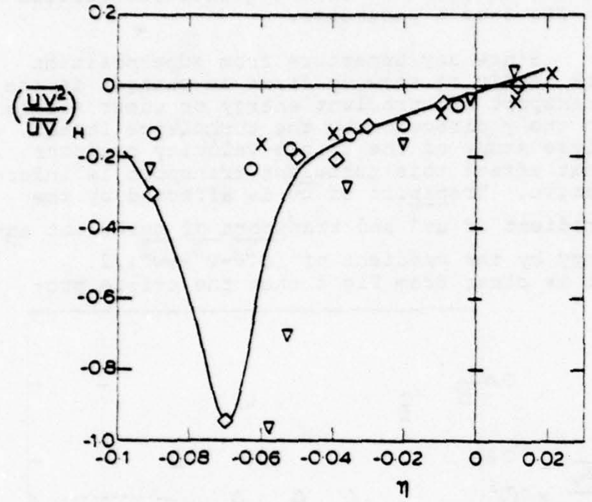

Fig 9 Transport velocity of hot-zone $\overline{uv}$, $\overline{uv^2}/uv \equiv V_\tau$. Symbols as in Fig 7.

$$V_\tau = \overline{uv^2} / uv \qquad (2)$$

analogous to the transport velocity for turbulent energy defined by

$$V_q = (\overline{u^2v}+\overline{v^3}+\overline{vw^2})/(\overline{u^2}+\overline{v^2}+\overline{w^2}) \qquad (3)$$

The results in Figs 8 and 9 suggest that the structure parameter $uv_H/(\overline{u^2}+\overline{v^2})_H$, and more noticeably the transport velocities V_q and V_τ, unlike the interaction parameter $\Delta\tau/\tau_{max}$, have not reached an equilibrium state by x = 12 h. Fig 8 suggests that even the shape has not settled down by x = 12 h, irrespective of the behaviour of the velocity scale. In contrast, the interaction in a duct has reached an equilibrium state at a downstream distance about twice that at which the layers meet, corresponding to x = 12 h in the jet. It is not clear why changing from a weakly-turbulent flow (the duct) to a highly-turbulent one (the jet) should reduce the distance to the meeting point by a greater factor than the total distance to full development. Our results for x > 12 h have not yet been fully analysed.

A correlation of structure parameters and transport velocities in terms of $\Delta\tau/\tau_{max}$ (or a similar "interaction parameter") may be acceptable for engineering purposes. Such a correlation will have to be based on an optimization of flow predictions as well as on the present results, and this has not yet been done. The alternative to such a correlation on local interaction parameters would be transport equations for V_τ, which is an essential part of a modelled transport equation for τ, and possibly for other structural parameters. Recent work at Imperial College in rapidly-changing shear layers distorted by extra strain rates suggests that V_τ cannot be correlated on local parameters in that case, but streamwise rates of change are much larger in distortions than in interactions.

CONCLUSIONS

Preliminary analysis of conditionally-sampled measurements of the two mixing layers that merge to form a jet show that, as in the case of merging boundary layers in a duct, the turbulence properties of marked fluid in one shear layer are not greatly altered by interaction with the other layer. If the alterations in turbulence structure were negligible, as in the duct, the flow could be calculated by assumptions of superposition or "time-sharing" of the two turbulence fields. In fact the structural changes in the jet are significant but probably small enough to be correlated, for engineering purposes in terms of a simple interaction parameter.

ACKNOWLEDGEMENTS

Dr. K.K. Chaudhry (Indian Institute of Technology, Delhi) and Dr. O.O. Mojola (University of Ife, Nigeria) assisted with the early stages of this work, and Mr. D.H. Wood performed a large part of the data analysis. The work was supported by the Science Research Council grant B/SR/8978.

REFERENCES

1. Bradshaw, P., Dean, R.B., and McEligot, D.M., "Calculation of Interacting Turbulent Shear Layers: Duct Flow", *ASME Journal of Fluids Engineering*, Vol. 951, 1973, pp. 214 - 219.

2. Morel, J., and Torda, T.P., "Calculations of Free Turbulent Mixing by the Interaction Approach", *AIAA Journal*, Vol. 12, 1972, pp. 533-540.

3. Bradshaw, P., Ferriss, D.H., and Atwell, N.P., "Calculation of Boundary Layer Development Using the Turbulent Energy Equation", *Journal of Fluid Mechanics*, Vol. 28, 1967, pp. 593-616.

4. Gutmark, E., and Wygnanski, I., "The Planar Turbulent Jet", *Journal of Fluid Mechanics*, Vol. 73, 1976, pp. 465-495.

5. Castro, I.P., and Bradshaw, P., "The Turbulence Structure of a Highly Curved Mixing Layer", *Journal of Fluid Mechanics*, Vol. 73, 1976, pp. 265-304.

6. Launder, B.E. (Ed.), *Studies in Convection*, Vol. 1, Academic Press, London, 1975, pp. 79-166.

7. Chandrsuda, C., Mehta, R.D., Weir, A.D., and Bradshaw, P., "Effect of Free Stream Turbulence on Large Structure in Turbulent Mixing Layers", Imperial College unpublished paper, 1976.

8. Brown, G.L., and Roshko, A., "On density Effects and Large Structure in Turbulent Mixing Layers", Journal of Fluid Mechanics, Vol. 64, 1974, pp. 775-816.

9. Bradshaw, P., Ferriss, D.H., and Johnson, R.F., "Turbulence in the Noise-Producing Region of a Circular Jet", Journal of Fluid Mechanics, Vol. 19, 1964, pp. 591-624.

10. Dean, R.B., and Bradshaw, P., "Interacting Turbulent Shear Layers in Duct Flow", Journal of Fluid Mechanics, Vol. 78, 1976, pp. 641- .

NUMERICAL SOLUTION OF THREE-DIMENSIONAL FREE TURBULENT SHEAR FLOWS

Youn H. Oh and Julius E. Harris

NASA Langley Research Center
Hampton, Virginia 23665

ABSTRACT

Numerical results are presented for three-dimensional compressible turbulent jet and wake flows. An alternating direction implicit numerical procedure is used to solve the finite-difference form of the parabolic elliptic Navier-Stokes equations. A coordinate transformation maps the boundaries at infinity into a finite computational domain in order to properly specify infinity boundary conditions as well as contain the downstream growth of the viscous flow field in a fixed computational grid. Turbulence closure is achieved through an algebraic mixing length eddy viscosity model.

Numerical results for supersonic flow are presented for an axisymmetric jet, an elliptical jet, an elliptical wake, and two interacting rectangular jets. Experimental data were not available for comparison with the numerical results. However, the results compare well with empirical results for free shear flows.

NOMENCLATURE

A,B	Constants in coordinate transformation (see eqs (17))
a_1,a_2,a_3	Constants in mixing length model
c_1	Constant (see eq (19))
$\tilde{e}$	Turbulent kinetic energy; $(\tilde{u}'^2 + \tilde{v}'^2 + \tilde{w}'^2)/2$
f_I,f_{II},f_{III}	Constants in mixing length model (see eqs (16))
$\tilde{K}$	Mean kinetic energy; $(\tilde{u}^2 + \tilde{v}^2 + \tilde{w}^2)/2$
L^*	Reference length
M	Mach number
N_R	Reynolds number $\tilde{\rho}_\infty^* \tilde{u}_\infty^* L^* / \tilde{\mu}^*$
N_{Pr}	Prandtl number
N_{Pr_t}	Turbulent Prandtl number (see eq (12))
p	Pressure
r	(see eq (19))
R	Gas constant
S	Sutherland's constant
t	Width parameter (see eq (19))
$\tilde{T}$	Temperature
$\tilde{u},\tilde{v},\tilde{w}$	Velocity components in x-, y- and z-directions, respectively
$U_j\ (x,y,z)$	$\dfrac{\tilde{u}\ (x,y,z) - \tilde{u}_\infty}{\tilde{u}_j - \tilde{u}_\infty}$
$U_m\ (x,y,z)$	$\dfrac{\tilde{u}\ (x,y,z) - \tilde{u}_\infty}{\tilde{u}_m - \tilde{u}_\infty}$
x,y,z	Coordinate directions
x_{c_1},x_{c_2}	Ends of core (see Fig. 1)
$\hat{y}$	$y - y_j$
α_2,α_3	(see eq (15))
β_2,β_3	See Fig. 1; also eq (16b)
γ	Ratio of specific heats
δ_2,δ_3	Jet/wake widths
$\tilde{\Delta}$	Dilitation; $\frac{\partial\tilde{u}}{\partial x} + \frac{\partial\tilde{v}}{\partial y} + \frac{\partial\tilde{w}}{\partial z}$
$\varepsilon_{12},\varepsilon_{13},\varepsilon_{23}$	Eddy viscosities, see eqs (10)
$\varepsilon_{T2},\varepsilon_{T3}$	Eddy diffusivities, see eqs (10)
η,ζ	Transformed y- and z- coordinate
ℓ_2,ℓ_3	Mixing lengths
λ	Ratio of free stream velocity to primary flow, $\frac{\tilde{u}_\infty}{\tilde{u}_j}$
$\tilde{\mu}$	Viscosity
$\tilde{\rho}$	Density

Subscripts

∞	Free stream

PRECEDING PAGE BLANK-NOT FILMED

j	Jet
m	Maximum value
.05, .5, .95	$U_m(x,y_{.05},z) = .05$, $U_m(x,y,z_{.95}) = .95$, etc.
H	$U_j(0,y_H,z) = .5$, $U_j(0,y,z_H) = .5$
c	Center of curvature for input profile (y_H,z_H)

Superscripts

~	Mass weighted average; e.g., $\tilde{u} = \frac{\overline{\rho u}}{\bar{\rho}}$
—	Temporal average
'	Fluctuating component; e.g., $u' = u - \tilde{u}$
*	Dimensional quantity

INTRODUCTION

The mathematical character of the parabolic-elliptic Navier-Stokes (PENS) equations allows direct application of well-tested parabolic marching procedures to certain three-dimensional, turbulent free-shear flows while retaining the elliptical character of the Navier-Stokes equations in planes normal to the marching direction. The PENS equations can be applied to several turbulent flows of current interest; for example, three-dimensional interacting jet, wake, and vortex flows. The alternating direction implicit (ADI) numerical procedure and resulting block tridiagonal algorithm used in the present analysis is structured such that three-dimensional turbulent flows can be numerically solved with computer resources (storage/processing time) equivalent to current time-asymptotic techniques for the two-dimensional Navier-Stokes equations with turbulence modeling. One primary restriction is placed on the PENS equations in that the velocity component in the marching direction must be positive definite. The system is formally correct for supersonic flows; however, for subsonic flows the static pressure distribution or its gradient in the marching direction must be specified if the problem is to be well-posed mathematically.

Recently McDonald and Briley (Ref. 1) and Hirsh (Ref. 2) independently developed similar procedures for solving the PENS equations. The ADI procedure was used in References 1 and 2 to solve the PENS equations for laminar flow in linearized form. Hirsh (Ref. 2) considered the static temperature equation in contrast to the assumption of constant total temperature made in Reference 1 (constant total temperature assumption yields algebraic relationship between the velocity and temperature) as well as introduced an algebraic transformation to map the boundaries at infinity for the elliptic plane into a bounded computational domain. Related studies include Caretto, Curr, and Spalding (Ref. 3), Patankar and Spalding (Ref. 4), and Lewellen, Teske, and Donaldson (Ref. 5) for subsonic flows and Rudman and Rubin (Ref. 6), Nardo and Cresci (Ref. 7), Rubin and Lin (Refs. 8 to 10) and Lubard and Helliwell (Refs. 11, 12) for supersonic and hypersonic flows. Reviews of References 3 to 12 are presented in References 1 and 2. with comparisons of the numerical procedures used to solve the PENS equations; for example, iterative point relaxation for the coupled nonlinear system, time relaxation for the uncoupled linearized difference system, and a semi-implicit predictor-corrector iterative procedure for the coupled nonlinear system.

The present work is a direct outgrowth of the numerical procedure presented in Reference 2 for laminar flows. In the present analysis the static temperature equation solved in Reference 2 is replaced by the total enthalpy equation in order to correctly introduce the turbulence correlations into the averaged equations. The turbulence correlations are modeled through the mixing length eddy viscosity concept. The resulting computer program is utilized to study single axisymmetric, elliptic jets and wakes as well as interacting rectangular jets.

GOVERNING EQUATIONS

The elliptic character of the Navier-Stokes equations presents formidable computer resource requirements for three-dimensional compressible flows since the five dependent variables required for laminar flows must be stored for the entire three-dimensional region being computed. The consideration of the additional dependent variables required for turbulent flows places the computer storage and processing requirements well beyond the range of current computer systems for all but the simplest of flows. Consequently, simplifications based on the actual physics of the flow must be utilized to reduce the system of equations to a manageable level where they can be efficiently solved for applied problems. The first and most obvious simplification that might be considered for flows with a dominant flow direction, is classical boundary-layer scaling; however, the resultant system of equations is not sufficient to determine all the unknowns (see Ref. 2). The PENS equations are obtained from the Navier-Stokes equations by assuming that convection dominates the flow in one main-flow direction; consequently, all derivatives, associated with shear, taken with respect to the main-flow direction are assumed to be negligible.

Parabolic-Eliptic Navier-Stokes Equations

For the free shear flows discussed in the previous section one can assume, for the main-flow direction (x-coordinate; see Fig. 1) that diffusion is negligible in comparison to convection; consequently, the Reynolds equations governing the steady, compressible, turbulent flow can be written in Cartesian coordinate form as follows:

x-momentum

$$\frac{\partial}{\partial x}(\bar{\rho}\tilde{u}\tilde{u}) + \frac{\partial}{\partial y}\left(\bar{\rho}\tilde{v}\tilde{u} + \overline{\rho u'v'} - N_R^{-1}\frac{\partial \tilde{u}}{\partial y}\right)$$

$$+ \frac{\partial}{\partial z}\left(\bar{\rho}\tilde{w}\tilde{u} + \overline{\rho u'w'} - N_R^{-1}\frac{\partial \tilde{u}}{\partial z}\right) \tag{1}$$

$$= \frac{\partial}{\partial x}\left(-\bar{p} - \frac{2}{3}N_R^{-1}\Delta\right)$$

y-momentum

$$\frac{\partial}{\partial x}(\bar{\rho}\tilde{u}\tilde{v}) + \frac{\partial}{\partial y}\left(\bar{\rho}\tilde{v}\tilde{v} + \overline{\rho v'v'} - 2N_R^{-1}\frac{\partial\tilde{v}}{\partial y}\right)$$

$$+\frac{\partial}{\partial z}\left[\bar{\rho}\tilde{w}\tilde{v} + \overline{\rho v'w'} - N_R^{-1}\left(\frac{\partial\tilde{v}}{\partial z} + \frac{\partial\tilde{w}}{\partial y}\right)\right] \tag{2}$$

$$= \frac{\partial}{\partial y}\left(-\bar{P} - \frac{2}{3}N_R^{-1}\tilde{\Delta}\right)$$

z-momentum

$$\frac{\partial}{\partial x}(\bar{\rho}\tilde{u}\tilde{w}) + \frac{\partial}{\partial y}\left[\bar{\rho}\tilde{v}\tilde{w} + \overline{\rho w'v'} - N_R^{-1}\left(\frac{\partial\tilde{w}}{\partial y} + \frac{\partial\tilde{v}}{\partial z}\right)\right]$$

$$+\frac{\partial}{\partial z}\left(\bar{\rho}\tilde{w}\tilde{w} + \overline{\rho w'w'} - 2N_R^{-1}\frac{\partial\tilde{w}}{\partial z}\right) \tag{3}$$

$$= \frac{\partial}{\partial z}\left(-\bar{P} - \frac{2}{3}N_R^{-1}\tilde{\Delta}\right)$$

Where the time average of mass weighted fluctuating terms as well as the μ' correlations have been neglected. Present calculation $\tilde{\Delta}$ is neglected.

The continuity equation is written as

$$\frac{\partial}{\partial x}(\bar{\rho}\tilde{u}) + \frac{\partial}{\partial y}(\bar{\rho}\tilde{v}) + \frac{\partial}{\partial z}(\bar{\rho}\tilde{w}) = 0 \tag{4}$$

The total enthalpy equation is written as follows:

$$\frac{\partial}{\partial x}\left[\bar{\rho}\tilde{u}\tilde{T} + \tilde{\beta}\bar{\rho}\tilde{u}(\tilde{K} + \tilde{e})\right]$$

$$+\frac{\partial}{\partial y}\Big[\bar{\rho}\tilde{v}\tilde{T} + \tilde{\beta}\bar{\rho}\tilde{v}(\tilde{K} + \tilde{e})$$

$$+\bar{\rho}\widetilde{T'v'} + \tilde{\beta}\bar{\rho}(\tilde{u}\widetilde{u'v'} + \tilde{v}\widetilde{v'v'} + \tilde{w}\widetilde{v'w'})$$

$$-\tilde{\beta}N_R^{-1}\Big(-\frac{2}{3}\tilde{v}\tilde{\Delta} + \tilde{u}\frac{\partial\tilde{u}}{\partial y} + \tilde{v}\frac{\partial\tilde{v}}{\partial y} + \tilde{w}\frac{\partial\tilde{w}}{\partial y} \tag{5}$$

$$+\tilde{u}\frac{\partial\tilde{v}}{\partial x} + \tilde{v}\frac{\partial\tilde{v}}{\partial y} + \tilde{w}\frac{\partial\tilde{v}}{\partial z}\Big) - N_{Pr}^{-1}N_R^{-1}\frac{\partial\tilde{T}}{\partial y}\Big]$$

$$+\frac{\partial}{\partial z}\Big[\bar{\rho}\tilde{w}\tilde{T} + \tilde{\beta}\bar{\rho}\tilde{w}(\tilde{K} + \tilde{e})$$

$$+\bar{\rho}\widetilde{T'w'} + \tilde{\beta}\bar{\rho}(\tilde{u}\widetilde{u'w'} + \tilde{v}\widetilde{v'w'} + \tilde{w}\widetilde{w'w'})$$

$$-\tilde{\beta}N_R^{-1}\Big(-\frac{2}{3}\tilde{w}\tilde{\Delta} + \tilde{u}\frac{\partial\tilde{u}}{\partial z} + \tilde{v}\frac{\partial\tilde{v}}{\partial z} + \tilde{w}\frac{\partial\tilde{w}}{\partial z}$$

$$+\tilde{u}\frac{\partial\tilde{w}}{\partial x} + \tilde{v}\frac{\partial\tilde{w}}{\partial y} + \tilde{w}\frac{\partial\tilde{w}}{\partial z}\Big) - N_{Pr}^{-1}N_R^{-1}\frac{\partial\tilde{T}}{\partial z} = 0$$

The parameters $\tilde{\beta}$, $\tilde{K}$, and $\tilde{e}$ are defined as follows:

$$\left.\begin{aligned} \tilde{\beta} &= (\gamma - 1)\tilde{M}_\infty^2 \\ \tilde{K} &= (\tilde{u}^2 + \tilde{v}^2 + \tilde{w}^2)/2 \\ \tilde{e} &= (\overline{\rho u_i' u_i'})/\bar{\rho} \end{aligned}\right\} \tag{6}$$

The system of equations is closed by the definition of a perfect gas equation of state

$$\bar{P} = R\bar{\rho}\tilde{T} \tag{7}$$

and a viscosity-temperature relationship (Southerland)

$$\tilde{\mu} = \tilde{T}^{\frac{3}{2}}\left(\frac{1 + S}{\tilde{T} + S}\right) \tag{8}$$

together with the turbulence model.

The variables appearing in equations (1) to (8) have been nondimensionalized as follows:

$$\left.\begin{aligned} \tilde{u}_i &= \tilde{u}_i^*/\tilde{u}_\infty^* & \tilde{\mu} &= \tilde{\mu}^*/\tilde{\mu}_\infty^* \\ \bar{P} &= \bar{P}^*/(\tilde{\rho}_\infty^*\tilde{u}_\infty^{*2}) & S &= S^*/\tilde{T}_\infty^* \\ \tilde{\rho} &= \tilde{\rho}^*/\tilde{\rho}_\infty^* & R &= R^*/(\tilde{u}_\infty^{*2}/\tilde{T}_\infty^*) \\ \tilde{T} &= \tilde{T}^*/\tilde{T}_\infty^* & x_i &= x_i^*/L^* \end{aligned}\right\} \tag{9}$$

The system of equations, with the exception of the continuity equation (eq. (4)) is parabolic in x; consequently, marching integration can be used in the streamwise coordinate. The system is elliptic in character in the plane normal to the x-coordinate (y-z plane; see Fig. 1) since all second derivatives with respect to y and z are retained. Consequently, flows with swirl or cross-flow recirculation in the y-z plane can be correctly treated.

It should be noted that the continuity equation (eq. (4)) is hyperbolic in character and as such can be marched in x. However, since the continuity equation does not explicitly contain a diffusion term discontinuities or errors in the initial data plane (x = 0) will persist for large x-distances unless either carefully selected consistent initial data are used or an artificial diffusion term is added to equation (4) and utilized for several y-z planes downstream from x = 0. In the present paper the initial data were carefully selected; no explicit artificial diffusion term was utilized in conjunction with equation (4).

The PENS system of equations have been shown to be singular at M = 1, if $\partial\bar{p}/\partial x$ is treated implicitly, and singular for M < 1, if the pressure gradient is treated explicitly. However, if $\partial\bar{p}/\partial x$ is either neglected or specified as a function of x then the parabolic march in x can proceed without difficulty (Ref. 10). For M > 1 the problem is well posed and the parabolic march can proceed without difficulty.

Turbulence Closure

The three-dimensionality of the flow results in a number of turbulent correlations that must be modeled for the present set of governing equations. The specific correlations that must be modeled in order to close the system of governing equations are $\widetilde{u'v'}$, $\widetilde{u'w'}$, $\widetilde{v'w'}$, $\widetilde{v'v'}$, $\widetilde{w'w'}$, $\widetilde{T'v'}$, $\widetilde{T'w'}$, and $\tilde{e}$. Equation sets for obtaining some or all of these correlations are currently being developed (see for example Donaldson (Ref. 13), Hanjalic and Launder (Ref. 14), Bradshaw (Ref. 15), Launder, Reece, and Rodi (Ref. 16)); however, any attempt to solve a system of closure model equations simultaneously with the mean flow equations considered in the present paper would not be practical for the flows considered since the computer resource requirements would exceed current capabilities.

As a first step, a mixing length, eddy viscosity model is utilized in the present study as follows:

$$
\begin{aligned}
\widetilde{u'v'} &= -\epsilon_{12}\left(\frac{\partial\tilde{u}}{\partial y} + \frac{\partial\tilde{v}}{\partial x}\right) \\
\widetilde{u'w'} &= -\epsilon_{13}\left(\frac{\partial\tilde{u}}{\partial z} + \frac{\partial\tilde{w}}{\partial x}\right) \\
\widetilde{v'w'} &= -\epsilon_{23}\left(\frac{\partial\tilde{v}}{\partial z} + \frac{\partial\tilde{w}}{\partial y}\right) \\
\widetilde{T'v'} &= -\epsilon_{T2}\frac{\partial\tilde{T}}{\partial y} \\
\widetilde{T'w'} &= -\epsilon_{T3}\frac{\partial\tilde{T}}{\partial z} \\
\widetilde{v'v'} &= a_2\tilde{e} \\
\widetilde{w'w'} &= a_3\tilde{e} \\
\tilde{e} &= \sqrt{[\widetilde{u'v'}]^2 + [\widetilde{u'w'}]^2 + [\widetilde{v'w'}]^2}\,/a_1
\end{aligned}
\qquad (10)
$$

where

$$
\begin{aligned}
[\widetilde{u'v'}]_{y,z} &\equiv \widetilde{u'v'}\Big|_{y,z} \quad \text{for} \quad y \geq y_{\widetilde{u'v'}_{max}} \\
&\equiv \widetilde{u'v'}\Big|_{y_{\widetilde{u'v'}_{max}},z} \quad y < y_{\widetilde{u'v'}_{max}}
\end{aligned}
\qquad (11)
$$

and

$$\epsilon_{T2} = \epsilon_{12}/N_{Pr_t} \; ; \; \epsilon_{T3} = \epsilon_{13}/N_{Pr_t} \qquad (12)$$

The constants a_1, a_2, and a_3 are assigned values of .3, .5, and 5, respectively. The turbulent Prandtl number N_{Pr_t} is assigned a constant value of .9.

From mixing length theory the eddy viscosity becomes

$$\epsilon_{12} = \ell_2^2\left|\frac{\partial\tilde{u}}{\partial y}\right| \qquad (13)$$

$$\epsilon_{13} = \ell_3^2\left|\frac{\partial\tilde{u}}{\partial z}\right| \qquad (14)$$

where ε_{23} has been assumed to zero. Recently Gessner and Emery (Ref. 17) showed that the 7-equation model of Launder et al (Ref. 16) reduced to a form similar to the current model in the super equilibrium limit. The mixing lengths, ℓ_2 and ℓ_3 are obtained from the jet and/or wake widths, δ_2 and δ_3 in the x-y and x-z planes based on the results presented by Rudy and Bushnell (Ref. 18).

$$
\left.
\begin{aligned}
\ell_2/\delta_2 &= \alpha_2 \\
\ell_3/\delta_3 &= \alpha_3
\end{aligned}
\right\} \qquad (15)
$$

Rudy and Bushnell (Ref. 18) divided the shear layer into the following three characteristic regions: (see Fig. 1):

region I

$$
\left.
\begin{aligned}
\delta_2 &= f_I\,(y_{.05} - y_{.95}) \\
\delta_3 &= f_I\,(z_{.05} - z_{.95})
\end{aligned}
\right\} \qquad (16a)
$$

region II

$$
\left.
\begin{aligned}
\delta_2 &= f_{II}\,y_{.05} + (x - x_{c_2})\tan\beta_2 \\
\delta_3 &= f_{II}\,z_{.05} + (x - x_{c_3})\tan\beta_3
\end{aligned}
\right\} \qquad (16b)
$$

region III

$$
\left.
\begin{aligned}
\delta_2 &= 2f_{III}\,(y_{.05} + y_j) \\
\delta_3 &= 2f_{III}\,z_{.05}
\end{aligned}
\right\} \qquad (16c)
$$

Where $y_{.05}$ and $y_{.95}$ are defined as the y values where $U_m(x,y,z)$ equals .05 and .95, respectively.

The center of each jet or wake is located at $y = 0$ and the plane of symmetry for interacting jets or wakes is located at $y = -y_j$ (the half-distance between the two interacting jets or wakes). In a similar fashion $z_{.05}$ and $z_{.95}$ are defined as the greater of the two z values where $U_m\,(x,0,z)$ equals .05 and .95, respectively or $U_m\,(x, -y_j, z)$ equals .05 or .95, respectively for the interacting jet. The x-value defining the end of regions I and II are determined such that δ is continuous function of x. The following constants are specified for the present study: $\alpha_2 = \alpha_3 = .05$, $f_I = 1.425$, $f_{II} = f_{III} = 1.2$ and $\beta_2 = \beta_3 = 8^\circ$.

NUMERICAL PROCEDURE

An alternating direction implicit (ASI) procedure is used in the present stody to solve the system of equations. The ADI procedure is an outgrowth of the paper by Peaceman and Rachford (Ref. 19) and has been applied to laminar jet flows by Hirsh (Ref. 2).

Coordinate Transformation

Equations (1) to (5) are case in finite-difference form on the transformed region defined as follows (see Ref. 2):

$$\eta = \frac{Ay}{|1 + Ay|} \; ; \; \zeta = \frac{Bz}{|1 + Bz|} \qquad (17)$$

When the constants A and B are selected such that $U_j(x,y,z)$ has a value of .5 at η and $\zeta = .5$. This linear algebraic transformation removes the problem associated with boundary condition specification since $y = z = 0$ maps into $\eta = \zeta = 0$ and $y \to \infty$, $z \to \infty$ maps into $\eta \to 1$, $\zeta \to 1$ as well as assures that the jet or wake remain inside the preselected η, ζ computational comain for large x.

Linearization

The ADI procedure is a two-step, second-order implicit technique. The first step advances the solution from $x = x_i$ to an intermediate station between x_i and x_{i+1}. The solution is second-order accurate at $x_i + \Delta x/2$; consequently, in order to retain the second-order accuracy all nonlinear coefficients as well as the cross derivatives are calculated at the $x_i + \Delta x/2$ plane through the following extrapolation:

$$Q_{j,k}^{i+\frac{1}{2}} = \frac{[(\Delta x_+) - 2(\Delta x_-)]Q_{j,k}^{i} - (\Delta x_+)Q_{j,k}^{i-1}}{2(\Delta x_-)} \tag{18}$$

where Q represents any quantity to be extrapolated.

Computer Requirements

The coupled system of five linear algebraic equations in five unknowns are solved by an efficient block tridiagonal procedure (see Hirsh (Ref. 2)). The equations are solved in the transformed (η,ζ) plane for specified x locations. A uniform grid is generated in the η,ζ plane in order to retain second order accuracy. It should be noted that the grid in the x,y plane is varied in order to cluster the points in the regions of maximum shear. Variable x-march steps are utilized in order to minimize the computer processing time. The storage requirements for the present computer code with algebraic closure for a 41 x 41 grid point distribution in the η,ζ plane is 210 K_8 which includes the storage required for a self-contained graphic package. The processing time on a CDC CYBER 175 computer system is 10^{-3} sec/unknown/grid point (8.4 sec/x-station; 41 x 41; η,ζ grid).

RESULTS AND DISCUSSION

The present study was limited to co-flowing supersonic jets/wakes in order to avoid problems associated with sonic and/or subsonic flow (see Refs. 1 and 2). As previously noted, the initial data plane ($x = 0$) may be specified from either experimental data or from an analytical development. However, care must be exercised to assure that these data are smooth and satisfy the governing equations. There are no sufficient experimental data available for the present test cases (to the knowledge of the authors). Consequently, a subprogram was developed to generate the initial data required to initiate the x-march.

For the single jet, the subprogram generates the half velocity line in the quarter plane from the specification of three coordinates $(0, y_H, 0)$, $(0, 0, z_H)$, and $(0, y_c, z_c)$ which represent the height, width, and center of curvature for geometries with circular or elliptical arcs. The velocity profiles are next constructed in the quarter plane, using specified values of $\tilde{u}_j$, $\tilde{u}_\infty$, and t as follows:

$$\tilde{u}(0,y,z) = \frac{1}{2}[(\tilde{u}_j + \tilde{u}_\infty) \pm (\tilde{u}_j - \tilde{u}_\infty)\,\mathrm{erf}(c_1 r/t)] \tag{19}$$

where $c_1 = 1.81243$, t is the width between $U_j = .1$ and .9, and r is the minimum distance from the point (0, y, z) to the half velocity line. The sign (±) is selected as follows: the plus (+) sign is selected when the point (0, y, z) is on the core side of the half velocity line; the minus (-) sign when the point (0, y, z) is on the free stream side.

For the interacting jet case, the jet coordinate point $(0, y_j, 0)$ has to be specified (y_j is half the distance between the centerlines of the two jets). The y coordinates is first translated to $\hat{y}$ through the linear transform $\hat{y} = y - y_j$. Next, the streamwise velocity, $\tilde{u}$ is constructed from equation (19) for the quarter infinite plane ($\hat{y} \geq -y_j$, ; $z \geq 0$; eq. (19) where $\hat{y}$ replaces y). Then a new velocity field, u_2 based on an imaginary jet (located opposite to the symmetry plane) is constructed and superimposed as follows:

$$\tilde{u}(0, \hat{y}, z) = \tilde{u}_1(0, \hat{y}, z) + \tilde{u}_2(0, \hat{y}, z) - \tilde{u}_\infty \tag{20}$$

The static temperature field is then computed by assuming constant total enthalpy. The cross flow velocity field, (v, w) is initially assumed to be zero, and the static pressure is assumed independent of y and z ($p_{x=0} = \text{const.}$).

The parameters A and B (see eqs. (17)) are selected such that z_H maps to $\zeta = .5$ and y_H for the single jet or wake and $-y_j$ for the interacting jet are mapped to $\eta = -.5$.

Symmetry boundary conditions are imposed along the η and ζ axis for the single jet or wake. For the interacting jet case the symmetry condition is imposed along the $\eta = -.5$ plane. Dirchlet conditions on all dependent variables are specified at $\eta = \zeta = 1$.

An axisymmetric jet is presented as the first test case. This particular case was chosen to verify the numerical procedure and turbulence closure since results for axisymmetric turbulent jet flow are well documented in the literature. The present results are compared with empirical and two-dimensional mixing length results in Figures 2 and 3. The test conditions for the calculations are presented in Table 1.

Forstall and Shapiro (Ref. 20) compared the mixing length analysis of Squire and Trouncer with experimental data for coaxial subsonic jet flow and noted that the mixing length approach predicted the correct half-velocity growth; however, the axial velocity decay rate was underpredicted. The empirical law of velocity decay (Ref. 20) along the axis is independent of λ and downstream of the potential core satisfies the relationship

$$U_j(x,0,0) \propto x^{-1} \tag{21}$$

However, mixing length predicts $x^{-1/1.3}$ which is also independent of λ. The mixing length analysis predicts the correct empirical spreading law

$$y_{.5} \propto x^{(1-\lambda)} \tag{22}$$

The predicted rates of $x^{-1/1.3}$ and $x^{(1-\lambda)}$ are insensitive to the selected mixing length constants.

The numerical results obtained in the present analysis clearly agree with the expected trends. The laminar results presented on Figures 2 and 3 are included for comparison purposes.

Profiles of $\tilde{u}, \tilde{p}, 1-\tilde{T}$, and $\tilde{v}, \tilde{w}$ are presented at the $x = 0.2$ and $x = 60$ planes in Figure 4. Symmetry flow condition checks at $x = 60$ indicate that symmetry was achieved up to the seventh significant digit.

Elliptical jet, wake, and interacting jet flow results are presented in Figures 5, 6, and 7, respectively. Flow conditions for these three test cases are presented in Table 1. A 49 x 33 grid was used for the interacting jet case (Fig. 7).

The flow fields presented represent approximately 75 percent of the computed η,ζ plane. It should be noted that $\tilde{v}$, $\tilde{w}$, and $\tilde{p}$ have been magnified an order of magnitude more than $\tilde{u}$ and $\tilde{T}$ for clarity in the figures. Streamwise velocity decay and half width velocity growth are presented in Figures 8 and 9 for the single jet and wake. The streamwise velocity decay for the interacting jet case at $y = 0$ and $y = y_j$ are presented in Figure 10. The corresponding value of ℓ_2 is also presented. The variation of ℓ_2 with x represents an average value since problems were encountered in the computer code logic for this case. Experimental data are required for this particular case before the turbulence model can be verified or improved.

The results presented in Figures 2 to 10 clearly demonstrate that the present procedure is capable of solving three-dimensional free flows ($M > 1$) with pressure gradients in all three spatial coordinates. However, the present mixing length eddy viscosity turbulence closure limits the validity of the results near the axis of the flow for pressure which in turn results in questionable cross flow velocity fields in this region. The mixing length formulation cannot yield the correct turbulent energy variation in the region of $\tilde{u}_{max}$ (see Gessner and Emery (Ref. 17)). It appears that the two "turbulent equation"model (turbulent kinetic energy plus dissipation) is required to produce more nearly correct pressure and cross flow velocity fields in the region of u_{max}. This would require the solution of a coupled 7 x 7 block tridiagonal matrix in the present method for each cross plane instead of the present 5 x 5 system; however, a less strongly coupled approach might be utilized (see Naot and Launder (Ref. 22)).

The current computer code requires 210 K_8 memory for a 41 x 41 grid in the η,ζ plane. The computation time for the cases presented was lengthy (approximately 9000 sec; CYBER 175) due to the stability restrictions placed on the marching step due primarily to the turbulence model logic. Consequently, it appears from the present work that the addition of a more complicated system of partial differential equations for turbulence closure is not feasible in the present numerical procedure unless modifications can be made to remove the sensitivity of the results to disturbances in the initial data plane (artifical diffusion) as well as to significantly reduce the required computation time. Numerical experimentation on the present test cases indicates that disturbances develop near the edge of the jet or wake for $N_R > 10^3$ which amplify and destroy the solution. The CFL number limitation could be due to several factors such as (a) hyperbolic character of the continuity equation (no diffusion), (b) problems associated with selecting continuous length scales from the developing velocity profiles, and (c) failure to iterate each x-station to some prespecified convergence level (see Ref. 2). Future work will be directed towards a careful numerical analyses of each of these areas to determine whether closure model equations can be efficiently treated by the present ADI procedure.

CONCLUDING REMARKS

The alternating direction implicit method has been successfully applied to numerically solve the parabolic-elliptic Navier-Stokes equations for supersonic turbulent jets and wakes. A mixing length eddy viscosity model was used to provide turbulence closure. A coordinate transformation was utilized to allow specification of infinity boundary conditions on a finite computational domain as well as contain the downstream growth of the viscous flow field in a fixed computational grid.

The numerical results were compared with empirical and/or numerical results for two-dimensional free shear flows; experimental data were not available for the three-dimensional supersonic flows computed. In all cases the expected characteristics of the flow, such as centerline decay rate, spreading rate, and profile development were well predicted.

The initial data plane presented somewhat of a problem since experimental data were not available. However, the analytical data generated were found to be satisfactory for Reynolds numbers up to 10^3. Solutions for larger Reynolds numbers were not presented due to instabilities associated with either the initial data plane or the length-scale formulation.

The present computer code requires 210 K_8 storage and approximately 10^{-3} seconds/unknown/grid point processing time. These computer requirements precludes the extension of the method to two or more equation models for turbulence closure since the computation time and computer core storage requirements would be unrealistic. Consequently, the present method must be either improved computationally or replaced with a new approach for flows where the mixing length eddy-viscosity is inadequate.

REFERENCES

1. McDonald, H.; and Briley, W. R.: Three-Dimensional Supersonic Flow of a Viscous or Inviscid Gas. Journal of Computational Physics 19, 1975, pp. 150-178.

2. Hirsh, R. S.: Numerical Calculation of Supersonic Three-Dimensional Free-Mixing Flows Using the Parabolic-Elliptic Navier-Stokes Equations. NASA TN D-8195, 1976.

3. Caretto, L. S.; Curr, R. M.; and Spalding, D. B.: Comput. Meth. Engrg. 1, 1973, pp. 39-51.

4. Patankar, S. V.; and Spalding, D. B.: A Calculation Procedure for Heat, Mass and Momentum Transfer in Three-Dimensional Parabolic Flows. Int. J. Heat and Mass Trans., Vol. 15, No. 10, 1972, pp. 1787-1806.

5. Lewellen, W. S.; Teske, M.; and Donaldson, C. duP.: Turbulent Wakes in a Stratified Fluid, Part I: Model Development, Verification, and Sensitivity to Initial Conditions. Report No. 226, A.R.A.P. August 1972.

6. Rudman, S.; and Rubin, S. G.: Hypersonic Viscous Flow Over Slender Bodies With Sharp Leading Edges. AIAA Journal, Vol. 6, 1968, pp. 1883-1890.

7. Nardo, C. T.; and Cresci, R. J.: An Alternating Directional Implicit Scheme for Three-Dimensional Hypersonic Flows. J. Comput. Phys., Vol. 8, No. 2, October 1971, pp. 268-284.

8. Rubin, S. G.; and Lin, T. C.: Numerical Methods for Two- and Three-Dimensional Viscous Flow Problems: Application to Hypersonic Leading Edge Equations. AFOSR-TR-71-0778, U.S. Air Force, April 1971. (Available from DDC as AD 726 547).

9. Rubin, S. G.; and Lin, T. C.: A Numerical Method for Three-Dimensional Viscous Flow: Application to the Hypersonic Leading Edge. J. Comp. Phys., Vol. 9, No. 2, April 1972, pp. 339-364.

10. Lin, T. C.; and Rubin, S. G.: Viscous Flow Over a Cone at Moderate Incidence - I. Hypersonic Tip Region. Computers and Fluids, Vol. 1, No. 1, 1973, pp. 37-57.

11. Lubard, S. C.; and Helliwell, W. S.: Calculation of the Flow on a Cone at High Angle of Attack. AIAA Paper No. 73-635, July 1973.

12. Helliwell, W. S.; and Lubard, S. C.: An Implicit Method for Three-Dimensional Viscous Flow With Application to Cones at Angle of Attack. Computers and Fluids, Vol. 3, No. 1, 1975, pp. 83-101.

13. Donaldson, C. duP.: A Progress Report on an Attempt to Construct an Invarian Model of Turbulent Shear Flows. AGARD-CP-93 on Turbulent Shear Flows, London, Paper B-1, 1971.

14. Hanjalic, K.; and Launder, B. E.: A Reynolds Stress Model of Turbulence and its Application to Thin Shear Flows. J. Fluid Mech., Vol. 52, 1972, pp. 609-638.

15. Bradshaw, P.: The Understanding and Prediction of Turbulent Flow. Aeronautical J., July 1972, pp. 403-418.

16. Launder, B. E.; Reece, G. J.; and Rodi, W.: Progress in the Development of a Reynolds-Stress Turbulence Closure. J. Fluid Mech., Vol. 68, 1975, pp. 537-566.

17. Gessner, F. B.; and Emery, A. F.: A Reynolds Stress Model for Turbulent Corner Flows - Part 1: Development of the Model. J. of Fluid Eng., Transactions of the ASME, June 1976, pp. 261-268.

18. Rudy, D. H.; and Bushnell, D. M.: A Rational Approach to the Use of Prandtl's Mixing Length Model in Free Turbulent Shear Flow Calculations. NASA SP-321, Free Turbulent Shear Flows, Volume I - Conference Proceedings, 1972.

19. Peaceman, D. W.; and Rachford, H. H., Jr.: The Numerical Solution of Parabolic and Elliptic Differential Equations. J. Soc. Indust. Appl. Math., Vol. 3, No. 1, 1955, pp. 28-41.

20. Forstall, W., Jr.; and Shapiro, A. H.: Momentum and Mass Transfer in Coaxial Gas Jets. J. of Appl. Mech., 1950, pp. 399-408.

21. Squire, H. B.; and Trouncer, J.: Round Jets in a General Stream. R&M, No. 1974, Brit. A.R.C., 1944.

22. Naot, D.; and Launder, B. E.: Numerical Calculation of the Turbulent Swirling and Recirculating Flows With a Reynolds Stress Closure. Report ME-22/75, Ben Gurion University of the Negev, 1975.

TABLE 1. - TEST CONDITIONS

CASE	M_j	M_∞	λ	y_H	z_H	y_c	z_c	y_j	t	N_R	N_{Pr}	N_{Pr_t}	γ	s
1	1.8	1.2	2/3	1.0	1.0	0.	0.	0.	.4	10^3	.76	.9	1.4	.375
2	1.8	1.2	2/3	2.0	1.0	0.	0.	0.	.4	10^3	.76	.9	1.4	.375
3	1.2	1.8	1.5	2.0	1.0	0.	0.	0.	.4	10^3	.76	.9	1.4	.375
4	1.8	1.2	2/3	1.0	1.0	.8	.8	1.2	.4	10^3	.76	.9	1.4	.375

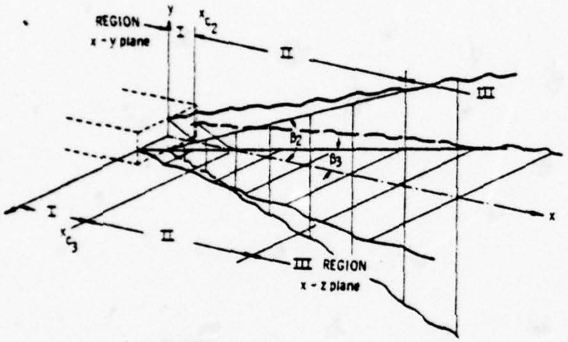

Fig. 1 Schematic illustration of mixing length.

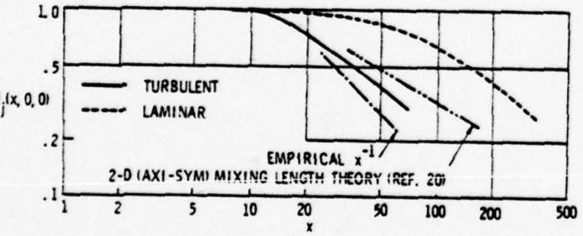

Fig. 2 Streamwise velocity decay along the axis of circular jet, laminar and turbulent.

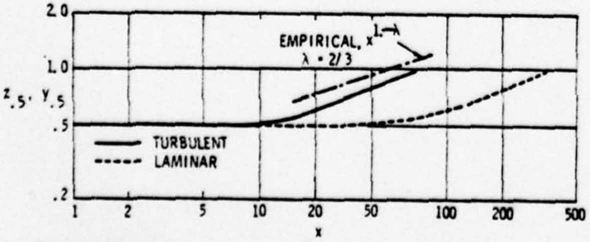

Fig. 3 Spreading of a half velocity line of circular jet, laminar and turbulent.

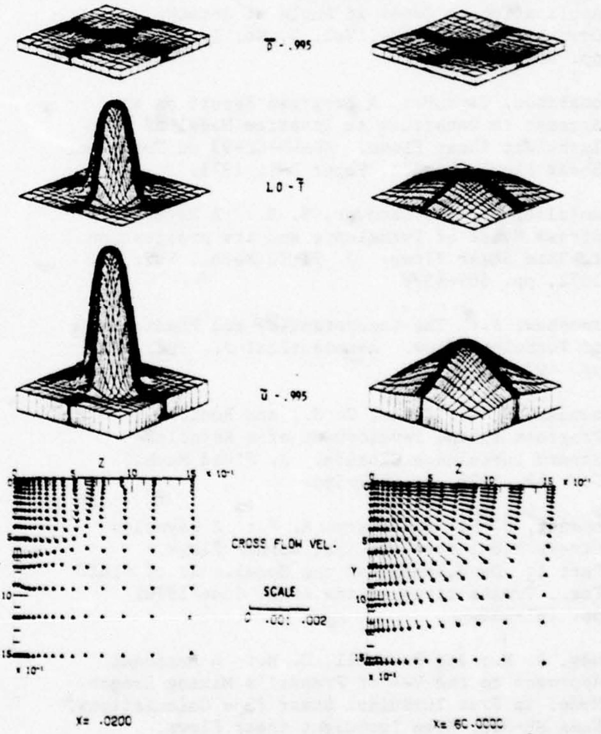

Fig. 4 Circular free turbulent jet flow fields at $\underset{\sim}{x}$=.02 and 60. Values at the axis; $\tilde{u}$=1.32577, $\tilde{T}$=.7818, $\bar{p}$=1.00001 at x=.02, and $\tilde{u}$=1.11087, $\tilde{T}$=.94009, $\bar{p}$=.99723 at x=60.

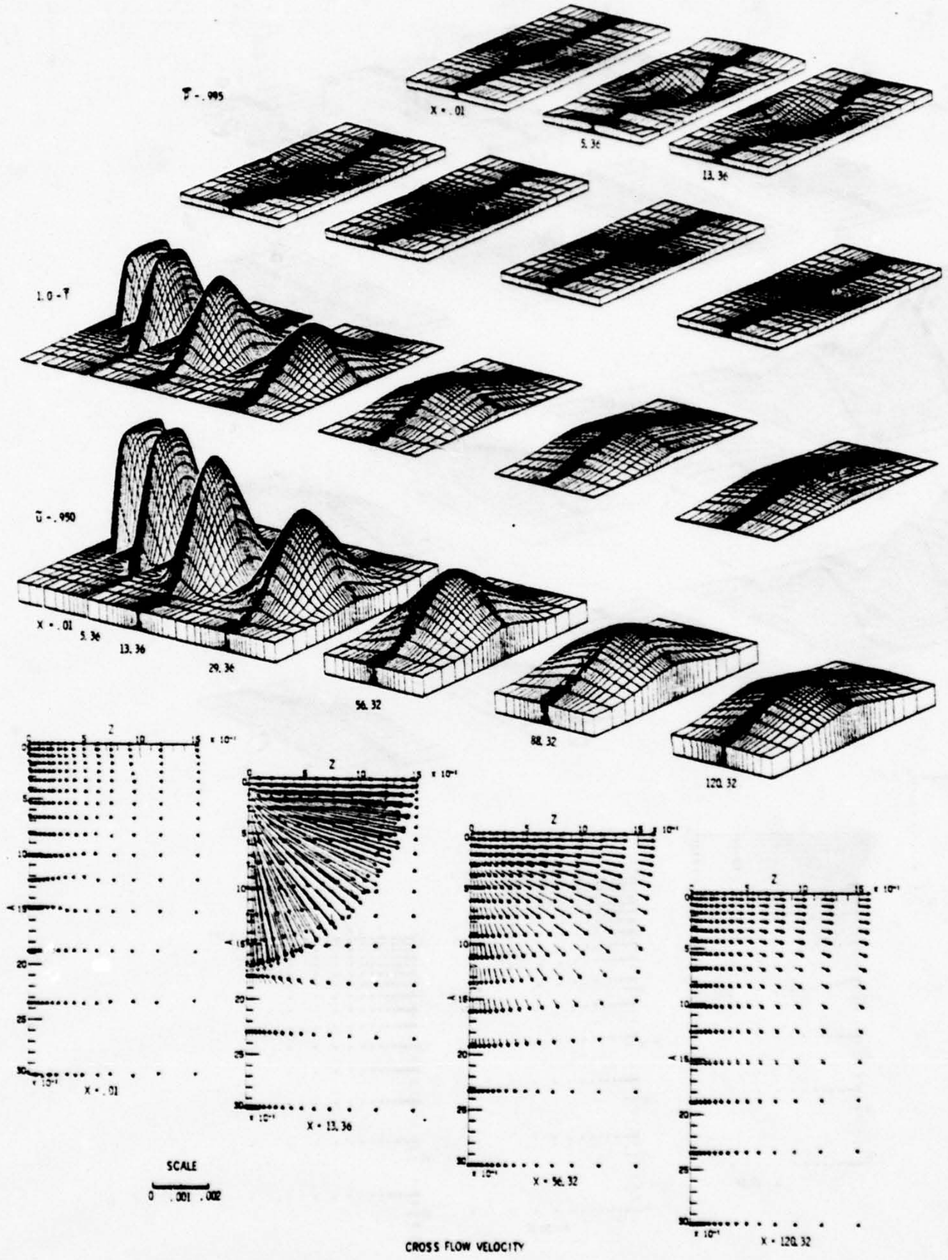

Fig. 5 Flow fields of elliptic free turbulent jet. Slenderness ratio of the initial jet = 2.
Values at the axis;

Marching steps	1	101	201	401	601	801	1001
x	.01	5.36	13.36	29.36	56.32	88.32	120.32
$\tilde{u}$	1.32581	1.32777	1.29153	1.20826	1.14170	1.10559	1.08550
$\tilde{T}$	.78176	.78098	.81372	.87702	.92065	.94247	.95413
$\bar{p}$	.99999	.98699	.98906	.99502	.99775	.99874	.99920

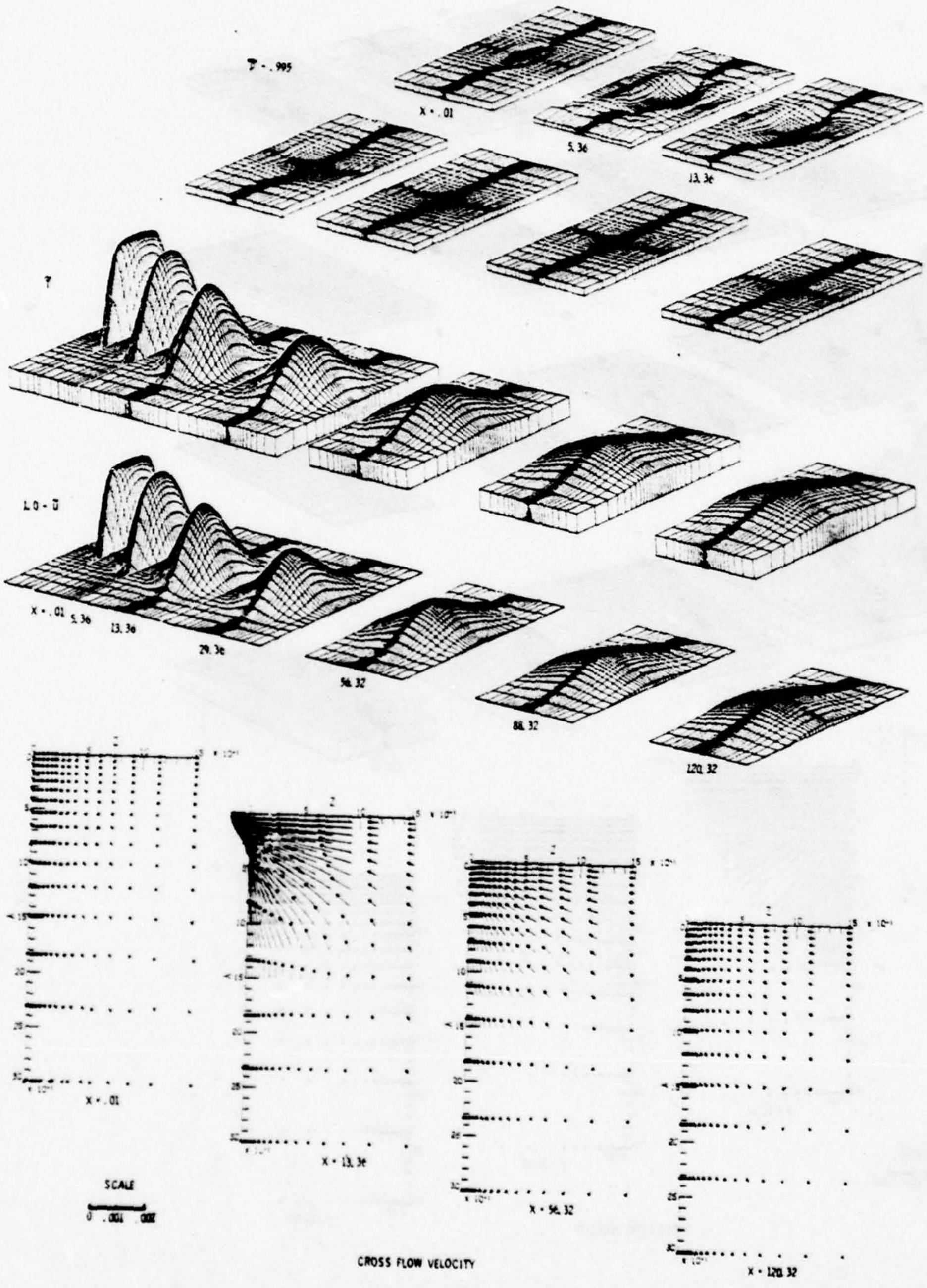

Fig. 6 Flow fields of elliptic free turbulent wake. Slenderness ratio of the initial wake = 2. Values at the axis;

Marching steps	1	101	201	401	601	801	1001
x	.01	5.36	13.36	29.36	56.36	88.32	120.32
$\tilde{U}$	.75452	.76858	.81842	.87872	.91897	.93997	.95149
$\tilde{T}$	1.27908	1.26026	1.20095	1.13367	1.08937	1.06620	1.05345
$\bar{P}$	.99991	.99038	.99340	.99713	.99858	.99917	.99954

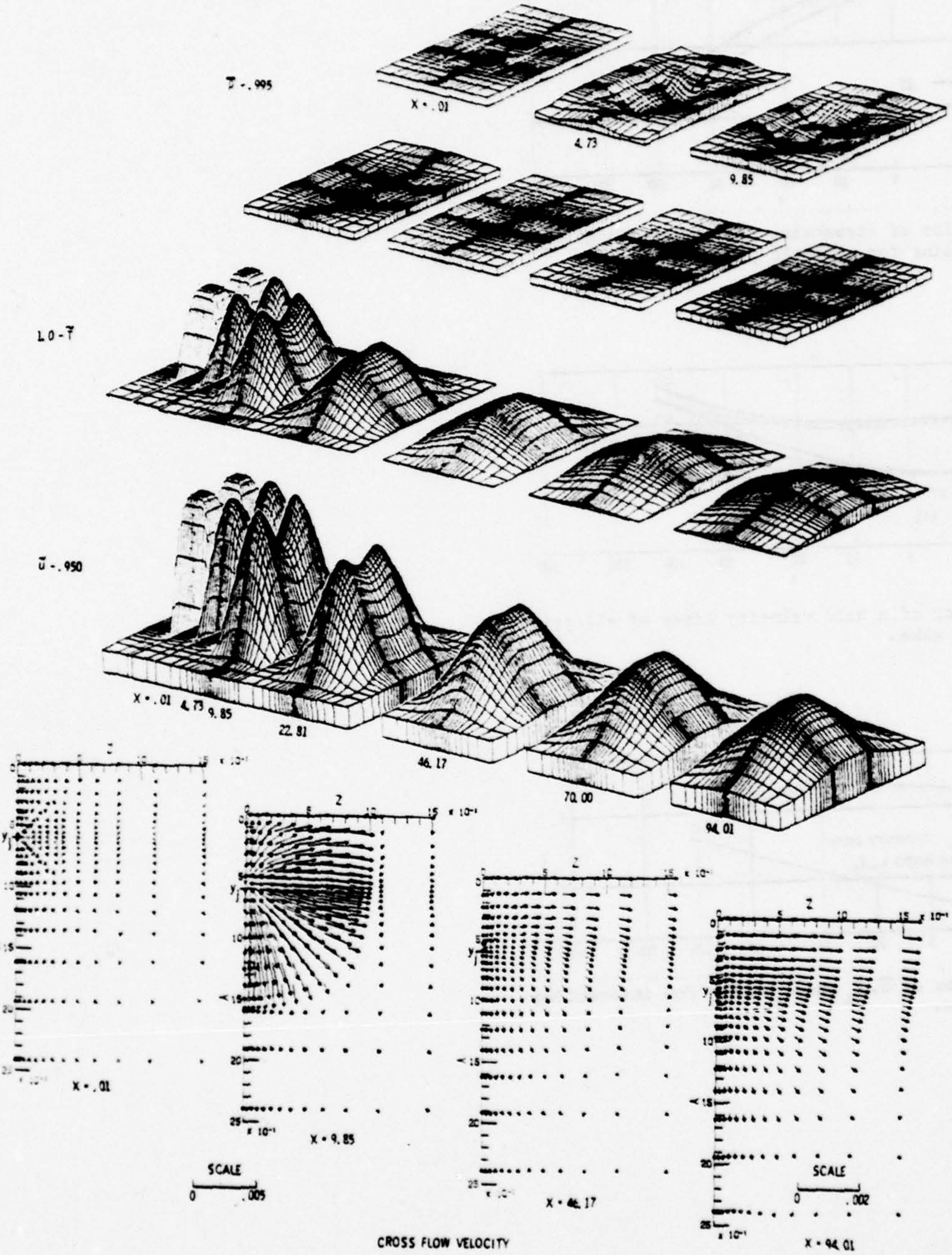

Fig. 7 Flow fields of interacting square jets. Computed values at the symmetry axis;

Marching steps	1	87	151	313	605	831	977
x	.01	4.73	9.85	22.81	46.17	70.65	94.01
$\tilde{u}$	1.17510	1.20886	1.22052	1.21557	1.18479	1.16390	1.14583
$\tilde{T}$	.89017	.85892	.85203	.87582	.90400	.91838	.93001
$\bar{p}$	.99957	.98954	.99372	.99677	.99938	.99787	.99846

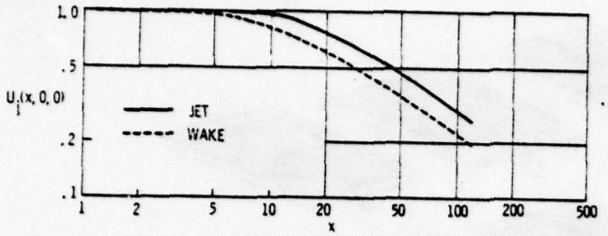

Fig. 8 Variation of streamwise velocities along the centerline for elliptic jet and wake.

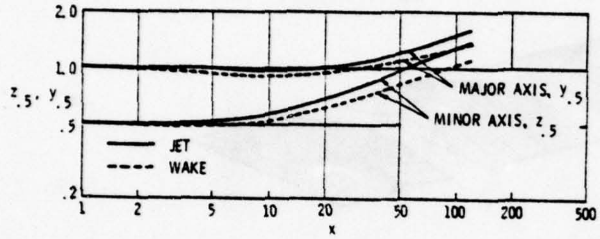

Fig. 9 Spreading of a half velocity lines of elliptic jet and wake.

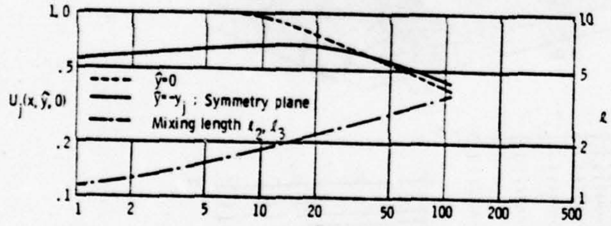

Fig. 10 Variation of $\tilde{u}$, ℓ_2 and ℓ_3 with x for interacting jet flow.

THE CALCULATION OF THREE-DIMENSIONAL TURBULENT FREE JETS

J.J. McGuirk and W. Rodi
Sonderforschungsbereich 80, University of Karlsruhe
Karlsruhe, Germany

ABSTRACT

The paper presents an application of the two-equation k-ε model to the problem of three-dimensional free jets issuing from rectangular orifices. The turbulence model has been modified so that plane and round jets may be predicted with the same empirical input. The continuity, momentum and turbulence equations are solved using the finite-difference procedure of Patankar and Spalding for three-dimensional parabolic flows and results are presented for aspect ratios of 1, 5, 10 and 20. The decay of axial velocity is well predicted. The behaviour of the half-widths however is not well predicted when no lateral velocities are specified at the orifice; the measured cross-over of jet major and minor axes is not obtained. The possible existence of a lateral velocity field at the orifice cross-section is examined and its ability to produce the observed jet inversion is demonstrated. Profile shapes in the orifice short-axis direction are in good agreement with measurements and, when inlet lateral velocities are specified, the long-axis profiles are also predicted fairly well. The measured "saddle-shape" of the profiles in this direction is, however, not obtained; this will require further changes to the turbulence model.

NOMENCLATURE

b_0 - orifice breadth
c_1, c_2, c - constants in turbulence model
d_0 - orifice depth
e - aspect ratio of jet = b_0/d_0
G - production of turbulent kinetic energy
k - turbulent kinetic energy = $1/2\ (\overline{u^2}+\overline{v^2}+\overline{w^2})$
L - turbulence length scale
P - mean static pressure
U, U_1 - mean velocity in x-direction
u, u_1 - fluctuating velocity in x-direction
V, U_2 - mean velocity in y-direction
v, u_2 - fluctuating velocity in y-direction
W, U_3 - mean velocity in z-direction
w, u_3 - fluctuating velocity in z-direction
x, x_1 - axial co-ordinate
y, x_2 - lateral co-ordinate (orifice short-axis)
z, x_3 - transverse co-ordinate (orifice long-axis)
ν - kinematic viscosity
ρ - fluid density
ε - dissipation of k
$\sigma_k, \sigma_\varepsilon$ - turbulent Prandtl Nos. for k, ε
δ_{ij} - Kronecker delta

Subscripts

m - centre-line value
$1/2, 3/4$ - half/three-quarter velocity location
0 - inlet value
a - ambient value
t - turbulent value
$\overline{}$ - time-averaged value (superscript)

INTRODUCTION

The development and testing of turbulence models has proceeded apace since the advent of efficient computer programs for the solution of fluid flow problems. Necessarily, the verification of the various models was first of all restricted to simpler flow situations for which the computer programs were more economic and better tested and for which measurements were readily available. Examples of this verification process may be found in the proceedings of the Stanford and Langley conferences ([1], [2]), where attention was given solely to two-dimensional wall boundary layers and free shear flows, respectively. Since relatively economic computer programs have recently become available also for 3D flows, it now seems opportune to extend the verification of those turbulence models which have performed well in the tests up to date to three-dimensional flow problems. Turbulence models involving closure at the two-equation level have been shown (see for example Launder et al. [3]) to provide appreciably better universality than lower order models, whereas the higher order closure schemes appear at the moment to be insufficiently well-developed to prove themselves superior even for two-dimensional flows. It is the purpose of the present paper therefore to apply and extend the k-ε two-equation model, which has performed successfully in a wide range of two-dimensional problems (see References [2] and [4]), to the prediction of a basic three-dimensional flow. As the first test case we have chosen the problem of three-dimensional free jets issuing into stagnant surroundings; the boundary-layer nature of this flow makes it particularly suitable for economic numerical calculations, yet the flow still exhibits many interesting and complex phenomena, as will now be discussed.

The schematics of a three-dimensional free jet issuing from a rectangular orifice are indicated in Fig. 1; this flow configuration was used in the experimental investigations of Sforza and co-workers ([5], [6]), Yevdjevitch [7], and most recently by Sfeier [8] who also reported measurements of the temperature field. Unfortunately no measurements of turbulence quantities are available. The experiments have

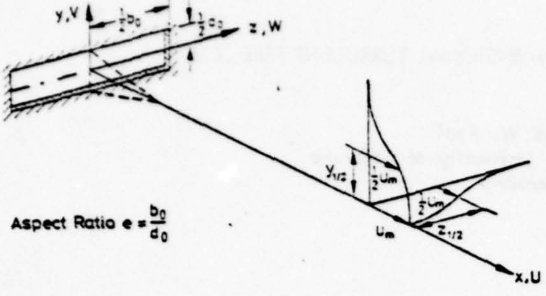

Fig. 1 Flow Configuration

shown that this flow possesses several interesting features which make it a particularly severe test case; when the aspect ratio e is large for example, the centre-line velocity decay measurements indicate that the initial behaviour is similar to that of a two-dimensional plane jet. Far downstream however, the flow will approach axi-symmetry and the flow development is akin to that of a round jet. It can thus be seen that this flow includes the two basic two-dimensional jet flows (plane and round) in its initial and final zones and the turbulence model should be able to predict these regions as well as the intermediate transition region. The measurements of the velocity half-widths (see Fig. 1) in the two lateral directions on the other hand indicate a behaviour very different to two-dimensional jets. The half-width in the direction of the long axis of the orifice actually decreases in magnitude initially whereas the minor axis half-width grows; at some distance downstream they cross over after which they both grow, but at slightly different rates, tending to approach each other as the jet tends to axi-symmetry. The initial decrease seems to be connected with the presence of lateral velocities at the orifice cross-section, as Sfeier [8] has shown that when the jet issues from a long rectangular channel as opposed to a sharp-edged orifice the major axis half-width does not decrease initially but remains practically constant. The cross-over still takes place however, so that the different behaviour of the two half-widths cannot totally be explained via the initial conditions. This inversion of major and minor axes of the jet is also accompanied by the appearance of so-called "saddle-shape" velocity profiles in the direction of the orifice long axis. The maximum velocity is displaced some way from the centre-plane, although again Sfeier's measurements show that this shape is much more pronounced for the jet out of a sharp-edged orifice. Both the jet inversion and the saddle-shape profiles seem to be indications of the presence of secondary motions in the plane of the jet cross-section, which Sforza [6] suggests are induced by a system of closed vortex rings generated at the orifice. In an experimental and theoretical investigation [9] into the behaviour of single, impulsively generated closed vortex loops of rectangular and elliptic shape, the process of inversion of major and minor axes was observed and predicted. The ring was also shown to distort out of the plane in which it had been formed, thereby creating a component of vorticity in the axial direction. The mechanism by which secondary motions in the jet cross-section may be produced was therefore clearly illustrated by this investigation, although in the case of steady flow out of a rectangular orifice the vortex rings are generated by a continuous rolling up of the vortex sheet representing the velocity discontinuity at the orifice. Such vortex rings, which have been observed in the case of a round jet (see Laufer [10]), interact with each other and form the coherent large-scale turbulence structure of the jet, at least in the initial mixing-layer region.

The brief description of the behaviour of 3D free jets given above shows that this is indeed a worthy 3D test case. The present paper makes a first step in the testing of turbulence models for 3D flows by applying one model to the prediction of 3D free jets. The details of the model and of the calculation procedure used are given in the next section; the results of the calculations and a discussion of the performance of the model follows, and in the final section a summary of the outcome of the present work is given together with suggestions for further testing.

MATHEMATICAL MODEL

Mean-Flow Equations

The mean-velocity distribution in constant-density three-dimensional free jets at high Reynolds numbers is governed by the following equations:

$$\frac{\partial U}{\partial x} + \frac{\partial V}{\partial y} + \frac{\partial W}{\partial z} = 0 \qquad (1)$$

$$\frac{\partial U^2}{\partial x} + \frac{\partial VU}{\partial y} + \frac{\partial WU}{\partial z} = -\frac{\partial \overline{uv}}{\partial y} - \frac{\partial \overline{uw}}{\partial z} \qquad (2)$$

$$\frac{\partial UV}{\partial x} + \frac{\partial V^2}{\partial y} + \frac{\partial WV}{\partial z} = -\frac{1}{\rho}\frac{\partial P}{\partial y} - \frac{\partial \overline{v^2}}{\partial y} - \frac{\partial \overline{vw}}{\partial z} \qquad (3)$$

$$\frac{\partial UW}{\partial x} + \frac{\partial VW}{\partial y} + \frac{\partial W^2}{\partial z} = -\frac{1}{\rho}\frac{\partial P}{\partial z} - \frac{\partial \overline{vw}}{\partial y} - \frac{\partial \overline{w^2}}{\partial z} \qquad (4)$$

where (1) is the continuity equation and (2), (3) and (4) are momentum equations in the x-, y-, and z-directions, respectively. All symbols are defined in Fig. 1 and in the Nomenclature. Equations (2) to (4) are written in a form valid for free boundary-layer type flows: in these flows the streamwise turbulent diffusion of momentum is negligible so that no Reynolds-stress gradients with respect to x appear; also the streamwise pressure gradient originally appearing in Eq. (2) is negligible when the surroundings are at constant velocity (here at rest).

In two-dimensional (plane or round) jets, the lateral momentum equation need not be solved because, when the streamwise pressure gradient is neglected, the lateral velocity can be determined from the continuity equation. In the three-dimensional case considered here this is not possible because now all three velocity components appear in the continuity equation. Therefore, all three momentum equations have to be solved.

Turbulence Model

In order to close the above set of equations, the Reynolds stresses in the momentum equations (2) to (4) have to be specified by means of a turbulence model. As was mentioned already in the Introduction, the present work employs and tests an extended version of the so-called k-ε model. In what follows, the standard k-ε model is briefly described first, and its extension is introduced subsequently.

The standard k-ε -model. In this model, the Reynolds stresses are calculated via the effective viscosity concept which may be written in general form as:

$$-\overline{u_i u_j} = \nu_t \left(\frac{\partial U_i}{\partial x_j} + \frac{\partial U_j}{\partial x_i} \right) - \frac{2}{3} \delta_{ij} k \;. \quad (5)$$

Here, tensor notation has been used for brevity; the conversion to the notation used above can be found in the Nomenclature. In Eq. (5), ν_t is a scalar effective (kinematic) viscosity and k is the turbulent kinetic energy (= 1/2 $\overline{u_i u_i}$).

The k-ε model characterizes the local state of turbulence by two parameters: the turbulent kinetic energy, k, and the rate of its dissipation, ε. The effective viscosity ν_t is related to these parameters by the Kolmogorov-Prandtl expression:

$$\nu_t = c_\mu \frac{k^2}{\varepsilon} \;, \quad (6)$$

where c_μ is an empirical constant. The distribution of k and ε over the flow field is calculated from the following semi-empirical transport equations for k and ε:

$$\frac{\partial Uk}{\partial x} + \frac{\partial Vk}{\partial y} + \frac{\partial Wk}{\partial z} = \frac{\partial}{\partial y}\left(\frac{\nu_t}{\sigma_k}\frac{\partial k}{\partial y}\right) + \frac{\partial}{\partial z}\left(\frac{\nu_t}{\sigma_k}\frac{\partial k}{\partial z}\right) + G - \varepsilon \quad (7)$$

$$\frac{\partial U\varepsilon}{\partial x} + \frac{\partial V\varepsilon}{\partial y} + \frac{\partial W\varepsilon}{\partial z} = \frac{\partial}{\partial y}\left(\frac{\nu_t}{\sigma_\varepsilon}\frac{\partial \varepsilon}{\partial y}\right) + \frac{\partial}{\partial z}\left(\frac{\nu_t}{\sigma_\varepsilon}\frac{\partial \varepsilon}{\partial z}\right) + c_1\frac{\varepsilon}{k}G - c_2\frac{\varepsilon^2}{k} \quad (8)$$

where G is the production of turbulence energy.

$$G = \nu_t \left[\left(\frac{\partial U}{\partial y}\right)^2 + \left(\frac{\partial U}{\partial z}\right)^2 \right] \quad (9)$$

and σ_k, σ_ε, c_1 and c_2 are further empirical constants. The values of the empirical constants are adopted from Launder and Spalding [4] and are given in Table 1. With these constants, the development of the plane jet is predicted correctly, but not that of the round jet (rate of spread is 40 % too high). Because plane and round jet form the limiting flow regimes in a three-dimensional jet, the k-ε model is extended below so that both jets can be predicted with the same empirical input.

Table 1

Empirical constants in the k-ε model (from [4])

c_μ	c_1	c_2	σ_k	σ_ε
.09	1.44	1.92	1.0	1.3

One further comment should be made here concerning the standard version of the model: the use of a scalar effective viscosity in Eq. (5) implies that the principal axes of stress and strain are co-aligned. This appears to be approximately valid for the shear stresses $\overline{uv}$ and $\overline{uw}$ in the streamwise momentum equation, but to a much lesser extent for the stresses appearing in the lateral momentum equations (3) and (4). These stresses, which all act in the cross-sectional plane of the jet, are influenced by mean rates of strain acting orthogonal to this plane; this cross-planar influence is known to be the cause of turbulence-driven secondary flows (for example in square ducts [11]) and, hence, such flows cannot be predicted with the standard k-ε model.

Extension of the k-ε model. In order to make the k-ε model applicable also to round jets, Rodi [12] devised correction functions for c_μ and c_2 which were used also by Launder et al. [3] in the round-jet predictions for the Langley conference. These functions relate c_μ and c_2 to the retardation parameter $y_{1/2}/U_m \, dU_m/dx$, which was used to distinguish strong jets (stagnant surroundings) from weak jets (in co-flowing stream). The functions were devised on an entirely empirical basis without physical interpretation or justification; in addition, they were designed to be switched on only for round jets and cannot predict the transition plane-round jet occurring in a 3D jet. Therefore, a different modification of the k-ε model is suggested below based on physical arguments and is valid for both plane and round jets. The form of the modification is, however, quite similar to the correction functions discussed above, mainly because the retardation parameter also distinguishes plane jets from round jets.

Correlation measurements in plane and round jets [13, 14] indicate that the lateral scale of the large eddies relative to the flow width is somewhat smaller, and that the coherence of the large eddies is weaker in the round than in the plane jet. Gutmark and Wygnanski [14] and Fiedler [15] explain this by the different decay rate of the velocity scale in the two jets: in the plane jet the velocity scale decays as $x^{-1/2}$ and in the round jet as x^{-1}. In the k-ε model, the characteristic length scale of the turbulence, L, is determined by the ε-equation since $\varepsilon \propto k^{3/2}/L$. This scale is perhaps not identical with the scale of the large eddies, but it is related to it. The above-mentioned influence of the decay rate of the velocity scale on the length scale is not accounted for in the ε-equation. In order to include this influence, it is therefore suggested here to modify the ε-equation in the following way.

According to the above arguments, the velocity decay rate affects merely the scale of eddies characteristic of a cross-section of the jet and not the lateral length scale distribution. Therefore, the ε-equation can be modified simply by making one of the empirical constants in the source terms a function of a suitable non-dimensional retardation parameter. The constant chosen is c_1 and the function is as follows:

$$c_1 = 1.14 - 5.31 \, \frac{y_{1/2}}{U_m} \frac{dU_m}{dx} \;. \quad (10)$$

In self-similar jets, the retardation parameter $y_{1/2}/U_m dU_m/dx$ takes a value of - .055 in the plane case and of - .087 in the round case. Therefore, the function (10) yields a different value of c_1 in the plane and round jet; the value for the plane jet being that used in the standard k-ε model ($= 1.44$). When function (10) is employed instead of a constant value of c_1 in the k-ε model, the predicted rates of spread agree with experiments for both plane and round jets. For the plane jet, the predicted turbulent kinetic energy level also agrees with experiments, for the round jet it is, however, somewhat low. For the 3D jet, function (10) with the retardation parameter evaluated only at the centreline is rather crude. However, preliminary test runs with this parameter determined locally along the z-axis produced little change in the results. It must be emphasized that the correction function (10) is valid only for jets in stagnant surroundings excluding the potential core region.

Finally, the influence of the streamwise velocity gradient on the length scale of turbulence may also be explained by Townsend's [16] notion that the large eddies are laterally compressed by the transverse strain rate produced by the entrainment; this transverse strain rate is directly related to the streamwise velocity gradient via the continuity equation.

Boundary Conditions and Details of Calculation Procedure

The previous sections have outlined a closed system of equations, but these must first be supplied with initial and boundary conditions for the free-jet problem before the solution can begin. Use has been made of the symmetry of the flow so that only one quadrant of the jet has been considered and two boundaries of the calculation domain consist therefore of symmetry planes. All variables have a zero normal gradient boundary condition along these planes apart from the lateral velocity perpendicular to the plane which is fixed at zero on the symmetry plane. The computer program used was originally capable of handling only wall or symmetry boundaries, and hence had to be modified for the present problem. This has as the other two boundaries of the calculation domain free boundaries along which the jet spreads into the surrounding fluid. The modifications entailed building into the program the ability to handle constant pressure boundary conditions as this is the proper specification for pressure in the ambient fluid. For U, k and ε, the free-stream values were fixed at the free edges of the grid and zero values for all three variables were used. The lateral velocity parallel to the free boundary was also fixed to zero, whereas for the velocity perpendicular to the edge a zero gradient condition was imposed. Since the jet spreads into the ambient fluid, some means has to be found for controlling the finite-difference grid so that this always covers the region of interest; in the present calculations this has been done so that the edge of the grid always lies outside the jet edge.

In deciding which inlet conditions to use, the case of jet flow out of an orifice and not out of a long rectangular channel as also investigated by Sfeier [8] was chosen for the present calculations. Consequently, a top-hat profile for the axial velocity has been used in all calculations. For the turbulence properties at inlet, no information is available from the experiments. It is known (see e.g. [2]) that the initial values of k and ε affect mainly the potential core length. Hence, in the present work the values of both variables were fixed as uniform across the jet; k corresponding to a low level of turbulence and ε being adjusted until the potential core length and initial rate of decay (first 15 orifice depths) were in agreement with the measured behaviour for the square jet; these values were then left unchanged for all other aspect ratios. Two specifications have been used for the lateral velocities at the initial plane: first, calculations were made with zero lateral velocities; however, the measured decrease of the half-width in the orifice long axis direction discussed in the Introduction was then not obtained. In an attempt to examine the effect of lateral velocities at the orifice on the predictions, further calculations were made with a non-zero lateral velocity field specified at the initial plane. The existence of such velocities may be due to two causes: firstly a jet issuing from a sharp-edged orifice will exhibit a vena-contracta effect and this would imply lateral velocities directed in towards the jet axis along both y and z directions. Secondly Owczarek and Rockwell [17] have shown that for rectangular orifices in finite-size settling chambers a further lateral motion is present for aspect ratios larger than 1. The cause is the differing streamline curvature of the flow inside the chamber as the fluid flows through the orifice. This produces pressure differences which lead to secondary flow in the plane of the orifice such that the velocity is inward in the direction of the orifice long axis and outward (away from the jet axis) along the orifice short axis. In the experiments this and the vena-contracta effect will obviously be superimposed and the actual lateral velocities will depend strongly on the details of the orifice and settling chamber. In the absence of measurements of any initial lateral motions, the only available experimental information is the initial rate of decrease of the z-direction half-width. The initial lateral velocity field was therefore specified as follows: the V-velocities were left at zero; the W-velocity field was given a linear shape from zero at the y-axis to a maximum value at the jet edge ($z=1/2\ b_0$) with no variation in the y-direction. The direction of the W-velocity was towards the jet axis and the maximum W-level was adjusted so that the initial rate of decrease of the half-width agreed with measurements; for $e = 10$ this maximum was 12 1/2 per cent of the jet axial velocity, for $e = 20$ this had to be increased to 15 per cent (an increased lateral motion is in accord with the explanation in [17]).

The resulting set of equations and boundary conditions was solved using a procedure based upon the algorithm developed by Patankar and Spalding [18] for three-dimensional parabolic differential equations. The solution procedure was modified as mentioned above to allow for the presence of free boundaries and to allow the finite-difference grid to expand with the jet. The rate of grid expansion was calculated from simplified forms of the continuity and axial momentum equations applicable near the jet edge; this method of grid control is similar to the calculation of entrainment used in the two-dimensional procedure of Patankar and Spalding [21]. The solution is obtained in a forward-marching, non-iterative manner; the pressure field is determined by first calculating an intermediate velocity field based upon estimated (upstream) pressures, and by then finding a correction to the pressure field so as to satisfy the continuity equation locally at all grid nodes. The constancy of the total axial momentum flux implied by a zero streamwise pressure gradient was used as a check on the numerical procedure.

The calculations were performed on a Univac 1108 computer. Grid refinement and forward step size tests were carried out and typical grids used had 12 or 17 nodes in the y-direction and 12, 17 or 22 nodes in the z-direction, maximum step sizes of 8 per cent of the jet width in the y-direction were used. A typical calculation using a 12 x 17 grid took approximately 600 steps to cover an axial distance of 150 orifice depths, requiring about 40 K words of core store and an execution time of 8 minutes (corresponding to a time requirement of .000 65 s/equation/grid node/step).

RESULTS AND DISCUSSION

In order to test the changes which had been made to the computer program (viz. the introduction of free boundaries), a flow problem related to the present situation was sought which possessed an analytical solution. For the case of a laminar rectangular free jet in a co-flowing stream, Pai and Hsieh [19] have obtained a solution of the linearized momentum equations and their results were used for comparison. As long as the inlet velocity difference between jet and ambient streams is small compared to the ambient velocity, the linearization should not introduce too great errors; in the test calculations the inlet jet velocity excess was ten per cent of the ambient velocity. Figure 2 shows the decay of the centre-line jet velocity excess for three different aspect ratios; the agreement is very good everywhere except in the initial region where the linearized solution is more likely to be in error. The spread of the three-quarter velocity widths for an aspect ratio of 5 is shown in Figure 3, the tendency to axi-symmetry can clearly be seen and is predicted slightly faster by the present method, on the whole, however, the agreement is satisfactory.

The computer program was then applied to turbulent jets issuing from sharp-edged orifices having aspect ratios of 1, 5, 10, and 20. Computations have been carried out with a constant value of c_1 as well as with the function (10). Predicted and measured decay of centre-line velocities are compared in Figure 4 for the aspect ratios 1, 5, and 20, and in Figure 5 for the aspect ratio 10. In all cases the agreement is very good; this manifests the ability of the present calculation method to predict correctly the influence of the orifice aspect ratio on the velocity decay. For aspect ratios greater than unity, the initial plane-jet decay behaviour ($U_m \propto x^{-1/2}$) and the asymptotic round-jet behaviour ($U_m \propto x^{-1}$) can clearly be observed in Figures 4 and 5. Evidently, the plane-jet region extends to larger downstream distances with increasing aspect ratios and this is also reproduced in the present calculations. Figure 5 shows predictions both with and without inlet lateral velocity. The effect on the velocity decay can be seen to be small: the decay in the plane-jet region is slowed down somewhat. Figure 4 also includes predictions with a constant value of $c_1 = 1.44$. As the jet with aspect ratio 1 begins spreading like a round jet fairly quickly, the difference to the prediction using the c_1-function is largest in this case: with $c_1 = 1.44$ the velocity clearly decays too fast. For the higher aspect ratio the round-jet regions covered by the calculation are much shorter, so that significant differences could not yet develop.

The predictions of the velocity half-widths in the y- and z-directions are given for an aspect ratio of 10 in Figure 6 and 20 in Figure 7. The first figure shows that without inlet lateral velocities only the development of $y_{1/2}$ is satisfactorily reproduced; for $z_{1/2}$ the measured decrease does not take place and there is therefore no cross-over. With the initial lateral velocity field adjusted as described in the previous section, the jet inversion does occur, and it occurs at approximately the correct axial location. The development of $z_{1/2}$ is in good agreement with the measurements and the $y_{1/2}$-spread is also slightly improved. The tendency of the half-widths to approach each other seems to be too slow in the present calculations. For an aspect ratio of 20, Figure 7 shows that adjusting the inlet lateral velocity to obtain the initial decrease again results in a reasonable prediction of the cross-over location and satisfactory agreement with the experiments over the full range of axial distance for which measurements are available.

The next three figures present comparisons of the mean velocity profiles with the measurements of Sfeier [8] for an aspect ratio of 10. Figure 8 gives profiles in the y-direction.

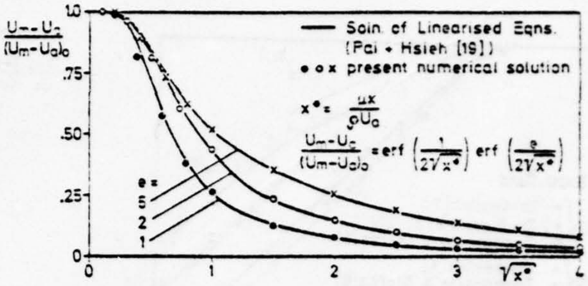

Fig. 2 Centre-line velocity decay, laminar jet problem

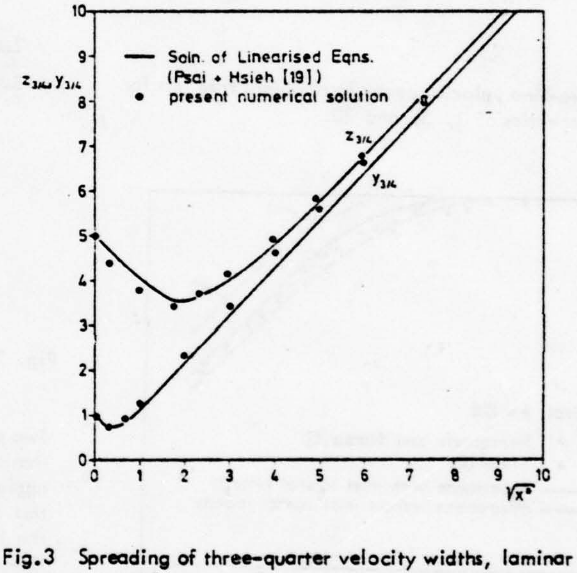

Fig.3 Spreading of three-quarter velocity widths, laminar jet problem, e = 5.

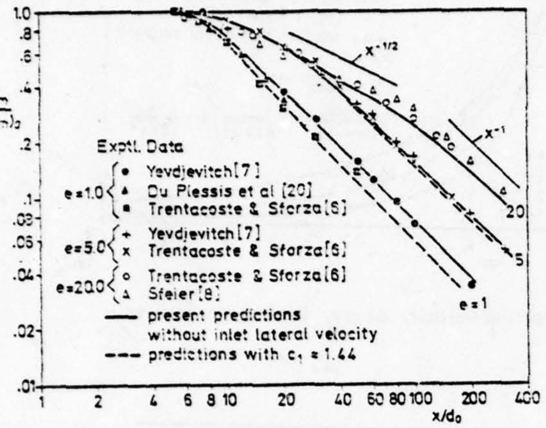

Fig. 4 Centre-line velocity decay in turbulent free jets for aspect ratios of 1, 5, and 20.

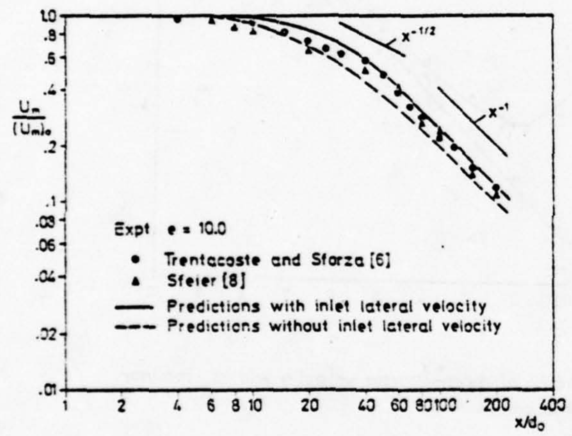

Fig. 5 Centre-line velocity decay for e = 10, effect of inlet lateral velocity distribution.

Agreement is good both with and without inlet lateral velocities, although slightly improved in the former case; certainly the tendency of the profiles to be self-similar after 10 orifice depths is present also in the predictions. For the z-direction profiles, good agreement is of course only obtained when the inlet lateral velocity is included (Figure 9) and the extent of disagreement when this is put to zero can be clearly seen in Figure 10. The approach to similarity is also reasonably well predicted as shown in Figure 9. One feature which is missing even with the modified initial conditions is the presence of the saddle-shape in the z-direction profiles. It seems clear that the inlet lateral velocity field used in the present calculations can explain some of the behaviour of the z-direction profiles (their overall width is well predicted), but some other mechanism is obviously responsible for the saddle-shape.

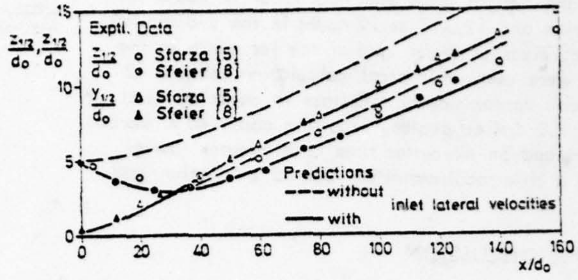

Fig. 6 Spreading of jet, half-widths for e = 10, effect of inlet lateral velocity.

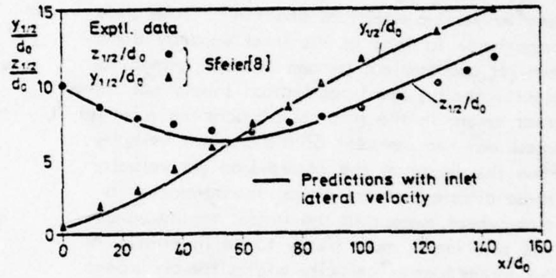

Fig. 7 Spreading of jet half-widths for e = 20.

Two possible causes may be mentioned here. The first is that the axial pressure gradient ignored here may not be negligible where there is significant lateral motion, and this may act to accelerate or decelerate some regions of the flow relative to others. The second possible cause, in line with the arguments presented in the Introduction, may be that there are other secondary flows superimposed upon those due to the orifice conditions. These additional, turbulence-driven secondary flows (representing a streamwise component of vorticity) may act to convect high momentum fluid from the central portions of the jet out towards the edges and thus create the saddle-shape. As stated earlier, however, the present version of the k-ε model is incapable of predicting such flows. It would have to be extended to allow a more realistic calculation of the stresses in the lateral momentum equations via a Reynolds stress model (algebraic or differential) as in the work of Launder and Ying [11] for square duct flow. This should form the next step in the development and testing of this turbulence model for three-dimensional flows.

SUMMARY AND CONCLUSIONS

The two-equation k-ε model in a modified form has been applied to the problem of three-dimensional free jets issuing from rectangular orifices. The velocity decay was predicted very well for all four aspect ratios considered and the transition from plane-jet-type decay ($\propto x^{-1/2}$) to round-jet-type decay ($\propto x^{-1}$) was reproduced accurately. For those calculations in which zero lateral velocities were specified as inlet conditions the development of the

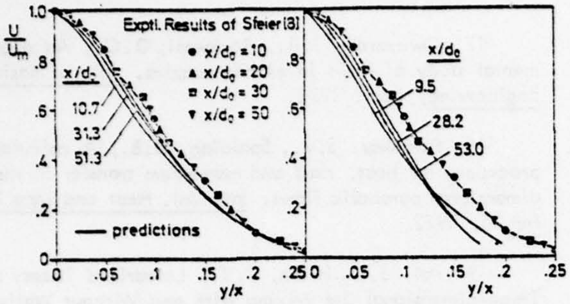

Fig. 8 y-direction velocity profiles with (left) and without (right) inlet lateral velocities

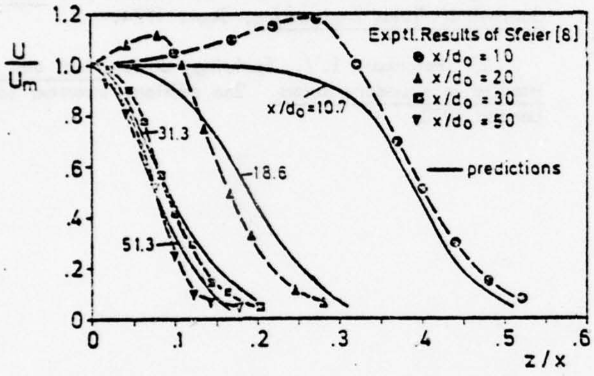

Fig. 9 z-direction velocity profiles with inlet lateral velocities

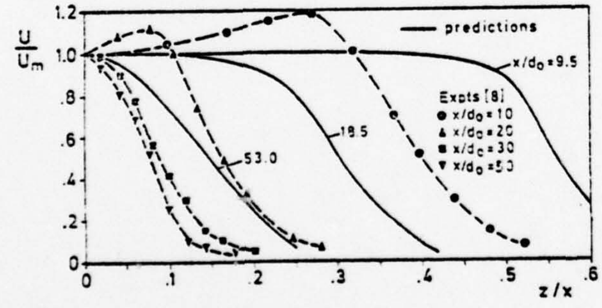

Fig. 10 z-direction velocity profiles without inlet lateral velocities

half-widths was not in agreement with experiments and the observed jet inversion was completely absent. When the transverse velocity at inlet was specified so as to produce the experimentally observed initial decrease of the z half-width, good agreement was obtained with the measured $y_{1/2}$ and $z_{1/2}$ for aspect ratios of 10 and 20.

It should be emphasized that, since the prediction of the z half-width depends strongly on the unknown lateral velocity conditions at the orifice, final judgement of the performance of the turbulence model is necessarily delayed. Further predictions must be made for a case where the inlet conditions have been fully measured.

One detail of the mean velocity profiles which was not obtained was the measured saddle-shape in the z-direction. It is suggested that this profile shape may be due to some turbulence-driven secondary flow in the plane of the jet. The present turbulence model is incapable of producing such a flow, however, and would have to be extended by including some form of Reynolds stress model.

ACKNOWLEDGEMENTS

The research reported in this paper was sponsored by the Sonderforschungsbereich 80. The numerical calculations were carried out on the UNIVAC 1108 computer at the University of Karlsruhe using a modified version of the program STABLE of CHAM Ltd., London; this is based on the solution algorithm of Reference [18].

REFERENCES

1 Proceedings of Conference on computation of turbulent boundary layers - AFDSR-IFP-Stanford, Calif., 1968.

2 Proceedings of Conference on Free Turbulent Shear Flows held at Langley Research Centre, Hampton, Virginia, July 1972, NASA Report SP-321.

3 Launder, B.E., Morse, A., Rodi, W., and Spalding, D.B., Prediction of Free Shear Flows - a comparison of six turbulence models. Paper at Langley Conference, 1972.

4 Launder, B.E., Spalding, D.B., The Numerical Computation of Turbulent Flows. Computer Methods in Applied Mechanics and Engineering 3, 1974.

5 Sforza, P.M., Steiger, M.H., and Trentacoste, N., Studies on Three-dimensional Viscous Jets. AIAA Journal 4, May 1966.

6 Trentacoste, N., Sforza, P.N., Further Experimental Results for Three-dimensional Free Jets. AIAA Journal 5, May 1967.

7 Yevdjevich, V.J., Diffusion of Slot Jets with Finite Orifice Length-Width Ratios. Hydraulics Papers, Colorado State University, Fort Collins, Colorado, March 1966.

8 Sfeier, A.A., The velocity and temperature fields of rectangular jets. Int. Jnl. Heat and Mass Transfer 19, 1976.

9 Viets, H., Sforza, P.M., Dynamics of Bilaterally Symmetric Vortex Rings. Physics of Fluids 15, Feb. 1972.

10 Laufer, J., New trends in experimental turbulence research. Annual Review of Fluid Mechanics 7, 1975.

11 Launder, B.E., Ying, W.M., Predictions of flow and heat transfer in ducts of square cross section. Heat and Fluid Flow 3, 1973.

12 Rodi, W., The prediction of free turbulent boundary layers by use of a two-equation model of turbulence. Ph.D. Thesis, University of London, 1972.

13 Gutmark, E. and Wygnanski, I., The planar turbulent jet, J. Fluid Mech. 73, pp. 465-493, 1976.

14 Wygnanski, I. and Fiedler, H.E., Some measurements in the self-preserving jet. J. Fluid Mech. 38, pp. 577-612, 1969.

15 Fiedler, H.E., On turbulence and mixing mechanism in free turbulent shear flows, in: Turbulent Mixing in Nonreactive and Reactive Flows. Project Squid Workshop, Plenum Press, New York and London, 1975.

16 Townsend, A.A., The structure of turbulent shear flow. Cambridge University Press, 1956.

17 Owczarek, J.A., Rockwell, D.O., An experimental study of flows in planar nozzles. Jnl. of Basic Engineering, Sept. 1972.

18 Patankar, S.V., Spalding, D.B., A calculation procedure for heat, mass and momentum transfer in three-dimensional parabolic flows. Int. Jnl. Heat and Mass Transfer 15, 1972.

19 Pai, S.I., Hsieh, T.Y., Linearized Theory of Three-dimensional Jet Mixing With and Without Walls. Jnl. of Basic Engineering, March 1970.

20 DuPlessis, M.P., Wang, R.L., Kahawita, R., Investigation of the near-region of a square jet. ASME Journal of Fluids Engineering, Sept. 1974.

21 Patankar, S.V., Spalding, D.B., Heat and mass transfer in boundary layers. 2nd edition, Intertext Books, London, 1970.

SESSION 2

FREE SHEAR FLOWS-2

Chairman: W. Rodi
Sonderforschungsbereich 80
University of Karlsruhe
Karlsruhe, Federal Republic of Germany

TURBULENT MIXING IN FREE SWIRLING JETS

by

E.W. Grandmaison[†] and H.A. Becker
Department of Chemical Engineering

Queen's University
Kingston, Ontario

ABSTRACT

A light scatter technique, marker nephelometry, was used to study the nozzle fluid concentration field of free swirling turbulent jets. Swirl was generated by guide vanes in a 7.14 cm diameter nozzle giving swirl numbers of 0.385, 0.667, 1.16 and 1.43. The parameters measured include those describing the self preserving forms of the mean concentration field, the intensity and integral scale of the concentration fluctuations, and the intermittency for the jets without internal recirculation (swirl number < 0.7). Results show that swirling jets without internal recirculation are very similar in structure. The data for the two jets with internal recirculation zones are given as contour maps describing the mean concentration and fluctuation intensity fields. The results as a whole describe jets with weak to moderate swirl and indicate the trends to be expected for jets with strong swirl.

NOMENCLATURE

Variables

b	concentration half-radius of jet ($r = b$ at $\overline{\Gamma} = \frac{1}{2}\overline{\Gamma}_c$), m
$E_{\gamma 1}(k_1)$	one-dimensional wave number spectral density function for concentration fluctuations, kg^2/m^5
f	frequency, s^{-1} = hz
G	jet source angular momentum flux, N·m
$G_\gamma(f)$	frequency spectral density function for concentration fluctuations, $kg^2 s/m^6$
I	jet source axial momentum flux, N
k_1	$= 2\pi f/\overline{U}_1$, wave number, m^{-1}
P	static pressure, Pa
P_∞	static pressure in ambient fluid far from the jet, Pa
r	radial position in jet (in cylindrical polar coordinates), m^{-1}
r_o	jet source port radius (here the nozzle radius), m
R	$= R(x, \phi, t)$, radial position of a point on the turbulent jet boundary, m
$\overline{R}$	mean jet radius defined on the turbulent boundary, m^{-1}
$\overline{U}_x$	mean axial velocity component, m/s
$\overline{U}_\phi$	mean tangential velocity component, m/s
$\overline{U}_1$	mean stream speed in the local mean flow direction (magnitude of the mean velocity vector), m/s
x	axial position in jet (in cylindrical polar coordinates), origin at the center of the jet source exit port, m
x_o	location of point of virtual origin of jet, m
Γ	jet source-fluid concentration, kg/m^3
γ	$= \Gamma - \overline{\Gamma}$, jet source-fluid concentration fluctuation, kg/m^3
$\overline{\delta}$	= prob ($\Gamma > 0$), intermittency factor
Λ_γ	longitudinal integral scale of concentration fluctuations, m
σ	standard deviation of R, a length scale for the convolutions of the jet boundary ('wrinkle amplitude'), m
ϕ	angular position in jet (cylindrical polar coordinates), rad

Dimensionless quantities

C	$= \overline{\gamma_A \gamma_B}/\hat{\gamma}_A \hat{\gamma}_B$, correlation function for concentration fluctuations at two points, A and B
$C(x, 0; x, r)$	correlation function for concentration fluctuations at points on and off the jet axis, separation distance r; the 'radial correlation coefficient'
$C(x, r, \phi; x, r, \phi + \pi)$	correlation function for concentration fluctuations at points on opposite sides of the jet axis, separation distance 2 r; the 'symmetrical correlation function'
S	$= G/Ir_o$, swirl number

[†] Present address: Domtar Research Centre, Senneville, Quebec

Overscri[illegible]

$(\overline{\ })$ time-average value
$(\hat{\ })$ root-mean-square value; square root of $\overline{(\ )^2}$

Subscripts

c centerline value
o value at jet source

INTRODUCTION

A swirling jet has a significant component of tangential local velocity at points off the jet centerline. This results in radial and axial pressure gradients which have a strong effect on the flow field. At sufficiently high levels of swirl, very large pressure gradients produce a reverse flow region near the nozzle and around the jet axis. This reverse flow characteristic has made the swirling jet a particularly useful device for shaping the reaction zone in chemical reaction systems, particularly in industrial flames.

The object of principal interest in the present study is the mixing field of the free turbulent swirling jet in effectively stagnant surroundings. The experimental system was of air mixing with air at constant density. The effects of swirl on the field are characterized (1) by the swirl number $S \equiv G/Ir_o$, where I and G are the fluxes of axial and angular momentum:

$$I = 2\pi \int_o^\infty (\rho\overline{U}_x{}^2 + \overline{P} - P_\infty)\, r\, dr$$

$$G = 2\pi \int_o^\infty \rho\overline{U}_x\overline{U}_\phi r^2\, dr$$

Swirl levels in the present work were in the range S = 0.39 to 1.43. The non-swirling jet, S = 0, has been amply investigated in other studies (2,3), the most recent of which (3) was done with the present apparatus.

A common type of swirl generator for jets (4--6) consists of guide vanes set in the exit section of the jet source, here a flow nozzle. The other most widely used device is based on tangential injection of the jet source fluid into the delivery chamber (1,7). Mathur and McCallum (4,5) have related the swirl number for vane-generated swirl to the angle θ between the guide vanes and the upstream flow; they found that for efficient hubless vanes

$$S = \frac{2}{3}\tan\theta. \qquad (1)$$

To ensure performance at the high level indicated by this result, the vanes should overlap in the axially-projected view (4,5). Direct measurements of the axial and angular momentum fluxes I and G indicate that (1) may be as much as 8% in error (4,5), a normally acceptable level of uncertainty in S. The four sets of swirl vanes used in the present work had blade angles θ of 30°, 45°, 60° and 65°, giving swirl numbers, as calculated from (1), of 0.39, 0.67, 1.16 and 1.43. The two lower levels of swirl were insufficient to induce a recirculation bubble or eddy in the core of the jet just downstream of the nozzle exit, but the two higher ones did provoke this phenomenon. The results will be discussed accordingly. In the case of low swirl, interest will be focussed on the essentially self-preserving flow established in the far region of the jet. In the case of swirl sufficient to cause recirculation, attention will be concentrated on the near region where the recirculation bubble is located.

APPARATUS

The jet source consisted of a flow-nozzle fitted to the exit of a wind tunnel settling chamber, providing an area contraction ratio of 150:1. The nozzle throat diameter was 7.14 cm. The swirl vanes were mounted in a short tubular extension attached to the nozzle. The system was operated at nozzle Reynolds numbers over 100,000.

The jet source air was marked with an oil condensation smoke to facilitate investigation of the nozzle fluid concentration field by marker nephelometry--a technique in which concentration fields and mixing processes are studied *in situ* by means of light scattering measurements on colloidal particles introduced in one of the streams entering a system. This technique has been fully discussed elsewhere (3,8,9). The light-scatter system and the instruments used here were those described in another paper in this Symposium (3).

RESULTS FOR JETS WITHOUT RECIRCULATION

Mean concentration

The axial decay of the centerline mean concentration in the two jets with weak swirl and, from (3), in a non-swirling jet, is shown in Fig. 1. The curves tend to straighten with downstream distance, suggesting asymptotic approach to a state of at least partial self-preservation in which

$$\overline{\Gamma}_o/\overline{\Gamma}_c = C_1(x - x_o)/r_o, \qquad (2)$$

where C_1 is the centerline concentration decay constant and x_o is the location of the virtual origin of the self-preserving flow. The values estimated for C_1 and x_o are given in Table 1. The variation of C_1 with the swirl number is described by

$$C_1 = 0.0923(1 + .124\, S + 1.2\, S^2) \qquad (3)$$

The jet spreading is characterized by the 'concentration half-radius' b,

$$r = b \text{ at } \overline{\Gamma}(x, r) = \tfrac{1}{2}\overline{\Gamma}(x, 0) \equiv \tfrac{1}{2}\overline{\Gamma}_c(x)$$

The behaviour of b at $x > 40\ r_o$, Fig. 2, is described by

$$b = C_2(x - x_o), \tag{4}$$

where C_2 is a characteristic spreading constant for the self-preserving flow. The estimated values of C_2, Table 1, are described by

$$C_2 = 0.105(1 + 0.124\ S + 1.2\ S^2) \tag{5}$$

If the mean velocity and mean concentration fields far enough downstream are self-preserving, then the conservation of axial momentum and jet source material gives

$$\rho\overline{U}_c{}^2 b^2 = (\text{const.})\ \rho U_o{}^2 r_o{}^2$$

$$\rho\overline{\Gamma}_c\overline{U}_c b^2 = (\text{const.})\ \rho\Gamma_o U_o r_o{}^2$$

Thus

$$C_3 = \overline{\Gamma}_c b/\Gamma_o r_o \tag{6}$$

should be a general constant in self-preservation. Equations (2) and (4) give $C_3 = C_2/C_1$, and Table 1 shows that $C_3 = 1.15$. Becker, et al (8) found $C_3 = 1.14$ in their study of a non-swirling free jet.

The radial mean concentration profiles for $x/r_o \geq 20$, presented in detail by Grandmaison (10), are fitted well within the experimental error by the following expressions

$$\overline{\Gamma} = \overline{\Gamma}_c \exp\ (-\ 0.693\ r^2/b^2),\ r < r_1 \tag{7}$$

$$\overline{\Gamma} = A_1\overline{\Gamma}_c \exp\ (-\ 0.693\ A_2 r^2/b^2),\ r > r_1 \tag{8}$$

where r_1, A_1 and A_2 are given in Table 1. These equations are of the general form of the Gaussian (normal) probability density function. In general, (7) applies quite accurately up to about $\overline{\Gamma} = 0.2\ \overline{\Gamma}_c$. This behavior has been observed in both free (2,3) and confined (11) non-swirling jets, and contrasts with velocity profiles which are generally slightly non-Gaussian; typically (11)

$$\overline{U}_x = \overline{U}_c \exp\ [-\ 0.693\ (r/x)^{1.85}].$$

Rms concentration fluctuation

The ratio of the rms concentration fluctuation to the mean concentration is often called the concentration fluctuation intensity. The intensity on the jet centerline, Fig. 3, is fitted by

$$\hat{\gamma}_c/\overline{\Gamma}_c = C_4/(1 + B\overline{\Gamma}_c/\Gamma_o), \tag{9}$$

where C_4 and B are given in Table 1. The apparent self-preserving value, about $\hat{\gamma}_c/\overline{\Gamma}_c = 0.22$, is the same as found by Becker, et al (2) for their non-swirling jet.

The radial profiles of the intensity, presented in detail by Grandmaison (10), are simply related to the mean concentration field and are quite well described by

$$\overline{\gamma^2}/\overline{\Gamma}^2 = 0.206\ \overline{\Gamma}_c/\overline{\Gamma} - 0.173 \tag{10}$$

Becker, et al (2) found the two constants to be 0.206 and 0.156 for their non-swirling jet.

Intermittency

The intermittent presence of source fluid at points towards the jet edge is characterized by the function

$$\delta = \{1 \text{ if } \Gamma > 0;\ 0 \text{ if } \Gamma = 0\}$$

The mean value of δ is the 'intermittency factor',

$$\overline{\delta} = \text{prob}(\Gamma > 0).$$

Radial profiles of $\overline{\delta}$ are usually quite well described by the Gaussian probability distribution function (or the error function), the parameters of which, $\overline{R}$ and σ, can be interpreted as the mean radial position of the turbulent jet boundary and a length scale for the turbulent ('large eddy') convolution of the boundary. We have

$$r = \overline{R} \text{ at } \overline{\delta} = \tfrac{1}{2},$$

and σ is the 'standard deviation' in the error function fitted to $\overline{\delta}(r)$. The physical significance of these concepts has been discussed in detail elsewhere (3,12,13).

Radial profiles of $\overline{\delta}$ measured in the present jets are reasonably well fitted by the error function (10). The values of $\overline{R}$ and σ are described by

$$\overline{R} = C_5(x - x_o), \tag{11}$$

$$\sigma = C_6(x - x_o), \tag{12}$$

where C_5 and C_6 are given in Table 1. The variations in the ratios of the various radial scales, namely $\overline{R}/b$, σ/b, and $\sigma/\overline{R}$, are in keeping with the variations in the radial profile of the mean concentration towards the jet edge as indicated by the different parameter values in (8), Table 1. Apparently swirl affects the large eddy structure so as to appreciably alter the jet characteristics in the intermittent region, but not in the non-intermittent core.

Spectrum

The frequency spectrum of the concentration fluctuations was measured at points on the jet centerline. One-dimensional wave-number spectra were estimated from these results by means of the transformation

$$k_1 = 2\pi f/\overline{U}_1,\ E_{\gamma 1}(k_1) = \overline{U}_1\ G(f)/2\pi. \tag{13}$$

It is here assumed that Taylor's hypothesis is satisfied, that the turbulence is weak enough so that the turbulent field is in effect convected past any point like a frozen pattern moving at the local mean velocity. The integral longitudinal length scale of the concentration fluctuations is then given by

$$\Lambda_\gamma = \pi\ E_{\gamma 1}(0)/2\ \overline{\gamma^2} \tag{14}$$

The full experimental results have been presented by Grandmaison (10). Typical spectra are shown in Fig. 4. The spectra are quite well fitted by the relation given by Becker, et al (2) for their non-swirling jet,

$$E_{\gamma 1}(k_1\Lambda_\gamma) = \frac{2}{\pi}\ [1 + 1.793\ (k_1\Lambda_\gamma)^2]^{5/6}, \tag{15}$$

which reduces to

$$E_{\gamma 1}(k_1\Lambda_\gamma) = 0.392\ (k_1\Lambda_\gamma)^{-5/3} \tag{16}$$

at the higher wave numbers in the experimental range. The (- 5/3) power-law behavior is indicative of a Kolmogoroff inertial-convective equilibrium subrange.

The integral scales are fitted by

$$\Lambda_\gamma = C_7(x - x_o), \tag{17}$$

where C_7 is given in Table 1. The values of Λ_γ are close to those of σ, as should be expected, since σ is also essentially an integral length scale of the turbulence.

Two-point correlation function

Measurements were made of the radial correlation function $C(x, 0; x, r)$ and of the symmetrical lateral correlation function $C(x, r, \phi; x, r, \phi + \pi)$. The full results are given by Grandmaison (10). Those for $S = 0.67$ are shown in Figs. 5 and 6, and those for $S = 0$ are in another paper in this symposium (3). Mild swirl shows very little effect here; the results are all very similar and undistinguishable from those for the non-swirling jet.

RESULTS FOR JETS WITH RECIRCULATION

Mean concentration and concentration fluctuation intensity

Radial profiles of mean concentration and concentration fluctuation intensity were measured at $x/r_o = 0.2$, 1, 2, 4, 6, 8, 10, 12, 16 and 20 for both swirl levels, $S = 1.16$ and 1.43. A form of self-preservation is not to be expected in this range of x/r_o which encompasses the zone of internal recirculation, so the forms of presentation used for the results on jets with weak swirl are inappropriate. We shall instead use the device of contour maps. These, Figs. 7 and 8, show little difference between the concentration fields at the two swirl levels. The radial maximum of the mean concentration is well off the jet centerline up to $x/r_o = 10$. This characteristic is represented by the dashed curves in Figs. 7 and 8 which follow the minima of $-\nabla\overline{\Gamma}$. We shall call the surface defined by these curves the 'recirculation envelope', for it is evident that it must quite closely follow the peak of the mainstream flow as defined by the off-axis minima of $-\nabla\underline{U}$, and thus the boundary of the recirculation eddy or 'bubble'. Inside this envelope the turbulent mixing is dominated by the recirculation of jet mainstream fluid from downstream, while on the outside it is dominated by the entrainment of ambient fluid into the mainstream. It is therefore not unexpected that jet source-fluid concentration fluctuation intensities inside the recirculation envelope are fairly low, for the mixing of jet fluid with other jet fluid from a little further downstream should give much smaller fluctuations than the mixing of jet fluid with ambient fluid.

Figures 9 and 10 show the variation of mean concentration and the concentration fluctuation intensity along the jet centerline and along the recirculation envelope. The data converge at the downstream limit of the recirculation eddy. The behavior of the centerline mean concentration further downstream is represented by (2) with the following parameter values:

S	1.16	1.43
C_1	0.31	0.21
x_o	9.5	24

Equation (3) gives $C_1 = 0.266$ for $S = 1.16$, so in this case the jet with recirculation is not very different from those without recirculation.

The fluctuation intensity $\hat{\gamma}/\overline{\Gamma}$ on the jet centerline appears to level off around $x/r_o = 60$ at a value of about 0.25. It may thereafter stay at this level, but it would not be surprising if it decayed slightly to about the same level indicated far downstream in the jets with weak swirl, about 0.22.

The well localized region, Fig. 10, where the intensities $\hat{\gamma}/\overline{\Gamma}$ measured on the jet centerline and on the recirculation envelope converge, roughly at $x = 9\ r_o$, can be taken as a practical definition of the downstream limit of the recirculation eddy. At the upstream end the recirculation actually penetrated into the nozzle exit tube. It should be noted that in general Γ_o is the concentration of jet source fluid in the source fluid, hence--in mass units--the density ρ_o. In the two jets with recirculation the value of Γ_o as simulated by the smoke marker was not represented at the nozzle exit plane. However, it was easily determined there by removing the swirl vanes.

Spectra

Frequency spectra of the concentration fluctuations were measured at points on the recirculation envelope at $x/r_o = 2, 4, 6, 8$ and 10. One-dimensional wave-number spectra and integral length scales were estimated from these by means of (13) and (14). The spectra--those for S = 1.43 are shown in Fig. 11--are not perceptibly different from those observed far downstream in jets with weak swirl, Fig. 4, or no swirl (2,3). The integral scales, Fig. 12, are fairly large and apparently indicate an unusually strong large-eddy activity, compared to the self-preserving region of weakly swirling or non-swirling jets.

DISCUSSION

The apparently close approach to structural self-preservation in weakly swirling jets--i.e., jets with no recirculation--as indicated here by the concentration field at $\Gamma_o / \overline{\Gamma}_c > 2$ is consistent with other investigators' observations (1,4--7,14,15) on the velocity field (components of mean velocity and rms fluctuation) over the same region, $x \leq 60\ r_o$. An interesting direct comparison of characteristics for the self-preserving state is possible in the case of the spreading constant C_2, here defined by (4) for the mean concentration field. The data of Kerr and Fraser (6), Rose (14) and Chigier and Chervinsky (15) for the 'velocity half-radius', shown collectively in Chigier and Chervinsky's Fig. 12, are well described by

$$C_2 = 0.084(1 + 2.4\ S),\ S < 0.8.$$

(the velocity half-radius is defined on the radial profile of the mean axial velocity component $\overline{U}_x$ by $r = b$ at $\overline{U}_x = \frac{1}{2}\overline{U}_c$).

Following is a comparison of values of C_2 given by this formula and by our data:

S	0	0.39	0.67
C_2, concentration field	0.105	0.130	0.171
C_2, velocity field	0.084	0.163	0.219

The values for S = 0 are in good agreement with past observations on the relative rates of spreading of momentum and source-fluid material or thermal energy in non-swirling jets; momentum spreads more rapidly, consistent with a value of about 0.7 for the turbulence Schmidt and Prandtl numbers. The values of C_2 for the swirling jets with S = 0.39 and 0.67, contrarily, seem to indicate a somewhat more rapid spreading of momentum. Measurements of the velocity field in our swirling jets are needed, however, before any firm conclusions can be drawn as to the relative spreading rates of momentum and scalar properties. Further, we need direct experimental measurements of the swirl number for our system in order to be confident of comparisons with other workers' results. Aside from these factors, it must also be recognized that two systems at the same swirl number will not necessarily perform identically, because the behavior may be influenced by the source velocity distribution as well as by the global input parameter S. We are inclined to believe that the relative spreading rates of momentum and material or energy in the far field of constant-density swirling jets should be similar to those in non-swirling jets. The contrary trend in the above table probably reflects error in our estimates of the swirl number and, perhaps, genuine differences in swirler performance. These questions are presently under investigation.

The present data give an internally consistent picture of the self-preserving region of weakly swirling jets. Increasing the swirl number increases the rates of entrainment and spreading, but has only small or insignificant configurational effects on the jet structure. The product $C_3 = \overline{\Gamma}_c b$ is a constant, as expected when the radial profiles of $\overline{\Gamma}$ are generally similar. The ratios between the length scales as b, $\overline{R}$, σ and Λ_γ indicate a more pronounced large-eddy structure in the presence of swirl, but the effect is not great (e.g., σ/b increases by up to 30%).

The results on the recirculation region of the jets with recirculation (S = 1.16 and 1.43) are fairly consistent with past work on the velocity field. We have evidence that the downstream limit of the recirculation eddy is around $x \approx 9\ r_o$; Syred and Beér (7, their Fig. 7a) present data that indicate $x \approx 10\ r_o$. At $x > 10\ r_o$ these jets fairly rapidly approach a self-preserving form similar to that observed in weakly swirling jets.

ACKNOWLEDGEMENTS

This work was supported by grants from the National Research Council of Canada.

REFERENCES

1. Chigier, N.A. and Beér, J.M., "Velocity and static pressure distributions in swirling air jets issuing from annular and divergent nozzles", Journal of Basic Engineering, Trans. ASME, Series D, vol. 86, 1974, pp. 788--798

2. Becker, H.A., Hottel, H.C., and Williams, G.C.,"The nozzle fluid concentration field of the round free jet", Journal of Fluid Mechanics, vol. 30, 1967, pp. 285--303

3. Grandmaison, E.W., Rathgeber, D.E., and Becker, H.A., "Some characteristics of concentration fluctuations in free turbulent jets", in this Symposium

4. Mathur, M.L. and MacCallum, N.R.L., "Swirling air jets issuing from vane swirlers. Part 1: free jets", Journal of the Institute of Fuel, vol. 40, 1967, pp. 214--225

5. Mathur, M.L. and MacCallum, N.R.L., "Swirling air jets issuing from vane swirlers. Part 2: enclosed jets", Journal of the Institute of Fuel, vol. 40, 1967, pp. 238--245

6. Kerr, N.M. and Fraser, D., "Swirl. Part 1: Effect on axisymmetrical turbulent jets", Journal of the Institute of Fuel, vol. 38, 1965, pp. 519--526

7. Syred, W. and Beér, J.M., "Combustion in swirling flows: a review", Combustion and Flame, vol. 23, 1974, pp. 143--201

8. Becker, H.A., Hottel, H.C. and Williams, G.C., "On the light-scatter technique for the study of turbulence and mixing", Journal of Fluid Mechanics, vol. 30, 1967, pp. 259--284

9. Becker, H.A., "Mixing, concentration fluctuations and marker nephelometry", Studies in Convection (ed. B.E. Launder), vol. 2, 1977

10. Grandmaison, E.W., Turbulent Mixing in Free Swirling Jets, Ph.D. thesis, Dept. of Chemical Engineering, Queen's University, Kingston, Ontario, 1973

11. Becker, H.A., Hottel, H.C. and Williams, G.C., "Mixing and flow in ducted turbulent jets", Ninth Symposium (International) on Combustion, Academic Press, 1963, pp. 7--19

12. Becker, H.A., Hottel, H.C. and Williams, G.C., "Concentration intermittency in jets", Tenth Symposium (International) on Combustion, The Combustion Institute, 1965, pp. 1253--1263

13. Corrsin, S. and Uberoi, M.S., "Free-Stream Boundaries of Turbulent Flows", NACA Report 1244, 1955

14. Rose, W.G., "A swirling round turbulent jet", Journal of Applied Mechanics, vol. 29, Trans. ASME, vol. 84, Series E, 1962, pp. 616--625

15. Chigier, N.A. and Chervinsky, A., "Experimental investigation of swirling vortex motion in jets", Journal of Applied Mechanics, Trans. ASME, vol.34, Series E, 1967, pp. 443--451

Table 1. Values of constants for the self-preserving region of weakly swirling jets

S	0	0.39	0.67
x_o/r_o	3.4	-6.8	-6.8
C_1	0.0923	0.113	0.149
C_2	0.105	0.130	0.171
C_3	1.14	1.15	1.15
C_4	0.219	0.235	0.227
B	0.520	0.006	0.075
C_5	0.192	0.273	0.326
C_6	0.0324	0.0525	0.0692
C_7	0.0420[†]	0.0649	0.0752
A_1	3.64	1.18	1.67
A_2	1.85	1.14	1.37
r_1/b	1.62	1.31	1.46
$\overline{R}/b$	1.83	2.10	1.91
σ/b	0.309	0.404	0.405
Λ_γ/b	0.400	0.499	0.440
$\sigma/\overline{R}$	0.169	0.192	0.212
Λ_γ/σ	1.30	1.24	1.09

[†] Virtual origin $x_o = 0$ in this case.

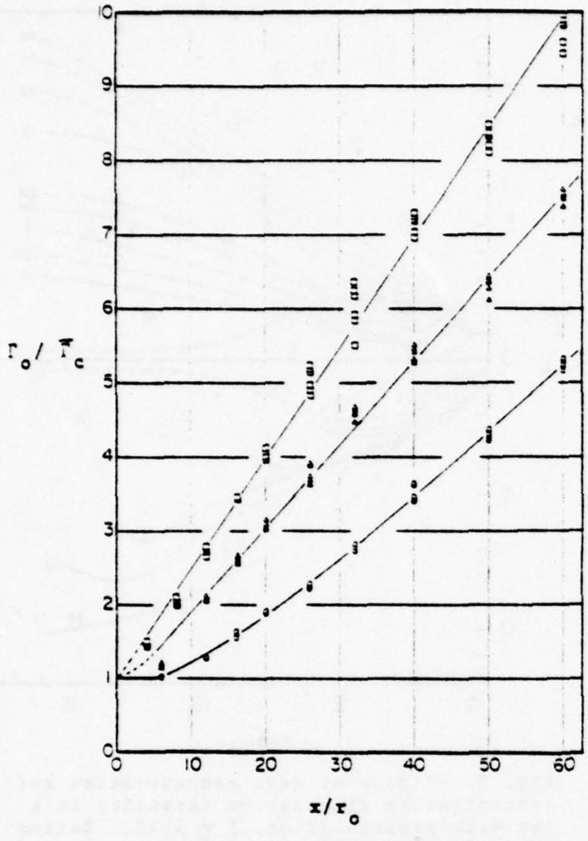

Fig. 1. Decay of the centerline mean concentration in jets with no recirculation. Swirl numbers S: bottom curve, 0; middle, 0.39; top, 0.67.

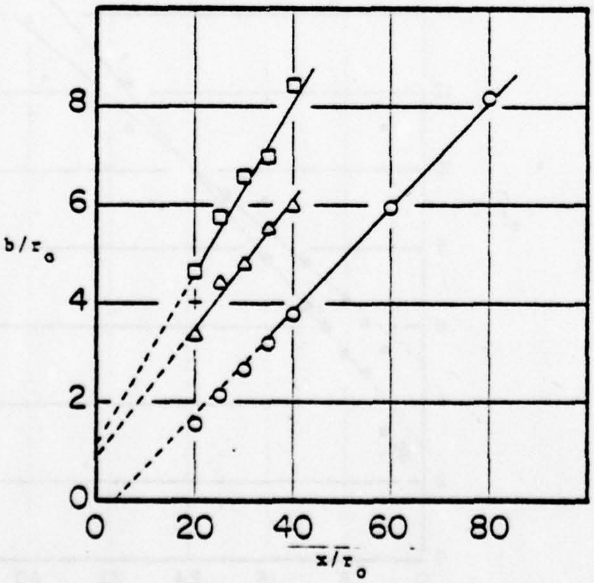

Fig. 2. Growth of the concentration half-radius in jets with no recirculation. Swirl numbers S: bottom curve, 0; middle, 0.39; top, 0.67.

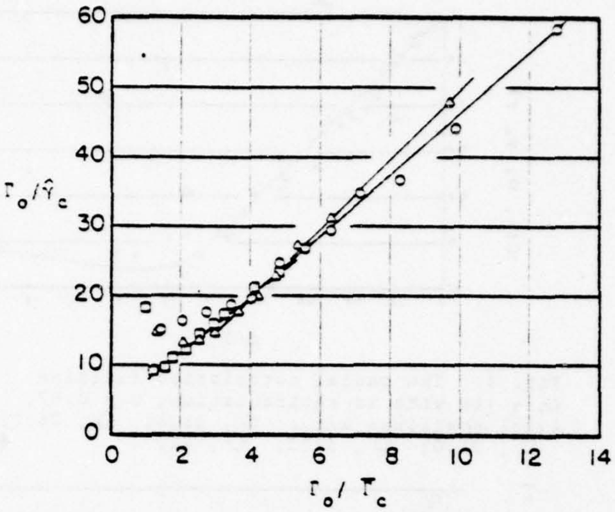

Fig. 3. Centerline variation of the concentration fluctuation intensity in jets with no recirculation. Swirl numbers S: □, 0; △, 0.39; ○, 0.67.

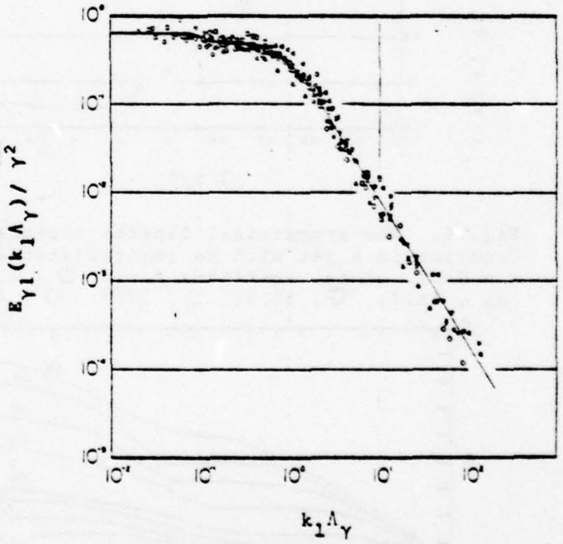

Fig. 4. One-dimensional wave-number spectrum of concentration fluctuations at points on the centerline of jets with no recirculation. The slope at $k_1\Lambda_\gamma > 2$ is (- 5/3). Axial positions x/r_o: { ○, 20; □, 40 | S = 0}; { △, 20; ▽, 30; ▽, 40 | S = 0.39}; { ◇, 20; ◁, 30; ×, 40 | S = 0.67}.

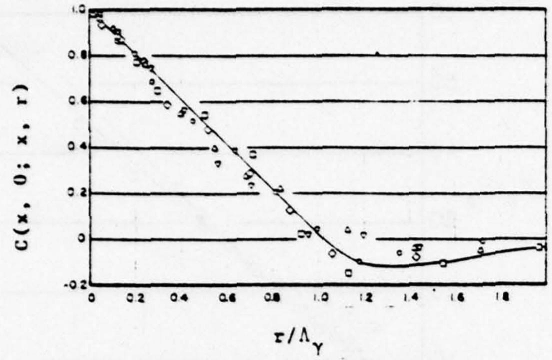

Fig. 5. The radial correlation function in a jet with no recirculation, S = 0.67. Axial positions x/r_o : ○, 21.6; △, 26.7; ▽, 32.0; □, 37.3; ◇, 42.7.

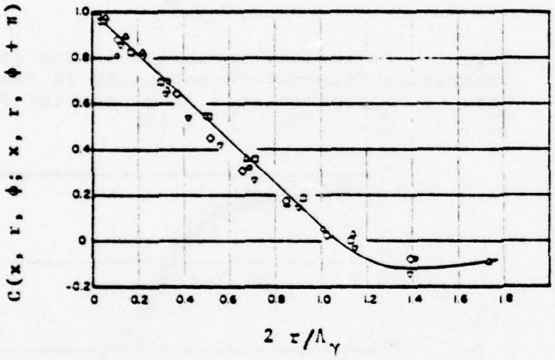

Fig. 6. The symmetrical lateral correlatio function in a jet with no recirculation, S = 0.67. Axial positions x/r_o: ○, 21.6; △, 26.7; ▽, 32.0; □, 37.3; ◇, 42.7

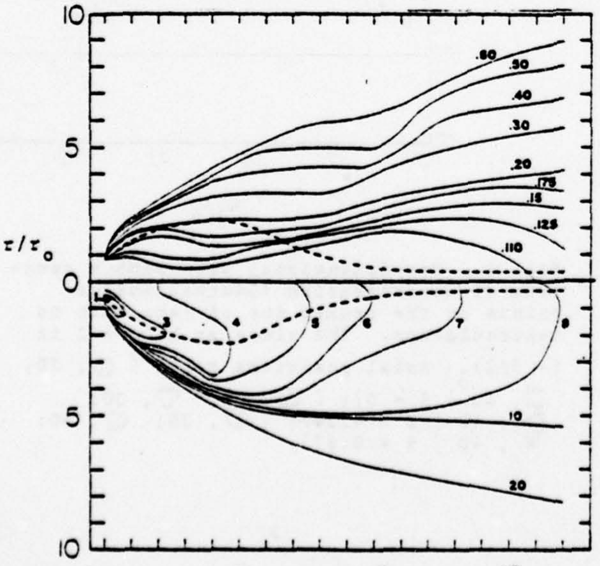

Fig. 7. Fields of mean concentration and concentration fluctuation intensity in a jet with recirculation, S = 1.16. Bottom half, $\Gamma_o/\overline{\Gamma}$; top half, $\hat{\gamma}/\overline{\Gamma}$.

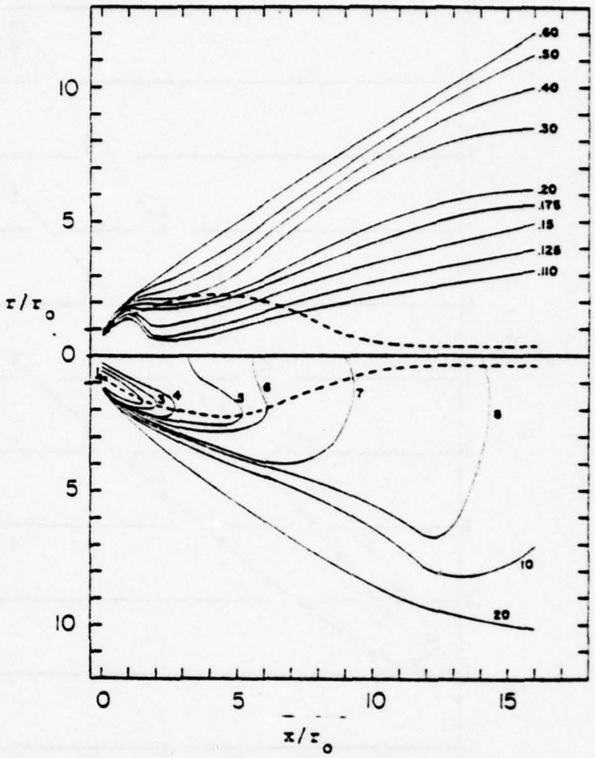

Fig. 8. Fields of mean concentration and concentration fluctuation intensity in a jet with recirculation, S = 1.43. Bottom half, $\Gamma_o/\overline{\Gamma}$; top half, $\hat{\gamma}/\overline{\Gamma}$.

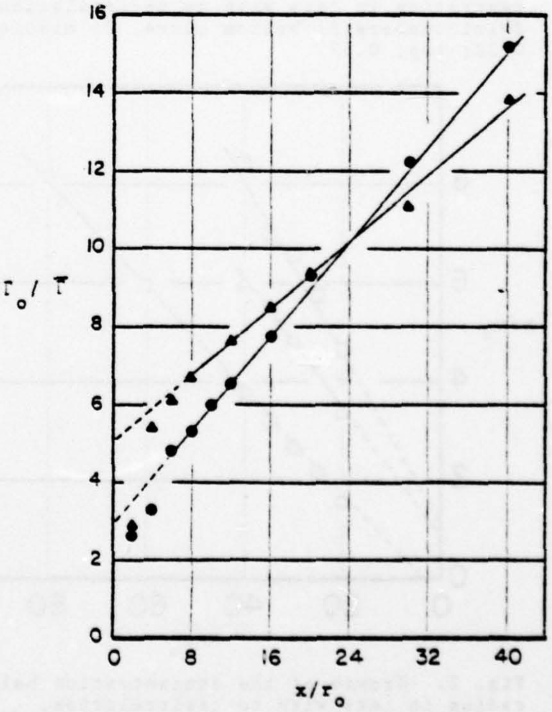

Fig. 9. Variation of mean concentration along the recirculation envelope. Swirl numbers S: ●, 1.16; ▲, 1.43.

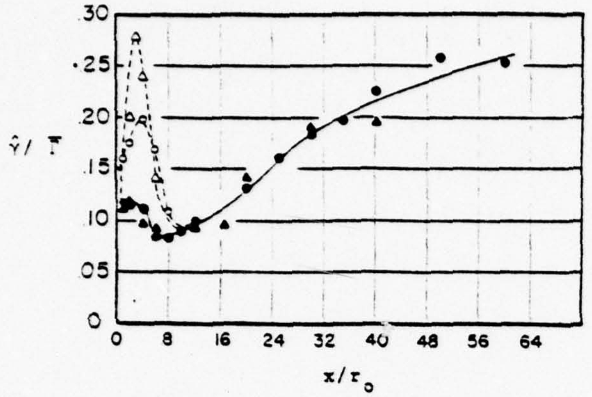

Fig. 10. Variation of concentration fluctuation intensity along the jet centerline (filled symbols) and along the recirculation envelope (open symbols). Swirl numbers S: ○●, 1.16; △▲, 1.43.

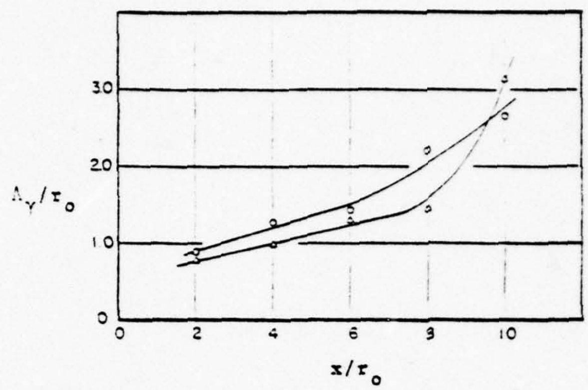

Fig. 12. The integral length scale at points on the recirculation envelope. Swirl numbers S: ○, 1.16; △, 1.43.

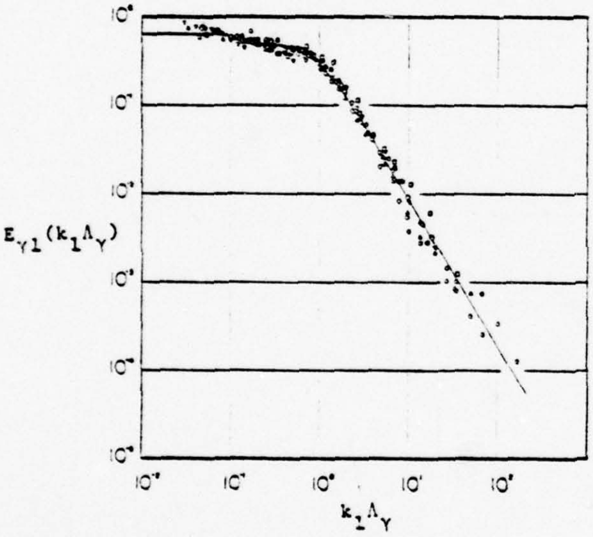

Fig. 11. One-dimensional wave-number spectrum at points on the recirculation envelope, S = 1.43. The slope at $k_1\Lambda_\gamma > 2$ is (- 5/3). Position coordinates (x/r_o, r/r_o): ▽, (2, 1.8); □, (4, 2); △, (6, 2); ◇, (8, 1.5); ○, (10, 0).

INFLUENCE OF EXTERNAL TURBULENCE ON MIXING OF AXISYMMETRIC COAXIAL JETS

by

Leo E. Fink

Sonderforschungsbereich 80, University of Karlsruhe
D-7500 Karlsruhe 1, Federal Republic of Germany

ABSTRACT

The flow configuration of an axisymmetric jet discharging into a co-flowing turbulent stream was chosen to investigate both theoretically and experimentally the influence of external turbulence on a thin shear layer A phenomenological description of the flow field leads to the formulation of an eddy viscosity term which takes account of the mutual interaction between internal and external turbulence. To verify the proposed turbulence model, experiments in a wind tunnel were performed. The experimental results show that the jet develops faster and at a nonlinear rate compared to the conventional jet. This behaviour is well predicted by the turbulence model which was incorporated into an integral method of flow computation.

NOMENCLATURE

A_1, B_1 = constants
b = thickness of grid bar, m
b = typical width of shear layer, m
c_i, c_z, c_A, c_D = constants
D = inside diameter of jet tube, m
$E(\mathbf{k})$ = energy spectrum of turbulence, m^3/s^2
$E_{11}(k_1)$ = 1 - dimensional turbulence spectrum m^3/s^2
$f(\eta)$ = similarity function for the excess momentum flux
$g(\eta)$ = similarity function for the excess velocity
H = kinematic excess momentum flux
I_i = definite integrals of the similarity functions
k = kinetic energy of turbulence, m^2/s^2
$k = 0.5\,(\overline{u'^2} + \overline{v'^2} + \overline{w'^2}$
$\mathbf{k}$ = wave number, 1/m, $\mathbf{k} = \{k_1, k_2, k_3\}$
k^+ = scale of kinetic energy of turbulence, m^2/s^2
L = macrolength scale of turbulence, m
L_{11} = macrolength scale, m
$L_{11}/D = E_{11}(k_1 D = 0)/\overline{u'^2} \cdot \pi/2 \geq L_{11,t}/D$

M = mesh spacing of grid, m
$r_{1/2}$ = half width of the $\overline{u'^2}$-profile, m
Re = Reynolds number $Re = U_0 D/\nu$
$\bar{u}$ = axial mean velocity, m/s
$\overline{u'^2}$, $\overline{v'^2}$, $\overline{w'^2}$ = Reynolds normal stresses, m^2/s^2
$\bar{u}_d$ = axial mean excess velocity, m/s
U^* = mean velocity scale $U^* = (\bar{u}_d)_{\mathbb{C}}$, m/s
U_∞ = velocity of the external flow, m/s
U_0 = jet exit velocity, m/s
$\bar{v}$ = lateral mean velocity, m/s
V = nondimensional velocity scale $V = U_\infty/U^*$
x = axial coordinate, m
$\bar{x}$ = axial distance from grid, m
Δx = distance between grid and jet outlet, m
y = lateral coordinate, m
$y_{1/2}$ = half width of the $\bar{u}_d$-profile, m
y_a = outer boundary of shear layer, m
ε = dissipation of turbulence kinetic energy, m^2/s^3
η = nondimensional lateral distance $\eta = y/y_{1/2}$
θ_1 = momentum thickness $\theta_1 = (H/U_\infty^2)^{1/2}$, m
ν = kinematic viscosity, m^2/s
ν_T = eddy-viscosity, m^2/s
ρ = fluid density, kg/m^3
σ = solidity ratio of grid
$\bar{\tau}$ = Reynolds shearstress $\bar{\tau} = \rho\overline{u'v'}$, N/m^2
τ^*/ρ = scale of the shear stress, m^2/s^2

Indizes:

A = initial zone
e = energy containing eddies
E = final zone
max = maximum value in the cross-section

PRECEDING PAGE BLANK-NOT FILMED

0 = value at the jet exit
℄ = line of symmetry
Z = intermediate zone
∞ = external flow

1. INTRODUCTION

In problems of disposal of sewage and other liquid waste (e.g. cooling waters) into turbulent environments such as rivers and canals, as well as the emission of gases into the atmospheric boundary layer, the dispersion of contaminents is controlled successively by different mechanisms.

In general, the contaminated fluid is discharged from an outlet structure as a jet which expands slowly into the external stream, whereby the concentrations in the jet become diluted. Some hundred jet outlet diameters downstream, the mean kinetic energy of the jet is fully transformed into turbulence kinetic energy which in turn continues to dissipate into heat. Thus, the turbulence motion of the external stream is the only mechanism to disperse contaminants in this far field.

Both for the far field and for the jet type flow near the point of release, well established mathematical models to simulate the diffusion process are at hand. But for the intermediate region, which is characterised by the simultaneous action of turbulence generated by the jet and in the external stream, no reliable predictions have been made up to now. As long as this gap remains unclosed, the initial conditions required for far field models must be assumed or empirically determined. It is the purpose of this paper to provide insight into some features of this intermediate zone of flow development.

First a phenomenological evaluation of the various kinds of interactions between the jet and the external turbulence is given. A physical concept, proposed by Slawson/Csanady [1], is used to deduce an eddy viscosity term, which takes account of the supplementary dispersive action due to the presence of external turbulence. The next section provides a description of the test rig and the results of the experiments of an isothermal axisymmetric jet discharging into an external stream, which was made turbulent by a grid. This is followed by the deriviation of a prediction model, based on the integral method and a turbulence hypothesis of the eddy viscosity type. Finally the predicted and the measured developments of the mean field scales are compared.

2. PHENOMENOLOGICAL CONSIDERATIONS

The process of mutual interaction between a shear layer and a turbulent external flow has only recently attracted broad attention. Only a limited amount of knowledge about the details and the mechanism of such flows is available today. For this reason, this investigation started with a simple 2-dimensional isothermal free shear flow for which the governing equations could be solved by means of established computational procedures. Due to its close resemblance to practical situations and the convenience with which such a configuration can be generated in the laboratory, the axisymmetric jet discharging into a co-flowing turbulent stream was chosen as the test case.

It is a widely accepted hypothesis, occuring as a common denominator in the theory of turbulence that, in general, processes which interact most effectively are those having length scales of the same order of magnitude. Relying on this hypothesis, many experimental facts could be explained such as the occurance of the stage of local isotropy, the energy cascade process in the wave number space or Richardsons's law for relative diffusion of particles.

The process of relative diffusion could be regarded in some sense, as the linear counterpart of jet diffusion in a turbulent external stream. The linearisation accounts for the fact that in pure diffusion processes scalar quantities are merely convected around by whirls of different scales, whereas in the case of the jet, eddies of the jet will be influenced dynamically by eddies inherent to the external turbulence.

Despite this essential difference, there is much to be learnt from the diffusion process in turbulent flows. Firstly, one has to distinguish between bodily convection of a diffusing cloud and diffusion relative to the centroid of the meandering pattern. The meandering is caused by the action of whirls or eddies that have dimensions very much greater than the characteristic width of the diffusion pattern. This meandering motion makes no real contribution to the diffusion of tracers relative to the axis of the cloud and hence to dilution.

On the other hand the diffusion is controlled by the action of such eddies which have typical sizes of the order of the width of the pattern. If the instantaneous local concentrations are averaged over times that are long compared to the typical period of the meandering motion, the effect of the different eddy sizes can no longer be separated. The flat and wide concentration distribution over the cross-section measured in this way mainly reflect the action of the largest eddies. This is best seen by taking a long-time exposure photograph.

In the following discussion it will be assumed that the macro length scale of the eddies of the external flow is not large enough to produce a distinguishable part of meandering upon the jet under consideration Thus, all measurements with averaging times greater than the typical time scale of the turbulence should lead to identical results.

Since there exists only a global view concerning the mutual interaction processes between shear layer turbulence and an external turbulent flow, it is reasonable to base these phenomenological considerations on a "region-model" as first proposed by Slawson /Csanady [1] in connection with the prediction of the behaviour of chimney plumes in the atmosphere. According to their proposal, the flow field of the jet is subdivided into three main zones of flow development (cf. Fig. 1), which are designated the initial, intermediate and final zone, respectively. For each of these zones, the dominant mechanisms of jet

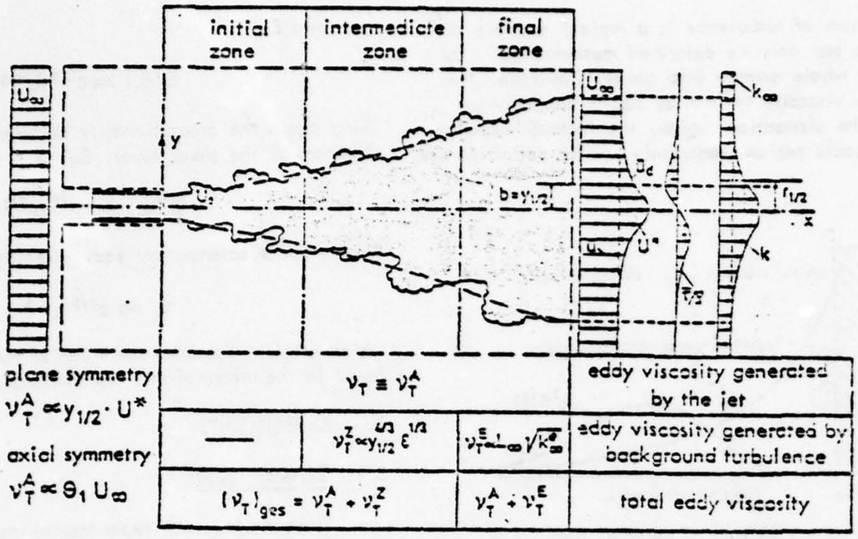

Fig. 1 Axial regions of jet development

diffusion will be described.

Such subdivisions of the flow field are often made in fluid mechanics, mainly in connection with an approximate mathematical description of compound and evolving flows. One of the greatest shortcomings of this procedure manifests itself in the lack of defintion of the axial boundaries of the various zones. Therefore continuous solutions which comprise two or more zones are generally not deducible. Another restriction to the generality of the analysis to follow is imposed by basing it on the eddy viscosity concept to represent the supplementary effect of the external turbulence on the jet diffusion. For each of the zones depicted in Fig. 1 both the fraction of the eddy viscosity generated in the jet itself and the additional part generated by the presence of the external turbulence will be determined.

The initial zone of the jet is characterized by a very coherent structure consisting of vortex-ring like vortices with typical dimensions of the jet tube diameter. Because these vortices possess a high level of kinetic and rotational energy, it seems plausible that they will be only slightly affected by a much more isotropic external turbulence of lower intensity. Therefore the fraction of the additional eddy viscosity should be vanishingly small in the initial zone.

In the course of the rolling up and folding processes, the vortices entrain turbulent ambient fluid. The fine scale structure of this entrained fluid should enhance the destabilisation of the vortices and lead to a higher rate of vortex pairing, whereby the length scale of the amalgamated vortex and hence the shear layer width becomes greater. Further downstream the coherence of the jet-generated vortices becomes weaker. As a consequence of the entrainment flow into the jet region, eddies of the external flow should have a great tendency to come near the edge of the jet. It seems reasonable therefore that as well as the fine scale part which leads via destabilisation to an enhanced jet enlargement, a direct interaction of the vortex stretching type between the energy containing eddies of the jet and the eddies of the external turbulence should also take place. In the following, it is supposed that this latter type of mutual interaction excerts the dominant external effect on jet diffusion.

According to the process of energy transfer in the wave number space, which is essentially accomplished by vortex stretching (see e.g. Tennekes/Lumley [2]), it is assumed that only such eddies of the external turbulence are effective in transfering energy to the eddies within the jet, which are slightly larger than the controlling eddies within the jet. Since the typical eddies within the jet are to a good approximation proportional to a typical scale of the jet width, b, say the half width $y_{1/2}$, it follows that the "active" eddies of the external turbulence should also be proportional to the actual half width.

To determine the portion of jet eddy viscosity, which is generated by the action of external turbulence, the energy content of the "active" eddies of the background flow must also be defined. Supposing that the energy of these eddies is "smeared" over a wave number band of width k (see e.g. Tennekes/Lumley [2]), the energy content should be proportional to both the maximum value of the spectual energy density E (k) in this interval and the wave number band width k. By virtue of the proportionality between the wave number and the reciprocal of the characteristic jet width, the additional eddy viscosity can thus be written as

$$\nu_T \propto b\sqrt{E(k)\cdot k} \propto \sqrt{b}\,\sqrt{E(1/b)}\,. \tag{1}$$

From this it becomes evident that the effects of the external turbulence depend on a complete description of the energy spectrum of the free stream turbulence.

The spectrum of turbulence is a typical example of processes which can only be described mathematically by subdividing the whole domain into zones. Therefore, the additional eddy viscosity defined by Eq. 1 can only be evaluated for the dissipation region, the inertial subrange and the large scale region separately (for definition see Fig. 2).

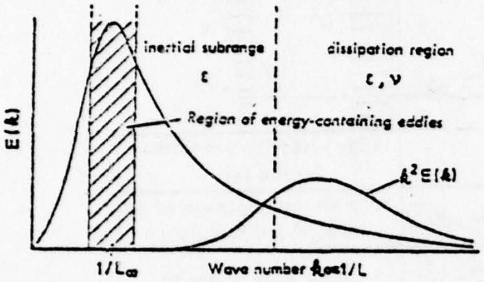

Fig. 2 Energy spectrum of external turbulence

It can be assumed that in most cases, the eddies in the dissipation region are too small and have an energy level too low to affect the eddies in the free shear layer. Thus, this range of the energy spectrum can remain out of consideration. Depending on the dimensions of the turbulence generator, there could exist a pronounced inertial subrange part in the turbulence spectrum. In grid turbulence the width of this region typically assumes one or two decades whereas in the atmosphere it is spread over more decades. If the initial thickness of the shear layer is small enough, the "active" eddies of the external turbulence initially pertain to the inertial subrange.

With growing jet width, larger eddies of the external stream become most effective. This selective process continues until the "active" eddies from outside are identical to the energy containing eddies. When this state is achieved, the final region (cf. Fig. 1) begins. The eddies of the external flow that are still larger than those which contain most of the energy, possess very little energy. They will not contribure to jet diffusion but they may be able to convect the whole jet aside.

The maximum effect upon jet diffusion is therefore arrived at when the energy containing eddies have become active. Although the jet continues to grow in width, the length scale of the "active" eddies from outside remain the same. The additional eddy viscosity in the final zone becomes uncorrelated to the actual shear layer width, and should be proportional to both the characteristic length scale and the energy content k^e_∞ of the energy containing eddies

$$\nu_T \propto L_\infty \sqrt{k^e_\infty}\,. \tag{2}$$

If the external flow is not evolving, the eddy viscosity defined by Eq. 2 assumes a constant value.

The numerical value of the eddy viscosity in the inertial subrange can be determined by substituting the functional relationship for the pertinent turbulence spectrum into Eq. 1

$$E(k) \propto \varepsilon^{2/3} k^{-5/3}. \tag{3}$$

Using again the proportionality between wave number and thickness of the shear layer, Eq. 3 can be rewritten as

$$E(k) \propto \varepsilon^{2/3}\, b^{5/3}. \tag{4}$$

Finally the supplementary eddy viscosity is given by

$$\nu_T \propto \varepsilon^{1/3}\, b^{4/3} \tag{5}$$

which closely resembles the relation for the eddy diffusivity found in the theory of relative diffusion.

3. EXPERIMENTS

3.1 General layout

Since no relevant experimental data were available from the literature, measurements were performed in a wind tunnel using different grids to produce distinct levels and scales of background turbulence (see Fig. 3). Jets of different momentum thicknesses were discharged from a long tube with D = 6 mm in the centre of the tunnel cross-section and coaxial to the main flow. To succeed in an unbiased evaluation of the influence of external turbulence upon jet mixing, the same jets were investigated with and without grids installed.

Mean velocities were measured with pitot tubes and axial turbulence fluctuations with single normal hot wires (DISA 55A22, 55D01). Time spectra of this velocity fluctuation were computed on a Fourier Analyser Type HP 5400 A in order to determine the longitudinal macro length scale $L_{11,1}$. Since the mean velocity profiles for both cases without and with external turbulence appeared to be self-similar to a good approximation (see Fig. 4), the relevant shear stress $\rho\,\overline{u'v'}$ could be computed using the transformed momentum equation. Assuming equality between the normal stress components $\overline{v'^2}$ and $\overline{w'^2}$, and a fixed ratio $\overline{u'^2}/\overline{v'^2} \approx 1.35$, the balance of turbulence kinetic energy k was estimated. In doing this, the dissipation term was approximated by $c_D \cdot k^{3/2}/L$ and the diffusion term by a gradient type model. Since the measurements show no significant variation of $L_{11,1}$ over the jet cross-section, the condition that the diffusion term over the cross-section must integrate to zero was used to determine the unknown value of c_D/L.

3.2 Characteristics of the external flow

The jet was introduced at a distance of 10 mesh lengths downstream of the bi-plane grid. The ratio of mesh size to thickness of the square wooden bars was M/b = 40/10 mm, corresponding to a solidity ratio of $\sigma = 0.43$.

The axial decay of the streamwise velocity fluctuation is well described by a power law

$$\frac{\overline{u'^2}}{U_\infty} \propto \left(\frac{\bar{x}}{M}\right)^{1.50}, \tag{6}$$

whereas the longitudinal macro length scale $L_{11,1}$ grows to the power of 0.5 (see Fig. 6). The state of homogeneity

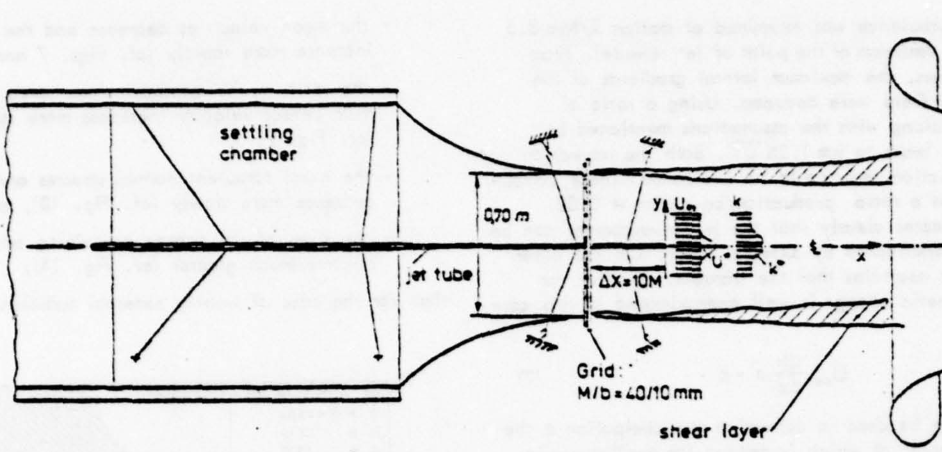

Fig. 3 Schematic layout of the experimental set up

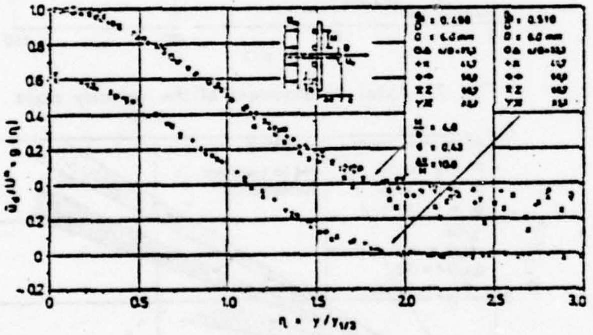

Fig. 4 Distribution of excess velocity in high (above) and low (below) turbulent external flow

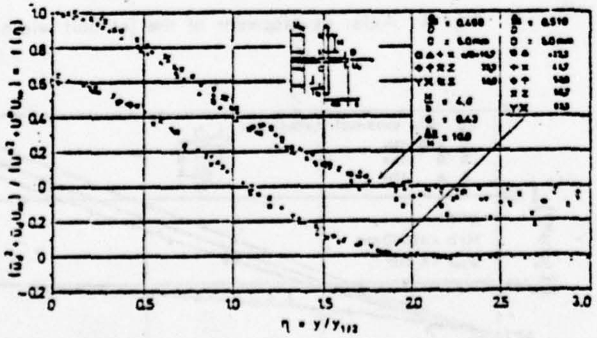

Fig. 5 Distribution of excess momentum flux in high (above) and low (below) turbulent external flow

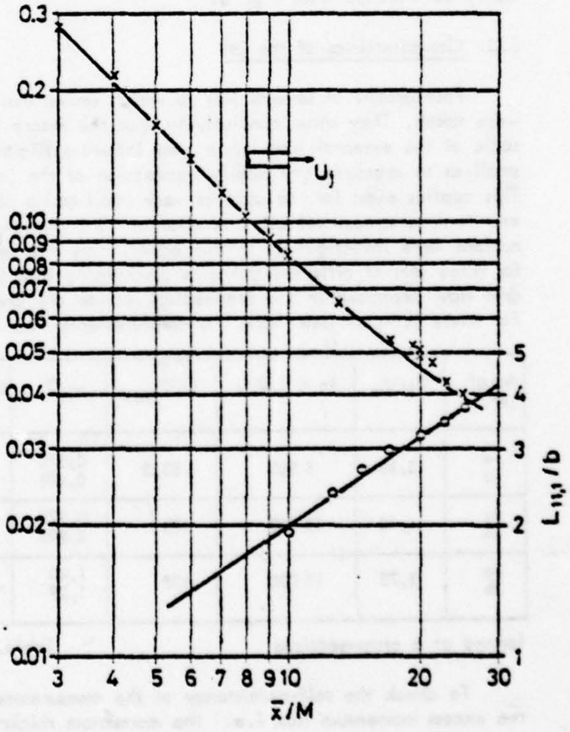

Fig. 6 Axial development of turbulence intensity and macro length scale of the external flow

of the grid turbulence was examined at station $\bar{x}/M \approx 8.5$ (viz. 1.5 M upstream of the point of jet release). From several traverses, the maximum lateral gradients of the mean velocity field were deduced. Using a ratio of $\overline{u'v'}/k \approx 0.3$ along with the assumptions mentioned in § 3.1, which leads to $k \approx 1.25\,\overline{u'^2}$, both the advection and the production term could be evaluated. These computations yielded a ratio production/advection ≈ 0.02. This fact indicates clearly that the jet development can be looked at as unaffected by external shear. On the other hand this fact acertains that the transport equation for turbulence kinetic energy is well approximated in this case by

$$U_\infty \frac{dk}{dx} = -\varepsilon \, . \tag{7}$$

Equation 7 can be used to determine the dissipation ε the axial development of which is needed for predictions in connection with the turbulence model for the intermediate zone (cf. Eq 5). After resolving k into the three normal stresses and in regard of the above mentioned relationships between the normal stresses, Eq. 7 can be written as

$$\frac{\varepsilon \Theta_1}{U_\infty^3} \approx -\frac{4}{3} \frac{d(\overline{u'^2}/U_\infty^2)}{d(x/\Theta_1)} \, . \tag{8}$$

The axial gradient of the streamwise normal stress can easily be deduced from Fig. 6.

3.3 Characteristics of the jet

Photographs of several jets to which smoke was added were taken. They show conclusively that the macro length scale of the external turbulence was indeed sufficiently small as to preclude any bodily convection of the jets. This applies even for the case of very small ratios of jet-exit to free stream velocity. A total of 13 jet-grid-combinations were investigated. In this paper, only the results for three jets of different strengths discharging into the grid flow described in the preceeding section are presented. For every jet-pair (see Table 1), measurements were performed at 6 cross-sections.

No of jet	U_0/U_∞	$Re = U_0 D/\nu$	$(x/D)_{max}$	Θ_1/D	$\Delta x/M$
1a 1b	3,10	8 500	83,3	0,510 0,498	10
2a 2b	4,50	13 000	125	0,975 0,895	10
3a 3b	5,75	15 700	125	1,40 1,29	10

Table 1

To check the self-consistency of the measurements, the excess momentum flux i.e. the momentum thickness was computed for every cross-section. It was found that the momentum flux was conserved to within 8 per cent of the initial value. The main experimental results can be summarized as follows.
The measurements show that, in the presence of a suitable external turbulence:

- the mean velocities decrease and the half widths increase more rapidly (cf. Figs. 7 and 8)
- the ratio of the maximum shear stress to the maximum defect velocity increases more rapidly (cf. Fig. 9)
- the axial turbulent normal stresses are greater and decrease more slowly (cf. Fig. 10), and
- the sizes of the energy containing eddies in the jet become much greater (cf. Fig. 11),

than for the case of weakly external turbulent flow.

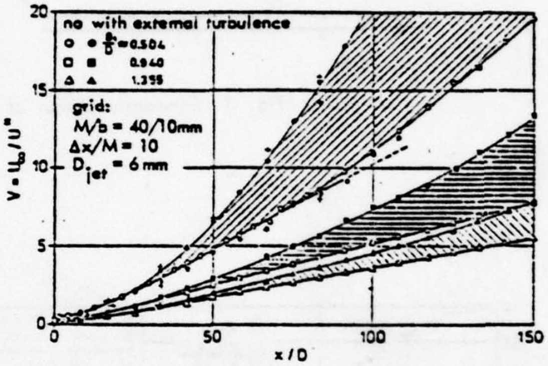

Fig. 7 Axial development of the velocity scale

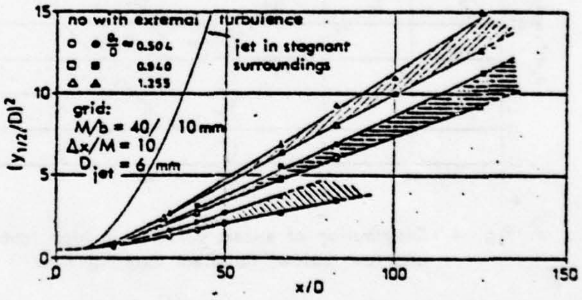

Fig. 8 Axial development of the jet half width

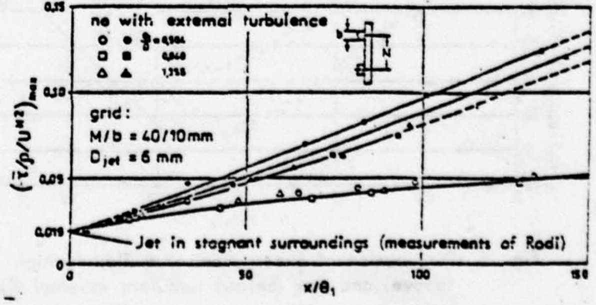

Fig. 9 Axial development of the shear stress parameter

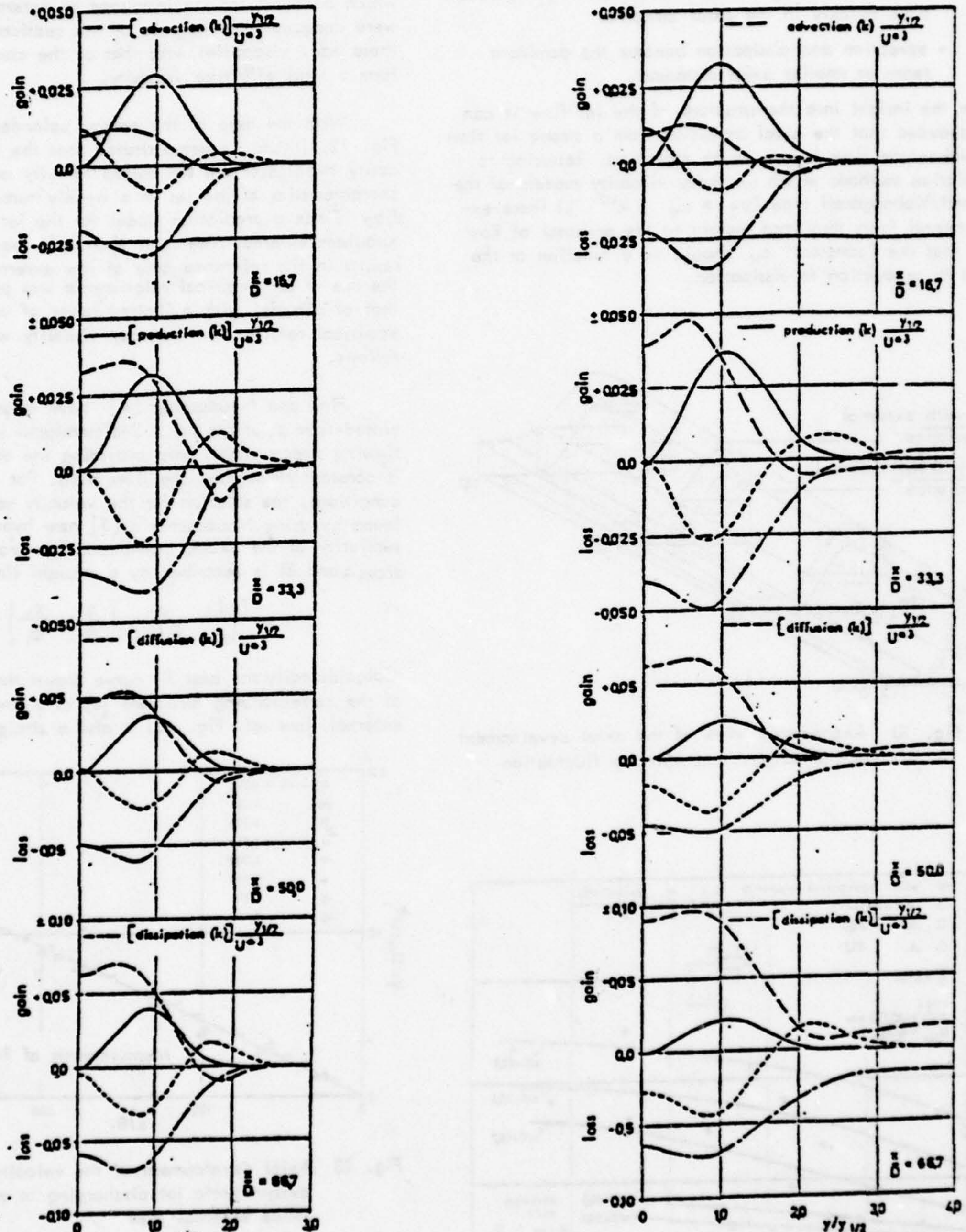

Fig. 12 Axial development of the energy balance across the jet of strength $\theta_1/D = 0.504$ in low turbulence (left) and high turbulence (right) external flow.

From the energy balance (see Fig. 12) it becomes obvious that in the presence of external turbulence

- production is higher near the jet exit but decreases more quickly in the axial direction
- advection and dissipation become the dominant terms at smaller axial distances.

From the insight into the structure of the jet flow it can be deduced that the axial transition from a strong jet flow to wake-type flow is very much enhanced. Referring to prediction methods which use eddy viscosity models of the Prandtl/Kolmogoroff type ($\nu_T = c_\nu \cdot k^{1/2} L$) these experimental facts thus lend weight to the proposal of Rodi [3] that the "constant" c_ν should be a function of the ratio of production to dissipation.

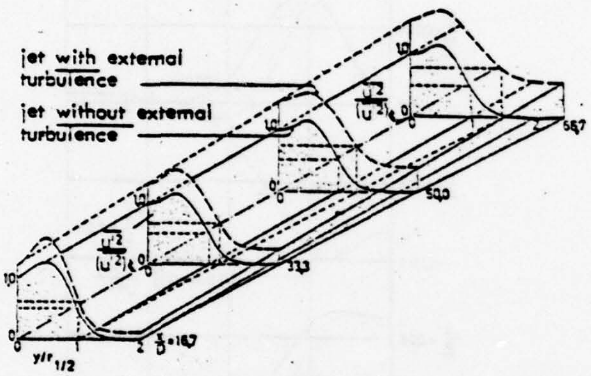

Fig. 10 Axonometric view of the axial development of the longitudinal velocity fluctuation

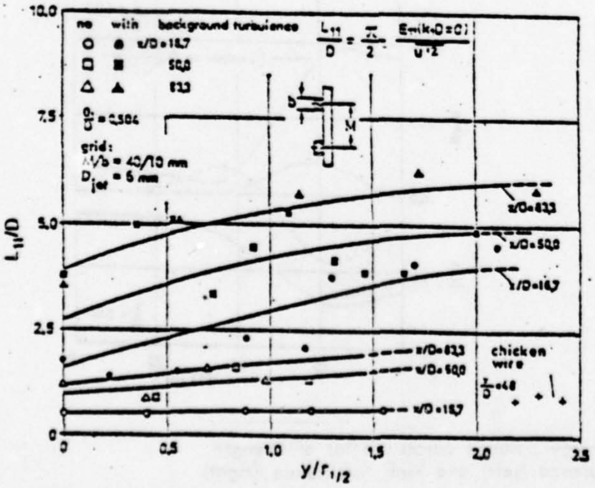

Fig. 11 Distribution of the macro length scale across the jet of strength $\theta_1/D \approx 0,504$

4. THE PREDICTION MODEL

In § 2 relationships for a supplementary eddy viscosity which accounts for the influence of external turbulence were deduced. The purpose of this section is to combine these eddy viscosities with that of the conventional jet to form a total effective viscosity.

With the help of the energy balances depicted in Fig. 12, it can be demonstrated that the known eddy viscosity hypotheses are not suited to fully account for the characteristics of the jet in a weakly turbulent external flow. Since a prediction model for the jet in a highly turbulent external flow must above all lead to realistic results in the reference case of low external turbulence, the use of an empirical relationship was preferred to that of a model with a limited range of validity. The empirical relation for the eddy viscosity was deduced as follows.

Fink and Naudascher [4] have derived reliable closed-form solutions for a 2-dimensional jet in a co-flowing stream which hold providing the effective viscosity is constant throughout the flow field. For axisymmetric conditions, the solution for the velocity scale which was found by using Naudascher's [5] new hypothesis for the similarity of the excess momentum flux profiles (see Appendices A and B) is described by a straight line.

$$V = \frac{I_1 I_3}{I_2} \frac{\nu_T}{\theta_1 U_\infty} \left(\frac{x}{\theta_1} - \frac{x_A}{\theta_1} \right) . \tag{9}$$

Coincidentally the best fit curve drawn through the data of the corresponding turbulent jet in a low turbulence external flow (cf. Fig. 13) is also a straight line passing through the origin. By comparing the slopes of the two curves it turns out that the eddy viscosity generated in the jet depends on its momentum-thickness and the free stream velocity

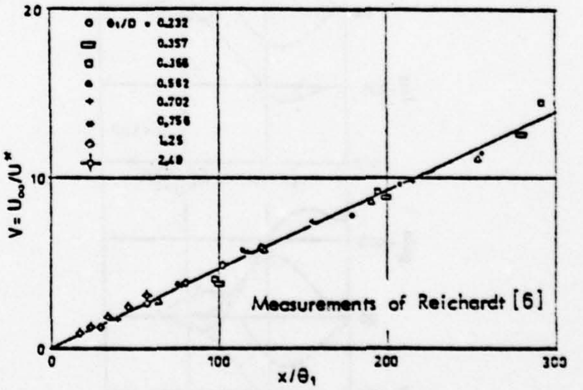

Fig. 13 Axial development of the velocity scale for the axisymmetric jet discharging in a low turbulence external flow

$$\nu_T = \frac{I_2}{I_1 I_3} \theta_1 U_\infty \frac{dV}{d(x/\theta_1)} . \tag{10}$$

With the aid of Eqs. 15 and 17 this relationship can be transformed to

$$\nu_T \sim U^* b \sqrt{1 + \frac{U_\infty}{U^*}} \; . \qquad (11)$$

This new relation affirms the conclusions drawn from the kinetic energy balance: viz. in the strong jet region ($U_\infty/U^* \ll 1$), the classical self-preservation assumption $\nu_T \propto U^* b$, which expresses a constant ratio between production and dissipation holds, whereas further downstream the effective viscosity decreases more slowly than the product of the mean flow scales U^* and b.

According to the basic assumption of the phenomenological argumentation presented in § 2, the dispersive effects provided by the cumulative action both of internal and external turbulence should be additive. Therefore the pertinent parts of the eddy viscosity will be added together to give a total effective viscosity for every zone. The results are summarized in Fig. 1. The difficulty of deducing a solution which comprises the initial and the intermediate zone of jet development is overcome by using the same total viscosity in both zones. This procedure introduces no great error since the supplementary eddy viscosity assumes only small values in the initial zone. Finally, the shear stress model of the first two zones reads

$$\frac{\overline{\tau}}{\varrho} = (c_A \Theta_1 U_\infty + c_Z b^{4/3} \varepsilon^{1/3}) \; \frac{\partial \bar{u}}{\partial y} \; . \qquad (12)$$

This turbulence model was inserted into the integral form of the mean energy equation, Eq. 21. After combination with the reduced momentum equation, Eq. 17, the following *differential* equation for the velocity scale V is obtained

$$\frac{dV}{dx/\Theta_1} = A_1 + B_1 \frac{V^{4/3}}{(1+V)^{2/3}}$$

$$A_j = \frac{I_1}{I_2} I_3 c_A$$

$$B_1 = \underbrace{\frac{I_1}{I_2} I_3 c_Z}_{B_1^*} \frac{\varepsilon^{1/3} \Theta_1^{1/3}}{U_\infty} \qquad (13)$$

5. COMPARISON OF PREDICTION AND MEASUREMENTS

As a preliminary step, the validity of the similarity hypotheses has to be assured. From Figs. 4 and 5 it can be seen that both the conventional excess velocity profile (used to reduce the energy equation) and the profiles of the excess momentum flux (used in the momentum and in the energy equation) retain their similarity despite the presence of a highly turbulent external stream. A more general test however can be made by evaluating both sides of Eq. 17 of Appendix A. This test provides evidence as to what extent the reduced momentum equation is compatible with the data. Figure 14 shows that the predicted linear relationship between the length and the velocity scale is well obeyed with the exception of an initial non-similarity region, which has become more extended in the case of a turbulent external flow. In either case, an empirical constant should be added to the right hand side of Eq. 17, in order to have better agreement with the data. This correction was used in all subsequent applications.

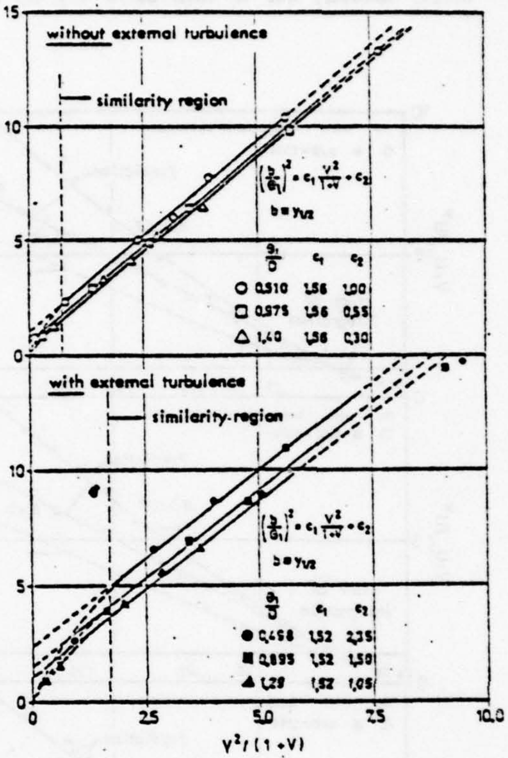

Fig. 14 Verification of the similarity assumptions

In order to determine the single free constant in the turbulence model, Eq. 13 was solved numerically for one of the jet cases. It was found convenient to fix the value of the compound coefficient B_1^* of Eq. 13 instead of that of c_Z. Using this constant, the predicted behaviour of the velocity scale for 6 jets of different strengths discharging into 3 different types of grid flows agrees fairly well with the data. The results for the three jets referenced in Table 1 are shown in Fig. 15. The value of $B_1 = 0$ in Fig. 15 refers to the low turbulence case, where the dissipation ε tends to zero.

To obtain some impression of the magnitude of the total eddy viscosity, the axial variation of the ratio of the supplementary viscosity to the self generated viscosity is also displayed in this Figure. It becomes evident that the supplementary viscosity takes on values of about 6 times that in the conventional jet.

The final zone has not yet been taken into consideration. According to the definition of this zone, the supplementary eddy viscosity should tend very closely towards a constant value in the case of a grid flow, since the turbulence Reynolds number Re = kL/ν does not change appreciably in the region of measurement. This would have entailed a constant axial growth rate of the velocity scale which, however, was not observed for any case.

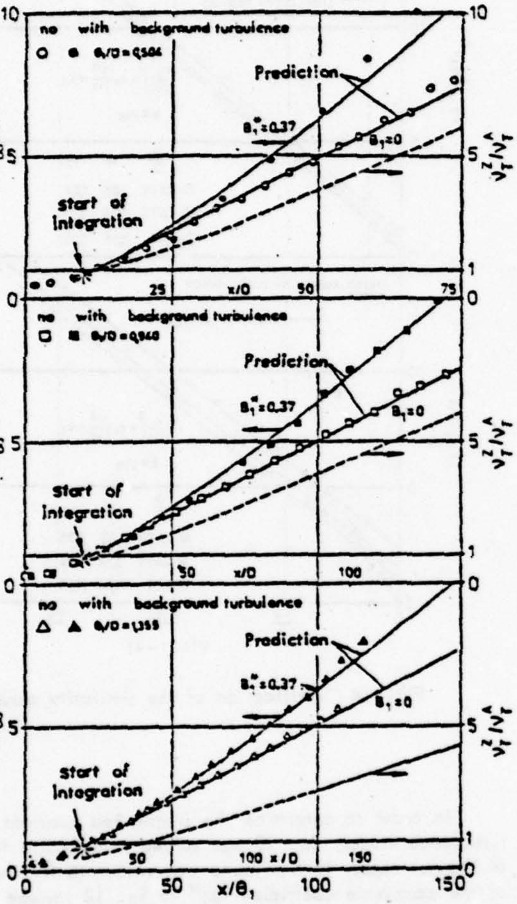

Fig. 15 Comparison of predicted and measured velocity scales for three jets

6. CONCLUSIONS

The existing knowledge concerning external turbulence effects upon the development of shear layers has almost exclusively been gained by investigating wall boundary layers. In this paper, the free shear layer of a axisymmetric jet discharging into a co-flowing external turbulent stream was studied. Bodily convection of the whole jet, which, in case of long averaging time, would imply a spurious rapid enlargement of the shear layer, was excluded by a proper choice of the macro length scale of the external flow ($L_{11,1}/D_{jet} = 5$). The measurements show that the effects of the external turbulence are already felt at the centre line where an increase of both turbulence kinetic energy and the length scale from about 10 jet diameters downstream of the exit was observed. The enhanced axial development of the jet is badly predicted by assuming a constant total eddy viscosity composed of a self-generated part and a supplement, which is only influenced by the characteristics of the energy containing eddies of the external turbulence. However, more reliable predictions could be achieved by using a phenomenological concept borrowed from the theory of relative diffusion, according to which the width of the jet corresponds to a wavelength in the inertial subrange of the external turbulence. Despite this partial success, the detailed mechanism of external turbulence effects on the shear layer of jets is not yet adequately understood.

This theme will be further pursued in the experimental program in our new wind tunnel, the test section of which is sufficiently large to reach the final zone of jet development. With a view to the application of conditional-sampling techniques, the jet fluid will be heated so as to make it distinguishable from the external flow.

ACKNOWLEDGEMENT

The author is grateful to SFB80 and to the DFG for their financial support. The computations were performed at the computer centre of the University of Karlsruhe.

REFERENCES

[1] Slawson, P.R., and Csanady, G.T., "The effect of Atmospheric Conditions on Plume Rise", J. Fluid Mech., Vol. 47, Part 1, 1971.

[2] Tennekes, H., and Lumley, J.L., "A First Course in Turbulence", The MIT Press, 1972.

[3] Rodi, W., "The Prediction of Free Turbulent Boundary Layers by Use of a Two-Equation Model of Turbulence, Ph.D. Thesis, University of London, 1972.

[4] Fink, L.E., and Naudascher, E., "On the Validity of a General Similarity Hypothesis for Jet and Wake Flows", Proceedings of the 9th Symposium on Naval Hydrodynamics, Vol. 2, AOR-203, Office of Naval Research, Department of the Navy.

[5] Naudascher, E., "On a General Similarity Analysis for Turbulent Jet and Wake Flows", The University of Iowa, IIHR Report, No. 106, 1967.

[6] Reichardt, H., "Zur Problematik der turbulenten Strahlausbreitung in einer Grundströmung", Mitteilungen aus dem Max-Planck-Institut für Strömungsforschung Göttingen, No. 35, 1965.

[7] Patankar, S.V., and Spalding, D.B., "Heat and Mass Transfer in Boundary Layers, A General Calculation Procedure", Intertext Books, London, 2nd Edition, 1970

APPENDIX A REDUCTION OF THE MOMENTUM EQUATION

For the case of negligible axial pressure gradient, the boundary layer form of the momentum equation for axi-symmetric flows reads

$$\frac{\partial \bar{u}^2 y}{\partial x} + \frac{\partial \overline{v}\bar{u} y}{\partial y} = \frac{\partial (y\, \bar{\tau}/\rho)}{\partial y}, \qquad (14)$$

if in addition the Reynolds normal stresses are neglected. Naudascher's new similarity hypothesis postulates the similarity of the profiles of the excess momentum flux.

$$\frac{\bar{u}_d{}^2 + \bar{u}_d U_\infty}{U^{*2} + U^* U_\infty} = f(\eta)\text{, where } \eta = \frac{y}{b(x)} \text{ and } b = y_{1/2}. \qquad (15)$$

After integration of Eq. 14 over the jet cross-section and substitution of the similarity hypothesis, Eq. 15, one obtains

$$\int_0^{\eta_a} \left(U^{*2} + U^* U_\infty\right) b^2 f\, \eta\, d\eta = H = \text{const}. \qquad (16)$$

This relationship can be nondimensionalised. The result is

$$\left(\frac{b}{\Theta_1}\right)^2 = \frac{1}{I_1} \cdot \frac{V^2}{1+V}, \text{ where } I_1 = \int_0^{\eta_a} f \eta\, d\eta = \text{const}. \qquad (17)$$

APPENDIX B REDUCTION OF THE ENERGY EQUATION

Applying the same simplifications as in the case of the momentum equation, the mean energy equation reads

$$\bar{u}^2 \frac{\partial \bar{u}}{\partial x} + \bar{u}\bar{v} \frac{\partial \bar{u}}{\partial y} = \bar{u} \frac{1}{y} \frac{\partial}{\partial y} \left(y\, \frac{\bar{\tau}}{\rho}\right). \qquad (18)$$

After intergrating over the jet cross-section and then by parts, one obtains

$$\frac{d}{dx}\left[\frac{1}{2}\int_0^{y_a} \bar{u}_d (\bar{u}_d^2 + \bar{u}_d U_\infty)\, y\, dy\right] + \int_0^{y_a} \frac{\bar{\tau}}{\rho} \frac{\partial \bar{u}_1}{\partial y}\, y\, dy = 0, \qquad (19)$$

where in addition the condition of constant excess momentum flux (Eq. 16) has been used to simplify the left hand side. For substitution into this equation, Naudascher's similarity hypothesis is solved for $\bar{u}_d$

$$\frac{\bar{u}_d}{U^*} = -\frac{1}{2} V + \sqrt{\frac{1}{4} V^2 + f(\eta)(1+V)} = g(\eta). \qquad (20)$$

If both the original form, Eq. 15, and this relationship are inserted, the mean energy equation assumes a very intractable form since it envolves elliptic integrals. Comparisons with direct numerical solutions of the momentum equation using the GENMIX computercode of Patankar/Spalding [7] have shown that adequately reliable predictions could be deduced if instead of Eq. 20 a linearized version is substituted for the isolated $\bar{u}_d$-terms in Eq. 19. With these simplifications, the reduced mean energy equation reads

$$\frac{1}{2} \frac{I_2}{I_1} \frac{d}{d(x/\Theta_1)} \left(\frac{1}{V}\right) = -\frac{1}{V} \frac{b}{\Theta_1} \int_0^{\eta_a} \frac{\tau/\rho}{U_\infty^2} \frac{\partial g}{\partial \eta}\, \eta\, d\eta, \qquad (21)$$

where $I_2 = \int_0^{\eta_a} f g \eta\, d\eta$

SOME MEASUREMENTS OF SPATIAL CORRELATIONS IN AN AXISYMMETRIC TURBULENT JET

X.B. Reed,Jr. (speaker)
L. Spiegel
S. Hartland

Technisch-Chemisches Laboratorium
Eidgenössische Technische Hochschule
Zürich, Switzerland

ABSTRACT

Extensive measurements of the six independent components of the spatial correlation tensor $R_{ij}(x_k|x_\ell)$ have been made in the fully developed turbulence ($z/d=50$) of an axisymmetric free jet. A portion of the results are reported here. The measurements were made in a submerged water jet using Laser-Doppler anemometry with frequency shifting. There is agreement between the subset of our results and the corresponding correlations of Wygnanski and Fiedler (31),who,following Corrsin and Uberoi (7,8),employed symmetrically placed hot wires,(i.e.,with no fixed wire) in an air jet.

NOMENCLATURE

d	outlet diameter of jet (6mm)
$\underset{\sim}{r}$	$(=\underset{\sim}{x}'-\underset{\sim}{x})$ displacement vector
$r_{1/2}$	radius to midpoint of mean axial velocity
(r,θ,z)	cylindrical coordinates
$\underset{\approx}{R}(\underset{\sim}{x}\|\underset{\sim}{x}')$	two-point correlation dyadic
$R_{ij}(x_m\|x_n')$	tensorial components of the two-point correlation
$\underset{\sim}{u}$	fluctuating velocity
u_r,u_θ,u_z	fluctuating velocity components (physical)
u_r',u_θ',u_z'	rms components of velocity
$\underset{\sim}{U}$	mean velocity
U_r,U_θ,U_z	mean velocity components(physical)
$\overline{u_r u_z},\overline{u_z u_r}$ etc.	single point correlations
(x,y,z)	Cartesian coordinates
γ	intermittency factor
η	$(=r/z)$ dimensionless radial distance.

INTRODUCTION

The free axisymmetric turbulent jet,as one of the standard shear flows,has received considerable attention since WWII and the post-war years (e.g. 1-4;5-18). Detailed measurements leading to the term-by-term determination of the turbulent energy balance have been made in the developing, as well as the fully developed,self-preserving jet; isotropy in the core has been obtained in some labs but not in others; and the failure of Taylor's hypothesis, the consequent equivocal nature of the concept of a convection velocity, and the notion of a convection velocity for each wave number, have been established, to list some among many of the advances. In addition, the role of coherent structures near the nozzle exit has been much investigated because of its obvious relevance to the jet-noise problem (e.g. 19-20).

Yet the spatial structure of the fully-developed turbulent jet, as manifested by the spatial correlation tensor of second order,has only been measured in isolated cases. There have been neither systematic nor exhaustive measurements of spatial correlations in the axisymmetric jet. The reason is obvious upon comparison with isotropic, or even homogeneous, turbulence (2,4,21): in the general shear flow, not only must all of the components of $\underset{\approx}{R}(\underset{\sim}{x}|\underset{\sim}{x}')$ be measured,they must be measured as functions of the three-dimensional vector $\underset{\sim}{x}$, as well as of all three components of the displacement vector $\underset{\sim}{r}=\underset{\sim}{x}'-\underset{\sim}{x}$ for each fixed $\underset{\sim}{x}$. The turbulent wake of a cylinder is one shear flow in which reasonably extensive measurements have been made (4,22-24).

The large eddy structure is of significance in any turbulent flow for a number of reasons(the classic is ref.25,see also refs 26-29,4,24)and has been extracted in the case of the fully developed turbulent wake of a circular cylinder (4,22-24,27-28)from the diagonal terms R_{11},R_{22} and R_{33} measured at three fixed points as functions of displacements in each of the three perpendicular directions alone; other measurements were also made to confirm,or assist in establishing the models. Similarly,spatial,as well as spatio-temporal correlations have been made in the turbulent boundary layer, again with

PRECEDING PAGE BLANK-NOT FILMED

the focus on the large eddy structure (30).

An extensive program of measurements of $\underline{\underline{R}}(\underline{x}|\underline{x}')$ within an axisymmetric, fully developed turbulent jet has been undertaken at the E.T.H. with the ultimate goal being the characterization of the large eddy structure. Only a sample of these results can be presented here.

EXPERIMENTAL BACKGROUND

The measurements were made with two Laser-Doppler anemometers (DISA-LDA Type 55L with electronic circuitry modified and up-dated in 1975), employing Bragg cells [1]. Optical frequency shifting is necessary in such highly intense turbulence, and it also offers the possibility of measuring in the highly intermittent outer regions of the jet. Frequency shifts from 400-600 kHz were used, depending on the local flow conditions and the slew rate of the tracker.

There were a number of other electronic accessories used in the course of research. A Wavetek Model 164 (30MHz) sweep generator was used in conjunction with a Tektronix Universal Counter DC 503, to calibrate the Doppler frequency. A Tektronix 7623 storage oscilloscope served several purposes, including fine adjustment of the optics on the basis of the quality of the Doppler signal. A Nelson Ross MF-9 spectrum analyzer with low and high frequency plug-ins PSA 036 and 235 was used for purely diagnostic purposes. A DISA signal conditioner was used as a low-pass filter to cut off noise above 200 Hz before the output signal was further processed. The correlations were calculated on a Hewlett-Packard 3721A correlator. Because of the importance of the low frequency contribution to the turbulent energy, (cf. 31 and 7), an RC circuit preceded the correlator input to eliminate the DC component by acting as a high-pass filter; the result was a flat frequency down to 0.012 Hz (3 dB point).

Dow Uniform Latex Particles 41950 (nominal diameter 1.099μm, density 1050 kg/m^3) were used as light-scattering centers. Concentrations were roughly 30 particles/mm^3. This may be compared with the $1/e^2$ measuring volumes of 0.01 mm^3 and 0.024 mm^3 for the 300 mm and 400 mm lens, respectively. It should be mentioned that beam expanders were employed to reduce the size of the measuring volumes. For our forward scattering, differential mode measurements, this range of particle concentrations was an experimentally determined optimum. The practical optimization procedure was as follows. A small amount was added to the system and after homogenization the rms axial velocity was measured. The number of scattering particles was then doubled and the measurement repeated. Initially, the introduction of additional particles reduced the rms value by increasing the proportion of the fluid mechanical signal at the expense of the electronic noise. At the other limit of very high particle concentrations, the addition of still more scattering particles increases the rms velocity by impairing the passage of the laser beams and the scattered light, which thus also reduces the S/N. Fortunately, the minimum in the rms (maximum in the S/N) was quite flat, and the desired concentration could be achieved without having to advance in increments that were impractically small. Over long periods of time, the latex spheres tended to accumulate on the walls of the glass tubing and test section with a concomitant loss in S/N. Efforts to sweep them free only led to clusters, which also reduced the S/N; these were visible as flashes of reflected/scattered light as they passed through the laser beams. Consequently, every few months, the system was shut down, washed, emptied and refilled with new distilled water and scattering particles.

The axis of the submerged jet coincided with the axis of a vertical circular glass cylinder, 600 mm in diameter and 1000 mm long; no wall effects were perceptible. To avoid optical difficulties, a square aquarium that was also filled with water enclosed the glass cylinder - otherwise, neither the velocity component nor its position of measurement could be directly recorded. The jet exit was 100 mm above the rounded metal base of the glass cylinder and the overflow weir at the top of the cylinder was axisymmetric, thereby minimizing end effects. The jet exited from a 6mm stainless steel tube after flowing initially through a settling chamber, thence into the bell-shaped inlet of a 4-to-1 contraction outfitted with a honeycomb and grids, and finally through a 16-to-3 contraction with a honeycomb and grids. A hemispherical distributor at the inlet to the settling chamber was designed, but early runs indicated that it would have been redundant. An overhead tank (2.8m) ensured a constant pressure at the inlet to the pump that preceded the settling chamber. The throughput was measured with an inductive flow meter to a precision of 0.1% and a systematic linearity error of 0.25%. The temperature was measured with an NTC resistor and controlled ("bang-bang") with a countercurrent heat exchanger; typical temperature deviations detected were smaller than 0.08K from the desired 294.9K and the temperature was presumably further homogenized in the settling chamber, contractions and accessories before the jet exit. A throughput of 1.63x10^{-4} m^3/s (585 lt/hr) yielded an exit velocity of 5.75 m/s or, at 294.9K, a jet Reynolds number of about 35.4x10^3.

Extensive precautions were taken to avoid vibrations, and their elimination was confirmed, not only indirectly through the usual barometers of the turbulence measurements, but also directly from a number of vibration measurements. An earlier version of the flow system had, in fact, to be modified to eliminate vibrations. Originally, a common frame supported all components, but separate frames

---

[1] We are indebted to Mr.R.Brunner for the design and construction of the high frequency power generator, as well as for occasional assistance with the electronics.

had to be constructed for the support of the test section, the optics and the feed tanks and pumps. Each was mounted on its own vibration-absorbing elements so that pump and building vibrations were not transmitted throughout the system.

The sending optics were mounted on precision elevating stages which, in turn, were mounted on precision two-dimensional lathe tables so that the optics could be translated in all three dimensions relative to the test section. The accuracy in the x,y(r,θ) plane was 0.1mm, that in the z-direction being 0.05mm. Careful measurements indicated that the bisector of the laser beams from the DISA optical unit did not coincide with the optical axis of the lens. Compensating displacements of the optical bench in the vertical and horizontal directions ensured that the bisector was perpendicular to the aquarium wall and thus that true x,y and z velocity components were measured at the true positions.

The experimental procedure was otherwise quite standard, although it might be mentioned that both flow and electronic equipment were turned on each morning about 45 minutes before measurements were begun.¶From the start, the investigation was focused on correlation measurements relevant to large-scale turbulent structures. Consequently, no premium was placed on our mean and rms velocities, nor were single-point correlations made. For one thing, single-point measurements and investigations of fine scale structures have been extensively studied in the literature (31,1-10,13-15). Nevertheless, preliminary measurements were made of some of these quantities, not only to establish the axisymmetry of the jet but also to locate the axis of the jet at each new horizontal plane (the z stages spanned only 60mm) and for each velocity component (upon rotation, the optical unit had to be readjusted). In what follows, our raw data are compared with literature values, primarily the more recent ones of Wygnanski and Fiedler (31).

The mean axial velocity profile is shown in Fig.1. The scatter of the data from the different planes is comparable to that of other authors. Some of Wygnanski and Fiedler's points (solid), which are on Hinze's curve, are included for comparison; there is also agreement between their $r_{1/2}$ - admittedly a coarse measure, but nevertheless one characterizing the whole curve in some sense - and ours. Some of the data were taken with the correlator, others with a PAR box-car integrator used as a simple integrator. The latter has a maximum integration time of 100s and, as is typical of analog equipment, only smooths (RC averages), with the result that somewhat greater scatter was obtained. The correlator performs true digital averaging, as well as permitting longer averaging times, and these data all lay nearer the average literature curve.

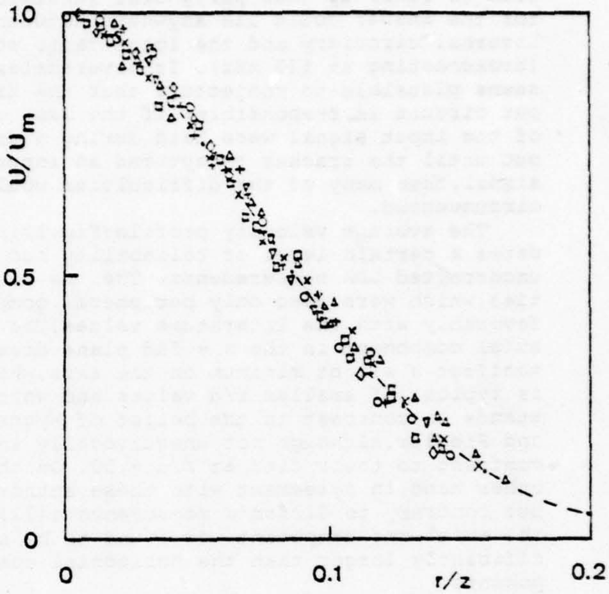

Figure 1: Mean axial velocity profile

◇ z/d = 31.5, ▫ z/d = 48.6
○ z/d = 31.8, + z/d = 50.0
△ z/d = 38.3, x z/d = 58.5
▽ z/d = 46.6
. Wygnanski ---- Hinze
& Fiedler

It was originally hoped that frequency shifting would enable LDA measurement in the highly intermittent region at the edge of the jet, where hot wires have notorious difficulties because of their rectification property and because of the radial velocity contribution, facts that remain unchanged by the duration of the averaging periods. Our hopes were not entirely fulfilled, atleast not for our raw data, for the values agree remarkably well with those of Wygnanski and Fiedler near the edge of the jet.

There the LDA measurements suffer from a relative lack of scattering particles in the ambient water. The turbulent bursts are long, but there are fewer of them. When the tracker drops out, the drop-out spikes become proportionally more important than the turbulent signal. It is thus natural that our rms values in the highly intermittent region are high. Moreover, the trackers seem to have a preferred frequency that depends upon the frequency range in which they are working, and when a tracker drops out it tends to this preferred frequency. There is thus a consistent bias given to the mean value, as well as an additional electronic contribution to the rms value. In the 0.225-1.5 MHz range, which was almost exclusively used, we ascertained a pronounced tendency for the tracker to jump toward the neighborhood of 500 kHz during dropouts. It would require a modest research program to clear up this peripheral question, for the answer could lie anywhere between the internal circuitry and the local radio station (broadcasting at 530 kHz). It nevertheless seems plausible to conjecture that the dropout circuit is responsible: if the last value of the input signal were held during a dropout until the tracker recaptured an input signal, then many of the difficulties would be circumvented.

The average velocity profile (Fig.1) indicates a certain level of reliability for the uncorrected LDA measurements. The rms velocities, which were also only peripheral, compare favorably with the literature values. The axial component in the z = 50d plane does manifest a slight minimum on the axis, which is typical of smaller z/d values and which stands in contrast to the belief of Wygnanski and Fiedler, although not unequivocally in contrast to their data at z/d = 50. On the other hand, in agreement with these authors but contrary to Gibson's measurements (12), the axial rms component was found to be significantly larger than the horizontal components.

Correlative measurement circumvents a number of potential questions concerning LDA, providing one is not concerned with the fine scales but with the large eddies. Doubtless for this reason, another set of preliminary measurements agrees very well with those of Wygnanski and Fiedler, namely, the single-point correlation $\overline{u_z u_x}$ shown in Figure 2.

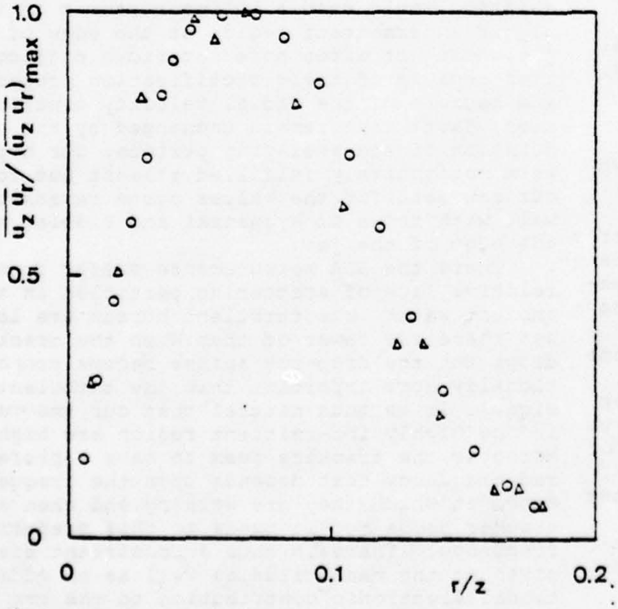

Figure 2: Shear stress distribution (z/d=50)
▲ Wygnanski and Fiedler
○ present investigation

LDA, as a non-disturbing method, offers special advantages for correlation measurements. Precisely at small separations where hot-wire probe wakes cause difficulty (32), however, a different set of questions arise which are associated with measuring volumes, their shapes and their relative orientations. Consequently, no microscales have been calculated, pending clarification (for a discussion of LDA, the state of the art and the integration of LDA measurements, see e.g. 33).

A final word on the correlation measurements themselves: A correlation profile consisted of a series of displacements of the moving point in increments of 2-10mm, depending upon the local slope of the profile. For each of the points in a profile, at least four correlations were measured at each spatial separation, and the resulting values were averaged to yield a single "data point"; if scatter were present, additional measurements were made. Integration times were a minimum of 120s. To try to develop a feel for the role of the integration time, as well as to eliminate it as a possible source of error, many correlations were averaged over 300s, 600s and even 900-1800s; occasionally 3600s were used.

In general, no appreciable changes were found for averaging times beyond 120s. In the highly intermittent region ($\gamma < 0{,}5$ say), the measurement is increasingly influenced by drop-out, the spikes of which are registered as an apparent turbulent fluctuation, as discussed above. The effect of these spikes could not be entirely eliminated, for they occur with a certain (average) frequency and therefore can not be removed by prolonged averaging.

Thus, for small values of γ, the correlator and the Doppler and turbulent signals had to be continuously monitored to preclude such difficulties.

RESULTS AND DISCUSSIONS

According to Wygnanski and Fiedler (p588,31), "The structure of the eddies is self-preserving from z/d = 40,...". Our correlations have all been made with at least one fixed point in the z/d = 50 plane after preliminary measurements had been made at z/d = 20,35,50,65 and 80. The correlations have all been made dimensionless with the peak value R_{zz} on the axis corresponding to $\overline{u_z^2}$ there. This somewhat unconventional choice permits a direct comparison of all correlations on the same basis and represents, moreover, a "normalization" with a correlative measurement of $(u_z')^2$.

The families of isocorrelation curves selected for presentation were $R_{zz}(\underset{\sim}{x}|\underset{\sim}{x}')$ and $R_{zr}(\underline{x}|\underline{x}')$, the former because of the importance of the mean flow direction and the latter because the Reynolds' stress, which is central to turbulence production, arises as a special case. We further limit ourselves here to the presentation of measurements of R_{zz} in a single θ plane and in a single z-plane and of R_{zr} in a single θ-plane, that is:

Series 1: $R_{zz}(\underline{x}|\underline{x}')$, with $\underline{x} \leftrightarrow (r, \theta=0, z=300)$
$r = 0,18$

and with $\underline{x}' \leftrightarrow (r', \theta'=\theta=0, z')$

Series 2: $R_{zz}(\underline{x}|\underline{x}')$ with $\underline{x} \leftrightarrow (r, \theta=0, z=300)$
$r=0,6,12,18,24$

and with $\underline{x}' \leftrightarrow (r', \theta', z'=z=300$

Series 3: $R_{zr}(\underline{x}|\underline{x}')$ with $\underline{x} \leftrightarrow (r, \theta=0, z=300)$
$r = 0,6,18$

and with $\underline{x}' \leftrightarrow (r', \theta'=\theta=0, z')$

For orientation see Fig.3.

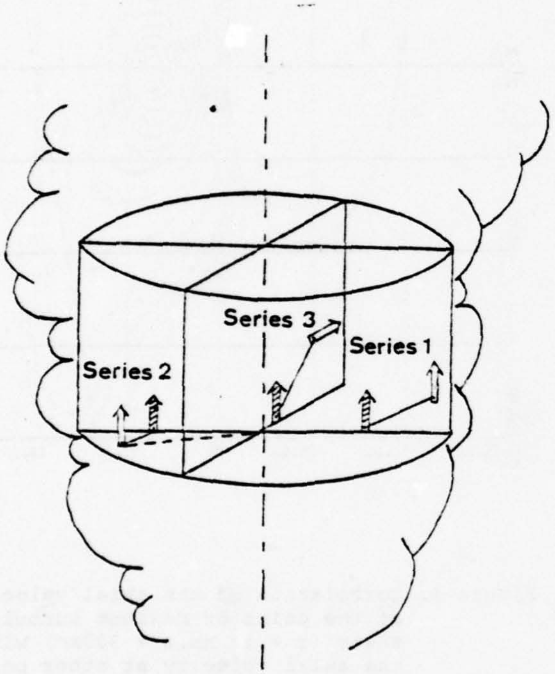

Figure 3: Orientation diagram for correlation measurements (hatched arrows denote fixed points)

Series 1 yields certain obvious information about the large eddy structure that would have been expected. In particular, although the R_{zz} correlation on the axis is not isotropic (Fig.4), the two share a number of common features. Thus, with the expected exception that the radial expansion of the jet with increasing axial distance due to the entrainment of ambient fluid and propagation of the turbulent fluid into its environment is greater than the corresponding eddy growth in wind tunnel turbulence due to the more rapid decay of the smaller eddies, the topography of the correlation on the axis strongly resembles that for isotropic turbulence. Such "second order" effects have not been taken into account to enable a more direct comparison, nor have recent correlation measurements of isotropic turbulence been used for comparison (32).

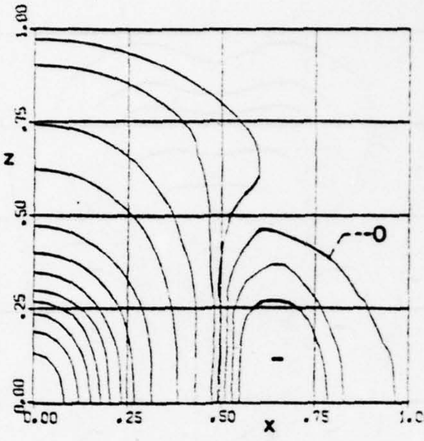

Figure 4: Isocorrelation curves for isotropic turbulence: $R_{zz}(\underline{r})$, $\underline{r} \leftrightarrow (x,o,z)$.
Here and in Figs 5-11, the correlations are measured in the positive direction from the zero isocorrelation in the following increments: 0.01, 0.02, 0.05, 0.1, 0.2, 0.3, 0.4, 0.5 0.6, 0.7, 0.8, 0.9, 1.0. In the negative directions the increments are: -0.01, -0.02, -0.05 -0.1. Negative portions of the isocorrelation figures are so denoted; the undesignated portions are understood to be positive. Distances are in arbitrary units.

Rather, because the comparison at most is a qualitative one, typical f and g curves (21) were used to produce the isocorrelation curves (cf. closing remarks of the section). The comparison is then between R_{zz} and R_{ii} (no sum) and between R_{zx} and $R_{ij}(i \neq j)$, and an appropriate norm would also be necessary for a quantitative comparison. Regardless of whether the f-curves have a zero or not (32), one tends to think of elliptic isocorrelations, but this is a property possessed only by the small eddies (Fig.4). The innermost isocorrelations on the axis of the jet (Fig.5) and elsewhere (Fig.6) are also elliptic, but even the smallest isocorrelation curve (Fig.5) is not truly an ellipse. The fixed point is clearly not centered in the closed curve; the corners are artifacts of the interpolation - line-plot procedure (see remarks at the end of the section), but the fore-aft asymmetry relative to the fixed point is real. That this occurs on the axis further underlines the lack of the isotropy in the core of the jet.

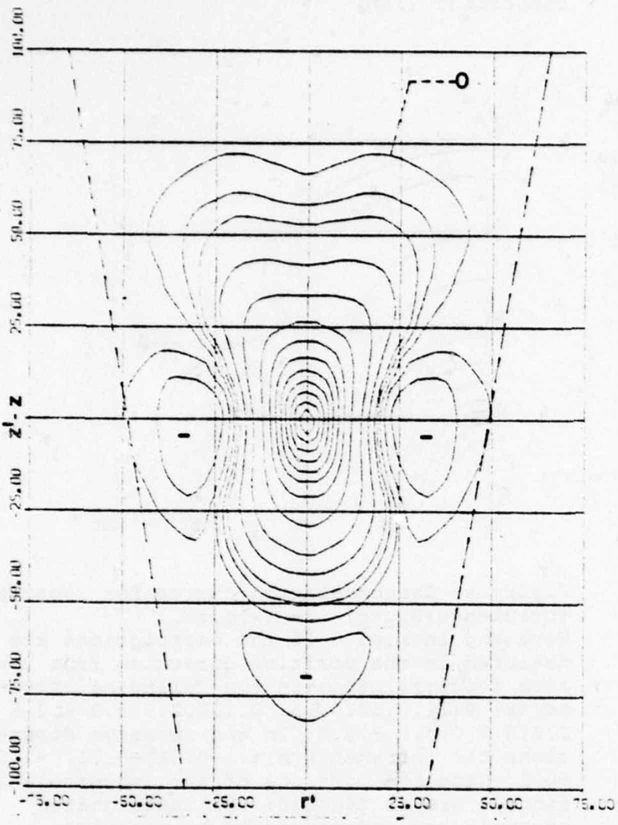

Figure 5: Correlation of the axial velocity on the jet axis at z/d=50(z=300mm) with the axial velocity at other points in a single vertical plane containing the jet axis : $R_{zz}(\underset{\sim}{x}|\underset{\sim}{x}')$, $(r,\theta,z)=(0,0,300)$, $(r',\theta',z')=(r',0,z')$ The $\gamma = 0.5$ levels are denoted by the dashed lines (31).Here and in all the remaining figures except Fig.12, distances are expressed in mm.

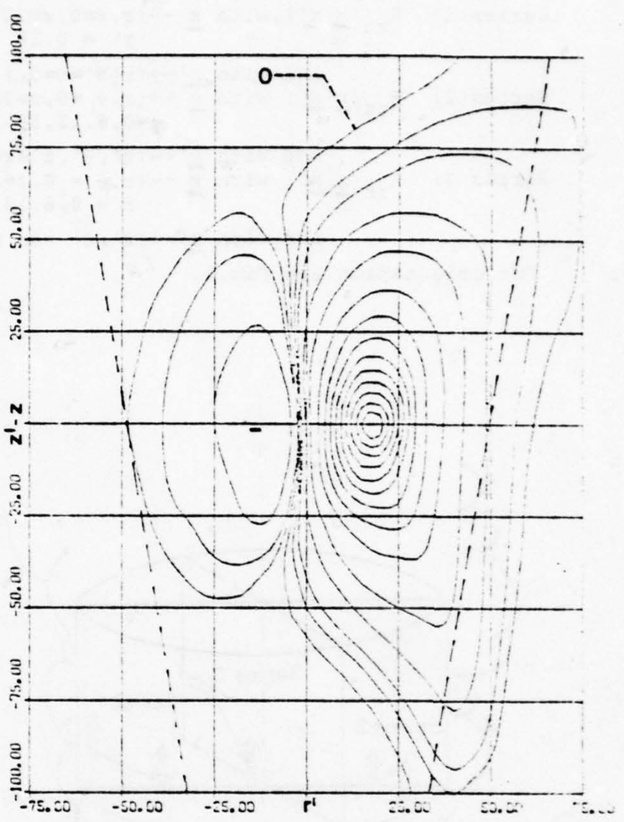

Figure 6: Correlation of the axial velocity at the point of maximum turbulent shear (r = 18 mm,z = 300mm) with the axial velocity at other points in the vertical plane defined by the fixed point and the jet axis: $R_{zz}(\underset{\sim}{x}|\underset{\sim}{x}')$, $(r,\theta,z)=(18,0,300)$, $(r',\theta',z')=(r',0,z')$

As the fixed point is moved radially outward, the eddy structure becomes longer and somewhat more diffuse, both in the radial and the axial directions, because there is less small structure to scramble the turbulence (Series 1). The negative troughs of R_{zz} that were symmetrically placed when the fixed point was on the axis(Fig.5) undergo dramatic changes when the fixed point is moved outwards. The negative trough on the axis side becomes deeper, as well as larger, whereas that in the intermittent region becomes extremely diffuse as attested to by the only other figure from this series (Fig.6), which was measured with the fixed point at the location of the maximum Reynolds' stress (r = 18).

It should be pointed out that the zero line, which may be quite sharply defined when it lies between well-defined positive and negative values, is not expected to be reliable at great distances from the fixed point; this comment applies to all figures. The $\gamma = 0.5$ line indicated on the figures is taken from Wygnanski and Fiedler, whose measurements in turn agreed with those of Corrsin and Kistler (9).

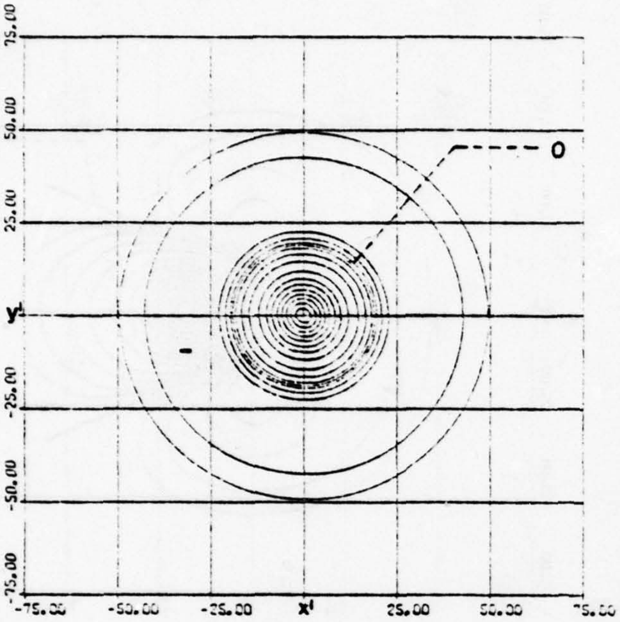

Figure 7: Correlation of the axial velocity on the jet axis with the axial velocity at other points in the same horizontal plane (z'=z=300mm): $R_{zz}(\underline{x}|\underline{x}')$, (x,y,z)=(0,0,300), (x',y',z')=(x',y',300)

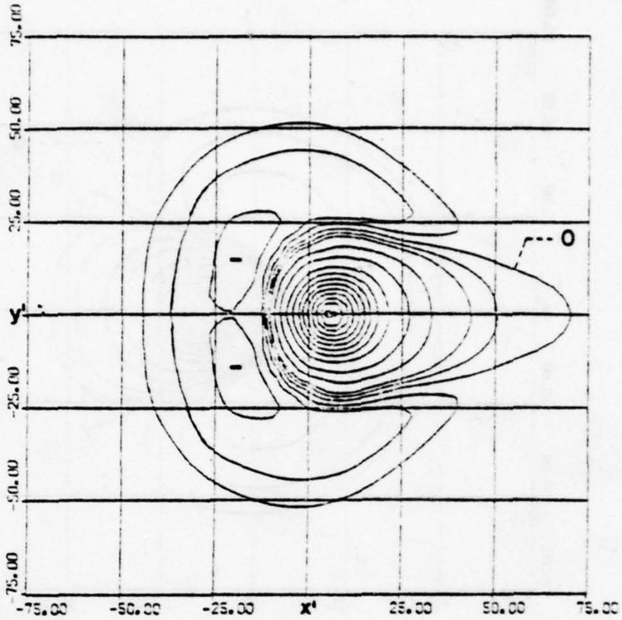

Figure 8: Correlation of the axial velocity at r = 6 mm with the axial velocity at other points in the same horizontal plane (z'=z=300 mm): $R_{zz}(\underline{x}|\underline{x}')$, (x,y,z)=(6,0,300), (x',y',z')=(x',y',300)

The correlations of the second series (see Fig.3) yield information about R_{zz} in the horizontal plane. The first figure (Fig.7) corresponds closely to the g-function of isotropic turbulence, as would be expected from axisymmetry. On the other hand, the locations of the zero circles and the (relative) depth of the negative "moat" that they delineate need not agree quantitatively with their isotropic counterparts. As the fixed point is moved radially outward in this series (Figs 8 to 11), the negative "moat" is "ruptured" and no longer fully encloses the positive massiv. The C-shaped negative portion of the correlation becomes both deeper and more diffuse, the further outward the fixed point is moved, just as the positive portion becomes more diffuse. The increased depth of the negative part is, however, bimodal rather than unimodal.

The R_{ij} (for i≠j) isotropic correlation is shown in Fig.12. The R_{zx} correlation in a vertical plane (see Fig.3) for the fixed point on the jet axis is topographically similar (Fig.13), which is presumably dictated by the zero value along the z-axis and along the x-axis (in fact, throughout the z'=z plane). It is clear, however, that this R_{zx} correlation (Fig.13) is distinct from its isotropic counterpart (Fig.12), above all by the absence in the former of symmetry about the $(2n-1)\pi/4$ lines in the (x,z) plane.

This lack of symmetry is, once again, due to the stretching in the downstream direction of the jet. As the fixed point is moved outward in Series 3, there is not a "continuous deformation" of Fig.13. Instead, the two positive lobes coalesce into a single positive massiv (Figs 14 and 15) and grow at the expense of the negative lobes, although all portions become more diffuse, as usual. It is interesting that the R_{zx} correlation at r=18 (Fig.15) resembles the R_{zz} correlation at r=0 (Fig.5), if the latter were rotated through a corresponding angle.

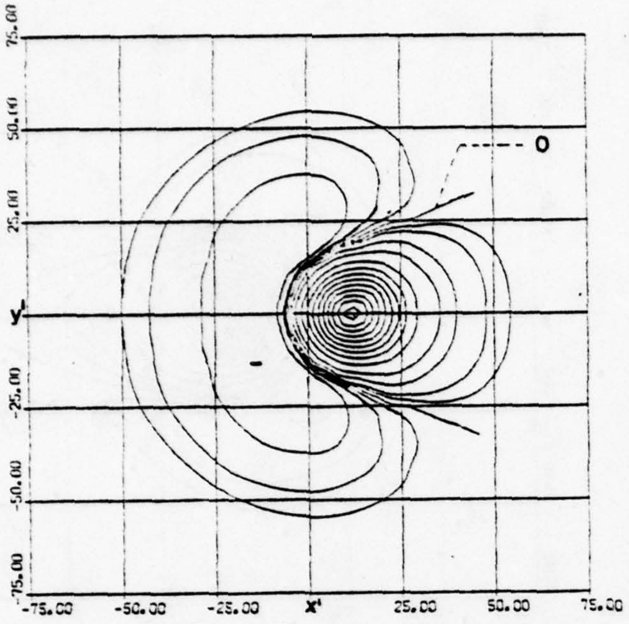

Figure 9: Correlation of the axial velocity at $r=12\text{mm}$ with the axial velocity at other points in the same horizontal plane ($z'=z=300\text{mm}$): $R_{zz}(\underset{\sim}{x}|\underset{\sim}{x}')$, $(x,y,z)=(12,0,300)$, $(x',y',z')=(x',y',300)$

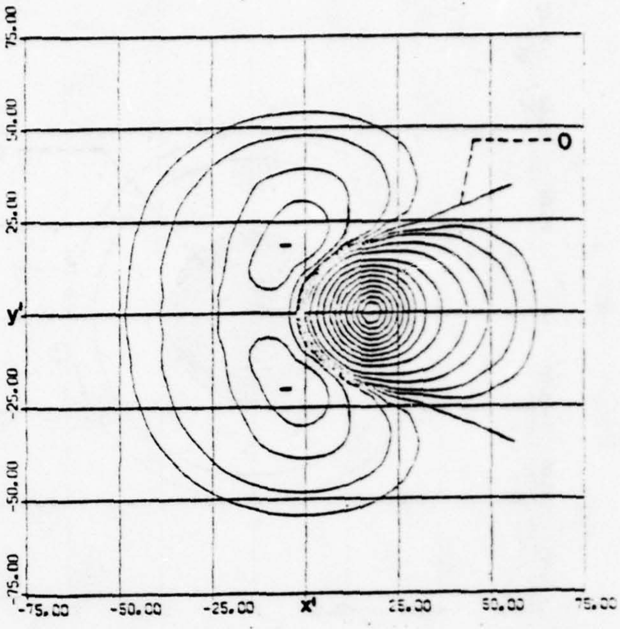

Figure 10: Correlation of the axial velocity at the point of maximum turbulent shear ($r=18\text{mm}$) with the axial velocity at other points in the same horizontal plane ($z'=z=300\text{mm}$): $R_{zz}(\underset{\sim}{x}|\underset{\sim}{x}')$, $(x,y,z)=(18,0,300)$, $(x',y',z')=(x',y',300)$

The correlation R_{zx} was chosen for presentation in Series 3 (Fig13-15) instead of R_{zr} in order to present a full vertical plane containing the jet axis. Although one could employ

$$u_x = \begin{cases} u_r, & \text{for } \theta = 0 \\ -u_r, & \text{for } \theta = \pi \end{cases}$$

to arrive at R_{zr}, it is an inherent feature of cylindrical coördinates that discontinuities arise at $r=0$. Thus, one may imagine leafing through a notebook of θ pages to emphasize how far removed $\theta = \pi$ is from $\theta = 0$. Or, expressed differently, $r \geq 0$ is a property of cylindrical coordinates, and we have put $\theta = 0$ and $\theta = \pi$ into juxtaposition, with the result that R_{zr} and its derivatives, as viewed in each of the corresponding versions of Figs 13-15 would appear to undergo a discontinuity.

The isocorrelation curves of Figs 5-11, 13-15 were produced as follows. The experimental data were taken along either a vertical or a horizontal straight line, so chosen that a maximum amount of information about the topography was obtained; in cases of doubt or when certain features required further illumination, additional lines were selected and further data were taken. Isocorrelation curves were drawn through these data. Although the curves for all figures were selected to have consistent corresponding altitudes, the values were expressed in volts. Upon conversion to velocity units and subsequently nondimensionalizing, however, inappropriate values for the altitudes were obtained. Consequently, programs were written to regenerate the figures with suitable isocorrelation values. A two-dimensional (spline) interpolation of correlation profiles on properly chosen sections of the original family of isocorrelations then yielded the present versions of the figures.

Because the original isocorrelation curves were drawn through the data, albeit smoothly, there is an associated error. Further, the interpolation scheme did not contain a smoothing procedure, which had several implications. There were slight abrupt corners

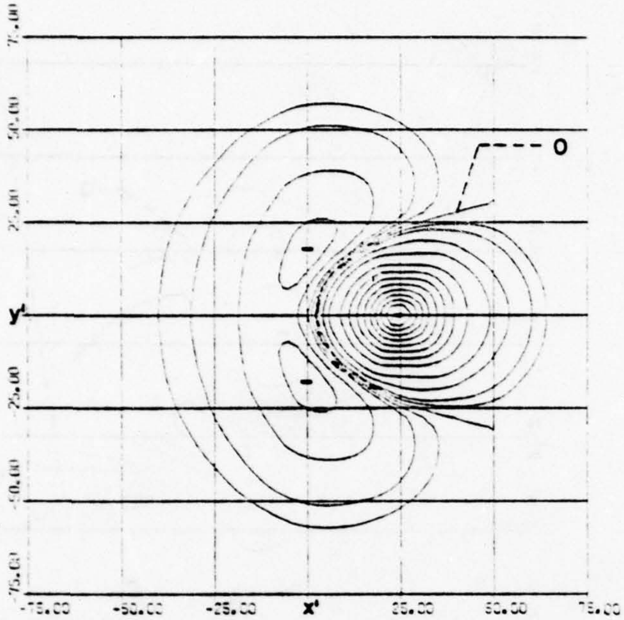

Figure 11: Correlation of the axial velocity at a point beyond the point of maximum turbulent shear (at r=24mm) with the axial velocity at the other points in the same horizontal plane (z'=z=300mm):
R_{zz} $(\underline{x}|\underline{x}')$, $(x,y,z)=(24,0,300)$
$(x',y',z')=(x',y',300)$

NB. The intermittency factor is 50% at r=48 mm.

and other noticeable irregularities in the isocorrelation curves. These could not be eliminated by employing spline-plot instead of line-plot, for ripples then appeared instead of corners and irregularities. Thus, although a spline-plot costed 100 times as much and produced a smooth isocorrelation, it did not produce a smoothed one. All figures were thus done with line-plot, and where such artifacts were especially displeasing to the eye, they were smoothed by hand. These small interpolation-plotting irregularities were, in any case, within the error bounds of the measurements and arose almost exclusively at small absolute values of the correlation, where it is well known that difficulties can arise (34).

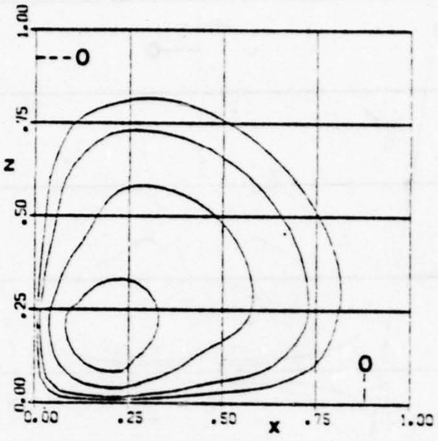

Figure 12: Isocorrelation curves for isotropic turbulence:
$R_{zx}(\underline{r})$, $\underline{r} \leftrightarrow (x,0,z)$

Here and in Figs 13-15, the isocorrelations are measured in the positive direction from the zero isocorrelation in the following increments : 0.01, 0.02, 0.05, 0.1, 0.15, 0.2, 0.25, 0.3, 0.35. In the negative direction the increments are : -0.01, -0.02, -0.05 -0.1. Distances are in arbitrary units.

REFERENCES

1. Abramovich, G.N. 1963 The Theory of Turbulent Jets MIT Press, Cambridge, Mass.
2. Hinze, J.O. 1959 Turbulence, McGraw-Hill, New York.
3. Tennekes, H. and Lumley, J.L. 1972 A First Course in Turbulence, MIT Press, Cambridge, Mass.
4. Townsend, A.A. 1976 The Structure of Turbulent Shear Flow (2nd ed.) Cambridge University Press, London.
5. Corrsin, S. 1943 NACA Wartime Report, No. 94.
6. Corrsin, S. 1957 Nat.Acad.Sci.Naval Hydrodyn. Publ.515.
7. Corrsin, S. and Uberoi, M. 1949 NACA TN 1865.
8. Corrsin, S. and Uberoi, M. 1951 NACA Report 1040.
9. Corrsin, S. and Kistler, A.L. 1955 NACA Report 1244.
10. Hinze, J.O. and Van der Hegge Zijnen, B.G. 1949 Appl.Sci.Res. 1a, 435.
11. Laurence, J.C. 1957 NACA Report 1292.
12. Gibson, M.M. 1963 J.Fluid Mech. 15, 161.
13. Sami, S. 1967 J.Fluid Mech. 29, 81.
14. Sami, S. Carmody, T. and Rouse, H. 1967 J.Fluid Mech. 27, 231.

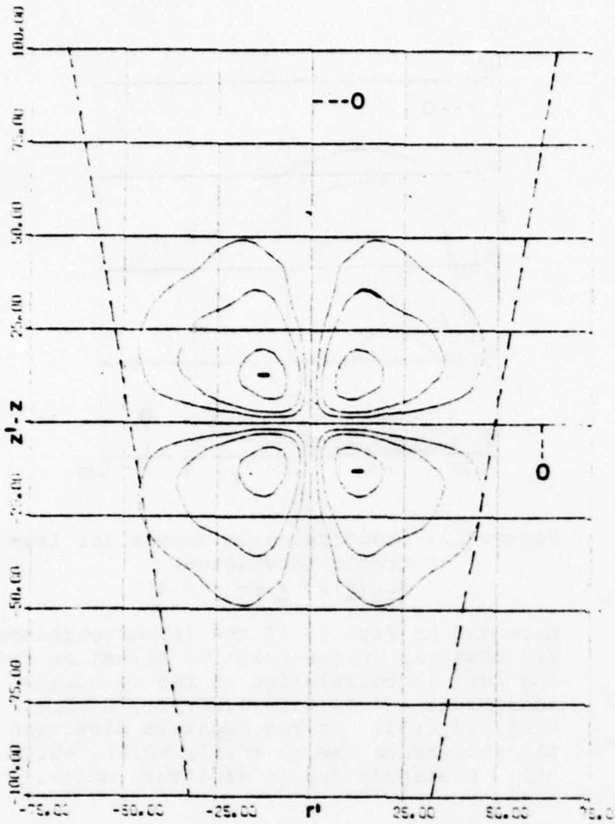

Figure 13: Correlation of the axial velocity on the jet axis (z=300m) with the horizontal velocity components at other points in the same vertical plane containing the axis: $R_{zx}(x|x')$, $(r,\theta,z)=(0,0,300)$ $(r',\theta,z')=(r',0,z')$

REFERENCES (continued)

15. Miller, D. R. and Comings, E.W. 1957 J. Fluid Mech. 3, 1.
16. Wills, J.A. 1964 J.Fluid Mech. 20,417.
17. Willmarth, W.W. and Wooldridge, C.E. 1962 J. Fluid Mech. 14, 187.
18. Davies, P.O.A.L., Fisher, M.J. and Barratt, M.J. 1963 J.Fluid Mech. 15, 337.
19. Crow, S.C. and Champagne, F.H. 1971 J. Fluid Mech. 48, 547.
20. Ffowcs Williams, J.E., Leppington, F.G., Crighton, D.G., and Levine, H. 1972 Aero.Res.Counc.Current Paper, no. 1195.
21. Batchelor, G.K. 1953 The Theory of Homogeneous Turbulence, Cambridge University Press, London.

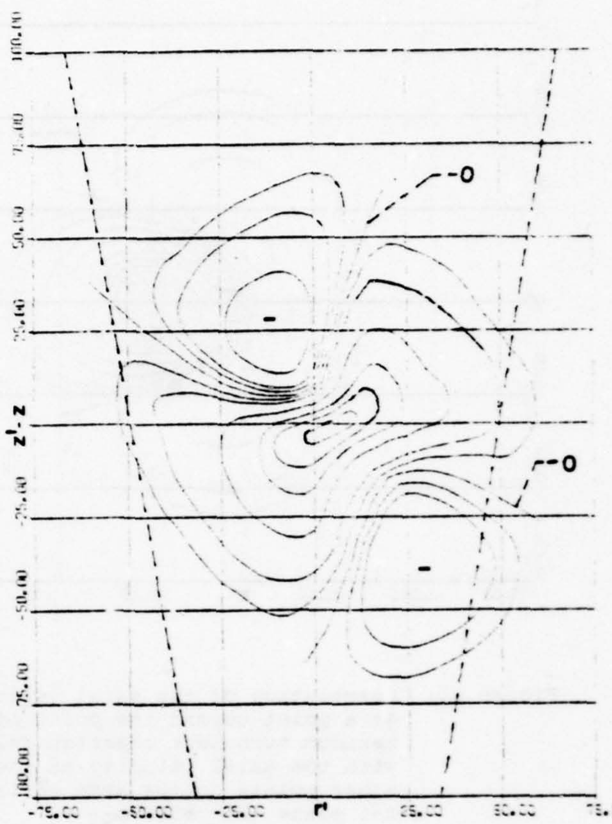

Figure 14: Correlation of the axial velocity at a point off the jet axis (r=6mm, z=300mm) with the horizontal velocity component at other points in the vertical plane defined by the fixed point and the axis: $R_{zx}(\underline{x}|\underline{x}')$, $(r,\theta,z)=(6,0,300)$, $(r',\theta',z')=(r',0,z')$

REFERENCES (continued)

22. Townsend, A.A. 1947, 1949 Proc.Roy.Soc. A190, 551, A197, 124; 1949 Aust.J.Sci.Res. 2, 451.
23. Townsend, A.A. 1966 J. Fluid Mech. 26, 689.
24. Grant, H.L. 1958 J. Fluid Mech. 4, 149.
25. Batchelor, G.K. 1949 Proc.Roy. Soc. A195, 513.
26. Batchelor, G.K. and Proudman, I. 1956 Philos.Trans. A248, 369.
27. Lumley, J.L. 1967 Proc. Int.Colloq.on the Fine Scale Structure of the Atmosphere and its Influence on Radio Wave Propagation (Dokl.Akad.Nauk. SSSR), p.166.

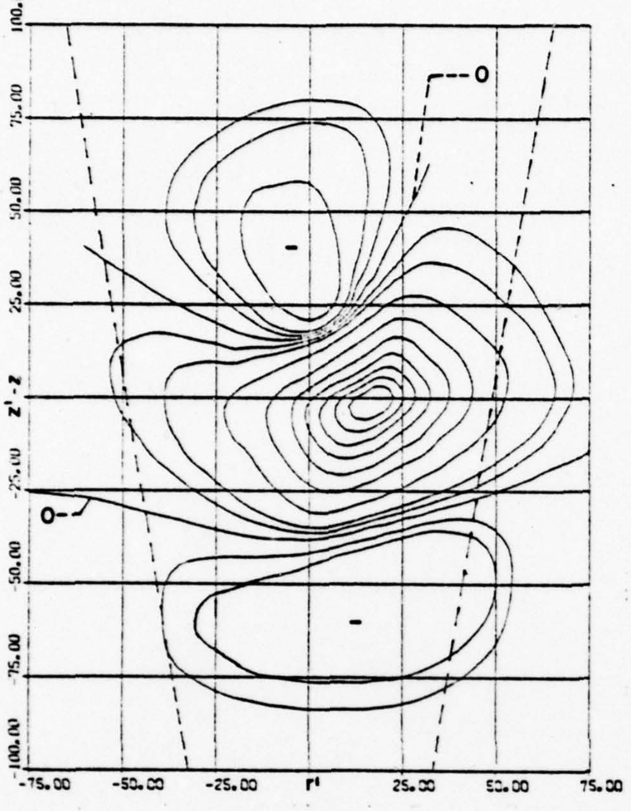

Figure 15: Correlation of the axial velocity at the point of maximum turbulent shear (r=18mm, z=300) with the horizontal velocity at other points in the vertical plane defined by the fixed point and the jet axis :
$R_{zx}(\underline{x}|\underline{x}'),\ (r,\theta,z)=(18,0,300),$
$(r',\theta',z')=(r',0,z')$

REFERENCES (continued)

28. Payne, F.R. and Lumley, J.L. 1967 Phys.Fluids Supplement - Boundary Layers and Turbulence, S 194.

29. Bakewell, H.P. and Lumley, J.L. 1967 Phys. Fluids 10, 1880.

30. Kovasnay, L.S.G., Kibens, V. and Blackwelder, R.F. 1970 J. Fluid Mech. 41, 283.

31. Wygnanski, I. and Fiedler, H. 1969 J.Fluid Mech. 38, 577.

32. Comte-Bellot, G. and Corrsin, S. 1971 J.Fluid Mech. 48, 273.

33. Durst, F., Melling, A., and Whitelaw,J.H. 1976 Principles and Practice of Laser-Doppler Anemometry, Academic, London.

34. Bendat, J.S. and Piersol, A.G. 1966 Measurement and Analysis of Random Data, Wiley,New York.

We are indebted to the Swiss Nationalfond for their support of this research.

PRECEDING PAGE BLANK-NOT FILMED

IMPINGING AXISYMMETRIC TURBULENT FLOWS: THE WALL JET, THE RADIAL JET AND OPPOSING FREE JETS

P. O. Witze
Sandia Laboratories
Livermore, California

H. A. Dwyer
Department of Mechanical Engineering
University of California, Davis

ABSTRACT

The results of an experimental and analytic study of impinging axisymmetric turbulent flows are presented. Three impinging-flow configurations are considered: a single axisymmetric turbulent jet impinging normal to a plate; two directly-opposing axisymmetric turbulent jets of equal momentum flux impinging against each other; and a constrained radial jet as produced by the radial flow from an annular orifice formed by two parallel circular disks. The purpose of the investigation is to characterize the structure of these flows, with the goal of identifying and analytically modeling the regions of physically similar flow behavior. The parameters of interest are the nozzle diameter, nozzle separation distance and the jet exit velocity. Hot-film anemometer measurements are presented for the mean velocity and turbulence intensity in the streamwise direction. Analytical models with varying degrees of empiricism are then used to describe the experimental results.

NOMENCLATURE

b = shear layer half-width, where $U = U_o/2$
m = spreading-rate of shear layer half-width
r = radial-direction coordinate
r_c = radius of radial jet core
r_j = nozzle radius
r_v = virtual origin radius of constrained radial jet
u' = streamwise direction turbulence intensity
U = streamwise direction mean velocity
V = lateral direction mean velocity
x = axial-direction coordinate
x_c = jet core length
x_v = axial distance measured from jet virtual origin
y = lateral-direction coordinate
y_j = distance from the nozzle exit to the impingement plane of impinging jets; nozzle half-width of constrained radial jets
y_v = distance from the jet virtual origin to the impingement plane
ρ = coordinate in a circular pipe
Λ = U_r/U_m for wall jet
λ = b_m/b_r for wall jet

Subscripts

m = conditions where the velocity is maximum
o = conditions on jet centerline
r = conditions for a wall jet as referenced to a radial jet

CHARACTERISTIC STRUCTURE

The coordinate system and nomenclature to be used to describe impinging axisymmetric jets is shown in Fig. 1. The flow field can be subdivided into three zones, the first being that of a free axisymmetric jet. In this zone the flow is unaffected by the presence of the opposing jet or wall, such that conventional free jet theory can be used. The second zone is the impingement region, in which pressure gradients come into play as the flow decelerates, changes direction, and then accelerates radially outward as either a radial or wall jet, which constitutes the third zone.

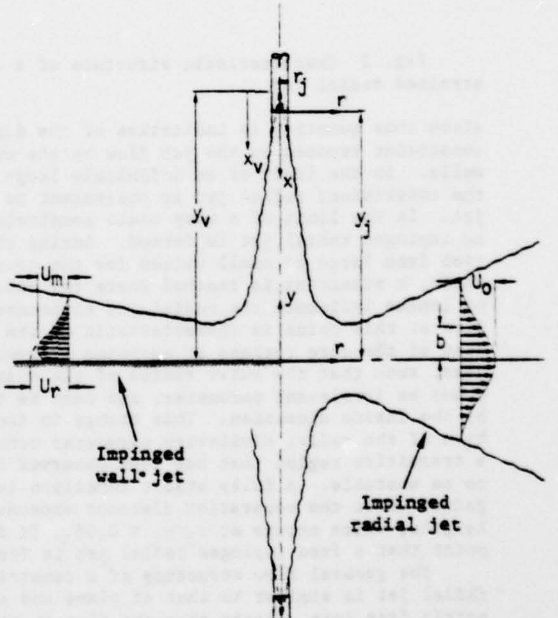

Fig. 1 Characteristic structure of opposing free jets and the impinging wall jet

Poreh and Cermak (1) have shown that the dimensionless parameters $(U_o/U_j)(y_v/r_j)$ and (x_v/y_v) characterize the mean velocity along the centerline of a jet impinging normal to a plate. The present study will show that these parameters also characterize the flow between two opposing free jets.

The impinged radial jet depicted in Fig. 1 is a special limiting case of a family of radial jet flows. If opposing axisymmetric nozzles are brought very close together, such that the separation distance is small relative to the thickness of the nozzle walls, a constrained radial jet is formed, as illustrated in Fig. 2. This represents another limiting form of radial jets, and is the axisymmetric counterpart of the more familiar plane jet. Unique to radial jets in general, however, is the appearance of a second geometric-similarity parameter. For the constrained radial jet this additional dimension is the nozzle radius r_j, where the nozzle half-width y_j is analogous to the typical characteristic nozzle dimension of orifice size. The ratio of these geometric factors r_j/y_j will be termed the "constraint ratio", since this quantity is indicative of the degree of constraint imposed on the jet flow by the nozzle walls. In the limit of an infinitely large radius, the constrained radial jet is equivalent to a plane jet. In the limit of a very small constraint ratio, an impinged radial jet is formed. During the transition from large to small values for the constraint ratio, a situation is reached where the nozzle walls no longer influence the radial-jet structure. The flow at this point is characteristic of the collision of the core regions of opposing axisymmetric jets, such that the outer radius of the nozzles becomes an irrelevant parameter, and must be replaced by the inside dimension. This change in the definition of the radial similarity parameter occurs during a transition region that has been observed by Luna (2) to be unstable. A fully stable condition is not regained until the separation distance exceeds two core lengths, which occurs at $r_j/y_j \approx 0.06$. It is at this point that a free impinged radial jet is formed.

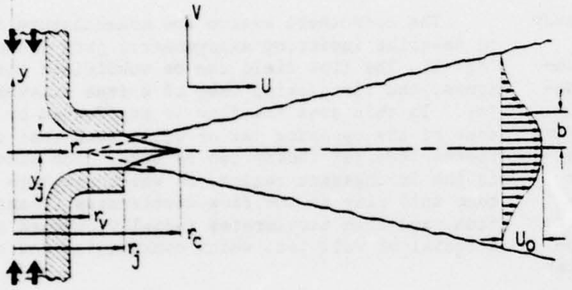

Fig. 2 Characteristic structure of a constrained radial jet

The general flow structure of a constrained radial jet is similar to that of plane and axisymmetric free jets, except that the flow in the constant-velocity inviscid core is not parallel, owing to the form of the continuity equation in cylindrical coordinates. For the radial-jet equations to be self-similar, Rodi (3) has shown that it is a necessary condition that db/dr, $(b/U_o)dU_o/dr$, and b/r all be constant. The first two criteria are comparable to the conditions necessary for self-similar plane and axisymmetric jet solutions, and are satisfied when $b \sim r - r_v$ and $U_o \sim 1/(r - r_v)$. The third criterion is unique to the radial jet, and requires that $r_v = 0$. Thus self-similar radial-jet equations can exist only for the special case where the virtual origin of the jet is located on the axis of symmetry, or in the limit where $r \gg r_v$. This is a significant result, since for a typical constrained radial jet $r_v \approx r_j$, although it will be shown that the singular occurrence of $r_v = 0$ can be achieved in the limit $r_j/y_j \to 0$, which is the case of the impinged radial jet. The condition that $r_v = 0$ is therefore a necessary condition for the occurrence of what might be called an "ideal" radial jet, implying that the jet is both well behaved and analytically self-similar.

The fact that the constrained radial jet is not a self-similar flow precludes the possibility of a purely analytic solution. However, experimental results to be presented below do provide the necessary information for an empirical analysis. It will be shown that the radial-jet half-width does grow linearly from the virtual origin, such that

$$b = m(r - r_v) \tag{1}$$

and that the velocity profiles across the shear layer have a self-similar form that can be expressed as

$$U/U_o = \text{sech}^2(0.881\ y/b) \tag{2}$$

Then, for conservation of total momentum it follows that

$$\frac{U_o}{U_j} = \sqrt{\frac{1.32\ r_j y_j}{mr(r - r_v)}} \tag{3}$$

for which there are two empirical quantities to be determined, m and r_v. However, it will be shown that, for well-designed nozzles producing constrained radial jets where the exit velocity from the orifice is *parallel, m is a universal constant having the value* 0.106; and for large values of r/y_j, $r_v \approx r_j$.

Wall Jet

The impinged wall jet differs from the impinged radial jet only in the nature of the boundary condition at the impingement plane. The flow can be idealistically described as emanating from a point source located on a flat surface, having an initial velocity component in the radial direction only. In practice, wall jets are formed by either impinging a free jet against a surface, or by injecting fluid out from the annular slot between a circular plate and a parallel flat surface. The flows created by these two means can be classified as impinged and constrained wall jets, respectively.

An analytic treatment of the turbulent wall jet was first given by Glauert (4), in which he subdivided the flow into two distinct regions. For the region near the wall he employed an eddy viscosity distribution that is consistent with the 1/7 power-law velocity profile; for the outer-flow region Prandtl's constant exchange coefficient eddy viscosity model was used. The resulting expression for the maximum velocity in the wall jet profile was

$$U_m \sim r^{-1.14} \tag{4}$$

and for the half-width of the jet,

$$b \sim r^{1.015} \tag{5}$$

Since the centerline velocity of an ideal radial jet decays as 1/r, the increase in decay rate expressed by Eq. (4) can be directly attributed to the wall shear stress. It is also significant to note that the virtual origin of the wall jet is found to occur at the axis of symmetry.

A summary of the velocity decay and spreading rates measured by several other authors is given in Table 1. Bakke (5) is the only one of those shown to have used a constrained wall jet. His results indicate no unique behavior when compared to the other impinged wall jet results. This can be explained by the constrained radial jet results to be presented in a later section: for Bakke's apparatus, $r_j/y_j = 4.20$, which is too small a constraint ratio to classify his wall jet as truly being "constrained".

Generalized Equations:	Half-Width $\frac{b}{L} = m\left(\frac{r}{L}\right)^p$		Maximum Velocity $U_m \sim (r)^{-q}$	
Experimenter	**L**	**m**	**p**	**q**
Glauert (4)	1	---	1.015	1.14
Bakke (5)	1	0.105	0.94	1.12
Brady and Ludwig (6)	r_j	0.062	1.028	1.143
Poreh, et al. (7)	y_v	0.098	0.90	1.10
Hrycak, et al. (8)	$2r_j$	*	0.95	1.12
Govindan & Subba Raju (9)	y_v	0.089	0.915	1.122† 1.238
Present Study	y_v	0.0946	1.01	1.12

* $m = 0.000405\ y_v/r_j + 0.0864$

† For $y_v/r_j < 16$ and $y_v/r_j > 16$, respectively

Table 1 Summary of wall jet experimental results

An approach to the wall jet less involved than Glauert's has been taken by Poreh and Cermak (1) and Abramovich (10), whereby they basically neglect the wall boundary layer, treating the flow as a hypothetical radial jet. An artificial reference velocity, U_r, is defined by extrapolating the velocity profile of the outer flow inward to the wall. It is then postulated that this reference velocity will behave like the centerline velocity of a free radial jet, with

$$\left(\frac{U_r}{U_j}\right)\left(\frac{y_v}{r_j}\right) \sim \left(\frac{y_v}{r}\right) \qquad (6)$$

where the previously given correlation parameters for the impinging jet region have been used.

Poreh and Cermak's experimental results tend to confirm Eq. (6), which is interesting in that the reference velocity U_r is found to decay at a slower rate than the maximum velocity U_m as measured by other authors. This result is supported by the observations of Hrycak, et al., (8) who found that

$$U_m \sim r^{-1.12} \quad \text{and} \quad U_r \sim r^{-1.00}$$

where the same set of experimental data was used to determine both relationships. Because U_r and U_m have different dependencies on the radial distance, then so must the half-width, such that b must be further delineated as being either b_r or b_m. Therefore, for a consistent pair of similarity parameters to exist, $U_r = \Lambda U_m$ and $b_r = b_m/\lambda$, where Λ and λ are proportionality constants. Taking Eq. (2) for the velocity profile in a radial jet, this gives

$$U/U_m = \Lambda\ \mathrm{sech}^2(0.881\ \lambda y/b_m) \qquad (7)$$

and it can further be shown that

$$\lambda = \ln(\sqrt{2\Lambda} + \sqrt{2\Lambda - 1})/0.881 \qquad (8)$$

EXPERIMENTAL RESULTS

A wide range of experimental conditions were included in this study, as summarized in Table 2. The jet flows were formed by commercial-grade dry air supplied from standard compressed-gas bottles. A laser beam was used to align the nozzles in the opposing free jet configuration. The mean velocity measurements were taken with a linearized constant-temperature anemometer. The linearizer output was digitized and processed with an on-line PDP-8 minicomputer. A single-sensor, hot-film probe was used throughout, oriented normal to the streamwise direction. This choice excluded the possibility of determining the lateral velocity component, which for impinged radial jets was found to be significantly large. However, because the relative turbulence intensity was also large, it is believed that the added sensitivity that an inclined sensor would have to the third fluctuating velocity component would seriously impair the accuracy of two-component measurements.

Constrained Radial Jet	U_j (m/s)	r_j (cm)	r_v (cm)	y_j (cm)†
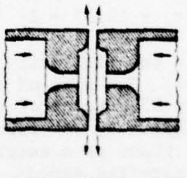	60.7	1.59	‡	0.0186
	30.5	1.59	1.46	0.02§
	30.8	1.59	1.52	0.0414
	30.2	1.59	1.57	0.0665
	29.6	1.59	1.58	0.0919
	30.5	3.18	3.15	0.0148*
	26.8	3.18	2.97	0.0363
Opposing Free Jets				
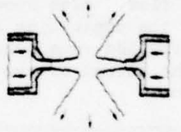	30.8	0.30	13.3	12.7
	30.5	0.30	10.2	9.53
	30.5	0.30	6.99	6.35
	61.3	0.30	13.3	12.7
	30.8	0.43	9.86	8.97
Impinging Wall Jet				
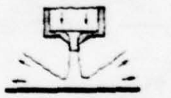	30.5	0.30	10.2	9.53

† Corrected for nozzle wall boundary-layer effects.

‡ Not measured. Assumed to be 1.46 cm.

§ Empirically selected because of non-analytic nozzle-wall boundary layer.

* Fully developed channel flow.

Table 2 Summary of experimental conditions

For a major portion of the shear flows studied, relative turbulence intensities were found to be in excess of 20 percent, at which point the nonlinear response of the anemometer to large directional fluctuations in velocity produces a systematic error. Additionally, when the turbulence intensity exceeds about 30 percent, there is a finite probability of a reversal in flow direction; this condition cannot be detected by the probe, and thus another systematic error results. While it is admittedly not possible to make accurate corrections for these conditions when the turbulence becomes too high, some improvement can be achieved in the mean velocity by applying the correction proposed by Corrsin (11). The corresponding error in the measurement of the turbulent fluctuation has been shown by Parthasarathy and Tritton (12) to be small for a linearized anemometer.

An experimental difficulty was encountered in the occurrence of a significant boundary layer on the inner walls of the jet nozzles. Since this manifests itself as a net mass and momentum deficit of the jet flow, techniques had to be developed to correct for the wall boundary-layer effect. For further details, see Witze (13).

Impinging Axisymmetric Jets

Velocity measurements taken along the centerline of opposing free jets are presented in Fig. 3. The theoretical curve shown is that of Warren (14), where

$$U_o/U_j = [0.0708\ (x/r_j - 12.5) + 1]^{-1} \qquad (9)$$

The data correlate well with the similarity parameters proposed by Poreh and Cermak. The size of the interaction zone is approximately 15 percent of the nozzle separation distance. The indicated non-zero mean velocity at the impingement plane is a result of directional ambiguity of the hot-film sensor. Turbulent fluctuations at the stagnation point are erroneously being interpreted as a mean flow. Also shown in Fig. 3 are measurements taken on the centerline of a jet striking a plate. The interaction zone size is apparently independent of the nature of the impingement plane boundary condition.

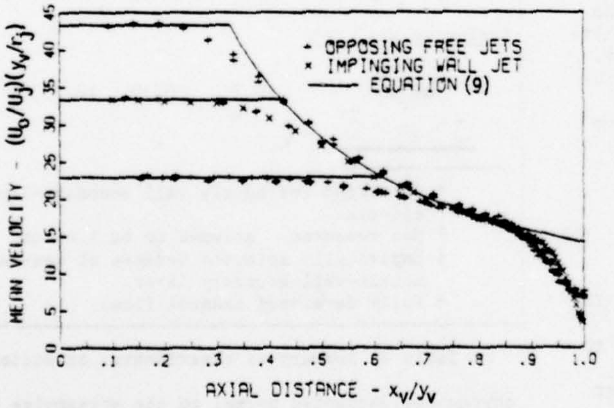

Fig. 3 Centerline velocity in impinging jets

The relative turbulence intensity measurements corresponding to the conditions presented in Fig. 3 are given in Fig. 4. For opposing free jets the data correlate closely within the interaction zone, confirming again the choice of similarity parameters. The turbulence intensities do not correlate in the free axisymmetric jet region because the parameter along the abscissa is incorrect for an unopposed jet, which would be x_v/r_j.

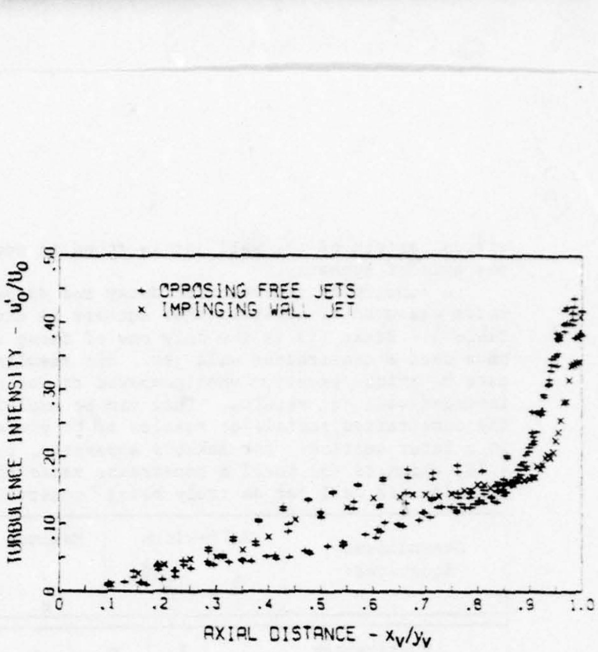

Fig. 4 Centerline turbulence intensity in impinging jets

Unlike the mean velocity results, the size of the turbulent interaction zone is clearly a function of the impingement plane boundary condition. For opposing jets the zone is the same size as for the mean velocity, at 15 percent of the half-separation distance, whereas the impinging wall jet zone is about 10 percent.

Radial Jets and the Wall Jet

Mean velocity profile data for a typical nozzle configuration producing a constrained radial jet are shown in Fig. 5, compared with the self-similar velocity profile given by Eq. (2). While the measured values are clearly self-similar, it is also evident that theory underpredicts the data by a considerable amount in the outer region. The apparent asymptotic trend of the data toward a non-zero edge velocity is due to the presence of a measurable lateral velocity component. This is a reasonable conclusion, since the orientation of the hot-film probe was such that the sensor was perpendicular to the (r,y)-plane, and thus responded to the total velocity vector $U_{meas} = (U^2 + V^2)^{1/2}$. Using the continuity equation, it can be estimated that $V/U_o \approx -0.12$ at the outer edge of the shear layer, which is very close to the magnitude of the asymptotic value indicated in Fig. 5.

Mean velocity profile data for a typical impinged radial jet are also shown in Fig. 5. Again, it is seen that the profiles are of a self-similar form, although there is considerably more scatter in the data than in the constrained-jet case. There is also some indication of an inexplicable dip in the profile at $y/b \approx 0.7$. Additionally, owing to the higher entrainment rate of the impinged jet, the disagreement between data and theory at the outer edge due to the lateral velocity component is even more pronounced.

Mean velocity profiles across the wall jet measured at four radial stations are shown in Fig. 6, where it is seen that the flow is self-preserving. Comparison with Glauert's theoretical curve (for Glauert's $\alpha = 1.3$) shows reasonable agreement between theory and data except in the wall boundary layer region. The less-full profile indicated by the data is most likely due to a non-fully-developed turbulent wall boundary layer. Comparison of data with the free radial jet profile as expressed by Eq. (7) also shows good agreement, with $\Lambda = 1.20$ such that $\lambda = 1.14$. Since only one nozzle radius and one nozzle-to-plate separation distance were used for the experiments, it is not known whether Λ is a universal constant.

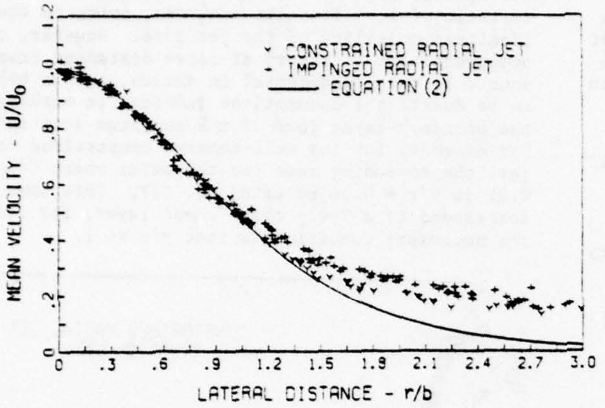

Fig. 5 Velocity profile in radial jets

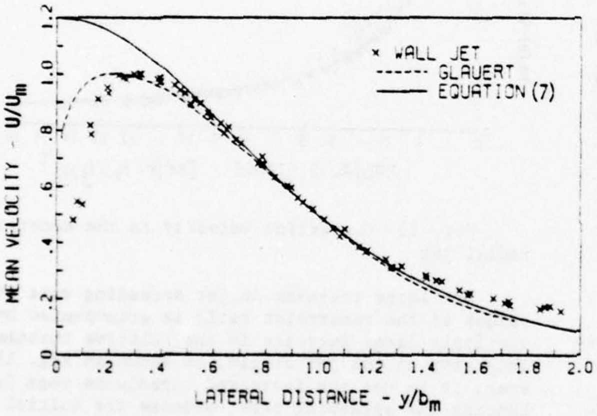

Fig. 6 Velocity profile in the wall jet

The turbulence intensity data corresponding to the mean velocity profile data just presented are given in Fig. 7. (The wall jet lateral distance has been normalized by b_m.) The constrained radial jet and wall jet profiles are quite similar, both peaking at $y/b \approx 1.5$. It should be pointed out that much of the indicated scatter in the profile data is due to a lack of similarity between different axial positions. Refer to Refs. (13) or (15) for a more explicit presentation of the turbulence profile data.

Radial jet half-widths are shown in Fig. 8 as determined from the profile measurements. The origin of each of the curves shown is approximately at the nozzle radius, such that the value of the abscissa at the origin is representative of the constraint ratio. A constant spreading rate of $m = 0.106$ is seen to exist for large constraint ratios, whereas, if the constraint ratio is reduced, the spreading rate increases until the impinged-radial-jet limit of $m = 0.37$ is reached. The limit of an infinite constraint ratio corresponds to a plane jet, for which Newman (16) has determined an average value of $m = 0.104$, based on a comprehensive review of the experimental literature up to 1965.

Also shown in Fig. 8 are the half-width measurements determined for the wall jet, for which it was found that

$$b/y_v = 0.0946\ (r/y_v)^{1.01} \tag{10}$$

Within the scope of the experiment the half-width is virtually linear with distance from the axis of symmetry, with a growth rate that is just slightly smaller than that found for the constrained radial jet.

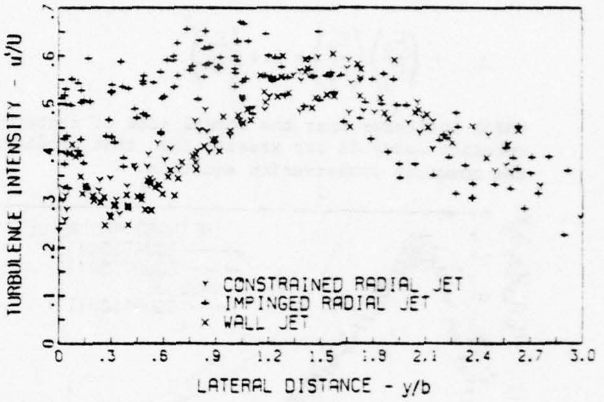

Fig. 7 Turbulence intensity profiles in impinged jets

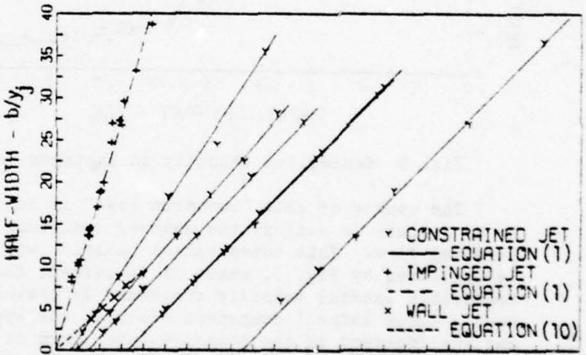

Fig. 8 Half-width of impinged jets. The ordinate and abscissa are ×100 for the impinged radial jet and wall jet data

Mean velocity measurements taken along the impinged radial jet centerline are shown in Fig. 9. The measured velocity in the stagnation region is known to be in error, as the stagnation-point velocity should be zero. The form of the similarity parameters is significant in that they are characteristic of the free-axisymmetric-jet conditions at the point of impact.

It has been shown that two of the requirements for self-similarity are satisfied by the impinged radial jet; namely, that the shear layer should grow linearly from a virtual origin located at $r = 0$. The remaining condition is that the centerline velocity should decay inversely with radial distance, which is a result of the condition that radial momentum be conserved. If it is assumed that the impinged radial jet's total radial momentum is equal to the sum of the momentum fluxes from the opposing axisymmetric nozzles, it can be shown that

$$\left(\frac{U_o}{U_j}\right)\left(\frac{y_v}{r_j}\right) = 1.89\left(\frac{y_v}{r}\right) \tag{11}$$

where Eq. (2) has been used for the velocity profile, with m = 0.37. This result is shown compared with centerline velocity data in Fig. 9. It is evident that Eq. (11) severely overpredicts the momentum in the flow. This discrepancy is due to more than just the assumed level of total momentum, however, since a nonlinear least-squares fit to the data results in

$$\left(\frac{U_o}{U_j}\right)\left(\frac{y_v}{r_j}\right) = 0.4\left(\frac{y_v}{r}\right)^2 \qquad (12)$$

which indicates that the actual rate of centerline velocity decay is far greater than that predicted by the momentum conservation equation.

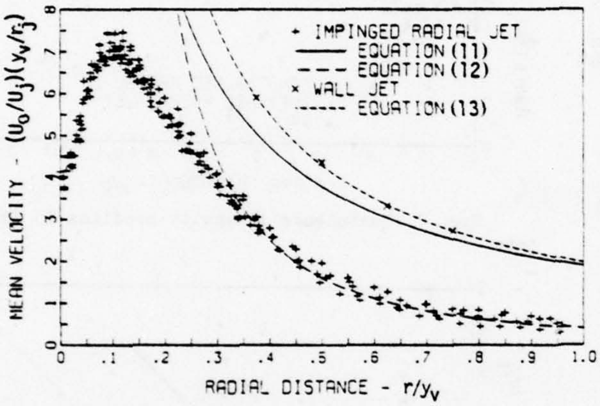

Fig. 9 Centerline velocity in impinged jets

The source of this "momentum loss" is believed to be failure to satisfy the assumed condition of parallel flow. This non-parallel behavior was clearly indicated by Fig. 5, where it is evident that a measurable lateral velocity component is present. Such a large lateral component violates the approximations inherent in the boundary-layer form of the governing equations used to model the flow. Indeed, a complete reassessment of the full Navier-Stokes equations is necessary, since additional terms corresponding to the high turbulence levels may also need to be retained.

Also shown in Fig. 9 is the maximum mean velocity in the wall jet, for which it was found that

$$\left(\frac{U_m}{U_j}\right)\left(\frac{y_v}{r_j}\right) = 1.97\left(\frac{y_v}{r}\right)^{1.12} \qquad (13)$$

where both the proportionality constant and the exponent were determined directly from the data. The value for the exponent is in close agreement with other reported values in Table 1.

Experimental measurements of centerline velocities in constrained radial jets are shown in Fig. 10. The similarity parameter used along the abscissa includes two empirically determined quantities, these being the spreading rate and virtual-origin location. The theoretical curve shown in the figure was computed using Eq. (3), where the core length is found from the condition that $U_o/U_j = 1$, giving

$$r_c = \frac{1}{2}\left[r_v + (r_v^2 + 5.29\ r_j y_j/m)^{1/2}\right] \qquad (14)$$

Agreement between data and theory is reasonably good, although in general the prediction is high. Within the initial region, this type of disparity is characteristic of most free-jet analyses, owing to the idealized modelling of the jet core. However, the overprediction of theory at large distances from the source is more fundamental in nature, and is believed to be due to the assumptions inherent in working with the boundary-layer form of the momentum equations. For example, for the well-behaved constrained radial jet, the spreading rate for the point where $U/U_o = 0.01$ is $y/r = 0.36$ by using Eq. (2). This does not correspond to a "very thin" shear layer, for which the necessary condition is that $y/r \ll 1$.

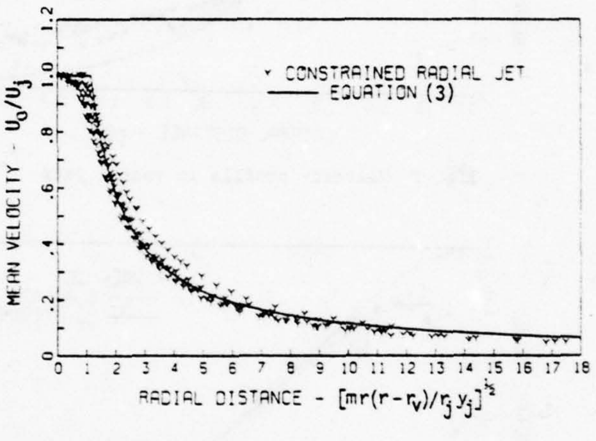

Fig. 10 Centerline velocity in the constrained radial jet

The large increase in jet spreading rate at small values of the constraint ratio is accompanied by a similarly large increase in the relative turbulence intensity at the jet origin, as shown in Fig. 11. However, it is not the increased turbulence that is enhancing the spreading rate, because the initial turbulence intensity levels at a jet's source do not influence the final self-preserving form of the shear layer, other than the location of the virtual origin. This is indicated by the asymptotic behavior of the relative intensity data, which are seen to converge to a value of approximately 32 percent, irrespective of the initial turbulence levels.

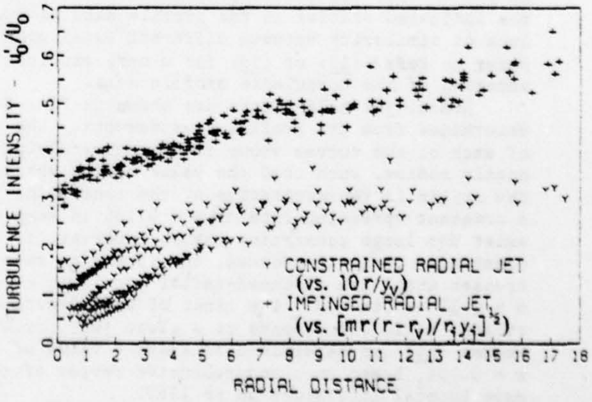

Fig. 11 Turbulence intensity in radial jets

Because the spreading rate does correlate with the nozzle constraint ratio, but not with the initial turbulence level, it can be concluded that the non-parallel nature of the initial jet conditions must be the property characterizing non-ideal radial-jet behavior. This hypothesis is consistent with the observed universal spreading rate of impinged radial jets, since it can be argued that colliding self-similar axisymmetric jets will produce self-similar radial-jet initial conditions that are both non-parallel and independent of the separation distance. Thus it is only when constraining nozzle walls are introduced that the self-similar initial conditions of impinging jets become altered, to the point that in the limit of large constraint ratios the initial flow becomes parallel, and a well-behaved constrained radial jet results.

CONCLUSIONS

The results of an experimental and analytic study of impinging axisymmetric turbulent flows have been presented. Three impinging-flow configurations were considered: a single axisymmetric turbulent jet impinging normal to a plate; two directly-opposing axisymmetric turbulent jets of equal momentum flux impinging against each other; and a constrained radial jet as produced by the radial flow from an annular orifice formed by two parallel circular disks.

A geometric parameter termed the constraint ratio, defined as the ratio of nozzle diameter to separation distance, has been shown to characterize radial-jet behavior. Large values of the constraint ratio typify "constrained" radial jets, for which the nozzle walls constrain the flow leaving the orifice to be parallel; a small constraint ratio is representative of two opposing free axisymmetric jets, the collision of which produces an "impinged" radial jet. It has been found that the well-behaved constrained radial jet spreads at the same rate as does the familiar plane jet, whereas the impinged radial jet spreads at a rate more than three times as fast. Neither type of radial jet is amenable to a self-similar analytic solution; however, while the impinged jet has been shown to require numerical solution techniques, an empirical solution for the constrained jet has been demonstrated.

A comparison between the impinged radial jet and an impinged wall jet has revealed that in both cases the impingement zone occupies only the inner 15 percent of the separation distance between the source nozzles and the impingement plane, with the pre-impingement region having the structure of an undisturbed free axisymmetric jet. On the other hand, the wall jet region is more similar to the free shear layer of the constrained radial jet than that of an impinged radial jet. With the exception of the immediate wall boundary layer region and its associated momentum losses, the outer region of the wall jet closely resembles the constrained radial jet in terms of the spreading rate, centerline velocity decay, and turbulence intensity, although the centerline velocity does decay at a slightly faster rate, due to shear stress losses at the wall.

REFERENCES

1 Poreh, M. and Cermak, J. E., "Flow Characteristics of a Circular Submerged Jet Impinging Normally on a Smooth Boundary," Sixth Midwestern Conference on Fluid Mechanics, 1959, University of Texas, Austin, pp. 198-212.

2 Luna, R. E., "A Study of Impinging Axisymmetric Jets and Their Application to Size Classification of Small Particles," Ph.D Thesis, Princeton University, 1965.

3 Rodi, W., "The Prediction of Free Turbulent Boundary Layers by Use of a Two-Equation-Model of Turbulence," Ph.D Thesis, University of London, 1972.

4 Glauert, M. B., "The Wall Jet," Journal of Fluid Mechanics, Vol. 1, Part 6, 1956, pp. 625-643.

5 Bakke, P., "An Experimental Investigation of a Wall Jet," Journal of Fluid Mechanics, Vol. 2, 1957, pp. 467-472.

6 Brady, W. G. and Ludwig, G., "Theoretical and Experimental Studies of Impinging Uniform Jets," Journal of the American Helicopter Society, Vol. 8, No. 2, 1963, pp. 1-13.

7 Poreh, M., Tsuei, Y. G., and Cermak, J. E., "Investigation of a Turbulent Radial Wall Jet," Journal of Applied Mechanics, Vol. 89, June 1967, pp. 457-463.

8 Hrycak, P., Lee, D. T., Gauntner, J. W., and Livingood, J. N. B., "Experimental Flow Characteristics of a Single Turbulent Jet Impinging on a Flat Plate," NASA TN D-5690, March 1970.

9 Govindan, A. P. and Subba Raju, K., "Hydrodynamics of a Radial Wall Jet," Journal of Applied Mechanics, Vol. 41, June 1974, pp. 518-519.

10 Abramovich, G. N., The Theory of Turbulent Jets, MIT Press, Cambridge, Mass., 1963.

11 Corrsin, S., "Investigation of Flow in an Axially Symmetrical Heated Jet of Air," NACA Wartime Report W-94, December 1943.

12 Parthasarathy, S. P. and Tritton, D. J., "Impossibility of Linearizing a Hot-Wire Anemometer for Measurements in Turbulent Flows," AIAA Journal, Vol. 1, No. 5, May 1963, pp. 1210-1211.

13 Witze, P. O., "A Study of Impinging Axisymmetric Turbulent Flows: The Wall Jet, the Radial Jet, and Opposing Free Jets," Ph.D Dissertation, University of California, Davis, 1974.

14 Warren, W. R., "An Analytical and Experimental Study of Compressible Free Jets," Report 381, 1957, Aeronautical Engineering Laboratory, Princeton University.

15 Witze, P. O. and Dwyer, H. A., "The Turbulent Radial Jet," Journal of Fluid Mechanics, Vol. 75, Part 3, 1976, pp. 401-417.

16 Newman, B. G., "Turbulent Jets and Wakes in a Pressure Gradient," Fluid Mechanics of Internal Flow, Edited by G. Sovran, Elsevier Publishing Company, Amsterdam, 1967, pp. 170-209.

NEAR FIELD VELOCITY MEASUREMENTS IN A FULLY PULSED SUBSONIC AIR JET

K. Bremhorst and W.H. Harch

Department of Mechanical Engineering,
University of Queensland, St. Lucia,
Qld. 4067, Australia

ABSTRACT

Measurements in the near field of streamwise mean and turbulent velocities are reported for a fully pulsed axi-symmetric subsonic air jet exhausting into still air. The mean velocity field follows the same scaling laws as a steady jet but the pulsing moves the effective origin well upstream from the jet exit. Entrainment rates were found to be significantly higher than for the steady jet and are a function of two length scales. Mean and turbulent velocity length scaling differ significantly. The measurements indicate that momentum is not conserved which is attributed to the existence of a significant pressure gradient for which case a modified thin flow conservation equation is presented. Ensemble averaging of the signals permitted the separation of the pseudo and intrinsic turbulence components.

NOMENCLATURE

a, a_1, a_2 - Effective origins for U_0; $r_{\frac{1}{2},U}$; $\sqrt{\overline{u_0^2}}$
A, A_1, A_2 - Slopes of laws for U_0; $r_{\frac{1}{2},U}$; $\sqrt{\overline{u_0^2}}$
A_s - Hot wire surface area
A, B, C - Hot-wire calibration constants
C_i - Instantaneous wire cooling velocity
d - Outlet orifice diameter
E - Hot-wire voltage
h - Film coefficient
K_U^1, K_P^1, K_δ^1 - Hot-wire small perturbation sensitivity to, U, P and T_E respectively
P, P_∞ - Static pressure in, and at edge of jet respectively relative to far field ambient pressure
Q, Q_E - Volume flow at any x and at exit respectively
r - Radial co-ordinate
$r_{\frac{1}{2},U}$ - Half-value radius of U
$r_{\frac{1}{2},u}$; $r_{\frac{1}{2},u_p}$ - Half-value radii of $\overline{u^2}$ and $\overline{u^2}_p$
R - Radius of control volume
R_W - Hot-wire resistance
t_p - Period of a pulsation cycle
T_E - Unheated wire equilibrium temperature
T_W - Heated wire temperature
u - Aggregate axial velocity fluctuation
u_0 - u on jet axis
u_p - Pseudo turbulence velocity fluctuation
u_{p_0} - Pseudo turbulence velocity fluctuation on jet axis
u^1 - Intrinsic velocity fluctuation
$\overline{u^2}(f)$ - Spectral component of $\overline{u^2}$ at frequency, f
U - Mean axial velocity
$\overline{U}$ - Mean flow velocity at jet exit evaluated from mass flow and ambient far field temperature and pressure
U_i - Instantaneous total axial velocity
U_m - Maximum anticipated velocity
U_p - Total pseudo turbulence velocity at a given instant from beginning of pulsation cycle.
U_0 - Mean axial velocity on jet axis
V, v - Mean and fluctuating radial velocity
w - Azimuthal velocity fluctuation
x - Streamwise directional co-ordinate with origin at exit plane of jet orifice
α, β, γ - Linearizer constants
ρ - Density
τ_p - Time from valve opening; same meaning if used as subscript
— - Overbar denotes time averaging over many pulsating cycles.

INTRODUCTION

The velocity field of a steady jet has already received considerable attention from both the theoretical and the experimental aspect. By comparison, little is known about the basic characteristics of pulsed jets. Crow and Champagne [1] in their study of the structure of a steady jet introduced a small pulsation and observed a significant increase in entrainment. Binder et al [2, 3] showed that for this case the entrainment increases with increasing level of pulsation and that the spread of the jet is dependent on the level of pulsation as well as the frequency of pulsation. Curtet and Girard [4] showed by flow visualization that such jets consist of periodically ejected vortex rings. The fully pulsed case represents the upper boundary on the

PRECEDING PAGE BLANK-NOT FILMED

AD-A055 654 PENNSYLVANIA STATE UNIV UNIVERSITY PARK DEPT OF MECH--ETC F/G 20/4
SYMPOSIUM ON TURBULENT SHEAR FLOWS HELD AT THE PENNSYLVANIA STA--ETC(U)
APR 77 N00014-77-C-0176

UNCLASSIFIED NL

2 OF 9
ADA
055654

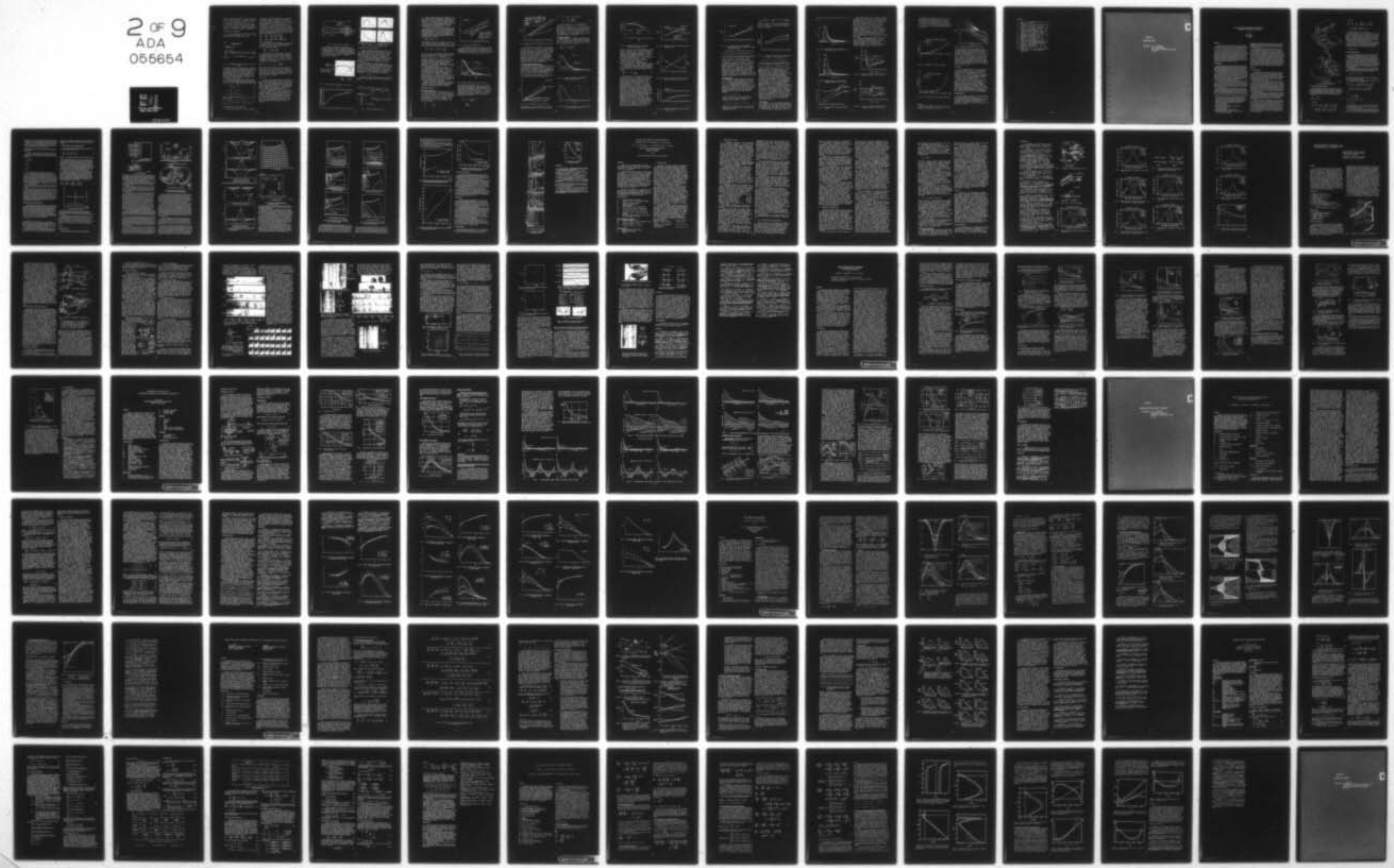

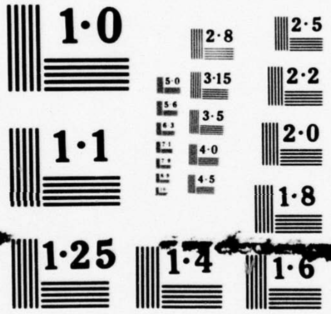

NATIONAL BUREAU OF STANDARDS
MICROCOPY RESOLUTION TEST CHART

level of pulsation as the flow at the jet exit is reduced to zero at the end of each cycle. The case of zero flow velocity exists in unsteady turbulent puffs studied by Kovasznay et al [5].

The purpose of this paper is to present mean and turbulent streamwise velocity data in the near field of a fully pulsed jet exhausting at subsonic speeds into stationary air. Within a limited range, the effect of pulsating frequency is considered.

TERMINOLOGY AND DEFINITIONS

A velocity transducer of sufficiently fast response will produce a signal similar to that of Fig.1, when placed at a fixed point in the flow.

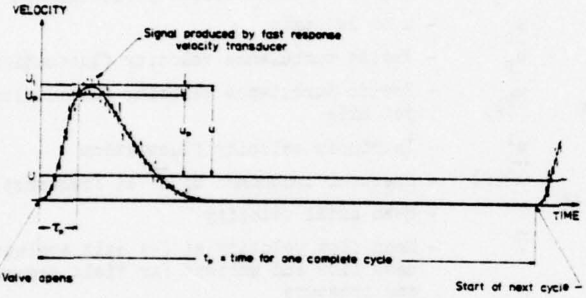

Fig. 1 Instantaneous velocity signal and its basic elements

The signal consists of a periodic component referred to as "pseudo turbulence" superimposed on which are fluctuations of much higher frequency referred to as "intrinsic turbulence". The latter contains all shear turbulence, turbulence due to the high flow Reynolds number as well as any unsteadiness associated with the pseudo turbulence. The sum of the pseudo and intrinsic turbulence is referred to as the "aggregate turbulence".

The total pseudo turbulence velocity, U_p, is found by ensemble averaging the total instantaneous flow velocity over a large number of cycles at time τ_p. Eqs. 1(a)-(d) define the various velocities used.

$$U = \lim_{T\to\infty} \frac{1}{T} \int_0^T U_i dt \tag{1a}$$

$$= \frac{1}{t_p} \int_0^{t_p} U_p dt \tag{1b}$$

$$U_p = \lim_{N\to\infty} \frac{1}{N} \sum_{n=1}^{N} U_{i,\tau_p,n}. \tag{1c}$$

where N = number of samples and $U_{i,\tau_p,n} = U_i$ at τ_p for the nth sample.

$$u^1 = U_i - U_p;\ u_p = U_p - U;\ u = U_i - U \tag{1d}$$

Also, $\int_0^{t_p} u_p\, dt = 0$, $\overline{u^1} = 0$, $\overline{u_p} = 0$ and $\overline{u} = 0$.

FLOW DESCRIPTION AND BASIC EQUATIONS

The flow was produced by the rapid opening and closing of a valve thereby periodically exhausting high pressure air from a receiver to atmosphere. As the valve opens, a compression wave is set up which travels downstream at sonic velocity and a corresponding rarefaction wave travels upstream. If the fluid exhausts at a sufficiently high velocity, it moves through the resultant pressure field producing an interaction between this and the fluid. Reconsideration of the basic time-averaged flow equations used in steady jet situations is, therefore, required. The axial and radial Navier-Stokes equation for compressible, axisymmetric flow without swirl and negligible molecular effects become

$$U\frac{\partial U}{\partial x} + V\frac{\partial U}{\partial r} = -\frac{1}{\rho}\frac{\partial P}{\partial x} - \frac{\partial \overline{u^2}}{\partial x} - \frac{1}{r}\frac{\partial r\overline{uv}}{\partial r} \tag{2}$$

$$U\frac{\partial V}{\partial x} - V\frac{\partial V}{\partial r} = -\frac{1}{\rho}\frac{\partial P}{\partial r} - \frac{\partial \overline{uv}}{\partial x} - \frac{1}{r}\frac{\partial r\overline{v^2}}{\partial r} + \frac{\overline{w^2}}{r} \tag{3}$$

where ρ is variable.

The usual thin flow approximations, Tennekes and Lumley [6], together with the approximation that ρ is a function only of x, leads to Eq.(4) which will slightly underestimate $\partial\overline{v^2}/\partial x$.

$$\frac{\partial \overline{v^2}}{\partial x} = -\frac{1}{\rho}\frac{\partial P}{\partial x} + \frac{1}{\rho}\frac{\partial P_\infty}{\partial x} \tag{4}$$

Substitution of this result into the axial momentum equation, Eq. (2), and integration across the jet using a cylindrical control volume of radius R sufficiently large so that at $r = R$, $U = 0$ and $\overline{uv} = 0$ yields Eq. (5) if at $r = 0$, $V = 0$ and $\overline{uv} = 0$. $\partial P_\infty/\partial x$ is assumed to be independent of the radial position for purposes of this integration.

$$\frac{\partial}{\partial x}\int_0^R (U^2 + \overline{u^2} - \overline{v^2})\, r\, dr = -\frac{R^2}{2\rho}\frac{\partial P_\infty}{\partial x} \tag{5}$$

Both ρ and P_∞ are functions of x. In the case of a steady jet, $\partial P_\infty/\partial x = 0$ thus yielding the familiar result where the integral of Eq. (5) is constant and proportional to the total jet momentum. Since $\partial P_\infty/\partial x$ will be negative, the pulsed jet momentum should increase with x until the far field condition of zero pressure gradient is reached.

JET FACILITY

A plenum chamber placed immediately upstream of the pulsating valve consisted of a cylindrical vessel with a free internal space 720 mm long x 260 mm diameter. Air left the vessel through a rounded, smooth transition piece which connected the plenum chamber and the pulsating valve (Fig. 2). A contraction with an exit diameter of 25.4 mm was placed after the rollers to give an axisymmetric free jet.

During continuous operation of the system the pressure fluctuations in the plenum chamber resulting from the pulsation of the flow never exceeded 3% of the mean plenum chamber gauge pressure which was 35 kN/m^2. Flow rates were measured well upstream of the plenum chamber with an orifice flow meter and were found to be independent of frequency of pulsation. Pressure fluctuation levels in the plenum chamber decreased with increasing frequency of pulsation.

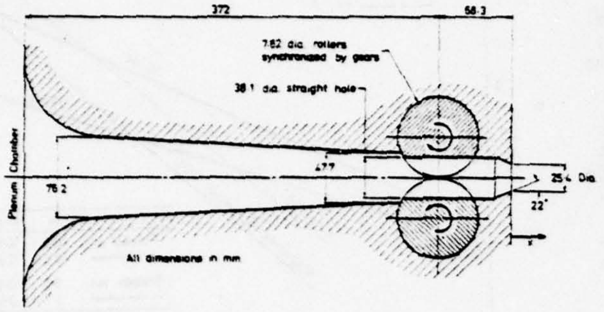

Fig. 2 Partial view of air supply

Stream static temperature was measured with a hot-wire operated at very low constant current thus responding essentially like a resistance thermometer. A typical signal at two exit diameters from the outlet is shown in Fig. 3. The peak to peak temperature fluctuation level as a function of distance from the outlet orifice is given in Fig. 4 and typical velocity signals in Fig. 5.

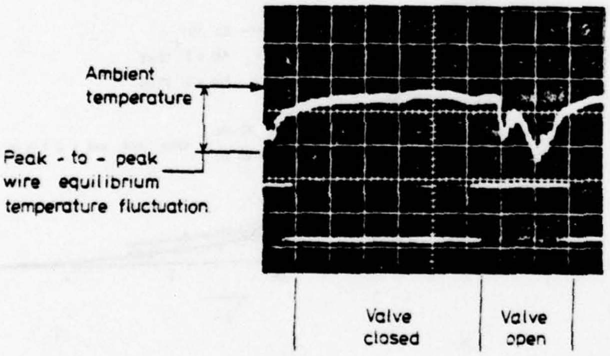

Fig. 3 Typical temperature signal at 25 Hz, x/d = 2

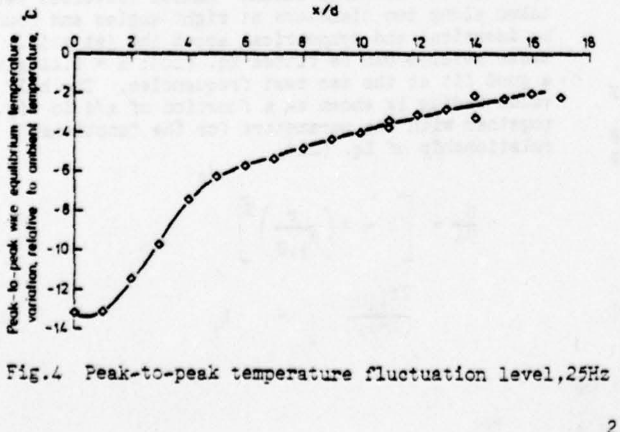

Fig.4 Peak-to-peak temperature fluctuation level,25Hz

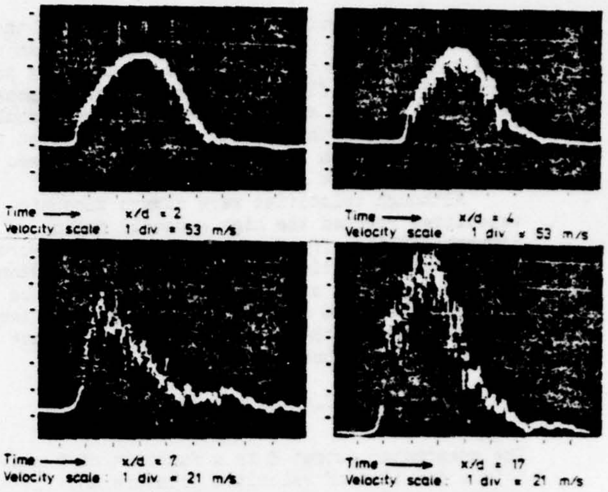

Fig. 5 Typical velocity signals, 10Hz

INSTRUMENTATION AND DATA ANALYSIS

Velocity measurements were performed with a constant temperature hot-wire anemometer which incorporated dynamic linearization in the feedback loop so that over the whole velocity range constant system bandwidth existed. The wire was 5 μm diameter x 1.4 mm long tungsten operated at an overheat ratio of 0.5. Due to the large fluctuating forces on the wire, a curved wire was used the response of which will, except for a scale factor, be similar to that of a straight wire.

For low subsonic velocities, Bremhorst and Gilmore[7] have shown that identical small perturbation responses of a hot-wire are obtained by the static and dynamic methods of calibration provided that a velocity wire output correlation appropriate to the velocity range is used for the static method. The one covering accurately the velocity range met in the present measurements is Eq. (6) by Siddall and Davies [8].

$$E^2 = A + B\sqrt{U_i} + CU_i \qquad (6)$$

The method of signal processing used to effectively linearize the wire output, Fig. 6, simply solves Eq.(6) for U_i

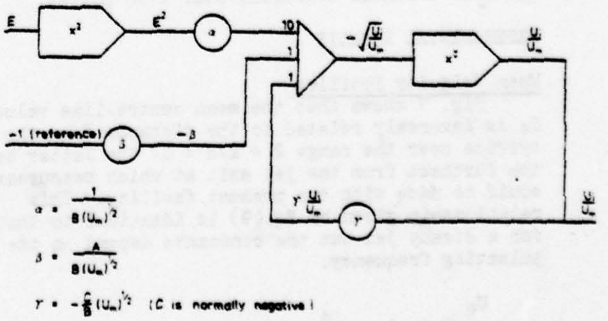

Fig. 6 Hot-wire linearizer circuit

Unless otherwise stated, it is assumed that the mean wire voltage is proportional to the mean streamwise velocity and the fluctuating voltage is proportional to the fluctuating part of the streamwise velocity. At the edges of the jet where turbulence levels are high, this approximation will lead to the usual errors which have already been discussed extensively in the literature.

Although velocities were always subsonic, peak velocities reached the high subsonic regime so that compressibility effects on the hot-wire measurements require consideration. Eq. (7) gives the instantaneous heat balance of a hot-wire in the absence of end conduction and operated in the constant temperature mode where the wire resistance and hence wire temperature are constant.

$$E^2/R_W = hA_s(T_W - T_E) \qquad (7)$$

The anemometer output E is a function of h and T_E and h is a function of velocity, pressure and T_E. For small variations from a reference state, the anemometer output may be corrected by application of Eq.(8)

$$dE = K_U{}^1 \frac{dU}{\overline{U}} + K_P{}^1 \frac{dP}{\overline{P}} + K_\delta^1 \frac{dT_E}{\overline{T}_E} \qquad (8)$$

$K_P{}^1 = K_U{}^1$ if h is a function only of Reynolds Number and the working fluid is a perfect gas. For the conditions used, $K_U{}^1/K_\delta{}^1 = -(\overline{T}_W-\overline{T}_E)/2\overline{T}_E$ at all velocities, $(\overline{T}_W-\overline{T}_E) = 125$ K, $\overline{T}_E = 293$ K and the resistance ratio was set by measuring the cold wire resistance at ambient conditions. Reference to Fig. 4 shows that the stream temperature was generally below the ambient temperature. The above is used at a later stage for the assessment of the measured mean velocity data.

The difference in temperature between the jet and the ambient air leads to heat transfer by turbulent mixing of the two fluids. Its effect on the turbulent velocity measurements is similar to that obtained when performing measurements in a heated or cooled jet. Again, no corrections for this were made but an error analysis showed that the measured intrinsic turbulence intensities would be up to 10% higher than the true ones in regions where a high correlation exists between the intrinsic velocity and temperature fluctuations.

Signal processing was performed on an EAI Pacer 600 hybrid computer which permitted the separation of pseudo and intrinsic turbulence components by suitable ensemble averaging over 1750 pulses.

EXPERIMENTAL RESULTS

Mean Velocity Profiles

Fig. 7 shows that the mean centre-line velocity U_0 is inversely related to the distance from the orifice over the range $2 < x/d < 17$ the latter being the furthest from the jet exit at which measurements could be made with the present facility. This relationship given by Eq.(9) is identical to that for a steady jet but the constants depend on the pulsating frequency.

$$\frac{U_0}{\overline{U}} = A \frac{d}{x + a} \qquad (9)$$

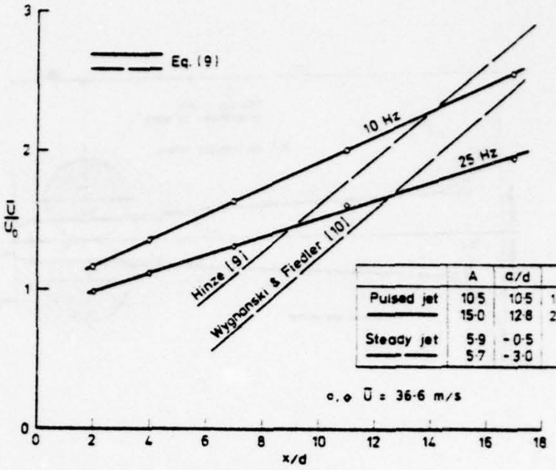

Fig. 7 Decay of mean axial velocity.

The considerable movement of the virtual origin upstream is consistent with that observed by Crow and Champagne [1] at low levels of jet perturbation. Radial distributions of mean velocity, Fig. 8, scale well with the half value radius $r_{\frac{1}{2},U}$ (r at which $U = \frac{1}{2}U_0$).

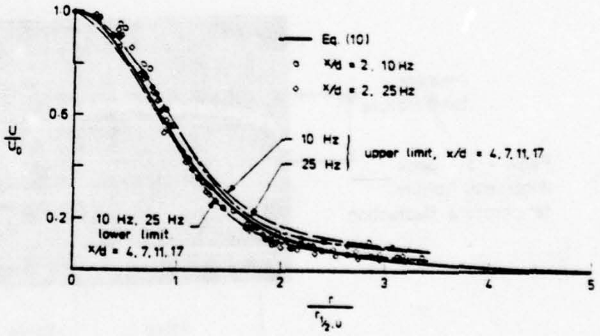

Fig. 8 Radial distributions of mean velocity.

The distributions obtained at x/d = 4, 7, 11 and 17 fall within the bands shown. Radial traverses were taken along two diameters at right angles and found to be identical and symmetrical about the jet axis. To these results can be fitted Eq. (10); α = 0.44 giving a good fit at the two test frequencies. The half value radius is shown as a function of x/d in Fig. 9 together with the parameters for the functional relationship of Eq. (11).

$$\frac{U}{U_0} = \left[1 + \alpha\left(\frac{r}{r_{\frac{1}{2},U}}\right)^2\right]^{-2} \qquad (10)$$

$$\frac{2r_{\frac{1}{2},U}}{(x+a_1)} = A_1 \qquad (11)$$

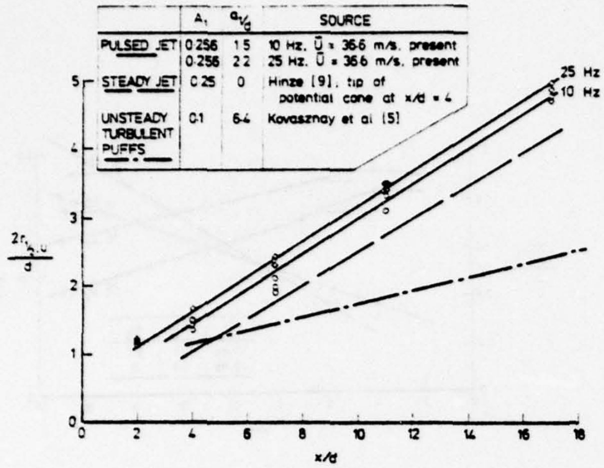

Fig. 9 Mean velocity half value radius as a function of x/d.

Some evidence of the existence of a potential cone is seen in Fig. 8 at x/d = 2 but has completely vanished at x/d = 4. Although the turbulence level of the flow upstream of the valve was only 2.5% when operating under steady jet conditions, the concept of a potential cone is probably not applicable because of the finite opening and closing times of the valve. Both the concept of a "mixing region" which would be applicable to the developing flow immediately downstream of the valve and that of a "fully developed jet" further downstream in the self-preserving region are still appropriate.

Volume Flow and Entrainment Rates

From the mean velocity distributions, the volume flow can be found by integration. The problem of calculating the entrainment rate, $d(Q/Q_E)/d(x/d)$, has already been discussed by Crow and Champagne [1] and Hinze [9]. To arrive at the experimental points of Fig. 10, velocity profiles were integrated to that r at which the velocity was less than 0.1 U_Q. This gave results almost identical to the fairing-in procedure used by Crow and Champagne [1].

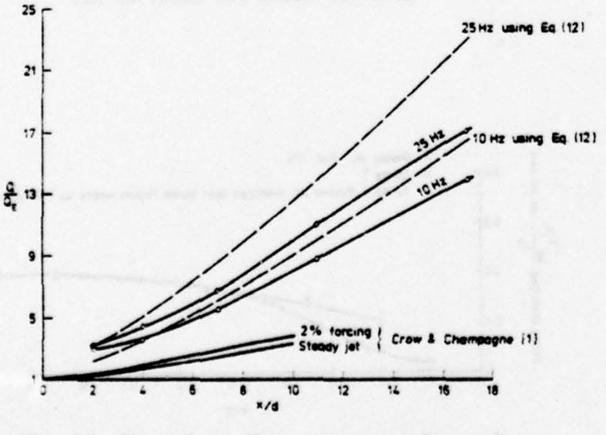

Fig. 10 Jet volume flow rate at various x/d

For comparison, the curve obtained by use of the functional relationship of Eq. (12), derived from Eqs. (9), (10) and (11) is also shown

$$\frac{Q}{Q_E} = \frac{AA_1^2}{\alpha}\,\frac{(x+a_1)^2}{d(x+a)} \qquad (12)$$

Unlike the steady jet, the entrainment now depends on "a" as well as "a_1". Since "a" is significantly different from "a_1", a constant entrainment rate is not obtained in the near field region. Approximate entrainment rates calculated from Fig. 10 are 1.05 and 1.3 for 10 Hz and 25 Hz respectively at the larger values of x/d which exceed that of 0.292 measured by Crow and Champagne [1] in the self-preserving region of a steady jet.

Turbulence Intensity

Radial profiles of aggregate turbulence levels are shown in Fig. 11(a). A functional relationship, Eq.(13), of the same form as that used for the mean velocity profiles of Fig. 8 again gives an acceptable fit to the data for x/d > 2 and α = 0.44.

$$\frac{\overline{u^2}}{\overline{u^2}_0} = \left[1 + \alpha\left(\frac{r}{r_{½,u}}\right)^2\right]^{-2} \qquad (13)$$

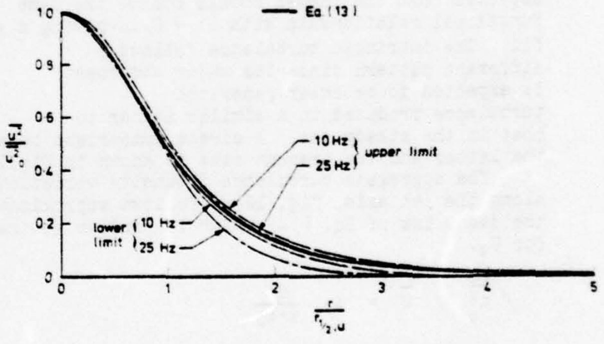

Fig. 11(a) Radial distributions of aggregate turbulence energy levels.

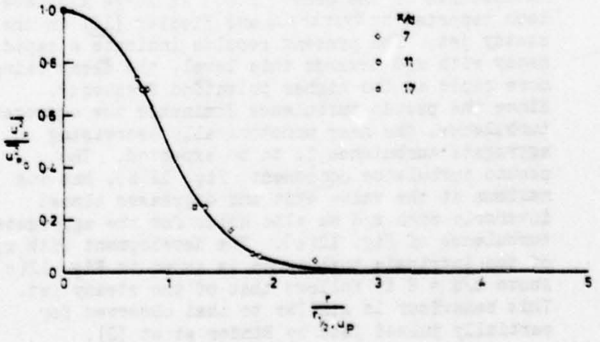

Fig. 11(b) Radial distributions of pseudo turbulence fluctuation energy levels, 25 Hz.

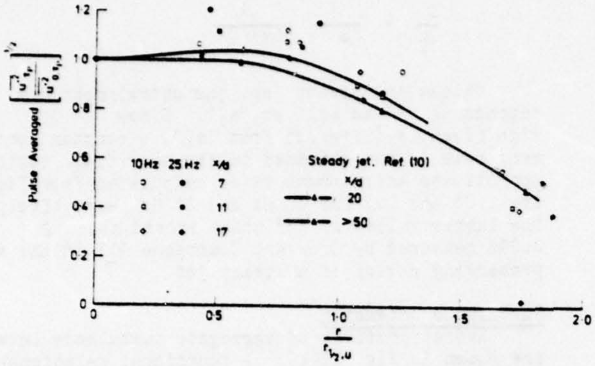

Fig. 11(c) Radial distributions of intrinsic turbulence intensity levels

Pseudo and intrinsic turbulence components are shown in Figs. 11(b) and 11(c). In each case the relevant half value radius was used to obtain the normalization. Since the pseudo turbulence is the major component of the aggregate turbulence, it is to be expected that the former should follow the same functional relationship with α = 0.44 giving a good fit, The intrinsic turbulence follows a different pattern since its major component is expected to be shear generated turbulence produced in a similar manner to that in the steady jet. A direct comparison between the latter and the present case is shown in Fig.11(c)

The aggregate turbulence intensity variation along the jet axis, Fig. 12(a) follows approximately the decay law of Eq. (14) which is similar to that for U_0.

$$\sqrt{\overline{u_0^2}} \; / \; \overline{U} = A_2 \frac{d}{x+a_2} \qquad (14)$$

Very high levels of turbulence intensity are indicated but this is to be expected since fluctuations in velocity are from zero to the maximum velocity about a small resultant mean velocity. These large fluctuations are, however, only in the axial direction. For increasing x/d, the jet pulsation gradually decays until in the limit an essentially steady jet is obtained. Turbulence intensities of the order of 0.3 at large x/d have been reported by Wygnanski and Fiedler [10] in the steady jet. The present results indicate a rapid decay with x/d towards this level, the decay being more rapid at the higher pulsation frequency. Since the pseudo turbulence dominates the aggregate turbulence, the near monotonically decreasing aggregate turbulence is to be expected. The pseudo turbulence component, Fig. 12(b), has its maximum at the valve exit and decreases almost inversely with x/d as also holds for the aggregate turbulence of Fig. 12(a). The development with x/d of the intrinsic turbulence is shown in Fig. 12(c). Above x/d = 8 it follows that of the steady jet. This behaviour is similar to that observed for partially pulsed jets by Binder et at [2].

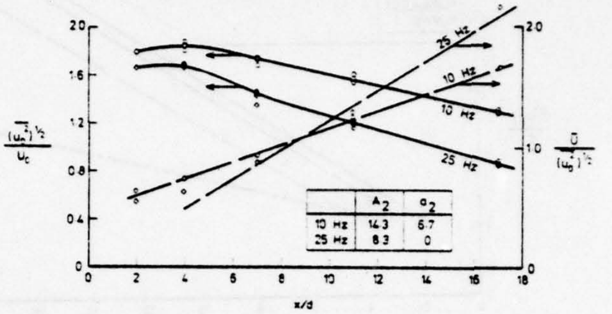

Fig. 12(a) Aggregate turbulence intensity variation along jet axis.

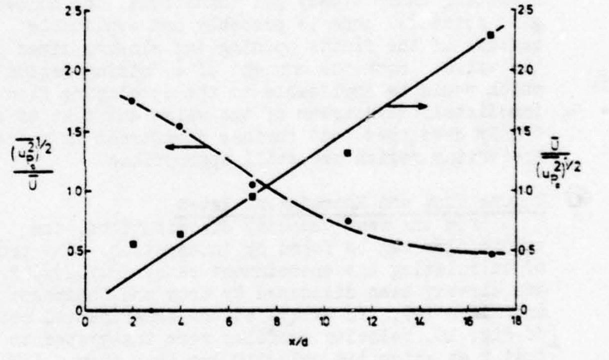

Fig. 12(b) Pseudo turbulence fluctuation intensity variation along jet axis, 25 Hz.

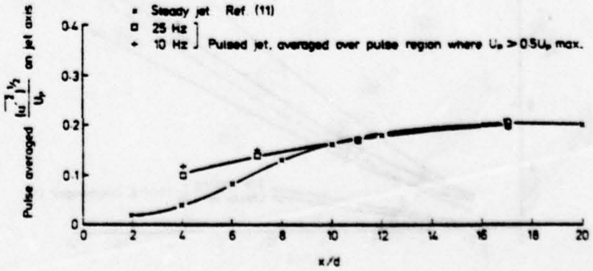

Fig. 12(c) Intrinsic turbulence intensity variation along jet axis.

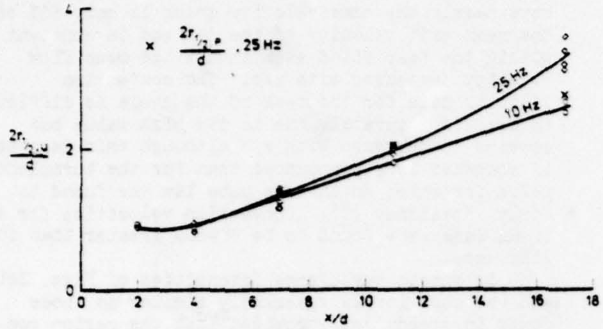

Fig. 13 Half value radii of axial aggregate turbulence and pseudo turbulence fluctuation energy distributions.

Half value radii of $\overline{u^2}$ and $\overline{u_p^2}$ (radii at which $\overline{u^2} = \frac{1}{2}\overline{u^2}_0$ and $\overline{u_p^2} = \frac{1}{2}\overline{u_p^2}_0$) are shown in Fig. 13. It is noteworthy that for the fully developed, steady jet $r_{\frac{1}{2},u} > r_{\frac{1}{2},U}$ while the converse is true for the fully pulsed case. Unlike the mean velocity situation (Fig. 9) $r_{\frac{1}{2},u}$ is not a linear function of x/d suggesting a degree of dissimilarity between the mean and fluctuating fields. This is further confirmed by the results of Fig. 12(a) which is the case corresponding to that of Fig. 7 for the mean velocity field. It is seen that both the effective origin and the rate of axial decay differ significantly from those applicable to the mean flow. Incomplete similarity in the near field is undoubtedly due to the fact that for the pulsating jet, the aggregate turbulence level is dominated by the pseudo turbulence which scales with x/d rather than (x+a)/d.

Momentum Balance

The simplified momentum equation applicable to free flows with a pressure gradient was derived as Eq. (5). Since the turbulence components enter Eq. (5), the approximate response of the hot-wire used to this stage requires reconsideration. Let C_i denote the instantaneous cooling velocity of the wire. Eq. (15) relates this to the other flow components when a mean flow exists only in the axial direction, sensitivity to flow along the wire is negligible and the wire lies in the azimuthal direction.

$$C_i^2 = (U + u)^2 + v^2 \tag{15}$$

Eq. (16) then gives the quantity which can be evaluated from the signal of a normal wire to represent the total momentum at any x/d

$$\int_0^R \overline{C_i^2}\, rdr = \int_0^R (U^2 + \overline{u^2} + \overline{v^2})\, rdr \tag{16}$$

Substitution of this result into Eq. (5) gives the conservation equation, Eq. (17), in terms of the measured quantity C_i^2.

$$\frac{\partial}{\partial x}\int_0^R \overline{C_i^2}\, rdr - 2\frac{\partial}{\partial x}\int_0^R \overline{v^2}\, rdr = -\frac{R}{\partial \rho}\frac{\partial P_\infty}{\partial x} \tag{17}$$

Reference to Fig. 14 shows that the first term of Eq. (17) is positive. If the term containing $\overline{v^2}$ is accepted to be small, the existence of a negative $\partial P_\infty/\partial x$ is established.

Fig. 14 Jet momentum evaluated from uncorrected hot-wire signal - First term of Eq. (17).

At x/d = 2, $\overline{v^2} = 0$ so that $\int_0^R \overline{C_i^2}\, rdr$ is directly proportional to the jet momentum at exit. If a zero pressure gradient did exit, the results of Fig. 14 indicate that $\int_0^R \overline{v^2}\, rdr$ would have to represent half the jet momentum at x/d = 2, which appears unlikely as $\overline{v^2}$ is not expected to be significantly above the value of a steady jet at the same mean velocity whereas the $\overline{u^2}$ is very significantly above the equivalent steady jet values because of the pseudo turbulence component.

Finally, it should be noted that hot-wire response errors due to pressures and temperatures different from the calibration conditions decrease the integrated C_i^2 values at low x/d relative to those at higher x/d as at all times the anemometer was calibrated and set up at temperatures and pressures similar to those obtained at large x/d. With the aid of Eq. (8) and the operating data given earlier, it is seen that corrected velocities at low x/d would be lower than the uncorrected values reported here. Unfortunately, precise correction is not possible without measured values of pressure, but if at x/d = 2 the pressure is 5% above atmospheric and the temperature on average is 6°C below ambient as obtained from Fig. 4, the corrected velocity would be 15% below that reported here thus considerably enhancing the case for a non zero pressure gradient as at x/d = 17 virtually no correction is required.

Pulse Details

In addition to the time averages over many complete pulses, data were obtained at a given point within each pulse. The position within each pulse was determined by a fixed delay relative to a timing pulse obtained from the rotary valve drive shaft.

The total pseudo turbulence as a function of position within the pulse is shown in Figs. 15(a) and (b).

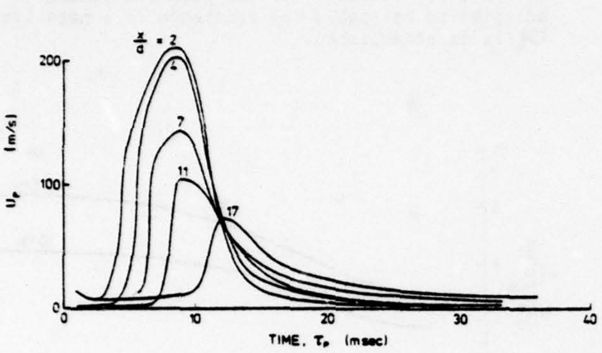

Fig. 15(a) Axial variation of total pseudo turbulence velocity , x/d = 7, 25 Hz.

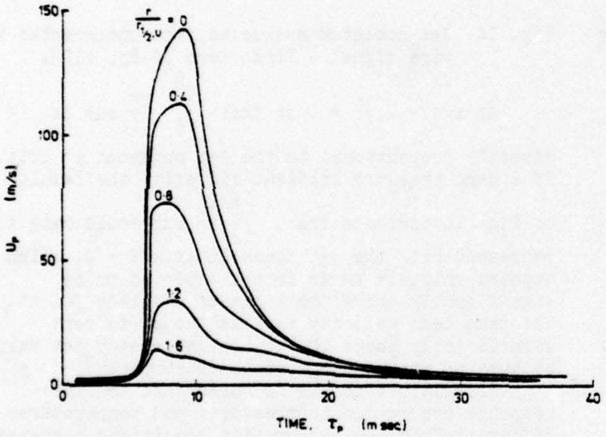

Fig. 15(b) Radial variation of total pseudo turbulence velocity, x/d = 7, 25Hz.

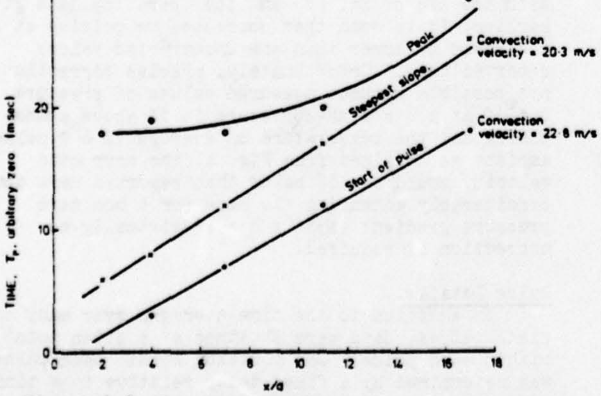

Fig. 15(c) Propagation of various pulse features, 25Hz.

From the data of Fig. 15(a) convection velocities of various pulse features can be calculated. These are shown in Fig. 15(c) from which it is seen that the commencing point of the pulse and the steepest slope have nearly the same velocity which is only 60% of the mean exit velocity of the jet and is constant within the near field even though the mean flow velocity decreases with x/d. The convection velocity data for the peak of the cycle is difficult to measure accurately due to its high value but appears to decrease with x/d although this decrease is somewhat less pronounced than for the turbulent puffs for which an inverse cube law was found to apply, Kovasznay [5]. Convection velocities for the 10 Hz case were found to be 50-60% greater than for the 25Hz case.

Intrinsic turbulence intensities of Figs. 16(a) and (b) show levels remarkably similar to those found in steady jets provided that the region containing the pulse front is excluded as the statistical samples there are unreliable due to insufficient samples. It is from such data that the results of Figs 11(c) and 12(c) were obtained.

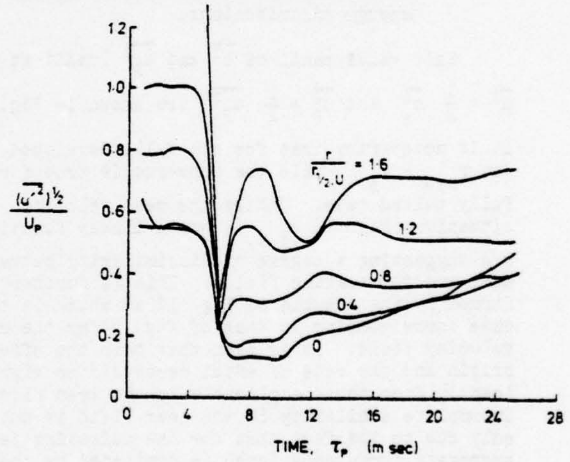

Fig. 16(a) Intrinsic turbulence intensity variation throughout a pulse, x/d = 7, 25Hz.

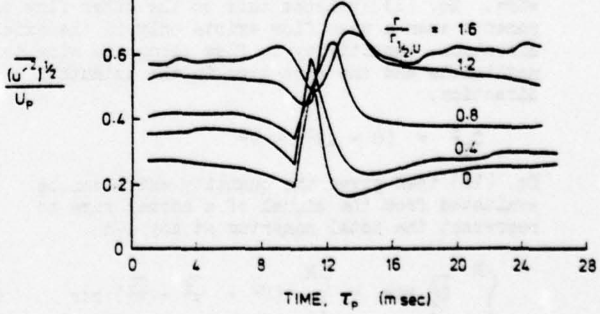

Fig. 16(b) Intrinsic turbulence intensity variation throughout a pulse, x/d =17, 25Hz.

The skewness and flatness data Fig. 17(a) and (b), also compare well with steady jet data. The r/x rather than r/(x+a) normalization is considered justified as the effective origin for the mean velocity half value radius data is approximately at x/d = 2 (Fig. 9). Inclusion of this minor correction would produce an even better agreement between the two cases.

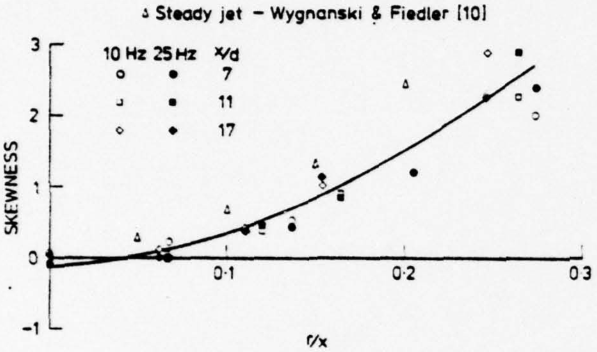

Fig. 17(a) Skewness of intrinsic turbulence

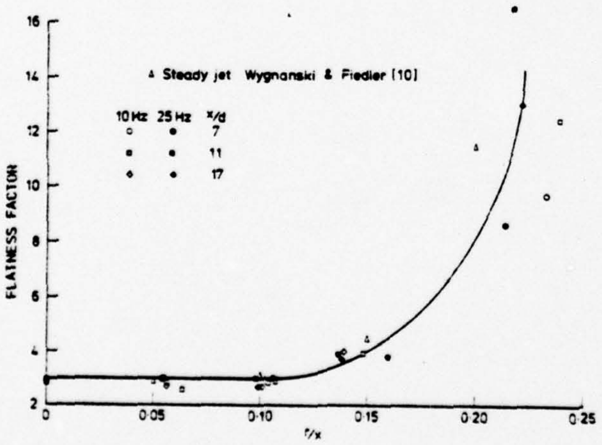

Fig. 17(b) Flatness factor of intrinsic turbulence.

Spectra

The steady progression of the flow from a low turbulence pulse train to a near steady jet flow is typified by the spectra of Fig. 18.

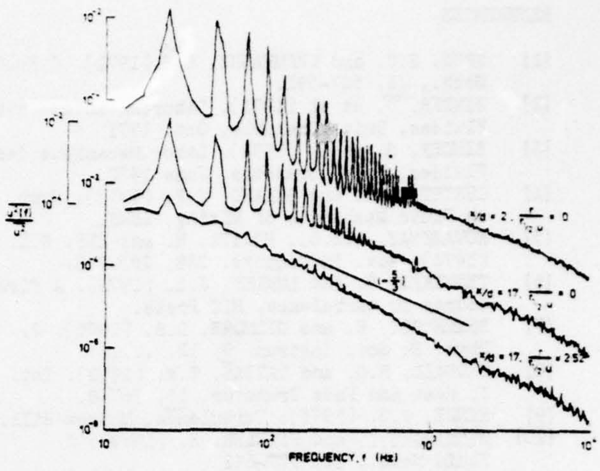

Fig. 18 Aggregate turbulence spectra, 25Hz.

For the latter case the pulsed component forms a less dominant part of the low frequency spectrum with the high frequencies tending towards the general universal spectral shape with its -5/3 fall off. Comparison of the two spectra at x/d = 17 also shows that the pulsed component is still evident in the core of the flow but at the edge of the jet it has almost vanished. The fundamental and associated harmonics are only indicative in width and relative power as no attempt was made to optimize the digital data analysis for maximum definition of these sharp peaks. Spectra for other positions in the flow are available in Harch [12].

CONCLUSION

The mean velocity field of a fully pulsed subsonic air jet issuing into still air can be described by the same functional relationships used for steady jets. The main effects of the jet pulsation are to move the effective jet origin well upstream of jet exit and to significantly increase entrainment rates, the higher pulsating frequency yielding the higher entrainment rate.

Length scaling for the streamwise turbulence differs significantly from that of the mean velocity. This is due to an x/d dependence of the pulsating component whereas the shear generated turbulence has an (x+a)/d dependence. Results indicate that momentum is not conserved in the near field of the fully pulsed jet. Assumption of a non-zero streamwise pressure gradient at the edge of the jet yielded a modified integral momentum equation which is consistent with the hot-wire measurements.

ACKNOWLEDGEMENTS

Mr. T.C. Smith's assistance with the programming of the hybrid computer and the receipt of an Australian Research Grants Commission grant to assist with this work are gratefully acknowledged. One of the authors, W.H. Harch is also grateful for a Commonwealth Postgraduate Scholarship received for the duration of the work.

REFERENCES

[1] CROW, S.C. and CHAMPAGNE, F.H.(1971). J.Fluid Mech., 48, 547-591.

[2] BINDER, G. et al (1971). Labor.Mecanique des Fluides, Univ. Grenoble, Oct. 1971

[3] BINDER, G. et al (1972). Labor.Mecanique des Fluides, Univ. Grenoble, June 1972.

[4] CURTET, R.M. and GIRARD, J.P. (1973). Symp. on Fluid Mechanics of Mixing, ASME.

[5] KOVASZNAY, L.S.G., FUJITA, H. and LEE, R.L. (1974). Adv. in Geophys. 18B, 253-263.

[6] TENNEKES, H. and LUMLEY, J.L. (1972). A first course in turbulence, MIT Press.

[7] BREMHORST, K. and GILMORE, D.B. (1976). J. Phys. E: Sci. Instrum. 9, 12, ...

[8] SIDDALL, R.G. and DAVIES, T.W. (1972). Int. J. Heat and Mass Transfer, 15, 367-8.

[9] HINZE, J.O. (1975). Turbulence, McGraw-Hill.

[10] WYGNANSKI, I. and FIEDLER, H. (1969). J. Fluid Mech., 38, 577-612.

[11] CORRSIN, S. and UBEROI, M.S. (1950). NACA Report 998.

[12] HARCH, W.H. (1977), Ph.D. Thesis, University of Queensland, St. Lucia, Queensland, Australia.

3

SESSION 3

IMPINGING JETS

Chairman: A. K. Runchal
Dames and Moore
Los Angeles, California 90017
U.S.A.

COMPUTATIONS AND MEASUREMENTS OF TWO-DIMENSIONAL TURBULENT JET IMPINGEMENT FLOWFIELDS*

by

W.W. Bower[†]
D.R. Kotansky**
G.H. Hoffman***

ABSTRACT

The interaction of the lift jets and the ground is an important consideration with regard to the design of VTOL aircraft. A key element of this ground effect problem is turbulent jet entrainment, which causes otherwise static air to be set into motion and leads to aerodynamic loads on airframe surfaces. As a first step toward gaining an understanding of this phenomenon, a combined theoretical and experimental analysis of two-dimensional turbulent jet impingement flowfields has been undertaken. Both planar and axisymmetric jets in close ground effect have been modeled using the incompressible Reynolds equations in combination with a one-equation turbulence model. Distributions of the flow properties are computed as functions of Reynolds number based on jet exit properties and height of the jet exit plane above ground. For the planar impinging jet, flowfield properties are presented for various flow configurations, and comparisons are made with the computed distributions.

INTRODUCTION

During the past ten years, a sizeable research effort has been devoted to the design of jet- and fan-powered vertical-takeoff-and-landing (VTOL) aircraft. At the McDonnell Douglas Corporation, current VTOL aircraft development programs include the AV-8A and AV-8B Harrier direct-lift jet fighter and the McDonnell Aircraft model 260 lift-cruise-fan-augmented, multi-purpose aircraft.

Major problems of VTOL flight occur during takeoff and the transition to cruise. Principally, unpredictable forces can be produced on the airframe through the interaction of the lift jets and the ground, a so-called ground effect problem. These forces, which occur as the result of a flowfield induced by the propulsive lift jets, can be either positive or negative. In the former case, additional lift is provided, but in the latter case, a nominally designed propulsion system may not have sufficient thrust for an adequately controlled takeoff.

The task of predicting the aerodynamic interference effects of the lift jet, the airframe, and the ground is not a simple one either experimentally or theoretically. The numerous variables which affect the flowfield make it difficult to economically study an aircraft configuration through wind tunnel tests alone. On the other hand, the flow is so complex that a rigorous analytical treatment is not possible at the present time.

The objective of the VTOL aircraft flowfield investigation in progress at the McDonnell Douglas Research Laboratories (MDRL) is to gain fundamental knowledge of the flowfield associated with a two-dimensional lift jet in ground effect. This includes a more complete understanding of the effect of turbulent jet entrainment on the static pressure variation on the upper surface from which the jet discharges. Solutions of the two-dimensional flow equations are presently tractable, and the knowledge gained may then be applied to achieve a better understanding of the more complex three-dimensional lift-jet flowfields associated with VTOL aircraft.

Toward achieving this objective, MDRL has undertaken a combined theoretical and experimental research effort. The analytical phase is a solution of the two-dimensional, time-averaged conservation equations, in conjunction with a turbulence model, to describe the turbulent flowfield associated with a single, two-dimensional lift jet emanating from a static upper surface and striking the ground. The primary configuration for theoretical analysis is the unvectored planar lift jet, which was selected since the vectored configuration can be studied in future work still using a two-dimensional approach. An unvectored axisymmetric lift jet has also been analyzed theoretically, but when this configuration is vectored, the flowfield becomes three-dimensional. The experimental phase of the MDRL effort is the acquisition of detailed flowfield measurements for the planar jet to establish the validity of the computed flow variables. Although data have been reported for a single axisymmetric jet striking a ground plane (1-4), an extensive set of measurements for the planar configuration is not available.

ANALYSIS

The Flow Configurations

The two-dimensional impinging-jet flows of interest in the present paper are shown schematically in Fig. 1. For the planar configuration, the jet exits from a slot of width D in a contoured upper surface a distance H above the ground plane. The region of interest extends a distance W from the jet centerline. For the axisymmetric configuration, the jet issues from a nozzle of diameter D located a distance H above the impingement surface. The region of interest extends radially a distance W from the axis.

For both geometries, the jet flowfield can be divided into three regions: a free-jet region in which the flow is essentially the same as that of a jet issuing into an unbounded medium; the impingement region, in which the flow changes direction with a large pressure gradient; and the wall-jet region in which the flow spreads out over the impingement surface with zero pressure gradient. The fluid surrounding the jet is entrained at the boundaries of all three regions, causing otherwise static air to be set into motion. If the jet discharges from a bounding upper surface, this motion results in locally reduced static pressures and an aerodynamic load on the surface.

For the configurations of Fig. 1, a rigorous fluid dynamic analysis cannot be made using purely inviscid-flow calculation techniques, even with the addition of empirical or boundary-layer corrections. In fact, a turbulent boundary-layer procedure cannot simply be patched into an inviscid scheme since there are pressure gradients in both coordinate directions with no single dominant direction of flow.

In the present approach, the time-averaged continuity and Navier-Stokes equations for steady, two-dimensional, incompressible flow are used to describe the mean motion of the fluid in the turbulent jet impingement problem. As a result of the averaging procedure, unknown turbulent stress terms arise in the time-averaged momentum equations. To solve for the turbulent shear stress, a turbulent-kinetic-energy equation is used in combination with a constitutive equation that relates the square root of the turbulent kinetic energy to the turbulent viscosity. The resulting coupled nonlinear elliptic, partial-differential equations that describe the flow are solved for the fluid properties employing finite-difference procedures.

---

*The theoretical research on planar jets was conducted under the Office of Naval Research Contract N00014-76-C-0494. The experimental study of planar jets and the analysis of axisymmetric jets was conducted under the McDonnell Douglas Independent Research and Development Program.

[†] Research Scientist, McDonnell Douglas Research Laboratories
McDonnell Douglas Corporation
St. Louis, Missouri 63166

**Section Chief - Technology, McDonnell Aircraft Company
McDonnell Douglas Corporation
St. Louis, Missouri 63166

***Research Associate, Garfield Thomas Water Tunnel
Applied Research Laboratory, The Pennsylvania State University
University Park, Pennsylvania 16802

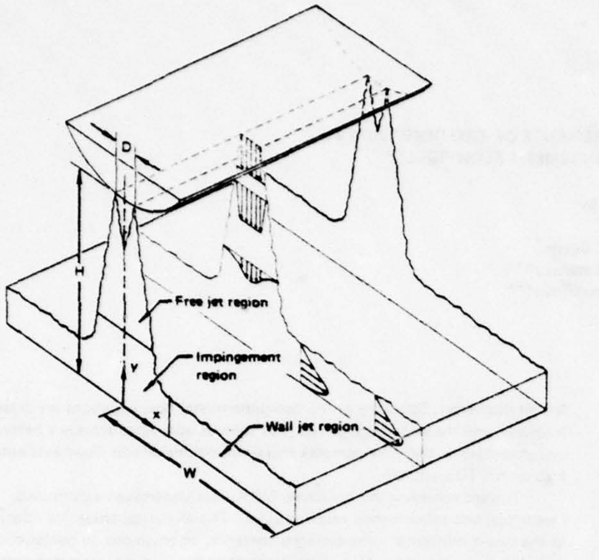

(a) Planar jet

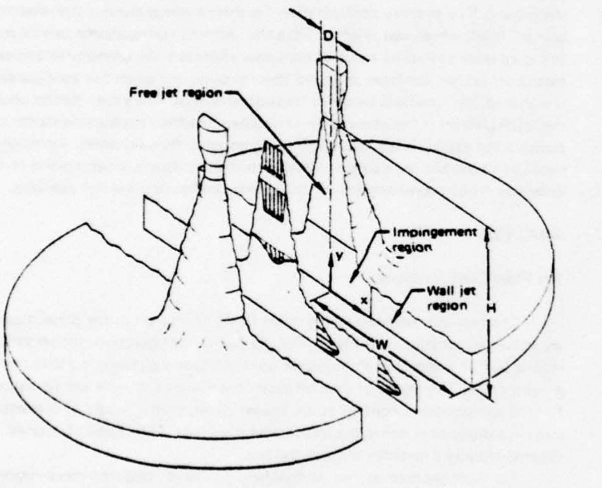

(b) Axisymmetric jet

GP77-0220-2

Fig. 1 Two-dimensional impinging jet flows

The Time-Averaged Conservation Equations

The governing equations which form the starting point of the analysis are those describing the conservation of mass and momentum for the steady, two-dimensional, incompressible flow of a Newtonian fluid with no body forces. To write the time-averaged forms of these equations to describe a turbulent flow, the usual Reynolds decomposition is used, and the following are obtained:

Continuity:

$$\frac{1}{x^j}\frac{\partial}{\partial x}(x^j u) + \frac{\partial v}{\partial y} = 0 \tag{1}$$

x - Momentum:

$$u\frac{\partial u}{\partial x} + v\frac{\partial u}{\partial y} = -\frac{1}{2}\frac{\partial p}{\partial x} + \mu_{eff}\left[\frac{\partial^2 u}{\partial x^2} + j\frac{\partial}{\partial x}\left(\frac{u}{x}\right) + \frac{\partial^2 u}{\partial y^2}\right]$$
$$+ 2\frac{\partial u}{\partial x}\frac{\partial \mu_{turb}}{\partial x} + \frac{\partial \mu_{turb}}{\partial y}\left(\frac{\partial u}{\partial y} + \frac{\partial v}{\partial x}\right) + j\frac{2\mu_{turb}u}{x^2} \tag{2}$$

y - Momentum:

$$u\frac{\partial v}{\partial x} + v\frac{\partial v}{\partial y} = -\frac{1}{2}\frac{\partial p}{\partial y} + \mu_{eff}\left[\frac{\partial^2 v}{\partial x^2} + \frac{j}{x}\frac{\partial v}{\partial x} + \frac{\partial^2 v}{\partial y^2}\right]$$
$$+ 2\frac{\partial v}{\partial y}\frac{\partial \mu_{turb}}{\partial y} + \frac{\partial \mu_{turb}}{\partial x}\left(\frac{\partial u}{\partial y} + \frac{\partial v}{\partial x}\right) \tag{3}$$

with j = 0 for planar flow, and j = 1 for axisymmetric flow.

The previous equations were written in dimensionless form by introducing the normalizing parameters D (the jet width at the entrance plane to the solution domain), V_o (the jet centerline velocity at the same station), and ρ (the constant fluid density). Dimensionless variables were obtained by dividing lengths by D, velocities by V_o, the effective and turbulent viscosities by $\rho V_o D$, and the static pressure by $1/2\rho V_o^2$. This introduces the Reynolds number based on jet properties at the entrance plane to the solution domain, $Re = V_o D/\nu$.

In Eqs. (2) and (3), the so-called Reynolds equations, the Reynolds stresses are related to the gradients of the mean velocity components through definition of a turbulent viscosity, μ_{turb}. The effective viscosity, μ_{eff}, is the sum of the molecular and turbulent components, given below in dimensionless form.

$$\mu_{eff} = \frac{1}{Re} + \mu_{turb}. \tag{4}$$

The Turbulence Model Equation

There are various turbulence modeling techniques which can be used to compute μ_{turb} and thereby close the system of Eqs. (1) through (3). These techniques are described in detail by Reynolds (5) in a recent review article.

The most familiar representation of turbulence is the zero-equation model in which the turbulent viscosity is related to the time-averaged velocity field, generally using a mixing length. The zero-equation model deteriorates in accuracy, however, for flows with significant turning, high entering turbulence levels, a stagnation-point region, or boundary-layer separation. In the jet impingement problem under consideration, all of these flow phenomena occur and should be taken into account. For this reason, a more advanced one-equation model of turbulence was adopted.

The essence of the one-equation model is to derive from the instantaneous Navier-Stokes equations a partial-differential equation describing the kinetic energy of the turbulent fluctuations of the flow, which is defined by

$$k = \frac{1}{2} < (u')^2 + (v')^2 + (w')^2 >. \tag{5}$$

The latter, which has been normalized by V_o^2, is related through a phenomenological equation to the turbulent viscosity.

In the present analysis, the one-equation turbulence model of Wolfshtein(6) was selected to compute k; its dimensionless form is

$$u\frac{\partial k}{\partial x} + v\frac{\partial k}{\partial y} = \mu_{turb}\left[2\left(\frac{\partial u}{\partial x}\right)^2 + \left(\frac{\partial u}{\partial y} + \frac{\partial v}{\partial x}\right)^2 + 2\left(\frac{\partial v}{\partial y}\right)^2\right]$$
$$+ \frac{1}{x^j}\frac{\partial}{\partial x}\left(x^j \Gamma_{k,eff}\frac{\partial k}{\partial x}\right) + \frac{\partial}{\partial y}\left(\Gamma_{k,eff}\frac{\partial k}{\partial y}\right) - \frac{C_D k^{3/2}}{\ell_D}. \tag{6}$$

where

$$\Gamma_{k,eff} = \frac{1}{Re} + \frac{\mu_{turb}}{\sigma_{k,turb}}. \tag{7}$$

The turbulent viscosity is computed from

$$\mu_{turb} = c_\mu k^{1/2}\ell_\mu. \tag{8}$$

In the previous equations, C_D, $\sigma_{k,turb}$, and c_μ are constants which have been evaluated by Wolfshtein(6). The variable ℓ_D is the length scale for dissipation, and ℓ_μ is the length scale for viscosity.

The required length-scale distributions depend on the geometry of interest. Therefore, it is not possible to specify general relations which are applicable to all flow configurations. This feature is a disadvantage of one-equation models of turbulence and is the reason more detailed two-equation models have been developed in which a length-scale distribution is computed with a partial differential equation. In the work described here, the ℓ_D and ℓ_μ variations used for the planar impinging jet with a bounding upper surface are those reported in Ref. 7, and the variations used for the axisymmetric impinging jet without a confining upper surface are those used by Wolfshtein (6).

The Vorticity/Stream-Function Form of the Conservation and Turbulence Model Equations

Equations (1), (2), (3), and (6) are not solved in the primitive-variable (u, v, and p) form in which they are written, but rather in terms of the time-averaged vorticity ω and stream function ψ, which are defined by the following equations:

$$\omega = \frac{\partial v}{\partial x} - \frac{\partial u}{\partial y} \tag{9}$$

$$\frac{1}{x^j}\frac{\partial \psi}{\partial y} = u \tag{10}$$

$$\frac{1}{x^j}\frac{\partial \psi}{\partial x} = -v. \tag{11}$$

The vorticity is normalized by V_o/D and the stream function by V_oD.

A vorticity transport equation is derived by differentiating Eq. (2) with respect to y, differentiating Eq. (3) with respect to x, subtracting the former from the latter, and introducing the defining equation for vorticity. This eliminates the static pressure as an unknown. Conservation of mass is ensured through definition of the stream function, which is determined from a Poisson equation obtained by combining Eqs. (9) through (11). The velocity components appearing in the turbulence model equation are also rewritten in terms of the stream function. For brevity, these equations are not presented here but can be found in Ref. 7 for the case of planar flow.

The boundary conditions on ω, ψ, and k which are applied to the governing equations are presented in subsequent sections when specific geometries are considered.

Once the vorticity, stream function, and turbulent viscosity variations are computed, the velocity component distributions must be calculated. The velocity components are readily obtained from the definition of the stream function. The pressure field is computed through a solution of the Poisson equation for pressure. This equation is derived by differentiating Eq. (2) with respect to x, differentiating Eq. (3) with respect to y, and adding the two equations. For planar flow this equation is also presented in Ref. 7. The boundary conditions that are imposed are given by the two momentum equations, Eqs. (2) and (3). Thus, the pressure is determined to within a constant, the value of which is set by fixing the pressure level at one point in the flow.

Conformal Mapping of the Flowfield Equations

To solve the governing equations for a flow with a contoured upper boundary, which simulates the lower surface of a fuselage, an inverse conformal mapping procedure is introduced. In this technique, which was originally devised at MDRL by G.H. Hoffman, a finite-difference computational plane with coordinates (ξ,η) is specified. The distance between nodes in the ξ direction is a, and the distance in the η direction is b, where a and b are not necessarily equal. As an option, stretching functions can then be introduced in each coordinate direction, $\mu = f_1(\xi)$ and $\lambda = f_2(\eta)$, and a mapping plane (μ,λ) can be determined which permits finer resolution of the flowfield where gradients of the computed variables are severe. Finally, a conformal mapping given by

$$\mu + i\lambda = F(x + iy) \tag{12}$$

is introduced which specifies the physical plane (x,y). Laplace's equation is satisfied by both x and y and is solved for each variable subject to the required boundary conditions. The latter follow from physical constraints when they are known at the boundaries and from integration of the Cauchy-Riemann relations for x and y when the boundary distributions are not known.

The unique feature of Hoffman's mapping scheme is that instead of specifying the coordinate distributions in the physical plane and accepting whatever computational plane results, a numerically convenient computational plane is specified, and the corresponding computational plane within the specified physical boundaries is computed. For this reason, the mapping scheme is an inverse procedure.

Finite-Difference Solution of the Governing Equations

With conformal mapping, the elliptic partial-differential equations that describe the flow can be written in the form

$$\alpha\frac{\partial^2\phi}{\partial\xi^2} + \gamma\frac{\partial\phi}{\partial\xi} + \beta\frac{\partial^2\phi}{\partial\eta^2} + \delta\frac{\partial\phi}{\partial\eta} = \sigma, \tag{13}$$

where α, γ, β, and δ denote the nonlinear coefficients, and σ denotes the source term.

For the two Poisson equations ($\phi = \psi$ or $\phi = p$) Eq. (13) can be solved numerically without difficulty using the conventional central-difference finite-difference algorithm. For the vorticity transport equation, $\phi = \omega$, and for the Wolfshtein turbulence-model equation, $\phi = k$, this is not the case. The coefficients γ and δ for these equations contain the Reynolds number as a multiplicative factor, and, as a result, with the standard central-difference algorithm, the discretized system of equations is diagonally dominant for only a limited range in the coefficients γ and δ. Diagonal dominance is necessary to obtain convergence in the iterative solution of the discretized system of equations.

Consequently, in the present work the vorticity transport equation and the turbulent-kinetic-energy equation are solved using the augmented-central-difference (ACD) algorithm developed by G.H. Hoffman at MDRL (8). The essence of this method can be illustrated by considering the derivative $\partial\phi/\partial\xi$ of Eq. (13). Using the five-point, finite-difference stencil shown in Fig. 2 and point-of-the compass notation, this derivative can be evaluated at point P using the following truncated Taylor-series representation and standard central-difference approximation to the first derivative:

$$\left.\frac{\partial\phi}{\partial\xi}\right|_P = \frac{\phi_E - \phi_W}{2a} - \frac{a^2}{6}\left.\frac{\partial^3\phi}{\partial\xi^3}\right|_P - \frac{a^4}{5!}\left.\frac{\partial^5\phi}{\partial\xi^5}\right|_P . \tag{14}$$

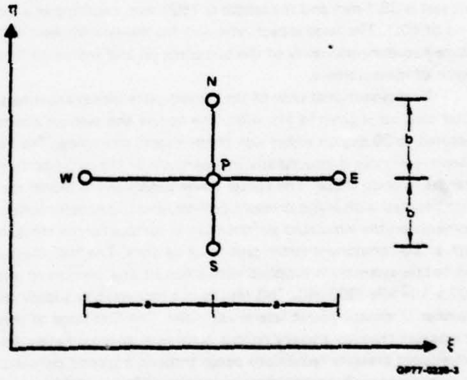

Fig. 2 Five-point finite-difference stencil

In the ACD scheme, the derivative $\partial^3\phi/\partial\xi^3$ is retained and is expressed in terms of lower-order derivatives by differentiating Eq. (13) with respect to ξ. The derivative $\partial\phi/\partial\eta$ in Eq. (13) is represented in an analogous fashion with the ACD algorithm.

The finite-difference equations are solved using point relaxation. The computing sequence is illustrated in Fig. 3. For each flow variable ϕ (ω, ψ, k, and p), a local residual is defined by $r_\phi = |\phi_{N+1} - \phi_N|$, where N is the iteration counter. The following maximum permissible residuals, $r_{\phi,\max}$, are set for each variable: $r_{\omega,\max} = 10^{-3}$, $r_{\psi,\max} = 10^{-4}$, $r_{k,\max} = 10^{-4}$ and $r_{p,\max} = 10^{-6}$. Convergence is said to be achieved when $r_\phi < r_{\phi,\max}$ everywhere in the flowfield.

RESULTS

The Planar Impinging Jet

Measured Flow Properties. The planar impinging-jet flowfield, shown

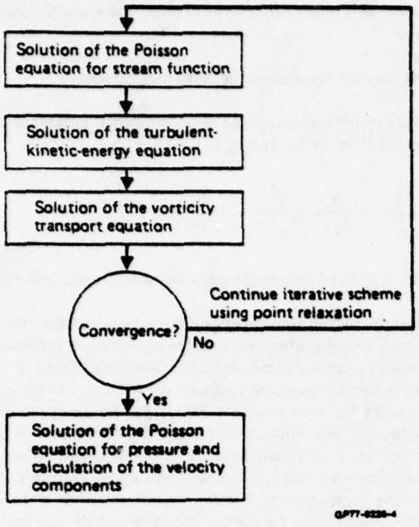

Fig. 3 Calculating sequence

schematically in Fig. 1(a), has received major emphasis in the MDRL experimental and theoretical research effort. Recently a test program to measure the flow properties for this configuration and a contracted research effort for the Office of Naval Research to compute the corresponding flows were completed. Representative preliminary results are presented in this section.

In the experimental program two basic geometries, a flat-plate model and a curved-plate model, were tested in simulated close ground effect using an adjustable-height ground board. Details of the test apparatus and model hardware are shown in Fig. 4.

The general configuration is illustrated in Fig. 4(a). The width of the jet exit slot is 38.1 mm and the length is 1524 mm, resulting in a jet slot aspect ratio of 40:1. The large aspect ratio and the model endplates are utilized to assure two-dimensionality of the turbulent jet and entrained flowfield in the region of measurement.

A cross-sectional view of the curved-plate model showing the selected outer contour is given in Fig. 4(b). The nozzle and plenum assembly can be vectored to 30 deg on either side of the model centerline. The high-pressure plenum assembly is structurally independent of the outer body to facilitate changes in body shape. The center lower panels of the model are densely instrumented with static pressure orifices, and if desired induced forces and moments on the simulated airframe under-surface can be measured directly with a two-component strain gage force balance. The high-pressure plenum and nozzle assembly is supplied with clean air at a pressure in excess of 2.07×10^3 kPa (300 psi). This results in a low-velocity supply to the upper chamber eliminating large lateral velocities. The first stage of pressure reduction occurs through a heavy porous plate with approximately 4% open area. Subsequent pressure reductions occur through a second porous plate and a jet exit screen with approximate porosities of 30% and 60% respectively.

Extensive static pressure measurements, jet plume total pressure surveys, and hot-wire anemometer measurements were completed during the test program. These data show the extreme influence of the ratio of distance above ground to jet exit slot width and the surprisingly strong significance of body under-surface shape.

In Fig. 5 the static pressure distributions on the under-surface of the flat-plate model and on the ground surface below the flat-plate model are shown for three values of H in close ground effect. From Fig. 5(a) the sensitivity of the under-surface pressure to H is readily apparent. The maximum induced negative pressure measured was approximately 6.2 kPa (0.9 psi), and in all other runs the induced static pressures were substantially smaller. These small pressure signals necessitated the use of a 1.0 psid transducer in the scanivalve pressure system for model surface pressures.

Ground-plane static pressure profiles, Fig. 5(b), indicate some surprising results. For $H \leq 2$, ground-plane pressures on either side of the stagnation point are below ambient. This suggests a strong acceleration in the impingement flow to either side of the stagnation point, probably a result of flow separation on the upper surface near the jet exit. Prediction of these induced negative pressures on the ground plane constitutes a severe test for any computational procedure.

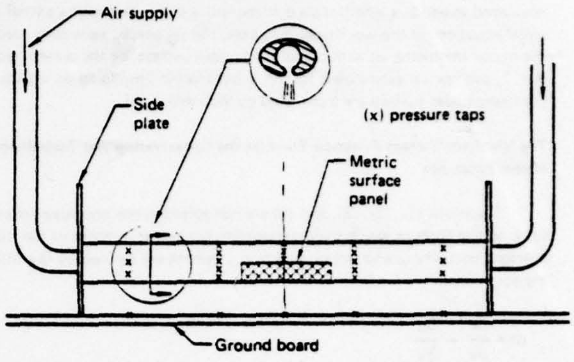

(a) Test configuration and instrumentation detail

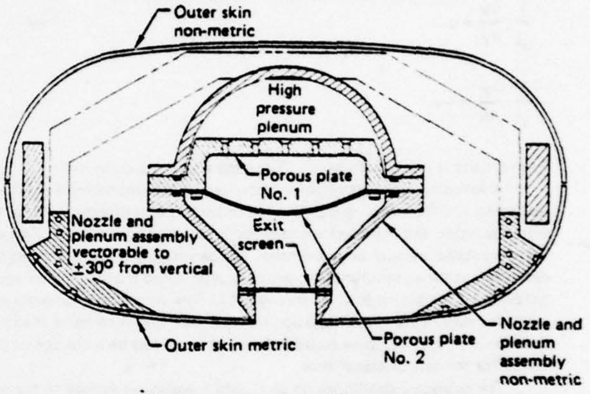

(b) Cross-section view of the test model

Fig. 4 Description of the planar lift-jet/airframe/ground interaction experimental configuration

It should be noted that both the upper-surface and ground-board static pressure variations indicate flow symmetry about the jet centerline. Jet dynamic pressure profiles measured at three stations below the exit plane further substantiate that a planar flow was in fact achieved during the test. Specifically, spanwise jet velocity variations were within ± 10% across the 1.5 m (60 in.) span of the jet. In addition, these profiles revealed a fairly well behaved core flow persisting down to approximately four diameters from the exit plane.

Figure 6 presents the model under-surface and ground-plane static pressure distributions in the flowfield of the curved-plate model in close ground effect. The test conditions for the data shown correspond to those for the flat-plate model of Fig. 5. The sensitivity of the induced pressures on the model under-surface to H, Fig. 6(a), are of the same order of magnitude as for the flat-plate case. However, the magnitudes of the induced negative pressures on the curved-plate model are significantly lower (more than a factor of two), which clearly indicate the advantages of under-surface curvature to reduce induced suck-down loads. The below-ambient ground-board pressures are again evident in Fig. 6(b) for $H = 1$, but they are of a greatly reduced magnitude from those of the flat-plate model flowfield.

Computed Flow Properties. Calculations of the fluid properties for both the flat-plate and curved-plate flowfields have been made using the analysis technique described in the previous section. The physical and computational planes used, along with the boundary conditions imposed on the primary flow variables (stream function, vorticity, and turbulent kinetic energy), are shown in Fig. 7.

Since only normal impingement is considered, geometric symmetry about the jet centerline exists so that only half the flowfield need be solved. The stream function and vorticity are antisymmetric about the centerline, and the turbulent kinetic energy is symmetric. Boundary conditions imposed on ψ, ω, and k follow from assumed profiles at the jet exit plane; from the no-slip, impermeable-wall constraint at the solid surfaces; from symmetry at the jet centerline; and from the assumption of developed flow at the right boundary. The latter assumption

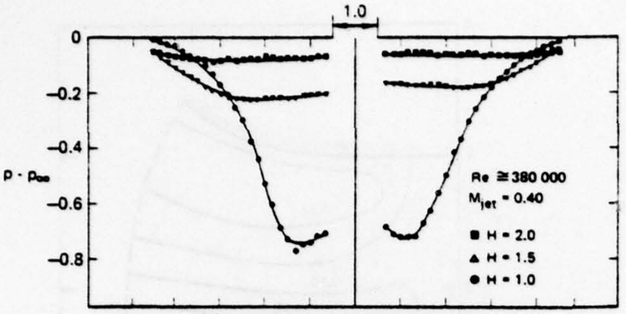

(a) Under-surface static pressure profiles

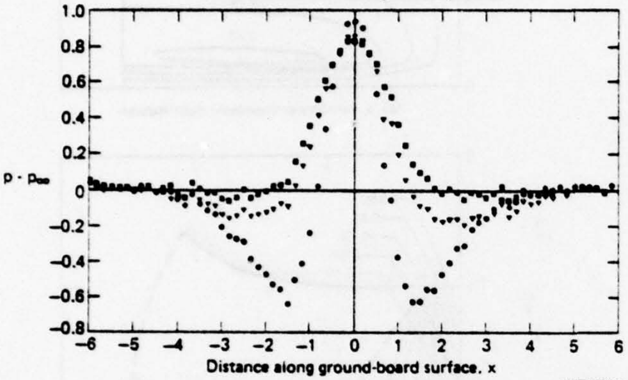

(b) Ground-board static pressure profiles

Fig. 5 Measured pressure distributions for the flat-plate model in close ground effect

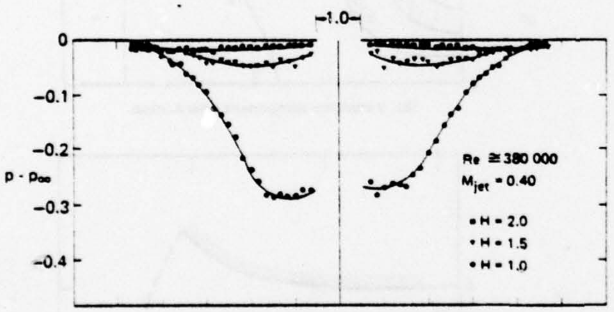

(a) Under-surface static pressure profiles

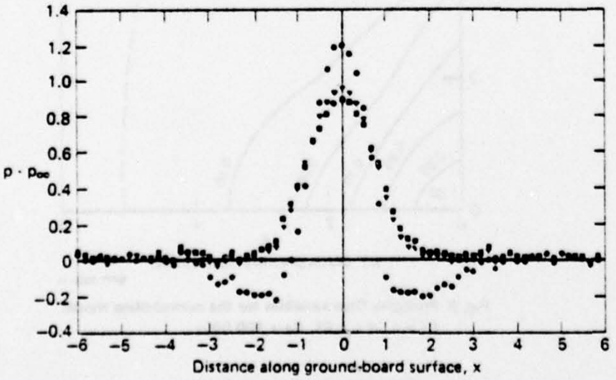

(b) Ground-board static pressure profiles

Fig. 6 Measured pressure distributions for the curved-plate model in close ground effect

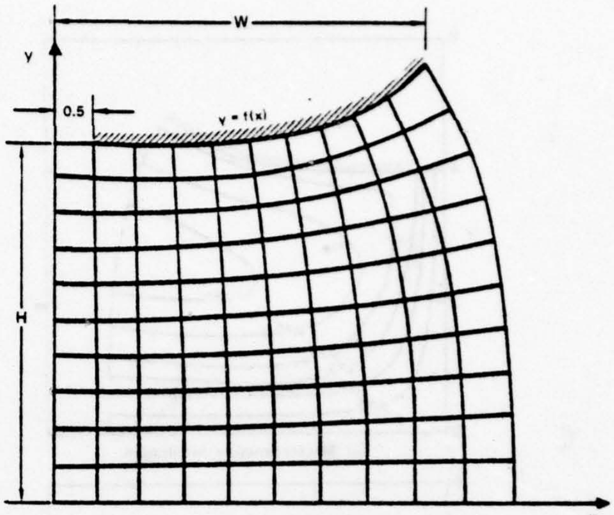

(a) Physical plane

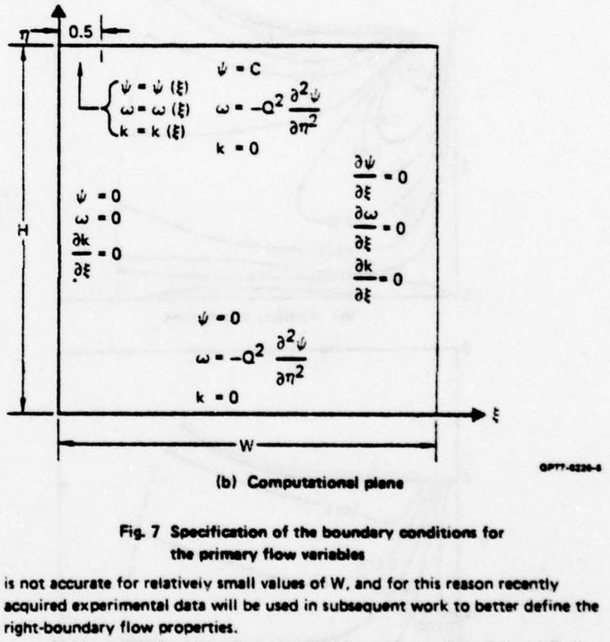

(b) Computational plane

Fig. 7 Specification of the boundary conditions for the primary flow variables

is not accurate for relatively small values of W, and for this reason recently acquired experimental data will be used in subsequent work to better define the right-boundary flow properties.

Although solutions have been obtained for various values of H and Re for the flat-plate configuration, only solutions computed for the more interesting curved-plate geometry are presented here. In all cases a 41 by 41 finite-difference grid, uniform in each coordinate direction in the computational plane, was used.

For the curved-plate configuration with H = 4 and W = 4.68, Fig. 8 shows contour plots of the primary flow variables computed for a Reynolds number of 100 000. The stream function contour, Fig. 8(a), depicts the entrainment of fluid into the jet, and the vorticity distribution, Fig. 8(b), shows the convection of vorticity toward the right boundary and the development of the lower wall jet. Of particular interest is the plot of the turbulent kinetic energy, Fig. 8(c). Throughout the impinging jet, k decays in magnitude from the maximum value of 0.04 imposed at the jet entrance plane to the solution domain.

The primitive flow variables (velocity components and static pressure) are shown in Fig. 9. The x-velocity-component distribution, Fig. 9(a), further shows the entrainment into the jet and the growth of the wall jet along the impingement surface. The y-velocity-component profile, Fig. 9(b), illustrates the rate of decay of the jet centerline velocity as the stagnation point is approached, and the static pressure profile, Fig. 9(c), shows the corresponding rise in p.

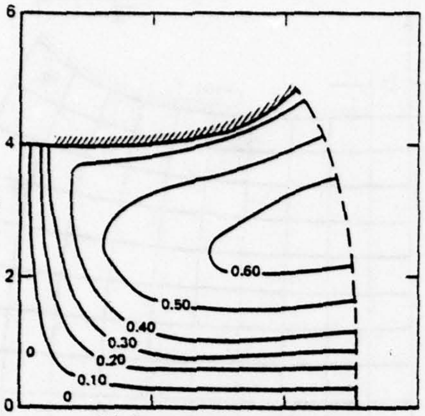

(a) Stream function distribution

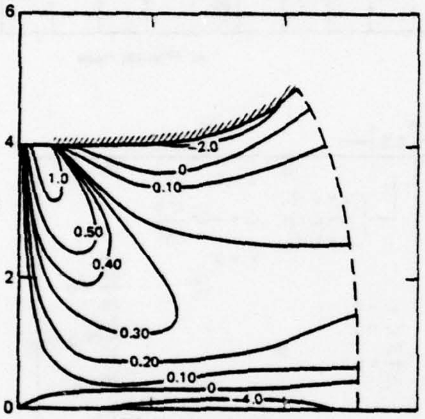

(b) Vorticity distribution

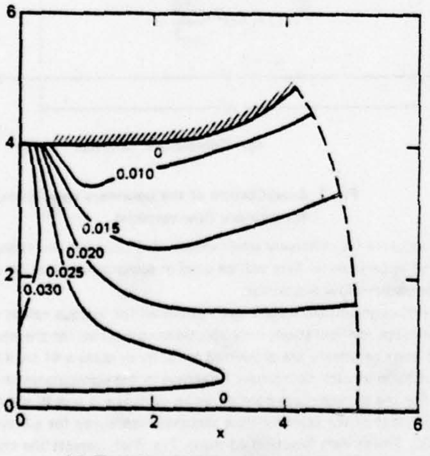

(c) Turbulent-kinetic-energy distribution

GP77-0226-9

Fig. 8 Primary flow variables for the curved-plate model (H = 4, W = 4.68, Re = 100 000)

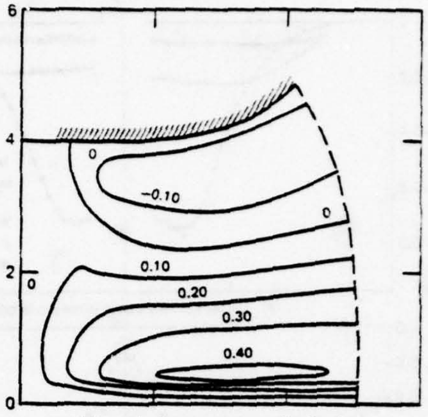

(a) x-velocity-component distribution

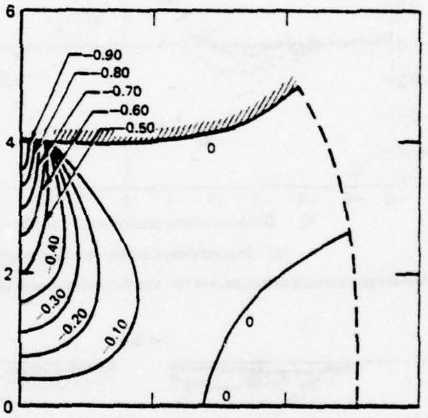

(b) y-velocity-component distribution

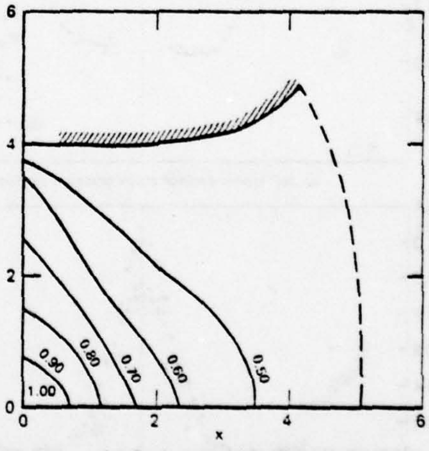

(c) Static pressure distribution

GP77-0226-10

Fig. 9 Primitive flow variables for the curved-plate model (H = 4, W = 4.68, Re = 100 000)

Comparison of Measured and Computed Flow Properties. Comparison of measured and computed flow variables of interest are shown in Figs. 10 through 12 for the curved-plate geometry with H = 4. The distribution of centerline turbulent kinetic energy as a function of y is shown in Fig. 10 as obtained experimentally for the lowest Reynolds number for which the flow was measured (Re = 130 000) and theoretically for the largest Reynolds number for which the flow was computed (Re = 100 000). The poor agreement is attributed to the inaccuracy of the proposed length scales given in Ref. 7, which were formulated on the basis of simple order-of-magnitude arguments. With the present availability of the impinging jet data, these length scale distributions can be modified to bring the experimental and theoretical distributions in better agreement. The excessive turbulence level within the jet results in a decay of the magnitude of the jet centerline velocity which is greater than that observed experimentally, as shown in Fig. 11.

The computed and measured lower-wall static pressure variations for the curved-plate flowfield with H = 4 are shown in Fig. 12. The theoretical drop in p is not as severe as that measured, which may, in part, be also due to incorrect turbulence modeling near the stagnation point.

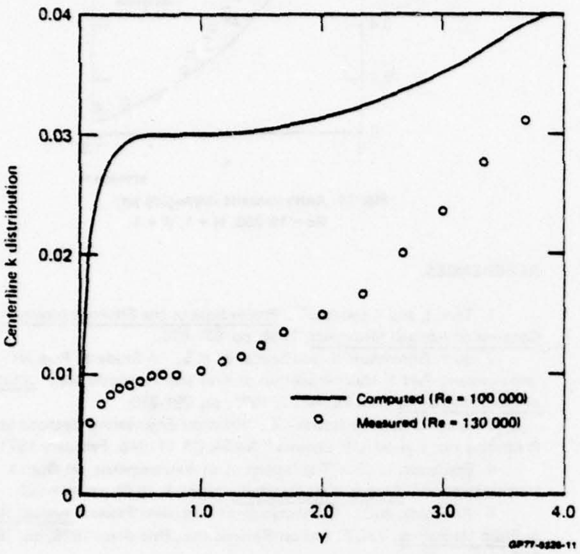

Fig. 10 **Comparison of computed and measured centerline turbulent-kinetic-energy distributions for the curved-plate model with H = 4**

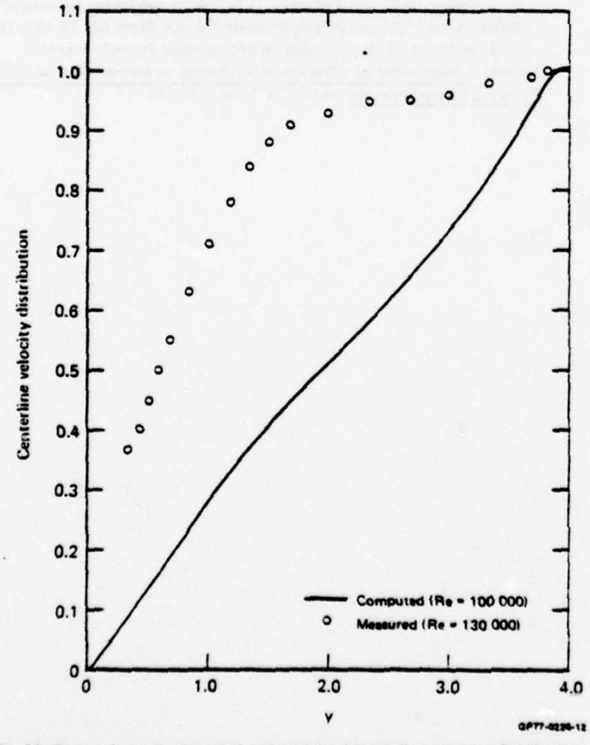

Fig. 11 **Comparison of computed and measured centerline velocity distributions for the curved-plate model with H = 4**

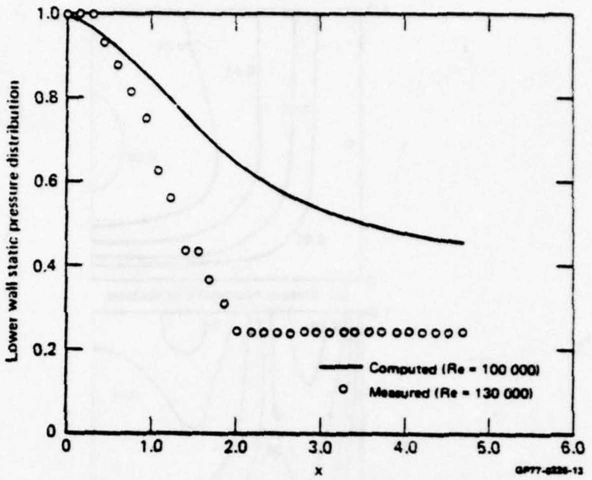

Fig. 12 **Comparison of computed and measured wall static pressure distributions for the curved-plate model with H = 4**

The Axisymmetric Impinging Jet

The axisymmetric impinging-jet flowfield, shown schematically in Fig. 1(b), has been studied only theoretically in the MDRL research program on jet impingement flowfields. Compared to the planar case, a relatively large number of experimental studies of this configuration have been reported.

The configuration studied analytically is the same as that shown in Fig. 7 except that the solid upper surface has been replaced by a free boundary parallel to the lower wall through which a developed turbulent jet enters the computational domain normal to the boundary with no vorticity or turbulent fluctuations. Thus, no conformal mapping is required ($\xi = x, \eta = y$), and the boundary conditions are the same as those shown in Fig. 7(b), with the following imposed along the upper boundary for $x \geqslant 0.5$: $\partial\psi/\partial y = 0$, $\omega = 0$, and $k = 0$.

The primary flow variables and velocity components computed on a square solution domain with H = 1, W = 1, and Re = 10 000 are shown in Fig. 13. The profiles are very similar to those computed by Wolfshtein(6) and Bower and Kotansky(7) for a planar jet with a free upper boundary. A comparison of the computed jet static pressure variation along the axis and that measured by Gray and Kisielowski(3) is shown in Fig. 14.

CONCLUSIONS

A procedure for solving the Reynolds equations in conjunction with a one-equation turbulence model has been applied to a single two-dimensional incompressible jet impinging normal to the ground. This is a configuration for which purely inviscid techniques do not provide information on jet entrainment and for which inviscid and boundary layer schemes cannot be patched together since the boundary layer assumptions are grossly violated.

For the planar jet case, results of a test program are presented which reveal a strong dependence of the flowfield on the ratio of distance above ground to jet exit slot width and on body under-surface shape. Fluid properties computed for the planar jet emanating from a curved-plate upper surface do not agree in magnitude with those measured. The differences are attributed to the inaccuracy of the required turbulence length scales which were postulated on the basis of simple physical arguments without the benefit of data. For the axisymmetric jet case, the computed flowfields are qualitatively similar to those computed by Wolfshtein(6) for the analogous planar impinging jet.

As the next step in the current MDRL research effort, work will be directed toward modifying the length scale distributions in order to provide a more accurate prediction scheme. Comparisons with additional test data will be made, and parametric studies will be carried out to better define the role entrainment plays in two-dimensional jet impingement flows.

ACKNOWLEDGMENT

The authors acknowledge the contributions of Dr. F.W. Roos (MDRL) in the acquisition of the planar jet test data and Dr. M.I.O. Ero (Purdue University) in the formulation of the turbulent axisymmetric jet theoretical model.

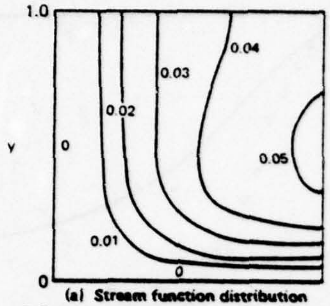

(a) Stream function distribution

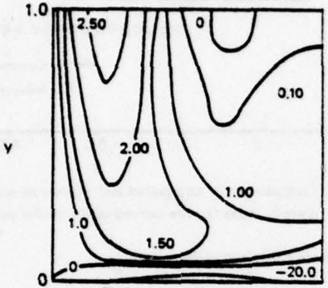

(b) Vorticity distribution

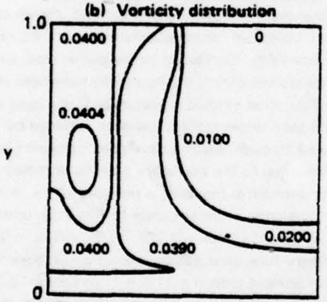

(c) Turbulent-kinetic-energy distribution

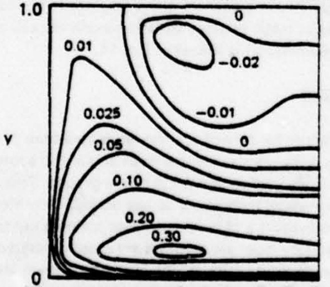

(d) x - component-of-velocity distribution

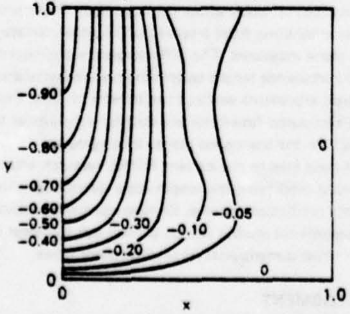

(e) y - component-of-velocity distribution

GP77-0228-14

Fig. 13 Axisymmetric impinging jet; Re = 10 000, H = 1, W = 1

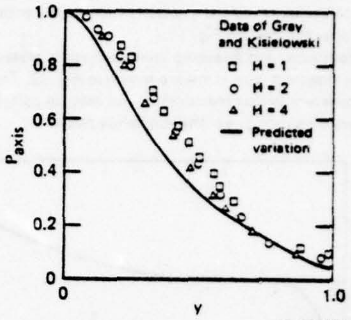

GP77-0228-15

Fig. 14 Axisymmetric impinging jet; Re = 10 000, H = 1, W = 1

REFERENCES

1 Tani, I. and Komatsu, Y., Proceedings of the Eleventh International Congress of Applied Mechanics, 1966, pp. 672-676.

2 du P. Donaldson, C. and Snedeker, R.S., "A Study of Free Jet Impingement. Part 1. Mean Properties of Free and Impinging Jets," Journal of Fluid Mechanics, Vol. 45, Part 2, 1971, pp. 281-319.

3 Gray, L. and Kisielowski, E., "Practical Engineering Methods for Predicting Hot Gas Jet-Lift Engines," NASA CR 111845, February 1971.

4 Bradbury, L.J.S., "The Impact of an Axisymmetric Jet Onto a Normal Ground," Aeronautical Quarterly, Vol. 23, 1972, pp. 141-147.

5 Reynolds, W.C., "Computation of Turbulent Flows," Annual Review of Fluid Mechanics, Vol. 8, Annual Reviews Inc., Palo Alto, 1976, pp. 183-208.

6 Wolfshtein, M. "Convection Processes in Turbulent Impinging Jets," Report SF/R/2, Department of Mechanical Engineering, Imperial College of Science and Technology, November 1967.

7 Bower, W.W. and Kotansky, D.R., "A Navier-Stokes Analysis of the Two-Dimensional Ground Effects Problem," AIAA Paper No. 76-621, 1976.

8 Hoffman, G.H., "Calculation of Separated Flows in Internal Passages," Proceedings of a Workshop on Prediction Methods for Jet V/STOL Propulsion Aerodynamics, Vol. 1, 1975, pp. 114-124.

FLOW AND HEAT TRANSFER CHARACTERISTICS OF A TURBULENT SLOT JET IMPINGING ON A MOVING WALL

A.R.P. van Heiningen, A.S. Mujumdar and W.J.M. Douglas

Department of Chemical Engineering
McGill University
Montreal, Canada

and

The Pulp and Paper Institute of Canada

ABSTRACT

Results of an experimental study of local heat transfer under partially confined turbulent slot jets impinging on a moving surface are presented.

A photo-fabrication technique was used to deposit a 0.27 µm gold-film on a pyroceram substrate to act as a fast response temperature sensor. The sensor was mounted flush on the surface of a rotating porous stainless steel drum. Instantaneous heat transfer rates were determined numerically by solving the governing transient heat conduction equation. For slow rotation, i.e. for low surface-to-jet velocity ratios the heat transfer results were not influenced by the surface motion, demonstrating negligible influence of wall motion.

Finally, the results of a numerical prediction using a two-equation model of turbulence for a stationary impingement surface are presented and discussed in the light of the experimental results obtained.

NOMENCLATURE

b	coefficient in equation (1)
C_p	specific heat at constant pressure
H	nozzle to plate distance
k	thermal conductivity
L	nozzle width
T_j	jet temperature at nozzle exit
T_p	average drum surface temperature
U_r	rotational velocity of the drum
U_p	suction velocity through the drum surface
x	distance from stagnation point along the impingement surface

Non-dimensional Numbers

Nu	Nusselt number $= \alpha L/k$
Nu_0	Nusselt number at the stagnation point
Re	Reynolds number $= \rho U_j L/\mu$
St	Stanton number $= \alpha/(\rho C_p U_j)$

Greek Letters

α	heat transfer coefficient
μ	dynamic viscosity
ρ	density

1. INTRODUCTION

Impinging jets are commonly encountered in industrial equipment because of their favourable heat and mass transfer characteristics. Most of their major applications particularly in the drying of paper and textiles involve use of jets of various configurations impinging on moving surfaces. One such application involves the use of stationary multiple slot jets, separated by exhaust ports to reduce the adverse effects of "spent" air, impinging normally on the wet paper web which is supported on a large rotating roll. Mujumdar and Douglas (1) and Hardisty (2) among many others have reviewed the general literature with reference to application of impingement flows in paper drying.

In view of the lack of published work, experimental or analytical, on the flow and heat transfer characteristics of partially confined turbulent jets impinging on moving surfaces, the present study was undertaken to assess the importance of wall motion in determining the transfer rates. Although the eventual goal of this study is to examine the effects of suction applied at the impingement surface on both the flow and heat transfer characteristics, and the experimental set-up was designed to study the influence of this additional parameter, this paper will consider only the case of no suction or blowing at the moving surface.

Experimental heat transfer distributions for the case of "very slow" wall motion are compared with the generally accepted data for a turbulent slot jet impinging on a stationary plate. Furthermore, results of a numerical prediction for the stationary wall case are also presented and discussed. A two-equation turbulence model was used to solve the governing flow and energy equations in primitive variables (velocity-pressure).

The parameters included in the experimental study are:

Reynolds number, Re	13700 - 49100
Nozzle to plate spacing, H/L	2.6 and 6.0
Velocity of impingement surface, U_p	0.45 - 2.74 m/s
Nozzle width, L	0.62 and 1.41 cm

2. EXPERIMENTAL SET-UP

A schematic diagram of the experimental set-up is shown in Figure 1. Hot air enters the upper plenum chamber while ambient air enters the lower plenum chamber to maintain the rotating drum at a uniform temperature, i.e. to avoid continual heating of the drum. The lower plenum chamber (cold-side) and the cooling nozzle were also designed to acquire useable heat transfer data. Both chambers contain honeycomb to straighten the flow and a combination of screens to reduce the turbulence level down to an estimated value of less than 0.5 percent at the nozzle exit. The hot and cold air streams are exhausted via a ductwork designed to equalize the pressure drops in each arm. Unequal pressure drops were found to induce oblique impingement with the jet inclined towards the arm with a lower pressure drop.

Furthermore to eliminate undesirable interference between the hot and cold exit streams, teflon skimmer plates positioned within 3 mm of the drum surface separated the two streams (as shown in Figure 1). Although the drum is made of porous stainless steel (PSS) to allow application of suction this paper will be concerned only with the impermeable wall results. Care was taken to prevent air flow into and inside the drum. The drum surface was quite smooth (surface roughness of ~ 20 μm rms), i.e. the results obtained are considered valid for a smooth surface.

Electrical signals from the heatflux sensor, thermocouples and the pressure transducer mounted on the rotating drum are transmitted to stationary monitoring instrumentation via a low-noise, 14-channel slip-ring assembly (IEC Corp. Austin, Texas, model IEC-BX-14) mounted on the drum shaft.

Following are the key geometric dimensions of the physical set-up:

Diameter of the rotating drum	483 mm
Width of the upper nozzle	6.2 mm
Length of the rotating drum	229 mm
Width of the lower nozzle	14.1 mm
Length of the nozzle (both)	203 mm
Spacing between drum surface and cover plate	37 mm

The nozzles conformed to the specifications of the standard ASME long radius nozzle.

The thin-film heat flux sensor, shown schematically in Figure 2, was made using the photo-fabrication technique used extensively in manufacture of micro-circuits. A zig-zag pattern of gold film is deposited on the surface of a pyroceram 9606 (Corning Glass, Inc., Corning, N.Y.) substrate (89 mm x 6 mm x 3.2 mm). This substrate was selected to match the $\sqrt{kC_p\rho}$ value of the porous stainless steel used (Pall Canada, Montreal) since under transient conditions the thermal response is governed by the parameter $\sqrt{kC_p\rho}$ (3).

The thermal conductivity of PSS was measured using a simple apparatus described in Reference (4). The $\sqrt{\rho k C_p}$ values for the PSS and pyroceram 9606 are 2670 ± 110 and 2820 W $s^{1/2}/m^2/^\circ K$ respectively. These are close enough to justify assumption of surface temperature continuity over the sensor-drum interface. Note that a discontinuity will make the sensor to act like a skin-friction measurement device (5). The sensor was mounted flush with the drum surface and located centrally with the longest dimension parallel to the drum axis. The three gold strips, shown in Figure 2, are 0.25 mm x 70 mm and are 0.20 mm apart with a film thickness of 0.27 μm. To protect the gold film a 0.1 μm layer of SiO_2 was deposited by sputtering on the active surface of the sensor. The film resistance was measured to be 180 Ω at 20°C with a temperature sensitivity of 0.278 ± 0.003 Ω/°C over the temperature range, 20 - 100°C.

The instantaneous heat transfer (temperature) fluctuation was monitored by making the film one arm of a four-decade Wheatstone bridge circuit (J.C. Biddle Co., Cat. No. 601022) fed by a 1.35 volt mercury battery. The film can achieve a change of 0.44 mV/°C without appreciable self-heating. With an input noise level of about 2 μV the sensor can detect changes of 0.005°C. The film has negligible thermal inertia and hence responds to heat transfer fluctuations essentially instantaneously.

The heat flux probe was placed and held flush with the drum surface even at high rotational speeds. Care was taken to ensure that no flow separation took place along the edges of the pyroceram substrate. A 50 μm polyimide adhesive tape (Dodge Industries, Inc., Hoosick Falls, N.Y., Cat. No. 2345) was used to cover the small gap between the substrate and the drum.

To eliminate temperature gradients in the direction parallel to the drum axis it was found necessary to insulate the whole assembly (except the drum) with a 5 cm fiberglas layer. Also, the sides of the drum were blackened and heated each with two 250-volt infra-red heating lamps to counter the cooling due to exposure to ambient air. The temperature of the black drum side plate is monitored with an IR pyrometer. Air temperature at the nozzles and temperature of the cover plates at various locations is measured with strategically placed thermocouples. Velocity and temperature distribution in the exit ducts are measured with a moveable pitot tube and thermocouples respectively.

Finally, a calibrated pressure transducer (Kulite XTH-190-5) with a natural frequency of about 70 kHz is mounted centrally and flush with the drum surface 180° from the heat flux sensor.

Further details on the experimental set-up and procedures are available in Reference (6).

3. DATA ACQUISITION AND REDUCTION

The resistance of the heat flux sensor is measured with a 4-decade Wheatstone bridge. The bridge is balanced to correspond to the average resistance when the drum rotates. The bridge reading is converted into temperature using a pre-determined calibration curve. The unbalanced bridge voltage is amplified 2500 times (DANA model 2820, 2 μv rms RTI) and transmitted via a shielded cable to a GE-PAC 4020 digital computer for data acquisition, storage and reduction.

The signal is filtered, amplified and subsequently digitized by a 9 bit + sign, 2-channel, high-speed analog-to-digital-converter (ADC) before being stored on a disk. Extreme care was taken to reduce the electrical noise by shielding all the wires and grounding all instruments to a common ground. The sampling rate of the ADC was chosen to be about 500 measurements per rotation.

The gain of the second amplifier is adjusted so that the absolute value of the peak output signal would be slightly smaller than 5 volt, which is the maximum input of the ADC. The filter is set at a frequency range one decade higher than the ADC sampling rate to eliminate extraneous high frequency (> 10 kHz) noise.

The data stored on disk are transformed digitally into heat fluxes. The unsteady, one-dimensional heat conduction equation is solved using a modification of Schmidt's method. There is no heat loss from the back side of the sensor because the temperature at the back was equal to the average surface temperature as measured with the gold film. The penetration depth of the heat waves in the sensor material was always smaller than the thickness of the substrate for all rotational speeds considered.

Further information on the data reduction of a thin film heat flux sensor is given in (7). In order to identify the circumferential location of the sensor a lever was attached to the rotating drum which activates a microswitch when passing and produces a square wave voltage in the microswitch circuit. This signal is transmitted to the second channel of the ADC and recorded simultaneously with the sensor signal. The start of the square wave is used to label the position of the sensor. This allows averaging of the heat flux at each circumferential position over several rotations. The heat flux distribution under the hot and cold jet are converted into Nusselt numbers, printed and then plotted on a CALCOMP plotter. The pressure signal is displayed on a storage oscilloscope.

4. RESULTS AND DISCUSSION

Figures 3 and 4 show a typical output of the data acquisition and reduction system for the cold (lower) and hot jet (upper) impingement heat transfer, respectively. All pertinent information is included in each graphical output from the CALCOMP plotter. These figures refer to an essentially stationary impingement wall since the rotational speed was only 0.39 revolutions per second yielding a linear surface velocity of only 0.6 m/s which may be compared with jet velocities of 68 m/s and 78 m/s. These figures represent local Nusselt numbers averaged over 50 rotations. Averaging over a larger number of rotations did not make any measurable difference in the Nu distribution curves.

The instantaneous Nusselt number distribution over the drum circumference for a single rotation, however, displays the typical turbulent fluctuations (Figures 5 and 6). The heat flux sensor has an averaging area of only 1.15 mm, and thus these results have spatial and temporal resolution in local heat transfer distributions not attained previously for a turbulent impinging jet situation. Even under the worst case of the lowest rotational speed the circumferential heat conduction in the sensor is less than 1 percent of the convective heat flux. Thus the accuracy and spatial resolution of the sensor is unaffected by possible conduction effects.

Since the jet-to-surface velocity ratio is of the order 10^{-2}, the results shown in Figures 3 and 4 may be compared with published data for stationary impingement plates. This is supported by the work of Popiel et al. (8) and Metzger & Groghowsky (9) who studied the heat transfer between an impinging axisymmetric jet and a rotating disk.

It can be seen in Figure 3 that the present results in the impingement region compare well with the data of Cadek and Zerkle (10) who used a 0.90 mm diameter Gardon foil to measure the local heat flux distribution on the impingement surface. Cadek and Zerkle used an ASME long radius nozzle as used in this study. The greater differences between Cadek's data and the present data for $|X/L| > 7.5$ may be attributable at least partially to the presence of a recirculation zone in the present set-up owing to the cover plate. The curvature of the drum is expected to have negligible effect on the present results since its radius of curvature is two orders of magnitude larger than the width of the nozzle.

It is interesting to note that, although not shown in Figure 4, the present results for $H/L = 6$ are bounded on both sides by Cadek's data for $H/L = 4$ and $H/L = 8$. The slight asymmetry in the Nusselt number distribution under the hot jet may be due to slightly oblique impingement of the jet which could not be corrected for.

The heat transfer distribution curves are characterized by a central peak (at stagnation) with secondary peaks on either side, in accord with Cadek and Zerkle (10) and Gardon and Akfirat (11). As pointed out by Gardon and Akfirat the central peak is due to the high laminar stagnation heat transfer while the secondary peaks are caused by transition of the jet flow from laminar to turbulent regime. This hypothesis is supported by the instantaneous Nusselt number distributions (Figures 5 and 6). It can be seen that the intensity of Nusselt number fluctuations is relatively high in the regions of the secondary peaks and quite low in the stagnation region. A further confirmation of this phenomenon is obtained from the instantaneous pressure distribution sensed by the pressure transducer. Figure 7 is a reproduction of a typical pressure trace recorded on a storage oscilloscope. Strong pressure fluctuations occur in regions of the secondary peaks and in the "wall jet" region. The intense turbulent fluctuations far removed from the stagnation region may be associated with the high heat transfer values obtained in this work when compared with Cadek's data.

The influence of the Reynolds number on the heat transfer distribution for the nozzle-to-plate spacings, H/L, of 2.6 and 6.0 can be seen in Figures 8 to 11 together with 3 and 4. The values of the Nusselt numbers at the stagnation point over the Reynolds number range studied are very well correlated by

$$Nu_0 = b\sqrt{Re} \tag{1}$$

where b = 0.49±0.05 and 0.515±0.01 for H/L = 2.6 and 6.0 respectively. These values are in close agreement with the data of Cadek Zerkle (8). Miyazaki and Silberman (12) obtained analytically b = 0.45 when H/L > 1.5 for a jet with a flat velocity profile at the nozzle exit by neglecting the spreading and turbulence of the jet.

Comparison of the theoretical and the experimental values of b confirms that the stagnation point heat transfer is reasonably well described by the combination of potential flow and laminar boundary layer flow if the jet impacts before the end of the potential core. A better agreement is expected when the free stream velocity in the boundary layer calculation is derived from the experimental pressure distribution at the impingement wall.

As may be expected the coefficient b is slightly higher for H/L = 6.0 because at this nozzle-to-plate spacing the increase in heat transfer due to turbulence becomes more important than the decrease in heat transfer due to the mean axial velocity decay of the jet. The maximum heat transfer at the secondary peaks for H/L = 2.6 can be correlated as

$$Nu = (0.00263\pm0.00005)\ Re \tag{2}$$

Also, for H/L = 6 the maximum heat transfer of the secondary peaks are linearly proportional to the Reynolds number. As a result the secondary peaks become more dominant as the Re number increases. The locations of the secondary peaks were observed to be independent of the Reynolds number for a given H/L. These occurred at X/L = 7.5 and 5.5 respectively for H/L = 2.6 and 6, again in agreement with Cadek and Zerkle (10).

The average heat transfer for H/L = 2.6 is maximal when averaged from X/L = -12.5 to X/L = 12.5 and found to be proportional to $Re^{0.78}$. The influence of H/L can be seen from Figures 4 and 9.

It is interesting to note that the heat transfer distribution was unaffected when the rotational speed of the drum was increased to 1.8 rps (equivalent to a surface velocity of 2.74 m/sec) over the Reynolds number range considered here.

Numerical Prediction

Some preliminary numerical predictions were made of the flow and temperature fields of a partially confined turbulent slot jet impinging on a stationary flat surface. The flow field is confined by the two cover plates attached to the jet nozzle and mounted parallel to the impingement plate.

A computer program developed by Gosman et al. (13) was used to solve the full Navier-Stokes equations in their primitive form to compute the heat transfer under the impinging slot jet. The turbulent viscosity and the turbulent thermal conductivity were derived from the turbulent kinetic energy-energy dissipation, two-equation model and a constant turbulent Prandtl number respectively.

As can be seen from Figure 12, for Re = 22750 and H/L = 8, the predicted heat transfer distribution at the impingement plate compared favourably with the experimental data of Gardon and Akfirat (14) and Cadek and Zerkle (10) except for a deviation in the stagnation region. A better agreement with the experimental data was obtained in this region when the number of grid lines next to the impingement plate was increased. The deviation in the stagnation region is thought to be due to the inapplicability of the "log law" as a boundary condition in this region.

For smaller values of H/L the difference between the predicted and measured heat transfer is expected to increase as the turbulence model used here is unable to predict transition from laminar to turbulent flow. However, for the prediction of the heat transfer under an impinging jet which is fully turbulent before impact (say, H/L = 8) the two-equation turbulence model was found to be superior to a previously reported prediction obtained by Wolfshtein (15) with a one-equation model also shown in Figure 12.

CLOSURE

Results of this experimental investigation show that for low surface-to-jet velocity ratios the effect of motion of the impingement surface on the local heat transfer at the surface is negligible over the Reynolds number and nozzle-to-surface spacing ranges considered. Using a very fast response, photo-fabricated thin film sensor high resolution heat transfer distribution curves are obtained for a turbulent jet impinging on essentially stationary and on slowly moving surfaces. Comparison with earlier work on stationary impingement is favourable in the impingement region. However, considerable deviations are noted away from this region possibly due to the influence of partial confinement. Finally, it is postulated that unless the jet is fully turbulent before impact, the commonly used two-equation model of turbulence fails to predict the "wavy" heat transfer distribution curves for H/L < 8. For H/L > 8, the two-equation model, as expected, has a predictive capability superior to that of the one-equation model.

ACKNOWLEDGEMENT

The assistance of Dr. Mahesh Jain of the Department of Electrical Engineering, McGill University and Precision Photomasks, St. Hubert, Quebec, in the fabrication of the thin film sensor is gratefully acknowledged.

REFERENCES

1 Mujumdar, A.S. and Douglas, W.J.M., "Impingement Heat Transfer: A Literature Survey", TAPPI Meeting, New Orleans, La., Oct. 3, 1972.

2 Hardisty, H., "Industrial Drying Using Impinging Air Jets - Part I and II", University of Bath, School of Engineering Report No. 226 and 227, 1973.

3 Eckert, E.R.G. and Drake, R.M., Heat and Mass Transfer, McGraw-Hill, 1959.

4 Biceroglu, O., Mujumdar, A.S., van Heiningen, A.R.P. and Douglas, W.J.M., "Thermal Conductivity of Sintered Metal Powders at Room Temperature", Letters in Heat and Mass Transfer, 3, 3, 183, 1976.

5 Van Heiningen, A.R.P., Mujumdar, A.S. and Douglas, W.J.M., "On the Use of Hot Film and Cold Film Sensors for Skin Friction and Heat Transfer Measurements in Impingement Flows", Letters in Heat and Mass Transfer, 3, 6, 523, 1976.

6 Van Heiningen, A.R.P., "Heat Transfer Between an Impinging Slot Jet and a Porous Rotating Drum", Ph.D. Thesis, McGill University, Montreal, 1977.

7 Van Heiningen, A.R.P., Mujumdar, A.S. and Douglas, W.J.M., "A Fast Response Transient Heat Flux Sensor", To be published, 1977.

8 Popiel, Cz.O., Tuliszka, E., Boguslawski, L., "Heat Transfer from a Rotating Disk in an Impinging Round Air Jet", Paper NC 5.9, Vol. III, pp. 212, Proceedings of the Fifth International Heat Transfer Conference, Tokyo, 1974.

9 Metzger, D.E. and Groghowsky, L.D., "Heat Transfer Between an Impinging Jet and a Rotating Disk", Paper 76-WA/HT-2, 97th Winter Annual Meeting of the ASME, New York, 1976.

10 Cadek, F.F. and Zerkle, R.D., "Local Heat Transfer Characteristics of Two-Dimensional Impinging Air Jets - Theory and Experiment", Paper FC1.4, Proceedings of the Fifth International Heat Transfer Conference, Tokyo, 1974.

11 Gardon, R. and Akfirat, J.C., "The Role of Turbulence in Determining the Heat-Transfer Characteristics of Impinging Jets", International Journal Heat Mass Transfer, 8, 1261-1272, 1965.

12 Miyazaki, H. and Silberman, E., "Flow and Heat Transfer on a Flat Plate Normal to a Two-Dimensional Laminar Jet Issuing from a Nozzle of Finite Height", International Journal Heat Mass Transfer", 15, 2097-2107, 1972.

13 Gosman, A.D., Whitelaw, J.H. and Launder, B.E., "Flow, Heat and Mass Transfer in Turbulent Recirculating Flows - Prediction and Measurements", Short Course, McGill University, August 1976.

14 Gardon, R. and Akfirat, J.C., "Heat Transfer Characteristics of Impinging Two-Dimensional Air Jets", Journal of Heat Transfer Transactions ASME, 101-108, 1966.

15 Wolfshtein, M., "Convective Processes in Impinging Jets", Ph.D. Dissertation, London University, 1968.

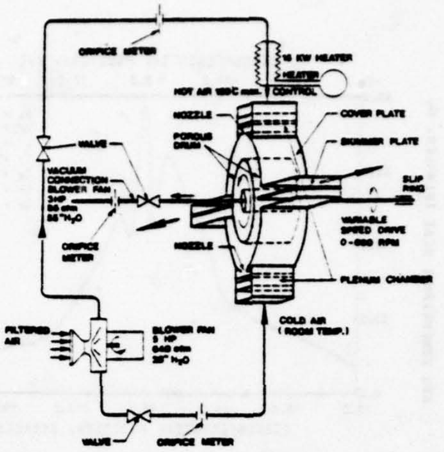

Fig. 1 Schematic of experimental set-up

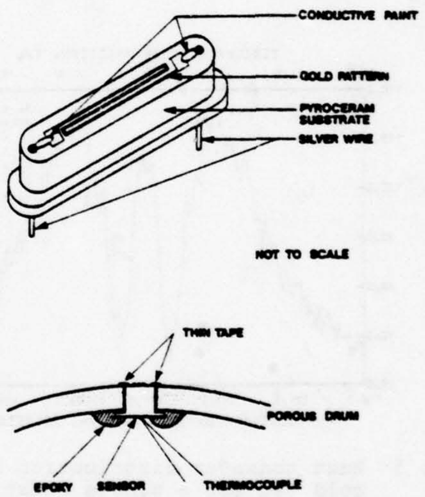

Fig. 2 Details of heat flux sensor

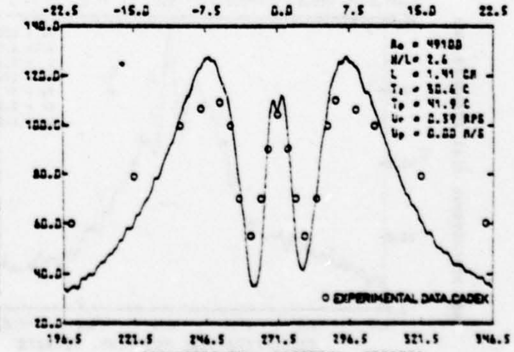

Fig. 3 Heat transfer distribution under the cold jet

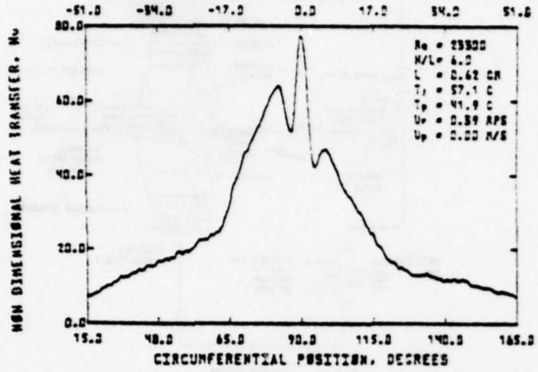

Fig. 4 Heat transfer distribution under the hot jet

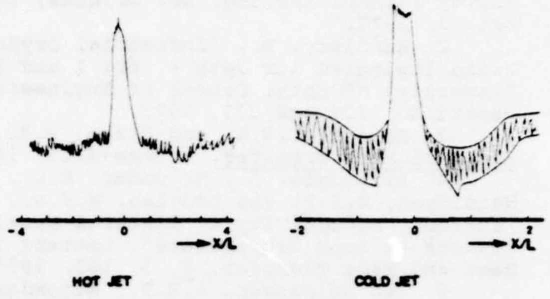

Fig. 7 Stagnation pressure distribution under hot and cold jets

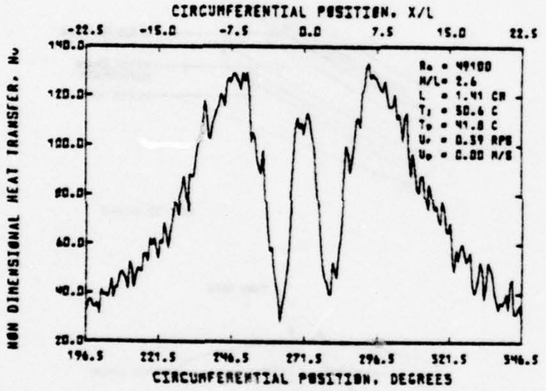

Fig. 5 Heat transfer distribution under the cold jet for a single rotation

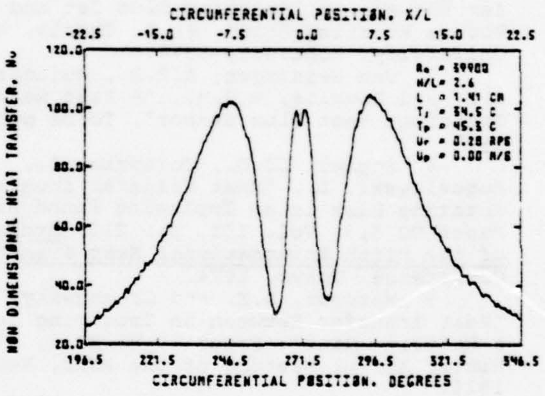

Fig. 8 Heat transfer distribution under the cold jet

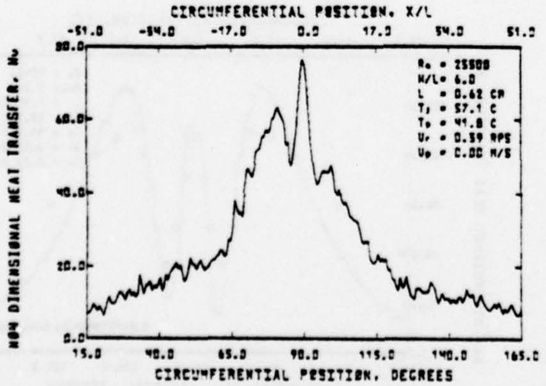

Fig. 6 Heat transfer distribution under the hot jet for a single rotation

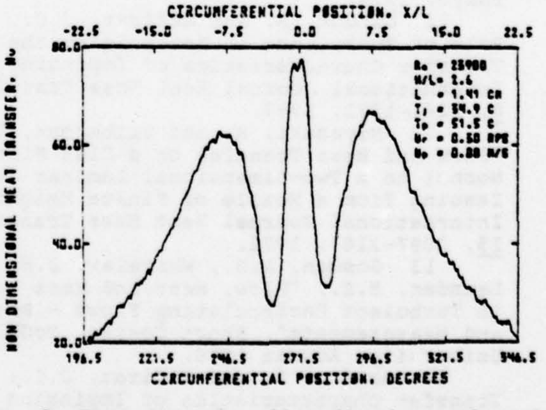

Fig. 9 Heat transfer distribution under the cold jet

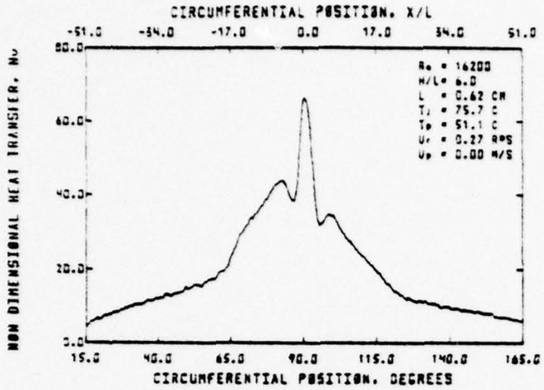

Fig. 10 Heat transfer distribution under the hot jet

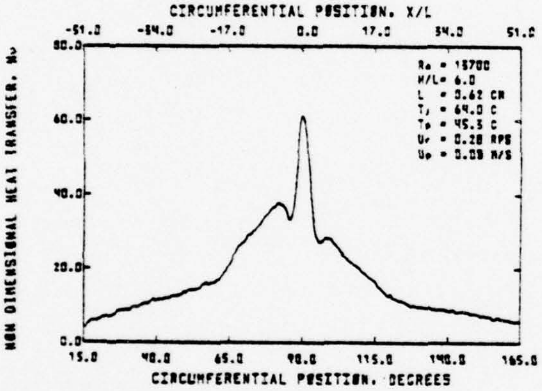

Fig. 11 Heat transfer distribution under the hot jet

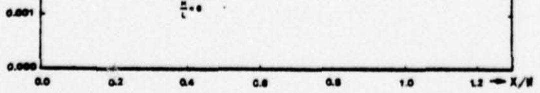

Fig. 12 Comparison of predicted and experimental heat transfer distribution

CHARACTERISTIC BEHAVIOUR OF TURBULENCE IN THE STAGNATION REGION OF A TWO-DIMENSIONAL SUBMERGED JET IMPINGING NORMALLY ON A FLAT PLATE

SEIICHI YOKOBORI, GRADUATE STUDENT
NOBUHIDE KASAGI, ASSISTANT PROFESSOR
MASARU HIRATA, PROFESSOR

DEPARTMENT OF MECHANICAL ENGINEERING
UNIVERSITY OF TOKYO ,TOKYO, JAPAN

ABSTRACT

It is further confirmed that the longitudinal vortex-like structures in large scales, in general, should be formed in the stagnation region of the two-dimensional, submerged jet impinging normally on a flat plate placed in the transition range between the potential core and the well-developed region of the jet. It is shown that the characteristics of these eddies have been made clear both qualitatively and quantitatively by using flow visualization techniques. These well ordered structures are to be closely connected with the three-dimensional distortions of a couple of shear vortex filaments upstream and that the interactions between these vortices in both sides predominate in the determination of the flow patterns at the stagnation region. In addition, the effects of these eddies on the enhancement of the heat transfer rate at that region are discussed.

NOMENCLATURE

B = width of slot nozzle, m
D = diameter of circular nozzle, m
F = frequency, 1/m s
H = nozzle-to -plate distance, m
n = sampling number
p = static pressure, Pa
$Re_B = UB/\nu$ = Reynolds number
T = average time interval of eddy generation, s
U = velocity at the nozzle exit, m/s
$u, v, w,$ = velocity components in x, y, z direction, m/s
x, y, z = rectangular coordinates (see Fig. 1), m

Greek Symbols

λ = average spacing of eddies, m
λ^* = non-dimensionalized spacing, λ/B
μ = viscosity, kg/m s
ν = kinematic viscosity, m^2/s
ρ = density, kg/m^3
σ = standard deviation

INTRODUCTORY REMARKS

It has been demonstrated by previous experimental investigations[1-10] that the rate of heat and mass transfer of submerged, plane or round jet impinging normally on a flat plate should be remarkably enhanced in the neighbourhood of the stagnation region. These enhancements, however, have been ambiguously considered mainly due to the effect of the turbulence which is produced in the upstream free shear layer and is transported downstream by the mean flow.

At the University of Tokyo, successive studies on the impinging jets have been conducted up to the present. Recently Kukita et al.[2] performed the experiments concerned with the structure of the two-dimensional stagnation flow field by using a flow-visualization technique in the air jet impinging normally on a flat plate. From the instantaneous photographic records of the flow field, they concluded that the unsteady three-dimensional phenomena should exist in the stagnation region of the submerged plane jet impinging normally on a flat plate and that the scales of eddies accompanied could appear much larger than the thickness of the laminar boundary layer which was calculated theoretically. In addition, they discussed the important relation between these characteristic turbulence behaviours and the comparatively high heat transfer rate of impinging jets. More detailed results, however, have not been obtained because of a lack of observations continuous in time, so a further investigation on the productive mechanism of these large-scale structures has been desired and expected to contribute to a better understanding of stagnation flow structure.

As for fluid-dynamic instabilities in the stagnation flow, various kinds of vigorous amplifications

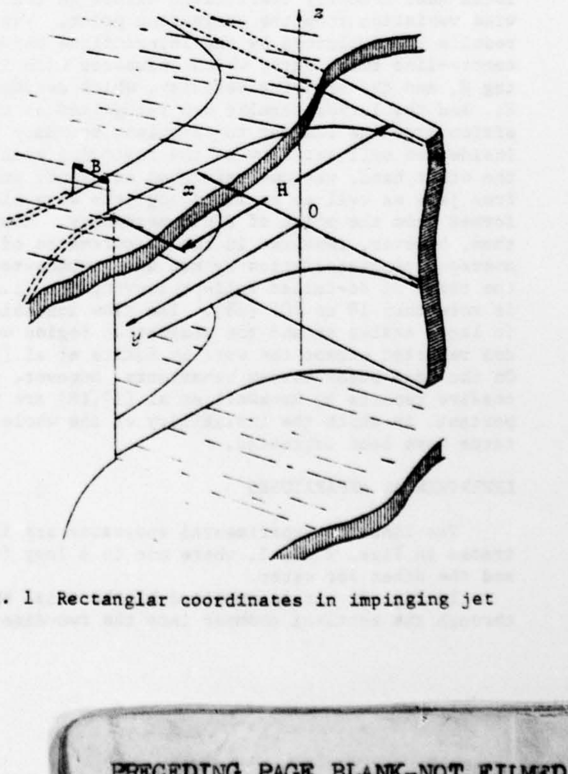

Fig. 1 Rectanglar coordinates in impinging jet

PRECEDING PAGE BLANK-NOT FILMED

of turbulences in that region have been reported recently[7]. For example, in the forward stagnation flow on a circular cylinder, more generally, on a blunt body, the vortex streets have been reported[3, 11] and their existence has been supported succesfully by the so-called "Vorticity Amplification Theory" proposed by Kestin et al.[12]. The similar spanwise quasi-perodic variation of flow structure has been observed in the re-attaching region of separated flows [13] and treated theoretically by Inger[14]. But the scales of turbulence coherent structures which will be discussed in this paper are much larger than those considered above, as indicated by Kukita et al.

In the past decade so-called well ordered structures in turbulent shear flows become of much interest to a number of reserchers, since such structures possess predominant roles on the turbulence production as well as the Reynolds stress generation(e.g. see Laufer[15]). It is, however, rather difficult to detect the unsteady three-dimensional fluid motions which occur discretely and exist for their characteristic lifetimes, if one depends only upon the conventional measuring probes fixed in space. In this paper the flow-visualization techniques, namely, the Smoke-Wire method and the Hydrogen-Bubble method, are applied to investigate the structure of stagnation flow region of a two-dimensional impinging jet without smearing out these structures in time averages. In addition, the combination technique of the Hydrogen-Bubble visualization and the pressure fluctuation measurement is developed and examined for the purpose of the detection scheme of large structures in turbulence.

PREVIOUS WORKS OF IMPINGING PLANE JET

Many studies on the plane, submerged impinging jet have made so far[2,4,5,8,9,10,16,17,18]. Most of the studies have been performed with increased demands of heat transfer problem. By the successive studies of Gardon et al.[4,5] two conclusions have been reported that the heat transfer coefficient at the stagnation point takes its maximum value when the ratio of H/B is about 8 to 10 and that the second peak of local heat transfer coefficient exists in the streamwise variation from the stagnation point. The former results are explained by the interactions between the centre-line turbulence, which increases with increasing H, and the arriving velocity, which decreases with H. And the latter results are recognized as the transition from the laminar to turbulent boundary layer inside the wall jet flow on the impinging wall. On the other hand, various reserches on plane, submerged free jets as well as on impinging jets were also performed from the point of fluid mechanics. Most of them, however, resulted in the measurements of time-averaged characteristics by hot wire anemometers in the range of so-called self-preserving jet (i.e. H/B is more than 10 to 20) [16]. The flow instabilities in large scales around the stagnation region were seldom reported except the work by Kukita et al.[2]. On the free shear vortex behaviours, however, the successive reports by Rockwell et al.[17,18] are very important, in which the instability of the whole patterns have been suggested.

EXPERIMENTAL APPARATUSES

Two kinds of experimental apparatus are illustrated in Figs. 2 and 3, where one is a loop for air and the other for water.

In Fig. 2, air is supplied by the axial blower through the settling chamber into the two-dimensional nozzle of 120 mm in width and 1300 mm in height. The aspect-ratio is 10.8 and the side panels of 240 mm wide are fixed at the both ends of the nozzle exit. The Reynolds number based on the nozzle width and the exit velocity ranges from 10^4 up to $2x10^5$.

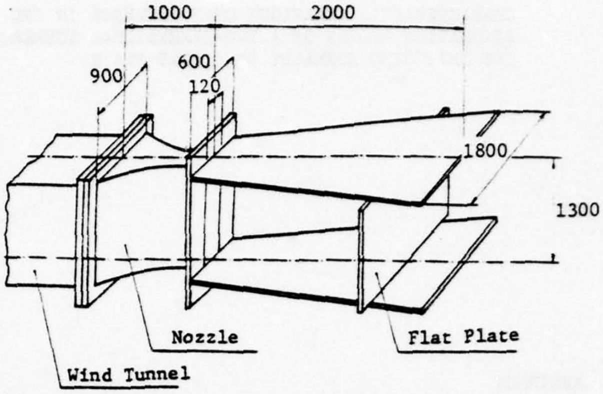

Fig. 2 Schematic of experimental apparatus of air jet

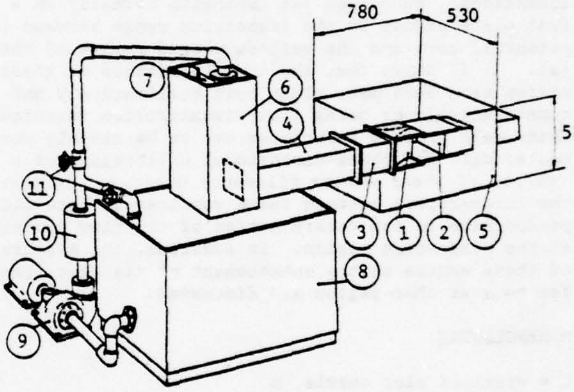

Fig. 3 Schematic of experimental apparatus of water jet

(1) Two-dimensional nozzle (2) Impinging plate
(3) Honeycomb chamber (4) Entrance duct
(5) Test tank made of acryl (6) Overhead tank
(7) Plates for controlling waterhead
(8) Tank (9) Volute pump (10) Absorber
(11) Valve for controlling flow rate

In Fig.3, water from a reservoir tank is pumped up through the damping chamber to the overhead-tank by a volute pump and is supplied through the honeycomb chamber into the nozzle, which is sandwiched by two parallel horizontal plates. The velocity at the nozzle exit can be controlled by varying the water head. In order to confirm the effect of the nozzle width on the flow pattern, two kinds of nozzles are constructed. The width of the nozzles are 5 and 15 mm respectively and the height is the same as 150 mm, so the aspect ratio becomes 30 and 10. The most experiment has been carried out by using the nozzle of 15 mm width for the sake of clear visualization. This water loop is made of acrylic resin so that the detailed flow pattern can be observed from any direction. The Reynolds number in this closed loop ranges from 10^3 to 10^4.

Using the experimental apparatus mentioned above, the ratio of the distance between the nozzle exit and the impinging plate to the nozzle width, H/B, has been varied in the range of about 2 to 10.

EXPERIMENTAL PROCEDURES

1) Flow Visualization Techniques

As flow visualization techniques, the Smoke-Wire method is applied to the air jet, while the Hydrogen-Bubble method in the water.

In the Smoke-Wire technique [19], a mixture of liquid paraffine and machine oil is painted initially on a fine nichrome wire of 70μm in diamater. This wire is placed at the desired region to be visualized without any disturbances to the flow field and is impulsively beated by a high D.C. charge accumlated by capacitor banks. After a fixed time interval from the instance of the smoke generation on the wire, an instantaneous photographic record of the smoke streaks is taken by flashing a stroboscope. This programmed sequence is automatically completed by the electric circuit developed which is triggered by the shutter of the camera. In this technique, photos can be taken from the different directions at the same time. This method has been used successfully to investigate three-dimensional structures of turbulence in boundary layer flows by the present co-authors [20,21].

The Hydrogen-Bubble method is now well known of its useful advantages for flow visualizations [22] and has been also used in the visual studies on turbulence (e.g. [23]). Presently this technique is applied to the water jet in order to investigate behaviours of large scale structures continuously in time. Bubble generating wires are positioned, in most cases, parallel to the z-axis, while in some cases parallel to the x-axis, and at most three wires are placed in the flow field at a time. In most of the present experiments bubbles are generated continuously by a constant D.C. charge, not periodically by controlling a power supply as has been demonstrated in the literature [26].

2) Measurement of Wall Static Pressure Fluctuation at Stagnation Region

A semi-conductor pressure transducer of 5mm diameter is fixed into the impinging plate, as shown in Fig.4, in order to detect the pressure fluctuation accompanied with the characteristic flow pattern. In addition, the Hydroben-Bubble technique is combined with this pressure fluctuation measurement for further cofirmation of spatially convected structures. The pressure hole is 2mm in diameter and 1mm in depth, in which silicone oil is filled up. The frequency response of this pick-up is flat up to 1kHz, but in order to eliminate the unwanted noise the output signal has been passed through a low-pass filter under 28Hz, which is enough higher than the frequencies of large scale flow structures in the water jet.

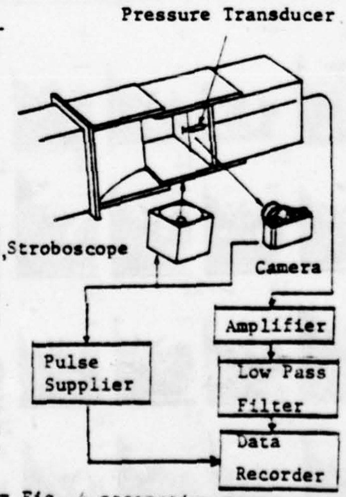

Fig. 4 stagnation pressure measurements

3) Velocity Measurement

In the air jet measurements, the velocity is measured by using a hot-wire anemometer as well as Pitot tubes. In the water jet measurements, relatively higher velocities are measured by Pitot tubes.

CLASSIFICATION OF FLOW FIELD OF PLANE FREE JET

Before the well-ordered structures at the stagnation region of the plane, submerged, impinging jet are discussed, it is important to summarize the general feature of flow field of the plane free jet. It can be classified roughly into three regions as follows:

(1) Potential Core Region

As far as about 4B downstream from the nozzle exit, the so-called potential core region exists where the flow is laminar without vorticity and is sandwiched by the free shear layers which include nascent stage vortices sheets. The length of the potential core is influenced by the upstream histories such as the shape of nozzle exit and the boundary layer thickness in the nozzle, since the development of the shear layer must depend strongly upon them. When this potential core region impinges directly on the flat plate, the flow patterns at the stagnation region are almost laminar-like and the large-scale turbulence can hardly be visualized.

(2) Transition Region

This region is a transition region from the potential core region (1) to the well-developed region (3). In this region, shear vortices develop and interact as has been indicated by Rockwell & Niccolls [17,18]. When the impinging wall is positioned within this region, the large-scale eddies become most vigorous and these eddies are observed very often as a pair which happen to look like the Taylor-Görtler vortices. The spatial scales of eddies become large with incresing the value of H/B. The typical photographs of these eddy structures along the stagnation line are shown in Fig. 5, where all photos have been taken from the x-direction. These results suggest that the mechanism of the generation of these large eddies can be closely connected with the behaviours of shear-vortices upstream.

(3) Well-developed Region

In the region more than 10 to 12B downstream from the nozzle exit, the jet grows up to the so-called self-preserving state with the complete development of the shear layer. Strictly speaking, the self-preserving region is said to be the region more than 40B downstream from the nozzle exit [24], but from a wider point of view it may be admitted to be defined as above mentioned. In this region the effect of upstream history on the flow-field can be neglected. When the impinging wall is located in this region, the well ordered vortex-pairs can be hardly found in the stagnation region. But the large-scale eddies happen to appear in a distorted shape accompanied with the small-scale turbulence of higher wave numbers. This occurrence, however, decreases with increasing of H/B.

From the remarks mentiond above, most of the experiments have been performed with the impinging plate located in the transition region of the jet.

QUALITATIVE OBSERVATION OF SHEAR VORTICES OF FREE JET REGION

In general, the flow fields of submerged, impinging jets can be classified into three regions as shown in Fig.6, namely, the free jet region, the impinging region and the wall jet region. Of these regions, the free jet region is defined as a region uninfluenced by the effect of impingement and it possesses the same characteristics as those of a free jet

Although the behaviours of the shear-vortex streets in the free jet have been extensively studied by Rockwell et al.[17,18], the free jet region of the impinging jet is examined by using the Hydrogen-Bubble method as shown in Fig.7. These photographs have been taken periodically by the moter-drive mechanism with the time interval of 0.25 second. The initial small disturbances generated by the linear instability of free shear layer grow finally into large shear-vortices, which are convected downstream in a certain characteristic frequency. In these photos, it can be recognized that there occur randomly both the symmetrical and asymmetrical formations of shear vortices.

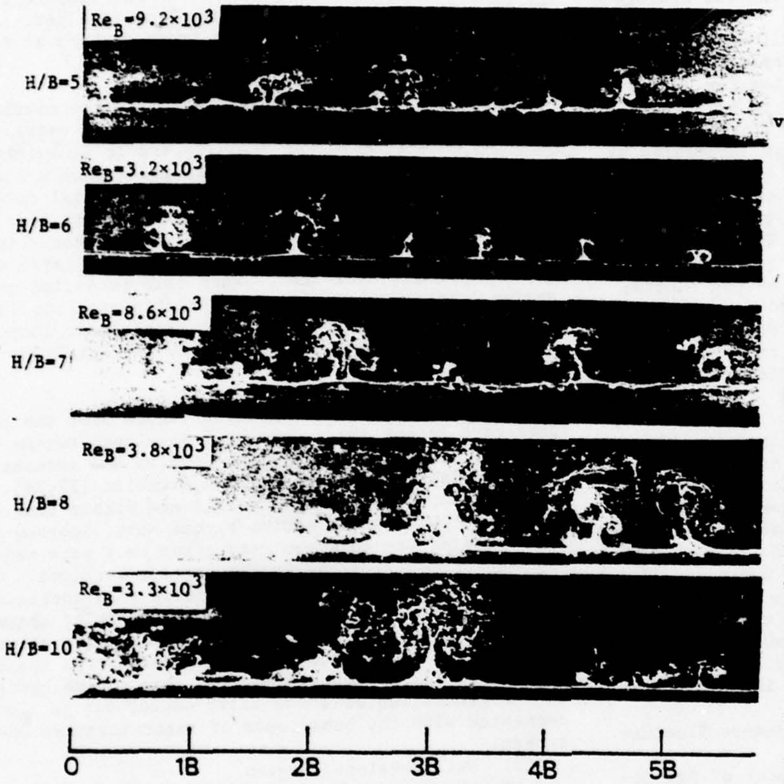

Fig. 5 Pair-vortex structures in stagnation region visualized in water jet with a bubble generating wire flush with the wall

Successively the three-dimensional distortions of shear vortices have been visualized emphatically. The instantanious photograph in Fig.8, taken from the x-direction, shows the stretchings of the shear-vortex filaments. These filaments are formed by the mass concentration due to the strong vorticitiessince the bubbles are generated continuously on the wire. The distortion of large wavelength grows downstream accompanied with the generation of the disturbances of higher wave numbers, but this large structure can be identified clearly until it rushes into the impinging region.

These behaviours of shear vortices have been also visualized as shown in Fig.9, where the photograph is takén from the backside of the impinging plate. In the same way as before, three-dimensional stretchings of shear vortices can be confirmed. Moreover, from the additional analysis of the high-speed 16 mm movies, it is observed that the profiles of the distortions of both side shear vortices likely appear to be in inverse phases, even though the shear vortices may impinge on the wall asymmetrically as shown in Fig.7. So there exist both the region where the shear vortices approach considerably and the region where the vortices are apart, almost periodically along the geometrical stagnation line. In addition, the trembling motion of the stagnation line in the x-direction can be seen, which must be explained as the result of the asymmetrical impinging of upstream shear-vortices. The vortex filaments, however, seldom appear to be convected directly to the opposite side beyond the geometrical stagnation line.

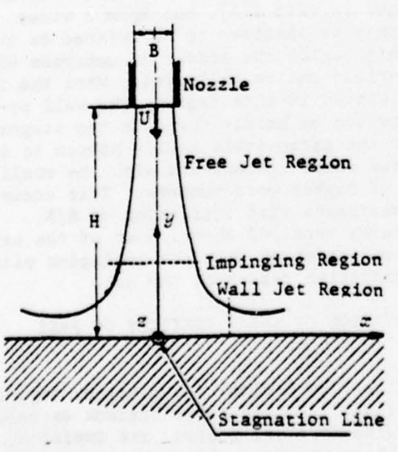

Fig.6 Classification of flow field of impinging jet

Fig. 7 Visualization of shear vortices

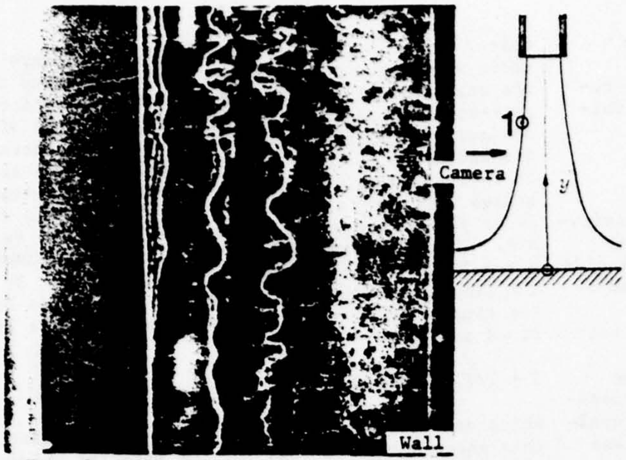

Fig. 8 Stretching of shear-vortex filament

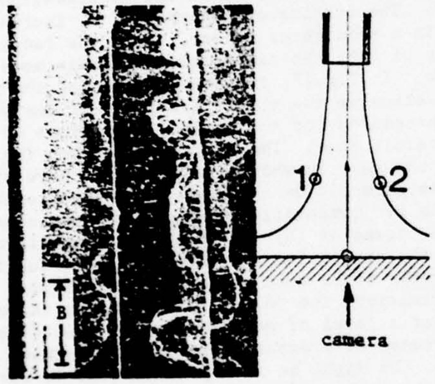

Fig. 9 Stretching of shear-vortex filament

BEHAVIOURS OF LARGE-SCALE EDDIES IN STAGNATION REGION OF IMPINGING JET

It is confirmed that the coherent structures of turbulence eddies in the stagnation region exist in all visual experiments, where the Reynolds number ranges from 10^3 up to 2×10^6 with water and air loops, when the impinging plate is located in the transition region of the jet. Typical photographs are represented in Fig.10 in the air and water jets. A series of photos in the water jet have been taken, and it is recognized that these pair-vortex structures appeared discretely in time and space. At the same time these streamwise pair-vortex structures change their characteristics, such as scales and wavenumbers of turbulence included, according to the wall-position, i.e. H/B, as shown in Fig.7.

As a characteristic length scale, the mean spacing of generations of large eddies in the z-direction have been measured on the photographs taken from the x and y directions. The typical photograph of vortex streets is shown in Fig.11 in which the bubbles are generated on two wires. It is observed that the vortex filaments of these eddies appear both sides of the stagnation line almost symmetrically and this suggests the continuity of the vortex filament across the stagnation line. In addition the vortex-like structure must be streched in the streamwise direction by the flow acceleration in the stagnation flow region. The measured values of the mean spacing, λ^*, non-dimensionalized by B, are represented versus the Reynolds number in Fig. 12. In these figures, the open symbols are present results in the water jet, while the solid symbols are the individual values measured by present authors from some limited numbers of photographs taken by Kukita et al.[2] for air jet experiments. Present results have been obtained within an error of 5% by analyzing more than 100 photographs and the standard deviations are 30 to 40% of the ensemble mean as indicated by the length of the vertical lines on the symbols in the figures. The triangular symbol in Fig. 12 is the result measured by using the smaller nozzle of 5mm in

air jet, H/B=6, $Re_B=(5\sim10)\times10^4$ from Kukita et al.[2]

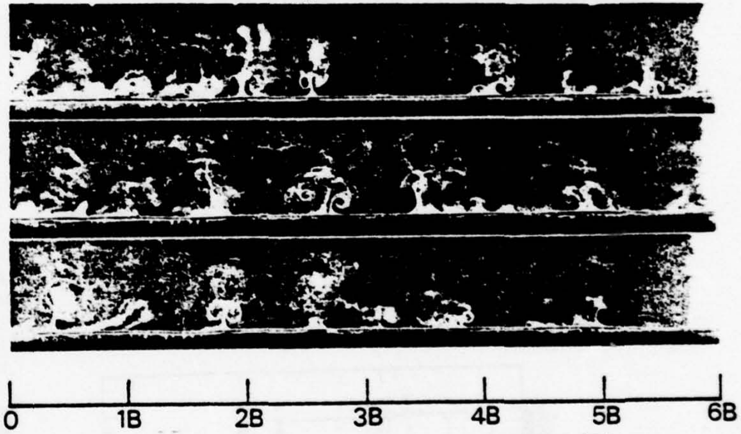

water jet
H/B=6, $Re_B=3.2\times10^3$

Fig. 10 Pair-vortex structures in stagnation region

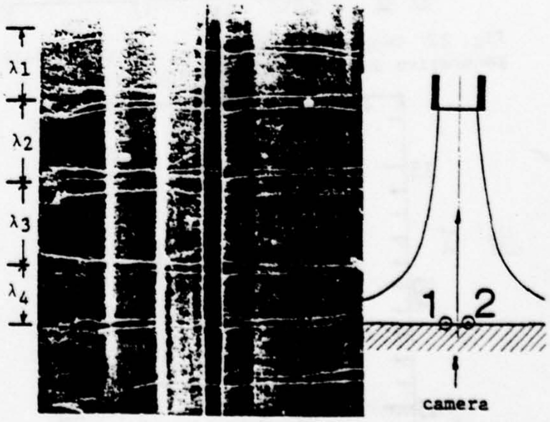

Fig.11 Pair-vortex streets

with. From these results, the spacing of vortices generation is concluded to be a weak function of Reynolds number, and the empirical correlation is obtained from the measurements in the water jet as follows:

$$\lambda^* = \lambda/B \propto Re_B^{-0.046} \qquad (1)$$

This conclusion might be reasonably understood, reviewing the findings that the large eddy structures in turbulence should be almost independent of the Reynolds number of the main flow field as has been discussed by Roshko[25].

The dependency of the average spacing on the nozzle-plate distance is shown in Fig.13, where the Reynolds number is maintained almost constant. The non-dimensional spacing seems to increase with increasing H/B and this result is in accordance with the qualitative obserbation in Fig.7 that the scales of these structures increase in the same way.

As a general descreption, the average value of the spacing of vortex-pair generations is about 0.8 - 0.9 times the nozzle width and is the order as same as the wavelength of shear-vortex distortion which is mentioned previously.

Secondly, in order to examine the time scale of these vortex-like structures, the frequency of their generation per unit length in the z-direction has been measured from the high-speed movies taken from behind the impinging wall. Fig.14 shows a example of a history table of vortices on the stagnation line in the water jet when $Re_B = 2.3\times10^3$ and $H/B = 6.0$. The circle symbol is the occurrence of pair-vortex structure, while the cross denotes the collapse. In some cases lacking in either symbol, it has been difficult to identify the occurrence or collapse clearly because of the ambiguity of flow-visualisation movies. Although these phenomena appear randomly in time and space, it can be also recognized that there are some cases where they occur almost at the same time along the stagnation line. In counting the generation of pair-vortex structure, the difficulty because of the ambiguity of motion pictures increase with increasing H/B and Re_B. So there might be included some errors in the following quantitative results of the time scales obtained in this way. Fig.15 shows the frequency of generation per unit spanwise length, F, versus H/B. This frequency appears to have its maximum around H/B = 7 and to decrease with increasing H/B. By using the frequency of generation and the spacing in Fig.13, the time scale of these well-ordered structure is defined as follows·

$$T = 1/F\lambda = 1/F\lambda^* B \qquad (2)$$

which can be roughly interpreted as a mean lifetime of this phenomenon. In Fig. 16, the measured values of this lifetime are represented in the nondimensional form, TU/B. The spacing of generation, λ, increases gradually in a monotonous manner, so in the range of large value of H/B, the time scale increases more than F decreases. In Fig.17, the measurements of the pressure fluctuation at the stagnation point of the water jet are represented for the various conditions of the nozzle-plate distance. The traces of (A) and (B) correspond to the case in which the potential core of the jet impinges directly on the plate, and the pressure fluctuations are comparatively small. On the other hand, in the cases of (C) and (D), where the plate is located in the transition resion of the jet, the fluctuations appear to be much intence and vigorous. From a rough estimation, the velocity fluctuation is considered to be at a level of more than 20 %. The considerable differrence of pressure fluctuations between (A), (B) and (C), (D) might be mainly attributed to the existance of the large eddy structure at the stagnation region.

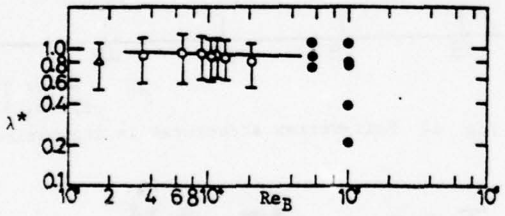

Fig. 12 Dependency of spacing of vortex-pair generation on Reynolds number H/B=6.0

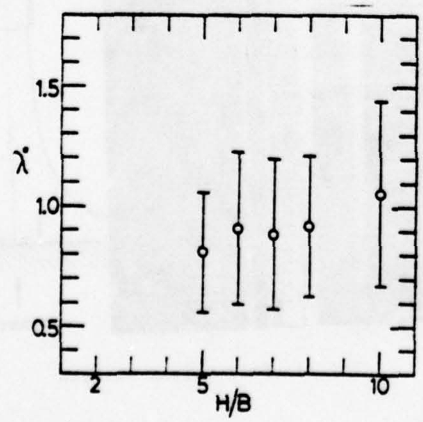

Fig. 13 Dependency of spacing of vortex-pair generation on nozzle-plate distance $Re_B=(8\sim9)\times10^3$

In order to investigate the pressure fluctuation pattern accompanied with the vortex-like structure, the Hydrogen-Bubble technique is integrated and the typical examples are shown in Fig.18, where H/B = 6.0 and $Re_B = 1.2\times10^4$. Since the bubble generating wire is located downstream the pressure hole, its effect on the pressure measurement can be neglected. The pattern recognition of the eddy structure in the pressure fluctuation must be much complicated, because the trembling motion of the instantaneous stagnation line as well as the shear vortices fluctuation might contribute simultaneously. Presently the visual analyses of the pressure fluctuation patterns are performed when the large eddies exist right above the pressure hole and also

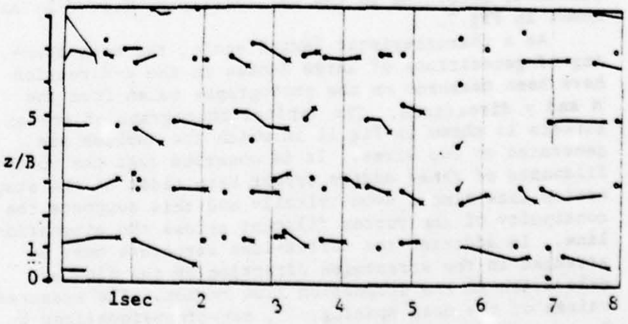

Fig. 14 Time table of pair-vortex along stagnation line in water jet, $Re_B=2.3\times10^3$, H/B=6.0

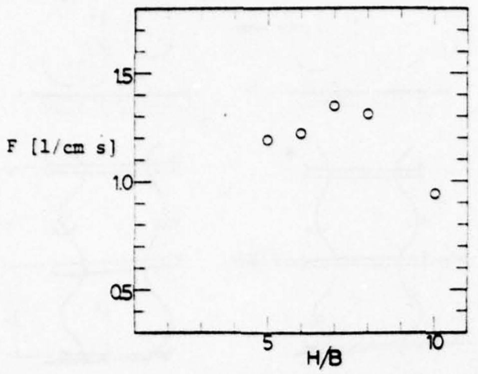

Fig. 15 Frequency of vortex-pair generation in water jet, $Re_B=2.3\times10^3$

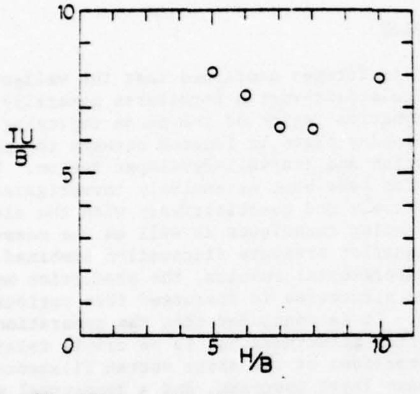

Fig. 16 Time scale of pair-vortex structure in water jet, $Re_B=2.3\times10^3$

wander from the hole. The pattern analysis has been carried out during the time span of the time scale of this phenomenon which can be estimated assuming the value of TU/B to be 5 to 10, resulting 10 to 5 Hz in this case. As a qualitative description of pressure fluctuation pattern, the stagnation pressure tends to decrease during the interval the pair-vortex exists, while it is likely to increase in the region between the neighbouring vortex structures.

Considering the characteristic behaviours of the stagnation flow field of the impinging jet reported here, the mechanism of the enhancement of heat and mass transfer can be explained much clearly. From the stagnation pressure measurements in Fig.17, the turbulence intensity must be recognized very high with the impinging plate located in the transition region, as has been reported elsewhere[16]. This corresponds to the high transport rate of heat and mass under this condition of impinging wall location[e.g. 4,5]. Moreover the enhancement of transport rate must be based on the occurrence of streamwise pair-vortex structures in the large scales which are more than several times the laminar boundary layer thickness calculated theoretically. The boundary layer of passive quantities should be extremely broken and renewed when these phenomena occur in the stagnation region. Although the scales of these structures increase with increasing H/B as shown in Fig.5, the frequency of generation in time and space decreases rapidly beyond the value of H/B=7. This fact may clearly explain the general variation of heat transfer coefficient with H/B which has been reported by the several researchers[e.g. 4,5].

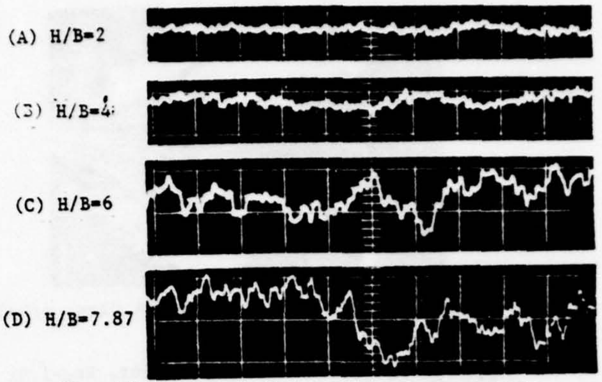

Fig. 17 Pressure fluctuation at stagnation point ($Re_B=1.05\times10^4$, ordinate; p', $0.054\times(\frac{1}{2}\rho U^2)$/div., abscissa; t, 0.5sec/div.)

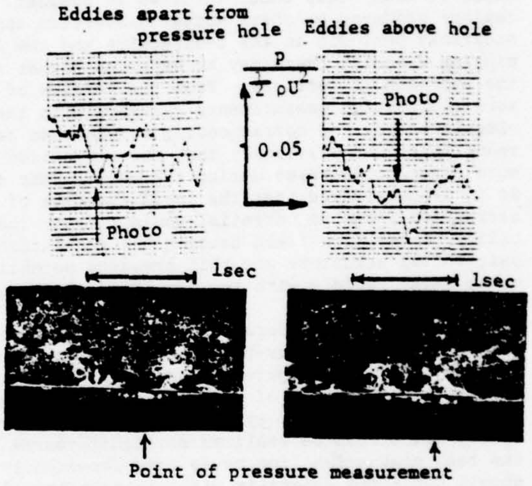

Fig. 18 Pressure fluctuation measurements combined with Hydrogen-Bubble method

RELATION BETWEEN STRETCHING OF SHEAR-VORTICES UPSTREAM AND LARGE-SCALE EDDY STRUCTURE IN STAGNATION REGION

The production mechanism of these well-ordered structures in the stagnation region is discussed in connection with the three-dimensional stretching of vortex filaments upstream. The scales of shear vortices (see Figs. 7 and 19), which increase with the development of shear layer, affect the whole flow field in a comparatively long timespan, inducing the trembling motion of the stagnation line. In addition, these developed shear vortices may influence the increased scales of the streamwise pair-vortices in the stagnation region as shown in Fig. 5. On the other hand, the wavelength of distortions of vortex filaments (see Figs. 8 and 9) is the same order as the spacing of vortex-pair generation in the stagnation region, so this fact strongly suggests the connection between the shear vortex distortion and the pair-vortex formation.

Therefore the stagnation region is investigated by using three bubble generating wires simultaneously as shown in Fig. 20, which has been taken from behind the impinging plate. In this photograph, it is possible to recognize that the streamwise vortices should often ex-

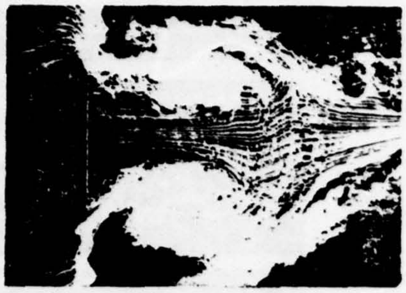

Distance between nozzle and smoke wire. x/B=2.0

Fig. 19 Shear vortices in air jet, Re_B=1.0x 10^5, H/B=8.0

ist in the region where the distance between the filaments of both sides shear vortices is smaller. These regions produced by shear vortex distortion appear considerably periodic in the z-direction and the local impinging velocity there may be expected higher due to the approach of vortices. From the results of pressure fluctuation measurements combined with the flow-visualization, the corresponding results has been already mentioned previously that the stagnation pressure tends to decrease during the vortex-pair exists. So it is considered that the local increase of the stagnation pressure potential would trigger the instability of the flow field causing the generation of the pair-vortex structure and this pressure potential would decay rapidly with the development of the vortex structure.

From these considerations, a conceptual model for the mechanism of vortex-pair structures in the stagnation region is constructed as shown in Fig. 21. In this figure two kinds of configurations of shear vortices are supposed, i.e. symmetrical and asymmetrical cases, and it can be realized straightforwards that the real stagnation line moves time-dependently and should not agree generally with the geometrical stagnation line. But the fundamental mechanism in both cases is considered to be the same as is discussed above.

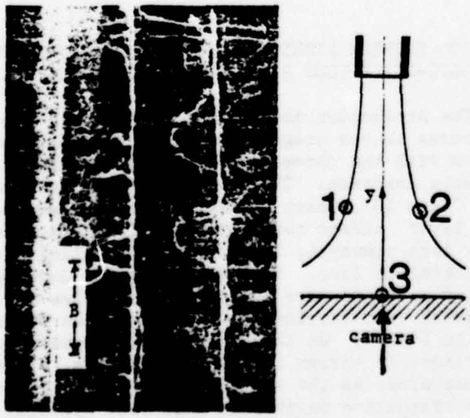

Fig. 20 Relation between streatching of upstream shear vortices and pair-vortex structures in stagnation region, Re_B=3.0x 10^3, H/B=6.0

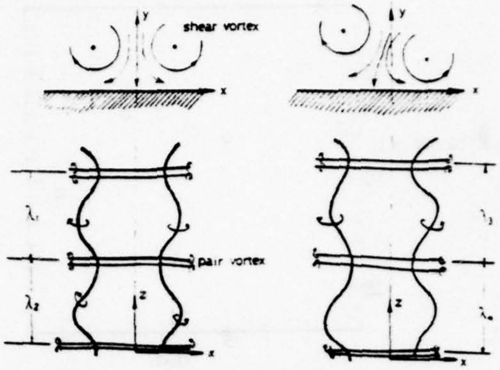

Fig. 21 Conceptual model for mechanism of vortex-pair generation

CONCLUSION

It is further confirmed that the well-ordered large-scale pair-vortex structures generally exist in the stagnation region of the plane impinging jet, when the impinging plate is located between the potential-core region and the well-developed region. These flow structures have been extensively investigated both qualitatively and quantitatively with the aid of flow-visualization techniques as well as the measurement of the stagnation pressure fluctuation combined. From these experimental results, the production mechanism of these structures is discussed from various points of view. It is concluded that the generation of the pair-vortex structures has to be deeply related with the distortions of the shear vortex filaments in the free shear layer upstream, and a conceptual model for the mechanism of the vortex generation is presented. In addition, it is emphasized that these phenomena should have an important role on the enhancement of heat and mass transfer of the impinging jet.

ACKNOWLEDGEMENT

The authors are grateful to Drs. T. Nakatogawa and Y. Kukita and Mr. K. Aruga for their useful discussions in the early stage of this work.

REFERENCES

1 Nakatogawa, T., Nishiwaki,N., Hirata, M. and Torii, K., "Heat Transfer of Round Turbulent Jet impinging Normally on Flat Plate," Proceedings of the 4th International Heat Transfer Conference, Vol. 2, FC 5'2, 1970.

2 Kukita, Y. and Hirata, M., "Flow-Pattern and Heat Transfer at the Stagnation Region of Turbulent Impinging Jet," (in Japanese) Proceedings of the 7th Turbulence Symposium, Institute of Space and Aeronautical Science, University of Tokyo, 1975, pp.99-104.

3 Kestin, J. and Wood, R. T., "The Mechanism which Causes Free-Stream Turbulence to Enhance Stagnation-Line Heat and Mass Transfer," Proceedings of the 4th International Heat Transfer Conference, FC 2'7, 1970.

4 Gardon, R. and Akfirat, J. C., "Heat Transfer Characteristics of Impinging Two-Dimensional Air Jets," Journal of Heat Transfer, Trans. ASME, Series C, Vol. 88, No. 1, Feb., 1966, pp. 101-108.

5 Gardon, R. and Akfirat, J. C., "The Role of Turbulence in Determining the Heat-Transfer Charac-

teristics of Impinging Jets," International Journal of Heat and Mass Transfer, Vol. 8, 1965, pp. 1261-1272.

6 Kataoka, K. and Mizushina, T., "Local Enhancement of Heat Transfer in an Impinging Round Jet by Free-Stream Turbulence," Proceedings of the 5th International Heat Transfer Conference, FC 8.3, 1974.

7 Schlichting, H., "A Survey of Some Recent Research Investigations on Boundary Layers and Heat Transfer," Journal of Applied Mechanics, Trans. ASME, Series E, Vol. 38, No. 2, June 1971, pp. 289-300.

8 Baines, W. D. and Keffer, J. F., "Shear Stress and Heat Transfer at a Stagnation Point," Internatinal Journal of Heat and Mass Transfer, Vol. 19, 1976, pp. 21-26.

9 Sparrow, E. M. and Lee, L., "Analysis of Flow Field and Impingement Heat/Mass Transfer Due to a Nonuniform Slot Jet," Journal of Heat Transfer, Trans. ASME, Series C, Vol. 97, No. 2, May, 1975, pp. 191-197.

10 Sparrow, E. M. and Wong, T. C., "Impingement Transfer Coefficients Due to Initially Laminar Slot Jets," International Journal of Heat and Mass Transfer, Vol. 18, 1975, pp. 597-605.

11 Roshko, A. and Thomke, G. J., "Observations of Turbulent Reattachment Behind and Axi-Symmetric Downstream Facing Step in Supersonic Flow," AIAA Journal, 1966, Vol. 4, pp. 975-980.

12 Inger, G. R., "Three-Dimensional Disturbances in Reattaching Seperated Flows," Proceedings of the 1974 Heat Transfer and Fluid Mechanics Institute (by Davis and Wilson), Stanford University Press, 1974, pp. 74-90.

13 Sadeh, W. Z., Sutera, S. P. and Maeder, P. F., "An Investigation of Vorticity Amplification in Stagnation Flow," Zeitschrift für angewandte Mathmatik und Physik, Vol. 21, 1970, pp. 717-742.

14 Sadeh, W. Z., Sutera, S. P. and Maeder, P. F., "Analysis of Vorticity Amplification in the Flow Approaching a Two-Dimensional Stagnation Point," Zeitschrift für angewandte Mathematik und Physik, Vol. 21, 1970, pp. 699-716.

15 Laufer, J., "New Trends in Experimental Turbulence Research," Annual Review of Fluid Mechanics, Vol. 7, 1975, pp. 307-325.

16 Russel, P. J. and Hatton, A. P., "Turbulent Flow Characteristics of an Impinging Jet," Proceedings of the Institute of Mechanical Engineers 1972, Vol 186, 52/72.

17 Rockwell, D. O. and Niccolls, W. O., "Natural Breakdown of Planar Jets," Journal of Basic Engineering, Trans. ASME, Series D, Vol. 94, No. 4, Dec., 1972, pp. 720-730.

18 Rockwell, D. O. and Niccolls, W. O., "Large Amplitude Axial Excitation of Planar Jet Flow," Journal of Fluids Engineering, Trans. ASME, Series I, Vol. 97, No. 3, Sept., 1975, pp. 380-382.

19 Gaby, L. I., "Hot-Wire Smoke Streams for Visualization of Air Flow Patterns," Journal of Scientific Instruments, Vol. 43, 1966, pp. 334.

20 Kasagi, N. and Hirata, M., "Transport Phenomena in Near-Wall Region of Turbulent Boundary Layer around a Rotating Cylinder," 1975, ASME Papers, 75-HT/WA-58.

21 Kasagi, N. and Hirata, M., "Bursting Phenomena in Turbulent Boundary Layer on a Horizontal Flat Plate Heated from Below," Proc. 1976 ICHMT Seminar on Turbulent Buoyant Convection, Dubrovnik, 1976, pp. 27-38.

22 Schraub, F. A., Kline, S. J., Runstadler Jr., P. W. and Littel, A., "Use of Hydrogen Bubbles for Quantitative Determination of Time-Dependent Velocity Fields in Low-Speed Water Flows," 1965, ASME, Trans., Series D, Vol. 87, pp. 429-444.

23 Kim, H. T., Kline, S. J. and Reynolds, W. C., "The Production of Turbulence Near a Smooth Wall in a Turbulent Boundary Layer," Journal of Fluid Mechanics, Vol. 50, 1971, pp. 133-160.

24 Gutmark, E. and Wygnanski, I., "The Planar Turbulent jet," Journal of Fluid Mechanics, Vol 73, 1976, pp. 465-495.

25 Roshko, A., "Structure of Turbulent Shear Flows: A New Look," AIAA Journal, Vol. 14, No. 10, Oct. 1976, pp. 1349-1357.

SELECTIVE AMPLIFICATION OF FLUCTUATIONS IN A TURBULENT IMPINGING JET

by

E. Gutmark*, I. Wygnanski** and M. Wolfshtein*

* Technion, Israel Institute of Technology, Haifa

** University of Tel-Aviv (currently at the University of Southern California, Los-Angeles)

ABSTRACT

Measurements of power spectra in the stagnation region of the axisymmetric impinging jet were made in order to cast some light on the vortex stretching mechanism in the flow approaching stagnation. A loudspeaker was used to force on the jet a wave of a predominant length and control its amplitude. The development of the oscillatory motion, as the flow approaches stagnation, could then be easily observed. The measurements were made at low speeds. The Reynolds number based on diameter of the nozzle was $12000 \leq Re \leq 60000$ and the relative amplitude of forcing was changed from 2% to 10%.

A "filter characteristic" of the jet stagnation region was determined by additional measurements with different forcing frequencies. This function exhibits the influence of this region on vortices of different scales. It was proved that the stagnation region functions as a low pass filter.

Forcing the jet at a frequency higher than the neutral one yields an increase in the axial turbulent intensity which is proportional to the level of forcing. Forcing at a frequency lower than the neutral frequency yields higher increase in the axial turbulent intensity than the previous one. The effect of the same forcing frequencies on the mean velocity is quite different. Forcing at the higher frequency increases the axial mean velocity proportionally to the level of forcing, while forcing at the lower frequency has no effect on the mean velocity.

INTRODUCTION

This paper is concerned with the structure of turbulence in turbulent stagnation flows and impinging jets, and the influence of controlled disturbances on this structure. The structure of turbulence in stagnation region determines the characteristics of the mean flow and heat transfer in this region, and is therefore of much interest. The influence of turbulence in this flow was initially observed in heat transfer experiments. Kestin, Maeder and Sogin (1) reported that the heat transfer rates in the stagnation region rose by nearly 40% when the turbulence level of the free stream was increased from 0.5% to 2.7%. The heat transfer coefficient in the latter case was 80% higher than that theoretically predicted for steady laminar flow. The heat transfer augmentation is most probably caused by the rapid distortion of the flow and the concimmitant stretching of vortices whose axes are normal to the plane of symmetry. Sutera, Maeder and Kestin (2) predicted an augmentation of turbulence level in the flow approaching stagnation as a result of this stretching process. They also showed that the augmentation depends critically on the initial scale of the oncoming vortices, because those eddies which are originally small may simply dissipate by the action of viscosity following the stretching process. There must, therefore, exist a neutral scale below which the turbulence dissipates as the flow approaches stagnation. Thus stagnation flow acts like a low-pass filtering amplifier. The impingement of an axisymmetric jet onto a flat surface was studied experimentally by Donaldson, Snedeker and Margolis (3) with the explicit purpose of obtaining the heat transfer coefficient in the vicinity of the stagnation point. When the surface was 30 diameters downstream from the nozzle, the heat transfer close to the stagnation point was 120% higher than that predicted by laminar flow theory. It was therefore suggested to introduce a turbulence correction factor to the data. Bradbury (4) studied the impinging jet in context with ground erosion which is caused by lifting jets from VTOL aircraft. He thus measured the distribution of pressure on the surface as a function of the distance from the nozzle and the initial velocity of the jet. Sadeh, Sutera and Maeder (5) experimented with two-dimensional stagnation flow by mounting a plate normal to a stream in a wind tunnel. The level of turbulence in the impinging stream was varied by the introduction of rods upstream of the plate. Furthermore, the scale and orientation of the large eddies could be altered by changing the direction of the rods, the spacing between them and the direction of their axes in relation to the distorting flow. The results, however, were not sufficiently definite because the experiment involved a transfer of energy from a wide spectrum of eddies which exist in a turbulent flow to another wide spectrum of eddies having a somewhat different scale. Hunt (6) applied the theory of "Rapid Distortion" to turbulent flow around a circular body. Assuming that the residence time of the particles is smaller than the turbulent time scales he calculated the effect of changes in the mean velocity and the upstream spectral distributions on the turbulence, the r.m.s. values of the turbulent components and their spectral distributions in the downstream region of the flow. Hunt obtained two asymptotic solutions for the much smaller or much larger turbulence scale compared with the cylinder typical dimensions, and an approximate solution for the case of similar turbulence scale and cylinder dimensions.

Gutmark et al (7) studied the impingement of a plane turbulent jet on a surface, believing that the

PRECEDING PAGE BLANK-NOT FILMED

high level of turbulence which is present in a fully developed jet will be helpful in determining the mechanism associated with the stretching of vortices near stagnation. A general trend of energy transfer towards the large scale eddies was identified as the flow approached stagnation. Yet it was difficult to identify the influence of stretching on different frequencies.

The present experiment was designed in order to study the vortex stretching mechanism in a flow approaching stagnation. Following Crow and Champagne (8), a loudspeaker was used to superimpose a wave of a predominant length on a round jet, and control its amplitude. The development of the oscillatory motion as the flow approaches stagnation could then be easily observed. The measurements were made at low speeds for which the flow could be considered incompressible.

EXPERIMENTAL APPARATUS

A schematic diagram of the apparatus and the coordinate system used is shown in figure 1.

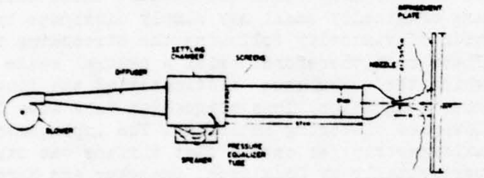

Fig. 1 A Schematic of Experimental Apparatus.

The jet is issued at the velocity $-W_o$ from a circular nozzle with diameter -d and impinges normally on a plate in a distance -h from it. The coordinate system originates at the stagnation point. The z direction coincides with the axis of the jet and the radial direction, parallel to the surface is r.

The air is filtered and compressed by a centrifugal blower. It then passes through a rectangular settling chamber in which a 12" loudspeaker is installed. The speaker produces pressure fluctuations which are manifested as velocity fluctuations at the exit of the nozzle. The speaker is activated by a Krohn-Hite signal generator (Model 5100 A) and a Dynaco power amplifier. The settling chamber resonates at discrete forcing frequencies which are independent of the exit velocity W_o and are therefore most suitable as forcing frequencies. For the Reynolds number range of interest the surging amplitude had a maximum at a frequency of 84 Hz. The nozzle velocity was varied by altering the r.p.m. of the blower which was driven by a DC motor.

The nozzle diameter is 25 mm and the jet emerges with a uniform velocity profile and 0.2% turbulence level. The Reynolds number in which the investigation was carried out was varied from 12000 to 60000. The jet impinged on a large plexiglass plate which was installed on a traversing mechanism capable of moving in all three directions. A hot wire probe was mounted on a plug at the center of the plate. An independent traversing mechanism enabled the probe to move in a direction normal to the surface. Measurements in the stagnation region outside the axis of symmetry were made by traversing the entire plate in the radial direction.

All data was acquired using Disa 55D01 constant temperature anemometers together with Disa 55D10 linearizers. The linearizers were calibrated at known conditions in the core of the jet. The signal was recorded on a digital tape and processed on a VARIAN 620i computer with a memory of 16k. The accuracy of the analog to digital conversion was 12 bit and the sampling rate was 20k for each of the two channels used. The difference of sampling time between the two channels was 10μsec. At each point 100 samples were made, 0.3 second each. Some of the digitally obtained results were checked using convnetional analog instrumentation. Spectral measurements were made with a Honeywell SAICOR, model SAI - 52B, digital spectrum analyzer. The smoothes output of the analyzer was plotted on an X-Y plotter.

MEAN VELOCITY AND FLUCTUATING COMPONENTS

All the measurements described in this chapter were made along the axis of the jet, namely, along the stagnation stream line. The stagnation plate was 10 diameters downstream of the nozzle. In order to study the effect of the stagnation region on vortices of various scales without the interference of other energy transfer mechanisms, the loudspeaker generated sinusoidal oscillations that were superimposed on the jet in a narrow-band and with no harmonics. These oscillations were of relatively high level of energy referring to the turbulent fluctuations in the jet. Initially the measurements were made in the "natural" jet (without additional oscillations) as a reference to those that were performed in the "forced" jet (with additional oscillations). Forcing frequencies above and under the neutral frequency were used. (The neutral frequency is defined as that frequency at which the energy remains constant at all distances from the wall). Two levels of forcing amplitude were used, namely 2% and 10% of the nozzle velocity.

Mean Velocity

The distribution of the non-dimensional mean velocity along the axis in both forced and unforced cases are shown in figure 2.

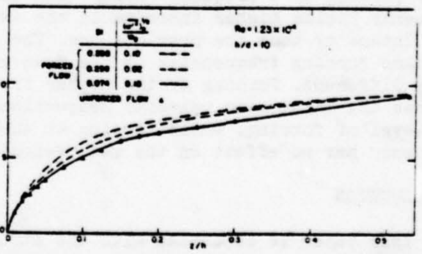

Fig. 2 The Mean Longitudinal Velocity of Forced and Unforced Jets.

At high amplitude forcing the mean velocity increases proportionally to the forcing intensity. At low intensity forcing the mean velocity remains unaltered compared to the unforced jet. It may be guessed that the energy lost from the high Strouhal number forcing is transferred wholly or partially to the mean velocity, which is therefore higher, while low Strouhal number forcing maintains the energy in the oscillatory flow and therefore do not affect the mean flow. This guess is only hypothetical without additional support gained from measurements of the whole flow field and investigation of the effects of different forcings on the jet's width and characteristics off the axis.

Fluctuating Components of the Turbulent Velocity

The distribution of the axial and radial turbulent intensities normalized with respect to the nozzle velocity is given in Figure 3.

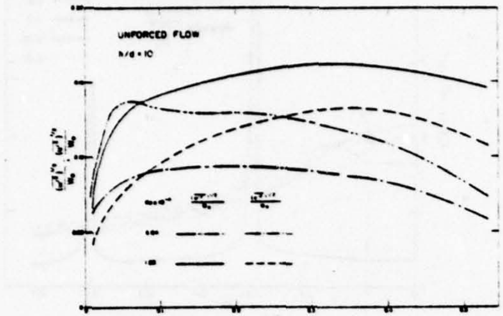

Fig. 3 The Two Components of the Velocity Fluctuations of an Unforced Jet.

Both axial and lateral intensities in the higher Reynolds number flow have lower values than their corresponding values at lower Reynolds number in the free jet region and at the outer edge of the stagnation region. As the impingement plate is approached, $z/h < 0.08$, these relations are reversed. At $Re = 6.4 \times 10^4$ the axial component is intensified from $z/h = 0.1$ as exhibited by the hump in the corresponding curve.

The effect of forcing on the turbulent intensities of the jet are shown in Figure 4.

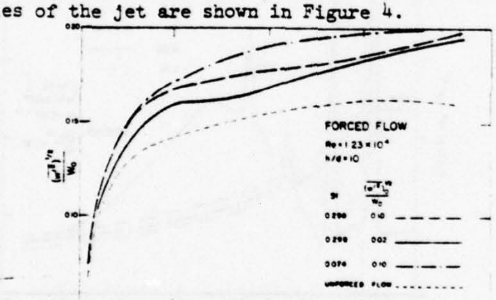

Fig. 4
The Two Components of the Velocity Fluctuations of a Forced Jet.

Both high and low amplitude forcings at a frequency higher than the neutral one bring the turbulent intensity in the free jet region to a level of 20% of the mean nozzle velocity. Forcing the jet at $St = 0.298$ when $Re = 1.23 \times 10^4$ yields an increase in the axial turbulent intensity which is proportional to the level of forcing. Forcing at $St = 0.074$ while the other parameters are kept constant yields a higher increase in the axial turbulent intensity than $St = 0.298$ at the same level of forcing.

POWER SPECTRA

Axial Fluctuations on the Axis of the Jet

Spectral analysis constitutes the bulk of the experimental effort because through it one may learn how the energy is transferred from one scale to another as the flow approaches stagnation. In figure 5

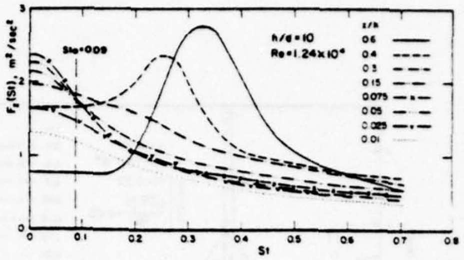

Fig. 5 Spectral Distribution of the Longitudinal Velocity Fluctuations.

the power spectra of the longitudinal fluctuations $F_z(St)$ along the axis of the jet, in the unforced case, are plotted as a function of the distance from the stagnation point. In the free jet region, $z/h = 0.6$, most of the turbulent energy is concentrated around $St = \frac{fd}{W_0} = 0.33$.

As the flow approaches stagnation the energy shifts towards lower Strouhal-number. The intensity of the fluctuations at $St > 0.09$ is reduced, while the intensity of the fluctuations at $St < 0.09$ increases monotonically as the flow approaches stagnation. Around this value a node in the power spectra distribution is formed. Of course in the immediate vicinity of the plate the amplitude of all fluctuations decays.

The distribution of the energy level of the longitudinal fluctuating component in different frequencies (or Strouhal-numbers) is described in Figure 6.

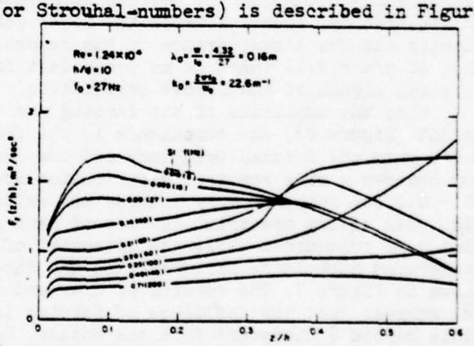

Fig. 6 The Longitudinal Velocity Fluctuations at Different Wave-Numbers.

The "neutral" frequency $f_o = 27$ Hz ($St_o = 0.09$) is clearly noticed in the graph. This frequency corresponds to a wave-length of $\lambda_o = \frac{\overline{W}_{M1}}{f_o} = 0.16$ m, where $\overline{W}_{M_1}$ is the mean velocity on the jet axis at the beginning of the stagnation region. Fluctuations in a frequency lower than the neutral one are intensified as the stagnation plate is approached and those at frequencies higher than the neutral decay gradually towards the plate. Forcing was applied at two Strouhal-numbers (1) $St = 0.3$ (higher than the neutral) and (2) $St = 0.07$ (lower than the neutral). The forcing at the plane of the nozzle was almost perfectly sinusoidal with an R.M.S. amplitude of 2% $(\overline{(w'^2)}_o^{1/2}/W_o = 0.02)$; In Figure 7 the power spectra of the axial velocity fluctuations are plotted for various distances from the stagnation plate, and at forcing Strouhal number of 0.3.

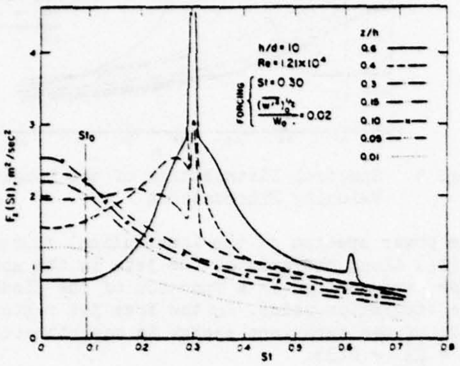

Fig. 7 Spectral Distribution of the Longitudinal Velocity Fluctuation of a Forced Jet.

There is a very weak second harmonic oscillation visible at St = 0.6. No other harmonics were visible in this case. Since the flow was forced at St = 0.3 which is the preferred mode of the free jet, there is a very strong peak in the power spectra at z/h = 0.6. At z/h = 0.4 one observes a shift in the spectral energy towards the lower Strouhal-numbers and the disappearance of the second harmonic. At z/h = 0.15 there is no trace left from the original signal of the forced oscillation.

When the amplitude of the forcing was increased to 10% (Figure 8), the turbulence in the free jet locks onto the forcing frequency and one can no longer observe a wide spectral distribution around St = 0.3 but rather a very narrow and extremely high peak of the spectrum. The second harmonic is also more pronounced while the intensity of the background turbulence is lower than the intensity shown in Figure 7. The results of Crow and Champagne (8) suggest that the influence of forcing is negligible beyond 8 diameters from the nozzle. In the present case the initial disturbance amplitude has a profound effect on the spectra. While the peak in the spectrum corresponding to the preferred mode (St = 0.3) disappears at z/h = 0.2 ($\frac{h-z}{d} = 8$) for 2% forcing amplitude (Figure 7) it is still very strong at the same point on the axis when the jet was forced at an initial amplitude of 10% (Figure 8).

As the flow approaches the plate the second harmonic disappears at z/h = 0.2 while a trace of the forced oscillation is still visible at z/h = 0.05.

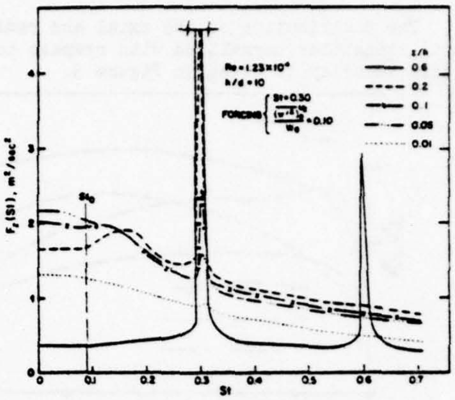

Fig. 8 Spectral Distribution of the Longitudinal Velocity Fluctuations of a Forced Jet.

A very different spectral distribution was obtained (Figure 9) when the forcing frequency was lowered to 21 Hz (i.e. St = 0.07) while maintaining the amplitude of $(\overline{w'^2})_o^{1/2}/W_o = 0.10$, keeping the jet velocity W_o, and h unchanged.

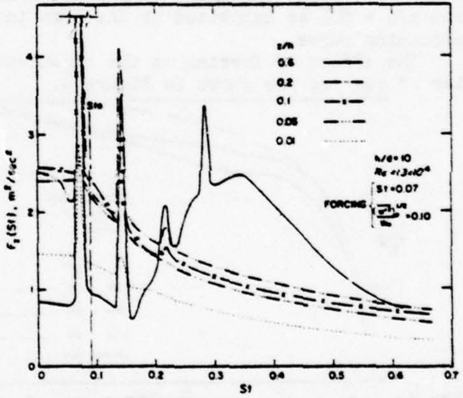

Fig. 9 Spectral Distribution of the Longitudinal Velocity Fluctuations of a Forced Jet.

There are 3 higher order harmonics visible at St = 0.14, 0.21, 0.29. The third harmonic is higher than the second because it is near St = 0.3. Two of them which are above the neutral Strouhal-number disappear at $z/h \leq 0.1$ while the forcing frequency and the first harmonic are clearly visible even at z/h = 0.01. Since the forcing frequency was now at St = 0.07 the background turbulence did not lock onto the forced oscillations, inspite of the fact that their amplitude was 10% at the nozzle. Moreover, a broad band peak at St = 0.3 remains.

It should be emphasized that although the natural augmentation of the jet is most efficient at St = 0.3, the forced fluctuations at St = 0.07 were maintained in the stagnation region. This fact indicates that it is, possible to distinguish between the augmentation produced by the jet and that which is caused by the stagnation. Measurements in the wall-jet region of the impinging jet showed that the energy level of the low frequency fluctuation is still high and the high frequency fluctuations decay completely.

Filter Characteristics

The measurements of power spectra which were described in the preceding chapters proved that the stagnation region has a low-pass filtering effect on the eddies' structure in the flow. In order to establish the precise filtering function of the stagnation region, the resultant spectra of forcings in a wide Strouhal number range, were measured at two locations in the stagnation region. The forcing amplitude was varied between 5% to 20%.

The power spectrum of the forcing wave was measured at the exit of the nozzle for each case to assure that it consisted of a single sharp peak at the forcing Strouhal number. The line joining all the peak's maxima depicts the forcing level. The envelope of all the end-points of the power spectra peaks, F_z, measured at a certain point on the stagnation region, has been called the "filter characteristic" at this location. The value of the filter characteristic measured at z/h = 0.05 normalized with respect to a forcing level of 10% at the nozzle is shown in Figure 10.

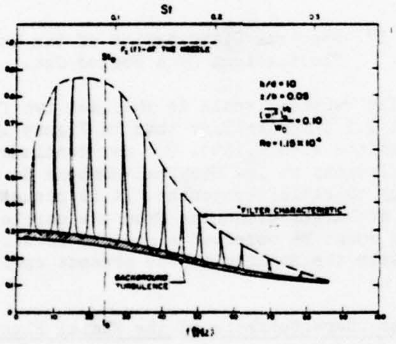

Fig. 10 An Example for the Filter-Characteristic of the Longitudinal Fluctuations.

The filter characteristics were measured for several combinations of parameters: Two forcing amplitudes - 5% and 10% maintaining constant the Reynolds number (Re = 1.15 x 10^4) and h/d = 10, then a higher Reynolds number (Re = 2.64 x 10^4) with 10% forcing amolitude and h/d = 10, and finally with the original Re = 1.15 x 10^4 and a larger plate to nozzle distance h/d = 14.5. The four "filter-characteristics" which were measured at z/h = 0.05 and the two measured at z/h = 0.15, with different parameters combinations are given in Figure 11.

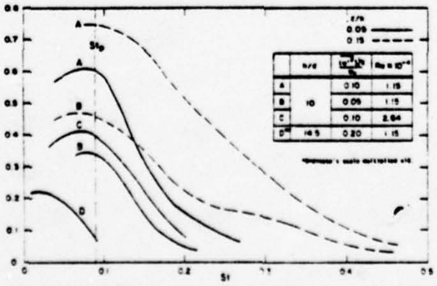

Figure 11. The "Filter-Characteristics" of the Longitudinal Fluctuations.

For the last case the amplitude of the forcing had to be increased to 20% in order to obtain satisfactory response level at the location of measurement in the stagnation region. We tried to define a set of non-dimensional variables in order to exhibit similarity of the results, but probably because of the non-linearity of the augmentation process we couldn't obtain it. Therefore the "filter-characteristics" are presented as a function of the non-dimensional frequency (Strouhal-number). In this figure, the value of the "filter-characteristics" are those which were measured above the level of the background-turbulence level, i.e., the abscissa is overlapping this spectral distribution. Each one of the "filter-characteristics" is related to the forcing level at the nozzle. The considerable difference between the "filter-characteristic" level which corresponds to the high forcing level (10%) and that which is the result of the lower forcing level (5%) at z/h = 0.05; 0.15 indicated that the jet's response to the forcing applied to it, is non-linear with respect to the forcing level. This fact is attributed to the "lock-in" effect which was described in the preceding chapter. Comparison of the forcing height in the free jet region of low level forcing (Figure 7) and high level (Figure 8) shows that as a result of the "lock-in" at the high level forcing, the energy in that forcing frequency is almost double than that of the low level. That means that in spite of the fact that the natural augmentation of the jet brings the turbulence intensity in both cases to the same level, at the high level forcing a double amount of energy is concentrated as a result of the "lock-in" process. It is obvious that this process is stronger at the higher Strouhal-numbers as can be seen in Figure 11. In the same figure the Reynolds-number effect is demonstrated at the high level forcing, where the "filter-characteristic" level decreases as the Reynolds number increases. The related phenomenon of the weakening or disappearance of the orderly eddy structure in a free jet with higher Reynolds-number was already reported by Bradshaw, Ferriss and Johnson (9) and was mentioned by Crow and Champagne (8) as well.

Increasing the nozzle to plate distance to 14.5 nozzle diameters has a profound effect on the "filter-characteristic" level in the stagnation region. The forcing level had to be increased to 20%(at the nozzle) in order to maintain a trace of the forcing signal in the spectrum. Even at this high forcing level the "filter-characteristic" is more than an order of magnitude lower than the other "filter characteristics".

Radial Fluctuations on the Axis of the Jet.

The stretching process at the stagnation region acts in a different way on the axial and radial fluctuating components. Measurements in the stagnation region of a two-dimensional impinging jet showed high unisotropy in this region.

Initially the power spectra of the radial fluctuations in the unforced jet, were measured (Figure 12)

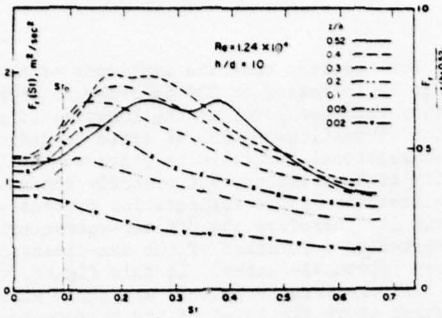

Fig. 12 Spectral Distribution of the Radial Velocity Fluctuations.

Their average level is lower than that of the axial fluctuations and is 70% from their value in the free jet region at St = 0.3. The v' spectra are much more evenly distributed at various Strouhal-numbers than the spectra of w' are (Figure 5).

The energy variation of the fluctuations at different Strouhal-numbers as they approach the stagnation plate is given in Figure 13.

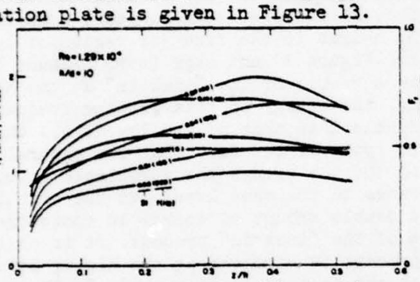

Fig. 13 The Radial Velocity Fluctuations at Different Wave-Numbers.

Unlike the augmentation of the axial fluctuations at low Strouhal-numbers (Figure 6) and a neutral one which was identified there, here there is no augmentation and all frequencies are decaying as the plate is approached.

The effect of forcing on the radial fluctuations is rather slow and not as dramatic as it is on the axial component of the fluctuations (Figure 14).

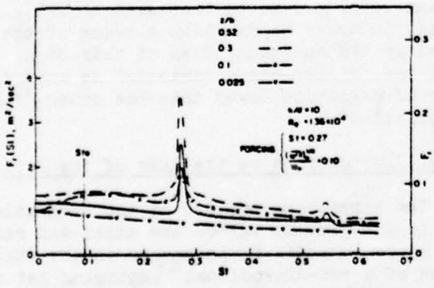

Fig. 14 Spectral Distribution of the Radial Velocity of a Forced Jet.

In the vicinity of the nozzle the peak in the v' power spectra is non-existent. It increases slowly in the free jet region in the downstream direction and attains a maximum at z/h = 0.3 which for St = 0.27 amounts to 20% of the w' fluctuations for this case. This indicates that the transfer of energy from w' to v' is not a very efficient prosess and the tendency to isotropy must of necessity be slow.

A first harmonic at St = 0.6 is also visible for $0.3 < z/h < 0.52$. It disappears at z/h = 0.1 while no trace of the fundamental disturbance can be seen at z/h = 0.025. Forcing at St = 0.06 and maintaining the other parameters constant, had no effect on the radial fluctuations at all. The power spectra of v' in Figure 15 are almost identical to those of Figure 12.

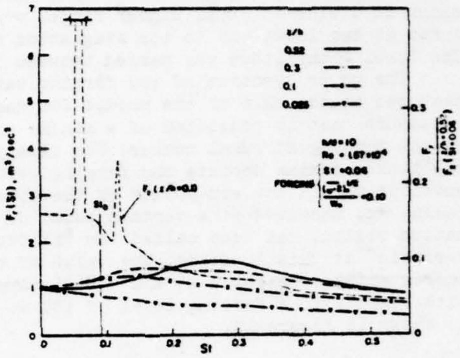

Fig. 15 Spectral Distribution of the Radial Velocity Fluctuations of a Forced Jet.

The vertical scale in the last two firgures is about 2.5 times smaller than in Figure 12 to allow for comparison with $F_z(St)$. One may conclude that axial oscillations at low Strouhal-numbers do not transfer energy to radial component. It is plausible, however, that at larger distances from the nozzle v' fluctuations would be observed since the wave-length associated with the forcing in the present case is larger than h.

Filter Characteristic of the Radial Fluctuations.

The "filter characteristic" of the radial fluctuating component is defined in the same manner as for the axial fluctuations. The measurements were made at two points in the stagnation region: z/h= 0.05, 0.15 and with two forcing levels: high (10%) and medium (5%).

The radial "filter characteristics" are given in Figure 16 and are compared to the axial results.

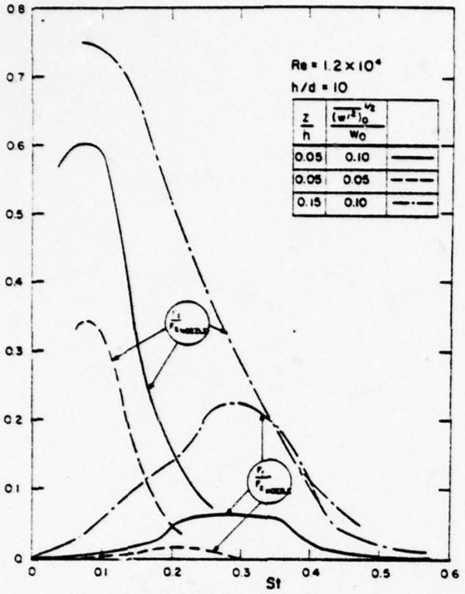

Fig. 16 The "Filter-Characteristics" of the Longitudinal and Radial Fluctuations.

Their value is given above the background fluctuations spectrum and are related to the forcing level at the exit. Their profile is characteristic to a Band-Pass Filter, whose center frequency is around St=0.3. The low energy level of the fluctuations in the low Strpuhal-numbers range is due to the fact that only a small amount of energy is transferred from the axial fluctuations to the radial in this range. The decay of fluctuations in the high Strouhal-numbers range is caused by the strong action of the dissipation. The maximum height of the radial filter characteristic is appreciably lower than that of the axial one, yet their values at the high Strouhal-numbers range (St > 0.3) are similar. The influence of the forcing level on the radial fluctuations is stronger than in the axial fluctuations. In the range of St > 0.3 the traces of the medium level forcing do not exist while those of the higher level are in their maximum value. The absence of those traces may result from the strong action of the dissipation.

CONCLUDING REMARKS

The stagnation region of the impinging jet was investigated concentrating on the vortex stretching mechanism in the flow approaching stagnation. The non-dimensional parameters of this flow are the Strouhal-numbers - $St = \frac{f \cdot d}{u}$, the Reynolds number and the plate to nozzle distance.

The concentration of energy at the larger scales was demonstrated in spectral measurement and the neutral scale that separates the range of scales which lose energy from the scales which gain it, was determined. By using a loudspeaker a wave of a predetermined length and amplitude could be superimposed on the flow. Waves whose scales were lower and larger than the neutral scale were superimposed on the jet at the nozzle and their response was checked in the stagnation region at two points. In this way the "filter characteristic" of the stagnation region of the jet was determined. This function describes the influence that the stagnation region has on vortices of different scales. It was shown that the stagnation region has lowpass filter characteristics that allow only scales larger than the neutral one to survive. A conjecture was proposed that the energy used to force small scales which cannot survive in the stagnation region, was delivered wholly or partially to the mean flow and thus augmented it.

Additional measurements in the stagnation region off the axis, along the divergent stream lines could allow a better understanding of the phenomena discussed in this work. Nevertheless, the mechanism governing the flow in the stagnation flow is now sufficiently understood to enable the investigation of the influence of the stretching of vortices on heat transfer in the stagnation region. The method of forcing the jet with a wave of predetermined frequency and amplitude can be used to investigate the heat transfer rates and perhaps to control them.

REFERENCES.

1. Kestin,J,Maeder,P.F. and Sogin,H.H.,"The Influence of Turbulence on the Transfer of Heat to Cylinders near the Stagnation Point". Z. angew. Math. Phys. Vol.12, 1961, p.115.
2. Sutera,S.P.,Maeder,P.F. and Kestin,J."On the Sensitivity of Heat Transfer in the Stagnation-point Boundary Layer to Free-stream Vorticity",Journal of Fluid Mechanics,Vol.16,No.4,1963,pp.497-520.
3. Donaldson.C.D.,Snedeker,R.S.and Margolis,D.P."A study of Free Jet Impingement.Part 2. Free Jet Turbulent Struncture and Impingement Heat TRansfer", Journal of Fluid Mechanics, Vol. 45, No.3,1971, pp.477-512.
4. Bradbury,LJ.S.,"The Impact of an Axisymmetric Jet onto a Normal Ground",Aeronautical Quarterly, Vol. 23,May 1972, pp.141-147.
5. Sadeh,W.Z.,Sutera,S.P.and Maeder,P.F.,"An Investigation of Vorticity Amplification in Stagnation Flow",Z.angew.Math.Phys.,Vol.21,1970,pp.717-742.
6. Hunt,J.C.R.,"A Theory of Turbulent Flow Round Two-dimensional Bluff Bodies",Journal of Fluid MechanicsVol.61, No. 4 1973, pp.625-706.
7. Gutmark,E.,Wolfshtein M. and Wygnanski,I."The plane Turbulent Impinging Jet",TAE-226,May 1976, Technion, Haifa,Israel.
8. Crow,S.C.and Champagne,F.H.,"Orderly Structure in Jet Turbulence",Journal of Fluid Mechanics, Vol.48, No.3, 1971, pp. 547-591.
9. Bradshaw,P,Ferriss,D.H.and Johnson,R.F.,"Turbulence in the Noise-produeing Region of a Circular Jet". Journal of Fluid Mechanics,Vol.19.1964,pp.591-624.

EXPERIMENTAL INVESTIGATION ON THE TURBULENCE STRUCTURE OF AN IMPINGING, PULSATING JET

Peter Leister
Sonderforschungsbereich 80, Universität Karlsruhe
Karlsruhe, West Germany

ABSTRACT

A turbulent round free jet with a nozzle exit velocity consisting of a constant and a periodic (sinusoidal) component impinging normally on a rough flat plate was investigated. Measurements of instantaneous and time averaged velocities in the flow field and wall pressure and wall shear stress were performed. By correlation technique periodic and stochastic parts of fluctuations were separated. The behaviour of these parts was studied in the free jet region and the wall jet region. Interactions between pulsation and turbulence seem to be possible only within the free jet region and the free shear layer of the wall jet region. The wall boundary layer turbulence is not affected by pulsation. The different behaviour of instantaneous magnitudes when pulsation is present is explained by the transfer mechanism of kinetic energy of pulsation into turbulent energy. From measurements it is concluded that the transfer is easiest if eddies are available with frequencies of comparable order as the pulsation frequency.

NOMENCLATURE

D	nozzle
f	pulsation frequency
H	nozzle to plate distance
I^*	ratio of momentum flux = $\dot{M}_o/\dot{M}_{op}$
k_s	equivalent sand roughness
$\dot{M}_o$	momentum flux at nozzle exit
$\bar{p}_w$	wall pressure
R	correlation
Re_D	nozzle Reynoldsnumber = $\bar{u}_o D/\nu$
r	radial direction
u	velocity in x-direction
v	velocity in r-direction
Sr	Strouhalnumber = $f D/\bar{u}_o$
T	time intervall of sample
t	time
x	streamwise direction (free jet region)
y	continuous time series
z	wall separation

Greek symbols

α	amplitude of pulsation = $u_{o\,max}/u_o$
δ	wall boundary thickness ($\delta = z$ where $v(z) = v_m$)
ζ	wall coordinate in z-direction starting at $z = \delta$
θ	time shift in correlation
ν	kinematic viscosity
τ_o	wall shear stress

Subscripts

m	on jet axis
p	periodic
s	stochastic
t	total
w	wall
o	nozzle
1	signal of probe at fixed position
2	signal of probe at variable position

Superscripts

–	time averaged value
*	dimensionless
′	turbulent (stochastic) part

INTRODUCTION

Impinging jets are a widely used tool in the area of heat and mass transfer processes such as tempering of glass, turbine blade cooling and drying. Beyond that erosion of ground by hovercrafts or of beds of flumes caused by ship-propellers may be treated as impinging jet problems. To apply pulsating jets seems at a first glance to be of theoretical interest. Yet known investigations in this field had real practice aims in mind. (1) reports of a pulsating jet to study improvement of ejector pumps. (2) measured reaction and mixing processes of pulsating jets in burning chambers, (3) investigated thrust improvement by pulsation of nozzle engines, (4) report about coherent turbulence structures in a jet with periodic exit velocity as a problem of noise generation, while (5) studied the behaviour of pulsating jets, to be applied in fluidics (pneumatic logic elements). The common feature of these results is that jets with an artifical periodic exit velocity tend to have a faster spreading and decay of mean velocity of the jet´s center line, while turbulence levels increase. In (6) increased erosion rates are described comparing a pulsating jet impinging on the loose sand bed with continuous jet. The essential reason of this effect could not be explained since no magnitude of turbulence were measured. It was the aim of (7) to explain this phenomenon. Main results concerning the behaviour of time averaged and instaneous

PRECEDING PAGE BLANK-NOT FILMED

magnitudes are reported here.

EXPERIMENTAL SETUP

The investigations were carried out at an air jet issuing from a round nozzle of .03 m diameter and impinging on an artificially roughened plate, the equivalent sandroughness of which was determined elsewhere (7). Nozzle to plate distance could be varied within $3 < H/D \leq 16.66$ (Fig. 1). The pulsation was produced by a special rotating piston which superimposed an additional portion of supplying air delivered by the fan to the continuous part and subtracting a portion of the latter one cyclically producing in this way a pulsating velocity at the nozzle. The frequency of pulsation could be varied within $1 \leq f \leq 45$ Hz and the amplitude within $0 < \alpha \leq 80$ %. Before entering the fan the ambient air passed through a heat exchanger to provide nozzle exit temperature at ambient level. The installed traversing mechanism allowed to set the used probes at each point of the flow field.

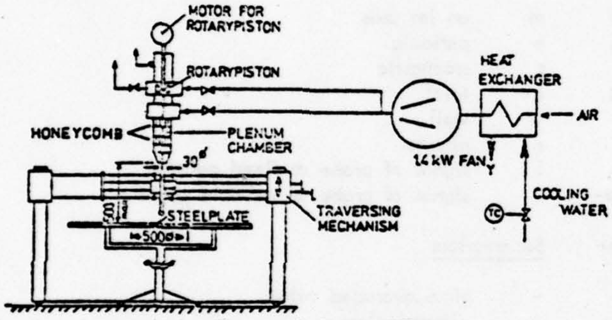

Fig. 1 Experimental setup

Both time averaged magnitudes of the flow field and at the plate and instantaneous velocity fluctuations could be measured by the measured equipment shown in Fig. 2

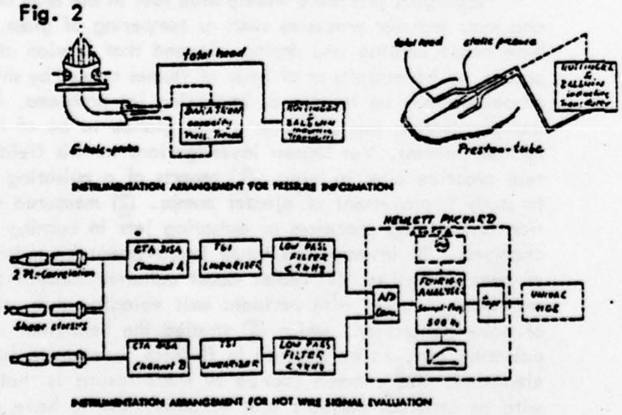

Fig. 2 Instrumentation arrangement

Averaged velocities were measured as well by a 4-hole-pitot tube sensitive to flow direction as by a hot wire anemometer. Time averaged wall pressures and wall shear stress were measured by a modified Preston tube. Velocity fluctuations were measured by two linearized constant-temperature anemometers with single wires and X-wires. Correlations of both the low pass filtered signals were performed by a Fourier analyser with a sampling frequency of 500 Hz and averaging over 100 samples. The hot wire anemometers were calibrated in the nozzle when the jet was blowing without pulsation but with a background turbulence of .3 %.

EXPERIMENTAL RESULTS

General Remarks

In turbulent, continuous free jets the exit momentum flux is the only invariant magnitude other flow field magnitudes can be related to both in the region of flow establishment and the region of established flow (Fig. 3). To compare the pulsating jet with a continuous one both must have equal nozzle momentum flux. If the nozzle velocity varies harmonically about a time mean value

$$u_o(t) = \bar{u}_{op}(1 + \alpha \sin 2\pi f t) \tag{1}$$

equal momentum flux at the nozzle exit requires:

$$2\pi \int_0^{D/2} \frac{1}{T} \int_0^T \bar{u}_{op}^2 (1 + \alpha \sin 2\pi f t)^2 \, dt \, r dr = 2\pi \int_0^{D/2} \bar{u}_o^2 r dr \tag{2}$$

and with $\bar{u}_{op}$ and $\bar{u}_o$ constant across the nozzle area:

$$\bar{u}_{op} = \bar{u}_o / \sqrt{1 + \frac{\alpha^2}{2}} \tag{3}$$

Hence in a pulsating jet the time independent part of nozzle exit velocity is $1/\sqrt{1+\alpha^2/2}$ times smaller than the nozzle exit velocity of a continuous jet. Based on equation (3) the experiments were carried out.

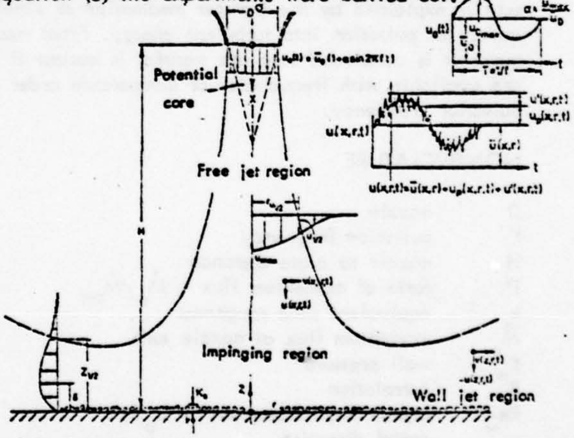

Fig. 3 Definition sketch

Time averaged velocities

Free jet region. Fig. 4 shows the centerline velocity $\bar{u}_m$ of a pulsating jet (f = 15 Hz, α = 34 %) and of a continuous jet with an exit velocity of 30 m/s. The faster decay of the pulsating jet is evident. The "potential core" region is shortened to 3.5 nozzle diameters. After a certain transition region the centerline velocity behaves like that in a continuous jet diminuished by a constant factor (parallel shifting). If impinging plates are present the decrease of centerline velocity is at small nozzles/plate distances nearly the same as in a continuous jet whilst for large H/D this decay tends to be slower in the pulsating jet.

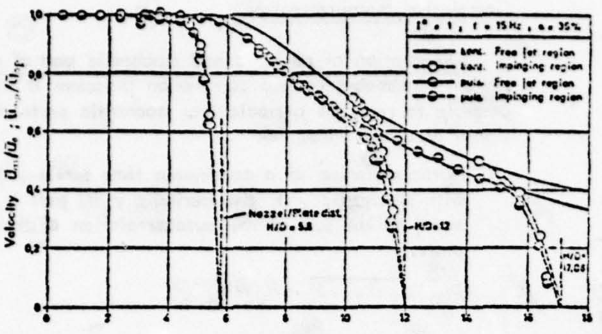

Fig. 4 Velocity decay on jet axis

In the radial distribution the streamwise velocities exhibit an increase in the outer region of the jet. The jet is broader than a continuous one. The profiles show a self-preserving behaviour for x/D ⩾ 6. In Fig. 5 several velocity profiles are displayed in the similarity coordinates. The measurements group very well around the curve for the continuous profiles, if the length scale $r_{u\,1/2}$ is increased from .0848 x for the continuous jet to .1 x for the pulsating jet. These results are in good agreement with those of (1, 2, 3, 4, 5) for pulsating free jets.

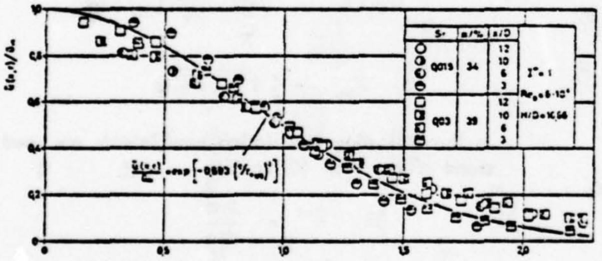

Fig. 5 Radial distribution of axial velocity in free jet region (Similarity coordinates)

Wall jet region. Of most interest is to study the behaviour of the wall jet region under the influence of pulsation. Fig. 6 displays the development of the maximum velocity $\bar{v}_m$ parallel to the wall, e.g. the velocity on the wall jet axis, both for a nozzle to plate distance H/D = 16.66 and for H/D = 5.8. It is clearly to be seen that adjacent to the stagnation point and in the impingement region (r/D < 3) the maximum velocity is smaller than that of a continuous jet due to the decreased arrival velocity $\bar{u}_m$ (x = H) of the free pulsating jet. But for r/D > 4 the ratio $\bar{v}_m/\bar{u}_o$ reaches the value of the continuous jet and becomes independent from H/D. Velocity profiles in the wall jet region were measured at several stagnation point distances r/D, (H/D, f, ∝ , $\bar{u}_o$ as in Fig. 6). It was found that towards the outer edge of the free shear layer of the wall jet the velocities $\bar{v}$ are significantly greater than in a continuous jet. This may be a continuation of the behaviour in the free jet region. In the wall boundary layer of the wall jet the velocity profiles of the pulsating jet merge into that of a continuous jet when wall separation z is decreased. In Fig. 7 the velocity profiles are shown in the "Glauert" co-ordinates. The shift of the profiles away from the wall is due to the rough wall. In the outer region the faster pulsating wall jet is evident.

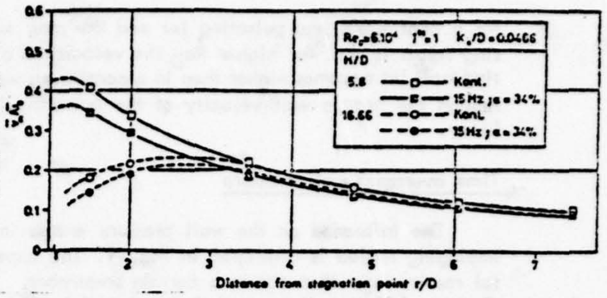

Fig. 6 Development of maximum velocity $\bar{v}_m$ parallel to the wall

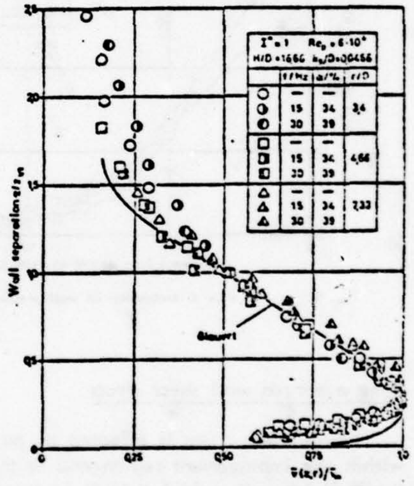

Fig. 7 Velocity profiles wall jet region similarity coordinates

To find out a dependency of the velocity on the nozzle Reynolds number Re_D in the wall jet region as it is known for the continuous jet - though a weak one - velocity profiles were measured at r/D = 7, H/D = 5.8 for several Re_D- values. Fig. 8 displays this tendency

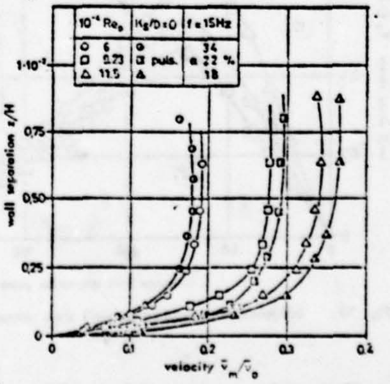

Fig. 6 Influence of Re_D-number on velocity profiles

for a continuous and pulsating jet and the most surprising result is that for higher Re_D the velocity in a pulsating wall jet becomes higher than in a continuous wall jet though the nozzle exit velocity of the pulsating jet is lower.

Time averaged wall pressure

The influence on the wall pressure excess in the impinging region is displayed in Fig. 9. The experimental results show that above a certain Sr-number ($Sr \geq 6 \cdot 10^{-3}$) wall pressure is decreased in the stagnation point region but for $r/D > 1$ wall pressure values exceed that of a continuous impinging jet. The influence of pulsation amplitude is negligible within $15 < \alpha < 80\,\%$.

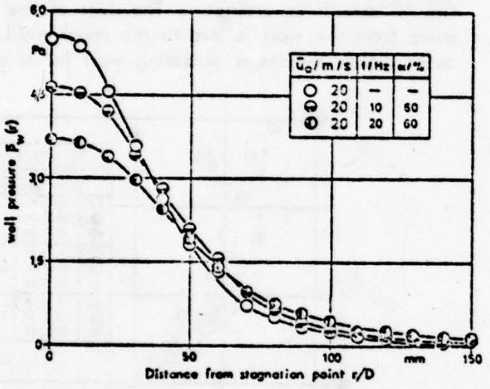

Fig. 9 Influence of frequency on wall pressure

Time averaged wall shear stress

Wall shear stress is effected by pulsation in that within the impingement region and at the beginning of the wall jet region ($r/D < 3$) it is decreased and the maximum is shifted slightly away from the stagnation point (Fig. 10). This influence is measured only if $Sr \geq 6 \cdot 10^{-3}$. The influence of pulsation amplitude is small. For $r/D > 3$ wall shear stress tends to reach the value of a continuous wall jet.

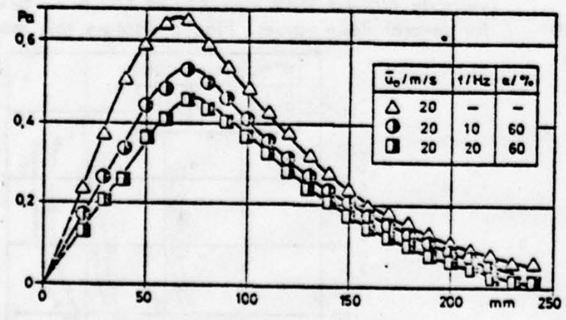

Fig. 10 Influence of frequency on wall shear stress

Correlation measurements

Separation of periodic and stochastic part of a signal. By means of two correlation theorems it was possible to separate periodic and stochastic parts of the signal of a hot wire.

- Autocorrelation of a continuous time series y (t) with stochastic $y_s(t)$ and periodic $y_p(t)$ part is equal to the sum of the autocorrelation of these parts.

$$R_{yy}(\theta) = \overline{y(t) \cdot y(t+\theta)} = R_{y_p y_p}(\theta) + R_{y_s y_s}(\theta)$$

$$= \lim_{T \to \infty} \frac{1}{T} \int_{-T/2}^{T/2} y_p(t)\, y_p(t+\theta)\, dt + \lim_{T \to \infty} \frac{1}{T} \int_{-T/2}^{T/2} y_s(t) \cdot y_s(t+\theta)\, dt \qquad (4)$$

- Crosscorrelation of a pure periodic time series $y_p(t)$ and a pure stochastic time series $y_s(t)$ is equal to zero.

$$R_{y_p y_s}(\theta) = \overline{y_p(t) \cdot y_s(t+\theta)} = \lim_{T \to \infty} \frac{1}{T} \int_{-T/2}^{T/2} y_p(t)\, y_s(t+\theta)\, dt = 0 \qquad (5)$$

With equation (4) and (5) it can be shown that the crosscorrelation of the stochastic parts of two time series involving each a harmonic part gives:

$$\frac{\overline{y_{1s} \cdot y_{2s}}}{\sqrt{\overline{y_{1s}^2}}\sqrt{\overline{y_{2s}^2}}} = \frac{R_{12} - R_{1_p 2_p}}{\sqrt{R_{11}(0) - R_{1_p 1_p}(0)} \cdot \sqrt{R_{22}(0) - R_{2_p 2_p}(0)}} \qquad (6)$$

with

$$R_{1_p 2_p} = \frac{1}{2} \sqrt{R_{1_p 1_p}} \sqrt{R_{2_p 2_p}}$$

In the following correlation coefficients are used instead of equation (4) or (5)

$$R^* = \frac{R_{yy}(\theta)}{R_{yy}(0)} \qquad (7)$$

and

$$R^+_{12} = \frac{R_{12}(\theta)}{R_{12}(0)} \qquad (8)$$

respectively.

These correlation evaluations were performed within the Fourier analyser (Fig. 2) except of eq. (6) which was evaluated "manually" - regarding the capacity of the computer - by means of the auto- and crosscorrelation signals.

Auto- and space-time-correlations of the axial velocity fluctuation in free jet region

In Fig. 11 autocorrelation coefficients of the total axial velocity fluctuations $u_p + u'$ is shown versus time shift $\theta \bar{u}_0/D$ both for a continuous and pulsating jet (lower sequence) and for $x/D = 10$ and $x/D = 13.66$ (from left to right). The parameter is the radial position r of the single hot wire. The known behaviour of a continuous jet is characterized by an increase of time scale both in radial and in axial direction. In the pulsating jet such a development is not displayed. Pulsation dominates the flow with a certain damping in radial direction. The integral time scale seems to be enlarged but not changed in axial or radial direction. To prove a possible increase of scale by pulsation, two point correlations of $(u_p + u')$ were performed with two single hot wire probes, one of them kept fixed at the jet's axis the other moved towards the edge of the jet, crosscorrelating both signals. This leads to lateral space-time correlations (Fig. 12), where the envelope of the maxima of crosscorrelation curves as a function of probe separation exhibits the development of length scale. For the pulsating jet the results seem to confirm an increase of length scale.

It is of greatest interest to persue the fluctuations within the impinging region to get information about the interactions of pulsation and turbulence while axial fluctions are transferred into radial fluctuations within this region. Yet is is very difficult to measure with single or X-wires in this region. Therefore hot wire measurements were performed only within the wall jet region. The auto- and 2-point-correlations of the $(v_p + v')$ fluctuations (where in the wall jet v are the axial fluctuations) were performed only within the free shear layer of the wall jet. (For 2-point-correlations the fixed probe was held on the wall jet's axis.) Fig. 13 and 14 show the results of these measurements. They confirm the results of the free jet region. To prove an enlargement of scale of the stochastic part of velocity fluctuations eq. (6) was applied for the correlation results to the wall jet region. Fig. 15 shows obvious an enlargement of length scale by pulsation.

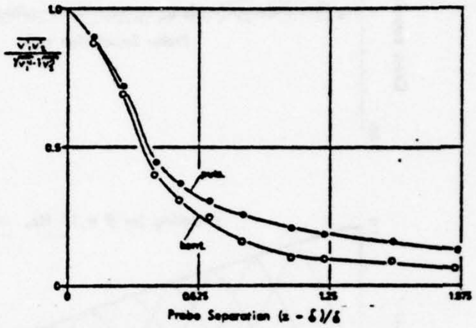

Fig. 15 Increase of lateral space-time-correlation of axial stochastic component (wall jet region H/D = 16.66; r/D = 8 free shear layer)

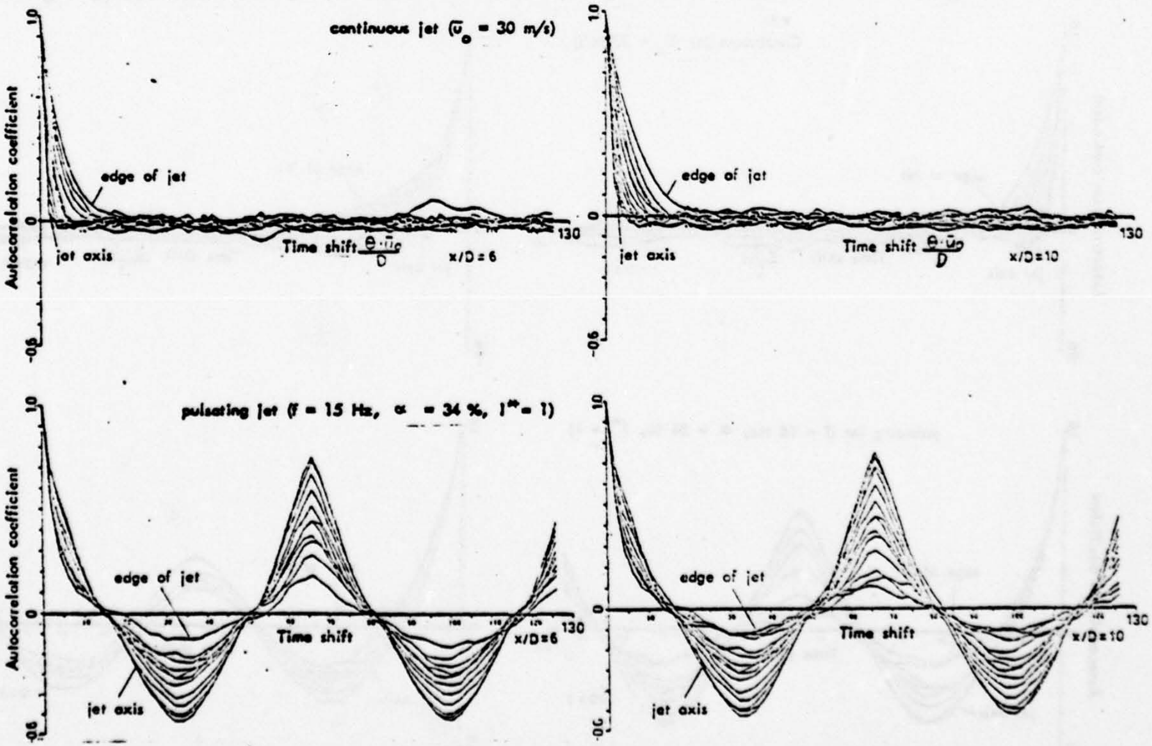

Fig. 11 Autocorrelation of axial velocity fluctuations in free jet region

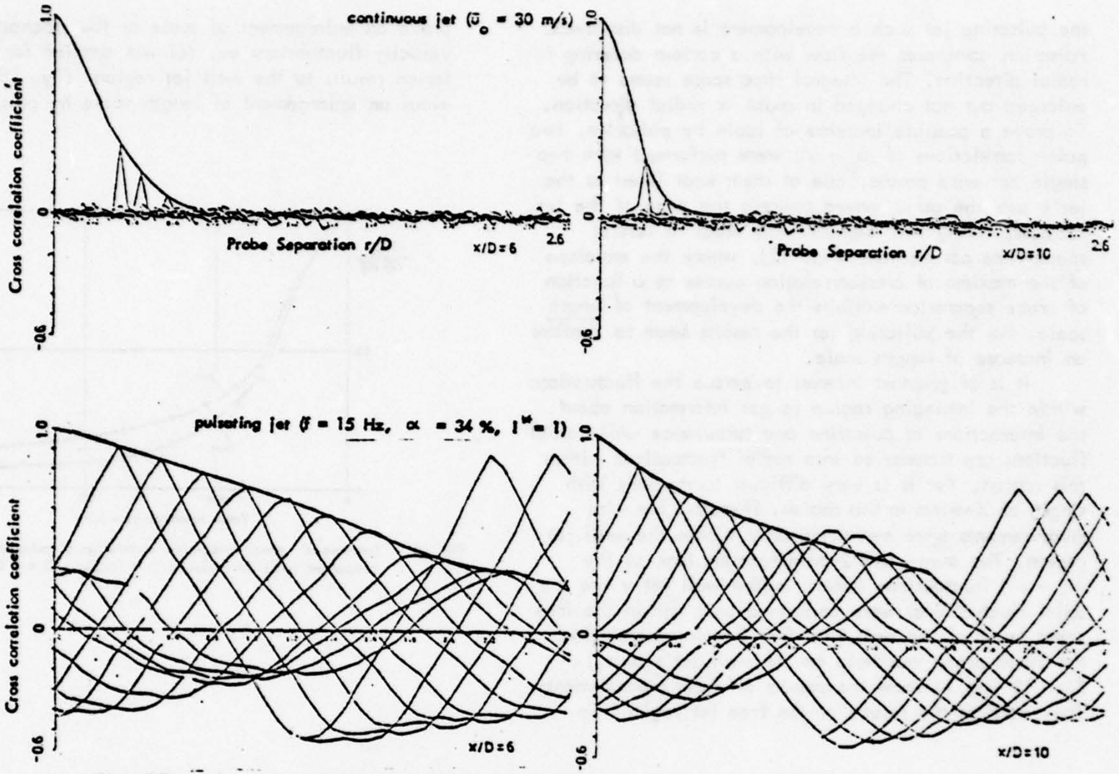

Fig. 12 Lateral space time correlation of the axial velocity fluctuations in free jet region

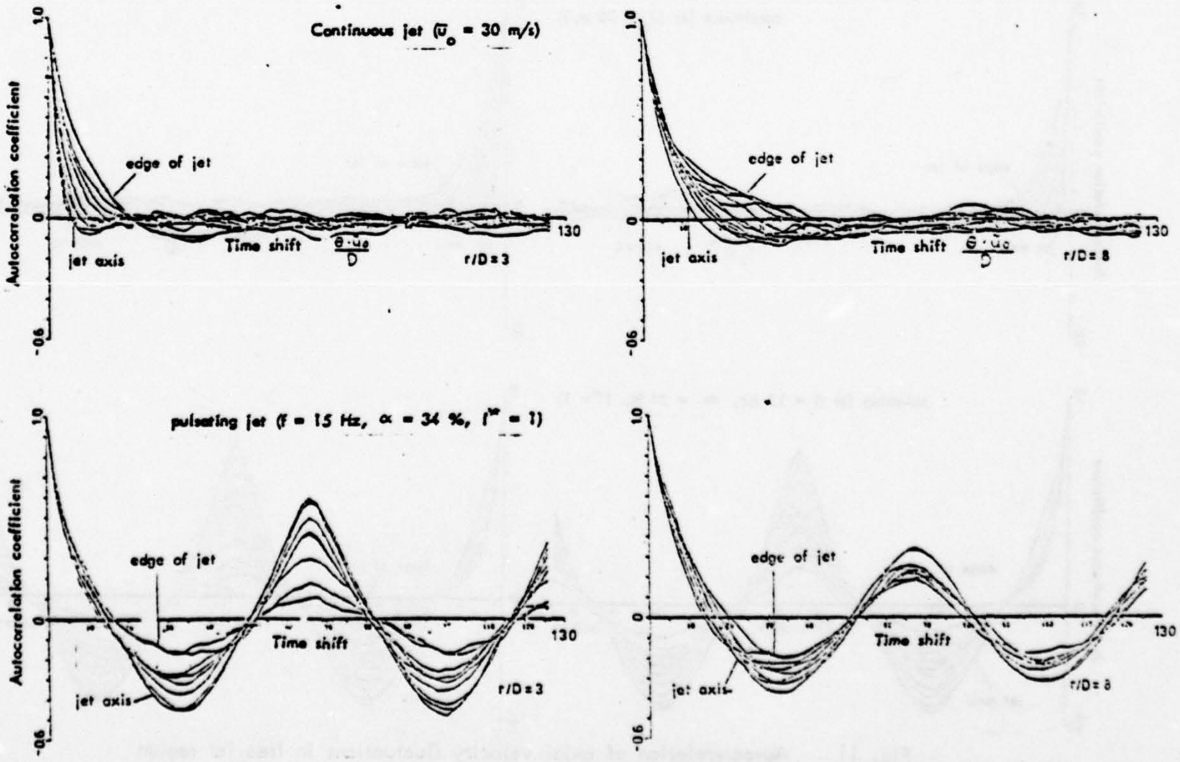

Fig. 13 Autocorrelation of axial velocity fluctuations in wall jet region (free shear layer)

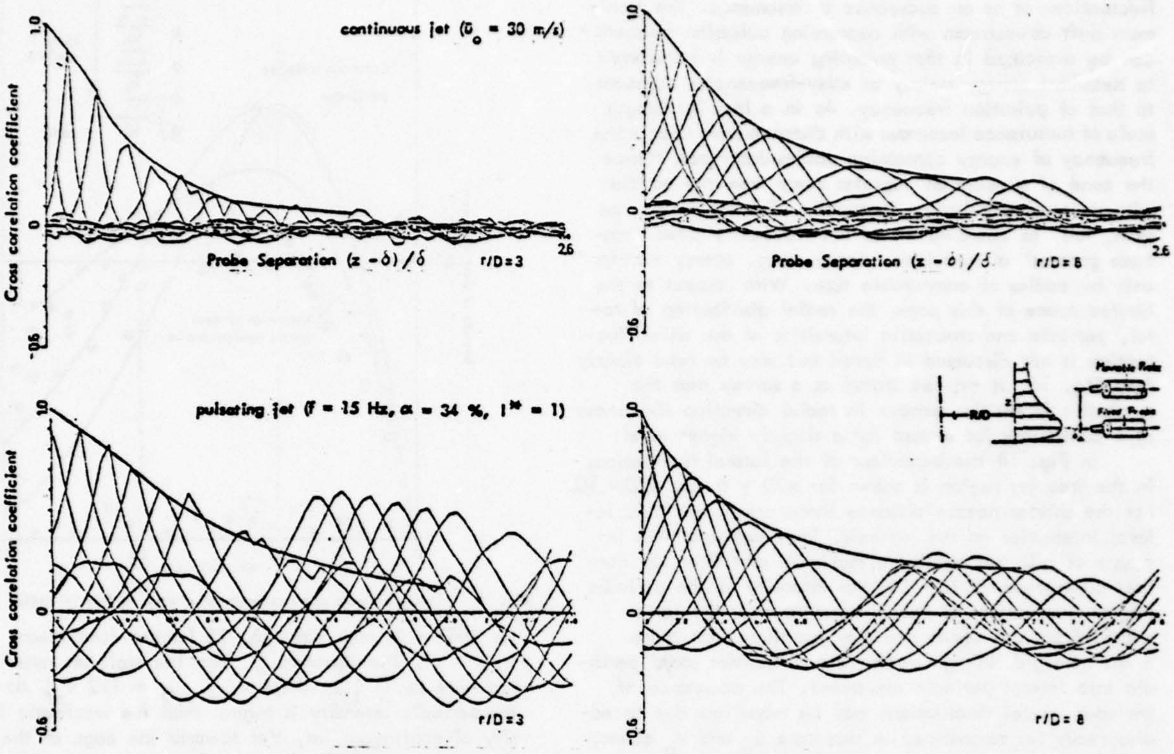

Fig. 14 Lateral space-time-correlation of the axial velocity fluctuations in wall jet region (free shear layer)

Intensities of velocity fluctuations

Free jet region. Applying eq. (4) to the autocorrelation results at zero time shift leads to

$$\overline{u_t^2} = \overline{u_p^2} + \overline{u'^2}$$

$$\overline{v_t^2} = \overline{v_p^2} + \overline{v'^2} \qquad (9)$$

and the crosscorrelation of X-wire signals - under consideration of X-wire evaluations after (8) - leads to

$$\overline{u_t v_t} = \overline{u_p v_p} + \overline{u' v'} \qquad (10)$$

in Fig. 16 the separation of eq. (9) was performed for the axial fluctuations in the free jet region. They are presented as intensities related on the mean centerline velocity. The most surprising result is not only that the high intensity - impressed to the flow in the nozzle as periodic intensity - consists at larger nozzle distances (x/D = 13.6) mainly of periodic intensity but also that within $8 < x/D < 13.66$ the total and the periodic intensities on the jet axis exhibit a maximum. Fig. 17 confirms this finding comparing it with the results of (1, 3, 4, 5). From this figure it is to conclude that the lower the pulsation frequency the farther downstream this maximum occurs. The occuring maximum of axial intensities is according to (3, 4, 5) to be interpreted as a stimulation of axial

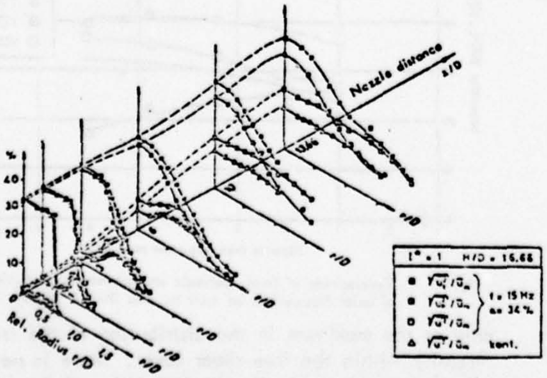

Fig. 16 Isometric view of total, periodic and stochastic intensities of axial fluctuations in free jet region

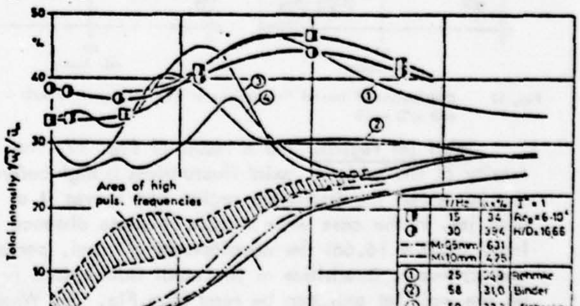

Fig. 17 Stimulation of total intensity of axial velocity fluctuation on jet axis (free jet region)

fluctuations or as an occurance of resonance. The maximum shift downstream with decreasing pulsation frequency can be explained in that pulsating energy is transferred to turbulent energy mainly at eddy-frequencies adjacent to that of pulsation frequency. As in a free jet length scale of turbulence increases with distance from nozzle the frequency of energy containing eddies decreases. Hence the zone of stimulation migrates away from the nozzle with decreasing pulsation frequency. This result may be seen, too, as confirmation of the frequently cited "cascade process" of turbulence decay, e.g. energy transfer only by eddies of comparable size. With respect to the limited space of this paper the radial distribution of total, periodic and stochastic intensities of the axial fluctuation is not discussed in detail but may be read clearly from Fig. 16. It may be stated as a survey that the stochastic intensities behave in radial direction like those in a continuous jet except for a slightly higher level.

In Fig. 18 the behaviour of the lateral fluctuations in the free jet region is shown for x/D = 6 and x/D = 10. For the shorter nozzle distance there are no periodic lateral intensities on the jet axis. They increase with increase of r/D and exhibit a maximum at r/D ≈ .5. Farther downstream (x/D = 10) the intensity of the periodic lateral fluctuations is nearly constant over the jet's width. From this result one may conclude that there exists no rigid linkage mechanism to transfer axial periodic into lateral periodic movement. The occurance of periodic lateral fluctuations may be more less due to eddies ready for resonance. In this case u_p and v_p cannot be in phase and hence crosscorrelations $\overline{u_p v_p}$ must be small. Results of X-wire measurements prove this (Fig.19) where the total shear stresses $\overline{u_t v_t}$ in the free pulsating jet are not significantly higher than in a continuous jet and the periodic shear stress $\overline{u_p v_p}$ are nearly zero.

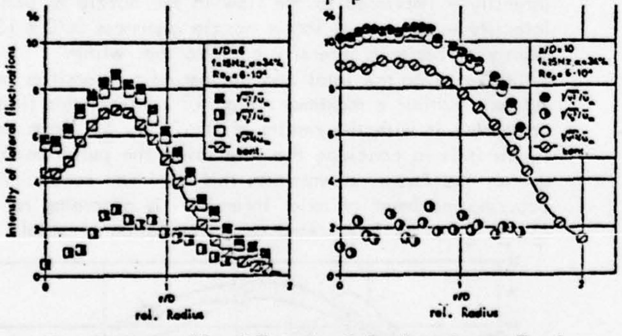

Fig. 18 Distribution of lateral fluctuations in free jet region at x/D = 6 and x/D = 10

<u>Wall jet region.</u> As a result of Fig. 17, the intensity of the periodic axial fluctuations is high before the jet enters the impinging region and leaves it as a wall jet. In the case when nozzle to plate distance is large (H/D = 16.66) the development of total, periodic and stochastic intensities of the axial fluctuations $(v_p + v')$ on the wall jet axis can be read from Fig. 20. Whereas the total intensity $\sqrt{\overline{v_t^2}}/\bar{v}_m$ remain nearly constant along the jet axis the periodic intensity $\sqrt{\overline{v_p^2}}/\bar{v}_m$ decays monotonously. The stochastic intensity $\sqrt{\overline{v'^2}}/\bar{v}_m$ increases and is slightly higher than in a continuous wall jet. The lateral distribution (z - direction) of the axial intensities becomes evident from Fig. 21 at the beginning of the wall

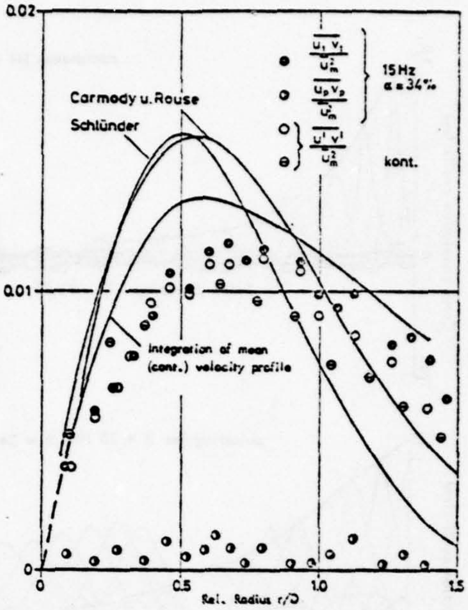

Fig. 19 Total, periodic and stochastic shear stress in free jet region (x/D = 10)

jet (r/D = 3) and from Fig. 22 farther downstream (r/D = 8). The distance ζ from the wall jet axis is related here to $\zeta_{1/2}$ where $v(\zeta_{1/2}) = 1/2\ \bar{v}_m)$. At r/D = 3 the periodic intensity is higher than the stochastic intensity of continuous jet. Yet towards the edge of the free shear layer $\sqrt{\overline{v_p^2}}/\bar{v}_m$ decays. The remaining stochastic intensity is higher over the whole width of the wall jet than in a continuous case. Farther downstream (r/D = 8) the periodic intensity has been damped on the axis far below the value of the stochastic intensity of a continuous jet. The remaining stochastic intensity of the pulsating wall jet is nearly constant for the whole width of the free shear layer. In Fig. 23 the distribution of the different fractions of the lateral fluctuations are shown versus the wall separation farther downstream of the wall jet. In this figure a part of the wall boundary layer is included in the measurement results. Periodic intensities $\sqrt{\overline{u_p^2}}/\bar{v}_m$ occur

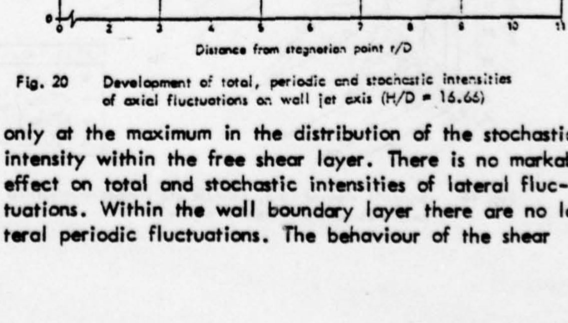

Fig. 20 Development of total, periodic and stochastic intensities of axial fluctuations on wall jet axis (H/D = 16.66)

only at the maximum in the distribution of the stochastic intensity within the free shear layer. There is no markable effect on total and stochastic intensities of lateral fluctuations. Within the wall boundary layer there are no lateral periodic fluctuations. The behaviour of the shear

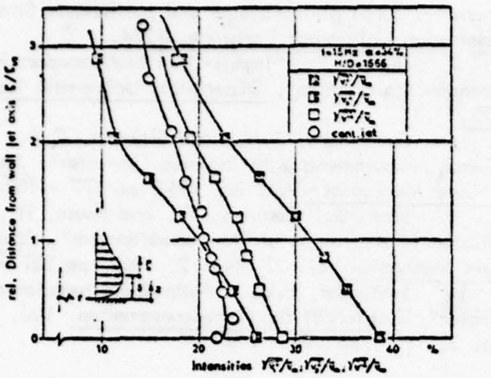

Fig. 21 Lateral Distribution of total, periodic and stochastic intensities of axial fluctuations (wall jet region; free shear layer; r/D = 3).

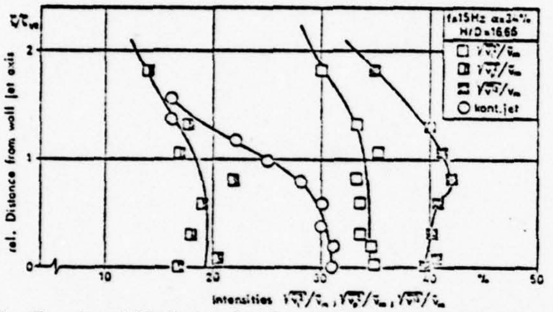

Fig. 22 Lateral Distribution of total, periodic and stochastic intensities of axial fluctuations (wall jet region; free shear layer; r/D = 3).

stress in the wall jet at r/D = 8 is demonstrated in Fig. 24 where the left half is valid for the continuous wall jet whereas the right half represents a pulsating wall jet. Within the free shear layer the total shear stress $\overline{v_t u_t}$ is increased more than in a free jet region, because a significant periodic shear stress $\overline{v_p u_p}$ is present. This suggests that in the wall jet region the periodic axial fluctuations are more in phase with periodic lateral fluctuations than in the free jet. Yet the stochastic shear stress $\overline{v'u'}$ in pulsating wall jet is slightly decreased. This result is not plausibly explainable. Within the wall boundary layer the measurements exhibit no differences in shear stress between continuous and pulsating wall jet. If the impinging plate is situated at a distance from the nozzle which corresponds to the length of the potential core of a continuous jet (as it is usually applied in heat or mass transfer processes) the intensities of the axial fluctuations of the axis of the pulsating wall jet exhibit a distinct maximum at r/D = 4 as well for the total and periodic intensities as for the stochastic intensities (Fig.25).

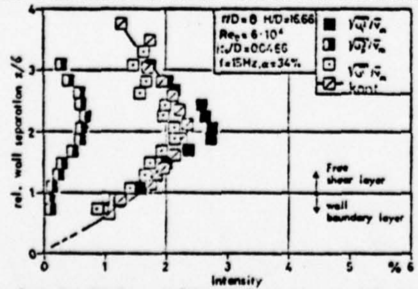

Fig. 23 Intensity distribution of lateral fluctuation in wall jet region

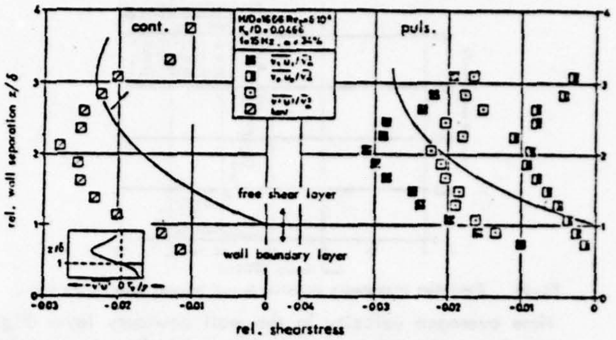

Fig. 24 Distribution of total, periodic and stochastic shear stress (H/D = 16.66)

At the begin of the wall jet (r/D = 2) the intensities are higher than in a continuous wall jet whereas farther downstream (r/D = 8) the total intensities on the wall jet axis are equal to the stochastic intensities of a continuous jet. The occuring maximum in Fig. 25 may be explained in a similar way like the stimulation process in the free jet region. Since at H/D = 5.8 no large eddies could be produced within the free jet region these low-frequent eddies can occur only in the free shear layer of the wall jet. Therefore the resonance phenomenon appears in the wall jet. To study the interactions between pulsation and turbulence within the wall boundary layer measurements of the axial fluctuations at H/D = 5.8, r/D = 7 were performed at a smooth plate in order to measure immediately at the wall. In Fig. 26 the stochastic local intensities $\sqrt{\overline{v'^2}}/\bar{v}(z)$ for a continuous and a pulsating wall jet are displayed versus the wall separation z/δ at three different Reynoldnumbers. The most surprising result is that

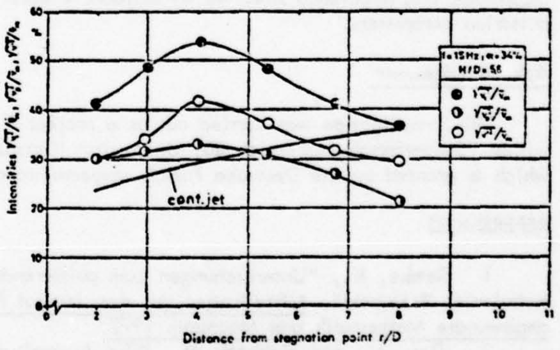

Fig. 25 Development of total, periodic and stochastic intensity of axial fluctuations on wall jet axis (H/D = 5.8)

stochastic intensities are not affected by pulsation within the wall boundary layer, though within the free shear layer of the wall jet this occured markably (Fig. 20 - 25). This result confirms the conclusions of the measurements within the free shear layer in that transfer from pulsating energy to turbulent energy is obtainable if eddies of frequencies adjacent to the pulsation frequency are present. As in the wall boundary layer the largest eddies are one order of magnitude smaller than those in the free shear layer their frequencies are too high to interact with pulsation. From this result the unexpected behaviour of the

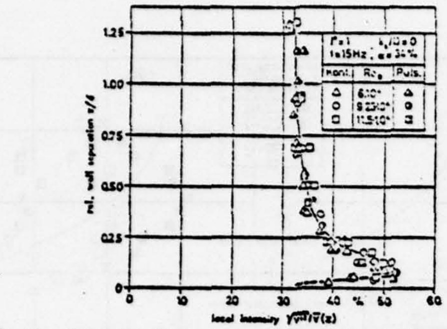

Fig.-26. Distribution of stochastic intensities in wall boundary layer (H/D = 5.8)

time averaged velocity in the wall boundary layer (Fig. 8) may be explained in that at increasing Re_D-numbers the inertia effects of the pulsating fluctuations exceed and support the time mean velocity, so that the decrease of axial mean velocity with increasing r/D is slower in a pulsating jet as in a continuous wall jet especially at high Re_D-numbers and the velocity lastly may become higher (Fig. 8).

CONCLUSIONS

The behaviour of the turbulence structure of a free jet under the influence of pulsation - that in the enlargement of lifetime of eddies with frequencies adjacent to the pulsation frequency - can be observed in the wall jet region of an impinging jet only within the free shear layer but not yet within the wall boundary layer. As one result of the different influence of pulsation on these both types of shear layers the decrease of mean velocity in the wall boundary layer with increasing stagnation point is slower than in a continuous wall jet. Hence pulsation offers a tool to influence both the behaviour of mean magnitudes and turbulence structure by suitable choice of pulsation parameters.

Acknowledgement

This investigation was carried out as a project B 2 within "Sonderforschungsbereich 80, Universität Karlsruhe" which is granted by the Deutsche Forschungsgemeinschaft.

REFERENCES

1 Remke, K., "Untersuchungen zum pulsierenden, turbulenten Freistrahl", Mitteilungen aus dem Institut für angewandte Mathematik und Mechanik 1972.

2 Gal, J., and Eickhoff, H., "Zur Ausbreitung pulsierender, runder, turbulenter Freistrahlen und Freistrahlflammen", Chemie-Ingenieurtechnik Vol. 42, No. 2, 1970, pp 73 - 76.

3 Favre-Marinet, M. et.al., "Jets instationaires, Etude 2 Structure Des Jets Pulsants", Université Grenoble Institut pour Mecanique, Oct. 1971 et Juin 1972.

4 Crow, S.C., and Champagne, F.M., "Orderly structures in jet turbulence", Journal of Fluid Mechanics Vol. 26, 1971, pp 547 - 591.

5 Olivari, D., "Analysis of an axisymmetric turbulent pulsating jet", Von Kharman Institute for Fluid Dynamics Technical Note 104, 1974.

6 Westrich, B., "Erosion eines gleichförmigen Sandbettes durch gleichförmige und pulsierende Strahlen", Dissertation Universität Karlsruhe, 1974.

7 Leister, P., "Impuls- und Stofftransport in pulsierenden Prallstrahlen", Dissertation Universität Karlsruhe 1977.

8 Champagne, F.H., and Sleicher, C.A., "Turbulence measurements with inclined hot-wires", Journal of Fluid Mechanics, Vol. 28, 1967, pp 177 - 182.

9 Sami, S., Carmody, T., and Rouse, H., "Jet diffusion in the region of flow establishment", Journal of Fluid Mechanics Vol. 27, No. 2, 1967, pp 231 - 252.

10 Schlünder, E.U., "Ausbreitung turbulenter Freistrahlen", Zeitschrift für Flugwissenschaften, Vol. 19, No. 3, 1971, pp 108 - 113

SESSION 4

SECOND AND HIGHER ORDER CLOSURES

Chairman: W. C. Reynolds
Stanford University
Stanford, California 94305
U.S.A.

A CRITICAL EVALUATION OF INVARIANT SECOND-ORDER CLOSURE MODELS FOR SUBSONIC BOUNDARY LAYERS

M. W. Rubesin,[1] A. J. Crisalli,[2] M. J. Lanfranco,[3] and M. Acharya[2]

ABSTRACT

Computations based on several second-order turbulence models, including full Reynolds stress and two-equation models, are compared with a number of boundary-layer experiments. In general, the models represent the data reasonably well, with skin friction tending to be somewhat overpredicted in the far downstream region of the adverse pressure gradient experiments. A discussion of the behavior of the ARAP full Reynolds stress model in predicting the components of the Reynolds stress tensor is given. It is concluded that compatibility at the wall may necessitate the use of more than one length scale.

NOMENCLATURE

a,b = modeling constants, ARAP model
C_f = local skin-friction coefficient, $2\tau_w/\rho_e U_e^2$
c_s = modeling constant, LRR model
D_{ij} = $\overline{u_i{}^{,m} u_{j,m}}$
e = turbulent kinetic or mixing energy
H = shape factor, δ^*/θ
k = $q^2/2$
ℓ = length scale, Ng-Spalding model
M = Mach number
p = pressure
q^2 = $\overline{u_1^2} + \overline{u_2^2} + \overline{u_3^2}$
u_i or u,v,w = fluctuating velocity components
u',v',w' = RMS velocity components
U = mean velocity
w = dissipation rate, Wilcox-Traci model
x,y,z = Cartesian coordinates
δ_{ij} = Kronecker delta
δ = value of y for which $U = 0.99\, U_e$
δ^* = displacement thickness
ε = turbulence dissipation rate, LRR model
ε_d = dissipation function, Jones-Launder model
θ = momentum thickness
Λ = algebraic length scale, ARAP model
μ = viscosity
ν = kinematic viscosity
ρ = density
τ = shear stress

Superscripts

—— = time average
' = root mean square
, = derivative in tensor notation
m = tensor notation index

Subscripts

, = derivative in tensor notation
e = boundary-layer edge condition
i,j,k,m = tensor notation indices
w = wall conditions
∞ = free-stream conditions upstream of pressure gradient

INTRODUCTION

Modern highly maneuverable aircraft often operate at conditions where separated flows exist over large portions of their surface (1). Under the impetus to

---

[1] Ames Research Center, Moffett Field, CA.

[2] National Research Council, Research Associates, Ames Research Center, Moffett Field, CA.

[3] Informatics Inc., Palo Alto, CA.

design aircraft that occasionally operate in this manner, methods of predicting the quantitative character of these separated flow regions are currently enjoying an accelerated rate of development. These methods exploit the power of larger electronic computers and can consider such enormously complicating factors as the strong interaction between largely inviscid and viscous portions of the flow fields, the three-dimensional character of the boundary layer and separated flow regions, the presence of rotational flows and vortices, and the compressibility of the air. A major limitation in the rate of development of these computational methods has been the pace of the evolution of reliable models of the turbulence mechanisms that exist under these rather complex flow conditions.

Of the alternative methods of modeling turbulence, the use of single point, Reynolds averaged momentum and energy equations supplemented by one or more differential equations for establishing values of the Reynolds stress and heat fluxes has proved the most practical for flow fields at Reynolds numbers of aerodynamic interest. The literature is replete with methods of "closing" the turbulence equations for certain of the second-order turbulence quantities (2). The bulk of the methods, however, apply strictly only to incompressible, constant property flows and most contain simplifications, such as the concept of the eddy viscosity, that impose rather gross assumptions when consideration is given to three-dimensionality in boundary layers or to the mean strain field in separated regions. Further, most of the numerical methods utilized invoke the "law of the wall" for boundary conditions near the surface to avoid integrating the turbulence equations all the way to the surface where costly fine mesh resolution is required. This manner of handling the surface boundary condition is not appropriate close to points of separation where the "law of the wall" loses much of its meaning. Further, most methods also avoid making modeling modifications that may be required when the turbulence Reynolds numbers become relatively low near surfaces.

For application to the separated flows indicated earlier it is necessary to relax some of these restrictions in turbulence modeling. Ames has for the past few years been sponsoring and participating in the development and refinement of two different second-order closure methods for the single point full Reynolds stress and heat flux equations for a compressible fluid. One model is an outgrowth of the invariant second order-closure model originally proposed by Donaldson (3), that has been developed by Donaldson, Sullivan, and others of the Aeronautical Research Associates of Princeton (4,5). It uses the primitive variables of velocity, density, and pressure, and their second and higher order correlations, as the dependent variables of the model. Because the correlations involving density and viscosity fluctuations are expressed explicitly in the formulation, the modeling equations are quite complex, though complete. The second model, developed by David Wilcox of DCW Industries (6-8) has as its genesis the elegantly simple model of Saffman (9). The dependent variables in this model are mass averaged in the manner originated by Favre (10), and the resulting equations are almost as simple in form as those for incompressible flow, containing just a few new terms involving fluctuating pressure-strain and velocity-density correlations. Most of the effects of density fluctuations are contained implicitly in the mass averaged dependent variables. Both of these models have been programmed by their originators into boundary layer codes that compute directly to the surface where the inner boundary conditions are applied.[4]

The role the authors have in this turbulence model development program is to perform detailed comparisons of the computed results with experimental data with the view of critically assessing the models at their current state of development as engineering tools, of identifying modeling weaknesses, participating with the model originators in devising modeling changes, and, finally, of expanding the models to conditions more general than exist within a boundary layer, such as a code for numerically solving the time-averaged Navier-Stokes equations. Because of certain restrictive features in the current turbulence models, the model assessment and refinement process has been restricted largely to boundary layer data. The Aeronautical Research Associates of Princeton (ARAP) model, at this time, contains an algebraically defined turbulence length scale appropriate only to boundary layers. Thus, comparisons with the fundamental experiments involving homogeneous flows (11-14) cannot be made without introducing a new length scale equation appropriate for such flows, probably in the form of a partial differential equation that will reduce to or be equivalent to the one used in boundary layers when boundary-layer conditions prevail. This process is taking place currently, but the progress will not be reported here. Also, the most advanced version of the Wilcox model is restricted to a two-equation eddy diffusivity model that also is most appropriate in boundary-layer flows. Thus, although the models treated here are applicable to more general flows, the data comparisons cited will be confined to attached two-dimensional boundary-layer flows.

In (15), the authors compared the computations based on the ARAP Reynolds stress and Wilcox eddy diffusivity models with data obtained in boundary layers at supersonic speeds and in adverse pressure gradients. The Mach numbers at the boundary-layer edges and the magnitudes of the impressed adverse pressure gradients were such to combine to give increasing values of local surface shear with downstream distance. To gain insights in the boundary-layer mechanisms as separation is approached, it is necessary to examine experiments where the local shear is reduced with downstream distance. The low-speed experiment of Samuel and Joubert (16) is ideally suited for this task in that an increasingly adverse pressure gradient was applied to the boundary layer and the turbulence mechanisms were accurately defined as the data contained direct measurement of the individual Reynolds stresses. Because it is dangerous to rely on a single experiment, comparisons are also made with these turbulence models and other experiments containing direct measurement of the Reynolds stresses, i.e., the classic flat-plate experiment of Klebanoff (17), the adverse pressure gradient experiment of Bradshaw (18), and the slightly favorable pressure gradient data of Acharya (19).

DESCRIPTION OF MODELS

In addition to the ARAP and DCW models which the authors are dealing with directly, several other second-order turbulence models will be used in the

---

[4] The Wilcox code has been particularized to an eddy viscosity version that can be adapted to make calculations based on eddy viscosity models other than those of Wilcox or Saffman. In this form of the code, the "law of the wall" is used as the inner boundary condition in keeping with the techniques of the originators of the other models.

comparisons with experimental data. All of these models will now be briefly described. Because the emphasis will be on full Reynolds stress modeling, the full Reynolds stress models will be described somewhat more fully than the two-equation eddy-viscosity models, which for the most part will be referred to the literature.

The ARAP model is a full Reynolds stress model for compressible turbulent boundary layers. The dissipation term in the $\overline{u_iu_j}$ Reynolds stress equations incorporates the effects of both anisotropic and isotropic dissipation. It is given by

$$D_{ij} = a\overline{u_iu_j}/\Lambda^2 + b\delta_{ij}q^3/3\Lambda\nu \tag{1}$$

where Λ is an algebraic length scale defined as the minimum of 0.65y and 0.17δ.

The redistribution term, or the exchange between the individual Reynolds stresses, is modeled after Rotta (20), as

$$\overline{pu_{i,j}} + \overline{pu_{j,i}} = -\rho q(\overline{u_iu_j} - \delta_{ij}q^3/3)/\Lambda \tag{2}$$

Although ARAP has also included another term (not shown) on the right side of (2) which reflects the influence of the mean strain term as discussed by Chou and Rotta, this term will not be included in the calculations which follow. More will be said about this later. The velocity diffusion of Reynolds stresses is modeled as

$$\overline{u_iu_ju_k} = 0.1q\Lambda[(\overline{u_iu_j})_{,k} + (\overline{u_ju_k})_{,i} + (\overline{u_ku_i})_{,j}] \tag{3}$$

Of course, there are many other modeled terms, mainly due to compressibility effects, but they are outside the scope of this paper and will not be given here.

The incompressible full Reynolds stress model developed by Launder, Reece, and Rodi (21), and hereafter called LRR, will be used at only one juncture in this paper. It presents an interesting contrast to the ARAP model. Instead of an algebraic length scale, it employs a length scale based on the turbulence dissipation rate, ε, which is computed from a differential equation. Another difference is that LRR assumes the dissipative motions to be isotropic, i.e.,

$$2\nu D_{ij} = 2\delta_{ij}\varepsilon/3 \ . \tag{4}$$

This model uses a more elaborate modeling of the redistribution term which, in addition to the above discussed terms used by ARAP, includes the effects of a special near-wall correction term. Diffusion of turbulent velocity fluctuations is approximated by

$$\overline{u_iu_ju_k} = -c_s k[\overline{u_iu_\ell}(\overline{u_ju_k})_{,\ell} + \overline{u_ju_\ell}(\overline{u_ku_i})_{,\ell} + \overline{u_ku_\ell}(\overline{u_iu_j})_{,\ell}]/\varepsilon \tag{5}$$

which also presents an interesting contrast to the ARAP model. Finally, a very important difference is that, unlike ARAP, LRR does not integrate through the viscous sublayer, thereby necessitating that the inner boundary values of $\overline{u},\varepsilon$ and the Reynolds stress components be preassigned.

The remaining three models to be used in the comparisons are relatively well known two-equation eddy-viscosity models which employ two parameters to compute eddy viscosity. The first parameter is the turbulent kinetic or mixing energy e and the second parameter is either a dissipation function ε_d, length scale ℓ, or dissipation rate w. The three models, whose detailed descriptions can be found in (22,23 and 6) are the Jones-Launder e-ε_d model, the Ng-Spalding e-ℓ model, and the Wilcox-Traci e-w model.

DISCUSSION OF COMPARISONS

The data of several boundary-layer experiments will now be used to test the performance of the models and to discover possible avenues of improvement. The first experiment to be considered will be that of Samuel and Joubert consisting of an incompressible turbulent boundary layer on a flat plate subjected to an increasingly adverse pressure gradient. Figure 1 shows the measured and predicted local skin-friction coefficients. The measured values are based on Stanton tube data and Clauser Plots of the mean velocity data in the wall region. The comparison shows that the turbulence model calculations predict the general behavior of the data quite well, although they do not fall off as rapidly in the far downstream region. In Fig. 2, a comparison is given of the shape factor, the ratio of displacement thickness to momentum thickness. Again the computations show the trends of the data quite well, the computed results being within 10% of the data. To gain some insight into the reasons for increased differences between the computations and data with downstream distance, profiles of the mean and fluctuating data are examined at a station x = 2.89 m in Figs. 3-5. The mean velocity at this station is shown in Fig. 3. It is observed that the calculated profiles are somewhat fuller than the data and this is consistent with the lower predicted shape factor. The predicted and measured turbulent shear stress distributions are shown in Fig. 4. The higher predicted values of the peak turbulent shear are consistent with the higher predicted skin-friction coefficients. However, the overall agreement with the turbulent shear profile is generally good. The three normal turbulent velocity fluctuations are shown in Fig. 5 in comparison with the results from the ARAP full Reynolds stress model. The ARAP model yields excellent values of v', but underestimates u' to some extent, especially near the surface, and completely misses w' in magnitude and character. More will be said about this later in the paper.

The next experiment to be considered is Bradshaw's "Flow C" which consists of an incompressible boundary layer induced by a suddenly applied adverse pressure gradient ($U_e \propto x^{-0.255}$). Figure 6 shows the measured and predicted local skin-friction coefficients. Note that the convexity of Bradshaw's C_f graph is opposite to Samuel and Joubert's due to the former being decreasingly adverse while the latter is increasingly adverse. All the models except one show reasonably good agreement with the data. As was also observed in the Samuel and Joubert experiment, the predicted skin-friction coefficients do not fall off rapidly enough in the far downstream region (except for Ng-Spalding) but the discrepancy here is much less. Apparently, an increasingly adverse pressure gradient makes greater demands on the modeling than does a decreasingly adverse one. In Fig. 7, it is seen that the agreement of the model prediction of H vs x with the experimental data is generally quite good, although they tend to be a bit low in the far downstream region just as in the Samuel and Joubert experiment. In Figs. 8, 9 and 10 we have plotted profiles of various quantities at a single station lying well in the downstream region. Figure 8 shows the mean velocity profiles of the experiment and the models at this station. The agreement is excellent. Figure 9 shows the turbulent shear profile. All the models again overshoot the peak experimental values to varying extents, although they all capture the qualitative trend of the data. Figure 10 shows the measured values of the normal components of the Reynolds stress tensor, and the predictions of these quantities by the ARAP model. As in the previous experiment, the predicted $\overline{v^2}$ shows good agreement while the $\overline{u^2}$ and $\overline{w^2}$ components are far lower than the data.

Figures 11 to 15 show data from Klebanoff's experiment consisting of an incompressible turbulent boundary layer on a flat plate with zero pressure gradient. All measurements were taken at a single downstream station. Figures 11 and 12 show the predicted and measured velocity and turbulent shear profiles. All the models agree with the experimental data to within the experimental error.

Figures 13 and 14 show the profiles of the diagonal components of the Reynolds stress tensor as measured by Klebanoff and as predicted by the full Reynolds stress models ARAP and LRR. While the ARAP model again approximately duplicates $\overline{v^2}$ and underpredicts $\overline{u^2}$ and $\overline{w^2}$, it is observed that LRR shows good agreement with all three diagonal components.

A possible explanation for the better performance of LRR in this regard may lie in the fact that LRR includes the influence of mean strain rate on the redistribution term, while in ARAP we omitted this influence. However, preliminary runs of the ARAP program which did include this influence, modeled in a form roughly similar to that in LRR, show that it does not correct the distribution of the normal Reynolds stresses. Another possible explanation, which may be significant, is the fact that in LRR the approximately correct values of $\overline{u^2}$, $\overline{v^2}$ and $\overline{w^2}$ at the edge of the viscous sublayer are input as inner boundary conditions in order to avoid integrating through the viscous sublayer. This suggests that the cause of ARAP's incorrect distribution of $\overline{u^2}$, $\overline{v^2}$, $\overline{w^2}$ may be incorrect behavior of the model near the wall. This is supported by the following argument. Letting

$$\left.\begin{aligned} u &= a_1 y + a_2 y^2 + \dots \\ w &= b_1 y + b_2 y^2 + \dots \end{aligned}\right\} \qquad (6)$$

we see, by the continuity equation that

$$v = c_2 y^2 + \dots \qquad (7)$$

Here a_i, b_i and c_i are functions of x and t. At the wall, where molecular diffusion and dissipation are the predominant physical mechanisms, the equations for the Reynolds stresses in the ARAP model reduce to

$$\partial^2(\overline{u_1^2})/\partial y^2 - 2a\overline{u_1^2}/\Lambda^2 = 0 \qquad (8)$$

$$\partial^2(\overline{u_2^2})/\partial y^2 - 2a\overline{u_2^2}/\Lambda^2 = 0 \qquad (9)$$

$$\partial^2(\overline{u_3^2})/\partial y^2 - 2a\overline{u_3^2}/\Lambda^2 = 0 \qquad (10)$$

$$\partial^2(\overline{u_1 u_2})/\partial y^2 - 2a\overline{u_1 u_2}/\Lambda^2 = 0 \qquad (11)$$

In these equations let $\Lambda = dy$ where d is an unknown slope. Then substituting the power series expansions (6) and (7) into (8-11), and letting $y \to 0$ yields $d = a^{1/2} = 1.80$ from (8), $d = (a/6)^{1/2} = 0.74$ from (11), $d = a^{1/2} = 1.80$ from (10) and $d = (a/3)^{1/2} = 1.04$ from (11) (here we have set $a = 3.25$ as in the program). This suggests that in order for this model to be consistent at the wall, three different length scales in the vicinity of the wall are necessary, i.e., $\Lambda = 1.80y$ for $\overline{u^2}$ and $\overline{w^2}$, $\Lambda = 0.735y$ for $\overline{v^2}$ and $\Lambda = 1.04y$ for $\overline{uv}$. In the current ARAP program only one length scale is used, i.e., $\Lambda = 0.65y$ (near the wall). Of the three length scales computed above this is closest to the one for $\overline{v^2}$ which may explain why the ARAP model correctly predicts $\overline{v^2}$. The next closest is the $\overline{uv}$ length scale. This and the fact that $\overline{v^2}$ and $\overline{uv}$ are the only Reynolds stress components occurring in the unmodeled $\overline{uv}$ equation may explain why the ARAP model agrees fairly well with $\overline{uv}$. Perhaps a general conclusion which can be drawn from this is that the correct prediction of all Reynolds stress components by a low Reynolds number model hinges upon the model satisfying the necessary wall compatibility conditions.

Klebanoff also gave values of the dissipation terms $\overline{u_{1,1}u_{1,1}}$, $\overline{u_{1,2}u_{1,2}}$ and $\overline{u_{1,3}u_{1,3}}$. The first quantity was obtained by using the Taylor hypothesis

$$\overline{u_{1,1}u_{1,1}} = \overline{u_{,t}u_{,t}}/U_e^2 \qquad (12)$$

and the measured quantities on the right-hand side. The second and third quantities were obtained by measuring the spatial correlations in the following relation and its analogue in the z direction.

$$\overline{u_1(y)u_1(y+\Delta)}/u_1'(y)u_1'(y+\Delta) = 1 - \overline{u_{1,2}u_{1,2}}\Delta^2/2U^2 \qquad (13)$$

Although the relations (12) and (13) are not strictly valid in a wall boundary layer, Klebanoff gave sufficient supporting arguments that we may take his measurements of these quantities as being accurate, at least tentatively. These measurements are of value because they provide the modeler with a direct test of a modeled term, i.e., D_{11}. Figure 15 shows the measured values of $\delta^2 D_{11}/2U_e^2$ along with the values of this quantity computed from (1). This comparison suggests that the model (1) produces values of D_{11} which are too high by a factor of 5 or more near the wall. This observation can be supported by the following independent analytic argument. Substituting the power series (6) and (7) into the right side of the dissipation model (1) and using the definition of Λ, and the value of the constant $a = 3.25$, and letting $y \to 0$ yields $7.7\,\overline{a_1^2} + O(y^3)$. Since $\overline{a_1^2} = \overline{u_{1,2}u_{1,2}}$ at $y = 0$, i.e., $= \overline{a_1^2} = D_{11}$ at $y = 0$, we now see that the modeled D_{11} yields a value at the wall which is 7.7 times the actual D_{11} at the wall. The above analysis suggests that the constants a and b in the current dissipation model may be too high, at least insofar as D_{11} is concerned.

Figures 16 to 18 show data from the experiment of Acharya. This experiment includes effects of a slight favorable pressure gradient and mild compressibility ($M = 0.6$). Because of the latter, only the ARAP program and a compressible version of the Wilcox-Traci program are shown in the comparisons. In Figs. 16 and 17 we see that the measured and predicted velocity and turbulent shear profiles agree very well. In Fig. 18 we see that of the three normal components of the Reynolds stress tensor, $\overline{v^2}$ is predicted most accurately. On the other hand, the predicted $\overline{v^2}$ here shows greater error when compared to the experimental data than the previous comparisons did. Whether this is due to a modeling problem related to compressibility effects or to an unfortunate combination of experimental and modeling errors is at this point an open question. More data containing direct measurements of Reynolds stress components in both compressible and incompressible boundary layers is needed.

Finally, in Fig. 19 the ability to model compressible flows is indicated with reference to the local skin-friction data from the experiment of Lewis, Gran and Kubota (24). This consists of a supersonic ($M = 4.0$) turbulent boundary layer with strong adverse, followed by favorable, pressure gradients. In addition to the ARAP and Wilcox-Traci predictions, a 0-equation eddy-viscosity model has been plotted. Based on this and other compressible experiments, we have concluded that higher order models generally do a comparable job, and in some cases a better job, relative to algebraic eddy-viscosity models in predicting skin friction in attached boundary layers.

CONCLUDING REMARKS

Several second-order turbulence models, including full Reynolds stress and two-equation eddy-viscosity models, were applied to a number of boundary-layer experiments. The comparisons of the model predictions with data from the adverse pressure gradient experiments of Samuel and Joubert and Bradshaw and the zero pressure gradient experiment of Klebanoff showed that the models yielded reasonable predictions of skin friction, shape factor, mean velocity profiles, turbulent shear and other quantities. In the far downstream region of the two adverse pressure gradient experiments, the models yielded values of skin friction which were, to varying degrees, too high, the effect being more pronounced in the Samuel and Joubert experiment than in the Bradshaw experiment.

The Wilcox-Traci and ARAP models, which can handle compressibility effects, were also compared with the compressible flow experiments of Acharya and Lewis, Gran and Kubota and were shown to yield good predictions of the above-mentioned quantities.

A direct comparison, using only experimental values, was made of the dissipation quantity D_{11} as measured by Klebanoff and as modeled by ARAP in (1). In the final analysis, such direct term-by-term comparison of modeled terms is the best and most rigorous test of any modeling assumption. Unfortunately, the necessary measurements for such comparisons are hard to come by and even harder to perform accurately. However, this area of experimentation deserves more emphasis. Related to this is the need for more direct measurements of components of the Reynolds stress tensor in both incompressible and compressible boundary layers.

The discussion centered on the ARAP model because it is a full Reynolds stress model which integrates through the viscous sublayer. It was seen that this model does a fine job of predicting skin friction, mean velocity profiles, $\overline{v^2}$, $\overline{uv}$, etc. while incorrectly predicting two components of the Reynolds stress tensor, i.e., $\overline{u^2}$ and $\overline{w^2}$. It was argued that this behavior stems from the fact that the modeled equations for $\overline{u^2}$ and $\overline{w^2}$ do not satisfy the necessary wall compatibility conditions. On the other hand, the model does yield reasonable values for $\overline{v^2}$ and this is probably the most important for computing $\overline{uv}$, thereby explaining the generally good performance of this model in other respects. However, the correct prediction of all components of the Reynolds stress tensor will probably necessitate more than one length scale, especially near the wall.

We believe that the comparisons of this report along with the results of many other comparisons not shown here, indicate that higher order closure methods can produce predictive models which are valid over a broad range of flow situations and, in the special case of wall boundary layers with mild pressure gradients, are comparable in performance to algebraic eddy viscosity models, notwithstanding that the latter have been finely tuned for many years to predict just this type of flow.

REFERENCES

1 Peake, D. J., "Controlled and Uncontrolled Flow Separation in Three Dimensions," Report LR-591, July 1976, National Research Council Canada, National Aeronautical Establishment.

2 Launder, B. E. and Spalding, D. B., "Mathematical Models of Turbulence," Academic Press, London and New York, 1972.

3 Donaldson, C. duP. and Rosenbaum, H., "Calculation of Turbulent Shear Flows Through Closure of the Reynolds Equations by Invariant Modeling," ARAP Report No. 127, Dec. 1968, Aeronautical Research Associates of Princeton, Inc., Princeton, N.J.

4 Varma, A. K., Beddini, R. A., Sullivan, R. D., and Donaldson, C. duP., "Application of an Invariant Second-Order Closure Model to Compressible Turbulent Shear Layers," AIAA Paper 74-592, June 1974, Palo Alto, Calif.

5 Sullivan, Roger D., "GYC: A Program to Compute the Turbulent Boundary Layer on a Rotating Cone," ARAP Working Paper 76-2, Aug. 1976, Aeronautical Research Associates of Princeton, Inc., Princeton, N.J.

6 Wilcox, D. C. and Traci, R. M., "A Complete Model of Turbulence," AIAA Paper 76-351, July 14-16, 1976, San Diego, Calif.

7 Chambers, T. L. and Wilcox, D. C., "Critical Examination of Two-Equation Turbulence Closure Models," AIAA Paper 76-352, July 14-16, 1976, San Diego, Calif.

8 Wilcox, D. C. and Chambers, T. L., "Streamline Curvature Effects on Turbulent Boundary Layers," AIAA Paper 76-353, July 14-16, 1976, San Diego, Calif.

9 Saffman, P. G., "A Model for Inhomogeneous Turbulent Flow," *Proceedings of the Royal Society (London) A*, Vol. 137, 1970, pp. 417-433.

10 Favre, A., "Equations des Gaz Turbulents Compressibles," *J. Mecan.*, Vol. 4, No. 3, Sept. 1965, pp. 361-390.

11 Champagne, F. H., Harris, V. G., and Corrsin, S., "Experiments on Nearly Homogeneous Turbulent Shear Flow," *Journal of Fluid Mechanics*, Vol. 41, part 1, 1970, p. 81.

12 Comte-Bellot, G. and Corrsin, S., "Simple Eulerian Time Correlation of Full and Narrow-Band Velocity Signals in Grid-Generated 'Isotropic' Turbulence," *Journal of Fluid Mechanics*, Vol. 48, part 2, 1971, p. 273.

13 Tucker, H. J. and Reynolds, A. J., "The Distortion of Turbulence by Irrotational Plane Strain," *Journal of Fluid Mechanics*, Vol. 32, part 4, pp. 657-673.

14 Uberoi, M. S., "Energy Transfer in Isotropic Turbulence," *The Physics of Fluids*, Vol. 6, No. 8, 1963, p. 1048.

15 Rubesin, M. W., Crisalli, A. J., Lanfranco, M. J., and Acharya, M., "A Critique of Some Recent Second-Order Turbulence Closure Models for Compressible Boundary Layers," AIAA Paper 77-128, Jan. 24-26, 1977, Los Angeles, Calif.

16 Samuel, A. E., and Joubert, P. N., "A Boundary Layer Developing in an Increasingly Adverse Pressure Gradient," *Journal of Fluid Mechanics*, Vol. 66, part 3, 1974, pp. 481-505.

17 Klebanoff, P. S., "Characteristics of Turbulence in a Boundary Layer with Zero Pressure Gradient," Report 1247, 1955, NACA.

18 Bradshaw, P., "The Response of a Constant-Pressure Turbulent Boundary Layer to the Sudden Application of an Adverse Pressure Gradient," ARC Reports and Memoranda No. 3575, 1969.

19 Acharya, M., "Effects of Compressibility on Boundary-Layer Turbulence," AIAA Paper 76-334, July 1976.

20 Rotta, J., "Statistische Theorie Nicht-Homogener Turbulenz, I. Mitteilung," Zeischrift fur Physik, Vol. 129, 1951, pp. 547-572.

21 Launder, B. E., Reece, G. J., and Rodi, W., "Progress in the Development of a Reynolds-Stress Turbulence Closure," Journal of Fluid Mechanics, Vol. 68, part 3, 1975, pp. 537-566.

22 Jones, W. P. and Launder, B. E., "The Prediction of Laminarization with a Two-Equation Model of Turbulence," International Journal of Heat and Mass Transfer, Vol. 15, 1972, pp. 301-314.

23 Ng, K. H. and Spalding, D. B., "Turbulence Model for Boundary Layers Near Walls," Physics of Fluids, Vol. 15, No. 1, 1972, pp. 20-30.

24 Lewis, J. E., Gran, R. L., and Kubota, T., "An Experiment on the Adiabatic Compressible Turbulent Boundary Layer in Adverse and Favorable Pressure-Gradients," Journal of Fluid Mechanics, Vol. 51, part 4, 1972, pp. 657-672.

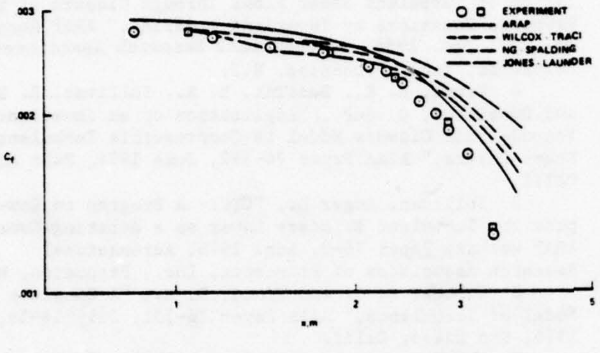

Fig. 1 Local skin friction coefficient, experiment of Samuel and Joubert (16)

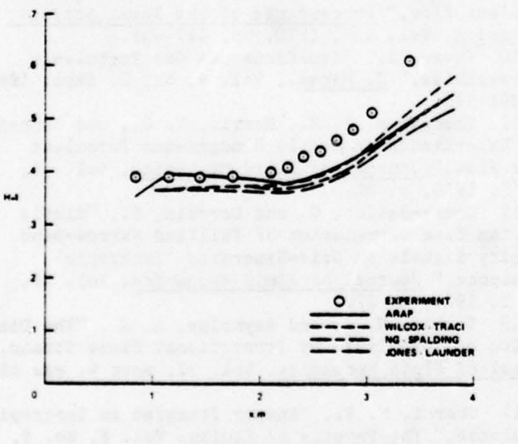

Fig. 2 Shape factor, experiment of Samuel and Joubert (16)

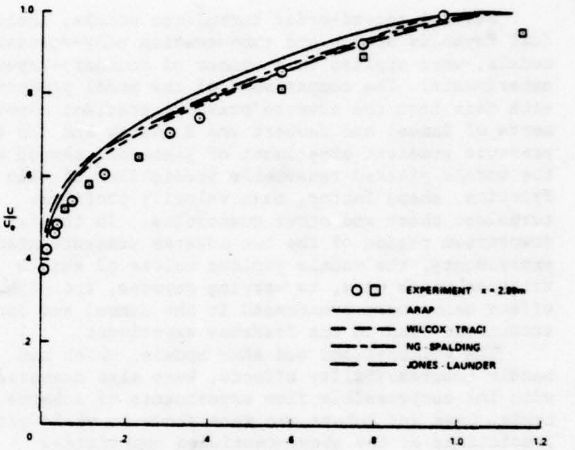

Fig. 3 Mean velocity profile, experiment of Samuel and Joubert (16)

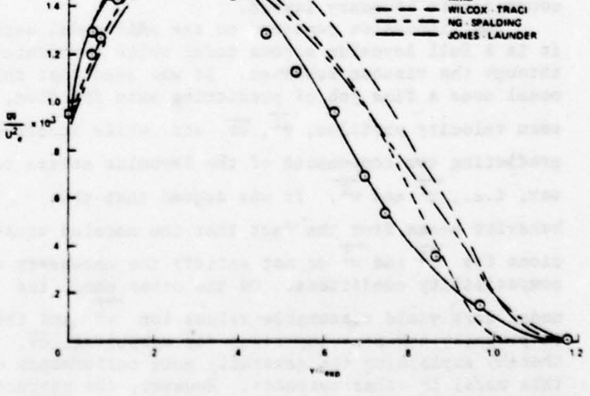

Fig. 4 Turbulent shear stress profile, experiment of Samuel and Joubert (16)

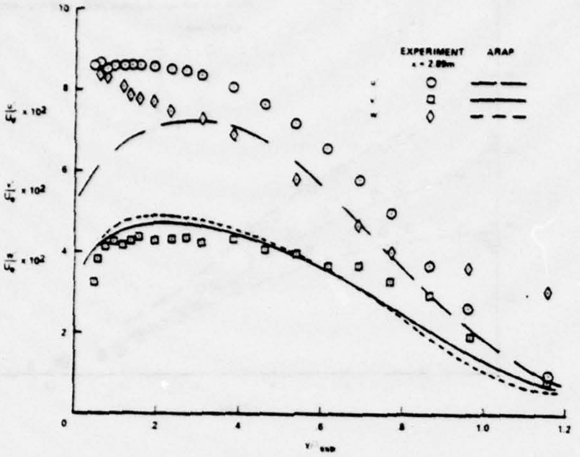

Fig. 5 Normal turbulence intensities, experiment of Samuel and Joubert (16)

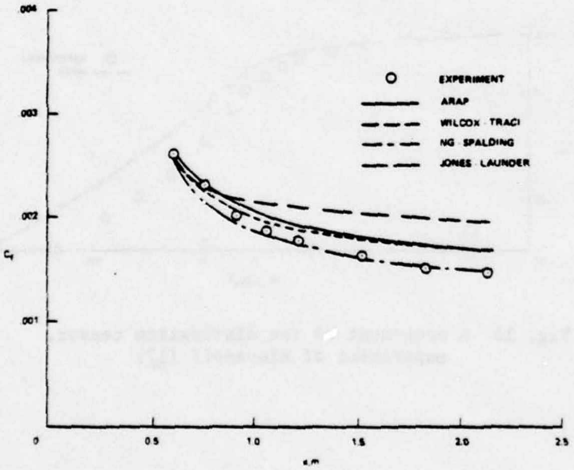

Fig. 6 Local skin friction coefficient, experiment of Bradshaw (18)

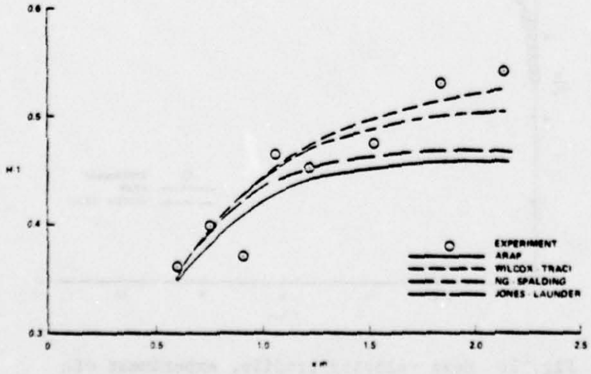

Fig. 7 Shape factor, experiment of Bradshaw (18)

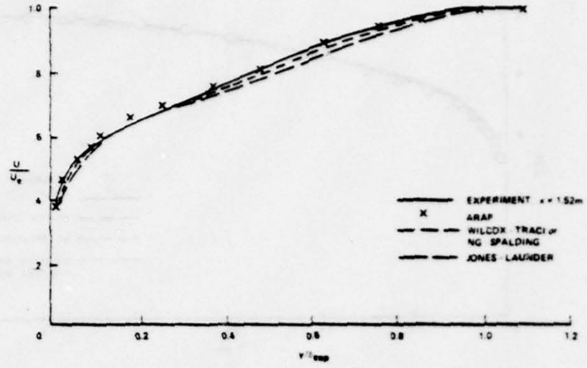

Fig. 8 Mean velocity profile, experiment of Bradshaw (18)

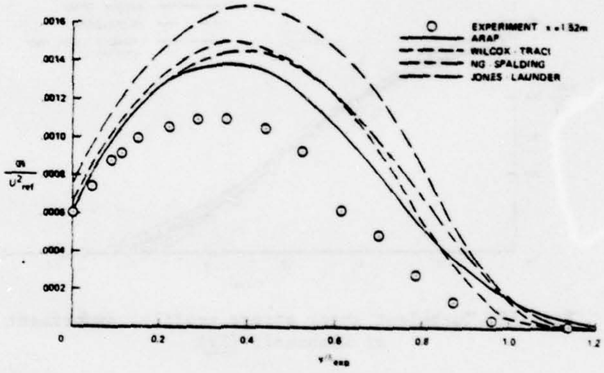

Fig. 9 Turbulent shear stress profile, experiment of Bradshaw (18)

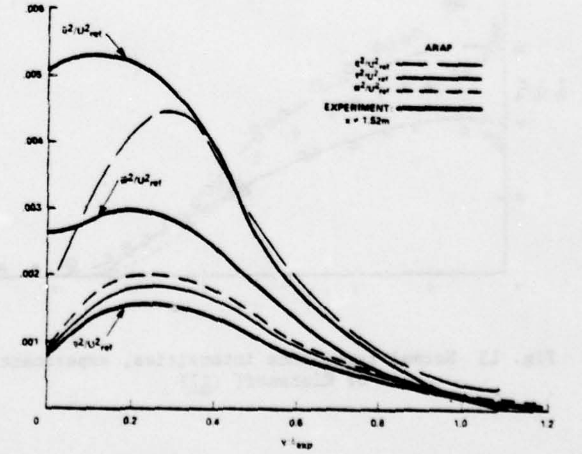

Fig. 10 Scaled diagonal components of the Reynolds stress tensor, experiment of Bradshaw (18)

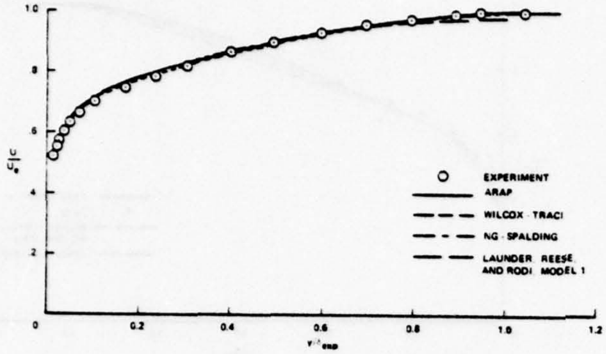

Fig. 11 Mean velocity profile, experiment of Klebanoff (17)

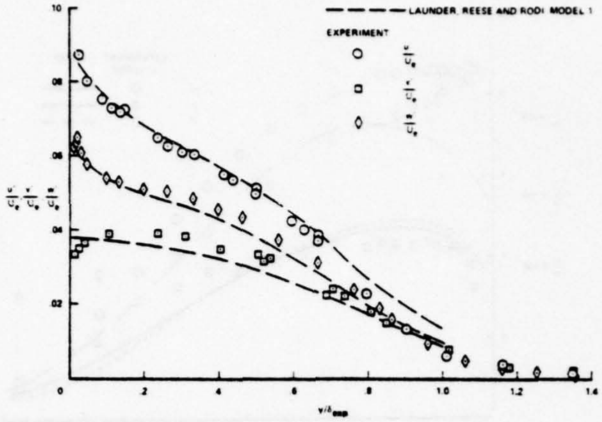

Fig. 14 Normal turbulence intensities, experiment of Klebanoff (17)

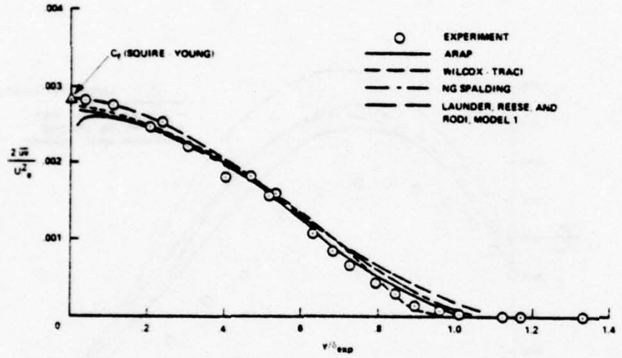

Fig. 12 Turbulent shear stress profile, experiment of Klebanoff (17)

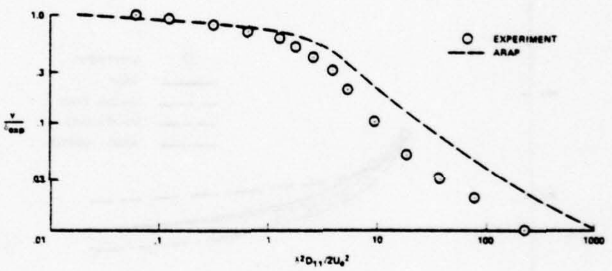

Fig. 15 A component of the dissipation tensor, experiment of Klebanoff (17)

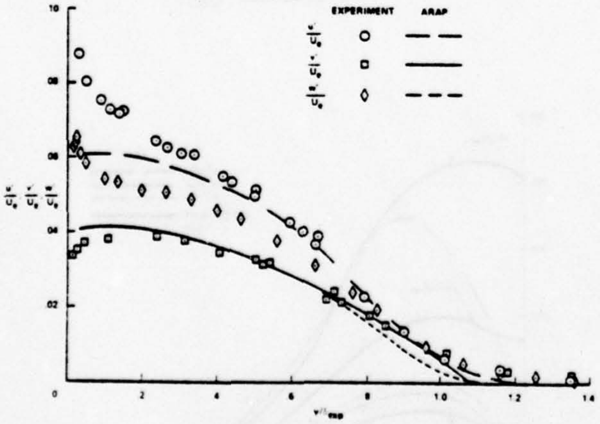

Fig. 13 Normal turbulence intensities, experiment of Klebanoff (17)

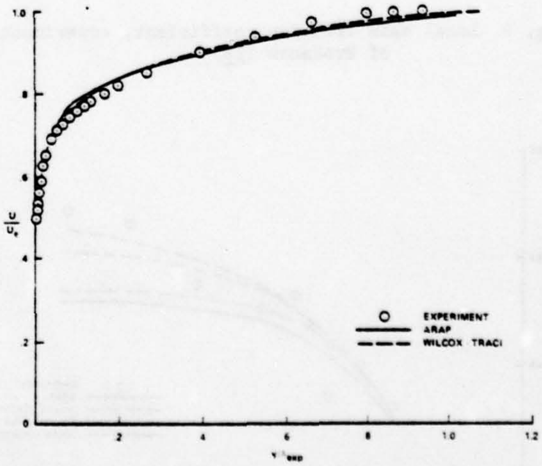

Fig. 16 Mean velocity profile, experiment of Acharya (19)

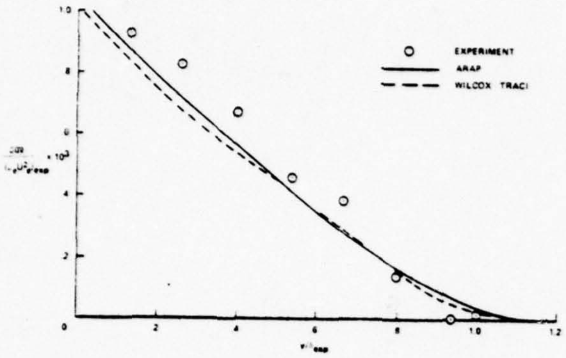

Fig. 17 Turbulent shear stress profile, experiment of Acharya (19)

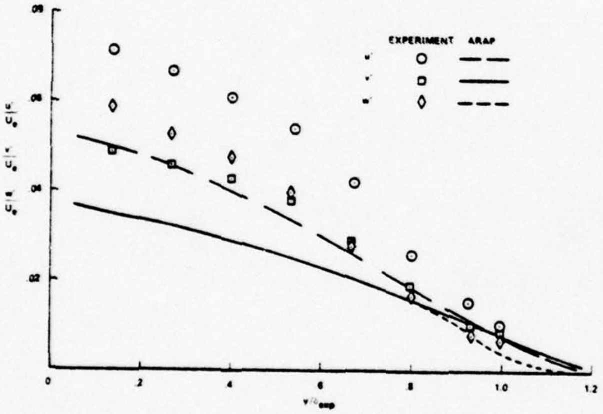

Fig. 18 Normal turbulence intensities, experiment of Acharya (19)

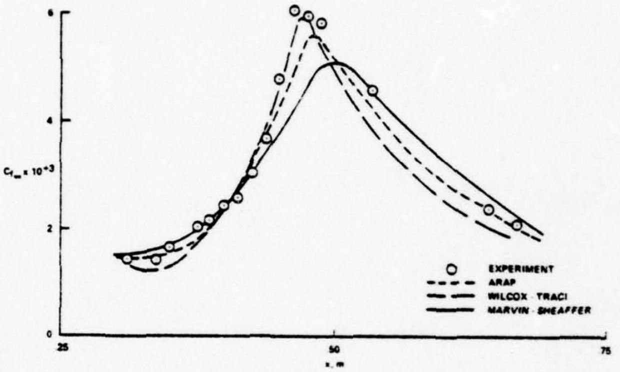

Fig. 19 Local skin friction coefficient based on free-stream dynamic pressure, experiment of Lewis *et al.* (24)

TEST OF SECOND ORDER CLOSURE MODEL
IN A COMPRESSIBLE TURBULENT WAKE

J.P. Bonnet - Th. Alziary de Roquefort

Centre d'Etudes Aérodynamiques et Thermiques
Université de Poitiers
43, route de l'Aérodrome
86000 Poitiers
(France)

ABSTRACT

Turbulence measurements in the supersonic wake behind a flat plate held at zero incidence are presented. A constant temperature hot wire anemometer is used to measure the $\overline{u'^2}$, $\overline{T'u'}$ and $\overline{T'^2}$ profiles in the wake for several x stations. A numerical study is made with a second order closure model based on the"invariant modeling" of Donaldson, using transport equations of $\overline{u}$, $\overline{T}$, $\overline{u'^2}$, $\overline{v'^2}$, $\overline{w'^2}$, $\overline{u'v'}$, $\overline{T'^2}$, $\overline{T'u'}$, $\overline{T'v'}$. Adjustment of the model is made by comparison with experimental results in the case of incompressible wake. The relative importance of different terms is studied on the basis of numerical results. Some production terms which are generally neglected may be larger than 30% of the convective terms and must be taken in account even in the far wake. For the supersonic wake, the agreement is good for mean velocity but rather poor for turbulent quantities.

NOMENCLATURE

E = bridge voltage of the anemometer
F and G = fluctuation sensitivities
R = Reynolds number
P = Prandtl number
M = Mach number
p = pressure
u_i (or u,v,w) = velocity component
(directions x, y and z)
x_i (or x,y,z) = coordinate system
T = temperature
ρ = density
μ = viscosity
k = thermal conductivity
σ = ratio of mean density to mean temperature = - $\frac{\bar{\rho}}{\bar{T}}$
C_p = specific heat at constant pressure
γ = ratio of specific heats
$q^2 = \overline{u'^i u'_i}$ = kinetic turbulent energy
Λ, λ, macrō and micro-scale lengths of turbulence
θ = momentum thickness
C_1, C_2 ..., a, b turbulence models parameters

Subscripts

t total conditions
o axis conditions
∞ free stream conditions (reference conditions)
$(\ )_{,\ell}$ derivative with respect to x_ℓ coordinate

Superscripts

$(\ )'$ fluctuations about mean value
$\overline{(\ )}$ time averaged quantity

I - INTRODUCTION

The turbulent wake behind a flat plate is a strongly nonequilibrium shear flow and has been used by Launder et alii {1} and Pope and Whitelaw {2} as a critical test to judge the validity of numerical methods for prediction of turbulent flows. For incompressible flow the most promising methods, which have already achieved some noticeable success, are based on solutions of the Reynolds stresses transport equations. In principle these methods can be extended to compressible flows but, due to the lack of experimental results, the modelization of some terms is very empiric. Several methods using the transport equations for second order correlations are currently being explored (See reviews by Bradshaw {3}, Mellor and Herring {4}, Reynolds {5}). In an attempt to test the applicability of this class of methods to the study of the supersonic wake of a thin flat plate we choose to apply the models proposed by Donaldson et alii {6}. This method makes a systematic use of a macro-scale of turbulence which depends only on the flow geometry instead of using a length-scale or dissipation transport equation. In a first step the choice of the macro-scale and the adjustment of some coefficients of the model was made by comparison between the numerical predictions and the experimental results of Chevray and Kovasznay {7} for the incompressible wake of a thin flat plate. In a second step, the program predictions were compared with experimental results for a supersonic wake at $M_\infty = 2$ and very high Reynolds number. A detailed comparison of all terms appearing in the equations was made on the basis of the numerical results, and allowed to draw conclusions about the importance of some production terms which are generally neglected in thin shear flows computation.

II - MEASUREMENTS IN THE SUPERSONIC WAKE OF A FLAT PLATE

1. Flow realization

The experiments were performed in a supersonic blowdown wind tunnel at Mach 2. The test section dimensions were 15×15 cm and the maximum running time was about one minute. The wake was generated by a

PRECEDING PAGE BLANK-NOT FILMED

flat plate fitted at zero yaw along the nozzle axis, the leading edge being in the subsonic region upstream of the throat in order to minimize the perturbations. The plate was 0.3 cm thick, 15 cm wide, with a length L of 80 cm in the supersonic region. The trailing edge was bevelled to a 3 deg. double wedge angle.

The adjustable walls of the test section enables to obtain in the wake a nearly constant static pressure (Δp about 1%). The wake whose initial thickness was about 2 cm can be observed as far as 100 cm downstream of the trailing edge. Two dimensionality of the flow was checked by making measurements off the center span position and was found satisfactory. The Reynolds number R (based on the length L in the supersonic region and freestream conditions) is 6.5 10^7 and this high value enables to have a fully turbulent boundary layer far upstream from the trailing edge and indeed a fully turbulent wake, since its beginning. During the run the stagnation pressure was held constant with typical fluctuations less than 1% but the total temperature decreases at a rate of about .7 K/s. This variation of temperature gives a change of the Reynolds number of ±3% during the measurements.

2. Experimental techniques

For each run the data were collected along the coordinate y normal to the wake. The displacement of the probe in the y direction and the data acquisition were monitored by an IBM 1800 computer. Traverses are made for several distances x measured from the trailing edge along the flow direction. The mean flow was studied with pitot tube, static pressure and total temperature probes. A special dual support was used for simultaneous measurements of hot wire signal and total pressure and, in this case, the distance between the two probes in the z direction was 5 mm.

The turbulence properties were investigated with a single 5 μm diam Pt-Rd hot wire operating at constant temperature. The choice of the CTA technique instead of the constant current anemometer was made on account of the short running time of the wind tunnel and the large total temperature variation. The CCA technique needs a compensation of the frequency response according to the time constant of the wire, and, in our situation, the necessary electronic adjustments during the run leads to numerous difficulties. It is well known that the CTA gives good frequency response provided that the gain be sufficiently high and the overheat ratio not too low. In the present case the lowest overheat ratio was 1.1 and the AC gain was set at 800 on a DISA 55 M01 anemometer. Both calculations, based on the papers of Perry and Morrison {8} and Wood {9}, and measurements of the effective time constant, using the square wave technique, are in agreement and give in the worst case a value of 4.5 10^{-6}s. Anemometer output spectrums show low energy levels at frequencies above 200 KHz in agreement with the results of Demetriades {10}, Kistler {11} and Rose {12} in similar situations. A spectrum was taken for each wire in order to detect any strain gage effect which appears on the spectrum as peaks above 100 KHz. The wire was rejected if not satisfactory.

In a classical way the basic equation of voltage fluctuations for a normal wire in supersonic flow can be written

$$\frac{E'}{\overline{E}} = F\,\frac{(\rho u)'}{\overline{\rho u}} + G\,\frac{T_t'}{\overline{T_t}}$$

The sensitivity coefficients were obtained by direct calibration in a supersonic free jet. Its small dimensions (10 mm diam) allow continuous operations with the same dynamical and thermal conditions encountered in the wake. The sensitivity coefficients were determined by varying the stagnation pressure and temperature and using a least square method on about 300 values of p, T_t and E at a fixed Mach number. The experimental conditions are in the range $1.2 \leq M \leq 2$ where the Mach number influence can be neglected. This calibration operation was repeated for each wire overheat ratio.

The profiles of $\overline{E'^2}$ were determined for 7 to 10 different overheat ratios between 1.1 and 2. The values of $\overline{(\rho u)'^2}/(\overline{\rho u})^2$, $\overline{(\rho u)'T_t'}/\overline{\rho u}\;\overline{T_t}$ and $\overline{T_t'^2}/\overline{T_t}^2$ where then computed by a regression analysis from the equation :

$$\frac{\overline{E'^2}}{G^2\overline{E}^2} = \frac{\overline{T_t'^2}}{\overline{T_t}^2} + 2\,\frac{F}{G}\,\frac{\overline{(\rho u)'T_t'}}{\overline{\rho u}\;\overline{T_t}} + \left(\frac{F}{G}\right)^2 \frac{\overline{(\rho u)'^2}}{(\overline{\rho u})^2}$$

With the assumption of small pressure fluctuations $p'/\overline{p}$ with respect to density $\rho'/\overline{\rho}$ or temperature $T'/\overline{T}$ fluctuations, one can obtain in a classical way the values of $\overline{u'^2}/\overline{u}^2$, $\overline{T'u'}/\overline{T}\overline{u}$ and $\overline{T'^2}/\overline{T}^2$.

3. Results

Some low frequency perturbations at about 3 Hz were found in the wake at all downstream stations. A study with two total pressure probes located symmetrically to the axis shows a strong negative correlation i.e. the wake moves as a whole in the y direction. This low frequency flapping of the wake interacting with the transverse displacement of the probe gives rise to quasi-periodic fluctuations in the output signal. For the total pressure these perturbations were removed by taking the measurements over 512 or 1024 points equally spaced in the y direction and by using later a digital filtering technique. Symmetry of the wake was found very good either for the filtered values or for mean values taken over a long time. In all cases the measurements were taken on both sides of the wake.

The measured total temperature in the wake was found nearly constant. On the center line near the trailing edge the total temperature was only 5 deg. K below the level in the external flow and the difference decreases downstream. This results from the fact that the wall temperature of the thin flat plate follows the evolution of the total temperature in the external flow, being only slighly higher than the recovery temperature (i.e. the plate is cooled by the flow).

The velocity profiles given in Fig.1 were issued from the Mach number profiles with the hypothesis of constant total temperature. The momentum thickness θ was computed for each x station as a test of the absence of any pressure gradient. Differences as high as 7% are observed but without any significant tendancy and they are supposed due to insufficient accuracy in the velocity measurements. The mean value of θ is 1.28 mm which gives R_θ = 1.04 10^5. All data are presented in dimensionless form using θ and the undisturbed flow velocity u_∞ as reference quantities. The temperatures are referenced to $T_\infty = \overline{u}_\infty^2/C_p$.

Turbulence measurements for $\overline{u'^2}$, $\overline{T'u'}$ and $\overline{T'^2}$ are given on figures 2 to 4. The measured values of the total temperature fluctuations were found very small so that there is a strong correlation between u' and T'

$$T'/\overline{T} \approx (\gamma-1)\,M^2\,u'/\overline{u} \quad .$$

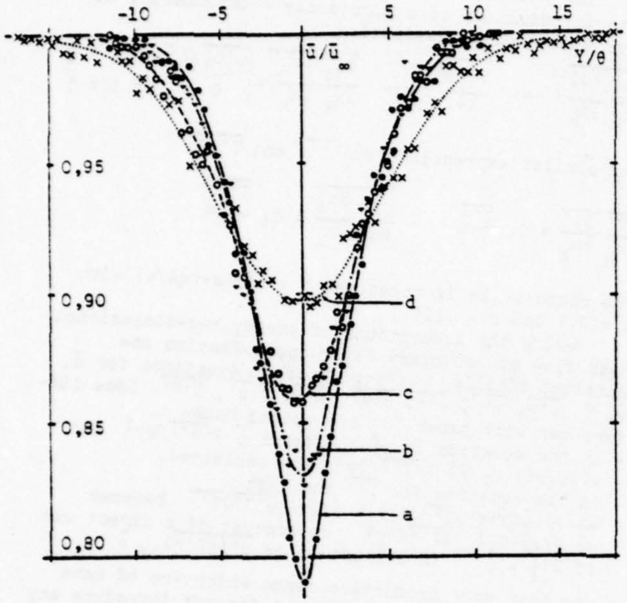

Fig. 1 Mean velocity distribution in the wake (experimental data)
For notations see fig. 2

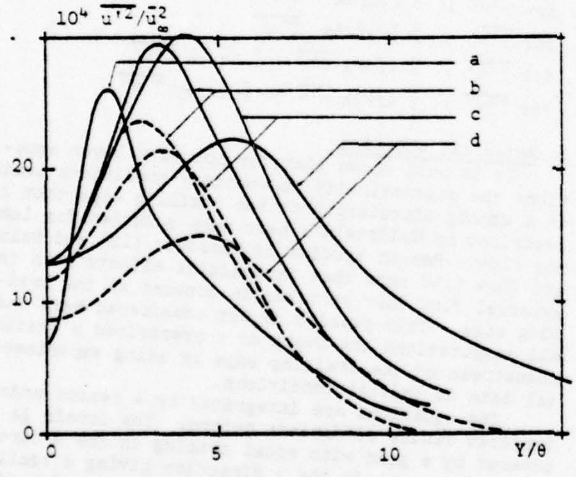

Fig. 2 Intensity of streamwise component of velocity fluctuations in the wake

—— experimental data

- - - model predictions

(a) $x/\theta = 48.$

(b) $= 92.$

(c) $= 134.$

(d) $= 266.$

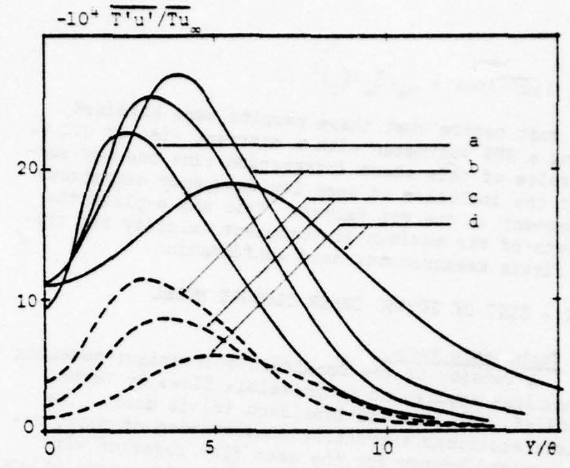

Fig. 3 Intensity of velocity temperature correlation in the wake
(for notations see Fig. 2)

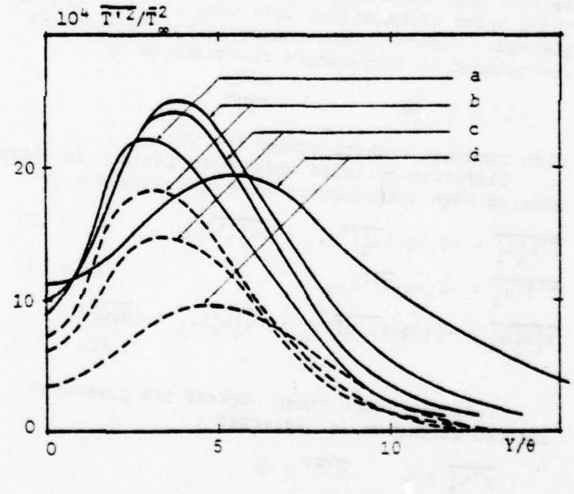

Fig. 4 Intensity of temperature fluctuations in the wake
(for notations see Fig. 2)

This situation, named by Morkovin the "strong Reynolds analogy", is explained by the nearly adiabatic flow over the flat plate which gives a nearly constant total temperature in the wake. As x increases the maximum moves away from the center-line. A rather unexpected result is the increase of the maximum which occurs between $x/\theta = 48$ and $x/\theta = 134$. Clearly this does not agree with the dynamic equilibrium hypothesis tested by Demetriades (15) which requires

$$(\rho\overline{u'^2})\max = \rho_\infty(\bar{u}_\infty-\bar{u}_0)^2 .$$

One must notice that these results were obtained using a RMS voltmeter with a constant time of 0.1 s. In spite of this short integration time one may suspect the inclusion of some low frequency extraneous component in the rms values. This may explain the growth of the maximum of turbulent velocity and these firsts measurements need confirmation.

III - TEST OF SECOND ORDER CLOSURE MODEL

1. Turbulence model

A version of the Donaldson's invariant modeling technique applied to compressible flows by Varma, Beddini, Sullivan and Donaldson {6} is used. The basic equations expressing conservation of mass, momentum and energy for the mean flow together with the transport equations for second order correlations $\overline{u'_iu'_j}$ and $\overline{T'u'_i}$ are derived. They involved second, third and fourth-order unknown correlations which are expressed in terms of second order ones and mean flow properties following Donaldson's proposals.

Keeping in view the moderate value of the Mach number, the divergence of velocity fluctuations is neglected ($\partial u'_i/\partial x_i = 0$) and the pressure fluctuations are also neglected in comparison to that of density and temperature ($\bar{\rho}T' + \rho'\bar{T} = 0$). Fourth and third order correlations involving μ' or k' are neglected. Viscosity and conductivity fluctuations are related to temperature fluctuations by

$$\mu' = T'\frac{\partial\mu}{\partial T} \qquad k' = \frac{\mu' C_p}{P}$$

with constant Prandtl number $P = .72$.

Diffusion by third order correlations is approximated with introduction of a macro-scale Λ by :

$$\overline{T'u'_\ell u'_i} = -C_1\Lambda q\{(\overline{u'_iT'})_{,\ell} + (\overline{u'_\ell T'})_{,i}\} \qquad (C_1 = .1)$$

$$\overline{T'T'u'_\ell} = -C_2\Lambda q(\overline{T'^2})_{,\ell} \qquad (C_2 = .1)$$

$$\overline{u'_iu'_ju'_k} = -C_3\Lambda q\{(\overline{u'_iu'_j})_{,k} + (\overline{u'_iu'_k})_{,j} + (\overline{u'_ju'_k})_{,i}\} \qquad (C_3 = .1)$$

Following most other workers the pressure-induced diffusion is neglected :

$$\overline{p'u'_i} = 0 \qquad \overline{p'T'} = 0$$

Donaldson's models are adopted :

$$\overline{p'\frac{\partial T'}{\partial x_k}} = -C_6\frac{\bar{\rho}q}{\Lambda}\overline{u'_kT'}$$

$$\overline{T'T'T'} = 0$$

$$\overline{u'_iu'_{j,k}} = \frac{1}{2}(\overline{u'_iu'_j})_{,k}$$

$$\overline{T'u'_{i,j}} = \frac{1}{3}\delta_{ij}\overline{T'u'^\ell_{,\ell}}$$

The pressure-strain correlations are approximated with Rotta's proposal taking also in account the effect of the mean rate of strain in the simplest way (see for example ref. {1} and {4})

$$\overline{p'\left(\frac{\partial u'_i}{\partial x_k} + \frac{\partial u'_k}{\partial x_i}\right)} = -\frac{\bar{\rho}q}{\Lambda}\left(\overline{u'_iu'_k}-\delta_{ik}\frac{q^2}{3}\right) + C_9\bar{\rho}q^2\left(\frac{\partial\bar{u}_i}{\partial x_k} + \frac{\partial\bar{u}_k}{\partial x_i}\right)$$

The modelisation of dissipation terms is made with introduction of a *microscale* λ *considering* either anisotropic dissipation

$$\overline{\frac{\partial u'_i}{\partial x_k}\frac{\partial u'_j}{\partial x_k}} = \frac{\overline{u'_iu'_j}}{\lambda^2} \quad \text{or} \quad \overline{\frac{\partial u'_i}{\partial x_k}\frac{\partial u'_j}{\partial x_k}} = \begin{cases}\overline{u'_iu'_j}/\lambda^2 & \text{if } i = j\\ 0 & \text{if } i \neq j\end{cases}$$

and similar expressions for $\overline{T'^2}$ and $\overline{T'u'}$

$$\overline{\frac{\partial T'}{\partial x_k}\frac{\partial T'}{\partial x_k}} = C_4\frac{\overline{T'^2}}{\lambda^2} \qquad \overline{\frac{\partial T'}{\partial x_k}\frac{\partial u'_i}{\partial x_k}} = C_5\frac{\overline{T'u'_i}}{\lambda^2}$$

The micro-scale is taken as $\lambda^2 = \Lambda^2/(a+bq\Lambda/\nu)$ with $a = 2.5$ and $b = .125$.

Using the assumptions of steady two-dimensional mean flow and boundary layer approximation one obtained finally a system of 10 equations for $\bar{u}$, $\bar{v}$, $\bar{T}$, $\overline{u'^2}$, $\overline{v'^2}$, $\overline{w'^2}$, $\overline{u'v'}$, $\overline{T'^2}$, $\overline{T'u'}$, $\overline{T'v'}$. Some differences with paper {6} are quoted below :

- in the equation for $\bar{T}$ the terms $\bar{\mu}\,\partial^2\overline{v'^2}/\partial y^2$ and $\gamma(\partial\mu/\partial T)(C_p/P)\,\partial^2\overline{T'^2}/\partial y^2$ are neglected.
- in the equation for $\overline{T'^2}$ the term $-\partial/\partial y(\bar{\rho}C_2\Lambda q\,\partial\overline{T'^2}/\partial y) + \partial/\partial y(\sigma\overline{v'T'})\overline{T'^2}$ becomes $-\bar{\rho}\,\partial/\partial y(C_2\Lambda q\,\partial\overline{T'^2}/\partial y)$ on account of a direct use of $u'^\ell_{,\ell} = 0$ in evaluation of $\overline{u'^\ell(T'^2)_{,\ell}}\,\bar{\rho}$
- one keep some production terms which are of same order as convective terms and dit not introduce any computational difficulty namely :

. for $\overline{u'^2}$: $2\bar{\rho}\,\partial\bar{u}/\partial x\,\overline{u'^2}$
. for $\overline{v'^2}$: $2\bar{\rho}\,\partial\bar{v}/\partial y\,\overline{v'^2}$
. for $\overline{u'v'}$: $\bar{\rho}\,(\partial\bar{u}/\partial x + \partial\bar{v}/\partial y)\,\overline{u'v'}$
. for $\overline{T'^2}$: $2\bar{\rho}\,\partial\bar{T}/\partial x\,\overline{T'u'}$
. for $\overline{T'u'}$: $\bar{\rho}\,\partial\bar{T}/\partial x\,\overline{u'^2} + \bar{\rho}\,\partial\bar{u}/\partial x\,\overline{T'u'}$
. for $\overline{T'v'}$: $\bar{\rho}\,\partial\bar{T}/\partial x\,\overline{u'v'} + \bar{\rho}\,\partial\bar{v}/\partial y\,\overline{T'v'}$

2. Numerical solution

It is well known that for boundary layer equations the discontinuity in boundary conditions leads to a strong singularity at the trailing edge that is described by Goldstein's near wake solution for laminar flow. Recent studies of Messiter {13} and Melnik and Chow {14} show that interaction effects with the external flow must be taken in account at the trailing edge. This problem is not considered here and all computations are begun at a prescribed x station downstream of the trailing edge by using experimental data as initial conditions.

The equations are integrated by a second order implicit finite difference method. The domain is covered by a grid with equal spacing in the x direction and unequal in the y direction giving a smaller mesh size near the center-line. Discretization of x derivatives is made with second order three points upwind differences. Non linearity and coupling of the equations is handled by a Gauss-Seidel iterative scheme at every x step, keeping only one variable as unknown in each equation. This leads to the succesive solution (in the order $\bar{u}$, $\bar{v}$, $\bar{T}$, $\overline{u'^2}$, $\overline{v'^2}$, $\overline{w'^2}$, $\overline{u'v'}$, $\overline{T'^2}$, $\overline{T'u'}$, $\overline{T'v'}$) of nine sets of linear equations with tridiagonal matrices instead of using a unique tridiagonal matrix with 9x9 submatrices as elements. The test of convergence was a relative change on $\bar{u}$ and $\bar{T}$ less than 10^{-4} for all nodes. The use of three x stations allows to begin the iterative process at each step with a third order prediction which is very efficient in saving time of computation. A typical run time on IBM 370-168 is 0.3 s per x step for 200 to 250 points in the y direction.

The program was checked in two manners. First, the constancy of the momentum thickness for a zero pressure gradient was satisfied better than 10^{-3} for 400 x steps. Secondly a special program uses the solution vectors after the integration, in order to give energy budget for each equation. The relative importance of various terms can then be "*a posteriori*" examined.

3. Application to incompressible flow

In a first step, the numerical program was applied to the wake of a thin flat plate examined by Chevray and Kovasznay {7}. Initial data were taken at x = 20 cm ($x/\theta = 34.4$). In the absence of data for $\overline{w'^2}$ we used the measurements of Tsen et alii {16} for the ratio $\overline{w'^2}/\overline{u'^2}$ (.35 on the center-line, .40 for the maximum value of $\overline{w'^2}$). The best results were obtained with $\overline{\partial u'_i/\partial x_k \, \partial u'_j/\partial x_k} = 0$, if $i \neq j$ and $C_3 = .1$, $C_9 = .05$. The macro-scale Λ was taken as $\Lambda = .3|\tilde{Y}_1 - \tilde{Y}_2|$

where $\tilde{Y}_1$ is the location such that

$$|\bar{u}(\tilde{Y}_1) - \bar{u}_o| = .5|\bar{u}_e - \bar{u}_o|$$

(idem for $\tilde{Y}_2$). A slightly better agreement is obtained if one use for Λ a function of x and y such

$$\Lambda = .2|\tilde{y}_1 - \tilde{y}_2| + .15|y|$$

but this is a quite empirical choice and it would be more rational to use a transport equation for a length-scale rather than refine its expression.

Profiles of mean velocity are compared with measurements at x = 50 cm, 150 cm, 240 cm on fig. 5, and the agreement is generally good.

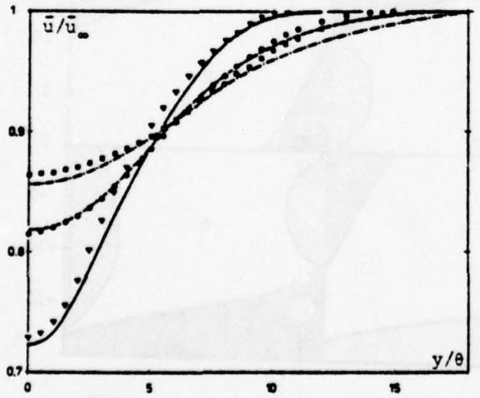

Fig. 5 - Mean velocity profiles in the symmetric incompressible wake

Experimental data {7}		model predictions
x/θ = 86.	▼	————
= 258.	●	--------
= 414.	◘	—·—·—·

Comparison for normal and shear stresses is made on figure 6 to 8. The result is seen to be good for $\overline{u'v'}$ but the normal stresses are not well predicted near the center line $\overline{u'^2}$ being too small and $\overline{v'^2}$ too large. A similar discrepancy was observed by Launder, Reece and Rodi {1} using a dissipation transport equation and a more sophisticated model for the pressure-strain correlations.

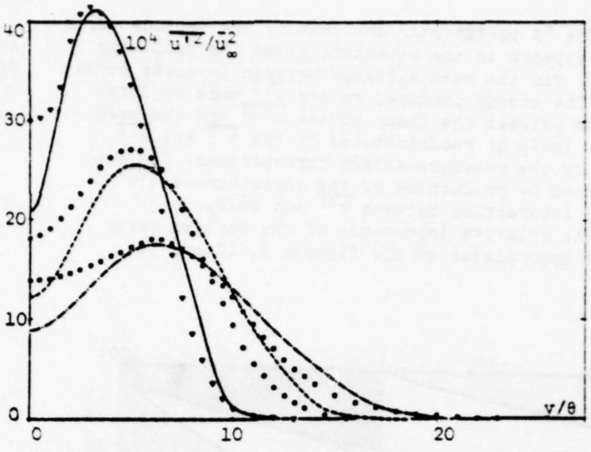

Fig. 6 - Intensity of the streamwise component of velocity fluctuations
For notations, see fig. 5

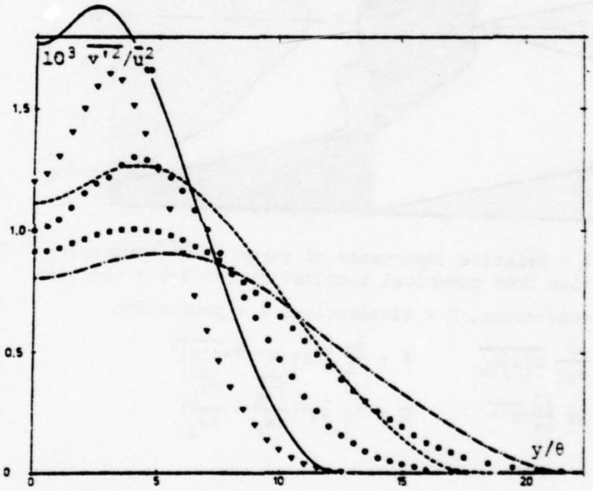

Fig. 7 - Intensity of the normal component of velocity fluctuations
For notations, see fig. 5

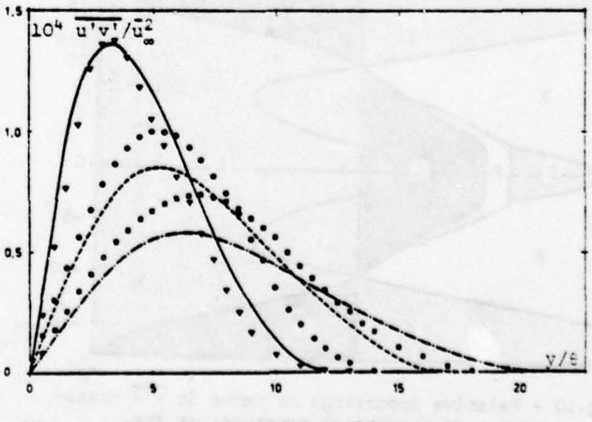

Fig. 8 - Distribution of Reynolds stress
For notations see fig. 5

The "*a posteriori*" analysis of the various terms which appears in the equations gives the following picture for the main exchange between Reynolds stresses. The energy produced on the $\overline{u'^2}$ mode by interaction between the shear stress $\overline{u'v'}$ and the mean strain $\partial\bar{u}/\partial y$ is redistributed on the $\overline{v'^2}$ and $\overline{w'^2}$ mode, by the pressure-strain correlations. The loop is closed by production of the shear stress $\overline{u'v'}$ trough interaction between $\overline{v'^2}$ and $\partial\bar{u}/\partial y$.

The relative importance of the various terms can be appreciated on the figures 9, 10 and 11.

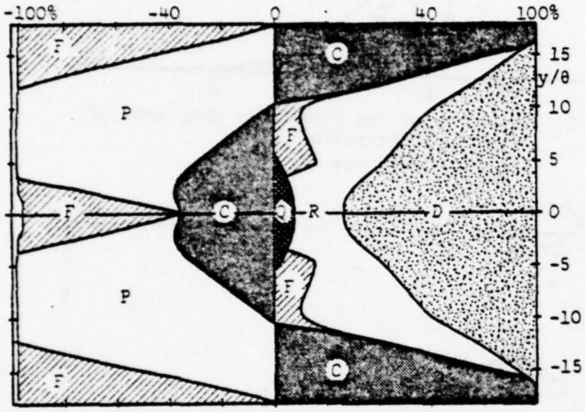

Fig.9 - Relative importance of terms in $\overline{u'^2}$ transport equation from numerical computation for $X/\theta = 414$ {7}

C = convection, D = dissipation, P = production

$F = \frac{\partial}{\partial x_i}\overline{u'_i u'_j u'_k}$ $\qquad R = \frac{\bar{\rho} q}{\Lambda}(\delta_{ij}\, q^2/3 - \overline{u'_i u'_j})$

$Q = 2\bar{\rho}\,\frac{\partial\bar{u}}{\partial x}\,\overline{u'^2}$ $\qquad G = C_9\,\bar{\rho} q^2 (\frac{\partial\overline{u_i}}{\partial x_k} + \frac{\partial\overline{u_k}}{\partial x_i})$

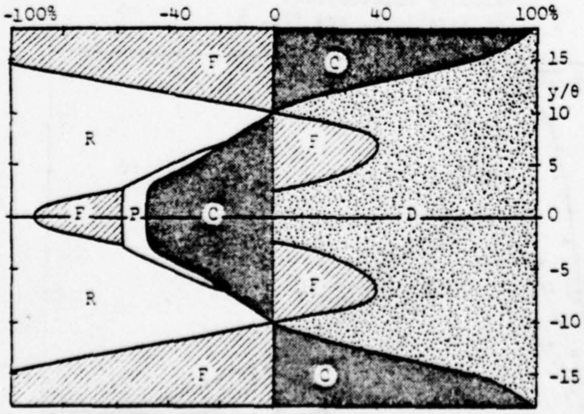

Fig.10 - Relative importance of terms in $\overline{v'^2}$ transport equation from numerical computation for $x/\theta = 414$ {7}
For legend, see fig. 9.

The following conventions are used in these graphs : in the equations all the terms are written on the same side of the equal sign.

- the terms are related to sum of the positives ones
- the values are plotted in an additive manner (i.e. the value is proportionnal to the difference of the abscissae of the limiting curves)

One can draw the following conclusions :

- equation for $\overline{u'^2}$.
  The redistribution plus dissipation balance production terms apart near the axis where they balance diffusion and convection. Even for the last x station ($x/\theta = 414$) the x production $2\rho\overline{u'^2}\,\partial\bar{u}/\partial x$ is not very small and can be larger than 10% of the dissipation term near the axis. The effect of the mean strain rate in the model for pressure-strain correlation is very small.
- equation for $\overline{v'^2}$.
  The redistribution terms ensure energy production balancing dissipation plus diffusion. Near the axis diffusion plus convection balance only dissipation. The production term $2\rho\,\partial\bar{v}/\partial y\,\overline{v'^2}$ is about 10% of the dissipation near the axis. The contribution of the mean strain rate in the model for pressure-strain correlation is negligible.
- equation for $\overline{u'v'}$.
  The production terms are essentially balanced by pressure-strain correlation . The effect on the mean strain rate in the pressure-strain correlation is about 15% of the entire production.

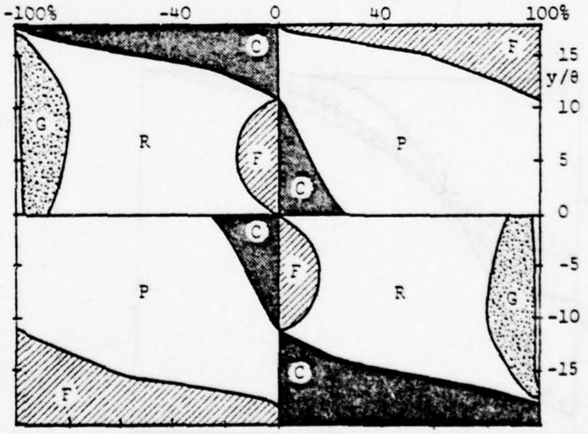

Fig.11 - Relative importance of terms in $\overline{u'v'}$ transport equation from numerical computation for $X/\theta = 414$ {7}.
For legend, see fig. 9.

Another confrontation for the incompressible case is presented on figures 12, 13, 14 and 15. The experimental results used are those obtained at C.E.A.T. of Poitiers by Tsen, Lemonnier and Garem {17} concerning the dissymetric wake of a flat plate with strong adverse pressure gradient.

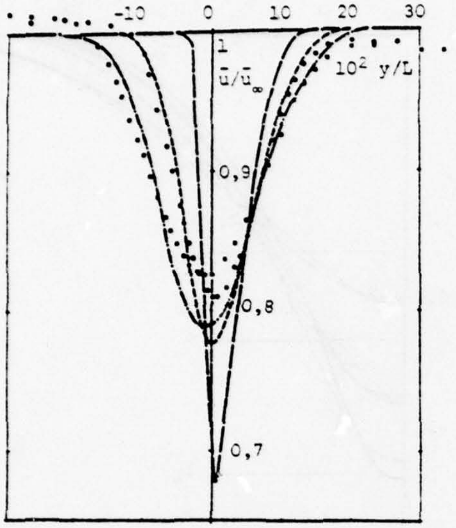

Fig. 12 - Mean velocity profiles in asymmetric incompressible wake with adverse pressure gradient
Experimental data from Tsen {17} ; model predictions

X/L = 0,17 ————————
X/L = 1,8 □ - - - - - - - - -
X/L = 3,5 ● —·—·—·—·—

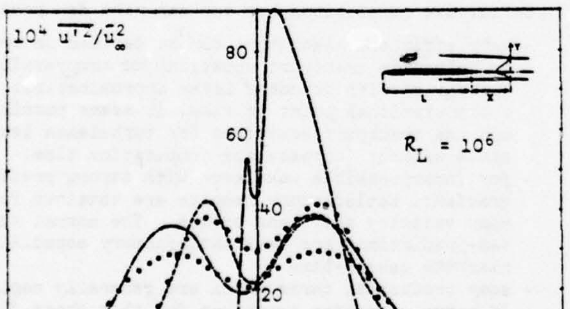

Fig. 13 - Intensity of the streamwise component of velocity fluctuations
For Notations, see fig. 12

Some characteristic features of this very intricate case are predicted by the model. Vanishing of the assymmetry is well represented and a rather good agreement is obtained between measurements and predictions for $\bar{u}$ and $\overline{u'v'}$. The major discrepancy is observed on the v' component for which the computed level is 25% to low near the axis.

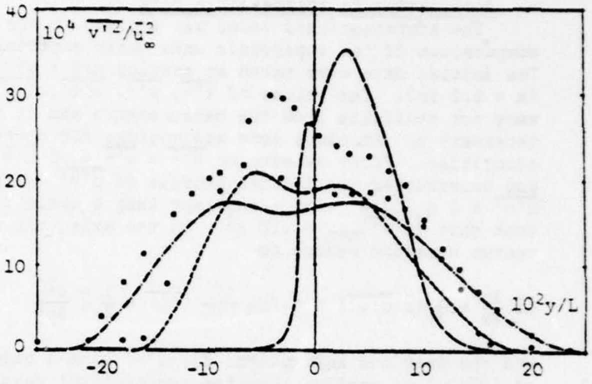

Fig. 14 - Intensity of the normal component of velocity fluctuations
For notations, see fig. 12.

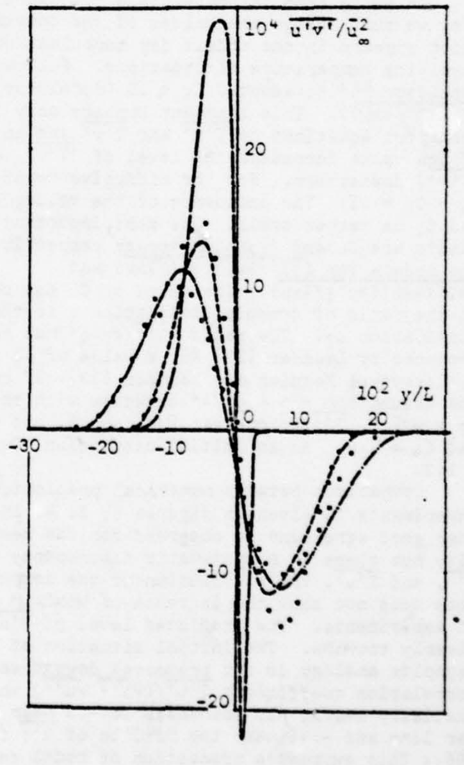

Fig. 15 - Distribution of Reynolds stress
For notation, see fig. 12

These results for incompressible flows seem sufficiently encouraging to attempt an application to the computation of a supersonic wake, keeping the values of Λ, C_3 and C_9 adopted in the above calcultions.

4. Application to compressible flow

The aforementioned model was applied to the computation of the supersonic wake under experiment. The initial data were taken at station $x/\theta = 48.$ ($x = 6.2$ cm). The values of $\overline{v'^2}$, $\overline{w'^2}$, $\overline{u'v'}$, $\overline{T'v'}$ were not available from the measurements and it was necessary to introduce some assumptions for these quantities. First we adopted $\overline{v'^2} = \overline{w'^2} = .5\ \overline{u'^2}$ and constructed the initial profile of $\overline{u'v'}$ using $\overline{u'v'} = \ell\ q\ \partial\bar{u}/\partial y$ with a constant length scale ℓ such that $|\overline{u'v'}|_{max} = .16\ q^2$. On the axis, the momentum equation reduce to

$$\bar{\rho}\bar{u}\ \frac{\partial\bar{u}}{\partial x} + \frac{\partial}{\partial y}(\bar{\rho}\ \overline{u'v'}) + C_1\Lambda\sigma q\ \frac{\partial^2}{\partial y^2}\ \overline{T'u'} = \frac{1}{R}\ \bar{\mu}\ \frac{\partial^2\bar{u}}{\partial y^2}$$

and the previous assumptions for $\overline{u'v'}$ give a value of $(\partial\bar{u}/\partial x)_{y=0}$ smaller than the experimental measurements of $\bar{u}$. For comparison some runs were made with a greater value of ℓ giving $|\overline{u'v'}|_{max} = .18\ q^2$ or with a more isotropic initial state taking $\overline{v'^2} = \overline{w'^2} = .75\ \overline{u'^2}$. Taking into account the situation of strong Reynolds analogy, the initial data for $\overline{T'v'}$ are given by $\overline{T'v'} = -u\ \overline{u'v'}$.

In going from incompressible to compressible flow we must assign the values of the constants which appears in the models for turbulent quantities involving temperature fluctuations. Following Donaldson {6} we adopted $C_6 = .9$ (model for $p'\ (\partial T'/\partial x_k)$). This constant appears only in the transport equations of $\overline{T'u'}$ and $\overline{T'v'}$ and an increase of its value decreases the level of $|\overline{T'u'}|$ and $|\overline{T'v'}|$ downstream. For the diffusive terms we took $C_1 = C_2 = .1$. The influence of the values of C_1 and C_2 is rather small. The most important coefficients are C_4 and C_5 which appear respectively in the models for $(\partial T'/\partial x_k)(\partial T'/\partial x_k)$ and $(\partial T'/\partial x_k)(\partial u'_i/\partial x_k)$. The value of C_4 can be related to the ratio of dynamic dissipation ε to thermal dissipation ε_T. The ratio $\varepsilon\overline{T'^2}/\varepsilon_T\ q^2$ has been introduced by Launder {18} and a value of .5 suggested by Dekeyser, Beguier and Launder {19}. If one makes the assumption $\varepsilon \sim \nu\ q^2/\lambda^2$ together with the model $\varepsilon_T = \nu/P\ C_4\ \overline{T'^2}/\lambda^2$ one get $P/C_4 \sim 0.5$, and we adopted $C_4 = 1.4$. As an initial assumption, C_5 was set $= 1.2$.

Comparison between numerical predictions and experiments is given on figures 2, 3, 4, 16. A rather good agreement is observed for the mean velocity but there is a systematic discrepancy for $\overline{u'^2}$, $\overline{T'^2}$, and $\overline{T'u'}$. The x evolution of the computed values does not show the increase of maximum observed in experiments. The predicted level of $\overline{T'u'}$ seems clearly too low. The initial situation of strong Reynolds analogy is not preserved downstream and the correlation coefficient $\overline{T'u'}/(\sqrt{\overline{T'^2}}\ \sqrt{\overline{u'^2}})$ which is initially nearly -1, increases to -.2 near the center line and -.45 near the maximum of $\overline{u'^2}$ for $x/\theta = 266$. This express a production of total temperature fluctuations which seems unlikely and was not observed in experiments. One must notice that some exploratory computations made with differents values for C_1, C_2, C_4, C_5, C_6 show that the results for $\bar{u}$, $\overline{u'^2}$, $\overline{v'^2}$, $\overline{w'^2}$, $\overline{u'v'}$ are not very sensitive to these constants and the dynamical quantities are nearly independent of quantities involving temperature fluctuations.

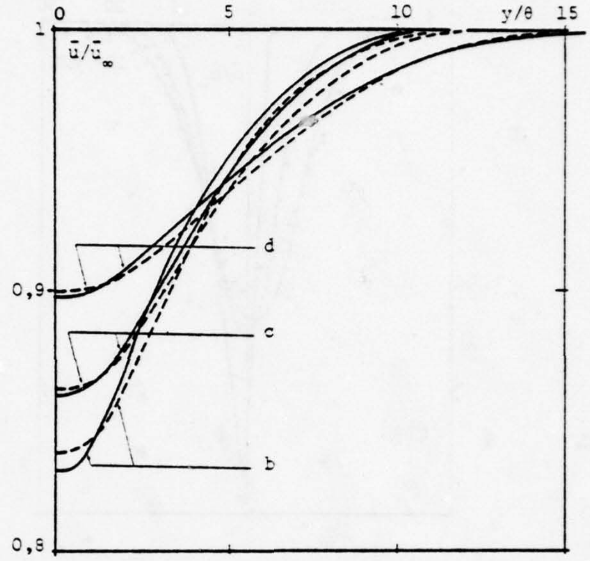

Fig. 16 - Mean velocity profiles in supersonic wake

———————— experimental data
- - - - - - - - model predictions

(b):$x/\theta = 92$; (c):$x/\theta = 134$; (d):$x/\theta = 266$

IV - CONCLUSIONS

In the present state it seems premature to draw definitive conclusions but one can make few remarks :

- very efficient algorithms can be devised in order to solve the transport equations for compressible turbulence with boundary layer approximations. From a computational point of view, it seems possible to add the transport equations for turbulence length scale without increase the computation time.
- for incompressible wake even with strong pressure gradient, satisfactory results are obtained for mean velocity and shear stress. The normal stresses-predictions are less satisfactory especially near the center-line
- some production terms which are generally neglected in normal stresses equations for thin shear flow are not entirely negligible
- for the compressible wake under experiments the agreement with numerical predictions was good for the mean velocity but a serious discrepancy exists with the first hot wire measurements
- the strong Reynolds analogy situation which occurs very often in the moderate Mach number flows is not preserved by the model. An improvement based on a direct use of the total enthalpy equation is under investigation

The authors gratefully acknowledge the financial support from the "Direction des Recherches et Moyens d'Essais" under contracts 75-228 and 76/371.

REFERENCES

1 B.E. Launder, G.J. Reece and W. Rodi, "Progress in the Development of a Reynolds-Stress Turbulence Closure", Journal of Fluid Mechanics, Vol. 68, P.3, pp. 537-566, 1975

2 S.B. Pope and J.H. Whitelaw, "The calculation of Near-Wake Flows", Journal of Fluid Mechanics, Vol. 73, P.1, pp. 9-32, 1976

3 P. Bradshaw, "The Understanding and Prediction of Turbulent Flow", Aeronautical Journal, Vol. 16, pp. 403-418, 1972

4 G.L. Mellor and H.J. Herring, "A Survey of Mean Turbulent Field Closure Models", AIAA Journal, Vol.11, n°5, pp.590-599, 1972

5 W.C. Reynolds, "Recent Advances in the Computation of Turbulent Flows", Adv. Chem. Engng, USA, pp.193-246, 1974

6 A.K. Varma, R.A. Beddini, R.D. Sullivan and C. du P. Donaldson, "Application of an Invariant Second Order Closure Model to Compressible Turbulent Shear Layers", AIAA Paper, n°74/592, 1974

7 R. Chevray and L.S.G. Kovasznay, "Turbulence Measurements in the Wake of a Thin Flat Plate", AIAA Journal, Vol.7, n°8, pp.1641-1642, 1969

8 A.E. Perry and G.L. Morrison, "A Study of the Constant Temperature Hot-Wire Anemometer", Journal of Fluid Mechanics, Vol.47, P.3, pp.251-267, 1976

9 N.B. Wood, "A Method for Determination and Control of the Frequency Response of the Constant-Temperature Hot-Wire Anemometer", Journal of Fluid Mechanics, Vol.67, P.4, pp.769-786, 1975

10 A. Demitriades, "Turbulence Correlations in a Compressible Wake", Journal of Fluid Mechanics, Vol.74, P.2, pp.251-267, 1976

11 A.L. Kistler, "Fluctuation Measurements in a Supersonic Turbulent Boundary Layer", Physics of Fluids, Vol.2, n°3, pp.290-296, 1959

12 W.C. Rose, "The Behaviour of a Compressible Turbulent Boundary Layer in a Shock-Wave-Induced Adverse Pressure Gradient", NASA Report n° TN D-7092, 1973

13 A. Messiter, "Boundary Layer Flow Near the Trailing Edge of a Flat Plate", SIAM Journal of Applied Mechanics, Vol.18, pp.241-257, 1970

14 R. Melnik and R. Chow, "Asymptotic Theory of Two-Dimensional Trailing Edge Flows", Grumman Research Department, Report RE-510 J, 1975

15 A. Demitriades, "Turbulence Measurements in a Supersonic Two-Dimensional Wake", Physics of Fluids, Vol.13, n°7, pp.1672-1678, 1970

16 L.F. Tsen and J. Fayet, "Calcul des sillages subsoniques tenant compte de l'énergie turbulente", Contrat DRME n° 71/349/1, rapport final, Sept. 1972

17 L.F. Tsen, H. Garem and P.E. Lemonnier, "Mesures des tensions de Reynolds dans le sillage (SDPI) d'une plaque plane en incidence à 5°, en gradient de pression positif", Contrat DRME n° 71/349/2, 1973

18 B.E. Launder, "Heat and Mass Transport in Turbulence", in "Topics in Applied Physics Turbulence", Bradshaw-Springers, 1976, Chap.6

19 I. Dekeyser, C. Beguier, B.E. Launder, "Rapport des dissipations dynamique et thermique dans les écoulements turbulents", 13ème Colloque AAAF Aérodynamique Appliquée, Lyon, Nov. 1976

NUMERICAL PREDICTION OF AXISYMMETRIC FREE SHEAR FLOWS WITH A SECOND-ORDER REYNOLDS STRESS CLOSURE

B. E. LAUNDER
DEPARTMENT OF MECHANICAL ENGINEERING
UNIVERSITY OF CALIFORNIA
DAVIS, CALIFORNIA 95616

and

A. MORSE
DEPARTMENT OF MECHANICAL ENGINEERING
IMPERIAL COLLEGE
LONDON SW7 2BX

ABSTRACT

The paper deals with the application of the Reynolds stress closure of [2] to the calculation of the axisymmetric jet in stagnant surroundings with and without swirl. A technique for handling the numerical solution of the equations with the Patankar-Spalding 2-dimensional parabolic scheme is first presented including a practice for reducing the sensitivity of the solution to the forward step.

Solutions to the round, non-swirling jet display a rate of spread that is 50% too large when constant coefficients, optimized for plane flows, are used. The origin of the discrepancy is shown to be the source terms in the dissipation rate equation, a 1% change in either of the source-term coefficients altering the rate of spread by about 4%. It is found that in swirling flows the usually neglected shear stress $\overline{uw}$ exerts a strong influence on $\overline{uv}$ and hence on the rate of spread. With the present model of how mean strain affects the pressure-strain correlation, however, the predicted $\overline{uw}$ has the <u>wrong sign</u> and thus the numerical solutions display a reduced rate of spread in contrast to the strong augmentation found in practice.

NOMENCLATURE

c_1, c_2	coefficients in pressure-strain model
c_s, c_ϵ	diffusion coefficients in stress and dissipation equations
$c_{\epsilon 1}$, $c_{\epsilon 2}$	source-term coefficients in dissipation equation
D_{ij}	tensor defined following equation (1)
$\mathcal{D}_{ij}$	net diffusion rate of stress component $\overline{u_iu_j}$
k	turbulence kinetic energy
p	static pressure
P	production rate of turbulence energy
P_{ij}	production rate of stress component $\overline{u_iu_j}$
r	radial coordinate
U, V, W	mean velocities in axial, radial and circumferential directions
u, v, w	fluctuating velocities in axial, radial and circumferential directions
U_i, u_i	mean and fluctuating velocities (tensor notation) in direction x_i
$\overline{u_iu_j}$	kinematic Reynolds stress
x	axial coordinate
x_i	Cartesian distance coordinate
α, β, γ	coefficients in ϕ_{ij} model linearly related to c_2
δ_{ij}	Kronecker delta
ε	kinematic dissipation rate of turbulence energy
ϵ_{ij}	dissipation rate of stress component $\overline{u_iu_j}$
ϕ_{ij}	pressure-strain correlation of stress component $\overline{u_iu_j}$
ρ	fluid density
ω	normalized stream function

INTRODUCTION

The last few years have seen extensive progress in the development and application of second-order turbulence closures. In these schemes the non-zero Reynolds-stress components are themselves the subjects of a set approximated transport equations which are solved simultaneously with those for the mean flow. Models of this type have allowed the successful prediction of numerous turbulence phenomena that are beyond the scope of simpler schemes based on St. Venant's effective viscosity concept. As examples we may cite successful predictions of: the non-coincidence of the surfaces of zero shear stress and zero mean strain [1]; the great sensitivity of near-wall flows to surface curvature [2,3]; the occurrence of turbulence-driven secondary flows in ducts [4,5]; and the effects of gravitational forces on stratified flows [6-8].

Schemes of this kind appear to offer the best prospect, over the next decade, for practical computations of complex shear flows. It needs to be emphasized however that a good deal more testing is needed in various types of strain field before the reliability of the available models may be thoroughly assessed.

PRECEDING PAGE BLANK-NOT FILMED

Axisymmetric shear flows provide an important subclass of flows that have so far received only slight attention in the context of second-order closures. They also provide two well-documented flow phenomena that effective-viscosity models notably fail to predict. Measurements of the axisymmetric jet in stagnant surroundings show its rate of spread to be 20-25% less than that of the plane 2-dimensional jet. Two-equation viscosity models (with empirical coefficients tuned to predict the latter flow accurately) predict virtually the same spreading rate for the two flows [9,10], however. If swirl is imparted to the round jet, experiments show a monotonic and pronounced increase in the rate of spread as the level of swirl is raised. The same two-equation viscosity models, however, predict hardly any effect unless one (or more) of the coefficients in the model is specifically tuned as a function of the swirling flow Richardson number to bring accord with measurement.

Our initial aim in undertaking the research reported here was to discover whether, by adopting a more soundly based closure of second-order type, these anomalies in predicting axisymmetric flows could be removed. The basic model adopted for study was that applied by Launder, Reece and Rodi [2] (hereafter LRR) - generally with good accuracy - to a range of plane thin shear flows. The research has gone through a number of phases and though the conclusions to emerge at each stage have tended to be rather negative we feel they are not less useful for that. The first task, that of obtaining numerically accurate solutions to the thin-shear-flow (parabolic) form of the governing equations, itself proved to be a far from trivial task exacerbated by the use of the normalized stream function as cross-stream independent variable [11]. When numerically satisfactory solutions were obtained it became clear that the predictions were in fact worse than with a 2-equation viscosity model, the rate of spread being fully 50% greater than measured.

Bradshaw [12] had suggested that small extra strain rates (generally neglected in thin-shear-flow computations) were responsible for the difficulty of predicting the round jet and the effects of streamwise curvature. LRR had confirmed that their model was indeed sensitive to secondary strains associated with streamwise curvature. It was thus decided to include all the small (but non-zero) terms in the momentum, stress and dissipation rate equations that had hitherto been omitted. While considerably adding to the complexity of the calculation, the overall effect of these terms on the spreading rate was negligible - at least for the round jet without swirl. Attention therefore shifted to identifying the process (or processes) in the LRR closure that were inadequately approximated and to devising a generally satisfactory remedy. It emerges from our study that the two poorly predicted flow phenomena discussed above appear to be due to quite separate shortcomings in the model. The incorrect spread in the nonswirling round jet arises mainly from the dissipation rate equation while the failure to display the correct effects of swirl is largely due to shortcomings in the model for the pressure-strain correlation in the Reynolds stress equations.

Section 2 of the paper presents the equations in tensor and axisymmetric form and describes the method adopted for solving the equations in the latter system. The predictions themselves - and their shortcomings - are discussed in Section 3 while the concluding section draws together the main findings to emerge and with it the writers' thoughts on directions for further development of second-order closures.

THE MODEL EQUATIONS AND THEIR SOLUTION

The LRR Reynolds Stress Closure

In the free-shear-flow version of the closure proposed in [2] the kinematic Reynolds stresses are obtained from the following set of transport equations:

$$\frac{D\overline{u_i u_j}}{Dt} = P_{ij} + \phi_{ij} - \frac{2}{3}\varepsilon\delta_{ij} + \mathcal{D}_{ij} \qquad (1)$$

where the four terms appearing on the right side of equation (1) denote respectively: stress creation due to mean shear; redistributive or randomizing action of the pressure-strain correlation; direct dissipation by viscous action; and diffusive transport. In mathematical form the pressure-strain correlation is approximated as

$$\begin{aligned}\phi_{ij} \equiv -c_1\frac{\varepsilon}{k}(\overline{u_i u_j} - \frac{2}{3}\delta_{ij}k) - \alpha(P_{ij} - \frac{2}{3}\delta_{ij}P) \\ -\beta(D_{ij} - \frac{2}{3}\delta_{ij}P) + \gamma k(\frac{\partial U_i}{\partial x_j} + \frac{\partial U_j}{\partial x_i})\end{aligned} \qquad (2)$$

where $k \equiv \overline{u_k u_k}/2$, the turbulence kinetic energy;

$$\varepsilon \equiv \nu\overline{\left(\frac{\partial u_i}{\partial x_k}\right)^2};\ P_{ij} \equiv -\left[\overline{u_i u_k}\frac{\partial U_j}{\partial x_k} + \overline{u_j u_k}\frac{\partial U_i}{\partial x_k}\right];\ P \equiv P_{kk}/2;$$

$$D_{ij} \equiv -\left[\overline{u_i u_k}\frac{\partial U_k}{\partial x_j} + \overline{u_j u_k}\frac{\partial U_k}{\partial x_i}\right]$$

and the coefficients α, β and γ are uniquely related to a quantity c_2 by:

$$\alpha \equiv (8+c_2)/11;\quad \beta \equiv (8c_2-2)11;\quad \gamma \equiv (30c_2-2)/55$$

In [2], two models were adopted for the net diffusive transport of stress, $\mathcal{D}_{ij}$. The version proposed in [1]:

$$\mathcal{D}_{ij} = c_s'\frac{\partial}{\partial x_k}\left[\frac{k}{\varepsilon}(\overline{u_i u_\ell}\frac{\partial\overline{u_j u_k}}{\partial x_\ell} + \overline{u_j u_\ell}\frac{\partial\overline{u_k u_i}}{\partial x_\ell} + \overline{u_k u_\ell}\frac{\partial\overline{u_i u_j}}{\partial x_\ell})\right] \qquad (3)$$

and the simpler version proposed by Daly and Harlow [13]

$$\mathcal{D}_{ij} = c_s\frac{\partial}{\partial x_k}(\frac{k}{\varepsilon}\overline{u_k u_\ell}\frac{\partial\overline{u_i u_j}}{\partial x_\ell}) \qquad (4)$$

Although equation (3) appeared superior on physical grounds, LRR found in practice that equation (4) produced equally as satisfactory results for the flows considered. Thus because the transformation of equation (3) to axisymmetric coordinates produces a great many terms the present work has mainly adopted the simpler form given by equation (4).

Closure in the LRR model is completed through the following equation for ε, the turbulence energy dissipation rate:

$$\frac{D\varepsilon}{Dt} = c_{\varepsilon 1}\frac{P\varepsilon}{k} - c_{\varepsilon 2}\frac{\varepsilon^2}{k} + c_\varepsilon\frac{\partial}{\partial x_k}(\frac{k}{\varepsilon}\overline{u_\ell u_k}\frac{\partial\varepsilon}{\partial x_\ell}) \qquad (5)$$

$$\begin{aligned} U\frac{\partial\overline{u^2}}{\partial x} + V\frac{\partial\overline{u^2}}{\partial r} = {} & -2(1-\alpha)\overline{uv}\frac{\partial U}{\partial r} - \frac{2}{3}\varepsilon - c_1\frac{\varepsilon}{k}\left(\overline{u^2}-\frac{2}{3}k\right) + 2\frac{(\alpha+\beta)}{3}P + \frac{c_s}{r}\frac{\partial}{\partial r}\left[\frac{rk\overline{v^2}}{\varepsilon}\frac{\partial\overline{u^2}}{\partial r}\right] \\ & \boxed{-2(1-\alpha)\overline{u^2}\frac{\partial U}{\partial x} - \beta\left(-2\overline{u^2}\frac{\partial U}{\partial x} - 2\overline{uw}\frac{\partial W}{\partial x}\right) + 2\gamma k\frac{\partial U}{\partial x}} \end{aligned} \tag{6a}$$

$$\begin{aligned} U\frac{\partial\overline{v^2}}{\partial x} + V\frac{\partial\overline{v^2}}{\partial r} - 2\frac{W}{r}\overline{vw} = {} & -2(1-\alpha)\overline{vw}\,\frac{W}{r} - \frac{2}{3}\varepsilon - c_1\frac{\varepsilon}{k}\left(\overline{v^2}-\frac{2}{3}k\right) - \beta\left(-2\overline{uv}\frac{\partial U}{\partial r} - 2\overline{vw}\frac{\partial W}{\partial r}\right) + \frac{2}{3}(\alpha+\beta)P \\ & + \frac{c_s}{r}\frac{\partial}{\partial r}\left[\frac{rk}{\varepsilon}\left(\overline{v^2}\,\frac{\partial\overline{v^2}}{\partial r} - \frac{2\overline{vw})^2}{r}\right)\right] - \frac{2c_s k}{r\varepsilon}\left[\overline{vw}\,\frac{\partial\overline{vw}}{\partial r} + \overline{w^2}\frac{(\overline{v^2}-\overline{w^2})}{r}\right] \\ & \boxed{-2(1-\alpha-\beta)\overline{v^2}\,\frac{\partial V}{\partial r} + 2\gamma k\,\frac{\partial V}{\partial r}} \end{aligned} \tag{6b}$$

$$\begin{aligned} U\frac{\partial\overline{w^2}}{\partial x} + V\frac{\partial\overline{w^2}}{\partial r} + 2\frac{W}{r}\overline{vw} = {} & -2(1-\alpha)\overline{vw}\,\frac{\partial W}{\partial r} - \frac{2}{3}\varepsilon - c_1\frac{\varepsilon}{k}\left(\overline{w^2}-\frac{2}{3}k\right) - \beta 2\overline{vw}\frac{W}{r} + \frac{2}{3}(\alpha+\beta)P \\ & + \frac{c_s}{r}\frac{\partial}{\partial r}\left[\frac{rk}{\varepsilon}\left(\overline{v^2}\,\frac{\partial\overline{w^2}}{\partial r} + 2\frac{(\overline{vw})^2}{r}\right)\right] + 2\frac{c_s k}{r\varepsilon}\left[\overline{vw}\,\frac{\partial\overline{vw}}{\partial r} + \frac{\overline{w^2}(\overline{v^2}-\overline{w^2})}{r}\right] \\ & \boxed{-2(1-\alpha)\left(\overline{uw}\,\frac{\partial W}{\partial x} + \overline{w^2}\frac{V}{r}\right) + 2\beta w^2\,\frac{V}{r} + 2\gamma k\frac{V}{r}} \end{aligned} \tag{6c}$$

$$\begin{aligned} U\frac{\partial\overline{uv}}{\partial x} + V\frac{\partial\overline{uv}}{\partial r} - \frac{\overline{uw}W}{r} = {} & -(1-\alpha)\overline{v^2}\,\frac{\partial U}{\partial r} - c_1\varepsilon\frac{\overline{uv}}{k} - \beta\left(-\overline{u^2}\,\frac{\partial U}{\partial r} - \overline{uw}\,\frac{\partial W}{\partial r}\right) + \gamma k\frac{\partial U}{\partial r} + \frac{c_s}{r}\frac{\partial}{\partial r}\left[\frac{rk}{\varepsilon}\left(\overline{v^2}\,\frac{\partial\overline{uv}}{\partial r} - \frac{\overline{vw}\,\overline{uw}}{r}\right)\right] \\ & - \frac{c_s k}{r\varepsilon}\left[\overline{vw}\,\frac{\partial\overline{uw}}{\partial r} + \overline{w^2}\,\frac{\overline{uv}}{r}\right] + \boxed{(1-\alpha)\left(\overline{uv}\,\frac{V}{r} + \overline{uw}\,\frac{W}{r}\right) - \beta\overline{uv}\,\frac{V}{r} - \overline{vw}\,\frac{\partial W}{\partial x}} \end{aligned} \tag{6d}$$

$$\begin{aligned} U\frac{\partial\overline{vw}}{\partial x} + V\frac{\partial\overline{vw}}{\partial r} + (\overline{v^2}-\overline{w^2})\frac{W}{r} = {} & -(1-\alpha)\left(\overline{v^2}\,\frac{\partial W}{\partial r} - \overline{w^2}\frac{W}{r}\right) - c_1\varepsilon\frac{\overline{vw}}{k} - \beta\left(\frac{\overline{v^2}W}{r} - \overline{uw}\,\frac{\partial U}{\partial r} - \overline{w^2}\,\frac{\partial W}{\partial r}\right) + \gamma k\left(\frac{\partial W}{\partial r} - \frac{W}{r}\right) \\ & + \frac{c_s}{r}\frac{\partial}{\partial r}\left[\frac{rk}{\varepsilon}\left(\overline{v^2}\,\frac{\partial\overline{vw}}{\partial r} + \overline{vw}\frac{(\overline{v^2}-\overline{w^2})}{r}\right)\right] + \frac{c_s k}{r\varepsilon}\left[\overline{vw}\,\frac{\partial}{\partial r}\,(\overline{v^2}-\overline{w^2}) - 4\overline{w^2}\,\frac{\overline{vw}}{r}\right] \\ & \boxed{-(1-\alpha)\left(\overline{uv}\,\frac{\partial W}{\partial x} - \overline{vw}\,\frac{\partial U}{\partial x}\right) - \beta\overline{vw}\,\frac{\partial U}{\partial x}} \end{aligned} \tag{6e}$$

$$\begin{aligned} U\frac{\partial\overline{uw}}{\partial x} + V\frac{\partial\overline{uw}}{\partial r} + \frac{\overline{uv}W}{r} = {} & -(1-\alpha)\left(\overline{uv}\,\frac{\partial W}{\partial r} + \overline{vw}\,\frac{\partial U}{\partial r}\right) - c_1\varepsilon\frac{\overline{uw}}{k} - \beta\overline{uv}\,\frac{W}{r} + \frac{c_s}{r}\frac{\partial}{\partial r}\left[\frac{k}{\varepsilon}\left(\overline{v^2}\,\frac{\partial\overline{uw}}{\partial r} + \frac{\overline{vw}\,\overline{uv}}{r}\right)\right] \\ & + \frac{c_s k}{r\varepsilon}\left[\overline{vw}\,\frac{\partial\overline{v^2}}{\partial r} - \overline{w^2}\,\frac{\overline{uw}}{r}\right] \boxed{-(1-\alpha)\left(\overline{u^2}\,\frac{\partial W}{\partial x} + \overline{uw}\,\frac{\partial V}{\partial r}\right) - \beta\left(\overline{uw}\,\frac{\partial V}{\partial r} - \overline{w^2}\,\frac{\partial W}{\partial x}\right) + \gamma k\,\frac{\partial W}{\partial x}} \end{aligned} \tag{6f}$$

Table 1: Stress Transport Equations for Axisymmetric Thin Shear Flows with Swirl

The model contains six coefficients that are assigned constant values as follows:

c_1	c_2	c_s[1]	(c_s')	$c_{\varepsilon 1}$	$c_{\varepsilon 2}$	c_ε
1.5	0.4	0.22	0.11	1.45	1.90	0.18

Transformation of Equations (1), (2) and (4) to the case of axisymmetric thin shear flows enables the stress-transport equations to be written in the form shown in Table 1[2]. The terms contained in the broken-line boxes are the nominally second-order generation and pseudo-generation terms, the latter arising from the modeling of the mean-strain part of the pressure-strain correlation. These terms exert most effect on the turbulence structure near the axis since they remain finite there while the primary generation terms vanish. The equations also contain convection terms of a type not present in Cartesian coordinates. These need to be retained as they are similar in form to the primary production terms. Indeed in the $\overline{uv}$ equation when swirl is present the "additional" convection term $\overline{uv}W/r$ is usually the largest term appearing.

The diffusion processes in all the stress equations except that for $\overline{u^2}$ contain two types of terms: one of gradient type and the other of source-term form. Since the turbulent shear stresses $\overline{uv}$ and $\overline{uw}$ vary linearly with radius near the axis both the gradient and the source contributions to the diffusion tend to infinity as the axis is approached. They are of opposite sign, however, and their difference in fact goes to zero.

The dissipation rate transport equation for an axisymmetric thin shear flow takes the form:

$$U\frac{\partial \varepsilon}{\partial x} + V\frac{\partial \varepsilon}{\partial r} = c_{\varepsilon 1}\frac{\varepsilon}{k}P - c_{\varepsilon 2}\frac{\varepsilon^2}{k} + \frac{c_\varepsilon}{r}\frac{\partial}{\partial r}\left[\frac{rk\overline{v^2}}{\varepsilon}\frac{\partial \varepsilon}{\partial r}\right] \qquad (7)$$

Finally, the momentum and continuity equations for this class of flows may be written:

$$\frac{\partial U}{\partial x} + \frac{\partial V}{\partial r} + \frac{V}{r} = 0 \qquad (8)$$

$$U\frac{\partial U}{\partial x} + V\frac{\partial U}{\partial r} = -\frac{1}{r}\frac{\partial}{\partial r}(r\overline{uv}) - \frac{\partial}{\partial x}\left(\frac{P_o}{\rho} + \overline{v_o^2}\right) - \frac{\partial}{\partial x}\int_{r_o}^{r}\frac{[W^2+(\overline{w^2}-\overline{v^2})]}{r}\,dr \; \boxed{-\frac{\partial}{\partial x}(\overline{u^2}-\overline{v^2})} \qquad (9a)$$

$$U\frac{\partial W}{\partial x} + V\frac{\partial W}{\partial r} + \frac{VW}{r} = -\frac{1}{r}\frac{\partial}{\partial r}(r\overline{vw}) - \frac{\overline{vw}}{r} \; \boxed{-\frac{\partial \overline{uw}}{\partial x}} \qquad (9b)$$

It should be noted that P, the turbulence energy production rate appearing in Equations (6) and (7), will differ slightly according to whether or not the secondary generation terms are included. In all cases P is half the sum of the generation rates in the $\overline{u^2}$, $\overline{v^2}$ and $\overline{w^2}$ equations.

Solutions of the Equations

The well-known finite-difference procedure of Patankar and Spalding [11] formed the basis of the numerical solution scheme. The application of this method to the treatment of axisymmetric flows with a second-order closure is not straightforward, however. The difficulties had been recognized (but not overcome) by Rodi [10] and occupied many months in the present study before a fully satisfactory treatment was devised.

The problems arose chiefly from the fact the method of [11] adopts a dimensionless stream function ω as cross-stream variable. Variables such as $\overline{uv}$ and $\overline{uw}$ vary linearly with r near the axis and hence as $\omega^{1/2}$, which conflicts with the implied linear internodal variation built into the numerical procedure. Further problems were associated with achieving equality of $\overline{v^2}$ and $\overline{w^2}$ at the axis and the inclusion of the secondary generation terms. Morse [14] provides a detailed discussion of the numerical treatment. The following summary should, however, suffice to allow anyone familiar with the basic numerical scheme to introduce the appropriate modifications.

1. Dependent variables whose value goes to zero at the axis are multiplied by a power of radius so that they approach constant values as $r \to 0$. Thus quantities such as $\overline{uv}$ which vary linearly with radius are replaced by $\overline{uv}/r$ while $\overline{vw}$ which varies as r^2 is replaced by $\overline{vw}/r^2$. Due to the non-standard form of these equations, the diffusion coefficients appearing in the finite difference approximations involve ratios of the radii of the grid nodes and the adjacent control-volume faces.
2. The only satisfactory method found to ensure the exact equality of $\overline{v^2}$ and $\overline{w^2}$ on the axis was to solve an equation for $(\overline{w^2}-\overline{v^2})$; the equation was transformed as indicated above so that $(\overline{w^2}-\overline{v^2})/r^2$ was the operand of the diffusion term. The individual normal stresses were obtained by solving equations for $\overline{u^2}$ and for the turbulence kinetic energy, k; these were of standard form and presented no difficulties.
3. The secondary source terms required the finite-difference approximation of the axial mean velocity gradient. This was obtained by assuming the profile to be of the same non-dimensional shape at the upstream and downstream ends of a forward step. In this way $\partial U/\partial x$ could be expressed in terms of the radial variation of U, the spreading rate of the shear flow and the velocity changes at the flow boundaries. The profile of radial velocity (which ordinarily never appears in the Patankar-Spalding procedure) may then be obtained from the continuity equation. The assumption of profile similarity in computing $\partial U/\partial x$ does not, it

---

[1] In fact the value of c_s was published as 0.25 in error rather than 0.21. The value 0.22 was arrived at by Morse [14] from an independent optimization.

[2] Morse [14] gives the more general set appropriate to non-axisymmetric elliptic flows in cylindrical polar coordinates.

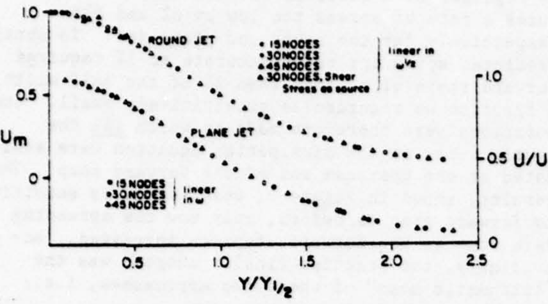

Figure 1: Exploration of grid dependence and technique for handling shear stress in momentum equation equation.

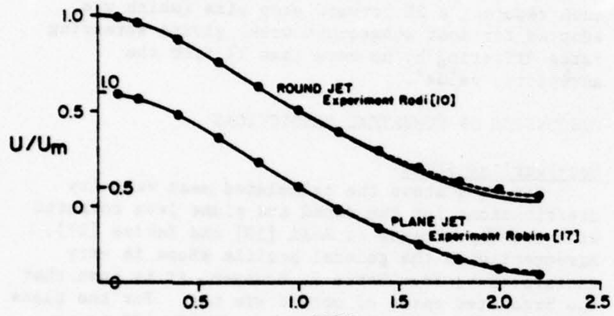

Figure 3: Predictions of velocity profile in round and plane jet. ——— usual thin shear flow form; - - - - including secondary production terms.

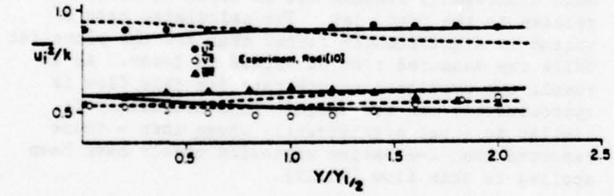

Figure 4: Normal stress profiles in round jet. ——— usual thin shear flow form; - - - including secondary production terms.

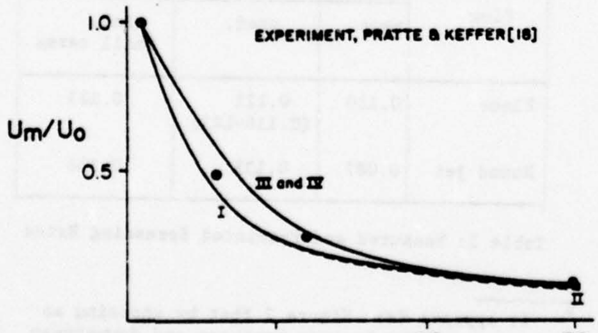

Figure 5: Decay of center-line velocity in swirling jet in stagnant surroundings. I: usual thin shear flow form; II: including secondary production, effect of $\overline{uw}$ excluded; III: including $\overline{uw}$; IV: including secondary effects in momentum equations.

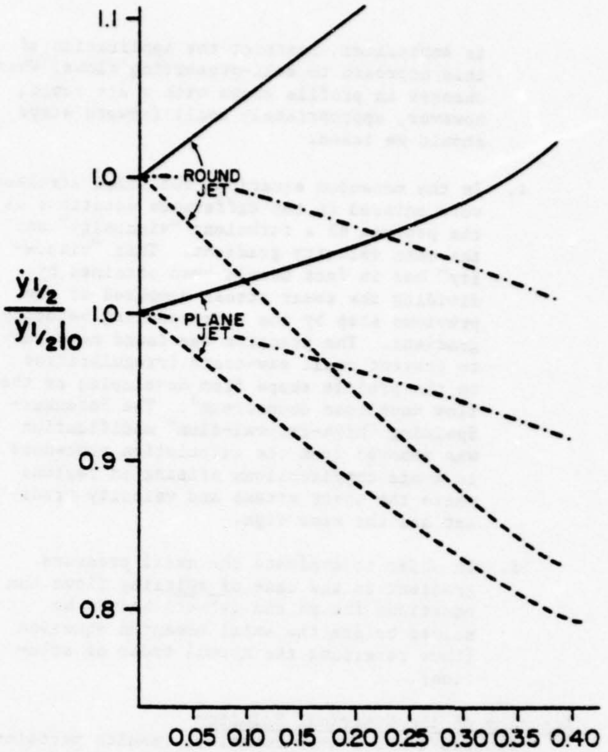

Figure 2: Dependence of spreading rate on source-term treatment in dissipation equations. - - semi-implicit (linearized) sources; ——— upstream sources; —·—·— "arithmetic mean" treatment.

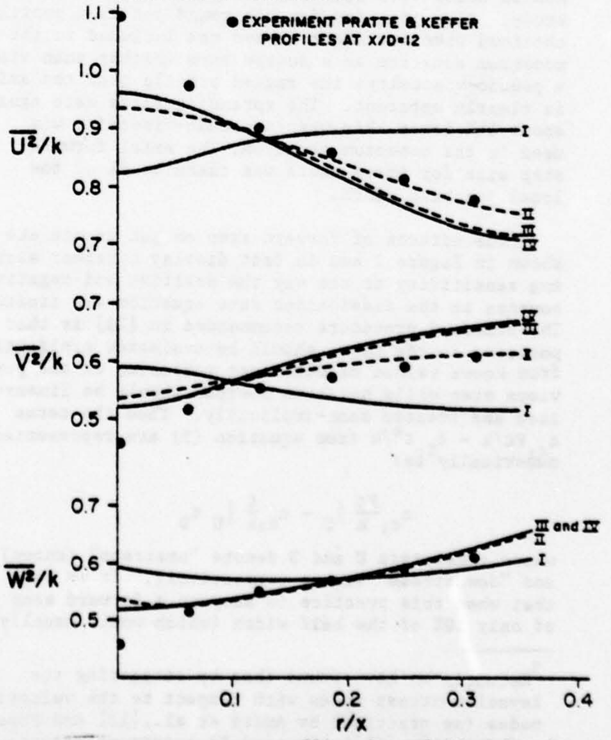

Figure 6: Normal stress profiles in swirling jet in stagnant surroundings; x/D = 12. For legend see Figure 5.

is emphasized, restrict the application of this approach to self-preserving flows. Where changes in profile shape with x are rapid, however, appropriately small forward steps should be taken.

4. In the momentum equations the shear stresses were entered in the difference equations as the product of a turbulent "viscosity" and the mean velocity gradient. This "viscosity" had in fact merely been obtained by dividing the shear stress computed at the previous step by the corresponding velocity gradient. The practice was found necessary to prevent small saw-tooth irregularities in the profile shape from developing as the flow developed downstream[3]. The Patankar-Spalding "high-lateral-flux" modification was removed from the calculation procedure to avoid complications arising in regions where the shear stress and velocity gradient had the same sign.

5. In order to evaluate the axial pressure gradient in the case of swirling flows the equations for rW and $(\overline{w^2}-\overline{v^2})$ had to be solved before the axial momentum equation (thus reversing the normal order of solution).

Accuracy of the Numerical Solution

Figures 1 and 2 show numerical results pertaining to the fully-developed region of the axisymmetric and plane jets in stagnant surroundings. From Figure 1 the implied profile shapes for 15, 30 and 45 cross-stream nodes are scarcely distinguishable. The calculated spreading rates were however about 1½% lower with 15 nodes than for 30 or 45 nodes; for this reason 30 nodes were selected for the main part of the study. Also included for the round jet is a profile obtained when the shear stress was included in the momentum equation as a source term (rather than via a pseudo-viscosity; the ragged profile near the axis is clearly apparent. The spreading rates were again about 1½% lower than when a pseudo-viscosity was used in the momentum equation. The axial forward step size for these tests was taken as 5% of the local jet half width.

The effects of forward step on jet growth are shown in Figure 2 and in fact display a rather alarming sensitivity to the way the positive and negative sources in the dissipation rate equation are treated. The standard procedure recommended in [11] is that positive source terms should be evaluated explicitly from known values of dependent variables at the previous step while negative sources should be linearized and treated semi-implicitly. Thus the terms $c_{\varepsilon_1} P\varepsilon/k - c_{\varepsilon_2} \varepsilon^2/k$ from equation (5) are represented numerically as:

$$c_{\varepsilon_1} \frac{P\varepsilon}{k}\Big|_U - c_{\varepsilon_2} \frac{\varepsilon}{k}\Big|_U \varepsilon_D \qquad (10)$$

where subscripts U and D denote "upstream" (known) and "downstream" values respectively. It is seen that when this practice is adopted a forward step of only 10% of the half width (which would usually be regarded as a cautious forward step size) produces a rate of spread too low by 8% and 6½% respectively for the round and plane jet. To obtain predicted spreading rates accurate to 1% required forward steps of no more than 2% of the half width - a fraction we regarded as prohibitively small. Computations were therefore made in which all the source terms in the dissipation equation were evaluated at the upstream end of the forward step. The results, shown in Figure 2, were nearly as sensitive to forward step as before, only now the spreading rate rose as the forward step was increased. Accordingly, the practice finally adopted was the "arithmetic mean" of these two approaches, i.e.:

$$c_{\varepsilon_1} \frac{P\varepsilon}{k}\Big|_U - \frac{1}{2} c_{\varepsilon_2} \frac{\varepsilon}{k}\Big|_U (\varepsilon_U + \varepsilon_D) \qquad (11)$$

Clearly with this formulation the sensitivity is much reduced, a 5% forward step size (which was adopted for most subsequent work) giving spreading rates differing by no more than 1% from the asymptotic value[4].

DISCUSSION OF NUMERICAL PREDICTIONS

Non-Swirling Flows

Figure 3 shows the calculated mean velocity distributions for the round and plane jets compared with the experiments of Rodi [10] and Robins [17]. Agreement with the general profile shape is very satisfactory; from Table 2, however, it is seen that the predicted rates of spread are not. For the plane jet the rate of spread is approximately 10% higher than the mean of experimental values for this flow. The slightly higher numerical value obtained in the present study than in the LRR work seems to be due to the larger forward steps taken in the latter. The main discrepancy brought out in Table 2, however, relates to the round jet. The calculated rate of spread is significantly larger than for the plane jet while the measured rate of spread is lower. As a result the predicted growth rate for this flow is approximately 50% too large! This deficiency is similar to - but significantly worse than - those reported when 2-equation viscosity models have been applied to this flow [9, 10].

Flow	$dy_{1/2}/dx$		
	meas.	pred.	inc. small terms
Plane	0.110	0.123 (0.116-LRR)	0.123
Round jet	0.087	0.135	0.136

Table 2: Measured and Predicted Spreading Rates

---

[3] Recently we have found that by staggering the Reynolds-stress nodes with respect to the velocity nodes (as practised by André et al.,[15] and Pope and Whitelaw [16]) the need to construct pseudo-viscosities is avoided.

[4] It appears from Figure 2 that by choosing an unequal weighting between upstream and downstream values of ε the sensitivity could be reduced substantially further. This was not done in the present work, however, for there appears no guarantee that the same fractional weighting would be the best one for all flows.

There seemed little hope that such a large discrepancy could be attributable to secondary strain effects. Nevertheless all the non-zero secondary terms in the stress and dissipation equations were added to the numerical solution. The results are indicated by the broken line in Figure 3 and by the right hand column in Table 2: such small effect as there is on the rate of spread is in fact in the wrong direction. The normal-stress terms appearing in the mean momentum equations were also included and likewise caused negligible effects on the growth rates.

Next, a comprehensive study was made of the sensitivity of the predictions to each of the turbulence-model coefficients. The results are summarized in Table 3. The entries show the percentage change in rate of spread brought about by raising the value of the indicated coefficient by 10% with the remainder held at their standard value. For this comparison the plane mixing layer in stagnant surroundings has also been included, the entries in the table indicating the percentage change in the width characterized by locations where the mean velocity was 90% and 10% of that of the external stream. For this flow predictions with the standard constants are in satisfactory agreement with measurement.

Flow	c_1	c_2	c_s	c_{ε_1}	c_{ε_2}	c_ε
Round jet	-9.4	-4.9	-8.2	-28.6	+52.0	-0.2
Plane jet	-5.8	-4.2	-3.3	-32.6	+43.8	-0.3
Mixing jet	-5.5	-4.8	-0.2	-32.1	+31.5	-1.7

Table 3: Percentage Response of Rate of Spread to 10% Increase in Turbulence Model Coefficient

Broadly, the dissipation sources control the magnitude of turbulence energy and thus the associated coefficients exert considerable influence on the rate of spread. The pressure-strain coefficients c_1 and c_2 affect the destruction and generation of shear stress but are not as influential as the dissipation-source coefficients. The diffusion coefficients mainly change the shape of the calculated profiles. The table suggests that a reoptimization of the coefficients could not foreseeably enable all three flows to be predicted correctly for the effects of changing each coefficient are of similar magnitude in the different flows. The coefficient c_s produces an unexpectedly large effect in the round jet, but significant variations in this quantity produce large distortions to the shear stress and, hence, to the velocity profile.

The non-dimensional profiles of the Reynolds normal stresses for the round jet are shown in Figure 4. Here the effect of the secondary generation term is more pronounced raising the levels of streamwise fluctuations on the axis and reducing the other two components. Agreement with the experimental profiles is somewhat worse for the case where the secondary strains are included, though considering experimental uncertainties the agreement is probably satisfactory. The distributions of these normalized stress profiles is scarcely altered by changes in the source-term coefficients in the dissipation equation. We may thus conclude that the defects in the prediction of the round jet stem principally from the source-term model in the dissipation equation rather than from the approximations used for the pressure-strain or diffusion processes.

Swirling Flows

The first computations made of swirling flows attempted a simulation of the swirling jet in stagnant surroundings studied by Pratte and Keffer [18]. Although these authors report initial profiles of all six Reynolds-stress components, their initial shear stress measurements displayed what appeared to be a number of spurious features. For this reason the initial profiles of $\overline{uw}$ and $\overline{vw}$ were estimated from the mean strain field by application of the following turbulent viscosity formula:

$$\mu_t = 0.06\,\rho k^{\frac{1}{2}} r_{\frac{1}{2}} \qquad (12)$$

The resultant profiles of $\overline{uv}$ and $\overline{vw}$ were roughly in accord with the reported data.

At first only the primary-generation terms were included and we did not account for the effects of the third component of shear stress, $\overline{uw}$. The resultant decay of axial velocity shown as curve I in Figure 5 is in fairly close agreement with the experiment. It must be remembered, however, that in the absence of swirl the predicted rate of spread of the jet was 50% too large. The relatively close agreement shown in Figure 5 is therefore a manifestation of a further <u>weakness</u> in the model: the failure to display the strong effect of swirl on the rate of spread that experiments unmistakably indicate. The "small" terms, hitherto omitted, were then included in three stages: first, secondary generation terms in the stress equations were added - but excluding any term containing $\overline{uw}$ (II); next all terms in which $\overline{uw}$ appeared were also included (III); finally the secondary terms in the mean momentum equations were added (IV). The effects of including these terms are shown in Figures 5 and 6, the curves being labelled as indicated above. From these comparisons it emerges that:

(i) The first group of secondary-generation terms produces only a very minor effect on the rate of decay of the jet. They do however have a significant and beneficial effect on the prediction of the non-dimensional normal-stress profiles shown in Figure 6.

(ii) The introduction of the $\overline{uw}$ equation has a dramatic effect on the decay of the jet in the initial region, the mean rate of decrease of center-line velocity being reduced by 40%! There are also changes produced, again generally beneficial, in the normal stress profiles.

The main cause of the slower decay for III is the appearance in the $\overline{uv}$ equation (eq(6d)) of the term $(1-\alpha)\overline{uw}W/r$ on the right side of the equation and (especially) the extra convection term $-\overline{uw}W/r$ on the left. The calculated values of $\overline{uw}$ are predominantly negative; thus, since $\overline{uv}$ is positive, the extra terms act to reduce the magnitude of this shear stress and thus to delay the rate of decay of mean velocity.

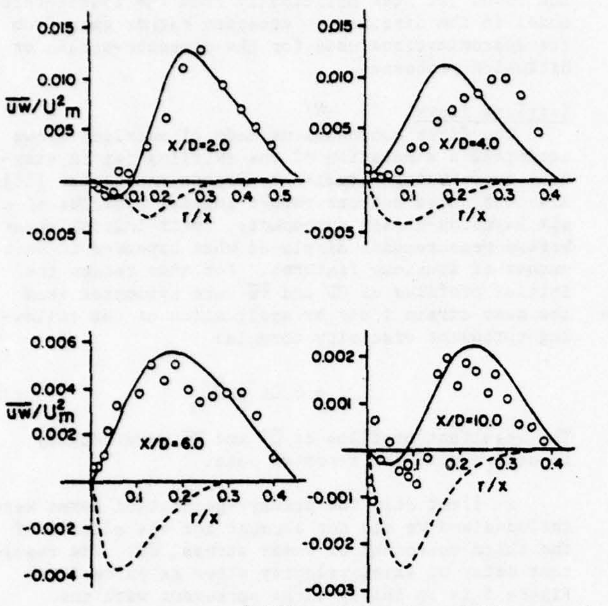

Figure 7: Development of $\overline{uw}$ profiles in swirling jet in stagnant surroundings: ---- prediction, standard form for ϕ_{ij}; —— prediction with mean-strain contribution to ϕ_{ij} for $\overline{uw}$ and $\overline{vw}$ reduced by 60%; o o experiment, Morse [14]

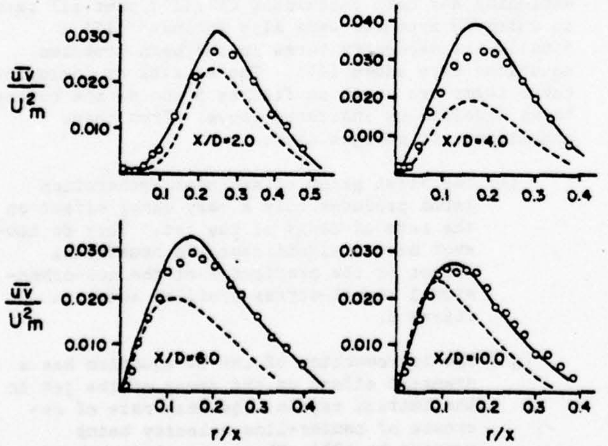

Figure 8: Development of $\overline{uv}$ profiles in swirling jet in stagnant surroundings; for legend see Fig. 7.

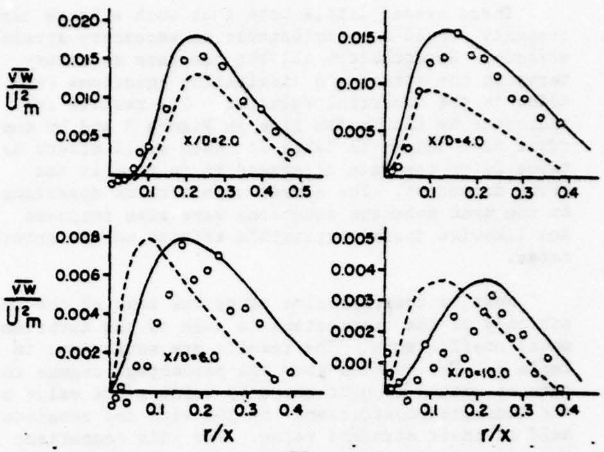

Figure 9: Development of $\overline{vw}$ profiles in swirling jet in stagnant surroundings; for legend see Fig. 7.

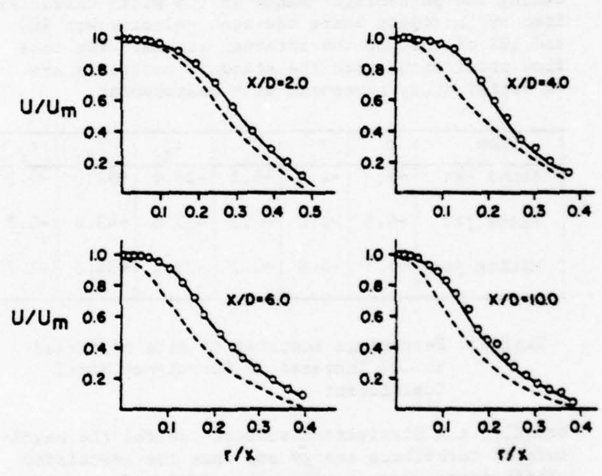

Figure 10: Development of axial velocity profile in swirling jet in stagnant surroundings; for legend see Fig. 7.

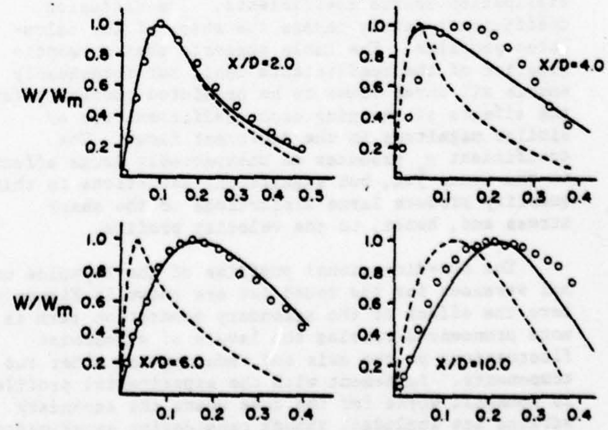

Figure 11: Development of circumferential velocity profile in swirling jet in stagnant surroundings; for legend see Fig. 7.

Here we should mention that in practice the action of $\overline{uw}$ is opposite from that indicated by the above predictions. The values of this correlation are found from measurements [14, 18] to be large and positive. Thus the secondary generation in fact makes $\overline{uv}$ larger, promoting a faster rate of decay in swirling jets than in non-swirling ones. Several workers have proposed computational schemes for swirling flows in which agreement with the observed effects on the spreading rate is secured by making the quantity $c_{\varepsilon 1}$ or $c_{\varepsilon 2}$ (or their counterparts in some other quasi-length-scale equation) dependent on the level of swirl [19, 20]. In view of the above results however we can see that this practice is physically very wide of the mark. The real sources of the poor agreement are (i) the great sensitivity of the $\overline{uv}$ correlation to the presence of swirling velocities (that cannot, in any event, be adequately represented in terms of an effective viscosity), coupled with (ii) the failure of the present model to give realistic values of the $\overline{uw}$ correlation.

Evidently a major re-think is needed in modeling the mean-strain contribution to the pressure-strain correlation. The present work has not produced any general proposals. It has, however, explored the effects of various modifications to the original stress closure an example of which is displayed in Figures 7-11. The experimental data are those obtained by Morse [14]; besides mean axial and swirl velocities, all six Reynolds stress components were measured. Only the shear-stress components are shown here however for it is these which exert direct effect on the mean flow. The computations began at $x/D = 0.5$ where a complete set of initial profiles was provided. Two sets of predictions are shown: the broken lines indicate predictions obtained with essentially the model presented in Section 2; the solid lines are those which result when the mean-strain contribution to Φ_{ij} is reduced by 60% in the $\overline{uw}$ and $\overline{vw}$ equations (by reducing α, β, and γ in these equations). From Figure 7 it is seen that this change entirely alters the character, distribution and sign of $\overline{uw}$, which in turn raises the level of $\overline{uv}$ in much better agreement with the experimental values, Figure 8. The modification to the pressure-strain correlation also significantly improves the profiles of the shear stress $\overline{vw}$ opposing the swirling motion, Figure 9. As a result, the prediction of the spread of the axial and swirling mean velocity field shown in Figures 10 and 11 is generally very satisfactory.

CONCLUDING REMARKS

The present contribution has identified two major weaknesses in the second-order closure of Reference [2] when applied to the prediction of the round jet, with and without swirl. The first, which has previously been commented on or alluded to by a number of workers [2, 16, 10], relates to the modeling of the source terms in the dissipation equation. The physical source of the error is that existing equations, based on local values of turbulence correlations, do not seem able to mirror the inherent time lag between the input of new turbulence energy at low wave numbers and the occurrence of a significant response in the dissipation rate. Although the use, in the ε equation, of the turbulence anisotropy in place of the energy production:dissipation ratio (as proposed by Lumley and Khajeh Nouri [21]) seems physically well founded, our own experiences suggest such a formulation to be even less satisfactory in practice.

The shortcomings of the modeling of the pressure-strain processes emerged only towards the end of the present study when the equation for $\overline{uw}$ was added. Until then it had seemed probable that the dissipation equation was also responsible for the failure to predict swirl effects correctly. In many respects the identification of the failure as due to the pressure-strain model is encouraging. For, rational approximations can be devised for Φ_{ij} and the approximations refined in a systematic way. Lumley [22] has, in fact, proposed a far more elaborate model of mean strain effects than used in the present work. We have hitherto had no reason to adopt it because, on the one hand, the scheme added a large number of additional coefficients that would need to be tuned and, on the other, the simpler scheme proposed in [2] seemed entirely adequate. Now that the latter premise has been swept away it is time to look for more general formulations.

ACKNOWLEDGEMENTS

The research reported above has been supported by the Science Research Council through research grant B/RG/1863. The numerical computations were performed at the University of London and Imperial College Computer Centers. The authors' names are in alphabetical order.

BIBLIOGRAPHIC REFERENCES

1. Hanjalić, K. and Launder, B. E., "A Reynolds Stress Model of Turbulence and Its Application to Thin Shear Flows", Journal of Fluid Mechanics, Vol. 52, 1972, p. 609.

2. Launder, B. E., Reece, G. J., and Rodi, W., "Progress in the Development of a Reynolds Stress Turbulence Closure", Journal of Fluid Mechanics, Vol. 68, 1975, p. 537.

3. Irwin, H. P. A. H. and Arnot-Smith, P., "Prediction of the Effect of Streamline Curvature on Turbulence", Phys. Fluids, Vol. 18, 1975, p. 624.

4. Launder, B. E. and Ying, W. M., "Prediction of Flow and Heat Transfer in Ducts of Square Cross Section", Proc. Inst. Mech. Engrs., London, Vol. 187, 1973, pp. 37-73.

5. Naot, D., Shavit, A., and Wolfshtein, M., "Numerical Calculations of Reynolds Stresses in a Square Duct with Secondary Flow", Wärme-und Stoffübertragung, Vol. 7, 1974, p. 151.

6. Wyngaard, J. C. and Coté, O. R., "The Evolution of a Convective Planetary Boundary Layer - a Higher Order Closure Model Study", Advances in Geophysics, Vol. 18, 1974.

7. Mellor, G., "Analytic Prediction of the Properties of Stratified Boundary Layers", Journal of Atmospheric Science, Vol. 30, 1973, p. 1061.

8. Launder, B. E., "On the Effects of a Gravitational Field on the Turbulent Transport of Heat and Momentum", Journal of Fluid Mechanics, Vol. 67, 1975, p. 569.

9. Rodi, W. and Spalding, D. B., A Two-Parameter Model of Turbulence and Its Application to Free Jets" Wärme-und Stoffübertragung, Vol 3, 1970, p. 85.

10. Rodi, W., "The Prediction of Free Turbulent Boundary Layers by use of a 2-Equation Turbulence Model", Ph.D. Thesis, University of London, 1972.

11. Patankar, S. V. and Spalding, D. B., Heat and Mass Transfer in Boundary Layers, 2nd Edition, Intertext, London, 1970.

12. Bradshaw, P., "The Effects of Streamline Curvature on Turbulent Flow" AGARDograph No. 169, 1973.

13. Daly, B. J. and Harlow, F. H., "Transport Equations of Turbulence", Phys. Fluids, Vol. 13, p. 2634.

14. Morse, A., "Axisymmetric Turbulent Shear Flows With and Without Swirl", Ph.D. Thesis, University of London, 1977.

15. André, J. C., DeMoor, G., Lacarrère, P., and duVachet, R., "Turbulence Approximation for Inhomogeneous Turbulent Flows", Journal of Atmospheric Sciences, Vol. 33, 1976, p. 476.

16. Pope, S. B. and Whitelaw, J. H., "The Calculation of Near-Wake Flows", Journal of Fluid Mechanics, Vol. 73, 1976, p. 9.

17. Robins, A., "The Structure and Development of a Plane Turbulent Jet", Ph.D. Thesis, University of London, 1971.

18. Pratte, B. D. and Keffer, J. F., "The Swirling Turbulent Jet", Trans. ASME J. Basic Eng., Vol. 95, 1973.

19. Koosinlin, M. L. and Lockwood, F. C. "The Prediction of Turbulent Boundary Layers on Rotating Axially-Symmetric Bodies", Imperial College, Mechanical Engr. Rep BL/TN/A/46, 1971.

20. Lilley, D. G., "Prediction of Inert Turbulent Swirl Flows", AIAA J., Vol. II, 1973, p. 955.

21. Lumley, J. L. and Khajeh Nouri, B. J., "Computational Modeling of Turbulent Transport", Adv. in Geophysics, Vol. 18, 1974.

22. Lumley, J. L., "Prediction Methods for Turbulent Flow: Introduction", Von Karman Institute Lecture Series No. 76, 1975.

THEORETICAL STUDY OF THE REYNOLDS STRESS EQUATIONS

by

A. Lin and M. Wolfshtein
Department of Aeronautical Engineering
Technion- Israel Institute of Technology
Haifa, Israel

ABSTRACT

The paper is concerned with the transport equations for the Reynolds stress in incompressible shear flow. The various terms in the equations are analyzed. A new model for the two-point double-velocity correlation tensor is suggested and used to obtain approximations to the pressure interaction and decay terms. The model is applied to the three cases of homogeneous shear flow, accelerating grid turbulence, and irrotational strain. The results show good agreement with experimental data.

NOMENCLATURE

English Symbols

A,B,C,E	Constants in the redistribution.
D_{ij}	Semi-production function tensor.
e_{ij}	Instantaneous rate of strain tensor.
f_i	Isotropic functions in two point correlation.
G	Green function.
k	Turbulence energy.
ℓ	Turbulent length scale.
M_{ij}	Micro-scale tensor.
P_{ij}	Pressure-velocity interaction tensor.
p	Instantaneous pressure.
Q_{ij}	Two-point double-velocity correlation tensor.
$\underset{\sim}{\xi}$, r	Separation vector, separation distance.
$\bar{R}_t$	Reynolds number of turbulence.
S_1, S_2	Source terms in the pressure equation.
S_{ijk}, $S_{i,jk}$	Single-point and two-point triple-velocity correlation tensors.
t	Time
T_{ij}	Turbulent diffusion tensor.
u_i	Instantaneous velocity vector.
U_{ij}	Reynolds stress tensor.
$\underset{\sim}{x}$, x_i	radius vector.

Greek Symbols

α	Dissipation constant.
δ_{ij}	Kronecker delta.
$\varepsilon_{ij}, \varepsilon_{ij_1}, \varepsilon_{ij_2}$	Dissipation tensor.
λ	Microscale.
Λ	Dissipation weighting function.
ν	Kinematic viscosity.
ξ	Normalised separation radius.
ρ	Density.
π_{ij}	Reynolds stress production tensor.
$\theta, \phi_1, \phi_2, \phi_3$	Parameters of pressure-interaction tensor.

Greek Symbols (cont'd)

∇^2_r	Laplacian operator in separation-radius coordinates.

Superscripts

$\bar{(\ )}$	Mean.
$(\ )'$	Fluctuating.

INTRODUCTION

A variety of contemporary turbulence models are based on approximations to the Reynolds stress equations. Such approximations require specification of the triple velocity correlations, the pressure-velocity correlations and the r.m.s. spatial velocity derivatives, which represent turbulent diffusion, redistribution, and dissipation respectively. Wolfshtein et al(1) used two-point double-velocity correlations in order to calculate the redistribution and dissipation. The "quasi-isotropic" model of the two-point correlation(2) was used in the calculations. However, this work suffered from two deficiencies: (i) The quasi-isotropic model cannot satisfy the dynamic equations of the two-point correlation, as this model has three degrees of freedom only.

In the present paper a new model for the two-point correlations is presented, which answers the above deficiencies. This model is used to calculate the redistribution and dissipation of the Reynolds stresses. After some substitutions and manipulations a newer form of the Reynolds stress equations is obtained, and solved for a number of simple cases.

This paper is restricted to stationary, incompressible flow. The triple velocity correlation is not discussed in this paper.

THE REYNOLDS STRESS EQUATION

An exact transport equation for the Reynolds stresses U_{ij} is easily derived(1) and has the following form:

$$\frac{DU_{ij}}{Dt} = \pi_{ij}+T_{ij}+P_{ij}+\varepsilon_{ij} \tag{1}$$

where the terms on the righthand side are:

Production:

$$\pi_{ij} = -\left(U_{ik}\frac{\partial\bar{u}_j}{\partial x_k} + U_{jk}\frac{\partial\bar{u}_i}{\partial x_k}\right) \tag{1a}$$

Turbulent diffusion:

$$T_{ij} = -\frac{\partial}{\partial x_k}\overline{u'_i\, u'_j\, u'_k} \tag{1b}$$

Pressure interaction:

$$P_{ij} = \frac{1}{\rho}\overline{u_i'\frac{\partial p'}{\partial x_j}} + \overline{u_j'\frac{\partial p'}{\partial x_i}} \qquad (1c)$$

Decay:

$$\varepsilon_{ij} = \nu\left(\frac{\partial^2 u_{ij}}{\partial x_k^2} - 2\,\overline{\frac{\partial u_i}{\partial x_k}\,\frac{\partial u_j}{\partial x_k}}\right) \qquad (1d)$$

The pressure interaction is very often split into two terms: The pressure diffusion $\frac{1}{\rho}\left(\frac{\partial}{\partial x_i}\overline{p'u'_j} + \frac{\partial}{\partial x_j}\overline{p'u'_j}\right)$ and the traceless redistribution $\frac{1}{\rho}\overline{p'e_{ij}}$ where e_{ij} is the rate of strain $\partial u_i/\partial x_j + \partial u_j/\partial x_i$. The decay is sometimes called dissipation, although the use of this name is justified only for the trace of ε_{ij}, the dissipation of turbulence energy to thermal energy. The first term on the righthand side of (1d) has the appearance of a diffusion term and is usually added to T_{ij} as laminar diffusion.

It is clear that the production term, π_{ij}, is properly defined to allow its calculation. The diffusion term is difficult to calculate, and is usually assumed to be represented by gradient-like expressions as laminar diffusion. The pressure interaction and the decay terms may be calculated if the two-point double-velocity correlation is known. Indeed the present paper is concerned with a new model for the two-point correlation and its application to the calculation of the decay and pressure interaction.

THE PRESSURE INTERACTION TERM P_{ij}

The pressure-velocity interaction term in the Reynolds stress equations is

$$P_{ij} = \frac{1}{\rho}\left(\overline{u_i'\frac{\partial p'}{\partial x_j}} + \overline{u_j'\frac{\partial p'}{\partial x_i}}\right) \qquad (2)$$

Traditionally this term is split into two parts: (i) a gradient-like part which is referred to as pressure-diffusion, and (ii) a pressure-strain correlation which has no trace, and has therefore been called redistribution. It has already been shown that this splitting is not always useful, and an alternative procedure is to obtain a formal solution to the pressure Poisson equation, which has been discussed in the literature (Chou$^{(3)}$, or Naot et al.$^{(2)}$

$$\frac{1}{\rho}\nabla^2 p = -(S_1 + S_2) \qquad (3)$$

$$S_1 = 2\frac{\partial \bar{u}_k}{\partial x_k}\frac{\partial u_k}{\partial x_\ell}$$

$$S_2 = \frac{\partial^2}{\partial x_k \partial x_\ell}(u_k u_\ell - U_{k\ell})$$

where p and u_i denote the instantaneous pressure and velocity, $\bar{u}$ is the mean velocity, and $U_{k\ell}$ is the single point double velocity correlation. A formal solution of eqn (3) is given by

$$4\pi\frac{p}{\rho} = \iiint_V G\,S_1 dV + \iiint_V G\,S_2 dV \qquad (4)$$

where V is a control volume characterised by zero fluctuations on its envelope, and $G(\underset{\sim}{X}, \underset{\sim}{r})$ is the Green function.

It is clear that S_1 vanishes when the mean velocity gradient vanishes, while S_2 remains finite in all turbulent flows.

An equation for the pressure-velocity correlation may be obtained from eqn (4). Using an $(\underset{\sim}{x}, \underset{\sim}{r})$ coordinate system$^{(4)}$, and applying the Gauss theorem, the following expressions are obtained:

$$P_{ij} = P_{ij_1} + P_{ij_2} + P_{ij_3} + P_{ij_4} \qquad (5)$$

$$P_{ij_1} = -\frac{2}{3}\pi_{ij} \qquad (5a)$$

$$P_{ij_2} = -\frac{1}{2\pi}\iiint_V \frac{\partial \bar{u}_{k_B}}{r_\ell}\left(Q_{j\ell}\frac{\partial^2 G}{\partial r_k \partial r_i} + Q_{i\ell}\frac{\partial^2 G}{\partial r_k \partial r_j}\right)dV \qquad (5b)$$

$$P_{ij_3} = +\frac{1}{3}\left(\frac{\partial S_{ikk}}{\partial x_j} + \frac{\partial S_{jkk}}{\partial x_i}\right. \qquad (5c)$$

$$P_{ij_4} = \frac{1}{4\pi}\iiint_V \left(S_{i,k\ell}\frac{\partial^3 G}{\partial r_k \partial r_\ell \partial r_j} + S_{j,k}\frac{\partial^3 G}{\partial r_k \partial r_\ell \partial r_i}\right)dV \qquad (5d)$$

where $S_{ik\ell}$ and $S_{i,k\ell}$ are single and two points triple velocity correlations and G is the Green's function.

In the above splitting of eqn (5) into terms no distinction is made between pressure diffusion and redistribution. This practice follows Neot et al$^{(2)}$. However, the model of eqn (5) recommended by Neot et al could not account for the pressure diffusion, as all the terms in the model did not have any trace. This deficiency will be removed in the present paper.

Another conventional classification of eqn (5) is obtained by noting that the terms P_{ij_1} and P_{ij_2} contain mean velocity gradients. Therefore they must vanish in homogeneous flows, and have been called forced interaction. On the other hand, P_{ij_3} and P_{ij_4} do not contain mean velocity gradients and may be finite even in homogeneous flows. They have been called free or natural interaction.

Classification of the terms in P_{ij} is easy. Thus P_{ij_1} is proportional to the Reynolds stress generation, π_{ij}, which is a given function of the Reynolds stresses and velocity gradients. Such a term was present in earlier models as well$^{(2,5)}$, yet in the present formulation this term is exact.

The second term, P_{ij_2}, is a volume integral of the two-point correlations. This term will be estimated in the following section of the paper. The third part, P_{ij_3} is a spatial derivative of the triple velocity correlations. Evidently, similar terms constitute the turbulent diffusion of the Reynolds stresses, and this term constitutes the pressure-diffusion.

Finally, P_{ij_4} is a volume integral of the triple-velocity two-point correlation. This term may be approached in two ways. Firstly, examination of P_{ij_4} suggests that it is related to the single-point triple-velocity correlations, and must therefore be considered as additional pressure diffusion. Another approach is to substitute a model for the two-point triple-velocity correlation in eqn (5d). If the homogeneous isotropic model is used, the following expression is obtained:

$$P_{ij_4} = -2\left(\frac{2k}{3}\right)^{3/2}\delta_{ij}\int_0^\infty \frac{1}{r}\,\frac{dh}{dr}\,dr \qquad (6)$$

where h is the isotropic homogeneous triple velocity correlation function and r is the separation distance. Eqn (6) suggests that P_{ij_4} has a component of the form $\delta_{ij}k^{3/2}/\ell$ which represents isotropic dissipation.

In summary it may be assumed that P_{ij_4} may be divided into dissipation and diffusion terms, of the form

$$P_{ij_4} = P_{ij_{41}} + P_{ij_{42}} \tag{7}$$

$$P_{ij_{41}} = -\Lambda_1 \frac{\nu k}{\lambda^2}(1 + \alpha_2 R_t) \tag{7a}$$

where Λ_1 and α_2 are constants, λ is the length scale of the turbulence, $R_t = \sqrt{k}\ \lambda/\nu$, and $P_{ij_{42}}$ is a diffusion like term.

THE TWO-POINT CORRELATION

As was mentioned above, P_{ij_2} may be calculated by substitution of a suitable expression for the two two-point double-velocity correlation in eqn (5b). Thus, Rotta[6] used the isotropic homogeneous two-point correlation while Naot et al[7] used the quasi-isotropic model. The latter model was based on the assumption of local isotropy, and required the prescription of three arbitrary scalar functions in order to determine the two-point correlation tensor. Yet, even if symmetry of the tensor is assumed, the six differential equations governing the two-point correlation must be satisfied. Moreover, the assumption of local isotropy does not seem justified in shear layers, especially near solid walls. The above two deficiencies were removed in the present research by the development of a now two-point correlation model, based on the following assumptions:

(i) The two-point double-velocity correlation tensor, Q_{ij}, is dependent on the Reynolds stresses at the two points, U_{ij_A} and U_{ij_B}

(ii) The two points "A" and "B" are of equal importance.

(iii) Q_{ij} is a linear function of U_{ij_A}, U_{ij_B}, and $U_{ij_A}\,U_{k\ell_B}$. It follows that

$$Q_{ij}(\underline{x},\ \underline{r}) = \frac{3}{2k} U_{rs}(\underline{x})\, U_{p_t}(\underline{x}+\underline{r}) \cdot g_{rsptij}(\underline{x}, \underline{r}) \tag{8}$$

(iv) The sixth order tensor relating Q_{ij} to U_{ij} is isotropic and its components depend on the generalized distance $\xi = r\sqrt{1+\alpha R_t}$ where α is a constant. This form of ξ is so chosen as to yield the proper asymptotic behaviour of the dissipation.

Applying all of the above assumptions Q_{ij} is given by

$$Q_{ij}(\underline{x},\ \underline{r}) = \frac{1}{\frac{2}{3}k}(U_{ij_A}k_B + U_{ij_B}k_A)f_1$$

$$+ \frac{1}{\frac{2}{3}k}(U_{mn_A}e_m e_n k_B e_i e_j + U_{mn_B}e_m e_n k_A e_i e_j)f_2$$

$$+ \frac{1}{\frac{2}{3}k}(U_{mn_A}e_m e_n k_B + U_{mn_B}e_m e_n k_A)f_3\ \delta_{ij}$$

$$+ \frac{1}{\frac{2}{3}k}(U_{im_A}k_B e_m e_j + U_{im_B}k_A e_m e_j + U_{jm_A}k_B e_m e_i + U_{jm_B}k_A e_m e_i)f_4$$

$$+ \frac{1}{\frac{2}{3}k}\ k_A k_B\ e_i e_j\ f_5$$

$$+ \frac{1}{\frac{2}{3}k}\ k_A k_B\ \delta_{ij}\ f_6$$

$$+ \frac{1}{\frac{2}{3}k}(U_{ij_A}e_m e_n U_{mn_B} + U_{ij_B}U_{mn_q}e_m e_n)f_7$$

$$+ \frac{1}{\frac{2}{3}k}U_{mn_A}e_m e_n U_{pq_B}e_p e_q e_i e_j\ f_8$$

$$+ \frac{1}{\frac{2}{3}k}U_{mn_A}e_m e_n U_{pq_b}e_p e_q\ f_9\ \delta_{ij}$$

$$+ \frac{1}{\frac{2}{3}k}[(U_{im_A}e_m e_j + U_{jm_A}e_m e_i)U_{pq_B}e_p e_q + (U_{im_B}e_m e_i)U_{mn_A}e_m e_n]f_{10}$$

$$+ \frac{1}{k}[U_{im_A}\ U_{mj_B} + U_{jm_A}]f_{11}$$

$$+ \frac{1}{k}[U_{mp_A}U_{mq_B} + U_{mp_B}U_{mq_A}]e_p e_q e_i e_i\ f_{12}$$

$$\frac{1}{k}[U_{mp_A}U_{mq_B}]\ \delta_{ij}\ e_p e_q\ f_{13}$$

$$+ \frac{1}{k}(U_{im_A}U_{mj_B} + U_{im_B}\ U_{mj_A})f_{14}$$

$$\frac{1}{k}[U_{im_A}U_{mp_B}e_p e_j + U_{jm_B}U_{mp_A}e_p e_i)f_{15} \tag{9}$$

Kinematic conditions for Q_{ij} may be obtained by its differentiation, and application of the continuity equation. The following relations between the f-functions are obtained:

$$\frac{d}{dr}(f_2+f_3+f_4) = \frac{1}{r}(f_2+2f_3+f_4)$$

$$\frac{d}{dr}(f_1 + f_4) = -\frac{1}{r}(2f_3 + f_4)$$

$$\frac{d}{dr}(f_5 + f_6) = -\frac{1}{r}f_4$$

$$\frac{d}{dr}(f_{11}\qquad) = -\frac{2}{r}(f_7+f_{13}) \tag{9a}$$

$$\frac{d}{dr}(f_7 + f_{10}) = \frac{2}{r}(f_7 - f_9)$$

$$\frac{d}{dr}(f_8+2f_{10}+f_9) = \frac{4}{r}(2f_{10}+f_9)$$

$$\frac{d}{dr}(f_{12}+f_{13}) = \frac{1}{r}(2f_{13}-3f_{10})$$

$$\frac{d}{dr}(f_{15}) \qquad = 0$$

The f_i-functions are dependent on the generalised coordinate ξ only. They must satisfy the following boundary conditions:

$$f_1(0)=1$$

$$f_2(0)=f_3(0)=\ldots\ldots=f_{14}(0)=0$$

$$f_1(\infty)=f_2(\infty)=\ldots\ldots=f_{14}(\infty)=0$$

Unlike the quasi-isotropic model, the present model is not isotropic, and may be used even in the immediate vicinity of solid walls.

FINAL EXPRESSION FOR P_{ij_2}

Substitution of the expression for Q_{ij}, eqn (9) into eqn (5b) allows calculation of P_{ij_2}, provided that the Green Function "G" as well as the distribution of the mean velocity and the Reynolds stress around the central point "A" is known. The Green function for regions remote from solid walls may be taken as 1/r where r is the separation distance between the points A and B. When the point A approaches the wall (and the macro scale is large compared to the distance from the wall) a "wall-Green-function" should be used defined as

$$G = \frac{1}{r} - \frac{1}{r^*} \qquad (10)$$

where r^* is the separation distance between B and the mirror immage of A. Yet, such formulations will not be discussed in the present paper.

The substitution in eqn (5b) still requires the Reynolds stress and velocity gradient distribution. These may be obtained by Taylor series expansion. Very often, one or two terms in the expansion are sufficient (when the macro-scale is small compared to the scale of the mean velocity). If the first term in the expansion is taken (this implies that Q_{ij} and the velocity gradient are assumed to be constant in the region where the two point correlation is finite) and $G=1/r$, the following expression for P_{ij_2} is obtained:

$$P_{ij} = A\pi_{ij} + BD_{ij} + C\,\frac{\pi_{\ell\ell}}{3}\,\delta_{ij} + E\,\frac{2k}{3}\,\bar{e}_{ij} \qquad (11)$$

where δ_{ij} is given in eqn (12) and

$$D_{ij} = -(U_{ik}\frac{\partial \bar{u}_k}{\partial x_j} + U_{jk}\frac{\partial \bar{u}_k}{\partial x_i} \qquad (12)$$

$$\bar{e}_{ij} = \frac{1}{2}\left(\frac{\partial \bar{u}_i}{\partial x_j} + \frac{\partial \bar{u}_j}{\partial x_i}\right)$$

The quantities A,B,C,E are dependent on the local structure of the turbulence, and are given in Table 1 below, which gives the values obtained by other researchers as well. In all but the simplest case of isotropic homogeneous turbulence A,B,C and E are dependent on a single parameter, ϕ. In the present case three parameters, ϕ_1, ϕ_2, ϕ_3 are required. These parameters may be considered as macro-scale functions, and may vary from one flow to another, or even inside a given flow. Yet, some typical values have been suggested for them and the resulting A,B,C,E are listed in Table 2 below. It may be seen that all researchers recommend fairly similar values apart from the values recommended by Reynolds$^{(8)}$ for A and B.

THE DECAY TERM

The decay, as defined in eqn (1d) is readily divided into two parts:

$$\varepsilon_{ij_1} = \nu\,\frac{\partial^2 U_{ij}}{x_k{}^2} \qquad (13a)$$

$$\varepsilon_{ij_2} = -2\nu\,\overline{\frac{\partial u'_i}{\partial x_k}\,\frac{\partial u'_j}{\partial x_k}} \qquad (13b)$$

As already mentioned, ε_{ij} does not cause any difficulty, and will not be discussed here any more. The second term, ε_{ij}, is dependent on the two point correlation:

$$\varepsilon_{ij_2} = 2\nu(\nabla_r^2\,Q_{ij})_{r=o} = -2\nu\cdot M_{ij} \qquad (14)$$

where ∇_r^2 is the Laplacian operator in the $\underset{\sim}{r}$ coordinate system, and M_{ij}, the micro-scale tensor is given by

$$M_{ij} = \left(\frac{2k}{3\lambda^2}\right)_{ij} \qquad (15)$$

The elements of M_{ij} may be easily calculated from the two point correlation, eqn (9). The result is

$$M_{ij} = -\,\varepsilon\left[\Lambda\,\frac{U_{ij}}{\frac{2}{3}k} + (1-\Lambda)\delta_{ij}\right] \qquad (16)$$

where

$$\varepsilon = -\,\frac{1}{3}M_{ii} = -\,\frac{20}{9}\,\frac{k}{\lambda^2{}_3}\,(1+\alpha R_t) \qquad (16a)$$

$$\Lambda = \frac{44/50}{\lambda_1{}^2\left(\frac{1}{\lambda_1^2} + \frac{1}{\lambda_3^2} + \frac{1}{\lambda_6^2} + \frac{1}{\lambda_{14}^2}\right)} - \frac{16/50}{\lambda_3^2\left(\frac{1}{\lambda_1^2} + \frac{1}{\lambda_3^2} + \frac{1}{\lambda_6^2} + \frac{1}{\lambda_{14}^2}\right)}$$

$$\lambda^2_{14} - \frac{1/10}{\lambda^2_{14}\left(\frac{1}{\lambda_1^2} + \frac{1}{\lambda_3^2} + \frac{1}{\lambda_6^2} + \frac{1}{\lambda_{14}^2}\right)} \qquad \frac{1}{\lambda^2{}_e} = -\,\frac{1}{2}\left(\frac{d^2 fe}{dr^2}\right)_{r\to o} \qquad (16b)$$

and fe are the model ¨ functions as given in eqn (9).

	A	B	C	E
Hom Iso				$-\ 2/15$
Quasi Iso$^{(2)}$	$\frac{8\phi-6}{105}$	$\frac{64\phi+22}{105}$	$\frac{-72\phi+54}{105}$	$\frac{144\phi+18}{105}$
Launder et al$^{(5)}$	$\frac{3\phi-2}{33}$	$\frac{2}{11}(4\phi+1)$	$-\frac{3}{11}(3\phi-2)$	$\frac{6}{55}(15\phi+1)$
Reynolds$^{(8)}$	$\frac{11}{30}$	$\frac{7\phi+20}{30}$	$-\frac{3}{5}\phi$	$\frac{6}{5}(1+\phi)$
Present	$\frac{8\phi_1-5-\phi_3}{105}$ $-\ \phi_2/90$	$\frac{64\phi_1+22+\phi_3}{105}$ $-\ \phi_2/35$	$\frac{-72\phi_1+54-8\phi_3}{105}$ $-\ \phi_2/70$	$\frac{144\phi+18-16\phi_3}{105}$ $-\frac{13}{55}\phi_2$

Table 1: Formulae for Coefficients in P_{ij_2}

$$\phi_1 = \int_o^\infty f_3\,dr/r \qquad \phi_2 = \int_o^\infty (f_{11}+f_7)\,dr/r \qquad \phi_3 = \int_o^\infty (f_{13}-f_{14})\,dr/r$$

	Parameter values	A	B	C	E
Hom.Iso					-0.133
Quasi Iso (2)	$\phi = -0.5$	-0.0952	-0.0952	0.857	-0.514
Launder (5) et al	$\phi = -0.4$	-0.0970	-0.109	+0.873	-0.545
Reynolds (8)	$\phi = -1.5$	-0.550	0.317	0.900	-0.600
Present	$\phi_1 = -0.5$ $\phi_2 = 1$ $\phi_3 = 0.01$	-0.0969	-0.124	0.842	-0.752

Table 2: Typical numerical values for coefficients in P_{ij_2}

It is worth while to note that the non-isotropic formulation of M_{ij} may be interpreted as a sum of "return to isotropy" term, and a regular decay term, as follows:

$$M_{ij} = \varepsilon\Lambda\left(\frac{U_{ij}}{\frac{2}{3}k} - \delta_{ij}\right) + \varepsilon\delta_{ij} \tag{17}$$

In principle, M_{ij} may be calculated by differentiation of the transport equation governing the two-point correlation. The resulting equation is

$$\frac{DM_{ij}}{Dt} = A_1\left(M_{ik}\frac{\partial\bar{u}_j}{\partial x_k} + M_{jk}\frac{\partial\bar{u}_i}{\partial x_k}\right) - e_5\frac{\nu}{\lambda_3^2}M_{ij}(1+e_3R_t) \tag{18}$$

$$A_1 = -1.642$$

$$e_5 = 3.6$$

where pressure-velocity and triple velocity correlations were neglected.

FINAL FORM OF THE EQUATIONS

The final form of eqn (1) may now be written, by substitution of P_{ij} from eqn (5a), (11), (5c), (7) and ε_{ij} from eqn (13a), (14). Examination of these terms shows that the distinction between the terms made above is not necessarily the only one. Apparently P_{ij_1} and P_{ij_2} are production terms, while P_{ij_3}, $P_{ij_{42}}$ and ε_{ij_1} are turbulent terms and $P_{ij_{41}}$ is a decay term, and the first part of ε_{ij_2} is a redistribution, or "return to isotropy" term. It is therefore convenient to regroup the terms to transport $\hat{T}_{ij}$, production $\hat{\pi}_{ij}$, and decay $\hat{\varepsilon}_{ij}$. These quantities are defined in the following equations

$$\hat{T}_{ij} = -\frac{\partial S_{ijk}}{\partial x_k} + \frac{1}{3}\left(\frac{\partial S_{ikk}}{\partial x_j} + \frac{\partial S_{jkk}}{\partial x_i}\right) + P_{ij_{41}} + \nu\frac{\partial^2 U_{ij}}{\partial x_k^2} \tag{19a}$$

$$\hat{\pi}_{ij} = \left(A + \frac{1}{3}\right)\pi_{ij} + BD_{ij} + \frac{C}{3}\pi_{\ell\ell}\delta_{ij} + E\,\frac{2k}{3}\,\bar{e}_{ij} \tag{19b}$$

$$\hat{\varepsilon}_{ij} = -\,GU_{ij} - \frac{2}{3}kH\,\delta_{ij} \tag{19c}$$

where

$$G = \frac{20\Lambda}{3}(1 + \alpha R_t)\frac{\nu}{\lambda_3^2} \tag{20a}$$

$$H = \left[\frac{3\Lambda_1}{2}(1 + \alpha_1 R_t) + \frac{20}{3}(1 - \Lambda)(1 + \alpha R_t\right]\frac{\nu}{\lambda_3^2} \tag{20b}$$

Contraction of the above terms yields the corresponding terms of the energy equation:

$$\hat{T}_{ii} = -\frac{\partial S_{iik}}{\partial x_k} + \frac{2}{3}\frac{\partial S_{ikk}}{\partial x_i} + P_{ii_{41}} + 2\nu\frac{\partial^2 k}{\partial x_i^2} \tag{21a}$$

$$\hat{\pi}_{ii} = \left(A+B+C+\frac{1}{3}\right)\pi_{ii} \tag{21b}$$

$$\hat{\varepsilon}_{ii} = -\,2k(G+H) \tag{21c}$$

The problem is to solve equations (18), (1) and (19). Various such solutions will be described in the following sections.

HOMOGENEOUS TURBULENT SHEAR FLOW

This flow was experimentally investigated by Rose(9), Champagne et al(10), and Rose(11). The flow is generated by placing a special grid mode of parallel rods in a duct. The flow passing through the grid is unidirectional with uniform axial velocity gradient. The components of U_{ij} are uniform in the cross section, but they vary in the axial direction. The scale of turbulence usually grows in the axial direction.

The governing equations for the Reynolds stress in this flow may be easily written. Neglecting $\hat{T}_{ij}$, the equations are

$$\bar{u}_1\frac{d}{dx_1}\,U = \left(\tilde{A}\,\frac{\tilde{U}}{k} - \tilde{B}\right)\frac{2}{3}k \tag{22}$$

$$\frac{2}{3}k\,\tilde{U} = U$$

$$\tilde{U} = \begin{pmatrix} U_{11} \\ U_{22} \\ U_{33} \\ U_{12} \end{pmatrix} \quad \tilde{B} = \begin{pmatrix} H \\ H \\ H \\ -\frac{E}{2}u' \end{pmatrix} \quad \tilde{A} = \begin{pmatrix} -G & 0 & 0 & -\left(\frac{2}{3}+2A+\frac{2}{3}C\right)u' \\ 0 & -G & 0 & -\left(2B+\frac{2}{3}C\right)u' \\ 0 & 0 & -G & -\frac{2}{3}C\,u' \\ -Bu' & -\left(A+\frac{1}{3}\right)u' & 0 & -G \end{pmatrix}$$

The solution of the above equation reaches an equilibrium when

$$\tilde{U}_{11} = G\,\frac{1+3A+C}{(A+B+C+{}^1/_3)\bar{e}_{12}} + H\,\frac{{}^2/_3+2A-B}{(A+B+C+{}^1/_3)\bar{e}_{12}}$$

$$\tilde{U}_{22} = G\,\frac{3B+C}{(A+B+C+{}^1/_3)\bar{e}_{12}} + H\,\frac{-{}^1/_3-A+2B}{(A+B+C+{}^1/_3)\bar{e}_{12}}$$

$$\tilde{U}_{33} = G\,\frac{C}{(A+B+C+{}^1/_3)\bar{e}_{12}} + H\,\frac{-{}^1/_3-A-B}{(A+B+C+{}^1/_3)\bar{e}_{12}}$$

$$\tilde{U}_{12} = -\,\frac{3}{2}\,\frac{(H+G)}{(A+B+C+{}^1/_3)\bar{e}_{12}} \tag{23}$$

However, this solution is possible only when $\det(\tilde{A})=0$, and as this condition is satisfied only for one particular value of $R_t=0.148$ this solution is of limited interest. A fully developed solution may be obtained for $\tilde{U}$, as follows:

$$\tilde{U}_{11}=\frac{3H+4\bar{e}_{12}(3A+C+1)\tilde{U}_{12}}{3H+\frac{4}{3}\bar{e}_{12}(3A+3B+3C+1)\tilde{U}_{12}}$$

$$\tilde{U}_{22}=\frac{3H+4\bar{e}_{12}(3B+C)\tilde{U}_{12}}{3H+\frac{4}{3}\bar{e}_{12}(3A+3B+3C+1)\tilde{U}_{12}} \qquad (24)$$

$$\tilde{U}_{33}=\frac{3H+4\bar{e}_{12}C\,\tilde{U}_{12}}{3H+\frac{4}{3}\bar{e}_{12}(3A+3B+3C+1)\tilde{U}_{12}}$$

The fourth equation, for $\tilde{U}_{12}$, will not be given here, due to its complexity. It is a third order polynomial equation, which has at least one real positive root provided that $H \geq 0.51$. The tensor $\tilde{U}$ appears to reach an equilibrium condition at the end of the duct of Champagne et al(10). A better approximation is obtained when the scale λ is allowed to vary in the axial direction. The following equation may be derived from eqn (18):

$$\bar{u}_1\frac{dm}{dx}=2A_1e_{12}m-m(G+H+F)+\frac{2}{3}(A+B+C+\frac{1}{3})m\bar{e}_{12}\tilde{U}_{12} \qquad (25)$$

where

$$m=M_{ii}/h^2\ \frac{2}{3}k=(\frac{h}{\lambda_3})^2 \qquad (26)$$

$$F=e_5\frac{\nu}{\lambda^2}(1+e_3R_t) \qquad (27)$$

and h is the duct width.

An asymptotic solution of eqn (25) may be easily obtained, if U is assumed to be constant

$$m=m_o\exp\frac{x}{\bar{u}_1}[2A_1\bar{e}_{12}+\frac{2}{3}(A+B+C+\frac{1}{3})2\bar{e}_{12}\tilde{U}_{12}-(H+F+G)] \qquad (28)$$

The experimental data of Champagne et al indicates that $A_2 \approx -1$ and $A_1 \approx -1.643$.

Finally eqs (22) and (25) were solved numerically, using A,B,C, and E as given in Table 2, A_1 and e_5 as given in eqn (18), and

$\Lambda = 0.6$ $\Lambda_1 = -2.0$ $\alpha = 0.315$
$\alpha_1 = 0.617$ $e_3 = 1.53$

The calculated results (Fig. 1) are in good agreement with the data.

ACCELERATING GRID TURBULENCE

Usually, grid turbulence is not isotropic, and the streamwise fluctuations U_{11} have larger magnitude than the cross stream fluctuations, U_{22} and U_{33} which are nearly equal to one another. The off-diagonal components of the Reynolds stresses are zero. The ratio of U_{11} to U_{22} may be changed by acceleration of the flow, and such experiments were reported by Uberoi and Wallis(12) and Compte-Bellot and Corrsim(13). In the experiments the acceleration was produced by imposing a streamwise velocity gradient, given by

$$\dot{u}=\frac{\bar{u}_1}{\partial x_1}=-\frac{1}{2}\frac{\partial\bar{u}_2}{\partial x_2}=-\frac{1}{2}\frac{\partial\bar{u}_3}{\partial x_3} \qquad (29)$$

The experimental data suggest that the influence of the acceleration on the structure of the turbulence is very fast. Therefore it is reasonable to neglect $\hat{T}_{ij}$ and $\hat{\varepsilon}_{ij}$. In this case the following set of equations is obtained:

$$\bar{u}_1\frac{dU}{dx_1}=\frac{d\bar{u}_1}{dx_1}M\,U \qquad (30)$$

$$U=\begin{matrix}U_{11}\\U_{12}\end{matrix}\qquad M=\begin{matrix}-2(A+B)-\frac{2}{3}(C+1)+\frac{E}{3} & \frac{2}{3}(C+E)\\ -\frac{2}{3}C-\frac{E}{6} & A+B+\frac{2C+1+E}{3}\end{matrix}$$

Obviously specification of $\bar{u}_1(x)$ is required. However, by transforming the independent variable to $\bar{u}_1$ the equation becomes

$$\bar{u}_1\frac{dU}{d\bar{u}_1}=M\,U \qquad (31)$$

with the solution

$$\frac{U_{11}}{U_{11,i}}=(1-V_2)W_2(\frac{\bar{u}_1}{\bar{u}_{1,i}})^{\omega_1}+(1-V_1)W_1(\frac{\bar{u}_1}{\bar{u}_{1,i}})^{\omega_2} \qquad (32a)$$

$$\frac{U_{22}}{U_{22,i}}=(W_2-1)W_1(\frac{\bar{u}_1}{\bar{u}_{1,i}})^{\omega_1}+(W_1-1)W_2(\frac{\bar{u}_1}{\bar{u}_{1,i}})^{\omega_2} \qquad (32b)$$

where

$$V_1=\frac{2(C+E)}{3(\omega_1+b_1+b_3)}\qquad V_2=\frac{2(C+E)}{3(\omega_2+b_1+b_3)}$$

$$W_1=\frac{\omega_1+b_1+b_3}{2\sqrt{b_1^2-b_2^2}}\qquad W_2=\frac{\omega_2+b_1+b_3}{2\sqrt{b_1^2-b_1^2}}$$

$$b_1^1=\frac{3A+3B+1}{2}+\frac{2C-E}{3}\qquad b_2^2=\frac{(C+E)(4C+E)}{9}\qquad b_3=\frac{3A+3B+1}{6}$$

$$\omega_1=-b_3-\sqrt{b_1^2-b_2^2}\qquad \omega_2=-b_3+\sqrt{b_1^2-b_2^2}$$

Comparison of these equations with the data of Uberoi and Wallis(12) suggests the following values for the constants:

$A=-0.097$ $B=-0.122$ $C=-0.95$ $E=-0.71$

These values are fairly new to those recommended in the use of the homogeneous shear flow.

Finally eqn (1), (18), and (19) were run for the three experimental cases reported by Uberoi and Wallis. As no scale measurements were reported by these authors the initial scales were guessed in such a way which ensured good agreement with the data. The Reynolds stress and length scale distribution computed for Uberoi and Wallis's medium size mesh are shown in Fig. 2, and show good agreement with the data. Further the ratio U_{11}/U_{22} is shown in Fig. 3 for the mesh Reynolds numbers. Again the comparison with the experimental data is good.

STRAINED TURBULENT FLOW

Tucker and Reynolds(14) and Reynolds and Reynolds and Tucker(15) have studied the irrotational straining of turbulence in variable geometry ducts. Their ducts were so constructed as to make the diagonal components of the rate of strain, $\bar{e}_{ij}$, uniform in the entire duct. Thus e_{ij} is given by

$$\bar{e}_{ij}=\begin{matrix}\frac{\partial\bar{u}_1}{\partial x_1} & 0 & 0\\ 0 & \frac{\partial\bar{u}_2}{\partial x_2} & 0\\ 0 & 0 & \frac{\partial\bar{u}_3}{\partial x_3}\end{matrix} \qquad (33a)$$

where

$$-\frac{\partial\bar{u}_3}{\partial x_3}=\frac{\partial\bar{u}_1}{\partial x_1}+\frac{\partial\bar{u}_2}{\partial x_2} \qquad (33b)$$

The governing equations for this case are given below (with $\hat{T}_{ij}$ neglected):

$$\bar{u}_1\frac{d}{dx}R=-M\,R \qquad (34a)$$

where

$$R=\begin{array}{c} k \\ D_2 \\ D_3 \end{array} ; \quad M=\begin{array}{ccc} G+H & -(a+C)\bar{e}_{22} & -(a+C)\bar{e}_{33} \\ 2(a-E)(\bar{e}_{11}-\bar{e}_{22}) & G+\frac{2}{3}a(\bar{e}_{11}-2\bar{e}_{22}) & \frac{2}{3}a\bar{e}_{33} \\ 2(a-E)(\bar{e}_{11}-\bar{e}_{33}) & -\frac{2}{3}a\bar{e}_{22} & G+\frac{2}{3}a(\bar{e}_{11}-2\bar{e}_{33}) \end{array} \qquad (34b)$$

$D_2= U_{11}-U_{22}$ $D_3=U_{11}-U_{33}$ $a=A+B+\frac{1}{3}$

As in the case of homogeneous shear, conditions for equilibrium are unstable, but $\tilde{R}=R/\frac{2}{3}k$ may reach an equilibrium. Analysis of this case is difficult. Therefore only some special cases were solved, as summarised in Table 3 below. In these solutions it was assumed that $R_t<<1$ and $\lambda/h=0.006$.

$\bar{e}_{11}$	$\bar{e}_{22}$	$\bar{e}_{33}$	$\tilde{U}_{11}$	$\tilde{U}_{22}$	$\tilde{U}_{33}$
0	4.45	-4.45	1.85	0.35	0.70
2.6	2.6	-5.2	0.57	0.93	1.50
-1.3	2.6	-1.3			

Table 3: Reynolds stress distribution in plane strain

These values are practically identical with the experimental data.

The solution of the governing equations for U_{ij} when ($R_t<< 1$) is the sum of three exponential functions with the eigenvalues of M as exponential coefficients. Examination of the data of Tucker and Reynolds(14) shows that the exponential coefficient is 0.7 which corresponds to the larger eigenvalue of M for this case. The other two eigenvalues happen to be negligibly small in this case.

As in the previous cases the development of the turbulence in this flow was calculated numerically. The calculated Reynolds stresses are compared with the experimental data for $\bar{e}_{11}=0$ in Fig. 4 and show fairly good agreement. Comparison of calculated normalised Reynolds stresses $\tilde{U}$ with experimental data for various strain parameters F_e (as defined by Reynolds and Tucker(15)) are shown in Fig. 5. Again the agreement is good.

CONCLUSIONS

1. A new model for the double-velocity two-point correlation is presented. This model is not isotropic and may therefore be used near solid walls. Further, this model may satisfy the dynamic equations for the two-point correlations.
2. A new formulation for the pressure-velocity interaction term in the Reynolds stress equations is presented. This formulation is based on integration by parts of the volume integrals of P_{ij}, and on substitution of the new two-point correlation model. The analysis shows very clearly the contribution of the pressure-velocity interaction to apparent diffusion, production and decay terms.
3. The present model may be used near walls, and in the viscous sublayer.
4. Application of the model to some simple flows shows good agreement between theoretical and experimental data.

[1] Wolfshtein, M., Naot, D., and Lin, A. (1975), Models of turbulence, in: Topics in Transport Phenomena, Hemisphere Pub. Co.

[2] Naot, D., Shavit, A., and Wolfshtein, M.(1973), Phys. Fluids, 16, 738.

[3] Chou, P.Y (1945), Quart. App. Math. 3, 38.

[4] Wolfshtein, M. (1970), Israel J. Tech., 8, 87.

[5] Launder, B.E., Reece, G.J., and Rodi, W. (1975), J. Fluid Mech., 68, 537.

[6] Rotta, J.C. (1972), Proc. 13th Int. Cong. Theoretical App. Mech., Moscow.

[7] Naot, D., Shavit, A., Wolfshtein, M. (1974), Warme und Stoff Ubertragung, 7, 151.

[8] Reynolds, W.C. (1975), Dept. Mech. Eng., Stanford U., Rept. No. TF-4.

[9] Rose, W.G. (1966), J. Fluid Mech., 25, 97.

[10] Champagne, F.H., Harris, V.G., and Corrsin, S.(1970), J. Fluid Mech., 41, 81.

[11] Rose, W.G. (1970), J. Fluid Mech., 44, 767.

[12] Uberoi, M.S., and Wallis, S. (1966), J. Fluid Mech., 24, 539.

[13] Comte-Bellot, G., and Corrsin, S. (1966), J. Fluid Mech., 25, 657.

[14] Tucker, H.J. and Reynolds, J.A. (1968), J. Fluid Mech., 32, 657.

[15] Reynolds, J.A. and Tucker, H.J. (1975), J. Fluid Mech., 68, 673.

THE CLIPPING APPROXIMATION FOR INHOMOGENEOUS TURBULENCE

J.C. ANDRE, G. DE MOOR, P. LACARRERE, G. THERRY, and R. du VACHAT

Direction de la Météorologie, EERM/GMD, 73-77 rue de Sèvres, 92100 - Boulogne, France

ABSTRACT

A new treatment of third order moments is proposed for the study of inhomogeneous turbulence: the equations for the rate of change of third order correlations should be used in conjunction with the quasi-normal approximation and with the enforcement of some generalized Schwarz inequalities ("clipping" mechanism) relating third and second order moments, the clipping mechanism being intended to preserve realizability. Together with rather classical formulations for pressure and dissipative terms, this approximation is used for numerical modeling of a penetrative convection experiment and of an asymmetric channel flow experiment.

NOMENCLATURE

$a_\cdot$, $c_\cdot$ = dimensionless constants

e = eddy kinetic energy (per unit mass)
p = pressure difference from reference state
P = eddy kinetic energy generation
P_{ij} = Reynolds stress generation
P_{iT} = heat flux generation
Q_o = kinematic heat flux
t = time
T = temperature
T_* = convective temperature scale
$\underline{u} = (u_1,u_2,u_3) = (u,v,w)$ = velocity
u_T, v_T, w_T = r.m.s. velocities
u_* = friction velocity
w_* = convective velocity scale
$\underline{x} = (x_1,x_2,x_3) = (x,y,z)$ = position
z_i = inversion height
D/Dt = Lagrangian derivative following the mean motion
$\underline{\beta}$ = buoyancy coefficient ($\underline{\beta} = -\underline{g}/T_o$, with g = gravity acceleration, T_o = standard temperature)
δ_{ij} = Kronecker symbol
ε = eddy kinetic energy dissipation
ε_T = temperature variance dissipation
ρ = (constant) density

INTRODUCTION

In second order turbulence modeling, one is faced to three kinds of closure problems due respectively to (i) presso-correlations, (ii) dissipative terms, and (iii) third order moments.

The invariant modeling technique (1) provides a rational method for generating approximations to pressure terms (i); furthermore, though there is no general agreement about which one is the "best", simple versions of these approximations are now considered to be valuable for a large number of flows (2). On the other hand, much attention has been recently devoted to problem (ii) for which, again, invariant modeling is a very efficient guide; as a result, a few equations for dissipative terms are now available for practical use (3,4). Unfortunately, for third order terms (iii) invariant modeling alone is not very useful, because it results into many undetermined constants (1); yet, a good description of, say, energy fluxes is of primary importance for a correct modeling of such simple flows as the convective mixed layer (4) or asymmetric shear flows (2). Moreover, it is easy to show that abridged invariant proposals (with only one undetermined constant) are unable to yield realistic third order moments (4,5). So, for problem (iii), one has to resort to some kind of physical model. Such a model has been used by Zeman (4) and Zeman and Lumley (6); here, we propose another approach to the problem of third order moments.

SECOND ORDER MODELS

Second order equations

For a thermally stratified flow at high Reynolds number, the set of second order equations, as derived from the Boussinesq system, read (see e.g. 7)

$$\frac{\partial \overline{u}_k}{\partial x_k} = 0 \tag{1}$$

$$\frac{D\overline{u}_i}{Dt} = -\frac{\partial \overline{u'_i u'_k}}{\partial x_k} - \frac{1}{\rho}\frac{\partial \overline{p}}{\partial x_i} + \beta_i \overline{T} \tag{2}$$

$$\frac{D\overline{T}}{Dt} = -\frac{\partial \overline{u'_k T'}}{\partial x_k} \tag{3}$$

PRECEDING PAGE BLANK-NOT FILMED

$$\frac{D\overline{u'_iu'_j}}{Dt} = -\left(\overline{u'_ku'_i}\frac{\partial\overline{u}_j}{\partial x_k} + \overline{u'_ku'_j}\frac{\partial\overline{u}_i}{\partial x_k}\right) + \left(\beta_j\,\overline{u'_iT'} + \beta_i\,\overline{u'_jT'}\right)$$

$$\underbrace{-\frac{1}{\rho}\left(\overline{u'_i\frac{\partial p'}{\partial x_j}} + \overline{u'_j\frac{\partial p'}{\partial x_i}}\right)}_{(i)} \underbrace{-\frac{2}{3}\varepsilon\delta_{ij}}_{(ii)} \underbrace{-\frac{\partial\overline{u'_ku'_iu'_j}}{\partial x_k}}_{(iii)} \qquad (4)$$

$$\frac{D\overline{u'_iT'}}{Dt} = -\left(\overline{u'_ku'_i}\frac{\partial\overline{T}}{\partial x_k} + \overline{u'_kT'}\frac{\partial\overline{u}_i}{\partial x_k}\right) + \beta_i\,\overline{T'^2}$$

$$\underbrace{-\frac{1}{\rho}\overline{T'\frac{\partial p'}{\partial x_i}}}_{(i)} \underbrace{-\frac{\partial\overline{u'_ku'_iT'}}{\partial x_k}}_{(iii)} \quad . \qquad (5)$$

$$\frac{D\overline{T'^2}}{Dt} = -2\,\overline{u'_kT'}\frac{\partial\overline{T}}{\partial x_k} \underbrace{-\varepsilon_T}_{(ii)} \underbrace{-\frac{\partial\overline{u'_kT'^2}}{\partial x_k}}_{(iii)} \qquad (6)$$

The principal notations are defined in the nomenclature list. The overbar is used for averaging, the prime for deviation from the mean. Einstein summation over repeated subscripts is implied, while non repeated subscripts run from 1 to 3. The closure problems announced in the introduction are quoted below.

Modeling the pressure terms

As usually done, we split the pressure term appearing in the Reynolds stress equations (4) into a transport term and a deviatoric term; following Launder (3), we neglect the former and model the latter according to

$$\frac{1}{\rho}\overline{p'\left(\frac{\partial u'_i}{\partial x_j} + \frac{\partial u'_j}{\partial x_i}\right)} = -c_4\frac{\varepsilon}{e}\left(\overline{u'_iu'_j} - \frac{2}{3}\delta_{ij}\,\overline{e}\right)$$

$$-c_5\left(P_{ij} - \frac{2}{3}\delta_{ij}P\right) \qquad (7)$$

where P_{ij} is the total (dynamic and thermal) generation of Reynolds stress $\overline{u'_iu'_j}$, and P the total generation of eddy kinetic energy $\overline{e}$. The c_4-term is intended to describe the classical "return-to-isotropy" while the c_5-one tends to isotropize the turbulence production tensor (this last term describing shear and buoyant contributions to presso-correlations).

In a similar way we retain, for the pressure term appearing in the heat flux equations (5)

$$\frac{1}{\rho}\overline{p'\frac{\partial T'}{\partial x_i}} = -c_6\frac{\varepsilon}{e}\overline{u'_iT'} - c_7P_{iT} \qquad (8)$$

where P_{iT} is the net generation of heat flux.

Modeling the dissipative terms

For dissipative terms, one can adopt the Kolmogorov idea which allows to express them, on dimensional grounds, in terms of the turbulent kinetic energy $\overline{e}$, the temperature variance $\overline{T'^2}$, and some mixing length l; however l is too much dependent upon the particular flow which is considered, but current work is being performed to derive equations for the time-rate of change of dissipative terms. Here we use a rather classical approximation of the ε-equation (2), but we keep a dimensional formulation for the dissipation of temperature variance ε_T, because ε_T-equations do not seem presently as reliable as ε-ones (1).

The equation we use for ε reads

$$\frac{D\varepsilon}{Dt} = a_1\frac{\partial}{\partial x_k}\left(\frac{e}{\varepsilon}\overline{u'_ku'_l}\frac{\partial\varepsilon}{\partial x_l}\right) - a_2\frac{\varepsilon}{e}\overline{u'_ku'_l}\frac{\partial\overline{u}_l}{\partial x_k}$$

$$+ a_{2T}\frac{\varepsilon}{e}\beta_k\,\overline{u'_kT'} - a_3\frac{\varepsilon^2}{e} \qquad (9)$$

In the right hand side of (9), we find the simplest modeling of the terms that survive at high Reynolds number, namely, from left to right: diffusion, shear production, buoyant production and molecular destruction of kinetic energy dissipation. Furthermore, it is assumed that the dissipative time scale defined by $\overline{e}$ and ε (evaluated from (9)) is also relevant for temperature variance dissipation,

$$\varepsilon_T = c_2\frac{\varepsilon}{e}\overline{T'^2} \qquad (10)$$

CLIPPING APPROXIMATION FOR THIRD ORDER MOMENTS

Since we do not use the invariant modeling technique to express the third order moments, we have to consider the equations for their rate of change. It is easy to derive these equations with some algebra; not surprisely, they involve three kinds of new unknown terms, namely presso-correlations, "dissipative" terms, and fourth order moments.

Closure problems in third order equations

Concerning presso-correlations, if we neglect the transport part and drop shear and buoyant contributions (at least as a first step), the modeling can be done through an extension of the "return-to-isotropy" concept. In the $\overline{u'_iu'_ju'_k}$ and $\overline{u'_iT'^2}$ equations, this obviously amounts to a "return-to-zero" term proportional to these variables themselves; for $\overline{u'_iu'_jT'}$ - the isotropic value of which is not zero but ($\overline{u'_ku'_kT'}\delta_{ij}$) / 3 - the problem can be handled as follows (Launder 1976, private communication). One can split the pressure term (minus its transport part) into a (trace free) "redistribution" term and a "source" term:

$$\overline{p'\left(\frac{\partial u'_iT'}{\partial x_j} + \frac{\partial u'_jT'}{\partial x_i}\right)} = \overline{p'\left(\frac{\partial u'_iT'}{\partial x_j} + \frac{\partial u'_jT'}{\partial x_i} - \frac{2}{3}\delta_{ij}\frac{\partial u'_kT'}{\partial x_k}\right)}$$

$$+\frac{2}{3}\delta_{ij}\,\overline{p'\frac{\partial u'_kT'}{\partial x_k}} \qquad (11)$$

In the right hand side of (11), the first term can then be modeled as a "return-to-isotropy" term while the second one can be taken proportional to $\overline{u'_k u'_k T'}$:

$$\overline{p'\left(\frac{\partial u'_i T'}{\partial x_j}+\frac{\partial u'_j T'}{\partial x_i}\right)} = -c_9\frac{\varepsilon}{\overline{e}}\left(\overline{u'_i u'_j T'}-\frac{1}{3}\delta_{ij}\,\overline{u'_k u'_k T'}\right) + c'_9\frac{\varepsilon}{\overline{e}}\,\overline{u'_k u'_k T'}\,\delta_{ij} \qquad (12)$$

Moreover, numerical experiments have suggested that a better overall agreement was achieved by using a "return-to-zero" modeling for all pressure terms, i.e. by taking $c'_9 = -c_9/3$.

In the absence of sufficient knowledge of their effects, the "dissipative" terms will be neglected. As a tentative justification of this assumption, it can be noticed that in the asymmetric channel flow of Hanjalic and Launder (8), these effects are indeed found to be negligeable as compared to the "return-to-isotropy" effects if Lumley's model (1) is retained for dissipative terms.

To model fourth order correlations, the more natural way is to use the quasi-normal approximation:

$$\overline{a'b'c'd'} = \overline{a'b'}.\overline{c'd'} + \overline{a'c'}.\overline{b'd'} + \overline{a'd'}.\overline{b'c'} \qquad (13)$$

where a, b, c, and d stand here for u_i or T.

Clipping mechanism for third order moments

It is well known that the quasi-normal approximation alone is unsuitable for turbulence modeling, since it leads to the unphysical development of negative energy and variances, and more generally to non realizable statistics (e.g. 9). This defect can be ascribed to an excessive growth of third order correlations, which is due to an unsufficient damping effect by the fourth order correlations. It appears thus necessary to aid to the quasi-normal approximation a damping mechanism of third order moments; such a damping mechanism is suggested below.

Using Schwarz inequalities, it is easy to show that third order correlations must verify (15)

$$\overline{a'b'c'}^2 \leqslant \overline{a'^2}\left(\overline{b'^2c'^2} - \overline{b'c'}^2\right) \qquad (14)$$

and symmetrical conditions in a, b, c; using the quasi-normal hypothesis, these conditions read

$$\left|\overline{a'b'c'}\right| \leqslant \mathrm{Min}\left\{\begin{matrix}\left[\overline{a'^2}\left(\overline{b'^2}.\overline{c'^2}+\overline{b'c'}^2\right)\right]^{\frac{1}{2}},\\ \left[\overline{b'^2}\left(\overline{a'^2}.\overline{c'^2}+\overline{a'c'}^2\right)\right]^{\frac{1}{2}},\\ \left[\overline{c'^2}\left(\overline{a'^2}.\overline{b'^2}+\overline{a'b'}^2\right)\right]^{\frac{1}{2}}\end{matrix}\right\} \qquad (15)$$

However nothing in the quasi-normal approximation makes it necessary that these inequalities be satisfied. Our "clipping" approximation (10) consists in enforcing (15) at each time step and at each grid point by cutting off the value of $\overline{a'b'c'}$ whenever it exceeds the right hand side of (15). This mechanism constitutes of course only a minimum damping effect for third order correlations, since it acts only to prevent the development of impossibly large values; but numerical experiments show it produces realizable turbulent flows in the sense that the development of negative variances or the violation of ordinary Schwarz inequalities for Reynolds stresses is made impossible.

BASIC SET OF EQUATIONS

Due to the overwhelming complexity bound to three-dimensionality, we are mainly interested in turbulent flows which have only one direction of inhomogeneity. Denoting by z this direction (the gravity direction in buoyant problems) and assuming the mean velocity has no z-component, the quasi-normal system modified by the clipping inequalities can be recapitulated as follows:

$$\frac{\partial\overline{u_i}}{\partial t} = -\frac{\partial\overline{u'_i w'}}{\partial z} - \frac{1}{\rho}\frac{\partial\overline{p}}{\partial x_i} \quad (\text{ with } \overline{u_3} = \overline{w} = 0) \qquad (16)$$

$$\frac{\partial\overline{T}}{\partial t} = -\frac{\partial\overline{w'T'}}{\partial z} \qquad (17)$$

$$\frac{\partial\overline{u'_i u'_j}}{\partial t} = -\frac{\partial\overline{u'_i u'_j w'}}{\partial z} - c_4\frac{\varepsilon}{\overline{e}}\left(\overline{u'_i u'_j} - \frac{2}{3}\delta_{ij}\,\overline{e}\right) - (1-c_5)\left\{\overline{u'_i w'}\frac{\partial\overline{u_j}}{\partial z} + \overline{u'_j w'}\frac{\partial\overline{u_i}}{\partial z} - \beta\left(\overline{u'_i T'}\delta_{3j} + \overline{u'_j T'}\delta_{3i}\right)\right\} - \frac{2}{3}c_5\left(\overline{u'_k w'}\frac{\partial\overline{u_k}}{\partial z} - \beta\,\overline{w'T'}\right)\delta_{ij} - \frac{2}{3}\varepsilon\delta_{ij} \qquad (18)$$

$$\frac{\partial\overline{u'_i T'}}{\partial t} = -\frac{\partial\overline{u'_i w'T'}}{\partial z} - \overline{u'_i w'}\frac{\partial\overline{T}}{\partial z} - c_6\frac{\varepsilon}{\overline{e}}\,\overline{u'_i T'} - (1-c_7)\left(\overline{w'T'}\frac{\partial\overline{u_i}}{\partial z} - \beta\,\overline{T'^2}\delta_{3i}\right) \qquad (19)$$

$$\frac{\partial\overline{T'^2}}{\partial t} = -\frac{\partial\overline{w'T'^2}}{\partial z} - 2\,\overline{w'T'}\frac{\partial\overline{T}}{\partial z} - c_2\frac{\varepsilon}{\overline{e}}\,\overline{T'^2} \qquad (20)$$

$$\frac{\partial\varepsilon}{\partial t} = a_1\frac{\partial}{\partial z}\left(\frac{\overline{e}}{\varepsilon}\overline{w'^2}\frac{\partial\varepsilon}{\partial z}\right) - a_2\frac{\varepsilon}{\overline{e}}\,\overline{u'_i w'}\frac{\partial\overline{u_i}}{\partial z} + a_{2T}\frac{\varepsilon}{\overline{e}}\beta\,\overline{w'T'} - a_3\frac{\varepsilon^2}{\overline{e}} \qquad (21)$$

$$\frac{\partial \overline{u_i'u_j'w'}}{\partial t} = -\overline{u_i'w'^2}\frac{\partial \overline{u_j}}{\partial z} - \overline{u_j'w'^2}\frac{\partial \overline{u_i}}{\partial z} - \overline{w'^2}\frac{\partial \overline{u_i'u_j'}}{\partial z}$$

$$- \overline{u_j'w'}\frac{\partial \overline{u_i'w'}}{\partial z} - \overline{u_i'w'}\frac{\partial \overline{u_j'w'}}{\partial z} - c_8\frac{\varepsilon}{e}\overline{u_i'u_j'w'}$$

$$+ \beta(\overline{u_i'u_j'T'} + \overline{u_i'w'T'}\,\delta_{3j} + \overline{u_j'w'T'}\,\delta_{3i})$$

$$\left|\overline{u_i'u_j'w'}\right| \leqslant \text{Min} \left\{ \begin{matrix} \left[\overline{u_i'^2}(\overline{u_j'^2}.\overline{w'^2}+\overline{u_j'w'}^2)\right]^{\frac{1}{2}}, \\ \left[\overline{u_j'^2}(\overline{u_i'^2}.\overline{w'^2}+\overline{u_i'w'}^2)\right]^{\frac{1}{2}}, \\ \left[\overline{w'^2}(\overline{u_i'^2}.\overline{u_j'^2}+\overline{u_i'u_j'}^2)\right]^{\frac{1}{2}} \end{matrix} \right\} \qquad (22)$$

$$\frac{\partial \overline{u_i'u_j'T'}}{\partial t} = -\overline{u_i'u_j'w'}\frac{\partial \overline{T}}{\partial z} - \overline{u_i'w'T'}\frac{\partial \overline{u_j}}{\partial z} - \overline{u_j'w'T'}\frac{\partial \overline{u_i}}{\partial z}$$

$$- \overline{w'T'}\frac{\partial \overline{u_i'u_j'}}{\partial z} - \overline{u_i'w'}\frac{\partial \overline{u_j'T'}}{\partial z} - \overline{u_j'w'}\frac{\partial \overline{u_i'T'}}{\partial z}$$

$$+ \beta(\overline{u_i'T'^2}\delta_{3j} + \overline{u_j'T'^2}\delta_{3i}) - c_9\frac{\varepsilon}{e}\overline{u_i'u_j'T'}$$

$$\left|\overline{u_i'u_j'T'}\right| \leqslant \text{Min} \left\{ \begin{matrix} \left[\overline{u_i'^2}(\overline{u_j'^2}.\overline{T'^2}+\overline{u_j'T'}^2)\right]^{\frac{1}{2}}, \\ \left[\overline{u_j'^2}(\overline{u_i'^2}.\overline{T'^2}+\overline{u_i'T'}^2)\right]^{\frac{1}{2}}, \\ \left[\overline{T'^2}(\overline{u_i'^2}.\overline{u_j'^2}+\overline{u_i'u_j'}^2)\right]^{\frac{1}{2}} \end{matrix} \right\} \qquad (23)$$

$$\frac{\partial \overline{u_i'T'^2}}{\partial t} = -\overline{w'T'^2}\frac{\partial \overline{u_i}}{\partial z} - 2\,\overline{u_i'w'T'}\frac{\partial \overline{T}}{\partial z} - \overline{u_i'w'}\frac{\partial \overline{T'^2}}{\partial z}$$

$$- 2\,\overline{w'T'}\frac{\partial \overline{u_i'T'}}{\partial z} + \beta\overline{T'^3}\,\delta_{3i} - c_{10}\frac{\varepsilon}{e}\overline{u_i'T'^2}$$

$$\left|\overline{u_i'T'^2}\right| \leqslant \left[\overline{T'^2}(\overline{u_i'^2}.\overline{T'^2}+\overline{u_i'T'}^2)\right]^{\frac{1}{2}} \qquad (24)$$

$$\frac{\partial \overline{T'^3}}{\partial t} = -3\,\overline{w'T'^2}\frac{\partial \overline{T}}{\partial z} - 3\,\overline{w'T'}\frac{\partial \overline{T'^2}}{\partial z}$$

$$\left|\overline{T'^3}\right| \leqslant (2\,\overline{T'^2}^3)^{\frac{1}{2}} \qquad (25)$$

NUMERICAL SIMULATION OF TURBULENT FLOWS

As preliminary tests of the clipping approximation, it is useful to consider the particular cases of turbulence driven either by buoyancy alone (set u_i=0 in the system (16)-(25)) or by shear alone (set T=0 in this system). As such case studies, we retained the numerical simulation of two laboratory experiments: the Willis and Deardorff (11) penetrative convection experiment, and the Hanjalic and Launder (8) asymmetric channel flow experiment.

The numerical schemes and boundary conditions used are described with some details in André et al. (12). We use a staggered grid with first and third order moments calculated at the same main levels and second order ones at the intermediate levels; the time integration scheme we retained is the Euler-backward (Matsuno) one. Thanks to the staggered grid, boundary conditions (in the vicinity of the walls) have to be expressed only for second order moments and dissipations. These are taken according to the similarity theory, using as basic ingredients: the (positive) kinematic heat flux Q_o at the bottom of the convective layer and the inversion height z_i in the convection experiment (11), or the friction velocities u_* in the shear driven experiment (8).

Initial conditions differ from case to case for the mean quantities ($\overline{u_i}$ and $\overline{T}$); for simplicity, all second and third order correlations are initially set to zero (except at the boundary levels where they are taken according to the initial values of Q_o, z_i, u_*). As a result the model needs some time interval to build up realistic values of turbulent quantities (of the order of 500 time steps).

The free constants of the model were determined on the basis of experimental data, existing litterature and computer optimisation (with "feed-back" between the two experiments); the values retained presently (admittedly, this is not the final word) are the following:

$c_2 = 2.7$; $c_4 = 4.5$; $c_5 = 0$; $c_6 = 6.4$;
$c_7 = 0.2$; $c_8 = c_9 = c_{10} = 9.$; $a_1 = 0.13$;
$a_2 = 1.44$; $a_{2T} = 0.7$; $a_3 = 2.$.

Simulation of the penetrative convection experiment

In this laboratory experiment (see Willis and Deardorff 11), a layer of water is heated from below. The initial conditions for mean temperature are a constant temperature (T = 21 C) in the first 50 cm and an overlying stable layer with a lapse rate of 0.16 C/cm (case S1) or of 0.36 C/cm (case S2). At the lower boundary we impose the kinematic heat flux $\overline{w'T'} = Q_o(t)$ chosen so as to fit the experimental conditions. The time step used is 0.3 sec. As suggested by Willis and Deardorff (11), the profiles of the various quantities should be steady if made dimensionless by the proper scales. Our model was found to be consistent with this hypothesis and that is the reason why we shall present our results in dimensionless form.

Figure 1 compares the computed and experimental profiles of mean temperature for case S2. It can be noted that the model recovers the thermally unstable layer near the lower boundary, the nearly adiabatic layer higher up, with increasing stability as the inversion level is approached, and the cooling of the upper layer ("overshoot").

Figure 2 shows the vertical profiles of the turbulent heat flux $\overline{w'T'}$ for cases S1 and S2; the height is scaled with z_i, and the heat flux with its surface value Q_o. As was to be expected, the negative value of $\overline{w'T'}$ in the "overshoot" is found to be larger for case S1 than for case S2.

The vertical velocity variance $\overline{w'^2}$, made dimensionless by the square of the convective velocity $w_* = (\beta Q_o z_i)^{1/3}$, is plotted in figure 3 as a function

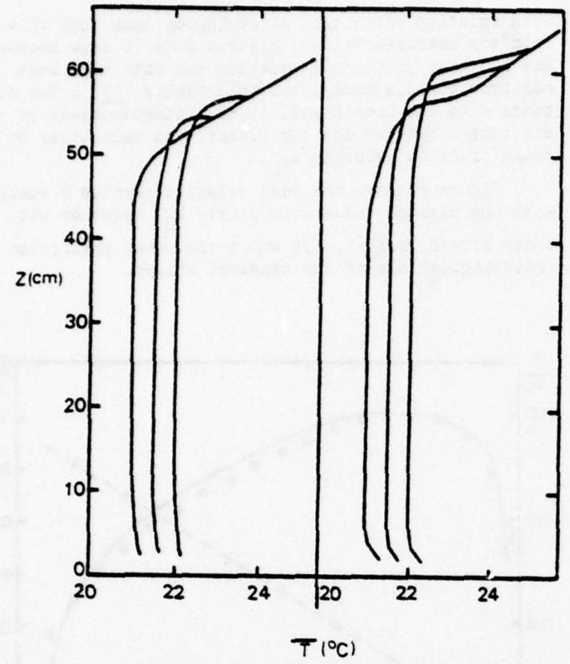

Figure 1 : Evolution of the mean temperature profile for case S2. Left: laboratory measurements; right: numerical results. From left to right: t = 150 sec; t = 255 sec; t = 360 sec after the beginning of experiment.

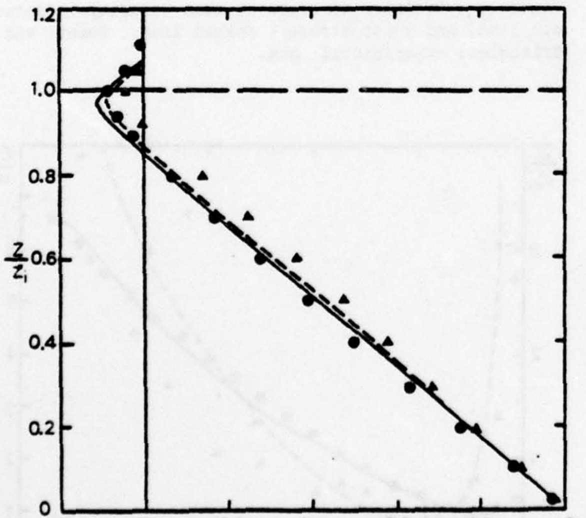

Figure 2 : Vertical profiles of dimensionless heat flux. Continuous line: S1 model data; points: S1 experimental data; dashed line: S2 model data; triangles: S2 experimental data.

of z/z_i. It can be seen that the overall shape of the profiles is recovered in the two cases, with higher values in case S2 than in case S1 (in agreement with experiment).

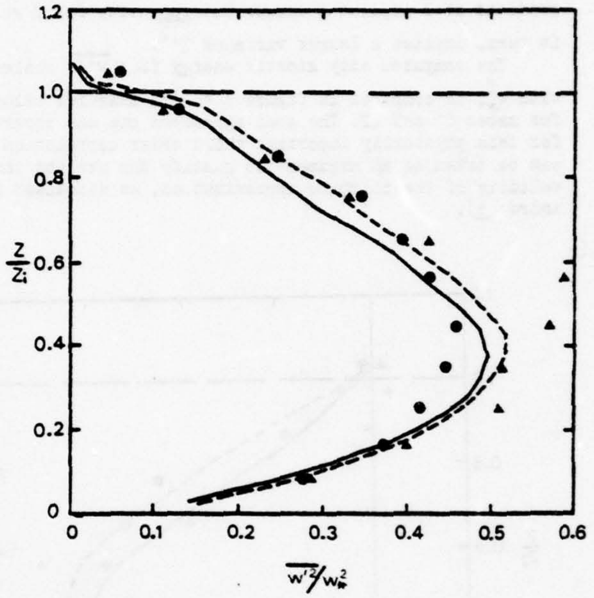

Figure 3 : Vertical profiles of dimensionless vertical velocity variance. Symbols as in figure 2.

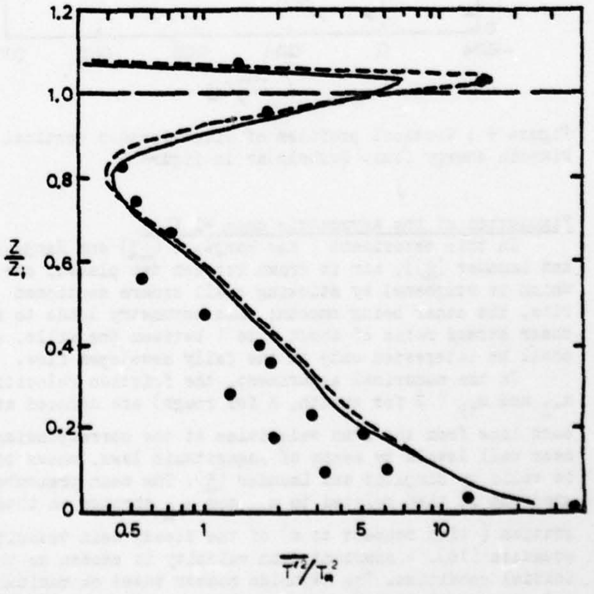

Figure 4 : Vertical profiles of dimensionless temperature variance. Symbols as in figure 2.

Figure 4 <u>shows</u> the vertical profiles of the temperature variance $\overline{T'^2}$, scaled with T_*^2, where $T_* = Q_0 / w_*$. The numerical model gives the same shape and order of magnitude as the laboratory measurements. It can be seen that in case S2 the temperature variance reaches a higher maximum value: this was to be expected since a larger gradient of $\overline{T}$ implies a larger hetero<u>rog</u>eneity for T which, in turn, implies a larger variance $\overline{T'^2}$.

The computed eddy kinetic energy flux $\overline{w'e}$, scaled with w_*^3, is compared in figure 5 to its measured values for cases S1 and S2. The good agreement one can observe for this physically important third order correlation can be taken as an argument to justify the use and the validity of the clipping approximation, as discussed by André (<u>5</u>).

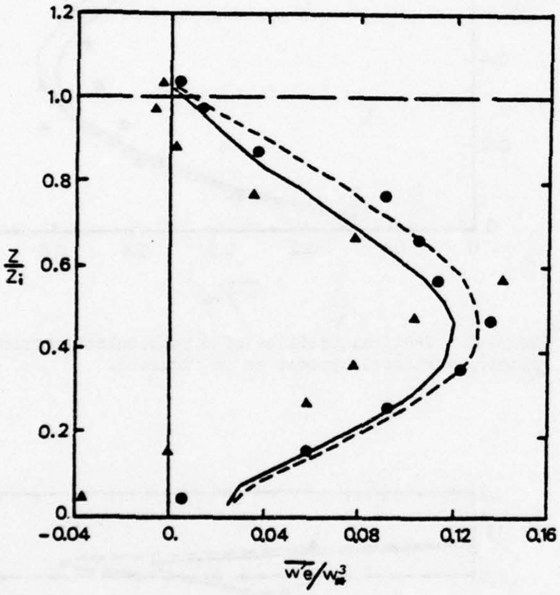

Figure 5 : Vertical profiles of dimensionless vertical kinetic energy flux. Symbols as in figure 2.

Simulation of the asymmetric channel flow

In this experiment (see Hanjalic (<u>13</u>) and Hanjalic and Launder (<u>8</u>)), air is drawn between two plates, one of which is roughened by sticking small square sectioned ribs, the other being smooth; this asymmetry leads to a shear stress ratio of about 5 to 1 between the walls. We shall be interested only in the fully developed flow.

In the numerical experiment, the friction velocities u_{*S} and u_{*R} (S for smooth, R for rough) are deduced at each time from the mean velocities at the corresponding near wall levels by means of logarithmic laws, shown to be valid by Hanjalic and Launder (<u>8</u>). The mean pressure gradient is then related to u_{*S} and u_{*R} through an integration (with respect to z) of the steady mean velocity equation (16). A constant mean velocity is chosen as the initial condition. The Reynolds number based on maximum velocity and half distance between the walls is typically 56000. The time step used is 0.00005 sec. After about 1000 time steps, the "numerical flow" becomes steady, with friction velocities differing by less than 10 % from the measured values. Figures 6 to 10 show measured and computed profiles (experimental data have been deduced from the diagrams shown in Hanjalic (<u>13</u>)). The distance z to the smooth wall is made dimensionless by the distance D between the two plates, and velocities by the rough friction velocity u_{*R}.

Figure 6 shows the mean velocity profile (scaled with the maximum value of velocity u_m) together with the shear stress profile, for which the model prediction is indistinguishable of the measured values.

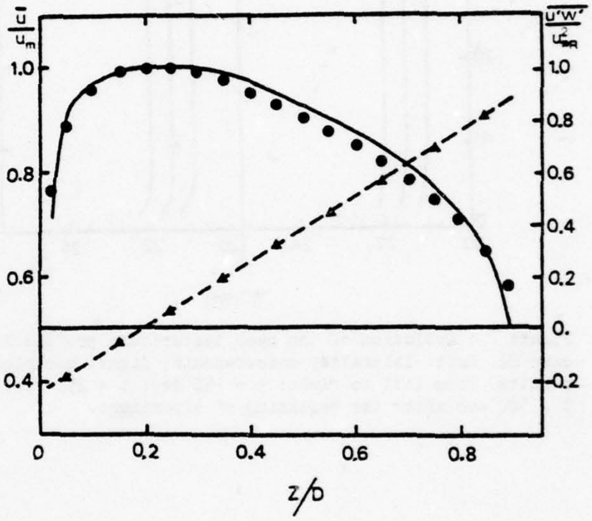

Figure 6 : Profiles of computed mean velocity (continuous line) and shear stress (dashed line). Points and triangles: experimental data.

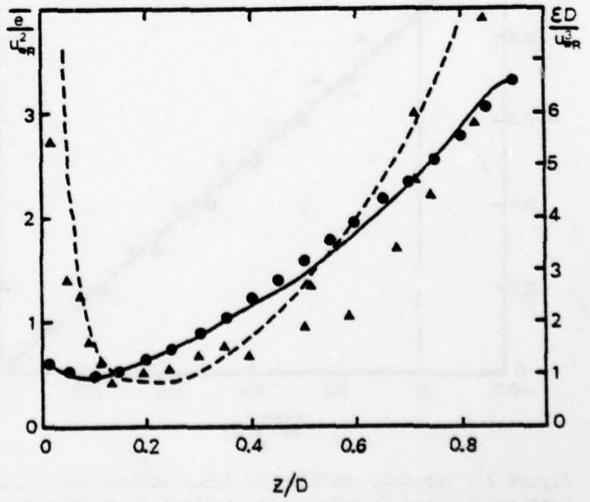

Figure 7 : Profiles of computed eddy kinetic energy (continuous line) and dissipation (dashed line). Points and triangles: experimental data.

Figure 7 compares the computed and experimental profiles of mean eddy kinetic energy and of its dissipation rate. For dissipation, data were obtained by a balance in the energy budget, and also by other methods (8). Both predicted profiles appear quite satisfactory, though, as shown by figure 8 which displays dimensionless r.m.s. velocities u_T, v_T, w_T, kinetic energy is not well distributed among its components. One can hope to remedy to this difficulty by taking into account near-wall effects in the model for presso-correlations (2). This is presently being done, along the semi-empirical way proposed by Launder et al. (2).

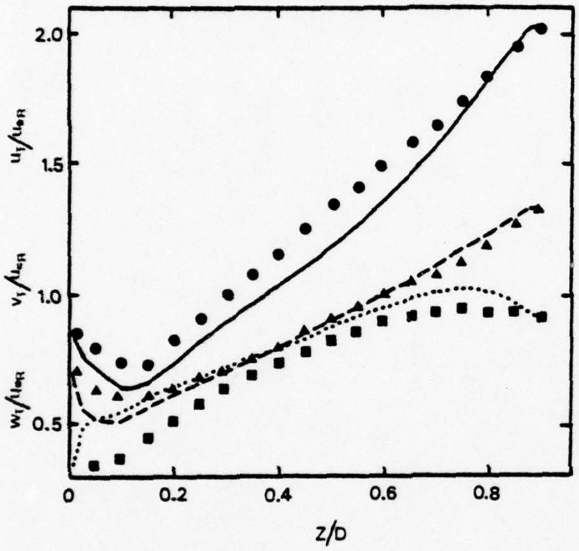

Figure 8 : Profiles of computed r.m.s. velocities (continuous, dashed, and dotted lines). Points, triangles, and squares: experimental data.

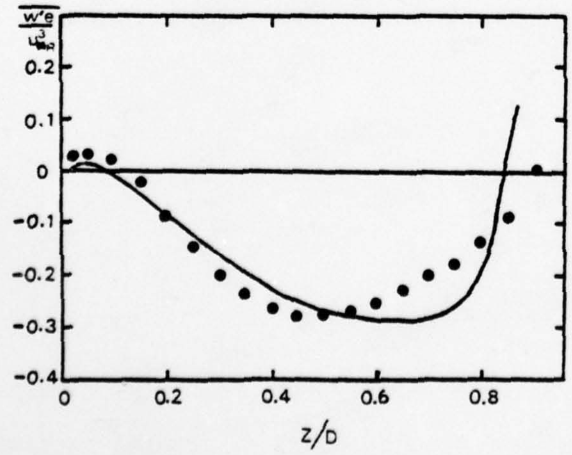

Figure 9 : Profile of computed eddy kinetic energy flux. Points: experimental data.

Figures 9 and 10 show the model results for two third order correlations, namely the kinetic energy flux (figure 9) and the shear stress flux (figure 10). One can see that the computed profiles are in rather good agreement with experimental data.

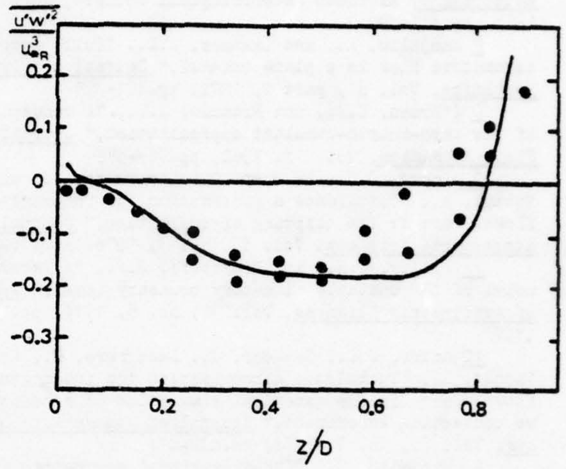

Figure 10 : Profile of computed shear stress flux. Points: experimental data.

CONCLUSION

The clipping approximation has been shown to be able to give good predictions of second and third order moments in two very different types of turbulent flows. Of course, much work remains to be done, particularly in the field of pressure effects (including near-wall effects) and dissipation parametrizations. Moreover, further testing has to be done for other type of flows, specially for those where buoyancy and shear play a comparable role. Nevertheless, this approximation appears suitable for realistic modeling of turbulent flows, and particularly those of geophysical interest, as was shown by the successful numerical simulation of the diurnal part of Day 33 from Clarke et al. Wangara experiment (14) (see André (5)).

BIBLIOGRAPHIC REFERENCES

1 Lumley, J.L., "Prediction methods for turbulent flows," Lecture Series 76, March 1975, von Karman Institute for Fluid Dynamics, Rhode-St-Genèse, Belgium

2 Launder, B.E., Reece, G.J., and Rodi, W., "Progress in the development of a Reynolds-stress turbulence model," Journal of Fluid Mechanics, Vol. 68, part 3, 1975, pp.537-566

3 Launder, B.E., "On the effects of a gravitational field on the turbulent transport of heat and momentum," Journal of Fluid Mechanics, Vol. 67, part 3, 1975, pp.569-581

4 Zeman, O., "The dynamics of entrainment in planetary boundary layers: a study in turbulence and parametrization," Ph. D. Thesis, 1975, The Pennsylvania State University, University Park, Penn.

5 André, J.C., "A third-order-closure model for the evolution of a convective planetary boundary layer," Seminars on the Treatment of the Boundary Layer in Numerical Weather Prediction, European Center for Medium Range

Weather Forecast, 1976, pp.203-233

6 Zeman, O., and Lumley, J.L., "Modeling buoyancy driven mixed layers," *Journal of Atmospheric Sciences*, Vol. 33, No. 10, 1976, pp.1974-1988

7 Donaldson, C. du P., "Construction of a dynamic model of the production of atmospheric turbulence and the dispersal of atmospheric pollutants," *Workshop on Micrometeorology*, American Meteorological Society, Boston, 1973, pp.313-392

8 Hanjalic, K., and Launder, B.E., "Fully developed asymmetric flow in a plane channel," *Journal of Fluid Mechanics*, Vol. 51, part 2, 1972, pp.301-335

9 O'Brien, E.E., and Francis, G.C., "A consequence of the zero-fourth-cumulant approximation," *Journal of Fluid Mechanics*, Vol. 13, 1962, pp.369-375

10 André, J.C., De Moor, G., Lacarrère, P., and du Vachat, R., "Turbulence approximation for inhomogeneous flows. Part I: The clipping approximation," *Journal of Atmospheric Sciences*, Vol. 33, No. 3, 1976, pp.476-481

11 Willis, G.E., and Deardorff, J.W., "A laboratory model of the unstable planetary boundary layer," *Journal of Atmospheric Sciences*, Vol. 31, No. 5, 1974, pp.1297-1307

12 André, J.C., De Moor, G., Lacarrère, P., and du Vachat, R., "Turbulence approximation for inhomogeneous flows. Part II: The numerical simulation of a penetrative convection experiment," *Journal of Atmospheric Sciences*, Vol. 33, No. 3, 1976, pp.482-491

13 Hanjalic, K., "Two-dimensional asymmetric flow in ducts," Ph. D. Thesis, 1970, University of London, London, Great-Britain

14 Clarke, R.H., Dyer, A.J., Brook, R.R., Reid, D.G., and Troup, A.J., "The Wangara experiment: boundary layer data," Paper No. 19, 1971, Division Meteorological Physics CSIRO, Aspendale, Australia

15 du Vachat, R., "Realizability inequalities in turbulent flows", to be published in *The Physics of Fluids*, April 1977

SESSION 5

NUMERICAL METHODS

Chairman: H. McDonald
Scientific Research Associates, Inc.
Glastonburg, Connecticutt 06033
U.S.A.

5

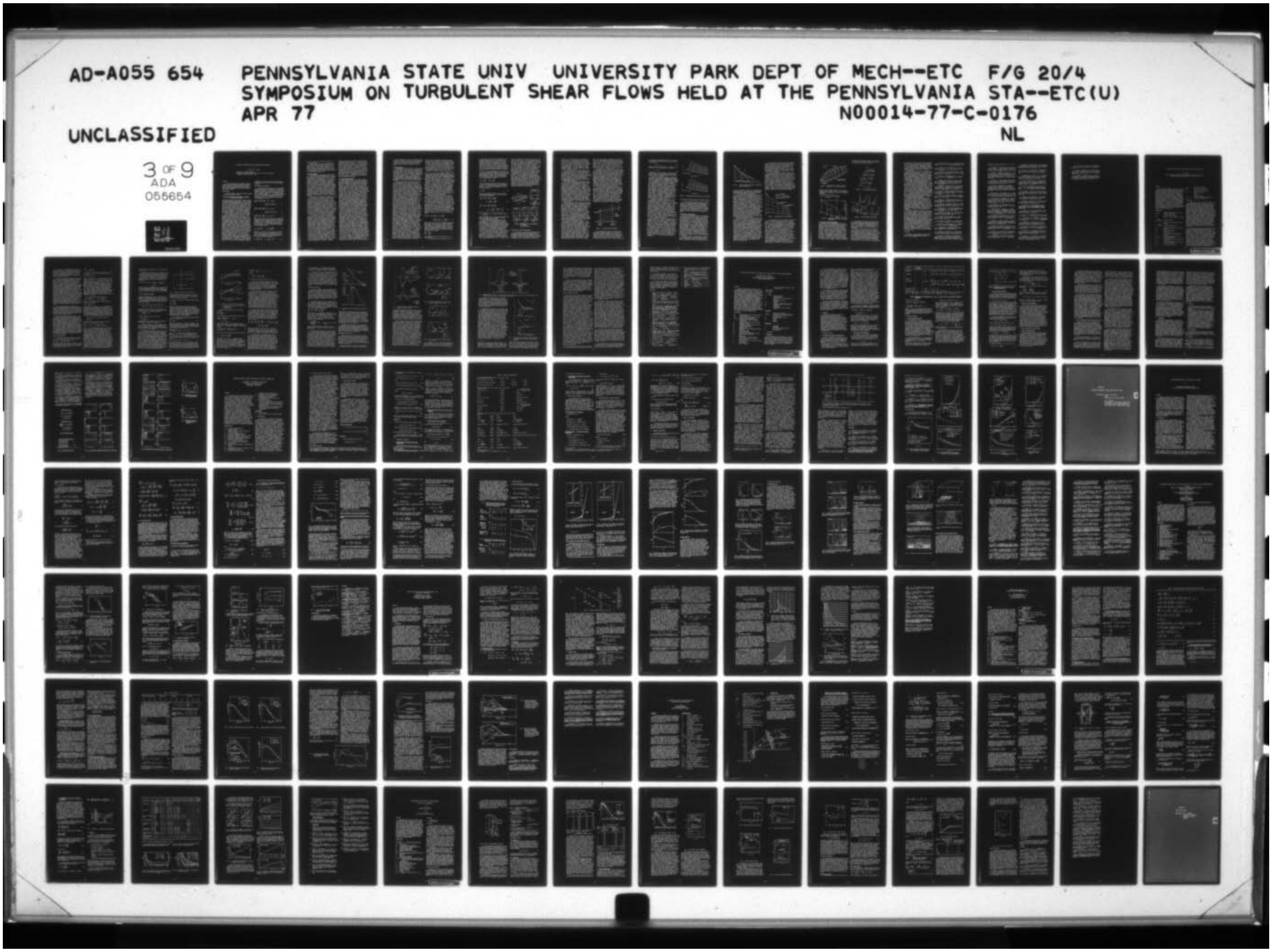

AD-A055 654 PENNSYLVANIA STATE UNIV UNIVERSITY PARK DEPT OF MECH--ETC F/G 20/4
SYMPOSIUM ON TURBULENT SHEAR FLOWS HELD AT THE PENNSYLVANIA STA--ETC(U)
APR 77 N00014-77-C-0176
UNCLASSIFIED NL

3 OF 9
ADA
055654

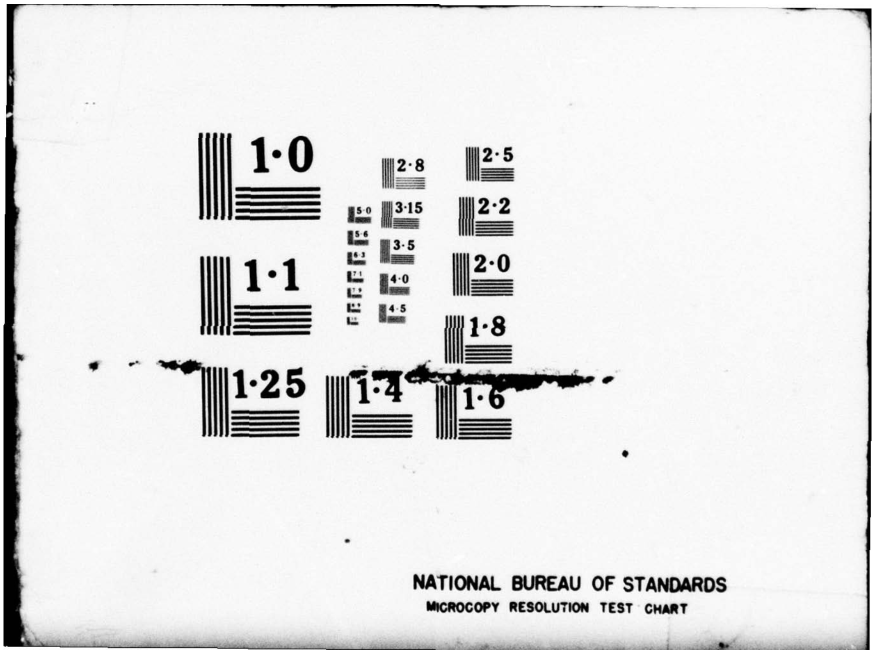

NATIONAL BUREAU OF STANDARDS
MICROCOPY RESOLUTION TEST CHART

ADVANCES IN TURBULENT BOUNDARY LAYER CALCULATION METHODOLOGY

by

J.F. Nash* & V.C. Patel**

* Sybucon Inc., Atlanta, Georgia
** Division of Energy Engineering and Institute of Hydraulic Research
University of Iowa, Iowa City, Iowa.

ABSTRACT

A review is made of recent advances in the computation of three-dimensional turbulent boundary layers. Emphasis is placed upon those areas which have received the greatest attention, but problem areas are also identified where further research is most urgently needed.

INTRODUCTION

In 1967, Spalding [1] proposed a Reynolds number to characterize research effort

$$\frac{\text{(size of team)(speed of work)(density of effort)}}{\text{(viscosity of subject)}}$$

and surmised that this must attain a critical value before the augmentation and spread (turbulent mixing) of information becomes appreciable. It can be safely said that for three-dimensional turbulent boundary layers the critical value has not been reached since there is little evidence of any instability! There is little doubt, however, that the subject is highly viscous and that the size and density of effort, as well as the speed of the prime worker, the computer, are all on the increase. Our European colleagues have huddled together in two recent conferences on this topic (Euromech 33, Berlin 1972, and Euromech 60, Trondheim 1975) and reached similar conclusions.

Since the publication of our review of three-dimensional turbulent boundary layers [2] in 1972 some progress has been made on the modeling of turbulence on the one hand, and on the computation of complex turbulent flows on the other. For the present purposes we shall confine our attention largely to the computational aspects. Although a number of fundamental studies are being conducted on the relatively well documented case of thin two-dimensional boundary layers, the main thrust in boundary-layer research appears to be shifting towards more complex flows. In two dimensions this has led to work on the development of turbulence models with wider applicability, interacting shear layers, viscous-inviscid interactions, and even separated flows, although some of these cannot really be treated within the framework of boundary-layer theory alone. The three-dimensional boundary layer is a complex flow of a somewhat different variety. Here, the problems of arbitrary surface geometry and the specification of the relevant initial and boundary conditions are just as complicated as the problem of the solution of the mean-flow equations. Indeed, from a purely computational point of view, the three-dimensional laminar boundary layer is just as complex as its turbulent counterpart, and both demand a considerable amount of ingenuity.

DEVELOPMENTS IN THE THEORY

In the conventional treatment of a thin boundary layer developing on a surface of small curvatures the equations of momentum and continuity are written in a coordinate system (x,y,z) such that lines of constant x and z form an orthogonal net on the surface, y=0, and y is measured normal to it. Denoting the pressure impressed by the external flow on the boundary layer by p(x,z) and the velocity components in the (x,y,z) direction by (U,V,W), the boundary-layer equations for incompressible flow are:

$$\frac{U}{h_1}\frac{\partial U}{\partial x} + V\frac{\partial U}{\partial y} + \frac{W}{h_3}\frac{\partial U}{\partial z} + (K_{13}U - K_{31}W)W + \frac{1}{h_1}\frac{\partial}{\partial x}\left(\frac{p}{\rho}\right) - \frac{\partial}{\partial y}\left(\frac{\tau_x}{\rho}\right) = 0 \tag{1}$$

$$\frac{U}{h_1}\frac{\partial W}{\partial x} + V\frac{\partial W}{\partial y} + \frac{W}{h_3}\frac{\partial W}{\partial z} + (K_{31}W - K_{13}U)U + \frac{1}{h_3}\frac{\partial}{\partial z}\left(\frac{p}{\rho}\right) - \frac{\partial}{\partial y}\left(\frac{\tau_z}{\rho}\right) = 0 \tag{2}$$

$$\frac{1}{h_1}\frac{\partial U}{\partial x} + \frac{\partial V}{\partial y} + \frac{1}{h_3}\frac{\partial W}{\partial z} + K_{31}U + K_{13}W = 0 \tag{3}$$

Here, $h_1(x,z)$ and $h_3(x,z)$ are the metric coefficients associated with the x- and z-direction, respectively; K_{13} and K_{31} are the geodesic curvatures of the lines of constant x and z, respectively; ρ is the fluid density; τ_x and τ_z are the shear stresses in the x- and z-directions. The two curvatures are related to the metric coefficients by

$$K_{13} = \frac{1}{h_1 h_3}\frac{\partial h_1}{\partial z}, \qquad K_{31} = \frac{1}{h_3 h_1}\frac{\partial h_3}{\partial x} \tag{4}$$

Equations (1) through (3) apply directly to laminar flows, but also to turbulent boundary layers if (U,V,W) are regarded as the time-averaged velocities and the shear stresses are written as the sums of the viscous and Reynolds stresses, i.e.

$$\tau_x = \mu\frac{\partial U}{\partial y} - \rho\overline{uv}, \qquad \tau_z = \mu\frac{\partial W}{\partial y} - \rho\overline{vw} \tag{5}$$

where (u,v,w) are the velocity fluctuations in the (x,y,z) directions.

Before describing the recent developments in the treatment of the equations listed above it is useful to review briefly several aspects of more general nature. These concern the selection of a coordinate system, some special classes of flow for which the equations become somewhat simpler, and the models available for the closure of the equations of the turbulent boundary layer.

Coordinate Systems

In the calculation of boundary-layer development on arbitrary three-dimensional bodies, such as finite wings, fuselages and ship forms, an important problem that has to be resolved first is the choice of a convenient coordinate system. The locally orthogonal system considered above is quite general insofar as it offers a wide variety of choices including the intrinsic or streamline coordinates. However, several recent workers have suggested the use of the even more general nonorthogonal coordinates although only a few isolated attempts have been made to incorporate them in a computation procedure. In either case, the freedom of choice of a coordinate system for a particular problem is restricted somewhat by the nature of the geometry under consideration and by the availability of the necessary boundary conditions. A convenient coordinate system can usually be identified for certain classes of problems, while for others it may not be immediately obvious.

In calculation methods based on integral equations of the boundary layer, it has been customary to adopt the streamline coordinate system. This is largely due to the fact that the physical inputs concerning the velocity profile shapes, friction formulae and other auxiliary relations required for closure of the equations are best formulated by reference to the streamlines outside the boundary layer. The major drawback of this approach is that the coordinate system changes whenever the external flow is altered by changes in the orientation of the surface or the characteristics of the oncoming stream. Even with integral equations, however, it is possible to revert to the more general coordinate systems discussed earlier provided suitable transformations are made prior to the solution of the equations.

On the basis of our collective experience to date it is possible to identify certain general guidelines for the selection of a coordinate system and also point out those areas which need further attention. First of all, parabolicity of hyperbolicity of the governing differential equations suggests that one set of coordinate lines should be pointed roughly in the "downstream" direction. For most practical purposes, downstream may be taken as the general direction of the flow outside the boundary layer. Secondly, an attempt should be made to ensure the coincidence of coordinate lines with lines or geometrical boundaries along which the flow characteristics are known or can be invented with some physical justification. Finally, as a favor to the potential user, it is desirable to include the construction of the coordinate system as a part of the boundary-layer computation procedure and ensure that the pressure distribution on the surface can be prescribed readily. It is unlikely that all of the above requirements can be met by a computation procedure which is at the same time general enough to be used for a variety of surface configurations of interest. However, substantial progress can be made in this direction by learning and making use of the large body of knowledge in differential geometry. It is worth noting that most calculation procedures for three-dimensional boundary layers currently under development utilize ad hoc coordinate systems. On the other hand the solution should properly be independent of the coordinate system used to generate it. It is therefore interesting to surmise on the influence of the choice of coordinates on the final results irrespective of the other numerical and physical contents. Suitable checks have simply not been applied to ascertain this effect, but it is imperative that such investigations be carried out to establish the credibility of the computation procedures.

Quasi-Two Dimensional Flows

Although the equations of the general three-dimensional boundary layer can be found in many early papers and textbooks, their complexity deterred the early investigators from tackling them with complete generality. There has therefore been a continuing interest in identifying types of flow for which the equations take some simple forms by virtue of geometric symmetries, and also types of flow where valid approximations can be made. Notable examples of such special cases in the first category are: two-dimensional flows, axially symmetric flows, infinite-yawed-cylinder flows, the flow along an attachment line, and the flow along a plane of symmetry. In the second cateogry are the well known approximation of small crossflow and the flow near a stagnation point. The particular forms of the equations for these special cases have been discussed elsewhere [2]. Here we shall simply consider their relevance to the solution of the complete three-dimensional boundary-layer equations. Continued experimental and theoretical studies of these cases are obviously important not only because they provide valuable information for the understanding of the complete problem but also supply the necessary initial and boundary conditions for its solution. Thus, for example, the solutions of Howarth [3], Squire [4] and Darcy [5] for the boundary layer near a stagnation point can be used to initiate the complete solution of the boundary layer on a blunt-nosed body, while the attachment-line flow investigated by Cumpsty and Head [6,7] determines the initial conditions along the leading edge of a swept wing. On the other hand, the flow along a plane of symmetry, which can be computed independently using the simpler equations, can provide the boundary conditions for calculation on, say, ship forms, bodies of revolution at incidence, and fuselages, all of which contain at least one plane of symmetry. This particular case is therefore of great practical significance. This is amply demonstrated by the recent computations performed by Wang [8] for the laminar boundary layers on the planes of symmetry of prolate spheroids at incidence. Wang's work suggested that a considerable amount of information on the overall behavior of the boundary layer, including separation, could be extracted by examining the results of these relatively simple computations. Secondly, these plane-of-symmetry solutions proved to be of great value in formulating the methods required to calculate [9,10,11] the boundary-layer development over the entire body. Although some data exist [12; 13,14] on the behavior of a turbulent boundary layer along a plane of symmetry, additional detailed studies are needed to improve our understanding of this special case. Some progress has been made in this direction in the recent study of Head and Prahlad [15]

It should be noted that the basic difference between the plane-of-symmetry flow and the much explored two-dimensional flow is the existence of convergence or divergence of streamlines on either side of the symmetry plane, although the crossflow itself is zero.

Turbulence Models

A considerable amount of effort has been devoted in recent years to the development of comprehensive turbulence models. Most of the recent work has been reviewed in some detail by Launder and Spalding [16] and Reynolds [17]. We do not propose to repeat this effort here even for the case of the three-dimensional turbulent boundary layer. Instead, we shall examine the models that have actually been utilized in three-dimensional boundary-layer computations and summarize some of the important similarities and differences in the results that have been obtained to date.

By far the most common turbulence model that has been employed so far is the isotropic eddy-viscosity model (see, for example, [18,19,20,21,22, 23,24,25]) or its half-brother, the mixing length model. While there are a great many conceptual objections to this so-called zero-equation model, there are some justifications for its present widespread use, the most obvious one being simplicity. It was initially thought that the model offerred a distinct advantage since the basic numerical procedures could also be used to study laminar and transitional boundary layers. However, such possibilities also exist with even the most advanced turbulence models since the turbulence can be "switched off" if desired. The performance of the eddy-viscosity and mixing-length models has been compared against several sets of well known experimental data. These include the obstacle flow of East and Hoxey [13], the curved-channel experiments of Vermeulen [26] and the infinite swept-wing measurements of Bradshaw and Terrell [35] and van den Berg et al [24]. Among the main conclusions to be drawn from these studies are the following: (a) Although the precise variations of the eddy-viscosity and mixing-length across the boundary layer, and the numerical methods used to solve the equations, differ from one investigator to another, the basic predictions of the methods are quite similar. This is indeed a testimony to the increasing numerical expertise in this business. (b) These models give reasonably accurate predictions of the flows considered insofar as the mean velocity profiles and the general development of the boundary layer is concerned provided the regions near separation are excluded. (c) As evidenced by the Stanford-style competition at Trondheim [28] and other attempts, none of the turbulent-flow methods has succeeded in the prediction of flow separation with any degree of accuracy even for such special cases as the infinite swept wing. The prediction of separation lines, such as those observed in front of obstacles or on bodies of revolution at incidence, appears even more remote. The difficulty is compounded by the lack of a generally accepted definition of separation. (d) The somewhat encouraging results obtained with the eddy-viscosity models have led to their extension to computation of flows over quite complicated geometries such as complete wings [29] and ship hulls [18,21]. Some caution is advised in the interpretation of these results, however, in view of the observation that the models have been tested against data of a somewhat limited nature. The overall reliability of the methods for performing routine calculations in aerodynamic and hydrodynamic applications therefore needs to be demonstrated by comparison with a much wider variety of experimental data. It appears that such data may soon become available.

In the more advanced turbulence models the Reynolds stresses are deduced from additional differential equations which, in turn, are obtained from the transport equations of one or more of the following quantities: the turbulent kinetic energy $(k = \frac{1}{2}(\overline{u^2} + \overline{v^2} + \overline{w^2})^{1/2}$, the rate of energy dissipation (ε), and the Reynolds stresses themselves. The various terms in the exact transport equations are approximated (modeled) by making suitable hypotheses, justifying them on the basis of experimental data and/or physical reasoning, so that the end result is an equation, or set of equations, which relate the Reynolds stresses occurring in the mean-flow equations to the rest of the unknowns, namely the mean velocity components. In the context of two-dimensional boundary layers, where $\overline{uv}$ is the only unknown Reynolds stress, the resulting models are classified as one-equation or two-equation models [16,17], depending on the number of additional differential equations generated to affect the closure of the mean-flow equations. Such a classification is rendered somewhat meaningless in the case of three-dimensional turbulent boundary layers where there are two unknown Reynolds stresses ($\overline{uv}$ and $\overline{vw}$), and the additional relationships may consist of combinations of differential and algebraic equations.

The geneology of the models based on the turbulent kinetic-energy equation and the transport equations for the Reynolds stresses, as they relate to the problem of three-dimensional turbulent boundary layers, was outlined in our previous review [2]. The earliest attempt to generalize the then flourishing turbulent kinetic-energy method of Bradshaw et al. [30] to the case of three-dimensional boundary layers was made by Nash [31]. There it was shown that the two-dimensional version of the model could easily be adopted to three dimensions by making appropriate modifications in the convection and production terms, leaving the diffusion and dissipation terms unchanged. This results in an equation for the magnitude of the Reynolds stress, $\tau\ [\equiv \rho(\overline{uv}^2 + \overline{vw}^2)^{1/2}]$, which is assumed to be proportional to the turbulent kinetic energy:

$$\frac{U}{h_1}\frac{\partial\tau}{\partial x} + V\frac{\partial\tau}{\partial y} + \frac{W}{h_3}\frac{\partial\tau}{\partial z} + 2a_1\ [\rho\overline{uv}\frac{\partial U}{\partial y} + \rho\overline{vw}\frac{\partial W}{\partial y} + \frac{\partial}{\partial y}(a_2\tau) + \frac{\tau^{3/2}}{\rho^{1/2}L}] = 0 \qquad (6)$$

Here, $2a_1$ ($\equiv \tau/\rho k = 0.30$) is a constant, and a_2 and L are the same functions of y/δ, as in the two-dimensional case; a_2 is a diffusion parameter and L is identified with the dissipation length. In order to close the mean-flow equations, Nash introduced the additional assumption that the resultant turbulent shear stress acts in the same direction as the resultant mean rate-of-strain:

$$\frac{\overline{uv}}{\overline{vw}} = \frac{\partial U/\partial y}{\partial W/\partial y} \qquad (7)$$

The corresponding result for laminar flow is, of course, exact.

In the subsequent work of Bradshaw [32], the last assumption was avoided by consideration of the transport equations of the two Reynolds stresses. Numerical experiments performed to compare the two assumptions showed little difference in the predictions of the mean-flow parameters for several representative cases. Although some doubt has been cast on this observation in some recent publications, there is as yet no definitive evidence to indicate that the directional response of the shear stress has a significant effect on the computation of the mean flow.

The third turbulence model we shall consider is that due to Launder and Spalding [33] which is a generalization of an earlier two-dimensional model developed at Imperial College. Here, the turbulent Reynolds stresses are related to the corresponding mean rate-of-strain by an isotropic eddy viscosity, ν_T, in the usual manner, namely

$$-\overline{uv} = \nu_T \frac{\partial U}{\partial y}, \quad -\overline{vw} = \nu_T \frac{\partial W}{\partial y} \tag{8}$$

However, instead of specifying the distribution of ν_T across the boundary layer as in the conventional approach, it is related to the turbulent kinetic-energy, k, and its rate of dissipation, ε, via the well known relation

$$\nu_T = c_\mu \frac{k^2}{\varepsilon} \tag{9}$$

where c_μ is a constant (=0.09). In turn, k and ε are obtained from the modeled transport equations (in Cartesian coordinates)

$$U \frac{\partial k}{\partial x} + V \frac{\partial k}{\partial y} + W \frac{\partial k}{\partial z} = \frac{\partial}{\partial y} \left(\frac{\nu_T}{\sigma_k} \frac{\partial k}{\partial y}\right) + \nu_T \left\{ \left(\frac{\partial U}{\partial y}\right)^2 + \left(\frac{\partial W}{\partial y}\right)^2 \right\} - \varepsilon \tag{10}$$

$$U \frac{\partial \varepsilon}{\partial x} + V \frac{\partial \varepsilon}{\partial y} + W \frac{\partial \varepsilon}{\partial z} = \frac{\partial}{\partial y} \left(\frac{\nu_T}{\sigma_\varepsilon} \frac{\partial \varepsilon}{\partial y}\right) + c_1 \frac{\varepsilon}{k} \nu_T \left\{ \left(\frac{\partial U}{\partial y}\right)^2 + \left(\frac{\partial W}{\partial y}\right)^2 \right\} - c_2 \frac{\varepsilon^2}{k} \tag{11}$$

where c_1 (=1.44), c_2 (=1.92), σ_k (=1.0) and $\sigma_\varepsilon \left(\equiv \frac{k^2}{\sqrt{c_\mu}(c_2 - c_1)} = 1.1\right)$ are all empirical constants (see, for example, [16]). It will be noted that this model also implies the coincidence of the shear stress and rate-of-strain vectors.

The three transport-equation models listed above apply only to the fully-turbulent region of the boundary layer. The sublayer and transition zones adjacent to the surface require special treatment. This usually takes the form either of matching the fully-turbulent flow solution to the conditions at the wall using some generalized form of the law of the wall, or of introducing further empirical modifications into the turbulence model and continuing the calculation down to the surface. Significant uncertainties are present in both approaches.

Of the three advanced turbulence models discussed above, the most widely tested and utilized is that of Nash and Patel [2]. The general level of agreement with experimental data obtained with this model is well illustrated by Figure 1, taken from several such comparisons shown in [2]. Neither of the other two models has been tested sufficiently to indicate its superiority. It will be recalled that the modification of Bradshaw, as incorporated in our model, does not give significant improvements in performance. The Launder-Spalding model was used recently by Spalding, Singhal, Rodi and Rastogi to compute all of the seven test cases at the "Trondheim Trials." However, its performance was judged to be somewhat inconsistent insofar as its results deviated considerably from the various integral and differential methods tested there [34]. The test cases at Trondheim consisted of four hypothetical cases for which no experimental data exist; of the remaining three, two were of the infinite-swept-wing type [35,27]. Moreover, only one differential method (Spalding, et al.) was able to complete the computations for all seven cases. Conceptually, the advanced turbulence models represent an improvement upon the usual eddy-viscosity approach. However, it is clear that only the eddy-viscosity methods of Cebeci [21] and Chang and Patel [18] and the turbulent kinetic-energy method of Nash and Patel [2,36] have computationally progressed to a level where meaningful comparisons can be made with experimental data gathered from quite different and general flow geometries.

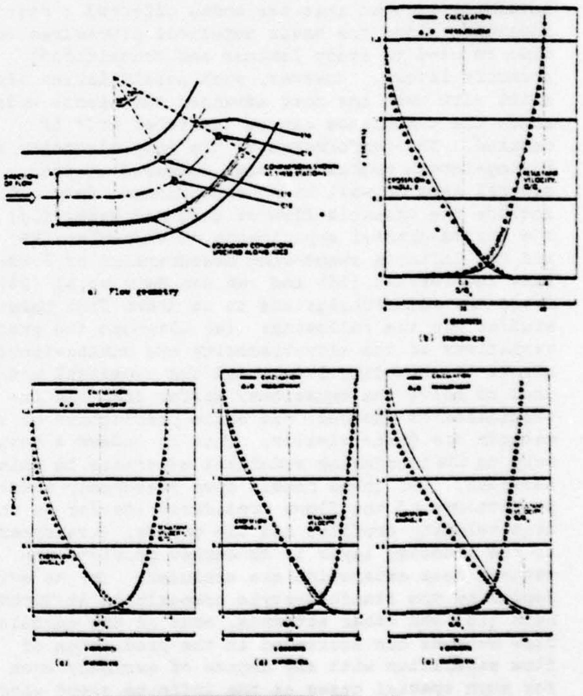

FIGURE 1. COMPARISON WITH THE MEASUREMENTS OF VERMEULEN
Nash and Patel [2]

DEVELOPMENTS IN SOLUTION METHODOLOGY

The development of appropriate methods for solving the partial differential equations describing turbulent boundary layers has run parallel to, but not always in step with, the development of the underlying theory. Often, particularly in the early days of boundary layers, a great volume of theory has existed without adequate means for translating it into solutions. On the other hand, more recently there seem to have been periods when the sophistication of solution methods outstripped the sophistication of the theory. Furthermore, at any one time, it has usually been possible to identify inappropriate combinations: of a good theory and a poor computation method, or a poor theory and a superior computation method. Certainly there are examples of both in existence today.

In the early days of turbulent boundary layers the need was for methods for solving the equations in a two-dimensional domain. This was true both for two-dimensional flows, as such, and also for axisymmetric flows, boundary layers with small crossflow, and boundary layers on infinite yawed cylinders. The last two classes of flow involve components of velocity and shear stress normal to the domain, but not derivatives normal to the domain; hence a two-dimensional domain suffices.

This factor, together with the relatively high ratio of ingenuity to computer facilities, provoked the emergence of integral methods of solution [37]. The objective in these methods was to reduce the boundary-layer equations to a set of ordinary differential equations which could be integrated in the downstream longitudinal direction. A further, and essential practical, objective was to keep the number of resulting equations to a minimum. In the case of incompressible two-dimensional or axisymmetric flows this proved relatively easy. Whether or not the ordinary differential equations were derived formally by taking moments of the original partial differential ones, and whether or not profile families were explicitly specified, it emerged that reasonable precision could be achieved using only small numbers of dependent variables and an equally small number of resulting equations. These equations would usually be solved by hand.

Compressibility presented a complicating factor to which the proponents of integral methods responded with some measure of success. Particularly in the case of adiabatic walls certain integral methods could be extended to compressible flow without undue difficulty. Flows with heat transfer, however, presented major problems. Three-dimensionality presented even more serious complications. One reason for this lay in the difficulty of representing the vector velocity profile by a suitable functional form. It became apparent that larger and larger numbers of disposable parameters would be required in order to provide the necessary generality [2], and for each additional parameter an additional governing equation is required. Other reasons involved the representation of the turbulent shear stress in the three-dimensional flow.

Conceptually, the integral approach, in its broadest sense, can be used to solve sets of equations of almost any degree of complexity. However a point of complexity occurs beyond which this approach ceases to provide an economically competitive mode of solution. Thereafter, at least as the issue is judged at this time, direct numerical solution of the partial differential equations offers more prospect of success. Actually, there is not a sharp dividing line between integral methods and direct numerical methods. Rather the two approaches lie towards opposite ends of a continuum. Integral methods involve the use of complicated functional forms to approximate the solution over significant portions of the domain. Direct numerical methods involve division of the domain into a much larger number of elements over which the solution is approximated by more primitive functional forms. By far the most popular method of direct numerical solution: the finite-difference method, seeks to determine the solution at discrete node points in the domain. This is the approach that we shall concentrate on here, but it is worth mentioning that it is not the only approach; possibly, in the last analysis, it may not turn out to be the best one.

Introduction of the boundary-layer approximations into the original, more general, set of partial differential equations produces a new set of equations which are non-elliptic: they may be parabolic or hyperbolic, depending on details of the turbulence modeling. Be that as it may, the non-ellipticity offers the possibility of integrating the equations by means of a forward-marching procedure. In flows to which a two-dimensional integration domain is appropriate (see above) the forward marching procedure advances "downstream" relative to the major velocity components parallel to the domain. A solution is sought along a normal to the body surface, at a station some distance downstream of another station where the solution is already known from an earlier stage of the calculation or from specified initial conditions.

In terms of the finite-difference framework, the solution sought, at the downstream station, is represented by values of a vector: F, say, at discrete node points along the normal (Figure 2). The elements of F will generally be the principal dependent variables: the velocity components (excluding the normal one, V, which is usually calculated retrospectively from the continuity equation), the local static temperature, certain turbulence parameters, and so forth. Sometimes transformed versions of some of the variables are used, e.g. stream function. In the simplest case of two-dimensional, incompressible, laminar flow, the vector may degenerate to a scalar; in other cases it contains two or more elements.

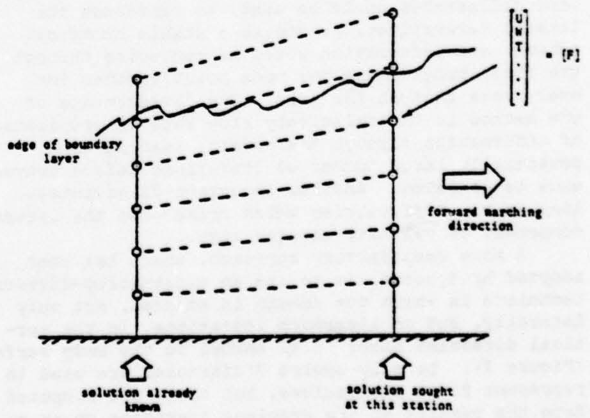

FIGURE 2. FORWARD-MARCHING PROCEDURE

Finite-difference methods can be divided into two classes according to whether the vectors, for different node points along the normal, are calculated individually (explicit methods), or collectively (implicit methods). More specifically the difference between the two classes can be stated as follows. If the solution along the normal is itself represented by a vector Q, whose elements are the F's, then the forward-marching procedure leads to an equation for Q of the form

$$PQ = R \tag{12}$$

where P is a square matrix and R is a vector of the same order as Q. The solution is, of course,

$$Q = P^{-1}R \tag{13}$$

(assuming that P has an inverse). Explicit methods are such that P is a diagonal matrix, which has a trivial inverse: implicit methods are such that inversion of P is non-trivial.

In place of the simple concept of upstream and downstream, first-order, three-dimensional boundary-layer theory offers zones of dependence and influence [38,2]. Determination of the solution along a normal to the body surface, at some station, involves a calculation extending over the zone of dependence of that station, and marching towards it. One of the most important properties of zones of dependence is that conditions at more than one station on the body affect the solution at the station to which the zone refers. The forward-marching procedure must consequently deal with a sequence of two-dimensional arrays of solution vectors (F) rather than with a sequence of one-dimensional arrays (G) of those vectors. It therefore becomes necessary to scan the zone of dependence, in some manner, to capture the lateral passage of information from one vector solution to another. The success of this scanning process is a strong determining factor in the success of the method as a whole.

One method of scanning would consist, simply, of a succession of passes, through the zone of dependence from one end to the other: i.e. always in the same direction. This method would be adequate so long as the component of mean velocity in the direction of scan were everywhere positive. Backward differences could be used, to represent the lateral derivatives, providing a stable numerical scheme, and information would be convected through the zone, progressing one node point further for every pass through the zone. One disadvantage of the method is the relatively slow rate of propagation of information through the domain, leading to a potentially large number of iterations before convergence is achieved. Another important disadvantage lies in the difficulties which arise when the lateral component of velocity changes sign.

A more satisfactory approach, which has been adopted by Sybucon, is to use an alternating-direction technique in which the domain is scanned, not only laterally, but on alternate iterations, in the vertical direction also: i.e. normal to the body surface (Figure 3). Locally upwind differences are used to represent first derivatives, but these are computed from the results of the previous iteration so as to avoid stability problems when the direction of scan is "upstream" relative to the lateral velocities. An important advantage of the alternating-direction-implicit (ADI) method is the fast convergence achieved, and a major contributing factor is the provision of a numerical mechanism - the vertical scanning iterations, during which the solution is sought along a lateral line - for the rapid lateral transfer of information.

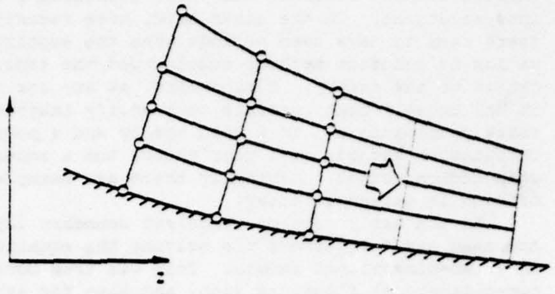

(a) Horizontal Scan

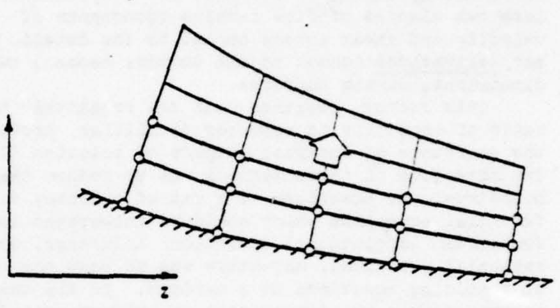

(b) Vertical Scan

FIGURE 3. ALTERNATING-DIRECTION-IMPLICIT (ADI) SCHEME

APPLICATIONS OF THREE-DIMENSIONAL CALCULATION METHODS

In this section we propose to survey the applications of the three-dimensional boundary-layer calculation procedures that have been discussed. The emphasis will be placed on illustrating the types of problems that can be handled in aeronautics as well as naval hydrodynamics rather than on a comparative evaluation of different methods. Illustrative examples are drawn largely from the work of the authors and their collaborators over the past few years.

Applications in Aeronautics

One of the first applications of the older explicit method of Nash and Patel [36] for calculating three-dimensional turbulent boundary layers was to the supercritical wing of the NASA modified-F8 research airplane [39]. The wing geometry was highly three-dimensional, but was approximated by two segments which could be described by polar coordinate systems (see Figure 4). A boundary-layer calculation was performed first for the inboard segment, and then a subsequent calculation was performed for the outboard segment. Interfacing of the solution was prescribed along a line common to both segments. A considerable amount of hand-work was necessary in the calculations because only primitive methods of handling the geometry and pressure distribution were available at that time. Nevertheless, much was learned from the exercise, and the experience gained provided the groundwork for later, more satisfactory wing programs.

The first series of calculations on the NASA F-8 wing were done using wind-tunnel pressure distributions. Some additional ones were performed using pressures measured in flight, and the original inten-

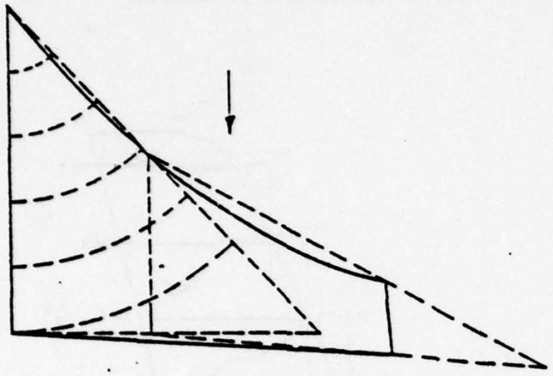

FIGURE 4. CONICAL COORDINATES FOR FINITE SWEPT WING
Nash and Scruggs [39]

tion was to compare the results with boundary-layer measurements from the flight tests. Unfortunately, only preliminary boundary-layer data were measured before the flight program was cancelled.

A later series of calculations was made for the Lockheed C5 wing, using an improved version of the explicit method. This later method was arranged to handle a large number of segments of the wing, each bounded by streamwise cuts. The calculation started with the inboard segment and proceeded outboard, one segment at a time, with appropriate interfacing. A significant feature of this method, which also proved useful in subsequent work, was the use of a non-rectangular grid (placed on the planform of the wing) combined with a rectangular coordinate system for describing the velocities and shear-stress components. Such a scheme allows the use of yawed panels but avoids the complexities of a fully non-orthogonal coordinate system. The results of the calculations made for the C5 wing were compared with flight boundary-layer measurements, and the comparisons were good, bearing in mind the difficulties of making reliable observations under flight conditions. The comparisons certainly lay claim to be the ones made at the highest-ever Reynolds number.

Another application of the explicit method was to the rotor of a helicopter in forward flight [40]. The rotor is, of course, a high-aspect-ratio configuration, but significant radial momentum transport occurs, partly because of the changing conditions along the blade (the inboard sections may be in a locally reversed-flow environment) and partly because of centrifugal effects. One of the objectives of the series of calculations performed was to determine the precise importance of these spanwise phenomena. This objective was partially achieved, but the calculations, as a whole, were of little use because they were based on the assumption of quasi-steady flow. It was believed naively, at that time, that the effects of time-dependence would be small at representative advance ratios. However it soon emerged that the calculations predicted extensive boundary-layer separation under conditions where the actual rotor was unstalled. The lessons learned provided the incentive for the extension of the method to unsteady flows.

The newer implicit methods for three-dimensional boundary layers are likely to be applied much more extensively because of their lower computation times, and also because more sophisticated geometry- and pressure-handling schemes have been built in. The implicit method developed at Sybucon, which treats both laminar and turbulent boundary layers in steady compressible flow, has, so far, been applied to airplane wings and fuselages.

One of the features of the method is the use of a local orthogonal coordinate system erected on each of many panel elements into which the body surface is segmented. In the case of a wing, the panels are formed by first dividing the wing into strips by means of vertical cuts, parallel to the center-plane of the aircraft (Figure 5), and then dividing each strip into an equal number of segments by means of lines of roughly constant percentage of local chord. In the case of a fuselage, the initial series of vertical cuts is made at right angles to the longitudinal axis of the aircraft, and the subsequent segmentation along lines of roughly constant angular position around the periphery (Figure 6). In both cases, the panel elements consist of warped quadrilaterals whose geometry can be described readily by the local coordinate system.

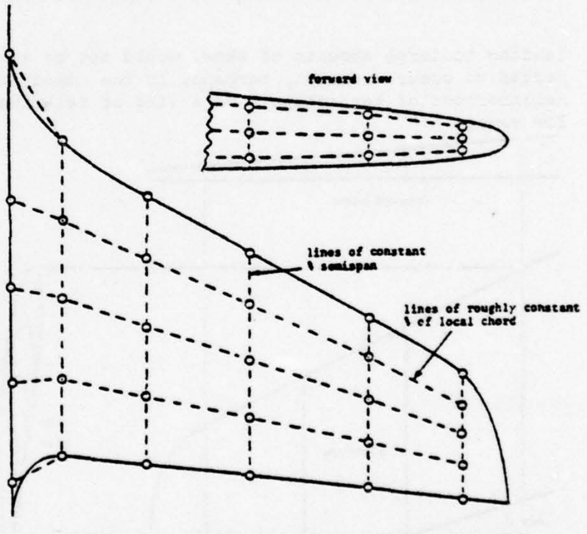

FIGURE 5. REPRESENTATION OF WING GEOMETRY

A wing calculation, which illustrates the application of the method is shown in Figures 7 through 9. Figure 7 shows the wing geometry: a thick, tapered swept wing, with a leading-edge sweep of approximately 26°. Flight pressure data exist for the wing in question, consisting of measurements along four streamwise rows: designated Rows A, B, C, and D (with Row A closest to the tip, and Row A closest to the wing root). Figure 8 shows the pressure coefficient along the four rows, for a Mach number of 0.84, at which a shock of significant strength exists over the two interior rows and a bifurcated shock over the outboard row. Figure 9 shows an overview of the results of the calculation. Separation is predicted to occur over part of the span, as indicated by the boundary plotted on the planform sketch. Inset are three representative velocity profiles, plotted in the form of streamwise and crossflow components. Two of the profiles exhibit a small degree of skew (of opposite sign in the two cases); the third profile is almost coplanar. Substantial streamline rotations,

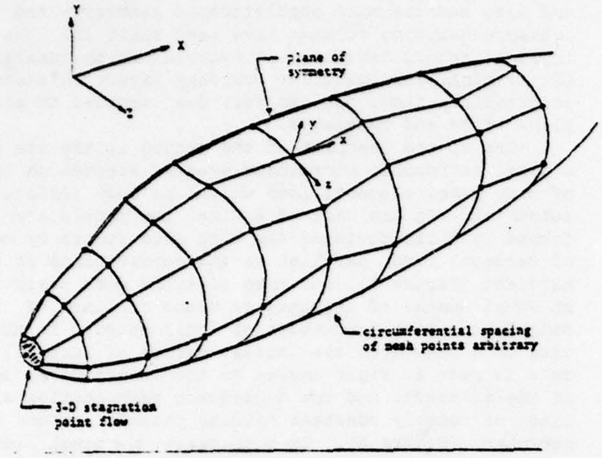

FIGURE 6. REPRESENTATION OF FUSELAGE GEOMETRY

leading to large amounts of skew, would not be expected to occur - except, perhaps, in the immediate neighborhood of separation - on a wing of relatively low sweep.

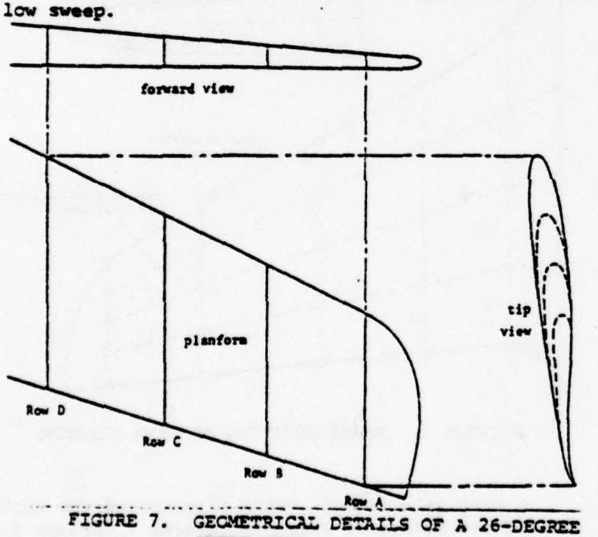

FIGURE 7. GEOMETRICAL DETAILS OF A 26-DEGREE SWEPT WING

Applications in Naval Hydrodynamics

The shapes of basic interest in naval hydrodynamics are of course different from those in aeronautics and therefore require somewhat different geometry-handling techniques in the computation procedures. Of the few configurations of common interest, however, the one that poses challenging problems in three-dimensional boundary-layer theory, as well as general viscous flow phenomena, is the flow past bodies of revolution at incidence. The interest in naval applications stems from the need to predict the performance of underwater vehicles, while that in aerodynamics relates to missiles and projectiles. Although the speed ranges are quite different in these, the basic viscous-flow phenomena of boundary-layer development, transition, separation and vortex formation remain essentially the same. The boundary layer aspects can now be handled with the available calculation procedures.

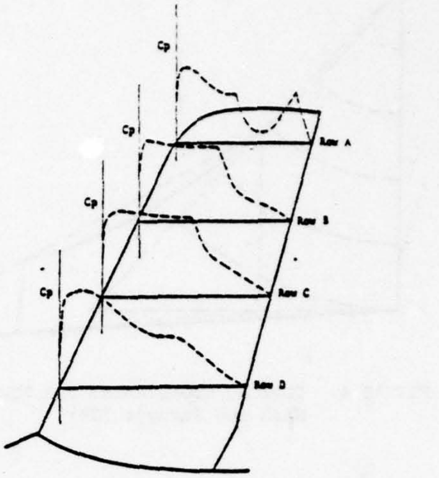

FIGURE 8. WING PRESSURE DISTRIBUTION

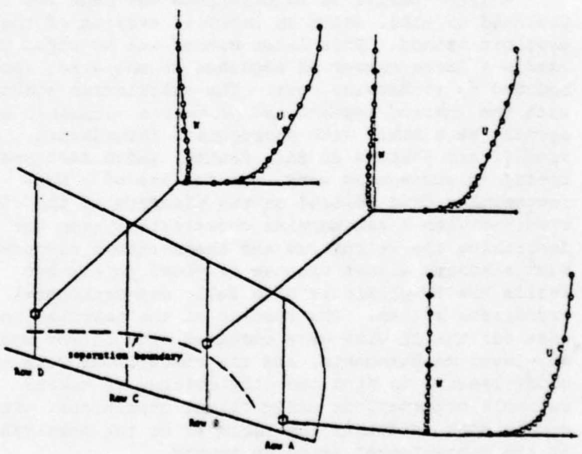

FIGURE 9. TYPICAL BOUNDARY LAYER RESULTS

Three-dimensional boundary layers on surface ships are also receiving increased attention. The ship problem possesses certain peculiarities [41] which are not encountered in aeronautical applications. The presence of a free surface and the characteristic geometry are the main sources of the differences.

Methods for the calculation of the potential flow on a ship hull have not reached the level of sophistication achieved by those in current use in the aeronautical industry due largely to the difficulty of accounting for the free-surface effects. Solutions employing linearized free-surface boundary conditions and thin-ship theory do not provide the level of accuracy needed for boundary-layer computations, while methods developed for the idealized zero-Froude-number case, in which the free surface is regarded as a rigid plane, serve a limited purpose and ignore the influence of surface waves altogether. In view of this, the computation of ship boundary layers can proceed only with some inherent uncertainity. It should, however, be remarked that research on higher-order wave theory, with boundary conditions on the hull satisfied exactly and the presence of the boundary layer and the wake taken into account, is actively under way.

The surface waves influence the boundary-layer development in two ways [42,43]. The locally strong pressure gradients associated with the waves may lead to rapid changes in the boundary-layer thickness and even localized pockets of separation. Secondly, the streamline curvatures due to the waves produce complex patterns of secondary flows which are known to significantly influence the flow further beneath the free surface. These possibilities are of course not encountered in aeronautical applications.

The computation of the boundary layer over most of the hull (the parallel middle-body) can be handled quite adequately using the usual techniques. Special attention is however needed in treating the flow over the bow and the stern. The boundary layer over the bow is known to be highly sensitive to geometry. At the bow, large changes in streamline curvatures lead to large changes in the crossflow within the boundary layer and, under certain circumstances, the boundary layer rolls up into a pair of so-called bilge vortices [44]. It has been observed that the bilge vortices can be eliminated by attaching a bulb to the bow [45]. Some of the available three-dimensional boundary-layer computation methods can be used to study these interesting and important phenomena.

The boundary-layer thickness over the stern often becomes of the same order of magnitude as the local radii of curvature of the surface, and localized flow separations and vortices induced by the rapid changes in surface geometry and the free surface introduce additional complexities. The use of conventional thin boundary-layer theory is therefore questionable over this region. Further study of the boundary-layer characteristics over the stern is however required in order to develop methods for the prediction of viscous resistance and the design of appendages.

The initial attempts at calculating three-dimensional boundary layers on ship hulls [46,47,48,49] utilized integral methods, with the additional assumption of small crossflow. The two attempts made so far to adopt differential methods are those of Chang and Patel [18] and Cebeci, Kaups and Moser [21]. In both cases, however, attention was restricted to the zero-Froude-number case. In the former, the full three-dimensional boundary-layer equations were solved in a convenient surface-orthogonal coordinate system [50] for a hypothetical parabolic ship, while the latter calculations were performed in streamline coordinates with the assumption of small crossflow for the reflex model of a cargo ship tested in a wind tunnel by Larsson [51]. The relative success of these exploratory computations suggests that it is now possible to perform meaningful ship boundary-layer calculations at least in regions where the boundary-layer remains thin.

REFERENCES

1 Spalding, D.B., "Theories of the Turbulent Boundary Layer," Applied Mechanics Reviews, Vol. 20, No. 8, 1967, pp. 735-740.

2 Nash, J.F. and Patel, V.C., "Three-Dimensional Turbulent Boundary Layers," SBC Technical Book, Atlanta 1972.

3 Howarth, L., "The Boundary Layer in Three-Dimensional Flow. Part II: The Flow Near a Stagnation Point," Phil. Mag., Vol. 44, 1951, p. 1433.

4 Squire, L.C., "The Three-Dimensional Boundary-Layer Equations and Some Power Series Solutions," British ARC, R.&M. No. 3006, 1957.

5 Davey, A., "Boundary-Layer Flow at a Saddle Point of Attachment," J. Fluid Mech., Vol. 10, 1961, p. 593.

6 Cumpsty, N.A. and Head, M.R., "The Calculation of Three-Dimensional Turbulent Boundary Layers. Part II: Attachment-Line Flow on an Infinite Swept Wing," Aeron. Quart., Vol. 18, 1967, p. 150.

7 Cumpsty, N.A. and Head, M.R., "The Calculation of Three-Dimensional Turbulent Boundary Layers. Part III: Comparison of Attachment-Line Calculations with Experiment," Aeron. Quart., Vol. 20, 1969, p. 99.

8 Wang, K.C., "Three-Dimensional Boundary Layer Near the Plane of Symmetry of a Spheroid at Incidence," J. Fluid Mech., Vol. 43, 1970, p. 187.

9 Wang, K.C., "Separation Patterns of Boundary Layer over an Inclined Body of Revolution," AIAA Journal, Vol. 10, 1972, p. 1044.

10 Wang, K.C., "Laminar Boundary Layer Over a Body of Revolution at Extremely High Incidence," Physics of Fluids, Vol. 17, 1974, p. 1381.

11 Wang, K.C., "Boundary Layer Over a Blunt Body at High Incidence with Open-Type of Separation," Proc. Roy. Society, London, Vol. A340, 1974, p. 33.

12 Johnston, J.P., "The Turbulent Boundary Layer at a Plane of Symmetry in a Three-Dimensional Flow," ASME, J. Basic Eng., Vol. 82, 1960, p. 622.

13 East, L.F. and Hoxey, R.P., "Low-Speed Three-Dimensional Turbulent Boundary Layer Data, Part I.," British RAE, Tech. Rept. 69041, 1969.

14 Crabbe, R.S., "Measurements in a Laterally Strained Turbulent Boundary Layer," McGill Univ., Mech. Eng. Rept. 71-2, 1971.

15 Head, M.R. and Prahlad, T.S., "The Boundary Layer in a Plane of Symmetry", to be published, 1975.

16 Launder, B.E. and Spalding, D.B., "Mathematical Models of Turbulence," Academic Press, 1972.

17 Reynolds, W.C., "Computation of Turbulent Flows," Annual Review of Fluid Mechanics, Vol. 8, 1976, p. 183.

18 Chang, K.C. and Patel, V.C., "Calculation of Three-Dimensional Boundary Layers on Ship Forms," Iowa Inst. of Hydraulic Res., Rept. IIHR 178, 1975.

19 Cebeci, T., Mosinskis, G.J. and Kaups, K., "A General Method for Calculating Three-Dimensional Incompressible Laminar and Turbulent Boundary Layers. I. Swept Infinite Cylinder and Small Cross Flow," Douglas

Aircraft Co., Rept. No. MDC-J5694, 1972. Also AIAA J. Vol. 12, 1974, p. 779.

20 Cebeci, T., "Calculation of Three Dimensional Boundary Layers, II. Three-Dimensional Flows in Cartesian Coordinates," Douglas Aircraft Co., Rept. No. MDC-J6517, 1974. Also AIAA J., Vol. 13, 1975, p. 1056.

21 Cebeci, T., Kaups, K. and Moser, A., "A General Method for Calculating Three-Dimensional Incompressible Laminar and Turbulent Boundary Layers. III. Three-Dimensional Flows in Curvilinear Orthogonal Coordinates," Douglas Aircraft Co., Rept. No. MDC-J6867, 1975.

22 East, J.L., "An Exact Numerical Solution of the Three-Dimensional Incompressible Turbulent Boundary Layer Equations," Ph.D. Thesis, Virginia Polytechnic Inst. and State Univ., 1970.

23 Michel, R., Cousteix, J. and Quémard, C., "Application d'un schéma amélioré de longueur de mélange à l'étude des couches limites turbulentes tridimensionelles," Specialists' Meeting on Turbulent Shear Flows, London, paper 7 (AGARD Conf. Proc. no. 93), 1971.

24. Pierce, F.J. and Klinksiek, W.F., "An Implicet Numerical Solution of the Turbulent Three-Dimensional Incompressible Boundary Layer Equations," Virg. Poly. Inst. and State Univ., Rept. VIP-E-71-14, 1971.

25 Fanneløp, T.K. and Humphreys, D., "The Solution of the Laminar and Turbulent Three-Dimensional Boundary Layer Equations with a Simple Finite Difference Technique," F.F.A., Aero. Res. Inst. Sweden, Stockholm, Rept. No. 126, 1975.

26 Vermeulen, A.J., "Measurements of Three-Dimensional Turbulent Boundary Layers," Ph.D. Thesis, Cambridge University, 1971.

27 Berg, van den B., Elsenaar, A., Lindhout, J.P.F. and Wesseling, P., "Measurements in an Incompressible Three-Dimensional Turbulent Boundary Layer, Under Infinite Swept-Wing Conditions, and Comparison With Theory," J. Fluid Mech., Vol. 70, p. 127, 1975.

28 Fanneløp, T.K., and Krogstad, P.A., "Three-Dimensional Turbulent Boundary Layers in External Flows: a Report on Euromech 60," J. Fluid Mech., Vol. 71, 1975, p. 815.

29 Cebeci, T., Kaups, K., Ramsey, J. and Moser, A., "Calculation of Three-Dimensional Compressible Boundary Layers on Arbitrary Wings," Douglas Aircraft Company, Rept. No. MDC-J6866, 1975.

30 Bradshaw, P., Ferris, D.H. and Atwell, N.P., "Calculation of Boundary-Layer Development Using the Turbulent Energy Equation," J. Fluid Mech., Vol. 28, 1967, p. 593.

31 Nash, J.F., "The Calculation of Three-Dimensional Turbulent Boundary Layers in Incompressible Flow," J. Fluid Mech., Vol. 37, 1969, p. 625.

32 Bradshaw, P., "Calculation of Three-Dimensional Turbulent Boundary Layers," J. Fluid Mech., Vol. 46, 1971, p. 417.

33 Launder, B.E. and Spalding, D.B., "The Numerical Computation of Turbulent Flows," Computer Methods in Applied Mechanics and Engineering, Vol. 3, 1974, p. 269.

34 East, L.F., "Computation of Three-Dimensional Turbulent Boundary Layers: Euromech 60, Trondheim 1975," Aero. Res. Inst., Sweden, Rept. FFA-TN-AE-2111, 1975.

35 Bradshaw, P. and Terrell, M.G., "The Response of a Turbulent Boundary Layer on an Infinite Swept Wing to the Sudden Removal of the Pressure Gradient," British NPL, Aero-Rept. No. 1305, 1969.

36 Nash, J.F. and Patel, V.C., "A Generalized Method for the Calculation of Three-Dimensional Turbulent Boundary Layers," Proceeding of Project SQUID Workshop, Atlanta, 1971, p. 170.

37 Kline, S.J., Morkovin, M.V., Sovran, G. and Cockrell, D.J., "Computation of Turbulent Boundary Layers - 1966," Proc. AFOSR-IFP-STANFORD Conference, 1968.

38 Raetz,G.S., "A Method of Calculating Three Dimensional Laminar Boundary Layers of Steady Compressible Flows," Northrop Aircraft Inc., Rept. No. NAI-58-73, 1957.

39 Nash, J.F. and Scruggs, R.M., "Three-Dimensional Compressible Boundary Layer Computations for a Finite Swept Wing," NASA CR-112158, 1972.

40 Hicks, J.G. and Nash, J.F., "The Calculation of Three-Dimensional Turbulent Boundary Layers on Helicopter Rotors," NASA CR-1845, 1971.

41 Landweber, L., "Characteristics of Ship Boundary Layers," Proc. Eighth Symposium on Naval Hydrodynamics, Office of Naval Research, Pasadena, 1970, p. 449.

42 Chow, S.-K., "Free Surface Effects on Boundary Layer Separation on Vertical Struts," Ph.D. dissertation, University of Iowa, 1967.

43 Tzou, T.-S., "Secondary Flow Near a Simulated Free Surface," M.S. Thesis, University of Iowa, 1966.

44 Tatinclaux, J.C., "Experimental Investigation of the Drag Induced by Bilge Vortices," Schiffstechnik, Vol. 17, 1970, p.

45 Takahei, T., "Investigation on the Flow Around the Entrances to Full Hull Forms," Proc. 11 International Towing Tank Conference, Tokyo, 1966.

46 Webster, W.C. and Huang, T.T., "Study of the Boundary Layer on Ship Forms," J. Ship Research, Vol. 14, 1970, p. 153.

47 Gadd, G.E., "The Approximate Calculation of Turbulent Boundary Layer Development on Ship Hulls," Trans. Roy. Inst. of Naval Architects, Vol. 113, 1971 p. 59.

48 Kerczek, C. von, "Calculation of the Turbulent Boundary Layer on a Ship Hull at Zero Froude Number," David Taylor Naval Ship Research & Development Center, Unpublished Report, 1972.

49 Adee, B.H., "An Analysis of Ship Resistance," University of Washington, Seattle, Rept. UWME-BHA-75-01, 1975

50 Miloh, T. and Patel, V.C., "Orthogonal Coordinate Systems for Three-Dimensional Boundary Layers, with Particular Reference to Ship Forms," *J. Ship Research*, Vol. 17, 1973, p. 50.

51 Larsson, L., "Boundary Layers of Ships. III. An Experimental Investigation of the Turbulent Boundary Layer on a Ship Model," Swedish State Suipbuilding Experimental Tank, Report No. 46, 1974.

NUMERICAL DIFFICULTIES IN THE CALCULATION OF COMPLEX TURBULENT FLOWS

by

I.P. CASTRO

CENTRAL ELECTRICITY GENERATING BOARD, MARCHWOOD ENGINEERING LABORATORIES,
MARCHWOOD, SOUTHAMPTON, HAMPSHIRE, SO4 4ZB, ENGLAND.

ABSTRACT

In this Paper the numerical accuracy of a finite-difference technique typical of many used for the calculation of elliptic turbulent flows is discussed. The size of the inevitable truncation terms are investigated both analytically and by direct comparison between predictions and experiment. A classic turbulent shear flow is considered first and it appears that although local errors can be large the general features of the flow are well predicted. Flow down a rearward facing step and over a two-dimensional fence are investigated next. It is clear that inadequate turbulence models are not the sole, or even perhaps the major, cause of discrepancies between prediction and experiment. In particular, it is concluded that numerical errors in regions of difficult geometry (e.g. sharp corners) can be severe so that it seems naive to suppose that the more common numerical methods using 'blanket' grids of the size often used are capable of accurate predictions.

NOMENCLATURE

$A_{E,W,N,S}$	Convective coefficients in finite-difference equations.
C_D	Turbulence model constant.
h_+	Specified by grid geometry, see Figure 1.
$k = \frac{1}{2}\overline{q^2}$ $= \frac{1}{2}(\overline{u^2}+\overline{v^2}+\overline{w^2})$	Turbulence energy.
K	Constant in the conduction/diffusion equation.
$L_\varepsilon \equiv \frac{C_D k^{3/2}}{\varepsilon}$	Dissipation length scale.
P,p	Mean, fluctuating parts of the static pressure.
Re_m	Mesh Reynolds number.
r	Stokes radius.
S_o	Source term in finite-difference equations.
$\Gamma_{E,W,N,S}$	Diffusion coefficients in finite-difference equations.
U,V	Mean velocities in x and y directions respectively.
u,v,w	Fluctuating components of velocity in x, y and z directions.
$\overline{uv}$	Turbulent shear stress.
x,y,z	Cartesian co-ordinates.
$\Delta x, \Delta y$	Mesh spacings, see Figure 1.
ε	Turbulence dissipation rate.
$\nu = \mu/\rho$	Kinematic viscosity.
ρ	Density.
μ	Laminar viscosity.
μ_e, μ_t, μ_h	Effective, turbulent and numerical viscosities, respectively.

INTRODUCTION

Numerical prediction of turbulent thin shear flows is now commonplace. There are a number of accurate numerical procedures, mostly finite-difference techniques, which have been shown to be successful and most of the difficulties associated with such predictions relate directly to the lack of total physical understanding and consequent inadequacies in the various turbulence models used. However, in the case of complex turbulent flows, defined loosely as those which fail to satisfy the boundary layer approximation and which are, therefore, in general elliptic, the situation is not so clear. Not only are the problems of providing realistic turbulence models greatly increased, but the numerical techniques are also severely tested. In recent years a number of programs for solving complicated fluid flow problems have been developed but it is unfortunate, although perhaps inevitable, that there is a general dearth of accurate and sufficiently detailed experimental data against which to test calculation methods. This is particularly true for isothermal complex turbulent flows and whilst this situation remains the accuracy of prediction methods must clearly remain in some doubt.

The problem which leads to the greatest discussion among fluid dynamicists concerns the modelling of the turbulence. The fact that extra rates of strain, additional to the basic shear, $\partial U/\partial y$, can lead to large charges in the Reynolds stresses, much larger, in fact, than the explicit extra terms in the transport equations would suggest, is by now well established (Launder et al. (1); Bradshaw, (2)). It is generally recognised therefore that only methods based on modelled forms of the full transport equations are likely to have sufficient physical content to be able to cope with complex flows. Although such models are now being developed (e.g. Hanjalic & Launder (3); Launder et al. (1)) they have as yet only been extensively tested for the calculation of thin shear flows or, at least, flows which are essentially parabolic; their adequacy for more complex flows remains to be demonstrated.

PRECEDING PAGE BLANK-NOT FILMED

The accuracy of a numerical prediction rests, however, not only on the excellence or otherwise of the turbulence model but, even more basically, on the accuracy of the numerical techniques used to solve the equations which embody the model. It is this aspect of complex turbulent flow prediction which is the main concern of this Paper.

One of the main questions that has arisen in the past concerns the importance of numerical viscosity errors. Nearly all elliptic finite-difference techniques use upwind differencing for the convective terms. This is often defended on physical grounds, with some justification, but is anyway usually necessary at quite moderate Reynolds numbers to ensure proper convergence. The significance of the consequent first order errors in laminar flows has been demonstrated in the literature (Roache (4), Blowers (5)) but relatively little attention has been paid to the possible importance of such errors in turbulent flows. It is often stated (Gosman et al. (6)) or just implicitly assumed, that since typical turbulent eddy viscosities are much larger than the laminar viscosity, numerical viscosities will not be important. However, there seems to be no convincing evidence that this is, in fact, generally the case. In addition, since the calculation of turbulent flows usually necessitate a non-uniform grid there are inherent in most of the common numerical techniques errors proportional to the difference between consecutive mesh spacings. In laminar flows these (mathematically first order) errors are usually less important than numerical viscosity errors.

We have investigated these problems, not by rigorous mathematical analysis of the finite-difference equations - this has been done in the past (Cheng (7)) but does not necessarily lead to direct insight into the likely importance of such errors in an engineering calculation - but rather by the application of a well known and typical finite-difference procedure to a few carefully chosen turbulent flows.

The particular method used was similar to that described by Patankar & Spalding (8), Harlow & Welch (9) and others for solving two or three-dimensional elliptic equations using velocity and pressure as the main dependent variables; it is a much used method and was, for example, employed by Pope & Whitelaw (10) in their recent calculations of near wake flows. A straightforward two-equation eddy viscosity turbulence model (Rodi (11); Launder & Spalding (12)) was used since the basic aim was to investigate the performance of the numerical method. Whilst it was not thought that the model contained sufficient insight to enable it to cope with complex flows, the use of a more sophisticated approach was, for our purpose, not necessary. The relevant details of the turbulence model and, more particularly, the numerical techniques are described in the following section.

THE CALCULATION METHOD

The equation expressing conservation of momentum in, say, the x-direction for a turbulent flow is

$$U\frac{\partial U}{\partial x} + V\frac{\partial U}{\partial y} = -\frac{1}{\rho}\frac{\partial P}{\partial x} - \frac{\partial \overline{uv}}{\partial y} - \frac{\partial \overline{u^2}}{\partial x} + \nu\nabla^2 U \qquad (1)$$

with the usual notation. Closure is effected by the well known 'eddy viscosity' method, in which the shear stress is related to the local mean rate of strain by a turbulent eddy viscosity, i.e.

$$-\overline{\rho uv} = \mu_t\left(\frac{\partial U}{\partial y} + \frac{\partial V}{\partial x}\right) \quad . \qquad (2)$$

μ_e, defined as the effective eddy viscosity, is given by $\mu_e = \mu_t + \mu$, where μ is the laminar viscosity. μ_t is specified by

$$\mu_t = \rho k^{\frac{1}{2}}.L_\varepsilon = C_D\rho k^2/\varepsilon \qquad (3)$$

where k is the turbulent kinetic energy and L_ε is the length scale related to ε, the rate of energy dissipation by viscosity. L_ε is typical of the size of the larger (but not the largest) eddies in the flow. Exact equations expressing transport of k and ε can be derived from the Navier-Stokes equations and modelled forms of these (as in Launder & Spalding (12)), are used to calculate k and ε for insertion in equation (3). This two-equation model is undoubtedly better than, say, a simple mixing length type prescription for μ_e since it takes convection and diffusion of k into account. However, the basic limitation is imposed by (2), which implies that the shear stress responds immediately to changes in the mean strain rate; inspection of the exact shear stress transport equation shows that it does not.

The normal stresses are determined by

$$-\overline{\rho u^2} = 2\mu_e\frac{\partial U}{\partial x} - \frac{2}{3}\rho k \quad , \quad -\overline{\rho v^2} = 2\mu_e\frac{\partial V}{\partial y} - \frac{2}{3}\rho k$$

which is clearly better than the simple form directly analogous to equation (2),

$$-\overline{\rho u^2} = 2\mu_e\frac{\partial U}{\partial x} \quad , \text{ etc.,}$$

although the $(2/3)\rho k$ terms are, in the momentum equations, simple scalars which can be included in the pressure terms and subtracted out after a solution has been obtained. The triple velocity correlation terms occurring in the exact equations for k and ε are all modelled by simple gradient diffusion hypotheses. This is a widely used approach, although it takes no account of the experimental observation that transport processes tend to be dominated by large scale eddy motions.

In addition to the continuity condition,

$$\frac{\partial U}{\partial x} + \frac{\partial V}{\partial y} = 0 \quad ,$$

there are then four partial differential equations which can all be written in the form

$$\frac{\partial}{\partial x}(\rho U.\phi) + \frac{\partial}{\partial y}(\rho V.\phi) = \frac{\partial}{\partial x}\left(\Gamma_x\frac{\partial \phi}{\partial x}\right) + \frac{\partial}{\partial y}\left(\Gamma_y\frac{\partial \phi}{\partial y}\right) + S_o \qquad (4)$$

where ϕ is the particular variable of interest (U,V,k or ε), $\Gamma_{x,y}$ are the exchange coefficients (involving Prandtl numbers in the k and ε cases) and S_o is a 'source' containing all the remaining terms. The convective terms are written in their 'conservative' forms although note that U, for example, is not a conserved quantity in the sense that vorticity is in a two-dimensional flow. Note also that in the case of the momentum equations the source term, S_o, contains the pressure gradient. The joint problems of determining the pressure field and satisfying continuity are dealt with by deriving and solving a pressure perturbation equation, as described by Patankar & Spalding (8); the important point to note here is that although this process is in many ways the core of the whole technique and injudicious setting up of the pressure equation can lead to severe difficulties in obtaining convergence of the whole system of equations, from the point of view of solving the individual momentum equations the pressure gradients are treated simply as known sources.

Generally equations like (4) are replaced by their differential form, or by integrating over finite areas. The present method employs the latter technique; the important sources of numerical error are not essentially different in either scheme. To identify these truncation errors attention is concentrated on the U momentum equation, for which the finite-difference equation is

$$(\rho U.U\Delta y)_w^e + (\rho V.U\Delta x)_s^n = (\mu_e \frac{\partial U}{\partial x}.\Delta y)_w^e + (\mu_e \frac{\partial U}{\partial y}.\Delta x)_s^n$$

$$+ S_o.\Delta x\Delta y \quad , \qquad (5)$$

where the limits of integration are the boundaries of the cell surrounding the central node, Figure 1, and the source term, which in this case is the analogous finite-differenced equivalent of the volume integral of

$$-\frac{1}{\rho}\frac{\partial P}{\partial x} + \frac{\partial}{\partial x}(\mu_e \frac{\partial U}{\partial x}) + \frac{\partial}{\partial y}(\mu_e \frac{\partial V}{\partial x}) \quad ,$$

is taken as constant over the cell. Note that the k terms in the normal stress simulation have here been absorbed into the pressure term. Linear variations of the flow parameters are assumed and since the cell boundaries are placed half-way between adjacent nodes, equation (5) becomes

$$A_eU_e - A_wU_w + A_nU_n - A_sU_s - S_o\Delta x\Delta y = T_e(U_E - U_P)$$

$$- T_w(U_P - U_W) + T_n(U_N - U_P) - T_s(U_P - U_S) \qquad (6)$$

where the A's are convective flow rates across cell boundaries given by $A_e = \rho U_e \Delta y$, etc. and the T's are diffusive flow rate coefficients given by

$$T_e = \frac{\mu_{e_e}.\Delta y}{h_+} \text{, etc.}$$

The above equation is recast in the form

$$A_pU_p = \sum_{EWNS} AU + S_u \quad ,$$

and solved for U_P everywhere using a standard Alternating Direction Implicit (ADI) scheme.

In common with previous workers (Fromm & Harlow (13); Lilly (14); Gosman et al. (6); Deardorff (15), etc.) the program uses a staggered mesh in which velocities are defined at cell boundaries and pressures and other variables at cell centres.

In evaluating the convective terms, the U values on the cell boundaries are related to the values at adjacent nodes, so that when central differencing is used $U_e = (U_E + U_P)/2$, etc. see Figure 1. Since only the four points adjacent to the central node are used, there are on a non-uniform mesh inevitable truncation errors (in the double differential terms) which Blowers (5) calls '1½' order errors. They are proportional to the difference between adjacent mesh intervals, as a simple Taylor series expansion shows, and there is no way of avoiding this type of error short of using at least a 7-point replacement of the Laplacian or of treating the inner first differentials as additional variables and so increasing the number of equations (as in the Keller Box method used by Cebeci & Smith (16)). As Blowers (5) has pointed out, this source of error on a non-uniform mesh is often entirely ignored; this may be because it is often a less significant source of error than the true first order errors which can occur even on a uniform grid. Attention is turned to these next.

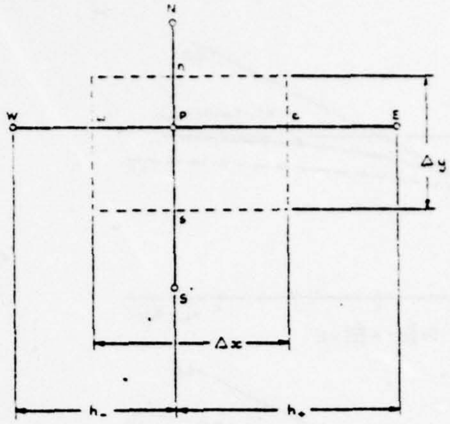

Fig. 1 Geometry of control cell around node P

It is well known that if the mesh Reynolds number defined as

$$Re_m = \frac{\rho U_p \Delta x}{\mu_e}$$

exceeds 2 at any one of the grid nodes the finite-difference matrix obtained by central differencing ceases to be diagonally dominant so that the usual techniques used to solve it, typified by ADI, are unstable and will not converge. The common way of avoiding this problem is to use upwind differencing for the convection terms, or, at best, a hybrid scheme in which central differences are used wherever possible ($Re_m < 2$) and upwind differences are used elsewhere.

By consideration of the simple advection-diffusion equation in one-dimension, i.e.

$$U\frac{\partial \phi}{\partial x} - K\frac{\partial^2 \phi}{\partial x^2} = 0 \quad , \qquad (7)$$

where ϕ is a scalar and U is taken as constant, it is sometimes argued that at high Peclet (Reynolds) numbers upwind differencing leads to more accurate results and is, anyway, more physically realistic. The usual central difference (CD) scheme for (7) is

$$U\left[\frac{\phi_{j+1} - \phi_{j-1}}{2\Delta x}\right] - \frac{K}{\Delta x^2}(\phi_{j+1} - 2\phi_j + \phi_{j-1}) = 0$$

where Δx is the (uniform) mesh spacing between the nodes j-1, j, j+1, etc. With the boundary conditions $\phi_{j+1} = 0$ and $\phi_{j-1} = 1$, ϕ_j is thus given by $\phi_j = \frac{1}{2}(1 + \frac{1}{2}Re_m)$, where $Re_m = (U\Delta x)/K$. In the corresponding case of the usual upwind difference (UD) scheme, ϕ_j is given by

$$\phi_j = (1 + Re_m)/(2 + Re_m), \quad (Re_m > 0) \quad .$$

The analytic solution is $\phi_j = \frac{1}{2}(1 + \mathrm{Tanh}(\frac{1}{4}Re_m))$, and these three results are plotted against Re_m in Figure 2a. Clearly for $Re_m > 2\frac{1}{2}$ the errors from UD are less than those from CD, although only for $Re_m > 20$ are UD errors less than about 5%. In the high Reynolds number limit UD does give the correct solution, $\phi_j = 1$.

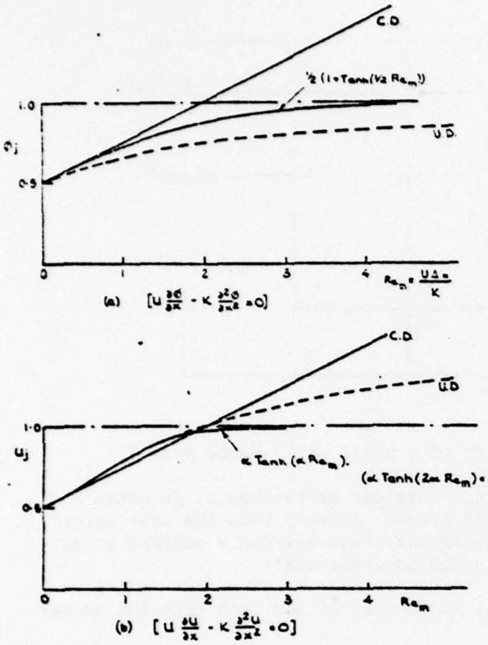

Fig. 2 Accuracy of finite-difference schemes for
(a) the one-dimensional convection/diffusion equation
(b) Burgers equation

Similar considerations apply to the Burgers equation

$$U\frac{\partial U}{\partial x} - K\frac{\partial^2 U}{\partial x^2} = 0 \quad .$$

The CD scheme, with the non-linear term written as

$$\tfrac{1}{2}\frac{\partial(U^2)}{\partial x} \equiv \tfrac{1}{2}\frac{U^2_{j+1} - U^2_{j-1}}{2\Delta x} \quad , \qquad \text{leads to}$$

$$U_j = \tfrac{1}{2}(1 + \tfrac{1}{2}Re_m) \quad ,$$

where, in this case, the velocity scale in Re_m is defined as half the sum of the boundary values ($U_{j-1} = 1$, $U_{j+1} = 0$). The common UD version of the convective term is

$$\tfrac{1}{2}\left[\frac{U_j(U_j + U_{j+1})}{2\Delta x} - \frac{U_{j-1}(U_j + U_{j-1})}{2\Delta x}\right], \; U > 0 \qquad (8)$$

and, with the same boundary conditions, this leads to

$$U_j = \tfrac{1}{2} - \frac{2}{Re_m} + \left[\frac{5}{4} + \frac{4}{Re_m^{\,2}}\right]^{\frac{1}{2}} \quad .$$

The analytic solution is $U_j = \alpha\text{Tanh}(\alpha Re_m)$, where $\alpha\text{Tanh}(2\alpha Re_m) = 1$. These are compared in Figure 2b. Again it is clear that the CD scheme is inappropriate for large Re_m, but in this case the UD scheme does not give the correct result either: indeed, as $Re_m \to \infty$, $U_j \to 1.618$. Although this is the UD scheme usually used (and it is therefore the one employed in the present work) it is not the only possibility. An obvious alternative is

$$\frac{U_j^{\,2} - U_{j-1}^{\,2}}{2\Delta x} - \frac{K}{\Delta x^2}(U_{j+1} - 2U_j + U_{j-1}) = 0 \quad ,$$

leading to

$$U_j = -\frac{1}{Re_m} + \left(1 + \frac{1}{Re_m} + \frac{1}{Re_m^{\,2}}\right)^{\frac{1}{2}} \quad ,$$

which does have the correct behaviour as Re → ∞.

In the actual solution procedure, of course, the convective term is effectively linearised since U_j and U_{j-1} multiplying the bracketed parts of (8) are replaced by the 'old' velocity values provided by the previous iteration, but this in no way alters the arguments above, since there we are in effect considering the final converged solution - always assuming that such convergance is possible.

The most important aspects of the above considerations are, firstly, that Central Differencing, if it were possible, would not necessarily lead to more accurate results. This has been demonstrated rigorously by Cheng (7). For a scheme of formal numerical accuracy of $O(\Delta x)^n$ the size of the truncation errors is $O(\Delta x.Re)^n$ so that for mesh Reynolds numbers greater than unity 'difference schemes of higher order formal accuracy do not promise smaller truncation error'. Secondly, however, although upwind difference schemes as usually applied to the convection-diffusion scalar equation do lead to asymptotically correct predictions at high Reynolds numbers, the analagous scheme, when applied to the non-linear Burgers equation, does not. In the simple one-dimensional case above, the error is only less than 10% for mesh Reynolds numbers below about 5½.

It can be readily shown that the size of the first order truncation term arising from upwind differencing is at least as large as the real viscous diffusion term. A common modification, first proposed by Spalding and used by, for example, Gosman et al. (6) is therefore to ignore the latter term altogether when using upwind differencing and this does lead to reduced errors. In the case of the U-momentum equation the numerical technique, based on such a modified hybrid scheme, then solves, in effect:

$$U\frac{\partial U}{\partial x} + V\frac{\partial U}{\partial y} = -\frac{1}{\rho}\frac{\partial P}{\partial x} - \frac{\partial\overline{uv}}{\partial y} - \overline{\frac{\partial u^2}{\partial x}} + \nu\nabla^2 U + \frac{1}{\rho}\frac{\partial}{\partial x}\left[(\tfrac{1}{2}\mu_{n_x} - \mu_e)\frac{\partial U}{\partial x}\right]$$
$$+ \frac{1}{\rho}\frac{\partial}{\partial y}\left[(\tfrac{1}{2}\mu_{n_y} - \mu_e)\frac{\partial U}{\partial y}\right] \qquad (9)$$

where $\mu_{n_x} = \rho|U|\Delta x$ if $(\rho|U|\Delta x)/\mu_e > 2$ and is $2\mu_e$ otherwise and similarly for μ_{n_y}. Note that since μ_e is in general a function of x and y the errors are not simply (½Re-1) times the real diffusion terms, as they would be in the laminar flow-equivalent of equation (9).

Now in the case of the transport equations for k and ε, the convection and diffusion terms are often small compared with the source terms, particularly in flows which satisfy the boundary layer approximation. It would seem reasonable therefore to suppose that the error terms corresponding to those in equation (9) are small, except possibly in regions where transport terms are comparable with, or greater than, the source terms. However, such arguments cannot necessarily be applied to the momentum equations in which the convection, 'pseudo-diffusion' and 'pseudo-source' terms are all invariably of similar order. Indeed, in zero-pressure gradient boundary layer type flows the x-component source and 'diffusion' terms in the U-momentum equation are insignificant. It is therefore quite possible that truncation errors in the upwind differenced equivalent of the momentum equations are significant.

The only positive way of determining the truth of such a statement is to make careful checks of the size of truncation errors arising in particular cases and, of course, to make detailed comparisons of prediction with experiment wherever possible. In complex flows the latter procedure is not easy since it is not always possible to 'unscramble' the effects of numerical errors from the effects of inadequacies in the turbulence model. The following sections describe the results of some numerical computations using the calculation procedure outlined above (with the modified hybrid differencing scheme) for a few carefully chosen flows.

THE PLANE MIXING LAYER

To the usual boundary layer approximation and for sufficiently high Reynolds numbers the plane two-dimensional mixing layer is an exactly self-preserving flow. It is, of course, not usual to use an elliptic scheme for predicting this flow, but such a procedure has the particular advantage (for the present purpose) of highlighting any numerical errors specific to such schemes; it is generally recognised that a two-equation eddy viscosity model is adequate for flows of this kind.

It is possible in this case to estimate the size of the numerical viscosity errors from first principles. Taking the U-momentum equation as an example and assuming that the lateral grid spacings are sufficiently fine to ensure that the only numerical viscosity errors are the longitudinal ones, equation (9) becomes to the boundary layer approximation

$$U\frac{\partial U}{\partial x} + V\frac{\partial U}{\partial y} = -\frac{\partial \overline{uv}}{\partial y} + \tfrac{1}{2}\Delta x\frac{\partial}{\partial x}\left(U\frac{\partial U}{\partial x}\right) \quad ,$$

where, since it is insignificant compared with the other terms, we have ignored the $\partial/\partial x\{\mu_e(\partial U/\partial x)\}$ term, and the x-step (Δx) has been taken as uniform. For the real flow to be self-preserving $U = U_o f(\eta)$, $\overline{uv} = U_o{}^2 g(\eta)$ and $\eta = y/x$. If the error term is normalised by the maximum value of the shear stress gradient it can be shown that

$$E \equiv \frac{\tfrac{1}{2}\Delta x\,\frac{\partial}{\partial x}\left(U\frac{\partial U}{\partial x}\right)}{\left|\frac{\partial \overline{uv}}{\partial y}\right|_{max}} = \alpha\frac{\Delta x}{x} \quad ; \quad \alpha = \frac{\eta}{2g'_{max}}\cdot(\eta f f'' + \eta f'^2 + 2ff')$$

and dashes denote differentiation with respect to η. Standard data can be used to calculate α across the mixing layer.

The program predicted the self-preserving nature of the flow quite well; normalised profiles of mean velocity and turbulent energy are shown in Figure 3, compared with standard experimental results (Liepmann & Laufer (17); Castro (18)). However, inspection of the U-momentum equation revealed significant errors. After the converged solution had been obtained (converged in the sense that the residuals of each of the equations were no larger than the rounding error limits of the computer) the various terms in the momentum equation were calculated, to second order accuracy. The resulting 'out-of-balance', or numerical error, term, normalised by the maximum shear stress gradient, is shown in Figure 4 together with the analytic estimate of E derived above. Clearly the errors can be locally quite large, particularly at the front end of the grid where $\Delta x/x$ is necessarily larger, and the actual errors are close to those anticipated by the analysis. It is notable that the integrated error over the whole mixing layer is small and that despite the locally large values of E at, say, x = 0.23 units, the basic mean velocity profiles do not seem to be seriously affected. It is not obvious why this should be so, although errors in the turbulent energy balance are rather lower since the source terms are dominant over most of the flow.

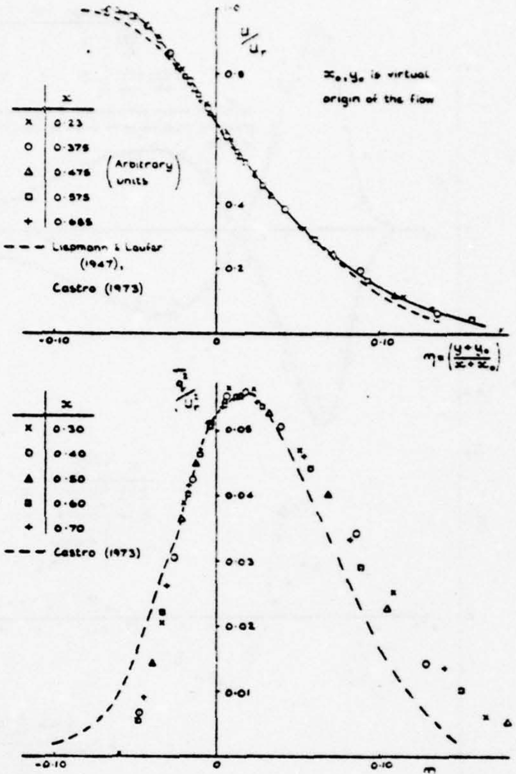

Fig. 3 Plane mixing layer predictions versus experiment

As expected the errors reduce as x increases and $\Delta x/x$ decreases. This procedure of comparing results at different downstream stations amounts in this self-preserving flow to a grid-dependency check and it seems that the basic results are virtually grid-independent, despite the fact that local imbalance in the U-momentum equation, at least, can be quite large.

THE REARWARD FACING STEP

Although by our definition flow down a rearward facing step is complex it is considerably simpler than many of the flows that are currently being calculated by methods such as the present one. Even in this case, however, there is little reliable experimental data for the cavity flow region, although its length and the subsequent flow development are rather better documented (Bradshaw & Wong (19)).

For flows like this the only way of performing grid-dependency checks is to actually refine the grid.

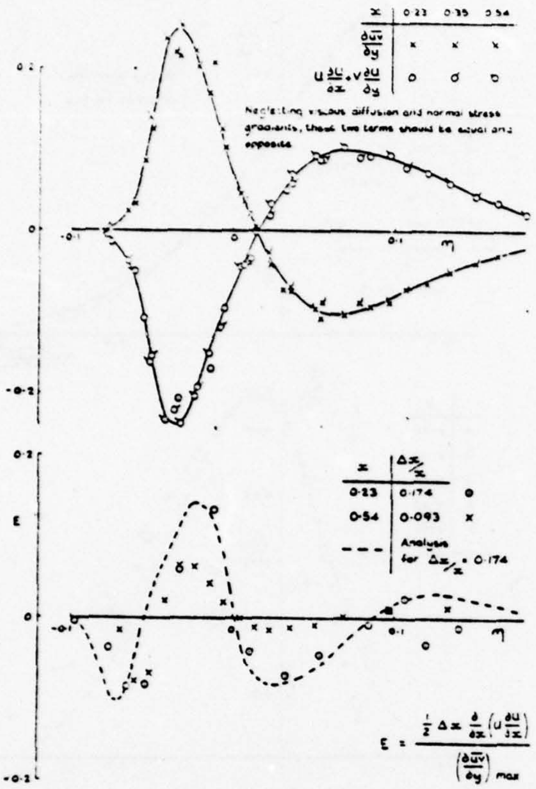

Fig. 4 Plane mixing layer U–momentum balance and numerical viscosity errors

To maximise the possible variations in mesh spacing in the region of greatest flow variation, the step was placed at x = 0 and its height was 1/3 of the height of the grid. Most of the tests were designed to investigate the effect of y–grid (lines of constant y) variations in the region of the separated shear layer; the smallest y–mesh spacing ranged from 2% of the step height in Grid 1 (40 x 39) to 10% in Grid 3 (40 x 16) and for all grids the x–mesh (40 nodes) was identical.

Figure 5 shows typical variations of mean velocity and turbulent energy in cases where the upstream flow was uniform and laminar (Figure 5a) or turbulent and sheared (Figure 5b). In the latter case the input profiles, at x = 0, defined an ordinary zero pressure gradient turbulent boundary layer with a thickness equal to the step height. The effect of mesh spacing on mean velocity seems fairly small so that the reattachment point was only about 16% further downstream for the finest grid than for the coarsest, although this figure increased to 20% in the case of a uniform upstream flow. The largest differences are in the turbulence quantities, like the turbulent energy, within the recirculation zone. Although these differences may not, from a practical engineering point of view, seem at first sight very significant they are generally symptomatic of numerical viscosity effects, since the mesh spacings in all cases were kept as uniform as possible to reduce the 1½ order to a minimum. It was thought at first that within the recirculation region at say, x/h = 2, longitudinal convection and diffusion may well be important so that numerical viscosity errors could be large even in the k and ε equations. Figure 6 shows the momentum balance at this location for Grids 1 and 3 (with a boundary layer upstream flow) and whilst the general form is similar in both cases it is clear that the shear layer

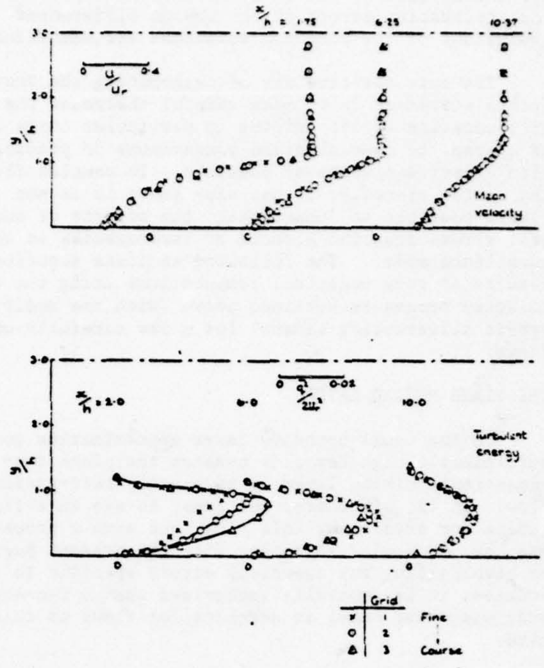

Fig. 5a Step flow predictions for various grids; uniform, laminar flow at inlet

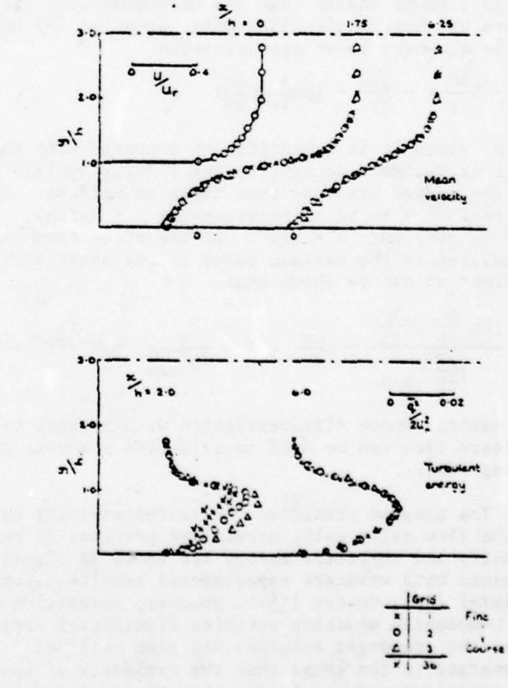

Fig. 5b Step flow predictions: turbulent boundary layer at inlet

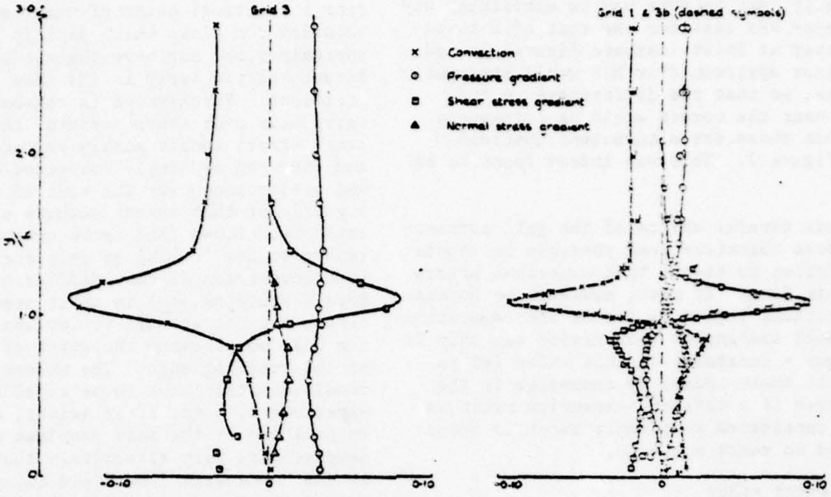

Fig. 6 Momentum balance at x/h = 2.0 for step flow with boundary layer at inlet (Fig. 5b) for various grids. Ignoring viscous diffusion, the terms should sum to zero.

is much thicker for the coarse grid run. However, close inspection of the mesh Reynolds number and consequent errors in this region revealed that they were broadly no worse than in the plane mixing layer prediction discussed previously and practically independent of the grid. It became evident that the increased shear layer thickness originated almost entirely from the much larger errors arising close to separation at the corner of the step.

In predictions of laminar flow situations similar to the present case Blowers (5) found that grid detail in the region of sharp corners was very critical. Some of his difficulties arose because he was solving the vorticity-stream function equations but it was quite clear that any numerical errors arising at the separation corner were convected downstream and had an almost overwhelming effect on the rest of the flow field. Figure 7 shows profiles of turbulent energy just downstream of the step at x/h = 0.055 and 0.475 and it is obvious that the differences first occur very close to the step. By increasing the maximum expansion ratio from 1.5 to 2 (3 at one point) it was possible to rearrange Grid 3 (40 x 16) so as to reduce the mesh spacing near the corner to 2% of the step height, the same values as in the larger and finer Grid 1. Results of a prediction with this arrangement, Grid 3b, are included in Figures 5 to 7. Despite the fact that the 1½ order truncation errors must be considerably larger for Grid 3b than Grid 1, the predictions with these two grids are very close, so it is certain that the larger numerical errors near the corner on Grid 3 are the major cause of the discrepancies between the latter prediction and those with Grids 1 and 3b. Blowers (5) concluded that, with the vorticity-stream function formulation, the mesh spacing near the corner, h, had to be of the same order as the Stokes radius, r, refined by

$$r = \nu/\sigma\bar{U}$$

where $\bar{U}$ is a typical velocity near the corner. For laminar flow at high Reynolds numbers r becomes very small and it is impractical to reduce the mesh spacing to O(r), but in a turbulent flow ν is replaced by ν_e, which is usually considerably larger than ν. In the present case h/r was estimated to be about 2 for Grid 3 and 0.4 for Grids 1 and 3b so it does seem that this ratio must be no larger than unity, at least. Fortunately it is often possible for this to be arranged but if the expansion ratios are to be kept low this may require a grid with a large number of nodes, partic-

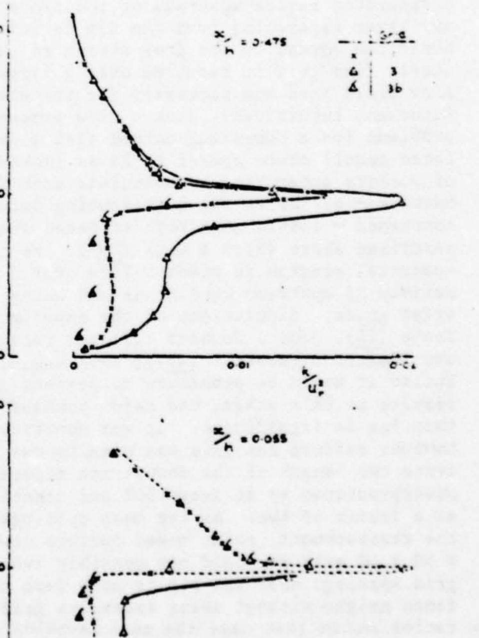

Fig. 7 Turbulent energy profiles just downstream of separation, for the boundary layer upstream flow case

ularly in the main flow direction. These considerations, incidentally, may go some way to explaining why the grid dependency was less for the case of a turbulent boundary layer at inlet (compare Figures 5a and 5b). For a laminar upstream flow h/r would presumably be rather greater, so that the differences in the energy profiles near the corner would be correspondingly greater than those for a turbulent upstream flow, shown in Figure 7. This was indeed found to be the case.

Provided that careful choice of the grid parameters is made it does therefore seem possible to obtain sufficient resolution to ensure that numerical errors are small for this flow. It must, however, be emphasised that the critical region is around the separation corner. The x-mesh spacing in this region was only 2% of the step height - increases in this value led to effects similar to those caused by increases in the y-spacing - so even if a constant expansion ratio as large as 2 were considered reasonable about 13 nodes would be required to reach $x/h = 10$.

SURFACE MOUNTED FENCE FLOWS

Flow over a fence in either a laminar or a sheared turbulent stream is obviously a rather more complex flow than the rearward facing step. Not only is there a separated region upstream of the fence but the boundary layer separating from the tip is initially in a direction normal to the free stream so that a particularly fine grid is required over a larger area of the flow field than was necessary for the step flow. Although, intuitively, such a flow presents serious problems for a numerical method (let alone the turbulence model) there appear to be an increasing number of workers attempting to calculate such flows with methods - as far as the differencing techniques are concerned - little more sophisticated than those described above (Hirt & Cook (20)). We have used the numerical program to predict flow over a fence for a variety of upstream conditions and using various different grids. Simulations of the experiments of Arie & Rouse (21), Good & Joubert (22) and recent work of our own (Castro & Fackrell (23)), have been undertaken. Whilst it would be premature to present detailed results at this stage, the major conclusion of the work thus far is significant. It was consistently true that however refined the grid was made in the region of the fence the length of the downstream separation zone was underpredicted by at least 50% and sometimes by as much as a factor of two. As the mesh spacings were reduced, the reattachment point moved further downstream. With a 40 x 40 grid we could not sensibly reduce the finest grid spacings near the tip to much less than 1% of the fence height without using excessive grid expansion ratios and in that case the mesh Reynolds numbers in both directions were O(10) to O(100) near the tip of the fence. Unlike the rearward facing step case, the transverse V-velocities are of course of the same order as the longitudinal velocities and it appears that the resulting numerical errors near separation are unavoidable unless special techniques are employed. Rimon (24) found very similar problems in his calculations of low Reynolds number flow round a disc. Even though he was able to use central differencing, the high body curvature at the edge of the disc, leading of course to extreme gradients of vorticity, had profound effects on the numerical accuracy and, incidentally, the stability of the numerical scheme.

COMMENTS AND CONCLUSIONS

It has been shown that common methods of differencing the equations governing elliptic turbulent flow lead to truncation errors which, although they do not, from a practical point of view, seriously affect accuracy for flows which satisfy the boundary layer approximation, can nevertheless be locally quite significant, particularly in the case of the momentum equations. Furthermore in regions of complex flow, in particular near sharp corners, the size of these truncation errors cannot easily be reduced to insignificance and they can be simply convected downstream leading to bad predictions over the rest of the flow field. It is significant that recent authors using elliptic calculation techniques (and hence upwind differencing) often resort to the 'trick' of only starting the calculation just downstream of the 'difficult part'. For example, Pope & Whitelaw (10) in their predictions of near wake flows, did not attempt to include the flow upstream of the body but located the start of the x-grid downstream of the trailing edge. The necessary inlet boundary conditions then have to be supplied by reference to experimental data, if it exists, or intuition. This was in fact one of the main problems in their work and they demonstrated very effectively the extreme sensitivity of the downstream flow field to, particularly, the transverse velocity profile used at the inlet. Provided sufficient experimental information is available, this technique is perhaps acceptable, but the fact that it is now being used at all is itself an indication of the problems that exist with 'blanket' type grids which cover the whole flow region.

What is equally clear, however, and is well known in the literature, is that the use of simple central differencing, if it could be achieved, would not necessarily improve the overall accuracy. Numerical analysts (Phillips (25); Fromm (26); Roache (4); Hirt (27), etc) have shown that the non-linear computational instabilities which arise have their origin in space-trunction errors - we are not concerned here with the similar problems in time differencing. The only way to avoid the difficulty is to ensure that the finite difference scheme satisfies all the integral constraints on quantities of physical importance such as mean kinetic energy and mean-square vorticity (Arakawa (28)). The only well known difference methods, appropriate to the vorticity/stream function formulation of the equations of motion, which obey at least some of the conservation laws are due to Arakawa (28). His second order scheme can be used on a staggered grid (Lilly (14)) and in that form is similar to the 'marker-and-cell' method used by the Los Alamos group (as is the method used by Hirt & Cook (20)). Although the stability of the second order Arakawa scheme is usually greater than that of centred difference approximations with no conservation properties, 'psuedo-viscosity' does, in practice, have to be added to maintain stability at high Reynolds numbers.

On the other hand, finite-element approximations usually satisfy the conservation laws automatically - indeed, Arakawa's (28) method has recently been shown to be directly related to finite-element methods, Jesperson (29). In addition, Orszag (30) has convincingly demonstrated that Galerkin (spectral) methods are much more accurate than even Arakawa's fourth-order finite difference scheme. It is no doubt considerations of this sort that are leading some workers to consider these methods as viable alternatives to finite differencing, but the development of such methods for complex turbulent flows is likely to be slow.

As an engineering tool finite-difference methods will clearly be used for some time, and the main message of the present work is that particular caution must be exercised in applying such methods to complex flow problems. Whilst it is possible to use many of the available techniques to predict a wide range of complex fluid flow phenomena, numerical accuracy can be a serious problem if simple upwind or even central differencing is used.

Unless special treatment of the complicated areas, particularly separation corners and the like, is incorporated (embedding a much finer mesh in such regions, whilst retaining a coarser mesh elsewhere, for example) large numerical errors can occur and spoil the accuracy of the predictions downstream.

Whilst doubt about numerical accuracy remains there is little point in detailed discussion on the necessary physical input for a particular complex flow: it is essential to demonstrate, in any comparison with experiment, that numerical errors are insignificant before blaming all the differences on inadequate turbulence models.

REFERENCES

1. Launder, B.E., Reece, G.J. & Rodi, W. J. Fluid Mech., Vol. 68., 1975, pp 537-566.
2. Bradshaw, P. 'Effects of streamline curvature on turbulent flow' AGARDograph No. 169, 1973.
3. Hanjalic, K. & Launder, B.E., J. Fluid Mech., Vol. 52, 1972, pp 609-638.
4. Roache, P.J. J. Comp. Phys., Vol. 10, 1972, pp 169-184.
5. Blowers, R.M. 'The calculation by finite differences of steady two-dimensional laminar flow in a T-junction'. Ph.D Thesis, University of Surrey, 1973.
6. Gosman, A.D., Pun, W.M., Runchal, A.K., Spalding, D.B. & Wolfshtein, M. "Heat & Mass Transfer in Recirculating Flows", Academic Press, 1969.
7. Cheng, Sin-I, The Physics of Fluids Supplement, Vol. 12 Part II, 1969, pp 34-41.
8. Patankar, S.V. & Spalding, D.B. Int. J. Heat Mass Transfer, Vol. 15, 1972, pp 1787-1806.
9. Harlow, F.H. & Welch, J.E. The Physics of Fluids, Vol. 8, 1965, pp 2182-2189.
10. Pope, S.B. & Whitelaw, J.H. J. Fluid Mech., Vol. 73, 1976, pp 9-32.
11. Rodi, W. 'The prediction of free turbulent boundary layers by use of a two-equation model of turbulence', Ph.D Thesis, Imperial College, London, 1973.
12. Launder, B.E. & Spalding, D.D. "Mathematical Models of Turbulence", Academic Press, 1972.
13. Fromm, J.E. & Harlow, F.H. The Physics of Fluids, Vol. 6, 1963, pp 975-982.
14. Lilly, D.K. Mon. Weath. Rev., Vol. 93, 1965, pp 11-26.
15. Deardorff, J.W. J. Fluid Mech., Vol. 41, 1970, pp 453-480.
16. Cebeci, T. & Smith, A.M.O. "Analysis of Turbulent Boundary Layers", Academic Press, 1974.
17. Liepmann, H.W. & Laufer, J. Technical Notes, Nat. Adv. Comm. Aero., Washington, No. 1257, 1947.
18. Castro, I.P. 'The turbulent structure of a highly curved mixing layer', Ph.D Thesis, Imperial College, London.
19. Bradshaw, P. & Wong, F.Y.F. J. Fluid Mech., Vol. 52, 1972, pp 113-135.
20. Hirt, C.W. & Cook, J.L. J. Comp. Physics, Vol. 10, 1972, pp 324-340.
21. Arie, M. & Rouse, H. J. Fluid Mech., Vol. 31, 1956, pp 129.
22. Good, M.C. & Joubert, P.N. J. Fluid Mech., Vol. 31, 1968, pp 547-582.
23. Castro, I.P. & Fackrell, J.E. "An investigation of two-dimensional fence flows with emphasis on wind tunnel blockage effects", CEGB Report R/M/N901.
24. Rimon, Y. The Physics of Fluid Supplement, Vol. 12 Part II, 1969, pp 65-75.
25. Phillips, N.A. 'The Atmosphere and Sea in Motion', Rockefeller Institute Press, New York, 1959, pp 501-504.
26. Fromm, J.E. The Physics of Fluid Supplement, Vol. 12 Part II, 1969, pp 3-12.
27. Hirt, C.W. J. Comp. Physics, Vol. 2, 1968, pp 339-355.
28. Arakawa, A. J. Comp. Physics, Vol. 1, 1966, pp 119-143.
29. Jesperson, D.C. J. Comp. Physics, Vol. 16, 1974, pp 383-390.
30. Orszag, S.A. J. Fluid Mech., Vol. 49, 1971, pp 75-112.

A COMPUTER PREDICTION METHOD FOR TURBULENT FLOW AND HEAT TRANSFER IN PISTON/CYLINDER ASSEMBLIES

A.D. Gosman and A.P. Watkins
Mechanical Engineering Department
Imperial College of Science and Technology
London SW7 2BX, England.

ABSTRACT

A method is described of calculating the flow and temperature fields produced by the cyclic compression and expansion of a gas by a rapidly oscillating piston contained in a cylinder. The method operates by solving the governing differential conservation equations on a computational mesh which expands and contracts with the motion of the piston. An implicit, iterative finite-difference procedure is employed, a novel feature of which is a two-stage process for adjusting the temperatures and pressures so as to procure rapid convergence. The effects of turbulence are characterised by solving additional conservation equations for the kinetic energy of turbulence and its dissipation rate. Applications of the method are described to the problems of an axially-symmetric piston oscillating in a cylinder which is either closed or equipped with a centrally-located valve. Certain features of the predictions of the time-varying flow and turbulence fields are displayed and are shown to be in qualitative agreement with the few available experimental measurements.

NOMENCLATURE

A_c	coefficients of finite-difference equation
a	cell boundary area
C_p, C_v	constant pressure and constant-volume specific heats, respectively
C_μ, C_1, C_2	constants of the turbulence model, assigned values 0.09, 1.44 and 1.92 respectively
f	spatial differencing weighting factors
F_b	boundary heat flow
G	generation of turbulent kinetic energy
h	stagnation enthalpy
k	turbulent kinetic energy
$\dot{m}$	mass flow rate
M	coefficient of finite-difference equation
p	pressure
Pe	cell Peclet number
r	radial co-ordinate
s, S	source term in differential and finite-difference eqns respectively
t	time
T	temperature
u	axial velocity in Eulerian frame
$\tilde{u}$	axial velocity relative to moving co-ordinate frame
u'	turbulent fluctuation in mean flow velocity
v	radial velocity
V	cell volume
z	axial co-ordinate
z_p	instantaneous distance between cylinder and piston heads

Greek symbols

$\beta = (\partial\rho/\partial T)_p$	
$\gamma = (\partial\rho/\partial p)_T$	
Γ	effective viscosity
δt	time increment
ε	dissipation rate of turbulent kinetic energy
ϕ	any dependent variable
μ	viscosity
ρ	density
σ_h	turbulent 'Prandtl/Schmidt' numbers
σ_k	assigned values 0.9, 1.0 and 1.2
σ_ε	respectively
θ	crank angle
ξ	non-dimensional axial co-ordinate $(=z/z_p)$

Subscripts

c	member of grid cluster
P,N,S,E,W	nodal points of finite-difference grid
n,s,e,w	cell boundary locations of finite-difference grid
b	external boundary of grid
eff	effective
f	field
p	piston
t	turbulent

Superscripts

$-$	volume-mean
$'$	correction
$*$	approximate or temporary value
n	new time level
o	old time level

1. INTRODUCTION

1.1 Background

The often-conflicting requirements of improving economy and reducing pollutent emissions have prompted designers and researchers in the field of reciprocating internal combustion engines to turn to computational procedures as an additional aid for determining the nature of the in-cylinder processes. This paper is concerned with a phase in the development of such a procedure.

PRECEDING PAGE BLANK-NOT FILMED

The authors commenced work in this area in 1973, when a method was developed of predicting laminar flow in a piston/cylinder assembly using a finite-difference technique which employed a novel computational mesh which expands and contracts with the motion of the piston: details of the method (which we have called RPM, standing for reciprocating piston motion) and some applications are provided in [1] and [2]. Subsequently improvements and extensions were made, the former including a way of enhancing economy by making block adjustments to the pressure and temperature fields based on overall conservation requirements, and the latter the incorporation of a mathematical model of turbulence, so as to allow the more practically-interesting turbulent flows to be simulated. Some preliminary calculations of turbulent flows are described in [3] and [4]. An early variant of the laminar RPM was also used by Chong et al [5] in an independent study.

Other methods have subsequently emerged for predicting in-cylinder flows including those of Diwakar et al [6], who use an explicit finite-difference procedure to solve the equations for inviscid or laminar flow on an expanding/contracting grid, and Boni [7] who employed the semi-implicit 'Arbitrary Lagrangian-Eulerian (ALE)' method of Hirt et al [8] to solve for combusting flow, with a constant eddy viscosity representation of turbulence effects.

All of the foregoing studies have focussed on two-dimensional flows of either plane or axisymmetrical kinds, although the methods used are all capable of being extended to three dimensions. The reasons why the extension has not been made are probably the very large increase in computing time and storage requirements which it would entail, coupled with uncertainties about the accuracy of prediction attainable for turbulent flow.

1.2 Contents

This paper is intended to describe the essentials of the present method and some representative results of turbulent-flow computations, giving about equal weight to both topics. Section 2 below presents the differential equations of the mathematical model in terms of conventional Eulerian co-ordinates and then in the expanding/contracting co-ordinate frame. Section 3 outlines the method of solution, including the block adjustment procedure mentioned above. In section 4 we show and discuss predictions for the two situations illustrated in Fig 1, namely an oscillating piston contained in either a closed cylinder, or in one whose head is equipped with a centrally-located valve operating in a simulated four-stroke cycle.

2. MATHEMATICAL MODEL

2.1 Conservation equations in Eulerian form

The flow is assumed to be governed by the differential conservation equations of mass, momentum and energy which, for the axially-symmetrical situations considered here, may be expressed in terms of: the velocity components[1] u and v in the axial (z) and radial (r) directions respectively; the pressure p; and the stagnation enthalpy $h \equiv C_v T + p/\rho + (u^2 + v^2)/2$, where C_v, T and ρ are respectively the constant-volume specific heat, temperature and density of the fluid. When the flow is laminar, these assumptions are unambiguous, as are the appropriate forms of the equations; but turbulence brings with it problems of both interpretation (see for example [9] and [10]) and formulation, topics to which we can scarcely do justice here. Instead, we shall simply confine ourselves to the following statements: firstly, it is impractical to attempt to calculate all the details of the turbulent motion because of the excessively fine grids which would be required. Secondly, if the process of ensemble averaging [11] is applied to the equations, they then assume a form closely similar to the time-smoothed equations of a 'steady' turbulent flow [12], the effects of turbulence appearing in the form of correlations of fluctuating quantities, which are often referred to as turbulent fluxes. Finally, we may assume (but without much justification) that the turbulent fluxes of momentum (i.e. the Reynolds stresses) and thermal energy can be calculated through scalar eddy diffusivities which are in turn determined by solving additional differential conservation equations for the (ensemble-averaged) kinetic energy of turbulence k and its dissipation rate ε. This 'turbulence modelling' approach, which was originally developed and applied to steady turbulent flows [13] has achieved some success for them [14]: however uncertainties exist about its validity for the quite different circumstances of in-cylinder flows.

Within the above framework, the complete equation set may be compactly represented in terms of a single *general equation for an arbitrary dependent variable* ϕ:

$$\frac{\partial \phi}{\partial t} + \frac{\partial}{\partial z}(\rho u \phi) + \frac{1}{r}\frac{\partial}{\partial r}(r \rho v \phi) - \frac{\partial}{\partial z}(\Gamma_\phi \frac{\partial \phi}{\partial z})$$

$$- \frac{1}{r}\frac{\partial}{\partial r}(r\Gamma_\phi \frac{\partial \phi}{\partial r}) + s_\phi = 0 \qquad (1)$$

and the accompanying table 1 below, which gives the definitions of the 'effective diffusivity' coefficients Γ_ϕ and 'source/sink' terms s_ϕ for the individual conservation equations. The new quantities appearing in this table include the 'effective viscosity' μ_{eff} which is defined by:

$$\mu_{eff} = \mu + \mu_t = \mu + C_\mu \rho k^2/\varepsilon \qquad (2)$$

where C_μ and the quantities $C_1, C_2, \sigma_h, \sigma_k$ and σ_ε are 'constants' of the turbulence model whose values, which we have taken from [15], are given in the Nomenclature. The quantities s' stand for additional terms containing density fluctuations, whose modelling is the subject of current research.

2.2 The coordinate transformation

The purpose of the coordinate transformation is to avoid the inconvenience that, in Eulerian space, the size of the calculation domain varies with time. It was demonstrated in [1] that this can be circumvented by replacing the axial coordinate z by:

$$\xi \equiv z/z_p \qquad (3)$$

where z_p is the (time-varying) distance between the cylinder head and piston surfaces (see Fig 1). The transformation is straightforward and leads to the

---

[1] We do not consider here flows which may have a third component w in the circumferential direction, commonly referred to as 'swirl'. Calculations have however been performed with swirl simulation, which will be reported elsewhere.

Equation	Dependent Variable	Γ_ϕ	s_ϕ
u momentum	u	μ_{eff}	$\frac{\partial}{\partial z}(\mu_{eff}\frac{\partial u}{\partial z}) + \frac{1}{r}\frac{\partial}{\partial r}(r\mu_{eff}\frac{\partial v}{\partial z}) - \frac{\partial p}{\partial z} - \frac{2}{3}\frac{\partial}{\partial z}(\mu_{eff}\nabla.\underline{u} + \rho k) + s'_u$
v momentum	v	μ_{eff}	$\frac{\partial}{\partial z}(\mu_{eff}\frac{\partial u}{\partial r}) + \frac{1}{r}\frac{\partial}{\partial r}(r\mu_{eff}\frac{\partial v}{\partial r}) - 2\mu_{eff}\frac{v}{r^2} - \frac{\partial p}{\partial r} - \frac{2}{3}\frac{\partial}{\partial r}(\mu_{eff}\nabla.\underline{u}$ $+ \rho k) + s'_v$
continuity	1	0	s'_p
total energy	$\tilde{h}$	μ_{eff}/σ_h	$\frac{\partial p}{\partial t} + \frac{\partial}{\partial z}\{\mu_{eff}(1 - \frac{1}{\sigma_h})\frac{\partial}{\partial z}(\frac{u^2+v^2}{2})\} + \frac{1}{r}\frac{\partial}{\partial r}\{r\mu_{eff}(1 - \frac{1}{\sigma_h})$ x $\frac{\partial}{\partial r}(\frac{u^2+v^2}{2})\} + \frac{\partial}{\partial z}\{\mu_{eff}(\frac{1}{\sigma_k} - \frac{1}{\sigma_h})\frac{\partial k}{\partial z}\} + \frac{1}{r}\frac{\partial}{\partial r}\{r\mu_{eff}(\frac{1}{\sigma_k} - \frac{1}{\sigma_h})\frac{\partial k}{\partial r}\}$ $+ s'_h$
turbulence energy	k	μ_{eff}/σ_k	$G - \rho\varepsilon + s'_k$
dissipation rate	ε	$\mu_{eff}/\sigma_\varepsilon$	$\frac{\varepsilon}{k}(C_1 G - C_2\rho\varepsilon) + \rho\varepsilon\nabla.\underline{u} + s'_\varepsilon$

Note: $\nabla.\underline{u} \equiv \frac{\partial u}{\partial z} + \frac{1}{r}\frac{\partial}{\partial r}(rv)$; $G \equiv \mu_{eff}\left[2\{(\frac{\partial u}{\partial z})^2 + (\frac{\partial v}{\partial r})^2\} + (\frac{\partial u}{\partial r} + \frac{\partial v}{\partial z})^2 + 2(\frac{v}{r})^2\right] - \frac{2}{3}\nabla.\underline{u}(\mu_{eff}\nabla.\underline{u} + \rho k)$

Table 1 Definitions of the coefficients Γ_ϕ and S_ϕ of eqn (1) for the different conservation equations

following variant of eqn (1):

$$\frac{1}{z_p}\frac{\partial}{\partial t}(\rho z_p\phi) + \frac{1}{z_p}\frac{\partial}{\partial \xi}(\rho\tilde{u}\phi) + \frac{1}{r}\frac{\partial}{\partial r}(r\rho v\phi)$$

$$- \frac{1}{z_p}\frac{\partial}{\partial \xi}(\frac{\Gamma_\phi}{z_p}\frac{\partial \phi}{\partial \xi}) - \frac{1}{r}\frac{\partial}{\partial r}(r\Gamma_\phi\frac{\partial \phi}{\partial r}) + s_\phi = 0 \qquad (4)$$

where $\tilde{u} \equiv u - \xi u_p$ is the local relative velocity between the fluid and the coordinate frame, u_p being the instantaneous piston velocity. This equation, it should be noted, looks very similar to its Eulerian counterpart, a fact which greatly facilitates solution.

3. SOLUTION PROCEDURE

3.1 Finite-difference equations

For the purpose of deriving the finite-difference equations (fdes) the transformed coordinate space is overlaid with a grid of nodes formed by the intersections of arbitrarily-spaced coordinate lines (Fig 2) at which the scalar variables p, h, k and ε are calculated; while the velocities, shown as arrows in the diagram, are located mid-way between the pressures which drive them. Each of the variables is imagined as being surrounded by its own control volume or 'cell' over which eqn (4) is integrated, with the aid of approximations, in both space and time. The desirable features which we sought, and which have guided our choice of approximations, have been accuracy and stability to arbitrary specifications of the grid and time intervals.

In terms of the notation of Fig 2 for a typical grid node[†] P enclosed in its cell and surrounded by its neighbours N, S, E and W, the finite-difference approximation to eqn (4) is written:

$$M_P^o(\phi_P^n - \phi_P^o) + \sum_C A_c^n(\phi_p^n - \phi_c^n) + S_P = 0 \qquad (5)$$

where: the superscripts 'o' and 'n' denote 'old' and 'new' values at times t and t + δt respectively, δt being the time increment; the summation is over the nodes N, S, E and W of the cluster; and the coefficients are defined by:

$$M_P^o \equiv (\rho V)_P^o/\delta t;\quad A_W \equiv (\rho\tilde{u}af)_w;\quad A_S \equiv (\rho vaf)_s;$$

$$A_E \equiv -(\rho\tilde{u}af)_e;\quad A_N \equiv -(\rho\tilde{u}af)_n;\quad S_P \equiv \int_{V_P} s_\phi\, dV. \qquad (6)$$

The subscripts n, s, e and w in the above definitions refer to the cell boundaries, values of the quantities required at these locations being obtained by linear interpolation where necessary. The f's are weighting factors, whose specification follows from the choice of spatial differencing approximations, which in turn influence both accuracy and computational stability. The latter, and to some extent the former, is enhanced [16] by the following specification:

$$f_w \equiv \begin{cases} (1 + 2/Pe_w)/2 & , \text{ for } |Pe_w| \leq 2 \\ 1 & , \quad Pe_w > 2 \\ 0 & , \quad Pe_w < -2 \end{cases} \qquad (7)$$

where $Pe_w \equiv (\rho\tilde{u})_w z_p\delta\xi_{PW}/{}_w$ and similar formulae exist for the remaining f's.

Finite-difference equations for the individual variables of Table 1 may be generated from eqn (5) by insertion of the appropriate expressions for the associated Γ and S_P: the S_P's are given in Table 2, albeit in an abbreviated form (the full expressions are lengthy) in which some of the terms are either swept into the quantities S'_P or left unexpanded. Since eqn (5) is of implicit form, the fdes for each variable consist of a simultaneous set. Solution is possible by a variety of means, but our differencing practices give rise to equations which are suitable for solution by iteration, which is our current preference.

[†] In the case of the velocities the same notation applies, the convention being that they take the label of the grid node at which they point.

ϕ	S_P
u	$(p_P - p_W)a_{e/w} + S'_{P,u}$
v	$(p_P - p_S)(a_n + a_s)/2 + S'_{P,v}$
h	$(M_P p_P)^n - (M_P p_P)^o + S'_{P,h}$
k	$V_P^n(G_P - \rho_P \varepsilon_P)^n + S'_{P,k}$
ε	$V_P^n \left[\varepsilon_P(C_1 G_P - C_2 \rho_P \varepsilon_P)/k_P + \rho_P \varepsilon_P(\nabla . u)_P\right]^n$
	$+ S'_{P,\varepsilon}$

Table 2 Definitions of the quantity S_P for the individual variables

3.2 The calculation of pressure

In order to complete the formulation we require a method of calculating pressure. Here we follow the lead of Chorin [17] and others in using a guess-and-correct pressure which invokes the continuity equation, whose finite-difference representation is:

$$M_P^n - M_P^o + \dot{m}_e - \dot{m}_w + \dot{m}_n - \dot{m}_s = 0 \qquad (8)$$

where the $\dot{m}$'s are mass flow rates, e.g. $\dot{m}_e \equiv (\rho \tilde{u} a)_e$, $\dot{m}_s \equiv (\rho v a)_s$, etc. In the present application however it is necessary to take into account a number of special features, notably the strong coupling which may exist between the pressure and temperature fields; and the sometimes disproportionate influences on these fields of both the compress/expansion process itself and the fluid motions which it induces. We do this by means of a two-stage procedure, in which the pressures and temperatures are first globally adjusted by amounts $\overline{p}'$ and $\overline{T}'$ respectively to allow for compression/expansion and then local adjustments are made to allow for the effects of fluid motion.

The global adjustments are obtained from global continuity and energy equations. The former is obtained by replacing M_P^n in eqn (8) by:

$$M_P^n = M_P^* + \beta_P^* \overline{p}' + \gamma_P^* \overline{T}' \qquad (9)$$

and then summing over the entire field to yield:

$$\sum_F (M_P^* - M_P^o) + \overline{p}' \sum_F \beta_P^* + \overline{T}' \sum_F \gamma_P^* + \sum_B \dot{m}_b = 0 \qquad (10)$$

Here the * superscript denotes a value based on the current iterate, the final term represents the nett outward mass flow across the boundaries (which is of course zero if the cylinder is closed) and the quantities β_P and γ_P are defined as:

$$\beta_P \equiv (\partial\rho/\partial P)_T; \qquad \gamma_P \equiv (\partial\rho/\partial T)_p \qquad (11)$$

and evaluated from the equation of state for the gas. The global energy equation is obtained from a simplified version of the finite-difference energy equation, the simplifications being allowed by the fact that the global adjustments tend to zero as the solution is approached. Thus, with the aid of eqn (5) and Table 2 we write:

$$\overline{T}' \sum_F C_p M_P^o + \sum_F M_P^o(h_P^* - h_P^o) + \sum_B F_b + \sum_F \left[(M_P^* + \gamma_P \overline{T}' + \beta_P^* \overline{p}')(\overline{p}' + P^*) - M_P^o p_P^o\right] = 0 \qquad (12)$$

where F_b is the outward-directed heat flow from boundary cells. Equations (10) and (12) are easily solved simultaneously for $\overline{p}'$ and $\overline{T}'$, this calculation being imbedded in the overall calculation cycle, as will be described below.

The second-stage local temperature adjustments are obtained simply by solving the fdes for h. As for the local pressures, following the practice of [18] we obtain equations for these by replacing the mass flows in (8) by, for example:

$$\dot{m}_w = \dot{m}_w^* + \frac{\partial \dot{m}_w}{\partial(p_W - p_P)}(p'_W - p'_P) \qquad (13)$$

where the p's are local pressure corrections and we approximate:

$$\frac{\partial \dot{m}_w}{\partial(p_W - p_P)} \approx \frac{\rho a^2_{e/w}}{(M_P^o + \sum_C A_C^n)} \qquad (14)$$

where the right-hand side comes from the u momentum equations. We obtain, after also replacing M_P from (9):

$$M_P^* - M_P^o + \sum_C A_C (p'_P - p'_C) + \sum_C \dot{m}_C^* + \gamma_P^* \overline{T}' + \beta_P^* \overline{p}' = 0 \qquad (15)$$

which is the required equation: its form, it should be noted, is similar to that of eqn (5).

3.3 Summary of solving procedure

Starting from a prescribed variation of the piston position with time and initial prescriptions of the flow and temperature fields, the RPM method generates predictions at each succeeding time interval in the following sequence of steps: (i) a first approximation to the pressure and temperature fields is obtained by solving the global eqns (10) and (12); (ii) temporary fields of u and v are then obtained by solving their respective momentum equations; (iii) solution of the pressure correction eqn (15) allows the local pressures to be adjusted and the velocities to be brought into continuity balance (iv) the fields of h, k and ε are then updated by solving their respective equations. This sequence is repeated from step (i) until the current solution satisfies the difference equations to the required degree. Normally the calculations are carried through as many simulated piston cycles as are required to eliminate 'start-up' effects, i.e. to produce a solution which is periodic. The results which are described below were obtained in this way.

3. SOME APPLICATIONS OF THE PROCEDURE

3.1 Flow in a closed cylinder

The first turbulent-flow predictions generated with the RPM procedure were for a closed cylinder (diagram (a) of Fig 1), but with conditions otherwise similar to those which might prevail in a practical engine or compressor. The results about to be described were taken from a parametric study, reported in [3] in which quantities such as engine speed, compression ratio etc. were varied. Here we show just one set of results, for a speed of 2000 rpm, compression ratio of 14:1 and bore:stroke ratio of 1.0. They were obtained, after grid-refinement tests, on a 21 x 21 non-uniformly-spaced grid at 6° crank angle intervals.

Although the predictions contain information on the instantaneous temperature distribution and local heat transfer rates to the walls (prescribed as isothermal) we shall focus here on the hydrodynamic aspects. The sequence of diagrams of Fig 3 show the predicted velocity fields (in the form of vectors) and the corresponding turbulence intensity distributions (in the form of contours of $\sqrt{2k/3}/\overline{u}_p$ where $\overline{u}_p$ is the mean piston velocity) at various crank angles, measured from BDC. The plots are to scale and the direction of the piston motion is indicated by the superimposed arrows.

The vectors reveal that over the greater part of the cycle the flow is essentially in a state of uniform compression/expansion, with a small peak in the near-wall velocities which is characteristic of oscillating flows at high frequencies. Recirculation occurs at BDC and TDC, but the single toroidal vortices which are formed are very weak and the vectors have been drawn larger than scale to show them.

The turbulence intensity contours indicate small spatial variations in the central region and somewhat steeper gradients near the walls: not surprisingly, the peak levels are generated near the corner where the piston slides along the cylinder wall. Two perhaps unexpected features are observed: firstly, apart from the fore-mentioned maximum, the turbulence levels within the cylinder are the same order as or greater than those near the walls; and secondly, the level tends to increase as the fluid is compressed and decreases when it expands. The explanation of these features appears to lie in the generation of turbulence by normal stresses; at least their existence can be attributed to this within the context of the present turbulence model. More detailed considerations, which we shall report elsewhere, reveal that although the trends which we predict may be correct (no experimental data has been found to either confirm or refute them) the magnitudes are probably overpredicted. Fortunately, as we shall see below, this 'compression-generated turbulence' as we shall term it, is probably overshadowed by other sources in real engines.

3.2 Flow in a cylinder with a centrally-located valve

Following the above study, the computer model was 'equipped' with a single inlet/exhaust valve centrally located in the cylinder head (diagram (b) of Fig 1) and opened and closed in a sequence simulating a typical four-stroke engine cycle. Parametric explorations were made of the effect of engine speed, compression ratio, etc. on the flow and heat transfer characteristics, in the absence of combustion. The results are described in a preliminary way in [4]; here we shall show the flow predictions for just one set of conditions, for which the speed, compression ratio and bore:stroke ratio were 2000 rpm, 14:1 and 1 respectively.

The valve was represented in the computer model as an annular orifice of time-varying area, with a prescribed discharge coefficient and external pressure.

During the intake stroke the following characteristics of the incoming flow were ascribed constant values: the flow angle and velocity distribution; the turbulence intensity and length scale; and the gas temperature. Some effort was made to assign 'realistic' values to those quantities, but there is little data available for guidance (a point to which we shall return later). The grid-independent results reported herein were obtained with a 21 x 21 non-uniformly spaced grid and with time intervals corresponding to 6° of crank angle. The periodic state was achieved in about 5 complete cycles, starting from rest.

A series of plots showing the predicted flow patterns at various stages in the four-stroke cycle are shown in Fig 4: the crank angle, measured from TDC of the inlet stroke, is shown beside each plot as is the fractional open area f_v of the valve. Because the range of velocity in these circumstances may be very large, some of the vectors are drawn out of scale to avoid obscuring the diagram: such vectors are marked thus (⟶). The number of diagrams which can be shown is necessarily limited, but we have attempted to select ones which are representative. The sequence commences with the inlet stroke, where the incoming fluid, which enters at an angle of 30° with the cylinder head, provokes a large toroidal vortex rotating in a clockwise sense: the velocities are large, exceeding that of the piston over most of the volume. The vortex persists throughout the entire intake and compression phases, although its strength diminishes during compression. The vortex motion is very quickly suppressed early in the expansion stroke (which seems to be a characteristic feature of these flows) and the velocity field reverts to the nearly one-dimensional behaviour observed in the closed case. Finally, during the exhaust phase a sink flow pattern in observed, although more detailed plots reveal the existence of small vortices adjacent to the head of the valve and to the junction of the cylinder head and wall.

The corresponding turbulence intensity contours are also shown in Fig 4. It is immediately noticeable that the levels are very large indeed[1], being far in excess of the values observed in the closed case. The turbulence is clearly generated during the inlet stroke, where it mainly eminates from the shear layers on either side of the conical jet of incoming air and is then convected and diffused throughout the cylinder. Presumably it is these transport processes which are responsible for the appearance of the zone of high energy near the centre of the vortex. As the fluid is compressed the turbulence decays, the contribution of compression-generated turbulence evidently being too small to prevent this, and the decay persists throughout most of the expansion phase. Finally, there is an increase in turbulence level near the valve when it opens for the exhaust process, the shear generated by the outgoing flow being responsible for this.

How well do these predictions accord with reality? Fortunately, Witze [9] has recently made hot-wire anemometer measurements in a similar configuration which allow some assessment to be made, albeit with important qualifications which we shall discuss below. Figs 5 and 6 show respectively his measurements of mean resultant velocity u_R ($\equiv \sqrt{u^2+v^2}$) and turbulence intensity (defined in this instance as $\sqrt{u_R'^2}/\overline{u}_p$) at a point near the valve (the approximate location is indicated in Fig 1(b)) together with the RPM predictions for the same point and another nearby one. (In deducing u'_R from k for this comparison we have assumed isotropy). If we focus first on the measurements and predictions at the same location, it can reasonably be claimed that there is some measure of agreement, especially for the mean velocity, but during certain stages of the cycle the trends are totally

---

[1] When assessing these values it should be borne in mind that the local fluid velocity is sometimes much greater than $\overline{u}_p$.

different, especially around $\theta = 360^\circ$ which is TDC of the compression stroke. The measurements indicate a peak in both velocity and intensity at this stage, whereas the predictions show these as falling and the velocity as reaching its minimum value. It is difficult to say which behaviour is correct, although it is equally difficult to conceive of a mechanism for generating the experimentally-indicated increase in velocity. As for the rise in turbulence intensity, although it is tempting to identify this as compression-generated turbulence, the measured levels are much higher than those which were predicted to occur in the closed case.

The second set of predictions in the above figures has been provided to show how the large spatial gradients within the cylinder volume give rise to appreciable changes in magnitude when the monitoring location is shifted radially outwards by a small amount (~ 1/15 of the cylinder radius). Alternatively, and perhaps more significantly, the same effect might well be produced by small differences between the assumed and actual inlet conditions. The likelihood that such differences actually existed is large (for example, the flow angle probably varies with valve lift, rather than staying constant as we have assumed) and points to the need for detailed specification of inlet conditions.

Although we have been unable to uncover any other source of data for two-dimensional configurations, it is of interest to note that the measurements obtained by Lancaster [10] in a similar configuration to that of Witze, but with a conventional head equipped with separate inlet and exhaust valves, exhibit trends which are reproduced by the RPM predictions. For example, the qualitative behaviour of the mean velocity is the same, as is the tendency for the turbulence intensity variation to follow that of the mean velocity. Also predicted is the observed proportionality between the (absolute) turbulence intensity and the engine speed. A detailed account of these comparisons will appear elsewhere.

3.3 Discussion

The results described herein should suffice to demonstrate that the RPM procedure is capable of solving the strongly-coupled equations of motion, energy and the turbulence model in a time-varying domain. No especial difficulties were encountered in obtaining the solutions, although it should be said that the simultaneity and non-linearity of the equation set necessitated the use of under-relaxation. The computing times required were typically about 7 min on a CDC 6600 machine for 180° of piston motion, using the grid and time intervals specified above, but there is ample scope for reducing the times by optimisation of the algorithm and coding. As expected, the method was stable to much larger grid and time intervals, which enabled very short run times during the setting-up of new cases.

As for the accuracy of prediction, it is clearly too early to make an assessment, although the comparisons thus far are encouraging. Much work remains to be done in assessing and improving the turbulence modelling and in making comparisons with experimental data. Both of these activities are currently hampered by the paucity of data available; indeed it is probably true to say that this is a limiting factor to the further development of computer models. Ideally, measurements are required which possess the following features: firstly, they should focus on configurations which are two-dimensional, for apart from being more economical to measure and calculate, success in predicting these is a necessary prerequisite to the prediction of three-dimensional cases, with which they share many features. Secondly, the boundary conditions should be well-defined, especially those during intake; and thirdly, the cylinder volume should be more extensively mapped than hitherto, for it is now clear that the spatial variations are too large to be characterised by just a few measuring locations.

Notwithstanding the current uncertainties, it seems worthwhile to extend the range of phenomena encompassed by the model, as we are now doing. Mention has already been made of the incorporation of swirl simulation, which is done by solving an additional momentum equation for the tangential direction. Simultaneously the grid specification has been generalised to allow more flexibility in geometrical configuration and these two developments have been combined in calculations of swirling flow in the type of 'bowl in piston' arrangement which features in some designs of Diesel and stratified-charge engines. A report is currently being prepared on this work. A further extension which is currently in progress is the modelling of combustion, but this is still at an early stage.

4. CONCLUSIONS

1. A calculation procedure has been developed for solving the differential conservation equations for turbulent flow and heat transfer in piston/cylinder assemblies.
2. Predictions for an oscillating piston in a closed cylinder indicate essentially one-dimensional flow and the existence of compression-generated turbulence, produced by the action of normal stresses. No experimental data has been found for comparison.
3. Calculations with a centrally-located valve indicate that the induction flow strongly influences the velocity and turbulence structure throughout the entire four-stroke cycle. The intake-generated turbulence is predicted to be much more intense than that generated by compression, at least for the the present piston/cylinder configuration.
4. Comparisons with the measurements of Witze [9] reveal qualitative agreement in many respects, but quantitative comparisons and the pinpointing of sources of discrepancies are both hindered by uncertainties in the experimental conditions.

5. ACKNOWLEDGEMENTS

The authors gratefully acknowledge the encouragement and assistance of the Perkins Engine Co. Thanks are also due to Dr. P. Witze for providing early access to his experimental data.

6. REFERENCES

1 Watkins, A.P. "Calculation of flow and heat transfer in the combustion chamber of a reciprocating engine". M.Sc. Thesis, University of London, 1973.

2 Gosman, A.D. and Watkins, A.P. "A calculation procedure for flow and heat transfer in piston/cylinder assemblies". Imperial College Mech. Eng. Dept. Report, Dec. 1975.

3 Gosman, A.D. and Watkins, A.P. "Calculations of turbulent heat transfer in a closed piston/cylinder

system". Imperial College Mech. Eng. Dept. Report, March 1976.

4 Gosman, A.D. and Watkins A.P. "Simulation of flow and heat transfer during a four-stroke motored engine cycle". Imperial College Mech. Eng. Dept. Report, March 1976.

5 Chong, M.S., Milkins, E.E. and Watson, H.C. "The prediction of heat and mass transfer during compression and expansion in I.C. engines" SAE transactions 760761, 1976.

6 Diwakar, R., Anderson, J.D., Griffin, M.D. and Jones, E. "Inviscid solutions of the flow field in an internal combustion engine". Dept. of Aerospace Engr. Report, Univ. of Maryland, 1976.

7 Boni, A.A., Chapman, M., Cook, J.L. and Schneyer, G.P. "Computer simulation of combustion in a stratified charge engine". Proc. Sixteenth (International) Symposium on Combustion, Aug. 1976.

8 Hirt, C.W., Amsden, A.A. and Cook, J.L. "An arbitrary Lagrangian-Eulerian computing method for all flow speeds" J. Comp. Phys., Vol. 14, 1974, pp. 227-253.

9 Witze, P.O. "Preliminary hot-wire measurements in a motored engine with an axisymmetric cylinder geometry", private communication, July 1976.

10 Lancaster, D.R. "The effects of engine variables on turbulence in a spark-ignition engine". General Motors Research Publication GMR-2062R, Feb. 1976.

11 Bendat, J.S. and Piersol, A.G. Measurement and analysis of random data, Wiley, New York, 1967.

12 Hinze, J.O. Turbulence, McGraw-Hill, New York, 1959.

13 Launder, B.E. and Spalding, D.B. Mathematical Models of Turbulence, Academic Press, London, 1972.

14 Gosman, A.D., Khalil, E.E. and Whitelaw, J.H. "The calculation of two-dimensional turbulent recirculating flows". To be published in Proc. Symposium on Turbulent Shear Flows, Penn. State University, April 1977.

15 Gosman, A.D. and Pun, W.M. "Lecture notes for a course entitled calculation of recirculating flows", Imperial College Mech. Eng. Dept. Report, Dec. 1973.

16 Raithby, G.D. and Torrance, K.E. "Upstream-weighted differencing schemes and their application to elliptic problems involving fluid flow" Computers and Fluids, Vol. 2, 1974, pp. 191-

17 Chorin, A.J. "Numerical solution of the Navier-Stokes equations" Math. Comp., Vol. 22, 1968, p. 745.

18 Caretto, L.S., Gosman, A.D., Patankar, S.V. and Spalding, D.B. "Two calculation procedures for steady, three-dimensional flows with recirculation". Proc. Third International Conf. on Numerical Methods in Fluid Mech., Vol. 2, Springer Verlag, July 1972, pp. 60-68.

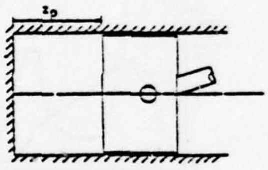

(a) Closed case

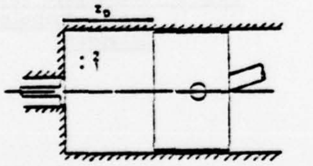

(b) Valve case

Fig. 1 Calculation Domain

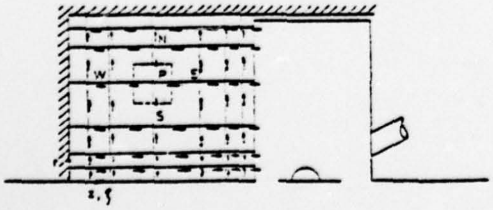

Fig. 2 Finite-difference Grid

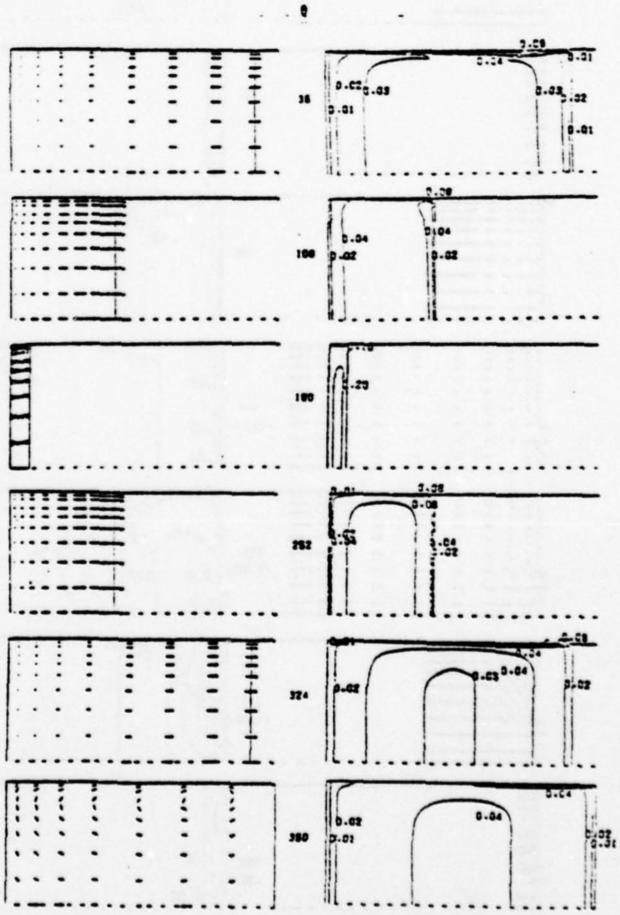

(a) Velocity field (b) Turbulence intensity

Fig. 3 Velocities and Turbulence Intensities - Closed Case

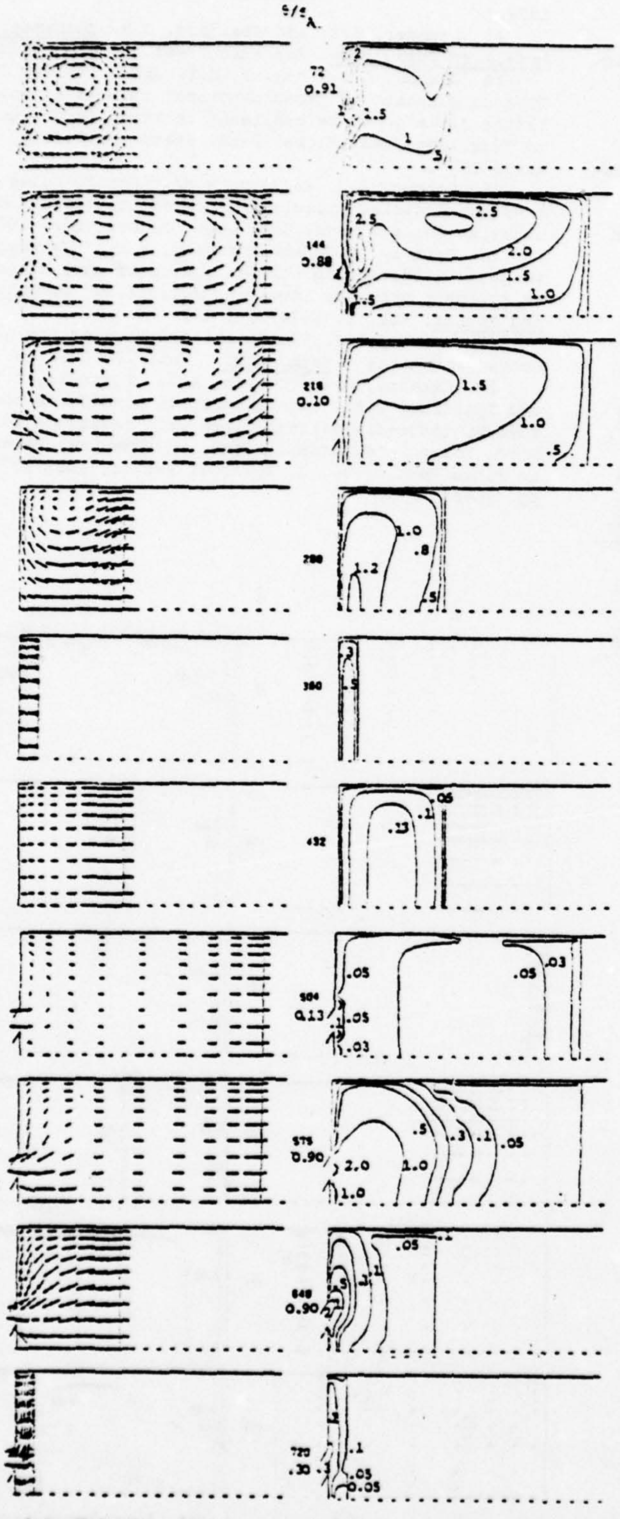

(a) Velocity field (b) Turbulence intensity

Fig. 4 Velocities and Turbulence Intensities - Valve Case

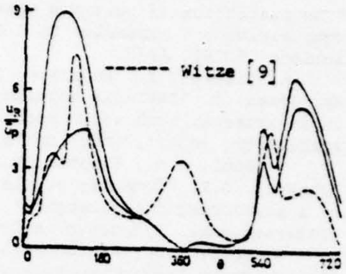

Fig. 5 Comparison with Witze Data - Mean Velocity

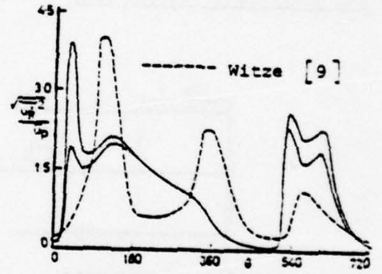

Fig. 6 Comparison with Witze Data - Turbulence Intensity

TURBULENT BOUNDARY LAYER STUDIES USING POLYNOMIAL INTERPOLATION

S. G. RUBIN, P. K. KHOSLA, AND S. RIVERA
Polytechnic Institute of New York
Aerodynamics Laboratories
Farmingdale, New York

ABSTRACT

For laminar flows, higher-order differential methods derived from polynomial spline interpolation and Hermitian collocation have significantly reduced the numbers of mesh points required to achieve accuracy equal to that of conventional second-order finite-difference methods. This study is intended to evaluate the applicability of two of these techniques for simulating the thicker, higher-shear turbulent boundary layer on a flat plate, with and without mass transfer. Coupled velocity-stream function solutions are obtained with displacement thickness normalized and transformed boundary layer variables. The fourth-order spline 4 and sixth-order Hermite 6 formulations are considered. Single layer and two-layer eddy viscosity models are used for closure. The results obtained here with relatively coarse meshes compare favorably with experimental data, and lead us to believe that, with appropriate closure modelling, more general turbulent shear flows can be simulated with comparable reductions in computer requirements.

NOMENCLATURE

a,b = interval boundary points
A = damping length
f_j = boundary layer variable related to stream function
F = Van Driest damping function
G_j = defined by equation (2f)
h_j = mesh width across the boundary layer
I_{tr} = transition intermittency factor
K_j = defined by equations (2d) and (2e)
ℓ = turbulent mixing length
m_j = $(V_\eta)_j$ first spline derivative
M_j = $(V_{\eta\eta})_j$ second spline derivative
N+1 = grid points
Re = Reynolds number based on characteristic length
t = $(\eta-\eta_{j-1})/h_j$
u_e = velocity at the edge of boundary layer
V_j = longitudinal velocity
x = coordinate along the flow
y = coordinate across the flow
α = exponent in the transformation
β = pressure gradient parameter
δ = displacement thickness
Δ = parameter appearing in spline 4
ϵ = eddy viscosity
ν = kinematic viscosity
σ = h_{j+1}/h_j characteristic of non-uniform grid and equals 1 for uniform grid
ξ = independent boundary layer coordinate along the flow
η = coordinate across the boundary layer
ζ = transformed variable defined by equation (6)

Subscripts

w = wall values
e = values at the edge of boundary layer

1. INTRODUCTION

The numerical evaluation of turbulent shear flows has been limited, in many cases, by both the availability of appropriate closure models and the significant increase in computer storage and calculation time over that required for laminar flows. Generally, large numbers of mesh points must be specified in order to accurately describe the thick turbulent shear layer, the thin laminar sublayer, and the large gradients, near the edge of the viscous sublayer, associated with typical eddy viscosity behavior. In this paper, we are concerned only with the latter difficulty, i.e., computer storage and time; we rely on existing closure models, which are reasonable for the simple geometries considered here. The present analysis represents a series of numerical experiments to test the applicability of two higher-order collocation (differential) methods (1-5) that have previously been very successful for the evaluation of laminar boundary layer flows with and without mass injection (3), potential flows (2), Burgers equation (2) and the incompressible laminar Navier-Stokes solution for the flow in a driven cavity with Reynolds numbers of up to 1000 and relatively coarse grids (4,5).

These earlier analyses were concerned with the development of a variety of second, fourth and sixth order numerical procedures as obtained by polynomial (spline) interpolation or by Hermitian collocation. Two of these methods, the fourth-order[1] accurate Spline 4 (2) and the sixth-order[1] accurate Hermite 6 (3-5) formulations will be tested here and assessed relative to second-order accurate[1] central finite-differencing. In the earlier laminar studies, it was generally found that Spline 4 required one-quarter the number of mesh points, in each coordinate direction, as did the finite-difference method in order to achieve equal accuracy. This led to reductions of from 50% to 75% in computer storage and time. Hermite 6 required even fewer points than Spline 4 to achieve equal accuracy and led to even further computational efficiency. The purpose of the present study is to determine the applicability of higher-order collocation as a tool for calculating thicker, higher shear turbulent boundary layers. The incompressible flow over a flat plate with and without mass injection will be considered. The single layer eddy viscosity model used previously by Michel (6) or the two-layer Cebeci-Smith (7) formulation are applied for closure. The equations are solved in (1) normalized laminar boundary layer coordinates, (2) displacement thickness normalized coordinates, (3) a transformed laminar coordinate frame and (4) a combination of (2) and (3). The second system limits the boundary layer growth; the third procedure leads to the desirable accumulation of mesh points in the laminar sublayer, with a uniform mesh in the transformed plane. For procedures (1) and (2) this can be accomplished only with a variable mesh. For procedure (1) the turbulent boundary layer thickness must also be monitored in order to maintain the accuracy of the solution, but complex transformations are avoided. The procedure (4) has the advantages of both (2) and (3).

For the spline 4 formulation, the resulting boundary layer problem leads to a 3x3 block tridiagonal system for the coupled momentum and continuity equations. For Hermite 6 the system is 4x4, but solutions can be obtained by an unconditionally stable and rapid iterative procedure that involves a pair of 2x2 block tridiagonal systems. This procedure, which will be described in detail in a future paper, can also be applied to Spline 4 so that the 3x3 system is replaced by a combined 2x2 and simple tridiagonal formulation[2]. Finite difference calculations involve a single 2x2 block system.

2. COLLOCATION ANALYSIS

Higher-order collocation formulas are derivable from polynomial (spline) interpolation or Hermite (Taylor series) expansion techniques. The accuracy of the resulting procedure depends on the order of the polynomial or the truncation error in the series expansion. In References (1-5), the complete derivations for a variety of methods are described. These will not be repeated here and only the relevant equations for two procedures, Spline 4 and Hermite 6, will be described.

Consider the domain $[a,b]$ in the ζ-coordinate direction. Divide the domain into N intervals, so that at the mesh points $\zeta=\zeta_j$, $j=1, N+1$; $\zeta_1=a$ and $\zeta_{N+1}=b$. The mesh width $h_j=\zeta_j-\zeta_{j-1}$, and $\sigma=h_{j+1}/h_j$ is the ratio of successive mesh widths. At the mesh points, the function $V(\xi,\zeta)=V(\xi,\zeta_j)=V_j$ and the derivatives $(V_\zeta)_j$ and $(V_{\zeta\zeta})_j$ are denoted by m_j and M_j, respectively. In conventional (differential) finite-difference methods, the governing system of equations involves only the unknown functional values V_j. All derivatives are given as functions of V_j. In the higher-order spline or Hermite methods, collocation at the mesh points couples V_j, m_j and M_j. The higher the order, the stronger is the coupling. The couplings for the three methods to be considered here are given below, see References (1-4) for more complete derivations.

Finite-Differences

$$m_j = (V_{j+1}+(\sigma^2-1)V_j-\sigma^2 V_{j-1})/(\sigma(1+\sigma)h_j) \tag{1a}$$

$$M_j = 2(V_{j+1}-(1+\sigma)V_j+\sigma V_{j-1})/(\sigma(1+\sigma)h_j^2) \tag{1b}$$

Spline 4

$$a_{33}K_{j+1}+b_{33}K_j+c_{33}K_{j-1}+a_{31}V_{j+1} +b_{31}V_j+c_{31}V_{j-1}= 0 \tag{2a}$$

---

[1] For uniform meshes.

[2] If the continuity and momentum equations are uncoupled, Spline 4 reduces to a pair of tridiagonal equations and Hermite 6 becomes a 2x2 block plus a single tridiagonal equation. This approach is not desirable however as it requires an excessive number of iterations, at each streamwise location, to converge.

The coefficients are tabulated in Table 1. In addition,

$$m_j=-h_{j+1}(2K_j+K_{j+1})/6+(V_{j+1}-V_j)/h_{j+1} \quad (2b)$$

$$m_j=h_j(2K_j+K_{j-1})/6+(V_j-V_{j-1})/h_j \quad (2c)$$

and

$$K_j=2m_{j-1}/h_j+4m_j/h_j-6(V_j-V_{j-1})/h_j^2 \quad (2d)$$

$$K_j=-4m_j/h_{j+1}-2m_{j+1}/h_{j+1}+6(V_{j+1}-V_j)/h_{j+1}^2 \quad (2e)$$

$$M_j=K_j+\frac{\Delta}{6}(K_{j+1}-(1+\sigma)K_j+\sigma K_{j-1})=K_j+G_j \quad (2f)$$

where

$$\Delta=(1+\sigma^3)/(\sigma(1+\sigma)^2) \ .$$

Also, on any interval $[j-1,j]$, we obtain the following interpolation polynomial for $V(\xi,\eta)$

$$\begin{aligned}V(\xi,\eta)&=K_{j-1}(1-t)^3h_j^2/6+K_jt^3h_j^2/6\\&+(V_{j-1}-K_{j-1}h_j^2/6)(1-t)+(V_j-K_jh_j^2/6)t\\&+G_jh_j^2t^3(1-t)^2/2+G_{j-1}h_j^2t^2(1-t)^3/2\ , \quad (2g)\end{aligned}$$

where $t=(\zeta-\zeta_{j-1})/h_j$. With $\Delta=0$, from the integral of (2g) over $[j-1,j]$ we also obtain

$$\int_{\zeta_{j-1}}^{\zeta_j}Vd\zeta=f_j-f_{j-1}=(V_j+V_{j-1})h_j/2-(K_j+K_{j-1})h_j^3/24 \quad (2h)$$

This is a more accurate formula for f_j than that used in earlier studies (3-5).

Hermite 6

$$\begin{aligned}a_{33}M_{j+1}+b_{33}M_j+c_{33}M_{j-1}+a_{31}V_{j+1}+b_{31}V_j+c_{31}V_{j-1}\\+a_{34}m_{j+1}+b_{34}m_j+c_{34}m_{j-1}=0 \quad (3a)\end{aligned}$$

$$\begin{aligned}a_{43}M_{j+1}+b_{43}M_j+c_{43}M_{j-1}+a_{41}V_{j+1}+b_{41}V_j+c_{41}V_{j-1}\\+a_{44}M_{j+1}+b_{44}m_j+c_{44}m_{j-1}=0 \quad (3b)\end{aligned}$$

The coefficients are given in Table 1.

The truncation errors for each of these formulations are given in References (3) and (5).

3. GOVERNING EQUATIONS

A. Displacement Thickness Normalized Coordinates

After appropriate normalization and transformation, the governing boundary layer equations become

$$(1+\epsilon)V_{\eta\eta}+(\epsilon_\eta+(\frac{\delta^2}{2})_\xi f+\delta^2f_\xi)V_\eta+\beta(1-V^2)=\delta^2VV_\xi \quad (4a)$$

$$f_\eta=V \quad (4b)$$

where $V(\xi,\eta)=V=u/u_e$; u is the streamwise velocity and e denotes conditions at the boundary layer edge. $\beta=\delta^2(u_e)_x/u_e$; for the flat plate, $\beta=0$. $f=f(\xi,\eta)$ is a normalized stream function and $\lim_{\eta\to\infty}f(\xi,\eta)-\eta-\beta_o$. $\xi=x$; $\eta=yR_e^{1/2}/\delta$; $R_e=u_e/\nu$; x,y denote the axial and normal coordinate directions; ν is the molecular viscosity and ϵ is the turbulent eddy viscosity. δ is a modified displacement thickness defined as

$$\delta=\beta_o^{-1}R_e^{1/2}\int_o^\infty(1-V)dy \quad (5)$$

The constant β_o depends on the pressure gradient parameter β. For laminar flow over a flat plate, $\beta_o=1.21678$, since the turbulent boundary layer thickness is approximately six to eight times the displacement thickness. In this coordinate frame, the boundary layer is confined to the region $\eta<8$.

B. Laminar Boundary Layer (or Gortler (8)) Variables

These are recovered from (4a) simply by setting $\delta=(2\xi)^{1/2}$; this is the laminar value of (5). Equation (4b) is unchanged. Since y grows approximately as $\xi^{0.8}$, in this coordinate frame η grows as $\xi^{0.3}$.

C. Transformed Laminar Variables

With $\delta=(2\xi)^{1/2}$, we transform the η or normal coordinate such that

$$\eta=a_o\zeta/(1+b_o\zeta)^c \quad (6)$$

The boundary layer edge η_e is prescribed as $\zeta=1$; therefore, $a_o=\eta_e(1+b_o)^c$. For the present calculations $c=-109$, $b_o=0.05$ and $\eta_e=60$.[3]

The governing equations (4) become

$$\begin{aligned}(1+\epsilon)\zeta_\eta^2V_{\zeta\zeta}+((1+\epsilon)\zeta_{\eta\eta}+[\epsilon_\eta+f+2\xi f_\xi]\zeta_\eta)V_\zeta\\+\beta(1-V^2)=\xi(V^2)_\xi \quad (7a)\end{aligned}$$

and

$$f_\zeta\zeta_\eta=V\ . \quad (7b)$$

This transformation allows for an accumulation of mesh points in the laminar sublayer when a uniform mesh is prescribed in the ζ-plane; however, the boundary layer edge η_e is

---

[3] This transformation and the associated constants were suggested to us by Dr. Stephen Wornom of the NASA Langley Research Center.

TABLE I: MATRIK COEFFICIENTS[4]

<u>Finite-Differences (2x2)</u> $w_1=V,\ w_2=f,\ d_1=\alpha_5,\ d_2=0.$

$a_{11}=(2\alpha_3+h_j\alpha_4)/(\sigma(1+\sigma)h_j^2)$ $a_{12}=0$ $a_{21}=0$ $a_{22}=0$

$b_{11}=\alpha_1-(2\alpha_3/\sigma h_j^2)+(\sigma-1)\alpha_4/\sigma h_j$ $b_{12}=\alpha_2$ $b_{21}=h_j/2$ $b_{22}=1$

$c_{11}=(2\alpha_3-\sigma h_j\alpha_4)/(1+\sigma)h_j^2$ $c_{12}=0$ $c_{21}=h_j/2$ $c_{22}=-1$

<u>Spline 4 (3x3)</u> $w_1=V,\ w_2=f,\ w_3=K,\ d_1=\alpha_5,\ d_2=0,\ d_3=0$

$a_{11}=\alpha_4/\sigma(1+\sigma)h_j$ $a_{12}=0$ $a_{13}=\dfrac{(\alpha_3\Delta(1+\sigma)-\sigma h_j\alpha_4)}{6(1+\sigma)}$

$a_{21}=0$ $a_{22}=0$ $a_{23}=0$

$a_{31}=6$ $a_{32}=0$ $a_{33}=-\sigma^2h_j^2$

$b_{11}=\alpha_1+(\sigma-1)\alpha_4/\sigma h_j$ $b_{12}=\alpha_2$ $b_{13}=\alpha_3(1-\Delta(1+\sigma)/6)$

$b_{21}=-h_j/2$ $b_{22}=1$ $b_{23}=h_j^2/24$

$b_{31}=-6(1+\sigma)$ $b_{32}=0$ $b_{33}=-2\sigma(1+\sigma)h_j^2$

$c_{11}=-\sigma\alpha_4/(1+\sigma)h_j$ $c_{12}=0$ $c_{13}=\dfrac{\sigma(\Delta\alpha_3(1+\sigma)+h_j\alpha_4)}{6(1+\sigma)}$

$c_{21}=-h_j/2$ $c_{22}=-1$ $c_{23}=-h_j^2/24$

$c_{31}=6\sigma$ $c_{32}=0$ $c_{33}=-\sigma h_j^2$

<u>Hermite 6</u> $w_1=V,\ w_2=f,\ w_3=M,\ w_4=m,\ d_1=\alpha_5,\ d_2=0,\ d_3=0,\ d_4=0$

$a_{11}=0$ $a_{12}=0$ $a_{13}=0$ $a_{14}=0$

$a_{21}=0$ $a_{22}=0$ $a_{23}=0$ $a_{24}=0$

$a_{31}=\dfrac{5\sigma+3}{\sigma^3(1+\sigma)}$ $a_{32}=0$ $a_{33}=h_j^2/6\sigma$ $a_{34}=\dfrac{-h_j(5\sigma+4)}{3\sigma^2(1+\sigma)}$

$a_{41}=6(\sigma^2-\sigma-1)/\sigma^2$ $a_{42}=0$ $a_{43}=h_j^2(\sigma+1)(\sigma-2)/5$ $a_{44}=h_j(14+10\sigma-10\sigma^2)/5\sigma$

$b_{11}=\alpha_1$ $b_{12}=\alpha_2$ $b_{13}=\alpha_3$ $b_{14}=\alpha_4$

$b_{21}=-2h_j/5$ $b_{22}=1$ $b_{23}=-h_j^3/60$ $b_{24}=h_j^2/10$

$b_{31}=-a_{31}-c_{31}$ $b_{32}=0$ $b_{33}=-h_j^2(1+\sigma)^2/3\sigma$ $b_{34}=5h_j(\sigma-1)(1+\sigma)^2/3\sigma^2$

$b_{41}=-a_{41}-c_{41}$ $b_{42}=0$ $b_{43}=-3h_j^2(\sigma-1)(1+\sigma)^3/5$ $b_{44}=h_j[32+4(\sigma-1)(4\sigma^4+9\sigma^3+4\sigma^2-\sigma+4)]/5\sigma$

$c_{11}=0$ $c_{12}=0$ $c_{13}=0$ $c_{14}=0$

$c_{21}=-3h_j/5$ $c_{22}=-1$ $c_{23}=0$ $c_{24}=-3h_j^2/20$

$c_{31}=\dfrac{\sigma(5+3\sigma)}{1+\sigma}$ $c_{32}=0$ $c_{33}=\sigma h_j^2/6$ $c_{34}=\dfrac{\sigma h_j(5+4\sigma)}{3(1+\sigma)}$

$c_{41}=6\sigma^2(\sigma^2+\sigma-1)$ $c_{42}=0$ $c_{43}=\sigma^2h_j^2(2\sigma-1)(\sigma+1)/5$ $c_{44}=\sigma^2h_j(14\sigma^2+10\sigma-10)/5$

---

[4] See equations (10) for values of $\alpha_1,\ldots,\alpha_5$.

not confined and grows with ξ.

D. Transformed Displacement Thickness Coordinates

If the displacement thickness normalized equations are used, with δ prescribed by (5), and the same mapping (6) is applied, (7a) becomes

$$\zeta_\eta^2(1+\varepsilon)V_{\eta\eta}+\left((1+\varepsilon)\zeta_{\eta\eta}+\left[\left(\left(\frac{\delta^2}{2}\right)_\xi+\delta^2 f_\xi\right)+\varepsilon_\eta\right]\zeta_\eta\right)V_\zeta$$
$$+\beta(1-V^2)=\delta^2 V V_\xi \tag{8a}$$

In this system, we achieve mesh point accumulation as well as growth control. The edge value of $\eta_e=10$[5] applies for all values of ξ.

4. EDDY VISCOSITY MODELS

Two closure models that have been reasonably successful in approximating surface boundary layers have been given by Michel (6) and Cebeci-Smith (7). These have been used for the present calculations. In the latter, which is a two-layer model, the slope of the eddy viscosity is discontinuous at the juncture of the inner and outer regions. This did not lead to any apparent difficulty with the higher-order formulations.

Single Layer With Injection

$$\varepsilon=R_e^{3/2}F^2\ell^2|u_\eta|/\delta$$

where

$$F=1-\exp[-\eta/A]\ ,\quad \eta=yR_e^{\frac{1}{2}}/\delta$$

$$A=26[R_e^{\frac{1}{2}}\delta(u_\eta)_{\eta=0}]^{-\frac{1}{2}}\exp(-5.9v_w^+)\ ,$$

$$v_w^+=J[R_e^{\frac{1}{2}}\delta/(u_\eta)_{\eta=0}]^{\frac{1}{2}}\ ,\quad J=v_w/u_e$$

$$\ell=0.085\delta\eta_e R_e^{-\frac{1}{2}}[\tanh(0.41\eta/0.085\eta_e)]\ ;$$

η_e is the boundary layer thickness.

Two-Layer With Injection And With Transition

$$\delta=(2\xi)^{\frac{1}{2}};\quad y=(2\xi)^{\frac{1}{2}}\eta R_e^{-\frac{1}{2}};\quad \zeta=\eta;$$

Inner region:

$$\varepsilon=\varepsilon_i=I_{tr}L^2R_e^{3/2}(2\xi)^{-\frac{1}{2}}|u_\eta|$$

$$L=0.41\eta R_e^{-\frac{1}{2}}(2\xi)^{\frac{1}{2}}[1-\exp(-\eta/A)]$$

$$A=26[(2R_e\xi)^{\frac{1}{2}}(u_\eta)_{\eta=0}]^{-\frac{1}{2}}\exp(-5.9v_w^+)$$

Outer region:

$$\varepsilon_o=0.0168I_{tr}(2R_e\xi)^{\frac{1}{2}}\int_o^\infty(1-V)d\eta$$

I_{tr} is the transition intermittency factor given as

$$I_{tr}=1-\exp\left(-G(\xi-\xi_{tr})^2\right) \tag{9}$$

$G=(R_e^2/1200)(R_e\xi_{tr})^{-1.34}$; ξ_{tr} is the location where transition is initiated. Calculations were considered with I_{tr} from (9) and with a step transition from laminar conditions, so that $I_{tr}=1.0$. After a short distance downstream of ξ_{tr}, the solutions were undistinguishable so that fully turbulent conditions were virtually unsensitive to the transition modelling.

5. COUPLED BOUNDARY LAYER EQUATIONS

The governing equations (4) or (7) are coupled with the collocation formulae (1) for finite-differences, (2) for Spline 4 or (3) for Hermite 6. This leads to a coupled (2x2) or (3x3) or (4x4) block tridiagonal system, respectively. The unknowns are V_j, f_j and, when necessary, M_j and/or m_j.

In order to obtain these coupled systems, we first apply quasi-linearization for the nonlinear terms in (4a) or (8a). The viscosity coefficients are treated iteratively. The streamwise (ξ) derivatives are approximated by either backward (first-order) differencing, or Crank-Nicolson (second-order) differencing, or a higher-order formulae described in Reference (3). All of these procedures are implicit and except for the latter, they are unconditionally stable. For the boundary layer problems considered here, the streamwise gradients are much less significant than the surface normal variations and therefore the choice of streamwise differencing is not important. For purposes of simplicity, the coupled systems shown herein use first-order backward differencing. The quasi-linearized collocation form of (8a) becomes

$$\alpha_1V_j+\alpha_2f_j+\alpha_3M_j+\alpha_4m_j=\alpha_5 \tag{10a}$$

where

$$\alpha_1=-2\bar{V}_j(\bar{\beta}+\bar{\delta}^2/2\Delta\xi) \tag{10b}$$

$$\alpha_2=\frac{\bar{\zeta}_\eta}{2\Delta\xi}[3\bar{\delta}^2-(\delta^2)^{n-1}]\bar{m}_j \tag{10c}$$

$$\alpha_3=\bar{\zeta}_\eta^2(1+\bar{\varepsilon}) \tag{10d}$$

In some calculations the M_j contribution from $\bar{\varepsilon}_\eta$ in α_4 was included directly in α_3.

---

[5] The constant α in the transformation of case (C) is now more appropriately, $\alpha=-90$. The solutions are quite sensitive to the choice of the constants α and β.

$$d_4=(1+\tilde{\epsilon})\zeta_{\eta\eta}+\zeta_\eta[\tilde{\epsilon}_\eta+(\frac{\tilde{\delta}^2}{2\Delta\xi}-\frac{(\delta^2)^n}{2\xi})\tilde{f}_j+\frac{\tilde{\delta}^2}{\Delta\xi}(\tilde{f}_j-f_j^n)] \quad (10e)$$

$$d_5=-\tilde{\beta}(1+\tilde{V}_j^2)-\frac{\tilde{\delta}^2}{2\Delta\xi}(\tilde{V}_j^2+(V_j^2)^n)+\frac{\zeta_\eta}{2\Delta\xi}[3\tilde{\delta}^2-(\delta^2)^n]\tilde{m}_j\tilde{f}_j \quad (10f)$$

The superscript n denotes the previous streamwise (ξ) location. Variables without superscripts are the unknown quantities at the new location n+1; the superscript tilde (~) denotes the latest iterative value at n+1. Two iterations are generally required at each streamwise location.

The streamfunction equation (8b) is of the form

$$f_j-f_{j-1}+b_{21}V_j+c_{21}V_{j-1}+b_{23}M_j+c_{23}M_{j-1}+b_{24}m_j+c_{24}m_{j-1}=d_2 \quad (10b)$$

The final systems for finite-differences (2x2), Spline 4 (3x3) and Hermite 6 (4x4) are of the form

$$AW_{j+1}+BW_j+CW_{j-1}=d \quad (11)$$

where $A=\{a_{ik}\}$, $B=\{b_{ik}\}$, $C=\{c_{ik}\}$ are the matrix coefficients of the vector $W=w_k$. d is the vector d_i. The matrix and vector coefficients are given in Table 1 for each of the formulations. The simple displacement thickness normalized form is recovered with $\zeta=\eta$. The laminar variables are recovered with $\zeta=\eta$ and $\delta=(2\xi)^{1/2}$.

The appropriate boundary conditions for each of the formulations are given below. The truncation errors associated with these and other higher-order developments are given in (3) and (4).

6. BOUNDARY CONDITIONS

The general boundary conditions for all the methods are as follows:

$$u_1=u(0)=0;\ f_1=f(0)=f_w \text{ and } u_{N+1}=u(\eta_e)=1,$$

where $f_w=0$ for a non-permeable surface. The additional spline boundary conditions are obtained from the governing boundary layer equation and the two point relationships of the type given in equations (2b)-(2e). The derivations are given in more detail in (4) and (5). In the present paper, the boundary condition for M_1 is obtained from the equation as

$$M_1=u_{\eta\eta}(0)=-\beta .$$

For Spline 4, this leads to the following expressions for K_1:

$$\sigma\neq1\ ;\ K_1=-\beta-\Delta\left(K_3-(1+\sigma)K_2+\sigma K_1\right)/6$$

$$\sigma=1\ ;\ K_1=-\beta-(-K_4+4K_3-5K_2+2K_1)/12$$

or for general σ,

$$K_1=-\beta-h_2^2(u^{iv})_1/12 .$$

The ~~former~~ are obtained by extrapolation. The latter uses the equation (4a) at the wall and is more desirable for coarse grids. For finer grids near the surface the two conditions lead to similar results.

The value m_1 is given by

$$m_1=-\frac{h_2}{3}(K_1+.5K_2)+u_2/h_2 \quad \text{(Spline 4)}$$

and

$$m_1=\frac{5}{3h_2}u_2-\frac{2}{3}m_2+\frac{h_2}{12}(M_2-3M_1)-\frac{h_2^2}{36}(u_{\eta\eta\eta})_1+O(h_2^5) \quad (12) \quad \text{(Hermite 6)}$$

$u_{\eta\eta\eta}$ can either be obtained by extrapolation or by differentiating the governing equation at the wall. In the present paper this derivative is simply obtained from equation (4a) and has been applied for the calculations shown herein.

7. SOLUTION PROCEDURE

The block-tridiagonal system (11) is solved by a now standard two-pass inversion procedure (9). In view of the large numbers of zeros appearing in the matrices A, B, C, it should be possible to optimize the inversion formulae. This was not considered here, so that the higher-order calculations can be made more efficient and thereby further enhance their advantages over conventional lower-order procedures.

The Hermite 6 (4x4) block-tridiagonal system was actually solved by an iterative unconditionally stable predictor-corrector method. In this solution procedure, a pair of (2x2) block systems must be evaluated. This leads to a significant reduction in computer operation counts and, therefore, time. The details of this procedure will be the subject of a future paper. The (3x3) Spline 4 system was solved by both the coupled and predictor-corrector procedures. For the latter, only simple tridiagonal equations need be inverted and the calculation times are less than that required for the coupled solutions. The results are, of course, identical.

8. RESULTS

The calculations for a flat plate geometry with and without surface mass transfer are presented. The Cebeci-Smith two-layer closure modelling with transition intermittency was used with the Görtler transformed and displacement thickness coordinates. The single layer eddy viscosity without transition modelling was used with all other coordinate systems; solutions were obtained with and without mass transfer. The results are virtually insensitive to the transition modelling after a very short distance downstream of the transition point. It is significant, however, that the numerical formulations described herein do provide accurate turbulent results even with a step change from laminar to turbulent flow conditions, or a step change from zero to finite uniform surface injection. The higher-order procedures do not suffer any apparent loss of accuracy or stability with these discontinuous flow conditions.

Our goals for this numerical experiment are to evaluate the calculated resluts as obtained with finite-difference, Spline 4 and Hermite 6 formulations, and to assess the merits of the transformed coordinate systems described herein, in order to forecast their utility for more complex geometries to be considered in future studies. Of particular interest are computer times and storage to achieve equal accuracy, ease of application for other configurations and three-dimensional flows, and a conclusion as to the minimum mesh point requirements, with the optimum procedure considered here, to achieve 5% accuracy for the flat plate geometry.

Typical solutions for the skin friction coefficient $C_f=2m(0,\xi)\zeta_{\eta}(o)/\delta R_e^{1/2}$, the velocity profile $V(\xi,\eta)$ and in certain cases the displacement thickness δ are shown in figure 1 for laminar or Görtler variables; i.e., $\eta=\zeta$, $\delta=(2\xi)^{1/2}$, figure 2 with the displacement thickness normalization; i.e., $\eta=\zeta$, δ from equation (5), and figure 3 with the transformed (see equation (6)) displacement thickness normalization. The effects of surface mass transfer are depicted in figure 4. The surface velocity gradient $m(0,\xi)=m_1(\xi)$ is evaluated from the spline formula (2) for spline 4, the expansion formula (12) for Hermite 6 and the following second-order accurate three-point end difference formula (13) for the finite-difference calculations:

$$m_1(\xi)=[(1+\sigma)^2V_2(\xi)-V_3(\xi)]/\sigma(1+\sigma)h_2 \qquad (13)$$

In certain cases the two-point formula (14) derived in Reference (5),

$$m_1(\xi)=V_2(\xi)/h_2-\beta h_2/2 \qquad (14)$$

provides more accurate finite-difference results. This condition will be described more fully in an expanded version of this paper to be published.

The solutions with Görtler variables and the Cebeci-Smith eddy viscosity model allow for transition intermittency. All other solutions, with either single or two-layer closure, assume a step change from laminar to turbulent flow conditions. The results indicate that a short distance downstream of the transition location $R_{e_{\xi tr}}=5.45\times10^5$, transition modelling is no longer important. Solutions are shown in the range $0.5\times10^6\leq R_{e_\xi}\leq 2\times10^6$. The profiles are shown at $R_{e_\xi}=10^6$ and the c_f values at this location are tabulated in Table II. The experimental data at this location is in the range $c_f=3.45-3.55$ (7,10). The displacement thickness normalization controls the numerical growth of the boundary layer, and as seen with the velocity profiles on figure 2 a quasi-similarity for $V(\xi,\eta)$ as a function of y/δ is achieved for $R_{e_x}\geq10^6$. As x increases, changes in the profile are confined to the sublayer region very close to the surface. Based on these results it appears that with this normalization the turbulent boundary layer, even for very large R_{e_x}, can be described with a minimal number of mesh points. The Spline 4 solutions with 21 and even 11 mesh points are remarkably accurate. Similar conclusions apply to the Hermite 6 calculations, although these have not been as extensive and further study is in progress. The finite-difference calculations require upwards of 61 mesh points to achieve comparable accuracy. Therefore, as in earlier laminar studies, it appears that factors of three to six in the number of mesh points can be saved by use of the higher-order interpolation procedures. This translates into savings of from 25% to 75% in computer times for two-dimensional flows.

The solutions with Görtler variables (figure 1) and transformed variables (figure 3) also lead to a significant mesh point reduction with the Spline 4 formulation (Hermite 6 was not considered in the transformed variables). The latter solutions are quite sensitive to the transformation constants, e.g., see Table II, and therefore extreme care is required with the use of coordinate transformations. For the former, boundary layer growth, i.e., $\eta_e(x)$, requires either large numbers of mesh points or large values of σ and therefore increased truncation errors.

In view of these experiences we tend to favor the displacement thickness normalization without transformation and with moderately

TABLE II: TYPICAL SOLUTIONS FOR c_f AT $R_{ex}=1.014\times10^6$

		N	h_2	σ	F.D.	S4	H6	Closure Model
G.V.†		141	0.001	1.063	3.46	3.46	-	C-S†
		61	0.2	1	5.48	3.89	3.48	C-S
		61	0.2	1	4.82	3.75	-	M‡
		21	0.05	1.5	5.14	3.16	-	M
δ†		61	.00363	-	3.59	3.47	-	M
		21	.005	1.4	4.44 (4.44)‡	3.39	3.52	M
		11	.1432	1.4	12.05 (8.67)‡	3.21	-	M
δ_T†	$\alpha=-90$	21	0.05	1	3.31 (3.62)‡	3.50	-	M
	$b_o=.05$	11	0.1	1	2.43 (4.05)‡	3.40	-	M
	$\alpha=-109$	21	0.05	1	-	3.66	-	M
	$b_o=.05$	11	0.1	1	-	3.68	-	M

† G.V. is Görtler Variables; δ is displacement thickness normalization; δ_T is δ normalization with transformation; C-S is Cebeci-Smith; M is Michel without transition intermittency.

‡ Finite-difference values using equation (14).

large σ values; i.e., $\sigma\leq1.5$. This approach would also be most desirable for three-dimensional calculations where δ may vary significantly in the secondary or azimuthal direction. Coordinate transformations may be highly sensitive to flow variations in this direction.

Finally, a typical solution with surface mass transfer is shown on figure 4. The injection is started discontinuously and this does not lead to any difficulties with the Spline 4 calculations. The free stream Reynolds number is 1.2×10^6 and injection is started at $x=0.65$. The velocity profiles and friction coefficient agree quite well with the data (7). It is important to note that arbitrary laminar or turbulent initial conditions have been assumed and that experimental data has not been used at any point in the calculation. With Görtler variables, Spline 4 solutions with 21 mesh points and $\eta_e=25$ appear to be quite acceptable for the range of R_{ex} depicted. δ-transformed solutions (not shown) are comparable to those found with zero mass transfer. As a final experiment, the injection was discontinuously terminated at $R_{ex}=1.229\times10^6$. The boundary layer thins down rapidly, c_f increases, and the solutions are quite reasonable. There is no data for these flow conditions.

In conclusion, it has been possible to numerically simulate turbulent boundary layers, with and without discontinuous mass transfer, with large reductions in the numbers of mesh points typically required for finite-difference calculations. With a displacement thickness normalization that stems the boundary layer growth, as few as 11 points provide 5-7% accuracy, and with 21 points the results are well within the experimental scatter. Future studies will include other coordinate transformations, additional Hermite 6 calculations, a consideration of conservation form equations and applications to free shear flow.

REFERENCES

1 Rubin, S.G. and Graves, R.A., "Viscous Flow Solutions With a Cubic Spline Approximation," Computers and Fluids, Vol. 3, No. 1, 1975, pp. 1-36.

2 Rubin, S.G. and Khosla, P.K., "Higher Order Numerical Solutions Using Cubic Splines," AIAA Journal, Vol. 14, No. 7, 1976, pp.851-858.

3 Rubin, S.G. and Khosla, P.K., "Higher-Order Numerical Methods Derived From Three-Point Polynomial Interpolation," NASA CR-2735, 1976.

4 Rubin, S.G. and Khosla, P.K., "Numerical Methods Based on Polynomial Spline Interpolation," Proceedings of Fifth Int'l. Conference on Numerical Methods in Fluid Dynamics, Enschede, The Netherlands, Springer-Verlag,

Heidelberg, 1976, pp. 370-377.

5 Rubin, S.G. and Khosla, P.K., "Polynomial Interpolation Methods for Viscous Flow Calculations," to appear in the Journal of Computational Physics.

6 Michel, R., Qumard, C. and Durant, R., Proceedings of Computation of Turbulent Boundary Layers, AFOSR-IFP Conference, Stanford University, 1968.

7 Cebeci, T. and Smith, A.M.O., "Analysis of Turbulent Boundary Layers," Academic Press, N.Y., 1974.

8 Rosenhead, L., "Laminar Boundary Layers," Oxford at the Clarendon Press, 1963.

9 Rosenberg D.U., "Methods for the Numerical Solution of Partial Differential Equations," American Elsevier Publishing Co. Inc., N.Y., 1969.

10 Wilghardt, K., Proceedings of Computation of Turbulent Boundary Layers, AFOSR-IFP Conference Stanford University, 1968.

ACKNOWLEDGMENT

This research was supported by the Air Force Office of Scientific Research under Grant No. AFOSR 74-2635, Project No. 9781-01.

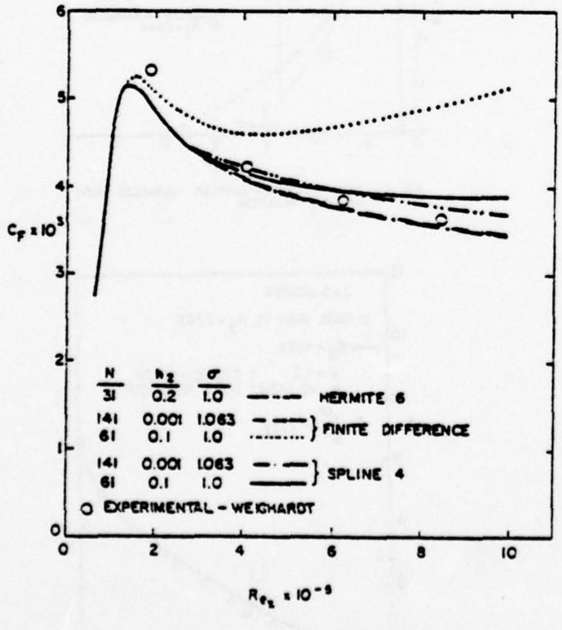

FIG. 1a SKIN FRICTION - GÖRTLER VARIABLES WITH TRANSITION INTERMITTANCY

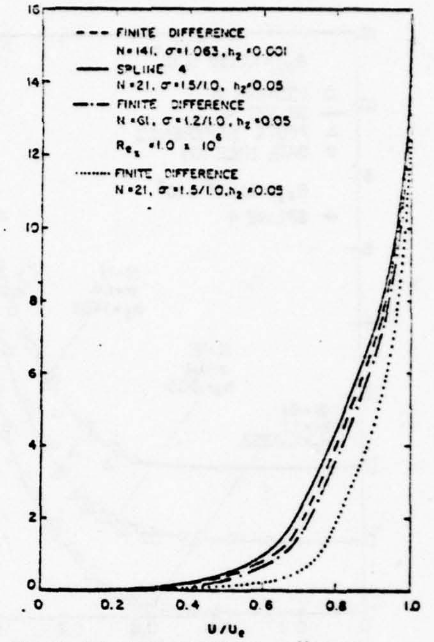

FIG. 1b VELOCITY PROFILES - GÖRTLER VARIABLES

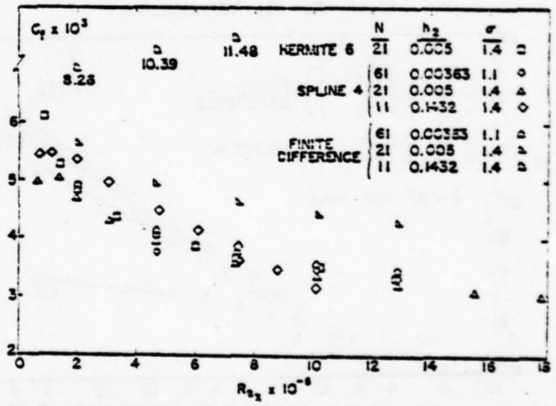

FIG. 2a SKIN FRICTION - DISPLACEMENT THICKNESS (δ) NORMALIZATION-STEP TRANSITION

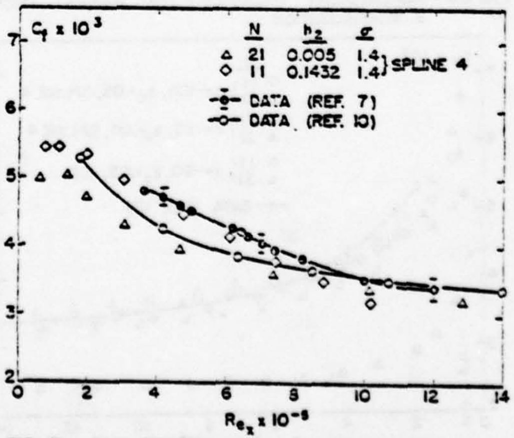

FIG. 2b SKIN FRICTION WITH δ NORMALIZATION-COMPARISON WITH DATA-STEP TRANSITION

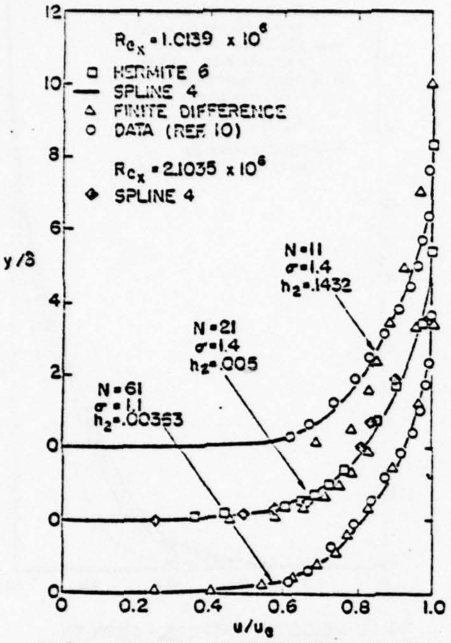

FIG. 2c VELOCITY PROFILES - DISPLACEMENT THICKNESS (δ) NORMALIZATION

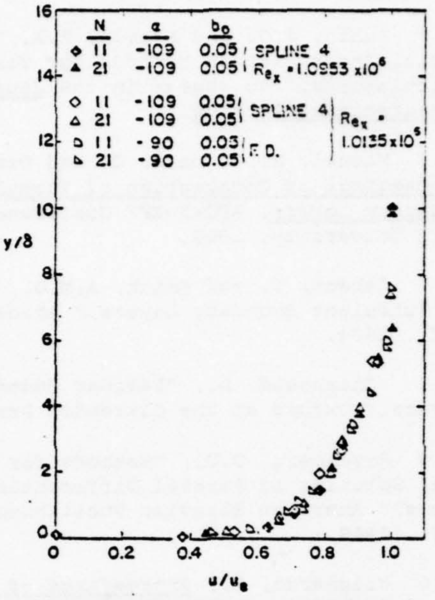

FIG. 3b VELOCITY PROFILES - TRANSFORMED δ NORMALIZATION

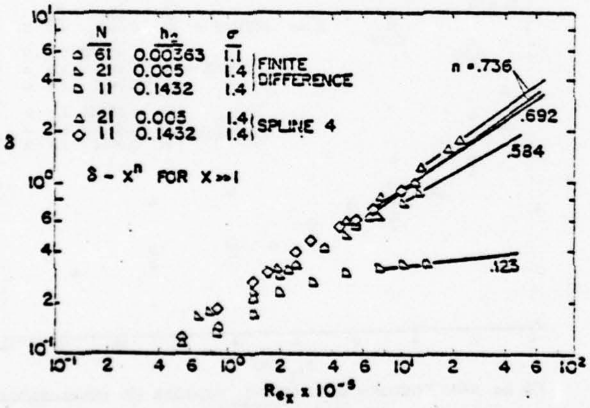

FIG. 2d DISPLACEMENT THICKNESS - DISPLACEMENT THICKNESS δ NORMALIZATION

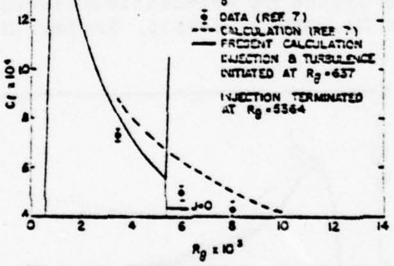

FIG. 4a SKIN FRICTION - GORTLER VARIABLES WITH UNIFORM INJECTION

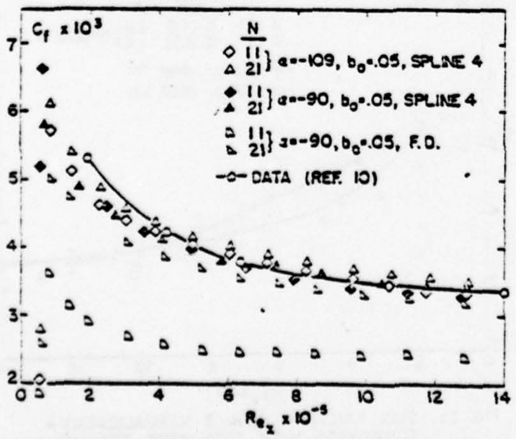

FIG. 3a SKIN FRICTION - TRANSFORMED δ NORMALIZATION - STEP TRANSITION

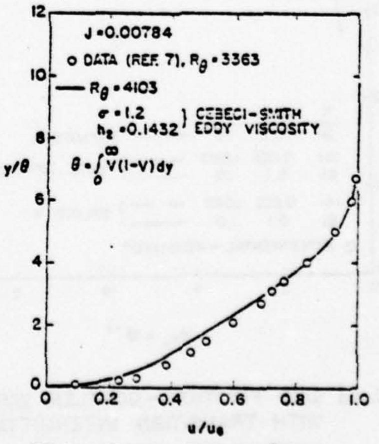

FIG. 4b VELOCITY PROFILE - GÖRTLER VARIABLES WITH UNIFORM INJECTION

SESSION 6

PLANETARY BOUNDARY LAYERS AND BUOYANT FLOWS

Co-chairmen: C. duP. Donaldson
ARAP
Princeton, New Jersey 08540

J. L. Lumley
Department of Aerospace Engineering
The Pennsylvania State University
University Park, Pennsylvania 16802

A TURBULENCE MODEL APPLIED TO GEOPHYSICAL FLUID PROBLEMS

BY

GEORGE MELLOR AND TETSUJI YAMADA*
Princeton University, Princeton, New Jersey 08540

ABSTRACT

Empirical constants in a second moment closure model centered on hypotheses by Rotta and Kolmogorov were established from laboratory experiments on flows of engineering interest. The same model has now been applied to laboratory experiments of geophysical interest, and a number of simulations in atmospheric and oceanic fluid dynamics. The latter include: the near-surface, atmospheric boundary layer; the entire, diurnally varying atmospheric boundary layer; dispersion of a point source pollutant in the atmospheric boundary layer; development of oceanic surface mixed layers and bottom layers; global atmospheric simulations.

The model and the basis for the necessary empirical constants will be reviewed critically; simulations and data comparisons, some of which have previously been described in the literature, will be collected and reviewed.

1. INTRODUCTION

Our experience at Princeton University with second moment turbulence modeling began at the time of the 1968 Stanford Conference on Turbulent Boundary Layer Computation (Kline et al, 1) with a simple Prandtl type model based on the solution of the turbulent kinetic energy equation. At that time, this model, Bradshaw's model and our older eddy viscosity model did very well in predicting all of the data compiled for the conference. Thus it was not clear that more complicated models based on hypotheses by Rotta (2) and Kolmogorov (3) and requiring consideration of all components of the Reynolds stress tensor could be justified on the basis of improving predictions.

The first results from the second moment calculations of Donaldson and Rosenbaum (4) (using Rotta's energy redistribution hypothesis but not the Kolmogorov isotropic dissipation hypothesis) when applied to wakes and jets and subsequent studies by Hanjalic and Launder (5) were encouraging but the newer models involved more empirical constants than did the older models which, on this basis alone, would facilitate agreement with data.

Our interest in the Rotta-Kolmogorov model (Mellor and Herring 6) was greatly enhanced by data obtained by So and Mellor (7, 8) which demonstrated the effect of wall curvature on turbulent flow. On stable, concave walls the Reynolds stress was virtually extinguished in the outer half portion of a turbulent layer and reduced significantly in the inner portion. With no empirical adjustment involving curvature, the model quantitatively predicted this rather dramatic occurrence (So 9, Mellor 10). The same model, when extended in - it now seems - a rather straightforward manner, predicted the observed stabilizing and destabilizing effect of density gradients in a gravity field (Mellor 11) according to data by Businger et al (12). All empirical constants were obtained from neutral flow data where turbulent energy production is in balance with dissipation. Numerical solutions are not needed for this purpose.

Yamada and Mellor (13), Lewellen et al (14) and others have now made persuasive predictions of stratified laboratory flows and atmospheric boundary layers which are strongly influenced by diurnally varying density stratification.

The empirical content of these models resides in various turbulent length scales; a major assumption is that all of the scales are proportional to a single master length scale. The experience generated thus far indicates that this is a viable assumption.

Surprisingly, although the length scale proportionality constants are important, many results are either independent or not very sensitive to willful variations in the master length scale itself. Thus, we have tried to separate our study of the turbulence model into two parts: first, the study of the single point moment equations, their various length scale constants of proportionality and, second, consideration of the master length scale itself.

We have been uncomfortable in dealing with a master length scale equation (closure assumptions seem less rational and empirical constants are not as directly related to data as are the length scale proportionality constants) and for some time were content with algebraic prescriptions. However, following Rotta once again, a turbulence length scale equation can be approached via the equations for the turbulence spectra or the equations for the two-point correlation functions. When the separation distance, r, approaches zero we obtain the single point, moment equations discussed previously and lose all length scale information. Thus the approach suggested by Rotta was to consider the integral of the correlation functions over r-space. Conceptually complicated assumptions are required to close the resultant equations. Nevertheless, we believe it best to proceed

---

*Present address: Atmospheric Physics Section, Argonne National Laboratory, Argonne, Ill. 60439

Research supported by the Air Force Office of Scientific Research under Grant No. AFOSR 75-2756. Computing time granted by NOAA/Geophysical Fluid Dynamics Laboratory was used in this research.

on this fact rather than adopt an equation for the dissipation in the manner of other currently active models; our reasons will be discussed below.

2. THE BASIC MODEL

If one writes down the single point equations for the moments of velocity and temperature, unknown higher moment terms appear. The model we have adopted (Mellor and Herring 6) to determine these unknowns is based on the energy redistribution hypothesis of Rotta in the form

$$\overline{p\left(\frac{\partial u_i}{\partial x_j}+\frac{\partial u_j}{\partial x_i}\right)} = -\frac{q}{3\ell_1}\left(\overline{u_i u_j}-\frac{\delta_{ij}}{3}q^2\right)+C_1 q^2\left(\frac{\partial U_i}{\partial x_j}+\frac{\partial U_j}{\partial x_i}\right), \tag{1}$$

and the Kolmogorov hypothesis of local, small-scale isotropy such that the dissipation is modeled according to

$$2\nu\overline{\frac{\partial u_i}{\partial x_k}\frac{\partial u_j}{\partial x_k}} = \frac{2}{3}\frac{q^3}{\Lambda_1}\delta_{ij} . \tag{2}$$

In the above, U_i is the mean velocity, u_i and p the turbulent velocity and pressure, $q^2 = \overline{u_i{}^2}$, ℓ_1 and Λ_1 are length scales and C_1 is a non-dimensional constant. The above model was then extended (Mellor 11) to include temperature (or any scalar) such that

$$\overline{p\frac{\partial\theta}{\partial x_j}} = -\frac{q}{3\ell_1}\overline{u_j\theta}. \tag{3}$$

$$(\alpha+\nu)\overline{\frac{\partial u_j}{\partial x_k}\frac{\partial\theta}{\partial x_k}} = 0, \tag{4}$$

and the temperature variance dissipation is

$$2\alpha\overline{\frac{\partial\theta}{\partial x_k}\frac{\partial\theta}{\partial x_k}} = 2\frac{q}{\Lambda_2}\overline{\theta^2}, \tag{5}$$

where $\overline{\theta^2}$ is the temperature variance and ℓ_2 and Λ_2 are length scales. It is an intrinsic part of the model, and ultimately, perhaps, its greatest weakness, that all lengths are assumed to be proportional to a single, master length scale.

Higher order terms (see definition of "order" below) can be added to the above (Launder et al 15, Launder 16, Wyngaard 17); to (1) one could add $C_2\,(P_{ikkj} + P_{jkki} - (2\delta_{ij}/3)\,P_{\ell kk\ell}) + C_3\,(P_{ikjk} + P_{jkik} - (2\delta_{ij}/3)\,P_{\ell k\ell k}) + C_4\beta(g_i\overline{u_j\theta} + g_j\overline{u_i\theta} - (2\delta_{ij}/3)g_k\overline{u_k\theta})$ where $P_{ijkm} \equiv -\overline{u_i u_j}\;\partial U_k/\partial x_m$. β is the coefficient of thermal expansion and g_i is the gravity vector; to (3) one could add $C_5\,g_j\beta\overline{\theta^2} + C_6\,\overline{\theta u_k}\partial U_k/\partial x_j + C_7\,\overline{\theta u_k}\partial U_j/\partial x_k$. In a rotating flow other terms containing the rotation vector can be added along with other higher order terms (Lumley 33). However, we have resisted added complexity for the following reasons: (a) In ref. (10), the above model met with instant and rather surprising success in predicting the very dramatic, stabilizing or destabilizing effects of density stratification in a gravity field. Similar effects of flow curvature were equally well predicted; (b) It is not at all clear that in the vicinity of walls, terms involving a unit vector, λ_i, normal to a wall should not be included in the list of additional terms. One would wish it not be thus but wishes do not govern turbulent flow. (c) The data base is not sufficient or accurate enough to determine many constants. (d) We are motivated to minimize complexity and the number of empirical constants.

Thus, the model represented by (1)-(5) is relatively simple. Our expection of the model is that it will accurately predict mean velocity and temperature fields and do a reasonable job of estimating turbulent moments.

To complete the model we must add closure expressions for $\overline{u_k u_i u_j}$, $\overline{pu_j}$, $\overline{u_i u_j\theta}$ and $\overline{p\theta}$. The choice is ambiguous as discussed in (6) and (11).

However, we choose

$$\overline{u_k u_i u_j} = \frac{3}{5}\,\ell q\;S_q\left(\frac{\partial\overline{u_i u_j}}{\partial x_k} + \frac{\partial\overline{u_i u_k}}{\partial x_j} + \frac{\partial\overline{u_j u_k}}{\partial x_i}\right), \tag{6}$$

$$\overline{u_k u_i\theta} = -\,\ell q\;S_{u\theta}\left(\frac{\partial\overline{u_k\theta}}{\partial x_j} + \frac{\partial\overline{u_j\theta}}{\partial x_k}\right), \tag{7}$$

$$\overline{u_k\theta^2} = -\,\ell q\;S_\theta\,\frac{\partial\overline{\theta^2}}{\partial x_k}, \tag{8}$$

and have thus far set $\overline{pu_j} = \overline{p\theta} = 0$. Expressions for $\overline{pu_j}$ and $\overline{p\theta}$ could be invented but it would be difficult *to discriminate them from the expressions in (6) and* (7). This will be particularly true when the model is further simplified below. $S_q, S_{u\theta}, S_\theta$ are empirical numbers.

We now cite the equations for the mean velocity U_i and temperature Θ. They are

$$\frac{\partial U_k}{\partial x_k} = 0, \tag{9}$$

$$\frac{DU_j}{Dt} + \varepsilon_{jk\ell}f_\ell U_k = \frac{\partial}{\partial x_k}(-\overline{u_k u_j}) - \frac{\partial P}{\partial x_j} - g_j\beta\Theta, \tag{10}$$

$$\frac{D\Theta}{Dt} = \frac{\partial}{\partial x_k}(-\overline{u_k\theta}), \tag{11}$$

where $D()/Dt \equiv U_k\partial()/\partial x_k + \partial()/\partial t$ and f_k is the Coriolis vector.

Now, if the closure assumptions are inserted into the mean, turbulent moment equations we have the complete model as follows:

$$\frac{D\overline{u_i u_j}}{Dt} + f_k(\varepsilon_{jk\ell}\overline{u_\ell u_i} + \varepsilon_{ik\ell}\overline{u_\ell u_j})$$

$$= \frac{\partial}{\partial x_k}\left[\frac{3}{5}\,\ell q\, S_q\left(\frac{\partial\overline{u_i u_j}}{\partial x_k} + \frac{\partial\overline{u_i u_k}}{\partial x_j} + \frac{\partial\overline{u_j u_k}}{\partial x_i}\right)\right]$$

$$-\overline{u_k u_i}\frac{U_j}{\partial x_k} - \overline{u_k u_j}\frac{\partial U_i}{\partial x_k} - \beta(g_j\overline{u_i\theta} + g_i\overline{u_j\theta})$$

$$\frac{q}{3\ell_1}\left(\overline{u_i u_j} - \frac{\delta_{ij}}{3}q^2\right) + C_1 q^2\left(\frac{\partial U_i}{\partial x_j} + \frac{\partial U_j}{\partial x_i}\right) - \frac{2}{3}\frac{q^3}{\Lambda_1}\delta_{ij}, \quad (12)$$

$$\frac{D\overline{u_j\theta}}{Dt} + f_k\varepsilon_{jk\ell}\overline{u_\ell\theta}$$

$$= \frac{\partial}{\partial x_k}\left[\ell q\, S_{u\theta}\left(\frac{\partial\overline{u_j\theta}}{\partial x_k} + \frac{\partial\overline{u_k\theta}}{\partial x_j}\right)\right]$$

$$-\overline{u_j u_k}\frac{\partial\Theta}{\partial x_k} - \overline{\theta u_k}\frac{\partial U_j}{\partial x_k} - \beta g_j\overline{\theta^2} - \frac{q}{3\ell_2}\overline{u_j\theta}, \quad (13)$$

$$\frac{D\overline{\theta^2}}{Dt} = \frac{\partial}{\partial x_k}\left[\ell q\, S_\theta\frac{\partial\overline{\theta^2}}{\partial x_k}\right] - 2\overline{u_k\theta}\frac{\partial\Theta}{\partial x_k} - 2\frac{q}{\Lambda_2}\overline{\theta^2} \quad (14)$$

3. THE SIMPLIFIED MODEL

Although we have used the complete model in the numerical solution of problems (Mellor and Yamada 18, Briggs, Mellor and Yamada 19), the model is still too complicated for practical application to geophysical fluid dynamics problems. It will be appreciated that the model must be extended to include other scalar quantities besides temperature (in the atmosphere, water vapor and liquid water along with other chemical constituents; in the oceans, salinity and other chemical constituents) and the numerical effort can quickly get out of hand.

A process of simplification has been described by Mellor and Yamada (18) in some detail. Briefly it involves evaluating all terms in the model equations as a product of q^3/Λ and powers of a where $\Lambda = O(\Lambda_1)$ and $a^2 = O(a_{ij}^2)$. a_{ij} is the non-dimensional measure of anisotropy in the expression

$$\overline{u_i u_j} = \left(\frac{\delta_{ij}}{3} + a_{ij}\right)q^2$$

Similar parameters are introduced for the temperature variables. We then evaluated terms in (12), (13) and (14) in powers of a and eliminated terms of order a^2. All of this is suggested by the kinetic theory of gases wherein a is related to the Knudson number and is generally a very small number. For turbulent flows a_{ij}^2 0.15 and is not overly small. Nevertheless the procedure contributes some discipline to the process of simplification and provides a self consistent model. What we have called a "Level 3" model[1] is as follows:

$$\frac{Dq^2}{Dt} - \frac{\partial}{\partial x_k}\left[\ell q S_q\frac{\partial q^2}{\partial x_k}\right] = -2\overline{u_k u_i}\frac{\partial U_i}{\partial x_k} - 2\beta g_k\overline{u_k\theta} - 2\frac{q^3}{\Lambda_1},$$

$$\overline{u_i u_j} = \frac{\delta_{ij}}{3}q^2 - \frac{3\ell_1}{q}\left[(\overline{u_k u_i} - C_1 q^2\delta_{ki})\frac{\partial U_j}{\partial x_k}\right. \quad (15)$$

$$\left. + (\overline{u_k u_j} - C_1 q^2\delta_{kj})\frac{\partial U_i}{\partial x_k} - \frac{2}{3}\delta_{ij}\overline{u_k u_\ell}\frac{\partial U_\ell}{\partial x_k}\right]$$

$$-\frac{3\ell_1}{q}\beta(g_j\overline{u_i\theta} + g_i\overline{u_j\theta} - \frac{2}{3}\delta_{ij}g_k\overline{u_k\theta})$$

$$-\frac{3\ell_1}{q}f_k(\varepsilon_{jk\ell}\overline{u_\ell u_i} + \varepsilon_{ik\ell}\overline{u_\ell u_j}), \quad (16)$$

$$\frac{D\overline{\theta^2}}{Dt} - \frac{\partial}{\partial x_k}\left[\ell q S_\theta\frac{\partial\overline{\theta^2}}{\partial x_k}\right] = -2\overline{u_k\theta}\frac{\partial\Theta}{\partial x_k} - 2\frac{q}{\Lambda_2}\overline{\theta^2} \quad (17)$$

$$\overline{u_j\theta} = -\frac{3\ell_2}{q}\left[\overline{u_j u_k}\frac{\partial\Theta}{\partial x_k} + \overline{\theta u_k}\frac{\partial U_j}{\partial x_k} + \beta g_j\overline{\theta^2}\right]. \quad (18)$$

A Further Simplification

We have made one further simplification which is not directly justified by our ordering analysis and that is to neglect the material derivative and diffusion terms in (17) so that a balance between temperature variance and dissipation remains (the resultant model has been termed a "Level two and half" model by users). This is motivated by practical matters; otherwise if one includes other scalars like water vapor, for example, one finds a need to write a differential equation for the variance of water vapor, the variance of temperature and an equation for the cross correlation of temperature and water vapor. The situation quickly gets out of hand if more scalars are added to the list to be computed.

A close reexamination of our ordering analysis indicates that this further simplification might be justified for all stable flows and slightly unstable flows; error is more likely as one approaches the free-convection limit. Thus, this is a cautionary note on a problem which further experience may or may not alleviate.

The Boundary Layer Approximation

If now the boundary layer approximation is made and $g_i=(0,0,-g)$, our model reduces further to

---

[1] In ref (18) a mistake was made. The last term in equation (21) of that paper and subsequently all terms labeled $_1q^2$ or $_f$ should be purged since they are of order a^2. The mistake is embarassing since the original purpose of the ordering analysis was to eliminate terms.

$$\frac{D}{Dt}\begin{bmatrix}U\\V\\0\end{bmatrix}+\frac{\partial}{\partial z}\begin{bmatrix}\overline{uw}\\\overline{vw}\\0\end{bmatrix}=-\begin{bmatrix}\partial P/\partial x\\\partial P/\partial y\\\partial P/\partial z\end{bmatrix}+\begin{bmatrix}fV\\-fU\\g\beta\Theta\end{bmatrix}, \qquad (19a,b,c)$$

$$\frac{D\Theta}{Dt}-\frac{\partial\overline{w\theta}}{\partial z}=0, \qquad (20)$$

$$\frac{D}{Dt}\left(\frac{q^2}{2}\right)-\frac{\partial}{\partial z}\left[\ell q\ S_q\frac{\partial}{\partial z}\left(\frac{q^2}{2}\right)\right]=P_{xx}+P_{yy}+\beta g\overline{w\theta}-\frac{q^3}{\Lambda_1}, \qquad (21)$$

$$\begin{bmatrix}\overline{u^2}\\\overline{v^2}\\\overline{w^2}\end{bmatrix}=\frac{q^2}{3}\begin{bmatrix}1\\1\\1\end{bmatrix}+\frac{\ell_1}{q}\begin{bmatrix}4P_{xx}-2P_{yy}-2\beta g\overline{w\theta}\\-2P_{xx}+4P_{yy}-2\beta g\overline{w\theta}\\-2P_{xx}-2P_{yy}+4\beta g\overline{w\theta}\end{bmatrix}, \qquad (22a,b,c)$$

$$-\begin{bmatrix}\overline{uv}\\\overline{wu}\\\overline{wv}\end{bmatrix}=\frac{3\ell_1}{q}\begin{bmatrix}P_{yx}+P_{xy}\\(\overline{w^2}-C_1q^2)\partial U/\partial z-\beta g\overline{u\theta}\\(\overline{w^2}-C_1q^2)\partial V/\partial z-\beta g\overline{v\theta}\end{bmatrix}, \qquad (23a,b,c)$$

$$-\begin{bmatrix}\overline{u\theta}\\\overline{v\theta}\\\overline{w\theta}\end{bmatrix}=\frac{3\ell_2}{q}\begin{bmatrix}\overline{uw}\partial\Theta/\partial z+\overline{w\theta}\partial U/\partial z\\\overline{vw}\partial\Theta/\partial z+\overline{w\theta}\partial V/\partial z\\\overline{w^2}\partial\Theta/\partial z-\beta g\overline{\theta^2}\end{bmatrix}, \qquad (24a,b,c)$$

$$0=-2\overline{w\theta}\frac{\partial\Theta}{\partial z}-2\frac{q\overline{\theta^2}}{\Lambda_2} \qquad (25)$$

where $P_{ij}\equiv-\overline{wu_i}\,\partial U_j/\partial z$. To simplify the discussion below, the Coriolis terms have been excluded. They may be shown to be small in the atmospheric boundary layer and the other flows discussed below.

For computational purposes equations (22), (23) and (24) may be greatly simplified to read

$$(-\overline{wu},-\overline{wv})=\ell q\ S_M\left(\frac{\partial U}{\partial z},\frac{\partial V}{\partial z}\right), \qquad (26a,b)$$

$$-\overline{w\theta}=\ell q\ S_H\frac{\partial\Theta}{\partial z}\ , \qquad (26c)$$

where

$$S_M=\frac{3A_1(\overline{w^2}-C_1q^2)/q^2+9A_1A_2\ell\beta g\overline{w\theta}/q^3}{1+9A_1A_2\ell^2\beta g\ (\partial\Theta/\partial z)/q^2}, \qquad (27a)$$

$$S_H=\frac{2A_2\overline{w^2}/q^2}{1+3A_2B_2\ell^2\beta g(\partial\Theta/\partial z)/q^2}, \qquad (27b)$$

and $\overline{w^2}$ is given by (22c).

4. THE EMPIRICAL CONSTANTS FROM NEUTRAL DATA

It is fundamental to current second moment models that all length scales be everywhere proportional to each other. Therefore we set

$$(\ell_1,\Lambda_1,\ell_2,\Lambda_2,)=(A_1,B_1,A_2,B_2)\ell\ , \qquad (28)$$

where ℓ is the master turbulent length scale. The constants A_1, B_1, A_2, B_2 and C_1 must be determined from data. This can be accomplished without resort to a trial and error process (sometimes termed "computer optimization") by appealing to data where turbulent energy production and dissipation are balanced. This occurs in the overlap (law of the wall) region near walls and in homogeneous shear flow data where diffusion is zero and where at some downstream point in the flow, it happens that $\partial q^2/\partial x=0$.

Previously (11), we had determined that $(A_1, B_1, A_2, B_2, C_1)=(0.78, 15.0, 0.79, 8.0, .056)$. In this paper, we have exerted more effort in collecting and intepreting data; hopefully these results will also be useful to other modelers.

Interpretation of wall data requires some care. We wish to correctly identify the outer asymptotes of the "inner", viscous wall functions (law of the wall coordinates) which describe the various turbulent flow properties and which will match with the inner asymptotes of the "outer" functions. It is the latter which our model is supposed to simulate. The large Reynolds number asymptotic behavior of turbulent wall flows has been discussed by Yajnik (20) and Mellor (21). Perry and Abel (22) have provided a nice experimental illustration of the matter which we repeat here in Fig. 1. It is seen that we need to determine a quantity like u'/u_t when $y^+>80$. In general, data is not as well resolved in the near wall regions as in Fig. 1. Therefore there is error in interpretation. However, it is believed that this kind of error is considerably smaller than the variations among the different data sets related to measurement error and systematic departures for small Reynolds numbers.

The values for turbulent velocity variances are collected in Table I and for turbulent thermal variances in Table II. In Table I, aside from Reynolds number and u_τ/U_o, the independent data may be thought to be u'/u_t, v'/v_t and w'/u_t, the remaining two quantities are derived. In Table II, $-\overline{w\theta}/U_o\Delta\Theta, \theta'/\Delta\Theta$ and P_{rt} are independent whereas the remaining two variables are derived.

If we now turn to the model as represented by equations (22), (23) and (24) and simplify the equations to the conditions governing the data in Table I and II, namely that the flow is two-dimensional, bouyancy effects are negligible and production equals dissipation so that $q^3/\Lambda_1=-\overline{uw}\,\partial U/\partial z$, then the following relation may be obtained from (22), (23), (24) and (28):

$$\frac{\partial U}{\partial z}=\frac{u_\tau}{\ell}\ , \qquad (29a)$$

$$\overline{u^2}=(1-2\gamma_1)q^2\ , \qquad (29b)$$

$$\overline{v^2}=\overline{w^2}=\gamma_1q^2\ , \qquad (29c)$$

$$B_1 = (q/u_\tau)^3, \tag{29d}$$

$$A_1 = B_1(1/3-\gamma_1)/2\ , \tag{29e}$$

$$C_1 = \gamma_1 - (3A_1B_1^{1/3})^{-1} \tag{29f}$$

$$\frac{\partial\Theta}{\partial z} = -\frac{\overline{w\theta}}{u_\tau}\frac{Prt}{\ell}\ , \tag{30a}$$

$$A_2 = A_1(\gamma_1-C_1)(\gamma_1 Prt)^{-1}, \tag{30b}$$

$$B_2 = (u_\tau^2\,\overline{\theta^2}\,/\overline{w\theta}^2)B_1^{1/3}Prt^{-1}, \tag{30c}$$

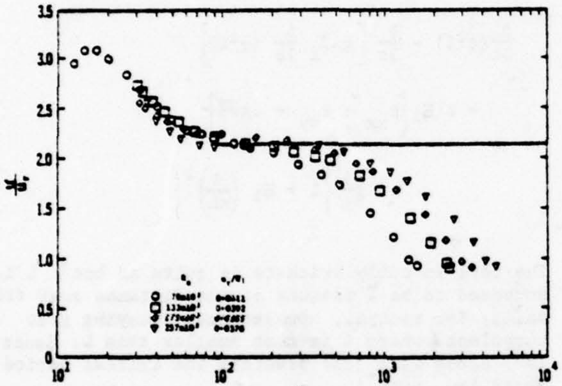

Fig. 1. Longitudinal turbulent intensity in a pipe as observed by Perry and Abel (22). The horizontal line is the estimated outer asymptote of the inner function (law of the wall coordinates). The Reynolds number is based on the pipe diameter.

We first note that (29a) and (30a) when integrated, yield the logarithmic law of wall when $\ell = \kappa z$. For *homogeneous shear flow* ℓ *does not vary in the z-direction.* Taken together, (29a) and (30a) include a definition of the turbulent Prandtl number, Prt. Note that the turbulent Prandtl number will vary with stratification; in this discussion, only the neutral value is considered.

We must choose values of B_1, γ_1, Prt and B_2 from Table I and II. It is not a simple choice and perhaps the principal value of the tables is to show that considerable uncertainty exists; if we bias our choice toward one set of data, that set will be predicted well but another set may not be. For example, there is an obvious difference between the wall data and the homogeneous shear flow data.

The first choices we have made are $B_1 = 16.6$ and $\gamma_1 = .222$. From (29e,f) we obtain $A_1 = 0.92$ and $C_1 = 0.08$. From (29b,c,d) this yields $q/u_\tau = 2.55$ $u'/u\tau = 1.9$ and $v'/u\tau = w'/u\tau = 1.2$. The fact that v' and w' are not equal is not well supported by the data and as discussed earlier, the model could be complicated to permit $v' \neq w'$. The choice of additional terms is not clear, however, and the further choice of the additional constants they would introduce would be less clear.

The choice of turbulent Prandtl number is quite ambiguous from Table II. This quantity has been measured by other besides those listed in Table II. A 1962 survey (ref 23) infers that, near a smooth wall, $0.74 < Prt < .92$. Gowen and Smith (24) obtain $.8 < Prt < 1.0$ for smooth pipes and $1.0 < Prt < 1.2$ for rough pipes at a radius Reynolds number of 20,000. (For large enough Reynolds number, Prt should not depend on roughness). Atmospheric boundary layer data, to be discussed below, indicates $Prt = 0.74$ in the neutral case. Here we choose $Prt = 0.80$ so that (30b) yields $A_2 = 0.74$. Finally we choose $B_2 = 10.1$[2]. This yields $u\tau^2\ \overline{\theta^2}/\overline{w\theta}^2 = 3.1$, which may be compared with the corresponding data in Table II. Perhaps, it is better to consider the correlations $(-\overline{uw})/(u'w')$ and $(-\overline{w\theta})/(w'\theta')$ which can be calculated from the above constants and equations (29b,c,d) and (30c); we obtain 0.44 and 0.42 for comparison with that data. It should also be noted that the ratio $B_2/B_1 = 0.61$ may be compared with the similarity prediction of $B_2/B_1 = 2/3$ for decaying, homogeneous temperature and velocity fields (Hinze, 25) which apparently agrees with the measurements of Gibson and Schwartz (26). However, these measurements cover a rather short decay history.

Summarizing, we find now that

$$(A_1,B_1,A_2,B_2,C_1) = (0.92,\ 16.6,\ 0.74,\ 10.1,\ 0.08)$$

which differ just a bit from the values cited previously on the basis of more limited information.

Stabilization by Flow Curvature and Density Stratification

The model has not yet been described completely, but enough has been determined to demonstrate the surprising capability of the model to predict the stabilization of turbulent fields by curvature and density stratification. The data obtained by So and Mellor (7) was a clear demonstration of the fact that the stabilizing curvature could literally extinguish turbulence. The effect of curvature as predicted by the model has been described in ref (7), (9) and (10) and was our first indication that the model could predictively extend far beyond the neutral data on which it is based. However, this paper is meant to emphasize geophysical fluid problems for which we turn to the near surface, atmospheric boundary layer data of Businger et al (12).

For the purpose of direct comparison of data with model prediction we neglect the material derivative and diffusion terms in (21), yielding

$$\frac{q^3}{\Lambda_1} = -\overline{uw}\,\frac{\partial U}{\partial z} - \overline{vw}\,\frac{\partial V}{\partial z} + \beta g\overline{w\theta}. \tag{31}$$

This should be a valid simplification near surfaces, at least for neutral and stable flows. The result is

---

[2] Neither the neutral data nor the density stratifical data discussed below justify third significant figure accuracy. However, it will appear that the turbulent Prandtl number at the critical Richardson number is about unity. With $B_2 = 10.1$ the model will yield this value exactly. However, any value, say $B_2 = 10 \pm 0.5$, would be justified by the neutral data and adequately predict the stratified data of Businger et al (12).

that the stability coefficients, S_M and S_H, in (27a,b) may be written,

$$S_M = 3A_1 \frac{\gamma_1 - C_1 - (6A_1 + 3A_2)\Gamma/B_1}{\gamma_1 - \gamma_2\Gamma + 3A_1\Gamma/B_1}(\gamma_1 - \gamma_2\Gamma) \tag{32a}$$

$$S_H = 3A_2(\gamma_1 - \gamma_2\Gamma), \tag{32b}$$

where

$$\gamma_1 \equiv (1/3) - (2A_1/B_1), \quad \gamma_2 \equiv (B_2/B_1) + (6A_1/B_1), \tag{33a,b}$$

$$\Gamma \equiv R_f/(1-R_f), \tag{34a}$$

and

$$R_f \equiv -\beta g\overline{w\theta}/(P_{xx}+P_{yy}), \tag{34b}$$

is the flux Richardson number. The gradient Richardson number is

$$R_i = \frac{\beta g\,\partial\Theta/\partial z}{(\partial U/\partial z)^2 + (\partial V/\partial z)^2} = \frac{S_M}{S_H} R_f \,. \tag{35}$$

Fig. 2 is a plot of S_M (R_i) and S_H (R_i). A critical Richardson number is determined by the condition, $\gamma_1 - \gamma_2\Gamma = 0$, or using (33a,b) and (34) yields

$$R_{fcr} = \frac{\gamma_1}{\gamma_1+\gamma_2} = \frac{B_1-6A_1}{B_1+3B_2+12A_1} \,. \tag{36}$$

For (A_1, B_1, B_2) = (0.92, 16.6, 10.1) we have $R_{fcr} = 0.19$ and also $R_{icr} = 0.19$ as the critical Richardson numbers beyond which turbulence and mixing cease to exist.

For comparison with the near surface layer data we now assume $\ell = \kappa z$. The data are cast in Monin-Obukhov similarity form, $\phi_M(\zeta)$, $\phi_H(\zeta)$ where

$$\phi_M \equiv \frac{\kappa z}{u_\tau}\frac{\partial U}{\partial z} = \left[B_1(1-R_f)S_M{}^3\right]^{-1/4} \tag{37a}$$

$$\phi_H \equiv \frac{\kappa z u_\tau}{H}\frac{\partial \Theta}{\partial z} = \left[B_1(1-R_f)S_H{}^4/S_M\right]^{-1/4} \tag{37b}$$

$$\zeta \equiv \frac{z}{u_\tau{}^3/(\kappa g\beta H)} = \phi_M R_f \,, \tag{38}$$

where $u_\tau{}^2 = (\overline{uw}^2 + \overline{vw}^2)^{1/2}$ and $H = -\overline{w\theta}$ near the surface.

Figs. 3a and 3b compare the model results with the data of Businger et al (12). Note that the point $R_f = R_{fcr} = 0.19$ in Fig. 2 is mapped into the straight lines $\phi_M = \phi_H = \zeta/R_{fcr}$ as $\zeta \to \infty$. Note from (36) that the prediction of R_{fcr} does not depend on $\ell(z)$.

Lewellen and Teske (27) have also shown a favorable comparison of their model with this data. They included the diffusion term and did get better agreement then we did for ϕ_M in the unstable region where diffusion is liable to be important. However, they had to insert a specific Richardson number parameterization into their model to obtain the correct critical Richardson number.

5. THE TURBULENT LENGTH SCALE EQUATION

We have postponed consideration of the equation for the master length scale ℓ so that the other elements of the model were first justified on the basis of neutral data and a direct test of the model's predictive power; i.e. the prediction of turbulent stabilization in a density stratified flow. The factor S_q in (21) must also now be determined.

Following Rotta (2), we appeal to the integral of the two-point correlation function. The closure assumptions are complicated and we consider the result less convincing than the previous assumptions and more likely to be amended in the future. The version we use as of this writing is

$$\frac{D}{Dt}(q^2\ell) - \frac{\partial}{\partial z}\left[g\ell S_\ell \frac{\partial}{\partial z}(q^2\ell)\right] = \ell E_1\left[P_{xx} + P_{yy} + \beta g\overline{w\theta}\right] - \frac{q^3}{B_1}\left\{1 + E_2\left(\frac{\ell}{\kappa L}\right)^2\right\} \tag{39}$$

The term in curly brackets is quite ad hoc[3]. L is supposed to be a measure of the distance away from walls. For neutral, homogeneous, decaying grid turbulence where ℓ is much smaller than L. Equation (39) along with (21) predicts the initial period decay law, $q^2 \propto t^{-1}$.

We specify L according to

$$L^{-1}(\underset{\sim}{r}) = \frac{1}{2\pi}\iint \frac{dA(\underset{\sim}{r}_o)}{|\underset{\sim}{r}-\underset{\sim}{r}_o|^3} \tag{40}$$

and is similar to ideas offered by Shir (28) and Launder et al (15). $\underset{\sim}{r}$ is any point in the fluid domain bounded by solid wall at $\underset{\sim}{r}_o$; $dA(\underset{\sim}{r}_o)$ is an elemental wall area. For a boundary layer flow near an infinite plane wall, $L = z$; for channel flow, $L^{-1} = z^{-1} + (2h-z)^{-1}$ where 2h is the distance separating the channel walls. It can, by the way, be shown that a third term at the right of (39) - here represented by $E_2(q^3/B_1)(\ell/\kappa L)^2$- is absolutely necessary, but the one chosen here is one of several alternatives (Ng and Spalding 29, Wolfstein 30, Mellor and Herring 6, Lewellyn et al 14, Rotta 31) All can say in the present case is that, as we will see, it works well.

While one cannot assert great confidence in equation (39) we prefer it rather than the differential equation for dissipation (Daly and Harlow 32, Hanjalic and Launder 5, Lumley and Khajeh-Nouri 33). Since the dissipation is modeled here according to (2), the dissipation transport equation could supply the needed length scale. The dissipation transport equation is an equation for the curvature of the two point, velocity correlation function as the separation distance approaches zero. Alternately

---

[3] We have also used $(\kappa^{-1}\partial\ell/\partial x_i)^2$ in place of $(\ell/\kappa L)^2$ which also worked well except in the near vicinity of mixed layer interfaces.

it is an equation for the integral of the spectral density function after multiplication by the square of the wavenumber, thus weighting the integral so that large wave number and small scale turbulence is emphasized. Thus, it seems fundamentally wrong to us to use an equation which describes the small scale turbulence to determine the required turbulent macrosocale. Operationally, however, the terms in the dissipation transport equation and equation (39) are special cases of a more general length scale equation (Mellor and Herring 6, Lewellen et al 14).

In subsequent discussions we will mention some calculations using an algebraic expression of the form, $\ell = \ell_0 \kappa z/(\kappa z+\ell_0)$ where $\ell_0 \equiv \alpha \int_0^\infty |z| q dz / \int_0^\infty q dz$, is used in place of equation (39). For boundary layers; this works very well, but it is limited to boundary layers and the empirical constant, α, would depend on the type of layer, a conventional layer or an Ekman layer, etc.

Table I: Observed Values of turbulent velocity variables where production is balanced by dissipation. Primes represent r.m.s. values and $u_\tau^2 \equiv -\overline{UW}$. U_0 is either the center line velocity or the mainstream velocity. R is pipe radius and h is the half channel width.

		$\frac{u_\tau}{U_0}$	$\frac{u'}{u_\tau}$	$\frac{v'}{u_\tau}$	$\frac{w'}{u_\tau}$	$\frac{q}{u_\tau}$	$\frac{-\overline{uw}}{u'w'}$
Pipe	$\frac{U_0 R}{\nu} 10^{-4}$						
Laufer (34)	25.0	.0346	2.2	1.70	1.00	2.95	.45
Perry & Abel (22)	12.8	.0370	2.12	—	1.03		.46
Bremhorst & Bulleck (35)	3.5	.0398	1.9	—	1.26		.42
Channel	$\frac{U_0 h}{\nu} 10^{-4}$						
Laufer (36)	3.1	.0377	1.88	1.19	1.03	2.45	.52
Laufer (36)	6.2	.0367	1.76	1.14	1.03	2.12	.55
Comte-Bellot (37)			2.1	1.30	1.03	2.9	.62
Boundary Layer	$\frac{U_0 \delta}{\nu} 10^{-4}$						
Klebanoff (38)	7.4	.0377	2.02	1.41	1.03	2.66	.48
So & Mellor (7)	2.0	.042	1.70	1.18	1.00	2.30	.58
Young et al (39):							
Flat surface	4.6	.039	2.25	—	1.15		.39
Wave surface	5.1	.042	2.4	—	1.3		.32
" "	8.8	.049	2.4	—	1.3		.32
Homogeneous Shear Flow							
Rose (40)		.0066	1.66	1.35	1.26	2.48	.48
Champagne et al (41)		.0105	1.70	1.29	1.20	2.45	.49

Table II: Observed Values of turbulent thermal variables where production is balanced by dissipation. Primes represent r.m.s. values.

	$\frac{U_0 R}{\nu} 10^{-4}$	$\frac{-\overline{w\theta}}{U_0 \Delta\Theta}$	$\frac{\theta'}{\Delta\Theta}$	P_{rt}	$\frac{-\overline{w\theta}}{w'\theta'}$	$\frac{u_\tau^2 \overline{\theta^2}}{\overline{w\theta}^2}$
Pipe Flow						
Bremhorst & Bulleck (35)	3.5	.0020	.102	—	.41	3.0
Boundary Layer	$\frac{U_0 \delta}{\nu} 10^{-4}$					
Young et al (39):						
Flat surface	4.6	.0015	.075	.95	.46	3.8
Wave surface	5.1	.0032	.12	.55	.48	2.48
" "	8.8	.0035	.11	.55	.50	2.37

6. BOUNDARY CONDITIONS

For the mean velocity and temperature boundary conditions, one either specifies stress and heat flux

$$-\overline{wu}_i(x,y,z_0) \equiv \tau_{0i} = \left(q\ell S_M \frac{\partial U}{\partial z}\right)_{z=z_0} \qquad (41)$$

$$-\overline{w\theta}(x,y,z_0) \equiv H = \left(q\ell S_H \frac{\partial \Theta}{\partial z}\right)_{z=z_0} \qquad (42)$$

or, near solid surfaces at rest, the numerical solution is matched to

$$U_i(x,y,z) = \frac{\tau_{0i}}{\kappa u_\tau} \ln\left(\frac{z-z_0}{z_{MS}}\right) \qquad (43)$$

$$\Theta(x,y,z)-\Theta(x,y,z_0) = \frac{HP_{rt}}{\kappa u_\tau} \ln\left(\frac{z-z_0}{z_{HS}}\right) \qquad (44)$$

where $u_\tau^2 \equiv (\tau_{0i}^2)^{1/2}$, i=x,y, and z_{MS} and z_{HS} are the roughness parameters; for smooth surfaces $z_{MS} u_\tau/\nu = \exp(-4.9\kappa)$ whereas z_{HS}/z_{MS} is a function of Prandtl number. Also we have

$$q^2(x,y,z_0) = B_1^{2/3} u_\tau^2 \qquad (45)$$

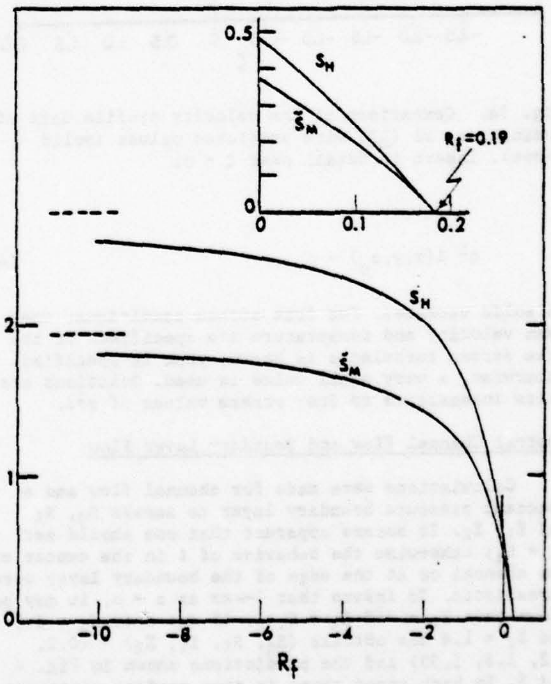

Fig. 2. The stability functions, S_M and S_H, of equations (26a,b,c) when turbulent production is balanced by dissipation. Inset is a detail near $R_f = 0$.

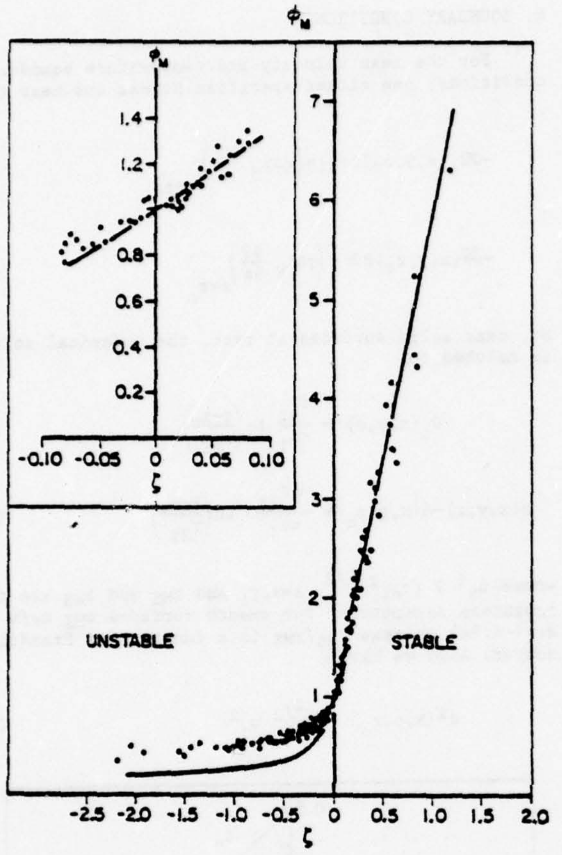

Fig. 3a. Comparison of the velocity profile data of Businger et al (12) with predicted values (solid curve). Insert is detail near $\zeta = 0$.

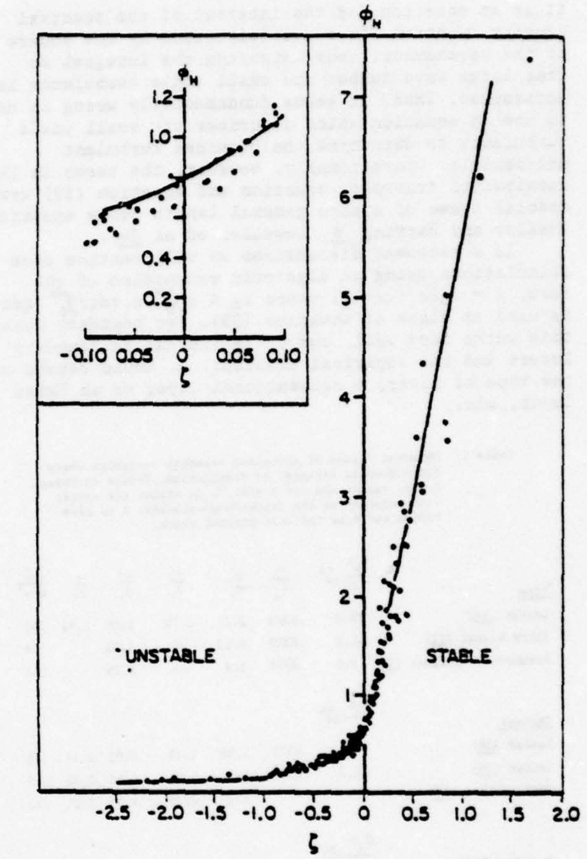

Fig. 3b. Comparison of the temperature profile data of Businger et al (12) with predicted values (solid curve). Insert is detail near $\zeta = 0$.

$$q^2 \ell(x,y,z_o) = 0 \tag{46}$$

on solid surfaces. For free stream conditions, the mean velocity and temperature are specified. If the free stream turbulence is known, that is specified. Otherwise, a very small value is used. Solutions are quite insensitive to free stream values of $q^2\ell$.

Neutral Channel Flow and Boundary Layer Flow

Calculations were made for channel flow and a constant pressure boundary layer to assess S_q, S_ℓ and E_1, E_2. It became apparent that one should set $S_\ell = S_q$; otherwise the behavior of ℓ in the center of the channel or at the edge of the boundary layer were unrealistic. To insure that $\ell \sim \kappa z$ as $z \to o$, it may be shown that $E_2 = \kappa^2 B_1 S_\ell + E_1 - 1$. If one sets $S_q = 0.2$ and $E_1 = 1.8$ one obtains $(S_q, S_\ell, E_1, E_2) = (0.2, 0.2, 1.8, 1.33)$ and the predictions shown in Fig. 4 and 5. In both cases there is near perfect agreement with measured values of $-\overline{uw}(z)$ and $q(z)$; for the channel flow case, the Reynolds stress distribution is linear and is now shown.

The outer free stream turbulence level has been set at $q/u\tau = .07$ as estimated from ref (38) but this may be a bit low. Two boundary conditions for $q^2\ell$ have been specified and correspond to the solid and dashed lines in Fig. 5.

The separate components u', v' and w' are not shown since they do not enter into the determination of E_1. Agreement with data is quite good in this respect except that we predict $v' = w'$ as discussed earlier. Away from walls this is in agreement with the data, but near walls there is some disagreement in accordance with Table I.

Free Convection

With no alteration in the model, calculations were performed to compare with the free convection experiment of Willis and Deardorff (42) wherein a heat flux was imposed at the bottom surface of a tank of water after a linear temperature gradient had been established in the tank. Since there is no shear production the Richardson number changes abruptly from $+\infty$ to $-\infty$ at $z = z_i$, the inversion height.

The calculated temperature and heat flux very nearly overlie the data in Fig. 6 and have not been plotted. A possible exception is that the small, negative flux overshoot near $z=z_i$ is underestimated by a factor of 4 or 5. Note that the experimental heat flux was determined by integrating the temperature tendency and might be subject to error.

Predictions of u', w' and θ' are shown in Figs. 7 and 8 and agree surprisingly well with the data. Readers might wish to compare these predictions with those by Lewellyn et al (14) and Zeman and Lumley (44).

It should be noted that Willis and Deardorff also obtained data for $\overline{wq^2}/2$. If $\overline{pw}$ were zero, one could compare that data with the diffusion represented by $q\ell\, S_q \partial(q^2/2)/\partial z$ in (21) (even though we formally neglected pressure diffusion, it must be considered a part of the diffusion term of (21) if observation indicates that $pw \neq 0$) in which case the model appears to underestimate the measured $\overline{wq^2}$. However, a very recent paper by Champagne et al (43) indicates that $\overline{pw}$ is larger and of the opposite sign of $\overline{wq^2}/2$ for unstable flows. Now, it is reasonable to expect that S_q is Richardson number dependent as is, analogously, S_M and S_H. However, it appears too early from the point of view of available data to make a useful determination of S_q (R_i). In any event, it does not appear that predictive accuracy would be greatly affected.

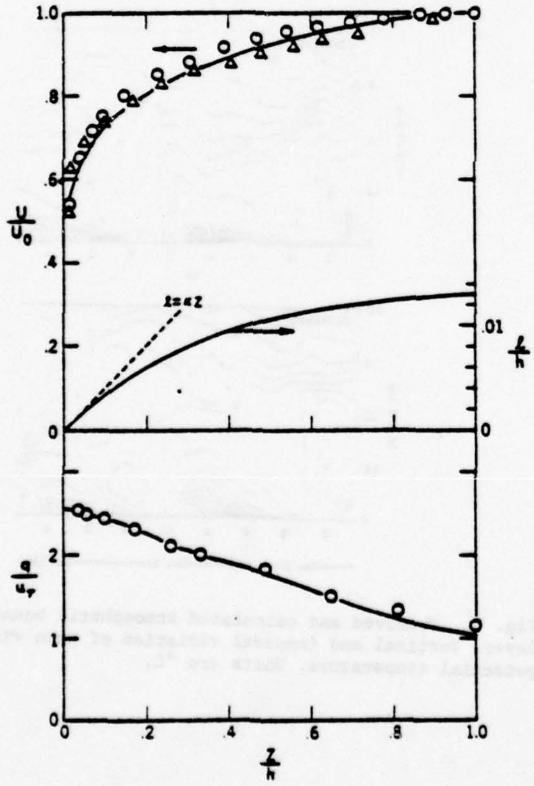

Fig. 4. Channel Flow. Comparison of predicted mean velocity and turbulent intensity (solid lines) with data by Laufer (36) and Hanjalic as recorded in ref. (15). The circles are Laufer's data.

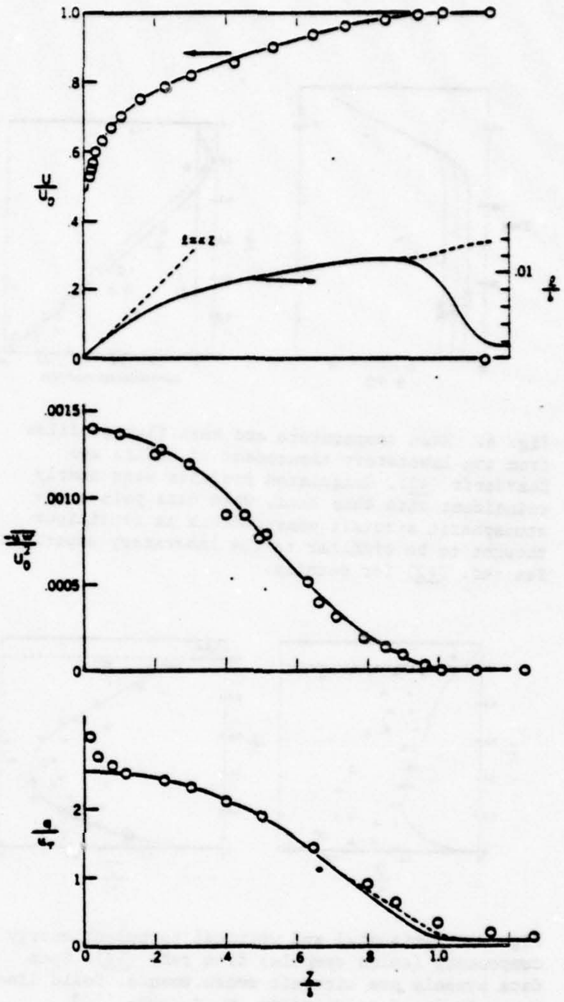

Fig. 5. Boundary Layer. Comparison of the predicted mean velocity and turbulent intensity with data by Klebanoff (38).

Forced Convection

The experiment whereby a shear stress was impulsively applied to the top surface of stable, salinity stratified water, thereby mixing the top layer, has been performed by Kato and Phillips (45). Qualitively, the mixing process is inhibited by the stratification such that an abrupt density change occurs across the interface separating strongly turbulent and quiescent fluid. Using a simpler version of the present model (an algebraic length scale recipe and neglect of the turbulent kinetic energy tendency and diffusion terms), Mellor and Durbin (46) predicted this data quite well and we expect that prediction will prevail when this latest version of the model is applied. In ref (46), other examples of mixed layer dynamics are explored and a favorable comparison with ocean observations in the North Pacific is included.

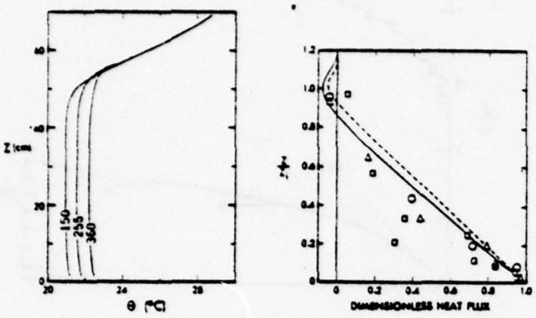

Fig. 6. Mean temperature and heat flux profiles from the laboratory experiment of Willis and Deardorff (42). Calculated profiles were nearly coincident with this data. Open data points are atmospheric aircraft measurements in conditions thought to be similiar to the laboratory experiment. See ref. (42) for details.

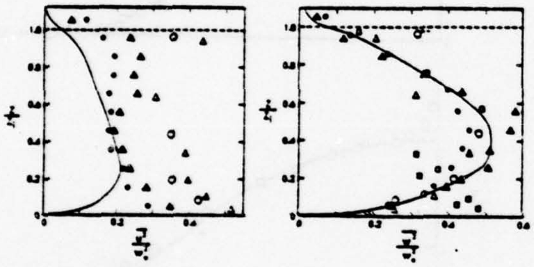

Fig. 7. Horizontal and vertical turbulent energy components (solid symbols) from ref. (42). Open data symbols are aircraft measurements. Solid lines are calculated predictions. $w_* \equiv (g\beta H z_i)^{1/3}$.

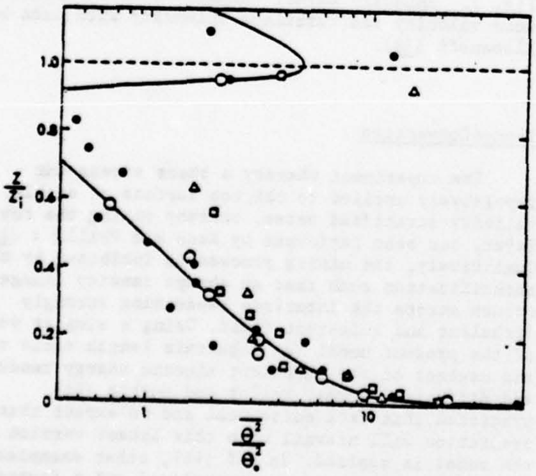

Fig. 8. Temperature variance (solid symbols) from ref. (42). Open data symbols are aircraft measurements. Solid lines are calculated predictions. $\theta_* \equiv H/w_*$.

8. ATMOSPHERIC SIMULATIONS

The Wangara Data Set

The present model has been compared with atmospheric boundary layer data of Clarke (47) - which is called the "Wangara Data". The temperature variables in the previous equations must now be interpreted as virtual potential temperature.

Comparison of simulations and observations by Yamada and Mellor (13) are shown in Fig. 9, 10 and 11. The calculations shown in these figures used an algebraic length scale equation but have been repeated using (39) with little change in the result. The calculations assume horizontal homogeneity so that altitude and time are the only independent variables.

A feature of the velocity field prediction is the appearance of "the nocturnal jet" around midnight and near z=200m. Between midnight and 0600 hours the cooling of near surface air is underestimated. This may be attributed to a small amount of mixing due to internal waves; currently the model does not include non-linear wave effects. The major effect of the diurnal surface heating cycle can best be seen in Fig. 12 where we show contours of calculated turbulent kinetic energy. Further details are provided in ref (13).

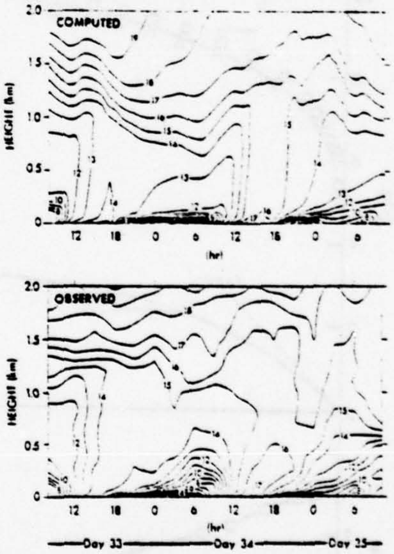

Fig. 9. Observed and calculated atmospheric boundary layer. Vertical and temporal variation of mean virtual potential temperature. Units are °C.

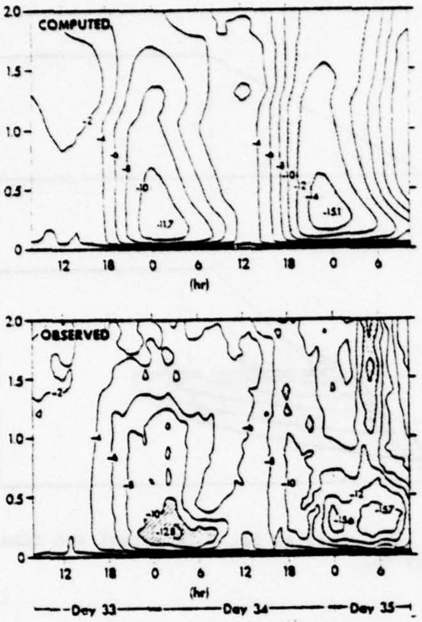

Fig. 10. Observed and calculated atmospheric boundary layer. Vertical and temporal variations of the eastward mean wind component. Units are m sec^{-1}.

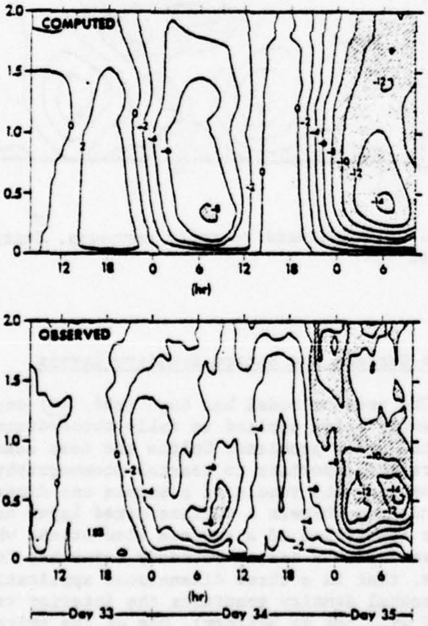

Fig. 11. Observed and calculated atmospheric boundary layer. Vertical and temporal variation of the northward mean wind component.

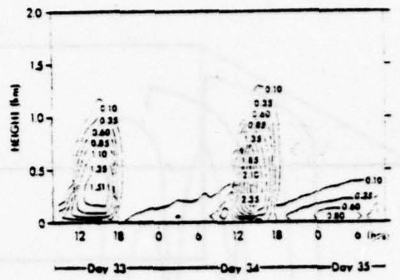

Fig. 12. Time and space variation of computed q^2 (twice the turbulent kinetic energy, units are m^2 s^{-2}). The stippled areas indicate regions where $10^{-3}m^2s^{-2}<q^2<10^{-2}m^2s^{-2}$.

Pollutant Dispersion

Model equations developed for temperature may also be applied to any scalar such as a chemically inert pollutant.

Using the horizontally homogeneous wind field generated for the Wangara data, Yamada (48) has made a fully three dimensional calculation of the dispersion of a pollutant point source located at various distances from the ground. Fig. (13a,b) illustrates dispersion of a source located at z=40m during the early morning and afternoon hours. The morning, low level inversion confines pollutants to near surface altitudes whereas vertical mixing in the afternoon is vigorous as would be deduced from Fig. 12. Other calculations which include an assessment of ground level concentration as influenced by source height will be found in ref. (48).

One finding of interest is that the effect of lateral diffusion terms in the mean concentration equation is negligible except very close to the source. Lateral dispersion is dominated by vertical variability of mean wind speed and direction. Horizontal mean advective dispersion creates mean vertical concentration gradients which are subsequently mixed through vertical diffusion.

Global Atmospheric Simulations

The present model, with the algebraic length scale equation described previously, has now been incorporated into the General Circulation Models of NOAA's Geophysical Fluid Dynamics Laboratory. Currently, one such model represents the global atmosphere with horizontal resolution of about 4° latitude and longitude and 18 vertical levels; the first 5 levels are assigned to the lower 2km.

These calculation produce an enormous amount of numbers. Calculations extracted from a paper by Miyakoda (49) are shown in Fig. 14, 15 and 16. They are zonally averaged plots of temperature, zonal velocity and $K_M \equiv \ell q\ S_M$. Synoptic detail is therefore averaged out of the plots. Nevertheless, one can identify the troposphere, tropopause and stratosphere in Fig. 14; in Fig. 15, the jet streams are evident.

Thus far the model only includes the effect of water vapor. Liquid water and cloud structure (Sommeria and Deardorff 50, Mellor 51) is a matter of current research.

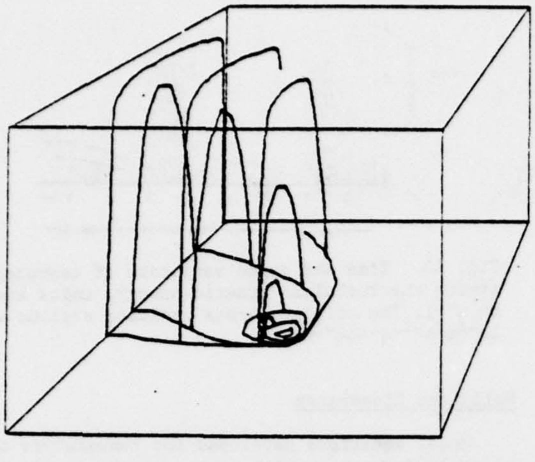

Fig. 13a. Simulations of Pollutant dispersion from a source at 40m above ground level. The mean wind, temperature and turbulence field is the same as in Fig. 9, 10 and 11 at 1500 hours on day 33. The box represents a 40km x 40km x 1200m domain.

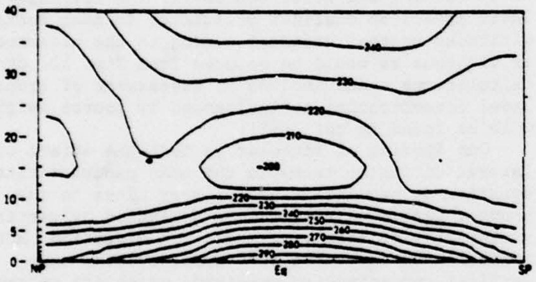

Fig. 14. Zonal averaged, virtual potential temperature contours from a global atmospheric simulation by Miyakoda and Sirutis (49). The time is in March. Units are °K.

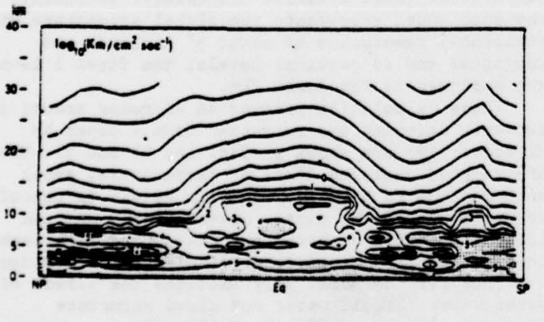

Fig. 16. Contours of the log of the eddy viscosity.

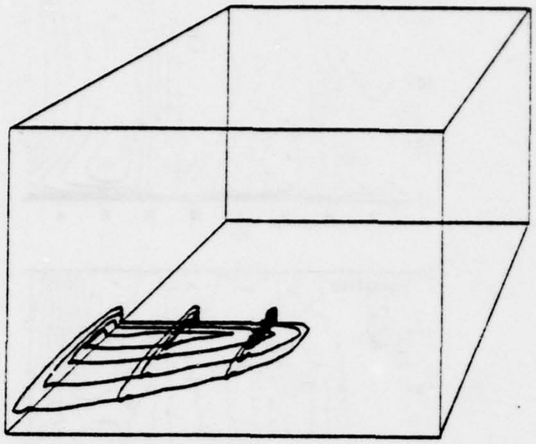

Fig. 13b. Same as Fig. 13a except the time is 0600 on day 34.

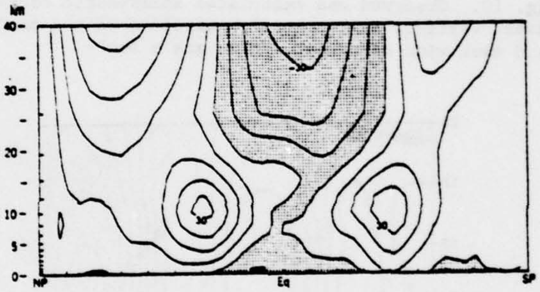

Fig. 15. Eastward velocity contours. Units are m sec^{-1}.

Ocean Surface and Bottom Boundary Layers

The present model has been (ref. 46) and is currently being applied to fully three-dimensional, coastal ocean problems. Unlike the deep ocean, bottom layers are important to coastal oceanography. In Fig. 17, we show the result of a simple one dimensional calculation wherein a surface mixed layer has formed after imposition of a surface wind stress while, at the same time a bottom boundary layer has formed. (Note, that in a three dimensional application with horizontal density gradients the interior velocity field will not be uniform). One of the impressive features of the length scale equation, (39), is that a length scale distribution appropriate to the surface layer develops while simultaneously providing a length scale appropriate to the bottom layer. In the region between layers, the value of the length scale remains equal to that which was initially specified.

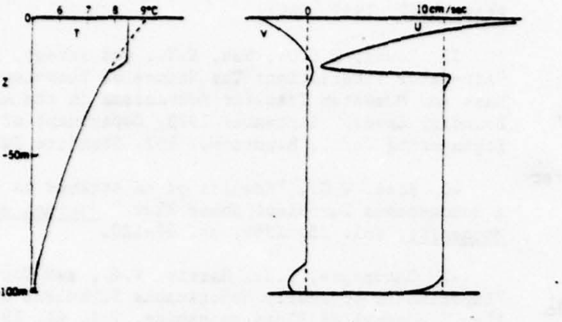

Fig. 17. Illustration of the development of surface currents after a 15 knot wind has blown for two days. At the same time, a bottom boundary layer is allowed to develop. The dashed curves are the initial conditions while the solid lines are two days later.

9. CONCLUSION

A turbulent model has been developed which is relatively simple and which can be applied to a wide variety of engineering and geophysical flows.

We separate the study of the model into the group of closure assumptions proposed by Rotta - and here extended to include temperature (or any other scalar) and density stratification - and the master length scale equation . The latter inspires the least confidence but performs exceptionally well.

The rules of the game we are playing - at least for the present - are to obtain all empirical constants from neutral data and then see if the model can predict stabilization or destabilization of turbulent fields due to density stratification in a gravity field and, in separate studies, due to flow curvature and other body force like effects. The constants in equation (28), one of which is not independent, are unambiguously related to simple neutral flow data and computer solutions are not required to identify these constants. The remaining constants are von Karman's constant, κ, and the four constants in equation (47); one of these is not independent (we have an intuitive feeling that a mathetical constraint also exists for the condition, $S_q = S_\ell$, but, thus far, it has not been revealed to us). Trial and error computer solutions have determined these.

The model and the fixed set of constants seems to perform well in predicting diverse neutral flows. The same model, with no alteration, appear to predict density stratified flows in a manner which far exceeds prior expectation.

REFERENCES

1 Kline, S.J., Morkovin, M.V., Sovran, G., and Cockrell, D.J., Proceedings of the Stanford Conference on Computation of Turbulent Boundary Layers, AFOSR-IFP, 1968.

2 Rotta, J.C., "Statistische Theorie Nichthomogener Turbulenz," Zeitschrift fur Physik, Vol. 129, 1951, pp. 547-572; also Vol. 131, 1951, pp. 51-77

3 Kolmogoroff, A.N., "The Local Structure of Turbulence in Incompressible Viscous Fluid for Very Large Reynolds Number," C.R. Academy of Sciences, USSR, Vol. 30, 1941, p. 301 (translation, Friedlander, S.K., and Topper, L., "Turbulence: Classic Papers on Statistical Theory," Interscience, New York, 1961).

4 Donaldson, C. duP., and Rosenbaum, H., "Calculation of the Turbulent Shear Flows Through Closure of the Reynolds Equations by Invariant Modeling," ARAP Rept. 127, 1968, Aeronautical Research Associates of Princeton, Princeton, N.J.

5 Hanjalic, K., and Launder, B.E., "Fully Developed Asymmetric Flow in a Plane Channel," Journal of Fluid Mechanics, Vol. 52, 1972, p. 689.

6 Mellor, G.L., and Herring, H.J., "A Survey of the Mean Turbulent Field Closure Models," AIAA Journal, Vol. 11, 1973, pp. 590-599.

7 So, R.M.C., and Mellor, G.L., "Experiments on Convex Curvature Effects in Turbulent Boundary Layers," Journal of Fluid Mechanics, Vol. 60, 1973, pp. 43-63.

8 So, R.M.C., and Mellor, G.L., "Experiments on Turbulent Boundary Layers on a Concave Wall," The Aeronautical Quart, Vol. XXVI, 1975, pp. 25-40.

9 So, R.M.C., "A Turbulent Velocity Scale for Curved Shear Flows," Journal of Fluid Mechanics, Vol. 70, 1975, pp. 37-57.

10 Mellor, G.L., "A Comparative Study of Curved Flow and Density, Stratified Flow," Journal of Atmospheric Science, Vol. 32, 1975, pp. 1287-1282.

11 Mellor, G.L., "Analytic Prediction of the Properties of Stratified Planetary Surface Layers," Journal of Atmospheric Science, Vol. 30, 1973, pp. 1061-1069.

12 Businger, J.A., Wyngaard, J.C., Izumi, Y., and Bradley, E.F., "Flux Profile Relationships in the Atmospheric Surface Layer," Journal of Atmospheric Science, Vol. 28, 1971, pp.181-189.

13 Yamada, T., and Mellor, G.,,"A Simulation of the Wangara Atmospheric Boundary Layer Data," Journal of Atmospheric Science, Vol. 32, 1975, pp. 2309-2329.

14 Lewellan, W.S., Teske, M.E., and Donaldson, C. duP., "Variable Density Flows Computed by a Second-Order Closure Description of Turbulence," AIAA Journal, Vol. 14, 1976, pp.382-387.

15 Launder, B.E., Reece, G.J., and Rodi, W., "Progress in the Development of a Reynolds-Stress Turbulence Closure," Journal of Fluid Mechanics, Vol. 68, 1975, pp.537-566.

16 Launder, B.E., "On the Effect of a Gravitational Field on the Turbulent Transport of Heat and Momentum," Journal of Fluid Mechanics, Vol. 67, 1975, pp. 569-581.

17 Wyngaard, J.C., "Modeling the Planetary Boundary Layer-Extension to the Stable Case," Boundary Layer Meteorology, Vol. 9, 1975, pp. 441-460.

18 Mellor, G.L., and Yamada, T., "A Hierarchy of Turbulence Closure Models for Planetary Boundary Layers," Journal of Atmospheric Science, Vol. 31, 1974 pp. 1791-1806.

19 Briggs, M., Mellor, G., and Yamada T., "A Second Moment Turbulence Model applied to Fully Separated Flow," Proceedings: 1976 SQUID Workshop on Turbulence in Internal Flows, (in press).

20 Yajnik, K.S., "Asymptotic Theory of Turbulent Shear Flows," Journal of Fluid Mechanics, Vol. 42, 1970, pp. 411-427.

21 Mellor, G.L., "The Large Reynolds Number Asymptotic Theory of Turbulent Boundary Layers, International Journal of Engineering Sciences, Vol. 11, 1972, pp. 851-873.

22 Perry, A.E., and Abell, C.J., "Scaling Laws for Pipe-Flow Turbulence," Journal of Fluid Mechanics, Vol. 67, 1975, pp. 257-271.

23 Kestin, J., and Richardson, P.D., "Heat Transfer across Turbulent Incompressible Boundary Layers," Colloque international sur "La mecanique de la turbulance," Marseille 1961.

24 Gowen, R.A., and Smith, J.W., "Turbulent Heat Transfer from Smooth and Rough Surfaces," International Journal of Heat and Mass Transfer, Vol. 11, 1968, pp. 1657-1673.

25 Hinze, J.O., "Turbulence - An Introduction to its Mechanism and Theory," McGraw-Hill Book Company.

26 Gibson, C.H., and Schwartz, W.H., "The Universal Spectra of Turbulent Velocity and Scalar Fields," Journal of Fluid Mechanics, Vol. 16, 1965, pp. 365-384.

27 Lewellen, W.S., and Teske, M., "Prediction of the Monin-Obukhov Similarity Functions from an Invariant Model of Turbulence, Journal of Atmospheric Science, Vol. 30, 1973, pp. 1340-1345.

28 Shir, C.C., "A Preliminary Study of Atmospheric Turbulent Flows in the Idealized Planetary Boundary Layer, Journal of Atmospheric Science, Vol. 30, 1973, pp. 1327-1339.

29 Ng, K.H., and Spalding, D.B., "Turbulence Model for Boundary Layers near Walls," Physics of Fluids, Vol. 15, 1972, pp. 20-30.

30 Wolfstein, M., "On the Length-Scale of Turbulence Equation," Israel Journal of Technology, Vol. 8, 1970, pp. 87-99.

31 Rotta, J.C., "Turbulent Shear Layer Prediction on the Basis of the Transport Equations for the Reynold Stresses," Proceedings of the 13th International Congress of Theoretical and Applied Mechanics, Moscow University, pp. 295-308.

32 Daly, B.J., and Harlow, F.H., "Transport Equations in Turbulence," The Physics of Fluids, Vol. 13, 1970.

33 Lumley, J.L., and Khajeh-Nouri, B., "Modeling Homogeneous Deformation of Turbulence," Advances in Geophysics, Vol. 18A, 1974, pp. 162-192.

34 Laufer, J., "The Structure of Turbulence in Fully Developed Pipe Flow," NACA Rep. 1174, 1954.

35 Bremhorst, K., and Bullock, "Spectral Measurements of Turbulent heat and Momentum Transfer in Fully Developed Pipe Flow," International Journal of Heat and Mass Transfer, Vol. 16, 1973, pp. 2141-2154.

36 Laufer, J., "Investigation of Turbulent Flow in a Two-Dimensional Channel," NACA Technical Note 2123.

37 Comte-Bellot, G., "Ecoulement Turbulent Entre deau Parois Parelleles," Publ. Sci. Tech., Ministere de l'Air, No. 419.

38 Klebanoff, P.S., "Characteristics of Turbulence in a Boundary Layer with Zero Pressure Gradient," Rept. 1247, 1955, NACA.

39 Young, M.B.O., Hsu, E.Y., and Street, R.L., "Air-Water Interaction: The Nature of Turbulent Heat Mass and Momentum Transfer Mechanisms in the Air Boundary Layer," September 1973, Department of Civil Engineering Tech., Report No. 163, Stanford University.

40 Rose, W.G., "Results of an Attempt to Generate a Homogeneous Turbulent Shear Flow," Journal of Fluid Mechanics, Vol. 25, 1966, pp. 97-120.

41 Champagne, F.H., Harris, V.G., and Corrsin, S., "Experiments on nearly Homogeneous Turbulent Shear Flow," Journal of Fluid Mechanics, Vol. 41, 1970, pp. 31-141.

42 Willis, G.E., and Deardorff, J.W., "A Laboratory Model of the Unstable Planetary Boundary Layer," Journal of Atmospheric Science, Vol. 31, 1974, pp. 1297-1307.

43 Champagne, F.H., Friehe, C.A., LaRue, J.C., and Wyngaard, J.C., "Flux measurements, Flux Extimation Techniques and Fine-Scale Turbulence Measurements in the Unstable Surface Layer over Land," Unpublished manuscript.

44 Zeman, O., and Lumley, J.L., "Turbulence and Diffusion Modeling in Buoyancy Driven Mixed Layers," Third Symposium on Atmospheric Turbulence, Diffusion and Air Quality, October, 26-29, Raleigh, N.C.

45 Kato, H., and Phillips, O.M., "On the Penetration of a Turbulent Layer into a Stratified Fluid," Journal of Fluid Mechanics, Vol. 37, 1969, pp. 643-655.

46 Mellor, G.L., and Durbin, P.A., "The Structure and Dynamics of the Ocean Surface Mixed Layer," Journal of Physical Oceanography, Vol. 5, 1975, pp. 718-728.

47 Clarke, R.H., Dyer, J.A., Brook, R.R., Reid, D.G. and Troup, A.J., "The Wangara Experiment: Boundary Layer Data," Tech. Paper 19, Div. Meteor. Phys. CSIRO, Australia.

48 Yamada, T., "A Numerical Experiment on Pollutant Dispersion in a Horizontally-Homogeneous Atmospheric Boundary Layer," Submitted for publication to the Journal of Atmospheric Environment.

49 Miyakoda, K., and Sirutis, J., "Comparative Integrations of Global Models with Various Parameterized processes of Subgrid-Scale Vertical Transports," Submitted for publication to Beitrage zur Physik der Atmosphare.

50 Sommeria, G., and Deardorff, J.W., "Subgrid Scale Condensation in Cloud Models," Journal of Atmospheric Science, Vol. 34, (to be published; Feb. 1977).

51 Mellor, G.L., "The Gaussian Cloud Model Relations," Journal of Atmospheric Science, Vol. 34, (to be published; Feb. 1977).

THE TEMPERATURE SKEWNESS BUDGET IN THE LOWER ATMOSPHERE, AND ITS IMPLICATIONS FOR TURBULENCE MODELING

J. C. Wyngaard
Cooperative Institute for Research in Environmental Sciences
University of Colorado/NOAA
Boulder, Colorado 80309
and
Wave Propagation Laboratory
National Oceanic and Atmospheric Administration
Boulder, Colorado 80302

and

A. Sundararajan
Department of Meteorology
University of Oklahoma
Norman, Oklahoma 73069

ABSTRACT

Recent research has shown that carrying rate equations, rather than parameterizations, for third moments in turbulence models gives improved simulations of buoyancy-driven flows. Little is known about these rate equations, or budgets, so we present an analysis for the case of temperature fluctuations. Data from the convective atmospheric boundary layer show clearly how temperature skewness is maintained. The budget behaves much like that for temperature variance, with molecular destruction important; this refutes recent assumptions in the literature that it is negligible. The Corrsin arguments for the inertial range of the temperature spectrum are extended to the third moment, giving a cospectral prediction which *is consistent* with the data. The third moment flux is shown to be approximately Gaussian.

NOMENCLATURE

C	cospectrum of θ^2 and θ
Co	one-dimensional form of C
D	thermal diffusivity
f	frequency, Hz
F	one-dimensional temperature spectrum
g	accel. of gravity
k	von Karman constant
ℓ	turbulent integral scale
L	Monin-Obukhov length
M	molecular destruction rate of $\overline{\theta^3}/3$
N	molecular destruction rate of $\theta^2/2$
Q_0	surface temperature flux
S	temperature skewness, $\overline{\theta^3}/(\overline{\theta^2})^{3/2}$
t	time
T_*	surface temperature scale = $-Q_0/u_*$
u	turbulent velocity scale
u_*	surface friction velocity
u_i	turbulent velocity vector = $(u_1,u_2,u_3)=(u,v,w)$
U_i	mean velocity vector = (U_1, U_2, U_3)
z	distance from surface
z_i	boundary layer thickness

Greek symbols

β	one-dimensional spectral constant
γ	one-dimensional cospectral constant
ε	dissipation rate of turbulent kinetic energy
θ	fluctuating temperature
Θ	mean potential temperature
κ	wavenumber
ρ'	fluctuating density
ρ_0	background density
ϕ	temperature spectrum
ϕ_h	nondimensional mean temperature gradient

INTRODUCTION

The second moment turbulence models which have been developed for calculation of shear flows usually do not perform as well in buoyancy-driven turbulence. When typical models are applied to the convective atmospheric boundary layer (ABL), for example, the mean field predictions often seem reasonable but important features of the turbulence field are often strikingly incorrect. While this situation is not widely discussed in the turbulence community (buoyancy effects are unmentioned in Reynolds' (1) survey of computation of turbulent flows, for example), it has strong implications for geophysical turbulence modeling.

Flows met in nature, outside the laboratory, are apt to have relatively large length scales ℓ and small velocity scales u, so that small density fluctuations ρ' have large dynamical effects. The ratio of characteristic buoyancy and inertia forces for the turbulence is apt to be of order one:

$$\frac{\rho' g \ell}{\rho_0 u^2} \sim 1 \tag{1}$$

In the convective ABL we might have $u \sim 1$ m/sec, $\ell \sim 300$ m; then from Eq. (1) buoyancy and inertia effects will be equal for a temperature fluctuation level of only 0.1 C.

Strong buoyancy effects are the rule in the ABL. The convective case, which occurs in the daytime over land and can also be driven by the moisture flux over water, is typically capped by a stably-stratified (inversion) layer which cannot support turbulence and thus determines the ABL depth. Stable stratification typically extends to the surface at night over land, and in flow over cooler water.

Second-moment models for geophysical turbulence, as for shear flows, require parameterizations for three types of terms: the molecular destruction rates, the turbulent pressure covariances, and the third moment divergence (transport) terms. Recent ABL applications (e.g. Wyngaard (2), Zeman and Lumley (3)) have shown the need for including buoyancy effects in these parameterizations. The Zeman-Lumley work is particularly significant; in their study of a buoyancy-driven ABL they abandon the usual gradient-diffusion parameterization for transport, which is known to be a poor model in buoyant flows (Wyngaard (4)). Instead, they carry rate equations for these third moments. These new equations have buoyant terms, also third moments, and thus buoyancy effects on transport are explicitly included. The Zeman-Lumley approach gives a remarkably good simulation of turbulence structure in the convective ABL.

The lack of high-quality turbulence data from buoyant flows, very apparent before these recent developments, can be only more conspicuous now. Third-moment budgets were discussed in the context of turbulence modeling by Hanjalic and Launder (5) and by André et al (6,7). However, there were *no* data available for testing their hypotheses about these budgets.

With this background, we present here measurements of a particularly simple third moment budget, that for temperature, and examine some of its implications for turbulence modeling.

THE $\overline{\theta^3}$ BUDGET IN LARGE RE TURBULENCE

Neglecting phase changes, radiation, and dissipative heating, the temperature fluctuation θ satisfies (Lumley and Panofsky (8))

$$\theta_{,t} + \Theta_{,j}u_j + \theta_{,j}U_j + \theta_{,j}u_j - \overline{\theta_{,j}u_j} = D\,\theta_{,jj} \qquad (2)$$

where U_i, u_i; Θ, θ are mean and fluctuating parts of the velocity and temperature, D is the thermal diffusivity, a comma denotes differentiation and repeated indices are summed. In the ABL we interpret Θ as the mean *potential* temperature. Multiplying by θ^2 and averaging gives the θ^3 budget:

$$\frac{1}{3}(\overline{\theta^3})_{,t} = -\Theta_{,j}\,\overline{u_j\theta^2} - \frac{1}{3}(\overline{\theta^3})_{,j}U_j - \frac{1}{3}(\overline{\theta^3 u_j})_{,j} + \overline{\theta^2}(\overline{\theta u_j})_{,j} + D\,\overline{\theta_{,jj}\theta^2} \qquad (3)$$

The molecular term can be written

$$D\,\overline{\theta_{,jj}\theta^2} = \frac{1}{3}D(\overline{\theta^3})_{,jj} - D\overline{(\theta^2)_{,j}\theta_{,j}} \qquad (4)$$

The first term on the right of Eq. (4), representing molecular diffusion, is negligible compared to other terms in Eq. (3) in turbulence of large Reynolds and Peclet number (Tennekes and Lumley (9)). Thus the budget becomes

$$\frac{1}{3}(\overline{\theta^3})_{,t} = \underset{(a)}{-\Theta_{,j}\,\overline{u_j\theta^2}} - \underset{(b)}{\frac{1}{3}(\overline{\theta^3})_{,j}U_j} - \underset{(c)}{\frac{1}{3}(\overline{\theta^3 u_j})_{,j}} + \underset{(d)}{\overline{\theta^2}(\overline{\theta u_j})_{,j}} - \underset{(e)}{D\overline{(\theta^2)_{,j}\theta_{,j}}} \qquad (5)$$

The terms are (a) production by temperature gradient; (b) mean advection; (c) turbulent transport; (d) production by heat flux gradient; and (e) molecular destruction. We will now examine the budget in two flows.

a) Atmospheric surface layer

In a horizontally homogeneous surface layer term (b) in Eq. (5) vanishes, while (d) is of order z/z_i times the leading terms, with z the distance from the surface and z_i the ABL depth. Thus it reduces to

$$\frac{1}{3}(\overline{\theta^3})_{,t} = \underset{(a)}{-\Theta_{,3}\,\overline{w\theta^2}} - \underset{(c)}{\frac{1}{3}(\overline{\theta^3 w})_{,3}} - \underset{(e)}{D\overline{(\theta^2)_{,j}\theta_{,j}}} \qquad (6)$$

Here we use the notation $x_3=z$, $u_3=w$.

The surface layer θ field is positively skewed; Fig. 1 shows data on $S=\overline{\theta^3}/(\overline{\theta^2})^{3/2}$. Here z is nondimensionalized with the Monin-Obukhov length L (see Haugen (10) for discussion of this scaling). Because S is positive we interpet terms which make a positive contribution to the right side of Eq. (6) as gain terms, and negative ones as losses.

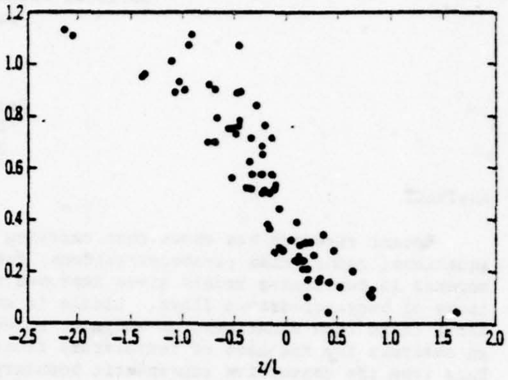

Fig. 1 Temperature skewness in the surface layer. Data from 1968 Kansas experiment.

Surface-layer data on terms (a) and (c) in Eq.(6) are presented in Figs. 2 and 3. We have used Monin-Obukhov scaling, with $u_*T_*=-Q_0$, the surface temperature flux. The data were taken in daytime (unstable) *conditions, with Q_0 positive (upward). Fig. 2 shows* the nondimensionalized (multiplied by $-kz/(u_*T_*^3)$) term (a). It is positive, indicating (a) is also positive and hence a gain term.

The data on $\overline{w\theta^3}$ are presented in Fig. 3. Each line connects data from (usually) three levels (5.7, 11.3 and 22.6 m) during the same 60-min run. Note that the slopes are fairly consistent, with a sign that indicates that term (c) is also a gain. A more subtle feature of Fig. 3 is the apparent departure from Monin-Obukhov similarity. At fixed z/L (-0.5, say) there is a consistent run-to-run spread in

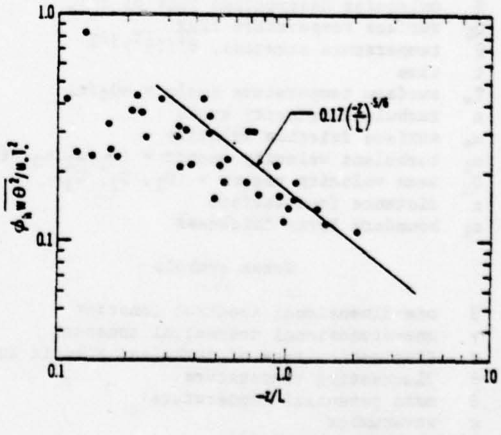

Fig. 2 Production rate by temperature gradient; Kansas data.

values of $\overline{w\theta^3}/u_* T_*^3$, indicating it depends on more than z/L. While interesting, this is beyond the scope of our paper and will not be pursued here.

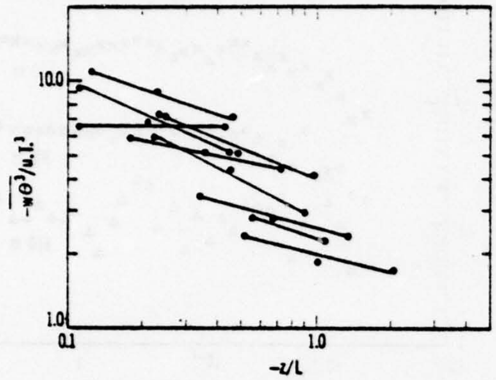

Fig. 3 Vertical flux of $\overline{\theta^3}$; Kansas data.

Since both terms (a) and (c) in Eq. 6 are gains, it follows that (e) is the loss which balances the budget, which substantiates our earlier interpretation as molecular destruction. Thus

$$\overline{(\theta^2)_{,j}\theta_{,j}} = 2\overline{\theta_{,j}\theta_{,j}\theta} = 2\overline{(\theta_{,j}\theta_{,j} - \overline{\theta_{,j}\theta_{,j}})\theta} \tag{7}$$

is positive, so that activity in the fluctuating temperature gradient field in the unstable surface layer tends to be concentrated in the hot spots. Viewed another way,

$$\overline{(\theta^2)_{,j}\theta_{,j}} = -\overline{\theta_{,jj}\theta^2} \tag{8}$$

is positive, which indicates that locally high cooling rates ($\theta_{,jj}$ negative), due to conduction in the hot spots, dominate the warming effects in cooler regions.

There is an analogy here with the budget of temperature variance, which in the surface layer is

$$\frac{1}{2}(\overline{\theta^2})_{,t} = -\Theta_{,3}\,\overline{w\theta} - \frac{1}{2}(\overline{\theta^2 w})_{,3} - D\overline{\theta_{,j}\theta_{,j}} \tag{9}$$

The terms have the same interpretation as those in Eq. (6), and have been measured (Wyngaard and Coté (11)). The molecular destruction rate has the property

$$N = D\overline{\theta_{,j}\theta_{,j}} = D\int \kappa^2\,\phi(\underline{\kappa})\,d\underline{\kappa} \tag{10}$$

where ϕ is the temperature spectrum,

$$\overline{\theta^2} = \int \phi(\underline{\kappa})\,d\underline{\kappa} \tag{11}$$

Corrsin (12) proposed that in an inertial range ϕ depends only on κ, N, and ε, the dissipation rate of turbulent kinetic energy. Thus on dimensional grounds the one-dimensional temperature spectrum F has the form

$$F = \beta\,N\,\varepsilon^{-1/3}\,\kappa_1^{-5/3} \tag{12}$$

which agrees with measurements. The constant $\beta \sim 0.8$-1.0, according to data.

For $\overline{\theta^3}$ we define a molecular destruction rate M:

$$M = \overline{D(\theta^2)_{,j}\theta_{,j}} = D\int \kappa^2 C(\underline{\kappa})\,d\underline{\kappa} \tag{13}$$

$$\overline{\theta^3} = \int C(\underline{\kappa})\,d\underline{\kappa} \tag{14}$$

with C the cospectrum of θ^2 and θ. Extending Corrsin's arguments to the inertial range of C, we have $C = C(M,\varepsilon,\kappa)$, which gives for the one-dimensional cospectrum

$$Co = \gamma\,M\,\varepsilon^{-1/3}\,\kappa_1^{-5/3} \tag{15}$$

The linear dependence on M seems essential on physical grounds. Clearly $\overline{\theta^3}$ in a jet, for example, can be made to change sign by changing the jet temperature, while keeping the temperature fluctuations dynamically passive. Thus M and Co should change sign together, as they do in Eq. (15). Similar scaling has been proposed for higher-order turbulence spectra (Van Atta and Wyngaard (13)).

Before leaving the surface layer, we briefly consider the behavior of S in the limiting case of very unstable conditions (large -z/L). There a state of "local free convection" is observed; buoyancy effects dominate, and u_* is no longer an important parameter. Similarity scaling then becomes very simple (Wyngaard (4)). In our case, we should find S→constant. This is tested against data in Fig. 4; S does seem to approach a constant under very unstable conditions.

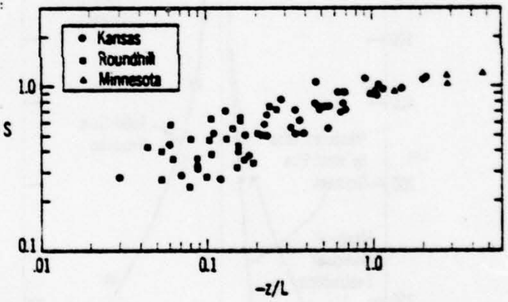

Fig. 4 A test of the local free convection prediction S→constant.

b) The mid-regions of the ABL

Temperature fluctuations are positively skewed throughout most of the convective boundary layer. Fig. 5 shows data taken during the 1973 Minnesota experiments; the individual profiles are averages over several hours during the quasi-steady mid-day period. Each profile is consistent with an S value near 1 in the surface layer, a decrease to a minimum near mid-layer, and an increase at greater heights due to entrainment effects near the inversion base at z_i.

Above the surface layer in the convective ABL $\Theta_{,3}$ is so small that term (a) in the budget, Eq. 5, becomes negligible. The appropriate form here is

$$\frac{1}{3}(\overline{\theta^3})_{,t} = \underset{(c)}{-\frac{1}{3}(\overline{\theta^3 w})_{,3}} + \underset{(d)}{\overline{\theta^2}(\overline{\theta w})_{,3}} - \underset{(e)}{D\overline{(\theta^2)_{,j}\theta_{,j}}} \tag{16}$$

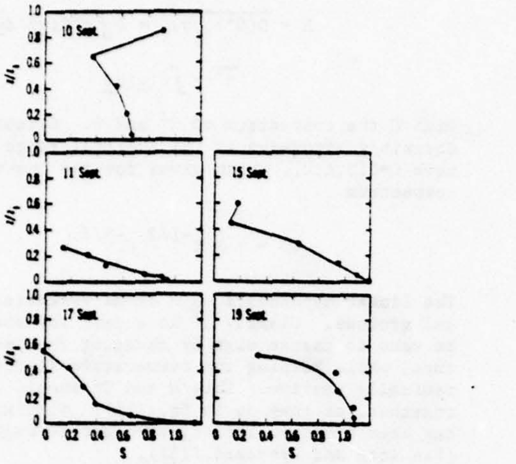

Fig. 5 S profiles in the convective ABL; Minnesota data.

We have measured (c) and (d) at 152, 305, and 610 m in run 6A1 of the 1973 Minnesota experiments (Kaimal et al (14)), with the results shown in Fig. 6.

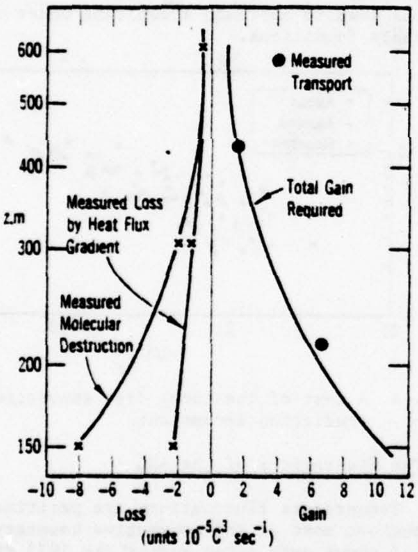

Fig. 6 Terms in the $\overline{\theta^3}/3$ budget, from Minnesota data.

Term (e), M, was obtained from the inertial range of the θ^2-θ cospectrum using Eq. (15) with γ assumed to be 1.0. Fig. 7 shows these cospectra in the form $f^{5/3}$ times the frequency cospectrum for the 75-min run. They show constant inertial range levels, which agree with Eq. (15) if we can take $\kappa_1=2\pi f/U_1$ by Taylor's hypothesis.

Both the time derivative term and the production term (a) were an order of magnitude less than the others, justifying their neglect. Thus the right side of Eq. (16) should balance, and Fig. 6 shows it does so remarkably well.

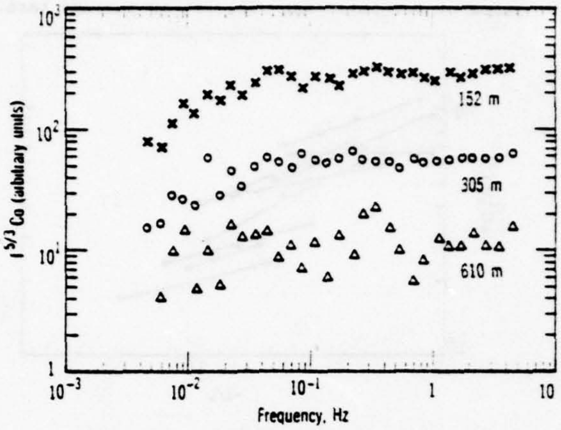

Fig. 7 Measured inertial range cospectra of θ^2 and θ, Minnesota data.

SOME IMPLICATIONS FOR TURBULENCE MODELING

Our measurements show that molecular destruction has a dominant role in the $\overline{\theta^3}$ budget. This contradicts the assumption by Andre et al (6,7) that it is negligible. It also casts doubt on the neglect of viscous effects by Hanjalic and Launder (5) in the $\overline{u_i u_j u_k}$ budget.

Zeman and Lumley (3) included molecular destruction in their $\overline{\theta^3}$ budget, and parameterized it as

$$M = 2\,\frac{\overline{\theta^3}}{\overline{\theta^2}}\,N \tag{17}$$

which is equivalent to

$$\frac{M}{N(\overline{\theta^2})^{1/2}} = 2S \tag{18}$$

Our results, although not extensive enough to test this critically, indicate this can significantly underestimate M, as shown in Table 1.

Table 1. Test of Zeman-Lumley M parameterization

z,m	$\frac{M}{N(\overline{\theta^2})^{1/2}}$	2S	ratio
152	1.88	1.50	1.25
305	1.45	0.69	2.1
610	0.92	0.45	2.0

A potential advantage of carrying third moment equations in a turbulence model, in addition to the advantages they bring through the explicit inclusion of buoyancy effects, is that their transport terms, being fourth moments, might be amenable to the "quasi-Gaussian" approximation. As applied to the $\overline{\theta^3}$ budget, this says

$$\overline{w\theta^3} = 3\,\overline{w\theta}\,\overline{\theta^2} \tag{19}$$

which is tested against Kansas, Minnesota and oversea (AMTEX) data in Fig. 8. The data scatter about the quasi-Gaussian prediction, being slightly lower near the surface and greater aloft.

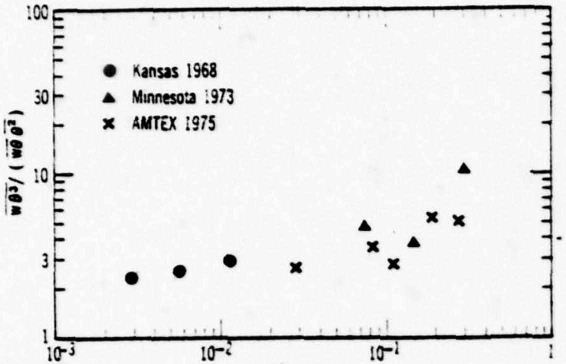

Fig. 8 A test of the quasi-Gaussian approximation $\overline{w\theta^3} = 3\,\overline{w\theta}\,\overline{\theta^2}$.

ACKNOWLEDGMENTS

The authors are grateful to D. A. Haugen and J. Young for supplying the Minnesota data, to D. Lenschow for the AMTEX data, and to J. Tillman for the Roundhill data. We also thank Ms. J. Trebing for expertly typing the manuscript.

REFERENCES

1 Reynolds, W. C., "Computation of Turbulent Flows," Annual Review of Fluid Mech., Vol. 8, 1976, pp. 183-208.

2 Wyngaard, J. C., "Modeling the Planetary Boundary Layer—Extension to the Stable Case," Boundary-Layer Meteorol., Vol. 9, 1975, pp. 441-460.

3 Zeman, O. and Lumley, J. L., "Modeling Buoyancy Driven Mixed Layers," J. Atmos. Sci., Vol. 33, 1976, pp. 1974-1988.

4 Wyngaard, J. C., "On Surface-Layer Turbulence," in Workshop on Micrometeorology, D. A. Haugen, Ed., Amer. Meteorol. Soc., Boston, 1973, pp. 101-149.

5 Hanjalic, K. and Launder, B. E., "A Reynolds Stress Model of Turbulence and its Application to Thin Shear Flows," J. Fluid Mech., Vol. 52, 1972, pp. 609-638.

6 André, J. C., DeMoor, G., LaCarrère, P., and DuVachat, R., "Turbulence Approximation for Inhomogeneous Flows: Part I. The Clipping Approximation," J. Atmos. Sci., Vol. 33, 1976, pp. 476-481.

7 _____, "... Part II. The Numerical Simulation of a Penetrative Convective Experiment," J. Atmos. Sci., Vol. 33, 1976, pp. 482-491.

8 Lumley, J. L. and Panofsky, H. A., "The Structure of Atmospheric Turbulence," Interscience, New York, 1964.

9 Tennekes, H. and Lumley, J. L., "A First Course in Turbulence," MIT Press, Cambridge, 1972.

10 Haugen, D. A., Ed., "Workshop on Micrometeorology," Amer. Meteorol. Soc., Boston, 1973.

11 Wyngaard, J. C. and Coté, O. R., "The Budgets of Turbulent Kinetic Energy and Temperature Variance in the Atmospheric Surface Layer," J. Atmos. Sci., Vol. 28, 1971, pp. 190-201.

12 Corrsin, S., "On the Spectrum of Isotropic Temperature Fluctuations in an Isotropic Turbulence," J. Appl. Phys., Vol. 22, 1951, pp. 469-473.

13 Van Atta, C. and Wyngaard, J. C., "On Higher-Order Spectra of Turbulence," J. Fluid Mech., Vol. 72, 1975, pp. 673-694.

14 Kaimal, J. C., Wyngaard, J. C., Haugen, D.A., Coté, O. R., Izumi, Y., Caughey, S. J., and Readings, C. J., "Turbulence Structure in the Convective Boundary Layer," J. Atmos. Sci., Vol. 33, 1976, pp. 2152-2169.

BUOYANCY EFFECTS IN ENTRAINING TURBULENT BOUNDARY LAYERS: A SECOND-ORDER CLOSURE STUDY

OTTO ZEMAN AND J. L. LUMLEY
Pennsylvania State University
Department of Aerospace Engineering
University Park, PA 16802

ABSTRACT

A second-order modeling technique is used to investigate the structure of turbulent boundary layers under stable, neutral and unstable conditions. Special attention is paid to the evening transition from a convective to a stable regime of an atmospheric entraining boundary layer capped by an inversion.

The second-order closure scheme utilizes the turbulent transport model which incorporates buoyancy effects (Zeman and Lumley, 1976). The importance of the buoyancy contributions in the turbulent transport model for the process of entrainment and for the turbulence decay during the evening transition is discussed.

1. INTRODUCTION

A planetary boundary layer undergoes diurnal oscillations which are a consequence of the variability of solar radiation. Typically, on a sunny day a convective mixed layer develops and grows as it entrains stable air from above. Sometimes during the afternoon, the convective activity weakens as the insolation diminishes in magnitude and the entrainment ceases at the mixed-layer top. Later, at sunset, the turbulent heat flux at the ground reverses direction and the boundary layer transits into a stable regime. The transition from the unstable to the stable regime is a complex event whereby the structure of the boundary layer undergoes drastic changes (see for example Businger (1973)). The stable layer often generates internal gravity waves and the interaction of buoyancy and Coriolis forces with turbulence may lead to oscillatory motion with alternating periods of turbulence and calm during the night (Gifford 1952).

This paper is a preliminary report on the application of the second-order technique to the evening transition of the atmospheric boundary layer (ABL). The purpose of the paper is to shed some light on the details of the ABL during the transition and also to outline some of the problems that modelers face when attempting to model the stably stratified turbulence. The second-order model described here is an extension of the shear-free convective model (Zeman, 1975; Zeman and Lumley, 1976) to horizontally turbulent shear flows in a stratified atmosphere. In the past, Wyngaard (1975) successfully used a somewhat similar model for modeling the stable ABL.

In the following section we shall outline the basic equations pertaining to the problem; in section 3 we shall describe modeling of the pressure terms, energy dissipation, and destruction of temperature variance. Section 4 describes the model for the third-order fluxes (or transport terms) and the way buoyancy affects the transport of second-order quantities in a stably stratified atmosphere. In section 5 we discuss some aspects of modeling stably stratified turbulent flows. In section 6 we present preliminary results of simulation of the evening transition in an ABL.

2. MODEL EQUATIONS

We are concerned with a barotropic, horizontally homogeneous dry ABL in which radiative effects are neglected. In the Boussinesq approximation the rate equations for the second-order quantities at high Reynolds number (Wyngaard, 1975) reduce to

$$\begin{aligned}\frac{\partial\overline{u_i u_k}}{\partial t} = &-\overline{u_i u_j}U_{k,j} - \overline{u_k u_j}U_{i,j} + \beta_i\overline{\theta u_k} + \beta_k\overline{\theta u_i}\\ &+ 2\epsilon_{ipq}\Omega_q\overline{u_k u_p} + 2\epsilon_{kpq}\Omega_q\overline{u_i u_p}\\ &- \left(\overline{u_i u_j u_k} + \frac{2}{3}\frac{\delta_{ik}}{\rho}\overline{pu_j}\right)_{,j} - \Pi_{ik} - \frac{2}{3}\epsilon\delta_{ik}\ ,\end{aligned} \tag{1}$$

$$\begin{aligned}\frac{\partial\overline{\theta u_i}}{\partial t} = &-\overline{\theta u_j}U_{i,j} - \overline{u_i u_j}\Theta_{,j} + \beta_i\overline{\theta^2} + 2\epsilon_{ijk}\Omega_k\overline{\theta u_j}\\ &- (\overline{u_i u_j\theta})_{,j} - \Pi_i\ ,\end{aligned} \tag{2}$$

$$\frac{\partial\overline{\theta^2}}{\partial t} = -2\overline{\theta u_j}\Theta_{,j} - (\overline{\theta^2 u_j})_{,j} - 2\overline{\epsilon_\theta}\ , \tag{3}$$

and the equations for the mean wind components $U_i = (U,V,0)$ and the mean potential temperature Θ are

$$\begin{aligned}\frac{\partial U}{\partial t} &= -(\overline{u_1 u_3})_{,3} + f(V - V_g)\ ,\\ \frac{\partial V}{\partial t} &= -(\overline{u_2 u_3})_{,3} - f(U - U_g)\ ,\\ \frac{\partial\Theta}{\partial t} &= -(\overline{\theta u_3})_{,3}\end{aligned} \tag{4}$$

where we make the standard assumption concerning the geostrophic equilibrium which, in turn, allows us to eliminate the mean pressure gradients. In (4) U_g and V_g are the prescribed components of the geostrophic wind and f is the Coriolis parameter taken to be 10^{-4} $\sec^{-1}$.

In equations (1) through (3) $\overline{u_i u_j}$, $\overline{\theta u_i}$ and $\overline{\theta^2}$ are ensemble averaged one-point second moments of the fluctuating velocities $u_i = (u_1,u_2,u_3)$ and temperature

PRECEDING PAGE BLANK-NOT FILMED

θ; $\overline{\epsilon}$ and $\overline{\epsilon_\theta}$ are the mean rates of turbulence energy dissipation and of the destruction of $\overline{\theta^2}/2$ respectively. Although not entirely justified in stably stratified turbulence, we take $\overline{\epsilon}$ to be isotropically distributed among the component energies. We shall discuss the soundness of the isotropy assumption for $\overline{\epsilon}$ later in this paper. The term Π_{ik} represents the deviatoric part of the pressure term (Lumley and Khajeh-Nouri 1974), which is

$$\Pi_{ik} = \frac{1}{\rho}\{\overline{p,_i u_k} + \overline{p,_k u_i} - \frac{2}{3}\delta_{ik}(\overline{pu_j}),_j\} ,$$

Similarly, Π_i in equation (2) is the pressure gradient-temperature correlation term

$$\Pi_i = \overline{p,_i \theta}/\rho \quad ,$$

Here, p is fluctuating pressure. The parameter Ω_D is the angular velocity of the frame of reference and $\beta_i = (0,0\ g/\Theta_o)$ is the buoyancy parameter. The mean-temperature Θ_o is taken to be 273°K.

Equations (1) through (3) contain unknown quantities $\overline{\epsilon}$, $\overline{\epsilon_\theta}$, the pressure terms Π_{ik} and Π_i and the third-order fluxes. The second-order closure technique consists in approximating these unknown quantities in order to close the system of equations. The next two sections deal with the problem of closure.

3. THE MODELS FOR PRESSURE TERMS AND VISCOUS TERMS

The pressure and viscous term models used in the present study have been developed earlier by Zeman and Tennekes (1975), Zeman (1975), Lumley (1975), and Zeman and Lumley (1976). The pressure terms can generally be divided into two parts: the non-linear return-to-isotropy part which is associated with inertial interactions within the turbulence field and the "rapid" part which reflects the interactions between turbulence and the mean field quantities, such as mean shear and Coriolis and buoyancy forces. Apart from the usual symmetry and incompressibility constraints ($\Pi_{ii} = 0$, $\Pi_{ik} = \Pi_{ki}$), in a homogeneous isotropic approximation it is convenient to utilize the integral constraint (see e.g. Zeman 1975). This enables us to eliminate almost all the free constants in the "rapid" part of the pressure term model, assuming that we keep only terms linear in second-order quantities. In strongly inhomogeneous and anisotropic flows such as a nocturnal ABL we may disregard the homogeneous approximation and resort to matching the model to a known flow. Recently it has become evident that non-linear terms may have to be added in the rapid pressure terms to satisfy the so-called realizability conditions. This aspect of modeling will be discussed later.

The pressure term model

The following are the pressure term models Π_{ik} and Π_i used in this study:

$$\begin{aligned}\Pi_{ik} = C_1\overline{\epsilon}b_{ik} - 2q^2[\alpha_o S_{ik} + \alpha_1(S_{ij}b_{jk} + S_{jk}b_{ij} \\ - \frac{2}{3}S_{ji}b_{ij}\delta_{ik}) + \gamma_1(R_{ij}b_{jk} - R_{jk}b_{ij})] \\ + \frac{3}{10}\beta_j(\overline{\theta u_i}\delta_{jk} + \overline{\theta u_k}\delta_{ji} - \frac{2}{3}\overline{\theta u_j}\delta_{ik}) \quad , \quad (5)\end{aligned}$$

$$\begin{aligned}\Pi_k = C_\theta\frac{\overline{\epsilon}}{q^2}\overline{\theta u_i} + \frac{4}{5}a_m[(U_{i,j} - 2\epsilon_{ij\ell}\Omega_\ell) \times (\delta_{ki}\overline{\theta u_j} \\ - \frac{1}{4}(\delta_{ij}\overline{\theta u_k} + \delta_{jk}\overline{\theta u_i}))] + \frac{1}{3}\beta_i\delta_{ik}\overline{\theta^2} \quad . \quad (6)\end{aligned}$$

Here, $b_{ij} (= \overline{u_i u_j}/q^2 - \frac{1}{3}\delta_{ij})$ is the departure-from-isotropy tensor, S_{ij} is the mean strain rate tensor defined as

$$S_{ij} = \frac{1}{2}\{U_{i,j} + U_{j,i}\} \quad ,$$

and the skew-symmetric rotation tensor R_{ij} is defined as

$$R_{ij} = \frac{1}{2}\{U_{i,j} - U_{j,i}\} - 2\epsilon_{ijk}\Omega_k \quad .$$

The terms on the right-hand sides of equation (5) and (6) are respectively the return-to-isotropy terms (Rotta's terms), "rapid" terms due to mean shear (in square brackets), and "rapid" terms due to buoyancy (terms associated with β_i). The numerical values of the constants in (5) and (6) are as follows:

$$C_1 = 3.5 \quad \alpha_o = \frac{1}{5}, \ \alpha_1 = 0.31, \ \gamma_1 = 0.22$$

$$C_\theta = 7.5 \quad a_m = -0.56$$

Briefly, the set of constants C_1, α_1 and γ_1 were determined by the methods outlined by Zeman and Tennekes (1975): if in the neutral surface layer the Reynolds stresses are known, with certain assumptions, we can form three independent stress equations, where the only unknowns are C_1, α_1 and γ_1. Similarly, there are two independent heat flux equations which enable us to determine C_θ and a_m (Zeman 1975). The set of constants in (7) corresponds to the surface layer data from the Kansas experiment (Wyngaard et al, 1974). It is to be added, that the strictly invariant homogeneous approximations to the "rapid" part due to mean shear yield $\alpha_o = 1/5$, $\alpha_1 = 3/4$, $\gamma_1 = 0$ and $a_m = 1.0$, (these make the rapid part independent of the rotation part R_{ik} of the mean deformation tensor). These homogeneous values, however, force the turbulence field to take on unrealistic values of Reynolds stresses and heat fluxes.

Modifications to the forms of Π_i and Π_{ik} necessitated by the realizability conditions and the recently advanced return-to-isotropy model of Lumley and Newman (1977) are discussed in section 5.

Viscous terms

The models for $\overline{\epsilon}$ and $\overline{\epsilon_\theta}$ used in this study are those described by Zeman (1975) and Zeman and Lumley (1976). The following forms reflect the recent findings of Newman and Warhaft at The Pennsylvania State University (personal communication):

$$\begin{aligned}\frac{\partial\overline{\epsilon}}{\partial t} = -3.8\frac{\overline{\epsilon}^2}{q^2} + \frac{\overline{\epsilon}}{q^2}[-aU_{i,j}\overline{u_i u_j} + \frac{bII\overline{\epsilon}}{1 + 3\sqrt{II}} + \\ 3.8\beta_i \times (\overline{\theta u_i} - \frac{21}{4}\frac{\overline{\theta u_j}b_{ij}}{1 + 3\sqrt{II}}) - (\overline{\epsilon u_j}),_j \qquad (8)\end{aligned}$$

$$\begin{aligned}\frac{\partial\overline{\epsilon_\theta}}{\partial t} = 3.0\frac{\overline{\epsilon_\theta}^2}{\overline{\theta^2}}(1 + 0.25r) - c\frac{\overline{\epsilon_\theta}}{\overline{\theta^2}}\overline{\theta u_j}\Theta,_j \\ + d\overline{\theta u_j}\,\overline{\theta u_j}\frac{\overline{\epsilon}^2}{q^6} - (\overline{\epsilon_\theta u_j}),_j \quad . \qquad (9)\end{aligned}$$

$$K_{ij}G_{j,3} \equiv \left\{\begin{array}{cccccccccc}
.92K_m & & & 1.83K_{13} & & & & & & \\
 & .92K_m & & & 1.83K_m & & & & & \\
 & & 2.4K_m & & & & 3.9\beta T_3K_m & & & 3.2\beta^2T_3^2K_t \\
 & & K_{13} & 2.0K_m & & & 2\beta T_3K_{13} & 2\beta T_3K_m & & \\
 & & K_{23} & & 2.0K_m & & 2\beta T_3K_{23} & & 2\beta T_3K_m & \\
 & & & & & 1.1K_m & & & & \\
 & & .9T_3\overline{\theta u_3} & & & & 2.0K_m & & & 1.65\beta T_3K_t \\
 & & & .9T_3\overline{\theta u_3} & & & 1.1K_{13} & 1.1K_m & & \\
 & & & & .9T_3\overline{\theta u_3} & & 1.1K_{23} & & 1.1K_m & \\
 & & & & & & 2K_\theta & & & K_t
\end{array}\right\}\left\{\begin{array}{c}
\overline{u_1^2}_{,3} \\
\overline{u_2^2}_{,3} \\
\overline{u_3^2}_{,3} \\
\overline{u_1u_3}_{,3} \\
\overline{u_2u_3}_{,3} \\
\overline{u_1u_2}_{,3} \\
\overline{\theta u_3}_{,3} \\
\overline{\theta u_1}_{,3} \\
\overline{\theta u_2}_{,3} \\
\overline{\theta^2}_{,3}
\end{array}\right\}.$$

Table I. The eddy coefficient matrix K_{ij} ($\beta \equiv \beta_3$).

Here, the first terms on the right hand side of (8) and (9) are the isotropic decay terms, r in (9) is the ratio of the thermal to mechanical time scale ($r = (\overline{\theta^2}/\overline{\varepsilon}_\theta)/(q^2/\overline{\varepsilon})$). The presence of the mechanical time scale q^2/ε in the $\overline{\varepsilon}_\theta$ equation (through the term 0.25r) provides a weak but necessary coupling between the mechanical and thermal fields in isotropic turbulence. The second term in (8) reflects the production of $\overline{\varepsilon}$ (or the enstrophy) due to deformation of the turbulence field by the mean field (terms involving the mechanical production of the *kinetic* energy $q^2/2$, $U_{i,j}\overline{u_iu_j}$, and the *buoyant production of* $q^2/2, \beta_i\overline{\theta u_i}$). *The effect of* the large-scale anisotropy on the rate of $\overline{\varepsilon}$ is reflected by the term involving the second invariant II of the anisotropy tensor b_{ij} ($II = b_{ij}b_{ij}$). In analogy with the ε-equation, the $\overline{\varepsilon}_\theta$-equation contains the $\theta^2/2$ production term $\overline{\theta u_j}\Theta_{,j}$, and the term $\overline{\theta u_i}\;\overline{\theta u_i}$ which is a measure of anisotropy of the thermal field. Matching the model to experimental data, Zeman (1975) found the constants in equation (3) to be $a = 0.95$ and $b = 30.0$, Newman (personal communication) found the constants $c = 0.97$ and $d = 30.0$ in equation (9).

There has been some discussion in the literature (e.g., Reynolds 1976) as to which form of the $\overline{\varepsilon}$ model (or $\overline{\varepsilon}_\theta$) is more appropriate: the model containing the mean field quantities ($U_{i,j}$, $\Theta_{,j}$) or the turbulence quantities which are the result of the deformation by the mean field, i.e., II and $\overline{\theta u_i}\;\overline{\theta u_i}$. It has now become evident that both the mean field and the large-scale turbulence field have to be represented in the models of $\overline{\varepsilon}$ and $\overline{\varepsilon}_\theta$. The models in equations (8) and (9) were verified in a wide range of disparate turbulent flows and in this respect they are universally valid.

4. TRANSPORT MODEL

Due to the complexity of the transport model, we resort in this paper to merely showing the specific form of the model for the dry horizontally homogeneous ABL. The interested reader is referred to papers by Zeman and Lumley (1976) and Lumley (1975) which deal with the transport model in some detail.

Briefly, in order to form a rational transport model we approximately solved the rate equations for the third-order fluxes (required in equations (1) and (2)) by applying the so-called quasi-Gaussian eddy-damped approximation to the fourth-order terms, and neglecting the temporal terms and the terms containing mean shear and mean temperature gradient (with the exception of the $\overline{\theta^2u_i}$ where $\Theta_{,j}$ is retained). We then arrived at approximate solutions which allowed us to express explicitly the third-order quantities in terms of turbulence scales, the Brunt-Väisälä frequency $(\beta_j\Theta_{,j})^{1/2}$ and the gradients of the second-order quantities. The final, tensorial form of the transport model for the ABL is

$$F_i = -K_{ij}G_{j,3} \quad . \tag{10}$$

where, F_i is the column vector of the vertical fluxes of the second moments G_i and K_{ij} is the eddy coefficient tensor. We need vertical fluxes of all component of Reynolds stresses $\overline{u_iu_j}$, all three flux components of the heat flux vector $\overline{\theta u_i}$ and the scalar flux $\overline{\theta^2u_3}$. The fluxes $\overline{\varepsilon u_3}$ and $\overline{\varepsilon_\theta u_3}$ are treated separately. We designate

$$F_i = \{\widetilde{\overline{u_1^2u_3}}, \widetilde{\overline{u_2^2u_3}}, \widetilde{\overline{u_3^3}}, \overline{u_1u_3^2}, \overline{u_2u_3^2}, \overline{u_1u_2u_3},$$

$$\overline{\theta u_3^2}, \overline{\theta u_1u_3}, \overline{\theta u_2u_3}, \overline{\theta^2u_3}\}$$

and correspondingly

$$G_i = \{\overline{u_1^2}, \overline{u_2^2}, \ldots \text{ etc.}\} \quad ,$$

and obtain the eddy coefficient matrix as shown in Table 1. The first three components of the vector F_i, $\widetilde{\overline{u_\alpha u_\alpha u_3}}$ are the fluxes of the components of energy; these include the pressure flux $2/3\ \overline{pu_3}/\rho$.

The fundamental coefficients in Table I are defined as follows:

$$K_m = T_3(\overline{u_3^2} + 0.31\beta_3T_\theta\overline{\theta u_3}) \quad ,$$

$$K_t = T_{eff}(\overline{u_3^2} + .62\beta_3T_\theta\overline{\theta u_3})/(1 + \tfrac{1}{3}\beta_3\Theta_{,3}T_3T_{eff}) ,$$

$$K_\theta = T_3\overline{\theta u_3}/(1 + \tfrac{1}{3}\beta_3\Theta_{,3}T_3T_{eff}) \quad ,$$

$$K_{13} = T_3(\overline{u_1u_3} + \beta_3T_\theta\overline{\theta u_1}) \quad ,$$

and $K_{23} = T_3(\overline{u_2u_3} + \beta_3T_\theta\overline{\theta u_2})$,

$$T_{eff} = 1/(1/T_3 + 2.0/T_\theta) \text{ and } T_\theta = \overline{\theta^2}/\overline{\varepsilon_\theta} \quad .$$

Here $T_3 = \chi q^2/\overline{\varepsilon}$ is the relaxation time scale pertaining to the third-order moments of the turbulent field. The constant χ relates T_3 to the fundamental time scale of turbulence $q^2/\overline{\varepsilon}$. We find that values of χ in the range of 0.10 to 0.13 yield realistic levels of the third-order fluxes in a convective ABL (Zeman and Lumley 1976). Hanjalic and Launder (1972) used $\chi = 0.07$. This value is consistent with our results because we model molecular terms and the pressure flux term $\overline{pu_i/\rho}$ $(= -\frac{1}{5}q^2u_i)$. Inclusion of the latter terms has the effect of reducing the time scale T_3.

For flux $\overline{\varepsilon u_3}$ and $\overline{\varepsilon_\theta u_3}$ we used simple scalar models

$$\overline{\varepsilon u_3} = -K_m\overline{\varepsilon}_{,3} \quad ,$$

$$\overline{\varepsilon_\theta u_3} = -\frac{1}{2}K_t\overline{\varepsilon_\theta}_{,3} \quad .$$

The existence of the off-diagonal terms in K_{ij} is an indication that the third-order fluxes are coupled primarily through the buoyancy parameter β_i; hence a flux of one quantity can be affected by a gradient of another one. The contributions of the off-diagonal terms have been shown to be of importance in convective ABL's (Zeman 1975); this is not necessarily true for the nocturnal layer, where the vertical fluxes are suppressed and the turbulence state is more or less determined by the local properties of the turbulence field. The implicit buoyancy contributions to the eddy coefficients in equation (11) have, however, a physical significance in stably stratified inhomogeneous turbulence. It may be shown that the eddy coefficients in equation (11) have approximately the same functional dependence on z/L as the quasi-homogeneous eddy coefficients K_M and K_H which relate the second-order fluxes $\overline{u_1u_3}$ and $\overline{\theta u_3}$ to their respective mean gradients $U_{,3}$ and $\Theta_{,3}$. The general form of the eddy coefficent K as a function of z/L is

$$K(z/L) = f(z/L)\,(1 - \alpha\, z/L) \quad , \tag{12}$$

for $z/L \ll 1$. Here, L is the Monin-Obukhov length and the numerical values of α range between 3.0 and 7.0

It follows that the generation of both the second and third-order fluxes by turbulent mixing will cease at about the same value of the parameter z/L. This particular property of the transport model is the key to understanding why isolated patches of turbulence may develop from an initially continuous turbulence field. A discussion of the structure of stably stratified turbulence is the subject of the next section.

5. PECULIARITIES OF STABLY STRATIFIED TURBULENCE-MODIFICATION TO THE MODEL

Turbulence under the influence of strong negative buoyancy forces is unlike the well-behaved turbulence that we encounter in neutral and convective boundary layers. There exists some evidence (Woods, 1969), that isolated patches of turbulence can exist in a stably stratified fluid and assume after a long time a two-dimensional structure with the vertical motions virtually nonexistent (the so-called fossil turbulence). Evidently, the buoyancy force field and the resulting large anisotropy alter the mechanism of the return-to-isotropy tendency and the spectral cascade. Although modeling of the direct effect of buoyancy on the internal mechanisms of turbulence is presently beyond our capabilities, it is plausible to appeal to the large scale anisotropy parameters as an indirect measure of the buoyancy effects. It is therefore desirable to subject to careful scrutiny the behaviour of the model equations in the limit of small vertical fluctuations as measured by the variance $\overline{u_3^2}$. In this context, Schumann (1976) advanced the notion of realizability for the Reynolds stress models; he showed that as a component of the Reynolds stress tensor $\overline{u_iu_j}$ approaching zero, the time derivative $\partial/\partial t(\overline{u_iu_j})$ approaches zero as well. He also intimated that the linear pressure term model Π_{ik} such as that in equation (5) does not assure realizability. Lumley and Newman (1977) constructed a return-to-isotropy model which is realizable for neutral homogeneous turbulence.

Inspection of the second-order model proposed here indicates that the model is not realizable in the sense of Schumann for small vertical turbulence energy $\overline{u_3^2}$. To illustrate this we shall analyze the shear stress and vertical heat flux equations. In the limit of vanishing vertical turbulent velocity u_3, all the second order moments containing u_3 are negligible compared to their horizontal counterparts. Neglecting Coriolis and transport effects we obtain from equations (1), (2), (5) and (6)

$$\frac{\partial\overline{u_1u_3}}{\partial t} = -U_{,3}[-\frac{1}{5}q^2 + \alpha_1(\overline{u_2^2} - \frac{1}{3}q^2) + \gamma_1(\overline{u_1^2})] + (1 - 0.3a_g)\beta_3\overline{\theta u_1} \quad , \tag{13}$$

and

$$\frac{\partial\overline{\theta u_3}}{\partial t} = (1 - \frac{1}{3}C_T)\beta_3\overline{\theta^2} - \frac{a_m}{5}\overline{\theta u_1}U_{,3} \quad . \tag{14}$$

It is evident that since $\overline{\theta u_1}/\overline{\theta u_3} < 0$, in stably stratified shear turbulence, the strictly invariant model (in which $a_m = a_g = 1$, $C_T = 1$, $\alpha_1 = 3/4$ and $\gamma_1 = 0$) may lead to unphysical results or nonrealizability in the sense of Schumann. Apart from the buoyancy terms, for typical values of $\overline{u_1^2}/\overline{u_2^2} = 2.0$ we obtain $\partial\overline{u_1u_3}/\partial t = +\frac{1}{5}q^2U_{,3}$ which is not admissible. The realizability is, however, substantially improved by using the model discussed in section (2) of this paper where $\gamma_1 > 0$.

As it appears now the most troublesome equation from the viewpoint of realizability is the heat flux equation where the buoyancy term has a tendency to maintain a spurious positive heat flux. Wyngaard (1975) presented a plausible physical argument, suggesting that the rapid part of the pressure term $\Pi_i^\beta = C_T\frac{1}{3}\beta_3\overline{\theta^2}\,\delta_{i3}$ should counteract the buoyancy term $\beta_3\overline{\theta^2}$ in (14) in such a manner that in the limit of large positive Richardson's number R_i, the effect of $\beta_3\overline{\theta^2}$ be entirely eliminated. He proposed an ad hoc formula $C_T = C_T(R_i)$ with the limit $C_T \to 3$ as $R_i \to \infty$.

There are many ways to modify Π_i^β and we can only guess at some plausible form. It is evident that in some way Π_i^β has to be a function of anisotropy of the thermal turbulence field, with Π_i^β departing from its isotropic value $1/3\ \beta_3\overline{\theta^2}\delta_{i3}$ as anisotropy increases. We chose to make Π_i^β a function of large scale anisotropy rather than a function of the mean field quantities. In this paper we used the interim model

$$\Pi_i^\beta = (\frac{1}{3}\delta_{i3} - \frac{5b_{i3}}{1 + 18|\text{II}|})\beta_3\overline{\theta^2} \quad , \tag{15}$$

which yields approximately the limit $\Pi_3^\beta \to 1.0$ as $\overline{u_3^2} \to 0$. In free convection (15) assures that $\Pi_3^\beta \to 0$ as $\overline{u_3^2} \to q^2$. The decrease of Π_3^β with increasing intensity of vertical motion makes sense physically: the temperature variance spectrum $E_\theta(\underline{k})$ in wavenumber space $\underline{k} = (k_1, k_2, k_3)$ becomes distorted with more variance residing in horizontal wavenumbers k_1 and k_2 as the eddies become elongated in the vertical direction and the integral

$$\Pi_3^\beta = \frac{1}{4\pi}\beta_3 \int_{-\infty}^{\infty} \frac{k_3^2}{k^2} E_\theta(\underline{k})d\underline{k}$$

becomes smaller compared to its isotropic value $\frac{1}{3}\beta_3\overline{\theta^2}$. The same argument was put forth by Wyngaard (1975) to justify the effect of stable stratification on Π_3^β. We note that the model in (15) also generates terms Π_1^β and Π_2^β in equations for θu_1 and θu_2. These, however, are small compared to Π_3^β.

The models for $\bar{\varepsilon}$ and $\bar{\varepsilon}_\theta$ are always realizable; however, for a strictly two-dimensional turbulence (2D), with $\overline{u_3^2}$ identically zero, we arrive at a few paradoxes. First, in 2D turbulence at large Reynolds number, the kinetic energy q^2 is approximately invariant and the quantity $\bar{\varepsilon}q^2/\varepsilon^2 \to -\infty$ and the internal time scale $q^2/\bar{\varepsilon}$ becomes meaningless. Secondly, the rate equation for $\bar{\varepsilon}$ (eq. (8)) cannot "know" whether the turbulence field is in a 2D or 3D mode.

In view of the foregoing the second-order model in the present form presupposes the existence of a three-dimensional inertial subrange and the model realizability in the 2D limit may not be physically meaningful; nevertheless the realizable model leads to better numerical stability and it prevents generation of spurious second-order moments. Furthermore, Lumley and Newman (1977) have shown that a realizable return-to-isotropy model leads to a better agreement with experimental data in anisotropic homogeneous turbulence.

6. THE NUMERICAL EXPERIMENT

Here, we present some preliminary computations of the ABL structure during the evening transition. We begin with a weakly convective mixed layer capped by an inversion (the inversion strength $\gamma = 0025°C/m$) one hour before sunset. During the convective regime the prescribed surface heat flux is approaching zero shortly before sunset. From that point on it is assumed that the radiative cooling produces a constant cooling rate of the air at the lower boundary, i.e., in the stable regime the surface heat flux is determined rather than prescribed.

At the upper boundary of the computation domain all second order quantities and mean wind shear were set at zero. The potential temperature gradient was set at $\partial\Theta/\partial z = \gamma$. At the lower boundary (at the height $x_3 = 5m$) the second-order quantities were specified in agreement with the surface layer values given by Wyngaard (1975). The boundary values in the convective regime were modified to handle the free convective limit described by Zeman and Lumley (1976). The geostropic wind was fixed at $U_g = 11.5m/sec$ and $V_g = 0$. The coordinate x_1 was aligned in the West-East direction at the latitude of 45° North, and x_2 in the South-North direction. The finite difference scheme employed for the numerical solution is described in Zeman (1975). Since the magnitude and direction of the wind at the lower boundary varied, the values of the Reynolds stresses and heat fluxes at the lower boundary had to be readjusted during the computation. This was done every 10th time step (or 10 seconds).

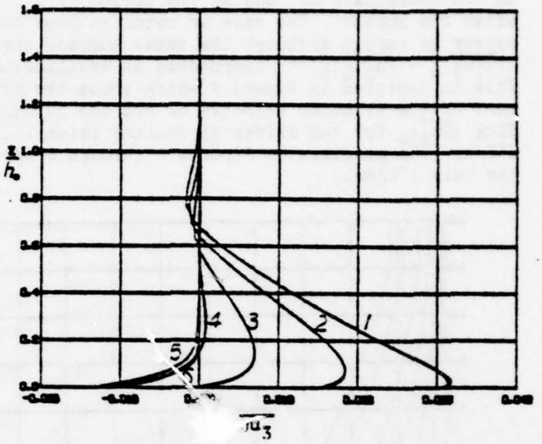

Fig. 1 Profiles of the kinematic heat flux $\overline{\theta u_3}$ in Cm/sec during the evening transition shown at 30 min. intervals beginning one hour before sunset (curve 1). The height is normalized by the initial height $h_o = 650m$ of the convective ABL.

In figure 1 we present the development of heat flux profiles during the evening transition at intervals of approximately 30 minutes beginning one hour before the transition. We note that the initially positive heat flux (curve 1) has a small region of negative heat flux at the top of the mixed layer which signifies the entrainment. As the surface flux moves through the transition (curve 3) the upper regions with larger time scales tend to maintain their convective structure. As the cooling at the ground advances the heat flux eventually approaches an equilibrium with the upper-region flux decaying to zero. The x_1-component of the horizontal heat flux is approximately a mirror image of the vertical heat flux $\overline{\theta u_3}$. The x_1-component of the Reynolds shear stress, $\overline{u_1u_3}$ is shown in Figure 2. After the transition $\overline{u_1u_3}$ decreases rapidly in magnitude as the momentum flux in the boundary layer is curtailed.

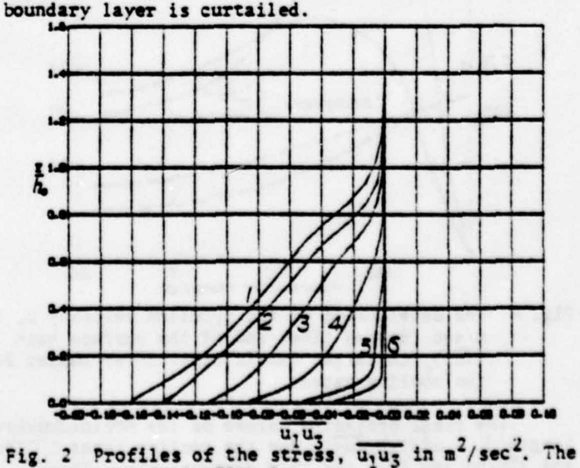

Fig. 2 Profiles of the stress, $\overline{u_1u_3}$ in m^2/sec^2. The same as in Fig. 1.

The development of the stable layer is accompanied by a build-up of the x_2-component V of the mean wind (shown in Figure 3) and the corresponding shear stress $\overline{u_2u_3}$ in the x_2 direction. The wind vector at the surface rotates from 5 to 26 degrees (with respect to the coordinate x_1) during the period of 1 1/2 hours after the sunset. The rate of rotation does not appear to vanish although the total surface stress $((\overline{u_1u_3})_0^2 + (\overline{u_2u_3})_0^2)^{1/2}$ approaches an equilibrium value. This is depicted in Figure 4 which shows the development of the friction velocity u_* and the surface heat flux $(\overline{\theta u_3})_0$ for two different cooling rates, 1°C/hr and 2°C/hr (the profiles in Figures 1 through 3 are for the rate 1°C/hr).

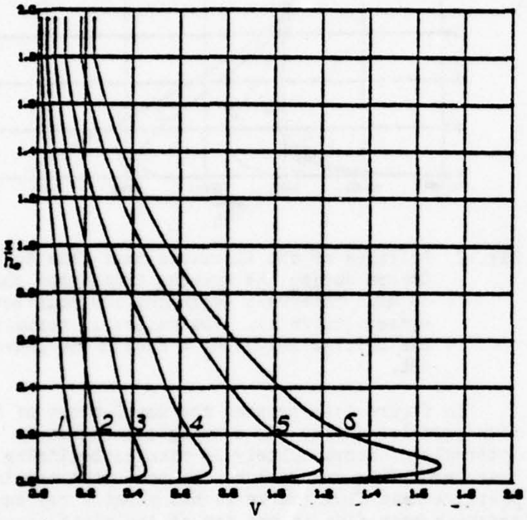

Fig. 3 Profiles of the x_2 component of wind velocity in m/sec. The same as in Figure 1.

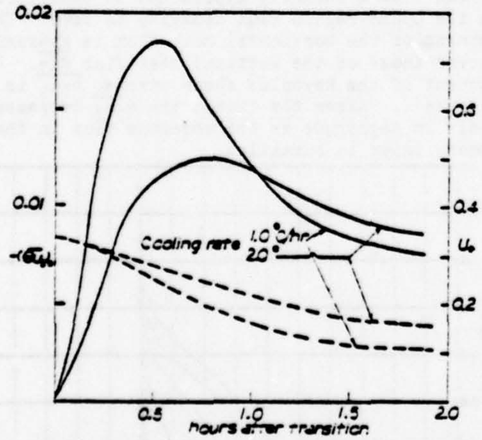

Fig. 4 The development of the friction velocity u_* in m/sec (dashed line) and of the surface heat $(\overline{\theta u_3})_0$ in cm/sec (solid line) after sunset for two cooling rates.

The final projected values of the Monin-Obukhov length $L = u_*^3/\beta_3 k(\overline{\theta u_3})_0$ for the cooling rates 1°C/hr and 2°C/hr are 35 m and 15 m respectively. These values are in approximate agreement with the results of Wyngaard (1975).

For cooling rates above 2°C/hr the numerical scheme exhibited instability in the upper regions of the computation domain. This we suspect is due to nonrealizability of the shear stress components $\overline{u_1u_3}$ and $\overline{u_2u_3}$. We note that equation (13) contains the buoyancy term $\beta\overline{\theta u_1}$ which has an effect analogous to the term $\beta\overline{\theta^2}$ in the vertical flux equation (equation (14)). The nonrealizability of $\overline{u_1u_3}$ (or $\overline{u_2u_3}$) leads to negative energy production and eventually to a numerical instability in the regions where turbulence, in effect, cannot exist.

Hence, the pressure term model Π_{ik} has to be modified in such a manner as to make the components $\overline{u_1u_3}$ and $\overline{u_2u_3}$ realizable in the limit $\overline{u_3^2} \to 0$. This however involves both the rapid distortion term due to mean shear and the rapid term due to buoyancy. At present we have little guidance as to a plausible form of the modification.

CONCLUSION

In this paper we have demonstrated the feasibility of a generalized second-order model. The model presented covers a wide range of flow conditions from a free convective ABL to a stable ABL. The stable ABL presents perhaps the most severe test for the model and the problems of modeling stably stratified turbulence are far from being resolved.

This work was supported in part by the U.S. Environmental Protection Agency through its Select Research Group in Meteorology and in part by the U.S. National Science Foundation, Atmospheric Sciences . Section. John L. Lumley's contribution evolved during a period spent at the Institut de Mécanique Statistique de la Turbulence, Université d'Aix-Marseille II, and at the Laboratoire de Mécanique des Fluides, Ecole Centrale de Lyon made possible by the support of the John Simon Guggenheim Memorial Foundation and the Délegation Générale à la Recherche Scientifique et Technique (France); the evolution of his ideas benefitted greatly from the collaboration of J. Seiss which is hereby gratefully acknowledged.

REFERENCES

Batchelor, G. K., 1969: Computation of the energy spectrum in homogeneous two-dimensional turbulence. *Physics of Fluids*, **12**, II, 233-239.

Businger, J. A., 1973: Turbulent Transfer in the Atmospheric Surface Layer. *Workshop on micrometeorology*, D. A. Haugen, editor, *Amer. Met. Soc.*, 67-98.

Chimonas, G., 1972: The stability of coupled wave-turbulence system in a parallel shear flow. *Boundary-Layer Meteo.*, **2**, 444-452.

Gifford, F. A., 1952: The break-down of a low level inversion studied by means of detailed soundings with a modified radiosonde, *Bull, A.M.S.*, **33**, 373-397.

Hanjalic, K. and B. E. Launder, 1972: A Reynolds stress model of turbulence and its application to thin shear flow. *J. Fluid Mech.*, **52**, 609-638.

Lumley, J. L., 1975: Prediction methods for turbulent flows. Notes, von Karmán Institute, Rhode-St.Genèse, Belgium, March 3-7, 1975.

Lumley, J. L., B. Khajeh-Nouri, 1974: Computational modeling of turbulent transport: *Advances in Geophysics*, **18A**, 169-192.

Lumley, J. L. and G. R. Newman, 1977: The return to isotropy of homogeneous turbulence. To be published in *Journal of Fluid Mech*.

Reynolds, W. C., 1976: Computation of Turbulent Flows. *Annual Review of Fluid Mechanics*, **8**, 183-208.

Schumann, U., 1976: Realizability of Reynolds stress turbulence models. Submitted to *Physics of Fluids*.

Woods, J. D., 1969: On Richardson's number as a criterion for laminar-turbulent-laminar transition in the ocean and atmosphere. Radio Science 4, 1289-1298.

Wyngaard, J. C., 1975: Modeling the planetary boundary layer-extension to the stable case. *Boundary-Layer Meteo.*, **9**, 441-460.

Wyngaard, J. C., O. R. Coté, and K. S. Rao, 1974: Modeling the atmospheric boundary layer. *Advances in Geophysics*, Vol. 18A, Acad. Press, 193-212.

Zeman, O., 1975: *The Dynamics of Entrainment in Planetary Boundary Layers: A Study in Turbulence Modeling and Parameterization*. Ph.D. Thesis, The Pennsylvania State University.

Zeman, O. and J. L. Lumley, 1976: Modeling buoyancy driven mixed layers. *J. Atmos. Sci.*, **33**, 1974-1988.

Zeman, O. and H. Tennekes, 1975: A self-contained model for the pressure terms in the turbulent stress equation of a neutral atmospheric boundary layer, *J. Atmos. Sci.*, **32**, 1808-1813.

ALGEBRAIC STRESS MODELING IN A BUOYANCY CONTROLLED TURBULENT SHEAR FLOW

Francesco Tamanini
Factory Mutual Research Corporation
Factory Mutual System
Norwood, Massachusetts 02062

ABSTRACT

The paper presents an application of the algebraic stress modeling (ASM) technique to the prediction of the flow in a turbulent round buoyant jet. In the ASM approach, algebraic formulas are obtained for the Reynolds stresses, $\overline{u_iu_j}$, and for the components of the turbulent heat flux, $\overline{tu_i}$. In the model used here, transport equations are solved for the turbulence kinetic energy, k, its dissipation, ε, and the mean square temperature fluctuations, g. The study shows that buoyancy increases the rate of dissipation of g above the values indicated by previous recommendations for the modeling of that quantity. As a possible explanation for this result it is suggested that buoyancy introduces anisotropy in the fluctuations at the dissipation scale. With reference to the production of k, the contribution from the secondary components of the strain tensor is found to be non-negligible. Finally, it is observed that the modeling of buoyant flows still presents uncertainties and that additional work is necessary to properly account for the effect of buoyancy on the production of ε and the dissipation of g.

NOMENCLATURE

a_g = acceleration of gravity, m/s^2
A_u, A_t, B_u, B_t = constants in eqs (19) and (20)
c_p = specific heat, joules/kg C
$c_1, c_2, c_k, c_{t1}, c_{t2}, c_g, c_{g2}, c_\varepsilon, c_{\varepsilon 1}, c_{\varepsilon 2}, c_{\varepsilon 3}$ = model constants
C = convection term
D = diffusion term
f_1 = "memory" factor in eq (14)
F_0 = buoyancy flux, m^4/s^3
g = mean square temperature fluctuations, $(\text{deg K})^2$
H = enthalpy flux defined by eq (21), joules/s
k = turbulence kinetic energy, m^2/s^2
K = entrainment coefficient defined in eq (22)
$\dot{M}$ = total mass flux, kg/s
P_γ = rate of production of γ per unit mass of fluid
r = radial coordinate, m
T, t = mean and fluctuating temperature, deg K
U_i, u_i = mean and fluctuating velocity components in the i-direction, m/s
W = jet momentum, kg m/s^2
x = longitudinal coordinate, m
X_k, X_{kg} = functions defined in eqs (5.3) and (6.3) in Table 1
γ = dummy variable, represents k, ε or g
ΔT = excess temperature above ambient $(T-T_0)$, deg K
ε = dissipation of turbulence kinetic energy, m^2/s^3
ε_γ = rate of dissipation of γ per unit mass of fluid
μ = viscosity, kg/m s
ρ = density, kg/m^3
σ = Prandtl number

Subscripts

c = centerline
i, j = indexes referring to coordinate axes
is = isotropic
x, r, θ = longitudinal, radial, tangential component
τ = turbulent
j = nozzle fluid conditions
0 = room conditions

Superscripts

— indicates time average
' indicates fluctuating component

INTRODUCTION

Over the past ten years significant progress has been made in the development of turbulence models which are suitable for engineering applications[1]. In most such models the turbulent transport of momentum and energy is evaluated by introducing the effective turbulent viscosity, μ_T, and the turbulent Prandtl number, σ_T. While the latter quantity is customarily assigned a constant value or evaluated through an empirical formula to account for wall effects, the modeling of μ_T has seen increasing sophistication.

In the early mixing length approach, μ_T is obtained as the product between a length scale (the mixing length) which is prescribed as a constant fraction of the scale of the flow, and a velocity scale, which is inferred from the mean velocity profile. With the advent of so-called two-equation models of turbulence, the mean flow-related prescription for the two scales has been replaced with an algebraic expression involving two properties of the turbulence, which in turn are obtained by finding the solution to a modeled form of their transport equations. The turbulence kinetic energy, k, and its dissipation, ε, are often selected as the two properties to characterize the turbulence field[2].

The k-ε approach represents an improvement over the mixing length technique because it is more general and relaxes the assumption of local equilibrium of the turbulence by allowing for diffusion of the quantities (k and ε) determining the magnitude of μ_T. If one needs to make estimates of the level of fluctuations of a scalar quantity as in the case, for example, when chemical reaction is involved, an additional model transport equation is used for the mean square fluctuations, g, of temperature or concentrations.

A limitation common to the mixing length and the two-equation schemes is that they both postulate isotropy of the turbulent fluctuations. When buoyant

PRECEDING PAGE BLANK-NOT FILMED

forces interact with the flow, larger levels of anisotropy are expected and the modeling of the turbulence requires evaluation of the Reynolds stresses and the components of the turbulent energy (or mass) flux. The drawback of this approach is in the increased complexity of the model and the larger amounts of computing time required to solve the transport equations for the second order correlations which are taken into account[2,3].

In this study we have preferred to follow a suggestion for algebraic stress modeling (ASM) made by Rodi[4]. As implied by its name, this technique involves finding algebraic solutions for the Reynolds stress equations by introducing an additional modeling assumption for the terms representing convection and diffusion. The final scheme amounts to an improved version of the k-ε-g formulation: the improvement is represented by the fact that the large-scale anisotropy of the flow is taken into account through the replacement of some of the constants of the standard k-ε-g model with known functions of gradients of the mean velocity and temperature fields and ratios of production and dissipation of k and g. Meroney[5] has shown that the ASM approach is much more economical than a full Reynolds stress model, while sacrificing little in terms of accuracy.

In this paper we discuss the application of the technique to the case of axisymmetric thermal plumes. First, a brief presentation is made of the model equations, followed by a discussion of the experimental data with which the model predictions have been compared, and an assessment of the model performance as well as a detailed examination of the character of the turbulence in the flow. Finally, areas in which the modeling needs to be improved are discussed.

THEORETICAL MODEL

The equations used by the model are listed in Table 1; details on their derivation can be found in Reference[6]. A complete list of symbols is given in the nomenclature: it should be noted that capital letters or overbars indicate mean quantities, while lower case letters or primes refer to fluctuating components. We now proceed to discuss the less obvious aspects of the theoretical formulation.

Conservation of Mass, Momentum and Energy

Equations (1)-(3) express conservation of mass, longitudinal momentum and energy for a boundary layer flow. These equations have been obtained neglecting turbulent correlations which involve density fluctuations. As can be noted, the turbulent shear stress in the momentum equation and the radial turbulent heat flux in the energy equation are left in their exact form, in anticipation of the fact that we will derive model expressions for all second-order correlations.

In what might appear to be inconsistent with the boundary layer assumption, we have retained the longitudinal gradients of the quantity $\overline{u_x^2-u_r^2}$ in eq (2) and of the longitudinal heat flux, $\overline{tu_x}$, in eq (3). The reason for this will be further discussed later: at this point, it is sufficient to state that in a thermal plume the term $\overline{tu_x}$ gives a non-negligible contribution to the total energy flux. Even though the corresponding term in the momentum equation is not as important, overall consistency of the model motivated its retention.

Turbulent Correlations

Transport equations are solved for three turbulence quantities: turbulence kinetic energy, k, dissipation of turbulence kinetic energy, ε, and mean square temperature fluctuations, $g \equiv \overline{t^2}$. The structure of the model equations is the same for all three quantities and is given by eq (4) in Table 1 (with γ=k,ε, or g). The terms appearing in that expression represent convection, diffusion, production and dissipation of the quantity in question (k, ε or g).

The modeling of turbulent diffusion (second term in brackets in the right hand side of eq (4)) relies on a proposal for gradient-driven diffusion made by Launder et al[7]. We believe that this choice is appropriate for the flow modeled in this study, even though it is understood that, for more complex situations, the direct effect of buoyancy on turbulent transport may have to be included [3].

With regard to the terms representing production (P_γ) and dissipation (ε_γ), some require modeling, while some can be treated exactly. Let us now examine these terms separately for the three quantities k, ε and g and introduce the algegraic stress modeling assumptions for the second-order correlations $\overline{u_i u_j}$ and $\overline{tu_i}$.

Turbulence kinetic energy (k). The dissipation of k is ε by definition: the problems related to its modeling are, therefore, shifted to the ε-equation. The production P_k is also treated exactly because it involves calculable correlations and mean field gradients. The source P_k is evaluated by the model as:

$$P_k = \frac{1}{2} \sum_i P_{ii} \tag{8}$$

where the sources of the Reynolds stresses $\overline{u_x^2}$, $\overline{u_r^2}$, $\overline{u_\theta^2}$ are given by:

$$P_{xx} = -2\, \overline{u_x^2}\, \frac{\partial U_x}{\partial x} - 2\, \overline{u_x u_r}\, \frac{\partial U_x}{\partial r} - \frac{2}{\rho}\, a_g\, \overline{\rho' u_x} \tag{9.1}$$

$$P_{rr} = -\, 2\, \overline{u_r^2}\, \frac{\partial U_r}{\partial r} \tag{9.2}$$

$$P_{\theta\theta} = -\, 2\, \overline{u_\theta^2}\, \frac{U_r}{r} \tag{9.3}$$

Note the presence of the last term in eq (9.1) representing production of $\overline{u_x^2}$ due to buoyancy.

Equations (9.1)-(9.3) are written by neglecting the component $\partial U_r/\partial x$ of the strain tensor. In a departure from the common practice of boundary layer treatments, we have kept the terms involving $\partial U_x/\partial x$ and $\partial U_r/\partial r$ even though they should be small with respect to $\partial U_x/\partial r$. It will be shown that some of the quantities related to these terms give rise to production of k which is by no means negligible.

Because of the cylindrical geometry, the third-order correlation $2\, \overline{u_r u_\theta^2}/r$ should appear in P_{rr} and, with the opposite sign, in $P_{\theta\theta}$. We have neglected these higher order correlations but without being too confident that it is appropriate to do so. A clarification of this issue should not be postponed, particularly considering the fact that the k-ε model is known to require special adjustments when applied to axisymmetric forced jets[2].

Dissipation of turbulence kinetic energy (ε). In dealing with the terms P_ε and ε_ε representing production and dissipation of ε, both of which require modeling, we follow standard k-ε practice[2,7] and write:

Table 1. Conservation Equations and ASM Formulas Used by the Model

$$\frac{\partial(\overline{\rho}U_x)}{\partial x} + \frac{1}{r}\frac{\partial(r\overline{\rho}U_r)}{\partial r} = 0 \tag{1}$$

$$\overline{\rho}U_x\frac{\partial U_x}{\partial x} + \overline{\rho}U_r\frac{\partial U_x}{\partial r} = \frac{1}{r}\frac{\partial}{\partial r}\left[r\left(\mu\frac{\partial U_x}{\partial r} - \overline{\rho}\,\overline{u_x u_r}\right)\right] - \frac{\partial}{\partial x}\left[\overline{\rho}\left(\overline{u_x^2} - \overline{u_r^2}\right)\right] + a_g\left(\rho_0 - \overline{\rho}\right) \tag{2}$$

$$\overline{\rho}U_x\frac{\partial T}{\partial x} + \overline{\rho}U_r\frac{\partial T}{\partial r} = \frac{1}{r}\frac{\partial}{\partial r}\left[r\left(\frac{\mu}{\sigma}\frac{\partial T}{\partial r} - \overline{\rho}\,\overline{tu_r}\right)\right] - \frac{\partial}{\partial x}\left[\overline{\rho}\,\overline{tu_x}\right] \tag{3}$$

$$\overline{\rho}U_x\frac{\partial \gamma}{\partial x} + \overline{\rho}U_r\frac{\partial \gamma}{\partial r} = \frac{1}{r}\frac{\partial}{\partial r}\left[r\left(\frac{\mu}{\sigma_\gamma} + \overline{\rho}\,c_\gamma\frac{k}{\varepsilon}\overline{u_r^2}\right)\frac{\partial \gamma}{\partial r}\right] + \overline{\rho}\left(P_\gamma - \varepsilon_\gamma\right) \tag{4}$$

$$\frac{\overline{u_x u_r}}{k} = \frac{k}{\varepsilon}(1-c_2)\left(-\frac{\overline{u_r^2}}{k}\frac{\partial U_x}{\partial r} - a_g\frac{\overline{\rho' u_r}}{\overline{\rho}k}\right)\Bigg/\left[X_k + \frac{k}{\varepsilon}(1-c_2)\left(\frac{\partial U_x}{\partial x} + \frac{\partial U_r}{\partial r}\right)\right] \tag{5.1}$$

$$\frac{\overline{u_i^2}}{k} = \left[(1-c_2)\frac{P_{ii}}{\varepsilon} + \frac{2}{3}c_2\frac{P_k}{\varepsilon} + \frac{2}{3}(c_1-1)\right]\Big/X_k \tag{5.2}$$

$$X_k = \frac{P_k}{\varepsilon} + c_1 - 1 \tag{5.3}$$

$$\overline{tu_x} = \frac{k}{\varepsilon}\left[-\overline{u_x^2}\frac{\partial T}{\partial x} - \overline{u_x u_r}\frac{\partial T}{\partial r} + (1-c_{t2})\left(-\overline{tu_r}\frac{\partial U_x}{\partial r} - \frac{1}{\rho}a_g\,\overline{t\rho'}\right)\right]\Bigg/\left[X_{kg} + \frac{k}{\varepsilon}(1-c_{t2})\frac{\partial U_x}{\partial x}\right] \tag{6.1}$$

$$\overline{tu_r} = \frac{k}{\varepsilon}\left[-\overline{u_r u_x}\frac{\partial T}{\partial x} - \overline{u_r^2}\frac{\partial T}{\partial r}\right]\Bigg/\left[X_{kg} + \frac{k}{\varepsilon}(1-c_{t2})\frac{\partial U_r}{\partial r}\right] \tag{6.2}$$

$$X_{kg} = \frac{1}{2}\left(\frac{P_k}{\varepsilon} - 1\right) + \frac{1}{2}\frac{k}{g}\frac{\varepsilon_g}{\varepsilon}\left(\frac{P_g}{\varepsilon_g} - 1\right) + c_{t1} \tag{6.3}$$

$$-\frac{1}{\rho}\overline{\rho' u_i} = \frac{1}{T}\overline{tu_i} \quad ; \quad -\frac{1}{\rho}\overline{t\rho'} = \frac{1}{T}g \tag{7}$$

$$P_\varepsilon = \frac{\varepsilon}{k}\left[c_{\varepsilon 1}P_k - \left(c_{\varepsilon 3} - c_{\varepsilon 1}\right)a_g\frac{1}{\rho}\overline{\rho' u_x}\right] \tag{10}$$

$$\varepsilon_\varepsilon = c_{\varepsilon 2}\frac{\varepsilon^2}{k} \tag{11}$$

The above expressions are based on little more than dimensional analysis; therefore, one should not be excessively optimistic in estimating their performance in a buoyant flow.

The constant $c_{\varepsilon 3}$ was introduced for the sake of generality, since there is no a priori argument saying that the sources of k associated with mean strain and buoyancy should be equally effective as sources of ε. In fact, Hossain and Rodi[8] have observed that different values of $c_{\varepsilon 3}$ are required to match experimental data on horizontal and vertical buoyant jets. The choice, made in this study, to set $c_{\varepsilon 3} = c_{\varepsilon 1}$ should be regarded as subject to possible revision as more information becomes available on the performance of the model in different situations involving buoyant flows.

Mean square temperature fluctuations (g). **The source of temperature fluctuations is given by:**

$$P_g = -2\,\overline{tu_x}\frac{\partial T}{\partial x} - 2\,\overline{tu_r}\frac{\partial T}{\partial r} \tag{12}$$

As for the case of P_k, no modeling is necessary since the terms appearing in the definition of P_g are all calculable. Note that the contribution from the longitudinal component of the turbulent heat flux is taken into account.

In the modeling of the dissipation, ε_g, we follow the standard k-ε-g approach, which was first proposed by Spalding[9] as:

$$\varepsilon_g = c_{g2}\frac{\varepsilon}{k}g \tag{13}$$

There is indication that eq (13) may not be adequate to model ε_g; the unusually high value (2.80) used in this work for the constant c_{g2} tends to confirm that opinion. In Reference[6] we suggest the possibility that the increase in the value of c_{g2} is due to the fact that buoyancy distorts the turbulence all the way down to the dissipation scale. To account for such effect we propose to write:

$$c_{g2} = c_{g2,is} \frac{8}{81} \sum_i f_i^{-2} \left(\frac{\overline{u_i^2}}{k}\right)^{-3} \tag{14}$$

where the constant $c_{g2,is}$ can be obtained from data on the decay of temperature fluctuations in isotropic turbulence. The functions f_i (for $i=x,r,\theta$) are "memory" factors, which are as yet unknown, but probably depend on the flux Richardson number, R_f, and the ratios, P_k/ε and P_g/ε_g.

The proposal of eq (14) is still at an early stage of development; it might turn out that the modeling of the functions f_i is so complex as to make the solution of a separate transport equation for ε_g a more attractive alternative. It should be mentioned that Zeman and Lumley[3] and Meroney[5] have already undertaken the latter approach and that Launder[10] also argues for it.

Reynolds stresses $(\overline{u_i u_j})$. The starting point for the modeling of the Reynolds stresses is represented by the transport equation for $\overline{u_i u_j}$ developed by Launder et al[7]. Rodi's proposal[4] for algebraic stress modeling eliminates from the equation the terms containing derivatives of $\overline{u_i u_j}$ by assuming:

$$(C-D)_{ij} = \frac{\overline{u_i u_j}}{k} (C-D)_k \tag{15}$$

where the quantity in the left-hand side represents the net balance between convection (C) and diffusion (D) of the Reynolds stress, $\overline{u_i u_j}$. Rodi[4] has shown that eq (15) can be obtained by neglecting gradients of $\overline{u_i u_j}/k$ across the flow. In the case of k, convection minus diffusion equals production minus dissipation; with a little algebra one can see that introducing the above assumption in the model equation for $\overline{u_i u_j}$ leads to the algebraic expressions given as eqs (5.1)-(5.3) in Table 1.

As anticipated in the introduction, the model can now account in some approximate way for the anisotropic distribution of turbulence kinetic energy among its components (eq (5.2)) as well as for the direct effect of buoyancy on the shear stress (eq (5.1)). The constants c_1 and c_2, which appear in the final expressions, arise from the modeling of the pressure-velocity correlations. The values selected for these constants are 1.5 and .6 respectively[7].

Turbulent heat flux components, $\overline{tu_i}$. In order to obtain expressions for the correlations $\overline{tu_i}$ we use the model transport equation for these quantities proposed by Launder[11], and apply Rodi's concept for algebraic stress modeling in the form:

$$(C-D)_{\overline{tu_i}} = \overline{tu_i} \left[\frac{1}{2\overline{u_i^2}} (C-D)_{\overline{u_i^2}} + \frac{1}{2\overline{t^2}} (C-D)_{\overline{t^2}} \right] \tag{16}$$

After introducing eq (16) in the transport equation for $\overline{tu_i}$ and taking advantage of eq (15) it is possible to obtain the algebraic expressions for $\overline{tu_x}$ and $\overline{tu_r}$ given as eqs (6.1)-(6.3) in Table 1. This operation uses the fact that the terms representing production and dissipation of $g \equiv \overline{t^2}$ can be substituted for those indicating convection and diffusion of g in the right hand side of eq (16).

The values of 3.5 and .5 are assigned to the two constants, c_{t1} and c_{t2}, appearing in the ASM formulas for the two components of the turbulent heat flux, $\overline{tu_x}$ and $\overline{tu_r}$. These two constants are similar to c_1 and c_2, arising in the $\overline{u_i u_j}$-equation, since they appear in the modeling of the pressure-temperature correlations. For the correlations involving density fluctuations, we assume that the flow follows the perfect gas law and, therefore, adopt the relationships given as eq (7) in Table 1.

As a consequence of the extension of the ASM approach to the modeling of $\overline{tu_i}$, there is no need to prescribe separately the value of the turbulent Prandtl number, σ_τ. Instead, σ_τ can be calculated from:

$$\sigma_\tau = \frac{\overline{u_x u_r}}{\overline{tu_r}} \left(\frac{\partial T}{\partial r}\right) \Big/ \left(\frac{\partial U_x}{\partial r}\right) \tag{17}$$

Choice of Model Constants

The model outlined in the preceding sections contains 11 constants, for which values must be selected. In our earlier work [6] we have not undertaken a systematic optimization effort, since we have considered only a limited number of flows, namely, forced and buoyant axisymmetric jets. As a general rule, we have adopted the values which users of k-ε-g or Reynolds stress techniques seem to agree upon and we have made changes only where strictly necessary. The final set used for the calculations performed in the course of this study is shown in Table 2. The laminar Prandtl numbers σ_k, σ_ε and σ_g in the three versions of eq (4) for k, ε and g do not significantly affect the results of the prediction. In any case, their values are not subject to choice since the exact equations for k, ε and g show that: $\sigma_k = \sigma_\varepsilon = 1$ and $\sigma_g = \sigma$ (= .7).

Of the constants in Table 2, c_{g2} is the only one taking a value significantly different from those that have appeared in the literature. Spalding[9] for his predictions of concentration fluctuations in a round forced jet adopted $c_{g2} = 1.79$ and recently [8,11] there has been a tendency toward the use of values as low as 1.25. We have already commented on the possibility that small-scale anisotropy is responsible for the spread among the values for c_{g2}; however, we did not make use of eq (14) in this study.

A related question arises in connection with the choice of the constant $c_{\varepsilon 3}$. If the turbulence is isotropic at the scale at which dissipation takes place, $c_{\varepsilon 3}$ must be equal to zero [6]. The fact that our predictions indicate $c_{\varepsilon 3} = c_{\varepsilon 1} = 1.44$ may mean that the assumed small-scale isotropy does not exist or that inadequate modeling of some other term requires a "wrong" value for $c_{\varepsilon 3}$ to offset that error. Whatever the final conclusion, it is clear that this point needs to be resolved.

Boundary and Initial Conditions

Five differential equations for U_x, T, k, ε and g are solved using the Patankar-Spalding method[12] for parabolic flows. The transverse velocity U_r is obtained from the continuity equation. In the case of the round buoyant jet predicted here the dependent variables assume the ambient values ($U_x = k = \varepsilon = g = 0$, $T = T_0 = 302$ K) at the outer edge of the initial shear layer and the nozzle values ($U_x = U_{x,1} = .674$ m/s, $T = T_1 = 573$ K) at the inner edge. When the inner edge reaches the jet axis, the symmetry condition is imposed on the radial derivatives of the variables.

Table 2. Model Constants

$\overline{u_i u_j}$-formulas/k-equation			$\overline{tu_i}$-formulas		g-equation		ε-equation			
c_1	c_2	c_k	c_{t1}	c_{t2}	c_g	c_{g2}	c_ε	$c_{\varepsilon 1}$	$c_{\varepsilon 2}$	$c_{\varepsilon 3}$
1.5	.6	.21	3.5	.5	.3	2.8	.15	1.44	1.92	1.44

Establishing a set of initial conditions is easy for velocity and temperature (top-hat profiles were selected in the nozzle flow) but presents problems with regard to the turbulence quantities. The turbulence model used here cannot cope with low-Reynolds number turbulence, much less transition. Therefore, to be rigorous one should use the model starting at a station where the turbulence is fully developed and where radial profiles of k, ε and g are available. We follow the practice to begin the calculation at the nozzle lip by assuming laminar flow. Turbulence is then "turned on" at an arbitrary distance from the nozzle by selecting initial profiles for k, ε and g given by:

$$k = 10^{-4}\, U_x^2 \tag{18.1}$$

$$\varepsilon = k^{3/2}/r_1 \tag{18.2}$$

$$g = 10^{-4}\, (T_1 - T)(T - T_0) \tag{18.3}$$

where r_1(= .0318 m) is the nozzle radius. The location for the beginning of the turbulent calculation is then adjusted so that the virtual origin of the computed flow matches that given by the experiment.

Note that the retention of laminar diffusion in eqs (2)-(4) does not represent an attempt to account for low turbulence Reynolds number effect, but is required to insure sufficient diffusion in the first steps of the turbulent calculation, when the flow is still essentially laminar.

EXPERIMENTAL DATA

Recently there has been renewed interest in turbulent buoyant jets and experimental investigations of the structure of the turbulence in axisymmetric plumes have finally appeared[13,14]. This follows a 20-year interval during which Yih's measurements[15] for the profiles of mean temperature and vertical velocity have remained practically unchallenged. In the present study we have used the data by George et al[13], since we believe them to be more reliable. To justify this choice, however, we will describe the points on which the three cited studies agree and try to explain the differences.

The profiles of mean excess (over the ambient) temperature (ΔT) and vertical velocity (U_x) are usually presented in dimensionless form by giving their Gaussian fits:

$$\left(\frac{x}{F_0}\right)^{1/3} U_x = A_u \exp\left[-\,B_u\,(r/x)^2\right] \tag{19}$$

$$a_g \left(\frac{x^5}{F_0{}^2}\right)^{1/3} \frac{\Delta T}{T} = A_t \exp\left[-\,B_t\,(r/x)^2\right] \tag{20}$$

where the buoyancy flux F_0 is related by $F_0 = a_g\, H/(c_p \rho_0 T_0)$ to the enthalpy flux, H, which in turn is given by:

$$H = 2\pi\, c_p \int_0^\infty \bar{\rho} U_x\, \Delta T \left(1 + \frac{\overline{tu_x}}{U_x \Delta T}\right) r\, dr \tag{21}$$

The following values are reported for the four constants A_u, B_u, A_t and B_t by References [13]-[15]:

	A_u	B_u	A_t	B_t
George et al[13]	3.4	55	9.1	65
Nakagome and Hirata[14]	-	39	-	63
Yih[15]	4.7	96	11	71

The three sets of data are in substantial agreement only with reference to the rate of spread of the temperature profile (constant B_t). Part of the difference between the values for A_t reported by George et al[13] and Yih[15] is due to the fact that the former evaluated H and, therefore, F_0 including the turbulent contribution (cf eq (21)) while the latter did not. If $\overline{tu_x}$ is neglected, the F_0 associated with George et al's data is reduced by 17 percent and the fit to the temperature data requires $A_t = 10.3$ instead of 9.1. One can conclude that the mean temperature profile is well established.

The situation is quite different for the velocity measurements. Yih's measurements, which were obtained using a fan anemometer, imply that the velocity profile is narrower than the temperature profile. The other two studies [13,14] come to the opposite result. In our opinion these are closer to the truth, since they involved a more reliable technique based on hot-wire anemometry with a procedure for the interpretation of the signal, which accounts for the instantaneous value of the temperature. Note that what is given by George et al[13] for B_u is a "recommended" value, which takes into account the possible overestimate of the one-wire probe near the edges of the plume. A fit through the actual data points would give $B_u = 45$, which is in good agreement with the value reported by Nakagome and Hirata[14].

Even though a final judgment probably must wait for measurements obtained with a velocity probe which does not suffer directional ambiguity, the above considerations are the basis for our choice of George et al's results for the comparisons with the model predictions discussed in the following section.

NUMERICAL PREDICTIONS

The model predictions for the radial profiles of mean and fluctuating components of vertical velocity and temperature are shown in dimensionless form in Figs 1-4. As can be seen, there is overall good agreement between theory and experiment for all four quantities. The calculated profiles of mean variables essentially reach the self-preserving state at about eight diameters, while those of the fluctuating components require more time. The model predicts that at the last station at which measurements were made by George et al[13], i.e., 16 diameters from the source, all profiles are self-preserving. However, since the

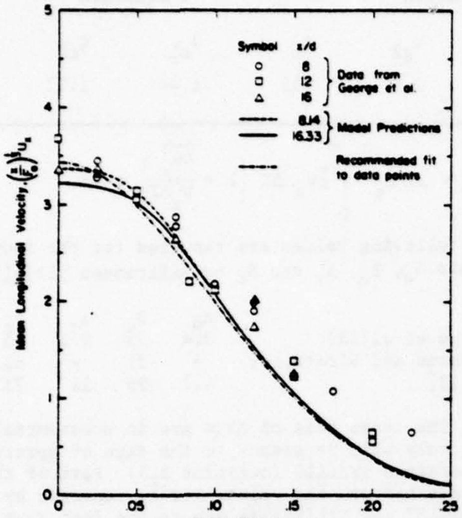

Fig. 1 Radial distribution of mean vertical velocity

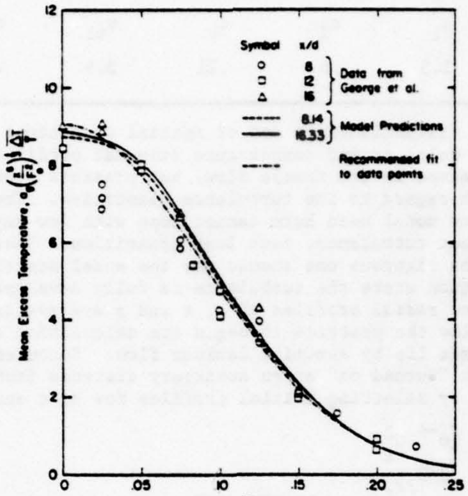

Fig. 2 Radial distribution of mean excess temperature

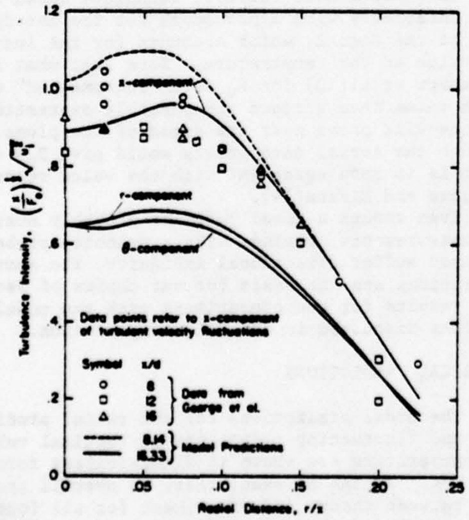

Fig. 3 Radial profiles of three components of turbulence intensity

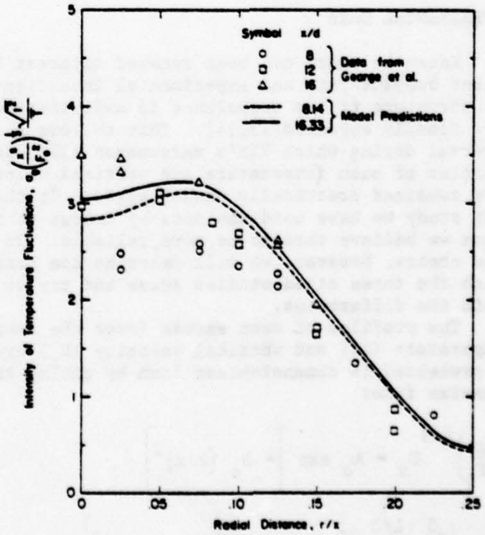

Fig. 4 Radial profiles of the intensity of temperature fluctuations

theory is not capable of accurately modeling the initial growth of the turbulence, the departure, which we believe to be small, of the conditions of the experiment from self-preservation should be judged on the basis of the data itself and not on the results of the prediction.

The calculated profile of shear stress shown in Fig 5 implies that the turbulent transport of momentum is greater than that calculated and measured for a round forced jet by about 45 and 90 percent respectively[6]. This result is contrasted by the observation that the longitudinal component of the turbulence intensity is of similar magnitude in the two cases $\left((\overline{u_x^2})^{1/2}/U_{x,c} \cong .28\right.$ on the axis of both flows and the rest of the radial profiles are also very similar$\left.\right)$. It is reasonable to infer that the action of buoyancy probably does not have a very strong effect on the level of the components of the turbulence kinetic energy.

The situation is quite different with reference to the temperature field. The relative intensity of temperature fluctuations, $(\overline{t^2})^{1/2}/\Delta T$, is measured by George et al[13] as being about .38 on the axis, while forced jet data for the same quantity seem to indicate a much lower value (~.22, cf Reference[6]). This result is particularly remarkable since buoyancy does not enter directly in the g-equation and should be evaluated by remembering the unusually large value of dissipation ($c_{g2} = 2.8$ in eq (13)), which is required to obtain a predicted level of temperature fluctuations in line with the experiment.

The turbulent Prandtl number, σ_T, gives an indication of the relative intensities of heat and momentum transport. The values plotted in Fig 5, which were calculated using eq (17), are in the range .7-.8 usually recommended for computing heat transfer in non-buoyant round jets.

A further indication of the fact that the buoyant jet has more vigorous lateral transport than the forced jet is given by the entrainment data plotted in Fig. 6. We have chosen to present these results by using the entrainment coefficient K, defined by Ricou and Spalding[16] as:

$$K = \frac{d\dot{M}}{dx} \Big/ \left(\rho_0 W\right)^{1/2} \qquad (22)$$

where $\dot{M}$ is the mass flux in the plume and W is the total momentum, given by:

$$W = 2\pi \int_0^\infty \overline{\rho}\, U_x^2 \left(1 + \frac{\overline{u_x^2} - \overline{u_r^2}}{U_x^2}\right) r\,dr \qquad (23)$$

The value of K calculated for the thermal plume is about .55, as indicated by the dashed line in Fig 6. If one neglected the turbulent contribution to W, which amounts to 8.3 percent of the total momentum, the asymptotic value of K would be about .57. The results for the forced jet, taken from Reference [6] and also shown in Fig 6, indicate in that case a much lower value of K=.29 and, therefore, a difference of almost a factor of two. This result points to the fact that alterations of the turbulence structure due to buoyancy can have a profound impact on overall characteristics of the flow, even though other indicators of the intensity of the fluctuations are less dramatically affected.

Since turbulence is "stretched' by gravity in the longitudinal direction, one would expect temperature and velocity fluctuations in that direction to be highly correlated. Therefore, a quantity of interest is the longitudinal component of the turbulent heat flux. The prediction of the model, presented in the form of a correlation coefficient, is shown in Fig 7. The data by George et al[13] indicate that this coefficient is roughly constant and equal to ~.67, while the data by Nakagome and Hirata[14], which have more scatter, imply a value of about .5. As can be seen, the numerical predictions fall somewhere between these two sets of data. Selecting a value of .3, instead of .5, for c_{t2} would make the calculated correlation coefficient agree almost exactly with George et al's measurements. This indication is in agreement with the recommendations contained in the recent review by Launder[10] and suggests that only 30, instead of 50 percent, of the heat flux generated by mean strain and buoyancy is directly removed by the pressure fluctuations.

Note that the numerical model predicts that 12 percent (the data of George et al would indicate 17 percent) of the total longitudinal heat flux is contributed by the turbulent fluctuations. If the corresponding turbulent term in the energy equation (cf eq (3) in Table 1) were neglected, the calculated mean temperatures would be too large by 10-20 percent, because the total heat flux, H, is conserved in the thermal plume and there is no contribution to H due to

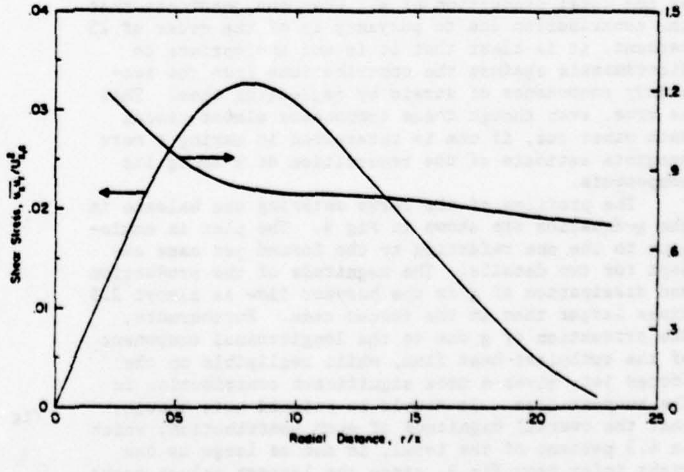

Fig. 5 Calculated radial profiles of turbulent shear stress and Prandtl number

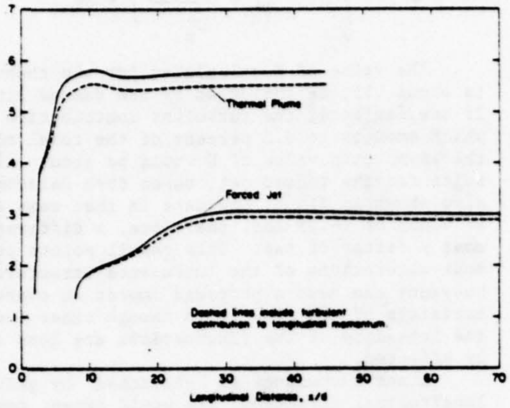

Fig. 6 Calculated variation of the entrainment coefficient with distance from the source for forced [6] and buoyant jets (d=nozzle dia)

turbulence at the beginning of the calculation, where the flow is assumed to be laminar.

Before concluding, it is appropriate to consider the relative magnitudes of the different terms entering in the transport equations for k and g. We will do so by discussing the profiles in Figs 8 and 9 and by making reference to the forced jet case, studied elsewhere[6]. With regard to the balance for the turbulence kinetic energy (Fig 8), the results in Reference [6] show that the normalized magnitude of the dissipation in the thermal plume is very close to that obtained for the forced jet. The production terms, however, are quite different: the total k-production is some 20 percent lower than the total dissipation for the forced jet, 30 percent higher for the buoyant jet.

The interesting result is that direct buoyancy effects, through the term $-a_g \overline{\rho' u_x}/\overline{\rho}$, are only partially responsible for the excess production of k; the rest of this excess comes from higher levels of shear. In addition, there is a non-negligible effect due to the secondary components of the strain tensor.

The term $-\overline{u_x^2}\,(\partial U_x/\partial x)$, for example, has an overall negative contribution which amounts to 17 percent of the total production of k. When one considers that the contribution due to buoyancy is of the order of 23 percent, it is clear that it is not appropriate to discriminate against the contributions from the secondary components of strain by neglecting them. This is true, even though these components almost cancel each other out, if one is interested in making a more accurate estimate of the repartition of k among its components.

The profiles of the terms entering the balance in the g-equation are shown in Fig 9. The plot is analogous to the one referring to the forced jet case except for two details. The magnitude of the production and dissipation of g in the buoyant flow is almost 2.5 times larger than in the forced case. Furthermore, the production of g due to the longitudinal component of the turbulent heat flux, while negligible in the forced jet, gives a more significant contribution in the buoyant case. It should be pointed out, though, that the overall magnitude of such contribution, which is 6.3 percent of the total, is not as large as one might infer from Fig 9, since the largest values occur near the axis. Despite this result, which shows the overall effect not to be too important, we would argue that the term should be included, since its magnitude may be much greater in buoyant flows other than the one examined here, particularly considering that the term in question can be evaluated using the ASM approach with very little effort.

CONCLUSIONS

We have presented theoretical predictions of an axisymmetric buoyant jet, which are based on an improved version of the k-ε-g technique. The improvement was obtained by finding approximate algebraic solutions to model equations for the Reynolds stresses and for the components of the turbulent heat flux. This algebraic stress modeling (ASM) approach allows for departures of the large-scale eddies from isotropy, without requiring the solution of a large number of differential equations. In addition, the production of turbulence kinetic energy directly associated with buoyancy can be evaluated with no further assumptions.

Since the formulation of the model was such that terms, which are usually neglected in boundary layer treatments, could be evaluated with little additional effort, some of these terms were included in the computations. As a result, we found that:

1 The longitudinal component of the turbulent heat flux accounts for 12-17 percent of the total heat flux in the plume;

2 The secondary components of the strain tensor give a significant contribution to the production of turbulence kinetic energy;

3 The source of temperature fluctuations associated with the longitudinal turbulent heat flux, while only 6.3 percent of the total in the case considered, can be of greater importance in other situations.

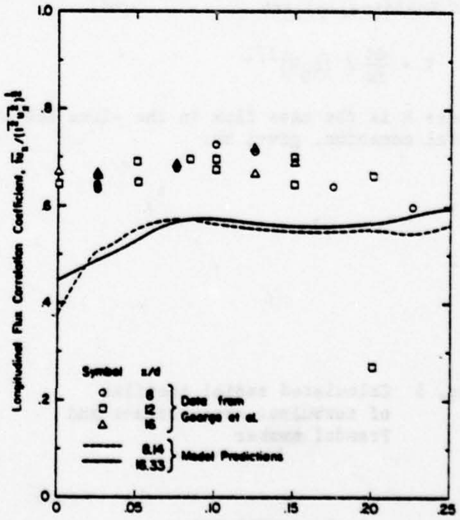

Fig. 7 Radial profile of vertical component of turbulent heat flux

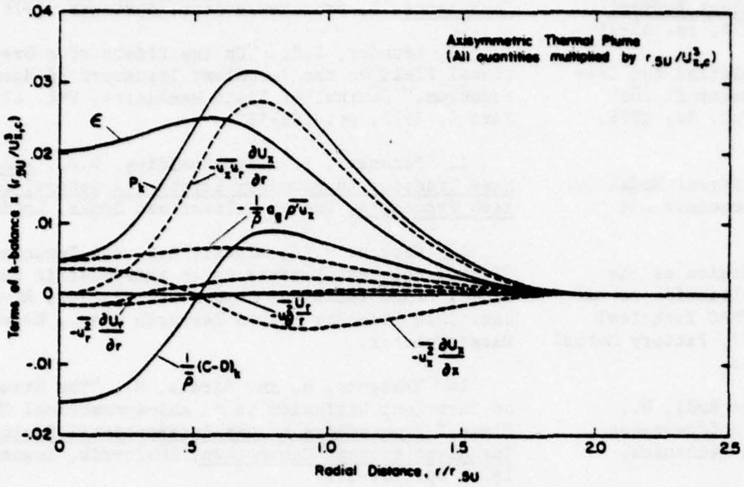

Fig. 8 Radial distribution of production/dissipation terms in the k-equation. The radius $r_{.5U}$ represents the distance from the axis at which the vertical velocity U_x reaches half its centerline value.

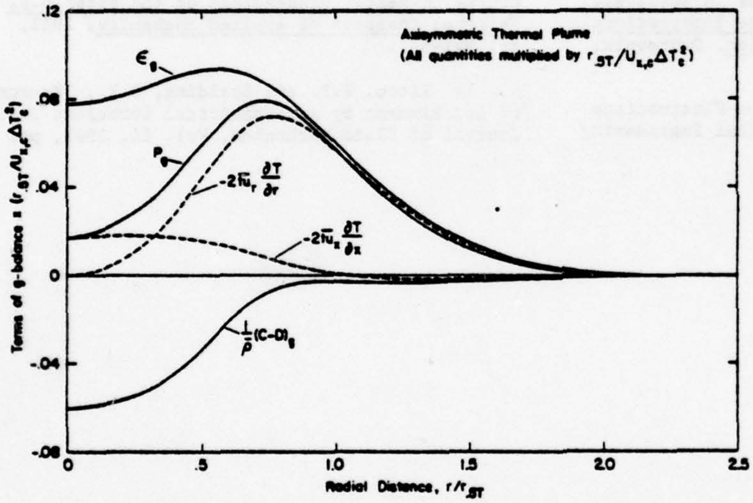

Fig. 9 Radial distribution of production/dissipation terms in the g-equation. The radius $r_{.5T}$ represents the distance from the axis at which the excess temperature ΔT reaches half its centerline value.

Somewhat unexpected was the need to increase the magnitude of the dissipation of temperature fluctuations by choosing a large value (2.80) for the constant c_{g2}. We postulate that part of such increase is due to buoyancy-induced anisotropy at the scale, where dissipation takes place. Related to this question is the modeling of the term representing production of ε due to buoyancy; if turbulence were isotropic at the dissipation scale, such a term should be negligible. The fact that our calculations indicate that it cannot be neglected seems to further challenge the assumption of small-scale isotropy. We realize that this result is not conclusive; however, it raises some questions as to the extent of the improvements of the modeling technique which are required when buoyancy is present.

ACKNOWLEDGMENTS

The author is grateful to John de Ris of Factory Mutual Research Corporation for continuous advice and encouragement. The study was internally sponsored and the support of the Research Corporation is acknowledged.

REFERENCES

1 Launder, B.E. and Spalding, D.B., Mathematical Models of Turbulence, Academic Press, London and New York, 1972.

2 Launder, B.E., Morse, A., Rodi, W. and Spalding, D.B., "Prediction of Free Shear Flows-A Comparison of the Performance of Six Turbulence Models," Proceedings Of The Conference On Turbulent Shear Flows, NASA Langley Research Center, NASA SP-321 (N73-28154-173), July 1972, pp. 361-426.

3 Zeman, O. and Lumley, J.L., "A Second-Order Model for Buoyancy-Driven Mixed Layers," Proceedings of the International Seminar on Turbulent Buoyant Convection, Dubrovnik, Yugoslavia, 1976, pp. 65-76.

4 Rodi, W., "A New Algebraic Relation for Calculating the Reynolds Stresses," Zeitschrift für Angewandte Mathematik und Mechanik, Vol. 56, 1976, pp. 219-221.

5 Meroney, R.N., "An Algebraic Stress Model for Stratified Turbulent Shear Flows," Computers and Fluids, Vol. 4, 1976, pp. 93-107.

6 Tamanini, F., "An Improved Version of the k-ε-g Model of Turbulence and Its Application to Axisymmetric Forced and Buoyant Jets," FMRC Technical Report No. 22360-4, RC-B-63, Feb. 1977, Factory Mutual Research Corp., Norwood, Massachusetts.

7 Launder, B.E., Reece, G.J. and Rodi, W., "Progress in the Development of a Reynolds-Stress Turbulence Closure," Journal of Fluid Mechanics, Vol. 68, Part 3, 1975, pp. 537-566.

8 Hossain, M.S. and Rodi, W., "Influence of Buoyancy on the Turbulence Intensities in Horizontal and Vertical Jets," Proceedings of the International Seminar on Turbulent Buoyant Convection, Dubrovnik, Yugoslavia, 1976, pp. 39-51.

9 Spalding, D.B., "Concentration Fluctuations in a Round Turbulent Free Jet," Chemical Engineering Science, Vol. 26, 1971, pp. 95-107.

10 Launder, B.E., "Heat and Mass Transport by Turbulence," Chapter 6 in Topics in Applied Physics - Turbulence, P. Bradshaw editor, Springer, 1976.

11 Launder, B.E., "On the Effect of a Gravitational Field on the Turbulent Transport of Heat and Momentum," Journal of Fluid Mechanics, Vol. 67, Part 3, 1975, pp. 569-581.

12 Patankar, S.V. and Spalding, D.B., Heat and Mass Transfer in Boundary Layers. A General Calculation Procedure, 2nd ed., Intertext Books, London, 1970.

13 George, W.K., Alpert, R.L. and Tamanini, F., "Turbulence Measurements in an Axisymmetric Buoyant Plume," FMRC Technical Report No. 22359-2, RC-B-53, Jan. 1976, Factory Mutual Research Corp., Norwood, Massachusetts.

14 Nakagome, H. and Hirata, M., "The Structure of Turbulent Diffusion in an Axi-symmetrical Thermal Plume," Proceedings of the International Seminar on Turbulent Buoyant Convection, Dubrovnik, Yugoslavia, 1976, pp. 361-372.

15 Yih, C.S., "Free Convection Due to a Point Source of Heat," Proceedings of the First U.S. National Congress of Applied Mechanics, 1952, pp. 941-947.

16 Ricou, F.P. and Spalding, D.B., "Measurements of Entrainment by Axisymmetrical Turbulent Jets," Journal of Fluid Mechanics, Vol. 11, 1961, pp. 21-32.

A MATHEMATICAL MODEL FOR THE PREDICTION OF PLUME RISE IN STRATIFIED FLOWS

by

Michael Schatzmann
Sonderforschungsbereich 80
University of Karlsruhe, W. Germany

ABSTRACT

In this paper a mathematical model is presented for the prediction of spreading and rising of submerged round buoyant jets discharged into a stratified, flowing ambient fluid. This is the type of flow that exists in the emission of hot chimney gases into the atmosphere or of cooling water into the ocean or lakes.

The model is based on the differential equations for the conservation of mass, momentum, concentration and thermal energy. These are transformed by vector operations in a streamwise coordinate system and integrated in the angular and radial directions using symmetry and similarity assumptions. The resulting set of non-linear first-order differential equations differs from the equations developed by other authors who have also applied the integral method (sec. 2).

In order to achieve closure a new entrainment function is derived by combining the mean kinetic energy equation with the integral form of the s-momentum equation (sec. 3). This function contains five empirically fitted coefficients, held constant over all subsequent predictions. Adding the equation of state for air in a potential atmosphere, the set of equations can be solved numerically.

As a consequence of the assumptions used in the derivation, the simulation model is restricted to initially round, buoyant or non-buoyant jets with two-dimensional trajectories discharged continuously into non-recirculating flows with approximately uniform background velocity. However, ambient turbulence and density stratification due to non-uniform temperature or salinity distribution are permitted, even if the density gradient changes layerwise, in contrast to other models. Furthermore, the density difference between jet and ambient flow may be large because the common Boussinesq assumption was not used.

The mathematical model was tested by comparing the results with published data for about 80 different jet flows. These flows range from the simple momentum jet to buoyant plumes in stratified cross-winds with temperature inversion. Section 5 gives some examples of the good agreement between prediction and experiment.

NOMENCLATURE

A_i	entrainment coefficients
b	nominal jet radius (equ. 2.17)
C	circumference of the jet
c	concentration ($c = \bar{c} + c'$)
c_D	drag coefficient
c_p	specific heat at constant pressure
D	jet diameter
E	entrainment rate (equ. 2.25)
$\mathbb{F}$	local densimetric Froude number
$\mathbb{F}r$	Froude number (sec. 5)
$\vec{g}$	gravity vector
$\vec{i}, \vec{j}, \vec{k}$	unit vectors (x, y, z-system)
$\vec{i}_s, \vec{i}_r, \vec{i}_\phi$	unit vectors (i, r, ϕ-system)
L_∞	macro scale of the energy-containing eddies
p	pressure
R	local jet radius, $R = \sqrt{2} \cdot b$
$r_{1/2}$	half-width of the mean excess velocity profile
s, r, ϕ	coordinates of the streamwise system
T	absolute temperature
u, v, w	local velocity components in the s, r, ϕ-directions, respectively. ($u = \bar{u} + u' = u_g + u_d + u'$, etc.)
u_∞	free-stream velocity
u_g, v_g, w_g	free-stream velocity components in the s, r, ϕ-directions, respectively
u_d, v_d, w_d	excess velocity components in the s, r, ϕ-directions, respectively
$\overline{v'^2_\infty}$	free-stream turbulence intensity
$\bar{x}, \bar{y}, \bar{z}$	coordinates of the Cartesian system located at the jet exit

x, y, z	coordinates of the Cartesian system located at point $P(s_o, 0)$
z_{max}	maximum height of rise
Δz	local jet diameter, $\Delta z = 2 \cdot R(s)$
ε	dimensionless entrainment function (equ. 3.19)
θ	angle of the jet trajectory (fig. 2.1)
λ	spreading ratio (equ. 2.17)
ρ	density, $\rho = \bar{\rho} + \rho' = \rho_{\infty} + \rho_d + \rho'$
$(\ )_i$	at diffuser outlet ($s = 0$)
$(\ )_o$	at end of flow establishment zone ($s = s_o$)
$(\ )_{\infty}$	free stream value
$(\ )_p$	quantity of the potential system (sec. 4)
$\overline{(\ )}$	time averaged value
$(\ )'$	fluctuating component
$(\ )_d$	excess component, e.g. $u_d = \bar{u} - u_g$
$(\ )_g$	free-stream component, e.g. $u_g = \bar{u} - u_d$
$(\ )^*$	excess component at the jet center line, e.g. $u^* = u_d(s, 0)$

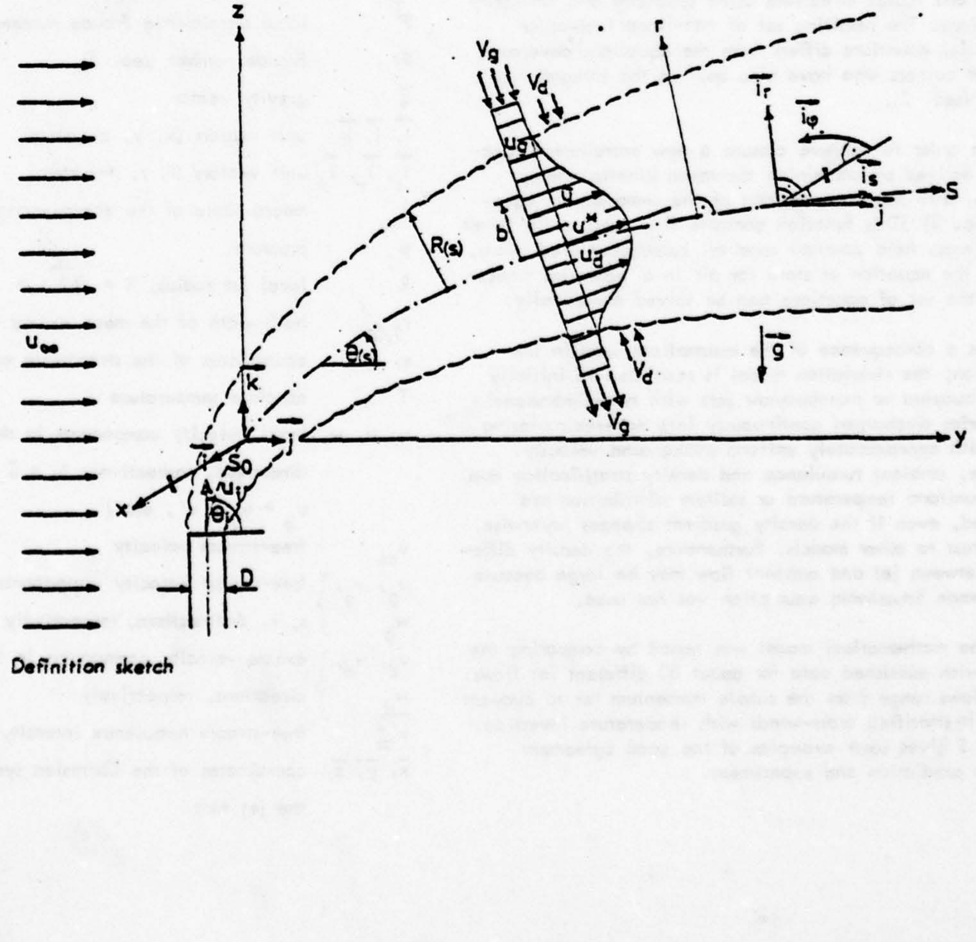

Fig. 2.1: Definition sketch

1. INTRODUCTION

The emission of noxious gases into the atmosphere or of sewage into rivers and lakes is often unavoidable for technical reasons. Furthermore, it would be very wasteful not to use natural recycling processes. However, to protect our environment it is necessary that

- only such pollutants are exhausted which are degradable,
- the total amount of each pollutant is matched to natures ability to degrade these pollutants,
- the local concentrations of each pollutant remains below a tolerable value.

To fulfill these requirements interdisciplinary research is needed. Biologists and chemists must investigate the effects of certain concentrations of pollutants on human life and the ecological system in general. Fluid mechanics engineers and physicists have to predict the plume path and the dilution so as to design optimal discharge equipment and to give the basis for ecological assessment.

2. DERIVATION OF THE INTEGRAL FORM OF EQUATIONS GOVERNING THE JET BEHAVIOR

From a mathematical point of view the spreading of a jet is an initial value problem, which is exactly described by the basic differential equations of fluid mechanics and the appropriate boundary conditions. By applying the principles of conservation of mass, momentum and thermal energy to a turbulent flow which is steady with respect to the mean motion, the following equations in general vector form are obtained /16/:

continuity equation of mass:

$$\overline{v}\cdot\operatorname{grad}\varrho+\varrho\cdot\operatorname{div}\overline{v}=0 \tag{2.1}$$

continuity equation of momentum:

$$\varrho\cdot\left(\frac{1}{2}\cdot\operatorname{grad}\overline{v}^2-\overline{v}\times\operatorname{rot}\overline{v}\right)=-\operatorname{grad}\varrho+\varrho\cdot\overline{g} \tag{2.2}$$

continuity equation of a scalar quantity:

$$\overline{v}\cdot\operatorname{grad}(\varrho\cdot c)+\varrho\cdot c\cdot\operatorname{div}\overline{v}=0 \tag{2.3}$$

continuity equation of thermal energy:

$$\overline{v}\cdot\operatorname{grad}(\varrho\cdot T)+\varrho\cdot T\cdot\operatorname{div}\overline{v}=0 \tag{2.4}$$

with velocity vector $\vec{v}$, density ϱ, concentration c, temperature T, pressure p and gravity vector $\vec{g}$ (see fig. 2.1).

After resolving the local pressure gradient into the hydrostatic pressure gradient and the remaining difference gradient, grod p_d, introducing a system of orthogonal curvilinear coordinates (s, r, ø) as done by Hirst /11/ it follows:

continuity equation of mass:

$$\varrho\left[\frac{1}{1-\varkappa}\cdot\frac{\partial u}{\partial s}+\frac{1}{r}\frac{\partial}{\partial r}(r\cdot v)+\frac{1}{r}\frac{\partial w}{\partial\varphi}-\frac{v}{1-\varkappa}\cdot\frac{\varkappa}{r}-\frac{w}{1-\varkappa}\cdot\frac{1}{r}\frac{\partial\varkappa}{\partial\varphi}\right]+\frac{u}{1-\varkappa}\cdot\frac{\partial\varrho}{\partial s}+v\frac{\partial\varrho}{\partial r}+\frac{w}{r}\cdot\frac{\partial\varrho}{\partial\varphi}=0 \tag{2.5}$$

momentum equation in s-direction:

$$\varrho\cdot\left\{u\cdot\frac{\partial u}{\partial s}+v\cdot\frac{\partial u}{\partial r}\cdot(1-\varkappa)+\frac{1}{r}\left[w\frac{\partial u}{\partial\varphi}(1-\varkappa)-u\cdot w\frac{\partial\varkappa}{\partial\varphi}-u\cdot v\cdot\varkappa\right]\right\}=(\varrho_\infty-\varrho)\cdot g\cdot\sin\Theta\cdot(1-\varkappa)-\frac{\partial p_d}{\partial s} \tag{2.6}$$

momentum equation in y-direction:

$$\begin{aligned}&\varrho\cdot\left\{u\cdot\frac{\partial u}{\partial s}+v\cdot\frac{\partial u}{\partial r}\cdot(1-\varkappa)+\frac{1}{r}\left[w\cdot\frac{\partial u}{\partial\varphi}\cdot(1-\varkappa)-u\cdot w\cdot\frac{\partial\varkappa}{\partial\varphi}-u\cdot v\cdot\varkappa\right]\right\}\cdot\cos\Theta\\&-\varrho\cdot\left\{u\cdot\frac{\partial v}{\partial s}\cdot\sin\varphi+v\cdot\frac{\partial v}{\partial r}\cdot(1-\varkappa)\cdot\sin\varphi+u\cdot\frac{\partial w}{\partial s}\cdot\cos\varphi+v\cdot\frac{\partial w}{\partial r}\cdot(1-\varkappa)\cdot\cos\varphi\right.\\&\quad+\frac{1}{r}\left[w\frac{\partial v}{\partial\varphi}(1-\varkappa)\cdot\sin\varphi-w^2\cdot(1-\varkappa)\cdot\sin\varphi+u^2\cdot\varkappa\cdot\sin\varphi+w\frac{\partial w}{\partial\varphi}(1-\varkappa)\cos\varphi\right.\\&\qquad\left.\left.+v\cdot w\cdot(1-\varkappa)\cdot\cos\varphi+u^2\cdot\frac{\partial\varkappa}{\partial\varphi}\cdot\cos\varphi\right]\right\}\cdot\sin\Theta\\&=-\frac{\partial p_d}{\partial s}\cdot\cos\Theta+\frac{\partial p_d}{\partial r}\cdot(1-\varkappa)\cdot\sin\varphi\cdot\sin\Theta+\frac{1}{r}\frac{\partial p_d}{\partial\varphi}\cdot(1-\varkappa)\cdot\cos\varphi\cdot\sin\Theta\end{aligned} \tag{2.7}$$

momentum equation in z-direction:

$$\begin{aligned}&\varrho\cdot\left\{u\frac{\partial u}{\partial s}+v\frac{\partial u}{\partial r}\cdot(1-\varkappa)+\frac{1}{r}\left[w\frac{\partial u}{\partial\varphi}(1-\varkappa)-u\cdot w\frac{\partial\varkappa}{\partial\varphi}-u\cdot v\cdot\varkappa\right]\right\}\cdot\sin\Theta\\&+\varrho\cdot\left\{u\frac{\partial v}{\partial s}\cdot\sin\varphi+v\frac{\partial v}{\partial r}\cdot(1-\varkappa)\cdot\sin\varphi+u\frac{\partial w}{\partial s}\cdot\cos\varphi+v\frac{\partial w}{\partial r}\cdot(1-\varkappa)\cdot\cos\varphi\right.\\&\quad+\frac{1}{r}\left[w\frac{\partial v}{\partial\varphi}\cdot(1-\varkappa)\cdot\sin\varphi-w^2\cdot(1-\varkappa)\cdot\sin\varphi+u^2\cdot\varkappa\cdot\sin\varphi+w\frac{\partial w}{\partial\varphi}(1-\varkappa)\cos\varphi\right.\\&\qquad\left.\left.+v\cdot w\cdot(1-\varkappa)\cdot\cos\varphi+u^2\frac{\partial\varkappa}{\partial\varphi}\cdot\cos\varphi\right]\right\}\cdot\cos\Theta\\&=(\varrho_\infty-\varrho)\cdot g\cdot(1-\varkappa)-\frac{\partial p_d}{\partial s}\cdot\sin\Theta-\frac{\partial p_d}{\partial r}\cdot(1-\varkappa)\cdot\sin\varphi\cdot\cos\Theta-\frac{1}{r}\frac{\partial p_d}{\partial\varphi}(1-\varkappa)\cos\varphi\cdot\cos\Theta\end{aligned} \tag{2.8}$$

continuity equation of a scalar quantity:

$$u\cdot\frac{\partial c}{\partial s}+v\cdot\frac{\partial c}{\partial r}\cdot(1-\varkappa)+\frac{w}{r}\cdot\frac{\partial c}{\partial\varphi}\cdot(1-\varkappa)=0 \tag{2.9}$$

continuity equation of thermal energy:

$$u\cdot\frac{\partial T}{\partial s}+v\cdot\frac{\partial T}{\partial r}\cdot(1-\varkappa)+\frac{w}{r}\cdot\frac{\partial T}{\partial\varphi}\cdot(1-\varkappa)=0 \tag{2.10}$$

The unknowns u, v, w, ϱ, p_d, c and T are dependent upon s, r and ø, as is the shorthand notation $\varkappa = r\cdot\sin\phi\cdot d\Theta/ds$ resulting from the coordinate transformation.

Although the equations become more complicated, the field quantities must be resolved into their mean and turbulent parts ($u = \bar{u} + u'$ etc.) and the mean quantities into their background and excess components. If the system is to be integrated, this is the only way to insert the boundary conditions correctly. We define (see fig. 2.2):

$$\begin{aligned}\bar{u}&=u_g+u_d\\\bar{v}&=v_g+v_d\\\bar{w}&=w_g+w_d\\\bar{\varrho}&=\varrho_\infty+\varrho_d\\\bar{T}&=T_\infty+T_d\\\bar{c}&=c_\infty+c_d\end{aligned} \tag{2.11}$$

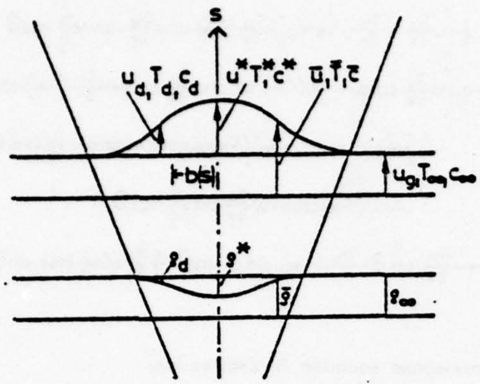

Fig. 2.2: Splitting of the mean quantities into excess and background components

Supposing the free-stream velocity u_∞ is approximately uniform, using the common Markovin-Hypotheses for flows of small Mach numbers /14/, assuming axial symmetry for the mean excess and turbulent quantities and substituting the unknown pressure gradient grad p_d by an empirical function for the pressure forces per jet segment ds, the following set of equations is obtained after integrating with respect to ϕ from $\phi = 0$ to $\phi = 2\pi$ /16/:

continuity equation of mass:

$$\frac{\partial}{\partial s}\left[\bar\varrho\cdot(u_g+u_d)\right]+\frac{1}{r}\frac{\partial}{\partial r}(r\cdot\bar\varrho\cdot v_d)-\frac{1}{2}\cdot\left(\frac{\partial u_g}{\partial s}\right)\cdot\frac{1}{r}\frac{\partial}{\partial r}(r^2\cdot\bar\varrho)=0 \tag{2.12}$$

s-momentum equation:

$$\begin{aligned}\frac{\partial}{\partial s}\left[\bar\varrho\cdot u_d\cdot(u_g+u_d)\right]+\frac{1}{r}\frac{\partial}{\partial r}(r\bar\varrho\cdot u_d\cdot v_d)-\frac{1}{2}\left(\frac{\partial u_g}{\partial s}\right)\frac{1}{r}\frac{\partial}{\partial r}(r^2\bar\varrho\cdot u_d)\\+\frac{1}{r}\frac{\partial}{\partial r}(r\cdot\bar\varrho\cdot\overline{v'u'})=(\varrho_\infty-\bar\varrho)\cdot g\cdot\sin\Theta\end{aligned} \tag{2.13}$$

y-momentum equation:

$$\begin{aligned}&\left\{\frac{\partial}{\partial s}\left[\bar\varrho\cdot u_d\cdot(u_g+u_d)\right]+\frac{1}{r}\frac{\partial}{\partial r}(r\cdot\bar\varrho\cdot u_d\cdot v_d)-\frac{1}{2}\left(\frac{\partial u_g}{\partial s}\right)\frac{1}{r}\frac{\partial}{\partial r}(r^2\cdot\bar\varrho\cdot u_d)\right.\\&\left.+\frac{1}{r}\frac{\partial}{\partial r}(r\cdot\bar\varrho\cdot\overline{v'u'})\right\}\cdot\cos\Theta-\left\{\bar\varrho\cdot u_d\cdot(u_g+u_d)+\frac{1}{2}v_d\frac{1}{r}\frac{\partial}{\partial r}(r^2\bar\varrho\cdot v_d)\right.\\&\left.-\frac{1}{2}\cdot\frac{1}{r}\cdot\frac{\partial}{\partial r}\left[r^2\cdot\bar\varrho\cdot(v_d+\overline{v'^2})\right]\right\}\cdot\sin\Theta\cdot\frac{\partial\Theta}{\partial s}\\&+\frac{1}{2}u_\infty\cdot\sin\Theta\cdot\left[\frac{1}{r}\frac{\partial}{\partial r}(r\cdot\bar\varrho\cdot v_d)-v_d\cdot\frac{\partial\varrho}{\partial r}\right]\cdot\sin\Theta=0\end{aligned} \tag{2.14}$$

z-momentum equation:

$$\begin{aligned}&\left\{\frac{\partial}{\partial s}\left[\bar\varrho\cdot u_d\cdot(u_g+u_d)\right]+\frac{1}{r}\frac{\partial}{\partial r}(r\cdot\bar\varrho\cdot u_d\cdot v_d)-\frac{1}{2}\cdot\left(\frac{\partial u_g}{\partial s}\right)\cdot\frac{1}{r}\frac{\partial}{\partial r}(r^2\bar\varrho\cdot u_d)\right.\\&\left.+\frac{1}{r}\frac{\partial}{\partial r}(r\cdot\bar\varrho\cdot\overline{v'u'})\right\}\cdot\sin\Theta\\&+\left\{\bar\varrho\cdot u_d\cdot(u_g+u_d)+\frac{1}{2}\cdot v_d\cdot\frac{1}{r}\frac{\partial}{\partial r}(r^2\cdot\bar\varrho\cdot v_d^2)\right.\\&\left.-\frac{1}{2}\cdot\frac{1}{r}\cdot\frac{\partial}{\partial r}\left[r^2\cdot\bar\varrho\cdot(v_d^2+\overline{v'^2})\right]\right\}\cdot\cos\Theta\cdot\frac{\partial\Theta}{\partial s}\\&-\frac{1}{2}u_\infty\cdot\sin\Theta\cdot\left[\frac{1}{r}\cdot\frac{\partial}{\partial r}(r\cdot\bar\varrho\cdot v_d)-v_d\cdot\frac{\partial\varrho}{\partial r}\right]\cdot\cos\Theta=(\varrho_\infty-\bar\varrho)\cdot g\end{aligned} \tag{2.15}$$

continuity equation of a scalar quantity (either c or T):

$$\begin{aligned}\frac{\partial}{\partial s}\left[\bar\varrho\cdot c_d\cdot(u_g+u_d)\right]+\frac{1}{r}\frac{\partial}{\partial r}(r\bar\varrho v_d\cdot c_d)-\frac{1}{2}\cdot\left(\frac{\partial u_g}{\partial s}\right)\frac{1}{r}\frac{\partial}{\partial r}(r^2\cdot\bar\varrho\cdot c_d)\\+\frac{1}{r}\frac{\partial}{\partial r}(r\cdot\bar\varrho\cdot\overline{v'c'})+\bar\varrho\cdot(u_g+u_d)\cdot\frac{\partial c_\infty}{\partial s}=0\end{aligned} \tag{2.16}$$

In addition use has been made of the boundary layer approximation of Prandtl and terms of small magnitude have been dropped. Introducing Gaussian similarity profiles for the mean excess quantities, that is

$$\begin{aligned}\bar u-u_g&=u_d(s,r)=u^*(s)\cdot e^{-\left(\frac{r}{b(s)}\right)^2}\\\bar T-T_\infty&=T_d(s,r)=T^*(s)\cdot e^{-\left(\frac{r}{\lambda\cdot b(s)}\right)^2}\\\bar c-c_\infty&=c_d(s,r)=c^*(s)\cdot e^{-\left(\frac{r}{\lambda\cdot b(s)}\right)^2}\end{aligned} \tag{2.17}$$

and approximately

$$\bar\varrho-\varrho_\infty=\varrho_d(s,r)=\varrho^*(s)\cdot e^{-\left(\frac{r}{\lambda\cdot b(s)}\right)^2}$$

the variables depending on s and r can be substituted by a product of two separate functions depending either on s or r. Using the Leibnitz-Rule for the differentiation of an integral with variable limits /4/

$$\int_{\alpha(s)}^{\beta(s)}\frac{\partial}{\partial s}\left[f(s,r)\right]dr=\frac{d}{ds}\int_{\alpha(s)}^{\beta(s)}f(s,r)\,dr-\frac{d}{ds}\left[\beta(s)\right]\cdot f(s,\beta)+\frac{d}{ds}\left[\alpha(s)\right]\cdot f(s,\alpha) \tag{2.18}$$

the equations can be integrated from r = 0 to the assumed outer edge of the jet $R = \sqrt{2}\cdot b$ or to $R \to \infty$, if the value of the integrand becomes zero at the edge, respectively.

Using the boundary conditions

$$\begin{aligned}&u_d(R)=\varrho_d(R)=c_d(R)=T_d(R)=0\\&\overline{v'u'}(R)=\overline{v'c'}(R)=\overline{v'T'}(R)=0\\&\overline{v'^2}(R)=\overline{v_\infty'^2}\quad\text{mit } R=\sqrt{2}\cdot b\end{aligned} \tag{2.19}$$

the following equations are obtained /16/:

continuity equation of mass:

$$\frac{d}{ds}(\varrho_\infty\cdot u^*\cdot b^2)+2b^2\cdot u_\infty\cdot\cos\Theta\cdot\frac{d\varrho_\infty}{ds}+\lambda^2\cdot\frac{d}{ds}(u_\infty\cdot\cos\Theta\cdot\varrho^*\cdot b^2)+\frac{\lambda^2}{\lambda^2+1}\cdot\frac{d}{ds}(\varrho^*\cdot u^*\cdot b^2)=2\varrho_\infty\cdot E \tag{2.20}$$

s-momentum equation:

$$\frac{d}{ds}\left\{u^*b^2\cdot\left[u^*\cdot\left(\frac{1}{2}\varrho_\infty+\frac{\lambda^2}{2\lambda^2+1}\varrho^*\right)+u_\infty\cdot\cos\Theta\cdot\left(\varrho_\infty+\frac{\lambda^2}{\lambda^2+1}\varrho^*\right)\right]\right\}=-\lambda^2\cdot b^2\cdot\varrho^*\cdot g\cdot\sin\Theta \tag{2.21}$$

Θ-equation:

$$\frac{d\Theta}{ds}=-\frac{\lambda^2\cdot b^2\cdot\varrho^*\cdot g\cdot\cos\Theta+u_\infty\cdot\varrho_\infty\cdot E\cdot\sin\Theta+\frac{1}{\pi}\cdot\sqrt{2}\cdot c_D\cdot\varrho_\infty\cdot b\cdot u_\infty^2\cdot\sin^2\Theta}{b^2\cdot u^{*2}\cdot\left(\frac{1}{2}\varrho_\infty+\frac{\lambda^2}{2\lambda^2+1}\cdot\varrho^*\right)+b^2\cdot u^*\cdot u_\infty\cdot\cos\Theta\cdot\left(\varrho_\infty+\frac{\lambda^2}{\lambda^2+1}\cdot\varrho^*\right)-2b\varrho_\infty\cdot v_\infty'^2} \tag{2.22}$$

continuity of a scalar tracer:

$$\frac{d}{ds}\left[\lambda^2\cdot b^2\cdot\left(u_\infty\cos\Theta\cdot\varrho_\infty\cdot c^*+\frac{1}{2}u_\infty\cos\Theta\cdot\varrho^*\cdot c^*+\frac{1}{\lambda^2+1}u^*\cdot\varrho_\infty\cdot c^*+\frac{1}{\lambda^2+2}\cdot u^*\cdot\varrho^*\cdot c^*\right)\right]=-\left(\frac{dc_\infty}{ds}\right)\cdot b^2\cdot\left(2u_\infty\cdot\cos\Theta\cdot\varrho_\infty+\lambda^2\cdot u_\infty\cdot\cos\Theta\cdot\varrho^*+u^*\cdot\varrho_\infty+\frac{\lambda^2}{\lambda^2+1}\cdot u^*\cdot\varrho^*\right) \tag{2.23}$$

continuity equation of thermal energy:

$$\frac{d}{ds}\left[\lambda^2\cdot b^2\cdot\left(u_\infty\cdot\cos\Theta\cdot\varrho_\infty\cdot T^*+\frac{1}{2}u_\infty\cdot\cos\Theta\cdot\varrho^*\cdot T^*+\frac{1}{\lambda^2+1}u^*\cdot\varrho_\infty\cdot T^*+\frac{1}{\lambda^2+2}\cdot u^*\cdot\varrho^*\cdot T^*\right)\right]=-\left(\frac{dT_\infty}{ds}\right)\cdot b^2\cdot\left(2u_\infty\cdot\cos\Theta\cdot\varrho_\infty+\lambda^2\cdot u_\infty\cdot\cos\Theta\cdot\varrho^*+u^*\cdot\varrho_\infty+\frac{\lambda^2}{\lambda^2+1}\cdot u^*\cdot\varrho^*\right) \tag{2.24}$$

The quantity $\lambda = 1.16$ accounts for the different rates of spreading of mass and momentum, b is the nominal jet radius defined by equation (2.17) and E represents the volume of ambient fluid which entrains into the jet due to turbulence. E is defined by

$$E(s)=-\frac{1}{2\cdot\pi}\cdot\oint_C v_z(R)\cdot dC=-v_z(R)\cdot R \tag{2.25}$$

The Θ-equation results from the combination of the momentum equations in the y and z directions and describes the variation of the angle of inclination with respect to s. That the cross-correlations $\overline{v'u'}$, $\overline{v'c'}$ and $\overline{v'T'}$ vanish outside the jet (equ. 2.19) is the logical consequence of the assumed shear-free condition u_∞ = const and of the additional supposition that the temperature and concentration gradients in the ambient stream are small. Background turbulence, however, is not excluded provided it is produced beyond the direct vicinity of the jet, as e.g. in the case of a plume exhausted to the atmosphere by a tall chimney.

It is quite interesting to note that in the equations there is no obvious indication of the state of turbulence within the jet, but it would be wrong to conclude that the jet *behaviour would not be affected by turbulence.* The dominant influence of turbulent motions on the development of the field quantities is hidden in the entrainment expression E, which depends totally on the state of self-generated and ambient turbulence.

With (2.20) to (2.24) a set of five ordinary differential equations is obtained for the seven unknowns: excess velocity $u^*(s)$, nominal jet radius $b(s)$, angle of inclination $\theta(s)$, excess density or density defect $\varrho^*(s)$, excess temperature $T^*(s)$, excess concentration $c^*(s)$ and entrainment $E(s)$. In order to achieve closure, two additional functions must be specified:

- an equation of state $\varrho = \varrho\,(T,\ c)$ and
- an entrainment hypothesis $E = E(u^*,\ b,\ \theta,\ \varrho^*,\ T^*,\ c^*)$

After defining the initial conditions $u^*(s_0)$, $b(s_0)$, $\theta(s_0)$ $\varrho^*(s_0)$, $T^*(s_0)$ and $c^*(s_0)$ the system of equations can be solved numerically (s_0 indicates the end of the zone of *establishment*). If information is required about the jet development with respect to y and z, the integrals

$$y=\int_{s_0}^{s}\cos\Theta(s)\cdot ds \tag{2.26}$$

and

$$z=\int_{s_0}^{s}\sin\Theta(s)\cdot ds \tag{2.27}$$

must also be solved.

Using temporarily the common Boussinesq approximation and assuming the ambient fluid to be free of turbulence and of density stratification, the equations above can be compared with those published by Abraham /1/, Chan and Kennedy /5/, Fan /7/, Hoult, Fay and Forney /12/, Keffer and Baines /13/ or Hirst /11/, who also applied the integral method. Contrary to expectations, however, their equations are not identical with the formulae developed here. This difference is due to the following:

- Hirst, in deriving his mathematical model, infringed the Leibnitz rule for the differentiation of an integral with variable limits (see equ. 2.18)
- all other above-mentioned investigators, who derived their equations by using a control volume, balanced the fluxes incompletely.

Both errors lead to the same results. For example, the integral form of the continuity equation of mass becomes

$$\frac{d}{ds}\int_0^R(u_s+u_z)\cdot r\cdot dr=\frac{1}{2}\frac{d}{ds}\left[b^2\cdot(u^*+2u_\infty\cdot\cos\Theta)\right]=E \tag{2.28}$$

instead of the exact relation

$$\frac{d}{ds}\int_0^R u_z\cdot r\,dr=\frac{1}{2}\frac{d}{ds}(b^2\cdot u^*)=E \tag{2.29}$$

Fig. 2.3 shows the physical plausibility of (2.29) for a simple round jet in a coflowing stream. The flux of ambient fluid $E = -v_d(R)\cdot R = v_d(R_K)\cdot R_K$, which flows into the control volume due to turbulent fluctuations inside the jet, only increases the excess velocity section, marked by A. On the contrary equation (2.28) calculates purely the volume flux within the jet, dQ/ds, which yields

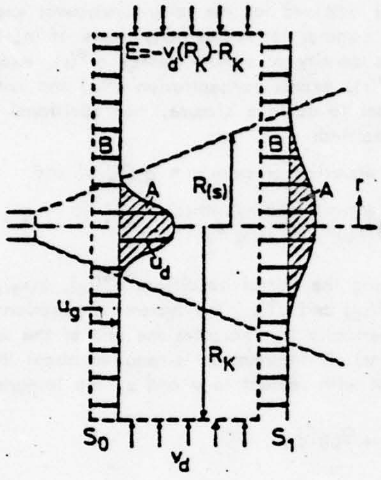

Fig. 2.3: Entrainment for a round jet in a coflowing stream

uniquely in the special case of $u_\infty = 0$ the correct continuity equation of mass. As a consequence "entrainment" takes another meaning. The entrainment hypothesis now has to express not only the amount of ambient fluid mixed into the jet by means of turbulence but also the increase of mass flux due to convection (flow section B).

The analysis of turbulent jet flows requires a turbulence or entrainment hypothesis. This empirical input to the mathematical model together with skilful data-fitting in order to fix the constants may explain why Hirst, Fan etc. nevertheless obtained reasonable agreement between theory and experiment. It is to be expected, however, that the use of more accurate equations will diminish the amount of empirical input necessary and will improve the accuracy of the predictions.

3. DERIVATION OF A NEW ENTRAINMENT FUNCTION

Integrating the differential form of the mean kinetic energy equation in the same way as the equations developed in sec. 2 yields:

$$\frac{d}{ds}\left[u^{*2}\cdot b^2\cdot\left(u^*+\frac{3}{2}u_a\right)\right] = -\frac{6}{\lambda^2+1}\cdot u^{*3}\cdot b\cdot\frac{\lambda^2\cdot\sin\theta}{F^2} - 24\cdot u^*\cdot\frac{1}{b^2}\cdot\int_0^\infty \overline{v'u'}\cdot e^{-\left(\frac{r}{b}\right)^2}\cdot r^2\cdot dr \qquad (3.1)$$

For substituting the unknown shear-stress term, another equation is required which also contains only mean quantities and the cross-correlation $\overline{v'u'}(s, r)$. This relation is obtained by indefinitely integrating the s-momentum equation with respect to r or its dimensionless form $\eta = r/b$, respectively

$$\eta\cdot\frac{\overline{v'u'(s,\eta)}}{u^{*2}} = F_6(\eta)\cdot\varepsilon + F_7(\eta)\cdot\frac{\lambda^2\cdot\sin\theta}{F^2} + \left[F_8(\eta)\cdot\sin\theta\cdot b\cdot\frac{d\theta}{ds} + 2\cdot F_9(\eta)\cdot\varepsilon\cdot\cos\theta\right]\cdot\frac{u_a}{u^*} \qquad (3.2)$$

The functions F_i are dependent on η, F is the local densimetric Froude number, defined by:

$$F^2 = \frac{u^{*2}}{\frac{\rho^c}{\rho_0}\cdot g\cdot b} \qquad (3.3)$$

In order to facilitate the derivation, Boussinesq approximated equations have been used.

Combining (3.1), (3.2) and (2.20) a differential equation for the dimensionless entrainment function is obtained

$$\varepsilon = \frac{\frac{db}{ds} + \left(\frac{\lambda^2-2}{\lambda^2+1} - 12\cdot I_2\right)\frac{\lambda^2\cdot\sin\theta}{F^2} + \left[\left(\frac{1}{4} - 12\cdot I_4\right)\sin\theta\cdot b\cdot\frac{d\theta}{ds} + \frac{3}{2}\frac{db}{ds}\right]\cdot\frac{u_a}{u^*}}{1+12\cdot I_1 + (1+24\cdot I_3)\cdot\frac{u_a}{u^*}\cdot\cos\theta} \qquad (3.4)$$

where I_i are dimensionless integration constants.

From a mathematical point of view $\varepsilon = -v_d(R)\cdot R/u^*\cdot b$ is a boundary condition; since for n-th order differential equations boundary conditions of order n-1 are required, it is necessary to specify the gradients in this equation. This will be carried out successively from the simplest to the most difficult flow configuration by using empirical information.

Beginning with the momentum jet discharged into a quiescent ambient, equation (3.4) reduces to

$$\varepsilon = \frac{\frac{db}{ds}}{1+12\cdot I_1} \qquad (3.5)$$

As it is known from experiments, the jet width increases proportional to the streamwise coordinate s, that is:

$$\frac{db}{ds} = \text{const.} \qquad (3.6)$$

Following the data of Albertson et al / 2/, the constants are db/ds = 0,114 and $A_1 = 0.057$. Thus the integral constant must be $I_1 = 1/12$ which can be confirmed by calculating

$$I_2 = \int_0^\infty F_6(\eta)\cdot e^{-\eta^2}\cdot\eta\cdot d\eta = \int_0^\infty\int_0^\eta e^{-\eta^2}\cdot\eta\cdot d\eta\cdot e^{-2\eta^2}\cdot\eta\cdot d\eta \qquad (3.7)$$

For a simple buoyant jet ($u_\infty = 0$, $\theta = \pi/2$) the basic form of the entrainment function becomes

$$\varepsilon = \frac{\frac{db}{ds} + \left(\frac{\lambda^2-2}{\lambda^2+1} - 12 \cdot I_2\right) \cdot \frac{\lambda^2}{F^2}}{1 + 12 \cdot I_1} \qquad (3.8)$$

Since a universal ε -relation is desired, the equation for a more difficult flow configuration must always include those for simpler cases, i.e. for F → ∞ the ε -formula for a buoyant jet should reduce to (5.15). Therefore it should have the following form

$$\varepsilon = \frac{2 \cdot A_1 + \left(\frac{\lambda^2-2}{\lambda^2+1} - 12 \cdot I_2\right) \cdot \frac{\lambda^2}{F^2}}{2} \qquad (3.9)$$

and the already well known entrainment hypothesis of Fox /9/

$$\varepsilon = A_1 + A_2 \cdot \frac{1}{F^2} \qquad (3.10)$$

is thereby obtained.

In the case of a jet in a co-flowing stream (3.4) becomes

$$\varepsilon = \frac{\frac{db}{ds} + \frac{3}{2} \frac{u_\infty}{u^*} \cdot \frac{db}{ds}}{1 + 12 I_1 + (1 + 24 I_2) \cdot \frac{u_\infty}{u^*}} \qquad (3.11)$$

Measurements of Fink /8/ suggest that the gradient db/ds could be substituted by

$$\frac{db}{ds} = \frac{\text{Konst.}}{b} \qquad (3.12)$$

However, renouncing possible better solutions in favour of finally obtaining a generalised entrainment function, this approach will not be followed. Instead the first gradient in the numerator of (3.11) was again replaced by $2 \cdot A_1$ and the second one was deleted, this yields:

$$\varepsilon = \frac{2 \cdot A_1}{2 + A_3 \cdot \frac{u_\infty}{u^*}} \qquad (3.13)$$

The coefficient A_3 was determined in an optimization process by comparing the theoretical predictions with experimental data of coaxial jets.

Extending the procedure above to a momentum jet in a cross flow yields:

$$\varepsilon = \frac{2 \cdot A_1 + \left(\frac{1}{4} - 12 \cdot I_1\right) \frac{u_\infty}{u^*} \cdot \sin\theta \cdot b \cdot \frac{d\theta}{ds}}{2 + A_3 \cdot \frac{u_\infty}{u^*} \cdot \cos\theta} \qquad (3.14)$$

The term containing the gradient dθ/ds takes into account that the streamwise component of the free-stream velocity $u_g = u_\infty \cdot \cos\theta$ changes in the zone of inclination. Since the entrainment rate is thereby effected only secondarily, the term has been neglected. Instead, an additional term must be formulated which accounts for the incremental inflow of ambient fluid due to the action of the cross-flow induced counter-rotating vortex pair. This vortex pair, typical of this kind of flow, has been suppressed by applying the symmetry assumption in the derivation of the shear-stress relation (3.2). Since the size of the vortex pair must be proportional to the jet width, and its intensity must depend on the magnitude of the velocity component $v_g = u_\infty \cdot \sin\theta$, the following approach has been made

$$E_{zus} = A_4 \cdot b \cdot u_\infty \cdot \sin\theta \qquad (3.15)$$

which when non-dimensionalized reads as follows:

$$\varepsilon_{zus} = A_4 \cdot \frac{u_\infty}{u^*} \cdot \sin\theta \qquad (3.16)$$

Numerical experiments showed that the most suitable combination of the ε -function and (3.16) is:

$$\varepsilon = \frac{2 \cdot A_1 + 2 \cdot A_2 \cdot \frac{\sin\theta}{F^2}}{2 + A_3 \cdot \frac{u_\infty}{u^*} \cdot \cos\theta} \cdot \left(1 + A_4 \cdot \frac{u_\infty}{u^*} \cdot \sin\theta\right) \qquad (3.17)$$

If in addition to the jet flow the ambient fluid is also turbulent, another additional entrainment term must be specified. Investigations on chimney plumes made by Slawson and Csanady /18/ show that background turbulence affects above all the far-field of a jet, where the energy-containing eddies of atmospheric turbulence can interact with the large scale structures of the jet turbulence. From dimensional reasoning this suggests the following relation:

$$E_\infty = A_5 \cdot L_\infty \cdot \sqrt{\overline{v'^2_\infty}} \qquad (3.18)$$

However, due to a lack of sufficient experimental information, this approach has not yet been tested.

Adding (3.17) and (3.18), the final form of the entrainment function is obtained:

$$\varepsilon = \frac{A_1 + A_2 \cdot \frac{\sin\theta}{F^2}}{1 + 0{,}5 \cdot A_3 \cdot \frac{u_\infty}{u^*} \cdot \cos\theta} \cdot \left(1 + A_4 \cdot \frac{u_\infty}{u^*} \cdot \sin\theta\right) + A_5 \cdot \frac{L_\infty}{b} \cdot \frac{\sqrt{\overline{v'^2_\infty}}}{u^*} \qquad (3.19)$$

and this has been used for all subsequent predictions. The five empirically fitted coefficients are:

$A_1 = 0.057$
$A_2 = -0.67$
$A_3 = 10.0$
$A_4 = 2.0$
$A_5 = ?$

For more details see /16/.

4. THE EQUATION OF STATE IN A POTENTIAL ATMOSPHERE

Since air is a compressible fluid, the pressure p_∞ in the atmospheric boundary layer becomes smaller with altitude. This has the additional complication that the temperature of a rising plume not only decreases due to mixing with the cooler surrounding air, but also due to expansion. In order to avoid those difficulties caused by the compressibility of air, it is very common to introduce a fictious "potential temperatur" $T_{\infty p}$, which is defined as the temperature a parcel of air of temperature T_∞ and pressure p_∞ would have if it were brought adiabatically to a certain reference pressure $p_{\infty o}$ /15/. This then leads to a so-called potential atmosphere of uniform pressure distribution and makes possible the calculation of jets in both compressible and incompressible fluids using the same mathematical model.

For an atmosphere in hydrostatic equilibrium the potential temperatur gradient $dT_{\infty p}/dz$ can be derived from the real temperatur gradient dT_∞/dz by

$$\frac{dT_{\infty p}}{dz} = \frac{T_{\infty p}(z)}{T_\infty(z)} \cdot \left(\frac{dT_\infty}{dz} + \frac{g}{c_p}\right) \tag{4.1}$$

where the quotient of potential and real temperature

$$\frac{T_{\infty p}(z)}{T_\infty(z)} = \left(\frac{p_{\infty o}}{p_\infty(z)}\right)^{\frac{R_a}{c_p}} \tag{4.2}$$

is nearly unity for $z < 500$ m /16/. The adiabatic temperature gradient of the real system $dT_\infty/dz = -g/c_p = -0.00975$ °K/m is called "the adiabatic lapse rate". By applying (4.1), the potential density

$$\rho_{\infty p}(z) = \rho_{\infty p01} \cdot \frac{T_{\infty p01}}{T_{\infty p}(z)} \tag{4.3}$$

and its gradient

$$\frac{d\rho_{\infty p}}{ds} = -\frac{\rho_{\infty p}}{T_{\infty p}} \cdot \frac{dT_{\infty p}}{dz} \cdot \sin\theta \tag{4.4}$$

can be obtained, where $\rho_{\infty p01}$ and $T_{\infty p01}$ (see fig. 4.1) are reference values. The computer program can accomodate an atmosphere in which different temperature gradients exist in different layers.

The density defect at the jet axis can be obtained by using the universal gas law. This yields

$$\rho_p^* = -\rho_{\infty p} \cdot \frac{T_p^*}{T_{\infty p} + T_p^*} \tag{4.5}$$

and the derivation ρ^* with respect to s becomes

$$\frac{d\rho_p^*}{ds} = -\frac{\rho_{\infty p} + \rho_p^*}{T_{\infty p} + T_p^*} \cdot \left(\frac{dT_p^*}{ds} + \frac{dT_{\infty p}}{dz} \cdot \sin\Theta\right) + \frac{\rho_{\infty p}}{T_{\infty p}} \cdot \frac{dT_{\infty p}}{dz} \sin\Theta \tag{4.6}$$

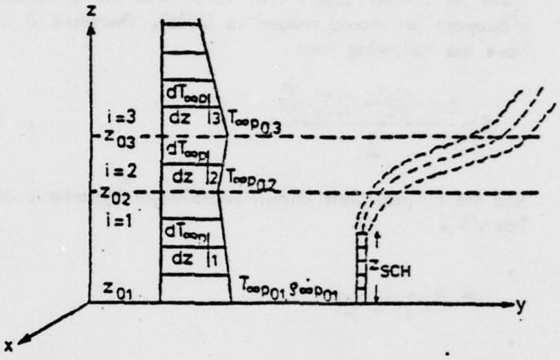

Fig. 4.1: Modelling of atmospheric boundary conditions

5. RESULTS

Finally, the system of equations has been extended by using the chain rule, nondimensionalising and then solving numerically by applying the method of Runge-Kutta.

Reformulating the equations in dimensionless form yielded the following initial dimensionless numbers which determine the development of all jet properties:

- the Froude number $\mathrm{IFr} = u^*_j/\sqrt{g \cdot D}$
- the velocity ratio u_∞/u^*_j
- the angle of discharge θ_j
- the potential temperature ratio $T^*p_j/T_{\infty p j}$
- *the potential temperature gradient* $d(T_{\infty p}/T_{\infty p j}) / d(z/D)$
- the relative intensity of background turbulence $\sqrt{\overline{v_\infty'^2}}/u_\infty$
- the relative scale of energy-containing eddies L_∞/D

Density differences due to concentrations have been simulated by varying adequately the initial temperature ratio. The densimetric Froude number IF is a dependent variable, composed of the Froude number IFr and the potential density ratio $\rho^*p_j/\rho_{\infty p j} = f(T^*p_j/T_{\infty p j})$.

Table 5.1 contains *data of a selection of about* 80 different jet flows which have been used to test the accuracy of the predictions.

Flow configuration	Run	Measurements of	Figure	$F = \frac{u_i^*}{\sqrt{g \cdot d}}$	θ_i	$\frac{T^*_{oi}}{T_{\infty oi}}$	$\frac{\varrho^*_{oi}}{\varrho_{\infty oi}}$	$\frac{D}{T_{\infty oi}} \cdot \frac{dT_\infty}{dz}$	$\frac{u_\infty}{u^*_i}$	$\frac{\sqrt{\overline{v'^2_\infty}}}{u_\infty}$	$\frac{L_\infty}{D}$	$F = \frac{u^*_i}{\sqrt{\left\lvert\frac{\varrho^*_{oi}}{\varrho_{\infty oi}}\right\rvert g D}}$
Simple Momentum Jet	1 - 1	Albertson et al /2/	5.1	62,60	90°	0	0	0	0	0	0	∞
	1 - 2	Wygnanski et al /18/	5.1	100,20	90°	0	0	0	0	0	0	∞
	1 - 3	Fan /7/	5.1	15,32	90°	0	0	0	0	0	0	∞
	1 - 4	Becker et al /3/	5.1	520,86	90°	0	0	0	0	0	0	∞
Simple Buoyant Jet	2 - 1	Hayashi et al /10/	5.2	0,727	90°	0,111	-0,1000	0	0	0	0	2,3
	2 - 2	Hayashi et al /10/	5.2	1,612	90°	0,111	-0,1000	0	0	0	0	5,1
	2 - 3	Hayashi et al /10/	5.2	7,107	90°	0,111	-0,1000	0	0	0	0	22,5
	2 - 4	Hayashi et al /10/	5.2	15,62	90°	0,111	-0,1000	0	0	0	0	49,4
	2 - 5	Hayashi et al /10/	5.2	30,9	90°	0,111	-0,1000	0	0	0	0	97,6
	2 - 6	Hayashi et al /10/	5.2	52,9	90°	0,111	-0,1000	0	0	0	0	167,1
Buoyant Jet in Stratified Ambient	3 - 4	Fan /7/	5.3	2,87	43,6°	0,018	-0,018	$1,7 \cdot 10^{-4}$	0	0	0	21
	3 - 5	Fan /7/	5.3	2,73	39,1°	0,018	-0,018	$1,7 \cdot 10^{-4}$	0	0	0	20
	3 - 6	Fan /7/	5.3	6,22	45°	0,015	-0,015	$7,4 \cdot 10^{-5}$	0	0	0	51
	3 - 7	Fan /7/	5.3	4,09	0°	0,024	-0,023	$1,9 \cdot 10^{-5}$	0	0	0	26
Jet in Co-Flowing Stream	4 - 2	Fink /8/	5.4	106,7	0°	0	0	0	0,2857	0	0	∞
Jet in Non-Stratified Cross-Flow	5 - 1	Chu et al /6/	5.5	12,12	90°	0	0	0	0,125	0	0	∞
	5 - 2	Chu et al /6/	5.5	12,20	90°	0	0	0	0,05154	0	0	∞
	5 - 3	Chu et al /6/	5.5	6,30	90°	0	0	0	0,0303	0	0	∞
	5 - 4	Chu et al /6/	5.5	15,30	90°	0	0	0	0,02272	0	0	∞
Buoyant Jet in Non-Stratified Cross-Flow	6 - 8	Fan /7/	5.6	5,97	90°	0,023	-0,023	0	0,25	0	0	40
	6 - 9	Fan /7/	5.6	5,97	90°	0,023	-0,023	0	0,125	0	0	40
	6 - 10	Fan /7/	5.6	5,97	90°	0,023	-0,023	0	0,0833	0	0	40
	6 - 11	Fan /7/	5.6	8,03	90°	0,042	-0,041	0	0,0625	0	0	40
Buoyant Jet in Stratified Cross-Flow	7 - 14	Slawson et al /17/	5.7	2,74	90°	0,340	-0,254	$-2,3 \cdot 10^{-4}$	0,435	0	0	5,43
	7 - 18	Slawson et al /17/	5.7	2,74	90°	0,369	-0,269	$-4,7 \cdot 10^{-5}$	0,551	0	0	5,27
Buoyant Jet in Stratified Cross-Flow with Temperature Inversion	7 - 19	Slawson et al /17/	5.8	2,74	90°	0,344	-0,256	$+2,0 \cdot 10^{-4}$ $-8,5 \cdot 10^{-4}$ $+6,9 \cdot 10^{-4}$	0,456	0	0	5,41

Tabelle 5.1: Summary of experimental data used for verification

The following figures give some examples of the good agreement between theoretical and experimental results.

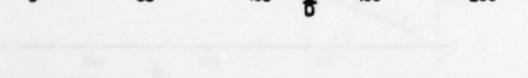

Fig. 5.1: Center line velocity and concentration decay for the simple momentum jet (data from ref. /2/, /3/, /7/, /19/).

Figure 5.1 presents the velocity and concentration decay at the center line of simple momentum jets.

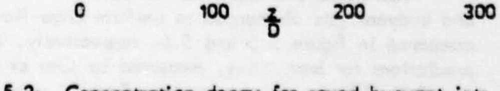

Fig. 5.2: Concentration decay for round buoyant jets (data from ref. /10/)

Figure 5.2 shows the concentration decay for buoyant jets discharged into uniform quiescent ambient fluids with densimetric Froude numbers ranging from 2.3 to 167. The experimental data are due to Hayashi and Ito /10/.

The measured and predicted trajectories and half-widths for buoyant jets discharged at various angles to stably stratified ambients are compared in figure 5.3.

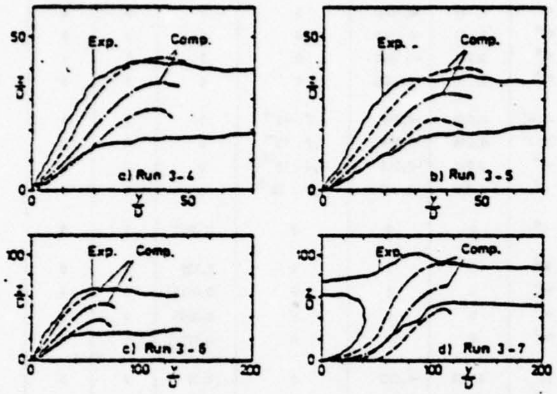

Fig. 5.3: Buoyant jets discharged at various angles to a stably stratified ambient fluid (data from ref. /7/)

Fig. 5.4 shows the decrease of the center line excess velocity and the increase of the momentum half width for a non-buoyant jet discharged into a co-flowing stream. The experimental data are obtained from the work of Fink /8/. Because of the assumptions used in deriving equation (3.13) the underestimation of the calculated half-width values is to be expected.

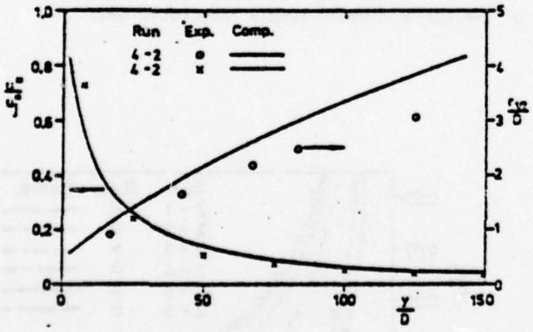

Fig. 5.4: Momentum jet discharged into a co-flowing stream (data from ref. /8/).

Predictions and experimental data for non-buoyant and buoyant jets discharged to uniform cross-flows are compared in figure 5.5 and 5.6, respectively. Again the predictions for both flows, measured by Chu et al /6/ and Fan /7/, are quite accurate. Equally good agreement has been obtained for other velocity ratios and densimetric Froude numbers (see /16/).

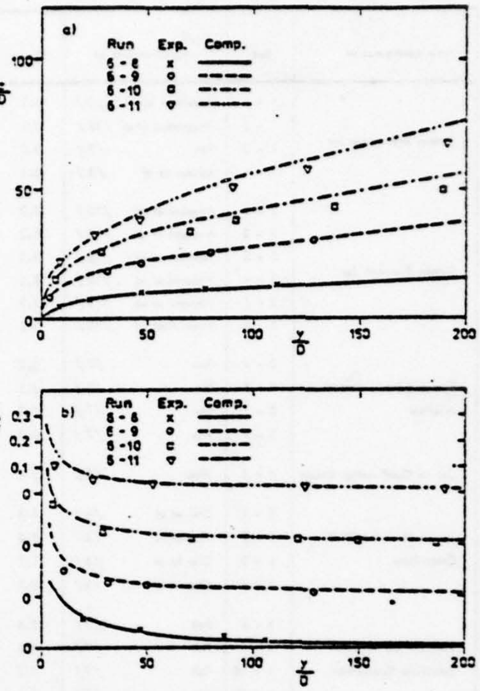

Fig. 5.6: Trajectories and center line concentration decay for buoyant jets discharged normally into uniform cross-flows (data from ref. /7/).

Figure 5.7 and 5.8 show comparisons between the trajectories of chimney plumes observed by Slawson and Csanady /17/ and those predicted with the present mathematical model. The predictions are good, even if the temperature gradient changes layerwise, as fig. 5.8 indicates.

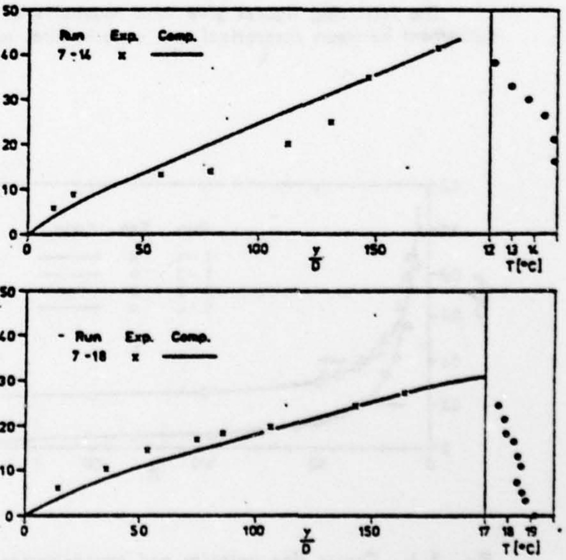

Fig. 5.7: Trajectories for buoyant chimney plumes discharged into stratified cross-winds (field measurements by Slawson et al /17/).

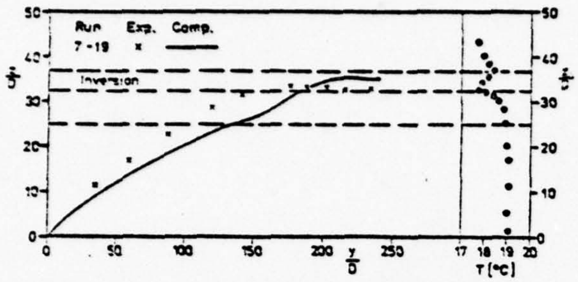

Fig. 5.8: Trajectory for a buoyant chimney plume discharged into a stratified cross-wind with temperature inversion (field measurements by Slawson et al /17/).

ACKNOWLEDGEMENT

The author is grateful to DFG and SFB 80 for the financial support. The computations were performed on the UNIVAC 1108 computer of the University of Karlsruhe.

REFERENCES

/1/ Abraham, G.: The Flow of Round Buoyant Jets Issuing Vertically into Ambient Fluid Flowing in a Horizontal Direction. Delft Hydraulics Laboratory, Publ. Nr. 81, 1971

/2/ Albertson, M.L., Day, Y.B., Jensen, R.A., and Rouse, H.: Diffusion of Submerged Jets. Trans. Am. Soc. Civ. Eng., Vol. 115, pp. 639-697, 1950

/3/ Becker, H.Y., Hottel, H.C., and Williams, G.C.: The Nozzle-Fluid Concentration Field of the Round, Turbulent, Free Jet. Journ. of Fluid Mech., Vol. 30, pp. 285-303, 1967

/4/ Bronstein, I.N. and Semendjajew, K.A.: Taschenbuch der Mathematik. Teubner-Verlag, Leipzig, S. 349, 1966

/5/ Chan, T.L., and Kennedy, J.F.: Turbulent Nonbuoyant or Buoyant Jets Discharged into Flowing or Quiescent Fluids. Iowa Inst. of Hydr. Research, Report No. 140, 1972

/6/ Chu, V.H., and Goldberg, M.B.: Buoyant Forced Plumes in Cross-flow. Journ. of the Hydr. Div., Proc. ASCE, HY9, pp. 10805-10808, 1974

/7/ Fan, L.N.: Turbulent Buoyant Jets into Stratified or Flowing Ambient Fluids. California Institut of Technology, Report No. KH-R-15, Pasadena, 1967

/8/ Fink, L.: Der axialsymmetrische Strahl in einer turbulenten Grundströmung. Sonderforschungsbereich 80 an der Universität Karlsruhe, Bericht Nr. SFB80/ET/20, 1974

/9/ Fox, D.G.: Forced Plume in a Stratified Fluid. Journ. of Geoph. Res., Vol. 75, pp. 6818-6835, 1970

/10/ Hayashi, T., and Ito, M.: Initial Dilution of Effluent Discharging into Stagnant Sea Water. Int. Symp. on Disch. of Sew. from Sea Outfalls, Paper No. 26, London 1974

/11/ Hirst, E.A.: Analysis of Round, Turbulent, Buoyant Jets Discharged to Flowing Stratified Ambients. Oak Ridge National Laboratory, Report No. ORNL-4685, Oak Ridge, 1971

/12/ Hoult, D.P., Fay, J.A., and Forney, L.J.: A Theory of Plume Rise Compared with Field Observations. Journ. of Air Poll. Contr. Ass., Vol. 19, pp. 585-590, 1969

/13/ Keffer, J.F., and Baines, W.D.: The Round Turbulent Jet in a Cross-Wind. Journ. of Fluid Mech., Vol. 15, pp. 481-496, 1963

/14/ Markovin, M.V.: Effects of Compressibility on Turbulent Flows. Colloques Internat. C.N.R.S. 108, Paris 1962.

/15/ Plate, E.J.: Aerodynamic Characteristics of Atmospheric Boundary Layers. US Atomic Energy Commission, Division of Technical Information, Oak Ridge, Tennessee, 1971

/16/ Schatzmann, M.: Auftriebsstrahlen in natürlichen Strömungen - Entwicklung eines mathematischen Modells. Sonderforschungsbereich 80 an der Universität Karlsruhe, Bericht Nr. SFB80/T/86, 1976

/17/ Slawson, P.R., and Csanady, G.T.: The Effect of Atmospheric Conditions on Plume Rise. Journ. of Fluid Mech., Vol. 47, pp. 39-49, 1971

/18/ Slawson, P.R., and Csanady, G.T.: On the Mean Path of Buoyant, Bent-Over Chimney Plumes. Journ. of Fluid Mech., Vol. 28, pp. 311-322, 1967

/19/ Wygnanski, I., and Fiedler, H.: Some Measurements in the Self-Preserving Jet. Journ. of Fluid Mech., Vol. 38, pp. 577-612, 1969

AN EXPERIMENTAL INVESTIGATION OF A TURBULENT THERMAL PLUME ALONG AN ISOTHERMAL WALL

by

J. A. Liburdy
Memphis State University

and

G. M. Faeth
The Pennsylvania State University

ABSTRACT

Measurements were made on a turbulent thermal plume resulting from a line source of heat along the base of a vertical isothermal wall. Results were obtained for various values of thermal energy flux in the plume, and distances above the source, within the weakly buoyant region of the plume. The results include profiles of mean velocity and temperature excess and the turbulent quantities u', v', w', t', $\overline{u'v'}$, $\overline{u't'}$, and $\overline{v't'}$. Mean and turbulent quantities exhibited local similarity, in terms of the local plume thermal energy flux and the height above the source, in the region away from the wall. The measurements are compared with earlier results for natural convection, the adiabatic wall plume, and the free line plume. The results are also examined in terms of proposed mixing length and higher order turbulence models.

NOMENCLATURE

$C_1, C_2, C_3, C_4, C_{q1}, C_{q2}, C_\mu, C'_\mu$	turbulence modeling constants
C_p	specific heat
Gr_x	local Grashoff number, $g\beta x^3 \Delta T_m / \nu^2$
g	acceleration due to gravitational force
k	turbulent kinetic energy
L	momentum mixing length
Pr_t	turbulent Prandtl number
Q_x	thermal energy flux in plume, Eq. (1)
q	$\overline{t'^2}$
$R_{x'y'}$	correlation coefficient, $\overline{x'y'}/(\overline{x'^2})^{1/2}(\overline{y'^2})^{1/2}$
T	temperature
t	time
t'	temperature fluctuation
U	mean vertical velocity
u', v', w'	fluctuating velocity components, vertical, normal to wall, horizontal and parallel to wall
x	height along wall
y	distance normal to wall
β	coefficient of thermal expansion
ΔT	temperature excess, $T - T_\infty$
δ	plume width, $U = .01\ U_m$
$\delta_{1/2}$	plume half width, $U = .5\ U_m$
ε	rate of dissipation of k
μ_t	turbulent viscosity
ν	kinematic viscosity
ρ	density
$\sigma_k, \sigma_t, \sigma_\varepsilon$	turbulent Prandtl numbers for k, $\overline{t'^2}$, and ε

Subscripts

m	maximum value
∞	ambient condition

INTRODUCTION

Turbulent thermal wall plumes are produced by a line source of heat along the base of a vertical or inclined surface. Wall plumes are encountered above fires spreading up a surface, above baseboard heating elements, and in other confined natural convection processes. The present investigation considered the thermal plume along a vertical wall during the initial stages of wall heating, when the wall temperature is equal to the ambient temperature (the isothermal wall plume).

The structure of the plume was examined experimentally. Measurements were made of mean velocity, mean temperature excess, turbulent velocity components, Reynolds stress, temperature fluctuations, and temperature-velocity correlations. Various source strengths and positions above the source were considered; however, experiments were limited to the fully turbulent region far above the source, where property variations (aside from the buoyant contribution of the density change) and gaseous radiation can be ignored.

The measurements are examined in the context of various methods of turbulence modeling. This includes integral methods (1-3), mixing length models (4), and second-order closure models (5,6) that have been applied to natural convection processes and plumes.

Existing turbulence data on wall plumes are limited to measurements of streamwise turbulent velocity intensities in a thermal plume rising along a vertical adiabatic surface (3), mean velocity and temperature excess data are available for both the free line plume (1) and the adiabatic wall plume (3). More information on mean quantities and turbulence characteristics is available for related flows, and the present results will be compared with these measurements, e.g., natural convection from a heated vertical plate (6-9), and wall jets (10).

APPARATUS AND PROCEDURE

Figure 1 is a sketch of the test wall, along with its dimensions. The rear wall of the apparatus was cooled by water circulation. The noncooled side walls and floor panel were employed to minimize the effect of drafts and to provide a region of two-dimensional flow near the centerline of the cooled wall.

PRECEDING PAGE BLANK-NOT FILMED

The thermal source was provided by an array of diffusion flames, located along the front lower edge of the wall. The flames were fueled with carbon monoxide in order to avoid water condensation on the instrumentation. The heat source strength was varied by adjusting the fuel flow rate, using a pressure regulating valve in conjunction with a critical flow orifice for metering and stability.

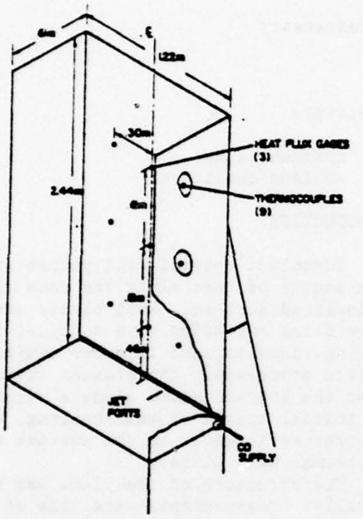

Fig. 1 Sketch of the experimental apparatus

The cooling passages were attached to the rear side of the test wall. Wall temperatures were monitored with thermocouples mounted in recesses cut from the back of the wall at the positions indicated in Fig. 1. By rapidly circulating the coolant from a large storage drum in the vicinity of the test area, it was possible to maintain the wall ±.3K of the ambient temperature at all thermocouple locations.

Mean temperatures within the plume were measured with a chromel-alumel thermocouple constructed from 0.0254 mm diameter wires. All other measurements were made with tungsten hot wire sensors, 0.00508 mm in diameter with approximately 1 mm of exposed length. The hot wires were calibrated for the gas temperature range at all overheat ratios used in the tests, in a heated air stream. The calibrations were correlated using a temperature dependent Nusselt number-Reynolds number relationship similar to that proposed by Collis and Williams (11).

The hot wire measurements employed two Thermo Systems, Inc., Model 1050 anemometers, a Model 1015C correlator, and a Model 1060 true r.m.s. meter. All signals were processed with a Hewlett-Packard, Model DY2401B, integrating digital voltmeter, using one minute intervals of integration, timed with a Model 2509A, digital clock.

The quantities that were measured, and the procedures used for each measurement are summarized in Table 1. In order to establish confidence in the measurements, tests were repeated, various overheat ratios were used, and results were crosschecked using different methods. Within the range of test conditions reported here, all measurements were repeatable within 15%.

TABLE 1. MEASUREMENT TECHNIQUES

Technique	Quantity
Single-wire, constant temperature at various overheat ratios	$U, \overline{u'^2}$
Fine-wire thermocouple	ΔT
Single-wire, constant current	$\Delta T, \overline{t'^2}$
Single-wire, constant temperature at three overheat ratios	$U, \overline{u'^2}, \overline{u't'}, \overline{t'^2}$
Cross-wire, constant temperature	$U, \Delta T, \overline{u'^2}, \overline{v'^2}, \overline{w'^2}, \overline{u'v'}$
Cross-wire, constant current at low overheat ratio	$\overline{v't'}, \overline{t'^2}$

The two-dimensionality of the flow was also examined. Within 0.14 m on either side of the centerline, temperatures varied less than 1% and velocities varied less than 10%, in no systematic way, for all test conditions.

EXPERIMENTAL RESULTS

Test Conditions

The test conditions are summarized in Table 2, along with the property values used to reduce the data. Vertical distances are measured from the base of the wall, which corresponds to the exit plane of the fuel jets. The thermal energy flux in the plume was determined by numerically integrating the velocity and temperature excess profiles, using the following expression

$$Q_x = \int_0^\infty \rho U C_p \Delta T \, dy \qquad (1)$$

In the region considered in the tests, the maximum temperature excess was only 13.2 K, which minimized the corrections of the hot wire measurements.

Mean Quantities

The mean velocity and temperature excess profiles are plotted as a function of y/x in Figs. 2 and 3, where x is measured from the base of the wall and includes no virtual origin correction. For comparison, the figures also include profiles obtained by Rouse, et al (1), for free line plumes; Grella and Faeth (3) for the adiabatic wall plume; and Cheesewright (9) for natural convection on a vertical isothermal surface for the range $Gr_x = 3\text{-}8.7 \times 10^{10}$ (which agree with more recent measurements by Smith (6)). Cheesewright (9) presents his data in terms of $(y/x)Gr^{\cdot 1}$, however, y/x alone is nearly as satisfactory over his test range, for the outer portions of the flow.

The plumes are wider than the natural convection flow, with the isothermal wall plume profiles falling between those of the free line plume and the adiabatic wall plume, in the outer regions. It appears that the surface tends to stabilize lateral motion and mixing, causing flows with the region of maximum buoyance concentrated nearer to the wall, by virtue of their boundary conditions, to be narrower. The velocity profiles for the isothermal wall plume are very similar to the profiles measured for radial wall jets by Poreh, et al (10), although the y/x coordinate system does not provide the best correlation of the wall jet data.

TABLE 2. SUMMARY OF TEST CONDITIONS

Test	x (m)	Q_x (W/m)	U_m (m/s)	ΔT_m (K)
1	.47	59.8	.349	5.29
2	.47	156.4	.463	9.74
3	.47	283.8	.575	13.20
4	.94	116.2	.429	3.91
5	.94	239.2	.520	6.38
6	.94	325.1	.516	8.54
7	1.82	130.9	.400	2.58
8	1.82	305.7	.594	3.90

Nominal ambient conditions: 306K, $97.3 kN/m^2$

Properties: $\rho = 1.11 kg/m^3, g = 9.801 m/s$
$C_p = 1.004 kJ/kgK, \nu = 16.9 \times 10^{-6} m^2/s$

Assuming similarity of mean and turbulent quantities, Rouse et al (1) determine *a simple correlation* for the variation of U_m and ΔT_m with distance from the source for a free line plume. Similar to the free line plume, thermal energy flux in the plume is conserved in the adiabatic wall plume, and Grella and Faeth (3) found that a similar expression was valid at the high Reynolds number limit, where the wall friction factor can be assumed to be constant or small but varying. The same approach can be applied for the isothermal wall plume, if it is also assumed that the Stanton number is constant or small but varying (12). However, since the thermal energy flux varies for the isothermal wall plume, instead of complete similarity of mean quantities, local similarity is obtained, based on the local thermal energy flux in the plume. The variation of the local thermal energy flux in the isothermal wall plume must be determined by evaluating the rate of heat transfer to the wall, the procedure for this is described elsewhere (12).

The variation in maximum mean quantities with distance from the source is summarized in Table 3 for the three plumes. The maximum velocity and temperature parameters are reasonably constant over the present test range, when Q_x is taken as the local thermal energy flux. Parameters for the adiabatic wall plume and free line plume are also given in the table, and exhibit about the same degree of variation over the test range. For a given thermal energy content and position, the maximum velocity and temperature excess are greatest for the adiabatic wall plume, and least for the free line plume. Therefore, although the wall provides a momentum and energy sink, reduced mixing as a result of wall stabilization of the flow more than offsets this loss.

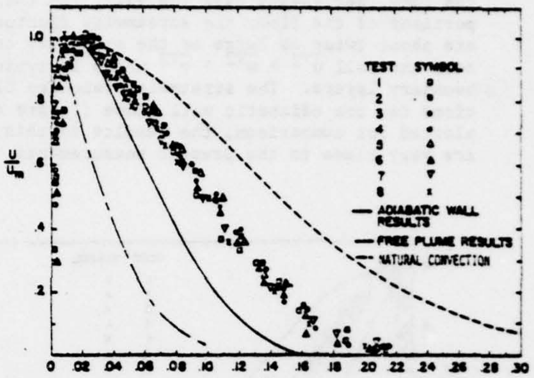

Fig. 2 Mean velocity profiles

TABLE 3. SUMMARY OF FLOW PARAMETERS

Test	$\frac{U_m}{(g\beta Q_x/\rho C_p)^{1/3}}$	$\frac{g\beta x\Delta T_m}{(g\beta Q_x/\rho C_p)^{2/3}}$	$Gr_x \times 10^{-8}$
1	2.91	5.55	.62
2	2.80	5.38	1.14
3	2.86	4.91	1.55
4	2.87	5.27	3.67
5	2.73	5.31	5.98
6	2.45	5.80	8.01
7	2.57	6.22	17.56
8	2.88	5.34	26.5
Averages:	2.76 ± .17	5.47 ± .39	
Adiabatic Wall Plume (3):	3.09 ± .07	7.91 ± .25	
Free Line Plume (1)[a]:	2.27	4.12	

[a] For the free line plume, Q_x is one-half the total energy flux in the plume.

The previous results indicate that these flows spread in a more or less linear fashion with distance from the source. The free line plume and the adiabatic wall plume have a constant maximum velocity and the maximum temperature is proportional to x^{-1}. The isothermal wall plume has nearly the same characteristics, except since Q_x decreases with distance from the source, U_m decreases slowly (approximately proportional to $x^{-.07}$), and ΔT_m decreases more rapidly than the adiabatic flows (approximately proportional to $x^{-1.14}$)(12). For natural convection on an isothermal surface, ΔT_m is constant by definition and U_m is proportional to $x^{1/2}$(9).

Turbulence Measurements

The turbulence measurements were limited to test conditions 2, 3, 4, and 5. Figure 4 illustrates the fluctuating velocity components, normalized by the maximum streamwise velocity. The data is plotted in terms of y/x, and $y/\delta_{1/2}$, which simplifies comparisons with other flows. The results are similar for the different test conditions. The velocity fluctuations are nearly constant across the bulk of the flow, decreasing near the wall. In the outer portions of the flow, the streamwise fluctuations are about twice as large as the other two components; near the wall $\overline{u'^2} > \overline{w'^2} > \overline{v'^2}$ which is typical of boundary layers. The streamwise velocity fluctuations for the adiabatic wall plume (3) are also plotted for comparison, the results in this case are very close to the present measurements.

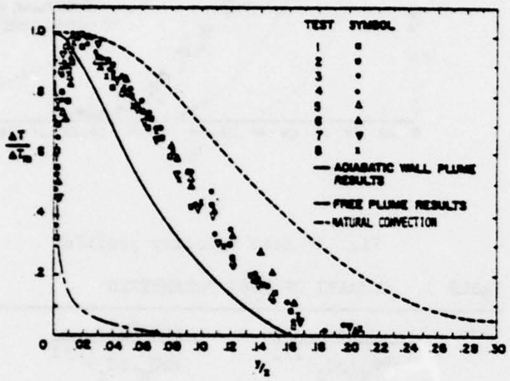

Fig. 3 Mean temperature excess profiles

Figure 4 also illustrates natural convection results for $Gr_x = 4.93 \times 10^{10}$, reported by Smith (6) (in this case the plot is in terms of $y/\delta_{1/2}$). These measurements have similar trends as the present results, but the intensities are higher in comparison to U_m. Although not directly comparable, the wall jet measurements of Poreh, et al (10), are also shown, these values are still higher than the buoyant flows.

Turbulent kinetic energy profiles are illustrated in Fig. 5. In the outer portions of the flow k is approximately constant and $\overline{u'^2}:\overline{v'^2}:\overline{w'^2} = (1.24:.42:.34)k$. Smith did not determine w', however, if it is assumed that w' = v', the ratios for natural convection in the outer region are $\overline{u'^2}:\overline{v'^2}:\overline{w'^2} = (.94:.53:53)k$.

Profiles of Reynolds stress are presented in Fig. 6 along with results for natural convection and the radial wall jet. The present values are nearly constant across much of the flow, with a small peak near the inflection point of the velocity profile. In keeping with the lower values of k for the present flow, the Reynolds stresses are lower than the other two cases illustrated in the figure. The stresses do not change sign at the maximum velocity position, and this characteristic is also observed for the wall jet. The measurements for natural convection do not extend to the maximum velocity position, however, these results also show little tendency to approach zero at $\frac{\partial U}{\partial y} = 0$. The wall jet results, and the present measurements extrapolated suggest that sign reversal occurs between $\frac{\partial U}{\partial y} = 0$ and the wall, due to the asymmetric mean velocity profile. The buoyant flows have additional buoyant generation of $\overline{u'v'}$ near the wall, which further impedes the Reynolds stress from approaching zero as the sign of the velocity gradient changes, than is the case for the wall jet which exhibits a more peaked Reynolds stress profile.

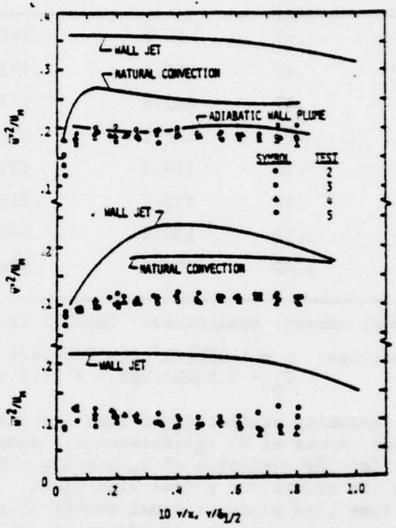

Fig. 4 Fluctuating velocity components

The temperature fluctuation intensities are illustrated in Fig. 7, along with the measurements for natural convection obtained by Smith (6). For the wall plume, temperature fluctuations reach a maximum near the wall, and slowly decline in the outer region. The natural convection values show a much sharper peak in the temperature fluctuation profile, and are generally lower than the present values.

The correlation coefficients $R_{u'v'}$, $R_{u't'}$, and $R_{v't'}$ are illustrated in Fig. 8, along with results for natural convection and the radial wall jet. The velocity correlation coefficient, $R_{u'v'}$, is nearly constant across much of the present flow and the values are generally somewhat lower than the natural convection measurements, which also exhibit little variation with position. The present values of $R_{u'v'}$ are similar to those reported by Poreh, et al (10) for the wall jet in the outer regions of the flow.

The streamwise velocity correlation, $R_{u't'}$, is very high near the wall for the present flow. This behavior has also been observed near the centerline of free plumes, where values of $R_{u't'}$ in the range .6-.7 have been reported. For most locations $R_{u't'}$ is generally lower than the natural convection measurements, falling in the range .4-.6.

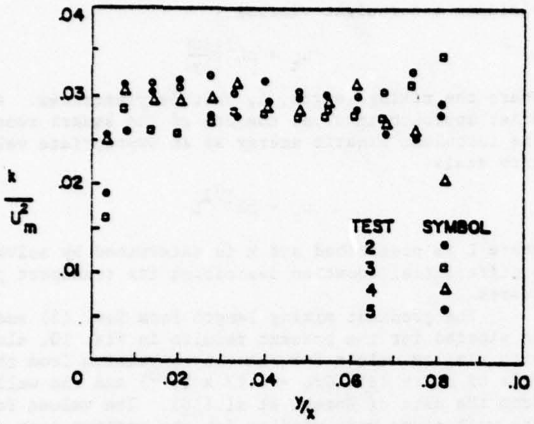

Fig. 5 Turbulent kinetic energy profiles

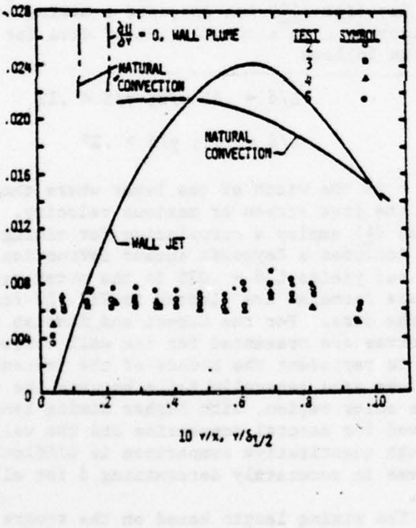

Fig. 6 Reynolds stress profiles

The values of $R_{v't'}$ for the wall plume and natural convection are generally similar. Again, due to the asymmetrical temperature profile, the correlation does not change sign at the maximum temperature position.

For the present measurements, the fact that $R_{u'v'}$ and $R_{v't'}$ do not change sign near the wall, and show little tendency to do so, and very high values of $R_{u't'}$ were observed, should be treated with care; the mean gradients are large in this region and wall effects are present so that measurements are less reliable than those in the outer portions of the flow. These measurements, however, suggest potential difficulties with eddy viscosity models of this flow, since these models cannot simulate the behavior of $\overline{u'v'}$ and $\overline{v't'}$ observed in the present tests.

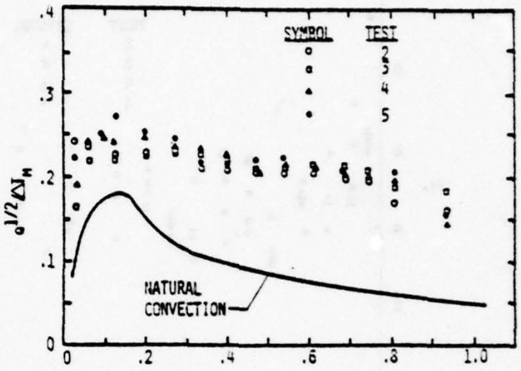

Fig. 7 Fluctuating temperature intensities

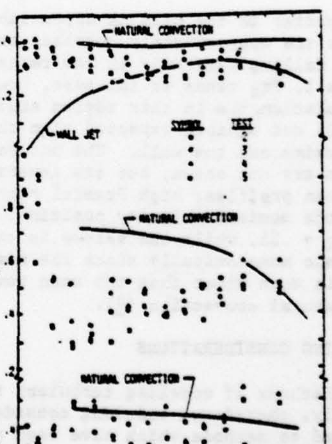

Fig. 8 Correlation coefficient profiles

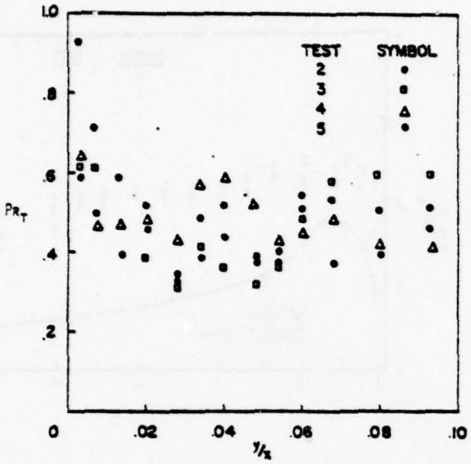

Fig. 9 Turbulent Prandtl number profiles

Figure 9 is a plot of the ratio of momentum to heat transport by turbulence. This ratio is an effective Prandtl number defined as

$$Pr_t = \overline{u'v'}\,\frac{\partial T}{\partial y}\Big/\overline{v't'}\,\frac{\partial U}{\partial y} \tag{2}$$

The scatter in the data is appreciable, however, the values are approximately constant over much of the flow, falling generally in the range 0.4-.6. Near the wall, Pr_t tends to increase, however, the values are questionable in this region since both $\overline{u'v'}$ and $\overline{v't'}$ do not exhibit expected sign changes between the maxima and the wall. The natural convection values are not shown, but are generally dominated by the mean profiles; high Prandtl number values occur near the maximum velocity position, e.g., $Pr_t = 4$ at $y/\delta_{1/2} = .25$, while the values in the outer region decrease monotonically since the mean velocity profile is much wider than the mean temperature profile for natural convection (9).

MODELING CONSIDERATIONS

Methods of modeling turbulent flows are evolving rapidly, therefore, modeling considerations were limited to methods which have been applied to buoyant flows along vertical surfaces. This includes mixing length models for natural convection, e.g., Kebeci and Khattab (4), Mason and Seban (14), and Noto and Matsumoto (15). A k-ε model has also been applied to natural convection by Plumb and Kennedy (5) and this model is considered as well. More recent models proposed by Launder (16) and Gibson and Launder (17) have thus far been only applied to horizontal flows far from surfaces, and while these methods are of interest, they have not been considered in the following.

Mixing Length Models

A mixing length model can be developed using a stress-mean gradient relationship (18), as follows

$$\overline{u'v'} = L^2\left|\frac{\partial U}{\partial y}\right|\frac{\partial U}{\partial y} \tag{3}$$

yielding a turbulent viscosity

$$\mu_t = \rho L^2\left|\frac{\partial U}{\partial y}\right| \tag{4}$$

where the mixing length, L, must be prescribed. Another approach involves the use of the square root of the turbulent kinetic energy as an appropriate velocity scale

$$\mu_t = \rho k^{1/2} L \tag{5}$$

where L is prescribed and k is determined by solving a differential equation describing its transport processes.

The gradient mixing length from Eqs. (3) and (4) is plotted for the present results in Fig. 10, along with similar values for natural convection from the data of Smith (6) ($Gr_x = 4.93 \times 10^{10}$) and the wall jet from the data of Poreh, et al (10). The values for the wall plume were similar for the various test conditions and the present mixing lengths are averages for Tests 2-5. Mixing lengths are plotted for the whole width of the flow but between the wall and the maximum velocity position the square of the mixing length calculated from Eq. (3) is negative and a mixing length is not properly defined. The mixing length is also infinitely large at the maximum velocity position for the wall plume and wall jet, and large values are encountered in the vicinity of this region.

Escudier (19) has proposed a mixing length relationship from a compilation of data for flows near walls as follows

$$L/\delta = .41\ y/\delta;\quad y/\delta \leqslant .22 \tag{6}$$

$$L/\delta = .09;\quad y/\delta > .22 \tag{7}$$

where δ is the width of the layer where the velocity is 1% of the free stream or maximum velocity. Cebeci and Khattab (4) employ a correlation for mixing length which includes a Reynolds number correction near the wall, but yields $L/\delta = .075$ in the outer region. Both of these formulae are plotted in Fig. 10 for comparison with the data. For the Cebeci and Khattab equation, two curves are presented for the wall correction in order to represent the bounds of the present data. The plume data generally falls between the two models in the outer region, with higher mixing length values observed for natural convection and the wall jet, although quantitative comparison is difficult due to problems in accurately determining δ for all three flows.

The mixing length based on the square root of the turbulent kinetic energy was also evaluated. The trends are the same as those observed in Fig. 10, however, the values are 20-30% lower. Thermal mixing lengths have similar characteristics, except the values are larger in the outer region, as dictated by Pr_t.

Higher Order Models

In their analysis of turbulent natural convection along an isothermal wall, Plumb and Kennedy (5) employed transport equations for k, ε, and q, as follows

$$\rho\frac{Dk}{Dt} = \frac{\partial}{\partial y}\left(\frac{\mu_t}{\sigma_k}\frac{\partial k}{\partial y}\right) + \mu_t\left(\frac{\partial U}{\partial y}\right)^2 - \rho\varepsilon + \rho g\beta\overline{u't'} \tag{7}$$

$$\rho\frac{D\varepsilon}{Dt} = \frac{\partial}{\partial y}\left(\frac{\mu_t}{\sigma_\varepsilon}\frac{\partial \varepsilon}{\partial y}\right) + C_1\frac{\varepsilon}{k}\mu_t\left(\frac{\partial U}{\partial y}\right)^2 - C_2\frac{\rho\varepsilon^2}{k} + C_3\rho g\beta\overline{u't'} \tag{8}$$

$$\rho \frac{Dq}{Dt} = \frac{\partial}{\partial y}\left(\frac{\mu_t}{\sigma_q}\frac{\partial q}{\partial y}\right) + C_{q1}\mu_t\left(\frac{\partial T}{\partial y}\right)^2 - C_{q2}\rho\frac{\varepsilon}{k}q \qquad (9)$$

where

$$\mu_t = C_\mu \rho k^2/\varepsilon \qquad (10)$$

Following an agrument given by Launder and Spalding (18), Plumb and Kennedy (5) also proposed

$$\overline{u't'} = C_4(qk)^{1/2} \qquad (11)$$

From the data obtained in the present investigation, it is possible to estimate values for C_μ, C_4, C_{q1}, and C_{q2}. In this treatment, wall effects are not considered and it should be noted that dissipation rates and diffusion quantities are not yet available for this flow. The constant C_4 can be determined directly from the present data, computation of the remaining parameters is considered in the following.

The results shown in Fig. 5 indicate the k/U_m^2 is approximately constant for a good portion of the flow. Furthermore, the energy loss from the plume to the wall is not very large over the present test range (12), and Q_x does not vary to great degree with height above the source. In these circumstances, the results given in Table 3 indicate that U_m, and therefore k, does not vary significantly with position along the wall. Since diffusion and convection of k is small, the value of C_μ can be estimated by neglecting these terms in Eq. (7) to obtain

$$C_\mu = C'_\mu\left[1 - g\beta\overline{u't'}/(\overline{u'v'}\,\frac{\partial U}{\partial y})\right] \qquad (12)$$

where

$$C'_\mu = (\overline{u'v'}/k)^2 \qquad (13)$$

The parameter C'_μ represents the nonbuoyant contribution to C_μ in the present flow.

Figure 7 indicates that $q/\Delta T_m^2$ is nearly constant for much of the flow. However, from Table 3, $\Delta T_m \propto x^{-1}$ if the small reductions in Q_x with height above the source are ignored. Therefore the evaluation of C_{q1} and C_{q2} must consider convection, although diffusion effects have been ignored. The term involving C_{q1} in Eq. (9) represents production of q, as follows

$$C_{q1}\mu t\left(\frac{\partial T}{\partial y}\right)^2 = -2\rho\left(\overline{v't'}\,\frac{\partial T}{\partial y} + \overline{u't'}\,\frac{\partial T}{\partial x}\right) \qquad (14)$$

Assuming that Q_x is constant, Eq. (14) may be solved for C_{q1} to yield

$$\frac{C_{q1}Pr_t}{2} = 1 - \sqrt{\frac{\overline{u'^2}}{\overline{v'^2}}}\left(\frac{R_{u't'}\Delta T}{R_{v't'}\Delta T_m}\right)\left[\frac{\partial(\Delta T/\Delta T_m)}{\partial(y/x)}\right]^{-1} \qquad (15)$$

where the last term in this expression is due to convection. Equation (9) can be solved for C_{q2} to yield

$$\frac{C_{q2}C_\mu}{C_{q1}Pr_t^2} = \frac{\overline{v't'}^2}{kq}\left[1 - 2\sqrt{\frac{\overline{t'^2}}{\overline{v'^2}}}\left(\frac{U\Delta T}{C_{q1}R_{v't'}Pr_t\Delta T_m^2}\right)\left(\frac{\partial(\Delta T/\Delta T_m)}{\partial(y/x)}\right)^{-1}\right] \qquad (16)$$

Profiles of C'_μ, C_μ, C_4, C_{q1}, and C_{q2} are illustrated in Fig. 11; the values shown are averages for Tests 2-5. The maximum temperature and velocity locations are close to one another, and C_μ, C_{q1}, and C_{q2} are large in this region. Between the wall and the maximum velocity position, C_μ is generally small, but it is negative since the turbulent shear stress did not change sign at the maximum velocity position. In the same region, C_4, C_{q1}, and C_{q2} exhibit large variations. Experimental errors in the near wall region may be a factor in this behavior, but the results also suggest basic problems with an eddy viscosity model for the present flow, which is typical of asymmetric flows in general.

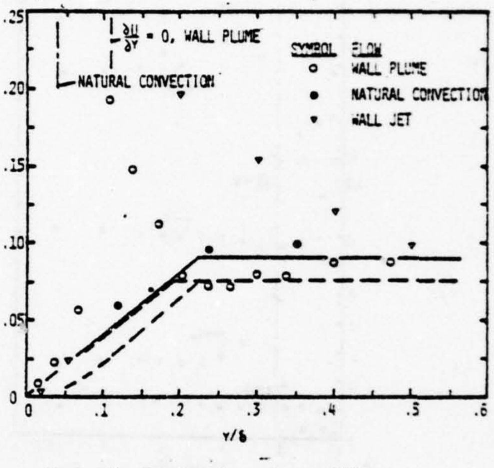

Fig. 10 Mixing length profiles

TABLE 4. MODELLING CONSTANTS

	Isothermal Wall Plume	Natural Convection Plumb and Kennedy (5)
C_μ	.125	.09
C'_μ	.06	—
C_4	.5	.5
C_{q1}	4.5	2.8
C_{q2}	2.6	1.7
C_{q1}/C_{q2}	1.73	1.65

The results shown in Fig. 11 indicate that the modeling parameters tend to approach constant values in the outer portions of the flow. These values are summarized in Table 4, along with the values used in the same region by Plumb and Kennedy (5) during their natural convection calculations. Plumb and Kennedy close C_μ based on a value recommended by Jones and Launder (20) for nonbuoyant flows, the value measured in the present study is about 40% higher, while the nonbuoyant contribution, represented by C'_μ is lower by a similar amount. Plumb and Kennedy chose C_4 from the natural convection measurements of Smith (6), the present measurements give essentially the same value of this parameter. The values for C_{q1} and C_{q2} used in Ref. 5 were selected on the basis of turbulent plume results for axisymmetric flows. The values of these parameters found in the present study are higher. This is due to the fact that both C_{q1} and C_{q2} are proportional to Pr_t^{-1}, which approaches 2.0 in the present flow but is generally lower in axisymmetric flows (18). The ratio C_{q1}/C_{q2} is nearly independent of Pr_t and the present value of this ratio is nearly equal to the value found in the earlier work (5).

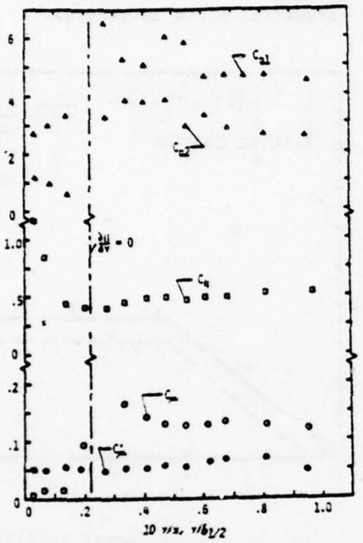

Fig. 11 Profiles of model constants

CONCLUDING REMARKS

The present measurements for an isothermal wall plume were conducted sufficiently far from the source so that weakly buoyant approximations could be applied to the flow. In this region, mean quantities in the isothermal wall plume exhibited local similarity based on height above the source and the local thermal energy flux in the plume to about the same extent that similarity has been observed for other plumes. The isothermal wall plume is thicker than natural convection boundary layer and the adiabatic wall plume, since its point of maximum buoyancy is displaced from the wall. The flow is thinner than the half width of a free line plume, however, since the presence of the wall stabilizes lateral mixing and meandering of the flow. When compared to the free line plume, the isothermal wall plume has greater velocities and temperatures at a given condition, due to its reduced entrainment, in spite of direct losses to the wall.

The local similarity integral model provides a reasonably good correlation of the mean properties of the flow. Temperature and velocity distributions can be determined from Figs. 1 and 2, and U_m and ΔT_m can be determined for Table 2 for given values of Q_x and x.

Turbulence quantities exhibited similarity over the test range. The values of $\overline{u'^2}/U_m^2$, k/U_m^2, etc., were lower than those measured by Smith (6) for natural convection, but $q^{1/2}/\Delta T_m$ was somewhat higher. In the outer regions of the flow $\overline{u'^2}:\overline{v'^2}:\overline{w'^2}$ had the ratios 1.24:.42:34, rather than the values .94:53:53 that have been found for nonbuoyant shear layers (16) suggesting a buoyant contribution which increases the streamwise velocity fluctuations.

The modeling parameters that could be calculated from the present data were relatively constant in the outer portions of the flow, but exhibited changes near the wall and near the maximum velocity position, since Reynolds stresses did not approach zero at $\frac{\partial U}{\partial y} = 0$. Mixing lengths in the outer region agree reasonably well with values in current use, and the turbulent Prandtl number approached 0.5 which is typical of plane flows not influenced by a wall.

Since the present mixing length parameters, and modeling constants are reasonably normal, it is expected that mixing length models (4, 14, 15) and k-ε-q models (5) should be about as successful for the present flow as they were for natural convection. However, $\overline{u'v'}$ and $\overline{v't'}$ were not observed to approach zero at the velocity and temperature maxima, and an eddy viscosity model cannot properly represent this behavior. Present experimental errors are highest near the wall, and this behavior could be the result of experimental difficulties, however, it would be desirable if models based on the transport equations for $\overline{u_i'u_j'}$ and $\overline{u_i't'}$, similar to those used for buoyant horizontal flows (16, 17), were employed for this flow. Notably, Smith (6) completed some preliminary calculations along these lines which indicate that $\overline{u'v'}$ reaches zero quite close to the wall for natural convection.

ACKNOWLEDGMENT

This research was supported by the United States Department of Commerce, National Bureau of Standards, Grant No. 5-9020, under the technical management of Dr. John Rockett of the Programmatic Center for Fire Research.

REFERENCES

1. Rouse, H., Yih, C., and Humphreys, H., "Gravitational Convection from a Boundary Source", Tellus, Vol. 4, 1952, pp. 201-210.

2. Lee, S. L. and Emmons, H. W., "A Study of Natural Convection Above a Line Fire", Journal of Fluid Mechanics, Vol. 11, 1961, pp. 353-368.

3. Grella, J. J. and Faeth, G. M., "Measurements in a two-Dimensional Thermal Plume Along a Vertical Adiabatic Wall", Journal of Fluid Mechanics. Vol. 71, 1975, pp. 701-710

4. Cebeci, T. and Khattab, A., "Prediction of Turbulent-Free-Convective-Heat Transfer From a Vertical Flat Plate, ASME Transactions, Series C, Journal of Heat Transfer, Vol. 97, No. 3, Aug. 1975, pp. 469-471.

5. Plumb, O. A. and Kennedy, L. A., "Application of a k-ε Turbulence Model to Natural Convection From a Vertical Isothermal Surface", ASME Paper 76-HT-17, Aug. 1976.

6. Smith, R. R., "Characteristics of Turbulence in Free Convection Flow Past a Vertical Plate", Ph.D. Thesis, 1972, Queen Mary College, University of London.

7. Lock, G. and Trotter, F., "Observations on the Structure of a Turbulent Free Convection Boundary

Layer", *International Journal of Heat and Mass Transfer*, Vol. 11, 1968, pp. 193-202.

8. Kutateladze, S. S., Kirdyaskim, A., and Ivankin, V., "Turbulent Natural Convection on a Vertical Plate and in a Vertical Layer", *International Journal of Heat and Mass Transfer*, Vol. 15, 1972, pp. 193-202.

9. Cheesewright, R., "Turbulent Natural Convection from a Vertical Plane Surface", ASME Transactions, Series C, *Journal of Heat Transfer*, Vol. 90, 1968, pp. 1-8.

10. Poreh, H., Tsuei, Y. G., and Cermak, J. E., "Investigation of a Turbulent Radial Wall Jet", ASME Transactions, Series E, *Journal of Applied Mechanics*, Vol. 89, 1967, pp. 457-463.

11. Collis, D. G. and Williams, M. J., "Two-dimensional Convection from Heated Wires at Low Reynolds Numbers", *Journal of Fluid Mechanics*, Vol. 6, 1959, pp. 357-384.

12. Liburdy, J. A. and Faeth, G. M., "Heat Transfer and Mean Structure of a Turbulent Thermal Plume Along a Vertical Isothermal Wall", to be published.

13. George, W. K., Alpert, R. L., and Tamanini, F., "Turbulent Measurements in an Axisymmetric Buoyant Plume", FMRC Serial No. 22359-2, Jan. 1976, Factory Mutual Research Corp., Norwood, Mass.

14. Mason, H. B. and Seban, R. A., "Numerical Predictions for Turbulent Free Convection from Vertical Surfaces", *International Journal of Heat and Mass Transfer*, Vol. 17, 1974, pp. 1329-1336.

15. Noto, K. and Matsumoto, R., "Turbulent Heat Transfer by Natural Convection Along an Isothermal Vertical Flat Surface", ASME Transactions, Series C. *Journal of Heat Transfer*, Vol. 97, 1975, pp. 621-624.

16. Launder, B. E., "On the Effects of a Gravitational Field on the Turbulent Transport of Heat and Momentum", *Journal of Fluid Mechanics*, Vol. 67, 1975, pp. 569-581.

17. Gibson, M. M. and Launder, B. E., "On the Calculation of Horizontal, Turbulent, Free Shear Flows Under Gravitational Influence", ASME Transactions, Series C, *Journal of Heat Transfer*, Vol. 98, 1976, pp. 81-87.

18. Launder, B. E. and Spalding, D. B., *Mathematical Models of Turbulence*, Academic Press, London, 1972, pp. 23-45, p. 49.

19. Escudier, M. P., "The Distribution of Mixing-Length in Turbulent Flow Near Walls", Heat Transfer Section Report TWF/1, 1966, Imperial College, London.

20. Jones, W. P. and Launder, B. E., "The Prediction of Laminarization with a 2-Equation Model of Turbulence", *International Journal of Heat and Mass Transfer*, Vol. 15, 1972, pp. 301-314.

SESSION 7

REACTING FLOWS

Chairman: H. A. Becker
Queen's University
Kingston, Ontario
Canada

AD-A055 654 PENNSYLVANIA STATE UNIV UNIVERSITY PARK DEPT OF MECH--ETC F/G 20/4
SYMPOSIUM ON TURBULENT SHEAR FLOWS HELD AT THE PENNSYLVANIA STA--ETC(U)
APR 77 N00014-77-C-0176

UNCLASSIFIED NL

4 OF 9
ADA
055654

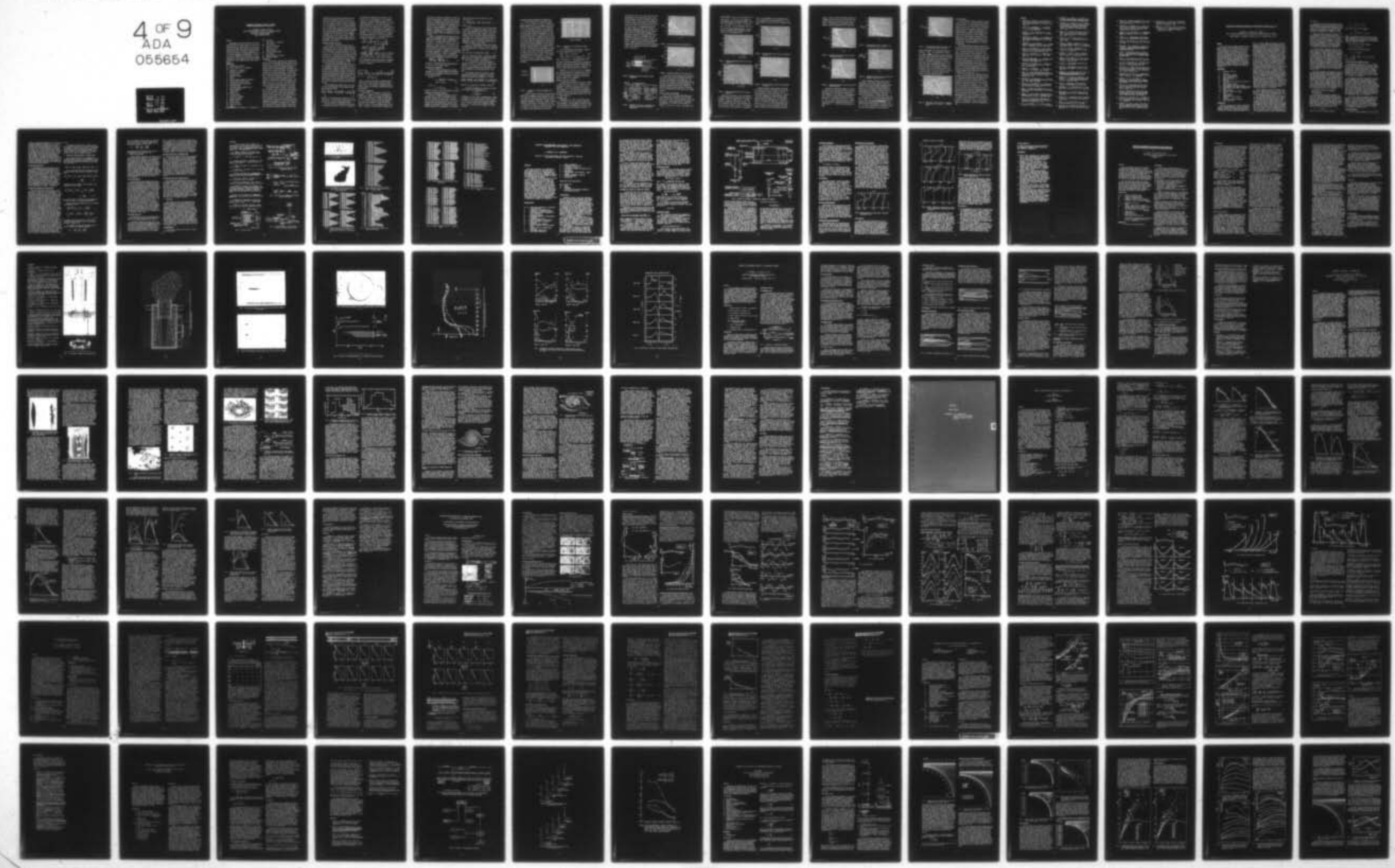

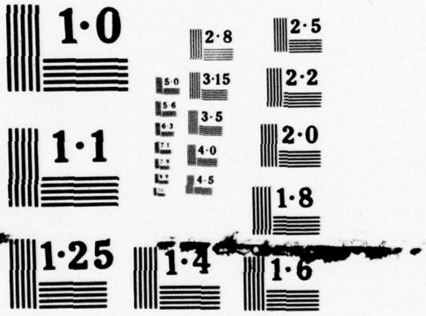

NATIONAL BUREAU OF STANDARDS
MICROCOPY RESOLUTION TEST CHART

MEASUREMENT AND NUMERICAL MODELING OF TURBULENT SCALAR MIXING AND REACTION IN CO-AXIAL JETS

G. K. Patterson, Associate Professor*
Win-Chung Lee and Steven J. Calvin, Jr., Graduate Students
Department of Chemical Engineering
University of Missouri-Rolla
Rolla, Missouri 65401

ABSTRACT

Measurements of the scalar diffusion and mixing between the inner and outer streams of a co-axial jet have been made, and a modification of the k_e-ϵ turbulence model has been used to model the fluid dynamics, diffusion and mixing. Data was also obtained from which the distribution of reaction conversion of one of the mixing components was determined. The reaction was also simulated with the modified k_e-ϵ model. Measurements of the average velocities and turbulence were made to validate comparison with other investigations.

NOMENCLATURE

$\bar{C}_c$	concentration at center
$\bar{C}_i$	average concentration of component - i
$\overline{c_i^2}$	segregation of component - i
x_j	distance in direction - j
ψ	stream function
μ_t	turbulent viscosity
ρ	density
σ_a	turbulent Schmidt number for property - a
$\bar{K}$	average reaction rate constant
k	fluctuating reaction rate constant
k_e	turbulence energy
ϵ	turbulence energy dissipation rate
$\bar{T}$	average temperature
β	reactant ratio
H_R	reaction heat
E_a	activation energy
F	conversion of reactant
A	degree of mixedness
$\bar{U}$	average velocity
$\bar{U}_a$	annular velocity
$\bar{U}_j$	center jet velocity
r	radius
$\overline{u_1^2}$	turbulence
γ	interdiffusion of reactants
C_p	heat capacity
$\mathcal{D}$	molecular diffusivity
P	creation rate term
D	decay rate term
N_S	molecular Schmidt number
R	gas constant
r_o	outside radius of jet nozzle
Re	Reynolds number

INTRODUCTION

Of the devices for promoting mixing between components of fluid, the simplest and most studied is the turbulent jet. Much has been done to measure the flow dynamic variables (related to momentum transport) of turbulent jets of various geometries. References 1-15 represent only a sample of the useful flow dynamic data available for free and confined jets. Less has been done to measure the variables related to scalar transport in such jets, particularly the fluctuating components of the scalar quantities needed to gain insight into the mechanism of turbulent transport. References 1, 2, 4, 6, 12, 16, and 17 are among the few known to the authors where both average and fluctuating scalar quantities were measured in mixing jets.

Of greatest interest, of course, is the mixing jet with chemical reaction between the mixing components. That is, however, a very complex system and no studies are known to the authors where experimental data have been obtained for both the average and fluctuating concentrations of the scalar components. A few investigations where average concentrations and/or temperatures were measured in a jet with reacting components are represented by References 18-21. Besides the simultaneous large scale turbulent diffusion and small scale mixing processes, measured by the average

---

*Now at Lawrence Livermore Lab., Livermore, Ca.

concentration and fluctuating concentration (hereafter called segregation) profiles, occuring in a mixing jet, there are also the creation of segregation by large scale turbulent diffusion, the destruction of segregation - as well as average concentration - by the reaction, the generation of both large scale and small scale temperature gradients, measured by the average temperature profile and fluctuating temperature profile, and effects of both temperature and composition on density and viscosity. Experimental measurements and attempts to model these various aspects of the mixing jet with reaction will be discussed in what follows.

TURBULENT DIFFUSION AND MIXING

In this paper, turbulent diffusion refers to transport from points of higher average concentration or temperature to points of lower average concentration or temperature as treated by Zakkay, et al. (22), Flint, et al. (23), Baldwin and Walsh (24), and Hedman and Smoot (25). Mixing refers to the reduction of the local level of a fluctuating quantity by the combination of fluid element stretching and molecular diffusion as described by Corrsin (26, 27), Brodkey, et al. (28, 29), Hiby (30), and Rosensweig (31, 32).

Turbulent diffusion has been modeled through use of the Lagrangian approach to the spread of the mixing components by random turbulent motion (23, 24, 33) but most often by assuming a gradient transport mechanism with an eddy diffusivity (34-38) to account for the combination of molecular diffusion and turbulent convection represented by the $\overline{u_i c_j}$-correlations. This approach has, of course, long been used for turbulent heat transport but most often with a constant eddy diffusivity or a prescribed distribution of eddy diffusivities.

For the modeling work reported here, the following form of two-dimensional scalar component conservation equation was used:

$$\frac{\partial \bar{C}_1}{\partial x_2}\frac{\partial \psi}{\partial x_1} + \frac{\partial \bar{C}_1}{\partial x_1}\frac{\partial \psi}{\partial x_2} = \frac{1}{\rho}\frac{\partial}{\partial x_1}\left(\frac{\mu_t}{\sigma_{\bar{C}_1}}\frac{\partial \bar{C}_1}{\partial x_1}\right) + \frac{1}{\rho}\frac{\partial}{\partial x_2}\left(\frac{\mu_t}{\sigma_{\bar{C}_1}}\frac{\partial \bar{C}_1}{\partial x_2}\right) + P_{\bar{C}_1} \qquad (1)$$

where $P_{\bar{C}_1}$ is the production term (negative of the reaction rate). The two diffusion terms account for the molecular and turbulent fluxes mentioned above.

The rate of mixing is sometimes called the decay of segregation and relates to the rate of decrease of the amplitude of concentration fluctuations. Both Corrsin (26, 27) and Rosensweig (31, 32) proposed equations for relating segregation decay rate to the turbulence properties. Since segregation may be convected (diffused) by the large scale turbulence, Spalding (1971) has proposed that a gradient diffusion model be applied to the segregation of a component in the same manner as to the average concentration of the component. If the transport equation for instantaneous concentration C_i is first multiplied through by fluctuating concentration c_i, the equation may be rearranged and simplified to (written for c_1):

$$\bar{U}_1 \frac{\partial \overline{c_1^2}}{\partial x_1} + \bar{U}_2 \frac{\partial \overline{c_1^2}}{\partial x_2} = \underbrace{\mathcal{D}\nabla^2 \overline{c_1^2} - 2\,\overline{u_1 c_1}\,\frac{\partial \bar{C}_1}{\partial x_2} - \frac{\partial}{\partial x_1}\overline{u_1 c_1^2} - \frac{\partial}{\partial x_2}\overline{u_2 c_1^2} - 2\,\overline{u_2 c_1}\,\frac{\partial \bar{C}_1}{\partial x_2}}_{\text{diffusion of } \overline{c_1^2}}$$
$$+ \underbrace{2\mathcal{D}\left[\overline{\left(\frac{\partial c_1}{\partial x_1}\right)^2} + \overline{\left(\frac{\partial c_1}{\partial x_2}\right)^2}\right]}_{\text{decay of } \overline{c_1^2} \text{ by mixing}} - \underbrace{2\bar{K}\left(\overline{c_1^2}\,\bar{C}_2 + \overline{c_1 c_2}\,\bar{C}_1 + \overline{c_1^2 c_2}\right)}_{\text{decay of } \overline{c_1^2} \text{ by reaction}} \qquad (2)$$

The two-dimensional conservation equation for segregation would then take the following form if written similarly to Equation 1:

$$\frac{\partial \overline{c_i^2}}{\partial x_2}\frac{\partial \psi}{\partial x_1} + \frac{\partial \overline{c_1^2}}{\partial x_1}\frac{\partial \psi}{\partial x_2} = \frac{1}{\rho}\frac{\partial}{\partial x_1}\left(\frac{\mu_t}{\sigma_{c_1^2}}\frac{\partial \overline{c_i^2}}{\partial x_1}\right) + \frac{1}{\rho}\frac{\partial}{\partial x_2}\left(\frac{\mu_t}{\sigma_{c_i^2}}\frac{\partial \overline{c_i^2}}{\partial x_2}\right)$$
$$- D_{Ti} - D_{Ri} + P_{Di} \qquad (3)$$

where D_{Ti} and D_{Ri} are the rates of segregation decay caused by mixing and by chemical reaction, respectively, and P_{Di} is the creation of segregation brought about by large scale (gradient) turbulent diffusion of the component.

CREATION OF SEGREGATION

The definition of segregation is highly scale-dependent. If streams of A and B are completely separated, small regions in each stream are considered to contain zero segregation in terms of either component. If, however, a region covering both streams is considered, the segregation in terms of either component is non-zero, since both components exist in the region. According to the derivation by Brodkey (39), the product of the overall concentration of each component, when separation is complete, equals the segregation. Put another way, a mixture of two components which are totally immiscible, would have a segregation equal to the product of the average concentrations of the two components. If more than one component is present, then the segregation of each component is determined as if it were mixed with only one other component (the other components are lumped together).

Creation of segregation occurs when the scale of separation of components (scale of segregation (39)) becomes smaller than the region of consideration. That occurs, for instance, when ambient fluid is entrained into a jet of fluid. At the jet outlet the segregation in terms of either fluid is zero if the region considered is significantly smaller than the jet radius or half-width. As ambient fluid is entrained downstream, segregation is created at a rate determined by the entrainment rate. The rate of segregation creation may be determined from a conservation equation for average concentration product as follows:

$$\frac{\partial(\overline{C}_1\overline{C}_2)}{\partial x_1}\frac{\partial\psi}{\partial x_2} + \frac{\partial(\overline{C}_1\overline{C}_2)}{\partial x_2}\frac{\partial\psi}{\partial x_1} = P_{D_1} \qquad (4)$$

Of course, no diffusion terms are included because this is not a true transport equation.

DESTRUCTION OF SEGREGATION

The rate of decay of segregation by turbulent stretching of fluid elements combined with molecular diffusion may be represented by the Corrsin equation for the isotropic mixer:

for $N_S \gg 1$

$$D_T = 2\overline{(\partial c_i/\partial x_j)^2} = 2\,\overline{c_i^2}/[4(k_e/\varepsilon) + (\nu/\varepsilon)^{1/2}\,\ln N_S\,] \qquad (5)$$

for $N_S \leq 1$

$$D_T = 3\,\overline{c_i^2}\,\varepsilon/4k_e \qquad (6)$$

Equation 5 applies to liquids and Equation 6 to gases.

GENERATION OF TEMPERATURE GRADIENTS

Generation of temperature gradients by endo- or exothermic reaction leads to enhancement of local, small-scale gradients which may have a controlling effect on local reaction rates (40-42). This has not yet been conclusively demonstrated, because the enhancement level depends on the degree of correlation between concentration and temperature. For a second-order reaction this may be expressed as follows (written for C_1):

$$P_{\overline{C}_1} = -\overline{K}(\overline{C}_1\overline{C}_2 + \overline{c_1c_2}) - \overline{kc_1}\,\overline{C}_2 - \overline{kc_2}\,\overline{C}_1 - \overline{kc_1c_2} \qquad (7)$$

where $K = f(T)$.

Positive values of each of the last three terms of Equation 7 will enhance the reaction rate and vice versa. Since exothermic reaction causes local temperature increases which usually increase K, there is a tendency to drive the correlation $\overline{kc_i}$ toward negative in the small scale (reaction interface thickness) but toward positive in the intermediate scale (scale of segregation). Which of these terms dominates and the importance of $\overline{kc_1c_2}$ is not yet known.

Here it is assumed that the opposite $\overline{kc_i}$-effects are compensating and that $\overline{kc_1c_2}$ is of smaller importance than the average terms. The reaction rate is then computed from:

$$P_{\overline{C}_1} \cong -K_o\,\exp(-E_a(\overline{T}-T_o)/R\overline{T}T_o)(\overline{C}_1\overline{C}_2 + \overline{c_1c_2}) \qquad (8)$$

where $\overline{K} = K_o\,\exp(-E_a(\overline{T}-T_o)/R\overline{T}T_o)$. Considerable experimental work will be required to adequately define the $\overline{kc_i}$- correlations in order to use Equation 7.

If K_o in Equation 8 is large, many methods of numerical solution will become unstable because of the product of a very large and a very small number. In that case the equilibrium reaction assumption (20,37), which corresponds to infinite reaction rate must be made.

The turbulent diffusion of the thermal energy generated by the reaction is modeled by a transport equation of the same form as Equation 1 as follows:

$$\frac{\partial\overline{T}}{\partial x_2}\frac{\partial\psi}{\partial x_1} + \frac{\partial\overline{T}}{\partial x_1}\frac{\partial\psi}{\partial x_2} = \frac{1}{C_p}\frac{\partial}{\partial x_1}\left(\frac{\mu_t}{\rho\sigma_T}\frac{\partial\overline{T}}{\partial x_1}\right) + \frac{1}{C_p}\frac{\partial}{\partial x_2}\left(\frac{\mu_t}{\rho\sigma_T}\frac{\partial\overline{T}}{\partial x_2}\right) + P_{\overline{T}} \qquad (9)$$

where $P_{\overline{T}} = H_{R_i}\,P_{\overline{C}_i}$, and H_{R_i} is the heat of reaction.

The effects of temperature on density and viscosity for gases are given approximately by

$$\rho = \rho_o(T_o/\overline{T})$$

$$\mu = \mu_o(\overline{T}/T_o)^{1/2} \qquad (10)$$

Fluctuations of ρ and μ are not considered here. Changes in composition during reaction can also affect density and viscosity, but in many reactions, such as combustion in air, a diluent renders overall composition change effects minor. Such effects can frequently be ignored with care.

RELATIONSHIP BETWEEN SEGREGATION AND CORRELATIONS

In order to make use of the conservation Equations 1, 2, and 8, some form of closure is needed to connect the correlations of fluctuating concentrations $\overline{c_1c_2}$ and $\overline{c_1^2c_2}$ to the segregation $\overline{c_1^2}$ (if component-1 is to be considered). O'Brien and coworkers (40, 43, 44) have done considerable work toward obtaining the needed closure through the development of a theoretical probability density distribution for the concentration fluctuations. Lockwood and Nagib (37) used a truncated normal density distribution for concentration in their model for combustion which makes use of the equilibrium reaction assumption for fast reaction. Donaldson (41) considered effects of various types of simplified probability density distributions on reaction rate, but comparisons with experimental data were not made. A more simplified approach was developed by Patterson (45) using a very crude probability density distribution as shown in Figure 1. The assumed concentration profile is compared in Figure 2 to a more realistic one. This distribution corresponds to the case for almost complete segregation of the components.

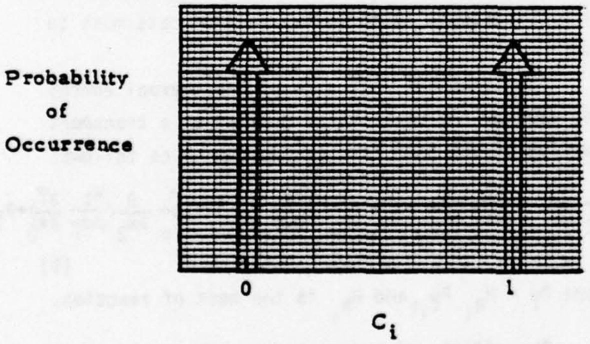

Figure 1. Illustration of pdf for segregated components.

As shown in Figure 2, diffusion of the mixing components during segregation decay was simulated by simply allowing the regions of each component to overlap. That should be a good approximation only when reaction between the components is very fast. Actually, through comparison with the data of Vassilatos and Toor (46) for second-order reaction in a turbulently mixed tubular reactor, it was shown that even for relatively slow reactions good simulation was achieved (45).

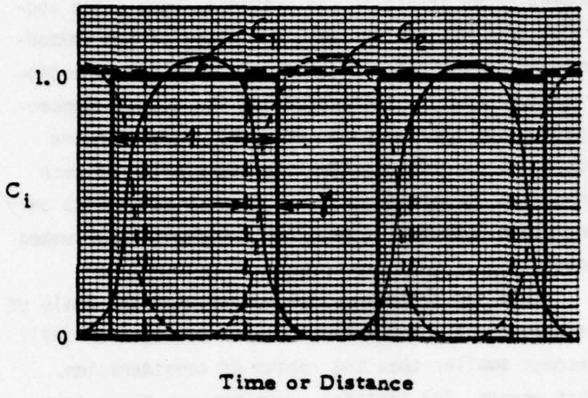

Figure 2. Illustration of simple model of interdiffusion.

For the concentration distribution of Figure 2, the closure relationships are as follows:

$$\overline{c_1c_2} = -\overline{c_1^2}\,(1 - \gamma)/(\beta(1+\gamma)) \qquad (11a)$$

$$\overline{c_1^2c_2} = 2(\overline{c_1^2})^{3/2}\,\gamma(1-\gamma)^{1/2}/(\beta(1+\gamma)^{3/2}) \qquad (11b)$$

where $\beta = \bar{C}_{10}/\bar{C}_{20}$ and $\gamma = (\beta\bar{C}_1\bar{C}_2 - \overline{c_1^2})/(\beta\bar{C}_1\bar{C}_2 + \overline{c_1^2})$. Best results were obtained when $\overline{c_1^2c_2}$ was assumed zero instead of using the above relationship, even though that was inconsistent with the model. Equation 11 was tested for $585<K<10^{11}$ ℓ/mole·sec and for $1.0<\beta<5.75$.

Equations 1, 3, 4, 5 or 6, 8, 9, 10, 11 combined with the usual equations for stream function, vorticity, turbulence energy and dissipation rate now constitute a closed model for second-order reaction between turbulently mixing components.

NUMERICAL SOLUTION OF THE MODEL

The model described above was solved for a number of conditions both for a free jet of component -1 with entrainment of component -2 and for a coaxial jet of components -1 and -2 with entrainment of the annular fluid, component -2. The solutions were obtained for cylindrical and plane jets by use of a two-dimensional relaxation routine as described by Gosman, et al. (47) for steady state flow.

EXPERIMENTAL WORK

Measurements of $\bar{C}_1$, $\overline{c_1^2}$, $\bar{U}_1$ and $\overline{u_1^2}$ were made using a co-axial air jet with and without reaction of dilute components. The jet geometry is shown in Figure 3 and the electronic instrumentation in Figure 4. The ratio of outer-to-inner jet velocities was about 1.5.

The average velocity in the inner jet was 650 cm/sec. Measurements of velocity, which were made by laser-Doppler anemometry using the differential mode, were obtained in order to assure normal jet development. The average velocity and turbulence profiles are compared with the results of Durao and Whitelaw (8) in Figures 5 and 6. The suspended particles were NaCl made by atomization from a 1.0 N solution. The concentration measurements were made with the same light source as for laser-Doppler anemometry by measuring the intensity of scattered light from the measurement volume, with the exception that salt particles were produced from a 0.05 N solution. The technique is similar to that described in References 1 and 2. Recently Melling (48) has analyzed the scattered light technique for concentration measurement in detail and discussed difficulties for measurement of $\overline{u_1c}$ - correlations.

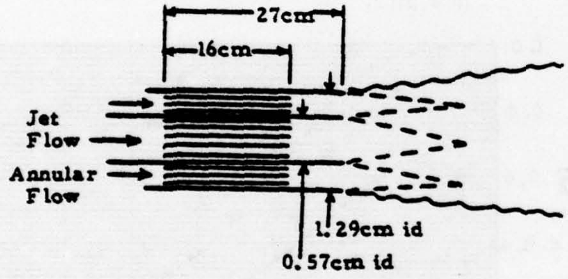

Figure 3. Diagram of co-axial jet used in these experiments.

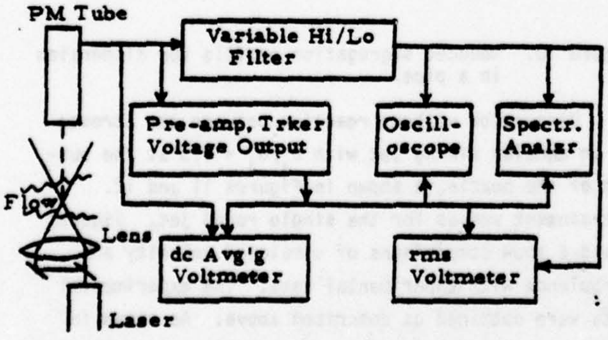

Figure 4. Schematic of electronic instrumentation used for velocity and concentration measurements.

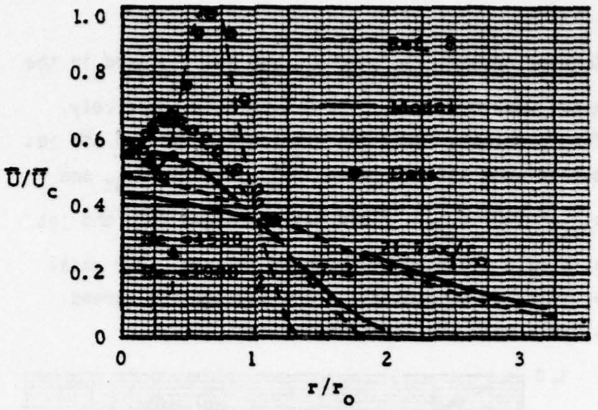

Figure 5. Velocity profiles for the co-axial jet.

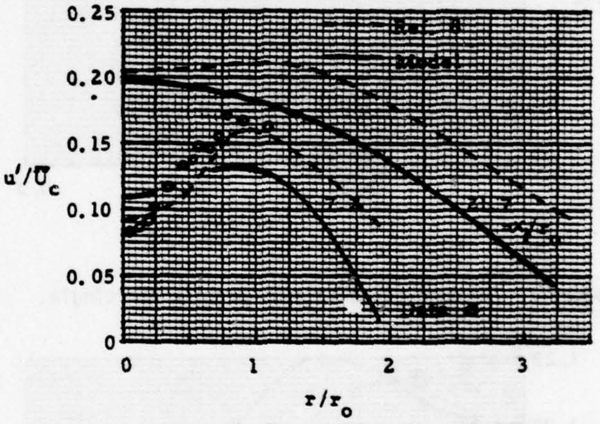

Figure 6. Turbulence profiles for the co-axial jet.

In the case of reaction between mixing components, the co-axial jet was used with hydrogen chloride in the axial jet and ammonia in the annular jet. The scattered light intensity from the generated particles was used as an indication of reaction completion. The relationship between scattered light intensity and ammonium chloride formed was obtained by integration of a far downstream profile where reaction was assumed complete.

RESULTS OF MODEL AND EXPERIMENT

Figures 7 and 8 show comparisons between the average concentration and segregation data of Becker, Hottel, and Williams (1) and the computed results using the model for a single round free jet. The results are presented in the reduced variables $\overline{C_1}/\overline{C_{1c}}$ and $\sqrt{\overline{c_1^2}/c_{1c}^2}$ versus $r/(x_1 - 4.8r_0)$. The values of the

Schmidt numbers σ_T, $\sigma_{\overline{u^2}}$, σ_ε, $\sigma_{\overline{C}}$, and $\sigma_{\overline{c^2}}$ used in the model were 0.6, 1.0, 1.3, 0.6, 0.6, respectively. The turbulence level and dissipation rate in the jet outlet were assumed to be $\overline{u^2}_{out} = 0.01\ \overline{U}^2_{out}$ and $\varepsilon_{out} = 0.01\ \overline{U}^2_{out}$. Fluid was entrained into the jet at a rate dictated by momentum balance. The axial profiles of concentration and segregation agreed closely with the experimental data.

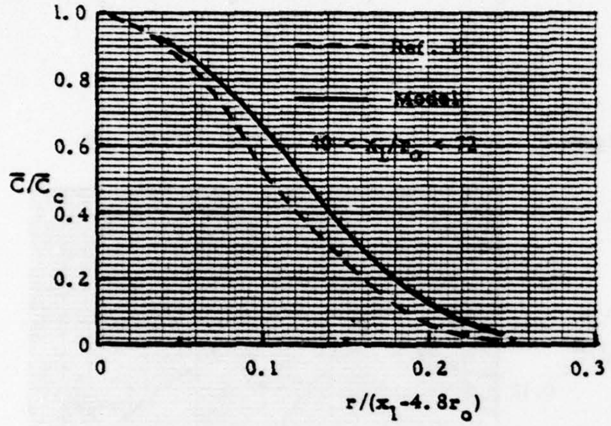

Figure 7. Reduced concentration profile for single, round jet.

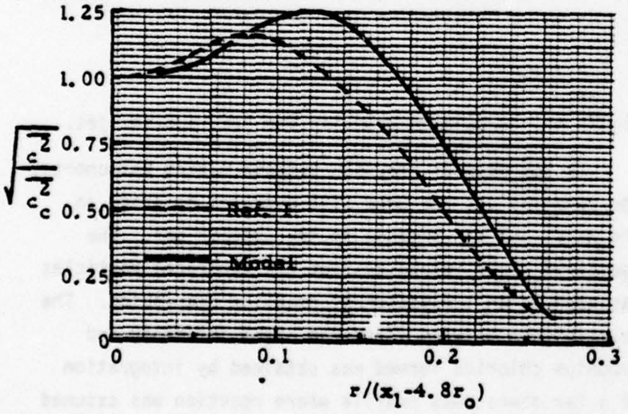

Figure 8. Reduced segregation profile for single, round jet.

Comparison of dispersion in pipe flow measured by Becker, Rosensweig, and Gwozdz (2) with results of the model is shown in Figures 9 and 10. The same values of σ_i were used in the model as above. The jet of dispersing fluid was at the same average velocity as the main stream in the pipe. The concentration profiles and rate of decrease on the centerline were in close agreement with the experimental data, but the segregation values were generally low. This may be because a point source was not simulated in the model.

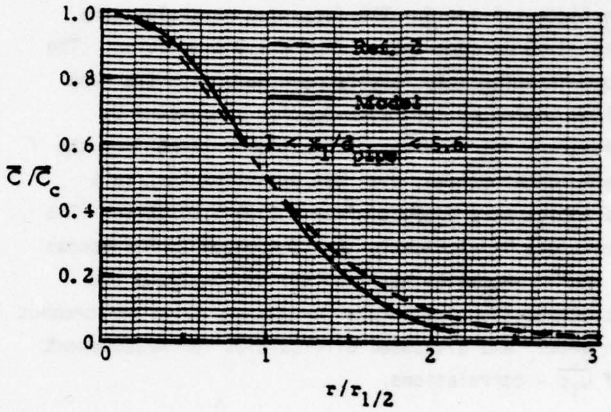

Figure 9. Reduced concentration profile for dispersion in a pipe.

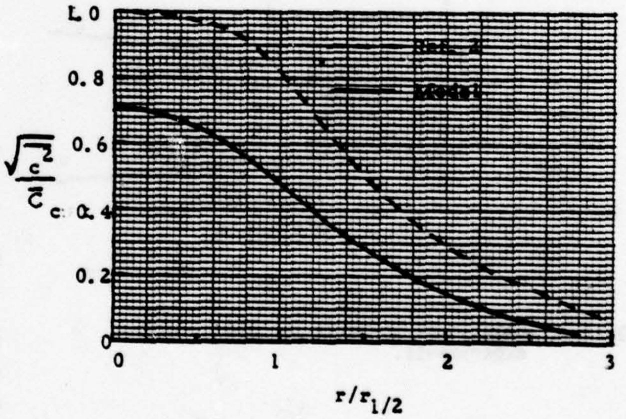

Figure 10. Reduced segregation profile for dispersion in a pipe.

Dispersion without reaction between the streams of an annular mixing jet with $\overline{U}_a/\overline{U}_j = 1.5$ at the outlet of the nozzle is shown in Figures 11 and 12. Entrainment was as for the single round jet. Figures 5 and 6 show comparisons of simulated velocity and turbulence with experimental data. The experimental data were obtained as described above. As shown in Figure 11, the centerline concentrations agree closely (except for $x_1/r_0 = 4.6$) with the experimental data, but the curves are not of the same shape. The model appears to develop a normal distribution profile too rapidly. Figure 12 shows that the model predicts the segregation profiles with the correct qualitative behavior and again the centerline levels are close to correct. The skewness of the experimental data is probably caused by unaccounted for exit conditions.

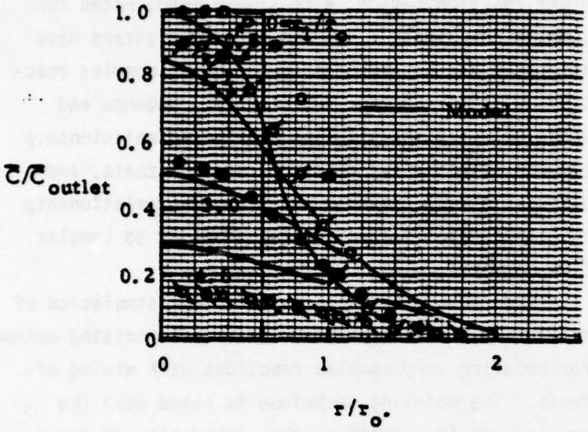

Figure 11. Concentration profiles for the co-axial jet with no reaction.

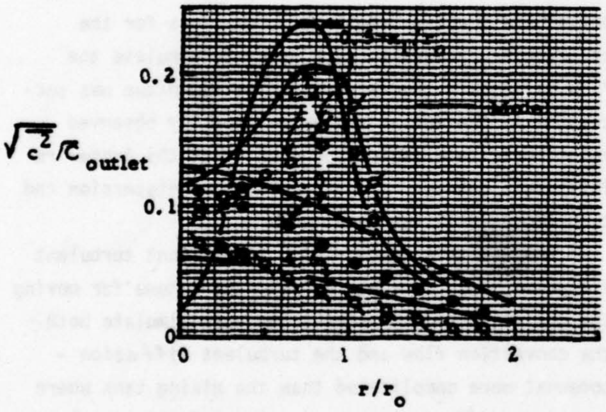

Figure 12. Segregation profiles for the co-axial jet with no reaction.

Simulation of second-order reaction in an annular mixing jet with the same nozzle sizes and outlet velocities as above, was done for reduced kinetic rate constants of 10 and 1000 sec^{-1}, corresponding to $\overline{K}\,\overline{C}_{20}$. Figure 13 shows the concentration profiles and Figure 14 the segregation profiles for $\overline{K}\,\overline{C}_{20}$ = 10. Also, in Figure 13 are shown curves for concentration profiles for assumed perfect local mixing (segregation = 0). A significant difference may be seen.

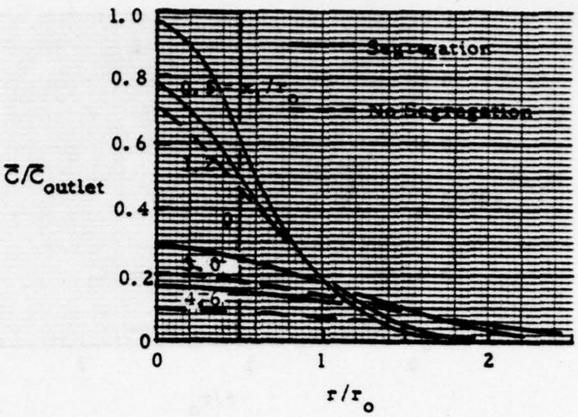

Figure 13. Concentration profiles in co-axial jet with reaction; $K\,\overline{C}_{20}$ = 10 sec^{-1}.

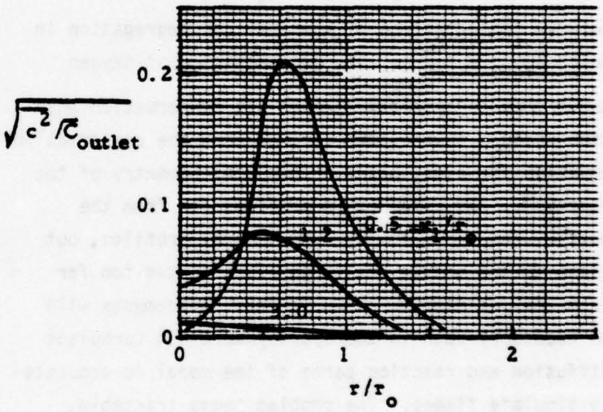

Figure 14. Segregation profiles in co-axial jet with reaction; $K\,\overline{C}_{20}$ = 10 sec^{-1}.

Figure 15 compares simulation results for the same annular jet and $\overline{K}\,\overline{C}_{20}$ = 1000 sec^{-1} with the concentration data for the ammonia-hydrogen chloride reaction, where hydrogen chloride concentration is given as $\overline{C}_1$. Qualitatively the model predicts the correct behavior as compared to the data, but dispersion deviates as in the case of no reaction. The reason for the deviation is probably the same.

Only preliminary work has been done to apply the model presented here to strongly exothermic reactions such as flames, but Figure 16 gives one comparison of computed and experimental(19) temperatures for a town gas-air turbulent diffusion flame produced by a single jet into air. The reaction conversion was calculated by using the equilibrium assumption and the relationship

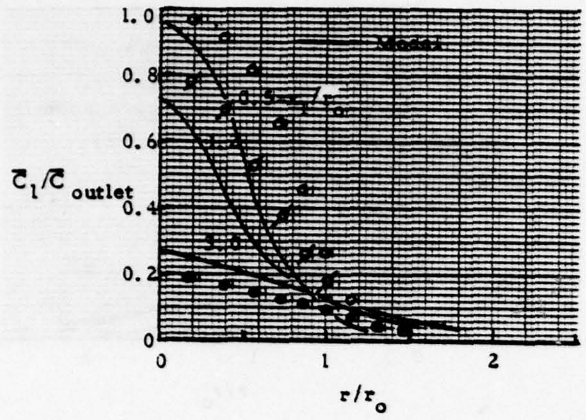

Figure 15. Concentration profiles for co-axial jet with reaction; $\overline{K}\,\overline{C}_{20} = 1000$ sec^{-1}.

between concentration of the fuel and segregation in which $\overline{C}_{fuel} = \sqrt{\overline{c^2_{fuel}}}$. The concentration of oxygen could then be computed through its conservation equation using a source term derived from the conservation equation for fuel, based on the stoichiometry of the reaction. The temperature profiles far from the nozzle were close to the experimental profiles, but close to the nozzle the temperature peaked too far from the jet center. Many further refinements will be necessary both in the hydrodynamic and turbulent diffusion and reaction parts of the model to accurately simulate flames. The problem seems tractable, however, from these preliminary results.

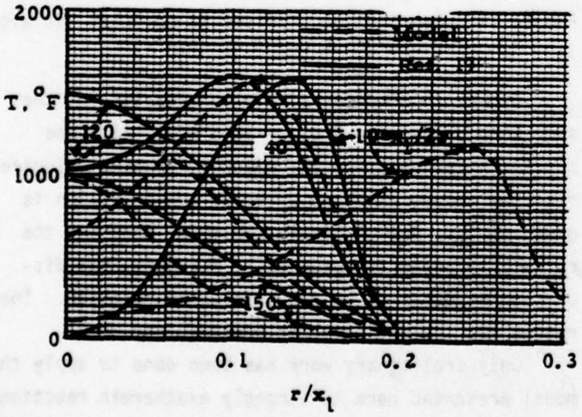

Figure 16. Comparison of model results with temperature profiles in a town gas diffusion flame.

COMPLEX REACTIONS

The most difficult problem in modeling turbulent mixing with reaction is how to handle multiple simultaneous reactions. The relationships of the type of Equations 8 and 11 which result from a single second-order reaction become excessively complicated for complex reactions. A number of investigators have attempted various schemes for handling complex reactions with mixing (49, 50, 51, 52). DeGance and Johns (50, 51) investigated a proposed relationship between selectivity, reaction rate constants, and diffusivities. They did not apply the relationship to higher than first-order reactions or to complex flow patterns.

The random coalescence-dispersion simulation of mixing (52) presently offers the most promising method for modeling very complex reactions with mixing effects. The modeling technique is based upon the merging, mixing, reacting, then separation of sites which represent portions of the turbulent fluid. The technique was used to model a competitive-consecutive second-order reaction in a mixing tank with both propeller and turbine impellers. The sites for the coalescence-dispersion were moved to simulate the flow patterns in the reactors. The technique was successful in predicting the experimentally observed selectivity to a desired product, when the proper relationship between rate of coalescence-dispersion and turbulence level was used. (53).

For use in a reactor with significant turbulent diffusion, such as a mixing jet, the scheme for moving the coalescence-dispersion sites must simulate both the convection flow and the turbulent diffusion - somewhat more complicated than the mixing tank where turbulent diffusion may be ignored. Future developments should show that a combination of $k_e - \epsilon$ modeling of the turbulent flow and turbulent diffusion as described above with the random coalescence-dispersion method will make the modeling of complex reactions with turbulent mixing quite feasible. If strong temperature effects on the flow field occur, iteration between the coalescence-dispersion computation of reaction conversion and the $k_e - \epsilon$ flow field computation will be necessary. It must also be recognized that the method will require long computer run-times.

REFERENCES

1. Becker, H. A., Hottel, H. C., and Williams, G. C., "The Nozzle-Fluid Concentration Field of the Round, Turbulent Free Jet," J. Fluid Mech., 30, 1967, 285.
2. Becker, H. A., Rosensweig, R. E., and Gwozdz, J. R., "Turbulent Dispersion in a Pipe Flow," A.I.Ch.E. J., 12, 1966, 964.
3. Bradbury, L. J. S., "The Structure of a Self-Preserving Turbulent Plane Jet," J. Fluid Mech., 23, 1965, 31.
4. Catalano, G. D., Morton, J. B., and Humphris, R. R., "Experimental Investigation of an Axisymmetric Jet in a Coflowing Airstream," A.I.A.A. J., 14, 1976, 1157.
5. Champagne, F. H., and Wygnanski, I. J., "An Experimental Investigation of Coaxial Turbulent Jets," Intern. J. Heat Mass Trans., 14, 1971, 1445.
6. Corrsin, S., and Uberoi, M. S., "Further Experiments on the flow and Heat Transfer in a Heated Turbulent Air Jet," NACA Report 998, 1947.
7. Corrsin, S., and Uberoi, M. S., "Spectra and Diffusion in a Round Turbulent Jet," NACA Report 1040, 1949.
8. Durao, D., and Whitelaw, J. H., "Turbulent Mixing in the Development Region of Coaxial Jets," J. Fluids Eng., Trans ASME, 1973.
9. Forstall, W., and Shapiro, A. H., "Momentum and Mass Transfer in Coaxial Gas Jets," J. Appl. Mech., 17, 1950, 399.
10. Gutmark, E., and Wygnanski, I., "The Planar Turbulent Jet," J. Fluid Mech., 73, 1976, 465.
11. Owen, F. K., "Laser Velocimeter Measurements in Free and Confined Coaxial Jets with Recirculation," Paper 75-120, A.I.A.A. 13th Aero. Sci. Mtg., Pasadena, Ca. 1975.
12. Rozinsky, E. H., and Brighton, J. A., "Confined Jet Mixing for Non-separated Conditions," J. Basic Eng., Trans. ASME, 1971, D93.
13. Rosler, R. S., and Bankoff, S. G., "Large-Scale Turbulence Characteristics of a Submerged Water Jet," A.I.Ch.E. J., 9, 1963, 672.
14. Sami, S., " Balance of Turbulence Energy in the Region of Jet-Flow Establishment," J. Fluid Mech., 29, 1967, 81.
15. Tomich, J. F., and E. Weger, "Some New Results on Momentum and Heat Transfer in Compressible Turbulent Free Jets," A.I.Ch.E. J., 13, 1967, 948.
16. Lee, W.-C., "Light-Scattering Measurements of Turbulence and Concentration," M.S. Dissertation, University of Missouri-Rolla, 1966.
17. Lee, J., and Brodkey, R. S., "Turbulent Motion and Mixing in a Pipe," A.I.Ch.E. J., 10, 1964, 187.
18. Hawthorne, W. R., Wedell, D. S., Hottel, H. C., 3rd Symp. on Comb., Flame, and Explosion Phen., ed. by Williams and Wilkins, Baltimore, 1949.
19. Lockwood, F. C., and Odidi, A. O. O., "Measurement of Mean and Fluctuating Temperature and of Ion Concentration in Round Free-Jet Turbulent Diffusion and Premixed Flames," 15th Symp. (Intern.) on Combustion, The Combustion Inst., 1975, p. 561.
20. Becker, H. A., "Effect of Concentration Flucuations in Turbulent Diffusion Flames," 15th Symp. (Intern.) on Combustion, The Combustion Inst., 1975, p. 601.
21. Shea, J. R., III, "A Chemical Reaction in a Turbulent Jet," Ph.D. Dissertation, Cal. Inst. Techn., 1975.
22. Zakkay, V., Krause, E., and Woo, S. D. L., "Turbulent Transport Properties for Axisymmtric Heterogeneous Mixing," A.I.A.A. J., 2, 1964, 1939.
23. Flint, D. L., Kada, H., and Hanratty, T. J., "Point Source Turbulent Diffusion in a Pipe," A.I.Ch.E. J., 6, 1960, 325.
24. Baldwin, L. V., and T. J. Walsh, "Turbulent Diffusion in the Case of Fully Developed Pipe Flow," A.I.Ch.E. J., 7, 1961, 53.
25. Hedman, P. O., and Smoot, L. D., "Particle-Gas Dispersion Effects in Confined Coaxial Jets," A.I.Ch.E. J., 21, 1975, 372.
26. Corrsin, S., "The Isotropic Turbulent Mixer," A.I.Ch.E. J., 3, 1957, 329.
27. Corrsin, S., "The Isotropic Turbulent Mixer-II. Arbitrary Schmidt Number," A.I.Ch.E. J., 10, 1964, 870.
28. Brodkey, R. S., "Mixing in Turbulent Fields," in Turbulence in Mixing Operations, ed. by R. S. Brodkey, Academic Press, New York, 1975.
29. McKelvey, K. N., Yieh, H.-N., Zakanycz, S., and Brodkey, R. S., "Turbulent Motion, Mixing, and Kinetics in a Chemical Reactor Configuration," A.I.Ch.E. J., 21, 1975, 1165.
30. Hiby, J. W., "Mischung in Turbulenter Rohrstromung," Verfahrenstechnik, 4, 1970, Dec.
31. Rosensweig, R. E., "Idealized Theory for Turbulent Mixing in Vessels," A.I.Ch.E. J., 10, 1964, 91.
32. Rosensweig, R. E., "Isotropic Turbulent Mixing with Boundary Source," Can. J. Chem. Eng., 44, 1966, 255.
33. Kirmse, D. W., "A Monte-Carlo Study of Turbulent Diffusion," Ph.D. Dissertation, Iowa State University, 1964.
34. Shetz, J. A., "Turbulent Mixing of a Jet in a Co-Flowing Stream," A.I.A.A. J., 6, 1968.
35. Spalding, D. B., "Concentration Fluctuations in a Round Turbulent Free Jet," Chem. Eng. Sci., 26, 1971, 95.

36. Lumley, J. L., "Modeling Turbulent Flux of Passive Scalar Quantities in Inhomogeneous Flows," Phys. Fluids, 18, 1975, 619.

37. Lockwood, F. C., and Naguib, A. S., "The Prediction of the Fluctuations in the Properties of Free, Round-Jet, Turbulent, Diffusion Flames," Combustion Flame, 24, 1975, 109.

38. Launder, B. E., and Spalding, D. B., Mathematical Models of Turbulence, Academic Press, London, 1972.

39. Brodkey, R. S., The Phenomena of Fluid Motions, Addison-Wesley, Reading, Mass., 1967, p. 332.

40. Dopazo, C., and O'Brien, E. E., 4th Intern. Coll. on Gas Dyn. of Exp. and Reactive Sys., La Jolla, Ca., 1973.

41. Donaldson, C. duP., "Modeling of the Scalar Correlations," in Turbulent Mixing in Nonreactive and Reactive Flows, ed. by S.N.B. Murthy, Plenum, New York, 1975.

42. Borghi, R., "Computation Studies of Turbulent Flows," in Turbulent Mixing in Nonreactive and Reactive Flows, ed. by S. N. B. Murthy, Plenum, New York, 1975.

43. Dopazo, C., "A Probabalistic Approach to Turbulent Flame Theory," Acta Astron., 3, 1976, 853.

44. Lin, C.-H., and O'Brien, E. E., "Turbulent Shear Flow Mixing and Rapid Chemical Reactions: An Analogy," J. Fluid Mech., 64, 1974, 195.

45. Patterson, G. K., "Model with No Arbitrary Parameters for Mixing Effects on Second-Order Reaction with Unmixed Feed Reactants," Proc. ASME Mixing Symp., Atlanta, Georgia, 1973.

46. Vassilatos, G., and Toor, H. L., "Second-Order Chemical Reactions in a Non-Homogeneous Turbulent Fluid," A.I.Ch.E. J., 11, 1965, 666.

47. Gosman, A. D., Pun, W. M., Runchal, A. K., Spalding, D. B., and Wolfshtein, M., Heat and Mass Transfer in Recirculating Flows, Academic Press, London.

48. Melling, A., "A Technique for Simultaneous Velocity and Concentration Measurements," unpub. manus. of the Dept. of Mech. Eng., Imperial College, London, 1976.

49. Stein, W., "Umsatz und Selektivitat bei zusammengesetzten Reaktionen in Schlaufenreaktoren mit uberlagerten Umlaufen verschiedener Umlaufzeit," Chemie Ing. Tech., 43, 1971, 466.

50. DeGance, A. E., and Johns, L. E., "The Sensitivity of the Selectivity to Transport Parameters in Batch Heterogeneous Reaction Systems," Chem. Eng. J., 7, 1974, 227.

51. DeGance, A. E., and L. E. Johns, "The Construction of a Homogeneous Representation of Slurry Reactions Under Conditions of Imperfect Contacting," 69th Annual A.I.Ch.E. Meeting, Chicago, 1976.

52. Patterson, G. K., "Applications of Random-Coalescence Dispersion," 4th Intern. Symp. on Chem. Reactor Eng., Heidelberg, 1976.

53. Canon, R. M., Smith, A. W., Wall, K. W., and Patterson, G. K., "Turbulence Level Significance of the Monte-Carlo Interaction Parameter," Chem. Eng. Sci., 1977.

INVESTIGATION OF COMBUSTION INSTABILITIES IN SWIRLING FLOWS USING REAL TIME L.D.V.

A.K. GUPTA,* D.S. TAYLOR, and J.M. BEÉR.*

DEPT. OF CHEMICAL ENGINEERING AND FUEL TECHNOLOGY, SHEFFIELD UNIVERSITY, ENGLAND.

*PRESENT ADDRESS: DEPARTMENT OF CHEMICAL ENG., MIT, CAMBRIDGE, MASS. 02139.

SUMMARY

A real time laser velocimetric system has been developed using a light frequency shifting, a electronic counter, and a real time electronic clock having a time resolution of 0.77 μ sec. The overall velocity response of the anemometric system was investigated using a velocity synthesiser and was found to be better than 1000 Hz. The naturally occuring three dimensional time dependent instability called precessing vortex core associated with strongly swirling flows have been investigated in the isothermal and combustive conditions using the real-time L.D.V. The present measurements show good agreement with those obtained using hot wire anemometry under isothermal conditions. The frequency of the PVC under combustive conditions was found to be generally higher than that found under isothermal conditions.

NOMENCLATURE

A_T	tangential inlet area.
f	frequency
G_x	flux of axial momentum
G_ϕ	flux of angular momentum
L	length of swirler
M_i	input mass flow of air
p	pressure
Δp	total pressure drop across swirl generator
Q	flow rate
r	radius, radial distance
R	swirl generator radius at the exit.
S.F.	time dependent swirl number: frequency based
S.P.	time dependent swirl number: pressure drop based.
S_1, S_2	stream surfaces
S	time mean average swirl number
t	time
u	axial velocity
v	radial velocity
w	tangential or swirl velocity.
ρ	density.
Ω	inlet flux of angular momentum
θ	polar co-ordinate

INTRODUCTION

Swirl is commonly used for flame stabilization in high intensity combustors. There is now enough evidence to suggest that assumptions of flow axi-symmetry made with many types of swirling flows are true only for low swirl and Reynolds number (1,2,3,4,5). At a swirl number greater than 0.6 (so as to cause local recirculation) as the Reynolds number is increased an instability develops called the vortex breakdown phenomenon; it is first revealed as a small closed bubble of circulating fluid on the burner axis (3,6). As the Reynolds number is further increased, a large three dimensional time dependent instability, called the precessing vortex core (hereafter P.V.C.) develops. In this the central forced vortex region of flow is displaced from the axis and starts to precess about the axis of symmetry. This phenomenon is very regular in nature and can cause other instabilities to arise (5,7). This transition has considerable implications not only for the stability of swirl burners but also for the rates of mixing, hence combustion intensity and flame length. The PVC in diffusion flames can extend the range of stable burning well into the region of fuel lean mixture ratios (1). Besides the flame stability and combustion intensity the large PVC in combustion systems is undesirable as resonant coupling between the PVC frequency and the furnace or cavity can easily occur (2). In general, under isothermal conditions, previous studies with a hot wire anemometer and the frequency amplitude spectral analysis in a reverberant room showed that the frequency of the PVC increases linearly with Reynolds number (8). Also there only appears to be one PVC present in most swirl burners (1,7). The spatial distribution of pressure fluctuations measured with a probe coupled condenser microphone at the burner exit showed a sharp peak towards the centre of the PVC (4). The peak frequency of the fundamental harmonic was found to increase linearly with the air flow rate. In many swirling flows, therefore the PVC dominates the flow and causes very high levels of velocity fluctuation (previously thought to be turbulence).

The PVC frequently occurs in isothermal flows, particularly inside long devices $L/_D > 1$) or at the exit (6,9). Combustion has significant effect upon the PVC and may be strongly characterised by the mode of fuel introduction into the burner (1,2,7):

(a) Pre-mixed Combustion excites the frequency and amplitude of the PVC substantially, the amplification depends principally upon the mixture ratio.

(b) Diffusion type flames produced by axial or tangential fuel entry (at mixture ratios around stoichiometric) damp the frequency some what (at high Re) and amplitude by more than an order of magnitude. This damped PVC does not greatly affect the aerodynamics of the swirling flow. The frequency and amplitude of the PVC are not greatly affected by the air/fuel mixture ratio. At very weak mixture ratio (>50) there is a sudden transition or vortex breakdown(s) to a conjugate state with a large, virtually undamped

PVC present.

Measurements of the rotating temperature field, associated with the PVC, under conditions approaching vortex breakdown showed high temperatures near to the centre of the PVC (∿ 1250°C) (1). Precessing vortex cores cause large regular fluctuations in pressure (typically 0.12 atmospheres) accompanied by large temperature fluctuations (up to 1100°C in 3 m sec.)

Previous reported results were made with a hot wire anemometer in the non-reacting (isothermal) swirling flows and a pitot probe coupled to a pressure transducer in the combustive case. This can give erroneous results due to the presence of a physical probe in particular when the diameter of the probe is similar to the dimensions of the PVC. In addition to the problem of disturbance to the flow, the pitot probe also suffer from (a) low frequency response, (b) low amplitude response, and (c) the presence of a standing wave under certain flow conditions.

In a recent paper by cherdron et at (10) asymmetric flows with sudden expansion geometries were studied using a flow visualisation technique and laser doppler anemometry. These self-induced disturbances are generated at the edge of expansion, and amplified in the shear layers. The frequency spectra of velocity was obtained by using a Fast Fourier Analyser (Hewlett Packard 5440A) in conjunction with a tracker (BBC - Goerz LSE 01). The resulting output could either be displayed on a x-y plotter or punched onto paper tape for subsequent computer processing. The spectral content of the fluctuations in velocity were related to the dimensions of the two unequal regions of flow recirculation. It was shown that the intensity of fluctuating energy in the low Reynolds number flows studied can be larger than the corresponding turbulent flows.

This paper, therefore, investigates the naturally occuring three dimensional time dependent instability associated with strongly swirling flows in the isothermal and combustive cases with a newly developed Real Time Laser Anemometer. A real time LDA has been specially developed using a light frequency shifting, electronic particle pulse counter and a real time electronic clock having a time resolution of 0.76778 μ sec. Results are also reported from that carried out on a Real Time Laser Anemometry (RTLA) oscillating velocity synthesiser and an oscillating pipe flow. The results show that effectively any regular perturbation present in the flow, in the presence of a high level of background noise, can be extracted.

2. EXPERIMENTAL APPARATUS AND TECHNIQUES

The Swirl Burner

The experimental swirl burner consisted of a cylindrical tube 34 mm diameter, and 100 mm. long, Fig. 1. Air was supplied through eight 1.04 mm wide tangential inlet slits in the wall. Natural gas was used as the fuel: composition, 94.4% CH_4, 3.22%, C_2H_2, 0.6% C_3H_8, 1.46% N_2; the remainder being higher hydrocarbons. The mode of fuel injection into the burner could be varied from axial at the base of the burner to tangential half way up the burner.
The definition of swirl number used (11), was

$$S = G_\phi / G_x R$$

where the axial flux of angular momentum

$$G_\phi = \int_0^R (wr)\, \rho\, u 2\pi r dr.$$

and the axial flux of linear momentum

$$G_x = \int_0^R 2\pi u^2 \rho r dr + \int_0^R 2\pi p r dr$$

However in the present study as the detailed experimental measurements of various velocity profiles and static pressure were not available, the swirl number, based upon geometrical parameters for this particular burner was obtained as follows:

Input axial flux of angular momentum

$$G_\phi = M_i\, (M_i\, R/_{\rho_i}\, A_T)$$

Input axial flux of linear momentum

$$G_x = M_i\, (M_i/\rho_i R^2)$$

Thus $S = \dfrac{G_\phi}{G_x R} = \dfrac{\pi R^2}{A_T} = 1.56$ for the swirl burner used here.

The Real Time Laser Anemometric System

The anemometric system shown in Fig. 2 consists essentially of two major parts - An electronic converter unit which processes raw photomultiplier signals into batches of digital information and a digital processor which is essentially capable of storing or processing data from the converter. In the present apparatus the latter is a Digital LS1-11 PDP 11/03 mainframe with 8K of Memory in 16 bits and a parallel line interface DL V11 through which electrical connection is made to the converter.

The Electronic converter is essentially a pulse-counting anemometer which has capability of processing three raw photomultiplier signals simultaneously. Each signal is amplified and gated against a high frequency oscillator which in effect times the usable portion of the input burst. Each of the three channels therefore presents its output as two pulse trains which are counted and stored on a pair of 16 bit binary registers. The leading edge of the first channel to excite is also used to provide a pulse which updates a latch linked to a1.3MHz real time clock. This allows each event to be timed to the nearest microsecond, and to be presented on two 16 bit latches as the most and least significant points of a 32 bit word.

As soon as an event has terminated, data is present as a total of eight 16-bit words in appropriate registers. These words are then transferred to the computer via a short routine which accepts as many words as required via a multiplexer whose select address is sequenced by the program. Data presents in the order X, Real Time, Y and Z, so that curtailment of the program can be used to transfer less than the full complement of available data.

Velocity Synthesiser

This device has been assembled in order to source a complete through-system excercise to facilitate both program and hardware development, Fig. 3. In effect the device replaces one converter board allowing synthesis of one channel response plus the real time clock function. The module contains an oscillator to provide a basis for the real-time clock, (nominally 1 MHz), one to source events at about 1 KHz with an approximate 10 per cent duty cycle, and a further voltage controlled oscillator which produced a frequency around 1 MHz which could be modulated by an audio frequency signal supplied from an external signal generator. The whole arrangement developed a regular series of signals with a varying cycle count which was interpreted by the rest of the system as a particle stream with velocity modulated in amplitude frequency and waveform identical to the signal applied by the external signal generator.

The Oscillator Pipe Flow

A predetermined regular perturbation in axial velocity was obtained by using an oscillating diaphragm driven by an eccentric 3-phase motor, Fig. 4. The column of air inside the cavity oscillates at a frequency depending upon the motor speed. The motor speed, which was nominally 1000 r.p.m., was detected using a photoelectric detector, a trigger unit and a counter, Fig. 4. The Amplitude and shape of the waveform in the pipe flow could be controlled by adjusting the air flow through the pipe. High frequency oscillations in the pipe flow were obtained using a loud speaker driven by a power amplifier. This arrangement was able to produce oscillations in the pipe flow upto about 350 Hz. The shape of the regular perturbation in signal to the amplifier.

The High level Program for Data Reduction

Raw data acquired via the multiplexer from the converter unit was stored in the core memory of the PDP 11/03 as a series of 16 bit binary numbers. Since this machine does not yet have a direct physical connection with the main PDP8 machine, it was necessary to dump this data on paper tape after each run. The PDP 11/03 was equipped with binary-decimal convert routine which allowed all acquired data to be punched as a punctuated series of 5-digit decimal numbers. These tapes were then transferred by the PDP8 system to a series of Files identifiable by OS/8 Basic, through which all results were subsequently calculated. The high level program first reduced all data of an input group to an instantaneous velocity and a real time value in milliseconds with the first time reading equal to zero. The program then selected a time interval which was set at twice the cycle time of a frequency which was rather smaller than that expected from circumstantial evidence. The real time reading associated with each velocity value was then divided by the preselected interval and the remainder taken as an indication of where in that cycle (or pair of cycles) the particular velocity reading would lie. Each velocity reading would then be used to update one of 40 accumulator registers so that each register would always contain the mean of all those valves that had been assigned to it. In this way, allocation of every item of raw data would lead to population of the 40 slots which would reconstruct two complete cycles of a periodic input velocity wave only if the selected cycle time was exactly equal to the period of that wave. In all other cases, the distribution within the 40 registers would be more or less incoherent giving rise to essentially random pattern of velocity distribution.

The program was equipped with a graphic routine for the teletype so that the eye could be used to judge the symmetry or otherwise of the results. In addition, the program was made to reiterate by stopping up the search frequency by a fixed increment so that the eye could be used to detect the appearance of a coherent waveform in the series of graphs so produced.

3. THEORETICAL CHARACTERIZATION OF SWIRLING FLOWS

For swirling flows with PVC a nondimensional frequency parameter similar to that suggested by Cassidy and Falvey (6) can be derived (ignoring viscous terms and considering momentum equation parallel to the mean flow) as follows:

$$r\rho\frac{\partial w}{\partial t} + r\rho\left(v\frac{\partial w}{\partial r} + \frac{1}{r}w\frac{\partial w}{\partial \theta} + ru\frac{\partial w}{\partial x} + \frac{wv}{r}\right) = \frac{\partial P}{\partial \theta} \quad \ldots(1)$$

With the continuity equation, integration over an arbitrary control volume and the use of Ganss's theorm gives

$$\frac{\partial}{\partial t}\int_V r\rho w\,\partial V + \int_S \rho r w\left(v\frac{\partial r}{\partial n} + wr\frac{\partial \theta}{\partial n} + v\frac{\partial x}{\partial n}\right)\partial S + \int_V \rho w\,\partial V = \int_V \frac{dPdV}{\partial \theta} \quad \ldots (2)$$

choosing the control volume V, the tube length L, and diameter D, Eqn. (2) becomes

$$\frac{\partial}{\partial t}\int_V r\rho w dV - \int_{S_1} \rho r w u dS + \int_{S_2} \rho r w u dS + \int_V \frac{\rho v w r dV}{r} = -\int_V \frac{\partial P\,\partial V}{\partial \theta} \quad \ldots (3)$$

The second integral is the flux of angular momentum into the tube. This is an independent variable-Ω.

Forming dimensionless quantities from all variables transforms eqn. (3) to

$$\left(\rho\frac{Q^2}{\Omega D}\right)\left(\frac{fD^3}{Q}\right)\frac{d}{dt}\int_{\bar{V}} \bar{r}\bar{w}d\bar{V} - 1 + \left(\frac{\rho Q^2}{\Omega D}\right)\cdot\left\{\int_{\bar{S}_2} \overline{\rho w u d\bar{s}} + \int_{\bar{V}} \overline{vw}d\bar{V}\right\} = -\left(\frac{\Delta P D^3}{\Omega}\right)\int_{\bar{V}} \frac{\partial \bar{P}}{\partial \theta}d\bar{V} \quad \ldots\ldots (4)$$

The dimensionless parameters fD^3/Ω, $\Delta PD^3/\Omega$, $\Omega D/_{\rho Q}{}^2$ with the $L/_D$ ratio may then be used to correlate experimental frequency data.

If we define our second swirl parameter as the ratio of frequency and momentum parameters

$$S.F. = \frac{fD^3}{Q} \times \frac{\rho Q^2}{\Omega D} = \frac{\rho f D^2 Q}{\Omega}$$

This swirl parameter (12) was shown to be constant over a wide range of different flow rates and L/D ratios ($1.6 \leq L/_D \leq 7.2$). Similar comments apply to the pressure parameter i.e. the ratio

$$S.P. = \frac{\Delta PD^3}{\Omega} \times \frac{\rho Q^2}{\Omega D} = \frac{\Delta PD^2Q^2}{\Omega^2}$$

suggesting that either parameter may be used for characterization of such swirling flows.

4. RESULTS AND DISCUSSION

Under isothermal conditions a hot wire was placed at the burner exit at about $^r/_R = 0.67$; a signal as shown in fig. 5(a) was obtained. The frequency of this PVC was found to increase linearly with flow rate tangentially through the burner. When fuel was introduced axially to the burner, it was entrained immediately into the PVC. A photograph of the flame under fuel lean conditions, as shown in Fig. 5(b), showed that the burning essentially occurs in and around the PVC. It has been shown before (9) that the non dimensionalized frequency parameter $fD_e{}^3/Q_o$ tends to a constant value at high Reynolds number both for the combustive and isothermal flows. A pitot tube coupled to a pressure transducer was used as sensor under combustive conditions (9) which can have a poor frequency and amplitude response particularly at high frequencies.

Velocity Synthesiser

To check the frequency response of the laser anemometry hardware a velocity synthesiser was devised. Both the frequency and the amplitude could be varied in this synthesiser. The input waveforms to the synthesiser were varied from few Hz up to 1000 Hz and the corresponding waveforms obtained using the RTLA system described in section 2. The resulting output waveforms are depicted in Fig. 6 and correspond to the input frequencies of 50 Hz, 101.6 Hz, 202.9 Hz, and 1000.7 Hz which were measured using a counter timer. However, at low frequencies, when the time cut frequency in the computer program did not match exactly with the input frequency, to the velocity synthesiser the presence of a regular wave form could still be observed as seen in Fig. 7. At higher frequencies a more accurate time cut is required to extract the waveform. For example at 500 Hz, one m sec difference in time cut gives a waveform completely out of phase. Under isothermal or combustive conditions in swirl burners therefore one requires an approximate idea of the frequency. Once an approximate waveform is extracted from the raw data, a true waveform can then be obtained by re-analysing the data closer to the approximate waveform frequency in small steps.

Oscillatory Pipe flow

Oscillations in velocity were obtained using either a loud speaker driven by a power amplifier or by an oscillating diaphragm driven by a motor.

Oscillatory frequencies of about 16 Hz in the pipe flow with the motor driven diaphragm and about 350 Hz with the loud speaker arrangement could easily be obtained. The shape of the waveform could be altered by adjusting the air flow rate through the pipe. The results are depicted in 8 and 9, and represent the waveforms present in the flow using a oscillating diaphragm, Fig. 8 and a loud speaker, Fig. 9. As expected a good waveform is obtained at low frequencies, Fig. 8. At high frequencies, however, the response is poor and can be due to number of errors e.g. agglomeration in seeded particles giving low frequency response and also amplitude and phase lag, error in time cut frequency, and the errors due to the variation in frequency over the time duration of the measurement. Other sources of errors are mentioned in ref. 13. Despite the various errors so introduced, a reasonable shape of the waveform can be extracted.

Swirling Flow with PVC - isothermal Case

The PVC signal obtained using hot wire anemometer, Fig. 5, showed the presence of a low frequency waveform. A high frequency low amplitude signal superimposed on the low frequency can also be seen. With the RTLA one would expect to see a basic low frequency PVC signal superimposed on a low amplitude high frequency signal. This is indeed what was obtained here, Fig. 10. The measurement control volume in Fig. 10 was 6 mm away from the burner exit and at $^r/R \simeq 0.7$. The centre of the PVC was found by locating the position of the zero velocity. As the MCV was moved radially outward or inward at the burner exit random fluctuations (i.e. no characteristic waveform) were found, as expected. Maximum amplitude of velocity oscillations were found with the MCV at the centre of the PVC.

Swirling Flow with PVC - Combustive Case

The influence of combustion upon the PVC was investigated by introducting natural gas either axially at the base of the burner or tangentially half way up the burner. The amplitude of the PVC was damped with axial mode of fuel injection in agreement with the previous findings (1,7). However, with tangential fuel entry high amplitude of oscillations of PVC were found, Fig. 11. The type of flame obtained with this is an intermediate between the axial fuel entry at the base of the burner and the pre-mixed swirling type. The flame extended typically about 1 - 2 burner exit diameters. The measurements taken with the RTLA with MCV at 6 mm downstream of the burner exit showed the presence of the expected waveform.

5. CONCLUSIONS

The naturally occuring three dimensional time dependent instability called the precessing vortex core (PVC) associated with strongly swirling flows in the isothermal and combustive cases have been investigated with a newly developed real time laser anemometric system. The overall frequency response of the anemometric system was found to be better than 1000 Hz. This technique has many advantages over the conventional type of probes and investigate the interaction of combustion and thePVC. The data obtained can be used to design combustion system to mismatch the frequency of the PVC and the natural frequency of the combustion chamber this avoiding low frequency high amplitude oscillations in the burner-combustion chamber installation. The present measurements showed a good agreement between the hot wire measurements and the real time LDV in the isothermal state. The frequency of the PVC under combustive conditions was found to be generally high.

Acknowledgements

This work was supported by the SRC and is gratefully acknowledged.

REFERENCES

1 Syred, N., Gupta, A.K., and Beér, J.M: Temperature and Density Gradient Changes Arising with the Precessing Vortex Core and Vortex Breakdown in Swirl Burners. Proc. 15th Symposium (Intl.) on Combustion, Tokyo, 1974: pp. 587-597.

2 Syred, N., Hanby, V.I., and Gupta, A.K.: Resonant Instabilities Generated by Swirl Burners. J. Inst. Fuel, 46, 1973. pp. 402-407.

3 Sarpkaya, T.: J. Fluid Mech. 45, 1971. pp. 545.

4 Gupta, A.K., Syred, N., and Beér, J.M.: Noise Sources in Swirl Burners. J. Applied Acoustics, 9, 1976. pp. 151 - 163.

5 Syred, N., and Beér, J.M.: Astronaut Acta 17, 1972, pp 783-801.

6 Cassidy, J.J., and Falvey, H.T.: J. Fluid Mech, 41, 1970, pp. 727-736.

7 Syred, N., and Beér, J.M.: 14th Symposium (Intl.) on Combustion, the Combustion Institute, 1973. pp. 523.

8 Gupta, A.K., Syred, N., and Beér, J.M.: J. Inst. Fuel, March, 1973. pp. 119-123.

9 Syred, N., and Beér, J.M.: Proc. European Symposium on Combustion, Academic Press, 1973. pp. 542.

10 Cherdron, W., Durst, F., and Whitelaw, J.H. "Asymmetric Flows and Instabilities in Symmetric Ducts with Sudden Expansions". Sonderforschungsbereich 80, Ausbreitungs Und Transportvorgänge in Strömungen, Universität Karlsruhe, Report No. SFB 80/E/84, Oct., 1976.

11 Beér, J.M. and Chigier, N.A.: Combustion Aerodynamics, Applied Science Publishers Ltd., London, 1972.

12 Chanand, R.C. "Observation of Oscillatory Motion in Certain Swirling Flows". J. Fluid Mech., 21, 1965 pp. 111 - 127.

13 Gupta, A.K., and Beér, J.M. Dept. of Chem. Eng. and Fuel Tech. report No. CEFT/102/10/75, 1975.

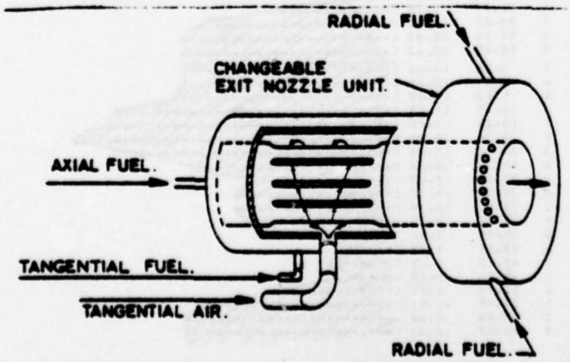

Fig. 1 The Swirl burner

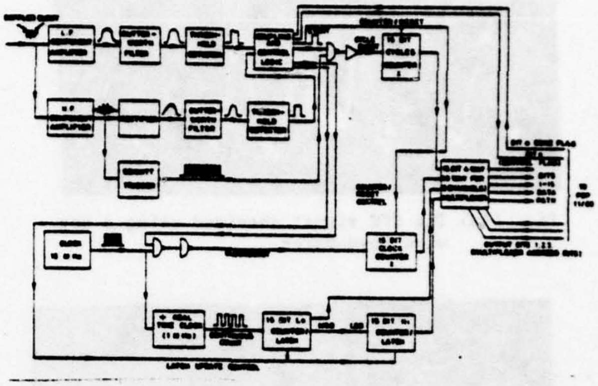

Fig. 2 Block diagram of the Real Time Laser Anemometer System.

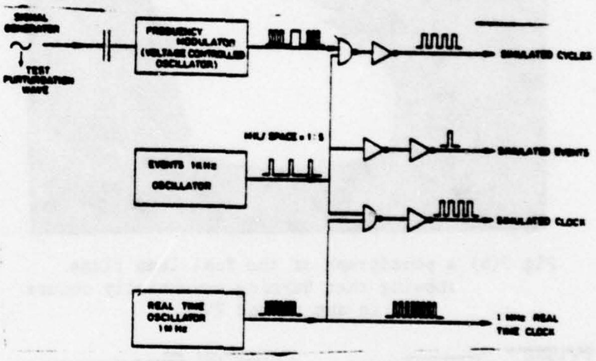

Fig. 3 Real Time Laser Anemometer oscillatory velocity Synthesiser

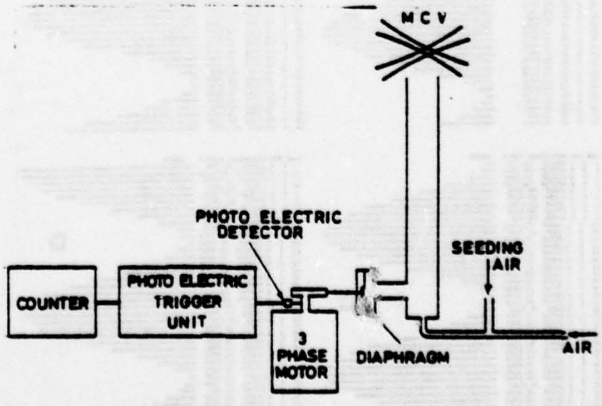

Fig. 4 A Block diagram of the oscillatory pipe flow using an eccentric motor.

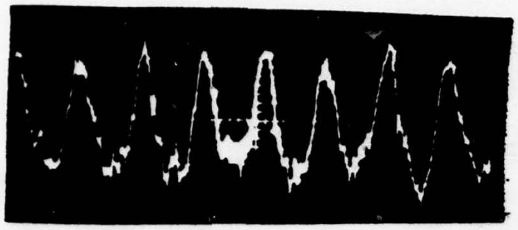

Fig. 5(a) The PVC signal obtained using a hot wire anemometer.

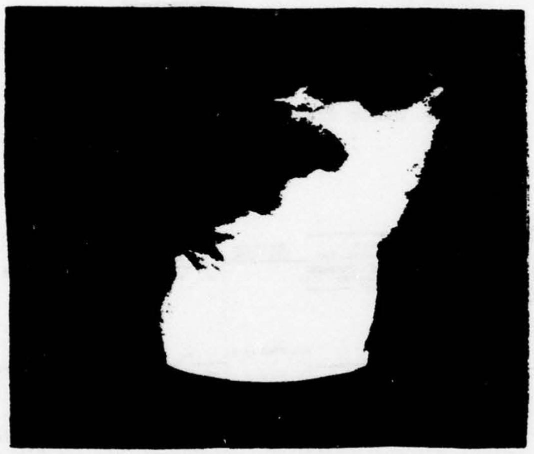

Fig 5(b) A photograph of the fuel lean flame showing that burning essentially occurs in and around PVC.

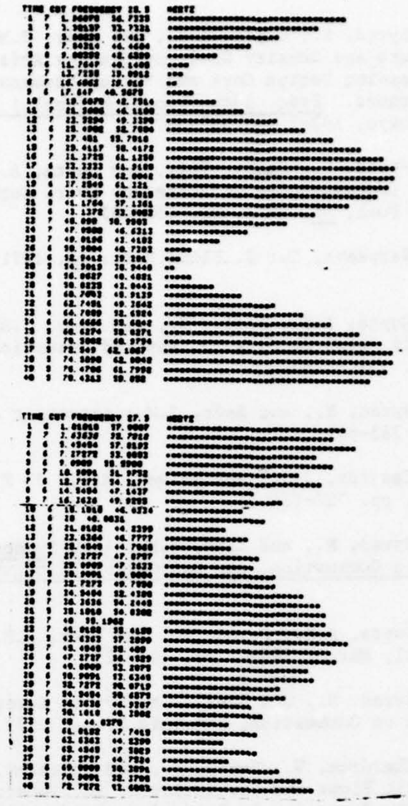

Fig. 7 Graphic displays of 25.5 Hz wave form using a velocity synthesiser at 25.5 Hz and 27.5 Hz.

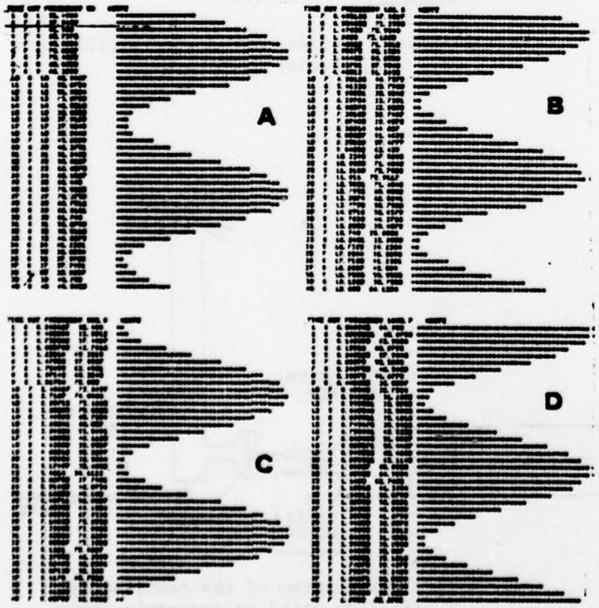

Fig 6 Graphic displays of the waveforms using a velocity synthesiser at (a) 50 Hz, (b) 101.6 Hz, (c) 202.9 Hz, and (d) 1000.7 Hz.

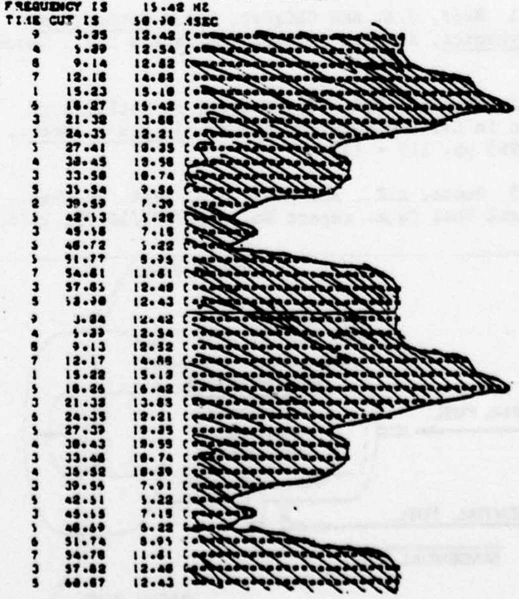

```
FREQUENCY IS    15.42 HZ
TIME CUT IS     60.90 MSEC
   9     3.35   12.42 (
   4     6.39   12.34 (
   8     9.14   12.82 (
   7    12.18   14.88 (
   1    15.23   15.10 (
   6    18.27   15.42 (
   3    21.32   13.88 (
   5    24.35   12.21 (
   5    27.41   10.35 (
   4    30.45   10.58 (
   3    33.50   10.74 (
   5    36.54    9.56 (
   2    39.59    7.39 (
   5    42.63    5.22 (
   3    45.68    7.15 (
   5    48.72    5.22 (
   5    51.77    8.95 (
   7    54.81   11.61 (
   3    57.85   12.48 (
   5    60.90   12.43 (
   9     3.34   12.42 (
   4     6.39   12.34 (
   8     9.13   12.32 (
   7    12.17   14.88 (
   1    15.22   15.12 (
   5    18.26   16.42 (
   3    21.30   13.85 (
   6    24.35   12.21 (
   5    27.39   10.35 (
   4    30.43   10.59 (
   3    33.48   10.74 (
   4    36.52   10.39 (
   3    39.56    7.91 (
   5    42.61    5.22 (
   3    45.65    7.15 (
   5    48.69    6.22 (
   6    51.74    8.95 (
   7    54.78   11.61 (
   3    57.82   12.48 (
   5    60.87   12.43 (
```

Fig. 8 Graphic display of the waveform using oscillatory diaphragm.

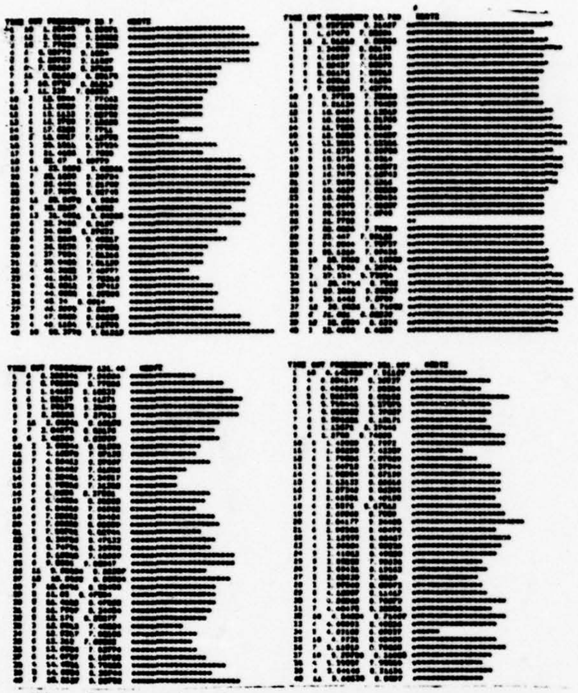

Fig. 9 Graphic display of the waveforms using a loud speaker.

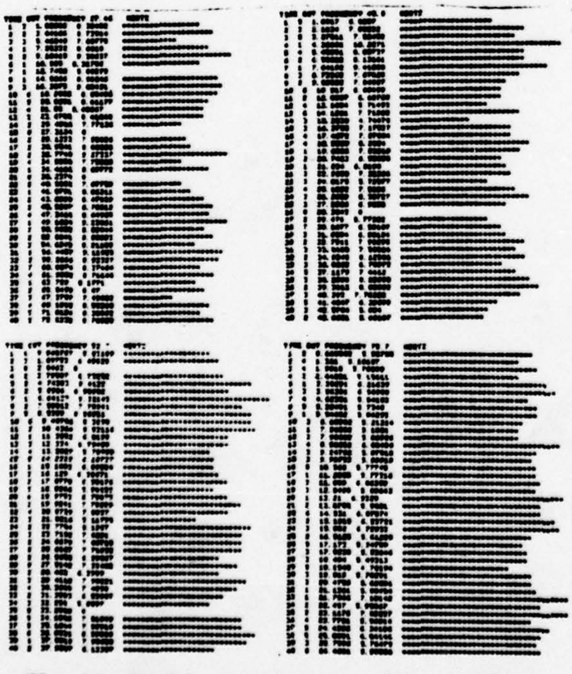

Fig. 10 Graphic display of the PVC - isothermal case

```
TIME CUT FREQUENCY 38.8   HERTZ
 1  4  1.28866  10.0496
 2  3  2.57732  9.99264
 3  3  3.86598  9.30640
 4  2  5.15464  10.33
 5  4  6.4433  10.9967
 6  7  7.73196  10.9426
 7  4  9.02062  11.2166
 8  4  10.3093  11.1140
 9  4  11.5979  10.5216
 10  3  12.8866  9.92309
 11  4  14.1752  10.306
 12  2  15.4639  10.1425
 13  2  16.7526  9.96696
 14  3  18.0412  6.8828
 15  4  19.3299  11.933
 16  1  20.6185  11.1900
 17  1  21.9072  8.68528
 18  5  23.1959  9.41458
 19  4  24.4845  11.1649
 20  3  25.7732  10.9922
 21  0  27.0618  0
 22  2  28.3505  9.34978
 23  6  29.6392  9.99277
 24  2  30.9278  9.67244
 25  1  32.2165  9.98013
 26  6  33.5051  10.7382
 27  2  34.7938  10.5287
 28  5  36.0825  10.734
 29  3  37.3711  11.5728
 30  1  38.6598  9.70974
 31  1  39.9484  11.6127
 32  4  41.2371  10.4909
 33  3  42.5258  10.2035
 34  1  43.8144  12.2904
 35  6  45.1031  9.84258
 36  1  46.3917  11.9361
 37  4  47.6804  9.78876
 38  3  48.9691  9.99133
 39  1  50.2577  12.5946
 40  4  51.5464  11.1933

TIME CUT FREQUENCY 42.2   HERTZ
 1  6  1.18483  4.93286
 2  4  2.36967  5.07485
 3  3  3.5545  5.96006
 4  2  4.73933  5.38716
 5  3  5.92417  5.34986
 6  3  7.109  5.08811
 7  2  8.29384  5.09841
 8  6  9.47867  5.15951
 9  3  10.6635  5.12805
 10  2  11.8483  5.38161
 11  1  13.0332  5.27873
 12  2  14.218  5.58273
 13  6  15.4028  5.57737
 14  1  16.5877  5.57769
 15  3  17.7725  5.48449
 16  0  18.9573  0
 17  3  20.1422  5.58882
 18  2  21.327  5.60087
 19  4  22.5118  5.38619
 20  5  23.6967  5.44799
```

Fig. 11 Graphic display of the PVC - Combustive Case

PREDICTION AND EXPERIMENTAL VERIFICATION OF TWO-DIMENSIONAL TURBULENT FLOW WITH COMBUSTION

A. PRZEKWAS and M. ZEMBRZUSKI

Institute of Power Engineering and Fluid Mechanics, Technical
University of Wrocław, Poland

ABSTRACT

The paper describes the mathematical model calculations of turbulent flow with combustion and the experimental measurements of velocity, concentrations and temperatures in the turbulent partially premixed town gas /air flame in cylindrical combustion chamber/.

The problem of calculation of a time-average reaction rate of one-step reaction in turbulent premixed flame was treated. An application of bimolecular Arrhenius - type function of the local time-average properties to the calculation of combustion rate gives any satisfactory results. The rigorous calculations need such a combustion model which includes a turbulent velocity, temperature and concentrations fluctuations. And to this end there were done the initial experimental measurements of the temperature fluctuations in premixed confined flame. The measurement of temperature fluctuations in selected measuring sectios of combustion chamber are reported.

NOMENCLATURE

a,b,c - functions appearing in conservation equation
A - constant in Arrhenius Law
C - constants in turbulence model
E - activation energy, constant in wall function
f - mixture fraction
g - time-mean-square of fluctuation
h - enthalpy
i - stochiometric ratio
k - kinetic energy of turbulence
m - mass fraction of species
p - pressure
R - universal gas constant
r - radial distance from the burner axis
S - source term in conservation equation
T - time mean temperature
u,v - time mean velocities
x - axial coordinate
y - distance from the wall
α - relaxation factor
ε - turbulence energy dissipation rate
μ - viscosity
ρ - gas density
τ - thermocouple time constant, shear stress
ϕ - general dependent variable
ψ - stream function
ω - vorticity

Subscripts and superscripts

eff - effective
fu - fuel
ox - oxygen
ξ - turbulent
- turbulent fluctuating component
— - time-averaged value

INTRODUCTION

Turbulent fluid flows with chemical reaction in combustion chambers are common in wide range of industrial practice. Combustion processes of gas-fuels occour in gaseous-rocked engines, glass-making and metal industries and in combustion chambers of steam boilers. In combustion devices, it is becoming increasingly important to have a knowledge of the velocity, temperature and concentrations distributions in a turbulent reacting flow in combustion chamber. At the present time many papers treat the numerical methods of turbulent flow with chemical reaction in application to prediction of combustion chambers.

In the numerical calculations of a complicated physical-chemical flow process with combustion important is as well physical models e.g. turbulent transport of flow properties and chemical kinetic , as numerical problems connected with boundary condition description, aproxymation and stability conditions.

The discussed problem is concerned with the nature of turbulent mixing and the question of description of the time-averaged rate at which chemical reaction proceed between the fuel and oxydant when

PRECEDING PAGE BLANK-NOT FILMED

the turbulent fluctuations ocoour. Experimental knowledge about the local structure of the flame zone where the combustion of premixed fuel/air actually takes place is very limited. The prediction and the computation of the consumption of fuel is rather difficult because the interaction between the turbulence and reaction phenomena is expected to be strong, specially in the more practical cases.

In this paper a numerical modelling approach is described and experimental investigation of partially premixed town gas/ /air fuel combustion in cylindrical combustion chamber with rear and forward facing steps. Measurement are reported of the mean velocity, temperature and concentration of fuel.

To the precise calculation of cobustion rate in turbulent premixed flame necessary are investigations tends towards understanding the combustion process including turbulent fluctuations. However, this experimental investigations are very difficult due to the lack of a practical measuring device. Such device must be small enough to measure local conditions, it must have a good frequency response and first of all, it must be able to surrive in high temperatures in combustion chamber. The very promissing instrument for measuring mean and fluctuating velocities and temperatures is lasser. But its development is still in a early stage.

In the paper initial measurement results of temperature fluctuations in flame in a selected sections of combustion chamber using the thermocouple are reported.

MATHEMATICAL MODEL OF PHYSICAL PROCESS

A swirlless flow with recirculation and chemical reaction in a combustion chamber is described with elliptic differential equations of momentum, mass and energy balance. To the description of two-dimensional flow the momentum equations changes availing the stream function and vorticity definitions. Now, when the methods of pressure calculation are known it is possible to use the so called primitive variables /u,v,p or p/ solving directly momentum equations /1/.

The method of numerical solving of two-dimensional elliptic differential equations described by Spalding and co-workers /2/ is well known and wide employed. The basic model equation is:

$$a\left[\frac{\partial}{\partial x}(\rho u\phi)+\frac{1}{r}\frac{\partial}{\partial r}(\rho r v\phi)\right]-\frac{\partial}{\partial x}\left[b\,\frac{\partial(c\phi)}{\partial x}\right]-\frac{1}{r}\frac{\partial}{\partial r}\left[br\,\frac{\partial(c\phi)}{\partial r}\right]-S_\phi=0$$

where dependent variable stands for ϕ the stream function ψ, vorticity ω/r, stagnation enthalpy $\bar{H}$, representative function $\varphi = m_{fu} - m_{ox}/i$, mass fraction of fuel m_{fu}, turbulence energy k and turbulence energy dissipation rate ε. Coefficients a,b,c occuring in equation as well as source terms are described in available bibliography. Below are discussed only the source terms of the turbulence equations and of the mass fraction of fuel equation, where the combustion model ocoour.

Described above the differential equations necessitates the specification of boundary condition at each surface of the solution domain. The flow domain taken to the calculations is a half-section of axial symetrical adiabatic combustion chamber. On the symetry axis variables /exept ω/r and ψ/ have zero normal gradients. At the exit all axial gradients was assume to be small. At the fuel and air entrance all quantitites are known. The specific heat was calculated in dependence on the temperature and gas composition /fu-ox-comb.gas/, and the density from perfect gas equation. Non-isothermality and gas compositon influences on flow only through the density, and the effective viscosity includes the influence of turbulence on mean flow.

Turbulence model

Closure of the time-mean equation system is effected by means of a turbulence k-ε model /3/ which involves the solution of two conservation equations of turbulent kinetic energy and energy dissipation rate. Source terms for these equations are respectively:

for k: $\rho\varepsilon - P$

for ε: $(C_{\varepsilon 1}\rho\varepsilon - C_{\varepsilon 2}P)\varepsilon/k$

where $P=\mu_{eff}\left[2\left(\left(\frac{\partial u}{\partial x}\right)^2+\left(\frac{\partial v}{\partial r}\right)^2+\left(\frac{v}{r}\right)^2\right)+\left(\frac{\partial u}{\partial r}-\frac{\partial v}{\partial x}\right)^2\right]$

The values of the constants used in turbulence model calculations were identical as in the paper /1/. Boundary conditions of k and ε with the assumption of logarythmic velocity distribution near the wall we can write

$$[u]_N=\frac{\tau/\rho}{\varkappa}\ln\left[E\,\frac{[y]_N(\tau/\rho)^{1/2}}{\nu}\right]$$

$$[k]_N=\frac{(\tau/\rho)}{C_\mu^{1/2}} \qquad [\varepsilon]_N=\frac{(\tau/\rho)^{3/2}}{\varkappa\,[y]_N}$$

where point N is located at a node Δy away from the point on the wall. Constant E = 9.0 is a function of wall roughness, and $\varkappa$ = 0.42.

On the basis of calculated distributions of kinetic energy and dissipation rate and assume turbulent viscosity isotrophy we can say

$$\mu_t = C_\mu\rho k^2/\varepsilon$$

Combustion model

The calculation results of turbulent flow with chemical reaction principally depend on assumed combustion model.

Usually, it is supposed in combustion calculations, that the combustion rate of fuel per unit volume is governed by the Arrhenius-type relation for simple one-step chemical reaction:

$$S_{m_{fu}} = m_{fu}\, m_{ox}\, \rho^2 A \exp(-E/RT)$$

This relation gives good results for steady or laminar combustion but for turbulent one is rather rough. In turbulent both

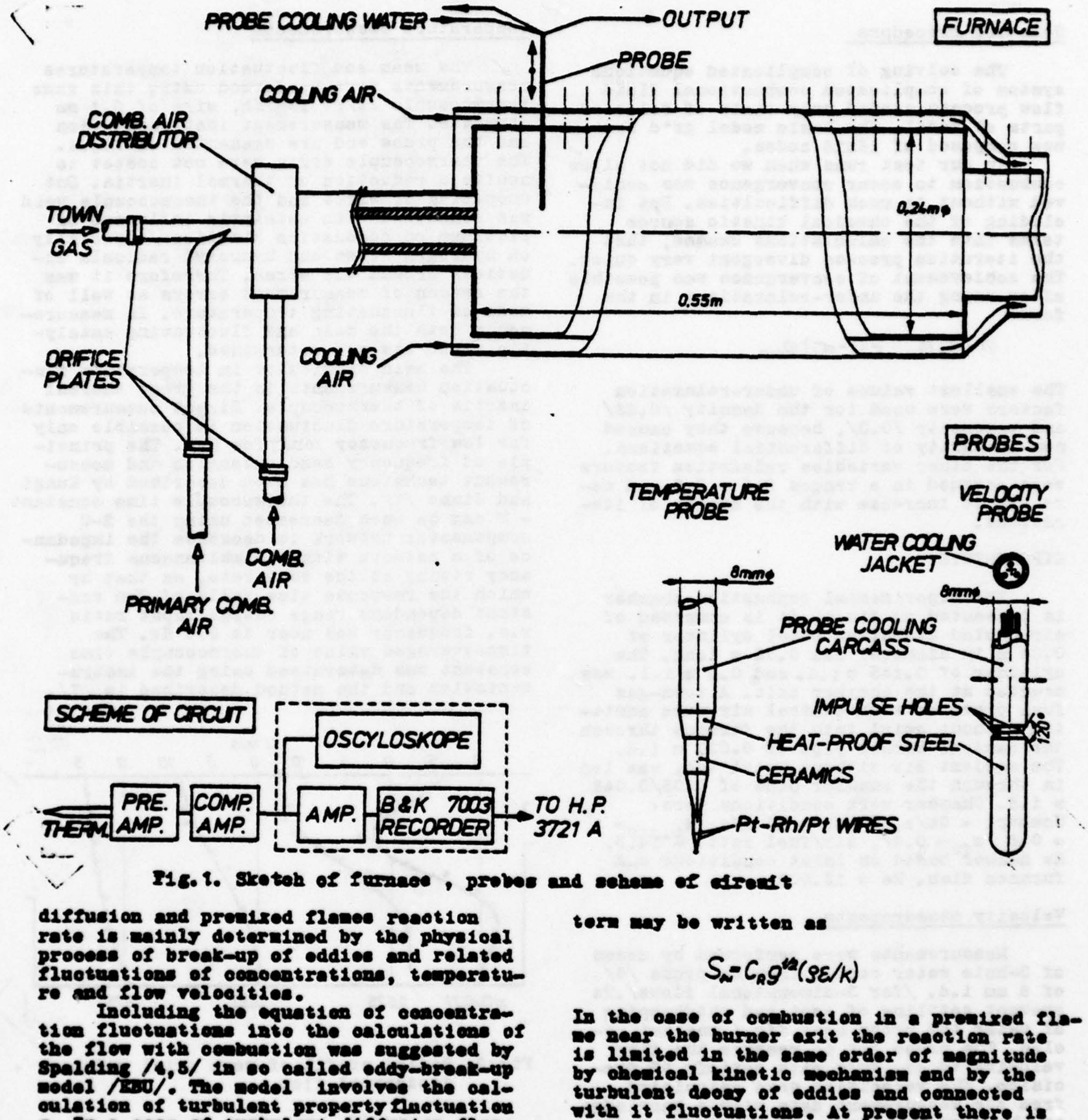

Fig. 1. Sketch of furnace, probes and scheme of circuit

diffusion and premixed flames reaction rate is mainly determined by the physical process of break-up of eddies and related fluctuations of concentrations, temperature and flow velocities.

Including the equation of concentration fluctuations into the calculations of the flow with combustion was suggested by Spalding /4,5/ in so called eddy-break-up model /EBU/. The model involves the calculation of turbulent property fluctuation g. In a case of turbulent diffusion flame calculations with infinitely fast reaction quantity g states for mean squared fluctuations of mixture fraction F'^2. If a finite reaction rate is assume, g is fuel concentration fluctuation. The fundamental EBU-model assumption is pressume that the rate of combustion of fuel is proportional to the rate of dying away of the fuel concentration fluctuation, and that the fluctuations of temperature and oxygen concentration are perfectly corelated with the fuel concentration. The eddy-break-up source term may be written as

$$S_{\sim} = C_R g^{1/2}(\varrho\varepsilon/k)$$

In the case of combustion in a premixed flame near the burner exit the reaction rate is limited in the same order of magnitude by chemical kinetic mechanism and by the turbulent decay of eddies and connected with it fluctuations. At present there is any adequate and verificated model of turbulent combustion in premixed flames, specially for hydrogen rich fuels.
Practical and theoretical experiments tend towards understanding the combustion mechanism in turbulent premixed flame are required.

Therefore in the paper to the average combustion rate determination the rough combustion model using the Arrhenius relation was assumed.

Solution procedure

The solving of complicated equations system of complicated combustional fluid flow process needed many tests of selected parts of model. The basic model grid system was composed of 16x18 nodes.

In our test runs when we did not allow combustion to occur convergence was achieved without to much difficulties. But including of the chemical kinetic source terms into the calculations caused, that the iteration process divergent very quick. The achievement of convergence was possible after using the under-relaxations in the form:

$$\phi = \alpha_\phi \phi_{NEW} + (1-\alpha_\phi)\phi_{OLD}$$

The smallest values of under-relaxation factors were used for the density /0.25/ and viscosity /0.3/, because they caused non-linearity of differential equations. For the other variables relaxation factors were assumed in a ranges 0.6 ÷ 0.9 and were set to increase with the number of iterations.

EXPERIMENTS

The experimental combustion chamber is presented on fig.1. It is composed of air-cooled stainless steel cylinder of 0.24 m in diameter and 0.55 m long. The cylinder of 0.145 m i.d. and 0.2 m i.l. was mounted at the chamber exit. A town-gas fuel premixed with central air were admitted without swirl into the furnace through the central burner pipe of 0.032 m i.d. The ambient air without swirl too, was led in through the annular pipe of 0.08/0.048 m i.d. Chamber work conditions were: Ucentr. = 6m/s, U amb = 13 m/s, $m_{t.gas}$ = = 0.6 /m_{fu} = 0.4/, air/fuel ratio = 14.0, Re number based on inlet conditions and furnace diam. Re = 12.000.

Velocity measurements

Measurements were performed by means of 3-hole water cooled impulse probe /6/ of 8 mm i.d. /for 3-dimensional flows/. To prevent settling of soot and outdropping of water the probe head fig.1 was not cooled. The probe let to measure the flow velocity to ca. 2m/s with satisfy 5% precision. The velocities were calculated from the measurement data with a knowledge of the concentrations and temperature distributions.

Concentration measurements

The average species concentrations were measured using a gas chromatograph with He as a carrying gas and molecular sieves /Am.Sc.Inc./ determining H_2, O_2, N_2, CH_4, CO and CO_2. The gas samples were collected with an uncooled quartz mikroprobe at particular positions in the combustion chamber.

Temperature measurements

The mean and fluctuation temperatures measurements were performed using this same thermocouple Pt/Pt 15% Rh, wire of 0.1 mm diameter. The measurement instrumentation and the probe end are presented on fig.1. The thermocouple wires were not coatet to achive a reduction of thermal inertia. But uncoating of wires and the thermocouple weld was connected with catalytic influence of platinum on combustion kinetics /especially on hydrogen atoms and hydroxyl radicals kinetics/ around the wires. Therefore it was the reason of measurement errors as well of mean as fluctuating temperature. In measurements both the mean and fluctuating catalytic.error was not determined.

The main difficulty in temperature fluctuation measurements is the great thermal inertia of thermocouple. Direct measurements of temperature fluctuation is possible only for low frequency /only few Hz/. The principle of frequency band extension and measurement technique has been described by Kungi and Jinno /7/. The thermocouple time constant – τ can be much decreased using the R-C compensator network to decrease the impedance of a network with a simultaneous frequency rising at the same rate, as that by which the response time falls of. The constant dependens range output/input ratio v.s. frequency was near to 200 Hz. The time-averaged value of thermocouple time constant was determined using the instrumentation and the method described in /7/.

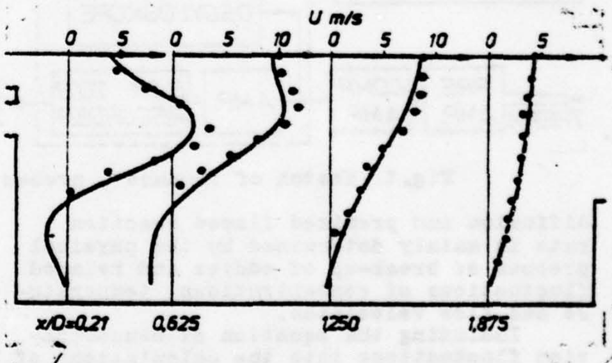

Fig.2. Radial profil of mean axial velocity isothermal flow

SOME RESULTS

There were any difficulties in the turbulent combustionless flow calculations, and the above described method calculation results are according to the experimental measurements. Fig.2 shows the calculated axial velocity profiles and measurements of mean velocities. It can be seen that in central stream zone the results are in good agreement. In the recirculation region it was not possible to measure unmistakenly and precisely the recirculation flow velocity, because of their low values.

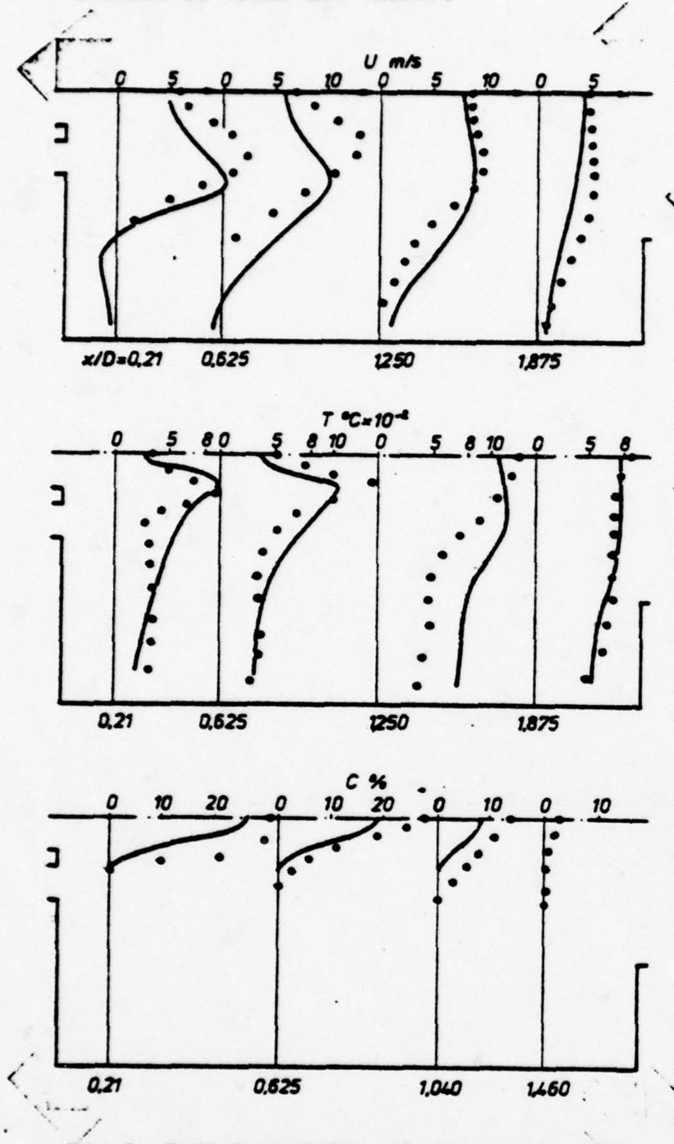

Fig.3. Radial profiles of mean axial velocity, temperature and mass fraction of fuel.

Calculated values of axial velocity, temperature and fuel concentration are compared with measurements on Fig.3. /in selected measurement sections/. The examination of the calculation and measurements results shows, that there are significant differences in a magnitude of the two sets of velocity, temperature and fuel concentration results. /m_{fu} - is the summ of combustible fuel components/. The reason of the results divergences in the central flame zone /combustion occure/ was, that in turbulent combustion calculations the mean volumetric reaction rate has been detrmined by the Arrhenius relation. The additional reason of divergences was rough choice of the chemical-kinetic constants in combustion rate relation. In the turbulent combustion calculations more adequate would be described above the EBU model, or including the concentration and temperature fluctuations directly in Arrhenius relation.

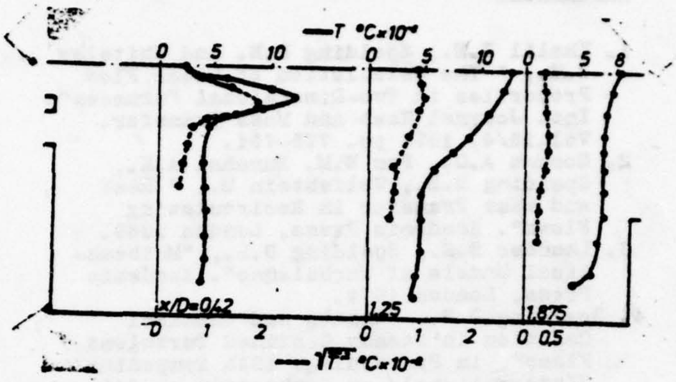

Fig.4. Radial profiles of mean and fluctuating temperatures

Therefore the initial temperature fluctuations measurements were performed in selected measurement sections of combustion chamber. It was done to achieve even a qualitative information about the structure of turbulent premixed flame. The measurement results of the rms temperature fluctuations and the mean temperatures are shown on Fig. 4. Alike the earlier papers e.g. /8/ treating of temperature fluctuation measurements in round free-jet flames it was remarked, that the maximum temperature fluctuations along the radius in section, in which the central cone combustion zone is visable, occur just outside the region of mean temperature maximum. In the farther part of combustion chamber position of these maxima were found nearly the combustion chamber axis. The maximum temperature fluctuations values on the chamber axis occur outside the central lighting flame zone.

CONCLUSIONS

1. It was presented an attempt of application of mathematical model to the calculations of turbulent.partially permixed flame with recirculation in combustion chamber and experimental measurement results.
2. The adopted combustion model to the reaction rate in turbulent flame gives any positive results. The continuation of systematical and more precise experiments of combustion mechanism in turbulent premixed flames are required
3. Basing on initial qualitative measurements of the temperature fluctuations in a confined flame it is possible to notice theirs significant increase in the combustion zone. The precise measurements of temperature fluctuationd will be the subject of farther experimental works.

Acknowledgments

We thank the National Science Foundation for financial support and Mr M.Pec for experimental assistance.

REFERENCES

1. Khalil E.E., Spalding D.B. and Whitelaw J.H., " The Calculation of Local Flow Properties in Two-Dimensional Furnaces". Int. Journal Heat and Mass Transfer. Vol.18/4, 1975 pp. 775-791.
2. Gosman A.D., Pun W.M. Runchal A.K., Spalding D.B., Wolfshtein M., " Heat and Mass Transfer in Recirculating Flows". Academic Press, London 1969.
3. Launder B.E., Spalding D.B., "Mathematical Models of Turbulence". Academic Press, London 1972.
4. Spalding D.B., "Mixing and Chemical Reaction in Steady Confined Turbulent Flame", in Proceedings 13th Symposium /International/ on Combustion pp.649-657. Combustion Institute, USA, 1971.
5. Mason H.B., Spalding D.B., "Prediction of Reaction Rates in Turbulent Premixed Boundary-Layer Flows", in Combustion Institute European Symposium, ed by Weinberg F.J., Academic Press 1973, pp. 601-606.
6. Hiett G.F., Powell G.E., " Three-dimesional Probe for Investigation of Flow Patterns", The Engineer, January 1962, 26, pp.165-170.
7. Kungi M. and Jinno H., "Measurements of Fluctuating Flame Temperature", 17th Symposium /International/ on Combustion, Butterworths, 1959, pp. 942-948.
8. Lockwood F.C., and Odidi A.O., "Measurements of Mean and Fluctuating Temperature and of Ion Concentration in Round Free-Jet Turbulent Diffusion and Premixed Flames" 15th /International/ Symposium on Combustion. Tokyo 1974, pp.561-570.

TURBULENT FLOW STRUCTURES AND RECIRCULATION PATTERNS ASSOCIATED WITH CYCLONE COMBUSTORS AND THEIR EFFECT ON FLAME STABILISATION.

by

A.C. Styles, N. Syred and S.E. Najim.

Department of Mechanical Engineering & Energy Studies
University College
Cardiff.

ABSTRACT

This paper examines in detail the combustion aerodynamics and burning behaviour of a cyclone combustor with the flame stabilised internally, close to the walls by the combined processes of aerodynamic recirculation of heat and active chemical species, and extremely long residence times and some heat re-radiation from the walls. This mode of burning has applications in burning either poor quality fuels weak mixtures of rich fuels such as natural gas and as a part of a multi-stage, low pollution combustor.

This work shows that the main flow pattern consists of a swirling flow which slowly descends down the device, is deflected radially inwards by the base and then slowly ascends up the device. Between these two layers a long thin annular recirculation zone is formed on whose boundary the flame is stabilised. Measurements of species concentration, mean temperature and velocity are presented.

NOMENCLATURE

a.r.z. - Annular recirculation zone
c.r.z. - Central recirculation zone
D_e - Diameter of combustor exhaust
D_o - Diameter of main section of combustor
D_t - Diameter of each of the eight tangential inlets.
P.V.C. - Precessing vortex core
r - Radius
r_o - Radius of main section of combustor
Re - Reynolds number based on exhaust diameter and mean velocity in this region
S - Swirl number based on input and outlet conditions
T - Temperature ^{o}C
U - Axial velocity
W - Tangential velocity
X - Axial distance from base plate
ϕ - Mixture Ratio -Vol.Flowrate of Air/Flowrate of Fuel x Stoichometric Mixture Ratio (at S.T.P. conditions).

Superscripts

' - Indicates fluctuating quantities

INTRODUCTION

Although cyclone combustors have been in operation for many years, principally for the combustion of low quality solid fuels, the widescale use of such devices has been restricted by the problems of ash slagging and rapid erosion of the furnace walls by chemical reactions with the refractory linings(1-13). However, in recent years there has been a revival of interest in these combustors for such diverse applications as

(a) The burning of low calorific value gas (5-7,15)
(b) Enhancing the output of cement kilns (16).
(c) The burning of wet vegetable refuse such as cotton husks or grape pressings.
(d) Incineration of such products as car tyres, used lubricant oil, pungent fumes from industrial processes and domestic refuse.
(e) As part of a multi-stage low pollution combustion system.

A number of differing types of cyclone combustors are in use, as reviewed in reference 1. They have one basic characteristic which distinguishes them from swirl burners, in that the flame front is located inside the device close to the outer walls. Flame stabilisation occurs due to a combination of three main factors:-

(a) Heat re-radiation from the chamber walls (often enhanced by the refractory nature of the walls).
(b) Aerodynamic recirculation of heat and active chemical species by a long thin annular recirculation region located close to the walls.
(c) The exceptionally long residence time of fluid particles in the device.

Conversely the swirl burner produces a large torroidal recirculation zone in the exhaust region around which the flame is stabilised. Thus the differentiation between the two type of combustor may be considered to the difference between burning in the exhaust region (swirl burner) and internal burning close to the wall (cyclone combustor). Nevertheless the cyclone combustor is quite capable of producing a large torroidal recirculation zone in the exhaust region (providing this region is centrally located and unobstructed) due to the high level of swirl generated in the device.

The work reported in this paper is concerned with a fundamental study of the combustion processes occurring inside a cyclone combustor using natural gas as fuel. The design of this combustor is based upon that of a cyclone dust separator modified to enhance flow stability, reduce pressure drop and improve flame stability.

THE COMBUSTOR

The combustor used is shown in Fig.1 and consists basically of a long cylindrical tube 2 diameters long constructed out of welded steel sections. A premix of air and natural gas enters near the top of the combustor through eight circular tangential inlets. These gases are prevented from leaving the combustor by an annular sleeve surrounding the exit, and are deflected downwards towards the base of the device. At the base of the device the swirling flow is deflected radially inwards along the baseplate, then separates from the base forming a vortex core region which then leaves the device through the annular sleeve. Thus the flows in the combustor consist essentially of two concentric swirling flows moving in different axial directions. Between these concentric swirling flows a long thin annular region of recirculation is formed which permits flame stabilisation to occur close to the wall.

Relevant dimensions of the burner are as follows

Diameter of Combustion Chamber	D_O	153 mm
Diameter of Exit	D_e	78 mm
Diameter of each tangential inlet (18 in total)	D_t	18.7 mm
Length of Combustion Chamber	L_c	309 mm
Length of Outlet Sleeve	L_s	125 mm

The swirl number based on inlet conditions of this device was 4.21. A full scale perspex model of this combustor was also constructed for the flow visualisation experiments.

Water model studies using 2 mm diameter polystyrene beads and a thin collimated light source were used to qualitatively assess the various flow patterns obtained. Velocity levels were obtained with a laser Doppler anemometer using 2 watt Argon laser and a particle counting signal processing unit. Mean temperatures were measured with a small diameter bare wire thermocouple coated with hexamethyldisiloxane to reduce catalytic effects. Species concentration measurements were taken from the combustion chamber using peristaltic pump and a small diameter quartz probe designed to give a sonic throat velocity, thus quenching any reactions. Analysis of these samples was then carried out on a Pye Unicam gas chromatograph. The temperature and concentration measurements were taken through a series of closely spaced ports in the main body of the combustor.

RESULTS AND DISCUSSION

A schematic diagram of the aerodynamics of the combustor derived from the water model studies and visual observation of the combustion processes are represented in Fig.2. Two distinct regions of swirl are evident - a wall flow rotating slowly about a fast moving inner vortex. Between these conjugate rotating flow lies a long thin annular region of recirculation in which high levels of heat and mass transfer occur. This annular recirculation zone (henceforth a.r.z) is in the form of a thin cylindrical wedge, Fig.2 and appears to be non continuous lengthwise, with low frequency eddies and mixing processes continually causing heat and mass transfer across this region. This is further illustrated by the water model photograph in the axial radial plane shown in Fig.3. Near to the exit, at the lip of the sleeve a slight escape of incoming fluid occurs due to its entrainment into the central vortex Figs.2 and 3. As the inner vortex passes through the annular sleeve towards the exhaust a large central torroidal recirculation zone is formed on the axis in a manner analogous to that which occurs with swirl burners Fig.2 and 4 (1). This central recirculation zone (henceforth c.r.z) is quite capable of supporting natural gas combustion, the result being virtually identical to that produced by swirl burners of similar swirl number. This c.r.z. reduces the effective outlet area of the device and increases the residence time of the flow inside the combustor. The c.r.z. only extends to the rear of the outlet sleeve. Inside the combustor the water models reveal the existence of a "dead" zone of low turbulence inside the inner vortex region close to the axis. Associated with the c.r.z. formed in the exit is the formation of a precessing vortex core (henceforth P.V.C.) which rotates about the boundary of the c.r.z. Fig.2,4 & 5. Outside the burner under certain conditions an instability associated with the P.V.C. occurs called the radial axial eddy Figs.2 (17).

The formation of the P.V.C. is important in premixed combustion systems owing to the capacity for resonant coupling with various acoustical and other modes of combustion instability (20). Measurements of the frequencies of the P.V.C. under isothermal conditions showed a near linear increase with Re and the non-dimensionalised results so obtained are shown in Fig.6 where they are compared with results obtained from other systems and the present combustor operated with only two and four inlets open so as to increase the swirl number. As may be seen the frequency parameter soon tends to a constant value at high Re for all systems considered. The results from this system seem to be clearly consistent with those obtained from other swirling flow systems. When combustion occurred in the exhaust region at near stoichometric mixture ratios the frequency of the P.V.C. was nearly doubled at high Re, a mode of behaviour similar to that which occurs with swirl burners (18). Under conditions of weak burning ($\phi > 1.5$), the combustion conditions considered in this paper, the frequency of the P.V.C. was only affected by combustion at low Re, thus correlating with other measurements made which showed that the combustion process was fully complete by the exhaust sleeve region and gases entering this region were of near uniform radial temperature and concentration profiles.

The combustion case considered in this paper occurs when a weak mixture of natural gas is burnt in this combustor ($\phi = 1.68$), and is considered to represent a combustion state which could occur in the incineration of low calorific value waste gases (it has been shown in reference 7 that the burning processes of Carbon Black Waste Gas in cyclone combustion may be simulated by burning weak mixtures of natural gas and air of equivalent overall heat output in the same combustor). The flame burns in the expected position in a long thin annular flame front located close to the outer walls and extending from the inlets down to the base plate of the device. Under the conditions at which measurements were taken the flame was close to blow off. Blow off did not occur in the conventional sense, but the flame collapsed radially inward at weaker mixture ratios to form a thin annular flame front with poor burning characteristics on the boundary of the inner vortex core region in a manner analogous to that found in references 6 and 7.

Temperature and concentration profiles were taken at the six zones indicated on Fig.2. The temperature profiles Fig.7, show that maximum temperature levels of up to 1100°C are obtained. The flame front is located about 25 mm from the wall along the length of the burner at $r/r_o \simeq 0.67$. Combustion is initiated in the annular region between the exit sleeve and the outer wall just below the tangential inlets. In this region the flame seems to extend to the sleeve boundary. In the main body of the combustor the flame front position scarcely seems to alter until at distances less than about 50 mm of the base plate flow (clearly shown by the water models) final burnout of the flame occurring at $r/r_o \simeq 0.28$ around the central vortex core region. Over much of the main body of the combustor from $X/D_o \simeq 0.2$ to the exhaust sleeve a region of near uniform temperature exists between $0.67 < r/r_o < 0.28$ due to the close radial position of the descending, burning, swirling flow and the ascending, burnt out swirling flow towards the exhaust, the two flows only being separated by the long, thin annular recirculation zone. For simplicity in laboratory experiments this combustor was not lined with refractory and thus the contribution of heat re-radiation to the flame stabilisation process is virtually negligible over the whole length of the combustor as shown by the low wall temperatures recorded, Fig.7, typically between 100 - 500°C. The flame front is located further away from the walls of this combustor than found in other work with differing types of cyclone combustor (6,7). This is due to two main effects:

(a) The lack of a refractory wall which would have improved the flame stabilisation process on the outside of the flame, has moved the flame radially outwards somewhat and improved the blow off limits by increasing substantially the heat re-radiation to the outside of the flame.

(b) The limited size and strength of the annular reverse flow zone. It is felt that the size and strength of this region can be substantially increased by fairly simple combustor modifications.

Species concentration measurements along the length of the burner, Fig.8 ($\phi = 1.68$) show that complete burnout of all the fuel has been achieved by the exhaust sleeve. In the flame front region close to the wall a high methane concentration exists ($\simeq$ 4-6%) persisting all the way down the combustor to the base plate. Close to the base plate the high methane concentrations in the region from $1.0 < r/r_o < 0.36$ indicate how the final burnout process is occurring in this region and also around the central vortex core region as the outer flow reaches the base plate and is deflected around towards the exit sleeve. It is apparent that final burnout of methane in the central vortex core region does not occur until $X/D_o \simeq 1.1$. Only very small concentrations of CO and H_2 were measured in the flame front region, typical values being of the order of 0.1 to 0.3% Fig.8. The highest concentrations of CO were usually found between $0.7 < X/D_o$, the peak of the CO concentrations lying just outside the flame front position generally.

A similar result was obtained with the H_2 concentrations. Nearto the base plate at $X/D_o < 0.2$ much more uniform concentrations of CO exist, typically around 0.1% (H_2 concentrations are here negligible) due to the convection of CO down the annular gap between the wall and the flame front. Final burnout of the CO then occurs in the vortex core region.

Tangential and axial velocity profiles inside the combustor are shown in Fig.9(a) and (b) in the isothermal state. The tangential velocity profiles are very much as to be expected in showing that the profiles are typically a free/forced vortex combination with the boundary of the vortex core region moving from about $r/r_o \simeq 0.33$ at a point near the exhaust ($X/D_o = 1.1$) to $r/r_o \simeq 0.14$ at a point near the base plate ($X/D_o = 0.6$).

The region of highest tangential velocity,at the vortex core boundary,is nearly double that close to the wall. The axial recirculation zone (Fig.9(b))closely corresponds to the point of inflexion of the tangential velocity profiles between the wall and central vortex core flow. The flame front boundary region also closely corresponds to this region.

The axial velocity profiles confirm the water model results and show a slow moving downward descending flow and a central faster moving flow. Between these two regions a recirculation zone exists with moderately high levels of turbulence (typically 20-40%). Turbulence levels are not as high as in the exit region of a swirl burner due to the high level of mean swirl velocity existing in this region.

In the central vortex core region axial velocities are very low,and no regions of reverse flow on the axis exists inside the cyclone chamber.

CONCLUSIONS

This paper has demonstrated the complex interaction problems occurring between combustion and the aerodynamic flow patterns occurring in cyclone combustors. The mode of combustion considered here, basically a wall burning mode,is stabilised principally by the mechanism of a long thin annular recirculation zone and very long residence times. This study has indicated that considerable room for improvement exists, particularly in the strengthening of the annular recirculation zone.

Dependant upon the application the exhaust flow, associated c.r.z. and P.V.C., may be superfluous (i.e. where only a wall burning mode is desired) and thus it is sensible to eliminate these flows where possible due to instability problems associated with the P.V.C. It is significant that certain Russian designs of cyclone combustors fit de-swirl vanes in the exhaust region to eliminate such problems (12). The author has also encountered instability problems in large designs of multi-inlet cyclone combustor (2.03 m diameter by 6.4 m long) for burning Carbon Black waste gas (21). Similar remedies were adopted.

ACKNOWLEDGMENTS

The authors gratefully acknowledge the generous financial support of the Science Research Council, U.K. in this work. S.E. Najim is directly sponsored by the Iraqui Government.

Thanks are also due to the Technical staff of University College for their support and also to Dr. D.S. Taylor of Sheffield University for his invaluable assistance with the laser Doppler particle counting system.

A. C. [illegible]
N. Syred

REFERENCES

1. Syred, N., Beer, J.M., Combustion and Flame, Vol.23, p.143, 1974.

2. Agrest, J., J.Inst.Fuel, Vol.38, p.344, August 1965.

3. Schmidt, K.R., V.D.I.-Berichte, Vol.146, p.90,1970.

4. Agrest, J., Institut Francais des Combustibles et de l'Energie, p.543, 1964.

5. Hurley, E.G. "Burning of Low Calorific Value Gases" Proc.Conference on Incineration of Municipal and Industrial Waste, Brighton, U.K. Vol.1, Paper 15, p.259, 1969, organised by the Institute of Fuel.

6. Syred, N., Dahmen, K.R., "The Combustion of Low Calorific Value Waste Gases". Proc.2nd. European Symposium on Combustion, organised by the European section of the Combustion Institute, Orleans, France, 1975, pp.414-419.

7. Syred, N., Dahmen, K.R., "Burning and Flame Stabilisation Problems Associated with the Combustion of Low Calorific Value Gas/Air Mixtures" Paper submitted to A.S.M.E. 1976.

8. Baluer, E.D. and Troyankin, Y.V., Thermal Eng. Vol.14, No.1, p.84, 1967.

9. Baluer, E.D. and Troyankin, Y.V., Thermal Eng. Vol.14, No.2, p.99, 1967.

10. Troyankin, Y.V., and Baluer, E.D., Thermal Eng. Vol.16, No.6, p.49, 1969.

11. Tager, S.A. et al, Thermal Eng. Vol.18, No.4, p.80 1971.

12. Tager, S.A. Thermal Eng. Vol.18, No.7, p.120, 1971

13. Marshak, Y.L. Thermal Eng. Vol.14, No.11, p.84,1967.

14. Syred, N., Dahmen, K.R. "The Effect of High Levels of Confinement upon the Aerodynamics of Swirl Burners" Paper submitted to A.I.A.A. journal, 1977.

15. Syred, N., Dahmen, K.R. Paper presented to the Fluid Mechanics of Combustion meeting held at the NASA Lewis Research Centre, Cleveland, Ohio, March 1976

16. Private Communications Dr. T.M. Lowes, A.P.C. Research Centre, Notts. U.K.

17. Syred, N., Beer, J.M. Astronautics Acta, Vol.17, No.415, p.783, 1972.

18. Syred, N., Beer, J.K. Proc. 14th Int. Symp. on Combustion, The Combustion Institute, Pittsburgh, Pa. p.537, 1973.

19. Syred, N., Gupta, A.K., Beer, J.M. Proc.15th Int. Symposium on Combustion, The Combustion Institute, Pittsburgh, Pa., p.587, 1975.

20. Syred, N., Manby, V.I., Gupta, A.K. J.Institute Fuel, p.402, December 1973.

21. Cassidy, J.J.Falvey, H.T. J.Fluid Mechanics, Vol.41, pt.4, p.727, 1970.

22. Private communications K.R. Dahmen, Continental Carbon Co., Houston, Texas, 1976/77.

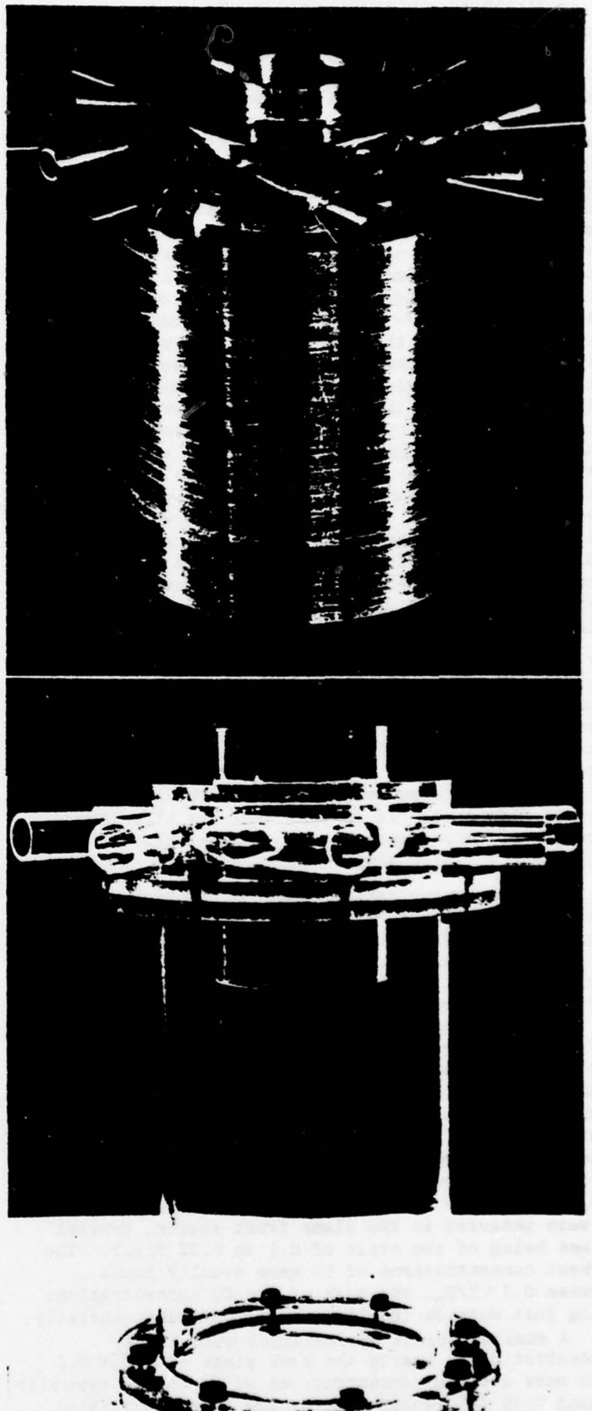

Fig. 1. Photograph of Combustor and Perspex Model.

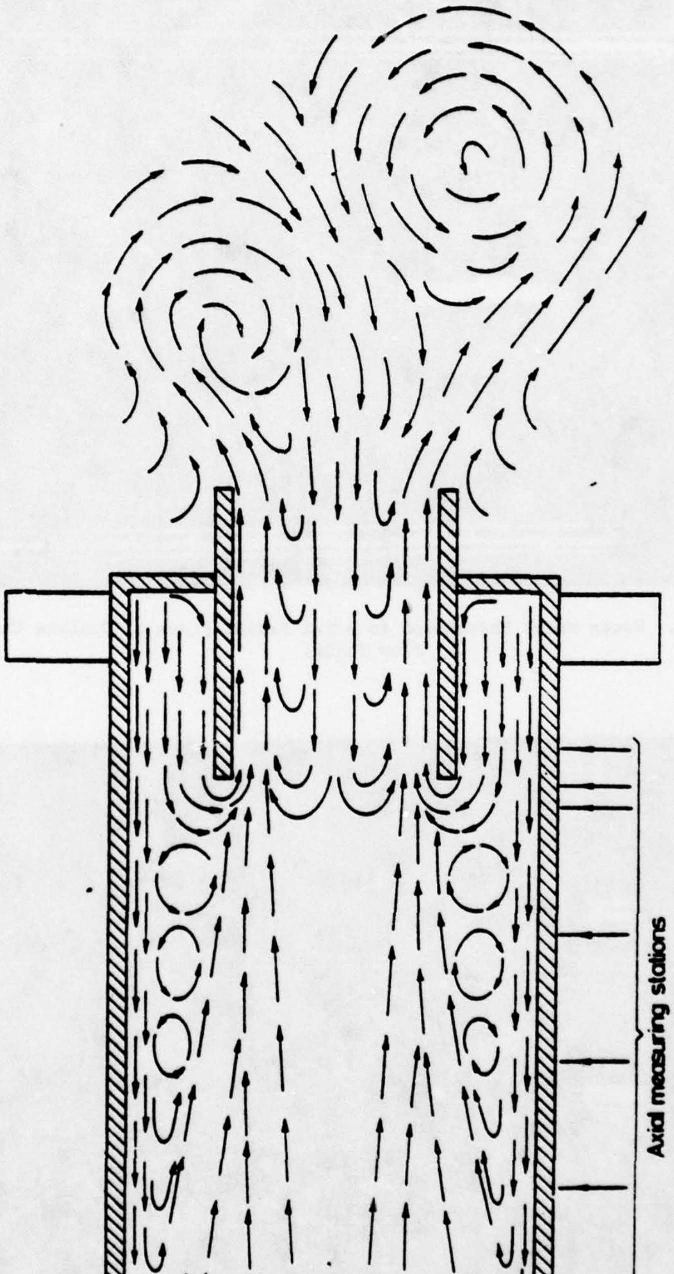

Fig.2. Schematic Model of Flow Patterns in Cyclone Combustor derived from Water Model Experiments.

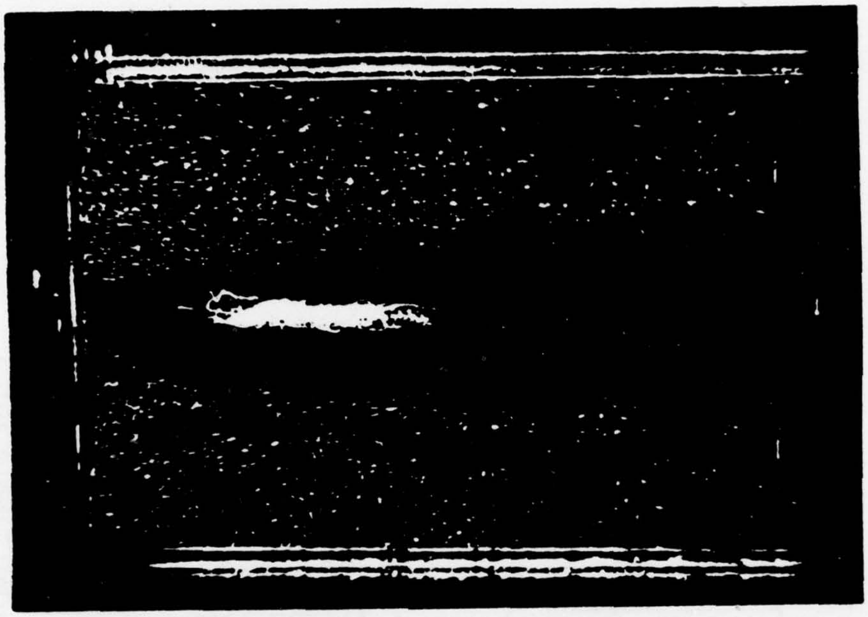

Fig.3. Water Model Photograph in Axial Radial Plane of Cyclone Chamber Flow Field.

Fig.4. Water Model Photograph in Axial Radial Plane in Exit of Cyclone Chamber.

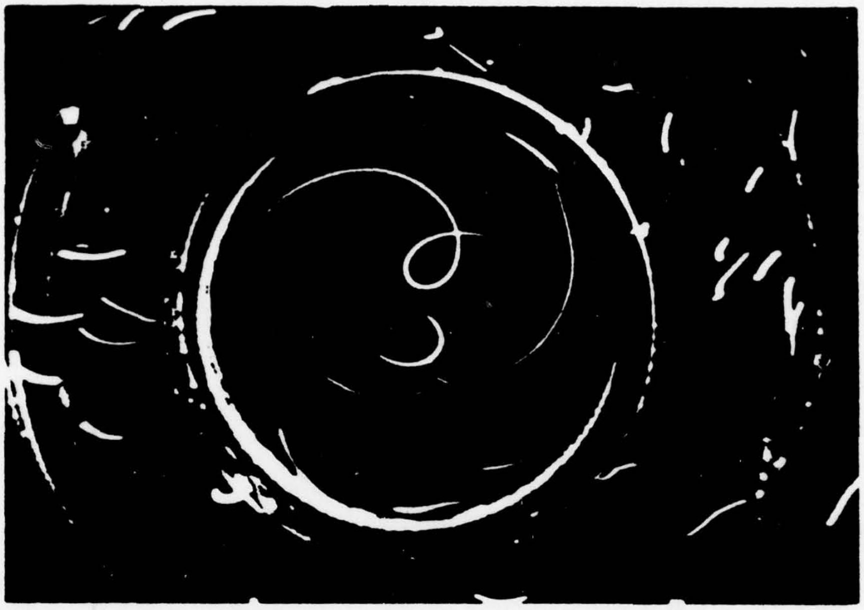

Fig.5. Water Model Photograph of P.V.C. in exhaust region of Cyclone Chamber.

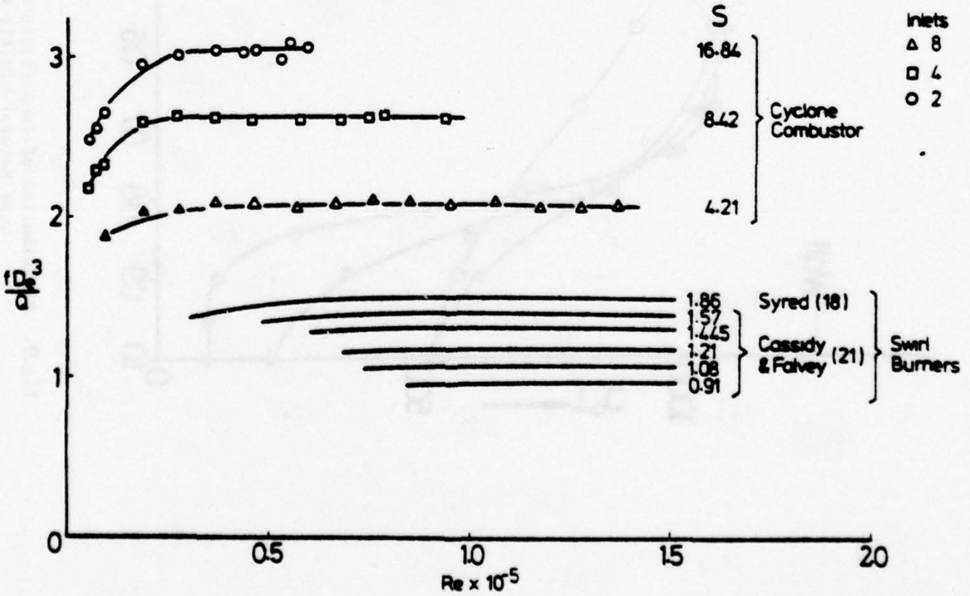

Fig.6. Variation of Non-Dimensionalised P.V.C. frequency with Reynolds Number.

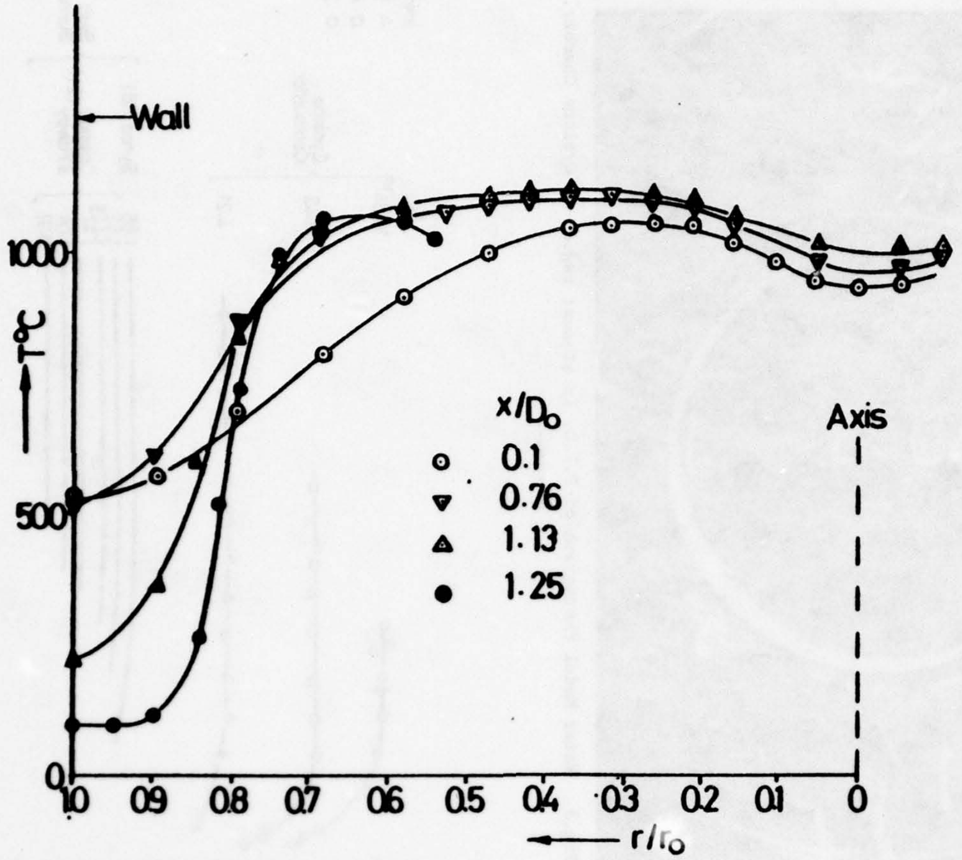

Fig.7. Distribution of temperature throughout Cyclone Combustor when burning weak Natural Gas/Air Mixtures (ϕ= 1.68)

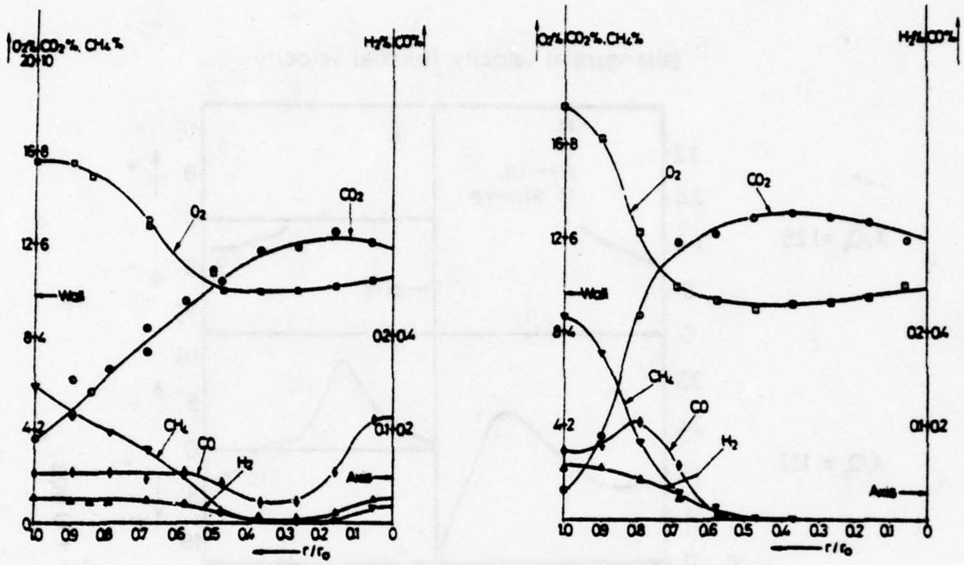

Fig 8(a) X/D0 =0.1

Fig. 8(b) X/D0 =0.76

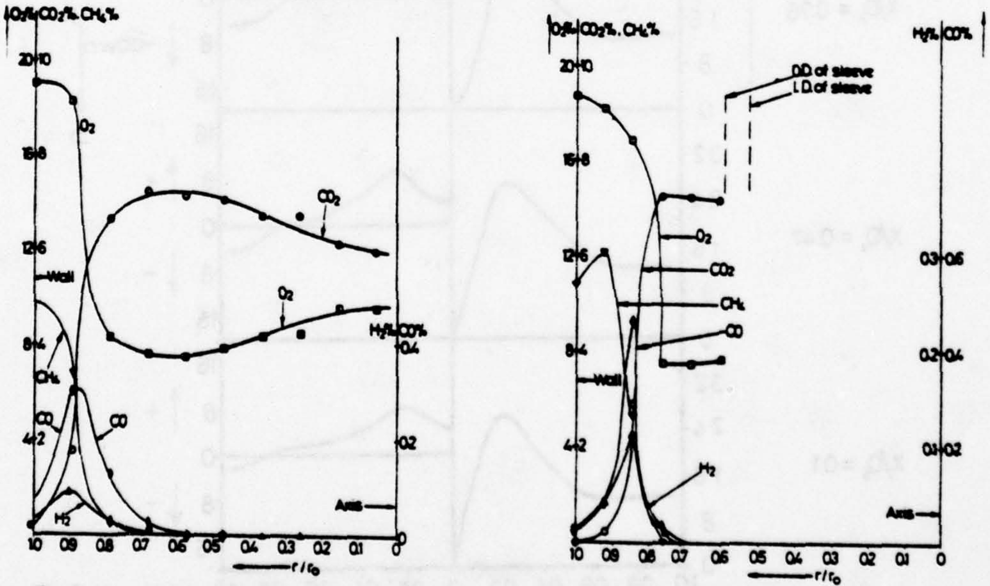

Fig 8 (c) X/D0 = 1.13

Fig. 8 (d) X/D0 = 1.25

Fig.8. Distribution of Species Concentration at Differing Axial Stations throughout Cyclone Combustor when burning Weak Natural Gas/Air Mixtures ($\phi = 1.68$).

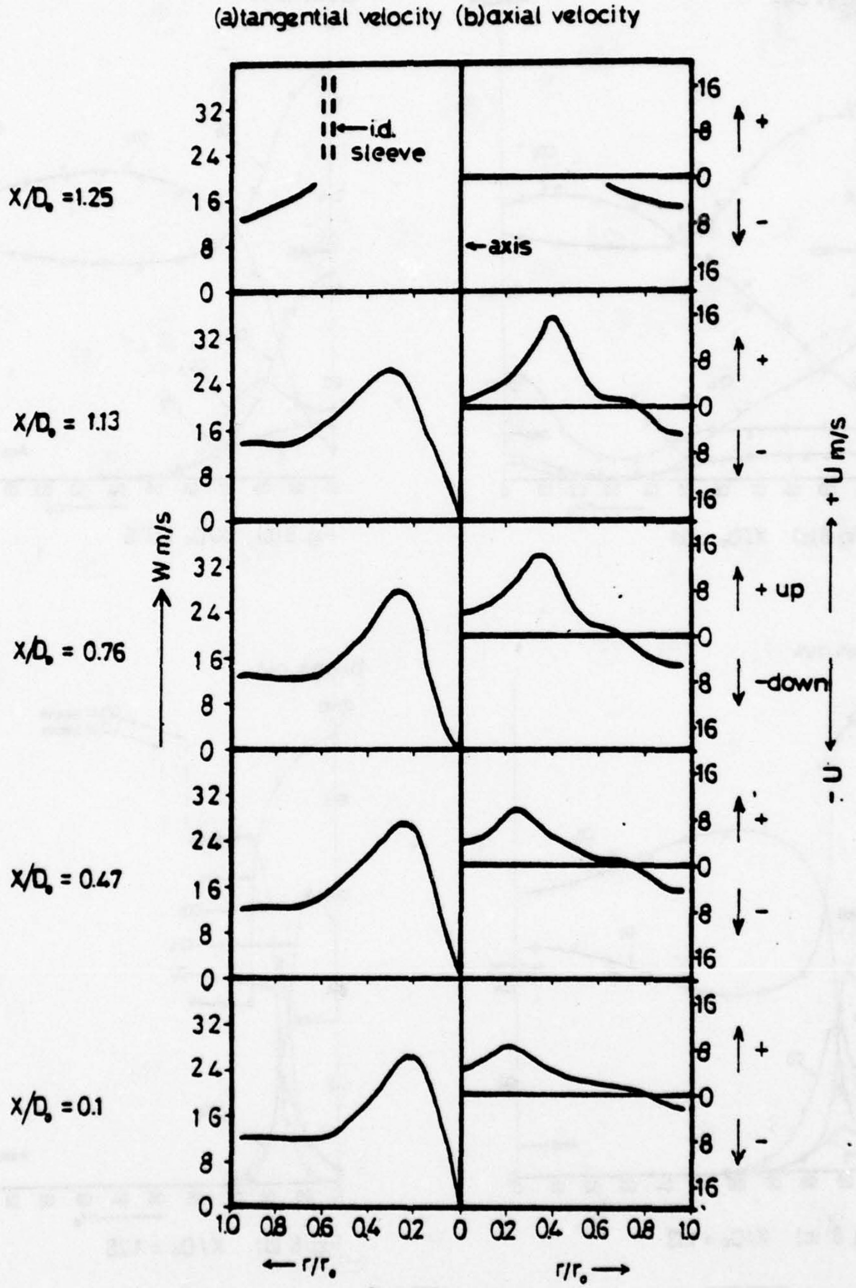

Fig.9. Distribution of Velocity in Cyclone Chamber (Isothermal Flow).

NUMERICAL AND EXPERIMENTAL STUDIES OF AN AXISYMMETRIC COMBUSTOR

D.G. ELLIMAN*, D.E. FUSSEY AND N. HAY,

Department of Mechanical Engineering, The University
of Nottingham, Nottingham, U.K.

(* Present address : Rolls-Royce Limited, Derby, U.K.)

ABSTRACT

A ducted axisymmetric combusting flow stabilised by a flat disc baffle has been investigated with a 2-D axisymmetric numerical method, based on the K-ε-g turbulence model and a simple reaction model. The numerical results have been compared with experimental measurements of the distributions of velocity, temperature and equivalence ratio. The diagnostics included a 7-hole pitot probe, thermocouple and gas-sampling probes. A simple fluctuations model was found to be essential in the prediction of the temperature field, although a simple mixing model predicted successfully the time mean mixing of fuel and air.

NOMENCLATURE

f = mixture fraction = m_f(fuel) - m_f(oxygen)/i

g = rms fluctuation of species or f

i = stoichiometric oxygen/fuel ratio

K = Kinetic energy of turbulence, per unit mass

m_f = mass fraction

Re_d = Reynolds number, based on combustor diameter

ε = rate of dissipation of K

η = weighting factor

ϕ = Equivalence Ratio = fuel/oxygen ratio x i

INTRODUCTION

There is an urgent need for successful prediction procedures for gas turbine and other combustors because of the complexity of the problem of designing a system for minimum pollutant emission, and the high cost of rig testing programmes.

The problem of computing a combusting flow in a gas turbine combustor is prodigious as a result of the influences of swirl, a complex geometry, droplets, radiation and the interaction of turbulence and chemical kinetics. This research was conceived with the objective of comparing measurements and numerical models of a simplified combustor. A 2-D axisymmetric geometry, with a flat disc baffle was chosen, since this would be simple to model using existing finite difference methods.

EXPERIMENTAL METHODS

The combustion rig

A model combustor was built which incorporated a highly turbulent flame stabilised by a recirculating region. (See Figure 1). Small physical dimensions were required to minimise the effects of radiation, and to ensure economy in the consumption of fuel at an acceptable combustion intensity, whereas a large size was desirable to reduce probe blockage effects. As a compromise, the test section was 153 mm internal diameter by 400 mm length. These overall dimensions gave a blockage ratio (probe area/flow area) of less than 0.5%. The baffle was 125 mm in diameter to ensure a large recirculation zone diameter to probe diameter ratio, and was machined with a 45 deg lip to ensure accurate knowledge of the position of the dividing streamline. A maximum heat release of 700 kW was achieved, giving an intensity of 113 MW/m^3. The use of a rear-entry traverse unit dictated that the flow should be exhausted from the rig in a radial direction, and in order to minimise any loss of axisymmetry, eight separate exhaust ports were arranged symmetrically around the periphery of a 30 deg nozzle attached to the rear of the working section. The exhaust flows were quenched by the injection of water sprays. The baffle and flame-tube were water-cooled.

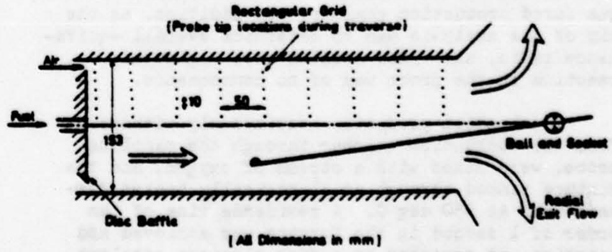

Fig 1. Schematic of experimental apparatus

Bottled methane was used as a fuel and was fed from a manifold through a pressure control valve. The rear-entry traverser was based on a design developed at N.G.T.E. (The National Gas Turbine Establishment). This traversed the rig in spherical polar co-ordinates originating from a spherical bearing at the rearmost axial point of the combustor. It allowed the whole test section to be investigated without the need for further access holes. In practice, measurements were made on a rectangular grid in cylindrical polar co-ordinates originating at the baffle centre.

The velocity probe

In order to measure the local velocity in a flow with a simple pitot tube, it is necessary to orientate the tube in the direction of flow. In a recirculating flow this direction is not generally known. Moreover, the difficulties of designing a fully articulating traversing system, particularly for use in a ducted flow, would be enormous. The problem may be overcome by the use of a direction sensitive pitot probe.

The N.G.T.E. 7-hole probe (1) was designed for traversing combustion chambers in the environment of a stoichiometric hydrocarbon-air flame. The head of the probe is made from platinum/20% rhodium alloy. Using the 7-hole probe a wide range of incident flow angle (up to ± 90 deg) can be detected. The calibration comprises three curves, which cover all orientations of the flow vector.

The exposed bead thermocouple probe

A simple exposed bead thermocouple probe mounted on a water-cooled stem was used to measure local temperatures in the combustor. An exposed bead design was chosen because it has a low blockage ratio and permits traversing close to walls. The errors associated with such probes can be large, especially in high temperature regions, and where an appreciable conduction path to the cooling jacket exists. Temperature traverses, however, proved to be repeatable and the errors were estimated by an extended correction procedure (2). The probe was checked by calibration against a double-shielded and aspirated thermocouple probe. After the correction procedure, the measurements agreed within 2%.

The sampling probe

The customary sampling difficulties associated with fuel condensation and blockage by carbon particles in water-cooled probes were not apparent in this gas fired combustion chamber. In addition, as the aim of the analysis was to determine overall equivalence ratio, and trace species were neglected, reaction in the probe was of no consequence.

Combustion products, continuously withdrawn from the combustion chamber through the sampling probe, were mixed with a stream of oxygen, and the mixture passed through an electrically heated furnace held at 950 deg C. A residence time of the order of 1 second in the furnace was achieved and reaction was promoted by a fine platinum catalyst. The gas sample was then analysed using a two-channel chromatograph to determine local equivalence ratio.

THE NUMERICAL MODEL

The 2-D axisymmetric flow was modelled by the finite-difference program GASEL, which was loaned by CHAM Limited. The sloping lip and the detailed geometry of the exit nozzle and discrete radial exit holes were, however, not incorporated.

The K-ε turbulence model and an "instant reaction" model were used. In the initial calculations a constant value of specific heat was employed, this being arranged to give the correct adiabatic flame temperture for a fully burned stoichiometric mixture of methane and air. Variable specific heat given as a cubic polynomial function of temperature for each species was later introduced. The density of the mixture was obtained from the equation of state, and the heat release from the mass fraction of fuel consumed.

Real turbulent flames differ from the predictions of simple mixing models in that fuel and oxygen are found to co-exist at points within the flame but at different instants in time. The phenomenon is referred to as unmixedness. This is not inconsistent with high kinetic rates and gives rise to a thick reaction zone or flame 'brush'.

Spalding (3) proposed a transport equation for the scalar root mean square of the concentration fluctuation of a species (g) in a non-combusting case. In a combusting case a complication arises since the source of the g equation for a given species will include terms involving the correlations of the fluctuating components of the reacting species. If g is considered instead as the mean square fluctuation of the mixture fraction f, however, the difficulty is avoided as a result of the lack of a source term in this equation. The prediction of a diffusion flame using this model was reported by Gosman (4).

The maximum and minimum values of f at a given point, f+ and f-, are represented by:

$$f^{+} = f + g^{\frac{1}{2}}$$

$$f^{-} = f - g^{\frac{1}{2}}$$

with the limitation that $f^{+} \leqslant 1$

$$f^{-} \geqslant 0.$$

In order to progress further with the model it is necessary to make an assumption of the form of the fluctuations with time. A Gaussian probability distribution function (pdf) would seem most realistic, with delta functions at $f = 0$ and $f = 1$, as employed in (5) and (6). However, this involves fairly lengthy algebraic manipulation without giving predictions of any greater realism than are obtained using a simple deterministic triangular waveform corresponding to a uniform pdf. Indeed Lockwood (5) achieved quite similar results with the simplest assumption of all, a square wave fluctuation. A weighting factor η is introduced ($0 < \eta < 1$) to prevent f^{+} exceeding unity, or f^{-} falling below zero, whilst maintaining f and $g^{\frac{1}{2}}$ at the values calculated.

Thus $\bar{f} = \eta f^{+} + (1-\eta) f^{-}$, where $\bar{f}$ represents the average value of the mixture fraction, and a similar expression is used for other properties. As a consequence, mean temperatures are reduced, since finite values of fuel and oxygen may co-exist in this model. It gives very plausible predictions for very modest computational effort and was therefore adopted in this work. Choice of this model was reinforced by Khalil (7) who found it to be the best of three models tested.

EXPERIMENTAL RESULTS

Measurements of velocity, temperature and equivalence ratio were made at the three conditions specified below in table 1.

The degree of axisymmetry of the flame developed within the combustion chamber was investigated by rotating the exposed bead thermocouple probe through 360 deg about the combustion chamber axis at selected locations. The variation did not exceed 10% of the mean.

Condition	1	2	3
Re_d	5×10^4	8×10^4	5×10^4
$\phi_{overall}$	0.9	0.9	1.6

Table 1. Experimental conditions

The experimental results may be subject to errors arising mainly from the following effects:-

(a) lack of axisymmetry (< ± 10%)

(b) errors of thermocouple calibration (< ± 2.5%)

(c) errors in equivalence ratio analysis (< ± 10%)

(d) errors in 7-hole probe measurements (< ± 10%)

(e) probe interaction with the flame.

A selection of the results obtained are now presented and discussed.

Temperature distribution

Detailed measurements of the combusting flow were made at condition 1. The measured contours of temperature are shown in figure 2. The dominant features are a cool central fuel jet, a cool film of air along the wall, and an annular flame stabilised by a recirculating flow of very hot gases downstream of the baffle. The reaction zone is obviously diffuse, as would be expected in a highly turbulent diffusion flame, giving the characteristic flame 'brush'. The temperatures are very much lower than the stoichiometric value for the fuel used which is in the region of 2100K for an atmospheric inlet temperature.

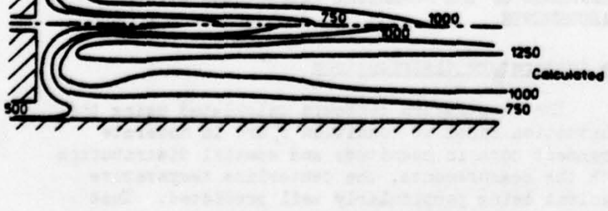

Fig. 2. Contours of Temperature at Condition 1 (K)

Equivalence ratio distribution

The equivalence ratio measurements for the same condition are shown in figure 3. The information obtained from the gas analyser represents the time-averaged equivalence ratio, and gives no indication of the local combustion efficiency. That is, the analyser is unable to differentiate between unburned fuel and combustion products, and is unable to follow temporal fluctuations in concentration. The fuel-air ratio in the rich region along the combustor axis could not be quantified as it was found to be impossible to burn completely all the excess fuel in the furnace for equivalence ratios in excess of about 1.5.

Fig. 3. Contours of Equivalence Ratio at Condition 1

The velocity distributions

The velocity distribution in the combustion chamber is presented as contours of axial and radial velocity in figures 4 and 5 respectively. In order to interpret the 7-hole probe output a local density is required. This was calculated from the measured values of temperature and equivalence ratio using a mean molecular weight and equation of state. In the 'out of range' regions the equivalence ratio was taken as that fuel-rich ratio which would produce the measured temperature on complete combustion. This latter assumption is, of course, uncertain and the actual equivalence ratio could lie anywhere between 1.5 and infinity. However, the resulting error in the density, and therefore the velocity, is unlikely to be greater than ±5% except in regions of very low temperature where the density is a stronger function of equivalence ratio.

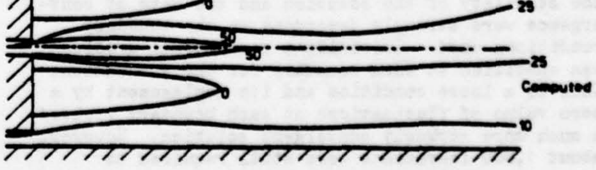

Fig. 4. Contours of Axial Velocity at Condition 1 (m/s)

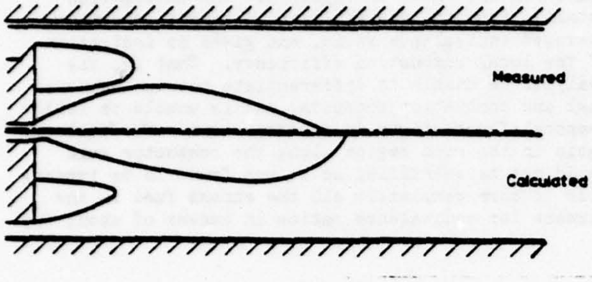

Fig. 5. Zero Radial Velocity Contours at Condition 1

Two concentric contra-rotating toroidal vortices are in evidence behind the baffle. The recirculation zone extends to approximately one diameter downstream. The length is about half that measured in the cold flow situation without a central jet. The jet along the axis and the annular jet near the wall initially begin to decay in velocity. Downstream of the recirculation zone, however, the expansion of the gases following combustion causes an acceleration across the reaction zone which tends to check this decay.

Only the zero radial velocity contours are shown in figure 5 because the radial components are small compared with the axial components for most of the flow. The coincidence of the large region of recirculating flow extending from the baffle tip with the high temperature region of figure 2 is a notable feature of the velocity field, which is presented in figures 4 and 5.

NUMERICAL RESULTS

The program was accepted as having converged when the sum of the mass residuals was less than 1×10^{-5} of the inlet mass flow, further iterations producing negligible changes in the calculated flowfield. A 20 x 20 non-uniform grid was found to be adequate, further refinement having almost no influence on the results at convergence. Typically, about 400 iterations were required to achieve the convergence criterion for the simple mixing model. The addition of the g equation for the fluctuations model had an adverse effect on the solution stability. At first convergence was so slow and uncertain, that only a very poor solution existed after 1,000 iterations. The situation did not improve with changes to the under-relaxation parameters, and both the stability of the solution and the rate of convergence were strongly dependent on the boundary conditions used. Initially a zero normal gradient was specified at each boundary for the g equation. This is a loose condition and its replacement by a zero value of fluctuations at each boundary yielded a much more strongly convergent solution. However, about 1,000 iterations were still required to achieve a converged solution.

The use of a zero value for g at the inlet boundaries is a reasonable approximation as clearly no concentration fluctuations can occur in a one-component environment. The approximation may also be used at the outlet if this is located sufficiently far downstream to have negligible influence on the region of interest. At the wall the fluctuations must be damped to zero, although the actual form of variation close to the boundary there is uncertain. In a turbulent flow it seems probable that fluctuations occur down to the laminar sublayer, making a zero value a very poor approximation unless an extremely fine grid is employed. A zero value at the axis of symmetry would be appropriate in an equilibrium flow as the radial concentration gradient is zero at this boundary. In a turbulent recirculating flow, however, fluctuations are convected and diffused to the axis making a zero value here improbable.

The limits of the flame 'brush' predicted for each of the three conditions are plotted in figure 6. The stoichiometric contour predicted by the simple mixing model is also shown. The results for conditions 1 and 2, which have different Reynolds numbers, are very similar indicating a relatively weak Reynolds number effect. Condition 3, however, which has a different equivalence ratio, exhibits a flame 'brush' which diverges more rapidly from the axis than that predicted at the other conditions. It is encouraging that these predictions are in qualitative agreement with the measurements.

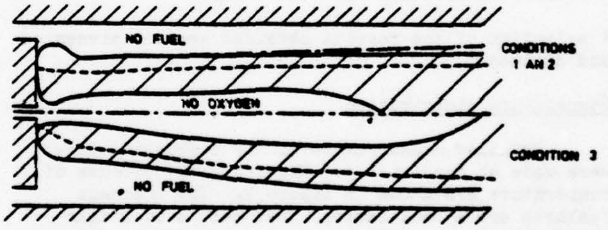

▨ Flame 'brush' predicted by fluctuations model.

— — — Stoichiometric contour predicted by simple mixing model.

—·—·— Boundary at condition 2, where this does not coincide with that at condition 1.

Fig. 6. Diagram Showing the Flame 'Brush' Predicted Using a Fluctuations Model

COMPARISON OF THE NUMERICAL PREDICTIONS WITH THE MEASUREMENTS

The temperature distributions

The temperature contours calculated using the fluctuation model at condition 1 are in moderate agreement both in magnitude and spatial distribution with the measurements, the centerline temperature gradient being particularly well predicted. That the bulk temperatures are correctly predicted is especially encouraging when it is remembered that the stoichiometric temperature for adiabatic combustion of the fuel is about 2100K. The most serious areas of disagreement lie in the presence of a hot 'streak' at a radius of about 20 mm, and in the cool jet predicted along the combustor wall. Several explanations for the discrepancies in the region of the cool wall can be suggested. It is possible that the flame has been distorted locally by the presence of the probe. This effect is particularly pronounced where the probe body lies downstream of the measured point. In addition, a flame is easily stabilised around the probe itself. Another possibility is that a cyclic instability was present in the flame. The mean measurements taken were of course unable to differentiate between a steady temperature, a cyclic instability about the measured mean, and a cool jet containing intermittent eddies of hot gas. Should a cyclic instability have been present the use of a stready flow program such as GASEL was inappropriate, and poor predictions inevitable. A third possibility is that the fluctuation model was unable to model the fluctuations in the areas of disagreement. As these areas lie close to the boundaries which were poorly specified in the solution of the g equation this possibility deserves closer examination.

The temperature profiles shown in figure 7 generally indicate good agreement near the mean radius of the combustion chamber, the temperature being over-predicted near the axis, and under-predicted near the wall. The peaks in the profile seem intuitively to be inappropriate and it is clear that a smoother curve would give greatly improved predictions. The level of fluctuation in the region of these peaks has been reduced by the influence of the zero value of g at the near boundary, and it thus seems certain that this is a significant shortcoming of the model specification. The agreement at the wall is forced in the temperature boundary specification. The good temperature prediction near the axis, however, seems at first to contradict the supposition that a poor boundary condition at this point is responsible for the spurious 'hot streak'. In fact, a high level of fluctuation may be tolerated in a very fuel rich environment before the temperature is affected significantly.

An ideal temperature calculated from the measured equivalence ratio is shown by the crosses in figure 7. This temperature assumes complete combustion, no heat loss, and perfect mixing. In fact this is not necessarily a maximum temperature as heat will be transferred by diffusion and turbulent mixing from the hottest regions of the flame towards the wall, and this effect is neglected. This temperature is in reasonable agreement with the thermocouple measurement within about 25 mm of the wall. This would suggest that fuel rich eddies are not present in this region.

The ideal temperature curve rises rapidly, however, towards the mean stoichiometric contour. This temperature profile is a function solely of the mean mixing between the fuel and air in a manner analogous to the simple reaction model. The prediction of the simple mixing model is shown also on figure 7 for comparison with the calculated 'ideal' temperature. The agreement is surprisingly good when the complex interlinkage of the predicted temperature field with the velocity and turbulence parameters is considered.

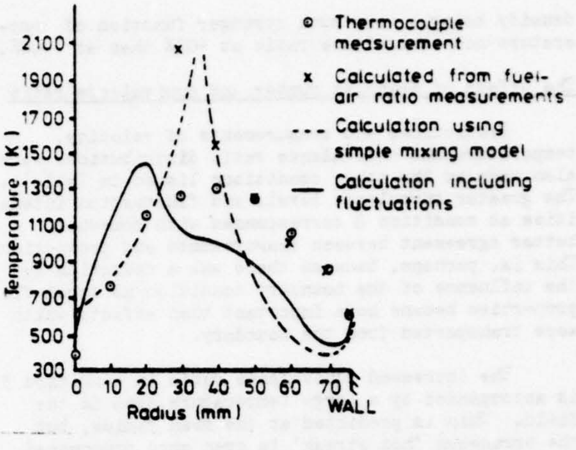

(a) 100 mm from baffle (within recirculation zone)

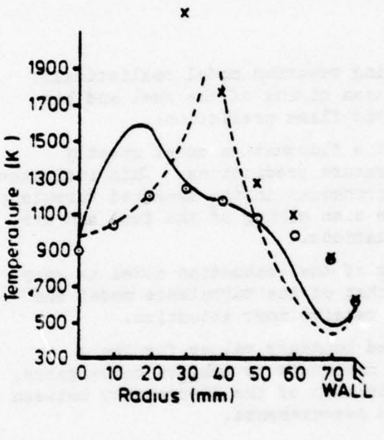

(b) 250 mm from baffle (outside recirculation zone)

Fig. 7. Temperature Profiles at Condition 1

The equivalence ratio distribution

The mean equivalence ratio contours shown in figure 4 are in qualitative agreement with the measurements. The discrepancy in the vicinity of the wall is again seen, however. The measured equivalence ratio is much greater here than that predicted.

The velocity distribution

Predicted contours of axial and radial velocity are presented together with the measured distributions in figures 4 and 5. Again, the predicted overall flow pattern is in qualitative agreement. The axial extent of the recirculating flow is predicted almost exactly. Axial velocities near the centerline are also well predicted. Towards the wall, however, the axial velocities are significantly overpredicted. The measured velocity can be up to twice that predicted, the greatest discrepancy lying in the air jet. That the error in the temperature prediction near the wall has a disproportionate effect on the velocity profile in comparison with the effect of the 'hot streak' predicted near the axis is a result simply of the density being a very much stronger function of temperature and equivalence ratio at 400K than at 1400K.

The effect of Reynolds number and equivalence ratio

Predictions and measurements of velocity, temperature and equivalence ratio distributions were also made at the other conditions listed in Table 1. The greater turbulence levels and fluctuation intensities at condition 2 corresponded with somewhat better agreement between measurements and predictions. This is, perhaps, because there was a reduction in the influence of the boundary condition as local flow properties became more important than effects which were transported from the boundary.

The increased equivalence ratio in condition 3 is accompanied by a large temperature drop in the field. This is predicted at the mean radius, but the erroneous 'hot streak' is even more pronounced at condition 3. The change in fuel jet velocity is well predicted, as is the recirculation zone and the greater angle of divergence of the flame brush.

CONCLUSIONS

1. The simple mixing reaction model realistically predicts the time mean mixing of the fuel and air but gives unrealistic flame predictions.
2. The addition of a fluctuation model greatly improves the temperature predictions. This indicates that the dominant processes in the measured turbulent diffusion flame are mean mixing of the fuel and air and temporal fluctuations.
3. The shortcoming of the combustion model is very much greater than that of the turbulence model and should, therefore, receive most attention.
4. Poorly specified boundary values for the g equation, although necessary to achieve convergence, were responsible for much of the discrepancy between the predictions and measurements.

ACKNOWLEDGEMENTS

We should like to thank CHAM Ltd. for the loan of the computer code GASEL and Mr. J. J. Macfarlane of the N.G.T.E. for the loan of the 7-hole pitot probe. The research was supported by the Science Research Council and Rolls-Royce Limited and was carried out in the laboratories of the Department of Mechanical Engineering, University of Nottingham.

REFERENCES

1. Macfarlane, J. J., "An omni-directional velocity vector probe suitable for use in gas turbine combustors. Design development and preliminary tests in a model combustor". ARC CP No. 1254, HMSO, 1973.
2. Elliman, D. G., "Experimental and Numerical Studies of an Axisymmetric Combustor", Ph.D. Thesis, University of Nottingham, 1977.
3. Spalding, D. B., "Concentration fluctuations in a round, turbulent free jet", Chem. Eng. Sci. vol. 26, 1971, pp.95-107.
4. Gosman, D. A. & Lockwood, F. C., "Prediction of the influence of turbulent fluctuations on flow & heat transfer in furnaces", Imperial College, London, Rep. HTS/73/52, 1973.
5. Lockwood, F. C. & Naguib, A. S., "The prediction of the fluctuations in the properties of free, round jet, turbulent diffusion flames", Combustion and Flame, vol.24, 1975, pp.109-124.
6. Elgobashi, S. E., "Characteristics of Gaseous Turbulent Diffusion Flames in Cylindrical Chambers", Ph.D. Thesis, University of London, 1974.
7. Khalil, E. E., Spalding, D. B. & Whitelaw, J. H., "The calculation of local flow properties in two dimensional furnaces", Int. J. Heat and Mass Transfer, vol.18, 1975, pp.775-791.

COHERENT STRUCTURES IN COMBUSTION

A. J. Yule, N. A. Chigier and D. Thompson
Department of Chemical Engineering and Fuel Technology
University of Sheffield
Mappin Street, Sheffield S1 3JD
England

ABSTRACT

It is proposed, on the basis of experimental evidence, that many combustion flows contain coherent burning structures, or 'flamelets', which interact as they are convected downstream. Photographic evidence for gas diffusion and liquid spray flames indicates that these flamelets are associated with coherent large eddies in these flows. The coherent structures are particularly evident for a gas diffusion flame impinging on a flat plate which contains three-dimensional flamelets. These flamelets have a wide range of sizes and trajectories at a fixed point which results in a typical intermittent, turbulent form for temperature fluctuations. Models are proposed for eddies/flamelets in transitional and turbulent regimes of various flows. It is described how coherent large eddies can result in reduced efficiency of combustion and high levels of emission of pollutants. Recognition of their existence provides an opportunity for more accurate modeling of combustion flows.

INTRODUCTION

Turbulent flow is of primary importance in most combustion processes. Gaseous and liquid spray flames have a wide range of complexity varying from axisymmetric free flames to strongly three-dimensional flows in combustion chambers. However, in all cases turbulence controls the entrainment of oxidant, macroscale mixing, back-mixing and the microscale mixing of reactants and hot products. Reliable modeling and design of combustion systems thus requires a fundamental understanding of turbulence structure and turbulence-flame interaction. At the present time the most detailed knowledge of turbulence structure has been derived for non-burning flows. Davies and Yule (1) and Roshko (2) have reviewed the results of experiments which have given an improved understanding of the structures of non-burning turbulent shear flows. In these experiments specific features of the turbulence have been examined in a Lagrangian, or quasi-Lagrangian, frame of reference by using flow visualization and various conditional sampling techniques. Standard techniques of time averaging point measurements were shown to be inadequate for obtaining a clear physical understanding of turbulent flows which contain important repetitive events and eddies. There is sufficient evidence from these various experiments to show that the structures of non-burning mixing layers, jets and wakes are strongly influenced by large eddies in the turbulence. Furthermore these eddies may be far more repetitive in their structures and interactions than was previously inferred from the signals which they produce at fixed points in the flow.

In certain of these experiments these eddies appear to remain coherent for significant downstream distances and growth in eddy scale occurs by the merging or coalescing of adjacent eddies. This contrasts with the classical turbulence model of eddies breaking down and decaying into smaller and smaller eddies, although the breakdown of large eddies has also been observed in certain situations. Information on coherent eddy structures in burning flows is scarce although their presence should be expected on the basis of the cold flow experiments. The objective of this paper is to provide information on the occurrence and nature of coherent eddy structures in burning flows and on their roles in the process of turbulence-flame interaction. This is achieved by combining photographic evidence for various flames with available data for non-burning and burning flows. It is now apparent that the reliable prediction of combustion flows requires significant advances over the present methods of solving time average conservation equations by using classical closure techniques. Thus several new approaches to modeling combustion flows have been investigated, these have the common feature of including time dependency and models of eddy structures (3), (4).

EVIDENCE OF COHERENT STRUCTURES IN COMBUSTION

In some cases evidence of the important roles of coherent structures is more readily obtainable for burning flows than for non-burning flows. This is because luminous flames can provide very clear visualisations of regions of molecular scale fuel/oxidant mixing. Such regions necessarily form parts of any coherent large eddy components of diffusion flames and will also be deformed and convected by these eddies. Thus if large scale structured volumes of reacting flow can be observed to move as coherent regions this is evidence for the existence of large coherent eddies in the same flow.

For reasons of clarity the coherent regions of reaction associated with eddies in the flow will be referred to as 'flamelets' (5). We thus define an eddy as a vorticity-containing region of fluid which moves as a coherent structure. A flamelet is defined as a region of burning which can be observed to move downstream as a coherent structure. In practice a flamelet will form part of an eddy, however the precise structure and position of a flamelet relative to an eddy varies according to the structure of the eddy and its position in the main flame. Thus the visualization of a flamelet in a flow will not necessarily always provide a full indication of the shape of the eddy with which it is associated.

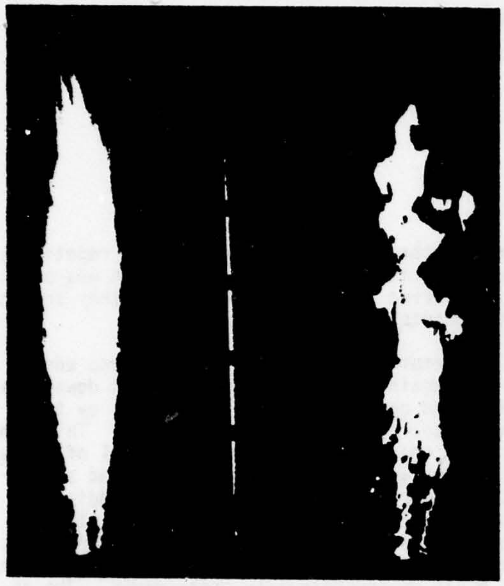

Fig. 1 Photographs of air blast atomized kerosene spray flame, exposure times 0.25 s and 0.004 s respectively.

The importance of studying and modeling the instantaneous rather than the time mean structure of a flow is demonstrated by comparing long and short time exposure photographs. For example Fig. 1 compares 0.25 s and 0.004 s exposure photographs of the same kerosene spray flame with a disk stabilizer. The left hand photograph has the brush appearance which is seen in long exposure photographs of turbulent flames, but the right hand photograph, which 'freezes' most of the motion, reveals that the actual instantaneous luminous flame region is very much smaller than the overall flame envelope. This phenomenon has been reported for other types of flame (6).

Examination of a series of photographs and cine films of flows of the type shown in Fig. 1 revealed that the large tongues of flame or flamelets, at the edges of the spray, are convected downstream and remain coherent and grow in scale as they move until extinction occurs at the end of the visible flame. In fact the flamelets have a substantial degree of coherence azimuthally, but they have a helical rather than axisymmetric structure. This observation correlates with the helical large scale structures which have been predicted by stability analysis for the downstream regions of cold round jets (7). The Reynolds number for this spray is 2 x 10^4 (based on orifice diameter and atomizing air velocity). On the basis of cold jet data (8) one should expect the complete length of the flame to be turbulent, apart from the first 50 mm, approximately, near the orifice. Also the measurements of velocity and temperature in these sprays (9), show intensity levels which are similar to those measured in, supposedly turbulent, gas diffusion flames. However the laminarizing effect of burning, which is discussed later, can be important so that the possibility exists that stabilizing viscous forces are maintaining an orderly, easily observed structure for the helical eddies. These sprays are stabilized by a region of recirculation near the orifice and this region is also likely to influence the structure and perhaps the instability mode for the large eddies/flamelets downstream. Certainly many gas diffusion flames, in the absence of a stabilizing disk, do not have such obvious helical structures in the flame.

The eddy structures in liquid spray flames are particularly important because of their roles in fuel droplet/turbulence interaction and thus in the determination of the local regimes of flow and combustion around droplets. The smaller droplets in the spray follow the gas flow, are carried along by the eddies and vaporize in the eddies. Burning, for these droplets, is a cloud combustion process which is basically similar to that found in gas diffusion flames. Larger droplets, however, do not follow the gas streamlines but instead can cross fuel/oxidant/products interfaces or even leave the large eddies completely. This process can both improve the efficiency of burning and the stability of the spray flame and also affect pollutant levels. For example soot particles can result from large droplets which leave the flame and burn individually but are quenched before burning has been completed.

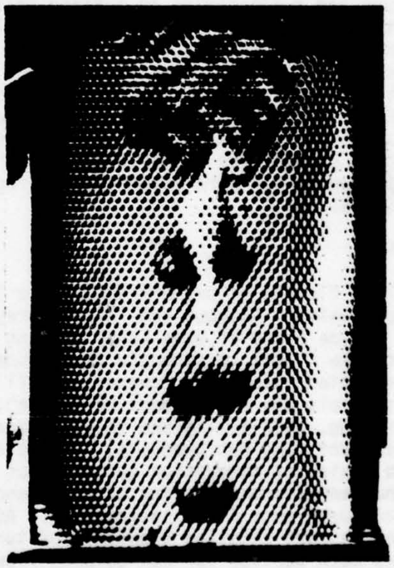

Fig. 2 Schlieren photograph of propane diffusion flame, burner diameter = 5 mm R_e = 10^3

Axisymmetric gas diffusion flames have a wide range of structures and hence a wide range of visual appearances, depending on the Reynolds number of the fuel jet and the properties of the fuel. Fig. 2 shows a schlieren visualization of a propane flame in which approximately the first twenty orifice diameters of flow contains vortex rings similar to those found in non-reacting flows. A combination of the laminarizing and expansion effects of combustion and also buoyancy effects, produces differences between this vortex ring structure for burning and non-burning flows of the same jet of gaseous fuel. Thus one can note, qualitatively, that the length of the region in which vortex rings are found, and thus the length of the transition region, is greater for the burning than the non-burning case. As in cold jets, these vortex rings coalesce with their neighbours and this process results in a less orderly structure for the fuel/oxidant/products interfaces in the vortices thus causing changes in the observed flame structure. This process can be observed in the upper part of Fig. 2. As schlieren type techniques indicate density gradients in the flow they produce visualizations which differ from direct visualizations of the luminous flame regions. The primary reaction regions, or flamelets, associated with the vortex rings in Fig. 2 are smooth tongues of flame which partially, or completely encircle the outer interface between the vortex ring and the surrounding air.

As with non-reacting round jets (8), the length of the transition region, containing these vortex rings, decreases as the Reynolds number is increased but coherent eddy structures can also be observed in the turbulent region of the flow, although with less clarity than the vortex rings. At higher Reynolds numbers the flamelets associated with the turbulent eddies, are observed as bulges of flame at the edges of the flow which do not have the smooth-spiral shapes found in the transition region. Small regions of burning gas frequently detach themselves from the flame and larger detached islands of burning gas separate at the end of the main flame.

Coherent flame and eddy structures are also observed in many large scale industrial processes. For example Fig. 3 shows flares burning surplus natural gas at a BP installation in the Middle East. Large eddies are produced by the combination of forced convection, buoyancy forces and also wind/jet interaction. The gas has a significant content of higher hydrocarbons, which can form soot easily during combustion. In addition, the relatively long period between ignition and completion of combustion allows significant radiative heat transfer to the unburnt gas, which can cause cracking. These factors account for the formation of considerable quantities of soot but it is interesting to note that the soot containing eddy does not disperse rapidly but maintains its coherence for a considerable distance.

Fig. 3 Natural gas flares, BP installation, Middle East.

In addition to the coherent structures in the free flames, discussed above, there is also strong evidence for the existence of coherent eddies and flamelets in combustion flows interacting with walls. In particular coherent structures are clearly visible in the flow produced by a gas diffusion flame impinging on a flat plate and this flow is discussed in more detail in the next section. Many practical combustors with swirling flow contain regions of recirculation which are similar in structure to the vortex ring-type eddies which are observed to be convected downstream in free flames.

Direct photographic evidence of coherent structures in flames is supported by quantitative point measurements. For example velocity and temperature spectra and correlations using laser anemometers and thermocouples indicate the presence of quasi-periodic streets of vortex rings in the transitional regions of flames. For turbulent flames the importance of the large eddies can be deduced from measurements which indicate unmixedness and also measurements of the statistics of large temperature 'spikes' (10) which can be related to the shapes, coherence and convective properties of flamelets and eddies in the flow. This type of measurement indicates that coherent large eddies influence flame structure even in the apparently complex burning of premixed flames downstream of turbulence grids. Other workers (11) have used schlieren techniques to show the deformation of flame regions by the eddies in this type of flow.

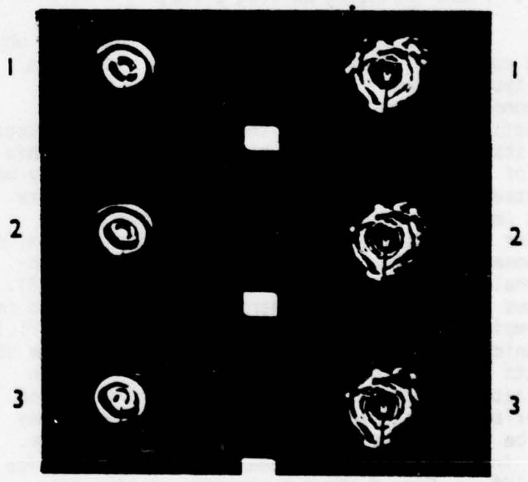

Fig. 4 Sequence of frames of flame impinging on flat plate, $R_e = 10^3$ and $R_e = 3 \times 10^3$.

BURNING JET IMPINGING ON FLAT PLATE

Fig. 4 shows two sequences of frames from cine films of a diffusion flame on the lower surface of a flat plate, produced by an axisymmetric jet of propane impinging on the plate from below. In these experiments the burner orifice diameter is 5 mm and the orifice is 100 mm vertically below the centre of a 740 mm diameter steel plate. Physically similar flame structures can also be observed for a wide range of these parameters, for example the same phenomenon has been observed by Milson and Chigier (12) using apparatus which was an order of magnitude larger. Fig. 4 shows that for $R_e = 10^3$ the flame on the plate consists of a street of toroidal flamelets, which indicates a street of vortex rings. These rings of flame increase in diameter with time until burning is completed and they are no longer visible. At $R_e = 3 \times$

10^3 evidence of instability can be seen in these rings. Fig. 5 shows the flame for $R_e = 10^4$ and it is seen that although a toroidal structure is still noticeable in the flow, the coherent structures now have the appearance of individual, three-dimensional cells of burning gas or flamelets. These structures are also visible at higher Reynolds numbers.

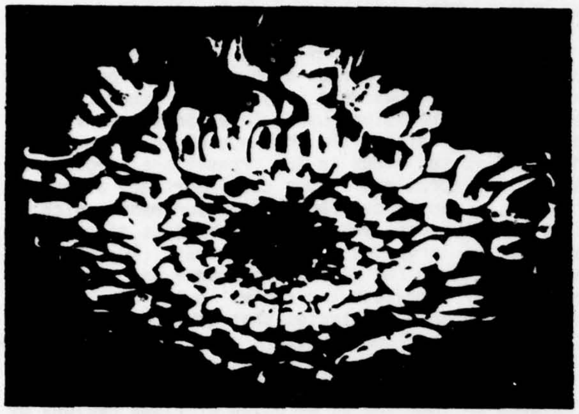

Fig. 5 Flame impinging on flat plate, $R_e = 10^4$.

At the present time it is not clear why these coherent flamelets are so clearly visible in this type of flow. Possibilities include the improvement of flame visualization produced by soot production and quenching at the flat plate or perhaps some stabilizing influence which is peculiar to this type of flow. This type of flow is not completely unexpected as it is known (13) that non-burning smoke rings impinging on a flat plate break down into a similar three-dimensional cell-structure and a similar phoenomenon is also found in the breakdown of transitional vortex rings in non-burning round jets (8). It thus appears that the coherent structures found in the impinging flame flow are formed by basically fluid mechanical processes and they do not arise because of effects peculiar to combustion processes. Thus an examination of this flow can provide information on eddy-flamelet interactions and structures which may also be relevant to other types of combustion flow.

An initial study has been made of the flow for $R_e = 10^4$. Fig. 6 shows a sequence of cine film frames with the center of each frame showing a point 200 mm from the centre of the plate. The individual flamelets are on average elongated in the flow r (radial) direction and they grow in scale as they move downstream. A randomness in the movements and dimensions of the flamelets is evident in the films. The flamelets grow in scale as they move towards the edge of the plate, both individually and also by amalgamating with neighbouring flamelets (both in the azimuthal and radial directions). In addition, flamelets are occasionally seen to move more quickly than average and they overtake and pass above other structures without merging with them. There is no visual evidence in these films of the eddies, which these flamelets delineate, breaking down into smaller scales which invites comparison with the growth in eddy scale in two-dimensional non-reacting mixing layers which was observed by Roshko (2).

The clarity with which the boundaries of the individual flamelets can be seen in the films permits a quantitative analysis of flamelet dimensions by measuring from consecutive frames using a film editor.

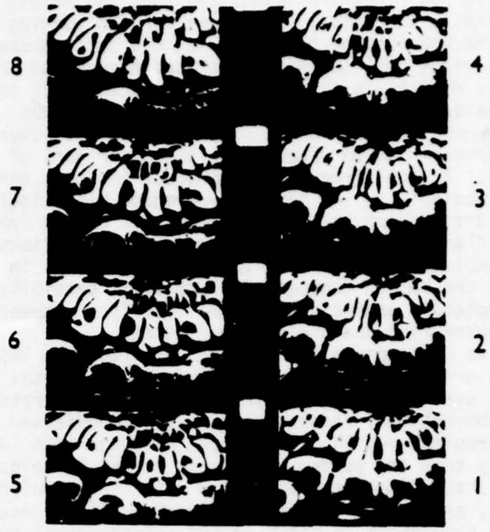

Fig. 6 Close-up of impinging flame, $R_e = 10^4$. Flamelets are moving from top to bottom in each frame, interval between frames = 0.016 s.

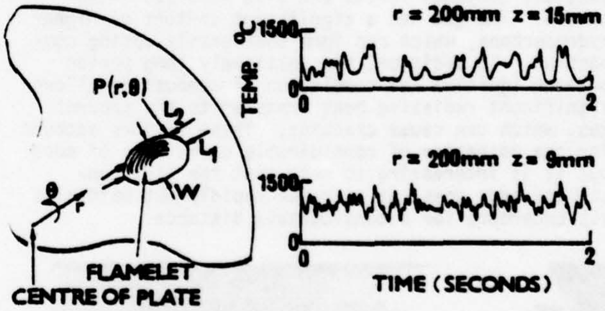

Fig. 7 Notation for impinging flame showing temperature time histories measured at two positions, $R_e = 10^4$.

Fig. 7 shows the notation for this analysis in which L_1 and W are the dimensions of a flamelet in the r and θ directions when its leading edge just passes through the line perpendicular to the plate through P(r, θ). In addition measured time histories of fluctuating temperatures are shown in Fig. 7 for positions in the centre and outer edge of the flame, halfway to the edge of the flat plate. These time histories were measured by a 25 μm diameter Pt/Pt - 13% Rh thermocouple. The temperature fluctuations have the intermittent appearance which is usually found in turbulent flames. The average flamelet length $\overline{L_1}$ increases almost linearly, with distance from the centre of the plate with $\overline{L_1} = 0.3$ r. In the cold mixing layer experiments of Roshko (2) the average longitudinal large eddy scale was also found to increase as $0.3x$ approximately where x is the distance downstream. Fig. 8 shows histograms of the length L_1 and width W for flamelets passing through one point 200 mm from the centre of the plate. It is seen that the average aspect ratio of the flamelets is approximately 2 and there is also a wide range of lengths and widths for the flamelets passing through any fixed point in the flow.

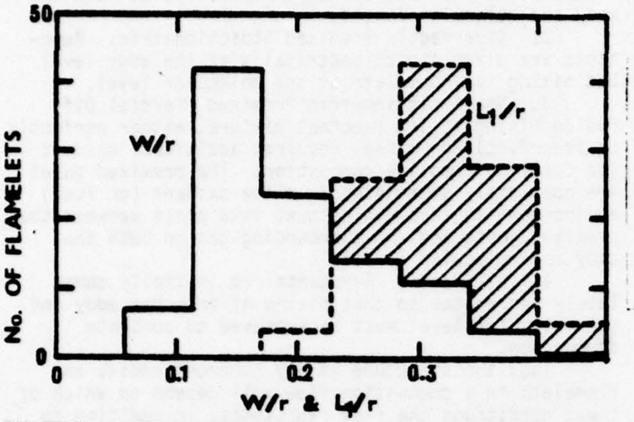

Fig. 8 Histograms of flamelet length and width at $r = 200$ mm, 150 flamelets measured, $R_e = 10^4$.

This spectrum of sizes contributes to the random, intermittent appearance of temperature fluctuations measured at fixed points but the random trajectories of the flamelets also contributes significantly to this effect. The effect of these random trajectories can be quantified by computing the histogram for the intercept dimension L_2 of the flamelets. This dimension is the length of the radial line through $P(r, \theta)$ intercepting the boundaries of the flamelet. This histrogram is shown in Fig. 9 and a very wide range of dimensions is evident. Variations in eddy dimensions and trajectories in the z direction (perpendicular to the plate) will have an important influence on the intermittent temperature signal at the outer edge of the flow. However, it was not possible to measure flamelet boundaries accurately in the z direction using this photographic technique. It thus appears that, for a wide range of flow parameters, the flame impinging on a flate plate contains coherent flamelets which indicate the presence of coherent eddies. The randomness in the structures and trajectories of these flamelets results in typical turbulent forms for point time histories of temperature fluctuations.

TRANSITIONAL AND TURBULENT FLOW

It is clear from the above that there is abundant evidence supporting the existence of coherent eddies and their associated flame structures (flamelets) in several types of flame. The photographic evidence indicates that the coherent eddy/flamelets found in combustion do not have a similar 'universal' structure for all types of flow. In particular, for diffusion flames,one can identify a range of coherent structures including: (i) Unstable laminar flow which contains an oscillating laminar diffusion flame (ii) Streets of axisymmetric vortex rings with smooth tongues of flame at their interfaces (iii) Other orderly vortex structures, including helical vortices, which also produce relatively smooth tongues of flame (iv) Individual coherent, three-dimensional eddies which produce randomly moving cell-like flamelets (as in the flame impinging on a flat plate) (v) Eddies containing coherent 'ragged' regions of burning which often form islands of burning which are separated from the main flame. This range of types is due to the dependence of the eddy structure on the local relative importance of inertial, viscous and buoyancy forces in the flow. There must also be a dependence of the eddy structure on the history of that eddy from its point of formation. By comparison with data (8), (14) for non-reacting cold flows, the local existence of large eddies which have an orderly vortex structure with associated smooth flamelets is indicative of a local transitional structure for the combustion flow. Thus viscous forces have an important stabilizing influence on this case. As viscous forces become relatively less important the orderliness of these vortex-eddies decreases, as they become increasingly three-dimensional and unstable. Thus the existence of regions of ragged flame moving as coherent structures is indicative of a flow which is closer to the usually accepted conditions of fully developed turbulent flow. For this case there are significantly energetic scales of motion present which are smaller than the large eddy scale.

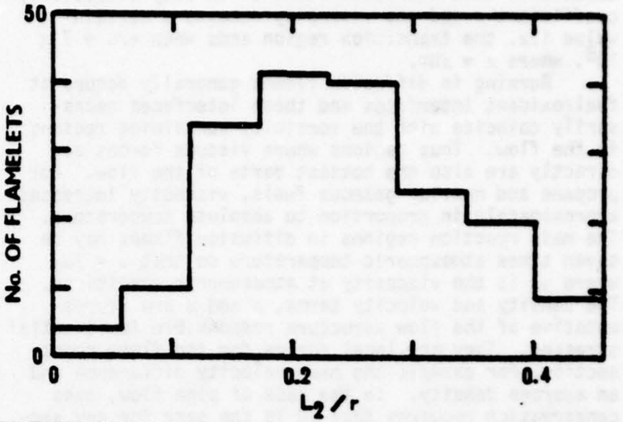

Fig. 9 Histogram of radial intercept length of flamelets for impinging flame, $r = 200$ mm, $Re = 10^4$.

The accepted test for the local existence of fully developed turbulence is that the turbulence structure has Reynolds number similarity. This criterion cannot be simply applied to most combustion flows, including those discussed above, because of the additional dependence of flame structure on variables such as the chemical kinetics, buoyancy forces, flame stabilization/ignition conditions and a range of complicating factors which occur with spray flames.

In addition flow in turbulent regions must be affected by any burning which occurs in Reynolds number dependent regions nearer to the burner nozzle. It can be demonstrated that many practical combustion flows may not contain fully developed turbulence, at least for a significant length of the flame. The length of the transition region for cold jets and mixing layers has been studied both experimentally and theoretically. Relationships for the length of the transition region, x_T, vary, probably because of differences in initial jet orifice conditions. For cold mixing layers Bradshaw (14) suggested $x_T = 7 \times 10^5 \mu/\rho U$ where ρ is the gas density and U is the jet orifice velocity. In approximate physical terms one can say that the flow locally contains fully developed turbulence when the local ratio of an eddy diffusivity coefficient ϵ and the viscosity exceeds a certain value i.e. the transition region ends when $\epsilon/\mu = 7 \times 10^5$, where $\epsilon = \rho U x$.

Burning in diffusion flames generally occurs at fuel/oxidant interfaces and these interfaces necessarily coincide with the vorticity-containing regions in the flow. Thus regions where viscous forces act directly are also the hottest parts of the flow. For propane and heavier gaseous fuels, viscosity increases approximately in proportion to absolute temperature. The main reaction regions in diffusion flames may be seven times atmospheric temperature so that $\mu = 7\mu_0$ where μ_0 is the viscosity at atmospheric conditions. The density and velocity terms, ρ and U are representative of the flow structure responsible for inertial stresses. They are local scales for the flame cross-section, for example the mean velocity difference and an average density. In the case of pipe flow, mass conservation requires that ρU is the same for any section of the flow for both burning and non-burning conditions. However for free shear flows burning results in the expansion of gases in all directions and the rate of engulfment of cold fluid is modified so that one cannot simply predict this term.

Experiments indicate that local mean velocities in burning and non-burning flows do not differ greatly when buoyancy forces may be neglected. However thermal expansion decreases local mean densities, although to a much smaller extent than would occur if all the gas were at the flame temperature. Thus, as a first approximation, if it is assumed that the effect of combustion on inertial forces is much less than the effect on viscous forces then:

$$(x_T)_{flame} = 7(x_T)_{cold\ jet} \text{ or } (x_T/D)_{flame} = 4.9 \times 10^6 \ R_e^{-1}$$

where R_e is the Reynolds number based on the burner diameter D. This relation predicts, for example, that the flow in the first 0.3 m of flame from a 5mm diameter burner is not fully turbulent when $R_e = 10^4$. This implies that the impinging flame discussed above may not contain fully developed turbulent flow for half the flame length. In addition, if this criterion is applied to a variety of laboratory scale diffusion flames and also to some large scale industrial flames it is found that significant lengths of the visible flame regions may not contain fully developed turbulence. On the other hand it is reasonable to assume that many of these flames possess the important characteristics of turbulent flow although there may not strictly be fully developed turbulence present.

It can be argued that buoyancy forces in vertical free flames increase the convection velocities of vortices and thus decrease the residence time of the vortices at any position in the flow and also lengthen the transition region. In general, for diffusion flames, it is likely that burning can increase the distance required to establish fully developed turbulent flow by at least one order of magnitude, especially where a fully formed cylindrical flame interface is established on and downstream of the jet nozzle.

MODELS OF THE STRUCTURES OF COHERENT EDDIES AND FLAMELETS

Evidence for the existence of coherent eddies and flamelets is based largely on studies of gas and liquid spray diffusion flames. However, turbulent flames can conveniently be separated into four categories according to the initial degree of mixing between fuel and oxidant when they are introduced into the system. Distinction is made between mixing at the eddy and molecular levels as well as the extent to which a mixture is richer or leaner than the fuel/oxidant stoichiometric mixture ratio:

1. Perfectly Premixed Stoichiometric: Reactants are completely mixed, stoichiometrically, at both the eddy and molecular levels.
2. Imperfectly Premixed Stoichiometric: Reactants are mixed stoichiometrically at the eddy level but mixing is incomplete at the molecular level.
3. Non-Stoichiometric Premixed (Partial Diffusion Mixing): The reactant mixture, either perfectly or imperfectly premixed, requires additional oxidant (or fuel) to complete combustion. The premixed gases are completely segregated from the oxidant (or fuel) environment so that mixing must take place between the premixed gases and the surrounding gas on both the eddy and molecular levels.
4. Diffusion: Reactants are initially completely segregated so that mixing at both the eddy and the molecular level must be achieved to complete combustion.

Thus the structure of any coherent eddies and flamelets in a combustion flow will depend on which of these conditions the flow represents, in addition to the effects of viscous and buoyancy forces and flow geometry. Models for coherent eddies in diffusion flames are described below for the two extremes of orderly-transitional and fully turbulent flow.

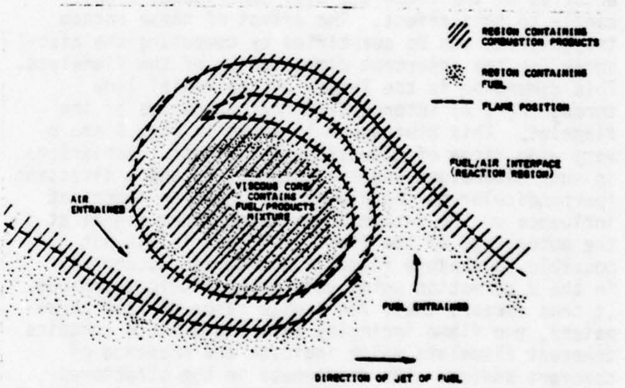

Fig. 10 Cross-section of transitional 'vortex' eddy in gas diffusion flame.

Model of the Transitional Vortex Eddy

The eddy, sketched in cross-section in Fig. 10, is an orderly vortex produced by the rolling-up of the vorticity containing interface at the edge of the flame. This represents a vortex ring, line vortex or helical vortex. For non-burning conditions the fuel/air interface is a double spiral around the vortex core. Fig. 10 represents this eddy before it has interacted with other eddies or developed instabilities. The flame coincides with the fuel/air interface region which has transverse concentration and temperature gradients and a local thickness which are dependent on the residence time of the vortex, the vortex strength, local diffusion coefficients and the local chemical kinetics. The chemical kinetics of the burning in this interface region are the same as those of steady laminar diffusion flames. The stretching of this fuel/air interface, due to the interactions of the vorticity which it contains, enhances the molecular mixing. Combustion proceeds near stoichiometric conditions. Preheating of fuel takes place mainly in the interface region where mixing is on the molecular scale, so that this region has much higher temperatures than the unmixed fuel and air regions. As the vortex is convected along,the velocities induced by the vorticity within it produce a continuous 'rolling-up' of the interface, an increase in the vortex dimensions and the continuous engulfment of additional air and fuel. Under 'cold' conditions the central core of vorticity increases its dimensions as $(\frac{\mu t}{\rho})^{\frac{1}{2}}$. Burning occurs near stoichiometric conditions and the vortex engulfs air and fuel in approximately equal quantities so that at a point along the interface all of the air engulfed at some previous time is consumed although there is still engulfed fuel remaining. This results in a region at the centre of the vortex which contains both unmixed cold fuel and also a mixture of fuel and hot products. The volume of this fuel/products region increases with increasing residence time of the vortex.

Fig. 10 indicates a continuous flame wrapped completely around the vortex and linked to adjacent vortices by the fuel/air interface. This may resemble a cross-section of one of the eddies found in the impinging flame (Fig. 6). In other situations flamelets are observed to emerge much shorter distances from the main flow. The length of the flamelet encircling the vortex varies depending on variables representing the vortex dynamics, the chemical kinetics and molecular scale mixing. For example this flamelet is sensitive to the ratio of the vortex circulation and the molecular diffusivity.

One consequence of this orderly structure is that soot and other pollutants collect in the central region of the vortex. If such a vortex retained its organized structure until it reached a point in the flow where there was no longer a supply of fuel to be entrained and subsequently entrained only air, the possibility exists that the fuel rich region in the vortex would never mix with air under conditions suitable for complete burning of the remaining fuel. In general these vortices do not remain coherent for the complete length of the flame, but instead the coalescing of neighbouring vortices and the three-dimensional breakdown of the vortices (8) results in their fundamental restructuring. This restructuring is important in transitional flows as it distorts existing interfaces in the vortices, accelerates molecular mixing rates and permits the mixing of fuel rich concentrations inside vortices with further air.

Model for Large Turbulent Eddy

It is likely that the randomly moving eddies observed in flames impinging on flat plates are representative of many of the features of coherent large eddies in fully developed turbulent flames with the exception that there are no observable medium eddy scales for the impinging flame. Thus one can consider three-dimensional eddies which are relatively elongated in the flow direction and which interact and coalesce in a similar manner to that observed for large eddies in cold flow experiments (1), (2) and (8).

A cross-section of such an eddy in a diffusion flame is sketched in Fig. 11. This eddy differs from the transitional eddy described above because of its three-dimensional structure, so that there is not complete coherence circumferentially around the flame, and also the existence of an irregular vorticity distribution within the eddy which can be considered as the existence of smaller eddy scales within the main eddy. Cold flow visualizations (8), (15) show that these large eddies engulf wedges of unmixed fluid in a similar fashion to the transitional vortices. However, as has been observed in dye injection experiments (15), the subsequent molecular scale mixing of the fluids engulfed from either side of the eddy is considerably more rapid for the case of the turbulent eddy than for the transitional eddy. Rapid mixing down to molecular scales is produced by vorticity stretching and interactions in the three-dimensional irregular vorticity field within the turbulent large eddy. The irregularity of the structure within the large eddy, whilst enhancing mixing, also introduces the possibility of a range of flamelet structures associated with the eddy. Thus in general a ragged flame-front can be expected to exist behind the fuel entrainment wedge with a smooth flame at the relatively regular interface which separates eddies. This structure is observed in many diffusion flames.

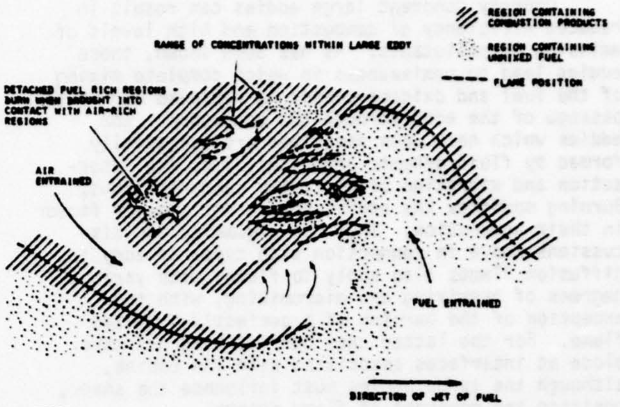

Fig. 11 Cross-section of large turbulent eddy in gas diffusion flame.

The likelihood exists of volumes of fuel detaching from the entrainment wedge and either existing, for some time, in a 'sea' of combustion products or burning as small detached islands of burning within the eddy. This phenomenon is also observed in practical flames. Regions of air will be engulfed by the eddy and exist within the eddy for some time, perhaps mixing with products but not with fuel within flammability limits.

Although micromixing within large eddies is rapid in cold flow experiments, there are conditions in the burning of fuel and oxidant which lead to significant differences from the cold flow case, e.g. the presence of products, the need for molecular mixing within flammability limits and the need for sufficient heat input. This requires mixing of fuel with very hot regions as well as with air if a separated 'island' of fuel in an eddy is to ignite and completely burn. Thus it is possible for part of the fuel engulfed by a turbulent eddy to exist, unburnt, in the eddy for a significant period before all of the conditions are met for combustion to be completed. As the eddies move downstream a point is reached at which the fuel supply at the centre of the flow is depleted so that eddies on either side of the flow meet. After this point the remaining unburned fuel in the entrainment wedges burn as large detached islands at the end of the main flame as can be observed in practice.

THE ROLES OF COHERENT EDDIES IN COMBUSTION

Orderly coherent large eddies can result in reduced efficiency of combustion and high levels of emission of pollutants. As has been shown, these eddies lead to unmixedness in which complete mixing of the fuel and oxidant cannot be achieved during the passage of the eddy through the combustor. The eddies which have been described are essentially formed by fluid dynamic processes, i.e. the interaction and migration of vorticity concentrations. Burning modifies the eddies but is not a major factor in their generation. Thus the arguments and discussions above in connection with types of eddy in diffusion flames also apply to flames with various degrees of premixing and micromixing, with the exception of the burning of a perfectly premixed flame. For the latter case burning need not take place at interfaces associated with the eddies, although the large eddies must influence the shape, position and movement of flame fronts.

THE ROLE OF COHERENT STRUCTURES IN POLLUTANT FORMATION IN DIFFUSION FLAMES

When coherent structures are regular components of turbulent diffusion flames their significance in emission of pollutants from such flames lies in the long period of diffusion-based combustion of each element of fuel. This contrasts with the model which would be relevant to combustion either in premixed conditions, or under conditions of small-scale turbulent mixing (where the period of combustion of each fuel element would be relatively small). The contrast is conveniently discussed in terms of the premixed flame and the coherent structure-interface flame. The two cases are illustrated in Fig. 12; each case is idealised to the extent that the premixed flame is considered to have homogeneous composition throughout the region under consideration, and the diffusion flame is considered to occur between regions which maintain their identity throughout the combustion process.

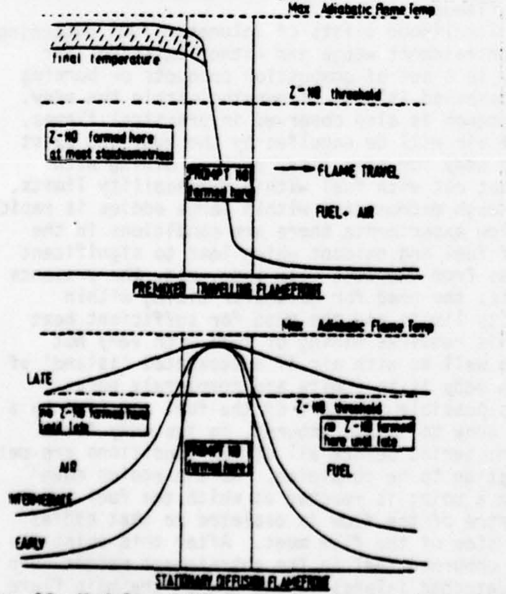

Fig. 12 Models of NO formation in premixed and diffusion type flames

The two processes of major importance in pollution control are the formation of nitric oxide and the persistence of carbon monoxide. Only the essential characteristics of the two processes will be discussed here, since they have been extensively discussed in the literature. These characteristics are:

Nitric Oxide. It is now generally recognised that nitric oxide is formed in flames by two distinct mechanisms, the so-called prompt-NO pathway and the Zeldovich 'chain mechanism'. The prompt-NO mechanism was first investigated in detail by Fenimore (16) and has since been extensively studied by Bachmaier, Eberius and Just (17) who report that prompt-NO formation during the combustion of a particular fuel under premixed conditions can be defined by the stoichiometry. In view of recent recognition that the chemical kinetics of premixed and diffusion flames combustion are very similar, the yield of prompt-NO per unit volume of fuel formed under diffusion flame conditions is expected to be similar to the yield obtained during combustion of that fuel in a premixed flame with near-stoichiometric fuel-air ratio.

The formation of nitric oxide via the Zeldovich mechanism ($N_2 + O = NO + N$, rate determining step, (rds) followed by the fast step $N + O_2 = NO + O$) has been studied extensively, the activation energy of the rds is 75.4 kcal. Although non-relaxation of the oxygen atom concentration to equilibrium has been regarded as a transient phenomenon leading to high nitric oxide formation rates in the immediate post flame region in some premixed flames, this need not be considered here since the relaxation of radical concentrations to equilibrium is thought to be rapid in diffusion flames. Consequently, nitric oxide formation by the Zeldovich mechanism in diffusion flames has an activation energy characteristic of the rds activation energy plus that empirically fitted to the dissociation of oxygen, i.e. 134.5 kcal.. This activation energy is very high, and the reaction may be regarded as extremely slow, below 1800 K. In the case of many flames with relatively small residence times at high temperature, the reaction can only provide significant levels of NO in pollutant emission terms when the temperature exceeds 1900 K.

Carbon Monoxide. Carbon monoxide formation is an integral part of the combustion of hydrocarbons. The species can co-exist in significant concentrations with carbon dioxide and oxygen at typical flame temperatures and CO burnout in combustion systems relies on the rapidity of oxidation down to c. 1200 K.

The following contrasts between NO formation in premixed and coherent structure-diffusion flames may be inferred:

Nitric oxide formation. The yield of prompt-NO from a premixed stoichiometric flame per unit volume of fuel burnt and that from an interface-combustion diffusion flame are considered similar - whatever the scale of turbulent eddy involved in the latter. The fuel-air ratio in the combustion interface is near to that in a stoichiometric flamefront, with passage of gas through the stoichiometric flamefront represented by 'ageing' of the interface as oxygen and fuel in the surrounding gas are depleted. The formation of prompt-NO is of secondary importance for practical purposes; there is limited scope for the drastic change in fuel type or fuel-air ratio required to minimise the yield, and its formation and emission seems inevitable.

In contrast, the yield of NO via the Zeldovich mechanism is a known function of temperature, oxygen concentration and residence time. Here, there is a marked contrast between the patterns of NO formation to be expected to occur in a premixed turbulent flame and in a large-scale structure interface flame. In the premixed flame, the flame envelope will be occupied by alternate regions of hot, burnt products, and unburnt fuel-air mixtures. Because of the high non-linearity of the temperature dependence of the Zeldovich mechanism the rate of formation of NO will be much greater than predicted by the time mean temperature (18), (19). In contrast, where large eddies occur, the temperature will only exceed the Zeldovich threshold in and near the relatively thin flamefront. Over much of the regions of air and fuel plus products involved, the temperature will be too low for Z-NO formation to occur during most of the period of combustion.

Thus it can be expected that if the coherent structures within a flame region are of fairly uniform size, and ignition occurs at a similar stage so that the time-mean flame envelope is well defined, the flame region can be constrained to give a low level of nitric oxide formation. Rapid dilution after the completion of combustion is necessary in order to minimise continuation of Z-NO formation in the post flame region.

Carbon monoxide formation. The formation and persistence of undesirably high levels of carbon monoxide is largely a problem of excessively rapid quenching, or maldistribution of fuel or air elements. Rapid quenching, can lead to carbon monoxide emission as a partly burnt coherent structure enters a region of high shear and low temperature, so that the structure is rapidly broken up and mixed with cold air. If this occurs, the temperature may fall below the range in which CO burnout is rapid in a very short time. Maldistribution of fuel and air elements can result in combustion of a group of elements moving together in the presence of insufficient oxygen for complete combustion. There is then potential for the core of the large region of gas with high CO content to survive intact for sufficient time for radiative cooling or impaction on a cold surface to assist CO freezout.

It is also noted that a fuel element completely surrounded by a flame envelope has high potential for carbon monoxide formation and 'storage'. CO formed at the combustion interface can diffuse into the unburnt fuel, where there is little, if any, oxygen available for reaction to complete conversion to carbon dioxide. This process effectively stores carbon monoxide and transfers it downstream towards the end of the flame region. In many flames, there is a much greater likelihood that coherent structures will disintegrate rapidly on mixing with cold air near the end of the flame than further upstream. In contrast, in premixed combustion the CO is formed in a region with stoichiometry characteristit of the whole gas input. Thus, if the mixture ratio is not fuel rich, CO burnout will occur throughout the flame region.

It must be re-emphasized that the premixed flame has been used as a contrast with the flame containing coherent structures in the interests of simplicity. The classical model of a turbulent diffusion flame implies similar characteristics to the premixed flame for the following reasons:

1. Each small element of fuel in the classical turbulent diffusion flame would burn rapidly after ignition- the flame region would thus consist mainly of alternate regions of cold, unburnt gas and hot gas in which Z-NO formation would occur.

2. A local fuel-air ratio can be ascribed to regions of gas sufficiently large to contain several fuel eddies- the instantaneous local fuel-air ratio for each region would not deviate greatly from its time mean value in well-structured flames.

It would therefore be valid to attempt to construct a model of NO formation in a turbulent diffusion flame with this structure on the basis of: (i) prompt NO formation in the flamefronts and (ii) Zeldovich NO formation in an average population of hot regions.

However, the observation of coherent structures as a regular phenomenon invalidates the basic concept of this model. The coherent structures can occupy regions which are a significant fraction of the total flame volume and persist for long periods. The transition period between the unburnt and fully burnt states, which is negligible for sufficiently small scale turbulent eddies of fuel, becomes of major importance in the combustion of large coherent structures. A more valid approach to the problem may then be evaluation of NO formation by a correctly chosen mean coherent structure in the flame under consideration.

The observations of coherent structures in flames reinforces the need for description of pollutant formation and emission in terms of a model which takes into account persistent chemical and temperature inhomogeneity. The magnitudes and persistence of the inhomogeneities which can arise are such that any model based on time averaging of any property must be regarded as purely empirical since it neglects to take into account the important physical structure of the flow.

CONCLUSIONS

Extensive photographic evidence proves that many types of flame contain coherent large eddies which produce regions of burning, or flamelets, in the flow. This evidence agrees with available data from point measurements. A combination of this evidence with observations for non-burning flows indicates that the range of eddy, and thus flamelet, structures which can be observed can be explained in terms of the relative local importance of viscous forces in the flow.

A flame impinging on a flat plate gives a particularly good visualization of coherent eddies, in combustion and it is found that local variations in eddy dimensions and trajectories can produce random fluctuations in point temperature measurements in the flow.

Coherent large eddies have important influences on macromixing and burning as the relatively organised structure which they impose on the flow determines the rate at which fuel, oxidant and products are mixed within flammability limits. For diffusion flames, burning takes place in relatively thin interface regions between fuel and oxidant similar to those found in steady laminar mixing.

These coherent large eddies can result in inefficient combustion and high levels of emission of pollutants. There is sufficient evidence to show that these large eddies are present in many practical combustion systems. These large eddies can be broken up by increasing the shear stresses in the flow in regions of steep velocity gradients and by the introduction of swirl.

ACKNOWLEDGEMENT

The authors express their appreciation to M. Wilde for his assistance in the photographic studies of flames.

REFERENCES

1 Davies, P. O. A. L. and Yule, A. J., "Coherent Structures in Turbulence," Journal of Fluid Mechanics, Vol. 69, Part 3, 1975, pp 513-537.

2 Roshko, A., "Structure of Turbulent Shear Flows : A New Look," AIAA Paper No. 76-78, January, 1976.

Spalding, D. B., "Development of the Eddy Breakup Model of Turbulent Combustion," Sixteenth Symposium (International) on Combustion, The Combustion Institute, Pittsburgh, 1977.

4 Donaldson, C. Du P., "On the Modeling of the Scalar Correlations Necessary to Construct a Second-Order Closure Description of Turbulent Reacting Flows," Turbulent Mixing in Nonreactive and Reactive Flows, Plenum Press, New York, 1975, pp. 131-153.

5 Williams, F. A., "Recent Advances in Theoretical Descriptions of Turbulent Diffusion Flames," Turbulent Mixing in Nonreactive and Reactive Flows, Plenum Press, New York, 1975 pp. 189-201.

6 Ballantyne, A. and Bray, K. M. C., "Investigations into the Structure of Jet Diffusion Flames using Time/Resolved Optical Measuring Techniques," Sixteenth Symposium (Int.) on Combustion, The Combustion Institute, Pittsburgh, 1977.

7 Mattingly, G. E. and Chang, C. C., "Unstable Waves in an Axisymmetric Jet Column," Journal of Fluid Mechanics, Vol. 65, Part 3, 1974, pp. 541-560.

8 Yule, A. J., "Observations of Late Transitional and Turbulent Flow in Round Jets," Symposium on Turbulent Shear Flows, Penn State University, April, 1977.

9 Styles, A. C. and Chigier, N. A., "Combustion of Air Blast Atomised Spray Flames," Sixteenth Symposium (International) on Combustion, The Combustion Institute, Pittsburgh, 1977.

10 Ho, C. M., Jakus, K. and Parker, K. H., "Temperature Fluctuations in a Turbulent Flame," Combustion and Flame, Vol. 27, 1976, pp. 113-124

11 Ballal, D. P. and Lefebvre, A. H., "Turbulence Effects on Enclosed Flames," Acta Astronautica, Vol. 1, 1974, pp. 471-483.

12 Milson, A. and Chigier, N. A., "Studies of Methane and Methane-Air Flames Impinging on a Cold Plate," Combustion and Flame, Vol. 21, 1973, pp.295-305

13 Magarvey, R. H. and MacLatchy, C. S., "The Disintegration of Vortex Rings," Canadian Journal of Physics, Vol. 42, 1964, pp. 684-689.

14 Bradshaw, P., "The Effect of Initial Conditions on the Development of a Free Shear Layer," Journal of Fluid Mechanics, Vol. 26, Part 2, 1966 pp.225-236.

15 Dimotakis, P. E. and Brown, G. L., "Large Structure Dynamics and Entrainment in the Mixing Layer at High Reynolds Number," Tech. Report CIT-7-PW, Aug. 1975, Project SQUID, Purdue University, West Lafayette, Indiana.

16 Fenimore, C. P., "Formation of Nitric Oxide in Premixed Hydrocarbon Flames," 13th Symposium (International) on Combustion, The Combustion Institute Institute, 1971, p. 373.

17 Bachmaier, F., Eberius, K. H. and Just, T., "The Formation of Nitric Oxide and the Detection of HCN in Premixed Hydrocarbon-Air Flames at one Atmosphere," Combustion Sci. Tech., Vol. 7, 1973, p. 77.

18 Thompson, D., "Formation of Nitric Oxide in Combustion Systems," Ph.D. Thesis, University of Sheffield, 1971.

19 Gouldin, F. C., "Role of Turbulent Fluctuations in NO Formations," Combustion Sci. Tech., Vol. 9, 1974, p 17.

SESSION 8

WALL FLOWS 1

Chairman: T. J. Hanratty
University of Illinois
Urbana, Illinois 61801
U.S.A.

BOUNDARY LAYER SHEAR STRESS IN SUBSONIC AND SUPERSONIC FLOW

by
V. A. Sandborn
Colorado State University

and
C. C. Horstman
NASA-Ames Research Center

ABSTRACT

A survey of shear stress distributions across turbulent boundary layers for a wide range of flow conditions has been made. Both the turbulent and viscous contributions to the shear stress are included. The study was directed toward establishing the basic characteristics for the shear distribution for different flow conditions. For the flows where equilibrium is established a model based on the theoretical solution of the boundary layer equation of motion for large Reynolds numbers is demonstrated. The limiting solution is found to be an accurate representation of measured shear distributions even at low Reynolds numbers.

The shear stress distribution for zero pressure gradient, turbulent boundary layers is found to be a near universal function of the local surface shear stress and boundary layer thickness. Both incompressible and supersonic flows demonstrate a remarkable degree of correlation. For pressure gradients, both increasing and decreasing, the limiting solution for large Reynolds number is found to predict the shear stress for the equilibrium flows.

For a typical incompressible, increasing pressure, nonequilibrium, turbulent boundary layer flow the outer region of the shear distribution was found to remain nearly constant with increasing pressure gradient. The effect of the pressure gradient is evident mainly in the inner region of the boundary layer. For compressible flows it was found that two different type pressure gradient flows exist depending on whether the mass flux gradient is positive or negative.

NOMENCLATURE

A	similarity constant, defined eq. (8)
a	constant describing the freestream velocity
B	similarity constant, defined eq. (9)
c_f	skin friction coefficient, $\tau_w/\rho_\infty U_\infty^2$
f	mean flow function
h	static enthalpy
p	pressure
U	mean longitudinal velocity
u	longitudinal turbulent velocity
U_τ	shear velocity, $\sqrt{\tau_w/\rho_e}$
v	vertical turbulent velocity
V	mean vertical velocity
x	distance in direction of mean flow
y	distance normal to surface
δ	boundary layer thickness or characteristic length
η	nondimensional vertical coordinate, y/δ
ν	kinematic viscosity
ρ	fluid density
τ	shear stress
ϕ	nondimensional mean flow function, U/U_e or $\rho U/\rho_e U_e$
ψ	nondimensional shear stress function, τ/τ_w
subscripts	
e	characteristic value
U	mean velocity
w	evaluated at the surface
ρU	mass flux
∞	evaluated in the freestream

INTRODUCTION

Theoretical evaluation of turbulent shear flows require a rational model between the turbulent motion and the mean flow. While predictions of shear flows have been greatly improved over the past few years, they still employ empirical relations between the turbulent and the mean motion. The empirical relations are at best first approximations which cannot be justified theoretically.

For turbulent boundary layers a model that relates the Reynolds turbulent shear stress and the mean flow is required. For low speed flows experimental information is available for comparison with predictions for a wide range of flow conditions. For small size boundary layers, such as encountered at supersonic speeds it has proven difficult to obtain reliable, direct measurements of the turbulent quantities, (1). An effort is being made to make available a large number of documented flows in order to improve the abilities of numerical prediction techniques.

The present paper examines a wide range of shear stress distributions for turbulent boundary layers. For the limiting case of large Reynolds number a solution for the shear stress in terms of the mean flow was obtained. The predicted shear stress distributions from the theoretical solution are found to agree within the accuracy of measurements for zero, favorable and adverse pressure gradient "equilibrium" flows. "Nonequilibrium" boundary layer shear stress distributions are also evaluated, although they cannot be predicted from the limiting theoretical solution.

TURBULENT BOUNDARY LAYER SHEAR STRESS

The equations of motion for a turbulent boundary layer can be written as

$$\rho U \frac{\partial U}{\partial x} + \rho V \frac{\partial U}{\partial y} = - \frac{\partial p}{\partial x} + \frac{\partial \tau}{\partial y} \qquad (1)$$

$$\frac{\partial p}{\partial y} + \frac{\partial \rho \overline{v^2}}{\partial y} = 0 \qquad (2)$$

where only τ and $\overline{V^2}$ contain turbulent quantities. For most boundary layer flows it appears that the y-direction equation, eq. (2), is independent of the x-direction equation, eq. (1). Thus, only eq. (1) is employed in boundary layer evaluations. The shear stress, τ, contains both the mean flow part and the turbulent shear stress

$$\tau \equiv \nu \frac{\partial U}{\partial y} + \tau_t \tag{3}$$

For incompressible flows the turbulent shear stress is the Reynolds shear stress, $-\rho\overline{uv}$. The "mass-weighted" average technique of Favre, (2) also leads to $-\rho\overline{uv}$ for the compressible turbulent shear stress. The earlier averaging techniques of Van Driest, (3), and Schubauer and Tchen, (4), give more complex relations for compressible flow. The present discussion will consider the turbulent shear stress as $-\rho\overline{uv}$, although for the major part of the analysis the total shear stress, τ, is employed directly as defined by eq. (1).

The boundary conditions for the shear stress require

$$\tau = \tau_w \quad \text{and} \quad \frac{\partial \tau}{\partial y} = \frac{\partial p}{\partial x} \quad \text{at} \quad y = 0 \tag{4}$$

The shear stress, τ, will approach zero at the outer limits of the boundary layer. For the similarity analysis it is convenient to require $\tau = 0$ at some characteristic distance, $y = \delta$, out in the flow. The sign of the pressure gradient determines the characteristic shape of the shear stress distribution. However, it will be demonstrated that two quite different boundary layers are produced by positive pressure gradients in compressible flows.

A relation between the shear stress and the mean flow can be obtained by considering the case of large Reynolds number. It was experimentally observed by Zoric and Sandborn, (5), that zero pressure gradient, turbulent boundary layers approach a similarity flow at large Reynolds numbers. For Reynolds numbers in excess of 10^7 it was demonstrated that both the mean and turbulent velocities reach values that can be correlated in terms of characteristic flow velocities and length. For the general case of compressible flow it has not been possible to experimentally prove the existence of similarity, however, the conditions of large Reynolds number are usually present.

For compressible flow a similarity may be assumed to exist in the form

$$\begin{aligned} \rho U &= \rho_e U_e \phi_{\rho U}(\eta) \\ U &= U_e \phi_U(\eta) \\ \tau &= \tau_e \psi(\eta) \end{aligned} \tag{5}$$

where $\rho_e U_e$ is a characteristic mass flow, U_e is a characteristic velocity and τ_e is a characteristic shear stress. The similarity variable η, is taken to be the vertical distance, y, divided by a characteristic length, δ_e. At this point the characteristic mass flow, velocity, shear stress and length can be left unspecified, although similarity restrictions place specific requirements on the parameters. In the practical case the characteristic length will be related to the shear layer thickness; the mass flow and velocity will be that of the freestream; and the shear stress will be related to a wall value. Employing the similarity conditions, eq. (5), in the x-direction equation of motion, eq. (1), and also using the continuity equation to solve for ρV gives the following relation

$$\psi' = \frac{\delta_e \rho_e U_e}{\tau_e} \frac{dU_e}{dx}[\phi_{\rho U}\phi_U - 1] - \frac{U_e}{\delta_e} \phi_U' \, [\delta_e \frac{d\rho_e U_e}{dx} \int_0^\eta \phi_{\rho U} d\eta$$

$$+ \rho_e U_e \frac{d\delta_e}{dx} \int_0^\eta \phi_{\rho U} d\eta] \tag{6}$$

where the prime denotes differentiation with respect to η. Integration of eq. (6) with respect to η produces an equation for the shear stress in terms of the mean flow parameters

$$\psi \equiv \tau/\tau_e = \frac{\delta_e \rho_e U_e}{\tau_e} \frac{dU_e}{dx} \left(\int_0^\eta \phi_{\rho U}\phi_U d\eta - \eta\right)$$

$$- \left(\frac{\delta_e U_e}{\tau_e} \frac{d\rho_e U_e}{dx} + \frac{\rho_e U_e^2}{\tau_e} \frac{d\delta_e}{dx}\right) \int_0^\eta \{\phi_U' \int_0^{\eta'} \phi_{\rho U} d\eta'\} d\eta + c \tag{7}$$

Equation (7) may be viewed as a particular limiting solution for the shear stress in turbulent boundary layers where the similarity specified by eq. (5) applies. It will be demonstrated that eq. (7) can be employed as a close approximation for a number of turbulent boundary layer flows. In the evaluation it has proven convenient to employ the local surface shear stress, $\tau_e = \tau_w$, as the characteristic shear and likewise $\delta_e = \delta$, $U_e = U_\infty$, and $\rho_e = \rho_\infty$. There is no attempt to theoretically justify these particular choices, and for the increasing pressure flows there is reason to suggest other values.

The assumption of similarity requires that eq. (7) be independent of x. Thus, the following restrictions are necessary.

$$\frac{\delta_e \rho_e U_e}{\tau_e} \frac{dU_e}{dx} = A \text{ (a constant independent of x)} \tag{8}$$

$$\frac{\delta_e U_e}{\tau_e} \frac{d\rho_e U_e}{dx} + \frac{\rho_e U_e}{\tau_e} \frac{d\delta_e}{dx} = B \text{ (a constant independent of x)} \tag{9}$$

These restrictions produce specific relations between the parameters for flows which are similar. As could have been foreseen, the need for four independent parameters was not necessary, since one can be eliminated between eqs. (8) and (9). However, it appeared that a better insight into the shear stress characteristics could be obtained by retaining the four parameters. The possible application of eq. (7) to flows that are not similar will limit the use of eqs. (8) and (9).

ZERO PRESSURE GRADIENT FLOW

Measurements of the shear stress across zero pressure gradient boundary layers for a wide range of flow conditions have been reported. Both subsonic and supersonic data are available. Figure 1 shows typical incompressible measurements of $-\rho\overline{uv}$ reported by Zoric and Sandborn, (5), for high Reynolds number and by Klebanoff, (6), for a lower Reynolds number. These data are correlated employing the wall shear stress and the boundary layer thickness. Within the accuracy of the measurements the two sets of data from widely different Reynolds number flows can be represented by the same nondimensional curve. The correlation suggests that the similarity relation, eq. (7), for the shear stress may be used for the low Reynolds number flows.

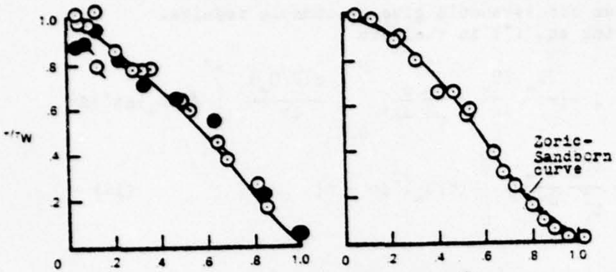

a) Zoric and Sandborn (5) b) Klebanoff (6)

Fig. 1 Incompressible, zero pressure gradient, shear stress distributions

Equation (7) for incompressible, zero pressure flow with $\tau_e = \tau_w$, $\delta_e = \delta$, and $U_e = U_\infty$ gives

$$\tau/\tau_w = 1 - \frac{U_\infty^2}{U_\tau^2}\frac{d\delta}{dx}\int_0^{\eta}\left\{\frac{d(U/U_\infty)}{d\eta}\int_0^{\eta'}(U/U_\infty)d\eta'\right\}d\eta \tag{10}$$

where $U_\tau^2 \equiv \tau_w/\rho$, and the boundary condition $\tau/\tau_w = 1$ at $\eta = 0$ was employed to evaluate the constant of integration. Evaluation of τ/τ_w from eq. (10) for the mean flow data of Zoric and Sandborn and of Klebanoff are shown as the faired curves on figure 1. The value of $d\delta/dx$ was not available for Klebanoff's data, so the boundary condition $\tau/\tau_w = 0$ at $\eta = 1$ was employed. For both sets of data it was found that eq. (10) accurately models the shear stress. Note that comparison of mean velocity profiles (in similarity coordinates, U/U_∞ vs η) for the two flows produce different distributions, (5). The use of a characteristic shear stress, τ_w, was found to give the best correlation for the shear distributions. For incompressible flow the "shear velocity," U_τ, is widely accepted as a characteristic velocity. However, for compressible flow a characteristic shear is more convenient, since the local density is important in the shear distribution.

Measurements of turbulent shear stress in compressible flows has proven extremely difficult. Based on the early work of Rotta, (8), Meier and Rotta, (9), employed an approximate similarity analysis to evaluate the shear stress distribution for supersonic flows with heat transfer. The basic similarity assumptions given in eq. (5) were employed along with the simplification that

$$df/dx = (f/f_e)\frac{df_e}{dx} \tag{11}$$

where $f = \rho U$, ρU^2, or ρUh. This simplification, eq. (11), eliminates the need to evaluate η-derivatives in the similarity relation. Figure 2 shows faired curves of the shear stress distributions evaluated by: Meier and Rotta (Mach no. 2.5 to 4.5); Bushnell and Morris (10) (Mach no. 4.67 to 6.50); Sturek, (11)(Mach no. 3.53); and Horstman and Owen, (12) (Mach no. 7.2). Each of the curves employed the similarity relation in the evaluation. It was not possible to identify either a consistent Mach-or Reynolds-number variation for the profiles shown. Individual sets of data, such as those of Meier and Rotta and Horstman and Owen, indicate small systematic variations. The remarkable correlation of shear stress distributions, shown in figure 2 appears to justify the similarity assumptions. Although the possibility still exists that the correlation is a result of the evaluation technique. A comparison of shear stress distribution evaluated from eq. (7) with the evaluation of Horstman and Owen, (12), for the $M = 7.2$ boundary layer gave nearly identical results.

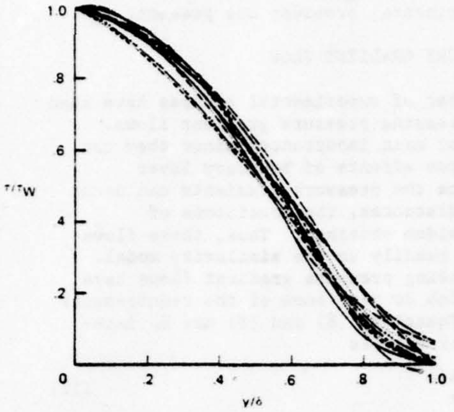

Fig. 2 Evaluation of the shear distributions for supersonic, zero pressure gradient flows. Curves identified in (7)

Figure 3 compares the supersonic shear distributions with the incompressible results of Zoric and Sandborn, (5). The incompressible similarity flow data agree very well with the supersonic distributions. The agreement is further justification of the basic concepts of the similarity model between the mean flow and the shear stress. Also shown on figure 3 are experimental measurements of the "turbulent shear stress" reported by Johnson and Rose, (13), for $M = 2.9$. The measurements agree with the similarity predictions in the outer region of the boundary layer, however there is a definite disagreement near the wall. Although the turbulent shear stress must go to zero at $\eta = 0$, the viscous shear stress is negligible for $\eta > 0.05$. The low values of the turbulent shear stress for small values of η are not accounted for by the viscous shear. While a

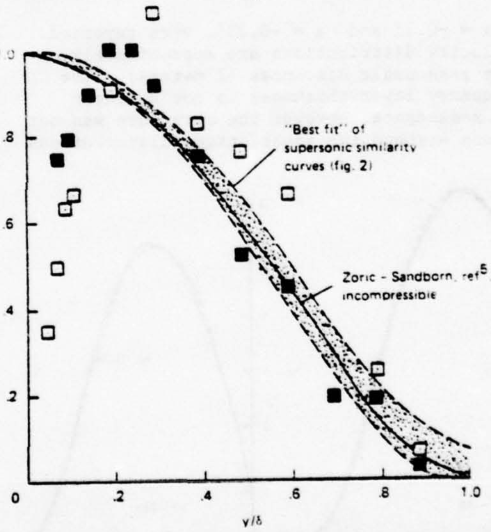

Fig. 3 Comparison of compressible and incompressible shear stress data (open points: hot wire, solid points: laser)

question may exist about the theoretical form of the turbulent shear stress, (14), it would appear more likely that experimental problems are present, (1).

INCREASING PRESSURE GRADIENT FLOW

A large number of experimental studies have been reported for increasing pressure gradient flows. These flows are of main importance, since they can produce the adverse effects of boundary layer separation. Since the pressure gradients can occur over very short distances, the conditions of similarity are seldom obtained. Thus, these flows will not conform readily to the similarity model.

A few increasing pressure gradient flows have been reported which do meet some of the requirements of similarity. Equations (8) and (9) may be integrated to give for example

$$U_e \propto \delta_e^{A/B} \tag{12}$$

If δ_e is a linear function of x-distance, (which was suggested by Zoric and Sandborn, (5), for the experimental, zero pressure gradient, similarity flow) then eq. (12) would correspond to the condition for laminar similarity studied by Falkner and Skan, (15).

Bradshaw, (16), has measured the mean and turbulent quantities for flows where

$$U_\infty \propto x^a \tag{13}$$

Two flows, $a = -0.15$ and $a = -0.255$, were reported. The mean velocity distributions are approximately similar over reasonable distances (2 meters). The measured boundary layer thickness is not a linear function of x-distance, however the curvature was not great. Figure 4 shows the shear stress distributions measured by Bradshaw. The shear measurements were reported as single faired curves for $a = -0.15$ and -0.255, in terms of $\tau/\rho U_\infty^2$ vs y/δ. Use of the dynamic pressure as the similarity "shear" is different from the wall shear employed in the present evaluation. If the skin friction coefficient, $c_f(= \tau_w/\rho U_\infty^2)$, were a constant, the wall shear stress or the dynamic pressure would produce the same result. For the particulur flows, c_f varies by 20% for $a = -0.15$, and by 15% for $a = -0.255$.

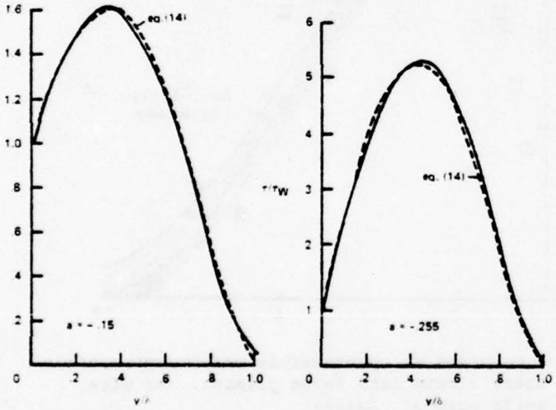

Fig. 4 Comparison of the similarity shear stress model with the increasing pressure gradient flows reported by Bradshaw, (16)

Thus, the use of either the wall shear or the dynamic pressure for correlation of the measurements of shear stress should give reasonable results. Employing eq. (7) in the form

$$\tau/\tau_w = 1 - \left[\frac{\delta U_\infty}{U_\tau^2}\frac{dU_\infty}{dx} + \frac{U_\infty^2}{U_\tau^2}\frac{d\delta}{dx}\right]\int_0^\eta \left\{\frac{d(U/U_\infty)}{d\eta}\int_0^{\eta'} (U/U_\infty)\,d\eta'\right\}d\eta$$
$$+ \frac{\delta U_\infty}{U_\tau^2}\frac{dU_\infty}{dx}\left[\int_0^\eta (U/U_\infty)^2 d\eta - \eta\right] \tag{14}$$

the shear distribution was computed from the mean velocity measurements. The comparison of the distribution, computed from eq. (14), is shown on figure 4. The boundary condition, $\tau/\tau_w = 0$ at $\eta = 1$, was employed for the calculations. In both flows it was found that the "correction" to $d\delta/dx$ in order to meet the outer boundary condition was less than 15%. The value of δ determined by Bradshaw for $U/U_\infty = 0.995$ was employed for the calculations. For these flows the similarity relation was found to be an accurate prediction of the shear stress.

The similarity model might have been expected to hold for the pressure gradient cases where the mean and turbulent velocities have reached an "equilibrium" condition. For the general case of "nonequilibrium" pressure gradient flows, difficulties in modeling the flow can be expected. It is generally known that the turbulent boundary layer flow responds very slowly to changes in the pressure. Horstman, (17), has demonstrated that the modeling of the shear can be improved by employing the concept of a "lag" in the turbulence development. A similar concept of velocity profile "relaxation" was suggested by Sandborn (18), to explain turbulent boundary layer separation data. Thus, it can be foreseen that the direct application of the similarity model based on local mean flow conditions is not likely to apply.

Figure 5 shows a typical nonequilibrium, increasing pressure gradient, incompressible, turbulent boundary layer shear stress distribution reported by

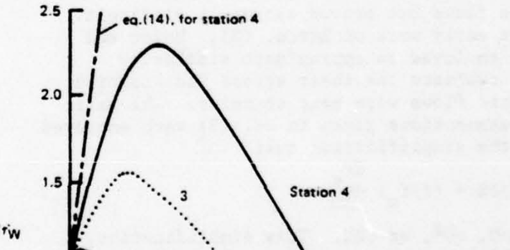

Fig. 5 Incompressible, increasing pressure gradient, turbulent boundary layer shear stress distributions

Sandborn and Slogar, (19). The direct evaluation of eq. (14), using the measured gradients is also shown for station 4. The similarity model greatly over-predicts the measured shear stress. The over-prediction comes from the pressure gradient term in eq. (14). This over-prediction demonstrates the apparent lag in the development of the boundary layer.

Evaluation of the nonequilibrium flow of Sandborn and Slogar suggests that upstream rather than local conditions are important. The characteristic shear stress was chosen as the value at the start of the nonequilibrium flow. Figure 6 shows a plot of the downstream shear stress distributions all referenced to the upstream surface shear stress. The local values of the boundary layer thickness were used for each profile. Use of the upstream surface shear stress produces a correlation of all the distributions in the outer region of the layer. The shear stress in the outer region apparently does not have time to adjust to the change in flow conditions. Only the region near the wall is altered by the increasing pressure.

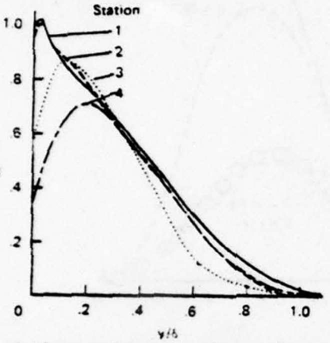

Fig. 6 Use of the upstream surface shear stress to correlate increasing pressure gradient measurements

For the data of Sandborn and Slogar the upstream boundary layer was in a decreasing pressure gradient, thus the outer part of the distribution is less in magnitude than that of a zero pressure gradient flow. The correlation suggests that the distribution of the shear stress in a rapidly changing pressure gradient might be modeled directly from the upstream velocity distribution, rather than the local velocity. Figure 7 demonstrates several possible "curve fits" of eq. (14) to the Sandborn-Slogar shear stress measurements at station 4. Direct use of the local pressure gradient with either the local or upstream velocity distribution produces a large overshoot in the predicted shear distribution. The results indicate the best model would be some average value of pressure gradient over the upstream approach to the measuring point. Only at the wall is the local pressure gradient required in order to produce the correct slope of the shear stress. Obviously, the assumptions of similarity in the present form are not accurate in the wall region. The present curve fitting was limited, in that the upstream mean velocity profile was not measured. Attempts to estimate the upstream conditions did not greatly alter the results shown on figure 7. Application of an upstream mean velocity profile for a favorable pressure gradient produced the over-prediction of the shear in the outer region similar to that seen on figure 7. As would be expected from previous boundary layer studies the model could be improved by use of an inner and outer matching technique.

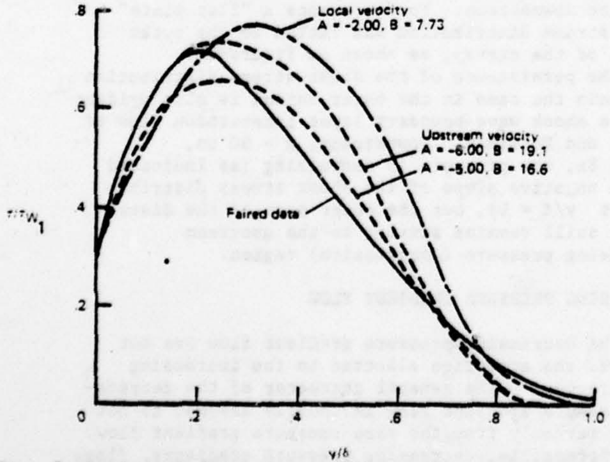

Fig. 7 Empirical fits of eq. (14) to the measurements of Sandborn and Slogar (19)
Computed value of $A = -8.48$ and $B = 25.1$

Experimental information on the shear stress distribution in compressible flows with pressure gradients have only become available in the past few years. The characteristic shape of the shear stress distribution found for increasing pressure gradients in incompressible flow is also evident in the compressible flows. A basic new case of increasing pressure flow must also be considered when compressibility is present. From eq. (7); two gradients, the mean velocity, and the mass flux, must be considered in compressible flows. These two gradients need not have the same sign, and for many supersonic flows they do not have the same sign. For convenience the supersonic, increasing pressure flows are identified as follows:

1. Adverse pressure gradient (both $\frac{dU}{dx}$ and $\frac{d\rho U}{dx}$ are negative)
2. Compression pressure gradient ($\frac{dU}{dx}$) is negative and $\frac{d\rho U}{dx}$ is positive)

The use of adverse pressure gradient is commonly employed in subsonic flows for the increasing pressure, since it can lead to the adverse effects of separation. In supersonic flows the freestream conditions will not be well-defined for the adverse pressure case due to the presence of shock waves. Obviously, near the wall the value of $d\rho U/dx$ must be negative, for flow separation to occur (from continuity $d\rho U/dx = -d\rho V/dy$, so ρV is a mass flux away from the surface region). The compression pressure flow produces a mass flux toward the surface, so that the boundary layer becomes progressively "thinner" and the surface shear stress increases. The compression pressure flow produces the opposite of separation. The typical shock wave-boundary layer interaction produces first the adverse pressure flow directly upstream of the shock, which may lead to boundary layer separation. In the region downstream of the shock interaction a compression type flow is observed.

Figure 8 shows computed shear stress distributions for two types of compression pressure gradient flows. The shock wave-boundary layer interaction flow of Kussoy and Horstman, (20), contains an adverse pressure region with a near separation upstream of the data shown. However, calculations of the shear stress in the adverse pressure region were questionable. The shear distributions were computed using the total pressure gradient along streamlines approach to evaluate the equation of motion, (21). The data of Sturek and Danberg, (22), shown in figure 8b is for isentropic compression. Evaluation of a number of other supersonic boundary layer studies produced similar shear stress distributions to those shown. In each case it was not possible to accurately evaluate the shear stress in the region of the shock wave.

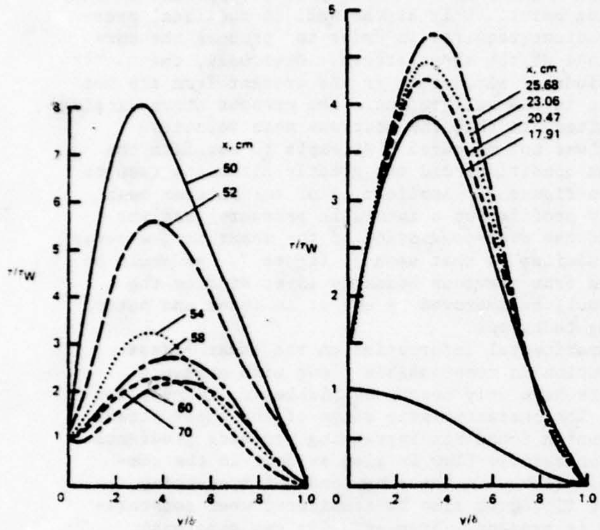

a) Kussoy-Horstman b) Sturek-Danberg

Fig. 8 Shear distributions for supersonic compression pressure gradients

In the adverse pressure region the shear distributions are expected to be similar to the incompressible date, figure 6. Hot wire and laser anemometer measurements of the turbulent shear stress were reported by Rose, (23), and Rose and Johnson, (13), for shock wave interaction flows. The measured distributions are similar to the data shown in figure 8 (for the outer region of the layer). The difficulty encountered near the wall for the zero pressure gradient case, figure 3, also appears to be present in the pressure gradient measurements.

For both the shock wave interaction and the isentropic compression the initial values of the shear stress are "processed" to much larger values. Accounting for changes in mean density, the turbulent component of the shear must increase in magnitude by factors of the order of 3 to 4. The main processing occurs very quickly through the shock wave and also over a few centimeters for the isentropic compression. Note that the application of the similarity model, eq. (7), to incompressible, increasing pressure gradient flows produce very large increases in the shear stress, due mainly to the pressure gradient term. Application of the similarity equation to the supersonic, increasing pressure gradient flows result in the same difficulty as observed for the incompressible flow. The local velocity gradient, eq. (8), produces too large an effect, as shown on figure 9. The obvious effect of the compression pressure gradient in a flow is to increase the magnitude of the turbulent shear stress. Bradshaw, (24), also noted the effect previously in the course of calculating compressible boundary layer flows. Apparently the equilibrium, adverse pressure gradient flows, figure 4, also increase the magnitude of the turbulent shear stress. However, for the nonequilibrium, adverse pressure gradient flow approaching separation, figure 6, the reduction of the wall shear stress leads to a marked decrease in the turbulent shear stress over the inner half of the boundary layer.

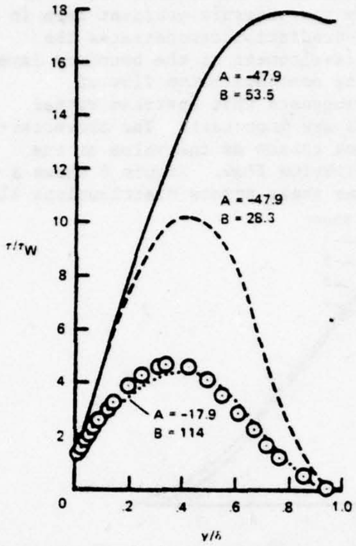

Fig. 9 Comparison of the shear stress predicted by the similarity model with a supersonic compression flow (22)

As shown on figure 9, the similarity model cannot be applied directly to the flow of Sturek and Danberg. Empirical curve fitting of eq. (7), using the local mean velocity and density functions, produced a reasonable approximation for the derived shear stress. For the empirical fit it was necessary to reduce the mean velocity gradient term (the constant A, eq. (8)) by a factor of 2.7 to obtain the approximate agreement.

Investigation of the application of an upstream similarity to the Sturek-Danberg flow is demonstrated in figure 10. The first upstream, x = 0, station was taken as the reference condition. This station was ahead of the isentropic compression ramp. Values of the wall shear stress, τ_{wo}, (at x = 0) and wall density, ρ_{wo}, (at x = 0), are employed as the characteristic shear and density. Not unlike the incompressible results, figure 6, the outer region of the shear distributions do not vary greatly with distance downstream. For reference a "flat plate" shear stress distribution was fitted to the outer region of the curves, as shown on figure 10.

The persistence of the shear stress distribution to remain the same in the outer region is also evident for the shock wave-boundary layer interaction flow of Kussoy and Horstman. Downstream, x > 60 cm, figure 8a, the pressure is decreasing (as indicated by the negative slope of the shear stress distribution at $y/\delta = 0$), but the outer part of the distribution still remains similar to the upstream increasing pressure (compression) region.

DECREASING PRESSURE GRADIENT FLOW

The decreasing pressure gradient flow has not received the attention allotted to the increasing pressure case. The general character of the decreasing pressure gradient flow is usually assumed to not differ markedly from the zero pressure gradient flow. For compressible, decreasing pressure gradients, flows exist where the mass flux gradient is opposite in sign

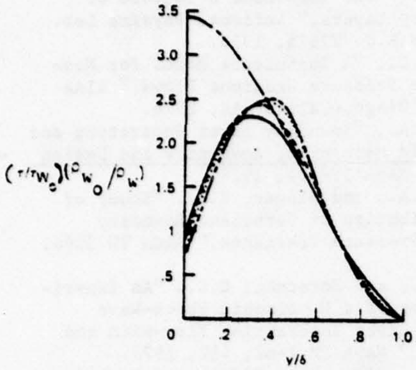

Fig. 10 Correlation of the compression flow shear stress distributions of Sturek and Danberg using upstream surface shear and density

to the mean velocity gradient. A division into a "favorable" pressure gradient (mean velocity and mass flux gradients are both positive) and an "expansion" pressure gradient (mean velocity gradient positive, and mass flux gradient negative) may be made. The increasing pressure gradient region measured by Kussoy and Horstman, (21), contains an "expansion" pressure gradient for $x > 74$ cm, figure 11. The expansion pressure gradient produced a marked increase in the shear stress in the outer region of the boundary layer for the particular flow.

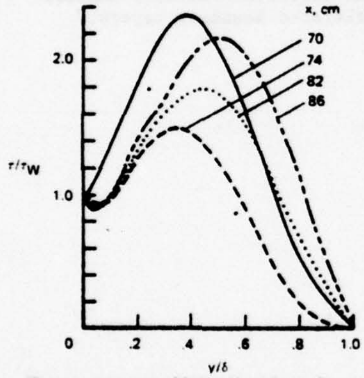

Fig. 11 Shear stress distribution in an "expansion" pressure gradient. Data of Kussoy and Horstman (21)

A favorable pressure gradient flow, at subsonic, compressible speeds in a constant area duct was reported by Sandborn and Seegmiller, (25). Figure 12 shows the shear stress distributions evaluated for Mach numbers of 0.2 and 0.5. The distributions were determined from a balance of the terms in the x-direction equation of motion. The flow developed over a distance of 2.5 meters, so that conditions of equilibrium might be expected. Evaluation of the shear stress, using eq. (7), employing local velocity measurements are compared with the direct values on figure 12. The boundary condition $\tau/\tau_w = 0$ at $y = \delta$ was also used in the evaluation. Direct evaluation of the constant B, eq. (9), differed by less than 15% from the value determined by the outer boundary condition. Also shown on figure 12 are the shear distributions obtained using the Meier-Rotta approximation, eq. (11). The outer edge boundary condition was also employed for the approximate calculation.

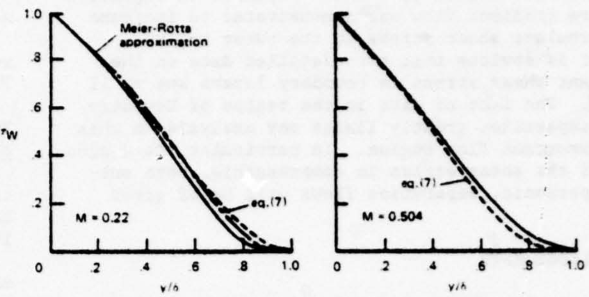

Fig. 12 Subsonic, decreasing pressure gradient, turbulent boundary layer, shear stress distributions

CONCLUSIONS

For equilibrium boundary layers, where the mean and turbulent flow have adjusted to the local conditions, a theoretical model between the mean and turbulent flow is obtained. The model is based on the limiting solution of the equation of motion for large Reynolds numbers, where similarity was observed to exist. The shear stress distribution for zero pressure gradient flows is demonstrated to be a near universal function of the local surface shear stress and local boundary layer thickness. Both incompressible and compressible, supersonic flows were found to produce nearly identical distributions. For both increasing and decreasing pressure gradient, equilibrium flows the theoretical model was shown to agree closely with experimental measurements.

For nonequilibrium, increasing pressure gradient flows the model based on local gradients is found to over-predict the shear stress. For a typical, incompressible, adverse pressure gradient, boundary layer it was demonstrated that the shear stress in the outer region of the layer does not change. The effect of the adverse pressure gradient was to decrease the surface shear stress, which led to a marked reduction in the turbulent shear stress in the inner part of the layer. The equilibrium, adverse pressure gradient results, both experimental and theoretically, indicate that increasing pressure gradients will increase the turbulent shear stress.

For compressible flows, two different types of pressure gradient flow are possible, depending on the sign of the mean velocity and mass flux gradients. For increasing pressure gradient flow separation of the boundary layer can only occur if the mean velocity and mass flux gradient are negative. For the case where the gradients are both negative the description, "adverse pressure gradient" was used. For the case where the mass flux is positive the description, "compression pressure gradient" was used. The compression pressure gradient of a shock wave-boundary layer interaction and also along an isentropic compression ramp were demonstrated. The compression pressure gradient produces a rapid "processing" of the turbulent shear stress to values 3 to 4 times greater than the upstream values. Evidence of similarity of the shear in the outer region of the layer, based on upstream conditions, was also observed for the compression pressure gradient flow.

Two types of decreasing pressure gradient flows were also encountered in supersonic flows. The favorable pressure gradient case (both mean velocity and mass flux gradients are positive), was observed, along with an "expansion pressure gradient" case (mass flux gradient negative). One example of an expansion pressure gradient flow was demonstrated to increase the turbulent shear stress in the outer region.

It is obvious that more detailed data on the turbulent shear stress in boundary layers are still needed. The lack of data in the region of boundary layer separation greatly limits any analysis in this very important flow region. In particular the evaluation of the shear stress in compressible, both sub- and supersonic, separation flows will be of great value.

ACKNOWLEDGEMENTS

Funds for the support of this study have been allocated by NASA-Ames Research Center, Moffett Field, California, under interchange NCA2-OR165-604, and previous funding.

REFERENCES

1 Sandborn, V.A., "Effect of Velocity Gradients on Measurements of Turbulent Shear Stress," AIAA Journal, Vol. 14, No. 3, 1976, pp. 400-402.

2 Favre, A., "Equations dus Gaz Turbulents Compressible," Journal Mecan., Vol. 4, No. 3, 1965, pp. 361-390.

3 Van Driest, F.R., "Turbulent Boundary Layer in Compressible Fluids," Journal of the Aeronautical Science, Vol. 18, No. 3, 1951, pp. 145-160.

4 Schubauer, G.B., and Tchen, C.M., Turbulent Flow, Princeton Aeronautical Paperbacks, Princeton University Press, 1961.

5 Zoric, D., and Sandborn, V.A., "Similarity of Large Reynolds Number Boundary Layers," Boundary Layer Meteorology, Vol. 2, No. 3, 1972, pp. 326-333.

6 Klebanoff, P.S., "Characteristics of Turbulence in a Boundary Layer with Zero Pressure Gradient," NACA Tech. Rept. 1247, 1955.

7 Sandborn, V.A., "A Review of Turbulence Measurements in Compressible Flow," NASA TM X-62,337, 1974.

8 Rotta, J., "On the Theory of the Turbulent Boundary Layer," NACA TM 1344, 1953.

9 Meier, H.V., and Rotta, J.C., "Experimental and Theoretical Investigations of Temperature Distributions in Supersonic Boundary Layers," AIAA Paper 70-744, Los Angeles, California, 1970.

10 Bushnell, D.M., and Morris, D.J., "Shear-Stress, Eddy-Viscosity, and Mixing-Length Distributions in Hypersonic Turbulent Boundary Layers," NASA TM X-2310, 1971.

11 Sturek, W.B., "Calculations of Turbulent Shear Stress in Supersonic Turbulent Boundary Layer Zero and Adverse Pressure Gradient Flow," AIAA Paper No. 73-166, Washington, D.C., 1973.

12 Horstman, C.C., and Owen, F.K., "Turbulent Properties of a Compressible Boundary Layer," AIAA Journal, Vol. 10, No. 11, 1972, pp. 1418-1424.

13 Rose, W.C., and Johnson, D.A., "A Study of Shock-Wave Turbulent Boundary Layer Interaction Using Laser Velocimeter and Hot Wire Anemometer Techniques," AIAA Paper No. 74-95, 1974.

14 Johnson, D.A., and Rose, W.C., "Laser Velocimeter and Hot Wire Anemometer Comparison in a Supersonic Boundary Layer," AIAA Journal, Vol. 13, No. 4., 1975, pp. 512-515.

15 Falkner, V.M., and Skan, S.W., "Some Approximate Solutions of the Boundary Layer Equations," Phil. Mag., Vol. 12, 1931, p. 865.

16 Bradshaw, P., "The Turbulent Structure of Equilibrium Boundary Layers," National Physics Lab. Aero Report 1184, A.R.C. 27675, 1966.

17 Horstman, C.C., "A Turbulence Model for Nonequilibrium Adverse Pressure Gradient Flows," AIAA Paper No. 412, San Diego, California, 1976.

18 Sandborn, V.A., "Boundary Layer Separation and Reattachment," Fluid Mechanics, Acoustics and Design of Turbomachinery, NASA SP-304, 1974.

19 Sandborn, V.A., and Slogar, R.J., "Study of the Momentum Distribution of Turbulent Boundary Layers in Adverse Pressure Gradients," NACA TN 3264, 1955.

20 Kussoy, M.I., and Horstman, C.C., "An Experimental Documentation of a Hypersonic Shock-Wave Turbulent Boundary Layer Interaction Flow-with and without Separation," NASA TM X-62, 412, 1975.

21 Bradshaw, P., "Anomalous Effects of Pressure Gradients on Supersonic Turbulent Boundary Layers," Aero Report 72-21, Imperial College, London, 1972.

22 Sturek, W.B., and Danberg, J.S., "The Supersonic Turbulent Boundary Layer in an Adverse Pressure Gradient-Experiment and Data Analysis," Turbulent Shear Flow, AGARD CP-93, 1971.

23 Rose, W.C., "The Behavior of a Compressible Turbulent Boundary Layer in a Shock-Wave-Induced Adverse Pressure Gradient," NASA TN D-7092, 1973.

24 Bradshaw, P., "The Effect of Mean Compressibility or Dilation on the Turbulence Structure of Supersonic Boundary Layers," Jour. Fluid Mech., Vol. 63, Pt. 3, 1974, pp. 449-464.

25 Sandborn, V.A., and Seegmiller, H.L., "Evaluation of Mean and Turbulent Velocity Measurements in Subsonic Accelerated Boundary Layers," NASA TN D-8367, 1976.

STRUCTURE AND DEVELOPMENT OF A TURBULENT BOUNDARY LAYER IN AN OSCILLATORY EXTERNAL FLOW

by Jean COUSTEIX, André DESOPPER and Robert HOUDEVILLE

Office National d'Etudes et de Recherches Aérospatiales (ONERA)
Centre d'Etudes et de Recherches de Toulouse (CERT)
31055 Toulouse, France

ABSTRACT

An unsteady turbulent boundary layer is experimentally studied in presence of an oscillatory free stream.

A statistical treatment of data enables us to separately analyse the periodic component and the turbulent fluctuation of the velocity measured by means of a hot wire anemometer. The longitudinal component of turbulence is studied by the determination of its intensity, of its statistical distribution and of its moments. Moreover, the variations of the shear stress profiles have been measured and are analysed.

A prediction method based on the resolution of the local equations is presented. Two turbulence schemes are used : a mixing length model and a transport equation model. An integral method of prediction is also presented. The results of these various methods are compared with the experimental data.

INTRODUCTION

For practical applications, in the field of the aerodynamics of helicopters or turbomachineries, it is very important to take into account the effects of the unsteadiness not only on the potential flow but also on the viscous flow, especially on the boundary layer.

In the last years, the attention has been turned in this direction. The understanding of the behaviour of a laminar boundary layer for which a lot of studies have been devoted (Ref. 1, 2) is now well advanced. But for the turbulent case, the results are less abundant (Ref. 3, 4) and consequently the knowledge of this problem is poor. Some boundary layer prediction methods have been extended to the case of an unsteady flow, but in almost all of these works we feel the need of experimental data to test the theoretical results (Ref. 5, 6, 7, 8).

Thus, we undertook a systematic study of the development of an unsteady turbulent boundary layer. Two main objectives are pursued :

. To get detailed experimental results on the effects of the unsteadiness on the characteristics of the turbulence and on the behaviour of the boundary layer.

. To use these results in order to check the validity of hypotheses introduced in some calculation methods and in order to check the validity of the results obtained by these methods.

This paper is devoted to the description of the results of a first stage of this work in which we study the development of a turbulent boundary layer in presence of an oscillatory external flow with a negligible longitudinal variation of the velocity.

EXPERIMENTAL STUDY

EXPERIMENTAL TECHNIQUE (FIG. 1)

The installation

A periodic flow is generated by means of a rotating vane set in the diffuser of a small subsonic wind tunnel of Eiffel type.

The development of the boundary layer is studied on the floor of the 100 mm x 110 mm test section. The velocity is measured with constant temperature hot wires anemometers. A probe is used as a reference in the external flow ; this probe is set at a fixed location above a second probe which is moved along a normal to the wall in order to explore the boundary layer.

The probings are made at four stations ; their abscissa are : $X_1 = 0$, $X_2 = 70$ mm, $X_2 = 140$ mm, $X_3 = 210$ mm.

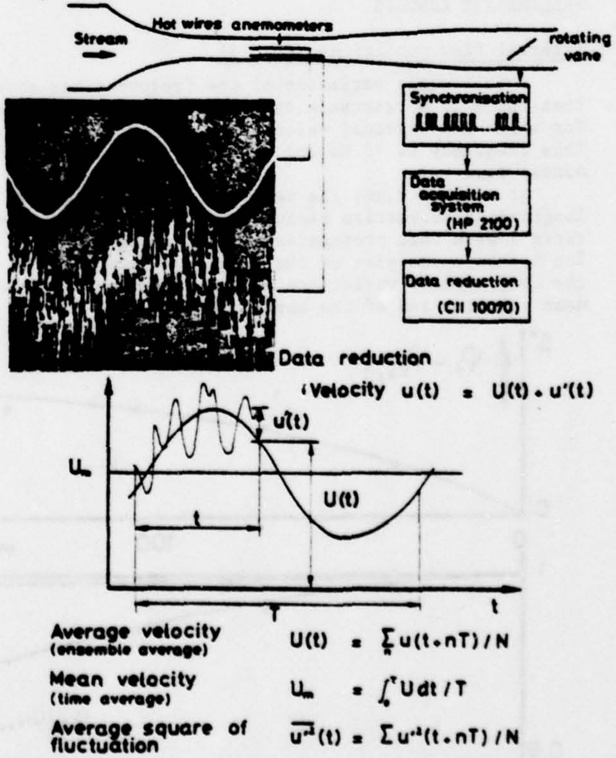

Fig. 1 – Experimental study of an unsteady turbulent boundary layer.

Data reduction

As the boundary layer is unsteady and turbulent, a statistical analysis of the data is needed to define an average quantity.

Here, we define an average quantity as an ensemble average ; it is clear that such an average is not equivalent to a time average.

An ensemble average must be taken over a great number of realizations of the same phenomenon. Since the flow is periodic, each period can be seen as one of these realizations. Therefore, to perform an ensemble average of a quantity f we calculate the sum of the values taken by f for instants, in the successive periods, corresponding to the same value of the phase angle in the external flow. A synchronization system connected to the rotation of the vane generates a train of stimuli and divides the period in 24 spaces ; this system enables us to recognize the phase angle.

The instantaneous velocity u is split in two parts : the average velocity U and the turbulent fluctuation u'. The average velocity U is determined as the ensemble average of u. The turbulent fluctuation u' is calculated by difference between u and U ; its ensemble average is zero. This fluctuation is studied with the aid of its intensity $(\overline{u'^2})^{1/2}$ or its higher order statistical moments or its probability density. As the flow is unsteady and periodic, the average velocity U or the turbulence intensity $(\overline{u'^2})^{1/2}$ are functions of the phase angle.

The use of a X-wires probe enable us to determine the shear stress defined as the ensemble average of the product $-u'v'$.

In the following sections we use also time averaged quantities. For example U_m is the time average of U, so that U/U_m varies around 1 in a period.

PRELIMINARY RESULTS

External flow conditions (Fig. 2)

A systematic variation of the frequency has shown that there is a resonance frequency of the wind tunnel for which the external velocity is nearly sinusoidal. This frequency is 43 Hz and is fixed for the experimental study.

At a given time, the velocity varies along the longitudinal direction because the rotating vane generates a wave that propagates with a finite celerity. The harmonic analysis of the velocity shows (Fig. 2) the longitudinal variations of the phase angle, of the mean velocity and of the amplitude.

Boundary layer flow (Fig. 3)

A first analysis of what happens in the boundary layer is obtained from the observation of the oscilloscope records which represent the evolution of the output voltage issued of the hot wire anemometer. Near the wall, the signal exhibits large fluctuations which are superimposed to a periodic signal. At higher distances of the wall, these fluctuations are dissymetrical and appear as peaks of large amplitude orientated in the negative direction. Moreover, the intensity of these fluctuations is larger in a part of the period : this phenomenon is due to the fact that the free boundary of the boundary layer varies in a periodic manner in time : sometimes the probe is plunged in the boundary layer, sometimes it is in the external flow.

Now, a large part of the discussion is devoted to the measurement of what is suggested by the observation of these photographs.

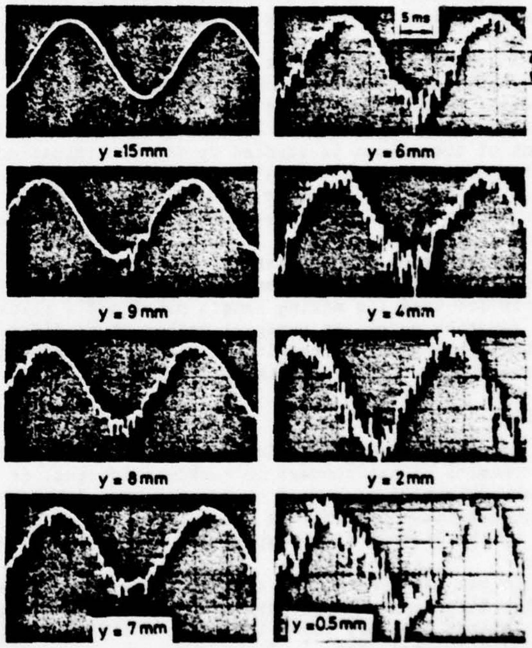

Fig. 3 – Oscilloscope records.

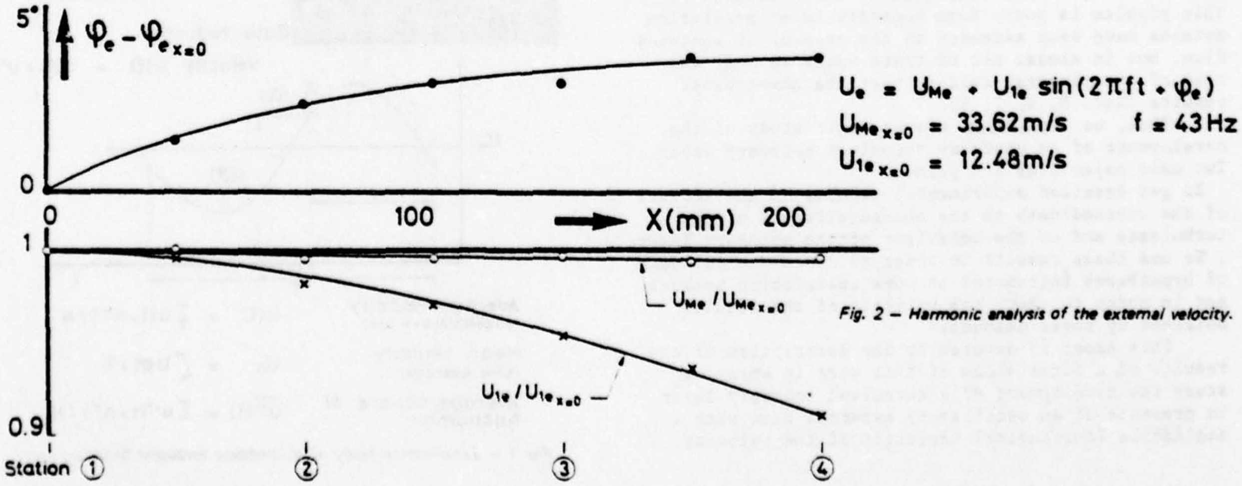

Fig. 2 – Harmonic analysis of the external velocity.

ANALYSIS OF THE RESULTS

Average velocity

Harmonic analysis of the velocity (Fig. 4). To emphasize the non linear effects in the boundary layer, an harmonic analysis has been performed. Concerning the fundamental frequency, the results are presented on the figure 4 where φ is the difference between the phase in the boundary layer and the phase in the external flow. The amplitude ΔU is reduced by the amplitude of the external velocity ΔU_e.

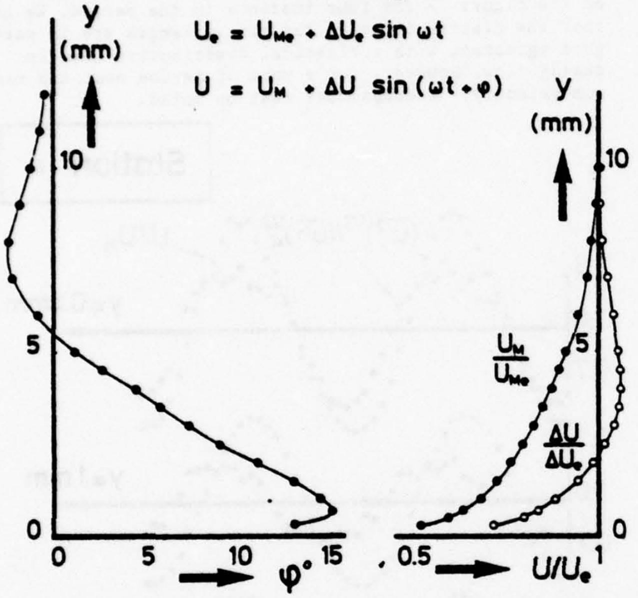

Fig. 4 – Harmonic analysis of the boundary layer average velocity.

We note that, in a region very near the wall, the phase angle is negative ; for higher values of the distance y normal to the wall the phase angle is positive ; near the free boundary of the boundary layer the phase angle is negative. One can be surprised by the positive values of the phase, but it must be remembered that the gradient $\frac{\partial U_e}{\partial t}$ of the external velocity is in advance of 90° with respect to the external velocity ; because in the boundary layer the inertial effects are smaller, it is not paradoxical that the phase angle is positive.

In a previous experiment (Ref. 9, 10), the observations were different ; the external velocity varied between 56 m/s and 114 m/s, so that the Strouhal number was smaller. Based on the mean value δ_{1m} of the boundary layer thickness δ_1 and on the mean velocity U_{em}, the Strouhal number $\omega \delta_{1m}/U_{em}$ was equal to 3.7 10^{-3}; in the present experiment it is 12.7 10^{-3}. We first noted that negative values of the phase angle were not measured in the external region ; but it may be because in this region the phase angle was so small that it could not be measured with a sufficient accuracy. It must be said that this fact was also present in the experiments of KARLSSON (Ref. 3). For laminar boundary layers, calculation or experiment indicate a similar fact and also show that the maximum of the phase lag presents a maximum when it is drawn as a function of the Strouhal number.

Secondly, in the previous experiment, the maximum positive value of the phase angle occured for a higher value of the reduced distance y/δ. Certainly, this fact is related to the variation of the Strouhal number. It is known that the ratio of the thickness of the "unsteady layer", i.e. the layer where the unsteady effects are significant, to the mean boundary layer thickness δ_m decreases as the Strouhal number increases: when the Strouhal number is very high, the unsteady effects are limited to a very thin layer near the wall. This is in agreement with our experimental observation: for a higher value of the Strouhal number, the maximum of the phase angle occurs for a lower value of y/δ.

The mean velocity profile is also presented on the figure 4. The pattern of this profile is very nearly that of a velocity profile for a steady boundary layer with zero pressure gradient.

Average velocity profiles (Fig. 5). On the figure 5, the average velocity profiles are presented as functions of the distance normal to the wall. Each profile is obtained for a given phase in the period of the external flow ; the velocity is reduced by its value at the outer boundary for the same value of the phase angle.

The observed variation of the profiles is due for a part, to the variation of the boundary layer thickness ; but the variation of their shape is related to the alternation of negative and positive external velocity gradient in a period. Subsequently, we note the evolution of the shape factor.

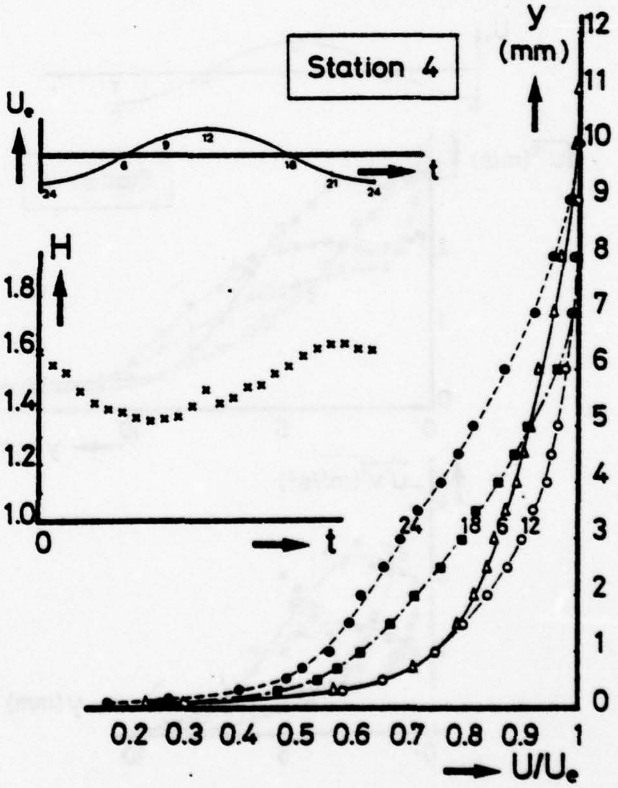

Fig. 5 – Boundary layer average velocity profiles.

Turbulence intensity and shear stress (Fig. 6,7,8,9)

The difference between the instantaneous velocity u and the average velocity U is the fluctuation u'. The standard deviation $(\overline{u'^2})^{1/2}$ defines the longitudinal component of the turbulent kinetic energy. Moreover, the use of a X-wires anemometer enables us to determine the shear stress $-\rho \overline{u'v'}$.

On the figure 6, the profiles of $(\overline{u'^2})^{1/2}$ and $-\overline{u'v'}$ are presented for various instants in the period. The first observation is that their evolutions are very similar (the similarity would be better if comparing the $\overline{u'^2}$ and $-\overline{u'v'}$ profiles). The evolution of the profiles is due partly to the periodic variation of the boundary layer thickness imposed by the unsteadiness of the flow, but it is clear that the variation of shape of the profiles is a direct consequence of the variable pressure gradient.

In order to compare the time variations of the average velocity U and of the turbulence intensity $(\overline{u'^2})^{1/2}$ these quantities are reduced by their time average U_m and $(\overline{u'^2})^{1/2}_m$ so that U/U_m and $(\overline{u'^2})^{1/2}/(\overline{u'^2})^{1/2}_m$ have variations around 1 ; these quantities are shown on the figure 7. In the external flow, turbulence intensity and average velocity are nearly in phase and their relative variations are almost equal. When the probe is displaced toward the wall, this is no longer true and we note a large difference in phase. This result is a consequence of the periodic variation of the free boundary : the fact that the maximum of thickness occurs in a part of the period near the minimum of velocity makes clear that the intensity of turbulence is higher in that part of the period at the distances y = 5 mm and y = 9 mm. For lower values of y the difference in phase is considerably reduced.

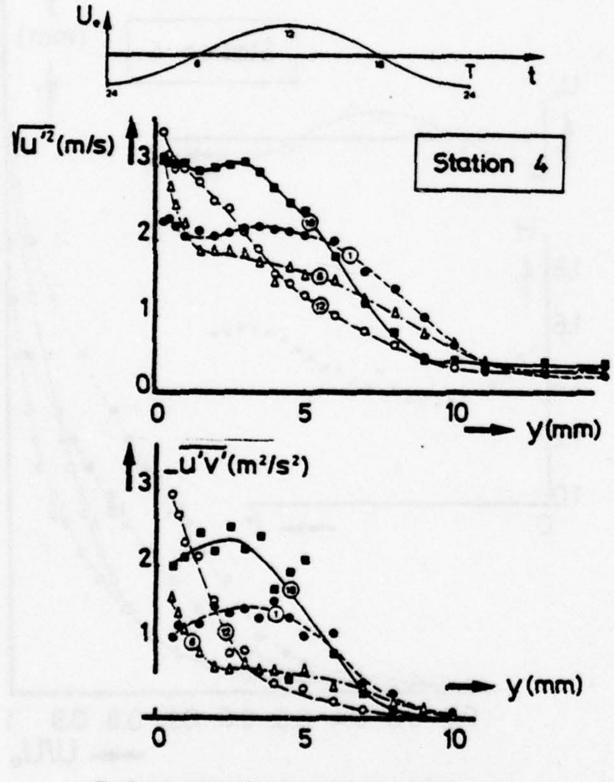

Fig. 6 – Intensity of turbulence and shear-stress profiles.

The measurements of the shear stress enable us to analyze quantities which implicitly play an important role in many calculation methods. For example, we determine the correlation coefficient $-\overline{u'v'}/(\overline{u'^2}.\overline{v'^2})^{1/2}$. It is represented on the figure 8 as function of time, for various distances to the wall at the station ④. In a rather thick region near the wall, the correlation coefficient is nearly equal to 0,5 : this value is very close to the value generally measured in a steady boundary layer. Obviously, this coefficient tends to zero in the outer region of the boundary layer because $\overline{u'v'}$ becomes zero and the turbulence intensity is small but non zero.

A classical scheme of turbulence is the mixing length model. We tried to directly analyze its validity by using the measurements of the shear stress and of the velocity. In this purpose, we must determine the derivative $\frac{\partial U}{\partial y}$, and then we calculate the mixing length by the ratio $l = -\overline{u'v'}/\frac{\partial U}{\partial y}$. To avoid a too great scatter in the results, the velocity profiles have been smoothed. The obtained evolution of the mixing length is presented on the figure 9 for four instants in the period. We note that the distributions of the mixing length are in rather good agreement with a classical distribution used in steady flow. However, for a part of period near the maximum velocity, discrepancies must be noted.

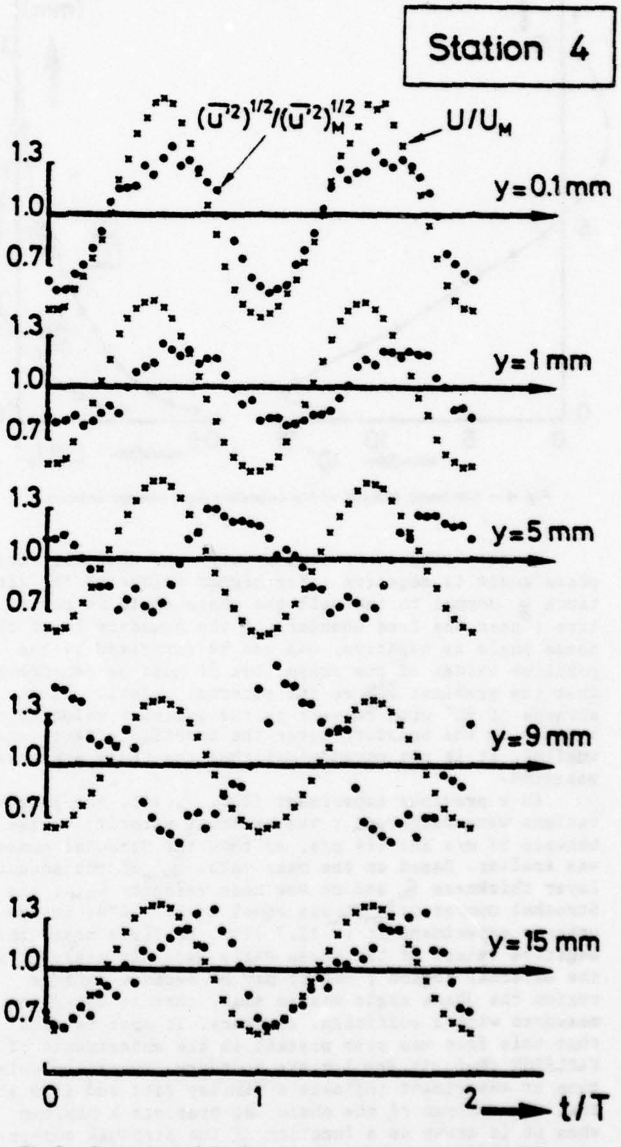

Fig. 7 – Comparison of the time variations of the turbulence intensity and of the average velocity.

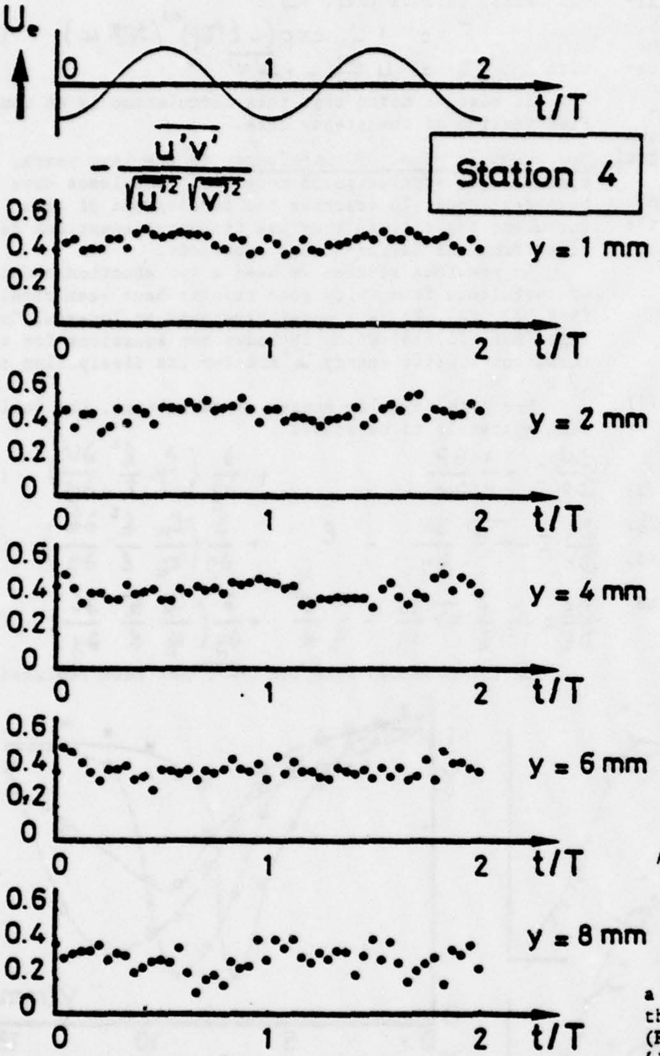

Fig. 8 – Correlation coefficient.

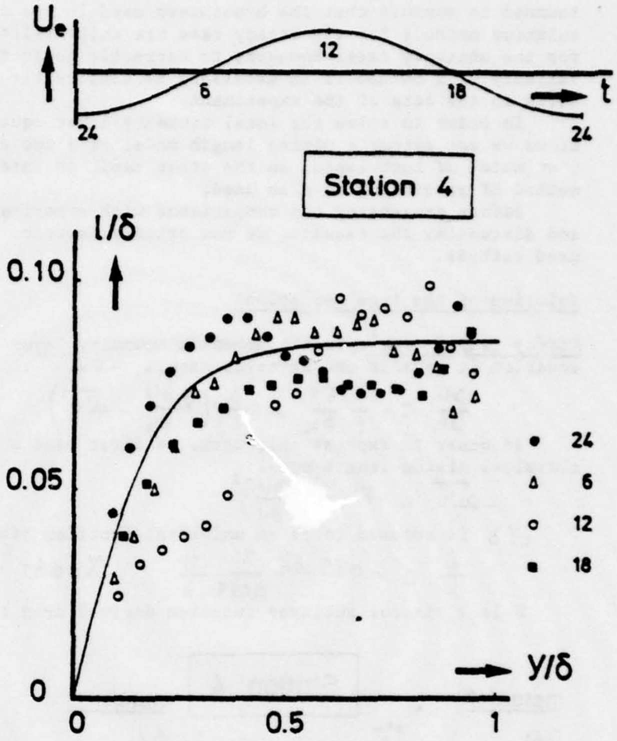

Fig. 9 – Mixing length distribution.

Statistical distribution of the velocity fluctuation (Fig. 10,11)

Further informations are obtained by studying the statistical distribution of the velocity fluctuations. The probability density of u' has been calculated and some results are presented on the figure 10. In abscissa the centered normalized variable $u'/(\overline{u'^2})^{1/2}$ is used. On the same graphs these functions are compared with a gaussian probability density. Qualitatively, the behaviour of this function is the same as in the case of a steady boundary layer : near the wall, it is nearly gaussian ; away from the wall it is skewed ; in the external flow it is again nearly gaussian as it is for the turbulence behind a grid. In steady flow, the skewness is a consequence of the intermittency phenomenon which is due to the random variation of the free boundary ; when the probe is in the outer flow the velocity is nearly constant and higher than in the turbulent spots : it corresponds to a peak in the density probability. Certainly this interpretation is still valid in the present case. It must be noted that the deformation occurs closer to the wall for the instant 19 : this can be explained by the fact that the average thickness of the boundary layer is thinner for this instant.

The instantaneous location of the free boundary is a random variable the distribution function of which is the intermittency factor γ . Under some assumptions (Ref. 11) it is related to the flatness factor by $\gamma = 3/F$ ($F = (\overline{u'^4}) / (\overline{u'^2})^2$) . This process is used here to bring some information about the variation of the free boundary (Fig. 11). Near the wall, the distribution of u' is nearly gaussian ; accordingly γ is about 1. The decrease of γ is representative of the random displacement of the free boundary. In the outer flow γ is again about 1 since the probability density is nearly gaussian. The figure 11 also shows that the free boundary is submitted to forced oscillations since the curve is dependent on the phase angle. However, if the distance y is reduced by the value $y_{\gamma=0.5}$ for which $\gamma = 0.5$ all the curves have the same shape. For comparison, we reported the points mesured by KLEBANOFF (Réf. 11) in the case of a steady flat plate boundary layer.

BOUNDARY LAYER CALCULATIONS

From the results of the presented experiments, it appears that the behaviour of the boundary layer and the structure of turbulence are not fundamentaly modified by the unsteady character of the flow. For example, the velocity profiles are correctly represented by profiles belonging to a family calculated in steady flow. We also saw that the correlation coefficient or the mixing length distribution are in pretty good agreement with the steady case. From these observations, it is well founded to suppose that the hypotheses used in the calculation methods for the steady case are still valid for the unsteady case. However, to correctly judge the validity of a method it is necessary to compare its results to the data of the experiment.

In order to solve the local boundary layer equations we use either a mixing length model or a two equation model of turbulence. On the other hand, an integral method of prediction is also used.

Before presenting the comparisons with experiment and discussing the results, we now briefly describe the used methods.

Solution of the local equations

Mixing length model. In the momentum boundary layer equation it appears the Reynolds stress $-\rho\overline{u'v'}$:

$$\frac{DU}{Dt} = -\frac{1}{\rho}\frac{\partial P}{\partial x} + \frac{\partial}{\partial y}\left(\nu\frac{\partial U}{\partial y} - \overline{u'v'}\right) \qquad (1)$$

In order to express this term, we first used a classical mixing length model :

$$-\overline{u'v'} = F^2 \ell^2 \left(\frac{\partial U}{\partial y}\right)^2 \qquad (2)$$

ℓ/δ is assumed to be an universal function of y/δ:

$$\frac{\ell}{\delta} = 0.085\, th \frac{\chi}{0.085}\frac{y}{\delta} \qquad \chi = 0.41 \qquad (3)$$

F is a viscous sublayer function derived from the VAN DRIEST formula (Réf. 12) :

$$F = 1 - \exp\left(-\ell(\tau\rho)^{1/2}/26\chi\mu\right) \qquad (4)$$

with $\tau = \mu\frac{\partial U}{\partial y} - \rho\overline{u'v'}$

It must be noted that this formulation is an unmodified version of the steady case.

Two equation model of turbulence. In the last years, various more sophisticated models of turbulence have been developed. To describe the development of some turbulent quantities, they use transport equations derived from the Navier-Stokes equations.

In previous studies we used a two equation model of turbulence from which good results have been obtained (Ref. 13, 14). It is a model developed at Imperial College (Ref. 15, 16) which includes two equations for the turbulent kinetic energy k and for its dissipation rate ε.

For high Reynolds number of turbulence, the following system is to be solved :

$$\frac{DU}{Dt} = -\frac{1}{\rho}\frac{\partial P}{\partial x} + \frac{\partial}{\partial y}\left(C_\mu\frac{k^2}{\varepsilon}\frac{\partial U}{\partial y}\right) \qquad (5)$$

$$\frac{Dk}{Dt} = -\overline{u'v'}\frac{\partial U}{\partial y} - \varepsilon + \frac{\partial}{\partial y}\left(\frac{C_\mu}{\sigma_k}\frac{k^2}{\varepsilon}\frac{\partial k}{\partial y}\right) \qquad (6)$$

$$\frac{D\varepsilon}{Dt} = -C_{\varepsilon_1}\frac{\varepsilon}{k}\overline{u'v'}\frac{\partial U}{\partial y} - C_{\varepsilon_2}\frac{\varepsilon^2}{k} + \frac{\partial}{\partial y}\left(\frac{C_\mu}{\sigma_\varepsilon}\frac{k^2}{\varepsilon}\frac{\partial \varepsilon}{\partial y}\right) \qquad (7)$$

In the momentum equation $-\overline{u'v'}$ has been replaced by

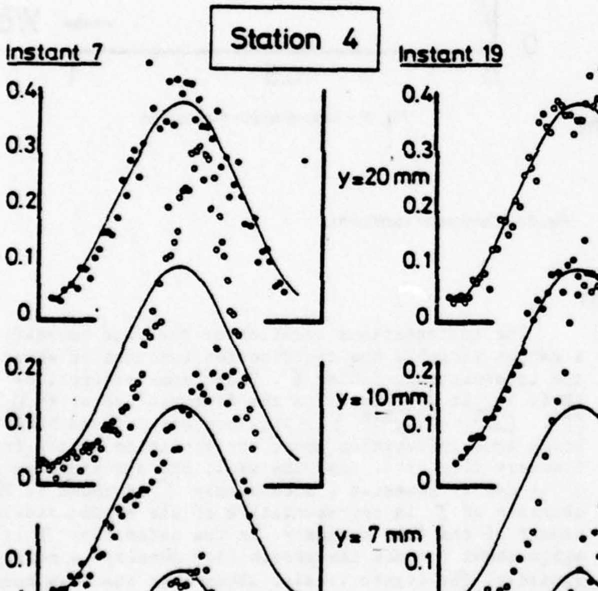

Fig. 10 – Probability density of the fluctuation u'.

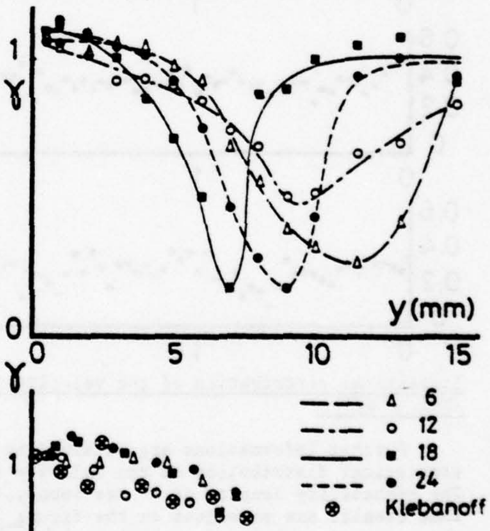

Fig. 11 – Flatness factor.

its expression :

$$-\overline{u'v'} = C_\mu \frac{k^2}{\varepsilon} \frac{\partial U}{\partial y} \qquad (8)$$

In these equations the values of the constants are :

$C_\mu = 0.09 \quad C_{\varepsilon_1} = 1.45 \quad C_{\varepsilon_2} = 2 \quad \sigma_k = 1.1 \quad \sigma_\varepsilon = 1.1$

With regard to the steady case, only the time derivatives in the convection terms have been added. It is important to note again that the modellisation used for the steady flow is unmodified.

As already said, this model is only valid for high Reynolds number of turbulence and is well adapted for the outer part of the boundary layer. Near the wall, this is no longer true because the turbulence Reynolds number decreases in this region and is zero at the wall. Therefore a special treatment is needed. Two possibilities have been used. The first option is to replace, near the wall, the transport equation system (Ref. 5, 6, 7) by the mixing length scheme and to solve the equations (Ref. 1, 2, 3, 4). This treatment is relaxed at a distance of the wall $y = y_r$ where the sublayer function F is nearly equal to 1 (F = 0,99), that is to say when the Reynolds number is high enough. The calculated condition at $y = y_r$ are used to determine the boundary conditions for the transport equation system ; at $y = y_r$ we impose the continuity of $U, \frac{\partial U}{\partial y}$ and τ . We assume that :

$$k = (\tau/\rho) / C_\mu^{1/2}$$

$$\varepsilon = \frac{C_\mu}{\tau/\rho} k^2 \frac{\partial U}{\partial y}$$

The second option is to introduce ad hoc modifications in the transport equations system as this has been done by JONES-LAUNDER (Ref. 16). We also used this low Reynolds number version of the transport equations. The boundary layer equations (continuity equation, momentum equation, turbulence model) are solved step by step by means of a finite difference method.

Solution of the global equations

The solution of the local equations enables us to get detailed informations on the development of the boundary layer. However, these calculations are time consuming and some difficulties can arise to correctly specify the initial or boundary conditions especially when using the transport equation model. In many practical applications it is only interesting to know the evolution of global quantities as the thickness δ_1 or the skin friction coefficient. Then an integral method can be efficient.

Such a method is based on the simultaneous solution of the global continuity and momentum equations. By neglecting the variation of the density, these equations are :

$$\frac{\partial \delta}{\partial x} - \frac{v_e}{u_e} = \frac{1}{u_e} \frac{\partial}{\partial x}\left[u_e(\delta - \delta_1)\right] \qquad (9)$$

$$\frac{C_f}{2} = \frac{\partial \theta}{\partial x} + \theta \frac{H+2}{u_e} \frac{\partial u_e}{\partial x} + \frac{1}{U_e^2} \frac{\partial}{\partial t}(U_e \delta_1) \qquad (10)$$

In this system, it appears five unknowns : $\frac{\partial \delta}{\partial x} - \frac{v_e}{u_e}$, C_f, δ_1, θ , δ . Therefore, we must use additional relations. As in the steady case, they can be gotten from the study of similarity solutions.

Similarity solutions. These solutions are very simple if we suppose that the Reynolds number tends to infinity. Under this condition, the similarity hypothesis is to assume that the defect velocity profile $(U_e - U)/U_e (C_f/2)^{1/2} = F'$ is only a function of the reduced distance $\eta = y/\delta$; δ is the boundary layer thickness and is function of t and x . In such similarity solutions, we only consider the outer part of the boundary layer where it is legitimate to neglect the effects of viscosity and to neglect the viscous stress with regard to the Reynolds stress. Therefore, if we use a mixing length model to express the Reynolds stress we get :

$$\tau = \mu \frac{\partial U}{\partial y} - \rho \overline{u'v'} \simeq -\rho \overline{u'v'}$$

$$-\overline{u'v'} = \ell^2 \left(\frac{\partial U}{\partial y}\right)^2$$

The similarity hypothesis enables to simplify the momentum equation. For this we consider that $(C_f/2)^{1/2}$ is a small parameter (because the Reynolds number tends to infinity) and only the terms of the same order as $(C_f/2)^{1/2}$ are retained. For the steady case the details of the algebra are given in Ref. 12. For the unsteady case, we follow exactly the same way and the momentum equation becomes :

$$\frac{\tau}{\tau_p} = \left(\frac{\ell}{\delta}\right)^2 F''^2 = 1 - \frac{F}{F_1} + P \eta F' \qquad (11)$$

with $F'' = \frac{dF'}{d\eta} \qquad F = \int_0^\eta F' d\eta \qquad F_1 = \int_0^1 F d\eta$

$$P = \frac{1}{F_1} + \beta^*$$

$$\beta^* = \beta_t + 2\beta_x \qquad \beta_x = -\frac{\delta}{\gamma U_e} \frac{\partial U_e}{\partial x} \qquad \beta_t = -\frac{\delta}{\gamma U_e^2} \frac{\partial U_e}{\partial t}$$

$$\gamma = (C_f/2)^{1/2} \qquad \eta = y / \delta(x,t)$$

This equation (11) is an ordinary differential equation for $F'(\eta)$ in which appears the only parameter $\beta^* = \beta_t + 2\beta_x$. We note that, with regard to the steady case, the only modification is that $\beta_t + 2\beta_x$ replaces $2\beta_x$. Therefore, the solution is exactly the same if it is considered as a function of β^*. For a practical use of these solutions, it is more convenient to replace the parameter β^* which characterizes the external velocity by a parameter which characterizes the shape of the profiles. For this, we use the Clauser parameter :

$$G = \int_0^1 F'^2 d\eta \Big/ \int_0^1 F' d\eta \qquad (12)$$

Use of similarity solutions for building the integral method. Now, we show how to use these solutions to get the additional relations needed for the closure of the integral method.

First, the thickness δ_1 is related to F_1 by :

$$\delta_1 / \delta = \gamma F_1 \qquad (13)$$

where F_1 is given by the similarity solution. It is a function of G that we represent by the formula :

$$F_1 = 0,613\ G - (3,6 + 76,86\ (1/G - 0,154)^2) / G$$

The similarity solutions enable us to express the entrainment coefficient. By using the similarity hypothesis the continuity equation is :

$$\frac{v}{\gamma U_e} = \beta_x \eta - \frac{\partial \delta}{\partial x}(\eta F' - F)$$

Written at the outer edge $(\eta = 1)$ this equation leads to :

$$\frac{\partial \delta}{\partial x} - \frac{v_e}{U_e} = \gamma P - \frac{1}{U_e} \frac{\partial \delta}{\partial t} \qquad \left(P = \frac{1}{F_1} + \beta^*\right) \qquad (14)$$

where P is a function of G determined by the similarity solutions that we represent by :

$$P = 0,074\ G - 1,0957 / G$$

We note that the entrainment coefficient $\frac{\partial \delta}{\partial x} - \frac{v_e}{U_e}$ is not represented by the same expression as in the steady case since it appears the term $\frac{1}{U_e} \frac{\partial \delta}{\partial t}$.

Finally, the law for the skin friction coefficient is deduced by the classical method of overlapping between the law of the wall and the defect velocity law. When $\eta \to 0$, since $\frac{\tau}{\tau_p} \to 1$, F' follows a logarithmic form :

$$F' = \frac{U_e - U}{\gamma U_e} = -\frac{1}{\chi} \ln \frac{y}{\delta} + D(G)$$

If we assume that the law of the wall is unmodified in unsteady flow, we have :

$$\frac{U}{\gamma U_e} = \frac{1}{\chi} \ln \frac{y \gamma U_e}{\nu} + 5.25$$

By adding the two formulae, we get the law for the skin friction coefficient :

$$\frac{1}{\gamma} = \frac{1}{\chi} \ln \frac{\gamma U_e \delta}{\nu} + 5.25 + D = \frac{1}{\chi} \ln \frac{U_e \delta_1}{\nu} + 5.25 + D - \frac{1}{\chi} \ln F_1 \quad (15)$$

where $D^* = D + 5.25 - \frac{1}{\chi} \ln F_1$ is a function of G represented by :

$$D^* = 2G - 4.25\, G^{1/2} + 2.12$$

Numerical technique. The system of the global equations (9,10) with the additional relations (13,14,15) is solved step by step by means of a finite difference technique.

COMPARISON WITH PRESENT EXPERIMENT

To calculate the development of the boundary layer the external velocity must be given. For this, we used the harmonic analysis of its distribution shown on the figure 4. Moreover, when the turbulence scheme is the transport equation model, the turbulence intensity and the dissipation rate in the outer flow must be specified. From the experiment, it is easy to determine the turbulence intensity (we took $k_e/U_e^2 = 5\,10^{-5}$). The value of the dissipation rate is more arbitrary but its influence is very small.

To solve the local equations, the velocity profiles must be specified in the planes $x = x_o$ and $t = t_o$: these data have been determined from the experiment. When using the transport equations model the profiles $k(y)$ and $\varepsilon(y)$ must be also fixed : they have been calculated by means of a mixing length formula from the velocity profiles.

The application of the integral method is more simple : it only needs the distributions of δ_1 and θ along the lines $x = x_o$ and $t = t_o$; they are known from the experiment.

It must be noted that in all these methods, the conditions in the plane $t = t_o$ are not important because a periodic solution independent on these conditions is obtained after a long enough time.

On the figure 12 are shown the calculated evolution of the thicknesses δ_1 and θ compared to the experimental data. The various methods lead to coherent results in good agreement with those of the experiment. At the first station there is no comparison because the experimental data are used as initial conditions.

The solution of the local equations enables us to get more detailed results as for example the evolution of the velocity, shear stress or turbulent kinetic energy profiles. The comparison of the velocity profiles (Fig. 13) shows that in all the used methods the deformation of these profiles is well reproduced. The results describing the evolution of the shear stress profiles (Fig. 15) are more scattered ; however the shape of these profiles and the general level of the shear stress are correctly calculated by the various methods.

In the mixing length scheme, the turbulent kinetic energy is not explicitly calculated. Therefore, for this quantity we have only reported the results obtained by means of the transport equation model (Fig. 14). In the experiment, only $\overline{u'^2}$ and $\overline{v'^2}$ have been measured. In order to determine the turbulent kinetic energy two hypotheses have been used : in the first case we suppose that $\overline{u'^2} = k$; in the second case we suppose that $\overline{w'^2} = 0{,}3k$ and the turbulent kinetic energy is calculated as $k = (\overline{u'^2} + \overline{v'^2})/1.4$. We see that these two means lead to close results. We also see that the transport equation model gives results in good agreement with experiment concerning the two treatments that have been used near the wall ; they do not give the same results but it is difficult to say if one is better than the other.

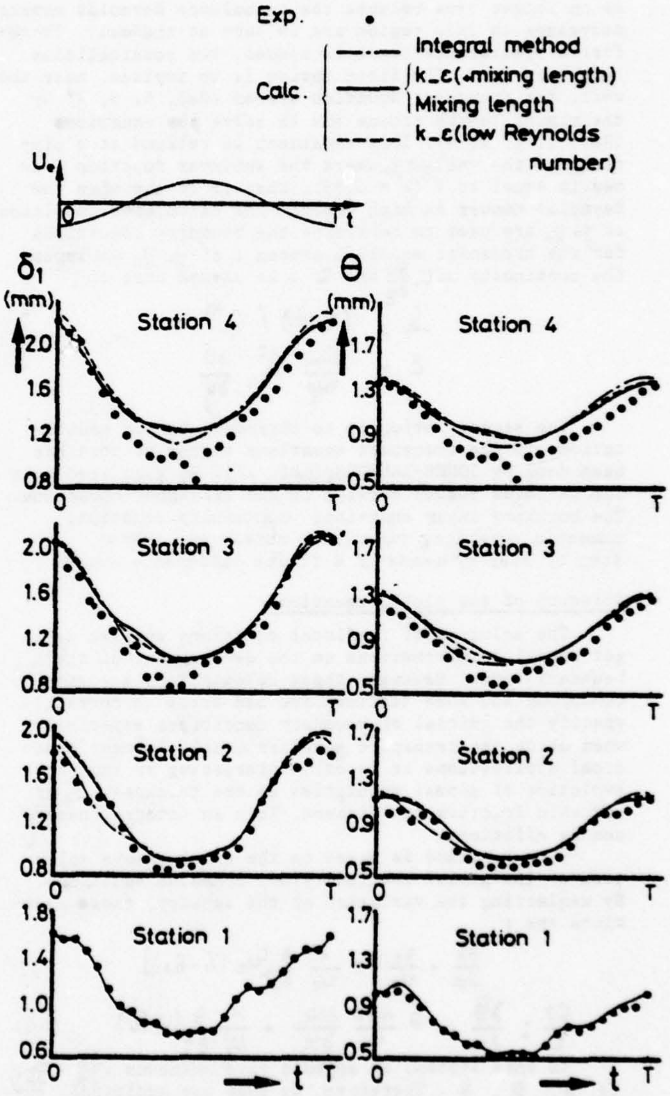

Fig. 12 – Boundary layer calculations – Integral thicknesses.

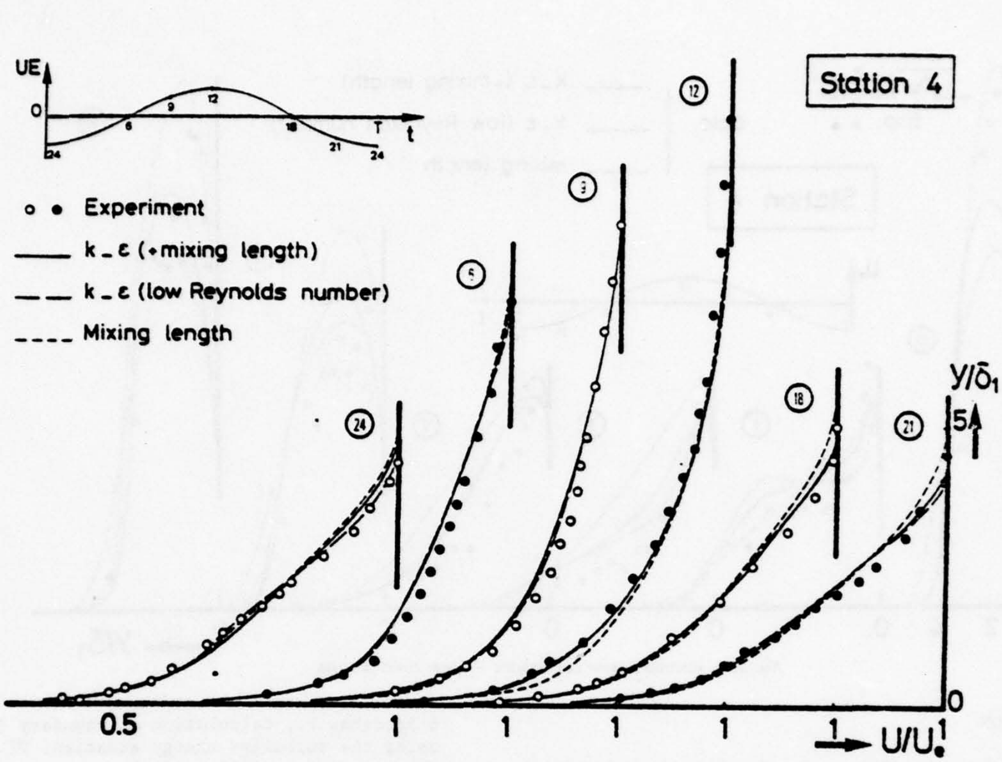

Fig. 13 – Boundary layer calculations – Average velocity profiles.

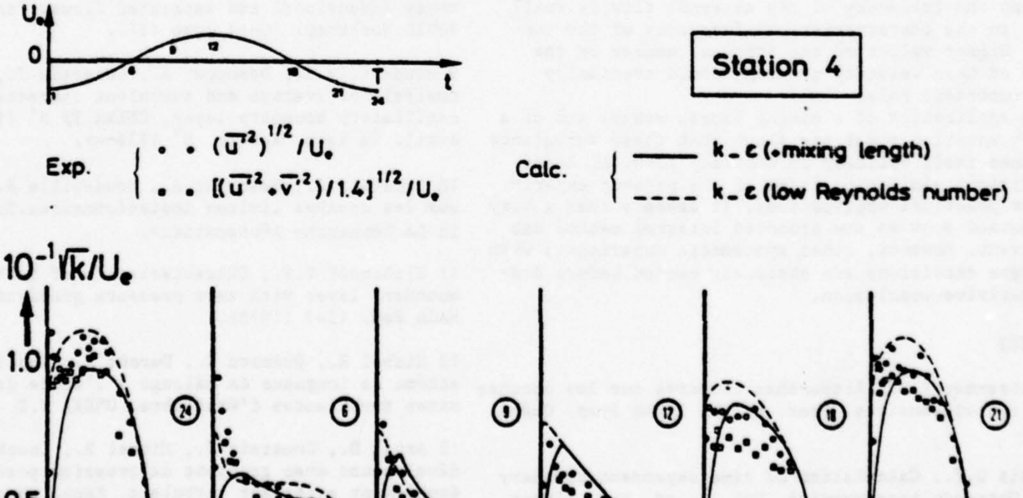

Fig. 14 – Boundary layer calculations – Turbulence intensity profiles.

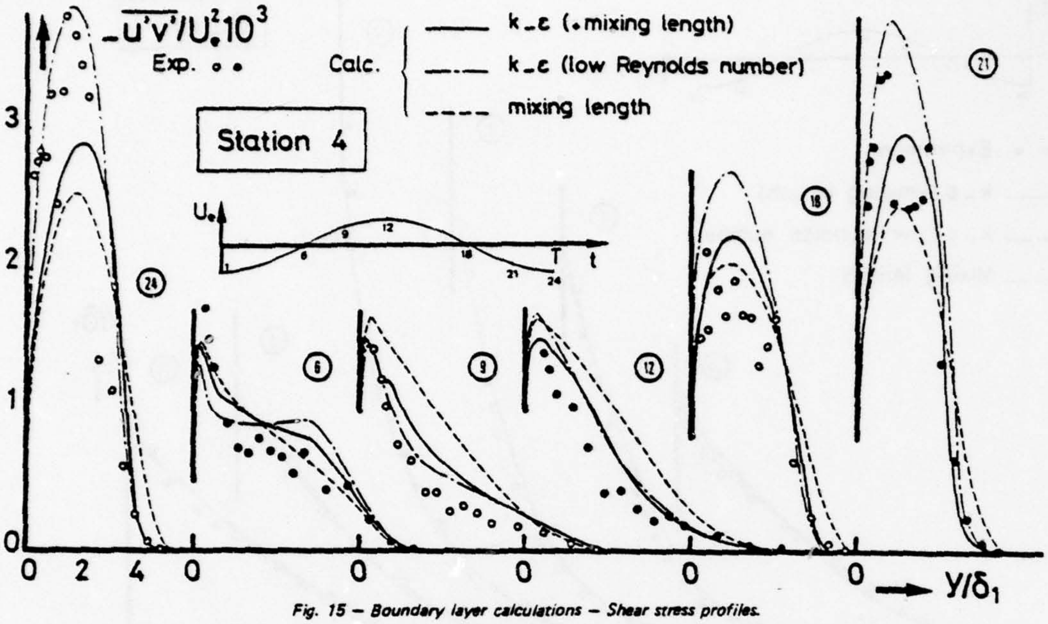

Fig. 15 – Boundary layer calculations – Shear stress profiles.

CONCLUSION

The experimental study of a turbulent boundary layer which is developing in presence of an oscillatory external flow has shown that the general behaviour of the boundary layer and that the structure of the turbulence are not fundamentally affected by the unsteadiness of the flow. However, it must be noted that in our experiment the frequency of the external flow is small compared to the characteristical frequency of the turbulence. Higher values of the Strouhal number or the presence of mean velocity gradient could eventually play an important role.

The application of a mixing length scheme and of a transport equation model has shown that these turbulence models keep their validity in unsteady flow, at least for conditions similar to those of the present experiment. For practical applications, it appears that a very simple method such as the proposed integral method can be efficient. However, other systematic experiments with more severe conditions are obsiously needed before drawing a decisive conclusion.

REFERENCES

1 Eichelbrenner E.A., Recherches récentes sur les couches limites instationnaires. Proc. of the IUTAM Symp. Québec 1971.

2 Telionis D.P., Calculation of time dependent boundary layers. Unsteady Aerodynamics, Vol. 1, ed. R.B. Kinney (1975), P. 155-190.

3 Karlsson S.K.F., An unsteady turbulent boundary layer. Journ. of Fluid Mech., Vol. 5, 1969, P. 622-636.

4 Charnay G., Mélinand J.P., Etude de la structure des couches limites turbulentes qui se développent en présence d'un écoulement extérieur pulsé. Contrat DRME 72-774 (1975).

5 Nash J.F., Carr L.W., Singleton R.E., Unsteady turbulent boundary layers in two dimensional incompressible flow. AIAA Journal, Vol. 13, N° 2 (Feb. 1975) P. 167-173.

6 Bradshaw P., Calculation of boundary layer development using the turbulent energy equation. VI. Unsteady flows. NPL Aero Report 1288, (1969).

7 Mc Croskey W.J., Philippe J.J., Unsteady viscous flow on oscillating airfoils. AIAA Paper, N° 74, 182.

8 Abbott D.E., Wu J.C., Fluid dynamics of unsteady, three dimensional and separated flows. Proceedings of a SQUID Workshop. 10-11 June 1971.

9 Houdeville R., Desopper A., Cousteix J., Experimental analysis of average and turbulent characteristics of an oscillatory boundary layer. ONERA TP N° 1976-30 (also avail. in Rech. Aerosp. N° 1976-4).

10 Cousteix J., Desopper A., Houdeville R., Recherches sur les couches limites instationnaires.To be published in La Recherche Aérospatiale.

11 Klebanoff P.S., Characteristics of turbulence in a boundary layer with zero pressure gradient. NACA Rep. 1247 (1955).

12 Michel R., Quémard C., Durant R., Application d'un schéma de longueur de mélange à l'étude des couches limites turbulentes d'équilibre. ONERA N.T. N° 154 (1969).

13 Arnal D., Cousteix J., Michel R., Couche limite se développant avec gradient de pression positif dans un écoulement extérieur turbulent. Rech. Aérosp. N° 1976-1.

14 Cousteix J., Progrès dans les méthodes de calcul des couches limites turbulentes bi et tridimensionnelles. 13e Colloque d'Aérodynamique Appliquée, Lyon (Nov. 1976).

15 Launder B.E., Prediction methods for turbulent flows. VKI Lecture Series 76 (1976).

16 Jones W.P., Launder B.E., The prediction of laminarization with a two equation model of turbulence. Int. Jour. of Heat and Mass transfer, Vol. 15, N° 2, (1972).

A STUDY OF THE RELAXATION PROCESS IN TURBULENT CHANNEL FLOW

V. Vasanta Ram, F. von Schulz-Hausmann
Ruhr University
Bochum, Federal Republic of Germany

ABSTRACT

This paper is devoted to the study of turbulent channel flow with a stepwise change in wall roughness. Object of the study was to gain insight into the processes that govern the relaxation behaviour of flow from one fully developed state to another. Experiments were conducted in a channel with the flow going over from a rough walled fully developed state to the smooth walled fully developed state. Measurements were made of the wall pressure gradient, the wall shear stress, of the mean and fluctuating velocities and of the Reynolds shear stress in the relaxation region. The experiments show that, to attain the fully developed downstream state, the wall pressure gradient needs only a short running length from the abrupt change, the mean velocity requiring a longer distance, and the Reynolds shear stress achieving this state still farther away downstream.

A theoretical framework is offered for study of the scaling behaviour of flows with relaxation. The salient parameter is found to be the ratio of friction velocities corresponding to the fully developed upstream and downstream states $u_{\tau a}/u_{\tau b}$. Based on a physical hypothesis, for the region away from the walls a relation is derived between the relaxation lengths and the parameter $u_{\tau a}/u_{\tau b}$.

NOMENCLATURE

h = half channel width, reference length
L_u = relaxation length for mean velocity, refered to h
L_τ = relaxation length for shear stress, refered to h
Re = $2hU/\nu$, Reynolds number
u, v = mean velocity components
u', v' = fluctuating velocity components
U = velocity along center line of channel
U_b = velocity at center line of channel in fully developed flow far downstream
u_τ = friction velocity
$u_{\tau *}$ = fictious friction velocity
x, y = coordinates
X, Y = dimensionless coordinates, refered to h
X_u = X/L_u
X_τ = X/L_τ
ν = kinematic viscosity
τ = Reynolds shear stress
$\sigma_1, \sigma_2, \sigma_3$ = Reynolds normal stresses

Subscripts

a upstream condition
b downstream asymptotic state
d departure from downstream asymptotic state, scaled as in eqn.(2)
r fully developed rough wall flow
s fully developed smooth wall flow
u universal function in fully developed flow, eqn.(1)

Superscripts

~ departure from downstream asymptotic state, eg., $\tilde{u} = u - u_b$
‾ averaged quantity, eg., $\overline{u'^2}$, $\overline{u'v'}$

INTRODUCTION

In his "Young Person's Guide to the Data" D. Coles, at the Stanford conference of 1968, observed (1): "Unfortunately the quality and completeness of the data deteriorate in this area, and the conclusions thus tend to be less conclusive." The reference was to a class of incompressible turbulent boundary layers that he titled "abnormal and relaxing flows" as opposed to "flows in or near equilibrium". Cole's remarks, although spoken in the context of boundary-layer flows, apply in spirit equally to all kinds of turbulent shear flow, even to the relatively simple category of channel and pipe flows. The turbulent shear flow becomes "abnormal" when its turbulence structure is disturbed from a state that it would naturally tend to assume for the flow in question, like the structure associated with the wall-wake combination for boundary layers or the fully developed state for channel flow. Examples for disturbances to the turbulence structure in channel flow are provided by those caused by abrupt changes of wall roughness or by other means like an oscillating ribbon in the experiments of A. Hussain and W. C. Reynolds (2).

Fully developed channel flows, like other simpler turbulent shear flows in or near equilibrium, have been studied extensively so that at present, although questions of basic character still remain to be answered, these flows may be regarded as predictable from an engineering viewpoint. Flows with a disturbance induced into their turbulence structure, on the other hand, are known to involve large and slowly decaying distortions in the mean flow, ref.eg., D. Coles (1). The present state of understanding of the dynamical processes in these flows seems to be very far removed from their counterparts for equilibrium flows. In such situations the reliability of prediction methods, when claimed to be applicable, also seems to be open to doubt. Furthermore, in contradistinction to flows in equilibrium, there is as yet, to the authors' knowledge, no consensus evolved on what factors could go to constitute a "standard relaxing flow", and if such a concept is desirable. The first mentioned of the authors of this paper felt that it might be meaningful to study relaxing flows from a point of view that attempts to identify the significant parameters and scales for the slowly decaying distortions in "standard relaxing flows". For wall flows the configuration of an infinite channel with a step change in roughness might be suitable as a standard, at least from an engineering point of view for assesment of prediction methods. For, the fully developed states both upstream of the step change and far downstream are well defined and possess simplifying features so that the relaxation process would be more tractable *to analysis and also* be experimentally realisable.

The response of a flow with constant shear stress subjected to a step change in surface roughness is the subject of a classical paper in 1965 by A. A. Townsend, whose book (3) contains further references on this and related topics. Work by R. A. Antonia and R. E. Luxton (4, 5, 6) represents an extensive investigation into this subject, their papers contain additional references. The flow in a channel with a step change in wall roughness does not seem to have received attention comparable to its counterpart in boundary layers. The only experiments the authors are aware of are by W. Jacobs (7) and by I. Tani, H. Makita (8). W. Jacobs' measurements, which were confined to pressure drop and mean velocity profiles, were conducted in a rather low aspect ratio (3:1) channel with only one of the mutually facing walls roughened, thus losing symmetry. The experiments of I. Tani, H. Makita in a channel of aspect ratio 10:1 with both the walls roughened are more extensive, covering both mean and turbulence quantities.

The present work was started with the object of gaining deeper insight into the physical mechanisms that govern the relaxation porcess. The study reported in this paper represents the current status in the course of this work and hence bears the character of an interim report.

EXPERIMENTS

The authors' experiments were conducted in a channel of aspect ratio 25:1. The dimensions of the channel are indicated in fig. 1 The mutually facing walls in the upstream section of the channelwere covered with *sandpaper*.

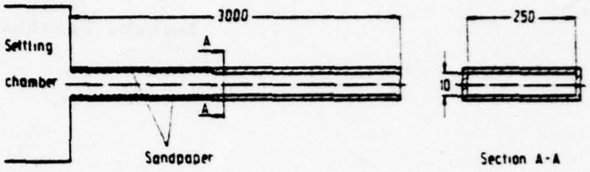

Fig. 1 Channel flow rig

(Drawing not to scale, dimensions in mm)

The following measurements were conducted:

a) Distribution of wall pressure;
b) *Mean velocity profiles;*
c) Profiles of r.m.s. values of fluctuating velocities $\sqrt{\overline{u'^2}}$, $\sqrt{\overline{v'^2}}$ and of Reynolds shear stress $\overline{u'v'}$;
d) Wall-shear stress as indicated by the reading of a sublayer fence.

Unfortunately no measurements of intermittency could be carried out.

Measurements b) and c) were conducted with the aid of a DISA constant temperature anemometer set with linearizer (Probe wire dia 5 μ, length 1.2 mm). For measurement of the Reynolds shear stress the technique of a single inclined hot wire (seeref.(9)) was employed. The probe was mounted on a manually operable precision mechanism which enabled rotation of the probe about its own axis.

The authors felt it desirable to get an estimate of the prevailing wall shear stress in the relaxation region by a method that does not involve extrapolation of Reynolds shear stress measurements, cf. (8). The Preston tube was not considered suitable for this purpose since the basis of its calibration, viz. the existence of a region obeying the log-law of the wall with a value of the Karman constant $\kappa = 0.41$, was doubted in the relaxation region, see (10). The technique of the sublayer fence was favoured because of experience that had been accumulated with this device (10). They were calibrated by measuring the pressure drop in the fully developed section of flow in a smooth-walled channel of the same dimensions as in fig. 1. To check the reliability of these measurements two sublayer fences, of *dimensions indicated in fig.* 2 with the fence height $h_f = 0.02$ mm and 0.03 mm ($u_\tau h_f/\nu \approx 25$-$35$), were used at each location. The difference in the values for wall shear stress as read off from their respective calibration curves was less than 0.05 N/m^2.

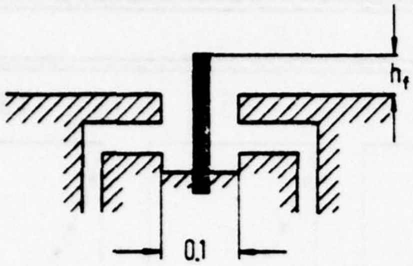

Fig. 2 Sublayer fence

The table below presents the data on the flow parameters for the measurements. The notations are as listed in the nomenclature.

Expt. No.	1	2	3	4	Tani, Makita
$\frac{U_s}{m/s}$	20.6	28.0	33.5	41.5	10
$Re_s \cdot 10^{-4}$	1.2	1.8	2.1	2.59	7.60
$\frac{u_{\tau s}}{m/s}$	1.03	1.52	1.85	1.90	0.43
$\frac{u_{\tau r}}{m/s}$	1.32	1.74	2.14	2.79	0.90
$\frac{u_{\tau r}}{u_{\tau s}}$	1.28	1.14	1.16	1.47	2.01

Experiments 1 through 3 were conducted with one kind of sandpaper (600 "Naßschleifpapier") whereas for experiment 4 one with a coarser grain (400 "Naßschleifpapier") was used to get a higher ratio $u_{\tau r}/u_{\tau s}$. The relaxation process was studied in greater detail for experiment 4. For purposes of comparison, data of I. Tani, H. Makita taken from (8) are given in the last column.

EXPERIMENTAL RESULTS

For purposes of economy in space and clarity only measurements of experiment no. 4 will be presented in detail. The flow in experiments 1 through 4 shows essentially the same pattern of behaviour. The pressure distribution, the center-line velocity $U(x)$ and the wall shear stress $\tau_w(x)$ as measured by the sublayer fence technique are shown in fig. 3. Fig. 4 is a presentation of the measured velocity and shear stress profiles, the former being plotted as velocity defect. The reference quantity $u_{\tau b}$ is the friction velocity corresponding to the wall shear stress in the fully developed smooth section far downstream, i.e., $u_{\tau s} = 1.895$ m/sec, cf. table.

The authors' experiments, in respect of gross features of flow, are in general agreement with the findings of I. Tani and H. Makita (8). Immediately downstream of the jump in wall roughness the pressure at the wall rises a little but within a very short distance $x/h \approx 7$, attains the constant negative gradient corresponding to the fully developed downstream state, fig. 3. Noteworthy in fig. 3, however, is the behaviour of the wall shear stress infered from the sublayer fence technique. The wall shear stress measured as here, attains its fully developed downstream value almost at the same order of distance as the pressure gradient. This is quantitatively different from the behaviour I. Tani and H. Makita (8) deduced from fitting their measured velocity profiles in the region near the wall to the logarithmic law.

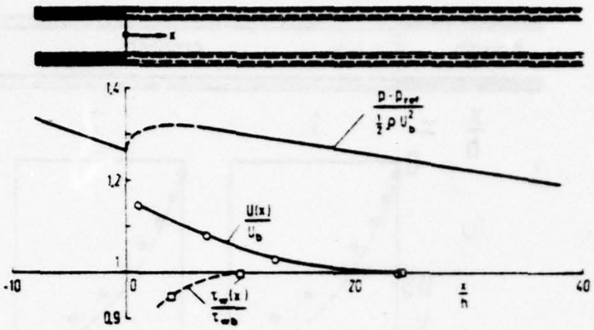

Fig. 3 Pressure gradient, center line velocity and wall shear stress

The rest of the data - one example for velocity and shear stress is shown in fig. 4 - support the findings of I. Tani and H. Makita, particularly the differential behaviour of layers closer to and away from the walls. In the authors' experiments, due to the size of the channel, measurements closer to the wall could not be taken, yet the rather slow attainment of the downstream equilibrium (fully developed) profiles away from the walls is evident from the plots in fig. 4. The Reynolds shear stress needs a distance of the order $x/h \approx 40$ beyond which no change is discernible. For purposes of discussion the velocity defect and the shear-stress profiles of fig. 4 have been replotted in fig. 5 with a fictious friction velocity $u_\tau^*(x)$ as reference. The quantity $u_\tau^*(x)$ has been obtained from the shear-stress measurements by fitting a straight line to the points in the center section (away from the walls) and extending the same up to the wall $y/h = 1$ where the value of the shear stress is read off as $\rho u_\tau^{*2}(x)$.

THEORETICAL FRAMEWORK

The flow in an infinitely long channel with a step change in wall roughness represents, in spite of its simple geometry, an intriguing flow situation. The energy and the length (or vorticity) scales characterising the turbulence structure have to undergo a change from one state to another. The salient forcing and balancing mechanisms effecting the transfer processes between scales are yet to be understood. The resul-

THIS PAGE IS BEST QUALITY PRACTICABLE
FROM COPY FURNISHED TO DDC

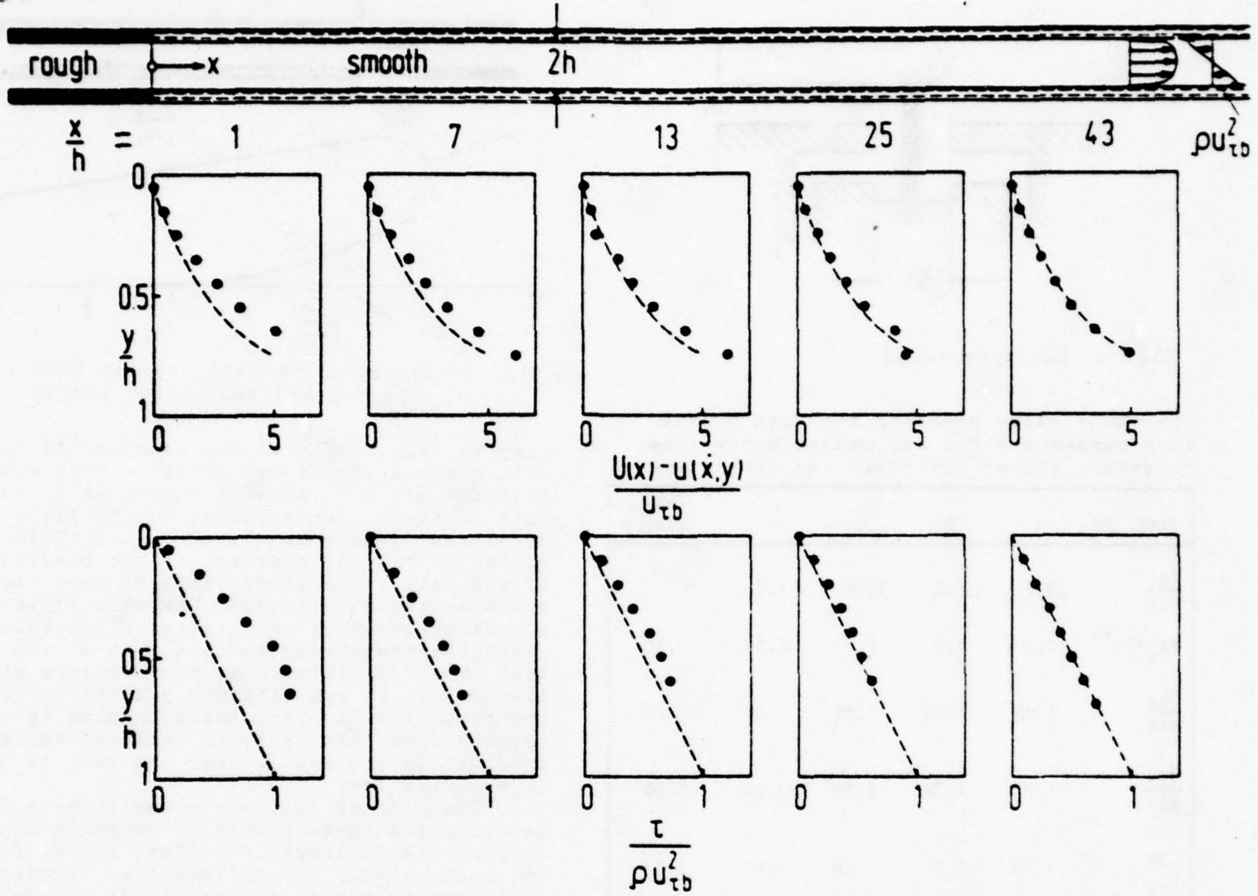

Fig. 4 Measured mean velocity and shear stress profiles.

$Re_s = 2.59 \times 10^4$. ------- Fully developed smooth profile

ting gross features of the flow are schematically indicated in fig. 6.

One approach to the problem would be through a turbulence model, the choice leaning towards one of the more sophisticated models advanced in recent years (the word "model" is used here in a sense that includes the "sub grid scale" methods). It is quite possible that some or all of these models - those by P. G. Saffmann (11), J.C. Rotta (12), J. L. Lumley (13), P. Bradshaw (15), W. C. Reynolds (16), B. E. Launder (14), D. B. Spalding (14), to quote a few,- contain those salient mechanisms with the proper emphasis, in which case their results might be expected to describe the flow situation. Although none of these models is really simple for computation there have been great strides taken during the last decades at solving the elliptic equations describing fluid motion, that their solution with these models should be within reach on a modern computing facility.

The authors of this paper have choosen a slightly different approach to the problem. Their objective is, as stated in the introduction, to attempt to deduce the significant scales involved in the relaxation process. This would call for suitable approximation of the governing equations based on order estimates. The order estimates are preferably carried out in the equations of motion and those derivable from them, although such a procedure could formally be applied to model equations too. An analysis of this kind would only serve to uncover the scales in the problem. Since the equations of motion alone are involved the scales should be verifiable through experiment, thus either supporting or refuting the structural hypothesis that underly the order estimates. For obtaining flow quantities like velocity and shear stress however, it is necessary to invoke a turbulence model.

Outline of analysis

The state of fully developed flow corresponding to the wall roughness in the downstream section of the channel is termed herein the downstream asymptotic state. The equations of motion are recast in terms of the departure of the flow quantities from their respective downstream asymptotic

THIS PAGE IS BEST QUALITY PRACTICABLE
FROM COPY FURNISHED TO DDC

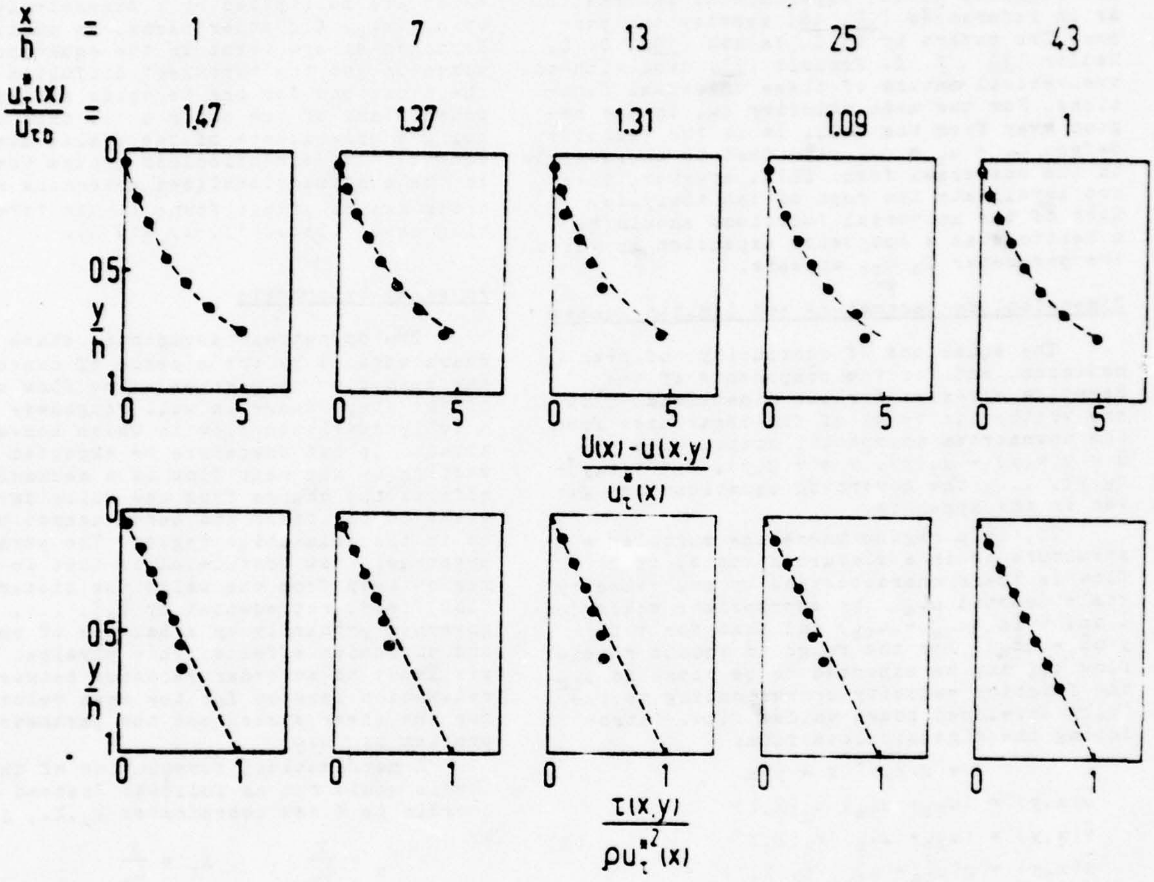

Fig. 5 Similarity plot of velocity defect and shear stress profiles of fig. 4

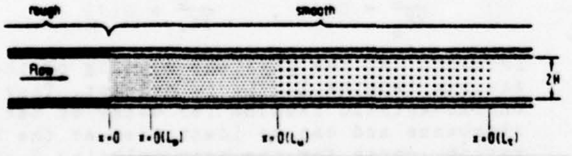

Physical quantity	Wall pressure gradient dp/dx	Mean velocity u(y)	Shear stress τ(y)
Relaxation length	L_p	L_u	L_τ

Note: Physical quantity reaches asymptotic value over a distance of the order of its relaxation length

Fig. 6 Scheme of the relaxation process in turbulent channel flow

states. All averaged quantities in the downstream asymptotic state are supposed to be characterised by one and only one velocity scale, viz., the friction velocity denoted $u_{\tau b}$. If, in a region where the disturbances have not died down the relevant scale of motion is $u_{\tau a}$, $(u_{\tau a} - u_{\tau b})$ represents the scale for the strength of the disturbance. This is a parameter in the problem. The relaxation length is defined as the length scale that characterises the decay of the disturbance. Order estimates of the terms in the equations of motion yield a relation between the relaxation length and the parameter.

The downstream asymptotic state

The downstream asymptotic state denoted by the subscript b is characterised by one and only one velocity scale. Further, all averaged quantities are independent of the streamwise coordinate x. Hence, the mean velocity, the Reynolds shear and normal stresses and higher order correlations are representable in terms of a set of universal functions u_u, τ_u, σ_{1u}, ..., of the coordinate $Y = y/h$ alone as follows:

$$u_b(y) = u_{\tau b}\, u_u(Y)$$
$$\tau_b(y) = \rho\, u_{\tau b}^2\, \tau_u(Y) \qquad (1)$$
$$\sigma_{1b}(y) = \rho\, u_{\tau b}^2\, \sigma_{1u}(Y)$$

THIS PAGE IS BEST QUALITY PRACTICABLE
FROM COPY FURNISHED TO DDC

In the present context the universal functions are regarded known, experimental information as in references (17, 18) serving the purpose. The papers by K. S. Yajnik (19), G. L. Mellor (20), F. E. Fendell (21) deal with the theoretical nature of these universal functions. For the mean velocity u_b, in the region away from the wall, it is the velocity defect $U_b - u_b = u_{\tau b}\, w(y)$ that is expressible in the universal form. This, however, does not invalidate the rest of the analysis. Each of the universal functions should be understood as a composite expansion in which the parameter $U_b/u_{\tau b}$ appears.

Dimensionless parameters and limiting cases

The equations of continuity, of mean momentum, and for the components of the Reynolds stresses for two-dimensional flow are written in terms of the departures from the downstream asymptotic state. With $\tilde{u} = u(x,y) - u_b(y)$, $v = \tilde{v}(x,y)$, $\tilde{\tau}_b = \tau(x,y) - \tau_b(y)$, ..., the governing equations are given in the appendix.

If, in a region where the turbulence structure is in a disturbed state, the flow is again characterised by one velocity scale denoted $u_{\tau a}$, the appropriate scale for $\tilde{u}$ and $\tilde{v}$ is $(u_{\tau a} - u_{\tau b})$ and that for $\tilde{\tau}$ is $\rho(u_{\tau a}^2 - u_{\tau b}^2)$. For the rough to smooth channel flow $u_{\tau a}$ may be expected to be close to $u_{\tau r}$, the friction velocity corresponding to the fully developed rough walled flow. Introducing the dimensionless forms

$$X = x/h, \quad Y = y/h$$

$$\begin{aligned} \tilde{u}(x,y) &= (u_{\tau b} - u_{\tau a})\, u_d(X,Y) \\ \tilde{v}(x,y) &= (u_{\tau b} - u_{\tau a})\, v_d(X,Y) \\ \tilde{\tau}(x,y) &= \rho(u_{\tau a}^2 - u_{\tau b}^2)\, \tau_d(X,Y) \\ \tilde{\sigma}_1(x,y) &= \rho(u_{\tau a}^2 - u_{\tau b}^2)\, \sigma_{1d}(X,Y) \end{aligned} \tag{2}$$

in the governing equations, the salient dimensionless parameters for the problem are obtained as $u_{\tau a}/u_{\tau b}$ and $\nu/(u_{\tau a} + u_{\tau b})h$. Three significant limiting forms of the equations can be distinguished according as

$$1)\ \frac{u_{\tau a}}{u_{\tau b}} \to \infty\,,\quad 2)\ \frac{u_{\tau a}}{u_{\tau b}} \to 1\,,\quad \text{or } 3)\ \frac{u_{\tau a}}{u_{\tau b}} \to 0\,.$$

Assesment of dominant terms

To assess the dominant terms in the equations the various dimensionless groups that arise in the governing equations are expanded in terms of a small parameter s_τ which is defined in the three limiting cases by

$$1)\ \frac{u_{\tau a}}{u_{\tau b}} = \frac{1}{s_\tau}\,,\quad 2)\ \frac{u_{\tau a}}{u_{\tau b}} = 1 + s_\tau\,,\quad 3)\ \frac{u_{\tau a}}{u_{\tau b}} = s_\tau\,,$$

s_τ always tending to zero.

In the region away from the walls effects of viscosity would be negligible so the terms with ν can be set equal to zero. Among the terms free from ν only the convection terms in the equations of mean momentum and the advective and the production terms in the equations for the Reynolds stress terms are multiplied by a dimensionless group of $u_{\tau a}/u_{\tau b}$. All other terms, in particular the Reynolds stress terms in the equations of mean momentum and the turbulent diffusion terms in the equations for the Reynolds stress components are of the order $O(1)$, this of course being a consequence of the scales used in eqn.(2). The dimensionless groups that appear in the nondimensionalized governing equations assume simple forms in the three limiting cases listed 1), 2) and 3).

Physical hypothesis

The downstream asymptotic state is characterised by the absence of convection by the mean flow (advection). The flow upstream of the step change in wall roughness is also a fully developed flow in which convection is absent. It can therefore be expected that convection by the mean flow is a mechanism that effects the change from one fully developed state to the other and hence cannot be ignored in the relaxation region. The physical hypothesis now postulated is that in the region away from the walls the disturbance flow field, represented by $\tilde{u}, \tilde{\tau}$, ..., is governed primarily by a balance of convective and diffusive effects. This physical hypothesis leads to an order relation between the relaxation lengths for the mean velocity and for the shear stress and the parameter of the problem $u_{\tau a}/u_{\tau b}$.

A mathematical formulation of the hypothesis would run as follows: Instead of the coordinate X new coordinates X_u, X_τ, defined by

$$X_u = \frac{X}{L_u}\,, \qquad X_\tau = \frac{X}{L_\tau} \tag{3}$$

are introduced. The scaling lengths L_u and L_τ are functions of the parameters $u_{\tau a}/u_{\tau b}$. They are to be choosen such that

$$\frac{\partial u_d}{\partial X_u} = O(1)\,, \qquad \frac{\partial \tau_d}{\partial X_\tau} = O(1) \tag{4}$$

From eqn.(4) the physical meaning of the scaling lengths L_u, L_τ is evident. They are characteristic lengths for decay of the disturbance and can be identified as the relaxation length for the mean velocity $\tilde{u}$ and for the shear stress $\tilde{\tau}$.

Invoking the physical hypothesis stated earlier in the governing equations enables the order of the dominant convective terms to be written with the scaling lengths L_u, L_τ as follows:
In the mean momentum equation:

$$\frac{U_b}{(u_{\tau a} + u_{\tau b})}\,\frac{1}{L_u} = 1 \tag{5a}$$

In the shear stress equation:

$$\frac{U_b(u_{\tau a} + u_{\tau b})}{(u_{\tau a}^2 + u_{\tau a}\, u_{\tau b} + u_{\tau b}^2)}\quad \frac{1}{L_\tau} = 1 \tag{5b}$$

THIS PAGE IS BEST QUALITY PRACTICABLE
FROM COPY FURNISHED TO DDC

In eqn.(5) the convection terms have been equated to 1 since the dominant diffusion terms are due to gradients in the y-direction and remain of the order 1.

Strictly speaking, the three limiting cases should be treated separately. However, a closer analysis shows that identical relations are obtained for $u_{\tau a}/u_{\tau b} \to 1$ and $u_{\tau a}/u_{\tau b} \to 0$. The relation retains its validity for $u_{\tau a}/u_{\tau b} \to \infty$ also, provided $u_{\tau a} << U_b$, which is generally the physical situation.

One consequence of the order estimates in eqn.(5) concerns the relation between the relaxation lengths L_u and L_τ. Eqn.(5) implies:

$$\frac{L_u}{L_\tau} = 1 - \frac{u_{\tau a}\, u_{\tau b}}{(u_{\tau a} + u_{\tau b})^2} , \qquad (6)$$

showing that L_τ is always greater than L_u. It is of further interest to study the behaviour of this ratio in the three limiting cases. One obtains:

1) $\frac{u_{\tau a}}{u_{\tau b}} \to \infty$; $s_\tau = \frac{u_{\tau b}}{u_{\tau a}}$:

$$\frac{L_u}{L_\tau} = 1 - \frac{s_\tau}{(1+s_\tau)^2} \cong 1 - s_\tau + 2s_\tau^2 - \ldots \qquad (7)$$

2) $\frac{u_{\tau a}}{u_{\tau b}} \to 1$; $s_\tau = \frac{u_{\tau a}}{u_{\tau b}} - 1$:

$$\frac{L_u}{L_\tau} = 1 - \frac{(1+s_\tau)}{(2+s_\tau)^2} \cong \frac{1}{2}\,(1 + s_\tau^2 + \ldots) \qquad (8)$$

3) $\frac{u_{\tau a}}{u_{\tau b}} \to 0$; $s_\tau = \frac{u_{\tau a}}{u_{\tau b}}$:

$$\frac{L_u}{L_\tau} = 1 - \frac{s_\tau}{(1+s_\tau)^2} \cong 1 - s_\tau + s_\tau^2 - \ldots \qquad (9)$$

DISCUSSION

One of the most distinguishing features of the channel flow with an abrupt change in wall roughness is clearly the rather slow evolution of the flow to its downstream asymptotic state in the mid region of the channel compared to the relatively rapid rate near the walls. Since, in the fully developed flow of either the rough or the smooth walled channel alone the velocity and shear stress profiles both in the mid region as well as near walls scale with one and the same quantity, viz., the wall friction, it is of interest to examine if the change in wall roughness induces two scales in the relaxation region, one in the mid region and another near the walls.

The plots in fig. 5 with the fictious velocity $u_\tau^*(x)$ as reference provides a partial answer to this question. It is seen that the mid region can indeed be scaled to a good approximation with a friction velocity different from the wall friction velocity. The fit on the universal curve (which is a straight line for the shear stress) is however not as good in the middle of the relaxation region as it is in the early or very late stages of the relaxation process.

The flow near the walls can be expected to scale with the wall friction velocity. Comparison of the wall pressure gradient and the wall friction curves in fig. 3 indicates that the wall shear stress could have been infered from the measured pressure gradient to within 5 per cent at $x/h \cong 5$. This is at variance with the plotted wall shear distribution of I. Tani and H. Makita (fig.9 in ref.(8)). In ref.(8) the deviation of the local wall shear stress from that in the fully developed downstream state tends on the whole to be larger and persists farther downstream. This might in part be due to the procedure adopted in ref.(8) to calculate the wall shear from the velocity profile. In particular, to the authors of this paper it seems likely that, whereas in the wall region the velocity profile obeys a logarithmic distribution, the constant may attain the value $\kappa = 0.41$ only farther downstream. Some evidence for this kind of behaviour of the wall layer is in ref.(10). Measurements in boundary layers by R. A. Antonia and R. E. Luxton (4) also indicate that for some distance downstream of the step change in wall roughness the wall layer does not show a belance between production and dissipation of turbulent energy. Since a balance between these quantities is associated with the law $u/u_\tau = (1/0{\cdot}41)\ln(yu_\tau/\nu) + C$ in the equilibrium layer, in the absence of this balance a departure from this constant 0.41 is plausible.

The concrete theoretical result in this paper is the scaling behaviour of the disturbance in the mid region of the channel, eqn. (5). For verification of this result by comparison with experiment careful interpretation of the theory is necessary, the significance of the quantities introduced in the theory requiring particular attention.

It is important to note that the result is in essense a statement on the manner in which the derivatives $\partial\tilde{u}/\partial x$ and $\partial\tilde{\tau}/\partial x$ scale under the physical hypothesis in a region where the scales for the strength of the disturbances in velocity and shear stress are $(u_{\tau a} - u_{\tau b})$ and $\rho(u_{\tau a}^2 - u_{\tau b}^2)$ respectively. It is therefore not ad hoc clear how $u_{\tau a}$ can be determined from a measured quantity in the experiment. The ambiguity involved is amply illustrated by an example. One could choose either the rough walled value $u_{\tau r}$ or the fictious quantity $u_\tau^*(x)$ at some station x.

For the present the authors have choosen for $u_{\tau a}$ the rough walled value $u_{\tau r}$ so that $\tilde{u}$ and $\tilde{\tau}$ are refered to $(u_{\tau r} - u_{\tau b})$ and $\rho(u_{\tau r}^2 - u_{\tau b}^2)$ respectively, and L_u and L_τ are calculated from eqn. (5) with this choice. Since the theoretical framework covers only the derivatives, the scaled quantities of $\tilde{u}$ and $\tilde{\tau}$ were first plotted against X/L_u and X/L_τ and the curves were shifted parallel to themselves. This resulting plots are shown in fig. 7 and 8. It is seen that the shape of the curves in these variables has remained

THIS PAGE IS BEST QUALITY PRACTICABLE
FROM COPY FURNISHED TO DDC

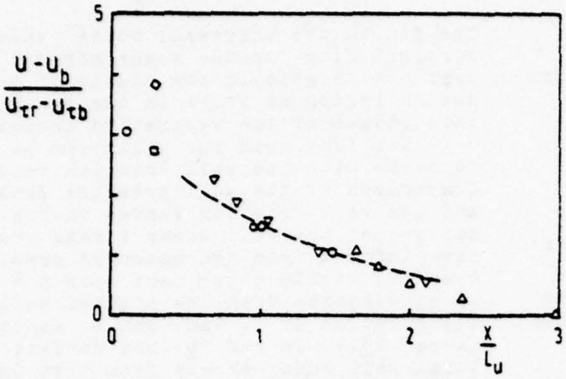

Fig. 7 Velocity in the relaxation region in scaled variables

Expt. No	4		3	Tani/ Makita	
y/h	0,05	0,45	0,45	0	0,4
Symbol	◇	○	□	▽	△

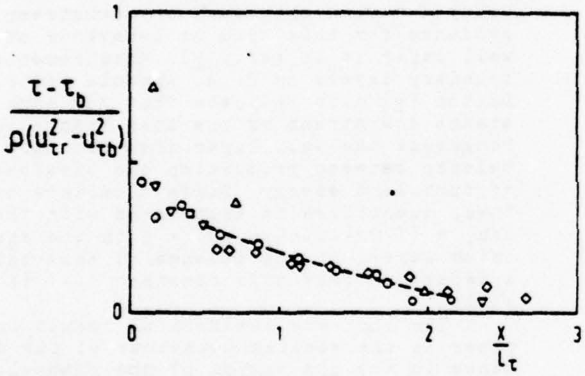

Fig. 8 Shear stress in the relaxation region in scaled variables

Expt. No	4		3	Tani/ Makita	
y/h	0,2	0,4	0,5	0,2	0,4
Symbol	◇	○	□	▽	△

roughly the same in all the experiments. From these plots it appears that the balance of convection and diffusion may be the primary mechanism for the relaxation process in the mid region of the channel.

ACKNOWLEDGEMENTS

The authors wish to thank Dr. H. Makita for making available to them copies of figures in ref. (8) to original size. They also thank Professor K. Gersten for helpful discussions.

REFERENCES

1 Coles, D. E., "The young person's guide to the data," Computation of Turbulent Boundary Layers, Proceedings 1968 AFOSR-IFP-Stanford Conference, Vol. II, Stanford University, 1969, pp. 1-45.

2 Hussain, A.K.M.F., Reynolds, W. C., "The mechanics of an organised wave in turbulent shear flow. Part 2: Experimental results," Journal of Fluid Mechanics, Vol. 54, 1972, pp 241-261.

3 Townsend, A. A., "The Structure of Turbulent Shear Flow," 2nd ed., Cambridge University Press, Cambridge, 1976.

4 Antonia, R. A., Luxton, R. E., "The response of a turbulent boundary layer to a step change in surface roughness. Part 1. Smooth to rough," Journal of Fluid Mechanics, Vol. 48, 1971, pp. 721-761.

5 Antonia, R. A., Luxton, R. E., "The Response of a turbulent boundary layer to a step change on surface roughness. Part 2. Rough to smooth," Journal of Fluid Mechanics, Vol. 53, 1972, pp. 737-757.

6 Antonia, R. A., Luxton, R. E., "Characteristics of turbulence within an internal boundary layer," Advances in Geophysics, Vol. 18 A, Academic Press, New York, 1974, pp. 263-285.

7 Jacobs, W., "Umformung eines turbulenten Geschwindigkeitsprofiles," Zeitschrift für angewandte Mathematik und Mechanik, Bd. 19, 1939, pp. 87-100.

8 Tani, I., Makita, H., "Response of a turbulent shear flow to a stepwise change in wall roughness," Zeitschrift für Flugwissenschaften, Bd. 19, 1971, pp. 335-339.

9 Fujita, H., Kovasznay, L.S.G., "Measurement of Reynolds stress by a single rotated wire anemometer," Revue of Scientific Instruments, Vol. 39, 1968, pp. 1351-1355.

10 Wauschkuhn, P., Vasanta Ram, V., "Die turbulente Grenzschicht hinter einem Ablösungsgebiet," Zeitschrift für Flugwissenschaften, Bd. 23, 1975, pp. 1-9.

11 Saffmann, P. G., "A model for inhomogeneous turbulent flow," Proceedings of the Royal Society London, Series A, Vol. 317, 1970, pp. 417-433.

12 Rotta, J. C., "Recent attempts to develop a generally applicable calculation method for turbulent shear flow layers," Proceedings of the AGARD Conference on turbulent shear flows London, 1971.

13 Lumley, J. L., Khajeh-Nouri, B., "Computational modelling of turbulent transport," Advances in Geophysics, Vol. 18 A, Academic Press, New York, 1974, pp. 169-192.

14 Launder, B. E., Spalding, D. B., "Mathematical models of turbulence," Academic Press, New York, 1972.

15 Bradshaw, P., Ferris, D. H. and Atwell, N. P., "Calculation of Boundary Layer Development using the Turbulent Energy Equation," J. Fluid Mechanics, Vol. 28, Part 3, 1967, pp. 593-616.

16 Reynolds, W. C., "Recent advances in the computation of turbulent flows," Advances in Chemical Engineering, Vol. 9, Academic Press, New York, 1974.

17 Laufer, J., "Investigation of turbulent flow in a two-dimensional channel," NACA TR 1053, 1951.

18 Comte-Bellot, G., "E'coulement turbulent entre deux parois parallèles," Publications Scientifiques et Techniques du Ministère de L'Air no. 419, 1965.

THIS PAGE IS BEST QUALITY PRACTICABLE
FROM COPY FURNISHED TO DDC

19 Yajnik, K. S., "Asymptotic theory of turbulent shear flows," Journal of Fluid Mechanics, Vol. 42, 1970, pp. 411-427.

20 Mellor, G. L., "The large Reynolds number asymptotic theory of turbulent boundary layers.

21 Fendell, F. E., "Singular perturbation and turbulent shear flow near walls," Journal of Astronautical Sciences, Vol. XX, 1972, pp. 129-165.

22 Bush, W. B., Fendell, F. E., "Asymptotic analysis of turbulent channel flow for mixing length theory," SIAM Journal on Applied Mathematics, Vol. 26, 1974, 413-427.

23 Rotta, J. C., "Turbulente Strömungen," B. G. Teubner, Stuttgart, 1972.

24 Tennekes, H., Lumley, J. L., "A first course in turbulence," MIT Press, Cambridge, Mass, 1972.

25 Schlichting, H., "Boundary layer theory," McGraw-Hill, New York, 1968.

26 Van Dyke, M., "Perturbation methods in fluid mechanics, "Annotated ed., Parabolic Press, Stanford, 1975.

APPENDIX

Governing equations

The governing equations for the problem are the equations of continuity, mean momentum and for components of the Reynolds stresses, written in terms of the departure from the downstream asymptotic state. Denoting this departure by a tilde, eg. $\tilde{u} = u(x,y)-u_b(y)$, $\tilde{\tau} = \tau(x,y)-\tau_b(y)$ these equations, taken from literature (23,24,25), are:

$$\frac{\partial \tilde{u}}{\partial x} + \frac{\partial \tilde{v}}{\partial y} = 0$$

$$(u_b+\tilde{u})\frac{\partial \tilde{u}}{\partial x} + \tilde{v}\left(\frac{du_b}{dy} + \frac{\partial \tilde{u}}{\partial y}\right) + \frac{1}{\rho}\tilde{p}_x -$$

$$- \nu\left(\frac{\partial^2 \tilde{u}}{\partial x^2} + \frac{\partial^2 \tilde{u}}{\partial y^2}\right) + \frac{1}{\rho}\left(\frac{\partial \tilde{\sigma}_1}{\partial x} - \frac{\partial \tilde{\tau}}{\partial y}\right) = 0 \qquad (10)$$

$$(u_b+\tilde{u})\frac{\partial \tilde{v}}{\partial x} + \tilde{v}\frac{\partial \tilde{v}}{\partial y} + \frac{1}{\rho}\tilde{p}_y -$$

$$- \nu\left(\frac{\partial^2 \tilde{v}}{\partial x^2} + \frac{\partial^2 \tilde{v}}{\partial y^2}\right) + \frac{1}{\rho}\left(- \frac{\partial \tilde{\tau}}{\partial x} + \frac{\partial \tilde{\sigma}_2}{\partial y}\right) = 0$$

In eqn.(10) $\tilde{p}_x$ and $\tilde{p}_y$ denote the departure of the pressure gradients from values in fully developed flow.

$$\tilde{p}_x = \frac{\partial p}{\partial x} - \rho\frac{u_{\tau b}^2}{h}$$
$$\tilde{p}_y = \frac{\partial p}{\partial y} + \frac{d\sigma_{2_b}}{dy} \qquad (11)$$

Among the higher order equations only that for the shear stress $\tau = -\rho\overline{u'v'}$ is given below:

$$(u_b+\tilde{u})\frac{\partial \tilde{\tau}}{\partial x} + \tilde{v}\left(\frac{d\tau_b}{dy} + \frac{\partial \tilde{\tau}}{\partial y}\right) + (\tau_b + \tilde{\tau})\frac{\partial \tilde{u}}{\partial x} -$$

$$- \sigma_{2_b}\frac{\partial \tilde{u}}{\partial y} - \tilde{\sigma}_2\left(\frac{du_b}{dy} + \frac{\partial \tilde{u}}{\partial y}\right) - (\sigma_{1_b} + \tilde{\sigma}_1)\frac{\partial \tilde{v}}{\partial x} +$$

$$+ (\tau_b + \tilde{\tau})\frac{\partial \tilde{v}}{\partial y} + \tilde{P} + \tilde{T} + 2\rho\nu\tilde{D} -$$

$$- \nu\left(\frac{\partial^2 \tilde{\tau}}{\partial x^2} + \frac{\partial^2 \tilde{\tau}}{\partial y^2}\right) = 0 \qquad (12)$$

where P, T and D are abbreviations for correlations involving pressure fluctuations, triple correlations of velocity fluctuations and correlations between gradients of the fluctuating velocities respectively.

THIS PAGE IS BEST QUALITY PRACTICABLE
FROM COPY FURNISHED TO DDC

MEASUREMENT OF MEAN FLOW AND TURBULENCE STRUCTURE IN AN AXISYMMETRIC PIPE FLOW WITH HIGH INITIAL SHEAR

J.T. TURNER.
SIMON ENGINEERING LABORATORIES,
UNIVERSITY OF MANCHESTER, U.K.

and

G. LIGHTNING.
MANAGING DIRECTOR,
LIGHTNING GROUP OF COMPANIES,
MANCHESTER 1.

ABSTRACT

The paper describes an experimental study of the interaction between the time mean and turbulence properties in an axisymmetric pipe flow with particularly severe initial distortion. Every term in the time-meaned continuity equation and the more important turbulence contributions to the axial and radial momentum equations have been determined. The use of pressure probes and hot wire anemometry under these adverse flow conditions has necessitated a careful study of the experimental errors inherent in the measurements. Consideration of the equations of motion enables certain interesting relationships between the mean flow and the turbulence structure to be derived : these expressions are confirmed by the data.

NOMENCLATURE

C_p	static pressure coefficient
C	integration constant
k	calibration constant, disc probe
p	static pressure
P	total pressure
r	radial position coordinate
R	pipe radius (or universal gas constant)
R_e	Reynolds number based on diameter and area mean velocity
S	turbulence correction factor (equation 5)
T	absolute temperature
u	turbulent velocity component
U	instantaneous velocity (vector)
z	axial coordinate
ρ	fluid density
τ	shear stress
ψ	integral turbulence function
ν	kinematic viscosity

Suffices

act	actual value
a,b	denote conditions at different axial positions
d	indicated by disc probe
eff	effective value
meas	measured value
r	radial component
w	wall condition
z	axial component

NB. time average denoted by overbar

INTRODUCTION

Our purpose has been to investigate the structure of an axisymmetric pipe flow with initially high levels of turbulence and mean velocity shear. Given the nature of the problem, it was realised at the outset that measurement of the flow structure would be difficult. Accordingly, the decision was taken to check the data (and the instrumentation) by applying the continuity and momentum equations for the mean and turbulent flow properties respectively.

In a previous exploratory investigation (1), the decay of a highly turbulent velocity distribution along a circular pipe was examined. Total pressure tubes were used to determine the mean flow structure and an attempt was made to relate the decay process to the axial pressure distribution along the pipe wall. Neither the turbulence structure of the flow nor the static pressure distribution over the pipe cross-section were measured and no corrections were applied to the pressures indicated by the total pressure probes.

Other relevant work has been described by Chao and Sandborn (2) who made relatively detailed measurements in a turbulent wall jet : their data will be referred to subsequently. Similarly Chaturvedi (3) presented useful background information concerned with the shear flow produced by an axisymmetric enlargement in a circular pipe.

The correction of pressure probes and hot wire anomometers for the effects of turbulence level and velocity shear have been discussed at length in the literature. Goldstein (4), Becker and Brown (5), in particular, have considered the response of total pressure probes in a turbulent flow and suggested methods for correcting the observed total pressure value. The response of a hot wire anemometer at high turbulence levels has been considered by, for example, Champagne (6), Rodi (7), Turner (8). The correction procedures are complex and frequently appear to be based on somewhat tenuous arguments : the preferred methods employed in the present study together with some justification for their use will be discussed at a later stage.

APPARATUS

Experiments were performed using a closed circuit airflow rig with a 102 mm (4 inch) diameter working section of approximately 50 diameters length. The fixed speed two-stage centrifugal fan exhausted

PRECEDING PAGE BLANK-NOT FILMED

into a 305 mm (12 inch) diameter return pipe then through a well designed contraction of 20 : 1 area ratio into the working section. In-circuit filters within the rig ensured relatively clean air conditions suitable for hot wire measurements. The working pipe length was made up of short (305 mm) sections : these were flanged and spigotted together and incorporated instrument access plugs every 102mm along the length. The working section and the contraction were made to a high standard of accuracy in machined aluminium.

To produce the test flow, a sharp edged orifice plate designed according to British Standard 1042 was inserted into the working section just after the contraction outlet. Although the principal reason for adding the 64 mm (2.5 inch) diameter orifice plate was to produce the severely distorted axisymmetric inlet flow, corner tappings were also included so that an accurate measurement of the mass flow rate could be obtained for comparison with the other data.

A range of instrumentation has been employed in the study. Standard pressure measuring probes such as forward facing total pressure tubes, surface pressure probes for the determination of skin friction at the wall and disc static pressure probes were supplemented by single and double hot wire probe measurements. Since the initial flow (close to the orifice plate) possessed both high turbulence levels and appreciable streamline curvature, parallel investigations were required with each instrument to study the influence of these factors. Much of this calibration work was carried out in a separate closed circuit wind tunnel having a 127 mm (5 inch) square section and low background turbulence level.

EXPERIMENTAL RESULTS AND THEIR VALIDITY

Traverses were made across successive diametral planes downstream of the orifice plate using forward facing total pressure tubes, disc static pressure probes, and hot wires. Additionally, the static pressure variation along the pipe wall was obtained and surface pressure tubes were used to determine the axial wall shear stress distribution assuming the calibration given by Patel (9).

Turbulent velocity fluctuations can be expected to alter the response of a total pressure or static pressure probe - see Goldstein (4), Becker and Brown (5). Fig.1 illustrates how the magnitude(and direction) of the instantaneous velocity vector is influenced by these fluctuations. Neglecting angular changes in sensitivity of the total pressure probe

$$U_{eff} = \{(U_1 + u_1)^2 + u_2^2 + u_3^2\}^{1/2} \tag{1}$$

and

$$P_{meas} = p + \frac{1}{2}\rho U_{eff}^2 \tag{2}$$

Thus, the actual time meaned velocity $(\overline{U}_1)_{act}$ in the axial direction can be determined. Making a further assumption that the turbulence is isotropic and considering only first order terms

$$\overline{U}_{1eff} = \left(1 - \frac{3}{2}\cdot\frac{\overline{u_1^2}}{\overline{U}_1^2}\right)\left\{\frac{2RT}{\overline{p}_{act}}\cdot(\overline{P} - \overline{p})_{meas}\right\}^{1/2} \tag{3}$$

Laufer (10) derived a similar relationship to this and more detailed treatments have been given by Hinze (11), Becker and Brown (5).

Note that the subscript (act) denotes the actual

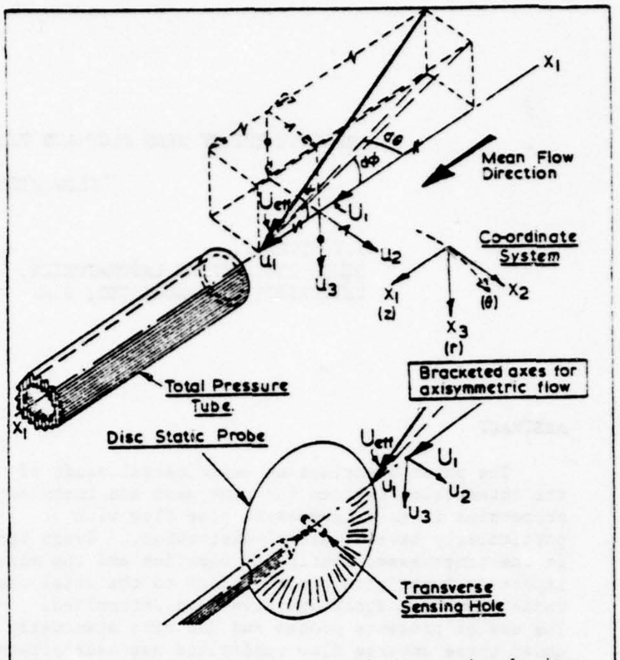

Fig.1. Schematic to show coordinates and velocity components.

value. Since the local in-stream static pressure differs significantly from that at the wall, it was necessary to use a miniature disc static probe to determine the static pressure distributions along the *flow. The probe was calibrated* at low turbulence level using an equation of the form

$$p = \frac{p_d - kP_{act}}{1+k} \tag{4}$$

as recommended by Bryer, Walshe and Garner (12).

Fig.2 shows the measured static pressure variations up to a distance of 40 diameters from the orifice.

Although it is clear that these static pressure measurements must also be affected by the turbulence, no corrections have been applied in view of the inherent difficulties of such a procedure. Attempts to determine the influence of the turbulence level on the calibration constant k in (4) were generally unsuccessful.

Substituting (4) into (3) yields the result

$$\overline{U}_{1act} = \left\{2RT\left(\frac{\overline{P}_{meas} - S\overline{p}_d}{k\overline{P}_{meas} + S\overline{p}_d}\right)\right\}^{1/2}$$

$$S = \overline{\{(\overline{U}_1 + u_1)^2 + u_2^2 + u_3^2\}} / \overline{U}_1^2 \tag{5}$$

Fig 3 shows the observed velocity distributions calculated using(1,2) i.e. uncorrected for the turbulence level or radial static pressure variations. A particularly interesting feature is that the non-dimensional velocity profiles for axial distances from 8 diameters onwards intersect at a fixed non-dimensional radius r/R = 0.71.

The mass flow rate along the pipe may now be estimated by integrating the velocity profiles for each axial position. Fig 4 shows how the separate corrections for the effect of turbulence and radial

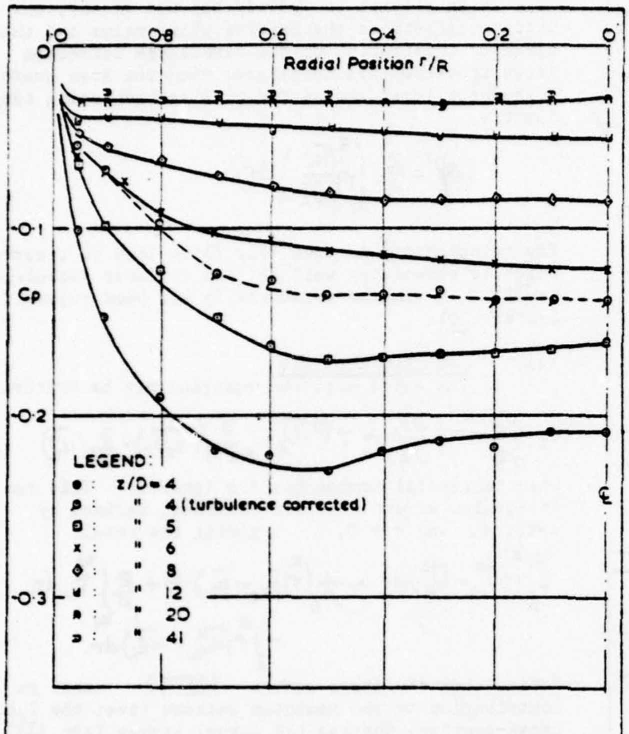

Fig.2. Variation in static pressure across the flow. Data obtained with disc static probe.

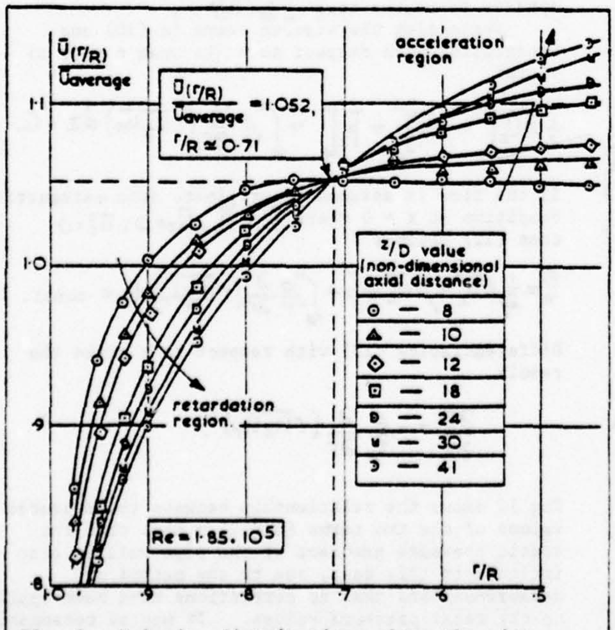

Fig. 3. Velocity distributions along the pipe.

static pressure variations on the total pressure probe (curve C), and the radial static pressure variations only (curve B), alter the crude estimates derived from (1) (curve A). Incorporation of these two corrections leads to an obvious improvement in the estimated mass flow rate at each section when compared with the reference mass flow rate yielded by the standard orifice plate.

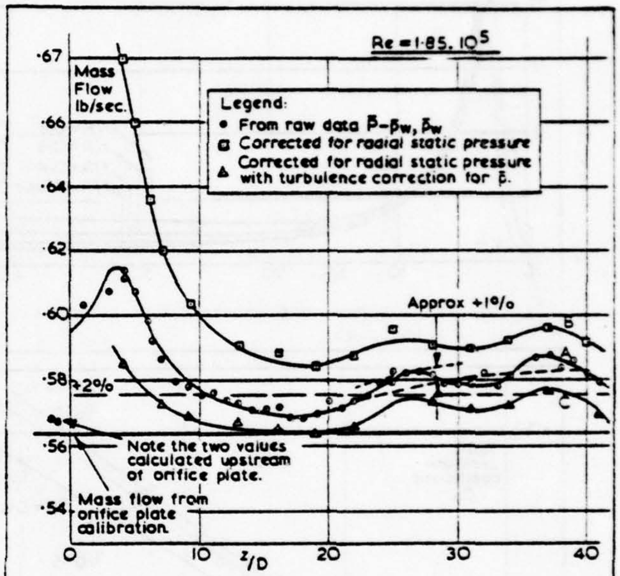

Fig.4. Mass flow estimates as a function of axial position. The effect of successive corrections to measured data.

DISCUSSION

(i) Normal stress and static pressure.

Comparison between the measured distributions of the longitudinal turbulence intensity (fig 5) and the static pressure coefficient

$$C_p = (\overline{p - p_\infty}) \Big/ \tfrac{1}{2}\rho \overline{U}_z^2 \qquad (6)$$

reveals a linear relationship between them - see fig 6. This suggests that the two parameters are correlated by an expression of the form

$$C_p = m_1 \sqrt{\overline{u_z^2}} \Big/ \overline{U}_z \, . \qquad (7)$$

Examination of the radial momentum equation, however, leads to the conclusion that the expected result should be

$$C_p = m_2 \, \overline{u_z^2} \Big/ \overline{U}_z \, . \qquad (8)$$

No explanation for this difference has yet been found although a careful study of the data given by Chao and Sandborn (2), and Miller and Comings (13) for entirely different flow systems reveals the same dependence as (7).

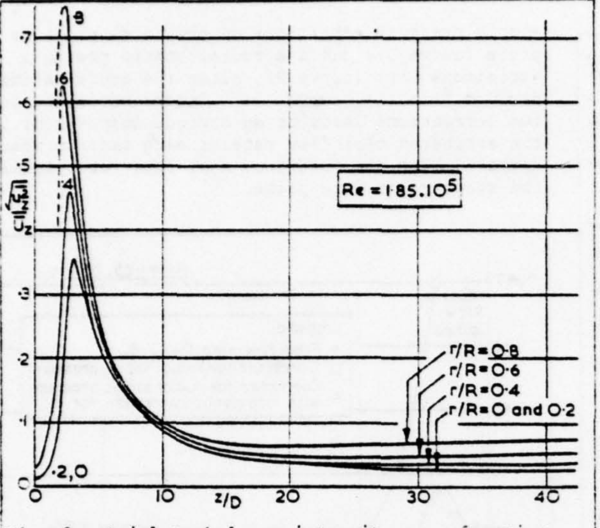

Fig. 5. Axial turbulence intensity as a function of position.

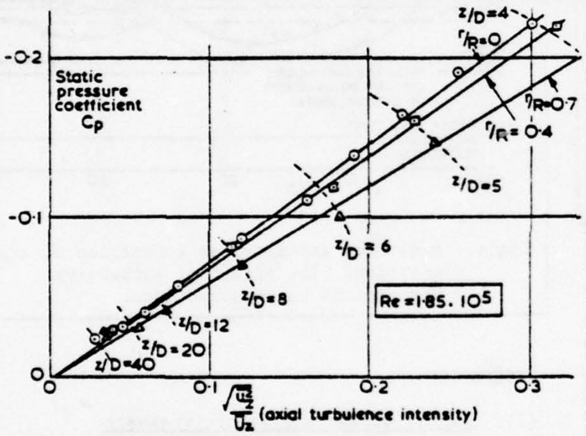

Fig. 6. Correlation between static pressure and axial turbulence intensity.

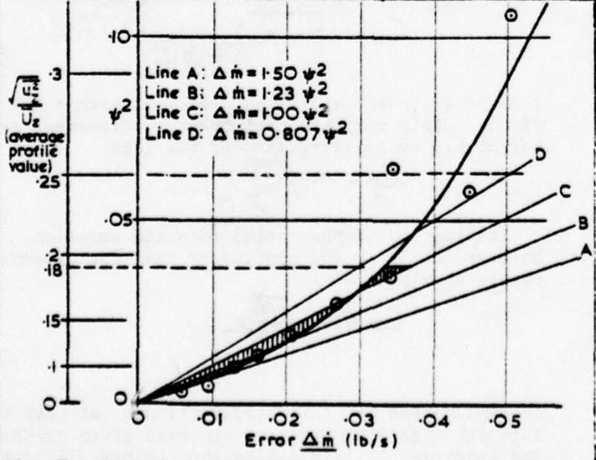

Fig. 7. Dependence of error in mass flow estimate upon turbulence level.

In an attempt to justify the use of (2), the difference between the orifice plate value and that given by integration of the turbulence corrected pitot traverses was correlated with the area averaged turbulence level across the pipe section using the function

$$\psi^2 = \frac{2}{R^2}\int_0^R r\left(\frac{\overline{u_z^2}}{\overline{U}_z^2}\right)dr\,. \tag{9}$$

The relationship is seen (fig 7) to lead to a curve which is especially well defined at lower turbulence levels. A similar relationship has been reported by Laufer (10).

(ii) Momentum analysis

The axial momentum equation may be written

$$\overline{U}_z\frac{\partial\overline{U}_z}{\partial z} = -\frac{1}{\rho}\cdot\frac{\partial\overline{p}_z}{\partial z} + \nu\nabla^2\overline{U}_z - \frac{1}{r}\frac{\partial}{\partial r}(r\overline{u_z u_r}) - \frac{\partial}{\partial r}(\overline{u_z^2}) \tag{10}$$

when tangential components are ignored. This can be integrated around a control surface, defined by $z = z_1, z_2$ and $r = 0, R$, giving the result

$$\frac{1}{2}\int_0^R r(\overline{U}_{z_2}^2 - \overline{U}_{z_1}^2)dr = -\frac{1}{\rho}\int_0^R r(\overline{p}_{z_2} - \overline{p}_{z_1})dr + \frac{R}{\rho}\int_{z_1}^{z_2}\tau_w dz - \int_0^R r(\overline{u_{z_2}^2} - \overline{u_{z_1}^2})dr. \tag{11}$$

Notice that the shear stress $(\overline{u_z u_r})$ makes no contribution to the momentum balance (over the full cross-section) whereas the normal stress term $(\overline{u_z^2})$ can be dominant in decaying flows.

Further consideration of (10) reveals some interesting features of the flow. Firstly, consider the magnitude of the measured terms as shown in figures 8 and 9 relating to conditions at the pipe centre-line and $r/R = 0.7$ respectively. The principal difference after some 7 to 8 diameters appears to be the term $\frac{1}{2}\frac{\partial}{\partial z}(\overline{U}_z^2)$.

Neglecting the viscous terms in (10) and integrating with respect to z (between z = 0, a) yields

$$\frac{1}{2}\rho\overline{U}_z^2\Big]_0^a + \rho\overline{u_z^2}\Big]_0^a + \overline{p}_z\Big]_0^a + \int_0^a\frac{\rho}{r}\cdot\frac{\partial}{\partial r}(r\overline{u_z u_r})dz = C. \tag{12}$$

If the flow is assumed to originate from a stagnation condition at z = 0 where $\overline{p}_0 \equiv \overline{P}_0, \overline{U}_z = 0, \overline{u_z^2} = 0$, then (12) becomes

$$\overline{P}_0 = \frac{1}{2}\rho\overline{U}_z^2 + \rho\overline{u_z^2} + \overline{p} + \int_0^a\frac{\rho}{r}\cdot\frac{\partial}{\partial r}(r\overline{u_z u_r})dz = \text{const.} \tag{13}$$

Differentiating (13) with respect to z gives the result

$$\frac{\partial\overline{P}}{\partial z} = -\frac{\rho}{r}\cdot\frac{\partial}{\partial r}(r\overline{u_z u_r})\,. \tag{14}$$

Fig 10 shows the relationship between the measured values of the two terms in (14) - note that the static pressure gradient at the pipe wall is also included in this data, due to the method of measurement and that no corrections have been applied to the total pressure values. It may be reasonable to assume that elimination of the static pressure gradient would superimpose all the results on the same

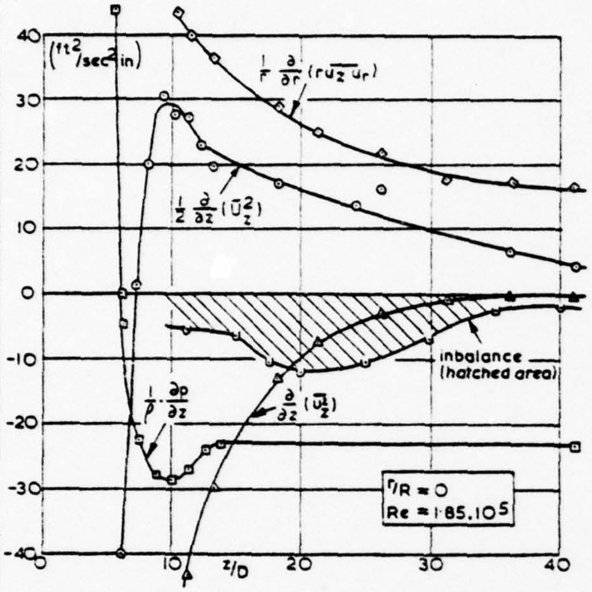

Fig.8. Measured terms in the momentum equation (along the centre-line).

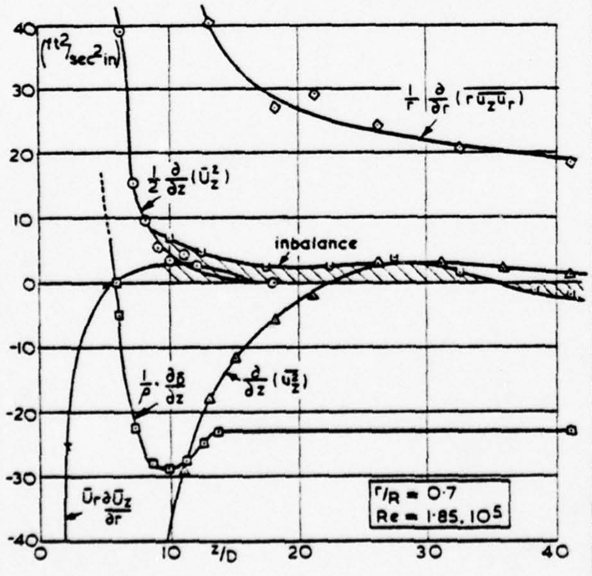

Fig.9. Measured terms in the momentum equation (at 70% radius).

straight line. It will be observed that the analytical result (14) shows reasonable agreement with the data.

In the fully developed pipe flow situation, the gradients of total and static become equal and the shear stress just balances the static pressure gradient. Thus, the straight line distributions should intersect at the point defined by these conditions. This is seen from fig 10 to be approximately satisfied by the measured values.

The experiments and a more complete treatment are contained in Lightning (14).

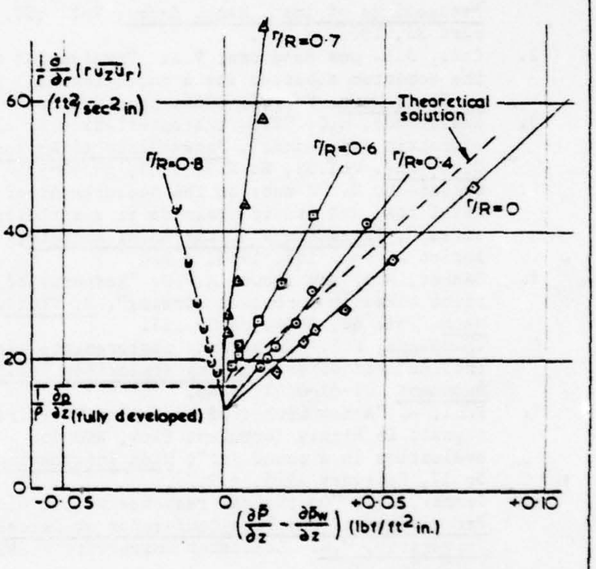

Fig.10. Correlation between total pressure gradient and in-stream shear stress.

CONCLUSION

Standard methods have been used to measure the time mean and turbulence properties of an axisymmetric shear flow in a pipe. The use of various correction procedures to remove the effects of turbulence and radial pressure gradients is shown to produce marked improvements in the accuracy of the data when tested using continuity.

Detailed measurements of the terms in the axial momentum equation reveal interesting features of the flow. In particular, strong correlations are found (i) between the in-stream static pressure depression (relative to the wall) and the axial component of the turbulence intensity, (ii) between the total pressure gradient in the axial direction and the shear stress and (iii) a new definition of total pressure is postulated. Examination of the data given by previous workers suggests that similar relationships may hold in other flow situations.

The experiments show how the decay of the initial turbulence structure affects the mean flow development and emphasise the need for extreme care when pressure probe and hot wire data is obtained in areas of high mean velocity shear and turbulence.

ACKNOWLEDGEMENTS

The authors are pleased to acknowledge that these experiments were carried out in the Department of Engineering, University of Manchester. The project was supported by a grant from the Science Research Council and the second named author was in receipt of a James Clayton Postgraduate Award from the Institution of Mechanical Engineers during his period of research.

REFERENCES

1. Livesey, J.L., Turner, J.T., and Glasspoole, W.F. "The decay of turbulent velocity profiles", Proceedings of Inst. Mech. Engrs. Vol. 180, part 3J, 1965, p.127.
2. Chao, J.L. and Sandborn, V.A. "Evaluation of the momentum equation for a turbulent wall jet", J. Fluid Mech. Vol.26, 1966, pp 819-828.
3. Chaturvedi, M.C. "Flow characteristics of axi-symmetric expansions", Proceedings of Am.Soc. Civil Eng. Vol.89, No HY3, 1963, pp 61-92.
4. Goldstein, S. "A note on the measurement of total head and static pressure in a turbulent stream", Proceedings of the Royal Society, Series A, Vol. 155, 1936, p 570.
5. Becker, H.A. and Brown, A.P.G. "Response of pitot tubes in turbulent streams", J. Fluid. Mech. Vol. 62, 1974, pp 85-114.
6. Champagne, F.H. "Turbulence measurements with inclined hot wires", Boeing Scientific Res.Lab. Document D1-82-0491, 1965.
7. Rodi, W. "A new method of analysing hot-wire signals in highly turbulent flow, and its evaluation in a round jet", DISA Information No 17, February 1975, p.9.
8. Turner, J.T. "On the yaw response of hot wires", Proceedings of the Disa Conference at Leicester University, U.K. Leicester University Press, 1972, Vol. 2.
9. Patel, V.C. "Calibration of the Preston tube and limitations on its use in pressure gradients", J.Fluid Mech. Vol.23, 1965, p.185.
10. Laufer, J. "The structure of turbulence in fully developed pipe flow", N.A.C.A. Tech. Note 2954, 1953.
11. Hinze, J.O. "Turbulence-an introduction to its mechanism and theory", McGraw-Hill, New York, 1959.
12. Bryer, D.W., Walshe, D.E., and Garner, M.A. "Pressure probes selected for three dimensional flow measurement", Aeronautical Research Council R and M. 3037, 1958.
13. Miller, D.R. and Comings, E.Q. "Static pressure distribution in the free turbulent jet", J. Fluid Mech. Vol.3, 1957, p. 1.
14. Lightning, G. "The momentum balance equation in turbulent fluid pipe flow", University of Manchester, Ph.D. thesis, December 1976.

Investigation of the longitudinal length scales of turbulence in a strongly accelerated water flow.

C.J. Bates, Dept. of Mechanical Engineering and Energy Studies,
University College, Cardiff.
S.Wales, United Kingdom.

ABSTRACT

Detailed experimental studies have been conducted to investigate the characteristics of the turbulent flow at both the entrance and throat of a 0.5 area ratio perspex Venturimeter, water being the working fluid. The flow is one with a high Reynolds number and low centreline percentage turbulence intensity, so that Taylor's hypothesis has been deemed to be satisfied. This assumption has enabled both the Eulerian length scales of turbulence to be estimated, these scales being known as the macroscale and microscale respectively. The results obtained from the autocorrelation coefficient profiles, show that the macroscale varies appreciably with both Reynolds number and radial position. Furthermore the microscale was found to be roughly constant over the central core region of the flow.

NOMENCLATURE

$D = 2R_1$ = Inlet Pipe Diameter

$d = 2R_2$ = Venturimeter Throat Diameter

Je = Eulerian Integral Time Scale or Time Macroscale

N = Sample Size

r = Radial Position

$R(\tau)$ = Eulerian Autocorrelation Coefficient

Re = Pipe Reynolds Number

T = Time Length of Sample = $(N-1) \times \tau$

t = Time

$\bar{u}$ = Time Averaged Mean Velocity

u' = Fluctuating Velocity Component

Λf = Length Macroscale

λ = Length Microscale

τe = Time Microscale

τ = Time Increment

INTRODUCTION

The flow at both the inlet and throat sections of a 0.5 area ratio conical Venturimeter has been subjected to a detailed experimental study using laser Doppler anemometry (LDA). During this study the Venturimeter was installed in a 254 mm diameter water pipeline, the measurement points being located D/2 upstream from the Venturimeter and half way along the Venturimeter throat. Details of the lengths of steel and perspex pipes comprising the pipeline are shown in Figure 1, the water being supplied from a 19.812 m constant head tank and the flowrate controlled by a butterfly valve located just prior to the pnuematically controlled flow diverter. Further details of the flow installation are available in the literature (1).

The main characteristics of the flow are such that the pipe Reynolds number is high, ranging from 30,000 up to 500,000, and the associated centreline percentage turbulence intensity is low, ranging up to 3% and 5% at the throat and inlet positions respectively. The percentage turbulence intensity increases towards 10% as the wall is approached, due to this Taylor's criterion has been taken to be satisfied. Displacements in the direction of flow have therefore been replaced by equivalent displacements in time using a suitable transformation. During its passage through the Venturimeter convergence the flow is subjected to a rapid acceleration, due to the associated high rates of shear, the velocity profile undergoes a rapid transition (2).

Details of LDA are available in the literature, during this study the experimental results were obtained from an on-line real time data acquisition system. This system incorporates a PDP 11/40 minicomputer linked to a DISA frequency tracker via a Microconsultants analogue to digital converter. A line diagram of the data processing equipment is shown in Figure 2. With this arrangement parameters such as the sampling rate and sample size are controlled by the software, so that real time measurements may be made without recourse to a large digital computer. As a result several complete runs may be completed and analysed in detail before the measuring point is moved to another position. Initial tests were conducted to determine the sample size necessary for convergence of both the mean velocity and percentage turbulence intensity. For this low turbulence flow a sample size of 3000 was found to be necessary, consequently throughout this study 4500 points have been used and ensemble averages formed over four separate runs. With real time sampling parameters such as mean velocity, percentage turbulence intensity, flatness and skewness factors and the associated velocity probability density distribution may be determined at each measuring position (3). Further details of this LDA/computer combination, together with the statistical techniques employed during the measurement of these parameters are available in the relevant literature (4),(5). The results discussed herein relate to the variation of both the longitudinal length scales of turbulence, these scales being known as the longitudinal integral scale or length macroscale and the Eulerian dissipation scale or length microscale.

EXPERIMENTAL MEASUREMENTS

(a) Radial variation of the length macroscale (Λf)

Using digital techniques the Eulerian autocorrelation coefficient may be written as:

$$R(\tau) = \frac{\sum_{t=0}^{T-\tau} u'(t)\ u'(t+\tau)}{\sum_{t=0}^{T} u'(t)\ u'(t)} .$$

$R(\tau)$ may be used to define both length and time scales of turbulence, the macroscale for length being given by:

$$\Lambda f = \bar{u}\ Je$$

$$\text{where } Je = \int_0^\infty R(\tau)\ d\tau$$

The length macroscale gives an indication of the mean eddy length in the flow direction. Radial variations of $R(\tau)$ at a Reynolds number of 220,000 are shown in Figures 3 and 4 for both the inlet and throat positions respectively. As expected the exponential decay may be clearly seen, in the main core of the flow the rate of decay decreases as r/R increases. Comparison of the profiles at both measuring positions shows that after the convergence the rate of decay is more rapid. Integration of these experimental profiles enables both the time and length macroscales to be estimated, Figure 5 shows the radial variation of the non-dimensional macroscale $\frac{\Lambda f}{2R}$ for two widely varying Reynolds numbers. From Figure 5 it is clear that the eddy length increases with both radial position and Reynolds number. It is interesting to note that at the centreline ($r/R = 0.0$) the eddy lengths are approximately equal and over the inner core region $r/R \leq 0.4$ the inlet eddy lengths are greater than the throat lengths, whereas the converse is true for greater values of r/R. A five to one reduction in Reynolds number reduces the length scale by a factor of three over the central core and somewhat less over the remaining region.

(b) Microscale variations (λ)

The radius of curvature of the autocorrelation profiles near the origin give an indication of the size of the smaller eddies which are primarily responsible for the dissipation of energy, this size is known as the microscale. In order to measure the initial shape of the profiles fast sampling rates are necessary, together with a large store if the complete profile is to be determined, although it is possible to form a composite profile using a range of sampling rates(6). The results using this technique have proved to be extremely consistent, the discontinuity at each overlap point being virtually zero. Providing a good estimate of the initial section of the profile has been obtained, the length macroscale may be estimated from the parabola introduced by Taylor (7), the approach being as follows:

$$\frac{1}{\tau e^2} = \lim_{\tau \to 0} \left(\frac{1-R(\tau)}{\tau^2}\right)$$

$$\text{and } \lambda = \bar{u}\ \tau e$$

Both $R(\tau)$ and τ are obtained from the real time analysis. Measurements of the initial curvature of the $R(\tau)$ curve, using a sampling rate of 0.0005 s, shows that R(0.0005) increases as r/R_1 increases, this trend is to be expected because of the shape of the profiles shown in Figure 3. For the $r/R_1 = 0.8$ radial position $\lambda/2R_1$ was found to be 0.0089 and the corresponding length scale ratio $\lambda/\Lambda f = 0.015$. At the $r/R = 0.0$ position $\lambda/2R_1$ and $\lambda/\Lambda f$ were found to be 0.00685 and 0.024 respectively. Additionally $\lambda/2R_1$ was found to be virtually constant in the region $r/R_1 \leq 0.4$.

CONCLUSIONS

Few measurements of the longitudinal scales of turbulence for high Reynolds number water flows are available in the literature, more data has been published for air flows where hot-wire anemometry has been widely used. The real time LDA/minicomputer data acquisition system has considerable potential for use during detailed studies of turbulence, irrespective of the type of fluid under investigation. Although results for a Reynolds number of 220,000 have been presented in detail, a wide range of Reynolds number has been investigated (3), (6). From Figures 3 and 4 it is clear that the decay rate of the autocorrelation profiles varies considerably with radial position, the decay rate being greater at the throat section where the velocity is highest. The initial slopes of the curves show that the higher frequencies in the flow are found over the central core region. This observation has been confirmed by the microscale measurements.

Morton and Clark (8) have presented the results obtained from a space correlation study in a 25 mm diameter water pipe line, using two separate LDA systems, the maximum Reynolds number being 18,100. Their results showed that $\frac{\Lambda f}{2R}$ was in the range from 0.26 to 0.197 for the $r/R_1 = 0.0$ position, furthermore $\frac{\Lambda f}{2R}$ decreased with increasing Reynolds number. Martin and Johanson (9) using hot-film anemometry at the centreline of a 152.4 mm diameter water flow reported values of $\frac{\Lambda f}{2R}$ for a Reynolds number range from 19,000 up to 160,000. Their results show that $\frac{\Lambda f}{2R}$ increases from 0.0379 up to 0.112 for the Reynolds number range investigated. For the Reynolds number of 220,000 considered during the present study the centreline values for $\frac{\Lambda f}{2R}$ were 0.275 and 0.367 for the inlet and throat locations respectively. At the lower Reynolds number of 44,000 values of 0.0912 and 0.124 were recorded for each respective location. For the higher Reynolds number $\frac{\Lambda f}{2R}$ was found to vary appreciably with radial position at both the inlet and throat locations, values of 0.585 and 1.20 were obtained for the inlet $r/R_1=0.8$ and throat $r/R_2=0.801$ positions respectively. Figure 5 shows that the length macroscale increases with increasing Reynolds number for all radial positions at both inlet and throat sections. Furthermore the absolute size of the macroscale is larger at the inlet for $r/R \leq 0.4$ and smaller over the region $0.4 < r/R \leq 0.801$, this latter region experiences the most significant changes in mean velocity in order to change the inlet power law profile into the "flat topped" throat profile.

Over the inlet position central core region, $r/R_1 \leq 0.4$, the length microscale was found to be roughly constant, $\frac{\lambda}{2R_1}$ had a maximum equal to 0.0089 at $r/R_1 = 0.8$. The non-dimensional scale ratio $\frac{\lambda}{\Lambda f}$ was found to be 0.0249 and 0.0152 at the $r/R_1 = 0.0$ and 0.8 radial positions respectively.

The results presented show that detailed turbulence measurements may now be achieved in flow situations which had previously proved too difficult. Additionally measurements may now be attempted for a range of fluids in the same pipeline using one data processing instrument, this would enable the similarity of the turbulence to be investigated. As more experimental data is reported the success of the modelling techniques at present employed during the study of shear flows and turbulence in general may be evaluated (10). For example the assumption of a Gaussian velocity probability density distribution at the measuring point has not received much experimental support to date.

REFERENCES

1. Bates, C.J., "Experimental pipe flow analysis using a laser Doppler anemometer", Disa Information, No.16, July 1974, pp.5-10.

2. Bates, C.J.,"Flow measurements using a laser Doppler anemometer", Proceedings Int.Conference on Fluid Flow Measurement in the mid-1970's, Glasgow, National Engineering Laboratory, April 1975, Paper F3.

3. Bates, C.J.,"A laser Doppler anemometry study of a 0.5 area ratio perspex Venturimeter" submitted to ASME, Journal of Fluids Engineering, November 1976.

4. Bates, C.J., and Hughes, T.D.R. "Real time statistical LDV system for the study of a high Reynolds number, low turbulence intensity flow", J. Physics E: Scientific Instruments, Vol.9, 1976, pp. 955-958.

5. Yanta, W.J. and Smith, R.A.,"Measurement of Turbulence - Transport Properties with a laser Doppler Velocimeter", Paper No.73 - 169, AIAA 11th Aerospace Sciences Meeting, Washington DC, 1973.

6. Bates, C.J.,"Macroscale estimates at the entrance and throat of a conical Venturimeter", submitted to Journal of Physics E: Scientific Instruments, December, 1976.

7. Taylor, G.I., "The spectrum of turbulence", Proceedings Royal Society, London, Vol.164A, 1938, pp.476-490.

8. Morton, J.B. and Clark, W.H., "Measurements of two-point velocity correlations in a pipe flow using laser anemometers", Journal of Physics. E: Scientific Instruments, Vol.4, 1971, pp.809-814.

9. Martin, G.Q. and Johanson, L.N.,"Turbulence characteristics of liquids in pipe flow", American Institute of Chemical Engineers Journal, Vol.11, No.1, Jan.1965, pp.29-33.

10. Hinze, J.O., Turbulence , 2nd.ed. McGraw-Hill, 1975.

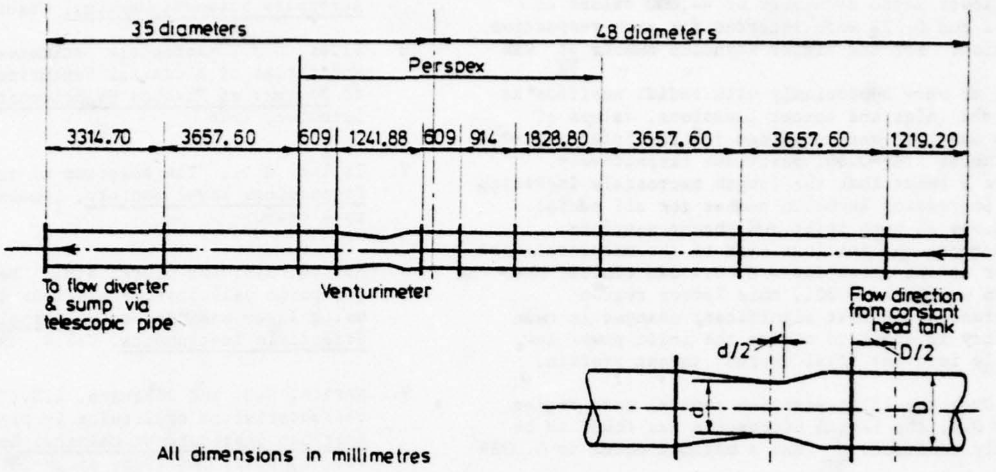

Fig.1. Water pipeline arrangement with 0.5 area ratio venturimeter installed, enlargement shows main measuring positions

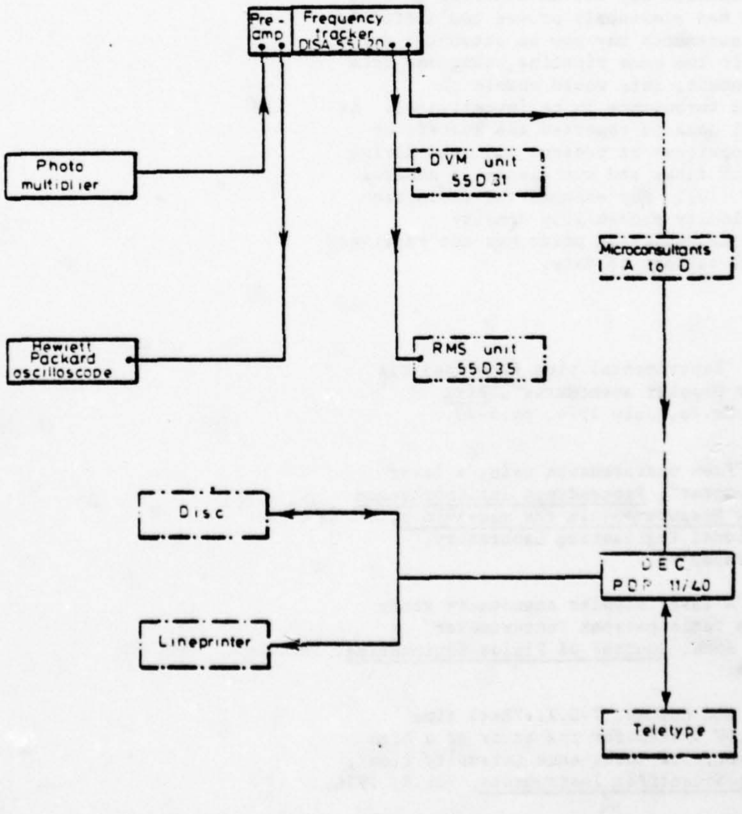

Fig. 2. Signal processing system

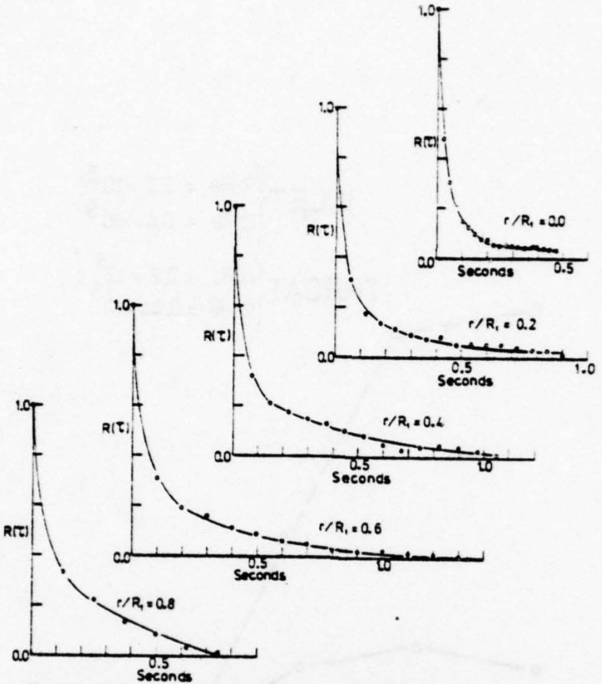

Fig.3. Variation of time correlation profile with inlet radial position, $R_E = 2.2 \times 10^5$

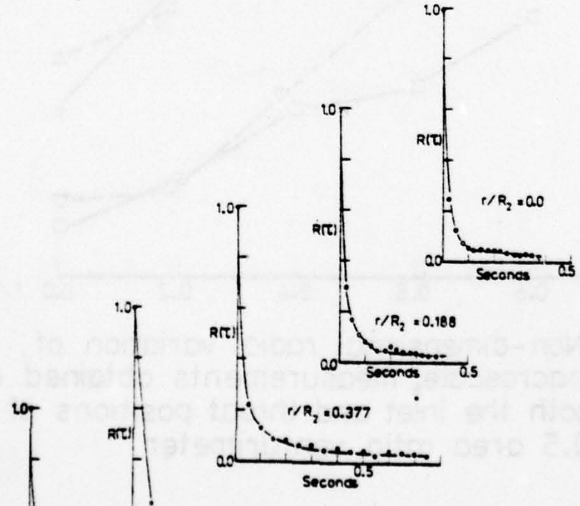

Fig. 4. Variation of time correlation profile with throat radial position, $R_E = 2.2 \times 10^5$

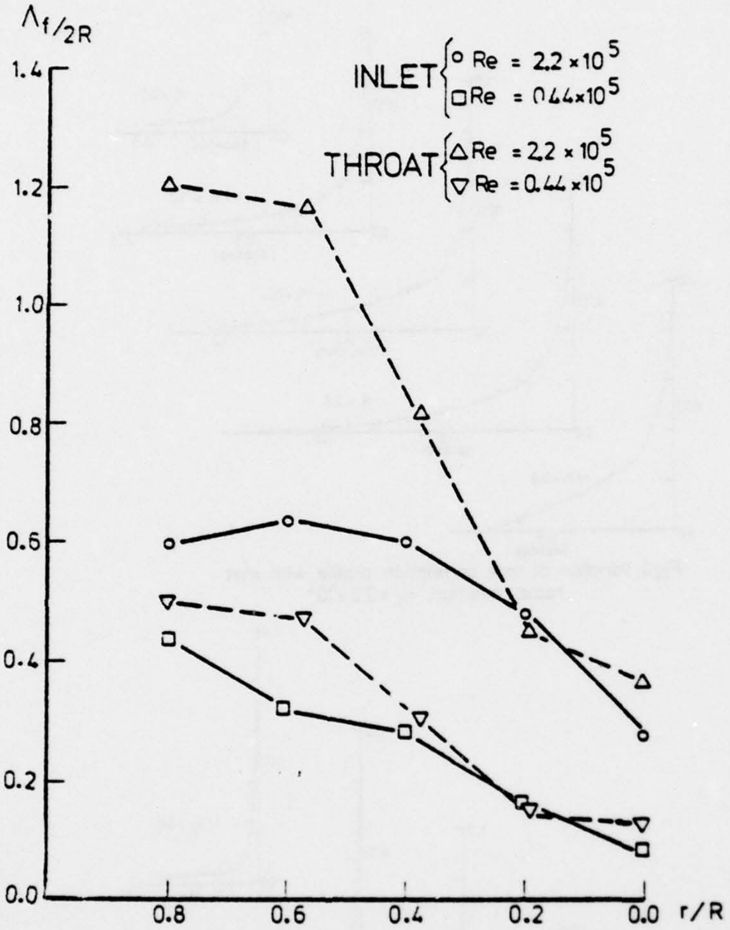

Fig. 5. Non-dimensional radial variation of macroscale, measurements obtained at both the inlet and throat positions of a 0.5 area ratio venturimeter

ANISOTROPIC EDDY VISCOSITIES IN THE TURBULENT FLOW THROUGH A ROD BUNDLE

KLAUS REHME
Institut für Neutronenphysik und Reaktortechnik
Kernforschungszentrum Karlsruhe
D 75oo Karlsruhe, Postfach 364o

ABSTRACT

Experiments were performed in a wall and a corner channel of a rod bundle in order to obtain detailed information of eddy viscosities in the radial and circumferential directions. The paper contains the description of the test section, the experimental results, and a comparison of the results with calculations by the VELASCO computer code (6).

NOMENCLATURE

D	rod diameter; m
D_h	hydraulic diameter; m
F	factor; -
h	length of the test section; m
L	length of the velocity profile; m
n	anisotropy factor; -
P	rod pitch; m
r	radius; m
Re	Reynolds number; -
$\bar{u}$	time-mean velocity; $m\ s^{-1}$
u'	velocity fluctuating in the axial direction; ms^{-1}
u_m	velocity averaged over a channel; $m\ s^{-1}$
u^*	shear velocity; $m\ s^{-1}$
v'	velocity fluctuating in the radial direction; ms^{-1}
w'	velocity fluctuating in the circumferential direction; ms^{-1}
W	distance between rod and channel wall + rod diameter; m
ε	eddy viscosity; $m^2 s^{-1}$
ε^+	dimensionless eddy viscosity; -
ϕ	angle; deg
μ	viscosity; $kg\ m^{-1}\ s^{-1}$
ρ	density; $kg\ m^{-3}$
τ_w	wall shear stress; Nm^{-2}

Subscripts

r	radial
ϕ	circumferential

INTRODUCTION

Computer codes used to predict the thermodynamic and fluid dynamic performance of rod bundles with longitudinal turbulent flow require experimental knowledge of the turbulent transport properties. Anisotropic eddy viscosities are used in the most advanced codes applied to rod bundles (1,2). The anisotropy of the momentum transport is described by different eddy viscosities in the radial direction, i.e., normal to the walls, and in the circumferential direction, i.e., parallel to the walls, respectively.

The eddy viscosity in the radial direction is defined by

$$\varepsilon_r = \frac{-\rho \overline{u'v'}}{\partial \bar{u}/\partial r} \qquad (1)$$

with ρ as the fluid density, $\overline{u'v'}$ as the time-mean correlation of the velocity fluctuations in the main direction of the flow (u') and in the direction normal to the wall (v') respectively, $\bar{u}$ is the time-mean fluid velocity, and r is the coordinate normal to the wall. As a dimensionless quantity the radial eddy viscosity can be written as

$$\varepsilon_r^+ = \frac{\varepsilon_r}{L \cdot u^*} \qquad (2)$$

with L as the length of the velocity profile measured normal to the wall between the wall and the position of maximum velocity and u^* as the local shear velocity defined by

$$u^* = \sqrt{\frac{\tau_w}{\rho}} \qquad (3)$$

with τ_w as the shear stress at the wall.

Likewise, the eddy viscosity in the circumferential direction is defined by

$$\varepsilon_\phi = \frac{-\rho \overline{u'w'}}{\frac{1}{r}\frac{\partial \bar{u}}{\partial \phi}} \qquad (4)$$

with w' as the velocity fluctuation in the circumferential direction. As a dimensionless quantity the circumferential eddy viscosity yields

$$\varepsilon_\phi^+ = \frac{\varepsilon_\phi}{L \cdot u^*} \qquad (5)$$

In channel flows the eddy viscosities in the radial and circumferential directions are non-isotropic; this fact is taken into account by an anisotropy factor n

$$n = \frac{\varepsilon_\phi^+}{\varepsilon_r^+} \qquad (6)$$

Up to now, experimental information on the value of the anisotropy factor and its local dependence has been very poor for non-circular channels. Information is available only for simple ducts, circular tubes and parallel plates, for which values between 2 and 3 habe been measured.

For rod bundles some results are known of the radial eddy viscosity from the experiments by Kjellström (3) and Trupp (4). Kjellström also reported a few values of the anisotropy factor n, but his results scatter widely and no conclusions can be drawn on the basis of those values. On the other hand, the anisotropy factor strongly influences the results calculated by the codes. Especially the circumferential variation of the mean flow velocity averaged normal to the walls, the variation of the wall shear stresses, and, hence, the resulting variation of the wall temperatures depend on the anisotropy factor (5). For instance, the calculations with the VELASCO code (6) for a rod bundle with a pitch-to-diameter ratio of the rods P/D = 1.1 show that the ratio of $\tau_{w_{max}}/\tau_{w_{min}}$ changes from 1.86 to 1.06, if the anisotropy factor is changed from 1 to 30 (5).

Precise experimental results on the anisotropy factor and its local distribution are therefore necessary to verify the assumptions made or to adjust the codes.

EXPERIMENTAL SETUP

In this investigation experiments were performed in a wall and a corner subchannel of a rod bundle. Since the temperature gradients are the highest in those channels of nuclear fuel elements, knowledge of the transport properties is most important for those channels. On the other hand, experiments in central subchannels are difficult to perform, since the flow will always be affected by the channel walls, as the results of different investigations show (3,4).

A rectangular channel (180x686 mm) with 4 rods (157.5 mm O.D.) in parallel is used for the experiments (Fig. 1), which results in a pitch-to-diameter ratio of P/D = 1.071 and a wall-to-diameter ratio of W/D = 1.072. The choice of these dimensions means an enlargement of 25:1 compared to the actual dimensions in a nuclear fuel element. The rods were fabricated of aluminium tubes; the outer surfaces of the tubes were machined. The measured mean roughness depths of the surfaces amounted to only 0.6 µm; the outer surface was very smooth. The rectangular channel was fabricated from plexiglass, so that one of the short walls is adjustable to allow the channel dimensions to be changed for different geometries. The overall length of the test section is h = 7000 mm; it was made up of 4 portions of L_T = 1750 mm each for both the channel and the rods. This makes the length-to-diameter ratios

$$\frac{h}{D_{rod}} \approx 45$$

$$\frac{h}{D_{h wall}} \approx 143$$

$$\frac{h}{D_{h\ corner}} \approx 176.$$

Small pins of 2 mm O.D. were used as spacers at four levels to fix the rods inside the channel. The measurements were performed with air as the fluid at the open outlet, 30 mm downstream from the outlet. The air is taken in through a silencer and a filter (1µm particle size) by a radial blower ($\dot{m}$ = 4.2 kg s^{-1}; Δp = 0.1 bar) and enters the test section through a honeycomb grid (Fig. 1).

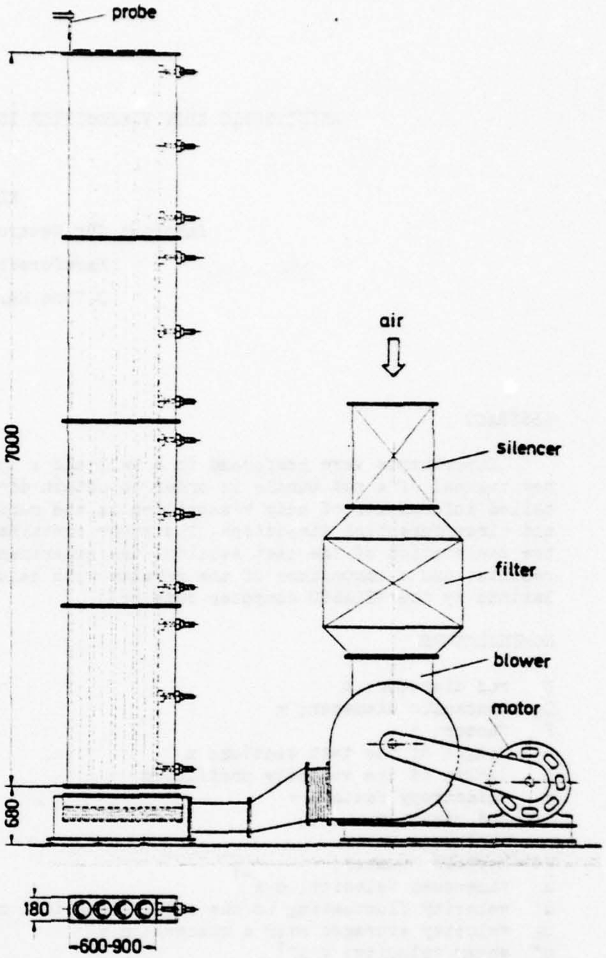

Fig. 1 Sketch of the test rig

Measurements were taken of

(a) the time-mean value of the fluid velocity by Pitot tubes,
(b) the turbulent shear stresses in the radial and circumferential directions,
(c) the distribution of turbulence intensities and, hence, the kinetic energy of turbulence by hot-wire measurements (b) and (c) (DISA), and
(d) the distribution of the wall shear stresses by Preston tubes.

In order to achieve the necessary accuracy of the measured values and their gradients, the flow cross section to be investigated was covered by a network of mesh points. The distribution of the locations where the measurements were taken is shown in Fig. 2 as an example for the wall channel. Measurements were taken along the rod wall between 0 and 90 deg: 5 deg each and along the channel wall between 0 and 84.4 mm: 5 mm each for a different number of points normal to the walls, depending on the width of the flow cross

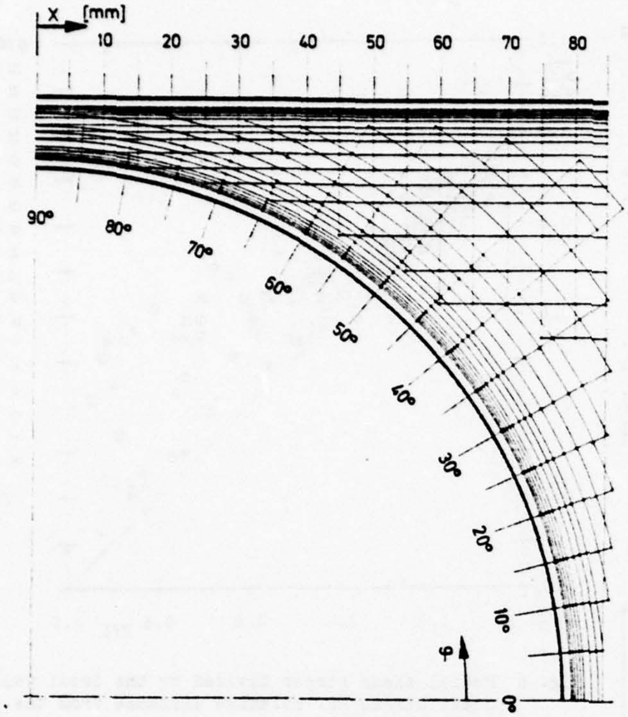

Fig. 2 Distribution of the positions at which measurements were taken (wall channel)

section between 1o and 2o points. Thus, measurements were taken at a total of 5oo positions in each channel by the technique used in earlier measurements on annuli (7,8). The hot-wire measurements were performed by the single-wire method in six different positions against the flow, as suggested by Kjellström (3). For evaluation of the results Kjellström's method was used. The difficulty in solving the set of six simultaneous equations with respect to the shear stress $\overline{v'w'}$ was overcome by disregarding this correlation, as reported already by Kjellström (3). Since the measurement of all values at all positions takes a long time, nearly 3 months, the density of the air at the outlet changes with the conditions of the weather (temperature and barometer readings). Therefore, the speed of the blower was adjusted by controlling the revolutions per minute of the motor such that at a fixed point in the channel the fluid velocity measured by a Pitot tube remained constant ($u = 27.74\ ms^{-1}$). Details of the test section and the measuring technique can be taken from (9).

RESULTS

The Reynolds number of this study based on the hydraulic diameter D_h and the velocity averaged across the subchannel

$$Re = \frac{\rho \cdot u_m \cdot D_h}{\mu} \qquad (7)$$

was $Re = 8.7x1o^4$ in the wall channel and $Re = 6.1x1o^4$ in the corner channel, respectively.

Time-mean Velocity, Turbulence Intensity

Typical results of this investigation are shown in Figs. 3, 4 and 5. Most of the results given in this paper stem from the investigation in the wall channel. The velocity distribution measured by Pitot tubes is shown in Fig. 3 as lines of constant velocity

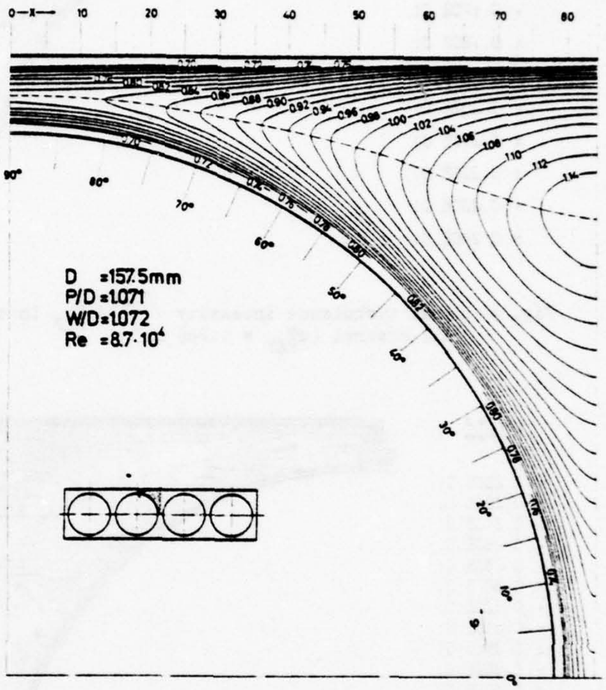

Fig. 3 Velocity field $\bar{u}/\bar{u}_{REF}$ measured in the wall channel ($u_{REF} = 27.74\ ms^{-1}$)

(isotachs). The velocity distribution does not show any disturbances which could be attributed to secondary flows. The velocities measured are related to the velocity kept constant ($u = 27.74\ ms^{-1}$) by a fixed Pitot tube. The average fluid velocity over the cross section ($u_m = 25.64\ ms^{-1}$) was calculated by an integration of the velocity distribution measured. The ratio of the maximum velocity (on the symmetry line) and the maximum velocity in the gap between rod and channel wall is 1.38.

Fig. 4 shows the measured axial turbulence intensities in the wall channel, which were made dimensionsless by the wall shear velocity on the rod at 5 deg (u^*_{REF}). All positions are indicated in Fig. 3. The contour map of lines of equal intensity shows that the intensity is the highest near the walls, as is to be expected, but that the intensity drop towards the center of the flow on lines normal to the wall depends on the circumferential position at the wall. The contour lines indicated some influence of secondary flows in the channel, especially at 25 and 6o deg. This influence of secondary flows is more pronounced in the map of the kinetic energy of turbulence in the corner channel (Fig. 5), which was made dimensionless by the square of the wall shear velocity at 5 deg (u^*_{REF}).

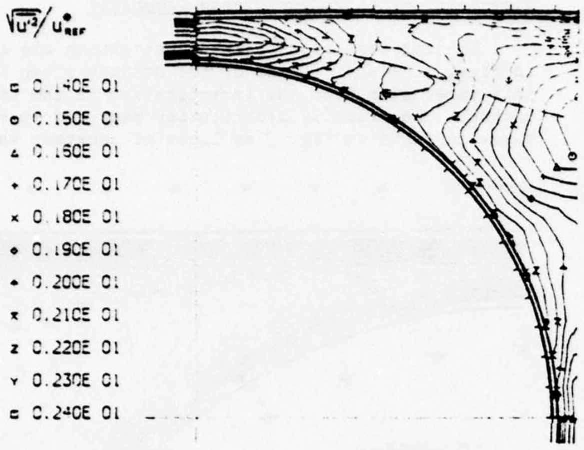

Fig. 4 Axial turbulence intensity $\sqrt{\overline{u'}^2}/u^{x}_{REF}$ in the wall channel (u^{x}_{REF} = 1.2o9 ms^{-1})

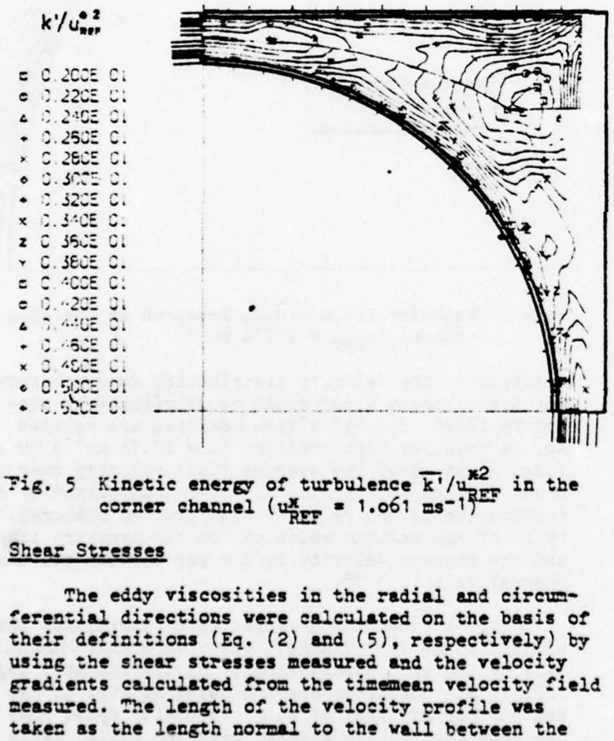

Fig. 5 Kinetic energy of turbulence $\overline{k'}/u^{x2}_{REF}$ in the corner channel (u^{x}_{REF} = 1.o61 ms^{-1})

Shear Stresses

The eddy viscosities in the radial and circumferential directions were calculated on the basis of their definitions (Eq. (2) and (5), respectively) by using the shear stresses measured and the velocity gradients calculated from the timemean velocity field measured. The length of the velocity profile was taken as the length normal to the wall between the wall and the position of maximum velocity. Fig. 3 shows this position as a dotted line. Some of the basic data for the calculation of the eddy viscosities are plotted in Fig. 6 and 7. Fig. 6 shows the radial turbulent shear stresses measured in the wall channel in the part adjacent to the rod vs. the relative distance from the wall. The shear stresses are related to the local wall shear stress. For comparison, a straight line is plotted in the figure to indicate the linear variation of the shear stress in a circular tube. In the case of a rod bundle, the variation of the radial shear stress across the channel is not linear but, depending on the circumferential position, follows a curve which is always higher than the circular tube line. The results show some scatter; especially for ϕ = 3o and 55 deg the measurements are obviously in error. The higher scatter near the center line may be partly due to the effect of the coordinates chosen, by which some portion of the circumferential shear stress is taken as a radial shear stress, except in the regions near 0° and 9o°, respectively. In these regions near the gaps the shear stress profile compares quite well with the profiles to be expected.

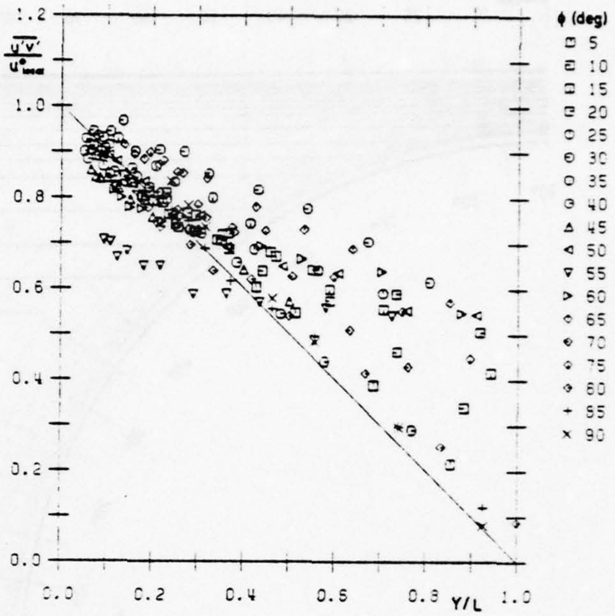

Fig. 6 Radial shear stress divided by the local wall shear stress vs. relative distance from the wall measured in the part of the wall channel adjacent to the rod

The experimental data of the circumferential shear stress are plotted in Fig. 7 as a contour map of lines

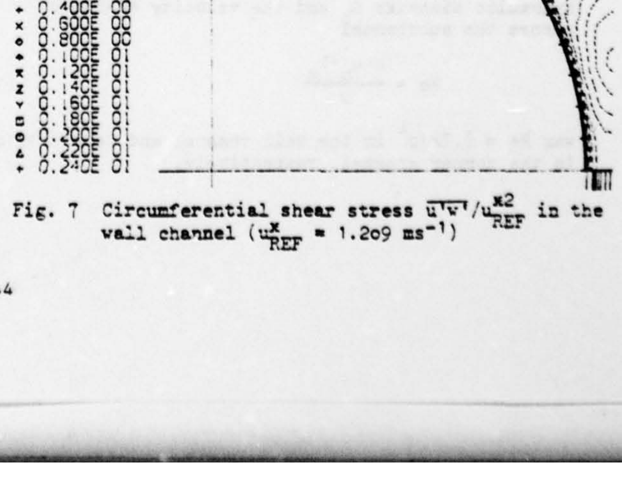

Fig. 7 Circumferential shear stress $\overline{u'v'}/u^{x2}_{REF}$ in the wall channel (u^{x}_{REF} = 1.2o9 ms^{-1})

of equal shear stress. For the circumferential positions below $\phi = 40$ deg the shear stresses are negative, as indicated by dotted lines in the figure. At about $\phi = 40$ deg the circumferential shear stress is zero; this is the region where the velocity gradient in circumferential direction is zero, too, as may be taken from Fig. 3. The circumferential shear stress is positive for $\phi > 40$ deg, goes through a maximum at about $\phi = 65$ deg, and approaches zero again very close to $\phi = 90$ deg. This indicates that there is only a very weak influence on the flow in the subchannel measured from the neighbouring subchannel. This statement is confirmed by the measurements for zero circumferential shear stress at the symmetry line, where the measured data are close to the symmetry line. In this figure the direction of the circumferential shear stresses measured from the rod and the channel, wall, respectively, is not the same for the positions near the center line of the flow cross section. It was therefore decided to subdivide the flow channel at the line of maximum time-mean velocity and to use r/ϕ coordinates in the part of the channel near the rod and x/y coordinates in the part near the channel wall.

Eddy Viscosities

From the original experimental results (not smoothed) the radial and circumferential eddy viscosities were calculated. The calculated values of the dimensionless eddy viscosities normal to the walls are plotted in Figs. 8 and 9 for the two parts of the wall subchannel vs. the relative wall distance. The geometry is indicated in the figures. The results in both parts of the subchannel show the same behaviour. Compared with the circular tube results by Reichardt (10), indicated as a full line, the radial eddy diffusivities are higher in the rod bundle. Close to the wall the measured data agree quite well with the circular tube values. The very high values near the center line may partly be due to the effect of the coordinates chosen, by which some position of the circumferential

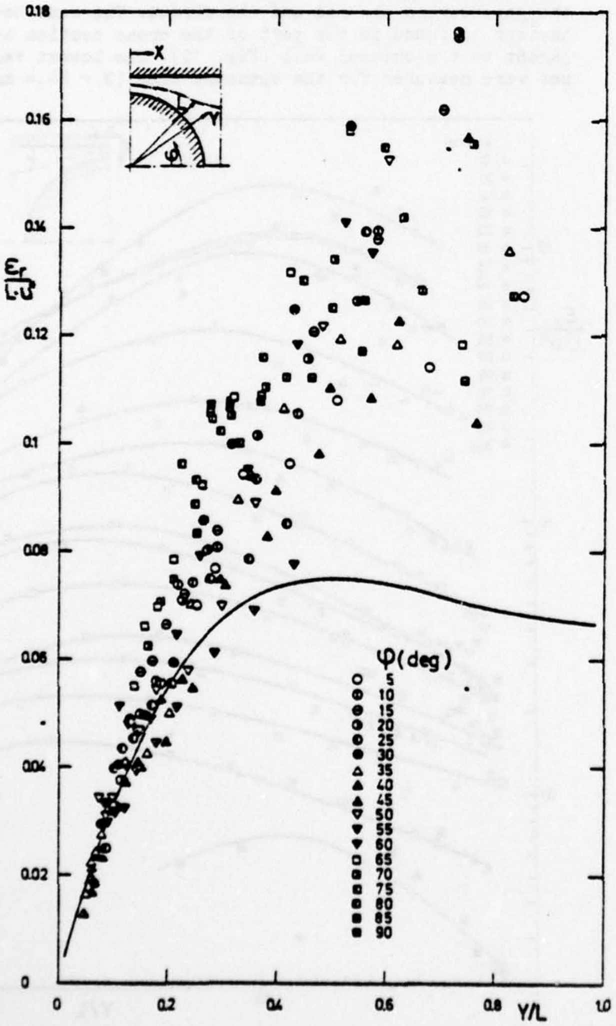

Fig. 8 Dimensionless radial eddy viscosity vs. relative distance from the wall measured in the part of the wall channel adjacent to the rod

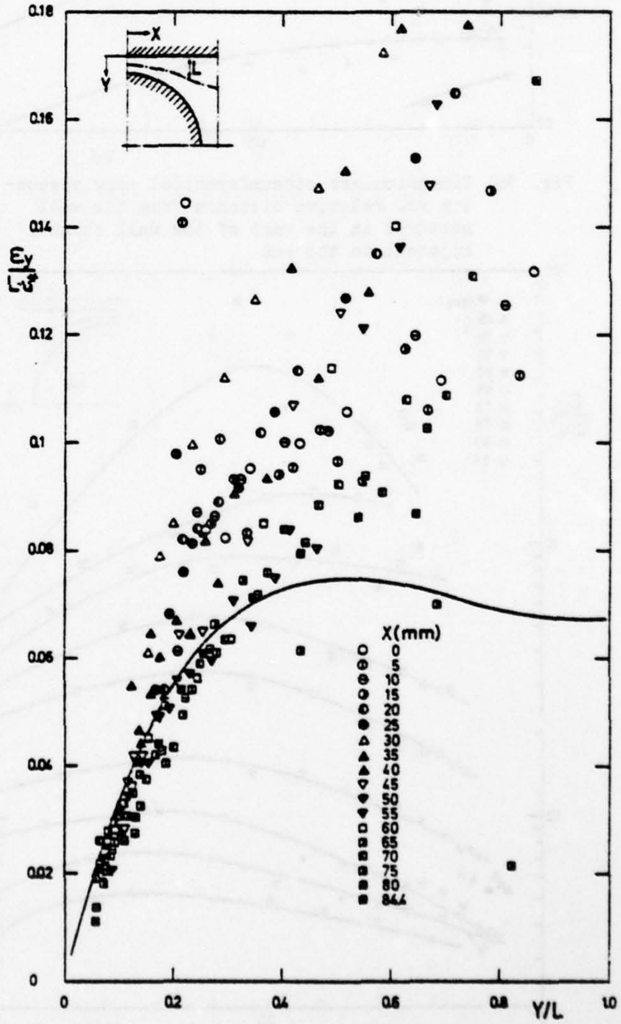

Fig. 9 Dimensionless radial eddy viscosity vs. relative distance from the wall measured in the part of the wall channel adjacent to the shroud

shear stress is taken as a radial shear stress, except in the regions near ϕ = 0 and 9o deg, respectively. The large scatter in the region near the center line also happens because of the small velocity gradients approaching zero at the center line. From the data shown we can conclude that the radial eddy diffusivity is almost independent of the circumferential position.

The latter is not true for the dimensionless circumferential eddy viscosity plotted in Figs. 1o and 11 for the part of the channel near the rod and in Fig. 12 for the part near the channel wall. The circumferential eddy viscosity shows a strong dependence on the position in the cross section and assumes very high values in the gaps of up to 2o and higher. This means that the circumferential eddy viscosity becomes higher by a factor of 26o compared with the maximum value of the radial eddy viscosity in a circular tube (ϵ^+ = o.o75). From the gap region at ϕ = 0 deg the circumferential eddy viscosities decrease to values comparable to the radial eddy viscosity at $\phi \gtrsim$ 4o deg, increasing again for $\phi >$ 4o deg to a maximum value in the gap between the rod and the shroud. The same behaviour is found in the part of the cross section adjacent to the channel wall (Fig. 12). The lowest values were measured for the symmetry line (X = 84.4 mm).

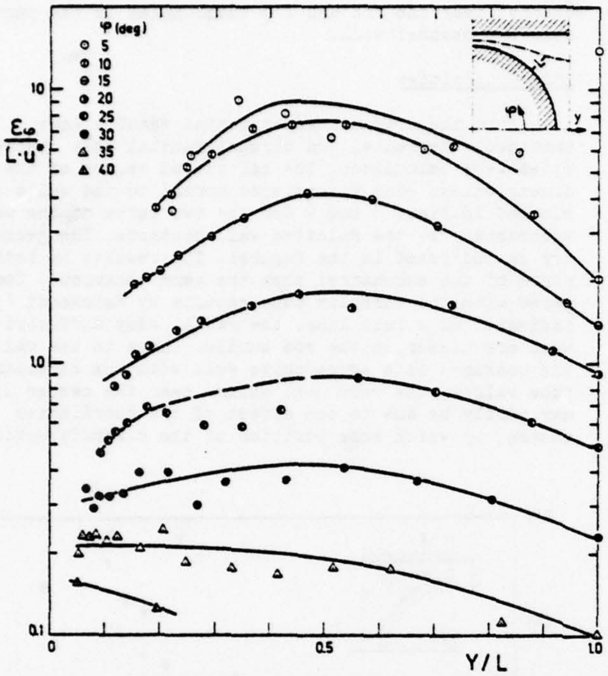

Fig. 1o Dimensionless circumferential eddy viscosity vs. relative distance from the wall measured in the part of the wall channel adjacent to the rod

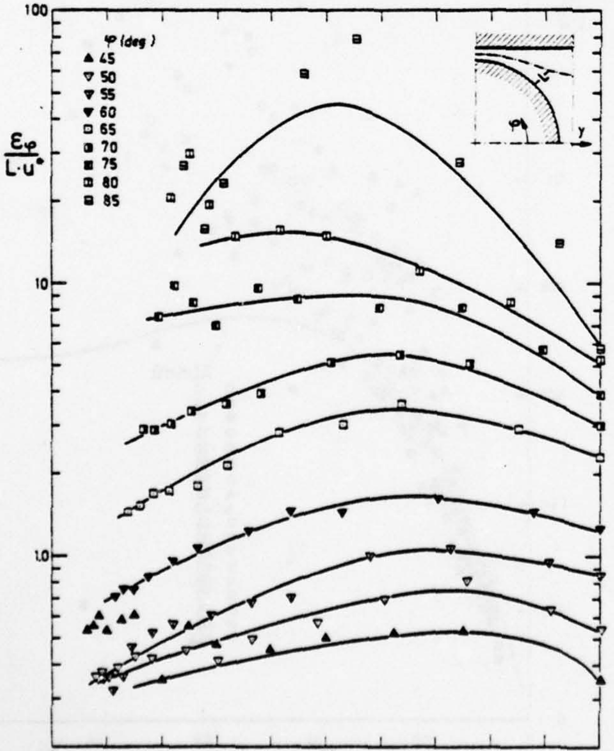

Fig. 11 Dimensionless circumferential eddy viscosity vs. relative distance from the wall measured in the part of the wall channel adjacent to the rod

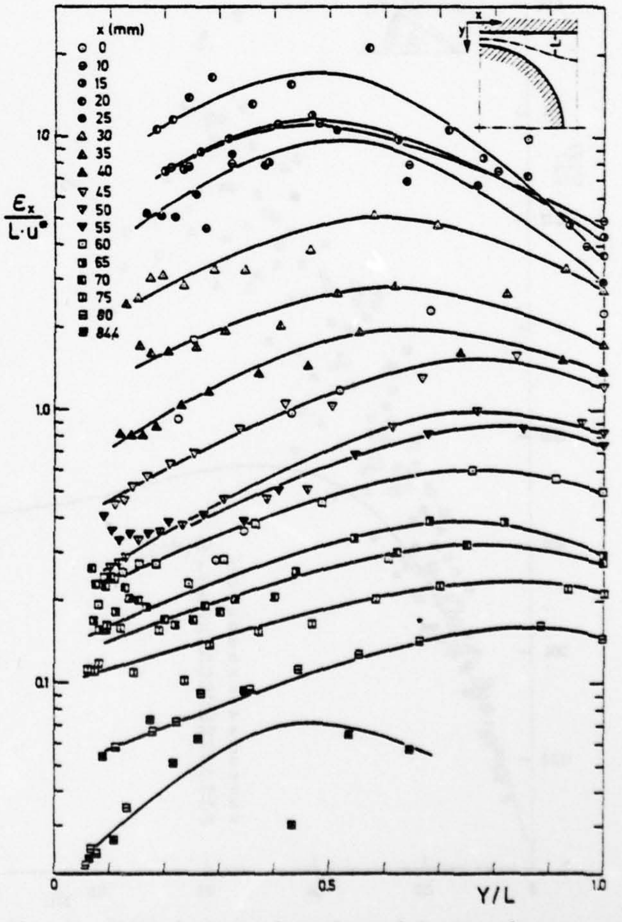

Fig. 12 Dimensionless circumferential eddy viscosity vs. relative distance from the wall measured in the part of the wall channel adjacent to the shroud

In the direction to the gap the circumferential eddy viscosities increase to a maximum value at x = 2o mm. The data for x < 2o mm remain at nearly a constant level. The dependence of the circumferential eddy viscosity on the relative distance from the wall is similar for nearly all positions measured. The values first increase to a maximum value with increasing distance from the wall and decrease slightly when approaching the center line.

This strong dependence of the circumferential eddy viscosity and, therefore, the anisotropy factor on the circumferential and radial positions is in contrast to the assumptions in the codes. In VELASCO (6) this circumferential eddy viscosity is assumed to be constant in the radial and circumferential directions.

COMPARISON BETWEEN THE RESULTS AND CALCULATIONS BY VELASCO

A number of calculations were performed with the VELASCO code developed by Eifler and Nijsing. The velocity field calculated by the code is plotted in Fig. 13. The lines of constant velocity are related to the same velocity as in Fig. 3, so the values in both figures are comparable. It is obvious that the measured velocity field is much more uniform than the calculated field. The ratio of the maximum velocity divided by the maximum velocity in the gap between rod and shroud is 1.62 for the predictions compared with a value of 1.38 for the measurements.

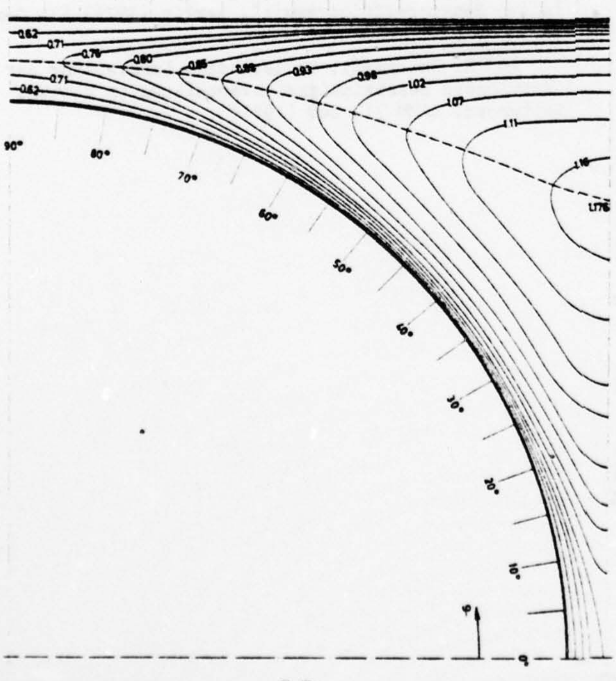

Fig. 13 Velocity field $\bar{u}/\bar{u}_{REF}$ calculated by VELASCO (u_{REF} = 27.74 ms^{-1})

The differences between the measurements and the calculations are quite pronounced for the wall shear stresses (Fig. 14). The plot shows the wall shear stresses related to the maximum wall shear stress for both walls: r/φ rod wall and x/y channel wall. The position of maximum wall shear stress was measured at the channel wall, whereas this position is calculated to be at the rod wall. Again, the measured wall shear stresses are much more uniform than those calculated. The ratio of maximum to minimum wall shear stress is clearly overestimated in the calculations. This ratio is 1.35 (measurements) and 1.74 (calculations) at the rod wall and 1.44 (measurements) and 1.61 (calculations) at the shroud wall, respectively.

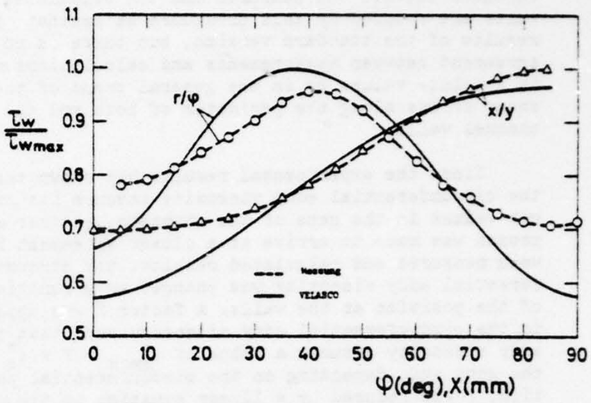

Fig. 14 Comparison of experimental and computed distributions of wall shear stresses

The main reason for this large discrepancy is felt to lie in the assumptions for the circumferential eddy viscosities in the VELASCO code. VELASCO assumes ε_ϕ^+ = o.154, constant in the radial and circumferential directions. This value is equivalent to twice the maximum of the radial eddy viscosity in a circular tube.

In order to adjust the VELASCO code to the measured results, different assumptions were applied to the code. Some results for the resulting wall shear stress distribution calculated are shown in Fig. 15.

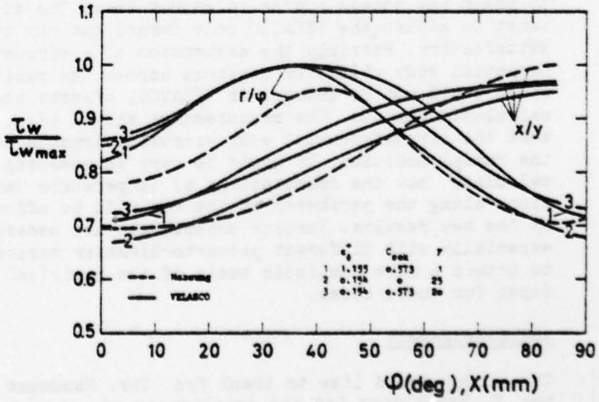

Fig. 15 Comparison of experimental and computed distributions of wall shear stresses

In the first case, the standard value of ε_ϕ^+ = o.154 was increased to ε_ϕ^+ = 1.155, that is, by a factor of 7.5. The assumption in the VELASCO code for the secondary flow remained unchanged in this case. The dif-

AD-A055 654   PENNSYLVANIA STATE UNIV UNIVERSITY PARK DEPT OF MECH--ETC F/G 20/4
SYMPOSIUM ON TURBULENT SHEAR FLOWS HELD AT THE PENNSYLVANIA STA--ETC(U)
APR 77   N00014-77-C-0176

UNCLASSIFIED   NL

5 OF 9
ADA
055654

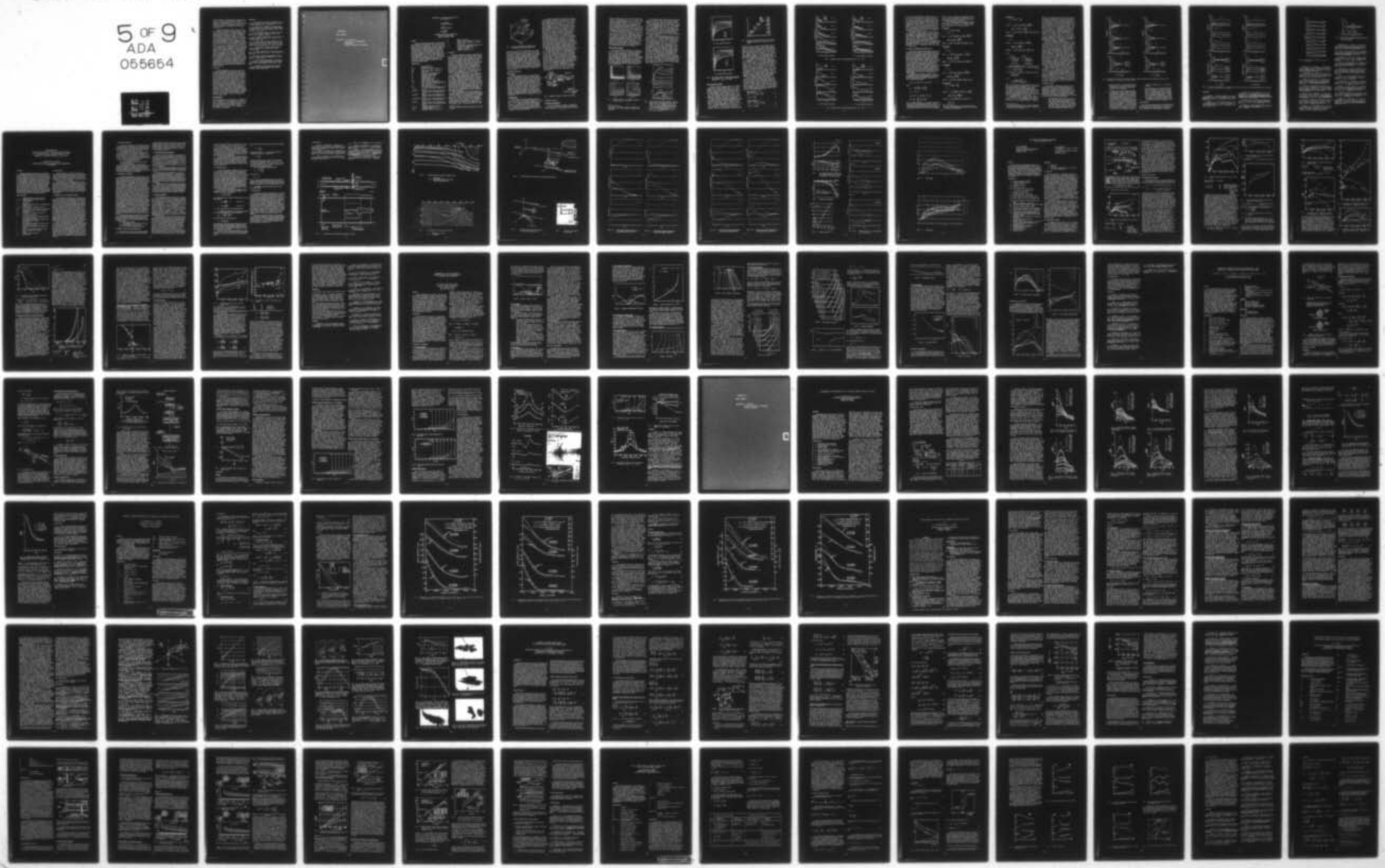

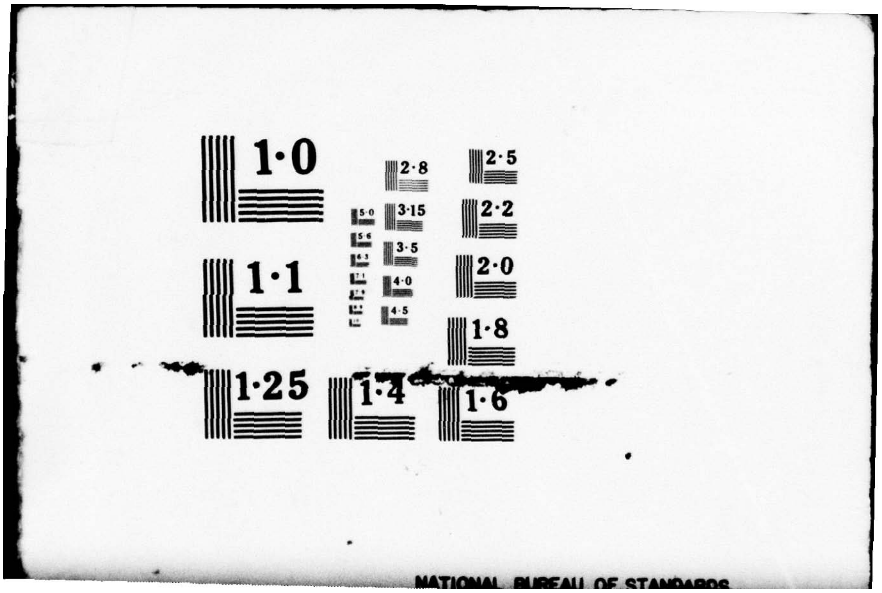
1·0
2·8
2·5
5·0
5·6
3·15
2·2
3·5
2·0
4·0
1·1
4·5
1·8
1·25
1·4
1·6
NATIONAL BUREAU OF STANDARDS

ferences between the measured and the calculated results are reduced by this procedure as against the results of the standard version, but there is no agreement between measurements and calculations either in absolute values or in the general trend of the shear stress along the perimeter of both rod and channel walls.

Since the experimental results had shown that the circumferential eddy viscosity assumes its highest values in the gaps of the channels, another approach was made to arrive at a closer agreement between measured and calculated results: the circumferential eddy viscosity was changed as a function of the position at the walls. A factor F was applied to the circumferential eddy viscosity such that the eddy viscosity assumes a value of $\varepsilon^+_{\phi max} = F \times \varepsilon^+_\phi$ in the gaps and, depending on the circumferential position, F was reduced by a linear equation to the standard value $\varepsilon^+_\phi = 0.154$ at the positions of maximum velocity, i.e., at $\phi = 45$ deg (r/ϕ) and at $x = 84.4$ mm (x/y), respectively. The agreement between calculated and experimental shear stresses was not substantially improved. The closest agreement was obtained by neglecting the secondary flow ($C_{sek} = 0$) and applying a factor of $F = 25$ to the circumferential eddy viscosity. The agreement (line 2 in Fig. 15) of calculated and measured wall shear stresses is satisfactory at the channel wall and at the rod wall in the region between $\phi = 45$ and $\phi = 90$ deg. However, there is a considerable deviation in the region $\phi = 0 \div 45$ deg at the rod wall. Quite similar results were obtained by comparing the variations of measured and calculated maximum velocities and local mean velocities, respectively, i.e., the velocity averaged over the profile length between the wall and the position of maximum velocity.

CONCLUSIONS

Detailed measurements of the eddy viscosities in the circumferential and radial directions were obtained in rod bundle subchannels for the first time by this investigation. Thus, applying the experimental results to the codes used for the prediction of flow and temperature distributions makes it possible to check the models and/or to adjust them. The attempt to adjust the VELASCO code turned out not to be satisfactory. Possibly the assumption of a circumferential eddy viscosity constant across the radius, which could not be changed in VELASCO, affects the calculated results. The measurements showed (Fig. 12) that the circumferential eddy viscosity depends on the radial position. It would be very interesting to calculate how the computations of temperature variations along the perimeter of the rod will be affected by the new results. Further experiments are necessary, especially with different pitch-to-diameter ratios, to obtain a more realistic basis of the empirical input for these codes.

Acknowledgement

The author would like to thank Mrs. Chr. Hausmann and Mrs. M. Mangelmann for the development of computer programs to calculate the eddy viscosities and the velocity averaged across the channel. The author would also like to express his gratitude to Messrs. E. Mensinger and G. Wörner for their cooperation in performing the experiments.

REFERENCES

1 R. Nijsing and W. Eifler, Temperature field in liquid-metal-cooled rod assemblies, Progress in Heat and Mass Transfer, Vol. 7, 115 (1973)

2 H. Ramm and K. Johannsen, A phenomenological turbulence model and its application to heat transport in infinite arrays with axial turbulent flow, J. Heat Transfer 97C, 231 (1975)

3 B. Kjellström, Studies of turbulent flow parallel to a rod bundle of triangular array, Report AE-487 (1974), Studsvik, Sweden

4 A.C. Trupp, The structure of turbulent flow in triangular array rod bundles, Ph.D. Thesis, Univ. of Manitoba, Canada (1973)

5 W. Eifler and R. Nijsing, Calculation of velocity distribution and wall shear stresses for axial turbulent flow in an infinite array of parallel rods, Wärme- und Stoffübertragung 2, 246 (1969) (in German)

6 W. Eifler and R. Nijsing, VELASCO-Velocity field in asymmetric rod configurations, Report EUR-4950e (1973)

7 K. Rehme, Turbulent flow in smooth concentric annuli with small radius ratios, J. Fluid Mech. 64 (2), 263 (1974)

8 K. Rehme, Turbulence measurements in smooth concentric annuli with small radius ratios, J. Fluid Mech. 72 (1), 189 (1975)

9 K. Rehme, Hot-wire anemometry in subchannels of rod bundl-s, KTG-Fachtagung "Experimentiertechnik in der Reaktor-Fluiddynamik", Berlin (1976) (in German)

10 H. Reichardt, Vollständige Darstellung der turbulenten Geschwindigkeitsverteilung in glatten Leitungen, ZAMM 31, 208 (1951)

SESSION 9

WALL FLOWS 2

Chairman: J. C. Rotta
Institut Fur Aerodynamik
Guttingen
Federal Republic of Germany

9

Measurements of Developing Turbulent Flow in a Square Duct

F. B. Gessner
Associate Professor

J. K. Po
Research Assistant

A. F. Emery
Professor

Department of Mechanical Engineering
University of Washington
Seattle, Washington 98195

ABSTRACT

This paper presents and analyzes a comprehensive set of mean flow and turbulence data taken in the entrance region of a square duct. At the location where peaking of the axial centerline velocity occurs, the results show that certain Reynolds stress components and mean rates of strain are elevated above their counterparts for fully-developed flow. Analysis of the data indicates that two recently proposed pressure-strain models can be used to model local pressure-strain behavior in both the two-dimensional and three-dimensional regions of the flow. Further analysis shows that the dissipation rate can be modeled in terms of a suitably-defined length scale and either the resultant primary *shear stress* or the turbulence kinetic energy.

NOMENCLATURE

a	duct half width
a'	diagonal half width
c_1, c_2	empirical instants, equation (5)
$a_{\ell j}^{mi}$	fourth-order tensor, equation (5)
AS	aspect ratio
D	duct width or dissipation rate
k	turbulence kinetic energy
ℓ_p	Prandtl's mixing length
P	production rate
PS	pressure-strain effect
R	redistribution rate
Re	Reynolds number ($Re \equiv U_b D/\nu$)
U,V,W	mean-velocity components in the x, y, and z directions, respectively (Fig. 1)
U_b	mean bulk velocity
U_o	mean centerline velocity
u,v,w	fluctuating velocity components in the x, y, and z directions, respectively (Fig. 1)
$\overline{u^2}, \overline{v^2}, \overline{w^2}$	Reynolds normal stress components referred to the xyz coordinate system (Fig. 6)
$\overline{uv}, \overline{uw}, \overline{vw}$	Reynolds shear stress components referred to the xyz coordinate system Fig. 6)
$\overline{uv'}, \overline{uw'}, \overline{v'w'}$	Reynolds shear stress components referred to the xy'z' *coordinate system* (Fig. 6)
$\overline{v'^2}, \overline{w'^2}$	Reynolds normal stress components referred to the xy'z' coordinate system (Fig. 6)
x,y,z	Cartesian coordinates (Fig. 1)
x,y',z'	Cartesian coordinates (Fig. 6)
x_s	starting length
α, β, γ	empirical constants, equation (5)
α_2	empirical constant
δ	boundary layer thickness ($\delta \equiv \delta_{.995}$)
δ_c	boundary layer thickness at corner bisector (Fig. 1)
δ_y, δ_z	boundary layer thicknesses in the y and z directions, respectively (Fig. 1)
ε	isotropic dissipation rate
ν	kinematic viscosity
ϕ	diffuser half angle (Fig. 2)

INTRODUCTION

Developing turbulent flow along a streamwise corner is a topic of interest to those who study complex, three-dimensional flows. This particular flow situation not only provides a natural vehicle for examining the validity of higher-order closure models which have been formulated in recent years, but is also of interest to a design engineer who must include corner effects in his analysis. Incompressible turbulent corner flows are characterized by the presence of transverse mean circulatory flows (secondary flows) which alter the primary flow and local wall shear stress behavior in the corner region (Fig. 1). The occurrence of secondary flow is the direct result of Reynolds stress gradients in the corner region induced by the three-dimensionality of the flow.

The analysis of fluid motion along a streamwise corner is concerned primarily with evaluating local skin friction behavior and heating rates in the corner region. These objectives can best be accomplished by means of numerical computations which enable one to predict local flow behavior without the need for extensive experimentation. A particular code will be successful, however, only if the overall system of equations includes a Reynolds stress model which properly describes the local turbulence structure. The formulation of an adequate Reynolds stress model, in turn, can only be accomplished if reliable experimental data are available for purposes of comparison with model predictions.

Previous experimental work on incompressible, developing corner flows was initially oriented towards obtaining information on entrance length requirements [1,2][1] and secondary flow development [3] in rectangular ducts. These results have been supplemented recently with additional mean-flow and turbulence data for zero [4-6], favorable [7-9], and adverse [6] pressure gradient flow conditions. Some data on transitional flow behavior in rectangular ducts are also available [10]. Although the results of these

---

[1] Numbers in brackets designate References at the end of paper

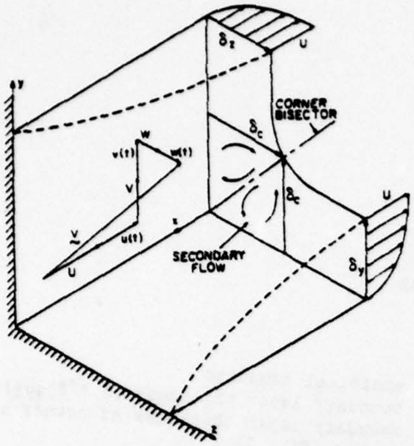

Fig. 1 Velocity components and boundary layer thicknesses for turbulent corner flow

studies have provided useful information on developing flow behavior in the vicinity of a corner, they are often of limited value for comparison with model predictions. In many of these studies, for example, it is not possible to determine actual inlet conditions from the measurements which are presented. Furthermore, the results of some studies indicate significant flow asymmetry about a corner bisector when none should actually exist on the basis of symmetry considerations. The present study was undertaken, therefore, in order to provide a reliable set of data which does not suffer from these shortcomings. All of the data that will be presented were obtained by Po [11] in the entrance region of a square duct at Re = 250,000.

EXPERIMENTAL APPARATUS

Test Facility

The test facility consists of a Formica-lined square duct approximately 22 m in length, as shown in Fig. 2. The duct is preceded by a contraction and a settling chamber with screens, filters, and honeycomb. The joint between the contraction and duct is smooth, and no tripping device was installed at the duct inlet. The distance between opposite walls of the duct was maintained at 0.254 m ± 0.25 mm over the length of the duct, and adjacent walls were set perpendicular to within ± 0.05 deg. The bottom wall was maintained level to within ± 0.4 mm over its length. The top wall is made of removable sections so that a traversing mechanism can be positioned at different streamwise locations. Other details of the overall flow system and duct configuration are given by Page [12].

Instrumentation

Static pressure taps are located on opposite walls of the duct at 1D intervals between x/D = 1 and x/D = 26, and then at 2D intervals between x/D = 26 and x/D = 84. Axial mean velocities were measured by means of a miniature Kiel probe (United Sensor KAC-8) in conjunction with a wall static pressure tap. Differential pressures were measured with an E. Vernon Hill Type A micromanometer with minor scale divisions of 0.0254 mm (0.001 in).

Turbulence measurements were made with hot-wire probes similar in design to configurations recommended by Comte-Bellot and her co-workers [13,14] for minimal prong interference effects. The sensing element of each probe was tungsten wire, 3.8 μ (0.00015 in) in diameter, and wire length-to-diameter ratio varied between 250 and 450. The longitudinal normal stress component was measured by means of a single wire normal to the flow which was calibrated before and after each data run in the potential core of a free jet. The remaining Reynolds stress components were measured by means of a single inclined wire oriented at a nominal angle of 45 deg relative to the axial flow direction. The inclined wire probe was calibrated in both the jet and in fully-developed pipe flow before and after each data run following the technique described by Gessner [15]. The hot-wire probes were operated by means of a Thermo-Systems, Inc. Model 1010 Constant Temperature Anemometer. The bridge output voltage was fed into a DISA Turbulence Processor Model 52B25, and mean square voltages were read on a DISA Digital Voltmeter Model 55D31. The Reynolds stress components were evaluated from response equations developed by Hill and Sleicher [16].

The Kiel probe and hot-wire probes were mounted on a traversing mechanism for probe translation in the yz plane (refer to Fig. 1). Probe positioning in the y and z directions was accurate to within ± 0.1 mm. Both normal and inclined wire probes were mounted with the probe stem parallel to the axial flow direction. By means of a bevel gear arrangement the inclined wire probe was rotated in 45-deg increments to orient the wire in the xy and xz planes, and in planes which bisect these planes (8 angular positions). This arrangement permitted $\overline{v^2}$, $\overline{w^2}$, $\overline{uv}$, $\overline{uw}$, and $\overline{vw}$ to be measured simultaneously at each point with the same wire. Because all turbulence data were taken at points where wall interference effects are negligible ($y/a \geq 0.05$, $z/a \geq 0.05$), no corrections were applied to measured Reynolds stress values.

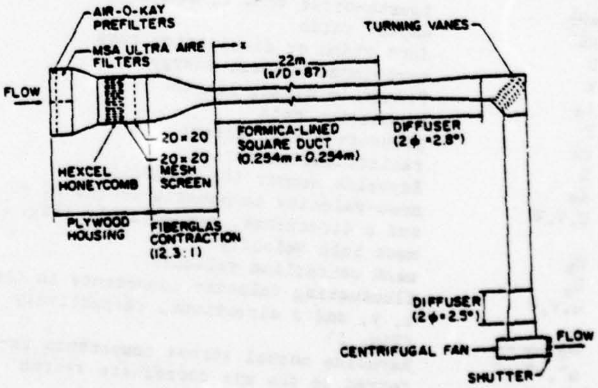

Fig. 2 Schematic diagram of overall flow system

EXPERIMENTAL RESULTS

Preliminary Measurements

Initial measurements were made in the near entrance region of the duct in order to determine inlet flow conditions. The virtual origin of the wall bisector boundary layer was found by extrapolating values of δ evaluated at $x/D = 0.2$, 1, 2, and 4 from velocity profiles measured at these locations. The virtual origin was located at $x_s/D = -0.65$, which indicates that flow at $x/D = 0$ is essentially uniform. Turbulence intensity measurements in the near entrance region indicated a core flow turbulence level less than 0.0035. These results can be compared with those of Ahmed [9] who made extensive measurements in the entrance region of a square duct over a moderate Reynolds number range ($4.7 \times 10^4 \leq Re \leq 1.4 \times 10^5$). His results also indicate a core flow turbulence level in the near entrance region less than 0.0035 for the Reynolds number range investigated. Tatchell [17] has shown, however, that close agreement between Ahmed's results and model predictions based on assumed uniform flow at $x/D = 0$ is possible only when a starting length $x_s/D = -6.25$ is applied to the computations. It thus appears that flow at the inlet of Ahmed's duct was partially developed, and caution must be observed, therefore, when comparisons are made with his results.

Mean Velocity Profiles

The isotach patterns[2] measured in a quadrant of the flow at $x/D = 8$, 16, 24, 40, and 84 are shown in Fig. 3. The profiles exhibit excellent symmetry about the corner bisector and are indicative of the presence of two secondary flow cells centered about the bisector, as shown in Fig. 1. The non-existence of additional secondary flow cells in the near entrance region has been confirmed in a previous study [12]. Figure 3(a) shows that isotachs beyond the corner region are essentially parallel and free of the ripples which exist in Ahmed's patterns at $x/D = 6.36$ and 12.9.

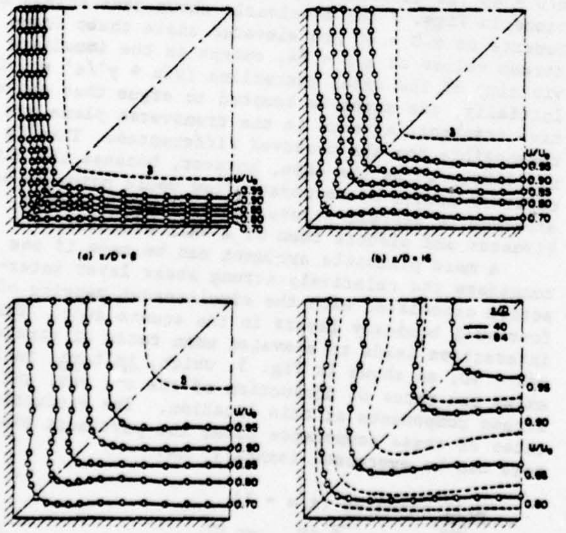

Fig. 3 Isotach patterns in the entrance region of a square duct, $Re = 2.5 \times 10^5$

In the region beyond the location where the wall and corner boundary layers begin to merge (simultaneously at $x/D = 32$), Fig. 3(d) shows that corresponding isotachs shift markedly between $x/D = 40$ and a location downstream where the flow reaches an apparent fully-developed state ($x/D = 84$). The isotachs at $x/D = 84$ (dashed lines) are more distorted than their counterparts at $x/D = 40$, which implies that the strength of the secondary flow increases between these two locations. This conjectured behavior is in accord with the results of an earlier related study [15] in which secondary flow velocity components were measured directly.

Figure 4 shows the streamwise variation of the axial mean velocity component measured along the wall bisector $z/a = 1.0$ at fixed distances from the wall over the interval $0.02 \leq y/a \leq 1.0$. The distributions indicate a local peaking of the axial velocity on the duct centerline ($y/a = z/a = 1.0$) at $x/D = 40$, an effect similar to that noted by Dean [18] and Comte-Bellot [19] in their experimental studies of developing turbulent flow in high aspect ratio rectangular ducts. The centerline velocity distribution for the square duct peaks at a higher value because of increased core flow acceleration induced by simultaneous boundary layer development on all four walls. The peaking also occurs downstream of the location where the boundary layers begin to merge ($x/D = 32$), indicating that further adjustment of the flow takes place after the core flow becomes non-existent, presumably because of shear layer interaction effects which lead to a non-equilibrium condition at $x/D = 32$. Figure 5 shows that these effects lead to mean rates of strain at $x/D = 40$ which exceed those observed at $x/D = 84$.

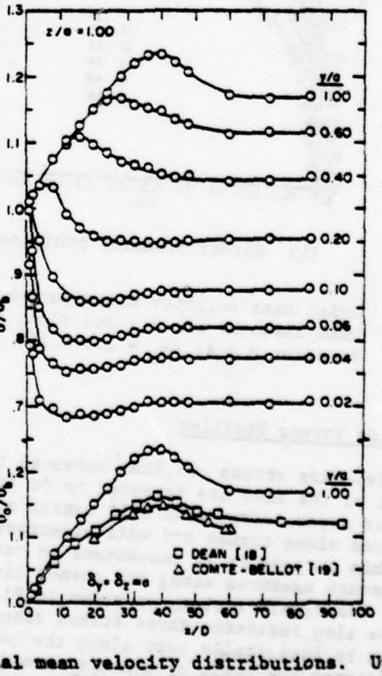

Fig. 4 Axial mean velocity distributions. Upper set shows profile development along the wall bisector $z/a = 1$ of a square duct, $Re = 2.5 \times 10^5$. Lower set represents distributions along axial centerline: ○ square duct, $Re = 2.5 \times 10^5$; □ rectangular duct, $AS = 12.0$, $Re = 1.0 \times 10^5$; △ rectangular duct, $AS = 13.3$, $Re = 2.4 \times 10^5$.

---

[2] An isotach is defined as a line of constant axial mean velocity in a plane normal to the axial flow direction.

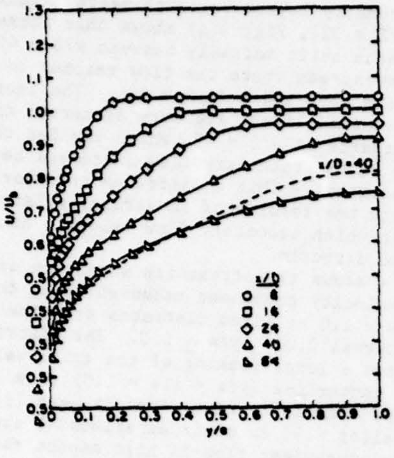

(a) Wall bisector profiles

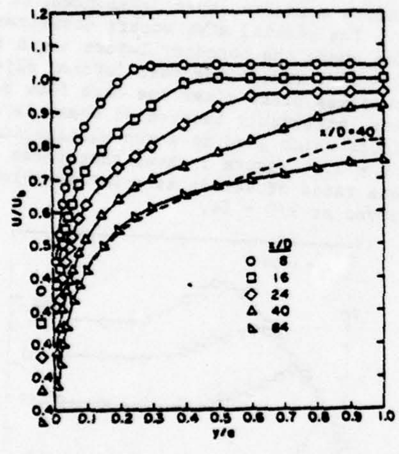

(b) Corner bisector profiles

Fig. 5 Axial mean velocity distributions along the wall bisector $z/a = 1$ and along the corner bisector $y = z$; $Re_b = 2.5 \times 10^5$

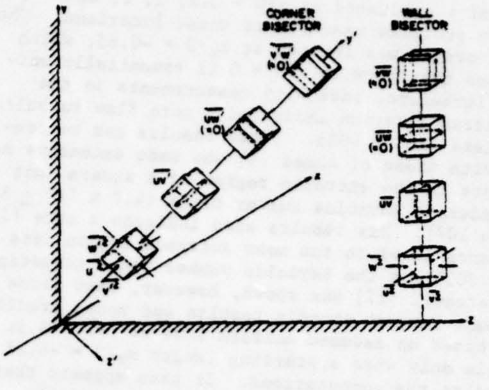

Fig. 6 Reynolds stress components acting on planes normal and parallel to corner and wall bisectors

Reynolds Stress Profiles

Reynolds stress profiles measured in a complete octant of the flow are reported by Po [11]. In the present paper, discussion will center on profiles measured along corner and wall bisectors of the duct. For this purpose it is convenient to refer stress components measured along the corner bisector to an xy'z' coordinate system, as shown in Fig. 6. This figure also indicates those stress components which should be identically zero along the corner and wall bisectors on the basis of symmetry considerations.

Normal stress and shear stress component profiles measured at different streamwise locations along the duct are shown in Figs. 7 and 8. Within the inner region of the developing boundary layer (y/δ_y or $y/\delta_c < 0.5$), all stress components on the corner bisector are generally lower than their counterparts on the wall bisector. This behavior is apparently the result of the fluid retaining some of its statistical properties as it is convected inward toward the corner by the secondary motion. This apparent memory-retention of flow in the transverse plane eventually leads to a plateau-like behavior of the stress components along the corner bisector after the boundary layers have merged (refer to results at x/D = 40 and 84). Figures 7a and 7b also show that the corner has an inhibiting influence on the anisotropy between normal stress components in the transverse plane, i.e., $|\overline{v'^2} - \overline{w'^2}|$ is generally less than $|\overline{v^2} - \overline{w^2}|$ in the vicinity of the corner at each streamwise location.

A comparison of $\overline{u^2}$, $-\overline{uv}$ and $-\overline{uv'}$ stress components measured at x/D = 84 with their counterparts at x/D = 40 (as indicated by the dashed-line distributions in Figs. 7 and 8) clearly shows that stress components at x/D = 40 are elevated above their downstream values at x/D = 84, except in the immediate vicinity of the axial centerline (y/a = y'/a' = 1.0). Initially, one might be tempted to argue that convective transport effects in the transverse plane are responsible for the observed differences. This is not likely to be the case, however, because the circulatory nature of secondary flow would normally be expected to depress stress levels along a corner bisector and elevate them on a wall bisector.

A more plausible argument can be made if one considers the relatively strong shear layer interaction associated with the simultaneous merging of four wall boundary layers in the square duct. This interaction leads to elevated mean rates of strain at x/D = 40, as shown in Fig. 5, which, in turn, influences the rates of production of the $\overline{u^2}$, $-\overline{uv}$, and $-\overline{uv'}$ stress components at this location. The production rates of these components along the pertinent bisectors can be expressed (exactly) as:

Wall bisector (z/a = 1)

$$P(\overline{u^2}) = -2\left(\overline{u^2}\frac{\partial U}{\partial x} + \overline{uv}\frac{\partial U}{\partial y}\right) \tag{1}$$

$$P(-\overline{uv}) = \overline{v^2}\frac{\partial U}{\partial y} \tag{2}$$

Corner bisector (y = z)

$$P(\overline{u^2}) = -2\left(\overline{u^2}\frac{\partial U}{\partial x} + \overline{uv'}\frac{\partial U}{\partial y'}\right) \tag{3}$$

$$P(-\overline{uv'}) = \overline{v'^2}\frac{\partial U}{\partial y'} \tag{4}$$

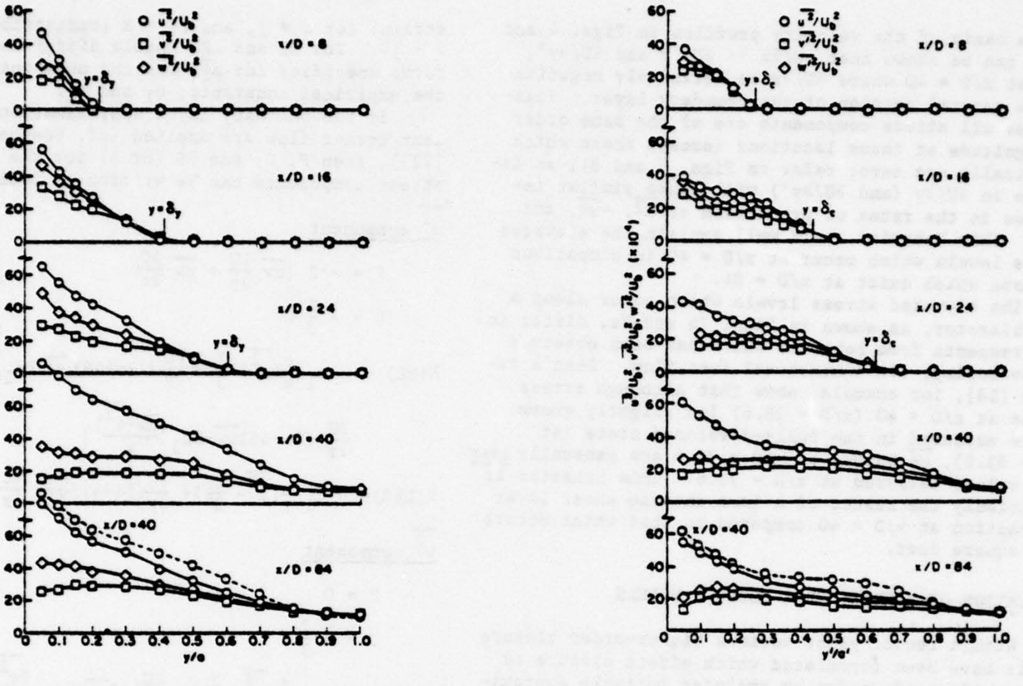

(a) Wall bisector profiles

(b) Corner bisector profiles

Fig. 7 Reynolds normal stress distributions, Re = 2.5 x 10^5

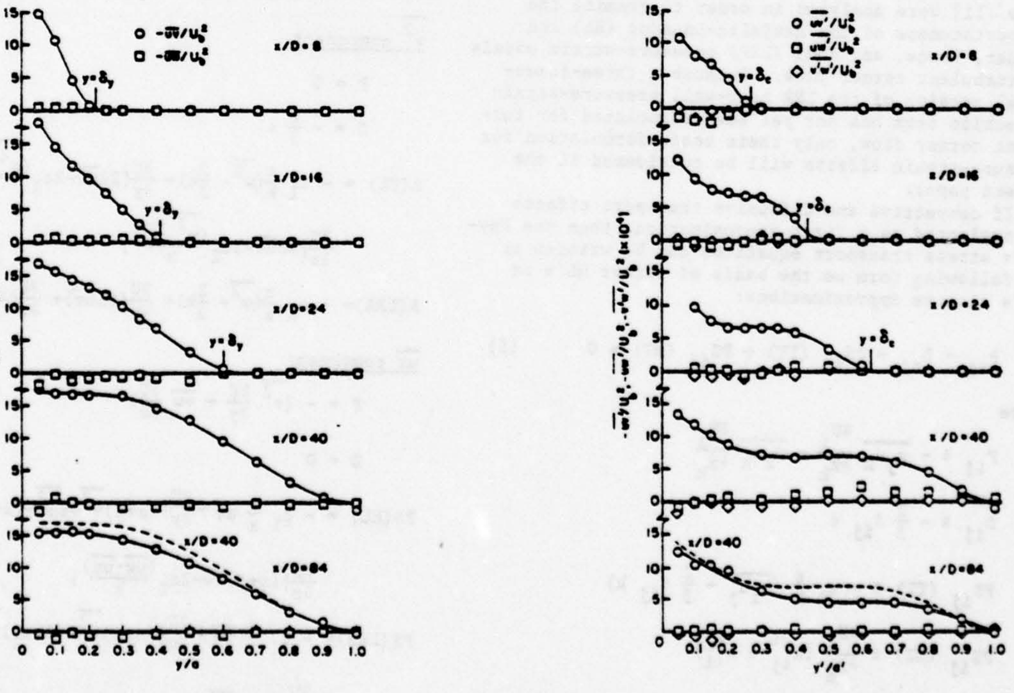

(a) Wall bisector profiles

(b) Corner bisector profiles

Fig. 8 Reynolds shear stress distributions, Re = 2.5 x 10^5

On the basis of the velocity profiles in Figs. 4 and 5, it can be shown that $\partial U/\partial x \ll \partial U/\partial y$ and $\partial U/\partial y'$, even at $x/D = 40$ where $\partial U/\partial x$ is definitely negative in the central portion of the boundary layer. Inasmuch as all stress components are of the same order of magnitude at these locations (except those which identically are zero; refer to Figs. 7 and 8), an increase in $\partial U/\partial y$ (and $\partial U/\partial y'$) will cause similar increases in the rates of production of $\overline{u^2}$, $-\overline{uv}$, and $-\overline{uv'}$. This behavior could well explain the elevated stress levels which occur at $x/D = 40$ in comparison to those which exist at $x/D = 84$.

The elevated stress levels which occur along a wall bisector, as shown in Figs. 7a and 8a, differ in some respects from behavior which has been observed in developing, two-dimensional duct flow. Dean's results [18], for example, show that although stress values at $x/D = 40$ ($x/D = 38.6$) lie slightly above values measured in the fully-developed state (at $x/D = 93.6$), $\overline{u^2}$ values at $x/D = 38.6$ are generally less than values measured at $x/D = 93.6$. This behavior is undoubtedly the result of a less intense shear layer interaction at $x/D = 40$ compared to that which occurs in a square duct.

EVALUATION OF HIGHER-ORDER CLOSURE MODELS

Within recent years various higher-order closure models have been formulated which effect closure to the equations of motion by applying suitable approximations to the Reynolds stress transport equations. One of the more promising models is one proposed by Hanjalic and Launder [20]. This model has recently been modified and extended by Launder, Reece, and Rodi [21] to include near-wall pressure-strain effects in its formulation. In the present study, the data of Po [11] were analyzed in order to examine the appropriateness of the Hanjalic-Launder (HL) and Launder, Reece, and Rodi (LRR) pressure-strain models for turbulent corner flow. Because a three-dimensional version of the LRR near-wall pressure-strain correction term has not yet been formulated for turbulent corner flow, only their basic formulation for pressure-strain effects will be considered in the present paper.

If convective and diffusive transport effects are neglected as a first approximation, then the Reynolds stress transport equations can be written in the following form on the basis of either HL's or LRR's closure approximations:

$$P_{ij} + D_{ij} + PS_{ij}\ (TT) + PS_{ij}\ (MT) = 0 \qquad (5)$$

where

$$P_{ij} \equiv -\overline{u_j u_k}\frac{\partial U_i}{\partial x_k} - \overline{u_i u_k}\frac{\partial U_j}{\partial x_k}$$

$$D_{ij} \equiv -\frac{2}{3}\delta_{ij}\,\varepsilon$$

$$PS_{ij}\ (TT) \equiv -c_1\frac{\varepsilon}{k}(\overline{u_i u_j} - \frac{2}{3}\delta_{ij}\,k)$$

$$PS_{ij}\ (MT) \equiv \frac{\partial U_\ell}{\partial x_m}(a_{\ell j}^{mi} + a_{\ell i}^{mj})$$

with $P \equiv$ production rate, $D \equiv$ (isotropic) dissipation rate, PS (TT) $\equiv$ pressure-strain effects caused by "turbulent-turbulent" interactions, and PS (MT) $\equiv$ pressure-strain effects caused by "mean flow-turbulent" interactions, where PS = PS (TT) + PS (MT) (pressure strain) for $i \neq j$, and PS = R (redistribution) when $i = j$[3]. The HL and LRR models differ only in the forms specified for $a_{\ell j}^{mi}$ and the numerical values of the empirical constants: c_1 and c_2.

If the boundary layer approximations for turbulent corner flow are applied (cf. Gessner and Emery [22]), then P, D, and PS (or R) for the individual stress components can be written as follows:

$\overline{u^2}$ component

$$P = -2\,(\overline{uv}\frac{\partial U}{\partial y} + \overline{uw}\frac{\partial U}{\partial z})$$

$$D = -\frac{2}{3}\varepsilon$$

$$R(HL) = -c_1\frac{\varepsilon}{k}(\overline{u^2} - \frac{2}{3}k) + \frac{\partial U}{\partial y}[(2\alpha+4\beta)\overline{uv} - 2c_2\frac{(\overline{uv}\cdot\overline{u^2})}{k}] +$$

$$\frac{\partial U}{\partial z}[(2\alpha+4\beta)\overline{uw} - 2c_2\frac{(\overline{uw}\cdot\overline{u^2})}{k}]$$

$$R(LRR) = -c_1\frac{\varepsilon}{k}(\overline{u^2} - \frac{2}{3}k) + \frac{\partial U}{\partial y}(2\alpha+4\beta)\overline{uv} + \frac{\partial U}{\partial z}(2\alpha+4\beta)\overline{uw}$$

$\overline{v^2}$ component

$$P = 0$$

$$D = -\frac{2}{3}\varepsilon$$

$$R(HL) = -c_1\frac{\varepsilon}{k}(\overline{v^2} - \frac{2}{3}k) + \frac{\partial U}{\partial y}[4\beta\overline{uv} - 2c_2\frac{(\overline{v^2}\cdot\overline{uv})}{k}] +$$

$$\frac{\partial U}{\partial z}[2\beta\overline{uw} - 2c_2\frac{(\overline{v^2}\cdot\overline{uw})}{k}]$$

$$R(LRR) = -c_1\frac{\varepsilon}{k}(\overline{v^2} - \frac{2}{3}k) + \frac{\partial U}{\partial y}(4\beta+2c_2)\overline{uv} + \frac{\partial U}{\partial z}(2\beta\overline{uw})$$

$\overline{w^2}$ component

$$P = 0$$

$$D = -\frac{2}{3}\varepsilon$$

$$R(HL) = -c_1\frac{\varepsilon}{k}(\overline{w^2} - \frac{2}{3}k) + \frac{\partial U}{\partial y}[2\beta\overline{uv} - 2c_2\frac{(\overline{w^2}\cdot\overline{uv})}{k}] +$$

$$\frac{\partial U}{\partial z}[4\beta\overline{uw} - 2c_2\frac{(\overline{w^2}\cdot\overline{uw})}{k}]$$

$$R(LRR) = -c_1\frac{\varepsilon}{k}(\overline{w^2} - \frac{2}{3}k) + \frac{\partial U}{\partial y}(2\beta\overline{uv}) + \frac{\partial U}{\partial z}(4\beta+2c_2)\overline{uw}$$

$\overline{uv}$ component

$$P = -(\overline{v^2}\frac{\partial U}{\partial y} + \overline{vw}\frac{\partial U}{\partial z})$$

$$D = 0$$

$$PS(HL) = -c_1\frac{\varepsilon}{k}\overline{uv} + \frac{\partial U}{\partial y}[(\alpha+\beta)\overline{v^2} + \beta\overline{u^2} + \gamma k - 2c_2\frac{(\overline{uv})^2}{k}] +$$

$$\frac{\partial U}{\partial z}[(\alpha+\beta)\overline{vw} - 2c_2\frac{(\overline{uw}\cdot\overline{uv})}{k}]$$

$$PS(LRR) = -c_1\frac{\varepsilon}{k}\overline{uv} + \frac{\partial U}{\partial y}[(\alpha+\beta)\overline{v^2} + (\beta+c_2)\overline{u^2} + \gamma k] +$$

$$\frac{\partial U}{\partial z}(\alpha+\beta)\overline{vw}$$

---

[3] The term "redistribution" is not appropriate when $i \neq j$ because no redistribution actually occurs among the shear stress components.

$\overline{uw}$ component

$$P = -\left(\overline{vw}\,\frac{\partial U}{\partial y} + \overline{w^2}\,\frac{\partial U}{\partial z}\right)$$

$$D = 0$$

$$PS(HL) = -c_1\frac{\varepsilon}{k}\overline{uw} + \frac{\partial U}{\partial y}\left[(\alpha+\beta)\overline{vw} - 2c_2\frac{(\overline{uv}\cdot\overline{uw})}{k}\right] + \frac{\partial U}{\partial z}\left[(\alpha+\beta)\overline{w^2} + \beta\overline{u^2} + \gamma k - 2c_2\frac{(\overline{uw})^2}{k}\right]$$

$$PS(LRR) = -c_1\frac{\varepsilon}{k}\overline{uw} + \frac{\partial U}{\partial y}(\alpha+\beta)\overline{vw} + \frac{\partial U}{\partial z}\left[(\alpha+\beta)\overline{w^2} + (\beta+c_2)\overline{u^2} + \gamma k\right]$$

$\overline{vw}$ component

$$P = 0$$

$$D = 0$$

$$PS(HL) = -c_1\frac{\varepsilon}{k}\overline{vw} + \frac{\partial U}{\partial y}\left[\beta\overline{uw} - 2c_2\frac{(\overline{uv}\cdot\overline{vw})}{k}\right] + \frac{\partial U}{\partial z}\left[\beta\overline{uv} - 2c_2\frac{(\overline{uw}\cdot\overline{vw})}{k}\right]$$

$$PS(LRR) = -c_1\frac{\varepsilon}{k}\overline{vw} + \frac{\partial U}{\partial y}(\beta+c_2)\overline{uw} + \frac{\partial U}{\partial z}(\beta+c_2)\overline{uv}$$

where

$$\begin{array}{llll} c_1 & \equiv 2.8 & c_1 & \equiv 1.5 \\ c_2 & \equiv 0.45 & c_2 & \equiv 0.4 \\ \alpha & \equiv (10-8c_2)/11 & \alpha & \equiv (10+4c_2)/11 \\ \beta & \equiv -(2-6c_2)/11 & \beta & \equiv -(2+3c_2)/11 \\ \gamma & \equiv (2-6c_2)/55 & \gamma & \equiv -(30c_2-2)/55 \\ & \text{(HL model)} & & \text{(LRR model)} \end{array}$$

From the equations for $\overline{u^2}$, $\overline{v^2}$, and $\overline{w^2}$, it follows that the dissipation rate, ε, can be expressed as

$$\varepsilon = -\left(\overline{uv}\,\frac{\partial U}{\partial y} + \overline{uw}\,\frac{\partial U}{\partial z}\right) \tag{6}$$

or, equivalently, in terms of a length scale as [22]

$$\varepsilon = \frac{[\overline{uv}^2 + \overline{uw}^2]^{3/4}}{\ell_p} \tag{7}$$

with

$$\ell_p \equiv \frac{[\overline{uv}^2 + \overline{uw}^2]^{1/4}}{[(\partial U/\partial y)^2 + (\partial U/\partial z)^2]^{1/2}}$$

where ℓ_p can be regarded as an extended form of Prandtl's mixing length. In equation (7), ε is modeled in terms of the resultant primary shear stress $(\overline{uv}^2 + \overline{uw}^2)^{1/2}$ and an isotropic length scale, ℓ_p, in a manner which does not account for possible viscous effects on the dissipation rate. This is permissible in the present study because the local turbulence Reynolds number ($\equiv k^{1/2}\ell_p/\nu$) was greater than 400 at all measuring points in the flow.

Distributions of P, D, and PS (or R) computed for the individual stress components along a wall bisector ($z/a = 1.0$) in the developing flow region of the duct ($x/D = 24$) are shown in Fig. 9.[4] From the figure it is evident that both the HL and LRR formulations model pressure-strain effects on the individual components very well. The figure indicates, for example, that energy received by the $\overline{u^2}$ component is redistributed to the $\overline{v^2}$ and $\overline{w^2}$ components, and that the production of $-\overline{uv}$ is offset by losses resulting from pressure-strain effects in the flow. The results shown in Fig. 9 also provide indirect confirmation of equation (7) for modeling ε, inasmuch as the sum of terms (S) is essentially zero over most of the boundary layer. Additional comparisons not included in this paper show that essentially the same level of agreement exists when ε is modeled in terms of k and α_2, i.e., when $\varepsilon = (\alpha_2 k)^{3/2}/\ell_p$ with $\alpha_2 = 0.26$ on the basis of values for c_1 and c_2 prescribed by Hanjalic and Launder [20]. The tail-up or tail-down behavior of S as the wall is approached is attributable primarily to the neglect of near-wall pressure-strain effects in equation (5).

In order to determine whether equations (5) and (7) model local behavior in the vicinity of a corner, distributions of P, D, and PS (or R) were evaluated for all six Reynolds stress components along the traverse $z/a = 0.1$ at $x/D = 24$. Figure 10 shows that local "source-sink" behavior is modeled remarkably well for each stress component. The modeling of pressure-strain effects by either the HL or LRR formulation leads to an almost exact balance of terms for each component. These results imply that either model may be used to predict local pressure-strain behavior in both the two-dimensional and three-dimensional regions of the flow. Note also that source-sink effects on $\overline{vw}$ cannot be modeled properly unless both "turbulent - turbulent" and "mean flow-turbulent" interactions are modeled in the pressure-strain term. This dependency implies that methods of closure in which only return-to-isotropy effects ("turbulent - turbulent" interactions) are modeled cannot be used to predict local flow behavior in the corner region.

Figure 10 shows that, at times, the production of $-\overline{uv}$ may be either positive or negative along the traverse $z/a = 0.1$. This behavior is the result of the local turbulent shear stress following the sign (+ or -) of the local mean velocity gradient. This can best be demonstrated by comparing $-\overline{uv}$ stress distributions measured at $x/D = 84$ (Fig. 11) with the isotach patterns shown in Fig. 3d. Along a traverse over which the sign of $-\overline{uv}$ changes (e.g., along $z/a = 0.2$), Fig. 12 shows that the mechanisms which lead to a loss or gain in $-\overline{uv}$ are directly correlated with the sign of $-\overline{uv}$ itself.

CONCLUDING REMARKS

This paper has presented and analyzed some recently acquired data in the entrance region of a square duct. The scope of the results presented is necessarily constrained by space limitations, and more extensive tabulated data are available from the authors upon request. On the basis of the results presented in this paper, the following conclusions may be drawn for developing turbulent flow in a square duct with uniform flow inlet conditions:

1. The simultaneous merging of four wall boundary layers leads to a relatively strong shear layer interaction downstream of the location where the boundary layers initially merge ($x/D = 32$). At $x/D = 40$ the axial centerline velocity peaks at a higher value than that observed in two-dimensional duct flow, and elevated mean rates of strain

---

[4] The distributions shown in Fig. 9 and in subsequent figures have been normalized by the duct half-width, a, and the bulk flow velocity, U_b.

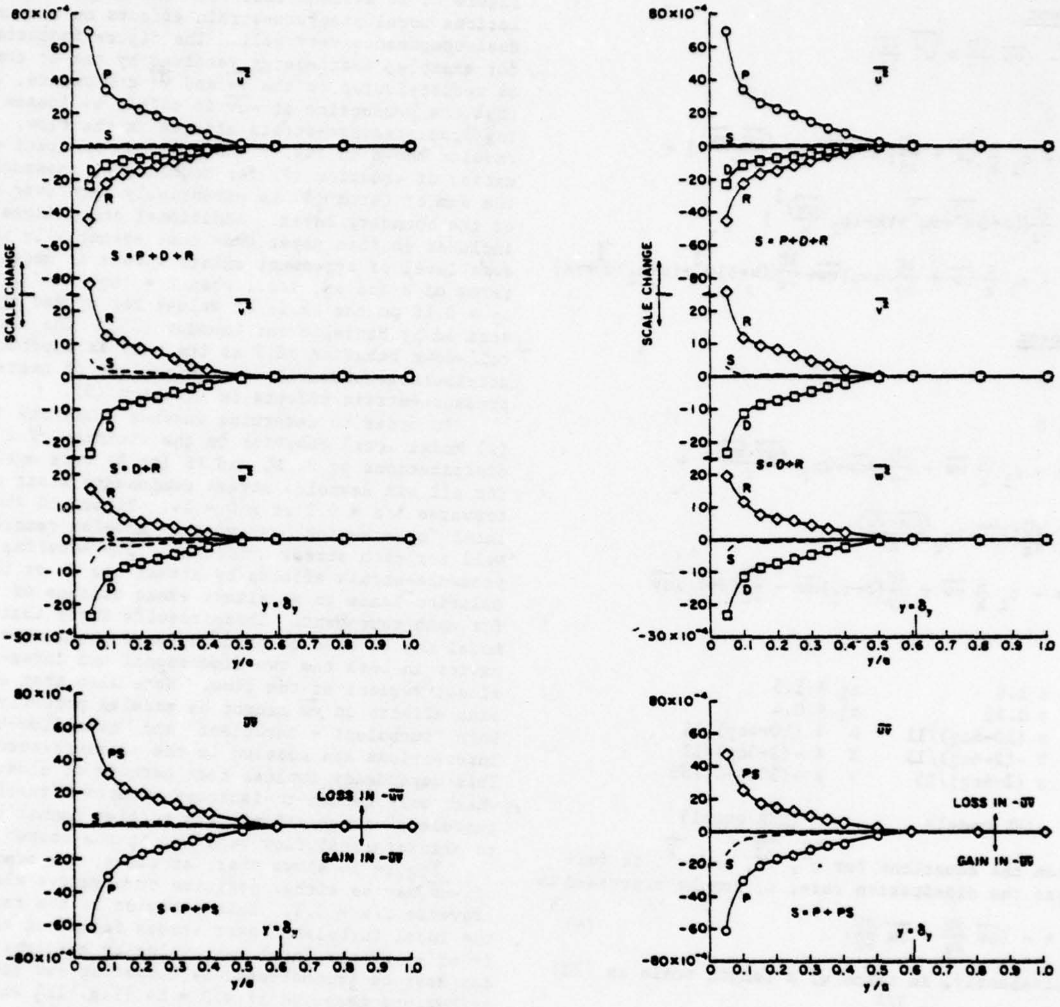

(a) HL model

(b) LRR model

Fig. 9 Production, dissipation, and pressure-strain effects on Reynolds stress components along the wall bisector z/a = 1; x/D = 24, Re = 2.5 x 10^5

exist in the flow. Certain Reynolds stress components ($\overline{u^2}$, and $-\overline{uv}$) are also elevated in comparison to values which exist when the flow is fully developed.

2. Convective and diffusive transport effects in the Reynolds stress transport equations are negligible in comparison to source-sink effects in this equation. The HL and LRR pressure-strain models can be used to model local pressure-strain behavior in both the two-dimensional and three-dimensional regions of the flow. The empirical constants, c_1, and c_2, as defined for two-dimensional flow, are also adequate for modeling local pressure-strain behavior in the three-dimensional corner region. A near-wall pressure strain correction term must be included in the Reynolds stress transport equations if local behavior in the immediate vicinity of a corner or bounding wall is to be modeled properly.

3. The dissipation rate is modeled reasonably well at the points not too close to a wall when ε is expressed in terms of the resultant primary shear stress and an extended form of Prandtl's mixing length. The same level of agreement exists where ε is modeled in terms of the turbulence kinetic energy by means of an empirical constant which is uniquely related to the values of c_1 and c_2 prescribed by Hanjalic and Launder [20].

ACKNOWLEDGEMENT

This study was sponsored by the National Science Foundation under NSF Grant GK-39956. The authors would like to express their appreciation to the National Science Foundation for their support of this work.

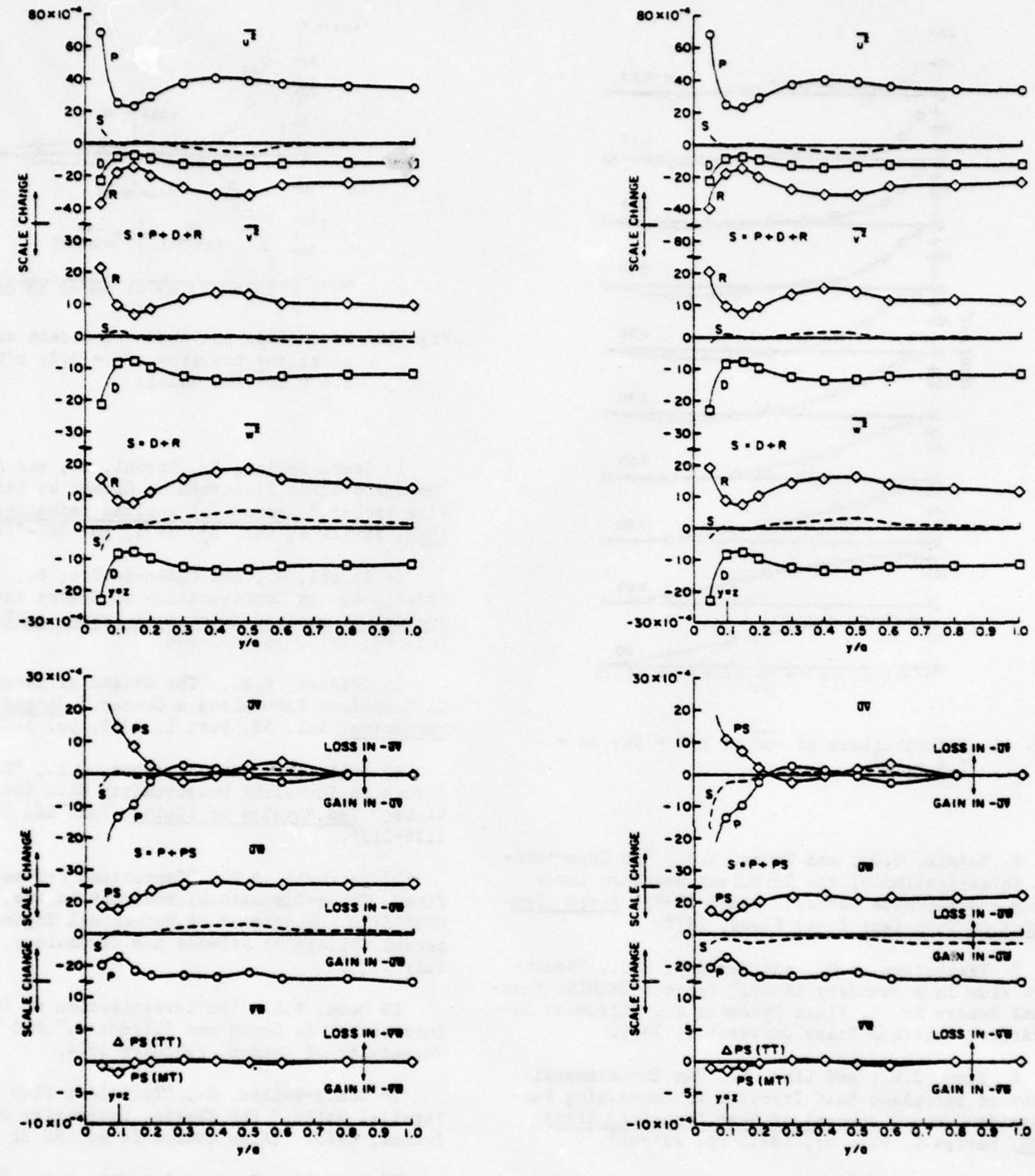

(a) HL model (b) LRR model

Fig. 10 Production, dissipation, and pressure-strain effects on Reynolds stress components along the traverse $z/a = 0.1$; $x/D = 24$, $Re = 2.5 \times 10^5$

REFERENCES

1 Agarwala, P., "The Hydrodynamic Entry Length in Rectangular Ducts," MS Thesis, Department of Chemical Engineering, University of Washington, Seattle, Washington, 1967.

2 Bromfield, F.S., "The Hydrodynamic Entry Length in Rectangular Channels," PhD Thesis, Department of Chemical Engineering, University of Washington, Seattle, Washington, 1964.

3 Pletcher, R.H., and McManus, H.N., Jr., "Secondary Flow in the Entrance Section of a Straight Rectangular Duct," Developments in Mechanics, Proceedings of the Eighth Midwestern Mechanics Conference, Pergamon Press, New York, 1965.

4 Perkins, H.J., "The Formation of Streamwise Vorticity in Turbulent Flow," Journal of Fluid Mechanics, Vol. 44, Part 4, 1970, pp. 721-740.

5 Bragg, G.M., "The Turbulent Boundary Layer in a Corner," Journal of Fluid Mechanics, Vol. 36, Part 3, 1969, pp. 485-503.

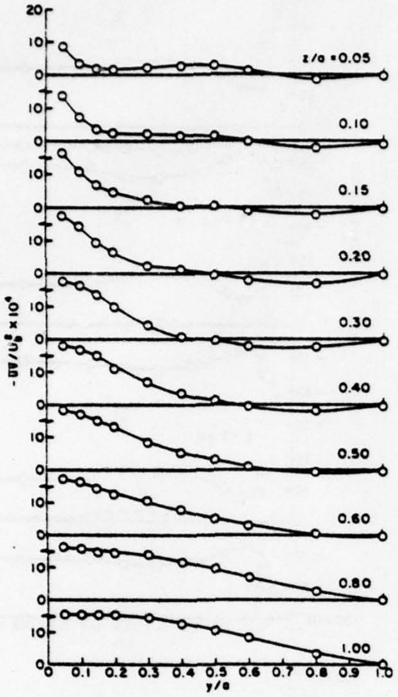

Fig. 11 Distributions of $-\overline{uv}$ at x/D = 84; Re = 2.5 x 10^5

6 Mojola, O.O., and Young, A.D., "An Experimental Investigation of the Turbulent Boundary Layer Along a Streamwise Corner," AGARD CP-93, Agard Symposium on Turbulent Shear Flows, 1972.

7 Veenhuizen, S.D., and Meroney, R.N., "Secondary Flow in a Boundary Layer," Project THEMIS, Technical Report No. 3, Fluid Dynamics and Diffusion Laboratory, Colorado State University, 1969.

8 Yang, J.W., and Liao, N., "An Experimental Study of Turbulent Heat Transfer in Converging Rectangular Ducts," Journal of Heat Transfer, Trans. ASME, Series C, Vol. 95, 1973, pp. 453-457.

9 Ahmed, S., "Turbulent Flow in Non-Circular Ducts," PhD Thesis, Department of Mechanical Engineering, University of Waterloo, 1971. (See also International Journal of Heat and Mass Transfer, Vol. 14, 1971, pp. 365-375.)

10 Legkiy, U.M., and Makarov, A.S., "Some Regularities of the Flow of the Mixed Boundary Layer in Entry Lengths of Rectangular Ducts," Fluid Mechanics-Soviet Research, Vol. 2, No. 1, January-February 1973.

11 Po, J.K., "Developing Turbulent Flow in the Entrance Region of a Square Duct," MS Thesis, Department of Mechanical Engineering, University of Washington, Seattle, Washington, February 1975.

12 Page, R.J., "An Experimental Study of Developing Turbulent Flow in a Square Duct," MS Thesis, Department of Mechanical Engineering, University of Washington, Seattle, Washington, March 1971.

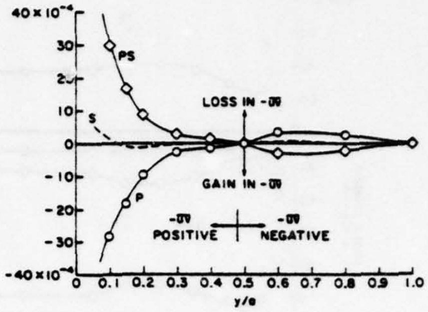

Fig. 12 Production and pressure-strain effects on $-\overline{uv}$ along the traverse z/a = 0.2; x/D = 84, Re = 2.5 x 10^5 (HL model)

13 Comte-Bellot, G., Strohl, A., and Alcaraz, E., "On Aerodynamic Disturbances Caused by Single Hot-Wire Probes," Journal of Applied Mechanics, Trans. ASME, Series E, Vol. 38, 1971, pp. 767-774.

14 Strohl, A., and Comte-Bellot, G., "Aerodynamic Effects Due to Configuration of X-Wire Anemometers," Journal of Applied Mechanics, Trans. ASME, Series E, Vol. 40, 1973, pp. 661-666.

15 Gessner, F.B., "The Origin of Secondary Flow in Turbulent Flow Along a Corner," Journal of Fluid Mechanics, Vol. 58, Part 1, 1973, pp. 1-25.

16 Hill, J.C., and Sleicher, C.A., "Equations for Errors in Turbulent Measurements With Inclined Hot-Wires," The Physics of Fluids, Vol. 12, 1969, pp. 1126-1127.

17 Tatchell, D.G., "Convection Processes in Confined, Three-Dimensional Boundary Layers," Report HTS/75/20, Department of Mechanical Engineering, Imperial College of Science and Technology, London, July 1975.

18 Dean, R.B., "An Investigation of Shear Layer Interaction in Ducts and Diffusers," PhD Thesis, University of London, February 1974.

19 Comte-Bellot, G., "Turbulent Flow Between Two Parallel Walls," PhD Thesis, University of Grenoble France, 1963. (Also available as ARC 31 609.)

20 Hanjalic, K., and Launder, B.E., "A Reynolds Stress Model of Turbulence and Its Application to Thin Shear Flows," Journal of Fluid Mechanics, Vol. 52, Part 4, 1972, pp. 609-638.

21 Launder, B.E., Reece, G.J., and Rodi, W., "Progress in the Development of a Reynolds Stress Turbulence Closure," Journal of Fluid Mechanics, Vol. 68, Part 3, 1975, pp. 537-566.

22 Gessner, F.B., and Emery, A.F., "A Reynolds Stress Model for Turbulent Corner Flows, Part I: Development of the Model," Journal of Fluids Engineering, Trans. ASME, Series I, Vol. 98, 1976, pp. 261-268.

MEASUREMENTS OF
THE MEAN VELOCITY AND OF THE REYNOLDS STRESS TENSOR IN A THREE-DIMENSIONAL TURBULENT BOUNDARY LAYER INDUCED BY A CYLINDER STANDING ON A FLAT WALL

R. DECHOW and K. O. FELSCH

Universität Karlsruhe, Institut für Strömungslehre und Strömungsmaschinen,
D - 7500 Karlsruhe

ABSTRACT

Extensive experiments were carried out in a three-dimensional incompressible turbulent boundary layer growing in front of a cylinder standing on a flat wall in a wind tunnel. Beginning with the quasi two-dimensional boundary layer far in front of the cylinder the development of the boundary layer profiles were investigated along a streamline of the free stream up to the region behind the "three-dimensional" separation. At 14 different stations, profiles were measured of the mean velocity vector, the 6 components of the turbulent stress tensor, the static pressure and in addition the wall shear stress vector. The turbulence measurements were carried out with a single hot wire probe and with a rotatable X-probe, whose axis could be aligned with the direction of the local mean velocity. From this data the direction of the velocity gradient and of the turbulent shear stress were evaluated. The applicability of different shear stress models is checked and discussed.

NOMENCLATURE

c	wall-parallel component of the mean velocity
c_1, c_2, c_3	fluctuating velocity components (see fig. 5)
c_p	pressure coefficient
ℓ_{mix}	mixing length
s	magnitude of the mean velocity in the boundary layer (see fig. 4 and 5)
s_1, s_2, s_3	fluctuating velocity components (see fig. 5)
u_{Bez}	reference velocity ($u_{\delta_1} = 22{,}7$ m/s; $u_{\tau_1} = 0{,}879$ m/s)
u_δ	mean velocity at the edge of the boundary layer
u_τ	friction velocity
u, v, w	components of the mean velocity (see fig. 4)
x, y, z	boundary layer co-ordinates
α	flow angle at the edge of the boundary layer relativ to the tunnel axis (see fig. 4)
β	flow angle inside the boundary layer relative to the wall (pitch, upwash) (see fig. 4)
ν_e	eddy viscosity
γ	flow angle inside the boundary layer relative to the x-y-plane (yaw) (see fig. 4)
γ_G	angle of the velocity gradient vector relative to the x-y-plane
γ_τ	angle of the wall-parallel component of the shear stress vector relative to the x-y-plane
ρ	density
$\lvert\tau\rvert$	magnitude of shear stress vector
τ_w	wall shear stress

1. INTRODUCTION

For the development of better calculation methods for three-dimensional turbulent boundary layers more data are urgently needed, in particular concerning the behaviour of the turbulence properties. Recent meetings on this subject, (e.g. Euromech 60 in Trondheim 1975) confirm this necessity. The purpose of this paper is to contribute new data to this subject.

V. d. BERG et. al. [1] and ELSENAAR et. al. [2] have made complete measurements in a three-dimensional boundary layer of the infinite swept wing type; in the present case data of a more general type are to be presented, obtained in a three-dimensional boundary layer in front of an obstruction mounted upon a flat plate. As in the case of EAST et. al. [3] (who only made measurements of the mean velocity) the obstruction is a cylindrical body, and the boundary layer on the flat plate in front of the body is to be investigated.

2. DESCRIPTION OF THE WORKING SECTION

The measurements were carried out in the boundary layer wind tunnel of the Institut für Strömungslehre und Strömungsmaschinen of the University of Karlsruhe. Figure 1 shows the sketch of the working section which is a rectangular duct of 1500 mm × × 300 mm cross section and 3000 mm length. The cylinder diameter is 320 mm with a streamlined afterbody which prevents separation. The cylindrical body extends from the floor to the roof, the working area being near to the floor. The boundary layer probes are mounted in a probe-holder which is movable normal to the walls and can be rotated around the axis normal to the walls by a traversing mechanism. The probe-holder fits through slots in the upper wall of the working section and can be shifted together with the traversing gear along the slots whose direction is parallel to the tunnel axis. In addition a part of the roof plate is movable spanwise together with the probe. The floor plate is designed in a similar manner with pressure taps and the possibility of inserting flush-mounted hot films. This design of the working section allows every point of the working area to be reached by the probes.

Figure 2 shows some streamlines in the working section: the wall streamlines were determined from an oil flow pattern, whereas the lines in the free stream are drawn from direction measurements with a Conrad-tube. The quasi two-dimensionality at the start of the region of the three-dimensional separation can easily be seen. In this region there exist large gradients of the mean velocity in all directions and the vector of the mean velocity carries a component normal to the wall which is not negligible. These two facts are important: the first for the critical examination of the results of this work, the second for the applicability of the different measurement techniques.

3. MEASURING PROGRAM

In addition to the direction of the streamlines in the free stream the magnitude of the velocity and the static pressure were also measured, as was the static pressure at the wall. The isobars in the free stream and at the wall are shown in figure 3, where one can see the large differences near the cylinder.

One streamline in the free stream was chosen (see fig. 2) along which the boundary layer profiles were investigated at 10 separate stations (No. 1 – 10). In addition, 2 stations (No. 11 and 12) on a streamline further removed from the cylinder and 2 stations (No. 13 and 14) on the median plane were chosen. At these 14 stations the following variables were measured:

I) the vector of the mean velocity,
II) the 6 components of the Reynolds stress tensor,
III) the static pressure and
IV) the value and direction of the wall shear stress.

For presentation purposes a streamline coordinate system is used whose x-axis is aligned with the direction of the mean velocity at the edge of the boundary layer and projected onto the wall at every station. Figures 4 and 5 show the symbols used for the mean velocity and the fluctuating velocity components.

4. EXPERIMENTAL METHODS

In the free stream area the value of the mean velocity u was measured with a Pitot-tube and a static pressure probe after evaluation of its direction with a Conrad-tube. Inside the boundary layer the value of the mean velocity vector s, the yaw angle γ and the turbulence intensity $\sqrt{\overline{s_1^2}}$ were measured with a boundary layer type single hot-wire sensor with gold plated ends. The pitch angle β and the remaining 5 components of the stress tensor were measured with a X-probe. The design of the probe holder allowed yawing around the y-axis, pitching relative to the wall and turning around the probe axis without the probe tip leaving the measurement point. It was thus possible to align the probe axis with the local direction of the mean velocity s. Figure 6 shows the X-probe in the test section. Due to this alignment the two wires of the X-probe are equally sensitive to the fluctuating component in the direction of the local mean velocity and to the component normal to the mean velocity which lies in the plane formed by the wire and the mean velocity. By turning the X-probe around its axis in steps of 45 degrees combined with suitable processing of the signals the 6 components of the Reynolds stress tensor can be evaluated. After calibration and linearisation of the wire signals this kind of evaluation needs no further assumptions and corrections and is the consistent application of the X-probe methods described by HINZE [4] and BRADSHAW et. al. [5], it seems to be comparatively accurate. This is of course only valid, if influence of temperature, dust, electronic drift, mal-positioning of the probe, imperfections in the manufacturing of the probe and last but not least the influence of the non-uniform flow field are properly taken into consideration.

The static pressure inside the boundary layer was evaluated with the usual disc-probe; pressure taps were used for the wall pressure. The value of the wall shear stress was measured with a Preston-tube. The direction of the wall streamlines was evaluated in 3 different ways:

I) from the oil flow pattern,
II) by extrapolating the direction of the mean velocity at a wall distance y = 0,2 mm and
III) with a turnable flush-mounted hot-film probe.

5. PRESENTATION OF THE MEASUREMENTS

In this section the most important results of the measurements will be shown. For the whole data set see DECHOW [6]. In the first part the governing flow parameters are shown along the streamline described in section 3 and marked in figure 2. This will explain the nature of the flow at the edge of the boundary layer and will be helpful for the later understanding of the boundary layer data. These are presented in the second part, where 4 of the 14 profiles measured are described.

5.1. Flow Parameters Along the Streamline

Figure 11 shows the flow parameters plotted against the x-coordinate, which follows the projection of the streamline on the wall. Along this streamline the development of the boundary layer was investigated at the stations 1 to 10 (see figure 2). The measurements at stations 11 to 14 were made for comparison purposes. In the upper part of figure 11 the pressure coefficient c_p is drawn; $c_{p\delta}$ is the pressure at the edge of the boundary layer, c_{p0} its value at the wall. The wall pressure on the centerline c_{p0} (z = 0) is included for comparison.

The lower part shows the mean velocity u_δ and the friction velocity u_τ, both made dimensionless with their values at station 1. In this part only one value on the centerline (z = 0) is included for u_τ and u_δ.

The figure shows a small deceleration of the velocity up to the line of three-dimensional separation (x ≈ 520 mm) and an acceleration after this line. In the region of acceleration the friction velocity grows much faster than the velocity at the edge. This follows the development of the static pressure, which drops sharper at the wall than at the edge. The velocity profiles will show later a strong acceleration near the wall in this region. All these facts are well matched.

The directions relative to the tunnel of the free streamline, that is the angle α, and of the near-wall streamlines, that is the sum of α and the yaw angle γ near or at the wall, are shown in figure 12. Again there is a strong change at the wall in the region near the so-called three-dimensional separation. The different measurement show different directions in this region. This can be interpreted by the different measuring methods and by the nature of the flow.

5.2. Boundary Layer Profiles

Only 4 representative stations are here selected to indicate the results of the measurements taken at the 10 stations on the streamline (see figures 7a to 10c). In each of these figures the parameters are non-dimensionalised and plotted against the wall distance y in mm. The components u, v and w of the mean velocity are plotted in the upper figures (fig. 7a – 10a) non-dimensionalised by u_δ. The turbulence intensities were measured in components s_1, s_2 and s_3 relative to the mean velocity s. They will be shown here after conversion to components c_1, c_2 and c_3 relative to the mean velocity component c parallel to the wall (see fig. 5). Figures 7b – 10b show the rms-values of the intensities c_1, c_2 and c_3 non-dimensionalised by the friction velocity u_τ. In figures 7c – 10c the shear stress components $\overline{c_1 c_2}$, $\overline{c_2 c_3}$ and $\overline{c_2 c_3}$ are plotted, this time non-dimensionalised with u_τ^2.

The three diagrams of figure 7 show the profiles at station 1, which lies about 1500 mm downstream of the beginning of the working section. The mean velocity profile is a quasi two-dimensional one; the profiles of the fluctuating components and of the shear stress ($\overline{c_1 c_2}$) are in good agreement with the flat plate boundary layer data of KLEBANOFF [7]. Figures 8, 9 and 10 belong to stations 5, 7 and 10 and the increasing influence of three-dimensionality can clearly be seen. The data at stations 5 and 7 correspond well to the measurements of v.d. BERG et. al. [1] and ELSENAAR et. al. [2], whereas at station 10 (fig. 10a,b,c) the shape of the profiles deviates widely from that observed normaly in three-dimensional boundary layer because of the extreme conditions existing in this region, as described in section 5.1. At this station the vector of the mean velocity has in the middle part of the boundary layer a component v normal to the wall of about 10 % of u_δ : as the wall is approached v first tends to zero and then changes its direction. In addition the w component grows. This results in the above – mentioned acceleration of the flow near the wall which is produced by a secondary boundary layer originating in the horseshoe vortex at the bottom of the cylinder. A discussion of the behaviour of the stress tensor follows in the next section together with the other related parameters.

As already shown in figure 3 the static pressure at the wall and in the free stream differ in the region near the three-dimensional separation. The profile of the pressure coefficient at station 10 is shown in figure 13. Due to the possibility of errors, these measurements should be interpreted carefully, nevertheless the data do show a large deviation from the assumption of constant pressure inside the boundary layer.

6. FURTHER RESULTS

In order to make possible a comparison with existing calculation methods and existing data, other related parameters were computed from the present measurements. It is especially important to include information about the nature of the turbulent shear stresses. In contrast to the two-dimensional case one has to take into account the vectorial nature of the mean velocity and of the shear stress in a three-dimensional boundary layer, i.e. the direction of the different parameters must be considered. Several calculation methods for turbulent boundary layers use empirical equations for the shear stress and relate it to the mean velocity gradient, e.g. the eddy-viscosity or the mixing-length hypotheses. If these equations are to be used in the same way for three-dimensional turbulent boundary layers, the directions of the shear stress and the velocity gradient must be taken into consideration.

If it is assumed that the shear stress component $\overline{c_1 c_3}$ has no influence on the mean velocity profile, the magnitude of the resultant shear stress can be computed by:

$$|\tau| = \rho \cdot \sqrt{\overline{c_1 c_2}^2 + \overline{c_2 c_3}^2}$$

and its angle relative to the x-y-plane of the boundary layer co-ordinates is given by:

$$\gamma_\tau = \operatorname{arc\,tg}\left(\frac{\overline{c_2 c_3}}{\overline{c_1 c_2}}\right) + \gamma \qquad (\text{for } \overline{c_1 c_2} < 0)$$

or

$$\gamma_\tau = \operatorname{arc\,ctg}\left(\frac{\overline{c_1 c_2}}{\overline{c_2 c_3}}\right) + \gamma \qquad (\text{for } \overline{c_1 c_2} > 0) .$$

(N.B. $\overline{c_2 c_3}$ is greater than zero in all measured profiles.)

For computing the magnitude of the velocity gradient vector only the components parallel to the wall are considered:

$$\left|\frac{\partial c}{\partial y}\right| = \sqrt{\left(\frac{\partial u}{\partial y}\right)^2 + \left(\frac{\partial w}{\partial y}\right)^2}$$

and its angle relative to the x-y-plane is thus:

$$\gamma_G = \operatorname{arc\,tg} \frac{\partial w}{\partial y} \Big/ \frac{\partial u}{\partial y} .$$

Other authors have already shown, that the direction of the mean velocity gradient vector and the direction of the resultant shear stress do not agree in three-dimensional boundary layers (see [2]): this is also the case in the boundary layer investigated here, where very large discrepancies are found.

Figures 14, 15 and 16 indicate the magnitude of the discrepancies in the present flow and also contain the yaw angle measured at stations 5, 7 and 10 (note that in figure 16 the scale has been altered).

The eddy-viscosity relates the shear stress and the velocity gradient via:

$$\nu_e = \frac{|\tau|}{\rho} \cdot \frac{1}{\left|\frac{\partial c}{\partial y}\right|}$$

non-dimensionalising with u_δ and a displacement thickness δ_{1u} (formed from the velocity u) it follows that:

$$k_2 = \frac{\nu_e}{u_\delta \cdot \delta_{1u}}$$

which is often constant for the central part of two-dimensional boundary layer profiles. Figure 17 shows k_2 versus y/δ (δ = = boundary layer thickness) for all 10 stations along the streamline and it may be noted that only at the stations 1, 2 and 3 is the shape similar to the two-dimensional case.

For the mixing length the defining relation is

$$\ell_{mix} = \sqrt{\frac{|\tau|}{\rho} \cdot \frac{1}{\left|\frac{\partial c}{\partial y}\right|}}$$

and near the wall:

$$\ell_{mix} = k_1 \cdot y$$

with $k_1 = 0.41$ for two-dimensional boundary layers. Figure 18 shows the mixing length versus the wall distance (both non-dimensionalised with δ) for all the 10 stations. Again there exists a large deviation in comparison with the two-dimensional profile at station 1.

A comparison with other shear stress models in [6] has shown similar results.

7. CONCLUSIONS

The measurements presented in this paper give a comprehensive description of the investigated three-dimensional turbulent boundary layer. Due to the extreme care taken with regard to the measurement techniques the accuracy and reliability of the present data are believed to be comparatively good. The nature of the turbulent shear stress is the most interesting part of the results, indicating that the shear stress models used in two-dimensional computation methods can not be applied to three-dimensional turbulent boundary layers without additional new empirical input. No correlation could be found between the wall-parallel shear stress and the velocity gradient $\partial c/\partial y$. In the boundary layer investigated in the present work noticeable gradients exist also in other directions: it therefore seems necessary to examine the relationship between all three components of the shear stress and all components of the velocity gradient vector; to do this however, further measurements are necessary.

Other results presented here indicate that the applicability of the boundary layer simplifications to three-dimensional turbulent boundary layers (at least those near separation) should be discussed. Further, the results show a good agreement with Elsenaar's data from an infinite swept wing, but the three-dimensional effects are noticeably stronger in the present case.

8. REFERENCES

1 Berg, B. v. d. and Elsenaar, A., "Measurements in a Three-Dimensional Incompressible Turbulent Boundary Layer in an Adverse Pressure Gradient under Infinite Swept Wing Conditions", NLR TR 72092 U, 1972.

2 Elsenaar, A. and Boelsma, S. H., "Measurements of the Reynolds Stress Tensor in a Three-Dimensional Turbulent Boundary Layer under Infinite Swept Wing Conditions", NLR TR 74095 U, 1975.

3 East, L. F. and Hoxey, R. P., "Low-Speed Three-Dimensional Turbulent Boundary Layer Data", Part I and II, RAE T. R. 69041 and 69137, 1969.

4 Hinze, J. O., "Turbulence", 2nd ed., McGraw-Hill, 1975.

5 Bradshaw, P. and Johnston, R. F., "Turbulence Measurements with Hot-Wire Anemometers", NPL Notes on Applied Science, 33. 1963.

6 Dechow, R., "Mittlere Geschwindigkeit und Reynoldsscher Spannungstensor in der dreidimensionalen turbulenten Wandgrenzschicht vor einem stehenden Zylinder", Strömungsmechanik und Strömungsmaschinen, Mitt. d. Inst. für Strömungslehre und Strömungsmaschinen, Univ. Karlsruhe, Heft 21, 1977.

7 Klebanoff, P. S., "Characteristics of Turbulence in a Boundary Layer with Zero Pressure Gradient", NACA Report 1247, 1955.

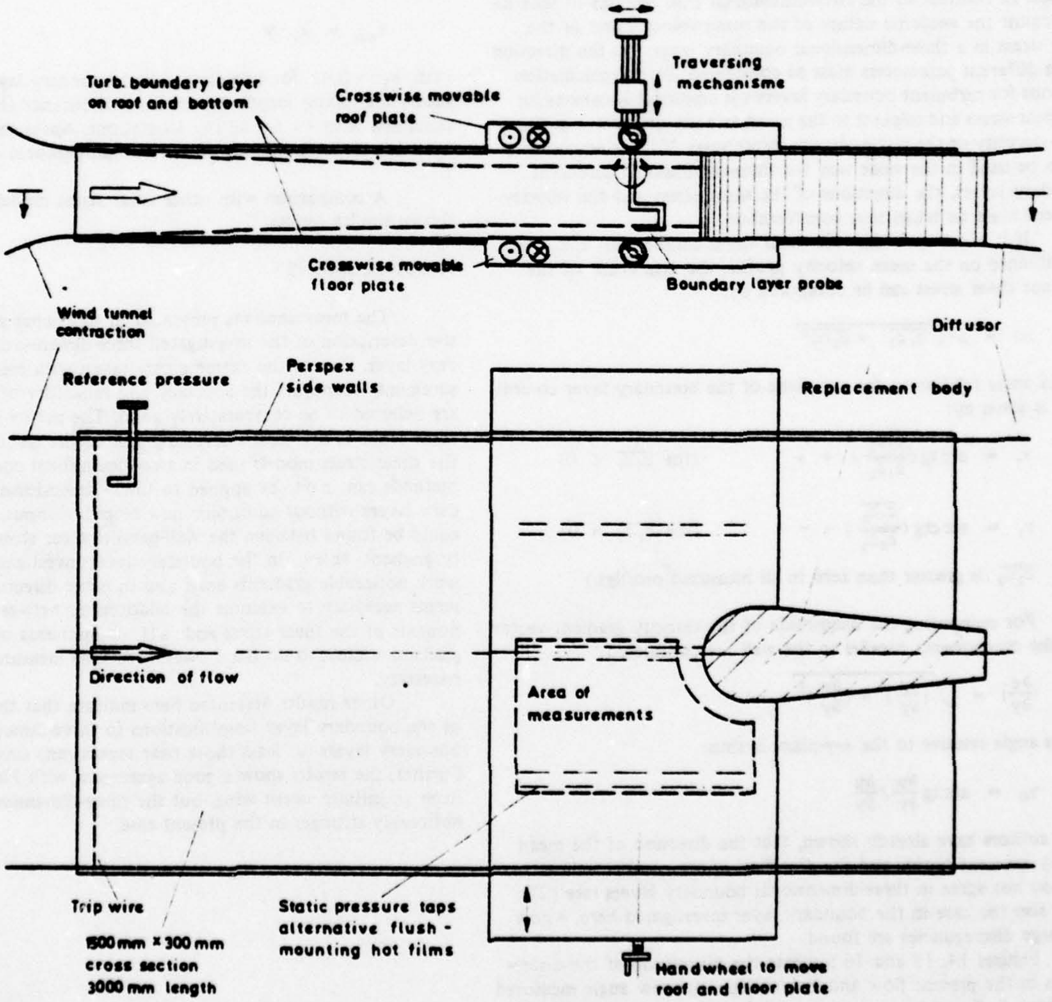

FIG. 1 Working section for three-dimensional boundary layer research

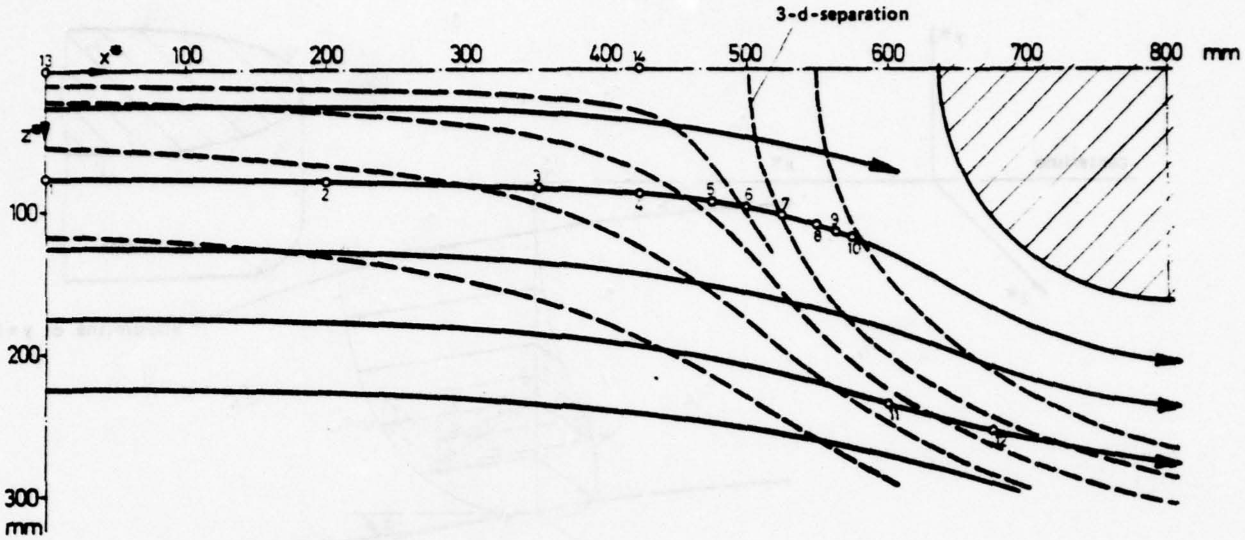

FIG. 2 Streamline pattern and positions of measuring stations

—— Streamlines at y = δ

– – – Wall streamlines (from oil flow pattern)

○ 4 Positions of measuring stations

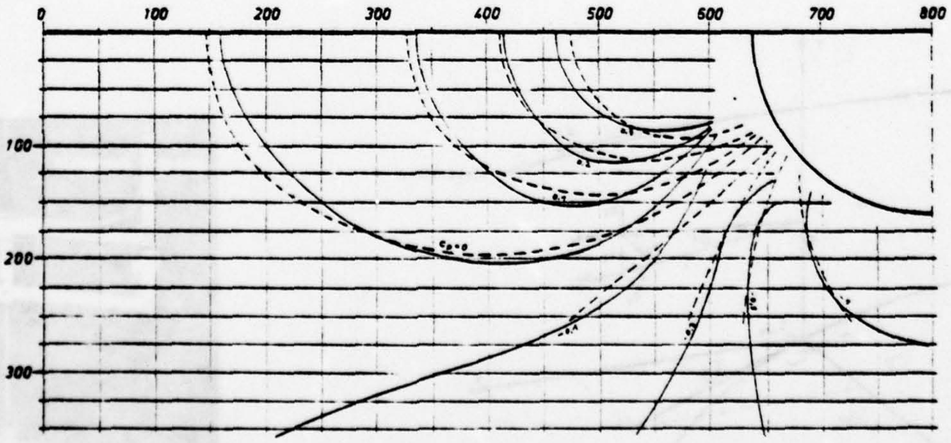

FIG. 3 Static pressure at the wall and in the free stream

—— Pressure at y = 100 mm

– – – Wall pressure

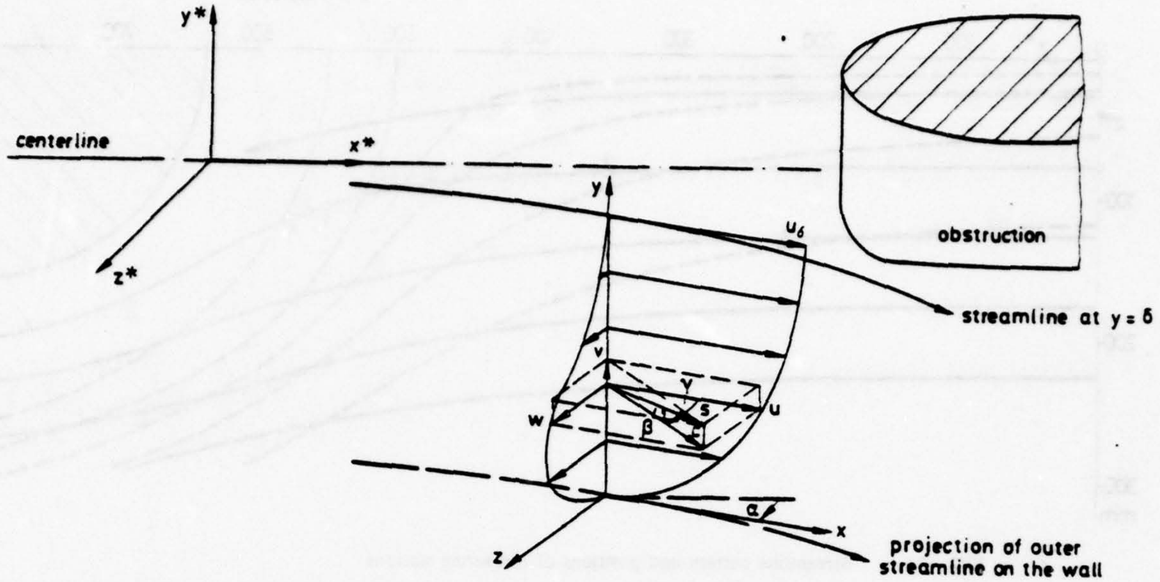

FIG. 4 Coordinates and mean velocities in a three-dimensional boundary layer

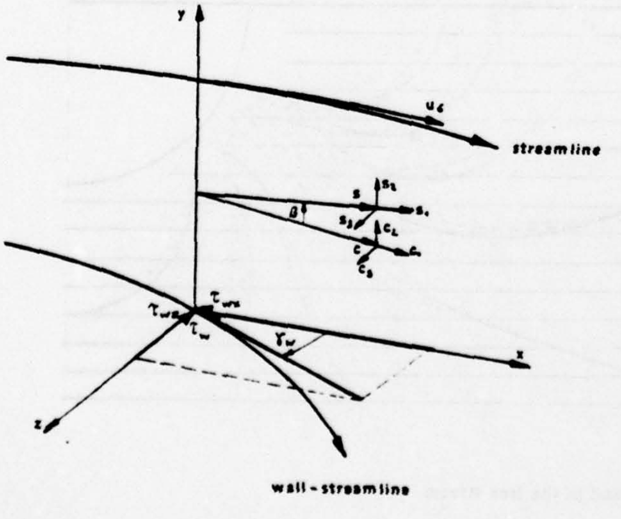

FIG. 5 Fluctuation velocities and wall shear stress in a three-dimensional boundary layer

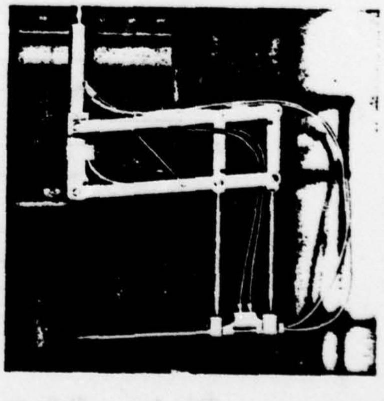

FIG. 6 X-Probe and probe holder in the test section

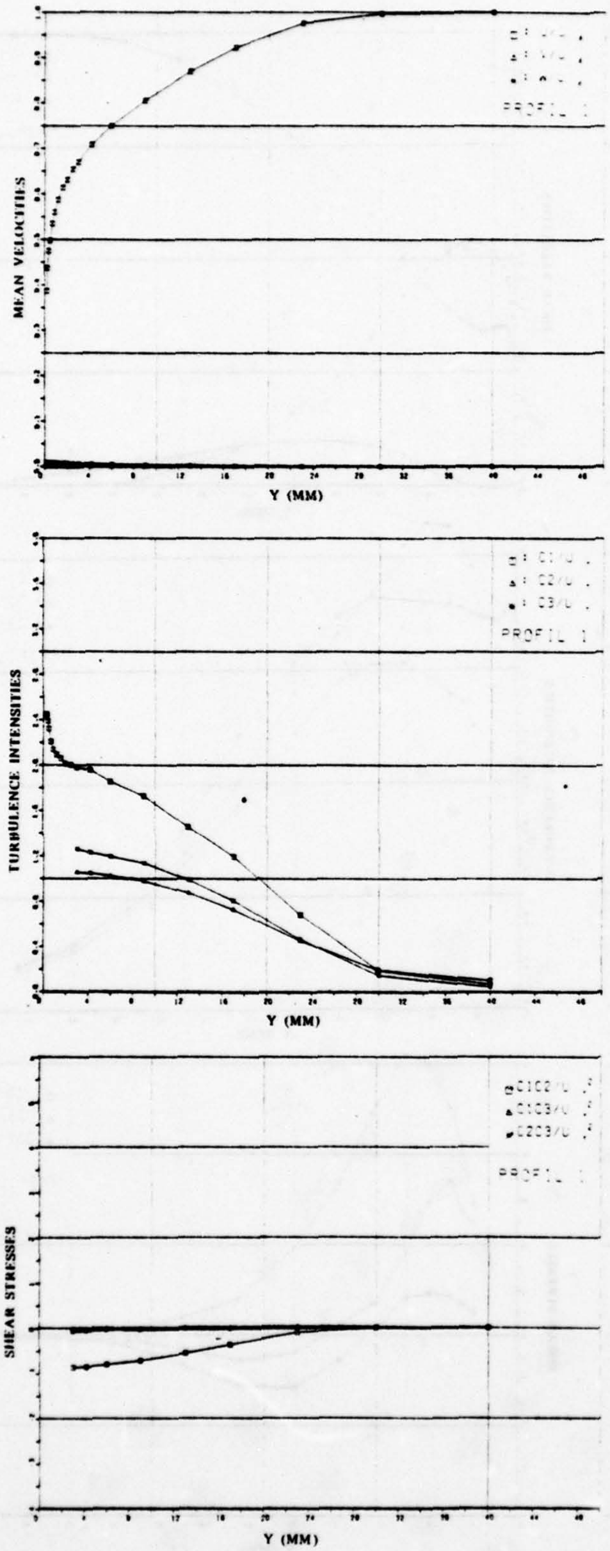

FIG. 7 a–c Mean velocities, turbulence intensities and turbulent shear stresses, POSITION 1

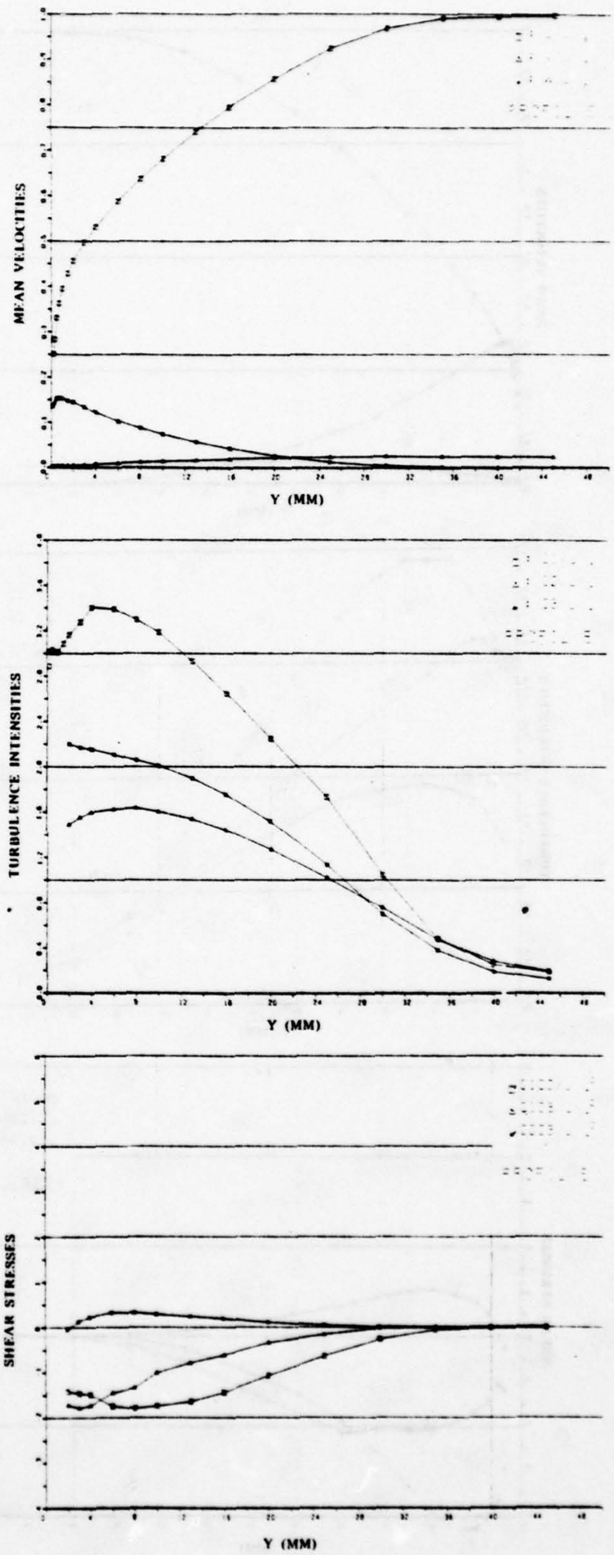

FIG. 8 a–c Mean velocities, turbulence intensities and turbulent shear stresses, POSITION 5

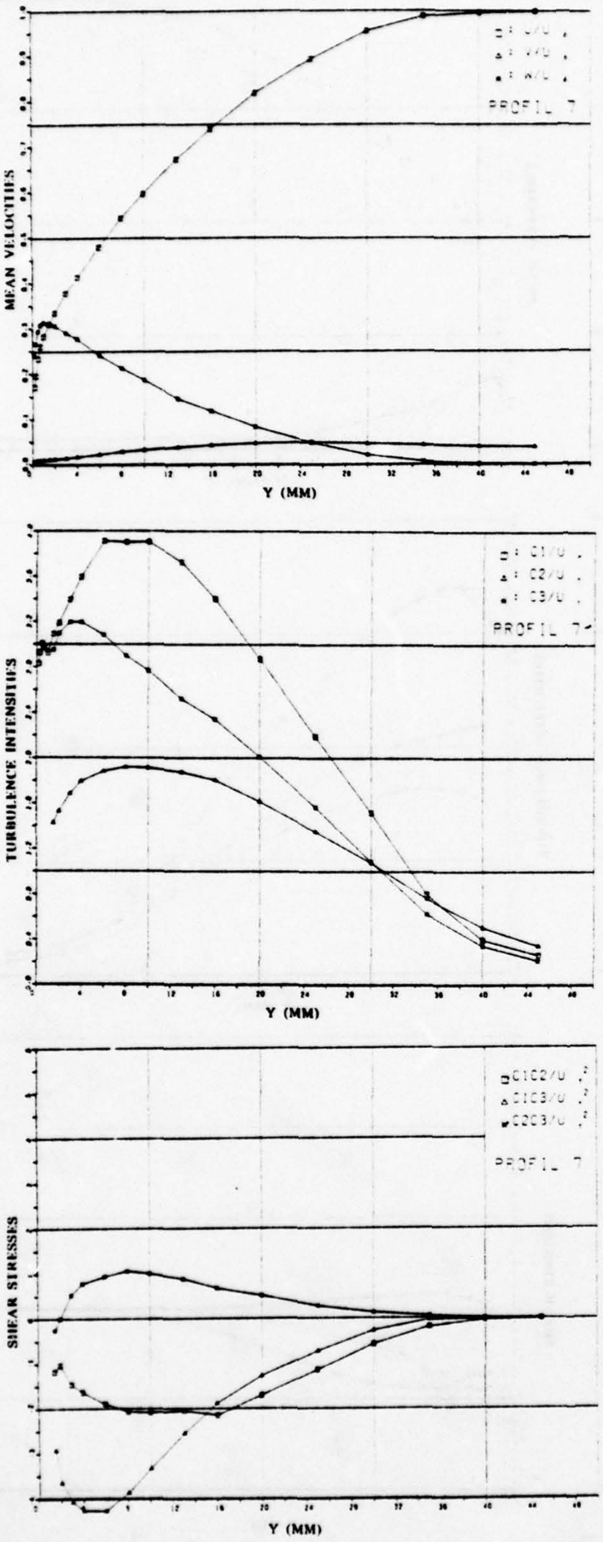

FIG. 9a–c Mean velocities, turbulence intensities and turbulent shear stresses, POSITION 7

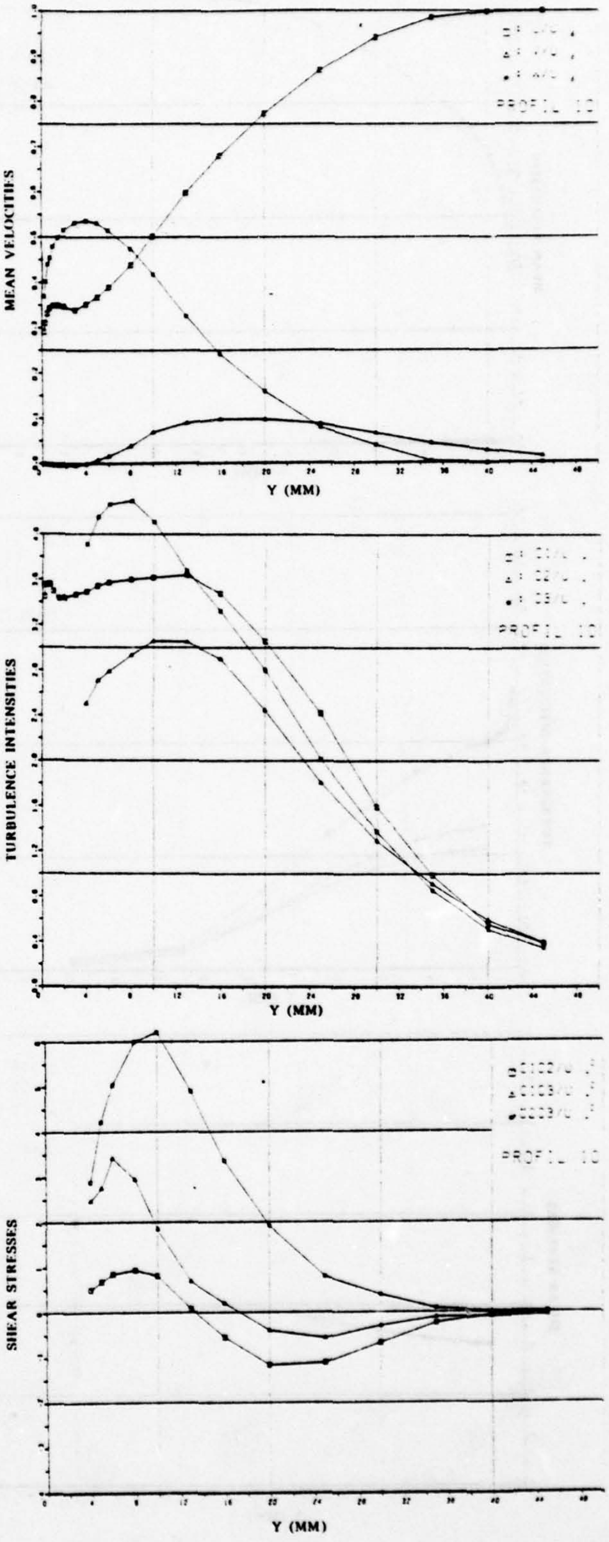

FIG. 10a–c Mean velocities, turbulence intensities and turbulent shear stresses, POSITION 10

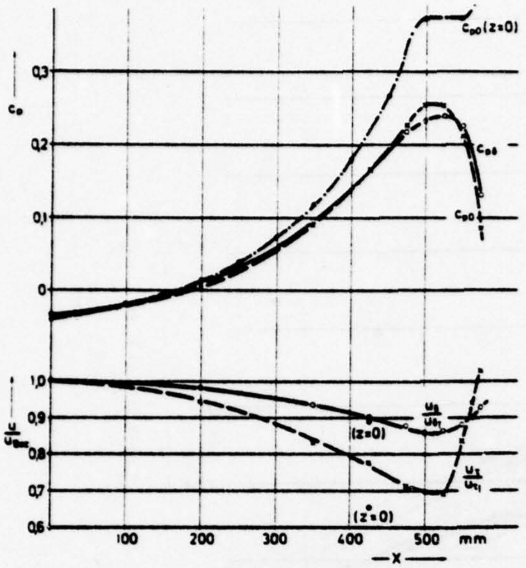

FIG. 11 Static pressure coefficient, free stream velocity and friction velocity along the streamline (positions 1 – 10) and on centerline

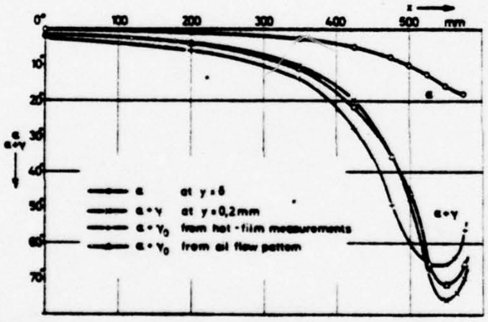

FIG. 12 Direction of the streamlines

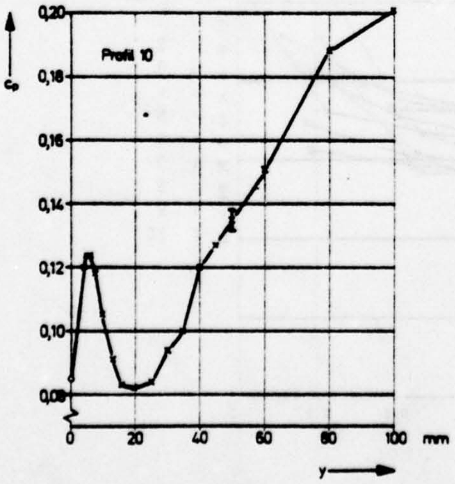

FIG. 13 Pressure coefficient $c_p(y)$

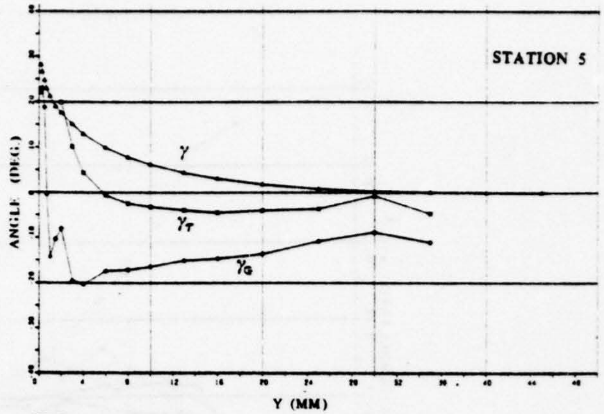

FIG. 14 ▲

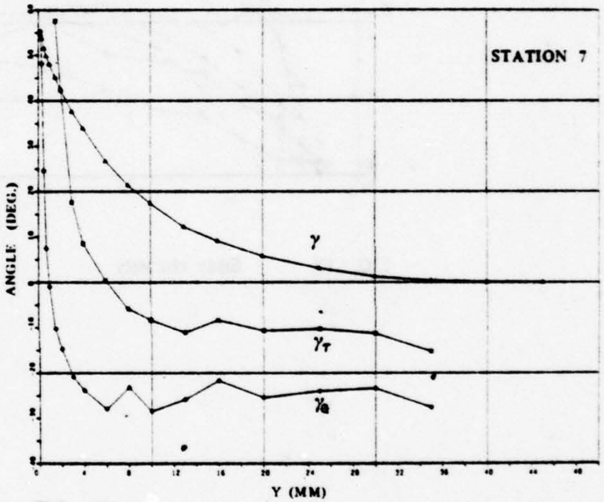

FIG. 15 ▲

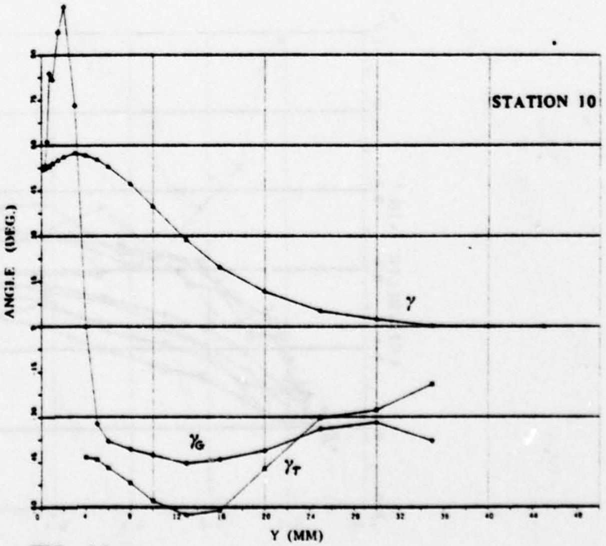

FIG. 16 ▲

FIG. 14 – 16 Direction of velocity (γ), velocity gradient (γ_G) and shear stress (γ_τ)

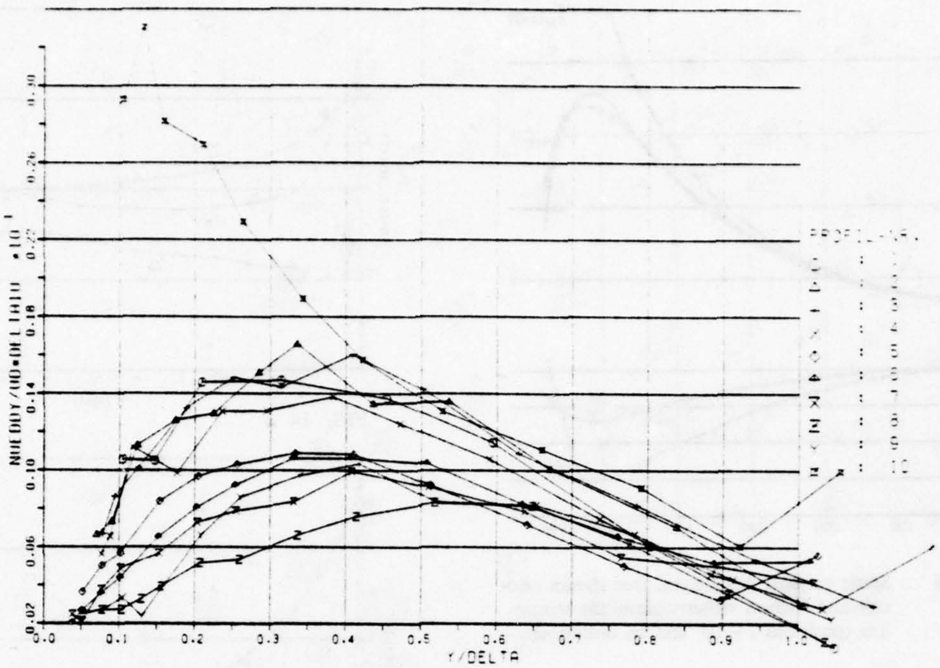

FIG. 17 Eddy viscosity

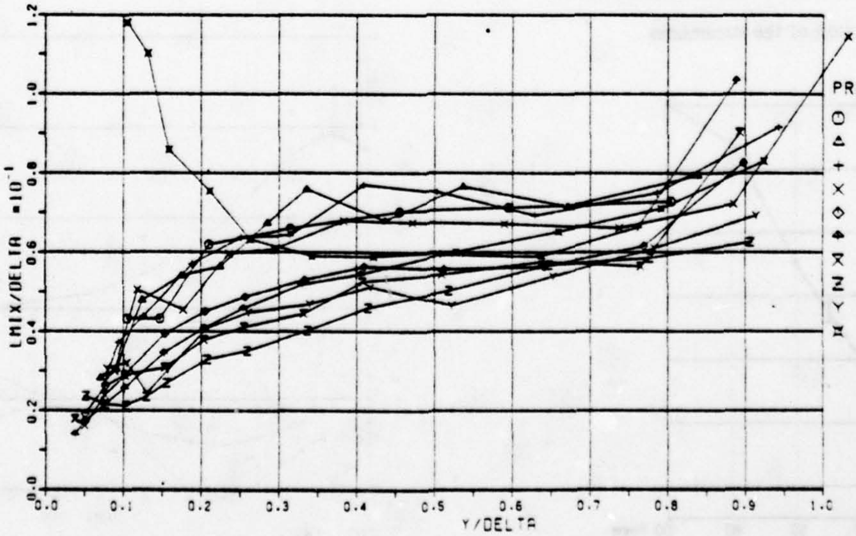

FIG. 18 Mixing length

SOME EFFECTS OF LONGITUDINAL WALL-CURVATURE ON TURBULENT BOUNDARY LAYERS

by

B. G. Shivaprasad
Project Assistant
Aeronautical Engineering Department
Indian Institute of Science
Bangalore, India

B. R. Ramaprian
Research Scientist and Adj. Assistant Professor
Iowa Institute of Hydraulic Research
University of Iowa
Iowa City, Iowa

ABSTRACT

Some results of an experimental study of the effect of mild longitudinal wall-curvature on turbulent boundary layers are presented. The use and limitations of curvature-buoyancy analogy are examined. The effects of curvature on the turbulent shear stress are discussed. Lastly, data on the effects of curvature on some aspects of the fine scale structure of turbulence are presented and correlation between the fine scale structure and the turbulent fluctuations is discussed.

NOMENCLATURE

a	structure parameter $\lvert\overline{uv}\rvert/\overline{q^2}$
c_μ	universal constant in Eq. (3)
f_p	frequency of bursts
f_{ra}	frequency of runs
L_p, L_r	length scales based on f_p and f_{ra} ($= U/f_p$ and U/f_{ra} respectively)
L_ε	dissipation length scale
l_k	Prandtl-Kolmogorov length scale
l_m	mixing length for curved boundary layer
l_o	mixing length for flat wall boundary layer
$\overline{q^2}$	twice the turbulent kinetic energy per unit mass
R	radius of curvature of the wall
R_{gc}	curvature Richardson number: $2\left\{\frac{U}{r^2}\frac{\partial}{\partial y}(Ur)\right\}/\left(\frac{\partial U}{\partial y}\right)^2$
R_θ	momentum thickness Reynolds number
r	local radius of curvature of the streamline
T_u, T_v	integral time scales of u and v fluctuations
U	mean velocity in the streamwise direction
U_∞	velocity at the edge of the boundary layer
u	turbulent velocity fluctuation in the longitudinal direction
v	turbulent velocity fluctuation in the radial direction
y	radial distance from the wall
β	constant in Eq. (1)
δ	boundary layer thickness based on 99 per cent of free stream angular momentum $(Ur)_\infty$
ε	dissipation rate
ζ	spanwise component of vorticity
η	non-dimensional distance y/δ
λ	Taylor-microscale
δ	density of the fluid
Ψ	stream function

SUBSCRIPTS

c	curved wall
F	flat wall
+,-	positive or negative part of the velocity fluctuation respectively

INTRODUCTION

In 1969, Bradshaw [1] predicted that even mild streamline curvature can significantly affect the structure and development of turbulent boundary layers. He also proposed a model based on analogy between streamline curvature and buoyancy, for assessing the effect of curvature on the distribution of the length scale across the boundary layer. He used this model for predicting boundary layer development over a mildly curved surface. The model was also used later by Eide and Johnston [2] in their prediction procedure. Experimental data on curved wall boundary layers have been obtained in the recent past by So and Mellor [3], Ellis and Joubert [4], and Meroney and Bradshaw [5]. Data on the effect of streamline curvature on free turbulent shear flows have been very recently reported by Castro and Bradshaw [6]. The investigation reported in this paper is a part of a more extensive study of the effect of curvature on turbulent boundary layers involving the measurement of both the mean and turbulent flow quantities. A complete account of this study is reported in [7].

The mean flow studies indicated that while the flow near a mildly curved wall still follows the universal log law, the wake structure is affected significantly by curvature [8]. In fact, it was found that mild curvature produces a much larger effect than what one anticipates from an interpolation between the effects of zero and strong curvature. It is this observation that prompted the authors to carry out a detailed study of the structure of turbulence in curved boundary layers. The study reported here included an investigation of the effect of curvature on the different length scales, the Reynolds shear stress and the fine scale structure of turbulence in the boundary layer.

THE EXPERIMENTAL PROGRAM

The experiments were carried out in a wind tunnel having a curved test section 25 cm high x 10 cm wide. A schematic diagram of the test section is shown in Fig. 1. The test facility is described in detail in [7]. The convex and concave walls of the test section had radii of 249 cm and 259 cm respectively. The value of δ/R for both the walls was approximately 0.013. It was ensured that the boundary layers on the

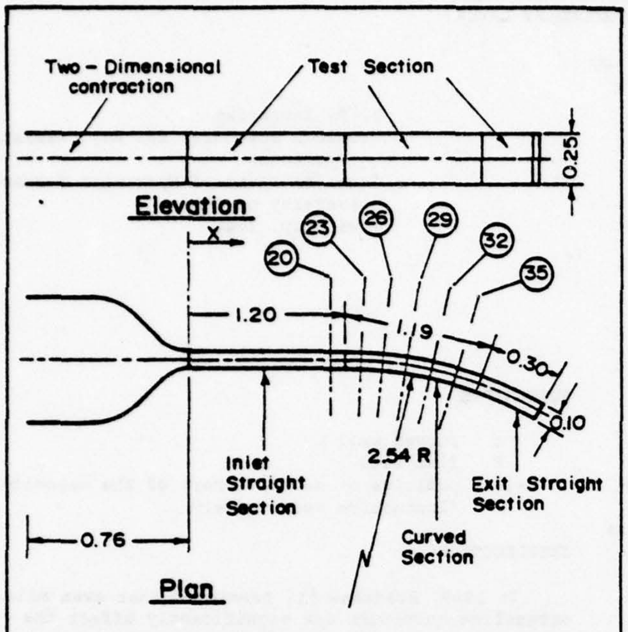

Station No.	20	23	36	29	32	35
X(m) Convex	1.03	1.28	1.50	1.73	1.96	2.18
X(m) Concave	1.03	1.29	1.52	1.76	1.98	2.22

All dimensions are in meters

Fig. 1. Lay out of the test section.

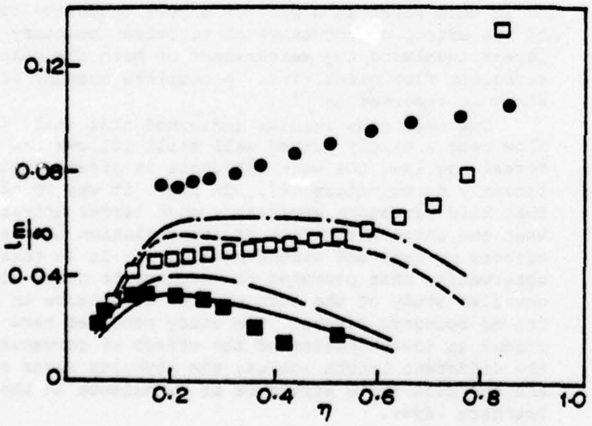

Fig. 2. Mixing length distribution over the convex wall.

from Calculation		from expt	
β=7	β=10		
		●	flat wall
—·—	- - - -	□	convex wall
— — —	———	■	So and Mellor [3] (at 58 cm downstream of beginning of curvature)

two walls were separated by a core of non-turbulent fluid even at the last measuring station along the curved section. All the experiments were carried out under nominally zero pressure gradient, two-dimensional conditions. The momentum thickness Reynolds number of the (flat wall) boundary layer at inlet to the curved section was about 2500. The free stream velocity at inlet to the curved section was approximately 22m/sec. Measurements reported in this paper were made at Stations 20 and 35 (See Fig. 1).

The total head in the boundary layer was measured using a round total head tube of 0.8 mm outside diameter. The same tube was used as a Preston tube for measuring the wall shear stress. Turbulence measurements were made using constant current hot-wire anemometry and other associated instrumentation. The overall frequency response of the system was flat in the range of 4 Hz - 8 kHz. For studying the fine scale structure of turbulence, suitably conditioned turbulence signal traces on the oscilloscope were photographed on 35 mm film using a drum camera. Autocorrelation curves from which the integral time scales were calculated were obtained by first recording the data on analog tape and later processing them digitally. The details of acquisition and processing of data are described in [7].

RESULTS AND DISCUSSION

Curvature-buoyancy Analogy

Based on the concept of an analogy between buoyancy and streamline curvature, Bradshaw proposed the following expressions for estimating the mixing length

$$l_o/l_m = 1 + \beta R_{gc} \quad \text{for convex wall } (R_{gc}>0)\ldots \quad (1)$$

and

$$l_m/l_o = 1 - 2 R_{gc} \quad \text{for concave walls } (R_{gc}<0) \quad (2)$$

$$(\text{valid for } -0.5<R_{gc}<0)$$

Using Eq. (1) and (2) and the mixing length distribution corresponding to the fully developed flat wall boundary layer at Station 20, the mixing length distributions over the curved walls were calculated. The results are shown in Fig. 2 and 3 along with the experimental data. The flat wall data are also shown in these figures. The large decrease in mixing length over the convex wall is very clearly seen. Comparison between the calculated and measured values of mixing length are shown also for the zero pressure gradient curved boundary layer data of So and Mellor [3]. With regard to the convex wall boundary layer, the calculated l_m distributions are shown for two alternate values of β, viz. β=7 (value used by Bradshaw [1] and β=10 (value used by Eide and Johnston [2]). It is seen that β=7 gives reasonably good results for the inner region ($y/\delta<0.2$) though the effect of curvature is quite small in this region. In the region $0.2<y/\delta<0.6$, the estimates using β=10 show better agreement with experimental results. In the outer region ($y/\delta>0.6$), however, Eq. (1) does not appear to be useful for calculating the mixing length over a mildly curved surface. Over a strongly curved surface, such as in the case of the experiments of Ref. 3 ($\delta/R \approx 0.1$), the shear stress in the outer region is nearly zero (See Fig. 10) and consequently, the inaccuracy in the estimation of the mixing length will not seriously affect the accuracy of a prediction procedure. For the concave wall boundary layer, the use of Eq. (2) seems to be satisfactory for mild wall-curvature. With stronger

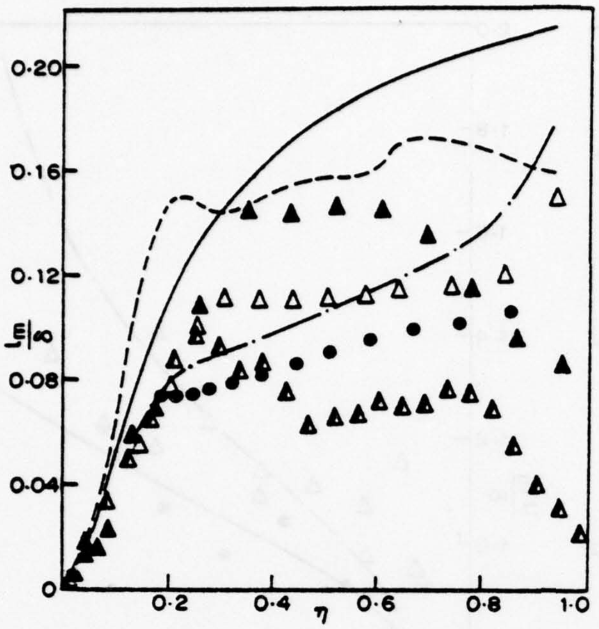

Fig. 3. Mixing length distribution over the concave wall

from Calculation using Eq. (1)	from expt.		
	●	flat wall	present experiments
— · —	△	concave wall	
———	▲	crest	from So and Mellor [3] at 90 cm downstream of beginning of curvature
- - - - - - -	◭	trough	

curvature, the flow situation becomes complicated as a system of longitudinal vortices comes into existence. As a consequence of this, the boundary layer thickness varies in the spanwise direction in a cyclic manner with a periodicity corresponding to the wave number of the vortex system. This vortex system was either non-existent or too weak to be detected in the present experiments with mild curvature. It was, on the other hand, quite prominent in the experiments of So and Mellor and therefore, in Fig. 3, comparisons in the case of their experiments are made for two spanwise locations at the same longitudinal station. These locations correspond to the crest and trough of the spanwise distribution of boundary layer thickness. It is seen that Eq. (2) is a poor representation of the actual mixing length distribution beyond $y/\delta = 0.1$.

The mixing length is just one of the many length scales that have been used in turbulence modeling. Other length scales characteristic of the more detailed structure of turbulence have, often, been used in turbulent flow prediction. It is, therefore, interesting to assess the performance of Eq. (1) and (2) with regard to these scales. The following length scales were studied in the present investigation.

(i) the Prandtl-Kolmogorov length scale l_k defined by:

$$-\overline{uv} = C_\mu (\overline{q^2})^{\frac{1}{2}} l_k \frac{\partial U}{\partial y} \tag{3}$$

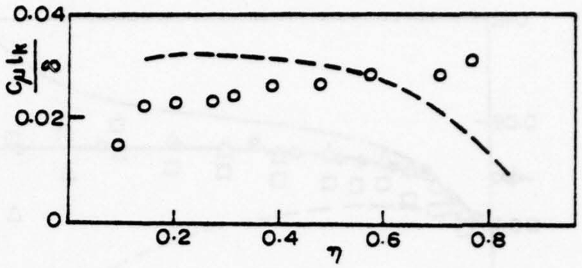

Fig. 4. Prandtl-Kolmogorov length scale distribution over the convex wall

o, from experiment; ---, from Calculation using Eq. (1)

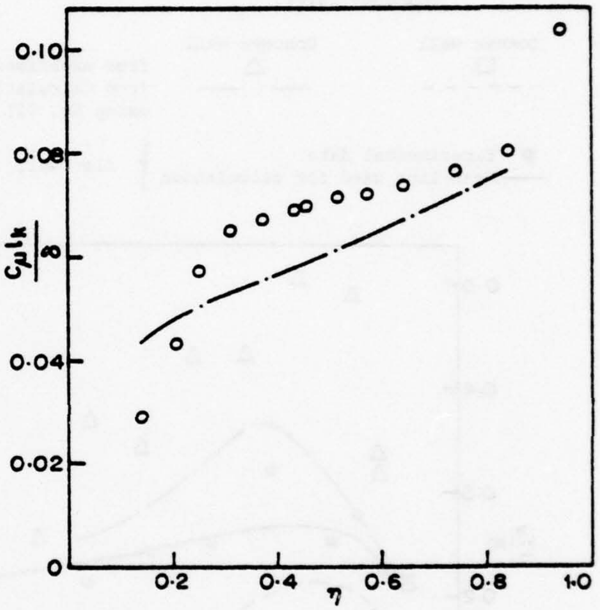

Fig. 5. Prandtl-Kolmogorov length scale distribution over the concave wall

o, from experiment; — · —, from calculation using Eq. (2).

(ii) the Taylor-microscale λ being defined by

$$\lambda^2 = U^2 \, \overline{u^2} / \overline{\left(\frac{\partial u}{\partial t}\right)^2} \tag{4}$$

(iii) the dissipation length scale L_ε defined by

$$L_\varepsilon = (\overline{q^2})^{3/2}/\varepsilon \tag{5}$$

(iv) the integral length scales (UT_u) and (UT_v) of the u and v fluctuations where T_u and T_v are integral time scales obtained as the area under the autocorrelation curves of u and v respectively.

In each case, the length scale distribution measured over the flat wall at station 20 was used to calculate the corresponding distribution over the curved wall from Eq. (1)/ Eq. (2). The calculated length scale

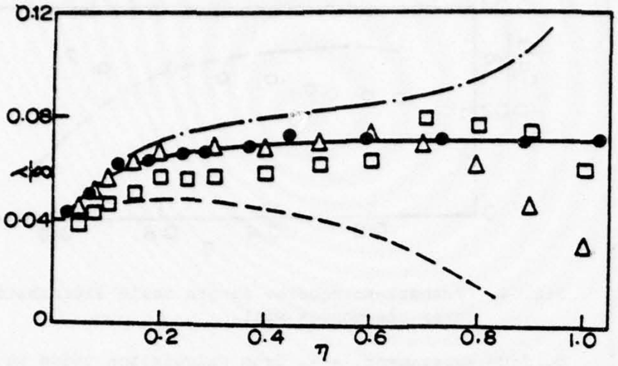

Fig. 6. Taylor-microscale distribution across the boundary layer.

Convex wall	Concave wall	
□	△	from experiment
- - - - - -	—·—	from Calculation using Eq. (1) & (2)

● Experimental data
—— Mean line used for calculation } flat wall

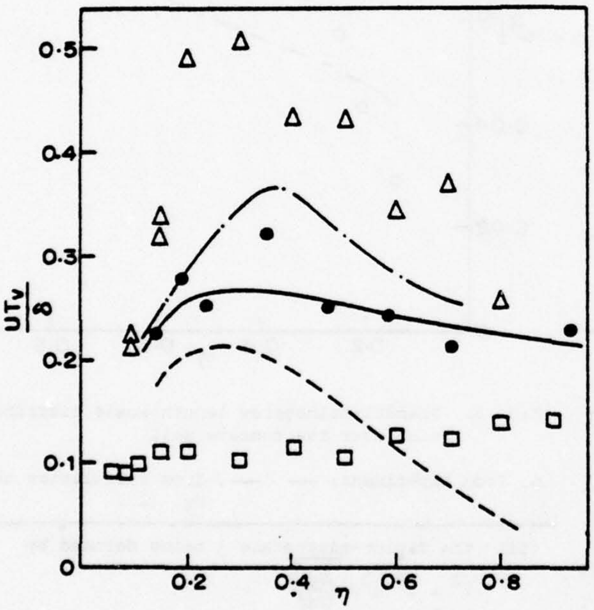

Fig. 7. Distribution of the integral length scale of v-fluctuations. Symbols as in Fig. 6.

distributions are compared with measurements in Figs. 4-9. An examination of these figures reveals that even in the case of mild curvature, the buoyancy curvature analogy in the form of Eq. (1) and (2) is reasonably satisfactory in predicting only the gross features of the flow. It is seen to become increasingly inadequate to account for the effect of curvature on the more detailed aspects of the flow. For example, the mixing length and Prandtl-Kolmogorov length scales are reasonably well predicted while the integral length scale (especially UT_v), the microscale and the dissipation length scale are not predicted

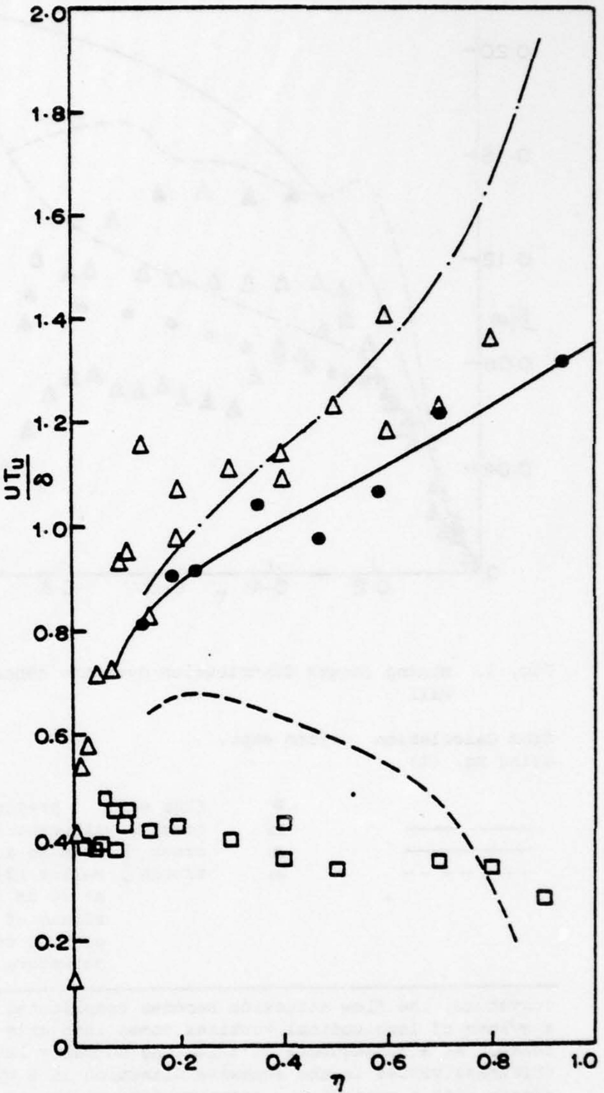

Fig. 8. Distribution of the integral length scale of u-fluctuations. Symbols as in Fig. 6.

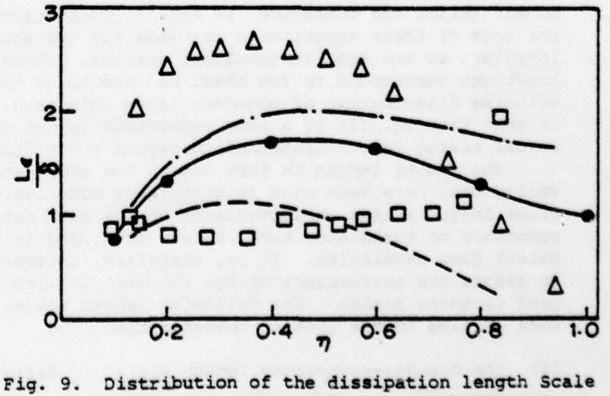

Fig. 9. Distribution of the dissipation length Scale across the boundary layer. Symbols as in Fig. 6.

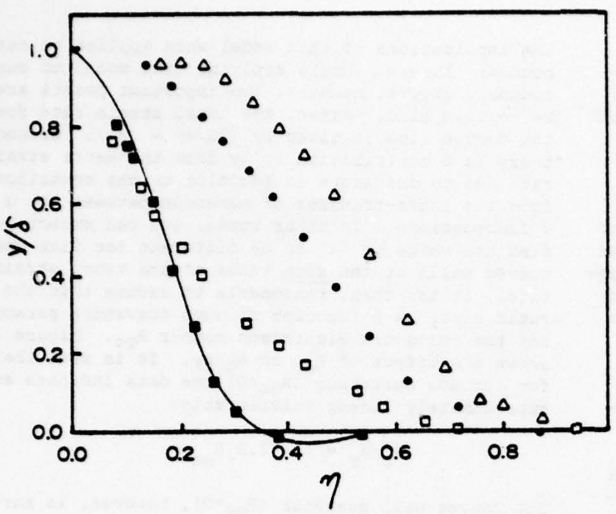

Fig. 10. Distribution of the Reynolds Shear Stress across the Boundary Layer.

□ Convex Wall; △ , Concave Wall; ● , flat wall

—■— , typical data from [3] for convex wall

well. Thus, it appears that the best use of Eq. (1) and (2) is for calculation procedures which use a relatively coarse basic turbulence model. With more complex turbulence models, the analogy in the form of Eq. (1) and (2) appears to be unrealistic. It is, however, to be emphasized that the present study revealed the limitations of only Eq. (1) and (2) and not those of the concept of the analogy itself.

Reynolds Shear Stress and Turbulence Modeling

Figure 10 shows the distribution of the Reynolds Shear Stress across the curved boundary layers. It is seen that convex curvature decreases the shear stress by as much as 50% (especially in the outer region) while concave curvature increases it by about 20% when compared with the flat wall boundary layer. While these trends are the same as those observed by So and Mellor in their experiments with much stronger curvature, ($\delta/R \approx 0.1$) the present results are significant since they indicate that even mild wall-curvature (especially convex curvature) can produce a spectacular effect on the Reynolds shear stress.

It is also seen from the Fig. 10 that the shear stress decreases rapidly across the convex wall boundary layer. In fact, it is seen that, with strong wall-curvature, the shear stress is practically zero in the outer half of the boundary layer. The steep drop across the boundary layer over the convex wall suggests that it may be useful to consider the outer part of the boundary layer as an inviscid but rotational flow. This concept was employed by Narasimha and Srinivasan [9] in a study of relaminarizing boundary layers, in which case also the shear stress is very small in the outer layer. Only a preliminary calculation based on their approach is attempted here to see whether the outer region of the flow can be treated as a rotational inviscid flow. For this purpose, the stream function and vorticity distribution across the boundary layer at an upstream station (Station 29) was obtained from the experimental velocity profile by using the relations

$$U = \frac{\partial \Psi}{\partial y} \qquad (6)$$

and

$$\frac{\partial U}{\partial y} + U = \zeta(\Psi) \qquad (7)$$

Similarly, at the downstream station (Station 35) the distribution of the stream function was obtained from the experimental velocity profile. The streamline corresponding to the outer edge of the boundary layer at station 29 was located at station 35 by matching the stream functions at the two stations. Taking this as the starting point of integration at station 35 and using the measured velocity at this point as the initial value of U the vorticity conservation Eq. (7) was integrated in the radially inward direction. The integration was done numerically by using a step-by-step procedure. The velocity distributions across the boundary layer obtained by this method are shown in Fig. 11. The two cases shown correspond to the present convex wall experiment and the zero pressure gradient convex wall experiment of So and Mellor. The experimentally obtained velocity distributions are also plotted in these figures, as well as the inviscid irrotational velocity distribution given by Ur=constant. It can be seen that, both in the case of the present experiment and the experiment of So and Mellor, the calculation based on rotational inviscid flow assumption accounts for a large part of the deviation from the irrotational velocity distribution in the outer layer at least up to a y/δ of 0.5. The discrepancy observed near the wall (viz. U not going to zero exactly at y=0) is because, the assumption of inviscid

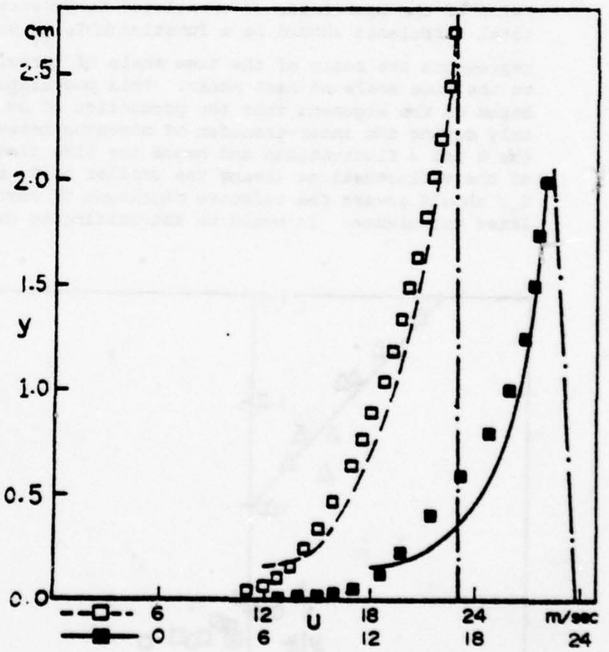

Fig. 11. Comparison of the measured mean velocity distribution with rotational inviscid calculation.

from calculation	from expt.	
- - - - -	□	present expts.
———	■	expts. of So and Mellor [3]
—·—		inviscid, irrotational theory.

flow is not valid near the wall and the integration cannot strictly be carried out in this region. However, in view of the satisfactory agreement observed in the outer region, one could approach the problem of the boundary layer over a convex surface by dividing the boundary layer into two regions (i) a region of shear with curvature effects represented by Eq. (1) with β=10 and an outer region of rotational inviscid flow. This may be conceptually superior to the use of an overall value of $\beta \approx 7$ over the entire boundary layer which is probably justified by comparisons between predictions and experimental data of the development of the gross boundary layer parameters (for e.g., as was done by Bradshaw [1] and Eide and Johnston [2]). Also, the fact that the time scales are smaller over the convex wall (as could be seen from Fig. 7 and 8) can be used to advantage in developing quick calculation procedures. Since the time scales are small, local models, such as the mixing length model (with curvature correction) could be employed for the inner layer with the outer layer being treated as an inviscid rotational flow. From the nature of the argument employed, one can expect this two-layer approach to be increasingly more useful, as wall-curvature inreases. However, this two-layer approach, suggested here, is only a possible scheme and problems of matching, etc., have to be looked into, before developing it into a useful prediction procedure.

Implications of a time scale model with regard to curved boundary layers. Ramaprian [10] proposed that the structure parameter a $(=|\overline{uv}|/\overline{q^2})$ representing the ratio of the magnitudes of correlated turbulence to total turbulence should be a function of $T_v \frac{\partial U}{\partial y}$ which represents the ratio of the time scale of turbulence to the time scale of mean shear. This postulate was based on the argument that the production of $\overline{uv}$ occurs only during the inter-transfer of momentum between the u and v fluctuations and hence the life time T_v of the v-fluctuations (being the smaller of T_u and T_v) should govern the relative magnitude of correlated turbulence. It would be interesting to examine the implications of this model when applied to curved boundary layers. While applying this model to curved boundary layers, however, two important points are to be kept in mind. First, the total strain rate for the curved flow is given by $(\partial U/\partial y - U/r)$. Secondly, there is a contribution to $\overline{uv}$ from the extra strain rate due to curvature in addition to the contribution from the inter-transfer of momentum between the u and v fluctuations. In other words, one can expect to find the value of 'a' to be different for flat and curved walls at the same value of the total strain rate. It is, then, reasonable to assume that the ratio a_c/a_F is a function of some curvature parameter, say the curvature Richardson number R_{gc}. Figure 12 shows the effect of R_{gc} on a_c/a_F. It is seen that for concave curvature (R_{gc}<0) the data indicate an approximately linear relationship:

$$a_c/a_F = 1 - 2.2\, R_{gc} \tag{8}$$

The convex wall behavior (R_{gc}>0), however, is markedly different. The large decrease in a_c/a_F at small positive values of R_{gc} is an important observation but the authors are unable to explain this at present.

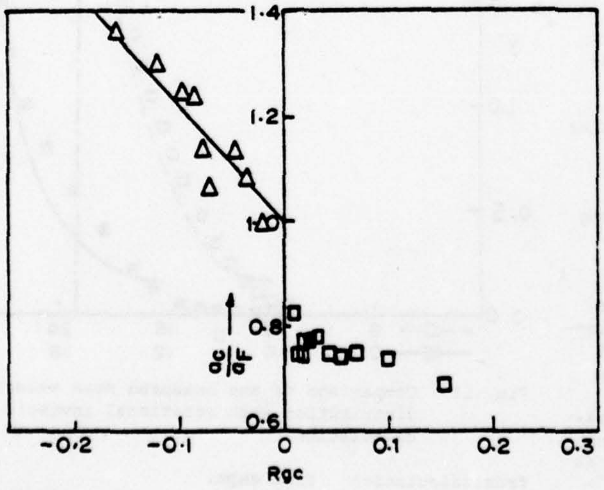

Fig. 12. Effect of curvature Richardson number on the Structure parameter.
□ , convex wall; △ , concave wall; —, least square fit: $a_c/a_F = 1 - 2.2\, R_{gc}$

Fine Scale Structure

It is now well known (See Kim et al., [11] and Rao et. al. [12]) that the fine scale structure of turbulence is intermittent. In order to understand the effect of curvature on this intermittency or "bursting" behavior, a detailed study of the turbulence signals u and v was made, after first filtering them using a narrow band pass filter. The center frequency of the filter was set at 3 kHz, which corresponded to the peak in the dissipation spectrum. (This was confirmed by approximate measurement of the dissipation spectrum.) The average frequency of "bursting" f_p was obtained from the oscilloscope trace of the filtered signal photographed using a drum camera. Also, the frequency of "runs" f_{ra}, [the "run" being defined as the interval of positive (or negative) amplitude between successive zero crossings] was obtained from the photographed oscilloscope traces of the unfiltered u and v signals.

In fact, the relevant quantity to be studied is not the frequency; rather, it is the distance between the high frequency regions in the flow as would be seen by an observer moving with the local stream at the convection velocity. Assuming that this convection velocity is U, this distance L_p can be defined as $L_p = U/f_p$. Similarly a relevant quantity to be used with the split signals is the distance L in the flow at which the fluctuations would reverse in direction at a given instant and is given by $L_r = U/f_{ra}$. Both these lengths are shown plotted in Fig. 13. It is seen that these length scales generally increase across the boundary layer. However, the increase is quite large in the case of the convex wall. It is interesting to note that the scales are very nearly the same for all the walls in the region close to the wall. This indicates that although the fine scale structure of turbulence near the wall is not significantly affected by mild curvature, the manner in which this structure is transported across the boundary layer is affected by curvature;—especially concave curvature. Further, if one assumes that the fine scale structure rich in vorticity is driven by the large eddy system, one can say that the effective size of this system grows considerably with distance from the wall in the case of the concave wall; whereas in the

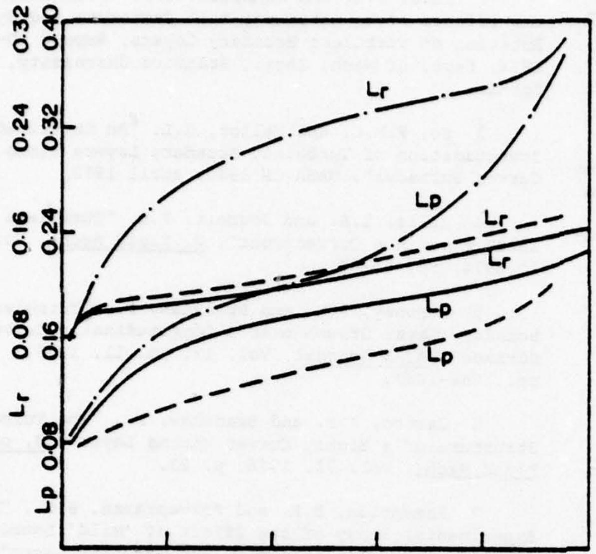

Fig. 13. Distributions of L_p and L_r across the boundary layer.

---, convex wall; — —, concave wall; ——, flat wall. (All the lines are mean through data points. Ordinates are in arbitrary units)

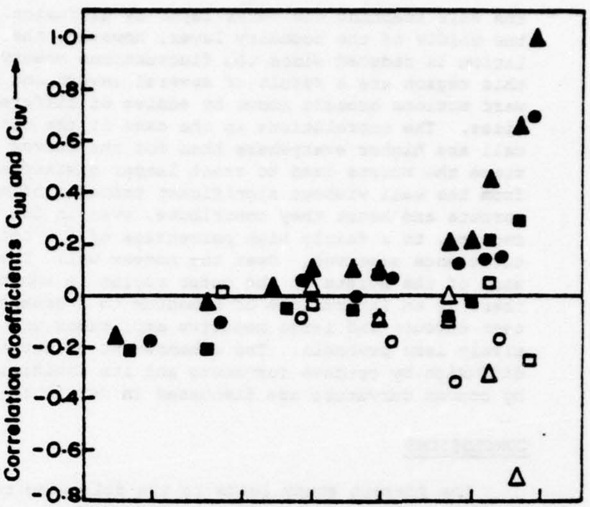

Fig. 14. Correlation of u and v fluctuations with bursts.

C_{uu}	C_{uv}	
●	○	flat wall
■	□	convex wall
▲	△	concave wall

case of the convex wall the effective eddy size grows at a much slower rate.

Another interesting feature observed during the experiments was that the u-signal in the outer part of the concave boundary layer often contained very large negative amplitudes. Also, these large negative peaks were found to be associated with a significant amount of high frequency activity. These features were observed in the outer part of the boundary layer over all the three walls (flat, convex and concave). However, they were found to be very much more pronounced over the concave wall than over the convex wall, with the flat wall behavior falling in between. The coincidence between the occurrence of high frequency activity and deceleration peaks suggested a possible correlation between "bursts" and deceleration. This correlation was studied quantitatively by using an analog correlator.

For quantifying the correlation, we first define the quantities R_{uu-}, R_{uu+}, R_{uv-}, and R_{uv+} as follows:

$$R_{uu-} = \frac{\overline{u_- u_{bp}}}{\sqrt{\overline{u_-^2}}\sqrt{\overline{u_b^2}}} \; ; \quad R_{uu+} = \frac{\overline{u_+ u_{bp}}}{\sqrt{\overline{u_+^2}}\sqrt{\overline{u_b^2}}} \; ;$$

$$R_{uv-} = \frac{\overline{v_- u_{bp}}}{\sqrt{\overline{v_-^2}}\sqrt{\overline{u_b^2}}} \; ; \quad R_{uv+} = \frac{\overline{v_+ u_{bp}}}{\sqrt{\overline{v_+^2}}\sqrt{\overline{u_b^2}}} \qquad (9)$$

where u_b and u_{bp} represent respectively the full and positive half of the filtered u-signal. From the above definition, it is clear that the range of variation in the magnitude of R_{uu-} etc. is 0 to 0.5. We now define another set of correlation coefficients as:

$$C_{uu} = 2 \left[\frac{-R_{uu-} - R_{uu+}}{-R_{uu-} + R_{uu+}}\right]$$

$$C_{uv} = 2 \left[\frac{-R_{uv-} - R_{uv+}}{-R_{uv-} + R_{uv+}}\right] \qquad (10)$$

From the above definition, it is seen that C_{uu} is a measure of the correlation between the u-bursts and u_- fluctuations, while C_{uv} is a measure of the correlation between the u-bursts and the v_- fluctuations. C_{uu} and C_{uv} will have a value of +1, 0 or -1 depending on whether there is total correlation, zero correlation or anti-correlation. The distributions of C_{uu} and C_{uv} across the boundary layers are shown for the three walls in Fig. 14. The figures indicate that there is a large correlation between the bursts and the negative u-fluctuations near the outer edge of the boundary layer and the correlation decreases and remains small over the middle part of the boundary layer. In fact, in the region close to the wall (note that the horizontal axis is in logarithmic coordinates) the correlation is slightly negative indicating a slight correlation between the bursts and the positive u-fluctuations. It is also seen from Fig. 14 that the correlation coefficient C_{uv} behaves approximately like $-C_{uu}$. This is to be expected since the u and v fluctuations have predominantly a negative correlation to each other. Figure 14 also shows that both C_{uu} and C_{uv} are generally larger in magnitude over the concave wall than over the convex wall.

The observed large correlation between u_- (or v_+) and the bursts at large distances from the wall is to be expected, since the large negative fluctuations observed near the outer edge of the boundary layer are essentially due to the bursts produced at the wall reaching the outer layer by diffusion. In the middle of the boundary layer, however, the correlation is reduced since the fluctuations observed in this region are a result of several inward and outward motions brought about by eddies of different sizes. The correlations in the case of the concave wall are higher everywhere than for the convex wall since the bursts tend to reach larger distances away from the wall without significant transfer of momentum enroute and hence they contribute, even in the middle regions, to a fairly high percentage of the total turbulence observed. Over the convex wall, the diffusion of the bursts to the outer region is inhibited; there is an interchange of momentum to a greater extent enroute and large negative amplitudes are relatively less probable. The enhancement of outward diffusion by concave curvature and its inhibition by convex curvature are discussed in detail in [7].

CONCLUSIONS

The present study leads to the following conclusions:

(i) Equations (1) and (2) proposed by Bradshaw are reasonably satisfactory to describe the effect of mild streamline curvature on coarse length scales such as the mixing length. However, they fail to describe curvature effects on length scales representative of the more detailed structure of turbulence.

(ii) Reynolds shear stress is significantly reduced by convex curvature and enhanced by concave curvature. The rapid decrease of the shear stress across the convex wall boundary layer allows one to treat the flow in the outer region of the boundary layer as rotational and inviscid.

(iii) The time scale model of Ref. 10 can be extended to concave wall boundary layers by appropriately accounting for the effect of curvature Richardson number on the structure parameter $|\overline{uv}|/\overline{q^2}$

(iv) Mild wall curvature does not affect the production of bursts. It, however, affects the outward diffusion of these bursts.

REFERENCES

1 Bradshaw, P., "The Analogy Between Streamline Curvature and Buoyancy in Turbulent Shear Flow", *J. Fluid Mech.*, Vol. 36, part 1, 1969, pp. 177-191.

2 Eide, S.A. and Johnston, J.P. "Prediction of the Effects of Longitudinal Wall Curvature and System Rotation on Turbulent Boundary Layers, Report PD-19, 1974, Dept. of Mech. Engg., Stanford University, California.

3 So, R.M.C. and Mellor, G.L. "An Experimental Investigation of Turbulent Boundary Layers along Curved Surfaces", NASA CR 1940, April 1972.

4 Ellis, L.B. and Joubert, P.N. "Turbulent Shear Flow in a Curved Duct", *J. Fluid Mech.*, Vol. 62, 1, 1974, pp. 65-84.

5 Meroney, R.N. and Bradshaw, P., "Turbulent Boundary Layer Growth over a Longitudinally Curved Surface", *AIAA Journal*, Vol. 13, No. 11, 1975, pp. 1448-1453.

6 Castro, I.P. and Bradshaw, P., "The Turbulence Structure of a Highly Curved Mixing Layer", *J. of Fluid Mech.*, Vol. 73, 1976, p. 23.

7 Ramaprian, B.R. and Shivaprasad, B.G., "An Experimental Study of the Effect of 'Mild' Longitudinal Curvature on the Turbulent Boundary Layer" Report 76 FM 2, 1976, Dept. of Aero. Engg., Indian Institute of Science, Bangalore, India.

8 Ramaprian, B.R. and Shivaprasad, B.G., "Mean Flow Measurements in Turbulent Boundary Layers along Mildly Curved Surfaces", to appear in AIAA Journal 1977.

9 Narasimha, R. and Sreenivasan, K.R. "Relaminarisation in Highly Accelerated Turbulent Boundary Layers", *J. Fluid Mech.*, Vol. 61, part 3, 1973, pp. 417-447.

10 Ramaprian, B.R. "Turbulence Measurements in an 'Equilibrium' Axi-symmetric Wall-jet," *J. Fluid Mech.*, Vol. 71, part 2, 1975, pp. 317-338.

11 Kim, H.T., Kline, S.J. and Reynolds, W.C., "The Production of Turbulence near a Smooth Wall in a Turbulent Boundary Layer," *J. of Fluid Mech.*, Vol. 50, 1971, p. 133.

12 Rao, K.N., Narasimha, R. and Badrinarayanan, M.A. "The 'Bursting' Phenomenon in a Turbulent Boundary Layer" *J. Fluid Mech.*, Vol. 48, part 2, 1971, pp. 339-352.

MEASUREMENTS IN THE THICK AXISYMMETRIC TURBULENT BOUNDARY LAYER AND THE NEAR WAKE OF A LOW-DRAG BODY OF REVOLUTION

by

V.C. Patel, Y.T. Lee & O. Güven
Institute of Hydraulic Research and
Division of Energy Engineering
The University of Iowa
Iowa City, Iowa 52242

ABSTRACT

Detailed measurements of pressure distributions, mean velocity profiles and Reynolds stresses were made in the thick, axisymmetric boundary layer and the near wake of a low-drag body of revolution. The data shed some light on the joint influence of transverse and longitudinal surface curvatures and pressure gradients on the boundary-layer development and on the manner in which an axisymmetric boundary layer becomes a fully-developed wake. Apart from giving a complete set of data on such an important flow configuration, the measurements should provide a fairly rigorous test case for some of the recent turbulence closure models which claim a level of generality not achieved by the older phenomenological models.

INTRODUCTION

In some previous work at Iowa [1], measurements were made in the thick axisymmetric boundary layer over the tail region of a spheroid whose tail was modified by attaching a short conical piece in order to avoid separation. Those measurements have been used [2,3] in the development of simple integral entrainment methods for the calculation of thick boundary layers in which there exists a substantial variation of static pressure in the direction normal to the surface. Since the measurements indicated that a proper theoretical treatment of the flow in the tail region should consider the interaction between the boundary layer and the external potential flow, a more refined iterative technique was developed [4,5]. During the course of this latter study it became apparent that a successful interaction scheme must also take the flow in the near wake of the body into consideration. The lack of detailed mean-flow and Reynolds-stress data in the near wake of an unseparated body of revolution provided the incentive to perform the experiment described here.

EXPERIMENTAL ARRANGEMENT

Wind Tunnel and Model

The experiments were performed in the large wind tunnel of the Iowa Institute of Hydraulic Research. The working section of the tunnel is 7.3 m long with a cross-section in the form of a 1.5 m octagon provided by throating a 3.7 m square approach section.

The selection of the model shape was based on a number of considerations and the experience gained from the previous experiments [1]. First of all, it was desirable to select a practically important configuration rather than a simple geometric shape. Secondly, in order to highlight the influence of strong transverse surface curvature it was necessary to maintain a thick boundary layer over an extended region of the body. Third, it was essential to avoid separation in the tail region so that the near wake could be explored in detail. Finally, in order to avoid the experimental [1] and theoretical [5] difficulties encountered in earlier work with a conical tail, it was thought convenient to consider a cusped-tail body so that the transition from the boundary layer to the wake would be smooth.

Parsons and Goodson [6] have considered a variety of shapes within a five-parameter family of bodies of revolution and used well known potential-flow and boundary-layer calculation methods and optimization *techniques to recommend optimum low-drag shapes.* The so-called F-57 body was selected out of these shapes as one which gave minimum resistance (at zero incidence and practical Reynolds numbers) and, at the same time, met most of the requirements set out above. The coordinates of this body are given by

For $0 \leq X \leq X_m$ (fore-body):

$$\frac{r_o}{r_m} = \{-1.1723(\frac{X}{X_m})^4 + 0.7088(\frac{X}{X_m})^3 + 1.0993(\frac{X}{X_m})^2 + 0.3642(\frac{X}{X_m})\}^{1/2}$$

For $X_m \leq X \leq L$ (pointed aft-body):

$$\frac{r_o}{r_m} = \{-0.11996\,\xi^5 - 2.58278\,\xi^4 + 3.52544\,\xi^3 + 0.17730\,\xi^2\}^{1/2}$$

where $\xi = \frac{L-X}{L-X_m}$, X is the axial distance measured from the nose, r_o is the local radius, X_m is the axial location of the maximum radius r_m, and L is the total length of the body. The location of maximum radius is thus $X_m/L = 0.4446$ and the length to maximum diameter ratio, $L/2r_m = 4.2735$.

For the present experiments, a model was constructed with L = 1.219 m (4.0 ft) so that $r_m = 0.1426$ m (0.4680 ft). The model was made hollow and in two parts in order to accomodate a scanivalve which was connected to the forty eight, 0.117 cm (0.046 in) diameter, pressure taps on the surface. Thirty two pressure taps lay on a single generator on the surface while the remainder were spaced circumferentially at three axial locations, X/L = 0.104, 0.445 and 0.771, for use in model alignment. The main body of the model was made of seasoned wood but metal nose- and tail-pieces, 5.08 cm and 12.70 cm in length, respectively, were used to provide accuracy and durability. The major features of the model are shown in Figure 1. The longitudinal slope (dr_o/dX) and longitudinal curvature (κ) of the surface are also shown for later reference.

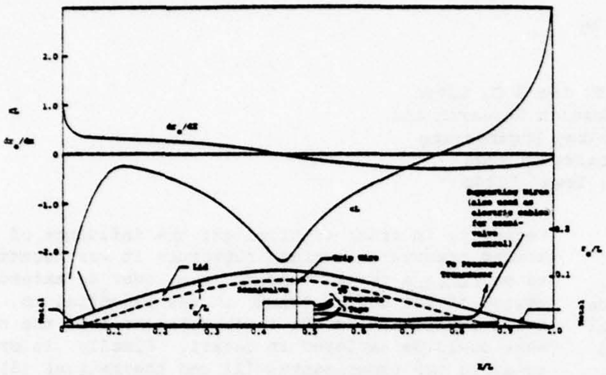

FIGURE 1. DETAILS OF THE F-57 BODY

Model Alignment

The model was mounted in the wind tunnel by means of eight 0.84 mm diameter steel wires in tension, four at each end (Figure 1). Each wire was provided with a screw coupling so that its length could be adjusted and the model located at the desired position.

The model was placed in the tunnel with its axis along the tunnel axis. Minor adjustments were then made to obtain axisymmetric flow conditions. Several means were employed to ascertain axial symmetry:

1. The static pressures measured along the circumference at the three axial locations were used to guide the preliminary positioning of the model.
2. Three 1.651 mm outside-diameter Preston tubes were then mounted on the surface at $X/L = 0.771$ at 120-degree intervals. The final position of the model was achieved by making small adjustments in the lengths of the rear support wires until the Preston tubes gave identical readings.
3. The final check on axial symmetry was provided by traversing a total pressure tube and a hot wire right across the wake of the body at $X/L = 1.10$ and 1.20. Satisfactory symmetry was observed in terms of the total pressure, the average velocity and the turbulence intensity.

All measurements reported here were made without further adjustments, the model being kept in the tunnel until the experiment was completed.

Instrumentation

The measurements in the boundary layer and the wake of the model were made with basically the same traverse mechanism as was described in [1]. The range of axial distances over which measurements could be made was, however, extended for the present experiments by making suitable modifications to the traverse mounting system situated outside the wind tunnel.

The total and static pressures were measured using probes of standard design, made from hypodermic tubing, and micro-manometers. In view of the uncertainities experienced earlier [1] in making static pressure measurements across the thick boundary layer where the mean-flow streamlines diverge appreciably from the surface, a special mechanism was built to rotate the head of the static probe into the direction of the local on-coming stream. Such a device was of course not required for the total pressure measurements due to the yaw-insensitivity of the pitot tube. Preston tubes of different diameters were used in conjunction with the calibration of Patel [7], to measure the wall shear stress on the body. As indicated earlier, the surface pressure distribution was measured by means of the pressure taps on the model. The scanivalve was located inside the model primarily to avoid flow interference associated with a large number of pressure tubes running from the model to outside the tunnel. The scanivalve was driven by power supplied through the rear cables supporting the model. Thus, only one pressure tube had to be taken out of the model. The flow disturbance caused by this was considered negligible.

Mean velocities and the Reynolds stresses within the boundary layer and the wake were measured by means of single-wire and cross-wire probes using the two-channel, constant-temperature 'Old-Gold-Model, Type 4-2H-Hot-Wire Anemometer' and 'Type 2 Mean-Product Computer', designed and manufacturered at the Iowa Institute of Hydraulic Research. For the purposes of the present experiments, these instruments were modified to make them compatible with the gold-plated series of probes made by DISA. In order to ascertain that proper matching had been achieved and, at the same time, to establish measurement procedures to be used, a series of preliminary tests was conducted in fully-developed turbulent flow in a 5.08 cm diameter pipe. The measurements on the body of revolution were commenced only after achieving consistent and satisfactory agreement with the data of Laufer at a pipe Reynolds number of 50,000.

Transition Device

The computations of Parsons and Goodson had indicated that transition on the F-57 body would occur naturally at $X/L = 0.475$, i.e. a short distance downstream of the location of maximum diameter, over a range of Reynolds numbers. Surface pressure distributions and other flow diagnostics on the model at a Reynolds number of 1.2×10^6 ($Re = U_oL/\nu$, where U_o is the velocity of the freestream approaching the body, L is the axial length of the body and ν is the kinematic viscosity) indicated that in reality transition occurred as a result of laminar separation followed by a turbulent reattachment; the bubble being in the neighborhood of the predicted location of transition. In order to eliminate this somewhat unsteady separation bubble and establish well defined conditions for the subsequent development of the turbulent boundary layer, a circular trip wire of 1.664 mm diameter was wrapped around the body at $X/L = 0.475$.

MEAN FLOW MEASUREMENTS

All measurements reported here were made at a Reynolds number, based on the approach velocity U_o and the body length L, of 1.2×10^6, which corresponded to a nominal approach velocity of 15.24 m/s (50 fps). U_o and the static pressure p_o at the end of the tunnel contraction were monitored throughout the experiments and have been used as reference conditions to nondimensionalize the data.

Surface Pressure Distribution

The static pressure distribution on the body surface is shown in Figure 2. Also shown for comparison in the potential-flow pressure distribution computed using the method of Landweber [8]. The close agreement between the two over most of the body indicated that the influence of wind-tunnel blockage is quite small. The departure of the measured pressure distribution from the theoretical one over the rear 25 percent of the body length is a result of the large thickness of the boundary layer in that region and its interaction with the external inviscid flow.

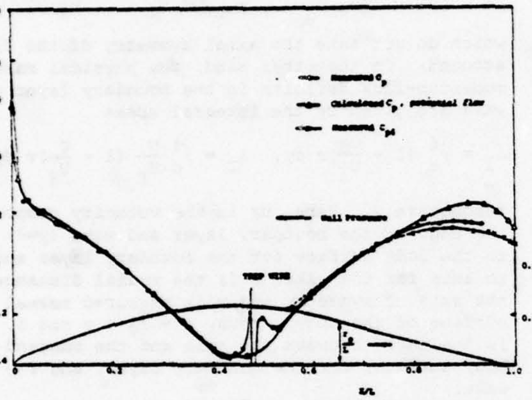

FIGURE 2. PRESSURE DISTRIBUTIONS ON THE BODY

Upstream Laminar Boundary Layer

A single set of measurements was made in the laminar boundary layer upstream of the trip wire at the axial location X/L = 0.433. The velocity profile obtained by means of a flattened pitot tube is shown in Figure 3 along with two members of the Pohlhausen family of profiles, the values of the Pohlhausen parameter Λ being chosen to span the value of -1.65 estimated from the local boundary layer thickness, which was 1.93 mm, and the local pressure gradient.

Static Pressure Field

Figure 4 shows the variation of static pressure across the boundary layer and the wake at several axial positions in the range 0.551 < X/L < 2.472. The convex longitudinal curvature of the body surface in the range 0.45 < X/L < 0.76 apparently leads to the substantial increase in static pressure along the outward normal not only within the boundary layer but also for some distance beyond the edge of the boundary layer (which was determined from the distribution of total pressure and is indicated by the dotted line y = δ). As the longitudinal curvature becomes concave and the boundary layer thickens as a result of the decreasing transverse radius r_0 over the rear one-quarter of the body length, the trends of the static pressure variation are reversed, indicating that the mean streamlines are concave. The data in the near wake suggest that the streamlines become nearly straight within a short distance downstream of the tail.

The axial variation of static pressure at the edge of the boundary and wake inferred from these

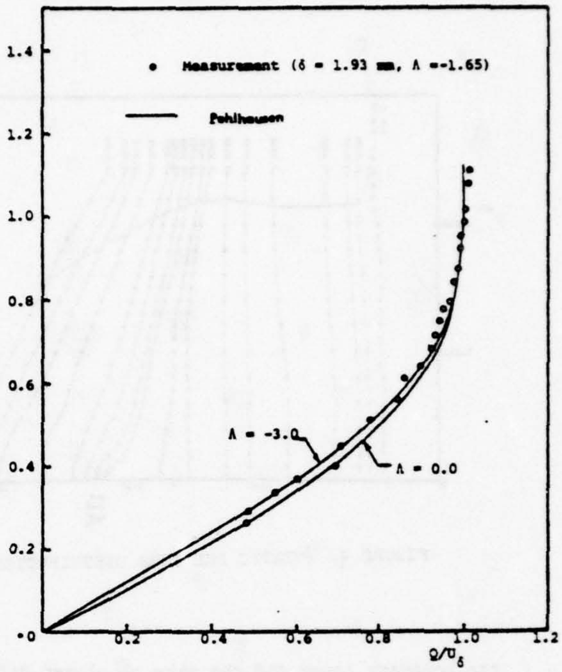

FIGURE 3. VELOCITY PROFILE AT X/L = 0.433

measurements is shown in Figure 2. The magnitude of the pressure difference between the wall and the edge of the boundary layer and wake is apparent from this figure.

The present data have been used to assess the importance of the static pressure variation across the near wake in the prediction of the overall drag coefficient of bodies of revolution using the conventional Squire-Young type formulas [8]. Further analysis of the pressure measurements in the thick boundary layer over the tail would undoubtedly shed some light on the magnitude of the extra terms in the momentum integral equation which were found to be important in the previous experiments and analysis [2,5].

Mean Velocity Profiles

Figure 5 shows the mean velocity profiles across

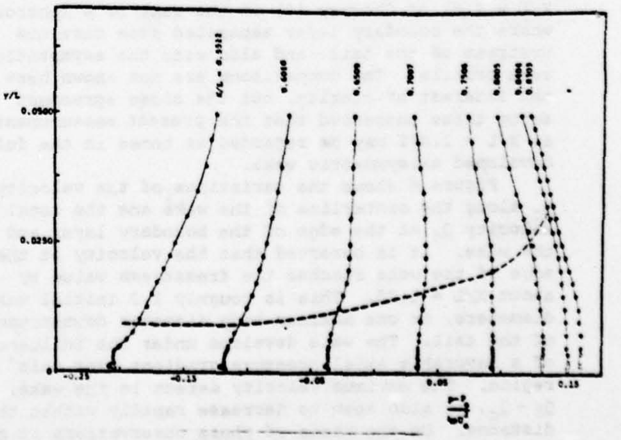

FIGURE 4 (continued)

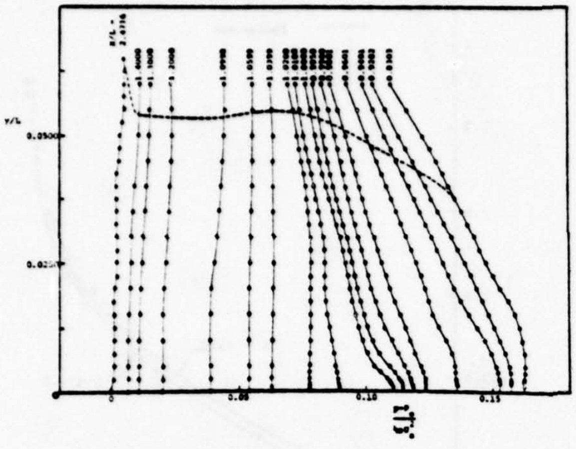

FIGURE 4. STATIC PRESSURE DISTRIBUTIONS

the boundary layer and the wake at eleven different axial stations. Here, U and V are the components of velocity in the directions tangent and normal to the body surface, respectively, and Q is the resultant velocity, i.e. $(U^2 + V^2)^{1/2}$. Q was measured by means of single hot-wire probe and was also obtained from the separate pitot and static probe traverses. It is seen that the two sets of data are in close agreement. The U and V components were measured by means of a crosswire probe. It is known that this technique is not altogether satisfactory insofar as accuracy of the mean flow quantities is concerned. Nevertheless, the data show the relative magnitudes of the two components and indicate that the normal component attains maximum values in the neighborhood of X/L = 0.92, where it is roughly 12 to 13 percent of the tangential component. The implication of this with regard to the validity of the thin boundary layer assumptions is obvious.

The velocity profile measured at the most downstream station in the wake, namely X/L = 2.472, was compared with the most downstream measurements (at X/L = 4.6) of Chevray [9] in the wake of a spheroid, where the boundary layer separated some distance upstream of the tail, and also with the asymptotic wake profile. The comparisons are not shown here in the interest of clarity, but the close agreement among these suggested that the present measurements at X/L = 2.472 may be regarded as those in the fully-developed axisymmetric wake.

Figure 6 shows the variations of the velocity Q_c along the centerline of the wake and the total velocity Q_δ at the edge of the boundary layer and the wake. It is observed that the velocity at the edge of the wake reaches the freestream value by about X/L = 1.25. This is roughly 2.3 initial wake diameters, or one maximum body diameter downstream of the tail. The wake develops under the influence of a favorable axial pressure gradient over this region. The maximum velocity defect in the wake, $Q_\delta - Q_c$, is also seen to decrease rapidly within this distance. On the basis of these observations it may be conjectured that the so-called near wake is confined to this region, and we may expect the measurements further downstream to conform with the well-known asymptotic wake behavior.

Some Integral Parameters

The velocity profiles deduced from the pitot and static traverses were integrated to determine the various types of integral parameters discussed earlier in [1]. Only the most significant ones will be presented here. The overall shape of the velocity profile is best described by the so-called 'planar' displacement and momentum thicknesses:

$$\bar{\delta}_1 = \int_0^\delta \left(1 - \frac{U}{U_\delta}\right) dy, \quad \bar{\delta}_2 = \int_0^\delta \frac{U}{U_\delta}\left(1 - \frac{U}{U_\delta}\right) dy$$

which do not take the axial symmetry of the flow into account. On the other hand, the physical mass- and momentum-flux deficits in the boundary layer and the wake are given by the integral areas

$$\Delta_1 = \int_0^\delta \left(1 - \frac{U}{U_\delta}\right) r\, dy, \quad \Delta_2 = \int_0^\delta \frac{U}{U_\delta}\left(1 - \frac{U}{U_\delta}\right) r\, dy$$

respectively. Here, U_δ is the velocity component at the edge of the boundary layer and wake $(y=\delta)$ tangent to the body surface for the boundary layer and parallel to axis for the wake, r is the radial distance from the axis of symmetry and y is measured normal to the surface of the body. Thus, $r = r_o + y \cos\phi$, where ϕ is the angle between the axis and the tangent to the body surface, for the boundary layer, and r=y for the wake.

The variations of $\bar{\delta}_2$ and Δ_2 with X/L in the turbulent boundary layer and the wake, and the corresponding shape parameters, defined by

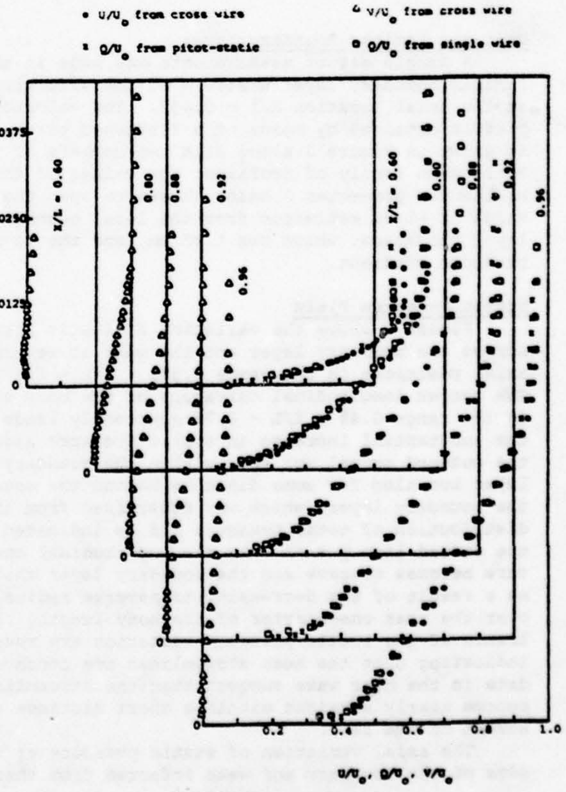

FIGURE 5 (continued)

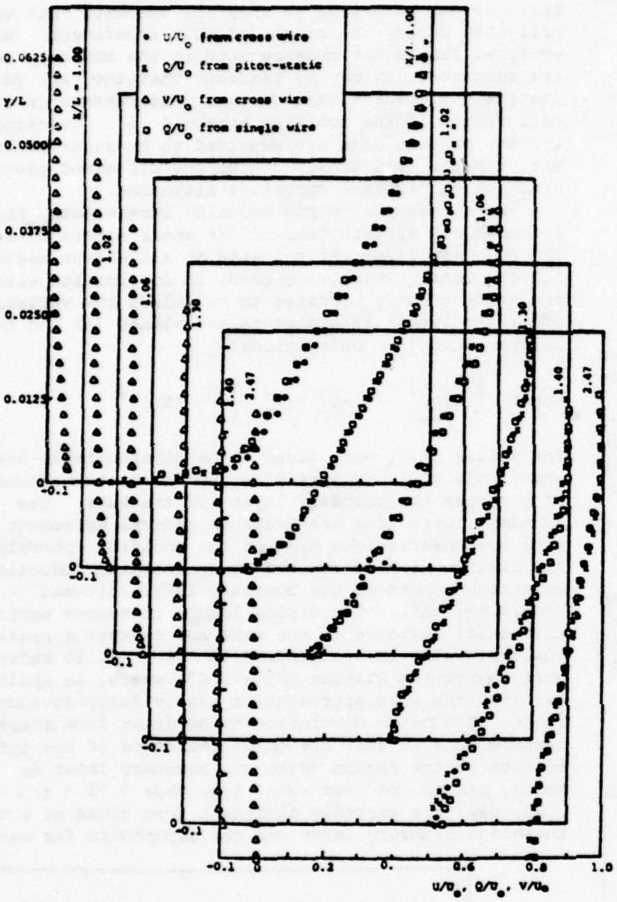

FIGURE 5. MEAN VELOCITY PROFILES

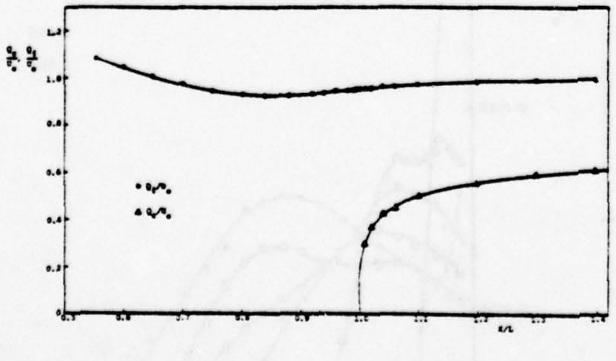

FIGURE 6. VELOCITY AT Y = δ AND WAKE CENTERLINE

$$\bar{H} = \bar{\delta}_1/\bar{\delta}_2, \quad H = \Delta_1/\Delta_2$$

are shown in Figure 7. It should be noted that the total drag coefficient C_D of the body is related to the asympotic value $\Delta_{2\infty}$ of the momentum-deficit area in the far wake via

$$C_D = \frac{D}{\frac{1}{2}\rho U_o^2 S} = \frac{4\pi\Delta_{2\infty}}{S}$$

where D is the drag force and S is a representative area of the body. $\bar{\delta}_2$, on the other hand, has no physical significance, but the parameter $\bar{H}$ indicates the shape of the velocity distributions.

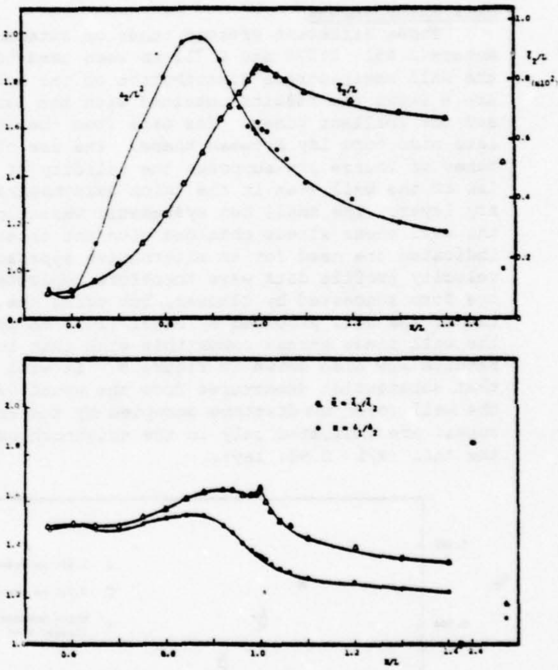

FIGURE 7. INTEGRAL PARAMETERS

Finally, the normal distance by which the external inviscid-flow streamlines are displaced outward due to the presence of the boundary layer and the wake, i.e. the displacement thickness δ^*, may be obtained from the relation [1]

$$r_o \delta^* (1 + \frac{1}{2}\frac{\delta^*}{r_o}\cos\phi) = \Delta_1$$

for the boundary layer, and

$$\frac{1}{2}\delta^{*2} = \Delta_1$$

for the wake. The displacement surface deduced in this manner is shown in Figure 8 along with the physical edge of the boundary layer and the wake. It should be emphasized here that this figure is drawn to scale without any distortion so that it clearly illustrates what is meant by a thick boundary layer. It is particularly interesting to note the magnitude of the displacement effect of the boundary layer over the rear one-quarter of the body and that in the near wake. The implication of this with regard to the boundary layer and near wake computations is discussed later on.

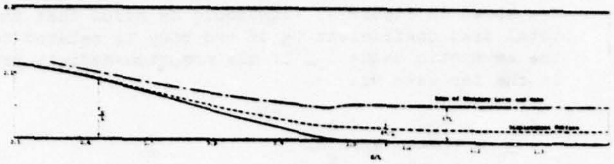

FIGURE 8. DISPLACEMENT SURFACE

Wall Shear Stress

Three different Preston tubes of external diameters 1.651, 1.270 and 0.711 mm were used to measure the wall shear-stress distribution on the body. Figure 9 shows the results obtained with the largest and the smallest tubes. The data from the intermediate size tube lay between these. The use of Preston tubes of course pre-supposes the validity of the usual law of the wall even in the thick axisymmetric boundary layer. The small but systematic variation in the wall shear stress obtained with the three tubes indicated the need for an alternative approach. The velocity profile data were therefore replotted in the form suggested by Clauser, but using the extended law of the wall proposed by Patel [10], to determine the wall shear stress compatible with that law. These results are also shown in Figure 9. It will be seen that substantial departures from the usual law of the wall (over the distance occupied by the Preston tubes) are indicated only in the neighborhood of the tail ($X/L > 0.94$, say).

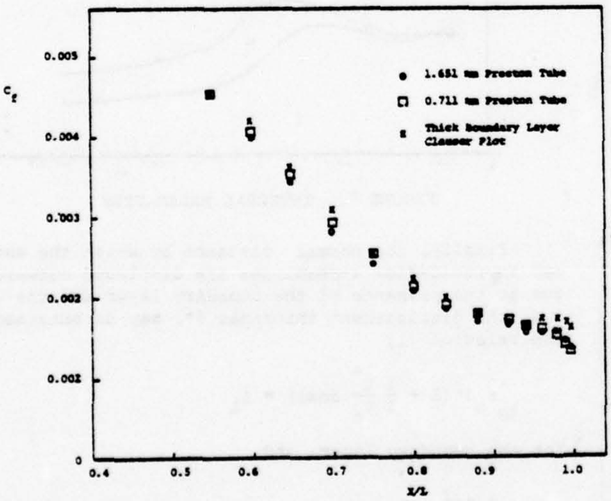

FIGURE 9. WALL SHEAR STRESS

TURBULENCE MEASUREMENTS

Hot wire traverses were made at six axial stations in the boundary layer and five stations in the wake. The mean-velocity profiles obtained in this manner were discussed earlier. Here we shall briefly mention the measurements of the non-zero Reynolds stresses, namely $\overline{u^2}$, $\overline{v^2}$, $\overline{w^2}$, and $\overline{uv}$. Limitations of space do not permit us to show all the data that were collected during the course of this experiment. However, as far as the measurements in the boundary layer are concerned, it may be remarked that they are qualitatively similar to the earlier measurements in the tail region of the modified spheroid [1]. Quantitatively, the present data are expected to be quite different from the earlier set due to the different pressure gradient and surface curvature histories.

As an example of the Reynolds stress data, Figure 10 shows the distribution of the shear stress $\overline{uv}$ across the boundary layer and the wake at all eleven measuring stations. These were used, in conjunction with the mean-velocity profiles to calculate the variation of mixing length according to the planar (ℓ) and the axisymmetric (ℓ_A) definitions

$$-\overline{uv} = \ell^2 \left(\frac{\partial U}{\partial y}\right)^2, \qquad -\overline{uv} = \ell_A^2 \left\{\frac{1}{r}\frac{\partial}{\partial y}(Ur)\right\}^2$$

The values of ℓ_A were found to be substantially lower than those of ℓ. Figure 11 shows the distributions of ℓ across the boundary layer and the wake. The boundary layer data are again in general agreement with the observations made on the modified spheroid [1] insofar as they indicate a substantial reduction of mixing length as the boundary layer thickens towards the tail. The mixing length increases again with axial distance in the wake and reaches a nearly constant value in the range $0.08 < \ell/\delta < 0.10$ at the most downstream station $X/L = 2.47$, where, as indicated earlier, the wake approaches a nearly fully-developed state. The major conclusion to be drawn from these measurements is that the characteristics of the turbulence in the region where the boundary layer is thick, and in the near wake, i.e. over $0.75 < X/L < 1.25$, say, are markedly different from those of a thin turbulent boundary layer and the asymptotic far wake.

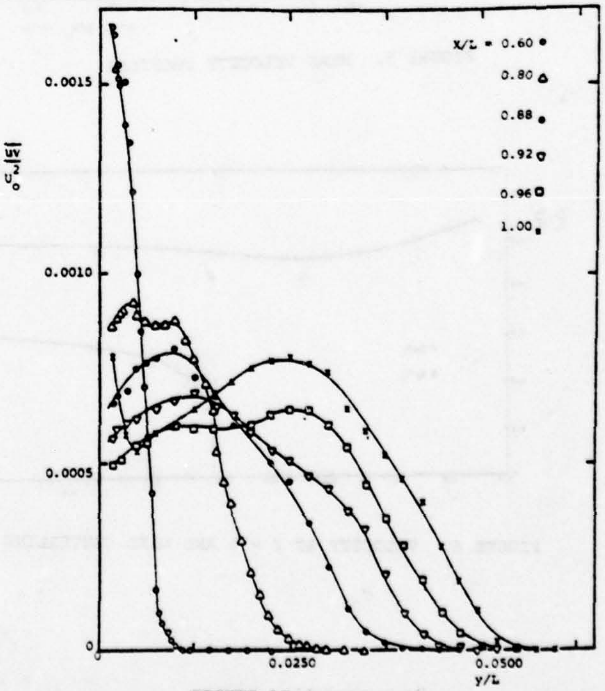

FIGURE 10 (continued)

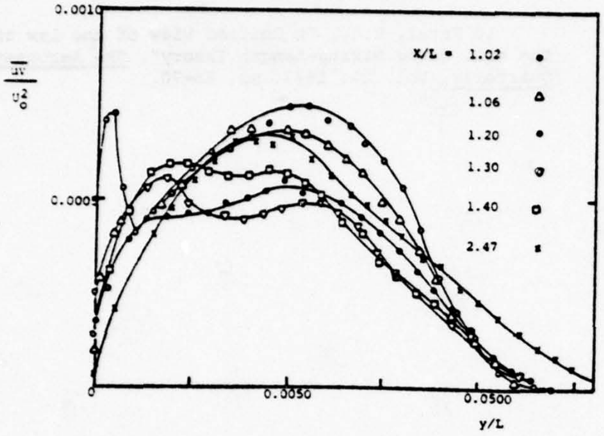

FIGURE 10. REYNOLDS STRESS DISTRIBUTIONS

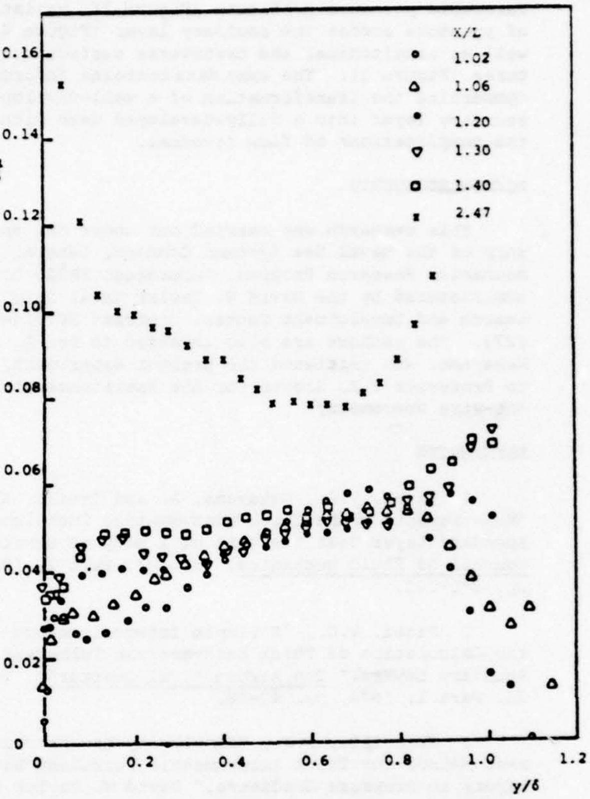

FIGURE 11. MIXING LENGTH DISTRIBUITONS

DISCUSSION AND CONCLUSIONS

It would be obvious by now that the main thrust of this presentation is to point out the existence of this detailed set of mean-flow and turbulence measurements in the thick boundary layer and the near wake of a low-drag body of revolution. Further analysis of the data is obviously needed in order to elucidate the various preliminary observations that have been made. Such an analysis is presently in progress. In particular we shall be examining the following: (a) Comparison of present data with those of previous related investigations. (b) The performance of the presently available advanced turbulence models in the prediction of the thick boundary layer over the tail region of the body (c) The modifications which may be required in these models to account for the rather strong extra rates of strain generated by the longitudinal ($\kappa\delta$) and transverse (δ/r_o) surface curvatures. (d) The possibility of continuing a boundary layer calculation through the near wake to recover the well known asymptotic behavior. (e) The verification of the various procedures that are available, including the one proposed by Nakayama, Patel and Landweber [4,5], to account for the interaction between the boundary layer, the wake and the external inviscid flow. The magnitude of the boundary layer and wake displacement effect shown in Figure 8 would appear to indicate that the conventional method of performing interactive calculations, in which the boundary layer is represented by adding the displacement thickness to the body surface and the wake is either ignored altogether or replaced by a set of singularities, may not be appropriate. Comparative computations need to be performed in order to estimate the shortcomings in such methods.

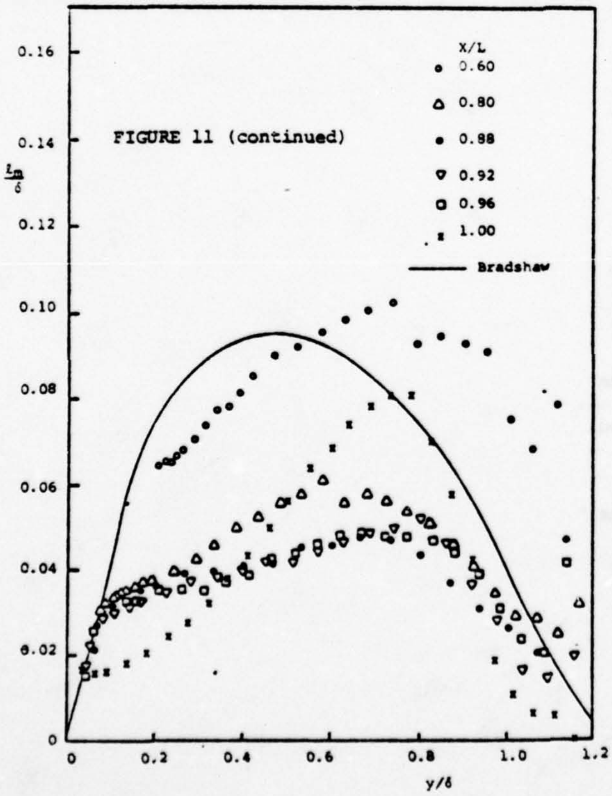

FIGURE 11 (continued)

Finally, it should be observed that the data from this experiment can be used to verify some of the newly emerging turbulence closure models which claim a wider range of applicability. The boundary layer data contain all the complicating factors of adverse and favorable pressure gradients (Figure 2), variation of pressure across the boundary layer (Figure 4) as well as longitudinal and transverse surface curvatures (Figure 1). The wake data contains information concerning the transformation of a well-developed boundary layer into a fully-developed wake without the complications of flow reversal.

ACKNOWLEDGEMENTS

This research was carried out under the sponsorship of the Naval Sea Systems Command, General Hydromechanics Research Program, Subproject SR023 01 01, administered by the David W. Taylor Naval Ship Research and Development Center, Contract N00014-75-C-0273. The authors are also indebted to Dr. A. Nakayama, who initiated the present experiment, and to Professor J.R. Glover for his assistance with hot-wire anemometry.

REFERENCES

1 Patel, V.C., Nakayama, A. and Damian, R., "Measurements in the Thick Axisymmetric Turbulent Boundary Layer Near the Tail of a Body of Revolution," Journal of Fluid Mechanics, Vol. 63, Part 2, 1974, pp. 345-362.

2 Patel, V.C., "A Simple Integral Method for the Calculation of Thick Axisymmetric Turbulent Boundary Layers," The Aeronautical Quarterly, Vol. 25, Part 1, 1974, pp. 47-58.

3 Granville, P.S., "Similarity-Law Entrainment Method for Thick Axisymmetric Turbulent Boundary Layers in Pressure Gradients," David W. Taylor Naval Ship Research and Development Center, Rept. 4525, 1975.

4 Nakayama, A., Patel, V.C. and Landweber, L., "Flow Interaction Near the Tail of a Body of Revolution. Part I: Flow Exterior to Boundary Layer and Wake," ASME, Journal of Fluids Engineering, Vol. 98, Series 1, No. 3, 1976, pp. 531-537.

5 Nakayama, A., Patel, V.C. and Landweber, L., "Flow Interaction Near the Tail of a Body of Revolution. Part II: Iterative Solution for Flow Within and Exterior to Boundary Layer and Wake," ASME, Journal of Fluids Engineering, Vol. 98, Series 1, No. 3, 1976, pp. 538-549.

6 Parsons, J.S. and Goodson, R.E., "The Optimum Shaping of Axisymmetric Bodies for Minimum Drag in Incompressible Flow," Automatic Control Center, School of Mech. Eng., Purdue Uni., Rept. ACC-72-5, 1972.

7 Patel, V.C., "Calibration of the Preston Tube and Limitations in Its Use in Pressure Gradients," Journal of Fluid Mechanics, Vol. 23, Part 1, 1965, pp. 185-208.

8 Landweber, L., "Potential Flow About Bodies of Revolution and Symmetric Two-Dimensional Forms," Iowa Institute of Hydraulic Research, University of Iowa, Report BuShips Index NS 715-102, 1959.

9 Chevray, R., "The Turbulent Wake of a Body of Revolution," ASME, Journal of Basic Engineering," Vol. 90, Series D, 1968, pp. 275-284.

10 Patel, V.C., "A Unified View of the Law of the Wall Using Mixing-Length Theory", The Aeronautical Quarterly, Vol. 24, 1973, pp. 55-70.

COMPUTATIONS OF TURBULENT BOUNDARY LAYER DEVELOPMENT OVER A YAWED, SPINNING BODY OF REVOLUTION WITH APPLICATION TO THE MAGNUS EFFECT

W. B. Sturek, H. A. Dwyer, L. D. Kayser, C. J. Nietubicz, R. P. Reklis, and K. O. Opalka

U. S. Army Ballistic Research Laboratory
Aberdeen Proving Ground, Maryland 21005

ABSTRACT

Many projectiles used by the Army are slender bodies of revolution which are launched at high spin rates. Magnus forces and moments are generated by the distorted boundary layer which results from a spinning body at angle of yaw. The Ballistic Research Laboratory (BRL) is conducting and supporting theoretical and experimental Magnus research efforts. The theoretical effort involves: (1) numerical calculation of the fully three-dimensional boundary layer with the added complication of interaction between surface spin and cross flow velocity; (2) three-dimensional inviscid flow calculations over a body plus boundary layer displacement surface with no plane of symmetry. Several types of experimental data, such as surface pressures, Magnus forces, boundary layer surveys, flow visualization, and skin friction, were obtained to evaluate and provide guidance to the theoretical effort. Comparison of the theory to experimental data shows the agreement to be very good.

NOMENCLATURE

c_f	skin friction coefficient
c_p	specific heat at constant pressure
C_n	normal force coefficient
C_Y	Magnus (side) force coefficient
D	diameter of base of model
h	static enthalpy
k_t	turbulent conductivity
ℓ	mixing length
p	pressure
P	spin rate, radians per second
Pr_t	turbulent Prandtl number, $c_p\varepsilon/k_t$
r	local radius of model
Re_ℓ	Reynolds number based on model length
u,v,w	velocities in boundary layer coordinates
V	velocity along model trajectory
x	surface coordinate in longitudinal direction
y,Y	coordinate perpendicular to local surface
z	cylindrical coordinate along model axis
α	angle of attack
ε	turbulent eddy viscosity
δ	boundary layer thickness
δ^*	boundary layer displacement thickness
Δp	centrifugal pressure gradient contribution to side force
η	transformed y coordinate
μ	molecular viscosity
ξ	transformed x coordinate
ρ	density
τ_x	longitudinal velocity wall shear contribution to side force
τ_ϕ	circumferential velocity wall shear contribution to side force
ϕ	coordinate in circumferential (azimuthal) direction

Subscripts

e	edge of boundary layer
w	model wall conditions
x	quantity in x direction
∞	free stream reference condition
ϕ	quantity in azimuthal direction

Superscripts

'	fluctuating quantity
-	time averaged quantity

INTRODUCTION

Many projectiles used by the Army are slender bodies of revolution which are launched at high spin rates. Magnus forces and moments are generated by the distorted boundary layer which results from a spinning body at angle of yaw. Recent Army interest in achieving increased range and greater payload capacity in artillery projectiles has led to designs with long, slender ogives, increased projectile length, and boat-tailed afterbodies. These designs have resulted in decreased drag with a resulting increase in range; however, the aerodynamic stability of these shapes is less than more conventional designs. This means that these new shapes are more susceptible to a Magnus induced instability. The Magnus force is small (Figure 1), typically 1/10 to 1/100 of the normal force; however, its effect is important because the Magnus moment acts to undamp the projectile throughout its flight. Thus, it is desirable to minimize the Magnus moment in order for the projectile to fly at a small average angle of attack and achieve the greatest range capability.

Magnus has been modeled theoretically as resulting from spin induced distortion of the boundary layer. This effect is illustrated schematically in Figure 2 where a cross-sectional view of a body of revolution is shown. The body is at angle of attack as indicated by the cross flow velocity. In the view where there is no surface spin, the profile of the edge of the boundary layer is symmetric with respect to the plane of the angle of attack. In the view where the surface is spinning, the profile of the boundary layer is asymmetric with respect to the plane of the angle of attack—thus, the inviscid pressure distribution (which responds to the aerodynamic shape composed of the model + boundary-layer-displacement-surface) is asymmetric and yields a net side force.

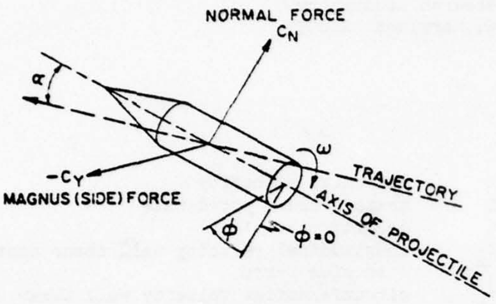

Fig. 1 Magnus and normal forces on a spinning projectile

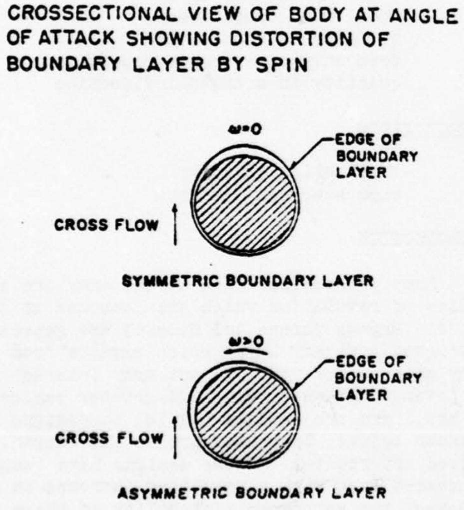

Fig. 2 Schematic illustration of spin induced boundary layer distortion

The U.S. Army Ballistic Research Laboratory has placed increased emphasis on research into the Magnus effect. In this paper, recent results of an effort to develop a method for computing Magnus effects for use in projectile design will be discussed and results of related experimental studies will be presented.

THEORETICAL APPROACH

Background

Since the Magnus effect is a viscous phenomena, computation of the boundary layer development is the foundation for computations of the Magnus force. The boundary layer we are considering is fully three dimensional with the added complication of the interaction of surface spin with the cross flow velocity. The inviscid flow also requires special attention since, in order to compute the Magnus force, the inviscid flow computation technique must be able to compute the three-dimensional flow over a body + boundary-layer-displacement-surface with no plane of symmetry.

Boundary Layer Computations

The basic equations defining the three dimensional compressible, turbulent boundary layer flow over an axisymmetric body of revolution described by the relation r = r(x) are listed below. The coordinate system is shown in Figure 3.

Continuity

$$\frac{\partial}{\partial x}(r\overline{\rho u}) + \frac{\partial}{\partial y}(r\bar{\rho}\hat{v}) + \frac{\partial}{\partial \phi}(\overline{\rho w}) = 0 \qquad (1)$$

x-Momentum

$$\bar{\rho}\left[\bar{u}\frac{\partial \bar{u}}{\partial x} + \hat{v}\frac{\partial \bar{u}}{\partial y} + \frac{\bar{w}}{r}\frac{\partial \bar{u}}{\partial \phi} - \frac{\bar{w}^2}{r}\frac{\partial r}{\partial x}\right] = -\frac{\partial \bar{p}_e}{\partial x} + \frac{\partial}{\partial y}\left[\mu\frac{\partial \bar{u}}{\partial y} - \overline{\rho u'v'}\right] \qquad (2)$$

φ-Momentum

$$\bar{\rho}\left[\bar{u}\frac{\partial \bar{w}}{\partial x} + \hat{v}\frac{\partial \bar{w}}{\partial y} + \frac{\bar{w}}{r}\frac{\partial \bar{w}}{\partial \phi} + \frac{\overline{uw}}{r}\frac{\partial r}{\partial x}\right] = -\frac{1}{r}\frac{\partial \bar{p}_e}{\partial \phi} + \frac{\partial}{\partial y}\left[\mu\frac{\partial \bar{w}}{\partial y} - \overline{\rho v'w'}\right] \qquad (3)$$

Energy

$$\bar{\rho}\left[\bar{u}\frac{\partial \bar{h}}{\partial x} + \hat{v}\frac{\partial \bar{h}}{\partial y} + \frac{\bar{w}}{r}\frac{\partial \bar{h}}{\partial \phi}\right] = \bar{u}\frac{\partial \bar{p}_e}{\partial x} + \frac{\bar{w}}{r}\frac{\partial \bar{p}_e}{\partial \phi} + \mu\left[\left(\frac{\partial \bar{u}}{\partial y}\right)^2 + \left(\frac{\partial \bar{w}}{\partial y}\right)^2\right] - \overline{\rho u'v'}\frac{\partial \bar{u}}{\partial y} - \overline{\rho v'w'}\frac{\partial \bar{w}}{\partial y} + \frac{\partial}{\partial y}\left[\frac{\mu}{Pr}\frac{\partial \bar{h}}{\partial y} - \overline{\rho v'h'}\right]. \qquad (4)$$

where $\hat{v} = \bar{v} + \frac{\overline{\rho'v'}}{\bar{\rho}}$ and the bar indicates a time averaged quantity.

In order to obtain closure for this system of equations, the following models of the turbulence terms have been introduced:

Turbulent Shear Stress

$$-\overline{\rho u'v'} = -\overline{\rho v'w'} = \bar{\rho}\,\ell^2\left[\left(\frac{\partial \bar{u}}{\partial y}\right)^2 + \left(\frac{\partial \bar{w}}{\partial y}\right)^2\right] = \varepsilon\left[\left(\frac{\partial \bar{u}}{\partial y}\right)^2 + \left(\frac{\partial \bar{w}}{\partial y}\right)^2\right]^{\frac{1}{2}}$$

where ε is introduced as the turbulent eddy viscosity and the mixing length, $\ell = .09\,\delta \tanh[(.4/.09)(y/\delta)]$. Van Driest damping is used to account for the effect of the laminar sublayer.

Turbulent Heat Transfer

$$-\overline{\bar{\rho} v' h'} = \frac{k_t}{c_p} \frac{\partial \bar{h}}{\partial y}$$

The turbulent Prandtl number is introduced as

$$Pr_t = c_p \varepsilon / k_t = 0.90$$

The numerical technique used to solve these equations is an implicit technique developed by Dwyer(1,2) that takes into consideration the changes in direction of the cross flow velocity that occurs on the side of the model where the inviscid cross flow opposes surface spin. This technique correctly models the cross flow convection process occurring within the boundary layer. In order to improve the speed and accuracy of the numerical solution, several coordinate transformations are employed:

Mangler Transformation of Axisymmetric Growth,

$$\xi = \int_0^x r^2 dx;$$

Blasius Type Transformation of Normal Growth,

$$\eta = \left(\frac{p_\infty}{p_e}\right)^{\frac{1}{2}} \left(\frac{\rho_\infty u_\infty}{2\mu_\infty \xi}\right)^{\frac{1}{2}} \int_0^y \frac{\rho}{\rho_\infty} r dy; \quad \text{and}$$

Coordinate Stretching to Allow Closer Grid Spacing Near the Wall (3),

$$n_j = 100\,(1.5 \exp\left[(j-1)(1/60)(1/.05)\right] - 1)/$$
$$(1.5 \exp (1/.05) - 1)$$

where $j = 1, 2, 3, \ldots\ldots 61$

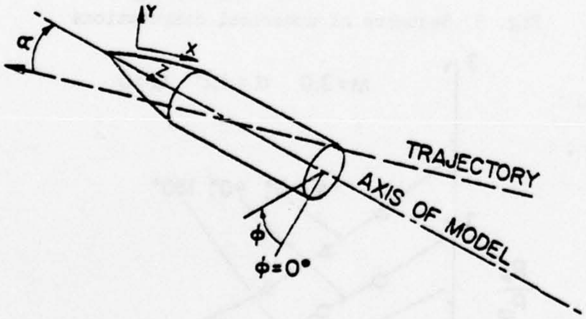

Fig. 3 Coordinate system

In computing the boundary layer development, the effect of turbulence is turned on gradually over three longitudinal steps. The computation grid in the azimuthal plane is in 10 degree increments. Three interations are performed at each station for turbulent computations. For comparison with experiment, the location of boundary layer transition is fixed at the location of the boundary layer trip on the experimental model.

Three Dimensional Displacement Surface

The three dimensional displacement surface is not merely the vector sum of the longitudinal and circumferential components of the boundary-layer displacement thicknesses. Instead, the differential equation derived by Moore (4):

$$\frac{\partial}{\partial x}\left[\rho_e u_e r\,(\delta^*_{3D} - \delta^*_x)\right] + \frac{\partial}{\partial \phi}\left[\rho_e w_e\,(\delta^*_{3D} - \delta^*_\phi)\right] = 0 \qquad (5)$$

must be solved for δ^*_{3D}, the three dimensional boundary-layer displacement thickness where

$$\delta^*_x = \int_0^\delta \left(1 - \frac{\rho u}{\rho_e u_e}\right) dy \text{ and } \delta^*_\phi = \int_0^\delta \left(1 - \frac{\rho w}{\rho_e w_e}\right) dy$$

Dwyer (5) has shown that equation (5) is of the general form

$$P \frac{\partial \delta^*_{3D}}{\partial x} + Q \frac{\partial \delta^*_{3D}}{\partial \phi} = R_1 \delta^*_{3D} + R_2 \qquad (6)$$

The singularity in δ^*_{3D} and δ^*_x at $x = 0$ can be avoided by starting the computations at a small, finite value of x and computing approximate starting conditions. Equation (6) can then be solved as an ordinary differential equation, providing the differencing in the circumferential direction is carried out from $\phi = 0$ to 180° and from $\phi = 0$ to -180° in order to obey the zone of influence defined by

$$\frac{dx}{d\phi} = r \frac{u_e}{w_e}.$$

An example of computed values of δ^*_{3D} for the SOC model is shown in Figure 4. The effect of spin is to decrease the thickness of the boundary layer where surface spin and inviscid crossflow are in the same direction and to increase the thickness of the boundary layer where surface spin and inviscid crossflow oppose.

Inviscid Computations

The development of a numerical technique for computing the three dimensional inviscid flow field over a yawed, pointed, body in supersonic flow was a very important step in the development of a capability for computing Magnus effects(6). The program uses MacCormack's(7) "shock capturing" numerical technique. This is a second order accurate scheme that uses a predictor-corrector technique to solve the equations of motion in an implicit marching scheme. The unique feature of the program developed by Sanders for the Magnus problem is that the flow field is computed about an axisymmetric model plus displacement surface which, due to the distortion of the boundary layer by surface spin, has no plane of symmetry.

Sequence of Computations

The sequence of computations which must be run in order to compute Magnus effects is indicated in Figure 5. Each block indicates a separate computer program along with its required input information and the output. The two main programs are outlined in asterisks.

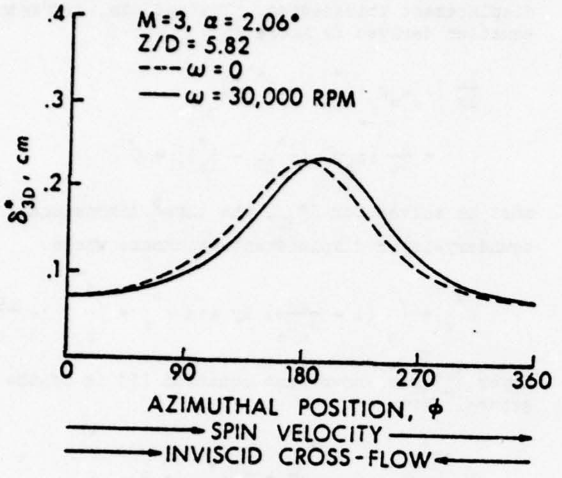

Fig. 4 Computations of δ^*_{3D} for the SOC model, $\omega = 30{,}000$ RPM

In order to start the computations, an initial plane of profile data at the tip of the model and inviscid flow boundary conditions are required. The initial profile data are computed for the limiting condition of the conical tip of the model. The inviscid flow boundary conditions are computed using the program developed by Sanders (6). An example showing the computed wall pressure distribution compared to experimental data for several azimuthal stations is shown in Figure 6. Also shown is the outline of the model shape, a six caliber long secant-ogive-cylinder. As seen in the figure, excellent agreement is obtained between theory and experiment for the moderate angle of attack considered here. It is seen that the boundary layer experiences a significant history of favorable and adverse pressure gradients in both the longitudinal and circumferential directions.

In order to start the boundary layer computation for the spinning model, initial profile data are generated for the limiting case of the laminar boundary layer at the tip of a non-spinning cone. These data, along with the outer boundary condition of the inviscid flow, enable the marching technique to begin for specific conditions of Mach number, angle of attack, wall temperature, spin rate, and free stream properties. The output of the boundary layer program consists of wall shear and centrifugal pressure gradient contributions to the Magnus effect and the longitudinal and circumferential components of the boundary layer displacement surface as functions of longitudinal and circumferential position over the entire surface of the model.

The output of the boundary layer program is input to the program which solves for the three dimensional boundary layer displacement thickness, δ^*_{3D}. Input data for this program are in the surface coordinate system used for the boundary layer computations. The output of this program is transformed into a cylindrical coordinate system in order to

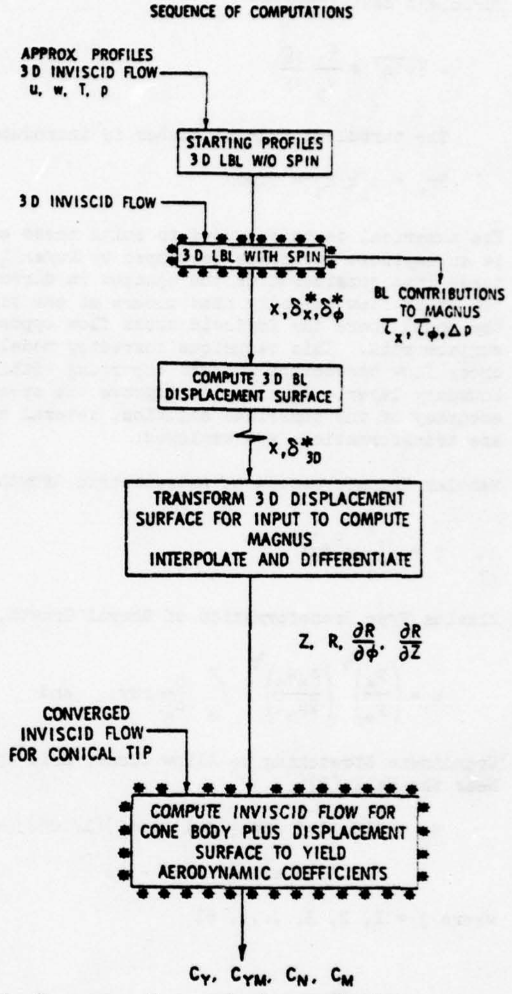

Fig. 5 Sequence of numerical computations

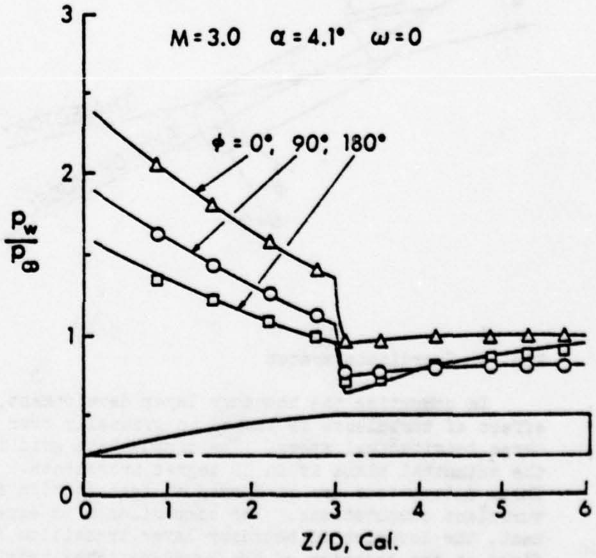

Fig. 6 Surface pressure distribution on the SOC model

facilitate computation of the inviscid flow. The output consists of the surface coordinates of the model plus δ^*_{3D} as well as the local derivatives of the surface coordinate in the axial and circumferential directions.

The final step is the computation of the inviscid flow over the newly defined body which is of completely arbitrary configuration with no plane of symmetry. The starting conditions consist of the inviscid flow field for the asymptotic cone tip of the original model. Pitch and yaw plane force and moment aerodynamic coefficients are the final outputs obtained.

Boundary Layer Components of Magnus

Due to spin induced asymmetry in the computed velocity profiles, three contributions to the Magnus effect are generated within and at the surface of the spinning model which are in addition to the boundary layer displacement effect sensed by the outer inviscid flow. These components are: (1) longitudinal velocity wall shear, $\tau_x = \mu\,(\partial u/\partial y)_{y=0}$; (2) circumferential velocity wall shear, $\tau_\phi = \mu\,(\partial w/\partial y)_{y=0}$; and (3) centrifugal pressure gradient, $\Delta p = \int_0^y \rho\,\frac{w^2}{r}\,dy$. For a non-spinning model, the net contribution of each of these components would be zero. However, due to the asymmetry induced by surface spin, a small contribution to a side force is obtained. The relative magnitudes of these components of the Magnus force are shown in Figure 7.

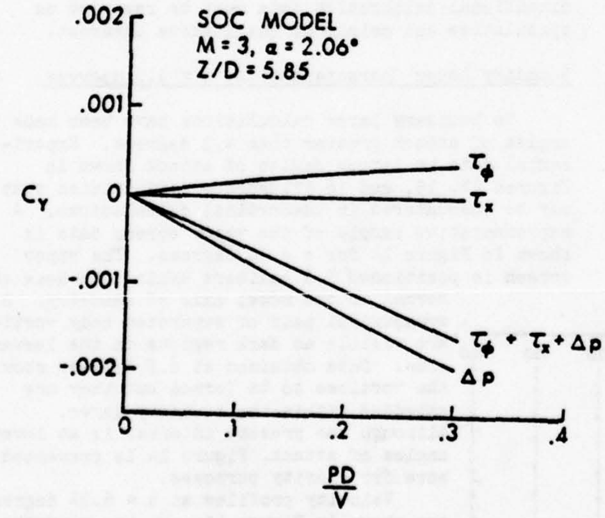

Fig. 7 Turbulent boundary layer contributions to Magnus force

EXPERIMENTS

General

The purpose of the experimental studies is to provide data that will be useful in evaluating and help guide the development of the theoretical effort. The experimental studies consisted of: (1) boundary layer profile measurements; (2) optical studies; (3) Preston tube skin friction measurements; (4) strain-gage balance force measurements; (5) wall static pressure measurements.

Experimental results were obtained in the BRL Supersonic Wind Tunnel No. 1 which is a continuous flow, flexible nozzle tunnel capable of Mach numbers 1.5 to 5.0; the test section size is 38 cm high by 33 cm wide. Data were obtained at Mach 3.0, a Reynolds number (Re_ℓ) of 7.6×10^6 and at both spinning and non-spinning conditions.

The model tested was the six caliber secant-ogive-cylinder with geometry as shown in the pressure distribution plot of Figure 6. The model was equipped with a boundary layer trip located 0.7 caliber from the nose to insure a consistent turbulent flow for all tests.

Boundary Layer Measurements

Measurements of the total head pressure through the boundary layer were made with a flattened impact pressure probe 0.15 cm wide by 0.015 cm high. Data were obtained on the cylindrical section at 3.33, 4.44, and 5.56 calibers from the nose and azimuthally around the model in 30 degree increments and at yaw angles from 0 to 6.3 degrees. At each position, surveys were made at both zero RPM and 20,000 RPM; the spin rate of 20,000 RPM corresponds to a pd/v of 0.19. The impact pressure probe was brought from outside the boundary layer down to, and contacting, the model surface for the zero RPM case; for the 20,000 RPM spin rate the probe was brought down to within approximately 0.01 cm from the surface. The probe axis was aligned longitudinally with the model axis. Some uncertainty is inherent in the profile data due to the probe not being aligned with the local flow direction within the boundary layer. This uncertainty would be greatest near the surface of the model and at longitudinal stations near the forward portion of the model. However, the large gradients present in a turbulent boundary layer would confine the greatest effect of flow angularity to a very small region near the surface which cannot be probed accurately using a total head probe. Also, these measurements were obtained at small angles of attack. Local Mach numbers within the boundary layer were determined from the Rayleigh pitot formula assuming a constant static pressure through the boundary layer. The boundary layer data for this paper uses measured values of wall static pressure.

Wall shear stress was obtained for the non-spinning model using the Preston tube technique. The Preston tube is a circular total head probe mounted flush with the model surface and sized to lie within the logarithmic portion of the law-of-the-wall velocity profile. The wall shear stress was computed from the measured impact and surface pressures and using the correlation relations of reference (8).

Vapor screen flow visualization experiments using the technique described in reference (9) were performed. The purpose of this phase was to obtain a better understanding of the surrounding flow field and in particular determine the presence of vortices both imbedded in the boundary layer and separated from the model surface. Vapor screen pictures were obtained at each ½ caliber position for angles of yaw of 2, 4, 5, 6, and 10 degrees both with and without spin.

Force Measurements

Measurements of Magnus and normal force were obtained using the strain-gage balance technique. The model is free to rotate on internally mounted bearings and equipped with a single row of turbine blades so that spin-up can be achieved. Turbine air is supplied to the model through the sting and the model is brought up to speeds as high as 40,000 RPM. The turbine air is then cut off and data are acquired as the model spin rate decays.

DISCUSSION OF THE THEORETICAL AND EXPERIMENTAL RESULTS

Boundary Layer Characteristics, $\alpha < 4.2$ degrees

A comparison of theoretical and experimental velocity profiles is shown in Figure 8 for 2 degrees angle of attack and zero spin rate. The agreement is considered to be good and is actually comparable to that obtained for supersonic two-dimensional flow measurements. On the leeward side, near $\phi = 180°$, the theoretical velocities are greater than the experimental measurements near the surface and the theoretical velocities are smaller than the experimental velocities near the edge of the boundary layer. On the windward side, near $\phi = 0°$, the situation is reversed. These differences in profile shape will give compensating effects when computing integral parameters. Figure 9 compares theoretical and experimental velocity profiles at 4.2 degrees angle of attack. The differences between theoretical and experimental profile shape are similar to those at $\alpha = 2$ degrees except that they are more pronounced; also, the variation in boundary layer thickness from the windward to the leeward side is greater for the 4.2 degree case.

The effect of spin on velocity profiles is shown in Figure 10 where profiles on the side where cross flow and spin are in the same direction (ϕ = 0-180) are compared with profiles on the opposite side of the model (ϕ = 180-360) where the cross flow is in the opposite direction of spin. On the windward side of the model (ϕ = 0-90), there is almost no measurable effect of spin. On the leeward side (ϕ = 120 vs 240 and 150 vs 210), the profile shapes differ substantially. The effect of cross flow in opposition to model surface rotation (e.g. $\phi = 210$) is to decrease the fullness of the profile which, of course, will result in a larger displacement thickness. It is of interest to note that the primary effect of spin is to change the profile shape rather than to change the total thickness.

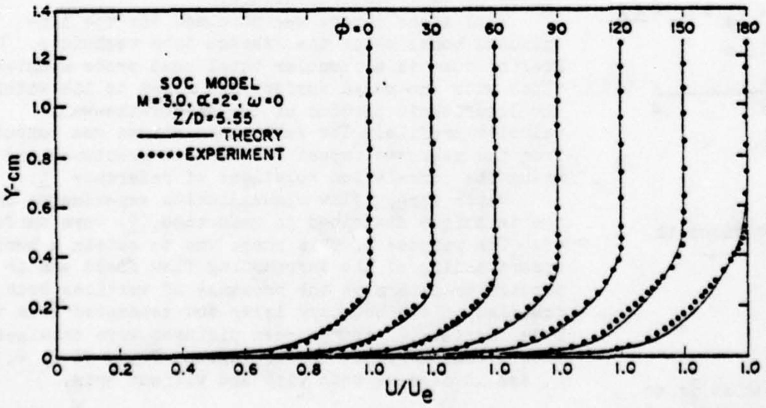

Fig. 8 Velocity profiles, theory compared with experiment

Values for the longitudinal component of displacement thickness are compared in Figure 11. The agreement between theory and experiment is generally good; however, it is seen at the forward station ($Z/D = 3.33$) that theoretical thicknesses are slightly greater than experiment ($\phi \approx 0$) and at the aft station theoretical thicknesses are slightly smaller than experiment. This situation indicates that the boundary layer actually grows at a faster rate than predicted by theory; however, this is not particularly surprising since the turbulence model did not provide for any adjustment as a function of pressure gradient. The effect of spin on displacement thickness δ^*_x can be seen in Figure 12 where the increment of δ^*_x due to spin is plotted on an expanded scale for $\alpha = 4.2$ degrees. The effect on displacement thickness is seen to be significant only in the vicinity of the leeward side (ϕ = 180 degrees). The agreement between theory and experiment is encouraging evidence that the numerical technique accurately models the effect of surface spin.

Measured values for skin friction coefficient obtained using the Preston tube technique are compared to theory in Figure 13. The skin friction coefficient is referenced to free stream static properties upstream of the model rather than the more conventional approach of using local properties at the edge of the boundary layer. The agreement indicated is within ± 10%. This is considered quite good since the Preston tube is expected to yield an accuracy of ± 10% for two dimensional flat plate boundary layer flow. The use of the Preston tube to obtain measurements in a three dimensional boundary layer flow using two dimensional calibration data must be regarded as speculative and mainly of qualitative interest.

Boundary Layer Characteristics, $\alpha > 4.2$ degrees

No boundary layer calculations have been made for angles of attack greater than 4.3 degrees. Experimental data at larger angles of attack shown in Figures 14, 15, and 16 illustrate difficulties that may be encountered in theoretical calculations. A representative sample of the vapor screen data is shown in Figure 14 for $\alpha = 10$ degrees. The vapor screen is positioned 5.5 calibers behind the nose and normal to the model axis of symmetry. A symmetrical pair of separated body vortices are visible as dark regions on the leeward side. Data obtained at 6.3 degrees show the vortices to be formed but they are embedded within the boundary layer. Although the present interest is at lower angles of attack, Figure 14 is presented here for clarity purposes.

Velocity profiles at $\alpha = 6.34$ degrees are shown in Figure 15. On the windward side of the model, the profiles seem well behaved; however, on the leeward side (ϕ = 180-240), profiles differ drastically with each other. For example, at $\phi = 180$ degrees the profile shows a fullness typical of profiles seen in a favorable pressure gradient; at $\phi = 210$ degrees, the profile is less full and seems to be tending toward separation, typical of profiles in an adverse pressure gradient. The displacement thickness at $\phi = 210$ degrees is actually greater than that at $\phi = 180$ degrees even though the total thickness is smaller than that at ϕ = 180 degrees. Another characteristic, which at first appears abnormal, is the large difference in boundary layer thicknesses at ϕ = 210 and 240 degrees. Displacement thicknesses at α = 6.34 degrees are shown in Figure 16. The significant difference from the 4.2 degrees case is the dip or decrease in δ^* near ϕ = 180 degrees. It is believed that the above phenomena are caused by the existence of longitudinal separation type vortices which are beginning to develop. Such vortices could create local areas of favorable and adverse pressure gradients that would cause the complex flows illustrated by Figures 15 and 16.

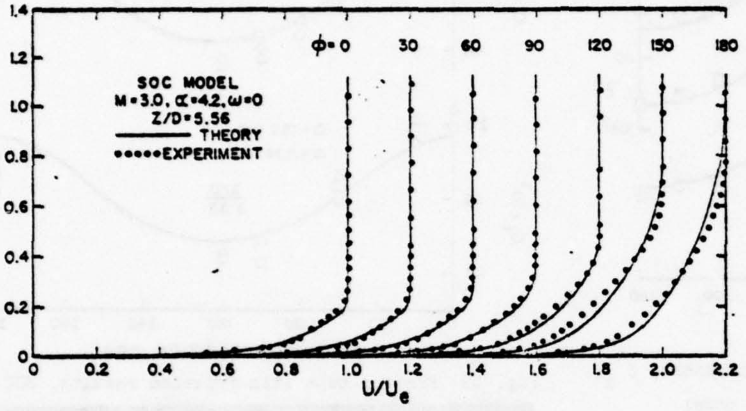

Fig. 9 Velocity profiles, theory compared with experiment

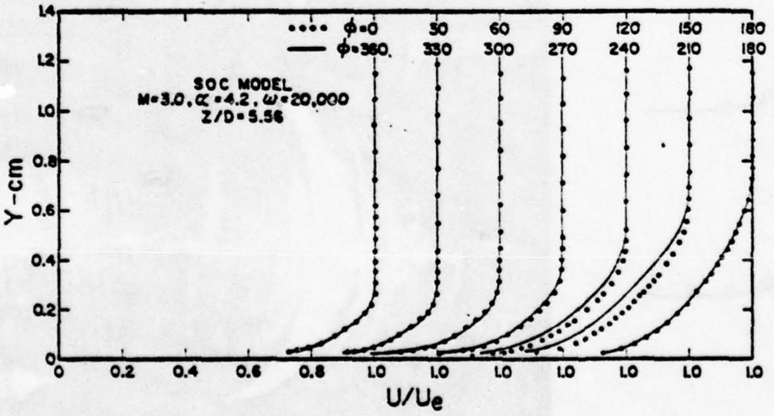

Fig. 10 Experimental velocity profiles, effects of spin

Magnus Characteristics

One criterion which can be used to gage the success of the theory is the accuracy with which Magnus forces and moments can be predicted. Figure 17 is a comparison of theoretical and experimental Magnus forces; in addition, the magnitude of the four components of the Magnus force are shown. The contributions of τ_ϕ and Δp oppose and are of comparable magnitude, while the contribution of τ_x is minimal. The arithmetic sum of the three boundary layer components is indicated by $C_{YBL} = \tau_x + \tau_\phi + \Delta p$. The total computed Magnus force shown here is the arithmetic sum of the contributions due to τ_x, τ_ϕ, Δp, and δ^*_{3D}. It is worthwhile to emphasize that this marks the first time that computations of the Magnus effect have been carried out in a conceptually "exact" manner for the turbulent boundary layer on a realistic projectile configuration. The agreement between the calculated Magnus force and experimental strain-gage balance force measurements is extremely good. The theoretical computations accurately reproduce the non-linear trend of Magnus with angle of attack. This non-linear behavior is due primarily to the increasing dominance of the contribution of δ^*_{3D} as the angle of attack increases.

CONCLUDING REMARKS

A combined theoretical-experimental study of the Magnus effect on yawed, spinning projectiles has been discussed. The overall objective of this effort is to develop a method for computing Magnus effects that could be used in the design of artillery projectiles. Numerical techniques have been developed for computing: (1) the three-dimensional turbulent boundary layer development over a yawed, spinning body of revolution; (2) the three-dimensional boundary-layer displacement surface for an arbitrary body of revolution; and (3) the three-dimensional inviscid flow field over a yawed, pointed body of completely general configuration with no plane of symmetry. The computations have been compared to experimental measurements of Magnus force and turbulent boundary layer profile characteristics. The general impression obtained in comparing the computations to experimental data is that the numerical techniques are working quite well and yielding very impressive agreement with experimental data. The results for Magnus force are considered extremely encouraging. The comparisons with detailed profile characteristics do reveal minor differences. It is believed that additional accuracy can be achieved by improved or more complex turbulence modeling which accounts for both favorable and adverse pressure gradients. Other refinements in the boundary layer computation such as correction for transverse curvature and inclusion of boundary region effects should be incorporated.

The ability to predict the point of transition may be a factor in the accuracy of the theoretical model. The location of transition was fixed by the use of boundary layer trips for all the experiments described; therefore, the theoretical results do not reflect any error which might be caused in predicting the location of the transition line around the model.

The higher angle of attack experiments suggest that problems will be encountered in extending the theory to angles of attack greater than 5 degrees.

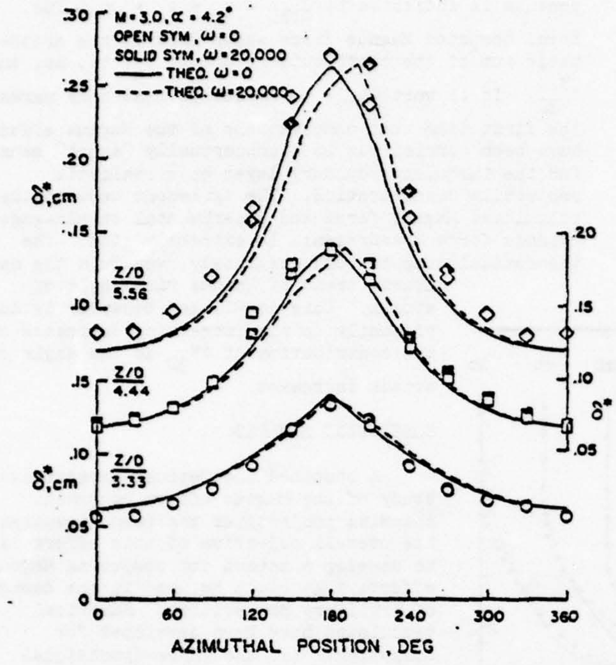

Fig. 11 Boundary layer displacement thickness, δ^*_x, compared with experiment, SOC model

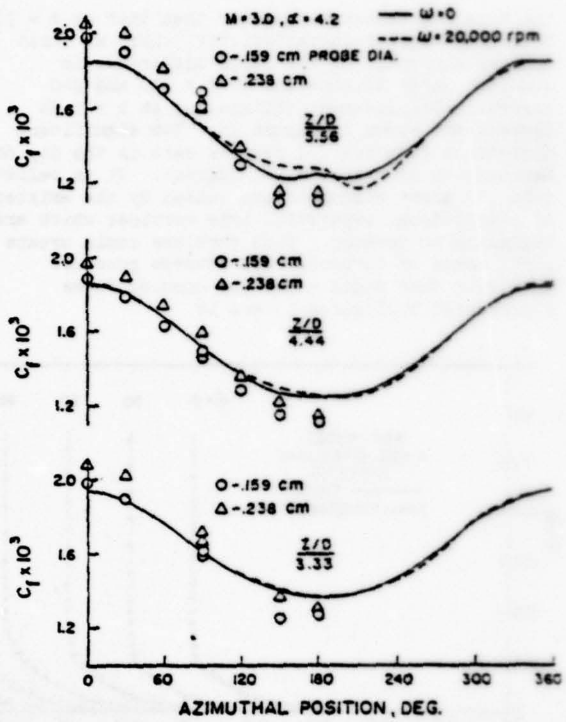

Fig. 13 Preston tube skin friction results, SOC model

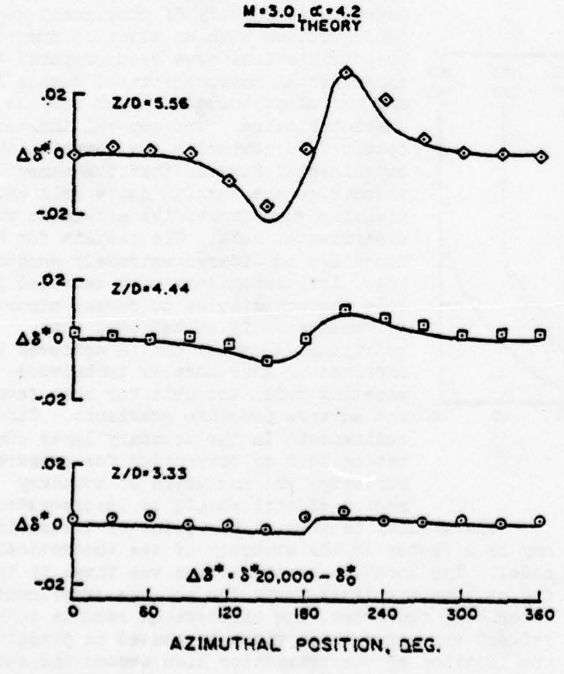

Fig. 12 Increment of displacement thickness, $\Delta\delta^*_x$, due to spin, SOC model

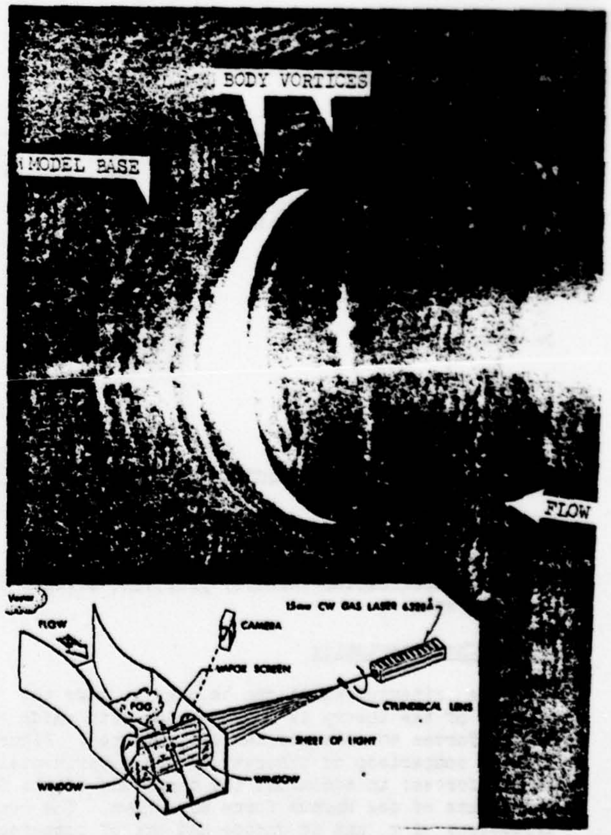

Fig. 14 Vapor screen photograph, SOC model, M = 3.0, α = 10 deg.

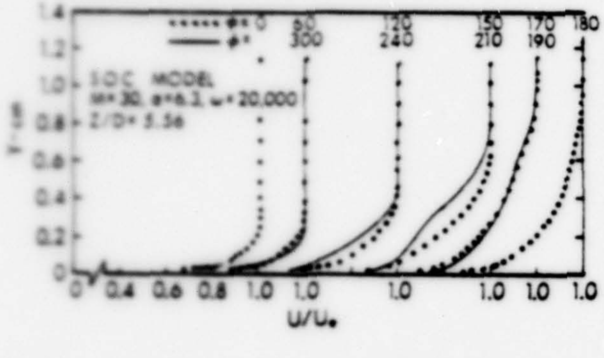

Fig. 15 Experimental velocity profiles, effects of spin, α = 6.3 deg.

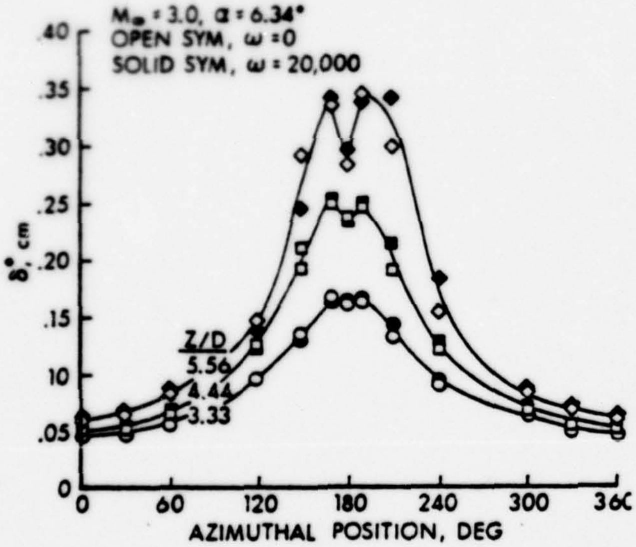

Fig. 16 Experimental boundary layer displacement thickness, SOC model, α = 6.3 deg.

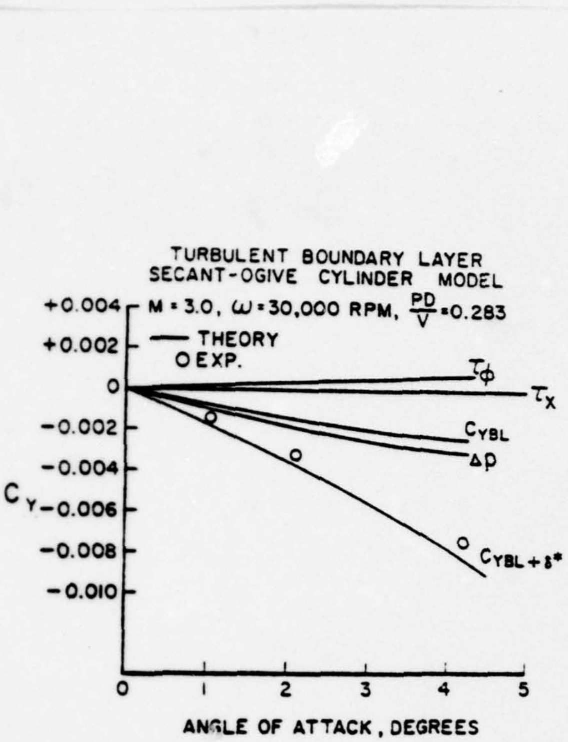

Fig. 17 Magnus force vs angle of attack, theory compared with experiment

REFERENCES

1 Dwyer, H. A., "Three Dimensional Flow Studies Over a Spinning Cone at Angle of Attack," BRL Contract Report No. 137, February 1974, U.S. Army Ballistic Research Laboratories, Aberdeen Proving Ground, Maryland. AD 774795.

2 Dwyer, H. A., and Sanders, B. R., "Magnus Forces on Spinning Supersonic Cones. Part I: The Boundary Layer," BRL Contract Report No. 248, July 1975, U.S. Army Ballistic Research Laboratories, Aberdeen Proving Ground, Maryland. AD A013518. Also *AIAA Journal*, Vol. 14, No. 4, May 1976, p. 498.

3 Blottner, F. G., "Variable Grid Scheme Applied to Turbulent Boundary Layers," Journal of Computer Methods in Applied Mechanics and Engineering, 1975.

4 Moore, F. K., "Displacement Effect of a Three-Dimensional Boundary Layer," NACA TN 2722, June 1952.

5 Dwyer, H. A., "Methods for Computing Magnus Effects on Artillery Projectiles," BRL Contract Report to be published, U.S. Army Ballistic Research Laboratories, Aberdeen Proving Ground, Maryland.

6 Sanders, B. R., "Three-Dimensional, Steady, Inviscid Flow Field Calculations With Application to the Magnus Problem," PhD Dissertation, University of California, Davis, California, May 1974.

7 MacCormack, R. W., "Numerical Solution of the Interaction of a Shock Wave With a Laminar Boundary Layer," Proceedings of the International Conference on Numerical Methods in Fluid Dynamics, Lecture Notes in Physics, Vol. 8, Maurice Holt, ed., Springer-Verlag, 1971.

8 Bradshaw, P., and Unsworth, K., "A Note on Preston Tube Calibrations in Compressible Flow," IC Aero Report 73-07, September 1973, Imperial College of Science and Technology, London, Great Britain.

9 Nietubicz, C. J., "Vapor Screen Technique Development at the Ballistic Research Laboratories," BRL Memorandum Report No. 2387, June 1974, U.S. Army Ballistic Research Laboratories, Aberdeen Proving Ground, Maryland. AD 784077.

SESSION 10

WALL FLOWS 3

Chairman: J. Mathieu
Ecole Centrale de Lyonnaise
Ecully, France

EXPERIMENTAL AND NUMERICAL STUDY OF CONSTANT DIAMETER DUCTED JET MIXING

P. H. OOSTHUIZEN AND M. C. WU
DEPARTMENT OF MECHANICAL ENGINEERING
QUEEN'S UNIVERSITY
KINGSTON, ONTARIO

ABSTRACT

Measurements of mean velocity and turbulence stress distributions in constant diameter, low-speed, isothermal, air-in-air ducted jet flow have been obtained. The conditions used in the tests were such that no regions of recirculating flow existed in the test-section. The measurements obtained are more extensive and complete than in any previous study. The ability of three commonly used turbulence models to predict the measured results has also been assessed. The turbulence models used were (a) an algebraic mixing-length model (b) a single differential equation model, the equation used being for the turbulence kinetic energy (c) a two differential equation model, the equations used being for the turbulence kinetic energy and the dissipation. These were used in conjunction with a numerical solution of the governing equations.

NOMENCLATURE

D = Working-section diameter
k = Turbulence kinetic energy
ℓ = Length scale
ℓ_m = Mixing length
U = Axial component of velocity
u = Fluctuating part of axial velocity
$\bar{U}_m$ = Average velocity across duct
U_c = Centre-line velocity
V = Radial component of velocity
v = Fluctuating part of radial velocity
x = Axial coordinate
R = Working-section radius
r = Radial coordinate
ε = Dissipation of energy
ν = Kinematic viscosity
ν_T = Eddy viscosity

INTRODUCTION

Ducted jet flows are of considerable practical interest having application in ejectors, in many combustion systems and in thrust augmentors. This type of flow is, however, also of importance in the general study of turbulent shear flows, involving, as it does, the interaction of a free-jet flow with a wall-bounded flow and the development of a type of developed duct flow from this interaction. Because it involves these various types of turbulent flow, which are often considered separately in simple turbulence models, experimental measurements in ducted-jet flows are useful for evaluating the adequacy of proposed turbulence models. It was particularly with the latter consideration in mind that the present study was undertaken. In this study, experimental measurements of mean velocities and turbulence stresses have been obtained in constant-diameter, low-speed, air-in-air ducted jet mixing, the flow conditions used having been so chosen that no regions of flow recirculation occurred in the test-section. The ability of some commonly used turbulence models to predict the observed experimental results has also been studied, the governing equations having been numerically solved.

A number of previous studies of ducted-jet mixing have, of course, been undertaken, reviews of much of this work being given in refs. 1 to 3. Many of these studies only involved the measurement of the wall pressure distributions with mean velocity profiles also being measured in a few instances. It is believed, however, that if the experimental study of ducted jet flows is to truly be of assistance in the development of turbulence models, then it is necessary to measure, in addition to the above quantities, at least some of the turbulence stressess since only then can the initial conditions be fully described when using more advanced turbulence models and only then can deficiencies in these models, if such exist, be fully evaluated. Extensive measurements of this type are not available although some such measurements have been given by Matsumato, Kimoto and Tshuchemato (4) and Razinsky (5). However, in the first of these studies, the jet diameter was so small compared to the duct diameter that little interaction between the jet and the wall boundary layer occurred in the region where the measurements were made. In the second of the studies mentioned, the results are rather sparse and different flow variables were measured on different cross-sectional planes which leads to some difficulty in comparing the results with numerical predictions. Further, the flow conditions used in some of the tests were such that there was a possibility that regions of reversed flow existed. While this is also likely to be true in some practical devices involving ducted-jet flow, it is felt that the adequacy of turbulence models for the prediction of non-separating flows should be thoroughly explored before testing them against results for flows involving recirculation.

It was with these perceived deficiencies in existing studies in mind that the present study was undertaken.

EXPERIMENTAL STUDY

The general layout of the experimental apparatus is shown schematically in fig. 1. The primary air-flow was supplied by a compressor through a pipe-line in which an orifice plate was mounted, this allowing the flow rate to be measured. The primary air entered the working-section through a convergent nozzle with an exit diameter of 20.6 mm. The test section, which was approximately 1 m long, had a constant diameter of 82.5 mm giving a diameter ratio of 4 to 1. The secondary air was drawn from the atmosphere into a settling chamber, which surrounded the primary flow delivery pipe, flowing into the test section from this chamber through an annular nozzle which was concentric with the primary flow nozzle. The temperatures of the primary and secondary flows were measured and found to be both essentially equal to the ambient temperature.

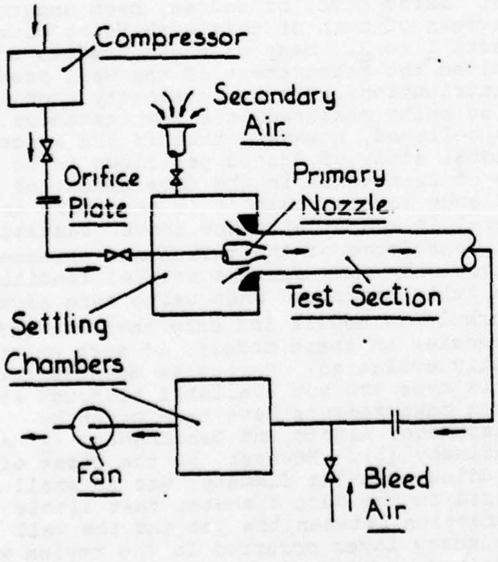

Fig. 1 Layout of apparatus

The test-section was connected at its exit end to a straight pipe which had the same diameter as the test section. An orifice plate mounted in this pipe allowed the total flow rate to be measured. This pipe discharged into a large settling chamber as shown in fig. 1, air being drawn from this chamber by a centrifugal fan which ran at a constant speed.

The primary and secondary flow rates could be independently varied. The primary flow rate was controlled by varying the rate at which air was delivered to the apparatus by the compressor. The secondary flow rate was controlled by varying the rate at which air was drawn through the test-section by the fan. Since the fan ran at a constant speed, this was accomplished by varying the amount of air bled into the apparatus from the atmosphere just upstream of the settling chamber to which the fan was connected.

The working section had a series of pressure taps mounted along its length, these being connected to a multi-tube manometer so allowing the wall pressure distribution to be measured. A series of ports, through which probes could be inserted into the flow, were also incorporated into the wall of the working section. Both Pitot and hot-wire probes were used in the present work. The probe being used at a particular time was mounted in a traversing gear, this assembly then fitting into the ports in the working section wall and so allowing the probe to be traversed diametrically across the working section. The radial position of the probe could be determined to an accuracy of better than 0.1 mm by means of a vernier system incorporated into the traversing gear.

The majority of the measurements were made using standard Disa cross-wire probes arranged to measure the U and V velocity components. These probes were used in conjunction with a Disa M and a Disa K hot-wire systems. Signal processing was carried out in analogue form using a Disa Turbulence Processor. Using this procedure, profiles of $\overline{U}$, $\overline{V}$, $\overline{uv}$, $\overline{u^2}$ and $\overline{v^2}$ were obtained. The hot-wire probes were calibrated in a separate rig, frequent checking of the calibration being undertaken during a test. In addition to the profile measurements using the cross-wire probes, additional measurements were made on the centre-line using both straight single-wire probes and a Pitot probe.

Table 1

Test Number	Primary Stream Velocity m/s	Secondary Stream Velocity m/s	Number of Sections at which Profiles were measured
1	62.5	29.9	7
2	62.5	19.2	6
3	60.7	15.2	8

Basically three tests were undertaken, the flow conditions in these tests being listed in Table 1. From this table it will be seen that the three tests involved primary stream to secondary stream velocity ratios of approximately 2 to 1, 3 to 1, and 4 to 1. In each of the tests complete profiles were measured using the cross-wire probes at the number of axial positions indicated in the Table. In addition, the centre-line velocity was measured at a larger number of axial positions and the wall pressure distribution was also measured.

EXPERIMENTAL RESULTS

Complete profiles for Test Number 3 are shown in figures 2 to 5 while mean axial velocity and $\overline{uv}$ profiles for the other two tests are shown in figures 6 to 9. In presenting these results, all velocities have been expressed relative to the mean velocity across the entire duct, $\overline{U}_m$. Measurements were taken on both sides of the centre-line and showed that axial symetry existed.

It should be noted from Table 1 that the tests all involved approximately the same primary stream velocity and different secondary stream velocities. Each test, therefore, involved a different $\overline{U}_m$. For this reason, the dimensionless variables expressed relative to $\overline{U}_m$, vary considerably from test-to-test in the initial jet-flow region.

As will be seen from the figures, the results, of course, show the same basic characteristics as those observed in previous studies. Near the inlet plane, the flow consists essentially of a free-jet along the axis of the working-section and a boundary layer on the wall with a "core" region between them. Interaction between these flows then occurs with an accompanying relatively rapid change in the form of the profiles and a form of duct flow is then attained. Now it will be noted that, in all three tests, the first profile was measured at least one full duct diameter downstream of the nozzle so that even the first profile only exhibits a relatively small "core" region. Nevertheless a definite region of almost uniform mean velocity and zero turbulence stress is clearly apparent in all the initial profiles.

For downstream of the inlet plane a duct-type flow exists in which the mean velocity and the turbulence shear stress vary continuously across the section. However, despite the fact that measurements were taken at greater downstream distances than in almost all previous studies, the flow characteristics in this region do not correspond to those that would exist is in fully-developed pipe flow, the mean velocity distribution near the centre-line being much flatter than in that type of flow and the turbulence stresses much higher. If the working-section

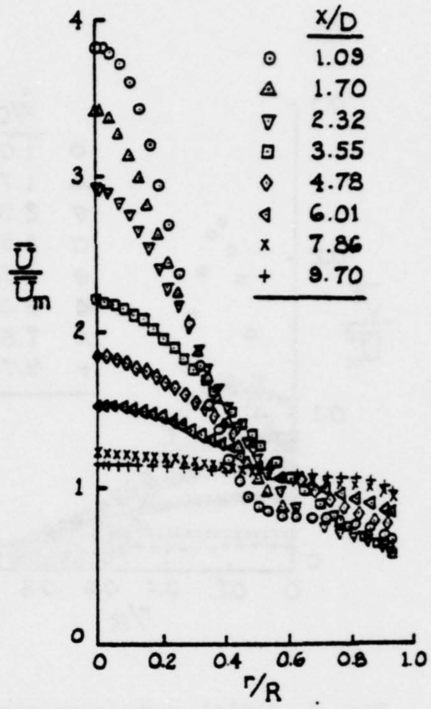

Fig. 2 Mean velocity distributions for 4 to 1 velocity ratio test

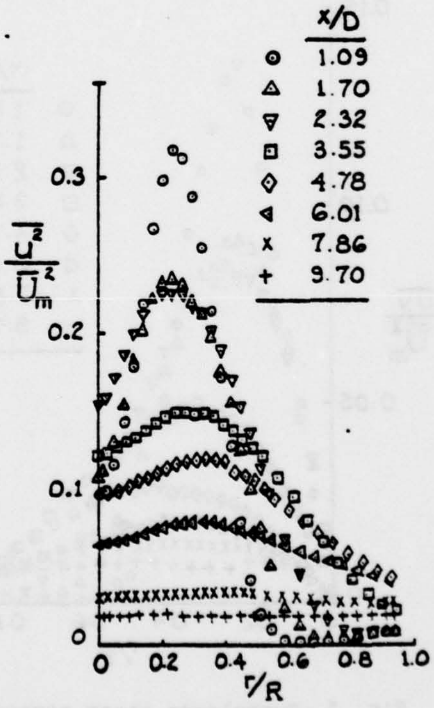

Fig. 3 Longitudinal turbulence stress distributions for 4 to 1 velocity ratio test

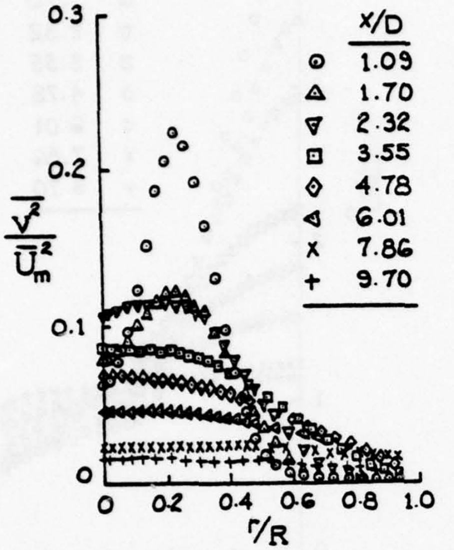

Fig. 4 Radial turbulence stress distributions for 4 to 1 velocity ratio test

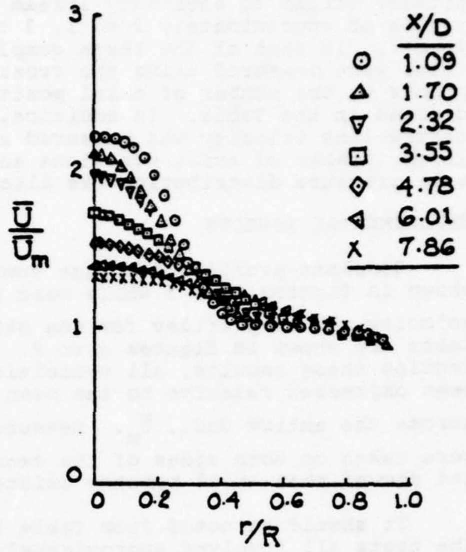

Fig. 6 Mean velocity distributions for 2 to 1 velocity ratio test

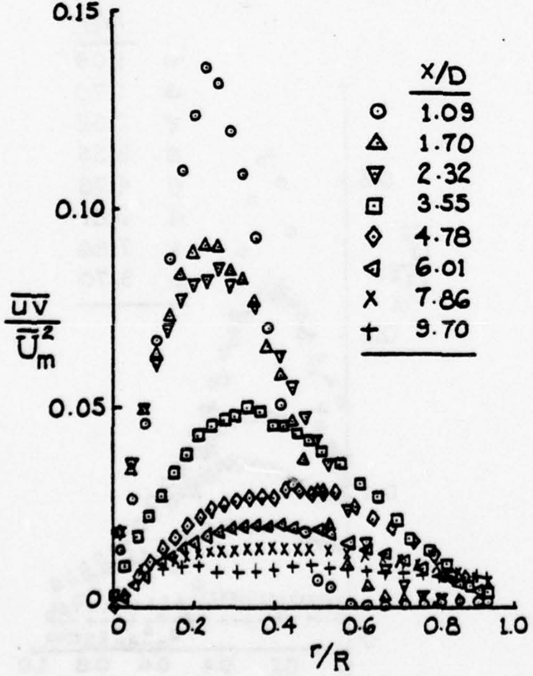

Fig. 5 Turbulence shear stress distributions for 4 to 1 velocity ratio test

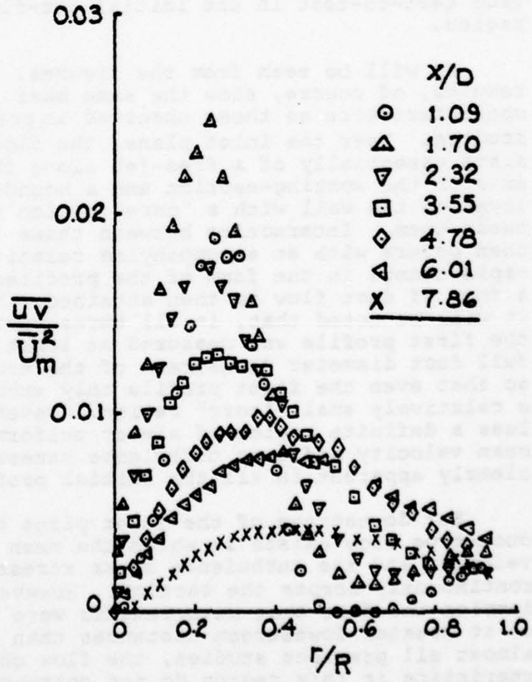

Fig. 7 Turbulence shear stress distributions for 2 to 1 velocity ratio tests

was very long, the fully developed pipe flow state would, presumeably, ultimately be reached. However, the rate at which the flow near the centre-line is tending towards this state is very low indication that such a state is unlikely to be achieved in most practical devices that involve ducted-jet flow. This observation also accounts for the fact that some earlier attempts at predicting ducted-jet flow were unsuccessful because these predictions were based on the use of simple algebraic turbulence models in which it was assumed that fully-developed pipe flow would be attained after a relatively short mixing zone.

NUMERICAL STUDY

As mentioned earlier, one of the main reasons for undertaking the present study was to provide data that could be used to assess the adequacy of various turbulence models. Some initial work on this has been undertaken using the boundary layer form of the governing equations, these being solved numerically using a relatively conventional forward-marching, implicit finite-difference scheme. Solutions have been obtained using this procedure in conjunction with three relatively simple turbulence models.

The three turbulence models used to obtain numerical solutions are as follows:
(i) Mixing Length Model: This algebraic model is basically the same as that used in ref. 3. The flow is assumed to consist of the various sub-regions shown in figure 10. Regions 2 and 4 are core-regions, i.e. regions of uniform velocity, while region 1 is assumed to consist of a boundary layer flow and region 3 to consist of a free-jet flow. In these latter two regions the mixing length distributions are assumed to be given by well-established equations for boundary layers and free jets respectively.

Region 6 is assumed to be a developed duct flow region in which the mixing-length distribution is taken to be independent of the downstream distance x. While region 6 is assumed to be a developed duct flow region, it was found in ref. 3 that in order to produce a reasonably good agreement between predicted and experimental results, much higher values for the mixing-length had to be assumed near the centre-line than would apply in fully-developed pipe flow. The reasons for this are, as previously discussed, apparent from a consideration of the present experimental results, these indicating that, in what is taken as region 6, a developed duct flow does not exist but the rate of change of flow variables with down-stream distance is so slow that a constant mixing-length can be assumed over moderate distances. However, because much higher turbulence shear stresses exist near center-line in this flow than in fully developed duct flow, much higher values for the mixing length have to be used.

The last region, region 5, is a transition region in which the mixing-length dis-

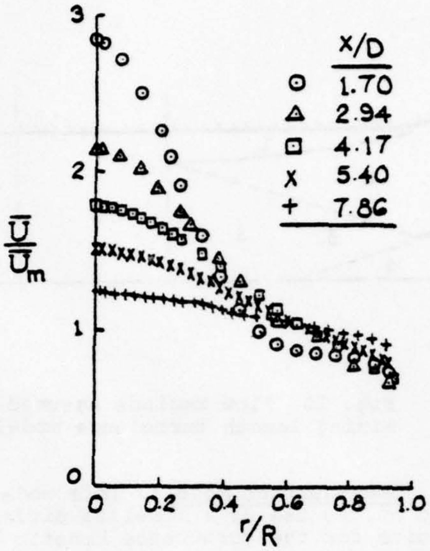

Fig. 8 Mean velocity distributions for 3 to 1 velocity ratio test

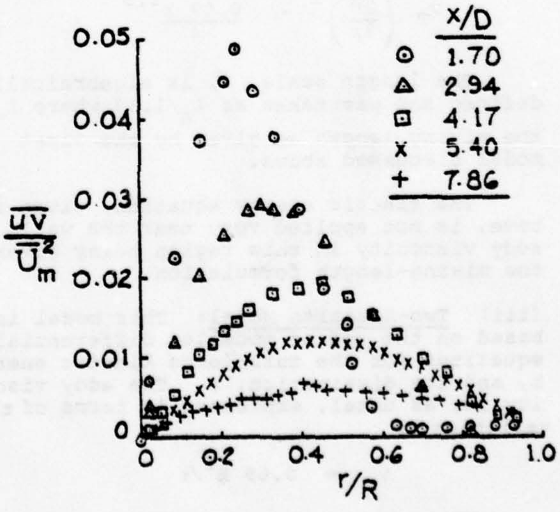

Fig. 9 Turbulence shear stress distributions for 3 to 1 velocity ratio test

tribution is assumed to change linearly from that applicable at the point where regions 1 and 3 meet to that applicable in region 5.

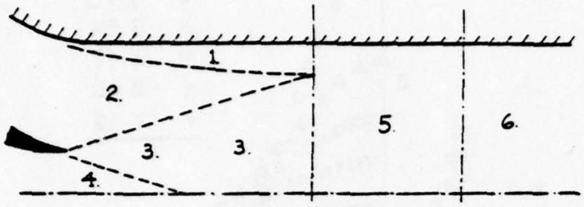

Fig. 10 Flow regions assumed in mixing length turbulence model

(ii) One-Equation Model: This model is based on the use of a modelled differential equation for the turbulence kinetic energy, k. The eddy viscosity is, as usual, expressed in terms of k and a length scale, ℓ, by

$$\nu_T = k^{0.5}\,\ell \qquad (1)$$

while the equation used to determine k is taken to be

$$\overline{U}\frac{\partial k}{\partial x} + \overline{V}\frac{\partial k}{\partial r} = \frac{1}{r}\frac{\partial}{\partial r}\left[r\,(\nu + \nu_T)\,\frac{\partial k}{\partial r}\right]$$

$$+ \nu_T\left(\frac{\partial \overline{U}}{\partial r}\right)^2 - \frac{0.09\,k^{1.5}}{\ell} \qquad (2)$$

The length scale, ℓ, is algebraically defined and was taken as $\ell_m/1.83$ where ℓ_m is the mixing length as given by the first model discussed above.

The kinetic energy equation, given above, is not applied very near the wall, the eddy viscosity in this region being given by the mixing-length formulation.

(iii) Two-Equation Model: This model is based on the use of modelled differential equations for the turbulence kinetic energy, k, and the dissipation, ε. The eddy viscosity is, as usual, expressed in terms of these variables by

$$\nu_T = 0.09\,k^2/\varepsilon \qquad (3)$$

While the equations used to determine k and ε are taken to be

$$\overline{U}\frac{\partial k}{\partial x} + \overline{V}\frac{\partial k}{\partial r} = \frac{1}{r}\frac{\partial}{\partial r}\left[r\,(\nu + \nu_T)\,\frac{\partial k}{\partial r}\right]$$

$$+ \nu_T\left(\frac{\partial \overline{U}}{\partial r}\right)^2 - \varepsilon \qquad (4)$$

and

$$\overline{U}\frac{\partial \varepsilon}{\partial x} + \overline{V}\frac{\partial \varepsilon}{\partial r} = \frac{1}{r}\frac{\partial}{\partial r}\left[r\,(\nu + \frac{\nu_T}{1.3})\,\frac{\partial \varepsilon}{\partial r}\right]$$

$$+ \frac{1.45\,\varepsilon\,\nu_T}{k}\left(\frac{\partial \overline{U}}{\partial r}\right)^2 - \frac{2\varepsilon^2}{k} \qquad (5)$$

The k-equation is, of course, essentially identical to equation (2).

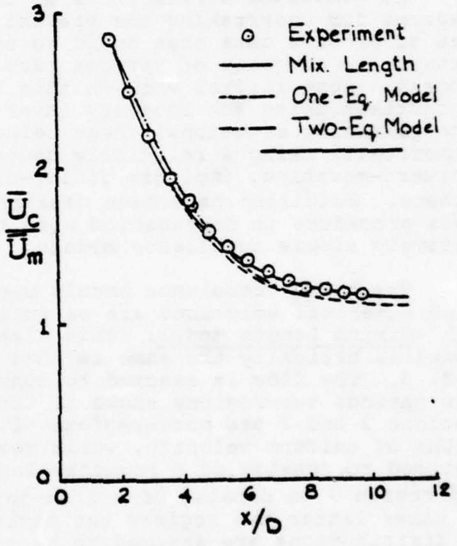

Fig. 11 Comparison between measured and predicted centre-line velocity distributions for 3 to 1 velocity ratio

As with the one-equation model, the above two equations are not applied very near the wall, the eddy viscosity in this region again being given by the mixing-length formulation.

Each of the above models have been used in conjunction with the momentum and continuity equations to obtain a prediction of the flow development. The numerical solution is based on the introduction of implicit finite difference approximations to the governing equations. The resulting set of approximate algebraic equations were then, as usual, solved by marching forward in the x-direction from one r-line to the next.

In order to carry out the solution, the conditions on some initial cross-sectional plane had to be prescribed. These were deduced from the actual measured conditions on the first plane on which measurements were

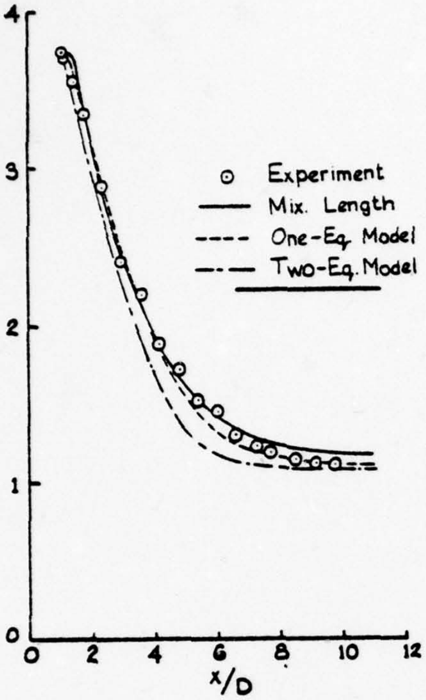

Fig. 12 Comparison between measured and predicted centre-line velocity distributions for 4 to 1 velocity ratio

taken. Now, as explained in the previous section, these measurements gave the distributions of $\overline{U}$, $\overline{V}$, $\overline{u^2}$, $\overline{v^2}$, and $\overline{uv}$. The mixing-length distribution on this plane could be deduced from the $\overline{U}$ distribution while the distribution of k was assumed to be approximately given by $3\,(\overline{u^2} + \overline{v^2})/2$. The approximate distribution of ε on the initial plane was deduced from the measured variations of $\overline{U}$ and $\overline{uv}$ and the approximate k distribution in conjunction with eq. (3).

Comparisons between measured and predicted centre-line velocity distributions are shown in figures 11 and 12. The agreement between the results shown in these figures is typical of that obtained in all comparisons between measured and predicted quantities, this agreement, basically, being relatively good and with no large differences existing between the predictions obtained using all three models. Taken overall, the mixing-length model appears to give the best agreement with the experimental results and the two-equation model the poorest agreement. However, it should be noted that both the mixing-length and the one-equation models incorporated empirical results deduced from earlier studies of ducted-jet flows in that the mixing-length distribution in the duct-flow region had been choosen to give agreement with the experimental results obtained in ref. 3. In contrast, the constants used in the two-equation model were derived entirely from studies of "simple" turbulent flows.

CONCLUSIONS

(i) While the experimental results obtained in the present study do not shed any fundementally new light on the processess involved in ducted-jet mixing, they are more comprehensive that those given in available studies and should prove useful for validation proposed turbulence models.

(ii) All three turbulence models considered in the present work gave reasonably good agreement with the experimental results. The fact that the two-equation model did not rely on empirical results for ducted-jet flow and still gave good agreement indicates that simpler models considered.

ACKNOWLEDGEMENTS

This work was supported by the National Research Council of Canada.

REFERENCES

1. Hill, P.G., "Incompressible Jet Mixing in Converging - Diverging Axisymmetric Ducts", Journal of Basic Engineering, Trans. of ASME, Vol. 89, Series D, No. 1, March 1976,

2. Hedges, K.R. and Hill, P.G., "Compressible Flow Ejectors Part 1 - Development of a Finite Difference Flow Model", Journal of Fluids Engineering, Trans. of ASME, Vol. 96, Series 1, No. 3, Sept. 1974, pp. 272 - 281.

3. Hedges, K.R. and Hill, P.G., "Compressible Flow Ejectors Part II - Flow Field Measurement and Analysis", Journal of Fluids Engineering, Trans. of ASME, Vol. 96, Series I, No. 3, Sept, pp. 282 - 288.

4. Matsumoto, R., Kimoto, K. and Tsuchimoto, W., "A Study of double Concentric Jets - 1st Report, Experimental Results for Air-Air Flow", Bulletin of the JSME, Vol. 16, No. 93, March 1973, pp. 529 - 540.

5. Razinsky, E., "Confined Mixing of a Confined Axisymmetric Jet", Ph.D. Thesis, Penn. State University, Dept. of Mech. Engineering June 1969.

COMPARISON OF SEVERAL TURBULENCE MODELS FOR PREDICTING FLOW PATTERNS WITHIN CONFINED JETS

K.N. TENNANKORE AND F.R. STEWARD

DEPARTMENT OF CHEMICAL ENGINEERING

UNIVERSITY OF NEW BRUNSWICK

ABSTRACT

Numerical solutions of the differential equations governing isothermal and nonisothermal confined jets have been obtained for three different models of the turbulence correlation terms. The models used were

1) mixing length model
2) k-ℓ turbulence model
3) k-ϵ turbulence model

A comparison of the predictions with experimental data taken in a confined jet system indicates that in the absence of a measured distribution of the kinetic energy of turbulence at the entrance section the mixing length model provided the best results for the isothermal case. For the nonisothermal jets, however, it was found that the k-ϵ model gives better prediction than the other two models in spite of the lack of measured distributions for the kinetic energy of turbulence at the entrance.

NOMENCLATURE

Ct	Craya-Curtet Number
Ct'	Craya-Curtet Number for nonisothermal confined jets
C_{μ_1}	constant in eqn (11)
C_{μ_2}	constant in eqn (12)
$C_{\epsilon_1}, C_{\epsilon_2}$	constants in eqn (14)
h	enthalpy
k	kinetic energy of turbulence
ℓ	mixing length
r	radial distance from the symmetry axis
u	axial velocity
u_m	centre-line axial velocity
v	radial velocity
w	tangential velocity
x	axial distance from the nozzle exit
ϵ	turbulence dissipation rate
ρ	density
ψ	stream function
ω	vorticity
μ_t	constant effective viscosity at the entrance section
μ_{eff}	effective turbulent viscosity
$\Gamma_{h_{eff}}$	effective turbulent conductivity divided by the heat capacity
σ_h	Prandtl number for turbulent heat transfer
σ_k	Prandtl number for the transport of kinetic energy of turbulence
σ_ϵ	Prandtl number for the transport of turbulence dissipation rate

Superscripts

'	fluctuating quantities
—	mean quantities

INTRODUCTION

Confined jet flows characterize the fluid dynamics prevalent in several industrial furnaces and combustion enclosures. Hence prediction of these flows from fundamental equations is of practical importance. The numerical solution procedure of Gosman et al (1) is widely used for this purpose. The scheme makes use of prescribed relations for the turbulence correlation terms appearing in the time-smoothed equations of motion in terms of mean variables. The relations which may be algebraic or differential equations are referred to as turbulence models. In this study, the performance of three turbulence models in the prediction of axisymmetric, confined, non-swirling jets (isothermal and non-isothermal) is evaluated by comparing the results of the numerical solution procedure with data taken on an experimental system.

THE SYSTEM

The experimental apparatus used consists of a right cylindrical duct of diameter 0.24 m with a nozzle at the centre of the lower end. The primary stream enters the duct through the nozzle while the secondary stream enters through the entire surrounding area covered with a fibermetal porous plate. The primary stream, being at a higher velocity, entrains the secondary stream forming the confined jet. Both the primary and secondary streams were air at room temperature for isothermal runs. The apparatus was provided with a heat exchanger for heating the primary stream before it enters the nozzle to conduct non-isothermal experiments. The details regarding the apparatus and measurement techniques can be found in the original thesis (2) or an earlier paper (3).

PRECEDING PAGE BLANK-NOT FILMED

THE EQUATIONS

The conservation equations which govern the system can be written in terms of the stream function, ψ, and the vorticity, ω (1).

$$a \frac{\partial}{\partial x}\left[\left(\phi \frac{\partial \psi}{\partial r}\right) - \frac{\partial}{\partial r}\left(\phi \frac{\partial \psi}{\partial x}\right)\right] - \frac{\partial}{\partial x}\left[b_1 \frac{\partial}{\partial x}(c\phi)\right] - \frac{\partial}{\partial r}\left[b_2 \frac{\partial}{\partial r}(c\phi)\right] + d_\phi = 0 \qquad (1)$$

where ϕ stands for any property such as ψ or ω; x is the axial distance and r the radial distance. The values of the coefficients for the different ϕ's are given in the table below.

Table 1. Coefficients for Equation (1)

ϕ	a	b_1	b_2	c	$d\phi$
ψ	0	$\frac{1}{\rho r}$	$\frac{1}{\rho r}$	1	$-\omega$
$\frac{\omega}{r}$	r^2	r^3	r^3	μ_{eff}	$-r^2\left[\frac{\partial}{\partial x}\left(\frac{\overline{u}^2 + \overline{v}^2}{2}\right)\frac{\partial \rho}{\partial r} - \frac{\partial}{\partial r}\left(\frac{\overline{u}^2 + \overline{v}^2}{2}\right)\frac{\partial \rho}{\partial x}\right]$
h	1	$\Gamma_{h_{eff}}\, r$	$\Gamma_{h_{eff}}\, r$	1	0

Here h is the enthalpy, $\overline{u}$ and $\overline{v}$ are mean axial and radial velocities, ρ is the density and μ_{eff} and $\Gamma_{h_{eff}}$ are the turbulent viscosity and the turbulent thermal conductivity divided by the heat capacity defined by

$$\mu_{eff} = \rho(\overline{u'v'})/\left(\frac{\partial \overline{u}}{\partial r}\right) \qquad (2)$$

and

$$\Gamma_{h_{eff}} = \rho(\overline{u'T'})/\left(\frac{\partial \overline{T}}{\partial r}\right) \qquad (3)$$

where T is the stream temperature and u',v' and T' are instantaneous fluctuations in u, v and T. The turbulent Prandtl number for heat transfer is defined as

$$\sigma_h = \mu_{eff}/\Gamma_{h_{eff}} \qquad (4)$$

Numerical solutions to these equations were obtained according to the procedure of Gosman et al (1) using three different models for the turbulent stress term, $\rho\, u'v'$. The models are as follows:

(1) Mixing Length Model

$$\rho\, \overline{u'v'} = \rho\, \ell^2 \left|\frac{\partial \overline{u}}{\partial r}\right| \left(\frac{\partial \overline{u}}{\partial r}\right) \qquad (5)$$

$$\ell = A_1 x \qquad (6)$$

where A_1 is a constant and x is the distance along the jet.

(2) k-ℓ Turbulence Model

$$\rho\, \overline{u'v'} = C_{\mu_1}\, \rho\, k^{1/2}\, \ell\left(\frac{\partial \overline{u}}{\partial r}\right) \qquad (7)$$

$$C_{\mu_1} = 0.08; \quad \ell = A_2\, x \quad \text{(Ref. 5)} \qquad (8)$$

where A_2 is a constant and k is the kinetic energy of the fluctuations or turbulence per unit mass defined by

$$k = (\overline{u'^2} + \overline{v'^2} + \overline{w'^2})/2 \qquad (9)$$

The kinetic energy of turbulence is determined by the differential equation which takes the conservation form (4)

$$r \frac{\partial}{\partial x}(\rho\, \overline{u}\, k) + \frac{\partial}{\partial r}(r\, \rho\, \overline{v}\, k) = \frac{\partial}{\partial r}\left(\frac{\mu_{eff}}{\sigma_k}\frac{\partial k}{\partial r}\right) + r\, \mu_{eff}\left(\frac{\partial \overline{u}}{\partial r}\right)^2 - \frac{r\, \rho\, k^{3/2}}{\ell} \qquad (10)$$

where

$$\mu_{eff} = C_{\mu_1}\, \rho\, k^{1/2}\, \ell \qquad (11)$$

and σ_k is the Prandtl number for the transport of kinetic energy of turbulence.

(3) k-ε Turbulence Model

$$\rho\, \overline{u'v'} = (C_{\mu_2}\, \rho\, k^2/\varepsilon)\left(\frac{\partial \overline{u}}{\partial r}\right) \qquad (12)$$

where ε is the turbulence dissipation rate and C_{μ_2} is a constant. k and ε are described by differential equations again in the conservation form.

$$r \frac{\partial}{\partial x}(\rho\, \overline{u}\, k) + \frac{\partial}{\partial r}(r\, \rho\, \overline{v}\, k) = \frac{\partial}{\partial r}\left(\frac{\mu_{eff}}{\sigma_k}\frac{\partial k}{\partial r}\right) + r\mu_{eff}\left(\frac{\partial \overline{u}}{\partial r}\right)^2 - r\rho\varepsilon \qquad (13)$$

$$r \frac{\partial}{\partial x}(\rho\, \overline{u}\, \varepsilon) + \frac{\partial}{\partial r}(r\, \rho\, \overline{v}\, \varepsilon) = \frac{\partial}{\partial r}\left(\frac{\mu_{eff}}{\sigma_\varepsilon}\frac{\partial \varepsilon}{\partial r}\right) + C_{\varepsilon_1}\, r\, \varepsilon\left|\mu_{eff}\left(\frac{\partial \overline{u}}{\partial r}\right)^2/k\right| - C_{\varepsilon_2}\, r\, \rho\, \varepsilon^2/k \qquad (14)$$

where

$$\mu_{eff} = C_{\mu_2}\, \rho\, k^2/\varepsilon \qquad (15)$$

The constant C_{ε_1} is taken to be 1.43 and C_{ε_2} is obtained from

$$C_{\varepsilon_2} = 1.92 - 0.0667\, f \qquad (16)$$

where

$$f = 0.072\, \frac{x}{\overline{u}_m}\left|\left(\frac{d\overline{u}_m}{dx} - \left|\frac{d\overline{u}_m}{dx}\right|\right)\right| \qquad (17)$$

and $\overline{u}_m$ is the centre-line axial velocity. The above relations are based on the suggestion of Launder et al (5).

Boundary Conditions

The boundary conditions for ψ, ω and h are as described in the procedure of Gosman et al (1). The following boundary conditions were employed for the kinetic energy of turbulence and the turbulence dissipation rate.

Duct entrance: The radial distribution of the kinetic energy of turbulence was calculated from the relation suggested by Launder et al (5) namely

$$k = \mu_t\left(\frac{\partial \overline{u}}{\partial r}\right)/0.3\, \rho \qquad (18)$$

where μ_t is a constant effective turbulent viscosity at the entrance section calculated according to the relation suggested by Gosman et al (1). The radial distribution of the turbulence dissipation rate was calculated as

$$\varepsilon = 0.09\ \rho\ k^2/\mu_t \tag{19}$$

Duct exit: The exit conditions for k and ε were obtained by assuming their axial gradients to be zero at the exit.
Symmetry axis and duct wall: The values of k and ε at the centre-line and near the wall were assumed to be the same as their value at the adjacent radial coordinate.

RESULTS

Numerical solutions were obtained for two values, 0.22 and 0.51, of the similarity parameter Ct, the Craya-Curtet number for the isothermal system (6) and for the same two values of the similarity parameter Ct', the modified Craya-Curtet number for the non-isothermal system (2). A value of 0.22 for the similarity parameter corresponds to large external recirculation outside the jet while a value of 0.51 corresponds to moderate external recirculation. The turbulent Prandtl number for heat transfer was taken to be 0.7 for non-isothermal calculations (2). Some of the numerical results are presented in Figures 1 - 5 along with experimental data for identical conditions.

Initially, a uniform primary stream velocity and a uniform secondary stream velocity were used in the numerical calculation as the boundary condition for the axial velocity at the duct entrance in order to calculate the boundary condition for the stream function. However, this was found to limit the accuracy of the predictions as shown in Figure 1.

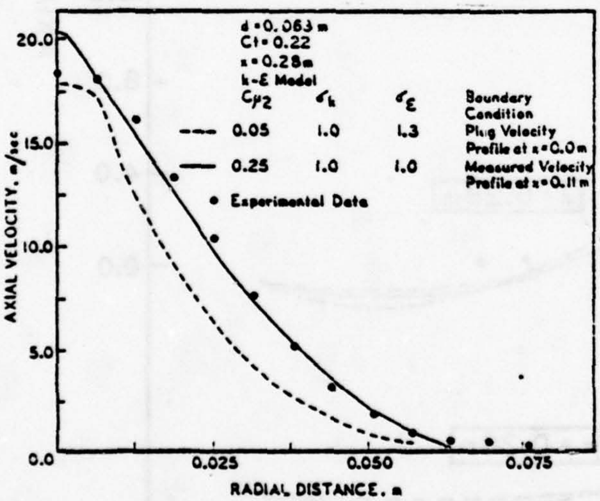

Fig 1 Comparison of the Predictions of Radial Profiles of Axial Velocity for the k-ε Model with the Experimental Data for Different Boundary Conditions for an Isothermal Confined Jet

When the measured velocity profile at an axial distance of 0.11 m from the nozzle exit was used to calculate the stream function distribution at that axial distance which was in turn used as the boundary condition for ψ, the prediction of the downstream velocity profiles was considerably improved. Figure 1 presents results for an isothermal confined jet using the k-ε turbulence model. The two cases presented consist of a plug flow profile at the duct entrance and the measured velocity profile at $x = 0.11$ m as the inlet boundary condition. The better prediction occurs when the measured velocity profile is taken as the boundary condition. The results given in this figure are typical of numerous comparisons. The calculated profiles in all other figures have used velocity and temperature profiles measured at an axial distance of 0.11 m as the boundary conditions. The radial distribution of k and ε at this axial location was obtained according to eqns (18) and (19) using the measured velocity profile.

Isothermal Confined Jets

A comparison of the predicted velocity profiles obtained with the three turbulence models described previously with the experimental data obtained from isothermal confined jets with Craya-Curtet numbers 0.22 and 0.51 are presented in Figs 2 and 3.

It is seen from Fig 2 that at smaller axial distances the predictions of the mixing length model and the k-ε model are approximately of the same order of accuracy while those of the k-ℓ model are somewhat poorer. At larger axial locations the predictions of the k-ε model are somewhat less accurate than those of the other two models. On the average the mixing length model seems to yield better predictions than the other two models over the entire jet. The mixing length model, however, predicts larger recirculation than indicated by an extrapolation of the experimental data. This may be due in part to the neglect of wall functions for the calculation of mixing length in the regions close to the wall.

The comparison of the predictions with the data for an isothermal confined jet of Ct equal to 0.51 presented in Fig 3 indicates that the results obtained with the mixing length model are better than those of the k-ℓ model which in turn are better than the results of the k-ε model.

Since the mixing length model could be derived from the differential equation for k by neglecting the convection and diffusion terms it appears that the inaccuracy in the predictions of the k-ℓ and k-ε models is due to the prescription of incorrect boundary conditions for k and ε at the entrance section. Thus the results imply that in the absence of measured values for k at the entrance section, the simple mixing length model is the most reasonable choice for predicting the flow patterns in isothermal confined jets since it requires the least calculational effort.

The results also indicate that the accuracy of the predictions at axial distances close to the exit (for instance 0.45 m in Fig 2) is considerably less than for the predictions at axial locations further upstream. This is considered to be partly due to the inadequacy of the calculation of the boundary conditions for ψ and ω at the duct exit where axial gradients for these variables are taken as zero. This assumption is especially in error for low values of Ct when large amounts of recirculation occur external to the jet extending into the exit region. This type of error should be reduced for a Ct of 0.51 and the predicted results in Fig 3 support this.

It is also seen from the results that the best values for the constants for the several models are not the same for the two different values of the similarity parameter, Ct.

Nonisothermal Confined Jets

The predicted velocity and temperature profiles for a nonisothermal confined jet with Ct' equal to

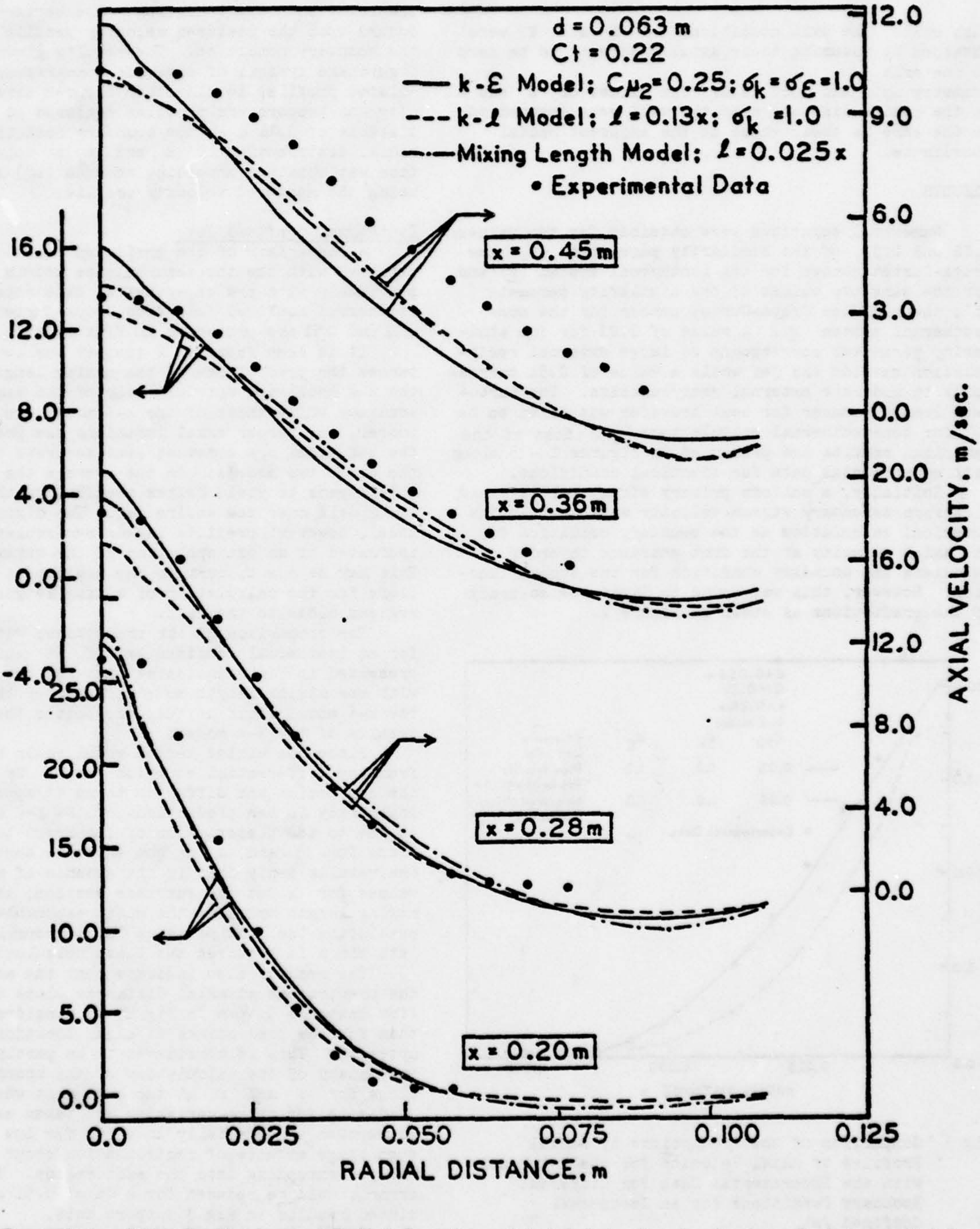

Fig 2 Comparison of the Predictions of Radial Profiles of Axial Velocity for Various Turbulence Models with the Experimental Data for an Isothermal Confined Jet of Ct equal to 0.22

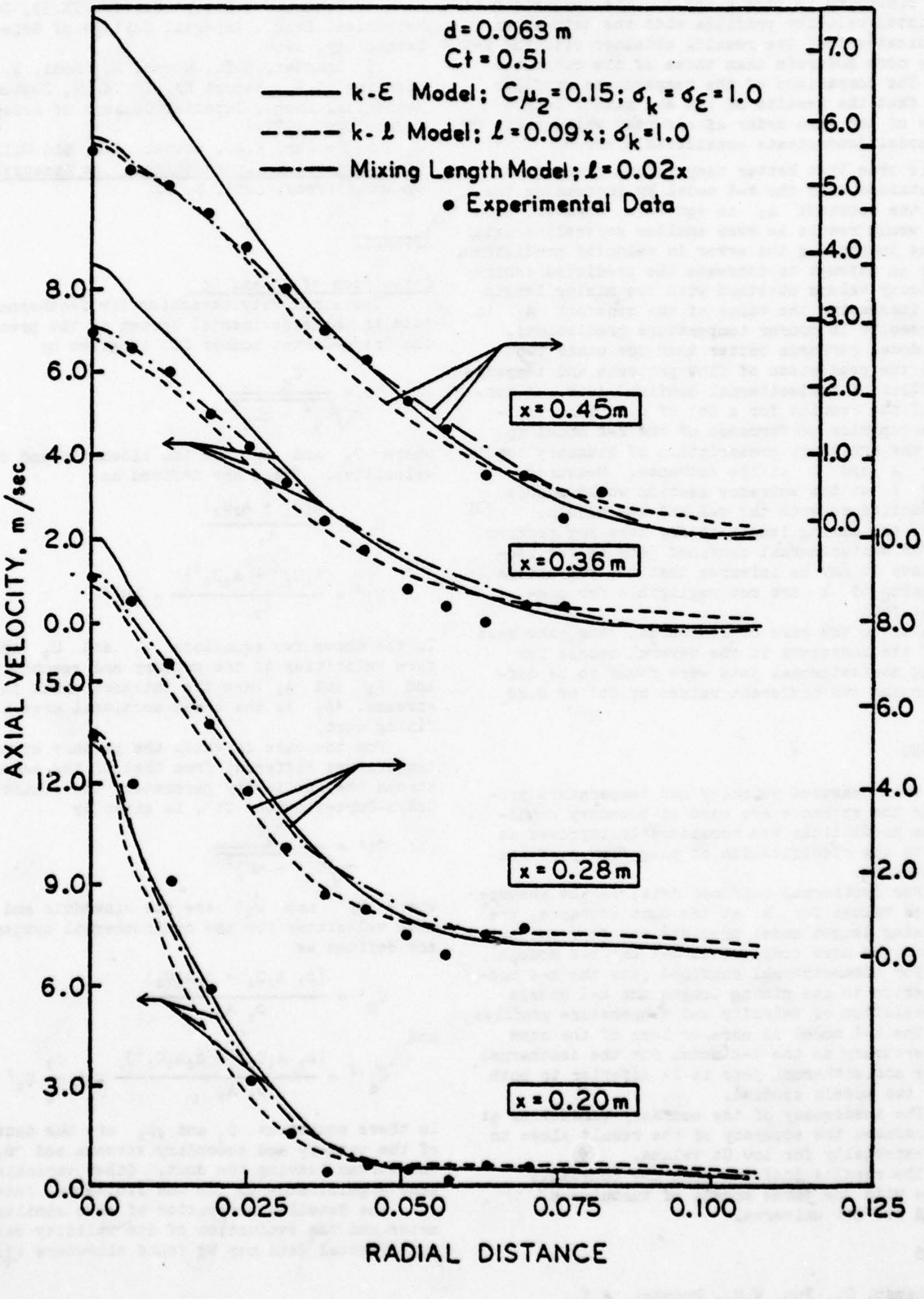

Fig 3 Comparison of the Predictions of Radial Profiles of Axial Velocity for Various Turbulence Models with the Experimental Data for an Isothermal Confined Jet of Ct equal to 0.51

0.51 are presented in Figs 4 and 5. The comparison of the predicted velocity profiles with the data shown in Fig 4 indicates that the results obtained with the k-ε model are more accurate than those of the other two models. The comparison of the temperature profiles indicate that the results of k-ε and mixing length model are of the same order of accuracy while those of the k-ℓ model demonstrate considerable error.

It is true that better temperature predictions can be obtained with the k-ℓ model by increasing the value of the constant A_2 in eqn (8). However, such a change would result in even smaller centreline axial velocities increasing the error in velocity predictions. Similarly an attempt to increase the predicted centreline velocity values obtained with the mixing length model by increasing the value of the constant A_1 in eqn (6) results in poorer temperature predictions. Thus k-ε model performs better than the other two models in the prediction of flow patterns and temperature profiles of nonisothermal confined jets. A comparison of the results for a Ct' of 0.22 also indicates the superior performance of the k-ε model in spite of the arbitrary prescription of boundary conditions for k and ε at the entrance. Measured values of k at the entrance section would enable better predictions with the k-ℓ and k-ε models.

Since the mixing length theory does not perform as well for nonisothermal confined jets as for isothermal ones it may be inferred that the convection and diffusion of k are not negligible for nonisothermal jets.

Similar to the case of isothermal jets, the best values of the constants in the several models for predicting nonisothermal jets were found to be different for the two different values of Ct' of 0.22 and 0.51.

CONCLUSIONS

1. When measured velocity and temperature profiles near the entrance are used as boundary conditions, the predictions are considerably improved as compared to the specification of plug flow profiles at the entrance.
2. For isothermal confined jets, in the absence of measured values for k at the duct entrance, the simple mixing length model predicts the flow pattern better than the more complicated k-ℓ and k-ε models.
3. For nonisothermal confined jets the k-ε model is superior to the mixing length and k-ℓ models in the prediction of velocity and temperature profiles.
4. The k-ℓ model is more or less of the same order of accuracy as the k-ε model for the isothermal case. For nonisothermal jets it is inferior to both the other two models studied.
5. The inadequacy of the boundary conditions at the exit reduces the accuracy of the result close to the exit especially for low Ct values.
6. The results indicate that the constants associated with the three models of turbulence considered are not universal.

REFERENCES

1 Gosman, D., Pun, W.M., Runchal, A.K., Spalding, D.B. and Wolfshtein, M., Heat and Mass Transfer in Recirculating Flows, Academic Press, New York, 1969.

2 Guruz, A.G., Ph.D. Thesis in Chemical Engineering, University of New Brunswick, 1974.

3 Guruz, A.G. and Steward, F.R., Paper Submitted to Combustion Science and Technology.

4 Rotta, J., Report No. TWF/TN/39, Dept. of Mechanical Engg., Imperial College of Science and Technology, 1968.

5 Launder, B.E., Morse, A., Rodi, W. and Spalding, D.B., Report No. TM/TN/19, Dept. of Mechanical Engg., Imperial College of Science and Technology, 1972.

6 Becker, H.A., Hottel, H.C. and Williams, G.C., Ninth Symposium (International) on Combustion, Academic Press, 1963, p. 7.

APPENDIX

Definition of Ct and Ct'

The similarity parameter for isothermal confined jets in the experimental system of the present study, the Craya-Curtet number Ct, is given by

$$Ct = \frac{U_k}{\sqrt{U_d^{\,2} - \tfrac{1}{2}U_k^{\,2}}} \qquad (20)$$

where U_k and U_d are the kinematic and dynamic mean velocities. These are defined as

$$U_k = \frac{(A_1U_1 + A_2U_2)}{A_3} \qquad (21)$$

and

$$U_d^{\,2} = \frac{(A_1U_1^{\,2} + A_2U_2^{\,2})}{A_3} - \tfrac{1}{2}U_2^{\,2} \qquad (22)$$

In the above two equations U_1 and U_2 are the uniform velocities of the primary and secondary stream and A_1 and A_2 are the entrance areas for these streams. A_3 is the cross-sectional area of the confining duct.

For the case in which the primary stream is at a temperature different from that of the secondary stream the similarity parameter, the nonisothermal Craya-Curtet number Ct', is given by

$$Ct' = \frac{U_k'}{\sqrt{U_d'^{\,2} - \tfrac{1}{2}U_k'^{\,2}}} \qquad (23)$$

where U_k' and U_d' are the kinematic and dynamic mean velocities for the nonisothermal system. These are defined as

$$U_k' = \frac{(\rho_1\, A_1U_1 + \rho_2A_2U_2)}{\rho_0\, A_3} \qquad (24)$$

and

$$U_d'^{\,2} = \frac{(\rho_1\, A_1U_1^{\,2} + \rho_2A_2U_2^{\,2})}{\rho_0\, A_3} - \tfrac{1}{2}\frac{\rho_2}{\rho_0}U_2^{\,2} \qquad (25)$$

In these equations ρ_1 and ρ_2 are the densities of the primary and secondary streams and ρ_0 that of the stream leaving the duct. Other variables have the same significance as for the isothermal case.

The detailed derivation of this similarity parameter and the evaluation of its validity based on experimental data may be found elsewhere (3).

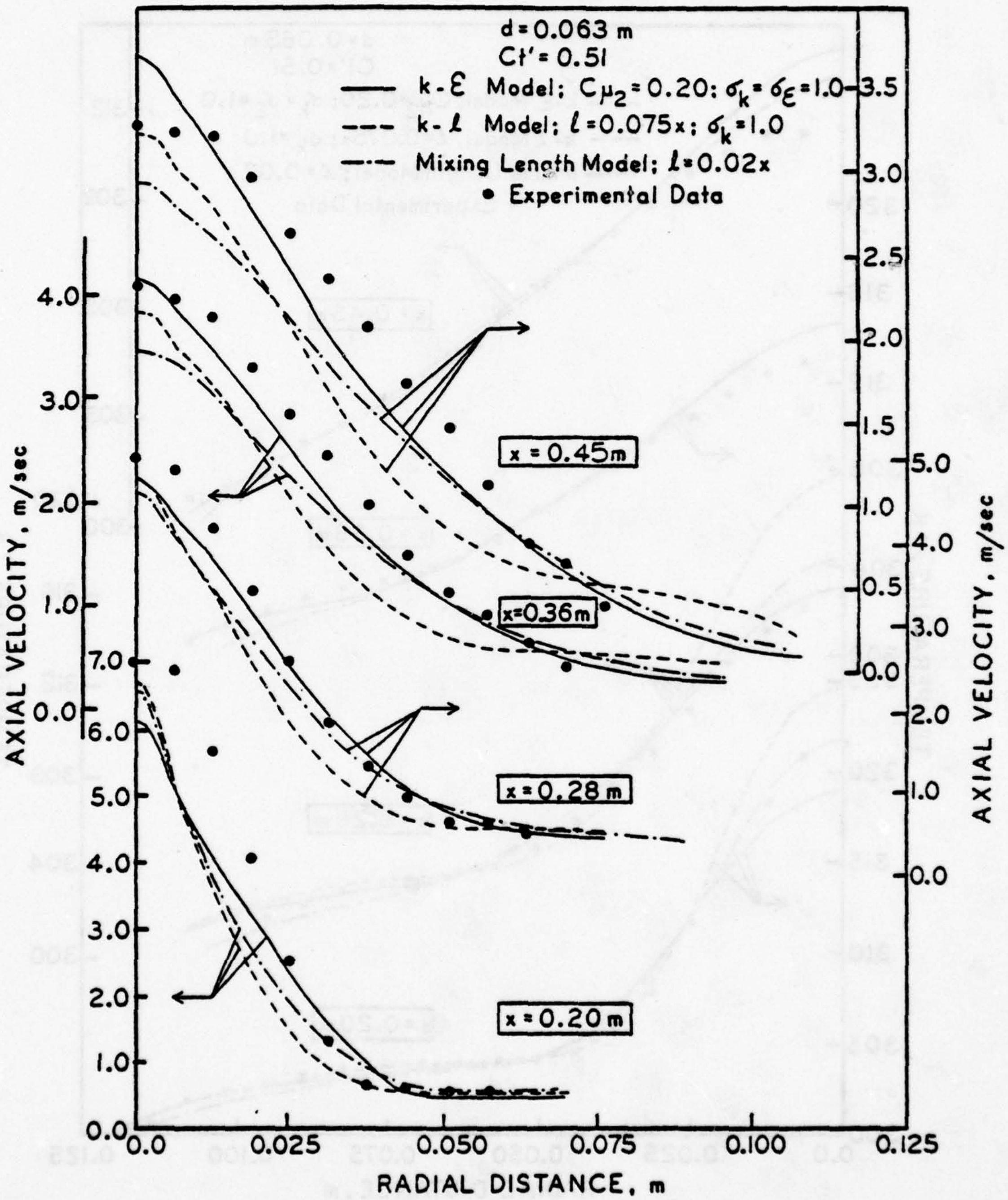

Fig 4 Comparison of the Predictions of Radial Profiles of Axial Velocity for Various Turbulence Models with the Experimental Data for a Nonisothermal Confined Jet of Ct' equal to 0.51

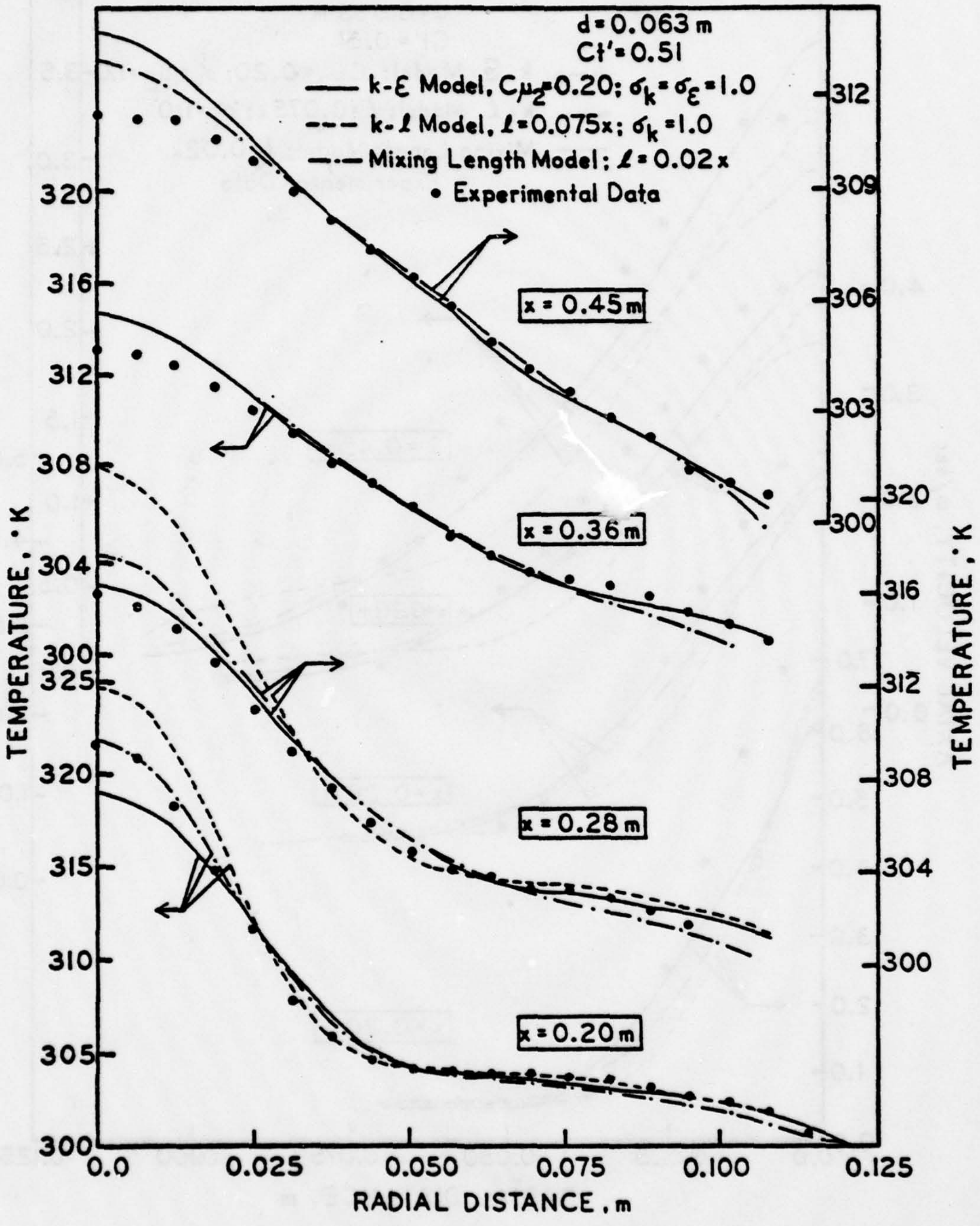

Fig 5 Comparison of the Predictions of Radial Profiles of Temperature for Various Turbulence Models with the Experimental Data for a Nonisothermal Confined Jet of Ct' equal to 0.51

Mixing Between a Round Jet and a Transverse Turbulent Pipe Flow

by

D. E. Rathgeber[†] and H. A. Becker

Department of Chemical Engineering
Queen's University
Kingston, Ontario

ABSTRACT

A light-scatter technique, marker nephelometry, was used to obtain air-in-air mixing data on the system resulting from the injection, at right angles through a port in the wall, of a round subsonic jet into a fully developed turbulent pipe flow. Though the pipe Reynolds number was also varied (68000 and 160000), the important input variables were M, the port to pipe mean speed ratio of the input streams (2.5 to 12.5), and D_o/D_p*, the port to pipe diameter ratio (0.020 to 0.058), both of which significantly affected the rate of jet deflection. Results also show, however, that the jet source fluid mean concentration along the jet trajectory* ξ *(defined as the locus of points of highest concentration in the longitudinal plane of bilateral symmetry) and the jet width are functions of only* ξ/MD_o*. Beyond* $\xi/MD_o = 5$*, radial profiles of the mean concentration and rms concentration fluctuations are similar in shape to those of a free jet, and the relative concentration fluctuation intensity along the trajectory is 0.4. The jet mixing field was also studied as to concentration fluctuation spectral density, integral scale, and intermittency.*

NOMENCLATURE

B	mean concentration half-radius, m
C	correlation coefficient for point concentration fluctuations at two points in space
D	diameter, m
$E_\gamma(k_1)$	one dimensional spectrum of point concentration fluctuations, kg^2m^5
f	frequency, 1/s
k_1	$=2\pi f/\bar{U}$, one dimensional wave number, m^{-1}
M	$= U_o/U_p$, ratio of the mean jet discharge velocity to the mean pipe velocity
$\bar{R}$	mean jet radius as defined by intermittency measurements, m
Re	$=UD/\nu$, Reynolds number
U	velocity, m/s
x,y,z	cartesian coordinates
δ	intermittency factor
Γ	concentration of the jet source fluid, kg/m^3
γ	$= \Gamma - \bar{\Gamma}$, fluctuating component of Γ, kg/m^3
Λ_γ	longitudinal integral spatial scale of the turbulent concentration fluctuations, m
ξ,η,ζ	curvilinear coordinates conforming to the jet shape
ν	kinematic viscosity, m^2/s
σ	standard deviation of the jet radius, R, as defined by intermittency measurements, m

Overscripts

$\bar{\ }$	(overbar) time-average value
$\hat{\ }$	time-average root-mean-square value

Subscripts

o	properties at the mouth of the jet port
p	properties of the pipe stream
ξ	properties on the ξ axis of the jet
+,-	properties on the ζ axis on the upstream and downstream sides of the jet respectively (see Fig. 1)

INTRODUCTION

The flow configuration of a round jet issuing at right angles into a larger subsonic stream commonly occurs in effluent dispersion operations and in industrial processes where streams are mixed for dilution, heat transfer, or chemical reaction. The mean velocity field of the jet has been studied experimentally (1-5) and several workers have also developed theoretical models for the jet trajectory (7-9). There have, however, been few investigations of the scalar fields in this type of system. Callaghan and Ruggeri (10) measured mean temperature profiles in the plane of bilateral symmetry of heated orifice jets issuing into a wind tunnel. Patrick (3) showed that the decay of jet source fluid concentration along the jet trajectory depends on the ratio of the jet to mainstream initial speeds and is more rapid than on the centreline of a simple free jet. Kamotani and Greber (4) demonstrated that mean temperature profiles in the plane of bilateral symmetry of heated jets are similar and fairly axi-symmetric when scaled by the temperature half-radius on the considered side of the jet, and that the lateral spread and decay of temperature with distance from the jet source is initially greater than in a simple free jet in stagnant surroundings.

In processes involving the mixing of streams, concern is often focussed on the stream composition in the mixing zone. The objective of the present work, therefore, was to advance knowledge of the concentration field of a round jet injected at right angles into a turbulent pipe flow. A pipe flow provides a well defined mainstream typical of many practical mixing processes and it is also

---

[†] Present address: Union Carbide Canada Ltd. Montreal, Canada

significantly different from the uniform, low-turbulence wind tunnel flows used by most other investigators. The jet issued from a round port in the pipe wall and the jet fluid concentration field was studied by a light-scatter technique called marker nephelometry (11,12,13) as to mean value, fluctuation intensity, scale, and intermittency. Jet trajectories, spreading rates, and dilution rates were correlated empirically with the dimensionless input parameters. Besides the quantitative results, photographs of the smoke-marked jet were taken to aid visualization of the flow structure.

FLOW PATTERN

The flow pattern that results when a round jet is injected into a transverse stream exhibits several prominent features. Near the source, the circular jet acts rather like a solid cylinder in that a positive pressure region occurs on the upstream side, the sides are subjected to shear, and if the stream speeds are great enough, wake effects produce recirculation on the downstream side (14). The jet entrance core (the initial region where the entrance velocity is preserved) is typically wasted within two or three entry port diameters, compared to about five diameters for a free jet, and the initially circular jet cross section is distorted to a kidney shape due the development of a pair of counter-rotating parallel vortices on the wake side. After the entrance core is consumed, a region is entered where the jet rapidly attains a direction and mean speed close to that of the transverse stream and the counter-rotating vortices expand over the whole jet cross section. The jet is thereby longitudinally bifurcated and exhibits lateral maxima of the source fluid concentration on either side of the plane of bilateral symmetry. Once fully deflected, the jet evolves into a flow structure dominated by the parallel vortex pair moving with the mainstream velocity, and this regime has been observed to extend beyond 1000 initial jet diameters downstream in a uniform wind tunnel flow (6). In this study, however, the pipe wall and the turbulence of the pipe flow disrupted such a regular vortex structure so that the far downstream phenomena appear to be dominated by dispersion due to the pipe-flow turbulence.

The mean velocity profile and turbulence of the pipe flow further complicate the situation, particularly near the jet source. Though the separate effects of these factors are not known quantitatively, presumably mainstream turbulence promotes jet dispersion (15) whereas the wall boundary layer allows greater jet penetration (16).

APPARATUS

The pipe flow was of air that passed through a 73 diameter-long horizontal straight run of aluminum industrial pipe, i.d. 16.15 cm. Straightening vanes and calming screens were provided at the inlet and pressure drop measurements showed the pipe wall to be aerodynamically smooth. Equilibrium pipe flow was closely approached over the last eleven diameters which constituted the test section, and it was here that the jet feed air was injected through a tubular entry piece, the mouth of which was flush and normal to the inner pipe wall. Two levels of pipe-stream mean velocity (U_p) were used, 6 m/s and 15 m/s, providing pipe Reynolds numbers of 68000 and 160000. Injection tubes were provided with inside diameters of 0.323 cm, 0.457 cm, 0.630 cm, and 0.932 cm, and each was at least 25 diameters long. The jet feed air was mixed with a light oil condensation smoke (17). Jet port Reynolds numbers were above 9000. Jet discharge speeds were less than 135 m/s so as to avoid appreciable compressibility effects.

The principles of marker nephelometry are given in other publications (11,12,13) and the particular details of the system used for this study have also been described (17). It suffices here to say that the light source was a 5 mW He-Ne laser which provided a control volume of about 5×10^{-4} cm^3. The mixing field was explored in cylindrical polar coordinates. Radial traversing was done by moving the receiving optics, angular traversing by rotating the pipe, and longitudinal traversing by moving the jet point of injection. Appropriate corrections were made for the finite probe size and for significant sources of noise (12, 13,17). The Schmidt number of the smoke particles in air was about 40,000 while that of air in air is about 0.7. The effect of this disparity under the present experimental conditions is, however, small (12,13) and the present results indeed accurately represent the gas/gas mixing process.

SYSTEM PROPERTIES

Coordinate Systems

Figure 1 shows the coordinate sytems used to describe the jet flow. Position in the pipe is defined by the cartesian coordinates x, y, and z with origin at the centre of the jet entrance port such that the x axis follows the jet injection tube centreline and the z axis is parallel to the pipe centreline. The curvilinear ξ, η, ζ coordinate system is natural to the jet shape. The ξ and ζ axes are in the x-z plane, and the curved ξ axis follows the lateral mean concentration maxima $\partial\overline{\Gamma}/\partial\zeta = 0$ along that plane. The ζ and η axes defined at any point on the ξ axis are straight, and the three axes are mutually perpendicular at their point of intersection. The η and y axes are parallel. The ξ axis appropriately indicates the jet trajectory.

Dimensional Considerations

Both input streams were essentially fully developed turbulent flows in frictionally smooth pipes. Thus, the integral scale of the pipe-flow turbulence was only dependent on the pipe diameter (18) and the relative turbulence intensity was nearly independent of the Reynolds number (19). Furthermore, the geometry of the system was fixed, compressibility effects were absent, and the streams were identical in physical properties. The pertinent input dimensionless parameters thus reduce to D_o/D_p, $M = U_o/U_p$, and a group such as z/D_o to define position. These are further simplified by adopting the approach of Pratte and Baines (6) wherein the jet is considered strong relative to the mainstream. The determining variables then reduce to D_o/D_p and z/MD_o (or ξ/MD_o). We then have, for example,

$$x/MD_o = f(D_o/D_p,\ z/MD_o) \qquad (1)$$

along the jet trajectory.

RESULTS

Jet Trajectory

A number of jet trajectories (ξ axes) for different D_o/D_p ratios are shown in Fig. 2. At each D_o/D_p, the rate of jet deflection is slightly greater at the higher pipe Reynolds number. This may be due to non-ideality in the pipe flow conditions or it may indicate an influence of the pipe Reynolds number. In any case, the effect is small enough to be of minor practical importance.

Comparison of the trajectories also shows that for the same pipe Reynolds number, higher rates of jet deflection are associated with increasing values of D_o/D_p. Though the effect is not large, the trend is clear and is expected when the mainstream entered by a transverse jet is confined and the jet source diameter is an appreciable fraction of the cross-flow dimensions.

The measured trajectories agree quite well with those of Kamotani and Greber (4) and Chassaing et al (5), but generally show greater deflection rates than those of Patrick (3) and Pratte and Baines (6). (The correlation of Pratte and Baines is also shown on the graphs.) Such discrepancies are, apparently, not uncommon because of variations in the cross-flow conditions and in the definitions of the jet trajectory used by different investigators (4). The present data are correlated reasonably well by

$$x/MD_o = 0.42\ (z/MD_o)^{0.20}\ (D_o/D_p)^{-0.39}. \qquad (2)$$

Jet Axial Distance ξ

Figure 3 shows the ξ position as a function of the z coordinate for the trajectories observed at the lower pipe Reynolds number. Similar data for the higher pipe Reynolds number are indistinguishable from those shown and the whole set is correlated by

$$\xi/MD_o = 1.0 + z/MD_o. \qquad (3)$$

The local properties of the jet will hereinafter be described in terms of the ξ coordinate.

Jet Width

A convenient scale for the jet width is the mean concentration half-radius, here defined as the distance normal to the ξ axis where the source fluid mean concentration is one-half that on the ξ axis. In the present work, measurements of the concentration half-radii were confined to the ξ axis only, where they are denoted as B_+ and B_- on the upstream and downstream sides of the jet respectively (see Fig. 1). The normalized concentration half-radii B_+/MD_o and B_-/MD_o are shown as a function of ξ/MD_o in Figs. 4 and 5; subtraction of 0.5/M in the ordinate values makes the data converge on a common origin near the jet port.

Figure 4 shows that a distinct change in the growth rate of B_+ takes place around $4 \leq \xi/MD_o \leq 5$, and a similar effect was observed by Pratte and Baines (6) for measurements of total jet width. Two equations have thus been found necessary to simply correlate B_+ with the flow conditions:

$$(B_+/D_o - 0.5)/M = 0.21\ (\xi/MD_o - 1.0)^{0.60} \qquad (4)$$

for $\xi/MD_o \leq 5$, and

$$(B_+/D_o - 0.5)/M = 0.24\ (\xi/MD_o)^{0.40} \qquad (5)$$

for $\xi/MD_o > 5$. A single equation describes B_-,

$$(B_-/D_o - 0.5)/M = 0.24\ (\xi/MD_o)^{0.49}. \qquad (6)$$

The values of B_- for the case $D_o/D_p = 0.058$, M = 2,42, Re_p = 160,000 are larger than those for the other situations so these data were not included in the derivation of (6). The reasons for this anomally are not quite clear, but the jet deflection here was exceptionally rapid and wall effects may have enhanced the jet spreading on the downstream side.

Generally, B_+ is smaller than B_-, particularly in the region $\xi/MD_o < 5$, and this reflects the wake forming tendency of the jet. Beyond $\xi/MD_o \approx 5$ there is little difference between the two half-radii and the jet expands at a decreasing rate.

Mean Concentration on the ξ Axis

The mean concentration of the jet source fluid on the ξ axis, $\overline{\Gamma}_\xi$, is shown in normalized form in Fig. 6 (subtracting 1/M from the ordinate values makes the data converge to zero at the port). Flow conditions were identical to those of the trajectory data (Fig. 2). A logarithmic plot of the same variables (not given here) shows $\overline{\Gamma}_\xi$ to behave in a manner similar to the mean concentration half-radius B_+ in that a marked reduction in the jet dilution rate occurs in the region $4 \leq \xi/MD_o \leq 5$. Thus two equations are again necessary to simply correlate the data:

$$(\overline{\Gamma}_o/\overline{\Gamma}_\xi - 1.0)/M = (\xi/MD_o - 0.73)^{0.74} \qquad (7)$$

for $\xi/MD_o \leq 5$, and

$$(\overline{\Gamma}_o/\overline{\Gamma}_\xi - 1.0)/M = 0.98 + 0.34\ \xi/MD_o \qquad (8)$$

for $\xi/MD_o > 5$. The jet source fluid concentration on the centreline of a self-preserving free jet in stagnant surroundings is given by (20)

$$\overline{\Gamma}_o/\overline{\Gamma}_\xi = 0.185\ \xi/D_o - 0.444 \qquad (9)$$

in the present notation. As M becomes large this approaches

$$\overline{\Gamma}_o/\overline{\Gamma}_\xi - 1.0)/M = 0.185\ \xi/MD_o \qquad (10)$$

so a comparison with free jet behavior can be made as shown in Fig. 6. Actually this comparison is not strictly valid, for as mentioned previously, the maximum mean concentration over the cross-section of the transverse jet in a cross-flow is displaced from the ξ axis. This disparity is not serious, however, since $\bar{\Gamma}_\xi$ is typically 60-80 % of the maximum value (illustrated in a following section).

For the present system, it is easily shown by a species balance that ordinate values of Fig. 6 must eventually approach $(D_p/D_oM)^2$ as the streams become completely mixed. Since such a fully mixed condition was never closely realized within the investigated region, the data show no tendency toward this asymptotic limit.

The results in Fig. 6 agree well with analogous temperature data obtained by Kamotani and Greber (4).

Relative Concentration Fluctuation Intensity on the Jet Trajectory

Figure 7 shows the relative concentration fluctuation intensity of the jet source fluid, $\hat{\gamma}/\bar{\Gamma}$ along the ξ axis as a function of the normalized distance ξ/MD_o. Apart from some scatter, the data for all conditions follow the same trend in that $\hat{\gamma}/\bar{\Gamma}$ increases from zero at the end of the jet core to a constant value of about 0.4 at $\xi/MD_o > 3$. The fact that $\hat{\gamma}/\bar{\Gamma}$ tends to constancy suggests that the turbulent flow structure of the jet tends towards self-preservation. This has also been suggested by Pratte and Baines (6) who observed that the shape of the jet cross-section changes little in the well developed region.

Figure 7 also indicates the asymptotic value, 0.23, reached on the centreline of a turbulent self-preserving free jet in stagnant surroundings.

Concentration Distribution Over the Jet Cross-Section

Figure 8 shows contour maps of the mean concentration over several flow cross-sections for one operating condition. Figure 9 similarly shows distributions of $\hat{\gamma}/\bar{\Gamma}$. Interestingly, the ratio of $\bar{\Gamma}$ on the ξ axis (Fig. 8) to the highest value in the cross-section apparently varies with distance from the injection port, reaching a minimum of about 0.6 in the zone $3 \leq \xi/MD_o \leq 6$, if the graph for $\xi/MD_o = 3.37$ is typical. Similarly, the ratio of $\hat{\gamma}/\bar{\Gamma}$ on the ξ axis (Fig. 9) to the minimum value in the cross-section also seems to depend on downstream location, reaching a maximum of 1.4 in the region $2 \leq \xi/MD_o \leq 6$.

Lateral Concentration in the Plane of Bilateral Symmetry

Figure 10 shows the mean concentration of the jet source fluid in the plane of bilateral symmetry normalized by the value on the ξ axis, $\bar{\Gamma}/\bar{\Gamma}_\xi$, as a function of the ζ coordinate made dimensionless by the concentration half-radius. The profiles are all alike and similar to those of temperature excess and excess mean velocity found by others (4,5) for jets in a cross-flow, as well as the Gaussian shaped distribution obtained in the self-preserving free jet in stagnant surroundings (20).

For the same flow conditions, Fig. 11 shows the root-mean-square concentration fluctuations normalized by the value on the axis, $\hat{\gamma}/\hat{\gamma}_\xi$. Beyond $\xi/MD_o = 4$, the profiles are quite symmetrical and self-similar, and they tend to those found in a self-preserving free jet in stagnant surroundings (20). Closer to the injection port, however, the concentration fluctuations are higher on the upstream side of the jet flow; presumably, this reflects the difference in local mixing conditions around the jet in the region of rapid deflection. Though not shown here, very similar results were also obtained for the case $D_o/D_p = 0.039$, $M = 4.9$, Re_p 68000.

The Integral Scale of the Concentration Fluctuations

The longitudinal integral spatial scale of the concentration fluctuations is defined as $\Lambda_\gamma = \int_0^\infty C \, d\xi$, where $C = \overline{\gamma_A \gamma_B}/\hat{\gamma}_A \hat{\gamma}_B$ is the correlation coefficient between concentration fluctuations at points $\Delta\xi$ apart. If it is assumed that the turbulence field remains frozen as it is translated past any point (ξ, η, ζ) with a local mean velocity $\bar{U}$ (a reasonable approximation on the ξ axis if not elsewhere), then it follows that Λ_γ is given by

$$\Lambda_\gamma = \frac{1}{2} \pi E_\gamma(0)/\hat{\gamma}^2, \tag{11}$$

where $E_\gamma(0)$ is the intercept at zero wave number of the one-dimensiomal spectral density function of the concentration fluctuations. In the present work, $E_\gamma(0)$ was estimated by measuring the fluctuation energy in the pass-band $(0, 0 + \Delta f)$ with low-pass filters, so that

$$\Lambda_\gamma = \frac{1}{4} \bar{U} \hat{\gamma}^2_{0,\Delta f}/ \hat{\gamma}^2 \Delta f. \tag{12}$$

The mean speed $\bar{U}$ was detected with a Kiel-type Pitot probe (22) oriented parallel with the local flow direction.

Figure 12 shows Λ_γ along the ξ axis in normalized form. The data are correlated reasonably well by

$$\Lambda_\gamma/MD_o = 0.10 \, (\xi/MD_o)^{0.40}. \tag{13}$$

Also shown is Λ_γ on the centreline of a turbulent free jet in stagnant surroundings where the previously published relation (20) $\Lambda_\gamma/D_o = 0.0445 \, x/D_o$ (x is the distance from the nozzle) is written as

$$\Lambda_\gamma/MD_o = 0.0445 \, \xi/MD_o \tag{14}$$

in the present notation.

Figure 13 shows that the ratio of the integral scale to the measured mean concetration half-radii, B_+ and B_-, approaches a constant value of about 0.25 - 0.30 beyond $\xi/MD_o = 5$.

Intermittency

Intermittency measurements are usually used to statistically describe the boundaries between turbulent and non-turbulent regions, and the the intermittency factor is defined as the fraction of time that a given point is inside the turbulent fluid. Since both input streams of the present study were turbulent, it is more appropriate to define the intermittency factor δ as the fraction of time that the concentration of the jet source fluid at a point is non-zero. To measure $\bar{\delta}$ it was only necessary to convert the instantaneous concentration signal Γ into a step function such that ($\delta = 1, \Gamma > 0; \delta = 0, \Gamma = 0$). Time averaging of the signal then gives

$$\bar{\delta} = \frac{1}{T}\int_0^T \delta.dt \equiv \text{prob. } (\Gamma > 0),\ T \to \infty \quad (15)$$

The instantaneous radial location of the jet boundary, assuming that it is uniquely defined, will be denoted by R, $R^2 = \zeta^2 + \eta^2$. The mean radial location of the boundary, $\bar{R}$, is considered to be where $\bar{\delta} = 1/2$. The depth of the intermittent zone is characterized by the standard deviation of R about $\bar{R}$, and if the distribution is normal

$$\sigma(\xi) = \{-\int_0^\infty (r - \bar{R})^2 \, (\partial\bar{\delta}/\partial r) \, d(r - \bar{R})\}^{\frac{1}{2}}. \quad (16)$$

A detailed account of the theory and measurement technique is given by Becker et al (23).

Lateral profiles of $\bar{\delta}$ were measured in the plane of bilateral symmetry at four downstream locations. Gaussian probability plots (not given here) show the data to be quite normally distributed in the range $0.20 \le \bar{\delta} \le 0.90$, and both $\bar{R}$ and σ were estimated from these graphs. The $\bar{\delta}$ profiles are shown in Fig. 14 where the ζ coordinate is normalized by $\bar{R}_+$ and $\bar{R}_-$ on the leading and trailing sides of the jet respectively. The profiles are quite symmetrical about the ξ axis ($\zeta = 0$) and somewhat broader than in a turbulent free jet in stagnant surroundings (20). Interestingly, $\bar{\delta}$ on the ξ axis decreases from unity near the jet source to about 0.9 at $\xi/MD_o = 2.5$, beyond which it eventually returns to unity.

An indication of the size of the convolutions of the jet boundary is provided by Fig. 15 which shows $\sigma/\bar{R}$ on both sides of the jet plotted as a function of the normalized ξ coordinate. This figure also shows the values typical of self-preserving free jets and wakes (23), and it is clear that the scale of the turbulent distortions in the boundary of the jet in a cross-flow is considerably greater than for these simpler flows, at least within the zone of rapid deflection ($2 \le \xi/MD_o \le 6$).

The concentration half-radii, B_+ and B_-, for the jet axial positions in Fig. 14 give $\bar{R}/B)_+ = \bar{R}/B_- = 1.2$, independent of ξ/MD_o; this is slightly less than the value 1.57 found in the self-preserving region of a turbulent free jet in stagnant surroundings (23).

Spectrum of the Point Concentration Fluctuations

The one-dimensional spectrum of the mean-square concentration fluctuations was measured with apparatus allowing analysis up to 20,000 Hz, but the signal was usually lost in noise before this limit and measurements were terminated somewhere well within the inertial convective subregime. For the one flow condition examined ($D_o/D_p = 0.058$, $M = 4.8$, $Re_p = 68000$), spectra were obtained at two points on the ξ axis where the local conditions were:

ξ/MD_o	$\hat{\gamma}/\bar{\Gamma}$	Λ_γ/D_o	$U_o/\bar{U}$
3.0	0.38	0.70	4.34
7.7	0.43	1.00	4.54

Two spectra were also obtained in the lower region of the lobes of the kidney-shaped cross-section (at about the 7 o'clock position in Fig. 8) at $\xi/MD_o = 3.0$ where the local conditions were:

$\bar{\Gamma}/\bar{\Gamma}_{max}$	$\hat{\gamma}/\bar{\Gamma}$	Λ_γ/D_o	$U_o/\bar{U}$
0.48	0.52	1.22	4.17
0.095	1.70	1.07	4.54

Here $\bar{\Gamma}/\bar{\Gamma}_{max}$ is the ratio of the mean concentration to the highest value in the cross-section (see Fig. 8). Figure 16 shows the spectra in normalized form. No unusual characteristics are apparent. All are well described by the following equations obtained from studies of a free jet in stagnant surroundings (20):

$$\frac{2\,E_\gamma(\Lambda_\gamma k_1)}{\pi\,E_\gamma(0)} = 0.594\,(1 + 1.455\,(\Lambda_\gamma k_1)^2)^{-\frac{5}{6}} \quad (17)$$

for $0.05 < \Lambda_\gamma k_1 < 2.2$, and

$$\frac{2\,E_\gamma(\Lambda_\gamma k_1)}{\pi\,E_\gamma(0)} = 0.395\,(\Lambda_\gamma k_1)^{-\frac{5}{3}}, \quad (18)$$

for $\Lambda_\gamma k_1 > 2.2$. The measurements extended down to 5 Hz ($\Lambda_\gamma k_1 = 0.045$), a value that should have been low enough to reveal any predominant frequency due to the counter-rotating vortices.

DISCUSSION

Figure 2 shows that the jet trajectory is reasonably well correlated with downstream position in the pipe when the dimensionless coordinates x/D_o and z/D_o are scaled by M, the ratio of the input stream speeds. This implies that the complications of the present study (eg. turbulent confined cross-flow with non-uniform mean velocity) were not so severe as to invalidate this approach of Pratte and Baines (6) to describing the jet path. Further support is provided by the fact that when the trajectory data are correlated by an equation of the more general form $x/D_o = \text{constant} \cdot (z/D_o)^a \, (D_o/D_p)^b \, (M)^c$, the result is an expression negligibly different from (2). It is not suprising that the observed trajectories show more rapid jet deflection than in uniform wind-tunnel cross-flows (3,6) since the jet mixing is undoubtedly enhanced by the cross-flow turbulence in the present system.

The increased deflection of the jet with increasing jet source diameter implies that the examined ratios of D_o/D_p may have been sufficiently large to produce adverse pressure gradients that inhibit jet penetration. Owing to the non-uniform mean velocity profile of the pipe stream, the larger jets are also subjected to stronger cross-flow effects over their initial development length of 2-3 source diameters and this may partly explain the slightly lower jet penetrations at the higher pipe Reynolds number. Such arguments are supported by the fact that the trajectories approach those of Pratte and Baines (6) as

D_o/D_p diminishes. In any case, changes in D_o/D_p and Re_p seem to have effected the jet deflection more through pressure effects than through the jet entrainment rate, since the mixing rate of the jets showed no dependence on these parameters.

Besides indicating the jet position relative to the pipe flow, Fig. 3 has two other interesting features. Close scrutiny shows that ξ/MD_o and z/MD_o are related in a very linear fashion beyond $\xi/MD_o \simeq 3\text{-}4$, suggesting that the jet is essentially totally deflected beyond this point. This compares with the observation of others (6) that the region of maximum deflection ends at about $4 \leq \xi/MD_o \leq 5$. Also, since the data extrapolate quite uniformly to $\xi/MD_o = 1.0$ at $z/MD_o = 0$, this distance $x \simeq \xi = 1.0\ MD_o$ represents the jet penetration before appreciable deflection takes place. It might be said then that the zone of maximum deflection occupies the region $1 \leq \xi/MD_o \leq 4$ for the present system. The third distinct region, termed the developed vortex zone, seems to commence at about $\xi/MD_o = 5\text{-}6$, and this is borne out by the mean concentration half-radius, B_+, and the jet source fluid mean concentration on the ξ axis, $\bar{\Gamma}_\xi$, both of which show distinct reductions in their longitudinal gradient at about $4 \leq \xi/MD_o \leq 5$ (see Figs. 4 & 6). There is some evidence that a degree of self-preservation or similarity exists in this far downstream region. Specifically, the relative concentration fluctuation intensity $\hat{\gamma}/\bar{\Gamma}$ on the ξ axis (Fig. 7), the normalized profiles of mean concentration and concentration fluctuation intensity on the ζ axis (Figs. 10 &11), the ratio of the integral scale to the concentration half-radii on the ζ axis, Λ_γ/B (Fig. 13), and the ratio of of the standard deviation of the jet radius to the mean radius, $\sigma/\bar{R}$ (Fig. 15), all become quite invariant beyond $\xi/MD_o = 6$.

The relative concentration fluctuation intensities, $\hat{\gamma}/\bar{\Gamma}$, observed in the jet flow beyond $\xi/MD_o = 5$ (Figs. 7 & 9) are considerably higher than the value of 0.23 observed on the centreline of a free jet in stagnant surroundings (20), but less than the value of 1.0 observed on the centreline of a diffusion plume in a turbulent pipe flow (18). Thus, the structure of a turbulent jet deflected by a cross-stream seems to be intermediate between these simpler flows.

Figure 13 shows $\Lambda_\gamma/B_+ \simeq \Lambda_\gamma/B_- \simeq 0.30$ for $\xi/MD_o > 5$, which is comparable to the value of 0.42 observed for the similar quantity in a free jet issuing into a quiescent medium (20). This suggests that the largest concentration eddies are comparable to the jet width. However, on combining the data of Fig. 13 and Fig. 15 and noting that $\bar{R} \simeq 1.2\ B$ (for the one case where $\bar{R}$ was measured; see the section on intermittency), we find that $\sigma/\Lambda_\gamma \simeq 1.6\text{-}2.0$ beyond $\xi/MD_o = 6$. This implies that the large concentration eddies in the jet in a cross-flow are elongated in the radial direction, whereas such eddies are stretched longitudinally in a free jet in stagnant surroundings (20). This behavior is perhaps consistent with the presence of the counter-rotating vortex pair.

Figure 14 shows that a state of intermittency exists right across the plane of bilateral symmetry between about $2 \leq \xi/MD_o \leq 7$. Presumably this reflects the bifurcation of the jet which has the effect of producing two roughly parallel swirling plumes separated by a diffuse region of low source fluid concentration (see Figs. 17 & 18). Further downstream and after the jet has been totally deflected, the distinction between the plumes becomes masked by general turbulent dispersion and $\bar{\delta}$ goes back to unity within the central region of the flow (Fig. 14). Though it is possible that each plume forms a distinct continuous convoluted boundary that separates it from the other, it is more likely that the intermittency observed here on the ξ axis was, rather, due to the presence of large eddies or "islands" of pipe stream fluid (larger than the light probe control volume) entrained into the central region of the jet.

One objective of the spectral density measurements (Fig. 16) was to determine whether the counter-rotating vortices would be evident in the spectrum. Since no indication was found, it is still not clear to what extent their scale and angular velocity depend on the flow conditions. Perhaps two-dimensional spectra obtained by sheet illumination (18) or two-point correlation function measurements would provide a better insight into this important feature of the turbulent jet deflected by a cross-flow.

ACKNOWLEDGMENTS

This work was funded by the National Research Council of Canada.

REFERENCES

1 Jordinson, R., "Flow in a Jet Directed Normal to the Wind," R and M 3074, Oct. 1956, Aeronautical Research Council, Great Britain.

2 Keffer, J. F. and Baines, W. D., "The Round Turbulent Jet in a Cross-Wind," Journal of Fluid Mechanics, Vol. 15, part 4, 1963, pp. 481-496.

3 Patrick, M. A., "Experimental Investigation of the Mixing and Penetration of a Round Turbulent Jet Injected Perpendicularly into a Transverse Stream," The Transactions of the Institution of Chemical Engineers, Vol. 45, No. 1, Jan. Feb. 1961, T16-T31.

4 Kamotani, Y. and Greber, I., "Experiments on a Turbulent Jet in a Cross Flow," American Institute of Aeronautics and Astronautics Journal, Vol. 10, No. 11, Nov. 1972, pp. 1425-1429.

5 Chassaing, P., George, J., Claria, A., and Sananes, F., "Physical Characteristics of Subsonic Jets in a Cross-Stream," Journal of Fluid Mechanics, Vol. 62, part 1, 1974, pp. 41-64.

6 Pratte, B. D. and Baines, W. D., "Profiles of the Round Turbulent Jet in a Cross Flow," Journal of the Proceedings of the American Society of Civil Engineers, HY-6, Nov. 1967, pp. 53-64.

7 Wooler, P. T., Burghart, G. T., and Gallagher, J. T., "Multiple Jets Exhausting into a Crossflow," Journal of Aircraft, Vol. 8, No. 6, June 1971, pp. 414-420.

8 Platten, J. L. and Keffer, J. F., "Entrainment in Deflected Axisymmetric Jets at

Various Angles to the Mainstream," Mech. Eng. Report No. TP6808, 1968, University of Toronto

9 Abraham, G., "The Flow of Round Buoyant Jets Issuing Vertically into Ambient Fluid Flowing in a Horizontal Direction," Proceedings of the Fifth International Water Pollution Research Conference, July-Aug. 1970.

10 Callaghan, E. E. and Ruggeri, R. S., A General Correlation of Temperature Profiles Downstream of a Heated Jet Directed Perpendicular to an Air Stream," Tech. Note No. 2466, 1951, Nat. Advisory Committee for Aeronautics.

11 Rosensweig, R. E., Hottel, H. C., and Williams, G. C., "Smoke-Scattered Light Measurement of Turbulent Concentration Fluctuations," Chemical Engineering Science, Vol. 15, Nos. 1 & 2, July 1961, pp. 111-129.

12 Becker, H. A., Hottel, H. C., and Williams, G. C., "On the Light-Scatter Technique for the Study of Turbulence and Mixing," Journal of Fluid Mechanics, Vol. 30, part 2, 1967, pp. 259-284.

13 Becker, H. A., "Mixing Concentration Fluctuations and Marker Nephelometry," Studies in Convection, Vol. 2, (ed. B. E. Launder), Academic Press, 1977.

14 McMahon, H. M., Hester, D. D., and Palfrey, J. G., "Vortex Shedding from a Turbulent Jet in a Cross-Wind," Journal of Fluid Mechanics, Vol. 48, part 1, 1971, pp. 73-80.

15 Weilland, R. H. and Trass, O., "Jet Penetration in Turbulent Streams," Canadian Journal of Chemical Engineering, Vol. 47, No. 4, Aug. 1969, pp. 443-444.

16 Bowely, W. W. and Sucec, J., "Trajectory and Spreading of a Turbulent Jet in the Presence of a Crossflow of Arbitrary Velocity Distribution," Report No. 69-GT-33, The American Society of Mechanical Engineers, 1969

17 Rathgeber, D. E., "Mixing Between a Round Jet and a Transverse Turbulent Pipe Flow," Ph. D. thesis, Dept. of Chem. Eng., Queen's University, Kingston, Ontario.

18 Becker, H. A., Rosensweig, R. E., and Gwozdz, J. R., "Turbulent Dispersion in a Pipe Flow," American Institute of Chemical Engineers Journal, Vol. 12, No. 5, Sept. 1966, pp. 964-972.

19 Laufer, J., "The Structure of Turbulence in Fully Developed Pipe Flow," Tech. Note No. 1174, 1954, Nat. Advisory Committee for Aeronautics.

20 Becker, H. A., Hottel, H. C. and Williams, G. C., "The Nozzle Fluid Concentration Field of the Round, Turbulent, Free Jet," Journal of Fluid Mechanics, Vol. 30, part 2, 1967, pp. 285-303.

21 Hinze, J. O., Turbulence, McGraw-Hill, New York, 1959, pp. 227.

22 Pankhurst, R. C. and Holder, D. W., Wind Tunnel Technique, Pitman, 1952, Fig. 92.

23 Becker, H. A., Hottel, H.C., and Williams, G. C., "Concentration Intermittency in Jets," Tenth Symposium (International) on Combustion, The Combustion Institute, 1965, pp. 1253-1263.

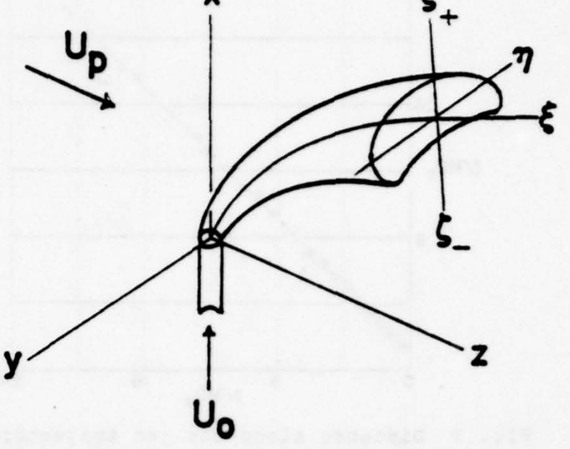

Fig. 1 Coordinate systems for the jet flow.

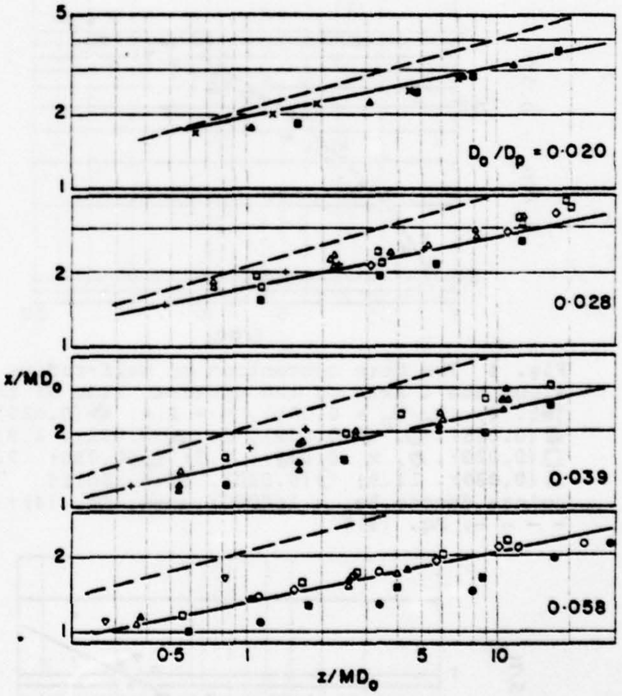

Fig. 2 Coordinates of the jet trajectory (ξ axis) for different M values: ●, ○, 2.4; ■, □, 4.9; ◆, ◇, 5.4; ▲, △, 7.5; ▽, 9.9; +, 11.9; ×, 12.4. Solid points denote Re_p = 160,000; ———, Eq. (2); – – – –, correlation of Pratte and Baines (6) obtained from visual studies of deflected jets.

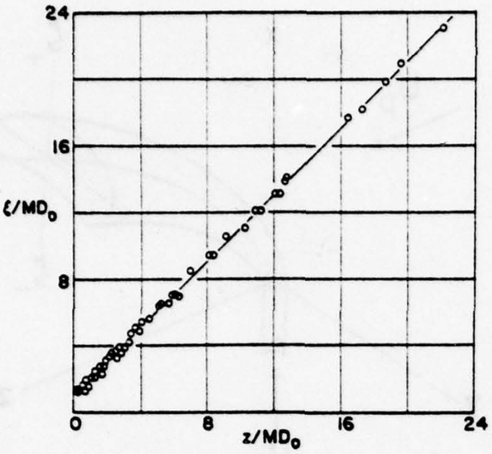

Fig. 3 Distance along the jet trajectory (ξ axis) as a function of distance downstream in the pipe for all four port sizes. Re_p = 68000, M = 2.4 - 12.4; ——, Eq. (3).

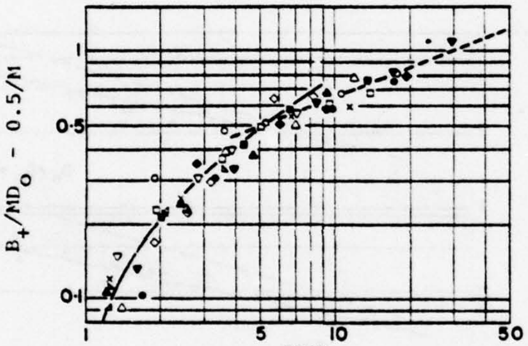

Fig. 4 The mean concentration half-radius along the ζ axis on the upstream side of the jet. ▼, (D_o/D_p = 0.058), M = 2.4; ◆(0.020), ■(0.028), ○, ●(0.039), △, ▲(0.058), 4.9; □(0.028), ▽, × (0.039), 7.5; ◺(0.058), 7.9; △(0.039), 11.9; ◇(0.020), 12.4. Solid points denote Re_p = 160000; ——, Eq. (4); – – – –, Eq. (5).

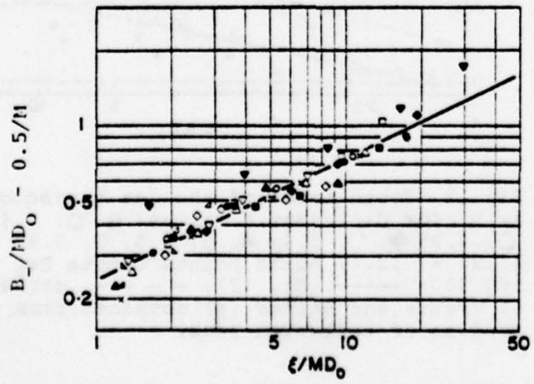

Fig. 5 The mean concentration half-radius along the ζ axis on the downstream side of the jet. Legend is identical to Fig. 4; ——, Eq. (6).

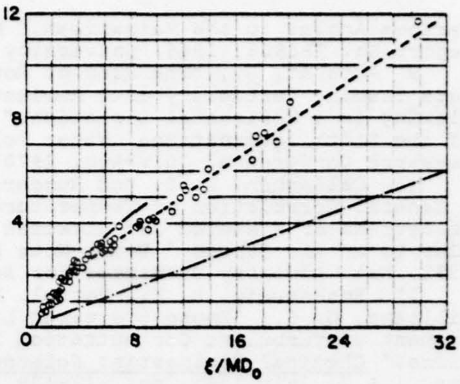

Fig. 6 The reciprocal of the mean concentration on the ξ axis. Operating conditions corresponded to those of Fig. 4; ——, Eq. (7); – – – –, Eq. (8); —— · ——, free jet behavior as represented by Eq. (10).

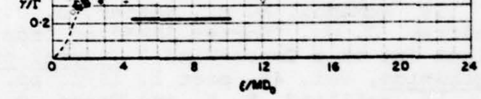

Fig. 7 The relative concentration fluctuation intensity on the ξ axis. + (D_o/D_p = 0.058), M = 2.4; ◆(0.020), ■(0.028), ○, ● (0.039), △(0.058), 4.9; □(0.028), ▽, × (0.039), 7.5; ◇(0.058), 9.9; ▲(0.028), ◿ (0.039), 11.9; Re_p = 160000 for ◆, ●, ×; ——, free jet centreline value (20).

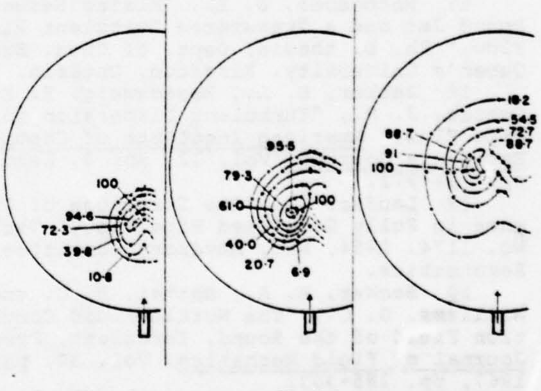

Fig. 8 The jet source fluid mean concentration, $\bar{\Gamma}$, across the jet at ξ/MD_o = 1.91, 3.37, and 9.26. Contours represent percentage of the maximum value (+); D_o/D_p = 0.028, M = 7.6, Re_p = 68000.

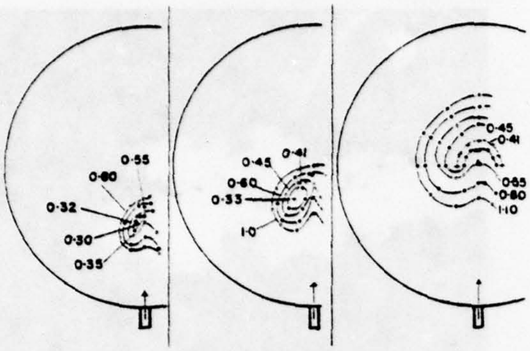

Fig. 9 The relative intensity of the jet source fluid concentration fluctuations, $\gamma/\bar{\Gamma}$, across the jet. Conditions are the same as in Fig. 8.

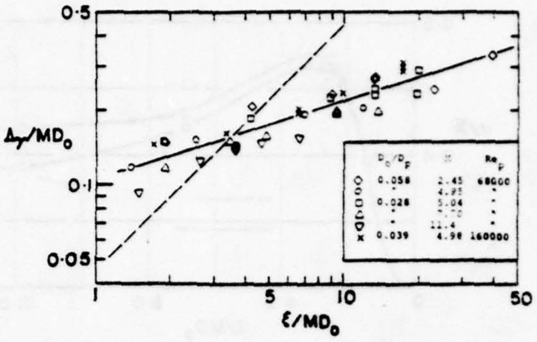

Fig. 12 The longitudinal integral scale of the concentration fluctuations, Λ_γ, on the ξ axis. ———, Eq. (13); – – – –, free jet behavior as represented by Eq. (14).

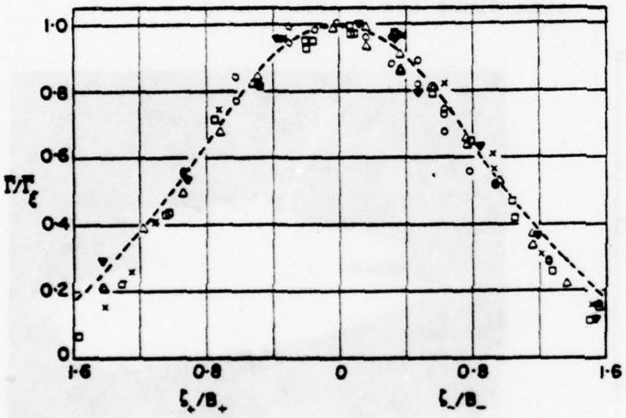

Fig. 10 The profile of the normalized mean concentration along the ζ axis for different ξ/MD_o: ▼, 1.7; ×, 3.0; □, 4.1; △, 7.5; ○, 12.5; D_o/D_p = 0.058, M = 4.9, Re_p = 68000; – – – –, free jet behavior (20).

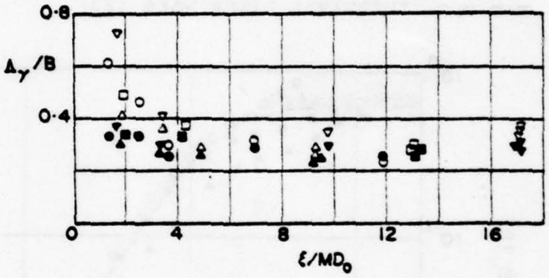

Fig. 13 The longitudinal integral scale of the concentration fluctuations, Λ_γ, on the axis normalized by the mean concentration half-radii B_+ (open points) and B_- (solid points). □, ■ (D_o/D_p = 0.028), ▽, ▼(0.039), ○, ● (0.058), M = 4.9; △, ▲ (0.028), M = 7.7; Re_p = 160,000 for ▽, ▼.

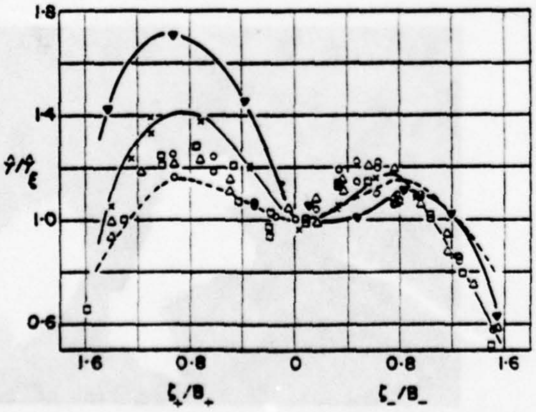

Fig. 11 The profile of the rms concentration fluctuation along the ζ axis. Legend and conditions are the same as in Fig. 10; – – – –, free jet behavior (20).

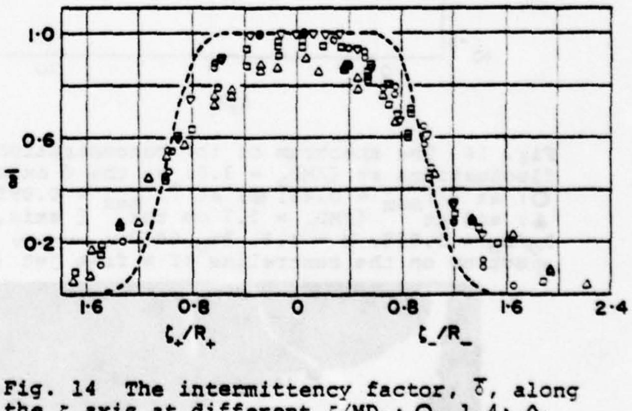

Fig. 14 The intermittency factor, $\bar{\delta}$, along the ζ axis at different ξ/MD_o: ○, 1.4; △, 2.5; □, 7.0; ▽, 12.0; D_o/D_p = 0.058, M = 4.9, Re_p = 68000; – – – –, free jet behavior (20).

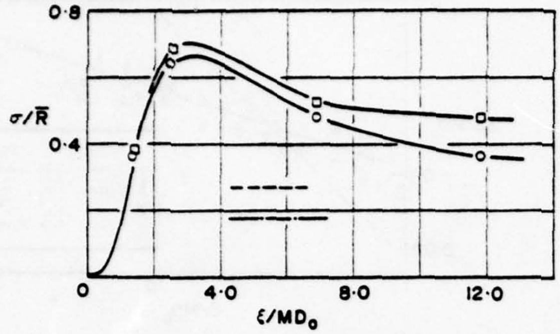

Fig. 15 The relative standard deviation of the mean jet radius on the ζ axis for the upstream (○) and downstream (□) sides of the jet. D_o/D_p = 0.058, M = 4.9, Re_p = 68000; —— · ——, turbulent free jet (23); – – – –, turbulent plane wake (23).

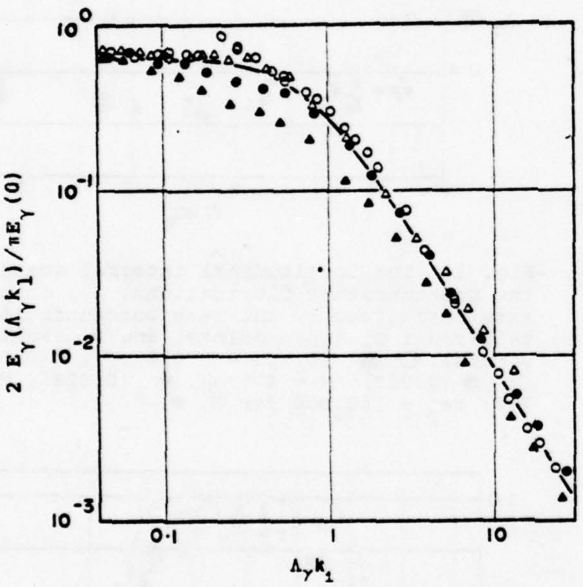

Fig. 16 The spectrum of the concentration fluctuations at ξ/MD_o = 3.0: on the ξ axis, ○; at $\overline{\Gamma}/\overline{\Gamma}_{max}$ = 0.48, ●; at $\overline{\Gamma}/\overline{\Gamma}_{max}$ = 0.095, ▲; and at ξ/MD_o = 7.7 on the ξ axis, △. D_o/D_p = 0.058, M = 4.8, Re_p 68000; ———, spectrum on the centreline of a free jet (20).

Fig. 18 A side view of the jet in Fig. 17.

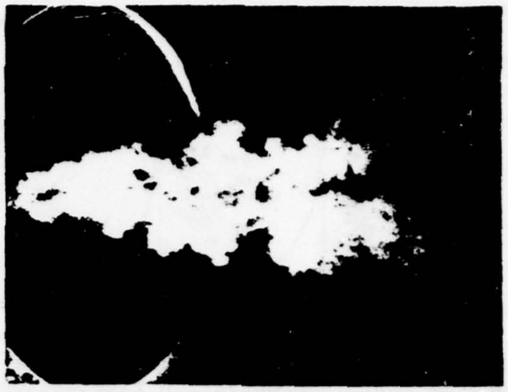

Fig. 17 Instantaneous picture of the smoke-marked jet viewed from the port discharge side along the ζ axis.

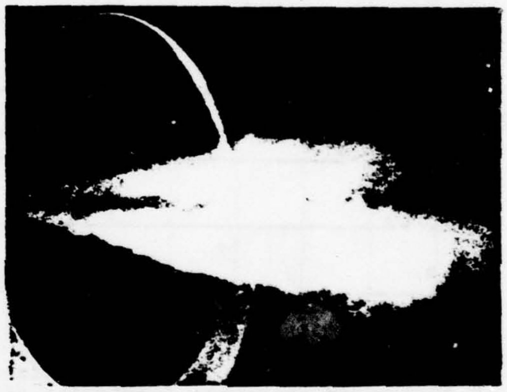

Fig. 19 A time-average version of Fig. 17 obtained by time-exposure.

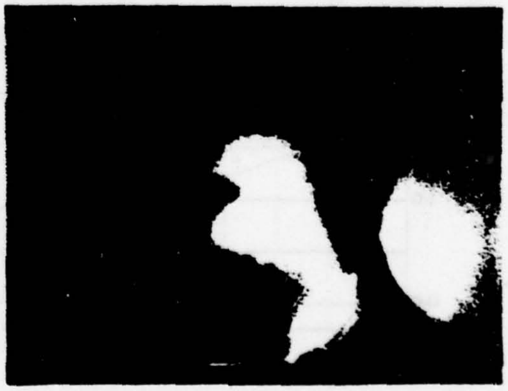

Fig. 20 The jet cross-section photographed by sheet illumination. The bright spots in the lower right corner are reflections.

A FAMILY OF TURBULENCE MODELS
FOR THREE-DIMENSIONAL THIN SHEAR LAYERS

J.C. Rotta
Deutsche Forschungs- und Versuchsanstalt für Luft- und Raumfahrt E.V.
Aerodynamische Versuchsanstalt Göttingen
Bunsenstrasse 10, 3400 Göttingen, W-Germany

ABSTRACT

The process of turbulent shear stress generation is studied on the basis of the transport equations, as derived from the Navier Stokes equations. The experimental observation that the vector of the shear stress is in general not parallel to the vector of the mean velocity gradient, is attributed mainly to the fluctuating pressure term. A new simple approximation to the part of the pressure strain term that depends on the mean rate of strain is proposed. It is used as a closure assumption for a family of turbulence models the most complicated of which consists of the transport equations for the shear stresses and the turbulent energy equation. Dropping the transport terms, three-dimensional versions of the eddy viscosity relationships and mixing length formulae are obtained, in which the eddy viscosity is nonisotropic.

INTRODUCTION

There exists a continued interest in prediction methods for three-dimensional boundary layers. As far as the laminar flow case is concerned, the problem is essentially a mathematical one. Vivid results have been presented by Geissler [1] and Wang [2], showing that useful numerical methods have been developed.

With computational methods for turbulent flow, physical problems are encountered. Several Euromech Colloquia have been devoted to three-dimensional turbulent boundary layers (Fernholz [3], Fanelöp & Krogstad [4]). Integral methods, which have proved to be successful with two-dimensional layers, are restricted in application to three-dimensional cases, mainly because of the great variety of mean cross flow profiles. Most investigators have concentrated their efforts on field methods based on partial differential equations. A systematic comparison of the performance of existing calculation methods was made at Euromech 60, the topic of which was "Three-dimensional turbulent boundary layers in external flows" (East [5]).

The literature on experiments on three-dimensional turbulent boundary layers was reviewed by Johnston [6]. With regard to calculation methods, the most important outcome of recent experiments is the evidence that the vector of the shear stress is not parallel to the vector of the mean velocity gradient in three-dimensional flow. In this paper an explanation for this behaviour is given, and relationships are proposed taking this fact into account. These relations are incorpotated in a family of existing turbulence models.

SHEAR STRESS TRANSPORT EQUATIONS

For a thin plane turbulent shear layer, the transport equations for the two components of the Reynolds stress tensor, $\tau_x = -\rho\overline{uv}$, $\tau_z = -\rho\overline{wv}$, can be derived from the Navier Stokes equations and are written as follows:

$$\left(U\frac{\partial}{\partial x} + V\frac{\partial}{\partial y} + W\frac{\partial}{\partial z}\right)(-\overline{uv}) = \overline{v^2}\frac{\partial U}{\partial y} - \overline{\frac{p'}{\rho}\left(\frac{\partial u}{\partial y} + \frac{\partial v}{\partial x}\right)} + \frac{\partial}{\partial y}\left(\frac{\overline{p'u}}{\rho} + \overline{uv^2}\right) , \qquad (1)$$

$$\left(U\frac{\partial}{\partial x} + V\frac{\partial}{\partial y} + W\frac{\partial}{\partial z}\right)(-\overline{wv}) = \overline{v^2}\frac{\partial W}{\partial y} - \overline{\frac{p'}{\rho}\left(\frac{\partial w}{\partial y} + \frac{\partial v}{\partial z}\right)} + \frac{\partial}{\partial y}\left(\frac{\overline{p'w}}{\rho} + \overline{wv^2}\right) . \qquad (2)$$

U, V, W are the mean and u, v, w the fluctuating velocity components in a rectangular Cartesian coordinate system x, y, z, where the y axis is normal to the plane of the shear layer. p' is the fluctuating pressure. (1) and (2) contain the usual thin layer simplifications, suppose steady high Reynolds number flow of constant density, ρ, and imply the conditions of local isotropy for the high wave number components of the fluctuating motion, but are exact otherwise (Rotta [7], p. 138).

The left hand side of each equation represents the rate of change of the Reynolds shear stress, caused by transport of shear stress due to mean velocity (convection). The third term on the right represents transport of shear stress in direction of the y axis due to turbulent interaction (turbulent diffusion). Usually, the dominant terms of (1) and (2) are the first and second terms on the right hand side. The first term represents generation of shear stress by the mean rate of strain and, accordingly, is a source term. The second term, which is the mean product of the fluctuating pressure and the fluctuating rate of strain (which after Bradshaw is called the pressure strain term for brevity) is known from two-dimensional flow studies to act as a sink term. In many if not most of all situations, the first and the second terms are nearly in equilibrium with each other. This fact explains the importance of the pressure strain terms in the process of shear stress generation.

The left hand side and the first term on the right of (1) and (2) are explicit, but closure assumptions are needed for the pressure strain terms and the diffusion terms, in order to use the equations with practical calculation methods. In the next paragraph, we shall discuss the closure assumptions for the pressure strain terms. Several relationships for the diffusion terms are proposed in the literature, so there is no need to discuss those assumptions in the present context.

THE PRESSURE STRAIN TERMS

The fluctuating pressure can be related to the fluctuating velocity field by the Poisson equation. According to the solution of this equation, the fluctuating pressure is expressed as the sum of two independent parts, the one, p'_M, being correlated with the mean rate of strain and the other, p'_T, being caused by interaction of velocity fluctuations. Consequently, the pressure strain term, too, is considered to consist of two parts.

Pressure strain dependence upon the mean rate of strain

The solution of the Poisson equation yields for the first part (Rotta [7], p. 143)

$$\overline{\frac{p'_M}{\rho}\frac{\partial u_i}{\partial x_j}} = -\frac{1}{2\pi}\int_{V(\underline{r})}\frac{\partial U_k}{\partial r_l}\frac{\partial^2}{\partial r_j \partial r_k}R_{il}\frac{d\underline{r}}{|\underline{r}|} + \frac{1}{2\pi}\int_{V(\underline{r})}\frac{\partial U_k}{\partial r_l}\frac{\partial^2}{\partial x_j \partial r_k}R_{il}\frac{d\underline{r}}{|\underline{r}|} \qquad (3)$$

where R_{il} denotes the two-point covariance

$$R_{il} = \overline{u_i(\underline{x})u_l(\underline{x}+\underline{r})}\ , \qquad (4)$$

$\underline{x}$ being the position vector of the fixed point, $\underline{r}$ the vector distance of the two points and $d\underline{r} = dr_1 dr_2 dr_3$.

The integration extends over all $\underline{r}$-space, $V(\underline{r})$, and the summation is taken over all components and directions k and l. The derivative $\partial U_k/\partial r_l$ is taken at position $\underline{x}+\underline{r}$, but may be replaced by the value at $\underline{x}$ for a first approximation. The second term on the right of (3) is due to inhomogenity of the turbulence field and may also be neglected for a first approximation. The considerations are, therefore, based on the simplified relationship

$$\overline{\frac{p'_M}{\rho}\frac{\partial u_i}{\partial x_j}} = -\frac{\partial U_k}{\partial x_l}\frac{1}{2\pi}\int_{V(\underline{r})}\frac{\partial^2}{\partial r_j \partial r_k}R_{il}\frac{d\underline{r}}{|\underline{r}|}\ . \qquad (5)$$

Applying (5) to the pressure strain terms of (1) and (2) yields formally

$$\overline{\frac{p'_M}{\rho}\left(\frac{\partial u}{\partial y}+\frac{\partial v}{\partial x}\right)} = -\frac{\partial U}{\partial y}\frac{1}{2\pi}\int_{V(\underline{r})}\left[\frac{\partial^2}{\partial r_y \partial r_x}R_{uv} + \frac{\partial^2}{\partial r_x^2}R_{vv}\right]\frac{d\underline{r}}{|\underline{r}|} - \frac{\partial W}{\partial y}\frac{1}{2\pi}\int_{V(\underline{r})}\left[\frac{\partial^2}{\partial r_y \partial r_z}R_{uv} + \frac{\partial^2}{\partial r_x \partial r_z}R_{vv}\right]\frac{d\underline{r}}{|\underline{r}|}\ , \qquad (6)$$

$$\overline{\frac{p'_M}{\rho}\left(\frac{\partial w}{\partial y}+\frac{\partial v}{\partial z}\right)} = -\frac{\partial U}{\partial y}\frac{1}{2\pi}\int_{V(\underline{r})}\left[\frac{\partial^2}{\partial r_y \partial r_x}R_{wv} + \frac{\partial^2}{\partial r_x \partial r_z}R_{vv}\right]\frac{d\underline{r}}{|\underline{r}|} - \frac{\partial W}{\partial y}\frac{1}{2\pi}\int_{V(\underline{r})}\left[\frac{\partial^2}{\partial r_y \partial r_z}R_{wv} + \frac{\partial^2}{\partial r_z^2}R_{vv}\right]\frac{d\underline{r}}{|\underline{r}|}\ . \qquad (7)$$

With the simplest assumption of isotropic distribution of the fluctuating velocity field, the integrals of (6) and (7) can be evaluated and one obtains:

$$-\frac{1}{2\pi}\int_{V(\underline{r})}\frac{\partial^2}{\partial r_x^2}R_{vv}\frac{d\underline{r}}{|\underline{r}|} = -\frac{1}{2\pi}\int_{V(\underline{r})}\frac{\partial^2}{\partial r_z^2}R_{vv}\frac{d\underline{r}}{|\underline{r}|} = \frac{4}{5}\overline{v^2}\ , \qquad (8)$$

$$-\frac{1}{2\pi}\int_{V(\underline{r})}\frac{\partial^2}{\partial r_y \partial r_x}R_{uv}\frac{d\underline{r}}{|\underline{r}|} = -\frac{1}{2\pi}\int_{V(\underline{r})}\frac{\partial^2}{\partial r_y \partial r_z}R_{wv}\frac{d\underline{r}}{|\underline{r}|} = -\frac{1}{5}\overline{v^2}\ , \qquad (9)$$

$$-\frac{1}{2\pi}\int\limits_{V(\underline{r})}\frac{\partial^2}{\partial r_y\partial r_z}R_{uv}\frac{d\underline{r}}{|\underline{r}|}=$$

$$=-\frac{1}{2\pi}\int\limits_{V(\underline{r})}\frac{\partial^2}{\partial r_y\partial r_x}R_{wv}\frac{1}{|\underline{r}|}=$$

$$=-\frac{1}{2\pi}\int\limits_{V(\underline{r})}\frac{\partial^2}{\partial r_x\partial r_z}R_{vv}\frac{d\underline{r}}{|\underline{r}|}=0 \quad . \tag{10}$$

From these relations it follows that the second term of (6) and the first term of (7) are zero, and that the vector of this part of the pressure strain term has the same direction as the mean rate of strain vector $\partial\underline{U}/\partial y$. The assumption of isotropic relations is, however, too simple. In the general case of a three-dimensional shear layer, each of the four integrals of (6) and (7) may have a different nonzero value.

The conditions come closer to reality if the estimation of the integrals is based on less restrictive symmetry concepts. Temporarily, rectangular Cartesian co-ordinates x_s, y_s, z_s are introduced, where at the point at which the pressure strain terms are to be determined, the x axis has the same direction as the resultant mean velocity $|\underline{U}| = U_r = (U^2 + W^2)^{1/2}$ at that point[1]. The vector $\underline{U}$ forms the angle γ with the x-co-ordinate, figure 1.

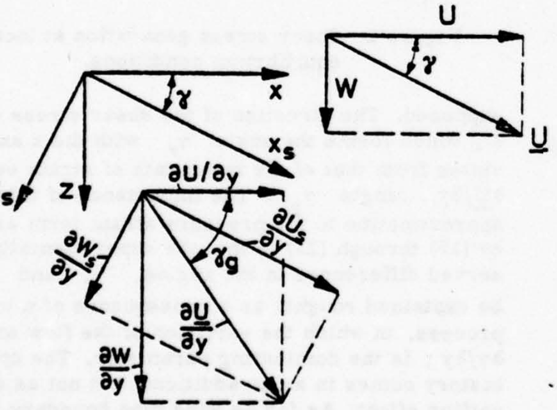

Figure 1 The co-ordinate systems. The y and y_s axes are normal to the xz plane.

The co-ordinates y_s and y are identical. By definition, the velocity components are $U_s = U_r$, $W_s = 0$ and $\partial U_s/\partial y = \partial U_r/\partial y$. If the mean velocity profiles are skewed, i. e. if the flow angle γ varies with y, the cross flow derivative is

$$\frac{\partial W_s}{\partial y} = U_r\frac{\partial\gamma}{\partial y} \quad , \tag{11}$$

and reduces to $\partial W_s/\partial y = 0$ for collateral mean velocity profiles (γ independent of y). The mean rate of strain vector, $\partial\underline{U}/\partial y$, forms the angle γ_g with the x co-ordinate.

Postulating symmetry of the turbulence structure with respect to the $x_s y_s$ plane and the $y_s z_s$ plane only, one is led contrary to (8) to the conclusion

$$-\frac{1}{2\pi}\int\limits_{V(\underline{r})}\frac{\partial^2}{\partial r_x^2}R_{vv}\frac{d\underline{r}}{|\underline{r}|} \neq -\frac{1}{2\pi}\int\limits_{V(\underline{r})}\frac{\partial^2}{\partial r_z^2}R_{vv}\frac{d\underline{r}}{|\underline{r}|} \quad , \tag{12}$$

whereas (10) is still valid. This suggests to approximate the part of the pressure strain term that depends on the mean rate of strain by

$$\overline{\frac{p'_M}{\rho}\left(\frac{\partial u_s}{\partial y}+\frac{\partial v}{\partial x_s}\right)} = \varkappa_{ss}\overline{v^2}\frac{\partial U_s}{\partial y} \quad , \tag{13}$$

$$\overline{\frac{p'_M}{\rho}\left(\frac{\partial w_s}{\partial y}+\frac{\partial v}{\partial z_s}\right)} = \varkappa_{nn}\overline{v^2}\frac{\partial W_s}{\partial y} \quad . \tag{14}$$

The values of the integrals are related to $\overline{v^2}$, because the integrals of (12) presumably provide the major contribution as is the case under isotropic conditions (see (8) and (9)). The dimensionless quantities $\varkappa_{ss}$ and $\varkappa_{nn}$ remain to be adjusted in accordance with experiments, since for the assumed turbulence field, it is not possible to evaluate the integrals explicitly like it can be done for isotropic turbulence; $\varkappa_{ss}$ must have the same value as in the two-dimensional case. The relations (13) and (14) represent the simplest approximation one can make of this term. The approximation is physically plausible, meets the requirement that it reduces to the two-dimensional form when $\partial W_s/\partial y = 0$, and makes provisions for the fact that the vector of this part of the pressure strain term is not parallel with the mean rate of strain vector. It is unlikely that any more refined assumptions can be put on a solid basis with the experimental data and the theoretical background presently available.

The expressions (13) and (14) are transformed to the arbitrarily oriented rectangular Cartesian co-ordinate system x, y, z, where W/U_r is used for $\sin\gamma$ and U/U_r is used for $\cos\gamma$. In this way we obtain

$$\overline{\frac{p'_M}{\rho}\left(\frac{\partial u}{\partial y}+\frac{\partial v}{\partial x}\right)} = \left(\varkappa_{xx}\frac{\partial U}{\partial y}+\varkappa_{xz}\frac{\partial W}{\partial y}\right)\overline{v^2} \quad . \tag{15}$$

---

[1] The vector $\underline{U}$ that is exactly the projection of the vector of local mean velocity in the plane $y = \text{const}$, is called mean velocity vector for brevity.

$$\overline{\frac{p'_M}{\rho}\left(\frac{\partial w}{\partial y}+\frac{\partial v}{\partial z}\right)} = \left(\kappa_{zx}\frac{\partial U}{\partial y}+\kappa_{zz}\frac{\partial W}{\partial y}\right)\overline{v^2} \quad , \qquad (16)$$

with the quantities

$$\kappa_{xx} = (\kappa_{ss}U^2 + \kappa_{nn}W^2)/U_r^2 \quad , \qquad (17)$$

$$\kappa_{xz} = \kappa_{zx} = (\kappa_{ss} - \kappa_{nn})UW/U_r^2 \quad , \qquad (18)$$

$$\kappa_{zz} = (\kappa_{ss}W^2 + \kappa_{nn}U^2)/U_r^2 \quad . \qquad (19)$$

According to (15) and (16), each component of the pressure strain term depends on $\partial U/\partial y$ as well as on $\partial W/\partial y$, in agreement with (6) and (7).

Pressure strain dependence upon turbulent interactions

The second part of the pressure strain term, which is due to the fluctuating pressure caused by fluctuating velocity interaction, is generally assumed to effect a redistribution of kinetic energy of the fluctuating velocities and a destruction of Reynolds shear stresses. The empirical relationship proposed by Rotta [8], which has been used successfully many times, provides

$$\overline{\frac{p'_T}{\rho}\left(\frac{\partial u}{\partial y}+\frac{\partial v}{\partial x}\right)} = -k_p\frac{\left(\overline{q^2}/2\right)^{1/2}}{L}\overline{uv} \quad , \qquad (20)$$

$$\overline{\frac{p'_T}{\rho}\left(\frac{\partial w}{\partial y}+\frac{\partial v}{\partial z}\right)} = -k_p\frac{\left(\overline{q^2}/2\right)^{1/2}}{L}\overline{wv} \quad , \qquad (21)$$

where $\overline{q^2}/2 = \left(\overline{u^2}+\overline{v^2}+\overline{w^2}\right)/2$ is the kinetic turbulent energy per unit mass, L a turbulence length scale of the large eddies, and k_p a dimensionless constant.

.SHEAR STRESS GENERATION AT LOCAL EQUILIBRIUM CONDITIONS

The foregoing considerations on the pressure strain term lead to striking conclusions with regard to experimental observations made in three-dimensional turbulent boundary layers. As already mentioned, the direction of the resultant of the components of the pressure strain term that depends on the mean rate of strain, is not the same as that of the mean rate of strain vector and, of course, also not the same as that of the vector $\underline{U}$, if different values for κ_{ss} and κ_{nn} of (13) and (14) are used. The direction of the resultant of the pressure strain term due to interaction of fluctuating velocities is the same as the direction of the shear stress vector. The resultant of the generation term of (1) and (2) points in the same direction as the mean rate of strain vector. Thus, if convection (left hand side of (1) and (2)) and diffusion are absent, the equilibrium between the generation term and the pressure strain term at a given point in the flow may be perhaps as sketched in figure 2. In this case, $\kappa_{nn} > \kappa_{ss}$ is supposed. The direction of the shear stress vector τ, which forms the angle γ_τ with the x axis, deviates from that of the mean rate of strain vector, $\partial\underline{U}/\partial y$, (angle γ_g). The importance of this simple approximation to the pressure strain term as given by (15) through (21) is that the experimentally observed differences in the angles, γ_τ and γ_g, can be explained roughly as a consequence of a local process, in which the variation of the flow angle, $\partial\gamma/\partial y$, is the dominating parameter. The upstream history comes in as an additional but not as a prevailing effect. As far as wing type boundary layers are concerned, the effects of convection (left hand side of (1) and (2)) and of diffusion are too weak to be alone responsible for the observed strong effect.

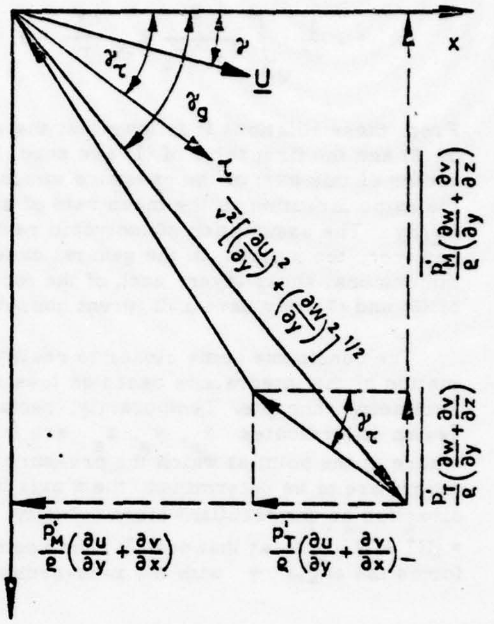

Figure 2 Shear stress generation at local equilibrium conditions.

In the following paragraphs, the above approximations are applied to several known turbulence models belonging to the same family insofar as one is derived from the other.

SEMI-EMPIRICAL SHEAR STRESS TRANSPORT EQUATIONS

The most complicated of the models mentioned here uses the shear stress transport equations in conjunction with the transport equation for the kinetic energy of the fluctuating velocities, $\overline{q^2}/2 = (\overline{u^2} + \overline{v^2} + \overline{w^2})/2$, perhaps together with a length scale equation (Rotta [9]). In this case, the turbulence field is described by the quantities $\overline{q^2}/2$, $\overline{uv}$, $\overline{wv}$, and L . Therefore, $\overline{v^2}$ is expressed in terms of $\overline{q^2}/2$. If now we define the dimensionless quantities

$$a_p = (1 - \varkappa_{ss})2\overline{v^2}/\overline{q^2} \quad , \tag{22}$$

$$T = \frac{1 - \varkappa_{nn}}{1 - \varkappa_{ss}} \quad , \tag{23}$$

equs. (1) and (2) become

$$(U \frac{\partial}{\partial x} + V \frac{\partial}{\partial y} + W \frac{\partial}{\partial z})(- \overline{uv}) =$$

$$= (a_{pxx} \frac{\partial U}{\partial y} + a_{pxz} \frac{\partial W}{\partial y}) \frac{\overline{q^2}}{2} + k_p \left(\frac{\overline{q^2}}{2}\right)^{1/2} \overline{uv} -$$

$$- \frac{\partial}{\partial y} \left\{ k_{q\tau} \left(\frac{\overline{q^2}}{2}\right)^{1/2} L \frac{\partial}{\partial y} \overline{uv} \right\} \quad . \tag{24}$$

$$(U \frac{\partial}{\partial x} + V \frac{\partial}{\partial y} + W \frac{\partial}{\partial z})(- \overline{wv}) =$$

$$= (a_{pzx} \frac{\partial U}{\partial y} + a_{pzz} \frac{\partial W}{\partial y}) \frac{\overline{q^2}}{2} + k_p \left(\frac{\overline{q^2}}{2}\right)^{1/2} \overline{wv} -$$

$$- \frac{\partial}{\partial y} \left\{ k_{q\tau} \left(\frac{\overline{q^2}}{2}\right)^{1/2} L \frac{\partial}{\partial y} \overline{wv} \right\} \quad , \tag{25}$$

where

$$a_{pxx} = a_p(U^2 + TW^2)/U_r^2 \quad , \tag{26}$$

$$a_{pxz} = a_{pzx} = a_p(1 - T)UW/U_r^2 \quad , \tag{27}$$

$$a_{pzz} = a_p(W^2 + TU^2)/U_r^2 \quad . \tag{28}$$

The diffusion is here assumed to depend on the gradient of the shear stress. A value between 0.2 and 0.25 appears suitable for a_p . The assumption of isotropic turbulence gives $a_p = 0.267$ and $T = 1$. The value of k_p follows from the requirement that, for two-dimensional flow, (24) and the turbulent energy equation are compatible with the logarithmic law of the wall (Rotta [7], p. 185).

PRANDTL'S EDDY VISCOSITY RELATIONSHIP

Prandtl [10] proposed a calculation method for two-dimensional shear layers which is based on the turbulent energy equation and the shear stress calculated from an eddy viscosity relationship, the eddy viscosity being determined from the square root of $\overline{q^2}/2$ and L :

$$\nu_T = k\left(\frac{\overline{q^2}}{2}\right)^{1/2} L \quad . \tag{29}$$

In conjunction with a length scale equation, this method was applied to plane and axisymmetric flows (Rotta & Vollmers [11], Vollmers & Rotta [12]).

The extended form of Prandtl's eddy viscosity relationship for three-dimensional flow is readily derived from (24) to (28), neglecting the convection and diffusion terms. Defining k as a_p/k_p , the eddy viscosity is obtained in tensor form:

$$(\nu_T)_{xx} = \nu_T(U^2 + TW^2)/U_r^2 \quad , \tag{30}$$

$$(\nu_T)_{xz} = (\nu_T)_{zx} = \nu_T(1 - T)UW/U_r^2 \quad , \tag{31}$$

$$(\nu_T)_{zz} = \nu_T(W^2 + TU^2)/U_r^2 \quad , \tag{32}$$

with the scalar eddy viscosity ν_T according to (29). It follows from (30) to (32) that the used approximation of the pressure strain term leads to a nonisotropic eddy viscosity. The following equations are obtained for the shear stresses:

$$- \overline{uv} = (\nu_T)_{xx} \frac{\partial U}{\partial y} + (\nu_T)_{xz} \frac{\partial W}{\partial y} \quad , \tag{33}$$

$$- \overline{wv} = (\nu_T)_{zx} \frac{\partial U}{\partial y} + (\nu_T)_{zz} \frac{\partial W}{\partial y} \quad . \tag{34}$$

If the eddy viscosity components are transformed to the x_s, y_s, z_s co-ordinates (putting $W = 0$), it is seen that the ratio of the transverse to streamwise component of the eddy viscosity, $(\nu_T)_{nn}/(\nu_T)_{ss}$, is equal to T . The ratio of the tangent of angle between the mean velocity vector $\underline{U}$ and the shear stress vector to the tangent of angle between the mean velocity vector and the mean rate of strain vector, usually denoted by N , equals the ratio of the eddy viscosities transverse and parallel to the local velocity vector. Thus for the eddy viscosity model, we have

$$N = \frac{\tan(\gamma_\tau - \gamma)}{\tan(\gamma_g - \gamma)} = T \quad . \tag{35}$$

East [13] and Elsenaar & Boelsma [14] have shown that the values of N , as determined from various boundary layer measurements, spread over a wide range but do not vary greatly accross the thickness of the layer for any particular profile. Values of T substantially less than unity are indicated and, tentatively, a value of the order of 0.5 may be suggested for boundary layer calculations until further information is available.

A nonisotropic eddy viscosity model was proposed by Fannelöp & Humphreys [15], which differs from the scheme given by (30) to (32). No physical support was adduced for their assumption.

MIXING LENGTH FORMULAE

If we now go a step further, in simplifying the turbulent energy equation, the three-dimensional version of the mixing length formula is obtained. Neglecting the transport terms (convection and diffusion), introducing (33) and (34) together with (30) to (32), and using a proper definition of the mixing length l in terms of L, (29) becomes

$$\nu_T = l^2\left[\left(\frac{\partial U}{\partial y}\right)^2 + \left(\frac{\partial W}{\partial y}\right)^2 + (T-1)\left(W\frac{\partial U}{\partial y} - U\frac{\partial W}{\partial y}\right)^2 / U_r^2\right]^{1/2} . \qquad (36)$$

This formula, which reduces to the well-known form for two-dimensional flow if W and $\partial W/\partial y$ are zero, represents together with (30) through (34) the mixing length formulae for three-dimensional thin layers.

Using these relations, one obtains for the magnitude of the shear stress vector in relation to the kinetic turbulent energy

$$\frac{|\tau|}{\rho\overline{q^2}} = a_1\left[\frac{\left(\frac{\partial U}{\partial y}\right)^2 + \left(\frac{\partial W}{\partial y}\right)^2 + (T^2-1)\left(W\frac{\partial U}{\partial y} - U\frac{\partial W}{\partial y}\right)^2/U_r^2}{\left(\frac{\partial U}{\partial y}\right)^2 + \left(\frac{\partial W}{\partial y}\right)^2 + (T-1)\left(W\frac{\partial U}{\partial y} - U\frac{\partial W}{\partial y}\right)^2/U_r^2}\right]^{1/2} . \qquad (37)$$

Actually, the quantity a_1 (= 0.15) is Bradshaw's [16] ratio of the magnitude of the shear stress to $\rho\overline{q^2}$ in two-dimensional boundary layers. Since

$$\frac{U\frac{\partial W}{\partial y} - W\frac{\partial U}{\partial y}}{U_r\left[\left(\frac{\partial U}{\partial y}\right)^2 + \left(\frac{\partial W}{\partial y}\right)^2\right]^{1/2}} = \sin(\gamma_g - \gamma) , \qquad (38)$$

it is seen from (37) that the ratio $|\tau| / \rho\overline{q^2}$ depends on the angle between the vector of the mean rate of strain and the vector of $\underline{U}$. Elsenaar & Boelsma [14] have determined $|\tau| / \rho\overline{q^2}$ from their measurements in a turbulent boundary layer under infinite swept wing conditions and found that this ratio decreases markedly in downstream direction. In figure 3, those values taken at $y/\delta = 0.4$ are plotted versus $\gamma_g - \gamma$ and compared with results, calculated from (37) for various values of parameter T. In fact, most of the test data display a stronger decrease with $\gamma_g - \gamma$ than the calculated values, but the latter agree at least qualitatively with the experiment.

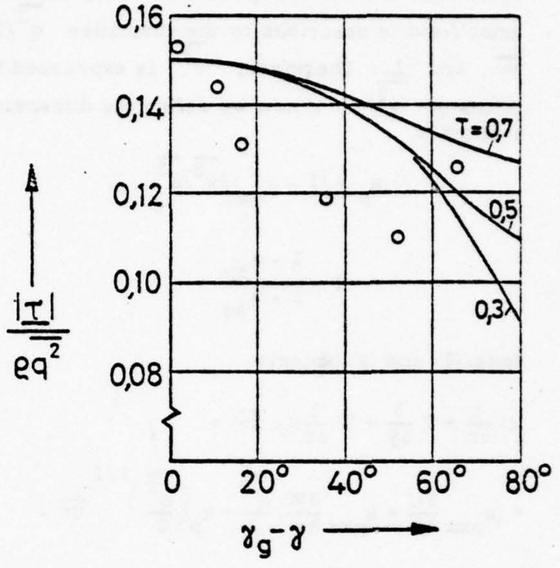

Figure 3 Variation of ratio shear stress to turbulent energy with angle $\gamma_g - \gamma$ and parameter T according to (37), $a_1 = 0.15$.

○ experiment (Elsenaar & Boelsma [14]) at $y/\delta = 0.4$.

There is another quantity which can be compared with the experiment. Elsenaar & Boelsma [14] calculated from their experiments the mixing length defined in the conventional manner as

$$l_{con} = \frac{(|\tau|/\rho)^{1/2}}{\left[\left(\frac{\partial U}{\partial y}\right)^2 + \left(\frac{\partial W}{\partial y}\right)^2\right]^{1/2}} . \qquad (39)$$

This value is roughly independent of wall distance y outside the wall region, but decreases in relation to the boundary layer thickness as the flow proceeds downstream. Values taken at $y/\delta = 0.5$ are plotted versus $\gamma_g - \gamma$ in figure 4. For two-dimensional boundary layers, l/δ in the outer part of the layer is found rather independent of the pressure distribution, and calculations with the mixing length formula based on this assumption give reasonably good results. This led us to calculate l_{con}/δ from (39) using (36)

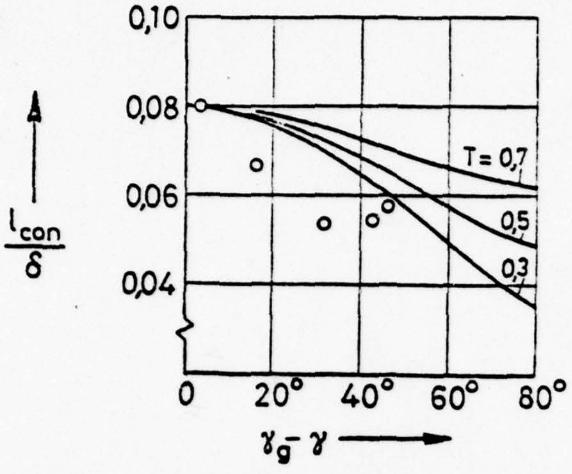

Figure 4 Variation of "conventional" mixing length according to (39) with angle $\gamma_g - \gamma$ and parameter T, $l/\delta = 0.08$.

○ experiment (Elsenaar & Boelsma [14] at $y/\delta = 0.5$.

and (30) to (34) with a constant value $l/\delta = 0.08$. It is seen from figure 4 that the calculated results for various values of T decrease with angle $\gamma_g - \gamma$ and are qualitatively in agreement with the experimental data, although the effect is again stronger in the experiments.

The qualitative agreement seen from figures 3 and 4 is an indication that the basic idea presented here is correct. In fact, both quantities, the ratio of shear stress to turbulent energy and the mixing length, are subject to a number of effects and are definitely influenced by the history of the flow. Thus more than qualitative agreement cannot be expected.

CONCLUSIONS

In the attempt to derive turbulence models for three-dimensional thin shear layer calculation from the transport equations for the shear stress, the attention is directed to the behaviour of the part of the mean product of fluctuating pressure and fluctuating rate of strain that depends on the mean rate of strain. If the turbulence field were isotropic, the vector of this quantity would be parallel with the mean rate of strain vector, as is assumed with calculation methods hitherto existing. However, the two vectors are not parallel in a nonisopropic field, thus providing the primary reason for the fact that the vectors of the shear stress and the mean rate of strain act in different directions when the mean velocity profiles are skewed.

Simple approximations to the pressure strain term are applied to close the transport equations for the shear stresses. One empirical quantity, T, is used in addition to those appearing in the two-dimensional transport equation. Neglecting the transport terms of the equations, a three-dimensional form of Prandtl's eddy viscostiy relationship is derived, which implies a nonisotropic eddy viscosity. Further simplification of the turbulent energy equation leads to the mixing length formulae for three-dimensional flow. According to these relationships, the ratio shear stress/turbulent energy and the conventionally defined mixing length decrease as the angle between local streamline and the vector of the mean rate of strain grows. The basic idea can also applied to Bradshaw's shear stress transport equations [17]. For a value $T = 1$, the equations reduce to the form prevailing up to now. It is obvious that the results calculated with any of the four models will come closer to experiments of wing boundary layers, if a value of T of about 0.5 is choosen rather than $T = 1$.

Acknowledgments

This study is part of a research work supported by the Deutsche Forschungsgemeinschaft. Essential thoughts were inspired at a joint investigation with G. R. Schneider [18]. I am grateful to him and to Prof. G. R. Inger for reviewing the manuscript and for helpful discussions.

REFERENCES

1 Geissler, W., "Berechnung der dreidimensionalen laminaren Grenzschicht an schrägangeströmten Rotationskörpern mit Ablösung," Ingenieur-Archiv, Bd. 43, 1974, S. 413-425.

2 Wang, K. C., "Separation Patterns of Boundary Layer over an Inclined Body of Revolution," A. I. A. A. Journal, Vol. 10, 1972, pp. 1044-1050.

3 Fernholz, H., "Three-Dimensional Turbulent Boundary Layers,": A Report on EUROMECH 33, Journal of Fluid Mechanics, Vol. 58, 1973, pp. 177-186.

4 Fannelöp, T. K., and Krogstad, P.Å., "Three "Three-Dimensional Turbulent Boundary Layers in External Flows: A Report on EUROMECH 60," Journal of Fluid Mechanics, Vol. 71, 1975, pp. 815-826.

5 East, L. F., "Computation of Three-Dimensional Turbulent Boundary Layers," TN AE-1211, 1975, The Aeronautical Research Institute of Sweden.

6 Johnston, J. P., "Experimental Studies in Three-Dimensional Turbulent Boundary Layers," MD-34, July 1976, Thermosciences Division Department of Mechanical Engineering, Stanford University, Stanford, Cal.

7 Rotta, J. C., "Turbulente Strömungen," B. G. Teubner, Stuttgart, 1972.

8 Rotta, J. C., "Statistische Theorie nichthomogener Turbulenz," Zeitschrift für Physik, Bd. 129, 1951, pp. 547-572.

9 Rotta, J. C., "Recent Attempts to Develop a Generally Applicable Calculation Method for Turbulent Shear Flow Layers," AGARD Conference Proceedings, No. 93, 1971, Turbulent Shear Flows, Fluid Dynamics Panel Specialists' Meeting, London, U.K., Sept. 1971, invited paper A-1 to A-11.

10 Prandtl, L., "Über ein neues Formelsystem für die ausgebildete Turbulenz," 1961, in Ludwig Prandtl, Gesammelte Abhandlungen (ed. W. Tollmien, H. Schlichting, and Görtler, H., Springer, Berlin, Göttingen, Heidelberg, pp. 874-887.

11 Rotta, J. C., and Vollmers, H., "Ähnliche" Lösungen der Differentialgleichungen für gemittelte Geschwindigkeiten, Turbulenzenergie und Turbulenzlänge," Deutsche Luft- und Raumfahrt, Forschungsbericht, 76-24, 1976, pp. 1-79.

12 Vollmers, H., and Rotta, J. C., "Similar Solutions for Turbulent Flows Described by Mean Velocity, Turbulent Energy, and Turbulent Length Scale," AIAA 9th Fluid and Plasma Dynamics Conference, San Diego, Cal., July 1976, AIAA paper No. 76-407, pp. 1-12.

13 East, L. F., "Measurements of the Three-Dimensional Incompressible Turbulent Boundary Layer Induced on the Surface of a Slender Delta Wing by the Leading Edge Vortex," Aeronautical Research Council Reports & Memoranda, No. 3768, 1973.

14 Elsenaar, A., and Boelsma, S. H., "Measurements of the Reynolds Stress Tensor in a Three-Dimensional Turbulent Boundary Layer Under Infinite Swept Wing Conditions," TR 74095 U, 1974, National Lucht- en Ruimtevaartlaboratorium.

15 Fannelöp, T. K., and Humphreys, D. A., "The Solution of the Laminar and Turbulent Three-dimensional Boundary Layer Equations with a Simple Finite Difference Technique," Rep. 126, 1975, The Aeronautical Research Institute of Sweden.

16 Bradshaw, P., Ferriss, D. H., and Atwell, N. P., "Calculation of Boundary-Layer Development Using the Turbulent Energy Equation," Journal of Fluid Mechanics, Vol. 28, 1967, pp. 593-616.

17 Bradshaw, P., "Calculation of Three-Dimensional Turbulent Boundary Layers," Journal of Fluid Mechanics, Vol. 46, 1971, pp. 417-445.

18 Rotta, J. C., and Schneider, G. R., "Theoretical Investigations of the Three-Dimensional Turbulent Boundary Layer on Swept Wings," IB 251-76 A 06, 1976, Deutsche Forschungs- und Versuchsanstalt für Luft- und Raumfahrt E. V., Aerodynamische Versuchsanstalt Göttingen.

THE EFFECT OF VELOCITY FLUCTUATIONS AND NONUNIFORMITIES IN THE FREE STREAM ON THE BOUNDARY LAYER DEVELOPMENT

H. U. Meier

Deutsche Forschungs- und Versuchsanstalt für Luft- und Raumfahrt E. V.
Aerodynamische Versuchsanstalt Göttingen
Bunsenstrasse 10, 3400 Göttingen, W-Germany

ABSTRACT

The influence of grid generated wind tunnel turbulence was studied. It was found that due to the position of the grids relatively to the boundary layer start, a momentum loss in the boundary layer can be added. This effect of large fluctuating velocity components and nonuniformity of the flow at the start of the boundary layer was investigated in detail.

The investigations led to some general remarks about the influence of the free stream turbulence level in low speed wind tunnel measurements.

NOMENCLATURE

c_f	skin friction coefficient, $c_f = 2\tau_w/(\rho_\infty U_\infty^2)$
d	diameter of rods
D	outer diameter (height) of a Pitot probe
M	mesh size of the grid
n	exponent for the decay of turbulence, Eq. (3)
p_d	dynamic pressure, $p_d = p_t - p_w$
p_t	Pitot pressure
p_w	static pressure, measured at the wall
RMS	Root Mean Square
Tu	turbulence level, $Tu = \left(\left(\overline{u'^2} + \overline{v'^2} + \overline{w'^2}\right)/3\right)^{1/2}/U_\infty$
Tu_1	turbulence level, $Tu_1 = \left(\overline{u'^2}/U_\infty^2\right)^{1/2}$
Tu_2	turbulence level, $Tu_2 = \left(\overline{v'^2}/U_\infty^2\right)^{1/2}$
Tu_3	turbulence level, $Tu_3 = \left(\overline{w'^2}/U_\infty^2\right)^{1/2}$
u_τ	shear stress velocity, $u_\tau = (\tau_w/\rho)^{1/2}$
U	mean velocity in x-direction
$\overline{u'^2}^{\,1/2}$	fluctuating velocity components in x-direction (RMS-value)
$\overline{v'^2}^{\,1/2}$	fluctuating velocity components in y-direction (RMS-value)
$\overline{w'^2}^{\,1/2}$	fluctuating velocity components in z-direction (RMS-value)
x, y, z	co-ordinates normal and parallel to the surface
x_G	distance from the grid to the leading edge
x_{LE}	distance from the leading edge to the measuring station
x_t	distance from the virtual origin of turbulence to the measuring station
x_{vo}	distance from virtual origin of turbulence to the leading edge
y^*	dimensionless wall distance, $y^* = yu_\tau/\nu$
δ	total boundary layer thickness
δ_2	momentum thickness, Eq. (5)
η	dimensionless wall distance, $\eta = y/\delta$
$\varkappa$	von Kármán constant, $\varkappa = 0.4$
ν	kinematic viscosity
π_1	wake factor, Eq. (1)
π_2	constant, Eq. (1)

ρ	density
τ	shear stress
ω	wake function, Eq. (1)
ω_2	additional velocity distribution, Eq. (1)

Subscripts

w	wall conditions
∞	free stream conditions

INTRODUCTION

The influence of wind tunnel turbulence on experimental results is a wellknown phenomenon. It is known that significant differences may exist between the wind tunnel and free flight test in quiescent stream. This is due to the change in the transition from laminar to turbulent boundary layer flow and the different structure of the turbulence in the boundary, which results e. g. in a change of the wall shear stress. However, the effect of grid-generated turbulence levels on the boundary layer development in the range of $Tu = 0.06\,\%$ to $1\,\%$ - a range which is representative for the turbulence levels in existing subsonic wind tunnels - is not investigated experimentally. Recent studies have been concentrated on relative high turbulence levels of the free stream in order to simulate the flow conditions of multistage turbomachineries. For this reason a theoretical [1] and experimental [2] investigation about the effect of low free stream turbulence $(Tu < 1\,\%)$ in subsonic incompressible flow along a flat tunnel wall, upon the boundary layer development was carried out at the DFVLR-AVA (Deutsche Forschungs- und Versuchsanstalt für Luft- und Raumfahrt-Aerodynamische Versuchsanstalt Göttingen). The basic turbulence level in the tunnel of $Tu \sim 0.06\,\%$ was increased by means of various grids having approximately identical mesh sizes.

In a preliminary investigation these grids were installed at the nozzle exit, approximately 20 mm in front of the leading edge of the flat tunnel side walls. This postulated highly turbulent flow at the leading edge which influences the boundary layer development considerably. To be able to investigate this effect systematically first a careful study of the decay of the turbulence intensity and its deviation from isotropy was made. Then velocity profiles in side wall boundary layers at different distances from the leading edge and turbulence levels were measured. The calculated boundary layer characteristics gave some information about the influence of the external turbulence.

EXPERIMENTAL SET-UP

A detailed description of the wind tunnel and applied measuring techniques is given in Ref. [2]. For convenience and better understanding the basic description is given again in this paper.

The low turbulence wind tunnel of the DFVLR-AVA is of an Eiffel type (Fig. 1). The settling chamber is equipped with dust filters and screens. The contraction ratio of the test section to the settling chamber is 1:15, in order to obtain a low turbulence level in the free stream. The test section is $0.3 \times 1.5\ m^2$. There is a small gap between the nozzle exit and the plane vertical wind tunnel wall (compare Fig. 2). This allows a new wall boundary layer to start at that location. At the end of the nozzle contraction grids can be installed (Fig. 2) in order to generate turbulence.

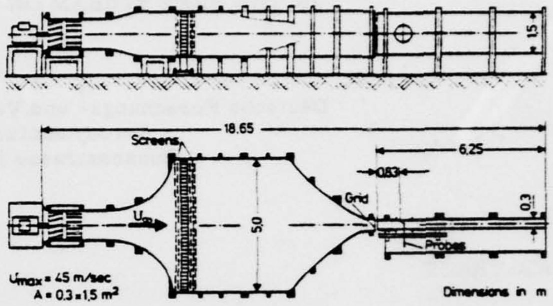

Fig. 1 Low turbulence wind tunnel of the DFVLR-AVA

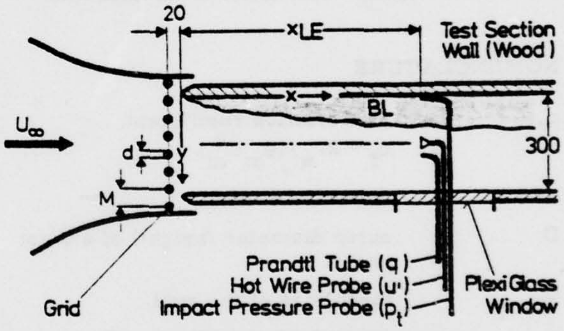

Fig. 2 Sketch of the test section

The tunnel walls are sufficiently divergent so that only negligible axial pressure and mean velocity gradients exist.

The transition from laminar to turbulent boundary layer flow was fixed 50 mm from and parallel to the leading edge by glueing a plastic tape with embossed large letter V's (tip against flow direction).

Mean Flow Measurements

The pressure data in the boundary layer were obtained with a flattened Pitot tube having a height of $D = 0.16$ mm. In order to take into account small variations of the free stream, the mean velocity $(U_\infty = 30\ m/s)$ was measured with a Prandtl tube.

The static pressure of the Prandtl tube was taken as the reference pressure for the Pitot tube. Thus in the data reduction procedure the actual free stream velocity could be used for example, to calculate the boundary layer integral values. All data were time averaged over a period of six seconds and then recorded at the identical time with a digital data logging system (AVA), essentially consisting of ten digital voltmeters with a special data storage.

Turbulence Measurements

All turbulence measurements were only carried out in the center line of the tunnel.

Velocity fluctuations in the flow direction (x-direction) were measured with a single hot wire, and in the y- and z-directions with X-hot wires. The hot wire probes were connected to a constant temperature anemometer unit from Thermosystems Inc. (TSI). The output was obtained from a Root Mean Square (RMS)-voltmeter from TSI which enabled measurements of the true RMS-values, $\left(\overline{u'^2}\right)^{1/2}$, $\left(\overline{v'^2}\right)^{1/2}$, $\left(\overline{w'^2}\right)^{1/2}$, to be determined from the fluctuating components u', v', w'. The application of a hot wire for flows with low turbulence levels requires a very careful calibration, as indicated RMS-values at zero velocity $(U_\infty = 0)$ are the sum of the instrumentation noise and signals due to the flow around the hot wire caused by natural convection. No way was found to overcome this problem using a proper calibration procedure. Thus the RMS-values for $U_\infty = 0$ were controlled by applying an extrapolation from the calibration curve. From a frequency analysis it was found that a relatively large contribution of the RMS-reading was due to high frequency noise. Due to the fact that these high frequencies $(f > 20\ \mathrm{kHz})$ cannot result from the flow unsteadiness, a low pass filter with a maximum frequency of 5 kHz was inserted.

The hot wires were recalibrated at each measuring station over the entire velocity range ($U_{\infty\,max} = 45$ m/s with no grid and $U_{\infty\,max} = 36$ m/s with the largest grid). The turbulence levels seemed to show no dependence on the free stream velocity for $U_\infty > 8$ m/s.

The change of the free stream temperature was less than 1 °C during one calibration run. Thus no temperature correction was incorporated into the calibration procedure.

Determination of Local Skin Friction

The wall shear stress τ_w was determined from the experimental velocity profile. The basis of the scheme is the comparison of calculated velocity profiles which are constructed essentially from the Law of the Wall and Coles's Law of the Wake. An additional distribution $\omega_2(\eta)$ proposed by J. C. Rotta is added for the wake in order to eliminate the abrupt change in the slope $\partial u/\partial y$ at the outer edge of the boundary layer. The entire profile then may be constructed following the relation

$$\frac{U}{u_\tau} = f(y^*) + \frac{\pi_1}{\chi}\,\omega(\eta) + \frac{\pi_2}{\chi}\,\omega_2(\eta) \quad . \qquad (1)$$

Here the function f represents the Law of the Wall and is a function of the dimensionless distance $y^* = yu_\tau/\nu$. (y is the wall distance, $u_\tau = (\tau_w/\rho)^{1/2}$ the shear stress velocity, and ν the kinematic velocity.) The best possible agreement between the measurements and calculation was accomplished by requiring that the Root Mean Square (RMS) deviation becomes a minimum. A detailed description of this method and the basic equations are given in Ref. [2].

RESULTS

Turbulence Measurements

The turbulence level in the wind tunnel was investigated with and without grids. Due to the fact that the grids were installed at the end of the nozzle exit the decay of grid generated turbulence in a rectangular channel was simulated. Three different grid sizes were used. The geometry was varied in such a way that the difference $(M - d)$, between the meshsize M and the wire diameter d was approximately constant. In Fig. 3 the measured turbulence levels in the wind tunnel with and without grids for different distances from the leading edge are shown. The pressure gradient in flow direction at $U_\infty \approx 30$ m/s was approximately zero. The black symbols are indicating

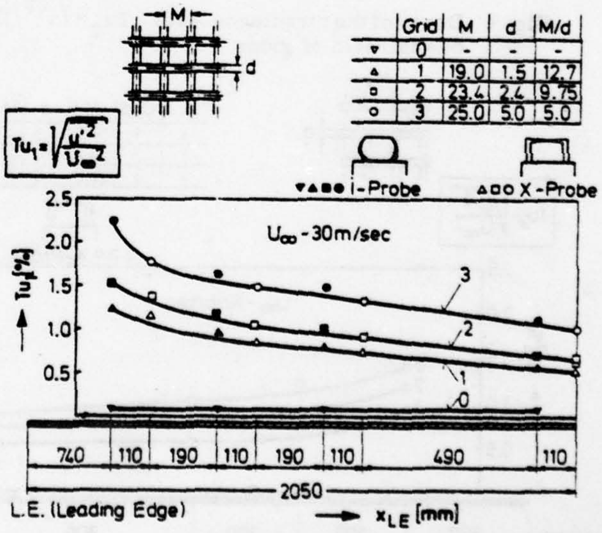

	Grid	M	d	M/d
▽	0	-	-	-
△	1	19.0	1.5	12.7
□	2	23.4	2.4	9.75
○	3	25.0	5.0	5.0

Fig. 3 Decay of the turbulence level $Tu_1 = \sqrt{\overline{u'^2}/U_\infty^2}$ downstream of grids

measurements with a single hot wire probe while the open symbols are representing results from a X-hot wire probe. The results of the single wire probe are slightly higher compared with those of the X-probe, but they are in the range of the expected accuracy.

In order to be able to proof the existence of quasi isotropic turbulence in the investigated tunnel flow, the v' and w' fluctuating velocity components were measured with X-hot wires. The results of these turbulence measurements are shown in Figs. 4 and 5. The decay of the fluctuating velocity components v', w' in y- and z-direction with increasing distance from the leading edge is similar to that of the u'-velocity component. However, as shown in Fig. 6, the measurements indicate that the ratio of the longitudinal to lateral turbulent intensities is consistently larger than 1.1 for distances $x_{LE} \leq 1\,500$ mm. This result is qualitatively in agreement with published results of anisotropic grid turbulence. Uberoi [3] found by measurements of turbulence behind a square-mesh biplane grid made of round rods that the RMS turbulent velocity fluctuations are characterized by

$$\left(\overline{v'^2}\right)^{1/2} = \left(\overline{w'^2}\right)^{1/2} = \frac{\left(\overline{u'^2}\right)^{1/2}}{1.18} . \qquad (2)$$

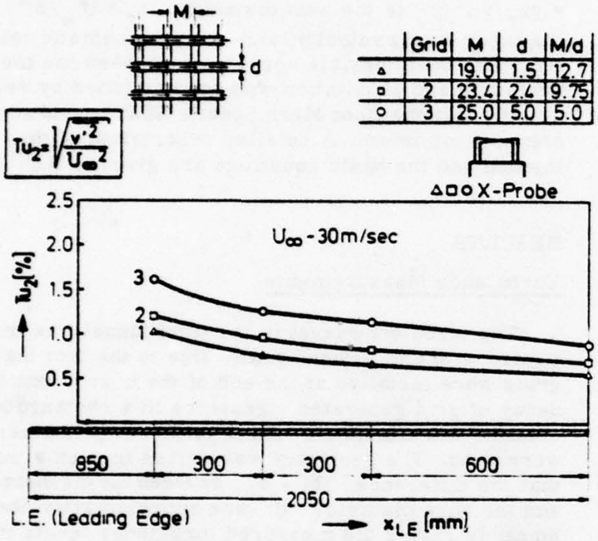

Fig. 4 Decay of the turbulence level $Tu_2 = \sqrt{\overline{v'^2}}/U_\infty$ downstream of grids

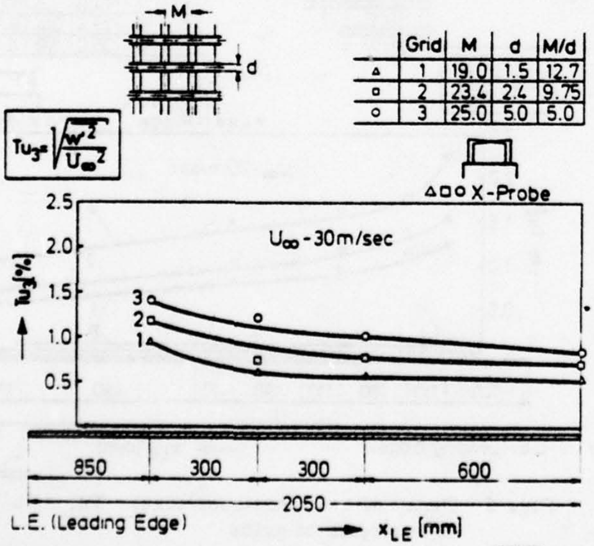

Fig. 5 Decay of the turbulence level $Tu_3 = \sqrt{\overline{w'^2}}/U_\infty$

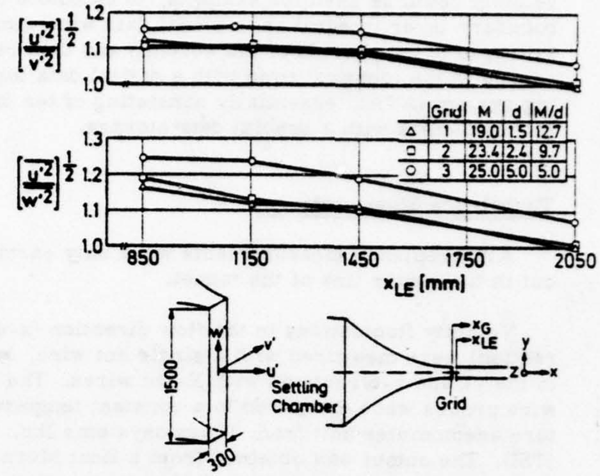

Fig. 6 Decay of the longitudinal to lateral turbulent intensity ratios

However, in our experiment the $\left(\overline{v'^2}\right)^{1/2}$ -component is greater than the $\left(\overline{w'^2}\right)^{1/2}$ -component. This result can be explained by the special geometry of the wind tunnel test section where the dimension in z-direction is about 5 times of that in y-direction. (The measurements of Uberoi were made in an axisymmetric nozzle.) As indicated in Fig. 6 the tunnel turbulence has become isotropic[1] by a distance of $x_{LE} \sim 2\,000$ mm only for the smaller grids 1 and 2. The turbulence generated by the largest investigated grid 3 is even for this long distance not isotropic. This result is not in agreement with experiments carried out by Portfors and Keffer [4] who found already isotropic turbulence at a distance from the leading edge of about 30 mesh lengths [30 M $\hat{=}$ ($x_{LE} \sim 600$ mm)]. Clearly, the experimental verification of a condition of isotropy depends upon the accuracy to which the three components of turbulent intensity can be determined. In

---

[1] Actually, true isotropy requires more than equality of the intensity components. Their energy spectra must be related through the isotropic expressions over the complete wave number range of turbulence. This was not proofed in the experiment.

[4] it is demonstrated that the experimental results depend strongly on the applied measuring technique and data reduction procedure. However, the authors of [4] found that for distances $x_G/M \leq 20$ (x_G distance from the grid to the measuring station) the ratios of the longitudinal to lateral components $\left(\overline{u'^2}\right)^{1/2} / \left(\overline{w'^2}\right)^{1/2}$ is greater than unity, while the RMS values of the velocity fluctuations $\left(\overline{u'^2}\right)^{1/2} / \left(\overline{v'^2}\right)^{1/2}$ are considerably smaller than unity. This was found neither by Uberoi nor in the here described experiments.

If simple theoretical relations for the decay of the turbulence intensity $Tu_1 = \left(\overline{u'^2}\right)^{1/2} / U_\infty$ shall be applied, the distance from the virtual origin ($Tu_1 = \infty$) to the grid has to be known. In order to find this virtual origin it was assumed - following Rotta [5] - that the decay of the RMS-values of the measured longitudinal velocity fluctuations $\left(\overline{u'^2}\right)^{1/2}$ is proportional to $(x_{LE})^{-n}$. (For our test conditions $x_G \sim LE$.) Comte-Bellot and Corrsin [6] found values for n in the range of $n = 1.2$ and and $n = 1.3$. In Fig. 7 the calculated values of $\left(\overline{u'^2}\right)^{-(1/n)}$, $(n = 1.3)$, for the three different investigated grids are plotted versus the distance from the leading edge x_{LE}. The points were approximated by straight lines and the distance x_{vo} from the grid to the virtual origin was found to be $x_{vo} \approx 250$ mm. The slope of the straight lines in Fig. 7 indicated that the measured turbulence data for the different grids could be correlated multiplying the distance $x_{LE} - |x_{vo}| = x_t$ with the grid-parameter M/d. The result is shown in Fig. 8.

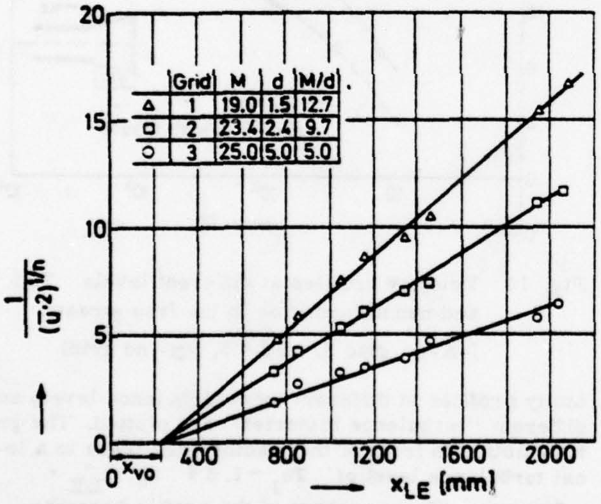

Fig. 7 Evaluation of the virtual origin x_{vo} of turbulence for different grids $(n = 1.3)$

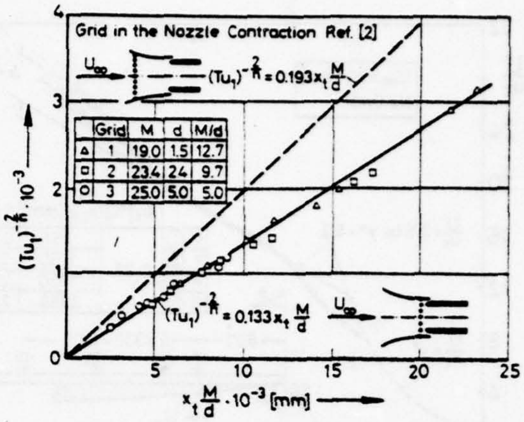

Fig. 8 Decay of Tu_1 downstream of different grids $(n = 1.3)$

The decay of turbulence intensity of all three grids can be correlated and described by the relation

$$(Tu_1)^{-2/n} = 0.133\, x_t \frac{M}{d} \quad . \tag{3}$$

It was found from this turbulence study, that an approximately constant, and low free stream turbulence level in flow direction cannot be established in the tunnel if the turbulence generators are installed at the nozzle exit and in addition close to the leading edge of the tunnel wall. In order to improve this situation, for the final experiments (compare Ref. [2]) the grids were placed inside the nozzle 570 mm in front of the leading edge of the flat tunnel side wall. Due to the remaining contraction (1: 1.4) the turbulent motion then undergoes selective change in its axial and transverse turbulent energy levels due to the directionally selective vortex line distorsion. The result obtained with the grids in this position is shown in Fig. 8 by the dotted line. It was found that the virtual origin was now approximately 500 mm in front of the leading edge. Due to fast decay of the turbulence level behind the grid the maximum value of Tu_1 at the leading edge was about 2 %, whereas with an even smaller grid at the nozzle exit Tu_1 was greater 10 %. Now the effect of the turbulence level and nonuniformity of the free stream on the boundary layer development was studied by means of profile measurements.

Boundary Layer Mean Flow Measurements

Knowing the turbulence intensities of the wind tunnel, boundary layer measurements were made with and without grids. The transition from laminar to turbulent boundary layer flow was fixed installing an artifical roughness at $x_{LE} = 50$ mm. In Fig. 9 and 10 the measured velocity profiles U/u_τ without and with grids are plotted versus the dimensionless wall

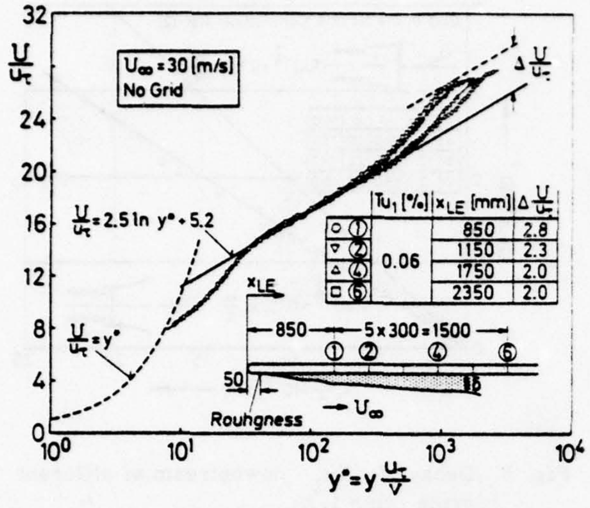

Fig. 9 Mean boundary layer velocity profiles for the free stream turbulence level Tu_1 = 0.06 % and different distances x_{LE}

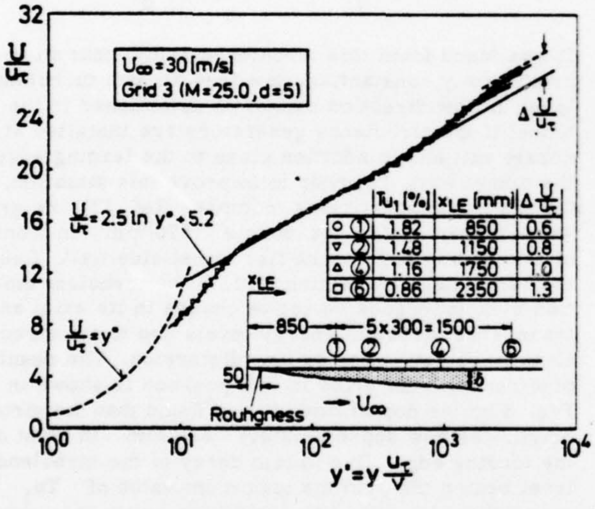

Fig. 10 Mean boundary layer velocity profiles for different free stream turbulence levels and distances x_{LE}

distance y^*. The boundary layer velocity profiles at very low turbulence levels in the free stream show in the outer part a large "overshoot" of the velocity ratio U/u_τ above the logarithmic velocity law. Fig. 9 indicates the magnitude of Coles's [7] wake component π_1, defined as the overshoot of the velocity profile above the logarithmic line

$$\pi_1 = \frac{\kappa}{2} \Delta \frac{U}{u_\tau} \quad (4)$$

(κ = 0.4, the von Kármán constant).

At low turbulence levels π_1 is seen to have approximately the same value that Coles found for the flat plate ($\pi_1 \sim 0.5$). The influence of the free stream turbulence on the wake component is clearly indicated by the velocity profiles in Fig. 10. The velocity overshoot decreases if the turbulence intensity is increased by very small amounts ($\Delta Tu_1 \sim 0.4$ %). It becomes clear from a further analysis of the measured boundary layer profiles that the main change will occur in the wake region of the profile. However, the results were obtained when the free stream turbulence at the leading edge was considerably higher than at the measuring station. Due to a high turbulence level of $Tu_1 > 10$ %, and to the nonuniformity of the flow using the grid 3 in front of the leading edge, a momentum loss in the boundary layer is inserted. This effect is demonstrated in Fig. 11 where the velocity profiles at different local turbulence levels and different "turbulence histories" are plotted. The grid assembling in front of the leading edge leads to a local turbulence level of $Tu_1 \sim 1.8$ % at x_{LE} = 850 mm. The overshoot of the profile becomes much smaller ($\pi_1/\kappa \approx 0.3$) while the boundary layer thickness is about 60 % larger compared to the low turbulence case ($Tu_1 \sim 0.06$ %). This dramatic change of the profile and the strong increase in the momentum thickness

$$\delta_2 = \int_{y=0}^{y=\delta} \frac{U}{U_\infty}\left(1 - \frac{U}{U_\infty}\right) dy \quad (5)$$

results from the momentum defect and the large fluctuating velocity components in the flow where the boundary layer starts. This effect is considerably diminished, when the grid is moved back about 500 mm

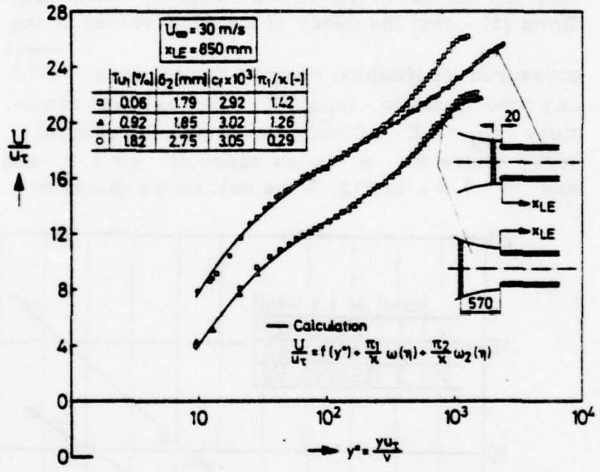

Fig. 11 Velocity profiles at different levels Tu_1 and nonuniformities in the free stream (-△-○- grid 3, M/d = 5, -□- no grid)

into the nozzle. Now the turbulence level at the measuring station is about $Tu_1 \sim 0.9\,\%$ and at the leading edge it is decreased to $Tu_1 \sim 1.5\,\%$ (compare Ref. [2] Fig. 3). If the three profiles in Fig. 11 are compared with each other the almost negligible changes in the local shear stress - compared to changes of the momentum thickness - become evident. An identical, qualitative result was obtained from profile measurements at larger distances obtained without and with grid (No. 3) as shown in Fig. 12. Due to the high turbulence intensity and the wake of one rod the boundary layer starts with a final amount of momentum loss, which appears as an additive constant for all distances.

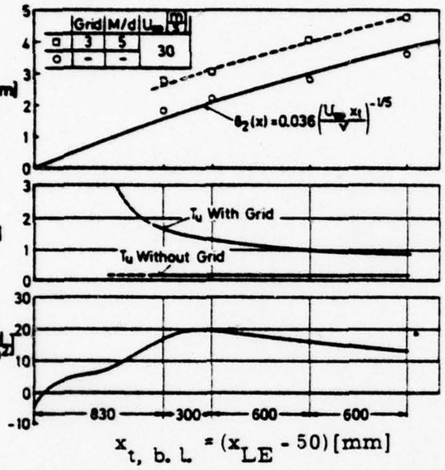

Fig. 12 Momentum thicknesses δ_2 for different turbulence levels and distances $x_{t,\,b.\,L}$ ($x_{t,\,b.\,L}$ = virtual origin of the turbulent boundary layer)

FINAL REMARKS AND CONCLUSIONS

The results of these preliminary tests imply that two effects, namely the

- different, but approximately constant turbulence levels of the free stream,
- and high, with increasing distance x_{LE} decreasing turbulence levels at the start of the boundary layer

influence the boundary layer development, and therefore should be separated. In the meantime measurements are carried out where the free stream turbulence was varied in the range of $Tu_1 \sim 0.06\,\%$ to $1\,\%$ and was approximately constant at all measuring stations. According to these measurements (Ref. [2]) and the here reported results, we learned for practical applications:

1. Turbulence levels in low speed wind tunnels of $Tu_1 \leq 0.2\,\%$ have no measurable influence on the wall shear stress and the shape parameter.
2. No further investigation of the "history effect" of the turbulence on wind tunnel experiments was carried out. However, the investigations so far clearly indicate that any artifical transition will change the boundary layer structure. Thus e. g. the momentum loss due a tripping wire on an airfoil can result in an increase of the displacement thickness which itself causes a change in the pressure distribution and, possibly the separation point of the profile. In any case the inserted momentum loss wall remain in the boundary layer.
3. An increase of the wind tunnel turbulence applying grids, will not simulate flow conditions at higher Reynolds numbers. Besides the change in the transition from laminar to turbulent flow, grid generated turbulence causes a change of the structure of the turbulent boundary layer.

ACKNOWLEDGMENT

The author wants to thank Mr. D. Baumgarten, who was responsible for the accomplishment of the measurements and data reduction.

REFERENCES

1 Aihara, Y., "Analytical Study of a Turbulent Boundary Layer Along a Flat Plate with External Flow Turbulence," IB 75 A 33, 1975, Deutsche Forschungs- und Versuchsanstalt für Luft- und Raumfahrt E. V., Aerodynamische Versuchsanstalt Göttingen.

2 Meier, H. U., "The Response of Turbulent Boundary Layers to Small Turbulence Levels in the External Free Stream," The Tenth Congress of the International Council of the Aeronautical Sciences, Ottawa, Can., October 1976, ICAS Paper No. 76-05, pp. 1-12.

3 Uberoi, M. S., "Small Axisymmetric Contraction of Grid Turbulence," Journal of Fluid Mechanics, Vol. 24, part 3, 1966, pp. 539-543.

4 Portfors, E. A., and Keffer, J. F., "Isotropy in Initial Period Grid Turbulence," Physics of Fluids, Vol. 12, 1969, pp. 1519-1521.

5 Rotta, J. C., "Turbulente Strömungen," B.G. Teubner Verlag, Stuttgart, 1971.

6 Comte-Bellot, G., "The Use of a Contraction to Improve the Isotropy of Grid-Generated Turbulence," Journal of Fluid Mechanics, Vol. 25, 1966, pp. 657-682.

7 Coles, D. E., "The Turbulent Boundary Layer in a Compressible Fluid," Rand Report R 403-PR, 1962, ARC 24-497, 1963.

ABOUT AN INTEGRAL METHOD FOR TURBULENT BOUNDARY LAYERS USING THE TURBULENT ENERGY EQUATION

M. JISCHA AND K. HOMANN
FACHBEREICH MASCHINENTECHNIK DER
UNIVERSITÄT ESSEN, GESAMTHOCHSCHULE, BRD

ABSTRACT

The present paper deals with the prediction of incompressible two-dimensional turbulent boundary layers. An integral method is developed based on the momentum and the mean kinetic energy equation. A third integral equation is added to calculate the dissipation integral. This equation is derived from the turbulent energy equation and takes into account the upstream history of the flow.

The Stanford data and an additional measured boundary layer with pressure gradients alternating in sign were used for testing. The method shows good agreement with the experimental values of the mean flow parameters even for strong departure from equilibrium.

NOMENCLATURE

a_1 : $-\overline{u'v'}/\overline{q^2}$
c : constant of Coles' profile
c_D : dissipation integral
c_E : entrainment function
c_f : skin friction coefficient
c_τ : shear stress integral
H, H_{12}, H_{32} : shape parameters of the mean velocity profile
n : parameter of shear stress profile
P : Coles' wake parameter
q^2 : turbulent kinetic energy
Re_2 : $u_\delta \delta_2/\nu$, Reynolds number
Re_τ : $u_\tau \delta/\nu$, Reynolds number
u_τ : skin friction velocity
u, v : velocity components in the x and y directions
w : Coles' wake function
x : longitudinal coordinate
y : transverse coordinate
β : dimensionsless pressure parameter
Γ : parameter of shear stress profile
δ : boundary layer thickness
δ_1 : displacement thickness
δ_2 : momentum loss thickness
δ_3 : energy loss thickness
ε : turbulent dissipation
η : y/δ, nondimensional transverse coordinate
κ : v.Kármán's constant
ν : kinematic viscosity
ρ : density
τ : shear stress

Subscripts

e : equilibrium value
E : conditions at the point of maximum shear
w : wall conditions.
δ : conditions at the outer edge of the boundary layer

Superscripts

A prime (') denotes a fluctuating quantity
A bar ($\overline{\ }$) denotes time mean

INTRODUCTION

The computation of turbulent phenomena is much more complicate than in the laminar case. The difficulties arise from the nonlinear convection terms of the basic Navier-Stokes equations. If these equations are written down for the mean quantities the number of unknowns exceeds the number of equations, so that the solution requires a certain amount of empiricism to combine the unknown correlations of the fluctuating velocity components with variables of the mean flow. Much success in this field has been achieved by establishing additional so called transport equations for the correlation terms. In this way the effects of the turbulence structure can be taken into account, but the closure problem still exists. Bradshaw et al. /1/ for instance propose a finite difference method with one transport equation for the rate of change of the turbulent kinetic energy $\overline{q^2}$, but models with more of such equations are widely in use /2,3,4,5/.

The progress in direct solution of the governing equations has turned away the attention from the integral prediction methods a little bit, although the various contributions to the 1968 AFSOR-IFP Stanford Conference /6/ had not shown the integral methods

PRECEDING PAGE BLANK-NOT FILMED

being remarkably worse than the direct methods or vice versa. Therefore and because of the essential simplifications in the numerical treatment the authors have tried to utilize transport equations for integral methods.

All of these methods use the momentum integral equation:

$$\frac{d\delta_2}{dx} + \frac{\delta_2}{u_\delta}\frac{du_\delta}{dx}(2+H_{12}) = \frac{c_f}{2} \tag{1}$$

This equation does not contain any direct information about the quantities of the turbulence field, therefore a second one is needed. The individual methods differ in this second equation which determines the unknown shape parameter of the velocity profile. According to this three different types of integral methods are in use:

A) Dissipation integral methods

B) Entrainment methods

C) Moment of momentum integral methods

The shape parameter equations introduce new functions which contain the required quantities of the turbulence field. In particular these functions read as follows:

A) Dissipation integral

$$c_D = \frac{2}{\rho\, u_\delta^3}\int_0^\delta \tau \frac{\partial \overline{u}}{\partial y}\, dy$$

B) Entrainment function

$$c_E = \frac{d\delta}{dx} - \frac{v_\delta}{u_\delta}$$

C) Shear stress integral

$$c_\tau = \frac{2}{\rho\, u_\delta^2}\int_0^\delta \tau\, dy$$

Furtheron all methods need three auxiliary relationships:

1. for the skin friction coefficient c_f
2. for a second shape parameter
3. for the functions c_D, c_E or c_τ .

It can easily be shown that the first and second follow directly from the turbulent velocity profile given by Coles /7/:

$$\frac{\overline{u}}{u_\tau} = \frac{1}{\kappa}\ln\frac{u_\tau y}{\nu} + c + \frac{P}{\kappa}(\eta) \tag{2}$$

Nevertheless nearly always empirical relationships were used, which are however in good agreement with those obtained by eq. (2). The essential difficulties arise from the third relation, because an information about the turbulent shear or the entrainment is required. The current status of science is shown briefly in the following table.

Method	1. Without history effects	2. Including history effects		
	Empirical relationships	2.1 Empirical relationships	2.2 Empirical differential equations	2.3 Transport equation
A	$c_D(H_{32}, Re_2)$ by Rotta/Truckenbrodt or Clauser/Walz, see Walz /8/	$c_D(H_{32}, Re_2, \beta)$ by Felsch /10/	Relaxation equation by Goldberg /12/	this work (turbulence energy)
B	$c_E(H)$ by Head /9/ $H = \frac{\delta-\delta_1}{\delta_2}$	$c_E(H, F)$ by Head and Patel /11/, F = correction function		by Hirst and Reynolds, see /6/ (turbulence energy) and by Green et al. /13/ (turbulence energy)
C			Relaxation equation by Nash and Hicks, see /6/	by McDonald and Camarata, see /6/ (turbulence energy)

The step from point 1 to 2.1 has been done first by Felsch /10/ for a method of type A. This method gave good results at the Stanford Conference. For a method of type B this step has been done by Head and Patel /11/ just after the conference.

Furtheron an empirical differential equation of a relaxation equation type has been used for a method of type A by Goldberg /12/ and a quite similar one for a method C by Nash and Hicks. Such empirical differential equations can be replaced by transport equations. This has been tried by Hirst and Reynolds for a method of type B and by McDonald and Camarata for a method of type C. Both methods have not been very successfull on the Stanford Conference, but recently Green et al. /13/ (method B) started a new attempt with better success by applying the turbulent energy equation at the point of maximum turbulent shear stress. A good deal of empiricism is envolved in these methods, because no analytical representation of the shear stress profile is used. Furthermore empirical relations must be established to connect shape parameter- and transport equation.

In this work the step 2.3 shall be carried out for method A.

DISSIPATION INTEGRAL METHOD

The shape parameter equation for dissipation integral methods reads in full:

$$\frac{dH_{32}}{dx} + H_{32}(1-H_{12})\,\frac{1}{u_\delta}\frac{du_\delta}{dx} + \frac{1}{\delta_2}\left(\frac{c_f}{2}H_{32} - c_D\right) = 0 \qquad (3)$$

The dissipation integral shall be evaluated solution of the turbulent energy equation which reads in integral form:

$$\frac{1}{2}\frac{d}{dx}\int_0^\delta \bar{u}\,\overline{q^2}\,dy + \int_0^\delta \overline{u'v'}\,\frac{\partial\bar{u}}{\partial y}\,dy + \int_0^\delta \varepsilon\,dy = 0 \qquad (4)$$

ε is the turbulent dissipation, the diffusion term disappears by integration. If the molecular shear stress is neglected, the dissipation integral and the production term of equation (4) can be related to each other:

$$c_D = \frac{2}{\rho\,u_\delta^3}\int_0^\delta \tau\,\frac{\partial\bar{u}}{\partial y}\,dy \approx -\frac{2}{u_\delta^3}\int_0^\delta \overline{u'v'}\,\frac{\partial\bar{u}}{\partial y}\,dy \qquad (5)$$

The integral statement dissipation = production is valid only for zero convection, the convection term indeed is the important history term.

In order to make use of the transport equation the unknown correlations must be modeled. We have chosen the modeling of Bradshaw et al. /1/, because this method belonged to the good differential methods at the Stanford Conference. Following Bradshaw we introduce

$$-\overline{u'v'} = a_1\,\overline{q^2}\ ; \quad \varepsilon = \frac{1}{L}\left(\frac{\tau}{\rho}\right)^{3/2}$$

as modeling assumptions, where τ is the turbulent part of the shear stress. With these assumptions eq. (4) becomes:

$$\frac{1}{2a_1}\frac{d}{dx}\int_0^\delta \bar{u}\,\frac{\tau}{\rho}\,dy - \int_0^\delta \frac{\tau}{\rho}\,\frac{\partial\bar{u}}{\partial y}\,dy + \int_0^\delta \frac{(\tau/\rho)^{3/2}}{L}\,dy = 0 \qquad (6)$$

Supplementary we use

a) an empirical relationship for the dissipation length given by Bradshaw et al. /1/,

b) the universal velocity profile (2),

c) a polynominal representation of the turbulent shear stress profile.

In a first attempt /14/ a one-parameter shear stress profile was used in the following form:

$$\frac{\tau}{\rho u_\delta^2} = \sum_{i=0}^{5} a_i\,\eta^i \qquad (7)$$

Together with the boundary conditions at $\eta = 0$

$$\tau = \frac{\partial^2\tau}{\partial\eta^2} = 0 \qquad (8)$$

and at $\eta = 1$

$$\tau = \frac{\partial\tau}{\partial\eta} = \frac{\partial^2\tau}{\partial\eta^2} = 0 \qquad (9)$$

one can obtain five of the six coefficients of eq. (7), so that

$$\frac{\tau}{\rho u_\delta^2} = \Gamma\,\eta\,(1-\eta)^3\,(3\eta + 1) \qquad (10)$$

In this equation Γ is a free parameter which can be equated to the unknown gradient of the shear stress profile at the wall and is determined by eq. (6). The dissipation integral c_D can be derived as

$$c_D = c_D\,(H_{32},\ Re_2,\ \Gamma) \qquad (11)$$

A comparison with Rotta's empirical function (see table) shows, that Γ accounts for the upstream history effects of the flow.

One can expect, that eq. (10) only holds for boundary layers with adverse pressure gradients, because the position of maximum shear is fixed to the point $\eta_E = 1/3$. Flat plate and accelerated boundary layers have their maximum in shear stress very close to the wall, and indeed the prediction method based on eq. (10) gave small but systematic departures from measurements in this cases. Therefore for the present work we introduced a second parameter n to account for the influence of the free stream pressure gradient at the position of maximum shear stress. A parameter was chosen, which did not affect the absolute value of τ_E to keep small the amount of empiricism which is connected with it. This is expressed by the prescription:

$$\left.\frac{\partial[\tau/(\Gamma\rho u_\delta^2)]}{\partial x}\right|_{\eta=\eta_E(x)} = 0 \qquad (12)$$

A two parameter model with the above quality can be obtained from eq. (10) by the simple transformation $\eta \rightarrow \eta^n$ so that:

$$\frac{\tau}{\rho u_\delta^2} = \Gamma\, \eta^n\, (1-\eta^n)^3\, (3\eta^n + 1) \qquad (13)$$

The exponent n can be related to η_E via:

$$\eta_E = (1/3)^{1/n} \qquad (14)$$

Fig. 1 shows two shear stress profiles for different values of n.

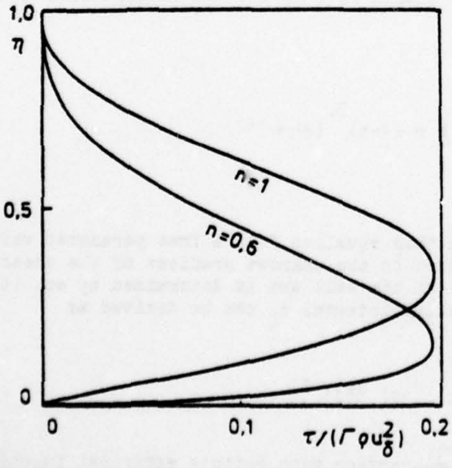

Fig. 1 Turbulent shear stress profile by eq. (13)

The findings of Mellor and Gibson /15/ allow the conclusion, that for equilibrium boundary layers n is a universal function of the pressure parameter β alone. This can also qualitatively be derived by applying the boundary layer equation at the wall, which gives:

$$\frac{\partial\tau}{\partial y} = \frac{dp_\delta}{dx} \quad \text{for } y = 0 \qquad (15)$$

Unfortunately the quantitative influence of the boundary conditions at the wall on the shape of the profile is not strong enough to derive a direct relationship between η_E and dp_δ/dx. (It is for the same reason, that we are allowed to neglect some of the original boundary conditions (8,9) in eq. (13)). Therefore in this work an empirical relationship between n and β shown in Fig. 2 is used even for non-equilibrium boundary layers.

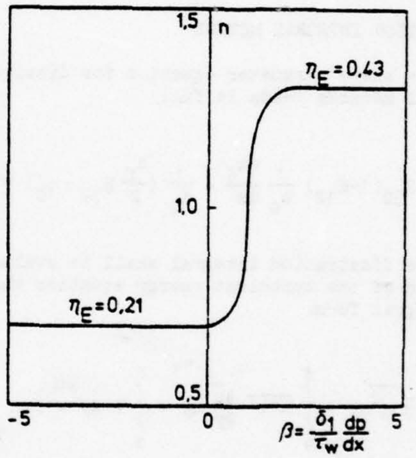

Fig. 2 Empirical relationship n(β)

Eq. (11) has to be completed:

$$c_D = c_D(H_{32}, Re_2, \Gamma, n) \qquad (16)$$

The burden of describing history effects is still carried by Γ alone, although β contains the free stream pressure gradient and is the only "upstream history parameter" of Felsch's method (see table) for instance. Nevertheless an additional differential equation like Goldberg's or a weighted form of eq. (4) could be used. Fig. 6 of the next chapture shows the effect of neglecting history effects in the n(β) - relationship. Present work deals with its improvement.

COMPARISON OF PREDICTED AND EXPERIMENTAL RESULTS

All Stanford test cases /16/ were used for calculations with the described method and good agreement between calculation and experiment was found except in cases with departures from two-dimensional conditions. No corrections were included in the computer program to deal with such effects.

In addition to the Stanford data the method was applied to a boundary layer with pressure gradients alternating in sign measured by Tsuji and Morikawa /17/.

Some attention must be paid to the starting values. We chose measured values of the momentum loss thickness δ_2 and the shape parameter H_{32}. The starting value of Γ was calculated by graphical differentiation of the measured $H_{32}(x)$ distribution, to eliminate the influence of wrong starting values in the present work. For practical calculations one of the empirical formulae of the table could be used. Free stream velocity and velocity gradient were seperately approximated by spline interpolation. If necessary the du_δ/dx development was cut into pieces to describe unsteady changes properly. The three ordinary differential equations were solved by a simple Runge-Kutta routine.

For this paper we chose five test cases of the Stanford catalogue and the boundary layer of Tsuji and Morikawa mentioned above. Figs. 3 to 8 show results for H_{12}-, c_f - and Re_2 - distributions.

The calculation of all (nearly 30) test cases took about one minute on a UNIVAC 1108 computer including the execution of a plotting routine. The comparison of the results with Bradshaw's et al. original method shows that the present method gives comparably good results. In spite of this some additional work especially on the somewhat artificial $n(\beta)$ - relationship seems to be necessary.

The predicted wrong curvature of the H_{12} and c_f development downstream the marked position in Fig.6 would change its sign, if a value of n according to the low upstream values of β was chosen.

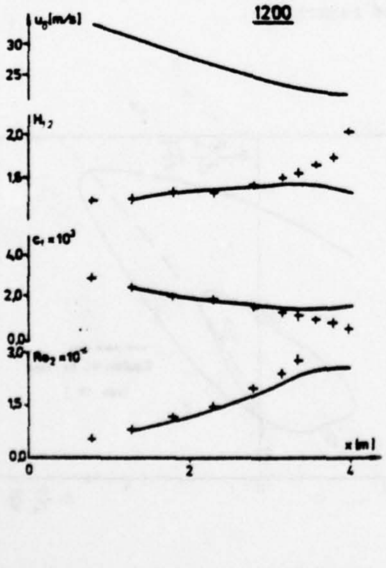

Fig. 3 Ludwieg and Tillmann, strong adverse pressure gradient

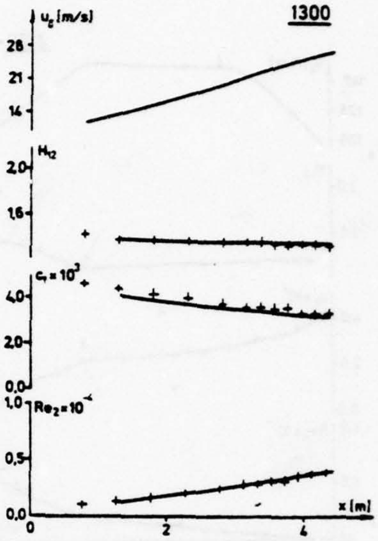

Fig. 4 Ludwieg and Tillmann, accelerating flow

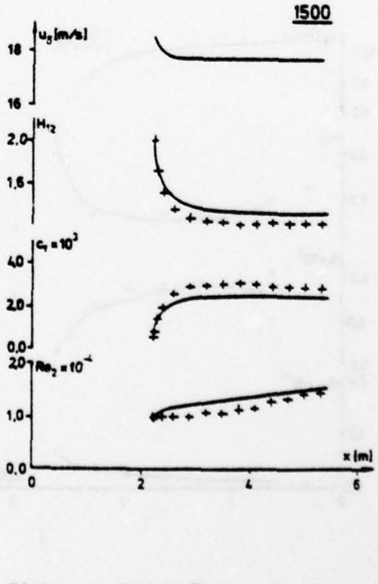

Fig. 5 Tillmann, ledge flow

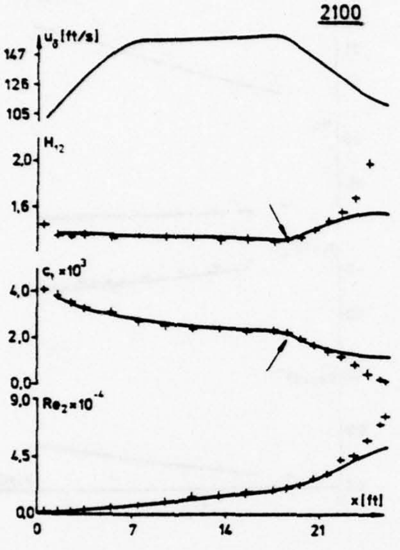

Fig. 6 Schubauer and Klebanoff, boundary layer on airfoil-like body

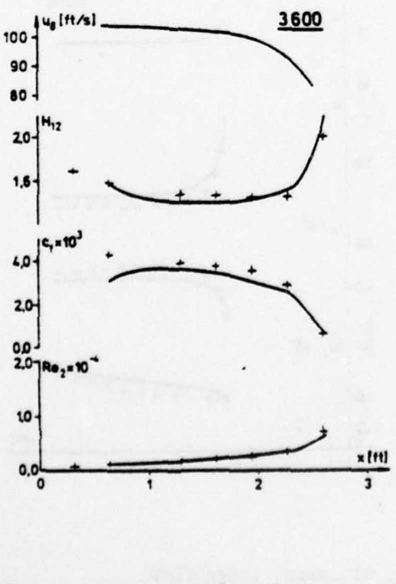

Fig. 7 Moses, case 1, boundary layer on cylinder in axially symmetric flow

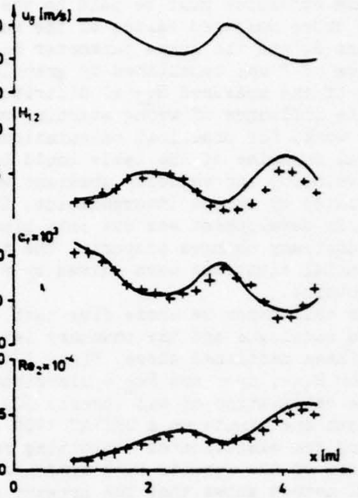

Fig. 8 Tsuji and Morikawa, pressure gradient alternating in sign

Finally Fig. 9 shows a computed G;β - plot for the boundary layer of Tsuji and Morikawa compared with Nash's equilibrium relationship. The strong departure from equilibrium conditions is pointed out clearly in this figure, so that the good results shown in Fig. 8 seem to be remarkable.

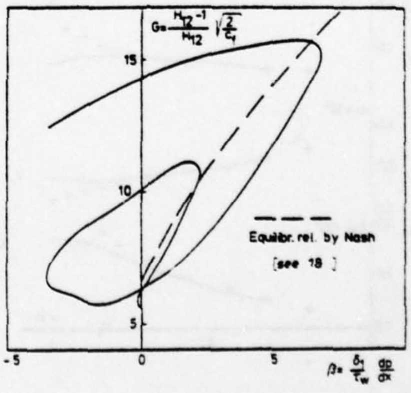

Fig. 9 Tsuji and Morikawa, $G = f(\beta)$, computed results

CONCLUDING REMARKS

At a state, where the present method is developed so far, that good predictions of experimental results can be expected in a broad spectrum of flow cases, we should try to demarcate it against the related methods. Compared to Felsch's algebraic and Goldberg's differential c_D- formula a more realistic description of turbulent shear stress transport was achieved by using a carefully modeled version of an exact transport equation with an amount of empiricism reduced to a minimum. In this sense step-by-step reduction of empiricism means to reobtain the universality of the original equations.

This general aim of the present work leads us to some critical remarks on Green's et al. method. Their ordinary differential equation for maximum shear stress (we should not call it an integral version of Bradshaw's method as Reynolds and Cebeci /19/ do) is related to the present one, because it was derived from the same transport equation. It can be interpreted as a weighted form of eq. (6) with $(\tau/\tau_E)^\infty$ as a weighting function. This choice of a weighting function reduces the initially available information to an unnecessary low degree, because only the development of maximum shear stress is described. In our opinion Green's equation seems to be a too small step in the right direction. The loss in information must be compensated by a lot of empirical relationships. Additionally the entrainment methods have the disadvantage that the connection between shape parameter and transport equation can be managed only empirically.

Finally from the present paper we can draw the conclusion, that consequent development of integral relationships can be a practical alternative to the partial differential methods, so that the extension to more complicated flows, like three dimensional flows or flows with heat and mass transfer seems to be a worthy task.

REFERENCES

1 Bradshaw, P., Ferris, D.H. and Atwell, N.P., "Calculation of Boundary Layer Development using the Turbulent Energy Equation," J. Fluid Mech., Vol. 28, Part 3, 1967, pp. 593-616.

2 Mellor, G.L. and Herring, H.J., "A Survey of the Mean Turbulent Field Closure Models," AIAA Journ., Vol 11, No. 5, 1973, pp. 590-599.

3 Launder, B.E. and Spalding, D.B., "Lectures on Mathematical Models of Turbulence," Academic Press, 1972.

4 Reynolds, W.C., "Recent Advances in the Computation of Turbulent Flows," Advances in Chemical Engineering, Vol. 9, Academic Press, New York, 1974.

5 Wolfshtein, M., Naot, D. and Lin, A., "Models of Turbulence," Me-746(N), June 1974, Ben Gurion Univ. of the Negev, Dep. of Mech. Eng., Beer-Sheva, Israel.

6 Kline, S.J., Sovran, G., Morkovin, M.V. and Cockrell, D.J., "Proc. Comp. of Turbulent Boundary Layers - 1968 AFOSR Stanford Conference, Vol. I, August 1968, Stanford Univ., California.

7 Coles, D., "The Law of the Wake in the Turbulent Boundary Layer," J. Fluid Mech., Vol. 1, Part 2, 1956, pp. 191-226.

8 Walz, A., "Strömungs- und Temperaturgrenzschichten", Verlag G. Braun, Karlsruhe, 1966.

9 Head, M.R., "Entrainment in the Turbulent Boundary Layer," R & M. 3152, 1958, Aeronautical Research Council.

10 Felsch, K.O., "Beitrag zur Berechnung turbulenter Grenzschichten in zweidimensionaler inkompressibler Strömung," DLR-FB 66-46, 1966.

11 Head, M.R. and Patel, V.C., "Improved Entrainment Method for Calculating Turbulent Boundary Layer Development," R & M. 3643, 1968, Aeronautical Research Council.

12 Goldberg, D., "Upstream History and Apparent Stress in Turbulent Boundary Layers," Rep. No. 85, 1966, Gas Turbine Lab., Inst. of Techn., Massachusetts.

13 Green, J.E., Weeks, D.J. and Brooman, J.W.F., "Prediction of Turbulent Boundary Layers and Wakes in Compressible Flow by a Lag-Entrainment Method", RAE TR T2231, 1973.

14 Jischa, M. and Homann, K., "Ein Integralverfahren unter Verwendung einer Transportgleichung", Will soon appear in ZAMM.

15 Mellor, G.L. and Gibson, D.M., "Equilibrium Turbulent Boundary Layers," J. Fluid Mech., Vol. 24, Part 2, 1966, pp. 225-253.

16 Coles, D.E. and Hirst, E.A., "Proc. Comp. of Turbulent Boundary Layers - 1968 AFSOR Stanford Conference Vol. II, Compiled Data", August 1968, Stanford Univ., California.

17 Tsuji, Y. and Morikawa, Y., "Turbulent Boundary Layer with Pressure Gradient Alternating in Sign," Aeronautical Quarterly, Febr. 1976.

18 Nash, J.F., "Turbulent Boundary Layer behaviour and the Auxiliary Equation NPL Aero Report 1137, 1965.

19 Reynolds, W.C. and Cebeci, T., "Calculation of Turbulent Flows," Topics in Applied Physics, Vol. 12, Editor: Bradshaw, P., Springer, New York, 1976, pp. 193-229.

20 Moses, H.L., "The Behaviour of Turbulent Boundary Layers in Adverse Pressure Gradients", Rep. No. 73, 1964, Gas Turbine Lab., Inst. of Techn., Massachusetts.

21 Nicoll, W.B. and Escudier, M.P., "Empirical Relationships between the Shape Factors H_{32} and H_{12} for Uniform - Density Turbulent Boundary Layers and Wall Jets," AIAA Journ., Vol. 4, 1966, pp. 940-942.

22 Ludwieg, H. and Tillmann, W., "Untersuchungen über die Wandschubspannung in turbulenten Reibungsschichten," Ing. Arch., Vol. 17, 1949, pp. 288-299.

APPENDIX

The equations of the present calculation method are:

Momentum integral equation:

$$\frac{d\delta_2}{dx} + \frac{\delta_2}{u_\delta}\frac{du_\delta}{dx}\,(2 + H_{12}) = \frac{c_f}{2} \qquad (17)$$

$$\text{with}\quad \delta_1 = \int_0^\delta \left(1 - \frac{\bar u}{u_\delta}\right)dy \;;\; \delta_2 = \int_0^\delta \frac{\bar u}{u_\delta}\left(1 - \frac{\bar u}{u_\delta}\right)dy$$

$$c_f = \frac{2\tau_w}{\rho u_\delta^2} \quad ; \; H_{12} = \delta_1/\delta_2$$

Shape parameter equation:

$$\frac{dH_{32}}{dx} + \frac{H_{32}}{u_\delta}\frac{du_\delta}{dx}\,(1 - H_{12}) = \frac{1}{\delta_2}\left(c_D - \frac{c_f}{2}H_{32}\right) \qquad (18)$$

$$\text{with}\quad \delta_3 = \int_0^\delta \frac{\bar u}{u_\delta}\left[1 - \left(\frac{\bar u}{u_\delta}\right)^2\right]dy$$

$$H_{32} = \delta_3/\delta_2 \quad ; \quad c_D = \frac{2}{\rho u_\delta^3}\int_0^\delta \tau\,\frac{\partial \bar u}{\partial y}\,dy$$

Integral relationship for the shear stress profile derived from eq. (6):

$$\frac{1}{2a_1}\frac{d}{dx}(\delta f_1 \Gamma) = \left(f_2 - \frac{3}{u_\delta}\frac{du_\delta}{dx}\,\delta f_1\right)\Gamma - f_3\,\Gamma^{3/2} \qquad (19)$$

The boundary layer thickness δ is determined from eq. (2):

$$\delta = \frac{\delta_1 u_\delta \kappa}{u_\tau(1+P)}$$

with $u_\tau = u_\delta\sqrt{\frac{c_f}{2}}$ and (see /7/):

$$2P - \ln(1+P) = \kappa\frac{u_\delta}{u_\tau} - \ln\frac{\delta_1 u_\delta}{\nu} - \kappa c - \ln\kappa$$

f_1 and f_2 are analytical functions of the shear stress and velocity profile:

$$f_1 = \sqrt{\frac{c_f}{2}}\,\frac{1}{\kappa}\left[-\frac{1}{(n+1)^2} + \frac{6}{(3n+1)^2} - \frac{8}{(4n+1)^2} + \frac{3}{(5n+1)^2}\right.$$

$$+ (\ln Re_\tau + \kappa c)\left(\frac{1}{n+1} - \frac{6}{3n+1} + \frac{8}{4n+1} - \frac{3}{5n+1}\right)$$

$$\left. + 2P\left(\frac{3}{n+3} - \frac{10}{n+1} + \frac{24}{4n+3} - \frac{9}{5n+3} - \frac{2}{n+4} + \frac{12}{3n+4} + \frac{6}{5n+4}\right)\right] ;$$

$$f_2 = \sqrt{\frac{c_f}{2}}\,\frac{1}{\kappa}\left[\frac{2}{5n} + 12P\left(\frac{1}{n+2} - \frac{6}{3n+2} + \frac{4}{2n+1} - \frac{3}{5n+2}\right.\right.$$

$$\left.\left. - \frac{1}{n+3} + \frac{2}{n+1} - \frac{8}{4n+3} + \frac{3}{5n+3}\right)\right]$$

For the evaluation of the integrals the wake function

$w(n) = 2n^2\,(3-2n)$ after Moses /20/ was used.

The dissipation term is represented by f_3. The dissipation length distribution of Bradshaw et al. /1/ was used with an additional correction factor. In a range $0{,}6 \leq n \leq 1{,}4$ the function f_3 can be approximated by

$$f_3 = -0{,}14\,n + 0{,}534$$

The correction factor already included in f_3 was adjusted to 0,8 and is proably due to different definitions of the boundary layer thickness.

The function $n = f(\beta)$ Fig. (2) with

$$\beta = -\frac{2\delta_1}{c_f}\frac{1}{u_\delta}\frac{du_\delta}{dx} \quad \text{is given by}$$

$$n = \begin{cases} 0{,}7 & \beta < 0 \\ 0{,}3\,[1 - \cos(\pi\beta/2)] + 0{,}7 \quad \text{for} & 0 \leq \beta \leq 2 \\ 1{,}3 & \beta > 2 \end{cases}$$

The connection between eqs. (18) and (19) is given by eq. (16) which reads:

$$c_D = 2\,\Gamma f_2(c_f, P, n)$$

c_D is only a strong function of n (via f_2) for small and negative values of β so that the lower boundary of n (= 0,7) could be adjusted carefully by numerical trial and error. The transition values of n and the upper limit should be taken as raw estimates, because experiments in this area with measurements of the shear stress profile and in equilibrium conditions are missing.

The auxiliary equations are:

$$H_{12} = \frac{-0{,}04855 + (0{,}775\,H_{32} - 1{,}1067)^{1/2}}{H_{32} - 1{,}431}$$

by Nicoll and Escudier /21/ and

$$c_f = 0{,}246\,Re_2^{-0{,}268}\;10^{-0{,}678\,H_{12}}$$

by Ludwieg and Tillmann /22/.

The following constants were used:

$a_1 = 0{,}15 \;;\; \kappa = 0{,}41 \;;\; c = 5{,}1.$

AD-A055 654 PENNSYLVANIA STATE UNIV UNIVERSITY PARK DEPT OF MECH--ETC F/G 20/4
SYMPOSIUM ON TURBULENT SHEAR FLOWS HELD AT THE PENNSYLVANIA STA--ETC(U)
APR 77 N00014-77-C-0176

UNCLASSIFIED NL

6 OF 9
ADA
055654

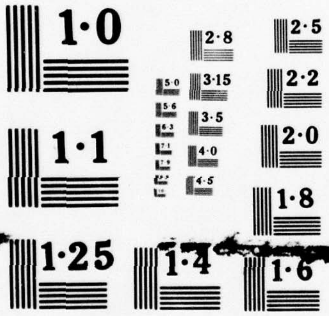

NATIONAL BUREAU OF STANDARDS
MICROCOPY RESOLUTION TEST CHART

SESSION 11

LARGE SCALE STRUCTURE

Chairman: L. Bradbury
Department of Mechanical Engineering
University of Surrey
Guildford, Surrey
England

ON THE LARGE-SCALE STRUCTURE IN TURBULENT FREE SHEAR FLOWS

J. T. C. LIU AND A. ALPER
DIVISION OF ENGINEERING
BROWN UNIVERSITY
PROVIDENCE, RHODE ISLAND 02912

ABSTRACT

The existence of organized structures in turbulent shear flow has been the subject of recent observational discoveries in both the laboratory and in the atmosphere and ocean. The recent work on modeling such structures in a temporally developing, horizontally homogeneous turbulent free shear layer (J. T. C. Liu and L. Merkine 1976 Proc. Roy. Soc. London, Ser. A, Vol. 352, pp. 213-247) has been extended to the spatially developing mixing layer, there being no available rational transformation between the two nonlinear problems. The basis for the consideration is the kinetic energy development of the mean flow, large-scale structure and fine-grained turbulence with a conditional average, supplementing the usual time average, to separate *the nonrandom from the random* part of the fluctuations. The integrated form of the energy equations and the accompanying shape assumptions, is used to derive "amplitude" equations for the mean flow, characterized by the shear layer thickness, the nonrandom and random components of flow which are characterized by their respective energy densities. In general, the large-scale structure augments the spreading of the shear layer and enhances the fine-grained turbulence by taking energy from the mean flow and transferring it to the turbulence as it amplifies and subsequently decays. The maximal amplitude of the large-scale structure is attained by the initially most amplified mode, however, the relative enhancement of the fine-grained turbulence is achieved by both the magnitude of the large-scale structure and its streamwise lifetime. Thus a greater enhancement of the turbulence is achievable by the lower frequency modes which have longer streamwise lifetimes. The large-scale structure can also be controlled by increasing the initial level of turbulence, which would render its decay more rapidly.

NOMENCLATURE

$U_i, \tilde{u}_i, u'_i$	dimensionless velocities of the mean, large-scale structure, fine-grained turbulence
$\mathcal{U}_i \equiv U_i + \tilde{u}_i$	
$P, \tilde{p}, p'$	dimensionless pressure of the mean, large-scale structure, fine-grained turbulence
$\mathcal{P} \equiv P + \tilde{p}$	
x_i	dimensionless coordinates (x, horizontal; y, vertical)
t	dimensionless time
$\overline{(\ )}$	average which produces a mean quantity, (the time average in the spatial problem, horizontal average in the temporal problem)
$\langle (\ ) \rangle$	conditional average
$\overline{u'_i u'_j}$	mean turbulent stresses
$\langle u'_i u'_j \rangle$	conditionally averaged turbulent stresses
$\tilde{r}_{ij} \equiv \langle u'_i u'_j \rangle - \overline{u'_i u'_j}$	modulated turbulent stresses
Re	Reynolds number

Other quantities are defined as they appear.

INTRODUCTION

Recent reviews of laboratory observations have pointed towards the omnipresence of large-scale organized structures in turbulent shear flows, with each type of shear flow having its own peculiar organized structure (1), (2), (3), (4), (5). Several international conferences have also been held in which such organized structures in turbulent flows were discussed (6), (7). It is apparent that turbulence in shear flows are not as random as originally thought to be and, in his Dryden Research Lecture, Roshko (4) reminds us that Dryden (8) had pointed out that it is necessary to separate the random from the nonrandom processes in turbulent flow. This view was also emphasized by Liepmann (9). Observations strongly suggest that the large-scale organized structures are important to the mixing and development of the shear flow and it is beginning to be recognized that the study of their dynamics is fundamental to any study of turbulent shear flows. Such studies being technologically important to combustion and reactive flows (7), (10) and jet noise (11), (12) to mention a few. Such organized structures are also observed to occur in regions of strong local shear provided by frontal systems and internal waves of a much larger scale in the atmosphere and in the ocean and are now thought to play an important role in the spectral cascading process and in mixing (13), (14). The observational unmasking of the large-scale organized structures in turbulent flows has, at least in the authors' view, given turbulence research new and exciting impetus.

We shall focus our attention to *free* turbulent flows in this paper in which the mean flow velocity profiles are inflexional. The presence of the large-scale structure is more or less attributable to the dynamical instability inherent in such flows (9), (12), (15), (16). Although the large-scale organized structure may be deterministic, it is conceivable that it is subjected to random forcing. Take the mixing region, for instance; the large-scale structure as a consequence of upstream forcing at a given frequency will propagate downstream at a phase velocity characteristic of that frequency. Suppose now a slower large-scale structure is first set up and subsequently a faster one is generated, a "*collision*" *of* the latter with the first will take place downstream as the faster one catches up with the slower one. It is not entirely inconceivable that this provides one of the explanations of the "pairing" or "vortex coalescence" process that has been observed (17). This essentially emphasizes the importance of studying the large-scale organized structure under well-controlled rather than under natural conditions (9), much in the same spirit of Schubauer and Skramstad (18), for purposes of physically isolating and understanding the mechanisms involved.

While it is generally important to understand the coalescence of large-scale organized structures in a turbulent shear flow, it seems logical that theoretical understanding of the interactions between a single, monochomatic large-scale structure with the fine-grained turbulence be obtained without complicating the picture with the more complicated dynamical effects. On the other hand, "vortex coalescence" is known to occur even without the presence of fine-grained turbulence and contributions towards its theoretical explanation can be made from purely dynamical considerations (19). We shall consider here the first major problem discussed above, that of the interaction between the large-scale structure and the disparately fine-grained turbulence in a free turbulent shear flow, in particular, the mixing region.

Our *aim* is towards physical understanding of the interactions between the disparate scales of motion which lead to the growth and development of the shear layer, rather than emphasizing numerical prediction or accuracy. This necessitates approximate considerations in order to achieve our aim, one which may be helpful towards the eventual incorporation of the large-scale structure dynamics in predictive schemes or towards well-controlled experimental unmasking of those mechanisms which contribute to the understanding of the development of organized structures in turbulent shear flows.

To proceed, we essentially follow earlier suggestions (8), (9), (20) and theoretically sort out the monochromatic large-scale organized structure from the random fine-grained turbulence by a conditional averaging procedure which has been described and realized in the laboratory elsewhere (21), (22), (23). This forms the starting point for the subsequent approximate considerations for the study of simultaneous interactions between the mean flow, the large-scale structure and the fine-grained turbulence. We have reported on our previous study of an idealized mixing region (24), in which the mean flow consisted of horizontally homogeneous, oppositely directed streams. The shear layer and interactions develop in *time* rather than in the streamwise distance. Since all mean quantities there are horizontally homogeneous, there is no streamwise "diffusion" in the mean and this comprises one of the natural simplifications of the problem (there being no backwards diffusion in time because of causality, of course). Another simplification in Ref. (24) was that the only non-equilibrium behavior of the fine-grained turbulence is due to interactions with the large-scale structure. The large-scale structure there develops in time and is horizontally periodic. The problem considered there, then, was the temporal problem and there does not exist a physically rational one-to-one transformation to the streamwise developing shear layer or spatial problem because of the causality condition, among others.

In this paper we shall present new results pertaining to the *spatial* problem. The locally equilibrium (with the mean) behavior of the fine-grained turbulence is also relaxed so that in our integrated energy considerations its evolution is due to the balance or inbalance between production from both the mean and large-scale structure and viscous dissipation rather than attributing its nonequilibrium behavior to the production mechanism from large-scale structure alone. In order to fix our ideas as to the physical picture which might emerge from our analysis, it would be helpful to recapitulate the interesting results reported by Binder and Favre-Marinet (23). A well-controlled large-scale structure was imparted upon the shear layer of a round jet and measurements were taken on the jet axis. In the absence of the large-scale structure the turbulence level on the jet axis gradually increased downstream. With the presence of the large-scale organized structure, the fine-grained turbulence level increased at a faster rate and became more vigorous with the downstream distance. Simultaneously, the large-scale structure amplified and subsequently decayed, as if having extracted energy from the mean flow and subsequently transferring it to the fine-grained turbulence. The spreading of the jet was also enhanced by the presence of the large-scale structure. Although geometrical effects in the experiments certainly play an important role, the qualitative physical situation should hold for the plane mixing region that we are to consider here.

FORMULATION

The explicity study of the large-scale organized structure coexisting with random fine-grained turbulence necessitates the splitting of a flow quantity into three components consisting of the mean motion and the nonrandom and random parts of the fluctuations. The usual time average, over a period at least that of the organized structure, produces the equations of mean motion. A second, conditional average then enables one to sort out the nonrandom part of the fluctuations from the random part, in contrast to and different from filtering. Such a splitting procedure, suitable for the present study is, of course, not new and has been discussed and utilized in the literature (2), (8), (9), (15), (16), (21), (22), (23), (25). However, the first systematic derivation of the conservation equations for the three component splitting procedure is attributable to W. C. Reynolds, as much as the two component splitting procedure was to O. Reynolds.

We shall consider an incompressible fluid. The velocity components and coordinates are made dimensionless by the corresponding characteristic scales appropriate to the problem. For instance, for the mixing region, the characteristic velocity is the free stream velocity and the characteristic length the initial boundary layer thickness. The pressure is made dimensionless by the free stream dynamic pressure and the time by that formed from the characteristic velocity and length. The conditional average is denoted by $<(\ )>$ and the usual time average by $\overline{(\ )}$. The mean flow quantities are denoted by capital symbols, the large-scale structure identified by the supercript tilde $\tilde{}$ and the random fine-grained turbulence by the supercript prime $'$. The conditional and time averages of the turbulence quantities are zero by definition. The conditional average of a large-scale organized quantity reproduces itself and its time average is zero. Because the two components of the fluctuations are not correlated, the time average of their products is zero. The conditional average of the products of two fine-grained turbulence quantities produces a mean Reynolds stress and a modulated stress, which are crucial to the interactions between the random fine-grained turbulence with the mean flow and the large-scale structure, respectively. The modulated turbulent stresses oscillate at the frequency of the large-scale organized structure.

Just as in the study of the two-component O. Reynolds turbulence problem, for all practical purposes, one is not interested in the details of the turbulence but in the stresses it sets up and the interaction with the mean flow in an averaged sense, in the explicit consideration of the large-scale structure one is also not interested in the details of the fine-grained turbulence but only in its modulated stresses and its mean stresses as it interacts with the large-scale and mean motions. Finally, the large-scale structure interacts with the mean flow through its own mean stresses. These can be best illustrated by writing down the momentum equations for the mean flow and the large-scale structure

$$\frac{\bar{D}U_i}{Dt} = -\frac{\partial P}{\partial x_i} + \frac{1}{Re}\frac{\partial^2 U_i}{\partial x_j \partial x_j} - \frac{\partial}{\partial x_j}(\overline{u_i'u_j'} + \overline{\tilde{u}_i\tilde{u}_j})$$

$$\frac{\bar{D}\tilde{u}_i}{Dt} + \tilde{u}_j\frac{\partial U_i}{\partial x_j} = -\frac{\partial \tilde{p}}{\partial x_i} + \frac{1}{Re}\frac{\partial^2 \tilde{u}_i}{\partial x_j \partial x_j}$$

$$- \frac{\partial}{\partial x_j}(\tilde{u}_i\tilde{u}_j - \overline{\tilde{u}_i\tilde{u}_j} + <u_i'u_j'>$$

$$- \overline{u_i'u_j'})$$

$$\frac{\partial U_i}{\partial x_i} = 0, \quad \frac{\partial \tilde{u}_i}{\partial x_i} = 0$$

where $\bar{D}/Dt$ is the substantial derivative following the mean flow, Re is the Reynolds number. In the absence of the large-scale structure, or if it were not sorted out from the random part, the problem reduces to the usual two-component turbulent flow problem. In the absence of the fine-grained turbulence, the problem then provides the starting point of nonlinear hydrodynamic theory in a laminar flow (26). It is clear then, the present problem is a cooperative blend of the two. Just as conservation equations for the mean turbulent stresses,

$$\overline{u_i'u_j'} ,$$

can be derived but with its accompanying closure problems (see, for instance, (27)), the conservation equations for the modulated turbulent stresses,

$$\tilde{r}_{ij} = <u_i'u_j'> - \overline{u_i'u_j'},$$

can also be similarly obtained (see, for instance, (28)) and similar problems with respect to closure also follows. Eddy viscosity models for

$$\tilde{r}_{ij}$$

has been used to some advantage in describing certain features of the large-scale organized structure (12), (15), (16), (28), however, some progress towards removing this stigma by bringing in the active participation of the fine-grained turbulence has recently been made in a paper which we have discussed earlier (24), where the temporal mixing region problem was discussed. The ideas follow some of the earlier works on nonlinear hydrodynamic stability theory for laminar shear flows (26), (29), (30), (31) which have been found helpful in explaining the large-scale organized structure in developing laminar shear flows. In this paper, we shall present our work on the spatially developing mixing region problem.

ENERGY INTEGRAL DESCRIPTION

The considerations alluded to in our discussion of Ref. (24) utilizes techniques of nonlinear hydrodynamic stability theory while bringing in the active interactions with the fine-grained turbulence. Such a consideration enables one to provide a gross description of the interaction processes among the three components of motion and has as its aim the derivation of the respective coupled "amplitude" (or "envelope") equations, with the accompanying shape assumptions for the vertical distributions (24), (26). The amplitude equations are derived from the kinetic energy equations in the mean.

For the spatially developing mixing region, the boundary layer approximations are applied to the mean energy equations of the three components of flow. The application of such approximations to the mean flow quantities and to the time-averaged random turbulence quantities has been the usual practice. Such approximations to the time-averaged large-scale organized structure quantities require some care. In the previous works on laminar flows such approximations were found unnecessary in that the streamwise derivatives of the time-averaged correlations of the organized structure could be evaluated (29), (31). In Ref. (31) it was found that the purely dynamical contributions were unimportant and this is confirmed in the present problem also. Rather than retaining these terms, they are neglected at the outset for simplicity. The appropriate kinetic energy equations are then

$$\frac{\bar{D}}{Dt}\frac{1}{2}U^2 = -\frac{\partial}{\partial y}U(\overline{u'v'} + \overline{\tilde{u}\tilde{v}}) - (-\overline{u'v'} - \overline{\tilde{u}\tilde{v}})\frac{\partial U}{\partial y}$$

$$\frac{\bar{D}}{Dt}\bar{q} = -\frac{\partial}{\partial y}[\overline{v'(p'+q)} + \overline{\tilde{v}\langle q\rangle}] + (-\overline{u'v'})\frac{\partial U}{\partial y}$$

$$+ \left[-\overline{\tilde{r}_{xx}\frac{\partial\tilde{u}}{\partial x}} - \overline{\tilde{r}_{xy}\left(\frac{\partial\tilde{u}}{\partial y} + \frac{\partial\tilde{v}}{\partial x}\right)} - \overline{\tilde{r}_{yy}\frac{\partial\tilde{v}}{\partial y}}\right] - \bar{\epsilon}$$

energy transfer from the large-scale structure

$$\frac{\bar{D}}{Dt}\bar{Q} = -\frac{\partial}{\partial y}[\overline{\tilde{v}(\tilde{p}+Q)} + \overline{\tilde{u}\tilde{r}_{xy}} + \overline{\tilde{v}\tilde{r}_{yy}}] + (-\overline{\tilde{u}\tilde{v}})\frac{\partial U}{\partial y}$$

$$- \left[-\overline{\tilde{r}_{xx}\frac{\partial\tilde{u}}{\partial x}} - \overline{\tilde{r}_{xy}\left(\frac{\partial\tilde{u}}{\partial y} + \frac{\partial\tilde{v}}{\partial x}\right)} - \overline{\tilde{r}_{yy}\frac{\partial\tilde{v}}{\partial y}}\right]$$

energy transfer to turbulence

where

$$q = \frac{1}{2}(u_i'u_i'), \quad Q = \frac{1}{2}(\tilde{u}_i\tilde{u}_i)$$

and $\bar{\epsilon}$ is the rate of viscous dissipation of the fine-grained turbulence. Viscous diffusion of the kinetic energies and dissipation of the mean flow and large-scale structure have been neglected. In the above, the respective diffusion and production from the mean flow terms are self-explanatory in the two fluctuation energy equations. The less familiar average energy transfer between the disparate scales are so indicated.

The integral kinetic energy equations are then

$$\frac{1}{2}\frac{d}{dx}\left[\int_{-\infty}^{0}U(U^2 - U^2_{-\infty})dy + \int_{0}^{\infty}U(U^2 - U^2_{+\infty})dy\right]$$

$$= -\int_{-\infty}^{\infty}(-\overline{u'v'} - \overline{\tilde{u}\tilde{v}})\frac{\partial U}{\partial y}dy$$

with the upper stream $U_{+\infty}$ is normalized to unity and subsequently the lower shear stream $U_{-\infty}$ taken as zero,

$$\frac{d}{dx}\int_{-\infty}^{\infty}U\bar{q}dy = \int_{-\infty}^{\infty}(-\overline{u'v'})\frac{\partial U}{\partial y}dy$$

$$+ \int_{-\infty}^{\infty}\left[-\overline{\tilde{r}_{xx}\frac{\partial\tilde{u}}{\partial x}} - \overline{\tilde{r}_{xy}\left(\frac{\partial\tilde{u}}{\partial y} + \frac{\partial\tilde{v}}{\partial x}\right)}\right.$$

$$\left.- \overline{\tilde{r}_{yy}\frac{\partial\tilde{v}}{\partial y}}\right]dy - \int_{-\infty}^{\infty}\bar{\epsilon}dy$$

$$\frac{d}{dx}\int_{-\infty}^{\infty}U\bar{Q}dy = \int_{-\infty}^{\infty}(-\overline{\tilde{u}\tilde{v}})\frac{\partial U}{\partial y}dy - \int_{-\infty}^{\infty}\left[-\overline{\tilde{r}_{xx}\frac{\partial\tilde{u}}{\partial x}}\right.$$

$$\left.- \overline{\tilde{r}_{xy}\left(\frac{\partial\tilde{u}}{\partial y} + \frac{\partial\tilde{v}}{\partial x}\right)} - \overline{\tilde{r}_{yy}\frac{\partial\tilde{v}}{\partial y}}\right]dy$$

Implicit in the above is that the mean shear flow is two dimensional, similarly with the large-scale organized structure which, in the subsequent shape assumption, will be taken as one whose vorticity axis is perpendicular to the streamwise direction. The recently observed spanwise periodicity (4) is not accounted here. The fine-grained turbulence, of course, is three dimensional.

The closure problem is obtained in the discussion of the shape assumptions. There, some of the detailed "microscopic" calculations of the modulated stresses and large-scale structure, prior to averaging, shall be done approximately.

Shape Assumptions

The mean flow is taken to be of the form

$$U = \frac{1}{2}(1 + \tanh\eta)$$

where $\eta = y/\delta(x)$ and $\delta(x)$ is the x-dependent shear layer thickness which will characterize the mean flow, to be determined jointly with the large-scale structure and the fine-grained turbulence problems.

The shape functions for the vertical distribution of the time-averaged fine-grained turbulence quantities are guided by measurements such as those of Wygnanski and Fiedler (32). The slight asymmetry of the profiles, though it could be accomodated here, is not taken into account. The Reynolds shear stress is taken to be of the form

$$-\overline{u'v'} = \frac{a_1}{\sqrt{\pi}}E(x)e^{-\eta^2}$$

and is related to the turbulent kinetic energy via the constant $a_1 = 0.3$, thus $\bar{q} = -\overline{u'v'}/a_1$. The factor $\sqrt{\pi}$ is a normalizing constant so that $\delta E(x)$ has the physical interpretation as being the total kinetic energy of the fine-grained turbulence across a slice of the entire shear layer. $E(x)$ is thus an energy density, the total energy per unit $\delta(x)$ and it characterizes the turbulence. Following Patankar and Spalding (33), and Bradshaw, Ferriss and Atwell (34), the dissipation of the fine-grained turbulence is taken to be

$$\epsilon = a_2\bar{q}^{3/2}/2\delta$$

where the value $a_2 = 1.5$ will be used.

Following earlier works (24), (26), (30), the vertical shape of the large-scale structure is given by a *local* linearized theory but with an amplitude $A(x)$ which is to be jointly solved with $\delta(x)$ and $E(x)$,

$$\begin{pmatrix} \tilde{u} \\ \tilde{v} \end{pmatrix} = A(x)e^{-i\beta\tau} \begin{pmatrix} \phi'(\eta;\beta) \\ -i\alpha\phi(\eta;\beta) \end{pmatrix} + \begin{pmatrix} \text{c.c.} \\ \text{c.c.} \end{pmatrix}$$

where α is the dimensionless complex wave number scaled by $\delta(x)$, β is the dimensionless physical frequency scaled also according to the local shear layer thickness $\delta(x)$ and is real, ϕ is the streamfunction and ϕ' refers to its η-derivative, c.c. denotes the complex conjugate. Here τ is the dimensionless time also referred to $\delta(x)$. The local shape functions are coupled to and diffused by the modulated turbulent stresses. The structure of these stresses warrants their shape assumption to be of the form (24),

$$\tilde{r}_{ij} = A(x)E(x)e^{-i\beta\tau}r_{ij}(\eta;\beta) + \text{c.c.}$$

Hence the vertical shape functions ϕ and r_{ij} forms a coupled local linear problem and in obtaining their equations A is taken exponential in x and E constant locally. An approximate method of solving the local temporal problem is outlined and argued in (24) and can be carried out similarly for the spatial problem here. Namely, the "inviscid" form of ϕ is first solved and then used in the algebraic r_{ij} equations as known functions. Additional closure assumptions are required for use in the equations for the modulated stress functions r_{ij}. For the mean stresses, these are $\overline{v'^2} = \overline{w'^2}$ and $\overline{v'^2}/(-\overline{u'v'}) \approx 2$ from, say, (32). For the modulated turbulent quantities these are patterned after closure assumptions for the mean quantities, with the pressure velocity correlation taken simply as

$$-\left[\langle u_j' \frac{\partial p'}{\partial x_i}\rangle - \overline{u_j' \frac{\partial p'}{\partial x_i}} + \langle u_i' \frac{\partial p'}{\partial x_j}\rangle - \overline{u_i' \frac{\partial p'}{\partial x_j}}\right]$$

$$= \frac{1}{T}\left[\tilde{r}_{ij} - \frac{1}{3}\tilde{r}_{ii}\delta_{ij}\right]$$

where T is the time-scale for "return to isotropy" and is taken as $T^{-1} = c\partial U/\partial y$ with $c \approx 1.445$. The modulated dissipation is taken to be

$$\tilde{\varepsilon} \equiv \langle\varepsilon\rangle - \bar{\varepsilon} \approx \frac{3}{2}\frac{a_2}{\delta}\sqrt{\bar{q}}\,\tilde{q}$$

where $\tilde{q} = \tilde{r}_{ii}/2$. Since the vertical shape function here is to be given by the local linear theory, the form for $\tilde{\varepsilon}$ as given above reflects a linearization with $\bar{q}$ there to be replaced by its local equilibrium value in the absence of the large-scale structure. Then

$$\tilde{\varepsilon} \approx \frac{\beta}{T}\tilde{q}$$

where the constant $\beta \approx 0.24$ (there is, of course, no confusion with the same symbol used for the frequency). This is similar to using the local homogeneous shear problem as a guide (see, for instance, (24)). These additional assumptions are used in the ϕ, r_{ij} problem which enters the main overall interaction problem for δ, E and A as quantities occurring under "interaction" integrals and are thus not considered to be sensitive. For completeness, we state the approximate ϕ, r_{ij} problem, with ϕ governed by the Rayleigh equation

$$(U - c)(\phi'' - \alpha^2\phi) - \phi U'' = 0$$

with appropriate boundary conditions, and r_{ij} by

$$i\alpha(U - c)\begin{bmatrix} r_{xx} \\ r_{yy} \\ r_{zz} \\ r_{xy} \end{bmatrix} + \begin{bmatrix} 2r_{xy} \\ 0 \\ 0 \\ r_{yy} \end{bmatrix}U' + \frac{1}{T}\left\{\begin{bmatrix} r_{xx} \\ r_{yy} \\ r_{zz} \\ r_{xy} \end{bmatrix} - \frac{1}{3}\begin{bmatrix} r_{ii} \\ r_{ii} \\ r_{ii} \\ 0 \end{bmatrix}\right\}$$

$$+ \frac{\beta}{3T}\begin{bmatrix} r_{ii} \\ r_{ii} \\ r_{ii} \\ 0 \end{bmatrix} = i\alpha\phi\begin{bmatrix} R'_{xx} \\ R'_{yy} \\ R'_{zz} \\ R'_{xy} \end{bmatrix} + \begin{bmatrix} -2i\alpha R_{xx}\phi' - 2R_{xy}\phi'' \\ 2i\alpha R_{yy}\phi' - 2\alpha^2 R_{xy}\phi \\ 0 \\ -R_{yy}\phi'' - \alpha^2\phi R_{xx} \end{bmatrix}$$

where the vertical shape functions of the mean stresses are

$$\begin{bmatrix} R_{xx} \\ R_{yy} \\ R_{zz} \\ -R_{xy} \end{bmatrix} = \begin{bmatrix} 0.45 \\ 0.34 \\ 0.34 \\ 0.17 \end{bmatrix}e^{-\eta^2} .$$

and the prime on the R_{ij} and ϕ denotes, again, differentiation with respect to η. Calculations for ϕ and r_{ij} are ultimately to be used in the integral over the large-scale structure and turbulence energy transfer mechanism,

$$\overline{\tilde{r}_{ij}\partial\tilde{u}_i/\partial x_j} .$$

It is clear that, to the present order of approximations, such a term is proportional to $|A|^2E$ and the "constants" of proportionality are functions of $\delta(x)$. The eigenfunctions ϕ are normalized so as to render $|A(x)|^2$ to be the corresponding energy density of the large-scale organized structure. Both $|A|^2$ and E are thus similarly interpreted.

The Interaction Problem

After the substitution of the shape functions into the energy integral equations, and with some straightforward algebraic dexterity, we obtain

$$I_1\frac{d\delta}{dx} = -I'_{rs}E - \tilde{I}_{rs}(\delta)\cdot|A|^2$$

$$I_3\frac{d\delta E}{dx} = I'_{rs}E + I_{wt}(\delta)\cdot|A|^2E - I_\varepsilon E^{3/2}$$

$$I_2(\delta)\,\frac{d\delta|A|^2}{dx} = \tilde{I}_{rs}(\delta)\cdot|A|^2 - I_{wt}(\delta)\cdot|A|^2E$$

with initial conditions $\delta(0) = 1$, $E(0) = E_o$, $|A(0)|^2 = |A|_o^2$. The physical interpretation of each term is obvious and can be reverted to the original conservation equations.

The integrals involving only the mean flow and time-averaged fine-grained turbulence quantities are constants,

$$I_1 = \frac{1}{16}\int_{-\infty}^{o}(1+\tanh\eta)^3 d\eta + \frac{1}{4}\int_{o}^{\infty}(1+\tanh\eta)\left[\frac{1}{4}(1+\tanh\eta)^2 - 1\right]d\eta$$

$$= -\,0.202$$

$$I_3 = \frac{1}{2\sqrt{\pi}}\int_{-\infty}^{\infty}(1+\tanh\eta)e^{-\eta^2}d\eta = 0.500$$

$$I'_{rs} = \frac{a_1}{2\sqrt{\pi}}\int_{-\infty}^{\infty}\operatorname{sech}^2\eta\; e^{-\eta^2}d\eta = 0.109$$

$$I_\varepsilon = \frac{a_2}{2\pi^{3/4}}\int_{-\infty}^{\infty}e^{-3\eta^2/2}d\eta = 0.465$$

The integrals involving the large-scale organized quantities are dependent on the local shear layer thickness $\delta(x)$ through their dependence on the spectral properties via local frequency parameter $\beta(\delta)$. The large-scale structure production integral is

$$\tilde{I}_{rs}(\beta) = \tilde{I}_{rs}(\delta) = \int_{-\infty}^{\infty} R\ell(i\alpha\phi\bar{\phi}')\operatorname{sech}^2\eta\, d\eta$$

where $R\ell$ denotes the real part and $\bar{\phi}$ is the complex conjugate of ϕ, and the large-scale structure — fine-grained turbulence interaction integral is

$$I_{wt}(\beta) = I_{wt}(\delta) = \int_{-\infty}^{\infty} R\ell\left[r_{xx}(-i\bar{\alpha}\bar{\phi}') + r_{xy}(\bar{\phi}'' + \bar{\alpha}^2\bar{\phi}) + r_{yy}(i\bar{\alpha}\bar{\phi}')\right]d\eta$$

with $I_{wt} > 0$. The details of the interpretation of the integrand are given in (24) for the temporal problem, and will not be repeated here. Finally,

$$I_2(\beta) = I_2(\delta) = \frac{1}{2}\left\{1 + \int_{-\infty}^{\infty}\tanh\eta\cdot\left[|\phi'|^2 + |\alpha|^2|\phi|^2\right]d\eta\right\}$$

and is very nearly constant.

The spectral properties of the interaction integrals associated with the large-scale structure are shown in Figure 1. They are numerically obtained as functions of $\beta(x) = \beta_o\delta(x)$, where β_o is the initial characteristic (dimensionless) frequency of the large-scale structure, $\beta(0) = \beta_o$.

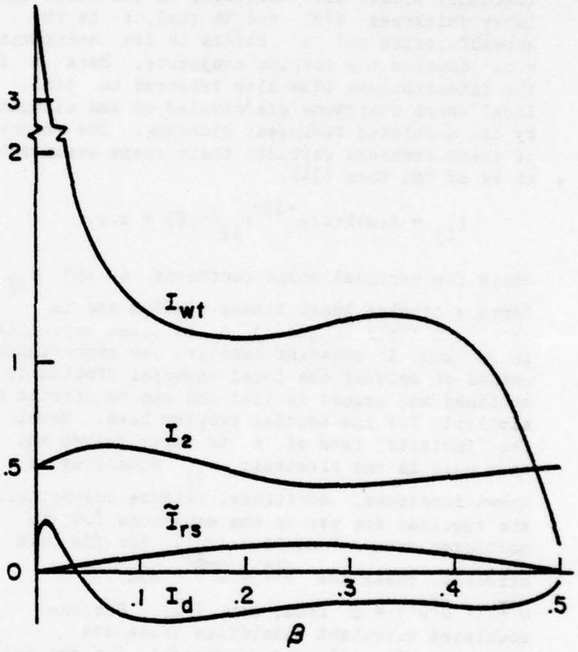

Figure 1. The spectral properties of the interaction integrals involving the large-scale structure.

The advection integral I_2 is very nearly constant and it will be approximated by 0.5 during the subsequent calculations since it was found that the problem is not sensitive to the variation of I_2. The Reynolds stress or production integral, $\tilde{I}_{rs}$, peaks at about $\beta \cong 0.21$, that value of β which corresponds to the maximal amplification in the local linear theory. The large-scale structure — fine-grained energy transfer integral I_{wt} shown here is different from that obtained for the temporal problem in Ref. (24) where the spectral properties were plotted as functions of the wave number. There the local turbulence was taken to be in equilibrium with the mean flow in order to isolate and illustrate the large-scale structure and fine-grained turbulence interaction and this rendered the modulated stresses to become singular as the local linear problem approached neutral. Here, because the fine-grained turbulence is not necessarily in equilibrium with the mean flow locally no such singularity occurred as $\beta \to 0.5$. Calculations of the properties beyond $\beta = 0.5$ were not obtained. The remaining integral, I_d, is shown only for illustrative purposes. It is associated with one of the streamwise large-scale structure diffusion terms,

$$\partial(\overline{u r_{xx}} + \overline{v r_{xy}})/\partial x.$$

Since $I_d << I_{wt}$ such streamwise diffusion terms contribute very little to the main features of the problem and they are neglected. There is no obvious rational transformation from a temporal to a spatial problem even in the present formulation.

RESULTS

With the large-scale structure interaction integrals interpreted as functions of $\beta = \beta_o \delta(x)$ and the single well controlled mode is specified to be β_o, the three first order nonlinear interaction equations are integrated subjected to the initial conditions $\delta(0) = 1$, $|A(0)|^2 = |A|^2_o$, $E(0) = E_o$. Energy densities corresponding to about 10^{-4} implies root mean square velocities of about a few percent of the free stream and this seems to be a reasonable value to be imposed upstream. The results are shown as functions of x, the streamwise distance normalized by the initial mixing layer thickness.

Physical Mechanisms for the Evolution of $\delta, |A|^2$, and E

In Figure 2, for the case of $\beta_o = 0.1$, two sets of curves are shown. The dashed curve indicates the shear layer growth accomplished by the energy transfer from the mean flow to the turbulence energy density E alone. Thus the development of E is due to the imbalance between production from the mean and viscous dissipation alone. With the imposition of the large-scale structure the mean flow spreading becomes enhanced as is the turbulence energy density. It can be seen that the large-scale structure energy density first amplifies and subsequently decays. All this is quite reminiscent of the observations of Binder and Favre-Marinet (23). In order to obtain physical insight into the behavior shown in Figure 2, we use the solution in a diagnostic manner by showing the relevant interaction terms that bring about the evolution of δ, E and $|A|^2$. In Figure 3 we illustrate the following terms: the viscous dissipation of turbulence energy

$$I_\epsilon E^{3/2}$$

shown as curve I, the turbulence production from the mean, $I'_{rs} E$ by curve II, the large-scale structure production from the mean $\bar{I}_{rs}|A|^2$ by curve III, and the energy transfer between the large-scale and turbulence $I_{wt}|A|^2E$ by curve IV. Initially III > IV and the large-scale structure amplifies and starts to decay when III < IV after $x \approx 85$. Of course, III itself decays because of the enhanced spreading caused by III itself. Initially when $|A|^2$ is still relatively small, the increase of E is due entirely to II > I. It continues to increase and becomes much enhanced due to IV and II in spite of the fact that I > II after x = 55. The spread of the shear layer thickness δ is significantly enhanced when both $|A|^2$ and the enhanced E (because of $|A|^2$) becomes important, the growth being contributed by both II and III.

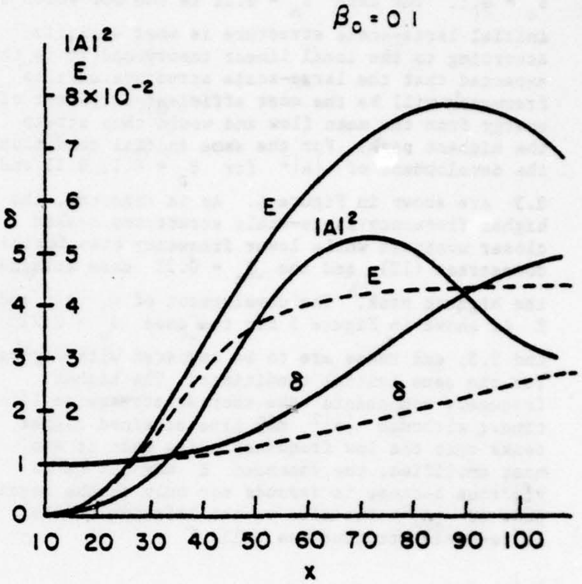

Figure 2. Streamwise development of δ, $|A|^2$ and E. Solid line: $\beta_o = 0.1$, $|A|^2_o = E_o = 10^{-4}$; Dotted line: $\beta_o = 0$, $|A|^2_o = 0$ and $E_o = 10^{-4}$.

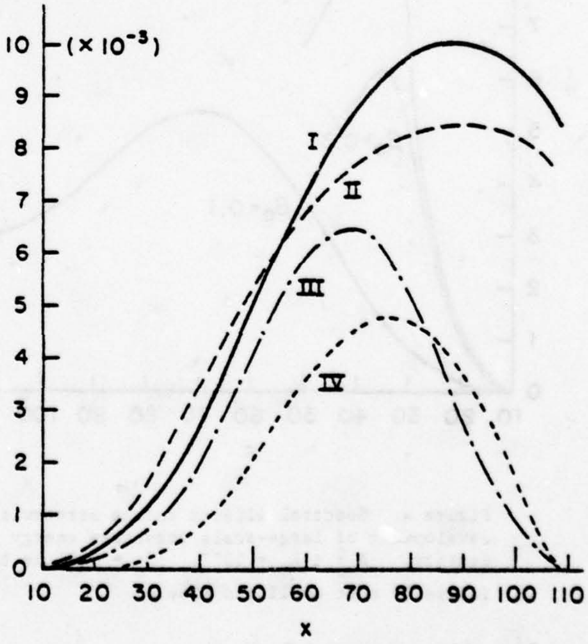

Figure 3. Energy transfer mechanisms, $\beta_o = 0.1$, $|A|^2_o = E_o = 10^{-4}$. I: $I_\epsilon E^{3/2}$, II: $I'_{rs}E$, III: $\bar{I}_{rs}|A|^2$, IV: $I_{wt}|A|^2E$.

The Spectral Dependence of the Interaction

Previously, the interaction was shown for $\beta_o = 0.1$. The case $\beta_o = 0.21$ is one for which the initial large-scale structure is most amplified according to the local linear theory and it is thus expected that the large-scale structure at this frequency will be the most efficient extractor of energy from the mean flow and would thus attain the highest peak. For the same initial conditions, the development of $|A|^2$ for $\beta_o = 0.1$, 0.21 and 0.3 are shown in Figure 4. As is expected, the higher frequency large-scale structures peaked closer upstream while lower frequency ones further downstream (12), and the $\beta_o = 0.21$ case attained the highest peak. The development of δ, $|A|^2$ and E is shown in Figure 5 for the case $\beta_o = 0.21$ and 0.3, and these are to be compared with Figure 2 for the same initial conditions. The higher frequency components have shorter streamwise lifetimes; although $|A|^2$ may have attained higher peaks than the low frequency modes when it was most amplified, the enhanced E may not be as vigorous because it depends not only on the magnitude of $|A|^2$ but also on the lifetime of the large-scale structure as well.

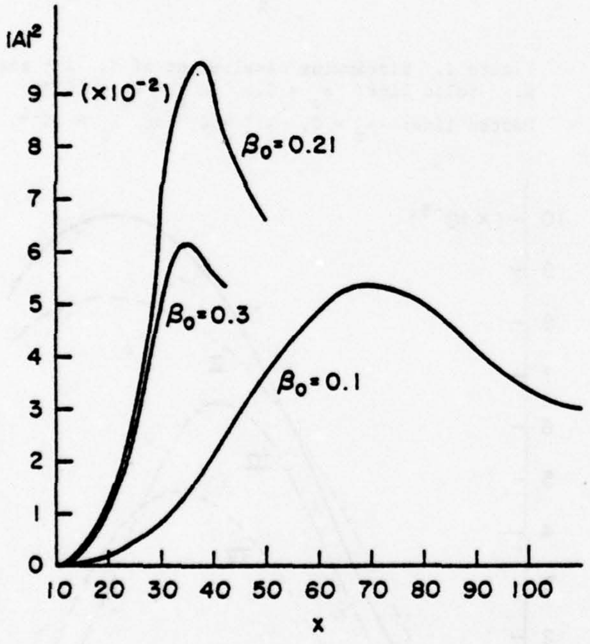

Figure 4. Spectral effects on the streamwise development of large-scale structure energy density, $|A|_o^2 = E_o = 10^{-4}$. ($\beta_o = 0.21$ is the initially most amplified case.)

Controlling the Large-Scale Structure

In addition to controlling the large-scale organized structure by direct imposition of definite spectral modes at a given strength, the use of fine-grained turbulence to control its development can also be achieved (12). In Figure 6 we show the $\beta_o = 0.21$ mode with fixed $|A|_o^2$ but with different initial conditions for E_o. The initially enhanced fine-grained turbulence suppresses the subsequent development of the large-scale structure, curve II, and in so doing, it achieves a lower subsequent enhancement as indicated by E_{II}.

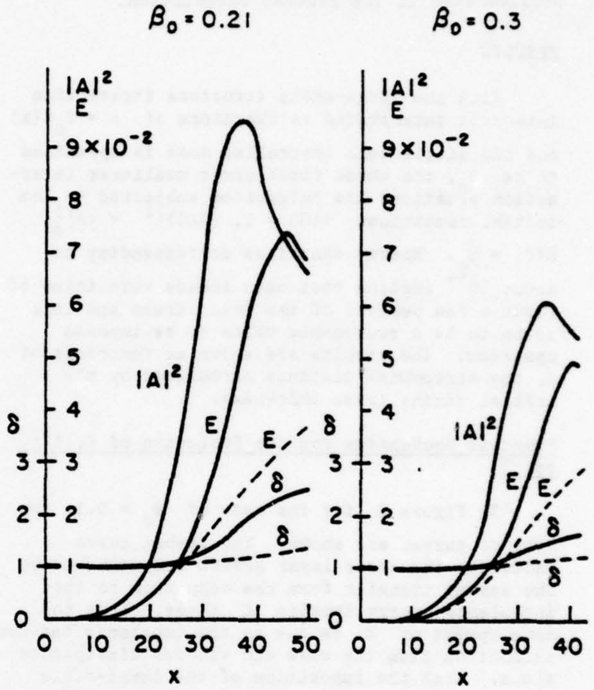

Figure 5. Spectral effects on the streamwise development of δ, $|A|^2$ and E. Solid line: $|A|_o^2 = E_o = 10^{-4}$; Dotted line: $\delta_o = 0$, $|A|_o^2 = 0$ and $E_o = 10^{-4}$. (Compare also with Figure 2.)

Discussion

The spatial nonlinear interaction problem has been obtained by consistantly interpreting the interaction integrals involving the large-scale structure, $\bar{I}_{rs}$ and I_{wt}, as functions of $\delta(x)$ through their dependence on $\beta(x) = \beta_o\delta(x)$ in the same spirit as (29), (30), and (31), as well as (24). In the temporal problem (24), the consequences of freezing these integrals as constants were further explored. The problem then became analytically tractable so as to enable us to obtain equilibrium states in the $|A|^2 - E$ plane and to study the nature of the singularity about such states. It was found that the $|A|^2 - E$ plane describes a stable spiral (24). The spiral behavior was sufficiently pronounced so as to resemble "bursts" or renewed large-scale structure activity after repeated cycles, which are not actually periodic, of amplification and decay. By a similar freezing of the interaction integrals in the spatial problem here, a spiral behavior about equilibrium points were also found but were not as pronounced as those in (24). The difference is not so much as between spatial and temporal problems, but that in (24) the local turbulence behavior was taken to be in equilibrium with the mean and this demanded a much larger I_{wt} for those modes of the large-scale structure approaching the neutral condition. In the present problem, the previous simplifying condition of local turbulence equilibrium with the mean is removed and this rendered I_{wt} to be finite as $\beta \to 0.5$. The results for the frozen interaction integrals are not presented here because of space limitations.

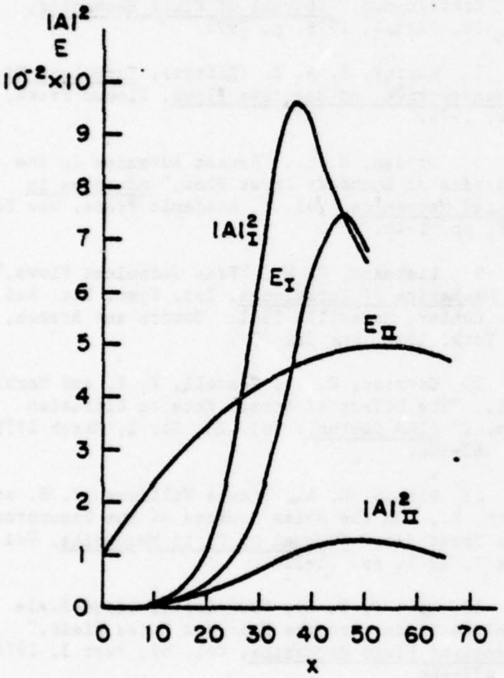

Figure 6. The effect of increasing the initial fine-grained turbulence energy level on the development of large-scale structure and turbulence energy densities. $\delta_o = 0.21$, I: $|A|_o^2 = E_o = 10^{-4}$; II: $|A|_o^2 = 10^{-4}$, $E_o = 10^{-2}$.

THE PROSPECTS FOR NUMERICAL SIMULATION

While much physical intuition could be gained about the interactions between large-scale structure and turbulence in a shear flow from the approximate energy integral considerations, much detail about the local structure is lacking. The analysis of the large-scale structure presented here resembles the analysis of nonlinear hydrodynamic stability theory in laminar flow (26), (29), (30), (31). Complementary to such analysis is the numerical simulation of finite-amplitude instabilities in laminar flow using the full nonsteady Navier-Stokes equations (see, for instance, (35), (36)). For the large-scale organized structure in a turbulent shear flow, a similar but more difficult numerical simulation could also be attempted. To this end, the senior author of the present paper recently posed the following problem.

To fix our ideas, let us revert to the temporal mixing layer problem of horizontally homogeneous and oppositely directed streams. The large-scale structure is horizontally periodic and develops in time. The "proper" dynamical dependent variable is the sum of the mean and the large-scale structure, denoted by the script notation

$$\mathcal{U}_i(x,y,t) = U(y,t) + \tilde{u}_i(x,y,t)$$

$$\mathcal{P}(x,y,t) = P(y,t) + \tilde{p}(x,y,t)$$

The full Navier-Stokes equations is then split into the mean and organized part and a turbulence part according to $\mathcal{U}_i + u_i'$ and $p = \mathcal{P} + p'$. Again denoting the conditional average by $<(\ )>$, we have for the dynamical variables

$$\frac{\partial \mathcal{U}_i}{\partial x_i} = 0$$

$$\frac{\partial \mathcal{U}_i}{\partial t} + \frac{\partial \mathcal{U}_i \mathcal{U}_i}{\partial x_i} = -\frac{\partial \mathcal{P}}{\partial x_i} - \frac{\partial <u_i'u_j'>}{\partial x_y} - \frac{1}{Re}\frac{\partial^2 \mathcal{U}_i}{\partial x_i \partial x_i}$$

and the coupled, yet unclosed, equation for the conditionally averaged stresses

$$\left(\frac{\partial}{\partial t} + \mathcal{U}_k \frac{\partial}{\partial x_k}\right)<u_i'u_j'> = -\underbrace{\left[<u_j'u_k'>\frac{\partial \mathcal{U}_i}{\partial x_k} + <u_i'u_k'>\frac{\partial \mathcal{U}_j}{\partial x_k}\right]}_{\text{production}}$$

$$+ \underbrace{<p'\left(\frac{\partial u_i'}{\partial x_j} + \frac{\partial u_j'}{\partial x_i}\right)>}_{\text{redistribution}}$$

$$\underbrace{-\frac{\partial}{\partial x_k}\left[<u_i'u_j'u_k'> + <p'(u_i'\delta_{jk} + u_j'\delta_{ik})> - \frac{1}{Re}\frac{\partial <u_i'u_j'>}{\partial x_k}\right]}_{\text{diffusion}}$$

$$\underbrace{-2\frac{1}{Re}<\frac{\partial u_i'}{\partial x_k}\frac{\partial u_j'}{\partial x_k}>}_{\text{dissipation}}$$

The viscous diffusion effects will subsequently be neglected. A possible closure scheme is obtained by a direct extension of Launder et al.'s model (27) for the mean stresses to the present conditionally averaged stresses $<u_i'u_j'>$. Again, reverting to the temporal mixing layer problem with a two-dimensional large-scale structure, such a model then provides eight equations for the eight unknowns $\mathcal{U}$, $\mathcal{V}$, $\mathcal{P}$ and $<u'v'>$, $<u'^2>$, $<v'^2>$, $<w'^2>$ and $<\epsilon>$. (Or, following Amsden and Harlow (35), the three dynamical variables are replaced by the vorticity and streamfunction.) $\mathcal{U}_i$ is horizontally periodic as are the conditionally averaged stresses $\langle u_i'u_j'\rangle$ and these decay far from the shear layer. Originally there existed the mean mixing layer with a set of consistent and compatible mean stresses and at $t = t_o$, a large-scale organized structure is imposed so that

$$\mathcal{U}_i(x,y,t_o) \equiv U_i(y,t_o) + \tilde{u}_i(x,y,t_o),$$

$$\langle u_i'u_j'\rangle(x,y,t_o) \equiv \overline{u_i'u_j'}(y,t_o) + \tilde{r}_{ij}(x,y,t_o).$$

Hence, the "initialization" calls for a compatible coexistence of the mean problem $U_i(y,t_o)$ and $\overline{u_i'u_j'}(y,t_o)$. The imposed $\tilde{u}_i(x,y,t_o)$ is then made compatible with $U_i(y,t_o)$, being, say, the solution to the Rayleigh equation with $U(y,t_o)$ as the mean profile and $\tilde{r}_{ij}(x,y,t_o)$ taken as zero. The problem yields the total quantities, $\mathcal{U}_i \equiv U_i + \tilde{u}_i$ and $\langle u_i'u_j'\rangle \equiv \overline{u_i'u_j'} + \tilde{r}_{ij}$, with the mean obtainable by horizontal averaging and the large-scale structure quantities by a subtraction of the mean from the total quantities. Of great interest, for instance, is the use of the numerical solution for diagnosing the energy transfer between the large-scale structure and the fine-grained turbulence, $\tilde{r}_{ij}\partial\tilde{u}_i/\partial x_j$ among others. The numerical problem here is certainly compounded compared to the relatively more straightforward laminar problem. Our colleague, T. B. Gatski, is courageously working on this problem and the results, when available, would be of great interest towards physically diagnosing the interaction problem. The extension of the temporally developing to the spatially developing mixing layer problem is certainly possible. However, much of the physics about the interaction could be gained from the simpler, temporal problem first before attempting the more difficult spatial problem.

ACKNOWLEDGMENTS

Various aspects of the research described in this paper are supported in part by the National Aeronautics and Space Administration, Langley Research Center, Grant NSG-1076, the National Science Foundation Grant ENG73-04104 and the Fluid Dynamics Program of the Office of Naval Research Contract N00014-76-C-0363. The authors express their thanks to Ruth Wattman for her assistance in the preparation of the manuscript.

REFERENCES

1 Laufer, J., "New Trends in Experimental Turbulence Research," Annual Review of Fluid Mechanics, Vol. 7, Annual Reviews, Palo Alto, 1975, pp. 307-326.

2 Mollo-Christensen, E., "Physics of Turbulent Flow," AIAA Journal, Vol. 9, No. 7, July 1971, pp. 1217-1228.

3 Mollo-Christensen, E., "Intermittency in Large-Scale Turbulent Flows," Annual Review of Fluid Mechanics, Vol. 5, Annual Reviews, Palo Alto, 1973, pp. 101-118.

4 Roshko, A., "Structure of Turbulent Shear Flows: A New Look," (Dryden Research Lecture), AIAA Journal, Vol. 14, No. 10, October 1976, pp. 1349-1357.

5 Willmarth, W. W., "Structure of Turbulence in Boundary Layers," Advances in Applied Mechanics, Vol. 15, Academic Press, New York, 1975, pp. 159-254.

6 Davis, P. O. A. L. and Yule, A. J., "Coherent Structures in Turbulence," Journal of Fluid Mechanics, Vol. 69, 1975, Part 3, pp. 517-537; and "Corrigendum," Journal of Fluid Mechanics, Vol. 74, Part 4, 1976, p. 797.

7 Murthy, S. N. B. (Editor), Turbulent Mixing in Nonreactive and Reactive Flows, Plenum Press, New York, 1975.

8 Dryden, H. L., "Recent Advances in the Mechanics of Boundary Layer Flow," Advances in Applied Mechanics, Vol. 1, Academic Press, New York, 1948, pp. 1-40.

9 Liepmann, H. W., "Free Turbulent Flows," The Mechanics of Turbulence, Int. Symp. Nat. Sci. Res. Center, Marseille 1961. Gordon and Breach, New York, 1964, pp. 211-227.

10 Carrier, G. F., Fendell, F. E. and Marble, F. E., "The Effect of Strain Rate on Diffusion Flames," SIAM Journal, Vol. 28, No. 2, March 1975, pp. 463-500.

11 Bishop, K. A., Ffowcs Williams, J. E. and Smith, W., "On the Noise Sources of the Unsuppressed High Speed Jet," Journal of Fluid Mechanics, Vol. 50, Part 1, 1971, pp. 21-31.

12 Liu, J. T. C., "Developing Large-Scale Wavelike Eddies and the Near Jet Noise Field," Journal of Fluid Mechanics, Vol. 62, Part 3, 1974, pp. 437-464.

13 Woods, J. D. and Wiley, R. L., "Billow Turbulence and Ocean Microstructure," Deep-Sea Research, Vol. 19, 1972, pp. 87-121.

14 Liu, J. T. C. and Merkine, L., "Energy Integral Description of the Development of Kelvin-Helmholtz Billows," Tellus, Vol. 28, No. 3, 1976, pp. 197-214.

15 Liu, J. T. C., "Nonlinear Development of an Instability Wave in a Turbulent Wake," Physics of Fluids, Vol. 14, No. 11, November 1971, pp. 2251-2257.

16 Reynolds, W. C., "Large-Scale Instabilities of Turbulent Wakes," Journal of Fluid Mechanics, Vol. 54, Part 3, 1972, pp. 481-488.

17 Winant, C. D. and Browand, F. K., "Vortex Pairing: The Mechanism of Turbulent Mixing-Layer Growth at Moderate Reynolds Number," Journal of Fluid Mechanics, Vol. 63, Part 2, 1974, pp. 237-255.

18 Schubauer, G. B. and Skramstad, H. K., "Laminar Boundary Layer Oscillations and Transition

on a Flat Plate," Rep. No. 909, 1948, National Advisory Committee on Aeronautics, Washington, D. C.

19 Kelly, R. E., "On the Stability of an Inviscid Shear Layer which is Periodic in Space and Time," Journal of Fluid Mechanics, Vol. 27, Part 4, pp. 657-689.

20 Townsend, A. A., The Structure of Turbulent Shear Flow, 1st ed., Cambridge University Press, 1956, p. 123.

21 Hussain, A. K. M. F. and Reynolds, W. C., "The Mechanics of an Organized Wave in Turbulent Shear Flow," Journal of Fluid Mechanics, Vol. 41, Part 2, 1970, pp. 241-258.

22 Kendall, J. M., "The Turbulent Boundary Layer Over a Wall with Progress Surface Waves," Journal of Fluid Mechanics, Vol. 41, Part 2, pp. 259-281.

23 Binder, G. and Favre-Marinet, M., "Mixing Improvement in Pulsating Turbulent Jets," Fluid Mechanics of Mixing, (E. M. Uram and V. W. Goldschmidt, eds.), American Society of Mechanical Engineers, New York, 1973, pp. 167-172.

24 Liu, J. T. C. and Merkine, L., "On the Interactions between Large-Scale Structure and Fine-Grained Turbulence in a Free Shear Flow," Proceedings of the Royal Society of London, Series A, Vol. 352, 29 December 1976, pp. 213-247.

25 Phillips, O. M., The Dynamics of the Upper Ocean, Cambridge University Press, 1966, p. 90.

26 Stuart, J. T., "On the Nonlinear Mechanics of Hydrodynamic Stability," Journal of Fluid Mechanics, Vol. 4, Part 1, 1958, pp. 1-21.

27 Launder, B. E., Reece, G. J. and Rodi, W., "Progress in the Development of a Reynolds Stress Turbulence Closure," Journal of Fluid Mechanics, Vol. 68, Part 3, 1975, pp. 537-566.

28 Reynolds, W. C. and Hussain, A. K. M. F., "The Mechanics of an Organized Wave in Turbulent Shear Flow. 3. Theoretical Models and Comparisons with Experiments," Journal of Fluid Mechanics, Vol. 54, Part 2, 1975, pp. 263-288.

29 Ko, D. R. S., Kubota, T., and Lees, L., "Finite Disturbance Effect in the Stability of a Laminar Incompressible Wake Behind a Flat Plate," Journal of Fluid Mechanics, Vol. 40, Part 2, 1970, pp. 315-341.

30 Liu, J. T. C. and Lees, L., "Finite-Amplitude Instability of the Compressible Laminar Wake: Strongly Amplified Disturbances," Physics of Fluids, Vol. 13, No. 12, December 1970, pp. 2932-2938.

31 Liu, J. T. C. and Gururaj, P. M., "Finite-Amplitude Instability of the Compressible Laminar Wake: Comparison with Experiments," Physics of Fluids, Vol. 17, No. 3, March 1974, pp. 532-543.

32 Wygnanski, I. and Fiedler, H. E., "The Two-Dimensional Mixing Region," Journal of Fluid Mechanics, Vol. 41, Part 2, pp. 327-362.

33 Patankar, S. V. and Spalding, D. B., "A Finite-Difference Procedure for Solving the Equations of the Two-Dimensional Boundary Layer," International Journal of Heat and Mass Transfer, Vol. 10, 1967, pp. 1389-1411.

34 Bradshaw, P., Ferriss, D. H. and Atwell, N. P., "Calculation of Boundary Layer Development Using the Turbulence Energy Equation," Journal of Fluid Mechanics, Vol. 28, Part 3, 1967, pp. 593-616.

35 Amsden, A. A. and Harlow, F. H., "Slip Instability," Physics of Fluids, Vol. 7, No. 3, March 1964, pp. 327-334.

36 Patnaik, P. C., Sherman, F. S., and Corcos, G. M., "A Numerical Simulation of Kelvin-Helmholtz Waves of Finite Amplitude," Journal of Fluid Mechanics, Vol. 73, Part 2, 1976, pp. 215-240.

OBSERVATIONS OF LATE TRANSITIONAL AND TURBULENT FLOW IN ROUND JETS

BY

A.J. YULE

Department of Chemical Engineering and Fuel Technology,
University of Sheffield, Sheffield, England.

ABSTRACT

Transitional and turbulent flows in the mixing layer region of a round jet are investigated for a range of Reynolds numbers by using flow visualization and hot wire techniques. Attention is focused on the vortices in the transition region and the large eddies in the turbulent region. The interaction and coalescence of vortex rings in the transition region is described. The transition region is characterized by a growth of three-dimensional flow due to a wave instability of the cores of the vortex rings. The merging of these distorted vortices produces large eddies in the turbulent region. Large eddies can remain coherent up to the end of the potential core region of the jet. A conditional sampling technique is used to measure eddies moving near the jet centreline. Their averaged structure is similar to that of a vortex ring. These sampled eddies contribute greatly to local velocity fluctuations and statistical correlations.

NOMENCLATURE

D = nozzle diameter.

f = frequency.

L = distance between centres of vortices.

P_u = normalised frequency spectra of u^2.

S_t = (fD/U_j)at spectra peak = Strouhal number based on frequency of P_u peak or vortex passing frequency.

R_e = U_jD/ν = jet Reynolds number.

t = time.

u,v,w = fluctuating velocity components in x, y and azimuthal directions.

U = mean velocity.

U_c = convection velocity.

U_j = jet exit velocity.

x,y,z = cartesian coordinate system based on nozzle lip.

x_T = transition distance.

η = y/x

τ = time delay in correlation or conditional sampling measurements.

ν = kinematic viscosity.

Subscripts

1 = fixed probe signal.

2 = moving (or sampling) probe signal.

s = conditionally sampled measurements.

INTRODUCTION

This investigation has the objective of obtaining a clearer understanding of the physical nature of the large scale structure in the mixing layer region of a round jet. Cold, round, free jets developing from thin, laminar nozzle boundary layers are considered, with the notation shown in Fig.1.

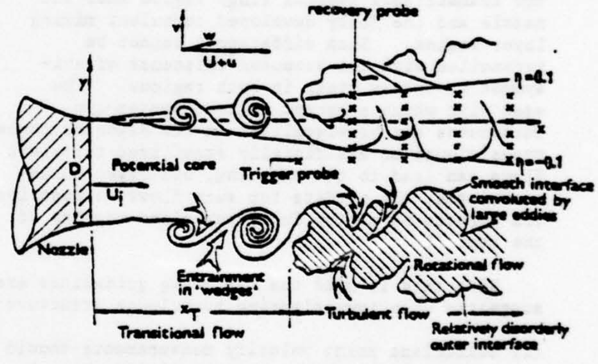

Fig.1 Notation for round free jet experiments.

The initial instability of the laminar shear layer near the nozzle is reasonably well understood both analytically (1) and experimentally (2). For all but the lowest Reynolds numbers, when other instability modes can occur, the initial instability manifests itself as the migration of vorticity to form periodic, circumferentially coherent, concentrations in the shear layer. This has the physical appearance of the rolling up of the laminar shear layer to form a periodic street of vortex rings.

The turbulent region of the mixing layer has been measured in many investigations by using hot wire techniques and these investigations (3) have indicated the importance of the large eddies in the turbulent flow. Experimental results obtained by conditional sampling (4), (5) and flow visualization (6) techniques have been used to infer that these eddies are similar to the vortex rings formed from

PRECEDING PAGE BLANK-NOT FILMED

the initial instability; however this evidence is not conclusive. These observations have much in common with the results of investigations (7), (8) of the eddy structures in two-dimensional mixing layers. It appears that the visualization and conditional sampling of eddies can be achieved in two-dimensional mixing layers with more ease than in the round jet. Line vortex-like large eddies have been found, and these generally grow in scale by coalescing with their neighbours. It has been argued (9) that the basic turbulent flow in a round jet may consist of a street of interacting and coalescing vortex rings analagous to the line vortices in the two-dimensional mixing layer. However, to the author's knowledge, the existence of vortex rings in the round jet has only been proved conclusively for a relatively short transitional, Reynolds number dependent, region near the nozzle. These initial vortex rings have been observed to coalesce. However, it is not clear that the region where this is observed is turbulent.

It has been proposed (4), (10) that many turbulent shear flows are dominated by coherent large eddies with fairly repetitive structures. Furthermore it has been proposed that these eddies have similar structures to the clearly observed vortex-structures found at lower Reynolds numbers, or in transitional regions of the same flow. However, a study of past experiments on round jet mixing layers indicates that there are substantial differences between the structures of the transitional (vortex ring) region near the nozzle and the fully developed turbulent mixing layer region. Such differences cannot be reconciled with the proposed existence of axi-symmetric vortex rings in both regions. The ease with which coherent laminar-vortex-type structures can be visualized in low Reynolds number transitional or artificially stabilized turbulent flows can lead to the tempting, but often unsubstantiated, use of data for such flows to describe the structures of the fully turbulent regions of the same flows.

With this in mind the following guidelines are suggested when investigating turbulence structure:

(i) Sufficient point velocity measurements should be made to demonstrate conclusively that the flow is locally turbulent, within accepted criteria.

(ii) Data for non-turbulent flows, for example those in which viscous forces are important, should not be used to describe the structures of turbulent flows without supporting data for the turbulent flows.

It is thus necessary to define criteria to distinguish between turbulent and non-turbulent regimes. In the absence of a universally accepted definition of turbulence it is not possible to define criteria which are applicable to all turbulent shear flows. In practise it is clear for the round jet whether local velocity time histories are associated with turbulent or transitional flow as is described below.

This investigation sets out to provide at least partial answers to the following problems:

(i) By what mechanisms does the initial vortex street break down to form turbulent flow?

(ii) Are coherent large eddies identifiable in the turbulent flow? What are the similarities and differences between them and the initial vortex rings?

(iii) Are there connections between the structure of the turbulent mixing layer and that of the vortex street near the nozzle?

TURBULENT AND TRANSITIONAL FLOW-DISCRIMINATION BY POINT MEASUREMENTS.

Point measurements of the mean and fluctuating velocity components were made in the mixing layer region of an air jet issuing from a 50.8 mm diameter nozzle for a range of jet Reynolds numbers, $9000 \leq R_e \leq 2 \times 10^5$. Cross-wires were used, with constant temperature anemometers and analogue linearizers. Data was either processed in real time, by using a Hewlett Packard Correlator, or it was stored and subsequently processed by using a data analysis computer. These experiments were intended to provide information on the locations of transitional and turbulent regions in the jet so that flow visualization and conditional sampling experiments could be planned. In addition they provide systematic quantitative data to aid the interpretation of visualizations of jet transition as a function of R_e.

Initial experiments showed that the mean velocity profile achieved its characteristic turbulent 'error function' shape in the mixing layer very near the nozzle and considerably before the local fluctuating velocity signals were turbulent in form. This is also found in the results of previous experiments on the transition of round jets (2) and two-dimensional mixing layers (11). Thus the existence of a similarity form for the mean velocity profile cannot be used as a sole criterion for proving that fully developed turbulent flow exists locally. Characteristics of the fluctuating velocity field were measured to discriminate between transitional and turbulent regions.

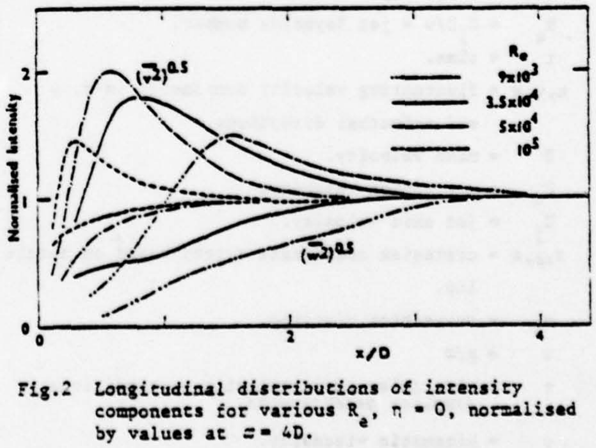

Fig.2 Longitudinal distributions of intensity components for various R_e, $\eta = 0$, normalised by values at $x = 4D$.

Figure 2 shows the distributions of $(\overline{v^2})^{\frac{1}{2}}$ and $(\overline{w^2})^{\frac{1}{2}}$ along $\eta = 0$ for different R_e. The measurements are normalised by their values at $x = 4D$. The distributions have basic similarities for all R_e. $(\overline{v^2})^{\frac{1}{2}}$ increases to a peak near the orifice and then decreases more slowly to the near constant value found in the fully developed turbulent mixing layer and $(\overline{w^2})^{\frac{1}{2}}$ increases gradually to its turbulent value which is reached at a similar distance downstream. The $(\overline{u^2})^{\frac{1}{2}}$ component increased rapidly to reach its turbulent value considerably before the other intensity components.

For a particular value of Re the asymptotic turbulent values of the three intensity components were the same to within 15%. The turbulent values of $(\overline{u^2})^{\frac{1}{2}}/U_j$ varied between 0.14 and 0.15 in the range of R_e investigated, thus indicating the existence of Reynolds number similarity. The value of x at which both $(\overline{v^2})^{\frac{1}{2}}$ and $(\overline{w^2})^{\frac{1}{2}}$ are within 5% of their turbulent values is plotted in Fig.3. This is one possible definition of the transition distance x_T.

Measurements of the Reynolds shear stress covariance $\overline{uv}(\tau)$ were made for the same jets. The measurement for $R_e = 21{,}000$ shown in Fig.4 are typical of the general trends found. There is a transition from a periodic correlation near the nozzle, where u and v are almost in quadrature, to a cusp shaped correlation at $x=4D$ which is indicative of significant high frequency components and is characteristic of low intermittency regions of turbulent shear flows. The shape of this latter turbulent distribution is retained downstream throughout the turbulent jet (in low intermittency regions). This distribution is also found in the turbulent regions for all the values of R_e and scales on local velocity and length scales. The covariances of other fluctuating quantities, e.g. $\overline{uu}(\tau)$ change at similar rates from periodic forms near the nozzle to their characteristic fully developed forms. The transitional jet flow ends when these turbulent forms of covariances (or spectra) are established and values of x_T estimated from these measurements are included in Figure 3. It is seen that this definition gives values of x_T which are typically 0.25D larger than values based on the measurements of $(\overline{v^2})^{\frac{1}{2}}$ and $(\overline{w^2})^{\frac{1}{2}}$. However one can reasonably assume that the jet mixing layer is locally turbulent when the peak values of $(\overline{v^2})^{\frac{1}{2}}$ and $(\overline{w^2})^{\frac{1}{2}}$ are within 15% of each other and the values are independent of x. It was also concluded that the attainment of similarity distributions of $(\overline{u^2})^{\frac{1}{2}}$ and U across the mixing layer (and also the attainment of a constant rate of spread for the mixing layer) could not be used as criteria for proving the local existance of fully developed turbulent flow.

Bradshaw (12) suggested that the assumption of a constant transitional Reynolds number, $x_T U_j/\nu = 7\times10^5$, may provide a reasonable estimate of x_T for his experiments. It can be seen from Fig.3 that $x_T U_j/\nu = 1.2 \times 10^5$ gives reasonable agreement with the present data.

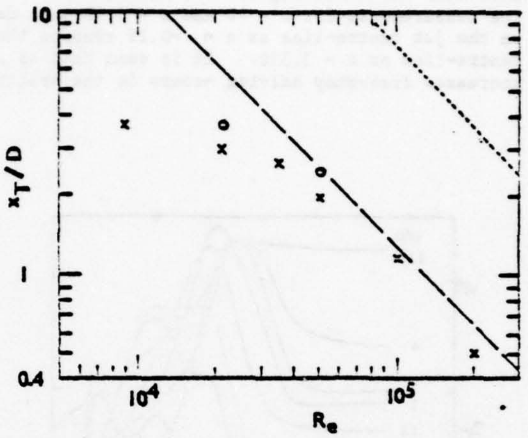

Fig.3 Transition distance as a function of Reynolds number (air jet),

------------ $x_T U_j/\nu = 7\times10^5$,

— — — — — $x_T U_j/\nu = 1.2\times10^5$

× intensity measurements.

o covariance measurements.

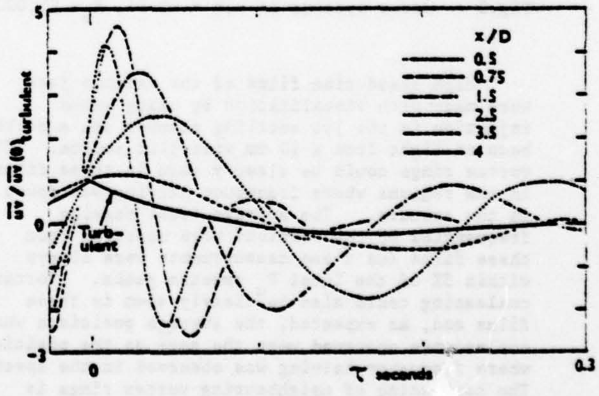

Fig. 4 Shear stress covariance with time delay, $\eta = 0$, $R_e = 21{,}000$.

VORTEX RINGS IN TRANSITION REGION OF AIR JET

The presence of vortex rings can be related to peaks in velocity frequency spectra measured in the jet potential core. Figure 5 shows the u spectra, P_u, for R_e = 21,000 for different x along the line η = −0.15 which is in the jet potential core near the inner edge of the mixing layer. The measurements for x = 4D and x = 5.5D were made on the jet centre-line as η = −0.15 crosses the centre-line at x = 3.33D. It is seen that as x increases frequency halving occurs in the spectra.

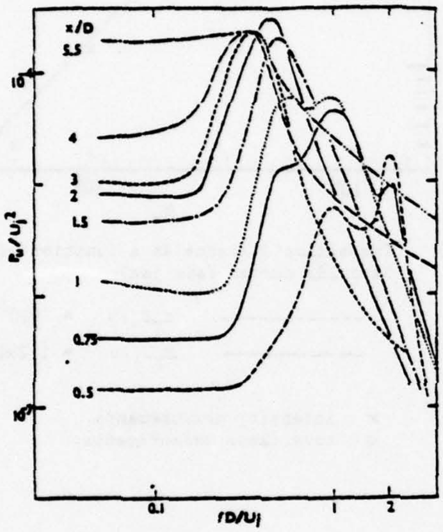

Fig.5 Power spectra of u, η = −0.15, R_e = 21,000

High speed cine films of the various jets were made with visualization by using smoke injection in the jet settling chamber and a narrow-beam of light from a 10 mm wide slit source. The vortex rings could be clearly seen in these films in the regions where frequency halving was found in the spectra. The average local passing frequencies of the vortices were measured from these films and these measurements were always within 5% of the local P_u spectra peaks. Vortex coalescing could also be clearly seen in these films and, as expected, the average positions where coalescence occurred were the same as the positions where frequency halving was observed in the spectra. The coalescing of neighbouring vortex rings is similar to that observed for line vortices in two-dimensional mixing layers (8) and it involves the engulfment of potential flow fluid.

The distribution of Strouhal numbers, $S_t(x)$, derived from u spectra are shown in Fig.6 for three values of R_e. Examination of the cine films of the jets combined with the spectra measurements and the knowledge of the locations of the transitional and turbulent regions yielded the following qualitative observations of the transitional flow:

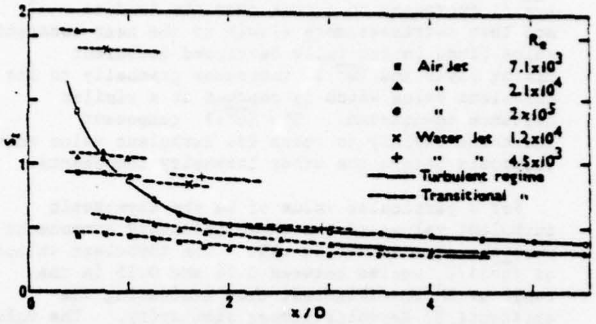

Fig.6 Strouhal numbers measured from potential core u spectra peaks for air jet and mean vortex passing frequencies for water jet.

(i) Ring vortices are not observable in the turbulent regions of the jets.

(ii) Peak-frequency halving, associated with coalescence, does not occur in the turbulent region.

(iii) The transitional flow can contain up to three vortex coalescing regions depending on R_e.

(iv) These regions overlap in a given jet, i.e. there are no fixed values of x at which coalescence *always occurs*.

(v) The initial orderly, spiral interface between jet and entrained ambient fluid in the vortex becomes increasingly disordered and diffuse as coalescence and the engulfment of new fluid occurs.

(vi) During the last observable coalescing of vortex rings, at the end of the transition region, potential core fluid and some fluid originally contained in the vortices, is ejected outwards between the vortices and this forms a diffuse, obscuring layer of smoke at the outer part of the jet.

(vii) Regions of diffuse smoke move as coherent structures in the turbulent region. The structures of these large turbulent eddies and their movements are more disorganised than those of the transitional vortex rings.

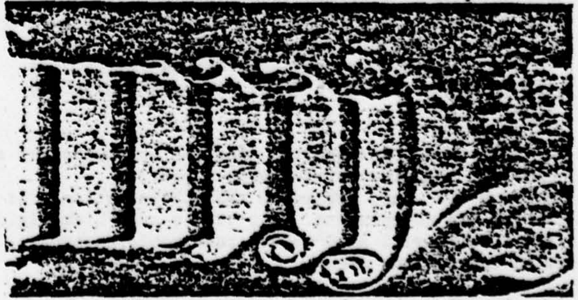

Fig.7 Submerged water jet visualised by pulsed formation of hydrogen bubbles across vertical diameter at orifice, R_e = 9000.

FLOW VISUALIZATION IN SUBMERGED WATER JETS.

Flow visualization of the transitional and turbulent flows is simplified by using water rather than air because of the lower velocity required to achieve a given Reynolds number. Hydrogen bubble visualizations of the transitional flow in a 50.8 mm diameter water jet were made for a range of R_e. Fig.7 shows a typical frame from a cine film for $R_e = 9000$. Two vortices are coalescing at the end of the transition region and the remains of the previous pair of coalescent vortices can be seen in the turbulent region as a relatively disorganised, diffuse region of bubbles on the right hand side of the frame. These diffuse regions generally remained observably coherent for several nozzle diameters downstream of the end of the transition region. Thus large eddies in the turbulent jet can be formed directly from the interaction of the transitional vortex rings. As with the smoke jet visualizations, these eddies were much less clearly observable than the vortex rings in the transition region.

The movements of vortices in the transition region were measured from the cine films. The structures of individual vortices and their movements during the coalescing process were neither strictly repetitive nor periodic. For example, although coalescing of the transitional vortices usually involved pairs of vortices, approximately one in six vortex coalescings involved three vortices and there was a less frequent occurrence of a single vortex stretching and disintegrating, without coalescing.

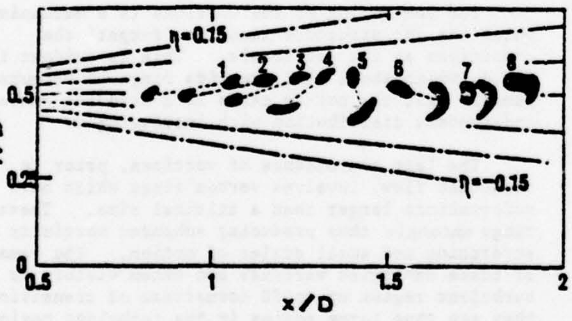

Fig.8 Movements of centres of coalescing vortices measured at intervals of 0.045s, Re=12,000.

Figure 8 shows the positions and approximate core shapes at intervals of 0.045s for a typical coalescence in the water jet with Re = 12,000. The second vortex ring accelerates, reduces its diameter and passes inside the first ring which simultaneously increases its diameter and decelerates. The cross-sections of the vortex cores, particularly that of the inner vortex, deform and stretch as they coalesce. During this process irrotational fluid from both sides of the mixing layer is engulfed to produce 'entrainment wedges' (Fig. 1 and Fig.7).

There is a significant random variation in the process of coalescence. For example, Fig.9. shows the probability distribution of the distances between 100 pairs of coalescing vortices as they pass $x/D = 1$ for $R_e = 12,000$. Fig.9 includes the distribution of vortex spacings in a two-dimensional mixing layer measured by Roshko (7) and these curves have some similarity. Roshko proposed that his mixing layer was a turbulent flow produced by the random motions of line vortices. However the region in which the present measurements were made in the round jet was not fully developed turbulence within the criteria described above. Thus it cannot be said, on the basis of this data, that the random movements of vortex rings effectively produce turbulent flow in a round jet. The differences between the transitional vortex ring flow and the fully turbulent flow are most clearly realised by studying the three-dimensional nature of the flow.

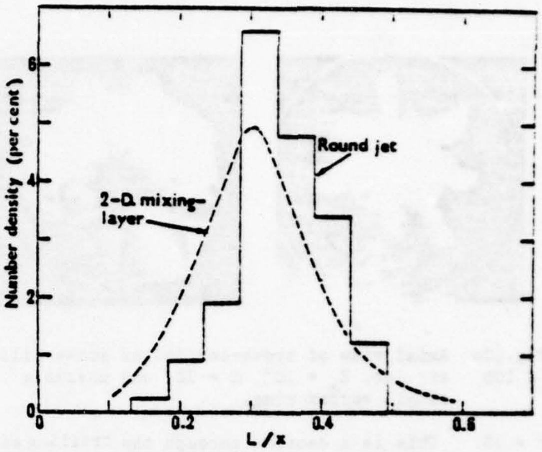

Fig.9 Probability distributions of vortex spacings in two-dimensional mixing layer (7) and round jet, $x/D = 1$, $R_e = 12,000$.

THREE-DIMENSIONALITY OF TRANSITION

The interactions of vortex rings during transition produce outwards jets of fluid. This fluid forms a relatively diffuse region at the outer part of the jet which moves more slowly than the vortices. This phenomenon indicates the importance of the three-dimensional instantaneous structure in the transitional and turbulent flows. As the u,v and w fluctuating velocity components are of the same magnitude in the turbulent region the instantaneous structures of the transitional and turbulent flows should be investigated and modelled in all three dimensions. There is no justification for restricting investigations or models to planes through the jet centre line and thus implicitly assuming a two-dimensional (axysymmetric) instantaneous turbulence structure.

The development of three-dimensional flow in the smoke filled air jet was investigated by filming the jet looking upstream with cross sections of the jet illuminated at different longitudinal positions. These films revealed that the growth of three-dimensionality in the transition region was basically an ordered growth of wave deformations of the cores of the vortex rings. Figure 10(a) is a front view of the jet with $Re = 10^4$ showing a cross-section at

Fig.10a & 10b Axial view of cross-section of smoke filled air jet, $R_e = 10^4$, $x = 3D$, and unstable single vortex ring.

$x = 3D$. This is a section through the trailing edge of the coalescing vortices at the end of the transition region. The fluctuating velocity field at this value of x has not yet reached all the properties of the fully developed turbulent flow which begins at $x = 4D$. Jets of fluid are shed from regions between vortices as seen in Fig.10a. These outward jets form the outer diffuse regions of smoke noted in side views of the jets.

The orderly lobed appearance of the smoke is attributable to the displacement of the vortex core (or coalescing cores) both radially and longitudinally into a standing wave pattern. The films showed that vortices were axisymmetric when they were formed near the nozzle and the amplitude of the wave deformation of the cores then increased with increasing x. This type of natural core instability has been investigated for single impulsively formed vortex rings by Widnall and Sullivan (13). For a given toroid diameter the number of core waves was found (13) to increase with decreasing thickness of the viscous core.

The similarity between the core wave instability in the transitional vortices in the jet and the instability of a single vortex ring can be seen by comparing Fig.10a with Fig.10b which is a front view of a single vortex ring 8D from a 50.8 mm diameter nozzle. The vortex has a convection velocity of 3 m/s and it thus has similar dimensions and convection velocity to the rings in Fig.10a. The circumferential waves in the outer potential flow of the vortices, as marked by the smoke, are in antiphase with the displacement of the vortex core.

GENERAL DESCRIPTION OF TRANSITIONAL JET STRUCTURE

The experiments outlined above allow a qualitative description of the events involved in the transition process and these events are sketched in Fig.11. Natural instability of the initial laminar shear layer produces a street of vortex-ring-like vorticity concentrations. As these vortex rings move downstream they generally coalesce with neighbouring rings so that the scale and separation of the vortex rings increases with distance from the nozzle. However, although point velocity measurements in this transitional flow exhibit periodic correlations and peaked spectra, there is considerable random variation in the movements and strengths of the coalescing vortices. Furthermore the vortex rings lose their phase agreement across the jet as they move downstream.

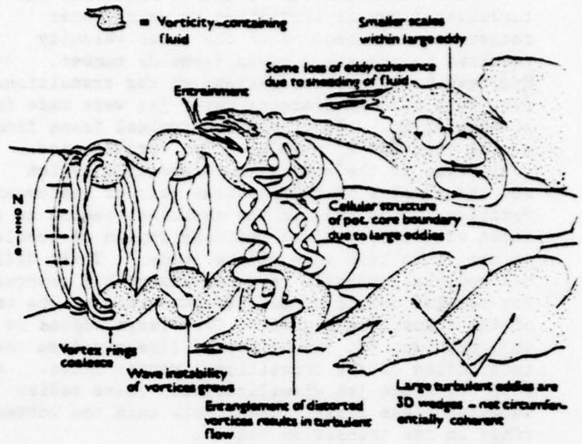

Fig.11 Physical structure of transitional jet.

The gradual increase of w fluctuations with distance from the nozzle is caused by the gradual, almost linear, growth of orderly wave deformations of the cores of the vortex rings. From one up to at least three regions of vortex coalescence can be observed in the transition region, depending on the jet Reynolds number and nozzle boundary layer thickness. Vortex ring coalescence cannot be observed downstream of the end of the transition region.

The coalescing of the vortices is a mechanism by which the jet structure tends to 'forget' the conditions at the jet nozzle. This is evident in Fig.6. which shows that the wide range of Strouhal numbers near the nozzle tends to a Reynolds number independent distribution with increasing x.

The last coalescence of vortices, prior to turbulent flow, involves vortex rings which have core deformations larger than a critical size. These rings entangle thus producing enhanced vorticity stretching and small scales of motion. The remains of these entangled vortices are often visible in the turbulent region up to 5D downstream of transition and they are thus large eddies in the turbulent region.

FLOW VISUALIZATION OF TURBULENT MIXING LAYER

Injection of dye into the mixing layer near the nozzle in the water jet provided visualization of deformations of the mixing layer interface produced by large eddies in the fully developed turbulent region. These visualizations were similar to those derived by Dimotakis and Brown (14) for high R_e turbulent two-dimensional mixing layers in a water channel. The dye had a relatively disordered and diffuse appearance at the outer edge of the mixing layer but there was a sharp convoluted interface at the inner, high velocity edge. The bulges of dye at the inner edge, marking the large eddies, have wedges of engulfed potential core fluid between them similar to those between vortices in the transition region. The entrainment wedges slope backwards at approximately 45° to the axial direction at the centre of the mixing layer. These wedges are the 45°

structures evident in many schlieren studies of turbulent jets. Films of the turbulent regions of both the air and water jets showed that the large eddies had a wide range of sizes and trajectories at any position and there was no obvious symmetry between structures on opposite sides of the jet. This suggests that the eddies lack the circumferential coherence of the transitional vortex rings. The dye injection experiment showed that large eddies coalesced with neighbouring eddies as they moved downstream. However this coalescing process differed from the clearly observed 'leapfrogging' coalescing of transitional vortex rings (Fig.8). The disappearance of the entrainment wedge separating the turbulent eddies was the only clear indication that coalescence had occurred. The observed process was similar to that described for large eddies in high R_e two-dimensional mixing layers (14). Intermittent outward jets of dye-containing fluid burst from the mixing layer. These outward jets appeared to accompany the coalescing process and they are similar to the outward jets seen in between vortices at the end of the transition region (Fig.10a). Visualizations of the jet downstream of the potential core exhibited similar outward bursts of fluid.

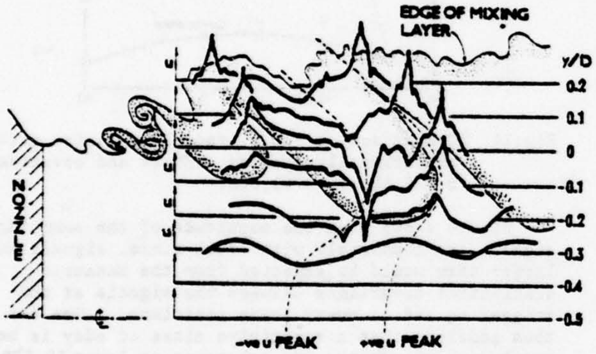

Fig.12 Velocity (u) time histories measured by array of hot wires in turbulent water jet.

Flow visualization techniques do not appear to be capable of providing quantitative data on large eddy structure and interaction in the turbulent region. Thus a conditional sampling technique was developed to study the eddies in more detail. Conditional sampling requires a triggering or conditioning criterion which is directly associated with the event or structure which is to be measured. The selection of suitable triggering criteria, derived from u fluctuations, was facilitated by simultaneously recording velocity time histories while filming the water jet with dye injection. Figure 12 shows u time histories measured by an array of hot wires at different radial positions at $x = 2D$ for $R_e = 50{,}000$. The flow was locally fully turbulent. The u measurements, shown on arbitrary scales, indicate the relationship between features of these signals and the shape of the edges of the mixing layer as indicated by the dye.

This type of analysis was made for a series of consecutive large eddies. There were considerable variations in the shape of the dye interface and the associated u time histories from one eddy to the next. Unusually large peaks in the u signals were found to be features which could be most easily correlated with the shapes of the dye patterns. The peaks ranged in magnitude from 1.5 to 3 times the local r.m.s. value of u. Thus, at the outer edge of the mixing layer, a series of large positive u peaks were found and these corresponded to regions of dye projecting from the jet. In the centre of the mixing layer ($y/D = 0$) both large positive and large negative peaks were found while at the high velocity edge of the mixing layer large negative u peaks corresponded to regions inside the dye (i.e. the rotational flow within the large eddy). In general large positive u peaks correspond to regions between eddies, i.e. the wedge of entrained fluid from the potential core. Large negative u peaks correspond to regions within the eddies. As is indicated in Fig.12 the positions of both the negative and positive u peaks advance and then retreat in phase as one moves out from the centre of the jet. In the central part of the potential core positive peaks in the u fluctuations roughly corresponded with the passing of the bulge of dye marking the large eddy and negative peaks corresponded to the interval between eddies passing. Examination of the hydrogen bubble time lines in Fig. 7 shows a similar relation between potential core u fluctuations and the passing of transitional vortices. However the u fluctuations outside the potential core were quite different for the turbulent and transitional vortex ring cases. The axisymmetric vortex rings at the beginning of the transition region produced skewness in u fluctuations but with opposite signs to that produced by the large turbulent eddies. Thus the vortex rings produced large negative u peaks at the outer edge of the mixing layer (sometimes producing reverse flow) and large positive u peaks at the inner edge where the instantaneous velocity exceeds U_j by up to 20% in the transition region but never more than 2% in the turbulent region. In the transition region vortex rings produced smooth low frequency velocity variations with larger gradients as the viscous cores passed. A detailed study (15) showed that the vortex rings had basically similar structures to classical single vortex rings with cores of solid body rotation. However in the turbulent region it was found that, although smooth velocity signals were measured in potential flow regions, the flow in the dye containing, rotational regions of the eddies produced higher frequency, lower amplitude u signals superimposed on the basic large amplitude peaks. These higher frequencies are the smaller scales of turbulence and they can be interpreted physically as being the interacting remnants of smaller eddies and vortices which merged at earlier times.

CONDITIONAL SAMPLING IN TURBULENT REGION

An extensive and continuing study has been made of the relationships between large u and v peaks and eddy structure and the use of these peaks to conditionally sample the large eddies in the turbulent jet. Parts of this work have been reported (5), (15) and a fuller description will be given at a later date. It is found that the large positive and negative u peaks occur at similar times as large peaks in v fluctuations. Thus the movements of fluid induced by the large eddies, which are responsible for these peaks, provide the major contribution to the shear stress uv. Conditional sampling (5) using the large u peaks near the centre of the mixing layer shows radial phase variations and the convection of the flow structures downstream. However the large variations in eddy structures and movements at any position results in very low levels of recovered signals. Conditional sampling of a particularly repetitive type of eddy produces reasonably high levels of recovered signal and an experiment of this type is described below.

The combined flow visualization/hot wire experiment showed that when a turbulent eddy moved unusually close to the jet centre-line the local potential core u fluctuations had unusually large positive and negative peaks. The probe positions used for conditional sampling are shown in Fig.1. The triggering hot wire probe, measuring u_1, was positioned in the air jet potential core at $x = 2D$, $\eta = -0.2$ for $R_e = 43{,}000$. Previous experiments showed that there was fully-developed turbulence for $x \geq 2D$. When u_1 had a negative peak with a magnitude greater than $2.8\,(\overline{u_1^2})^{\frac{1}{2}}$ an electronic triggering circuit was activated and the subsequent 0.01s of time history u_2 at the recovery probe was measured and stored. The final conditionally sampled signal u_s was derived by obtaining an ensemble average of at least 256 portions of the u_2 time history by using 256 consecutive large u_1 peaks. These triggering peaks represent 5% of the total u_1 negative peaks and thus 5% of the total number of large eddies responsible for the potential core fluctuations were sampled.

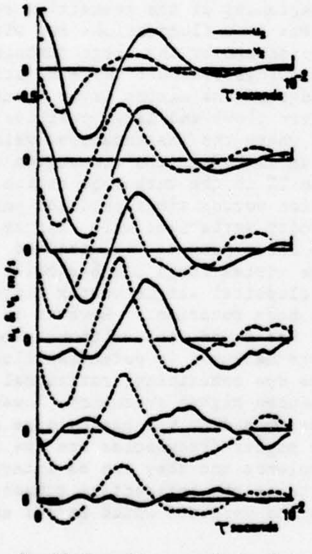

Fig.13 Conditionally sampled time histories of fluctuating velocity component at $x=2.5D$, $R_e = 43{,}000$. Triggered by -ve u_1 peaks greater than $2.8\,(\overline{u_1^2})^{\frac{1}{2}}$ at $x=2D$, $\eta = -0.2$.

Fig.13 shows the conditionally sampled time histories of the fluctuating velocity components u_s and v_s at $x = 2.5D$. The large negative u_s peaks at $\eta = -0.15$ and $\eta = -0.1$ correspond to the triggering peak which has been convected downstream from $x = 2D$. The large - ve u peaks in the potential core are seen to correspond to structures producing + ve u peaks in the centre and outer parts of the mixing layer and both large - ve and large + ve v peaks for the complete width of the mixing layer. Similar measurements at larger values of x showed that these sampled signals retained their shapes up to the end of the potential core ($x = 6D$) and they had a convection velocity $U_c = 0.72\,U_j$ for $-0.2 < \eta < 0$. The v_s signals retained 75% of their magnitude at the end of the potential core but the magnitude of the u_s signal dropped to approximately 40% of its value. Thus v component distributions associated with the sampled eddies were more coherent than the u distributions both spatially and with increasing existence times of the eddies.

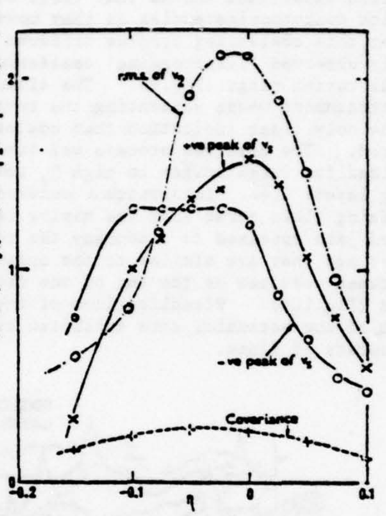

Fig.14 Comparison of r.m.s. radial intensity with conditionally sampled signals and covariance, $x = 2.5D$, $R_e = 43{,}000$.

Fig.14 shows that the magnitude of the sampling signals are comparable with local r.m.s. signals and larger than would be expected from the measured statistical covariance between the signals at the triggering and recovery probe positions. One can thus conclude that a repetitive class of eddy is being sampled which retains its coherence at least to the end of the potential core, is coherent for most of the width of the mixing layer, and is responsible for particularly large velocity fluctuations in the potential core.

The sampled signals at different values of x showed that, for longitudinal distances up to about 1.5D from the triggering position, it was reasonable to invoke the Taylor hypothesis of an unchanging convected eddy structure for the sampled eddies. Thus the u_s and v_s time histories at $x = 2.5D$ were converted into an approximate spatial velocity field in a coordinate system moving with the velocity $U_c = 0.72\,U_j$. In this moving frame of reference the transverse velocity component is v_s and the longitudinal velocity component is given by $U + u_s - U_c$. Fig.15 shows the directions and magnitudes (given by the length of each arrow) of the local velocity for the sampled eddies moving in this frame of reference. It is seen that the large negative u triggering peaks occurred between two large eddies on the inner side of the mixing layer which were on average, 1.3D apart at $x = 2.5D$. The general form of the cross section of the sampled eddies, with their longitudinally elongated cores, is very similar to that of laminar vortex rings.

These measurements do not imply that the sampled eddies are axisymmetric. In fact most evidence indicates that the eddies are strongly three-dimens-

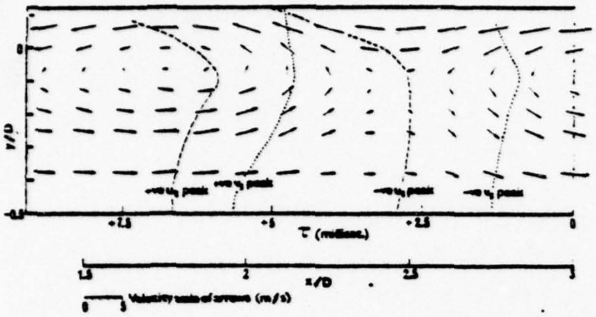

Fig.15 Conditionally sampled velocity field associated with large - ve u peaks at $\eta = -0.2$, $x = 2D$, $R_e = 43{,}000$.

ional and are coherent for only part of the circumference of the jet. For example the correlation coefficient for u fluctuations at $\eta = 0$ for diametrically opposite sides of the turbulent mixing layer is less than 0.05. Measurements of this correlation coefficient showed a gradual decrease in value in the transition regions of the jets from an initial value of approximately 0.9. This corresponds with the observed growth in three-dimensionality of the initially axisymmetric vortex rings. The conditional sampling technique inherently averages, and thus conceals, any randomness associated with the eddies. Thus although u and v fluctuations with higher frequency components than those associated with the large eddy scale are known to be present within the eddies, they are concealed by the sampling technique which produces the orderly velocity field seen in Fig.15. The spatial phase variations of the u and v peaks associated with the sampled eddies are included in Fig.15. It is seen that the sampled u and v signals appear to be approximately in quadrature for much of the width of the jet and this implies that there is little contribution to the shear stress $\overline{uv}$ by the sampled eddies. However examination of the u_s and v_s time histories at different radial positions, Fig.13, shows that asymmetries in these signals give small net positive contributions to the shear stress. It appears that the sampling technique is measuring an inner component of the coherent large eddies and other components, probably in the outer part of the mixing layer, are not important contributors to the large potential core fluctuations and are thus not measured. The interaction and merging of the sampled structures with other components of the motion may also give important contributions to the shear stress.

CONCLUDING REMARKS

It has been shown that transition in round jets can involve the entanglement of streets of vortex rings which have developed wave deformations of their viscous cores. The large scale structures produced by this process form coherent large eddies in the turbulent mixing layer region. It appears that much of the transitional flow is sufficiently orderly to be amenable to three-dimensional computer modelling. Coherent three-dimensional eddies are such dominating components of the turbulent mixing layer that their structures and interactions are essential aspects of future experimental and modelling studies of the round jet.

REFERENCES

1 Michalke, A. and Freymuth, P.,"The Instability and the Formation of Vortices in a Free Boundary Layer,"C.P.No.4,Part 2,A.G.A.R.D., 1966.

2 Wille, R., "Growth of Velocity Fluctuations Leading to Turbulence in a Free Shear Layer," A.F.O.S.R.Tech.Rep.,Hermann Fottinger Inst.,Berlin, 1963.

3 Bradshaw,P.,Ferriss,D.H. and Johnson,R.F., "Turbulence in the Noise Producing Region of a Circular jet," Journal of Fluid Mechanics,Vol.19, 1964, pp.591-624.

4 Davies, P.O.A.L. and Yule, A.J., "Coherent Structures in Turbulence," Journal of Fluid Mechanics, Vol.69,1975,pp.513-537.

5 Lau,J.C. and Fisher, M.J.,"The Vortex-Street Structure of "Turbulent" Jets. Part 1," Journal of Fluid Mechanics, Vol.67, 1975,pp.299-337.

6 Crow,S. and Champagne,F.H.,"Orderly Structure in Jet Turbulence," Journal of Fluid Mechanics,Vol. 48, 1971, pp.547-591.

7 Roshko,A., "Progress and Problems in Understanding Turbulent Shear Flows," Turbulent Mixing in Nonreactive and Reactive Flows, Plenum Press, N.Y., pp.295-311.

8 Browand,F.K.,"Ensemble-Averaged Large Scale Structure in the Turbulent Mixing Layer," Turbulent Mixing in Nonreactive and Reactive Flows, Plenum Press,N.Y.,1975,pp.317-321.

9 Laufer,J.,Kaplan,R.E. and Chu,W.T.,"On the Generation of Jet Noise,"Paper 131,A.G.A.R.D. Conference on Noise Mechanisms,Brussels,1973.

10 Roshko,A.,"Structure of Turbulent Shear Flows: A New Look," AIAA Paper No.76-78,January,1976.

11 Yule,A.J.,"Two-Dimensional Self-Preserving Turbulent Mixing Layers at Different Free Stream Velocity Ratios," R.& M.No.3683,1972,Aeronautical Research Council, London.

12 Bradshaw,P.,"The Effect of Initial Conditions on the Development of a Free Shear Layer," Journal of Fluid Mechanics,Vol.26,1966,pp.225-236.

13 Widnall,S.E. and Sullivan,J.P.,"On the Stability of Vortex Rings,"Proceedings of the Royal Society, A332,1973,pp.335-353.

14 Dimotakis,P.E. and Brown,G.L.,"Large Structure Dynamics and Entrainment in the Mixing Layer at High Reynolds Number," Tech.Report CIT-7-PU, Aug.1975, Project SQUID, Purdue University, West Lafayette, Indiana.

15 Yule,A.J.,Bruun,H.H.,Baxter,D.R.J. and Davies, P.O.A.L.,"Structure of Turbulent Jets,"ISVR Memo No. 506, April, 1974, University of Southampton.

ACKNOWLEDGEMENTS

Experiments were supported by the Science Research Council at the University of Southampton. The author thanks Prof. P.O.A.L.Davies for many useful discussions.

VORTEX PAIRING AND ORGANIZED STRUCTURES IN AXISYMMETRIC JETS UNDER CONTROLLED EXCITATION

K. B. M. Q. Zaman and A. K. M. F. Hussain

Mechanical Engineering Department
University of Houston
Houston, Texas

ABSTRACT

The conditions most favorable for vortex pairing in the near field of a circular jet have been investigated through hot-wire measurements in two circular air jets subjected to controlled excitation. Two distinct modes of vortex pairing, inferred from the subharmonic spectral component of the u-signal, have been identified. The first mode is attributed to the exit shear layer instability which scales on the exit free shear layer width, and the second (jet) mode scales on the jet diameter. Strongest pairing occurs at $St_\theta = 0.011$ in the 'shear layer mode' and at $St_D = 0.85$ in the 'jet mode'. At relatively high St_D, the shear layer mode (at $St_\theta = 0.011$) was observed to involve successive stages of pairing; however, only one pairing could be identified in the jet mode even though St_θ varied over a wide range. The data indicate that the two modes of vortex pairing are independent and excitation at one of the modes is sufficient to induce vortex pairing in the near field irrespective of whether the excitation corresponds to the other mode or not.

NOMENCLATURE

x = axial distance downstream from the jet exit plane
D = exit diameter
θ = momentum thickness of efflux boundary layer measured at 0.3 cm upstream from the exit
f_p = Frequency of controlled excitation producing sinusoidal surging at the exit
U = longitudinal mean velocity
u'_t = longitudinal total fluctuation intensity (rms)
u'_f = rms amplitude in the u' signal at f_p
$u'_{f/2}$, $u'_{f/4}$, $u'_{f/8}$ = rms amplitude in the u' signal at the successive subharmonic frequencies
u'_{ec}/U_{ec} = relative exit excitation level

$St_D = \frac{f_p D}{U_e}$

$St_\theta = \frac{f_p \theta}{U_e}$

$Re_D = \frac{U_e D}{\nu}$

Subscripts

e = jet exit
c = jet centerline

INTRODUCTION

The developing regions of free turbulent shear flows are dominated by large scale coherent structures which appear to play the key role in observed near field gross features like entrainment, mixing and aerodynamic noise production [1-5]. It is reasonable to suspect that the large scale coherent structures of the developing region persist in the so-called self-preserving regions of these shear flows. Thus, it is likely that the coherent structure in a turbulent shear flow never truly achieves independence of the initial condition in a finite flow length, and that turbulence self-preservation, though a valid concept for the asymptotic far-field, may not be achievable in laboratory flows.

The evolution of the large scale structure in free shear flows appears to occur through interactions (like pairing) of large-scale vortical motions [1,2,5-8], an anticascade phenomenon occuring simultaneously with the evolution of the small scale motions through vortex stretching. When the initial free shear layer is laminar, the initial vortical structure results from the (inviscid) instability and roll-up of the free shear layer, the initial size and spacing being determined by the most unstable eigenmode of the profile. It is possible that a free shear layer resulting from an initially turbulent boundary layer can also roll up into organized vortical structure which then evolve not unlike the initially laminar case.

The role of vortex pairing in mixing layer growth has been the subject of extensive recent studies. Winant and Browand [8] showed that any non-uniformity in strengths or spacing of two (or three) adjacent rolled up line vortices, formed in a water mixing layer, caused them to undergo successive stages of pairing to form progressively larger coherent structure downstream. They inferred that ingestion of non-turbulent fluid during the pairing process was the primary mechanism for entrainment and thus growth of the shear layer. Browand and Wiedman [9] has shown that significant Reynolds stress production is associated with the vortex pairing interaction process.

Browand and Laufer [1], from a flow visualization experiment in a circular water jet, hypothesized that the large scale structures just downstream of the potential core can be traced back to the upstream vortices whose generation depended on the exit shear layer instability. They observed difference in the statistical behavior (e.g. passage frequency, spatial coherence) between these initial rolled up vortices and the downstream large scale structures, and conjectured that independence of the large scale structure further downstream from the initial shear layer structure was achieved by successive stages of vortex pairing.

Davies and Yule [10] in a summary of the Colloquium on organized turbulence structures held at the University of Southampton in 1974, described Yule's own findings of coherent structures in axisymmetric jets from flow visualization experiments. Observation within the first ten diameters revealed the existence of interacting and coalescing ring vortices, and the large scale organized structures downstream in the turbulent round jet 'differed fundamentally from the laminar ring vortices nearer the nozzle from which they developed'.

Crow and Champagne [11] observed the existence of orderly 'vortical puffs' in axisymmetric jets, in addition to the slender vortex rings formed near the exit due to exit shear layer instability and roll up. They destroyed the 'surface ripples' by tripping the exit boundary layer and studied the effect of controlled excitation on the 'puff mode'. They found that the 'preferred mode', ie. the one producing maximum disturbance amplification downstream, occurred at $St_D = 0.30$. They also noticed pairing of the vortex puffs giving rise to a strong subharmonic structure when driven at twice the preferred mode, namely at $St_D = 0.60$.

The effect of acoustic excitation on the near flow structure of jets have been studied among others by Becker and Massaro [12], Rockwell [13], Vlasov and Gineveskiy [14] and the present authors [5]. Becker and Massaro [12] found that the Strouhal number (St_D) of the disturbance to which a given circular jet exit shear layer was most unstable varied approximately as the square root of the Reynolds number (Re_D). Rockwell [13] classified the plane jet flow under acoustic excitation into five regions depending on the ratio of excitation frequency (f_p) *to the natural vortex roll-up frequency* (f_N). *He* found that in two of these five regimes, the effect of excitation was very pronounced and clear vortex roll-up followed by coalescence phenomenon occurred. One of these two regimes corresponded to the case when the two frequencies matched and in the other the ratio between the two was about one third ie., $f_p/f_N = 1/3$. Vlasov and Ginevskiy [14] observed large amplification of centerline turbulence intensity at $St_D = 0.5$ but its suppression relative to the non-excited case at $St_D = 2.75$.

As reported in ref. [5], we had noticed the occurrence of a stable vortex pairing phenomenon in circular jets at $St_D = 0.85$ for three different nozzles over a moderate range of Re_D, the exit shear layer thickness in that range varying appreciably. This led us to suspect that the observed pairing phenomenon was not a consequence of the initial shear layer instability mechanism.

The present study evolved as a result of an effort to define the ranges of characteristic jet flow parameters favoring strong vortex pairing and to understand the role of exit shear layer instability on the vortex pairing mechanism in the jet.

As we shall see, the vortex pairing observed at $St_D = 0.85$ seems to be associated with a distinct mode of instability of circular jets, and independent of the initial shear layer instability.

EXPERIMENTAL PROCEDURE

The experiments have been carried out in a circular air jet facility consisting of two settling chambers in sequence. Sinusoidal perturbations in the exit profile are introduced at controlled frequencies and amplitudes with the help of a loudspeaker attached to the wall of the first chamber. The flow from the first settling chamber goes through a contraction and a diffuser into the second settling chamber before exiting through the nozzle into a large room with controlled temperature and humidity. The two settling chamber arrangement was introduced for eliminating any possible asymmetry introduced by the speaker. The exit mean and turbulence profiles were checked to be axisymmetric. The absence of any harmonic of the excitation frequency in the spectra of the exit velocity signal confirmed that the excitation was indeed pure tone (sinusoidal). The study was carried out with two nozzles (of Batchelor-shaw contour) of diameters 2.54 and 7.62 cms.

Probe traverses, with a traverse mechanism capable of movement in axial (x), transverse (y) and azimuthal (z) directions with a resolution of 0.00254 cm (.001 in) and in the angular (θ) direction in the x-y plane with a resolution of 0.01 degree, were done through remotely controlled stepping motors. A 4μ dia., 2.5 mm long tungsten hot-wire along with DISA equipment was used to obtain the instantaneous velocity signal. A Spectrascope SD335 spectrum analyzer (500 frequency lines) was used to obtain the velocity spectrum. The amplitudes (in dB) and frequencies (Hz) *of the spectral peaks were read* directly from the spectrum analyzer. The exit boundary layer thickness data were obtained/analyzed on-line with our laboratory minicomputer (HP 2100).

RESULTS AND DISCUSSION

The exit boundary layer momentum thickness $\theta = \int_0 U/U_c(1 - U/U_c)dy$ was used as the characteristic length scale of the free shear layer and was determined *at 3 mm upstream from the exit plane.* Before the start of the excitation studies, the $\theta = \theta(Ue)$ functions were determined from boundary layer traverses in the two nozzles for the entire ranges of available speed; these functions were found to be repeatable within 2%; excitation amplitudes used for vortex pairing studies produced no noticeable changes in these functions. Subsequently, for each nozzle the θ value at any Ue was found directly from the corresponding $\theta(Ue)$ plot. Even though the exit boundary layer was not fluctuation free, the fluctuation intensity profiles in the nozzle exit boundary layer could be attributed to oscillations of laminar boundary layer [15]. The exit velocity profile shape factor was essentially that of the Blassius profile, ie., 2.59. The exit boundary layer was thus assumed laminar for the entire range of speed used.

Investigation of the jet flow field revealed that pairing can occur with excitations at Strouhal numbers larger than $St_D = 0.85$. This, however, does not invalidate the findings reported in ref. [5]. It turns out that in order to detect these high Strouhal number pairing phenomenon, the probe has to be moved away from the centerline in the potential core towards the shear layer. As we will see, these pairings occur in the shear layer in the 'shear layer mode' as opposed to the 'jet mode' which involves the entire cross section.

Immediately downstream from the exit, the jet centerline is too far from the vortex core in the shear layer; the probe has to be close to the shear layer to capture the signatures of the passing rolled-up shear layer vortices or the associated coalescence event. We will present evidence which will suggest that a circular jet has two independent modes of instability and associated pairing: the shear layer mode and the jet mode.

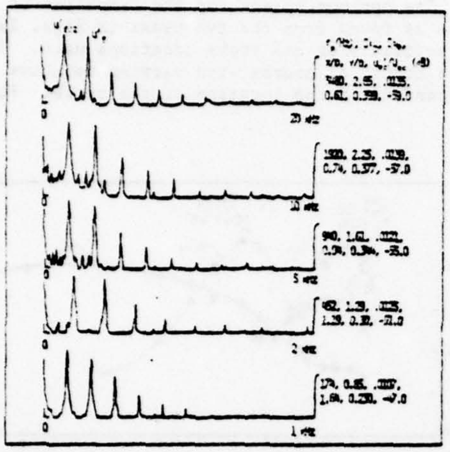

Fig. 1 Frequency spectra of the longitudinal velocity signal for shear layer mode excitations; jet dia: 2.54 cm. Vertical scales (log) are arbitrary and horizontal scales (linear) are indicated. The second peak in each plot represents the fundamental (f_p). Related information is indicated for each case.

Fig. 1 shows the one-dimenionsal frequency spectra of the longitudinal velocity u at the indicated off-centerline probe locations for the cases when vortex pairing can be inferred from the subharmonic amplitude. Note that for each location, the second peak in the spectra (from left) corresponds to the frequency of excitation while the subharmonic component can be attributed to the occurrence of pairing. (Even though the subharmonic component in a shear layer has been unambiguously related to vortex pairing, we intend to reaffirm this through flow visualization.) Note that for the five cases in Fig. 1 representing occurrence of vortex pairing (in the shear layer mode), the jet Strouhal number St_D ranges from 0.85 at Ue = 5.21 m/sec to 2.65 at Ue = 33.2 m/sec. However, the Strouhal number St_θ based on the shear layer exit momentum thickness θ is about 0.011 for all the cases. Similar data with the 7.62 cm dia. jet revealed occurrence of vortex pairing in the shear layer at a jet Strouhal number as high as St_D = 8.0 while the shear layer Strouhal number St_θ remained about 0.011. This is the 'shear layer mode' and is the same phenomenon studied by Freymuth [7], Winant and Browand [8], Brown and Roshko [2] and many others.

On the other hand, as first shown in ref [5], stable vortex pairing occurs in the jet at the jet Strouhal number St_D = 0.85 over a large range of jet Reynolds number (ie. independent of St_θ). This is the 'jet mode' and we have confirmed its occurrence at St_D = 0.85 over a St_θ range of 0.001-0.015.

These are the two 'modes' for a circular jet in which controlled excitation induces strong vortex pairing in the near field. We have failed to observe any indication of vortex pairing with excitations at Strouhal numbers significantly different from both St_D = 0.85 and St_θ = 0.011. In the following sections we present data to establish the occurrence of, as well as the characteristics of these two modes.

A series of experiments using hot-wire techniques were undertaken to find the nondimensional characteristic paramters controlling velocity fluctuation amplification and vortex pairing in circular jets. The experiments were carried out for each jet according to the following scheme. For a fixed excitation frequency f_p and probe location in the potential core, the amplitudes of the different harmonic contents in the longitudinal one-dimensional velocity spectrum were found out as a function of the exit speed. The relative exit excitation level u'_e/Ue was set at a preselected value, at a speed that resulted in the shear layer mode pairing; this level varied slightly with the exit speed and was higher at lower speeds and lower at higher speeds. The detailed considerations employed in choosing the excitation level and the probe locations will not be discussed here because they are not central to the results presented here. For a limited number of cases, similar amplitude variation data were obtained keeping the exit speed and relative excitation level the same but varying the excitation frequency. This latter scheme could not be used at all exit speeds because sinusoidal surging of adequate level could not be obtained at appropriate frequencies corresponding to each speed Ue.

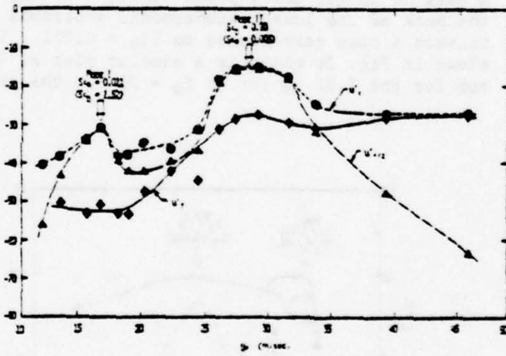

Fig. 2a Variations of the fundamental (u'_f) and subharmonic ($u'_{f/2}$) amplitudes and the total rms turbulence intensity (u'_t) as a function of exit speed Ue for the 2.54 cm jet; f_p = 1004 Hz; u'_{ec}/U_{ec} = 1%; U_{ec} = 19.0 m/sec; probe at x/D = 2.0 on the centerline.

Fig. 2a shows a typical plot of the fundamental and subharmonic amplitudes as a function of the exit speed Ue; the total turbulence intensity variation is shown for comparison. Note that the subharmonic amplitude peaks at two exit speeds. The total rms intensity, being a result of all the harmonic contents, also shows peaks at these conditions indicating that at these two states the subharmonic component is extremely strong and the rms value of the entire signal is essentially due to the subharmonic. The fundamental component varies much more monotonically. As we will see, whenever pairing occurs, the measured peak turbulence intensity is mostly due to the motions associated with the vortex pairing. Thus very little can be inferred about the jet sensitivity from the fundamental amplitude variation.

The striking feature of these two peaks in all similar plots is that the one on the left (Mode I) corresponds to a value of St_θ in the range 0.010 - 0.014 while the Mode II corresponds to a St_D value in the range 0.75 to 1.0. It is to be emphasized that, these two parameters could be varied over a wide range; viz., St_θ from 0.0001 to 0.20 and St_D from 0.02 to about 50.0. However, spectral data indicated that vortex pairing could be induced in the jet only when either $St_\theta = 0.011$ or $St_D = 0.85$.

$St_\theta = 0.011$ has been found by different investigators [16,17] to correspond to the frequency at which a given shear layer is most unstable. Given a shear layer without any particular applied disturbance, the roll-up into vortices tend to occur at the most unstable mode of the shear layer and this natural roll-up occurs at a frequency that corresponds to $St_\theta = 0.011$. This together with the fact that a constant St_θ is associated with the first peak (Fig. 2a) indicates that the first mode is associated with the jet exit shear layer instability and hence the name 'shear layer mode'. The second mode of vortex pairing (Mode II in Fig. 2a), on the other hand, always occurs at $St_D = 0.85$, scaling on the jet diameter D and hence named the 'jet mode'.

The shear layer mode, when St_D is high, is found to involve more than one stage of pairing; the peak of the subharmonic amplitude curve in such a case no longer corresponds to $St_\theta = 0.011$. However, the peak of the lowest subharmonic amplitude variation in such a case corresponds to $St_\theta = 0.011$. This is shown in Fig. 2b which is a similar plot as Fig. 2a but for the 7.62 cm jet at $f_p = 70$ Hz; the probe position is such as to bear identical geometric location as that used for the data in Fig. 2a. Note that the $u'_{f/4}$ spectral component has its peak at a velocity corresponding to $St_\theta = 0.011$. As we shall see later, the $u'_{f/4}$ component extracts energy from the $u'_{f/2}$ component as a result of which the peak of the subharmonic $u'_{f/2}$ in such a case is flattened out and its mean no longer corresponds to $St_\theta = 0.011$. Note that the second peak in Fig. 2b corresponds to $St_D = 1.0$.

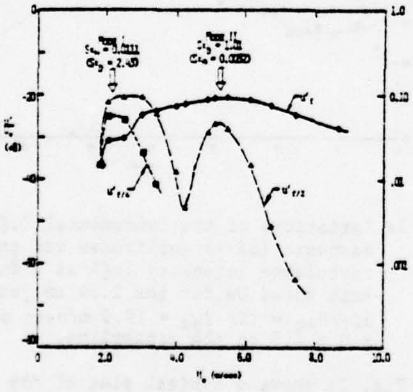

Fig. 2b Amplitude variations of u'_f, $u'_{f/2}$, $u'_{f/4}$ and u'_c with exit speed Ue for the 7.62 cm jet; $f_p = 70$ Hz; $u'_{ec}/U_{ec} = 3\%$, at $U_{ec} = 2.4$ m/sec; probe at $x/D = 0.67$ on the centerline.

The optimum speeds for the formation of the two modes as found from the two peaks in Figs. 2a, b are not artifacts of the probe locations used. These peaks occur, of course with varying relative amplitudes, independent of the location of the probe. Fig. 2c shows similar data obtained with the probe located on the centerline for the same flow condition as for Fig. 2b, but for probe location at $x/D = 2.0$ instead of at $x/D = 0.67$. The amplitudes of the different spectral components are plotted as a function of exit speed. In this case however, a third stage of pairing associated with the shear layer mode occurs for a small range of velocities and the peak of the $u'_{f/8}$ component now corresponds to $St_\theta = .0116$, while the $u'_{f/4}$ and $u'_{f/2}$ components have broader peaks.

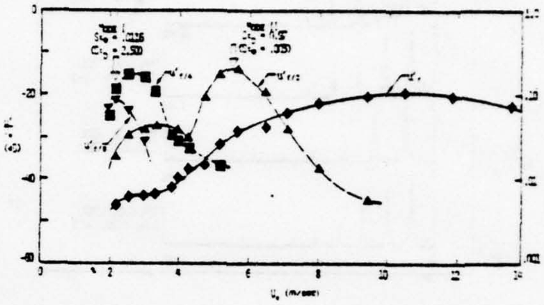

Fig. 2c Amplitude variation of u'_f, $u'_{f/2}$, $u'_{f/4}$, $u'_{f/8}$ and u'_c with exit speed Ue for the 7.62 cm jet; $f_p = 70$ Hz; $u'_{ec}/U_{ec} = 3\%$ at $U_e = 2.4$ m/sec; probe at $x/D = 2.0$ on the centerline.

The jet mode does not show any successive subharmonic beyond the first indicating that either only one pairing occurs in the jet mode or that a second pairing occurs so far downstream that no significant motion is induced by the pairing process at $x/D = 2.0$. It is not going to be easy to resolve this question as the random turbulence becomes so dominant after the first jet mode pairing that any other stage of pairing, even if present, will be obscured.

Data (similar to those in Figs. 2a-c) with different relative excitation amplitudes but for fixed probe location show (not presented here) that the Strouhal numbers for the two modes are the same as indicated above ie. $St_\theta = 0.011$ and $St_D = 0.85$. Note that the spectral components, including the fundamental, cannot be distinguished clearly from the background turbulence after 5 diameters downstream. Very near the exit, on the other hand, the subharmonic peaks become too weak to be distinguished from the background turbulence and electronic noise.

In order to further confirm the Strouhal numbers associated with the two modes of vortex pairing it is desirable to show the jet response for fixed velocities but varying frequencies of excitation. However, the frequencies of excitation, being determined by the cavity resonance frequencies of the settling chamber combination, cannot be varied continuously; also, amplitude of excitation achievable depends on the settling chamber resonance modes. However, for a limited number of cases at relatively lower frequencies (f_p) it was possible to obtain such data which also showed the existence of the two modes. Fig. 2d shows the (7.62 cm) jet response data as a function of

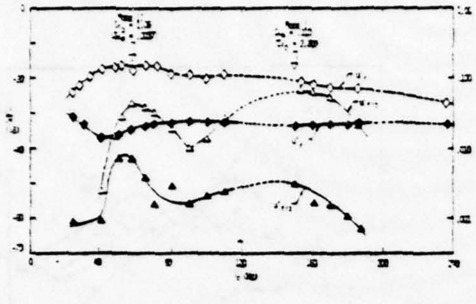

Fig. 2d Amplitude variations of u_f' and $u_{f/2}'$ with excitation frequency f_p for the 7.62 cm jet at constant Ue = 4.1 m/sec for two probe locations: (i) x/D = 0.20 and centerline (solid data points) (ii) x/D = 0.20 and U/U_c = 0.95 point near the shear layer (open data points).

excitation frequency at a fixed speed Ue = 4.1 m/sec; the dashed portion indicates frequency range where necessary exit excitation level was unattainable. A second probe was placed at the jet exit and the relative excitation level *was adjusted to the same* value at each frequency. This figure covers two experiments with the probe at two transverse locations but at the same downstream distance from the exit - one at the centerline (*open data points*) and the other near the shear layer at U/U_c = 0.95 (solid data points). Amplitude variation for only the fundamental and subharmonic frequencies are recorded and no noticeable $u_{f/4}'$ component could be discerned in the spectra. As is evident, the subharmonic curves are characterized by two distinct peaks - the one on the right now represents the shear layer mode and the other the jet mode.

From several plots similar to the ones in Figs. 2a-c, 12 for each of the two jets, the locii of the shear layer and the jet mode subharmonic peaks are shown on a St_D vs $Re_D^{1/2}$ plot in Fig. 3. For the jet mode, the region is terminated on the right because the second peak (Figs. 2a-c) becomes progressively broader with increasing Re_D and location of the second peak becomes ambiguous in such cases. Both the regions terminate on the left (Fig. 3) due to difficulty in measurements at low velocities and/or non-availability of very low excitation frequencies. The shear layer mode plot is limited on the right by the maximum speed available and/or maximum available excitation frequency of sufficient amplitude. Note that on a St_θ vs Re_θ plot, while the shear layer mode curves for the two jets would coincide, the jet mode curves for the two jets would be apart.

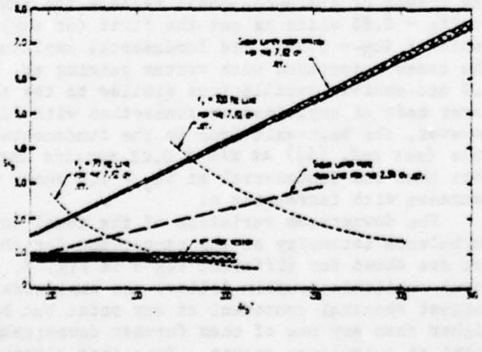

Fig. 3 Conditions for strong vortex pairing in the shear layer mode and the jet mode.

Fig. 3 also includes two constant frequency (f_p) lines for the 7.62 cm jet. It is clear that for excitation at f_p = 70 Hz, as the Reynolds number is varied, the subharmonic amplitude will be large at $Re_D^{1/2}$ = 113 and 170. However, at higher frequencies, for example at f_p = 310 Hz, the jet mode region cannot be reached with the maximum Re_D available; a plot similar to Fig. 2 for such f_p is characterized by only one peak corresponding to the shear layer mode at St_θ = 0.011.

In order to further understand the shear layer mode, the downstream spectral evolution in the shear layer was studied with the probe placed near the layer, viz at a location where U/U_c = 0.70. Fig. 4 shows the downstream variation of the rms of the total as well as of the spectral components for the 7.62 cm jet for excitation at St_θ = 0.011. The exit velocity and f_p were chosen such that St_D was quite high (3.77) *so* that no appreciable effect from the jet mode interfered with the shear layer data.

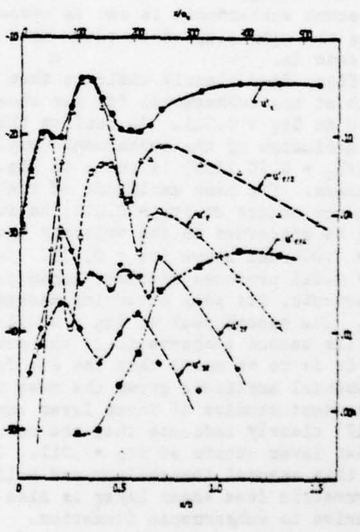

Fig. 4 Spectral evolution downstream along the U/U_c = 0.70 line for the 7.62 cm jet at St_θ = 0.011 (St_D = 3.77); f_p = 308 Hz; u_{ec}'/U_{ec} = 1%; U_e = 6.22 m/sec.

While the higher harmonic amplitudes show considerable scatter in the data due to background noise, the $u_{f/4}'$, $u_{f/2}'$ and u_f' spectral components exhibit well defined trends. The higher harmonics merely represent the existence of a non-sinusoidal signal with the period of the fundamental (or subharmonic) and thus has no bearing on the shear layer vortex scale size or spacing. The higher harmonics thus are of little significance in our discussion.

With increasing x, the fundamental amplitude increases, then saturates at $x/D \approx 0.13$ before starting to decay. The saturation and decay of the fundamental is associated with the growth of its harmonics, but more importantly with that of the subharmonic. The subharmonic extracts its energy from the fundamental and the maximum growth rate of the subharmonic roughly coincides with the maximum decay rate of the fundamental. The subharmonic grows to an amplitude larger than the fundamental due to addition of kinetic energy of two like signed vortices, saturates further downstream at $x/D \approx 0.30$ and then decays. The saturation of the subharmonic generates its own harmonics and thus contributes to u_f' which, as a result, exhibits a rise in its amplitude. The $u_{f/4}'$ component similarly grows at a maximum rate where the decay rate of $u_{f/2}'$ is maximum and saturates further downstream contributing energy to both u_f' and $u_{f/2}'$ components, both of which as a result exhibit rise in amplitude at that location. The spectral components give in to turbulence afterwards and no further pairing could be identified. Note that up to $x/D = 0.1$ the total velocity fluctuation is due to fundamental only. At $x/D = 0.3$ the fluctuation is essentially due to the subharmonic, which is stronger than the fundamental. However, the second subharmonic is not as strong because during the time elapsed to reach this stage transition sets in.

Figs. 2a-d clearly indicate that the maximum growth of the subharmonic for the shear layer mode occurs at $St_\theta \approx 0.011$. To confirm this, the streamwise evolution of the subharmonic amplitude (along the $U/U_c = 0.70$ line) is shown in Fig. 5 for a few St_θ cases. The peak amplitude at the subharmonic frequency occurs at $St_\theta = 0.011$; no subharmonic peaks could be discerned in the velocity spectra below $St_\theta \approx 0.004$ and above $St_\theta \approx 0.015$. Note also that $St_\theta = 0.011$ produces the most rapid growth of the subharmonic, its peak occurring nearest to the exit. The second peak at $St_\theta = 0.011$ also suggests that its second subharmonic is the strongest.

It is to be noted that the St_θ for which the fundamental amplitude grows the most is not 0.011. Independent studies of shear layer instability [16,17] clearly indicate that the natural roll-up of a shear layer occurs at $St_\theta \approx .011$. It thus appears that this natural instability and roll-up in an axisymmetric free shear layer is also the one most conducive to subharmonic formation.

The growth of the subharmonic for the jet mode as a function of x/D for different St_D's is plotted in Fig. 6; for all the cases shown here, the exit excitation level was kept constant at $u_{ec}'/U_{ec} = 3\%$. This figure confirms that for the jet mode, the maximum growth of the subharmonic occurs at $St_D = 0.85$. The subharmonic formation did not occur for cases below $St_D = 0.6$ and above $St_D = 1.6$. As will be seen, the latter case is associated with strong suppression of the centerline total turbulence intensity as compared to the non-excited case.

The fundamental amplitude variation along the jet centerline as a function of x/D for different St_D's is documented in Fig. 7. Maximum growth of the fundamental occurs at $St_D = 0.30$ which has also been found by Crow and Champagne [11] to be the jet 'preferred mode'. Crow and Champagne [11] also found the generation of a subharmonic at $St_D = 0.60$. They argued that $St_D = 0.60$, being double the preferred mode, was most susceptible to produce the (strongest) subharmonic in order for the disturbance to get back to the preferred mode. The pairing phenomenon being nonlinear, such an argument, applicable to a linear system, appears unjustified. Current data show that the growth of the subharmonic reaches its maximum at $St_D = 0.85$ which is not the first (or any) harmonic of $St_D = 0.30$. The fundamental amplitude for the cases associated with vortex pairing eg. $St_D = 0.85$, 1.0 etc exhibit oscillations similar to the shear layer mode as explained in connection with Fig. 4. However, the near-exit drop in the fundamental amplitude (see ref. [5]) at $x/D \approx 0.12$ remains unexplained. Note that the fundamental at $St_D = 1.6$ shows monotonic decrease with increasing x.

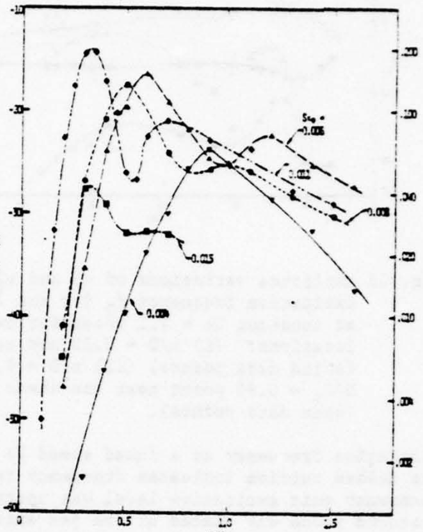

Fig. 5 Downstream variation of the subharmonic amplitude ($u_{f/2}'$) along the $U/U_c = 0.70$ line at different St_θ (ie. different Ue) for the 7.62 cm jet. $f_p = 308$ Hz; $u_{ec}'/U_{ec} = 1\%$ (constant). ▼ $St_\theta = 0.004$ ($St_D = 1.53$); ▲ 0.006 (2.48); ● 0.008 (3.02); ◆ 0.011 (3.77); ■ 0.015 (4.69).

The downstream variation of the total longitudinal turbulence intensity on the centerline for the 7.62 cm jet are shown for different St_D's in Fig. 8. The total amplitude roughly follows the amplitude of the largest spectral component at any point but becomes higher than any one of them further downstream where onset of turbulence occurs. Note that although $St_D = 0.30$ shows large amplitude (u_f') growth and is considered to be the preferred mode, the growth of the subharmonic at $St_D = 0.85$ results in comparable or even higher amplitude for the total fluctuation intensity. $St_D = 1.6$ shows a suppression of the centerline turbulence intensity, even below the

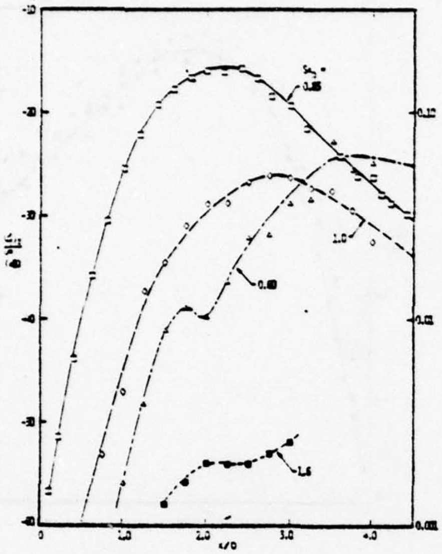

Fig. 6 Subharmonic amplitude variation with x/D along the jet centerline at different St_D's *for the* 7.62 cm jet. u'_{ec}/U_{ec} = 3% (constant); □ St_D = 0.85 (St_θ = 0.0025), Re_D = 32,000; ◇ St_D = 1.0 (St_θ = .0026), Re_D = 43,000; ■ St_D = 1.6 (St_θ = 0.0041), Re_D = 43,000; △ St_D = 0.60 (St_θ = 0.0016), Re_D = 41,600.

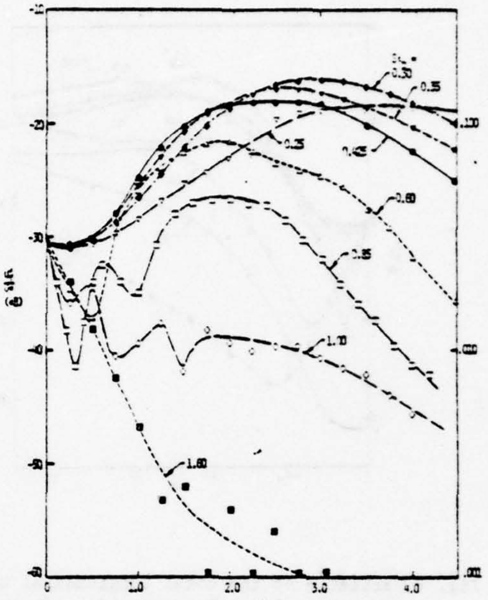

Fig. 7 Fundamental amplitude variation along the centerline of the 7.62 cm jet at different St_D. u'_{ec}/U_{ec} = 3% (constant). The different parametric values for each case in the order, St_D (St_θ), f_p, Re_D, are as follows: ▽ 0.25(.0006), 32 Hz, 50,000; ◆ 0.30(.00078), 32 Hz, 41,600; ▼ 0.35 (.00091), 37 Hz, 41,600; ● 0.425(.0011), 45 Hz, 41,600; △ 0.60(.0016), 64 Hz, 41,600; □ 0.85 (.0025), 70 Hz, 32,000; ◇ 1.0(.0026), 110 Hz, 43,000; ■ 1.6(.0041), 174 Hz. 42,800.

non-excited case. The suppression effect reported previously [5] is still unexplained. Recent data indicate that this suppression effect is dependent on Re_D. Vlasov and Ginevskiy [14] reported suppression at St_D = 2.75 but provided no explanation. This point constitutes a topic of our continuing research in this field.

The streamwise spectral evolution for the jet mode (7.62 cm jet) at St_D = 0.85 is shown in Fig. 9. Note that immediately downstream from the exit, the signal is due to the fundamental component which saturates due to the growth of the subharmonic through pairing. Pairing produces an intensification of the induced velocity and the subharmonic grows and reaches a maximum at x/D = 2½ before saturation. In this region the total signal is essentially due to the subharmonic. Saturation of the subharmonic contributes partially to u'_f component which as a result shows a rise again. The discussion here essentially follows that in connection with Fig. 4.

Fig. 10 documents only the subharmonic evolution at St_D = 0.85 along the jet centerline for three different cases: (i) for the 7.62 cm jet with laminar exit boundary layer when St_θ = .0025, (ii) same condition as in (i) except that the exit boundary layer was tripped to make it turbulent [see ref. 5 for details], (iii) for the 2.54 cm jet at St_D = 0.85 but St_θ = 0.0106. The subharmonic evolution for these three cases are essentially identical. Note that case (ii) eliminates shear layer structure and thus the effect of the shear layer mode on the jet mode. On the otherhand, case (iii) was chosen such that both the shear layer mode and the jet mode would occur simultaneously.

Figure 10 thus suggests that the jet mode is independent of the shear layer characteristics, and that the jet mode is independent of the shear layer mode. The jet mode is neither a legacy of the shear layer mode as commonly assumed nor does the shear layer mode affect the jet mode in any significant manner. It thus seems that the vortex pairing occurring at St_D = 0.85 is not initiated or governed by the initial shear layer instability.

Concluding Remarks

Vortex pairing in circular jets can occur in two distinct modes: the shear layer mode and the jet mode. The shear layer mode is associated with the exit shear layer instability mechanism and the strongest pairing occurs when the excitation frequency matches the natural roll-up frequency. Strouhal number based on exit boundary layer momentum thickness θ for this mode of vortex pairing is found to be St_θ = 0.011. In the jet mode of vortex pairing, the phenomenon scales on the jet diameter and most pronounced pairing occurs at St_D = 0.85. The velocity fluctuation intensity in the near field of

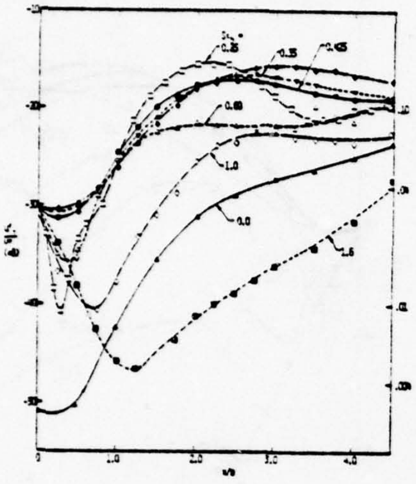

Fig. 8 Variation of the total longitudinal turbulence intensity along the centerline of the 7.62 cm jet at different St_D. $u'_{ec}/U_{ec} = 3\%$; other parametric values associated with each St_D are the same as indicated in Fig. 7. $Re_D = 41,600$ for the unpulsated case ($St_D = 0.0$).

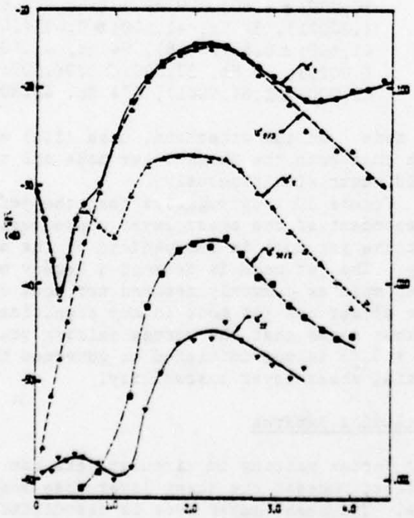

Fig. 9 Amplitude variation along the centerline of the different harmonic components in the u-signal of the 7.62 cm jet at $St_D = 0.85$ ($St_\theta = 0.0025$); $f_p = 70$ Hz; $Re_D = 32,000$; $u'_{ec}/U_{ec} = 3\%$.

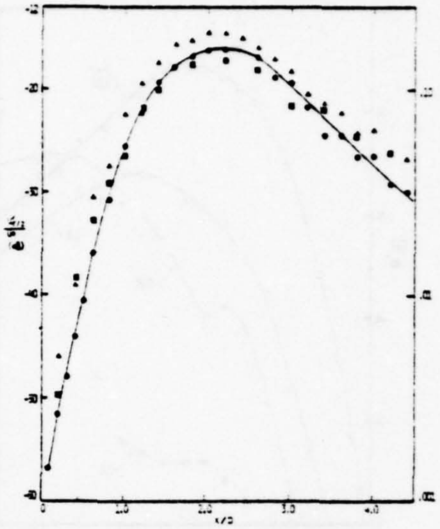

Fig. 10 The variation of the subharmonic ($u'_{f/2}$) amplitude along the jet centerline at $St_D = 0.85$ for three cases: (i) ● $St_D = 0.85$, $St_\theta = .0025$, $Re_D = 32,000$, $f_p = 70$ Hz for the 7.62 cm jet; (ii) ■ *same conditions* as in (i) except that exit boundary layer is made turbulent by tripping; (iii) ▲ $St_D = 0.85$, $St_\theta = .0107$, $Re_D = 8,900$, $f_p = 174$ Hz for the 2.54 cm jet.

a round jet reach relative maxima when it undergoes vortex pairing in either of the two modes.

When excited at the shear layer mode, and when the corresponding St_D is relatively high, the vortex rings rolled up shortly downstream from the exit is found to undergo more than one stage of pairing. It is plausible, in line of Laufer and Browand's [1], argument that the independence from the initial length scale (θ) and dependence on the jet diameter (D) as length scale further downstream may be achieved through successive stages of vortex pairing. However, as our data indicate, the jet mode of excitation can also initiate and govern the downstream coherent structures in a round jet. Although the instability mechanism involved in the jet mode is not yet well-understood, orderly structures scaling on the diameter of the jet seem to form in the near field without being influenced by the shear layer instability.

ACKNOWLEDGEMENT

This research is supported by the NASA Langley Research Center and the Office of Naval Research.

REFERENCES

[1] Browand, F. K. and Laufer, J., "The role of large scale structues in the initial development of circular jets," Proceedings of the Fourth Symposium on Turbulence Liquids, Sept., 1975, U. of Missouri-Rolla.

[2] Brown, G. and Roshko, A., J. Fluid Mech., 64, p. 775, (1974).

[3] Bishop, K. A., Ffowcs Williams, J. E., and Smith, W., J. Fluid Mech., 50, p. 21, (1971).

[4] Liu, J. T. C., J. Fluid Mech., 62, p. 437, (1974).

[5] Hussain, A.K.M.F. and Zaman, K.B.M.Q., "Effect of acoustic excitation on the turbulent structure of a circular jet," Proc. of the 3rd Interagency Symposium on Transportaion Noise, U. of Utah, Nov. 1975, pp 314-326

[6] Roshko, A., AIAAJ, 10, p. 1349, (1976).

[7] Freymuth, P., J. Fluid Mech., 25, p. 683 (1966).

[8] Winant, C. D. and Browand, F. K., J. Fluid Mech., 63, p. 237, (1974).

[9] Browand, F. K. and Wiedman, P. D., J. Fluid Mech., 76, p. 127, (1976).

[10] Davies, P.O.A.L. and Yule, A. J., J. Fluid Mech., 69, p. 513, (1975).

[11] Crow, S. C. and Champagne, F. H., J. Fluid Mech., 48, p. 547, (1971).

[12] Becker, H. A., and Massaro, T. A., J. Fluid Mech., 31, p. 435, (1968).

[13] Rockwell, D. O., J. Appl. Mech., Dec., 1972, p. 883.

[14] Vlasov, Y. V. and Ginevskiy, A. S., 1974, NASA TTF-15, 721

[15] Hussain, A.K.M.F. and Clark, A. R., "Upstream influence on the near-field of a plane turbulent jet," 1977, to be published.

[16] Sato, H., J. Fluid Mech., 7, p. 53, (1960).

[17] Hussain, A.K.M.F. and Zaman K.B.M.Q., "Edgetone effect produced by a hot-wire probe in a free shear layer," to be published.

THE EFFECTS OF THE LAMINAR/TURBULENT BOUNDARY LAYER STATES ON THE DEVELOPMENT OF A PLANE MIXING LAYER

John F. Foss
Department Mechanical Engineering
Michigan State University

ABSTRACT

The effect, of the laminar/turbulent boundary layer state on the mean and rms velocities of a developing plane mixing layer, has been investigated. The maximum Ux/ν allowed by the facility was 6.7×10^5; the maximum x station surveyed corresponds to approximately 2000 and 700 initial momentum thicknesses for the laminar and turbulent cases respectively. The use of commonly accepted non-dimensional representations of the data confirm (at least) an approximately self-preserving condition. They also suggest that the effects of the laminar/turbulent initial condition persist in the self-preserving region. A direct comparison of the data reveals that the persistence so observed is illusory. An interpretation of the reason for this misunderstanding is advanced.

NOMENCLATURE

Symbol	Definition
B	parameter used in transformation of laboratory to standard Gaussian coordinates, see (ζ)
E	Hot-wire voltage
E_o, K, n	coefficients in the hot-wire response equation (1)
H	δ_d/θ, boundary layer shape parameter
LBL	the case for which the boundary layer at x = 0 is laminar
m	parameter used in transformation of laboratory to standard Gaussian coordinates, see Table 2 for m_i where i=1,....4
p	static pressure
q	mean velocity vector in the undisturbed (streaming) fluid
Re_θ Re_x	Reynolds numbers based upon θ and x
S.P., St	designation of mixing layer from splitter plate (S.P.) and backward facing step (St)
S.D.	standard deviation defined for Gaussian fit to $\bar{U}/U$ data, see Table 2 for SD_i, i=1..4
TBL	the case for which the boundary layer at x = 0 is turbulent
u, v, w	velocity components in the mixing layer
u_τ	wall shear stress velocity $(\tau_w/\rho)^{1/2}$
U	i) component of q ii) reference velocity for mixing layer St $\lim_{y\to\infty} u(x,y)\to U$; S.P. $\lim_{y\to\pm\infty} u(x,y)\to U_1, U_2$
V	i) component of q ii) magnitude of the velocity vector in the xyplane $V^2=(u^2+v^2)$
x, y, z	longitudinal, lateral, and span wise position coordinates
x_o	apparent origin (defined for the specified width measure) of the mixing layer
y(r)	y location at which u/U = r
δ, δ_d, θ	boundary layer, displacement, and momentum thicknesses
δ_ω	vorticity thickness $\equiv (U_1-U_2)/\{(\partial\bar{U}/\partial y)$ at $y(0.5)\}$
σ_f	Gortler constant: $u/U = \mathrm{erf}\{\sigma_f(y-y(0.5))/(x-x_o)\}$
σ_p	standard deviation of Gaussian distribution
ζ $\equiv$	$my + B$, ζ is argument of standard Gaussian: mean = 0, $\sigma_p = 1$

Super and sub scripts

$\bar{(\ )}$ $\tilde{(\ )}$	temporal average and r.m.s. of ( )
$(\ )_i$	initial condition of ( ); ( ) at x = 0

INTRODUCTION

Plane mixing layers. The plane mixing layer is a comparatively simple, yet technologically important turbulent flow field. The literature on it is correspondingly vast. The recent identification of large scale, coherent motions in the layer (1), (2), and the recognition that these are possibly the controlling agents for its growth, has reinvigorated the interest in this flow. The technological importance of the plane mixing layer for aerodynamic and chemically reacting flows is made apparent in the reports of specialist's conferences on the respective subjects (3), (4). The latter contains an extensive review and interpretation of the available literature (on plane mixing layers) by Murthy (4).

The phenomena of self-preservation is of particular interest for the present study; the defining remarks by Townsend (5, p. 169) are useful for the clarification of its meaning and for later reference. "The principle, as distinct from the assumption, of self-preservation asserts that a moving equilibrium is set up in which the conditions at the initiation of the flow are largely irrelevant, and so the flow depends on one or two simple parameters and is geometrically similar at all sections."

Two general classes of plane mixing (or free shear) layers can be identified. Birch and Eggers (3) refer to these as: (i) layers which are created from a splitter plate (S.P.) with unsheared velocities U_1 and U_2, and (ii) layers which form downstream of a backward

PRECEDING PAGE BLANK-NOT FILMED

facing step (St.) and involve a single stream which enters a "quiescent" ambient fluid. For (i), a "simple parameter" would be a representation of the velocity ratio such as $(U_1-U_2)/(U_1+U_2)$. Superficially, case St may be described as the limiting condition of case S.P. where $U_2 \rightarrow 0$. However, their entrainment processes can be expected to be quite different.

The lack of an intrinsic length scale for the plane mixing layer means that an extrinisic scale, such as θ_i, must be used to characterize the relative magnitude of the downstream distance. Bradshaw (6) has explicitly examined such a dependence in the axismmetric mixing layer downstream of a 5 cm diameter jet orifice. Bradshaw identified quantitative requirements for the development length which is necessary to achieve a self-preserving flow; he has also cautioned* against the misuse of these criteria. From the defining remarks regarding self-preservation and from the recognition that δ_i, δ_{di} and θ_i are the available length scales to characterize the plane mixing layer, one could expect that the sole effect of the initial $(x = 0)$ conditions would be to alter the development length to achieve self-preservation.

Wygnanski and Fiedler (7) undertook a comprehensive investigation of a plane mixing layer in order to extend the data base, by including conditionally sampled measurements, beyond that provided by the earlier and widely accepted results of Liepmann and Laufer (8). Surprisingly, and strikingly given the above considerations, the two studies showed pronounced differences in even the simplest measure of the flow . . . the spreading rate of the mean velocity distributions in the "asymptotic" region. The inference was made that the asymptotic region was influenced by the conditions at the origin of the shear layer!

This possibility, and the desire to evaluate it by comparative measurements in the same (!) flow system provided the motivation for both the present investigation and that of Batt (9). Batt used a flow system which allowed the shear layer growth in the tripped and untripped S.P. and St configurations to be evaluated. The trip wire in Batt's experiment provided a "disturbed" ($\tilde{u}/U_i$ max. $= 12\%$) laminar ($\bar{u}/U_i$ vs y/δ_d is "identical" with that of the Blasius solution) boundary layer at $x = 0$. His results confirm that a residual effect of the boundary layer state is present in the (apparently) asymptotic region as defined by the longitudinal independence of the normalized $\bar{u}$ and $\tilde{u}$ distributions. A similarly motivated investigation has quite recently been executed by Browand (10) in a two stream mixing layer $(U_2/U_1=0.23)$. The effect of the initial condition was seen to persist over the range of his measurements. For $0 \leq x/\theta_i \leq 500$ the growth rate of the LBL condition was larger than that for a turbulent boundary layer at $x=0$. For $x/\theta_i \geq 500$ the growth rate of the T.B.L. condition was observed to approach that of the LBL condition.

Champagne et. al. (11) and Dimotakis and Brown (12) have advanced interpretations of the persistent initial condition effects. A partial summary of their observations suggests that: (i) non-universal, self preserving states may exist in which the initial condition affects the asymptotic state (11) or (ii) the approach to the asymptotic state may be extremely slow and that the apparent asymptotic states observed in laboratory flows are merely in the (slowly varying) intermediate stage of their development (12). They cite, as a reason for this, that the growth rate (e.g., $d\delta_\omega/dx$) is possibly a function of the vorticity distribution within the shear layer and since this distribution can be expected to change slowly, the approach to the final growth rate is correspondingly gradual. Champagne, et. al. (11) observe that the good agreement between their results and those of Patel (13) are encouraging in the search for the universal, asymptotic, shear layer. These introductory remarks are a condensed version of those prepared for a NASA report (Foss (14)). The reader is referred to this writing for a more complete summary of the extant literature and the present data.

THE PRESENT INVESTIGATION

The objectives of the present study may be readily formulated given the above considerations. Its principle objective is to provide sufficient measurements, of the spatial distributions for the first and second moments of the velocity in the developing region of a plane shear layer, that the influence of the laminar/turbulent initial boundary layer states can be assessed. The need for this study is implicit from an assessment of the previous investigations: there has been no direct comparison of the shear layers which result from the laminar/turbulent initial boundary layer conditions (in the same apparatus) for the St configuration. (It can be added that measurements beyond the region of rapid development were desired but that the above noted cautions regarding a "universal asymptotic state" are responsible for the stated interest in the developing region. Secondary purposes are: (i) to provide a data base with appropriate documentation that can serve as a test case for calculation methods* and (ii) to provide the basis for further studies which will seek to establish the governing phenomena which are responsible for the (presently) observed behavior of the time mean flow field.

EXPERIMENTAL FACILITY

A schematic representation of the experimental facility which is capable of providing a laminar or turbulent boundary layer at the initiation of the shear layer is shown in Figure 1. A large centrifugal fan (outlet dia = 40cm) is used to pressurize the 100 x 150cm plenum chamber which supplies air to the symmetrical contraction. The final flow control elements (straw-honeycomb and 30 mesh screen) result in a free stream fluctuation intensity of 0.2% at $x = 0$ for a flow velocity of 18.3mps. The fluctuations in the y and z directions are undoubtedly greater; they were not measured. An LVDT sensor monitored the position of the probe over the range ±76mm with a resolution of ±.03mm.

The laminar/turbulent boundary layer state was controlled by the suction/blowing condition of the discrete, rectangular (11 x 25mm) openings above the gap created by the end of the contraction and the leading edge of the smooth boundary layer plate. The details of this configuration are shown in Figure 2. The 1.8mm vertical displacement and the 10mm gap length were selected after a trial-and-error search for the minimum disturbances (at $x = 0$) for the laminar boundary layer (L.B.L.). A negative pressure of $[-0.95\rho U_i^2/2]$, similarly determined, was maintained in the super plenum for the L.B.L. condition. A positive pressure of $[0.1\rho U_i^2/2]$ was required to gain a fully turbulent boundary layer for all z locations. It is noteworthy that

---

*See the discussion on p. 39 of (3). Bradshaw notes that the required distance for the developing region, in terms of θ_i units and the R_x requirements may be sensitive to $(U\theta_i/\nu)$.

*The results of the measurements are available on ISM cards in a Fortran compatible format. They are available, at cost, upon request.

the discrete sections and tubing connections were both necessary and sufficient to gain a spanwise independent suction/blowing system. The initial attempt at boundary layer control with a similar configuration, viz., a simple gap opening into a plenum, produced both a Helmholtz resonant frequency (not observed in the present data) and a laminar boundary layer only over a short central span of the shear layer.

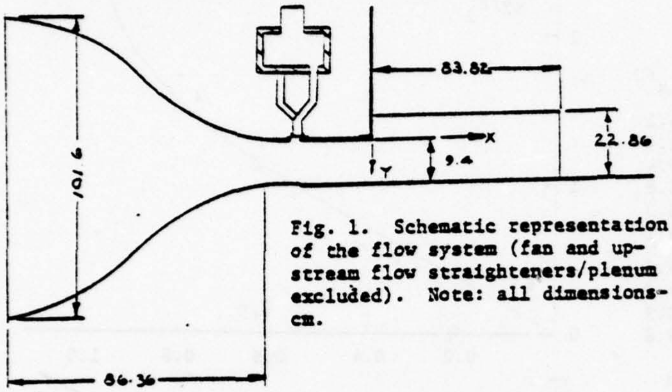

Fig. 1. Schematic representation of the flow system (fan and upstream flow straighteners/plenum excluded). Note: all dimensions-cm.

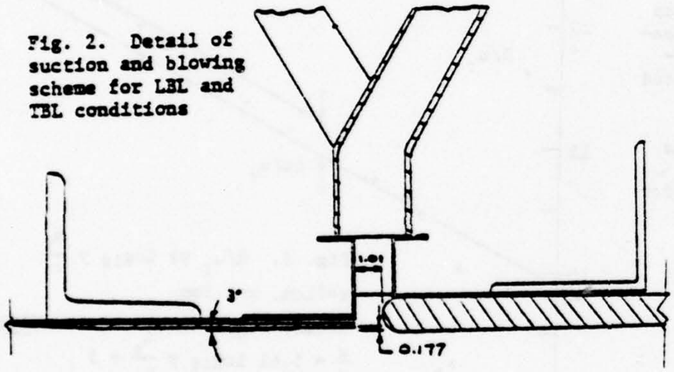

Fig. 2. Detail of suction and blowing scheme for LBL and TBL conditions

DATA ACQUISITION AND SIGNAL PROCESSING

The time mean and r.m.s. values of the velocity, which are presented in the results section, have been obtained using a single hot-wire probe set parallel to the z-direction. The probe configuration (Disa 55 F 11) is somewhat sensitive to pitch effects; however, the maximum error is approximately 5% (at 90 degrees), see Comte-Bellot, et. al., (15) which is considered to be satisfactory considering the objectives of the present study.

The calibration of the hot-wire was accomplished in the free stream of the flow from the main plenum. The total pressure was measured with a capacitive pressure transducer (Decker 308-3); the transducer linearity specifications and the V-p½ relationship combine to yield an accuracy of ± 0.18mps for $3 \leq V \leq 17$mps. The bridge voltage of the hot-wire anemometer (T.S.I. 1054-A) was conditioned by a 10Khz low pass filter and a 2 volt suppression in order to eliminate a substantial portion of the (high frequency) anemometer noise and to reduce the dynamic range (0-2 vs 0-4 volts) for the subsequent A/D conversion. The residual and amplified anemometer noise is nominally 3mv; as such it will, at most, effect the l.s.b. of the 5mv resolution A/D converter. An on-line T.I. 960A minicomputer was used to create and store an ensemble average of the samples collected over the specified time period. The calibration data were formed from 10^4 simultaneous samples of the hot-wire and pressure transducer voltages at a given flow speed. These values were averaged and 12-15 such data pairs were used to evaluate the constants E_o^2, K and n in the expression

$$E^2 = E_o^2 + KV^n \tag{1}$$

A constant value of the exponent n is supported by the results of Brunn (16) for the range $3 \leq V \leq 20$mps of interest in this work. The standard deviation of the calibration data was typically 0.06mps. (It is assumed for this calculation that the hot-wire voltage measurement and equation 1 are precisely correct.)

The L.B.L. flow field data were processed with the same routine; the hot-wire voltage was sampled and averaged for 10 seconds at each location of the traverse. In addition, an r.m.s. voltmeter (Disa 55 D35) was used to convert the voltage fluctuations into an analog voltage which was proportional to $\tilde{e}$ of the original signal. This analog voltage was recorded, along with the LVDT output signal, and the three average values were stored for further processing. The 10 second averaging time appeared to give satisfactory results and it was anticipated that a large number of (statistically independent) samples across the physical traverse would provide acceptable data. This was subsequently confirmed as regards the general trends of the velocity field behavior; however, detailed consideration of the growth characteristics of the layer were later inferred to require both longer sampling times and more spatial locations. The acquisition software was altered to allow an arbitrary sampling period and the TBL results were collected for 60 second time periods.

The r.m.s. velocity fluctuation $\tilde{u}$ was calculated from the measured $\tilde{e}$ by the relationship:

$$\tilde{u} = \tilde{e}\langle(dV/dE)\rangle \tag{2}$$

where $\langle(dV/dE)\rangle$ is evaluated from (1) at the ensemble average $\langle E\rangle$ value. The maximum error resulting from the constant slope assumption in this calculation is estimated by comparing $\tilde{u}$ with the average magnitude of $[V(E \pm \tilde{e}) - V(E)]$ for the largest $\tilde{e}\langle(dV/dE)\rangle$ values of the final data set. A representative value for the error is 0.8% for the x = 508mm traverse with the turbulent boundary layer initial condition. The fluctuating velocity is, of course, influenced by the transverse (v) component and the second order effects of u. A consideration of these higher order effects readily shows that the interpretation of the mean and r.m.s. voltages is both ambiguous and quite complex. No higher order corrections were made.

RESULTS

Boundary Layer Survey

Velocity traverses at selected span wise locations were used to document the boundary layer at x = -2mm. These data are to characterize the initial condition for the shear layer. A zero y position was inferred from the U(y) data and an integration routine was used to evaluate δ_d and θ for each traverse. The composite results are presented in Table 1.

A very substantial effort was required to completely eliminate the presence of turbulent bursts for the LBL condition. The problem was localized near z=42 and 58cm; interestingly, z=50cm was a region of very little disturbance. The problem was traced to slight irregularities in the surface and was controlled in that a completely laminar state existed for the LBL case. However, the laminar boundary layer at z=42cm was strongly disturbed with an r.m.s. fluctuation level higher than that of the turbulent boundary layer. The fluctuations of the LBL case were quite different from the (spectrally rich) fluctuations of the TBL case; *oscillograph traces of the two cases are presented in Figure 3.*

Table 1. Summary of Boundary Layer Data

	z	U(mps)	δ(mm)	θ(mm)x10^1	δ_d/θ	R_θx10^3	$\bar{u}_{max}/U$
LBL:	20	18.3	1.9	2.6	1.9	0.34	4.1
	42	18.3	2.4	3.0	1.9	0.39	11.4
	50	18.2	1.9	2.7	2.2	0.36	3.4
	58	18.3	2.2	3.1	2.3	0.40	6.8
	71	18.3	2.1	2.8	2.4	0.37	3.3
	86	18.3	2.2	2.9	2.3	0.37	6.1
TBL:	42	18.4	10.0	10	1.3	1.4	9.7
	50	18.4	6.5	6.6	1.5	0.9	9.7
	58	18.4	8.6	9.0	1.4	1.2	8.9
	71	18.4	7.5	8.1	1.5	1.1	9.8

The shear layer data were taken at the location of the minimum disturbance condition, z=71cm. The specific boundary layer conditions at this z location are presented in Figures 4 and 5. Close agreement between the present and the "standard" turbulent boundary layer, Coles (17), is evident. (u_τ was evaluated from the three "wall-law" points as plotted on a Clauser plot (18). u_τ=0.85mps.) The LBL/Blasius solution comparison suggests that the suction scheme results in a distorted profile $[u_\tau\delta_d/\nu]$(present) > $[u_\tau\delta_d/\nu]$(*Blasius*). *Figure 6 presents the* $\bar{u}/U$ data for the LBL and TBL cases.

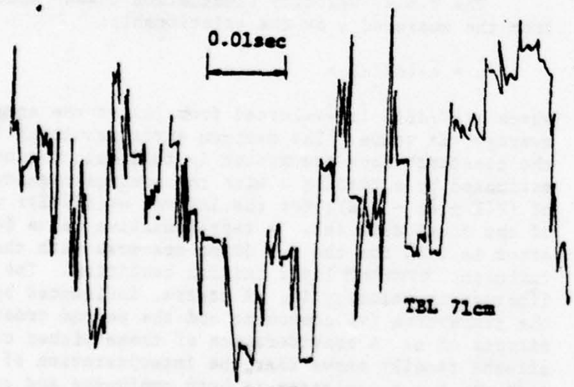

Fig. 3. Oscillograph traces of E(t) at u/U=0.5, x=0. (Amplitude is arbitrary and constant for all traces.)

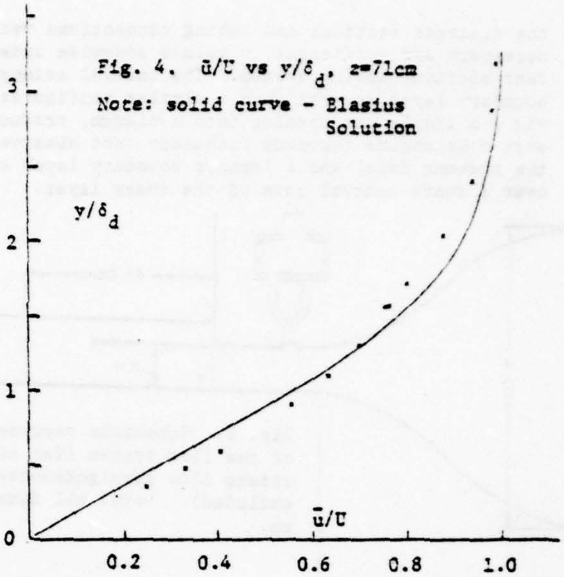

Fig. 4. $\bar{u}/U$ vs y/δ_d, z=71cm
Note: solid curve - Blasius Solution

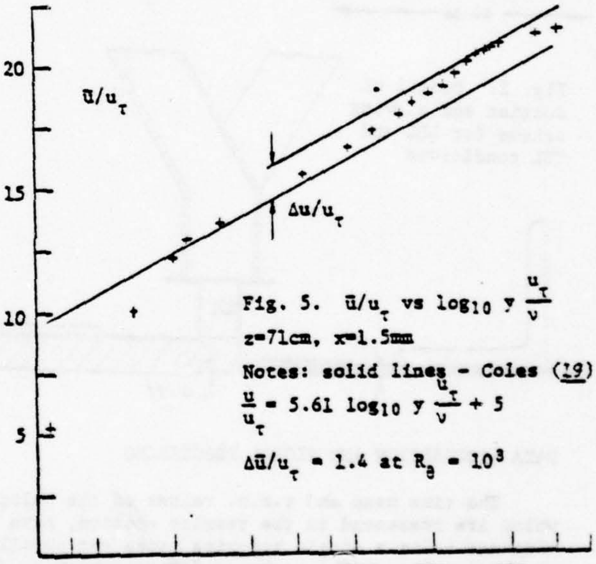

Fig. 5. $\bar{u}/u_\tau$ vs $\log_{10} y\frac{u_\tau}{\nu}$
z=71cm, x=1.5mm
Notes: solid lines - Coles (19)

$$\frac{u}{u_\tau} = 5.61 \log_{10} y\frac{u_\tau}{\nu} + 5$$

$\Delta\bar{u}/u_\tau$ = 1.4 at $R_\theta = 10^3$

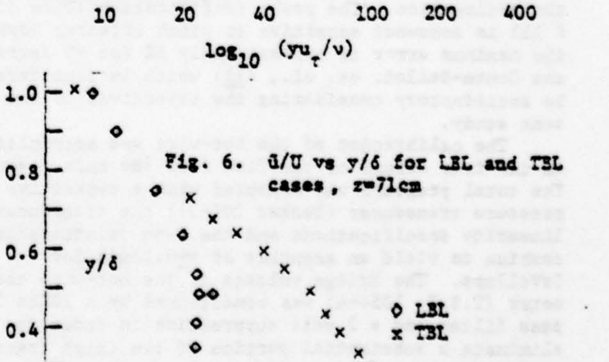

Fig. 6. $\bar{u}/U$ vs y/δ for LBL and TBL cases, z=71cm

Shear Layer Survey

The composite mean and r.m.s. values of the velocity are presented in Figures 7 and 8. The normalization of the y dimension, viz. $[y-y(.5)]/x$, is used to provide a compact presentation; the self-similar character of these data is considered in the next section. The maximum x location surveyed was $x=50.8$cm; this location is the farthest downstream location for which the infrequent turbulent signals, occurring at $y=5$cm, could be reliably traced to either the shear layer or the lower plate boundary layer. Hence, beyond this location, the shear fields of the two streams interact. The two streams interact much farther upstream in terms of the pressure fluctuations induced by their irregular boundaries. These fluctuations are observable as very low frequency, but substantial amplitude u fluctuations in the region of the flow between the two developing layers.

DISCUSSION OF RESULTS

Evaluation of Shear Layer Width

The evaluation of the plane mixing layer growth rate is facilitated by the definition of an appropriate width measure of the mean velocity field. If the flow is self-preserving, then all measures are in fixed proportion and the selection of a particular width measure may be arbitrarily made. If the developing shear layer is to be characterized, then judgement in the selection must be exercised. A desirable characteristic of the width measure is that it not rely upon the measurement of a specific velocity value; rather, it is preferable that it represent a smoothed measure of several independent velocity measurements. The momentum thickness (θ) utilized by Winant and Browand (2) is compatible with these criteria. However, it is inappropriate to calculate θ using single-wire measurements for the St case since $|V|$ does not approach zero as $y \to -\infty$ and (consequently) the integral of the experimental data is not well defined.

The use of an approximate analytic form which involves a width measure as a parameter is an appropriate response to the stated criteria; the use of the error function (erf) as the analytic form is adopted for this purpose. As will be quite evident, it is not assumed that the erf can be used to describe $\bar{u}$ for all y; indeed, this fitting process will allow the agreement between the data and this analytic expression to be evaluated. The fit, over the region of interest, is accomplished by using the measured $\bar{u}/U$ to evaluate ζ as:

$$\frac{u}{U} = 0.5 + \mathrm{erf}\,\frac{\zeta}{\sqrt{2}} \qquad (3)$$

where ζ is the argument of the Standard Gaussian cumulative distribution function

$$F(\zeta) = \frac{1}{\sqrt{2\pi}} \int_{-\infty}^{\zeta} \exp\left[\frac{-\alpha^2}{2}\right] d\alpha \qquad (4)$$

(Note that F has its mean value at $\zeta=0$ and the standard deviation of the distribution is obtained at $\zeta=1$.) Since the experimental data exists in pairs as $(u/U, y)$, it is possible to form the relationship

$$\zeta = my + B \qquad (5)$$

Consequently, m and B can be found from an application of a least squares relationship to the (ζ, y) pairs. Using (3) and (5), the centerline of the mean velocity traverse is seen to be

$$y(0.5) = -B/m \qquad (6)$$

and the quantity m^{-1} is seen to be the standard deviation of the spatial distribution, viz.,

$$\pm m^{-1} = y(0.5 \pm 0.341 \ldots) - y(0.5) \qquad (7)$$

The quality of the fit can be assessed by evaluating the standard deviation (S.D.) between the measured $\bar{u}/U$ and that computed from (3). This procedure has been carried out for four cases; the corresponding m and S.D. values are identified by the subscript numbers $1 \to 4$ which refer to a subset of the $\bar{u}/U$ values as described in Table 2.

The Görtler (19) solution can be written as

$$\frac{\bar{u}}{U} = 0.5 + \mathrm{erf}\,\sigma_f\left\{\frac{y-y(.5)}{x-x_o}\right\} \qquad (8)$$

which is related to m_1 by the expression

$$\sigma_f = \frac{m_1(x-x_o)}{\sqrt{2}} \qquad (9)$$

The vorticity width δ_ω, which is defined as

$$\delta_\omega \equiv U/\left(\frac{\partial u}{\partial y}\right)_{y(0.5)}$$

can be evaluated as

$$= \left\{\frac{\partial(u/U)}{\partial\zeta}\Big|_{\zeta=0}\left(\frac{\partial\zeta}{\partial y}\right)\right\}^{-1} = \sqrt{2\pi}/m_2 \qquad (10)$$

The full set of m^{-1} values are presented in Figure 9; the standard deviations are presented in Table 3. These results can be summarized as follows:

1) The Görtler solution and the high velocity side of the mixing layer are not well fit by the error function (SD≈3%) whereas the central region and the low velocity side of the shear layer are quite closely approximated by this analytic form (SD<1% ... for sufficiently large x).

2) The m_2^{-1} distributions suggest the x_o values:

$$x_o(\mathrm{TBL}) = +7.5\mathrm{cm},\ x_o(\mathrm{LBL}) = -4.1\mathrm{cm} \qquad (11)$$

3) The spread constants, evaluated from m_1^{-1} are:

$$\sigma_f(\mathrm{TBL}) = 10.19,\ \sigma_f(\mathrm{LBL}) = 13.6 \qquad (12)$$

which are somewhat different from the disturbed LBL cases for Wygnanski and Fiedler (8) and Batt (10): $\sigma_f=9$, and the "quiet" LBL case of Liepmann and Laufer (9): $\sigma_f=11$.

4) The δ_ω values, evaluated from m_2^{-1} are:

$$\delta_\omega(\mathrm{TBL})/(x-x_o)=0.19,\ \delta_\omega(\mathrm{LBL})/(x-x_o)=0.15 \qquad (13)$$

and these values are in the general range of other investigator's results; see Brown and Roshko (1). Their relative magnitude is in agreement with the conclusion of Batt (10), that the TBL case should have a greater spreading rate than the LBL condition.

5) The pronounced differences in m_3^{-1} and m_4^{-1} for both the TBL and LBL conditions suggest that the $\bar{U}/U$ distributions are strongly asymmetric. Consequently, the mean vorticity distribution considered by Dimotakis and Brown (12) is also asymmetric about the y(0.5) location.

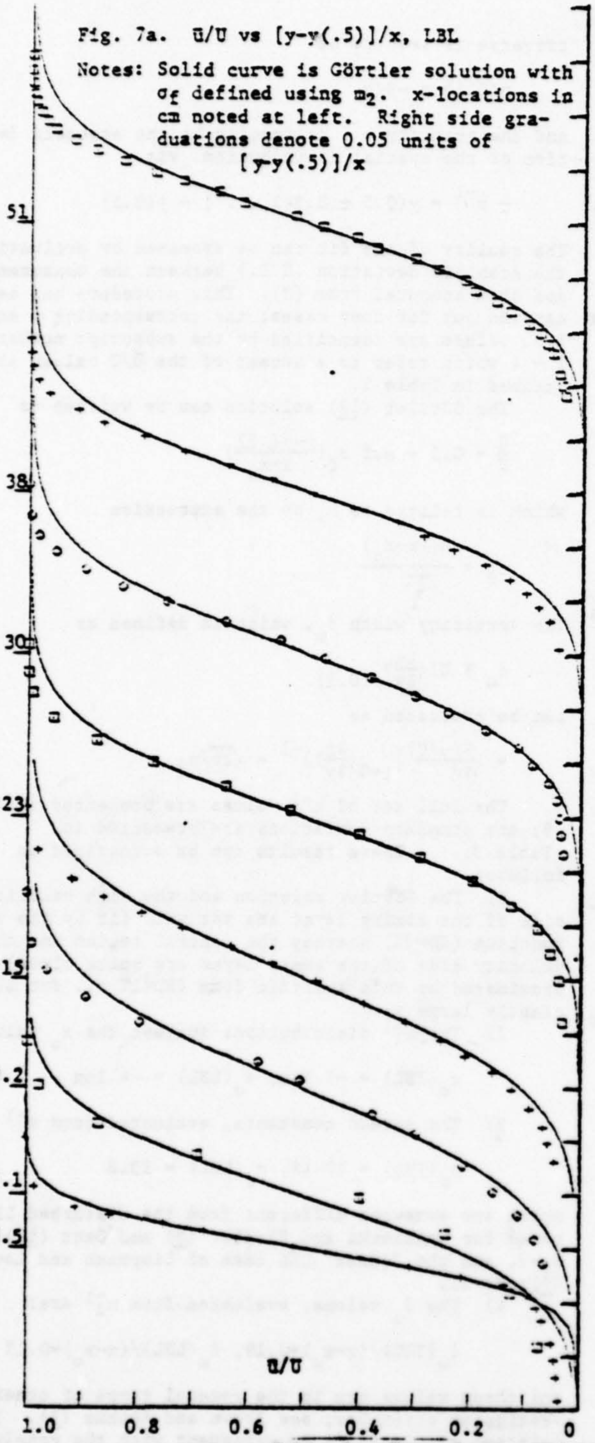
Fig. 7a. $\bar{u}/U$ vs $[y-y(.5)]/x$, LBL

Notes: Solid curve is Görtler solution with σ_f defined using m_2. x-locations in cm noted at left. Right side graduations denote 0.05 units of $[y-y(.5)]/x$

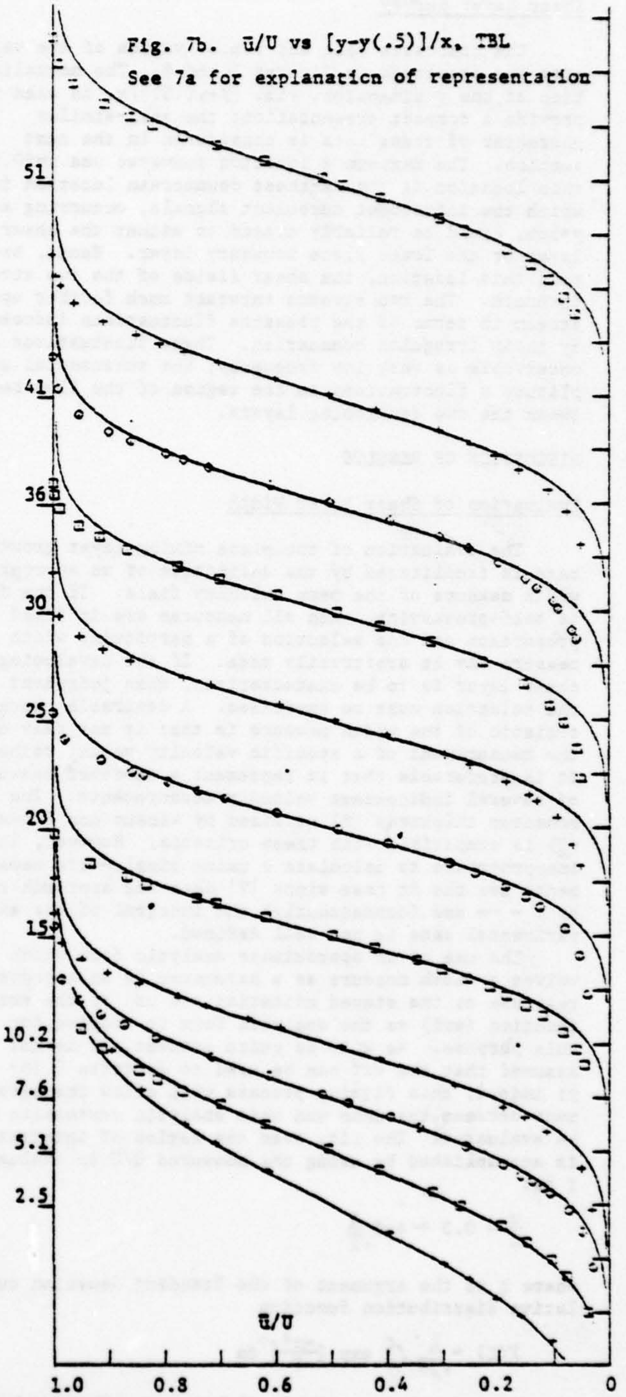
Fig. 7b. $\bar{u}/U$ vs $[y-y(.5)]/x$, TBL

See 7a for explanation of representation

Table 2. Shear layer regions used to define m and S.D. values

Sub	u/U Range	Definition/interpretation
1	$0.1 \le u/U \le 0.99$	Maximum range over which velocity magnitude data approximates $\bar{u}$ ($\bar{v}/\bar{u} \ll 1$ for $\bar{u}/U = 0.1$) and is appropriate for the Gaussian fit ($\bar{u}/U < 1.0$)
2	Three maximum u/U values which are <0.5 plus three minimum u/U values which are >0.5	approximation to u/U data which will define the $\partial\bar{u}/\partial y$ at y(0.5)
3	$0.1 \le \bar{u}/U \le 0.6$	low velocity region
4	$0.4 \le \bar{u}/U \le 0.99$	high velocity region

Fig. 8a. $\tilde{u}/U$ vs $[y-y(.5)]/x$, LBL case

Notes: x locations, in cm, of experimental data noted on left side, each mark on right is $\tilde{u}/U=0.05$

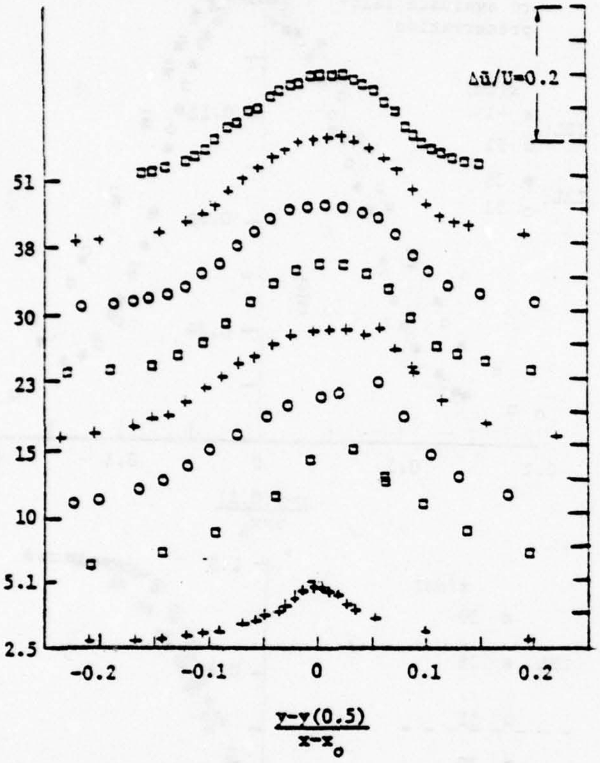

Fig. 8b. $\tilde{u}/U$ vs $[y-y(.5)]/x$, TBL case (see 8a for description of coordinates)

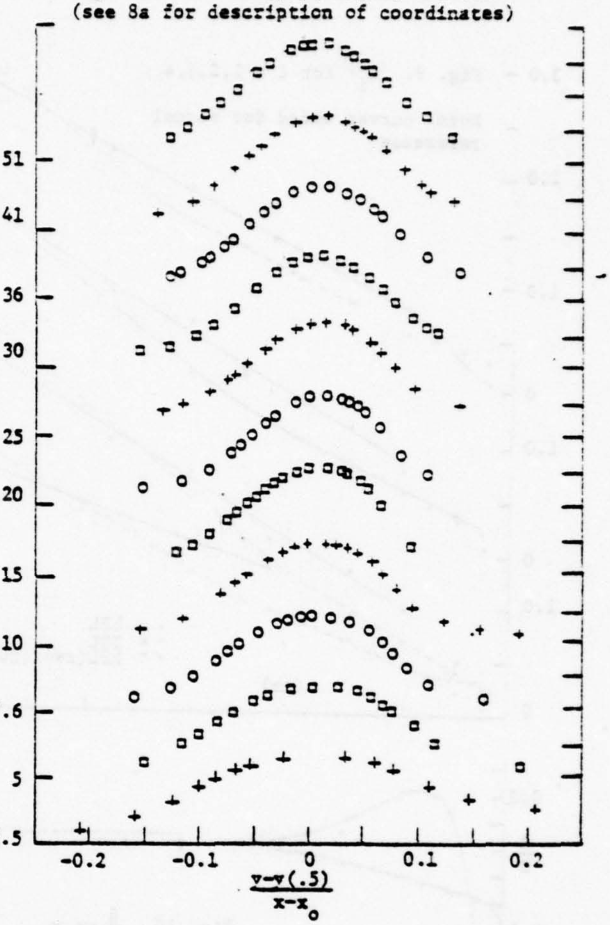

6. The $m^{-1}(x)$ distributions suggest that the development of the LBL and TBL cases are strongly different; the differences are also evident in the $\tilde{U}/U$ vs $[y-y(.5)]/x$ plots of Figure 7. The m^{-1} growth for the LBL case is extremely rapid near x=0 and it appears to reach its final state quite quickly. Conversely, the TBL case exhibits two distinct regions with a clear change in the otherwise constant slope (dm^{-1}/dx) at approximately 25cm or $300\theta_1$ units. Browand (11) noted a change in the growth rate of his TBL case at $x=(400 \div 500)\theta_1$ units. It is possible to infer that somewhat similar effects may be present in each flow since the effective time (τ) for the evolution of the layer will be approximately the same for the two conditions. ($\tau=x/U_c$ and since $U_c=(U_1+U_2)/2$, $\tau(\underline{11})/\tau(\text{present}) = (4.5/3)(0.5/0.62) = 1.2.$)

Self-Preservation

The observed linear growth of the shear layer width measure is a necessary, but not a sufficient condition for self-preservation. Other necessary conditions are evaluated below. The maximum $\tilde{u}/U$ value is independent of x for the self-preserving condition; Figure 10 presents the relevant data. This figure shows that the maximum fluctuation intensity distributions are dramatically different for the two cases in the region $0 \leq x \leq 25$cm and that the two seem to be tending toward their asymptotic limits by the end of the measurement region. The constant value $\tilde{u}/U=0.17$ has been added to the plot for visual reference. The apparent difference in the $\tilde{u}/U$ values may be a result of the inadequate averaging time of the r.m.s. voltage value for the LBL vs the TBL data. A more reliable comparison can be based upon the x-dependence of the normalized $\tilde{u}$ values for the separate LBL and TBL cases since the errors within each data set will be constant. This comparison is presented in Figure 11 where the similarity variable $\{[y-y(.5)]/(x-x_o)\}$ is used to evaluate the self-preserving character of the data. A similar representation of the mean velocity data is also presented in Figure 12. These data support the

Table 3 S.D. Values for the $\underline{\tilde{U}/U}$ regions 1-4

LBL Case (all x100)

x=	2.5	5.1	10	15	23	30	30	51
SD_1	2	2.8	4.3	3.3	2.5	3.6	3.5	3.5
SD_2	0.4	5.4	2.4	0.8	0.7	1.0	0.7	1.0
SD_3	0.9	2.0	1.0	0.5	0.6	0.7	0.6	0.8
SD_4	2.0	0.9	3.9	3.1	2.3	3.2	3.0	2.7

TBL Case (all x100)

2.5	5.1	7.6	10	15	20	25	30	36	41
1.4	1.5	3.1	3.5	2.3	2.8	3.7	3.2	2.3	2.9
0.6	0.7	0.4	0.6	0.5	0.6	0.8	0.7	0.7	0.8
0.5	0.2	0.4	0.6	0.3	0.9	1.0	1.2	0.9	0.7
1.1	1.5	2.5	3.2	1.9	2.0	2.9	2.8	1.1	2.2

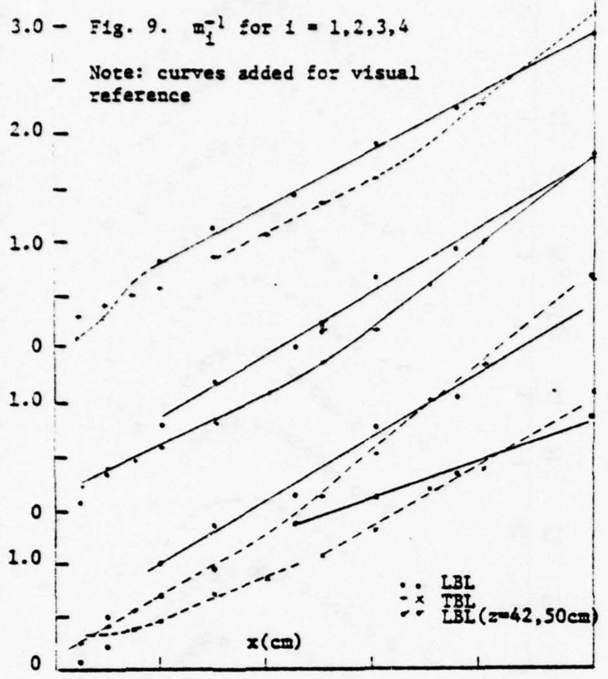

Fig. 9. m_i^{-1} for i = 1,2,3,4

Note: curves added for visual reference

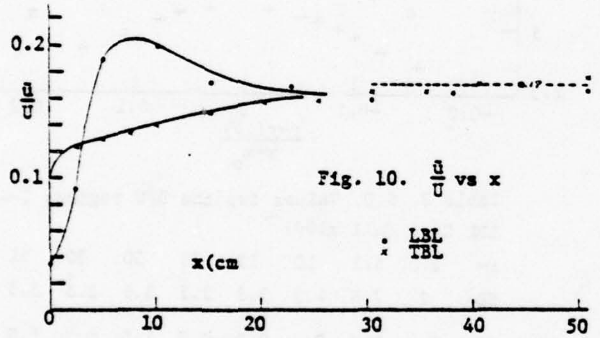

Fig. 10. $\tilde{u}/U$ vs x

interpretation that the flow has become self-preserving by Re_x=6.7x10^5 and that the turbulent boundary layer initial condition does result in a wider mixing layer. The ũ values can also be compared with the ũ data summarized by Champagne et. al. (11). The present data have been added to the plot taken directly from this reference; see Figure 13. A very close agreement between the TBL case and that of the Patel (13) and Champagne et. al. (11) studies is evident. The LBL data appear to be in agreement with the Liepmann and Laufer (8) results with the exception of the maximum ũ values for the present data.

Interpretation of the TBL and LBL Initial Condition Effects

The laminar/turbulent state of the boundary layer at x=0 clearly has a significant effect on the initial development of the plane mixing layer; the streamwise evolution of the fluctuation intensity and the mean velocity distributions are quite different for the two cases. The TBL case shows a pronounced change in its characteristics at $x/\theta_i \approx 300$ or 25cm whereas the LBL case is not similarly differentiated except for the ũ/U maximum values.

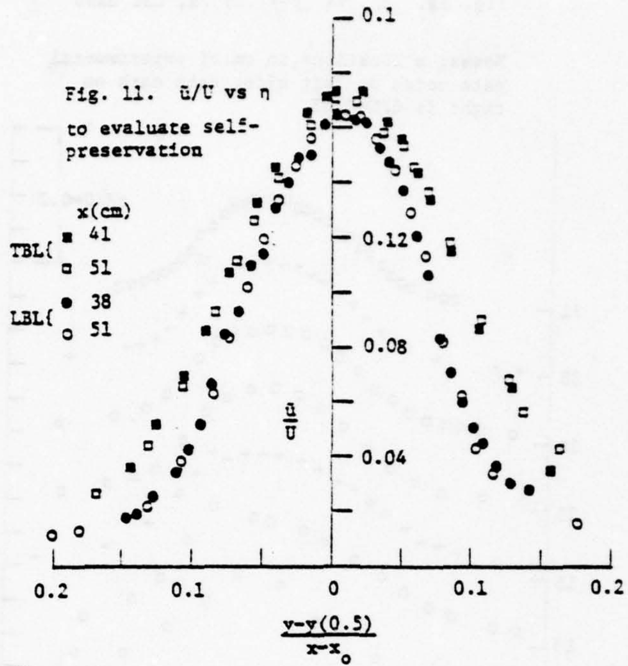

Fig. 11. ũ/U vs η to evaluate self-preservation

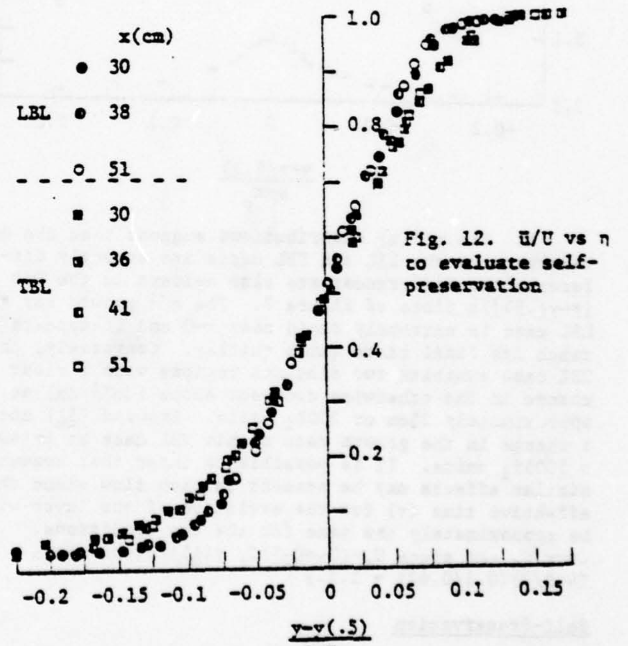

Fig. 12. Ū/U vs η to evaluate self-preservation

The quite interesting question about the initial condition effects on the asymptotic state cannot be definitively answered with these data; however, the data comparisons which involve the similarity coordinate $\{[y-y(.5)]/(x-x_o)\}$ do support the proposition that the effects persist in the region of self-preservation.

The present study is, however, not constrained to simply form comparative evaluations using the similarity coordinates. Since the same apparatus and the "same" flow speed* and streamwise locations were used for the measurements, a direct comparison of the experimental data is possible. The Ū and ũ data for

---

*U(LBL) = 18.59mps ≈ 1.02 U(TBL)

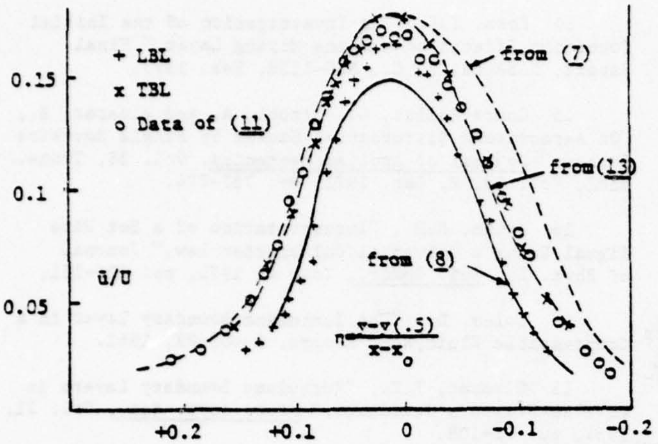

Fig. 13 ū/U vs η

Note original curve with (7), (8) and (13) data points added to original data of (11) taken directly from reference (11). Present data added to plot with ū/U<0.5 for η>0 convention of (11).

x=50.8cm are presented in Figure 14. This representation of the data provides a very strong contradiction to the earlier inferred influence of the initial conditions ... the flow fields from both the laminar and the turbulent initial conditions are essentially identical.*

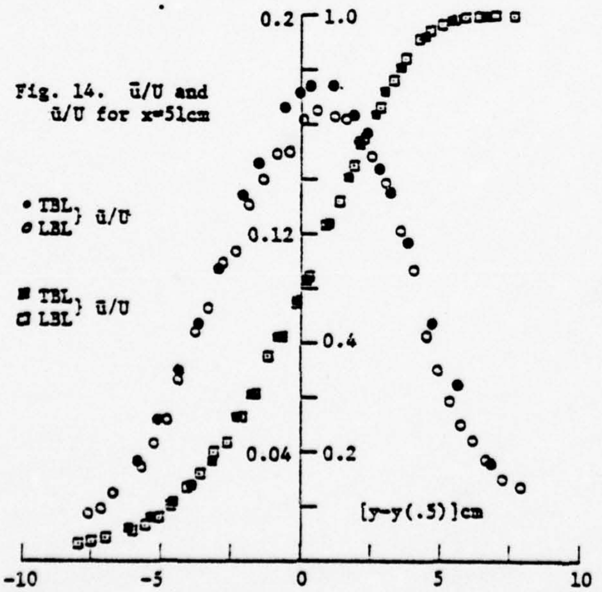

Fig. 14. ū/U and ũ/U for x=51cm

With this insight, it is not difficult to reevaluate the earlier evidence which seemed to suggest a continuing effect of the initial condition. Specifically, if one combines the self-preserving condition: dl/dx= constant (where l is a width measure of the shear layer), with the observation that a derivative is best evaluated from experimental data if the largest possible span of the independent variable is utilized, the use of x_o in the expression for the similarity variable is logical and evaluating it from an upstream extrapolation of the available data is reasonable. However, this commonly accepted procedure is not easily adapted to a situation where the x derivative of l ... in this case dm_2^{-1}/dx ... only slowly approaches its asymptotic value. By inference, this is the actual situation for the m_2^{-1} of, at least, the LBL case although it is too subtle an effect to be evident from Figure 9. The earlier quoted observation of Dimotakus and Brown (12) that ... the growth rate $d\delta_\omega/dx$ depends upon the vorticity distribution which is, in turn, related to δ_ω ... is quite useful in recognizing the cause for the gradual change in the m_2^{-1} slope for the LBL case. It is interesting to speculate on the reason for the apparent differences in the "time" to achieve an asymptotic state for the two initial boundary layer conditions. A related point of interest can be identified by comparing the tripped LBL data, e.g. (9), (11), with the present LBL and TBL cases. Such a comparison suggests that the character of the disturbance, and not its amplitude, is responsible for the substantial effect on the x_o inferred from the ū(x,y) in the developing region. (Note that $m_2^{-1}(x=25, z=42) = m_2^{-1}(x=25, z=71)$ see Fig. 9 and ũ(o,y,42)(max-LBL) = 3 ũ(o,y,71)(max-LBL) = 1.2 ũ(o,y,71)(max-TBL).)

The suggestion that is often made: that a quite large Re_x is required to observe a self-preserving condition, can be interpreted in the context of the present measurements. It is clear from an examination of Figure 9 that a large increase in the x values would be required to infer the same x_o for the LBL and TBL cases. Conversely, if a self-preserving flow is one in which the effects of the initial condition are lost, and if an experimental program which allows the two states to be obtained in the same apparatus is executed, then a certain determination that self-preservation has been obtained will result from "identical" Ū and ũ distributions. An added benefit is that the necessary Re_x value will be significantly smaller than that which would be required if the x_o value were to be precisely defined by the upstream extrapolation of l(x).

SUMMARY

Data to document the developing region of a plane mixing layer have been acquired for the two distinct initial conditions: a laminar and a turbulent boundary layer at x=0.

The initial development of these two flow fields is dramatically different; it is proposed that these data will constitute a viable reference case for the evaluation of calculation schemes.

The question of the initial condition effects on the self-preserving mixing layer has been addressed. It is proposed, on the basis of these data, that the initial condition is not relevant in the self-preserving state and that the apparent influence is a consequence of using an inappropriately evaluated similarity variable. The present data, when interpreted in the standard manner, reveal that the misinterpretation is quite easily made and that the correct evaluation requires the inference of very subtle changes in the slope of the width measure's x-dependence.

---

*The maximum r.m.s. fluctuation level at x=50.8cm was rechecked to evaluate the possible influence of an insufficient averaging time for the LBL case data. Several long term (30 sec.) analog voltage signals ũ were collected for both the LBL and TBL cases. These results confirmed that the ũ/U distribution for the TBL case was slightly wider but the amplitude difference was reduced to ≈3%. Maximum ũ values were ũ/U(TBL)=0.185 and ũ/U(LBL)=0.18.

ACKNOWLEDGEMENTS

Personal gratitude is expressed to Mr. Curtis Monroe, programmer, Ms. Mary Grace, typist, Mr. Frank Walker, draftsman and Mr. Dave Sigmon, electronics technician. The financial support of the High-Speed Aerodynamics Division of the NASA Langley Research Center, Mr. Michael Fischer and Mr. Jerry Heffner, grant monitors, and the Division of Engineering Research, MSU, Mr. J.W. Hoffman, Director, is gratefully acknowledged.

REFERENCES

1 Brown, G.L. and Roshko, A., "On Density Effects and Large Structure in Turbulent Mixing Layers," Journal of Fluid Mechanics, Vol. 64, Part 4, 1974, pp. 775-816.

2 Winant, C.D. and Browand, F.K., "Vortex Pairing: The Mechanism of Turbulent Mixing-layer Growth at Moderate Reynolds Number," Journal of Fluid Mechanics, Vol. 63, Part 2, Jan. 1974, pp. 237-255.

3 , "Free Turbulent Shear Flows, Vol. 1," Conference Proceedings, NASA SP-321, July 1972.

4 Murthy, S.N.B. (ed.), Turbulent Mixing in Non-Reactive and Reactive Flows, Plenum Press, New York, 1975.

5 Townsend, A.A., The Structure of Turbulent Shear Flow, 2nd Ed., Cambridge U. Press, Cambridge, 1976.

6 Bradshaw, P., "The Effect of Initial Conditions on the Development of a Free Shear Layer," Journal of Fluid Mechanics, Vol. 26, Part 2, 1966, pp. 225-236.

7 Wygnanski, I. and Fiedler, H.E., "The Two-Dimensional Mixing Region," Journal of Fluid Mechanics, Vol. 41, Part 2, April 1970, pp. 327-361.

8 Liepmann, H.W. and Laufer, Jr., "Investigations of Free Turbulent Mixing," NACA Report No. 1257, 1947.

9 Batt, R.G., "Some Measurements on the Effect of Tripping the Two-Dimensional Shear Layer," AIAA Journal, Vol. 13, No. 2, Feb. 1975, pp. 245-246.

10 Browand, F.K., "The Effect of Initial Conditions Upon the Growth of the Two-Dimensional Mixing Layer," APS Bulletin, Series II, Vol. 21, No. 10, Nov. 1976, p. 1221.

11 Champagne, F.H., Pao, Y.H. and Wygnanski, I. J., "On the Two-Dimensional Mixing Region," Journal of Fluid Mechanics, Vol. 74, Part 2, 1976, pp. 209-250.

12 Dimotakis, P.E. and Brown, G.L., "Large Structure Dynamics and Entrainment in the Mixing Layer at High Reynolds Number," Project SQUID Technical Report CIT-7-PU, August 1975.

13 Patel, R.P., "An Experimental Study of a Plane Mixing Layer," AIAA Journal, Vol. 11, No. 1, Jan. 1973, pp. 67-71.

14 Foss, J.F., "An Investigation of the Initial Condition Effects on a Plane Mixing Layer," Final Report, NASA La. R. C., NSG-1138, Feb. 1977.

15 Comte-Bellot, G., Strohl, A. and Alcaraz, E., "On Aerodynamic Disturbances Caused by Single Hot-Wire Probes," Journal of Applied Mechanics, Vol. 38, Trans. ASME, Vol. 93, E, Dec. 1971, pp. 767-774.

16 Brunn, H.H., "Interpretation of a Hot Wire Signal Using a Universal Calibration Law," Journal of Phys. E., Sci. Instr., Vol. 4, 1971, pp. 225-231.

17 Coles, D., "The Turbulent Boundary Layer in a Compressible Fluid," Rand Report, R-403-PR, 1962.

18 Clauser, F.H., "Turbulent Boundary Layers in Adverse Pressure Gradients," Jour. Aero. Sci., Vol. 21, 1954, pp. 91-108.

19 Görtler, H., "Berechnung von Aufgaven der freien Turbulenz auf Grund eines neuen Naherungsansatzes, Z. Anger. Math. Mech., Bd. 22, Nr. 5, Oct. 1942, pp. 244-254.

NUMERICAL SIMULATION OF TURBULENT MIXING LAYERS VIA VORTEX DYNAMICS[1]

W. T. Ashurst
Sandia Laboratories
Livermore, California

ABSTRACT

The simple concept of effective transport coefficients for turbulent flows is starting to be replaced with the realization that turbulent flows consist of structures which are created and destroyed and it is their interactions that produce the transport of mass, momentum, and energy. The bursting phenomena in boundary layers is one aspect of that structure and vorticity (or eddy) pairing <u>is</u> the structure of the turbulent mixing layer. This paper describes numerical experiments using discrete vortices, in order to determine to what detail they can simulate the planar turbulent mixing layer. Calculations involving several thousand vortices have duplicated the mixing layer growth, eddy pairing, turbulent shear stress profile, and root-mean-square velocity fluctuations of moderate Reynolds number flows. With the exception of the normal rms velocity fluctuation, good agreement is also found at high Reynolds number.

NOMENCLATURE

H = discrete vortex spacing
L = unit length in computer calculation
ℓ = spacing between eddies
M = number of vortices per unit length
N = number of vortices in computer system
P = pressure
r = distance from vortex center
Re = Reynolds number, $\Delta UL/\nu$
t = time
Δt = time step in computer calculation
U_1 = outer slow flow of mixing layer
U_2 = outer fast flow of mixing layer
$\bar{U}$ = average velocity, $(U_1 + U_2)/2$
ΔU = velocity difference, $U_2 - U_1$, and unit velocity in computer calculations
V = vortex induced velocity
X = flow direction
X_c = long range cutoff length
Y = normal to flow direction
δ_ω = shear layer vorticity thickness
Γ = sheet vorticity strength
κ = discrete vortex strength
ν = kinematic viscosity
σ = short range cutoff length and error function scale factor
θ = shear layer momentum thickness

INTRODUCTION

It has been realized recently that the structure of turbulent shear flows may be quite deterministic and very important to the overall flow. The flow visualization done by Browand, et al. (1) at moderate Reynolds numbers and that of Roshko, et al. (2) at "turbulent" Reynolds numbers have dramatically shown the free turbulent mixing layer to have a definite large-scale structure due to clusters of vorticity that pair together and hence thicken the mixing layer. While the time-average turbulent mixing layer thickness grows in a linear fashion, the instantaneous entrainment is distinctly nonuniform. This phenomenon is very crucial for combustion applications since chemical reactions will only occur when the reactants have been mixed to the appropriate composition. Therefore numerical simulation of turbulent mixing layers will be a valuable analytical tool for understanding many combustion systems (e.g., steady and non-steady intake flows).

Calculations using discrete vortices to study inviscid fluid motion have a long history—from Rosenhead's hand calculations in 1931 using a few vortices to recent computer calculations involving thousands of vortices (3). Most of these efforts were directed toward understanding the time evolution of finite-area vorticity regions or the initial breakup of the laminar shear layer (usually done for short times or small regions with periodic boundary conditions).

Previous numerical work using finite difference methods have been limited to low Reynolds number flow since the numerical grid must define regions whose thickness will decrease like (Reynolds number)$^{-1/2}$. Consequently the laminar instabilities have been thoroughly studied (4). Unfortunately, most combustion systems have high Reynolds number (turbulent) flow. Recently Chorin has suggested a novel numerical method for high Reynolds number flows (5). The inviscid flow is solved via discrete vortices (no finite difference mesh is required), while the viscous effects are incorporated via a random walk for each vortex.

I have applied this method to Stoke's first problem (infinite plane wall set in constant motion at zero time) in order to empirically determine the appropriate numerical parameters for non-steady viscous flow problems. Fig. 1 shows the exact velocity profile (at reduced time of 2) for a series of Reynolds numbers compared with ensemble averages from the vortex method. The agreement is quite good. (The disagreement at large Y/L is due to the short range cutoff (± L/2) used in the vortex interaction.) Over this time period (zero to 2) the calculated wall drag was within ten percent of the exact value (which is

---

[1] Work supported by ERDA.

proportional to $(\text{time})^{-1/2}$). Non-steady corner flow has also been treated (6) and comparison of these results with three-dimensional piston-cylinder experiments has been very encouraging.

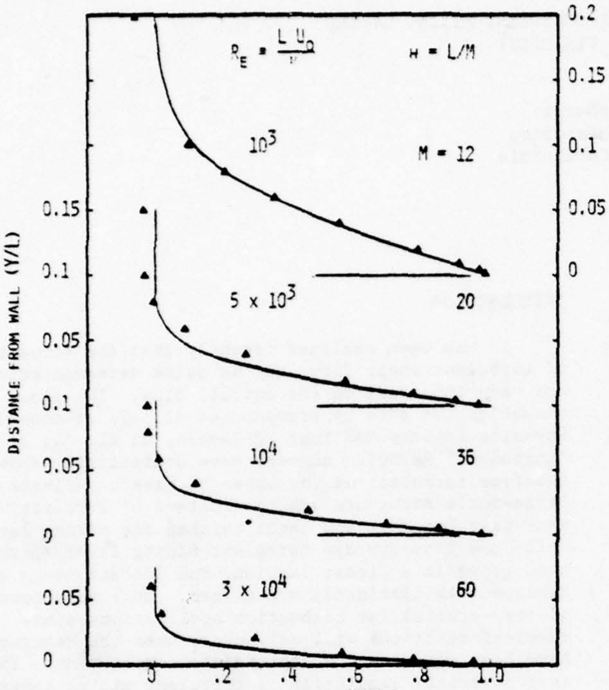

Fig. 1 Discrete vortex calculation of non-steady parallel flow near flat plate using random walk. Velocity profiles shown for time 2L/U after plate motion started (time step was 0.025 L/U).

Therefore, the goal of this work has been the application of Chorin's method to the free mixing layer with emphasis upon what features of turbulent flow are reproduced by the discrete vortex method.

NUMERICAL SIMULATION OF TWO-DIMENSIONAL MIXING LAYER

The ideal two-dimensional mixing layer can be defined by three parameters: 1) the velocity difference between the two flows that are to be mixed $\Delta U = U_2 - U_1$; 2) the average velocity $\overline{U} = (U_1+U_2)/2$ of the two streams; and 3) the kinematic viscosity of the working fluid ν. Good experimental technique eliminates other effects (e.g., flow non-uniformities, boundary layers on splitter plate and free stream turbulence, see Winant and Browand).

In the numerical simulation, the velocity difference defines the vorticity density of a vortex sheet that replaces the upstream wall $\Gamma/L = \Delta U$, where L is the length scale. The average velocity is produced with the addition of a linear potential $\overline{UX}$ throughout the system. The kinematic viscosity can be used to define a unit Reynolds number $Re = \Delta U\, L/\nu$. The splitter plate or upstream wall ends at the origin where the vorticity production per unit time is $\Gamma/t = \Delta U\, \overline{U}$ ($\rightarrow U^2/2$ for one flow at zero velocity).

The uniform sheet of vorticity could be replaced by discrete vortices of strength $\kappa = \Delta U\, L/M$ and spaced at distance $H = L/M$. Select the time step so that this array of discrete vortices will be convected a distance $H = \overline{U}\, \Delta t$ in one time step by the average velocity field. Therefore one discrete vortex passes the origin each time step and produces the proper vorticity production rate of $\kappa/\Delta t = \Delta U\, \overline{U}$.

Thus the numerical simulation consists of an upstream sheet of vorticity (of density ΔU) ending at the origin where a new discrete vortex (of strength $\Delta U\, \overline{U}\, \Delta t$) is created each time step. This new vortex and all the previously created ones are acted upon by the average velocity field $\overline{U}$. There are no outer walls.

Each discrete vortex produces an irrotational velocity field of $V_{\text{tangent}} = \kappa/2\pi r$ where r is the distance from the vortex center. In order to advance the solution from time t to $t + \Delta t$, the velocity at each vortex location must be determined. This velocity has three contributions: 1) the upstream sheet of vorticity; 2) the average velocity field; and 3) the 1/r interaction with all the other vortices in the system at that time. For N vortices this is a computational task proportional to N^2 (and N increases by one each time step!).

The above numerical scheme will be a solution to the inviscid or Euler equations for incompressible fluid flow. Previous numerical solutions using point vortices have had some difficulty with the velocity divergence at the vortex center. Chorin eliminated this problem by using a short range cutoff so that the induced velocity goes to a constant value for $r < \sigma$. The difference between the Euler equation solution and the numerical results approaches zero like σ^2.

Kelvin's circulation theorem shows that vorticity moves with the fluid element in an inviscid fluid. The effect of molecular viscosity is to diffuse or spread out concentrations of vorticity. Chorin's suggestion is that viscous diffusion of vorticity can be accomplished in the mean by adding a random walk component to each vortex each time step (5). The dispersion of this random walk can be defined in terms of the unit Reynolds number ($Re = \Delta U\, L/\nu$)

$$(\text{root mean square})/L = \frac{2}{Re}\,\frac{\Delta t\, \Delta U}{L}^{\,1/2}$$

For a given Reynolds number, the time step and number of vortices per unit length must be selected. From the laminar Stokes problem, it was found that a good choice for the average random component is a value equal to half of the short-range cutoff σ. (For the plane viscous wall, a discrete vortex and its negative image would be placed at $\pm\, \sigma/2$ with respect to the wall.) Computer generated movies showing the vortex displacement for each time step indicated that a reduced time step of ~ 0.05 was adequate.

RESULTS FOR MIXING LAYER

Mixing Layer Growth

The preliminary results for the mixing layer (using numerical parameters from Fig. 1) indicated that the random walk provides the laminar $\sqrt{X}$ growth rate of momentum thickness with a transition to the turbulent linear growth. Leaving out the random walk component still gave a transition to linear growth (approximate same location) but the early growth rate is more like an inverse fractional power. Thus the mixing layer linear growth rate is a consequence of the Euler equations.

To further investigate the dependence of vorticity coalescence and mixing layer growth upon Reynolds number, two different viscous flows have been studied at the same velocity parameter $\overline{U}/\Delta U = 1.05$.

Reynolds Number $\frac{\Delta UL}{\nu}$	Vortices per Length, M	Cutoff Length Short, σ/L	Long, X_c/L
250	8	0.02	80
1000	16	0.01	40

The time step for both flows was $\Delta t = L/(16\ \Delta U)$ where the unit length L equals 1 cm for comparison to the data of Winant and Browand (1).

Fig. 2 shows the time-average momentum thickness divided by downstream distance for the low Reynolds number flow. The approach to linear growth rate occurs at about the same location as the water channel results of Winant and Browand, ≈ 12 cm. The high Re flow had a transition at 6 L.

The averaging time for Fig. 2 was 64 reduced time units ($t\ \Delta U/L$) which corresponds to 24 seconds of real time if the velocity difference of Winant and Browand is used ($\Delta U = 2.62$ cm/s, $L = 1$ cm). A much longer calculation of 800 reduced time units (= five minutes real time with CDC 6600 computer time being 3000 times longer) has produced a momentum growth rate of $\Delta\theta/\Delta X = 0.021$. Using the error function for the mean velocity profile ($\sigma\theta/X \equiv 0.3989$ and $\delta_\omega' \equiv \sqrt{\pi}/\sigma$), the vorticity-thickness growth rate is $\delta_\omega/(X-X_0) = 0.093$ which falls within the experimental scatter shown in Fig. 10 of Brown and Roshko (2). The virtual origin is -3.8 L which agrees quite well with the results of Spencer and Jones (7).

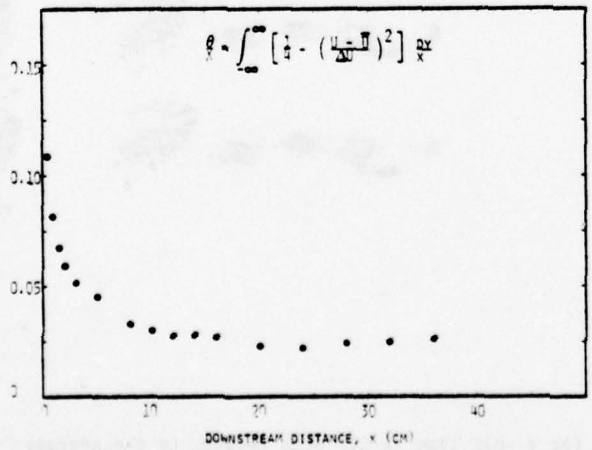

Fig. 2 Time average momentum thickness for 250 Re flow divided by downstream distance

Computer generated movies of the vortex motion clearly reveal vorticity coalescence and the large-scale vortex pairing. Seeding the two streams with different color tracer particles dramatically shows the aperiodic entrainment behavior. As Browand's movies indicate, the large-scale vortex pairing can most easily be seen while moving at the average flow speed $\overline{U}$. Fig. 3 presents streakline plots of the discrete vortices with respect to the average speed for a unit time period ($t = L/\Delta U$) with a field of view equal to 40 L; each succeeding plot is displaced two space units downstream and two units later in time.

From the first plots of each flow it can be seen that the first clusters of vorticity occur at the transition location. Neighboring clusters were first observed to roll around each other in the water channel experiments at the transition location (1). With the faster flow on the bottom, the rotation is counterclockwise and the downstream cluster slows down as it is raised by its interaction with the upstream cluster. The upstream cluster increases its velocity as it is pushed down by this interaction. The original clusters begin to lose their identity after rotating about ninety degrees. The water channel was long enough to observe four such pairings and Winant and Browand conclude "that the turbulent mixing layer grows through the combination of the large-scale vortical structures" (1).

Moore and Saffman (8) have proposed a model in which the vortices grow continuously by entraining irrotational fluid until their size to spacing reaches a critical value at which point the strain field rips the vortex apart to form larger vortices spaced at larger distances. They do not feel that vortex-pairing is a very important contribution to mixing layer growth. In Fig. 3 the beginning stages of the 250 Re flow does resemble a smearing process; however, farther downstream the clusters are clearly rolling around each other. Increasing the Reynolds number to 1000 shrinks the smearing region and the pairing clearly predominates.

The tangential velocity discontinuity has been studied recently by Acton (9) using 96 discrete vortices with a short range cutoff in a system two wavelengths long (periodic boundary conditions). The initial wavelength amplitude affects the time it takes for the cluster pair to roll up. Acton concludes that while it is possible to specify initial conditions so that a large vortex will ingest its smaller neighbor, as Moore and Saffman have proposed, this process takes much longer to complete and is likely to be beaten by the rollup pairing mechanism.

Thus the rollup pairing process is the mixing layer growth and is very important to the entrainment process of the surrounding non-turbulent fluid. The experimental movies of the dye in Winant and Browand's water channel and the computer movies of tracer particles reveal that the entrainment occurs by the engulfment of irrotational fluid between the pairing clusters of vorticity rather than by gradual lateral spreading of the rotational fluid.

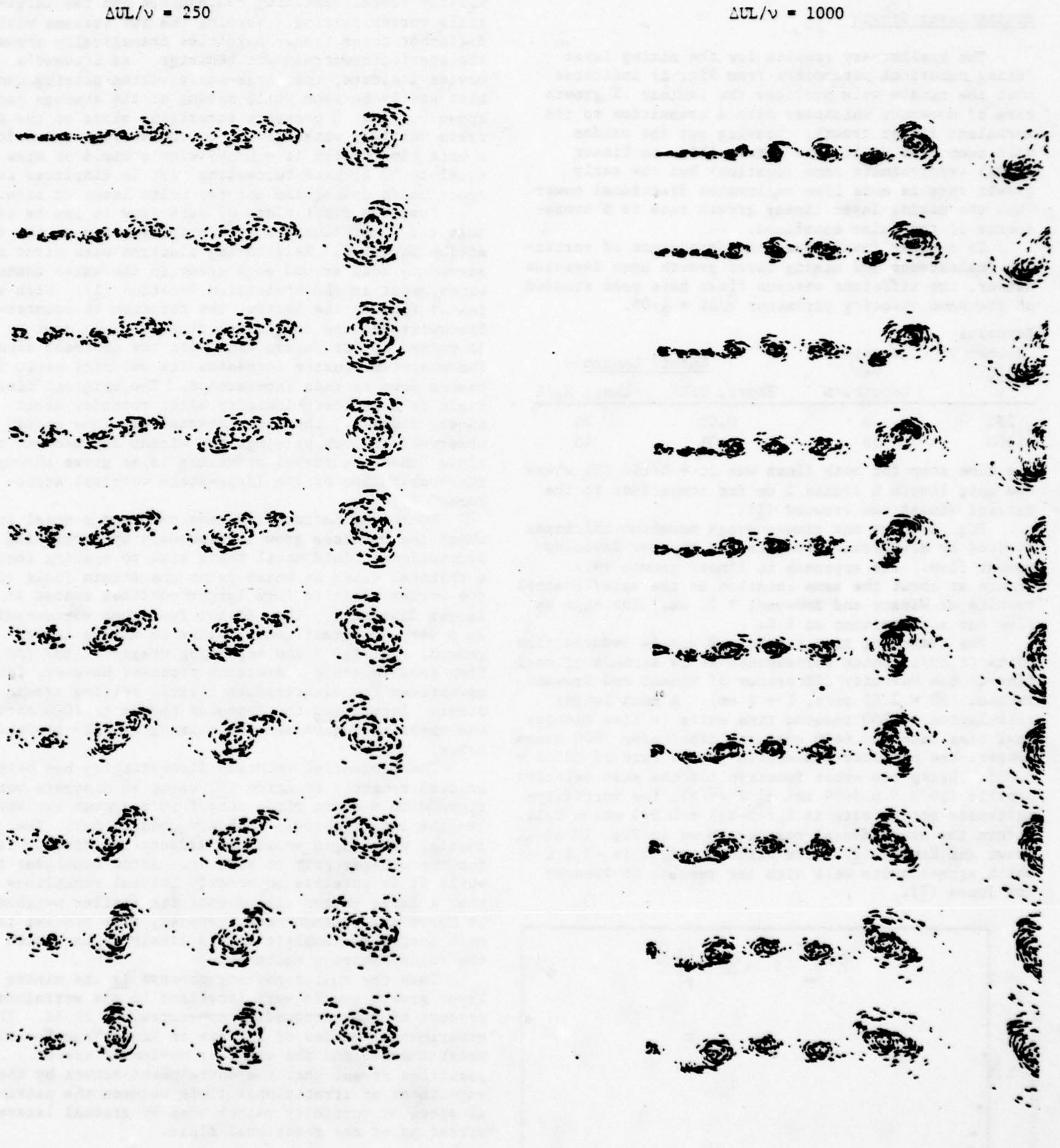

Fig. 3a Streakline plots of each discrete vortex for a unit time (L/ΔU) with respect to the average velocity. The field of view is equal to 40L. The top plots have the origin at the left with each succeeding plot displaced two units downstream and two units later in time. Left column is 250 Re flow and right column is 1000 Re.

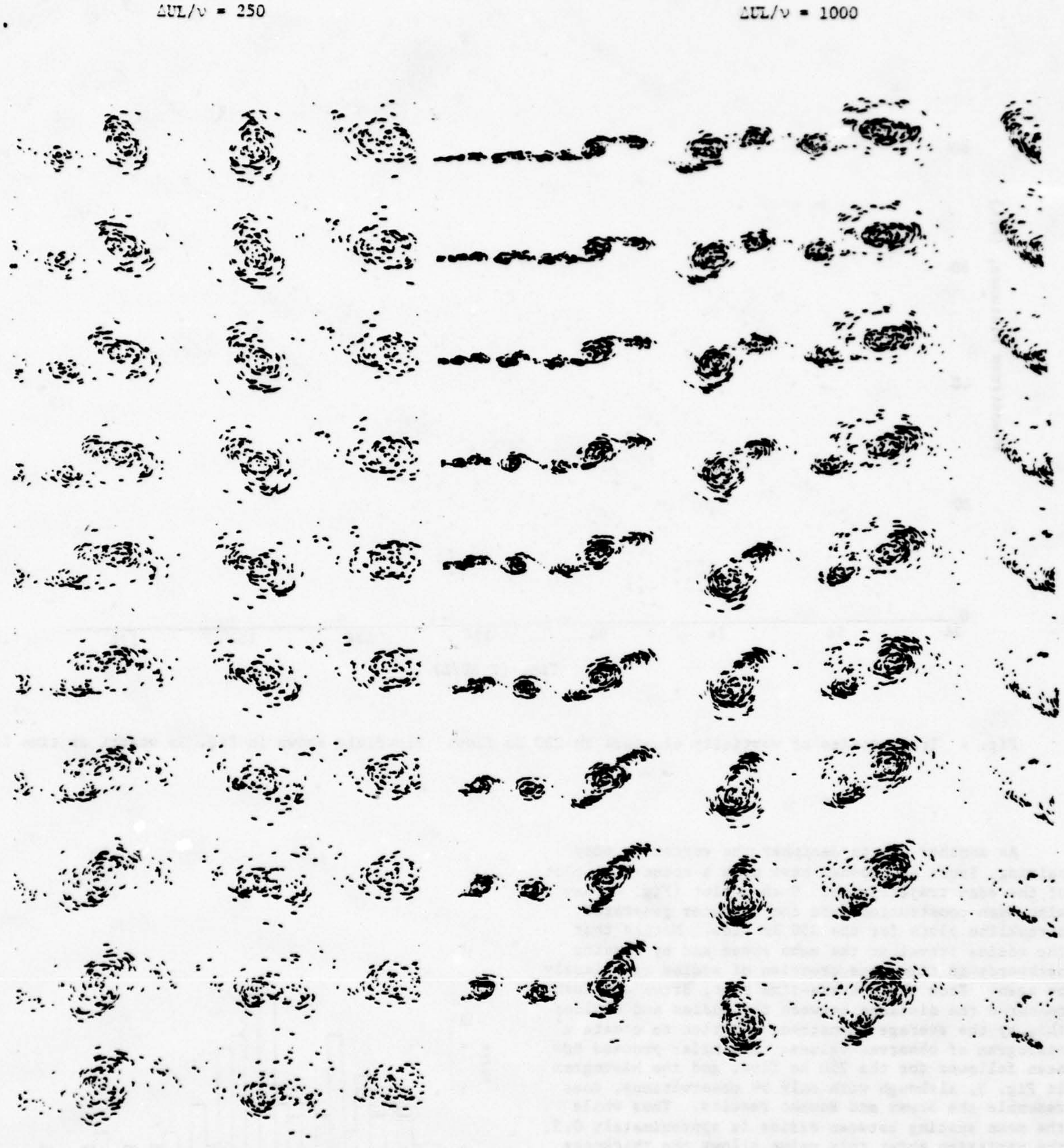

Fig. 3b Continuation of Fig. 3a with additional field of view for the 1000 Re flow (top right plot has origin at left and X = 60L at right).

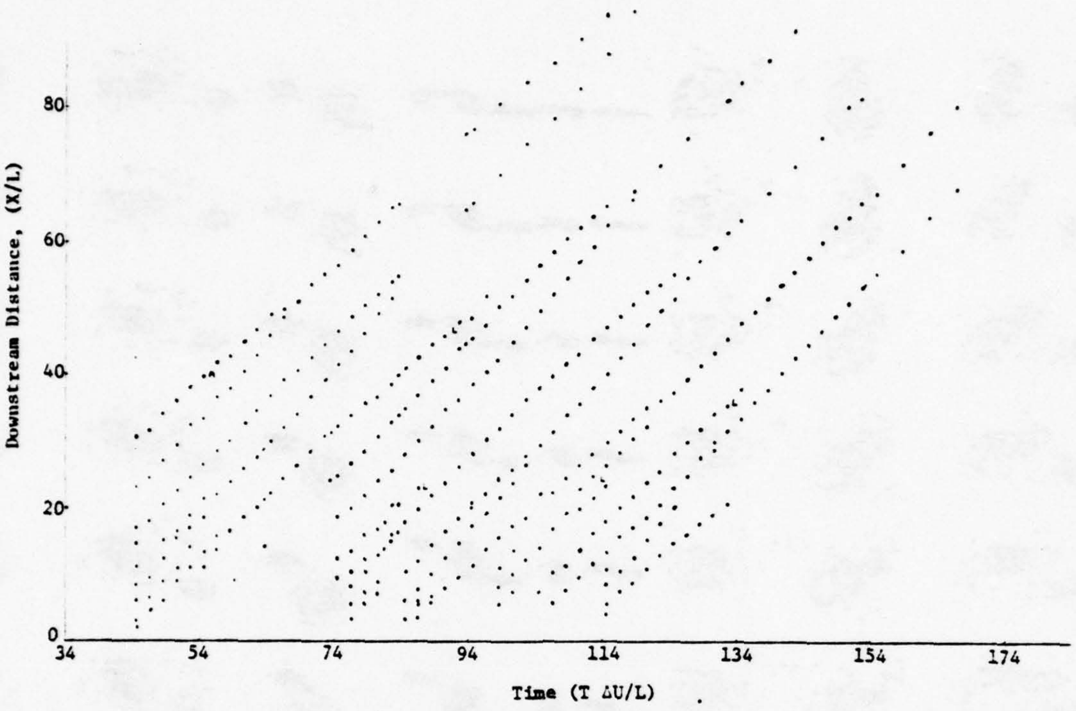

Fig. 4 Trajectories of vorticity clusters in 250 Re flow. Flowfield shown in Fig. 3a starts at time 124.

As another way to decipher the vortex or eddy pairing, Brown and Roshko have made a space-time plot of the eddy trajectories. Such a plot (Fig. 4) has also been constructed from the computer generated streakline plots for the 250 Re flow. Notice that the eddies travel at the mean speed and by tracing backwards in time, the creation of eddies can clearly be seen. From their space-time plot, Brown and Roshko measured the distance between the eddies and divided this by the average downstream location to create a histogram of observed values. A similar process has been followed for the 250 Re flow, and the histogram in Fig. 5, although with only 99 observations, does resemble the Brown and Roshko results. Thus while the mean spacing between eddies is approximately 0.3, the variation about this value allows the thickness of the layer to grow in a smooth linear fashion when measured over many eddy passings. Roshko has also shown that the space-time plot may be used to construct a histogram of eddy lifetimes (10). The resulting curve is fitted quite well by the exponential envelope previously used to describe velocity space-time correlation curves. Classically these correlations have been interpreted as an indication of eddy decay, whereas we can now see it is really the eddy mortality curve.

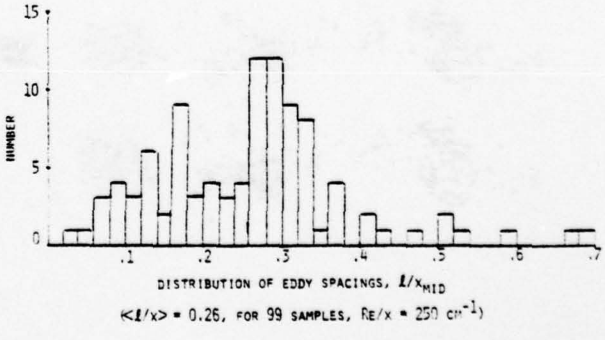

Fig. 5 Histogram of eddy spacings from Fig. 4

Velocity Results

The first extensive numerical simulation was done to correspond with the experimental conditions of the water channel used by Winant and Browand (1) and later Browand and Weidman (11). This is a moderate Reynolds number flow of 300 per cm, but they show good agreement with the Reynolds stress distribution from high Reynolds number experiments. However, the rms velocity fluctuations are glaringly different from high Re flow in that the normal (to flow) velocity fluctuations are larger than the longitudinal fluctuations (their results are reproduced in Fig. 6). Using a simple model of an infinite row of non-interacting vortices spaced at two different wavelengths and oscillating in the normal direction, they obtained the qualitative effect of the normal fluctuations exceeding the longitudinal ones.

They conclude that Reynolds-stress production is associated with the pairing process and is invariant to increasing Reynolds number while the small scale motion (i.e., velocity fluctuations) does change with Reynolds number.

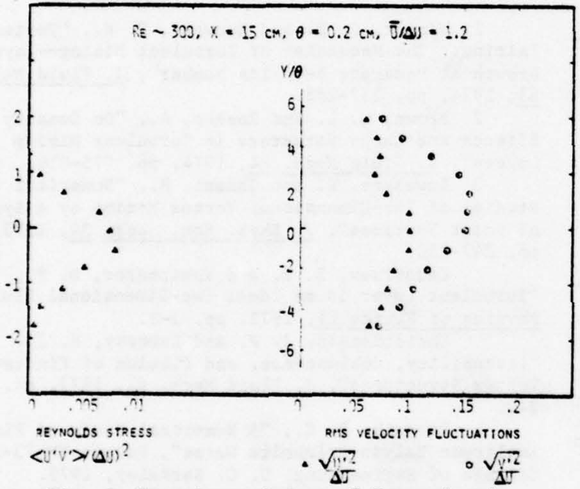

Fig. 6 Experimental data of Browand and Weidman (11)

The numerical results for Reynolds stress are twice the experimental value and the velocity fluctuations are the same in both directions; see Fig. 7.

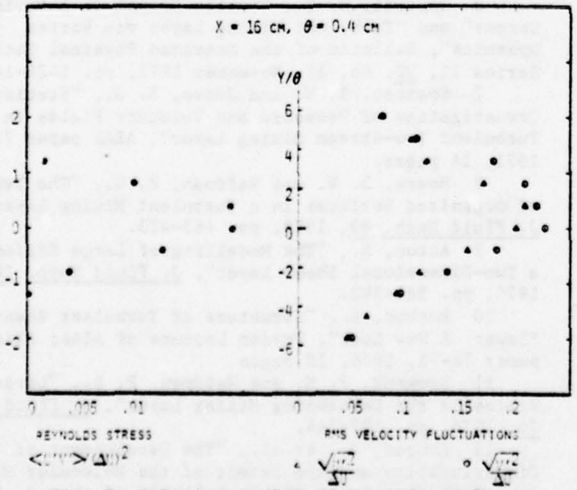

Fig. 7 Calculated flow with random walk

A second calculation was done where aging of the discrete vortices was included in an approximate manner by reducing the vortex interaction according to the exact solution for a single isolated vortex in a viscous fluid. The overall effect is not an exact solution of the Navier-Stokes equations but this has been done in the same spirit as Chorin's random walk approximation for vorticity diffusion. The discrete vortex velocity field is now a function of distance from the vortex center and the age of the vortex (time since it was created at the origin).

$$V(r,t) = \kappa[1 - \exp(-r^2/4\nu t)]/2\pi r$$

The results of the aging calculation are dramatically different. Fig. 8 shows the good agreement now obtained with the experimental Reynolds shear stress (dashed line). The separation in the rms velocity fluctuations is also reproduced quite well. Watching the computer movies reveals that there are two differing types of trajectories for the discrete vortex to follow: rising into the slow flow or falling into the fast flow. Downstream, aging produces a difference between vortices that have followed these two path types that is not present in the previous calculation (Fig. 7). Thus the small scale destruction of vorticity is evident in the velocity fluctuations. As the Reynolds number is increased even smaller length scales are activated (without disturbing the large scale structure (see Brown and Roshko (2)) and the normal velocity fluctuations become smaller than the longitudinal ones. The transition Reynolds number is not known.

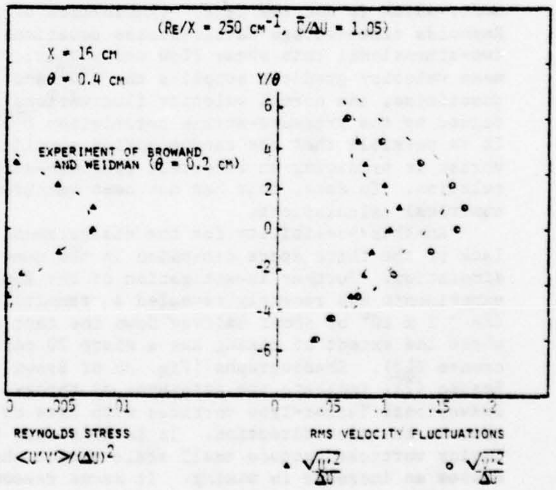

Fig. 8 Calculated flow with random walk and exponential spreading for each discrete vortex

Large Reynolds Number Mixing Layer

A preliminary calculation of a high Reynolds number flow has been made in order to approximate the conditions of Brown and Roshko (uniform density, U_1, U_2 = 380, 1000 cm/s, $\overline{U}/\Delta U = 1.11$, and $U_2/\nu = 5 \times 10^4\ \mathrm{cm}^{-1}$).

The numerical conditions are:

Reynolds Number $\frac{\Delta UL}{\nu}$	Vortices per Length, M	Cutoff Length		Time Step
		Short σ/L	Long X_c/L	$\Delta t\ \Delta U/L$
25,000	80	0.004	8	0.0125

So at $X = 8L$, the local Reynolds number is $\Delta U\ X/\nu = 2 \times 10^5$, which is about half of the experimental flow. This flow has been calculated for 64 reduced time units which is only 0.1 seconds real time with computer time being about two million times longer. The time-averaged velocities produce a good linear growth rate with a momentum thickness slope of $\Delta\theta/\Delta X = 0.023$. Again, using the error function for the mean velocity profile, this corresponds to a vorticity-thickness growth rate of $\delta_\omega/(X-X_0) = 0.102$, which is 16 percent above the experimental value.

This calculation included the aging effect on each discrete vortex, but due to the large Reynolds number and short residence time in the flow field ($0 \leq X/L \leq 10$), it probably was of very little importance. Between 4 and 10 L the time-average Reynolds shear stress and longitudinal rms velocity fluctuations agree quite well with the experimental data of Spencer and Jones (7). However, the normal rms velocity fluctuations are 50 percent larger (instead of *smaller*) than the longitudinal fluctuations.

It is not known what causes this lack of agreement between the experimental and numerical results. If the numerical simulation did not have a small enough length scale, then it seems that the longitudinal velocity fluctuations would also be in disagreement, which is not the case. Examination of the Reynolds time-average Navier-Stokes equations for the two-dimensional thin shear flow shows that, while the mean velocity gradient supplies the $\overline{U'V'}$ and $\overline{U'^2}$ quantities, the normal velocity fluctuations are maintained by the pressure-strain correlation $\overline{P\ \partial U'/\partial X}$. It is possible that the random motion supplied to each vortex is producing an incorrect pressure-strain correlation. To date, this has not been measured in the numerical calculations.

Another possibility for the disagreement is the lack of the third space dimension in the numerical simulation. Further investigation of the Roshko experiments has recently revealed a transition region ($Re \sim 2 \times 10^4$ or about halfway down the test section) where the extent of mixing has a sharp 20 percent increase (12). Shadowgraphs [Fig. 8b of Brown and Roshko (2)] indicate the existence of three-dimensional Taylor-type vortices with axes of rotation in the flow direction. It is felt that these Taylor vortices produce small scale motion which causes an increase in mixing. It seems reasonable that these Taylor vortices, which are not present at low Reynolds number such as the Winant and Browand conditions, could produce the experimentally observed normal and *spanwise* velocity fluctuations (which are about half of the longitudinal fluctuations) while not affecting the magnitude of the longitudinal velocity fluctuations found at low Reynolds number.

CONCLUSIONS

The method of discrete vortex simulation of the two-dimensional free mixing layer has been shown to have excellent agreement with moderate Reynolds number flows if the diffusion and decay of vorticity are included. In these calculations these effects were approximated by a random walk component and exponential aging for each vortex. Presently it appears that at high Reynolds number the mixing layer, while still predominately two-dimensional, has Taylor vortices with axes in the flow direction which slightly increase mixing but sharply decrease the normal velocity fluctuations when compared to moderate Reynolds number flow and numerical simulation results. However, the numerical simulation does provide computer generated movies which clearly show the aperiodic flow entrainment and vorticity coalescence. Further work will try to quantify the entrainment behavior in terms of concentration distributions which will have application to combusting flows.

ACKNOWLEDGMENT

Over the past two years I have enjoyed technical discussions with Don Chenoweth, Harry Dwyer, Alex Shestakov, and Alex Chorin.

REFERENCES

1 Winant, C. D. and Browand, F. K., "Vortex Pairing: The Mechanism of Turbulent Mixing--Layer Growth at Moderate Reynolds Number", *J. Fluid Mech. 63*, 1974, pp. 237-255.

2 Brown, G. L. and Roshko, A., "On Density Effects and Large Structure in Turbulent Mixing Layers", *J. Fluid Mech. 64*, 1974, pp. 775-816.

3 Kuwahara, K. and Takami, H., "Numerical Studies of Two-Dimensional Vortex Motion by a System of Point Vortices", *J. Phys. Soc. Japan 34*, 1973, pp. 247-253.

Kadomtsev, B. B. and Kostomarov, D. P., "Turbulent Layer in an Ideal Two-Dimensional Fluid", *Physics of Fluids 15*, 1972, pp. 1-3.

Christiansen, J. P. and Zabusky, N. J., "Instability, Coalescence, and Fission of Finite-Area Vortex Structures", *J. Fluid Mech. 61*, 1973, pp. 219-243.

4 Patnaik, P. C., "A Numerical Study of Finite Amplitude Kelvin-Helmholtz Waves", Report FM-73-3, College of Engineering, U. C. Berkeley, 1973.

5 Chorin, A. J., "Numerical Study of Slightly Viscous Flow", *J. Fluid Mech. 57*, 1973, pp. 785-796. (See also Shestakov, A. I., "Numerical Solution of the Navier-Stokes Equations at High Reynolds Numbers", UCRL-51894, Lawrence Livermore Laboratory (no date).)

6 Ashurst, W. T., "Vortex Growth in a Moving Corner" and "Turbulent Mixing Layer via Vortex Dynamics", Bulletin of the American Physical Society, Series II, *20*, No. 11, November 1975, pp. 1428-1429.

7 Spencer, B. W. and Jones, B. G., "Statistical Investigation of Pressure and Velocity Fields in the Turbulent Two-Stream Mixing Layer", AIAA paper 71-613, 1971, 14 pages.

8 Moore, D. W. and Saffman, P. G., "The Density of Organized Vortices in a Turbulent Mixing Layer", *J. Fluid Mech. 69*, 1975, pp. 465-473.

9 Acton, E., "The Modelling of Large Eddies in a Two-Dimensional Shear Layer", *J. Fluid Mech. 76*, 1976, pp. 561-592.

10 Roshko, A., "Structure of Turbulent Shear Flows: A New Look", Dryden Lecture of AIAA; AIAA paper 76-78, 1976, 12 pages.

11 Browand, F. K. and Weidman, P. D., "Large Scales in the Developing Mixing Layer", *J. Fluid Mech. 76*, 1976, pp. 127-144.

12 Konrad, J., et al., "The Development of Three-Dimensionality and the Extent of the Molecular Mixing in a Turbulent Shear Flow", Bulletin of the Am. Phys. Soc., Series II, *21*, No. 10, 1976, pg. 1229.

SESSION 12

GENERAL SESSION-1

Co-chairmen: L. H. Back
J.P.L.
Pasadena, California 91103
U.S.A.

J. J. D. Domingos
Instituto Superio Technico
Lisbon 1, Portugal

PREDICTION OF DIFFUSER FLOW AND PERFORMANCE FOLLOWING A NORMAL SHOCK WAVE-TURBULENT BOUNDARY LAYER INTERACTION

W A Kamal and J L Livesey
University of Salford
SALFORD M5 4WT
England

ABSTRACT

A diffuser flow model based on the simultaneous solution of the compressible boundary layer and the potential core is established. The model is designed for cases when the inlet flow is excessively disturbed, ie when the turbulence levels are sufficiently high to influence the flow regimes within the diffuser. This is achieved by allowing the model to account for the upstream history effects on the boundary layer development. A single integral parameter (I_G) is used to describe the inlet turbulence structure, together with the Mach number, Reynolds number and two boundary layer parameters in consideration of a more complete representation of the inlet flow conditions. Predictions of the model are compared with experimental data for the boundary layer growth in and performance of conical diffusers preceded by a shock-boundary layer interaction. Satisfactory agreement is obtained for unseparated geometries.

NOMENCLATURE

AR	diffuser area ratio at any x station
B	boundary layer blocked area fraction, $\approx\frac{2\delta^*}{R}$
C_f	skin friction coefficient, $\tau_w/\frac{1}{2}\rho_e U^2$
C_L	diffuser loss coefficient, $\mathcal{R}\bar{T}_e \ln(\bar{P}_1/\bar{P})/\frac{1}{2}\epsilon_3\bar{u}_1^2$
C_p	pressure recovery coefficient, $(\bar{p}-\bar{p}_1)/(\bar{P}_1-\bar{p}_1)$
D	entry pipe diameter
E	entrainment rate, eqn (4)
EL	entry pipe length/D
F	entrainment function, $E/\rho_e UR$
H	boundary layer shape parameter, δ^*/θ
$H_1, H_E, \bar{H}$	Δ/θ, θ_E/θ, $\int_0^\delta \frac{\rho}{\rho_e}(1-\frac{u}{U})dy/\theta$
I_G	inlet turbulence parameter, eqn (24)
M	local Mach number
P, p	total and static pressure
Q	characteristic velocity scale of the turbulence, eqn (24)
q	turbulent velocity, $q^2=\overline{u'^2}+\overline{v'^2}+\overline{w'^2}$
R	radius of duct at any station x
R_e	Reynolds number based on the average inlet velocity and pipe diameter
R_θ	Reynolds number based on free stream properties and boundary layer momentum thickness
r	radial distance from duct centre line or temperature recovery factor, $(T_r-T_e)/(T_t-T_e)$
$\bar{S}$	shear work integral, eqn (12)
T, T_t, T_r	Temperatures: static, total and recovery
U	axial velocity at edge of boundary layer
u	local axial velocity
u_*	friction velocity $\sqrt{\tau_w/\rho_e}$
u', v', w'	components of the turbulent velocity in the x, y and z directions
x	coordinate along the duct axis
X	non-dimensional axial distance, x/R_i
y	coordinate normal to the duct wall
z	coordinate parallel to the wall and normal to x-y plane
δ	boundary layer thickness
$\delta^*, \theta, \theta_E$	boundary layer displacement, momentum and energy thickness (planar definitions)
ϵ_3	$\int_{A_i}\rho u^3 dA/\overline{\rho u^3}A_i$
ρ, τ	local density and shear stress
ϕ	diffuser half angle
$\mathcal{R}$	gas constant

Subscripts

e	conditions at edge of the boundary layer
i	values at diffuser inlet station

Superscripts

$(\bar{\ })$	time mean of fluctuating quantity or mean value averaged over the cross section
$(\tilde{\ })$	non-dimensional length (normalized through R_i)

1. INTRODUCTION

A diffuser flow model designed for the case when the inlet flow is excessively disturbed, and particularly for a diffuser preceded by shock wave-turbulent boundary layer interaction is established. This type of flow is met in many practical design situations, e.g. supersonic jet air intakes, high speed centrifugal compressors and supersonic closed circuit wind tunnels. In this case the inlet flow is characterized by high subsonic or transonic Mach numbers, peaky velocity profiles which are in a rapid state of decay and high turbulence levels generated by the interaction and the following profile decay (1). The resulting turbulence structure, shown typically in fig (1) is markedly different from that of naturally developing pipe flow. In addition to the above case (2), the effects of the inlet turbulence structure on diffuser performance are evident in the cases of diffusers with artificially disturbed inlet flow (using vanes or centre bodies) (3), diffusers preceded by a parallel pipe when the inlet flow approaches fully developed conditions (4) & (5) and diffusers with decaying inlet velocity profiles (6). In all these cases, the improvement in pressure recovery and delay in stall inception were attributed to an improved turbulence structure at inlet, and its subsequent effect on velocity profile development (or boundary layer growth).

However, none of the diffuser performance prediction methods known to the authors (e.g. ref (7),

(8) and (9), considered the effects of the inlet turbulence structure, or included a turbulence parameter among its input quantities. This paper presents an attempt to overcome this evident shortcoming by considering the effects of upstream history on boundary layer development and the fact that the turbulent shear stresses lag in their development behind the mean velocity profile. An integral boundary layer approach was considered more appropriate for incorporating the additional inlet parameters and giving hopefully a sufficient description of the effects as to be an aid in design. Two methods have been developed:-

i. Method ENTS:- is a unification between the compressible turbulent boundary layer method of Green (10) and the method of Hirst & Reynolds (11). It is based on the ENTrainment principle and an explicit treatment of the Turbulence Structure via the turbulent kinetic energy equation which is transformed to give the streamwise development of the entrainment function (F).

ii. Method KEDEQ:- is a unification between the compressible boundary layer method of Livesey et al (12) and the method of Goldberg (13). The mean flow kinetic energy equation (Kinetic Energy Deficit eqn) is the boundary layer auxiliary equation, and the turbulence structure is treated implicitly. A simple diffusion-type eqn is used to specify the downstream development of the shear work integral ($\bar{S}$) relating it to the amount of Departure from EQuilibrium. No compressibility transformations are used, but Morkovin's hypothesis is invoked to extend to the compressible boundary layer correlations developed originally for the low speed flows.

2. THE DIFFUSER FLOW MODEL

The model is based on the simultaneous solution of the compressible boundary layers and the potential core. It is designed for the unstalled flow in a conical diffuser.

2.1 Basic assumptions

i) A steady one-dimensional isentropic core flow extends to the diffuser exit (Boundary layers do not merge).
ii) Boundary layers:- adiabatic, attached, thin at diffuser inlet, growing on a smooth wall under ordinary rates of strain (no shock waves or expansion fans) and anisoenergetic.
iii) Fluid is a perfect gas, flow is axisymmetric and the static pressure is function of axial distance only.

2.2 The model equations

i) Diffuser overall continuity equation:- Derived from the expression for continuity of the one-dimensional core flow and in a differential form reads

$$\frac{R-H\theta}{2}(1-M_e^2)\frac{d(\ell nU)}{dx}+\frac{dR}{dx}-H\frac{d\theta}{dx}-\theta\frac{dH}{dx}=0 \qquad (1)$$

ii) Boundary layer momentum integral equation
For an axially symmetric compressible flow, it takes the form

$$\frac{d\theta}{dx}+\theta\left|(2+H-M_e^2)\frac{d(\ell nU)}{dx}+\frac{d(\ell nR)}{dx}\right|=\frac{C_f}{2}$$

$$-\frac{1}{\rho_e U^2}\int_0^\delta\frac{\partial}{\partial x}(\overline{\rho v'^2}-\overline{\rho u'^2})\,dy \qquad (2)$$

The turbulence anisotropy term, which is the Normal Stress Contribution (N.S.C.) to the momentum balance, is usually neglected in boundary layer calculations. However, in most practical situations, the diffuser flow is usually extended up to and sometimes well inside the separation region. For the diffuser boundary layer growing under such severe adverse pressure gradients, the neglect of this term is unrealistic and leads to predictions in great error especially at large area ratios. Therefore, different empirical correlations for the N.S.C. are presented in the next section (section 2.3) and are included in the calculations. For the skin friction coefficient C_f, a modified version of the Ludwig & Tillmann correlation is employed,

$$C_f=0.246\frac{T_e}{T_m}\exp(-1.561\bar{H})\bar{R}_\theta^{-0.268} \qquad (3)$$

where $\bar{R}_\theta=\frac{\mu_e}{\mu_m}R_\theta$, μ_m = viscosity at temperature T_m

$$\frac{T_m}{T_e}=1+1.44rM_e^2 \text{ and } \bar{H}+1=(H+1)/(1+0.2rM_e^2)$$

The last two relations are obtained by employing Crocco's relation for the temperature distribution through the Boundary Layer.
iii) Boundary layer auxiliary equation
iv) History eqn.
If the diffuser continuity equation is viewed as giving the streamwise development of the centre line velocity U, and the momentum equation as the eqn for θ, then the auxiliary eqn is the one for the shape parameter H. The form of the auxiliary boundary layer equation depends on the method. It is the entrainment eqn in ENTS and the mean flow energy deficit eqn in KEDEQ. In either, a different turbulence describing quantity appears (F in ENTS & $\bar{S}$ in KEDEQ). The history eqn is then viewed as giving the downstream development of F or $\bar{S}$ (which characterize the turbulence structure of the boundary layer) and is different for each method as shown below:-
a. Method ENTS
iii)a. Aux. Boundary Layer eqn ≡ Entrainment eqn. For a compressible axisymmetric thin boundary layer flow the entrainment law can be written as

$$E=\frac{d}{dx}\left(R\int_0^\delta\rho u\,dy\right) \qquad (4)$$

which upon introducing the non-dimensional entrainment function $F=E/\rho_e UR$ and the mass flow thickness

$$\Delta=\delta-\delta^*=\int_0^\delta\frac{\rho u}{\rho_e U}dy \qquad (5)$$

takes the form

$$\frac{d\Delta}{dx}=F-\Delta\left|(1-M_e^2)\frac{d(\ell nU)}{dx}+\frac{d(\ell nR)}{dx}\right| \qquad (6)$$

and using the definition $H_1=\Delta/\theta$, it takes the final form

$$H_1\frac{d\theta}{dx}+\theta\frac{dH_1}{dx}=F-H_1\theta\left|(1-M_e^2)\frac{d\ell nU}{dx}+\frac{d(\ell nR)}{dx}\right| \qquad (7)$$

For the relation between the shape parameters H_1 & H a set of correlations given by Green (10) was employed. H_1 is indirectly related to H via the transformed shape parameter $\bar{H}$.

Although the physical, processes governing entrainment certainly involve the turbulence in the outer region of the boundary layer, conventional entrainment procedures employ some empirical assumptions to relate F to mean flow quantities. Now, with an explicit consideration of the turbulence structure, F is assumed to be determined primarily by the turbulence and following Hirst and Reynolds (11), F is assumed to vary linearly with a characteristic turbulent velocity Q chosen as $Q^2 = \frac{\int_0^\delta \rho u q^2 dy}{\int_0^\delta \rho u dy}$, thus the entrainment law becomes

$$E = K_1 \rho_e R Q \quad \text{or} \quad F = K_1 \frac{Q}{U} \tag{8}$$

iv) a. History eqn ≡ Turbulent kinetic energy eqn. An integral form of the T.K.E eqn is used to determine the streamwise evolution of the turbulence parameter Q and consequently the entrainment function F. For compressible flow, with a neglected free stream turbulence, it can be written as

$$\frac{d}{dx}\left|\frac{Q^2}{2} \int_0^\delta \rho u dy\right| = K_2 u_* \rho_e Q^2 \tag{9}$$

If Q is eleminated using eqn (8) and the definition of Δ (eqn 5) is introduced, eqn (9) takes the form

$$\frac{d}{dx}\left|F^2 \rho_e U^3 \Delta\right| = 2K_2\, u_* \rho_e U^2 F^2 \tag{10}$$

Replacing u_* by $U\sqrt{C_f/2}$, subtracting eqn (6) from an expansion of eqn (10) and rearranging, the history eqn can be reduced to

$$H_1 \theta \left|\frac{d(\ell nF)}{dx} + \frac{d(\ell nU)}{dx} - \frac{1}{2}\frac{d(\ell nR)}{dx}\right| = K_2\sqrt{\frac{C_f}{2}} - \frac{F}{2} \tag{11}$$

b. Method KEDEQ

iii)b. Aux. boundary layer eqn ≡ Kinetic energy deficit eqn. For an axisymmetric anisoenergetic boundary layer, it takes the form

$$\frac{d\theta_E}{dx} + \theta_E\left|\{3 + (r(\gamma-1)-1)M_e^2\}\frac{d(\ell nU)}{dx} + \frac{d(\ell nR)}{dx}\right|$$

$$= \frac{2}{\rho_e U^3} \int_0^\delta \tau \frac{\partial u}{\partial y} dy = 2\bar{S} \tag{12}$$

A suitable shape parameter is $H_E = \theta_E/\theta$. In reference (12), H_E was analytically correlated with H by assuming a power law velocity profile and employing Crocco's temperature distribution. The resulting correlation for subsonic Mach numbers and for H less than 5 takes the form

$$H_E = \frac{4H}{3H-1} + 0.0524\left(\frac{M_e}{H}\right) + 0.1308\left(\frac{M_e}{H}\right)^2 + 0.3584\left(\frac{M_e}{H}\right)^3 \tag{13}$$

$\bar{S}$ is the dimensionless turbulence energy production integral across the layer whose downstream development is specified by the history eqn.

iv)b- History eqn ≡ diffusion-type eqn for $\bar{S}$. The basic principle involved here is that the shear stress profile depends on the upstream history of the boundary layer and lags behind the mean flow such that an abrupt change in the mean velocity profile is followed by only a progressive change of the shear stress. Based on Goldberg's (13) observation that the mean flow appears to return to equilibrium at a rate proportional to the amount of departure from equilibrium, a "rate" eqn is assumed to specify the streamwise derivative of $\bar{S}$, which takes the form

$$\theta \frac{d\bar{S}}{dx} = K_3 (\bar{S}eqm - \bar{S}) \tag{14}$$

$\bar{S}eqm$ is related to its flat plate value using an empirical correlation involving a linear function of the pressure gradient as follows

$$\bar{S}eqm = \left|1-750(H-1)\frac{\theta}{U}\frac{dU}{dx}\right| \frac{0.0056}{R_\theta^{1/6}} \tag{15}$$

Here, an incompressible flat plate correlation was employed by invoking Morkovin's hypothesis.

The diffuser continuity eqn(1), the momentum integral eqn (2), the boundary layer aux. eqn (7 or 12) and the history eqn (11 or 14) constitute a system of four coupled, first order, non-linear ordinary differential equations with U, θ, H and F or $\bar{S}$ as the dependent variables. A single computer programme was written which embraces both methods with the auxiliary functions for each method included in separate subroutines as shown in appendix (1).

2.3 Correlations for the N.S.C. to the momentum balance. Assuming isotropic turbulence in the free stream, the normal stress term in the momentum eqn (2) reduces to

$$N.S.C = \frac{1}{\rho_e U^2} \frac{d}{dx}\left\{\int_0^\delta (\overline{\rho u'^2} - \overline{\rho v'^2}) dy\right\} \tag{16}$$

As a preliminary approach to including the N.S.C. term, available empirical correlations for the incompressible boundary layer which describe it in terms of mean flow parameters were employed, e.g.

i Ross' correlation (14)

$$N.S.C. = \frac{0.016}{U^2} \frac{d(\delta^* U^2)}{dx} \tag{17}$$

ii Goldberg's correlation

$$N.S.C. = 0.0365\,(H-1)\frac{d\delta^*}{dx} \tag{18}$$

iii Correlation by Lewkowicz et al (15)

$$N.S.C. = 4.75\, C_f (H-1.3)^2 \tag{19}$$

All such correlations could be used in the present model by once again invoking Morkovin's hypothesis that the direct effect of compressibility on the turbulence structure (especially on anisotropic quantities) should be very small in a subsonic mean flow.

However, it will be more logical to correlate the N.S.C. which is a turbulence anisotropy term comprising gradients of turbulent velocities using the characteristic turbulent velocity Q, which already appears in the model (method ENTS). On both dimensional and physical grounds, the integral in eqn (16) should finally reach the form

$$\int_0^\delta (\overline{\rho u'^2} - \overline{\rho v'^2}) dy = a \rho_e Q^2 \theta^* \tag{20}$$

where θ* is an arbitrary Boundary Layer thickness parameter, i.e. θ* can be either θ, δ*, Δ, θ_E etc. Consequently, a better correlation for the N.S.C. should take the form

$$N.S.C. = \frac{a}{\rho_e U^2} \frac{d}{dx} (\rho_e Q^2 \theta^*) \tag{21}$$

Employing the data of Strickland & Simpson (16) and choosing Δ as the boundary layer parameter, the value of a = 0.4 gave the best fit.

2.4 The inlet turbulence parameter I_G

To start the solution of the model, an initial value of the quantity describing the turbulence structure (F or $\bar{S}$) is required. In order to make possible the comparison between the predictions of both methods (ENTS & KEDEQ) at the same level of inlet turbulence, it was suggested that a single inlet turbulence parameter be used, to which F and $\bar{S}$ can be correlated. It is more logical and convenient to provide the designer with a single diffuser inlet turbulence parameter easy to estimate and/or measure, rather than leave him with the tedious task of estimating the entrainment rate or the shear work integral. The quantity found most suitable is $I_G = \frac{Q}{U}$ which can be considered as the mass averaged turbulence intensity across the diffuser inlet boundary layer. The F-I_G correlation can be obtained directly from eqn (8) as

$$F = K_1 I_G \tag{22}$$

and the value of $K_1 = 0.25$ recommended in reference (11) is used.

For the $\bar{S}$-I_G correlation, a theoretical expression is derived from a pipe flow analysis, which takes the form

$$\bar{S} = (C_1 . I_G)^2 |1 + C_2 . I_G| \tag{23}$$

The values of $C_1 = 0.7$ and $C_2 = 4.0$ gave the best fit to the available experimental data.

Finally, to allow the model to predict cases of diffusers with disturbed inlet flows where some free stream turbulence is expected to exist, the definition of I_G is slightly modified to

$$I_G = \frac{Q}{U} \quad \text{where} \quad Q^2 = \frac{\int_0^R \rho u q^2 r dr}{\int_0^R \rho u r dr} \tag{24}$$

The characteristic velocity of the turbulence is now obtained by integrating across the diffuser inlet section rather than across the boundary layer alone, thus I_G contains the turbulence energy in the free stream as well as in the boundary layer. Although the resulting Q will not be exactly that specified by the integral form of the T.K.E. eqn (eqn 9), the size of error involved will be minimal within the framework of the integral model.

For an incompressible flow, the diffuser inlet turbulence parameter reduces to

$$I_G = \frac{1}{\Lambda} \sqrt{2 \int_0^1 \left(\frac{u}{\bar{u}}\right)^3 I^2 \bar{r} d\bar{r}} \tag{25}$$

where Λ = profile peakiness = $U/\bar{u}$, $\bar{r} = r/R$

I = local turbulence intensity = q/u

Typical values of I_G in pipe flows

i) Incompressible fully developed pipe flow 6%
ii) Compressible " " " " 7-8%
iii) Following a shock boundary layer interaction 8-13%

Now, five input quantities (diffuser input parameters) are required by the model to specify a general inlet situation namely, M_i, R_e, θ_i, H_i and I_G.

Separation criteria

Two different flow detachment criteria were incorporated in the model to predict the point of possible separation (or first appreciable stall), namely

a) $H = 3.1$ which is normally used for conical diffusers.

b) $$\beta^* = \frac{X(1-H_i\bar{\theta}_i)^2(2H_i\bar{\theta}_i)^{0.536}}{2H\bar{\theta}\bar{R}^3} = 0.48$$

suggested in reference (7).

The calculations were extended beyond the separation point to assess the capability of the model for slightly separated diffusers.

3. THEORETICAL PREDICTIONS

3.1 Comparison between the predictions of both Methods

The two methods ENTS & KEDEQ differ fundamentally in their boundary layer approach and in their treatment of the turbulence structure. It is interesting to see how their predictions compare for the same diffuser geometry and inlet conditions. The very close agreement typically shown in figs (2) and (3) for four different inlet situations for the 5 and 12° diffuser respectively, indicates that both methods are generally of the same order of accuracy. Secondly, it confirms the relation between the two approaches for the treatment of the turbulence structure, a relation investigated in detail by McDonald (17). It also supports the validity of the various empirical and semi-analytical correlations used (especially between both F and $\bar{S}$ and I_G), and finally it confirms the fact that the effects of upstream history manifest themselves as changes in the local properties of the boundary layer and turbulence structure. The failure of earlier models that did not consider "boundary layer history" is interpreted as an incomplete specification of the inlet conditions.

3.2 Prediction of the effects of the diffuser inlet turbulence level

For the first time, a diffuser flow model which predicts the experimentally observed effects of the inlet turbulence level on the boundary layer growth in and performance of diffusers is established. Figs. (4) and (5) show that an increase in I_G leads to an increase in θ-growth, a decrease in H-growth and an improvement in pressure recovery; the sensitivity to a change in I_G being higher in the low I_G range. The following table demonstrates the effect of an increase of I_G in delaying separation

I_G	4%	8%	12%
X_{sep} (H-criterion)	3.6	5.3	8.2
X_{sep} (β^*-criterion)	3.7	4.1	4.5

12° diffuser $\theta_i = 0.01$ $H_i = 1.4$ $\bar{M}_i = 0.8$

Fig (3) coupled with the first separation criterion shows that, if the inlet turbulence is low enough, the flow in even a good diffuser will separate at quite an early stage (5° diffuser separates at AR=2.5 with I_G = 4%).

3.3 Model predicts the decay of a peaky profile in a pipe and possibly in a diffuser

The first measure of success of the model is its ability to predict the decay of a peaky velocity profile in a straight pipe, demonstrated in figs (6) and (7). In fig (6) the inlet turbulence level is kept constant while the initial profile peakiness is varied. As can be seen, the peakiest inlet profile has the highest rate of decay, but a residual difference in the value of the shape parameter still exists after ten diameters of the pipe length. When method KEDEQ is employed, however, the three curves close in much faster until there is practically no difference in H after approximately 8 diameters. Fig (7) shows that an increase of I_G leads to a much faster rate of decay. The H-growth curves in figs (2) to (5) confirm the dependence of the velocity profile development in a diffuser (growth or decay) on the sensitive balance between the initial values of H and I_G. Fig (4) shows that, if I_G is high in view of H_i, virtually zero growth of the profile can be maintained, with the consequence that a further increase in I_G will lead to profile decay. This is further substantiated in figs (2) and (3) where, at the same level of I_G, H either grows steadily or decays over a considerable part of diffuser length before it starts to grow again, depending on H_i. The above results are in line with the experimental findings of Livesey & Turner (6).

3.4 Prediction of the "Bradshaw effect"

Another success of the model is presented in fig (8) and more clearly in fig (9). Cockrell and Markland (4) reported that the diffuser pressure recovery ($\bar{C}_p$) which decreases as the boundary layer thickness at inlet increases, actually rises again when the inlet boundary layer is thick enough to approximate to fully developed pipe flow. Bradshaw (5) observed the same effect and suggested that the fully developed turbulence structure of the pipe flow is better able to transfer momentum radially than the smaller scale turbulence of moderately thick boundary layers. The velocity profile far down the diffuser is improved by turbulent mixing and separation is delayed. Figs (8) and (9) show that the model predicts just that. The interesting feature here, is that this is correctly predicted when the inlet turbulence parameter I_G is held constant. Fig (9) shows also that the phenomenon is expected to occur at a smaller θ_i and is followed by a considerable recovery in performance for the wider diffuser angles.

3.5 The insufficiency of blockage as the inlet boundary layer parameter

One of the achievements of the model is that it showed clearly that the usual practice of lumping the diffuser inlet velocity profile parameters into a single quantity (the blockage ratio B_i) is wrong. In fig (10), two different trends of variation of the pressure recovery C_p with B_i are obtained depending on whether θ_i or H_i is kept constant. The same is predicted for the separation point Xsep. In addition to M_i, R_e and I_G the model requires two inlet velocity profile parameters (to be chosen from θ_i, H_i and B_i) to initiate the solution. The use of B_i alone to specify the inlet situation is incorrect.

4. COMPARISON WITH EXPERIMENTAL DATA

For an assessment of the model, its predictions are compared with experimental data of diffusers preceded by a shock wave-boundary layer interaction in the inlet pipe; a case for which the model was originally designed. In the comparison, method ENTS was chosen so that the new correlation for the N.S.C. can be tested and the authors' own experimental data were employed in order to guarantee that the inlet conditions and the diffuser performance parameters are exactly those specified by the model. The comparison is made for three diffuser geometries (5,12 and 20 deg. total angle) with a sharp transition from the parallel pipe to diffuser cone. The diffuser inlet station is situated 1.5 diameters upstream of the geometrical throat to avoid the possible effects of the corner on inlet conditions. The boundary layer growth and performance data were measured at area ratios 2, 3 and 4 for all diffusers and additionally at AR = 1.5 for the 5° diffuser. Typical results of the comparison for the three diffusers with favourable (low inlet Mach number and blockage) and unfavourable inlet conditions are presented in figs (11) to (15).

The comparison for the two 5° diffuser test cases (fig 11) shows that the predictions are exceptionally good in view of the high values of inlet blockage involved which place them outside the class A restriction ($B_i > 0.05$). This success indicates that, with a proper treatment of the turbulence structure, the model could predict diffuser flows with moderate to very thick inlet boundary layers so long as a potential core still exists (which is observed experimentally). Fortunately, the predicted C_p seems to be relatively insensitive to small errors in the predicted boundary layer parameters. For favourable inlet conditions (case 509) the model under-predicts H at small area ratios, while at bigger ARs the predictions are very accurate. Apparently, the sharp corner results in the adverse pressure gradient at the early diffusion stages becoming stronger than that assumed by the theoretical model, thus leading to higher values of H than those predicted. For cases of high H_i and θ_i (e.g. case 517), these effects are less marked possibly because of the modifications of the pressure distribution at the corner by the thicker inlet boundary layer.

In fig (12) for the 12 deg. diffuser with unfavourable inlet conditions, the predictions of C_p (especially when using the new correlation for the N.S.C.) are adequate in view of the poor predictions of the boundary layer parameters. For favourable inlet conditions (fig 13) the trends are reversed with better predictions of θ and H while C_p is overestimated. One possible explanation is that in case 1210, δ^* is underestimated by the theory and consequently C_p is over-predicted. In case 1208, though θ is significantly underestimated and H over-estimated their product δ^* might be close to the actual value resulting in a better prediction of C_p. The effects of both the inlet sharp corner and separation could be employed to explain the observed variation in the accuracy of predicting the loss coefficient C_L with the change in inlet conditions (from favourable to unfavourable).

The comparison with the 20° diffuser data presented in figs (14 and 15) is practically irrelevant since for this geometry the flow over most of diffuser length is badly separated resulting in very inaccurate experimental data and an inapplicable theoretical model. As expected, the same trends as for the 12° diffuser are observed but the deviations are significantly greater. The only observation worth mentioning is that the C_p predictions are in great error even before the predicted separation point. The percentage error in C_p is much bigger at AR = 2 that at AR = 4. It appears that the experimental C_p curve has been shifted downwards from the theoretical one since the start of the diffusion. This suggests that the effects of the inlet sharp corner on the pressure gradient pattern rather than the effects of early separation are the major source of discrepancy. More specifically, the one-dimensional treatment of the potential core flow and the neglect of streamline curvature effects on the boundary layer development lead to the serious departure from the experimental values in the inlet zone.

Finally, from the comparison between theory and experiment (figs 11 to 15) the following general conclusions can be made:-

Prediction of the θ-growth:- For all geometries and inlet conditions investigated, the poorest predictions are those of the θ-growth. The major source of error is thought to be the use of a skin friction law (the Ludwig-Tillman correlation) which is not derived directly from the velocity profile law assumed. The appropriate way was to use a Coles-type velocity profile and to employ the asymptotic matching condition to obtain an equation for C_f, as is the case in the original Hirst and Reynolds method (11). Although a formulation of the velocity profile (wall-wake type) for compressible flow now exists (reference (18)), the incorporation of this profile would have complicated the mathematical treatment quite considerably.

The new correlation for the N.S.C. Of the three correlations employed, only the new correlation (eqn 21) responds to the severe adverse pressure gradients encountered at the early stages of diffusion, especially for cases of unfavouruable inlet conditions (yielding earlier separation). This is encouraging since the effects of the normal stresses are known to be measurable early before separation. The use of the new correlation leads to the best predictions of the pressure recovery performance for the 12° diffuser (see fig 12 and 13).

Separation criteria:- The δ^*-criterion is rejected on the following grounds:-

a) Although it is sensitive to geometrical variables, it is very insensitive to inlet conditions.

b) When the shock is moved closer to the diffuser inlet, thus worsening inlet conditions (increasing both M_i and H_i), the δ^*-criterion predicts a downstream shift of the separation point; which is the wrong trend. The H-criterion remains valid for this integral class of prediction methods.

REFERENCES

1 Livesey, J.L and Kamal W.A. "Shock-Boundary layer interaction influencing diffuser inlet flow structure", Paper submitted to Cancam 77.

2 Livesey, J.L. and Odukwe, A.O. "Some effects on conical diffuser performance of preceding normal shock boundary layer interaction", Proceedings of the IMechE 1974, Vol 188, pp.607-613.

3 Waitman, B., Reneau, L. and Kline, S. "Effects of inlet conditions on performance of two dimensional diffusers" J. of Basic Engg, vol.83, Sep. 1961, pp. 349-360.

4 Cockrell, D. and Markland, E. "Effects of inlet conditions on incompressible flow through conical diffusers" J. of the Royal Aero Society vol 66, Jan. 1962. pp.51

5 Bradshaw, P. "Performance of a diffuser with fully developed pipe flow at entry" J. Royal Aero. Society, vol 67 Nov. 1963, p.733.

6 Livesey, J.L. and Turner, J. "The effect of velocity profile decay on shear flow in diffusers". International J. of Mech. Sciences, vol 6, Feb. 1964, pp. 371-377.

7 Cocanower, A., Kline, S and Johnston, J. "A unified method for predicting the performance of subsonic diffusers of several geometries" Report PD-10, 1965, Thermoscience Division, Stanford University.

8 Nicoll, W. and Ramaprian, B. "A modified entrainment theory for the prediction of turbulent boundary layer growth in adverse pressure gradients" J. of Basic Engg; vol 91, Dec.1969, pp.649-655.

9 Means, J., Glance, P. and Klassen, H."Analytical investigation of conical diffusers" NASA TM X-2605, Aug. 1972.

10 Green, J. "The prediction of turbulent boundary layer development in compressible flow" J. of Fluid Mechanics, vol 31 part 4, 1968, pp.753-778.

11 Hirst, E and Reynolds W.C. "An integral prediction method for turbulent boundary layers using the turbulent kinetic energy equation" Rep. MD-21, Stanford University.

12 Livesey, J., Odukwe, A. and Kamal, W. "Compressible conical diffuser flow using the Energy Deficit boundary layer method", J. of Mech. Science, vol 17, no.4, 1975, pp.206-213.

13 Goldberg, P. "Upstream history and apparent stress in turbulent boundary layers". Rep.85, 1966, Gas Turbine Lab., Massachusetts Institute of Technology.

14 Ross, D. "Evaluation of the momentum integral equation for turbulent boundary layers", J. of Aeronautical Sciences, July 1953, p.502.

15 Lewkowicz, A., Hoadley, D. and Horlock, J. "Calculation of turbulent boundary layer development" In Proceedings of the AFOSR-IFP-Stanford Conference, 1968, pp.147-153.

16 Strickland, J. and Simpson, R. "The separating turbulent boundary layer" Tech. Rep. WT-2, Aug. 1973, Southern Methodist University.

17 McDonald, H. "The departure from equilibrium of turbulent boundary layers" Aeronautical Quarterly, vol.19 Feb. 1968, pp.1-19.

18 Sun, C. and Childs, M. "A modified wall-wake velocity profile for turbulent compressible Boundary layers" J. of Aircraft, vol 10, No.6, June 1973 p.381

APPENDIX (1)

Computing equations and solution procedure

The eqns are first non-dimensionalised using

$\bar{\theta} = \theta/R_i$, $X = x/R_i$, $\bar{R} = R/R_i$, $C = F$ or $\bar{S}$

$$\theta' = \frac{d\bar{\theta}}{dX}, \quad H' = \frac{dH}{dX}, \quad R' = \frac{d\bar{R}}{dX}, \quad U' = \frac{d(\ln U)}{dX}, \quad C' = \frac{dC}{dX}$$

then they are rewritten in the form

$$A_{i1}\theta' + A_{i2}H' + A_{i3}U' + A_{i4}C' = V_i$$

where i = 1,2,3,4 refer to the continuity, momentum integral, B.L. auxiliary and history eqns respectively.

1) $H\theta' + \theta H' - (1-M_e^2)(\bar{R}-H\bar{\theta})/2 \quad \bar{U}' = R'$

2) $G_1\theta' + G_2H' + G_3\bar{U}' + G_4C' = G_5$

3) $H_S\theta' + \bar{\theta}JH' + |KM_e(1+0.2M_e^2) + H_SN|\bar{\theta}U' = C - H_s\bar{\theta}(R'/\bar{R})$

4) $\alpha\bar{\theta}U' + \beta\bar{\theta}C' = \sigma C + \Omega$

where the functions $C, H_s, J, K, N, \alpha, \beta, \sigma, \Omega$ for each method are given by:-

	Method ENTS	Method XEDEO
C	F	S
H_S	H_1	H_E
J	$-1.2(\bar{H}-1)^{-7/3}/(1+0.2rM_e^2)$	$\partial H_E/\partial H$ } from
K	$-0.4rJM_e^2(\bar{H}+1)$	$\partial H_E/\partial M_e$ } eqn (13)
N	$(1-M_e^2)$	$\{3+\lvert r(\gamma-1)-1\rvert M_e^2\}$
α	H_1	$0.0375(H-1)/R_\theta^{1/6}$
β	H_1/F	1
σ	-0.5	-0.009
Ω	$K_2\sqrt{C_f/2} + \frac{H_1\bar{\theta}}{2}\frac{R'}{\bar{R}}$	$10^{-4}/(2R_\theta^{1/6})$

G_1, G_2, G_3, G_4 & G_5 vary according to the NSC correlation

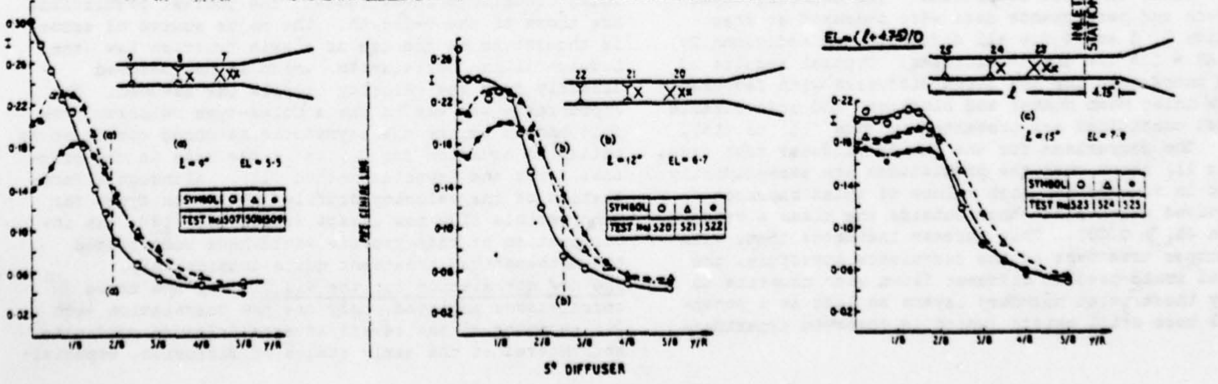

FIG. 1 VARIATION OF DIFFUSER INLET TURBULENCE INTENSITY DISTRIBUTION WITH SHOCK LOCATION AND ENTRY LENGTH.

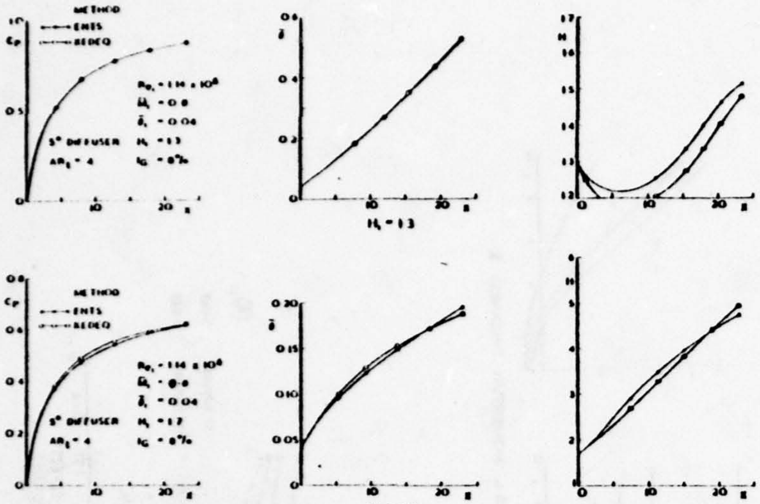

FIG 2 COMPARISON BETWEEN THE PREDICTIONS OF METHODS ENTS AND KEDEQ

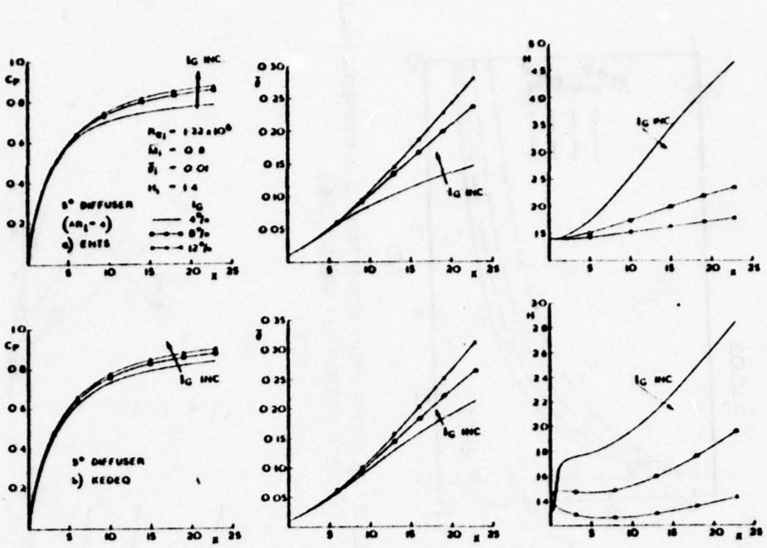

FIG 4 EFFECTS OF VARYING THE INLET TURBULENCE PARAMETER (I_G)

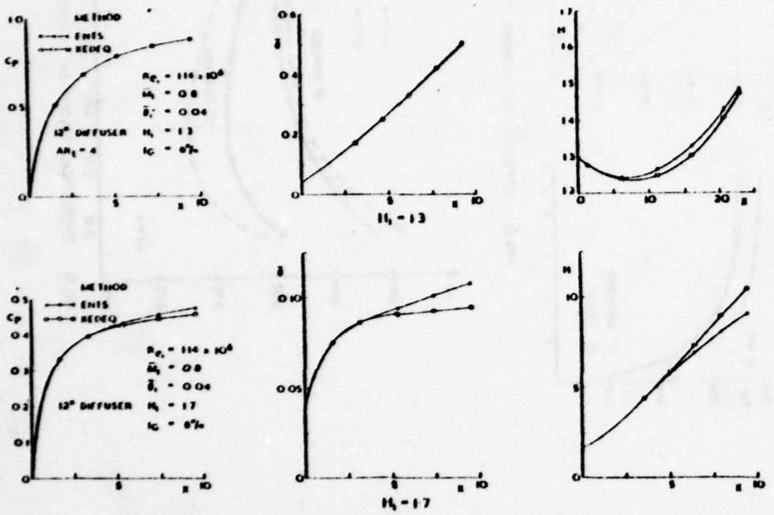

FIG 3 COMPARISON BETWEEN THE PREDICTIONS OF METHODS ENTS AND KEDEQ

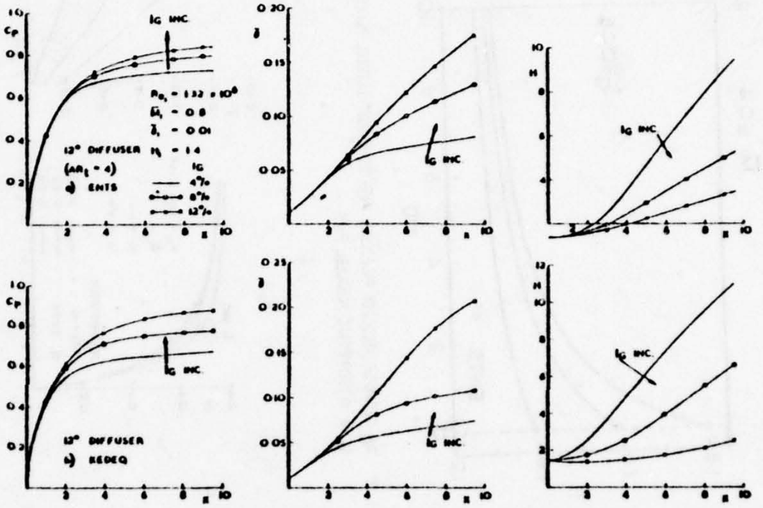

FIG 5 EFFECTS OF VARYING THE INLET TURBULENCE PARAMETER (I_G)

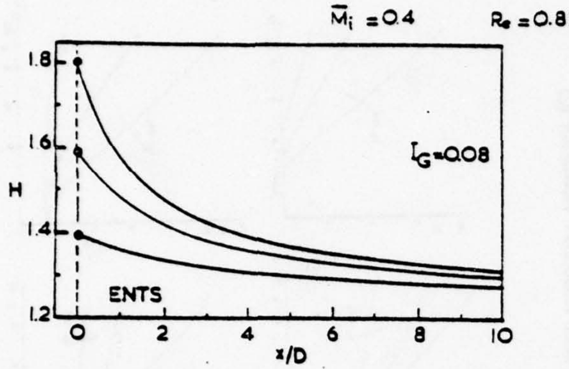

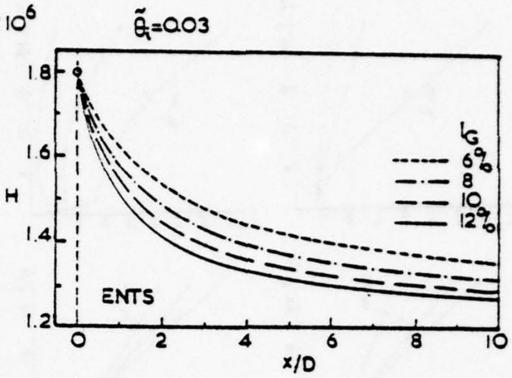

FIG. 6 THE DECAY OF VELOCITY PROFILES, WITH DIFFERENT INITIAL PEAKINESS, IN AN AXISYMMETRIC PARALLEL PIPE

FIG. 7 THE DECAY OF A PEAKY VELOCITY PROFILE IN AN AXISYMMETRIC PARALLEL PIPE AT DIFFERENT INLET TURBULENCE LEVELS

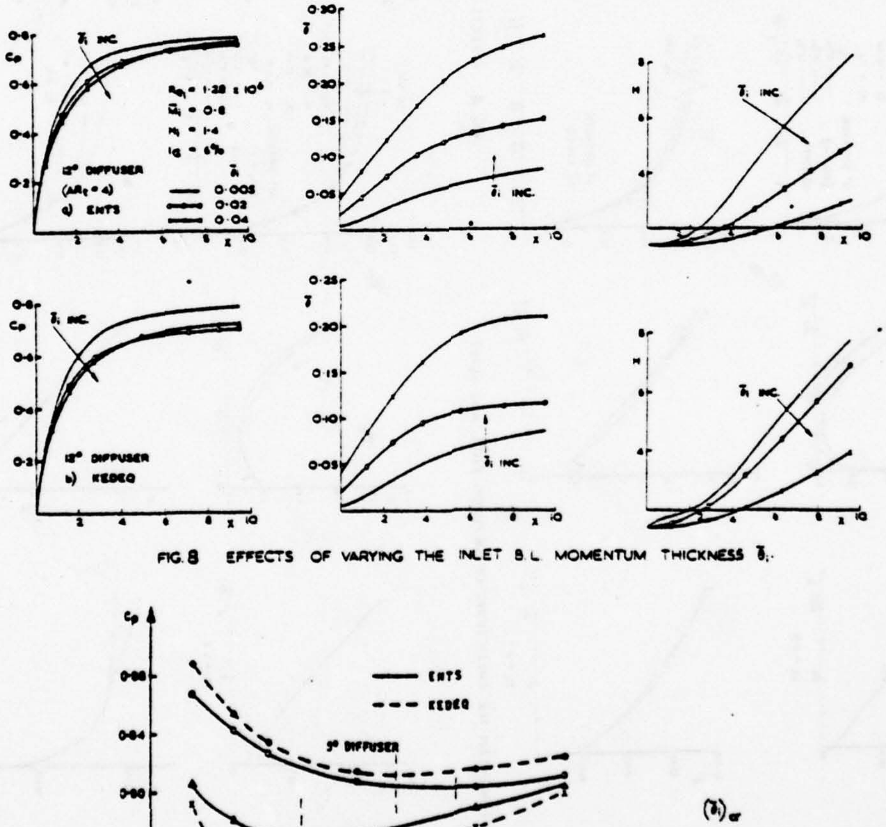

FIG. 8 EFFECTS OF VARYING THE INLET B.L. MOMENTUM THICKNESS $\bar{\theta}_i$.

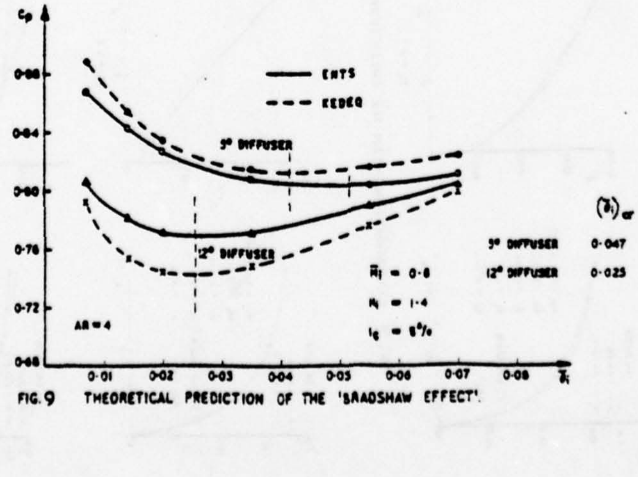

FIG. 9 THEORETICAL PREDICTION OF THE 'BRADSHAW EFFECT'.

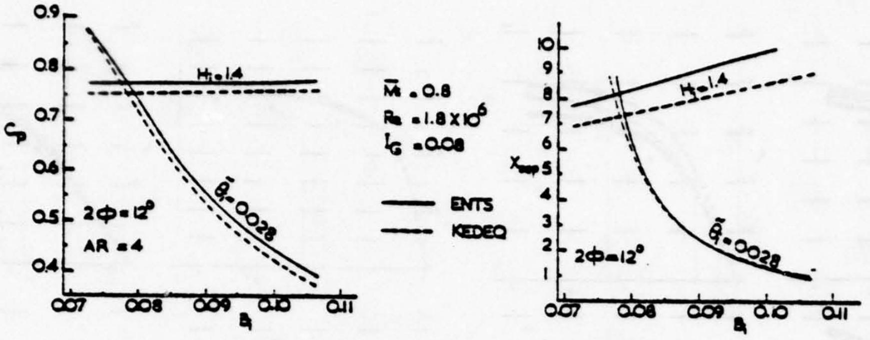

FIG. 10 PREDICTED VARIATION IN PRESSURE RECOVERY AND SEPARATION POINT WITH INLET BLOCKAGE

KEY TO FOLLOWING FIGURES (FIG 11 TO 15)

———	PREDICTIONS NEGLECTING THE N.S.C. TERM
—✱—✱—✱—	PREDICTIONS USING ROSS' CORRELATION FOR THE N.S.C.
—✱—✱—✱—	PREDICTIONS USING LEWKOWICZ ET AL CORRELATION FOR THE N.S.C.
—▣—▣—▣—	PREDICTIONS USING THE NEW CORRELATION FOR THE N.S.C.
- - - - - -	PREDICTED SEPARATION POINT USING THE H - CRITERION
—·—·—·	PREDICTED SEPARATION POINT USING THE β - CRITERION
⊙	EXPERIMENTAL POINTS.

FOR ALL CASES CONSIDERED $R_{\theta o} = 1.1 \times 10^6$

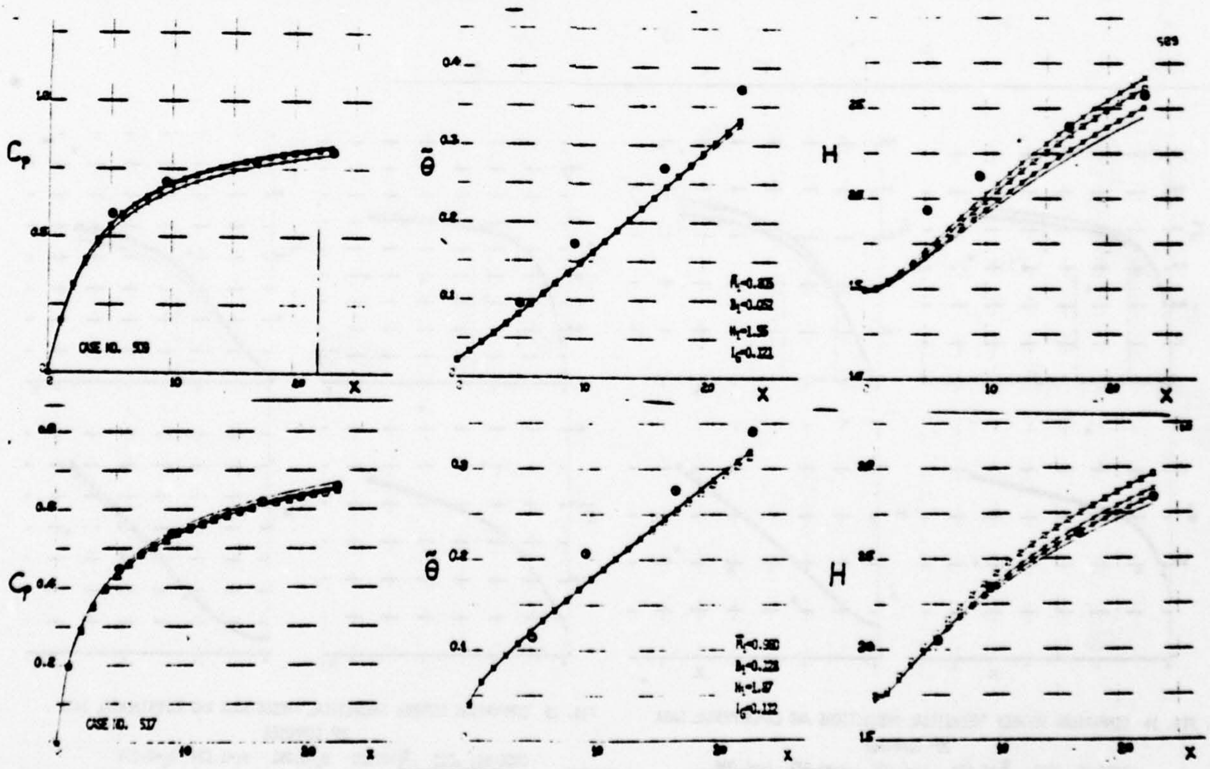

FIG.11. COMPARISON BETWEEN THEORETICAL PREDICTIONS AND EXPERIMENTAL DATA
5° DIFFUSER

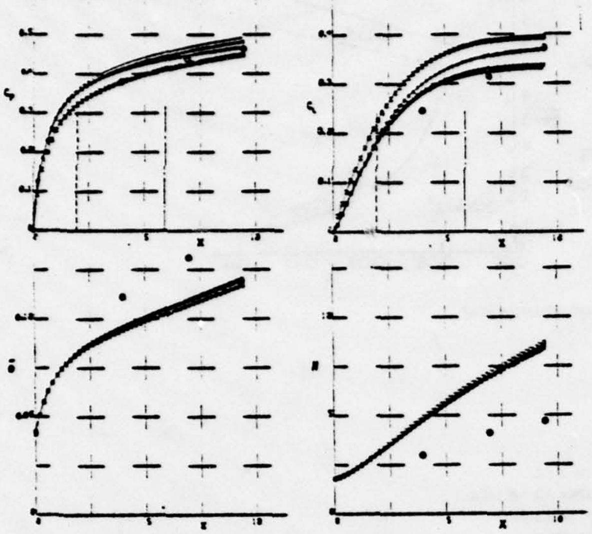

FIG. 12 COMPARISON BETWEEN THEORETICAL PREDICTIONS AND EXPERIMENTAL DATA
12° DIFFUSER
CASE NO. 1208 $\overline{M}_i$=0.909 B_i=0.125 H_i=1.960 I_G=0.097

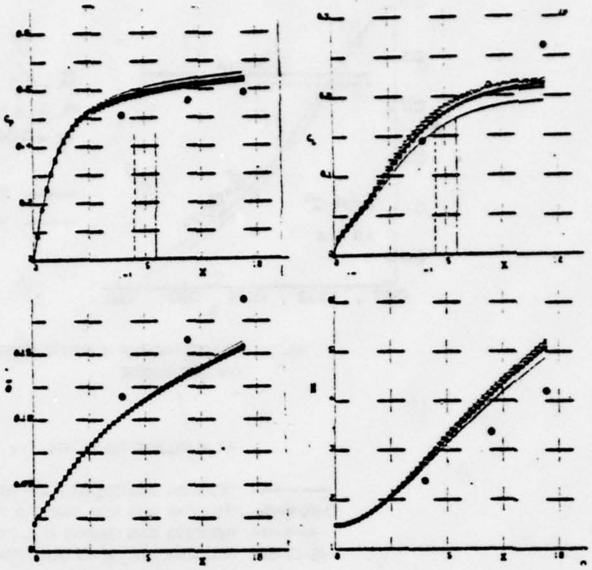

FIG. 13 COMPARISON BETWEEN THEORETICAL PREDICTIONS AND EXPERIMENTAL DATA
12° DIFFUSER
CASE NO. 1210 $\overline{M}_i$=0.811 B_i=0.047 H_i=1.550 I_G=0.117

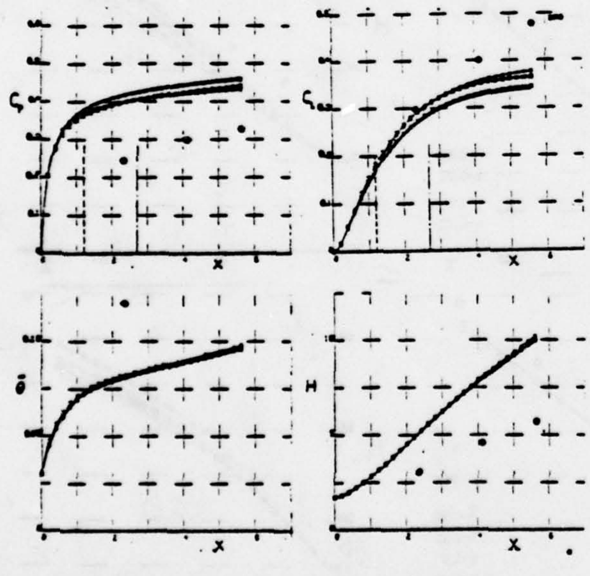

FIG. 14 COMPARISON BETWEEN THEORETICAL PREDICTIONS AND EXPERIMENTAL DATA
20° DIFFUSER
CASE NO. 2010 $\overline{M}_i$=0.932 B_i=0.093 H_i=1.932 I_G=0.096

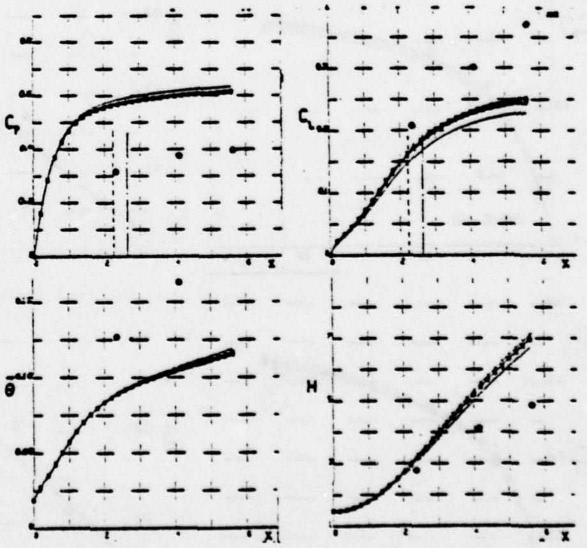

FIG. 15 COMPARISON BETWEEN THEORETICAL PREDICTIONS AND EXPERIMENTAL DATA
20° DIFFUSER
CASE NO. 2012 $\overline{M}_i$=0.820 B_i=0.051 H_i=1.524 I_G=0.094

SPATIALLY LOCALIZED, SHOCK-WAVE-INDUCED CONTINUOUS AND VERY FAST MIXING BETWEEN GASES AND LIQUID IN PARALLEL FLOW

(AN EXPERIMENTAL STUDY)

ENRIQUE DEVIS

UNIVERSIDAD DE LOS ANDES, BOGOTA, COLOMBIA

ABSTRACT

In many engineering applications the mixing of flows must be accomplished on a time scale short compared to the characteristic times for various kinetic processes associated with the mixed flow. The present investigation originated from considerations of the problem of the achievement of high power continuous wave laser operation with fluid mixing chemical lasers (1968). Later, the investigation extended to the problem of mixing a jet of liquid into a supersonic stream, in view of the possible applications in combustion starting from a liquid fuel as well as in other instances.

The fundamental mechanism was the action of a shock wave into a low-momentum, high-speed-of-sound fluid (liquid or gas) that produces a complex pattern and turbulent, supersonic shear flows over a stagnant bubble where recirculation of both fluids and final mixing or atomization occur in very short times (a few times 10^{-5} sec) and distances (about 1 cm).

The problems were studied in a shock tube and in different types of wind tunnels, using a chemiluminescent reaction (NO + O) to measure the mixing. Also, a correlation was found between this fenomena and the action of a shock wave into a boundary-layer.

EFFECT OF A SHOCK WAVE UPON STRATIFIED LAMINAE OF GASES IN A SHOCK TUBE.

The first step (Cornell University, 1968-1970) was to produce an interaction of an initially normal shock wave and a series of laminae of gases of different densities and molecular weights, namely, air and a mixture of helium and argon as shown in figure one.

A typical result is shown in that figure. The three laminae were separated by very thin lacquer membranes (the width was of the order of one wavelength of ordinary light); two sheets formed one membrane; their effect upon the flow was negligible. As the shock started the interaction, a time-dependent pattern developed that had the following main characteristics.

1 The helium-argon mixture decelerates to almost zero velocity (in a coordinate system that moves with the normal shock) after passing (or not) through its own normal shock A-D. After this, the helium flow is subsonic and thus the flow passage is divergent (the walls are A-C and D-E).

2 The air can pass through either the normal shock B-F or the first oblique shock AB and the second, BC. After the second one, the pressure rise equals that across the normal shock. The inclination of AB (α) is dictated near B by the Mach number and by the pressure in the "bubble", region 6, and so is the inclination of AC (β)- the flow direction in zone 2 near BC. The inclination of BC is dictated by α and by the pressure behind the normal shock that the flow behind BC must match. The inclination of the flow behind BC, γ , is not zero, and the Mach number is supersonic.

3 The pressure in the bubble is several times less than that after BC or the air-normal shock. An expansion fan centers at C and reduces the pressure to that of the bubble and at the same time terminates shock BC at C. This produces the first turn of the air towards the bubble. The pressure further downstream is still larger than that of the bubble, and that imbalance behind the bubble is maintained by a vortex-type of motion accompanied in many cases by isentropic compressions and expansions and irreversible compressions; the motion creates a flow of air into the bubble and induces and helps to maintain a movement inside it.

4 The first oblique shock AB is not straight and in some cases it starts at A as a compression fan (when the helium flow is subsonic). Thus the flow after it is rotational. AC constitutes the boundary between a nearly stagnant gas in the bubble and a rotational, supersonic flow of air over it. In figure 2 an important case can be seen where, in one half of the pattern, AC is a nearly straight line at an angle β , but in

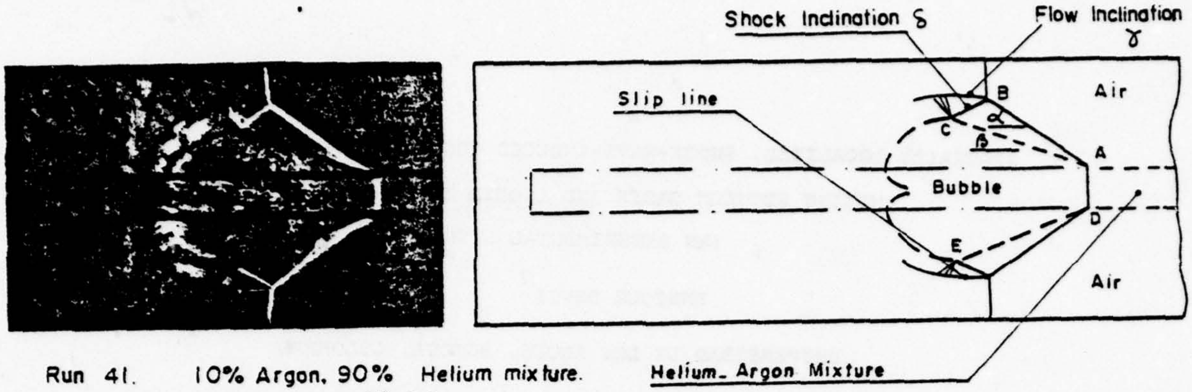

Run 41. 10% Argon, 90% Helium mixture.
Average Mach Nº : 3.1

Figure 1. A typical schlieren result

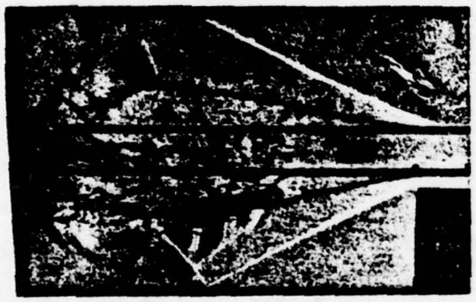

Run 96. 100% Helium
Mach at location : 2.8

Figure 2. Flow instabilities

(Flow instabilities show up along DE)

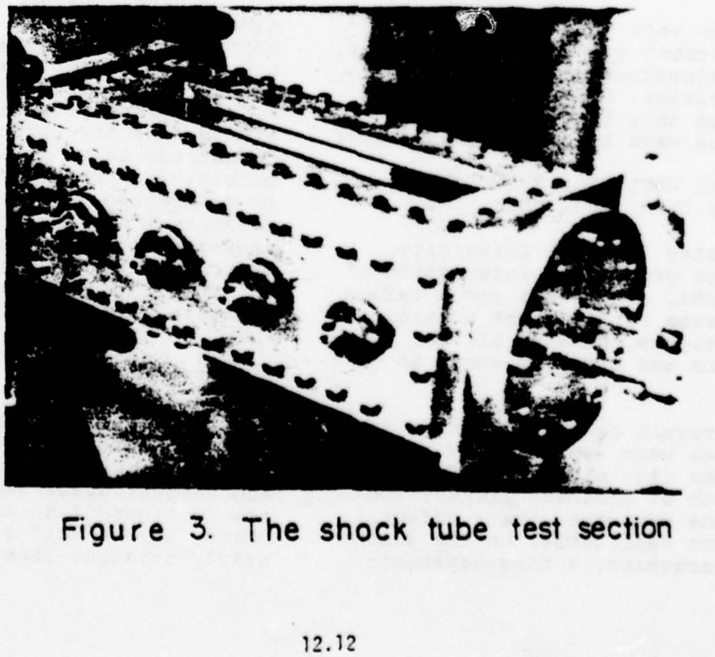

Figure 3. The shock tube test section

the other half instabilities have developed that can be clearly seen due to the membrane bits that are pushed along with the helium-air interface. These instabilities do not decay with time or along the flow, as could be expected in other supersonic flows; the many runs that were performed tend to indicate that after the pattern has traveled some distance along the test section these instabilities start to appear and produce a "leveling off" of the boundary AC, as can be seen in figure 2. The flow might become locally turbulent, as proposed in 1970, and is a shear flow.

5 During its transit through the test section, the pattern grows in size; the changes are greatest at the begining. However, angles α , β , δ , etc.,reach a steady state rather rapidly, and these values are in good agreement with theoretical predictions based upon the assumptions outlined in 1, 2 and 3 above, when turbulence has not set in. These predictions, in turn, are based upon instantaneuous valves of the Mach numbers which increase as the pattern moves. All these variations as well as most flow details and transient conditions from the time the normal shock hits the helium-argon lamina are analized extensively in reference 1.

6 Due to the necessarily short length of the test section the flow does not reach a steady state; this can only be accomplished in a wind tunnel. The bubble could continue growing indefinitely unless irreversibilities set in the form of turbulence and momentum transfer (from the air to the helium-argon) and mixing.

7 As the helium-argon mixture molecular weight increases the strength of the interaction decreases (but notice that as the molecular weight of the helium-argon exceeds that of air, still the Mach number is smaller and Cp/Cv is greater; the relative action of the two gases does not reverse).

8 As the Mach numbers increase, the strength of the interaction, vortices and mixing increases.

9 As both the ratio of the molecular weights of the two streams and the air Mach number are changed, the general geometry of the interaction changes; some of the main effects, such as the vortices or the centered expansion might not occur in some instances. The several cases that might occur are analyzed in reference 1. These of interest, however, are the ones so-far presented.

Apparatus and other Main Flow Conditions.

The equipment included a standard square-cross-section shock tube; a test section with two glass walls normal to the membranes; a schlieren system; a series of sensors that detect the passage of the normal shock, placed on the side wall, to trigger the schlieren system and to indicate at the osciloscope trace the passage of the shock over them; a pulse amplifier-scope-time delay-triggering spark-main spark electronic system; a helium-argon and air injection and continuous exhaust system (since leaks are unavoidable, the two laminae had to be continually "washed-off"). Initial Mach numbers used ranged from 1.5 to 3.5, and initial test-section pressures were about 90 torr and 200 torr. The experimental evidence comes from more than 100 successful runs (Ref. 1). Most runs failed due to the many delicate steps that had to be performed for a successful run.

A Note on Shock-Wave-Boundary Layer Interaction.

If one considers only either half of the symmetric interaction pattern then the helium-argon behaves as a boundary layer flowing along a wall, being acted upon by a shock wave, with the sole exception that the gas must have zero velocity at the symmetry line. This is so here and in the remaining of the present work.

Main Conclusion

When a shock-wave system passes through *laminae of different fluids, one having less* momentum and/or higher sound velocity, a strong interaction like that shown in Fig 1 might occur that includes recirculation of both fluids into a bubble attached to the shock pattern. It is important to notice that this conclusion might be extended to the case of a low-momentum liquid-instead of low-momentum gas, which is the basis for the third part of this work.

THE STEADY STATES IN WIND TUNNELS: THE MIXING OF STREAMS OF GASES.

The steady-state mixing was investigated from a theoretical viewpoint in reference 1. The main results show that, for the Mach number ranges and the types of gases employed, the equilibrium conditions after the irreversible process with an increase in pressure and mixing, do not differ greatly from those across a normal shock. The increase in entropy, in particular, is practically equal to the normal shock increment if one ignores the (important) entropy of mixing. The details of the derivations or results will not be presented here, for the sake of brevity.

This part of the work (Cornell University 1970-1971) had two main purposes. One, to investigate the steady state characteristics of the interaction pattern. Two, to measure the amount of mixing by employing a chemical reaction between the two streams.

The chemical reaction employed was one

with well known and investigated characteristics (at that time): the chemiluminescent reaction of nitric oxide and atomic oxigen. Of the many reactions that occur between these two and also with other species of the flow, it was shown that the following two were relevant:

$$NO + O \rightarrow NO_2 + \text{photon} \qquad (1)$$

$$k_1 = 3.8 \times 10^7 \pm 30\% \text{ cc mole}^{-1} \text{ sec}^{-1} \text{ at } 300 \text{ K}$$

$$NO + O + M \rightarrow NO_2 + M \qquad (2)$$

$$k_2 = (1.44 \pm .2) \times 10^{15} \exp (1930 \pm 100/RT) \text{ cc}^2 \text{ mole}^{-2} \text{ sec}^{-1} \ (307 < T < 505 \text{ K})$$

Reference 1 shows that other equations are not relevant and that polymerization of NO does not occur in the flow. The nitric oxide was introduced premixed with a nitrogen stream (and, later, air; no difference was observed due to pre-reactions with molecular oxigen or other gases) and the atomic oxigen was introduced along with the helium stream (Figure 4), and was generated by mixing a small stream of oxigen with helium and passing it through a radio-frecuency discharge at pressures below 70 torr, as shown in the same figure. Therefore, the pressure at the exit of the air mozzles had to be of the order of 30 torr, or less, in order to produce a nearly sonic stream of helium (or helium-argon). For an air Mach number of about 3 or less, as before, the air total pressure had to be atmospheric. Furthermore, the temperatures at which the reaction rate constants were known favor temperatures below atmospheric; thus it was correct to construct a wind tunnel that takes air from the atmosphere (no special preparations were necessary), mixes it with the helium-oxigen-atomic oxigen stream after passing through the shock waves, and evacuates the mixture using large capacity vacuum pumps in order to obtain continuous flows.

The mixing could be measured by obtainig the concentration of nitric oxide present in the resulting mixture, by employing the experimental fact that the chemiluminescence produced by reaction (1) in one of every million binary collissions follows the rule

$$I = k \cdot [O] \cdot [NO] \qquad (3)$$

that is, it is proportional to the concentration of the species; further, it has a short radiative life-time as compared to flow transit times.

Figure 5 shows a typical result. The main characteristics of the flow conditions are:

1 The shock wave pattern is produced by shocks I-H; shocks AB-BC are equivalent to those presented before, as well as the centered expansion at C. Shock inclinations differ very little from the theoretical predictions based upon normal shock val es at the given Mach numbers for helium and air

2 The increase in pressure as measured by the Mach numbers and the inclination of shocks ABC is equivalent to that across a normal shock.

3 The air Mach numbers (as measured by the inclination of Mach waves) in air were about 2.8 in many of the runs. This was in close agreement with pressure readings and with area ratios (taking into consideration the boundary-layer displacement thickness, ref. 1). The same can be said about the helium flow which enters sonically into the test section.

4 Static pressure readings away from shock waves were exhaustively performed and show that the pressure at the bubble is nearly equal to the total helium pressure; right after the bubble the pressure increases by some 40% (this is the region where the momentum transfer that allows the mixture to leave the bubble is "felt"), and then in the tail it decreases again to the exit pressure; the tail experiences a nearly sonic velocity as evidenced by shocks X and Y.

5 Shocks H-J and the one that starts as a compression fan at 0 and renders the flow horizontal would act as a "reflected shock" (I-H would be "incident")

6 The radio-frecuency discharge and the chemical reaction produce insignificant variations in flow temperatures.

7 The boundary AC, as expected, levels-off near C.

8 AC is the boundary between the bubble and the air flow, and it marks the limit of chemical reaction. Thus the mixing which occurs inside the bubble is mostly responsible for the reaction. However, near C along AC the chemiluminescense forms a "halo" that extends in the direction of B (Figure 5); it is suspected that this is caused by the turbulence, that levels-off AC and limits the size of the pattern, as it acts upon the boundary layer that flows on the two walls parallel to the plane of the paper in the figure and produces a diffussion of active species on those layers.

9 As will be shown later, the chemiluminescense in the tail is caused mostly by the delay of the chemical reactions and not by incomplete mixing. The two streams come out of the bubble already mixed in a proportion of nearly 6:1 air to helium-argon. The mixing occurs in the bubble and also along the turbulent boundary. The tail has virtually uniform composition.

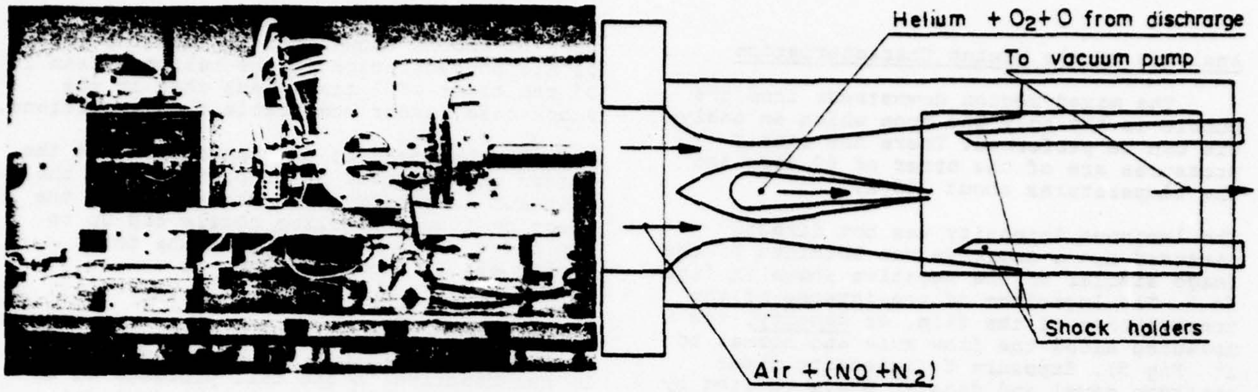

Figure 4. Part of the wind_tunnel instalation and a scheme of the test section

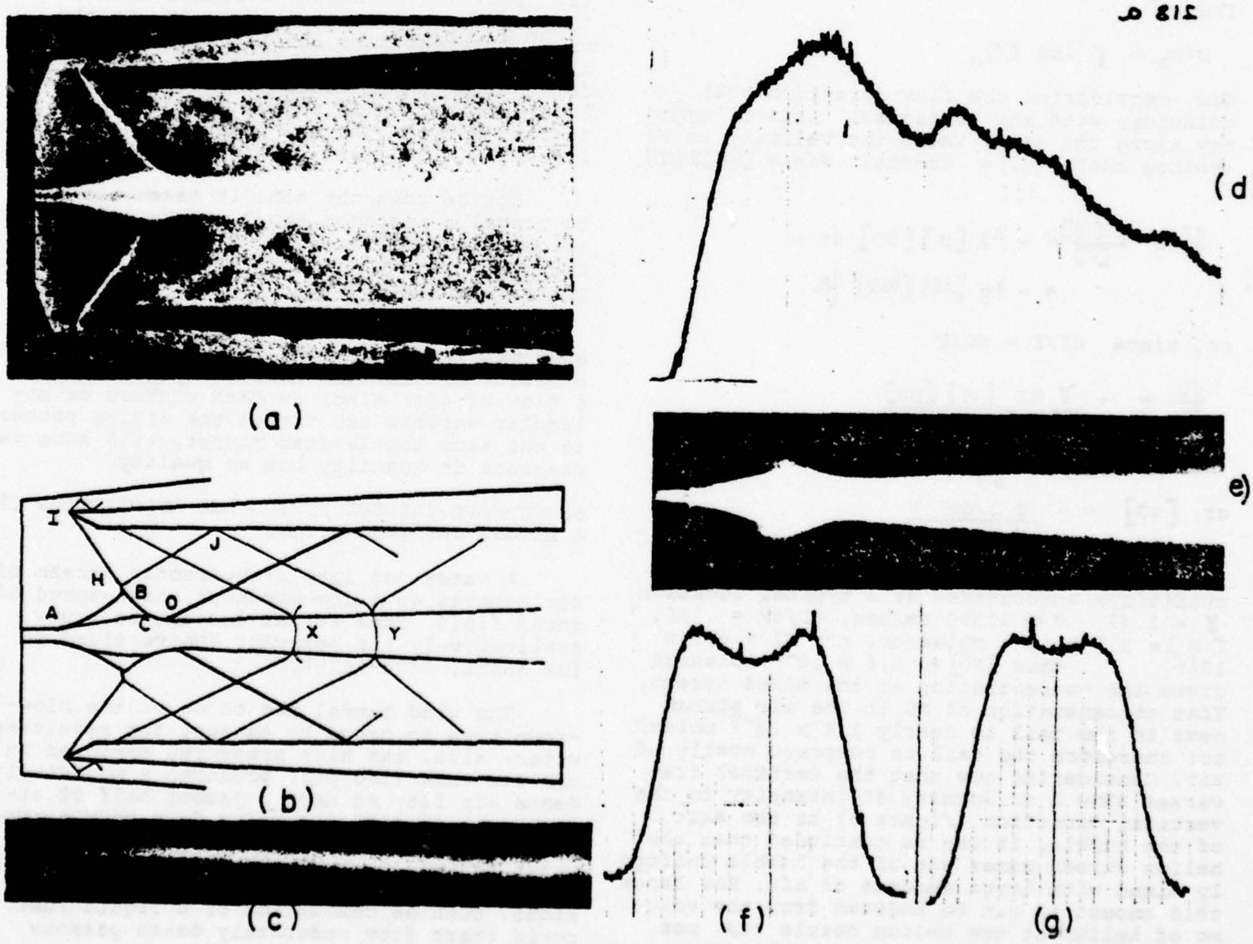

(a) (b) (c) (f) (g)

Figure 5 (a) A typical schlieren and chemiluminescence (b) Schematic of (a). (c) A typical result without shock (d) Densitometer trace along the flow axis. (e) The chemiluminescent reaction (f) vertical reading at bubble (g) At the neck

Analysis of the Mixing Characteristics

The mixed region downstream from the bubble is the only one upon which an analysis can be performed. There the static pressures are of the order of 60 torr and the temperatures about 250 K.

The luminous intensity was not directly measured but a negative was obtained of the image similar to the negative shown in figure 5. The logarithm of the inverse of the transmitance of the film, or density, was measured along the *flow axis* and *normal* to it (Fig 5). Exposure E (intensity times exposure time) and density D are related by

$$\frac{E}{E_o} = e^{(D-D_o)/\gamma}$$

where γ is a characteristic of the film. Thus

$$D-D_o = \gamma \log I/I_o$$

Now, considering the flow direction that coincides with the horizontal axis of symmetry along the tail, where the velocity is V, (notice that $[NO]$ = Constant since $[NO] \gg [O]$)

$$\frac{dI}{I} = \frac{d[O]}{[O]} = -k_2 [M][NO]\, dt =$$
$$= -k_2 [M][NO] \frac{dx}{V}$$

or, since $dI/I = dD/\gamma$

$$\frac{dD}{dx} = -\frac{\gamma k_2 [M][NO]}{V}$$

(notice that $\partial D/\partial y \sim 0$)

$$\text{or } [NO] = -\frac{(dD/dx)\, V}{\gamma k_2 [M]}$$

For one of the types of films used and the conditions encountered at a typical location, $\gamma = 1.47$, $V \sim 31500$ cm/sec, $dD/dx = .192$, $[M] = 3.8 \times 10^{-6}$ moles/cc, and $k_2 = 6.9 \times 10^{16}$ thus $[NO] \sim 1.6 \times 10^{-8}$ *moles/cc* gives the concentration at the mixed stream. That concentration of NO in the air stream next to the tail is nearly 1.4×10^{-8} moles/cc; therefore the tail is composed mostly of air. Considering now that the vertical traverses show a uniformity of intensity in the vertical direction (Figure 5) at the exit of the bubble, it can be concluded that the helium stream comes out of the bubble uniformly mixed with large amounts of air. How large this amount is can be deduced from the volume of helium at the helium nozzle tip, per unit of time, that enters the bubble (at sonic speed) and that of mixed gases before shocks X and Y, also at nearly sonic speed, and the order of magnitude is 6 to 1 (air to helium).

A comparison of a helium flow not acted upon by shocks shows (ref 1) that the ratio of air concentration in the helium stream is of the order of 7 times less than in the shock case, under comparable flow conditions.

Furthermore, if one considers that the oxigen atom removal is proportional to the emission intensity, then the extent of the reaction from the helium nozzle tip up to any point X can be found from the total number of 0 atoms removed, or

$$\int_{area} I\, dA$$

Following this method, it is found that: 1) the reaction in the tail proceeds at a rate equal to having the helium (oxigen) mixed with large amounts of air (and thus has a known concentration of NO, equal to that of the air stream), as was shown before, and 2) the reaction in the shock wave actually "ends" in a shorter distance than in this ideal, hypothetical case due to the very important fact that at least a part of the gases mix in the bubble and stay there for a time. The reaction thus occurs in a localized region of space, especially if it is fast enough (the one used here has a half life of 2×10^{-4} sec under our conditions).

Notice that the time it takes the air to travel a distance equal to the size of the bubble is about 2×10^{-5} sec; this is the order of magnitude of the time for complete mixing to occur.

Finally, it can be mentioned that the same mixing enhancement can be obtained with a series of multiple helium inyectors into a flow of air; also, as Mach numbers or molecular weights are varied the mixing proceeds in the same accelerated manner, with some variations in quantity but no quality.

SHOCK-WAVE INDUCED MIXING AND ATOMIZATION OF A LIQUID JET INTO A GAS.

A water jet into a supersonic stream of air behaves as a low-momentum, high-speed of sound fluid. Thus it was decided to study qualitatively its behavior (Universidad de los Andes, 1972-1975).

The wind tunnel had to be of the blow-down type in order to exhaust the resulting water; also, the high pressures employed in the air tank *(100 psi)* produced a moderately dense air flow at Mach 3 (about half of atmospheric density) starting from room temperature, and thus the interaction with the water jet would surely be strong enough. Further, it was thought that possible applications, such as combustion of a liquid fuel, could start from moderately dense gaseous (in the mixing zone) oxidants.

The air had no special preparation as it entered the tank from a reciprocating compressor ; it then passed from the large tank to a small one via a reduced diameter pipe

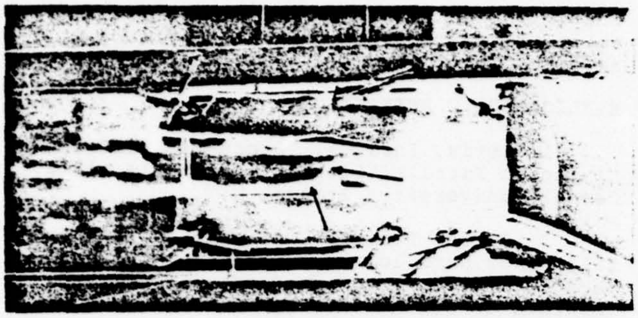

Fig. 5. The two-dimensional array; the "incident" shock and the bubble are pointed by arrows.

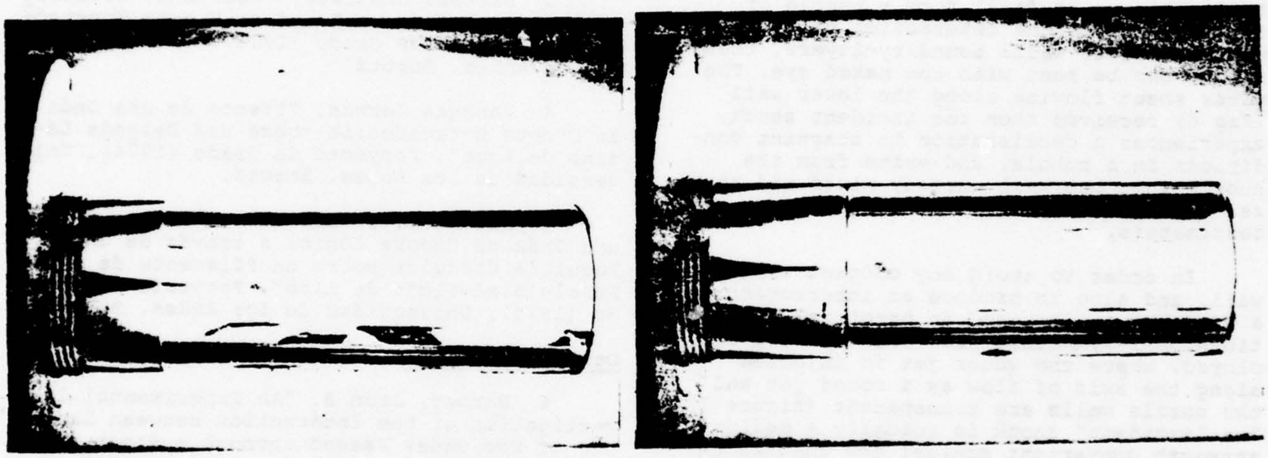

(a) (b)

Fig. 6. The axi-symmetrical array
(a) Conical shock produced by a change in wall inclination
(b) Conical shock produced by the same change plus a "jump" similar to that produced by a shock holder

Fig. 7. Two views of the main experimental apparatus.

(where condensation could occur, since flow temperatures were below freezing) and then to the nozzle. These ones had typical throat dimensions of 1 cm high by 2 cm deep. Appropriate flow conditions were verified by a schlieren system (ref 2,3).

The first step was to verify in a two-dimensional array that the same pattern was obtained. Figure 6 shows that it is so. The air flows at about 2.7 Mach number; the "incident" shock can not be seen through a schlieren system; but due to the fact that the small droplets that flow along the glass walls (that, by the way, was the cause for the schlieren to fail) form a bubble of their own below the interaction of the shock with the glass walls boundary-layers, these shocks can be seen with the naked eye. The water sheet flowing along the lower wall (Fig 6) received then the incident shock, experiences a deceleration to stagnant conditions in a bubble, and exits from the bubble into the tail already mixed and atomized with plenty of air, in about one or two centimeters.

In order to avoid any contact with a wall, and also to produce an interaction in a way that can be used in practical applications, axi-symmetric flow nozzles were employed, where the water jet is injected along the axis of flow as a round jet and the nozzle walls are transparent (figure 7) The "incident" shock is actually a medium-strength convergent conical one that is generated by a "jump" in the air path at Mach 2.8 at the wall or a change in wall direction.

As the photograph shows, a bubble is formed after a deceleration of the water, and, as in the cases before, it exits only after the air has transmitted enough momentum to it-after atomization. Thus, as both observations and the photographs suggest, the mixing of the water with air is very violent and very fast, and follows the same pattern analyzed before (Ref 4,5).

ACKNOWLEDGEMENTS

Doctor Terrill A Cool of Cornell University was thesis advisor in the first two parts of this investigation, and collaborated with suggestions, guidelines, and at times directly in the work. He was the director of the chemical laser research group where this work took place.

John Barber started some runs with a shock tube, also with Terrill Cool.

Fernando Prado, Santiago Harker, Germán Vanegas and Bernardo Breziner worked on special undergraduate projects covering the third part of this work, at the Universidad de Los Andes in Bogotá.

The National Aeronautics and Space Administration, the Ford Foundation, Cornell University and the Universidad de Los Andes collaborated in financing and providing a necessary aid in this project.

BIBLIOGRAPHIC REFERENCES

1 Devis, Enrique. "Shock-Wave Induced Mixing in Parallel Flow" Ph.D. Thesis, 1972, Cornell University. Ithaca, N.Y.

2 Prado, Fernando. "Diseño de unas instalaciones para lograr Túneles de Viento Supersónicos". Proyecto de Grado (1973). Universidad de los Andes. Bogotá.

3 Harker, Santiago. "Rediseño, Construcción y Pruebas de un Tunel de Viento Supersónico". Proyecto de Grado (1973). Universidad de los Andes. Bogotá

4 Vanegas Germán. "Efecto de una Onda de Choque Estacionaria sobre una Delgada Lámina de Agua". Proyecto de Grado (1974). Universidad de los Andes. Bogotá.

5 Breziner, B. Bernardo. "Efecto de una Onda de Choque Cónica a través de una Boquilla Circular sobre un Filamento de Agua Paralelo al Flujo de Aire". Proyecto de Grado (1975). Universidad de los Andes. Bogotá.

<u>Other References</u>

6 Barber, John B. "An Experimental Investigation of the Interaction Between Laminae of Two Gases Passed through a Shock Wave". Thesis (M.Sc.), Cornell University, 1969.

7 Hess, R.V. Interaction of Moving Shocks and Hot Layers. NACA TN 4002 (1957)

8 AGARD Conference Proceedings No. 4. Separated Flows (1966).

9 Crocco, L. and Lees, L. "A Mixing Theory for the Interaction Between Dissipative Flows and Nearly Insentropic Streams, "J. Aero.Sciences 19, No. 10, pp. 649-676 (1952).

10 Klein, F. S. and Herron, J.T. "Mass-Spectrometric Study of the Reaction of O Atoms with NO and NO_2, "J. Chem. Phys. 41 (1964).

11 Handbook of Supersonic Aerodynamics (NAVWEPS Report 1488) (1966).

12 Rad, W.J. "Some Numerical Results on Viscous Low-Density Nozzle Flows in the Slender-Channel Approximation," AIAAJ 9, p 811 (1971).

13 Ferri, A. "Review of Problems in Application of Supersonic Combustion", J. Roy. Aero. Soc. 68, 575 (1964)

14 Clyne, M. A. A. and Trush, B.A. "Mechanism of Chemiluminescent Combination Reactions Involving Oxygen Atoms," Proc. Roy Soc. A., 269, No. 1338 , 404 (1962)

15 Vandpee, M., Hill, K. D., and Kineyko, W.R. "Absolute Rate Constant Measurements for the Radiative Combination of Atomic Oxygen with Nitric Oxide", AIAAJ 9, 135 (1971)

16 Jonathan, N. and Petty, R. "Light Emission from Reaction of Atomic Oxygen with Nitric Oxide at Low Pressures", Trans. Faraday Soc. 64, pt. 5, 1240 (1968).

17 Resler, Edwin Louis. "High Temperature Gases Produced by Strong Shock Waves". Thesis (Ph.D), Cornell University, September 1951.

18 Bahn, G.S. Reaction Rate Compilation for the H-O-N System. Gordon and Breach, 1967.

19 Mees, C.E.K. and James, T.H. The Theory of the Photographic Process. 3rd ed., Macmillan, New York, 1966.

20 Polaroid Publication P444 (leaflet).

21 Pack, D.C. "The Reflection and Diffraction of Shock Waves", J. Fluid Mech. 549 (1963).

22 Cool, T.A. "Fluid Mixing Laser", Appl. Phys. Letters 9, 418 (1966).

23 Golomb, D. and Good, R.E. "Clusters in Isentropically Expanding Nitric Oxide and their Effect on the Chemiluminous NO-O Reaction", J. Chem. Phys, 49, p. 4177

24 Vanpee, M. and Kineyko, W.R. "Experiments on NO_2 Chemiluminescence Using Adiabatically Expanded NO", J. Chem. Phys. 52, p. 1619 (1970).

25 Fontijn, A., Meyer, C.B., and Schiff, H.I. 'Absolute Quantum Yield Measurements of the NO-O Reaction and its use as a Standard for Chemiluminescent Reactions", J. Chem. Phys. 40, No. 1 (1964)

26 Keyser, L. F., Levine, S. Z., and Kaufman, F. "Kinetics and Mechanism of NO_2 Fluorescence", J. Chem. Phys. 54, p. 355 (1971).

27 Gross, R.A. and Wallace Chinitz. "A Study of Supersonic Combustion", J. Aero Sc. 27, p 517 (1960)

28 Nicholls, J.A., Dabora, E. K., and Gealer, R.L. "Studies in Connection with Stabilized Gaseous Denotation Waves", 7 th. Int'l. Symposium on Combustion, 1958.

29 Markstein, G.H. "A Shock Tube Study of Flame Front-Pressure Wave Interaction", 6th Symposium (Int'l.) on Combustion, p. 387, Reinhold, New York.

30 Rudinger, G. "Shock Wave and Flame Interactions. Combustion and Propulsion." Third AGARD Coll. London: Pergamon.

31 Mark, Herman. "The Interaction of a Reflected Shock Wave with the Boundary-Layer in a Shock Tube". Thesis (Ph.D.), Cornell University, 1957.

32 Holden, M.S. "Theoretical and Experimental Studies of Separated Flows Induced by Shock-Wave-Boundary-Layer Interaction", AGARD CP No. 4, 1966, p. 147.

33 Cool, T.A. "Power and Gain Characteristics of High Speed Flow Lasers", J. Appl. Phys. 40, 3563 (1969)

34 Ribner, H.S., and Moore, F.K. "Unsteady Interaction of Disturbances with Shock Wave, with Applications to Turbulence and Noise", Heat Tr. and Fluid Mech Inst. (1953).

35 Witte, J. H. "Mixing Shocks in Two-Phase Flow", J. Fluid Mech. 36, 4, p. 639 (1969).

36 Rudinger, G. and Somers. L.M. "Behaviour of Small Regions of Different Gases Carried in Accelerated Gas Flows", J. Fluid Mech. 7,2, p. 161 (1960).

37 Jahn, R.G."The Refraction of Shock Waves at a Gaseous Interface." Princeton University Technical Report 11-19. 1955.

38 Shames, H. and Seashore, Ferris L. "Design Data for Graphical Construction of Two-Dimensional Sharp-Edge-Throat Supersonic Nozzles". NACA RM E8J12.

ON SOME ASPECTS OF TURBULENCE SUPPRESSION BY TRANSVERSE MAGNETIC FIELDS*

H. Branover, P. Gershon,

Department of Mechanical Engineering

Ben-Gurion University of the Negev

Beersheva, Israel

ABSTRACT

Results of direct measurements of turbulence intensity in duct flows placed in a transverse magnetic field have been reported by several authors during the last decade. It was established that while the integral characteristics (e.g., friction, mean velocity profile) of an initially turbulent flow begin to correspond to the laminar flow theory for a sufficiently strong magnetic field, local velocity fluctuations still remain at a very high level. Different explanations of this phenomenon have been suggested. Whether, and in what conditions, a transverse magnetic field is able to annihilate the velocity fluctuations remained an unsolved problem.

The present work describes a further experimental investigation of this problem. Turbulence intensity and correlation measurements have been performed in a mercury flow, by means of two-electrode and hot-film sensors. The apparatus was designed in such a manner as to make possible the verification of the hypothesis suggested for the explanation of the persistence of flow disturbances after laminarization.

An undisturbed laminarized flow was achieved. The analysis of the experimental data allowed us to draw a physical picture explaining the remaining disturbance phenomenon.

NOMENCLATURE

a,	semi-width of the cross-section side parallel to the magnetic field direction [m];
b,	semi-width of the cross-section side perpendicular to magnetic field direction [m];
B,	magnetic flux density [T];
Ha,	Hartmann number, $B \cdot b \cdot (\sigma/\mu)^{1/2}$;
L,	distance from the inlet section, [m];
N,	Stuart number, Ha^2/Re
r,	hydraulic radius, $ab/(a+b)$ [m];
Re,	Reynolds number, $U \cdot b/\nu$;
u',	rms value of the longitudinal velocity pulsations [m/s];
U,	mean flow velocity [m/s];

Greek Symbols

β,	aspect ratio of the channel's cross-section b/a;
μ,	dynamic viscosity [Kg/(m·s)];
ν,	kinematic viscosity [m^2/s];
σ,	electrical conductivity [S/m];

Subcripts

b,	based on the length b;
cr,	critical value.

INTRODUCTION

The very first investigations on MHD duct-flows already dealt with the turbulence suppression effect, both theoretically and experimentally. In the experimental works, the evaluation of the turbulence suppression was based upon the comparison of the measured friction factor value with the value predicted by the laminar flow theory. This permitted the establishment of the existence of critical ratios of the Hartmann to Reynolds numbers for ducts of different cross-sectional shapes.

An empirical expression was developed [1] for the relationship between the critical Ha/Re ratio and the aspect ratio $\beta = b/a$ of the cross-section:

$$(Ha/Re)_{cr} = [215 - 85 \cdot \exp(-0.35\beta)]^{-1}.$$

In the present work, the Hartmann and Reynolds numbers are based on the hydraulic radius $r = ab/(a+b)$, the length of the cross-section side perpendicular to the magnetic field being 2b and of the parallel side - 2a. For $b/a \gg 1$, $r \approx a$, while for $b/a \ll 1$, $r \approx b$.

The development of measurement techniques making possible direct (local) turbulence measurements in MHD ducts brought about new and surprising experimental evidence: even after the Ha/Re ratio exceeds the critical value, a high intensity of velocity fluctuations is still present in the flow. Typical results of such measurements [2] are presented in Fig. 1. This "remaining disturbances phenomenon" constitutes a very interesting paradox since it deals with a highly disturbed flow which, nevertheless, does not exhibit turbulent momentum transfer.

Further measurements [3,4,5] showed that the remaining disturbances persist a very long distance along the experimental channel, that they are strongly correlated in the field direction and that they are stronger in the middle of the duct than near the walls. The overall picture of the available experimental data regarding the level of the remaining disturbances is given in Table 1.

Two main hypotheses were suggested for the explanation of the phenomenon. The first [5] connected it with the trend, theoretically discovered earlier [6], of the MHD turbulence to become two-dimensional as a consequence of the unequal suppression of different velocity components by the magnetic

---

* This work was carried out under a contract from the Office of Naval Research, U.S.A., N00014-74-C-0228. Correlation measurements were supported also by a grant from the Israel National Academy of Sciences and Humanities, file P(B)31.

PRECEDING PAGE BLANK-NOT FILMED

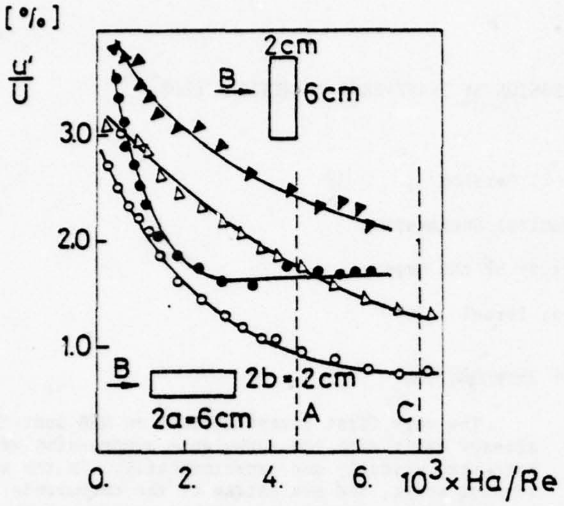

Fig. 1 Turbulence intensity measurements versus Ha/Re ratio in rectangular channels of different cross-sectional shapes
(1) β=3. :▲,L/a=10; ●,L/a=70;
critical Ha/Re ratio marked "A";
(2) β=0.33:Δ,L/b=10; o,L/b=70;
critical Ha/Re ratio marked "C".

field. Thus, the remaining disturbances were supposed to originate from the upstream turbulence, brought by the flow into the field region and "tuned" to a configuration which is less affected by the magnetic field.

According to the second hypothesis [3], the remaining disturbances come from the magnetic entrance region, where M-shaped mean velocity profiles exist [7]. In both cases, these disturbances would be close to two-dimensional in a plane perpendicular to the magnetic field and thus, should be only weakly influenced by it. At the same time, the scale of the disturbances is large and they are less affected by the viscous dissipation, a fact which explains their very slow decay.

The purpose of the present work was to check experimentally each of the two mentioned hypotheses. A particular question which had to be answered was whether a nondisturbed laminarized flow can be achieved at all in a straight, pressure gradient driven duct flow.

EXPERIMENTAL APPARATUS AND MEASURING TECHNIQUES

To make possible the experimental distinction between the two hypotheses described above, a special apparatus was built. It had to separate the influence of the turbulence entering the magnetic field from that of the vortex generating M-shaped mean velocity profiles in the magnetic entrance region. These requirements are met in the apparatus shown in Fig. 2.

One of its particular features is the shape of the inlet section of the channel, similar to that used in the classic Reynolds' experiment. This

TABLE I

Shape of the cross section	Aspect ratio β	Place of measurement L y/a z/b	Method*	Re	Interaction parameter at critical conditions $(N_b)_{cr}$	Disturbance level at critical conditions $(u'/U)_{cr}$	Authors
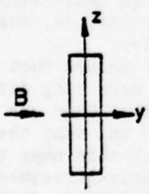	7.5:1	112a 0.6 0	t.e.	$7\cdot10^3$	1.07	0.8%	Slyusarev, 1971
	6:1	73a 0 0	h.w.	$1.02\cdot10^5$	12.5	1.3%	Hua & Lykoudis, 1974
	3:1	40a 0.9 0	t.e.	$1.74\cdot10^4$	1.55	1 %	Branover, Gelfgat, Kit & Platnieks, 1970
	3:1	40a 0 0	h.w.	$2.6\cdot10^4$	2.31	1.2%	Platnieks, 1971
	3:1	55a 0 0	t.e.	$2.6\cdot10^4$	2.26	1.4%	Kit & Platnieks, 1971
	3:1	70a 0 0	t.e.	$2.54\cdot10^4$	2.31	1.6%	Branover, Gelfgat, Kit & Tsinober, 1970
	1.2:1	16a 0 0	h.w.	$2.17\cdot10^4$	1.04	1.3%	Branover & Platnieks, 1971
Circular	1:1	$75R_0$ $R=0.9$ $\theta=0$	h.w.	$4\cdot10^3$	0.18	0.66%	Gardner & Lykoudis, 1971
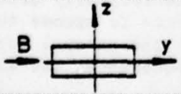	1:3	70b 0 0	t.e.	$1.4\cdot10^4$	0.67	0.8%	Branover, Gelfgat, Kit & Tsinober, 1970
	1:7.5	110b 0 0	t.e.	$6.6\cdot10^3$	0.35	0.5%	Branover, Slyusarev, & Shcerbinin, 1970
	1:5	193b 0.4 0.6	t.e.	$3.54\cdot10^3$	0.19	0.3%	Present work

* t.e.--two-electrode method; h.w.--hot-wire method

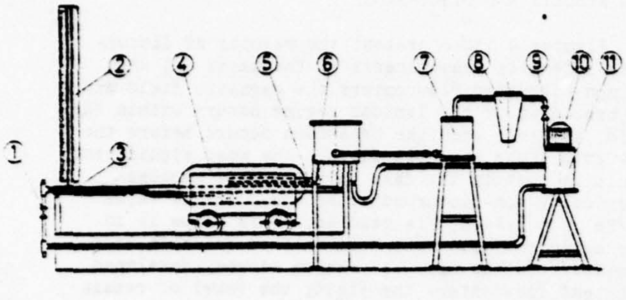

Fig. 2 Schematic of the experimental apparatus

(1) flow control valve; (2) manometers;
(3) Venturi tube; (4) electromagnet;
(5) test channel; (6) upper tank;
(7) buffer tank; (8) filter;
(9) control valve; (10) pump;
(11) lower tank.

feature insures the realization of a nondisturbed flow at supercritical Reynolds numbers. The insulated wall channel has a cross-section of 0.6×3 cm^2 ($\beta = 0.2$). The overall length of the channel is 69 cm (230 b). In a previous experimental work [8], the critical Reynolds number for a similar channel was found to be about 850 (based on the hydraulic radius).

The test channel is placed in the gap of the electromagnet so that the magnetic field is transverse to the axis of the channel and parallel to the larger side of the cross-section. The edge of the magnetic poles can be set anywhere between inlet and a point situated at a distance $L = 133$ b from the inlet. Experiments can also be run with whole entry section, including the converging nozzle, within the uniform magnetic field, so that there is no turbulence entering the field, nor M-shaped velocity profiles.

When the magnet is moved downstream with respect to the section where the breakdown of laminar flow occurs, turbulence is obviously brought into the magnetic field. For prevention of M-shaped velocity profiles in this latter case, the flow in a channel with $\beta \ll 1$ at relatively low Reynolds numbers seems to be the best choice. Let us analyze this question in a little more detail. In any MHD duct with arbitrary $0 < \beta < \infty$, the critical ratio of Hartmann to Reynolds numbers changes within a narrow interval: $7.4 \cdot 10^{-3} > (Ha/Re)_{cr} > 4.6 \cdot 10^{-3}$. At the same time, the sharpness of the M-profile is proportional to the Stuart number $N_b = Ha^2/Re$, based on the size, b, of the wall which is transverse to the magnetic field [7]. This number can be expressed as $(Ha/Re)_{cr} \cdot Ha \cdot b/a$. Furthermore, for laminarization, $Ha = (4.6...7.4)10^{-3} Re$. Hence, the critical Stuart number corresponding to laminarization is $(N_b)_{cr} = (4.6...7.4)^2 \cdot 10^{-6} \cdot Re \cdot \beta$, the lower coefficient corresponding to $\beta \gg 1$ and the higher one to $\beta \ll 1$. According to the assumption made before, regarding the conditions when the M-profiles are least developed, the measurements were made in an azimuthal field ($\beta \ll 1$) at small Reynolds numbers.

If we return to Table I, we note that the measured intensity of the remaining disturbances was lower for the lower values of $(N_b)_{cr}$. Surprisingly, attention was never paid to this obvious fact before. Figure 3 presents the relationship between the level of remaining disturbances and the critical Stuart number $(N_b)_{cr}$.

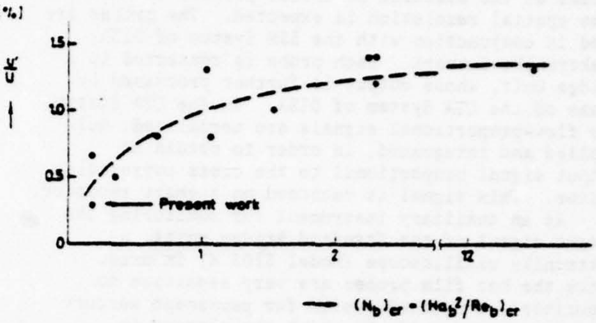

Fig. 3 The relationship between the level of remaining disturbances and the critical Stuart number $(N_b)_{cr}$.

The electromagnet is provided with rectangular 10×40 cm^2 poles, and can produce a field of maximum 0.7 Tesla in a gap of 4.2 cm. The field is uniform within 1% with the exception of 2 cm at each end of the pole piece.

For the turbulence intensity measurements, "two-electrode" probes were used. This method is based on the potential difference induced by an electroconductive flow between two electrodes perpendicular both to the field and flow directions; it was shown [9] to be qualitatively accurate, particularly for the flow configuration used in the present work and at Ha/Re ratios bigger than $3 \cdot 10^{-3}$.

Since for our investigation only the fluctuating velocity is of interest, the d.c. component in the potential difference (proportional to the average velocity) is filtered out, and the fluctuating component is amplified by a factor of 10^3 and measured by means of an rms voltmeter. The measured rms value, u', normalized by the potential difference corresponding to the average velocity, U, at the same magnetic field, is termed the "turbulence intensity". The electrode tips were situated on a line perpendicular to the larger side of the cross-section, at 1±0.05mm apart and at a distance of 0.7mm from this side (measured from the electrode closest to the wall).

For the turbulence intensity measurements, the noise level was determined by measuring the rms value of the probe output, using the whole amplifying chain, when the flow velocity was zero. This rms value, which included the common-mode signal picked up by the probe cables and the noise of the preamplifier, was subsequently deduced from the flow signal. The noise level was usually less than 10% of the pulsatile component of the probe output.

The spatial correlation measurements were performed by means of quartz coated hot-film probes of the Model 1210-20 Hg, manufactured by Thermo-Systems, Inc., U.S.A. (diameter of the sensor, 51μ; active sensor length, 0.1 cm; distance between supports, 0.2 cm).

Two identical probes were mounted on 94 cm long probe supports, which can slide, through mercury tight joints, along the whole test section of the channel. The sensing elements are situated on the center-line parallel to the magnetic field, symmetrically with respect to the center point of the cross-section.

The length of the hot film sensing area is comparable with the distance between the electrodes of the electric potential probes, so that the same spatial resolution is expected. The probes are used in conjunction with the 55M System of DISA Elektronik, Denmark. Each probe is connected to a Bridge Unit, whose output is further processed by means of the CTA System of DISA. In the CTA System, the flow-proportional signals are normalized, multiplied and integrated, in order to obtain an output signal proportional to the cross correlation factor. This signal is recorded on a chart recorder.

As an auxiliary instrument for monitoring the output signal of the Standard Bridge units, a Tektroniks oscilloscope (Model 5103 N) is used. Since the hot film probes are very sensitive to impurities, a special system for permanent mercury cleaning is operated, by which the mercury is bubbled through a strong acid solution. The extremely severe temperature regulation requirements imposed by the use of the hot-film technique in liquid metals have a weaker influence on spatial correlation measurements. However, the mercury temperature during the hot-film measurements was kept constant, within ±0.1 C, by means of a controlled cooling system.

Oscillographic recordings of the gradually suppressed velocity pulsations, as well as spectral measurements, reported elsewhere [1], have also been performed in the present investigation.

MAIN RESULTS AND DISCUSSION

Figures 4 and 5 present the results of disturbance intensity measurements in the cases (a) when the non-disturbed flow enters the magnetic field and the breakdown of the laminar regime occurs within the field, and (b), when the breakdown occurs before the flow enters the magnetic field. The most significant result is that in the case (a), the flow remains practically non-disturbed after the critical value $(Ha/Re)_{cr} = 7.4 \cdot 10^{-3}$ is reached. This value is in fair agreement with that derived from friction measurements. In the case (b), where already developed turbulent flow enters the field, the level of remaining disturbances is higher than in the first case, but is still essentially lower than in any previously reported works.

Since in this second case the difference from all the former experiments consists only in the lower $(N_b)_{cr}$, i.e., much less developed M-profiles at the magnetic entrance, it is most probably this entrance effect which accounts for the difference in results.

Thus, at the stage described, the possible conclusion was that the main reason for the remaining disturbances is the M-profile effect, while the trend of the entering turbulence to become two-dimensional may still play some role.

For a deeper insight into the problem, two-point correlations of the longitudinal velocity pulsations were measured. The results are plotted in Fig. 6,

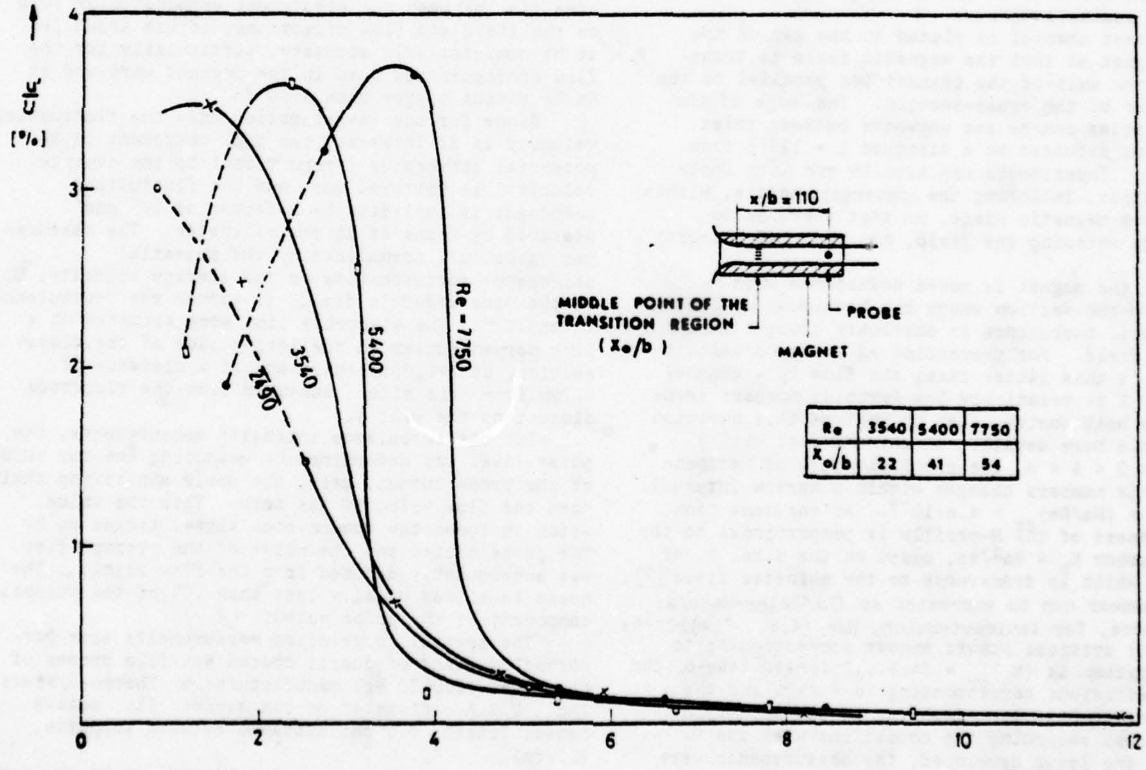

Fig. 4 Turbulence suppression in the case when non-disturbed flow enters the magnetic field.

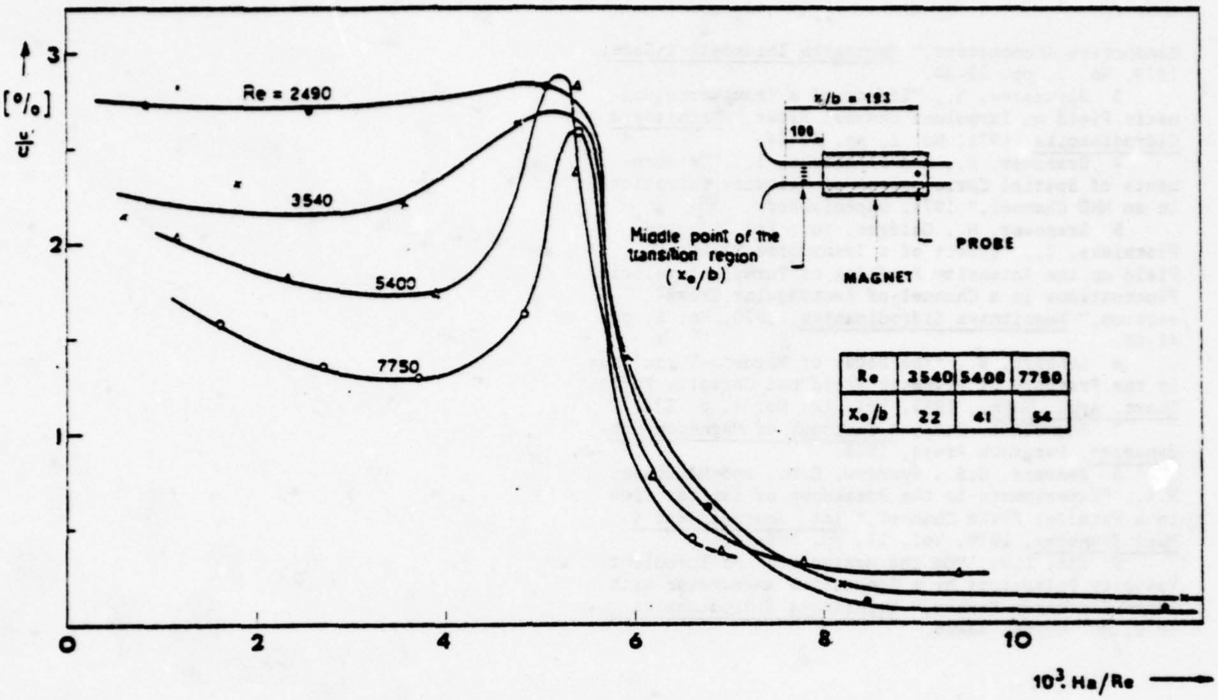

Fig. 5 Turbulence suppression in the case when the flow entering the magnetic field is already turbulent.

together with results obtained earlier [4] in a duct with $\beta > 1$. The corresponding intensity curves are presented at the bottom of the figure.

The correlation function obtained at $(Ha/Re)_{cr}$ in the present work, $(\beta = 0.2)$, is about two times lower than at $\beta > 1$. In our case, the correlation curve tends to continue downwards for $Ha/Re > (Ha/Re)_{cr}$, while at $\beta > 1$ it goes upwards. This again proves the assumption that the two-dimensional remaining disturbances are generated due to the M-effect. However, the comparison of the two correlation curves obtained in the present work shows that the increase of correlation in the case when the magnet covers the entrance (M-effect completely absent) is only slightly lower than in the second case. Thus, we have to conclude that the conversion of three dimensional turbulence to two-dimensional probably exists. If we now look at the bottom part of the graph, we see that when the maximal correlation is reached, the intensity already becomes close to zero (the situation is completely different at $\beta > 1$). This can be interpreted as an indication that the turbulence conversion effect, while existing, does not express itself significantly since the overall decay of all velocity components of the disturbed motion is faster.

This justifies the conclusion that the entrance effects (M-shaped mean velocity profiles) carry the main responsibility for the usually observed remaining disturbances in laminarized flows.

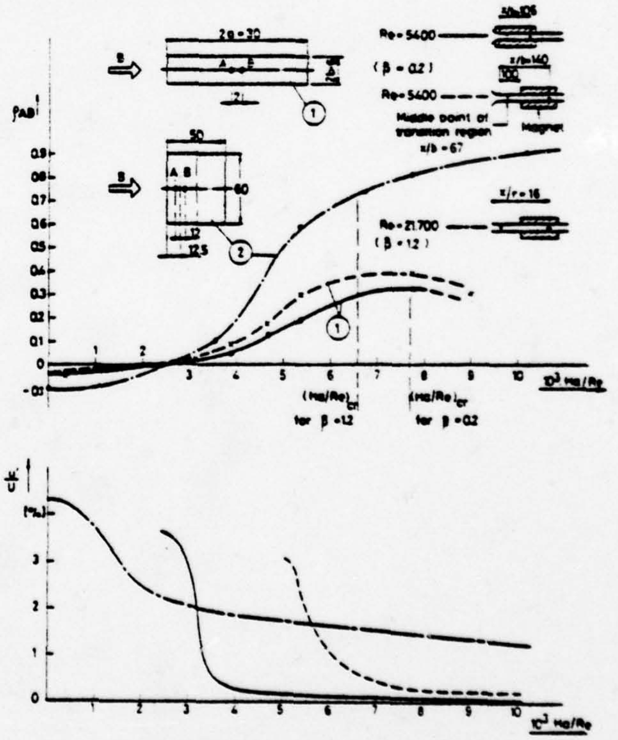

Fig. 6 Above: The correlation coefficient ρ_{AB} of the longitudinal velocity pulsations between two points situated on a magnetic field line. Results from [4] (β=1.2) are plotted for reference. Below: Corresponding turbulence suppression curves.

REFERENCES

1 Branover, H. and Gershon, P., "MHD Turbulence Study, Part II," Annual Report BGUN-RDA-100-76, April 1976, Ben-Gurion University of the Negev, Beersheva, Israel.

2 Branover, H., Gelfgat, Yu., Kit, L., and Tsinober, A., "On Some General Properties of MHD Turbulence in Pipes and its Investigation by Means of

Conductive Anemometers," Mechanika Zhidkosti i Gaza, 1970, No. 2, pp. 35-44.

3 Slyusarev, N., "Effect of a Transverse Magnetic Field on Turbulent Channel Flows," Magnitnaya Gidrodinamika, 1971, No. 1, pp. 18-24.

4 Branover, H., and Platnieks, I., "Measurements of Spatial Correlations of Velocity Pulsations in an MHD Channel," 1971, unpublished.

5 Branover, H., Gelfgat, Yu., Kit, L., and Platnieks, I., "Effect of a Transverse Magnetic Field on the Intensity Profiles of Turbulent Velocity Fluctuations in a Channel of Rectangular Cross-section," Magnitnaya Gidrodinamika, 1970, No. 3, pp. 41-49.

6 Lehnert, B., "The Decay of Magneto-Turbulence in the Presence of Magnetic Field and Coriolis Force," Quart. Appl. Math., 1955, Vol. 12, No. 4, p. 321.

7 Shercliff, J.A., A Textbook of Magnetohydrodynamics, Pergamon Press, 1965.

8 Beavers, G.S., Sparrow, E.M., and Magnuson, R.A., "Experiments in the Breakdown of Laminar Flow in a Parallel Plate Channel," Int. Journal Heat & Mass Transfer, 1970, Vol. 13, pp. 809-815.

9 Kit, L.G., "On the Measurement of Turbulent Velocity Pulsations by a Conductive Anemometer with Three-Electrode Sensor," Magnitnaya Gidrodinamika, 1970, No. 4, pp. 41-46.

THE EFFECT OF TURBULENT DIFFUSION ON GAS PARTICLE FLOW IN AN ELECTRIC FIELD

J. T. Jurewicz
The Institute of Paper Chemistry

and

D. E. Stock, C. T. Crowe
Department of Mechanical Engineering
Washington State University

ABSTRACT

A numerical study is made of the effect of fluid turbulence on the motion of charged particles in an electric field. Attention is focused on the turbulent diffusion of the particles in a steep concentration gradient and is motivated by the desire to better understand and predict the operation of electrostatic precipitators. The motion of the particles in the turbulent flow field is predicted using a pressure-velocity formulation for the gas flow and a Lagrangian formulation for the particle motion. Coupling between the gas and particles is obtained by iterative process between the two programs. Particle diffusion is incorporated into the calculation by assuming that turbulent diffusion acts as an average body force on the particles. A Fick's Law type relationship is used to define a diffusion drift velocity and the particle diffusivity is then related to the fluid turbulence through a turbulent Schmidt number. The results demonstrate known features of electrostatic separators and indicate that for extended duct lengths turbulent diffusion has an increasingly significant role in redistributing particle concentrations.

NOMENCLATURE

D	Duct spacing
d	Particle diameter
E	Electric field strength
F	Particle body force
f	Particle body force per unit mass
J	Mass flux
k	Correction factor for drag coefficient
Re	Reynolds number
Sc_T	Turbulent Schmidt number
t	Time
v	Velocity component
x	Axial positional variable
y	Transverse positional variable
ε	Material dielectric constant
ε_f	Fluid momentum diffusivity
ε_o	Permittivity of free space
ε_p	Particle eddy diffusivity
μ	Viscosity
ρ	Density
τ	Characteristic time
ω	Mass fraction

Subscripts

B	Body force
DIFF	Diffusion
eff	Effective
f	Fluid
o	Initial
p	Particle
T	Total

Superscripts

*	Mass average

INTRODUCTION

The flow of a mixture of gas and particulate matter is found in many industrial processes. Among these processes the flow in electrostatic precipitators has many unique features. The flow field is turbulent, the particle loading is usually low, and the particles are in the micron size range. Additionally, the particles are charged and acted upon by a combination of aerodynamic drag and electrostatic forces which often create steep particle concentration gradients in the direction perpendicular to the main flow. In such steep concentration gradients one would expect to find the effects of particle diffusion to be important. This paper presents an analysis of the gas-particle flow field found in electrostatic precipitators with special emphasis on the modeling of the turbulent diffusion of the particles.

It is convenient in this analysis to treat the gas flow field in the Eulerian frame of reference and to consider the particles in the Lagrangian frame of reference. Great advancement has been made in numerical modeling of two dimensional gas flow from the Eulerian frame of reference (1) and these advances can easily be incorporated into the proposed scheme. Particle motion, on the other hand, is more easily treated by following particle trajectories. This removes the need for averaging over both phases or the requirement for effective viscosities for the two phases. By treating the two phases in different manners, it has been possible to account for mass, momentum and germane heat and energy transfer between the phases (2).

In the past numerical modeling using the trajectory-gas flow scheme has incorporated the effects of mean flow field momentum, mass and energy coupling. However, no accounting was made of the effect of the fluctuating part of the flow on the particles or of the effect of particles on the fluctuating part of the gas. In the development presented, the effect of the fluctuating part of the gas flow field on the particles will be incorporated. Presently we know of no scheme which can be incorporated into a numerical program that accounts for the effect of the particles on the fluctuating part of the gas flow field.

NUMERICAL MODEL

The numerical model was developed by Crowe, Sharma, and Stock (2) and is based on the idea of treating droplets as sources of mass, momentum and energy to the gaseous phase. The following is a brief description of the basic features of the program. A more detailed description of the method of including fluid turbulence effects on the particles in an electric field is presented later.

Basic Concept

First the flow field is subdivided into a series of cells, as shown in Fig. 1. The example shown in the figure is the trajectories of charged particles being removed from the flow field by an applied electrostatic field. Each cell is regarded as a control volume for the gaseous phase and particles traversing a given cell in the flow field may be considered as:

1. A source (sink) of gaseous mass to the fluid cell if the droplet is evaporating or condensing.
2. A momentum augmentation (deficiency) to the fluid cell in the direction of the droplet motion.
3. A sink of thermal energy to the fluid cell.

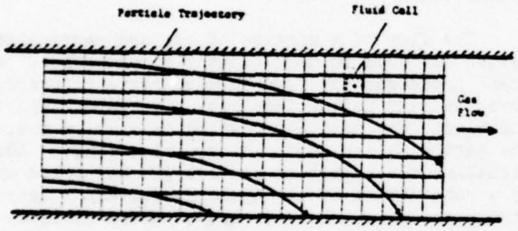

Fig. 1 Fluid cells and particle trajectories

For the specific application to charged particles in an electrostatic field, solid spherical particles in thermal equilibrium are considered in the remaining description. The reader is referred to the original reference (2) for the analysis of the energy coupling modes.

The finite difference equations for mass and momentum conservation are written for each cell incorporating the contribution due to the particulate or condensed phase. The gas flow field is analyzed utilizing an Eulerian approach which is the most straightforward for continuum flows. The entire flow field is then obtained by solving the finite difference equations for each cell with an extension of the TEACH program (1) developed at the Imperial College of Science and Technology in London.

The TEACH program uses a two equation model for turbulence closure. The turbulence field is described by the local intensity of turbulence and the dissipation rate. The finite difference form of the equation is incorporated into the model to yield the kinetic energy of turbulence and the dissipation rate as related to the local mean velocity field according to the scheme proposed by Launder and Spalding (3). From the turbulence intensity and dissipation rate in a cell, the effective viscosity is determined using the Prandtl-Kolmogorov formula.

Since little is known about the quantitative effect of particle size and concentration on the turbulence parameters, no attempt is made to include the effect of the particles on the turbulence field.

Particular trajectories are obtained by integrating the equation of motion for the particles in the gas flow field. This Lagrangian approach is the simplest method of analyzing the particulate phase. Recording the mass and momentum of the particles as they cross cell boundaries provides the source terms for the gas flow equations.

The equation of motion for the particles is given as

$$\frac{dv_p}{dt} = \frac{1}{\tau}(v_f - v_p) + f_B \tag{1}$$

where

$$\tau = \frac{\rho_p d_p^2}{18 \mu_f k} \tag{2}$$

is the particle characteristic relaxation time and f_B represents a body force per unit mass. The factor k is a modification to the drag coefficient which allows calculation of the aerodynamic drag for Reynolds numbers based on particle relative velocity up to 1000. Other forces acting on the particle — namely the pressure gradient, virtual mass and Basset terms — are neglected because they are of the order of the gas/particle density ratio which for most applications of interest is approximately 10^{-3}. The Saffman lift and Magnus forces are also neglected because the particles are not in a high shear region of the flow.

Since the solution scheme for the gas phase assumes constant fluid properties in each fluid cell, integration over time steps smaller than the cell dimensions yields

$$v_p = v_{p_o} e^{-t/\tau} + (v_f + \tau f_B)(1 - e^{-t/\tau}) \tag{3}$$

where v_{p_o} is the particle velocity at the start of the time step. The new particle location is determined by using a linear average of the velocities

$$X = X_o + (v_p + v_{p_o})\Delta t/2 \tag{4}$$

where X_o is the initial particle location for the time step.

It should be noted that Equation (1) was integrated only because the fluid properties were assumed constant within the cell boundaries. For a complete description of a particle moving in a turbulent velocity field, the fluid velocity v_f is a random function of space and time, and Equation (1) is not easily integrated.

Also, the body force term in Equation (1) becomes an effective drift velocity due to that force in Equation (3), τf_B. This fact is later used to include the effect of fluid turbulence and the applied electrostatic force on the particle motion and results in the definition of drift velocities due to turbulent diffusion and the electrical force.

The complete solution for the gas particle flow field is executed as illustrated in Fig. 2. The calculation begins by solving the gas flow field assuming no particles are present. Using this flow field, particle trajectories together with their size history along the trajectory are calculated. The mass and momentum source terms for each cell throughout the flow field are then determined. The gas flow field is solved again incorporating these source terms and the new flow field is used to establish new particle trajectories which constitute the effect of the gas phase on the particles. Calculating new source terms and incorporating them into the gas flow field equations constitutes the effect of the particles on the gas phase. This completes a cycle of mutual interaction or "two way" coupling between the gas and particles. After several iterations the gas flow equations are satisfied to within a predetermined value and a solution which accounts for the mutual interaction is complete.

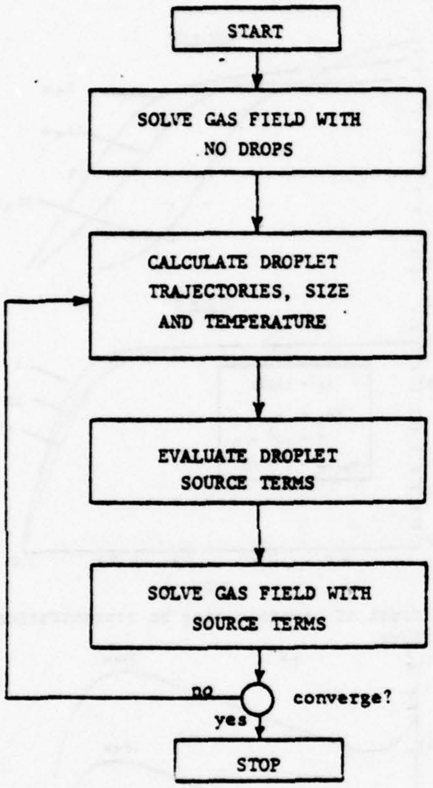

Fig. 2 Iteration scheme

Turbulent Diffusion

To this point, a major limitation of the numerical model is the inability to describe the effect of the fluid turbulence on the particle motion. In many applications, including electrostatic precipitators, steep concentration gradients exist and the role of turbulence in redistributing the concentrations is an important factor.

The task of including turbulent diffusion into the model is complicated because the gas phase numerical scheme deals with mean values of the velocity field rather than fluctuating components. Fluid properties including turbulence are treated as constants within a cell. Since the particles are tracked through the cells in a series of time steps smaller than the cell dimensions, they see only the mean values of the gas flow field and particle motion relative to the instantaneous turbulent fluctuations cannot be obtained.

To interface with the gas phase solution, turbulent diffusion is treated as an averaged effect on the particle motion. Jurewicz and Stock (4) assumed that turbulent diffusion can be treated as a body force acting upon the particles. Using this approach and considering diffusion as a body force in Equation (1) leads to a diffusion drift velocity term in Equation (3).

A first approximation for diffusion drift velocity is obtained from Fick's law of diffusion. The mass flux relative to the mass-averaged velocity is

$$J_p = \rho_p (v_p - v^*) \qquad (5)$$

where ρ_p is the particle mass concentration and v^* is the mass-averaged velocity defined by

$$v^* = \frac{\rho_p}{\rho_T} v_p + \frac{\rho_f}{\rho_T} v_f \qquad (6)$$

where the ρ's are mass concentrations. Assuming that the particle mass fraction ρ_p/ρ_T is relatively small and can be neglected, the ratio ρ_f/ρ_T becomes unity; and the mass-averaged velocity is equivalent to the fluid velocity. Equation (5) for the mass flux due to diffusion becomes

$$J_p = \rho_p (v_p - v_f) \qquad (7)$$

The term in parentheses represents an average diffusion velocity v_{DIFF}. Using Fick's law (5),

$$J = -\rho_T \varepsilon_p \frac{d\omega_p}{dy} \qquad (8)$$

where

$$\omega_p = \frac{\rho_p}{\rho_T} \qquad (9)$$

is the mass fraction of particles, and ε_p is the turbulent particle diffusivity; the diffusion velocity becomes

$$v_{DIFF} = -\frac{\varepsilon_p}{\omega_p} \frac{d\omega_p}{dy} \qquad (10)$$

The particle diffusivity is related to the fluid turbulence through the definition of the turbulent Schmidt number.

$$Sc_T = \frac{\varepsilon_f}{\varepsilon_p} \qquad (11)$$

where

$$\varepsilon_f = \frac{\mu_{eff}}{\rho_f} \qquad (12)$$

Although the turbulent gas-particle interaction defined in this manner is still an unresolved problem in turbulence, empirical values of Sc_T are available (6) and are prescribed in the numerical model.

$$v_{DIFF} = -\frac{\varepsilon_f}{Sc_T\, \omega_p} \frac{d\omega_p}{dy} \qquad (13)$$

and the particle velocity equation becomes

$$v_p = v_{p_o} e^{-t/\tau} + \left[v_f - \frac{\varepsilon_f}{Sc_T\, \omega_p} \frac{d\omega_p}{dy} \right] (1 - e^{-t/\tau}) \qquad (14)$$

Electric Field

An additional body force due to the electrostatic force acting on the charged particles is also included in the program. This requires the definition of another drift or migration velocity relation in Equation (3). The electrostatic force on a nonconducting particle charged by ion impaction on the particle surface and possessing a saturation charge is given by (7)

$$F_e = \frac{3\pi \varepsilon \varepsilon_o}{(\varepsilon + 2)} d_p^2 E_o E \qquad (15)$$

where ε_o is the permittivity of free space, ε is the material dielectric constant, E_o is the charging electric field, and E is the local electric field. The particle electrostatic drift velocity is

$$v_e = - \frac{18 \tau \varepsilon_o \varepsilon E E_o}{(\varepsilon + 2) \rho d_p} \qquad (16)$$

and the final relation for the total velocity of the particle is

$$v_p = v_{p_o} e^{-t/\tau} + \left[v_e - \frac{\varepsilon_{\varepsilon}}{Sc_T \omega_p} \frac{d\omega_p}{dy} - \frac{18\tau \varepsilon \varepsilon_o E_o E}{(\varepsilon + 2) \rho d_p} \right] (1 - 3^{-t/\tau}) \qquad (17)$$

APPLICATION TO ELECTROSTATIC PRECIPITATORS

Because of geometrical and electrical simplifications, only the second stage of a two-stage electrostatic precipitator shown in Fig. 3 is modeled. A high electrical potential is applied across the plates and the electric field lines are always perpendicular to the mean flow direction. Since a corona discharge is not present in the collection section, electric wind effects are neglected. These assumptions permit the restriction of the electrical and diffusion effects to the transverse direction. Also, the particles are assumed to obtain a saturation charge in the charging section and enter the collection region with a uniform concentration profile.

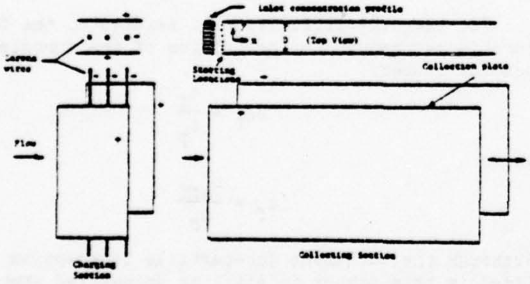

Fig. 3 Two-stage electrostatic precipitator

A numerical experiment was made of several parameters by varying each from a base line case defined by:

particle mass fraction	$= 5 \times 10^{-4}$
electric field strength	$= 10^5$ v/m
turbulent Schmidt number	= 0.4
turbulent intensity	= 0.05
particle diameter	= 15 µm
fluid Reynolds number	$= 1.02 \times 10^4$

The results are presented under separate headings.

Particle Size

Seven particle diameters were used to cover the range of sizes typical to the precipitation process (1 µm to 30 µm). Initially particle concentrations were uniform across the inlet and the changes that occurred at two downstream locations are shown in Fig. 4. Since the area under the relative concentration profiles is a measure of the fractional collection efficiency, the results demonstrate that larger particles are collected more readily. The increased particle migration velocities associated with the improved collection efficiencies are shown in Fig. 5 and 6.

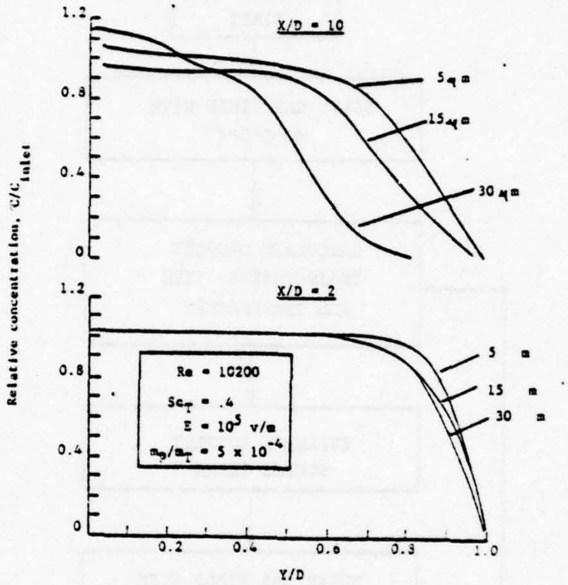

Fig. 4 Effect of particle size on concentration profiles

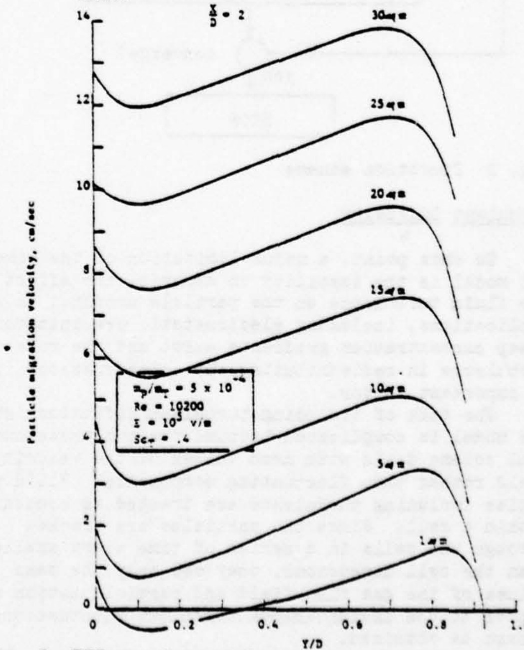

Fig. 5 Effect of particle size on migration velocity at X/D = 2

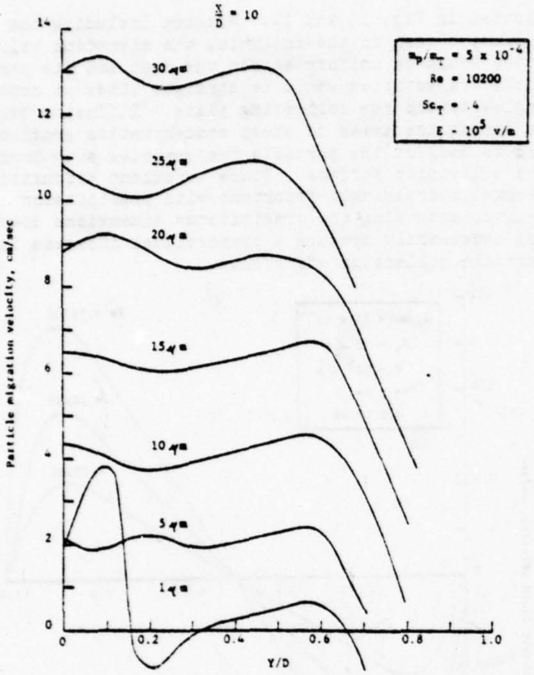

Fig. 6 Effect of particle size on migration velocity at X/D = 10

The shapes of the migration velocity profiles display several noteworthy features:

1. Although the profiles are similar for the various particle diameters, they are not uniform across the duct as is usually assumed in electrostatic precipitator analysis.

2. The migration velocity decreases near the collection surface and gradually increases across the duct until it rapidly drops off near the opposite wall. Later, this behavior is shown to be caused by secondary flow due to a developing velocity profile. It forces the small (1 μm) particles to travel in a direction opposite to the collecting force and may partially explain the difficulty in collecting small particles.

3. The rapid decrease in migration velocity at the wall opposite the collection surface is due to turbulent diffusion and is associated with the steep concentration gradients developed in this area.

The variation for the 1 μm particles at X/D = 10 is most likely due to the large grid size used in the calculations.

Particle Loading

Variation in the particle loading has little effect on the relative concentrations and migration velocity profiles, as seen in Fig. 7 and 8.

Reynolds Number

Results for variations in the duct Reynolds number are shown in Fig. 9, 10, and 11. The concentration profiles indicate an increase in collection efficiency with Reynolds number which is consistent with the form of the migration velocity profiles in Fig. 10. The migration velocities for the higher Reynolds number flow are lower near the collection surface and higher near the opposite wall. This behavior is due to the developing flow in the duct. Momentum is transferred to the center of the duct and is indicated by the transverse velocity components shown in Fig. 11. Since particles are influenced by the fluid velocity, the particle collection velocities are augmented on one side of the duct and diminished on the other.

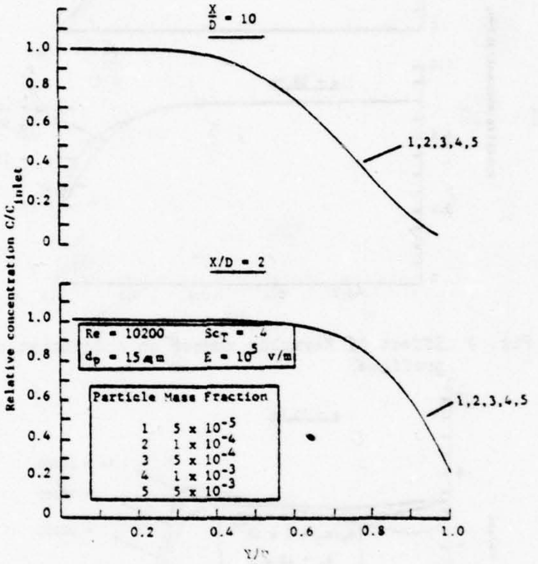

Fig. 7 Effect of particle loading on concentration profiles

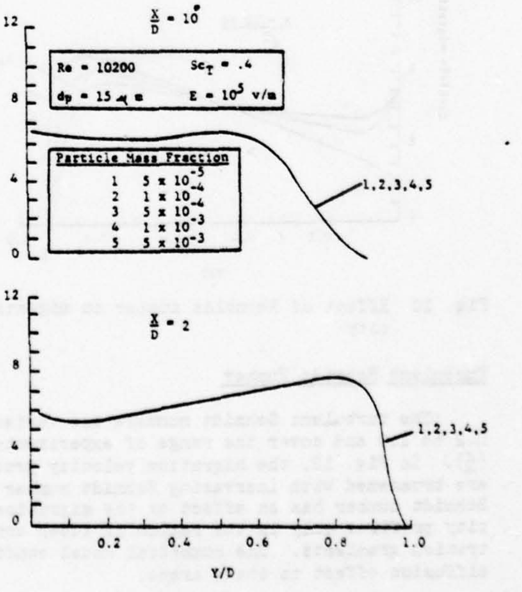

Fig. 8 Effect of particle loading on migration velocity

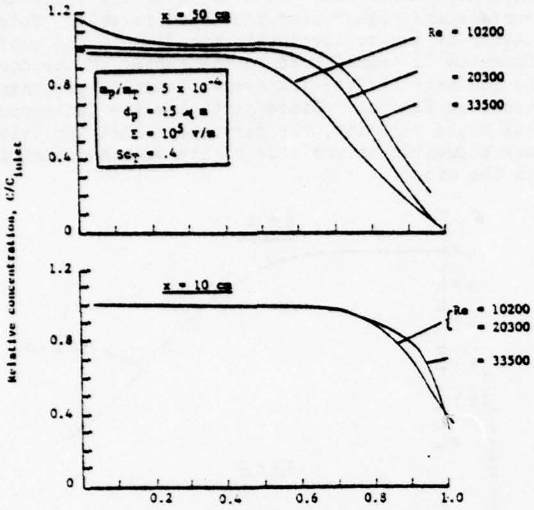

Fig. 9 Effect of Reynolds number on concentration profiles

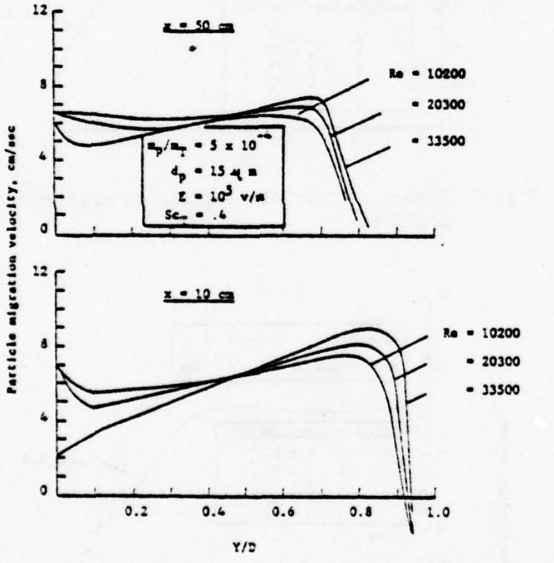

Fig. 10 Effect of Reynolds number on migration velocity

Turbulent Schmidt Number

The turbulent Schmidt numbers are varied from 0.2 to 1.0 and cover the range of experimental data (6). In Fig. 12, the migration velocity profiles are broadened with increasing Schmidt number and the Schmidt number has an effect on the migration velocity profiles only in the region of steep concentration gradients. The numerical model confines the diffusion effect to these areas.

Particle Trajectories

To summarize the capabilities of the numerical model, particle trajectories with the concentrations and migration velocity profiles superimposed are plotted in Fig. 13 and 14. Without including the diffusion term in the analysis, the migration velocities would be uniform across the duct and the particle trajectories would be straight lines at constant angles toward the collecting plate. Diffusion tends to smooth the areas of steep concentration gradients and to deflect the particle trajectories away from the collection surface. Since turbulent diffusion becomes increasingly important with precipitator length, extending the precipitator dimensions does not necessarily produce a proportional increase in particle collection efficiency.

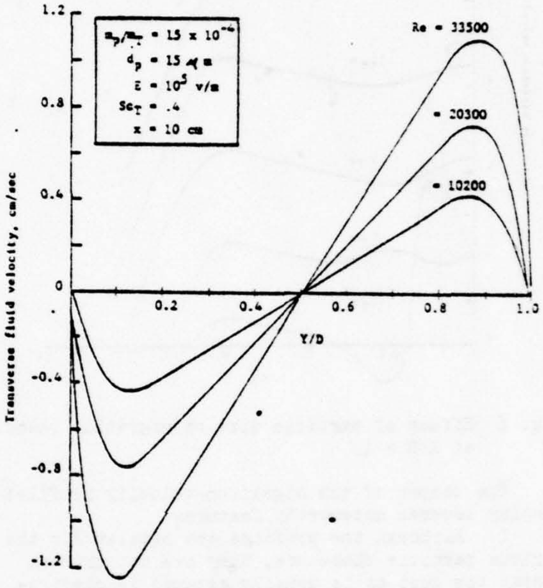

Fig. 11 Effect of Reynolds number on transverse fluid velocity

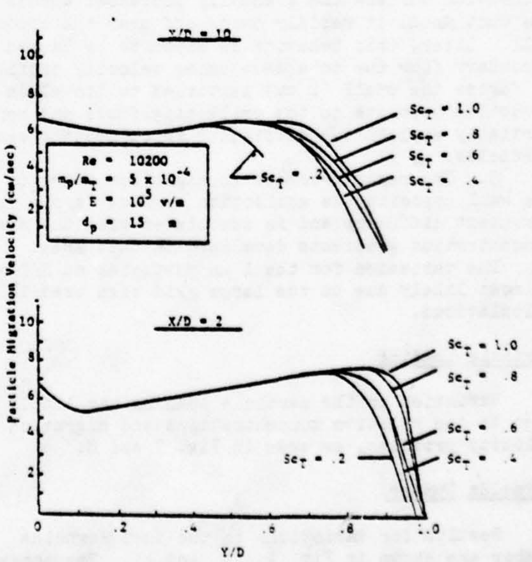

Fig. 12 Effect of Schmidt number on migration velocity

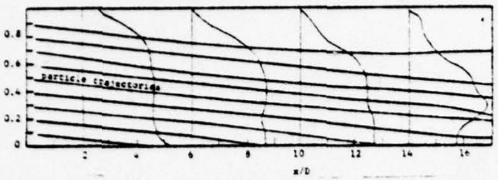

Fig. 13 Concentration profiles and particle trajectories

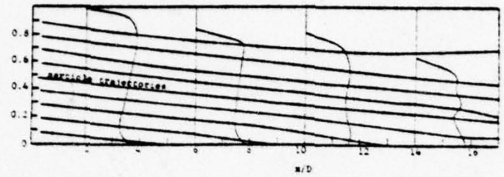

Fig. 14 Migration velocity profiles and particle trajectories

SUMMARY AND CONCLUSIONS

The model has demonstrated the basic features of the flow of charged particles in an electric field. These include several previously known characteristics of electrostatic separators. Larger particles are collected more readily than smaller ones and increasing the separator length does not lead to a corresponding increase in particulate removal. However, the cause of the latter is usually attributed to electrical and mechanical effects rather than turbulent diffusion as is shown here.

Other aspects were also demonstrated:

1. Turbulent diffusion is a significant factor in reducing the concentration gradients and redistributing the particles. In some areas the diffusion velocity was comparable with the transverse velocity created by electrostatic effects.

2. Secondary flow considerations are important when analyzing the motion of small particles. The smaller charge on the particles reduces their collection velocity to the order of the transverse fluid velocity component and makes the collection of small particles more difficult.

3. The migration velocity profiles used in most analyses of electrostatic separators are generally assumed to be constant. Diffusion and secondary flow effects have a substantial influence on the migration velocities which are shown not to have a uniform profile.

Although the numerical model provides a means of investigating many complex multiphase flow phenomena, it is still restricted by several assumptions. The diffusion model is limited to low particle loadings and relies on a prescribed value for the turbulent Schmidt number which is still an unresolved turbulence parameter. The model tends to place excessive importance on the concentration gradient rather than the fluid turbulence for controlling the diffusive effects on the particle. Therefore, a more fundamental relationship between the fluid point and particle diffusivities is required. The authors are presently investigating possible modifications.

ACKNOWLEDGMENT

This work was funded in part by the Electric Power Research Institute, Project RP 363-1.

REFERENCES

1. Gosman, A. D. and Pun, W. M., Lecture notes for a course entitled "Calculation of Recirculating Flows," Imperial College of Science and Technology, London, December 1973.
2. Crowe, C. T., Sharma, M. P. and Stock, D. E., "The Particle-Source-in-Cell (PSI-CELL) Model for Gas-Droplet Flows," to be published in the Journal of Fluids Engineering.
3. Launder, B. E. and Spalding, D. B., Mathematical Models of Turbulence, Academic Press (1972).
4. Jurewicz, J. T. and Stock, D. E., "A Numerical Model for Turbulent Diffusion in Gas-Particle Flows," paper number 76-WA/FE-33 presented at the ASME Winter Annual Meeting, NY, 1976.
5. Bird, R. B., Steward, W. E. and Lightfoot, E. N., Transport Phenomena, John Wiley and Sons, New York, 1960. pp. 495-504.
6. Lilly, G. P., "Effect of Particle Size on Particle Eddy Diffusivity," Industrial Engineering Chemistry Fundamentals, Vol. 12, 1973. pp. 268-275.
7. Oglesby, S., Jr., and Nicholas, B. G., "A Manual of Electrostatic Precipitator Technology, Part I — Fundamentals," Southern Research Institute, Birmingham, Alabama (NTIS No. PB196 360), August 1970, p. 102.

Application of Renormalization Theory of Critical Phenomena to Turbulent Fluctuations

S. Grossmann and E. Schnedler
Fachbereich Physik, Philipps-Universität
Renthof 6
D-3550 Marburg, Fed.Rep. of Germany

ABSTRACT

It is suggested to introduce a complex scalar field $\Psi(\vec{r})$ instead of the real vector velocity field $\vec{v}(\vec{r})$ to describe incompressible and viscous fluids. In terms of this field Ψ the inviscid Navier-Stokes-equation can be described canonically, i.e. as functional derivative of a Hamiltonian. The viscous term is added approxima/tely. By introducing noise and stochastic damping a Langevin equation and its corresponding Fokker-Planck-equation are obtained. The stochastic process approximately obeys detailed balance. This allows to calculate the stationary distribution function for the fluctuations in a homogeneous turbulent fluid.

Renormalization group equations for this distribution function are derived using Feynman graph techniques. The renormalization group transformation is defined by eliminating the long wave lengths step by step. This is opposite to the common procedure for critical phenomena, where the short wave length fluctuations are integrated out. If $d > 2$ a non trivial fixed point of the R.G.T. is found which is stable and attractive. The only existing "critical exponent" is the field dimension. Its anomalous part gives rise to a correction $\mu > 0$ in the exponent of the turbulence spectral function $E(k) = k^{-(5/3 + \mu)}$. The macroscopic part of the correlation function, Kolmogoroff's 5/3, is determined by the scaling behaviour of the noise parameter. μ is calculated by ε-expansion of the R.G.T. ($\varepsilon = d - 2$). One gets $\mu = \varepsilon^2/8$.

INTRODUCTION

The Problem Of A Turbulence Distribution Function

A solution of the Navier-Stokes-equation

$$\partial_t \vec{v} + (\vec{v} \cdot \mathrm{grad})\, \vec{v} = - \mathrm{grad}\, (P/\rho) + \nu \Delta \vec{v} \qquad (1)$$

for a turbulent fluid seems impossible, even when using a computer. This difficulty is commonly overcome by statistical methods. But the use of a statistical description requires the knowledge of a probability distribution functional for a turbulent fluid

$$w(\{v\}) = \exp(-\Phi(\{v\})).$$

A Boltzmann like ansatz, which assumes $\Phi(\{v\})$ to be governed by the energy

$$\Phi(\{v\}) \rightarrow \frac{1}{2} \int v^2(x) dV,$$

is leading to a deficiency. A Hamiltonian

$$H = \frac{1}{2} \int v^2(x) dV$$

does not lead to the Navier-Stokes interaction $(\vec{v} \cdot \mathrm{grad})\vec{v}$ canonically, i.e. as a functional derivative of the Hamiltonian. This interaction in turn would demand a term $\propto v^3$ in the Hamiltonian. But such a term is even worse, for it results in an unstable distribution function with infinite expectation values. Furthermore such a Hamiltonian would not be time reversal invariant and Galilean invariant.

But how might the distribution function look like ? Although $w(v(x))$ is locally Gaussian (Townsend, 1947) [1], experiments prove that the joint probability is certainly not, as e.g.

$$\langle (\vec{v}' - \vec{v})^4 \rangle / \langle (\vec{v}' - \vec{v})^2 \rangle^2 \neq 3,$$

$$\langle (\vec{v}' - \vec{v})^3 \rangle \neq 0, \qquad \text{and}$$

$$\langle (\partial^n v/\partial x^n)^4 \rangle / \langle (\partial^n v/\partial x^n)^2 \rangle^2$$

deviates increasingly more from 3 with increasing n, comp. G.K.Batchelor (1953), R. Betchov, C. Lorenzen (1974) [2].

ORDER PARAMETER FIELD

Introduction Of The Order Parameter Field

As is seems to be impossible to construct a Hamiltonian in terms of the Eulerian $\vec{v}$-field from which the Navier-Stokes-equation can be derived canonically, the idea arises to introduce another basic field in terms of which such a Hamiltonian of an incompressible fluid can be expressed. We use a scalar, complex "order parameter field" $\Psi(\vec{r},t)$. It has two degrees of freedom, $\mathrm{Re}\, \Psi = \alpha$ and $\mathrm{Im}\, \Psi = \gamma$, according to the transverse character of $\vec{v}$, and can be understood as a generalized potential, closely connected with Clebsch' potential [4]. The velocity v as well as the pressure P become observables in terms of Ψ.

E.g., the current of the Ψ-field

$$\vec{j} = \frac{1}{4\rho i} (\Psi^* \,\mathrm{grad}\, \Psi - \mathrm{c.c.}) \qquad (2)$$

determines the physical velocity field, as the velocity is the source free part of $\vec{j}(r,t)$

PRECEDING PAGE BLANK-NOT FILMED

$$\vec{v}(\vec{r},t) = \vec{j}(\vec{r},t) - \mathrm{grad}\ \phi(\vec{j}) \qquad (3)$$

where ϕ has to be determined by the solution of

$$\Delta\phi = \mathrm{div}\ \vec{j}\ . \qquad (4)$$

The observable pressure P can be calculated by

$$P = \frac{\rho}{2} v^2 + D_t\phi + \gamma D_t\alpha - \alpha D_t\gamma - u_o$$

$$D_t = \partial_t + \vec{v}\cdot\mathrm{grad}\ . \qquad (5)$$

Here u_o is the constant internal energy. Eq. (3) shows that $\vec{v}(\vec{r},t)$ is bilinear in terms of Ψ. The representation (2)-(5) arises from the flow of matter which takes place in each fluid flow.

The formal development of the Ψ-field theorie is based upon Pfaff's theorem (1814)[3] and a work by Clebsch (1857)[4], who first gave the generalized potential representation of v. A more physical picture of Ψ is obtained by starting with a variational principle for the Lagrangian density.

$$L = \frac{1}{2}\rho v^2 - \mathrm{const}$$

Incompressibility

$$\mathrm{div}\ \vec{v} = 0$$

is taken care of by a Lagrange parameter field $\phi(\vec{r},t)$.

The velocity fields admissable for variation must be further restricted by the fact that $\vec{v}(\vec{r},t)$ is generated by the flow of matter. Thus if a label $\alpha(\vec{r},t)$ is attached to each part of matter at some arbitrary but fixed time, this label will be a streaming invariant expressing "conservation of identity". This idea has been introduced already by Lin [5]. Thus

$$\partial_t\alpha + (\vec{v}\cdot\mathrm{grad})\ \alpha = 0$$

is a second constraint. It is taken care of by introducing another Lagrange parameter field $\gamma(\vec{r},t)$. So the variational principle with constraints for the perfect incompressible fluid reads

$$\delta\int_{t_1}^{t_2} dt \int_V dV\ [\frac{\rho}{2} v^2 - \phi\,\mathrm{div}\ \vec{v} - \gamma(\partial_t\alpha + \vec{v}\cdot\mathrm{grad}\alpha)] = 0$$

A variational principle which is symmetric in α and γ leads to Eq. (3) and

$$\partial_t\Psi + (\vec{v}\cdot\mathrm{grad})\ \Psi = 0 \qquad (6)$$

with $\Psi = \alpha + i\gamma$; $\vec{v}$ is to be considered as a functional of Ψ and Ψ^*, c.f. Eq. (3) together with Eq. (4). Eq. (6) implies the exact validity of the inviscid Navier-Stokes-equation ($\nu = 0$).

A viscous fluid may be described by adding a term $\nu\Delta\Psi$ to the equation of motion for the Ψ-field so that Eq. (6) now reads

$$\partial_t\Psi + (\vec{v}_b\cdot\mathrm{grad} - \nu\Delta)\Psi + \vec{v}_j(\Psi^*,\Psi)\cdot\mathrm{grad}\ \Psi = 0 \qquad (7)$$

where we divided $\vec{v}$ into two parts, $\vec{v}_b$ which is solely determined by the boundary, and $\vec{v}_j$ which is affected by fluctuations of Ψ via $\vec{j}$. Eq. (7) reproduces the viscous term of the Navier-Stokes-equation if one neglects mode coupling terms of higher order, which are expected to be of minor importance as compared with the kinetic coupling $\vec{v}_j(\Psi,\Psi^*)\cdot\mathrm{grad}\ \Psi$.

Eq. (7) exhibits a Landau-type interaction term $\propto\Psi^3$ and a competition between input $\vec{v}_b\cdot\mathrm{grad}\ \Psi$ and output $\nu\Delta\Psi$. This Ψ-field description was introduced by one of the authors [6].

Stationary Distribution Function For Turbulence Fluctuations

In order to derive a stationary distribution function for the fluctuating fields Ψ the following approach is suggested. At first add a stochastic force $\xi(\vec{r},t) = \xi^\alpha(\vec{r},t) + i\xi^\gamma(\vec{r},t)$ to the equation of motion (7). This noise is supposed to be due to and to represent properly the nonlinear pseudo stochastics of the Navier-Stokes-equations.

It is assumed to be of Gaussian type, i.e.

$$\langle\xi^a\rangle = 0$$

$$\langle\xi^a(\vec{r},t)\ \xi^{a'}(\vec{r}',t')\rangle = 2Q\,\delta_{a,a'}\,\delta(\vec{r}-\vec{r}')\delta(t-t')$$

As we know, the coupling of stochastic degrees of freedom has two consequences: a fluctuating term like $\xi(\vec{r},t)$ and an overall damping, generally assumed to read $\lambda\dot{x}$. Both are necessary if a Hamiltonian system shall approach to a steady state. We therefore add another term, a kinetic damping, due to the mode-mode interaction

$$-\lambda\frac{\delta H}{\delta\Psi}$$

to the equation of motion (7). One finds the following Langevin equation

$$\partial_t\Psi = -(1 - i\lambda)\ \vec{v}\cdot\mathrm{grad}\ \Psi + \nu\Delta\Psi + \xi\ . \qquad (8)$$

Stochastically equivalent to this Langevin equation is a Fokker-Planck equation for the probability functional $P(\{\Psi\},t)$ of the "stochastic" variable Ψ:

$$\partial_t P = \int dV\Big[\frac{\delta}{\delta\alpha}\{\vec{v}\cdot\mathrm{grad}(\alpha + \lambda\gamma) - \nu\Delta\alpha\}\ P + \frac{\delta}{\delta\gamma}\{\vec{v}\cdot\mathrm{grad}(\gamma - \lambda\alpha) - \nu\Delta\gamma\}\ P + Q\ (\frac{\delta^2}{\delta\alpha^2} + \frac{\delta^2}{\delta\gamma^2})\ P\Big] \qquad (9)$$

It is possible to find an (approximate) stationary solution of Eq. (9), $w(\{\Psi(\vec{r})\})\ D(\Psi)$. It is

$$w(\{\Psi\}) \propto \exp\Big[-\frac{1}{Q}\int dV\ \{\frac{\lambda}{2}\rho\ v^2(\Psi) + \frac{\nu}{2}\ |\mathrm{grad}\ \Psi|^2\}\Big]. \qquad (10)$$

$w(\{\Psi\})$ is suggested to play the role of a distribution function for the turbulence stochastics, if Q properly represents the energy input through the boundaries. The distribution function (10) contains a fourth order interaction $\propto\Psi^4$ of current-current type. As the functional variable is Ψ, the distribution is not Gaussian, although the weight $\propto v^2$ appears in the exponent.

Q is chosen to be

$$Q \propto (\rho\ell_b^3)\ v_b^2\ ,$$

ℓ_b = macroscopic length scale

v_b = macroscopic velocity scale on the length scale ℓ_b.

In 3 dimensions v_b can be connected with the energy dissipation

$$\varepsilon_{dis} = v_b^3/\ell_b \; :$$

$$Q = \varepsilon_{dis}^{2/3} \, \ell_b^{3+2/3} \quad . \qquad (11)$$

Both contributions of (10) are gauge invariant of the first kind ($\Psi \to e^{-i\,u\cdot kt}\Psi$). Other invariances are fulfilled as well.

The distribution in momentum space is given by

$$w(\{\Psi_k\}) = \exp(-\phi)$$

with

$$\phi = \int_k \frac{1}{2}\frac{\nu}{Q} k^2 \,|\,\Psi_k\,|^2 + \qquad (12)$$

$$\int_k \int_{k_1} \int_{k_2} \frac{\lambda}{\delta\rho Q} w(k_1,k_2;k)\, \Psi_{k_1+k/2}\, \Psi_{k_2+k/2}\, \dot{\Psi}_{k_1+k/2}\, \dot{\Psi}_{k_2-k/2}$$

$$w(k_1,k_2;k) = \vec{k}_1\cdot(\mathbb{1} - \vec{k}^0\,\vec{k}^0)\cdot\vec{k}_2 = \vec{k}_1\cdot P(k)\cdot\vec{k}_2 .$$

This result was derived by S. Grossmann (1975) [7].

THE RENORMALIZATION GROUP

The Physical Background

Consider a volume V_o which is containing a turbulent fluid. Turbulence is generated by the stirring boundaries of V_o.

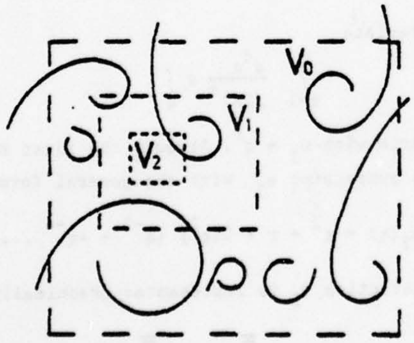

Now consider a smaller volume V_1 which is within V_o. The turbulent motion inside V_1 is similar to that inside V_o, and that in an even smaller volume V_2 is again similar to that in V_1 and so on. Considering a sequence of nested volumes of decreasing size means to follow the energy transport from the largest eddies to the smallest ones (Richardson, Kolmogoroff, ... [8]. As there is no typical length scale in the inertial subrange, i.e. as the turbulent motion in V_i is similar to that in V_{i+1}, there should exist a similarity relation for the static distribution functions for the turbulent motions in the different volumes V_i:

$$w \to w_{(1)} \to w_{(2)} \to \text{etc.}$$

A main result reported in the following will be the transformation law from $w_{(i)}$ to $w_{(i+1)}$. This similarity transformation contains the whole information about the scaling behaviour of the turbulent system.

Wavenumbers k with $k^{-1} \sim V_o$ are determined essentially by the boundaries. For larger k however the turbulence field is approximately isotropic and homogeneous and has lost the memory about the details of the boundaries. Be ℓ_b the extension of the isotropic turbulence, then $\ell_b \lesssim V_o^{1/3}$ and the velocity field $v(r) - \langle v(r)\rangle_{\ell_b}$ is the stochastic field which is supposed to be properly represented by the distribution function Eq. (10) or (12). The statistical turbulence field therefore has a lower momentum cut off, i.e. ϕ, Eq. (12), contains no Fourier components k with $k \lesssim 1/\ell_b \equiv \Lambda_o$.

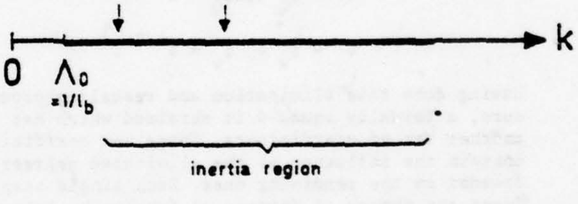

THE RENORMALIZATION GROUP TRANSFORMATION

The renormalization group transformation (R.G.T.) is the transformation from w to $w_{(1)}$, from $w_{(1)}$ to $w_{(2)}$ and so on,

$$w = \exp(-\phi(\Psi)) \xrightarrow[\text{R.G.T.}]{} w_{(1)} = \exp(-\phi_1(\Psi)) \xrightarrow[\text{R.G.T.}]{}$$

$$w_{(2)} = \exp(-\phi_2(\Psi)) \to \text{etc.}$$

i.e. the R.G.T. is defined by integrating out the wave numbers k with $k \in [\Lambda_o, \Lambda_1]$, etc.

This is equivalent to smoothing all degrees of freedom with Fourier components between Λ_o and Λ_1.

The renormalization group transformation defined by eliminating the long wave lengths step by step is opposite to the common procedure for critical phenomena, where the short wave length fluctuations are integrated out. The common R.G. procedure for critical phenomena is reported e.g. by Wilson and Kogut (1974) [9].

Our new interaction is then defined by

$$\exp(-\phi_1(\Psi)) = \int_{\substack{\Psi_k,\\ k\in[\Lambda_o,\Lambda_1]}} \exp(-\phi(\Psi_k)) \quad .$$

This is a quantitative version of the qualitative procedure of von Weizsäcker (1945), Oboukhoff and *Kolmogoroff* (1962), Gurvich and Yaglom (1967), Novikoff (1972), ... [10].

Having evaluated the partial trace, the result represents a system with a higher momentum cutoff $\Lambda_1 = s\,\Lambda_o$, with another velocity scale v_b' as well as another noise energy Q' and viscosity ν'. In order to compare this system with the initial one we rescale the momenta

$$k' = k/s, \text{ as } \Lambda_1 \leq k < \infty \rightarrow \Lambda_o \leq k' < \infty .$$

This means something like having a glance through a magnifying glass, so that V_1 looks like V_o.

To make the similarity complete not only the number of degrees of freedom have to be adjusted by rescaling k but also the field (velocity) scale must be adjusted. The rescaled fields are introduced by

$$\Psi_k' = \Psi_k/\zeta .$$

According to the changed boundaries of V_1 we have another noise energy Q'. Because of the similarity we demand that the Reynolds numbers of the flows in V_o and V_1 be equal. This results in adjusting also $\nu \rightarrow \nu'$

$$\begin{aligned} Q' &= z_Q\, Q, \; z_Q = s^{d+2/3} \\ \nu' &= z_\nu\, \nu, \; z_\nu = s^{4/3} . \end{aligned} \tag{13}$$

Having done this elimination and rescaling procedure, a formally equal Φ is obtained which has another set of coefficients. These new coefficients contain the influence of the eliminated degrees of freedom on the remaining ones. Each single step reduces the number of degrees of freedom by only a small amount. This justifies to calculate the renormalization group transformation perturbatively. Repeated application of the R.G.T. sums up the effects of all steps, thus finally many degrees of freedom are regarded.

Results Of The Renormalization Group Transformation

It turns out that the Navier-Stokes interaction of Eq. (12) with its transverse projector is reproduced by each renormalization step. Therefore it is possible to calculate the R.G.T. once and then iterate these equations.

The sequence of distributions turns out to converge, i.e. the coefficients of Φ do not change any more after some R.G.T.'s. The resulting coefficients are called a fixed point. The fixed point distribution function is interpreted as description of the inertial regime and expresses its universality.

The properties of the correlation function, particularly of the spectrum E(k) are evaluated by using the fixed point value of the field scaling parameter ζ^*. One finds a deviation of Kolmogoroff's 5/3 law if the formally extrapolated dimensionality is d > 2. This is due to the effect of the nonlinear interactions of the field fluctuations. It has not yet been possible to deduce the 5/3 exponent but only to show a method to determine deviations from 5/3.

Each renormalization step generates terms $\propto \mathbb{P}(0)$, which is a formally undefined expression. These terms arise due to the assumed translational invariance of the fully developed turbulence which is correct approximately only owing to the effects of the boundary. The transverse projector $\mathbb{P}(q)$, Eq. (12), was derived in Ref. [6] neglecting the boundaries when solving Eq. (4). The exact Green's function of the boundary value problem which solves Eq. (4) would lead to a non singular $\mathbb{P}$ at q = 0.

The fluctuation correction to Kolmogoroff's law has been calculated using an ε-expansion. It is ε = d − 2. We found

$$E(k) \propto k^{-(5/3+\mu)} \quad \text{with } \mu \approx \varepsilon^2/8 .$$

For d = 3 (ε = 1) this seems to be in good accordance with experimental results as given e.g. by van Atta and Park (1972) [11].

The Renormalization Group Equations

It is convenient to introduce dimensionless momenta

$$\left.\begin{aligned} &q = k/\Lambda_o, \text{ so } 1 \leq q \leq \infty \\ &\text{dimensionless fields} \\ &a_q = \sqrt{\nu/2Q}\; \Lambda_o^{(d+2)/2}\, \Psi_q, \\ &\text{and a dimensionless interaction constant} \\ &u = \lambda\, \Lambda_o^{d-2}\; Q/(2\rho\, \nu^2) \; . \end{aligned}\right\} \tag{14}$$

Then the distribution function Φ can be written as

$$\Phi(a_q) = \int_q u_2(q)\, |a_q|^2 + $$

$$+ \int_{q_1}\int_{q_2}\int_{\bar{q}_1}\int_{\bar{q}_2} u_4(q_1,q_2;\bar{q}_1,\bar{q}_2)\,\delta(\vec{q}_1+\vec{q}_2-\vec{\bar{q}}_1-\vec{\bar{q}}_2)\, a^*_{\bar{q}_1} a^*_{\bar{q}_2} a_{q_1} a_{q_2}$$

$$= \Phi_F + \Phi_I . \tag{15}$$

We abbreviate

$$\int_{q=1}^{\infty} \frac{d^d q}{(2\pi)^d} \equiv \int_q .$$

One starts with $u_2 = q^2$. Already the first R.G.T. gives a propagator u_2' with the general form

$$u_2(q) = q^2 + r + O(\varepsilon^2)\,(q^{-2} + \alpha q^{-4} \ldots) .$$

The interaction Φ_I is represented graphically

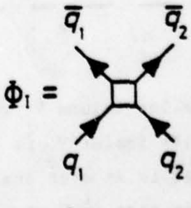

incoming arrows belong to a, momentum q_i, outgoing belong to a^*, momentum $\bar{q}_i$.

The interaction matrixelement is due to the particular form of the Navier-Stokes-equation

$$u_4\,(q_1,q_2;\bar{q}_1,\bar{q}_2) =$$

$$= \frac{1}{2}\,u\Big[\frac{1}{2}\,(\vec{q}_1 + \vec{\bar{q}}_1)\cdot P(\vec{q}_1 - \vec{\bar{q}}_1)\cdot P(\vec{q}_2 - \vec{\bar{q}}_2)\cdot \frac{1}{2}\,(\vec{q}_2 + \vec{\bar{q}}_2)$$

$$+ \frac{1}{2}\,(\vec{\bar{q}}_1 + \vec{q}_2)\cdot P(\vec{\bar{q}}_1 - \vec{q}_2)\cdot P(\vec{\bar{q}}_2 - \vec{q}_1)\cdot \frac{1}{2}\,(\vec{\bar{q}}_2 + \vec{q}_1)\Big] \qquad (16)$$

As the degrees of freedom with Fourier components between 1 and s shall be integrated, the fields a_q are splitted into one part $a_o(q)$, which contains the Fourier components between 1 and s, and another $a_1(q)$, which contains the Fourier components between s and ∞.

$\phi'(a')$ is then defined by

$$\exp\{-\phi'\,(a'_{q'})\} = \text{const}\,\exp\{-\phi_F(a_1)\}\times \qquad (17)$$

$$\times < \exp\{-\phi_I\,(a_o + a_1)\}>_{a_o,\ \text{Gauss}}\ .$$

Gaussian expectation values are calculated by the generalized Wick's theorem

$$\Big\langle a_{q_1}\,a_{q_2}\,\dots\,a_{q_n}\,a^*_{k_1}\,a^*_{k_2}\,\dots\,a^*_{k_m}\Big\rangle_{\text{Gauss}}$$

$$= \int_{\bar{a}_q} a_{q_1}\dots a_{q_n}\,a^*_{k_1}\dots a^*_{k_m}\,\exp(-\phi_F(a)) \Big/ \int_{\bar{a}_q} \exp(-\phi_F)$$

$$= \delta_{n,m}\,\overline{\vec{q}_1\,\vec{k}_1}\;\overline{\vec{q}_2\,\vec{k}_2}\dots\overline{\vec{q}_n\,\vec{k}_n} + \text{all}$$

possible different combinations, with the contraction defined by

$$\overline{\vec{q}_i\,\vec{k}_j} = \frac{\delta(\vec{q}_i - \vec{k}_j)}{u_2(q_i)}$$

$$\delta(\vec{k}_i - \vec{k}_j) = (2\pi)^d\ \delta^d(\vec{k}_i - \vec{k}_j)\ . \qquad (18)$$

From Eq. (17) $u_2\ u_4$, ... are calculated. A graphical representation of the two lowest perturbative orders in u to the propagator u'_2 is (each closed line represents a contraction, (18))

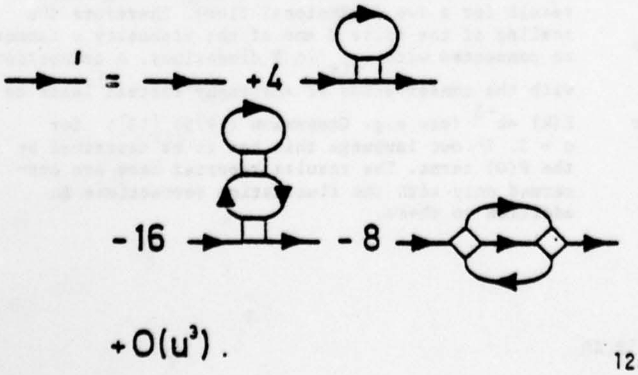

$+O(u^3)$.

The equivalent analytical formula reads

$$u'_2(q) = s^d\,\zeta^2\Big[\,u_2(sq) + 4\int_{p=1}^{s}\frac{u_4(s\vec{q},\vec{p};s\vec{q},\vec{p})}{u_2(p)}$$

$$-\,16\int\int_{p_1,p_2=1}^{s}\frac{u_4(s\vec{q},\vec{p}_1;\vec{p}_1,s\vec{q})\ u_4(\vec{p}_1,\vec{p}_2;\vec{p}_2,\vec{p}_1)}{u_2(p_1)\ u_2(p_1)\ u_2(p_2)} \qquad (19)$$

$$-8\int\int_{p_1,p_2=1}^{s}\frac{u_4(s\vec{q},\vec{p}_1;\vec{p}_2,s\vec{q}+\vec{p}_1-\vec{p}_2)\ u_4(s\vec{q}+\vec{p}_1-\vec{p}_2,\vec{p}_2;\vec{p}_1,s\vec{q})}{u_2(p_1)\ u_2(p_2)\ u_2(s\vec{q}+\vec{p}_1-\vec{p}_2)}\Big]$$

$+\ O\ (u^3)$.

The contributions to the interaction matrix element are calculated from

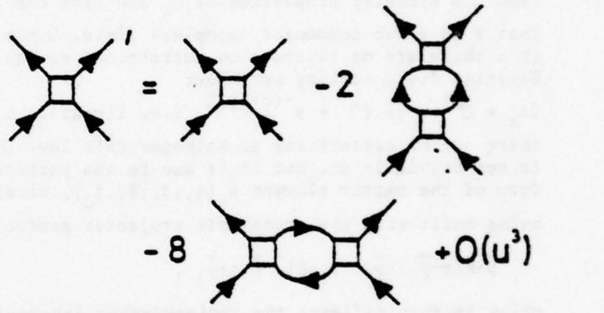

The equation for u'_4 reads:

$$u'_4(\vec{q}_1,\vec{q}_2;\vec{\bar{q}}_1,\vec{\bar{q}}_2) = s^{3d}\,\zeta^4\Big[\,u_4(s\vec{q}_1,s\vec{q}_2;s\vec{\bar{q}}_1,s\vec{\bar{q}}_2)$$

$$-8\int_{p=1}^{s}\frac{u_4(s\vec{q}_1,\vec{p};s\vec{\bar{q}}_1,s\vec{q}_1+\vec{p}-s\vec{\bar{q}}_1)\ u_4(\vec{p}+s\vec{\bar{q}}_2-s\vec{q}_2,s\vec{q}_2;\vec{p},s\vec{\bar{q}}_2)}{u_2(\vec{p})\ u_2(s\vec{q}_1+\vec{p}-s\vec{\bar{q}}_1)}$$

$$-2\int_{p=1}^{s}\frac{u_4(s\vec{q}_1,s\vec{q}_2;\vec{p},s\vec{q}_1+s\vec{q}_2-\vec{p})\ u_4(s\vec{\bar{q}}_1+s\vec{\bar{q}}_2-\vec{p},\vec{p};s\vec{\bar{q}}_1,s\vec{\bar{q}}_2)}{u_2(\vec{p})\ u_2(s\vec{q}_1+s\vec{q}_2-\vec{p})}\Big]$$

$$+\ O(u^3)\ . \qquad (20)$$

Eqs. (19) and (20) are the renormalization equations for the propagator u_2 and the interaction u_4. They are calculated perturbatively under the assumption that u is a small expansion parameter. u proves to be a small parameter in the vicinity of d = 2 ($u \propto \varepsilon = d - 2$) near the fixed point. Therefore the u-expansion is a perturbation expansion around the dimension d = 2.

Simplified, Two Parameter Renormalization Group Equations

In order to study some characteristic properties of the R.G. equations (19,20) a simplified though approximate two parameter version can be used. Only r, u are retained as parameters and a R.G.T. consists of transforming, r, u to r', u'. The two parameter

R.G. equation are

$$
\begin{aligned}
r' &= s^{-2}\left[r + 2u\,\frac{d-1}{1+r}\,C \right] \\
u' &= s^{d-2}\left[u - 2C\,\frac{u^2}{(1+r)^2} \right]
\end{aligned}
\qquad (21)
$$

with

$$C = \frac{1}{d}\int_1^s p^2 \quad .$$

To derive Eqs. (21) we used the projector properties of u_4, and its homogeneity: $u_4(sq_a) = s^2\, u_4(q_a)$. Furthermore we made a q^{-2} expansion, i.e. we omitted terms of order $p^2/(sq)^2$, where $p \in [1,s]$ and $sq \in [s,\infty)$.

The multiplicities of the graphs are derivable from the *symmetry properties of* u_4 *and* from the fact that Ψ is a two component (complex) field. Linear in u there are no fluctuation corrections to the Gaussian field scaling behaviour $(a'_k = \xi^{*-1}\, a_k)$: $\xi^* = s^{-(d+2)/2}$, i.e. linear in u there are no corrections to Kolmogoroff's law. This is not trivially so, but it is due to the particular form of the matrix element $u_4(q_1, q_2; \bar{q}_1, \bar{q}_2)$, namely being built with the transverse projector product

$$\vec{p}\cdot\mathbb{P}(\vec{p}-\vec{p}_1)\cdot\vec{p} \equiv \vec{p}_1\cdot\mathbb{P}(\vec{p}-\vec{p}_1)\cdot\vec{p}_1 \ ,$$

which in turn reflects the Navier-Stokes interaction. So the first order results in a mass renormalization $(\propto r|a_q|^2)$ only. Only second order terms contribute.

Eqs. (21) exhibit two fixed points. A trivial one is the Gaussian fixed point, $u^* = r^* = 0$.

In the neighbourhood of the fixed points the R.G.Eq.'s (21) can be linearized. The stability of the fixed point is determined by the eigenvalues of the linearized matrix which transforms, r, u to r', u'. One finds

$$\lambda_1 = s^{-2} < 1 \quad \text{and} \quad \lambda_2 = s^{\varepsilon} \ ,$$

which means that the Gaussian fixed point is attractive for $\varepsilon < 0$, i.e. $d < 2$, when iterating the linearized R.G.T.

The second fixed point is non-Gaussian

$$r^* = \varepsilon\,\frac{\ln s}{s^2-1} \approx \varepsilon/2, \text{ linear in } \varepsilon, s \text{ near to } 1,$$

$$u^* = \varepsilon\,\frac{\ln s}{2\,C} \approx 2\,\pi\,\varepsilon, \text{ linear in } \varepsilon.$$

The eigenvalues of the linear R.G.T. near this fixed point are $\lambda_1 = s^{-(2+\varepsilon)}$, $\lambda_2 = s^{-\varepsilon}$.

Thus this non-Gaussian fixed point is attractive for $\varepsilon = d - 2 > 0$. In particular there are non-Gaussian fluctuation contributions in 3-dimensional flows.

REDUCED AND PHYSICAL FIELDS

We have introduced reduced fields and momenta by Eqs. (14). As we know, c.f. Eqs. (13), Q and ν have to be scaled too. Consequently Ψ_k has another different scaling behaviour than a_k. As mentioned before boundary terms determine the $\mathbb{P}(0)$ terms. We know that the interaction differs for very small q from the transverse projector. This region is eliminated by each R.G. step in favour of an effective Q and ν. Now we recognize the "analytical" reason for renormalization of Q and ν when eliminating the low wave number degrees of freedom: the $\mathbb{P}(0)$ terms are determined by the boundaries and are supposed to be responsible for the scaling behaviour of Q and ν according to the changed boundaries. But as long as we cannot calculate these terms we connect the scaling behaviour of Q and ν with the conservation of energy dissipation Eq. (11) and find:

$$Q' = c\rho\varepsilon_{dis}^{2/3}\ \Lambda'^{-d-2/3} = s^{d+2/3} Q$$

as $\Lambda' = s^{-1}\,\Lambda$.

The scaling dimension of ν is determined by

$$Re' = Re = v_b \ell_b/\nu$$

and turns out to be

$$\nu' = s^{4/3}\ \nu.$$

Thus we find

$$\Psi'_{k'} = \frac{s^{(d+2/3)/2}}{s^{2/3}}\ \zeta^{*-1}\ \Psi_k \ .$$

For ζ^* we get up to the second order ε-expansion

$$\zeta^* \approx s^{-(d+2+\varepsilon^2/16)/2} \ .$$

From this it is easy to calculate the scaling behaviour of

$$E(k) = \frac{1}{2}\ \frac{\Omega_d}{(2\pi)^d}\ \frac{k^{d-1}}{\delta(\vec{k}-\vec{\bar{k}})}\ \langle v_k^*\ v_{\bar{k}}\rangle \ .$$

The field scaling of the non-Gaussian fixed point yields

$$E(k) = k^{-(5/3 + \varepsilon^2/8)}\ E'\ (\text{const}).$$

A detailed description of the R.G. procedure for turbulence fluctuations will be published [12].

It is known that two dimensional flow is different from three dimensional one. Especially conservation of energy dissipation contradicts the conservation of vorticity. (which is a rigorous result for a two dimensional flow). Therefore the scaling of the noise Q and of the viscosity ν cannot be connected with ε_{dis} in 2 dimensions. A connection with the conservation of enstrophy instead leads to $E(k) \propto k^{-3}$ (see e.g. Grossmann (1975) [13]) for $d = 2$. In our language this has to be described by the $\mathbb{P}(0)$ terms. The results reported here are concerned only with the fluctuation corrections in addition to these.

REFERENCES

[1] Townsend, A.A., Proc.Camb.Phil.Soc. 43, 560 (1947)

[2] Batchelor, G.K., "Theorie of Homogeneous Turbulence" ch. 8, The University Press Cambridge(1953)
Betchov, R., Lorenzen, C., Phys.Fluids 17, 1503 (1974)

[3] see e.g. Seliger, R.L., Whitham, G.B., Proc.Roy.Soc. London A 305, 1 (1968)

[4] Clebsch, A., J. reine angew. Mathem. 54, 293, (1857) and 56,1 (1859)

[5] Lin, C.C., see e.g. "Proc. of the Int. School of Physics, Enrico Fermi", Course 21, on Liquid Helium, Varenna, Ed.: G. Careri, Acad.Press (1963)

[6] Grossmann, S., Phys.Rev. A11, 2165 (1975)

[7] Grossmann, S., Z.Phys. B21, 403 (1975)

[8] Richardson, L.F., Proc.Roy.Soc. A 110, 709 (1926)
Kolmogoroff, A.N., C.R. (Doclady) Acad.Sci. USSR 30, 301 (1941)

[9] Wilson, K.G., Kogut, J., Phys.Rep. 12c, 75 (1974)

[10] von Weizsäcker, C.F., Z.Phys. 124, 614 (1948)
Oboukhoff,, A.M., J.Fluid Mech. 13, 77 (1962)
Kolmogoroff, A.N. J.Fluid Mech. 13, 82 (1962)
Gurvich, A.S., Yaglom, A.M., Phys. Fluids 10, Suppl. S 59 (1967)
see also Novikoff, E.A., Appl.Math.Mech. 35, 231 (1972)

[11] van Atta, C.W., Park, J., in "Statistical Models and Turbulence", Eds. M. Rosenblatt and C. van Atta, Lecture Notes in Physics, Vol.12, Springer Berlin etc. (1972) p. 402.

[12] Grossmann, S., Schnedler, E., to appear in Z.Phys. B (1977)

[13] Grossmann, S., Z.Phys. B 22, 401 (1975)

SESSION 13

RECIRCULATING FLOWS 1

Chairman: K. Owen
NASA Ames Research Center
Moffet Field, California
U.S.A.

13

MEASUREMENTS OF MEAN VELOCITY AND REYNOLDS STRESSES IN SOME REGIONS OF RECIRCULATING FLOW

W.D. Moss, S. Baker and L.J.S. Bradbury

(University of Surrey, Guildford, England)

ABSTRACT

The paper describes measurements of mean velocities and Reynolds stresses in recirculating flows associated with the flow past a number of simple bluff bodies. The principal instrument used was the pulsed-wire anemometer.

The main content of the paper concerns the flow behind a backward-facing step. The mean flow pattern is represented by streamlines; distributions of Reynolds stresses are given for the recirculating zone and for the mixing layer which is compared and contrasted with the plane mixing layer. Measurements for mean velocity and turbulence energy are compared with the predictions of a computer program based upon the turbulent viscosity concept.

The data represent interim results for a continuing program of work on flow past basic shapes; as an example of this work, results for a *forward-facing* step are briefly presented.

NOMENCLATURE

B	width of plate
c	constant
h	height of step
k	turbulence energy $(= \frac{1}{2}(\overline{u^2}+\overline{v^2}+\overline{w^2}))$
n	frequency of vortex shedding
p	static pressure
p_o	reference static pressure
U	mean velocity in x-direction
U_o	main stream mean velocity in x-direction
U_E	mean velocity in x-direction outside mixing layer
u	velocity fluctuation in x-direction
v	velocity fluctuation in y-direction
w	velocity fluctuation in z-direction
x	streamwise co-ordinate
y	transverse co-ordinate
$y_{m/2}$	transverse co-ordinate at which $U = \frac{1}{2}U_E$
z	spanwise co-ordinate
δ	boundary layer thickness
δ_1	displacement thickness
ε	rate of dissipation of turbulence energy per unit volume
η	$(y - y_{m/2}) / x$
ρ	density
ψ	stream function

INTRODUCTION

Regions of high turbulence and particularly those involving recirculating flows, where the velocities may undergo constant reversal of sign, have received less attention than those where these features are lacking. In many practical applications, however, it is these areas which are of interest. In particular, in civil engineering, when wind effects on buildings are considered, separation is invariably involved and it is generally the near region with its recirculating flows that is of greater interest than the far wake. There is, then, a compelling practical need for a fuller understanding of these regions, but difficulties in velocity measurement in these areas have inhibited the detailed study which is needed as a basis for the development of analysis.

Furthermore, mathematical methods for the prediction of turbulent shear flows have in the past concentrated upon thin shear layers of the boundary layer type. With the extension of such methods to flows governed by elliptic equations, the need for the corresponding experimental data is now more urgent.

The relatively recent development of the pulsed-wire anemometer has removed some of the difficulties associated with the desired measurements; it is well suited to highly turbulent and reversed flows and yields all three components of velocity fluctuations. The principal object of this paper, then, is to describe the use of this instrument in the investigation of the detailed flow patterns in the neighbourhood of a number of basic two-dimensional bodies set perpendicular to the main flow, all involving separation and, consequently, recirculating flows. For the reasons indicated above, the studies are directed mainly to the near region. The measurements were supplemented by others using X-array hot-wire anemometers for the measurement of shear stresses so that the quantities measured thus include mean velocities and Reynolds stresses in addition to surface pressure measurements.

A normal flat plate with free edges was among the first body shapes investigated with the pulsed-wire anemometer and served to afford comparative studies of the use of the hot-wire in recirculating flows. The measurements, largely already reported elsewhere, are briefly summarised here as a preliminary. The studies have now been extended to bodies typical of buildings in that they are set on a base plane parallel to the main flow, in contrast to the two-dimensional flat plate with its two free edges. One of the simplest of such shapes is a square step, perpendicular to the main flow and spanning the full width of a wind tunnel. For the present, attention is concentrated mainly upon a backward-facing step, where the studies of previous workers form a context for the present work. The results for a forward-facing step are indicated more briefly.

The underlying objective of the work has been not merely to examine the flow in particular simple cases, but rather to obtain a better fundamental understanding of bluff body flows generally, extending the work to bodies of less simple shape. The special case will have wider significance if the data presented serve to establish the basis for the treatment of a whole class of flows, as may be done if they are used to examine the applicability of a mathematical model of turbulence. Whilst, then, the authors' prime object in the present paper is to make available data for this purpose, the opportunity has been taken to compare some of the measurements for the backward-facing step with the predictions of a computer program based upon one such mathematical model.

EXPERIMENTS

The normal flat plate investigated was made of aluminium, width B = 50mm, having the sharp-edged cross-section shown (Fig.1) and being fitted with end plates to minimise the effect of the wall boundary layers on the two-dimensionality of the flow. It was set perpendicularly across the longer dimension of a wind tunnel, cross-section 762mm x 610mm, in a uniform air stream having a velocity U_0 of the order of 10m/s. Traverses were made using hot-wire and pulsed-wire anemometers, as appropriate, to measure mean velocities and turbulence intensities in and around the recirculating zone behind the plate.

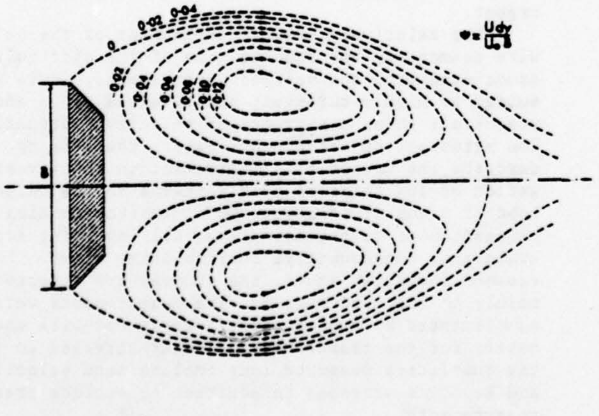

Fig.1 Flat Plate - Mean Streamlines

The model for the steps was constructed in acrylic sheet suitably stiffened and provided with pressure tappings (Fig.2). Its total length was 2m with a square step of height, h, 76mm, constructed at the half-distance. This model was set across the longer dimension of a larger wind tunnel, cross-section 1372mm x 1067mm. Preliminary tests showed that the flow at the centre of the model was effectively two-dimensional and, further, that the pressure distribution upstream of the step, to within a short distance of the edge, was very closely the same as for the case when the step was eliminated by continuing the plane at the same level throughout. A tapping 30mm from the edge could thus be used to provide a valid reference pressure p_0. The reference velocity U_0 was measured by a pitot-static tube set at a similar longitudinal station but in the uniform stream above the boundary layer. The velocity in the air stream approaching the model was again of the order of 10m/s: a little upstream of the step the turbulent boundary layer displacement thickness, δ_1, was approximately 0.1 times the step height.

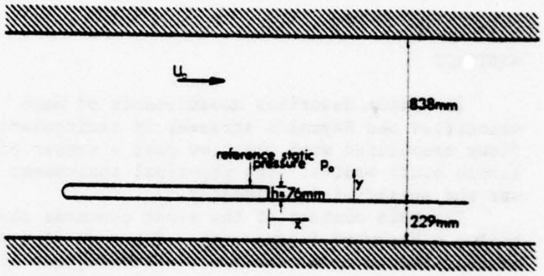

Fig.2 Backward-facing Step - Wind Tunnel Model

It was possible to use the same model for the experiments on the forward-facing step by simply reversing its direction in the tunnel.

Mean velocities and normal Reynolds stresses were measured with the pulsed-wire anemometer, the traverses being repeated with the probe set for each of the three principal directions to yield in turn longitudinal, transverse and spanwise components. Turbulent shear stresses were measured with an X-array hot-wire probe while the pressures at the tappings along the model surface were measured with an electrical micro-manometer.

FLAT PLATE

The detailed results for the plate have been reported more fully elsewhere (1, 2); the present account, therefore, is intended primarily to indicate their place in the development of the pulsed-wire anemometer for the investigation of such regions and to give emphasis to a comparison with the use of the hot-wire in similar situations.

From the traverses of mean velocity obtained with the pulsed-wire it was possible to evaluate the stream function along each traverse position and hence to draw mean stream lines (Fig.1). The greatest mean velocity in the reverse direction is about $0.5U_0$ while the total reverse flow rate per unit width is approximately $0.25U_0B$. Vortex shedding, although present, is in no way shown in this pattern which represents a time average over a period equal to many vortex-shedding cycles. A hot-wire outside the near-wake served, when its signals were processed by a correlator, to confirm the existence of vortex-shedding and to measure its frequency, indicating a Strouhal number, nB/U_0 of 0.14. Work is now in hand on conditional sampling whereby, using such a hot-wire as a synchronising signal, velocity samples may be taken by the pulsed-wire at the same phase in a series of vortex-shedding cycles. The sets of streamlines so obtained could thus show the mean form of the vortex at successive stages of its formation and movement downstream.

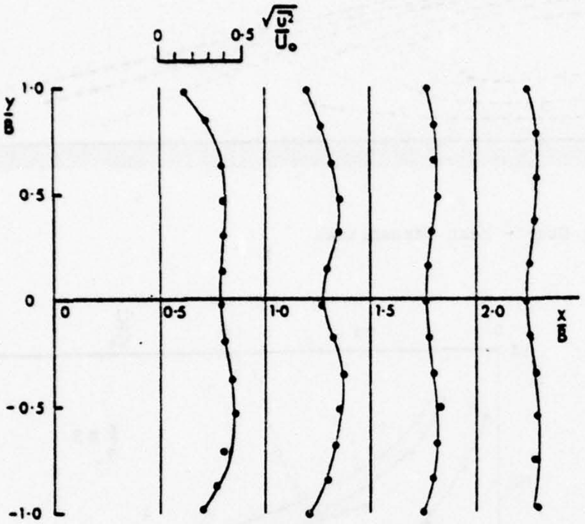

Fig.3 Flat Plate - Streamwise Turbulence Intensities

The high turbulence in the reverse-flow region is shown by the series of traverses of $\overline{u^2}$ (Fig.3), peak values approaching $0.5U_0$ with maximum centre-line values of $0.4U_0$. A point of particular interest was that while the spanwise w-component of turbulence tended to be very similar to this u-component, the magnitude of the transverse v-component was notably higher, often being of the order of twice as great. Such anisotropy is almost certainly associated with the vortex-shedding. It is perhaps worth noting that the presence of strong vortex shedding invalidates the application of existing turbulent flow prediction methods to flows of this type.

Comparative studies (2) of the hot-wire anemometer used in the same situation led to the conclusion that it would be incautious to make even qualitative use of hot-wire data in such highly turbulent flows.

BACKWARD-FACING STEP

In the present experiments, the Reynolds number of the flow over the backward-facing step was about 5×10^4 based on the step height. At this Reynolds number, the flow in the separation zone is highly turbulent and one would not expect any significant Reynolds number effects. In addition if the boundary layer thickness, δ, upstream of the step is small compared to the step height, h, then again one would not expect the ratio of boundary layer thickness to step height to have any significant effect on the flow structure in the separation zone. Thus, the flow structure could be a function only of the spatial co-ordinates x/h and y/h.

Fig.4 shows the surface pressure distribution over the faces of the step. On the face of the step the pressure coefficient is slightly negative with a value of about -0.05. The pressure then falls further to a minimum of about -0.08 ($\frac{1}{2}\rho U_o{}^2$) at about three step heights downstream of the step which corresponds to about half the length of the separation zone. The pressure then rises to a maximum of about 0.26 ($\frac{1}{2}\rho U_o{}^2$) before beginning to fall again, gradually approaching the free-stream static pressure far downstream. This pressure distribution compares closely with results of Tani, Iuchi and Komoda (3), who measured the pressure distributions for a range of ratios of boundary layer displacement thickness to step height of about 0.1 to 2.0. From their experiments, it seems that complete independence of boundary layer thickness had not been achieved even for the smallest ratios studied but the effect of boundary layer thickness seems not to have been very significant once the ratio was less than about 0.3. The effect of the upstream boundary layer on the flow structure in the present case, where the ratio of boundary layer thickness to step height is about 0.7, can therefore be expected to be small.

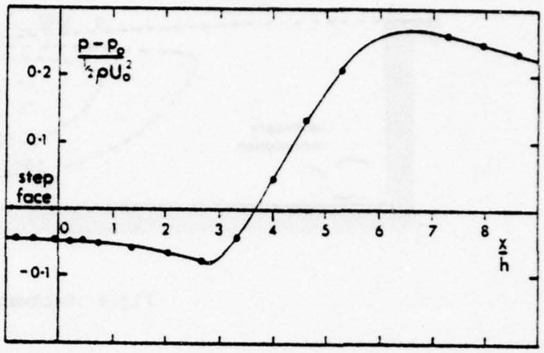

Fig.4 Backward-facing Step - Pressure Distribution

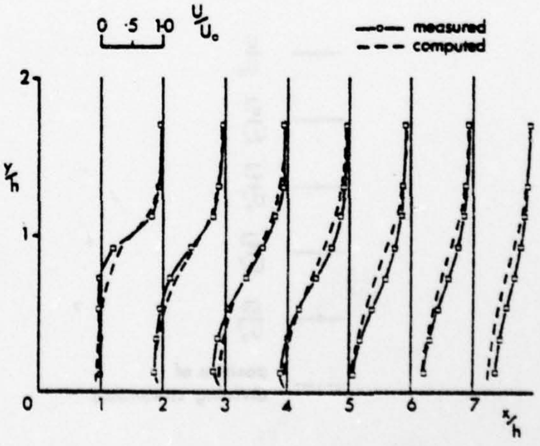

Fig.5 Backward-facing Step - Mean Velocities

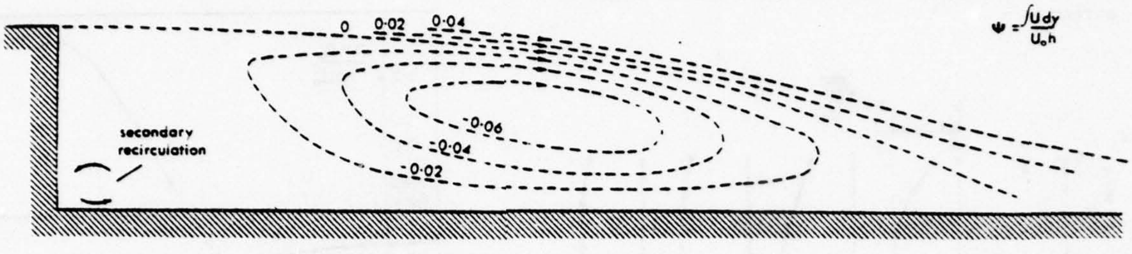

Fig.6 Backward-facing Step - Mean Streamlines

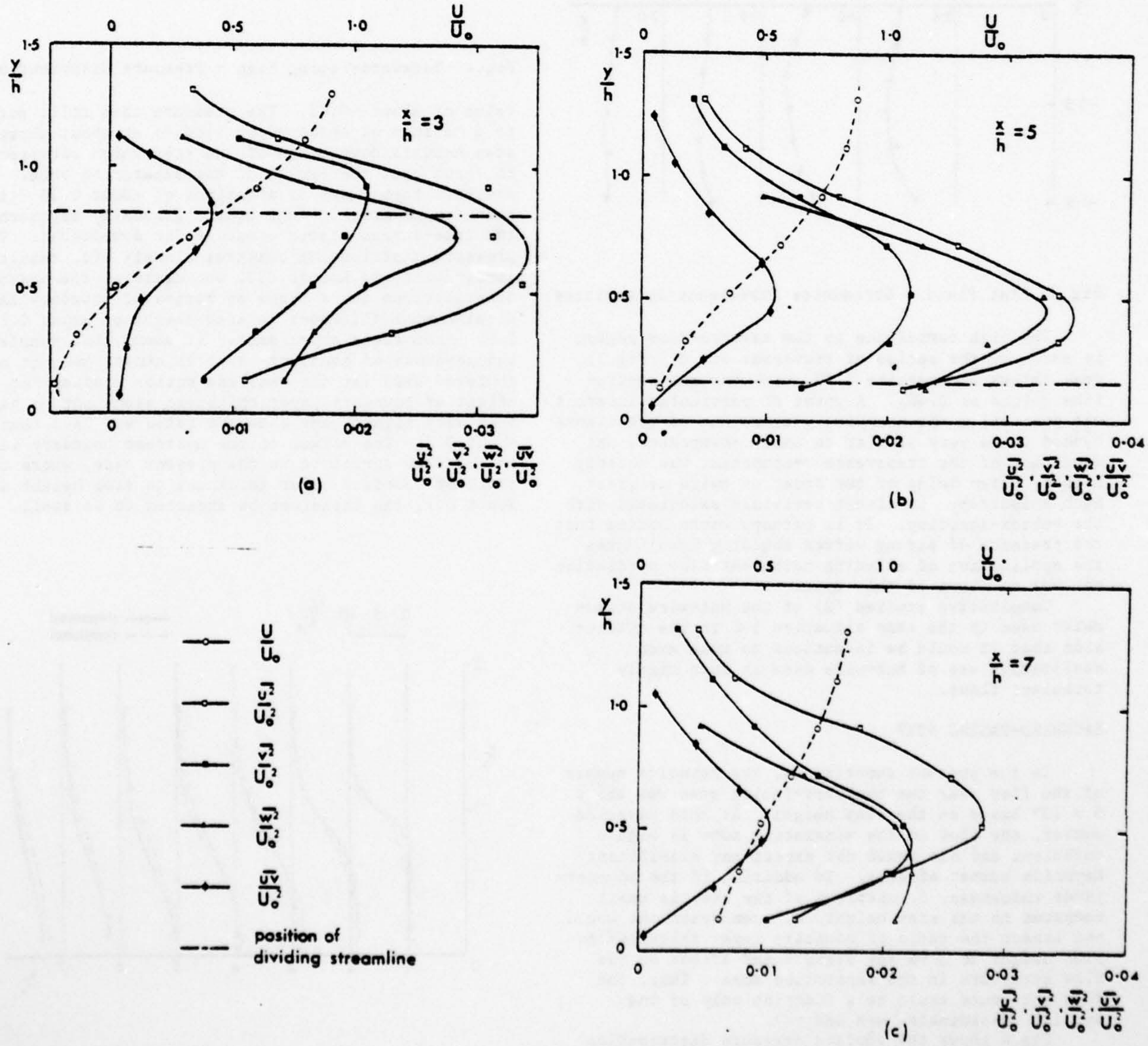

Fig.7 Backward-facing Step - Turbulent Stresses

It is of interest to note that Simmons (4) has suggested that if the velocity on the separated free stream lines in a bluff body flow is c U_o then, as might be inferred from a simple application of Bernoulli's theorem, a good approximation to the base pressure coefficient is $(1 - c^2)$. In the case of a backward-facing step, where the dividing streamline is initially nearly parallel to the main stream, c is likely to be of the order of unity and the base pressure coefficient correspondingly small.

Fig.5 shows the values of mean longitudinal velocities at a series of cross-sections in the recirculating zone. The overall pattern is similar to that found by Tani et al (3), but supplemented by the more reliable measurements now possible in the central zone with its continual reversals of flow. Mean streamlines plotted as contours of the stream function ψ, calculated from the values of mean streamwise velocity, are shown in Fig.6. They agreed well with the general pattern shown by the flow visualisation photographs prepared using the helium bubble technique. The maximum value of mean velocity in the reverse direction is slightly greater than $0.2U_o$ and the total reverse flow rate per unit width in the region is approximately $0.08U_oh$, so that the strength of the reverse flow is considerably less than that found behind the flat plate. In contrast to the flat plate, there is no evidence of vortex shedding; it would be desirable to study the spectra of the fluctuating velocities and whilst the possibility of doing this with the pulsed-wire anemometer using a random sampling technique has been demonstrated (5), the online computing facilities necessary were not available for this experiment.

Secondary recirculation, in the opposite sense, occurs in the corner at the bottom of the step. Although this could be detected clearly by the velocity measurements, the size of the probe was too great on the scale of the experiment to permit detailed examination.

When an oil film was applied to the downstream plane the area of re-attachment could be seen sharply defined in the pattern in the oil, perpendicular to the main flow. The flow thus appears to be two-dimensional; no evidence of the spanwise cell structure sometimes noted could be observed.

Fig.7 shows the distribution of $\overline{u^2}$, $\overline{v^2}$, $\overline{w^2}$ and $\overline{uv}$ at stations $\frac{x}{h} = 3$, 5 and 7 respectively with the distribution of mean velocity U and, where appropriate, the dividing streamline shown for comparison in each case. It should be noted that, since $\overline{uv}$ was measured with the X-array hot-wire probe, the values are only likely to be accurate in the regions where the turbulence level relative to the local velocities is less than about 30%. It will be seen that the maximum values of the Reynolds stresses are found in each case in the region where the transverse velocity gradient $\frac{\partial U}{\partial y}$ is close to a maximum. Further, the results confirm the observations of Tani et al (3) that the zone of maximum shear initially lies close to the dividing streamline but deviates outwards from it downstream.

The peak values of the stresses in the mixing layer increase at first with distance downstream approaching their maxima a little before the region of the re-attachment; thereafter they decrease, as observed by Bradshaw and Wong (6). It may be noted that, while $\overline{u^2}$ is in general the greatest of the normal stresses in the mixing layer and $\overline{v^2}$ the least, after re-attachment $\overline{w^2}$ retains a higher value close to the solid boundary than either $\overline{u^2}$ or $\overline{v^2}$. This perhaps may be seen as according with Bradshaw and Wong's statement that, at re-attachment, where the longitudinal rate of strain is high, $\overline{v^2}$ and $\overline{w^2}$ might be expected to increase near the surface while $\overline{u^2}$ tended to decrease, although there would be an opposing tendency for $\overline{v^2}$ to be reduced by the presence of the solid boundary while $\overline{u^2}$ and $\overline{w^2}$ increased.

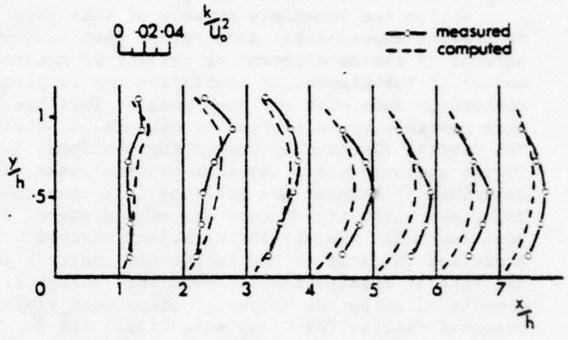

Fig.8 Backward-facing Step - Turbulence Energy

From the distribuiton of turbulence energy k $= \frac{1}{2}(\overline{u^2} + \overline{v^2} + \overline{w^2})$ shown in Fig.8, it may be seen that, although the values fall away from the peaks in the mixing layer, they remain throughout much of the recirculating region an appreciable fraction of those peak values, although the mean velocity locally may be very small. It is not, of course, possible to express the turbulence intensities in terms of the respective local mean velocities in the region, since these velocities may approach zero. The greatest values of longitudinal turbulent fluctuation encountered, almost $0.2U_o$, are less than half those found behind the flat plate.

A comparison may usefully be attempted between the present mixing layer and the plane two-dimensional turbulent mixing layer, which is one of the simplest shear flows and one which has received considerable study. In Figs.9 and 10, therefore, the mean velocities and longitudinal turbulent fluctuations are compared with the results of Champagne, Pao and Wygnanski (7) in whose studies air was exhausted at velocity U_E through a rectangular nozzle and allowed to mix at one of its boundaries with quiescent air, the remaining three boundaries being solid. The quantities $\frac{U}{U_E}$ and $\frac{\overline{u^2}}{U_E}$ for the mixing layer have been plotted against $\eta(=(y-y_{m/2})/x)$. (U_E is treated as the mean velocity in the main stream at the particular cross-section whereas for the plane mixing layer U_E is simply the exit velocity; $y = y_{m/2}$ where $U = \frac{1}{2}U_E$).

It will be seen that on the high speed side, U and, to a less marked extent, $\overline{u^2}$ show not dissimilar distributions for the two layers. The approximate nature of the comparison must be acknowledged; in the present case the mixing layer follows a curved path so that the velocity in the main flow outside the same layer is not constant and lines perpendicular to the solid boundary are not perpendicular to the centreline of the layer. In particular, on the low-speed side there is the recirculating region with its reversed flow rather than a simple quiescent zone. It cannot be suggested that the low-speed side is at all closely comparable, for the high levels of turbulence already noted in the separated zone are far higher than the corresponding values in the plane mixing layer. Nevertheless, the comparison for the high-speed side appears valuable and it is of interest too to note that the maximum value of $\overline{uv}/U_o^2$ measured in the mixing layer is approximately 0.01, comparable to the figure of Wygnanski and Fielder (8).

Whilst the immediate purpose of this paper is to present experimental data rather than to give an account of the development or testing of mathematical models of turbulence, an indication may be given of a comparison made with one such model. This has been made possible by collaboration with Dr. I. Castro of the Central Electricity Generating Board who applied to the present case a computer program based, as described by Launder and Spalding (9), upon the turbulent viscosity concept and making use of a two equation model whereby the turbulent viscosity is expressed in terms of the turbulence energy k and the rate of dissipation of turbulence energy ε. The computed figures are shown for comparison against the measured results for U and k in Figs.5 and 8. The overall mean pattern is well predicted together with the general levels of turbulence although in the latter case there is some difference in the detailed distribution. Many issues arise in the application of such program to problems of this type and no detailed treatment is attempted here.

FORWARD-FACING STEP

The work is being extended to other basic shapes. As an example, mean streamlines prepared from velocity measurements with a forward-facing step are shown (Fig.11). The two separated regions represent a more complex situation than that of the backward-facing step.

In the separated region downstream of the edge, the reverse flow rate per unit width, was of the order of $0.07U_oh$ and the maximum mean velocity encountered was about $0.3U_o$. The stresses in the mixing layer showed a behaviour similar to that of the backward-facing step in rising to a maximum near the position of re-attachment, with the line of maximum stress deviating from the dividing streamline downstream. On the other hand, the stresses were considerably greater in this case; in particular $\overline{uv}$ rose to $0.03U_o^2$ compared to $0.01U_o^2$, while $\overline{u}^2$ reached $0.10U_o^2$ compared to $0.04U_o^2$.

The reverse flow in the other recirculating region before the step was very much weaker, the flow rate per unit width being no more than $0.01U_oh$. (In Fig.11, the mean streamlines for this region are shown for intervals of 0.002 rather than 0.02 as for all other regions in order to give better definition to the flow pattern.) Again, the line of maximum stress in the mixing layer, which passed close to the top of the step, deviated from the dividing streamline which met the face of the step in a point of re-attachment at a height of 0.6h. The peak values of $\overline{u^2}$ rose along the mixing layer, approaching figures of $0.04U_o^2$ close to the top of the step while, in this case, no measured values of $\overline{uv}$ exceeded $0.004U_o^2$.

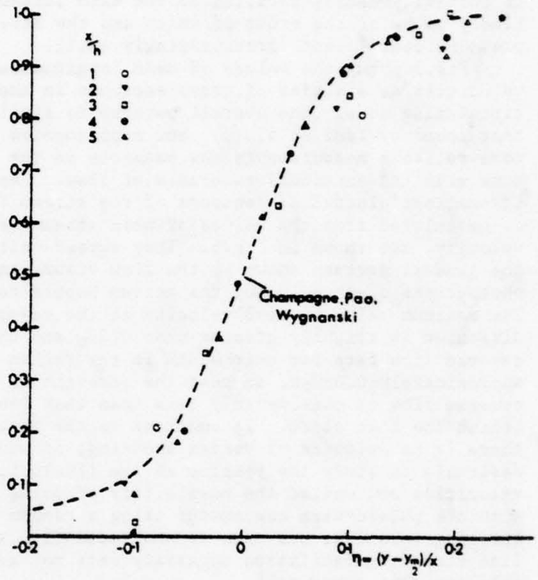

Fig.9 Backward-facing Step - Mean Velocities, Mixing Layer

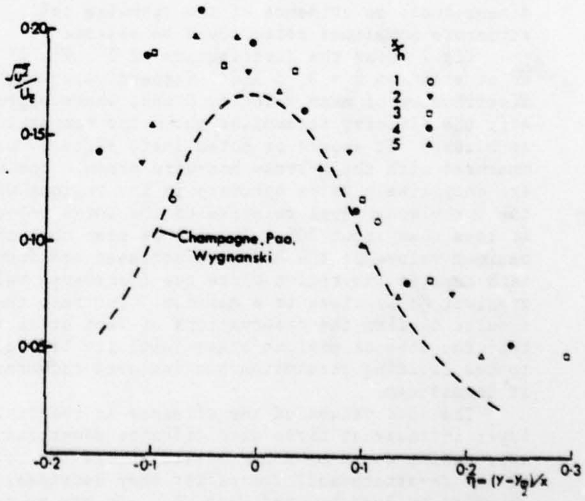

Fig.10 Backward-facing Step - Streamwise Velocity Fluctuations, Mixing Layer

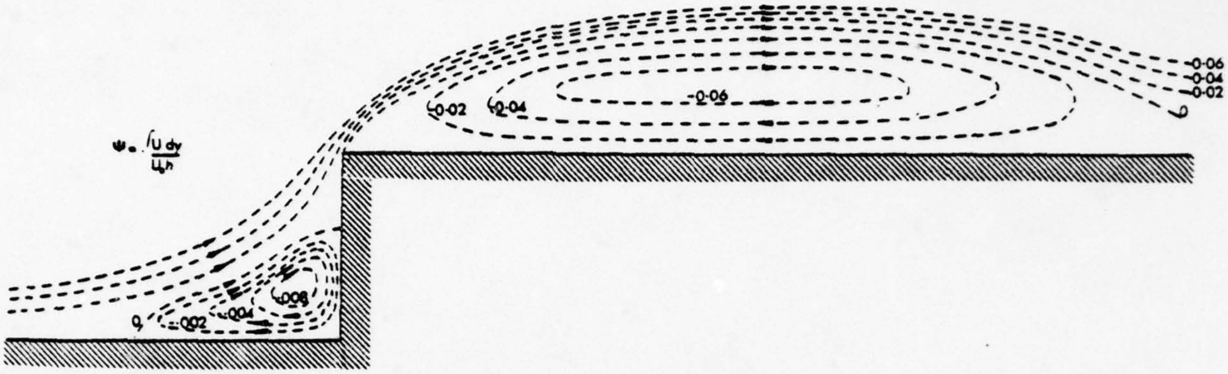

Fig.11 Forward-facing Step - Mean Streamlines

CONCLUDING REMARKS

This paper has described some preliminary results of studies of the flow over a number of bluff bodies. The work is intended to provide not only further information on the characteristics of the separation zones, but also to provide experimental test data with which to compare the turbulent flow prediction methods that are now being developed for application to recirculating flows. The results in this present paper represent only the earliest results of this work and a more extensive programme is now in progress to obtain more detailed information about the structure of turbulence in flows of this type.

REFERENCES

1 Bradbury, L.J.S. and Moss, W.D., "Pulsed Wire Anemometer Measurements in the Flow past a Normal Flat Plate in a Uniform Flow and in a Sheared Flow," Proceedings of the Fourth International Conference on Wind Effects on Buildings and Structures, Heathrow 1975, pp.485-496.

2 Bradbury, L.J.S., "Measurements with a Pulsed Wire and a Hot Wire Anemometer in the Highly Turbulent Wake of a Normal Flat Plate," Journal of Fluid Mechanics, Vol.77, Part 3, 1976, pp.473-497.

3 Tani, I., Iuchi, M. and Komoda, H., "Experimental Investigation of Flow Separation Associated with a Step or a Groove," Report No.364, April 1961, Aeronautical Research Institute, University of Tokyo.

4 Simmons, J.E.L., "The Relationship between the Base Pressure on a Bluff Body and the Velocity at Separation," Aeronautical Journal, Vol.78, July 1974, pp.330-331.

5 Gaster, M. and Bradbury, L.J.S., "The Measurement of the Spectra of Highly Turbulent Flows by a Randomly Triggered Pulsed-wire Anemometer," Journal of Fluid Mechanics, Vol.77, Part 3, 1976, pp.499-509.

REFERENCES (continued)

6 Bradshaw, P. and Wong, F.Y.F., "The Reattachment and Relaxation of a Turbulent Shear Layer," Journal of Fluid Mechanics, Vol.52, Part 1, 1972, pp.113-135.

7 Champagne, F.H., Pao, Y.H. and Wygnanski, I.J., "On the Two-dimensional Mixing Region," Journal of Fluid Mechanics, Vol.74, Part 2, 1976, pp.209-250.

8 Wygnanski, I. and Fielder, H.E., "The Two-Dimensional Mixing Region," Journal of Fluid Mechanics, Vol.41, Part 2, 1970, pp.327-361.

9 Launder, B.E. and Spalding, D.B., "Mathematical Models of Turbulence," Academic Press, London, 1972.

AD-A055 654 PENNSYLVANIA STATE UNIV UNIVERSITY PARK DEPT OF MECH--ETC F/G 20/4
SYMPOSIUM ON TURBULENT SHEAR FLOWS HELD AT THE PENNSYLVANIA STA--ETC(U)
APR 77 N00014-77-C-0176

UNCLASSIFIED NL

7 OF 9
ADA
055654

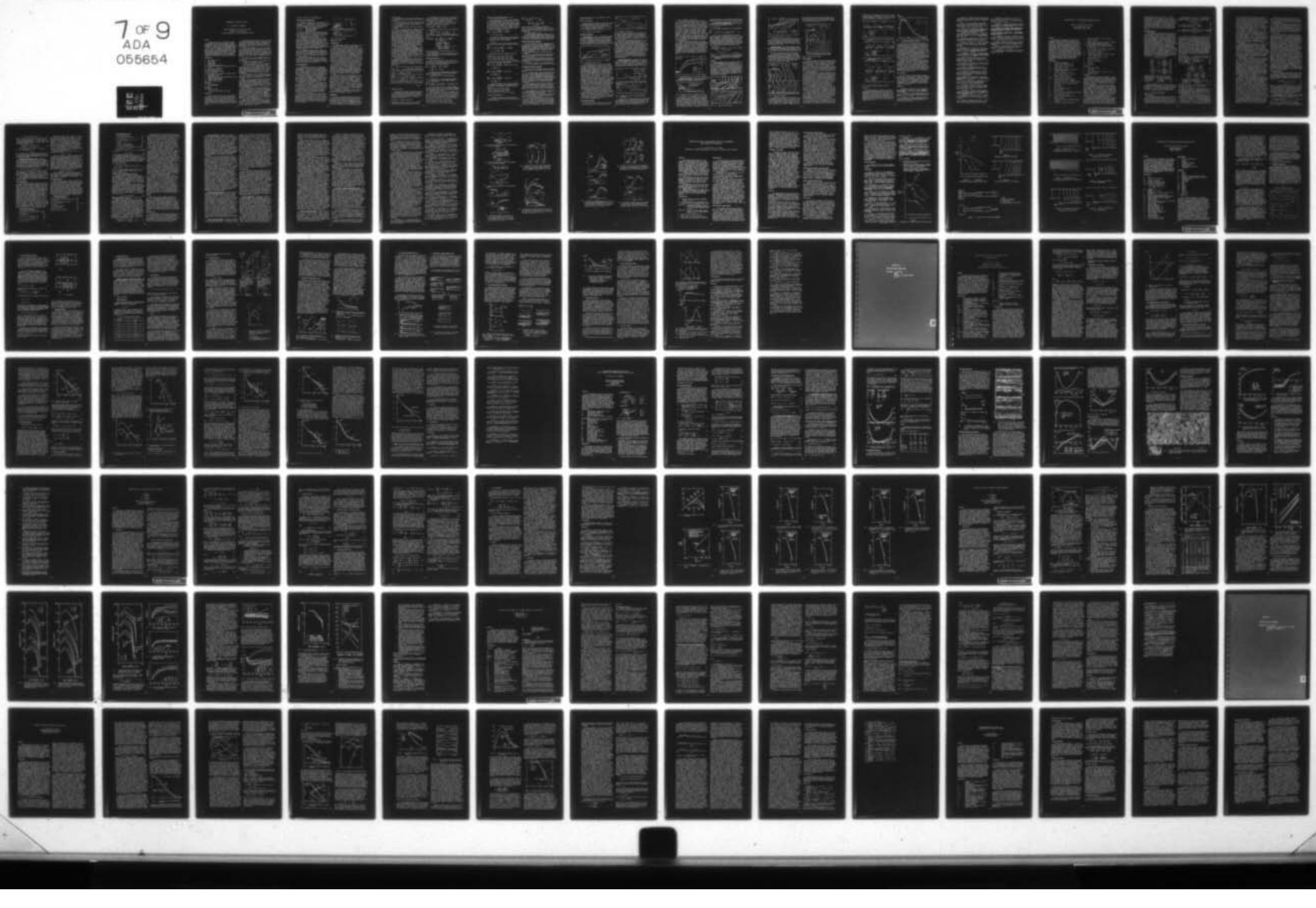

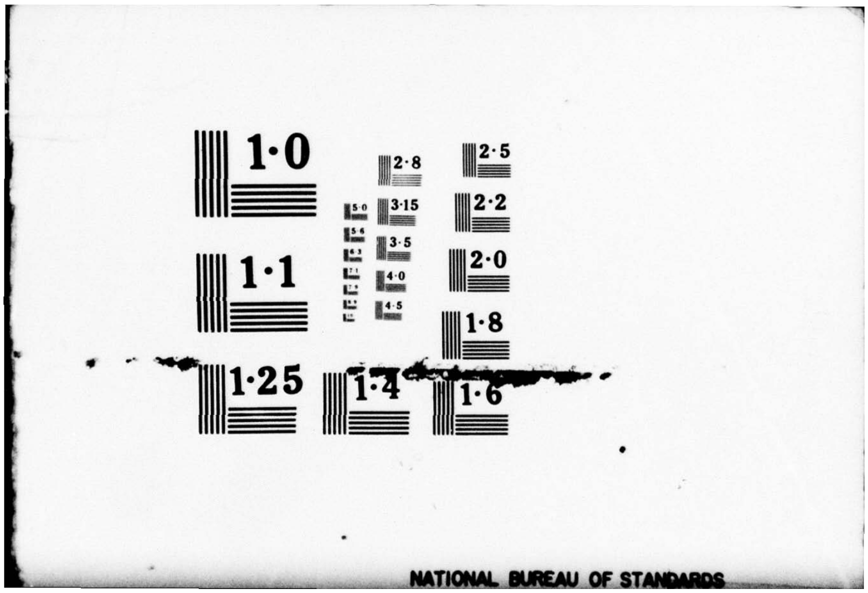
1·0
2·8
2·5
5·0
3·15
2·2
5·6
3·5
6·3
2·0
1·1
4·0
4·5
1·8
1·25
1·4
1·6
NATIONAL BUREAU OF STANDARDS

PERTURBATIONS OF TURBULENT PIPE FLOW

H. HA MINH and P. CHASSAING

Institut de Mécanique des Fluides de Toulouse
Laboratoire associé au CNRS
2, rue Charles Camichel - 31071 TOULOUSE CEDEX - France

ABSTRACT

The restructuration of a turbulent flow past a strong geometrical perturbation caused by a sudden enlargement is studied. The experimental results on the mean properties as well as the Reynolds stress are presented for three values of the enlargement factor ($\alpha = 0, 1, \infty$). The theoretical analysis based on mathematical models of turbulence is developed according to single point closure assumptions. The resulting numerical predictions are found to be in agreement with the experimental data if it is taken into consideration also the extent of the perturbation along with its intensity in the choice of the model.

NOMENCLATURE

$\underline{H}$	Step height (case A)
I	Unity tensor
L	Length scale
P	Mean pressure
r, y	Transversal co-ordinate
R_o, R_1	Radius upstream and downstream of the perturbation
$\underline{U}, V$	Mean velocity components
$\vec{V}$	Mean velocity vector
$\overline{u^2}, \overline{v^2}, \overline{w^2}, \overline{uv}$	Reynolds stresses/ρ
u', v', w'	r.m.s values
$\tilde{u}, \tilde{v}, \tilde{w}, \widetilde{uv}$	max. of $u', v', w', \overline{uv}$ in the same section
x	Longitudinal co-ordinate
α	Enlargement factor
δ	Boundary layer thickness or characteristic width
$\underline{\varepsilon}$	Turbulent dissipation rate
$\underline{\Sigma}$	Reynolds stress tensor/ρ
ν_T	Cinematic eddy viscosity

Subscripts

o	Inlet conditions
$\mathbb{c}$	Center line value

Overscript

T	Transposed tensor

Other symbols are difined in the text.

INTRODUCTION

Among the turbulent shear flows, the domain of thin shear layers has been studied by many workers, bringing out a number of prediction methods of acceptable accuracy. In most cases, this fact results mathematically from the parabolic nature of the equations, owing to Prandtl's assumptions, and physically from the existence of a quasi-equilibrium of turbulent energy.

For more complex shear flows, as occur, for example, when an extra rate of strain is acting, both physical analysis and numerical prediction become more complicated : one has now to consider diffusion and convection mechanisms and elliptic equations in co-ordinate space.

As noticed by BRADSHAW et al (1), it was legitimate to solve these previous difficulties by considering complex shear flows as perturbed versions of classical thin shear layers. Proceeding in this way, we can consider the problem as that of the rearrangement of a simple flow after some strong perturbation. The sudden enlargement of a circular duct is approached in such a way.

If we define (Fig.1) the enlargement factor α as $\alpha = (R_1 - R_o)/R_o$, two interesting limiting cases may be pointed out :

$\alpha \to 0$, obtained by putting $R_o \to \infty$ (the height of the step $H = R_1 - R_o$ remaining finite)

$\alpha \to \infty$, obtained by putting $R_1 \to \infty$ (R_o can't be reduced to 0 without losing physical significance)

In the first case, the readjustment of the flow regime takes place to form a similar type of flow to that existing before the perturbation. Such a configuration therefore allows the detailed study of the influence of external parameters (U_o, δ_o ..) on the development of the mixing zone associated with the perturbation.

In the second case, the flow regime readjusts itself to a "jet type" flow. This permits the influence of internal parameters (entrainment rate..) to be analysed.

These two limiting cases thus allow a more precise definition of the structure of the flow in general configurations(corresponding to finite values of α, about unity) where the readjustment of the flow over itself takes place after the development of a mixing layer influenced simultaneously by internal as well as external parameters.

Each of these three flows has been separately studied by a large number of workers, both experimentaly and theoretically. So far the case of enlargement of pipe flow is concerned, we can mention e.g. the papers of CHATURVEDI (2), RUNCHAL (3), HEBRARD (4). The separated flow over a step has been treated by TANI (5), GREEN (6), NARAYANAN et al (7), MASBERNAT (8) among several others and the round jet by CORRSIN (9), DAVIES et al (10), WYGNANSKI et al (11), RODI (12)... the list is far from being complete.

However these studies have not been carried on in the same way which is adopted in the present paper. That is the reason why shall return to experimental, theoretical and numerical considerations before discussing the comparison of the result.

PRECEDING PAGE BLANK-NOT FILMED

PHYSICAL ANALYSIS OF THE PERTURBED FLOWS

"Separated flow" configurations

The general configuration of a separated flow is given in Fig.1. The separation results from the sudden enlargement of a circular duct, in which a fully or partially developed flow exists. On the streamwise, one can distinguish three different regions :

$0 \leqslant x \leqslant x_1$	Recirculating region
$x_1 \leqslant x \leqslant x_2$	Reattaching region
$x_2 \leqslant x$	Recovering region

One can observe that, in the reattaching region although such a sensible reverse flow is not present at the outer boundary of the mixing zone, as in the first region, it is only in the third one that Prandtl's assumptions may be adopted.

Transversally, in case of partially developed flows, a "potential core" (zone "0") exists in the separation section which extends towards the wall in the form of a classical boundary layer, where the peaks of turbulent energy and dissipation are staying. For positive values of x, this zone gives rise to a mixing zone in which the mechanism of a production of turbulent kinetic energy would become amplified by the presence of a complete mean deformation rate ($\partial U/\partial r + \partial V/\partial x$).

As a result, the turbulent energy reaches high levels all the more increased as the dissipation collapses down from its initial value in the same time. This leads to a strong diffusion of the zone "2" into the flow : the rates of expansion reach values of about 0.3 (4)(13).

Beyond the reattachment area, the situation is modified due to the presence of the wall near which a new boundary layer "3" will progressively develop leading to equilibrium of the same type as those existing initially in the flow (zone "1").

"Jet" configuration

In this case, for identical inlet conditions, three different regions can also be distinguished longitudinally : in the first one, where a "potential core" remains, a third one, or self-preserving region, and a transition region. Of course, if the initial flow is fully developed, one can no longer speak of a "potential core" since all the energy transfer mechanisms take place throughout the cross section.

Transversally, in region I, a mixing layer appears in which the dissipation rate vanishes for the same reason as in the previous case. The production is also important but the diffusion is lower. (The rate of expansion is approximatively 0.16).

Beyond this, in region II, the flow reorganises to a jet type one which implies, in particular, the transformation of the form of turbulent energy profiles, by the shift of their maximums from the periphery towards the axis zone. This leads in region III to the classical self preserving profiles, the self preserving conditions being reached at different values of x according to the considered properties (U or $\overline{u^2}$, or $\overline{v^2}$, or $\overline{w^2}$, or $\overline{uv}$)

Taking into consideration this previous analysis it seems clear that the fundamental interest of the previous configurations lies in the study of general characteristics of a turbulent flow in rapid evolution between different equilibrium simple shear states. To examine this objective thoroughly, we have developed both experimental and theoretical approaches that we shall now discuss.

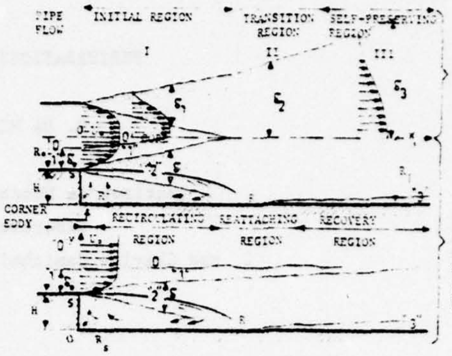

Fig.1 Flow configurations

EXPERIMENTAL STUDY

Installations

The experimental study on the perturbed flows has been developed on four distinct installations :

The first two of them are devoted to the plane separated flow over a step. In the first case, a subsonic (55 m/s) wind tunnel is equiped with a 10 cm high step. This quite large value allows a fine exploration of the recirculating zone. The thickness of the initial boundary layer can be varied by altering the rugosity of the bottom wall of the 12:1 convergent (the outer part of the velocity profile remains uniform). In the second case, a quasi-plane flow over a blunt body is obtained in an Eiffel's wind tunnel of 2.4 m in diameter and a 40 m/s maximum velocity. An elliptical two-dimensional profile with a bluff trailing edge (2H = 10 cm) is inserted between two parallel plane walls.

The second installation is conceived for the analysis of the round jet issuing from a pipe. It essentially consists of a seamless bronze duct of 4 cm in diameter ($2R_0$) and a $L = 175\ R_0$ length. One of the extremities is connected to a thermally stabilised compressed air generator through tranquilising, filtering sections and a convergent section. The axis of the tube is horizontally situated at a distance of 1.50 m above the ground level, the nearest wall of fluid flow.

The last installation, concerning recirculating flow consists of a first 7,2 cm in diameter duct, the length of which is adjustable between 0.3 m and 2 m. By varying the ratio L/R_0 it is possible to choose different levels of the initial boundary thickness. A second duct of 4 m length follows it coaxially. Its diameter can be fixed at 11.6 cm, 14.4 cm and 19.2 cm in order to obtain three different values of the enlargement factor α (0.61 ; 1 ; 1.66). Owing to the large flow rates, the system is fed by a group of ventilators powered by a variable speed motor, through different stages of tranquiliser sections.

A large number of experiments has been performed. The main characteristics of the runs that we shall discuss here and presented in table 1.

Measurements

The different measured parameters are related to the mean (U,P) and fluctuating ($\overline{u2}$, $\overline{v2}$, $\overline{w2}$, $\overline{uv}$) motion. The instrumentation consists of different pressure transducers (the probe diameters ranging from 1 mm to 3 mm) and DISA type 55 D hot wire anemometers, operating at constant temperature. After linearisation (55 D 10), mean values are processed with a time domain analyser

SOLARTRON 1860.

The measurement of the previous parameters in the above mentioned flow patterns posed a lot of difficulties due to :

i) The existence of locally high levels of turbulent intensities, associated with very steep gradients.

ii) The presence of zones where the velocity direction reverses.

Owing to these problems we have used a number of precautions.

As far the pressure values are concerned, corrections of static and dynamic values has been adopted (14) taking into consideration the high turbulent intensities. Due to the steep gradients, only normal or inclined single wire probes have been employed. A number of methods for increasing the hot wire measurement precision has been published including turbulence effects (12) (15) and directional properties of the probes (16) (17). Similar work has also been developed by the authors (18). For the sake of uniformity it must be yet pointed out that such corrections have not been introduced in the given results. However, for the $\overline{v^2}$, $\overline{w^2}$ and $\overline{uv}$ measurements by the rotated inclined hot wire technique, the angular sensitivity of each probe was specifically calibrated.

In the regions were the velocity vector locally reverses, the hot wire anemometer measurements lose all their significance since the thermal dissipation only depends on the square of some effective cooling velocity. The results given by this method in the reverse flow are therefore not given except to indicate them. Those obtained by the use of a Pitot tube, after detecting the correct sense of the local velocity, seem to be more accurate.

In conclusion, we think that, in spite of the precautions that we have taken and which can certainly be improved, the experimental results in such flow patterns are still having large errors. This fact must be kept in mind for the comparison with numerical predictions.

FLOW CONFIGURATION	FLOW CASE	α	U_0 (m/s)	$(R_e)_0$	INLET CONDI-TIONS	MESURED PARA-METERS	THEORETICAL MODELS EMPLOYED			
							EVM1	EVM2	RSTM3	RSTM5
PLANE SEPARATED FLOW	A	0 (H= 5cm) 1/7	15 20-30 12-55	10^5	$\frac{\delta^*}{h}$ = .05 to .5 .10	P , U P		•		
CONFINED SEPARATED FLOW	B	1 5/3	30 15	$7.2\,10^4$ $3.6\,10^4$	$\frac{\delta_0}{R_0}$ = .3 1.	P, U, $\overline{uv}$ $\overline{u^2}$, $\overline{v^2}$, $\overline{w^2}$	•	•	• (*)	
ROUND JET	C	$\frac{\alpha}{R_0 = 2\ \text{cm}}$	9.16 20.3 24	$1.1\,10^5$	$\frac{\delta_0}{R_0}$ = 1.	U, $\overline{uv}$ $\overline{u^2}$, $\overline{v^2}$, $\overline{w^2}$	•	•		•
Underlined values correspond to the presented results							(*) after reattachment			

Table 1

THEORETICAL ASPECTS

The theoretical problem, as seen here, consists in solving the local Reynolds' equations completed by some convenient closure assumptions. The mean steady state momentum equations of a Newtonian incompressible fluid, in the absence of external body forces may be written as :

$$\vec{\mathrm{div}}(\rho\vec{V} \otimes \vec{V}) = -\,\vec{\mathrm{grad}}\,P + \vec{\mathrm{div}}(\rho\overline{\overline{\Sigma}}_T) \qquad (1)$$

where $\otimes$ stands for the tensorial product and $\rho\overline{\overline{\Sigma}}_T$ represents the Reynolds stress tensor $(\overline{\rho v \otimes v})$.

All the models that we have used, include single point closure schemes, based either on a turbulent viscosity concept or on transport equations of turbulent stresses. We can therefore distinguish :

i) Eddy viscosity models (E.V.M.) for which the closure rests in the direct use of Reynolds tensor through the coefficient ν_T defined by :

$$\overline{\overline{\Sigma}}_T = \frac{\nu_T}{2}\,(\overrightarrow{\mathrm{grad}}\,\vec{V} + (\overrightarrow{\mathrm{grad}}\,\vec{V})^T) - 2\overline{\overline{I}}k \qquad (2)$$

Two proposals have been tested for the eddy viscosity ν_T that of :

. Prandtl Kolmogorov $\nu_T = C\mu\sqrt{k}\,L$ (3)

and . Chou $\nu_T = C\mu C_D \varepsilon^2/k$ (4)

ii) Reynolds' stresses transport models (R.S.T.M.), where the closure implies the following transport equations :

$$\begin{aligned}\vec{\mathrm{div}}[\rho\vec{V} \otimes \overline{\overline{\Sigma}}_T] = &-\rho[\overline{\overline{\Sigma}}_T \odot \overrightarrow{\mathrm{grad}}\,\vec{V} + (\overline{\overline{\Sigma}}_T \odot \overrightarrow{\mathrm{grad}}\,\vec{V})^T]\\ &- \overrightarrow{\mathrm{div}}\,\rho\overline{[\vec{v} \otimes \vec{v} \otimes \vec{v}]}\\ &+ \overline{\frac{p}{2}\,[(\overrightarrow{\mathrm{grad}}\,\vec{v} + (\overrightarrow{\mathrm{grad}}\,\vec{v})^T]}\\ &- [\overrightarrow{\mathrm{grad}}(\overline{p\vec{v}}) + (\overrightarrow{\mathrm{grad}}(\overline{p\vec{v}}))^T] + \mu\,\Delta\,\overline{\overline{\Sigma}}_T\\ &- 2\mu\,\overline{(\overrightarrow{\mathrm{grad}}\,\vec{v}) \otimes (\overrightarrow{\mathrm{grad}}\,\vec{v})^T} \qquad (5)\end{aligned}$$

where $\odot$ stands for the contraction product of two second order tensors.

The equations (5) have to be modelled through the classical assumptions for diffusion dissipation and redistribution terms.

Eddy viscosity models (E.V.M.)

Either of the schemes (3) or (4) requires the determination of the turbulent energy k. This is obtained by solving a modelised transport equation which can be written for axisymmetric flows :

$$\begin{aligned}\frac{Dk}{Dt} = &+\frac{\partial}{\partial x}\left[\frac{\nu_T}{\sigma_k}\frac{\partial k}{\partial x}\right] + \frac{1}{r}\frac{\partial}{\partial r}\left[r\,\frac{\nu_T}{\sigma_k}\frac{\partial k}{\partial r}\right]\\ &- \overline{uv}\,\frac{\partial U}{\partial y} - (\overline{u^2} - \overline{v^2})\,\frac{\partial U}{\partial x} - \varepsilon \qquad (6)\end{aligned}$$

The diffusion term is schematised according to a classical gradient type formula and the dissipation rate ε is obtained either :

- directly, from local isotropy assumption :

$$\varepsilon = C_D\,k^{3/2}/L \qquad (7)$$

where the length scale L is prescribed algebraically.

- or indirectly, by using a second transport equation modelised as :

$$\frac{D\varepsilon}{Dt} = \frac{\partial}{\partial x}\left(\frac{\nu_T}{\sigma_\varepsilon}\frac{\partial \varepsilon}{\partial x}\right) + \frac{1}{r}\frac{\partial}{\partial r}\left(\frac{\nu_T}{\sigma_\varepsilon}r\,\frac{\partial \varepsilon}{\partial r}\right) - C_1\,\frac{\varepsilon}{k}\,\overline{uv}\,\frac{\partial U}{\partial r} - C_2\,\frac{\varepsilon^2}{k} \qquad (8)$$

One can thus define, one or two transport equation models (E.V.M.1) and (E.V.M.2), which may be integrated in a more general way, in the models based upon transport equations of k and $k^m L^n$.

A certain number of constants are necessary introduced into the procedure. The values that we adopted are given in table 2, and correspond to those universally used in the literature. The numerical predictions were not therefore optimised over the experimental results for the particular flows previously described.

$C\mu$	C_D	σ_k	σ_ε	C_1	C_2
1.	0.09	1.	1.1	1.45	1.9

Table 2

Reynolds' stress transport models (R.S.T.M.)

For the perturbed flows that we have considered, the significant Reynolds' stresses are $\overline{u^2}$, $\overline{v^2}$, $\overline{w^2}$ and $\overline{uv}$. All the models that we have used employ a transport equation for the turbulent shear stress $\overline{uv}$. Among the different basic proposals that have been published and which have been reviewed, in ref.(19), we have more particularly used the closure schemes of LAUNDER et al (20). This leads to an equation which can be written, for the parabolic case, as :

$$\frac{D\overline{uv}}{Dt} = C_\tau \frac{1}{r}\frac{\partial}{\partial r}\left(r\,\frac{k\overline{v^2}}{\varepsilon}\frac{\partial\overline{uv}}{\partial r}\right) - C_\tau \frac{kw^2}{\varepsilon}\frac{\overline{uv}}{r^2}$$

$$- (1-\alpha)\,\overline{v^2}\,\frac{\partial U}{\partial r} - \beta\,\frac{\varepsilon}{k}\,\overline{uv} \qquad (9)$$

The closure can be definitively achieved either :

i) with the aid of some distribution assumption of the energy over the three components :

$$\overline{u_i^2} = a_i\,k$$

This gives rise to a three transport equation model (R.S.T.M.3) in which Eq.(9) takes the following form :

$$\frac{D\overline{uv}}{Dt} = C_\tau\,a_2\,\frac{1}{r}\frac{\partial}{\partial r}\left(r\,\frac{k^2}{\varepsilon}\frac{\partial\overline{uv}}{\partial r}\right) - C_\tau\,a_3\,\frac{k^2}{\varepsilon}\frac{\overline{uv}}{r^2}$$

$$- (1-\alpha)\,\dot{a}_2\,k\,\frac{\partial U}{\partial r} - \beta\,\frac{\varepsilon}{k}\,\overline{uv} \qquad (10)$$

The values of the new constants are given in table 3.

a_1	a_2	a_3	C_τ	α	β
1.	0.5	0.5	0.5	0.4	2.5

Table 3

ii) or by the use of three supplementary transport equations for the normal stresses (12)

$$\frac{D\overline{u^2}}{Dt} = \beta\,\frac{1}{r}\frac{\partial}{\partial r}\left(r\,\frac{k\overline{v^2}}{\varepsilon}\frac{\partial\overline{u^2}}{\partial r}\right) - 2\overline{uv}\,\frac{\partial U}{\partial r} - \omega\,\frac{\varepsilon}{k}\left(\overline{u^2} - \frac{2}{3}\,k\right)$$

$$+ \frac{4}{3}\,\alpha\,\overline{uv}\,\frac{\partial U}{\partial r} - \frac{2}{3}\,\varepsilon \qquad (11)$$

$$\frac{D\overline{v^2}}{Dt} = \beta\,\frac{1}{r}\frac{\partial}{\partial r}\left(r\,\frac{k\overline{v^2}}{\varepsilon}\frac{\partial\overline{v^2}}{\partial r}\right) - \omega\,\frac{\varepsilon}{k}\left(\overline{v^2} - \frac{2}{3}\,k\right)$$

$$- \frac{2}{3}\,\alpha\,\overline{uv}\,\frac{\partial U}{\partial r} - \frac{2}{3}\,\varepsilon \qquad (12)$$

$$\frac{D\overline{w^2}}{Dt} = \beta\,\frac{1}{r}\frac{\partial}{\partial r}\left(r\,\frac{k\overline{v^2}}{\varepsilon}\frac{\partial\overline{w^2}}{\partial r}\right) - \omega\,\frac{\varepsilon}{k}\left(\overline{w^2} - \frac{2}{3}\,k\right)$$

$$- \frac{2}{3}\,\alpha\,\overline{uv}\,\frac{\partial U}{\partial r} - \frac{2}{3}\,\varepsilon \qquad (13)$$

One can thus obtain the (R.S.T.M.5) based upon five transport equations for the quantities $\overline{u^2}$, $\overline{v^2}$, $\overline{w^2}$, $\overline{uv}$ and ε, the constants of which are given in table 4.

α	β	ω	C_1	C_2
0.42	0.25	2.75	1.43	1.9

Table 4

NUMERICAL CONSIDERATIONS

In general, the numerical problem consists in solving a system having the partial differential equations of the type :

$$\underbrace{a\left[\frac{\partial}{\partial x}(\rho U\phi) + \frac{1}{r}\frac{\partial}{\partial r}(r\rho V\phi)\right]}_{\text{Convection}} = \underbrace{S(\phi)}_{\text{Sources}}$$

$$+ \underbrace{\left[\frac{\partial}{\partial x}\left(b_1\,\frac{\partial\phi}{\partial x}\right) + \frac{1}{r}\frac{\partial}{\partial r}\left(b_2 r\,\frac{\partial\phi}{\partial r}\right)\right]}_{\text{Diffusion}} \qquad (14)$$

where ϕ stands for any transportable quantity. Putting $\phi=1$, and with a convinient choice of the coefficients, the above equation gives rise to the continuity equation, and can also have a number of particularities like :

i) the non linearity if $\phi = U$

ii) the parabolical character in space if $b_1 = 0$

Different computing programs have been developed to solve this problem (21)(22). They all require finite difference discretisation and we shall limit ourselves in this paper, to some particular and original points.

Solving the elliptical equations

Our method owes its origins to the common point of works done by GOSMAN et al (23), GREENPAN (24). The formulation is of the Poisson-Helmoltz type (ψ,ω). The discretisation is achieved by the integration over an elementary domain bounded by distinct lines of the network. For the convection terms, upstream difference schemes are used (21).

Three different boundary conditions have been considered :

i) Real distributions in the inlet section, which implicitely take into consideration the downstream influence of the flow.

ii) Cancelling of the longitudinal second order derivatives as the downstream conditions, according to the weakly elliptical character of the problem in the oulet section.

iii) Couette's values on the solid boundaries in order to avoid an extremely tight network in that zone.

Solving the parabolical equations

The results on flow problems governed by parabolical equations have been obtained by two distinct programs :

i) In confined domain, where the pressure and mean velocity are adapted using a predictor-corrector process. Centered finite differences are used for the first seven steps of the network and beyond, decentered schemes of the Dufort-Frankel type. The conditions at the walls are imposed by the use of a fictive limit at the outer boundary of the viscous sublayer where the velocity is described by the classical logarithmic distribution.

ii) In an infinite medium, where the equations are prealably transformed using the Von Mises variables (x,ψ). Following the ideas of PATANKAR et al (25) we have worked out an original version of computing the equations in which particular attention has been given on :

. the determination of the step Δx in function of the transverse network chosen, in order to obtain automatically the stability of the method.

. The regularisation of the flux at the free boundary of the jet whatever be the matching conditions imposed by the different profiles.

. The iterative procedure for the source terms implied by the downstream discretisation which brings out unknown values of the functions in the calculated section. This point is as important as the diffusion term of the momentum equation of the R.S.T. models is effectively considered as a source term (abandon of the eddy viscosity even as an intermediate variable in the calculation).

RESULTS AND DISCUSSION

Among the available results, we have chosen those whose parameters make the comparison easier. We shall successively discuss the three following points :

i) Streamwise variation (along x) of the characteristic values of different variables

ii) Transversal distributions (variation along r or y)

iii) Turbulent energy balances.

Streamwise variations

Axial velocity. The first representative parameter of the longitudinal effect of the perturbation is naturally the center line velocity $U_{\text{℄}}$. In the Fig.2 are shown the different relations obtained numerically as well as experimentally for each flow pattern. For the configuration B, the mean center line velocity has been arbitrarily located at the coordinate y = 2H.

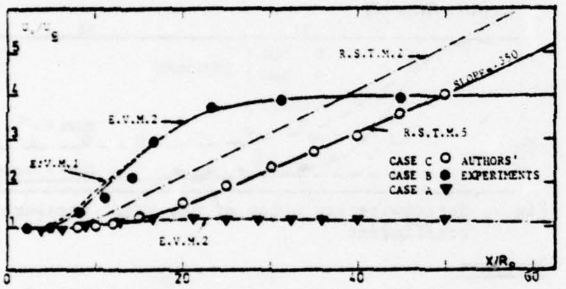

Fig.2. Streamwise variation of $U_{\text{℄}}$

One can notice that, in spite of the disappearance of the potential core in the case C, the velocity weakly decreases along the axis within the first sections. On the contrary, for the case B the sudden enlargement of the geometry leads to a rapid decrease of this parameter. Consequently, the comparison of these two configurations does not exhibit a simple link with the enlargement factor α. Furthermore, whereas, for case B, the ratio $U/U_{\text{℄}}$ tends to a finite constant value (4 when α equals 1) , it linearly varies with $(x-x^{*})$ for the case C. The value of the slope (0.350) deduced from R.S.T.5 model is very close to those obtained by several workers, see for instance WYGNANSKI et al (11) who has obtained, for very different exit conditions, 0.356. These characteristics are reached at downstream distances respectively equal to $20R_o$ and $40R_o$; the calculation shows in addition that, in case C the "pole" of the jet is located at the abscissa $x^{*} = 3R_o$. In the first configuration, after a small initial acceleration $(x \leqslant 5H)$, and a subsequent small deceleration $((U_{\text{℄}}/U_o)_{mini} = 0.88)$ the flow gradually gets back its initial velocity.

So far as the numerical predictions are concerned, one can note that, in case B, the influence of initial boundary layer thickness, as shown by the E.V.M.2, vanishes as the abscissa becomes $20R_o$. In case C, such types of models do not lead to satisfactory decrease of the center line velocity, except by the use of ad hoc empirical adjustements (26).

Axial turbulent energy

In Fig.3 are shown the evolutions of the axial turbulent energy ($k_{\text{℄}}$) for the two cases B and C.

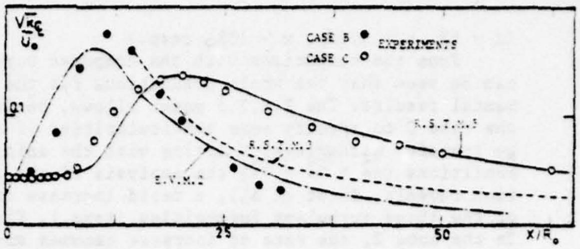

Fig.3. Streamwise variation $k_{\text{℄}}$

This quantity has been normalised by dividing by U_o^2 in order to compare the energy levels. For both cases the energy reaches a maximum value (corresponding to x = 11.5 Ro and 20 Ro resp.) , the level of which is higher for the separated flow than for the jet ($3.5\ 10^{-2}$ and $1.9\ 10^{-2}$ resp.)

Dealing with the numerical predictions, it can be noticed that the results computed from the R.S.T.5 model fit the experimental measurements better than those obtained with the E.V.model (in the case B). This could arise from many reasons : a relative inadaptation of the E.V.model to predict strongly perturbed flow, although limited in the space ; a better accuracy of the numerical values computed through a closer network in the parabolical case ; rather poor precision of the measurements (in case B) due to the lack of direct $\overline{w^2}$ values, and the consequent assumption needed for k $(\overline{v^2} = \overline{w^2})$. Such an approximation can be particularly wrong in the vicinity of the separation point where the energy distribution over the three components is highly anisotropic.

Turbulent intensities. The center line value of k does not correspond to the maximum of its distribution. The streamwise variations of the r.m.s peak values for each fluctuating velocity component, as indicated by $\tilde{u}$, $\tilde{v}$ and $\tilde{w}$ respectively, are then given, in the adimensional form (after division by Uo) in Fig.4.

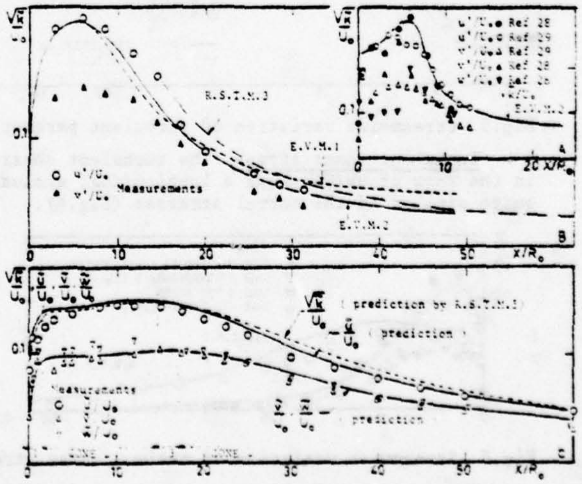

Fig.4. Streamwise variation of turbulent maximum intensities.

In the case A, the experimental results of HSU (28) and CHANDRSURA (29) are also plotted and clearly indicate the influence of different inlet conditions. One can also notice that each of the maxima, in the above cases, appear at different downstream distances.

($x = 6H$, $x \sim 5.6R_o$, $x \sim 15R_o$ resp.)

From the comparison with the computed curves, it can be seen that the whole predictions fit the experimental results. The R.S.T.5 model allows, besides, in the case C to specify some particularities of the energy transfer mechanisms. Starting with the anisotropic conditions ($\overline{u^2} > \overline{w^2} > \overline{v^2}$) the analysis of the computation reveals, first of all, a rapid increase of each of the three turbulent intensities.(zone 1. Fig.4c). In the zone 2, the rate of increase becomes smaller although the difference between the $\tilde{v}'$ and $\tilde{w}'$ values vanishes. The equality is achieved when u' reaches its maximum ($x \sim 15Ro$). Up to $x = 17Ro$, the v' and w' components are quite identical, and increase (zone 3) while u' has already started decreasing. Finally in the zone 4, the general evolution towards the characteristic distributions of the round turbulent jet takes place progressively.

In order to complete the analysis of the last flow pattern, we have plotted in Fig.5, the dimensionless values : $\tilde{u}/U_{\mathbb{C}}$,... One can thus conclude that the self preserving condition of the u' distribution is reached before those for v' and w'. The numerical values (50Ro and 64Ro resp.) are lower than those given by WYGNANSKI et al (11). We feel that this could be explained by the exit characteristics which are quite different in the two experiments : a quasi laminar flow on one hand, a fully developed pipe flow on the other.

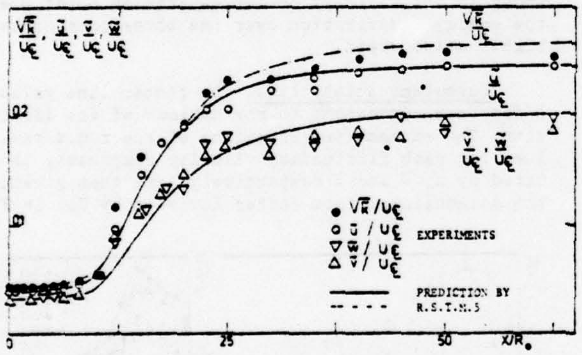

Fig.5. Streamwise variation of turbulent parameters.

Turbulent shear stress. The turbulent shear stress in the form of uv/U_o shows a longitudinal evolution quite similar to the normal stresses (Fig.6).

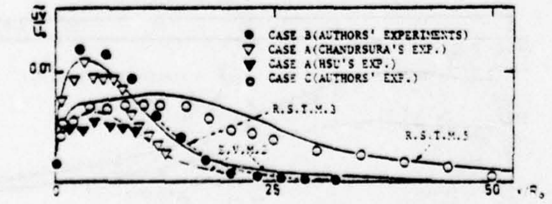

Fig.6. Streamwise variation of maximum shear stress.

The decrease of this parameter, yet stabilises earlier than that of the turbulent energy. Moreover, the corresponding levels of the results (28)(29) are about two times different in relation to the small thickness of the initial boundary layer in the second case. The differences which occur, between the prediction and the experiment for small values of x/Ro, are more difficult to interpret, due to the real difficulties in measuring precisely the maxima of fluctuating quantities subjected to steep spatial variations. These observations are equally valid on the normal stresses.

Total pressure and jet expansion. We conclude the presentation of the streamwise evolutions with that of the total center line pressure (Fig.7).

$$P_* = P_{\mathbb{C}} + \frac{1}{2}\rho U_{\mathbb{C}}^2 \qquad (15)$$

This parameter is deduced from the momentum equation :

$$\frac{dP_*}{dx} = -\rho \frac{d}{dx}(\overline{u_{\mathbb{C}}^2} - \overline{v_{\mathbb{C}}^2}) - \lim_{r \to o}\left[\frac{1}{r}\frac{\partial}{\partial r}(r\overline{uv})\right] \qquad (16)$$

In the case B, the extrapolation of the curve towards $x = 0$ (Fig.7) leads to the value -0.59, altogether comparable to that given by the Borda's formula (-0.56). In case C, the total pressure drop is lower since the dynamic pressure alone varies in that flow configuration according to the spanwise law of the jet. The computed value of the expansion rate corresponding to the self-preserving region is constant (0.085) and quite similar to the classical measured ones (12).

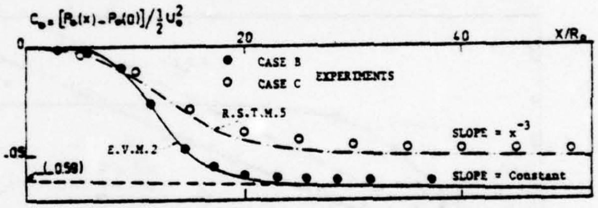

Fig.7. Streamwise variation of the total pressure coefficient.

Profiles

Velocity profiles. Some of the mean velocity profiles in the two recirculating flows are plotted in Fig.8 and 9. Downstream of the reattachment point, the velocity profiles are of the wake type, except in the vicinity of the wall. They inversely get transformed with respect to the evolution in the boundary layer upstream of the separation. The equilibrium form which corresponds to a first stage of flow restructuration is reached when $x = 35H$ - case A - and $30Ro$ - case B - These values are obtained from the examination of the logarithmic law at the wall.

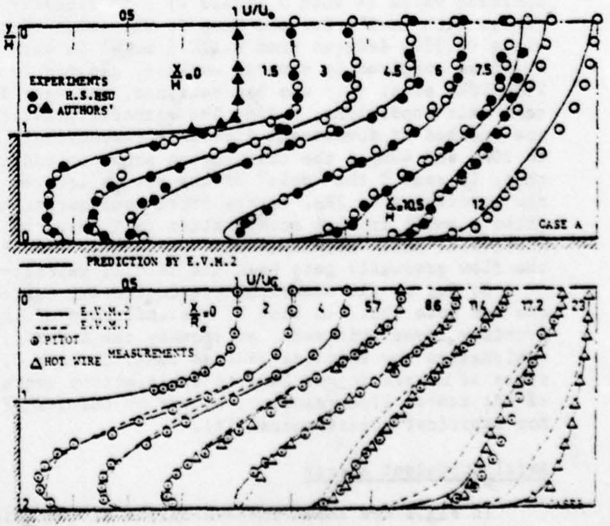

Fig. 8 - 9 : Mean velocity profiles.

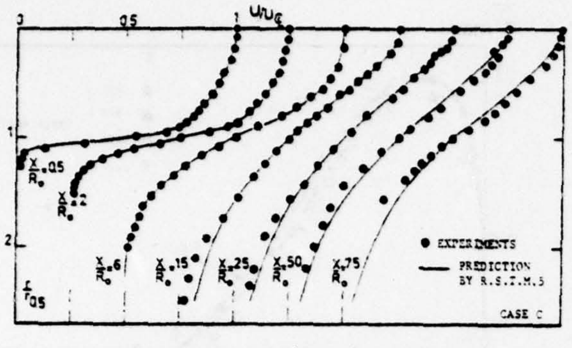

Fig.10. Mean velocity profiles (case C).

The result in the case C are given in Fig.10. In spite of the absence of reverse flow, one can observe a clear evolution from the pipe distribution towards the jet one (appearance of an inversion point). The similitude of the velocity profiles is almost achieved in the section $x/R_0 = 50$.

Reynolds stresses. The normal turbulent stresses are shown in Fig.11 and reveal some analogies between the restructuration mechanisms of the different flows:

1) Sudden increase of the maximum and center line values

ii) Shift of the peak values towards the axis.

It may be noticed that $\overline{u^2}$ reaches its maximum (along x) upstream of $u_{℄}$. This confirms a more regular distribution of the energy beyond the section where $\overline{v^2} = \overline{w^2}$. Dealing with the $\overline{v^2}$ component, it can be mentionned that in the two cases, the maximum value reaches the axis, which does not occur for $\overline{u^2}$ in the round jet, at least up to x = 200Ro.

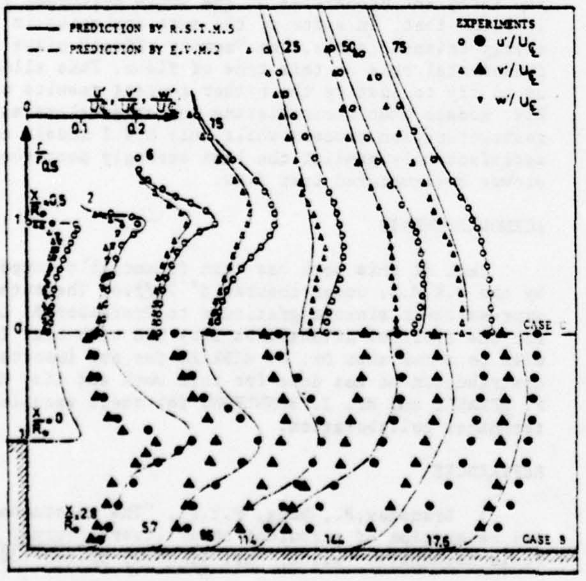

Fig.11. Turbulent intensities.

The tangential component is given in Fig.12. The maximum value of the distribution is roughly located at constant distances of about Ro from the axis. This result, already shown by (10) and (30) for the round jet with uniform initial velocity seems to indicate that this parameter is relatively insensitive to the inlet conditions. We can complete this remark by the fact that the linear part of the distribution (near the axis) associated with the duct flow, almost disappears in the two cases B and C when x = 4Ro.

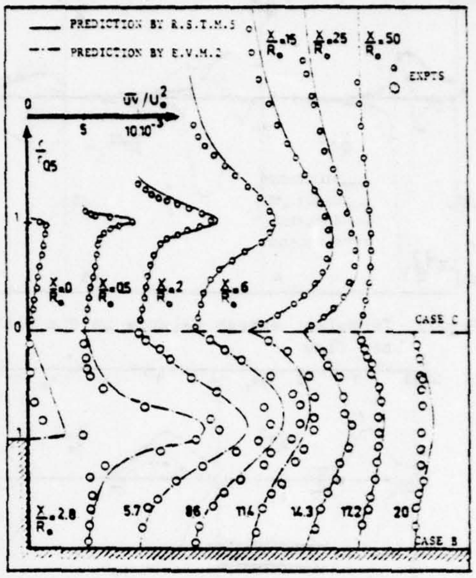

Fig.12. Turbulent shear stress.

Energy balance

To make the comparison easier, the energy balances have been plotted for each flow cases in three particular sections. The first one, located near the singularity, corresponds to roughly constant values of x/δ (x = 3H for cases A and B, x = 6Ro for case C). The second one is taken in the zone of decreasing turbulent intensity, that is slightly downstream of the reattachment point (x = 6H and x = 12Ro for cases A and B) and at x = 15Ro for case C. The last one is situated in the restructurating flow.

Certain analogies can be deduced between the three cases in Fig.13a.14a.15a in spite of the fact that the levels are not exactly the same. This upstream section is characterised by a strong production of turbulent energy associated with an intense mean deformation rate. The energy is partly convected by the mean velocity, partly diffused towards the axis and the outer boundary of the mixing layer. The rest of the production is dissipated at the same place. Thus the flow, in this section is far from equilibrium since convection, diffusion and dissipation are of the same order.

In the intermediate section Fig.13b.14b.15b, the production decreases in its amplitude but spreads out in space, due to the mixing layer expansion. The diffusion, still quite important, progressively decreases, while the dissipation tends to overtake the convection.

Finally we observe Fig.13c.14c.15c, that for the cases A and B, the peaks of production and dissipation shift towards the wall, while the diffusion gets reduced. Dealing with the longitudinal evolution of these energy balances, one can notice that although the reattachment takes place earlier in the case A (x = 6.4H instead of 9Ro for the B case), the restructuration is slower than in a confined flow. This point is confirmed by the results of the jet where the tendancy towards the restructuration takes place far away downstream. At x = 200Ro, the curves are quite similar to those obtained by WYGNANSKI et al (11) thus confirming the recovery of a classical jet type flow out-of-equilibrium, contrary to the cases A and B.

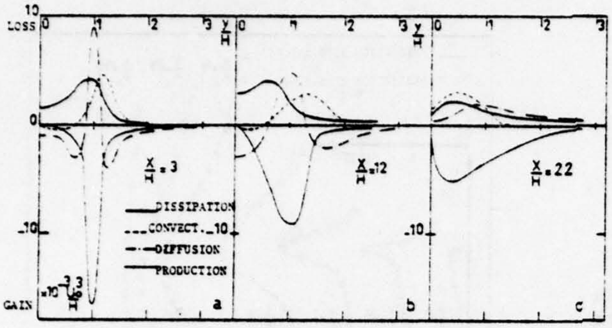

Fig.13. Turbulent energy balance in the plane separated flow

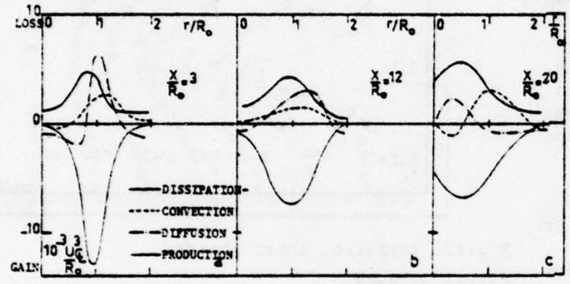

Fig.14. Turbulent energy balance in the confined separated flow

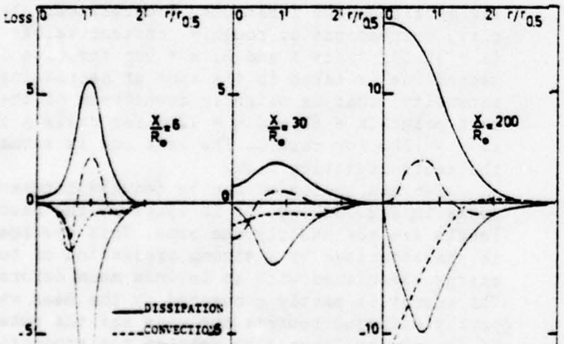

Fig.15. Turbulent energy balance in the jet.

CONCLUSION

The restructuration of turbulent flows after a strong boundary perturbation has been studied both experimentally and theoretically, on the basis of single point closure models. The comparison, between the three flow patterns analysed, indicate that the simple shear layer structure is achieved earlier in separated confined flow (B) than in the case of semi infinite one (A) and finally in the case of infinite domain (jet flow C).

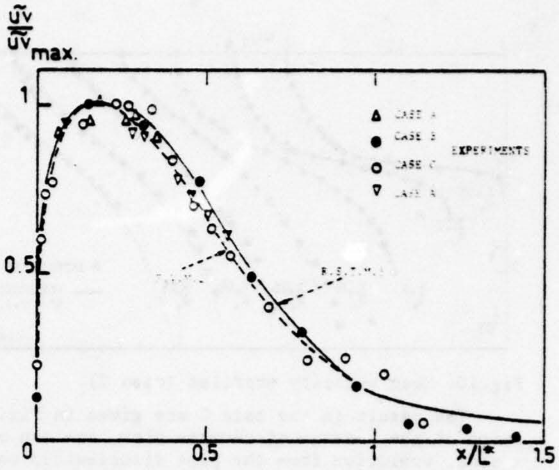

Fig.16. "Universal" streamwise variation of the dimensionless maximum shear stress.

If we focuss our attention on the mean velocity profiles, the previous classification corresponds to an increasing value of the number of scales necessary to define the flow after the relaxation (none for the case B, one transversal length scale for the case A, one velocity and one length scale for the last case). It seems therefore quite natural to introduce at least one extra scale to characterise the perturbed zone. If we choose for example the longitudinal distance L where the maximum turbulent shear becomes equal to its initial value, it is then possible to group the longitudinal variations for each case into one single curve (Fig.16). The above classification corresponds now to increasing values of this length scale.

Although this single parameter cannot represent the turbulent properties of the whole perturbed zone, it seems that, in spite of the sure analogies in the energy balance levels, the "memory effect" plays a fundamental role on this type of flows. This allows us to try to justify the rather correct results of the E.V. models when recirculating motion accelerates the restructuration process while only R.S.T models can satisfactorily predict the less strongly perturbed but slower restructured last flow.

ACKNOWLEDGMENTS

Part of this work has been financially supported by the D.R.M.E. under contrat n° 73/546. The authors express their sincere gratitude to Professor B. LAUNDER for the fruitful discussions they had with him. They wish to thank also Dr. P. HEBRARD for the important contribution he has done for this work and also Miss P. HERAULT and Mr. J. BONNEFONT for their excellent technical collaboration.

REFERENCES

1 Bradshaw,P., Wong, F.Y.F., "The reattachment and relaxation of turbulent shear layer" Journal of Fluid Mechanics, Vol.52, Part 1, 1972, pp.113-135

2 Chaturvedi,M.C., "Flow characteristics of axisymmetric expansions" Journal of the Hydraulics Division, May 1963, pp.61-62

3 Runchal,A.K. "Steady turbulent flow and heat transfer downstream of a sudden enlargement in a pipe of circular cross section" EF/TN/A/39 June 1971, Imperial College of London.

4 Hebrard,P. "Réponse d'un écoulement turbulent incompressible à la perturbation due à un décollement" Juillet 1973, Thèse d'Etat. Université P. Sabatier de Toulouse.

5 Tani,I., Iuchi,M., Komoda,H. "Experimental investigation of flow separation associated with a step or a groove" Report n°364, April 1961, Aeronautical Research Institut University of Tokyo.

6 Green,J.E., "Two dimensional turbulent reattachment as a boundary layer problem" Proceedings of A.G.A.R.D. Meeting on Separated flow (1966)

7 Narayanan, M.A., Khadgi,Y.N., Viswanath, P.R. "Similarities in pressure distribution in separated flow behind backward facing steps" Aeronautical Quaterly, Nov. 1974

8 Masbernat,L.,"Contribution à l'étude du décollement dans les écoulements turbulents de fluides incompressibles" Thèse de Doctorat, Toulouse, 1968.

9 Corrsin, S., Uberoi, M.S., "Further experiments on the flow and Heat Transfer in a heated turbulent air jet" April 1949 - NACA Technical note n°1865 Washington.

10 Davies,P.O.A.L., Fisher, M.J., Barratt,M.J., "The characteristics of the turbulence in the mixing region of a round jet" Journal of Fluid Mechanics (1963) Vol.15, part.3, pp.337-367

11 Wygnanski,I., Fiedler,H., "Some measurements in the self preserving jet" Journal of Fluid Mechanics (1969) Vol.38, Part.3, pp.577-612

12 Rodi,W.,"The prediction of free turbulent boundary layers by use of a two-equation model of turbulence" Dec.1972, Thesis P.D. university of London Imperial College of London.

13 Ha Minh,H., "Contribution à l'étude des écoulements turbulents décollés externes" Déc.1969, Thèse D.I. Université de Toulouse.

14 Barrat,M., "Détermination des pressions statiques dans les écoulements turbulents" C.R.A.S. série A, Janv.1962,n°5,p.467.

15 Guitton,D.E., "Correction of hot wire data for high intensity turbulence longitudinal cooling and probe interference" Mc Gill University Montreal Canada, n°69-12134 (1968)

16 Champagne,F.H., Sleicher,C.A.,"Turbulence measurements with inclined hot-wires" Journal of Fluid Mechanics (1967), vol.28, part.1

17 Saiy,M., PEERLESS,S.J., "Measurement of turbulent quantities in a two-stream mixing layer". Imperial College of London. BL/TN/A/56 (1972)

18 Chassaing,P., "Méthode de mesure par anémométrie à fil chaud" n°88 SA (Oct.1974)and "Etalonnage des propriétés directionnelles de sondes à fil chaud" n°80 SA (Fév. 1974)

19 Chassaing,P., Ha Minh,H.,"Modèles mathématiques de la turbulence. Schémas de base" Proceeding of Journées Franco-Polonaises, Gdansk. Nov.1976

20 Launder,B.E., Reece,G.J., Rodi,W., "Progress in the development of a Reynolds stress turbulence closure" Report HTS/73/31. Dec.1973. Imperial College of London.

21 Ha Minh,H., "Décollement provoqué d'un écoulement turbulent incompressible" Thèse d'Etat. Fév. 1976. Institut National Polytechnique de Toulouse.

22 Chassaing,P., Ha Minh,H., "N.S.E.P.T. une nouvelle solution des équations paraboliques de la turbulence" Rapport E.T.F. 14, 1976. Institut de Mécanique des Fluides de Toulouse.

23 Gosman,A.D., Pun,W.M., Runchal,A.K., Spalding D.B., Wolfshtein,M., "Heat and Mass transfer in recirculating flows" Academic Press, 1969

24 Greenpan,D., "Lectures on the numerical solution of linear singular and non linear differential equations" Prentice Hall (1968)

25 Patankar,S.V., Spalding,D.B., "Heat and mass transfer in boundary layers" Intertext books, London, 2nd Edition (1970)

26 Chassaing,P., Ha Minh,H., "Détermination numérique des caractéristiques moyennes d'un jet de tube turbulent : stabilité des calculs et choix des échelles" C.R.A.S. t.280, série B (1975) pp.699

27 Sami,S., Carmody,T., Rouse,H., "Jet diffusion in the region of flow establishment" Journal of Fluid Mechanics (1967) vol.27, part.2, pp.231-252

28 Hsu,H.C., "Characteristics of mean flow and turbulence at an abrupt two-dimensional expansion" Thesis P.D. University Iowa. Feb.1950

29 Chandrsura,C., "A reattaching turbulent shear layer in incompressible flow" Thesis P.D. University of London, Dec. 1975.

TURBULENCE MODELING OF SHOCK SEPARATED BOUNDARY-LAYER FLOWS

By

Thomas J. Coakley and John R. Viegas

Ames Research Center, NASA
Moffett Field, Calif., 94035

ABSTRACT

Computations of transonic and hypersonic shock-separated boundary-layer flows using zero-equation (algebraic), one-equation (kinetic energy), and two-equation (kinetic energy plus length scale) turbulence eddy viscosity models are described and compared with measurements. The computations make use of a new Navier-Stokes computer algorithm that has reduced computing times by one to two orders of magnitude. The algorithm, and how the turbulence models are incorporated into it, are described. Results for the transonic flow show that the unmodified one-equation model is superior to the zero-equation model in skin-friction predictions. For the hypersonic flow, a highly modified one-equation model that accurately predicts surface pressure and heat transfer is described. Preliminary two-equation model results are also presented.

NOMENCLATURE

C_F	skin-friction coefficient: TSBLI, $2\tau_w/\rho u_e^2$ HSBLI, $2\tau_w/\rho_\infty u_\infty^2$
C_H	Stanton number, $q_w/\rho_\infty u_\infty c_p(T_o-T_w)$
$c, \bar{c}$	sound speeds, $\gamma p/\rho$, $\gamma\bar{p}/\rho$
c_p, c_v	specific heats at constant pressure and volume, respectively
D	velocity divergence, $u_x + v_y + v/r$
E	total specific energy, $e + (u^2 + v^2)/2$
e	specific internal energy, $c_v T$
H_k, H_s	turbulence source functions
k	turbulence kinetic energy $\overline{\rho u_i'' u_i''}/2\rho$
L	length scale function 1-, 2-equation models
ℓ	length scale function 0-equation models
M	Mach number
p	static pressure
$\bar{p}$	combined pressure, $p + 2\rho k/3$
q_w	wall heat flux
R	HSBLI, center body radius; TSBLI, duct radius
Re_{x_o}	free-stream Reynolds number
R_T	turbulence Reynolds number, $\rho\sqrt{k}\,L/\mu$
r	radial coordinate
s	additional length scale defining turbulence variable
T, T_o	temperature, stagnation temperature
u,v	velocity components x and y direction
x	axial coordinate
x_o	TSBLI, axial location of foot of shock pressure rise measured from nozzle throat HSBLI, axial location of inviscid shock intercept with wall measured from apex of center body
y	distance normal to wall, HSBLI, r-R; TSBLI, R-r
γ	ratio of specific heats, c_p/c_v
δ	boundary-layer thickness
δ_o	boundary-layer thickness just ahead of shock, 1 in., Figs. 1 and 2
θ	shock generator angle, 15°, Fig. 2
μ	molecular viscosity
μ_T	turbulent eddy viscosity
ρ	density
τ_w	wall shear

Subscripts

e	boundary-layer edge
w	wall value
x,y	partial derivatives in x and y, $\partial/\partial x$, $\partial/\partial y$
∞	free-stream value

INTRODUCTION

Recent advances in computer algorithms (1) for the viscous gas-dynamics equations have reduced computing times by one to two orders of magnitude and have facilitated systematic studies of turbulence models for complex flows. This paper represents such a study and presents solutions for two shock-separated turbulent boundary-layer flows.

The experiments were conducted at Ames Research Center. The first of these (shown in Fig. 1) consists of a transonic normal shock-wave boundary-layer interaction (TSBLI) in a circular duct at an upstream Mach number of about 1.4 (2). The second flow (Fig. 2) consists of a hypersonic oblique-shock-wave boundary-layer interaction (HSBLI) in axially symmetric flow at Mach numbers of about 7 (3). The documentation for these flows includes surface measurements and mean and fluctuating flow-field measurements (2,4,5).

These flows are simulated by numerically solving the time-averaged compressible Navier-Stokes equations incorporating sets of zero-, one-, and two-equation models of turbulence. Zero-equation models constitute the simplest of a class of turbulence models in which the turbulent stress tensor and heat flux are modeled

PRECEDING PAGE BLANK-NOT FILMED

by means of an eddy visocity function. The more advanced members of the class are the one- and two-equation models in which additional field variables are introduced and used to represent the eddy viscosity function (6,7). Considerable success has been achieved with these advanced models in simpler flows where the zero-equation model has not been so successful (8-11). The purpose of this paper is to describe how these models have been incorporated into the Navier-Stokes code and to present initial applications using them.

ANALYSIS

Governing Equations

The differential equations used in this study are the time-dependent, mass-averaged Navier-Stokes equations for axially symmetric flow of a compressible fluid. Depending on the turbulence model used, these equations are augmented by additional equations; that is, the one-equation or kinetic-energy model employs one additional equation while the two-equation models employ two additional equations. All models use the eddy viscosity hypothesis, that is, the Reynolds stress, heat-flux and kinetic-energy flux terms are assumed related to the mean-flow velocity, temperature and kinetic energy gradients through an eddy transport coefficient that is simply added to the corresponding molecular viscosity or transport coefficient. The same hypothesis is used for the second field variable in the two-equation models. Additional conditions on the equations include the perfect gas assumption, constant specific heats, the Sutherland viscosity law, and zero bulk viscosity. The resulting equations, expressed in conservation form are written as follows:

$$U_t + F_x + r^{-1}(rG)_y = H \tag{1}$$

$$\left.\begin{aligned} U &= \begin{bmatrix} \rho \\ \rho u \\ \rho v \\ \rho E \\ \rho k \\ \rho s \end{bmatrix} \qquad F = \begin{bmatrix} \rho u \\ \rho u^2+\sigma_{xx} \\ \rho vu+\tau_{xy} \\ (\rho E+\sigma_{xx})u+\tau_{xy}v+q_{ex} \\ \rho ku+q_{kx} \\ \rho su+q_{sx} \end{bmatrix} \\ H &= \begin{bmatrix} 0 \\ 0 \\ \sigma_{\theta\theta}/r \\ 0 \\ H_k \\ H_s \end{bmatrix} \qquad G = \begin{bmatrix} \rho v \\ \rho uv+\tau_{xy} \\ \rho v^2+\sigma_{yy} \\ (\rho E+\sigma_{yy})v+\tau_{xy}u+q_{ey} \\ \rho kv+q_{ky} \\ \rho sv+q_{sy} \end{bmatrix} \end{aligned}\right\} \tag{2}$$

$$\left.\begin{aligned} &\sigma_{xx} = \bar{p}-2\mu_v(u_x-D/3) && q_{ex} = -\mu_e e_x \quad q_{ey} = -\mu_e e_y \\ &\sigma_{yy} = \bar{p}-2\mu_v(v_y-D/3) && q_{kx} = -\mu_k k_x \quad q_{ky} = -\mu_k k_y \\ &\sigma_{\theta\theta} = \bar{p}-2\mu_v(v/r-D/3) && q_{sx} = -\mu_s s_x \quad q_{sy} = -\mu_s s_y \\ &\tau_{xy} = -\mu_v(u_y+v_x) && D = u_x+v_y+v/r = \operatorname{div}\vec{u} \\ &E = e+(u^2+v^2)/2 && \bar{p} = p+2\rho k/3 \\ &e = c_v T && p = (\gamma-1)\rho e \\ &\qquad\qquad y = r-R && \end{aligned}\right\} \tag{3}$$

These equations are written explicitly for the hypersonic flow problem where R is the radius of the center body. For the transonic problem, R represents the radius of the duct and the equations may be obtained from the given ones by the transformation

$$y \to R - r,\ dy \to -dy,\ v \to -v \tag{4}$$

with all other variables unchanged.

Numerical Method

The numerical procedure used to solve these equations is the basic MacCormack method which has been modified and improved by the incorporation of a new algorithm called the Rapid Solver (1). We include here a brief description of the new method including its adaptation to the additional turbulence-model equations.

The field vector U in Eq. (1) is discretized on a computational mesh and advanced in time by means of a symmetric sequence of operators as indicated below.

$$\left.\begin{gathered} U(t+2\Delta t) = \mathscr{L}(2\Delta t)U(t) \\ \text{Outer Mesh} \\ \mathscr{L}(2\Delta t) = \begin{Bmatrix} \mathscr{L}_x(\Delta t)\mathscr{L}_y(\Delta t)\mathscr{L}_y(\Delta t)\mathscr{L}_x(\Delta t) & ;\text{HSBLI} \\ \mathscr{L}_x(\Delta t)\mathscr{L}_y(2\Delta t)\mathscr{L}_x(\Delta t) & ;\text{TSBLI} \end{Bmatrix} \\ \text{Inner Mesh} \\ \mathscr{L}(2\Delta t) = \begin{Bmatrix} [\mathscr{L}_x(\Delta\tau)\mathscr{L}_p(\Delta\tau)\mathscr{L}_h(\Delta\tau)\mathscr{L}_h(\Delta\tau)\mathscr{L}_p(\Delta\tau)\mathscr{L}_x(\Delta\tau)]^N & ;\text{HSBLI} \\ [\mathscr{L}_h(\Delta\tau)\mathscr{L}_p(\Delta\tau)\mathscr{L}_x(2\Delta\tau)\mathscr{L}_p(\Delta\tau)\mathscr{L}_h(\Delta\tau)]^N & :\text{TSBLI} \end{Bmatrix} \\ \Delta\tau = \Delta t/N \end{gathered}\right\} \tag{5}$$

In the outer or inviscid part of the mesh the mesh spacing in the y direction is relatively coarse, and the original, explicit, MacCormack operators $\mathscr{L}_x$ and $\mathscr{L}_y$ are used. In the inner or viscous part of the mesh, close to the wall, the mesh spacing is selected sufficiently fine to resolve the turbulent boundary layer in the viscous sublayer. This imposes severe time step limitations on the explicit operators and has motivated the adaptation of the Rapid Solver. In this algorithm the explicit operator, $\mathscr{L}_y$, is replaced by two new operators, $\mathscr{L}_h$ and $\mathscr{L}_p$, which dramatically reduce computing times. The operators used, defined by the equations they solve according to the concept of time splitting, are shown below. Also shown are the maximum stable time steps associated with each operator, and the total time step $2\Delta t$.

$$\mathscr{L}_x(\Delta t_x):U_t+F_x = 0 \quad ;\Delta t_x = \min[\Delta x/(|u|+c+\nu_x/\Delta x)] \tag{6}$$
$$\mathscr{L}_y(\Delta t_y):U_t+r^{-1}(rG)_y = H \quad ;\Delta t_y = \min[\Delta y/(|v|+c+\nu_y/\Delta y)] \tag{7}$$
$$\mathscr{L}_p(\Delta t_p):U^v_t-r^{-1}(rG^v)_y = H^v;\Delta t_p = \infty \tag{8}$$
$$\mathscr{L}_h(\Delta t_h) = \mathscr{L}_b(\Delta t_h)\mathscr{L}_a(\Delta t_h) \quad ;\Delta t_h = \min(\Delta y/|v|) \tag{9}$$
$$\mathscr{L}_a(\Delta t_h):\rho v^c_t+\bar{p}^c_y = 0 \quad ;\bar{p}^c_t+\rho\bar{c}^2(v^c_y+v^c/r) = 0 \tag{10}$$
$$\bar{p}^c = p^c+2\rho k/3 \quad ;\bar{c}^2 = \gamma\bar{p}^c/\rho \tag{11}$$
$$\mathscr{L}_b(\Delta t_h):U_t+r^{-1}(rG^c)_y = H^c \tag{12}$$

$$G^c = \begin{bmatrix} \rho v^c \\ \rho uv^c \\ \rho vv^c+\bar{p}^c \\ (\rho E+\bar{p}^c)v^c \\ \rho kv^c \\ \rho sv^c \end{bmatrix} \qquad H^c = \begin{bmatrix} 0 \\ 0 \\ \bar{p}^c/r \\ 0 \\ 0 \\ 0 \end{bmatrix} \tag{13}$$

$$U^v = \begin{bmatrix} \rho u \\ \rho v \\ \rho e \\ \rho k \\ \rho s \end{bmatrix} \quad G^v = \begin{bmatrix} \mu_v u_y \\ 4\mu_v v_y/3 \\ \mu_e e_y \\ \mu_k k_y \\ \mu_s s_y \end{bmatrix} \quad H^v = \begin{bmatrix} H_u \\ H_v \\ H_e \\ H_k \\ H_s \end{bmatrix} \tag{14}$$

$$\left.\begin{aligned} &\text{Outer Mesh}:\Delta t_c = \min(\Delta t_x,\Delta t_y/M_n) \\ &\text{Inner Mesh: } N = \operatorname{Int}[\Delta t_c/\min(\Delta t_h,\Delta t_x/M_n)+1] \\ &\qquad \text{HSBLI: } M_n = 1 \qquad \text{TSBLI}:M_n = 2 \\ &2\Delta t = 2\cdot\text{CFL}\cdot\Delta t_c \qquad\qquad \text{CFL} = .9 \end{aligned}\right\} \tag{15}$$

The source term, H^v, is $H-H^c$ plus the terms in $G-G^c$ that are not included in G^v, with $\bar{p}^c$ and v^c interpreted as $\bar{p}$ and v.

In Eq. (5) the number of operators and their sequencing order may be, to a certain extent, arbitrary. The number and sequencing of operators shown for the two problems has been chosen to minimize the number of computing operations in real time, t.

The operator $\mathscr{L}_h$ is called the hyperbolic operator because the equations it solves are hyperbolic in space-time. It is split into two subsidiary operators $\mathscr{L}_a$ and $\mathscr{L}_b$. The operator $\mathscr{L}_a$ solves the simplified set of equations for velocity, v^c, and combined pressure, $\bar{p}^c$, given by Eqs. (10) and (11), by a linearized method of characteristics. In this operation the local densities and sound speeds, $\bar{c}$, are considered constant over the time interval and an auxiliary network of grid points is constructed with spacings proportional to the local sound speed. This enables the pressures and velocities at each point in space-time to be computed by means of simple arithmetic and the solution advanced over the many characteristic time steps required to advance the solution the full time step $\Delta\tau = \Delta t/N$ which is a large fraction of the total time step, $2\Delta t$. The pressures and velocities, $\bar{p}^c$ and v^c, resulting from this computation are averaged in space and time and saved for use with the operator $\mathscr{L}_b$.

The operator $\mathscr{L}_b$, which solves Eq. (12), is the standard explicit MacCormack operator with one important difference. Use of the convection velocity v^c and combined pressure $\bar{p}^c$, time averaged over the relatively large time step $\Delta t/N$, in place of the local velocity and pressure v and p, evaluated basically at the original time level, allows the maximum stable time step to be increased from $\Delta t_y = \min[\Delta y/(|v| + c)]$ to $\Delta t_y = \min(\Delta y/|v|)$. This is a substantial increase because of the elimination of the sound speed, c, from the relationship.

The modification in the operator $\mathscr{L}_a$ arising from the additional turbulence model equations consists of using the combined pressure $\bar{p}^c = p^c + 2\rho k/3$ which includes the turbulence pressure, $2\rho k/3$, rather than the static pressure, p^c, alone. The modification is accomplished by combining the turbulent energy equation in Eq. (12) with the equation for p^c to form the equation for $\bar{p}^c$. Initial computations using only p^c, and placing $2\rho k/3$ in Eq. (8) for $\mathscr{L}_p$, were weakly unstable in that a high-frequency self-sustained oscillation in the pressure and velocity were observed at all mesh points very close to the wall.

The operator $\mathscr{L}_p$ is called the parabolic operator, and solves an essentially parabolic set of equations in time. It is implicit and uses the Thomas algorithm to invert a set of scalar tridiagonal matrices which include the diffusion terms, G^v, shown in Eq. (14). The source terms H_u and H_v for the velocity equations are generally small and are treated explicitly. The solutions for the velocities are advanced in time first. The solutions for the remaining variables are then advanced, using the updated velocities in the source terms which may be large and can cause instabilities if treated explicitly. The source terms for the turbulence model equations will be shown in detail later. The density is absent from the equations, having been fully updated by the $\mathscr{L}_h$ operator.

As stated earlier, the computational grid is divided into a coarse, outer mesh and a fine inner one. The mesh points in the outer mesh are uniformly spaced while those in the inner mesh are stretched exponentially in the y direction with the first mesh point away from the wall being at a value $y_2^+ = \sqrt{\rho\tau_w}y_2/\mu_w$, less than 5, placing it in the viscous sublayer. In the x direction, the grid point spacing is uniform in both inner and outer grids and is relatively coarse, Δx being about $0.5\delta_o$ in the hypersonic problem and $1\delta_o$ in the transonic problem. The value of δ_o for both problems is 1 inch. The specific number of grid points in the fine and coarse grids is as follows. For the HSBLI problem: 29 points in the x-direction, 45 points in the y-direction, and 20 points in the fine grid. The corresponding numbers in the TSBLI problem are 36, 30, and 20. A finer distribution of points was investigated in the early stages of this study. It was found that although considerably better resolution of the inviscid flow field and shock were possible, details of the surface-pressure, skin-friction and heat-transfer predictions using the coarse grid were in reasonable agreement with those of the fine grid computations.

Boundary and initial conditions used for the mean-flow variables are described in earlier studies (2,3). Boundary and initial conditions used for the turbulence variables will be described in the section on turbulence modeling.

The reduction in computing time resulting from the new algorithm is substantial, being about a factor of 10 for HSBLI problem and a factor of 60 for the TSBLI problem. Typical computing times to obtain fully converged solutions starting with the basic initial conditions are about 5 min on a CDC 7600 computer for the HSBLI problem, and 20 min for the TSBLI problem.

TURBULENCE MODELS

This section describes the various turbulence models that are under study. The reasons for studying eddy viscosity models, in contrast to other models, lies in their simplicity, their close relationships to one another, their wide use and proven capabilities for simpler flows, and what may be called their code compatibility. The first three items are covered in the book by Launder and Spalding (6) and will not be discussed here. The last item, code compatibility, deserves some comment. Code compatibility refers to the ease of incorporation into the Navier Stokes algorithm described in the previous section. Other turbulence models such as the Bradshaw one-equation model (12) and the Donaldson Reynolds stress model (13) appear to be more difficult to code. The reason for this rests in the nature of the parabolic operator $\mathscr{L}_p$. For the Bradshaw and Donaldson models, it is not clear that the stress and diffusion terms can be treated implicitly as easily as is done with the eddy viscosity models. If these terms are not treated implicitly the maximum stable time step for the operators will be reduced to impractically low values, as it is when the corresponding eddy viscosity terms are treated explicitly. Implicit methods that simultaneously solve the velocity, energy and turbulence equations using block tridiagonal matrix inversions are possible but are considerably more time consuming. The extension of the present Navier-Stokes algorithm (or any other compressible Navier-Stokes algorithm) to these important models would be an important advance.

Zero-Equation Models

For the zero-equation models the equations solved do not include the turbulence variables k and s, and the only modeling done is for the eddy diffusivities which are modeled algebraically. The expressions for the total viscosity, thermal energy diffusivity, and pressure are

$$\left.\begin{aligned} \mu_v &= \mu + \mu_T \\ \mu_e &= \gamma(\mu/Pr + \mu_T/Pr_T) = K_e/c_v \end{aligned}\right\} \tag{16}$$

$$\bar{p} = p \tag{17}$$

where μ_T is the turbulent eddy visocity, K_e is the total thermal conductivity, Pr and Pr_T are the molecular and turbulent Prandtl numbers equal to 0.72 and 0.9, respectively, and μ is the molecular viscosity given by the Sutherland viscosity law. Two types of zero-equation models are discussed, the equilibrium and nonequilibrium (or relaxation) models.

Equilibrium model. The standard or baseline model used by many investigators is expressed in terms of an inner and outer eddy viscosity function as

$$\mu_T = \left\{\begin{aligned} \mu_{T_{inner}} &= \rho\ell^2|u_y + v_x| &&; \ y \le y_c \\ \mu_{T_{outer}} &= .0168\rho u_e\delta^*/[1 + 5.5(y/\delta)^6]&&; \ y > y_c \end{aligned}\right\} \tag{18}$$

where y_c is the first point at which $\mu_{T_{inner}}$ exceeds $\mu_{T_{outer}}$. The function ℓ is the Prandtl mixing length modified by the van-Driest damping factor

$$\ell = \kappa y[1 - \exp(-\sqrt{\rho_w \tau_w}\, y/A^+ \mu_w)] \tag{19}$$

where $\kappa = 0.4$ and $A^+ = 26$ are the von Karman and van Driest constants, respectively. The edge velocity, u_e, is set to the maximum value of u for $y < y_{max}$, y_{max} being chosen slightly outside the boundary layer. The displacement thicknesses are

$$\left.\begin{aligned} \delta^* &= \int_0^{y_{max}} (1 - u/u_e)(r/R)dy \\ \delta_c^* &= \int_0^{y_{max}} (1 - \rho u/\rho_e u_e)(r/R)dy \end{aligned}\right\} \tag{20}$$

The boundary-layer thickness δ, appearing in Eq. (18), is assumed as

$$\delta = C_c \delta_c^* \tag{21}$$

with C_c being 1.735 for the HSBLI problem and 4.54 for the TSBLI problem. These constants were obtained by comparing experimental measurements and equilibrium boundary-layer solutions.

Nonequilibrium-relaxation model. Shang and Hankey were the first to apply the relaxation model to shock boundary-layer flows, and a number of investigators have subsequently experimented with different variations of it (2,14,15). The results reported here all use the original Shang-Hankey model called by Hung and MacCormack the upstream relaxation model (14). The eddy viscosity in this model is written

$$\mu_T = \mu_{T_{eq}} - (\mu_{T_{eq}} - \mu_{t_i})\exp[-(x - x_i)/\lambda_r] \tag{22}$$

where $\mu_{T_{eq}}$ is the local equilibrium eddy viscosity and the subscript i refers to a location selected slightly upstream of separation, $\lambda_r = C_r \delta_o$ is a relaxation length parameter, C_r being an arbitrary constant and δ_o the upstream boundary-layer thickness.

The zero-equation model results reported here use the above formulations, although many other variations have been tested.

One-Equation Model

The one-equation or kinetic energy model uses one additional partial differential equation to simulate turbulence. Several different versions of this model exist but only one is used in the present study. This model originated with Prandtl and Kolmogorov and was developed for incompressible flat plate boundary-layer flows by Glushko (8) who specified the low Reynolds number and the algebraic length scale functions. It was studied by Beckwith and Bushnell (9) in more complicated boundary-layer flows and was generalized (Rubesin, Ref. 16) to compressible flows using mass-averaged variables (Rubesin and Rose, Ref. 17). In a recent paper, initial tests using the full model as formulated by Rubesin, are described (18). In this paper a simpler version is used in which certain compressibility terms involving first derivatives of the strain rate tensor (or first derivatives of the temperature) are omitted. In Ref. 18 these terms were found to be of negligible importance. This model - which will be designated the G-R model and has only one turbulence source function H_k - is described below.

Glushko-Rubesin Model (G-R).

$$\left.\begin{aligned} H_k &= \mu_T S^2 + (\zeta M^2/\gamma - 2/3)\rho k D - C\mu_k k/L^2 \\ S^2 &= (u_y + v_x)^2 + 2[u_x^2 + v_y^2 + (v/r)^2] - 2D^2/3 \\ R_T &= \rho\sqrt{k}\, L/\mu \\ \mu_T &= \alpha\mu R_T \tilde{H}(R_T/R_o) \\ \tilde{H}(\tilde{R}) &= \left\{\begin{array}{ll} \tilde{R} & ;\tilde{R} < .75 \\ \tilde{R} - (\tilde{R} - .75)^2 & ;.75 < \tilde{R} < 1.25 \\ 1 & ;1.25 < \tilde{R} \end{array}\right\} \\ \alpha &= .2,\ C = 3.93,\ R_o = 110,\ \zeta = 0 \\ Pr_T &= .9,\ Pr_k = 2.5 \end{aligned}\right\} \tag{23}$$

The algebraic length scale function L specified by Glushko (8) is shown in Fig. 3 (models 1 and A). The boundary-layer thickness is defined in the same manner as the zero-equation model; that is, $\delta = C_c \delta_c^*$ (see Eq. (21)). The value of the compressibility parameter ζ, initially suggested by Rubesin was $\zeta = 8/11$. In Ref. 18 solutions for the TSBLI problem were found to be relatively insensitive to specific values of this parameter, and the initial choice, $\zeta = 8/11$, has been used here. This value was found to be too large in the HSBLI problem and subsequent investigations in this case use $\zeta = 0$.

The total kinetic energy diffusivity μ_k is represented as follows:

$$\mu_k = \mu + \mu_T/Pr_k \tag{24}$$

The total viscosity μ_v, and the thermal energy diffusivity μ_e, are represented as shown in Eq. (16), and the turbulence Prandtl numbers, Pr_T, and Pr_k are included in the summary of constants. Variations in the use of the Prandtl numbers Pr_T and Pr_k have been used in the earlier investigation (18) where the options of either including these parameters inside the argument of the eddy viscosity damping function $\tilde{H}$, or leaving them out were tested. The above formulation shows the Prandtl numbers left outside of the argument. The transformation from the above formulation to the optional one, for the Prandtl number Pr_T, is

$$\tilde{H}(R_T/R_o) \rightarrow \tilde{H}(R_T/Pr_T R_o) \tag{25}$$

The two usages will be reported in the results section of this paper as each case is discussed. For the one-equation (and two-equation) models, the combined pressure $\bar{p}$, replaces the static pressure p, as shown in Eqs. (3) and (11).

Two-Equation Models

The two-equation models presently under study are the models of Jones-Launder (10) and Wilcox-Traci (11). These models were selected because considerable experience has been gained in their application to simpler flows, and because they include low Reynolds number terms that permit integration to the wall. These models use two partial differential equations to simulate turbulence, the first equation being the turbulent kinetic energy equation, as in the one-equation model, and the second equation being used to define the turbulence length scale. The turbulence source functions, H_k and H_s, for these two models are described below.

Jones-Launder Model (J-L).

$$\left.\begin{aligned} H_k &= \mu_T S^2 - 2\rho k D/3 - 2\mu(\sqrt{k})_y^2 - \rho\varepsilon \\ H_\varepsilon &= [C_1(\mu_T S^2 - 2\rho k D/3) + 2\mu\mu_T k u_{yy}^2/\rho\varepsilon - C_2 f_2 \rho\varepsilon]\varepsilon/k \\ \varepsilon &= k^{3/2}/L = s \\ S^2 &= (u_y + v_x)^2 + 2[u_x^2 + v_y^2 + (v/r)^2] - 2D^2/3 \\ R_T &= \rho\sqrt{k}\, L/\mu = \rho k^2/\mu\varepsilon \\ \mu_T &= \mu C_\mu f_\mu R_T \\ f_\mu &= \exp[-2.5/(1 + R_T/50)] \\ f_2 &= 1 - 0.3\exp(-R_T^2) \\ C_\mu &= 0.09,\ C_1 = 1.55,\ C_2 = 2.0 \\ Pr_T &= 0.9,\ Pr_k = 1.0,\ Pr_\varepsilon = 1.3 \end{aligned}\right\} \tag{26}$$

Wilcox-Traci Model (W-T).

$$\left.\begin{aligned}
H_k &= (\alpha^*\bar{S} - \xi^* D - \beta^*\omega/\rho)\rho k \\
H_{\omega^2} &= \{\alpha\bar{S} - [\beta + 2\sigma(L_x^2 + L_y^2)]\omega/\rho\}\rho\omega^2 \\
\omega^2 &= (\rho\sqrt{k}/L)^2 = s \\
\bar{S} &= \{(u_y + v_x)^2 + 2[u_x^2 + v_y^2 + (v/r)^2]\}^{1/2} \\
R_T &= \rho\sqrt{k}\,L/\mu = \rho^2 k/\mu\omega \\
\mu_T &= \mu R_T \\
\alpha^* &= \alpha_\infty^*[1 - (10/11)\exp(-2R_T)] \\
\alpha &= \alpha_\infty[1 - (10/11)\exp(-R_T/2)] \\
\beta^* &= 9/100, \beta = 3/20, \xi^* = 5/2, \alpha_\infty^* = 3/10, \alpha_\infty = 1/3 \\
Pr_T &= 8/9,\ Pr_k = 2,\ Pr_\omega = 2 = 1/\sigma
\end{aligned}\right\} \quad (27)$$

The additional diffusivity μ_s for the two models is written

$$\mu_s = \mu + \mu_T/Pr_s \quad (28)$$

where the additional Prandtl number, Pr_s, is included in the summary of constants with Pr_T and Pr_k.

The Wilcox-Traci model is essentially the same as that described in Ref. 11. The production term in the Jones-Launder model has been generalized to compressible flows using the Navier-Stokes equations by the following replacement:

$$\begin{aligned}
\mathcal{P}_k &= -\tau^T u_y = \mu_T {u_y}^2 \rightarrow -\tau_{ij}^T u_{i,j} \\
&= \{\mu_T[(u_{i,j} + u_{j,i}) - 2u_{k,k}\delta_{ij}/3] - (2\rho k\delta_{ij}/3)\}u_{i,j} \\
&= \mu_T S^2 - 2\rho k D/3
\end{aligned} \quad (29)$$

where $\mathcal{P}_k$ is the turbulent energy production term, τ_{ij}^T is the Reynolds stress tensor, and $u_{i,j}$ the velocity gradient tensor.

Boundary Conditions and Special Procedures

The wall boundary condition on the turbulence kinetic energy is $k = 0$. This variable frequently may be driven negative in computations near the wall and near the edge of the boundary layer. In this case, k is set to zero in the one-equation model computations. The procedure is more complicated for the two-equation models and is described below.

The wall boundary condition on the additional turbulence variable depends on the model. The original J-L model used $s = \epsilon = 0$ but recent applications have used $\partial s/\partial y = 0$. Initial studies have not shown much difference in predictions using either of these two boundary conditions. The W-T model wall boundary condition on $s = \omega^2$ is, theoretically, $s \rightarrow \infty$ for smooth walls, but in practice is set equal to a large value. The condition is

$$\sqrt{s} = \omega = (\rho_w \tau_w/\mu_w \alpha_\infty^*) S_R \quad (30)$$

where the roughness function, S_R, is taken to be a large number; that is, 300-3000.

Boundary conditions that are used in boundary-layer codes at the edge of the boundary layer are not appropriate to the Navier-Stokes code where the turbulence equations are integrated, with the other equations, in the free stream. At the present time k and s are given very small values initially in the free stream and then held bounded above and below by constants. This type of procedure is also used in the main part of the boundary layer. The procedure there is to specify a lower bound on the kinetic energy at a given y location; this value presently being 1/100 its value at the inflow boundary at the same value of y. The bounds on s are determined by using the definition of s in terms of k and L and two limiting length scale distribution $\tilde{L}_{max}(y)$ and $\tilde{L}_{min}(y)$. The bounding relationships are then

$$\left.\begin{aligned}
k^{3/2}/\tilde{L}_{max} < s = \epsilon < k^{3/2}/\tilde{L}_{min} \ ; \quad J-L \\
\rho^2 k/\tilde{L}_{max}^2 < s = \omega^2 < \rho^2 k/\tilde{L}_{min}^2 \ ; \quad W-T
\end{aligned}\right\} \quad (31)$$

Initial tests with the two-equation models using the Navier-Stokes code on simple flat plate boundary-layer flows did not require this procedure for s. The need for it has arisen, however, in the more severe SBLI flows and is believed due to the fact that the variable s contains k to a positive power and L to a negative power. In an isolated region close to the wall near the reattachment point in the HSBLI problem, using the J-L model, the computed values of k and L can get very small; this makes the value of s very sensitive to small changes in k and L and causes the code difficulty. Introducing the bounds on s, as indicated, results in stable solutions.

The limiting length scale distributions $\tilde{L}_{max}$ and $\tilde{L}_{min}$ are taken to be fixed ratios (e.g., 0.1 and 5.0, respectively) of the length scale function defined at the inflow boundary. The latter function, which is also used to define the variable s at the inflow boundary in terms of k and L, is assumed proportional to the Glushko length scale function. The factor of proportionality is obtained by equating kinetic energy dissipation functions of the one- and two-equation models. (It is also obtained in other cases by equating eddy viscosity functions of the two models.)

For the one-equation models the inflow kinetic energy profile, in the TSBLI case, is assumed to be the Klebanoff distribution. In the HSBLI case, it is an equilibrium distribution obtained by integrating the equations from a location 1 ft upstream of the inflow boundary starting with a triangular distribution similar to the Klebanoff distribution and with a magnitude obtained from frequent trials. For the two-equation models, the inflow kinetic energy profile is the same as that used for the one-equation model.

At the inflow boundary, the static pressure p must be modified to include the effect of the turbulence pressure. This is done by assuming the combined pressure, $\bar{p} = p + 2\rho k/3$, to be constant across the boundary layer (in conformity with boundary-layer theory) and equal to the free-stream pressure. This introduces a variation in the static pressure and requires an adjustment in the density in order to retain the temperature profile which is obtained from a boundary-layer code. This is done by requiring the adjusted density and pressure to satisfy the perfect gas equation of state. In the TSBLI problem, these adjustments are small (1%) but in the HSBLI problem they are not so small, with the maximum turbulent pressure attaining values up to 10% of the free-stream pressure.

RESULTS

Results for the TSBLI problem are presented in Figs. 4-6, and those for the HSBLI are given in Figs. 7-9. The measurements are described in Refs. 2-4. Reference 18 describes initial tests with the one-equation model in which model parameters were systematically varied to ascertain model sensitivity to these parameters and to seek improved agreement with measurements. In that study, it was found that the shape of the length-scale function was by far the most important factor in controlling solution behavior. In this paper only the most significant results found in Ref. 18 are reported.

Transonic SBLI

For the transonic flow problem, computations using the two zero-equation turbulence models discussed in the text and two variants of the one-equation model will be compared with experimental measurements of surface pressure, skin friction, and velocity profiles. Comparisons of measured kinetic energy of turbulence profiles with calculations are also presented.

Surface predictions. Comparisons of computed skin-friction and surface-pressure distribution for the transonic SBLI are shown in Fig. 4 for a Reynolds number, just ahead of the shock, of 3.67×10^7. The experimental skin-friction results are from Ref. 2, while the wall-pressure measurements, normalized to the free-stream value about 15 in. ahead of x_o, are taken from some recent work of Mateer (private communication). The baseline model is the standard equilibrium model described earlier. Both this model and the zero-equation relaxation model predict the measured pressure distribution very well. Ahead of x_o, the measured and calculated baseline model and relaxation model skin-friction results agree; however, downstream of reattachment the calculations are in considerable disagreement with the experiment. Downstream of reattachment the relaxation model gives the poorest skin-friction prediction.

In Fig. 4 the two one-equation-model solutions shown also agree well with the measured pressure distribution. In addition, however, they both predict the measured rise in skin friction downstream of reattachment significantly better than do either of the zero-equation models shown. The one-equation model, labeled model 1, was chosen for this comparison because it represents the original Glushko-Rubesin model. It uses the length scale shown in Fig. 3, the option of including the Prandtl numbers Pr_T and Pr_k in the argument of the eddy viscosity damping function, $\tilde{H}$, and is model A1a0 of Ref. 18. This model, however, does not agree well with the skin-friction measurements near the upstream boundary and the predicted separation region is suspected of being too small. Recent measurements by Mateer (private communication) suggest that the length of the separated region in this case is larger ($\sim 2.5\delta_o$). Model 2 (model B1a4 of Ref. 18), represents a modified one-equation model. This model differs from model 1 primarily in that the length scale has been altered. The modification decreased the length scale slope in regions where the maximum kinetic energy increased with x and increased the slope in regions where this energy decreased with x. This has the effect of lowering the eddy viscosity in the region of rapid pressure rise and raising the eddy viscosity downstream of this region. This results in a larger separation bubble and good agreement with the measurements of the skin friction.

Velocity profile comparisons. Figure 5 shows comparisons between measured and computed velocity profiles for the TSBLI experiment at various locations downstream of the shock. Both zero-equation models yield similar results as do both of the variants of the one-equation model. All of the calculated velocities agree generally with the measurements, even to displaying the decrease in velocity near the centerline. Clearly, however, the one-equation model results are in better agreement with the measurements. Near the surface at $(x - x_o)/\delta_o = 4$, model 2 of the one-equation models has a slightly more "laminar-like" velocity profile which is consistent with the larger separation region shown in the previous figure. The separation bubble was so thin in this experiment that it was not possible to obtain measured velocities of the reversed flow. The computed bubble was also very thin, that is, $\sim 0.01\delta_o$, and this explains the apparent absence of a computed reversed flow profile in Fig. 5(a). At $(x - x_o)/\delta_o = 16$, profiles corresponding to the two one-equation models are coincident and appear as a single curve.

Kinetic energy comparisons. Computed and measured profiles of the kinetic energy of turbulence at various x locations are shown in Fig. 6. One-equation model 2 is used in this comparison. Similar results have been obtained with model 1 and are given in Ref. 18. The measured kinetic energy (Fig. 6(a)) was determined from a measurement of v' (see Fig. 12, Ref. 2) and the assumption that $u'^2:v'^2:w'^2 = 4:2:3$. This assumption was observed recently to be reasonable for equilibrium flows at high subsonic Mach numbers (19). It is apparent from Fig. 6 that the computed and measured profiles of the kinetic energy of turbulence are generally similar and that the trends with distance are in agreement. The experimental results do show a significant amount of free-stream turbulence downstream of the shock which has not yet been included in the calculations. Inclusion of this effect would tend to increase the calculated skin friction downstream of reattachment relative to the results shown in the preceding figures.

It is apparent from the calculated results that the shock wave has a very strong influence on the kinetic energy of the turbulence. Ahead of the shock, except for the peak of k being closer to the wall, the profile is not too different from Klebanoff's measurements. As the pressure rises rapidly, due to the shock, the turbulence energy increases and the peak moves away from the wall. Downstream of this rapid pressure rise, the peak turbulence decays with distance and a smaller peak begins to re-emerge adjacent to the wall. Far from the shock, one would expect to recover a profile similar to that at $(x - x_o)/\delta_o = -12$.

Hypersonic SBLI

For the hypersonic problem a number of zero- and one-equation variations have been tested, and a few preliminary tests using the two-equation models have been made. Results comparing two zero- and two one-equation model predictions will be discussed first. In these comparisons, the zero-equation models are the unmodified, equilibrium or baseline model, and the modified, nonequilibrium or relaxation model. The unmodified one-equation model, called model A, is the basic G-R model described in the text. It is identical to model 1 used in the TSBLI study, except that the Prandtl numbers Pr_T and Pr_k are excluded from the argument of the function, $\tilde{H}$, in Eq. (25). The modified one-equation model, called model B, is an extensively modified model in which the length scale L and the constant R_o in Eq. (23) have been adjusted so as to force agreement of predictions with measurements of surface pressure and heat transfer. The length scale functions for these two models are shown in Fig. 3. The process by means of which model B was developed is described more fully in Ref. 18.

Surface predictions. Predictions of surface pressure are compared with measurements in Fig. 7(a). In these comparisons, both the unmodified zero- and one-equation models overpredict the measured peak pressure, and fail to predict the plateau pressure rise. The separation bubble predicted by these two models is very thin (see Fig. 8). The reason for this is that the predicted eddy viscosity is too large in the neighborhood of the maximum pressure gradient, especially in the middle part of the boundary layer. This permits the high-speed fluid in the outer part of the boundary layer to exert, through elevated shear, too great a force in opposition to the pressure gradient. The high pressures downstream are thus prevented from strongly influencing the flow further upstream.

Predictions of surface pressure are improved using the modified zero-equation (or relaxation) model. In this case the eddy viscosity in the critical region of maximum pressure gradient is reduced, being now a combination of the low upstream value and the high local value. The improvements using this model appear limited, however, in that it has not been possible to achieve a higher pressure plateau or lower peak pressure by varying the relaxation constant C_r. In addition, as will be discussed below, this model is deficient in predicting skin friction and heat transfer.

The surface pressure prediction of the modified one-equation model B provides the best agreement with measurements. The modification by means of which this prediction was achieved was done by lowering the maximum value of the length scale upstream of the interaction to $L_{max} = 0.15\delta_o$, in conformity with recent experimental results of Backx and Richards (20) and then lowering it even more in the interaction zone, as shown in Fig. 3. This modification alone to the *outer* values of the length scale produced essentially the same surface pressures as shown for model B, although additional modifications to the *inner* length scale were required for the improved skin-friction and heat-transfer predictions of model B.

Skin-friction and heat-transfer predictions are shown in Figs. 7(b) and 7(c). In this case all the models predict a reattachment point ($C_f = 0$), downstream of the measured point. This seems to be an inherent characteristic of all models tested to date. The best prediction of reattachment is provided by the one-equation model A, and the worst is provided by the zero-equation relaxation model. The unmodified zero- and one-equation models (Baseline and Model A) overpredict maximum skin friction and show a delayed rise in surface heat transfer. The modified zero-equation (relaxation) model grossly underpredicts skin friction and heat transfer downstream of reattachment.

Improved predictions of C_f and C_H with the relaxation model can be made by lowering the value of the relaxation parameter, C_r, but in this case surface pressure predictions suffer. It is felt that surface pressure is the more important prediction variable since if pressure predictions are poor but C_f and C_H predictions good, then modeling changes improving pressure will more than likely adversely affect skin-friction and heat-transfer predictions. Conversely if surface pressure predictions are good then modeling changes to improve C_f and C_H can generally be made without adversely affecting pressure predictions.

The above effect is illustrated by the predictions of the one-equation model B, in which surface heat transfer is predicted accurately and best overall agreement in skin friction is achieved. The improved agreement is attained using the adjustment function g shown in Fig. 3. In this modification, the length scale in the separation zone, close to the wall, is greatly increased over its unmodified value, resulting in large increases in kinetic energy and eddy viscosity. The maximum value of the length scale in this adjustment is, however, unchanged. The adjustment was done by modifying g in such a way as to force agreement of heat transfer predictions with measurements. Initial attempts to force agreement with C_f were made but were unsuccessful in that the reattachment point could not be made to move upstream to coincide with the measured point. The severe adjustments to L embodied in the adjustment function g were found to have very little effect on surface pressure predictions.

Velocity profile predictions. Measured and computed velocity profiles are shown in Figs. 8(a)-8(e). The locations of these profiles, in terms of dimensionless distance, $(x - x_o)/\delta_o$, are also indicated and may be referred to Fig. 7. Figure 8(c) shows profiles of maximum flow reversal. In this case the locations of the corresponding measured and computed profiles differ by about a third of a boundary-layer thickness. In all other cases the locations are the same.

Comparing the profiles of maximum flow reversal (Fig. 8(c)), it is observed that the unmodified zero- and one-equation models fail to produce a profile that is even close to the measured one. The reason for this has already been identified: the eddy viscosity in the region of maximum pressure gradient, in the middle of the boundary layer, is too large. The modified zero- and one-equation models, on the other hand, are considerably better in their predictions. The characteristics of interest for these profiles are their curvature in the region of flow reversal and their maximum negative velocities. The one-equation model B provides the best predictions of these characteristics. This is explained by the modification to the inner length scale made to achieve improved heat-transfer predictions. The relatively large increases in kinetic energy and eddy viscosity close to the wall resulting from the modification directly account for the reduced profile curvature and maximum negative velocity.

Figure 8(b) compares profiles close to separation. Here again the one-equation model B provides the best predictions. The reason probably is due to the increased eddy viscosity close to the wall as explained previously.

Figures 8(d) and 8(e) compare profiles downstream of reattachment. In these cases the unmodified zero-equation or baseline model provides the best overall predictions, closely followed by the unmodified one-equation model A.

The modifications embodied in the one-equation model B, although complicated, have provided some insight into what is required in a good turbulence model. Modifications such as these should and will be tried for the zero-equation models, and will likely result in improved predictions. It is clear, however, that unless the modifications can be correlated with *flow-field variables* they will not be very useful or universal. Correlations of this type have been tried for the one-equation model without much success (18). For this reason the two-equation models are attractive because they automatically provide a length scale which embodies more physics of the flow than do the zero- and one-equation models. Preliminary results using a two-equation model will now be described.

Preliminary two-equation model predictions. Preliminary results using the Jones-Launder two-equation model are shown in Fig. 9. The model used is a variation of the original J-L model in that the low Reynolds number terms, $2\mu(\sqrt{k})_y^2$ and $2\mu\mu_T k u_{yy}^2/\rho\varepsilon$ in Eq. (26), are treated differently. The first term is replaced by $2\mu k/y^2$ (which is similar to the corresponding one-equation model term) and the second term is omitted entirely. Numerical difficulties in the initial development stages of the two-equation model code thought to be due to poor resolution of the derivatives in these terms led to this replacement. The upstream length scale function, $\tilde{L}_o$, used to define ε, and used in Eq. (31) to place bounds on ε, is 0.32 times the upstream length-scale function used for the one-equation model B. The bounding length scales are $\tilde{L}_{min} = 0.1\,\tilde{L}_o$ and $\tilde{L}_{max} = 2\,\tilde{L}_o$, and the boundary condition on ε is $\varepsilon_y = 0$ at the wall.

The solution presented for the two-equation model, near the reattachment point and downstream of it, is unsteady in time, oscillating with a frequency of about 3000 Hz. It is not known whether this unsteadiness is physical or numerical but experimental measurements of the flow also exhibited unsteadiness, with spikes in the energy spectrum at frequencies of 10000, 15000, and 20000 Hz.

Figure 9(a) shows the envelopes of the computed surface pressures taken over the last two cycles of oscillation. Figure 9(b) shows the computed surface pressure at the point of maximum excursion and are taken over the last four cycles of oscillation. The total number of cycles from the initial state is approximately nine, about twice the time required to achieve steady-state solutions for the one-equation models.

It is premature to make any conclusions from these results other than to state that the specific computer code and specific turbulence model used have the capacity to produce unsteady solutions that may simulate observed phenomena. It is quite possible that changes or improvements in the code or model will produce results in conflict with those presented here.

CONCLUDING REMARKS

This paper has described how one- and two-equation turbulence models have been incorporated into the new Navier-Stokes algorithm in use at the Ames Research Center, and has presented initial results using the models. The reductions in computing time resulting from the new algorithm permitted the initiation of a systematic study of turbulence models for complex flows. It is quite probable that turbulence models developed for simpler attached flows will not be adequate for accurate predictions of complex separated flows. The development of improved turbulence models is then essential for progress. The improvement will come only from a close coordination of experimental and computational research. This paper emphasizes the computational aspect of this research and illustrates some of the complexities involved.

The results presented indicate that the one-equation turbulence model is superior in some respects to the zero-equation models. For the transonic case, improved predictions of velocity profiles and skin-friction downstream of separation are achieved with few or no modifications to the basic one-equation model. For the hypersonic problem, where the extent of separation is greater, neither of the unmodified models does well. The modified zero-equation model discussed, and many others tested but not discussed, have not been a great improvement over the unmodified model. This does not mean that future modifications to the zero-equation models will not be successful. It simply means they are not yet known.

The one-equation model occupies a unique position within the class of eddy viscosity models. In essence it constitutes a bridge between the simple zero-equation models and the more complicated two-equation models. An apparent disadvantage of the one-equation model is the algebraic length scale but this in fact may be a strength, as discussed by Reynolds (7). The freedom to manipulate the length scale to fit data may result in knowledge leading to improvements in the one- and two-equation models, or it may lead in directions as yet unknown. The complicated adjustments in the one-equation model to achieve improved agreement with experiment in the hypersonic problem are simply an example of how knowledge can be gained in this way. It is hoped that similar adjustments will not be necessary for the two-equation models.

The results presented here are initial in nature and in no way suggest the so-called universal turbulence model. With due regard to the complexities involved, the position taken must be and is to test the best turbulence models available using the best computer algorithms available on the best documented flows available with confidence that the knowledge thus gained will ultimately lead to progress.

REFERENCES

1 MacCormack, R. W., "An Efficient Numerical Method for Solving the Time-Dependent Compressible Navier-Stokes Equations at High Reynolds Number," NASA TM X-73,129, July 1976.

2 Mateer, G. G., Brosh, A., and Viegas, J. R., "A Normal Shock-Wave Turbulent Boundary-Layer Interaction at Transonic Speeds," AIAA Paper 76-161, Jan. 1976.

3 Marvin, J. G., Horstman, C. C., Rubesin, M. W., Coakley, T. J., and Kussoy, M. I., "An Experimental and Numerical Investigation of Shock-Wave Induced Turbulent Boundary-Layer Separation at Hypersonic Speeds," In *Flow Separation*, AGARD-CCP-168, May 1975.

4 Kussoy, M. I. and Horstman, C. C., "An Experimental Documentation of a Hypersonic Shock-Wave Turbulent Boundary-Layer Interaction Flow - With and Without Separation," NASA TM X-62,412, Feb. 1975.

5 Mikulla, V. and Horstman, C. C., "Turbulence Stress Measurements in a Nonadiabatic Hypersonic Boundary Layer," *AIAA Journal*, Vol. 13, No. 12, Dec. 1975, pp. 1607-1613.

6 Launder, B. E. and Spalding, D. B., *Lectures in Mathematical Models of Turbulence*, Academic Press, London and New York, 1972.

7 Reynolds, W. C., "Computation of Turbulent Flows," *Annual Review of Fluid Mechanics*, Vol. 8, 1976, pp. 183-208.

8 Glushko, G. S., "Turbulent Boundary Layer on a Flat Plate in an Incompressible Fluid," *Bull. Acad. Sci. USSR, Mech. Ser.*, No. 4, 1965, pp. 13-23.

9 Beckwith, I. W. and Bushnell, D. M., "Detailed Description and Results of a Method for Computing Mean and Fluctuating Quantities in Turbulent Boundary Layers," NASA TN D-4815, 1968.

10 Jones, W. P. and Launder, B. E., "The Prediction of Laminarization with a Two-Equation Model of Turbulence," *Int. J. Heat Mass Transfer*, Vol. 15, Pergamon Press, 1972, pp. 301-314.

11 Wilcox, D. C. and Traci, R. M., "A Complete Model of Turbulence," AIAA Paper No. 76-351, AIAA 9th Fluid and Plasma Dynamics Conference, San Diego, Calif., July 14-16, 1976.

12 Bradshaw, P., Ferriss, D. H., and Atwell, N.P., "Calculation of Boundary-Layer Development using the Turbulent Energy Equation," *JFM*, Vol. 28, Part 3, 1967, pp. 593-616.

13 Varma, A. K., Beddini, R. A., Sullivan, R. D., and Donaldson, C. DuP., "Application of an Invariant Second-Order Closure Model to Compressible Turbulent Shear Layers," AIAA Paper No. 74-592, AIAA 7th Fluid and Plasma Dynamics Conference, Palo Alto, Calif., June 17-19, 1974.

14 Hung, C. M. and MacCormack, R. W., "Numerical Simulation of Supersonic and Hypersonic Turbulent Compression Corner Flows Using Relaxation Models," AIAA Paper 76-410, July 1976.

15 Shang, J. S. and Hankey, W. L., "Numerical Solution of the Navier-Stokes Equations for Compression Ramp," AIAA Paper 75-3, Jan. 1975.

16 Rubesin, M. W., "A One-Equation Model of Turbulence for Use with the Compressible Navier-Stokes Equations," NASA TM X-73,128, April 1976.

17 Rubesin, M. W. and Rose, W. C., "The Turbulent Mean-Flow Reynolds-Stress, and Heat Flux Equations in Mass-Averaged Dependent Variables," NASA TM X-62,248, March 1973.

18 Viegas, J. R. and Coakley, T. J., "Numerical Investigation of Turbulence Models for Shock Separated Boundary-Layer Flows," AIAA Paper 77-44, AIAA 15th Aerospace Sciences Meeting, Los Angeles, Calif., Jan. 24-26, 1977.

19 Acharya, Mukund, "Effects of Compressibility on Boundary-Layer Turbulence," AIAA Paper 76-334, 1976.

20 Backx, E. and Richards, B. E., "A High Mach Number Turbulent Boundary-Layer Study," *AIAA J.*, Vol. 14, No. 9, Sept. 1976.

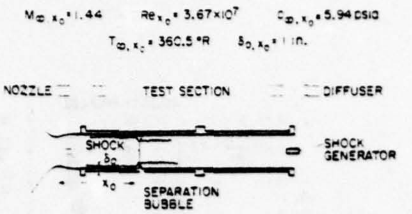

Fig. 1 Sketch of transonic normal shock boundary-layer interaction experiment

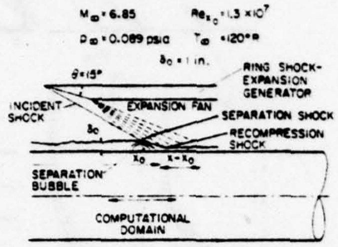

Fig. 2 Sketch of hypersonic oblique shock boundary-layer interaction experiment

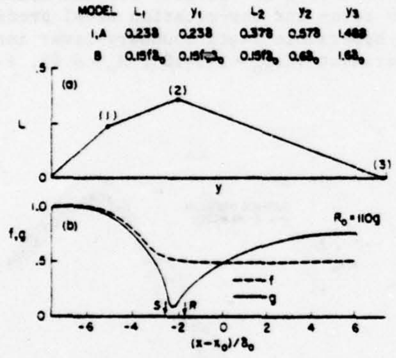

Fig. 3 Length scale functions used for one-equation models

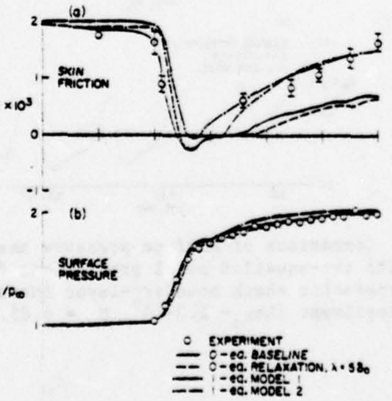

Fig. 4 Comparison of surface pressure and skin-friction measurements with zero- and one-equation model predictions for the transonic shock boundary-layer interaction experiment ($Re_{x_0} = 3.67\times10^7$, $M_\infty = 1.44$)

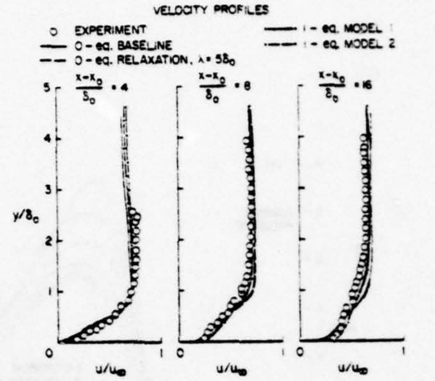

Fig. 5 Comparison of velocity profile measurements with zero- and one-equation model predictions for the transonic shock boundary-layer interaction experiments ($Re_{x_0} = 3.67\times10^7$, $M_\infty = 1.44$)

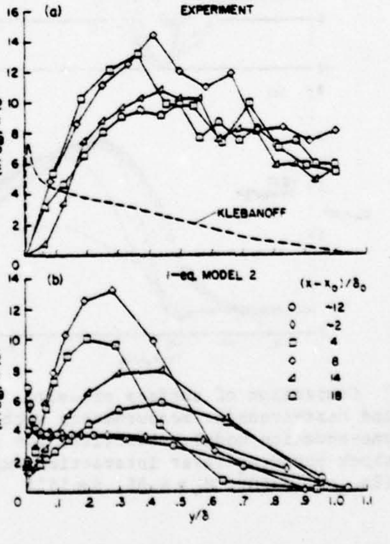

Fig. 6 Comparison of turbulent kinetic energy profile measurements with one-equation model 2 predictions for the transonic shock boundary-layer interaction experiment ($Re_{x_0} = 3.67\times10^7$, $M_\infty = 1.44$)

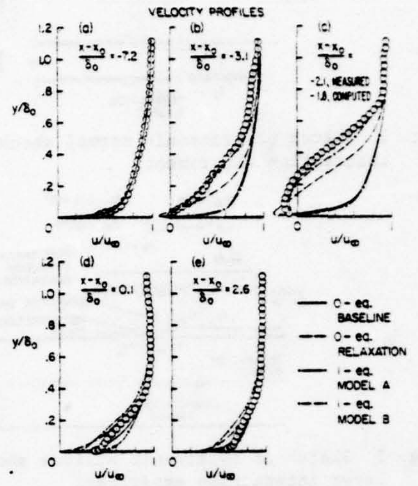

Fig. 8 Comparison of velocity profile measurements with zero- and one-equation model predictions for the hypersonic shock boundary-layer interaction experiment ($Re_{x_0} = 1.3\times10^7$, $M_\infty = 6.85$, $\theta = 15°$)

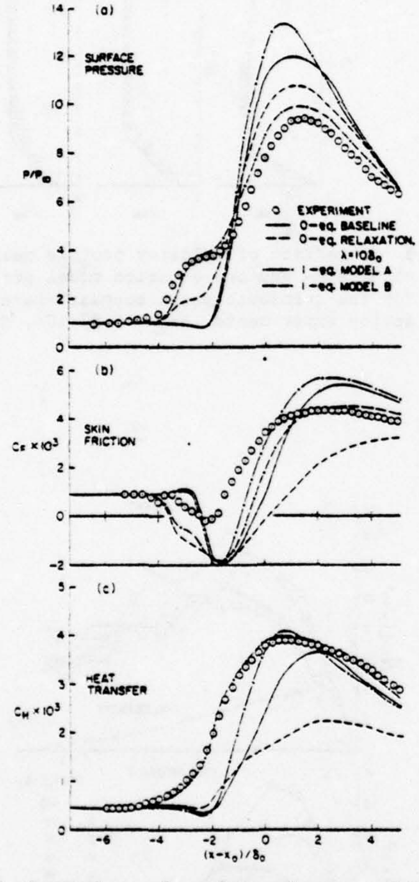

Fig. 7 Comparison of surface pressure, skin-friction and heat-transfer measurements with zero- and one-equation model predictions for the hypersonic shock boundary-layer interaction experiment ($Re_{x_0} = 1.3\times10^7$, $M_\infty = 6.85$, $\theta = 15°$)

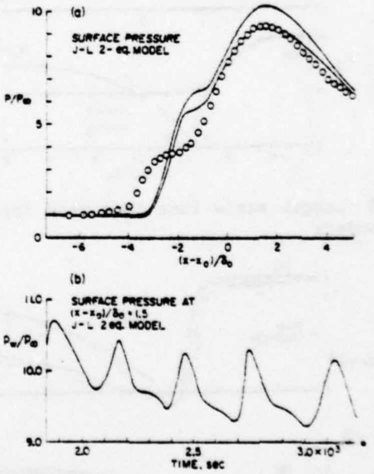

Fig. 9 Comparison of surface pressure measurements with two-equation model predictions for the hypersonic shock boundary-layer interaction experiment ($Re_{x_0} = 1.3\times10^7$, $M_\infty = 6.85$, $\theta = 15°$)

TURBULENT FLOW OVER A TWO-DIMENSIONAL STEP AND ITS DEPENDENCE UPON UPSTREAM FLOW CONDITIONS

T. W. Davies and D. J. Snell
Department of Chemical Engineering, University of Exeter, Devon, England

ABSTRACT

Previously reported work on two-dimensional separated flows (e.g. references 1 to 5) has shown wide discrepancies between results obtained on similar geometric configurations. The results presented in this paper show how variations in upstream conditions (almost inevitable from one experimental rig to another) can produce differences in flow characteristics large enough to explain such discrepancies.

The work was carried out in an open circuit wind tunnel having a working section of rectangular cross section containing a step.

The Reynolds No. of the flow in the approach to the step was about 10^5. Measurements were made with a DISA hot-wire anemometer system in the centre plane of the duct where the flow was truly two-dimensional.

The approach flow conditions studied included simple duct flow, duct flow with boundary layer suppression and duct flow with imposed shear.

Spatial distributions of mean velocity, turbulence intensity and shear stress are presented as functions of upstream velocity profile for two separate step heights.

NOMENCLATURE

$\overline{u}$ - local value of streamwise component of mean velocity

$\overline{u}_o$ - average value of the streamwise velocity of the flow approaching the step

$(\overline{u'^2})^{\frac{1}{2}}/\overline{u}_o$ - streamwise component of the turbulence intensity normalised w.r.t the mean approach flow velocity

$(\overline{u'v'})/\overline{u}_o^2$ - turbulent shear stress normalised w.r.t. the mean approach flow velocity.

ψ - mean value of stream function

ψ_t - mean value of total stream function across the duct upstream of the step

INTRODUCTION

A brief survey of published experimental data on two-dimensional separated flows created by downstream-facing step configurations reveals wide discrepancies in distributions of turbulence parameters. Figs 1 and 2 show a comparison of the maximum turbulence intensity and the maximum shear stress values published by Tani et al (1), Mueller et al (2), Chaturverdi (3), Abbott and Kline (4) and Denham (5).

There may be two reasons for the discrepancies shown in these figures:

(i) the different geometries used by each author does not allow strict comparison as attempted in figures 1 and 2.

(ii) the methods used by the various authors to collect and analyse their data (mostly hot-wire) were varied and prone to error.

The double step (or single step back-to-back) results of Chaturverdi should obviously be treated with reservation in view of the often asymmetric nature of such flows. However the flow geometries used by the remaining authors are very similar and this prompted a closer look at the influence of approach flow condition on the nature of the flow after separation in a downstream-facing step situation. Tani et al and Abbott and Kline declare their support to the popularly held view that the high degree of turbulence created upon separation swamps any contribution which may be made by the approach flow conditions to the nature of the recirculating flow. In both cases, however, some noticeable effect of approach flow conditions was measured.

EXPERIMENTAL ARRANGEMENTS

The present results were obtained as part of a wider study of separated flows using the open circuit wind tunnel sketched in figure 3. Interchangeable working sections consisted of rectangular ducts having height to width ratios of 9:1 to provide a two-dimensional flow over the central region. Working sections were made with step enlargements of various sizes. The condition of the flow approaching the step could be varied by means of a shear profile generator which could be inserted between the exit of the tunnel contraction and the entrance to working section. The generator was placed a sufficient distance downstream of the contraction so that it did not interfere with contraction performance and a sufficient distance upstream of the step so that the flow had settled down before reaching the separation plane. The shear profile generator was manufactured according to the design of Owen and Zienkiewicz (6) and consisted of an array of parallel tensioned wires the spacing of which controlled the amount of shear imparted to the flow.

ANEMOMETRY TECHNIQUE

Following the early efforts of Escudier (7) several attempts have been made to produce a technique which will allow the constant temperature hot-wire anemometer to be used in studies of highly turbulent flows. In the main these new techniques are based upon an analysis of a squared wire response equation and multiple measurements at a point. They differ in the method used to separate the mean and fluctuating velocity components. For example, the technique used by Rodi (8) achieved separation by making order of magnitude assumptions about velocity terms in a manner analogous to that used in a conventional hot-wire analysis. The results reported in this paper are based upon a technique developed by Davies (9) in which separation of velocity terms is achieved via assumptions about the nature of the wire signal. Refinements include a more accurate wire response equation (Siddall and Davies (11), Davies and Patrick (12)) and allowance for the effect of instantaneous flow reversal (di Gesso and Davies (10)). This technique appears to give plausible results when applied to a free jet (see diGesso and Davies (10)) but for the purpose of the present work the absolute accuracy achieved is secondary to the trends shown by the results.

RESULTS

The results given here are distributions of normalised mean streamwise velocity component, streamwise turbulence intensity component and shear stress for three separate approach flow situations and two different step heights. The approach flow conditions were

(i) unobstructed duct flow with natural boundary low growth between the wind tunnel contraction and the point of flow separation.

(ii) flow leaving the wind tunnel contraction passed through uniformly spaced wires (effective boundary layer suppression) before reaching the separation point.

(iii) flow leaving the wind tunnel contraction passed through a shear profile generator before reaching the separation point.

Power spectral density measurements, not reported here, showed that for all flow situations no periodicity was present in the approach flow.

Mean Velocity Distributions

The least spectacular effect of a change in the nature of the flow approaching the separation point was registered in the distributions of mean velocity, $\overline{u}/\overline{u}_o$.

Figure 4 shows three sets of normalised mean velocity profiles for the case of a flow from a 100 mm duct into a 150 mm duct via a 50 mm step. In all the figures showing distributions within the working section, the linear duct dimensions are distorted such that the cross stream distance is twice the downstream distance. This is to allow more clarity of presentation of profiles. Figure 5 shows normalised mean velocity profiles for flow from a 100 mm duct into a 175 mm duct via a 75 mm step. The full curves represent the situation of unobstructed duct flow approaching the separation point. The dashed curves show the results obtained when the shear profile generator was used with uniformly spaced wires. The dotted curves show the results obtained with a degree of shear introduced into the approaching flow.

Figures 6 and 7 show the normalised stream function distributions for uninterrupted flow over the 50 mm and 75 mm steps respectively.

Turbulence Instensity Distributions

Figures 8 and 9 show the distributions of streamwise turbulence intensity, $(\overline{u'^2})^{\frac{1}{2}}/\overline{u}_o$, for the 50 mm and 75 mm steps respectively and for the flow situations corresponding to those shown in figures 4 and 5 respectively i.e. full curves - natural boundary growth, dashed curves - boundary layer suppressed, dotted curves - upstream shear introduced.

Shear Stress Distributions

Figures 10 and 11 show the distributions of turbulent shear stress, $\overline{u'v'}/\overline{u}_o^2$, for the 50 mm and 75 mm steps respectively. Again the full curves show the situation prevailing when the flow enjoys an uninterrupted journey towards the point of separation. The dashed curves show the result obtained when the flow is passed through a uniformly spaced array of wires (no results for 75 mm step). The dotted curves show the distributions of shear stress associated with a uniformly sheared approach flow.

DISCUSSION

The effect of changes in the nature of the flow approaching the plane of separation are most noticeable in the distributions of turbulence intensity and shear stress across the shear layer. This result is in contrast to the view that turbulence generation upon separation is so dramatic that changing the flow approaching the separation plane can have little effect. This view was perhaps based on observations of changes in mean velocity profiles and compounded by uncertainties associated with measurement techniques in highly turbulent flows.

The effect of suppressing boundary layer growth by passing the approach flow through a uniformly spaced wire array is to deflect the "shear wedge" towards the step side of the flow. Reintroduction of a small degree of shear in the upstream flow appears to pull the "shear wedge" back somewhat towards the centre of the duct.

The variations in turbulence intensity and shear stress distribution brought about by the changes in the nature of the approaching flow are large enough to explain the discrepancies between previously reported results on very similar geometrical configurations. These discrepancies may have been caused by variations in approach flow conditions or by variations in the unspecified anemometry techniques employed by the various authors. We feel sufficiently confident in the anemometry technique employed by us that we can attribute the principal changes in flow parameters downstream of separation to the changes in flow parameters upstream of separation.

ACKNOWLEDGEMENTS

The authors are glad to acknowledge financial support from the Science Research Council.

REFERENCES

1 Tani, I., Inchi, M., and Komoda, H. "Experimental Investigation of Flow Separation Associated with a Step or a Groove", Report No. 364, 1961. Aeroanautical Research Institute, University of Tokyo.

2 Mueller, T.J., Korst, H.H. and Chow, W.L., "On the Separation, Reattachement and Redevelopment of Incompressible Turbulent Shear Flow", Journal of Basic Engineering, 1964, p.221.

3 Chaturverdi, M.C. "Flow Characteristics of Axisymmetric Expansions", Journal of the Hydraulic Division, Proceedings of the American Society of Civil Engineers, 1963, p.61.

4 Abbott, D.E., and Kline, S.J. "Experimental Investigation of Subsonic Turbulent Flow over Single and Double Backward Facing Steps", Journal of Basic Engineering, 1962, p. 317.

5 Denham, M.K. "The Development of a Laser Anemometer for Recirculating Fluid Flow Measurements", Ph.D. Thesis, Exeter University, 1974.

6 Owen, P.R. and Zienkiewicz, H.K. "The Production of Uniform Shear Flow in a Wind Tunnel", Journal of Fluid Mechanics, Vol. 2, 1957, p.521.

7 Escudier, M.P. "The Turbulent Incompressible Hydrodynamic Boundary Layer", Ph. D. Thesis, Imperial College, London University, 1967.

8 Rodi, W. "A New Method of Analysing Hot-wire Signals in Highly Turbulent Flow, and its Evaluation in a Round Jet", Report No. ET/TN/B/10, Mechanical Engineering Dept. Imperial College, London University, 1971.

9 Davies, T.W. "A Study of the Aerodynamics of the Recirculation Zone Formed in a Free Annular Jet", Ph.D. Thesis, Sheffield University, 1969.

10 diGesso, J.A., and Davies, T.W. "Hot-wire Anemometry in a Two-dimensional Separated Flow", Proceedings of a Conference on Fluid Flow Measurement in the Mid 1970s", N.E.L., East Kilbride, 1975, Paper F.1.

11 Siddall, R.G., and Davies, T.W. "An Improved Response Equation for Hot-wire Anemometry", International Journal of Heat and Mass Transfer, Vol. 15, 1972, p.367.

12 Davies, T.W., and Patrick, M.A. "A Simplified Method of Improving the Accuracy of Hot-wire Anemometry", Proceedings of a Symposium on Fluid Dynamic Measurements in the Industrial and Medical Environments, 1st ed., Vol. 1, Leicester University Press, 1972.

KEY TO FIGURES

——— unobstructed flow between contraction and working section.

----- approach flow passed through uniformly spaced wires thus diminishing boundary layer thickness at separation.

..... approach flow passed through shear profile generator and thus possessing uniform shear at separation.

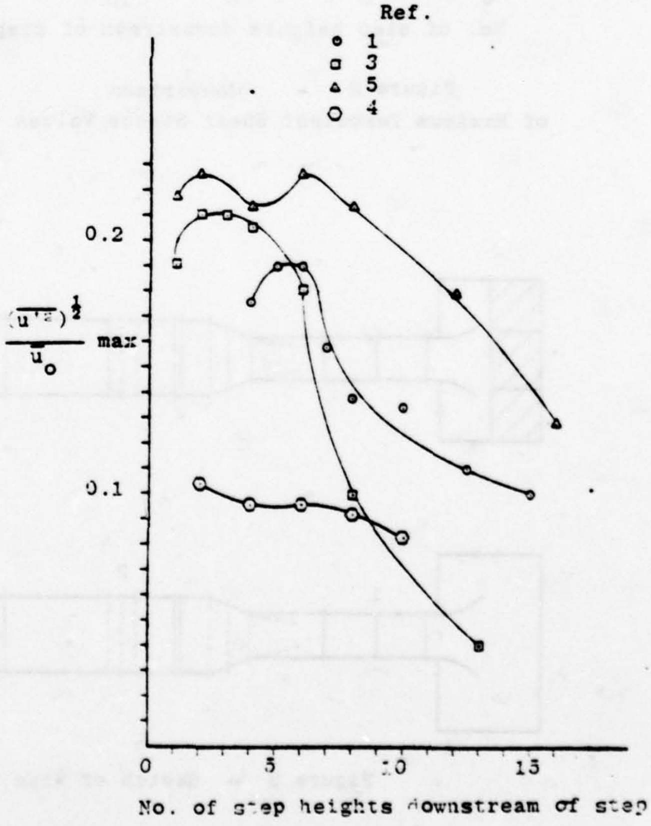

Figure 1
Comparison of Maximum Turbulence Intensities

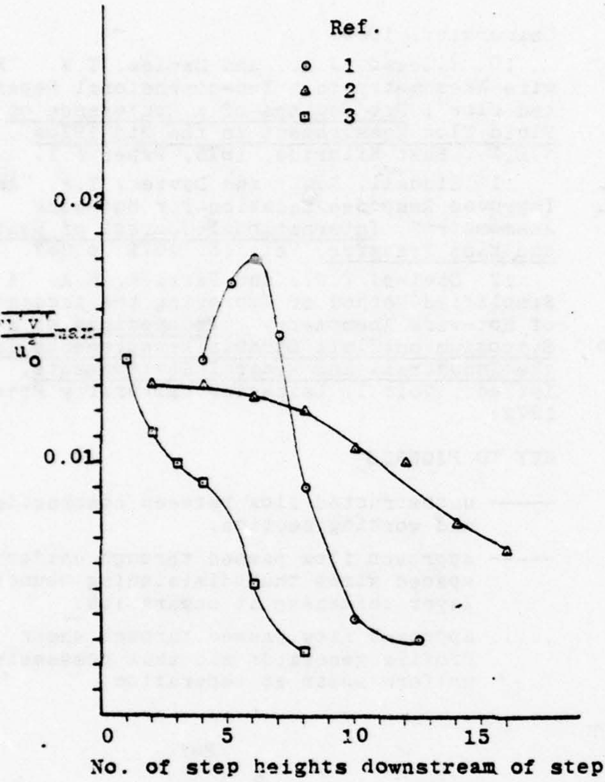

Figure 2 - Comparison of Maximum Turbulent Shear Stress Values

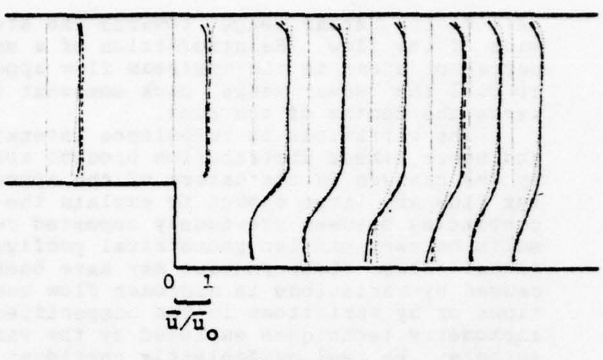

Figure 4
Profiles of $\overline{u}/\overline{u}_o$ for 50 mm step

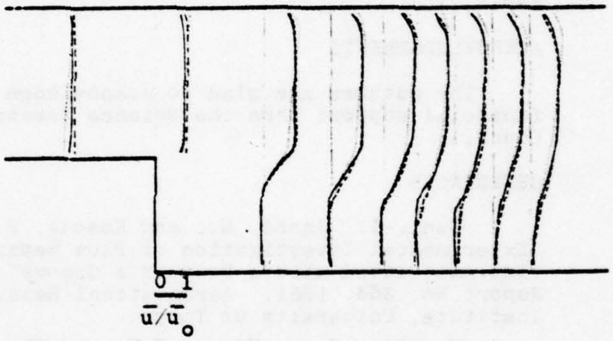

Figure 5
Profiles of $\overline{u}/\overline{u}_o$ for a 75 mm step

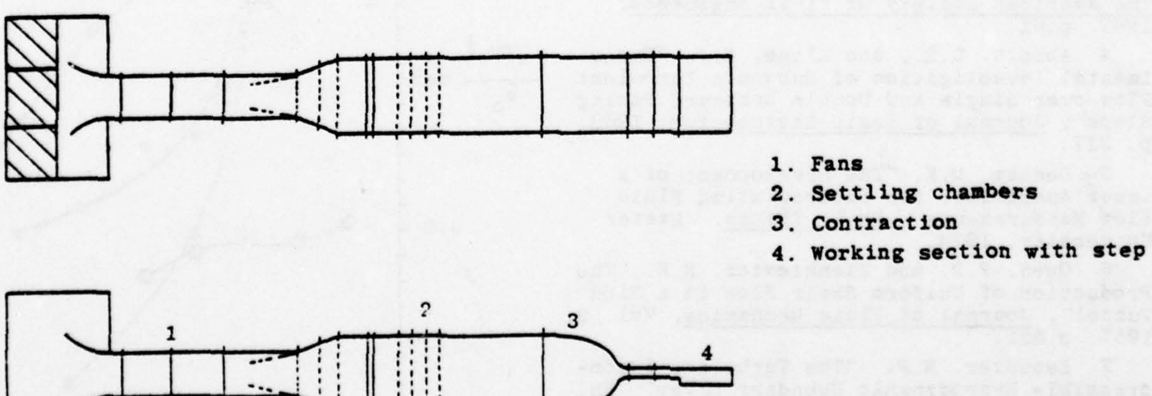

Figure 3 - Sketch of Wind Tunnel Arrangement

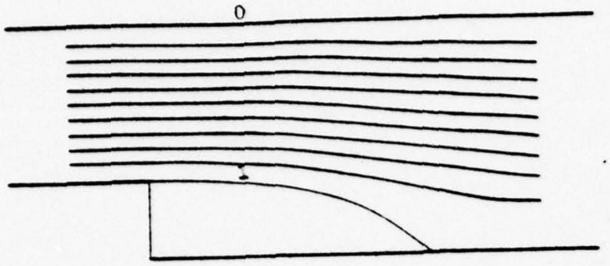

Figure 6 - Distribution of ψ/ψ_t for unobstructed flow over a 50 mm step

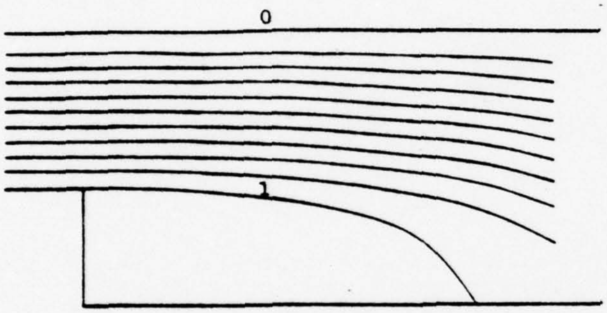

Figure 7 - Distribution of ψ/ψ_t for unobstructed flow over a 75 mm step

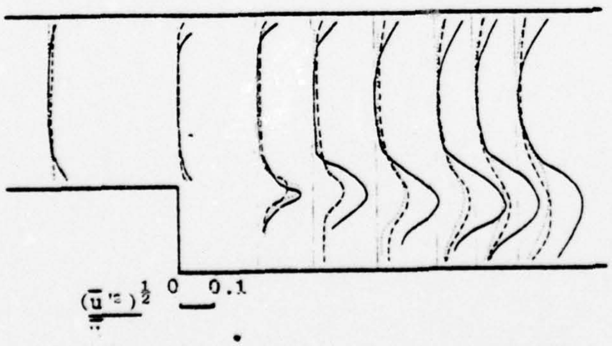

Figure 8 - Profiles of turbulence intensity for 50 mm step

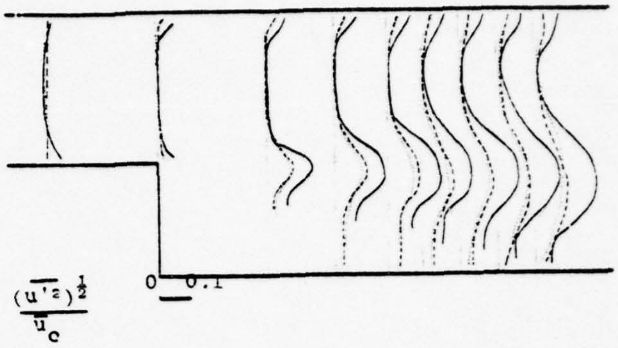

Figure 9 - Profiles of turbulence intensity for 75 mm step

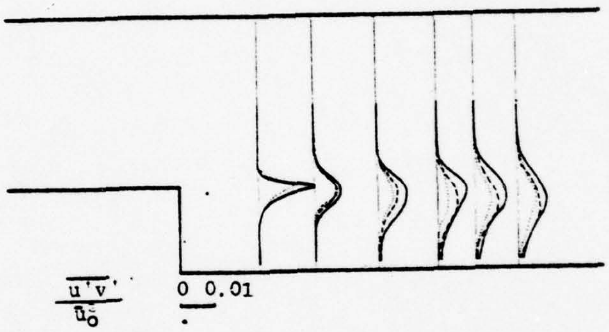

Figure 10 - Profiles of $\overline{u'v'}/\bar{u}_o^2$ for a 50 mm step

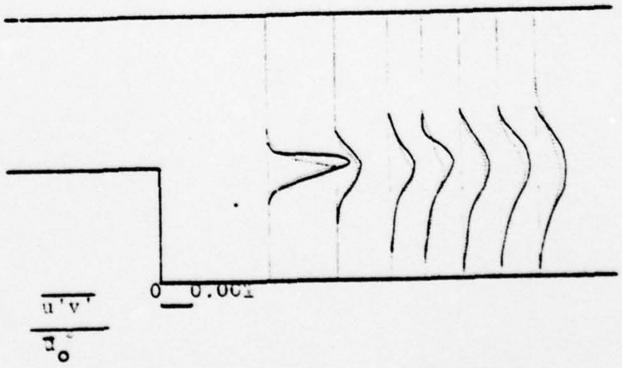

Figure 11 - Profiles of $\overline{u'v'}/\bar{u}_o^2$ for a 75 mm step

THE CALCULATION OF TWO-DIMENSIONAL TURBULENT RECIRCULATING FLOWS

A.D.Gosman, E.E. Khalil and J.H. Whitelaw

Imperial College of
Science and Technology
London, England.

ABSTRACT

The solution of two-dimensional, time-averaged conservation equations, in elliptic form, is reported for a range of boundary conditions corresponding to seven practical flow configurations. The solution procedure, which is embodied in the TEACH computer program, is described and numerical tests reported. The calculated properties of the seven flows are compared with experiment and demonstrate that the procedure, with a two-equation turbulence model, provides adequate precision for many engineering applications. The two-equation model is shown, however, to be deficient in detail.

NOMENCLATURE

a	area
A_p	coefficient in equation 6.
C_p	pressure coefficient.
C_1, C_2	constants in turbulence model.
C_D	constant in turbulence model.
C_t	Curtet number defined by: $\frac{1}{C_t{}^2} = \frac{1}{U_m^2 a} \int_a (P/\rho + U^2)\, da - \frac{1}{2}$
D, d	diameter.
E	constant in law of wall.
h	enthalpy.
k	kinetic energy of turbulence $= \frac{1}{2}(\overline{u}^2 + \overline{v}^2 + \overline{w}^2)$.
p	pressure.
P	pitch of ribbed roughness elements.
$Pr,_\phi$	Schmidt or Prandtl number for any variable ϕ.
r	radial distance from axis of symmetry.
Re	Reynolds number.
R	radius of duct.
S	swirl number defined as: $2\int (WU\rho r^2)\,dr / (R \int \rho U^2 r\,dr)$
S_ϕ	source or sink of variable ϕ.
St	Stanton number.
T	absolute temperature.
U	mean axial velocity.
$\tilde{u}$	axial normal stress, $(\sqrt{\overline{u}^2})$.
V	mean radial velocity.
$\tilde{v}$	radial normal stress, $(\sqrt{\overline{v}^2})$.
W	mean tangential velocity.
$\tilde{w}$	tangential normal stress, $(\sqrt{\overline{w}^2})$.
V_o	velocity vector.
x	axial coordinate
Y	radial coordinate.
y_1	distance normal to the wall.
y_a	width of the annular space.

Greek symbols

Γ_ϕ	exchange coefficient for ϕ
μ	viscosity
ρ	density
ε	dissipation of energy
ν	kinematic viscosity
τ	shear stress
ϕ	general dependent variable
Δ	rib height

Subscripts

a	annular
b	bulk
c	coolant
d	position of maximum tangential velocity
eff	effective (i.e. containing both laminar and turbulent effects)
fu	fuel stream
G	free stream
i	species
j	jet
lam	laminar
m	mean
max	maximum
min	minimum
tot	total
t	turbulent
W	wall
O	centreline

1. INTRODUCTION

In the classical literature, for instance Schlichting (1) and the papers referred to therein, turbulent recirculating flows receive slight attention due to the unavailability of appropriate solution techniques. However, the past two decades has seen the development of 'mathematical models' of such flows (2,3) which allow them to be described in terms of a closed set of differential equations; and of computer-based numerical methods capable of solving the equations, such as those described in references (4) and (5). The latter method in particular has allowed solutions to many important turbulent flows. For example, problems such as wall jets (6), wall jets with backward-facing steps (7) and diffusion flames in furnaces (8) were considered and, to an extent, explained by the procedure of reference (5). An important disadvantage of this method was, however, the use of stream function as dependent variable since it precluded convenient extension to three-dimensional flows.

PRECEDING PAGE BLANK-NOT FILMED

In recent years, numerical schemes for the solution of the two-or three-dimensional elliptic equations appropriate to recirculating flows, have been reported by many workers including Caretto et al. (9) and make use of the so-called primitive variables i.e. the numerical analysis has been performed with pressure and velocity as dependent variables and spatial coordinates as independent variables. These procedures appear to be more convenient to use than that of reference (5) but their applicability to a wide range of turbulent recirculating flow problems has not been reported and an assessment is, therefore, lacking. One purpose of this paper is to allow this assessment by making use of the procedure of reference (9) to solve equations appropriate to a range of two-dimensional recirculating flows. For this purpose, it is embodied in the 'TEACH' computer program described in (10).

The procedure described in reference (10) allows the solution of elliptic partial differential equations of the form:

$$\frac{\partial}{\partial x}(\rho U\phi) + \frac{1}{r}\frac{\partial}{\partial r}(\rho r V\phi) = S_\phi + \frac{\partial}{\partial x}\left(\Gamma_\phi \frac{\partial\phi}{\partial x}\right) + \frac{1}{r}\frac{\partial}{\partial r}\left(\Gamma_\phi r\frac{\partial\phi}{\partial r}\right) \qquad (1)$$

where r=1 converts the equation from the cylindrical form to the rectangular Cartesian form. The description of turbulent flows by equations of this type presumes that the time-mean values of the dependent variables of the turbulent flow, i.e. ϕ, can be represented by this form of equation together with appropriate boundary conditions. Since equation (1) represents a two-dimensional, time-average form of the Navier-Stokes equations, this implies that the flow must be two-dimensional, that the time dependence of the flow can be characterised by a turbulence model and that the turbulence model can have the form

$$\Gamma_\phi = \mu + \mu_t \qquad (2)$$

In time-averaging the Navier-Stokes equation, information has been lost and the solution of equation (1) with any turbulence model can serve only as an approximation. It is to be hoped that a convenient and general form of turbulence model exists which will allow the representation of the important characteristics of turbulent flows. A second purpose of this paper is, therefore, to determine the extent to which turbulent models of the type described in reference (3) can be used to represent turbulent flows. The present calculations have been performed with a 'two-equation' model (11, 12, 13, 14) and comments relating to the simplification or extension of this model are provided.

To achieve the two purposes stated in the previous paragraphs, seven flow situations with significant ellipticity are examined. Firstly, the influence of the finite-difference grid is determined; the influence of boundary conditions is then considered; and the turbulence model is appraised by comparing the calculated flow properties with available measurements. A sample number of calculations outside the range of experiments are also provided as an illustration of the use of the procedure for design purposes.

It may also be emphasised that the availability of experimental data in recirculating flows is considerably less than for boundary-layer flows. The reason is that, although conventional measuring techniques such as pressure and hot-wire probes may be used with satisfactory precision in boundary-layer flows, this is not so in regions of recirculation. It is not easy to assess the precision of measurements by these techniques in recirculating flows and, to an extent, this renders the assessment of turbulence models difficult. It is to be hoped that the increasing use of laser-Doppler anemometry will improve this situation in the near future.

The paper has been prepared in three main sections which describe respectively: the numerical procedure and general tests which have been carried out; the physical assumptions, their basis and their status with respect to alternatives; and the results of calculations. The paper ends with a discussion and conclusion section.

2. EQUATIONS AND SOLUTION PROCEDURE

2.1 Differential Equations

The set of partial-difference conservation equations (pdes) taken to govern the flows examined herein are compactly represented by equation (1) and the accompanying Table 1, which lists the dependent variables and the associated definitions of Γ_ϕ and S_ϕ: these, when substituted into equation (1) give rise to the familiar continuity, momentum (axial, radial and tangential) and thermal energy equations, together with those for turbulence energy and its dissipation rate. The task of the solution procedure is to solve this equation set with the appropriate boundary conditions (which, due to the elliptic nature of the pdes, take the form of prescriptions on ϕ or its normal gradient at all boundaries of the solution domain) and auxiliary algebraic equations such as (7) for μ_t.

Table 1

Conservation equations corresponding to equation 1

Conservation of	ϕ	Γ_ϕ	S_ϕ
mass	1	0	0
axial momentum	U	μ_{eff}	$\frac{\partial}{\partial x}\left(\mu_{eff}\frac{\partial U}{\partial x}\right) + \frac{1}{r}\frac{\partial}{\partial r}\left(\mu_{eff}\frac{r\partial V}{\partial x}\right) - \frac{\partial p}{\partial x}$
radial momentum	V	μ_{eff}	$\frac{\partial}{\partial x}\left(\mu_{eff}\frac{\partial U}{\partial r}\right) + \frac{1}{r}\frac{\partial}{\partial r}\left(\mu_{eff}\frac{r\partial V}{\partial r}\right) - 2\mu_{eff}\frac{V}{r^2}$ $\frac{\rho W^2}{r} - \frac{\partial p}{\partial r}$
tangential momentum	W	μ_{eff}	$-\left(\frac{\mu_{eff}}{r^2} + \rho\frac{V}{r} + \frac{1}{r}\frac{\partial\mu_{eff}}{\partial r}\right) W$
turbulent kinetic energy	k	$\frac{\mu_{eff}}{\sigma_k}$	$G_{k_1} - \rho\epsilon$
turbulence dissipate rate	ϵ	$\frac{\mu_{eff}}{\sigma_\epsilon}$	$\frac{\epsilon}{k}\left(C_1 G_{k_1} - C_2\rho\epsilon\right)$
stagnation enthalpy	h	$\frac{\mu_{eff}}{\sigma_h}$	0

$$G_{k_1} = \mu_{eff}\left\{2\left[\left(\frac{\partial U}{\partial x}\right)^2 + \left(\frac{\partial V}{\partial r}\right)^2 + \left(\frac{V}{r}\right)^2\right] + \left(\frac{\partial W}{\partial x}\right)^2 + \left[r\frac{\partial}{\partial r}\left(\frac{W}{r}\right)\right]^2 + \left(\frac{\partial U}{\partial r} + \frac{\partial V}{\partial x}\right)^2\right\}$$

2.2 Finite-Difference Equations

For the purposes of solution the flow domain is overlaid with a rectangular grid (Figure 1) whose intersection points or 'nodes' denote the location at which all variables, with the exception of the velocities, are calculated. The latter are computed at locations mid-way between the pressures which drive them, as indicated by the arrows in Figure 1. The nodes of a typical grid cluster are labelled as P, N, S, E and W.

The finite-difference counterpart[1] of the general pde (1) is derived by supposing that each variable is enclosed in its own control volume or 'cell', as illustrated in Figure 1. The pde is integrated over the control volume, with the aid of assumptions about the relations between the nodal values at ϕ and the rates of creation/destruction of this entity within the cells and its transport by convection and diffusion across the cell boundaries. The former is represented in linearised form as:

$$S_\phi \equiv \int_V s_\phi \, dV = S_O + S_P \phi_P \qquad (3)$$

and the transport by expressions of the form, for example;

$$\rho U_w \frac{(\phi_P + \phi_W)}{2} a_w - \Gamma_{\phi,w} \frac{(\phi_P - \phi_W)}{\delta x_{PW}} a_w \qquad (4)$$

when the quantity $Pe_w \equiv \rho U_w \delta x_{PW}/\Gamma_{\phi,w}$ is small and by

$$\rho U_w \phi_W, \quad U_w > 0$$

$$\rho U_w \phi_P, \quad U_w < 0 \qquad (5)$$

when Pe_w is large in magnitude. Here the subscripts P and W refer to the central and W nodes respectively, and w denotes the intervening cell boundary. Assembly of the above, and similar expressions for the remaining boundaries yields the fde;

$$(A_P - S_P) \, \phi_P = \sum_n A_n \phi_n + S_o \qquad (6)$$

where: $\sum_n$ denotes summation over the neighbouring nodes, N, S, E and W; $A_P \equiv \Sigma A_n$; and S_O and S_P are deduced from the S_ϕ's of Table 1. Equations of this kind are written for each of the variables, U, V, W, k, ε and h at every cell, with appropriate modifications being made to the total flux expressions (4) and (5) at cells adjoining the boundaries of the solution domain to take account of the conditions imposed there.

An equation for the remaining unknown pressure, is obtained by combining the continuity and momentum equations in the manner explained in Reference (9): this entails connecting changes in pressure, denoted by p' with changes in the velocities U', V' by approximate formulae derived from the momentum fdes. Substitution of these formulae into the continuity equation then yields a pde for p' similar to (6), with S_O now representing the local continuity imbalance in the prevailing velocity field.

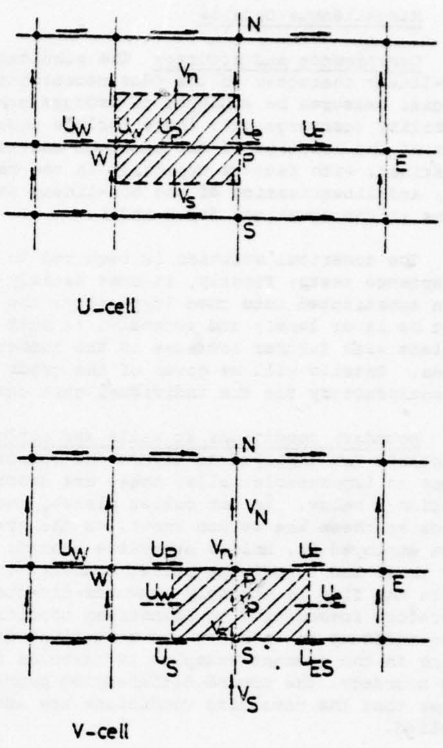

Fig. 1. Grid arrangement

2.3 Solution Algorithm

The fdes are solved by iteration, employing inner and outer iteration sequences. The outer sequence involves the cyclic application of the following steps: firstly, a field of intermediate axial and radial velocities, denoted by U* and V*, is obtained by solving the associated momentum equations using the prevailing pressures p*. Then continuity is enforced, by solving the equations for p' and thereby determining the required adjustments to the velocities and the pressures. The equations for the remaining variables are then solved in turn, and the whole process is repeated until a satisfactory solution is obtained.

The inner iteration sequence is employed to solve the equation sets for the individual variables. Solution is by a form of block iteration, in which a simple recurrence formulae, described in Reference 10 among others, is used to solve simultaneously for the ϕ's along each grid line, in the line-by-line counterpart of point Gauss-Seidel iteration. Complete convergence of the inner sequence is not necessary, and usually one to three applications of the block procedure suffices.

---

[1] Excluding the continuity equation, which receives special treatment.

2.4 Miscallenous Details

Convergence and accuracy The simultaneous and non-linear character of the fdes necessitates that special measures be employed to procure numerical stability (convergence): these include under-relaxation of the solution of the momentum and turbulence equations, with factors typically in the range 0.3-0.5; and linearisation of the non-linear source/sink terms in the equations for k and ε.

The numerical solution is required to pass two acceptance tests: firstly, it must satisfy the fdes when substituted into them (typically, the imbalance must be 1% or less); and secondly, it must be invariant with further increase in the number of grid nodes. Details will be given of the grids found to be satisfactory for the individual test cases.

Boundary conditions at walls and outlets Special practices are employed to impose the boundary conditions at impermeable walls: these are described in section 3 below. As for outlet planes, the conditions at these are seldom known, so the practice here employed is, unless otherwise stated, to locate (by trial and error) the outlet boundary in a region where the flow is strongly outwards-directed, and therefore insensitive to downstream conditions. It then suffices to estimate the streamline direction, which in the present examples is taken as normal to the boundary: the upwind differencing practice ensures that the remaining conditions are automatically applied.

3. PHYSICAL MODELLING

3.1 Turbulence Models

As can be seen from Table 1, the equations for turbulence energy and dissipation rate involve four constants. In addition, the equation

$$\mu_t = C_D \rho k^2/\varepsilon \qquad (7)$$

is necessary to close the set of equations; this involves one further constant. The five constants necessary for the turbulence model are shown in Table 2: they are identical with those recommended in reference (10).

Table 2. Turbulence model constants

constant	value
C_D	0.09
C_1	1.42
C_2	1.92
σ_ε	1.22
σ_k	0.9
κ	0.417
E	9.37
σ_h	0.9

The validity of the two-equation turbulence model has been tested previously for the case of recirculating regions downstream of blunt-body baffles. Pope and Whitelaw (14) demonstrated that, although it could not accurately represent the length of the recirculating region or the development of the downstream wake, it was only marginally less satisfactory than five-equation models. It can be expected, therefore, that the two-equation model will result in predictions of turbulent recirculating flows which are less than perfect; on the other hand, it is necessary to quantify the extent of any discrepancies which result from the model over a wide range of flow situations.

3.2 Wall Functions

In order to minimize computer storage and run times, the dependent variables at the wall were linked to those at the first grid node from the wall by equations which are consistent with the logarithmic "law of the wall". Thus, the resultant velocity parallel to the wall in question and at a distance y_1 from it corresponding to the first grid node was assumed to be represented by the 'law of the wall' equation

$$V_o C_D^{1/4} k^{1/2}/(\tau_w/\rho) = \frac{1}{\kappa} \ln\{E C_D^{1/4} k^{1/2} y_1 \rho/\mu\} \qquad (8)$$

from which the wall shear stresses were obtained in solving the momentum equations.

The calculations of turbulent kinetic energy and the rate of dissipation at the first grid node were determined in a manner consistent with the use of the law of the wall for the mean velocity components: details are given in references (10) and (11).

In the present numerical procedure, the above wall functions could readily be replaced by those appropriate to the viscous sub layer and previously employed in boundary layer procedures (11). An important consequence for the calculations of the following section would however be large increases in the required storage and run time.

4. RESULTS

The calculations presented in this section are intended to demonstrate that the present numerical procedure, embodying its two equation turbulence model, can be used for calculations in a range of flow configurations. These configurations are presented in an order which conforms approximately to increasing ellipticity of the equations which describe the flow, i.e. the turbulent diffusion in the x and y directions tend to the same magnitude. In each case, the geometry and flow arrangement are described and the results presented and compared with available measurements.

All of the calculations discussed below were performed with 20x20 grid nodes except that of 4.7 which required 30x30 nodes. The corresponding storage requirements, on a CDC 6600 ranged from approximately 20k words to 40k words. The corresponding calculation times ranged from approximately 100 to 600s and were longer than might normally be required since especially stringent convergence criteria were imposed. It should be emphasised that the location of the grid nodes to ensure grid-independent solutions requires experience and skill.

4.1 Swirling Pipe Flow

The experimental investigations of Weske and Sturov (15) relate to the flow of swirling air in a pipe. The degree of swirl was varied according to the rotational velocity of the inlet pipe and the measurements of three velocity components, obtained with a hot wire anemometer, were recorded at downstream locations for two values of the ratio of the maximum tangential velocity to the mean axial velocity at the inlet plane. The measured values of mean velocity components and the corresponding turbulence intensity were available at the inlet plane and were used as boundary conditions; the rate of dissipation in the inlet plane was calculated from the expression;

$$\varepsilon = k^{3/2} / 0.005D$$

which presumes the existence of a constant mixing length across the duct. The downstream boundary condition corresponded to zero x-gradients and were assigned at a value of x/D of 160. The calculated results were found to be comparatively insensitive to meshes greater than 16 x 16.

Figures 2 and 3 show the calculated values of the tangential component of velocity, W, for the two degrees of swirl and at downstream locations corresponding to x/D of 0.35 and 5.1 respectively; the corresponding profiles of turbulence kinetic energy are also presented. The measurements and calculations are in general agreement. Discrepancies exist close to the wall of the pipe and may be attributed to the two-equation turbulence model which is known to be imperfect for axisymmetric flows. The wall jet calculations of references (6) and (7) and the confined jet calculations of reference (8) showed similar trends. The discrepancy may be attributed, at least in part, to equation (7) which requires that the location of zero velocity gradient be identical with that of zero local shear stress.

Swirling flow in a pipe may also be achieved with the aid of vanes. An experiment of this type was carried out by Baker (16) who measured mean velocity components, with a direction-sensitive impact probe, at a number of values of x/D and with a swirl number, S, defined as $8\rho\int UWr^2 dr/(\rho U_m^2 D^3)$ of 0.55. Calculations were performed to compare with these results at x/D of 15 and 35. The inlet profile of the radial velocity component was assumed to decrease linearly with radius to a value of $-0.2U_m$ near the wall but numerical tests showed that the inlet profile did not influence the calculations of Figure 4 significantly; the inlet tangential velocity profile was assumed to increase linearly with the radius.

The assumed kinetic energy and dissipation rate profiles, which correspond to a mixing length assumption, did not have a significant influence on calculations downstream of x/D of 4 and did not, therefore, influence the results of Figure 4. The downstream boundary conditions, i.e. $\partial\phi/\partial x = 0$, were assigned at x/D of 100. Figure 4 compares measured and calculated values of the tangential velocity component at two downstream locations and

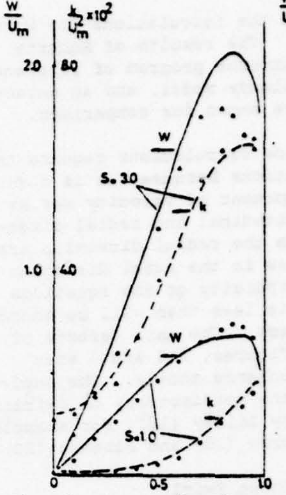

Fig. 2 Measured and calculated profiles of tangential velocity and kinetic energy in the swirling pipe flow of reference 15.

O,● S = 1.0
Δ,▲ S = 3.0
R_e = 3 x 10^4
$\frac{x}{D}$ = 5.1
——, --- present calculations

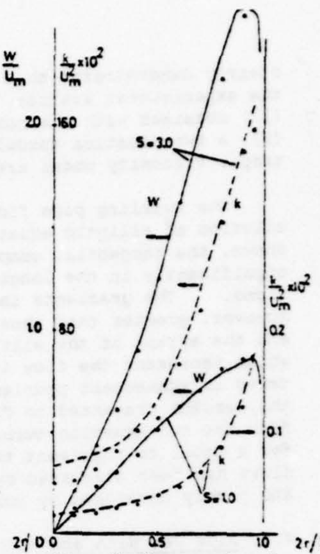

Fig. 3 Measured and calculated profiles of tangential velocity and kinetic energy in the swirling pipe flow of reference 15.

O,● S = 1.0
Δ,▲ S = 3.0
R_e = 3 x 10^4
$\frac{x}{D}$ = .35
——. --- present calculations

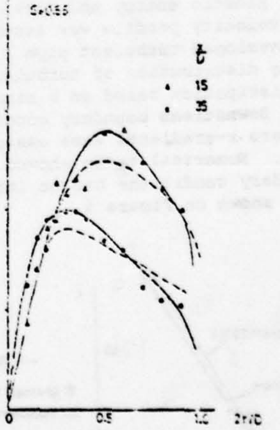

Fig. 4 Measured and calculated profiles of tangential velocity in the swirling pipe flow of reference 16.

S = 0.55
R_e = 5 x 10^4
▲,● measurements
—— --- calculations of reference 17
—— present calculations

clearly demonstrates that the calculations lie within the experimental scatter. The results of Roberts (17) obtained with the computer program of reference (5), a two-equation turbulence model, and an anisotropic viscosity model are shown for comparison.

The swirling pipe flow calculations require the solution of elliptic equations because, as is clearly shown, the tangential component of velocity varies significantly in the longitudinal and radial directions. The gradients in the radial direction are, however, greater than those in the axial direction and the extent of the ellipticity of the equations which represent the flow is less than will be encountered in subsequent problems. The main defects of the results presented on Figures, 2 3 and 4 stem from the two-equation turbulence models. The need for a model to represent the non-isotropy of swirling flows has been discussed by Lilley (18), for example, and partly developed by Morse (19) and Ribeiro (20).

4.2 Pipe Jet With and Without Swirl

The extent of mixing and recirculation was investigated by Barchilon and Curtet (21) and Craya and Curtet (22) for a jet of air in a pipe; this arrangement induced a secondary flow through the annulus formed between the jet nozzle and the pipe diameter and resulted in recirculation in the vicinity of the pipe wall for high values of jet to annulus velocity ratio. The investigations of reference (21) and (22) were carried out in a duct of diameter 0.162m and a nozzle diameter of 0.012m. The static and total head pressures were recorded at various locations in the flow for a variety of velocity ratios. The results are shown on Figures 5a and 5b in terms of the Curtet number and the ratio of mass flowing in the upstream direction to that in the downstream direction. The corresponding calculations are shown on the figures and were obtained from a knowledge of the mean jet velocity, U_m, and assumed inlet profiles of velocity, kinetic energy and dissipation rate. The initial velocity profile was assumed to be that of a fully developed turbulent pipe flow with a corresponding distribution of turbulent kinetic energy and dissipation based on a mixing length assumption. Downstream boundary conditions, corresponding to zero x-gradients were assigned at a value of x/D of 10. Numerical tests showed that these assumed boundary conditions had no influence on the calculations shown on Figure 5.

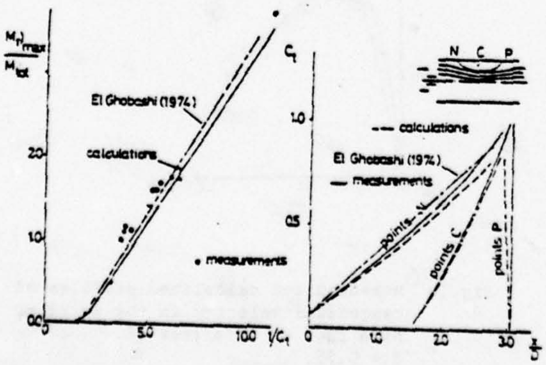

Fig. 5 Measured and calculated variations of recirculation, zero size and location with pipe jet flow of references 21 and 22.
$R_e = 8 \times 10^4$ ●,▲ Measurements — Calculations

The calculations are in reasonable agreement with the measurements although the latter, as might be expected from the simple instrumentation, show considerable scatter and are subject to an uncertainty which is difficult to specify. The experimental uncertainty is likely to be greatest at large Curtet number, due to the use of pitot tubes, and this is reflected in the experimental scatter. The calculations of El-Ghobashi (23), obtained with a k-ε turbulence model and a different numerical scheme, are in general agreement with the present results.

In the more recent measurements of Craya and Utrysko (24), a direction-sensitive pitot probe was used to measure the centre line axial velocity distribution and the profiles of the tangential velocity in a geometry similar to that described above; the swirl was induced in the jet flow with swirl numbers ranging from .0-.81. The boundary conditions were assumed to be similar to those used for the results of Figure 5 with the additional assumption of a linear profile of tangential velocity at the inlet plane: the influence of the assumed initial conditions did not extend beyond the first two grid lines, i.e. x/D of 0.15. Calculations were performed for a ratio of annulus to jet mass flow rate of 15 and for five swirl numbers. As indicated on Figure 6, the calculations agree with the experiments at low swirl numbers but agree less well as the swirl number increases to 0.81. The results correspond to Curtet numbers between 1.26 and 1.38 and, in keeping with Figure 5, did not reveal recirculation. Corresponding profiles of the tangential velocity component are shown on figure 7 and allows conclusions consistent with those appropriate to Figure 6.

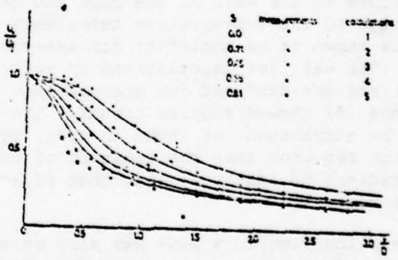

Fig. 6 Measured and calculated centreline distributions of mean axial velocity in the pipe jet flow of reference 24.
$R_e = 1.5 \times 10^4$ — present calculations
O,▲,▼,x,◻ measurements

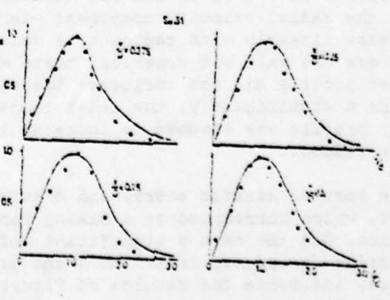

Fig. 7 Measured and calculated profiles of mean tangential velocity in the pipe jet flow of reference 24 for S = 0.81.
● measurements —— present calculations.

4.3 Flow Over A Backward-Facing Step

Abbott and Kline (25) observed turbulent flow downstream of a plane sudden expansion with the aid of smoke and, in the vicinity of the reattachment position, with tufts. The results tended to be qualitative but, as indicated on Figure 8, the repeatability of the determination of reattachment is remarkably good. The authors observed that the regions of recirculation on both sides of the symmetry plane were identical for small expansion ratio; however, for large values of expansion ratio, the two recirculation regions appeared to interact and to result in an asymmetric region of recirculation; indeed, at some conditions, two regions of recirculation were observed on one side of the symmetry plane and one on the other. For the symmetrical situation, the reattachment location tended to correspond to approximately 9h as the value of 2h/d increased above 0.8.

The calculations of figure 8 were obtained in the range of 2h/d for which symmetry had been observed and they are clearly in good agreement with the experiments. To obtain these calculations, a symmetry plane was assumed and profiles in the corner of the step, were assumed to conform to half of a fully developed channel flow. The imposed downstream boundary conditions were again zero x-gradients and were assigned at different downstream positions depending upon the value of 2h/d; the actual location was determined by trial and error with the criterion that they were far enough downstream not to influence the upstream calculations.

Although Abbott and Kline did not provide detailed measurements in the recirculation region, they can be provided by the calculation procedure. Figure 9 indicates velocity profiles corresponding to three values of 2 h/d.

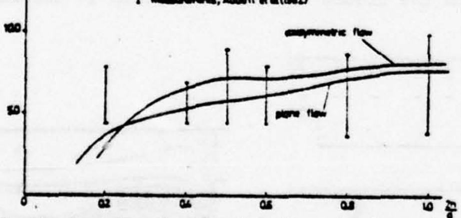

Fig. 8 Measured and calculated variation of recirculation zone length with expansion ratio in plane and axisymmetric flows. $R_e = 5 \times 10^4$ — present calculation I uncertainty bounds of measurements of reference 25.

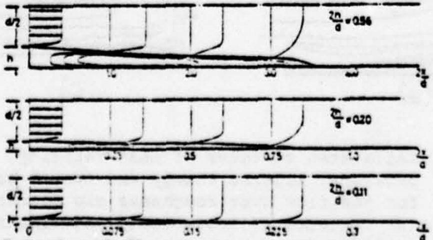

Fig. 9 Calculated flow patterns and velocity profiles in a plane sudden expansion at various expansion ratios.

4.4 Axisymmetric, Sudden Expansion Flow

The flow downstream of an axisymmetric, sudden enlargement was investigated by Back and Roschke (26) for a range of Reynolds numbers 10^2 to 10^4 based on the diameter of the smaller pipe. The expansion ratio was 0.385. Calculated values are compared with measurements, at turbulent Reynolds numbers, on Figure 8 which also present the calculations and measurements for the plane expansion of Abbott and Kline: the single measurement of Back and Roschke corresponds to a value of 2h/d of 1.6 and x_r/h of 8.5.

As an example of the information which can be obtained from the calculation procedure, Figure 10

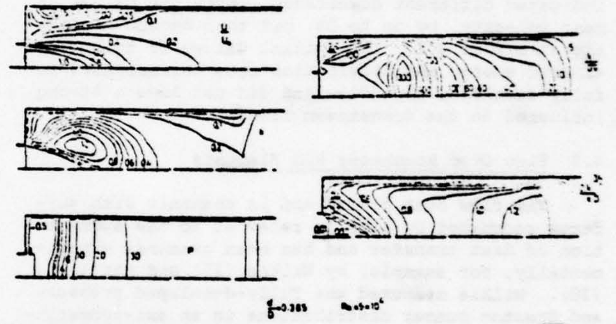

(a) Contours of isovelocity, kinetic energy and pressure for $\frac{d}{D}$=0.385 and R_e = 5 x 10^4.

(b) Contours of $k/\overline{uv}$ and ℓ/L for $\frac{d}{D}$= 0.385 and R_e = 5 x 10^4

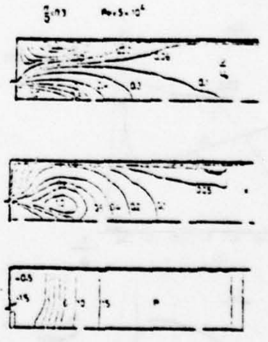

(c) Contours of isovelocity,kinetic energy and pressure for $\frac{d}{D}$ =0.3 and R_e =5x10^4

Fig. 10 Calculated flow properties in the sudden expansion geometry of reference 26.

has been prepared. Its presents contours of axial mean velocity, static pressure, turbulence, kinetic energy and length scale for the geometry of Back and Roschke and for a Reynolds number of $5x10^4$. There are no measuremonts with which to compare the calculations; they are, however, in accord with reasonable expectations. The calculations can readily be extended to indicate wall properties such as the shear stress and heat transfer coefficient, as will be demonstrated in later examples.

The above calculations were performed with a velocity profile of the form

$$U/U_o = (1-2r/d)^{1/7}$$

assumed in the inlet plane of the expansion and with zero x-gradients assumed at x/D of 16. Tests, with a uniform axial velocity profile at inlet indicated different downstream centreline values of mean velocity, by up to 5%, but then become negligible at x/D of 2.8. The initial values of turbulence kinetic energy and dissipation rate corresponded to fully developed pipe flow and did not have a strong influence on the downstream flow.

4.5 Flow Over Roughness Rib Elements

The flow over plates and in channels with surfaces roughened by ribs is relevant to the augmentation of heat transfer and has been examined experimentally, for example, by Wilkie (27) and Mantle (28). Wilkie measured the fully-developed pressure and Stanton number distributions in an axi-symmetrical arrangement with two ratios of pitch to rib height. Measurements and calculations are shown on Figure 11 and are in good agreement: there were no pressure measurements for the smaller pitch to rib height ratio. An indication of the regions of separated flows, obtained from the calculations, is also provided on Figure 11. The calculated flow properties were obtained by solving the conservation equations of mass, momentum, turbulent-kinetic energy and its dissipation rate and the stagnation enthalpy.

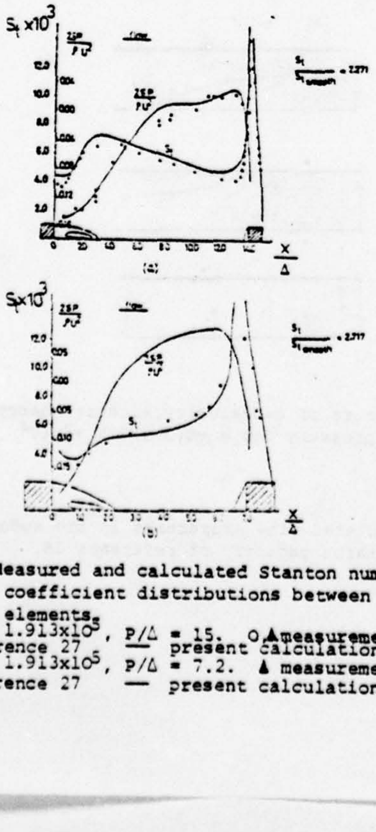

Fig. 11 Measured and calculated Stanton number and pressure coefficient distributions between two roughness rib elements.
(a) R_e = $1.913x10^5$, P/Δ = 15. ○▲measurements of reference 27 — present calculations.
(b) R_e = $1.913x10^5$, P/Δ = 7.2. ▲ measurements of reference 27 — present calculations.

No inlet profiles of mean velocity components, kinetic energy of turbulence and dissipation rate were reported in reference (27). The mean axial velocity profile at inlet was assumed to be that of fully developed channel flow; the radial component to be zero; and the kinetic energy distribution corresponded to k/U^2= 0.005. The influence of varying k/U^2 between 0.003 and 0.03 on the centreline velocity distribution was less than 4%. The dissipation rate was assumed to follow a mixing length hypothesis and the influence of this assumption diminished at downstream distances less than one rib height. The inner roughened wall was heated with T_w/T_b= 1.2 while the outer smooth wall was not heated.

Figure 12 presents detailed contours of mean velocity, static pressure, turbulence kinetic energy, and length scale for the smaller pitch to rib height ratio of Wilkie. Once again there are no measurements with which to compare and the calculations are provided to indicate the details with which calculated results can be obtained.

The measurements of recirculation-zone length obtained by Mantle are shown on Figure 13 together with calculations and the two are in good agreement. Although Mantle did not observe, with his wool tufts, reattachment for value of P/Δ less than 6.6, the calculations indicate reattachment to much lower values: for values of P/Δ less than around 2.5, the calculations did not exhibit recirculation.

Figure 13 also presents calculated values of overall Stanton number and pressure coefficient for a range of pitch to rib height ratios. It can be seen from the figure that, as the pitch is decreased

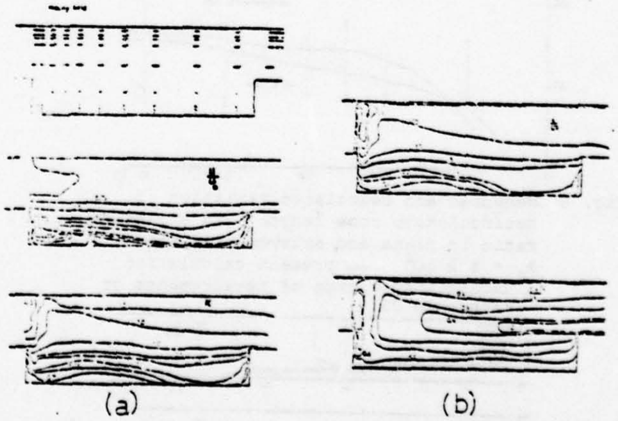

Fig. 12 Calculated contours of mean velocity, pressure, kinetic energy and length scale for the flow over roughness rib elements.
(a) Contours of isovelocity and kinetic energy.
(b) Contours of $k/\overline{uv}$ and ℓ/L.

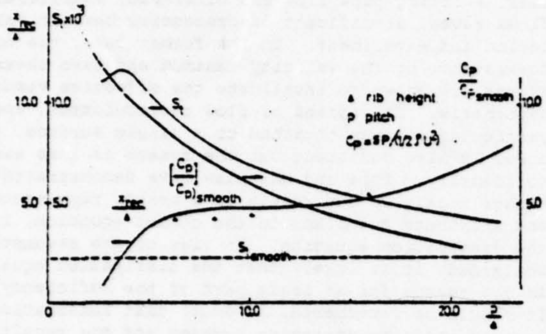

Fig. 13 Variation of recirculation zone length, overall Stanton number and pressure coefficients as a function of the ratio of rib pitch to height.
▲ measurements of reference 28.
— present calculations.

for the same rib height, the overall Stanton number and, therefore, the heat flux to the wall increases. Unfortunately, the required pressure drop, as indicated by the pressure coefficient, also increases and, for the lower values of P/Δ, the rate of increase of pressure drop is similar to the rate of increase of heat transfer rate.

4.6 Plane Wall-Jet Flows

Kacker and Whitelaw (29) used a hot-wire anemometer to measure mean velocity and turbulent kinetic energy downstream of wall jet geometries with four different velocity ratios of slot to free-stream velocity. In the particular case of a thick slot lip there is a substantial region of recirculation immediately downstream of the lip and this necessitates the solution of elliptic equations. Unlike the recirculation regions of previous flows, these are not bounded by surfaces on two sides.

Measured and calculated values of mean velocity and turbulence kinetic energy are presented on Figure 14 for two values of the velocity ratio and two downstream stations. The region of reversed flow is not large at the first downstream station where measurements are available and, at further downstream stations, the influence on the recirculation has disappeared. The calculations, however, encompass the region of recirculation and the results shown on the figures have been influenced by upstream recirculation.

The initial conditions, with the exception of dissipation rate which was calculated with the help of a mixing length assumption, were provided in reference (29): once again the downstream boundary conditions of zero x-gradients were located at a station such that upstream calculations were uninfluenced.

The measured and calculated values of velocity and kinetic energy are in good agreement: similar calculations, with a simple turbulence model, were obtained with a computer program based on the solution of equations for stream function and vorticity (5) but required a longer computing time and storage. In addition, these earlier calculations were in good agreement with measurements largely because the algebraic length-scale assumptions was formulated on the basis of the measurements.

4.7 Flow In The Wake Of A Disc

Durão and Whitelaw (30) reported values of axial velocity and the corresponding normal stress measured, by laser anemometry, in the wake of a disc surrounded by an annular jet. The measured axial distribution of velocity and a radial profile at x/D of 0.3 are shown on Figure 15 together with calculations ontained with the range of assumed values of the radial velocity component at the exit from the annular jet. Measured initial values of the axial velocity component and the corresponding normal stress were used in the calculations.

The radial velocity component was initially assumed zero and, as can be seen, the agreement between calculation and measurement is imperfect. In particular, the length of the recirculation region is calculated to be around 75% of the measured value and the minimum velocity is overestimated. The influence of finite radial velocity is also shown on the figure and is significant: thus, the absence of measured initial values of this radial component can be serious. In the present case, the radial values are likely to be very close to zero and the discrepancies between calculation and measurement can be attributed more to the turbulence model than to incorrect initial conditions.

There are also differences between calculations and measurements in the decay of the centreline velocity in the jet region and also at the outer edge of the jet. The former can be attributed to the turbulence model, as discussed by Pope and Whitelaw (14), but the latter is linked to the distribution of grid nodes in the outer region of the flow and to the radial location at which the free boundary condition is assigned. For the calculations of Figure 15, the outer grid boundary was located at 10D from the centreline and corresponded to $\partial\phi/\partial r$ of zero: the grid mesh was 30x30 with 16 grid nodes between the velocity maximum of figures 15b and the centreline. Tests with smaller numbers of grid nodes suggested that the distributions shown on Figure 15b were grid independent but the calculated profile in the outer region of the jet cannot be considered to be independent of radial location of the assigned boundary condition, even with this radial location at 10D. The inner region of the flow was not influenced by the location of the boundary condition and the outer region became less influenced with increasing downstream diameter.

5. CONCLUDING REMARKS

The results presented in the previous section demonstrate that the present solution procedure, together with conservation equations in time-averaged form and a two-equation turbulence model, can be used to represent a range of flows with adequate precision for many engineering applications. The procedure is acceptably economic of computing time and storage and can be adapted to a wide range of boundary conditions.

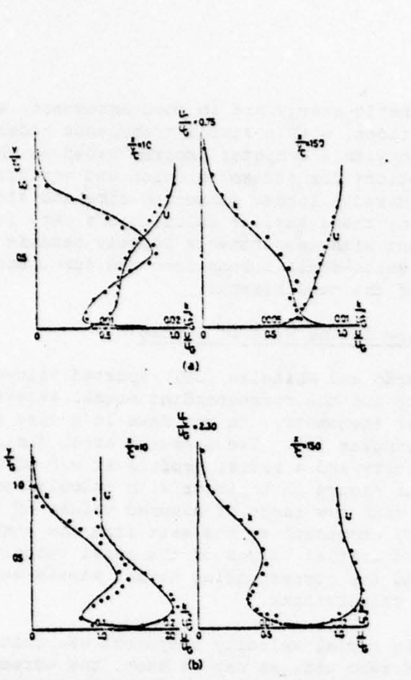

Fig. 14 Measured and calculated profiles of mean velocity and kinetic energy distribution of the wall jet of reference 29.
(a) U_C/U_G = 0.75 O,▲ measurements
— present calculations
(b) U_C/U_G = 2.3 O,▲ measurements
— present calculations

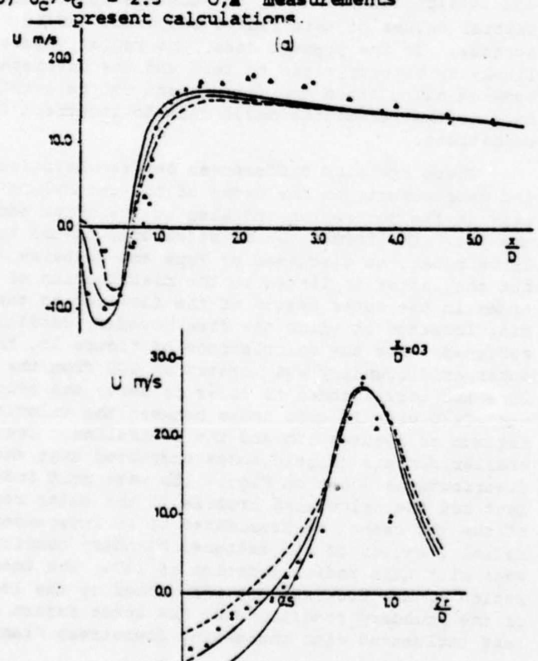

Fig. 15 Measured and calculated values of mean axial velocity in the wake behind the disc of reference 30.
O,▲ measurements
— calculation with inlet radial velocity=$0.05U_{inlet}$
— — calculation with inlet radial velocity=0.0
--- calculation with inlet radial velocity=$-0.05U_{inlet}$
(a) centre-line distributions
(b) radial profiles.

The two-equation turbulence model, although adequate for engineering purposes, does not allow precise representation of the present flows. In particular, swirling-pipe flow and bluff-body stabilised flows reveal significant discrepancies between calculation and experiment. In the former case, the non-coexistence of the velocity maximum and zero shear stress are shown to invalidate the effective viscosity hypothesis. In regions of flow recirculation, and particularly those attached to a single surface, the model is also deficient but the reason is less easy to identify. Pope and Whitelaw have demonstrated that higher models do not result in a better representation and attribute the blame to the common equation, i.e. the dissipation equation. In view of the assumptions contained, it is likely that the dissipation equation is the reason for at least part of the deficiency. It should be remembered, however, that information is lost in the time-averaging process and the resulting equations are bound to be less than exact.

ACKNOWLEDGEMENT

We are glad to have the opportunity to acknowledge support from the AERE, Harwell and from the Science Research Council.

REFERENCES

(1) Schlichting, H. Boundary layer theory, MacGraw Hill, 6th Edition, 1968.

(2) Harlow, F.H. and Nakayama, P.I. Turbulent transport equations. Physics of Fluids, 10, 1967, 323.

(3) Launder, B.E. and Spalding, D.B. Mathematical Models of Turbulence. Academic Press, 1972.

(4) Pun, W.M. and Spalding, D.B., A procedure for predicting the velocity and temperature distribution in confined, steady turbulent, gaseous diffusion flame. 18th International Astronautical Congress, Belgrade, 1967.

(5) Gosman, A.D., Pun, W.M., Runchal, A.K., Spalding, D.B. and Wolfstein, M. Heat and mass transfer in recirculating flow. Academic Press, 1969.

(6) Kacker, S.C., The influence of slot geometry on the two dimensional turbulent wall-jet. Ph.D. thesis, London University, 1970.

(7) Matthews, L. and Whitelaw, J.H. Plane jet flow over a backward facing step. Proc. Inst. of Mech. Eng. 187, 1973, 38.

(8) Elghobashi, S.E. and Pun, W.M., A theoretical and experimental study of turbulent diffusion flames in cylindrical furnaces. Proc. 15th Symposium (International) on Combustion, 1974, p. 1353, Combustion Institute, U.S.A.

(9) Caretto, L.S., Gosman, A.D., Patankar, S.V., and Spalding, D.B., Two calculation procedures for steady three-dimensional flows with recirculation. Proc. 3rd International Conference on Numerical Methods in Fluid Dynamics, Paris, 1972.

(10) Gosman, A.D. and Pun, W.M., Calculation of recirculating flows. Imperial College, Mech. Eng. Dept. Report.

(11) Launder, B.E. and Spalding, D.B. The numerical computation of turbulent flows. Computer methods in Applied Mechanics and Engineering, 3, 1974, 269.

(12) Launder, B.E., Morse, A., Rodi, W. and Spalding, D.B., The prediction of free shear flows - a comparison of the performance of six turbulence models, NASA Conference on free shear flow, Langley Field, Hampton, 1972.

(13) Jones, W.P. and Launder, B.E., Predictions of low Reynolds number phenomena with a two-equation

model of turbulence. Int. J. of Heat and Mass Transfer, 16, 1973, 1119.

(14) Pope, S.B. and Whitelaw, J.H., The calculation of near-wake flows. J. Fluid Mech. 73, 1976, 9.

(15) Weske, D.R. and Sturov, G. Ye., Experimental study of turbulent swirled flows in cylindrical tube. Fluid Mechanics, Soviet Research, 3, 1974, 77.

(16) Baker, D.W., Decay of swirling, turbulent flow of incompressible fluids in long pipes. Ph.D. thesis, University of Maryland, 1967.

(17) Roberts, L.W., Turbulent swirling flows with recirculation. Ph.D. thesis, London Univ., 1972.

(18) Lilley, D.G., Non-isotropic turbulence in swirling flows. Cranfield Institute of Technology Report, 1975.

(19) Morse, A. Private Communication, 1975.

(20) Ribeiro, M.M., The turbulence structure of free jet flows with and without swirl. Ph.D. thesis, London Univ., 1976.

(21) Barchilon, M. and Curtet, R. Some details of structure of an axisymmetric confined jet flow. Symposium on fully separated flows, Philadelphia. J. Basic Eng., D86, 1964, 777.

(22) Craya, A. and Curtet, R. Sur l'evolution d'un jet en espace confine, C.R.A.S., Paris, 236, 1953, 1134.

(23) ElGhobashi, S.E. Private communication, 1974.

(24) Craya, A. and Utrysko, B. Jets tournants en espace confine. Service de documentation scientifique et technique de l'arnement, Paris, 1967.

(25) Abbott, D.E. and Kline, S.J. Experimental investigation of subsonic turbulent flow over single and double backward facing steps. J. Basic Eng., D84, 1962, 317.

(26) Back, L.H. and Roschke, E.J. Shear-layer flow regimes and wall instabilities and reattachment lengths downstream of an abrupt circular channel expansion, Trans. ASME, J. Appl. Mech. 94, 1972, 677.

(27) Wilkie, D. Forced convection heat transfer from surfaces roughened by transverse ribs. Proc. 3rd Int. Heat Transfer Conference, 1966, 1, Chicago.

(28) Mantle, P.L. A new type of roughened heat transfer surface selected by flow visualization techniques. Proc. 3rd Int. Heat Transfer Conference, 1966, 45, Chicago.

(29) Kacker, S.C. and Whitelaw, J.H. The turbulence characteristics of two-dimensional wall jet and wall-wake flows. J. Applied Mechanics, E93, 1971, 239.

(30) Durão, D.F.G. and Whitelaw, J.H. Measurements in the region of recirculation behind a disc. Proc. 2nd Int. Workshop on laser velocimetry, Purdue Univ. 1974.

SESSION 14

SUB-GRID SCALE MODELLING

Chairman: J. Herring
NCAR
Boulder, Colorado 80303
U.S.A.

STUDIES OF SUB-GRID MODELLING WITH CLASSICAL CLOSURES AND BURGERS' EQUATION

BY

M. D. LOVE AND D. C. LESLIE

DEPARTMENT OF NUCLEAR ENGINEERING

QUEEN MARY COLLEGE, MILE END ROAD, LONDON E1 4NS

ABSTRACT

Studies with the Direct Interaction Approximation and Burgers' model turbulence of both the structure and performance of sub-grid models are reported. These suggest that the discrepancy between Lilly's evaluation of the Smagorinsky constant and the value required to stabilise practical calculations is not due to the effects of the filter nor to the unrealistic spectral form assumed; it may well be due to inhomogeneity. The investigation supports the standard eddy viscosity sub-grid model, and suggests that the performance will be improved if the local root mean square strain tensor is replaced by an average over a large volume. Further study will be needed to show whether this modification is appropriate for large eddy simulations of the Navier-Stokes equations.

NOMENCLATURE

A = non-dimensional constant in sinusoidal driving force for Burgers' equation
c = non-dimensional constant in Smagorinsky sub-grid model
c_i = non-dimensional constant in sub-grid model for Burgers' equation
DIA = Direct Interaction Approximation
$E(t)$ = Mean energy/unit length for Burgers' equation
$E(k,t)$ = energy/unit scalar wavenumber
f = forcing function in Burgers' equation
$G(\underline{x},\underline{x}')$ = filter function; $G(k)$ Fourier transform
g = general field variable; $\overline{g}$ = grid scale component; g' = sub-grid scale component
h = finite difference mesh interval
k = scalar wavenumber; $\underline{k}$ = vector wavenumber
K_1 = cut-off wavenumber
k_i = wavenumber in i direction
K_p = wavenumber peak in assumed spectral form
Ko = Kolmogorov constant
L = length of Burgers' flow field
p = scalar wavenumber, also kinematic pressure; $\underline{p}$ = vector wavenumber; $\overline{p}$ = grid scale kinematic pressure
R = residual stress in Burgers' equation
R_{ij} = residual stress in Navier-Stokes equations
r = scalar wavenumber; $\underline{r}$ = vector wavenumber
$S(k|p,r)$ = inertial transfer of energy/unit wavenumber into and out of wavenumber k
$\overline{S}$ = grid scale rate-of-strain tensor squared
$\overline{S}_{ij}$ = grid scale rate-of-strain tensor
$U(k)$ = backscatter of energy/unit wavenumber
u = fluid velocity in Burgers' equation
u_i = i component of fluid velocity; $\overline{u}_i$ grid scale component; u_i' sub-grid scale component
x_s = position of shock front
Δ = averaging length scale
ε = dissipation rate; $\overline{\varepsilon}$ = grid scale component
$\overline{\varepsilon}_{ev}$ = eddy viscosity dissipation rate
$\overline{\varepsilon}_{mv}$ = filtered molecular viscosity dissipation rate
$\overline{\varepsilon}_{rs}$ = resolvable scale dissipation rate
$\overline{\varepsilon}_{sgs}$ = sub-grid scale dissipation rate
ν = kinematic viscosity
ν_d = outscatter eddy viscosity coefficient
ν_e = eddy viscosity coefficient
ν_{Ti} = eddy viscosity coefficient in Burgers' equation
ω = frequency of sinusoidal driving force in Burgers' equation

Superscripts

Δ = triangle condition $|k-p| \leq r \leq k+p$
$\underline{W}$ = average of variable over length W

1. INTRODUCTION

Several numerical simulations of high Reynolds number three dimensional turbulent flows have been reported in the literature (1,2,7,17,and 18). These have all been Large Eddy Simulations, in which sub-grid models are used to represent the non-linear interactions between grid and sub-grid scales of motion. Despite the success of these calculations it is still not clear either how accurate the sub-grid modelling is, nor how accurate it needs to be.

Large Eddy Simulations are solutions of the spatially filtered Navier-Stokes equations and give the motions of the large eddies only. They assume that the velocity field can be divided into large and small eddies, and that the motions of the large eddies can then be calculated separately. This is possible because the motions of the large eddies are not sensitive to the details of the small dissipation eddies, which need not therefore be represented in the calculation. The method further assumes that the non-linear interactions between the large eddies and small eddies can be approximated in terms of the large eddies only, that is, by a sub-grid model. The first assumption is necessary because the great range in size of eddies present in a high Re flow means that the Navier-Stokes equations cannot be solved by a head-on computational attack. The second assumption is necessary to conserve energy in a purely large-eddy simulation.

Grid scale variables are defined by

$$\overline{g}(\underline{x},t) = \int_{\text{space}} g(\underline{x}',t)\, G(\underline{x},\underline{x}')d\underline{x}' \tag{1}$$

and sub-grid variables by

$$g'(\underline{x},t) = g(\underline{x},t) - \overline{g}(\underline{x},t)\ . \tag{2}$$

This follows the notation of Leonard (10), G denoting a filter function with characteristic length Δ. Filtering the Navier-Stokes equations according to eqn (1) we obtain

$$\frac{\partial}{\partial t}\overline{u}_i(\underline{x},t) + \frac{\partial}{\partial x_j}(\overline{u}_i\,\overline{u}_j + R_{ij}) - \nu\frac{\partial^2}{\partial x_j^2}\overline{u}_i = -\frac{\partial}{\partial x_i}\overline{p}(x,t)\quad , \tag{3}$$

where

$$R_{ij} = (\overline{\overline{u}_i\,\overline{u}_j} - \overline{u}_i\,\overline{u}_j) + \overline{u_i'\,\overline{u}_j} + \overline{u_j'\,\overline{u}_i} + \overline{u_i'\,u_j'}) \tag{4}$$

denotes the residual stresses. The dependent variables in eqn (3) vary smoothly over lengths of $O(\Delta)$ and thus permit the use of a relatively coarse mesh. Without filtering the mesh interval h would need to be smaller than the smallest dissipation eddy, demanding the use of a very fine mesh with far more grid points than can be accommodated on existing computers. The price paid for making the calculation tractable on a relatively coarse mesh is that the u_i' are unknown. To close the filtered equations of motion terms involving the u_i' must be approximated by expressions involving the $\overline{u}_i$. This is the technique of sub-grid modelling.

Although there are strong reasons for believing sub-grid models to be more universal than one point closure models (3), the choice of sub-grid model can nevertheless greatly influence the success of a large eddy simulation. A wide variety of subgrid models, filters, boundary conditions and finite difference schemes have been tried. Yet despite this neither the optimum choice of sub-grid model nor the reasons for making the choice are clear. This is because the complex interaction between the physics and the numerics in a large eddy simulation means that it is very difficult to unscramble the effects of the various processes present. This in turn implies that it is difficult to study the effectiveness of sub-grid modelling procedures by numerical calculations on the high Re Navier-Stokes equations. We have therefore examined the nature and effectiveness of sub-grid modelling by using a classical closure, the Direct Interaction Approximation or DIA (5, 8) and by numerical solution of Burgers' equation. The DIA gives approximate closed equations of motion for the evolution of the velocity covariance, and yields a detailed picture of the energy transfer. This permits us to explore the structure of the terms responsible for the sub-grid energy drain in large eddy simulations, but the investigation is limited to the ensemble average of the equations of motion. Burgers' equation is a one-dimensional analogue of the Navier-Stokes equations. Its one-dimensional character means that all scales of motion can be modelled in the computation, even if the (equivalent of the) Reynolds number is very high: moreover, a limited number of exact time-dependent solutions is known. These solutions can be compared with the corresponding coarse mesh solutions using sub-grid modelling techniques, and this comparison has been repeated both for single realizations and ensemble averages. This permits us to explore the effectiveness of the techniques.

2. APPLICATIONS OF CLASSICAL CLOSURES TO SUB-GRID MODELLING

2.1 The nature of the problem

The flow will be supposed to be homogeneous, and the analysis will be made in wavenumber space throughout. The sub-grid scales will be nearly homogeneous except near boundaries, but the grid scales cannot be so. The effect of inhomogeneity on sub-grid modelling is not known: indeed, it is one of the most important questions in this field of investigation. The classical closures are able to handle anisotropy, but for purposes of exposition we shall suppose that all scales are isotropic. We shall also use the spherically sharp filter

$$\begin{aligned} G(k) &= 1 \text{ if } k \le K_1 \\ &= 0 \text{ if } k > K_1 \end{aligned} \tag{5}$$

to illustrate the principles of the work. ($G(k)$ is the Fourier transform of the function $G(\underline{x}-\underline{x}')$ defined by equation (1)). With this simple filter, wavenumbers $< K_1$ belong to the grid scales and those with wavenumbers $> K_1$ to the sub-grid scales. Other filters have been studied and results for them are reported below, but the physics is particularly clear when the form (5) is used.

Energy transfer from one wavenumber to another and particularly from grid scales to sub-grid scales, is by interaction between a wavenumber triad k,p,r whose members can form a triangle. For isotropic turbulence the inertial transfer depends on scalar k,p,r only and the triangle condition reduces to

$$|k-p| \le r \le k+p\quad . \tag{6}$$

The equation of motion for $E(k,t)$, the energy per unit scalar wavenumber range is

$$\left[\frac{d}{dt} + 2\nu k^2\right]E(k,t) = \text{forcing term} + \frac{1}{2}\iint^{\Delta} S(k|p,r)dpdr\quad . \tag{7}$$

For a large eddy simulation, k will be in the grid scale range $k<K_1$. The "forcing term" which sustains the turbulence is local in wavenumber space and will be represented in the numerical scheme.

The second term on the right side of equation (7) represents inertial transfers into and out of wavenumber k. The affix Δ on the integral signs indicates that p r are constrained by the triangle condition (6): the region of integration is shown in figure 1. Superimposed on this figure are the lines $p,r = K_1$ which divide it into grid and sub-grid regions. The contribution from $p,r<K_1$ (region I in the figure) represents inertial transfers within the grid scales, and these will be explicitly included in the large eddy simulation. Contributions from the other three regions represent transfers between grid and sub-grid

scales.

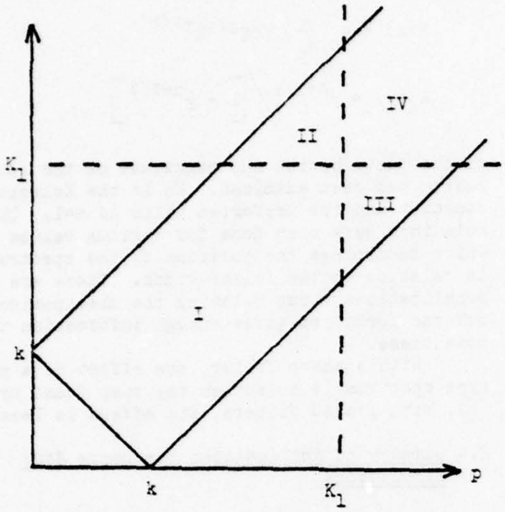

Fig 1 Regions of integration for the inertial transfer term.

The problem of sub-grid modelling is to portray the latter class of transfers as functionals of grid scale quantities such as E(k,t). To do this, we must know (or guess) the functional dependence of S(k|p,r) on E(k,t) and only the classical closures provide this sort of detail. This problem therefore provides a rather unique instance in which the complexity of these closures is positively necessary, in which they can provide results of practical value, and where no simpler method can.

2.2 The Smagorinsky-Lilly approximation

The need for some form of sub-grid model was clear to Smagorinsky (19) when he originated large eddy simulations, and he suggested that the transfer from grid scales should be approximated by

$$R_{ij} = \frac{1}{3} R_{kk} \delta_{ij} - 2 \nu_T \overline{S}_{ij} \tag{8}$$

where

$$\overline{S}_{ij} = \frac{1}{2} \left(\frac{\partial}{\partial x_j} \overline{u}_i + \frac{\partial}{\partial x_i} \overline{u}_j \right) \tag{9}$$

is the grid scale local rate-of-strain or deformation tensor, and ν_T is a turbulent viscosity. He therefore supposed that the variation of the drain term across the grid scales would be similar to that of the molecular dissipation. Smagorinsky postulated that ν_T was determined by ε, the instantaneous local rate of dissipation of turbulent energy per unit volume: his argument is reminiscent of Kolmogorov's. Dimensional analysis then suggests

$$<\nu_T> \propto <\varepsilon>^{1/3} \Delta^{4/3} \quad . \tag{10}$$

Here <> denotes an ensemble average and Δ is, as before, a measure of the averaging length of the filter. ε is not known directly, and Smagorinsky estimated it from the grid scale strain rate

$$\overline{S} = (2 \overline{S}_{ij} \overline{S}_{ij}) \quad .$$

If there is a long inertial range, it may be shown that

$$<\overline{S}> \propto <\varepsilon>^{2/3} \Delta^{-4/3} \quad . \tag{11}$$

Equation (10) is therefore modified to

$$\nu_T = c^2 \Delta^2 \overline{S}^{1/2} \tag{12}$$

where c is a non-dimensional constant.

To form an equation of motion compatible with (7) from the Smagorinsky-Lilly procedure, one must multiply the raw equation of motion ((3) plus (8) plus (12)) by $\overline{u}_i$ and then perform the ensemble averaging operation <> on the ensuing raw energy equation. The result for homogeneous turbulence is of the form

$$\text{sub-grid term} = - <\nu_T \frac{\partial}{\partial x_j} \overline{u}_i \cdot \left(\frac{\partial}{\partial x_j} \overline{u}_i + \frac{\partial}{\partial x_i} \overline{u}_j\right) \tag{13}$$

where "sub-grid term" is that part of the inertial transfers which is not explicitly represented in the large eddy simulation (see eqn (7)). Lilly evaluated this sub-grid term by

1. assuming

$$\text{sub-grid term} = - <\nu_T> <\frac{\partial}{\partial x_j} \overline{u}_i \cdot \left(\frac{\partial}{\partial x_j} \overline{u}_i + \frac{\partial}{\partial x_i} \overline{u}_j\right)>$$

$$= - c^2 \Delta^2 <\overline{S}>^{1/2} <\frac{\partial}{\partial x_j} \overline{u}_i \cdot \left(\frac{\partial}{\partial x_j} \overline{u}_i + \frac{\partial}{\partial x_i} \overline{u}_j\right)> \quad . \tag{14}$$

i.e. assuming that ν_T is a constant independent of x or k

2. postulating an inertial range spectrum at all finite wavenumbers.

With these assumptions, c is determined by energy conservation and can be calculated without knowing the detailed form of S(k|p,r). He found

$$c = 0.185 \quad . \tag{15}$$

Later workers have followed this lead, though some have preferred to estimate ε from the grid scale vorticity and Schumann (3) uses a modified formalism near boundaries. In practice, c must be chosen so that the computation conserves energy. The values so determined do not agree well with (15), c=0.10 being typical. The reason for the discrepancy has not been clear, and classical closures have been used to examine some of the possibilities.

2.3 Sub-grid modelling according to the DIA

All known classical closures give very similar results in this application: the DIA has been used throughout since it is the simplest and the best known. According to these closures

$$\text{sub-grid term} = - 2k^2 \nu_d(k) \overline{E}(k,t) + U(k) \quad . \tag{16}$$

Here $\overline{E}(k,t)$ is the grid scale component of E(k,t) and U(k) is the energy scattered back from the sub-grid scales to the grid scales: the first term on the right-hand side of (16) represents the outscatter (that is, the drain in the opposite direction). The fact that the classical closures give this division naturally and withought further approximation is one of the strongest reasons for thinking that they may be broadly correct. Eqn (16) is a statistically averaged relation. Therefore, though $\nu_d(k)$ may be dependent on k, it does not fluctuate from one realisation to the next.

With the approximations listed above, the Smagorinsky-Lilly procedure can be put into the form

$$\text{sub-grid term} = -\ 2k^2\nu_e\ \overline{E}(k,t) \tag{17}$$

and this differs from (16) in that the drain and the backscatter are rolled into one, and the resultant net eddy viscosity is supposed to be independent of k. Conversely the closures imply that the outscatter but not the backscatter, is of eddy viscosity form and that the drain or outscatter eddy viscosity might be k-dependent.

DIA gives explicit forms for $\nu_d(k)$ and $U(k)$ as functionals of $E(k,t)$ and the infinitesimal response function (see ref 8). They are mainly but not wholly determined by the spectral form in the sub-grid range of wavenumbers. Kraichnan (6) has applied these forms to the situation studied by Lilly, namely, a sharp filter with inertial range spectra at all wavenumbers. He finds that for $k \ll K_1$ (the cut wavenumber) ν_d is constant and $U(k)$ is very small. However, as k approaches K_1 both terms have singularities of order $(K_1-k)^{-2/3}$. These cancel, and the net eddy viscosity defined by

$$\nu_e(k) = \nu_d(k) - \frac{U(k)}{2k^2\overline{E}(k,t)} \tag{18}$$

has a finite cusp at $k=K_1$. It would therefore seem that the Smagorinsky-Lilly approximation can only be correct on the average and that it can be very wrong in detail. (Such a result can only be derived if one has a specific form for $S(k|p,r)$).

To test the universality of this finding the method has been applied to 3 "graded" filters, which fall smoothly rather than sharply from 1 to 0. The filters studied are a Gaussian, the tophat filter

$$G(\underline{k}) = B(k_1h)\ B(k_2h)\ B(k_3h)\ ;\ B\ (\xi) = \frac{\sin(\xi/2)}{(\xi/2)}$$

which is equivalent to the simplest finite difference scheme in configuration space, and the (cubical) box filter

$$\begin{aligned} G(k) &= 1 \text{ if } |k_1|,\ |k_2|,\ |k_3 \leq\ K_2 \\ &= 0 \text{ otherwise} \quad , \end{aligned}$$

which is used in the SUPERBOX code of Orszag and Patterson (16). The Gaussian is isotropic, and it may be shown that the effect of the anisotropy of the tophat filter is trivial: the effect of the much stronger anisotropy of the box filter needs further study.

Even when the grid scale spectrum is of purely inertial range form, the gentle fall of (e.g.) the Gaussian filter greatly softens the behaviour of ν_e. There is no cusp, and ν_d is virtually constant over the grid scale range. ν_e falls somewhat with increasing k, but not so much as to make its approximation with a constant value unreasonable.

The grid scale spectrum will certainly not be of inertial range form, and the effect of "production-type" spectra of the form

$$\begin{aligned} E(k) &= A_n\left(\frac{k}{K_p}\right) Ko\xi^{2/3}k^{-5/3} \\ A_n(y) &= y^{n+5/3} \Big/ \left[1 + y^{n+5/3}\right] \end{aligned} \tag{19}$$

on the distribution and magnitude of the eddy viscosity has been examined. Ko is the Kolmogorov constant and the preferred value is n=1. The calculations have been done for various values of ΔK_p, which determines the position of the spectral peak in relation to the filter width. There are now complications about relating the dissipation to $\overline{S}$, but the formalism gives enough information to overcome these.

With a sharp filter, the effect of a production type spectrum is to soften the cusp found by Kraichnan (6). With graded filters, its effect is less dramatic.

2.4 Summary of implications for Large Eddy Simulations

2.4.1. Although the closure gives explicit forms for the drain eddy viscosity $\nu_d(k)$ and the backscatter $U(k)$, no convincing representation has been found for the latter. It is therefore recommended that a net eddy viscosity $\nu_e(k)$ should be computed according to equation (18): this approach implies the use of a standard spectral form.

2.4.2. This form could be used directly in a wavenumber space calculation. This would be inconvenient in configuration space. Since ν_e does not vary strongly with k if the filter is graded and the spectrum is of production range form, the use of a (constant) average value is recommended, the average being defined so as to conserve energy. The effect of this recommendation is to endorse the representation of Smagorinsky and Lilly, provided only that Lilly's approximation (14) is reasonably accurate. The DIA leads immediately and without further approximation to the form (16), and the right-hand side of (14) proves to be a reasonable approximation to this form: however, it is the right-hand side of (13) which expresses the Smagorinsky-Lilly procedure.

2.4.3. Lilly's approximation (14) can be avoided, and the Smagorinsky-Lilly procedure brought closer to the results derived from the DIA if, in eqn (12), $\overline{S}^{1/2}$ is replaced by $\langle\overline{S}\rangle^{1/2}$. This realisation average may be approximated by an integration over a relatively large volume of space. As reported below, an integrated or non-local eddy viscosity has been compared with the more usual local form in coarse mesh calculations on Burgers' equation: the non-local version is found to be superior. This rather surprising finding should now be tested for Navier-Stokes turbulence.

2.4.4. The deduction from the DIA, that the dependence of ν_e on k is weak, agrees well with the computations of Leonard (11) on Navier-Stokes turbulence and our own computations on Burgers turbulence. In both cases it is found that the spectral distribution of the net drain across the grid scale wave numbers is similar to that of the dissipation by molecular viscosity.

2.4.5. Two of the four filters (the sharp and the Gaussian) are isotropic. The tophat filter is weakly anisotropic and it has been formally demonstrated, using the detailed account of energy transfer given by the DIA, that the effect of this anisotropy on the results is trivial. Since most finite difference schemes are similar to the tophat, this provides reassurance that no correction need be made for filter anisotropy in normal large eddy simulations (except perhaps near boundaries). However, the effect of the high anisotropy of the box filter may not be negligible.

2.4.6. In the first instance the DIA results were deduced assuming all scales to be isotropic. It has been formally demonstrated that these results are unaffected by any degree of grid scale anisotropy.

2.4.7. Values of the Lilly constant c have been inferred for all three graded filters and for a range of values of ΔK_D. These results permit the sub-grid model to be varied over the flow field.

2.4.8. With the tophat filter, the production-type spectrum (19) (n=1) centred in the middle of the grid scale range and Ko=1.41 (Lilly's value), c=0.162. This is only 12% lower than Lilly's value (15) for a sharp filter and a production-type spectrum. This shows that the effects of the filter and of spectral shapes are not responsible for the discrepancy between Lilly's result and practical calculations.

2.4.9. It is speculated that the discrepancy may be due to defects in the boundary conditions and/or the sub-grid model at the boundaries. This is supported by the work of Kwak et al (7) who find that Lilly's c-value gives good results in a Large Eddy Simulation of a homogeneous flow.

2.4.10. Sub-grid modelling of the pressure, the effects of grid scale inhomogeneity and of sub-grid scale anisotropy remain to be investigated.

3. NUMERICAL STUDIES OF BURGERS' EQUATION

3.1 Introductory remarks

The solutions to Burgers' equation

$$\frac{\partial}{\partial t} u(x,t) + u \frac{\partial}{\partial x} u - \nu \frac{\partial^2}{\partial x^2} u = f(x,t) \qquad (20)$$

display many qualitative similarities to Navier-Stokes turbulence. However there are important quantitative differences between the two flows. For example eqn (20) describes a one-dimensional shock wave process in which energy cascades from low wavenumbers to high wavenumbers where it is dissipated by viscous forces. The solutions to this equation display a k^{-2} inertial range at intermediate wavenumbers (see fig.2) while in Navier-Stokes turbulence the inertial range vaires as $k^{-5/3}$. Nevertheless, this separation of the low wavenumber energy-containing modes from the high wavenumber dissipation region by a universal inertial range, implies that the motion of the large scale structure in Burgers' model turbulence are unaffected by the details of the dissipation process. This in turn suggests that the large eddy simulation technique can also be applied in computing solutions to Burgers' equation, and that the application can give information on performance of sub-grid modelling techniques at high Re. We present results on the structure of the sub-grid drain term and compare coarse mesh solutions with corresponding exact and fine mesh solutions. These results are abstracted from more comprehensive limited circulation reports (13, 14).

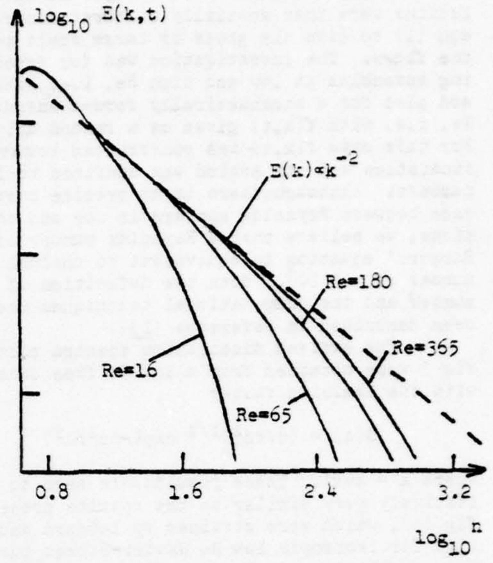

Fig. 2 Evolved velocity spectra for Burgers' equation at varying Re

Filtering eqn (20) according to eqn (1) we obtain

$$\frac{\partial}{\partial t} \overline{u}(x,t) = \frac{\partial}{\partial x} \{- \frac{\overline{u}^2}{2} + R + \nu \frac{\partial}{\partial x} \overline{u}\} + \overline{f}(x,t), \qquad (21)$$

where in complete analogy with eqns (3) and (4)

$$R = - \frac{1}{2} \{(\overline{u^2} - \overline{u}^2) + 2 \overline{\overline{u}\, u'} + \overline{u'^2} \} \qquad (22)$$

denotes the residual stresses. Multiplying eqn (21) throughout by u and then taking the ensemble average we find

$$\overline{\varepsilon} = \frac{d}{dt} \langle\frac{\overline{u}^2}{2} \rangle = \overline{\varepsilon}_{rs} + \overline{\varepsilon}_{sgs} + \overline{\varepsilon}_{mv} + \langle\overline{u}\, \overline{f}\rangle \quad . \qquad (23)$$

This is an equation of motion for the energy balance in the grid scale velocity field. The grid scale dissipation rates $\overline{\varepsilon}_{rs}$, $\overline{\varepsilon}_{sgs}$ and $\overline{\varepsilon}_{mv}$ are defined as

$$\overline{\varepsilon}_{rs} = - \frac{1}{2} \langle\overline{u} \frac{\partial}{\partial x}(\overline{\overline{u}^2} - \overline{u}^2)\rangle \qquad (24)$$

$$\overline{\varepsilon}_{sgs} = - \langle\overline{u} \frac{\partial}{\partial x} \{\overline{\overline{u}\, u'} + \frac{\overline{u'^2}}{2}\}\rangle \qquad (25)$$

and

$$\overline{\varepsilon}_{mv} = \nu\langle\overline{u} \frac{\partial^2}{\partial x^2} \overline{u}\rangle \quad . \qquad (26)$$

In eqn (21) the non-linear terms are responsible for the drain of energy from the flow field, whereas in the absence of filtering they are energy conserving.

3.2 Fine mesh calculations

The time evolution of ensembles of initially Gaussian velocity fields was computed from eqn (20) using periodic boundary conditions and with all length scales fully resolved. The results of these calculations were then spatially filtered according to eqn (1) to give the gross or large scale motions of the flows. The investigation was for freely decaying ensembles at low and high Re, i.e. with $f(x,t)=0$, and also for a stochastically forced ensemble at high Re, i.e. with $f(x,t)$ given as a random driving force. For this case $f(x,t)$ was constructed to have Gaussian statistics and its action was confined to low wavenumbers. Although there is no precise correspondence between Reynolds numbers in one and three dimensions, we believe that a Reynolds number of 180 in Burgers' equation is equivalent to channel Reynolds number of $\sim 5\ 10^5$. Both the definition of Reynolds number and the computational techniques used have been described in reference (13).

The evolved dissipation spectra plotted on fig 3 were obtained from a low Re free decay run (13) with the Gaussian filter

$$G(z) = (6/\pi\Delta^2)^{1/2} \exp(-6z^2/\Delta^2) \qquad (27)$$

where $z = x-x'$. These results are seen to be qualitatively very similar to the results presented in fig (4), which were obtained by Leonard and Patterson (11) for isotropic low Re Navier-Stokes turbulence. This similarly was also found to hold for the stochastically forced runs which were at high Re. The results of this run are shown on fig 5, which also shows that the magnitudes of $\overline{\varepsilon}_{rs}$ and $\overline{\varepsilon}_{mv}$ compared to $\overline{\varepsilon}_{sgs}$ are relatively smaller at high Re than at low Re, and that at high Re $\overline{\varepsilon}_{mv}$ has a high wavenumber tail absent at low Re. These figures suggest that the division of the energy transfers from the grid scales to the sub-grid scales is very similar in Burgers' model turbulence and three-dimensional turbulence. It is interesting that $\overline{\varepsilon}_{rs}$ peaks at a higher wavenumber than $\overline{\varepsilon}_{sgs}$. This suggests that $\overline{\varepsilon}_{rs}$ plays an important role in controlling high wavenumber excitations in large eddy simulations. In all three figures $\overline{\varepsilon}_{sgs}$ is seen to peak near the peak of $\overline{\varepsilon}_{mv}$, and the figures further suggest that $\overline{\varepsilon}_{sgs}$ has a similar structure to $\overline{\varepsilon}_{mv}$. The shape of the high wavenumber tail in fig.5 is influenced by the choice of filter. With for example $\Delta=L/32$ the tail is attenuated and $\overline{\varepsilon}_{mv}$ approaches the shape of $\overline{\varepsilon}_{sgs}$ more closely. These latter observations suggest that the sub-grid drain term can be usefully approximated by an eddy viscosity model.

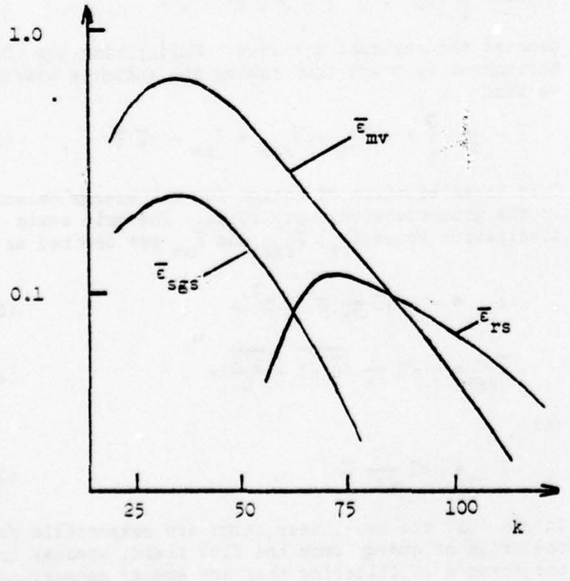

Fig 3 Dissipation spectra for Burgers' equation at low Re (Re=16)

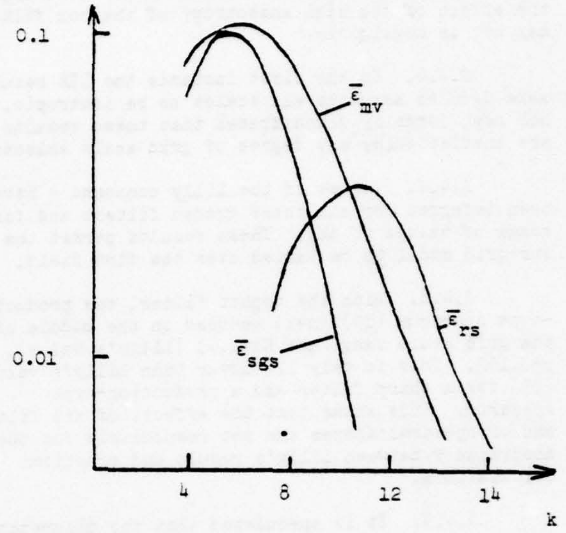

Fig 4 Dissipation spectra for isotropic low Re Navier-Stokes turbulence (Re$_\lambda$=30) (taken from Leonard and Patterson (11))

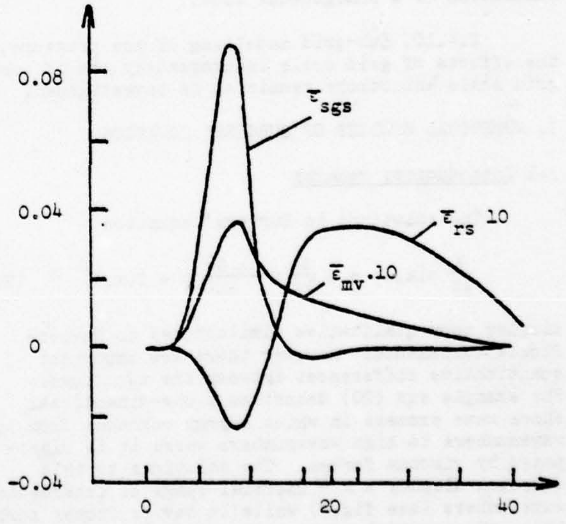

Fig 5 Dissipation spectra for Burgers' equation at high Re (Re=500).

3.3 Coarse Mesh calculations

Eqn (21) was solved on a coarse mesh with

$$f(x,t) = -A \sin 2\pi(x/L - t/To) \ ; \ \nu = 0 \ . \qquad (28)$$

An exact solution to eqn (20) exists for this case (4) which, if we scale all distances with L and all times with T_o, takes the form

$$u(x,t) = 1 + (2A/\pi)^{1/2} \sin\pi\,(x-t) \quad 0 \le x < x_s$$

$$= 1 - (2A/\pi)^{1/2} \sin\pi\,(x-t) \quad x_s < x \le 1\ . \qquad (29)$$

This solution describes a discontinuous travelling wave which sweeps periodically across the flow field. The location of the discontinuity x_s is determined by the condition

$$\int_0^1 u(x,t)dx = 1 - (2\pi)^{3/2} A^{1/2} \cos\pi(x_s-t) = 0\ ,$$

while the speed at which the shock fronts propagate is given by the average velocity of the adjacent fluid elements. In the comparisons of this solution with the coarse mesh calculations we set A=10 and used the following sub-grid models to close eqn (21):

Model 1: $R = \nu_{T1}\ \partial\overline{u}/\partial x \quad ; \qquad (30)$

Model 2: $R = \Delta^2/24\ \partial^2\overline{u}^2/\partial x^2 - \nu_{T2}\ \partial\overline{u}/\partial x \ ; \qquad (31)$

Model 3: $R = \Delta^2/12\ (\partial\overline{u}/\partial x)^2 - \nu_{T3}\ \partial\overline{u}/\partial x\ . \qquad (32)$

Each of these models is essentially a definition of a turbulent viscosity ν_{Ti}. In model 1 we simply lump all of the residual stress R into a single eddy viscosity term. The style of models 2 and 3 is to divide R into terms of $O(\Delta^2)$ and terms of higher order in Δ. This division is based on a Taylor series expansion of the type

$$g(z) = g(z) \int_{\text{space}} G(x)dx + \frac{1}{2}\frac{d^2}{dz^2} g(z) \int_{\text{space}} x^2 G(x)dx.$$

Using the expansion we find for the Gaussian filter defined in eqn (27)

$$(\overline{\overline{u}^2} - \overline{u}^2) \doteq \Delta^2/24\ \partial^2/\partial x^2 \overline{u}^2 \qquad (33)$$

and $$(\overline{\overline{u}\, u'}) = \Delta^2/24\ \overline{u}\ \partial^2/\partial x^2\ \overline{u} \quad . \qquad (34)$$

Model 2 only represents the term $\partial/\partial x(\overline{\overline{u}^2}-\overline{u}^2)$ appearing in R by the series expansion, while Model 3 represents both this term and the term $\partial/\partial x\ (\overline{\overline{u}\, u'})$ in this manner. In both models the remaining residual stress terms are lumped into the eddy viscosity term, which is supposed to approximate their role. There is no advantage in taking these expansions to higher order since this would imply the need for high order finite difference approximations which are difficult to implement, and also there are in any case serious doubts about the convergence of the series (14). Combined with eqn (21) Models 1 through 3 yield closed equations of motion for $\overline{u}$ once the form of the ν_{Ti} is specified. We effect the closure by assuming

$$\nu_{Ti} = c_i^{\,2}\ \Delta^2\ \overset{w}{\overline{|\partial\overline{u}/\partial x|}} \qquad (35)$$

where c_i is a constant and $\overset{w}{\overline{|\partial\overline{u}/\partial x|}}$ denotes the average over a length w of the quantity $|\partial\overline{u}/\partial x|$. C_i is determined by demanding

$$\int_0^L \overline{u}(x,t)\ \overline{F}(x,t)\ dx = \overline{\zeta}(t) = \frac{d}{dt} < \frac{\overline{u}^2}{2}\ (x,t)> \qquad (36)$$

at t=0. Here we have replaced the ensemble average <> by a volume average. In the limit w→0 eqn (35) tends to the one-dimensional equivalent of the Smagorinsky sub-grid model (see eqns (8) and (12)) based on the local value of the strain tensor; in the limit as w→L it tends to a non-local sub-grid model similar to that suggested by Direct Interaction (see §2).

Figure 6 shows the results from 4 computations

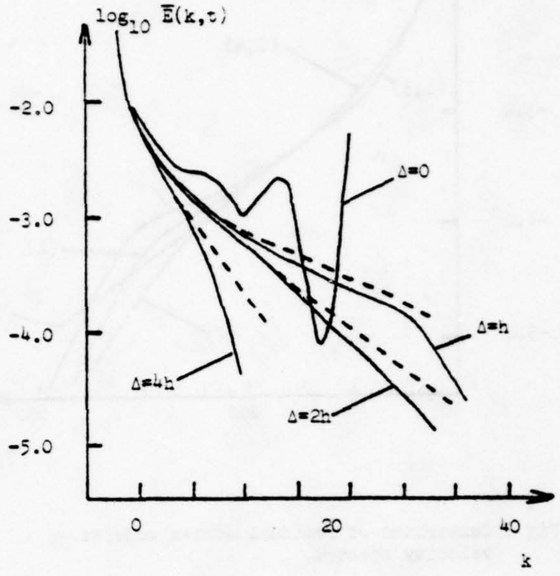

Fig 6 Optimisation of filter width

in which the time evolution of $\overline{u}(x,t)$ was computed from eqn (21) and (31) with w=L/2 and Δ=0, h, 2h and 4h. Setting Δ=0 is equivalent to ignoring the residual stress terms i.e. dispensing with both filter and sub-grid model. The gross distortion and erratic behaviour of the computed velocity spectrum at high wavenumbers for this case shows very clearly the need for sub-grid modelling. In the absence of the sub-grid drain term there is no mechanism for dissipating the energy which is transferred by the non-linear inertial forces from low wavenumbers to high wavenumbers. The consequence of this is the pile-up observed at the high wavenumber end of the spectrum, and ultimately a break down in the computation. For the remaining 3 choices of Δ the high wavenumber pile up is absent, though it is seen that in all cases there is some distortion at high wavenumbers. The figure suggests the choice of Δ ∿ 2h is optimum, which supports the findings of Kwak et al (7).

The coarse mesh velocity spectra shown on Fig.7 were obtained from computations using residual stress models 1 through 3 with w=L. We conclude from this figure that of the models studied residual stress model 2 gives the best representation of the sub-grid energy drain. This result was confirmed on repeating the calculations with varying w. Details of these latter calculations are given elsewhere (14). Fig.7 also suggests that there is not a lot to choose between the models. Models 1 and 2 give the best representation of the sub-grid terms and the choice between these models depends upon the price one is prepared to pay in computing time for the moderate improvement in accuracy which residual stress model 2 offers over residual stress model 1.

4th order finite difference schemes were used throughout, because the residual stress terms are of $O(\Delta^2) \sim O(h^2)$. Computations using 2nd order difference schemes give significantly poorer results than those reported above. Details of these calculations are

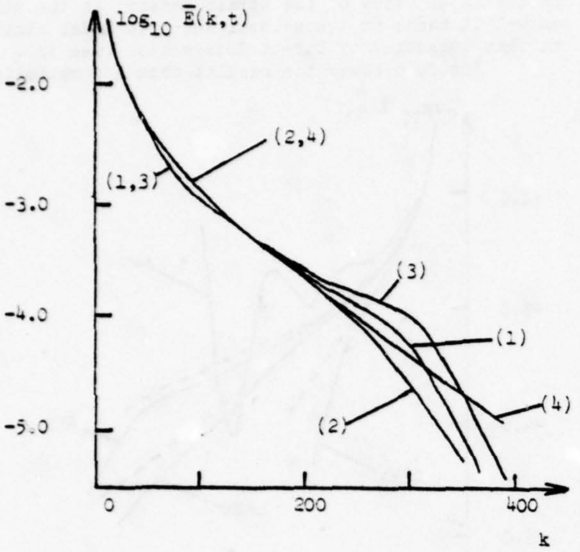

Fig 7 Comparison of residual stress models: velocity spectra

(1) residual stress model 1
(2) residual stress model 2
(3) residual stress model 3
(4) exact filtered spectrum

available elsewhere (15).

The results presented in Fig 8 were obtained using residual stress model 2 with $\Delta=2h$ and w varying from 0 through $L/2$. They show that a marked improvement occurs in the coarse mesh calculations when the eddy viscosity is averaged over a length of $O(4\Delta)$. These results favour the Direct Interaction or non-local sub-grid model, though a detailed numerical investigation (15) of the effect suggests the following explanation. In Burgers' model turbulence, energy transfers from the grid scales to the sub-grid scales are concentrated in the regions of high vorticity i.e. in the shock fronts. In the coarse mesh calculations distortions due to misrepresentations of the sub-grid drain terms spread out from the shock fronts, and a local eddy viscosity coefficient causes these localised regions of steepened velocity gradient to evolve into smaller shocks away from the main shock. These subsidiary shocks can be regarded as a genuine but unwanted feature of the coarse mesh solution. Their formation is inhibited by the use of a non-local eddy viscosity coefficient because this smooths over regions of weak vorticity, thereby feeding the calculation the information that the transfer of energy from the grid scales to the sub-grid scales is localised in regions of high vorticity, (which are the main shock fronts). This mechanism is not so obviously operative in Navier-Stokes turbulence, and therefore it cannot be assumed that the non-local eddy viscosity will necessarily be superior in this case also.

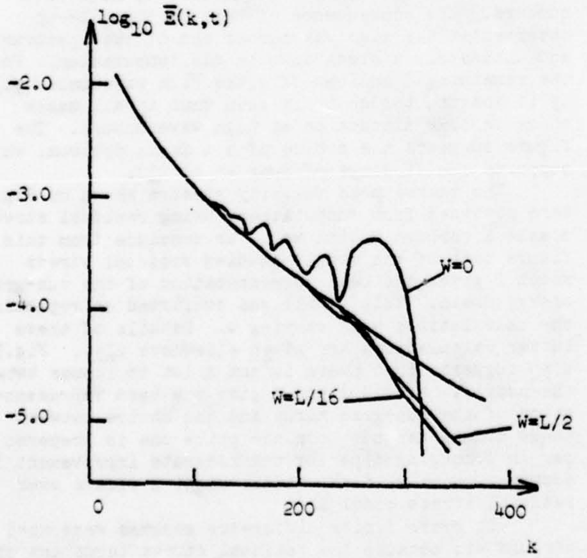

Fig 8 Local versus non-local eddy viscosities

The coarse mesh calculations reported above are for simple non-stochastic situations. They give information on the ability of the large eddy simulation technique to handle simple flow features. To provide a more rigorous test of the technique we have simulated on a coarse mesh the motions of the large scale components of the fine mesh calculations described in §3.2. The results of this investigation support the earlier findings on the optimum ratio of filter to mesh interval, choice of sub-grid model, and use of a non-local viscosity coefficient. Sampling errors were fairly large in these claculations and consequently the differences between results from the different models was less marked then for the periodic travelling wave solution. Also, since these flow fields consist of a chaotic mixture of shock waves, it was not possible to identify why the use of a non-local eddy viscosity coefficient gave superior results to the use of a local coefficient.

Figure 9 is for a free decay run with Re=180. It

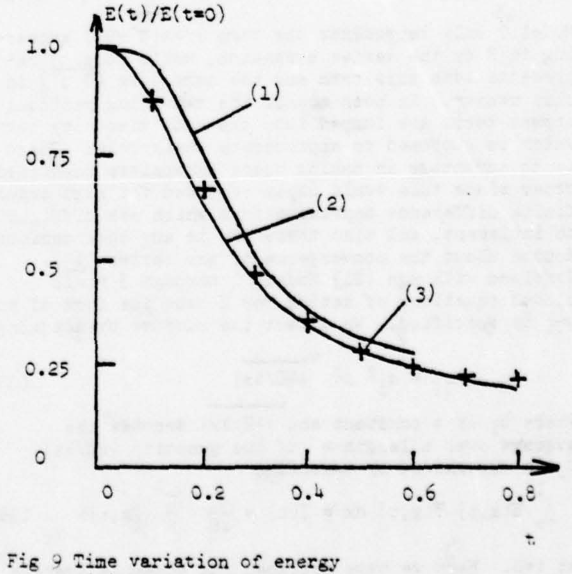

Fig 9 Time variation of energy
(1) exact field
(2) exact filtered field
(3) coarse mesh field

shows the rate of change of normalised total energy $E(t)/E(t=0)$ for the exact field, the exact filtered field and coarse mesh field with $C_2 = 0.2, \Delta = 2h, W = 4\Delta$ in the coarse mesh claculation. It is seen that the coarse mesh calculation reproduces the rate of change of energy in the exact filtered field very well. An interesting point to emerge from this figure is that neither the exact filtered or coarse mesh plots show the sharp kink at $t \sim 0.1$ shown by the exact field. This kink corresponds to the onset of shocks. During the first stage of evolution little dissipation takes place since the dissipation occurs predominantly in the shock fronts, which have yet to form. Energy cascades from low wavenumbers to high wavenumbers until high wavenumbers are excited and the viscous forces can begin to play a role. In the coarse mesh calculation this cascade appears as an apparent dissipation even in the early stages of evolution.

The coarse mesh spectrum plotted in fig 10 was obtained with residual stress model 2 and the parameter settings described above. It is seen that the coarse mesh calculation predicts the gross features of the fine mesh calculation satisfactorily, and in particular it predicts very accurately the motions of the lowest modes which contain the bulk of the energy. More significantly this figure implies that in more complex flows the top half of the wavenumber range in a large eddy simulation can be dominated by error, reducing the effective resolution by a factor of 2.

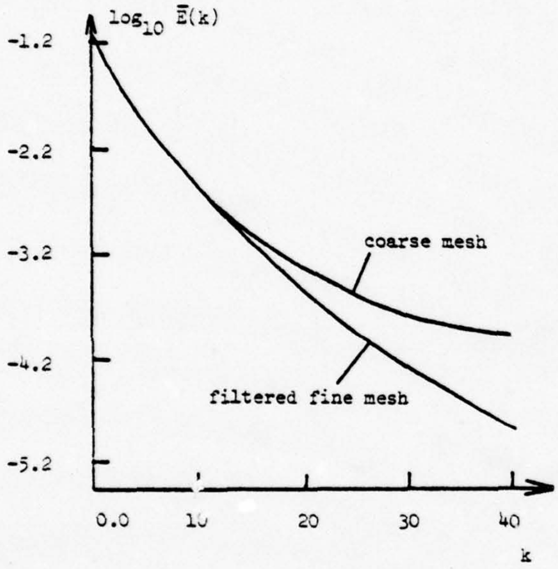

Fig 10 Coarse mesh and exact filtered velocity spectra

(1) coarse mesh field
(2) fine mesh field

3.4 Summary of implications for Large Eddy Simulations

3.4.1. Burgers' equation has been shown to yield useful information on sub-grid modelling at both low and high Re, and investigations using this equation support many of the earlier findings of Leonard and Patterson (11) and Kwak et al (7).

3.4.2. It has been shown that sub-grid modelling works, and that coarse mesh calculations can reproduce the gross features of both simple and complex flows at high Re. It seems however that error propagation in the high wavenumbers can reduce the effective resolution of a large eddy simulation by a factor of 2.

3.4.3. Both the coarse mesh calculations and the observed similarity between $\bar{\varepsilon}_{sgs}$ and $\bar{\varepsilon}_{mv}$ in the fine mesh calculations support the standard method of sub-grid modelling, provided only that the local root-mean - square strain tensor is replaced by the square root of an average over a large volume. Despite the agreement between this finding and §2.4.3 it is not clear that this modification is appropriate for Navier Stokes turbulence and its extension to this case will need careful study.

3.4.4. $\bar{\varepsilon}_{mv}$ and $\bar{\varepsilon}_{rs}$ peak at higher wavenumbers than $\bar{\varepsilon}_{sgs}$ which suggests they have an important role to play in controlling high wavenumber excitations. This is supported by the coarse mesh calculations which favour residual stress model 2 (see eqn (31)). This in turn favours fourth order differencing with explicit representation of the resolvable scale component of the residual stresses, which also supports the earlier findings of Kwak et al (7).

3.4.5. The need to pre-filter the governing equations has been demonstrated and the optimum filter width has been confirmed to be about twice the mesh interval.

4. CONCLUSIONS

It is clear that large eddy simulations offer great potential in the understanding and prediction of turbulent flows. Although much remains to be done before sub-grid modelling is properly understood, the results of this investigation have helped to put it on a firmer base. For the near future questions on the influence of inhomogeneity on both sub-grid models and large eddy simulations should perhaps be addressed with most urgency. We believe that large eddy simulations cannot play an effective role in design studies until this problem has been carefully studied.

5. ACKNOWLEDGMENTS

This work is supported by the British Science Research Council under Grant B/RG/3559.

We gratefully acknowledge the useful comments and assistance with the computations given by Mr. G. L. Quarini. We also thank Dr. A. Leonard for his kind permission to include fig 4 in this article.

6. REFERENCES

1. Deardorff, J. W., "A numerical study of three dimensional turbulent channel flow at large Reynolds numbers," Journal of Fluid Mechanics, Vol.41,1970, p.453.

2. Deardorff, J. W., "The use of subgrid transport equations in a three-dimensional model of atmospheric turbulence", Journal of Fluid Engineering, Sept. 1973, p.429.

3. Ferziger, J. H., "Large eddy numerical simulations of turbulent flows", to be published.

4. Jeng, D. T. "Forced model equation for turbulence", Physics of Fluids, Vol.12, No.10, 1969, p.2006.

5. Kraichnan, R. H., "Isotropic turbulence and

inertial range structure in the abridged LHDI approximation", Physics of Fluids, Vol.9, 1966, p.1728.

6. Kraichnan, R. H. "Eddy viscosity in two and three dimensions", Journal of Atmospheric Sciences, Vol.33, 1976.

7. Kwak, D., Reynolds, W. C., Ferziger, J. H., "Three dimensional time dependent computation of turbulent flow", TF-5, May 1975, Department of Mechanical Engineering, Stanford University,California.

8. Leslie, D. C., "Developments in the theory of turbulence", Clarendon Press, Oxford, 1973.

9. Leslie, D. C., and Quarini, G. L. "The application of classical closures to the formulation of sub-grid modelling procedures", to be published.

10.Leonard, A., "On the energy cascade in large eddy simulations of turbulent fluid flows" ,Advances in Geophysics, Vol. 18A, 1973, p.237.

11.Leonard, A., and Patterson, G. S.,"Numerical study of the energy loss of large eddies in turbulent flow simulations", to be published.

12.Lilly, D. K., "On the application of the eddy viscosity concept in the inertial sub-range of turbulence", NCAR-123, 1966, National Center for Atmospheric Research, Boulder, Colorado.

13.Love, M. D., "Techniques for solving Burgers' equation at low and high Re, with examples", QMC EP-6022, March 1976, Queen Mary College, London.

14.Love, M. D., "Techniques for solving Burgers' equation on a coarse mesh with examples", QMC EP-6023, October 1976, Queen Mary College, London.

15.Love, M. D., "A comparison of exact solutions and coarse mesh solutions with sub-grid modelling for the inviscid Burgers' equation", to be published.

16.Orszag, S. A., and Patterson, G.S."Numerical simulation of three-dimensional homogeneous isotropic turbulence", Physics Review Letters, Vol.28,No.76, 1972.

17.Schumann, U., "Ein Verfarhren zur direckten numerischen simulation turbulenter stromungen in platten-und ringspaltkanalen and uber seine anwendung zur untersuchung von turbulenz modellen", 1973, Dissertation, University of Karlsruhe.

18.Shaanan, S., Ferziger, J. H., Reynolds, W.C., "Numerical simulation of turbulence in the presence of shear", TF-6, August 1975, Department of Mechanical Engineering, Stanford University, California.

19.Smagorinsky, J., "General circulation experiments with the primative equations", Monthly Weather Review, Vol.93, No.3. p.99.

DIRECT NUMERICAL SIMULATION OF TURBULENT VELOCITY-, PRESSURE-, AND TEMPERATURE-FIELDS IN CHANNEL FLOWS

G. Grötzbach and U. Schumann

Kernforschungszentrum Karlsruhe
Institut für Reaktorentwicklung
Postfach 3640
7500 Karlsruhe
Federal Republic of Germany

ABSTRACT

A finite difference scheme for direct numerical simulation of turbulent velocity-, pressure-, and temperature-fields in plane channels and annuli is described. The fluid is incompressible and has constant density and diffusivities. The method is an extended and revised version of an earlier one. It now includes simultaneous simulation of the temperature field and employs a revised sub-grid scale model which has been extended to allow for moderately high Reynolds numbers (Re>10000) and poorly resolving grids. The purpose of this paper is to report and demonstrate the improved capabilities of the method.

NOMENCLATURE

a	dimensionless conductivity ($= 1/Pe_\tau$)
a_t	SGS turbulent conductivity
c	SGS model coefficient
D	distance between the walls
^jF	grid cell surface with normal in x_j-direction
IM,JM,KM	number of grid cells in x_1,x_2,x_3-direction
h	grid spacing $(\Delta x_1 \cdot \Delta x_2 \cdot \Delta x_3)^{1/3}$
p	kinematic pressure
$\dot{q}_w$	wall heat flux
R_1/R_2	inner/outer radius
t	time
T	temperature
u_i	velocity components
u_b	bulk velocity
u_o	wall shear stress velocity
x_i	coordinates, see Fig. 1
ν	kinematic viscosity ($= 1/Re_\tau$)
σ	correction factor
τ_w	wall shear stress
$\hat{y}$	any dimensionfull quantity y
y'	fluctuating part
$\langle y\rangle$	time mean value
$^V\bar{y}$	grid volume mean value
$^j\bar{y}$	surface mean value (taken over ^jF)
rms	root time mean square value

INTRODUCTION

Direct numerical simulation of turbulent flows is a new important tool to study the basic properties of turbulence. Here, we describe an improved and extended finite difference simulation of turbulent flows in plane channels and annuli. The geometry is shown in Fig. 1. The scheme is designed for Reynolds numbers

$$Re = \hat{u}_b\, \hat{D}/\hat{\nu} > 10\ 000 \qquad (1)$$

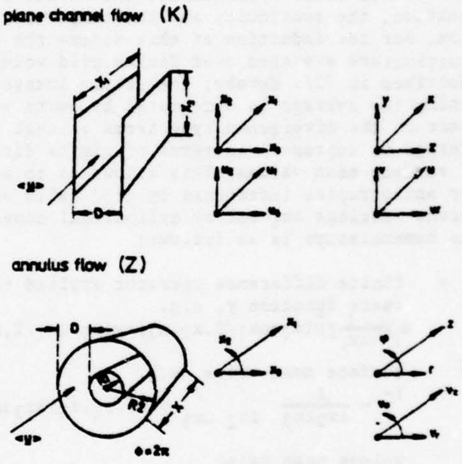

Fig. 1: Channel Geometry

In this stage we restrict ourselves to non-bouyant flows with constant viscosity ν and conductivity a so that the temperature is a passive scalar. The direct numerical simulation describes the time-dependent and three-dimensional large-scale turbulence under statistically steady-state conditions. The large scales are those which are resolved by the three-dimensional grid of the finite difference scheme. Typically up to 32 grid points can be used in each direction. The effect of the sub-grid scale (SGS) motion is accounted for by a SGS model. This approach has been developed by Deardorff /1/ and others and formed the basis of the code TURBIT-1 /2,3/ ("**TURB**ulenter **I**mpuls **T**ransport").

Further investigations have been concentrated on the following items /4/:

- development of a code "TURBIT-2" for simultaneous simulation of turbulent temperature fields in addition to velocity and pressure fields for plane channels and annuli.
- extension of the SGS model for SGS temperature transport and improvement of the existing models in order to allow for a wider range of Reynolds numbers (from moderate to very high) and to get reasonable results even on very coarse grids (which reduce the necessary computing time).
- verification of the accuracy of the temperature simulation by comparison with experiments.

As a result, TURBIT-2 has been established and several cases have been run in order to study the effect of the improved SGS model. For this purpose we used between 2048 and 32768 grid cells. The present code is capable of larger grids; however, the computing time required to attain steady state conditions becomes prohibitive long for more grid points; in earlier studies a grid with 32x32x64 = 65576 points has been used /2/. In the following we give some details of the method, summarize the experiences got up to now, and present some results obtained with respect to the temperature simulation.

THE METHOD USED IN TURBIT-2

Finite Difference Scheme

The code TURBIT-2 is based on a finite difference scheme which approximates the Navier-Stokes equation, the continuity and the temperature equation. For the deduction of this scheme the basic equations are averaged over finite grid volumes as described in /2/. Hereby, the triple integral defining the average is integrated by parts with respect to the divergence type terms so that the average is expressed in terms of finite differences of surface mean values. This allows us to account for anisotropies introduced by grid cells with different spacings Δx_i and by cylindrical coordinates. The nomenclature is as follows:

$\delta_j y$ finite difference operator applied to some space function y, e.g. (2)

$$\delta_1 y = \frac{1}{\Delta x_1} \left[\bar{y}(x_1+\Delta x_1/2, x_2, x_3) - y(x_1-\Delta x_1/2, x_2, x_3) \right]$$

${}^{j}\bar{y}$ surface mean value, e.g.

$${}^{1}\bar{y} = \frac{1}{\Delta x_2 \Delta x_3} \int_{\Delta x_2} \int_{\Delta x_3} y(x_1, z_2, z_3)\, dz_3\, dz_2 \tag{3}$$

${}^{v}\bar{y}$ volume mean value

$${}^{v}\bar{y} = \frac{1}{\Delta x_1 \Delta x_2 \Delta x_3} \int_{\Delta x_1} \int_{\Delta x_2} \int_{\Delta x_3} y(z_1, z_2, z_3) \cdot \cdot\, dz_3\, dz_2\, dz_1 \tag{4}$$

The resultant equations are

- averaged momentum (Navier-Stokes) equation

$$\frac{\partial}{\partial t}\, {}^{v}\bar{u}_i + \delta_j({}^{j}\overline{u_j u_i}) = -\delta_i\, {}^{i}\bar{p} + \delta_j\left(\nu\, {}^{i}\overline{\frac{\partial u_i}{\partial x_j}}\right) + \delta_{i1} P_x \tag{5}$$

- averaged mass (continuity) equation

$$\delta_i\, {}^{i}\bar{u}_i = 0 \tag{6}$$

- averaged temperature equation

$$\frac{\partial}{\partial t}\, {}^{v}\bar{T} + \delta_j({}^{j}\overline{u_j T}) = \delta_j\left(a\, {}^{j}\overline{\frac{\partial T}{\partial x_j}}\right) + {}^{v}\bar{Q} \tag{7}$$

The summation convention is assumed[1]. All quantities are made dimensionless by means of the length scale $\hat{D}$, the friction velocity $\hat{u}_0 = (\hat{\tau}_0/\hat{\rho}_0)^{1/2}$ ($\hat{\tau}_0$ = time mean wall shear stress - averaged over both walls, $\hat{\rho}_0$ = constant density), and the heat flux temperature $\hat{T}_0 = \hat{q}_0/[\hat{\rho}\, \hat{c}\, \hat{u}_0]$ ($\hat{q}_0$ = time mean wall heat flux, $\hat{c}$ = specific heat capacity). The dimensionless diffusivities are $\nu = \hat{\nu}/(\hat{u}_0 \hat{D})$ and $a = \hat{a}/(\hat{u}_0 \hat{D})$. The common Reynolds number Re and the friction coefficient c_f are related to $Re_\tau = 1/\nu$ by

$$Re_\tau = Re\, (\hat{u}_0/\hat{u}_b) = Re \sqrt{c_f/8} \tag{8}$$

The mean pressure gradient or driving force $P_x = 2$ is introduced so that the fluctuating pressure field p has a zero mean gradient in the axial direction. We assume that the axial mean temperature gradient is zero too. Otherwise a transformation has to be used as given in /4, p.65/.

The averaged products can be rewritten as

$${}^{j}\overline{u_i u_j} = {}^{j}\bar{u}_i\, {}^{j}\bar{u}_j + {}^{j}\overline{u_i' u_j'} \tag{9}$$

$${}^{j}\overline{u_j T} = {}^{j}\bar{u}_j\, {}^{j}\bar{T} + {}^{j}\overline{u_j' T'} \tag{10}$$

Where $u_i' = u_i - {}^{j}\bar{u}_i$, $T' = T - {}^{j}\bar{T}$. The second part of each sum forms the SGS fluxes.

So far, no approximations have been involved. Indeed, equations (5-7) are the conservation laws written in their integral form for grid volumes. However, the equations are as yet unclosed. The next step, therefore, is to express all quantities in terms of grid quantities. We employ a staggered grid as shown in Fig. 2. This allows us to retain the continuity equation in its exact form, eq. (6). The quantities not defined on the grid are approximated in a linear and second order manner using algebraic averages like $\bar{y}^j$, e.g.

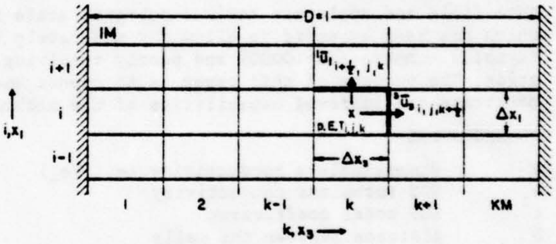

Fig. 2: Staggered Grid

$$\bar{y}^1 = \frac{1}{2} \left[\bar{y}(x_1+\Delta x_1/2, x_2, x_3) + y(x_1-\Delta x_1/2, x_2, x_3) \right] \tag{11}$$

This results in the following finite difference scheme which we write without space averaging bars; the superscript n refers to the time level ($t^n = n\Delta t$):

$$(u_i^{n+1} - u_i^{n-1})/(2\Delta t) = -\delta_j(\overline{u_j}^i\, \overline{u_i}^j)^n + \delta_j(\nu \delta_j u_i - {}^{j}\overline{u_i' u_j'})^{n-1} + \delta_{i1} P_x \tag{12}$$

$$(T^{n+1} - T^{n-1})/(2\Delta t) = -\delta_j(u_j\, \bar{T}^j)^n + \delta_j(a \delta_j T - {}^{j}\overline{u_j' T'})^{n-1} + \dot{Q}^n \tag{13}$$

The pressure p^n is determined from a Poisson-equation

$$\delta_i \delta_i p^n = \delta_i u_i^{n+1}/(2\Delta t) \tag{14}$$

so that the new time level velocities

$$u_i^{n+1} = u_i^{n+1} - (2\Delta t)\, \delta_i p^n \tag{15}$$

satisfy the continuity equation (6). Eq. (14) is solved using fast Fourier transform /5/. Eq. 12-13 correspond to a leap frog scheme which is started with an initial Euler step and interrupted by an

---

[1] for repeated lower indices

averaging step every n_L time steps (typically, n_L = 50). The actual code can be applied also for cylindrical coordinates and non equidistant grid spacings in the x_3-direction.

The Sub-grid Scale Flux Approximations

The general form of the model for the SGS stresses ${}^{j}\overline{u_i'u_j'}$ is as described in /2/; several improvements have been added /4/, however. The SGS heat flux ${}^{j}\overline{u_i'T'}$ has been modelled in an analogues manner /4/. The main characteristics are as follows:

First, the SGS fluxes are split into a fluctuating and a time mean part, e.g.

$$ {}^{j}\overline{u_j'T'} = \underbrace{{}^{j}\overline{u_j'T'} - \langle {}^{j}\overline{u_j'T'} \rangle}_{\text{"locally isotropic part"}} + \underbrace{\langle {}^{j}\overline{u_j'T'} \rangle}_{\text{"inhomogeneous part"}} \qquad (16) $$

and approximated by eddy diffusivity models

$$ {}^{j}\overline{u_j'T'} = -{}^{j}a_t\,\delta_j({}^{v}\bar{T} - \langle {}^{v}\bar{T} \rangle) - {}^{j}a^{*}_t\,\delta_j\,\langle {}^{v}\bar{T} \rangle \qquad (17) $$

$$ {}^{j}a_t = c_{T2}\,{}^{j}c_T\,({}^{j}F\,{}^{j}c_5\,{}^{v}\bar{E}')^{1/2}/\sigma_T \qquad (18) $$

$$ {}^{j}a^{*}_t = \delta_{3j}\,\ell\,\ell_H\,|\,\delta_3 \langle {}^{1}\bar{u}_1 \rangle\,|\,f_H\,(\text{mesh}) \qquad (19) $$

The corresponding eddy diffusivities /2/ of the SGS stresses are

$$ {}^{ij}\mu = c_2\,{}^{ij}c\,({}^{j}F\,{}^{j}c_5\,{}^{v}\bar{E}')^{1/2}/\sigma_1 \qquad (20) $$

$$ {}^{ij}\mu^{*} = \delta_{i1}\,\delta_{j3}\,\ell^2\,|\,\delta_3 \langle {}^{1}\bar{u}_1 \rangle\,|\,f\,(\text{mesh}) \qquad (21) $$

The "isotropic" eddy diffusivities ${}^{j}a_t$ and ${}^{ij}\mu$ are determined under the assumption of locally isotropic turbulence. Here, the characteristic length scale is derived from the surface area ${}^{j}F$ of the grid cell over which the average is defined, and the characteristic velocity from the SGS kinetic energy ${}^{v}\bar{E}'$. The coefficients ${}^{j}c_5$, ${}^{ij}c$, ${}^{j}c_T$ /2,4/ account for geometrical details of the mesh and the finite difference scheme and are of order one. The coefficients c_2 and c_{T2}, however, must be determined so that the energy or temperature variance dissipation due to the eddy diffusivities in the simulated gross-scale flow is of the same magnitude as the molecular dissipation in reality. For this purpose we assume the validity of the well known Kolmogorov-Spectrum for the kinetic energy E(k) (k = wave number) and its counterpart for temperature $E_T(k)$:

$$ E(k) = \alpha \langle \varepsilon \rangle^{2/3}\,k^{-5/3}, \quad E_T(k) = \beta \langle \varepsilon \rangle^{-1/3} \langle \varepsilon_T \rangle k^{-5/3} \qquad (22) $$

$$ \int_0^\infty E(k)\,dk = \frac{1}{2} \langle u_i'^2 \rangle, \quad \int_0^\infty E_T(k)\,dk = \langle T'^2 \rangle \qquad (23) $$

$$ \varepsilon = \nu(\partial u_i/\partial x_k)^2, \quad \varepsilon_T = 2a(\partial T/\partial x_k)^2 \qquad (24) $$

According to several experiments /4/ we assume the Kolmogorov- and Batchelor-constants α and β to be

$$ \alpha = 1.5 \quad , \quad \beta = 1.3 \qquad (25) $$

By means of these assumptions all coefficients c_2, c_{T2}, ${}^{j}c_5$, ${}^{ij}c$, ${}^{j}c_T$ can be evaluated /2,4/ without further approximations. Nevertheless, in /18,20/we use the coefficients σ_T and σ_1 to adjust the models numero-empirically and to account for the deficiencies of the theory. The values of the coefficients, c.., are dependent on the geometry of the mesh. Typical values of all SGS coefficients are listed in Tab. I. The value of c_2 is different from that given in /2/ which was erroneous due to a sign error in the underlying theory /5, see 4/. This (and the changes in the energy equation, see below) result in a reduction of the factor σ_1 from 3 /2/ to 1.4 /4/. The assumption of spectra of the Kolmogorov-type is not necessary. More realistic spectra which depart at small as well as at high wave-numbers have also been used /4,6/. The changes of c_2 introduced by these spectra remain less than 20 % for the cases considered up to now. They become important, however, for fine grids and small Reynolds numbers, where the grid scale becomes comparable to the Kolmogorov micro-scale.

The "inhomogeneous" eddy diffusivities ${}^{j}a^{*}_t$ and ${}^{ij}\mu^{*}$ are derived from the common mixing length models (ℓ, ℓ_H = mixing lengths for momentum and heat /4/). The crucial factors here are the damping functions f and f_H. They are designed so that for very coarse meshes the SGS model becomes equal to the common models for time averaged turbulence ($f, f_H \rightarrow 1$). For very fine resolution the functions go to zero since in this case all SGS fluxes are described by the isotropic parts. We use /4/:

$$ f(\text{mesh}) = \text{Min}\,(1, c_{10}[(\Delta x_1 \Delta x_2^{\,2} \Delta x_3)/F_o^{\,2}]^{1/2}) \qquad (26) $$

$$ f_H(\text{mesh}) = \text{Min}\,(1, [\bar{c}_{10} c_{T10} (\Delta x_1^{\,2} \Delta x_2^{\,2} \Delta x_3)^{2/5}/F_o]^{1/2}) \qquad (27) $$

The important parameter here is F_o, the grid surface required to make the SGS fluxes equal to the total turbulent fluxes. The coefficients c_{10} and c_{T10} are correction factors which have been adjusted numero-empirically, the coefficient c_{T10} depends also on the molecular Prandtl number.

The Sub-grid Scale Kinetic Energy Transport Equation

The SGS kinetic energy ${}^{v}\bar{E}' = \frac{1}{2}\,{}^{v}\overline{(u_i - {}^{v}\bar{u}_i)^2}$ is calculated integrating an additional transport equation as described in /2/. The following changes and extensions have been introduced /4/:

The production term, eq. (24,36) of /2/, has been extended to include the SGS energy production caused by the inhomogeneous part of the SGS stresses. This change has been found to be important in the near wall region, especially in annular channels, in order to predict a correct cross-stream energy profile.

The dissipation rate ε is now modelled by means of three terms $\varepsilon = \varepsilon_I + \varepsilon_{II} + \varepsilon_{III}$. The first term replaces the old model ($\bar{c}_3$ as in /2/):

$$ \varepsilon_I = c_3({}^{v}\bar{E}')^{3/2}/\text{Min}\,(h, c_{31}\ell) \qquad (28) $$

The inclusion of the minimum function makes the model suited for very coarse grids, in particular near the walls, where the mixing length ℓ becomes smaller than the mesh scale h. For small Reynolds numbers it has been found to be necessary to add the second term which describes the direct viscous dissipation:

$$ \varepsilon_{II} = \nu\,c_{32}\,{}^{v}\bar{E}'/[\overline{\text{Min}}(h_1, c_{31}\ell)]^2 \qquad (29) $$

The values of c_{31}, c_{32} have been determined /4/ from the empirical energy spectra proposed by Pao /7/. According to Jones and Launder /8/, finally the term

$$\varepsilon_{III} = 2\nu \left[\delta_3 ({}^{v}\overline{E}')^{1/2} \right]^2 \tag{30}$$

has been added, which accounts for the dissipation in the viscous sublayer. It is of negligible magnitude, however, for those Reynolds numbers and mesh sizes considered up to now. The relative magnitude of these three dissipation terms is shown in Fig. 3 for two examples.

Tab. I: SGS Coefficients for an Isotropic Grid ($\Delta x_1 = \Delta x_2 = \Delta x_3 = 1/16$), (Re=250000, Pr=0.7)

stress model		kinetic energy model	
c_2	0.0709	c_3	0.6336
$^1c_5$	0.8283	c_{31}	0.74
^{11}c	1.4744	c_{32}	20.0
^{12}c	0.8233	c_{20}	0.8044
c_{10}	2.0	**heat flux model**	
F	1.28	c_{T2}	0.1788
σ_1^o	1.4	^1c_T	1.0
		σ_T	1.4
		c_{T10}	1.0

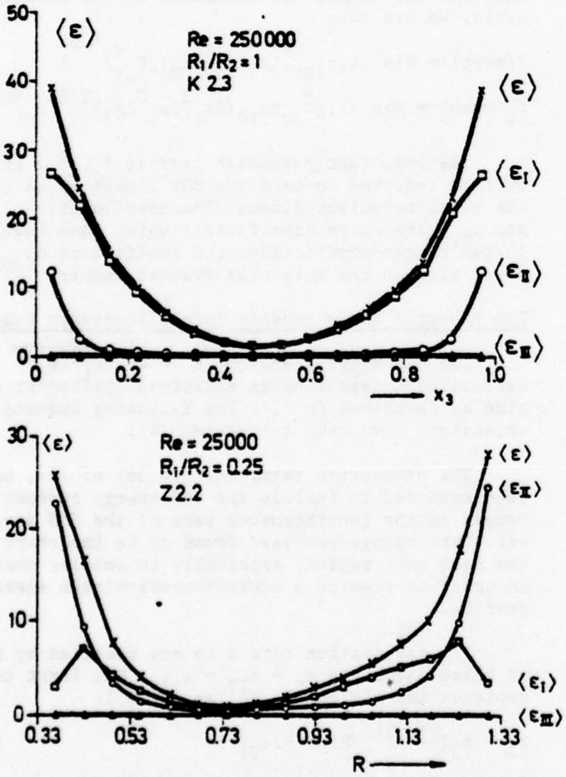

Fig. 3: Energy dissipation rate <ε> and its three parts for two cases, K2.3 and Z2.2

The Boundary Conditions

In x_1- and x_2-direction we assume periodicity with periodic lengths X_1 and X_2 (or angle, resp.), the values of which are listed in Tab. II.

In x_3-direction, at the walls we set the normal velocity to zero. In addition, the no-slip boundary condition requires prescription of the wall shear stresses $\overline{^3\tau_{wi}} = \nu \overline{^3\frac{\partial u_i}{\partial x_3}}$ and the normal wall heat flux $\dot{q}_w = \overline{^3 a \frac{\partial T}{\partial x_3}}$ as a function of the velocities and temperatures in the wall adjacent grid cells. The stresses are computed as in /2/ with two important changes /4/ which refer to eq. (45) of /2/. First, the time mean value $<\tau_w>$, which is equal to one in the present units for a steady state plane channel flow, is not prescribed this way rather than recalculated by proper averaging from the actual and recent velocity fields. Secondly. the wall roughness coefficient E can be a function of the equivalent sand-roughness height and the x_2-coordinate. This allows us to study secondary flows. The boundary condition in terms of the heat flux $\dot{q}_w$ is approximated for small Peclet numbers by

$$\dot{q}_w = -\frac{a}{\Delta x_3/2} ({}^{v}\overline{T}_1 - T_w) \tag{31}$$

(${}^{v}\overline{T}_1$ = first grid cell value, T_w = wall temperature). For large Peclet numbers we use

$$\dot{q}_w = <\dot{q}_w> ({}^{v}\overline{T}_1 - T_w)/< {}^{v}\overline{T}_1 - T_w > \tag{32}$$

where either $<\dot{q}_w>$ or T_w must be prescribed and the unknown part is determined from the logarithmic law of the wall /9/ averaged over the first grid cell

$$<{}^{v}\overline{T}_1> = -\frac{<\dot{q}w>}{<\tau_w>^{1/2}} \frac{1}{\kappa_H} \left[\ln(Re_\tau <\tau_w>^{1/2}) + \ln(\Delta x_3) - 1 \right] + B_T \tag{33}$$

($\kappa_H = 0.465$, B_T = function of wall roughness and Prandtl number /4/).

By setting $u_3^{n+1} = 0$ at the walls, instead of using (12), the Neumann boundary condition $\delta_3 P = 0$ at the wall follows from (15).

RESULTS

The purpose of this chapter is to demonstrate the general agreement between experiments and TURBIT-2 results.

Tab. II: Case Specifications

	K7	K2.2	K2.3	Z2.2
X_1	2	3.2	4	3.2
X_2	1	2	2	π
IM	16	32	64	32
JM	8	16	32	32
KM	16	16	16	16
R_1/R_2	1	1	1	0.25
Re	18700	25000	250000	25000
Pr	0.71	0.007	0.7	0.7
CPU-time IBM 370/168	40 min	3 h	18 h	7 h
problem time	6.05	4.24	4.23	4.51
no. of time steps	2128	2350	3224	2625

SGS Model Sensitivity

Several preliminary cases have been run in order to study the effect of the free SGS parameters σ_1, c_T, c_{10}, and c_{T10}, the values of which can be estimated to be of order one theoretically but remain to be fixed numero-empirically. For this purpose a rather coarse grid has been used (K7, see Tab. II). Typical results /4/ are a 15 % increase of the kinetic energy near the walls (which is the most sensitive measure) as a result of a 20 % increase of σ_1 and a 5 % decrease of the same quantity as a result of a 10 % increase of c_{10}. As shown in Fig. 4, the importance of the temperature model coefficients σ_T and c_{T10} are smaller. The values finally used are those listed in Tab. I. One should remind that an even weaker sensitivity is observed for finer grid resolutions.

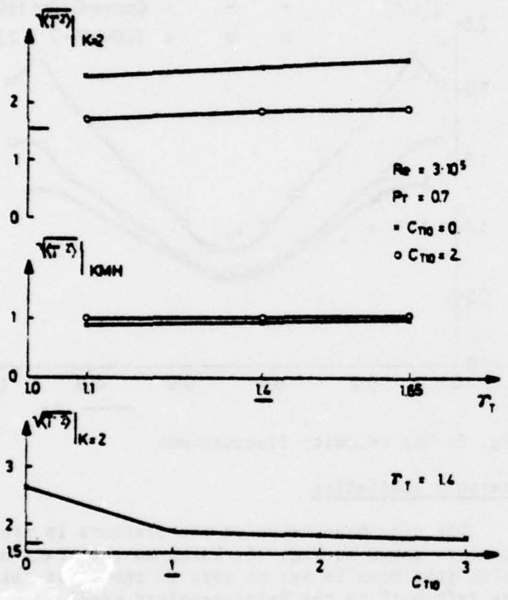

Fig. 4: Rms temperature fluctuations in the radial cells at K = 2 and K = KMH = KM/2 (channel middle) as a function of the SGS coefficients, case K7.

Flow Field and Velocity Statistics

Fig. 5 shows a typical resulting turbulent flow field for case Z2.2. This is an annulus (R1/R2 = 0.25) heated from the inner rod with an adiabatic outer wall. The contour lines and velocity vectors show the known quasi-random behaviour. The flow is from left to right. The velocity contour lines show some inclination against the flow direction towards the channel middle; this is observed in all plots of this type. The fluctuating kinetic energy is generally a rather smooth space-function except for some peaks (bursts?) near the walls, which are mainly contained in the directly resolved part of the flow field. As expected from experiments / 10, 11/, the kinetic energy is larger near the outer wall than near the inner one. This result was not so obvious in the older code-version /3/. The temperature fluctuations are larg near the heated inner wall only.

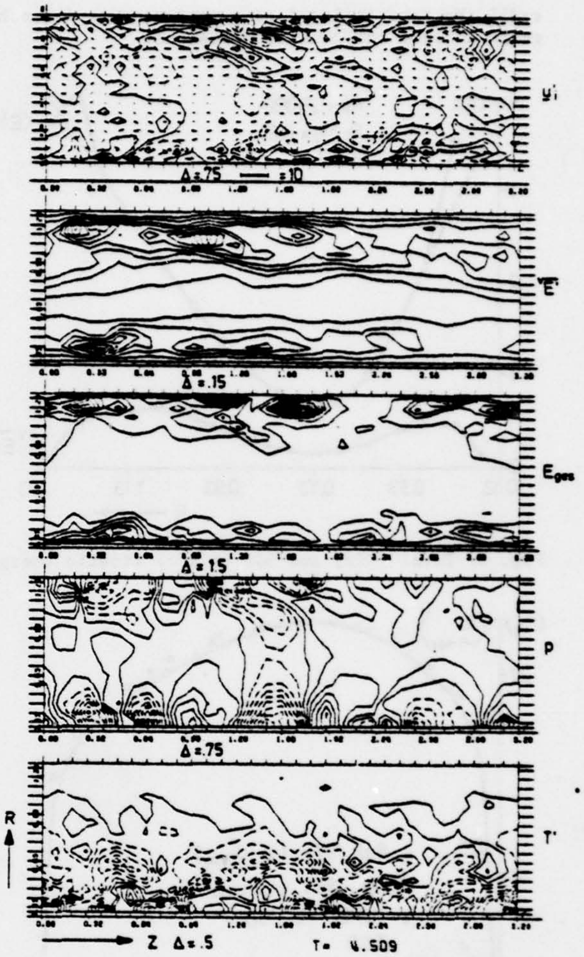

Fig. 5: Vector- and contour-line plots of the instantaneous resolved fluctuating velocities $u_i' = u_i - \langle u_i \rangle$, SGS kinetic energy $^v\overline{E}'$, total energy $E_{ges} = {}^v\overline{E}' + u_i'^2/2$, fluctuating pressure p and temperature T' in an annulus (Z2.2). Δ = contour line increment, dashed curves correspond to negative values.

The time mean value of the kinetic energy is shown in Fig. 6. Also plotted in this figure is the SGS part which amounts to less than 25 % of the total value. The corresponding dissipation rates are depicted in Fig. 3 mentioned above. Here we see the effect of the three model parts for two different Reynolds numbers. The direct viscous dissipation rate ε_{II} is not negligible especially near the walls. The computed velocity profile given in Fig. 7 shows very good agreement with the corresponding experimental results of Ball /12/ and Lee /13/. The difference between the measured and computed maximum value $\langle u_1 \rangle_{max}$ itself is less than 1 % if we refer to Lee. The results of Ball are smaller by 10 %, this seems to be a consequence of rather densly located spacers used by Ball in his annular channel. Fig. 8 shows the shear stress: The smaller values correspond to that part of the shear stress resolved directly by the large scale flow. We conclude that the major part of the momentum transport is accomplished by the resolved flow part. No experimental data are available for this ratio of radii. We have included some measurements for other radii to show the general agreement.

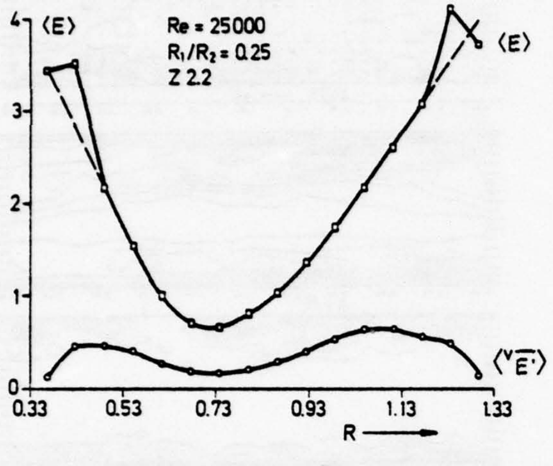

Fig. 6: Total (<E>) and SGS (<$^V\overline{E}$'>) kinetic energy

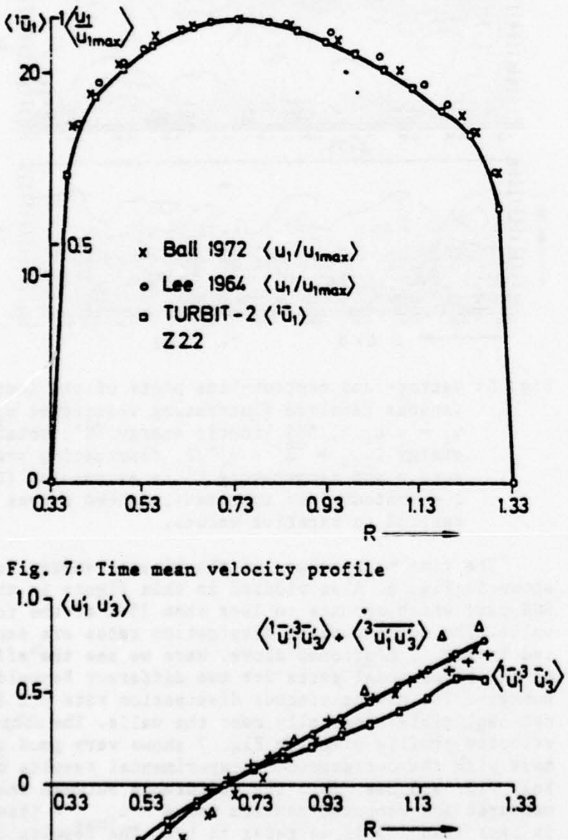

Fig. 7: Time mean velocity profile

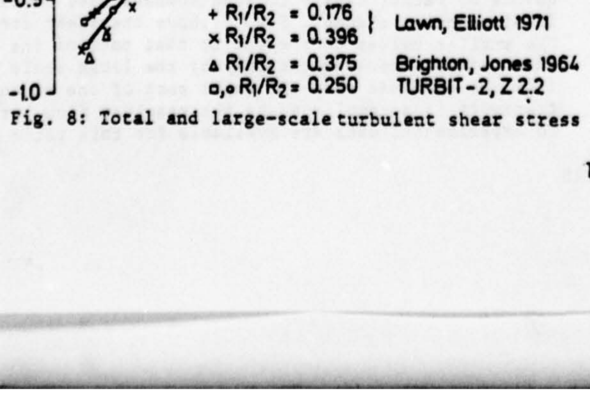

Fig. 8: Total and large-scale turbulent shear stress

For a plane channel we compare our computed rms velocity fluctuations with the measured results of Comte-Bellot /14/, see Fig. 9. The differences are less than about 20 %. Some of the differences might be attributable to the SGS part which has been computed from the SGS kinetic energy and added to the resolved part under the assumption of local isotropy. In all our simulations we observe a surprising result: The u_3-rms-values are larger than the u_2-values by a few percent in the middle of the channel. This might be a consequence of anisotropy and different resulting energy supply to these velocity components by means of the pressure fluctuations. It is not clear from experiments whether this effect is real, because the accuracy of the measurements is not sufficient for this purpose. Interestingly, this result is not discordant with the measurements of Comte-Bellot /14/.

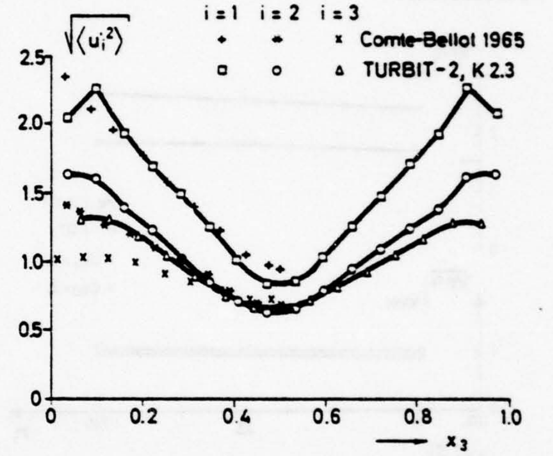

Fig. 9: Rms velocity fluctuations

Pressure Statistics

The time mean value of the pressure is not a constant as shown in Fig. 10. Using an arbitrary mean value (the mean is set to zero in the first cell near the left wall by the Poisson-solver used) we compare our computations with the experiments of Patterson et al. /15/. The rms pressure fluctuations are plotted

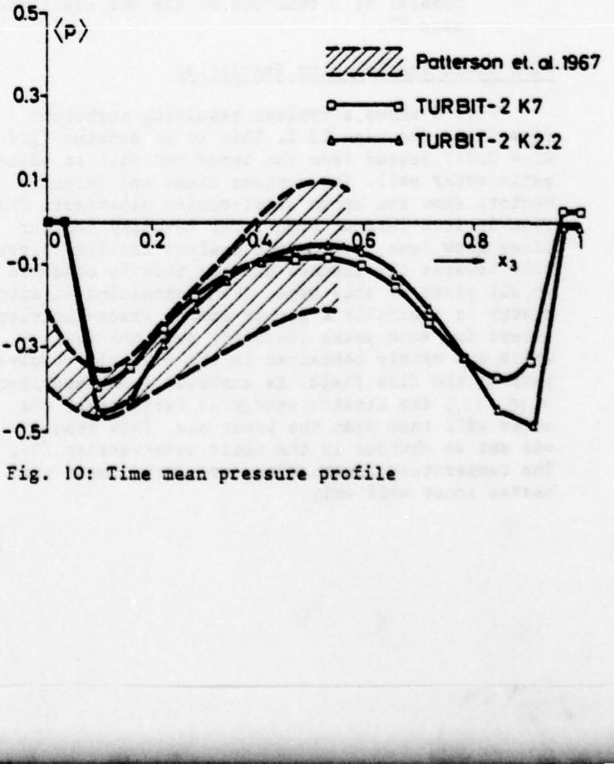

Fig. 10: Time mean pressure profile

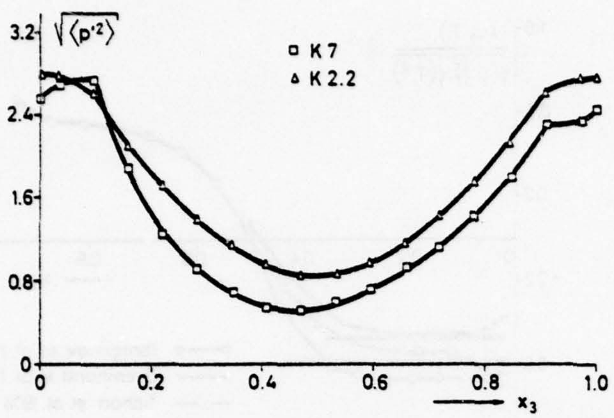

Fig. 11: Rms pressure fluctuations

in Fig. 11. The rms value at the wall, 2.7, corresponds well with experiments, see /3/. No internal measurements are known for this geometry. The case K7 gives rather small rms values, this is a consequence of too small periodicity lengths X_1 and X_2, which result in a filtering of the low frequency fluctuations.

Fig. 12 shows a contour-line plot of the instantaneous fluctuating pressure at the wall of a plane channel (K2.3) and the corresponding experimental result of Dinkelacker et al. /16,17/. Both plots are scaled so that the spatial dimensions are directly comparable. In both figures we observe a 45°-inclination. From the numerical results it is obvious that the pressure fluctuations are correlated over longer distances in the x_2- than in the mean flow-direction x_1. This finding agrees with earlier results /3/ and experiments /18/.

Temperature Statistics

The mean temperature profile, corresponding to Fig. 5 (Z2.2) is shown in Fig. 13. The agreement with experimental data /12,13,19/ is satisfactory except for the results of Ball, which depart probably due to the above mentioned spacers and a rather short thermal entry length. The Nusselt-number, calculated from this mean temperature profile, is Nu = 50,6. Experimental results deviate from this value by ± 15 % /4/.

For a plane channel with a rather coarse grid (K7), we show the rms temperature fluctuations in Fig. 14. In this case the fluid is heated by a volumetrical heat source within the fluid and cooled at both walls by prescribing constant and equal wall temperatures. No equivalent experimental data are known for a plane channel. We, therefore, refer to the pipe data of Bremhorst et al. /20/ which are in reasonable agreement. In Fig. 15 we show the correlation coefficient between the temperature- and the cross-stream velocity component for the same channel in comparison to several experiments /20-23/. The good agreement shows that the turbulent heat flux is correctly simulated. This is mainly a consequence of the inhomogeneous part (16,19) of the SGS heat flux model; it was found /4/ that neglection of the inhomogeneous SGS heat flux model results in higher temperature rms.

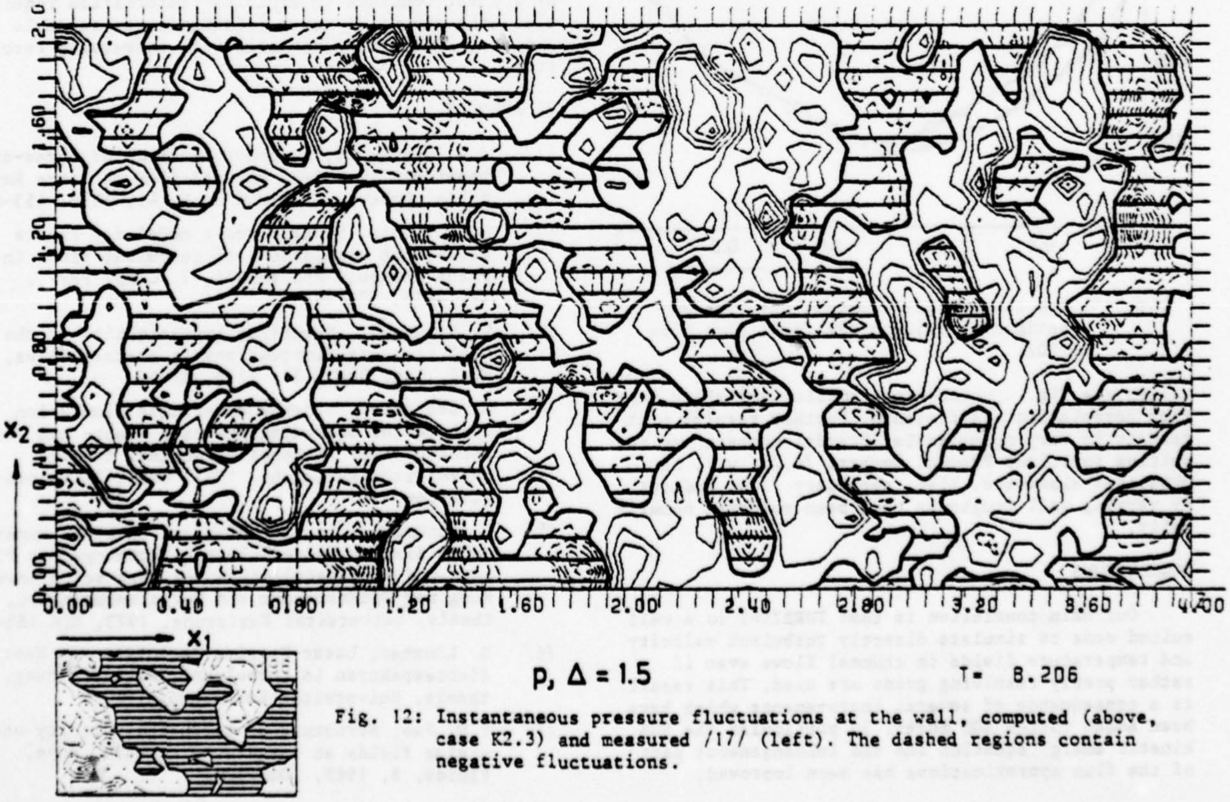

Fig. 12: Instantaneous pressure fluctuations at the wall, computed (above, case K2.3) and measured /17/ (left). The dashed regions contain negative fluctuations.

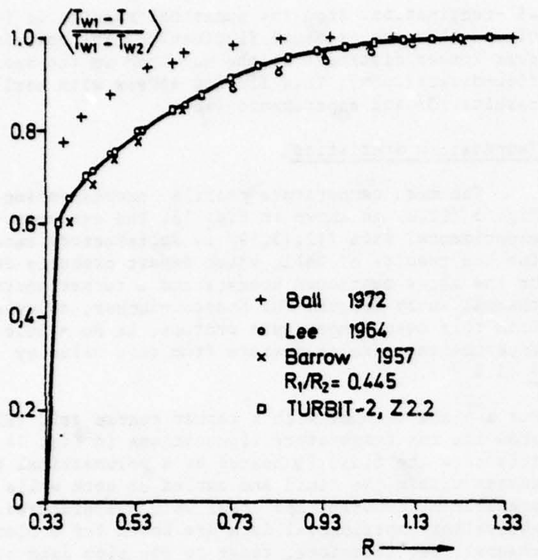

Fig. 13: Time mean temperature profile normalized by the wall temperatures at the inner and outer walls (T_{W1}, T_{W2}).

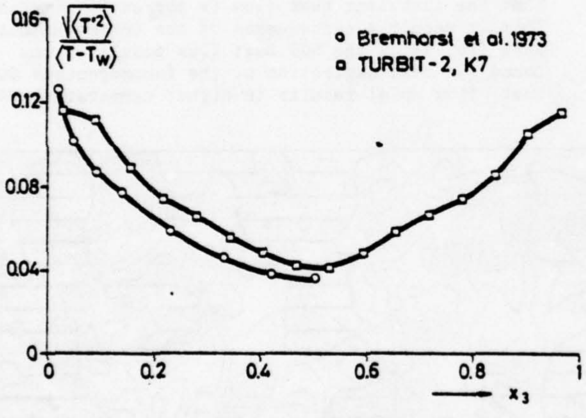

Fig. 14: Rms temperature fluctuations. The experimental results are for a pipe flow /20/.

values, see Fig. 4, which cause smaller turbulent heat flux correlation coefficients. Further results with respect to varying molecular Prandtl numbers and resulting turbulent Prandtl numbers /4,24/ will be published elsewhere. Also, secondary flows induced by varying wall roughness have been observed numerically.

CONCLUSIONS

Our main conclusion is that TURBIT-2 is a well suited code to simulate directly turbulent velocity and temperature fields in channel flows even if rather poorly resolving grids are used. This result is a consequence of several improvements which have been added to the SGS model. In particular the SGS kinetic energy equation and the inhomogeneous part of the flux approximations has been improved.

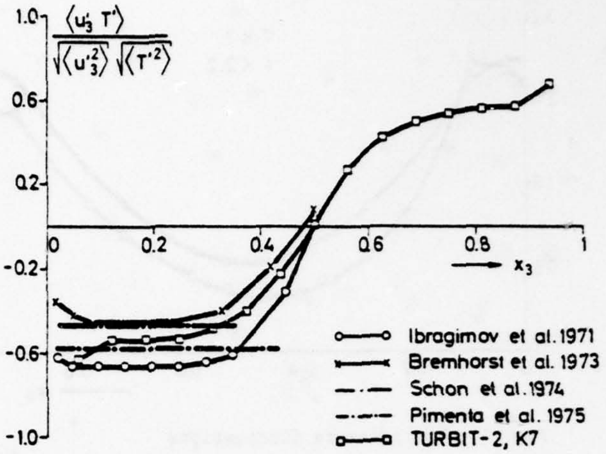

Fig. 15: Cross-stream velocity - temperature correlation coefficient

It has been shown that the resulting temperature fields are rather insensitive with respect to the model coefficients. The differences between the numerical results and experimental data are small in comparison with the scatter of the latter.

We are now able to produce results which can hardly be measured, like e.g. the pressure statistics and pressure-temperature correlations, using only a modest amount of computing time (e.g. 40 minutes for case K7). This achievement has to be payed for, however, by a small increase in empirical information required; also, the amount of novel information extractable from a direct simulation decreases with decreasing resolution.

REFERENCES

/1/ J.W. Deardorff, A numerical study of three-dimensional turbulent channel flow at large Reynolds numbers, J. Fluid Mech. 41, 1970, 453-480

/2/ U. Schumann, Subgrid scale model for finite difference simulations of turbulent flows in plane channels and annuli, J. Comp. Phys., 18, 1975, 376-404

/3/ U. Schumann, Numerical investigation of the wall pressure fluctuations in channel flows, Nucl. Eng. Des., 32, 1975, 37-47

/4/ G. Grötzbach, Direkte numerische Simulation turbulenter Geschwindigkeits-, Druck- und Temperaturfelder in Kanalströmungen, thesis, Universität Karlsruhe, 1977, KFK 2426 in preparation

/5/ U. Schumann, Ein Verfahren zur direkten numerischen Simulation turbulenter Strömungen in Platten- und Ringspaltkanälen und über seine Anwendung zur Untersuchung von Turbulenzmodellen, thesis, Universität Karlsruhe, 1973, KFK 1854

/6/ G. Lörcher, Laser-Doppler-Messungen von Energiedichtespektren in turbulenter Kanalströmung, thesis, Universität Karlsruhe, 1977

/7/ Y.H. Pao, Structure of turbulent velocity and scalar fields at large wave numbers, Phys. Fluids, 8, 1965, 1063-1075

/8/ W.P. Jones, B.E. Launder, The calculation of low Reynolds-number-phenomena with a two-equation model of turbulence,. Int. J. Heat Mass Transf. 16, 1973, 1119-1130

/9/ B.A. Kader, A.M. Yaglom, Heat and mass transfer laws for fully turbulent wall flows, Int. J. Heat Mass Transf. 15, 1972, 2329-2351

/10/ J.A. Brighton, J.B. Jones, Fully developed turbulent flow in annuli, J. Basic Eng. 86, 1964, 835-844

/11/ C.J. Lawn, C.J. Elliott, Fully developed turbulent flow through concentric annuli, 1971, CEGB-Report RD/B/N 1878

/12/ H.D. Ball, Experimental investigation of eddy diffusivities of air in turbulent annular flow, Ph. D. thesis, Kansas State Univ., 1972

/13/ Y. Lee, Turbulent flow and heat transfer in concentric and eccentric annuli, Ph. D. thesis, Univ. of Liverpool, 1964

/14/ G. Comte-Bellot, Ecoulement turbulent entre deux parois parallèles, Publications Scientifiques et Techniques du Ministère de l'Air, No. 419, 1965

/15/ G.K. Patterson, W.J. Ewbank, V.A. Sandborn, Radial pressure gradient in turbulent pipe flow, Phys. Fluids, 10, 1967, 2082-2084

/16/ A. Dinkelacker, M. Hessel, G.E.A. Meier, G. Schewe, Further results on wall pressure fluctuations in turbulent flow, Fed. Rep. Germany Hydroacoustics Symp., Proc. Ed. H. Merbt, Frauenhofer Ges. München, 3, 1975, 29-38

/17/ A. Dinkelacker, M. Hessel, G.E.A. Meier, G. Schewe, Investigation of pressure fluctuations beneath turbulent boundary layer by means of an optical method, submitted for publ. in a Suppl. to Phys. Fluids, 1976

/18/ J.M. Clinch, Measurement of the wall pressure field at the surface of a smooth wall pipe containing turbulent water flow, J. Sound Vib., 9, 1969, 398-419

/19/ H. Barrow, Fluid flow and heat transfer in an annulus with a heated core tube, Proc. IME, 169, 1957, 1113-1124

/20/ K. Bremhorst, K.J. Bullock, Spectral measurement of turbulent heat and momentum transfer in fully developed pipe flow, Int. J. Heat Mass Transf., 16, 1973, 2141-2154

/21/ M.Kh. Ibragimov, V.I. Subbotin, G.S. Taranov, Velocity and temperature fluctuations and their correlations in the turbulent flow of air in pipes, Int. Chem. Engng., 11, 1971, 659-665

/22/ J.F. Schon, J. Mathieu, A. Baille, J. Solal, G. Comte-Bellot, Experimental study of diffusion processes in unstable stratified boundary layers, Adv. in Geophys., 18B, 1974, 265-272

/23/ M.M. Pimenta, R.J. Moffat, W.M. Kays, The turbulent boundary layer: an experimental study of the transport of momentum and heat with the effect of roughness, Stanford Univ., 1975, Report HMT-21

/24/ G. Grötzbach, Erste Ergebnisse der direkten numerischen Simulation von Temperaturfeldern bei turbulenter Natriumströmung, 1976, KFK 1276/2, 129-6 - 129-11

IMPROVED METHODS FOR LARGE-EDDY SIMULATIONS OF TURBULENCE

by

N. N. Mansour
P. Moin
W. C. Reynolds
and
J. H. Ferziger

Department of Mechanical Engineering
Stanford University
Stanford, California 94305

ABSTRACT

By using Fourier transforms for evaluating spatial derivatives, we are able to improve the accuracy of the large-eddy simulation of homogeneous isotropic turbulence. Especially, the treatment of certain terms that arise in filtering the equations is considerably improved in both speed and accuracy. Use of vorticity as the principal variable is shown to be a viable and potentially useful alternative to the primitive variables. A method of deriving conservation properties of numerical schemes is given which is much simpler than previous methods and is widely applicable. The methods are applied to the computation of homogeneous isotropic turbulence, and it is found that the subgrid scale model is improved by using finite differences in place of "exact" derivatives.

1. INTRODUCTION

One of the promising approaches to solving "general" turbulence problems is "large-eddy simulation." The basic motivation for this approach is provided by the observation that the large-scale turbulent structures differ markedly from one flow type to another (e.g., jet vs. boundary layer), while the small-scale turbulent structures are quite similar. Thus, while there is little hope of concocting a "general" model for the large-scale structures, it is quite likely possible to do so for the small-scale motions. In large-eddy simulations, then, one contemplates calculating the large-scale turbulent motions with a relatively coarse time-dependent, three-dimensional computation which in turn uses some sort of model (the "subgrid scale model") for the smaller scales.

Kwak et al. [5] and Shaanan et al. [13] have shown that homogeneous turbulent flows can be simulated reasonably well with finite-difference methods using a relatively small number of mesh points (16 × 16 × 16 = 4096). Kwak used a fourth-order conservative method, while Shaanan used a modified staggered grid method, and, while both were successful, they also have their inconveniences. In order to assess the subgrid scale models used, to study the effect of various numerical schemes on them, and also for extensions to more complex flows, especially flows with inhomogeneities in turbulence intensity and length scale, it is important to obtain the maximum amount of computational accuracy possible with a given amount of memory and computer time. It is therefore important to seek new numerical methods which promise the improved accuracy.

In this paper we report our recent explorations into a number of computational methods which show promise in large-eddy simulations. The basic equations, in primitive variable form, are outlined in §2. The resetting of the problem in vorticity form is done in §3.

In §4 we introduce the spatial differencing methods and show how the modified wavenumber concept can be used to assess the accuracy of candidate schemes. In §5 we give the methods used for solving the Poisson equations (for the pressure in primitive variables, for the stream vector potential in vorticity variables) that arise in computing incompressible flows. Time-differencing is taken up in §7.

It is of utmost importance in any time-dependent flow computation that momentum and energy conservation be obtained exactly in a numerical sense. Failure to do so almost always results in computational instability. The demonstration that a method is conservative has usually been a tedious calculation in the past (especially for energy conservation) and has had to be done for each case separately. A straightforward method of demonstrating conservation for a class of methods is given in §6.

§8 describes the physical problem which will be considered and lists the parameters of the calculations. The results of these computations are given in §9.

2. DYNAMICAL EQUATIONS IN PRIMITIVE FORM

In the large-eddy simulation approach, the first and most fundamental step is defining the large-scale field. A general approach that recognizes the continuous nature of the flow variables is the "filter function" approach of Leonard [7]. If u is some flow variable, we can decompose it as follows:

$$u = \bar{u} + u' \tag{2.1}$$

where $\bar{u}$ is the large-scale component and u' is the residual field. Leonard defined the filtered field as

$$\bar{u}(\underline{x},t) = \int_D G(\underline{x}-\underline{x}')u(\underline{x}',t)d\underline{x}' \tag{2.2}$$

where $G(\underline{x}-\underline{x}')$ is the filter function and the integral is extended over the whole flow field. One can think of $\bar{u}$ as a *local* spatial average field.

We can apply (2.2) to the incompressible Navier-Stokes equations to get the dynamical equations of large-scale field.

$$\frac{\partial \bar{u}_i}{\partial t} + \frac{\partial}{\partial x_j}\overline{\bar{u}_i\bar{u}_j} + \frac{\partial}{\partial x_j}R_{ij} = -\frac{1}{\rho}\frac{\partial \bar{p}}{\partial x_i} + \nu\nabla^2\bar{u}_i \tag{2.3}$$

where we have decomposed u as in (2.1) and

$$R_{ij} = \overline{u_i'u_j'} + \overline{u_j'\bar{u}_i} + \overline{u_i'\bar{u}_j} \tag{2.4}$$

PRECEDING PAGE BLANK-NOT FILMED

R_{ij} depends upon small-scale quantities and must be modeled. We can write (2.3) in the following equivalent form:

$$\frac{\partial \bar{u}_i}{\partial t} + \overline{\bar{u}_j \left(\frac{\partial \bar{u}_i}{\partial x_j} - \frac{\partial \bar{u}_j}{\partial x_i} \right)} = - \frac{\partial \bar{P}}{\partial x_i} - \frac{\partial}{\partial x_j} \tau_{ij} + \nu \nabla^2 \bar{u}_i \quad (2.5)$$

where

$$\bar{P} = \bar{p}/\rho + \frac{1}{2} (\overline{\bar{u}_i \bar{u}_i}) + \frac{1}{3} R_{kk},$$

$$\tau_{ij} = R_{ij} - \frac{1}{3} R_{kk} \delta_{ij}$$

The rationale for choosing this form of the convective terms will be explained later.

The question arises as to how to handle the second term on the left-hand side. From Eq. (2.2) we have

$$\overline{\bar{u}_j \left(\frac{\partial \bar{u}_i}{\partial x_j} - \frac{\partial \bar{u}_j}{\partial x_i} \right)} = \int_{-\infty}^{+\infty} G(\underline{x}-\underline{x}') \bar{u}_j \left(\frac{\partial \bar{u}_i}{\partial x'_j} - \frac{\partial \bar{u}_j}{\partial x'_i} \right) d\underline{x}'$$

Previously (e.g., Kwak et al. [5] and Shaanan et al. [13]), we treated this term by using a Taylor series on the right-hand side. This is unnecessary, and for improved accuracy we Fourier-transform the above equation, to get:

$$\widehat{\overline{\bar{u}_j \left(\frac{\partial \bar{u}_i}{\partial x_j} - \frac{\partial \bar{u}_j}{\partial x_i} \right)}} = \hat{G} \widehat{\left[\bar{u}_j \left(\frac{\partial \bar{u}_i}{\partial x_j} - \frac{\partial \bar{u}_j}{\partial x_i} \right) \right]}$$

where $\wedge$ denotes a Fourier-transformed quantity; a $\wedge$ over a bracket means the transform of the bracketed quantity. Thus, given a velocity field, $\bar{u}_i$, one can compute the term in the brackets on the right-hand side of the above equation and multiply it by $\hat{G}$ and invert the transform to obtain the desired term.

In the calculations reported here, we take G to be a Gaussian function,

$$G(\underline{x}-\underline{x}') = \left\{ \sqrt{\frac{\gamma}{\pi}} \frac{1}{\Delta_A} \right\}^3 \exp \left\{ -\gamma (\underline{x}-\underline{x}')^2 / \Delta_A^2 \right\} \quad (2.6)$$

where γ is a constant and Δ_A is the filter width. For all calculations reported here, we have used $\gamma = 6$ and $\Delta_A = 2\Delta$, where Δ is the computational grid size. For a detailed investigation of the effects of choosing different Δ_A/Δ, see Moin et al. [9], where some numerical results are presented using a filter which corresponds to a sharp cutoff in Fourier space.

An eddy-viscosity model is used for τ_{ij}:

$$\tau_{ij} = - 2\nu_T \bar{S}_{ij} \quad (2.7)$$

where

$$\bar{S}_{ij} = \frac{1}{2} \left(\frac{\partial \bar{u}_i}{\partial x_j} + \frac{\partial \bar{u}_j}{\partial x_i} \right) \quad (2.8)$$

is the filtered strain rate tensor and ν_T is an eddy viscosity associated with the residual field motions. Smagorinsky [14] suggested the following model for ν_T:

$$\nu_T = (C_s \Delta_A)^2 (2\bar{S}_{ij} \bar{S}_{ij})^{1/2}$$

where C_s is a constant. In the calculations with the primitive equations reported here, we have used the following model:

$$\nu_T = (C_v \Delta_A)^2 \sqrt{\bar{\omega}_i \bar{\omega}_i} \quad (2.9)$$

where

$$\bar{\omega}_i = \varepsilon_{ijk} \frac{\partial \bar{u}_k}{\partial x_j}$$

is the large-scale vorticity and C_v is a constant. Note that in our earlier work (see Kwak et al. [5]) we found that, in the range of wavenumbers of interest, the two models are virtually equivalent. More will be said about the subgrid scale model in §9.

The governing equation for pressure field is obtained by applying the divergence operator to the dynamical equations of the large-scale field. Using the equation of continuity, one obtains

$$\nabla^2 \bar{P} = \frac{\partial}{\partial x_j} \left\{ - \overline{\bar{u}_j \left(\frac{\partial \bar{u}_i}{\partial x_j} - \frac{\partial \bar{u}_j}{\partial x_i} \right)} + \frac{\partial}{\partial x_j} (2\nu_T \bar{S}_{ij}) \right\} \quad (2.10)$$

Note that, since at the high Reynolds numbers considered here the direct viscous dissipation in the large-scale field is negligible compared to the subgrid-scale transfers, the viscous terms are neglected.

3. DYNAMICAL EQUATIONS IN VORTICITY FORM

In many flows of practical interest there are interactions between irrotational regions and turbulent regions. Examples of such flows are the shear layer, turbulent jet flows, and turbulent boundary layers with irrotational free stream flow. In such flows the regions are separated by a very thin superlayer across which there is normally a jump in the vorticity parallel to the layer. The dynamical equations for the vorticity seem to be the best choice for simulating such flows, since the vorticity would be identically zero in the irrotational region.

The appropriate equations can be derived by taking the curl of the filtered primitive equations (2.5) to get:

$$\frac{\partial \bar{\omega}_i}{\partial t} + \frac{\partial}{\partial x_j} (\overline{\bar{u}_j \bar{\omega}_i} - \overline{\bar{u}_i \bar{\omega}_j}) + \frac{\partial}{\partial x_j} W_{ij} = \nu \nabla^2 \bar{\omega}_i \quad (3.1)$$

where

$$W_{ij} = \overline{u'_j \bar{\omega}_i - u'_i \bar{\omega}_j + \bar{u}_j \omega'_i - \bar{u}_i \omega'_j + u'_j \omega'_i - u'_i \omega'_j} \; .$$

W_{ij} depends on small-scale quantities and hence must be modeled. We note that any model of W_{ij} should possess the following properties:

1. It should be antisymmetric, since W_{ij} is an antisymmetric tensor and therefore
$$\frac{\partial}{\partial x_i} \frac{\partial}{\partial x_j} W_{ij} = 0$$
It is therefore important to preserve the antisymmetry property of W_{ij}, since the dynamical equations for the vorticity do not contain a pressure-like term to adjust the divergence of the vorticity.
2. It should vanish in an irrotational region, since W_{ij} vanishes in such regions.
3. It should be an energy sink, since it represents the subgrid scale effects.

The curl of the model (2.7) could be used to model W_{ij}; this would give:

$$W_{ij} = - \varepsilon_{ijk} \frac{\partial}{\partial x_\ell} \left(2\nu_T \bar{S}_{k\ell} \right) \quad (3.2)$$

where $\bar{S}_k$ and ν_T are defined by Eqs. (2.8) and (2.9), respectively.

Another model has been used for W_{ij}:

$$W_{ij} = - \frac{\partial}{\partial x_j} \left(\nu_T \bar{\omega}_i \right) + \frac{\partial}{\partial x_i} \left(\nu_T \bar{\omega}_j \right) \quad (3.3)$$

where ν_T is defined as in Eq. (2.9). Both models satisfy all three criteria and have been tested (see §9).

4. NUMERICAL METHODS

In problems in which there are significant small-scale variations (high wave number components), the order of difference approximation in the conventional sense (ex. 2nd order, $O(\Delta^2)$) may not be the appropriate criterion for choosing a differencing method. Rather, one should look at the entire range of wave numbers up to π/Δ, the highest wave number that can be represented on a grid of size Δ. In order to make this point clear, we inquire how various numerical differencing schemes differentiate a simple Fourier wave $f(x) = e^{ikx}$. The correct answer is, of course, $f' = ikf$ for the first derivative and $f'' = -k^2 f$ for the second derivative. As a first case, consider the fourth-order differencing scheme:

$$\frac{\delta f}{\delta x} = \frac{f_{i-2} - 8f_{i-1} + 8f_{i+1} - f_{i+2}}{12\Delta} \tag{4.1}$$

(Throughout, we use δ to represent the numerical approximation of ∂), which was used in some of the calculations using the vorticity equations. For the Fourier wave discussed above, this scheme yields

$$f'_j = ik'f_j$$

where

$$k' = \frac{1}{6\Delta}\left[8\sin(\Delta k) - \sin(2\Delta k)\right] \tag{4.2}$$

is the modified wave number.

Next, consider the following fourth-order compact scheme (see Kopal [4], Orszag & Israeli [11], and Moin et al. [9]):

$$\frac{\delta u}{\delta x} = \frac{D_o u}{1 + \frac{1}{6}\Delta^2 D_+ D_-} \tag{4.3}$$

where D_o is the central difference operator.

$$D_o u_n = \frac{\left(u_{n+1} - u_{n-1}\right)}{2\Delta}$$

and D_+ and D_- are the forward and backward difference operators:

$$D_+ u_n = (u_{n+1} - u_n)/\Delta$$

$$D_- u_n = (u_n - u_{n-1})/\Delta$$

$$D_+ D_- u_n = (u_{n+1} - 2u_n + u_{n-1})/\Delta^2$$

This scheme was used in some of the calculations reported here, using the dynamical equations in primitive form. The above scheme is a three-point finite-difference scheme despite being fourth-order, and hence it appears attractive in boundary value problems with nonperiodic boundary conditions. However, the main disadvantage of this scheme in this case is that it requires an estimate of $\delta u/\delta x$ at the boundary. Here, x denotes the direction normal to the boundary.

Applying (4.3) to a Fourier wave, we obtain:

$$f'_j = i\tilde{k} f_j$$

where

$$\tilde{k} = \frac{\sin(k\Delta)}{\Delta}\left[\frac{3}{2 + \cos(k\Delta)}\right] \tag{4.4}$$

Finally, we have used the collocation or pseudo-spectral method (see Orszag [10] and Fox and Orszag [3]) in calculations using both primitive variable and vorticity equations. Applying this scheme to the simple Fourier wave discussed previously, we obtain:

$$f'_j = ikf_j \tag{4.5}$$

Figure 1 compares the modified wave numbers for $N = 16$ mesh points. It is clear that for a given number of mesh points, the ultimate accuracy can be obtained using the pseudo-spectral method; also, at high wave numbers, the compact scheme (4.3) is more accurate than the conventional fourth-order scheme (4.1). In this figure k'' is the modified wave number for the second-order difference operator, D_o.

5. NUMERICAL SOLUTION OF POISSON EQUATION

As was explained in §2, we obtain the pressure equation (2.10) by taking the numerical divergence of equation (2.5). This step must be done very carefully (see Kwak et al. [5] or Shaanan et al. [13]). One must set the pressure field at the current time step such that continuity is satisfied at the next time step. One way to achieve this goal is to use the same numerical differencing scheme for gradient and divergence operators. In general, however, this leads to a less accurate numerical scheme for the ∇^2 operator in the Poisson equation.

In the numerical simulation of the vorticity equation, we have to obtain the velocity field from the vorticity field in order to be able to advance in time. To do so, we will define a vector potential, ψ_k (see Lamb [6]), such that

$$\bar{u}_i = \epsilon_{ijk}\frac{\delta}{\delta x_j}\psi_k \tag{5.1}$$

ψ_i can be chosen to be solenoidal, i.e.,

$$\frac{\delta}{\delta x_i}\psi_i = 0 \tag{5.2}$$

Taking the numerical curl of (5.1) and using (5.2), we have

$$\frac{\delta}{\delta x_j}\frac{\delta}{\delta x_j}\psi_i = -\bar{\omega}_i \quad . \tag{5.3}$$

Solving the Poisson equation (5.3) and using (5.1), we get the velocity field from the vorticity field.

6. CONSERVATION PROPERTIES

As was pointed out by Phillips [12], numerical integration of the finite-difference analog of the Navier-Stokes equations may introduce nonlinear instabilities if proper care is not taken. Arakawa [1], working with the two-dimensional vorticity equation, showed that by properly conserving vorticity, energy and enstrophy $(\omega_i\omega_i)$, these instabilities disappeared. Lilly [8], working with the primitive variables, developed a spatial-differencing scheme that conserves momentum and energy. By conservation we mean that, in the absence of external forces and viscous dissipation, the only way that the momentum and kinetic energy in a control volume can change is by flow through the surface. This property must be retained in the numerical spatial-differencing method. In the simple case of periodic boundary conditions, we have:

$$\frac{\partial}{\partial t}\int_D \bar{u}_i\,dV = 0 \quad \text{(i.e., momentum conservation)} \tag{6.1}$$

$$\frac{\partial}{\partial t}\int_D \frac{1}{2}\,\overline{u}_i\overline{u}_i\,dV = 0 \quad \text{(i.e., energy conservation)} \tag{6.2}$$

It is usually easy to devise a numerical approximation to the dynamical equations in primitive form that conserves momentum, i.e., summation over the flow volume of the approximated equations would give the discrete equivalent of Eq. (6.1). However, the difficulties arise when trying to show energy conservation, since in general the identity

$$u_i \frac{\partial}{\partial x_j} u_i = \frac{\partial}{\partial x_j}\left(\frac{1}{2}\, u_i u_i\right) \tag{6.3}$$

does not hold in finite-difference form.

Writing the equations of motion in the following form (Tennekes and Lumley [15]):

$$\frac{\partial}{\partial t} u_i + u_j\left(\frac{\partial u_i}{\partial x_j} - \frac{\partial u_j}{\partial x_i}\right) = -\frac{\partial}{\partial x_i}\left(\frac{p}{\rho} + \frac{1}{2}\, u_i u_i\right) \tag{6.4}$$

$$\frac{\partial}{\partial x_i} u_i = 0 \tag{6.5}$$

and integrating over the flow volume, we get Eq. (6.1) by using integration by parts and the continuity equation (6.5). Multiplying Eq. (6.4) by u_i, the nonlinear terms on the left-hand side of the equation sum to zero by symmetry; then, integrating over the flow volume, we get Eq. (6.2) by using integration by parts and the continuity equation (6.5). We notice that written in the form shown by Eq. (6.4), we did not need the identity (6.3) to show energy conservation from the dynamical equations in primitive form; the conservation properties were obtained by making use of only integration by parts and the continuity equation.

Consider the numerical approximation of Eqs. (6.4) and (6.5);

$$\frac{\partial}{\partial t} u_i + u_j\left(\frac{\delta u_i}{\delta x_j} - \frac{\delta u_j}{\delta x_i}\right) = -\frac{\delta}{\delta x_i}\left(\frac{p}{\rho} + \frac{1}{2}\, u_i u_i\right) \tag{6.6}$$

$$\frac{\delta}{\delta x_i} u_i = 0 \tag{6.7}$$

where we are using $\delta/\delta x_i$ to denote the numerical approximations to the partial derivatives $\partial/\partial x_i$, and the same approximations are used in both equations (6.6, 6.7) for any given independent variable. In order to have long-term integration stability, Eq. (6.6) should numerically conserve momentum and energy.

If we follow the steps used in deriving the conservation properties from Eqs. (6.4) and (6.5), one realizes that the conservation properties will follow if we can establish numerical summation by parts. Consider the one-dimensional case, where we have, for periodic boundary conditions,

$$\int u(x)\,\frac{\partial}{\partial x} f(x)\,dx = -\int f(x)\,\frac{\partial}{\partial x} u(x)\,dx$$

The numerical analog of the above equation is:

$$\sum_{n=o}^{N-1} u(n)\,\frac{\delta}{\delta x_n} f(n) = -\sum_{n=o}^{N-1} f(n)\,\frac{\delta}{\delta x_n} u(n) \tag{6.8}$$

Expanding $u(n)$ in Fourier series, we get:

$$u(n) = \sum_{J=-N/2}^{N/2-1} \hat{u}(J)\,\exp(2\pi i J n/N)\ ;\ n = 0,1,\ldots,N-1$$

$$\hat{u}(J) = \sum_{n=o}^{N-1} u(n)\,\exp(-2\pi i J n/N)\ ;\ J = -\frac{N}{2},\ldots,\frac{N}{2}-1$$

Also,

$$\frac{\delta}{\delta x_n} f(n) = \sum_{J=-N/2}^{N/2-1} i k^*(J)\left\{\frac{1}{N}\sum_{n'=o}^{N-1} f(n') \cdot \exp(-2\pi i J n'/N)\right\}\exp(2\pi i J n/N) \tag{6.9}$$

where $k^*(J)$ is the modified wave number. $k^*(J)$ depends on the finite-difference scheme used, and examples have already been given in §4.

Substituting Eq. (6.9) into the left-hand side of Eq. (6.8) yields:

$$\sum_{n=o}^{N-1} u(n)\,\frac{\delta}{\delta x_n} f(n) = \frac{1}{N}\sum_{n=o}^{N-1}\sum_{n'=o}^{N-1}\sum_{J=-N/2}^{N/2-1} i k^*(J) u(n) \cdot f(n')\exp(-2\pi i J n'/N)\exp(2\pi i J n/N)$$

Now, changing the summation index in the last sum from J to $-J$, we see that this expression will agree with the right-hand side of Eq. (6.8), provided

$$k^*(J) = -k^*(-J) \tag{6.10}$$

$$k^*\left(-\frac{N}{2}\right) = 0 \tag{6.11}$$

Condition (6.10) is satisfied by all the methods under consideration, and $k^*(-N/2) = 0$ is true for the finite-difference methods (4.2) and (4.4). The pseudo-spectral method cannot differentiate between $f = \exp(i\pi x/\Delta)$ and $f = \exp(-i\pi x/\Delta)$, and, due to this confusion at $J = -N/2$, $k(-N/2)$ is set equal to zero for the pseudo-spectral method. Hence, summation by parts is obtained when (6.10) and (6.11) hold. Now, summing Eq. (6.6) over all mesh points, using the generalization of (6.8) to three dimensions and using Eq. (6.7) will yield the numerical equivalent of (6.1). Multiplying Eq. (6.6) by u_i, the nonlinear term in the left-hand side of (6.6) will sum to zero by symmetry; then summing over all mesh points, using as before the three-dimensional generalization of (6.8) and (6.7) will yield the numerical equivalent of Eq. (6.2).

Now that we have shown that the numerical approximation of the governing equations of motion written in the form (6.6) and (6.7) conserves the required properties, we would like to obtain the difference approximation to the vorticity equation.

In order to insure that the numerical vorticity equations are equivalent to the numerical primitive equations, the numerical curl must be applied to Eq. (6.6). Using the fact that numerically Div(curl $\vec{v}$) and Curl(grad S) will be identically equal to zero, if for any given direction the same numerical approximation is used for all operators $(\nabla_o, \nabla x, \nabla)$, and applying the numerical curl to Eq. (6.6) yields:

$$\frac{\partial}{\partial t}\omega_i + \frac{\delta}{\delta x_j}(u_j\omega_i - u_i\omega_j) = 0 \tag{6.12}$$

It is in this form that we will approximate the vorticity equations.

Note that by summing Eq. (6.10) over all grid points we get:

$$\frac{\partial}{\partial t}\sum_{\substack{\text{all grid}\\ \text{points}}} \omega_i = 0$$

Hence in the form (6.6), the primitive equations also conserve vorticity.

7. TIME DIFFERENCING

To advance time, a second-order Adams-Bashforth method was used. It has been shown by Lilly [8] that this method is weakly unstable, but the total spurious computational production of kinetic energy is small, and in problems with turbulence decay, it causes no problem.

The Adams-Bashforth formula for $\bar{u}_i$ at time step $n + 1$ is

$$\bar{u}_i^{n+1} = \bar{u}_i^{n} + \Delta t \left(\frac{3}{2} H_i^{(n)} - \frac{1}{2} H_i^{(n-1)}\right) + O(\Delta t^3)$$

where

$$H_i = \overline{-\bar{u}_j\left(\frac{\partial \bar{u}_i}{\partial x_j} - \frac{\partial \bar{u}_j}{\partial x_i}\right)} - \frac{\partial \bar{P}}{\partial x_i} - \frac{\partial}{\partial x_j} \tau_{ij}$$

Higher-order methods could be used, but there is no incentive to do so.

8. DECAY OF ISOTROPIC TURBULENCE

In order to assess the computational methods discussed earlier, we used them to simulate the simplest flow in turbulence, namely, the decay of homogeneous isotropic turbulence. The experimental grid turbulence of Comte-Bellot and Corrsin [2] were used as the "target" for our numerical predictions. This experiment approximates homogeneous isotropic turbulence, when viewed in a coordinate frame moving with the mean flow velocity.

Since the computation will treat the filtered field, we used a flow field which had the same filtered energy spectrum as that of the above experiment for our initial condition. The initial field was also constructed to be divergence-free and otherwise random.

The residual stress model constant (see (2.9)) was obtained by matching the computational rate of filtered energy decay to that of the experiment, as judged by consideration of the slope of the curve (Fig. 2). The values of the constants obtained using different numerical schemes were, in most cases, within ten per cent of each other.

9. RESULTS

The results presented here are the energy spectra obtained at the dimensionless time $U_0t/M = 98$, where $U_0 = 10$ m/sec is the experimental free-stream air speed, $M = 5.08$ cm is the size of the experimental turbulence-generating grid, and t is the time in seconds. The initial conditions were based on the data at $U_0t/M = 42$. Fig. 3 shows the energy spectrum obtained from pseudo-spectral calculations of the primitive equations using 16^3 mesh points. If the experimental curve is considered as the "target", we see that for $1 \leq k \leq 2.5$ the computed results are lower than the experimental values. Evidently the subgrid scale model takes too much energy from these wave numbers and too little from the other wave numbers. In this case, we used the pseudo-spectral approximation to calculate the subgrid scale terms as well as the other terms; thus the problem must lie with the subgrid scale model, the only significant approximation in the calculation. Fig. 4 shows the energy spectrum obtained using second-order central differencing to approximate all the derivatives appearing in the subgrid scale model. It can be seen that the computational points follow the experimental curve closely, except for a small accumulation of energy at the extreme end of the spectrum which was also present, to a lesser extent, in Fig. 3. One way to look at the difference between the results demonstrated by Figs. 3 and 4 is to regard them as corresponding to two different subgrid scale models. Although they are both versions of vorticity model (Eq. (2.9)), the second-order scheme produces a different approximation than does the pseudo-spectral method, due to truncation error. In this case, it turns out that the second-order approximation represents a subgrid scale model which does a better job in terms of agreement with the experiment.

Figure 5 shows the energy spectrum obtained from 32^3 pseudo-spectral calculations with the second-order differenced subgrid scale model. We see that the agreement with the experiment is quite good.

Figures 6 and 7 show the energy spectra obtained from the 16^3 compact scheme (Eq. (4.3)) calculations. In the result shown in Fig. 6, the compact scheme is used to compute the subgrid scale model (in addition to other quantities), while in the result shown in Fig. 7, the second-order scheme is used to calculate the subgrid scale terms. Again, we see that the second-order differenced model does a better job in terms of agreement with the experiment.

Figures 8-11 show the energy spectra obtained by using the dynamical vorticity equations. Fig. 8 is obtained by fourth-order finite-differencing the vorticity equation, using the curl of the vorticity model, Eq. (3.2), for the subgrid scale, with a 16^3 mesh. We obtain a good agreement with the experimental results up to wave number 2.5, after which the inaccuracy of the fourth-order differencing begins to take effect. This success is expected, since fourth-order finite-differencing the primitive equations produced good agreement with the filtered experimental results using the primitive variable version of this model (Kwak et al. [5]).

Figures 9 and 10 are results from a 16^3 computation using the pseudo-spectral method, and Eq. (3.3) as the subgrid scale model. We note the same behavior in Fig. 9 as that of Fig. 3; the computed spectrum falls lower than the experimental spectrum, indicating that the subgrid scale model using pseudo-spectral method to compute the spatial derivatives damps too much energy in the wave number range 1-2.5. Using second-order finite-differencing to compute the partial derivatives in the subgrid scale model, Eq. (3.3), we note a significant improvement in the computed spectrum. These results are consistent with the results obtained using the primitive variables. Fig. 11 shows the energy spectrum obtained from a 32^3 pseudo-spectral calculation using second-order finite-differencing to compute the partial derivatives in the subgrid scale model, Eq. (3.3). The results are similar to the 16^3 results.

Throughout this investigation, the Reynolds number based on Taylor's microscale, R_λ, was approximately 58.

10. CONCLUSIONS

This paper is aimed at providing understanding of what is necessary to compute at least simple turbulent flows, and provides the basis for attempting computation of more complex flows by large-eddy simulation.

Both the primitive variable and vorticity equations have been shown to provide satisfactory bases for the simulation of homogeneous isotropic turbulence; we can detect no significant difference in the results obtained with the two sets of equations for the cases treated. The choice of method is thus dictated by the particular problem to be treated. We believe that the vorticity approach is probably better for free shear flows, while the primitive equations are likely better for bounded flows.

As in our previous work, proper treatment of the $\overline{u_i u_j}$ term that arises in filtering the equations is found to be very important. However, the use of Fourier transform methods allows both more accurate and faster treatment of this term. This is a definite improvement over the earlier treatment (involving the "Leonard" stresses), which we believe should be used only when the use of transform methods is impossible.

A general approach to the derivation of conservation properties which is applicable to any numerical problem in incompressible fluid mechanics has been given and should simplify the analysis of numerical schemes.

We found, in agreement with earlier results, that, for the calculations treated herein, the optimum subgrid scale constant depends slightly on the numerical method used. The variation, which is not surprising, is in most cases only about ten percent and is not likely to have significant effects on the results computed in shear flows. The use of Fourier spatial differencing has allowed us to look more carefully at the subgrid scale model, and it was found that replacing exact derivatives with second-order differences (which is roughly equivalent to averaging the model spatially) produces improved behavior of the spectrum.

ACKNOWLEDGMENT

This work has been carried out in cooperation with the Ames Laboratory, NASA, under Contract NASA-NgR-05-020-622.

REFERENCES

1 Arakawa, A., "Computational Design for Long-Term Numerical Integration of the Equations of Fluid Motion: I. Two-Dimensional Incompressible Flow," Journal of Computational Physics, Vol. 1, No. 1, Aug. 1966, pp. 119-143.

2 Comte-Bellot, G., and Corrsin, "Simple Eulerian Time Correlation of Full and Narrow-Band Velocity Signals in Grid-Generated 'Isotropic' Turbulence," Journal of Fluid Mechanics, Vol. 48, Part 2, 1971, p. 273.

3 Fox, D. G., and Orszag, S. A. C., "Pseudospectral Approximation to Two-Dimensional Turbulence," Journal of Computational Physics, Vol. 11, No. 4, Apr. 1973, pp. 612-619.

4 Kopal, Z., Numerical Analysis, 2nd Ed., John Wiley and Sons, N. Y., 1961.

5 Kwak, D., Reynolds, W. C., Ferziger, J. H., "Three-Dimensional Time-Dependent Computation of Turbulent Flow," Report No. TF-5, May, 1975, Dept. of Mech. Engrg., Stanford University.

6 Lamb, H., Hydrodynamics, Dover, 1932, p. 208.

7 Leonard, A., "On the Energy Cascade in Large-Eddy Simulations of Turbulent Fluid Flows," Adv. in Geophysics, Vol. 18A, 1974, p. 237.

8 Lilly, D. K., "On the Computational Stability of Numerical Solutions of Time-Dependent Nonlinear Geophysical Fluid Dynamic Problems," Monthly Weather Review, Vol. 93, No. 1, Jan. 1965, pp. 11-26.

9 Moin, P., Mansour, N. N., Mehta, U. B., Ferziger, J. H., Reynolds, W. C., "Improvements in Large-Eddy Simulation Technique: Special Methods and High-Order Statistics," Report No. TF-10, Mech. Engrg. Dept., Stanford University, to be published.

10 Orszag, S. A., "Comparison of Pseudospectral and Spectral Approximation," Studies in Applied Mathematics, Vol. LI, No. 3, Sept. 1973, pp. 253-259.

11 Orszag, S. A., Israeli, M., "Numerical Simulation of Viscous Incompressible Flows," Annual Rev. Fluid Mechanics, Vol. 6, 1974, p. 281.

12 Phillips, N. A., "An Example of Nonlinear Computational Instability," The Atmosphere and Sea in Motion, Rockefeller Institute Press, New York, 1959, pp. 501-504.

13 Shaanan, S., Ferziger, J. H., Reynolds, W. C., "Numerical Simulation of Turbulence in the Presence of Shear," Report No. TF-6, Dept. of Mech. Engrg., Stanford University, 1975.

14 Smagorinsky, J., "General Circulation Experiments with the Primitive Equations. I. The Basic Experiment," Monthly Weather Review, Vol. 91, p. 99.

15 Tennekes, H., Lumley, J. L., A First Course in Turbulence, M.I.T. Press, 1972, p. 77.

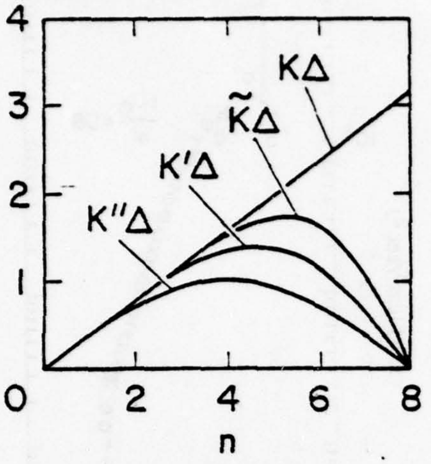

Fig. 1. Comparison of modified wave numbers K = 2πn/(NΔ).

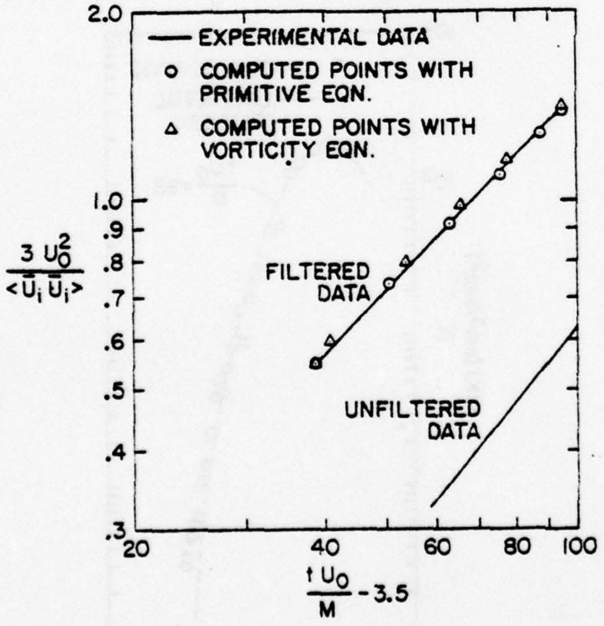

Fig. 2. Decay of mean square filtered velocity for 16 × 16 × 16 mesh. < > : average over all space.

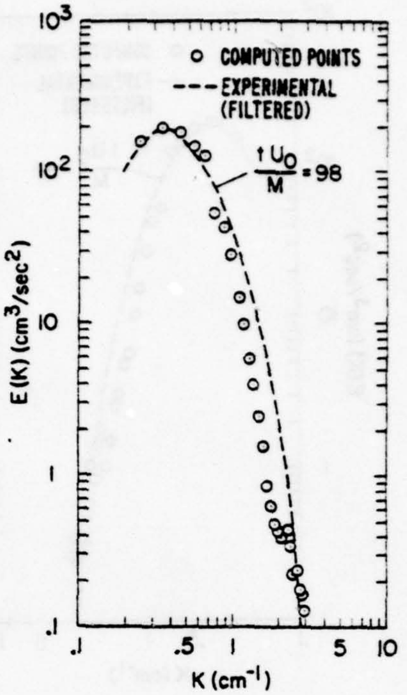

Fig. 3. Filtered energy spectra. Pseudo-spectral calculation with 16^3 mesh. $C_v = 0.213$, $\Delta = 1.5$ cm.

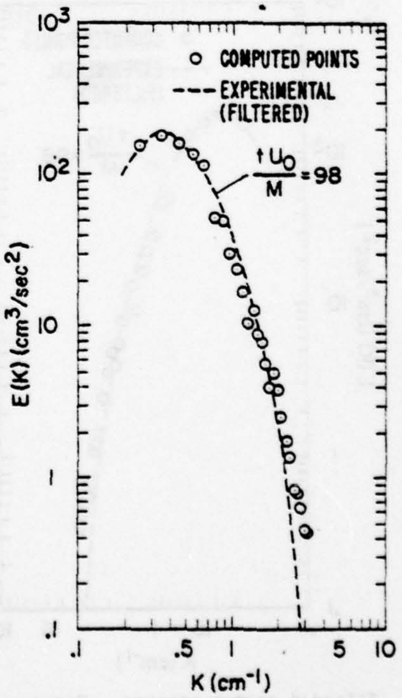

Fig. 4. Filtered energy spectra. Pseudo-spectral calculation with 16^3 mesh; 2nd-order differencing for subgrid scale term. $C_v = 0.22$, $\Delta = 1.5$ cm.

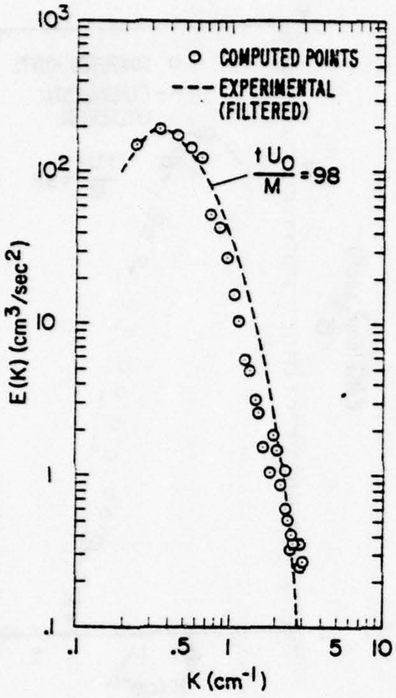

Fig. 5. Filtered energy spectra. Compact scheme (Eq. (4.3)) with 16^3 mesh. $C_v = 0.215$. $\Delta = 1.5$ cm.

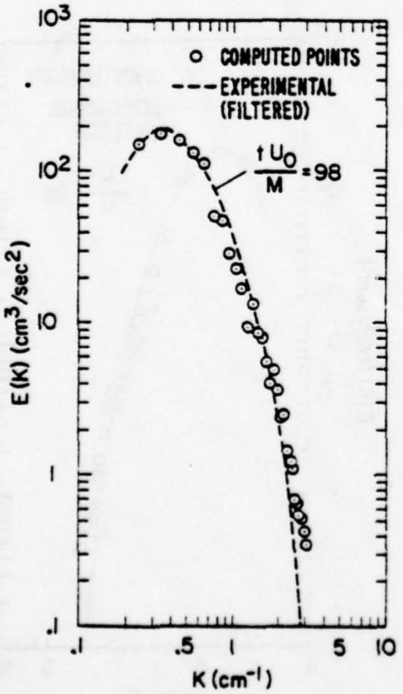

Fig. 6. Filtered energy spectra. Compact scheme (Eq. (4.3)) with 16^3 mesh; 2nd-order differencing for subgrid scale model. $C_v = 0.23$, $\Delta = 1.5$ cm.

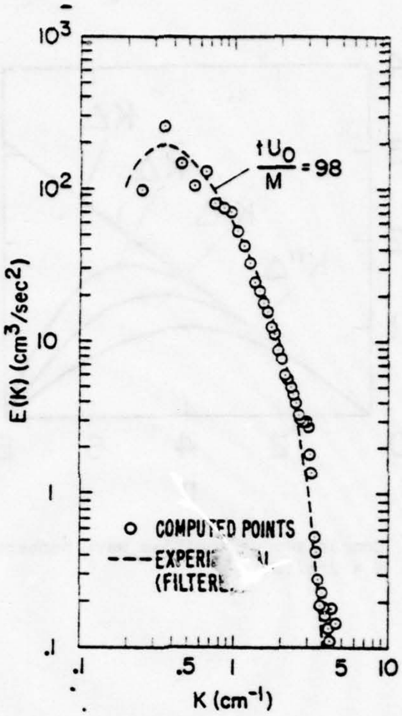

Fig. 7. Filtered energy spectra. Pseudo-spectral calculations with 32^3 mesh; 2nd-order differencing for S.G.S. $C_v = 0.19$. $\Delta = 1.0$ cm.

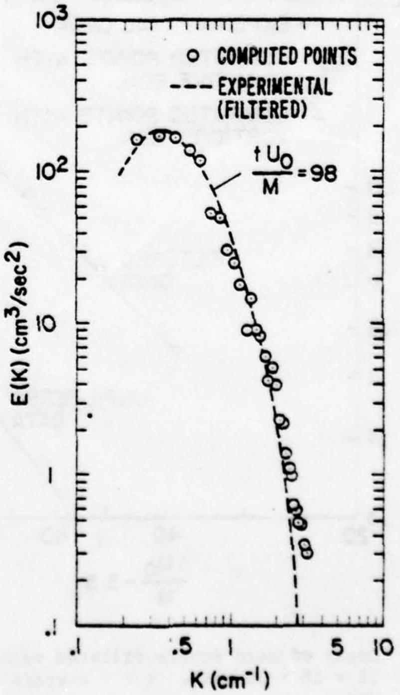

Fig. 8. Filtered energy spectra. 4th-order differencing (Eq. (4.1)) with 16^3 mesh; curl of vorticity model for S.G.S. $C_v = 0.235$. $\Delta = 1.5$ cm.

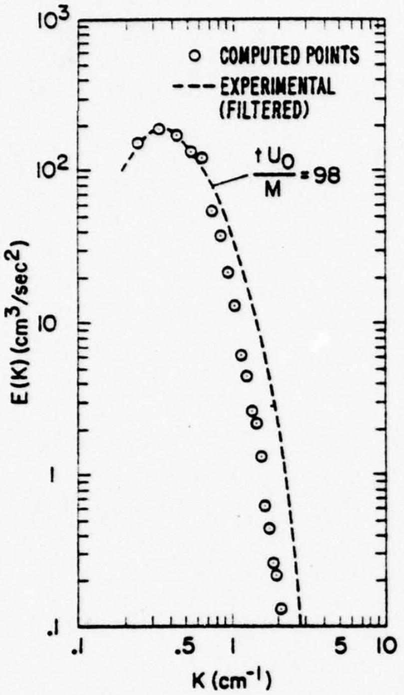

Fig. 9. Filtered energy spectra. Pseudo-spectral computation with 16^3 mesh; subgrid scale model (Eq. (3.3)). $C_v = 0.186$, $\Delta = 1.5$ cm.

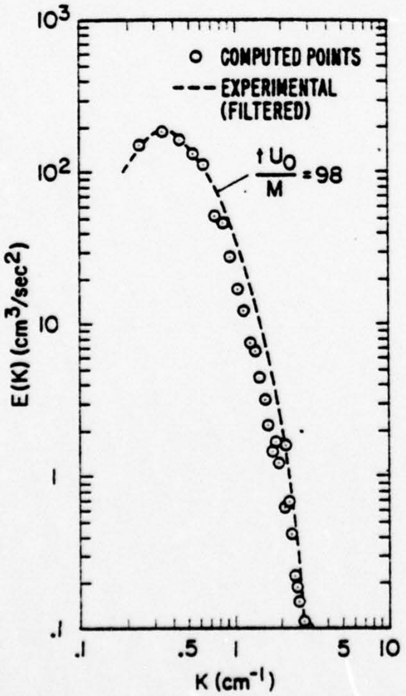

Fig. 10. Filtered energy spectra. Pseudo-spectral computation with 16^3 mesh; 2nd-order differencing for S.G.S. (Eq. (3.3)). $C_v = 0.188$, $\Delta = 1.5$ cm.

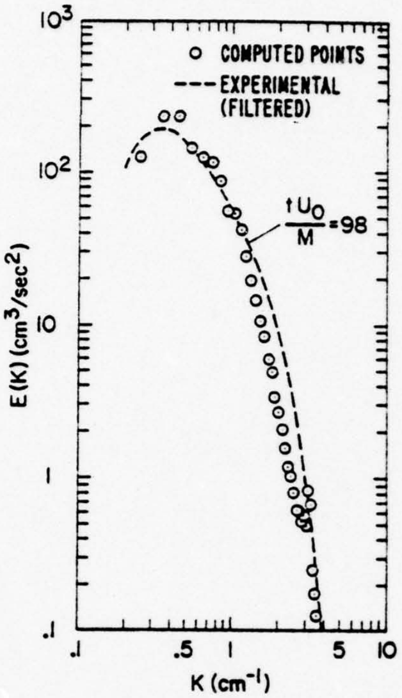

Fig. 11. Filtered energy spectra. Pseudo-spectral calculation with 32^3 mesh; 2nd-order differencing for S.G.S. (Eq. (3.3)). $C_v = 0.188$, $\Delta = 1.5$ cm.

LARGE EDDY SIMULATION OF HOMOGENEOUS ISOTROPIC TURBULENCE

by

J. H. Ferziger
U. B. Mehta
and
W. C. Reynolds

Department of Mechanical Engineering
Stanford University
Stanford, California 94305

ABSTRACT

This paper presents results from a comprehensive investigation of large-eddy simulations of homogeneous isotropic turbulence. Calculations have been made using 16^3 and 32^3 grid meshes, a number of flowfield filters, and two simple subgrid scale turbulence models. Particular attention has been paid to the degree of isotropy and the ability of the approach to predict higher-order statistical quantities (skewness and flatness). Directions for needed improvement in the simulation approach are indicated, and a plea is made to experimenters to process their data in a way which will facilitate comparison with large eddy simulations.

1. INTRODUCTION

Large eddy simulation is a three-dimensional time-dependent computational method in which one attempts to "capture" the large scale turbulent motions and model the small ones. This is necessary because computer resource availability limits the wavenumber range that can be covered in a simulation. One filters out the small scales, which necessarily removes some information about the flow field. This paper, which follows our earlier reports [1,2], further explores the sensitivity of various predicted quantities to the parameters of the large eddy simulation for homogeneous isotropic turbulence. Here we use the numerical technique of Kwak [1], with modifications to be mentioned. For evaluation of alternative methods, see our companion paper [3]. More details will be given in a forthcoming report [4].

Kwak [1] and Shaanan [2] each computed only one realization of homogeneous isotropic turbulence. When repeats of their calculations were made with different random initial fields, important differences were found in higher-order statistical quantities (e.g., skewness). Quantities closely related to the skewness play a key role in determining transfers among the Reynolds stress components, and it is important that the large eddy simulation predict them accurately. We therefore made a detailed study of how various computed quantities are affected by changes in the computational method and input parameters. This paper and Ref. [3] give selected results of that study.

In § 2 we review the analytical background of large-eddy simulation and discuss the selection of computational parameters; § 3 examines the effects on low order statistical quantities, energy and spectrum; § 4 discusses the effects on other statistical quantities. In § 5 we evaluate the basic approach, and made recommendations for future development.

2. MATHEMATICAL BACKGROUND

Following Leonard [5], the filtered value of a flow field variable $u(\underline{x},t)$ is defined by

$$\bar{u}(\underline{x},t) = \int_D G(\underline{x}-\underline{x}')u(\underline{x}',t)dx' \tag{2.1}$$

where the integration is carried out over the entire flow field. The filter $G(\underline{r})$ should be chosen to retain the large scale behavior of u while removing the small scale variations.

Computationally it is more convenient to compute the filtered value of a quantity by Fourier transforming (2.1), since $\hat{\bar{u}} = \hat{u}(k)\hat{G}(k)$. Thus, it is really the Fourier transform of the spatial filter that is of most interest. In [1,2] we claimed to use the Gaussian filter,

$$G(\underline{r}) = A \cdot \exp(-6r^2/\Delta^2) \tag{2.2}$$

where the factor 6 appears for convenience, and the constant A is adjusted for proper normalization. The exact continuous Fourier transform of (2.2) is a Gaussian in wavenumber space,

$$\hat{G}(\underline{k}) = e^{-k^2\Delta^2/24} \tag{2.3}$$

However, in numerical calculations the variables are defined only on a discrete grid and a discrete Fourier transform must be used. The discrete Fourier transform of (2.2) is not exactly a Gaussian in k-space; Fig. 1 compares the discrete transform of (2.2) with (2.3); (2.3) was used in [1,2].

Filters rejected in our earlier work are the "top hat" or "box" filters. The x-space top hat filter is

$$G = \begin{cases} 1/\Delta^3 & |x_i - x_i'| < \Delta/2 \quad i = 1,2,3 \\ 0 & \text{otherwise} \end{cases} \tag{2.4}$$

while the k-space top hat filter is a sharp-cutoff in wavenumber space:

$$\hat{G}(\underline{k}) = \begin{cases} 1 & |k_i| < k_c \\ 0.5 & |k_i| = k_c \\ 0 & |k_i| > k_c \end{cases} \quad i = 1,2,3 \tag{2.5}$$

Equation (2.4) was rejected because its Fourier transform $(k\Delta/2)^{-3}\sin^3(k\Delta/2)$ oscillates at high

PRECEDING PAGE BLANK-NOT FILMED

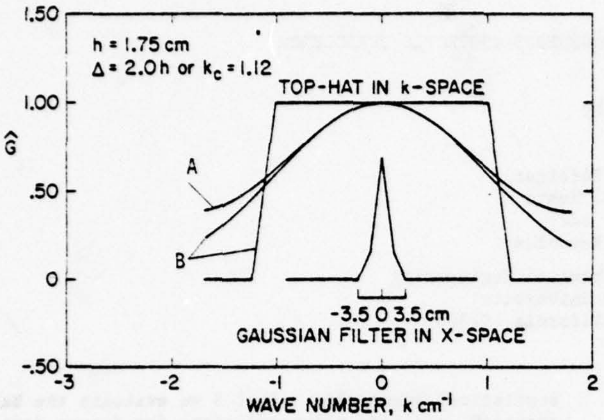

Fig. 1 Filters and their transforms;
(A) Discrete Fourier transform of Eqn. (2.2)
(B) Continuous Fourier transform

wavenumber and does not remove small scales sufficiently well; this is the filter implicitly used by those who have employed "box averages." Filter (2.5) retains all of the Fourier modes for $|k_i| < k_c$, and hence allows direct comparison of the energy spectrum for low wavenumbers with experiments. The spectral method of Orszag [6] is equivalent to the use of (2.5) with $k_c = \pi/h$, the highest wavenumber that can be supported by a mesh of size h. However, this filter poses problems unless special provisions are made for handling aliasing problems. There is no reason why k_c cannot be smaller than π/h, and if $k_c \leq 2\pi/(3h)$ the aliasing problem disappears entirely.

A related problem discussed in [1,2] revolves around the "Leonard stresses," $\overline{\bar{u}_i\bar{u}_j} - \bar{u}_i\bar{u}_j$, which arise when the Navier-Stokes equations are filtered. In [1,2] we approximated these using a Taylor series expansion of the $\underline{\bar{u}}$ field; (2.5) cannot be used in this approach. However, if instead one simply computes $\overline{\bar{u}_i\bar{u}_j}$ by computationally filtering the product $\bar{u}_i\bar{u}_j$ as described above, no such difficulty is encountered, and <u>any</u> filter can be used. This is the procedure we now employ.

The equations governing the large eddy field are obtained by filtering the (incompressible) Navier-Stokes equations, using $\underline{u} = \underline{\bar{u}} + \underline{u}'$,

$$\dot{\bar{u}}_i + (\overline{\bar{u}_i\bar{u}_j})_{,j} = -\bar{P}_{,i} + \nu\nabla^2\bar{u}_i - \tau_{ij,j} \tag{2.6}$$

Here an overdot denotes time differentiation, indices after commas denote the directions of partial differentiation, and the subscript summation convention is employed. Also

$$\tau_{ij} = R_{ij} - R_{kk}\delta_{ij}/3 \tag{2.7a}$$

$$\bar{P} = \bar{p}/\rho + R_{kk}/3 \tag{2.7b}$$

$$R_{ij} = \overline{u_i'u_j'} + \overline{u_j'\bar{u}_i} + \overline{u_i'\bar{u}_j}$$

The τ_{ij} represent the (negative) subgrid scale stresses, which must be modeled.

We have used two subgrid scale stress models of the form

$$\tau_{ij} = -2\nu_T\bar{S}_{ij} = -\nu_T(\bar{u}_{i,j}+\bar{u}_{j,i}) \tag{2.8}$$

The first is Smagorinsky's model [7]

$$\nu_T = (C_s\Delta)^2(2\bar{S}_{ij}\bar{S}_{ij})^{1/2} \tag{2.9}$$

The second uses rotation in place of strain rate,

$$\nu_T = (C_v\Delta)^2(\bar{\omega}_i\bar{\omega}_i)^{1/2} \tag{2.10}$$

where $\underline{\omega}$ is the vorticity of the filtered field. The constant (C_s or C_v) is the sole empirical constant in the simulation, and is adjusted to give the proper rate of energy decay for isotropic turbulence. Equation (2.10) may be of interest for eventual use in flows with irrotational regions (e.g., above a superlayer), which should be devoid of small-scale stresses. When using the top-hat k-space filter (2.5), we take $\Delta = \pi/k_c$.

In the work reported here we solved these equations using Kwak's [1] fourth-order energy-conserving finite difference method. Velocities are advanced in time explicitly using a second-order Adams-Bashforth method and the pressure is adjusted to maintain $\bar{u}_{i,i} = 0$ as required by continuity. This requires solution of a Poisson equation for $\bar{P}$. The only substantive changes from [1] are in the handling of the Leonard terms, as described above, and the inclusion of the viscous term (which is of minor importance).

A number of the simulation parameters affect the results. Those considered here are:

a) The number of grid points in each direction, N. We would like to use the smallest number of points that will yield an acceptable solution. FFT requirements dictate that N be a power of 2, and we have used $N = 16$ and 32.
b) The width of the filter, Δ, or in the case of (2.5) the cutoff wavenumber k_c. Here we seek an optimum. A large value of Δ (low k_c) averages away all of the significant information, leaving a meaningless computation. A small value of Δ (high k_c) means that excessive resources will be devoted to computing small scales. The optimum Δ (or π/k_c) should be related to the important turbulent length scale for the flow at hand, and hence will depend upon the flow being considered.
c) The computational mesh size, h. This must be such that all waves of importance in the filtered field can be accurately represented and differentiated.
d) The choice of filter; discussed above.
e) The treatment of the Leonard stresses; discussed above.
f) The subgrid scale model; we have used only algebraic models (2.9) and (2.10) to date, but more complex models could be employed.
g) Numerical methods; see [3] for further discussion.

In order to guide the selection of these parameters we have used a hierarchy of test levels:

a) Overall energy decay in isotropic turbulence. Although the model constant is adjusted to fit the decay rate, the <u>shape</u> of the decay curve should be predicted well.
b) The (filtered) energy spectrum. A calculation begun with the proper initial spectrum should produce the proper spectrum at a later time.
c) Higher-order statistics; from a practical point of view we are limited to those measured experimentally (usually only

skewness and flatness). It would be very rewarding if the computation could correctly predict the results of the experiments. In making comparisons with experiments, the major difficulty is in accounting for the filtering.

We have done a number of computations with various sets of parameters, and will look at these with respect to the above criteria in the following sections.

All calculations were carried out on a CDC 7600 computer. A typical calculation takes about 2 sec and 17 sec per time step, respectively, for 16^3 and 32^3 calculations. We have used of the order of 100 time steps.

3. ENERGY DECAY RATES AND SPECTRA

We have applied the approach outlined in § 2 to the decay of homogeneous isotropic turbulence. The experimental grid turbulence (2" mesh) data of Comte-Bellot and Corrsin [9] were used as the target. Periodic boundary conditions were used; this causes the motions on one side of the computational domain to be exactly correlated with those on the opposite face, which is of course artificial, but is a reasonable computational approach provided that the motions at the middle of the computational domain are uncorrelated from those at the ends. The calculations were started at point $T = U_oT/M = 42$ of [9] with a random field constructed to be divergence-free and to match the <u>filtered</u> experimental spectrum. The subgrid scale model constant (C_s or C_v) <u>was</u> determined by matching the computed energy ($\overline{u_i u_i}$ averaged over the computational field) to the <u>*filtered*</u> *experimental energy* at $T = 98$. The three-dimensional energy spectrum function $E(k)$ was calculated by summing the energy in shells in k-space (using the discrete Fourier representation of the $\underline{u}$ field) and then determining the energy per unit wavenumber. The numbers of points in each shell are shown by the histogram in Fig. 2. The parameters used are listed in Table 1. The number of grid points in each direction (N), the grid spacing (h), and the averaging interval (Δ) or the cut-off wavenumber (k_c) were the same in all three directions.

The effect of filtering, for the k-space top hat filter (2.5), is shown in Fig. 2. For the range of parameters that we were able to consider, the filtered field captures only about half of the total turbulence energy. This poses a problem when comparisons with experiments are to be made. Comparisons with properties that are sensitive to the small-scale field are impossible to make.

In flows of practical interest, quantities of engineering importance are low-order statistical quantities, i.e., skin friction, heat transfer, etc. The influence of the moderate-scale motions rejected by the filtering on these low-order quantities remains to be investigated for technically interesting flows. It may be that the large-scale motions which <u>are</u> correctly captured by large-eddy simulation suffice to predict these quantities. On the other hand, if it turns out that the moderate scales make important contributions to skin friction, heat transfer, etc., then it will be necessary to develop more complete subgrid scale models.

The evolution of the filtered spectrum without the subgrid scale terms is shown in Fig. 3. An energy build-up occurs at high wavenumber, and therefore it is essential that some subgrid scale model be included in any large eddy simulation.

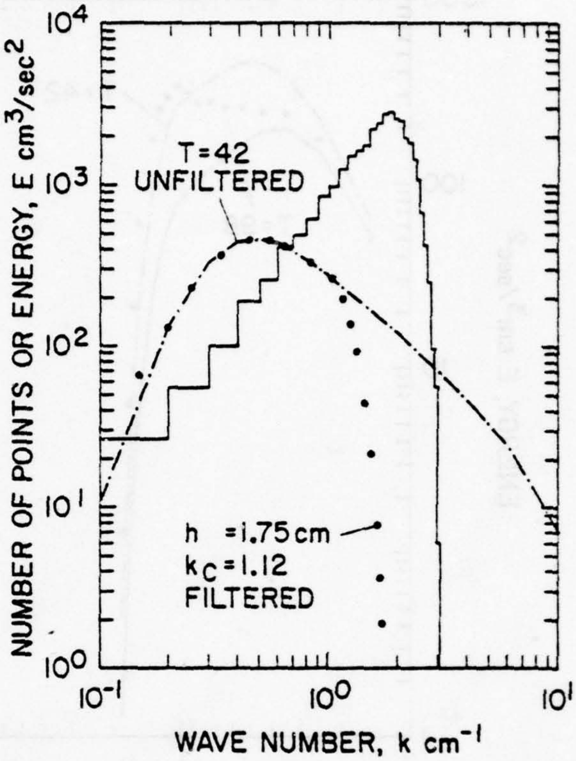

Fig. 2. Initial spectrum and wavenumber histogram showing number of Fourier modes in each spherical shell of thickness $\Delta k = 0.1$ cm^{-1}, for $N = 32$.

Table 1. Variation of Model Constant with Grid Size and Filter.

No.	Filter	h,cm	Δ/h	k_c	Model	C
16^3 runs						
1	CG	1.5	1.8	--	SM	0.238
2	CG	2.0	2.0	--	SM	0.230
3	DG	1.5	1.5	--	SM	0.231
4	DG	1.5	1.8	--	SM	0.226
5	DG	1.5	2.0	--	SM	0.222
6	DG	2.0	2.0	--	SM	0.225
7	THK	1.5	2.0	1.047	SM	0.199
8	THK	1.5	1.6	1.309	SM	0.213
9	THK	2.0	1.6	0.982	SM	0.223
10	THK	2.62	1.6	0.748	SM	0.236
11	DG	1.5	2.0	--	VM	0.251
12	DG	2.0	2.0	--	VM	0.254
32^3 runs						
13	DG	1.0	2.0	--	SM	0.213
14	DG	1.0	1.8	--	SM	0.214
15	DG	1.5	2.0	--	SM	0.219
16	DG	1.75	2.0	--	SM	0.222
17	THK	1.0	1.62	1.943	SM	0.188
18	THK	1.75	1.6	1.122	SM	0.215
19	DG	1.75	2.0	--	VM	0.252
20	THK	1.75	1.6	1.122	VM	0.243

DG - Discrete transform of spatial Gaussian
CG - Continuous transform of spatial Gaussian
THK - Continuous transform of k-space top-hat
SM - Smagorinsky's model
VM - Vorticity model

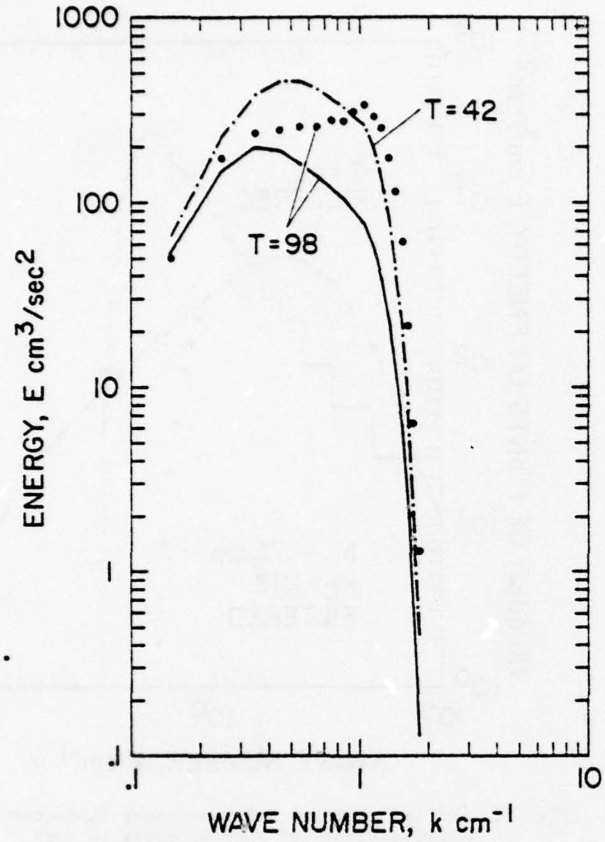

Fig. 3. Filtered energy spectrum evolution without subgrid scale model; N = 32, k_c = 1.12 cm^{-1}. Lines are experiments, dots are computed points.

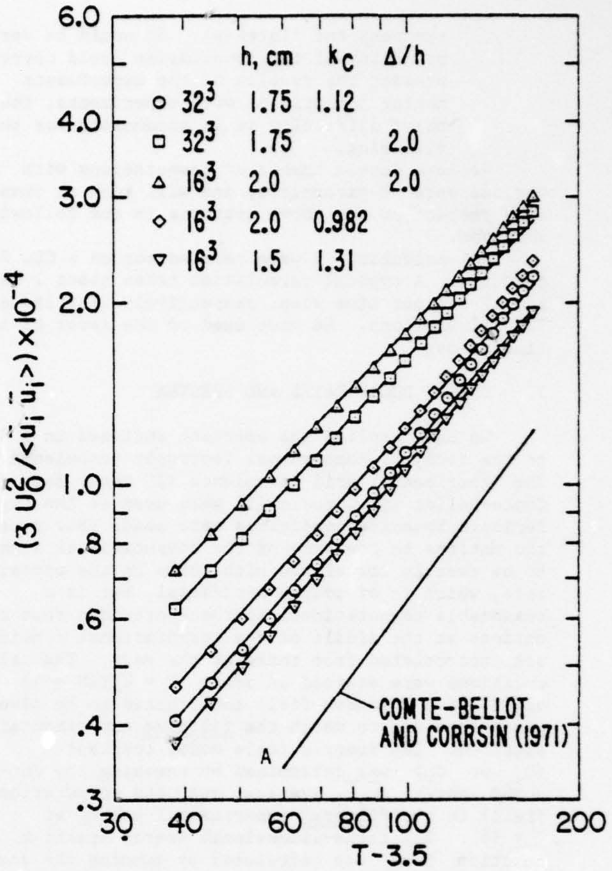

Fig. 4. Decay of filtered turbulent energy. Lines are filtered experiments, points are computations. Line A is unfiltered.

The decay of filtered turbulent energy with non-dimensional time T is shown in Fig. 4. Here the brackets < > denote an average over the entire computational field. Recall that the model constant was adjusted to give agreement at T = 98 ; the agreement at other times is quite good. Hence, it appears that even a simple subgrid model will give accurate predictions for the decay of the filtered energy.

The averaging interval Δ must be larger than the grid size h . We have explored a range of ratios Δ/h , and, as [1,2], find that Δ/h = 2 works well. Figures 5-7 show the predicted spectra for these tests. In these figures SM denotes Smagorinsky's model (2.9), and VM denotes the vorticity model (2.10). Figure 5 shows the rather surprising result that a 16^3 calculation does a remarkably good job of predicting the spectral evolution, provided that the computational parameters are carefully chosen. The top-hat filter allows a direct comparison between the computed results and the experiments at low wavenumbers, and does a better job of capturing the large-scale energy, which makes it the preferred filter from these points of view.

For each calculation the model constant was adjusted as described above. It is encouraging that there is only a slight dependence of the model constant upon the filter used, upon the number of mesh points, and upon the filter width or cut-off wavenumber. This has encouraged us to try the same models in other flows.

Examining the lower two sets of curves in Fig. 6 and 7, in the range $k > 2$ cm^{-1} , we see that the vorticity model removes less energy at high wavenumbers than Smagorinsky's model. But, in view of the uncertainty in the experimental spectrum, it is not possible to tell which of these models is better. Thus, the choice of model for the moment remains open.

In [1] and [2] we chose the grid size for a fixed N such that the maximum percentage of total energy was captured in the computations. Reference [1] used h = 1.5 cm and 1.0 cm respectively for N = 16 and 32 . We see from Figs. 5 and 6 that h = 2.0 and 1.75 cm respectively for N = 16 and N = 32 predict the energy spectra better. The reason for this will be discussed shortly.

4. OTHER STATISTICAL QUANTITIES

In the previous section we demonstrated that the spectrum can be predicted accurately. We would like to determine what else can be predicted using the simple subgrid scale models. In particular, it would be very desirable if quantities which govern transport rates in more complex flows could be correctly simulated.

The skewness of the velocity derivative is important as it is related to the inertial spectral transfer of energy, and in shear flows to the pressure-strain term, which effects transfer of

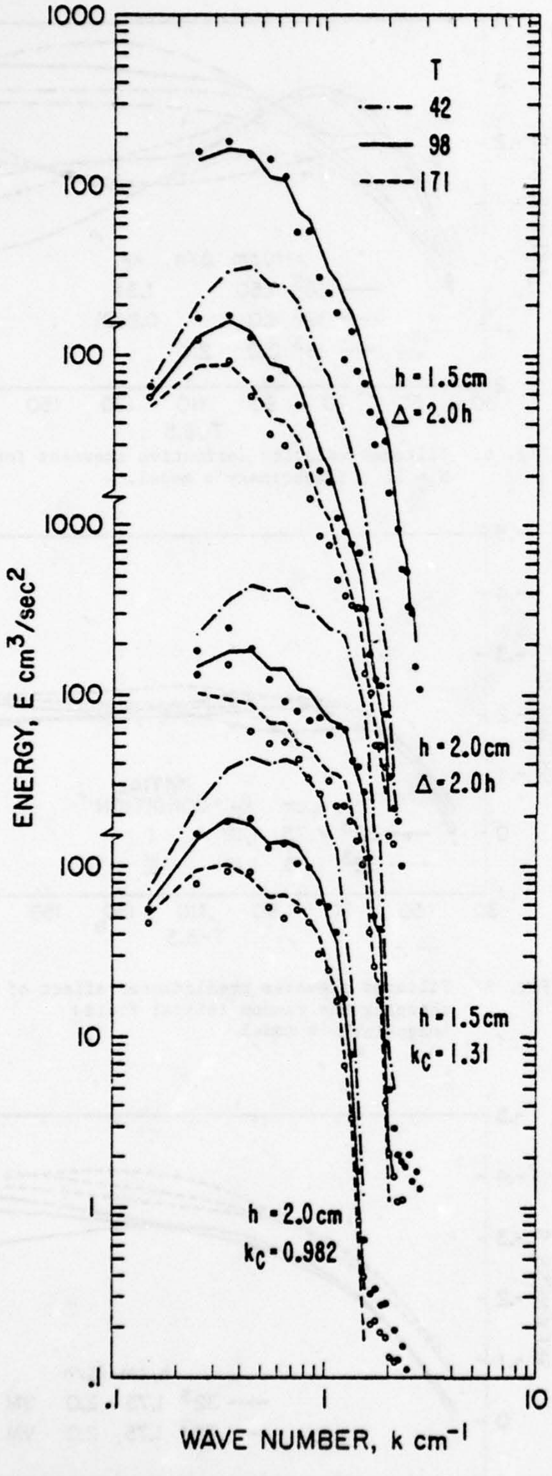

Fig. 5. Filtered energy spectra for N = 16, the top two sets use the discrete transform of the Gaussian spatial filter. Lines are experiments, points are computations; Smagorinsky's model.

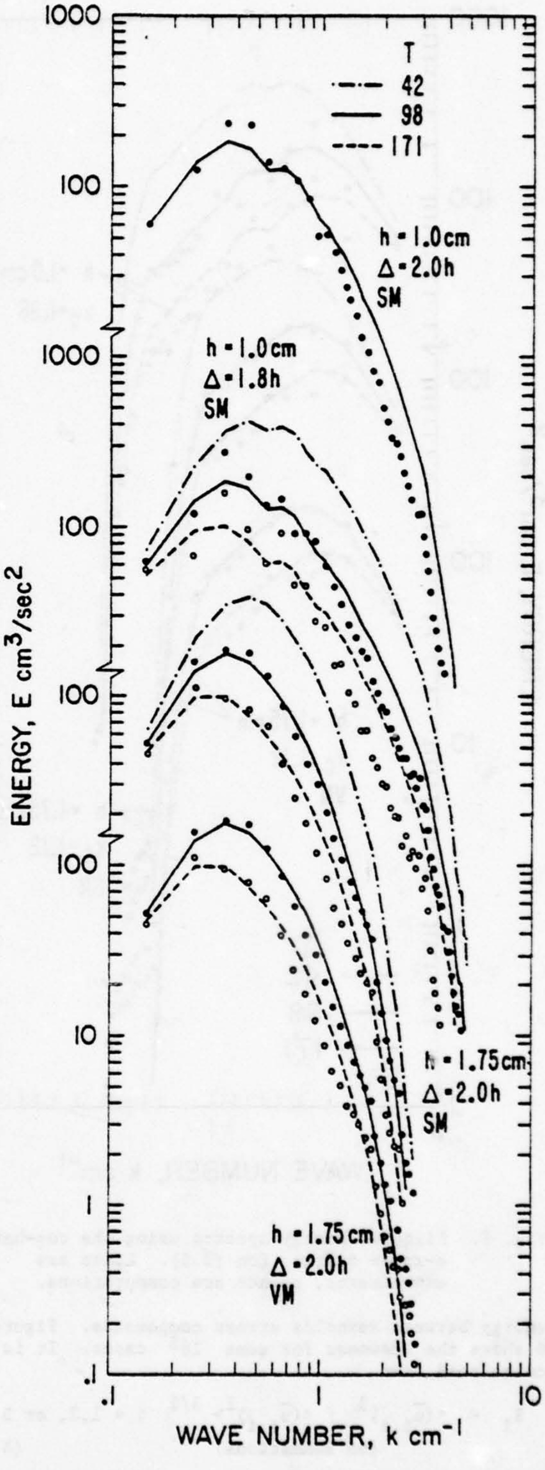

Fig. 6. Filtered energy spectra computed using the discrete transform of the Gaussian spatial filter, with N = 32. Lines are experiments, points are computations.

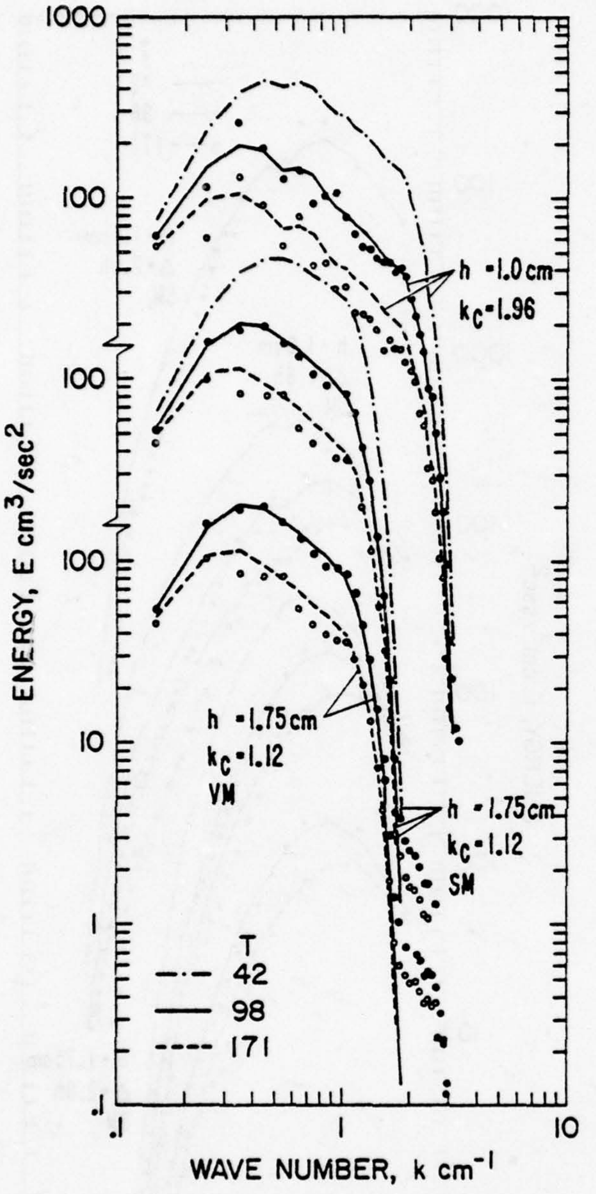

Fig. 7. Filtered energy spectra using the top-hat k-space filter, Eqn (2.5). Lines are experiments, points are computations.

energy between Reynolds stress components. Figure 8 shows the skewness for some 16^3 cases. It is calculated from

$$S_i = \langle(\bar{u}_{i,i})^3\rangle / \langle(\bar{u}_{i,i})^2\rangle^{3/2} \quad i = 1,2, \text{ or } 3 \quad \text{(no summations)} \tag{4.1}$$

In Figs. 8-10 there are three curves for each of a number of representative cases. The curves correspond to S_1, S_2, and S_3. Note the strong anisotropy of the skewnessess for the 16^3 calculations (Fig. 8). The skewness at first is small because the random initial field is nearly Gaussian. A negative

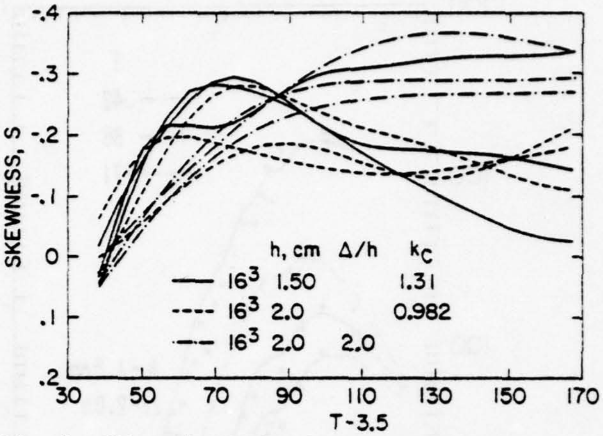

Fig. 8. Filtered velocity derivative skewness for N = 16 ; Smagorinsky's model.

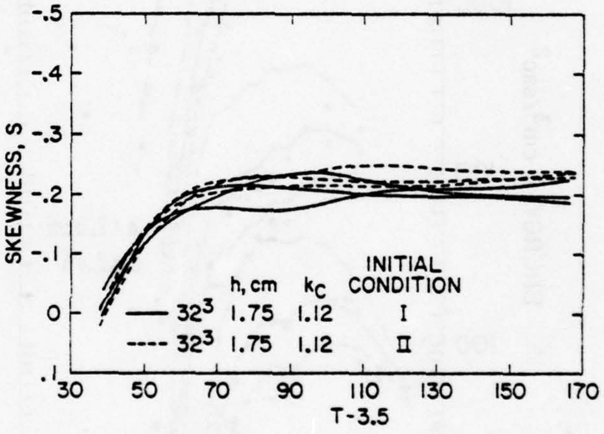

Fig. 9. Filtered skewness predictions; effect of changing the random initial field; Smagorinsky's model.

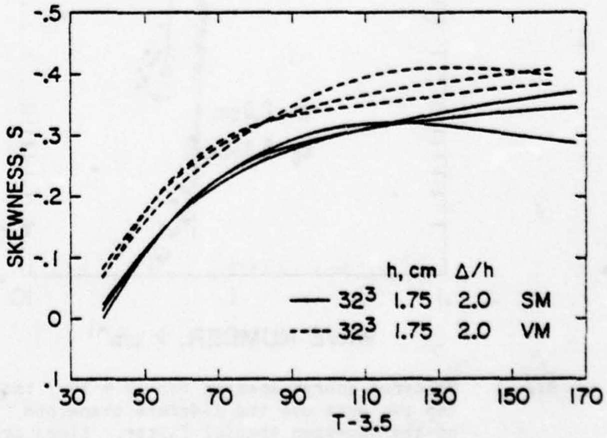

Fig. 10. Filtered skewness predictions--comparison of the two models.

skewness develops, in agreement with experiments, but quite different values are obtained with different sets of simulation parameters, and in some cases the simulation shows a subsequent drop in skewness that is not characteristic of experiments.

Figures 9 and 10 show representative results from 32^3 computations. Note that, with a careful choice of computation parameters, it is possible to obtain reasonably good isotropy among skewness components, especially in the 32^3 computations. Other runs with the same parameters but different initial conditions tend to have the same dispersion among S_1, S_2, and S_3, and approximately the same mean, so it is reasonable to make conclusions based on the cases shown; c.f. Fig. 9. The 16^3 calculations show so much variation that they should not be used to predict skewness. For 32^3 calculations, stable, reasonably isotropic predictions are obtained for $h = 1.75$ cm. For comparison, the integral scales reported experimentally vary from 1.3 cm to 4.9 cm, and thus is seems that a reasonable criterion for obtaining isotropy of skewness is that the computational domain be at least ten integral scales long.

On closer investigation, it appears that the bulk of any one skewness value is contributed by a few small spatial regions (3-6 for 16^3 and as many as 50 for the best 32^3 cases). These regions seem to be roughly a few integral scales in size, occupy only a few percent of the total volume, and are roughly spherical in shape. The detailed nature of these regions requires further investigation, but it seems that the primary requirement for statistically significant predictions of the skewness is that a sufficient number of these regions be captured; this is consistent with the above.

Comparing Figs. 9 and 10, we see that the Gaussian filter generally results in higher values of *the skewness* than the sharp cutoff filter, and the vorticity model generally produces higher values than Smagorinsky's model. All values of $-S$ for filtered field are considerably lower than the experimental values for the full field. Since the skewness is dominated by high wavenumbers, it is not surprising that the filtered skewness is less in magnitude than that of the actual flow.

We have also examined the isotropy of the computed flow fields by looking at the rms turbulent intensity ratios,

$$\frac{U}{V} = \sqrt{\frac{\langle \bar{u}_1^2 \rangle}{\langle \bar{u}_2^2 \rangle}} \quad \text{and} \quad \frac{W}{V} = \sqrt{\frac{\langle \bar{u}_3^2 \rangle}{\langle \bar{u}_2^2 \rangle}}$$

where again $\langle\ \rangle$ denotes an average over the full flow field. The results are shown in Fig. 11. Note that, *with the choice of computational parameters*, suggested above, reasonably isotropy is obtained.

Another check for isotropy was made by computing

$$\langle (\bar{u}_{1,1}^2) \rangle \ , \quad \langle \tfrac{1}{2}(\bar{u}_{2,1})^2 \rangle \ , \quad \text{and} \ \langle \tfrac{1}{2}(\bar{u}_{3,1})^2 \rangle$$

which should be equal in isotropic turbulence. The variation for the top-hap k-space filter averaged about 18%, while with the Gaussian filter the average variation was about 8%, for the largest computational domain.

The development of the flatness (or kurtosis) of the velocity derivatives is shown in Fig. 12. The initial field has a flatness of about 3, corresponding to a Gaussian distribution, but the changes produced by the two models are strikingly different. Experimentally one observes flatness greater than 3.0, and hence Fig. 12 might lead one to prefer the vorticity model over Smagorinsky's model. However, since filtering removes much high wavenumber information, which is important in the flatness, it really is difficult to make a judgment on this point.

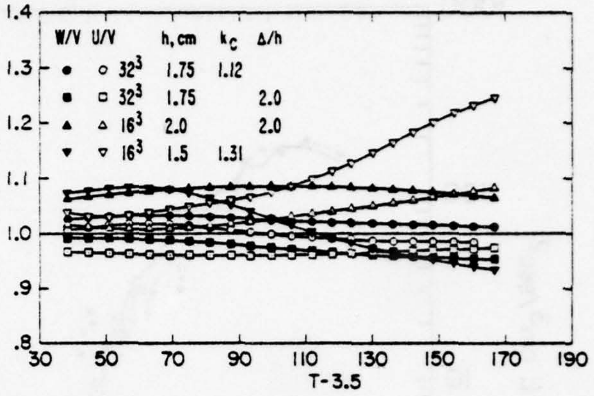

Fig. 11. Filtered turbulent intensity ratios.

We have also computed the autocorrelation functions, pressure-strain terms, dissipation rate, Taylor microscale, and integral scales. Both subgrid scale models give practically the same values for these quantities, but the selection of the filter and filter parameters greatly influences these values. We cannot make a direct comparison with the values found by [9] because there is no way to filter their values for comparison with our filtered quantities.

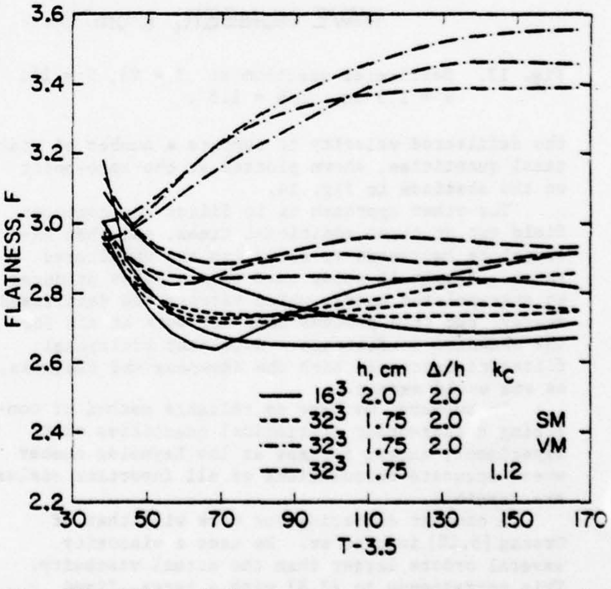

Fig. 12. Filtered flatness of the velocity derivatives.

We have explored two ways of defiltering our results in order to predict measured quantities. The first method is based on the fact that $\hat{\bar{u}} = \hat{u}\hat{G}$. Knowing $\hat{\bar{u}}$ and $\hat{G}$ we can divide to get $\hat{u}$. Figure 13 shows the result for one case which employed the Gaussian filter. A reasonable representation of the spectrum is obtained. Of course, for the top hat k-space filter the computation is unfiltered below k_c, and above k_c no defiltering is possible. We have used

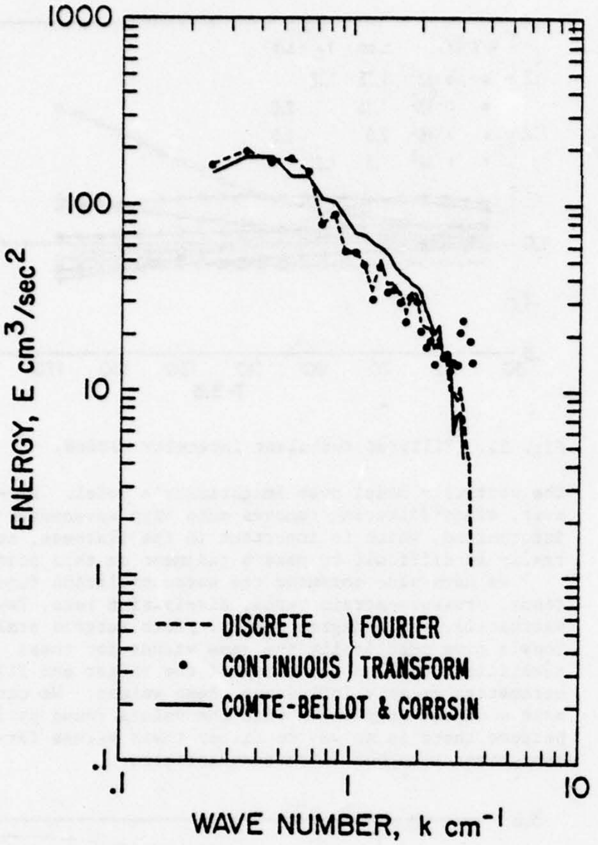

Fig. 13. Defiltered spectrum at T = 98; N = 16, h = 1.5 cm, $\Delta/h = 1.8$.

the defiltered velocity to compute a number of statistical quantities, shown plotted at the zero-point on the abscissa in Fig. 14.

The other approach is to filter the computed $\bar{u}$ field two or three additional times, and then extrapolate backwards to determine the unfiltered value. Figure 14 shows that this process produces an extrapolated energy which matches the defiltered energy; but this process does not work at all for the skewness or flatness. Note that additional filtering decreases both the skewness and flatness, as one would expect.

In summary, we have no reliable method of comparing higher-order statistical quantities with experiment, except perhaps at low Reynolds number where accurate calculations of all important scales are feasible.

A comment comparing our work with that of Orszag [6,10] is in order. He uses a viscosity several orders larger than the actual viscosity. This corresponds to (2.8) with a large, fixed ν_T. In some work he has used spectral methods; in a grid-based computation the counterpart is to use the top-hat k-space filter and a pseudospectral numerical technique such as described in [3].

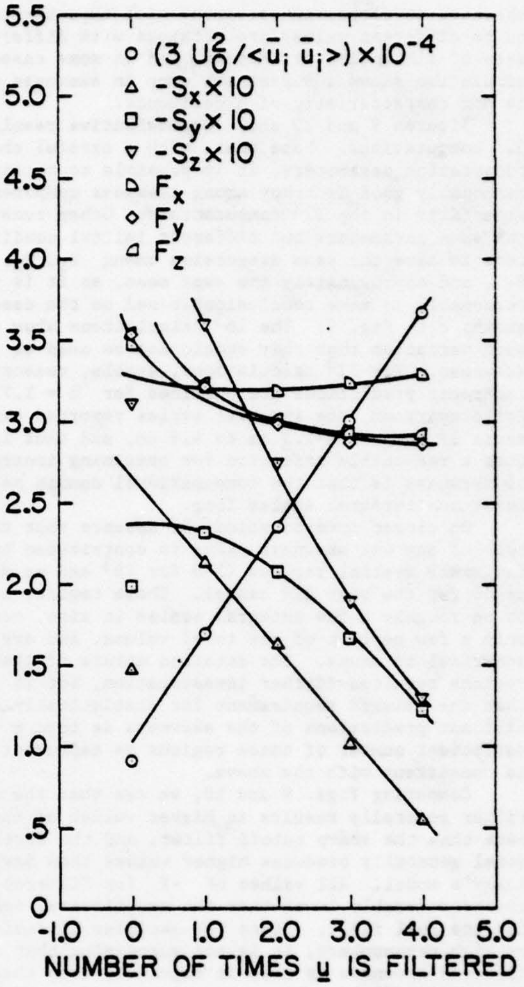

Fig. 14 Behavior of statistical quantities with defiltering or additional filtering. Discrete Gaussian filter, N = 16, $\Delta = 2h$, h = 2 cm; vorticity model.

5. CONCLUDING REMARKS

Based on the results presented here, we draw the following conclusions:

1. Large eddy simulations can predict lower-order statistics such as the (low wave-number portion) of the energy spectrum.
2. Filtering is essential to a successful calculation. Because of the necessity for filtering, not all of the flow energy is captured. Whether or not this is important in flows of engineering interest remains to to determined.
3. The Leonard stress terms may be handled by direct computation, with increased accuracy and efficiency, allowing use of the top hat k-space filter.
4. The top hat k-space filter captures more of the energy than the Gaussian and allows a direct comparison of the low wavenumber

part of the spectrum without defiltering. The Gaussian produces larger skewness magnitudes, which may be important in shear flow simulations.

5. The algebraic subgrid scale models are sufficient for predicting the spectra in homogeneous isotropic turbulence, and have the valuable property that the empirical constant need not vary substantially. Whether or not they will be sufficient for more complex flows remains to be determined.
6. The computational box size must be at least twice the distance at which the longitudinal and transverse correlations are negligibly small. This is of the order of ten integral scales.
7. If the Gaussian filter is used, the filter width Δ should be twice the mesh size h.
8. Higher-order statistics depend significantly upon the choice of filter and subgrid scale model.
9. The computations cannot be compared fully with experiments because of the filtering; we make a plea to experimenters to provide data in a form that could be filtered for comparison with large eddy simulations, or to carry out such filtering themselves.
10. While both the Smagorinsky and vorticity model predict the spectra and energy rather well, there are important differences in higher-order statistics, where neither does very well. There is insufficient basis for making a choice between these two models at this time.
11. Because of the difficulties in predicting higher-order statistical quantities, use of large eddy simulations to determine constants in simpler phenomenological models of turbulence should await further development of the approach.

These conclusions are all based on 16^3 and 32^3 calculations, and validation at 64^3 is recommended.

ACKNOWLEDGMENTS

This work has been carried out in cooperation with the Ames Laboratory, NASA, under Contract NASA-NgR-05-020-622.

REFERENCES

1 Kwak, D., Reynolds, W. C., Ferziger, J. H., "Three-Dimensional Time-Dependent Computation of Turbulent Flow," Report No. TF-5, May, 1975, Dept. of Mech. Engrg., Stanford University.

2 Shaanan, S., Ferziger, J. H., Reynolds, W. C., "Numerical Simulation of Turbulence in the Presence of Shear," Report No. TF-6, Dept. of Mech. Engrg., Stanford University, 1975.

3 Mansour, N. N., Moin, P., Reynolds, W. C., Ferziger, J. H., "Improved Methods for Large Eddy Simulations of Turbulence," proceedings of this conference.

4 Moin, P., Mansour, N. N., Mehta, U. B., Ferziger, J. H., Reynolds, W. C., "Improvements in Large-Eddy Simulation Technique: Special Methods and High-Order Statistics," Report No. TF-10, Dept. of Mech. Engrg., Stanford University, to be published.

5 Leonard, A., "On the Energy Cascade in Large-Eddy Simulations of Turbulent Fluid Flows," Adv. in Geophysics, Vol. 18A, 1974, p. 237.

6 Orszag, S. A., Israeli, M., "Numerical Simulation of Viscous Incompressible Flows," Annual Rev. Fluid Mechanics, Vol. 6, 1974, p. 281.

7 Smagorinsky, J., "General Circulation Experiments with the Primitive Equations. I. The Basic Experiment," Monthly Weather Review, Vol. 91, p. 99.

8 Reynolds, W. C., "Computation of Turbulent Flows," Annual Rev. Fluid Mechanics, Vol. 8, 1976, p. 183-208.

9 Comte-Bellot, G., and Corrsin, S., "Simple Eulerian Time Correlation of Full and Narrow-Band Velocity Signals in Grid-Generated 'Isotropic' Turbulence," Journal of Fluid Mechanics, Vol. 48, Part 2, 1971, p. 272.

10 Orszag, S. A. and Patterson, G. S., "Numerical Simulation of Three-Dimensional Homogeneous Isotropic Turbulence," Phys. Rev. Lett., Vol. 28, 1972, p. 76.

Three-Scale Sub-Grid Modeling of the Random Advection of a Passive Scalar

By Harvey A. Rose$^+$
Observatoire de Nice
Le Mont-Gros
06300 Nice, France

ABSTRACT

A subgrid model is presented for a passive scalar advected by a randomly prescribed frozen velocity field. In addition to an eddy diffusivity it has a term which describes the injection of noise from the subgrid scales, and a term which implicitly describes the coupling between the large eddies and the eddies just below the limit of resolution of the finite difference grid. The construction of the model is based upon an iterative procedure which first models away the dissipation range eddies, and then the eddies of a slightly larger size, etc. .

NOMANCLATURE

Symbol	Meaning
C	proportionality coefficient
E(k)	energy density of the velocity spectrum
f	fourier space shell ratio parameter
g(r)	kernel function for scalar flux
$\underline{j}$	vector valued scalar flux
$\underline{k},\underline{p},\underline{q},\underline{s}$	vector valued wavenumber variables
k,p,q,s	amplitudes of $\underline{k},\underline{p},\underline{q},\underline{s}$
k_d	energy dissipation range wavenumber
$k_d^{(n)}$	k_d reduced by n factors of f
k_o	cut in fourier space between supergrid and subgrid regions
m	exponent of 1/k in energy inertial range spectrum
N	number of fourier space shells
$\underline{r},\underline{r}'$	configuration space variables
t	time variable
$\underline{u}$	turbulent velocity field
$\underline{u}_<$	supergrid component of $\underline{u}$
$\underline{u}_>$	neargrid component of $\underline{u}$
U_{ij}	velocity covariance tensor
$\mathcal{U}_{ij}$	dimensionless form of U_{ij}
V_o	root mean square value of $\underline{u}$
$\beta(k)$	dimensionless eddy diffusivity
ε	energy dissipation rate per unit mass
μ	molecular diffusivity
μ_E	generic eddy diffusivity
$\mu^{(n)}(k)$	sequence of subgrid modeled eddy diffusivities
$\mu(k)$	final subgrid modeled eddy diffusivity
$\tau^{(n)}(k)$	sequence of diffusive time scales
$\tau(k)$	eddy turnover time
Ø	passive scalar field
Ø'	fluctuating component of Ø
$Ø_{NL}$	non-local contribution to Ø in subgrid model

Tensor Subscripts
i,j,m,n,x,y,z

TEXT

Introduction

Most turbulence models describe the enhancement of transport processes due to velocity fluctuations by a gradient-diffusion hypothesis(1),

$$\langle Ø' u_j \rangle = C \frac{\partial \langle Ø \rangle}{\partial r_j}$$

where Ø' and u are the fluctuating components of the property being transported and the velocity field respectively. This hypothesis has two serious deficiencies even in the simple case of almost homogeneous isotropic turbulence:

(a) The existence of a continuum of length scales, from that of the energy containing eddies to the Kolmogorov microscale, requires the "constant", C, to be replaced by an integral operator whose fourier transform has a peculiar cusp like behavior at the bottom of the inertial range (2,3).

(b) All detailed statistics of the small scales are lost when the original equations of motion are contracted by the process of taking the mean value. Their effect in the mean is represented by an eddy diffusivity, but the fluctuations about the mean which should be described by an "eddy noise", are ignored.

These deficiencies are distinct form the additional complications found in the analyses of strongly inhomogeneous flows, which often require that C not be determined by local flow properties, but rather by a transport equation for C (or for a length scale which determines C) itself.

In the context of the random advection of a passive scalar Ø, we show that these two effects, (a) and (b), are related, and that the crucial features which are omitted by a gradient-diffusion model are:

(A) A description of turbulence must incorporate, as a fundamental building block, the interaction of three contiguous scales of fluctuations (the use of two widely separated scales yields gradient-diffusion).

(B) The use of a constrained mean value operation, which is limited to a partial average over the fluctuations of intermediate size, produces a contracted

PRECEDING PAGE BLANK-NOT FILMED

description which makes explicit the injection of eddy noise from the small to the large scales of motion.

We present a model equation for the time evolution of ϕ in the special case of a frozen (time independent) velocity field. This model is limited in that it is only suitable for calculating the mean response of ϕ to an external disturbance. It is unsuitable for calculating the scalar correlation function, $\langle \phi\phi \rangle$, because only some of the factors which contribute to the eddy noise have been considered in detail. The linearity of the equation of motion for ϕ enables these two features to be separated and this is the reason why the passive scalar system was chosen.

The fourier representation of our model is found in equation (12). k_o is a cut in fourier space located at the boundary between the energy containing range and the inertial range of the prescribed advecting velocity field,u. It is used to decompose the set of all wavenumbers,k, as follows:

The supergrid region, with k such that $k \leq k_o$.

The subgrid region, with k such that $k > k_o$.

The neargrid region, with k such that $k_o < k \leq 2k_o$.

The energy spectrum of u is specified in the inertial range by the parameter m according to $E(k) \sim 1/k^m$. Our model refers explicitly to the supergrid passive scalar field and to the supergrid and neargrid velocity fields. The neargrid velocity field is considered to be random. A weakly wavenumber dependent eddy diffusivity, $\mu(k)$, appears which implicitly depends on m. It was assumed that the subgrid velocity field is both homogeneous and isotropic. No assumptions have been made concerning the supergrid velocity field.

There are two features of our model which distinguish it from the usual subgrid models. The first is the explicit retention of coupling between the supergrid scalar modes, and the neargrid velocity modes. This is one of the factors which contribute to eddy noise. We have called this coupling "eddy advection". The second feature is the uuϕ term in (12) which we have called "eddy mediated advection". It may be regarded as a non-local contribution to the scalar flux in configuration space. Eddy mediated advection represents the possibility of an exchange of scalar eddies between the supergrid and subgrid scales. Alternatively, it describes the apparent loss of local conservation of scalar density. This effect is an inherent property of measurements made on the passive scalar system with instruments which have a spatial resolution limited to eddies with size greater than $1/k_o$.

Though this model has no direct application to the study of real turbulence because of its assumptions about the subgrid velocity field and because it is a model for a linear system, we believe it is useful as an illustration of some of the features which a turbulence model should contain.

The mathematical method we will use is known as the renormalization-group, though no prior familiarity with it is assumed on the part of the reader. In the past few years it has proven to be a powerful tool for understanding critical phenomena (4). There are significant differences between these phenomena and that of turbulence and one does not expect to find, in the application of the renormalization-group to subgrid modeling, the spectacular success exhibited in calculating the properties of critical phenomena. Our model will remain a tentative one until it is closely compared with experiment.

Eddy Diffusivity Models

Consider a passive scalar field, $\phi(\underline{r},t)$, advected by a turbulent fluid with a solenoidal velocity field, $\underline{u}(\underline{r},t)$, a prescribed random function,

$$\frac{\partial \phi}{\partial t}(\underline{r},t) - \mu \nabla^2 \phi(\underline{r},t) = -u_j(\underline{r},t) \frac{\partial \phi}{\partial r_j}(\underline{r},t). \tag{1}$$

The summation convention for repeated latin subscripts, "j" assuming the values 1, 2 and 3 in (1), will be used. μ is the molecular diffusivity. The fourier transform of (1) is

$$\frac{\partial \phi}{\partial t}(\underline{k},t) + \mu k^2 \phi(\underline{k},t) = -ik_j \int_{\underline{p}+\underline{q}=\underline{k}} d^3p \, u_j(\underline{q},t)\phi(\underline{p},t) \,. \tag{2}$$

If $\underline{u}$ represents strong turbulence, then its energy spectrum E(k) has a long inertial range where $E(k) \sim 1/k^m$. The precise value of m is not relevant for our purposes, though the classical Kolmogorov value of 5/3 is used when presenting numerical results. Let the wavenumber k_o mark the bottom of this range, k_d the top, and let V_o be the r.m.s. value of $\underline{u}$,

$$\frac{1}{2} V_o^2 = \frac{1}{2}\langle u_j u_j \rangle = \int_0^\infty E(k)dk \gtrsim \int_0^{k_o} E(k)dk \,.$$

Typically, μ is small compared to V_o/k_o.

The philosophy behind many turbulence models, the subgrid models being a certain variety (5,6,7,8, 9,10,11,12,13,14), is that in calculations which are only concerned with smoothly varying quantities, the effect of the many, quickly evolving small scales of motion may be represented by enhanced transport coefficients in the original equation of motion. For the system described by (2), subgrid models would replace ϕ by its truncation at k_o,

$$\phi(\underline{r},t) = \int d^3k \, \phi(\underline{k},t) e^{i\underline{k}\,\underline{r}} \rightarrow \int_{k \leq k_o} d^3k \, \phi(\underline{k},t) e^{i\underline{k}\,\underline{r}} \,, \tag{3}$$

$\underline{u}$ by an analogous truncation, and μ would be replaced by an eddy diffusivity $\mu_E \gg \mu$, which must be of order V_o/k_o by dimensional analysis. The effect of these replacements is to drastically reduce the number of dynamic degrees of freedom. This reduction must somehow be made if the calculation is to fit on present day computers. Note that as an alternative to truncating in fourier space, it is common to work with a finite difference representation of (1) on a grid initially fine enough to resolve all the significant scales of motion. The fine grid is then replaced by a much coarser grid, simultaneously adjusting the equation of motion to compensate for the loss of spatial resolution. This adjustment also amounts to replacing μ by μ_E.

Though the detailed prescription for calculating μ_E depends on the particular model, the following reasoning is common. The fundamental property of strong turbulence is the transfer of energy form large eddies to small. For the passive scalar, the conserved quantity which plays an analogous role to energy is the mean square scalar fluctuation, called the scalar variance. It too is transferred to small eddies. The eddies of intermediate size, with wavenumbers $k_o < k < k_d$ serve as intermediaries in the transfer process. If the truncation indicated in (3) is made, the mechansim by which the now no longer referred to modes removed scalar variance from the large scale modes must be compensated for. Since the diffusive term, $\mu\nabla^2\phi$, removes scalar variance, it might be possible to realize this compensation by suitably enhancing the numerical value of μ. To estimate this enhancement, a dimensionally correct combination of large scale parameters is chosen. Clearly, k_o^{-1} is a relevant length scale, and $\langle|\partial u/\partial r|\rangle$ (with the spatial derivative evaluated in a coarse grid with mesh spacing $1/k_o$) is a relevant time scale, so that

$$\mu_E \sim \frac{1}{k_o^2}\langle|\partial u/\partial r|\rangle \ .$$

The above procedure captures some of the essential physics, but it has a fundamental inconsistency which results from following the detailed evolution of individual realizations of the supergrid modes, while at the same time compensating for the effect of the unresolvable subgrid modes only in the statistical mean. While it is true that the fine scale modes, say those with $k > 2k_o$, evolve so quickly that their effect on individual realizations may be replaced by an equivalent mean effect, there is a strong coupling between the supergrid modes and the neargrid modes which cannot be thus represented.

In place of the eddy diffusivity models, one is constructed which realizes the special properties of the neargrid scales. This is accomplished through the use of a constrained mean value operation which, in a sense to be precisely defined, only performs a partial average over the neargrid modes, and thus allows them to implicitly interact with the supergrid modes, in a realization dependent fashion.

Systematic Elimination of High Wavenumber Modes

Divide the set of equations represented by (2) into two subsets. The first contains those equations whose left hand member refers to a $\varnothing(\underline{k},t)$ such that $k \leq k_o$. The second contains all the others. In principle one can eliminate explicit reference to the latter set by solving them for the high k modes in terms of the low k modes, and then substituting the results into the first set wherever any reference is made to a high k mode (15). The resulting system can be further simplified by performing some kind of average over the high k velocity modes, whose statistics are presumed to be given. In practice, only an approximation to this algorithm can be accomplished.

To illustrate the kind of approximation used without being encumbered by the unwieldy algebra of many coupled equations, the following simple model will first be examined in detail,

$$dX(t)/dt + \alpha X(t) = -i(a_x+a_y)\cdot(X(t)+Y(t)) \qquad (4)$$

$$dY(t)/dt + 2\alpha Y(t) = -i(a_x+a_y)\cdot(X(t)+Y(t)) \ . \qquad (5)$$

X and Y are two functions of time, α is a positive constant, a_x and a_y are specified time independent random variables with zero mean and covariances $\langle a_x^2\rangle$ and $\langle a_y^2\rangle$ respectively. The identifications to be made with (2) are the following:

X is a scalar mode $\varnothing(k_x)$ with $k_x < k_o$

a_x is a frozen velocity mode $u(k_x)$

Y is a scalar mode $\varnothing(k_y)$ with $k_y > k_o$

a_y is a frozen velocity mode $u(k_y)$

α is the damping associated with μk_x^2

2α is the higher damping associated with μk_y^2

The equality of the right hand sides of equations (4) and (5) is of no consequence. The algebraic structure of (2) which is preserved by the above model is that both high and low wavenumber passive scalar modes may be advected by both high and low wavenumber velocity modes.

In the context of equations (4) and (5) a "subgrid model" is obtained by solving (5) for Y(t) in terms of X(t), and then substituting this solution into (4) to obtain a single equation for X(t). Though this can be done exactly, the corresponding operation in (2) is impossible. A full description of the approximations used to subgrid model equation (2) is given later. For the moment, let us content ourselves with only a brief sketch of the parallel development for equations (4) and (5).

Assuming that the subgrid modes evolve more quickly (a Markovian approximation) than the supergrid modes, and that the amplitude of the subgrid modes is smaller than those of the supergrid modes, it is plausible to use

$$Y(t) = -i(a_x+a_y)\cdot X(t)/2\alpha \qquad (6)$$

as an approximate solution to (5). Substitute (6) into (4) to obtain

$$dX(t)/dt + \alpha X(t) = -i(a_x+a_y)X(t) - (a_x+a_y)^2X(t)/2\alpha \ . \qquad (7)$$

Since a_y corresponds to a subgrid velocity mode, which is regarded as random, it is tempting to replace (7) by the equation which results from the substitutions

$$a_yX(t) \rightarrow \langle a_y\rangle X(t) = 0$$
$$a_ya_xX(t) \rightarrow \langle a_y\rangle a_xX(t) = 0$$
$$a_y^2X(t) \rightarrow \langle a_y^2\rangle X(t).$$

However, in a sense to be defined in the next section, only the latter two of the above are consistent with the properties in the mean of the original system, (4) and (5). With these substitutions we obtain

$$dX(t)/dt+(\alpha+\delta\alpha)X(t)=-i(a_x+a_y)X(t)-a_x^2X(t)/2\alpha \qquad (8)$$

where

$$\delta\alpha = \langle a_y^2\rangle/2\alpha$$

as a "subgrid model" for (4) and (5).

The interpretation of the various terms in (8) is:
(i) $\delta\alpha$ is the enhancement of the molecular diffusivity by the subgrid velocity modes,
(ii) ia_xX is the advection of the supergrid scalar field by the supergrid velocity field,
(iii) ia_yX is the random advection of the supergrid scalar field by the subgrid velocity field,
(iv) $(a_x^2/2\alpha)X$ represents the boosting of a supergrid scalar eddy into the subgrid regime by a supergrid velocity eddy (which gives the first a_x factor), and its return to the supergrid regime by its interaction with a second supergrid velocity eddy (which gives the second a_x factor).
The transformation of (7) into (8) might be described as a partial average over the subgrid velocity field statistics. The use of a partial subgrid average, as opposed to the use of an indiscriminate total average, is one way in which this model differs form the usual ones. As a consequence, the term described in (iii) appears which would otherwise be absent. The appearance of the unusual term in (iv) may be explained by saying that an average was performed over the subgrid scales with a probability distribution function con-

ditioned with respect to the values assumed by the supergrid scalar field. Physically this corresponds to the fact that the supergrid scalar eddies do not constitute an isolated system. There is a constant exchange, across the mathematical construct in fourier space at $k=k_o$ (or in the language of configuration space, an exchange from eddies resolved by the coarse finite difference grid to the unresolved eddies lying between the grid points), of scalar eddies which causes the subgrid scalar field to respond and react back on the supergrid scalar field.

To justify the above interpretation we must return to the original set of equations, (2), and perform the same manipulations which led to (8). Since $E(k)$ falls off exponentially for $k > k_d$ there will be a negligible contribution to $\delta\mu$ from this wavenumber range. Thus, for the purpose of constructing a subgrid model, the system represented by (2) may be truncated at k_d. However, even at k_d, it is clear that the approximation which led to (6) would be untenable if μ were small enough. For the analog of (6) to be valid, when Y corresponds to a subgrid scalar mode with wavenumber k, we must have $V_k/\mu k <$ 1 where V_k^2 is the energy per unit mass of the velocity modes in the neighborhood of k. This ratio, which may be thought of as a wavenumber dependent Reynolds number, assumes its largest value for $k=k_o$,

$$V_o/\mu k_o \tag{9}$$

For most problems of practical interest, this Reynolds number is much larger than one.

If we could solve for the subgrid modes in terms of the supergrid modes in such a way that the eddy diffusivity appeared in (9) instead of the molecular diffusivity, then the estimate in (9) would be lowered significantly. This can be partially realized by regarding the ultimate subgrid model as the product of two subsidiary calculations. The first calculation models away the modes between k_d and $k_d/2$. The effective Reynolds number for this preliminary calculation is much smaller than that in (9) because in place of V_o,

$$W = \sqrt{\int_{k_d/2}^{\infty} E(p)\,dp} \ll V_o$$

is used, and in place of k_o, $k_d/2$ is used. The system (2) is replaced by one with an upper cutoff of $k_d/2$, and with a diffusivity enhanced by the amount

$$\delta\mu \sim W/(k_d/2).$$

Next, the second calculation models away the modes between $k_d/2$ and k_o. The effective Reynolds number for this calculation is smaller than that in (9) because μ is replaced by $\mu + \delta\mu$.

The above process, whereby the subgrid model is produced in two stage, can be further subdivided by eliminating all of the subgrid modes in several stages. If we regard the original system as a ball in fourier space of radius k_d, then by removing the subgrid modes one shell at a time, beginning at k_d and working in to k_o, the effective diffusivity will be bootstraped up, bit by bit. When all the shells between k_o and k_d have been removed, the effective diffusivity has attained its full value, μ_E, of order V_o/k_o. In this way, the Reynolds number for the removal of a particular shell is always order unity, and the final subgrid model has been constructed with the use of a sequence of uniformly valid approximations.

It remains to be determined into how many shells fourier space should be divided in order that the most accurate subgrid model is produced. Clearly, two shells are better than one, and three better than two, but after we have passed to the limit of many shells, it is not a simple matter to decide upon the optimum number. Fortunately, the resulting model is not very sensitive to this decision. Later we shall discuss some criteria for making this choice. For the moment, simply assume that there are N shells with inner and outer radii $k_d^{(n)}$ and $k_d^{(n-1)}$ respectively, n=1,2,..., N, where

$$k_d^{(n)} = f^n k_d$$

and f is a parameter between zero and one. The superscript n=1 corresponds to the outer shell bounded by fk_d and k_d, and the value n=N is the innermost shell bounded by

$$k_o = f^N k_d \tag{10}$$

and k_o/f. A fractional decrease of radius size is the natural choice for an energy spectrum which obeys a power law.

After n shells have been removed there is an effective diffusivity denoted by $\mu^{(n)}(k)$, defined for $k \lesssim k_d^{(n)}$. If the velocity covariance, $U_{ij}(\underline{q})$,

$$\langle u_i(\underline{p})u_j(\underline{q})\rangle = \delta^3(\underline{p}+\underline{q})U_{ij}(\underline{q})$$

obeys a power law

$$U_{ij}(\underline{q}) = C\,\mathcal{U}_{ij}(\underline{q}/\lambda)/\lambda^{m+2}$$

where λ is any inverse length scale, $\mathcal{U}$ is a dimensionless function, and C is a dimensionfull constant with the dimensions

$$[C] = 1/T^2L^{m-3},$$

and if n is large enough such that

$$\frac{C^{1/2}}{\left[k_d^{(n)}\right]^{(m+1)/2}} \gg \mu,$$

then the relationship between $\mu^{(n+1)}(k)$ and $\mu^{(n)}(k)$ is simple. As a function of wavenumber normalized to $k_d^{(n+1)}$ and $k_d^{(n)}$ respectively, their functional forms are similar, with $\mu^{(n+1)}$ being larger than $\mu^{(n)}$,

$$\mu^{(n+1)}(\underline{k}) = \frac{1}{f^{(m+1)/2}}\mu^{(n)}(\underline{k}/f), \tag{11}$$

and $\mu^{(n)}$ is independent of the molecular diffusivity.

Equation (11) is exact, but the actual evaluation of $\mu^{(n)}$ is approximate. The limiting subgrid model obtained for f→1 is of particular interest because, for reasons to be discussed in the next section, it is believed that the models obtained for f near one are the most accurate. In addition, the analytic form of the resulting subgrid model is simple. Using approximations which parallel those leading to (8), we obtain

$$\frac{\partial\phi}{\partial t}(\underline{k},t) + \mu(k)k^2\phi(\underline{k},t) = -ik_j\int_{\substack{\underline{p}+\underline{q}=\underline{k}\\ p\lesssim k_o\\ q\lesssim 2k_o}} d^3p\, u_j(\underline{q},t)\phi(\underline{p},t) -$$

$$\frac{-k_j}{\mu(k_o)k_o^{(m+1)/2}}\int_{k_o < p \lesssim 2k_o} d^3p \int_{\substack{s \lesssim k_o \\ |\underline{k}-\underline{p}| \lesssim k_o \\ |\underline{p}-\underline{s}| \lesssim k_o}} d^3s \; \frac{s_n u_j(\underline{k}-\underline{p},t)u_n(\underline{p}-\underline{s},t)\emptyset(\underline{s},t)}{p^{(3-m)/2}} \quad , \tag{12}$$

as the final subgrid model in the limit of f → 1. The eddy diffusivity $\mu(k)$ is conveniently expressed in terms of the dimensionless function β defined by

$$\beta(\underline{k}/k_o) = (k_o^{m+1}/C)^{1/2}\mu(k).$$

For the spectral choice

$$U_{ij}(\underline{p}) = C(\delta_{ij} - p_i p_j/p^2)/4\pi p^{11/3} \quad ,$$

i.e. $m=5/3$, and $f=0.9$, it assumes the values $\beta(0)= .78$,

k/k_o	0.0	0.2	0.4	0.6	0.8	1.0
$\beta(k/k_o)/\beta(0)$	1.0	.96	.93	.91	.89	.88

Note that the value $m=3$ is a dividing point between two different regimes of behavior. The exponent $(3-m)/2 = 2-(m+1)/2$, simply expresses the competition between the decrease of p, for $p \sim k_d^{(n)}$, and the increase of $\mu^{(n)}$ with n in the determination of a typical diffusion time $\tau^{(n)}$,

$$\tau^{(n)} = \left[\mu^{(n)}(p)p^2\right]^{-1} \sim (k_d^{(n)})^{(m-3)/2}. \tag{13}$$

For the Markovian aspect of the approximation used in (6) to be valid, the subgrid scalar modes must be more quickly evolving than the supergrid modes, which implies that $\tau^{(n)} > \tau^{(n-1)}$, or that $m < 3$. This division at m=3, in the context of subgrid scale modeling, has been previously noted by Kraichnan (2) for different reasons.

Nature of the Approximations Used in Deriving the Model

The approximations used in obtaining (12) are of four different kinds. For simplicity their detailed description will be in the context of the transformation from (4) and (5) to (8). The first assumes that within the subgrid scales, the scalar variance decreases with increasing wavenumber. It is then reasonable to perturbatively solve (5) by inserting a formal expansion parameter, δ , in front of Y on the right hand side of the equation and solving for Y in terms of X as a power series in δ . The series is truncated, and δ is set equal to one. Secondly, it is assumed that the subgrid scalar modes are more quickly evolving than the supergrid modes, and we therefore make the approximation that Y(t) quickly decays to the steady state solution of (5). This is called a Markovian approximation. For example, the formal expansion of Y to zeroth order in δ , and subsequent Markovianization yields (6). The third approximation is an arbitrary one, and we have no justification for it except to say that without one like it we could not proceed. It may be regarded as an implicit constraint on the number of terms retained in the expansion in δ. We assume that a consistent model is produced by only retaining those terms in (4), after Y has been substituted for according to the first two approximations, which contain no more than two factors of the form a_x or a_y. For the real subgrid model it means that terms of the form uuØ are retained but that terms of the form uuuØ, uuuuØ, ... have been ignored.

The fourth and last approximation is concerned with the procedure for partial averaging. Since the goal of subgrid modeling is to replace the initial set of equations by a smaller set which is equivalent to the first modulo the calculation of statistical properties, we demand that the transformation induced by partial averaging leave these properties invariant. The precise criterion we have chosen is based on the Taylor series representation of the solution to (7). In this representation it is required that the mean value of X(t), with respect to a_y, be invariant up to and including terms of order a^2. This criterion allows us to replace (7) by (8). Note that this is consistent with the retention of terms of order a^2 in the third approximation. If the third approximation were expanded to retain terms of order a^4, which corresponds to terms of the form uuuuØ in the real subgrid model, then the invariance criterion would be extended to include terms of order a^4.

In addition to the questions concerning the details of the above approximations there remains the choice of the parameter f which determines in how many stages the modes between k_o and k_d are modeled away. The value of f would not matter if a subgrid model could be constructed with sufficient accuracy. This does not mean that the form of the resulting equations would look the same, only that they would yield the same numerical results for a given calculation of the supergrid scalar field. At the present time we do not have any quantitative estimates for the choice of f which would yield an optimal model. Such an estimate could be obtained by constructing the subgrid model which retained terms of the form uuuuØ, and then varying f until the changes produced by these additional terms is minimized. Qualitatively It is felt that the optimal value of f is closer to one than to zero because if the successive shells in fourier space that are being modeled away are thin, the effective diffusivity has time to adjust to the energy in the velocity modes being discarded.

Subgrid Modeled Scalar Transport

The unusual uuØ term in (12) has a simple interpretation in configuration space. If the inverse fourier transform of (12) is taken, and $\mu(k)$ replaced by its value at k_o, we obtain

$$\partial \emptyset(\underline{r},t)/\partial t = -\underline{\nabla}\cdot\underline{j}(\underline{r},t) \quad . \tag{14}$$

$\emptyset(\underline{r},t)$ is given by (3) and

$$\underline{j}(\underline{r},t) = -\mu(k_o)\,\underline{\nabla}\,\emptyset(\underline{r},t) + \emptyset(\underline{r},t)\underline{u}_<(\underline{r},t) + \emptyset(\underline{r},t)\underline{u}_>(\underline{r},t) + \emptyset_{NL}(\underline{r},t)\underline{u}_<(\underline{r},t) \quad , \tag{15}$$

with

$$\underline{u}_<(\underline{r},t) = \int_{p \lesssim k_o} d^3p\; \underline{u}(\underline{p},t)e^{i\underline{p}\cdot\underline{r}}$$

$$\underline{u}_>(\underline{r},t) = \int_{k_o < p \lesssim 2k_o} d^3p\; \underline{u}(\underline{p},t)e^{i\underline{p}\,\underline{r}}$$

$$\emptyset_{NL}(\underline{r},t) = -\int \frac{d^3\underline{r}'}{(2\pi)^3}\, g(\underline{r}-\underline{r}')\,\underline{\nabla}'\cdot\left[\emptyset(\underline{r}',t)\underline{u}\;(\underline{r}',t)\right]$$

where

$$g(\underline{r}) = \frac{1}{\mu(k_o)k_o^{(m+1)/2}} \int_{k_o < p \leq 2k_o} d^3p \; \frac{e^{i\underline{p}\cdot\underline{r}}}{p^{(3-m)/2}} \quad .$$

The first two contributions to the scalar flux, $\underline{j}$, are expected. They correspond to gradient diffusion and supergrid velocity field advective transport respectively. The third represents "eddy advection" by the neargrid velocity field, and it is looked upon as a random quantity. If we consider the subgrid model to be a description of the original passive scalar system based upon observations made through a microscope whose resolution is limited to objects with spatial dimension greater than $1/k_o$, then eddy advection is the advection of clearly seen scalar eddies by invisible velocity eddies. The last contribution to $\underline{j}$ is the supergrid advection of a non-local scalar density, ϕ_{NL}. Looking through our microscope, it would be described by the following sequence of events:

i) A velocity eddy is seen advecting a scalar eddy at spatial location $\underline{r}'$.

ii) The scalar eddy disappears form view.

iii) It reappears distributed at other space points $\underline{r}$, with a density ϕ_{NL} proportional to $g(\underline{r}-\underline{r}')$, being advected by visible velocity eddies.

Since this sequence represents the advection of a scalar eddy which has descended into the subgrid scales and then reemerged, let us call it "eddy mediated advection".

It is instructive to consider a numerical example of eddy mediated advection in fourier space. Let the superscale velocity field be given by

$$u_x(\underline{q}) = V\left[\delta(q_y-k_2) + \delta(q_y+k_2)\right]\delta(q_x)\delta(q_z)$$

$$u_y = u_z = 0 \; ,$$

with $k_2 < k_o$, and V a constant with the dimensions of velocity. Let there also be a time independent source of passive scalar, $S(\underline{q})$, on the right hand side of (12),

$$S(\underline{q}) = \left[\delta(q_x-k_1) + \delta(q_x+k_1)\right]\delta(q_y)\delta(q_z) \; ,$$

with $k_1 < k_o$. We wish to compare the various contributions to the damping of the passive scalar, ϕ. Since eddy advection represents the effect of a continuum of random velocity modes, its contribution is more or less additive and smoothly varying with the parameters k_1 and k_2. Let us therefore ignore it in the comparison between eddy diffusivity, supergrid advection, and eddy mediated advection. Consider the following two cases:

Case I.
$$\sqrt{k_1^{\,2} + k_2^{\,2}} \leq k_o$$

$$k_o < \sqrt{k_1^{\,2} + k_2^{\,2}} \leq 2k_o$$

There are six supergrid scalar modes, $\phi(\pm k_1,0,0)$ and $\phi(\pm k_1,\pm k_2,0)$. The latter four are implicitly coupled to the subgrid modes by eddy mediated advection. Omitting the effects of eddy advection, and approximating $\mu(k)$ by $\mu(k_o)$, we obtain the following set of equations from (12),

$$\mu(k_o)k_1^{\,2}\phi(k_1,0,0) = -ik_1V\left[\phi(k_1,k_2,0)+\phi(k_1,-k_2,0)\right] + 1$$

$$\mu(k_o)(k_1^{\,2}+k_2^{\,2})\phi(k_1,k_2,0) = -ik_1V\phi(k_1,0,0) - \frac{-k_1^{\,2}V^2\phi(k_1,k_2,0)}{\mu(k_o)k_o^{(m+1)/2}(k_1^{\,2}+4k_2^{\,2})^{(3-m)/4}}$$

and the equations for $\phi(k_1,\pm k_2,0)$ are identical. The delta functions in wavenumber belonging to the scalar modes have been suppressed. Solving these equations for $\phi(k_1,0,0)$ it is found that

$$\phi^{-1}(k_1,0,0) = \mu(k_o)k_1^{\,2} + \frac{2k_1^{\,2}V^2}{\mu(k_o)(k_1^{\,2}+k_2^{\,2}) + \dfrac{k_1^{\,2}V^2}{\mu(k_o)k_o^{(m+1)/2}(k_1^{\,2}+4k_2^{\,2})^{(3-m)/4}}} \quad .$$

Case II

$$k_o < \sqrt{k_1^{\,2} + k_2^{\,2}} \leq 2k_o$$

The point of view we adopt is that in the first case $\sqrt{k_1^{\,2}+k_2^{\,2}}$ is marginally less than k_o, and that the second case is obtained from the first by increasing k_1 by a small amount. There are two supergrid scalar modes, $\phi(\pm k_1,0,0)$ which are coupled to other modes only through eddy mediated advection:

$$\mu(k_o)k_1^{\,2}\phi(k_1,0,0) = \frac{-k_1^{\,2}V^2\phi(k_1,0,0)}{\mu(k_o)k_o^{(m+1)/2}(k_1^2+k_2^2)^{(3-m)/4}} + 1$$

$$\phi^{-1}(k_1,0,0) = \mu(k_o)k_1^2 + \frac{k_1^{\,2}V^2}{\mu(k_o)k_o^{(m+1)/2}(k_1^{\,2}+k_2^{\,2})^{(3-m)/4}} \quad .$$

Since in a typical supergrid realization $V = o(V_o)$ and k_1 and k_2 are both $o(k_o)$, the responses of ϕ in the above two cases are computed to be comparable. Physically, the responses should be identical since we have supposed the two cases to be marginally different when viewed from the full set of passive scalar equations. Though identical responses were not found it has been demonstrated how eddy mediated advection takes over for the loss of damping associated with the coupling of one supergrid scalar mode to another, which occurs when supergrid interactions boost an eddy into the higher wavenumbers of the subgrid scale. A subgrid model which only had an eddy diffusivity term would be forced to have a diffusivity which rose sharply for wavenumbers approaching k_o to compensate for the above effect.

Time Dependent Velocity Fields and the Transfer of Scalar Variance

The determination of what constitutes a realistic choice for the turbulent velocity field, $\underline{u}$, is not simple. It is common, in a problem like that of the passive scalar, to make the simplifying assumption that the physically realized $\underline{u}$ may be represented by a Gaussian process with the same mean and covariance. We shall soon question the validity of this assumption in the construction of a subgrid model, but first let us examine some of its qualitative consequences.

Since the resulting subgrid model, no matter how it is constructed, is used with a given realization of the supergrid velocity field, the subgrid velocity statistics should be conditioned with respect to that realization. This implies that $\langle \underline{u}(\underline{k},t)\underline{u}(\underline{p},t')\rangle_c$, where the subscript "c" stands for conditioned, with k and p greater than but comparable to k_o, is significantly inhomogeneous, i.e. the offdiagonal elements ($\underline{k}+\underline{p} \neq 0$) are comparable in magnitude to the diagonal elements ($\underline{k}+\underline{p}=0$). We therefore face the immediate difficulty of finding a suitable analytic expression which describes the corssover of $\langle \underline{u}(\underline{k})\underline{u}(\underline{p}) \rangle_c$ from an inhomogeneous, supergrid scale dependent, behavior for k and $p \gtrsim k_o$, to the presumed universal, Kolmogorov-like (16), behavior characteristic of fully developed turbulence in the limit of k and $p \gg k_o$. Though it is true that the unconditioned covariance assumes a universal behavior for wavenumbers much greater than some wavenumber determined by the external flow geometry, the covariance conditioned with respect to $\{ \underline{u}(\underline{k}) \mid k \lesssim k_o \}$ does not assume a universal behavior until wavenumbers much greater than k_o are attained. There is also the question of the time dependence assumed by $\langle \underline{u}(\underline{k},t)\underline{u}(\underline{p},t') \rangle_c$. Near k_o, the dependence on t and t' is also inhomogeneous in that it depends on (t+t') as well as (t-t'). For large wavenumbers, k, the decay of the unconditioned covariance with increasing $|t-t'|$ is determined by the Eulerian dephasing time, $1/kV_o$ (17). In contrast, the conditioned covariance has a different Eulerian dephasing time in which the r.m.s. subgrid velocity is used.

The principle difference between a physically realized turbulent velocity field and a Gaussian process with the same mean and covariance is that the former has statistical correlations beyond those implied by the covariance. Consider the subgrid modeling step in which the (n+1)th fourier space shell, modes with wavenumbers k satisfying

$$k_d^{(n+1)} < k \lesssim k_d^{(n)} ,$$

is removed. A partial average is performed over the velocity modes in this shell, conditioned with respect to all the velocity modes whose wavenumbers are smaller than $k_d^{(n+1)}$. If $k_o \ll k_d^{(n+1)}$, the Gaussian process modes with wavenumbers smaller than $k_d^{(n+1)}$ are almost statistically independent of the modes in the (n+1)th shell because in this wavenumber range the covariance is approximately diagonal. The corresponding physically realized velocity field modes are not independent. In particular, we speculate that the decay time for a typical velocity covariance in the (n+1)th shell, conditioned with respect to all velocity modes with wavenumbers smaller than $k_d^{(n+1)}$, is the eddy turn over time,

$$\tau(k) \sim (\epsilon^{1/3} k^{2/3})^{-1} ,$$

where ϵ is the energy dissipation rate per unit mass, and not the Eulerian dephasing time which is characteristic of a covariance conditioned with respect to the supergrid velocity modes. Therefore, even at the level of a crude, Gaussian, calculation which ignores the spatial and temporal inhomogeneities of the true subgrid velocity field, it is essential that the velocity covariance decays according to the eddy turnover time. The generalization of the subgrid model presented in (12) to this time dependent velocity field is straightforward, though the algebraic details have not yet been fully investigated. We believe that such a model, or perhaps a slightly more sophisticated one which roughly describes the crossover behavior for the velocity covariance, is suitable for calculations of $\langle \emptyset \rangle$, but of doubtful utility for calculations of $\langle \emptyset^2 \rangle$; it is the inhomogeneities in the large scale velocity and scalar eddies which determine the transfer of scalar variance across k_c, and its calculation is therefore sensitive to the modeling of these inhomogeneities and the associated crossover behavior of the velocity covariance.

Though we have little to say about the construction of a subgrid model which is suitable for the calculation of both $\langle \emptyset \rangle$ and $\langle \emptyset^2 \rangle$, let us mention one qualitative feature, the presence of a subgrid random scalar source, which has been omitted from (12). This source is distinct from the eddy advection term which injects noise into the supergrid scales due to the presence of a random subgrid velocity field. The physical process represented by this source is the collision of subgrid velocity and scalar eddies to yield random supergrid scalar eddies. Technically, such a term arises when the partial averaging criterion, which was used to replace (7) by (8), is supplemented by the demand that $\langle x^2 \rangle$ be invariant.

Summary

A subgrid model for the random advection of a passive scalar, $\emptyset$, has been presented in the special case of a frozen velocity field. Its application is limited to the calculation of the mean value of $\emptyset$ because only one of the contributions to the fluctuations of $\emptyset$ has been included.

There are two principle differences between this model and the usual subgrid models. These arise from the recognition of the strong coupling between the large (supergrid) eddies and the (neargrid) eddies lying just below the limit of resolution of the finite difference grid. One is the explicit injection of noise from the neargrid eddies into the supergrid eddies. The other is a spatially non-local contribution to the scalar flux.

The implications of our analysis are not confined to the class of models which are narrowly defined as "subgrid". Any model which attempts to describe scalar transport by simple advection and gradient diffusion will have difficulty in handling the above mentioned contributions to the scalar flux. The significance of our model lies not in the numerical value for the eddy diffusivity, which has been approximately calculated, but in its form, equations (12), (14) and (15), which allows for a new mode of scalar transport.

ACKNOWLEDGEMENTS

The inspiration for this work (but none of its deficiencies) came from Jackson Herring who pointed out the inconsistency between the usual subgrid models and the predictability studies, and to David Leslie whose seminar and preprint (10) provided the impetus to begin. I would also like to thank Robert Kraichnan for an informative conversation on subgrid modeling, and for a preprint (2) of his work on eddy viscosity. Thanks also go to Uriel Frisch for helping me to orgqnize my thoughts.

+This work was begun while the author was with the Advanced Study Program of the National Center for Atmospheric Research, Boulder, Colorado, which is sponsored by the National Science Foundation.

REFERENCES

1 Bradshaw, P., "The Understanding and Prediction of Turbulent Flow," Aeronautical Journal, Vol.76, July 1972, pp. 403-418.

2 Kraichnan, R.H., "Eddy Viscosity in Two and Three Dimensions," Journal of the Atmospheric Sciences, Vol.33, No.8, Aug. 1976, pp. 1521-1536.

3 Leith, C.E., Journal of the Atmospheric Sciences, Vol.28, 1971, pp. 145.

4 Wilson, K.G., "The Renormalization Group: Critical Phenomena and the Kondo Problem," Reviews

of Modern Physics, Vol. 47, No. 4, Oct. 1975, pp.773-840.

5 Deardorff, J.W., "A Numerical Study of Three-Dimensional Turbulent Channel Flow at Large Reynolds Numbers," Journal of Fluid Mechanics, Vol. 41, 1970, pp. 453.

6 Deardorff, J.W., "On the Magnitude of the Sub-Grid Scale Eddy Coefficient," Journal of Computational Physics, Vol. 7, No. 1, Feb. 1971, pp. 120-133.

7 Deardorff, J.W., Journal of the Atmospheric Sciences, Vol. 29, 1972, pp. 91.

8 Deardorff, J.W., Journal of Fluids Engineering (Tr. ASME), 1973, pp. 429-438.

9 Leonard, H., "Energy Cascade in Large-Eddy Simulations of Turbulent Fluid Flows," Advances in Geophysics, Vol. 18A, 1974, pp. 237.

10 Leslie, D.C., "The Application of Classical Closures to Subgrid Modeling," TU 11/75, 1975, Queen Mary College, London.

11 Lilly, D.K., "On the application of the Eddy Viscosity Concept in the Inertial Sub-Range of Turbulence," NCAR manuscript No. 123, 1966, Boulder, Colorado.

12 Lilly, D.K., "The Representation of Small-Scale Turbulence in Numerical Simulation Experiments," Proceedings of the IBM Scientific Computing Symposium on Environmental Sciences, IBM Form No. 320-1951, 1967, pp. 195-210.

13 Schumann, U., "Subgrid Scale Model for Finite Difference Simulations of Turbulent Floxs in Plane Channels and Annuli," Journal of Computational Physics, Vol. 18, No. 4, Aug. 1975, pp. 376-404.

14 Smagorinsky, J.S., "General Circulation Experiments With the Primitive Equations. I: The Basic Experiment," Monthly Weather Review, Vol. 91, 1963, pp. 99.

15 Ma, S. and Mazenko, G.F., "Critical Dynamics of Ferromagnets in 6-ϵ Dimensions: General Discussion and Detailed Calculation," Physical Review B, Vol. 11, No. 11, June 1975, pp. 4077-4100.

16 Kolmogorov, A.N., C.R. Academy of Science U.S.S.R, Vol. 30, 1941, pp. 301, 538.

17 Kraichnan, R.H., "Kolmogorov's Hypothesis and Eulerian Turbulence Theory," The Physics of Fluids, Vol. 7, No. 11, Nov. 1964, pp. 1723-1734.

SESSION 15

PASSIVE SCALAR TRANSPORT

Chairman: P. A. Libby
University of California, San Diego
La Jolla, California
U.S.A.

KINEMATIC AND THERMAL STRUCTURES OF A ROUND HEATED JET

R. Chevray and N. K. Tutu
Department of Mechanical Engineering
State University of New York
Stony Brook, New York 11794

ABSTRACT

Temperature and velocity fields in a round heated jet were investigated in detail. Both conventional and conditional (zone averages and point averages) measurements were performed. Filtered correlation measurements show that large scale turbulent motions are responsible for the bulk of momentum and heat transport, and also that small scales are more efficient in transporting heat than momentum. In no case is heat transported farther or more than momentum, however. These results are discussed in details, particularly with regard to the entrainment.

INTRODUCTION

Free turbulent shear flows have been a subject of considerable experimental investigation in the past. The axisymmetric jet, in particular, has been investigated as early as 1943 by Corrsin, Hinze and Van der Hegge Zijnen (1949) and later in more detail by Corrsin and Uberoi (1950). Although these experiments have clearly established the preferential lateral transport of scalar quantities like heat over vector quantities like momentum--as translated into the inequalities of the eddy diffusivities for momentum and heat--no light has been thrown upon the possible differences in transport mechanisms. From the discovery of intermittency in free turbulent shear flows by Corrsin (1943) and one of the first comprehensive studies of this phenomenon by Corrsin and Kistler (1954), it has been recognized that intermittency plays a dominant role in such flows. On the one hand, this double statistical structure requires for detailed studies that measurements be made either separately in turbulent and non-turbulent zones (conditional zone averages) or with respect to the interface location (conditional point averages). On another hand, to investigate the difference in the transfer mechanisms of heat and momentum, filtered correlation measurements $\overline{u_f v_f}$ and $\overline{v_f \theta_f}$ need to be made. These measurements, obviously require simultaneous and continuous signals for velocity components and temperature; techniques to obtain them were developed and used here.

FLOW FACILITY AND EXPERIMENTAL TECHNIQUES

The heated jet facility consists mainly of an airfoil blade fan driven by a 7.5 H.P. DC motor with a Morse [illegible] SCR speed control which maintains the speed constant within 1.5%. This discharges through a bank of 15 finned heaters (22.5 kw) into a diffuser the end cross section of which is circular. After settling chamber equipped with screens and honeycomb and a 16:1 contraction, the axisymmetric circular jet emerges with a diameter D of 22.5 cm into the room from the center of a flat circular plate 124 cm in diameter. From the diffuser onwards, the jet facility is insulated throughout with fiber glass and to produce as rectangular as possible an exit temperature profile a collar heater (which circulates air at the same temperature as that of the jet) is provided at the end of the contraction. In order to detect readily any buoyancy effect, the whole unit was installed horizontally. At 15 diameters downstream where both horizontal and vertical profiles were measured, no marked departure from symmetry was observed. Nominal values of the mean velocity and temperature (above ambient) at the jet exit were 25 m/s and 20°C, respectively, while the turbulence intensity was measured to be a little less than 0.5%. This gives us a value of 0.23×10^{-3} for the ratio of buoyant forces to the inertia forces $\{gL\Delta\Theta/(\Theta\bar{U}^2)\}$. Thus it is clear that the temperature could be treated as a dynamically passive scalar field. Previous measurements by Chevray and Tutu (1972) using the same jet facility and same exit conditions demonstrated the virtual identity of velocity spectra for the heated (non-isothermal) and isothermal jets.

Empirical expressions relating the heat transfer from cylinders to flow characteristics are usually used as a basis for hot-wire anemometry. In non-isothermal flows, due to temperature variations, however, these relations become "functionals" of fluid properties and as a result continuous signal of the velocity is not readily obtainable. Because of this difficulty, Wygnanski and Fiedler (1970) and Sunyach (1971) have conducted the comparative studies of the thermal and kinematic structures of free shear flows by measuring in both the heated and non-heated flows. Corrsin (1949) has presented a technique which permits measurements of mean velocity, mean temperature, velocity and temperature fluctuation levels, as well as turbulent heat transfer and shear to be made in heated flows; and Corrsin and Uberoi (1950) have used this technique to make measurements in a heated turbulent air jet. The procedure involved, however, is quite cumbersome and measurement errors are large, but more critically the method does not provide continuous and simultaneous signals for velocity and temperature. This becomes essential when it is required to obtain joint statistics of fluctuating velocity components and temperature or simply to compare directly the intermittency structures of the temperature and velocity fields. The instrument developed for this study and reported on earlier by Chevray and Tutu (1972) permits the aforementioned measurements to be made. Essentially, it consists of two hot-wire probes, one operated in low overheat constant current mode thus providing a signal directly proportional to temperature, whereas the second hot wire operated in constant temperature mode provides a signal containing information on both the temperature and velocity. The manner in which the signal depends on the temperature is determined by the heat transfer equation describing the behavior of the hot wire. Information on the velocity field alone can thus be obtained from this second hot wire by generating the proper function of temperature given by the first and conditioning the signal through an analog circuit. These functions were evaluated theoretically and verified experimentally for air. Dynamic compensation was provided so that a linear signal representative of the velocity field alone could be obtained. This technique was adapted to a cross wire configuration, thus permitting not only direct measurements of the shear stress and heat transfer but also the measurement of filtered correlations between velocity and temperature.

Another instrumentation problem of concern in this study is due to the well-known fact that measurements of components of the turbulent stress tensor in high intensity turbulent flows like free turbulent jets, mixing layers, etc. are not reliable. This is usually thought of as a consequence of truncating the series expansion of the hot-wire response equation

$$U_{eff} = \{U^2_{normal} + k^2U^2_{axial}\}^{\frac{1}{2}} \qquad (1)$$

where U_{eff} is the instantaneous effective cooling velocity, U_{normal} and U_{axial} are the components of the velocity vector normal and parallel to the hot wire, respectively, and k is the axial sensitivity of the hot wire. While Champagne and Sleicher (1967) have already given the corrections (valid for small turbulence intensities) to be applied to measurements owing to the influence of k, another important source of error is the resultant rectification of the velocity signal by the hot wire; the hot wire being sensitive only to the magnitude of the effective cooling velocity. Rectification occurs whenever the component of velocity normal to the hot wire crosses zero. Although for a hot wire held normal to the flow this will obviously happen only during flow reversals, this is not so for cross-wires which are inclined to the flow. Since U_{eff} is always positive, the errors due to rectification arise not because of truncation of the series expansion of the right-hand side of Eq. (1) but because during signal processing the modulus sign implicit on the right hand side of Eq. (1) is ignored. It is therefore clear that in high intensity turbulent flows, besides the axial sensitivity k and the sensitivity to the w component of velocity, rectivication is an additional source of error in conventional measurements with cross wires. Champagne and Sleicher (1967) have demonstrated that the error in second-order moments due to k is negative, Tutu and Chevray (1975) have shown that the errors due to the other two causes (independently) are of the same sign.

For all the measurements, two hot-wire probes were used. When only longitudinal velocity component and temperature were needed, a standard DISA 55A39 hot-wire probe was used. This probe has two mutually orthogonal hot-wire sensors that are perpendicular to the probe axis. For simultaneous measurements involving quantities other than the abovementioned, a cross wire was used with the temperature sensor located upstream from and perpendicular to both cross wires. In the constant temperature mode, all sensors were 3.8 µm diameter tungsten wires spot welded to the prongs. For temperature measurements, the sensor was etched from a spot welded Wollaston wire (10% Rh., Pt) having a diameter of .635 µm. This wire was operated in a constant current mode with a sensor current of 0.15 mA using a Flow Corporation 1900-1 constant current anemometer, thus acting as a simple resistance thermometer. At this low probe current the velocity sensitivity of the hot wire was smaller than the noise in the temperature signal. At zero flow velocity the frequency response was good up to (3dB down) 5.7 kHz and this increased to 10.7 kHz at a flow velocity of 5 m/sec. Thus there was no need for electronic frequency compensation of the temperature signal.

Throughout this investigation, DC coupling has been used for all measurements. Although this renders measurements more tedious it is well worth the advantage of eliminating the distortion in signals due to low frequency loss encountered in AC coupling. Most measurements were made digitally using Hewlett-Packard 2212A voltage to frequency (100,000 pulses/s/V) converters and modified (with seven digits and a 100 s gate time) Hewlett-Packard 5330A Preset Counters to perform a true integration. To minimize scatter, long integration times (five minutes) were used. For measurements of odd moments and cross correlations a DC electronic splitter was built in order to separate the signal into positive and negative parts for simultaneous integration.

GROSS CHARACTERISTICS--CONVENTIONAL, POINT AND ZONE AVERAGES

All the measurements were performed at x/D = 15; this choice was dictated more by experimental constraints than by any theoretical considerations. While Wygnanski and Fiedler's (1969) measurements in an isothermal round jet clearly show that the complete dynamical similarity is reached only about some 70 diameters downstream of the jet exit, at such large x/D values, a much larger exit temperature difference would be needed to permit temperature measurements to be made. This would obviously conflict directly with our requirement that the temperature field be dynamically passive. Figure 1 shows the mean longitudinal velocity and temperature profiles together with the measurements of Wygnanski and Fiedler (1969) made in the self-preserving region. This relatively flatter

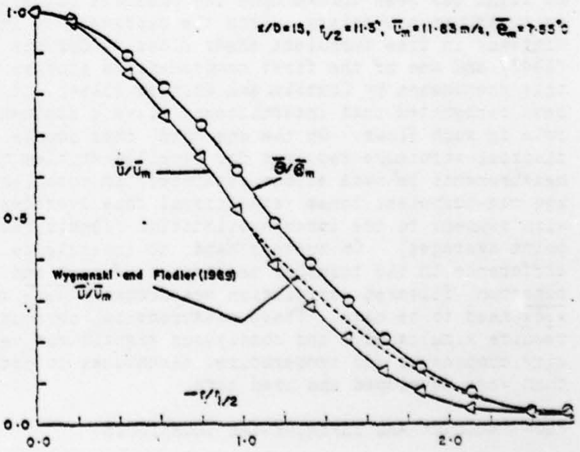

Figure 1. Longitudinal velocity and temperature profiles

distribution of temperature as compared to mean velocity is associated with the preferential transport of heat over momentum. It must be mentioned here that the temperature profile has been corrected for the contamination due to the influence of the velocity sensing hot-wire. This was done by measuring the mean temperature profiles with the velocity sensing hot wire on and off. The corrections were significant only for $r/r_{\frac{1}{2}} > 1.65$.

Velocity and temperature fluctuation intensities are presented in Fig. 2. The relatively large value of temperature fluctuations at the tails of the jet is due to fluctuations in the ambient temperature. Had we used AC coupling (with a cut off at 0.5 Hz, say) these very low frequency ambient temperature fluctuations would have been filtered out, and thus might have remained unnoticed. Again, in the outer regions of the jet the θ' profile was obtained by switching the velocity sensing wire off. In agreement with Wygnanski and Fiedler's (1969) measurements v' is everywhere less than u'. This is presumably because being an axis of symmetry, the center line of the jet serves as a constraint for the radial motions.

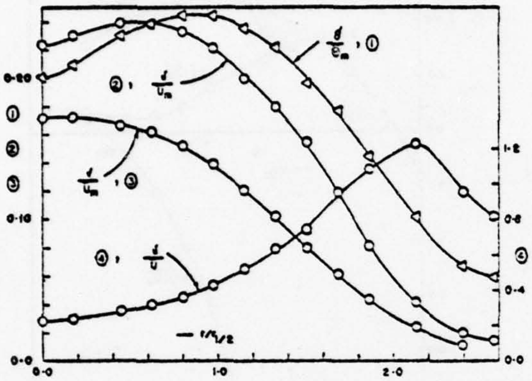

Figure 2. Velocity and temperature fluctuations at x/D = 15

To distinguish between the turbulent and nonturbulent states unambiguously, it is obvious that we must monitor a property of the flow which shows a jump across the turbulent/nonturbulent interface. An ideal detector probe would then be a vorticity probe giving us a continuous signal proportional to a component of vorticity. However such a probe would have at least four hot wires by itself with possibly an additional cross wire for u,v measurements and a single hot wire for temperature measurements. Obviously, not to mention the difficulties in building such an arrangement, there will be too many hot wires (and prongs) in a small volume to make any reliable measurements. Contrarily to what is generally thought, a two wire probe sensitive to $\partial U/\partial y$ is not a good substitute for a vorticity probe either, because although in the turbulent region $\partial\bar{U}/\partial y >> \partial\bar{V}/\partial x$, in the nonturbulent region $\partial\bar{U}/\partial y = \partial\bar{V}/\partial x$. Besides, and more importantly, instantaneous values $\partial U/\partial y$ and $\partial V/\partial x$ are *of the same order*; so, even in the turbulent region $\partial U/\partial y$ is not a good approximation for the vorticity component. For simplicity, therefore, it was decided to use $\partial u/\partial t$ as the basic signal from which to generate the intermittency function. Since the velocity fluctuations in the non-turbulent region are of a much lower frequency than the fluctuations in the turbulent zone, and since differentiation is nothing but selective amplification of high frequency components, $\partial u/\partial t$ should provide a good contrast between the turbulent and nonturbulent states. Moreover, assuming isotropy and Taylor's hypothesis, $\partial u/\partial t$ can also be visualized as being proportional to the square root of turbulent energy dissipation; thus a reasonably good detection can be expected from it.

Since the turbulence detector was designed and built (1972), many other turbulence detection schemes have appeared in the literature (i.e., Thomas, 1973; Paizis and Schwarz, 1974). The approach used here is described by Tutu (1976) and is basically the same as used by Kibens (1968). The actual circuit design, however, has been improved; in particular, the so-called 'hold time stage' (smoothing circuit) works on a completely different principle and is free of the defects and limitations of previous hold time stage as described by Tutu and Chevray (1976).

The time averaged value $\bar{I}$ of the intermittency function at a given point in space is called the intermittency factor and is usually denoted by γ. It is simply the fraction of time the flow is turbulent at a given location. Another important parameter that can be defined from I(t) is its "frequency" f_γ, which represents the number of turbulent bulges passing by a given location per unit time. Unfortunately, this has been referred to as the interface crossing rate in the literature, but it is important to note here that the interface crossing rate is $2f_\gamma$. Let $Q(\underset{\sim}{x},t)$ be a fluid mechanical property, then we can define its conventional average $\bar{Q}(\underset{\sim}{x})$, its turbulent zone average $\bar{Q}_t(\underset{\sim}{x}) = \bar{Q}$, and its nonturbulent zone average $\bar{Q}_n(\underset{\sim}{x}) = \bar{Q}$. Based on these three kinds of averages, three kinds of fluctuations arise:

$$q = Q-\bar{Q}; \quad q_t = Q-\bar{Q}_t; \quad q_n = Q-\bar{Q}_n$$

If $P(\underset{\sim}{x},t)$ is another fluid mechanical property, then three kinds of cross correlations suggest themselves.

$$\overline{pq} = \overline{(P-\bar{P})(Q-\bar{Q})}$$
$$\overline{\widetilde{p_t q_t}} = \overline{(P-\bar{P}_t)(Q-\bar{Q}_t)I}/\bar{I}$$
$$\overline{\widetilde{\widetilde{p_n q_n}}} = \overline{(P-\bar{P}_n)(Q-\bar{Q}_n)(1-I)}/\overline{(1-I)}$$

where, as it is clear, - denotes the conventional average, ≈ denotes the turbulent zone average, and ≈ denotes the non-turbulent zone average. The following relations are then easily proved.

$$\bar{Q} = \gamma\bar{Q}_t + (1-\gamma)\bar{Q}_n$$
$$\overline{pq} = \gamma\overline{\widetilde{p_t q_t}} + (1-\gamma)\overline{\widetilde{\widetilde{p_n q_n}}} + \gamma(1-\gamma)\{\bar{P}_t\bar{Q}_t + \bar{P}_n\bar{Q}_n - \bar{P}_t\bar{Q}_n - \bar{P}_n\bar{Q}_t\}$$
$$\overline{q^2} = \gamma\overline{\widetilde{q_t^2}} + (1-\gamma)\overline{\widetilde{\widetilde{q_n^2}}} + (1-\gamma)\{\bar{Q}_t-\bar{Q}_n\}^2$$

We call the terms in the braces 'switching terms' because they arise from the switching of mean level from turbulent to nonturbulent regions. Let

$$\hat{p}(\underset{\sim}{x},t) = \tfrac{1}{2}\left(\dot{I}(\underset{\sim}{x},t) + |\dot{I}(\underset{\sim}{x},t)|\right)$$

and $$\check{p}(\underset{\sim}{x},t) = \tfrac{1}{2}\left(|\dot{I}(\underset{\sim}{x},t)| - \dot{I}(\underset{\sim}{x},t)\right)$$

where $\dot{I}$ is the time derivative of I. $\hat{p}(t)$ is then a series of positive going δ-functions with each pulse occurring at the leading edge (downstream crossing--where I(t) changes from zero to unity). These functions can then be used to define the leading edge point average $\hat{Q}$ of Q and the trailing edge point average $\check{Q}$ of Q as

$$Q(\underset{\sim}{x}) = \lim_{T\to\infty}\left\{\int_{t_0}^{t_0+T} Q(\underset{\sim}{x},t)\hat{p}(\underset{\sim}{x},t)dt \div \int_{t_0}^{t_0+T}\hat{p}(\underset{\sim}{x},t)dt\right\}$$

$$= \overline{Q\hat{p}}/\overline{\hat{p}} = \overline{Q\hat{p}}/f_\gamma$$

$$\check{Q}(\underset{\sim}{x}) = \overline{Q\check{p}}/f_\gamma$$

We can also define a more general type of conditional point average, where the detector probe (from which $\hat{p}$ or $\check{p}$ is derived) and the sampling probe (which supplies Q) are separated by a certain distance $\underset{\sim}{r}$ in space and τ in time

$$\hat{Q}(\underset{\sim}{x},\underset{\sim}{r},\tau) = \overline{Q(\underset{\sim}{x}+\underset{\sim}{r},t+\tau)\hat{p}(\underset{\sim}{x},t)}/f_\gamma(\underset{\sim}{x})$$

Figure 3 shows the conditional zone averages of U and Θ across the jet. As expected, the fluid in the turbulent zones is seen travelling much faster than the fluid in the nonturbulent zones. The nonzero value of temperature in nonturbulent zones, and the observation that gradients of $\bar{\bar{\Theta}}$ and $\bar{\Theta}$ have the same sign, is rather curious. Its possible implications will be dissussed in the next section.

Again, in the turbulent zones the temperature distribution is much flatter than $\bar{U}_t$, showing that the scalar field is 'mixed' much better than the momentum. Figure 4 shows the fluctuation intensity of the longitudinal component of velocity in the two zones. As a comparison with Fig. 2 shows, for $r/r_{1/2} > 1.15$ the local turbulent intensities in the two zones are less than the unconditioned local turbulence intensity. The maximum value of about 0.7 for $u_t'/\bar{U}_t$ is much less than the maximum value of 1.2 for $u'/\bar{U}$; thus showing that the errors due to assumed simple linearized hot wire response are not as great as the unconditioned local turbulence intensity would indicate. The conditional averages of the radial component of velocity depicted in Fig. 5 show that as expected the nonturbulent fluid is moving in on an average while the turbulent fluid is moving out. Near the tails of the jet, the relatively large positive values of $\bar{V}_t$ indicate that once in a while the turbulent bulges are shooting out. Similarly, large negative values for $\bar{V}_n$ deep inside the jet show that the nonturbulent fluid is rushing in to be entrained, which suggests that perhaps there are deep crevices on the turbulent/nonturbulent interface in regions of high γ where significant entrainment is taking place. For high radial positions, the strange behavior of the unconditioned radial velocity $\bar{V}$ comes from the effects of rectification and distortion due to high turbulence intensity.

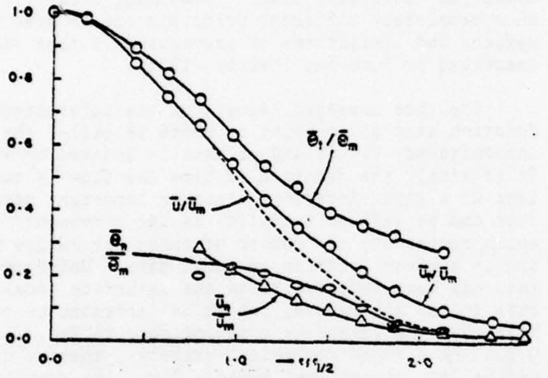

Figure 3. Conditional velocity and temperature profiles

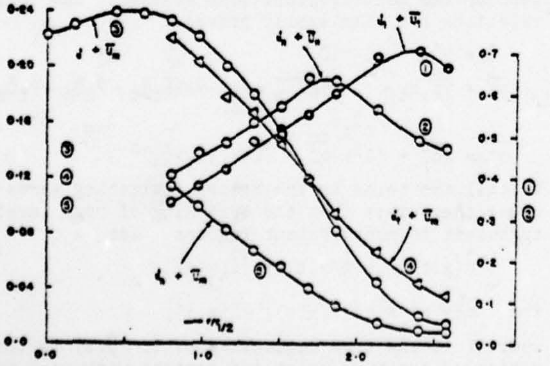

Figure 4. Zone averaged longitudinal velocity profiles

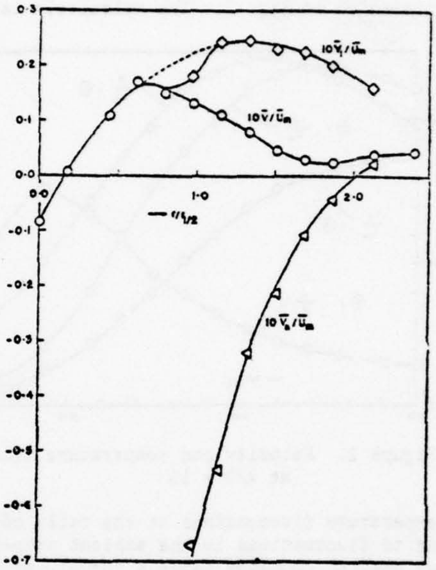

Figure 5. Zone averaged lateral velocity profile

Let $\underset{\sim}{\varsigma}$ be the velocity of the interface with respect to the fluid; if this propagation velocity is very small as compared to the fluid velocity at the interface, then the convection velocity of the interface can be assumed to be equal to (at least for the sake of qualitative interpretation of results) the fluid velocity at the interface. As Corrsin and Kistler (1954) and Phillips (1972) suggested, $|\underset{\sim}{\varsigma}|$ should be of the order Kolmogorov velocity scale $(\varepsilon\nu)^{1/4}$. For isotropic turbulence, an estimate for $|\underset{\sim}{\varsigma}|$ is

$$|\underset{\sim}{\varsigma}| \approx .5\sqrt{\nu\xi'}\ , \quad \xi' = \frac{\sqrt{5}v'}{\lambda_u}\ .$$

With the conditions at the center line of the jet at x/D = 15 these two estimates reduce to 0.188 m/sec and 0.06 m/sec, respectively. The measured longitudinal component of the point averaged fluid velocity at the interface is 1.24 m/sec at γ = 0.41, which is much larger than the estimated $|C_p|$. It therefore seems reasonable to interpret the point averaged velocity profile $\hat{U}(r)$ as the profile for the interface convection velocity. This leading as well as trailing edge velocity (longitudinal component) and temperature profiles are presented in Fig. 6. These reveal that on an average the fluid at the leading edge (front) is travelling with the same longitudinal velocity as the trailing edge (back). That the point averaged temperature profile is flatter than the point averaged velocity profile, giving yet another evidence that the temperature field is more homogeneous in the turbulent zones than the velocity field, was expected. The remarkable feature here, however, is that $\partial\hat{\Theta}/\partial r$ and $\partial\check{\Theta}/\partial r$ are both positive for $\gamma > 0.95$. This can only be explained if unusually large entrainment is taking place deep inside the jet in these regions of high γ, which is consistent with earlier observation (Fig. 5) of large negative values of $\hat{V}_n$ in the regions of high γ.

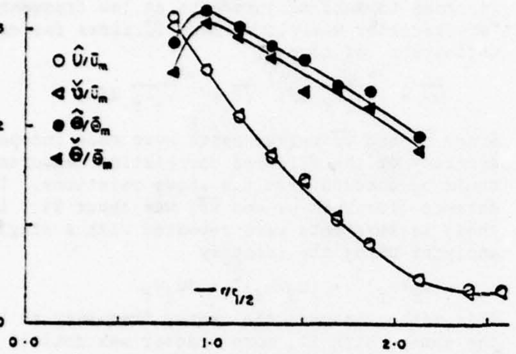

Figure 6. Point averaged temperature and velocity profiles

To find out the distribution of the radial component of fluid velocity near the interface and within the turbulent region, conditional point measurements with respect to the existence of the interface (at the point) at a certain time t before or after were made. For measurements near the leading edge, the velocity component V was sampled at fixed intervals after the interface was detected. To make measurements near the trailing edge, the tape (on which velocity and temperature signals were recorded and the intermittency function added) was run backwards and the above procedure was repeated. The results are plotted in Fig. 7 and show several interesting features. Chief among these, the radial velocities near the interface behave very differently at the 'fronts' than they do at the 'backs'. For $r/r_{1/2} < 1.66$ the fluid near the 'front' is moving inwards, while beyond $r/r_{1/2} = 1.66$ it is moving outwards. In contrast, however, the fluid near the trailing edge is on an average always moving inwards.

ENTRAINMENT AND PREFERENTIAL TRANSPORT

As the experimental results for the average turbulent Prandtl number indicate, the turbulent Prandtl number is very different from unity. It is different for different flows and as the results presented earlier indicate it even varies from location to location for the same flow. Although this behavior is far from being understood, it has been recognized early that the intermittency phenomenon plays a dominant role in such flows [Townsend (1956)], Mayer and Divoky (1966)]. It has also led investigators to believe that the transport mechanisms for momentum and scalar quantities are not identical. Townsend (1949) has suggested that, in the intermittent region gradient type diffusion (small scale fluctuations) would be mainly responsible for the transport of momentum while both gradient type diffusion and bulk convection (large scale fluctuations) would be responsible for the transport of heat. Recently, Fiedler (1975) has also suggested an ordinary gradient diffusion mechanism for momentum in a plane turbulent mixing layer. To be consistent with this model, however, the shear correlation $\overline{uv}$ should get most of its contribution from the small scale region. Useful as they are in problems of engineering relevance, the classical mixing length theories have, unfortunately, been unable to predict these transfer differences. Reynolds analogy and Prandtl's mixing length theory both imply identical temperature and velocity profiles ($\sigma_t = 1.0$). Taylor's (1932) vorticity transport theory, however, does predict differences between the temperature and velocity distributions, but this prediction, to be sure, is only qualitative. The inadequacies of these theories should not be surprising because as Taylor (1932) has shown, his theory is valid only when the mean and turbulent motions are confined to two dimensions. Among other objections to Prandtl's theory, because momentum of a fluid particle is not conserved during its motion, it is not valid in any case.

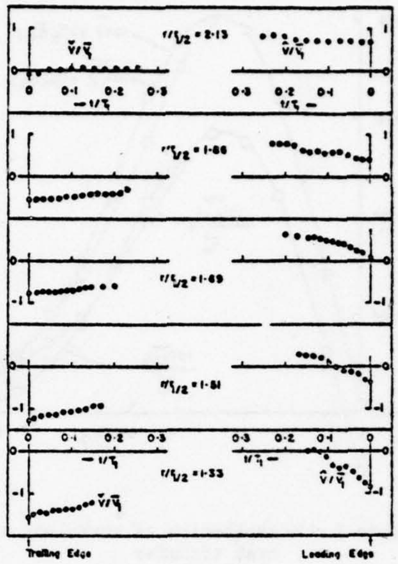

Figure 7. Point averaged lateral velocity distribution inside the turbulent bulge at x/D = 15

Corrected turbulent 'shear stress' and the lateral component of the turbulent heat transfer, both unconditioned and in the turbulent zones, are plotted in Fig. 8. That the turbulent zone values are less

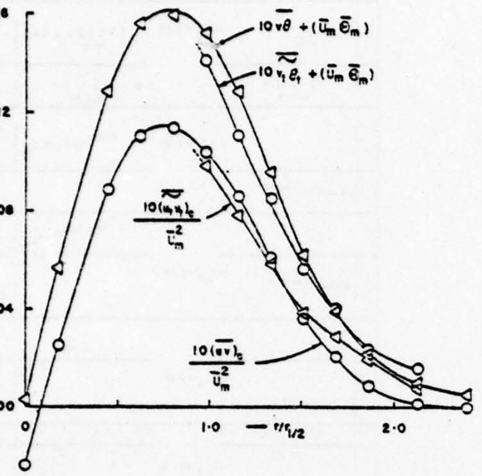

Figure 8. Distribution of turbulent shear and heat transfer

than the conventional averages in the central region is merely due to the 'switching terms' relating the two being of a certain sign. Since the nonturbulent zone averages for the 'shear stress' and heat transfer were too small (about an order of magnitude less) to be measured accurately, they were assumed to be effectively null. Distributions of $\overline{v\theta}$ and $\overline{uv}$ have similar shapes and reach their maximum values at approximately the same radial location. This suggests that the transport mechanisms for momentum and heat are perhaps not radically different. Mean velocity and temperature profiles presented earlier show the inflexion points to be roughly at $r/r_{\frac{1}{2}} = 1.1$ whereas $\overline{uv}$ and $\overline{v\theta}$ reach a maximum at approximately $r/r_{\frac{1}{2}} = 0.78$, thus demonstrating the weakness of a simple gradient type transport mechanism for either momentum or heat.

As pointed out by Corrsin and Uberoi (1950), the turbulent Prandtl number σ_t, defined as the ratio of "eddy diffusivities" for momentum and heat, does not have any fundamental physical basis; nevertheless it provides an empirical measure of the ratio of momentum to heat transfer. In terms of the various measured quantities it can be expressed as

$$\sigma_t = \frac{(\overline{uv}/U_m^2)\ \frac{\partial}{\partial r}(\bar{\Theta}/\bar{\Theta}_m)}{(\overline{v\theta}/\bar{U}_m\bar{\Theta}_m)\ \frac{\partial}{\partial r}(\bar{U}/\bar{U}_m)}$$

Its variation across the jet was computed from the least square curves fitted to the observed data. In qualitative agreement with Hinze and Van der Hegge Zijnen's (1949) indirect measurements, varying from .4 to .7, σ_t is hardly a constant across the jet. In view of the aforementioned inadequacy of a simple gradient type transport to describe this flow, this should not be surprising. It might be mentioned in this connection, that in view of the considerable scatter in their data, Corrsin and Uberoi (1950) concluded that σ_t was a constant across the flow but nonetheless, our average value of about 0.6 is less than their estimated value of about 0.7.

An additional means to study momentum and heat transport is to compare the size of eddies responsible for the bulk of the transport. Filtered correlations $\overline{u_fv_f}$ and $\overline{v_f\theta_f}$ serve just this purpose. Since simultaneous signal for u, v and θ were available, this was done by using two identical wave analyzers (HP 302A, bandwidth: 6Hz) set at the same center frequencies. In order to make measurements at low frequencies, the tape recorder was played back 32 times faster. By definition, of course,

$$\overline{uv} = \int_0^\infty \overline{u_fv_f}\,df;\quad \overline{v\theta} = \int_0^\infty \overline{v_f\theta_f}\,df\ .$$

Since $\overline{uv}$ and $\overline{v\theta}$ measurements were made independently, accuracy of the filtered correlation measurements could be checked from the above relations. The difference (for both $\overline{uv}$ and $\overline{v\theta}$) was about 9%. Later, these measurements were repeated with a single wave analyzer using the identify

$$(u_f+v_f)^2 - (u_f-v_f)^2 = 4u_fv_f.$$

This method insures the center frequency to be exactly the same. With it, more scatter was noticed at high frequencies, otherwise the results were unchanged. For these measurements shown in Fig. 9 no attempt has been made to convert frequency to wavenumber since on the one hand Taylor hypothesis is not applicable for our case and on the other hand the proper convection velocity is strongly dependent on wave number (Wygnanski and Fiedler, 1970).

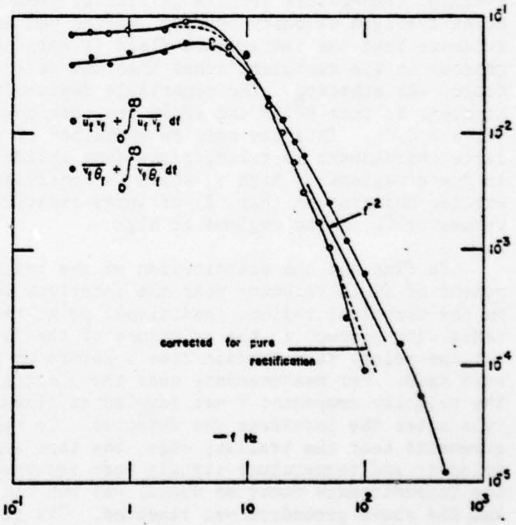

Figure 9. Filtered correlations at $r/r_{\frac{1}{2}} = 0.8$

From integration of the distributions of Fig. 9, $\overline{uv}$ gets about 70% of its contribution below 10 Hz while $\overline{v\theta}$ gets about 50%. Although the bulk of the transport (for temperature as well as momentum) is accomplished by the large scales, the small scales are more efficient in transporting heat than momentum. Thus gradient type diffusion is more important for heat than it is for momentum transport. Although this may look surprising at first, the physical reason for this can be translated to the fact that the "mixing length" for temperature is larger than it is for the momentum. This is because while a scalar is conserved during fluid motion (in the absence of molecular diffusivity) momentum is not; and since the momentum of a fluid particle associated with these small scale motions is continuously "bleeding", the effective mixing length is reduced.

$\overline{u_f v_f}$ drops sharply at 100 Hz, and since $\overline{v_f \theta_f}$ does not show such behavior, it was suspected that this strange cut off for $\overline{u_f v_f}$ might be due to the distortions in the velocity signals because of high turbulence intensity. In order to investigate this effect on the $\overline{u_f v_f}$ spectrum, $u(t)$ and $\theta(t-\tau)$ signals at the center line were assumed to simulate undistorted u and v signals. A delay line was used to delay the temperature signal, with a delay τ such that the correlation coefficient between $u(t)$ and $\theta(t-\tau)$ at the centerline was the same as R_{uv} at $r/r_{\frac{1}{2}} = 0.8$. The filtered correlation between these two signals was measured and served as the 'reference' (or true) spectrum. By analog means, these simulated signals were then distorted just as a cross wire would under conditions of pure rectification at $r/r_{\frac{1}{2}} = 0.8$. Filtered correlations were measured again and compared with the 'reference' spectrum. From these results, it is seen that the effect of pure rectification is to reduce the correlation $\overline{u_f v_f}$ algebraicly; this correlation is shown in Fig. 9. In the absence of molecular conductivity (and consequently molecular viscosity), the conservation equation for temperature reduces to $D\Theta/Dt = 0$; indicating that the temperature of a fluid particle is indeed conserved during its motion. Thus, considering the diffusion of temperature field by small scales only Prandtl's mixing theory should hold good. Also, it is clear that the only mechanisms responsible for the transport of heat (besides molecular diffusion) are bulk convection and turbulent diffusion (or more correctly convection by all scales). Neglecting molecular viscosity, the momentum equation reduces to $D\underset{\sim}{U}/Dt = -\frac{1}{\rho}\nabla p$. Thus it is immediately apparent that the momentum of a fluid particle is not conserved during its motion, but is continuously changing. It also shows that besides bulk convection and turbulent diffusion there is an additional mechanism for the momentum transport: namely, pressure forces. At first, it could be expected that due to an additional mechanism for transport, the velocity profile should be flatter than the temperature profile. This, however, has just the opposite effect. Because of continuous 'bleeding' of momentum from a fluid particle due to pressure forces, the effective mixing length for momentum is less than that for heat. Within the turbulent region, therefore, the transport due to pressure forces is achieved at the expense of transport due to convection, thus resulting in an overall reduction in the net momentum transport. Momentum, as opposed to heat, can be imparted to fluid in the nonturbulent region through pressure forces across the interface. Since this results in the momentum being distributed over more fluid volume (assuming that there is no negative entrainment heat cannot be transported across the turbulent/nonturbulent interface), this further makes the $\bar{U}_t$ profile steeper than the $\bar{\Theta}_t$ profile.

Using the classical mixing length arguments, the lateral component of the heat flux vector, q, and the turbulent shear stress, τ, are given by

$$\left.\begin{aligned} q &= -\rho c_p \ell^2 \left|\frac{\partial U}{\partial y}\right| \frac{\partial \bar{\Theta}}{\partial y} \\ \tau &\quad \sigma_t \rho \ell^2 \left|\frac{\partial U}{\partial y}\right| \frac{\partial U}{\partial y} \end{aligned}\right\} \qquad (2)$$

where c_p is the specific heat at constant pressure, ℓ is the "mixing length", and σ_t is the turbulent Prandtl number. If we restrict our attention to small scales, but which are large enough so that 'bleeding' of momentum and heat due to molecular actions can be neglected, we can write equations of the type (2) for individual length scales. This would result in a range of frequencies where the filtered correlations would behave as:

$$\overline{u_f v_f} \sim f^{-2}, \quad \overline{v_f \theta_f} \sim f^{-2}.$$

Between 45 Hz and 250 Hz, which, based on mean velocity would correspond to length scales between 3 cm and 17 cm (as compared to the microscale $\lambda = 4.95$ mm and Kolmogorov length $\eta = .09$ mm), $\overline{v_f \theta_f}$ does indeed drop as f^{-2}. If we define a turbulent Prandtl number $\sigma_t(f)$ for individual eddies as a function of frequency using filtered correlation measurements we see that for large eddies, bulk convection is an equally important and efficient mechanism for momentum transport. These eddies, being of a size comparable to the shear flow itself do not experience an appreciable inviscid drag, but as their size becomes smaller the inviscid drag (due to pressure forces) increases and σ_t consequently drops.

This preferential transport of a scalar has nonetheless to be viewed with the proper perspective; namely that it results in a more uniform distribution of the scalar property than the momentum within the flow field. It does not necessarily imply that relatively more scalar flux is transported laterally. It does not imply either as shown by Jenkins and Goldschmidt (1975) that the scalar is transported much further into the ambient fluid. To see this, let us split the round jet into two regions at the radial location where the heat flux and shear stress attain their maxima; all fluid elements in the central zone are losing both momentum and heat on an average, while fluid elements in the outer region are gaining these. Since in a turbulent jet the longitudinal momentum and heat flux is constant at every section, we define

$$m = \tau_{max}/(\text{Total longitudinal momentum flux})$$

$$h = q_{max}/(\text{Total longidutinal heat flux})$$

then the ratio m/h is a good measure of the relative transports of momentum and heat; from our measurements we get

$$m/h = 0.94$$

which is much higher than the turbulent Prandtl number of 0.61. If we consider the interfaces for velocity and temperature to be the same, the mass flow rate M_m which carries the momentum is:

$$M_m = \int_0^\infty \rho 2\pi r \bar{U} dr$$

while the mass flow rate M_h which carries the heat is

$$M_h = \int_0^\infty \rho 2\pi r \; \overline{I(t)U} \, dr.$$

Since $I(t) \leq 1$, it is obvious that $M_h < M_m$. So, contrary to the implications of the turbulent Prandtl number, momentum is distributed over more fluid mass than heat; and this also contributes in making the temperature profile relatively flatter.

Since the presence or absence of turbulence is independent of the magnitude of a passive scalar, there can be only one turbulent/nonturbulent interface which we designate the velocity interface. For the temperature, we will call interface the boundary across which there is a temperature variation--the fluid on one side of which being at the ambient temperature. Figure 10 shows the simultaneous traces of

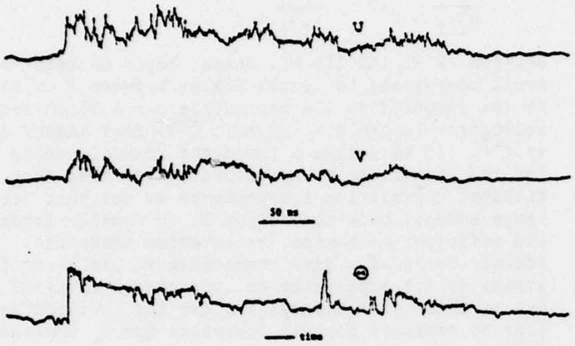

Figure 10. Simultaneous traces of U, V and Θ at $r/r_{\frac{1}{2}} = 1.33$

U, V and Θ signals at various locations in the jet. The difficulties in establishing the coincidence of temperature and velocity interfaces with absolute certainty are immediately apparent. Because of the contamination of the temperature signal (predominantly in regions of reserve flow) due to the influence of the velocity sensing hot wire, there exists sometimes large temperature excursions in the nonturbulent regions. Although these can usually be identified as such (because of their peculiar shape), it is not always so; and this makes the interface comparison difficult. As expected, the temperature signal shows a jump across the interface, whereas the velocity signal is comparatively smooth. By studying a large number of simultaneous U, Θ traces we concluded that within the present uncertainty inherent in our measurement technique, the temperature and velocity interfaces are coincident (Chevray and Tutu, 1972). Several other investigators have arrived at the same conclusion. Fiedler and Head (1966), by comparing the signals from the outputs of a hot wire anemometer and a photoelectric smoke detector found identity of smoke and turbulence distributions in a turbulent boundary layer. Based on this result Fiedler (1973) assumed the coincidence of temperature and velocity interfaces in a plane turbulent mixing layer. In their work on the wake of a heated flat plate, Kovasznay and Firasat Ali (1974) used the temperature signal to construct the intermittency signal [I(t)], thus implicitly assuming the coincidence of the temperature and velocity interfaces. All this might perhaps suggest that the identity of velocity and temperature interfaces is firmly established. This however is not the case. Were the interfaces for velocity and temperature different, it is clear that the temperature interface could only be outside the turbulent/nonturbulent interface. This can happen only if during certain times the instantaneous entrainment is negative; that is, the turbulent fluid becomes irrotational and mixes with ambient fluid. Since the dissipation of turbulent energy has to occur by molecular mechanisms, it follows that this "de-entrained" irrotational fluid will not exhibit temperature fluctuations characteristic of the turbulent fluid, but will instead exhibit low frequency fluctuations. When these are of the same order as the ambient temperature fluctuations, one is likely to conclude that the interfaces for velocity and temperature are the same even though they actually are not. Thus the presence of ambient temperature fluctuations in our experiments as well as those of other investigators (Jenkins and Goldschmidt, Kovasznay and Firasat Ali, Fiedler) prevents us from firmly establishing the coincidence of velocity and temperature interfaces.

Negative entrainment can occur only by two mechanisms: (a) bulk de-entrainment in which the lump of turbulent fluid is detached from the main body of turbulent fluid and decays by viscous dissipation and diffusion, and (b) reduction in the volume of turbulent flow by viscous dissipation and diffusion across the turbulent/nonturbulent interface--in this case the interface travels into the turbulent fluid. Since measurements to record the shape of turbulent bursts [either by direct flow visualization or by using a hot-wire rake similar to Kaplan and Laufer's (1968)] have been done only in a plane, whether lumps of turbulent fluid do detach from the main body of the turbulent flow has never been established. On another hand, as Corrsin and Kistler (1954) and Phillips (1972) argue, due to viscous diffusion and rapid production of vorticity stemming from the random rate of straining induced by the turbulence, the turbulent/nonturbulent interface always travels into the nonturbulent fluid (positive entrainment). In view of this argument (b) seems impossible and one is thus inclined to dismiss the idea of negative entrainment and consequently assume the identity of the interfaces for velocity and temperature. There are, however, two important experimental observations which strongly suggest that in free turbulent shear flows, there might be occurrences of instantaneous negative entrainment. First, by choosing the reference level for temperature measurements as the mean ambient temperature, the nonturbulent zone averaged profile of temperature should be a horizontal straight line $\bar{\Theta}_n = 0$ and this even in the presence of ambient temperature fluctuations. But as can be seen from Fig. (3) not only is $\bar{\Theta}_n$ large it also decreases with the radial coordinate r. Since the sign of $\partial\bar{\Theta}_n/\partial_r$ is same as that of $\partial\bar{\Theta}_t/\partial r$, these measurements would be consistent with the idea of negative entrainment. An obvious explanation could be that there exist an ambient temperature gradient set up in the room due to some hot air being recirculated. This would seem plausible were it not for the fact that the same trend is seen in all reported conditional measurements of temperature: Kovasznay and Firasat Ali (1974, wake of a heated flat plate), Fiedler (1973, plane turbulent mixing layer), Jenkins and Goldschmidt (1974, two dimensional plane jet), Davies, Keffer and Baines (1975, plane turbulent jet). Observation of this behavior for Θ_n has prompted Davies et al. (1975) to conclude that conduction heat transfer is taking place across the turbulent/nonturbulent interface (presumably because they rejected the notion of the negative entrainment). It is very unlikely however that this is happening. First of all, since the interface is not a material surface but is continuously propagating within the fluid medium, one has to be careful in talking about conduction heat transfer across the turbulent/nonturbulent interface. Assuming that the entrainment is only positive (if negative entrainment is allowed conduction across the interface will only be a second order effect), the velocity (or more properly vorticity) interface is travelling into the nonturbulent fluid with a velocity ζ which is of the order of $(\varepsilon\nu)^{1/4}$ (Corrsin and Kistler, Phillips). Let in an inertial coordinate system at time $t = 0$ both the vorticity and temperature interfaces be coincident; these are going to propagate into the nonturbulent fluid by actions of molecular viscosity and conductivity. If the molecular Prandtl number P_r is greater than unity, the thermal interface will always lag behind the velocity interface; if it is less than unity as for air, then the thermal interface will overtake the velocity interface. This however is not the case. Considering the conduction heat transfer from a plane wall kept at a constant temperature to a semi-infinite medium, it can be shown that the velocity of the thermal interface is proportional to $\sqrt{\alpha/t}$, where α is the molecular diffusivity and t is the time. Since the velocity of the vorticity interface is constant, it will soon overtake the thermal interface. Thus in the limit the velocity and thermal interfaces will be coincident, and as such there will be no conduction heat transfer across the turbulent/nonturbulent interface. This, of course, happens because the propagation of vorticity interface is accelerated by the random stretching of vortex lines, while no such mechanism exists for the thermal interface.

Another equally important observation has been made by Mobbs (1968). His experiments in a homogeneous turbulent flow surrounded by a potential flow moving with the same mean velocity (no mean shear and unstrained flow) have clearly demonstrated that there is a reduction in the volume rate (of flow) of turbulent fluid with the downstream distance. His subsequent measurements by subjecting the homogeneous free turbulent flow to a plane straining show that a reasonably high degree of anisotropy combined with straining by the mean flow is required before entrainment of nonturbulent fluid can occur at the interface. He thus concluded that "In free turbulent shear flows, the potential-turbulent flow boundary will advance into the nonturbulent fluid at a rate which depends on the local mean rate of strain and the local degree of anisotropy adjacent to the front. Contraction is expected to occur on those occasions when the boundary lies in a region of zero mean rate of strain, or when the anisotropy of the turbulence is low." Furthermore, he states, "It may be expected that the anisotropy of the turbulence adjacent to the bounding surface will be a maximum when the front is located near the point of maximum shear, and this will be the location most favorable to spreading of the turbulence." And this is consistent with our measurements showing large negative values of $\bar{V}_n$ and positive $\partial\hat{\Theta}/\partial r$ in the region of maximum shear.
Mobb's experiments clearly demonstrate that negative entrainment is possible. What is debatable, however, is whether there is negative entrainment occurring periodically in a given turbulent shear flow (the average entrainment rate is of course positive). This can only be resolved by a very careful interface comparison technique with negligibly small ambient temperature fluctuations. If it is found that the entrainment is indeed negative during certain durations, another important question to be settled will be the mechanism by which this happens; bulk de-entrainment or inward (into the turbulent region) propagation of the turbulent/nonturbulent interface. If one believes in the arguments of Corrsin and Kistler (1954) and consequent Phillips' (1972) assumption that the interface is always travelling into the nonturbulent fluid, bulk de-entrainment will be the only mechanism by which negative entrainment could occur.

CONCLUDING REMARKS

Within the present uncertainties in our measurement technique such as ambient temperature fluctuations, contamination of temperature signal by the velocity sensing hot-wire in regions of reverse flow, the velocity and temperature interfaces are coincident. There nevertheless exists a distinct possibility of instantaneous negative entrainment (and consequent occasional non-coincidence of temperature and velocity interfaces) on the basis of other previously published measurements in free turbulent shear flows.

From our conditional measurements, fluid particles in the turbulent zone are seen to move fast (as compared to the mean velocity) and outward, whereas fluid particles in the nonturbulent zones are moving slowly and inwards. Point measurements with respect to the interface suggest that jets of fluid are shooting out periodically from the central regions, thus greatly increasing the surface undulations of the interface. The measurements also suggest that the interface has crevices in zones of high γ where rapid entrainment is taking place.

The conventional turbulent Prandtl number was found to be a variable across the flow with a value of 0.61 at the location of maximum shear. Filtered correlation measurements show that large scale turbulent motions are responsible for the bulk of momentum and heat transport, and also that small scales are more efficient in transporting heat than momentum. Consequently, whereas bulk convection cannot be neglected for momentum transport, gradient type diffusion cannot be neglected for heat transport if it is included for momentum transport.

ACKNOWLEDGMENTS

Special thanks are due to E. E. O'Brien for his help in many capacities throughout this study. The financial support of the National Science Foundation under Grant No. GK30479 and KO40738 is gratefully acknowledged.

REFERENCES

Champagne, F. H. and Sleicher, C. A. (1967), J. Fluid Mech. 28, 177.

Chevray, R. and Tutu, N. K. (1972), Rev. Sci. Instr. 43, 1417.

Corrsin, S. (1943), NACA Rep. No. W-94.

Corrsin, S. (1949), NACA Tn No. 1864.

Corrsin, S. and Uberoi, M. S. (1950), NACA Rep. No. 998.

Corrsin, S. and Kistler, A. L. (1954), NACA Rep. No. 1244.

Davies, A. E., Keffer, J. F. and Baines, W. D. (1975), Phys. Fluids 18, 770.

Fiedler, H. and Head, M. R. (1966), J. Fluid Mech. 25, 719.

Fiedler, H. E. (1973), SecondIUTAM-IUGG Symposium on Turbulent Diffusion in Environmental Pollution, University of Virginia, USA.

Hinze, J. O. and Van der Hegge Zijnen, B. G. (1949), "Transfer of Heat and Matter in the Turbulent Mixing Zone of an Axially Symmetrical Jet", Appl. Sci.

Res., Vol. A1, pp. 435-461.

Jenkins, P. E. and Goldschmidt, V. W. (1975), Phys. of Fluids 19, 5, 613.

Kaplan, R. E. and Laufer, J. (1968), Proc. 12th Int. Congress of Applied Mech., 236.

Kovasznay, L. S. G., Kibens, V. and Blackwelder, R. F. (1970), J. Fluid Mech. 41, pp. 283-325.

Kovasznay, L. S. G. and Firasat Ali, S. (1974), Proceedings of Fifth Int. Heat Transfer Conf., Tokyo, II, 99.

Mayer, E. and Divorky, D. (1966), AIAA J. 4, 1995.

Mobbs, F. R. (1968), J. Fluid Mech. 33, 227.

Paizis, S. T. and Schwartz, W. H. (1974), Rev. Sci. Instr. 45, 348.

Phillips, O. M. (1972), J. Fluid Mech. 51, 97.

Sunyach, M. (1971), These Dr-es-Sc, Univ. Lyon.

Taylor, G. I. (1932), Proc. Roy. Soc. London A 135, 685.

Thomas, R. M. (1973), J. Fluid Mech. 57, 549.

Townsend, A. A. (1949), Aust. J. Sci. Res. Ser. A 2, 451.

Townsend, A. A. (1956), The Structure of Turbulent Shear Flow, Cambridge Univ. Press.

Tutu, N. K. (1976), Ph.D. Dissertation, SUNY, Stony Brook.

Tutu, N. K. and Chevray, R. (1975), J. Fluid Mech. 71, 785.

Tutu, N. K. and Chevray, R. (1976), Rev. Sci. Instrum. 47, 163.

Wygnanski, I. and Fiedler, H. (1969), J. Fluid Mech. 38, 577.

Wygnanski, I. and Fiedler, N. (1970), J. Fluid Mech. 41, 327.

TURBULENT TEMPERATURE AND THERMAL FLUX CHARACTERISTICS IN THE WAKE OF A CYLINDER

Gracio Fabris
Argonne National Laboratory
Argonne, Illinois

ABSTRACT

The far wake of a mildly heated cylinder was explored with a new four-wire probe and temperature was used as a tracer to reveal more of the flow structure. An extensive computer program for digital processing of output signals of the probe was developed. Full nonlinear response equations for the four sensors were solved simultaneously, yielding "true" instantaneous values of three components of velocity and temperature at any point of the turbulent wake. Additional special features are: full instantaneous corrections for free-stream velocity and temperature fluctuations, first-order corrections for D.C. drifts of the signals, complete elimination of all 60 Hz-related noise, instantaneous corrections for the streamwise displacement between the sensors, etc.

A number of conditionally sampled correlations was computed with respect to conventionally averaged flow, turbulent and potential zone averages, as well as the free stream conditions providing new physical insights into the structure of a two dimensional turbulent wake flow. This information is needed for development of prediction methods especially those trying to take in account large-scale intermittent features of the turbulent flow. The more important correlations involving temperature characteristics are presented in this paper in some detail.

NOMENCLATURE

D	diameter of a cylinder (6.2484 milimeters)
K	flatness factor
l_o	$=\sqrt{(x - x_o)D}$, self-similar length scale
q	fluctuating part of velocity
S	skewness factor
U,u,u'	total, fluctuating and RMS values of streamwise component of velocity
U_d	defect of streamwise component of velocity
U_∞,U_R	free stream velocity (6.46 meters per second)
V,v,v'	total, fluctuating and RMS values of lateral component of velocity
W,w,w'	total, fluctuating and RMS values of spanwise component of velocity
x	streamwise coordinate
x_o	$= -40$ D, virtual origin of the wake
y	lateral coordinate
z	spanwise coordinate
α	coefficient of thermal diffusivity
γ	intermittency factor
Θ,θ,θ'	total, fluctuating and RMS values of temperature overheat
Θ_R	maximum wake temperature overheat at $x/D = 200$ (0.4227 C)
$(\ )_R$	Reynolds averages; averages of fluctuating quantities computed with respect to conventional average as base
$(\ )_Z$	zone averages; averages of fluctuating quantities computed with respect to zone (heated or unheated) average as base
$\overline{(\ )}$	time averaged value

INTRODUCTION

Turbulent wake flow of a cylinder remains to be of great interest both technologically and fundamentally. Investigation of wake velocity and temperature fields simultaneously reveals interesting fluid phenomena and answers some heat transfer questions.

The last ten years have seen rapid development of large digital computers. Their power revolutionized prediction methods of turbulent flows leading to increasing number of equations with increasing number of turbulent characteristics. Of necessity terms and coefficients in these equations are based on intuitive assumptions. It is the task of experimentalists to provide more physical insights into the complex turbulent interactions. The new "conditional sampling" technique (1) combined with increasingly effective digital processing of data provide much more statistically significant detail data. For many applications, such structured data could be used for advanced prediction methods. Recently a method (2,3) has been put forward which extends prediction to the more physical conditioned turbulent averages.

To make better use of available digital processing of data it is essential to develop better experimental probes and data processing methods. An effort in this direction (4) generated a special four-wire probe that is practically interference free. Also, a method of processing the signals was developed to yield time series of uncontaminated instantaneous values of temperature and three velocity components at a point in a turbulent flow.

This paper presents information on the strucutre and statistics of turbulence correlations involving temperature in the two dimensional wake of a mildly heated cylinder.

EXPERIMENTAL APPARATUS AND TECHNIQUE

Flow Conditions

The experiments conducted were in a wind tunnel with 0.914 by 0.609 meter rectangular test section at a velocity of 6.46 meters per second. Measured turbulent fluctuation levels in the free stream were $u'/U_\infty = 0.00055$, $v'/U_\infty = 0.00042$ and $w'/U_\infty = 0.0007$ (after instantaneous compensation for spurious very low-frequency pressure induced fluctuations and 60 Hz noise, see (5)). A cylinder of diameter D = 6.2484 millimeters was slightly heated so that the maximum temperature at x/D = 400 was only 0.34 C and the wake exhibited no trace of buoyancy effects. The indicated rms free-stream temperature fluctuations were 0.0014 C (which was essentially electronic noise level).

The Four-Wire Probe

The probe is shown in Figure 1. It basically consists of an x-wire unit (sensors 1 and 2), a jawed sensor 3 (primarily for w component of velocity) and a temperature sensor 4 in front. Angular calibration was performed and the cosine law confirmed for all three jaw sensors. All sensors were made of Wollaston-processed Pt-10% Rh filaments 0.625 microns in diameter. When the overheat of the upstream sensor 3 was decreased to 150 C the thermal interference with sensors 1 and 2 was brought to a level of less than one per cent.

Processing of Signals

As part of signal processing the full response equations were written for all sensors taking into account the dependence of all flow properties. These equations were solved simultaneously using the Newton-Raphson technique to yield true instantaneous values of U, V, W, and Θ. Free stream velocity and temperature were measured by two additional probes and their values were subtracted simultaneously from the corresponding quantities in the wake. This improved the accuracy of measurements of true wake effects in low temperature and low velocity defect regions of the wake. All measurements were taken after at least six hours of steady running to minimize drifts for any given run. The first and the last acquisition of data was always carried out in the free stream. The running time of data acquisition at different wake positions was always recorded. It was assumed that any remaining D.C. drifts were slow and linear in time between the first and the last data acquisition and appropriate corrections were coded in for all channels.

The time span for 200 digitized samples coincided with exactly three periods of 60 Hz power line on which the acquisition was triggered. This fact was utilized to ensemble-average and educt the free stream signal to obtain the 60-cycle associated "noise" for each channel. These signals were then subtracted resulting in a substantially improved accuracy of measurements in low turbulence regions.

Correction for relative streamwise displacement of the sensors, based on instantaneous streamwise velocity was also introduced.

To assure that the system (probes, calibrations, processing, and correction technique) was functioning properly as a whole, it was checked extensively against established analog methods. For example, several u', v', and w' wake profiles have been measured each one using three different analog methods or probes. Also, the cold wake was rotated 90 degrees within the tunnel by mounting the cylinder vertically while the four-wire probe remained fixed and results were compared.

GOVERNING EQUATIONS

Derivation of the "turbulent" equations for mean and fluctuating thermal fields is given elsewhere (6). When simplifications are made for stationary two dimensional thin shear flow the mean conservation of heat reads:

$$(\overline{U}\frac{\partial}{\partial x} + \overline{V}\frac{\partial}{\partial y})\Theta = 1\,\frac{\partial\overline{u\theta}}{\partial x} - \frac{\partial\overline{v\theta}}{\partial y} + \alpha\frac{\partial^2\overline{\Theta}}{\partial y^2}\,, \qquad (1)$$

where the second term on the right dominates.

Because the temperature is a scalar, the dynamics of the mean square temperature fluctuations $\overline{\theta^2}$ is governed by a single scalar equation:

$$1/2(\overline{U}\frac{\partial\overline{\theta^2}}{\partial x} + \overline{V}\frac{\partial\overline{\theta^2}}{\partial y}) = -\overline{v\theta}\,\frac{\partial\overline{\Theta}}{\partial y} - -\overline{u\theta}\,\frac{\partial\overline{\Theta}}{\partial x} -$$

$$1/2\,\frac{\partial}{\partial x}\,(\overline{u\theta^2}) - 1/2\,\frac{\partial}{\partial y}\,(\overline{v\theta^2}) +$$

$$1/2\,\alpha\,\frac{\partial^2\overline{\theta^2}}{\partial xi\partial xi} - \alpha\overline{(\frac{\partial\theta}{\partial xi})(\frac{\partial\theta}{\partial xi})}, \qquad (2)$$

where Cartesian tensor notation is used in the molecular "dissipation" terms (second derivatives).

EXPERIMENTAL RESULTS

Data were recorded and processed for wake locations x/D = 200 and 400, each at twelve lateral profile positions. Prandtl number for air being near unity, a simple temperature threshold was effective in distinguishing between turbulent (heated) and potential (non-heated) parts of the flow. Careful processing of signals made possible the use of very low threshold levels of approximately four per cent of mean maximum wake overheat at any x position, e.g., 0.013 C at x/D = 400. Conditional averages were computed for the turbulent and potential zones of the time series and also as point averages at the front (downstream) and back (upstream) interfaces of the turbulent bulges. These were compared to normal time means ("Reynolds averaging") such as appear in the equations of the preceding section. The contrast between conditional fluctuations averages (with respect to local zone averaged properties as base) and the corresponding Reynolds averages revealed additional processes within the turbulent and potential parts of the flow, e.g. contributions to Reynolds stresses by the uncontaminated potential motions.

Instantaneous Quantities

Let us first focus on the instantaneous picture at a point to provide a "feel" for the nature of the flow under scrutiny, keeping in mind that no finite number of correlations can describe it fully. Figure 2 displays traces of instantaneous flow quantities, obtained by digital processing as previously described, at $x/D = 400$ and $y/D = 7.2$ corresponding to an intermittency factor of $\gamma = 0.65$. While the turbulent field is clearly random in character, some quasi-repeatable patterns are discernible. An exhaustive discussion on question of presence and importance of the nonrandom processes is given in (7). The fact that the coherent structures exhibit wide distribution of sizes and mutual distances and are obliterated by truly random turbulent processes has been responsible for rather late recognition of their existence (8, 9, 10).

Let us single out an isolated short turbulent bulge at time t = 150 ms on Figure 2. It has a lower streamwise velocity than the potential patches upstream and downstream of it. There is a virtual coincidence of the heated (turbulent) region and the region of rapidly changing lateral velocity. The front (downstream) part of this turbulent entity is moving rather rapidly toward the wake centerline (negative V) while its back part is moving in the opposite direction. The minimum of the streamwise velocity seems to occur approximately at the time of the maximum positive time derivative of the lateral velocity but with some shift to a region of the outward moving fluid. The trace of the spanwise velocity indicates increased movement in the spanwise direction compared to the upstream and downstream potential flow patches. The temperature increases on the downstream side of the turbulent bulge "ramp"-like (see (11)) while the decrease on the upstream side is rather abrupt.

More of less similar flow pattern is repeated a number of times. Differences in sizes, mutual time shifts and a degree of obliteration by smaller eddies are present as explained elsewhere (7). Generally, decreases of the streamwise velocity are somewhat more rapid than its increases. Changes to the outward motion are more rapid than changes to the inward motion. Gradients of the lateral velocity seem to be the highest. One could say that the sharpest gradients in lateral velocity correspond to "rolling over" of turbulent bulges by a faster moving potential flow that produces strong spanwise vorticity. Quite frequently sharp gradients are present in the spanwise velocity suggesting a possibility that some of strong vortices could turn from spanwise to lateral direction. In the literature (7) there is a talk of possible "vortex loop formed by pinching off and joining together of vortices from opposite sides of the street" (wake).

Temperature Distributions

Temperature distributions were extensively investigated for a similar geometry by LaRue (12) at downstream locations at $x/D = 400$ and 500. The locations being relatively close to each other and probably in the self-preserving region no differences were noticed in conditional levels of temperature in the turbulent bulges at two locations. We have done measurements at $x/D = 200$ and 400. Figure 3 compares these temperatures plotted in selfsimilar coordinates. Conventional averages show only slight discrepancy at two locations. The conditional temperatures in outer part of turbulent bulges show somewhat more measurable differences. At the first downstream location turbulent bulges move somewhat further outwards (in self-similar coordinates) and their average temperature is lower. A possible cause of this would be a relatively increased entrainment to outer parts of the bulges due to higher lateral and streamwise velocity differences between potential and turbulent bulges at $x/D = 200$ (see (5)).

We have also recorded average temperatures at "front" and "back" (downstream and upstream edges) of the turbulent bulges. These temperatures are of course just above the discrimination threshold temperature (equal to 0.013 C at $x/D = 400$). However, data (see Fig. 22 in (5)) show that temperature slopes $\partial\theta/\partial t$ are higher at the upstream edge of turbulent bulges. The average slope increases more and more as one moves further outwards from the wake centerline.

Streamwise and Lateral Velocities

Enhanced transfer of heat and momentum is due to large scale lateral eddy motion in the turbulent wake flow. Figure 4 displays various averages of the lateral velocities. The conventional average has a small negative value showing that there is a net inflow toward the wake centerline. Comparable measurements of this velocity are difficult to find in the literature. The potential cold flow moves towards the wake centerline and the average velocity of those less frequent potential lumps which penetrate farther inward increases with closeness to the wake centerline. Similar trends but with the opposite sign take place for the warm turbulent outward moving fluid. Fronts of the heated interfaces move faster toward the wake centerline than the average potential flow. This is an indication that turbulent bulges are being "rolled over" by faster moving potential flow. This picture is consistant with one for the outer part of turbulent boundary layers (1, 13).

Figure 5 displays the streamwise velocity defect at $x/D = 400$. As expected the patches of the potential flow move faster than the average flow at all lateral positions in the wake. This difference increases as the potential flow penetrates closer to the wake centerline. However, these inner potential patches move slower: in other words, they have been decelerated by interaction with even slower turbulent bulges. This deceleration has been accomplished through pressure fluctuations since the potential flow has not experienced shear stresses or "mixing."

The turbulent bulges in turn move slower than the average flow as should be expected. The maximum difference is not as high as that for the potential flow; this is a consequence of the profile shape of the conventional mean velocity defect. On the average, the front of a turbulent bulge moves faster than the potential flow, presumably encroaching upon the latter. On the average, the back is slower than potential average but faster than the average turbulent flow. This is interesting as some might expect the opposite namely that the potential flow would be more likely to "push" the back of turbulent bulges than to "suck" the front. Positive differences between the velocities of fronts and backs of turbulent bulges are consistent with the observed lengthening of the turbulent bulges.

Second Order Correlations

Figure 6 displays profile of temperature fluctuations. When fluctuations are computed with respect to the local conventional average temperature as base ("Reynolds average") their (conditional) value in heated fluid increases monotomically from the centerline. "Temperature fluctuations" in the "cold" potential flow reach very high values when computed in this way. Of course there should be no temperature fluctuations in potential flow and indeed when fluctuations are computed with respect to local zone average temperatures $\overline{\theta^2}$ *becomes neglegible.* This is one of the facts which corroborates the efficacy of the choice of the threshold value. Zone-averaged temperature fluctuations within turbulent bulges for γ F 1 remain significantly high with possibly an assymptotic behavior at the wake edge. The peak fluctuation appears to correspond approximately to the inflection points of the respective mean profile.

The $\overline{v\theta}$ correlation is shown in Figure 7. It is a very important correlation since it characterizes the lateral transport of heat per unit area of planes y = const. The lateral gradient of this correlation dominates the redistribution of the mean thermal energy lateraly in thin shear layers and its product with the lateral gradient of temperature is responsible for the main production rate of temperature fluctuations $\overline{\theta^2}$. The profile of $\overline{v\theta}$ has some similarity with the $\overline{\theta^2}$ profile. One can see that a considerable amount of heat is transferred by turbulent fluctuations within intermittent heated bulges. It is actually comparable to heat transferred by outward moving bulges themselves (product of conditional turbulent zone averages $\overline{V}$ and $\overline{\Theta}$).

Figure 8 displays correlation of fluctuations of temperature and the streamwise velocity component. In thin shear layers this correlation does not contribute significantly to heat transfer in the equations because its streamwise gradient is small.

Third Order Transport Corrélâtions

In this section streamwise and lateral transport of θ^2 and $v\theta$ will be discussed. These quantites appear in Reynolds-averaged equations for $\overline{\theta^2}$, $\overline{v\theta}$, and $\overline{u\theta}$, of which only the first is currently used. However, the analogy with the growing belief that the most consistant tractable set of equations for describing the turbulent velocity field would involve the Reynolds stresses as unknowns, conservation equations for $\overline{u\theta}$ and especially $\overline{v\theta}$ are likely to be considered in the near future. The present data would then provide a background for assumptions and/or useful test cases. The instantaneous quantity θ^2 is always positive and is similar to that of the turbulent kinetic energy $1/2\ q^2$. The full equation for θ^2 was given in a previous section. Figure 9 presents the lateral transport of square of temperature fluctuations. Conventionally averaged $\overline{v\theta^2}$ correlation shows that the square temperature fluctuations are generally transported away from the region of their high intensity. Conditional averages disagree with the "gradient transport law" and in fact exhibit intensive transfer of the squared temperature fluctuations toward the wake edge by the turbulent bulges.

Figure 10 indicates a streamwise transport of the squared temperature fluctuations. For the central part of the wake the correlation is positive indicating that the faster moving pieces of the fluid exhibit higher temperature fluctuations. At the wake edge this is true for slower moving fluid.

Figure 11 displays a profile of the $\overline{uv\theta}$ correlation. This correlation could be interpreted in several ways, e.g., as a correlation between instantaneous uv and temperature. Negative value of $uv\theta$ correlation in outer part of the wake probably means that contribution of the turbulent bulges (having mostly positive θ and netagive uv) predominates over contribution of the potential bulges. The $uv\theta$ correlation changes sign in a region closer to the wake centerline though none of the second order correlations does. Physical meaning of the reversal deserves more attention. Another way of looking at this correlation would be as streamwise transport of $v\theta$ flux. Specifically transport equation for $v\theta$ correlation can be written as it is sometimes done for the Reynolds stress. A third way of interpreting this correlation is as lateral transport of the $u\theta$ flux. It is in this way that the reversal of sign in $\overline{uv\theta}$ could be explained namely as transport of $u\theta$ away from maximum of $\overline{u\theta}$, at least as far as the conventional averages are concerned.

Figure 12 displays the $\overline{v^2\theta}$ correlation which represents lateral transport of $v\theta$. Conventional $v\theta$ correlation is positive at the upper side of the single wake and is transported away from the region where it is the highest, that is, toward the wake center and edge. Transport by heated bulges is substantial and positive while unheated bulges transport in the opposite direction.

Statistics of Time Derivatives of Temperature

It is the small scale of turbulence which is primarily responsible for dissipation of turbulent kinetic energy. Similarly the small scale of spatial temperature variations is responsible for the "dissipation" of temperature fluctuation intensity $\overline{\theta^2}$ by molecular action. In the small scale isotropic approximation $-6\alpha\overline{(\partial\theta/\partial x)^2}$ is used to calculate the rate of dissipation of the temperature fluctuations. Ratio of $\overline{(\partial\theta/\partial x)^2}$ to $2\overline{\theta^2}$ determines the Taylor microscale of the temperature fluctuations. Since in the far wake with relatively small turbulent intensities Taylor's hypothesis is rather well satisfied, investigation of the statistics of the $\partial\theta/\partial t$ fluctuations ($\sim U\ \partial\theta/\partial x$) should provide some insight into the small scale structure of thermal turbulence. Figure 13 displays profile of averaged squared time derative of temperature. Similarly with the profile of $\overline{\theta^2}$ is apparent while that is not the case with averaged squared time derivatives of three velocity components (see Figure 167 in (5)). By far the highest intensity of dissipation of temperature fluctuations is at the crests of the intermittent turbulent bulges. The values of $\overline{(\partial\theta/\partial t)^2}$ in the potential regions are negligible, again validating the efficacy of the threshold.

The assumption of isotropy of small scale temperature fluctuations has been checked in (14) and found to be true to an excellent degree. Our check (page 6.66 in (5)) of squared time deratives of components of velocity shows some disagreement with assumption of isotropy.

AD-A055 654 PENNSYLVANIA STATE UNIV UNIVERSITY PARK DEPT OF MECH--ETC F/G 20/4
SYMPOSIUM ON TURBULENT SHEAR FLOWS HELD AT THE PENNSYLVANIA STA--ETC(U)
APR 77 N00014-77-C-0176

UNCLASSIFIED NL

8 OF 9
ADA
055654

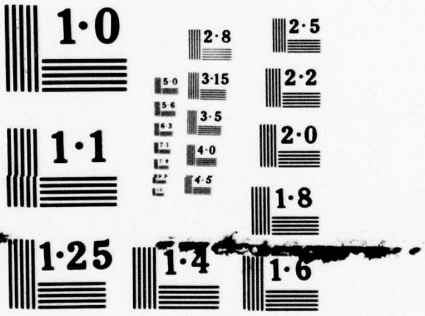

NATIONAL BUREAU OF STANDARDS
MICROCOPY RESOLUTION TEST CHART

Figure 14 presents the profile of the skewness factor of the time derivative of temperature. For the most part of the wake, the skewness factor has an almost constant value of minus one. This is an indication that a rather regular relationship might exist between upstream and downstream slope of the temperature trace ("ramps" seen in Figure 2) regardless of lateral position in the wake. As one approaches the top of turbulent bulges the skewness factor becomes more negative. Figure 15 displays the profile of the flatness factor of the time derivative of temperature. The value at the centerline is equal to eight. This is certainly the most pronounced deviation from Gaussiani of the turbulent quantities $\partial u/\partial t$, $\partial v/\partial t$, $\partial w/\partial t$, and $\partial\theta/\partial t$ whose K factor was computed at the centerline. It can be inferred that "dissipation" of thermal turbulence is an intermittant process within the fully turbulent flow (see 15). The value of $K_{\partial\theta/\partial t}$ decreases slightly away from the centerline still in the fully turbulent flow. In the intermittent flow the level of the conventionally computed $K_{\partial\theta/\partial t}$ increases dramatically toward the edge of the wake. This increase is only partially due to actual increase of the slope of the temperature trace in the intermittent turbulent fluid as seen in Figure 2, however, heavy contribution of the potential non-heated fluid to decrease the conventional standard deviation $(\partial\theta/\partial t)^2$ contributes even more to the sharp increase of the flatness factor. If $K_{\partial\theta/\partial t}$ is computed for intermittent heated flow only its value continues to drop as the wake edge is approached tending toward the Gaussian value of three.

SUMMARY AND CONCLUSIONS

A special four wire probe was made and a method of digital processing of its signals was developed yielding uncontaminated instantaneous values of three components of velocity and temperature at a point of a turbulent flow. The method of processing of the signals included instantaneous corrections for a wind tunnel free stream velocity and tempeature fluctuations, first order corrections for D.C. drifts of the signals, elimination of all 60 Hz related noise, and others.

The probe and the methods were used for conditional sampling in the turbulent far wake of a slightly heated cylinder. Instantaneous traces of U_d, V, W, and Θ in the intermittent region of the wake indicate that "deterministic" structures (large eddies) are present being more or less obliterated by smaller more random structures.

Conditional $\overline{U}$, $\overline{V}$ and $\overline{\epsilon}$ profiles show that the heated turbulent bulges move slower in the streamwise direction than the average flow while moving laterally outwards. The cold potential flow moves faster than the average flow and moves laterally inwards toward the wake centerline.

A number of conditional second and third order transport correlation involving temperature are given. Aim was to provide data to aid new prediction methods. High levels of temperature fluctuations, heat transfer and transport of thermal turbulence are present in the turbulent bulges in the intermittent region. While the concept of eddy diffusivity of $\overline{\theta^2}$ might be a rough approximation for the conventional profiles, it fails completely for the conditional profiles.

Dissipation of thermal turbulence is the most intense in the turbulent bulges. Statistics of $\partial\theta/\partial t$ fluctuations sharply deviate from Gaussianity. Negative values of the skewness factor may be associated with the "ramp" like trace of temperature. The flatness factor far exceeds Gaussian value even at the centerline suggesting an intermittent nature of the dissipation of the thermal turbulence in fully turbulent flow.

ACKNOWLEDGEMENT

Valuable guidance of Dr. M. V. Morkovin and Dr. J. L. Way during this research and help in writing of the paper is greatly appreciated. The research was supported under USAF OSR Grant No. AFOSR-73-2509.

REFERENCES

1. Kovaszney, L. S. G., Kibens, V., and Blackwelder, R. F., "Large Scale Motion in the Intermittent Region of a Turbulent Boundary Layer," Journal of Fluid Mechanics, Vol. 41, Part. 2, 1970, pp. 283-325.

2. Libby, P., "On the Prediction of Intermittent Turbulent Flow," Journal of Fluid Mechanics, Vol. 68, Part 2, 1975, pp. 273-295.

3. Libby, P. A., "Prediction of the Intermittent Turbulent Wake of a Heated Cylinder," The Physics of Fluids, Vol. 10, No. 4, April 1976, pp. 494-501.

4. Fabris, G., "A Probe and Method for Simultaneous Measurements of 'True' Instantaneous Temperature and Three Velocity Components in Turbulent Flow," submitted for publication, 1976.

5. Fabris, G., "Conditionally Sampled Turbulent Thermal and Velocity Fields in the Wake of a Warm Cylinder and Its Interaction with an Equal Cool Wake," Ph.D. Dissertation, Illinois Institute of Technology, Chicago, 1974.

6. Tennekes, H. and Lumley, J. L., "A First Course in Turbulence," MIT Press, Cambridge, Massachesetts, 1972.

7. Roshko, A., "Structure of Turbulent Shear Flows: A New Look," AIAA Journal, Vol. 14, No. 10, October 1976, p. 1349-1357.

8. Papailiou, D. D., "Turbulent Vortex Streets," Ph.D. Dissertation, Purdue University, 1971.

9. Bevilaqua, P. M. and Lykoudis, P. S., "Mechanism of Entrainment in Turbulent Wakes," AIAA Journal, Vol. 9, 1971, pp. 1657-1659.

10. Brown, G. and Roshko, A., "The Effect of Density Difference on the Turbulent Mixing Layer," AGARD Conference Proceedings, No. 93 on Turbulent Shear Flows, September 1971, pp. 21-1-23-12.

11. Antonia, P. A., Prabhu, A, and Stephenson, S. E., "Conditionally Sampled Measurements in a Heated Turbulent Jet," Journal of Fluid Mechanics, Vol. 72, Part 3, 1975, pp. 455-480.

12. LaRue, J. C., "The Temperature Characteristics in the Turbulent Wake of a Heated Rod," Ph.D. Dissertation, University of California, San Diego, 1974.

13. Hedley, T. B. and Keffer, J. F., "Some Turbulent/Non-Turbulent Properties of the Outer Intermittent Region of a Boundary Layer," Journal of Fluid Mechanics, Vol. 64, Part 4, 1974, pp. 645-678.

14. Freymuth, P. and Uberoi, M. S., "Structure of Temperature Fluctuations in the Turbulent Wake Behind a Heated Cylinder," The Physics of Fluids, Vol. 14, No. 12, December 1971.

15. Kuo, A. Y. and Corrsin, S., "Experiments on Internal Intermittence and Fine-Structure Distribution Functions in Fully Turbulent Fluids," Journal of Fluids Mechanics, 1971, Vol. 50, pp. 285-320.

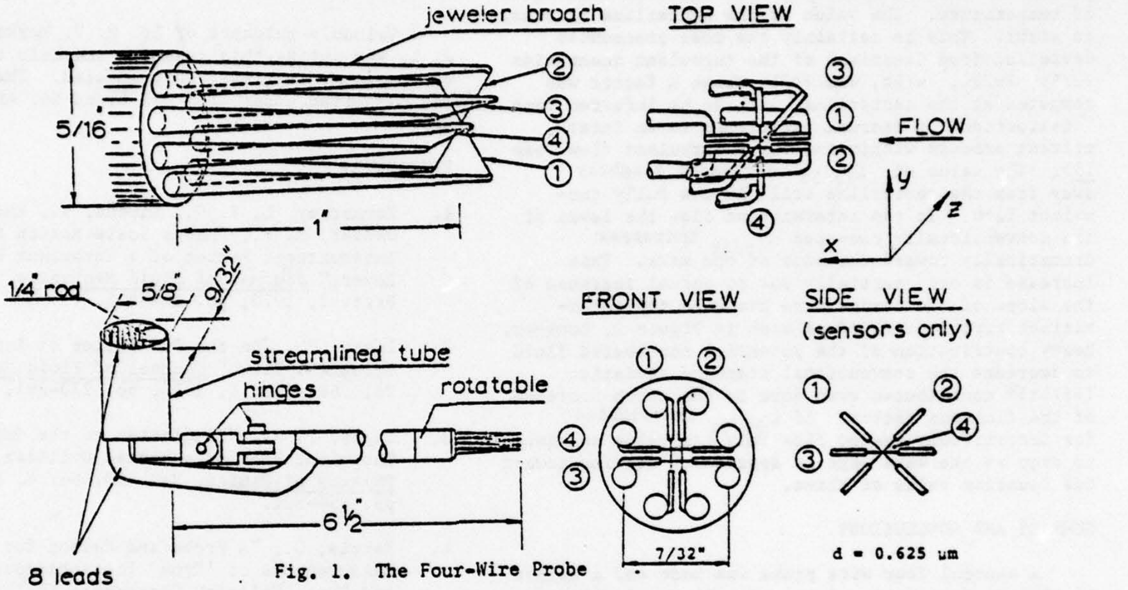

Fig. 1. The Four-Wire Probe

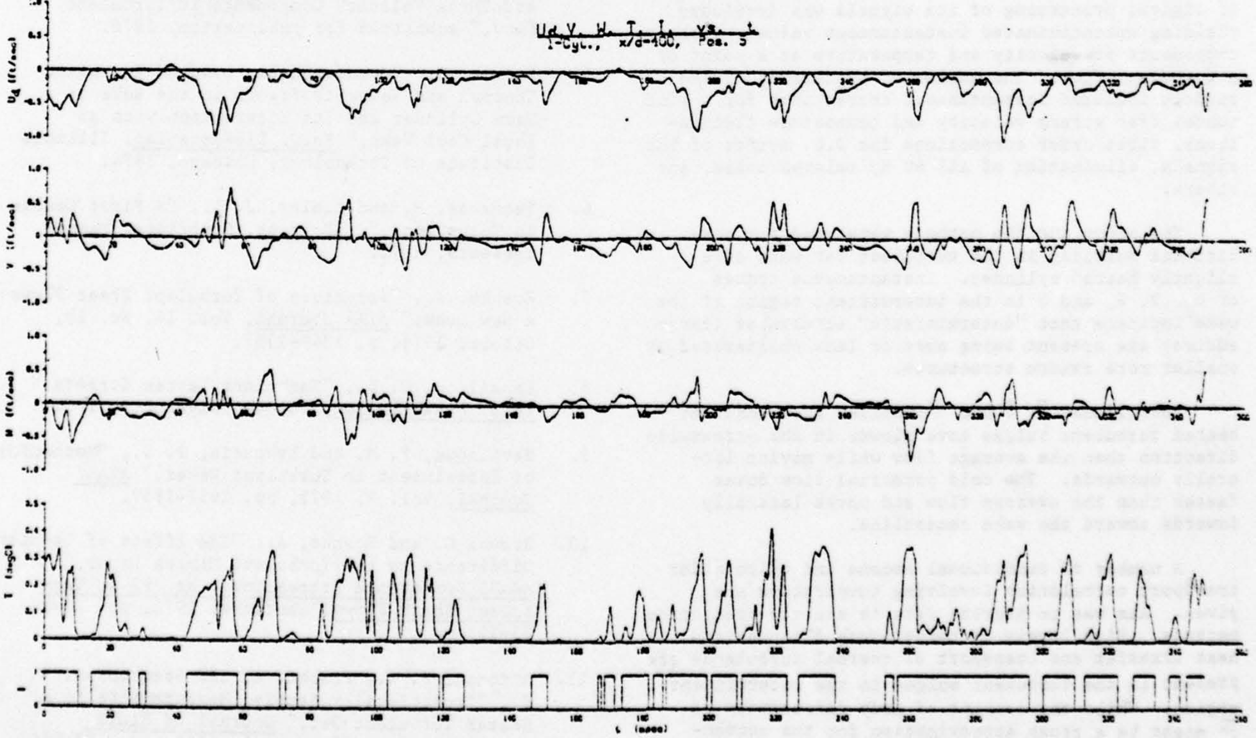

Fig. 2. Instantaneous Flow Quantities at x/D = 400, y/D = 7.2, γ = 0.65

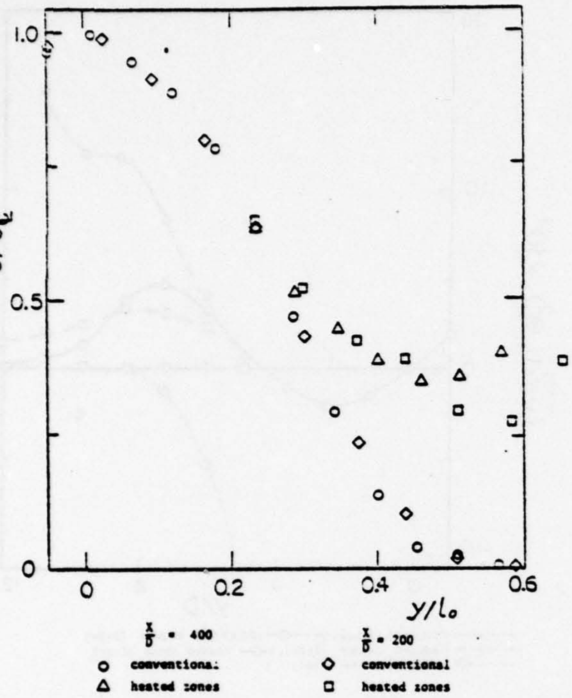

Fig. 3. Conditional Mean Temperatures

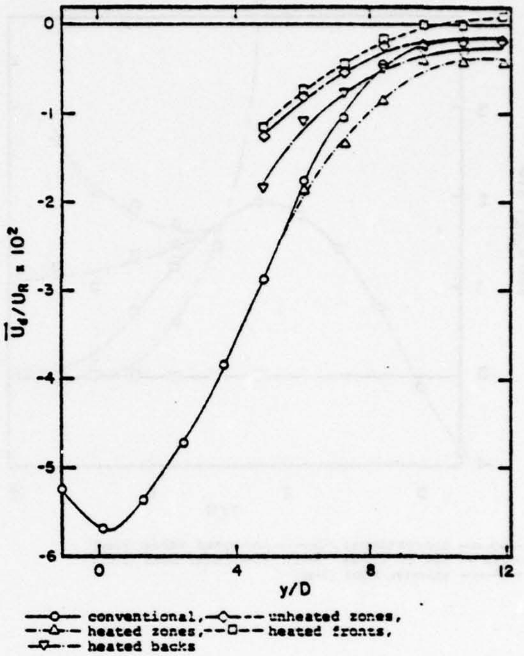

Fig. 5. Conditional Streamwise Velocities, x/D = 400

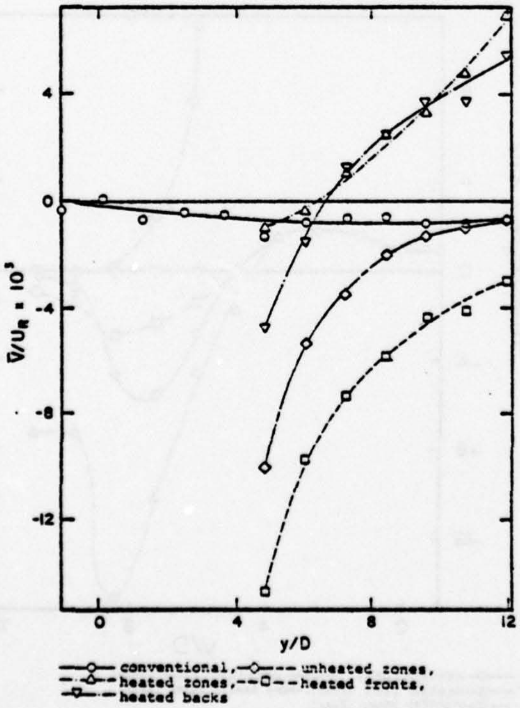

Fig. 4. Conditional Lateral Velocities, x/D = 400

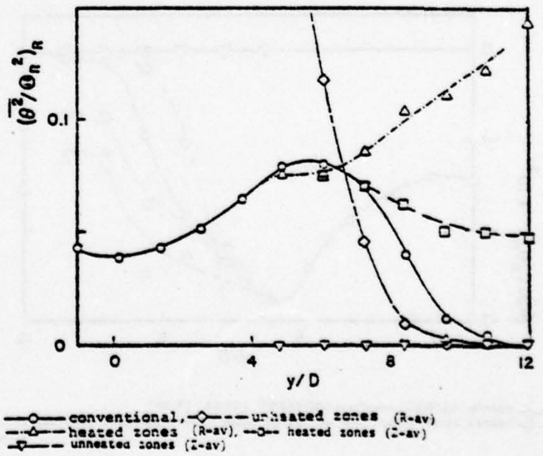

Fig. 6. Conditional Temperature Fluctuations, x/D = 400

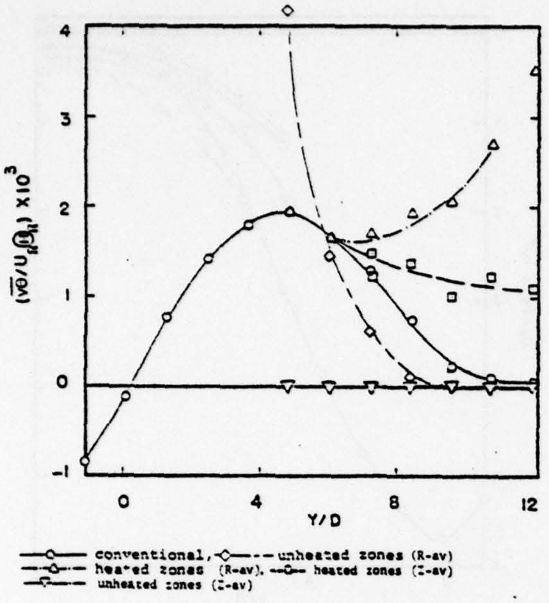

Fig. 7. $\overline{v\theta}$ Correlation; x/D = 400

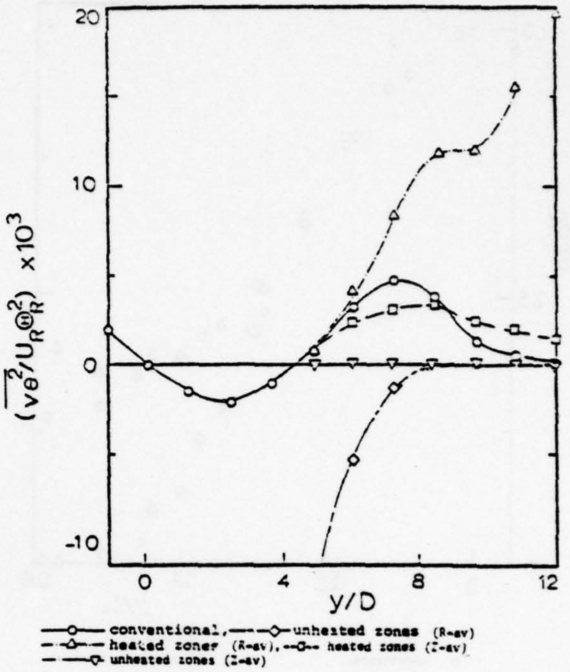

Fig. 8. $\overline{u\theta}$ Correlation; x/D = 400

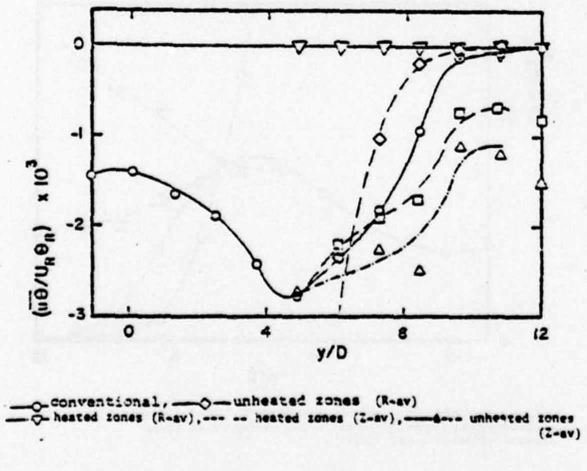

Fig. 9. Lateral Transport of θ^2; x/D = 400

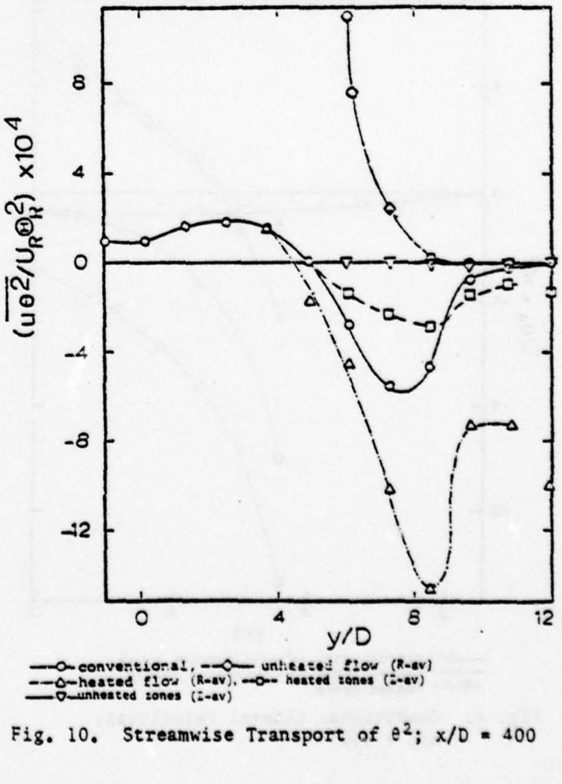

Fig. 10. Streamwise Transport of θ^2; x/D = 400

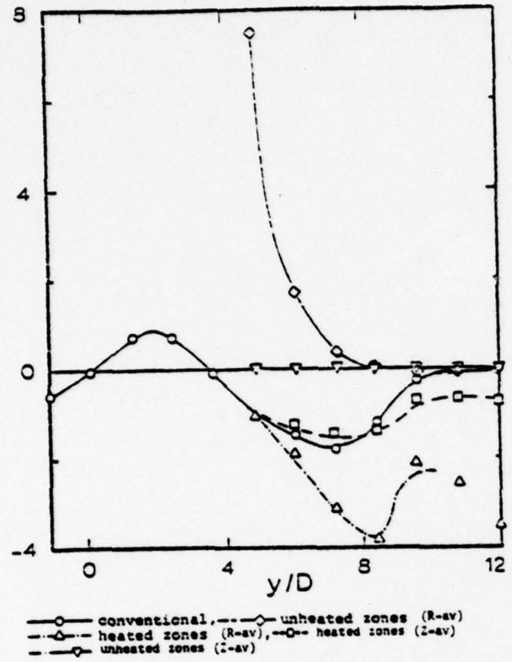

Fig. 11. Streamwise Transport of vθ; x/D = 400

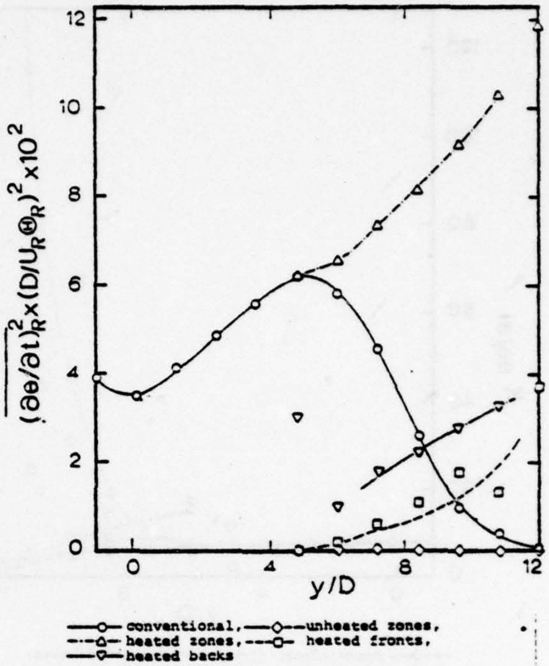

Fig. 13. Squared Time Derivative of Temperature; x/D = 400, R-Average

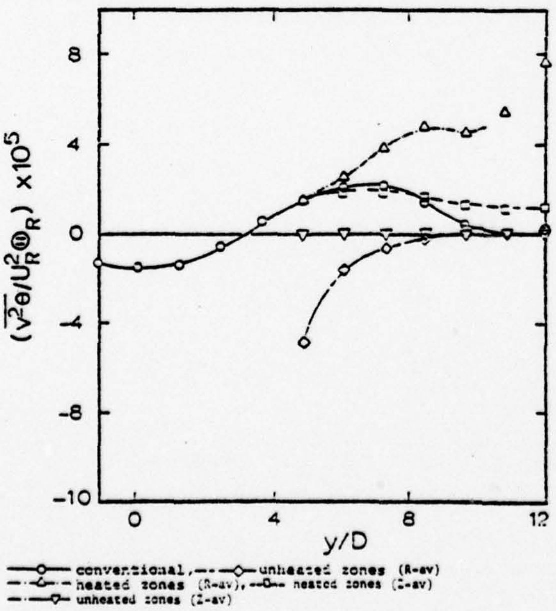

Fig. 12. Lateral Transport of vθ; x/D = 400, 1 Cylinder, R-Average

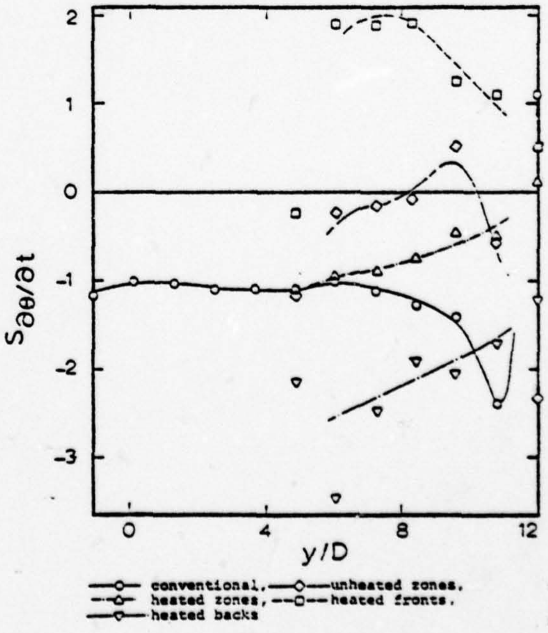

Fig. 14. Skewness Factor of Time Derivative of Temperature; x/D = 400

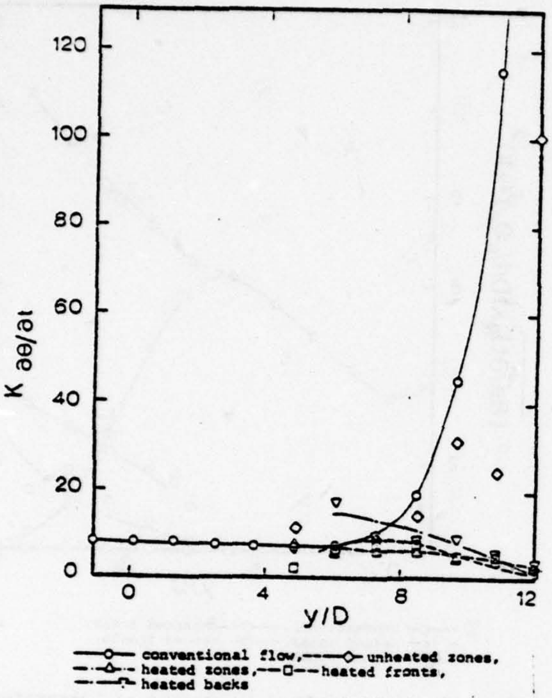

Fig. 15. Flatness Factor of Time Derivative of Temperature; x/D = 400

SOME CHARACTERISTICS OF CONCENTRATION FLUCTUATIONS IN FREE TURBULENT JETS

by

E.W. GRANDMAISON, D.E. RATHGEBER AND H.A. BECKER
DEPARTMENT OF CHEMICAL ENGINEERING
QUEEN'S UNIVERSITY
KINGSTON, ONTARIO

ABSTRACT

Becker, Hottel and Williams have determined many characteristics of the nozzle fluid concentration field of the round turbulent free jet: the mean concentration, concentration fluctuations, intermittency factor, spectrum and correlation functions, and integral scales. In the present work a much larger jet nozzle was used, 7.62 cm throat diameter compared to 0.635 cm in the reference, and the Reynolds number was correspondingly greater around 270,000 compared to 54,000. The same light-scatter technique and smoke marker were employed. Measurements were made up to 6 m downstream of the nozzle, at which point the turbulence scale was enormous compared to the observed control volume. The results support Becker, et al's findings and extend the range of the data. In particular, the spectrum of the concentration fluctuations has been measured into the viscous convective subrange where a (-1) power mode dependency on wave number is indicated, as expected for the slow diffusing smoke marker. Other new results include the skewness, kurtosis, and probability density function of the concentration fluctuations. The probability density, as expected, is essentially Gaussian on the jet centreline, but shows marked skewness towards the jet edges.

NOMENCLATURE

Variables

b	concentration half-radius of jet ($r = b$ at $\overline{\Gamma} = \frac{1}{2}\overline{\Gamma}_c$), m
$\mathcal{D}^*$	diffusivity of marker particles in fluid, m^2/s
e_k	turbulence kinetic energy per unit mass of fluid, m^2/s^2
$E_{\gamma 1}(k_1)$	one-dimensional wave-number spectral density function of concentration fluctuations, kg^2/m^5
f	frequency, s^{-1} = hz
$G_\gamma(f)$	frequency spectral density function of concentration fluctuations, $kg^2 s/m^6$
k_1	$= 2\pi f/\overline{U}_1$, wave number, m^{-1}
k_c	$= (\varepsilon/\nu^3)^{\frac{1}{4}}$, critical wave number for transition between (-5/3) and (-1) power-law modes of spectrum, m^{-1}
r	radial position in jet (in cylindrical polar coordinates), m
R	$= R(x, \phi, t)$, radial position of a point on the turbulent jet boundary, m
$\overline{R}$	mean jet radius defined on the turbulent jet boundary, m
$\overline{U}_1$	mean velocity component in the local mean-flow direction (magnitude of the mean velocity vector), m/s
x	axial position in jet (in cylindrical polar coordinates), origin at the center of the jet source exit port, m
Γ	jet source-fluid concentration, kg/m^3
γ	$= \Gamma - \overline{\Gamma}$, jet source-fluid concentration fluctuation, kg/m^3
δ	intermittency function, $\delta = 1$ if $\Gamma > 0$; $\delta = 0$ if $\Gamma = 0$
$\overline{\delta}$	= prob ($\Gamma > 0$), intermittency factor
ε	rate of dissipation of turbulence kinetic energy per unit mass of fluid, $m^2/kg\ s^3$
η	$= r/(x - x_o)$, dimensionless radial position, $x = x_o$ being the position of the virtual jet origin
Λ_x	longitudinal integral scale of velocity fluctuations on jet centerline, m
Λ_γ	longitudinal integral scale of concentration fluctuations on jet centerline, m
ν	kinematic viscosity, m^2/s
ξ	separation distance between points (x, r, ϕ) and $(x + \xi, r, \phi)$, m
σ	standard deviation of R, m
ϕ	angular position in jet (cylindrical polar coordinates), rad

Dimensionless quantities

C	$\equiv \overline{\gamma_A \gamma_B}/\hat{\gamma}_A \hat{\gamma}_B$, correlation function for concentration fluctuations at two points, A and B
$C(x, 0;\ x + \xi, 0)$	correlation function for concentration fluctuations at two points on the jet axis, separation distance ξ; 'the axial correlation function'

$C(x, 0; x, r)$ correlation function for concentration fluctuations at points on and off the jet axis, separation distance r; the 'radial correlation function'

$C(x, r, \phi; x, r, \phi + \pi)$ correlation function for concentration fluctuations at points on opposite sides of the jet axis, separation distance 2 r; the 'symmetrical lateral correlation function'

Re $= 2r_o U_o/\nu$, jet Reynolds number

S $= \overline{\gamma^3}/\hat{\gamma}^3$, skewness of the probability distribution of γ

K $= \overline{\gamma^4}/\hat{\gamma}^4$, kurtosis of the probability distribution of γ

Overscripts

$\overline{(\ )}$ time-average value

$\hat{(\ )}$ root-mean-square value; square root of $\overline{(\ )^2}$

Subscript

c centerline value

o value at jet source

INTRODUCTION

The fields of mean velocity, temperature, and source fluid concentration in a turbulent jet discharging through an essentially still, infinite medium have been mapped many times. The velocity and temperature fluctuations associated with the turbulent mixing have been examined by means of hot-wire anemometry (1,2,3). Concentration fluctuations were first characterized by Rosensweig, Hottel and Williams (4) who used this flow system to prove the feasibility of a light-scatter technique for studying the turbulent mixing of several streams, one of which is marked with colloidal particles. This technique was refined by Becker, Hottel and Williams (5) who subsequently used it (6) in a comprehensive study of mixing in a small air jet (6.35 mm nozzle dia.) at a moderately high Reynolds number (54000). Becker (7) has recently written a review article in which the name marker nephelometry is suggested for techniques in which concentration fields and mixing processes are studied *in situ* by means of light scattering measurements on colloidal particles introduced in one of the streams entering the system. Since spatial resolution in marker nephelometry is dependent on the scale of the turbulence relative to the observed control volume whose diameter is typically about 1 mm, it is advantageous to have this size ratio as large as possible if the signal is to represent point concentrations. One objective of the present work was, therefore, to check the accuracy of the previous measurements by studying a very large turbulent jet that easily satisfies the assumptions about negligible nozzle effects, full turbulence, and good spatial resolution.

Another objective was to determine the probability density function of the concentration fluctuations, and the associated skewness and kurtosis (3rd and 4th moments). Because of the large scale of the jets it was also possible to measure the spectrum of the concentration fluctuations beyond the wave number $k \approx (\varepsilon/\nu^3)^{1/4}$ where Batchelor's (8) k^{-1} viscous-convective subrange is postulated to begin for a slow diffusing species such as the present smoke marker. Although several investigators (9,10) have reported evidence of this sub-range, the data presented have been more indicative than conclusive. Our results are unfortunately no better in this respect. However, it does appear that with further extremely careful work, marker nephelometry should be capable of resolving this question.

APPARATUS

The jet source for most of the work was a 7.62 cm throat dia. round nozzle. Two other sources were also used to provide additional convenient conditions for measurements of high wave-number spectra and the probability density function; these consisted of long tubes of 1.27 cm and 5.08 cm inside diameter.

The principles of marker nephelometry have been described previously (4--7). A 5mW He-Ne laser was usually used as the light source in the present work, but a 500 mW Argon laser was employed for the high wave-number spectra. Control volumes were 1.0-1.5 mm^3 and, because of the great size of the jets, the corrections for volume-averaging were usually unnecessary. Intermittency was measured by the method of Becker, Hottel and Williams (11). Two-point correlation functions were measured with a Disa correlator, an analogue system. Spectra were measured from tape recordings of the amplified photomultiplier tube signal, by means of a Bruel and Kjaer frequency analyser. Various combinations of record-playback speed on the tape recorder allowed for spectrum measurements down to 1 Hz. Skewness was determined by measuring the correlation between the instantaneous square of the fluctuating signal and the signal itself. Kurtosis was measured by squaring the instantaneous fluctuation twice to yield the fourth moment. Probability density function was determined by digitizing and computer-analyzing the analogue tape-recorded signal.

The averaging times used for taking time-averages of signals were 60 sec for centreline measurements and up to 300 sec for measurements towards the edge of the jet. A time average of up to 20 min was required for the two-point correlations. The tape recordings for the spectra were 40--60 min long. The tape record length used in the probability density measurements was 10--17.5 min and the digital data samples ranged from 12000 to 21000 points, providing a good approximation to a statistical population.

The three jets were run at the following Reynolds numbers: 7.62 cm throat diameter, Re = 270,000; 5.08 cm dia, Re = 21,000; and 1.27 cm dia, Re = 45,000. All jets were operated in a large room free from drafts and disturbances.

EXPERIMENTAL RESULTS

Mean concentration field

Mean concentration along the jet centreline is expected to vary as x^{-1} in self-preservation. This behavior is approached asymptotically, Fig. 1. The data set is fitted by

$$\Gamma_o/\overline{\Gamma}_c = \{1,\ x/r_o < 5;\ 1 + 0.0923\,X - 0.047[1 - \exp(-\,0.0702\,X)],\ x/r_o > 5\}, \tag{1}$$

$X \equiv x/r_o - 5$. Thus

$$\Gamma_o/\overline{\Gamma}_c \simeq 0.0923(x/r_o - 3.35), \tag{2}$$

$x > 40\ r_o$. This may be compared with the earlier result of Becker, et al (6) obtained by marker nephelometry on a much smaller jet,

$$\Gamma_o/\overline{\Gamma}_c = 0.0925(x/r_o - 4.8), \tag{3}$$

$x > 35\ r_o$, based on data over the range $10\ r_o < x < 80\ r_o$.

The spreading of the jet is measured by the 'concentration half-radius' b,

$$r = b \text{ at } \overline{\Gamma}(x, r) = \tfrac{1}{2}\,\overline{\Gamma}_c(x),$$

which should vary as x in self-preservation. The data, Fig. 1, indicate that far downstream, about $x > 40\ r_o$,

$$b = 0.105(x - 3.35\ r_o). \tag{4}$$

Becker, et al (6) found

$$b = 0.106(x - 4.8\ r_o) \tag{5}$$

The radial profile of the mean concentration should be of the form

$$\overline{\Gamma} = \overline{\Gamma}_c\,f(\eta),\quad \eta \equiv r/(x - 3.35\ r_o)$$

in self-preservation, where $x = 3.35\ r_o$ is the virtual jet origin established by (2) and (4). The present data for $\eta < 0.17$ are fitted by

$$\overline{\Gamma} = \overline{\Gamma}_c \exp(-\,A\eta^2), \tag{6}$$

where A has the following values:

x/r_o	20	25	30	35	40	60	80
A	79.6	73.7	70.4	68.6	64.9	62.4	60.9

The failure of A to fully reach a constant value is perhaps due to a small non-ideality in the ambient conditions. However, the data for $x/r_o > 40$ are also quite well represented by A = 61.6, the self-preserving value reported by Becker, et al (6). The data for the outer region $\eta > 0.17$ (roughly $\overline{\Gamma}/\overline{\Gamma}_c < 0.15$) at $x > 40\ r_o$ are fairly well fitted by

$$\overline{\Gamma} = 10\,\overline{\Gamma}_c \exp(-\,141\,\eta^2). \tag{7}$$

Becker, et al there found $f = 2.93 \exp(-\,97\,\eta^2)$.

The data for $\eta < 0.17$ actually behave as though the virtual jet origin in respect to radial profile shape lies at $x = 6.7\ r_o$ instead of $3.35\ r_o$. Thus, if we define $\eta = r/(x - 6.7\ r_o)$, then A takes a constant value of 55.5.

The concentration fluctuation intensity

The concentration fluctuation intensity on the jet centerline is shown in Fig. 2 in a form suggested by Becker, et al (6). The linear region is fitted by

$$\hat{\gamma}_c = 0.219\,\overline{\Gamma}_c/(1 + 0.52\,\overline{\Gamma}_c/\Gamma_o), \tag{8}$$

and indicates that in self-preservation $\hat{\gamma}_c = 0.219\,\overline{\Gamma}_c$. Becker, et al found

$$\hat{\gamma}_c = 0.222\,\overline{\Gamma}_c/(1 + 0.6\,\overline{\Gamma}_c/\Gamma_o). \tag{9}$$

The radial profiles of $\hat{\gamma}$ appear to be self-preserving, within the scatter of the data, from $x = 20\ r_o$ onwards. They are well fitted by a functional form proposed by Becker, et al (6):

$$\overline{\gamma^2} = 0.196\,\overline{\Gamma}\,\overline{\Gamma}_c - 0.158\,\overline{\Gamma^2} \tag{10}$$

Their experimental values of the constants were very similar, 0.205 and 0.156.

Intermittency

Within the turbulent jet fluid $\Gamma > 0$ and outside it $\Gamma = 0$. Intermittency can therefore be characterized by the function

$$\delta = \{1,\ \Gamma > 0;\ 0,\ \Gamma = 0\}.$$

The time-average of δ,

$$\overline{\delta} = \text{prob}(\Gamma > 0),$$

is the intermittency factor. If the boundary of the turbulent jet fluid is not too strongly convoluted, then (11) its local radial position $r = R(\phi, x)$ is everywhere single-valued at any instant and $\overline{\delta} = 1 - F(R)$, where F(R) is the probability distribution function of R. Further, $\overline{R}(x)$ is the mean jet radius defined on the turbulent-jet boundary and

$$r = \overline{R} \text{ at } \overline{\delta} = \tfrac{1}{2}.$$

For a normal distribution

$$\overline{\delta} = \tfrac{1}{2}\,\text{erfc}[(r - \overline{R})/\sigma\sqrt{2}] \tag{11}$$

The radial length scale or "wrinkle amplitude" of the convolutions--essentially the scale of the "large eddies"--is measured by σ, the standard deviation of R. We have

$$\sigma^2 = \int_{-\infty}^{\infty} (R - \overline{R})^2 f(R)\, dR$$

$$= -\int_{0}^{\infty} (r - \overline{R})^2 \frac{\partial \overline{I}}{\partial r}\, dr, \qquad (12)$$

where $-\partial\overline{I}/\partial r$ is the value of the p.d.f. (probability density function), f(R), at r = R. The statement of this equation by Becker, et al (11) contains a printer's error; the lower limit of integration in their equation (2) should be $-\infty$, not 0.

The present data for $x > 20\ r_o$ are quite well represented by (11). The mean jet radius and the wrinkle amplitude are fitted by

$$\overline{R} = 0.192(x - 3.35\ r_o) \qquad (13)$$

$$\sigma = 0.0324(x - 3.35\ r_o), \qquad (14)$$

giving $\sigma = 0.168\ \overline{R}$. From (4), the equation of the concentration half-radius, $b = 0.547\ \overline{R}$. Becker, et al (6) found

$$\overline{R} = 0.189(x - 4.8\ r_o), \qquad (15)$$

$$\sigma = 0.0305(x - 4.8\ r_o) \qquad (16)$$

Skewness and kurtosis

The skewness S and kurtosis K,

$$S \equiv \overline{\gamma^3}/\hat{\gamma}^3,\ K \equiv \overline{\gamma^4}/\hat{\gamma}^4,$$

were measured over a radial traverse at $x = 40\ r_o$ in the jet from the 7.0 cm dia source. The results, Fig. 3, show that on the jet centerline the distribution of γ is essentially normal (Gaussian) since there S = 0 and K = 3. Elsewhere S is positive, and in the intermittent region both S and K depart strongly from their Gaussian values.

Probability density function

The p.d.f. of the concentration fluctuations, $f(\gamma)$, was measured at several radial positions at $x = 108\ r_o$ in the jet from the 1.27 cm dia source. The results for $\eta = 0$, 0.070 and 0.105 are shown in Fig. 4. The positions chosen represent the jet centerline, the point where $\hat{\gamma}$ is maximum, and the point r = b, all essentially in the turbulent jet core where $\overline{I} = 1$. As already indicated by the skewness and kurtosis, Fig. 4, it is evident that the concentration fluctuations here are fairly normally distributed.

Measurements were also made in the intermittently turbulent region. The strong positive skewness of the concentration fluctuations at low $\overline{I}$ posed a problem here as the peak of the p.d.f. tended to be lost in the background noise. Typical p.d.f.'s for passably good measurement conditions (i.e., fairly high $\overline{I}$) are shown in Fig. 5. The directly measured intermittency levels, 0.95 at $\eta = 0.140$ and 0.85 at $\eta = 0.160$, are confirmed by the fraction of sample points found to be at the system noise level.

Spectrum

The frequency spectral density function G(f),

$$\overline{\gamma^2} = \int_0^{\infty} G_{\gamma}(f)\, df,$$

is transformable into the one-dimensional wave-number spectral density function $E_{\gamma 1}(k_1)$ under the assumption of Taylor's hypothesis, giving

$$\overline{\gamma^2} = \int_0^{\infty} E_{\gamma 1}(k_1)\, dk_1,$$

$k_1 = 2\pi f/\ \overline{U}_1$. Since the Schmidt number of the smoke marker in air was very large, about 40000, the wave-number spectrum is expected to be of the form predicted by Batchelor (8) for slow-diffusing scalars. Thus, for systems at high Reynolds number, a Kolmogoroff inertial-convective subrange is expected in which $E_{\gamma 1}$ varies as $k_1^{-5/3}$, followed by a viscous-convective subrange where it varies as k_1^{-1}. The transition between these subranges is around $k_1 = k_c \equiv (\varepsilon/\nu^3)^{\frac{1}{4}}$. Finally, around $k_1 = (\varepsilon/\nu D^{*2})^{\frac{1}{4}}$ the marker concentration eddies should begin to dissipate by marker particle diffusion and $E_{\gamma 1}$ should fall very rapidly with k_1.

The critical wave number k_c at the transition between the (-5/3) and (-1) power-law modes can be estimated as follows. Kolmogoroff's hypothesis gives approximately (12,13)

$$\varepsilon = 0.1\ e_k^{3/2}/\Lambda_x.$$

On the jet centerline (1,6)

$$e_k = \frac{3}{2}\,(0.28\ \overline{U}_x)^2$$

$$\Lambda_x = 0.0395\ x,\ \Lambda_r = 0.0445\ x,$$

$$\overline{U}_x = 12.5\ U_o r_o/x.$$

Thus

$$k_c \Lambda_r = 0.1\ Re^{0.75} \qquad (17)$$

The one-dimensional spectrum was measured on the jet centerline. One set of data was taken over the range of x/r_o from 20 to 120 on the jet from the 7.6 cm dia nozzle operated at Re = 270,000, using the 5 mW He-Ne laser as the light source for marker nephelometry. These results, Fig. 6, confirm the (-5/3) power-law behavior over a wide wave-number range beyond $k_1\Lambda_\gamma = 2$, as previously observed by Becker, et al (6). However, the measurements could not be extended beyond $k_1\Lambda_\gamma = 100$ in wave number or much beyond $x = 120\ r_o$ in downstream distance because of low signal/noise ratios. Thus the hypothesized k^{-1} viscous-convective subrange of the spectrum was out of reach in these experiments.

An effort was then made to extend the accessible range of $k_1\Lambda_\gamma$ by all available means. The 5.08 cm dia tubular jet source was used because that system allowed observations at very large values of x/r_o within the laboratory space. The Reynolds number was decreased by a factor of 13, to 21000, to lower the critical wave number k_c. A 500 mW argon ion laser was used as the light source, raising the signal level by a factor of over 1000, about 100 due to the increase in power and the rest due to the shift in light wave length into the region of peak sensitivity of the photomultiplier tube. Spectra were then measured at x/r_o = 240 and 280 where the local mean velocity was 0.33 m/s and 0.28 m/s respectively. The results, corrected for noise and control-volume averaging as described by Becker, et al (5,7), are also shown in Fig. 6. The order-of-magnitude estimate of the critical wave number is, from (17), $k_c\Lambda_\gamma = 174$. The data do indeed show a visible tendency towards a (-1) slope beyond $k_1\Lambda_\gamma = 200$. Unfortunately measurements could not be made at $k_1\Lambda_\gamma$ higher than 600, owing to the limitations of the system.

Integral length scale

The integral longitudinal length scale of concentration fluctuations is given by

$$\Lambda_\gamma = \int_o^\infty C(x, r, \phi; x + \xi, r, \phi)\, d\xi. \quad (18)$$

Along the jet centerline application of Taylor's hypothesis gives

$$\Lambda_\gamma = \frac{\pi}{2} E_{\gamma 1}(0)/\overline{\gamma^2} \quad (19)$$

Values of Λ_γ so obtained from measurements of $E_{\gamma 1}(0)$, Fig. 1, are fitted by

$$\Lambda_\gamma = 0.0420\ x. \quad (20)$$

Becker, et al (6) obtained

$$\Lambda_\gamma = 0.0445\ x. \quad (21)$$

Two-point correlation function

The two-point correlation function was measured in three modes: (i) the longitudinal correlation function $C(x, 0; x + \xi, 0)$ for points on the jet centerline with the separation distance ξ; (ii) the radial correlation function $C(x, 0; x, r)$, with one point on the jet centerline and the other at radius r, separation distance r; and (iii) the symmetrical lateral correlation function $C(x, r, \phi; x, r, \phi + \pi)$ for points on opposite sides of the jet axis, separation distance 2 r.

The results on the longitudinal correlation function are shown in Fig. 7. This function was also estimated by Fourier transformation of the one-dimensional wave-number spectrum which was itself estimated from the frequency spectrum, as already described, under the assumption of Taylor's hypothesis. This hypothesis states that, if the turbulent velocity fluctuations are not too intense (say $\sqrt{e_k} << \overline{U}_1$), then the turbulence field in the neighborhood of any point is, to a good approximation, translated past that point like a frozen pattern moving at the local mean velocity. Observations of fluctuations at the point are then equivalent to spatial sampling of the field along a line in the direction of the mean motion. The fairly good agreement between the directly measured results in Fig. 7 and those inferred from the spectrum thus indicates that Taylor's hypothesis is fairly well satisfied on the jet centerline.

The present direct measurements of the longitudinal correlation function for concentration fluctuations are the first to be reported, the results of Becker, et al (6) being wholly based on Fourier transformation of the spectrum. The present direct data are well fitted by

$$C(x, 0; x + \xi, 0) = \exp(-\ 1.11\ \xi/\Lambda_\gamma). \quad (22)$$

The curve shown by Becker, et al in their Fig. 13 is fairly well fitted by this form with a constant of 1.15, the value producing coincidence at $\xi/\Lambda_\gamma = 1$.

The results on the symmetrical lateral correlation function, Fig. 8, agree very well with those of Becker, et al (6).

The radial correlation function, Fig. 9, shows a slightly slower decrease with separation distance than the symmetrical function. Becker, et al did not study this function in their work on the free jet (6), but they did observe the same trend in a mildly confined jet (14).

DISCUSSION

The present work and that of Becker, et al (6) were both very carefully done and due corrections were made for all significant sources of error. Their small jet allowed very good control of the boundary conditions, but the observed control volume could not be made as small as might be desired for some of the measurements and so an appreciable correction for volume-averaging was sometimes necessary. Measurement of the spectrum, in particular, could not be carried to wave numbers extending into the viscous-convective subrange.

The boundary conditions for the very large jets in the present study, by contrast, were certainly less ideal in that air currents in the required large rooms could not be as effectively suppressed or controlled. However, volume-averaging in the marker nephelometry was in nearly all measurements reduced to negligible proportions and spectrum measurements could be carried to much higher wave numbers.

The present results and those of Becker, et al (6) show good agreement in nearly all respects. The differences noted, principally in the shapes of the mean concentration profiles, appear to reach significant levels only in the outer fringe of the intermittently turbulent region where they may be due to non-ideality of the boundary conditions. The results thus indicate that in free jets at Reynolds numbers above 20,000 the turbulence is quite fully developed and any differences in structure are very minor. Further, the effect of volume-averaging in marker nephelometry is adequately described by the corrections of Becker, et al (5,7). In particular, the results support reference (5) as to (i) the theoretically-based correction of the spectral density function up to the end of the (-5/3) power-law subregime, and (ii) the empirical correction of the correlation function in terms of a displacement effect.

The present work shows that Taylor's hypothesis is reasonably valid on the jet centerline. The degree of weakness in the assumption can be quantitatively assessed by calculating the integral scale Λ_γ from direct measurements of the correlation function, using (18), and from the spectrum, by (19). The values estimated from the spectrum are about 10% high relative to the presumably true values given by (18). Wygnanski and Fiedler (1) found a similar discrepancy, about 9%, in the case of the longitudinal integral scale associated with axial velocity fluctuations.

The wholly new results reported here are all on the further statistical description of concentration fluctuations: the probability density function, the higher moments (skewness and kurtosis), and the viscous-convective subregime of the spectrum. The p.d.f.'s and the higher moments show that concentration fluctuations are essentially normally distributed on the jet centerline, but increasingly non-Gaussian away from the centerline to very strongly non-Gaussian at the jet edges. The radial profiles of skewness and kurtosis are very similar to those reported by Wygnanski and Fiedler (1) for the axial component of velocity fluctuation, u_x. Ribeiro and Whitelaw (15) have found that both u_x and the radial velocity fluctuation, u_r, have positively skewed distributions. The positive skewness of γ is therefore rather expected from that of u_r, and vice-versa, from simple physical reasoning.

The present evidence for the (-1) power-law, viscous-convective subrange is interesting but not wholly conclusive; to be quite convincing, the relevant data should cover a broader wave-number range. The apparent transition point from the (-5/3) power-law inertial-convective subrange, Fig. 6, is at about $k_1\Lambda_\gamma = 200$, which is very close to the order-of-magnitude estimate $k_c\Lambda_\gamma = 174$. The close agreement is fortuitous, particularly since $k_c \equiv (\varepsilon/\nu^3)^{\frac{1}{4}}$ is really defined for the three-dimensional spectrum and should be multiplied by an appropriate constant for the one-dimensional spectrum. Nevertheless, the transition still appears to occur within the expected region.

Evidence for the viscous-convective subrange has also been reported by Gibson and Schwarz (9) and Nye and Brodkey (10), but on very different systems and by different techniques. Their results suggest that the transition occurs at a wave number k_1 nearly an order of magnitude below k_c, which is rather different from our observation. It is possibly significant that neither of these studies was done at a sufficiently high Reynolds number to show a broad approximately (-5/3) power-law, inertial-convective subregime.

If work is to be done to further penetrate the high-wave number region of the spectrum by means of marker nephelometry, then the method of Becker, et al (5) for correcting the spectral density function for volume averaging needs calibrating in the (-1) power-law region. The existing experimental calibration (5) is wholly based on data in the (-5/3) power-law region. This was one of the factors that limited the present efforts to detect the viscous-convective subrange. It will, of course, never be possible to extend measurements to the region of diffusive dissipation of marker concentration fluctuations, simply because the signal/noise ratio in almost any feasible system is thoroughly degraded by marker shot noise at wave numbers well below those in question.

Finally, it should be understood that in this study, as well as in all others done in our laboratory, marker nephelometry has been used primarily to measure gas/gas mixing; i.e., mixing at a Schmidt number Sc on the order of unity, and not at that of the smoke marker, roughly 40000. Thus our system was, for example, arranged to measure effectively

$$\overline{\gamma^2} \simeq \int_0^{k_c} E_{\gamma 1}(k_1)\, dk_1,$$

and not

$$\overline{\gamma^{*2}} = \int_0^{\infty} E^*_{\gamma 1}(k_1)\, dk_1,$$

where the asterisk indicates values for marker/gas mixing and the omission of it means those for gas/gas mixing. The differences between these, and the questions of how to ensure that gas/gas mixing is simulated, have been discussed by Becker (7);

it suffices here to say that the experimental problem is not severe and poses no difficulties.

The present data on $\overline{\Gamma}$, $\overline{\gamma^2}$, $\overline{\gamma^3}/\hat{\gamma}^3$, $\overline{\gamma^4}/\hat{\gamma}^4$, $\overline{\delta}$, $f(\gamma)$, C, and Λ_γ--namely the mean concentration, the fluctuation variance, the skewness, the kurtosis, the intermittency factor, the probability density function, the two-point correlation function, and the integral length scale--thus all are appropriate to gas/gas mixing or, generally, the case Sc = 1. So also is the spectral density function up to the end of the (-5/3) power-law, inertial-convective subregime. However, around the critical wave number $k_1 = k_s$ the spectrum for Sc = 1 enters the final region of diffusive dissipation whereas that for Sc >> 1 enters the viscous-convective subrange. Thus the (-1) power-law region in Fig. 6 is peculiar to the marker/gas mixing and in this respect the ordinate would be better labelled $E^*_{\gamma 1}(k_1)$, to make the distinction explicit.

ACKNOWLEDGMENT

This work was supported by grants from the National Research Council of Canada.

REFERENCES

1. Wygnanski, I. and Fiedler, H., "Some measurements in the self-preserving jet", Journal of Fluid Mechanics, Vol. 38, part 3, 1969, pp. 577--612
2. Corrsin, S. and Uberoi, M.S., "Further Experiments on the Flow and Heat Transfer in a Heated Turbulent Jet", Report No. 998, 1950, Nat. Advisory Committee for Aeronautics
3. Corrsin, S. and Uberoi, M.S., "Spectra and Diffusion in a Round Turbulent Jet", Report No. 1040, 1951, Nat. Advisory Committee for Aeronautics
4. Rosensweig, R.E., Hottel, H.C. and Williams, G.C., "Smoke-scattered light measurement of turbulent concentration fluctuations", Chemical Engineering Science, Vol. 15, Nos. 1 and 2, July 1961, pp. 111--129
5. Becker, H.A., Hottel, H.C. and Williams, G.C., "On the light-scatter technique for the study of turbulence and mixing", Journal of Fluid Mechanics Vol. 30, part 2, 1967, pp. 259--284
6. Becker, H.A., Hottel, H.C. and Williams, G.C., "The nozzle-fluid concentration field of the round, turbulent, free jet", Journal of Fluid Mechanics, Vol. 30, part 2, 1967, pp. 285--303
7. Becker, H.A., "Marker nephelometry, concentration fluctuations, and turbulent mixing", Studies in Convection, Vol. 2 (ed. B.E. Launder), Academic Press, London, 1977
8. Batchelor, G.K., "Small-scale variation of converted quantities like temperature in turbulent fluid", Journal of Fluid Mechanics, Vol. 5, part 1, 1959, pp. 113--133
9. Gibson, C.H. and Schwarz, W.H., "The universal equilibrium spectra of turbulent velocity and scalar fields", Journal of Fluid Mechanics, Vol. 16, 1963, pp. 357--364
10. Nye, J.O. and Brodkey, R.S., "The scalar spectrum in the viscous-convective subrange", Journal of Fluid Mechanics, Vol. 29, part 1, 1967, pp. 151--163
11. Becker, H.A., Hottel, H.C. and Williams, G.C., "Concentration intermittency in jets", Tenth Symposium (International) on Combustion, The Combustion Institute, Pittsburgh, 1965, pp. 1253--1263
12. Launder, B.E. and Spalding, D.B., Mathematical Models of Turbulence, Academic Press, 1972
13. Patanker, S.V. and Spalding, D.B., Heat and Mass Transfer in Boundary Layers, Morgan-Grampian, London, 1967
14. Becker, H.A., Hottel, H.C. and Williams, G.C., "Concentration fluctuations in ducted turbulent jets", Eleventh Symposium (International) on Combustion, The Combustion Institute, Pittsburgh, 1967, pp. 791--798
15. Ribeiro, M.M. and Whitelaw, J.H., "Statistical characteristics of a turbulent jet", Journal of Fluid Mechanics, Vol. 70, part 1, 1975, pp. 1--15

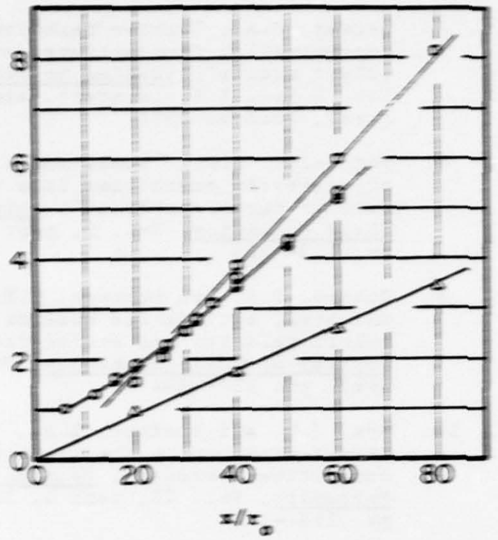

Fig. 1. Variation of centerline mean concentration $\overline{\Gamma}_c$, concentration half-radius b, and integral length scale Λ_γ with downstream distance x. Ordinates: ○, $\Gamma_o/\overline{\Gamma}_c$; □, b/r_o; △, Λ_γ/r_o.

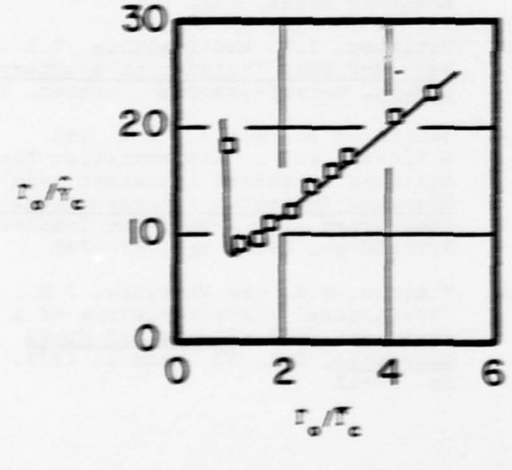

Fig. 2. Variation of concentration fluctuation intensity along the jet centerline.

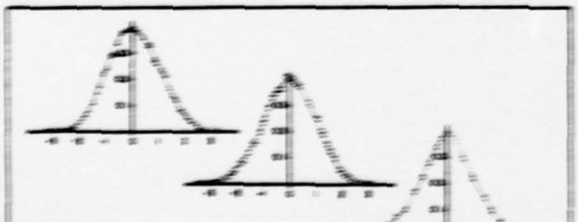

Fig. 4. The probability density function $f(\gamma)$ at $x = 108\ r_o$ and $\eta = 0.105$ (left), $\eta = 0.070$ (middle), and $\eta = 0$ (right).

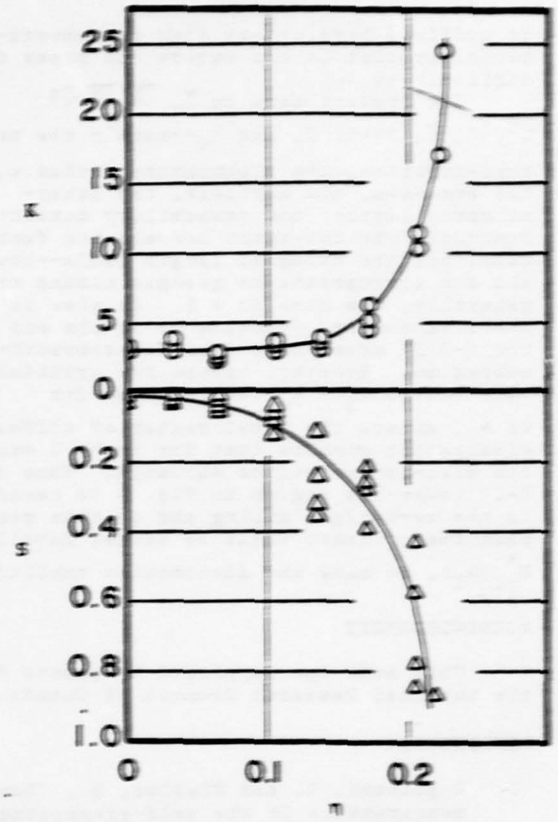

Fig. 3. Radial profiles of skewness and kurtosis at $x = 40\ r_o$ (both S and K are positive).

Fig. 5. The probability density function $f(\gamma)$ at $x = 108\ r_o$ and $\eta = 0.14$ (top) and $\eta = 0.16$ (bottom). The dashed regions are guessed extrapolations to $\gamma = -\overline{\Gamma}$ at which point $\Gamma = 0$.

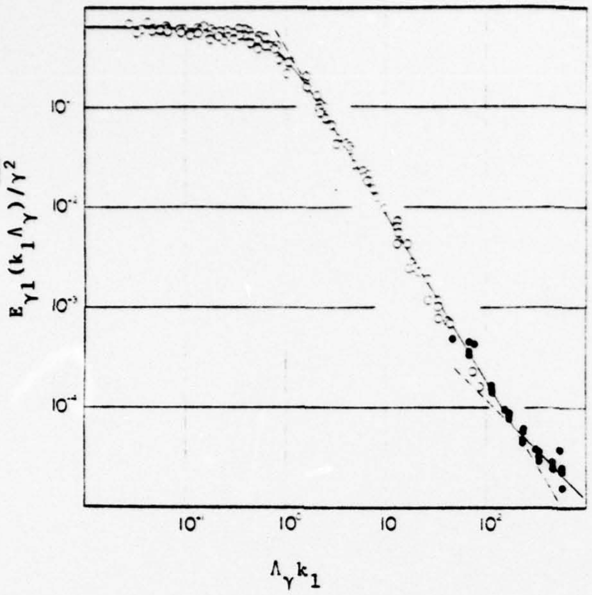

Fig. 6. The wave-number spectrum at points on the jet centerline. Open circles; x/r_o = 40 to 120; filled circles, x/r_o = 240 and 280. Straight-line fits of data: $k_1\Lambda_\gamma$ = 2--200, slope = - 5/3; $k_1\Lambda_\gamma$ = 200 to 600, slope = - 1.

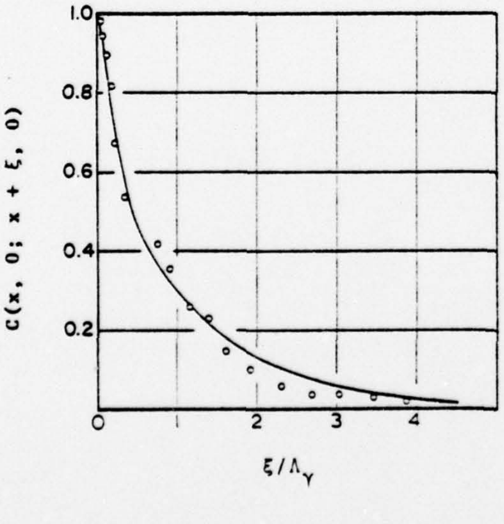

Fig. 7. The longitudinal correlation function on the jet centerline at the reference point x = 41 r_o. Circles denote direct measurements; the curve is from Fourier transformation of the wave-number spectrum.

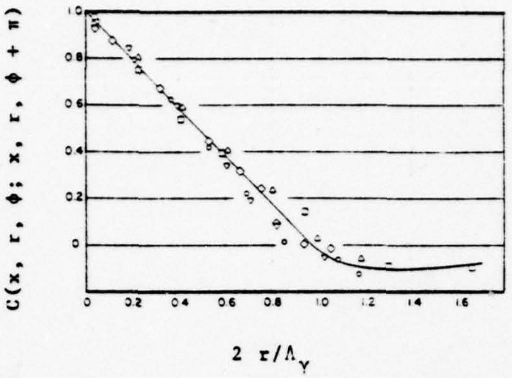

Fig. 8. The symmetrical lateral correlation function. Data for values of x/r_o of: ○, 20; △, 25; ▽, 31; □, 36; ◇, 41.

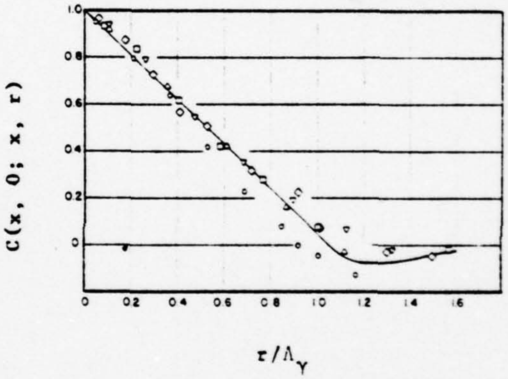

Fig. 9. The radial correlation function. Data for values of x/r_o of: ○, 20; △, 25; ▽, 31; □, 36; ◇, 41.

INTERPRETATION OF NEGATIVE PRODUCTION OF TEMPERATURE FLUCTUATIONS BY SPECTRAL ANALYSIS

L. FULACHIER and C. BEGUIER
Institut de Mécanique Statistique de la turbulence
Marseille, France

J.F. KEFFER
Department of Mechanical Engineering
University of Toronto, Canada

ABSTRACT

Spectral measurements have been made in a region of "negative production" of temperature fluctuations, produced by a slightly heated, two-dimensional jet superimposed upon a conventional mixing layer. The spectra of velocity and temperature are normal. In contrast, the cospectra of the lateral transport term indicate the presence of a dual population of the turbulent structure, distinct in size. It is shown that the large eddy component of the flow is responsible for the "negative production".

INTRODUCTION

In turbulent shear flows, the term describing the production of turbulent kinetic energy conventionally represents a transfer from the mean field to the turbulent motion.

The equations which govern these phenomena can be expressed as follows. For a steady, two-dimensional essentially incompressible turbulent motion the turbulent kinetic energy equation can be written,

$$d\frac{(\overline{q}^2/2)}{dt} = \overline{U}\,\frac{\partial(\overline{q}^2/2)}{\partial x} + \tilde{V}\,\frac{\partial(\overline{q}^2/2}{\partial y} = -\frac{\partial}{\partial y}\,\overline{v\left(\frac{p}{\rho} + \frac{q^2}{2}\right)}$$

$$-\frac{\partial}{\partial x}\,\overline{u\left(\frac{p}{\rho} + \frac{q^2}{2}\right)} + \pi - \varepsilon$$

where $\varepsilon = \nu\,\overline{(\partial u_i/\partial x_j)^2}$, is the dissipation of kinetic energy by viscosity, $\tilde{V} = \overline{\rho V}/\overline{\rho}$, is the lateral convection velocity expressed in a form which accounts for any slight density variations which could arise in the fluid due to slight heating by a contaminant such as heat (FAVRE, 1975) and the dynamic production terms are

$$\pi = -\left[\overline{uv}\,\frac{\partial \overline{U}}{\partial y} + (\overline{u^2} - \overline{v^2})\,\frac{\partial \overline{U}}{\partial x}\right].$$

The above term also appears, but with opposite sign in the equation of mean kinetic energy;

$$d\frac{(\overline{U}^2/2)}{dt} = \overline{U}\,\frac{\partial(\overline{U}^2/2)}{\partial x} + \tilde{V}\,\frac{\partial(\overline{U}^2/2)}{\partial y} = -\frac{\partial}{\partial y}\,(\overline{U}\,\overline{uv}) -$$

$$\frac{\partial}{\partial x}\,\overline{U}\,(\overline{u}^2 - \overline{v}^2) - \pi .$$

In the general case π is positive and the implication is that there is an increase in kinetic energy of the turbulent motion at the expense of the mean motion.

For the equivalent situation of a thermal field, of weak intensity superimposed upon the velocity field, the equations for the temperature fluctuation intensity, $\overline{\theta}^2$-stuff, can be written,

$$\frac{d(\overline{\theta}^2/2)}{dt} = \overline{U}\,\frac{\partial(\overline{\theta}^2/2)}{dx} + \tilde{V}\,\frac{\partial(\overline{\theta}^2/2)}{\partial y} = -\frac{\partial}{\partial y}\,\left(\overline{\frac{\theta^2 v}{2}}\right)$$

$$-\frac{\partial}{\partial x}\,\left(\overline{\frac{\theta^2 u}{2}}\right) + \pi_\theta - \varepsilon_\theta$$

where $\varepsilon_\theta = \alpha\,\left(\overline{\frac{\partial\theta}{\partial x_i}}\right)^2$, is the thermal dissipation or molecular smearing, α being the thermal diffusivity, and the corresponding thermal production terms are:

$$\pi_\theta = -\left[\overline{\theta v}\,\frac{\partial\overline{\Theta}}{\partial y} + \overline{\theta u}\,\frac{\partial\overline{\Theta}}{\partial x}\right]$$

We can construct an equivalent mean thermal energy field by multiplying the enthalpy equation by the mean temperature variation, $(\overline{\Theta} - \Theta_e)$, giving:

$$d\,\frac{(\overline{\Theta}-\Theta_e)^2/2}{dt} = \overline{U}\,\frac{\partial(\overline{\Theta}-\Theta_e)^2/2}{\partial e x} + \tilde{V}\,\frac{\partial(\overline{\Theta}-\Theta_e)^2/2}{\partial y}$$

$$= -\frac{\partial}{\partial y}\,[(\overline{\Theta}-\Theta_e)\overline{\theta v}] - \frac{\partial}{\partial x}\,[(\overline{\Theta}-\Theta_e)\overline{\theta u}] - \pi_\theta$$

As in the kinetic energy situation π_θ is generally positive and the expression for $\overline{\theta}^2$-stuff shows this as an increase in the level of fluctuation intensity. The net rate of change of $(\overline{\Theta}-\Theta_e)^2$ in the mean thermal energy equation within a given volume will be negative corresponding to a decrease in the mean temperature since $(\overline{\Theta}-\Theta_e)$ is positive in the present experiment. We note here that in our case heat is not considered to be an energy quantity, rather, as a passive scalar contaminant which effectively marks the fluid in a manner similar to an inert tracer.

PRECEDING PAGE BLANK-NOT FILMED

In several flows, where the mean velocity profile is asymmetric, it has been observed that a displacement occurs between the points where the tangential Reynolds stress and the gradient of mean velocity are zero (ESKINAZI and YEH, 1956; BRADSHAW and GEE, 1962 ; TAILLAND and MATHIEU, 1967 ; PALMER and KEFFER, 1972). In this zone the term describing the production of turbulent fluctuation intensity becomes negative and the implication is that a local transfer of energy from the turbulent to the mean motion takes place.

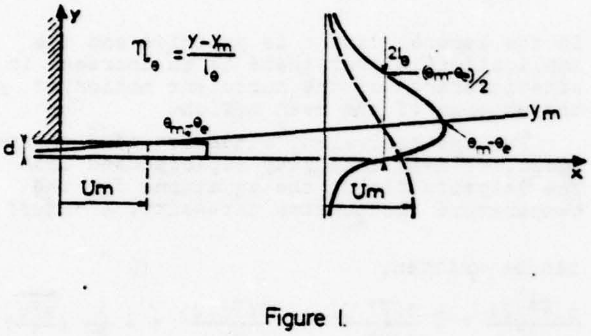

Fig. 1 Schematic of the flow

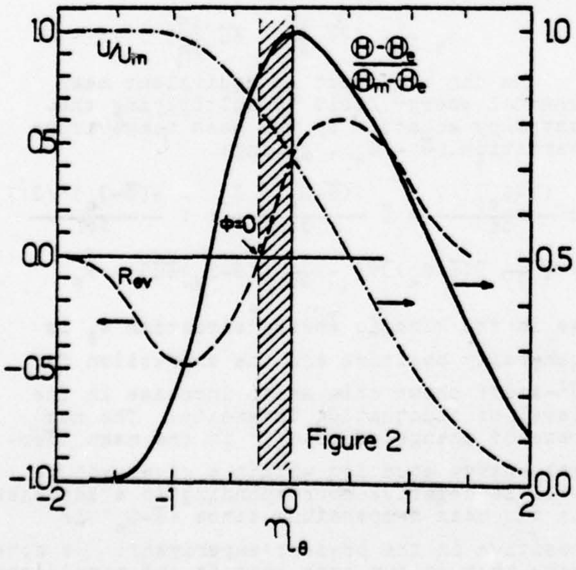

Fig. 2 Mean intensity profiles

A similar situation has been observed for an equivalent thermal field (BEGUIER, FULACHIER, KEFFER and DUMAS, 1975 ; BEGUIER, FULACHIER and KEFFER, 1976). Figure 1 shows a schematic of the flow which was studied, representing a slightly heated, two-dimensional jet, expanding into a quiescent medium on one side and into a uniform velocity stream on the other. The velocity of the jet and accompanying stream were equal thus producing a mixing layer with a jump in temperature at the free edge. The results, plotted in figure 2, showed that a displacement between the zeros of the lateral transport term $\overline{\theta v}$, and the mean temperature gradient $\partial\overline{\Theta}/\partial y$, existed and it was determined subsequently, that the production of thermal fluctuation intensity was negative in this region (FULACHIER, KEFFER and BEGUIER 1975) indicating a transfer of heat from the fluctuating to the mean field. A model for describing the lateral transport of enthalpy in the zone was developed.

The purpose of the present paper is to investigate the region of negative production in detail by examining the spectral components of the various fluctuating quantities and thus to suggest an explanation for the physical mechanisms which produce this effect.

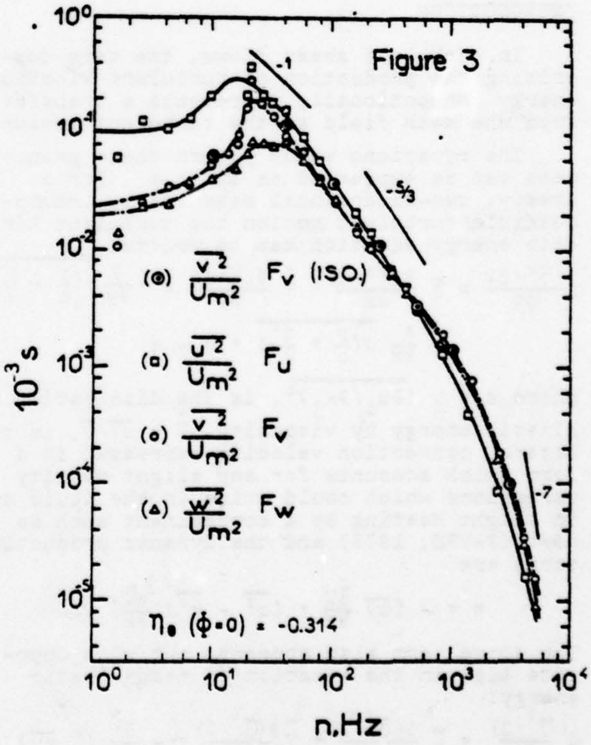

Fig. 3 Spectra of three components of Velocity at ϕ = 0.

EXPERIMENTAL RESULTS

Figure 3 presents the spectra of the three components of the velocity fluctuations, F_u, F_v and F_w as a function of frequency n, at the position $\eta_\theta = -0.314$ where the lateral transport of temperature, (in non-dimensional form),

$$\Phi = -\overline{\theta v}/(\Theta_m - \Theta_e)U_m$$

is zero. The areas have been normalized so that

$$\int_0^\infty F_\zeta \, dn = 1 .$$

Included as well is the spectrum of v, $(\overline{v^2}/\overline{U}_m^2)F_v$ (iso) calculated from the spectrum of u using the isotropic relation,

$F_v\,(\text{iso}) = \frac{1}{2}\,[F_u - n(\partial F_u/\partial n)]$ and it is seen that the flow is effectively isotropic for frequencies beyond 400 Hz. This corresponds to $k_1 \geq 1/\lambda_f$ where $k_1 = 2\pi n/\bar{U}$ and

$$\lambda_f = \bar{U}\,[2\overline{u^2}/\overline{(\partial u/\partial t)^2}]^{\frac{1}{2}} \simeq 5 \text{ mm},$$

the longitudinal microscale of the turbulence. The turbulent Reynolds number, $R_\lambda = (\overline{u^2})^{\frac{1}{2}}\lambda_f/\nu$ was about 600, high enough so that, between 80 and 800 Hz approximately, the spectrum for F_u obeyed the -5/3 law.

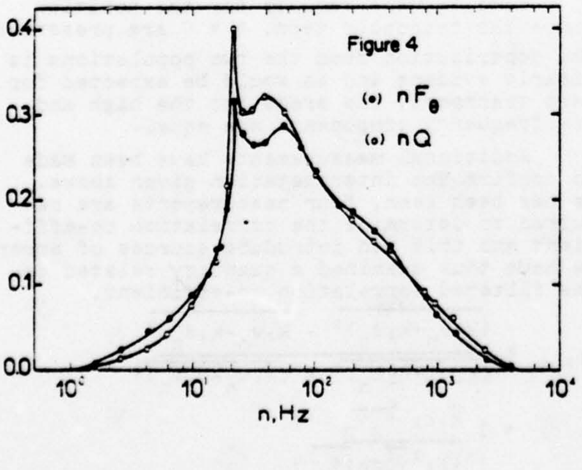

Fig. 4 Spectra of temperature and velocity vector at $\Phi = 0$

As the frequency approaches zero, it is found, similar to the results for the velocity mixing layer of WYGNANSKI and FIEDLER (1970), that

$$\overline{v^2}\,F_v \simeq \overline{w^2}\,F_w$$

and

$$\overline{u^2}\,F_u \simeq 5\,\overline{v^2}F_v .$$

Using the relation

$$L_\zeta = \frac{\bar{U}}{4}\,F_\zeta(n \to 0)$$

permits a determination of the macroscale ratio for the turbulence,

$$L_u/L_v \simeq 5\,\overline{v^2}/\overline{u^2} .$$

Figure 4 shows the results of applying the analogy of FULACHIER and DUMAS (1976), between the temperature and the velocity vector spectra,

$$Q = (\overline{u^2}F_u + \overline{v^2}F_v + \overline{w^2}F_w)/\overline{q^2} .$$

The results here have been obtained for a situation where the velocity and temperature fields are significantly different. Nevertheless it can be seen that the two spectra are approximately the same. The imperfect matching can be attributed mainly to experimental error.

The existence of a peak is evident at 22 Hz. This results from a resonance of the fan used to produce the jet flow. The effect on the spectra is very localized however and is virtually undetectable in the conventional log-log representation in figure 3. From these preliminary results it can thus be seen that, despite the rather unusual initial conditions, the spectra of the velocity and especially the temperature fluctuations behave normally.

In order to investigate the structure of the flow in the region of negative production, the co-spectra of the lateral transport terms, $E_{\theta v}$, has been measured. The quantity is defined in terms of the flux, so that

$$\int_0^\infty E_{\theta v}\,dn = \Phi$$

The magnitude of $E_{\theta v}(n)$ was obtained from the difference of two spectra as follows,

$$E_{\theta v}(n) = a[\overline{(k_1 v_n + k_2\theta_n)^2} - \overline{(k_1 v_n - k_2\theta_n)^2}] .$$

where the subscript n refers to the filtered value of a quantity and a, k_1 and k_2 are the coefficients of amplification. It is not necessary to determine these independently since the overall co-efficient $4ak_1k_2$ can be obtained from the normalizing relationship.

For the special situation in the flow where the transport term $\Phi = 0$, the above normalization method cannot be used and it is necessary to proceed in the following manner. A direct determination of the correlation coefficient, $R_{\theta_n v_n}$ between the filtered fluctuations θ_n and v_n is made from the four measured quantities contained in,

$$R_{\theta_n v_n} = \overline{\theta_n v_n} / (\overline{\theta_n^2}\ \overline{v_n^2})^{\frac{1}{2}}$$

The spectra, F_θ and F_v are then introduced to give the co-spectrum

$$E_{\theta v}(n) = \frac{(\theta^2 v^2)}{(\Theta_m - \Theta_e) U_m} R_{\theta_n v_n} (F_\theta F_v)^{\frac{1}{2}}$$

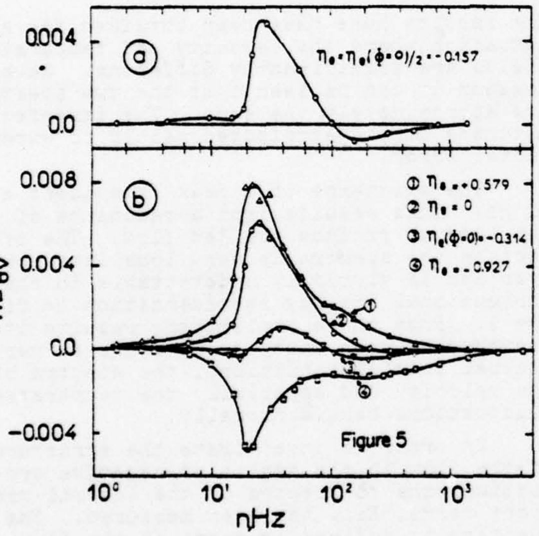

Fig. 5 Cospectra of lateral transport term

The evolution of $nE_{\theta v}$, taken across the flow, is presented in figure 5. In particular, the upper diagram, figure 5a, shows the co-spectrum for the location where the negative production is a maximum, i.e. $\eta_\theta = -0.157$ at which point

$$\partial[(\bar{\Theta} - \Theta_e)/(\Theta_m - \Theta_e)]/\partial\eta_\theta = 0.27$$

and $\Phi = -0.0060$. It can be seen from these results that the regions with opposite sign effectively serve to define the contributions from the low and high frequency components of the motion. The change in sign occurs at about 100 Hz which corresponds to $k_1 \simeq 1/L_u$. The portion of $E_{\theta v}$ corresponding to the highest frequencies is of the same sign as the mean temperature gradient whereas the lowest frequencies produce a transport having a sign opposite to that of the gradient. It can thus be inferred that the low frequency components, which are related to the largest eddies of the flow, are the main mechanism for the negative production of temperature fluctuation intensity.

The above results are similar to those found for the velocity field in an asymmetric plane jet (BEGUIER, 1969) or in a fully developed asymmetric flow in a plane channel (HANJALIC and LAUNDER, 1972). Their work supports the concept of a double structure in the flow where the high frequency components are related to the local gradient and the low frequency components to the large eddies. This has been described by a second order model of the turbulent transport for regions of negative production (HINZE 1970; BEGUIER, 1969; LAUNDER, 1968; FULACHIER, BEGUIER and KEFFER, 1975).

An examination of curves 1 and 4, in figure 5 b, taken outside the region of negative production where the gradients are approximately linear, shows the persistence of the double structure, as evidenced by the bimodal shape. The situation for the point of maximum temperature, curve 2 where the gradient is zero is consistent with the above results. The contribution to the co-variance from the smallest eddies is effectively zero which confirms that these higher frequency components are directly related to the gradient of mean temperature.

Finally, the results for the position where the transport term, $\Phi = 0$ are presented The contribution from the two populations is clearly evident and as would be expected for zero transport, the areas for the high and low frequency components are equal.

Additional measurements have been made to confirm the interpretation given above. As has been seen, four measurements are required to determine the correlation co-efficient and this can introduce sources of error. We have thus examined a quantity related to the filtered correlation co-efficient,

$$r_{\theta_n v_n} = \frac{\overline{(k_1 v_n + k_2 \theta_n)^2} - \overline{(k_1 v_n - k_2 \theta_n)^2}}{\overline{(k_1 v_n + k_2 \theta_n)^2} + \overline{(k_1 v_n - k_2 \theta_n)^2}}$$

$$= 2 \frac{k_1 k_2 \overline{\theta_n v_n}}{(k_1^2 \overline{v_n^2} + k_2^2 \overline{\theta_n^2})}$$

which requires only 2 measurements. The relationship of $R_{\theta_n v_n}$ to $r_{\theta_n v_n}$ is

$$r_{\theta_n v_n} = R_{\theta_n v_n} \left| \frac{(F_\theta F_v)^{\frac{1}{2}}}{(F_\theta + F_v)/2} \right| .$$

It should be noted that these terms are almost identical since for example if, $F_v = 2F_\theta$, $r_{\theta_n v_n} = 0.96\ R_{\theta_n v_n}$ and in the limit $r_{\theta_n v_n} \rightarrow R_{\theta_n v_n}$ is $F_v \rightarrow F_\theta$

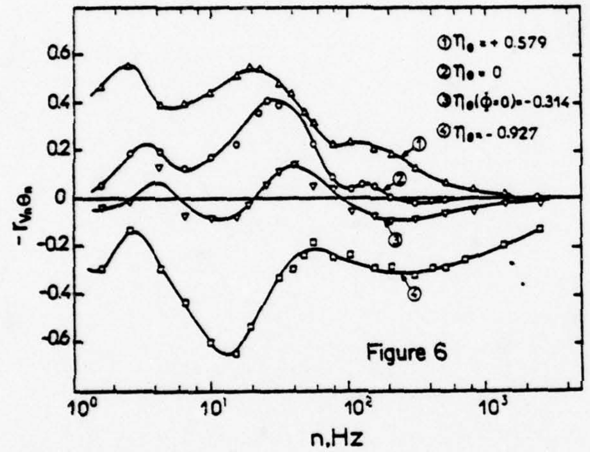

Fig. 6 Apparent spectal correlation co-efficient

The above variable was evaluated for the five locations across the flow as shown in figure 6. These results are seen to be generally consistent with the data in figure 5 in the sense that there is a change in the sign of the correlation term for $\Phi=0$ (curve 3) in the region beyond approximately 50 H. which defines the contribution from the low and the high frequencies.

Furthermore, the double structure, as marked by the temperature, while similar to that in figure 5 shows additionally a complex evolution of the large eddy structure as the flow is traversed. Even though this portion of the spectrum could be affected by the parasitic influence of the fan, there appears to be a consistent dependence of the low frequency structure upon the sign of the mean temperature gradient. This a maximum of $|r_{\theta_n v_n}|$ on one side of the mean temperature profile and a minimum as the other side at approximately the same frequency, the slight shift occurring primarily because of the difference in convection velocities on the two sides.

SUMMARY

The negative production of velocity fluctuations or of contaminant fluctuations such as temperature thus appear to be a direct result of the large eddy structure of the turbulent motion. Furthermore, the results support the concept that the tangential Reynolds stress or conversely, the lateral transport of a contaminant by the turbulence, must depend directly upon the double eddy structure in these regions.

REFERENCES

BEGUIER, C., 1969, Comptes Rendus, A 268, 69.

BEGUIER, C., FULACHIER, L., KEFFER, J.F., and DUMAS, R., 1975, Comptes Rendus, B 280, 493.

BEGUIER, C., FULACHIER, L., and KEFFER, J.F., 1976, J. Phys. 37, C1 - 187.

BRADSHAW, P., and GEE, M.T., 1962, Aero. Res. Counc. Lond. Rept.No. 3252.

ESKINAZI, S., and YEH, H., 1956, Jour. Aero. Sc. Vol. 23 No.1.

FAVRE, A., 1975, Proc. 5th Can. Cong. Appl. Mech. Fredericton.

FULACHIER, L., and DUMAS, R., 1976 J. Fluid Mech., 77,

FULACHIER, L., KEFFER, J.F., and BEGUIER, C., 1975, Comptes Rendus, B 280, 519.

HANJALIC, K., and LAUNDER, B.E., 1972, J.F.M., Vol. 51, Part 2, 301.

HINZE, J.O., 1970, Dutch J. Appl. Sci. Pis. 22, 163.

LAUNDER, B.E., 1968, Report BL/TN/2 - Imp. College, Lond.

PALMER, M.D., and KEFFER, J.F., 1972, J.F.M. Vol. 53, 593.

TAILLAND, A., and MATHIEU, J., 1967, J. Mech., 6, 103.

WYGNANSKI, I., and FIEDLER, H., 1970, J. Fluid Mech. 41, 327.

ACKNOWLEDGEMENTS

The work was carried out at the Institut de Mécanique Statistique de la Turbulence, a laboratory associated with CNRS. Financial support was also received from NATO and The National Research Council of Canada.

THE STRUCTURE OF TURBULENCE ASSOCIATED WITH AN INTERNAL THERMAL LAYER

by

H.Q. DANH* and R.A. ANTONIA⁺

* Department of Mechanical Engineering,
University of Sydney, N.S.W. 2006
AUSTRALIA

⁺ Department of Mechanical Engineering,
University of Newcastle, N.S.W. 2308
AUSTRALIA

ABSTRACT

Statistical properties are presented of velocity and temperature fluctuations associated with an internal thermal layer. This layer is formed when a fully developed turbulent boundary layer is subjected to a step change in surface heat flux. Upstream of the step, the wall heat flux is zero while downstream of the step, the magnitude of the heat flux is small enough for the temperature field to be treated as a passive contaminant of the flow.

Individual and joint probability density functions of longitudinal u and normal v velocity fluctuations and of the temperature fluctuation θ are presented both in the conventional sense and in the conditional mode, when only the heated or non-heated parts of the flow are considered. For the conditional measurements, the probability density function of θ is used to effectively locate the edge of the thermal interface.

Individual and joint probability densities of u and v in the heated part are better approximations to Gaussian distributions when compared with either conventional densities or those in the non-heated part of the flow. There is a strong similarity, especially in the heated flow, between p(u, v) and p(v, θ) except at small distances from the step or for large negative values of θ because of the relatively sharp cut-off in temperature. Contributions of conventional and conditional joint probability density functions of (u, v), (u, θ) and (v, θ) to the "ejection", "sweep" and "interaction" events are calculated at several distances downstream of the step. The contribution from the "ejection" event is larger than that from the "sweep" event while contributions from each event in the heated flow are generally 10-15% higher than conventional contributions.

NOMENCLATURE

Symbols

a, b - fluctuating quantities which stand for either u or v or θ
G - probability density function of the fitted Gaussian
p(a) - probability density function of quantity a
p(a, b) - joint probability density function of a, b
r_{ab} - correlation coefficient between a and b
Th - threshold on temperature fluctuation
U_1 - free stream velocity
u, v - velocity fluctuations in x, y direction, respectively
uv - Reynolds shear stress
uθ - longitudinal heat flux
vθ - transverse heat flux
x, y - directions parallel and normal to the wall
δ_o - boundary layer thickness at the heated step
γ_T - thermal intermittency factor, proportion of time for which flow is heated
θ - temperature fluctuation

Subscripts

$(\ )_h$ - quantity in the heated part of the flow
$(\ )_c$ - quantity in the non-heated part of the flow

Superscripts

$\overline{(\ )}$ - mean value
$(\ )'$ - conventional or conditional r.m.s. value
$(\ )^*$ - taken with respect to conditional mean
(e.g. $a_h^* = a_h - \overline{a}_h$ or $a_h^*.b_h^* = (a_h - \overline{a}_h)(b_h - \overline{b}_h)$)

INTRODUCTION

In the visual studies of Kline *et al.* (1) and Corino and Brodkey (2), attention was focused on the bursting phenomenon and the turbulence production process. From observations of the streaky sublayer structure, Kim *et al.* (3), Willmarth & Lu (4), Wallace *et al.* (5) have shown that the bursting process may be characterized by a sequence of events of sweeps of high streamwise momentum fluid into low momentum fluid near the wall alternating with ejections of the low momentum fluid away from the wall. The structure and generation of Reynolds shear stress and turbulent energy appears to be strongly dominated by this intermittent sweep-ejection cycle.

Recently, attention has been given to a comparison of the statistical properties of the instantaneous Reynolds shear stress uv with those of the instantaneous heat flux vθ. Venkataramani *et al.* (6) and Antonia and Sreenivasan (7) measured joint probability density functions of velocity and temperature fluctuations in a heated jet. Perry and Hoffmann (8) have made a preliminary study of the properties of uv and vθ in the case of a zero pressure gradient turbulent boundary layer with a heated (constant temperature) wall. In Perry and Hoffmann's study, the virtual origins for the thermal and momentum layers were made coincident and the authors reported marked similarity in behaviour of the uv and vθ fluxes. In this study, we investigate the behaviour of these fluxes in a thermal layer which grows downstream of a step change in surface heat flux but which is fully immersed within a self-preserving turbulent boundary layer. The interface associated

PRECEDING PAGE BLANK-NOT FILMED

with this thermal layer has been studied both qualitatively and quantitatively by Johnson (9) and Antonia *et al.* (10) but no attempt was made to investigate the similarity of heat and momentum transfer processes in the non self-preserving region immediately downstream of the step.

In this paper, the decision about the position of the thermal interface is determined from the probability density function of temperature. Individual and joint probability density functions of u, v and θ are presented for both heated and non-heated parts of the boundary layer. Contributions from "sweep" and "ejection" events are estimated for different streamwise stations, downstream of the step, and various positions across the layer.

EXPERIMENTAL TECHNIQUES AND CONDITIONS

Velocity and temperature fluctuations were measured in a developing thermal layer growing underneath a fully-developed turbulent boundary layer with zero pressure gradient. The boundary layer developed on the floor of a 38 cm x 23 cm working section of a low turbulence wind tunnel. The first 1.83 m section of the floor was unheated and this was followed by a heated section (constant surface heat flux) of 2.44 m length. The free stream velocity U_1 was 9.45 m/sec and the wall temperature T_w at the heated step was approximately 10°C above the ambient temperature T_1 of the free stream. At the position of the surface heat flux step the momentum boundary layer is self-preserving and has a thickness δ_o equal to 4.45 cm. Further details of experimental facilities and techniques may be found in Antonia *et al.* (10) and Danh (11).

Fluctuations u, v and θ were obtained with a combined X-wire/single wire arrangement. A miniature DISA X-wire (5 μm dia. Pt coated tungsten wires) operated by two channels of non-linearized DISA 55M10 constant temperature anemometers was used for the measurement of u and v. The temperature fluctuation θ was measured with a 1 μm diameter platinum "cold" wire, operated with an uncompensated constant current anemometer with a current value set at 0.2 mA. This wire was at a distance of 1 mm from the geometrical centre of the X-wire. Contamination of the X-wire signals by θ was removed using the method described in (12). Signals proportional to u(t), v(t) and θ(t) were recorded on a Philips Analog - 7FM tape recorder at speed of 38.1 cm/sec^{-1}. The tape recorder was later played back at 2.38 cm/sec and the signals were amplified and filtered (low-pass electronic filter with a sharp cut-off frequency set at 500 Hz) prior to digitization (with a 10 bit plus sign analogue to digital converter) at a sampling frequency of 1000 Hz. Amplification was required to ensure that the signals covered a major portion of the range (without ever exceeding it) of the digitizer. The digitized signals were processed on the DEC PDP 11/45 computer (16 bit processor, 92K memory) in the Faculty of Engineering (University of Sydney) computing centre. Records of 512000 samples (32 sec) were analysed to compute probability density functions.

The temperature θ was used to determine the appropriate threshold levels and hence the thermal intermittency factor γ_T. In Antonia *et al.* (10) analogue circuitry was used to discriminate between heated and non-heated fluid by comparing the temperature signal with a threshold voltage. This method however involves some degree of subjectivity on the part of the investigator. Digital processing of turbulence signals has enabled probability density functions of scalar quantities such as temperature or concentration to be accurately computed. These probability density functions provide a satisfactory determination of γ_T. Two methods of obtaining γ_T are used here. The first method is applied whenever γ_T is close to unity. When this occurs, the probability density function p(θ) should cut-off sharply at a level which corresponds to the nominal ambient temperature. When θ exceeds this "cut-off" value, the flow may be considered to be heated. The "cut-off" value is therefore taken as the appropriate threshold for θ and is then used to obtain conditional statistics of u and v in the heated part of the flow.

The second method is to fit the part of p(θ) which is near the ambient temperature cut-off with a Gaussian distribution as suggested by Bilger *et al.* (13). The method follows from the observation that the probability density function of temperature fluctuation in the wake of a slightly heated cylinder (14) and in a heated jet (Antonia and Sreenivasan (7)) has a bimodal shape with a spike structure appearing near the ambient temperature level of the freestream. This spike is assumed to be associated with the presence of freestream temperature fluctuations and electronic noise. It should therefore closely follow a Gaussian probability density G. The area under this Gaussian curve is assumed to be equal to $(1 - \gamma_T)$ and can be determined to an accuracy of better than ± 0.02 when there are about 10 data points to fit. With the assumption that the area under the Gaussian curve represents $(1 - \gamma_T)$, the threshold Th can be set so that $\int_{-\infty}^{Th} [p(\theta) - G]\, d\theta = \int_{Th}^{\infty} G\, d\theta$.

Unlike probability density functions of temperature in the wake or mixing layer (which may exhibit a trimodal shape, e.g. (15)) the distribution of p(θ) in the boundary layer does not exhibit a distinct two-peak structure. The absence of this structure is probably due to poorer signal to noise ratios of temperature fluctuations in the boundary layer as compared with those in the free stream layers. The lower signal to noise ratio may be speculatively attributed to the lower entrainment rate in the boundary layer than in free shear layers. In spite of the absence of a clear two-peaked structure, that part of p(θ) which is near the ambient temperature level may be satisfactorily fitted with a Gaussian curve. This suggests that the method of Bilger *et al.* may be used in the boundary layer when $\gamma_T < 1$ but the accuracy in determining γ_T and the conditional probability density is not expected to be as good as in the case of free shear layers. The values of γ_T determined from p(θ) are found to be in reasonable agreement with those presented in Antonia *et al.* (10) particularly when $\gamma_T \leq 0.5$ since, for this range of γ_T, the peak of p(θ) is also the peak of the fitted Gaussian curve. The value of Th determined by the method of Bilger *et al.* is used here to obtain conditional probability density functions of u, v and θ for either the heated ($\theta/\theta' >$ Th) or non-heated ($\theta/\theta' <$ Th) parts of the flow. Both conventional and conditional densities are normalized so that the area under each probability curve is equal to unity, i.e. $\int_{-\infty}^{\infty} p(a)\, da = 1$ or $\int_{-\infty}^{\infty} p(a_h^*)\, da_h^* = 1$.

PROBABILITY DENSITY FUNCTIONS OF VELOCITY AND TEMPERATURE

Probability density functions of u, v and θ at $x/\delta = 2.3$ are shown in Fig. 1 at $y/\delta_o = 0.092$ ($\gamma_T \simeq 0.68$). Although p(u) is nearly Gaussian, p(v) is distinctly non-Gaussian, presumably as a result of the constraint imposed by the wall. This departure from Gaussianity has been found (see (11) and the moments in Table 1) to decrease with increasing distance from the wall, at least in the fully turbulent region of the layer. The density $p(\theta)$ is highly non-Gaussian with correspondingly large skewness and flatness factors. A complete picture of the variation in $p(\theta)$ across the thermal layer at three x-stations has been presented by Danh (11).

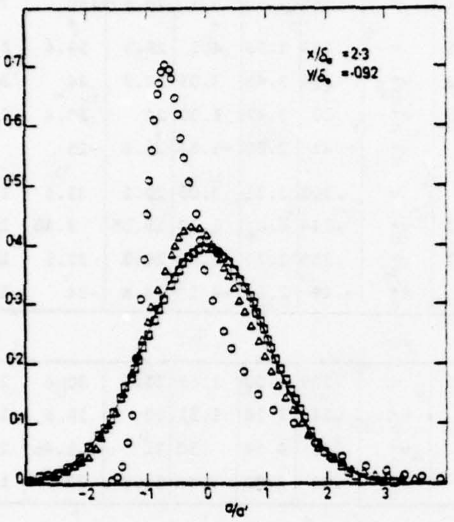

Fig. 1 Probability density functions of u, v and θ at $x/\delta_o = 2.3$ ($y/\delta = 0.092$). □, u; △, v; ○, θ; ——, Gaussian.

The main feature of these results is that the major departure from Gaussianity of $p(\theta)$ occurs very close to the wall and near the position of the thermal interface although the skewness of θ is of opposite sign in these two regions. It should be noted that the odd order moments of u are probably questionable very near the wall (e.g. odd order moments of u in Table 1 for $y/\delta = 0.038$ at $x/\delta_o = 2.3$) because of the non-linearity of the anemometer. When γ_T is very close to unity, little difference is expected between the conditional probability densities in the heated flow and the conventional densities. For $\gamma_T < 1.0$, conditional probability densities of u, v and θ are shown in Figs. 2-3 at $x/\delta_o = 2.3$. A noticeable feature of these figures is that $p(u_h^*)$ and especially $p(v_h^*)$ represent improved approximations to the Gaussian curve when compared with the conventional densities $p(u)$ and $p(v)$. Also, $p(u_h^*)$ is more closely Gaussian than $p(u_c^*)$ while $p(v_c^*)$ is more symmetrical than $p(v_h^*)$. These observations are clearly reflected in the results of Table 1 which show that, whereas there is little difference between even order moments of v_c^* and u_h^*, odd order moments of v_c^* are smaller than those of v_h^*. This trend is in general observable at all other stations x. The distribution of temperature $p(\theta_h^*)$ remains significantly different from the Gaussian density but the moments of θ_h^* are closer to the Gaussian values than are the conventional moments (Table 1). Moments of θ_c^* have been included in Table 1 mainly for the sake of completeness. Although $p(\theta_c^*)$ has been assumed to be Gaussian, the effect of imposing a threshold on θ has been considerable on the odd, but not the even, order moments of θ_c^*.

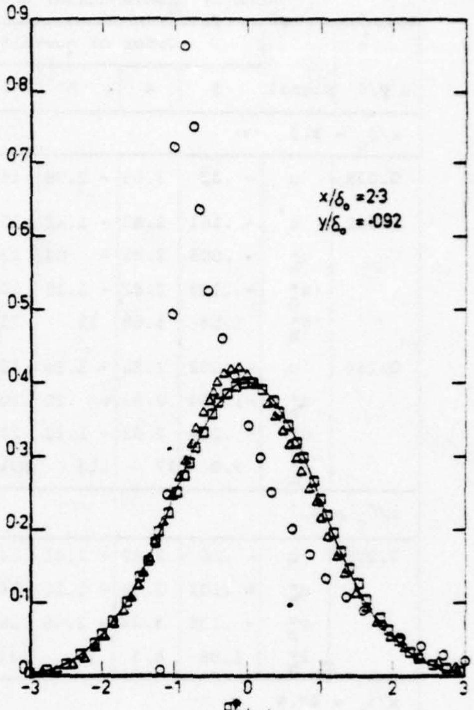

Fig. 2 Conditional probability density functions of u, v and θ in heated part of the flow at station $x/\delta_o = 2.3$ ($y/\delta = 0.092$). Symbols are as for Fig. 1.

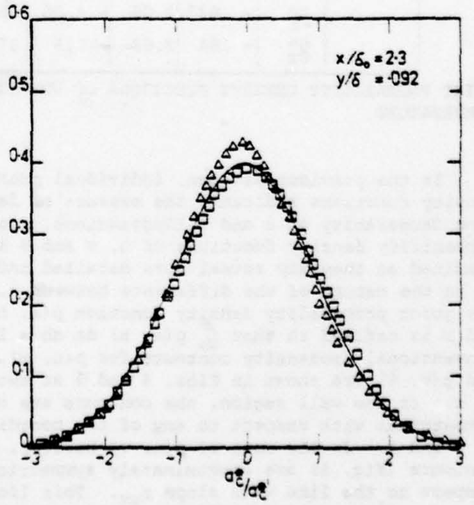

Fig. 3 Conditional probability density functions of u and v in non-heated flow at $x/\delta_o = 2.3$ ($y/\delta = 0.092$).

TABLE 1: Conventional and conditional high order moments of u, v and θ.

y/δ	Signal	Order of normalized moment						Signal	Order of normalized moment					
		3	4	5	6	7	8		3	4	5	6	7	8
$x/\delta_o = 2.3$														
0.038	u	- .32	3.05	- 2.95	16.3	- 28.8	128.4	v	.685	4.56	9.1	46.5	150	758
0.092	u	- .161	2.82	- 1.42	12.6	- 12	75.5	v	.354	3.58	4.1	26.5	59.4	343
	u_h^*	- .005	2.88	- .04	13.2	- .65	79.2	v_h^*	.264	3.48	3.05	24.5	44	300
	u_c^*	- .123	2.82	- 1.15	12.7	- 10.5	77.6	v_c^*	.10	3.47	1.30	24	20.4	276
	θ_h^*	1.54	5.68	19	75	312	1386	θ_c^*	-.48	2.60	-3.54	11.6	-25	77
0.254	u	- .232	2.82	- 1.94	12.8	- 15.68	78	v	.303	3.31	3.05	20.2	33.5	185
	u_h^*	- .044	2.63	- .30	10.4	- 1.48	51.3	v_h^*	.144	3.02	1.12	15.35	8.46	106
	u_c^*	- .224	2.83	- 1.92	13	- 16.0	80.7	v_c^*	.280	3.30	2.86	20.3	32.5	190
	θ_h^*	3.0	17	113	881	7580	70132	θ_c^*	-.49	2.9	-4.1	14.8	-34	109
$x/\delta_o = 5.7$														
0.209	u	- .26	2.92	- 2.41	14.65	- 23.6	110	v	.268	3.30	2.69	20.5	30.8	200
	u_h^*	- .102	2.94	- 1.12	14.45	- 12.7	103	v_h^*	.14	3.24	1.51	19	18.6	168
	u_c^*	- .235	3.04	- 2.46	16.9	- 29.2	154	v_c^*	.06	3.34	.50	21	1.46	211
	θ_h^*	1.98	8.3	36	183	1022	6155	θ_c^*	-.53	2.82	-4.4	14.8	37	117
$x/\delta_o = 42.9$														
0.176	u	- .23	2.44	- 1.74	10.26	- 14	64	v	.274	4.15	3.85	33.4	65	442
0.441	u	- .39	2.86	- 3.27	15	- 28.6	116	v	.29	3.02	2.86	18.9	36	212
	u_h^*	- .35	3.10	- 3.21	17	- 30	145	v_h^*	.244	3.46	2.88	24.5	44	305
	u_c^*	- .36	3.19	- 4.03	20.3	52	226	v_c^*	.006	3.51	.76	24.7	21.2	285
0.706	u	-1.106	4.32	-11.6	42.5	-155	628	v	.73	4.9	10.5	57.6	212	1202
	u_h^*	- .427	3.08	- 4.06	18.3	- 43.2	196	v_h^*	.217	3.43	1.84	21.0	15.5	180
	u_c^*	- .84	3.63	- 7.5	27.7	- 73.6	342	v_c^*	.36	4.27	4.7	39	80	606

JOINT PROBABILITY DENSITY FUNCTIONS OF VELOCITY AND TEMPERATURE

In the previous section, individual probability density functions indicated the measure of departure from Gaussianity of u and θ fluctuations. Joint probability density functions of u, v and θ are now examined as they may reveal more detailed information as to the nature of the difference between u, v and θ. The joint probability density function p(a, b) of a and b is defined so that $\iint_{-\infty}^{\infty} p(a, b)\, da\, db = 1$. Conventional isodensity contours for p(u, v), p(u, θ) and p(v, θ) are shown in Figs. 4 and 5 at two values of x. In the wall region, the contours are not symmetrical with respect to any of the coordinate axes u, v and θ. In the case of p(u, v) however, the contours (Fig. 5) are approximately symmetrical with respect to the line with slope r_{uv}. This line and its inverse r_{uv}^{-1} represent conditional means for jointly normal random variables and appear to be reasonable approximations to the measured conditional mean values of u and v except at large negative values of u and v.

Contours of p(u, θ) and p(v, θ) stretch out significantly into the (-u, +θ) and (+v, +θ) quadrants but are closely grouped together in the two quadrants that include the negative θ axis, mainly as a result of the ambient temperature cut-off.

As the distance from the wall increases (Fig. 5) the symmetry of p(u, v) with respect to the line of slope r_{uv} is impaired. Contours of largest p(u, v) values move well into the fourth (+u, -v) quadrant. The departure of measured conditional averages of u, v and θ from straight lines of slopes r_{uv}, $r_{v\theta}$ and $r_{u\theta}$ becomes particularly evident at large values of u, v and θ. Contours of p(v, θ) however remain essentially unchanged. This suggests that the maximum contribution to the average values of the shear stress $\overline{uv}$ and heat flux $\overline{u\theta}$ comes from the second quadrants [(u < o, v > o) and (u < o, θ > o)] because of the large amplitude but less probable fluctuations of u, v and θ, and the fourth quadrants [(u > o, v < o) and (u > o, θ < o)]. The results for p(u, θ) and p(v, θ) in Fig. 4 ($x/\delta_o = 2.3$) at $y/\delta = 0.254$ are probably not meaningful as the main source for θ at this location, characterized by a very small value of γ_T, is the combination of electronic noise and ambient temperature fluctuations. The contours become more symmetrical about the θ = o axis as a result of the small values of $r_{u\theta}$ and $r_{v\theta}$ (Table 2).

When $\gamma_T < 1.0$, contours for constant $p(u_h^*, v_h^*)$ show a closer degree of symmetry with respect to the

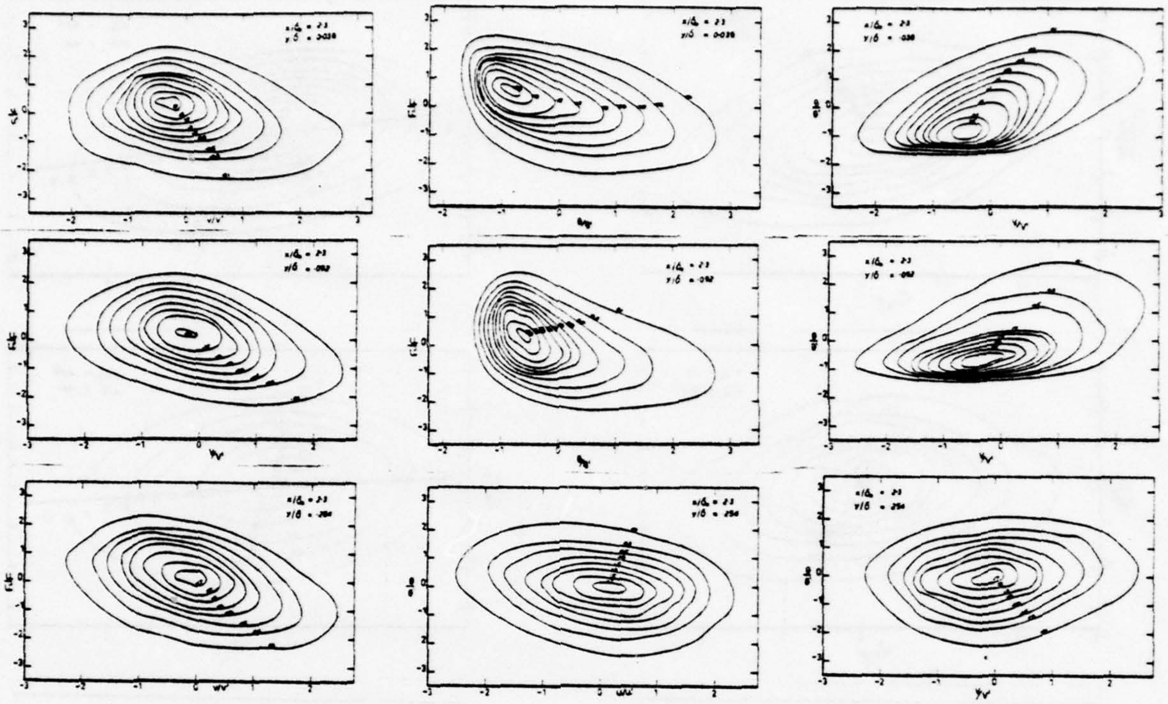

Fig. 4 Conventional isoprobability density contours for u, v, θ at $x/\delta_o = 2.3$.

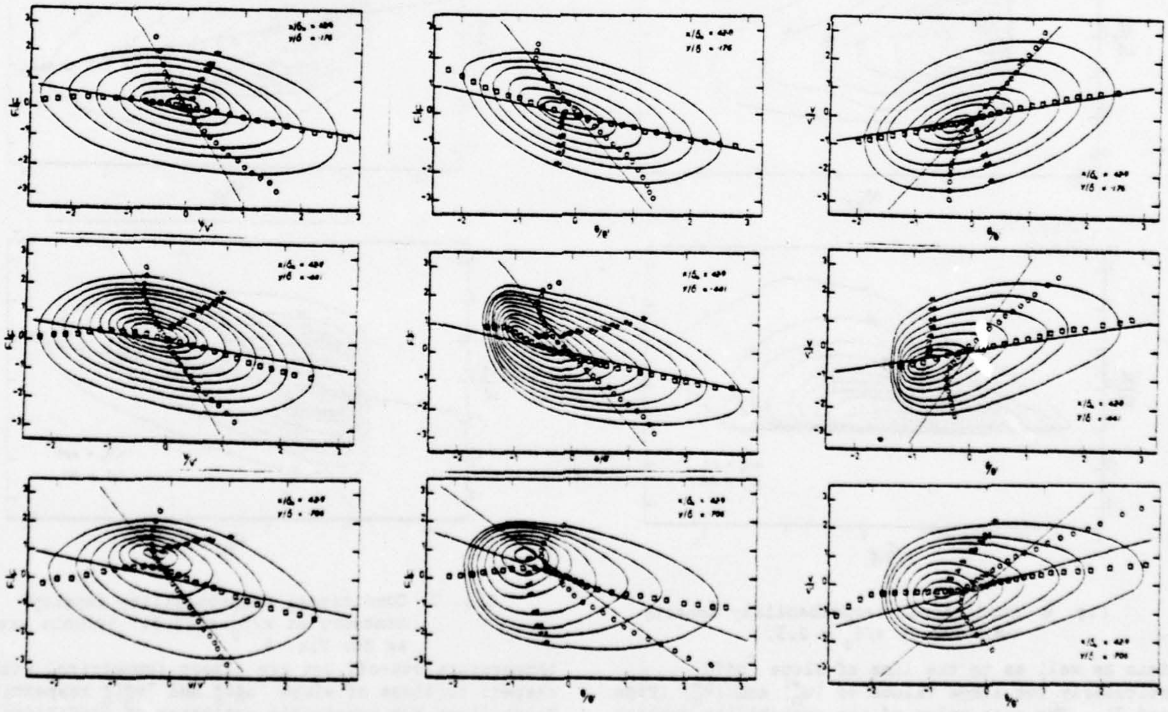

Fig. 5 Conventional isoprobability density contours for u, v, θ at $x/\delta_o = 42.9$. Symbols □, ○ represent conditional mean values of a (ordinate) and b (abscissa) respectively. Straight lines are Gaussian conditional means.

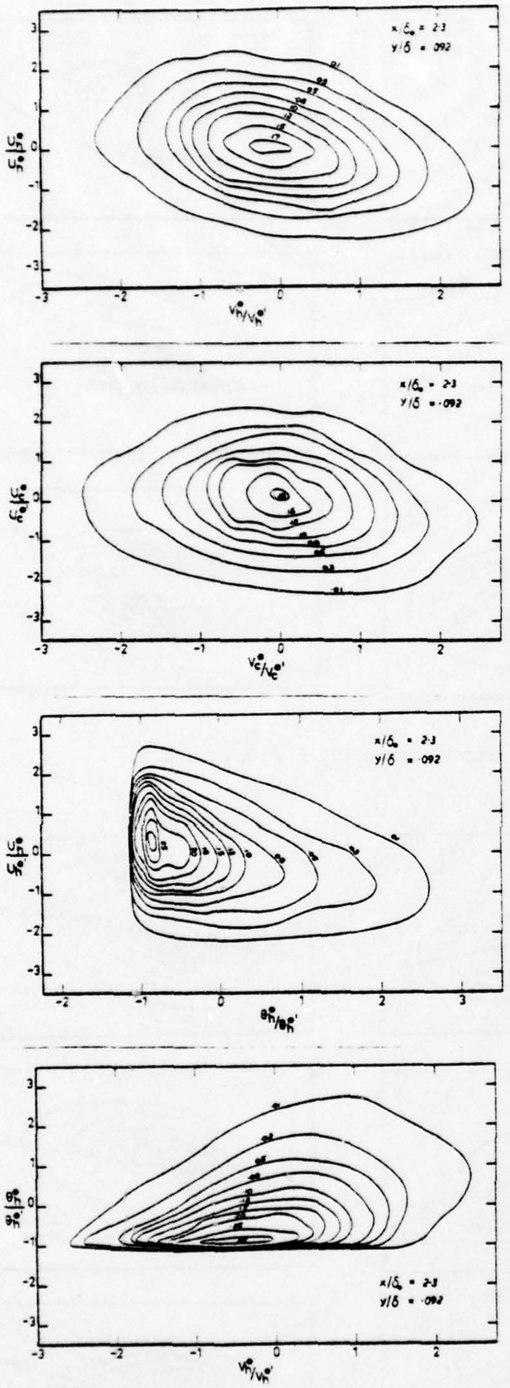

Fig. 6 Conditional isoprobability density contours at $x/\delta_0 = 2.3$.

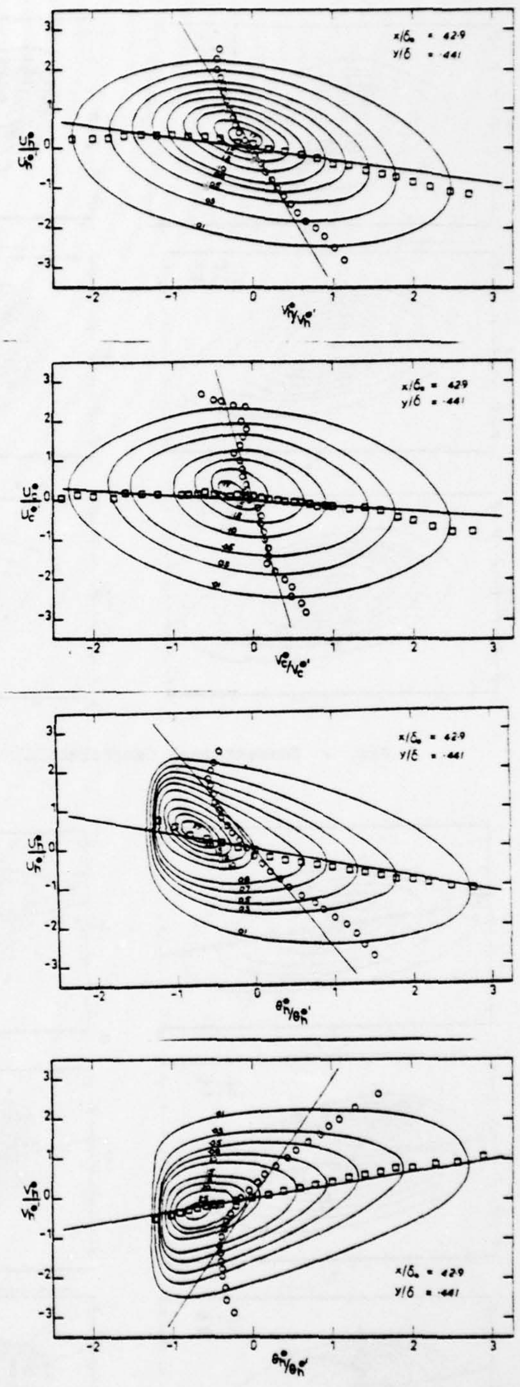

Fig. 7 Conditional isoprobability density contours at $x/\delta_0 = 42.9$. Symbols are as for Fig. 5.

origin as well as to the line of slope $^r u_h^* \theta_h^*$, particularly for large values of $|u_h^*|$ and $|v_h^*|$ (Figs. 6 and 7). The peak value of the probability density is closer to the origin, when compared with the conventional case. Contours of $p(u_h^*, \theta_h^*)$ and $p(v_h^*, \theta_h^*)$ remain constrained by the sharp ambient temperature cut-off but are almost symmetrical with respect to lines of slope $^r u_h^* \theta_h^*$ and $^r v_h^* \theta_h^*$ respectively. These lines are reasonable estimates of conditional mean values of u_h^* and v_h^* over a large range of values of θ_h^* as shown in Fig. 7.

An estimate of the contribution to $\overline{ab}$ from all four quadrants in the (a, b) plane is given in Table 2. As an example, the contribution from the (a > o, b > o) quadrant is calculated from $\overline{ab} = \int_0^\infty\int_0^\infty ab\, p^t(a, b)\, da.db$, where $p^t(a, b)$ is the joint probability density p(a, b), arbitrarily truncated at a = ± 3.4a' and b = ± 3.4b'[1].

TABLE 2: Percentage contribution to $\overline{ab}$ from different quadrants of (a, b) plane. (a) $x/\delta_o = 2.3$; (b) $x/\delta_o = 5.7$; (c) $x/\delta_o = 42.9$.

TABLE 2(a)

y/δ	a	b	I a>o b>o	II a<o b>o	III a<o b<o	IV a>o b<o	r_{ab}	γ_T
.038	u	v	- 31	+105	- 48	+ 74	-.24	1
	u	θ	- 20	+ 63	- 14	+ 70	-.42	
	v	θ	+ 69	- 11	+ 52	- 10	+.45	
.092	u	v	- 21	+ 83	- 28	+ 66	-.34	.68
	u	θ	- 12	+ 66	- 20	+ 65	-.37	
	v	θ	+ 74	- 13	+ 58	- 19	+.34	
	u_h^*	v_h^*	- 28	+ 86	- 32	+ 74	-.30	
	u_h^*	θ_h^*	- 24	+ 86	- 39	+ 77	-.36	
	v_h^*	θ_h^*	+ 82	- 18	+ 65	- 21	+.30	
	u_c^*	v_c^*	- 56	+124	- 64	+ 96	-.19	
.254	u	v	- 18	+ 79	- 23	+ 62	-.37	.06
	u	θ	- 54	+119	- 59	+103	-.19	
	v	θ	+146	- 85	+132	- 93	+.13	

TABLE 2(b)

y/δ	a	b	I a>o b>o	II a<o b>o	III a<o b<o	IV a>o b<o	r_{ab}	γ_T
.114	u	v	- 15	+ 73	- 20	+ 62	-.39	.99
	u	θ	- 11	+ 67	- 16	+ 61	-.43	
	v	θ	+ 68	- 13	+ 61	- 16	+.40	
.209	u	v	- 13	+ 72	- 18	+ 59	-.42	.55
	u	θ	- 12	+ 64	- 25	+ 73	-.34	
	v	θ	+ 70	- 12	+ 64	- 22	+.32	
	u_h^*	v_h^*	- 18	+ 72	- 23	+ 67	-.37	
	u_h^*	θ_h^*	- 22	+ 83	- 36	+ 75	-.27	
	v_h^*	θ_h^*	+ 79	- 20	+ 72	- 31	+.28	
	u_c^*	u_c^*	- 29	+ 91	+ 30	+ 78	-.28	

TABLE 2(c)

y/δ	a	b	I a>o b>o	II a<o b>o	III a<o b<o	IV a>o b<o	r_{ab}	γ_T
.176	u	v	- 26	+ 87	- 33	+ 72	-.30	1
	u	θ	- 15	+ 72	- 11	+ 54	-.40	
	v	θ	+ 80	- 27	+ 64	- 17	+.36	
.441	u	v	- 22	+ 88	- 32	+ 66	-.29	.88
	u	θ	- 11	+ 69	- 13	+ 55	-.40	
	v	θ	+ 76	- 17	+ 57	- 16	+.32	
	u_h^*	v_h^*	- 27	+ 92	- 36	+ 71	-.28	
	u_h^*	θ_h^*	- 14	+ 72	- 18	+ 60	-.39	
	v_h^*	θ_h^*	+ 77	- 21	+ 67	- 22	+.33	
	u_c^*	v_c^*	- 71	+138	- 83	+116	-.15	
.706	u	v	- 21	+ 92	- 36	+ 65	-.39	.33
	u	θ	- 17	+ 69	- 39	+ 87	-.69	
	v	θ	+ 71	- 27	+ 96	- 40	+.57	
	u_h^*	v_h^*	- 27	+ 91	- 41	+ 77	-.27	
	u_h^*	θ_h^*	- 35	+ 94	- 49	+ 90	-.29	
	v_h^*	θ_h^*	+ 92	- 37	+ 89	- 44	+.30	
	u_c^*	v_c^*	- 39	+119	- 60	+ 80	-.30	

Near the step (Table 2(a)) and at $y/\delta = 0.038$, contributions to $u\theta$ and $\overline{v\theta}$ from the ejection[2] quadrants are nearly identical, although contributions from the sweep quadrant are significantly larger for $\overline{u\theta}$ than for $v\theta$. This difference is reflected in the compensating increase in contributions from the interaction quadrants in the case of $\overline{u\theta}$. There is little similarity between contributions to $\overline{uv}$ from those to $\overline{u\theta}$ or $v\theta$, with contributions from all four quadrants being larger in the case of $\overline{uv}$ than for $\overline{u\theta}$ or $\overline{v\theta}$. As the distance from the wall increases (Table 2(a), $y/\delta = 0.092$), there is a decrease in contribution to $\overline{uv}$ from the sweep and, in particular, the ejection quadrants. On the other hand, contributions from these two quadrants are, in general, slightly increased in the case of $\overline{u\theta}$ and $\overline{v\theta}$, so that the similarity between contributions to $\overline{uv}$ and $\overline{v\theta}$ is significantly improved. This is especially true when only the heated part of the flow is considered.

At a short distance downstream from the step (Table 2(b)), the similarity between contributions to $\overline{uv}$ and $\overline{v\theta}$ from ejection and sweep quadrants is improved further. In the case of $\overline{u\theta}$, the contribution from the sweep event is larger than that for the ejection event at $y/\delta = .209$. When the effect of thermal intermittency is taken into account, contributions to $\overline{u\theta}$ become similar to those to $\overline{uv}$ or $\overline{v\theta}$. The results at $x/\delta_o = 42.9$ (Table 2(c)) provide further confirmation of the trends shown by Table 2(b).

The present contributions to uv, for all values of x/δ_o, are in general consistent with estimates made by Wallace *et al.*(5) and Brodkey *et al.*(16) obtained in the wall region of an oil channel flow. In the region immediately outside the sublayer, their results show that the ejection event contributes, on average,

---

[1] The truncation was necessary because of the limited storage capacity of the PDP 11/45 computer. The value of $\overline{ab}$ estimated from p^t agreed, to better than 10%, with the value obtained when the full range of (a, b) is used.

[2] Note that the ejection quadrant is the (-u, +θ) or second quadrant in the case of $\overline{u\theta}$ and the (+v, +θ) or first quadrant in the case of vθ.

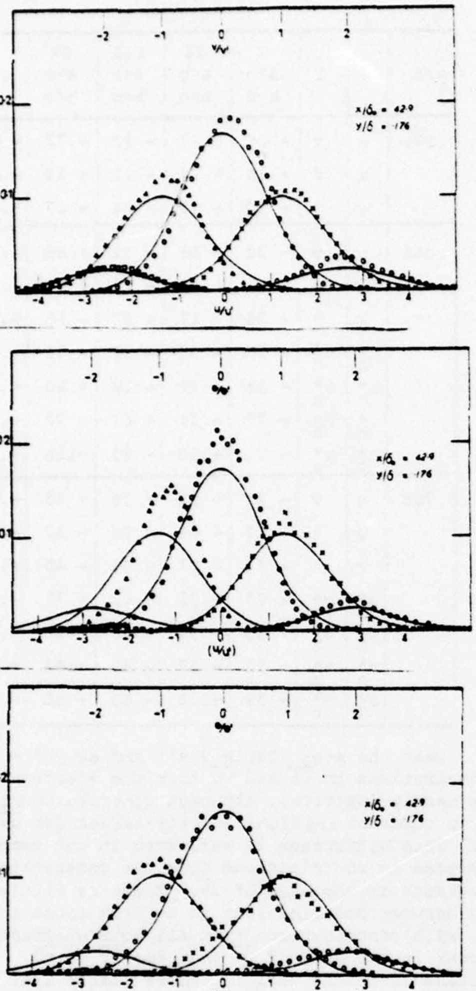

Fig. 8 Conditional probability densities of u, v, θ at $x/\delta_0 = 42.9$ ($y/\delta = .176$). Curves are Gaussian distributions.

about 25% more to the Reynolds stress than the sweep event while the interaction events contribute about 20% each to $\overline{uv}$. For a turbulent boundary layer with a relatively thick sublayer, Willmarth and Lu (4) and later Lu and Willmarth (17), obtained similar results for contributions to $-\overline{uv}$ from different events with the use of the "hole size" technique. Perry and Hoffmann (8) applied the "hole size" technique of Lu and Willmarth (17) to weighted joint probability density functions of (u, v) and (v, θ) and found that "ejections and sweeps" in Reynolds stress are usually accompanied by equivalent occurrences in heat flux. Contributions to $\overline{uv}$ and $\overline{v\theta}$ obtained by Perry and Hoffmann, obtained for a uniform temperature surface with no unheated starting length, are qualitatively similar to the present estimates. A quantitative comparison between the results is not justifiable since the use of the hole size technique tends to emphasize contributions from the ejection quadrant, especially in the case of $\overline{v\theta}$.

The deviation from Gaussianity of joint

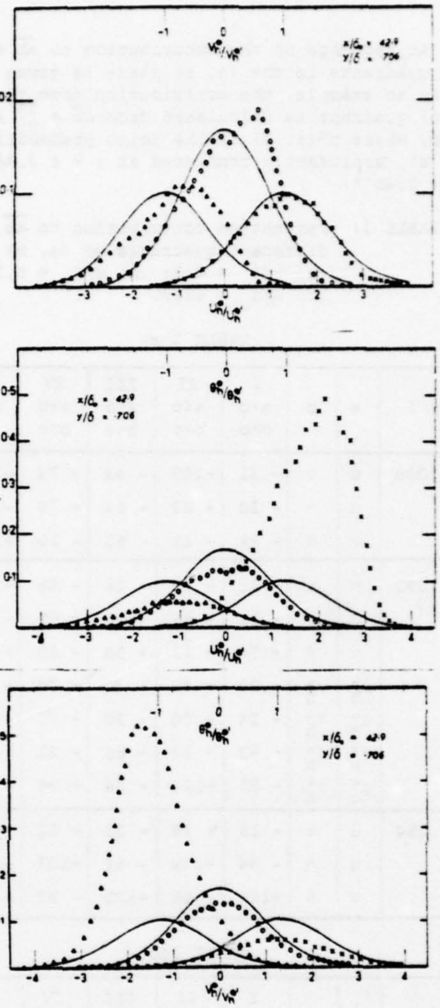

Fig. 9 Conditional probability densities in heated part of the flow of u, v, θ at $x/\delta_0 = 42.9$ ($y/\delta = .706$). Curves are Gaussian distributions.

probability density functions may be examined by taking cross-sectional cuts of the p(a, b) contours at either constant a or constant b values. In Fig. 8, conditional probability density functions of u and v are shown, at $x/\delta_0 = 42.9$ and $y/\delta = 0.176$, for given values of v or θ. In Fig. 9, the same type of information is presented, at the same station but for $y/\delta = .706$, in only the heated part of the flow. Also plotted in these figures is the bivariate Gaussian density function

$$p(a,b) = \frac{1}{2\pi\, a'b'(1-r_{ab})} \exp\{-\frac{1}{2(1-r_{ab}^2)}\left[\left(\frac{a}{a'}\right)^2 - 2r_{ab}\left(\frac{a}{a'}\right)\left(\frac{b}{b'}\right) + \left(\frac{b}{b'}\right)^2\right]\}$$

corresponding to the experimental value of the correlation coefficient r_{ab}. In the case of Fig. 9, a, b and r_{ab} in the expression for p(a, b) are replaced by a_h^*, b_h^* and $r_{a_h^* b_h^*}$ respectively.

Fig. 8 shows that for large |v|, p(u/v) is nearly Gaussian except near $u = o$. For smaller $|v|$, $p(u/v)$ follows the Gaussian curve more closely when v is positive than when v is negative. When $v = o$, the distribution for $u < o$ is more Gaussian than that for $u > o$.

Conditional densities $p(u/\theta)$ and $p(v/\theta)$ are reasonably Gaussian for positive values of θ. The approximation to Gaussianity breaks down completely for large negative values of θ, presumably because of the lower bound on θ which corresponds to the ambient temperature value. For moderately negative values of θ, $p(v/\theta)$ is better approximated by the Gaussian distribution than $p(u/\theta)$.

Conditional densities in the intermittent region of the layer (Fig. 9) indicate a fair approximation to Gaussianity for positive v_h^* and θ_h^*, at least in the case of $p(u_h^*/v_h^*)$ and $p(v_h^*/\theta_h^*)$. The Gaussian approximation is, however, not as good as in Fig. 8. The similarity between $p(u, \theta)$ and $p(v, \theta)$ is also less pronounced at $y/\delta = 0.706$ than at $y/\delta = 0.176$.

CONCLUSIONS

Although the probability density function of temperature in a heated boundary layer does not exhibit the bimodal shape observed in the case of a heated wake or heated jet, it still provides a satisfactory determination of the thermal intermittency factor. The departure of $p(\theta)$ from Gaussianity is more noticeable both in regions close to the wall and near the thermal interface. The probability density function of the longitudinal velocity fluctuation in the thermal layer is very nearly Gaussian when compared with the conventional $p(u)$, or the probability density $p(u^*)$ in the unheated - but still turbulent - part of the flow.

In the case of normal velocity fluctuations, the probability density function in the thermal layer is more Gaussian than the conventional density but the odd order moments of v in the unheated flow are closer to zero than those in the thermal layer.

At a small distance downstream of the heat flux step and very near the wall, the similarity between joint probability densities $p(u, v)$ and $p(v, \theta)$ is poor although $p(u, \theta)$ and $p(v, \theta)$ exhibit similar features. The similarity, in the inner region of the layer, between $p(u, v)$ and $p(v, \theta)$ improves quickly with increasing distance from the step. At the measuring station, furthest downstream from the step, the conditional density $p(u/v)$ is closely approximated by the bivariate Gaussian density while the approximation for $p(v, \theta)$ is reasonable only at large positive temperature fluctuations.

Estimates of contributions to the shear stress and heat fluxes show that, in the wall region, the ejection ($a < o$, $b > o$) and sweep ($a > o$, $b < o$) events provide positive contributions, well in excess of 100%. The contribution from the ejection event is however larger than that of the sweep event and a significant similarity exists between contributions to $\overline{uv}$ and $\overline{v\theta}$. At all stations contributions to $\overline{uv}$ from ejection and sweep events decrease slightly with increasing distance from the wall. Far downstream from the step, contributions to $\overline{uv}$ from the various events are nearly invariant with distance from the wall, but the contribution from the sweep event to $\overline{u\theta}$ and $\overline{v\theta}$ is found to increase as y increases. In the heated part of the flow, contributions from each event are generally 10-15% higher than conventional contributions. The similarity between $p(u, v)$ and $p(v, \theta)$ is improved when only the heated part of the flow is considered.

REFERENCES

1 Kline, S.J., Reynolds, W.C., Schraub, F.A. and Runstadler, P.W., "The Structure of Turbulent Boundary Layer," Journal of Fluid Mechanics, Vol. 30, Part 4, Dec. 1967, pp. 741-773.

2 Corino, E.R. and Brodkey, R.S., "A Visual Investigation of the Wall Region in Turbulent Flow," Journal of Fluid Mechanics, Vol. 37, Part 1, June 1969, pp. 1-30.

3 Kim, H.T., Kline, S.J. and Reynolds, W.C., "The Production of Turbulence Near a Smooth Wall in a Turbulent Boundary Layer," Journal of Fluid Mechanics, Vol. 50, Part 1, Nov. 1971, pp. 133-160.

4 Willmarth, W.W. and Lu, S.S., "Structure of Reynolds Stress Near the Wall," Journal of Fluid Mechanics, Vol. 55, Part 1, Sept. 1972, pp. 65-92.

5 Wallace, J.M., Eckelmann, H. and Brodkey, R.S., "The Wall Region in Turbulent Shear Flow," Journal of Fluid Mechanics, Vol. 54, Part 1, July 1972, pp. 39-48.

6 Venkataramani, K.S., Tutu, N.K. and Chevray, R., "Probability Distribution in a Round Heated Jet," Physics of Fluids, Vol. 18, Nov. 1975, pp. 1413-1420.

7 Antonia, R.A. and Sreenivasan, K.R., "Statistical Properties of Velocity and Temperature Fluctuations in a Turbulent Heated Jet," Tech. Note FM-3, 1976, Department of Mechanical Engineering, University of Newcastle.

8 Perry, E.A. and Hoffmann, P.H., "An Experimental Study of Turbulent Convective Heat Transfer from a Flat Plate," Journal of Fluid Mechanics, Vol. 77, Part 2, Sept. 1976, pp. 355-368.

9 Johnson, D.S., "Velocity and Temperature Fluctuation Measurements in a Turbulent Boundary Layer Downstream of a Stepwise Discontinuity in Wall Temperature," Journal of Applied Mechanics, ASME Transaction, Vol. 26, Sept. 1959, pp. 325-336.

10 Antonia, R.A., Danh, H.Q. and Prabhu, A., "Response of a Turbulent Boundary Layer to a Step Change in Surface Heat Flux," Charles Kolling Research Laboratory Tech. Note F-74, June 1975, Department of Mechanical Engineering, University of Sydney, to appear in Journal of Fluid Mechanics.

11 Danh, H.Q., "Turbulent Transfer Processes in Non-Isothermal Shear Flows," Ph.D. Thesis, Dec. 1976, Department of Mechanical Engineering, University of Sydney.

12 Antonia, R.A., Prabhu, A. and Stephenson, S.E., "Conditionally Sampled Measurements in a Heated Turbulent Jet," Journal of Fluid Mechanics, Vol. 72, Part 3, Dec. 1975, pp. 455-480.

13 Bilger, R.W., Antonia, R.A. and Sreenivasan, K.R., "The Determination of Intermittency from the Probability Density Function of a Passive Scalar," The Physics of Fluids, Vol. 19, No. 10, Oct. 1976, pp. 1471-1474.

14 LaRue, J.C. and Libby, P.A., "Temperature and Intermittency in the Turbulent Wake of a Heated Cylinder," The Physics of Fluids, Vol. 17, No. 5, May 1974, pp. 873-878.

15 Stephenson, S.E., "Experimental Investigation of a Heated Free Shear Layer," M.E.Sc. Thesis, Sept. 1976, Department of Mechanical Engineering, University of Sydney.

16 Brodkey, R.S., Wallace, J.M. and Eckelmann, H., "Some Properties of Truncated Turbulence Signals in Bounded Shear Flows," Journal of Fluid Mechanics, Vol. 63, Part 2, April 1974, pp. 209-224.

17 Lu, S.S. and Willmarth, W.W., "Measurements of the Structure of the Reynolds Stress in a Turbulent Boundary Layer," Journal of Fluid Mechanics, Vol. 60, Part 3, Sept. 1973, pp. 481-511.

THERMAL CHARACTERISTICS OF A TURBULENT BOUNDARY LAYER WITH INVERSION OF WALL HEAT FLUX

G. CHARNAY, J.P. SCHON, E. ALCARAZ and J. MATHIEU

Laboratoire de Mécanique des Fluides de l'Ecole Centrale
de Lyon, 36 route de Dardilly, 69130 Ecully, France

ABSTRACT

An experimental investigation of the thermal field downstream an inversion of a wall heat flux was carried out in a turbulent boundary layer. The external velocity U_1^o and the external temperature To are constant. The boundary layer investigated develops along a smooth flat plate which presents a step of temperature. Upstream the step the wall temperature is higher than To and approximately equal to To downstream. This research should bring additional information for modelling process for any region of the flow exhibiting special thermal characteristics which can not be explained with a first gradient model. Furthermore, the internal structure of the boundary layer can also be analyzed by thermal tagging effect and using conditional techniques.

NOMENCLATURE

fe = intermittency frequency for external frontier, s^{-1}
fi = intermittency frequency for internal frontier, s^{-1}
Ox_i = axis Ox_1 in the direction of the flow, axis Ox_2 normal to the wall,
p = fluctuating pressure, Kg m^{-1} s^{-2}
$Q + q(t)$ = fluctuating quantity
$\underline{q(t)}$ = fluctuation with zero mean
$\overline{Q + q}$ = (Q) conventional time average
$\overline{Q + q}^{*}$ = (Q^*) conditional zone average, * = e, i, f or c : see table II
$\widehat{Q + q}$ = ($\hat{Q}(\tau)$) conditional point average near front of bulges
$\overset{\frown}{Q + q}$ = ($\check{Q}(\tau)$) conditional point average near back of bulges
$\hat{Q}$ = point average at the front of interface, (τ=0)
$\check{Q}$ = point average at the back of interface, (τ=0)
q^* = ($Q + q(t) - Q^*$) local fluctuation
Sq = skewness factor of q, dimensionless
Tq = flatness factor of q, dimensionless
To = free stream temperature, deg. C.
Tp = wall temperature, deg C, ($X_1 < 0.7$ m)
Tṕ = wall temperature, deg C, ($X_1 > 0.7$ m)
Tm = extremum of temperature in a cross section, deg C
T = mean temperature, deg C
t = time, s
X_2^* = value of X_2 at T - Tm = (To - Tm)/2, $x_2 > \delta_T$, m
U_i = mean velocity, m/s
U_1^o = free stream velocity, m/s
u_i = fluctuating velocity, m/s
α = thermal diffusivity coefficient m^2/s
γ_e = intermittency factor for external frontier, dimensionless
γ_i = intermittency factor for internal frontier, dimensionless
δ = thickness of kinematic boundary layer, m
δ_T = value of X_2 at T = Tm, m
θ = fluctuating velocity, deg C
ν = kinematic viscosity, m^2/s
ρ = fluid density, Kg/m^3
τ = delay, s

1. INTRODUCTION

At present time, it is well known that in turbulent shear flows, no local connection can be found between the shear stress and the mean velocity gradient. In general rule, the signs of these two quantities are yet linked to each other, but even such a connection does not exist in restricted regions of flows exhibiting unsymmetrical boundary conditions. Such a situation was observed twenty years ago (1,2) and was investigated in wall jets (3-6).In order to predict such complex flows,new computing methods were developped (7,8).

The main purpose of the present paper is to display experimental informations in a more or less similar case where the heat flux is not connected with the mean temperature gradient, at least, in a restricted area. The boundary layer, under consideration, develops along a flat plate with a strong inversion of the wall heat flux. In the upstream part of the plate, the temperature of the wall is higher than the temperature of the surrounding flow ; on the contrary, in the downstream part, this situation is reversed. So far, only few detailed information is available, regarding this kind of flow (9-12). In this experimental research, the fluid motion is not affected by the temperature field.

In a first section (§ 3 and 4), the overall characteristics of the thermal field are presented. The mean temperature, turbulent heat flux, correlations of second, third and fourth order and thermal energy budget are determined. With a view of computing methods, special interest is given in this last thermal energy balance.

In the second section (§ 5 and 6), the behavior of the internal frontier, which is tagged by thermal effect downstream the wall temperature step, is analyzed. The statistical properties of such an interface are presented. For experimental facilities, the scheme of a thin limiting surface is supposed and the sign of the wall temperature step is reversed (the wall temperature increases at the step point). In this case, the discrimination between turbulent structures is based on a thermal threshold ; similar method was previously

PRECEDING PAGE BLANK-NOT FILMED

used in a disturbed boundary layer (13) and a wall jet (14). The intermittency factor, zone averages and conditional sampling of velocity and temperature are performed. For comparison, the statistical properties of the external edge of the overall boundary layer are analyzed.

In several practical configurations, similar situations can be encountered. The heat flux at the ground can suddenly be reversed when atmospherical winds blow from the sea to the seashore (15, 16) ; great urban centers can also generate reversal heat fluxes with respect to the surrounding country. This research should precisely contribute to model turbulent mechanisms in these very complex cases which requires a good deal of experimental data.

2. EXPERIMENTAL CONDITIONS AND TECHNIQUES

General description of the flow

The boundary layer investigated develops without longitudinal pressure gradient, along a smooth flat plate, 2 m. long and 0.5 m. wide. This plate presents a step of wall temperature at $X_1 = 0.7$ m. downstream the leading edge. The table I gives the experimental conditions for the two sections. In all cases, the difference between wall and external temperatures is about 20°C. Thus the influence of buoyancy effects on the kinematic field is weak enough to be neglected. The external stream has a mean velocity of 10 m./s and a residual intensity $(\overline{u_1^2})^{1/2}/U_1^{\,o}$ of 0.3 %

X_1 m		0.7	0.8.	0.9	1.05	14
T_w section 1: (§ 3,4)	Tp =To+23°C	T'p = To − 3°C				
T_w section 2: (§ 5,6)	Tp = To	T'p = To + 16°C				
δ mm		49	51	52	54	55

Table I. Experimental conditions

Data acquisition

All results were carried out by using hot wire technique. Analogic linear combinations of the signals issued from three anemometers permit simultaneous separation of the longitudinal and transverse components velocity and also the temperature at given point. Next these signals were digitally sampled. For each signal, the sampling rate is 10.000 samples/sec. and the resolution is 11 bits plus sign. The time of record is 10 s corresponding to 102400 samples.

The first step in processing the information consists to transform voltages in components of velocity and temperature. The three empirical curves of calibration are used for each "trio" of samples. In second part, several FORTRAN IV programs were used for obtaining conventional and conditional results. The intermittency function is estimated by means of a criterion based on the temperature.

Definitions

Classical relations (21) for conditionally averaging and sampling are utilized. The nomenclature and following table give respectively similar definition and notations that those of Hedley and Keffer (23).

X_2/δ	wall ⟶			Free stream
Frontier	Internal (I)		External (E)	
Superscript for averages	C	f	i	e

Table II Summary of superscript

3. OVERALL CHARACTERISTICS OF THE THERMAL FIELD

Mean temperature distribution

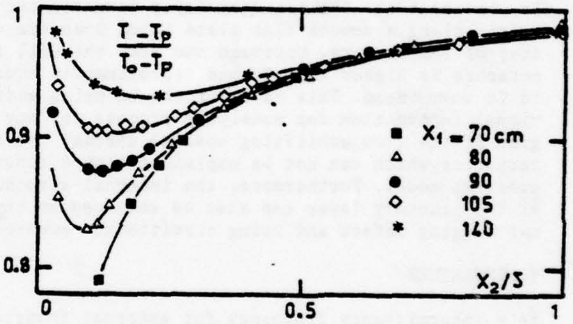

Fig.1. Distribution of the dimensionless mean temperature

Downstream the temperature step at the wall, the thermal field is strongly modified in the region next to the plate. At first, this influence is apparent on the mean temperature distribution (fig. 1). The temperature profile presented in a dimensionless form $(T - Tp)/(To - Tp)$ is given as a function of x_2/δ ; Tp stands for the upstream wall temperature, and To for that of the undisturbed stream. At four stations, the curves exhibit minimum values which are located farther and farther from the wall as we go downstream.

In the external part of the boundary layer ($x_2/\delta > 0.5$), the thermal properties are unaffected up to $x_1 < 1.4$ m.

Temperature fluctuation intensity

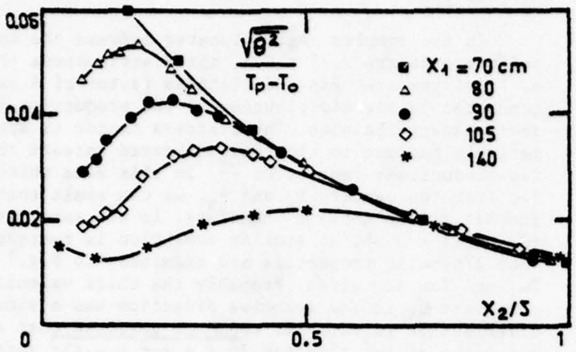

Fig.2. Distribution of the r.m.s. temperature fluctuation

Just downstream the temperature step, the temperature fluctuations strongly decrease, at least in the range of the values x_2/δ investigated. In fig.2., the distribution of $\sqrt{\overline{\theta^2}}/[Tp - To]$ is given versus x_2/δ. In a very narrow area, next to the wall, no experimental data are available at this time ; in fact, a thermal turbulent center should exist just beyond the viscous film, such a situation can be anticipated from the shape of the curves relative to the two last stations (x_1 = 1.05 m., x_1 = 1.4 m.). Obviously, the distribution of $(\overline{\theta^2})^{1/2}$ is directly connected to the production term in the equation governing the evolution of $\overline{\theta^2}/2$ which will be discussed later.

Turbulent heat flux

Upstream the temperature step, the heat flux, $\overline{u_2\theta}$, continually decreases with the distance from the wall x_2. Downstream the step, negative values of the heat flux near the plate must be interpreted as an heat exchange from the wall region to the surrounding flow (Fig. 3). In such a complex situation, the heat flux is not zero at a point where the mean temperature is maximum (Fig. 4).

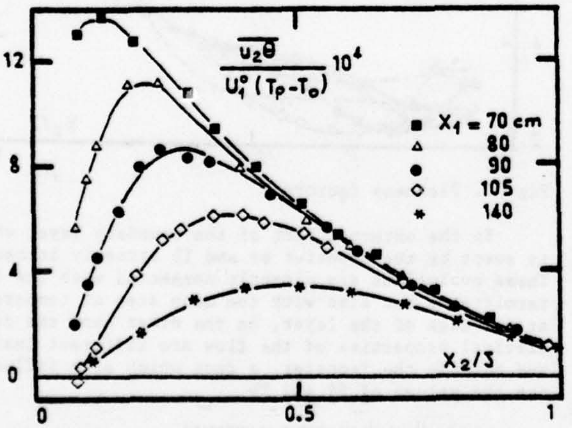

Fig. 3. Heat flux $\overline{u_2\theta}$ normal to the wall.

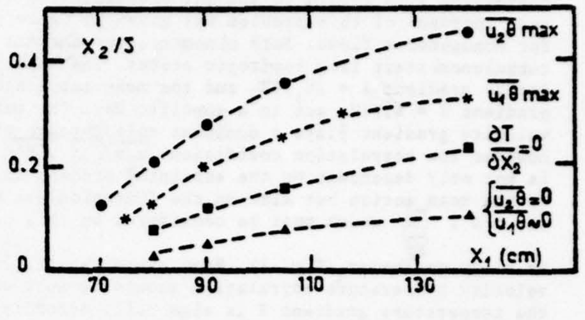

Fig. 4. Positions of the points where T, $\overline{u_2\theta}$, $\overline{u_1\theta}$ have particular values.

It would be relevant to review some experimental results which clearly invalidate any direct link assumed between the mean properties of a flow. In a wall jet, such a situation was pointed out (1) and properly explained later (8). At any rate, it is not possible to model these kinds of flows by using a first gradient approach. In any events, the memory of the turbulent structure has to be taken into account. Refering to qualitative explanations previously given by J. Mathieu (17) when kinematic properties are considered, a linear analysis should be convenient in order to predict qualitatively the anisotropic state of the turbulent structures strained by the mean flow. Such a state was approximatively determined from a Lagrangian approach by travelling along a mean streamline. Furthermore, the inhomogeneous field was supposed locally tractable by using theoretical results established for homogeneous one ; in computing methods (8), a transversal diffusion process is also introduced in order to take into account the interaction between turbulent structures travelling along various mean streamlines.

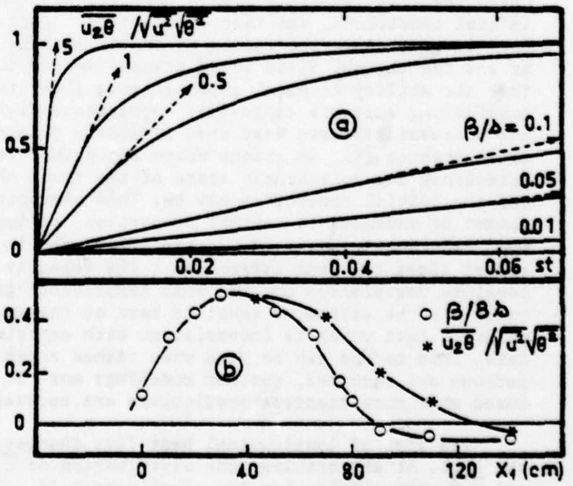

Fig. 5. Correlation coefficient $\overline{u_2\theta}/[\overline{u_2^2}\,\overline{\theta^2}]^{1/2} = Ru_2\theta$

(a) Computed values (18) with a linear approach, $\overline{q^2}_o$ = 1000 cm^2 s^{-2}, $\overline{\theta^2}$ = 0.05 deg^2

(b) for x_2 = 5 mm, ✱ measured values of $Ru_2\theta$, ○ measured values of β/s.

At first sight, a similar treatment seems to be convenient with regard to thermal properties. A linear approach of this problem was given by Gence (18) for homogeneous flows. Both kinematic and thermal turbulences start from isotropic states. The mean velocity gradient $s = \partial U_1/\partial X_2$ and the mean temperature gradient $\beta = \partial T/\partial X_2$ act in a specific way. The mean velocity gradient plays a dominant role through st ; however the correlation coefficient $\overline{u_2\theta}/[\overline{u_2^2} \cdot \overline{\theta^2}]^{1/2}$ is not only dependent on the straining process applied by the mean motion but also on the dimensionless ratio $\beta/s \cdot \frac{\overline{q_o^2}}{\overline{\theta_o^2}}$ which must be considered in this case as a new parameter (Fig. 5). From these results, the velocity temperature correlation should be null when the temperature gradient β is also null. Accordingly, if we consider an homogeneous field characterized by $s \neq 0$ and $\beta = 0$ and if an isotropic turbulence including both kinematic and thermal fluctuations is submitted to this shear flow, the velocity correlation $\overline{u_1u_2}$ starting from zero increases with st, whereas the velocity temperature correlation $\overline{u_2\theta}$ stands equal to zero. This behaviour is easy to understand in examining the equation which controls $\overline{u_i\theta}$

$$\frac{\partial}{\partial t}\overline{u_i\theta} + U_k\frac{\partial \overline{u_i\theta}}{\partial X_k} = -\overline{u_k\theta}\frac{\partial U_i}{\partial X_k} - \overline{u_i u_k}\frac{\partial T}{\partial X_k}$$

$$-\overline{\frac{\theta}{\rho}\frac{\partial p}{\partial X_i}} + \nu\overline{\theta\frac{\partial^2 u_i}{\partial X_k^2}} + \alpha\overline{u_i\frac{\partial^2\theta}{\partial X_k^2}}$$

when the initial values of $\overline{u_k\theta}$ and $\overline{u_iu_k}$ are zero

with $\partial U_i/\partial X_k \neq 0$ and $\partial T/\partial X_k = 0$ for any value of t. The evolution of the correlation term $u_i\theta$ depends on the two mean gradients s and β ; if $\beta = 0$ and if $s \neq 0$, $\overline{u_k\theta}$ starting from zero, the correlation $u_i\theta$ cannot be generated. It is difficult to imagine such a situation to be altered by non linear effects which specially generate random motions. With these initial conditions, the mean gradient s partially puts in order only the random kinematic motion, not at all the thermal field which stands isotropic. So far, the ability to model inhomogeneous flows by considering suitable tangential homogeneous field has successfully been used when kinematic properties are concerned (8). An unique curve approximatively determines the anisotropic state of the fluid whatever the initial conditions may be. This viewpoint cannot be extended to thermal properties, at least when only local values of β/s are introduced in the travel along the mean streamline ; the velocity temperature correlation and the mean temperature gradient would also be estimated equal to zero at the same point, a fact which is inconsistent with experimental data. This method can be used when rather rough estimations are required, another modellings must be introduced when more accurate predictions are necessary.

The sign of longitudinal heat flux changes near the wall. At any station, the distribution of $\overline{u_1\theta}$ and $\overline{u_2\theta}$ are similar but the coordinate X_2/δ of the extrema of these fluxes are very different from each other (fig. 4). Beyond the value $X_2/\delta = 0.5$, the ratio $u_1\theta/u_2\theta$ is approximately equal to the usual value 1.2.

Skewness and flatness factors of the temperature fluctuation

In the complex region located between the wall and the ordinate $X_2/\delta \approx 0.5$, the distributions (Figs. 6, 7) of the skewness and flatness factor of θ seem connected to the distribution of the production term in the energy balance. The flatness factor is approximatively maximum in the region located between the two productions centers of $\overline{\theta^2}$. In this area which is fed from two centers P_A and P_B, we can admit that two thermal random motions interfere. In the same area $(0 < X_2/\delta < 0.5)$, no similar evolution is remarked when kinematic properties are examined. In Fig.7 Tu_1 and Tu_2 are given. Probably the third velocity component u_3 in the spanwise direction has a similar distribution $Tu_3(X_2)$. It could be expected that the behaviour of the function $(\overline{u_1^2} + \overline{u_2^2} + \overline{u_3^2})^2$ versus X_2/δ would also have the same form. In this case, the analogy previously (19) proposed between $q^2 = u_2^2$ and θ^2 from spectral analysis would be involved at least when very detailed properties of the turbulent field are considered.

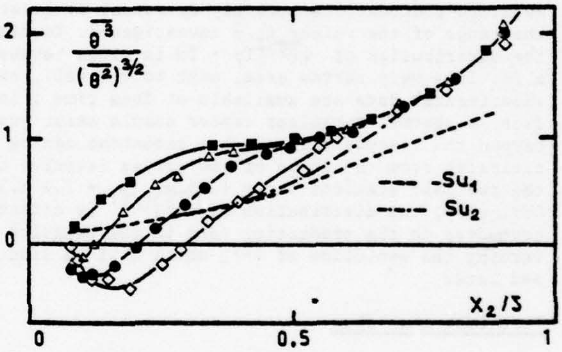

Fig. 6. Skewness factors

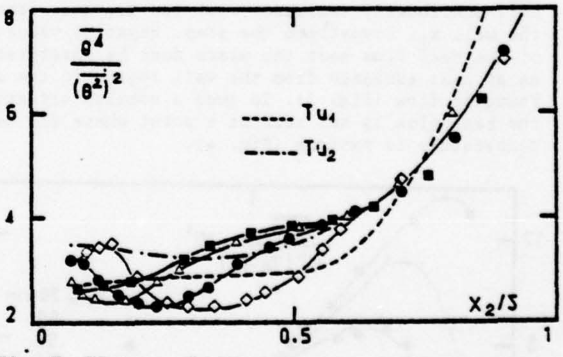

Fig. 7. Flatness factors

In the external part of the boundary layer which is swept by the frontier $S\theta$ and $T\theta$ strongly increase. These evolutions are directly connected with the intermittence but also with the mean step of temperature at the edge of the layer. on the other hand the statistical properties of the flow are different inside and outside the frontier, a fact which also influences the values of $S\theta$ and $T\theta$.

4. BUDGET OF TEMPERATURE VARIANCE

Both the turbulent kinetic energy balance and the turbulent thermal energy budget are equally important when predicting methods are concerned. In the case under consideration, no equilibrium state can exist downstream the temperature step, accordingly thermal scales Tm - Tp, Tp - To ; δ_T, $X_2^* - \delta_T$ cannot be successfully used in the disturbed area next to the wall ($0 < X_2/\delta < 0.5$).

For steady flows, the equation which controles $\frac{\overline{\theta^2}}{2}$ can be written

$$\underbrace{\frac{1}{2}U_1\frac{\partial\overline{\theta^2}}{\partial X_1}}_{}\!\!\overset{A_1}{}+\overset{A_2}{\frac{1}{2}U_2\frac{\partial\overline{\theta^2}}{\partial X_2}}+\overset{P_1}{\overline{u_1\theta}\frac{\partial T}{\partial X_1}}+\overset{P_2}{\overline{u_2\theta}\frac{\partial T}{\partial X_2}}$$

$$+\underbrace{\frac{1}{2}\frac{\partial\overline{u_1\theta^2}}{\partial X_1}}_{D_1}+\underbrace{\frac{1}{2}\frac{\partial\overline{u_2\theta^2}}{\partial X_2}}_{D_2}\underbrace{-\overline{\alpha\theta\left(\frac{\partial^2\theta}{\partial X_1^2}+\frac{\partial^2\theta}{\partial X_2^2}+\frac{\partial^2\theta}{\partial X_3^2}\right)}}_{\varepsilon}=0$$

The advection by the mean flow is taken into account by the two first terms A_1 and A_2 whereas the advection by the turbulent flow is represented by D_1 and D_2. The thermal field is smoothed by molecular effects through the three last terms, of course the smallest structures are the most influenced by conduction. $\overline{\theta^2}$ is produced by the interaction between the heat flux terms $\overline{u_1\theta}$ and $\overline{u_2\theta}$ and respectively components $\partial T/\partial X_1$ and $\partial T/\partial X_2$ of the mean temperature gradient ; if T is constant $\overline{\theta^2}$ can only decrease. We can already note that A_1, P_2, D_2 and ε are the dominant terms.

Production of $\overline{\theta^2}/2$ (fig. 8).

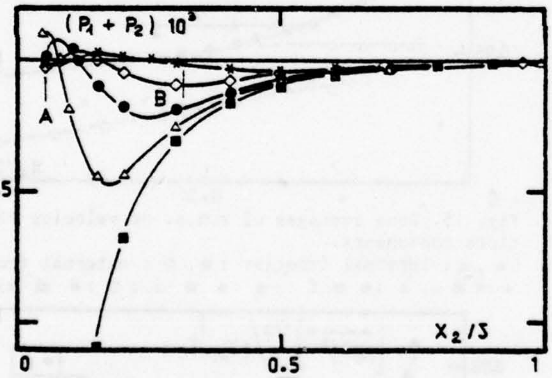

Fig. 8. Production term of $\overline{\theta^2}/2$.

The distribution of $P_1 + P_2$ versus X_2/δ is strongly modified by the step temperature at the wall. In a given section (X_1 = 1.05 m for example), the production is maximum at two points A and B, the first one is located near the wall, the other one B more outside, near the point where the slope of the mean temperature profile is maximum. Between A and B, a limited area appears where the thermal production - P is "negative" (20). The amount of "negative production" is very weak when compared with the overall production at the station. This countergradient heat flux is probably connected with the memory of the thermal turbulent structures.

Temperature fluctuation balance

The distribution of the terms which contributes to the evolution of $\overline{\theta^2}/2$ is given in Fig. 9 and 10. A comparison between two stations can be made, the first one located at the thermal step, the second one at 35 cm downstream.

In this last station, the production term is very weak and a complex situation exists specially characterized by a balance between molecular and advective effects, the turbulent diffusion having a small importance. A local equilibrium between production and "dissipation" is far from being realized, the influence of external region can be expected through travelling processes.

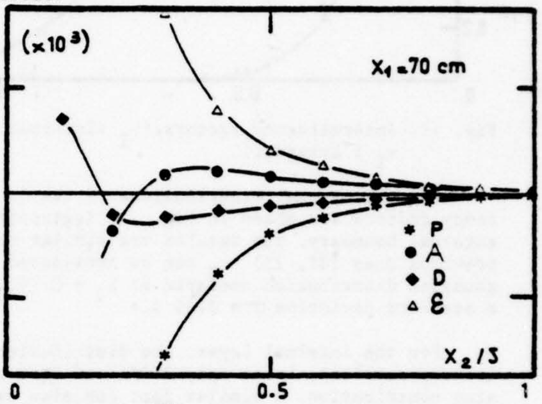

Fig. 9. Budget of $\overline{\theta^2}/2$ at the thermal step
(* : Production, △ : destruction, ● : advection, ◆ : diffusion).

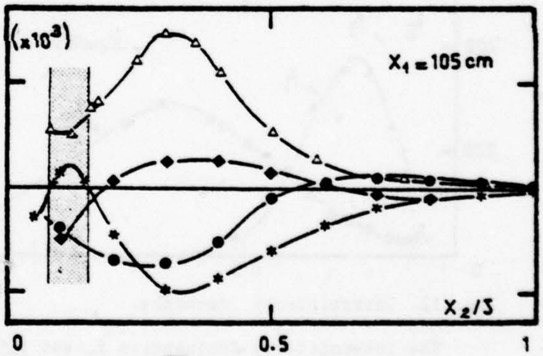

Fig. 10. Budget of $\overline{\theta^2}/2$ downstream the thermal step.

5. INTERMITTENCY AND ZONE AVERAGE

This section is devoted to the description of the boundary motion in connection with thermal effects at the temperature step. To carry out experimental investigations on the internal structure of the flow, an opposite temperature step is choosen. The statistical properties of the external edge of the flow are also studied. In this case, the first part of the plate $0 < X_1 < 0.7$ is tagged by heating.

Intermittency

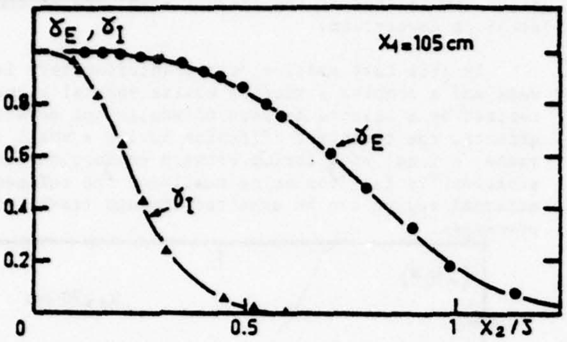

Fig. 11. Intermittency factors.(γ_I :Internal, γ_E : External)

The transversal distributions of the intermittency factors are shown in Fig. 11. Regarding the external boundary, the results are similar to the previous ones (21, 23). γ_E can be considered as a gaussian distribution centered at $X_2 = 0.79\ \delta$ with a standard deviation $\sigma = 0.28\ \delta$.

For the internal layer, the distribution of γ_I is unsymmetrical, it is very different from a gaussian contribution. A similar fact can also be observed in Johnson's work (9) and in a wall jet (14).

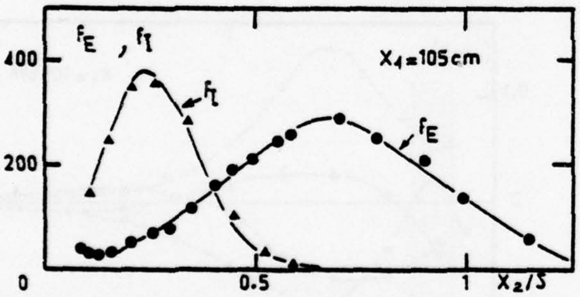

Fig. 12. Intermittency frequency.

The intermittency frequencies f_I and f_E are given in Fig. 12. The maximum values of f_I and f_E are in the same magnitude range.

Zone averages of kinematic and thermal characteristics

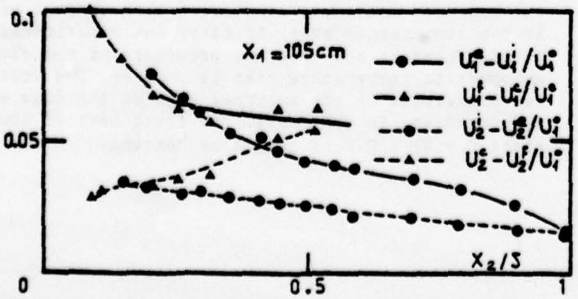

Fig. 13. Difference between conditional averages of velocity components (— longitudinal component, --- transverse component, ● : external frontier, ▲ : internal frontier.

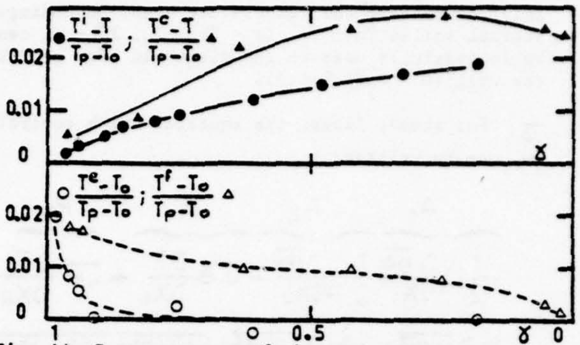

Fig. 14. Zone averages of the mean temperature

At first, the differences between the mean velocities inside and outside of the bulges are shown in Fig. 13. These differences are always of the same order of magnitude, the internal velocity step being higher.

The thermal field is analyzed in a slightly different way. In Figure 14, $(T^i - T)/To$ and $(T^c - T)/To$ are given as functions of X_2/δ. In the region swept by the edge of the boundary layer, no significant difference between T^e and To can be pointed out, similar situation has already been observed in a jet (2). On the contrary, two values T^f and To relative to the internal boundary are different from each other.

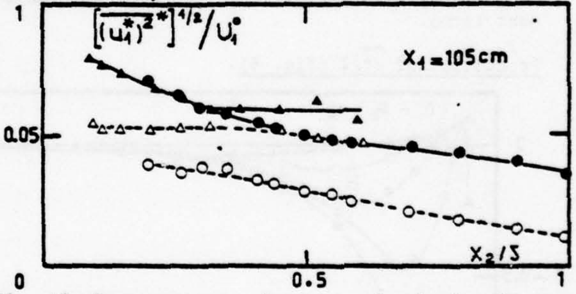

Fig. 15. Zone averages of r.m.s. of velocity fluctuations components.
(▲ , △ : internal frontier ; ●, ○ : external frontier ; ▲ :* ■ c, △ :* ■ f ; ● :* ■ i ; ○ :* ■ e)

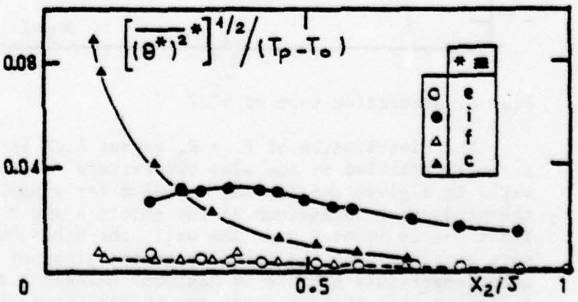

Fig. 16. Zone averages of r.m.s. of fluctuating temperature (—: inside the bulges ; ---:outside the bulges ; ▲ , △ : internal frontier ; ● , ○ : external frontier).

Using the same discrimination, turbulent properties can be measured in and out of the bulges.

The turbulent intensities $\left[\overline{(u_1)^2}\right]^{1/2}/U_1^o$ and $\left[\overline{(\theta)^2}\right]^{1/2}/(T_p\ To)$ are given in the Figs. 15 and 16.

This analyze puts forward the complex structure of the internal field, not only $\overline{(\theta^c)^2}^c$ is different from $\overline{(\theta^f)^2}^f$ but also the quantity $\overline{(u_1^c)^2}^c - \overline{(u_1^f)^2}^f$ is different from zero with a positive value. The ability to distinguish two internal fields is shown in Fig. 17 which relates to shear stress distribution.

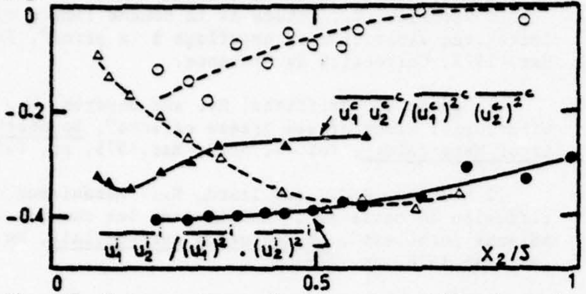

Fig. 17. Zone averages of shear stress (For legend see Fig. 16).

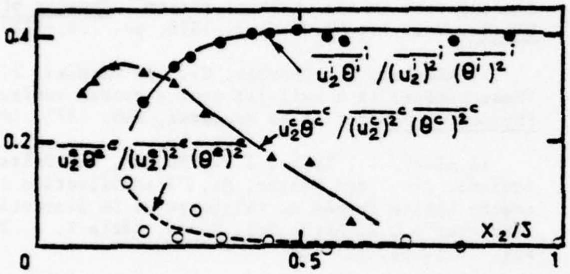

Fig. 18. Zone averages of transverse heat flux (For legend see Fig. 16).

The coefficient of velocity temperature correlation is high inside the bulges (Fig.18). This situation is rather similar to that encountered when examining the shear stress distributions. By contrast, the distribution of $\overline{u_2^c\,\theta^c}^c$ is different from that of $\overline{u_2^i\,\theta^i}^i$ which stands approximatively constant for a large range of X_2/δ. Perhaps, such a situation is generated by interferences between two thermal fields, the first one issued from the boundary condition upstream the temperature step, the second one from the boundary condition downstream. The data outside of the internal interface are not given because the contamination of the thermal signal by the velocity is important.

6. POINT AVERAGES

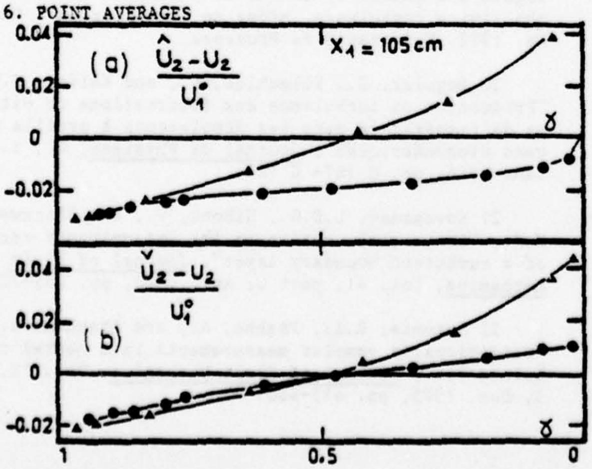

Fig. 19. Mean transverse velocity at the interfaces (a) : front, (b) : back ; ▲ : internal interface ; ● : external interface.

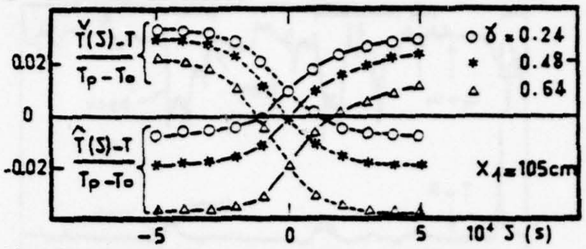

Fig. 20. Mean Temperature across the internal interface (— : front : --- : back)

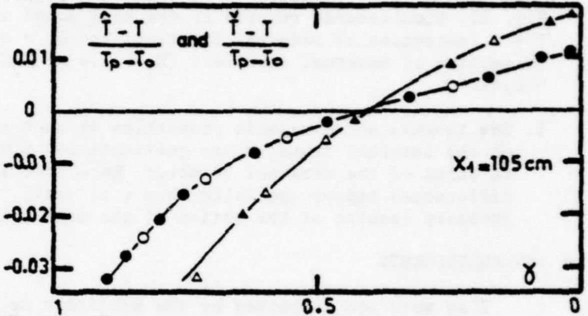

Fig. 21. Mean temperature at the interface (●, ○ : external ; ▲ , △ : internal).

The transversal velocities on the front and on the back of bulges are given as a function of γ (Fig. 19). The results are similar for the two frontiers except for $\gamma > 0.5$. For the external boundary, the results are in good agreement with those of Hedley and Keffer (23). Moreover, differences between the longitudinal components of the velocity at the front and at the back of the bulges remain small. The figure 20 shows the temperature distribution from the front to the back of the bulges relative from the internal interface. As for the external frontier, the temperatures are the same at the front and at the back (Fig. 21).

7. CONCLUSION

The thermal structure of a boundary layer downstream a wall temperature step is quite complex specially in a region where a turbulent heat flux exists in an oppositive direction to that of the mean temperature gradient. In this region, the negative production P of $\overline{\theta^2}/2$ excludes a local description of the field. On each side of this area, the production - P has two maximum values which partially determine the flatness factor distribution of θ.

This investigation also provides additional information, which are concerning the internal boundary which develops downstream the temperature step. In new prediction methods (24, 25), such a concept can be introduced. The main features are the following :

1. In the internal boundary layer specific kinematic properties can be detected inside and outside the bulges which are characterized by thermal effects.
2. Any connection between the motions of the two frontiers can be observed. From records, the internal temperature signal can be compared with the external velocity signal in Fig. 22. At the two frontiers the bulges are not detected exactly at the same

time, this time delay is probably connected to stretching process of the turbulent structures by the mean flow.

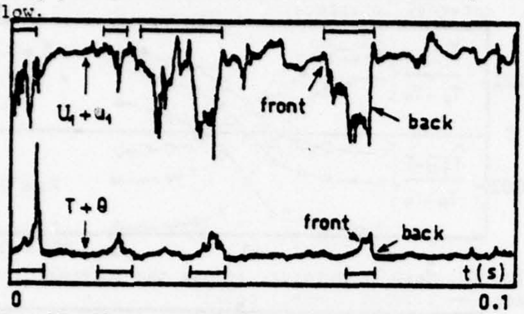

Fig. 22. Simultaneous records at the same point of $T + \theta$ (detection of internal frontier) and $U_1 + u_1$ (detection of external frontier) ($X_1 \sim 1{,}8$ m, $X_2/\delta \sim 0{,}6$).

3. The thermal and kinematic properties at each side of the internal frontier are qualitatively similar to those of the external frontier. More precisely, differences appear specially when γ is small, this probably results of the action of the mean field.

ACKNOWLEDGMENTS

This work was supported by the Ministère de la Qualité de la Vie - Environnement (Marché N°75-127).

The authors are grateful to M. J.P. MELINAND and Miss M. KREISS who assisted with measurements.

REFERENCES

1 Mathieu, J., "Contribution à l'étude aérothermique d'un jet plan évoluant en présence d'une paroi", Publications Scientifiques et Techniques, No 374, Jan. 1961.

2 Eskinazi, S. and Kruka, V., "The wall jet in a moving stream", Journal of Fluid Mechanics, Vol.20, part 4, Dec. 1964, pp. 555-579.

3 Bradshaw, P. and Gee, M.T., "Turbulent wall jets with and without external stream", NPL 3252, June 1960, Aeronautical Research Council.

4 Tailland, A. and Mathieu, J., "Jet pariétal", Journal de Mécanique, Vol. 6, No. 2, Mar. 1967, pp. 103-131.

5 Irwin, H.P.A.H., "Measurements in a self-preserving plane wall jet in a positive pressure gradient", Journal of Fluid Mechanics, Vol. 61, part 1, Oct. 1973, pp. 33-63.

6 Ramaprian, B.R., "Turbulence measurements in an equilibrium axisymmetric wall jet", Journal of Fluid Mechanics, Vol.71, part 2, Sept. 1975, pp. 317-338.

7 Launder, B.E., Reece, G.J., and Rodi, W., "Progress in the development of Reynolds stress turbulence closure", Journal of Fluid Mechanics, Vol.68, part 3, Apr. 1975, pp. 537-566.

8 Mathieu, J. and Jeandel, D., "in Prediction methods for turbulent flows", L.S.76, Mar.1975, Von Karman Inst.

9 Johnson, D.S., "Velocity and temperature fluctuation measurements in a turbulent boundary layer downstream a stepwise discontinuity in wall temperature", Journal of Applied Mechanics, Sept.1959, pp. 325-336.

10 Verollet, E., "Etude de la couche limite turbulente avec aspiration et chauffage à la paroi", Thesis Mar. 1972, Université de Provence.

11 Ogawa, Y., Griffiths, R., and Hoydysh, W., "A wind-tunnel study of sea breeze effects", Boundary Layer Meteorology, Vol. 8, No.2, Mar.1975, pp. 141-161

12 Michard, P.J., and Izard, N., "Mécanismes de diffusion de masse ou d'énergie dans les couches de mélange turbulent", La Recherche Aérospatiale, No.1, Jan. Feb.1976, pp. 27-35.

13 Charnay, G., Mathieu, J., and Comte-Bellot, G., "Response of a turbulent boundary layer to random fluctuations in the external stream", Physics of Fluids, Vol. 19, No.9, Sept. 1976, pp. 1261-1272.

14 Alcaraz, E., Charnay, G., and Mathieu, J., "Measurements in a wall jet over a convex surface", Physics of Fluids, to be appeared, Feb. 1977, 10 p.

15 Allet, C., Pages, J.P., Ravaut, M., Saïssac, J., Semiond, J.C., and Vergez, M., "Identification de la couche limite formée au voisinage de la discontinuité terre-mer", C.R. Acad. Sci. Paris, Série B, t. 281, Aug. 1975, pp. 121-123.

16 Mery, P., Schon, J.P., and Solal, J., "Comparison of thermally neutral and unstable shear flow in the wind-tunel and in the Atmosphere", Advances in Geophysics, Vol. 18 B, Academic Press, New-York, 1974, pp. 273-289.

17 Mathieu,J., "Remarks on turbulent flows with free stream boundaries", L.S. 36, Ap. 1971, Von Karman Inst.

18 Gence, J.N., Jeandel, D. and Mathieu, J., "Corrélations vitesse-température pour une turbulence isotrope soumise à un cisaillement et un gradient thermique moyens constants", C.R. Acad. Sci. Paris, Série B, t. 280, Feb. 1975, pp. 117-119.

19 Fulachier, L., "Contribution à l'étude des analogies des champs dynamique et thermique dans une couche limite turbulente, effet de l'aspiration", Thesis, Ap. 1972, Université de Provence.

20 Beguier, C., Fulachier, L., and Keffer, J.F., "Production de turbulence des fluctuations de vitesse ou de température dans les écoulements à profils moyens dissymétriques", Journal de Physique, C1, t.37, Jan. 1976, pp. C 187- C 189.

21 Kovasznay, L.S.G., Kibens, V., and Blackwelder, K.F., "Large scale motion in the intermittent region of a turbulent boundary layer", Journal of Fluid Mechanics, Vol. 41, part 2, Apr. 1970, pp. 283-325.

22 Antonia, R.A., Prabhu, A., and Stephenson, S.E. "Conditionally sampled measurements in a heated turbulent jet", Journal of Fluid Mechanics, Vol. 72, part 3, Dec. 1975, pp. 455-480.

23 Hedley, T.B., and Keffer, J.F., "Some turbulent/non-turbulent properties of the outer intermittent region of a boundary layer", Journal of Fluid Mechanics, Vol. 64, part 4, July 1974, pp. 645-673

24 Libby, P.A., "On the prediction of intermittent turbulent flows", Journal of Fluid Mechanics, Vol. 68, part 2, Mar. 1975, pp. 273-295.

25 Jenkins, P.E., and Goldschmidt, V.W., "A study of the intermittent region of a heated two-dimensional plane jet", HL 74-75, Oct. 1974, Purdue University.

SESSION 16

OPEN FORUM

5 Minute Presentations

OPEN FORUM PRESENTATION

SYMPOSIUM ON TURBULENT SHEAR FLOWS

Subsonic Separation from Bluff-Bodies

by

R. H. Page

Rutgers University, USA

Abstract:

The base drag of a bluff axisymmetrical body at zero degrees angle of attack is determined for turbulent subsonic flow. The elliptical nature of the problem is taken into account. Wall pressure attenuation takes place ahead of the location of separation. Turbulent mixing in the constant pressure region immediately downstream of separation is modeled with error function velocity profiles utilizing Goertler's similarity parameter and Hill's displaced origin. The energy transformation to the dividing streamline during deceleration from the constant pressure mixing region to the free stagnation point and during acceleration along the center line of the near wake are assumed to take place irreversibly and diabatically. This is a modified version of Korst's original escape criteria for a separated flow region. The wake velocity profile is modeled with a cosine function. An overall momentum, mass, and mechanical energy balance is shown to lead to solutions which give good agreement with experimental data from recent Rutgers research.

OPEN FORUM PRESENTATION

Calculation of Developing Turbulent Flows in Rectangular-Sectioned Ducts

G.J.Reece

Imperial College, London

ABSTRACT

Following the development of a generalised Reynolds-stress model of turbulence, and its application to one- and two-dimensional flows, reported by Launder, Reece & Rodi [1975], the model has been applied to developing flow in non-circular ducts. The near-wall modification to the pressure—strain terms in the Reynolds-stress equations has been generalised to three dimensions, and predictions made of the flow measured by Melling [1975]. Comparisons are drawn with the predictions made by Tatchell [1975], and it is shown that the use of a Reynolds-stress model, incorporated into the same solution procedure as used by Tatchell, produces considerable improvements in the predictions. Good agreement with Melling's data is also obtained in the case of those quantities not previously predicted.

OPEN FORUM PRESENTATION

The Determination of Momentum Heat and Mass Transport in Highly Turbulent Mixing Regions and the Application of Hydrocarbons as Tracer Gases in High-Velocity and High-Temperature Air-Jets.

by

H. Hardegen

DFVLR, Braunschweig

Abstract:

Mass transport in the mixing region of air jets usually is determined by injecting a tracer gas in one of the jets and analysing its downstream path.

Several physical phenomena, such as the averaging-effect, the displacement-effect, the discrimination of species in the sampling process, and the superrelevation of the pitot-pressure due to the fluctuating velocities cause an erroneous reading of the tracer gas concentration in the jet mixing-region. These effects increase with the turbulence intensity. Methods will be discussed to separate these effects and to eliminate them.

To observe the momentum, heat, and mass transport in the mixing region, it is necessary to record a large amount of data. It will be shown that the application of a modified and improved Total Hydrocarbon Analyser (with several auxiliary devices) in conjunction with hydrocarbons as tracer gases gives very good results, especially high accuracy, short measuring-time, low costs, easy operation, and good control of the measurement-series by an on-line computer.

Measurements on free jets up to $T_o = 1150$ K and low supersonic Mach numbers have been investigated.

OPEN FORUM PRESENTATION

Prediction of the Properties of Stratified, Turbulent, Wall Flow

by

M.M. Gibson

Imperial College, London

Abstract:

The effect of the wall on the turbulence structure of a buoyant boundary layer is modelled by means of simple approximations to the three components of the fluctuating pressure correlations which appear in the transport equations for stress and heat flux. Further approximations to the transport terms result in a set of algebraic equations which are used for a parametric study of the planetary surface layer and which form the basis of a "two-equation" transport model for buoyancy affected wall flows. The model explains, at least qualitatively, those features of wall-influenced buoyant flow which differ sharply from the behaviour of buoyant free shear layers. Numerical solutions have been obtained and the results are compared with published wind-tunnel measurements and data from the atmospheric boundary layer.

Abstract for "Open Forum" - Penn State, 18-20 April 1977

EXTRACTED LARGE EDDY STRUCTURE OF A FLAT-PLATE BOUNDARY LAYER, Loren A. Lemmerman* and Fred R. Payne, University of Texas at Arlington. Lumley's[1] decomposition of the velocity covariance into orthogonal eigen-functions is applied to a merged data set taken from Grant's [2] and Tritton's[3] measurements. Homogeneity in the transverse and flow directions specifies harmonic eigen-function behavior and reduces the data analysis space to one of four, rather than six, dimensions as in analysis of turbulent wake flow.[4]

A six-stage calculational procedure was devised: 1) Data augmentation, 2) data denormalization 3) Fourier transformation to a 7 x 7 wave-number grid 4) mass conservation to fill out the 9 x 9 correlation tensor; 5) eigen-solution of the 21 x 21 Hermitian matrix and 6) inverse transform of the largest, "dominant" eigen-function back to laboratory coordinates and interpretation as a "Large Eddy" structure. Calculations by Lemmerman[5] were performed on CDC Cybernet 7600.

Eigen-vector contributions to the Reynolds' stresses indicates that the "dominant" large eddy structure has at least two distinct scales. This conclusion is confirmed via well-separated peaks of the distribution of eigen-values, which are interpreted by Lumley as measures of mean square kinetic energy of the eigen-modes. Preliminary analysis indicates that results are like the "horseshoe" or "hairpin" eddies seen in flow visualization studies or extracted via " conditional sampling".

The next stage is to predict, via a suggestion of Lumley[6] as implemented by Payne[7], the structure of this flow from a "first principles" viewpoint. These approaches appear complimentary "conditional sampling/averaging" techniques. Applications of this methodology[8] to the "turbulence-modeling" problem[9] are briefly discussed. Work supported,in part, by NASA Ames Grant NSG-2077, Dr. Morris W. Rubesin, technical monitor.

---

* Now at Lockheed-Georgia Research Center

References

[1] Lumley, J. L., (1966) Doklady Akademia Nauk SSSR, Moscow
[2] Grant, H. L., (1958), Journal Fluid Mech., p.149
[3] Tritton, D. J., (1967), Journal Fluid Mechanics, p. 439
[4] Payne, F. R. & Lumley, J. L. (1967), Phy. Fluids, SII, p. S194
[5] Lemmerman, L.A. (1976) Ph.D. Dissertation, University of Texas at Arlington
[6] Lumley, J.L., (1965) Private Communication to F.R.P.
[7] Payne, F. R. (1968) Report ot USN/ONR
[8] Payne, F. R. (1975) "Research in Progress Report," 14th Mid-west Mech. Conf.
[9] Rubesin, M. W. (1975), "Subgrid or Reynolds Stress Modeling for Three-Dimensional Turbulent Computations," NASA SP-347.

Fred R. Payne

Fred R. Payne, Ph.D., P.E.
Professor, Aerospace Engineering

FRP/cme

"Prediction of Effects of Mean Streamline Curvature on Turbulence Structure"

by

D.D. Knight and P.G. Saffman
Applied Mathematics
California Institute of Technology
Pasadena, California 91125

As a preliminary step towards the understanding of the interaction of large structures in turbulent flows, the effects of mean streamline curvature on free turbulence structure has been investigated *using the turbulence model* equations of Saffman.

Two problems are considered - fully turbulent flow between concentric rotating cylinders, and the decay of an isolated turbulent line vortex. Quantitative agreement between theory and experiment is good.

OPEN FORUM PRESENTATION

Effect of Secondary Flow on Turbulence in an Open Channel Flow

by

Andreas Müller
ETH, Zürich (on leave at IIHR, University of Iowa)

Abstract:

The three dimensional effects of secondary flow vortices on a nominally two dimensional, fully developed open channel flow have been studied. A Laser-Doppler-Anemometer was used to measure the vertical and the longitudinal velocity components v(t) and u(t) in one horizontal ($y^+=1000$) and three vertical planes. The mean flow velocity was .70 m/sec, the water depth .025 m and the aspect ratio 1:6. The rough floor of the channel was initially formed by a flow over a moving bed with sediment transport. The secondary flow vortices of this flow caused a mild spanwise modulation of the floor height, about 10% to 40% of the roughness height. This floor profile was subsequently "frozen" by fixing it with cement.

The effect of the secondary flow on the flow parameters was studied by measuring both the mean and turbulent flow properties. It was found that a flow away from the wall was associated with an increase in turbulence and turbulent momentum exchange but with a reduction in the mean velocity, while a mean flow towards the wall was accompanied by exactly opposite effects. An estimate of the terms in the x-momentum equation at $y^+=1000$ indicates that $\overline{u'w'}$ is of the same order of magnitude as $\overline{u'v'}$. This agrees with the observation that $\partial U/\partial z$ is of the same order as $\partial U/\partial y$. The anisotropy of the turbulent fluctuations in the u'-v' plane was found to be particularly significant in regions of mean upward flow. This was revealed by detailed measurement of three different statistical distributions: the joint probability distribution $P(u',v')$ of u'(t) and v'(t) during the measuring period T_O, the density $D(u',v') = P(u',v').\ u'v'$ of the momentum flux in the u'-v' plane and the distribution $E_i(m,\tau)$ of the number of events of duration τ and momentum transport m, in each quadrant.

A Novel Procedure for Free Shear Flows

by

S. B. Pope

Imperial College of Science and Technology,
Mechanical Engineering Department,

Exhibition Road, London SW7 2BX.

ABSTRACT

. A finite-difference procedure is reported which calculates two-dimensional (plane or axisymmetric) free turbulent shear flows. It is intended, primarily, as a vehicle for developing and testing turbulence and combustion models and consequently it has been designed to be accurate, versatile and efficient. The k-ε turbulence model is used in conjunction with an effective viscosity hypothesis and equations for a conserved scalar, f, and its mean-square fluctuation are solved: it is emphasised, however, that these equations are incorporated for demonstration purposes - a major feature of the procedure is the ease with which other models can be built in.

Accuracy is achieved by solving the differential equations in normalised form in a physical coordinate system and by using a second-order-accurate difference scheme across the flow: stability is guaranteed by making the finite-difference equations fully implicit. In contrast to many other schemes, the simultaneous differential equations are solved simultaneously (by an iterative procedure) which adds both to accuracy and stability.

Results of calculations will be presented to demonstrate the use and accuracy of the procedure.

Effects of Secondary Contractions on Grid Turbulence*

J. C. Bennett+
United Technologies Research Center
East Hartford, Connecticut 06108

The use of a secondary contraction (a contraction downstream of the grid used to generate turbulence) has been made to obtain a turbulent motion which is nearly isotropic as possible. Both Uberoi and Wallis (Ref. 1) and Compte-Bellot and Corrsin (Ref. 2) have reported successful use of the secondary contraction. Subsequently, efforts were made to apply the technique to low Reynolds number grid turbulence (Ref. 3), the so-called "final period" turbulence. For the small Re region of the flow (large x/M), the contraction appears to have negligible effect on the turbulence.

A comparison of present and previous experimental results is made. Observable trends with contraction ratio and turbulent Reynolds number are made based on the experimental results. Possible implications for the effects of shear on turbulence of different scales are discussed.

References

1. Uberoi, M. S. and S. Wallis: Small Axisymmetric Contraction of Grid Turbulence. J. Fluid Mechanics 24, 539 (1966).
2. Compte-Bellot, G. and S. Corrsin: The Use of a Contraction to Improve the Isotropy of Grid-Generated Turbulence. J. Fluid Mechanics 25, 657 (1966).
3. Bennett, J. C.: Measurements of Grid-Generated, Nearly Isotropic Turbulence at Small Reynolds Numbers. PhD Thesis, Johns Hopkins University, (1976).

---

*Open Forum Presentation, Symposium on Turbulent Shear Flows, University Park, Pennsylvania, April 1977.

+Senior Research Engineer, Gas Dynamics Section.

Enclosure to
2-8050-220

A NOTE OF THE TURBULENT FREE SHEAR LAYER

by Stanley F. Birch

The reported variation in the spreading rate of a simple free shear layer has been the subject of much discussion in recent years. There have been many attempts to explain this variation, and some authors have even suggested that a unique asymptotic spreading rate may not be achievable in any realizable experimental apparatus. Such a suggestion strikes at the base of some of our most fundamental assumptions about turbulent flows and has wide ranging implications.

In order to resolve some of these difficulties, the present author has conducted an extensive re-examination of the available data. This has led to a number of conclusions which appear to be in conflict with some widely held views about the simple mixing layer. Some of these results are:

1. The available experimental evidence does indicate that the simple mixing layer has a unique asymptotic spreading rate which is largely independent of the experimental apparatus.

2. In spite of a considerable variation in the reported spreading rate, the available data show a high degree of internal consistency.

3. There is a significant difference in the developing region of a free mixing layer depending on whether the initial boundary layer is laminar or turbulent. In particular, it appears that the difficulty in achieving a fully developed mixing layer from an initially turbulent wall boundary layer may be a major reason for much of the present confusion.

Non-equilibrium Effects on the Turbulent Prandtl Number in Pipe Flow

B. E. Launder & D. S. A. Samaraweera

Experimental data of turbulent Prandtl number distributions in pipe flow show extensive scatter, some measurements indicating a fall in Prandtl number with distance from the pipe wall while others indicate a rise.

Second order closure predictions (in which transport equations are solved for the turbulent heat fluxes) have been obtained by the authors for various boundary conditions. The predicted distributions of Prandtl number display significant differences depending on whether the wall provides the heat source (or sink) or whether it is insulated. The result suggests that the differences reported in the experimental values are indeed genuine differences and not merely the result of experimental errors. The result also emphasizes that a second-order treatment intrinsically offers a more reliable means of calculating heat transfer rates than do methods based on the notion of an effective thermal conductivity.

"Some Recent Experimental and Prediction Results on the Structure of Turbulent Boundary Layers in the Vicinity of Separation"

by

Roger L. Simpson, Professor
Southern Methodist University
Dallas, Texas

Recently the results from an experimental study of a separating turbulent boundary layer due to an adverse pressure gradient were published in J. Fluid Mech. Measurements both upstream and downstream of the separation region were made using a directionally-sensitive laser anemometer. Several important results were obtained: (1) the law-of-the-wall velocity profile appears to be valid until there is intermittent backflow (intermittent separation location); (2) near separation the neglect of the normal-stress terms in the momentum and turbulence energy equations is not justified; (3) the separated flow outer region structure maintains some self-similarity downstream; and (4) no law-of-the-wall velocity profile for the backflow exists.

Based upon these observations, the Bradshaw et al. turbulent boundary layer prediction program was modified. Predictions were improved up to the beginning of intermittent separation. After intermittent separation, the turbulent shear layer and the free-stream flow interact to produce pressure gradient relief downstream. This allows the velocity components at the outer separated shear flow edge to be computed, which in turn makes possible computation of the inner region flow. The resulting backflow appears to serve the main purpose of satisfying the mass continuity requirement. Predictions are good for the boundary layer thickness distribution and mean velocity profiles and fairly good for other quantities.

TURBULENT NATURAL CONVECTION NEXT TO HEATED VERTICAL SURFACES

by

William K. George
and
Steven P. Capp

State University of New York at Buffalo
Department of Mechanical Engineering

In spite of numerous investigations over the past forty years of the naturally occurring turbulent flow next to heated vertical surfaces, there has not even been a consensus as to which scaling laws should be applied to the data. This is in direct contrast to the forced convection problem where the "law of the wall", "law of the wake", and the logarithmic friction law have for many years provided a framework for experiment and analysis.

In this presentation the fully developed turbulent natural convection boundary layers for constant wall temperature and constant wall heat flux surfaces will be analyzed using only parameters which occur naturally in the equations of motion or in the boundary conditions. Outer and inner flow regions will be identified and it will be shown that the inner region is a constant heat flux layer. A "law of the wall" and a "law of the wake" will be proposed for the inner and outer layers respectively. Conductive and thermo-viscous sublayers will be seen to exist next to the wall and a matched layer, the buoyant sublayer, will be shown to exist between the inner and outer layers. All predictions of universal velocity and temperature profiles, friction and heat transfer laws will be compared to the abundant experimental data.

UNIVERSITY OF TOKYO
DEPARTMENT OF MECHANICAL ENGINEERING
FACULTY OF ENGINEERING
BUNKYO-KU, TOKYO, 113 JAPAN
TELEPHONE (03) 812-2111

LARGE-EDDY STRUCTUTES IN TURBULENT SEPARATED FLOW DOWNSTREAM OF A REARWARD-FACING STEP

Nobuhide KASAGI, Assistant Professor
Masaru HITARA, Professor
Hiroyuki HIRAOKA, Undergraduate

ABSTRACT

So-called large eddy structures in turbulent shear flows are becoming of much interest to an increasing number of researchers, since such structures possess predominant roles on the turbulence production as well as Reynolds stress generation. It is, however, rather difficult to detect the unsteady three-dimensional events which occur discretely and exist for their characteristic lifetimes, if one depends only the conventional measuring devices fixed in space.

In the present study the Smoke-Wire method, which is adequate to the flow-visualization of the turbulent three-dimensional structures, is applied to the turbulent separated flow downstream of a rearward facing step. At the same time, the static pressure distribution as well as the local heat transfer coefficients have been measured and reported.

It is concluded that the relative locations of several characteristic lines, where the static pressure and the heat transfer rate have their maximum respectively and the wall shear stress equals to zero, are generally different each other. Moreover, from the visual observations of the instantaneous flow field, it is confirmed that the two kinds of longitudinal vortex-like structures in large scales should exist in the reattaching region and the region just behind the step. In the reattaching region, the free shear layer approaches to the solid surface accompanied with a strong recovery of pressure potential and this region is unstable in a fluid mechanic sense, but the scales of the turbulence eddies presently reported cannot be predicted by the linear stability theory or like that. A similar selective amplification of disturbances could be observed in a plane impinging jet, so the mechanisms of formation of such large scale eddies are discussed in comparison.

SESSION 17

GENERAL SESSION-2

Chairman: W. P. Jones
Department of Chemical Engineering
Imperial College
London SW7 2BX
United Kingdom

TRANSITION TO TURBULENCE IN CIRCULAR COUETTE FLOW

HARRY L. SWINNEY AND P. R. FENSTERMACHER
PHYSICS DEPARTMENT, CITY COLLEGE OF THE CITY UNIVERSITY OF NEW YORK
New York, New York 10031
and
J. P. GOLLUB
PHYSICS DEPARTMENT, HAVERFORD COLLEGE
Haverford, Pennsylvania 19041

ABSTRACT

The time-dependent behavior of a fluid contained between concentric cylinders with the inner cylinder rotating has been studied as a function of Reynolds number using laser Doppler velocimetry. Our records of the time dependence of the radial component of the local velocity are Fourier transformed to yield velocity power spectra. As the Reynolds number is increased these spectra reveal several transitions to new (previously undetected) flow states, each characterized by one or more discrete frequency components. At a higher, well defined Reynolds number all discrete spectral peaks disappear. Thus, we have observed three distinct dynamical regimes: periodic, quasiperiodic, and aperiodic. These same regimes are exhibited by simple nonlinear models with only a few degrees of freedom, a result which suggests that excitation of many degrees of freedom is not necessary to produce aperiodic flow in a fluid.

NOMENCLATURE

$C(\tau) \equiv \langle \Delta V_r(\vec{r},t)\, \Delta V_r(\vec{r}, t+\tau)\rangle$ - velocity fluctuation autocorrelation function
LDV - laser Doppler velocimetry technique
$P(\omega) = \frac{1}{2\pi}\int_{-\infty}^{\infty} C(\tau) e^{i\omega\tau}\, d\tau$ - velocity power spectrum
r_i - radius of inner cylinder
r_o - radius of outer cylinder
$R = r_i \omega_{cyl}(r_o - r_i)/\nu$ - Reynolds number
R_c - critical Reynolds number for the Taylor instability
$V_r(\vec{r},t)$ - radial component of the fluid velocity
ν - kinematic viscosity of fluid
ω - angular frequency in power spectrum (expressed in units of the angular frequency of the inner cylinder; thus, $\omega \equiv \omega(\text{rad/s})/\omega_{cyl}(\text{rad/s})$ is dimensionless
$\omega_1, \omega_2, \omega_3$ - sharp frequency components in the velocity power spectrum
ω_{cyl} - angular frequency of inner cylinder

INTRODUCTION

We have used laser Doppler velocimetry to investigate the various dynamical regimes exhibited by a fluid contained between concentric cylinders with the inner cylinder rotating (1). In these experiments the time dependence of the local radial velocity component is recorded digitally and then processed to obtain velocity power spectra. These spectra obtained at different Reynolds numbers are supplemented by a corresponding photographic study of the flow.

The velocity power spectra reveal the existence of several dynamical regimes which are not apparent in photographic studies or torque measurements and hence were not observed in previous studies. A periodic dynamical regime was observed with spectra characterized by one or more sharp frequency components at commensurate frequencies, while another regime, termed quasiperiodic, is characterized by spectral components at incommensurate frequencies. At a higher, well defined Reynolds number there is a transition to an aperiodic or chaotic regime where the spectrum contains no sharp frequency components and the corresponding velocity autocorrelation function decays. The observed chaotic regime is of course not fully developed turbulence, but we take its aperiodicity to be our operational definition of turbulence.

Background

In the more than half century since G. I. Taylor predicted and observed the transition from a simple laminar flow to a flow with horizontal toroidal vortices, the Taylor vortex instability has been extensively studied in many laboratories. As the Reynolds number is increased beyond the critical Reynolds number for the Taylor instability, R_c, a secondary instability is reached where transverse waves are superimposed on the horizontal vortices; at this transition the velocity field becomes time dependent. The onset of this wavy regime has been studied by a number of workers including Koschmieder (2), Snyder (3), Coles (4), and Donnelly and coworkers (5), among others. The work most relevant to the present study is the detailed photographic study by Coles, who found that the spatial state p/m, where p is the number of Taylor vortices and m is the number of tangential waves, is not a unique function of the Reynolds number. The particular state reached at a given R depends on the Reynolds number history. Coles measured the tangential wave velocity as a function of Reynolds number and found it to approach a constant value, independent of Reynolds number and spatial state." The tangential wave signal became lost in the noise at $R/R_c = 23$.

The present study is concerned primarily with the dynamical regimes exhibited by a single spatial state. Before describing this work we review briefly models that have been proposed to describe the transition to turbulence.

MODELS FOR THE TRANSITION TO TURBULENCE

In this paper we consider the transition to turbulence in systems which pass through a regime characterized by sharp temporal and spatial frequencies rather than a continuous spectrum; those shear dominated transitions which occur catastrophically with no intermediate periodic regime will not be discussed. Examples of the class of systems of interest here are, in addition to circular Couette flow, Rayleigh-Bénard convection and its many variants (6) and a symmetrically heated rotating fluid (7).

In 1944 Landau conjectured that the transition to turbulence may occur as an infinite sequence of discrete transitions to new periodic states, with each transition adding a new frequency to the motion (8). The Landau conjecture is not supported by experiment since turbulent flows are not characterized by discrete spectra.

A contrasting picture of the onset of turbulence was first suggested 14 years ago by Lorenz (9), whose highly truncated model of a symmetrically heated rotating fluid yielded a few transitions to different periodic regimes followed by a transition to aperiodic behavior. McLaughlin and Martin (10) found a similar sequence of events in their numerical modeling of convection, which was designed to explain the sharp onset of noise in the sensitive heat flux measurements of Ahlers (11) on liquid helium.

Ruelle and Takens (12) have argued that a sharp transition to aperiodic flow after a few periodic regimes is a consequence of the most general aspects of the nonlinear hydrodynamic equations, and other systems of highly nonlinear equations should show similar behavior. Ruelle and Takens predicted, using abstract topological reasoning, that after a fluid passes through at most three or four transitions to periodic regimes, then there will be a transition to a qualitatively different type of regime, where the behavior is truly random and the velocity autocorrelation function decays rather than oscillating.

These general hypotheses regarding the transition to turbulence by a sequence of instabilities do not supplant detailed numerical modeling of particular systems. For Couette flow Davey, DiPrima, and Stuart (13) and Eagles (14) have calculated the properties of the flow in the neighborhood of the onset of the wavy regime, but numerical analysis has not yet extended beyond the onset of the wavy regime.

EXPERIMENTAL PROCEDURE

Couette Flow Cell

The cell specifications are given in Table I. The inner cylinder is made of stainless steel and the outer cylinder is glass. The height of the inner cylinder is 0.30 m, although in the present work the cell was filled with fluid only to a height of 0.0625 m. The cell is mounted on an XYZ stage so it can be moved with respect to the laser beam probe. The cell is contained inside a box which has a proportional temperature controller that maintains the temperature at 27.50 ± 0.05°C.

The inner cylinder is powered through a belt drive by a synchronous motor which is driven by a stable oscillator. The rotation frequency of the inner cylinder (which ranged from 0.2 to 10 Hz in these experiments) is measured directly with an electronic timer and has an r.m.s. fluctuation of less than 0.3%.

Table I. Circular Couette Flow Cell

Inner cylinder radius, r_i	2.224×10^{-2} m
Outer cylinder radius, r_o	2.536×10^{-2} m
Ratio of radii, r_i/r_o	0.877
Fluid height	6.25×10^{-2} m
Height/gap	20.0
Fluid kinematic viscosity, ν	8.48×10^{-7} $m^2 s^{-1}$
Cell temperature	27.50±0.05° C
Number of axial vortices	17
Number of waves around annulus in wavy state	4
Diameter of LVD seed particles (approx. 10^{-4} wt. %)	4.8×10^{-7} m
Sample volume for velocity measurement	$\sim 2 \times 10^{-12}$ m^3
Critical Reynolds No., R_c	119 [(5)-Table A2]

The fluid is water, seeded with 4.8×10^{-7} m diameter polystyrene spheres for the laser Doppler velocimetry studies and with Kalliroscope suspension (15) for the photographic studies.

Laser Doppler Velocimetry (LDV) Optical System

The optical system (which in LDV terminology is called a reference beam backscatter system) is shown schematically in Fig. 1 (a). The collimated incident laser beam (0.1 W) is focused into the fluid with a 0.055 m focal length lens. The light backscattered at a 160° angle is collected by the same lens, passes through a pinhole aperture and beam splitter, and is focused onto a pinhole in front of the photomultiplier detector. The scattering volume, approximately 2×10^{-4} m long by 1×10^{-4} m diameter, is located

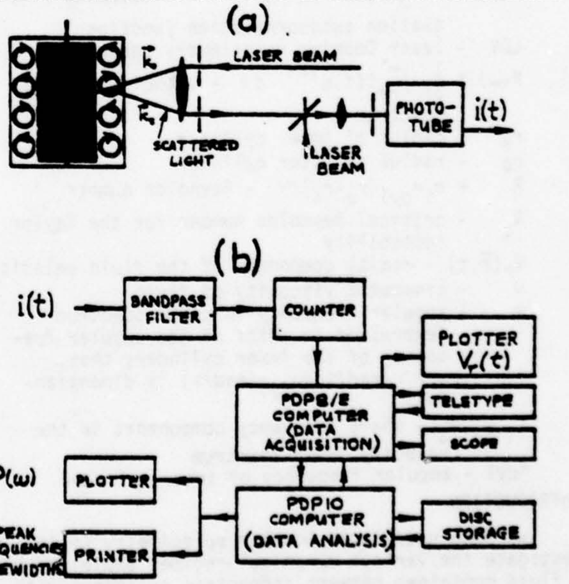

Fig. 1 Schematic of laser Doppler velocimetry system

(a) Optical system
(b) Digital data acquisition and analysis electronics

midway between the inner and outer cylinders for most of the measurements. The incident wavevector $\vec{k}_0$ and the scattered wavevector $\vec{k}_s$, both in a vertical plane which passes through the cylinder axis, are at equal angles with respect to the horizontal plane, so the momentum transfer-vector $\vec{q} = \vec{k}_0 - \vec{k}_s$ in in the horizontal plane; hence the scattered light is Doppler shifted by an amount

$$\omega_D = \vec{V} \cdot \vec{q} = V_r q = \left[\left(\frac{4\pi n}{\lambda_0} \right) \sin\frac{\theta}{2} \right] V_r , \qquad (1)$$

where n is the refractive index (1.333), λ_0 is the laser wavelength (4.88×10^{-5}m), θ is the scattering angle (160°) and $V_r(r,t)$ is the radial component of the fluid velocity. The Doppler shifted scattered optical field is mixed with unshifted laser light at the photocathode, and the photocurrent $i(t)$, being proportional to the square of the incident optical field, oscillates at the Doppler shift frequency. Thus measurements of this frequency in successive time intervals yield the time dependence of the radial component of the velocity of the fluid at a well defined point in the cell.

Data Acquisition and Analysis Electronics

The data acquisition system is diagrammed in Fig. 1(b). The photocurrent is bandpass filtered and the oscillations(typically 100KHz in the present experiment) are counted for a time Δt which is long compared to a period of oscillation, but short compared to the time scale of changes in the velocity. At the end of each time interval Δt the number of oscillations for that interval is deposited in the memory of a minicomputer (DEC PDP8/E). After the accumulation of either 1024 or 8192 points at successive time intervals, the resultant Doppler shift record, directly proportional to $V_r(t)$, is plotted and then transferred to a larger computer (DEC PDP10). Then the velocity power spectrum and the velocity autocorrelation function are computed and plotted, and another program calculates the positions and linewidths of the spectral lines. The immediate feedback of the spectral information serves as a valuable guide in the course of an experiment.

Spatial State

We have restricted our study primarily to a single spatial state, one with 17 axial vortices and, in the region where the waves exist, 4 azimuthal waves. Although several different states p/m other than the 17/4 state were found to be accessible, depending on the Reynolds number history of the system, the 17/4 state, once achieved, was stable indefinitely while the Reynolds number was varied throughout the range $2 < R/R_c < 45$. Thus it was possible to study the Reynolds number dependence of the dynamics of a single spatial state, without being concerned with the state switching problem that Coles has investigated (4). Switching between states was avoided by (a) using a short fluid height (height/gap=20), (b) rotating only the inner cylinder (Coles achieved some states by rotating and then stopping the outer cylinder), and (c) accelerating slowly when changing Reynolds number.

Although the present measurements were made primarily on the 17 vortex state, some measurements were also made on the 15 vortex state, and the same transitions between different dynamical regimes were observed for these two spatial states, as will be described below.

EXPERIMENTAL RESULTS

Time-Independent Flow

In the laminar state below R_c, V_r is zero, while in the Taylor vortex state (above R_c) V_r is periodic in the axial coordinate z but still time-independent. Gollub and Freilich (16) have studied the Reynolds number dependence of the amplitude of V_r in the Taylor vortex regime and have found that near R_c the $(R-R_c)^{1/2}$ dependence predicted by Landau is confirmed and the observed next order term in the perturbation expansion is consistent with a $(R-R_c)^{3/2}$ dependence as predicted by Davey (17).

Periodic Flow

The second instability, at $R/R_c = 1.3$, marks the onset of time dependence in V_r, which in the wavy regime oscillates as the azimuthal waves pass the fixed point probed by the laser beam. Figure 2 shows a portion of a record of $V_r(t)$ and the corresponding power spectrum (on a logarithmic scale) in the wavy regime at $R/R_c = 3.32$. (All power spectra are normalized so that $\int_0^{\omega_{max}} P(\omega) d\omega = \langle (\Delta V_r)^2 \rangle$, and the frequencies ω are expressed in units of the inner cylinder frequency; thus $\omega \equiv \omega(\text{rad/s}) / \omega_{cyl}(\text{rad/s})$.) The power spectrum contains a single fundamental which we call ω_1; this is the frequency of the azimuthal waves passing the point of observation. Although many harmonics are visible in the spectra obtained in the wavy regime, the higher harmonics are several orders of magnitude weaker in intensity than the fundamental and are visible only because of the high signal to noise ratio of the spectra. The relative amplitude of the peaks (particularly ω_1 and $2\omega_1$) is a strong function of z, as one would expect from the structure of vortex flow.

Quasiperiodic Flow

As the Reynolds number was increased a low frequency component, ω_2 (≈ 0.2) appeared in some runs at $R/R_c \approx 5$; ω_2 decreased with increasing R, vanishing at $R/R_c \approx 17$. Component ω_2 was clearly present in some runs but apparently absent in many others. This component is the only spectral feature that was not reproducible from run to run, and its physical significance is not understood. It may be a vacillation preceding a change in spatial state as Coles (4) has suggested.

At a higher, well defined Reynolds number, $R/R_c = 10.0 \pm 0.2$, a new previously undetected spectral component appears at a frequency $\omega_3 = (2/3)\,\omega_1$, as illustrated in Fig. 3 for $R/R_c = 13.3$. The component at ω_3 reproducibly appears when R is increased through $R/R_c = 10.0$ and disappears when R is decreased through $R/R_c = 10.0$. Its amplitude decreases continuously to zero as $R/R_c = 10.0$ is approached from above.

At larger Reynolds numbers the amplitude of ω_3 begins to decrease, and at $R/R_c = 19.8 \pm 0.1$ ω_3 disappears from the spectrum, as shown in Fig. 4. In the regime with ω_3 present the ratio ω_1/ω_3 decreases continuously (within the experimental resolution, better than 1%) from 1.63 at $R/R_c = 10.0$ to 1.41 at $R/R_c = 19.8$; hence ω_1 and ω_3 (and ω_2 as well) appear to be incommensurate.

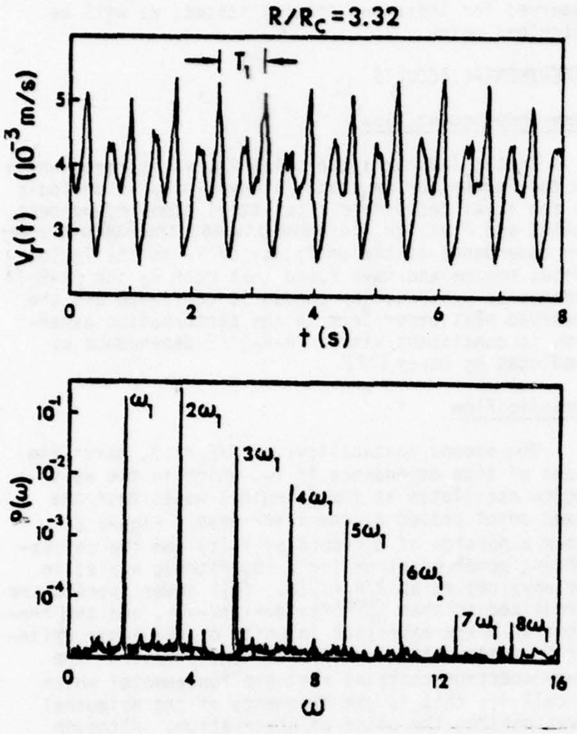

Fig. 2 The radial component of the fluid velocity $V_r(t)$ (measured at a point approximately midway between the inner and outer cylinders) and the corresponding power spectrum $P(\omega)$, in the wavy regime at $R/R_c=3.32$. The velocity plot shows only part of the velocity record (of 8192 points, 268 s duration) that was Fourier transformed to obtain the spectrum. T_1 is the period of the azimuthal waves that pass the point of observation and ω_1 is the corresponding frequency (relative to ω_{cyl}; hence ω is dimensionless). At this Reynolds number the amplitude of the azimuthal waves superimposed on the horizontal vortices is greater than one-half of an axial wavelength; hence spectra measured at any height in the fluid show an intense second harmonic.

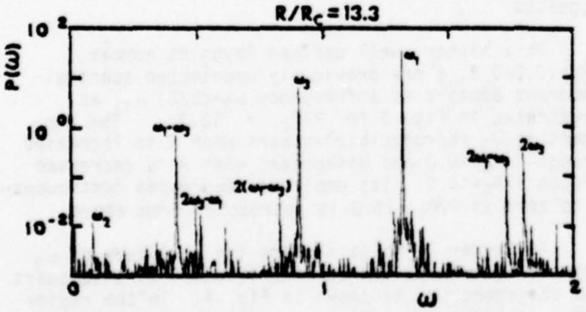

Fig. 3 The power spectrum of the radial component of the velocity at $R/R_c=13.3$.

Thus the regimes with ω_2 or ω_3 present are examples of quasiperiodic flow.

After ω_3 disappears ω_1 is the only sharp fundamental frequency component remaining in the spectrum. However, another spectral feature, a broad component, 100 times weaker in peak intensity than ω_1, is clearly present at $\omega \approx 0.45 \approx \omega_1/3$ (see Fig.4). The broad component first becomes discernible in the spectra at $R/R_c=17$.

Chaotic Flow

As the Reynolds number is increased through $R/R_c=22.4\pm0.2$ a dramatic change in the spectra occurs, as Fig. 5 illustrates: the amplitude of the sharp frequency component ω_1 decreases to zero, leaving only broad components located approximately at multiples of $\omega_1/3$. Thus $R/R_c=22.4$ marks a transition from a nearly periodic flow to a qualitatively different type of behavior, one characterized by a continuous spectrum or, equivalently, a decaying velocity autocorrelation function. The transition from a nearly periodic to chaotic flow is quite marked in the autocorrelation function, as shown in Fig. 6.

Spectra have been recorded up to $R/R_c=45$ and no further transitions have been observed.

Summary

The sharp frequency components observed in the velocity power spectra are plotted in Fig. 7. Components ω_1, ω_2, and ω_3 all had widths equal to the instrumental width, which in the highest resolution spectra (e.g., Fig. 3) was $\Delta\omega=0.001$ (full width at half maximum power). Such extremely high spectral resolution could not have been achieved without comparable long term stability in the rotation frequency

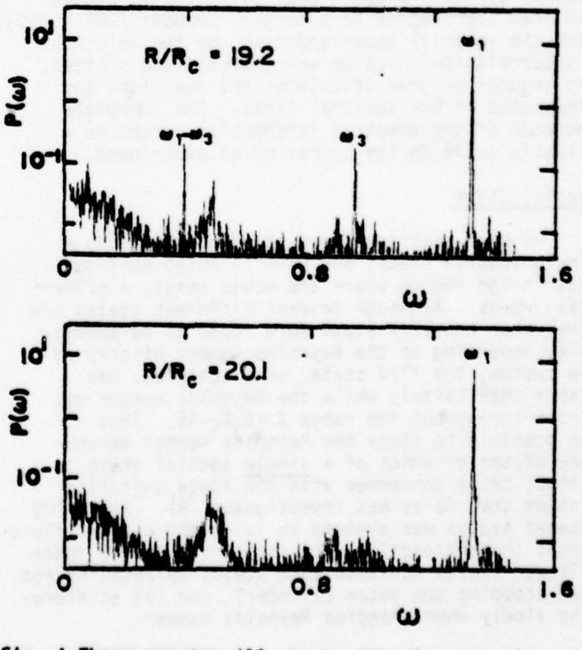

Fig. 4 These spectra illustrate the disappearance of ω_3 at $R/R_c=19.8\pm0.1$. Note that the spectra obtained both below and above R=19.8 contain a broad, weak component at $\omega \approx 0.45$.

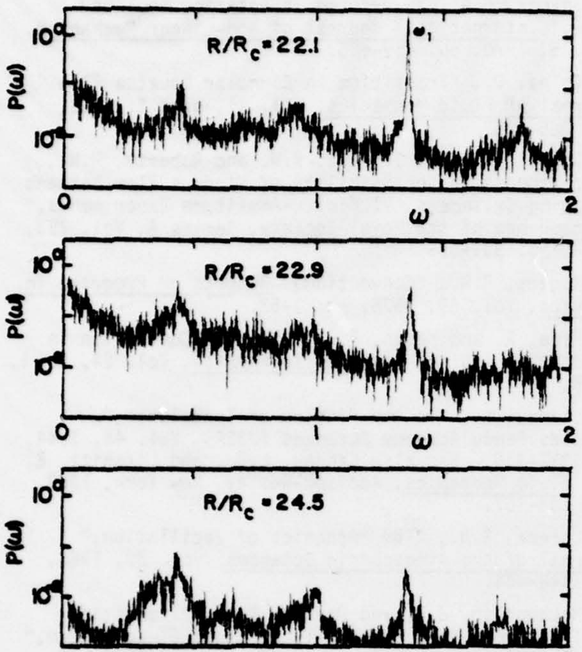

Fig. 5. These spectra at successively higher Reynolds numbers illustrate the disappearance of the sharp frequency component at ω_1, which occurs at $R/R_c = 22.4 \pm 0.2$. For $R/R_c < 22.4$, two components are centered at ω_1, a strong narrow component and a broad weak component. As $R/R_c \to 22.4^-$, the amplitude of the narrow spectral line rapidly goes to zero, and for $R/R_c > 22.4$ only the broad component remains.

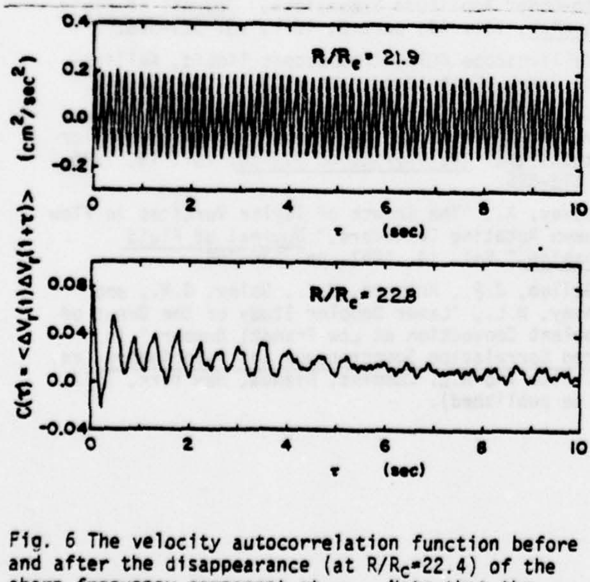

Fig. 6 The velocity autocorrelation function before and after the disappearance (at $R/R_c = 22.4$) of the sharp frequency component at ω_1. Note that the ordinate scales are different for the two graphs.

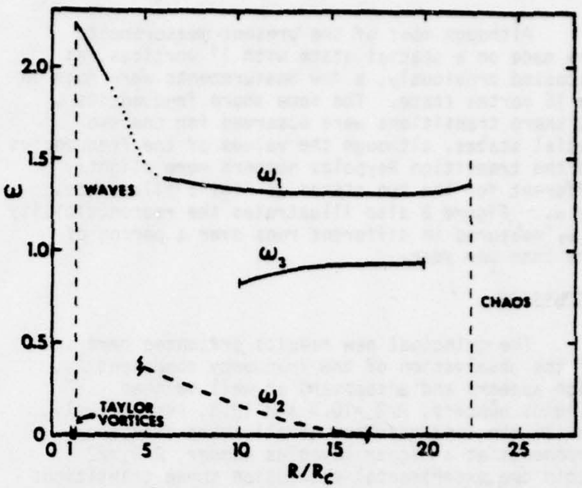

Fig. 7 The sharp frequency components observed in the power spectra of the radial component of the velocity. The time-independent Taylor vortex regime extends over a relatively small range in Reynolds number, from $R/R_c = 1$ to 1.3, a range which was not studied in the present work. We have also not studied the region $3.2 < R/R_c < 5.8$, which is indicated by the dotted part of the ω_1 curve. The values of ω_1 and ω_3 at any given Reynolds number reproduced from run to run with an accuracy of 1% or better, but, as discussed in the text, ω_2 was absent in many runs and its value was not reproducible. Sharp frequency components are observed only in the range from the onset of the wavy regime up to $R/R_c = 22.4$. The spectral features above $R/R_c = 22.4$ are quite broad.

of the inner cylinder. There is some indication that ω_1 may broaden slightly between $R/R_c = 19.8$ and 22.4, but this broadening, if it occurs, is comparable to our present resolution, and higher resolution (that is, longer velocity data records) will be required to determine whether ω_1 broadens before it disappears.

Our values for the wave frequency, ω_1, agree well with the values previously obtained by Coles (4) in an apparatus with the same radius ratio as ours [see his Fig. 6, a graph of ω_1/m vs R, where m is the number of azimuthal waves (4 in the present experiment)].

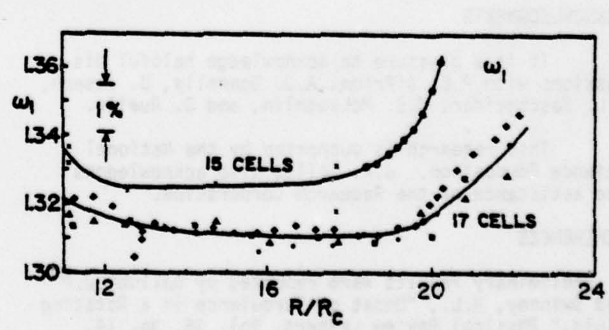

Fig. 8 A comparison of the values of ω_1 measured for the 17 and 15 vortex states. The same spectral features and sequence of events were observed for the two states. The different symbols indicate different experimental runs.

Although most of the present measurements were made on a spatial state with 17 vortices, as discussed previously, a few measurements were made on the 15 vortex state. The same sharp frequencies ω_j and sharp transitions were observed for the two spatial states, although the values of the frequencies and the transition Reynolds numbers were slightly different for the two states as Fig. 8 illustrates for ω_1. Figure 8 also illustrates the reproducibility of ω_1 measured in different runs over a period of more than one year.

DISCUSSION

The principal new results presented here are (1) the observation of the frequency component ω_3, which appears and disappears at well defined Reynolds numbers, $R/R_c=10.0$ and 19.8, respectively, and (2) the disappearance of all sharp frequency components at a higher Reynolds number, $R/R_c=22.4$. Within the experimental resolution these transitions exhibit no hysteresis. Also, the velocity was measured at several different radii and heights within the fluid, and the observed frequencies and transition Reynolds numbers were found to be independent of the laser probe position. In addition, the photographs of the flow obtained in the vicinity of the transitions at $R/R_c=10.0$ and 19.8 do not show any radical changes in the flow pattern, although the disappearance of ω_1 at $R/R_c=22.4$ can be seen as the loss of azimuthal waves.

In conclusion, we have observed in a circular Couette flow system three distinct dynamical regimes (periodic, quasiperiodic, and aperiodic) which are characteristic of nonlinear mathematical models with only a few degrees of freedom. The observed behavior is qualitatively consistent with the ideas of Lorenz and Ruelle and Takens, who suggested that a few nonlinearly coupled modes are sufficient to produce aperiodic motion. However, there is a small amount of broadband noise in the periodic regime that precedes the aperiodic regime. Whether this noise is important in the dynamics is not yet clear.

These experiments are continuing, and a more detailed report including photographs of the flow will be presented elsewhere. Also, a similar LDV study is underway (18) on the transition to turbulent convection in a fluid between parallel plates heated from below (Bénard system).

ACKNOWLEDGMENTS

It is a pleasure to acknowledge helpful discussions with R.C. DiPrima, R.J. Donnelly, D. Joseph, E.L. Koschmeider, J.B. McLaughlin, and D. Ruelle.

This research is supported by the National Science Foundation. J.P. Gollub also acknowledges the assistance of the Research Corporation.

REFERENCES

1 Preliminary results were reported by Gollub, J.P and Swinney, H.L., "Onset of Turbulence in a Rotating Fluid," *Physical Review Letters*, Vol. 35, No. 14, 1975, pp. 927-930.

2 Koschmeider, E.L., "Stability of Supercritical Bénard Convection and Taylor Vortex Flow," in *Proceedings of the Conference on Instability and Dissipative Structures in Hydrodynamics*, ed. by I. Prigogine and S.A. Rice, Wiley, New York, 1975, pp. 109-133

3 Snyder, H.A., "Waveforms in Rotating Couette Flow," *International Journal of Non-Linear Mechanics*, Vol. 5, 1970, pp. 659-685.

4 Coles, D., "Transition in Circular Couette Flow," *Journal of Fluid Mechanics*, Vol. 21, part 3, 1965, pp. 385-425.

5 Donnelly, R.J., Schwarz, K.W. and Roberts, P.H., "Experiments on the Stability of Viscous Flow Between Rotating Cylincers, VI Finite-Amplitude Experiments," *Proceedings of the Royal Society*, Series A, Vol. 283, 1965, pp. 531-556.

6 Rogers, R.H., "Convection," *Reports on Progress in Physics*, Vol. 39, 1976, pp. 1-63.

7 Hide, R. and Mason, P.J., "Sloping Convection in a Rotating Fluid," *Advances in Physics*, Vol. 24, No. 1, 1975, pp. 1-100.

8 Landau, L., "On the Problem of Turbulence," Comptes Rendu Academy Sciences (USSR), Vol. 44, 1944, pp. 311-316. See also Landau, L.D., and Lifshitz, E. M., *Fluid Mechanics*, Addison-Wesley, New York, 1959, pp. 103-107.

9 Lorenz, E.N., "The Mechanics of Vacillation," *Journal of the Atmospheric Sciences*, Vol. 20, 1963, pp. 448-464.

10 McLaughlin, J.B. and Martin, P.C., "Transition to Turbulence in a Statically Stressed Fluid System," *Physical Review A*, Vol. 12, 1975, pp. 186-203.

11 Ahlers, G., "The Rayleigh-Benard Instability at Helium Temperatures," in *Fluctuations, Instabilities, and Phase Transitions*, ed. by T. Riste, Plenum, New York, 1975, pp. 181-193.

12 Ruelle, D. and Takens, F., "On the Nature of Turbulence," *Communications in Mathematical Physics*, Vol. 20, 1971, pp. 167-192.

13 Davey, A, DiPrima, R.C., and Stuart, J.T., "On the Instability of Taylor Vortices," *Journal of Fluid Mechanics*, Vol. 31, part 1, 1968, pp. 17-52.

14 Eagles, P.M., "On Stability of Taylor Vortices by Fifth-Order Amplitude Expansions," *Journal of Fluid Mechanics*, Vol. 49, part 3, 1971, pp. 529-550.

15 Kalliroscope AQ1000 rheoscopic liquid, Kalliroscope Corp., Cambridge, Mass.

16 Gollub, J.P., and Freilich, M., "Optical Heterodyne Test of Perturbation Expansions for the Taylor Instability," *The Physics of Fluids*. Vol. 19, 1976, pp. 618-626.

17 Davey, A., "The Growth of Taylor Vortices in Flow Between Rotating Cylinders," *Journal of Fluid Mechanics*," Vol. 14, 1962, pp. 336-368.

18 Gollub, J.P., Hulbert, S.L., Dolny, G.M., and Swinney, H.L., "Laser Doppler Study of the Onset of Turbulent Convection at Low Prandtl Number," in *Photon Correlation Spectroscopy and Velocimetry*, ed. E.R. Pike and H.Z. Cummins, Plenum, New York, 1977, (to be published).

TURBULENT FLOW OVER WAVY SURFACES

Thomas J. Hanratty and C. A. Thorsness
Department of Chemical Engineering
University of Illinois
Urbana, Illinois

ABSTRACT

Measurements have been made of the variation of the wall shear stress accompanying the turbulent flow of a liquid along the surface of solid waves with a height of 0.30 mm and a length of 50.8 mm. These are of particular interest in that they show a clear-cut linear response and, consequently, provide a badly needed test of proposed solutions of the linear momentum equations that use different models for the wave induced Reynolds stresses. The use of a quasi-laminar assumption, whereby the wave induced changes of the Reynolds stresses are ignored, gives good agreement with measurements of the variation of the wall shear stress only for large values of the wave number, $\alpha v^*/\nu$ > ca 0.01. At smaller wave numbers it is necessary to use a model of the wave induced variation of the Reynolds stresses which takes account of the change of turbulence properties along the wave surface. For this purpose, we tentatively recommend a mixing length model suggested by Loyd, Moffat and Kays. An essential feature of this model is that variations of the thickness of the viscous wall region are induced by variation of the pressure gradient along the wave surface.

INTRODUCTION

This paper is concerned with the calculation of turbulent flows over wavy surfaces. It presents experimental data which allows an evaluation of different models for the wave induced variation of the Reynolds stress. For such flows the Reynolds stresses play an important role in determining the velocity field mainly in the viscous wall region ($\frac{yv^*}{\nu}$ < ca30). Consequently the results of our experiments provide a test for the accuracy of turbulence models close to a surface. Most of the recent computer calculations of turbulent flows past solid surfaces have used simple couette models for the viscous wall region. Yet in many instances the rate of response of the flow in the immediate vicinity of the wall to changes in external variables is critical and these calculations are not adequate because the couette model implies an instantaneous response; i.e., an equilibrium structure. The problem discussed in this paper is an example of a situation for which the assumption of an equilibrium flow close to the wall can lead to a large error in predicting the local shear stress and pressure on a solid surface and in predicting local heat and mass transfer rates.

The first analysis of flow over a wavy surface was carried out by Kelvin and Helmholtz. The surface was assumed to be of small enough amplitude that there is a linear response. A solution was obtained for an inviscid flow for which the velocity profile is uniform and for which the influence of turbulent stresses is negligible. Benjamin (1) extended this analysis by taking into account the influence of molecular viscosity and the shape of the average velocity profile. The analysis of Benjamin has been extensively used to evaluate the interaction between a turbulent fluid and waves on a liquid interface. However, in recent years considerable concern has been expressed regarding errors involved in the neglect of the wave induced Reynolds stresses. There has been need for experimental data which gives directly the forces on a wavy surface.

Studies of the pressure variation have proved inadequate because of difficulties in measurement for small amplitude waves and because pressure profiles are somewhat insensitive to the modelling of the Reynolds stresses. Therefore we have carried out a series of experiments in which we measured the shear stress variation along a solid wave of sinusoidal shape over which a turbulent fluid is flowing (10) (12). For very small amplitude waves a linear response is obtained in that the spatial variation of the wall shear stress is given by a single harmonic. For intermediate sized waves for which a separated flow does not exist higher order harmonics appear in the shear stress variation but not in the pressure variation.

From these data the amplitude and the phase of the different harmonics can be calculated. For small amplitude waves it is found that the quasi-laminar model of Benjamin is valid for small wave lengths. However, large errors can be made in using this analysis for intermediate and large wave lengths.

In order to improve the analysis Thorsness (12) explored different models for the Reynolds stresses which give attention to the viscous wall region. Of particular importance is the thinning and thickening of this region due to the induced pressure variations along the wave surface.

Our conclusions regarding modelling of the wave induced Reynolds stresses will be presented. We find that the eddy viscosity model of Kays and his co-workers to be useful, even though not in exact agreement with the results.

LINEARIZED MOMENTUM EQUATIONS

The boundary-layer coordinate system in which the momentum equations are formulated has the x-coordinate parallel to the two-dimensional wave surface and the y-coordinate perpendicular to it. The time averaged velocities, U, V, the turbulent stresses, R_{ij}, and the pressure gradients, $\partial P/\partial x$, $\partial P/\partial y$, are assumed to be composed of a component averaged over a wave length at a constant value of y and a component with a periodic spatial variation of the same wave length as the surface. For very small amplitude sinusoidal waves a linear response can be expected so that wave induced components have only a single harmonic. Consequently,

$$U = \overline{U}(y) + a\hat{u}(y)e^{i\alpha x} \tag{1a}$$

$$V = a\hat{v}(y)e^{i\alpha x} \tag{1b}$$

$$R_{ij} = \overline{R}_{ij}(y) + a\hat{r}_{ij}(y)e^{i\alpha x} \tag{1c}$$

$$\frac{\partial P}{\partial y} + \overline{\frac{\partial P}{\partial y}} + a\,\frac{d\hat{p}(y)}{dy}\,e^{i\alpha x} \tag{1d}$$

$$\frac{\partial P}{\partial x} + \overline{\frac{\partial P}{\partial x}} + ai\alpha\,\hat{p}(y)e^{i\alpha x} \tag{1e}$$

where $\hat{u}(y)$, $\hat{v}(y)$, $\hat{r}_{ij}(y)$ and $\hat{p}(y)$ are complex quantities, and a is the wave amplitude. Here, as throughout the rest of the paper, velocities have been made dimensionless with respect to a friction $v^* = \left(\frac{\overline{\tau}_w}{\rho}\right)^{1/2}$, defined in terms of a wave length averaged wall shear stress and lengths, with respect to ratio of the kinematic viscosity to the friction velocity, ν/v^*.

From the equation of conservation of mass a stream function ψ can be defined as

$$\psi = \int_0^y \overline{U}(y)dy + aF(y)e^{i\alpha x}, \tag{2}$$

$$\text{with } U = \frac{1}{h_y}\,\frac{\partial\psi}{\partial y}\,,\ V = -\frac{1}{h_x}\frac{\partial\psi}{\partial x}\,, \tag{3}$$

and the linearized metric functions given as

$$h_x = 1 + a\alpha^2 ye^{i\alpha x}, \quad h_y = 1. \tag{4}$$

For small values of $a\alpha$ the velocities can be represented as

$$U = \overline{U} + aF'e^{i\alpha x}, \quad V = -\,ia\alpha Fe^{i\alpha x}. \tag{5}$$

If $\hat{p}$ is eliminated between the x- and y-momentum equations the following relations are obtained defining F(y):

$$i\alpha\left[\overline{U}(F'' - \alpha^2 F) - \overline{U}''F + \alpha^2\overline{U}^2\right] = F^{IV} - 2\alpha^2 F'' - \alpha^4 F + 2\alpha^2\overline{U}'' - \alpha^4\overline{U} + \mathcal{R}, \tag{6}$$

$$\overline{U}''' + \overline{R}_{xy} = 0, \tag{7}$$

where

$$\mathcal{R} = i\alpha^3\overline{R}_{xx} + 3\alpha^2\overline{R}'_{xy} + i\alpha(\hat{r}'_{xx} - \hat{r}'_{yy}) + \alpha^2\hat{r}_{xy} + \hat{r}''_{xy}\,. \tag{8}$$

The velocity $\overline{U}(y)$ is taken to be the same as would exist if the surface were flat. This specification is consistent with the linearization assumption and is justified by the experimental result that the shear stress averaged along the wave surface is the same as what is measured for a flat surface. The no slip condition at the wave surface leads to the boundary conditions

$$F = 0,\ F' = 0 \text{ at } y = 0. \tag{9}$$

The requirement that flow far from the wave is that which would be present over a flat surface leads to the boundary conditions

$$F' = \overline{U}' \text{ and } F = \overline{U} \text{ for large } y. \tag{10}$$

The shear stress and pressure variation along the wavy surface can be calculated once a solution to (6) is obtained subject to boundary conditions (9) and (10). Since

$$\tau_w = \overline{\tau}(0) + a\hat{\tau}(0)e^{i\alpha x} = \frac{1}{h_y}\frac{\partial U}{\partial y}\bigg|_{y=0}\,, \tag{11}$$

the wave induced variation of the wall shear stress is

$$a\hat{\tau}(0)e^{i\alpha x} = aF''(0)e^{i\alpha x}\,. \tag{12}$$

By evaluating the x-momentum equation at y=0 the wave induced variation in the pressure at the solid surface is found to be

$$a\hat{p}(0)e^{i\alpha x} = -\frac{i}{\alpha}\left[F'''(0) + \alpha^2\overline{U}'(0)\right]ae^{i\alpha x}\,. \tag{13}$$

Equation (6) is similar to the Orr-Sommerfeld equation used in stability calculations except for the appearance of additional terms due to the use of curvilinear coordinates and due to the inclusion of Reynolds stresses. The inhomogeneous term on the left side of (6), which arises because of centripetal acceleration due to the bending of the mean flow in curvilinear coordinates, turns out to be of considerable importance.

The use of boundary-layer coordinates at large distances from the wave surface could limit the applicability of the solution to much smaller values of $a\alpha$ than is necessary. Consequently it would be more correct to match an inner solution in boundary-layer coordinates to an outer solution which is linearized around an average velocity profile defined in cartesian coordinates. If the matching is done at a location where the influences of viscous and turbulent stresses on the wave induced flow is negligible the values of $\hat{\tau}(0)$ and $\hat{p}(0)$ calculated in this way would be identical to those obtained by the solution of (6) to (13). The chief difference would be in the construction of the velocity field above the wave surface from the calculated results.

MODELS FOR THE TURBULENT STRESS

Constant Reynolds Stress Assumption - Model A

The quasi-laminar assumption of Benjamin (1) involves the proposal that the only influence of the turbulence is in the specification of the mean velocity profile $\overline{U}(y)$. Consequently, $\mathcal{R} = 0$ in (6). In this paper we explore an assumption which is essentially the same as this, Model A. The wave induced Reynolds stresses are taken as zero so that

$$\mathcal{R} = 3\alpha^2 \overline{R}'_{xy} = 3\alpha^2 (- \overline{U}'' - \overline{U}'' (0)) \qquad (14)$$

if normal stresses are neglected.

In boundary-layer coordinates this model is closely related to the assumption that Reynolds stresses are constant along a streamline discussed by Davis (3) for flow over wavy surfaces and by Deissler (4) in a different context.

Eddy Viscosity Assumption of Hussain and Reynolds - Model B

Hussain and Reynolds (6) approximated the wave induced Reynolds stress as the product of the wave induced rate of strain and a turbulent viscosity, ν_T, which is a specified function of y. If an isotropic relation is assumed between the turbulent stress tensor and the wave induced rate of strain, the following equation is derived for $\mathcal{R}$ in the boundary-layer system:

$$\mathcal{R} = \frac{\overline{\nu}_T}{\nu} (F^{IV} + 2\alpha^2 F'' + \alpha^4 F + 2\alpha^2 \overline{U}'' - \alpha^4 \overline{U}) + \frac{\overline{\nu}'_T}{\nu} (2F''' + 2\alpha^2 F' + \alpha^2 \overline{U}') + \frac{\overline{\nu}''_T}{\nu} (F'' + \alpha^2 F - \alpha^2 \overline{U}) \qquad (15)$$

This relation is particularly useful to examine the importance of $\mathcal{R}$ relative to other terms in (6). A conclusion derived from this comparison, noted in the thesis by Thorsness (12), is that $\mathcal{R}$ is not important for large y, where the variation of the wave induced velocity field is given by the inviscid Orr-Sommerfeld equation. Consequently, models of the wave induced Reynolds stress should pay particular attention to flow close to the surface, since errors made at large y will not greatly influence the calculated velocity field.

Mixing Length Assumption of Loyd, Moffat and Kays - Model D

A shortcoming of the eddy viscosity model of Hussain and Reynolds is that it does not take account of changes in turbulence properties along the wave surface. Thorsness (12) considered three models for $\mathcal{R}$ which attempt to consider this factor.

One of these includes only the influence of the change of the wall shear stress along the wave surface. Another is an adaptation of the mixing length model of Loyd, Moffat and Kays, which includes the influence of changes of both the pressure gradient and the shear stress along the wave surface. The third was the model of Mellor and Herring (8) which uses a differential equation for the turbulent energy to evaluate the Reynolds stress. Thorsness found that the mixing length model of Loyd, Moffat and Kays (7) did the best job in accounting for the influence of wave induced variations of the turbulence properties. Consequently we present here only a detailed treatment of this model.

The influence of a change of turbulence properties along the wave surface is introduced through a change in the eddy viscosity. We introduce a wave induced variation in eddy viscosity so that the Reynolds stress is related to the rate of strain through the relation

$$\mathcal{R}_{xy} = (\frac{\overline{\nu}_T}{\nu} + a \frac{\tilde{\nu}_T}{\nu} e^{i\alpha x}) 2e_{xy} \qquad (16)$$

Since turbulent stresses are important only close to the wave surface we make use of the boundary-layer assumption that normal stresses can be neglected. The Reynolds stress term in boundary-layer coordinates is then written as

$$\mathcal{R} = 3\alpha^2 \left[\frac{\overline{\nu}_T}{\nu} \overline{U}'\right]' + \alpha^2 \left[\frac{\overline{\nu}_T}{\nu} (F'' + \alpha^2 F - \alpha^2 \overline{U}) + \frac{\tilde{\nu}_T}{\nu} \overline{U}'\right] + \left[\frac{\overline{\nu}_T}{\nu} (F'' + \alpha^2 F - \alpha^2 \overline{U}) + \frac{\tilde{\nu}_T}{\nu} \overline{U}'\right]'' . \qquad (17)$$

According to the mixing length hypothesis of Loyd, Moffat and Kays,

$$\frac{\nu_T}{\nu} = \ell^2 \left| 2 e_{xy} \right| \qquad (18)$$

and

$$\ell = \kappa y \left[1 - \exp (- \frac{y\tau^{\frac{1}{2}}}{A})\right] \qquad (19)$$

for equilibrium boundary layers.

Here κ is the von Karman constant and $y\tau^{\frac{1}{2}}/A = D_M$ is a damping function which represents the influence of molecular viscosity on [illegible] mixing length. The coefficient in the damping function contains the local shear stress in the fluid and a scale factor, A, which governs the thickness of the viscous wall region where molecular viscosity is playing an important direct role in transmitting stress. The scale A increases with increasing negative pressure gradient, consistent with the laminarization reported by a number of investigators. We take A to be of the form

$$A = A_0 (1 + \frac{dp}{dx} k_1 + (\frac{dp}{dx})^2 k_2 + \ldots) \qquad (20)$$

for equilibrium flows where the pressure gradient is not changing. Loyd, Moffat and Kays have argued that for a nonequilibrium condition, such as exists in flow over waves, an effective pressure gradient should be used in (20), where

$$\frac{d (\frac{dp}{dx})_{eff.}}{dx} = \frac{(\frac{dp}{dx})_{eff.} - \frac{dp}{dx}}{k_L} \qquad (21)$$

This introduces a lag between the imposition of a non-zero pressure gradient and a change of the scale for the viscous wall region.

For flow over waves both positive and negative pressure gradients are experienced at the boundary. The magnitude of these wave induced pressure gradients varies with distance from the wave surface. However, the inner portion of the flow is very much like a boundary layer in that the pressure gradient is reasonably constant through a distance from the surface that includes the region where turbulent stresses are important. (See figure 5.23 of the thesis by Thorsness (12)). Consequently, it is not unreasonable to use the model developed by Loyd, Moffat and Kays for boundary layers to predict the influence of wall pressure gradients on the damping coefficient.

Another problem in using this model is the difficulty in estimating the variation of τ in the y-direction. Consequently, we have used the shear stress at the wall in the damping function,

$$\tau_w = 1 + aF'' (0) e^{i\alpha x} \qquad (22)$$

This has the effect of including all the influence of pressure gradient in the scale A, which for small amplitude waves can be represented as

$$A = \overline{A} + a\hat{A} e^{i\alpha x} \qquad (23)$$

The damping coefficient is thus

$$D_M = \frac{y\sqrt{1 + aF''(0)e^{i\alpha x}}}{\bar{A} + a\hat{A}e^{i\alpha x}} \tag{24}$$

If (21) is solved for a periodic pressure gradient the following relation is obtained from (20):

$$A = \bar{A} + a\,\frac{k_1\bar{A}i\alpha\hat{p}}{1 + i\alpha k_L}e^{i\alpha x} \tag{25}$$

so that

$$\hat{A} = \frac{k_1\bar{A}i\alpha\hat{p}}{1 + i\alpha k_L}\,. \tag{26}$$

An expression for the amplitude of the fluctuating eddy viscosity is obtained from (18),

$$\frac{\hat{\nu}_T}{\nu} = \left[\frac{F'' + \alpha^2 F - \alpha^2\bar{U}}{\bar{U}'} + \left(\frac{2\exp(-\frac{y}{\bar{A}})}{1 - \exp(-\frac{y}{\bar{A}})}\right)\left(\frac{y}{\bar{A}}\right)\left(\frac{F''(0)}{2} - \frac{\hat{A}}{\bar{A}}\right)\right]\frac{\bar{\nu}_T}{\nu} \tag{27}$$

The evaluation of $\hat{\nu}_T$ requires the specification of the parameters $\bar{A}$, k_1 and k_L. The scale $\bar{A}$ is obtained from data on the velocity profile for flow over a flat surface. A value of $k_L = 3000$ was suggested by Loyd, Moffat and Kays. From a correlation of data for favorable (negative) pressure gradients by Loyd, Moffat and Kays we obtain $k_1 = -30$. Because of the uncertainty in selecting k_1 and k_L we have carried out calculations with $k_L = 3000$ for three different values of k_1, including $k_1 = -30$, and for three different values of k_L with $k_1 = -30$.

SOLUTION OF THE MOMENTUM EQUATIONS

Mean Velocity Profile

The solution of the linearized momentum equations requires not only the specification of the wave induced Reynolds stress but also, of the mean velocity profile about which the problem is linearized. For the calculations presented in this paper we used a Van Driest mixing length equation to calculate the mean velocity profile:

$$\bar{U} = \int_0^y \frac{2\,dy}{1 + \sqrt{1 + \kappa^2 y^2\left[1 - \exp(-\frac{y}{\bar{A}})\right]^2}} \tag{28}$$

For large y this relation behaves as

$$\bar{U} = \frac{1}{\kappa}\ln y + B \tag{29}$$

Values of $\kappa = 0.41$ and $\bar{A} = 25$ used in our calculations give a value of $B = 5$ recommended in the literature.

Thorsness (12) also examined velocity profile relations proposed by Spalding and by Schlinger, as well as different combinations of κ and $\bar{A}$ in the Van Driest relation. He concluded that the calculations are relatively insensitive to the choice of the velocity profile function providing it gave a reasonable fit to experimental measurements.

Numerical Methods

A numerical scheme was used to solve the linearized momentum equation (6). Two independent solutions, f(y) and $\phi(y)$, to the homogeneous equation for F and, if needed, a third particular solution $f_p(y)$, to the complete inhomogeneous equation were generated by initializing the solutions at some appropriate distance from the surface and then integrating toward the surface. For models of the wave induced Reynolds stress in which it was necessary to know the pressure gradient and/or shear stress at the surface, an iterative procedure was used. The complete solution was then represented as

$$F(y) = Gf(y) + H\phi(y) + f_p(y), \tag{30}$$

where constants G and H are chosen so as to satisfy the two boundary conditions at y = 0.

The two homogeneous solutions chosen were those that decay at large values of y and the particular solution was set equal to $\bar{U}$ at large values of y so that boundary conditions (10) were satisfied. Far from the surface inertia terms dominate so that (6) reduces to

$$\bar{U}(F'' - \alpha^2 F) - \bar{U}''F + \alpha^2\bar{U}^2 = 0 \tag{31}$$

The solution $F = \bar{U}$ exactly satisfies this equation, justifying the choice of $f_p = \bar{U}$ at large values of y.

The behavior at large y of the "inviscid" homogeneous solution, $\phi(y)$, is obtained from the above equation by assuming $\bar{U}''$ is small and that $\bar{U}$ is approximately constant.

$$\phi(y) = e^{-\alpha y} \text{ for large } y \tag{32}$$

The "viscous" homogeneous solution, f(y), was generated by setting $f = f' = f''' = 0$ and letting either f'' real or f'' imaginary be equal to a small number. The final results were found to be insensitive to this choice and to the value of the assumed small number if the integration was started at large enough values of y.

A filtering scheme based on the work of Gersting and Jankowski (5) was developed to maintain the independence of $\phi(y)$, f(y), and $f_p(y)$. However, this was found to be unnecessary if double precision arithmetic was utilized on the IBM 360/75.

DESCRIPTION OF THE EXPERIMENTS

The wall shear stress measurements used to test the different model equations were obtained with two different wavy walls. One of these was constructed by Morrisroe (10) and consisted of a train of ten waves of length 2 in and amplitude 0.0114 in machined into a 1¼ in x 24 in x 27 in lucite slab. The other, a section used for mass transfer studies by Thorsness (12), consisted of ten waves having an amplitude of 0.0125 in and length of 2 in. The wave sections formed one wall of a 2 in x 24 in rectangular channel through which an electrolyte was circulated. They were preceded by a 27.5 ft length of channel so that studies were made with a fully developed turbulent velocity profile. Complete descriptions of the design of the channel and flow loop can be found in theses by Cook (2), Zilker (13) and Thorsness (12).

The variation of the shear stress along the wave surface was measured using electrochemical techniques developed in this laboratory (9) (11). The basic idea is to measure the rate of mass transfer to a small circular electrode mounted flush to the surface.

The wall shear stress is then related to the mass transfer coefficient K through the mass balance relation

$$\tau_w = \left(\frac{2\Gamma(4/3)K}{3}\right)^3 \frac{9L_e\mu}{D^2}, \qquad (33)$$

where D is the diffusion coefficient of the reacting species and L_e, the equivalent length equal to 0.82 times the diameter of the electrode.

The electrodes which were mounted along the middle wave of the wave section consisted of 0.020 in diameter platinum wires epoxied in holes drilled through the test section and sanded flush with the wave surface.

Mean velocity profiles were measured with a pitot tube using water as the test fluid and using a flat surface in place of the wave test section. Friction factors, defined as $f = \frac{2\tau_w}{\rho U_b^2}$, were determined by measuring the current to two 0.020 in diameter platinum wire electrodes mounted in the upper wall of the channel immediately above the removable test section. They were found to be in good agreement with results reported in other laboratories. The velocity profiles were in agreement with (29) using $\kappa = 0.41$ and $B = 5$.

EVALUATION OF THE MODELS FOR TURBULENT STRESS

Shear Stress Profiled

A typical measurement of the shear stress variation along a wave surface is shown in Fig 1. The line drawn through the data represents the best, in the least squares sense, fit of a sinusoidal curve with a wave length equal to that of the surface. It is noted that the maximum in the shear stress is upstream of the wave crest.

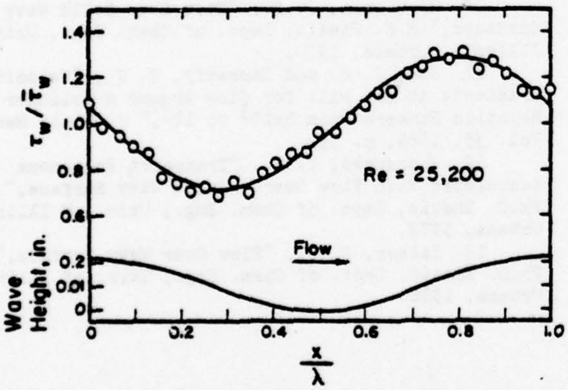

Fig. 1 Measured shear stress variation along the wave surface at Re = 25,200, based on the half width of the channel

Even though the magnitude of the variation in the wall shear stress is rather large, the data are fitted reasonably with a profile having a single harmonic. This suggests that the waves were of small enough amplitude that linear theory should be applicable. Further evidence for linear behavior is that the skin friction factors calculated from the average measured shear stress over the waves are essentially equal to those measured for a flat surface.

Fig 2 and 3 summarizes the measured shear stress distributions by plotting the phase angle and the amplitude of the fitted sinusoidal curves as functions of Reynolds number. The phase angle is measured with respect to the surface wave with shifts in the direction opposite the flow direction taken as positive.

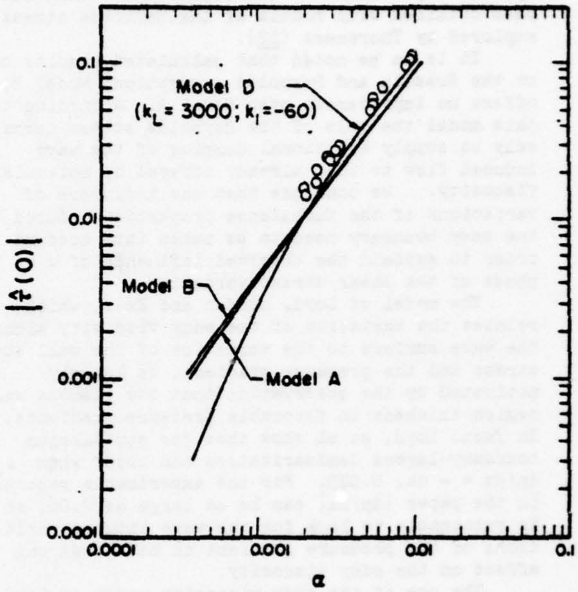

Fig. 2 Comparison of calculated and measured values of the amplitude of the wall shear stress variation

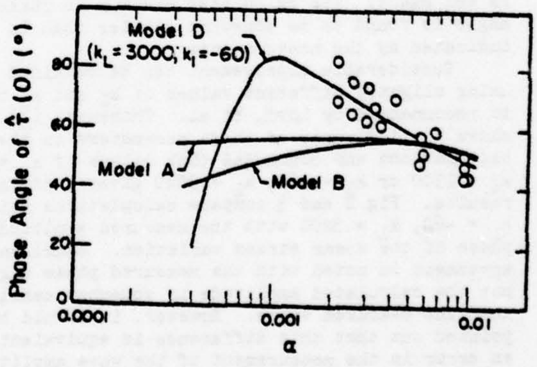

Fig 3 Comparison of calculated and measured values of the phase angle of the wall shear stress variation

Evaluation of the Quasi-Laminar Model

The comparison of measurements with Model A indicates that the quasi-laminar assumption can be used only for large α. This is to be expected since the thickness of the region over which wave induced velocity variations exist decreases with increasing α. At large enough α it is thin enough that turbulent stresses within it are negligibly small compared to viscous stresses.

Influence of Reynolds Stresses on the Wave Induced Flow

In order to obtain accurate solutions of the linear momentum equations in the range of α covered by our measurements it is necessary to include the influence of the wave induced variation of the Reynolds stress. Fig 2 and 3 indicate the type of improvement in the calculations that has been obtained with models of the Reynolds stress explored by Thorsness (12).

It is to be noted that calculated results based on the Hussain and Reynolds assumption, Model B, offers no improvement over Model A. According to this model the role of the Reynolds stress terms is only to supply additional damping of the wave induced flow to that already offered by molecular viscosity. We conclude that the influence of variations of the turbulence properties induced by the wavy boundary need to be taken into account in order to explain the observed influence of α on the phase of the shear stress variation.

The model of Loyd, Moffat and Kays, which relates the variation of the eddy viscosity along the wave surface to the variation of the wall shear stress and the pressure gradient, is largely motivated by the observation that the viscous wall region thickens in favorable pressure gradients. In fact, Loyd, et al show that for equilibrium boundary-layers laminarization can occur when $dp/dx = -$ ca. 0.023. For the experiments reported in the paper $|dp/dx|$ can be as large as 0.06, so it is reasonable to look for the wave induced variations of the pressure gradient to have a strong effect on the eddy viscosity.

The use of the eddy viscosity model of Loyd, Moffat and Kays with values of $k_1 = -30$ and $k_L = 3000$ recommended in their report gives better agreement with the measurements than does the Hussain and Reynolds model. However, the agreement is not exact. The calculated maximum in phase angle is found to be somewhat smaller than is indicated by the measurements.

Considerable improvement can be obtained by using slightly different values of k_1 and k_L than is recommended by Loyd, et al. Thorsness (12) shows the influence of these parameters on the calculations and concluded that values of $k_1 = -30$, $k_L = 1500$ or $k_1 = -60$, $k_L = 3000$ gives satisfactory results. Fig 2 and 3 compare calculations using $k_1 = -60$, $k_L = 3000$ with the measured amplitude and phase of the shear stress variation. Excellent agreement is noted with the measured phase angles, but the calculated amplitude is somewhat smaller than the measured value. However, it should be pointed out that this difference is equivalent to an error in the measurement of the wave amplitude of 0.051 mm. Recent measurements by Zilker (13) with larger amplitude waves have confirmed the measurements of the phase angle reported in this paper but have given slightly lower amplitudes of the first harmonic, in close agreement with the calculated curve shown in Fig 2. For this reason, we have more confidence in the measured phase angles and have chosen k_1 and k_L so as to have a close fit to these measurements.

On the basis of the above considerations we tentatively recommend that the Loyd, Moffat and Kays eddy viscosity model with values of $k_1 = -60$ and $k_L = 3000$ be used to extend the range of applicability of the quasi-laminar model to smaller wave numbers.

ACKNOWLEDGEMENT

This work was supported by the National Science Foundation under Grant ENG71-02362.

REFERENCES

1 Benjamin, T. B., "Shearing Flow Over a Wavy Boundary," J. Fluid Mech., Vol. 6, 1969, p. 161.

2 Cook, G. W., "Turbulent Flow Over Solid Wavy Surfaces," Ph.D. Thesis, Dept. of Chem., Univ. of Illinois, 1970.

3 Davis, R. E., "On Turbulent Flow Over a Wavy Boundary," J. Fluid Mech., Vol. 42, 1970, p. 721.

4 Deissler, R. G., "Evolution of a Moderately Short Turbulent Boundary Layer in a Severe Pressure Gradient," J. Fluid Mech., Vol. 64, 1974, p. 763.

5 Gersting, J. M. and Jankowski, D. F., "Numerical Methods for Orr-Sommerfeld Problems," Int. J. for Numerical Methods in Engineering, Vol. 4, 1972, p. 195.

6 Hussain, A. K. M. F. and Reynolds, W. C., "The Mechanics of a Perturbation Wave," Rept. FM-6, Thermosciences Div., Dept. of Mech. Eng., Stanford Univ., 1970.

7 Loyd, R. J., Moffat, R. J. and Kays, W. M., "The Turbulent Boundary Layer on a Porous Plate: An Experimental Study of the Fluid Dynamics with Strong Favorable Pressure Gradients and Blowing," Rept. HMT-13, Thermosciences Div., Dept. of Mech. Eng., Stanford Univ., 1970

8 Mellor, G. L. and Herring, H. J., "A Survey of the Mean Turbulent Field Closure Models," A.I.A.A. Journal, Vol. 11, 1973, p. 590.

9 Mitchell, J. E., and Hanratty, T. J., "A Study of Turbulence at a Wall Using an Electrochemical Wall-Shear Stress Meter," J. Fluid Mech., Vol. 26, 1966, p. 199

10 Morrisroe, P. E., "Flow Over Solid Wavy Surfaces," M.S. Thesis, Dept. of Chem. Eng., Univ. of Illinois, Urbana, 1970.

11 Son, J. S. and Hanratty, T. J., "Velocity Gradients at the Wall for Flow Around a Cylinder at Reynolds Numbers From 5×10^3 to 10^5," J. Fluid Mech., Vol. 35, 1969, p. 353.

12 Thorsness, C. B., "Transport Phenomena Associated With Flow Over a Solid Wavy Surface," Ph.D. Thesis, Dept. of Chem. Eng., Univ. of Illinois, Urbana, 1972.

13 Zilker, D. P., "Flow Over Wavy Surface," Ph.D. Thesis, Dept. of Chem. Eng., Univ. of Illinois, Urbana, 1976.

EXPERIMENTAL INVESTIGATION OF THE STRUCTURE OF NEAR-WALL TURBULENCE AND VISCOUS SUBLAYER

Kutateladze S.S., Khabakhpasheva E.M., Orlov V.V.,
Perepelitsa B.V., Mikhailova E.S.

ABSTRACT

The present paper presents the results of experimental studying near-wall turbulence in the immediate vicinity to the wall. The experiments comprise the measurements of velocity and temperature pulsations. The kinematic turbulence characteristics were measured using stroboscopic visualization technique enabling simultaneous measurements of all three components of instantaneous velocity vector in the region of the flow under examination to be carried out. The detailed experimental results on studying the parameters and structure of flow in the region of viscous and buffer zone ($0<y^+\leq 25$)are given. The contribution to the Reynolds shear stresses of near-wall flows of four types (u'<0,v'>0; u'>0,v'>0; u'>0,v'<0; u'<0,v'<0),where u' and v' are the streamwise and normal components of pulsation velocity is considered. The role of various-amplitude pulsations is analyzed as well as the mechanism of drag reduction by polymer additives. The statistical characteristics of temperature pulsations have been examined in a flow of water over the region of Reynolds numbers from $I\cdot IO^4$ to $6\cdot IO^4$. The main statistical characteristics of random processes have been obtained, as well as autocorrelation and spectral functions at various distances from the surface of heating. The analysis of the data obtained has shown that in a viscous sublayer the spectral density distribution is essentially independent of the distance from the wall.

NOMENCLATURE

x,y,z	-streamwise, normal wall, transverse Cartesian coordinates
U,V,W	-instantaneous velocity components in OX-, OY-, OZ-directions
u,v,w	-average velocity components
u',v',w'	-pulsation velocity components
u' v' w	RMS values of velocity pulsations
$\overline{u'v'}$, $\overline{u'w'}$; $\overline{v'w'}$	-Reynolds shear stresses
τ_w	-wall shear stress
y^+	$= yv_*/\nu$, dimensionless coordinate
ν	-kinematic viscosity
N	-total number of random process realizations
n_i	-number of i-process realization
ρ	-fluid density
T	-local average temperature
T_w	-wall temperature
σ_t	RMS value of temperature pulsations
A	-skewness coefficient
E	-flatness coefficient
H	-channel halfwidth

INTRODUCTION

The experimental investigation of the structure of near-wall turbulence in channels have been carried out at the Institute of Thermophysics for several years. These studies provided data on the kinematic turbulence parameters in the considerable part of the channel cross section including three characteristic regions of the near-wall turbulent flow: viscous sublayer, buffer zone and free stream with a logarithmic law of the average velocity distribution (I,2). The aim of the experiments described in what follows, is the detailed investigation of turbulence parameters in the zone directly near the wall and including the region of a viscous sublayer and that of intensive turbulence energy generation (a buffer zone). To study the mechanism of near-wall turbulence investigations in these regions is of primary importance.

At present along with the measurements of turbulent velocity pulsations the studies of temperature pulsations under the non-isothermal stream conditions are also carried out. Temperature pulsations measured in the direct vicinity to a wall enable us to obtain additional interesting information on the near-wall turbulence structure.

The present paper provides certain results of the experimental investigation of the near-wall turbulence parameters in a water stream with small additives of polyethylene-oxide and polyacrylamide. As is known, the introduction of high-polymer additives to a water stream may result in the considerable

drag reduction.
By the present numerous experimental results have been obtained on the influence of various factors on the value of drag reduction (2-6). At the same time the literature contains different points of view concerning the mechanism of this phenomenon. Studying the characteristic features of the near-wall turbulence structure provides important information to clarify the nature of the drag reduction by polymer additives.

1. Experimental Methods

a) Measurement of Turbulence Characteristics

The method of stroboscopic visualization of streams which has been developed at the Institute of Thermophysics for several years is based on photographing small tracers introduced into a flow at side flash lighting (1,2,7-9). As tracers, aluminium balls with a diameter of 3-5 μm are usually used. Such tracers follow the flow pulsations with good accuracy (10,11). In several studies small gas bubbles electrolytically obtained in the channel itself were also used. The simplest version of the optical scheme is represented in Fig.1.

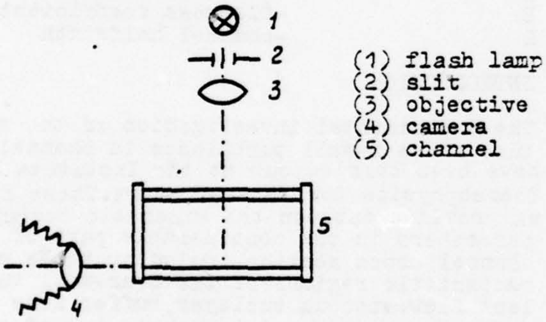

Fig.1 Optical scheme of photorecording for "two-coordinate" method

Immediately ahead a flash lamp a long slit diaphragm with a width of 0.1-0.2 mm is located which with the help of a rapid lens forms a thin "slit beam" in the investigated section. A camera which optical axis is normal to the slit beam plane is focused to the illuminated area. At a pulse of the flash lamp in the camera field of vision all tracers fallen inside the slit beam are observed as light points against the dark background. A series of flash lamp pulses provides a succession of positions of bright points—a discontinuous track. By the distance between two adjacent patterns two components of the instantaneous velocity vector are determined. At the same time the picture frame comprises a pattern of the thin stroke on the internal surface of the channel wall required for measuring the normal coordinate of each tracer. The set of tracks in one picture frame provides a field of instantaneous velocities in stream, and the totality of a sufficiently large number of the frames gives that of average velocities. The optical scheme shown in Fig.1 enables us to obtain two instantaneous velocity components at a time. With the help of this procedure many results have been obtained on studying the near-wall turbulence of water and dilute solutions of high polymers for streams with pressure gradient and for detached flows. At present this method has been further developed: a "three-coordinate" procedure of stroboscopic visualization has been elaborated, enabling simultaneous measurement of all three components of the instantaneous velocity to be performed. In this case one uses the effect of reflection of light emitted by tracers (tracers are secondary light sources) from the plane mirror surface of one of the walls bounding the region of flow under investigation. The effect of this reflection consists in that, in addition to a "real" trace an "imaginary" one appears in the semispace $y < 0$ (Fig.2).

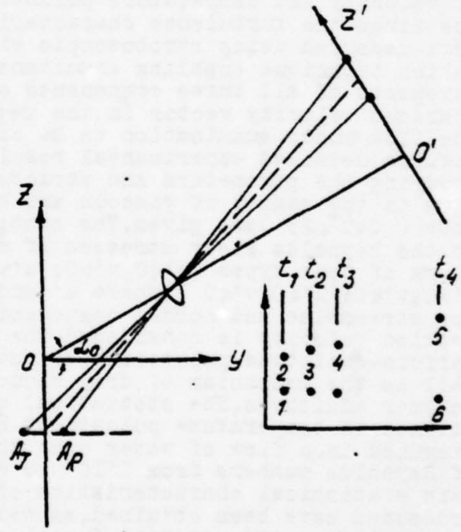

Fig.2 Optical scheme of photorecording for "three-coordinate" method
OZ-in the mirror plane; O'Z'-in the film plane; α_0-angle of lens dip

Under proper conditions of lighting and provided that the camera axis does not coincide with the OY-axis, two patterns of the discontinuous tracks are obtained on the film. In a simple case when the camera and tracers are situated in an optically-homogeneous medium, separated by a thin transparent wall, the y- and z-coordinates are expressed as functions of the camera inclination angle and the distance between the real and imaginary patterns of the tracers. When studying the streams of fluid in channels, to decrease astigmatism it is necessary to apply a prism with refractivity the closest possible to that of liquid (Fig.3). To operate over a wide velocity range and

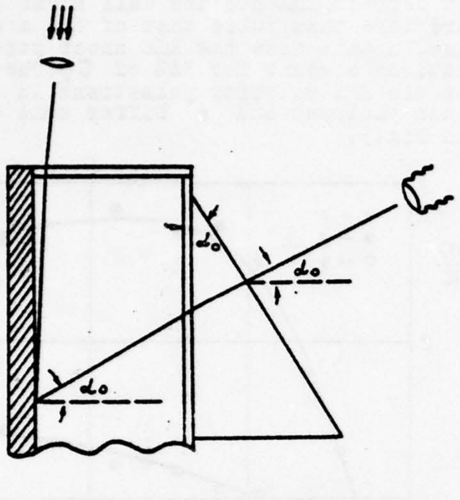

Fig.3 Optical photorecording scheme for "three-coordinate" method using correcting prism

to obtain information, providing the required accuracy in determining the instantaneous velocity values, great brightness of a light source, high and controlled frequency of flashes and the observance of strict time intervals between them are necessary. The electron stroboscope developed at the Institute ensures these requirements. It provides up to 800 kW pulse power and up to 20kHz pulse frequency. The number of pulses in a train and, hence, the succession of points forming a discontinuous track can be varied from 3 up to 12.

The choice of the train of pulses of the flash lamp is determined by the type of the stream being examined. If the stream-wise component of the instantaneous velocity vector is changed not only in its value but also in sign, such system of flashes is required that could enable us to determine the stream direction. For this purpose a system of flashes with inequal time intervals between them can be used. Such a system is also advantageous in the case when the instantaneous velocities in the stream region under examination differ by several times. For example, in studying the near-wall stream region the system of flashes t_2, t_3, t_4, t_8 was used, wherein the last time interval is 4 times as large as the preceding ones (Fig.2). At small stream velocity the coordinates of the track points (2), (3), (4) and (5) (corresponding to the time intervals t_2, t_3, t_4, t_8) were used. At a large flow velocity the point (5) may be hardly identified or be lying outside the frame. Then the instantaneous velocity is determined by the first three points (2), (3), (4) and their associated imaginary tracks. At a turbulent flow of liquid to obtain the averaged values of kinematic parameters with the required assurance, a large number of instantaneous velocity values should be measured. Hence, the procedure of measuring tracks should be automated wherever possible. A semi-automated system for measuring tracks comprising an optical-mechanical device with optical pickups of the displacement in two coordinate axes and an electron puncher unit ensures a possibility to carry out measurements of tracks to a high accuracy and tolerable time and labour consumptions. Then the information in terms of track coordinates from the punched tape is sent to the computer. To determine the average velocity profile the flow region under examination is divided to cells by subdividing the operational visual field to the appropriate zones in x, y and z. The mean velocity value is determined by averaging the instantaneous velocity values fallen into the proper cell in all frames. Velocity fluctuations are determined as deviations of the instantaneous velocity from the averaged velocity at a given point defined by the linear interpolation between the values in the centers of adjacent zones. The program provides for calculation of one-point velocity fluctuations momenta up to the 4-th order. Also calculated are the 2-nd order one-point mixed momenta and the histograms of instantaneous values of velocity fluctuations, wall shear stress and Reynolds stresses. At high density of tracks in each frame one may perform calculation of space correlations of all three velocity components. However, to obtain reliable values of the space correlation factors, mass experimental data should be processed, hence this information has been obtained only in several experiments. Computer processing enables us to carry out a more detailed analysis of flows as well. Thus, in a rectangular channel the contributions were defined introduced to the Reynolds shear stresses fluctuations u' and v' of various signs and amplitudes as well as some other characteristics enabling us to study a fine flow structure.

b) Temperature Pulsation Measurements

If the turbulent flow is heated through the channel wall, the velocity fluctuations in a viscous sublayer result in the pulsations in temperature. Hence, measurements of temperature pulsations can be used in studying the structure of turbulent liquid flows. To measure temperature pulsations and their mean values in a liquid flow a specially designed thermocouple probe was used. It should be noted that in the direct vicinity to a wall the use of thermocouple probes as compared with hot-wire ones is advantageous, since the overheating of their wires in relation to the environmental fluid and its associated heat-transfer with the channel wall results in considerable errors in this region. The probe was designed so that its influence on the temperature distribution in the near-wall flow region was as small as possible. The probe consists of an L-shaped stainless tube 2mm in diameter, ended in its horizontal section by a fastened two-channel glass cappilary 30 mm in length with welded nichrome-constantan thermo-electrodes 0.03 mm in diameter. The capillary ends in 10 mm greatly elongated cone not exceeding 0.1x0.2 mm in its overall size. The thermocouple junction is situated at a distance of about 1.5 mm from the glass capillary end. Upon mechanical treatment of the hot thermocouple junction its transverse size is ~10 m. This thermocouple design enables measurements to be carried out, starting from 0.03 mm distances from the surface. A micrometer screw makes it possible to registrate the probe displacements accurate to 0.01mm. Since the sensitivity of thermocouples used is tens of μV/°C, at a temperature difference $T_w - T_o$ of several degrees for further processing the signal should be amplified. For this purpose a special direct-current amplifier with up to 400 Hz transmission band and no more than 1.5 μV input-reduced noise level was used. The amplified signal upon transforming to a digital form, was stored in a computer magnetic memory. The sample size consists of 16 000 discrete units. With this sample size and frequency resolution, when calculating 3.12 Hz energetic spectrum, the normalized standard error for the energy spectra evaluation was about 15%.

2. Investigation of Water Flow Turbulence in Parallel-Walls Channel

The experimental installation with plexiglass test section 20x40 mm^2 was used. 20 calibres apart from the channel entrance at the internal channel side a mirror with a reflective covering was installed. The optical scheme of photorecording is shown in Fig.3. The inclination of the optical camera axis to XOY-plane was equal to $\alpha_o = 30°$. The size of the operational volume in the channel was 1.5 sm in OX-direction and 1 cm and 0.07 cm in OZ- and OY-directions, respectively.

a) Velocity Pulsations

The value of the dynamic velocity v_* was determined by averaging (with the help of a computer) the instantaneous values of U/y ratio near the channel wall. It should be noted that the unstable liquid flow nature in the viscous sublayer region results in considerable shear stress pulsations at the wall. Fig.4 represents the histogram of instantaneous values of U/y in $0 < y \leqslant 4.6$ region.

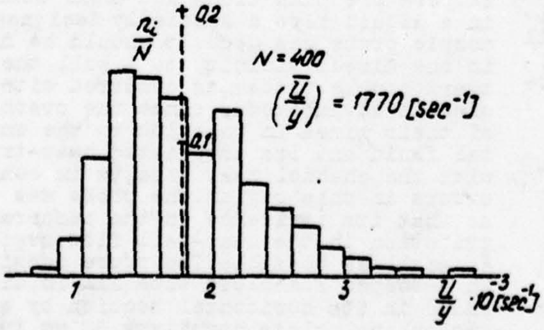

Fig.4 Distribution of instantaneous values of near-wall shear velocity gradient

At certain moments the wall shear stresses are more than twice that of the average value. In this case the RMS shear stress pulsations account for 30% of τ_w. The profiles of the RMS velocity pulsations in a viscous sublayer and a buffer zone are given in Fig.5.

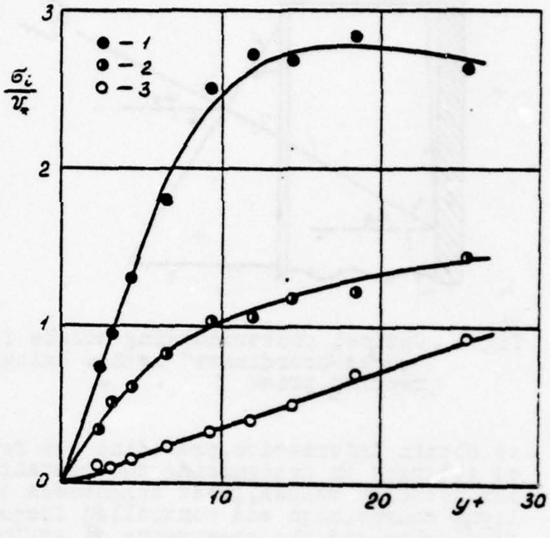

Fig. 5 RMS velocity fluctuations Re=21 000.

(1) σ_u/v_*; (2) σ_w/v_*; (3) σ_v/v_*

Data on the probability density of pulsations as well as measurements of their 3-d and 4-th momenta obtained in these experiments are given in details in (12,13) and essentially are in agreement with the data of other researchers. Hence, these data are not presented here and primary emphasis is placed on the detailed studying of the near-wall structure of turbulent shear stresses.

b) Certain Data on the Value and Structure of Reynolds Shear Stresses

The experimental data on the distribution of near-wall turbulent shear stresses are shown in Fig.6.

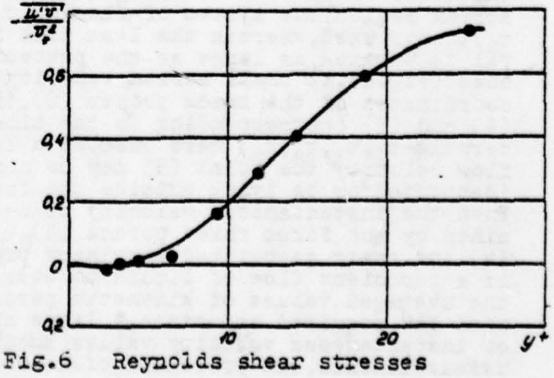

Fig.6 Reynolds shear stresses

The values $-\overline{u'v'}/v_*^2$ proved to be below those calculated from the profile of the mean velocity. This problem has been subjected to a specified analysis. From the considered possible reasons most probable seems to result from a three-dimensional flow in the channel examined (a rectangular 2:1 side ratio channel), which is pointed to by non-zero averaged values of v and w near the wall. The evaluation of terms in the Reynolds motion equation for a three-dimensional flow is in adequate agreement with this conclusion. This problem, however, requires further detailed analysis. Double correlation coefficients $\overline{u_i'u_j'}/\sigma_i\sigma_j$ are given in Fig.7.

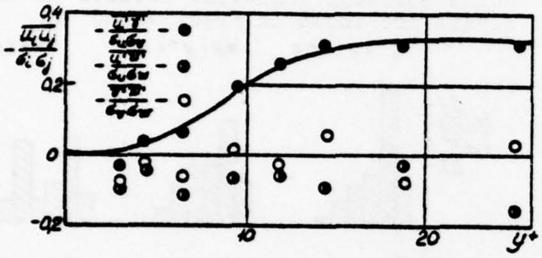

Fig. 7 Double-correlation coefficients

Within the viscous sublayer the correlation coefficient $\overline{u'v'}/\sigma_u\sigma_v$ is very small. With a removal from the wall it rapidly grows, at $y^+=15$ achieving the value approximately equal to 0.3. It is known, that in the developed turbulence area this value is equal to 0.42-0.43. Double-correlation coefficients $\overline{u'w'}/\sigma_v\sigma_w$ and $\overline{v'w'}/\sigma_v\sigma_w$ are close to zero. It should be noted, however, that the errors in the determination of correlation coefficients are rather high and in a viscous sublayer they are of the same order as the value under measurement. The average values of $\overline{u'v'}$ given in Figs.6 and 7 point to a large spread in the instantaneous values. In several experiments the instantaneous values of $\overline{u'v'}$ were found to be 30-50 times more than their average value. Investigations using various visualization techniques carried out recently (13-22) have made it possible to obtain much interesting information revealing characteristic features of the near-wall liquid flow. The experiments have shown that on a surface high- and low-velocity streamwise elongated regions exist. These streaks of decelerating liquid are gradually thickened and in the zone $5 \leqslant y^+ \leqslant 40$ a sharp burst of liquid from the wall takes place resulting in the initiation of stochastic motion over a large area (at present the mechanism of this phenomenon is treated in various ways). Instead of liquid carried out into the flow a new portion of liquid comes moving at a velocity exceeding the mean local one. The next stage can be conditionally treated as a non-stationary quasi-laminar flow. During this stage the deceleration of liquid occurs under the action of viscous forces. This stage is much more durable. Then a new burst of liquid from the wall takes place.

Along with ordered events, cases have been registered when portions of decelerated liquid receding from the wall are repelled back, and the incoming accelerating liquid is thrown away from the wall. There is a significant discrepancy between the quantitative estimations performed to define which of the stages found makes the greatest contribution to the value of Reynolds shear stresses (15, 16,23-25). As it has been noted above "burst" is characterized as a rule by a decelerating flow. At the same time after the "burst" liquid is directed to the near-wall region at a high velocity. Thus, these processes are characterized by various-sign velocity fluctuations and make a positive contribution to the value of Reynolds shear stresses. The cases when the portions of decelerating liquid move to the wall and the accelerating liquid is thrown away from it, result in negative instantaneous values of u'v'. According to our experimental results computer-aided calculations of the relations between the number of events with various combinations of signs in the velocity fluctuations (4 types) and the total number of the events registered were carried out. These values characterize the portion of time during which the near-wall liquid participates in one or another process of motion. The results of this processing are shown in Fig.8.

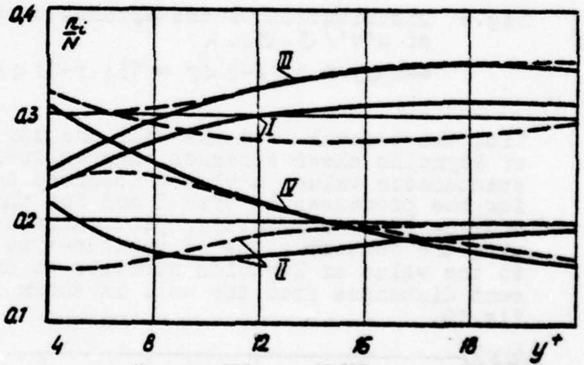

Fig.8 Probability of various types of motion in the near-wall region(--- data(24))

I-u' < 0, v' > 0; II-u' > 0, v' > 0;
III-u' > 0, v' < 0; IV-u' < 0, v' < 0;

From Fig.8 it is seen that near the wall ($6 < y^+ < 20$) the total probability of observations of flow with different-sign fluctuations is equal to 50-70%, i.e. it is 1.5 times as much as that for equal-sign velocity fluctuations flows. In this case the events of type I(u' < 0, v' > 0) are observed more rarely than those of type III(u' > 0, v' < 0). Fig.9 represents the histograms u'v' instantaneous values at different distances from the channel wall. The left-hand side of the histogram is contributed by the instantaneous values of u'v' products, characterized by different sign fluctuations. From the data obtained it is seen that near the wall the great instantaneous values of u'v' are related to process III, while "bursts" in this region followed by great u'v' are practically absent.

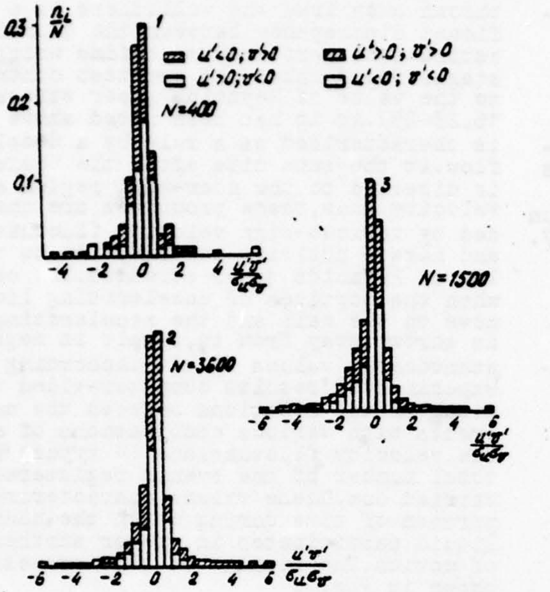

Fig.9 Distribution of instantaneous values of $u'v'/\sigma_u\sigma_v$.
4-0 < y ≤ 5; 2-5 < y ≤ 13; 3-13 < y ≤25

With the removal from the wall the structure of Reynolds shear stresses changes, great instantaneous values u'v' are observed both for the processes of type I and for those of type III. The resulting plot characterizing the contributions of various-type flows to the value of Reynolds stresses at different distances from the wall is shown in Fig.10.

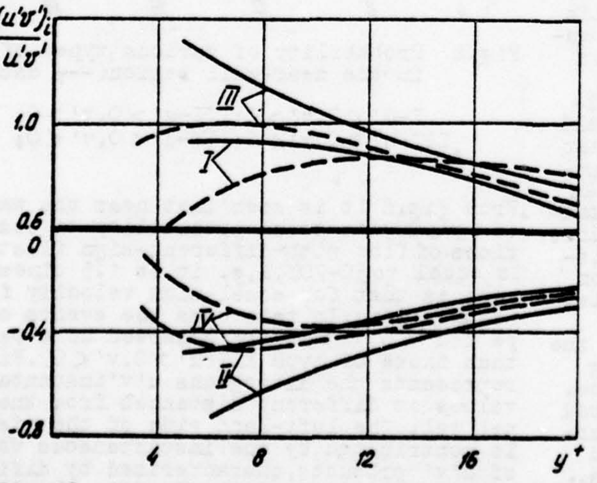

Fig.10 Contribution of various types of motion to Reynolds shear stresses. ---data(24); (I, II, III, IV see Fig.8)

In the direct vicinity of the wall the greatest contribution to Reynolds shear stresses is made by the flows with velocities exceeding the mean values. In this zone the processes of "bursting" of decelerating liquid portions from the wall are of less importance. In a buffer zone the contributions to the Reynolds stresses of the processes of type I and III become close in value and equal approximately 80%. The excess 60% are compensated by one-sign fluctuations products making a negative contribution to the Reynolds stresses value. A computer-aided analysis of the experimental data has been performed enabling us to define the contribution of different-amplitude fluctuations to the Reynolds stresses value. The results of this analysis are shown in Figs.11 and 12.

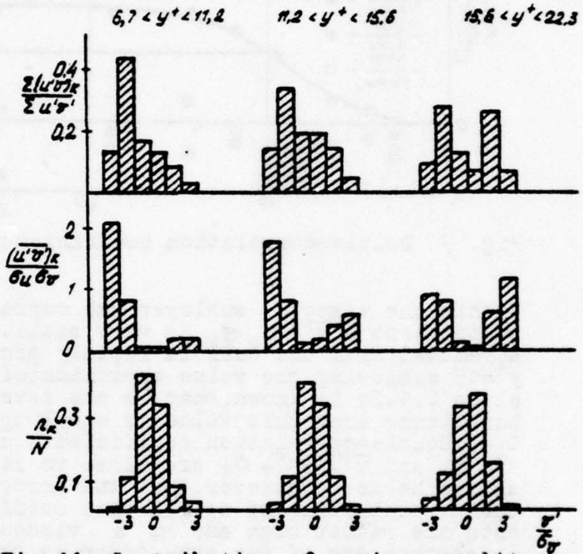

Fig.11 Contribution of various-amplitude fluctuations of v' to Reynolds stresses

Data presented at the bottom of the figures characterize the probabilities of different-amplitude fluctuations; centrally located is the mean value of Reynolds stresses versus the scale of fluctuations, and at the top is given the relative contribution of different-amplitude fluctuations to Reynolds stresses. From these figures it follows that about 70% of both the streamwise and normal velocity fluctuations have amplitudes under their RMS value. Their contribution to the value of Reynolds stresses is equal to 20-30%. At the same time the fluctuations with (1+2) σ_i amplitudes accounting for only 20-30% of the total number of fluctuations registered are responsible for 50-70% of the Reynolds stresses value. Great fluctuations both positive and negative resulting in very high instantaneous values of u'v' due to their small probability, however, contribute rather insignificantly to the value of Reynolds stresses. Near the wall high negative fluctuations of v' are apt to correspond to high positive fluctuations of u'. This is evidenced by the high mean value of u'v' determined for v' fluctuations in the range of $-3\sigma_v < v' < -2\sigma_v$.

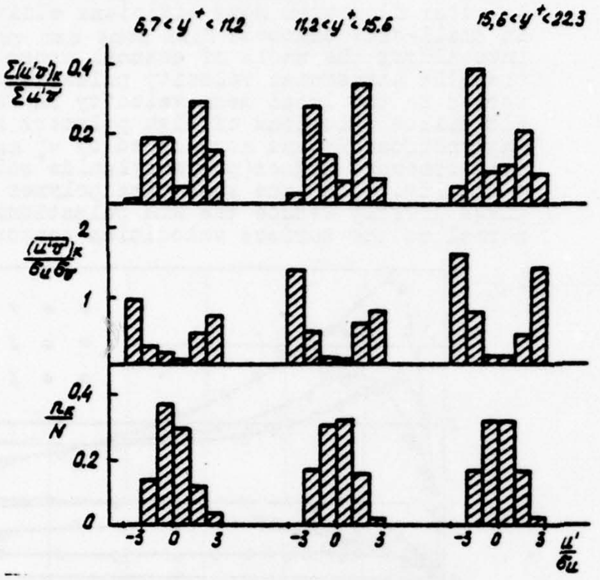

Fig.12 Contribution of various-amplitude fluctuations u' to Reynolds stresses

As is seen from the same histogram, in a viscous sublayer for high positive fluctuations of v' the situation is different. This shows that in the pulse transfer near-wall "bursts" are not decisive. With the removal from the wall the situation changes. The mean value of $\overline{(u'v')}_k$ for high positive fluctuations of v' and their contribution to the value of Reynolds stresses increase (Fig.11). Similar conclusions can also be made from Fig.12 representing the contribution of different-amplitude streamwise fluctuations to the value of Reynolds stresses. Thus, the quantitative data obtained characterizing the Reynolds stresses structure, show that for the pulse transfer near the surface predominant are the velocity fluctuations directed to the wall, emerging at "breaks" of liquid to the zone of viscous sublayer. At the same time with an increase in y^+ the role of fluctuations directed from the wall grows, and in the $15 < y^+ \leq 22$ region about half the total value of Reynolds stresses is associated with rather rare but powerful liquid "bursts" from the near-wall region.

3. Temperature Pulsations

The above analysis of near-wall turbulence exchange is in good agreement with the data obtained from the analysis of temperature pulsations. The present paper represents some results of measuring the statistical characteristics of temperature pulsations at a non-isothermal turbulent flow of water in a rectangular plane channel, over the range of Reynolds numbers from 10^4 to $60 \cdot 10^4$. The text section in these experiments comprised a rectangular channel 20x40 mm² three walls of which were made of plexiglass and one 40 mm in width of chrome-plated copper plate through which heat was transfered from an electric heater. The heat flux was chosen so that the temperature difference $T_w - T_o$ did not exceed 5-15 °C. Fig.13 shows distributions of the turbulent temperature pulsations in flow as well as the values of skewness coefficient and flatness factor.

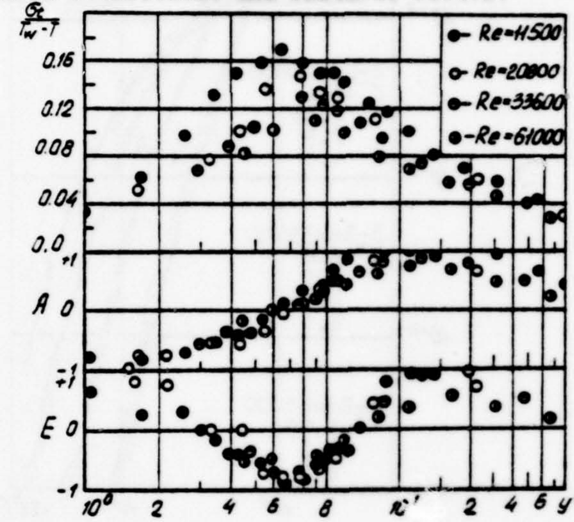

Fig.13 Distribution of temperature fluctuations intensity and skewness and flatness factors

In a viscous sublayer the skewness coefficient is negative and grows when approaching the wall, showing that a drastic penetration of cooled moles of liquid from the outer region of flow is observed. The amplitude of temperature pulsations caused by the penetration of the coldest liquid portions from the free stream is several times as much as that of hot bursts from the wall. Over the region of maximum temperature pulsation intensity, where the average temperature approximately equals $0.5 \cdot (T_w - T_o)$, the skewness coefficient changes its sign. It points to the appearance of hot bursts out of the sublayer whose amplitude exceeds that of temperature pulsations penetrating from the free stream. Spectra and autocorrelation functions were measured at various Reynolds numbers and different distances from wall beginning with 0.03 mm. The calculations results show that within a viscous sublayer $y^+ = 6$ spectra are essentially independent of the coordinate, Fig.14. Since the temperature pulsations in a turbulent flow are primarily caused by velocity pulsations, from the spectral uniformity of temperature pulsations in the viscous sublayer certain concepts on the sublayer structure given in (26,27) follow. According to this model the motion in sublayer takes the form of mutually independent perturbations with the same spectra, and the velocity distribution in a viscous sublayer is determined by linear equations.

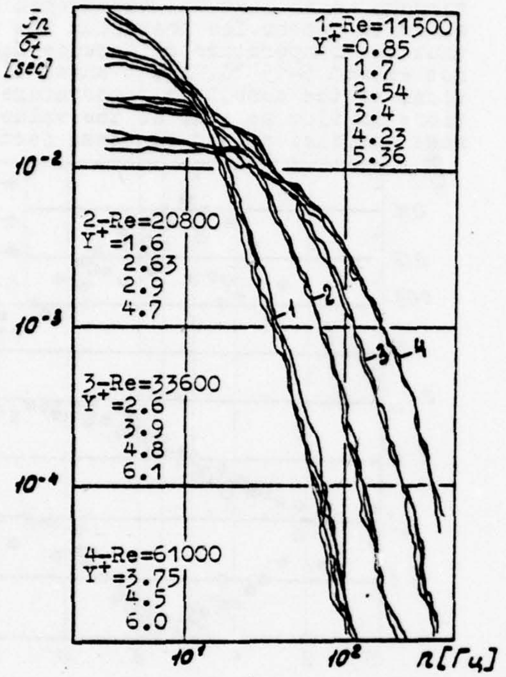

Fig.14 Spectral densities of temperature fluctuations in viscous sublayer

The distribution of the spectra outside the viscous sublayer ($y^+ \leqslant 6$) shows greater dependence on the y-coordinate. With an increase in y, still higher-frequency components appear in the spectra. If the given spectra are represented as a function of the wave number $k=2\pi f/u$, where u is the averaged local velocity value, then the spectral curves obtained are well grouped around one curve. Thus, outside the viscous sublayer the Tailor hypothesis on "frozen" turbulence for the temperature and velocity fields can be used.

4. The Effect of Polymer Additives

The study of near-wall turbulence of water with small additives of high polymers is very difficult. The generation of abnormal signals, low values of heat-transfer coefficients, variations in readings with time made a hot-wire anemometer impractical for this purpose. At the same time the stroboscopic flow visualization method enabled us to examine the profiles of mean velocity, the intensity of stream-wise and normal pulsations, the probability density of pulsations, the spatial correlations of streamwise velocity component and some other characteristics. The results of these studies are given in detail in (2,28-31). The experiments performed have shown that the influence of high polymer additives is not restricted to a narrow near-wall zone but extends into a major part of the channel. In this case the buffer zone where the molecular and turbulent viscosities are commensurable in value significantly grows in size. At water flow with most efficient additives in small-size channels this zone can extend into almost the whole of channel cross section. The streamwise velocity pulsations referred to the local mean velocity in water and dilute solutions of high polymers vary insignificantly and normalized by v_*^2 may be even somewhat higher (polyacrylamide solution Fig.15). At the same time polymer additives greatly reduce the RMS pulsations of normal to the surface velocities components.

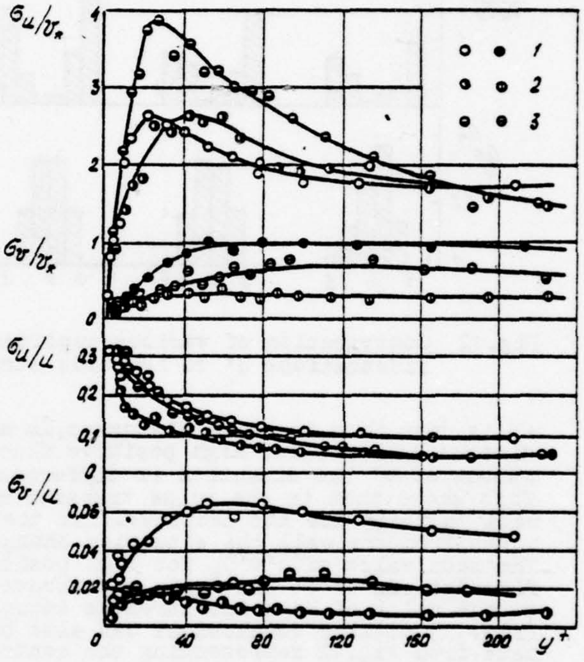

Fig.15 RMS velocity fluctuations in dilute solutions of polymers

1-water, Re=34 500; 2-polyethylene oxide solution, Re=2700, ζ/ζ_o=0.23; 3-polyacrylamide solution, Re=18 300, ζ/ζ_o=0.35

This reduction is observed both for the mean local velocity and the dynamic one. A decrease in σ_w is somewhat below that in σ_v. This can readily be seen in Fig.16.

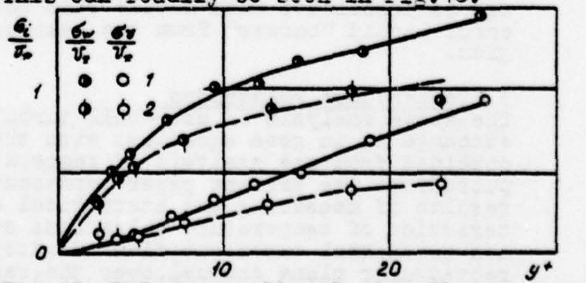

Fig.16 RMS near-wall velocity fluctuations 1-water, 2-polyacrylamide solution

One should take into consideration that the data of this figure refer to the flow of dilute solution undergone great destruction in a loop,when the drag reduction was equal only to 20%.Of considerable interest in a turbulent flow of polymer solutions are the double correlations $\overline{u'v'}$.They were defined both for a fresh solution of polyethylene oxide and for that after destruction.The experimental results are shown in Figs.17 and 18.

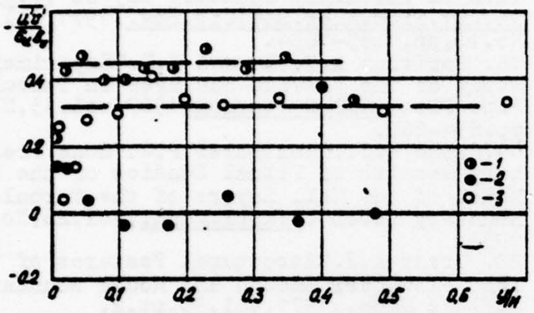

Fig.17 Double-correlation coefficients of velocity fluctuations

1-water;2-polyethylene oxide solution;3-the same after destruction

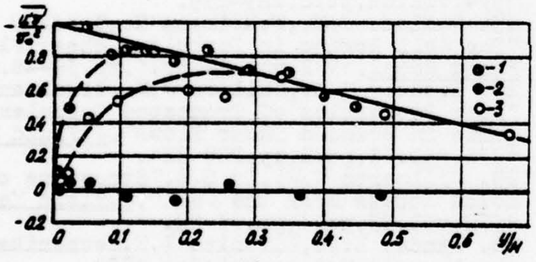

Fig.18 Reynolds stresses (notations as in Fig.17).

For the solution of polyethylene oxide destructed so that the velocity profile differs from the universal one insignificantly and the effect of drag reduction is small,the correlation coefficients $\overline{u'v'}/\sigma_u\sigma_v$ are close to the proper values for the water flow.In this case the drag coefficient at y/H >0.3 follows the relation $\tau/\tau_w=1-y/H$. For a fresh solution of polyethylene oxide over the total cross section the values $\overline{u'v'}/\sigma_u\sigma_v$ and $\overline{u'v'}/v_*^2$ are very small and outside the viscous sublayer the total shear stress $\tau=\tau_w(1-y/H)$ greatly exceeds the sum of viscous and Reynolds stresses.This experimental result shows that the Reynolds equations and hence Navie-Stokes ones do not describe the turbulent flow of dilute high polymer solutions even in the case when the solution viscosity is essentially the same as the water one and it does not vary with shear velocity(e.g. the examined solution of polyethylene oxide).Although we consider the obtained experimental result as the first direct evidence that the flow of dilute high polymer solutions does not obey the Navie-Stokes equation,this conclusion itself is not quite unexpected.These equations do not take into account the specific features of dilute high polymer solutions and primarily their elastic properties. The application of a simple rheological Maxwell equation with one characteristic relaxation time may qualitatively account for the effects observed in the experiments(2,32,33). The analysis of Reynolds stresses carried out in the same manner as for water shows, that with polymer additives the relative part of instantaneous values of u'v' products, whose pulsations have different signs (I and III in Fig.19)decreases.

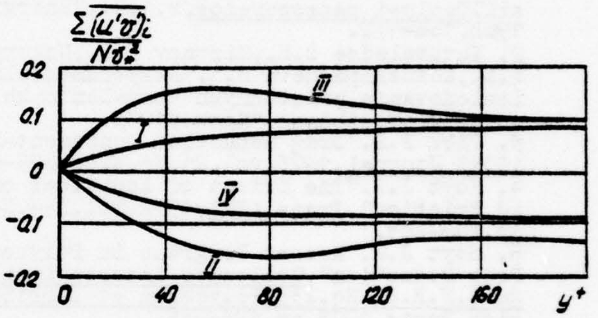

Fig.20 Contribution of various-types of motion to Reynolds stresses for polyethylene oxide dilute solution (I,II, III,IV as in Fig.8)

At the same time these values comprise bursts of decelerating liquid from the wall and break of liquid to the near-wall region of flow at larger than averaged velocities.As it has been noted earlier,just these processes mostly contribute to the value of Reynolds stresses.As a result,the Reynolds stresses associated with u'and v' pulsations of different and the same signs have been found to be rather close.(Fig.20).

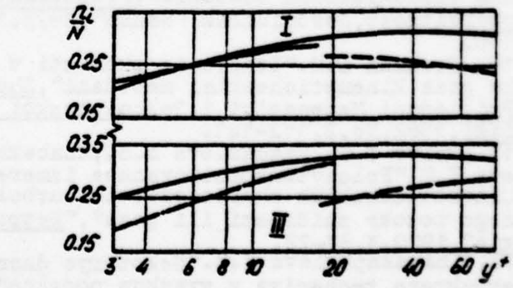

Fig.19 Probability of I and III types of motion. —— water;— — polyethylene oxide dilute solution;—·—·— polyacrylamide dilute solution

The reduction of "bursts" frequency results in the increase of macroscale of near-wall turbulence.This is also supported by the analysis of autocorrelation function of temperature pulsations (6).The decrease in the intensity of normal-to wall velocity pulsations and double-correlation coefficients,the increase in the time macroscale of turbulence at the outer boundary of viscous sublayer,i.e. a decrease in the intensity and frequency of bursts-all this results in decrease of turbulent energy generation in water with small polymer additives.

REFERENCES

1. Khabakhpasheva E.M.,Perepelitsa B.V.,Mikhailova E.S.,Orlov V.V.,Karsten V.M.,Efimenko G.I."Metodika i resultaty issledovaniy niya pristennoi turbulentnosti v usloviyakh teploobmena i povyshennogo urovnya pulsatsii".Teplo-i massoperenos,t.1,M.,"Energia", 1968,166-172.
2. Kutateladze S.S.,Mironov B.P.,Nakoryakov V.E.,Khabakhpasheva E.M."Eksperimentalnoe issledovanie pristennykh turbulentnykh techenii",Novosibirsk,"Nauka",1975.
3. Virk P.S."Drag Reduction Fundamentals", AIChE Journal,1975,vol.21,No.4,pp.625-636.
4. Hoyt J.W."The Effect of Additives on Fluid Friction",Trans.ASME,1972,vol.D94,No.2, pp.258-285.
5. Hoyt J.W."Recent Progress in Polymer Drag Reduction",Colloques internationaux du C.N.R.S. No.233,Polyméres et lubrification,Paris,1975,pp.193-215.
6. Khabakhpasheva E.M."Polymers and Turbulent Drag Reduction",Colloques internationaux du C.N.R.S. No.233,Polyméres et lubrification,Paris,1975,pp.217-224.
7. Orlov V.V.,Fedoruk Yu.M."Generator Tsuga svetovykh vspyshek bolshoi yarkosti dlya hydrodynamitcheskikh issledovanii",Teplophysika vysokikh temperatur,1968,No.4,764-766.
8. Orlov V.V."Experimentalnoe izuchenie pristennoi turbulentnosti v kanale",Zhurnal Prikladnoi Matematiki·i Tekhnicheskoi Phyziki,1966,No.4,124-126.
9. Orlov V.V. "Izmerenie kinematicheskikh characteristic turbulentnykh potokov metodom vizualizatsii techenia",Pristennaya turbulentnost,Novosibirsk,"Nauka",1973,180-190.
10. Trokhan A.M."Izmerenie skorosti v potoke gaza kinematicheskimi metodami",Zhurnal Prikladnoi Matematiki i Tekhnicheskoi Phyziki,1962,No.2,112-121.
11. Orlov V.V.,Mikhailova E.S.,Khabakhpasheva E.M."Poluavtomatizirovannoe izmerenie kinematicheskikh characteristik turbulentnogo potoka zhidkosti ili gaza","Metrologia",1970,3,67-72.
12. Khabakhpasheva E.M."Nekotorye dannye o strukture techeniya v vyazkom podsloe",Problemy teplophyziki i phyzicheskoi hydrodynamiki,Novosibirsk,"Nauka",1974,223-234.
13. Khabakhpasheva E.M.,Mikhailova E.S.Experimentalnoe issledovanie structury pristennoi turbulentnosti i vyazkogo podsloya. Novosibirsk,Institute of Thermal Physics, Siberian Branch of the USSR Ac.Sci.,1976, 33-57.
14. Kline S.J.,Reynolds W.C.,Schraub F.A., Runstadler P.W."The Structure of Turbulent Boundary Layers",J.Fluid Mech.,1967,vol.30, No.4,pp.741-743.
15. Kim H.T.,Kline S.J.,Reynolds W.C."The Production of Turbulence Near a Smooth Wall in a Turbulent Boundary Layer",J.Fluid Mech. 1971,vol.50,No.1,pp133-160.
16. Corino E.R.,Brodkey R.S."A Visual Investigation of the Wall Region in Turbulent Flow",J.Fluid Mech.1969,vol.37,No.1,pp.1-30.
17. Clark J.A.,Markland E."Flow Visualization in Turbulent Boundary Layers",J.Hydraul.Div.Proc.Amer.Soc.Civ.Eng.,1971,vol.97, No.10,pp.1653-1654.
18. Popivich A.T.,Hummel R.L."Experimental Study of the Viscous Sublayer in Turbulent Pipe Flow",AIChE Journal,1967,vol.13,No.5, pp.854-860.
19.Kline S.J.,Runstadler P.W."Some Preliminary Results of Visual Studies of the Flow Model of the Wall Layers of the Turbulent Boundary Layer",J.Appl.Mech.,vol.26,No.2, 1959.
20. Grass A.J."Structural Features of Turbulent Flow Over Smooth and Rough Boundaries", J.Fluid Mech.,1971,vol.50,pt.2.
21. Nychas S.J.,Hershey H.C.,Brodkey R.S."A Visual Study of Turbulent Shear Flow",J.Fluid Mech.,1973,vol.61,pt.3,pp.513-540.
22. Offen G.R.,Kline S.J."Combined Dye-streak and Hydrogen-bubble Visual Observations of a Turbulent Boundary Layer",J.Fluid Mech. 1974,vol.62,pt.2,223-239.
23. Wallace J.M.,Eckelmann H.,Brodkey R.S. "The Wall Region in Turbulent Shear Flow",J. Fluid Mech.,1972,vol.54,pt.1,pp.39-48.
24. Brodkey R.S.,Wallace J.M.,Eckelmann H. "Some Properties of Truncated Turbulence Signals in Bounded Shear Flows",J.Fluid Mech., 1974,vol.63,pt.2,pp.209-224.
25. Willmarth W.W.,Lu S.S."Structure of Reynolds Stress Near the Wall",J.Fluid Mech., 1972,vol.55,pt.1,pp.65-92.
26. Landau L.D.,Lifshits E.M.Mechanika sploshnykh sred.M.Gostekhizdat,1954.
27. Levich V.G.Phyziko-chimicheskaya hydrodinamika,M.Phyzmatgiz,1959.
28. Khabakhpasheva E.M.,Perepelitsa B.V."Polya skorostei i turbulentnykh pulsatsii pri malykh dobavkakh k vode vysokomoleculyarnykh vestchestv",In.Ph.Zh.,1968,t.14,No.4,598-601.
29. Khabakhpasheva E.M.,Perepelitsa B.V."Ob osobennosti pristennoi turbulentnosti v potokakh vody s vysokomoleculyarnymi dobavkami" In.-Ph.Zh.,1970,t.18,No.6,1094-1097.
30. Khabakhpasheva E.M.,Popov V.I.,Perepelitsa B.V."Heat Transfer in Viscoelastic Fluids",Proc.IV Intern.Heat Transfer Conference, Versailles,1970,vol.IV,Hn.2.
31. Khabakhpasheva E.M.,Perepelitsa B.V."Teploobmen pri turbulentnom techenii slabykh rastvorov vysokopolymerov",Teplo- i massoobmen,M.,"Energia",1972,t.3.
32. Pavlovsky V.A. "K voprosu o teoreticheskom opisanii slabykh vodnykh rastvorov polymerov".Dok.Akad.Nauk SSSR,1971,No.4,809-812.
33.Gorodtsov V.A.,Leonov A.I."Opisanie snizheniya soprotivleniya turbulentnogo treniya v uprugovyazkikh zhidkostyakh".,In.-Ph.Zh., 1973,t.25,No.6,1081-1089.

ASYMPTOTIC CORRELATIONAL MODELLING OF INHOMOGENEOUS TURBULENCE

B.A.Kolovandin

The Luikov Heat and Mass Transfer Institute,Minsk,USSR

ABSTRACT

The paper is concerned with the problem of universal (in the sense of the turbulent Reynolds number) and invariant (with respect to the form of a velocity field) description of inhomogeneous turbulence by means of a finite set of differential model equations for the *statistical moments*. The aim of the paper is to draw attention of constructors and users of correlational turbulence models to a principal obstacle to universal correlational description of turbulent flows. An approximate mathematically formalized technique which makes it possible to determine, in a straightforward manner, the unknown gradient-type moments included into the differential correlation equations is presented. A correlational model of inhomogeneous velocity field which conforms with the requirements of tensor invariance and, under author's supposition, invariance in the sense of the form of the turbulent velocity field is constructed. From the model a finite "closed" set of differential model moment equations referring to large-scale turbulence is generated. The invariance of the model with regard to the form of the tur*bulent velocity field* is demonstrated for different shear flows.

NOMENCLATURE

ℓu - scale of length of the turbulent field;

P - mean pressure;

p - pressure fluctuation;

$\overline{q^2} = \overline{u_i^2}$ - double kinetic energy of turbulence;

$\overline{u_i u_j'}$ - two-point velocity correlation;

u_i - components of velocity fluctuations;

U_i - ensemble averaged (mean) velocity components ($i=1,2,3$);

x_i - Cartesian coordinates;

x_1 - direction of mean flow;

x_2 - direction perpendicular to the mean flow;

$\xi_k=(x_k)_B-(x_k)_A$ - components of vector radius between A and B points;

ν - kinematic viscosity coefficient.

SUBSCRIPTS

, - denotes the covariant derivative with respect to x_i .

SUPERSCRIPTS

, - denotes the derivative in the ξ-space;

' - refers to B-point;

x - denotes the homogeneity of the turbulence.

NECESSARY CONDITIONS OF CORRELATIONAL MODELLING OF INHOMOGENEOUS TURBULENCE

Within the last decennia there have appeared numbers of papers on modelling of inhomogeneous turbulence based on the finite set of differential equations for the one-point statistical moments

$$U_{i,i} = 0 \tag{1}$$

$$\dot{U}_i + U_k \cdot U_{i,k} + (\overline{u_i u_k})_{,k} + P_{,i} - \nu U_{i,kk} = 0 \tag{2}$$

$$\dot{\overline{u_i u_j}} + U_k \cdot (\overline{u_i u_j})_{,k} + \overline{u_i u_k} \cdot U_{j,k} + \overline{u_j u_k} \cdot U_{i,k} + (\overline{u_i u_j u_k})_{,k} + \overline{u_i p}_{,j} + \overline{u_j p}_{,i} + 2\nu \overline{u_{i,k} u_{j,k}} - \nu(\overline{u_i u_j})_{,kk} = 0 \tag{3}$$

$$\dot{\overline{u_iu_ju_k}}+U_\ell\cdot(\overline{u_iu_ju_k})_{,\ell}+\overline{u_iu_ju_\ell}\cdot U_{k,\ell}+$$

$$+\overline{u_ju_ku_\ell}\cdot U_{i,\ell}+\overline{u_iu_ku_\ell}\cdot U_{j,\ell}+(\overline{u_iu_ju_ku_\ell})_{,\ell}-$$

$$-\overline{u_iu_j}\cdot(\overline{u_ku_\ell})_{,\ell}-\overline{u_iu_k}\cdot(\overline{u_ju_\ell})_{,\ell}-\overline{u_ju_k}\cdot(\overline{u_iu_\ell})_{,\ell}+$$

$$+\overline{u_iu_jp}_{,k}+\overline{u_ju_kp}_{,i}+\overline{u_iu_kp}_{,j},+2\nu(\overline{u_iu_{j,\ell}u_{k,\ell}}+$$

$$+\overline{u_ju_{i,\ell}u_{k,\ell}}+\overline{u_ku_{j,\ell}u_{i,\ell}})-\nu(\overline{u_iu_ju_k})_{,kk}=0$$

etc, (4)

where the tensor notation is employed.

For this set of equations to be closed, different authors introduce additional relations between the known and unknown moments. This is the way in which the finite set of closed modelling equations for the one-point statistical moments, i.e. the mathematical turbulence model in the correlational formulation is obtained. And any one of these models, by whatever way it is obtained, should satisfy some set of appropriate conditions which in particular involve: invariance with respect to the Galilean transformation, tensor invariance and invariance with respect to the form of the turbulent velocity field. The first two of these are obvious and typical of the known workable correlational models of turbulence. The third condition means that there should be the same degree of accuracy with which the turbulence model describes the statistical moments of the turbulent velocity field of any form, starting from the simplest one, which defines the decay of homogeneous and isotropic turbulence, to that which defines the shear turbulent flow of a certain complexity. It is quite evident that any correlational model of inhomogeneous turbulence, which claims to be classified as theory, should satisfy this necessary (though insufficient) conditions. As to the set of sufficient conditions, it should be specified by the complexity of that shear flow which is the most complex in the ierarchy of turbulent flows being described by this model. It should be kept in mind here that the degree of complexity of the most complex flow, among those considered, should be limited, since the finite set of equations for the moments cannot in principle provide complete statistical description of turbulent velocity field.

COMPLETENESS OF THE SET OF MODELLING EQUATIONS AND THE PROBLEM OF UNIVERSALITY OF THE MODEL WITH RESPECT TO THE TURBULENT REYNOLDS NUMBER

Proceeding from the third condition of invariance, the connection can be shown between the problem of universality with respect to the turbulent Reynolds number $R_\ell = \sqrt{q^2}\ell_u/\nu$ and the order of the highest moment described by the differential equation. Obviously, at homogeneous turbulence the set of equations (2)-(4), etc. transforms to the set of equations involving

- equation for the kinetic energy of turbulence $E=\overline{u_i^2}/2\equiv\overline{q^2}/2$

$$\dot{E}+\epsilon_u^x=0\,, \qquad (5)$$

where $\epsilon_u=\nu u_{i,k}u_{i,k}\equiv\nu E_{,kk}/2+\nu D_u$ is the dissipative function, $\overline{u_iu_j'}$ is the two-point correlation, $D_u=|(-\overline{u_iu_i'})^{,kk}|(\vec{\xi}=0)$ is the vorticity function,

- equation for the dissipative function etc

$$\dot{\epsilon}_u^x+F_u^x\cdot\epsilon_u^{x2}/2E=0, \qquad (6)$$

etc.,
where

$$F_u^x=14(S_\nu+S_u)/3(15\nu\epsilon_u^x)^{1/2},$$

$$S_\nu=-6(15\nu)^{1/2}\cdot|(D_{ii}')^{,kk}|(\vec{\xi}=0)/7D_u^{3/2},$$

$$S_u=-6(15\nu)^{1/2}\cdot|(D_{iki}')^{,k}|(\vec{\xi}=0)/7D_u^{3/2},$$

$$D_{ii'}=(-\overline{u_iu_i'})_{,kk},$$

$$D_{iki'}=(-\overline{u_iu_ku_i'})^{,kk}$$

and the superscript "x" refers to homogeneous turbulence so that $\epsilon_u^x=\nu D_u$.

Universality of the set of equations (5)-(6) in the sense of R_ℓ is "concealed" in the unknown function F_u^x the inertia part of which defines the non-linear interaction between the vortices of various scales ℓ_u. By the use of invariant relations of Loitsyansky |1| and Saffman |2| it can be easily shown that F_u^x may be a constant only at $R_\ell \ll 1$ and $R_\ell \gg 1$ which correspond, at the finite values of E, to small-scale and large-scale turbulence, namely

$$\lim_{R_\ell\to 0} F_u^x \to 14/5\,,$$

$$\lim_{R_\ell\to\infty} F_u^x \to 11/3 \qquad (7)$$

In the first case, $R_\ell \ll 1$, the characteristic turbulence scale is the Taylor microscale of turbulence

$$\ell_u^2 \equiv \lambda_u^2 = 10E/D_u, \qquad (8)$$

while in the second, $R_\ell >> 1$, the Taylor macroscale of turbulence

$$\ell_u \equiv L_u = 10(2)^{1/2} \cdot E^{3/2} / \nu D_u. \qquad (9)$$

Thus, any second-order correlational model satisfying the necessary condition of invariance with respect to the form of the field cannot claim of being able to universally describe turbulence in the sense of different turbulence scales since it cannot be closed for any value of R_ℓ. Applied to the wall flow it means that the second-order model fails to describe the whole region of the flow, from the wall to the outer boundary. In other words, the second-order model can be only asymptotical one, i.e. applicable either to very small-scale or very large-scale turbulence. Unfortunately, plenty of papers keeps appearing at present where the authors attempt to make use of the second-order model to describe the turbulent wall flows not containing any hint of its inapplicability in principle.

PROCEDURE OF UNKNOWN MOMENTS MODELLING

As far as the author is awarw, at present there are two methods of modelling the unknown gradient-type terms involved in the equations for the moments. One of them, the method of "physical modelling", pioneered by Kolmogorov |3|, postulates that the "work" of different unknown terms is to be considered on the basis of physical concepts and dimensional analysis. Thus, it presupposes separate consideration of each of the unknown terms. The main drawback of this method is connected to the absence of a clear physical meaning of the greater part of unknown terms and especially of the high-order moments. It is plain that for the success to be achieved with the method of physical modelling the author should possess intuition verging on art. The second, the method of "mathematical formalization" of unknown moments, whose originator seems to be Chou |4|, presupposes some formal transformation of the unknown moments which makes it possible to universally model any of the unknown moments irrespective of its order and physical meaning. An alternative† of such a method is the technique of modelling two-point moments set forth in a crude form by the author and Vatutin |5|. This technique envisages preliminary kinematic transformation of the unknown gradient-type moments with the use of the Burges variables which makes it possible to universally model any transformed moment. Thus, the second-order tensor of the dissipative function in equation (3) for the second moment $\overline{u_i u_j}$ is transformed as

$$\epsilon_u^{ij} \equiv \nu \overline{u_{i,k} u_{j,k}} = \bar{\bar{F}}_{ij}^{(1)} + \bar{\bar{F}}_{ij}^{(2)}$$

where $\bar{\bar{F}}_{ij}^{(1)} = \nu(\overline{u_i u_j})_{,kk}/4$ is the function defining "strong" inhomogeneity of the unknown moment ϵ_u^{ij}; $\bar{\bar{F}}_{ij}^{(2)} = \nu|(-\overline{u_i u_j'})_{,kk}|(\vec{\xi}=0)$ is the function which defines in general the properties of the unknown moment in homogeneous turbulence.

The function $\bar{\bar{F}}_{ij}^{(1)}$ is determined by equation (3) while for $\bar{\bar{F}}_{ij}^{(2)}$ it is sufficient to know the two-point correlation $u_i u_j'$ for two adjacent points, i.e. at $\xi_i^2/\ell_u^2 << 1$. Since turbulence between the two nearby points can be treated as quasi-homogeneous, the two-point correlation may be presented as

$$\overline{u_i u_j'} = H_{ij'} + N_{ij'}$$

where $H_{ij'}$ is the homogeneous two-point correlation, $N_{ij'}$ is the correcting function modelling the properties of "weak" inhomogeneity. Homogeneous two-point correlational tensors of any rank are determined here through the medium of Robertson's theory of invariants |7| by formally replacing all the "isotropic" invariants involved into the considered correlational tensor with the corresponding homogeneous invariants. Then the functions $H_{ij'}$ and $N_{ij'}$ are expanded into the Taylor power series with the part of the expansion factors being determined from the conditions of incompressibility. Omitting intermediate manipulations we shall write a set of modelling quasi-homogeneous correlations for nearby points in the form

$$\overline{u_i p'} = \{h_{20}^{(1)}(K_{ij} - \delta_{ij}) + h_{2\ell\ell}^{(1)} \cdot |2K_{mn} \cdot \xi_m \cdot \xi_n \times$$

$$\times \delta_{ij}/5 - \xi_\ell^2 (K_{ij} - 3\delta_{ij}/5|/3\} + (n_{10}^{(1)} +$$

$$+ n_{1\ell m}^{(1)} \cdot \xi_\ell \xi_m + \ldots) K_{ip} + \ldots,$$

$$\overline{u_i u_j'} = \{\bar{q}^2 |(1 - \xi_s^2 D_u/5\bar{q}^2) K_{ij} + (1-4c)\xi_i \xi_j \times$$

$$\times D_u/10\bar{q}^2 + c(K_{ik}\xi_k \xi_j + K_{jk}\xi_k \xi_i) D_u/5\bar{q}^2|\} + \ldots,$$

$$\overline{u_i u_j u_k'} = \{(-D'^{m}_{mnn'})(\vec{\xi}=0)|\xi_s^2 K_{ij} + K_{im}\xi_m \xi_j +$$

$$+ K_{jm}\xi_m \xi_j)\xi_k - 5\xi_s^2 (K_{ik}\xi_j + K_{jk}\xi_i)/2|\} +$$

$$+ (n_{10}^{(3)} + n_{1\ell m}^{(3)} \xi_\ell \xi_m + \ldots) K_{ijk} + \ldots$$

and so on,

---

† Recently Lumley |6| has developed a promising version of the method based on the so-called "functional expansion" of unknown gradient-type moments.

where

$$K_{ip}=3^{3/2}\overline{u_ip}/(\bar{q}^2)^{3/2},\qquad K_{ij}=3\overline{u_iu_j}/\bar{q}^2,$$

$$K_{ijk}=3^{3/2}\overline{u_iu_ju_k}/(\bar{q}^2)^{3/2}.$$

Thus, the unknown gradient-type moments are being modelled as follows

$$\bar{\bar{F}}_{ij\ldots k}=\bar{\bar{F}}^{(1)}_{ij\ldots k}+\phi^{(2)}(\overline{u_iu_j\cdots u_k},\ldots,\bar{q}^2,\ell_u) \tag{10}$$

where the scale ℓ_u is defined by (8) or (9) depending on which turbulence scale region determines the particular unknown moment of the gradient type $\bar{\bar{F}}_{ij\ldots k}$.

THE THIRD-ORDER MODEL OF INHOMOGENEOUS VELOCITY FIELD

Using modelling relations (10) one may construct the following moment model of inhomogeneous velocity field which satisfies the above conditions of invariance

$$\dot{\overline{u_iu_j}}+U_k\cdot(\overline{u_iu_j})_{,k}+\overline{u_iu_k}\cdot U_{j,k}+\overline{u_ju_k}\cdot U_{i,k}+(\overline{u_iu_ju_k})_{,k}+|(\overline{u_ip})_{,j}+(\overline{u_jp})_{,i}|/2+2\bar{h}^{(1)}\times$$
$$\times\,\nu D_u(3\overline{u_iu_j}/\bar{q}^2-\delta_{ij})+2\nu D_u'|6(3-2c)\overline{u_iu_j}/\bar{q}^2+(4c-1)\delta_{ij}|/15-(\nu/2)(\overline{u_iu_j})_{,kk}=0, \tag{11}$$

$$\dot{\overline{u_iu_ju_k}}+U_\ell\cdot(\overline{u_iu_ju_k})_{,\ell}+\overline{u_iu_ju_\ell}\cdot U_{k,\ell}+\overline{u_ju_ku_\ell}\cdot U_{i,\ell}+\overline{u_iu_ku_\ell}\cdot U_{j,\ell}+(\overline{u_iu_ju_ku_\ell})_{,\ell}-$$
$$-\overline{u_iu_j}\cdot(\overline{u_ku_\ell})_{,\ell}-\overline{u_iu_k}\cdot(\overline{u_ju_\ell})_{,\ell}-\overline{u_ju_k}\cdot(\overline{u_iu_\ell})_{,\ell}+|(\overline{u_iu_kp})_{,j}+(\overline{u_ju_kp})_{,i}+(\overline{u_iu_jp})_{,k}|/2-$$
$$-3\tilde{n}^{(3)}_{\ell\ell}\cdot D_u\cdot\overline{u_iu_ju_k}/\bar{q}^2-(\nu/4)\cdot(\overline{u_iu_ju_k})_{,\ell\ell}=0, \tag{12}$$

$$\dot{D}_u+U_k\cdot D_{u,k}+2D_u|6(3-4c)\overline{u_iu_k}/\bar{q}^2+4(2c+1)\times$$
$$\times\,\delta_{ik}|\cdot U_{i,k}/15-(2U_{i,k\ell\ell}\cdot\overline{u_iu_k}+U_{k,\ell\ell}\cdot\bar{q}^2{}_{,k})/4-$$
$$-|D_u(\tilde{n}^{(3)}_{\ell\ell}\cdot\overline{u_iu_iu_k}+\tilde{n}^{(1)}\cdot\overline{u_kp})/\bar{q}^2|_{,k}+$$
$$+F^{x}_u\cdot\nu D_u^2/\bar{q}^2-(\nu/2)\cdot D_{u,kk}=0, \tag{13}$$

$$(\overline{u_ip})_{,kk}+4U_{m,n}(\overline{u_iu_n})_{,m}+(\overline{u_iu_mu_n})_{,mn}+$$
$$+D_u(\tilde{n}^{(3)}_{mn}\cdot\overline{u_iu_mu_n}+\tilde{n}^{(1)}\overline{u_ip})/\bar{q}^2+$$
$$+\bar{h}^{(1)}\cdot\nu\cdot|D_u(3\overline{u_iu_k}/\bar{q}^2-\delta_{ik})|_{,k}=0, \tag{14}$$

$$(\overline{u_iu_jp})_{,kk}+4U_{m,n}\cdot(\overline{u_iu_ju_n})_{,m}+$$
$$+(\overline{u_iu_ju_mu_n}-\overline{u_iu_j}\cdot\overline{u_mu_n})_{,mn}=0 \tag{15}$$

where $c,\bar{h}^{(1)},\tilde{n}^{(1)},\tilde{n}^{(3)}_{k\ell}$ are unknown dimensionless factors.

The above third-order model can be closed accurate to the function $\bar{\bar{F}}^{x}_u(R_\lambda)$ being defined by homogeneous and anisotropic turbulence. Its analytical definition in the framework of the third-order model can be fulfilled for small values of the turbulent Reynolds number ($0<R_\lambda\leq 10$) for instance by the Deissler analysis |8|. This analysis is inapplicable, however, for moderate and high values of R_λ. The author and his colleagues |9| have made an attempt, therefore, to directly measure the moments S_ν and S_u in nearly nondecaying homogeneous turbulence realized in a wind tunnel. The experimental results indicate thus that within $60<R_\lambda<120$ the quantity F^{x}_u is a strongly varying function of R_λ asymptotically approaching the value given in (7) at $R_\lambda\gg 1$. Unfortunately, the range $0<R_\lambda<60$ has turned to be inaccessible for the present experiment. Until the function $F^{x}_u(R_\lambda)$ remains unknown for the arbitrary values of R_λ, the above third-order model cannot claim to be universal in the sense of R_λ.

ASYMPTOTIC MODEL OF THE LARGE-SCALE INHOMOGENEOUS VELOCITY FIELD

By estimating the order of values of different terms in modelling equations (11)-(15) and postulating the hypothesis of quasinormality to be valid† at $R_L\gg 1$, one may obtain an asymptotic model of the large-scale inhomogeneous velocity field. As was noted above, incorporation in the asymptotic model of the differential equations for the third and higher moments is incorrect. Therefore, for the third moments to be defined, we

---

† Since the validity of the hypothesis at $R_\lambda\ll 1$ is questionable, at present the author has a conservative attitude towards the possibility of constructing the model of small-scale turbulence using eqs.(11)-(15).

resort to the so-called equilibrium equations obtainable from differential equation (12) when only diffusion and dissipation terms are retained.

To be specific, we shall write down the asymptotic modelling equations in the approach of a two-dimension stationary boundary layer

$$U_1.U_{1,1}+U_2.U_{1,2}+(\overline{u_1u_2})_{,2}+(\bar{u}_1^2-\bar{u}_2^2)_{,1}+$$
$$+P_{,1}-\nu.U_{1,22}=0\ , \qquad (16)$$

$$U_1.(\overline{u_1u_2})_{,}+U_2.(\overline{u_1u_2})_{,2}+\bar{u}_2^2.U_{1,2}+|e+4(3-$$
$$2c)|\Phi_u.\overline{u_1u_2}/\bar{q}^2+(\overline{u_1u_2^2}+\overline{u_1p}/2)_{,2}=0,$$

$$U_1.(\overline{u_1u_3})_{,1}+U_2.(\overline{u_1u_3})_{,2}+|e+4(3-2c)|\ x$$
$$x\ \Phi_u.\overline{u_1u_3}/\bar{q}^2+(\overline{u_1u_2u_3})_{,2}=0 \qquad (17)$$

$$U_1.(\overline{u_2u_3})_{,1}+U_2.(\overline{u_2u_3})_{,2}+|e+4(3-2c)|\ x$$
$$x\ \Phi_u.\overline{u_2u_3}/\bar{q}^2+(\overline{u_3u_2^2}+\overline{u_3p}/2)_{,2}=0\ ,$$

$$U_1.(\bar{u}_2^2)_{,1}+U_2.(\bar{u}_2^2)_{,2}+\{|e+4(3-2c)|\ x$$
$$x\ \bar{u}_2^2/\bar{q}^2-|e+2(1-4c)|/3\}\Phi_u+(\bar{u}_2^3-$$
$$-\overline{u_2p})_{,2}=0,$$

$$U_1.(\bar{u}_1^2)_{,1}+U_2.(\bar{u}_1^2)_{,2}+2\overline{u_1u_2}.U_{1,2}+$$
$$+\{|e+4(3-2c)|.\bar{u}_1^2/\bar{q}^2-|e+2(1-4c)|/3\}+$$
$$+(\overline{u_2u_1^2})_{,2}=0, \qquad (18)$$

$$U_1.(\bar{u}_3^2)_{,1}+U_2.(\bar{u}_3^2)_{,2}+\{|e+4(3-2c)|\ x$$
$$x\ \bar{u}_3^2/\bar{q}^2-|e+2(1-4c)|/3\}\Phi_u+(\overline{u_2u_3^2})_{,2}=0,$$

$$(19)$$

$$U_1.\Phi_{u,1}+U_2.\Phi_{u,2}+4(3-4c).\Phi_u.\overline{u_1u_2}.U_{1,2}/5\bar{q}^2+$$
$$+55\Phi_u^2/3\bar{q}^2-|\Phi_u.(\overline{u_2u_k^2}/15a+\tilde{n}^{(1)}.\overline{u_2p})/\bar{q}^2|_{,2}=$$
$$=0,$$

$$\overline{u_ku_2}.(\overline{u_iu_j})_{,2}+\overline{u_iu_2}(\overline{u_ju_k})_{,2}+\overline{u_ju_2}.(\overline{u_iu_k})_{,2}+$$
$$+|(\overline{u_iu_jp})_{,k}+(\overline{u_iu_kp})_{,j}+(\overline{u_ju_kp})_{,i}|/2-$$
$$-\Phi_u.\overline{u_iu_ju_k}/a\bar{q}^2=0,$$

$$\overline{u_ip}=-(\tilde{n}_{mn}^{(3)}/\tilde{n}^{(1)}).\overline{u_iu_mu_n}\ ,$$

$$(\overline{u_iu_jp})_{,2}=-2(\overline{u_iu_2}.\overline{u_ju_2})_{,2}$$

where $e=30\tilde{n}^{(1)}$, $a=1/15\tilde{n}_{ss}^{(3)}$, $\Phi_u=\bar{q}^{2\ 3/2}/L_u$.

By substituting the moments $\overline{u_ip}$ and $\overline{u_iu_jp}$ (for simplicity we assume $\tilde{n}_{ij}^{(3)}=\tilde{n}_o^{(3)}\delta_{ij}$) in the equations for the velocity moments we shall rewrite non-numbered equations of the above set as follows

$$U_1.(\overline{u_1u_2})_{,1}+U_2.(\overline{u_1u_2})_{,2}+\bar{u}_2^2.U_{1,2}+|e+4(3-$$
$$-2c)|.\Phi_u.\overline{u_1u_2}/\bar{q}^2+(\overline{u_1u_2^2}-b.\overline{u_1u_k^2})_{,2}=0, \qquad (20)$$

$$U_1.(\overline{u_2u_3})_{,1}+U_2.(\overline{u_2u_3})_{,2}+|e+4(3-2c)|\ x$$
$$x\ \Phi_u.\overline{u_2u_3}/\bar{q}^2+(\overline{u_3u_2^2}-b.\overline{u_3u_k^2})_{,2}=0, \qquad (21)$$

$$U_1.(\bar{u}_2^2)_{,1}+U_2.(\bar{u}_2^2)_{,2}+\{|e+4(3-2c)|.\bar{u}_2^2/\bar{q}^2-$$
$$-|e+2(1-4c)|/3\}\Phi_u+(\bar{u}_2^3-2b\overline{u_2u_k^2})_{,2}=0, \qquad (22)$$

$$U_1.\Phi_{u,1}+U_2.\Phi_{u,2}+4(3-4c).\Phi_u.\overline{u_1u_2}.U_{1,2}/5\bar{q}^2+$$
$$+55\Phi_u^2/3\bar{q}^2-d|\Phi_u.\overline{u_2u_k^2}/\bar{q}^2|_{,2}=0, \qquad (23)$$

$$\bar{u}_1^3=3a.\bar{q}^2.\overline{u_1u_2}.(\bar{u}_2^2)_{,2}/\Phi_u, \qquad (24)$$

$$\overline{u_1u_2^2}=-a.\bar{q}^2.\overline{u_1u_2}.(\bar{u}_2^2)_{,2}/\Phi_u, \qquad (25)$$

$$\overline{u_1u_3^2}=a\bar{q}^2.|\overline{u_1u_2}(\bar{u}_3^2)_{,2}+2\overline{u_2u_3}.(\overline{u_1u_3})_{,2}|/\Phi_u, \qquad (26)$$

$$\bar{u}_2^3=-3a.\bar{q}^2.\bar{u}_2^2.(\bar{u}_2^2)_{,2}/\Phi_u, \qquad (27)$$

$$\overline{u_2u_1^2}=a.\bar{q}^2.\bar{u}_2^2.(\bar{u}_1^2)_{,2}/\Phi_u, \qquad (28)$$

$$\overline{u_2u_3^2}=a.\bar{q}^2.\bar{u}_2^2.(\bar{u}_3^2)_{,2}/\Phi_u, \qquad (29)$$

$$\overline{u_1u_2u_3}=a.\bar{q}^2.\bar{u}_2^2.(\overline{u_1u_3})_{,2}/\Phi_u, \qquad (30)$$

$$\overline{u_3u_2^2}=-a.\bar{q}^2.\overline{u_2u_3}.(\bar{u}_2^2)_{,2}/\Phi_u, \qquad (31)$$

$$\overline{u_3u_1^2}=a\bar{q}^2|\overline{u_2u_3}.(\bar{u}_1^2)_{,2}+2\overline{u_1u_2}.(\overline{u_1u_3})_{,2}|/\Phi_u\ , \qquad (32)$$

$$\bar{u}_3^3=3a.\bar{q}^2.\overline{u_2u_3}.(\bar{u}_3^2)_{,2}/\Phi_u, \qquad (33)$$

where $b=\tilde{n}_o^{(3)}/2\tilde{n}^{(1)}$, $d=\tilde{n}_{ss}^{(3)}-\tilde{n}_o^{(3)}$.

The set of equations (16)-(33) closed accurate to the unknown constants a,b,c,d, and e provides an approximate definition for the large-scale velocity field of inhomogeneous turbulent flows of the boundary-layer type.

EXAMPLES

A. Fully developed flat channel flow

At $P_{,1}$=const the equations for the moments are one-dimensional with the integral of equation (16) having the form

$$\overline{u_1u_2}=-v_*^2.(1-x_2/D),$$

where v_x is the friction velocity, D is the half-width of the channel. Assuming $\bar{u}_i^2=\bar{q}^2/3$ on the axis of the channel, the numerical values of the two unknown constants may be obtained: b=2, d=11/2.

For the set of the moment differential equations to be "splitted", we employ equilibrium approximation of equation (20)

$$U_{1,2}=-\varepsilon.\overline{u_1 u_2}.\Psi_u/\bar{u}_2^2 \qquad (34)$$

where $\Psi_u=|(e+12)/\varepsilon|\Phi_u/\bar{q}^2$,

$$\varepsilon=2(e+2)/3(e+12).$$

With account for the above, the system of dependable equations becomes

$$\bar{u}^2_{2,22}+(\bar{u}^2_{2,2}/\bar{u}^2_2-\Psi_{u,2}/\Psi_u)\bar{u}^2_{2,2}-(8\varepsilon/9\alpha)\ x$$

$$x\ \{|(1-3/2\varepsilon)-3(\bar{u}^2_2/E-\varepsilon)/8|.\varepsilon.E.\Psi_u^2/\bar{u}^2_2\ -$$

$$-\ (U_{1,2})^2/\varepsilon\}=0, \qquad (35)$$

$$E_{,22}+(\bar{u}^2_{2,2}/\bar{u}^2_2-\Psi_{u,2}/\Psi_u)E_{,2}-(13\varepsilon/9\alpha)\ x$$

$$x\ \{|(1-3/2\varepsilon)-6(\bar{u}^2_2/E-\varepsilon)/13|.\varepsilon.E.\Psi_u^2/\bar{u}^2_2\ -$$

$$-\ (U_{1,2})^2/\varepsilon\}=0, \qquad (36)$$

$$\Psi_{u,2}.(2\bar{u}^2_2-E)_{,2}=19.\Psi_u.(U_{1,2})^2/165\alpha, \qquad (37)$$

where $\alpha=-a(e+12)$.

Since the system of equations (35) - (37) is asymptotic, it is impossible to state the edge conditions on the both boundaries (with $x_2\to 0$, approximation of the large-scale turbulence is inapplicable). Therefore, the point $x_2=x_{2o}$ was chosen as an internal boundary, where equilibrium solution of equation (36) was fulfilled, i.e.

$$E_+^2=(1-y_o)^2/\varepsilon(1-3\varepsilon/2), \qquad (38)$$

where $E_+=E/v_x^2$, $y=x_2/D$.

Assuming a logarithmic velocity profile at the point $y=y_o$, i.e.

$$U_{+,y}(y_o)=1/\kappa y_o$$

we have

$$\sqrt{\Psi_{u+}}(y_o)=|\varepsilon(1-3\varepsilon/2)|^{1/2}.\kappa y \qquad (39)$$

where $U_+=U_1/v_x$, $\Psi_{u+}=\Psi_u.D/v_x$,

A system of equations (36)-(37) with the initial conditions (38) and (39) and equilibrium solution for R_2^+ was solved numerically. The constants α and y_o were determined by means of numerical experimentation based on the conditions $E^+_{,y}(1)=0$ and $E^+(1)=1$. The results are given in Figs.I-3

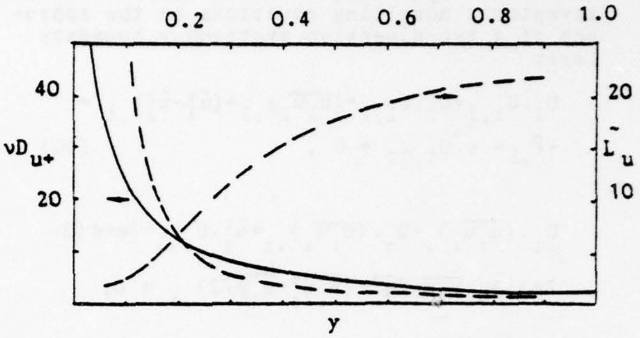

Fig.1. Distribution of dissipative function and macroscale of turbulence: - experiment |10-11|; --- numerical data, B=8.0.

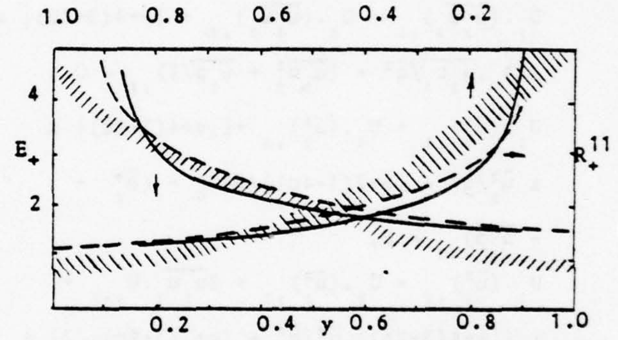

Fig.2. Fluctuating velocity distribution: ///// experiment |10-11|; — and--- numerical data at B=7.0 and B=8.0, respectively.

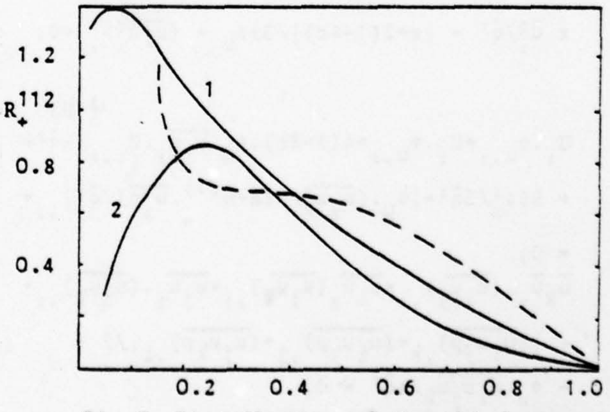

Fig.3. Distribution of the third moment $R_+^{112}=\overline{u_1^2 u_2}/v_x^3$: 1 - |10|, 2 - |11|, --- numerical data, B=8.0

B.Momentumless far wake

Assuming that at a sufficiently large distance from a self-propelled body there are conditions of similarity,one can represent the velocity field functions in the form

$$U_1=U_\infty+u_0(x_1).f(\eta),\quad E=e_0^2(x_1).g(\eta),$$

$$\bar{u}_i^2=e_0^2(x_1).g_i(\eta),\quad \Psi_u=|e_0(x_1)/\lambda_0(x_1)|.h(\eta),$$

$$\eta=x_2/\delta_0,$$

where $u_0,\delta_0,e_0,\lambda_0$ are velocity and length scales of the mean flow and fluctuations , respectively. The integral relations of the momentum

$$\int_{-\infty}^{+\infty} U_1(U_1-U_\infty)dx_2=-\int_{-\infty}^{+\infty}(\bar{u}_1^2-\bar{u}^2{}_2)dx_2 \qquad (40)$$

and of the mean flow energy

$$\left(\int_{-\infty}^{+\infty} U_1(U_1-U_\infty)^2dx_2\right)_{,x1}=-\left|\int_{-\infty}^{+\infty}(U_\infty-U_1)\times\right.$$

$$\left.\times\ (U_{1,2}\cdot\bar{u}_2^2/\Psi_u)_{,2}dx_2\right|/\varepsilon \qquad (41)$$

make it possible to find the decay "laws" of the scales u_0 and δ_0 with respect to x_1. Downstream decay of the fluctuation scales e_0 and λ_0 can be determined from equations for E and Ψ_u, which, with account of (34) and neglect of generation of fluctuations in the far wake by means of mean flow shear are of the form

$$g_{,\eta\eta}-2g_{2,\eta\eta}-(g_{2,\eta}/g_2-h_{,\eta}/h)(2g_2-g)_{,\eta}+$$

$$+\ \varepsilon.|(U_\infty/e_0)(\delta_0/\lambda_0)(h/g_2)\delta_0(2ge_{0,x1}/e_0-$$

$$-\ \eta.g_{,\eta}.\delta_{0,x1}/\delta_0)+\varepsilon(1-3\varepsilon/2)(\delta_0/\lambda_0)^2\times$$

$$\times\ (g/g_2)h^2|/\alpha(2b-1)=0, \qquad (42)$$

$$h_{,\eta}.(2g_2-g)_{,\eta}/h+\varepsilon\{|(d-2b+1)/d(2b-1)|\times$$

$$\times\ (U_\infty/e_0).(\delta_0/\lambda_0)(h/g_2)\delta_0(2g.e_{0,x1}/e_0-$$

$$-\ \eta.g_{,\eta}.\delta_{0,x1}/\delta)-(U_\infty/e_0)(\delta_0/\lambda_0)(h/g_2)\times$$

$$\times\ \delta_0(g.e_{0,x1}/e_0-g.\lambda_{0,x1}/\lambda_0-\eta.g_{,\eta}.\delta_{0,x1}/$$

$$\delta)/d+|(6d-22b+11)/6d(2b-1)|(1-3\varepsilon/2)\times$$

$$\times\ \varepsilon(g/g_2)(\delta_0/\lambda_0)^2.h^2\}/\alpha=0, \qquad (43)$$

A system of equations involving (42), (43),the equation of mean flow

$$f_{,\eta\eta}+(g_{2,\eta}/g_2-h_{,\eta}/h)-\varepsilon(U_\infty/e_0)(\delta_0/\lambda_0)\times$$

$$\times\ (h/g_2)\delta_0(fu_{0,x1}/u_0-\eta f_{,\eta}.\delta_{0,x1}/\delta_0)=0$$

and the equation for the mean square of transverse fluctuations

$$g_{2,\eta\eta}-4b.g_{,\eta\eta}/(8b-3)+(g_{2,\eta}/g_2-h_{,\eta}/h)\times$$

$$\times\ (g_2-4b.g/(8b-3)|_{,\eta}-\varepsilon\{(U_\infty/e_0)(\delta_0/\lambda_0)\times$$

$$\times\ (h/g_2)\delta_0(2g_2.e_{0,x1}/e_0-\eta.g_{2,\eta}.\delta_{0,x1}/\delta_0)+$$

$$+\ (g_2/g-\varepsilon)\varepsilon(g/g_2)(\delta_0/\lambda_0)^2h^2\}/\alpha(8b-3)=0$$

subject to $\nu_T=E/\Psi_u\equiv F(x_1)$ solved numerically under the initial conditions:

$$f(0)/u_0=1,\quad f_{,\eta}(0)=0,\quad g(0)/e_0^2=1,$$

$$g_{,\eta}(0)=0,\quad g_2(0)/e_0^2=2/3.$$

The laws of variation of the scale functions are of the form:

$$\delta_0\sim\lambda_0\sim x_1^{2/5},\quad (u_0/U_\infty)\sim x_1^{-6/5},$$

$$(e_0/U_\infty)\sim x_1^{-3/5}.$$

The results of calculation of different functions at $b=2$, $d=11/2$, $(1+2\pi)/q=33/32$, $2mR_s=$ $=-(\alpha.110\ln 4)/3$ where

$$m=\left|\int_{-\infty}^{+\infty} f\cdot(g_2.f_{,\eta}/h)_{,\eta}d\eta\right|/J_2,$$

$$J_2=\int_{-\infty}^{+\infty} f^2d\eta,\qquad R_s=e_0\lambda_0/\nu_T$$

$$\pi=\int_{-\infty}^{+\infty}\eta.g_{,\eta}.(g/g_2)d\eta\Big/\int_{-\infty}^{+\infty}(g^2/g_2)d\eta,$$

$$q=\int_{-\infty}^{+\infty}(g^3/g_2)d\eta\Big/\int_{-\infty}^{+\infty}(g^2/g_2)d\eta$$

are given in Fig. 4–6

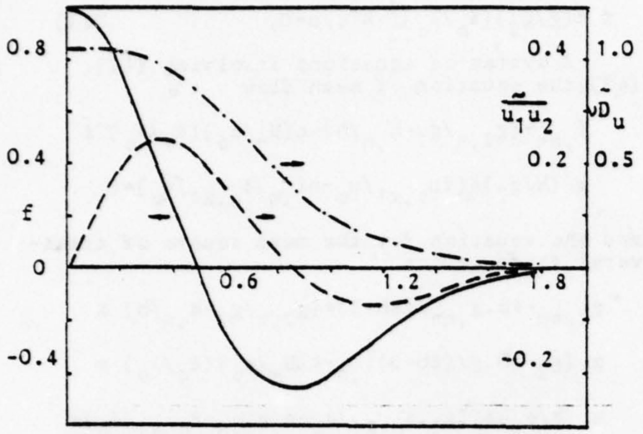

Fig.4. Radial profiles for the functions: — velocity difference f; --- Reynolds stress $\widetilde{\overline{u_1u_2}}=\overline{u_1u_2}/(u_oe_o)$ and -.-. dissipation function $\nu\tilde{D}_u=\nu D_u/(e_o^3/\delta_o)$.

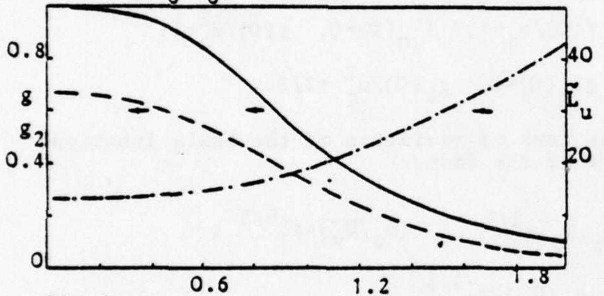

Fig.5. Radial profiles for the kinetic energy (solid line), intensity of transverse velocity fluctuations (dashed line) and macroscale of turbulence $\tilde{L}_u=L_u/\delta_o$ (dotted line).

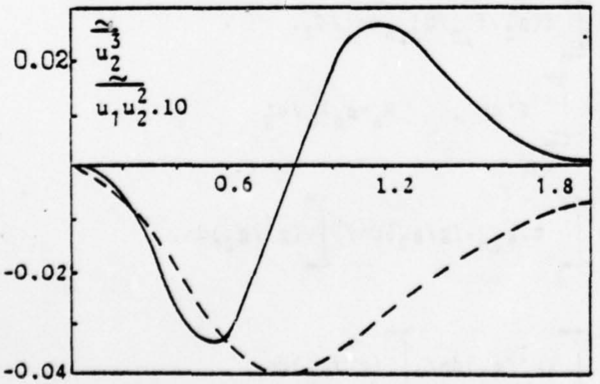

Fig.6. Radial profiles for the third moments: - $\widetilde{\overline{u_1u_2^2}}=\overline{u_1u_2^2}/u_oe_o^2$; --- $\tilde{\tilde{u}}_2^3=\overline{u_2^3}/e_o^3$.

Due to the confined space of the paper the author cannot give the results of calculation of other turbulent flows. But working long with the asymptotic large-scale model of turbulence (16)-(33), the author takes the liberty of asserting that this model is invariant with respect to the velocity field form, i.e. it allows the statistical moments of the turbulent flow velocity fields for various geometries to be calculated with the same degree of accuracy. However, the author has not yet attempted to extend this model to the elliptical flows.

ACKNOWLEDGEMENT

The author wishes to thank his colleague V.I.Brook-Levinson who carried out a great deal of numerical computations of different flows by the suggested asymptotical model.

REFERENCES

1 Loitsyansky,L.G., "Some fundamental laws of isotropic turbulent flow," Proceedings of Central Aero-Hydrodynamic Institute", 1939, Rep.No.440.

2.Saffman,J.P.G., "The large-scale structure of homogeneous turbulence," Journal of Fluid Mechanics, Vol. 27, 1967, pp.581-593.

3 Kolmogorov,A.N., "Equations of turbulent motion of incompressible fluid," Izvestiya AN SSSR, Ser. Fiz., Vol. 6, No. 1-2, 1942, pp.56-58.

4 Chou,P.-Y., "On velocity correlation and the solution of the equations of turbulent fluctuations", Quarterly of Applied Mathematics, Vol. 13, No.1, 1945, pp.38-54.

5 Kolovandin,B.A., Vatutin,I.A., "Statistical transfer theory in non-homogeneous turbulence," International Journal of Heat and Mass Transfer, Vol. 15, 1972, pp.2371-2383.

6 Lumley,J.L., "Prediction methods for turbulent flows," Von Karman Institute, Rhode St. Genese, Belgium, 1975.

7 Robertson,H.P., "The invariant theory of isotropic turbulence," Proceedings of the of the Cambridge Philosophical Society," Vol. 36, No. 2, 1940, pp.[illegible]09-223.

8 Deissler,R.G., "A theory of decaying homogeneous turbulence," Physics of Fluids, Vol. 3, No. 3, 1960, pp.176-187.

9 Kolovandin,B.A., Bulavko,A.A., and Dmitrenko,Yu.M., "Statistical transfer coefficients of homogeneous velocity and temperature fields," International Journal of Heat and Mass Transfer, Vol. 19, No. 12, 1976, pp. 1405-1413.

10 Laufer,J.,"The structure of turbulence in fully developed pipe flow", NACA, Rep. No. 1174, 1954.

11 Lawn, C.J., "The determination of the rate of dissipation in turbulent pipe flow", J. Fluid Mechanics, Vol. 48, part 3, 1971, pp.477-505.

SESSION 18

RECIRCULATING FLOW-2

Chairman: A. D. Gosman
Department of Mechanical Engineering
Imperial College
London SW7 2BX
England

THEORETICAL AND EXPERIMENTAL INVESTIGATIONS OF TURBULENT FLOWS WITH SEPARATION

F. Durst and A. K. Rastogi

Sonderforschungsbereich 80
Universität Karlsruhe
Karlsruhe, Germany

ABSTRACT

Theoretical and experimental studies are reported on a turbulent flow in a two-dimensional channel of aspect ratio 1:16 in which a square obstacle of half the channel height was located. A one dimensional laser Doppler anemometer was used to measure the mean longitudinal velocity distribution and the rms values of the longitudinal velocity fluctuations. The measurements were carried out along the channel centre from 20 channel heights upstream of the obstacle up to 33 channel heights downstream. Flow visualisation techniques were employed to observe the regions not covered by the LDA measurements. The governing partial differential equations were solved numerically and results are described in the theoretical part of the paper. In the separated flow region, the Reynolds equations were solved using the two-equation k- ε turbulence model and in the region downstream of the separation, the boundary layer equations were solved with both k-epsilon and the three-equation, k-ε-$\overline{uv}$ turbulence model. The calculations are compared with the measurements and demonstrate clearly that for turbulent flows with separation, the present state of turbulence modelling results in inaccurate predictions. Calculated values are presented for the increase in heat transfer rates and the pressure drop due to the obstruction.

NOMENCLATURE

A, B : finite difference coefficients
C's : empirical constants
D : channel height
H : obstruction height
k : kinetic energy of turbulence
P : pressure, main grid location
Q : heat transfer rate
T : temperature
U : mean longitudinal velocity
V : mean transverse velocity
$\overline{uv}$: turbulent shear stress
x : longitudinal coordinate
y : transverse coordinate

<u>Greek Symbols</u>

ε : dissipation of turbulent kinetic energy
ρ : density
μ : viscosity
σ : turbulent Prandtl number
ϕ : general dependent variable

<u>Subscripts</u>

av : average
n, s, e, w : north, south, east, west
p : main grid point
t : turbulent

INTRODUCTION

Most flows occurring in natural and technological environment are turbulent and contain regions of recirculation. These regions are characterised by strong streamline curvature, complex eddy structures and high turbulence intensities associated with high heat transfer rates and pressure losses. The complexity of flow within and near the region of recirculation hampered experimental studies in the past and this is indicated by the lack of measurements in the literature. A large proportion of the available experimental work is restricted to measurements of integral quantities such as the length of the recirculation zone, e.g. [1] or the rate of heat transfer along the test section walls [2]. A few detailed measurements have also been carried out using pitot tubes and hot wire anemometers [3]. However, because of the nonlinear response characteristics of these instruments, the accuracy of the results is questionable in the presence of high turbulence intensities and changes in flow direction. Further measuring errors are introduced due to the inherent flow disturbances caused by the measuring probes placed into separated flows.

The lack of detailed data on turbulent recirculating flows has hindered theoretical studies of such flow fields. Although reliable numerical schemes have been developed for solving the governing partial differential equations, the reliability of turbulence models in the separated regions has remained poor. Hence, advances in the development of prediction procedures for turbulent recirculating flows require dependable experimental results with which numerical predictions can be compared.

With the advent of laser Doppler anemometry there is now, in principle, no problem of instrumentation. In practice, however, the constructions of available test sections do not take into account the particular requirements of laser Doppler instruments and often prevent measurements of the relevant mean and turbulent quantities. Nevertheless, at present any reliable data, although incomplete, permit progress in the development of turbulence models for recirculating flows.

The present paper describes laser Doppler measurements of axial mean and fluctuating velocities in a two-dimensional water channel of aspect ratio 1:16, in which a square obstacle of half the channel height was located. The particular flow geometry was chosen because of its applicability to heat transfer equipment. Available solution procedures and turbulence models were employed to calculate the entire flow. Results of the calculations are compared with the measurements and the reliability of the existing turbulence models is commented upon. Suggestions for improvements are outlined.

EXPERIMENTAL INVESTIGATION

Flow visualisation and laser Doppler measurements were carried out in order to provide experimental information on turbulent flow with regions of separation. Such information is essential to develop reliable theoretical models for flow predictions.

The Experimental Equipment

The experimental investigation was carried out in a plane two-dimensional water channel with cross sectional dimensions of 50 mm x 800 mm providing an aspect ratio of 1:16. The main constructional details and dimensions of the test rig are schematically shown in Figure 1 together with the different measuring positions and the location of the flow obstacle. This obstacle was of square cross section (25 mm x 25 mm) and extended across the entire channel width. Regions of recirculation were observed in front, at the top and behind the obstruction.

The experimental rig contained a steel settling chamber into which water was pumped. The difference between the water levels in the plenum chamber and the outlet container provided the head for the flow through the test section. The water level in the settling chamber was controlled by the water supply through the pump and a level control in the outlet container.

The actual duct test section was constructed of perspex with glass side walls in order to provide little optical disturbance to the passage of the light beams. These could pass through the entire test section permitting laser Doppler measurements with forward scattered light.

The laser Doppler anemometer employed for the velocity measurements is schematically shown in Figure 1 b. It consisted of a 15 mW He-Ne-laser (Spectra Physics 124B), transmission optics comprising a rotating diffraction grating and a lens to focus and cross the laser beams in the test section centre plane. The light scattered by small particles suspended in the fluid was collected by a lens on the far side of the duct and focused at a pin hole in front of a photomultiplier (EMI 9558B). The output of the photomultiplier was processed by a TSI frequency tracker which provided an output voltage proportional to the frequency of the input signal. This output voltage was transferred to a data acquisition facility and processed there by a computer (Hewlett-Packard 5450A) to provide information on the mean frequency and the rms-frequency fluctuations. From this information the mean velocity and rms-velocity fluctuations were computed.

Laser Doppler measurements and flow visualisation.

The laser Doppler measurements described in the present paper covered the region from about 20 channel heights upstream of the flow obstacle to approximately 33 duct heights downstream. The duct length in front of the block was sufficient to permit fully developed turbulent duct flow to exist and initial LDA measurements were performed to ensure this.

The main measurements were carried out for a Reynolds number of 1.7×10^4, based on the channel height, D, and the bulk velocity, U_{av}. Figure 2 shows the measured mean velocity profiles and the distribution of rms-values of the longitudinal velocity fluctuations. The results show that the separation region extends from the upstream corner of the square obstacle to about 8 block heights downstream. The small recirculation region in front of the obstacle is indicated by its influence on the maximum of the measured rms-velocity fluctuations. The value of this maximum increases well before the flow reaches the block.

The flow rates along the centre plane were evaluated by integrating the measured mean velocity profiles, which was found to decrease near the flow obstacle (-7% maximum) due to three-dimensional effects which occurred inspite of the large aspect ratio of the employed test section. The acceleration of the side wall boundary layers and associated pressure fields caused a secondary flow to establish itself in planes perpendicular to the main flow. These were observed using flow visualisation techniques.

The flow visualisation experiments were carried out by injecting a solution of potassium permanganate in water, into parts of separated regions and observing the transport of the coloured fluid. Figures 3a and b show two photographs of the flow field around the block, indicating the separation regions in front, on the top and behind the flow obstacle. The small separation zone in front of the block was not explicitly shown by the LDA measurements.

THEORETICAL INVESTIGATION

The theoretical investigation consisted of calculating the measured flow situation numerically. The available finite difference calculation procedures for recirculating flows and boundary layers were employed to solve the governing partial differential equations. The two-equation k-ε turbulence model was employed to specify the turbulent viscosity. For boundary layer regions of the flow the three-equation $k\text{-}\varepsilon\text{-}\overline{uv}$ turbulence model was also used. Results of the calculations have been compared with the measurements reported in the previous section and the suitability of the existing k-ε turbulence model to separated turbulent flows is examined.

Governing Equations

The flow under consideration is governed by the two-dimensional form of the continuity and the time-averaged Navier Stokes equations. In the cartesian coordinate system these equations can be written in the following form:

$$\frac{\partial}{\partial x}(\rho U) + \frac{\partial}{\partial y}(\rho V) = 0 \qquad (1)$$

$$\frac{\partial}{\partial x}(\rho U^2) + \frac{\partial}{\partial y}(\rho UV) = -\frac{\partial P}{\partial x} + \frac{\partial}{\partial x}\left[(\mu_t + \mu)\frac{\partial U}{\partial x}\right] + \frac{\partial}{\partial y}\left[(\mu_t + \mu)\frac{\partial U}{\partial y}\right] \quad (2)$$

$$\frac{\partial}{\partial x}(\rho UV) + \frac{\partial}{\partial y}(\rho V^2) = -\frac{\partial P}{\partial y} + \frac{\partial}{\partial x}\left[(\mu_t + \mu)\frac{\partial V}{\partial x}\right] + \frac{\partial}{\partial y}\left[(\mu_t + \mu)\frac{\partial V}{\partial y}\right] \quad (3)$$

The eddy viscosity hypothesis has been used in the momentum equation. The eddy viscosity, μ_t, has to be specified by the turbulence model. Using the same hypothesis, the partial differential equation governing the transport of thermal energy has the form :

$$\frac{\partial}{\partial x}(\rho UT) + \frac{\partial}{\partial y}(\rho UT) = \frac{\partial}{\partial x}\left[\left(\frac{\mu_t}{\sigma_t} + \frac{\mu}{\sigma}\right)\frac{\partial T}{\partial x}\right] + \frac{\partial}{\partial y}\left[\left(\frac{\mu_t}{\sigma_t} + \frac{\mu}{\sigma}\right)\frac{\partial T}{\partial y}\right] \quad (4)$$

The complete flow domain can be divided into two regions : the recirculating flow region which extends from about 4 block heights upstream of the block to 10 - 12 block heights *downstream* and the boundary layer region which prevails in front of the block ($x/H < -4$) and beyond the recirculating flow region. In the region around the obstacle diffusion is equally important in both x and y directions, there exists no dominant direction of flow and the flow is influenced by the downstream conditions. Flow in this region is governed by the complete equations (1) to (4) and need to be solved by an iterative procedure so that downstream influences are included correctly. The calculation domain for the recirculating flow equations extended from 11 block heights upstream of the obstruction to 25 heights downstream. The region between $-11 \leq x/H \leq -4$ was *included in this* calculation only for the sake of convenience. In the region beyond the separated flow, there exists a dominant direction of flow and diffusion is important only in the cross stream direction. This region is governed by the differential equations (1), (2) and (4) without the diffusion terms in the x direction. These equations can be adequately solved by a forward marching type of solution procedure starting with suitable initial conditions.

The above set of partial differential equations has to be solved with the following boundary conditions :

$U = 0 = V$ along the walls

$T =$ constant along the walls

$\frac{\partial}{\partial x} = 0$ along the downstream edge of the recirculating flow calculation domain

In order to reduce computing times, calculations were not carried out right up to the wall and the velocities parallel to the walls at the wall nearest grid points were specified from the law of the wall. The law of the wall valid for turbulent boundary layers was used for all the regions in the present calculations.

Turbulence Model

The turbulent viscosity, μ_t, in equations (2) to (4) has been defined using the two-equation $k-\varepsilon$ model of turbulence [4]. According to this model,

$$\mu_t = C_\mu \rho k^2/\varepsilon \quad (5)$$

where C_μ is an empirical constant. k and ε in Eq. (5) are obtained by solving the following differential equations :

$$\frac{\partial}{\partial x}(\rho Uk) + \frac{\partial}{\partial y}(\rho Vk) = \frac{\partial}{\partial x}\left[\left(\frac{\mu_t}{\sigma_k} + \mu\right)\frac{\partial k}{\partial x}\right] + \frac{\partial}{\partial y}\left[\left(\frac{\mu_t}{\sigma_k} + \mu\right)\frac{\partial k}{\partial y}\right] + C_1 - \rho\varepsilon \quad (6)$$

where $G = \mu_t \left[2\left(\frac{\partial V}{\partial y}\right)^2 + 2\left(\frac{\partial U}{\partial x}\right)^2 + \left(\frac{\partial V}{\partial x} + \frac{\partial U}{\partial y}\right)^2\right]$

and represents generation of turbulent kinetic energy.

$$\frac{\partial}{\partial x}(\rho U\varepsilon) + \frac{\partial}{\partial y}(\rho V\varepsilon) = \frac{\partial}{\partial x}\left[\left(\frac{\mu_t}{\sigma_\varepsilon} + \mu\right)\frac{\partial \varepsilon}{\partial x}\right] + \frac{\partial}{\partial y}\left[\left(\frac{\mu_t}{\sigma_\varepsilon} + \mu\right)\frac{\partial \varepsilon}{\partial y}\right] + C_1\frac{\varepsilon}{k}C_1 - C_2\rho\varepsilon^2/k \quad (7)$$

Equations (6) and (7) have been derived from the Navier-Stokes equations and the assumptions made in obtaining their above forms have been reported elsewhere [5, 6]. Like the conservation equations for momentum, in the boundary layer calculations, Eqs. (6) and (7) do not contain the diffusion terms in x direction and G is produced only by $\partial U/\partial y$.

In the boundary layer flow domain, a three-equation turbulence model was also employed. This model specifies the turbulent shear stress through its transport equation which is also derived from the Navier-Stokes equations. With this turbulence model, therefore, the effective viscosity hypothesis is not employed in the longitudinal momentum equation. The transport equations for k and ε remain unchanged. The transport equations for longitudinal momentum and turbulent shear stress, as used with the three-equation model, have the following form :

$$\frac{\partial}{\partial x}(\rho U^2) + \frac{\partial}{\partial y}(\rho UV) = -\frac{\partial P}{\partial x} + \frac{\partial}{\partial y}\left(\mu\frac{\partial U}{\partial y}\right) + \frac{\partial}{\partial y}(-\rho\overline{uv}) \quad (2a)$$

$$\frac{\partial}{\partial x}(\rho U\overline{uv}) + \frac{\partial}{\partial y}(\rho V\overline{uv}) = \frac{\partial}{\partial y}\left[\left(\frac{\mu_t}{\sigma_s} + \mu\right)\frac{\partial}{\partial y}\overline{uv}\right] - C_s\left(\rho C_\mu k\frac{\partial U}{\partial y} + \frac{\rho\overline{uv}}{k}\varepsilon\right) \quad (8)$$

The *boundary* values for the turbulent quantities at the wall nearest grid points were also specified in accordance with the law of the wall. In the recirculating flow region k was obtained near the wall by solving the governing differential equation with G calculated using the wall shear stress, i.e. $G = \tau_w \frac{\partial U}{\partial y}$ in the boundary layer region. Following values were used for the empirical constants appearing in the turbulent transport equation :

$$C = .09,\ C_1 = 1.44,\ C_2 = 1.92,\ C_s = 2.8,$$

$$\sigma_t = 1.0,\ \sigma_k = 1.0,\ \sigma_\varepsilon = 1.3,\ \sigma_s = 0.9$$

Solution Procedures

Finite difference solution procedures are used in both recirculating flow and boundary-layer regions. The common features of these procedures are :

1. transformation of the partial differential equations in linear algebraic difference equations which connect the dependent variable at a grid point to its value at the neighbouring grid points
2. the above transformation uses "upwind differences" which makes the procedures unconditionally stable
3. the finite difference equations are solved by the method of successive substitution.

The algebraic details of the above features can be seen in references [7, 8]. Here only the details relevant to the present flow situation are reported.

Recirculating flow region. The solution procedure used for this region is embodied in the computer program *'Teach' developed at Imperial College, London. The* schematic layout of the finite difference grid is shown in Figures 4 and 5. The velocities are stored at the locations displaced from the main grid points (·) where P, k, T and ε are stored. The differential equation for each dependent variable (say ϕ) is integrated over the respective control volume (see Figure 4) and the following difference equation is obtained for each grid point in the calculation domain:

$$\phi_p = A_n \phi_n + A_s \phi_s + A_w \phi_w + A_e \phi_e + B \qquad (9)$$

A's in Eq. (9) consist of convection and diffusion through the control volume faces, e.g. A_n contains the convective and diffusive fluxes of through the north face of the control volume. It was found in the present investigation that it was very important how these coefficients were calculated for the velocity points adjacent to the obstruction corners (Figure 4). Considering the U velocity at point A in Figure 5, the south coefficient A_s in Eq. (9) should contain only half the convection since half of the south face of the control volume is blocked by the obstacle. Similarly the diffusion contribution to A_s should be such that it takes account of the fact that half of the south face is wall and only the other half exposed to the flow. Similar arguments are valid for the east coefficient A_e, considering the V velocity stored at the point B. These modifications resulted in very different solutions in the recirculating flow region in particular above the block. Without such modifications the calculated flow did not separate on the bottom face of the block and hence resulted in unrealistic calculations in the region downstream of the obstruction.

The rate of convergence of the finite difference equations was found to be slower in the region after the block as compared to the region upstream and over the obstacle. This observation was used to reduce the computing times considerably by freezing the solution in the upstream region after some iterations and by solving only the downstream region till converged solutions were obtained. In the end the complete flow region was calculated only for a few iterations to obtain the converged solution in the entire flowfield.

Boundary layer region. The method used for this region is embodied in the computer program 'GENMIX' and is explained in full detail in reference [7]. This procedure was used to calculate the flow redevelopment after the separated flow region created by the obstacle. GENMIX contains a forward marching procedure and requires initial condition for the dependent variables. The starting station was chosen at 10 obstacle heights downstream of the obstacle and the initial conditions were provided from the solutions obtained from the recirculating flow program 'Teach'. To obtain reliable initial conditions at this location, the recirculating flow calculation was done up to 25 block heights downstream of the block. The influence of these initial conditions was studied in order to define the precision to which they have to be specified.

RESULTS OF COMPUTATIONS

Computations were carried out to solve equations (1) to (7) between 11 block heights upstream and 25 block heights downstream using the recirculating flow program. A 50 x 27 finite difference grid (39 K words computer storage) provided grid independent solutions. Initial conditions at x/H = -11 for U and k ($\equiv 1.5\ \overline{u^2}$) were taken from the experiments while V = 0 and $\rho\,\varepsilon = \mu_t(\partial U/\partial y)^2$ were assumed to simulate the fully developed channel flow. About 300 iterations and 30 minutes of computing time were required to obtain the converged solutions on Univac 1108.

Figure 6a shows the computed and the measured streamline pattern around the obstruction. The points on this figure were obtained by locally integrating the measured U profiles. Agreement between the calculations and the measurements shown on Figure 6a is very satisfactory except over the bottom face of the block and the separated region behind the block. Measurements indicate that the separated region over the bottom face of the block joins with the separation region behind the block but the calculated separated streamline reattaches before the downstream edge of the block. This disagreement is partly due to the three-dimensional effects because of the obstruction in the measuring channel. Figures 6b and c show the computed values of heat transfer rates and the pressure drops along the channel walls. A constant wall temperature boundary condition was used. It is interesting to note that the calculations show, as expected, high heat transfer rates around the flow reattachment points on the top wall. More than 25 block heights downstream of the block the heat transfer rates are higher than those obtained in two-dimensional fully developed channel flow. The calculated pressure drop curves on Figure 6 c show that the flow at 3 block heights upstream of the block is affected by the obstruction and downstream of the block the pressure field becomes uniform fairly quickly. This is in accordance with the measurements [9] on relaxing boundary layers.

Figures 7 and 8 show the calculated and the measured longitudinal velocity profiles. Figure 7 indicates that velocity profiles upstream of the obstruction are faithfully predicted. The calculated longitudinal velocity profiles over and behind the obstruction do not compare very satisfactorily with those measured. The maximum negative velocity over the block (x/H = .5) is calculated to be half that measured and the discrepancy between the calculated and the measured values at 10 block heights downstream is of the order of 20-30% of the measured values.

Figure 8 shows the redevelopment of the flow after separation. The calculated profiles shown in Figure 8 have been obtained from the boundary layer program using different initial conditions at x/H = 10. These calculations were carried out with 45 cross-stream grid points and forward steps of 5% of the channel height. The computer storage required for these calculations was about 10 K words. It is clear that the calculated redevelopment continues to remain slow when the calculated velocity profiles are used as initial conditions. By using the measured velocity profiles at x/H = 10 as initial conditions and keeping all the other initial profiles the same, the calculated profiles compare much better with those measured although the redevelopment is still underpredicted. As shown in Figure 8 use of the three-equation model improves the calculated profiles further but not significantly. For the calculations with the three-equation model, initial profiles for $\overline{uv}$ were obtained from:

$$-\rho \, \overline{uv} = \mu_t \frac{\partial U}{\partial y}$$

Figure 9 shows some calculated profiles for kinetic energy of turbulence together with the measured quantity ($3/2 \, \overline{u^2}$) shown by points. Quantitative agreement between the calculations and the measured values shown on Figure 9 was not expected, but the *qualitative agreement* is worth noting. The calculated turbulence length scale is also shown at $x/H = 10$, *which suggests large scale eddies* beyond reattachment. Scales are also equally large in the separation zone. Further measurements on the turbulence quantities in many separated flows are required before the ability of the k-ε turbulence model in reproducing turbulent quantities can be evaluated. Considering the mediocre reproduction of the mean velocity profiles, prediction of turbulence quantities is not expected to be satisfactory. This has also been shown for some other flow configurations [10] .

CONCLUDING REMARKS

The results presented in the previous section demonstrate that the present state of the art in calculating the two-dimensional separated turbulent flows is satisfactory in *predicting the streamline patterns outside the separation zones*. Quantities of engineering interest such as the wall heat transfer rates and the static pressure drops are qualitatively well predicted. Considering the disagreement between the calculated and the measured mean velocity profiles, the wall heat transfer rates may not be quantitatively well predicted. As a result of errors in calculated profiles in the separated region, the flow redevelopment in the boundary layer region *after the flow reattachment* is also inaccurately predicted. The flow redevelopment is of practical interest because real problems deal with many ribs for heat transfer augmentation. It has also been shown that in the redevelopment region the three-equation turbulence model does not offer worthwhile advantages over the two-equation k-ε turbulence model, and it is more important to start with correct initial conditions.

The k-ε turbulence model has to be modified to obtain more accurate calculations in the separated flow regions. The present wall shear stress calculation is based on the law of the wall, valid for the normal boundary layers, which is then used to calculate the turbulence production near the wall. The wall-law should be replaced by more appropriate laws for separated flows. The turbulence equations should be solved more accurately near the walls, based on the complete differential equations valid up to the wall, rather than using the equilibrium conditions. This can be economically achieved by constructing the wall functions based on the complete observation equations. Further detailed turbulence measurements are of course, required to develop and test these suggestions.

REFERENCES

[1] Arie, M. and Rouse, H., Experiments in Two-Dimensional Flow over a Normal Wall, Journal of Fluid Mechanics, Vol. 1, Part 2, 1956, pp. 129-141.

[2] Krall, K.M. and Sparrow, E.M., Turbulent Heat Transfer in the Separated, Reattached, and Redevelopment Regions of a Circular Tube, Journal of Heat Transfer, Transactions ASME, 1966, pp. 131-136.

[3] Carmody, T., Establishment of the Wake Behind a Disc, Journal of Basic Engineering, Transactions ASME, Vol. 86, 1969, pp. 869.

[4] Launder, B.E. and Spalding, D.B., Mathematical Models of Turbulence. Academic Press, London and New York, 1972.

[5] Hinze, J.O., Turbulence. McGraw-Hill Book Company Inc., 1959.

[6] Hanjalic, K., Two-Dimensional Asymmetrical Turbulent Flows in Ducts, Ph.D. Thesis, University of London, 1970.

[7] Gosman, A.D. and Pun, W.M., Lecture notes for course entitled, Calculation of Recirculating Flow. Heat Transfer Report No. HTS/74/2, Imperial College, London, Dec. 1973.

[8] Patankar, S.V. and Spalding, D.B., Heat and Mass Transfer in Boundary Layers. 1st ed. Morgan Grampian, London, 1967, 2nd ed. Intertext, London, 1970.

[9] Wanschkuhn, P. and Vasanta Ram, V.I., Die turbulente Grenzschicht hinter einem Ablösungsgebiet. Zeitschrift für Flugwissenschaften 23, Heft 1, 1975.

[10] Pope, S.B. and Whitelaw, J.H., The Calculation of Near Wake Flows. Journal of Fluid Mechanics, Vol.73, Part 1, 1976, pp. 9-32.

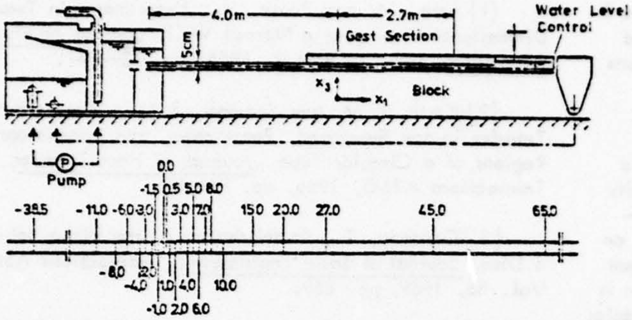

Figure 1a - Sketch of Water Channel and Indication of Measuring Positions

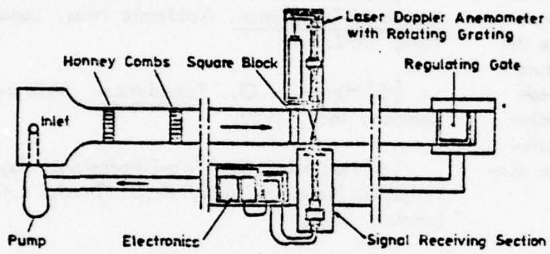

Figure 1b - Schematic Diagram of the LDA - System Located at the Duct Test Section

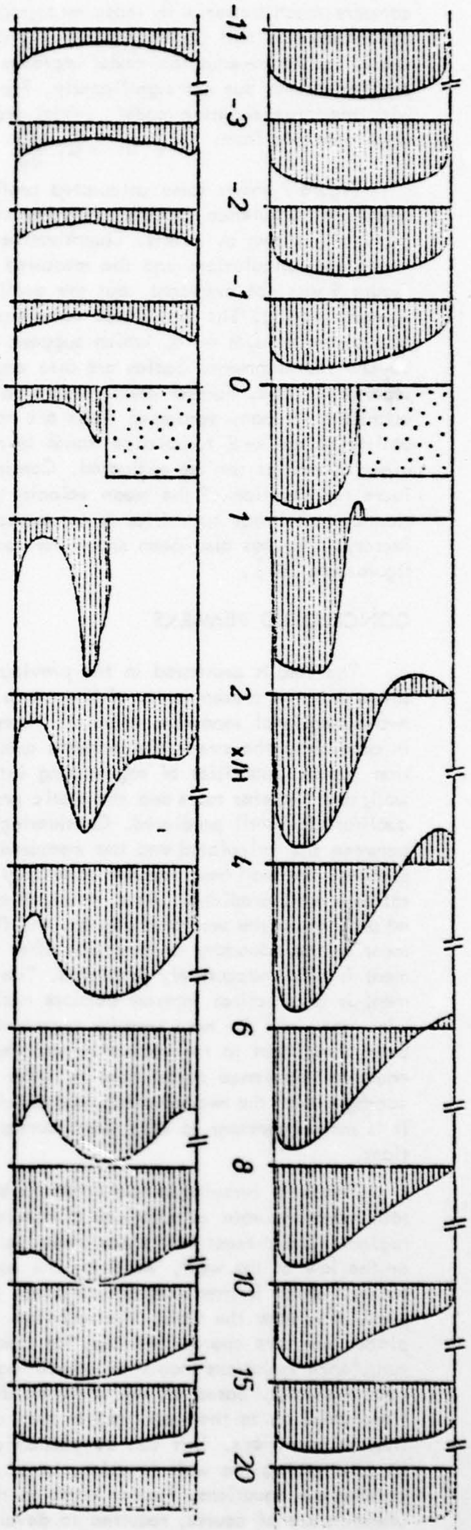

Figure 2: Measured profiles of mean velocity (1 cm = .24 m/sec) and rms fluctuations (1 cm = .072 m/sec) in longitudinal direction

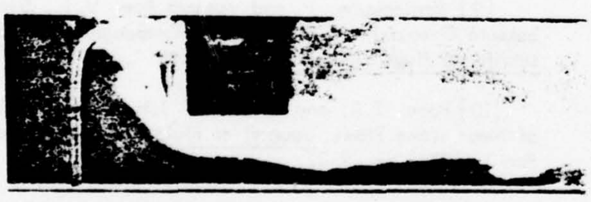

Figure 3a : Separation in front of the block

Figure 3b : Separation on top and behind the block

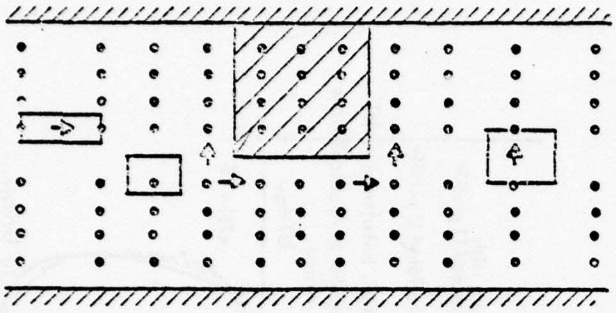

Figure 4 : Schematic layout of the finite difference grid

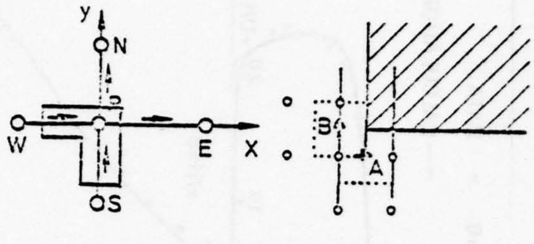

Figure 5 : Staggered grid and the block corner

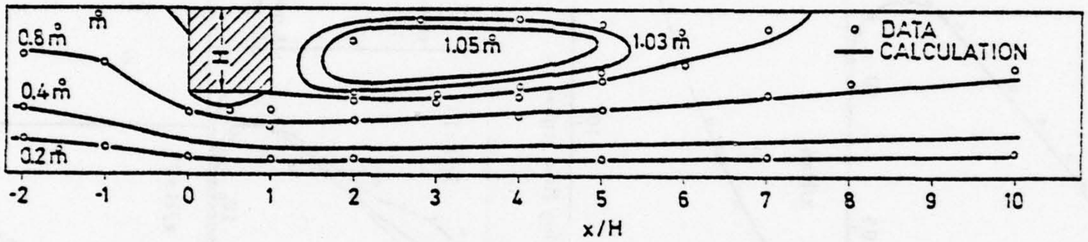

Figure 6a : Measured and computed stream lines around the block

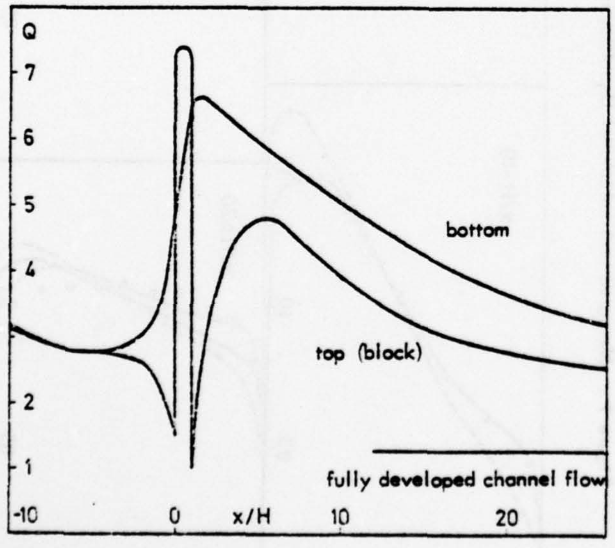

Figure 6b : Calculated heat transfer rates

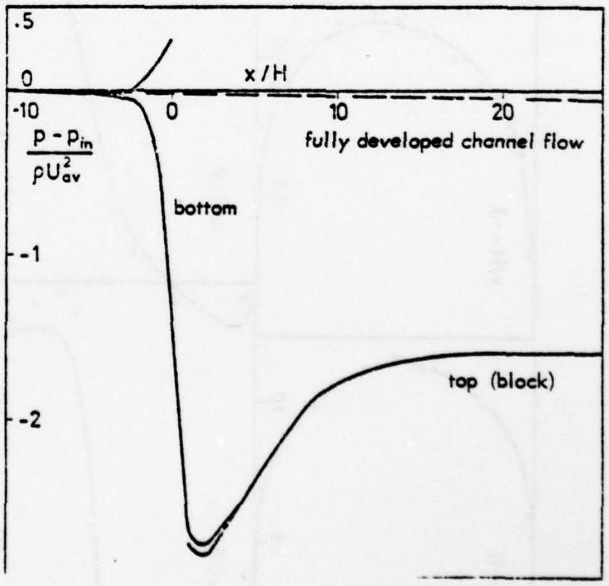

Figure 6c : Calculated pressure losses

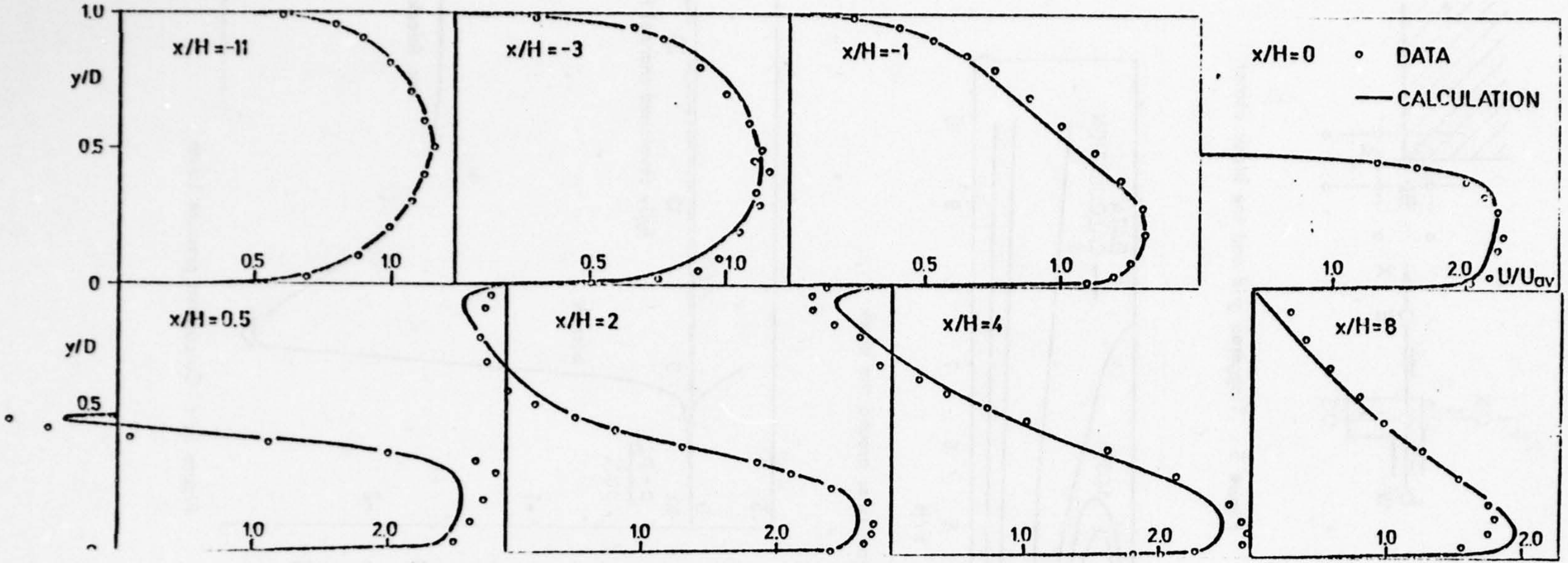

Figure 7 : Measured and calculated U profiles in the recirculating flow region

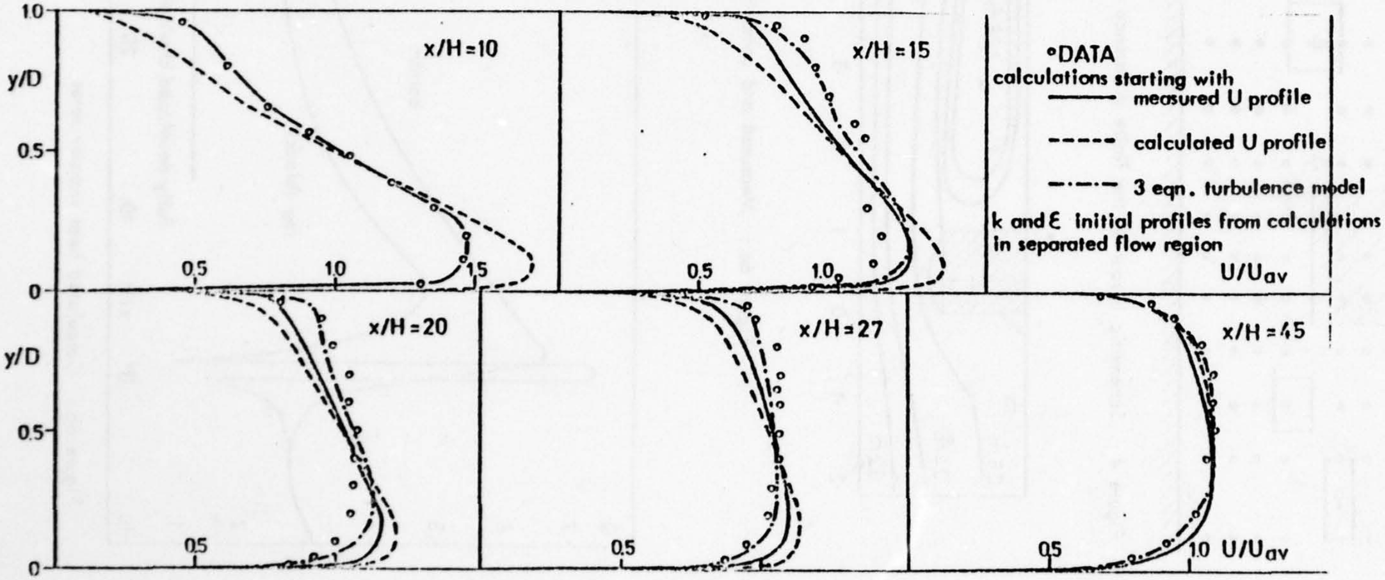

Figure 8 : Measured and calculated U profiles in the boundary layer region

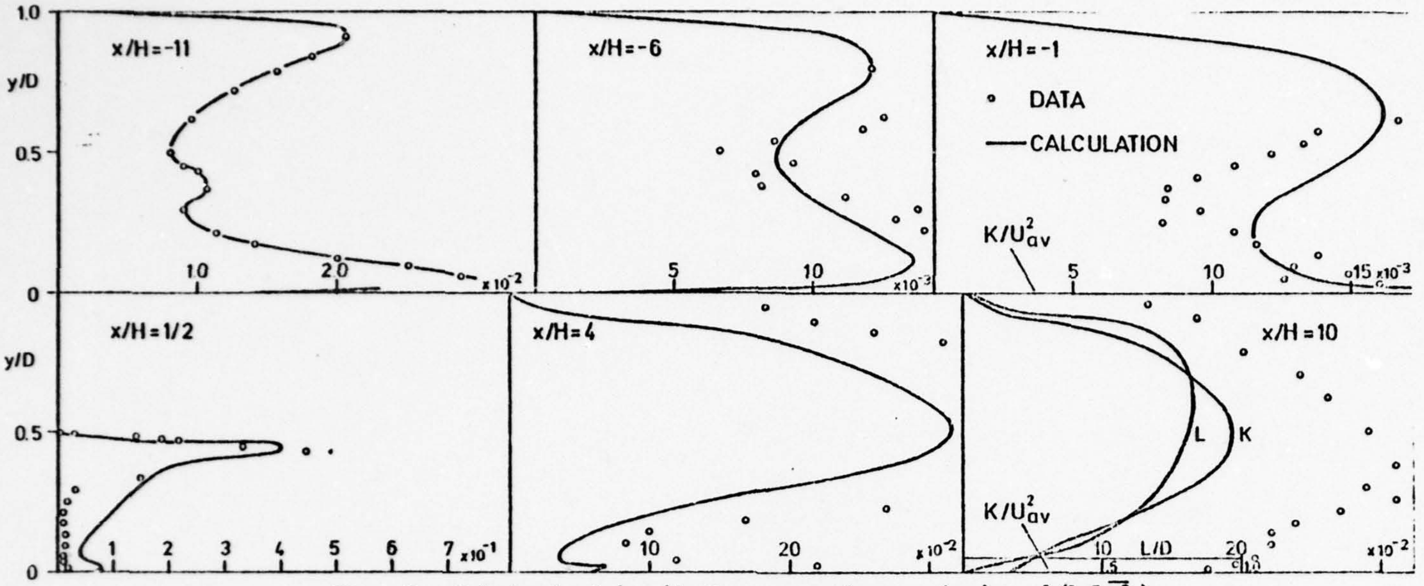

Figure 9 : Calculated turbulent kinetic energy and measured values of (1.5 $\overline{u^2}$)

SOME OBSERVATIONS ON THE NUMERICAL CALCULATION OF THE RECIRCULATION REGION OF TWIN PARALLEL SYMMETRIC JET FLOW

J. MILITZER[1], W. B. NICOLL, S. A. ALPAY

Department of Mechanical Engineering

University of Waterloo

Waterloo, Ontario, Canada

ABSTRACT

The present paper outlines the authors' experience in the numerical calculation of the recirculation zone between twin parallel jets issuing normally from a plane surface. Because of the relatively wide separation of the two jets at their points of inception, the authors found it uneconomic to use standard upwind or hybrid differencing schemes in their calculations. Rather, they found that adequate predictive accuracy could be obtained, at reasonable computation expense, with the skewed-upstream-differencing scheme of Raithby [6].

The adoption of this scheme was in itself not sufficient, however, to yield good predictions with k-ε turbulence model of Hanjalic [9]. The authors found it necessary to incorporate a streamline curvature effect on the generation terms in the turbulent kinetic energy and dissipation equations of a form suggested by Irwin and Arnot-Smith [7].

The resultant predictions display excellent agreement with the experimental data for the recirculation zone.

NOMENCLATURE

A_1, A_2, A_3	constants used in the correction factor for curvature effect on turbulence
B	width of the nozzle
C_D, C_1 and C_2	constants in the k-ε turbulence model
D	distance between the centre of the nozzles
D_k, D_ε	dissipation of kinetic energy and 'dissipation' of dissipation rate
F	curvature factor
G_k, G_ε	generation of turbulence kinetic energy and 'generation' of dissipation rate
G'_k	corrected generation rate of turbulence kinetic energy
k	turbulence kinetic energy
n	index of the iteration step
p	mean static pressure
R	radius of curvature
S_U, S_V	source terms in the momentum equations
S_c	correction factor for curvature effect on generation of turbulence
U_o	inlet velocity
U	mean velocity in the x direction
u	instantaneous velocity fluctuation in the x direction
V	mean velocity in the y direction
v	instantaneous velocity fluctuation in the y direction
x	cartesian coordinate
x_s	abscissa of the free stagnation point
y	cartesian coordinate

Greek Letters

ε	rate of dissipation of turbulence kinetic energy
ν_t	turbulent kinematic viscosity
ρ	density
$\sigma_k, \sigma_\varepsilon$	Prandtl numbers for the transport of k and ε respectively

INTRODUCTION

The objective of the present paper is to report the authors' experience in the prediction of a particular recirculating turbulent flow; specifically, we will report our experience with two numerical schemes, one hybrid and one upwind; and two turbulence models, one a widely utilized k-ε model and the other a simple modification of this model in which the generation of turbulence kinetic energy is dependent upon the streamline curvature and velocity gradient. As will be seen below, we regard our present conclusions as tentative; confirmation by other workers will be required. Nonetheless, we believe these conclusions to be of sufficient importance to justify their presentation now, since they do illuminate questions concerning the limitations on the predictive capacity of widely used methods.

The flow considered, shown in Fig. 1, is the recirculating turbulent incompressible flow produced by two plane parallel symmetric jets issuing normally from a single plane solid surface. The velocity field produced by such twin jets can be divided into three regions. The first, called the recirculation region, consists of two converging jet-like flows separated by two symmetric vortices. In this region a velocity profile measured in a plane parallel to the solid surface will display two velocity maxima and a velocity minimum with a negative value. In the second region, called the double jet region, the transverse velocity profile displays two velocity maxima separated by a positive valued minimum. Finally, there exists a third region in which the mean velocity distribution is similar to that generated by a single turbulent jet with a single velocity maximum. In the present paper we are concerned with the first region, that is, the recirculating region. Even within this region we shall not report in detail the experimental measurements; rather

---

[1] On leave from the Universidade de Sao Paulo, Departamento de Engenharia Mecanica, Sao Paulo, Brazil

PRECEDING PAGE BLANK-NOT FILMED

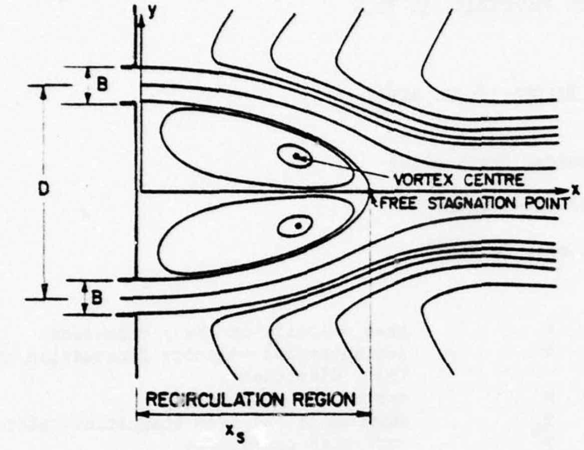

Fig. 1 Schematic of the symmetrical dual jet flow

we shall report here only sufficient data to allow the efficacy of the prediction method to be determined.[1]

In our view, the recirculation region of a twin-jet flow represents a particularly severe test of numerical prediction methods for two reasons. First, unlike many previously examined recirculating flows, the present flow is relatively unconstrained by bounding solid surfaces. As a consequence, there is little suppression of the effects of numerical diffusion, through the imposition of bounding streamlines via boundary conditions, compared with more constrained flows. Second, in the present flow the most severe misalignment of streamlines and the coordinate system occurs in regions of both high velocity and large velocity gradients; any tendency towards numerical diffusion is accentuated.

Despite this view, however, we should introduce a cautionary note concerning the generalization of our observations. At the present state-of-art, the predictive efficacy of any method for recirculating flows must be regarded as somewhat flow specific. In particular, we should not like any positive or negative conclusions about the prediction efficacy of a particular method <u>for a particular flow</u> to be generalized to a positive or negative conclusion in general. Rather we regard the present work as a very partial exploration of the boundaries of validity of particular types of calculation methods.

The Basic Problem

In the numerical calculation of turbulent recirculating flows there are two major sources of prediction error. They are the turbulent transport model utilized, and the numerical phenomenon called artificial or numerical diffusion. The latter source of error can be eliminated by the use of central differencing schemes and fine nodal point spacing.[1] This solution was not practical in the present problem for reasons of computation expense, and we were thus led to examine calculation procedures which utilized computationally less costly upwind or hybrid (upwind and central) differencing schemes.

The phrase artificial diffusion has been used in the literature in a generic sense to cover a variety of causes of over prediction of apparent diffusion. Therefore, it is useful for us to be specific about the sense in which we are using this phrase. In the present problem the main source of artificial diffusion in the recirculation zone is the misestimation of the convective terms in the high-velocity large-velocity-gradient regions, and our ultimate choice of prediction method has been based on the need to adequately represent these terms.

With regard to the turbulent transport model, various investigators [2,3,4,7,8] have commented upon the complexity of the turbulent structure and transport in flows with significant streamline curvature. In the present paper we initially used the k-ε model of Hanjalic [9]. This would appear to be the least complex model with the capacity to cope with recirculating flows [10], and it is a model which has been very extensively verified in a wide variety of non-recirculating flows. In addition it has been shown to yield reasonable results for some recirculating flows. As will be seen below, it did not prove adequate in the present problem, forcing us to modify it, in a crude manner, to account for streamline curvature effects.

The Mathematical Model

For a steady incompressible turbulent two-dimensional flow, the mass and momentum conservation equations can be expressed as:

$$\frac{\partial U}{\partial x} + \frac{\partial V}{\partial y} = 0 \qquad (1)$$

$$\frac{\partial}{\partial x}(U^2) + \frac{\partial}{\partial y}(UV) = \frac{\partial}{\partial x}(\nu_t \frac{\partial U}{\partial x}) + \frac{\partial}{\partial y}(\nu_t \frac{\partial U}{\partial y}) - \frac{1}{\rho}\frac{\partial p}{\partial x} + S_U \qquad (2)$$

$$\frac{\partial}{\partial x}(UV) + \frac{\partial}{\partial y}(V^2) = \frac{\partial}{\partial x}(\nu_t \frac{\partial V}{\partial x}) + \frac{\partial}{\partial y}(\nu_t \frac{\partial V}{\partial y}) - \frac{1}{\rho}\frac{\partial p}{\partial y} + S_V \qquad (3)$$

where ν_t represents the turbulent kinematic viscosity which is assumed to be adequately represented as a scalar quantity. Since the flow of present interest is a free shear flow, the molecular viscosity has been assumed negligible. The source terms include additional stress terms, namely:

$$S_U = \frac{\partial}{\partial x}(\nu_t \frac{\partial U}{\partial x}) + \frac{\partial}{\partial y}(\nu_t \frac{\partial V}{\partial x}) \qquad (4)$$

and

$$S_V = \frac{\partial}{\partial x}(\nu_t \frac{\partial U}{\partial y}) + \frac{\partial}{\partial y}(\nu_t \frac{\partial V}{\partial y}) \qquad (5)$$

---

[1] Detailed experimental data for all three regions and for both the symmetric and nonsymmetric cases may be found in Reference [1].

[1] We should note that convergence problems can arise when the nodal point spacing becomes too fine. This difficulty relates however, to the characteristics of the computer used. Presumably if cost is no impediment and if the required number of digits can be carried, the convergence problem would not exist.

AD-A055 654 PENNSYLVANIA STATE UNIV UNIVERSITY PARK DEPT OF MECH--ETC F/G 20/4
SYMPOSIUM ON TURBULENT SHEAR FLOWS HELD AT THE PENNSYLVANIA STA--ETC(U)
APR 77 N00014-77-C-0176

UNCLASSIFIED NL

9 OF 9
ADA
055654

END
DATE
FILMED
8-78
DDC

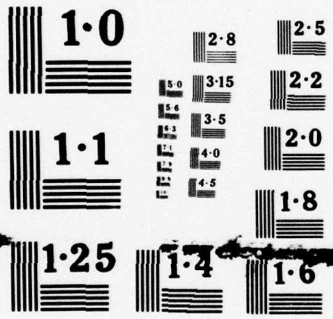

NATIONAL BUREAU OF STANDARDS

In the k-ε model the value of ν_t is assumed to be solely a function of the turbulence kinetic energy, k, and the rate of dissipation, ε. Dimensional analysis then yields:

$$\nu_t = C_D \frac{k^2}{\varepsilon} \qquad (6)$$

where C_D is a constant. The values of k and ε are assumed, in this model, to be determined by the k and ε transport equations (see Ref. [9]):

$$\frac{Dk}{Dt} = \frac{\partial}{\partial x}\left[\frac{\nu_t}{\sigma_k}\frac{\partial k}{\partial x}\right] + \frac{\partial}{\partial y}\left[\frac{\nu_t}{\sigma_k}\frac{\partial k}{\partial y}\right] + G_k - D_k \qquad (7)$$

and

$$\frac{D\varepsilon}{Dt} = \frac{\partial}{\partial x}\left[\frac{\nu_t}{\sigma_\varepsilon}\frac{\partial \varepsilon}{\partial x}\right] + \frac{\partial}{\partial y}\left[\frac{\nu_t}{\sigma_\varepsilon}\frac{\partial \varepsilon}{\partial y}\right] + G_\varepsilon - D_\varepsilon \qquad (8)$$

where D/Dt is the convective derivative and where G_k, D_k, G_ε, and D_ε are respectively the generation and dissipation of turbulence kinetic energy and rate of dissipation. The formulae expressing these quantities in terms of the mean flow field and k and ε may be determined by dimensional arguments similar to that used in the determination of ν_t, resulting:

$$G_k = \nu_t \left[2\left(\frac{\partial U}{\partial x}\right)^2 + \left(\frac{\partial U}{\partial y} + \frac{\partial V}{\partial x}\right)\frac{\partial U}{\partial y} + \left(\frac{\partial V}{\partial x} + \frac{\partial U}{\partial y}\right)\frac{\partial V}{\partial x} + 2\left(\frac{\partial V}{\partial y}\right)^2\right] \qquad (9)$$

$$D_k = \varepsilon \qquad (10)$$

$$G_\varepsilon = C_1 G_k \frac{\varepsilon}{k} \qquad (11)$$

$$D_\varepsilon = C_2 \frac{\varepsilon^2}{k} \qquad (12)$$

where C_1, C_2, σ_k, and σ_ε are assumed constants. Patankar [5] reports the following values for these constants: $C_D = 0.09$, $C_1 = 1.44$, $C_2 = 1.92$, $\sigma_k = 1.0$, and $\sigma_\varepsilon = 1.3$.

At this point we should observe that the above set of equations has been obtained at the expense of a variety of simplifying physical hypotheses. Hence the adequacy with which they can represent real flows cannot be determined <u>a priori</u>; rather only comparison of prediction and experiment can determine their adequacy. We make this observation because such validation is by its nature restricted in scope. Specifically, validation in flows in which the streamlines are near parallel or in flows in which the velocities in the regions of large streamline curvature are low, does not constitute validation for flows in which these conditions are not met. Indeed, various investigators have reported that the above equation set does <u>not</u> represent well the behaviour of many turbulent flows with large streamline curvature. This of course does not mean that the model is inadequate for a particular recirculating flow, since the prediction quality depends both on the quantities whose values are desired and on the influence of the recirculation region on the entire flow field under consideration.

As the present investigation proceeded, it became apparent that, for the twin jet flow recirculation region, the above mathematical model was not adequate. This inadequacy manifested itself in two ways. First, the predicted levels of turbulence kinetic energy were far too high. Indeed, the predicted levels were continuing to rise with further iterations in the solution procedure of Spalding-Patankar [5] and, as a consequence, the calculations were terminated before the converged values of k were obtained, although apparently the mean velocity field had converged. Second, the resultant mean velocity field was significantly in error. These observations are illustrated in Figures 2 and 3.

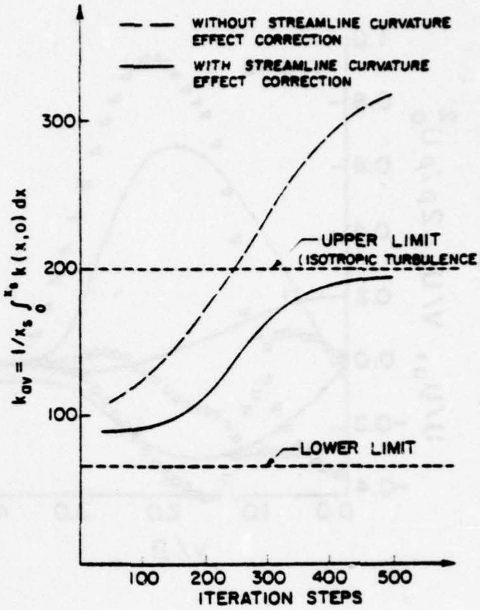

Fig. 2 Turbulence kinetic energy: convergence behaviour along the symmetry line in the recirculation region

On the basis of these results, the authors reexamined the turbulence model and the numerical procedure.

The Turbulence Model

As noted above, various authors have discussed the effects of streamline curvature on the turbulence structure. In particular, on the basis of their investigation of boundary layer flows over curved surfaces, So and Mellor [8] following Bradshaw [2] suggested that the appropriate parameter governing this effect was $(U/R)/(\partial U/\partial y)$, where R is the radius of streamline curvature. A simple generalization of this factor for a two-dimensional recirculating flow is:

$$F = \frac{\sqrt{U^2 + V^2}}{R\left(\frac{\partial U}{\partial y} + \frac{\partial V}{\partial x}\right)} \qquad (13)$$

where the radius of curvature, R, is given by:

$$\frac{1}{R} = \frac{UV\left(\frac{\partial V}{\partial y} - \frac{\partial U}{\partial x}\right)}{(U^2 + V^2)^{3/2}} \qquad (14)$$

The positive root is implied in both of the above expressions. It remains to incorporate the factor F into the k-ε turbulence model. Although, direct experiment data for the effect of F upon all second order

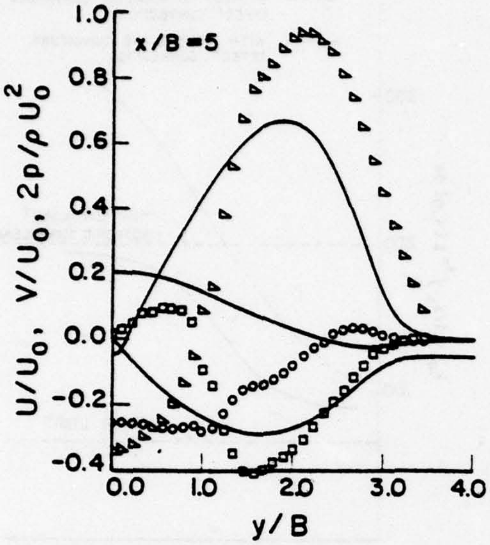

Fig. 3 Transverse velocity and static pressure profiles: the solid lines represent the predictions with the method of Ref. [5]; ▷ is the measured non-dimensional U velocity component, □ is the measured non-dimensional V velocity component and ○ is the non-dimensional static pressure

velocity fluctuation correlations are not available, Irwin and Arnot Smith [7] confirmed the strong correlation between F and the Reynolds stress $-\rho\overline{uv}$ as presented in Guitton's [4] data for a wall jet flow over a curved surface. Because the k-ε model implicitly assumes at least weak isotropy, and because the Reynolds stresses occur in the turbulent kinetic energy generation term, it is plausible to generalize Irwin and Arnot Smith's [7] findings to

$$G'_k = S_c G_k \tag{15}$$

where S_c is the correction factor for curvature. Irwin and Arnot Smith presented a correlation between F and $-\rho\overline{uv}$ in graphical form. A simple mathematical function which represents their graph adequately is:

$$S_c = A_1 \{1 - \exp [A_2(F - A_3)]\} \tag{16}$$

In the present work we have used the values:

$A_1 = 1.15$
$A_2 = 11.3$
$A_3 = 0.18$

For F values larger or equal to A_3, S_c is set to zero.

We should note that the value chosen for A_3 in the present investigation is consistent with the values reported by other investigators [7,8]; A_1 and A_2 were determined respectively from the apparent asymptote for large negative values of 1/R, and from the requirement that $S_c = 1$ at $1/R = 0$.

The substitution of G'_k for G_k in the turbulence kinetic energy and dissipation rate equations, as might be expected, did improve the predictions of turbulence kinetic energy within the recirculation zone, as shown in Figure 2. It did not unfortunately result in any significant improvement in the prediction of the mean velocity field.

At this stage we began to suspect that the difficulty lay not just in the turbulence model alone, but rather also in the numerical solution procedure. To this we now turn.

The Numerical Procedure

The results discussed above were obtained with the Spalding-Patankar method described in detail in Ref. [6]. Here we need only concern ourselves with the calculation of the momentum fluxes through the surfaces of the elemental control volume depicted in Figure 4. Without any loss of clarity we can consider only the convective flux through the westward facing surface; further for convenience the x-component of velocity is assumed positive. The convective flux may be determined from the product of the mass flow through the surface and an appropriate approximation of the actual value of the convected momentum. In the Spalding-Patankar method the former quantity is estimated from the expression $\rho(U_{W,n} + U_{P,n})/2$ where the second subscript, n, indicates the values obtained in the previous iteration. The value of the convected specific x-momentum is approximated as $U_{W,n+1}$ for large grid Reynolds numbers.[1] When U varies significantly over the distances Δx and Δy, and when V is of the same order as U, it is apparent that $U_{W,n+1}$ will be a poor estimate of the convected specific x-momentum. A better estimate can be obtained by replacing $U_{W,n+1}$ with some weighted average of $U_{NW,n+1}$, $U_{W,n+1}$ and $U_{SW,n+1}$; the precise weighting depending on the relative values of the x and y velocity components. We should observe here that the accuracy of the Spalding-Patankar estimation of convective momentum flux can be improved if Δx and Δy are reduced. Thus in problems where such reduction is economic, their method should provide an adequate answer. Whether or not such an approach is possible depends on the specific flow. In the present situation this was simply not possible, due to the large separation of the two injection slots. Indeed, with 40 grid lines in the cross flow direction with a spacing of 0.125B, and with 30 in the x direction with a spacing of 0.5B, the Spalding-Patankar predictions were almost completely unchanged when the turbulence model was replaced with a low constant value of effective viscosity, indicating that the artificial diffusion was completely dominating the predicted flow pattern.

An alternative approach, that is, an approach which sought to improve the estimated value of the convected quantity while maintaining a coarse grid, was followed by Raithby. The details of his skewed upstream differencing scheme (SUDS) have been reported by Raithby [6] and need not be repeated here; it will suffice to maintain that his method employs a weighted average of $U_{NW,n+1}$, $U_{W,n+1}$, and $U_{SW,n+1}$ to estimate the specific convected momentum in the example considered. Even though negative coefficients arise in the finite difference algebraic equations no major convergence problems were encountered.

---

[1] based on the velocity component, the grid spacing and the effective viscosity

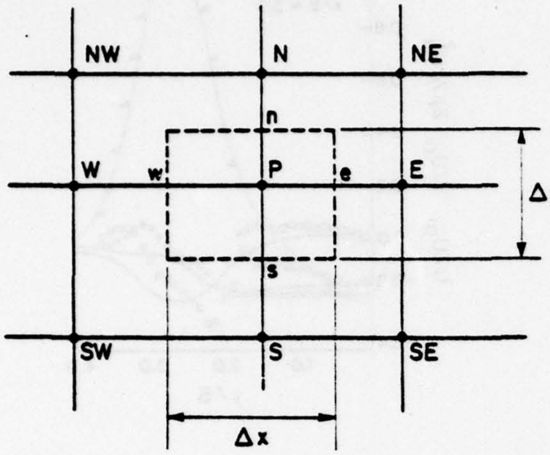

Fig. 4 A typical control volume used in the numerical calculations

Therefore, the final calculation procedure utilized Raithby's numerical calculation method and the modified k-ε turbulence model discussed previously. The following boundary conditions were specified.

i) Symmetry line: $V = 0$, $\partial U/\partial y = 0$, $\partial p/\partial y = 0$, $\partial k/\partial y = 0$ and $\partial \varepsilon/\partial y = 0$
ii) Inlet boundary: $V = 0$, $U = U_o$, $k = 1.81 \cdot 10^{-4} \cdot U_o^2$ and $\varepsilon = 1.35 \cdot 10^{-4} \cdot U_o^3/B$
iii) Free stream boundary: $\partial V/\partial y = 0$, $U = 0$, $p = 0$, $k = 1.81 \cdot 10^{-4}\, U_o^2$ and $\varepsilon = 1.47 \cdot 10^{-7}\, U_o^3/B$
v) Downstream boundary: $V = 0$, $\partial U/\partial x = 0$ and arbitrary values for k and ε.

The resultant predictions are compared with experimental data in the following section.

Comparison of Prediction and Experiment

The predicted velocity fields for various downstream stations in the recirculation zone are shown in Figure 5. Three quantities are presented: i) the x velocity component; ii) the y velocity component; and iii) the static pressure. The experimental data were obtained on an apparatus described in detail elsewhere [1]. The agreement between prediction and experiment is excellent; indeed the agreement is largely within the experimental uncertainty.

An overall comparison of prediction and experiment is shown in Figure 6, in which the upper half plane represents the predicted streamlines, and the lower half plane experimental streamlines. Again agreement is excellent, all features of the recirculating zone being well represented.

CONCLUSIONS

For the flow of present interest, the modified turbulence model and the calculation procedure of Raithby yield excellent predictions with a node spacing which results in economically feasible calculation expense.

ACKNOWLEDGEMENT

One of the authors, Julio Militzer, would like to acknowledge the financial support of 'Coordenacao do Aperfeicoamento de Pessoal de Nivel Superior (CAPES)' 'Fundacao de Amparo a Pesquisa do Estado de Sao Paulo (FAPESP)' both from Brazil. The third author, S. A. Alpay, gratefully acknowledges the support of the National Research Council of Canada, Grant No. 1644.

REFERENCES

1 Militzer, J., "Dual Plane Parallel Turbulent Jets: The Measurement and Prediction of the Mean Velocity Field", Ph.D. Thesis, U. of Waterloo, 1977.
2 Bradshaw, P., "The analogy between streamline curvature and buoyancy in turbulent flow", J. Fluid Mechanics, Vol. 36, pp. 177-191, 1969.
3 Bradshaw, P., "Review-complex turbulent flows", Journal of Fluids Engineering (ASME), June 1975.
4 Guitton, E., Ph.D. Thesis, McGill University, 1970.
5 Patankar, S.V., "Numerical prediction of three-dimensional flows", published in "Studies in Convection: Theory Measurement and Application", Vol. 1, edited by B.E. Launder, Academic Press, London, 1975.
6 Raithby, G.D., "Skew-upstream differencing schemes for problems involving fluid flow", Computer Methods in Applied Mechanics and Engineering, Vol. 5, pp. 151-162, 1976.
7 Irwin, H.P.A.H., and Arnot Smith, P., "Prediction of the effect of streamline curvature on turbulence", The Physics of Fluids, Vol. 18, No. 6, June 1975.
8 So, R.M.C. and Mellor, G.L., "Experiment on convex curvature effects in turbulent boundary layers", J. Fluid Mechanics, Vol. 60, pp. 43-62, 1973.
9 Hanjalic, K., "Two dimensional asymmetrical turbulent flow in ducts", Ph.D. Thesis, University of London (1970).
10 Launder, B.E. and Spalding, D.B., "Lectures in mathematical models of turbulence", Academic Press, 1972.

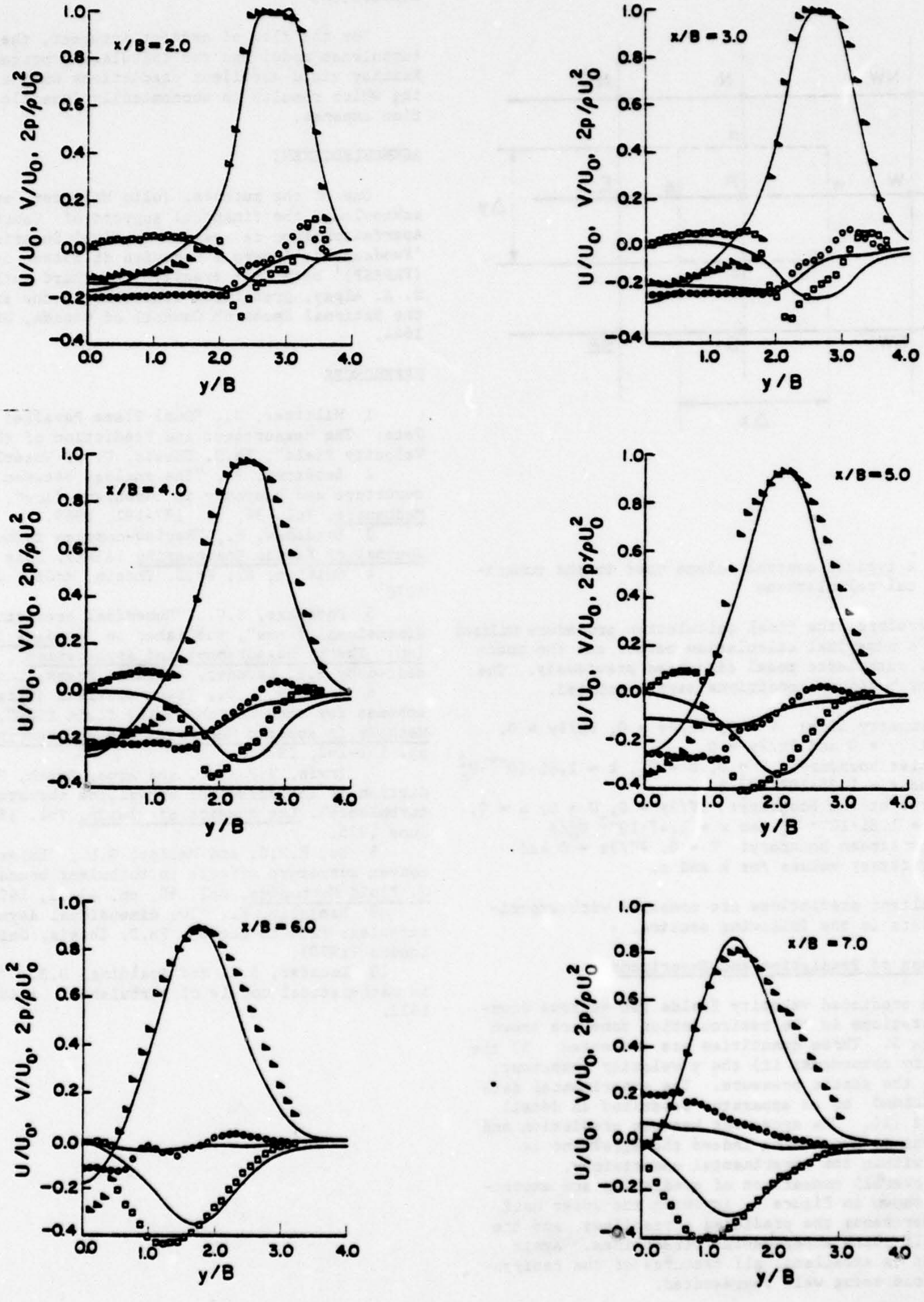

Fig. 5 Present predictions and experimental data for transverse velocity and static pressure profiles: the solid lines represent the predictions; ◣ is the measured non-dimensional U velocity component; □ is the measured non-dimensional V velocity component and ○ is the measured non-dimensional static pressure

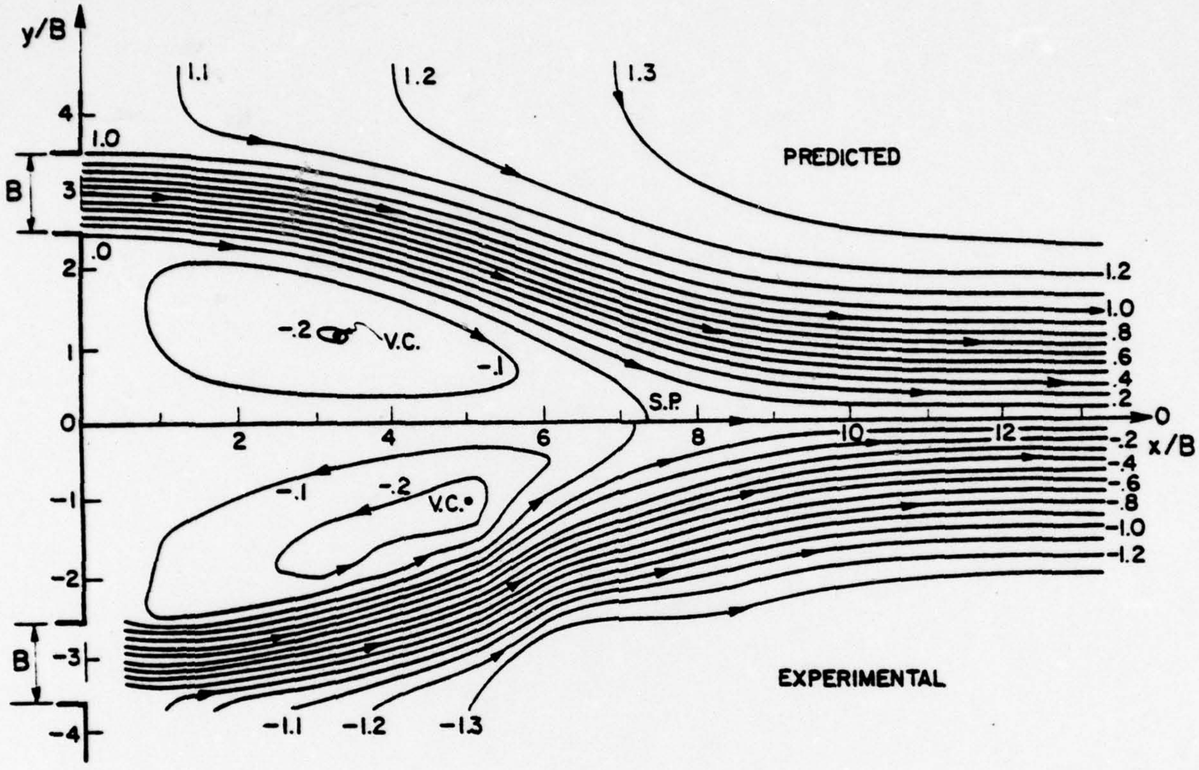

Fig. 6 Comparison of predicted and experimental streamline patterns

NUMERICAL ANALYSIS OF TURBULENT SEPARATED SUBSONIC DIFFUSER FLOW[1]

John C. Chien[2]

ARO, Inc.
Arnold Air Force Station, Tennessee 37389, USA

ABSTRACT

Separated subsonic diffuser flows are solved numerically with the steady state, incompressible Navier-Stokes equations. The effects of turbulence are introduced by a low Reynolds number two-equation k-ε model. A coordinate transformation and a general finite difference formulation with decay functions was employed to obtain convergent solutions for separated and non-separated diffuser flows with a fully developed non-uniform inlet condition. Solution of the flow field includes the prediction of the point of separation, the velocity, turbulent kinetic energy and total shear stress fields and the skin friction distribution.

NOMENCLATURE

A	Parameter
a	Constant
a_1, a_2	Coefficient
b	Constant
b_1, b_2	Coefficients
C_1, C_2	Coefficients
C_f	Skin friction coefficient
C_μ	Eddy viscosity coefficient
C	Transformation coefficient
d	Source term
F	Transformation parameter
G_i, G_j	Decay functions
h	Channel or 2-D diffuser height
JNM	Number of grid points along the r coordinate
k	Turbulent kinetic energy
R	Parameter, $k^2/(\nu\varepsilon)$
R_e	Reynolds number
R_i, R_j	Grid Reynolds number
$r, \tilde{r}$	Physical and transformed radial coordinate
$\tilde{r}_{max}$	Diffuser wall coordinate in transformed plane
$s(x)$	Diffuser wall coordinate in physical plane
u, v	Axial velocity and radial velocity components
$\overline{u}$	Average axial velocity at diffuser inlet
u', v', w'	Turbulent velocity components
x	Axial coordinate
y	Radial coordinate measured from the wall
α, β	Transformation parameters
δ	Index, zero for planar flow, 1 for axisymmetric flow or incremental
ε	Isotropic part of the total turbulent kinetic energy dissipation, $k^{3/2}/\ell$
η	Relaxation factor
2θ	Total diffuser divergence angle
ν	Molecular viscosity
ν_t	Eddy viscosity
σ_ε	Constant
τ	Shear stress
ϕ	Dependent variable
Ψ	Stream function
Ω	Vorticity

Subscripts

c	Centerline
I	Location of the beginning of the inlet section
max	Maximum
0	Sublayer-core region solution matching location
T	Total
w	Wall

---

[1] The research reported in this paper was sponsored by Arnold Engineering Development Center (AEDC), Air Force Systems Command (AFSC), Arnold Air Force Station, Tennessee, under Contract No. F406-75-C-0004 with ARO, Inc. Further reproduction is authorized to satisfy the needs of the U. S. Government.

[2] Research Engineer, Fluid Mechanics Section, Technology Applications Branch, Engine Test Facility.

PRECEDING PAGE BLANK-NOT FILMED

1.0 INTRODUCTION

Diffusers are an important component of many flow devices, such as propulsion systems, wind tunnels, test facilities, etc. Yet the prediction of diffuser flows remains as one of the most difficult fluid dynamics problems, especially when the inlet conditions to the diffuser are highly nonuniform. Since the optimum operating condition for a diffuser, i.e., maximum pressure recovery, has been shown experimentally to occur with *flow separation* (1), a realistic solution for the flow field can only be obtained by solving the full Navier-Stokes equations. In addition, the diffuser flows of practical interest are turbulent in nature. The performance of a diffuser depends not only on the shape of the inlet velocity profile but also on the turbulence level. The modeling of turbulence with the large pressure gradient existing in the diffuser flows requires a more sophisticated approach than the use of simple eddy viscosity models (2).

Currently, diffuser design information is obtained almost solely from empirical data (1, 3). Many of the available diffuser performance maps and correlations provide only static pressure recovery. Very few detailed turbulence properties of diffuser flows, established experimentally, are available even for nonseparated cases (2,4). Data for separated diffuser flows are even more sparse because conventional instruments, such as the hot wire anemometer, cannot provide meaningful measurement in regions where the flow direction reverses with time. This situation may improve in the future as the recently developed laser velocimeter (5,6) becomes more available and reliable so that the flow field data can be obtained for use in the development and verification of analytical prediction methods.

In the past, the flow in a diffuser has been analyzed by assuming that the diffuser flow field can be approximated by a thin boundary layer adjacent to the wall and an inviscid core in the center of the diffuser. The boundary layer and the inviscid core equations are then solved with or without interaction (7,8,9). No rigorous method is available to analyze diffuser flows with a highly nonuniform inlet profile with or without separation (10,11).

The purpose of the investigation reported herein is to develop numerical prediction methods for the calculation of turbulent, incompressible, separated, subsonic diffuser flows with nonuniform inlet conditions. The theory development, the turbulence models, the coordinate transformation and the numerical finite difference solution procedures are presented along with comparisons of the results with available experimental data. Complete details of the present work are available in (12).

2.0 GOVERNING EQUATIONS AND TURBULENCE MODELS

The basic equations which describe the motion of laminar or turbulent flow of an incompressible fluid are the Navier-Stokes equations. Usually, the time-averaged Reynolds equation is used to describe the turbulent flow. The Reynolds stresses introduced in the Reynolds equation are related to the velocity gradient and the turbulent kinetic energy fields through an eddy viscosity concept as (13,14,15).

$$\begin{aligned}
\overline{u'^2} &= -2\nu_t \frac{\partial u}{\partial x} + \frac{2}{3}k \\
\overline{v'^2} &= -2\nu_t \frac{\partial v}{\partial r} + \frac{2}{3}k \\
\overline{w'^2} &= -2\nu_t \frac{v}{r} + \frac{2}{3}k \\
\overline{u'v'} &= -\nu_t \left(\frac{\partial u}{\partial r} + \frac{\partial v}{\partial x}\right) \\
k &= \left(\overline{u'^2} + \overline{v'^2} + \overline{w'^2}\right)/2
\end{aligned} \tag{1}$$

The vorticity-stream function formulation can be obtained by taking the curl operation of the momentum equations and by defining the stream function from the continuity equation. The resulting equations are the vorticity equation:

$$\begin{aligned}
&\left\{\frac{\partial^2\Omega}{\partial x^2} + \frac{\partial^2\Omega}{\partial r^2}\right\} - \frac{1}{(\nu+\nu_t)}\left\{\left(u - 2\frac{\partial\nu_t}{\partial x}\right)\frac{\partial\Omega}{\partial x} + \left(v - 2\frac{\partial\nu_t}{\partial r} - \frac{\delta}{r}(\nu+\nu_t)\right)\frac{\partial\Omega}{\partial r}\right\} \\
&+ \frac{1}{(\nu+\nu_t)}\left\{\delta\Omega\left[\frac{v}{r} + \frac{1}{r}\frac{\partial\nu_t}{\partial r} - \frac{(\nu+\nu_t)}{r^2}\right] + \left(\frac{\partial^2\nu_t}{\partial x^2} - \frac{\partial^2\nu_t}{\partial r^2}\right)\left(\frac{\partial v}{\partial x} + \frac{\partial u}{\partial r}\right)\right. \\
&\left. + 2\left(\frac{\partial^2\nu_t}{\partial x\partial r}\right)\left(\frac{\partial v}{\partial r} - \frac{\partial u}{\partial x}\right)\right\} = 0
\end{aligned} \tag{2}$$

and the stream function equation:

$$\left\{\frac{\partial^2\psi}{\partial x^2} + \frac{\partial^2\psi}{\partial r^2}\right\} - \left(\frac{\delta}{r}\right)\frac{\partial\psi}{\partial r} + r^\delta\Omega = 0 \tag{3}$$

where Ω is the vorticity defined as

$$\Omega = \frac{\partial v}{\partial x} - \frac{\partial u}{\partial r} \tag{4}$$

The velocity is calculated from the relations

$$u = \left(\frac{1}{r}\right)^\delta \frac{\partial\psi}{\partial r} \tag{5}$$

$$v = -\left(\frac{1}{r}\right)^\delta \frac{\partial\psi}{\partial x} \tag{6}$$

The eddy viscosity introduced in Eq. (1) is calculated from a two-equation model developed in (16) but with the coefficient C_μ and the dissipation term near the wall determined differently (12). The eddy viscosity is determined in (16) from the Prandtl-Kolmogorov formula,

$$\nu_t = C_\mu \frac{k^2}{\varepsilon} \tag{7}$$

For low Reynolds number model, C_μ in Eq. (7) is redefined in the present study as

$$C_\mu = \frac{A}{3(a + A/b)} \tag{8}$$

where $A = \sqrt{2k}\, y/\nu$, y is measured from the wall, and a and b are constants. C_μ was determined from Eq. (7) with ν_t and (k^2/ε) distributions proposed by Mellor and Herring (17,18). The constant a is taken to be 1100 and b is determined as 0.27.

The TKE and its dissipation can be calculated from the following equation, The k-Equation:

$$\left\{\frac{\partial^2 k}{\partial x^2}+\frac{\partial^2 k}{\partial r^2}\right\}-\frac{1}{(\nu+\nu_t)}\left\{\left[u-\frac{\partial \nu_t}{\partial x}\right]\frac{\partial k}{\partial x}+\left[v-\frac{\partial \nu_t}{\partial r}-\delta\frac{(\nu+\nu_t)}{r}\right]\frac{\partial k}{\partial r}\right\}$$

$$+\frac{\nu_t}{(\nu+\nu_t)}\left\{2\left[\left(\frac{\partial u}{\partial x}\right)^2+\left(\frac{\partial v}{\partial r}\right)^2+\left(\frac{v}{r}\right)^2\delta\right]+\left(\frac{\partial u}{\partial r}+\frac{\partial v}{\partial x}\right)^2\right\} \tag{9}$$

$$-\frac{1}{(\nu+\nu_t)}\left\{\varepsilon+2\nu\frac{k}{y^2}\right\}=0$$

The ε-Equation:

$$\left\{\frac{\partial^2 \varepsilon}{\partial x^2}+\frac{\partial^2 \varepsilon}{\partial r^2}\right\}-\frac{1}{(\nu+\nu_t/\sigma_\varepsilon)}\left\{\left[u-\frac{\partial}{\partial x}\left(\frac{\nu_t}{\sigma_\varepsilon}\right)\right]\frac{\partial k}{\partial x}+\left[v-\frac{\partial}{\partial r}\left(\frac{\nu_t}{\sigma_\varepsilon}\right)-\frac{\delta}{r}\frac{\nu_t}{\sigma_\varepsilon}\right]\frac{\partial k}{\partial r}\right\}$$

$$+C_1\frac{\nu_t}{(\nu+\nu_t/\sigma_\varepsilon)}\frac{\varepsilon}{k}\left\{2\left[\left(\frac{\partial u}{\partial x}\right)^2+\left(\frac{\partial v}{\partial r}\right)^2+\left(\frac{v}{r}\right)^2\delta\right]+\left(\frac{\partial u}{\partial r}+\frac{\partial v}{\partial x}\right)^2\right\} \tag{10}$$

$$-C_2\frac{1}{(\nu+\nu_t/\sigma_\varepsilon)}\frac{\varepsilon^2}{k}=0$$

where $C_1 = 1.44$, $C_2 = 1.92\ (1-0.3\ \exp(-R^2))$, $\sigma_\varepsilon = 1.1$ and $R = k^2/(\nu\varepsilon)$.

Equations (2), (3), (5), (6), (7), (9), and (10) form a set of nonlinear partial differential equations for the unknowns Ω, ψ, u, v, ν_t, k and ε. Since the equations are elliptic in nature, the solution can be found only when the boundary conditions are given along a closed boundary of the computational domain. In the diffuser application, the domain is the flow field inside the diffuser and the boundaries are the diffuser wall, the inlet and the exit planes. In the present analysis, the domain is transformed into a rectangular grid and the numerical computations are performed in the transformed domain.

3.0 A COMPLETE COORDINATE TRANSFORMATION FOR A DIFFUSER FLOW

Both a body-aligned coordinate transformation and a sublayer stretching are necessary to provide good spatial resolution throughout a diffuser flow field. The complete coordinate transformation is achieved first by mapping the diffuser shape into a rectangular domain followed by a sublayer stretching (see Fig. 1). The complete transformation is given by

$$x = \tilde{x} \tag{11}$$

in the sublayer region,

$$r = S(x)\left\{1-\frac{\alpha}{\beta}\tan\beta(\tilde{r}_{max}-\tilde{r})\right\}\ ,\quad \tilde{r}_0 \le \tilde{r} \le \tilde{r}_{max} \tag{12}$$

in the core region,

$$r = S(x)\left\{1-\left[C(\tilde{r}_{max}-\tilde{r})+\ln\left[\cosh(\tilde{r}_0-\tilde{r})\right]+F\right]\right\},\quad 0 \le \tilde{r} \le \tilde{r}_0 \tag{13}$$

where r is measured from the centerline, s(x) represents the diffuser wall shape, $\tilde{r}_0$ is the transformed matching location and $\tilde{r}_{max}$ is the transformed wall shape. A typical coordinate transformation is shown in Fig. 2, with y and $\tilde{y}$ measured from the wall.

The ability of the coordinate transformation to provide good resolution in the transformed coordinate plane is demonstrated by considering the velocity and the turbulent kinetic energy distributions in a channel flow shown in physical coordinates in Fig. 3a. It can be seen that large gradients of the velocity and turbulent kinetic energy profiles exist near the wall. Poor resolution can be expected in the sublayer region when attempting to use a uniform coordinate system to describe the profiles. However, when Eqs. (12) and (13) are used to stretch the sublayer and the core region, sharp gradients in velocity profiles diminish as indicated in Fig. 3b. Thus, the detail velocity and turbulent kinetic energy profiles can be adequately described in the transformed coordinates. For this reason, the coordinate transformation plays an important role in obtaining an accurate numerical solution.

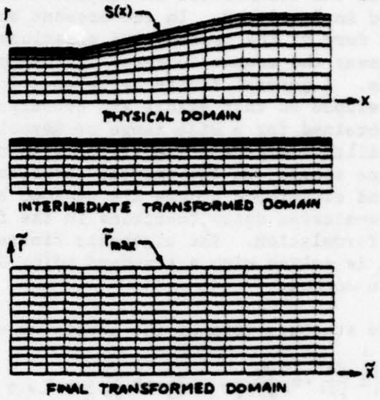

Fig. 1 A complete transformation for a diffuser

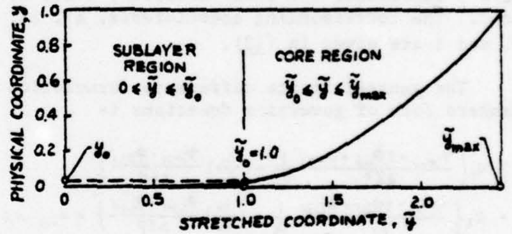

Fig. 2 Coordinate transformation with a sublayer stretching

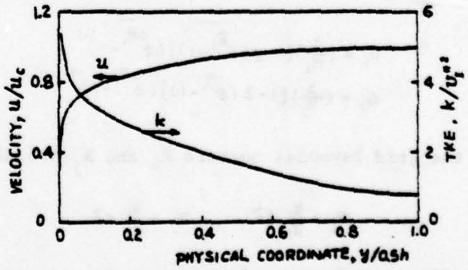

(a) Profiles in physical coordinate

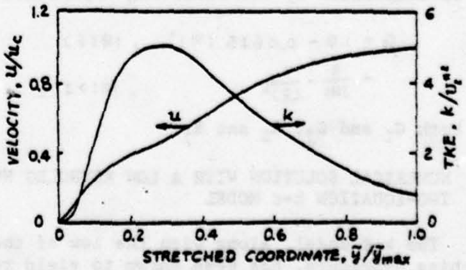

(b) Profiles in transformed coordinate

Fig. 3 Velocity and turbulent kinetic energy profiles in physical and transformed coordinates

4.0 FINITE DIFFERENCE FORMULATION AND NUMERICAL SOLUTION PROCEDURE

The governing equations and the turbulence models presented in the previous sections are a system of coupled nonlinear partial differential equations. The system cannot be solved analytically and, therefore, must be solved by numerical methods. The system of equations becomes even more complicated when it is written in the transformed coordinates such as those described in Section 3. In the present analysis, a standard form of the transformed equations is derived to represent the common features of the governing equations. A general finite difference formulation is then developed so that stable and convergent solutions can be obtained for a wide range of Reynolds number. The stability limitation associated with the central difference scheme and the accuracy problem inherent to the upwind difference scheme are avoided by the use of locally-evaluated decay functions in the finite-difference formulation. The algebraic finite difference equation is solved with a standard point Gauss-Seidel iteration method.

The standard form of the governing equations is

$$\left\{a_1\frac{\partial^2\phi}{\partial\tilde{x}^2}+a_2\frac{\partial^2\phi}{\partial\tilde{r}^2}\right\}-\left\{b_1\frac{\partial\phi}{\partial\tilde{x}}+b_2\frac{\partial\phi}{\partial\tilde{r}}\right\}+d=0 \qquad (14)$$

where ϕ represents the flow variables, i.e., Ω, ψ, k, and ε. The corresponding coefficients, a_1, a_2, b_1, b_2, and d are given in (12).

The general finite difference formulation of the standard form of governing equations is

$$\begin{aligned} a_1&\left\{\frac{\phi_{i+1,j}-2\phi_{i,j}+\phi_{i-1,j}}{\delta\tilde{x}^2}\frac{1}{G_i}-\left(\frac{b_1}{a_1}\right)\frac{\phi_{i+1,j}-\phi_{i-1,j}}{2\delta\tilde{x}}\right\}\\ +a_2&\left\{\frac{\phi_{i,j+1}-2\phi_{i,j}+\phi_{i,j-1}}{\delta\tilde{r}^2}\frac{1}{G_j}-\left(\frac{b_2}{a_2}\right)\frac{\phi_{i,j+1}-\phi_{i,j-1}}{2\delta\tilde{r}}\right\}+d_{i,j}=0\end{aligned} \qquad (15)$$

where the decay functions G_i and G_j are determined from (19)

$$\begin{aligned} G_i&=\left(\frac{2}{R_i}\right)\left[1-2\left(e^{R_i}-1\right)\right]\left(e^{2R_i}-1\right)^{-1}\\ G_j&=\left(\frac{2}{R_j}\right)\left[1-2\left(e^{R_j}-1\right)\right]\left(e^{2R_j}-1\right)^{-1}\end{aligned} \qquad (16)$$

and the grid Reynolds numbers R_i and R_j are defined as

$$R_i=\frac{b_1}{a_1}\delta\tilde{x} \quad , \quad R_j=\frac{b_2}{a_2}\delta\tilde{r} \qquad (17)$$

The calculation of the decay functions G_i and G_j can be simplified by the following approximation:

$$\begin{aligned} G&=1.0-0.0625\,(R)^2 \quad , \ |R|\le 2\\ &=\frac{2}{|R|}-\frac{1}{(R)^2} \quad , \ |R|>2\end{aligned} \qquad (18)$$

for both G_i and G_j, R_i and R_j.

5.0 NUMERICAL SOLUTION WITH A LOW REYNOLDS NUMBER TWO-EQUATION k-ε MODEL

The k-ε model, along with the law of the wall matching procedure, has been shown to yield reasonable results for flows in which the law of the wall is applicable, (12). However, the validity of the law of the wall is questionable in the vicinity of the separation point. In order to avoid using the law of the wall, the whole flow including the sublayer region is solved by the finite difference formulation so that the point of separation and the separated flow field can be predicted. The numerical formulation of the whole flow field requires the use of the low Reynolds number version of the k-ε model as well as a sublayer coordinate stretching techniques.

5.1 NUMERICAL RESULTS FOR A FULLY DEVELOPED CHANNEL FLOW

The calculated velocity profiles with Reynolds numbers, $\bar{u}h/\nu$, ranging from 1,657 to 207,000 are shown in Fig. 4. The profile shape changes from near parabolic at the low Reynolds number to a fuller profile at higher Reynolds number. At Reynolds number 1,657, the profile agrees well with the experimental data of Patel and Head (20). Results at higher Reynolds number also agree well with Laufer's data (21). The skin friction coefficient is presented in Fig. 5. The agreement between the numerical result and the experimental data (22) is very good.

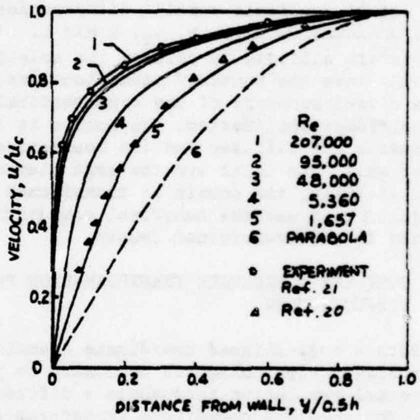

Fig. 4 Velocity distributions in a fully developed channel flow

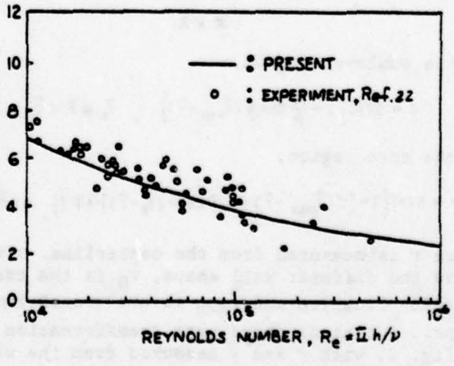

Fig. 5 Skin friction coefficient for fully developed channel flow

When the low Reynolds number k-ε model is used to calculate the eddy viscosity in the numerical iteration, it is necessary to use an underrelaxation factor on ν_t to provide smooth convergence. The optimum underrelaxation factor on ν_t was found to be (1/JNM), where JNM is the number of lateral grid points. The effect of the total number of grid points on the accuracy of the numerical solution is shown in Fig. 6. With only 41 grid points, the calculated total shear stress deviates substantially from the exact solution. On the other hand, the 101 point case is in excellent agreement with the exact solution. It was found that the TKE distribution is relatively sensitive to the grid arrangement, especially at high Reynolds number. When the grid arrangement is not adequate in the sublayer region, the error associated with the calculated TKE distribution is magnified and transmitted to the eddy viscosity through the Prandtl-Kolmogorov's formula, Eq. (7). Improvement in the coordinate stretching in the sublayer region and a better understanding of the grid arrangement could provide optimum use of the grid points.

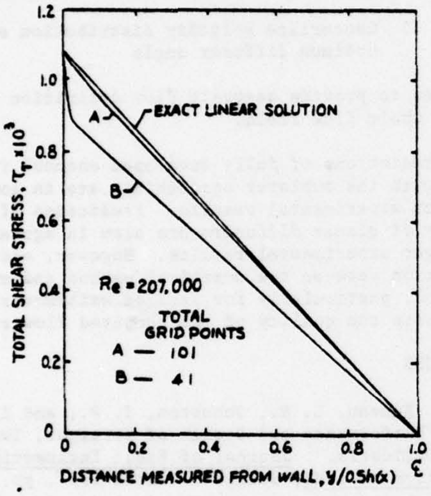

Fig. 6 Effect of total grid points on the total shear stress distribution for fully developed channel flow

5.2 NUMERICAL SOLUTION OF SEPARATED AND NONSEPARATED DIFFUSER FLOW

A series of preliminary calculation was made for a family of planar diffuser flows to illustrate the nature of the solution. The test case selected is a two-dimensional planar diffuser with a 4:1 aspect ratio, investigated by Reneau, et al. (1). The Reynolds number based on the inlet velocity $\overline{U}$ and the height h_I was 1.2×10^5. The inlet profile was a fully developed channel flow profile.

Fifty-one lateral grid points are used across the diffuser which includes both the core and the sublayer region. The number of grid points is considered adequate to provide a qualitative description of the flow field but not necessarily an accurate result. In the iteration process, the first 600 iterations are used to determine the flow field at the first three stations so that a fully developed channel flow profile can be obtained. With the inlet condition established, the next 600 iterations are used to compute the diffuser flow field. The calculated skin friction coefficient is shown in Fig. 7 for six different angles. Based on the skin friction distributions, flow separation does not occur in the first three cases, namely 2θ = 3.58, 7.15, and 14.25 deg. The point of separation, which appears in the last three cases, moves upstream as the diffuser angle increases. The skin friction coefficient near the exit corner ($x/h_I = 6$) in the separated region shows some oscillation, which indicates that the solution is not fully converged. However, the solution is stable upstream of the separation point.

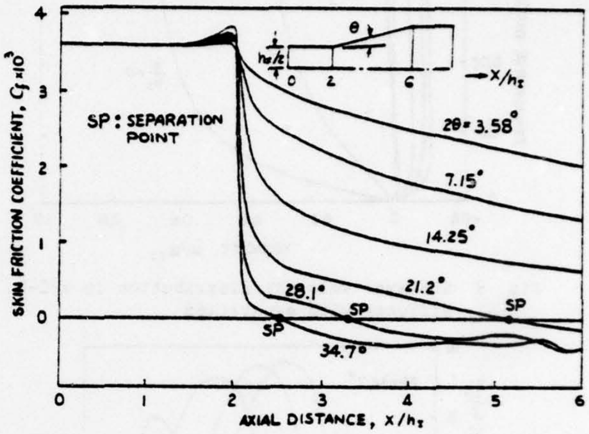

Fig. 7 Skin friction coefficient distributions in 2-D diffuser with a fully developed inlet velocity profile

The development of the velocity profile in the diffuser is shown in Fig. 8 for 2θ = 34.7 deg. As the axial distance increases, the fully developed channel flow profile gradually develops into a wake profile near the wall. For the separated profiles, the sublayer is so thin that it appears as if the velocity profile has a discontinuity near the wall. The velocity profile in the sublayer with an enlarged scale is shown in Fig. 9. The value of the reverse flow velocity near the wall at $x/h_I = 6$ is about 14 percent of the local centerline velocity. The predicted turbulent kinetic energy distribution is shown in Fig. 10. The distinctive feature of the turbulent kinetic energy distribution is that the location of the maximum TKE moves away from the wall in the diverging section. In general, the magnitude of the maximum TKE also increases in the diffuser diverging section. For 2θ = 34.7 deg, the maximum TKE at $x/h_I = 6$ is roughly doubled the maximum inlet computed value.

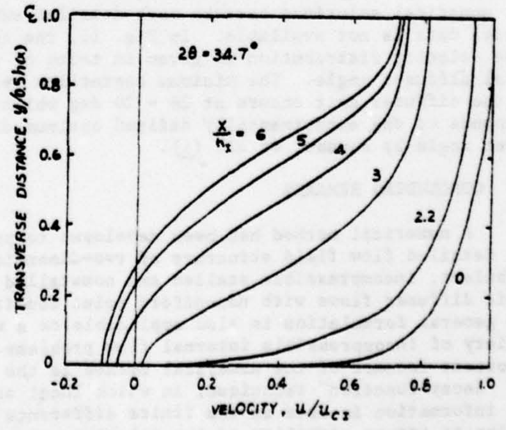

Fig. 8 Velocity distributions in a 2-D diffuser with separation

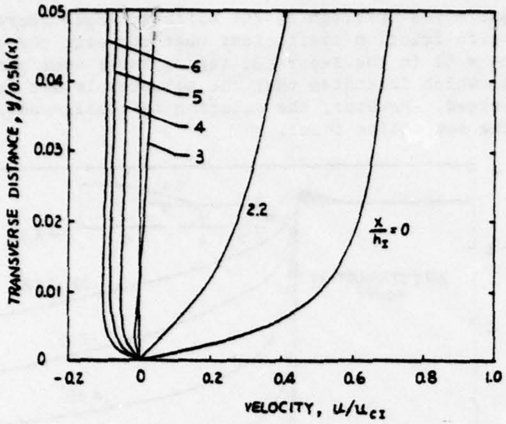

Fig. 9 Sublayer velocity distribution in a 2-D diffuser with separation

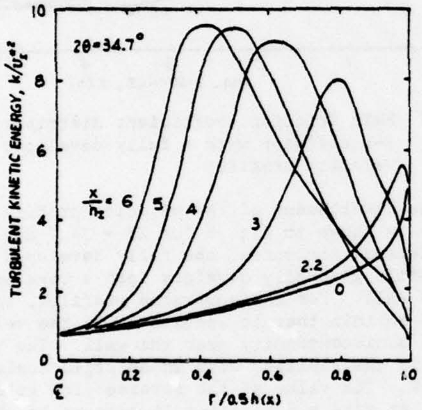

Fig. 10 Turbulent kinetic energy distributions in a 2-D diffuser with separation

Although there is no detailed flow field data available to verify the predicted flow field structure, the centerline velocity distribution is an indication of the pressure recovery. The data of (1) showed that the maximum pressure recovery occurred with a total diffuser angle of 20 deg. This experimental evidence is used to provide limited verification for the present numerical solutions because more detailed experimental data is not available. In Fig. 11, the centerline velocity distribution is given in terms of the total diffuser angle. The minimum centerline velocity at the diffuser exit occurs at 2θ = 20 deg which corresponds to the experimentally defined optimum diffuser angle by Reneau, et al. (1).

6.0 CONCLUDING REMARKS

A numerical method has been developed to provide the detailed flow field structure of two-dimensional, turbulent, incompressible stalled and nonstalled subsonic diffuser flows with nonuniform inlet conditions. The general formulation is also applicable to a wide variety of incompressible internal flow problems. An important feature of the numerical method is the use of the "decay function" technique, in which local analytical information is used in the finite difference formulation to insure stability of the solution. A coordinate transformation including sublayer stretching was developed to provide adequate flow definition throughout the whole flow field.

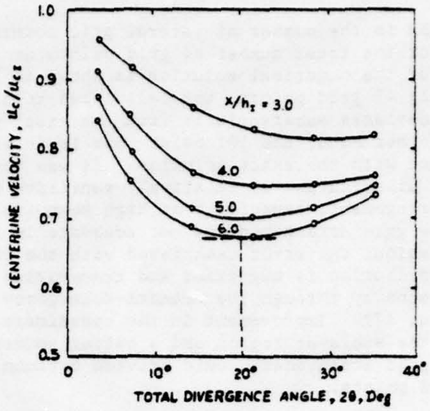

Fig. 11 Centerline velocity distribution and the optimum diffuser angle

Predictions of fully developed channel flows, obtained with the sublayer stretching, are in good agreement with experimental results. Prediction of the performance of planar diffusers are also in agreement with the meager experimental results. However, additional correlation between the numerical method and experiment is needed, particularly for stalled axisymmetric flows, to validate the quality of the computed flow structure.

REFERENCES

1 Reneau, L. R., Johnston, J. P., and Kline, S. J., "Performance and Design of Straight, Two-Dimensional Diffusers," Journal of Basic Engineering, Transaction of ASME, Series D, March 1967, pp. 141-150.

2 Boldman, D. R. and Newmann, H. E., "Experimental and Analytical Study of a Conically Diffused Flow with a Nearly Separated Boundary Layer," NASA TN D-7486, November 1973.

3 Dolan, F. X. and Runstadler, P. W., Jr., "Pressure Recovery Performance of Conical Diffusers at High Subsonic Mach Numbers," NASA CR-2299, August 1973.

4 Okwuobi, P. A. C. and Azad, R. S., "Turbulence in a Conical Diffuser with Fully Developed Flow at Entry," J. Fluid Mech. (1973), Vol. 57, Part 3, pp. 603-622.

5 Barnett, D. O. and Giel, T. V., Jr., "Application of a Two-Component Bragg-Diffracted Laser Velocimeter to Turbulence Measurements in a Subsonic Jet," AEDC-TR-76-36, May 1976.

6 Eckert, E. R. G., Editor, "Minnesota Symposium on Laser Anemometry Proceedings," October 22-24, 1975, Department of Conferences, Continuing Education and Extension, University of Minnesota, January 1976.

7 Bower, W. W., "An Analytical Procedure for the Calculation of Attached and Separated Subsonic Diffuser Flows," AIAA Paper No. 74-1173, AIAA 10th Propulsion Conference, San Diego, California, 1974.

8 Means, J. L., Glance, P. G., and Klassen, H. A., "Analytical Investigation of Conical Diffusers," NASA TM X-2605, August 1972.

9 Harsha, P. T. and Glassman, H. N., "Analysis of Turbulent Unseparated Flow in Subsonic Diffusers," ASME Paper 76-FE-26, 1976.

10 Wolf, S. and Johnston, J. P., "Effects of Nonuniform Inlet Velocity Profiles on Flow Regimes and Performance in Two-Dimensional Diffusers," Journal of Basic Engineering, Trans. of ASME, September 1969, pp. 462-474.

11 Anderson, O. L., "Finite-Difference Solution for Turbulent Swirling Compressible Flow in Axisymmetric Ducts with Struts," NASA CR-2365, February 1974.

12 Chien, John C., "Numerical Analysis of Turbulent Separated Subsonic Diffuser Flows," AEDC-TR-76-159, 1977.

13 Hinze, J. O., "Turbulence," McGraw-Hill Book Company, 1959.

14 Launder, B. E. and Spalding, D. B., "Lectures in Mathematical Models of Turbulence," Academic Press, 1972.

15 Harlow, F. H., Editor, "Turbulence Transport Modeling," AIAA Selected Reprint Series/Vol. XIV, 1973.

16 Launder, B. E., "Prediction Methods for Turbulent Flows," VKI Lecture Series 76, von Kármánn Institute for Fluid Dynamics, 1975.

17 Mellor, George L. and Herring, H. James, "Two Methods of Calculating Turbulent Boundary Layer Behavior Based on Numerical Solutions of the Equation of Motion," Proc. Computation of Turbulent Boundary Layer - 1968, AFOSR-IFP-Stanford Conference, Vol. I, Stanford University, 1969, 331.

18 Alber, Irwin E., "Similar Solutions for a Family of Separated Turbulent Boundary Layers," AIAA Paper No. 71-203, AIAA 9th Aerospace Sciences Meeting, 1971.

19 Chien, J. C., "A General Finite-Difference Formulation with Application to Navier-Stokes Equations," J. Computational Physics, Vol. 20, No. 3, March 1976.

20 Patel, V. C. and Head, M. R., "Some Observations of Skin Friction and Velocity Profiles in Fully Developed Pipe and Channel Flows," J. Fluid Mech., 38, 181, 1969.

21 Laufer, J., "Investigation of Turbulent Flow in a Two-Dimensional Channel," NACA Report 1053, 1951.

22 Dean, R. B., "Reynolds Number Dependence of Skin Friction in Two-Dimensional Rectangular Duct Flow and a Discussion of the "Law of the Wake"," IC Aero Report 74-11, December 1974, Imperial College of Science and Technology, London, England.

SOME POSSIBILITIES OF MATHEMATICAL MODELLING FLUID FLOW THROUGH AN ORFICE WITHIN PIPELINE AT HIGH REYNOLDS NUMBERS

B.Dobrowolski, Z.Kabza and A.Negrusz
Institute of Thermal Engineering and Fluid Mechanics
Technical University of Wrocław, Poland

Abstract – The paper presents an attempt of a numerical solution of the problem of turbulent flow through a pipeline with nozzle.A fundamental equation system for numerical calculations has been given in a non-dimensional form.Its solution has been based on a known numerical procedure for two-dimensional elliptical equations.Some theoretical examination results have been quoted for velocity pressure,and turbulence energy within the nozzle area.The mathematical model adequacy has been verified on the basis of experimental data for nozzle coefficient.

NOMENCLATURE

$a_0 \ldots a_6$ = coefficients in equation (15),
c_μ, c_1, c_2 = constans in turbulence model,
d = orifice diameter,m,
D = pipe diameter,m,
k = kinetic energy of turbulence, $= k^* U^2$, m^2/s^2,
p = pressure, $= p^* \rho U$, N/m^2,
p_1 = pressure at upstream corner tap, N/m^2,
p_2 = pressure at dowstream corner tap, N/m^2
Δp = pressure difference, $= \Delta p^* \rho U^2$, N/m^2,
r = radial distance from axis of symmetry,
  $= r^* D$, m,
Re = Reynolds number $= \rho U D/\mu$
$\dot{Q}$ = volumetric flow rate, m^3/s,
u = velocity component in z direction,
  $= U u^*$, m/s,
U = average upstream velocity, $= 4Q/\pi D^2$, m/s,
v = velocity component in r direction,
  $= U v^*$, m/s,
z = axial distance from inlet section,
  $= z^* D$, m,
z_0 = nozzle length,m.

Greek symbols
α = nozzle coefficient,
β = ratio of diameter, = d/D,
μ = viscosity coefficient of fluid,kg/ms,
ρ = density, kg/m^3,
σ_ϕ = effective Prandtl number for transport of ϕ,
ε = dissipation of energy, $= \varepsilon^* U^3/D$, m^2/s^3,
ω = vorticity, $= \omega^* U/D$, 1/s,
ϕ = general dependent variable,
ψ = stream function, $= \psi^* D^2 U$, m^3/s.

Subscripts
eff = effective (including the effect of turbulence)

Superscripts
$*$ = nondimensional,
k = number of iterations.

INTRODUCTION

Obstruction meters are commonly used for measuring the rate of flow of liquids transported in pipelines. Many a type of obstruction meters are known and used at present for pipelines of D>50mm diameter and within the Reynolds number range exceeding Re = 50,000.The best meters with respect to their metrological features have been standardized [1,2,3] .Data on obstruction meter optimum geometrical shape as well as their characteristic values (discharge coefficient, expansion factor,etc.)have been determined in standards on the basis of long-term experimental examination.New designs of obstruction meters are still needed for pipelines of D<50 mm diameter and for small and average Reynolds numbers ranging from 2,000 to 100,000; these new designs should make possible meter standardization.It seems that cyli-

PRECEDING PAGE BLANK-NOT FILMED

ndrical nozzles have met the requirements.

Koennecke [4] has carried out the first essential examination of cylindrical nozzles. Next, Jorissen [5,6] in 1950's, has confirmed Koennecke's results. In the 1970's author [7,8] worked up and thoroughly examined a new type of a cylindrical nozzle. The obtained results, confirmed by paralelly performed works of Japanese investigators [9] point to good metrological performance of this nozzle.

The main problem appearing when designing new nozzle types is the determination of nozzle optimum size at which nozzle coefficient is constant within a wide range of Reynolds number variation. This involves time- and money-consuming experimental investigations. A mathematical model of such a nozzle would make possible a qualitative and quantitative analysis of processes occurring within the nozzle area and a limitation of necessary test number as well as the explanation of physical phenomena within the nozzle area that are insufficiently known as yet.

Some results [10,11,12] are available, but they deal with laminar flow only. Thus a necessity exists of the extension of theoretical investigation on turbulent flows, too, because they are of a considerable importance in flow measurements.

FORMULATION OF THE PROBLEM AND PHYSICAL ASSUMPTIONS

The considered flow system is presented on Fig.1. It contains a section of a D-diameter pipeline with a cylindrical nozzle. The nozzle is of a length z and diameter d.

Despite the simplicity of the flow system complex physical processes take place here, being connected with a detachment of the stream from pipe wall, stream contraction and expansion in the nozzle area. This causes the formation of recirculation zones sized mainly in dependence on d/D and z/d relations as well as on Reynolds number Re.

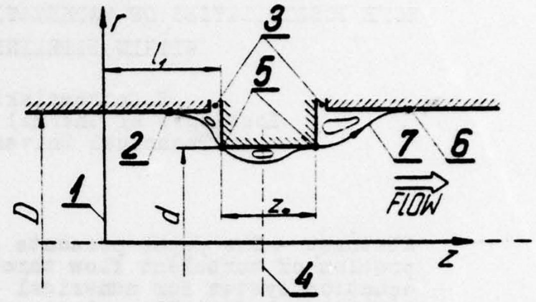

Fig.1. A flow system with a cylindrical nozzle

(1) Plane of inlet
(2) Last attachment point
(3) Pressure-tap locations
(4) Plane of vena-contracta
(5) Separation points
(6) Reattachment points
(7) Free streamline

The complexity of physical processes occurring within the nozzle area forces the application of elliptical differential equations for their description (at velocities characteristic for flow measurement).

In the subsequent part of this paper a mathematical model will be presented of a flow of liquid through a nozzle being based on the following assumptions

1. A fluid is incompressible and of a constant density
2. A fully-developed turbulent flow occurs at a distance l_1 before the nozzle (See Fig.1).
3. The flow is isothermal and axi-symmetric
4. Pipe walls and nozzle surface are impermeable.

A mathematical model should make it possible the determination of the velocity distribution in the flow area, pressure distribution and the nozzle coefficient. It is possible to determine such a relation of z/d at which the nozzle coefficient remains constant within a wide range of Reynolds number variation.

MATHEMATICAL MODEL

The transport equation

Steady, axially-symmetric isothermal flow of a viscous and incompressible liquid is described by known equations of continuous media motion complemented by the equation of continuity. These equations take–in cylindrical r, z coordinates– the following form

$$\rho\left(u\frac{\partial u}{\partial z}+v\frac{\partial u}{\partial r}\right)=-\frac{\partial p}{\partial z}+\left\{\frac{1}{r}\frac{\partial}{\partial r}\left(r\mu_{eff}\left(\frac{\partial v}{\partial z}+\frac{\partial u}{\partial r}\right)\right)+2\frac{\partial}{\partial z}\left(\mu_{eff}\frac{\partial u}{\partial z}\right)\right\} \qquad (1)$$

$$\rho\left(u\frac{\partial v}{\partial z}+v\frac{\partial v}{\partial r}\right)=-\frac{\partial p}{\partial r}+\left\{\frac{2}{r}\frac{\partial}{\partial r}\left(r\mu_{eff}\frac{\partial v}{\partial r}\right)-2\mu_{eff}\frac{v}{r^2}+\frac{\partial}{\partial z}\left(\mu_{eff}\left(\frac{\partial v}{\partial z}+\frac{\partial u}{\partial r}\right)\right)\right\} \qquad (2)$$

$$\frac{\partial u}{\partial z}+\frac{1}{r}\frac{\partial}{\partial r}(vr)=0 \qquad (3)$$

The quantity μ_{eff} appearing in the equations (1) and (2) is the so called effective viscosity being the sum of molecular viscosity μ and the turbulent one μ_t characterizing the turbulence status in a given point of the flow area, according to the equation.

$$\mu_{eff}=\mu+\mu_t \qquad (4)$$

The essence of the accepted turbulent flow modelling method is that additional turbulence–caused stresses are introduced into motion equations (1) and (2). A turbulent flow is thus treated as a laminar one with a variable viscosity characterized by parameters being time–averaged ones of a turbulent flow.

Turbulence model

A broad review of mathematical turbulence models is presented in [13]. Individual models are of various complexity and usability classes resulting from particular physical hypotheses accepted. On the basis of physical analysis of a phenomenon of flow through a nozzle (detachment of wall layer, recirculation zones) a turbulence model has been accepted, being based on elliptical differential equations for turbulence energy k and for dissipation of turbulence energy ε. A general form of the k~ε model has been given in [14]. Transport equations for k and ε – in cylindrical coordinates – are of the following form

$$\rho\left(u\frac{\partial k}{\partial z}+v\frac{\partial k}{\partial r}\right)=\frac{\partial}{\partial z}\left(\frac{\mu_{eff}}{\sigma_k}\frac{\partial k}{\partial z}\right)+\frac{1}{r}\frac{\partial}{\partial r}\left(r\frac{\mu_{eff}}{\sigma_k}\frac{\partial k}{\partial r}\right)+\mu_{eff}G-\rho\varepsilon \qquad (5)$$

$$\rho\left(u\frac{\partial \varepsilon}{\partial z}+v\frac{\partial \varepsilon}{\partial r}\right)=\frac{\partial}{\partial z}\left(\frac{\mu_{eff}}{\sigma_\varepsilon}\frac{\partial \varepsilon}{\partial z}\right)+\frac{1}{r}\frac{\partial}{\partial r}\left(r\frac{\mu_{eff}}{\sigma_\varepsilon}\frac{\partial \varepsilon}{\partial r}\right)+\frac{\varepsilon}{k}\left(c_1\mu_{eff}G-c_2\rho\varepsilon\right) \qquad (6)$$

where $G=2\left\{\left(\frac{\partial u}{\partial z}\right)^2+\left(\frac{\partial v}{\partial r}\right)^2+\left(\frac{v}{r}\right)^2\right\}+\left(\frac{\partial u}{\partial r}+\frac{\partial v}{\partial z}\right)^2$

Knowing local values of k and ε one may determine local value of turbulent viscosity from Prandtl and Kolmogorov formule

$$\mu_t=C_\mu\rho\,\frac{k^2}{\varepsilon} \qquad (7)$$

Value of constants appearing in the turbulence model and taken for calculations according to recommendations of [14], are, respectively $c_1 = 1.44$, $c_2 = 1.92$, $c_\mu = 0.09$, $\sigma_\varepsilon = 1.3$, $\sigma_k = 1.0$.

Generalized representation of the equations

Differential equations (1), (2), (3), (5) and (6) as well as algebraic expressions (4) and (7) form a closed system of equations describing isothermal flow of a viscous and incompressible liquid. The equations (1), (2) and (3) will further be transformed in order to eliminate the pressure by means of introducing stream function ψ and vorticity ω defined as follows

$$\omega=\frac{\partial v}{\partial z}-\frac{\partial u}{\partial r} \qquad (8)$$

$$u=\frac{1}{r}\frac{\partial \psi}{\partial r} \qquad (9)$$

$$v=-\frac{1}{r}\frac{\partial \psi}{\partial z} \qquad (10)$$

Differentiating equations (1), (2) ($\frac{\partial(\cdot)}{\partial r}$ and $\frac{\partial(\cdot)}{\partial z}$ respectively), and adding by sides we obtain an equation of vorticity transport. Introducing definition equation of stream function (9) and (10) into the equation (8) we obtain Poisson's equation for the stream function. Introducing simultaneously non–dimensional quantities

$$r^*=\frac{r}{D};\; z^*=\frac{z}{D};\; u^*=\frac{u}{U};\; v^*=\frac{v}{U};\; \omega^*=\omega\frac{D}{U}$$

$$\psi^* = \frac{\psi}{D^2 U} ; \; \varepsilon^* = \varepsilon \frac{D}{U^3} ; \; k^* = \frac{k}{U^2} ; \; P^* = \frac{P}{\rho U^2} \qquad (11)$$

we obtain vorticity transport equation and the Poisson's one in a non-dimensional form

$$\frac{\partial (u^* \omega^*)}{\partial z^*} + \frac{\partial (v^* \omega^*)}{\partial r^*} = \frac{\partial}{\partial r^*}\left(\frac{1}{r^*}\frac{\partial}{\partial r^*}(r^* R \omega^*)\right) + \frac{\partial^2}{\partial z^{*2}}(R\omega^*) + 2\frac{\partial^2 R}{\partial z^* \partial r^*}\left(\frac{\partial v^*}{\partial r^*} - \frac{\partial u^*}{\partial z^*}\right) + 2\left(\frac{\partial^2 R}{\partial z^{*2}}\frac{\partial u}{\partial r^*} - \frac{\partial^2 R}{\partial r^{*2}}\frac{\partial v^*}{\partial z^*}\right) \qquad (12)$$

$$\frac{\partial}{\partial z^*}\left(\frac{1}{r^*}\frac{\partial \psi^*}{\partial z^*}\right) + \frac{\partial}{\partial r^*}\left(\frac{1}{r^*}\frac{\partial \psi^*}{\partial r^*}\right) + \omega^* = 0 \qquad (13)$$

The quantity R appearing in the equation (12) is a reciprocal of effective Reynolds number

$$R = \frac{\mu_{eff}}{UD\rho} = \frac{1}{Re_{eff}} \qquad (14)$$

After introducement of non-dimensional quantities (11) into equations (5) and(6) we obtain non-dimensional equations for turbulence energy and its dissipation.It can be easily noticed the equations for $\omega^*, \psi^*, k^*, \varepsilon^*$ may be written down in a generalized form

$$a_0\left\{\frac{\partial u^* \phi}{\partial z^*} + \frac{a_1}{r^*}\frac{\partial}{\partial r^*}\left(\frac{r^*}{a_1} v^* \phi\right)\right\} = \frac{a_2}{r^*}\frac{\partial}{\partial r^*}\left(a_3 \frac{\partial a_4 \phi}{\partial r^*}\right) + \frac{\partial}{\partial z^*}\left(a_5 \frac{\partial a_6 \phi}{\partial z^*}\right) + S_\phi \qquad (15)$$

Coefficients of the equation (15) are tabulated in the Table No 1 below.

Table 1.Values of coefficients of the equation (15).

ϕ	a_0	a_1	a_2	a_3	a_4	a_5	a_6	S_ϕ
ω^*	1	r^*	r^*	$\frac{1}{r^*}$	$r^* R$	1	R	S^*_ω
ψ^*	0	–	r^*	$\frac{1}{r^*}$	1	$\frac{1}{r^*}$	1	ω^*
k^*	1	1	1	$r^* \frac{R}{\sigma_k}$	1	$\frac{R}{\sigma_k}$	1	$RG^* - \varepsilon^*$
ε^*	1	1	1	$r^* \frac{R}{\sigma_\varepsilon}$	1	$\frac{R}{\sigma_\varepsilon}$	1	$\frac{\varepsilon^*}{k^*}(C_1 RG^* - C_2 \varepsilon^*)$

NUMERICAL SOLUTION OF THE EQUATIONS

Finite difference equations and their solutions

A solution of the generalized differential equation (15) has been based on a method of finite differences for ununiform grids.A typical grid used in calculations can be seen on Fig.2.

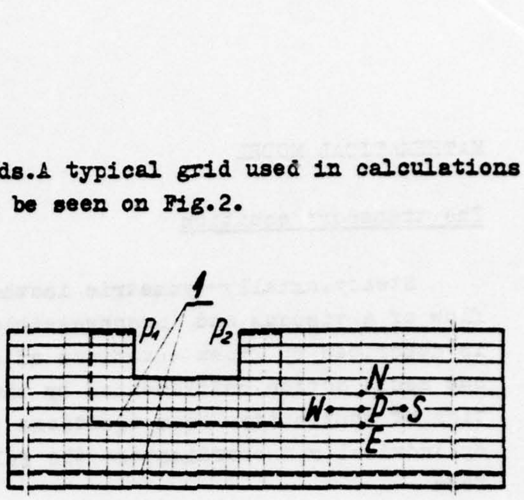

Fig.2. Example of the grid-distribution and typical interior mode P of the grid. (1) Path of pressure integration

Differential equation approximation by difference equations algorithms will not be presented in detail because they are standard [15] for this type of elliptical equations.A system of differential (15) has been transformed into a system of algebraic equations in the form

$$\phi_P = C_N \phi_N + C_S \phi_S + C_E \phi_E + C_W \phi_W + S_\phi \qquad (16)$$

For each variable ϕ and for every inner grid point a single, such type equation may be written down.Resulting systems of algebraic equations have been solved with Gauss - Seidel iteration method and the use of relaxation.The iterative process has been considered finished when the relation

$$\max\left|\frac{\phi^k - \phi^{k-1}}{\max|\phi^k|}\right| \leqslant 0.001 \qquad (17)$$

takes place for each variable in each grid point.

Boundary conditions

For the aims of solving a numerical problem one should know boundary conditions of differential equations.All the boundaries must have determined conditions for variables of the equation (15) because the basic equation system for numerical calculation is of an elliptic type.

<u>Pipe walls and nozzle surface.</u> Boundary conditions for vorticity and stream function are the same as for a laminar flow[11] .In the case of turbulence energy and its dissipation relations have been used of "wall function " given in [14].

<u>Symmetry axis.</u> From axial symmetry condition of a flow it has been taken

$$V^* = \omega^* = \frac{\partial v}{\partial z} = \frac{\partial u}{\partial r^*} = \frac{\partial k^*}{\partial r^*} = \frac{\partial \varepsilon^*}{\partial r^*} = 0 ; \; u^* = \frac{\partial^2 \psi^*}{\partial r^{*2}}$$

<u>A section before the nozzle.</u>Velocity profile and turbulence energy and its dissipation distribution have been determined from known dependences for a fully developed turbulent flow inside a pipe.Conditions for vorticity and stream function have been fixed on the basis of definition equations (8) and (9).

<u>A section behind the nozzle</u>. A condition $\frac{\partial \phi}{\partial z} = 0$ has been taken for every variable from the equation (15).

CALCULATION OF PRESSURES AND NOZZLE COEFFICIENT

The determination of velocity and effective viscosity by means of solving the equation system (15) makes it possible to calculate static pressure distribution within the area of flow.The method of pressure calculation is well-known [15,16] and consists in the determination of derivatives $\frac{\partial p}{\partial z}$ and $\frac{\partial p}{\partial r}$ appearing in equations (1) and (2). Pressure difference existing between any two points within the flow area may be determined in the following way

$$P_1 - P_2 = \int_s \left(\frac{\partial p}{\partial z} dz + \frac{\partial p}{\partial r} dr \right) \qquad (18)$$

where s is any continuous curve led between points 1 and 2.The s curve has then been approximated with sections paralell to the coordinate axes (see Fig.2).The knowledge of pressure difference on a nozzle makes it possible the calculation of nozzle coefficient– according to recomendation of the Standard [3] from the formula

$$\alpha = \frac{1}{\sqrt{2}} \frac{\beta^2}{\sqrt{\Delta p^*}} \qquad (19)$$

Quantity Δp^* is a non-dimensional pressure difference at a nozzle $\Delta p^* = (p_1 - p_2)/\rho U_1^2$,U is an average velocity in a section placed before the nozzle.

DISCUSION OF CALCULATION RESULTS

The presented mathematical model of a cylindrical nozzle has been used to determine velocity fields,pressure distribution and nozzle coefficient.Results of experimental examination of the cylindrical nozzle are presented in [7,8,9]. The above mentioned characteristic quantities have been chosen for numerical calculations as being important for obstruction meters performance.

Calculations have been caried out for an uniform grid shown on Fig.2 sized 11x31 in the radial and axial direction,respectively.

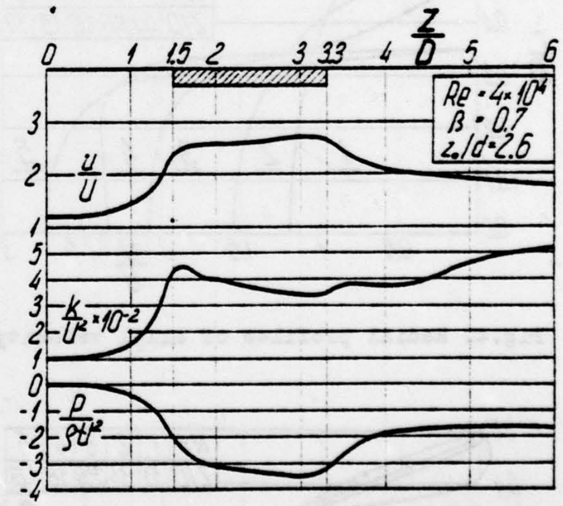

Fig.3. Centre-line distribution of axial velocity,kinetic energy of turbulence and static pressure.

On Fig.3,distribution of non-dimensional axial velocity,turbulence energy and pressure in the symmetry axis for Reynolds number Re = 4×10^4, as an instance and the relation $\beta = 0{,}7$ are presented. On the basis of curve runs one may notice that increase in velocity and a static pressure decrease may be observed near by the nozzle. The maximum velocity and the minimum pressure at the pipe axis is distant by 3D from the inlet section, i.e. in the vicinity of nozzle outlet plane. Quantitative experimental examinations [7,8,9] have shown that a nozzle of $\beta = 0.7$ shows good performance at $z/d = 2.6 \div 3$. This may be explained by the occurrence of a "vena-contracta" section in the cylindrical part of the nozzle. In order to analyse this question more completly profiles of axial velocity near by the nozzle inlet should be considered. Such profiles for areas before and within the nozzle have been shown on Fig. 4, whereas on Fig. 5 – the ones from behind the nozzle.

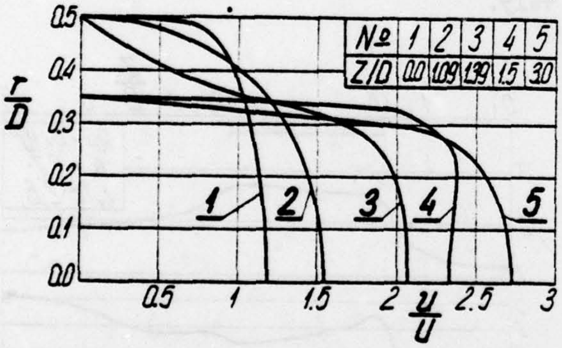

Fig.4. Radial profiles of axial velocity

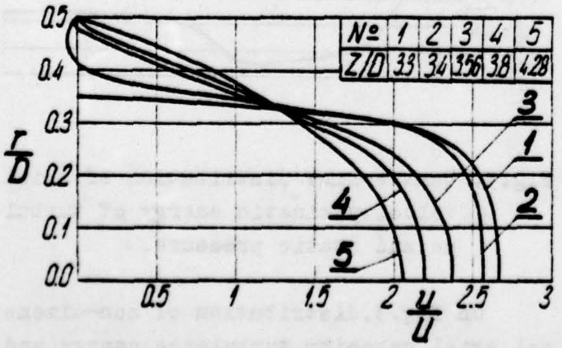

Fig.5. Radial profiles of axial velocity

The appearance of the maximum axial velocity in a considerable distance from the inlet edge of the nozzle may be explained by a peculiar velocity distribution at the nozzle inlet (maximum of the velocity near the wall). A recirculation zone may be observed behind the nozzle (See Fig.5, curve 1). This zone is relatively small because of rather high $\beta = 0.7$. Radial profiles of non-dimensional turbulence energy are shown on Fig.6.

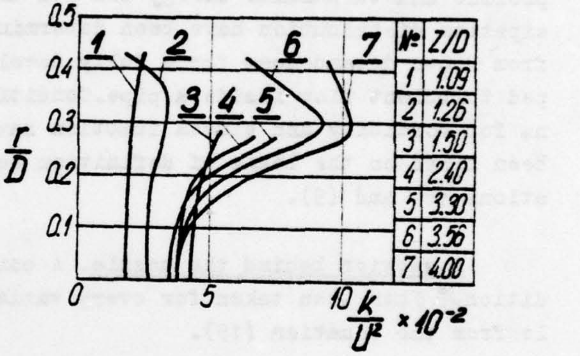

Fig.6. Radial profiles of kinetic energy of turbulence

In the behind-nozzle area a growth of turbulence energy may be observed. The maximum values of turbulence energy appear in the area of great velocity gradients.

A mathematical model has been verified on the basis of experimental data concerning a cylindrical nozzle coefficient taken from [7]. These data have been shown in Fig. 7. by a continuous line whereas calculation results by points. In both cases an increase of nozzle coefficient α accompanied by Reynolds number growth may be observed. A comparison between the calculation results and the experiments was the best at Re = 4×10^4. At higher and lower Reynolds numbers the maximum relative error of a calculated and experimentally measured nozzle coefficient has not exceeded 15 per cent. It must, nevertheless, be noticed that the nozzle coefficient is calculated on the basis of pre-

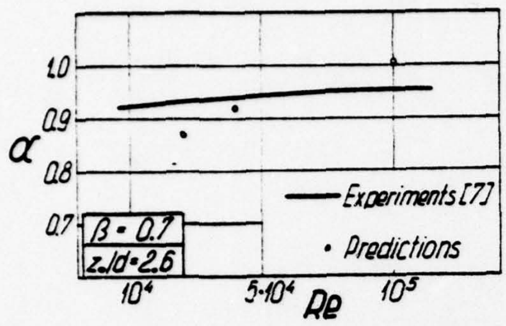

Fig.7.Comparision of predicted and experimental nozzle coeficients

ssure distribution so it is influenced by errors of presure determination.

Attempts are being performed now to improve the accuracy of calculations.As it has been shown on a fragmentary example a numerical analysis of metrologic properties of nozzles may be very useful and give valuable information enabling the designer to select optimum shape thus limiting considerably the number of experimental examination.The numerical analysis serves also as an instrument of a better recognition of phenomena occuring in such flows.

REFERENCES

1 ISO/TC-30 Secretariat - 138 291, Jan.1975

2 ASME Flow Measurement Power Test Codes,New York,1959

3 British Standard 1042.Methods for the Measurement of Fluid Flow in Pipes. British Standards Institution,1964

4 Koennecke,W.,"Neue Düsenformen fur kleinere und mittlere Reynoldszahlen".Forschung auf dem Gebiete des Ingenieurwesens No 9,1938,pp.109-125.

5 Jorissen,A.L.,Newton,H.T.,"Discharge Measurements by means of Cylindrical Nozzles",Trans.ASME,Vol.74,No.5,pp.825-835.

6 Jorissen,A.L.,"Discharge Measurements at low Reynolds Numbers Special Devices",Trans.ASME,Vol.78,No.2,pp.365-368.

7 Kabza,Z.,"Measurement of Flow rate in Pipes of Diameter below 50 mm by means of Cylindrical Nozzles",Doct.Diss,Technical University of Wrocław (Poland),1974.

8 Kabza,Z.,"Cylindrical Nozzles for Measurements of rate of Flow",Teploenergetika (USSR),No 10,1975,pp.82-85.

9 Komiya Kin-ichi,Nogashio Keiich, " Characteristics of a Cylinder Nozzle", Bull.Nat.Res.Lab.Metrol. No 28,1974,pp.15-20.

10 Mills,R.D.,"Numerical Solutions of Viscous Flow through a Pipe Orifice at low Reynolds Numbers".Journal Mechanical Engineering Science,Vol.10,No.2,1968,pp.133-140.

11 Coder,D.W.,Buckley,F.T.,"Implicit Solutions of Unsteady Navier Stokes Equation for Laminar Flow through an Orifice within a Pipe".Computer and Fluids,Vol.2, 1974,pp.295-315.

12 Zampaglione,D.,Greppi,M.,"Numerical Study of a Viscous Flow Through a Pipe Orifice,Meccanica,Vol.7,No.3,1972,pp.151-164.

13 Launder,B.E.,Spalding,D.B.,Mathematical Models of Turbulence,London,1972, Academic Press.

14 Launder,B.E.,Spalding,D.B.,"The Numerical Computation of Turbulent Flows". Computers Methods in Applied Mechanics and Engineering,Vol.3,1974,pp.269-289.

15 Gosman,A.D.,Pun,W.M.,Runchal.A.K., Spalding,D.B.,Wolfshtein,M., Heat and Mass Transfer in Recirculating Flows.London, 1969,Academic Press.

16 Carnaham,B.,Luther,H.A.,Wilkes,I.O., Applied Numerical Methods,London,1969, J.Wiley and Sons In.c.

THE CALCULATION OF SEPARATED BOUNDARY LAYERS

by

S. B. Pope

Imperial College of Science and Technology,

Department of Mechanical Engineering,

Exhibition Road, London SW7 2BX.

ABSTRACT

Separated boundary layers, such as those on the suction surface of airfoils at high angles of attack or in rapidly expanding diffusers, are considered. A finite-difference procedure is outlined which solves the flow equations in general orthogonal coordinates, thus facilitating the treatment of curved surfaces: the k-ε, two-equation turbulence model is used. Calculations of separated boundary layers in curved diffusers are presented from which the influence of geometric and turbulence model parameters are determined.

NOMENCLATURE

$C_{\varepsilon 1}$, $C_{\varepsilon 2}$, C_μ	turbulence model constants
D	initial duct width
E	wall law constant
k	kinetic energy of turbulence
L	length of curve in duct
ℓ_r	reattachment length (from start of curve)
ℓ_s	separation length (from start of curve)
P	rate of production of turbulent kinetic energy
p	pressure
t	time
U	velocity
x	position

Greek symbols

δ_{ij}	Kronecker delta
ε	rate of dissipation of turbulent kinetic energy
κ	wall law constant
μ	laminar viscosity
μ_{eff}	effective viscosity
ρ	density
σ_k, σ_ε	turbulence model constants
τ_{ij}	Reynolds stress tensor
τ_w	wall shear stress
ψ_{min}	minimum value of stream function

INTRODUCTION

The work reported here represents an initial investigation into the problems faced in calculating the flow properties of turbulent separated boundary-layers. In these flows, the adverse pressure gradient causes the boundary-layer to slow down and thicken until a reversed flow region occurs and the wall shear stress becomes negative: depending upon the behaviour of the free stream, the boundary-layer may or may not re-attach, forming a closed bubble of recirculation. The nett effect is to enhance the momentum transfer to the wall; and, consequently, the possible occurence and behaviour of separated boundary layers is of practical significance in engineering situations where the minimisation of losses is at a premium: diffusers and airfoils serve as examples.

Several recent papers have reported numerical solutions of the elliptic equations appropriate to turbulent recirculating flows by employing turbulence models to determine the Reynolds stresses: Pope and Whitelaw (1) calculated the flow behind discs in a uniform free-stream using both Reynolds-stress and mean-flow closures; Runchal and Spalding (2) calculated the flow downstream of a sudden enlargement in a circular pipe; and, Majumdar and Bhaduri (3) considered the flow in a recessed wall cavity. In these and other works the calculations were compared with the scarce experimental data available producing differing degrees of agreement. The discrepancies can be attributed both to difficulties in measurement and to the inadequacy of aspects of the turbulence models in certain circumstances (4).

The separated boundary-layers considered here are similar to the flows mentioned above but important differences make the task of their calculation more difficult. To appreciate these differences, consider the flow in a pipe with a sudden enlargement compared with the flow over an airfoil at a high angle of attack. In the pipe-step problem the separation is caused by the abrupt change in geometry and the structure of the turbulence is dominated by the thin shear-layer between the recirculation zone and the main flow. For the airfoil, on the other hand, the location of separation is determined by the flow itself, both by mean quantities (such as the axial pressure gradient) and by the turbulence which is created in the wall boundary-layer. Thus, an adequate representation of the turbulence in this instance is more difficult since, in near-wall regions, large variations in properties occur and low Reynolds number effects may be important: further, this flow can be expected to be more sensitive to turbulent structure and consequently errors in representing turbulence quantities can be expected to result in errors in mean flow quantities.

These above mentioned difficulties in calculating airfoil flows are difficulties in representing the physics of turbulence but additional, practical

PRECEDING PAGE BLANK-NOT FILMED

problems are posed by the airfoil geometry and flow situation. As the boundary-layer is of central importance to the flow as a whole, its accurate numerical treatment is of equal importance: however, in the Cartesian coordinate system used by most numerical procedures (e.g. 1-3) the curved airfoil surface passes through the finite-difference grid at an angle, hindering the accurate imposition of boundary conditions, introducing numerical diffusion and preventing the selective refinement of the grid near the surface to improve accuracy. The imposition of boundary conditions in the free-stream is also complicated since the potential flow solution for the inviscid free-stream is influenced by the boundary-layer thickness on the airfoil surface. Thus, with the considerable thickness of separated boundary-layers, the matching of the viscid and inviscid solutions in the free-stream poses an additional problem.

In the present work, a symmetric, curved, two-dimensional diffuser is considered. This choice avoids the difficulty associated with the free-stream boundary and allows attention to be focussed on the representation of the turbulent flow. A numerical procedure has been developed to solve the flow equations in general orthogonal coordinates which allows grid lines to be aligned with the curved boundaries. As a consequence, the near-wall region can be treated accurately. This procedure has been used in conjunction with a two-equation turbulence model to determine the influence of geometric and turbulence-model parameters on the calculated separated flow. The implications of these results for the accurate calculation of separated boundary-layers is discussed.

CALCULATION PROCEDURE

Turbulence Model

The k-ε turbulence model used in the procedure is presented here with summary justification: although the finite-difference procedure solves equations in general orthogonal coordinates, the equations are presented in customary Cartesian tensor notation in order not to detract from their physical significance.

The continuity and momentum equations for a high Reynolds number, constant density flow are:

$$\frac{\partial \rho}{\partial t} + \frac{\partial \rho U_i}{\partial x_i} = 0 \qquad (1)$$

and

$$\frac{\partial \rho U_j}{\partial t} + \frac{\partial \rho U_i U_j}{\partial x_i} = -\frac{\partial p}{\partial x_j} - \frac{\partial \tau_{ij}}{\partial x_j} \qquad (2)$$

where ρ is the density, U(x,t) is the averaged velocity at position x and time t, p is the pressure and τ_{ij} the stress tensor. The unknown Reynolds stresses, which at the high Reynolds number considered here are the only contributors to τ_{ij}, are determined from the k-ε turbulence model in conjunction with the isotropic viscosity hypothesis,

$$\frac{\partial \rho k}{\partial t} + \frac{\partial \rho U_i k}{\partial x_i} = \frac{\partial}{\partial x_i} \frac{\mu_{eff}}{\sigma_k} \frac{\partial k}{\partial x_i} + P - \rho \varepsilon \qquad (3)$$

$$\frac{\partial \rho \varepsilon}{\partial t} + \frac{\partial \rho U_i \varepsilon}{\partial x_i} = \frac{\partial}{\partial x_i} \frac{\mu_{eff}}{\sigma_\varepsilon} \frac{\partial \varepsilon}{\partial x_i} + \frac{\varepsilon}{k} (C_{\varepsilon 1} P - C_{\varepsilon 2} \rho \varepsilon) \qquad (4)$$

and

$$\tau_{ij} = -\mu_{eff}\left(\frac{\partial U_i}{\partial x_j} + \frac{\partial U_j}{\partial x_i}\right) + \frac{2}{3} \rho k \delta_{ij} \qquad (5)$$

Equations (3) and (4) account for the transport of the turbulent kinetic energy, k, and its rate of dissipation, ε. The production of kinetic energy and the effective viscosity are given by,

$$P = -\frac{\partial U_i}{\partial x_j} \tau_{ij} \qquad (6)$$

and

$$\mu_{eff} = C_\mu \rho k^2/\varepsilon \qquad (7)$$

and the constants C_μ, $C_{\varepsilon 1}$, $C_{\varepsilon 2}$, σ_k and σ_ε are ascribed the values 0.09, 1.45, 1.90, 1.0 and 1.3 respectively.

The closure provided by these equations was first used by Jones (5) although it stems from the earlier works of Chou (6) and Harlow and Nakayama (7). A description of the modelling of the turbulence equations is given by Launder and Spalding (8) and for a criticism of the effective viscosity hypothesis and dissipation equation (which contain the major assumptions), the reader is referred to previous work, (9, 4).

Solution Procedure

The solution procedure, which uses finite-difference means to solve equations (1) - (7) on an orthogonal grid, is a development of Gosman and Pun's (10) method. First, it is necessary to generate an orthogonal grid appropriate to the shape of the solution domain and this is accomplished by solving Laplace's equation numerically for the Cartesian coordinates of the specified grid line intersections. A typical grid used in the calculations reported here is shown on Figure 1. The initial width of the duct, D, is doubled by a sinusoidal

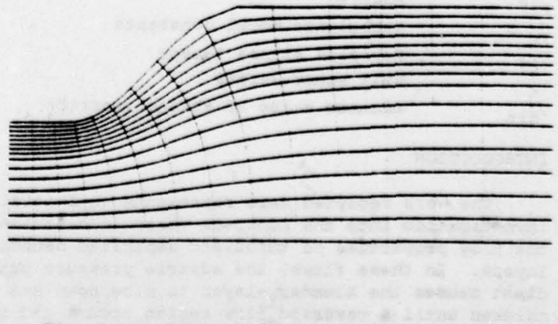

Fig. 1 Orthogonal finite-difference grid

curve of length L and, as the duct is symmetric, only half the flow need be calculated. It may be seen that more grid lines are placed close to the wall in order to provide greater accuracy in that important region.

The details of the finite-difference procedure to solve the flow equations in general orthogonal coordinates are reported elsewhere, (11). Briefly, by integrating the differential equations over grid cells, finite-difference equations are obtained for the two normal velocities, k and ε. These are solved iteratively together with a pressure correction equation which modifies the pressure field so that the converged solution also satisfies the continuity equation. The calculations reported here were performed on 20x16 grids, such as that shown on figure 1, and 150 iterations were required for convergence leading to 190 seconds of computation (CDC6600) using 21,000 words of memory.

Boundary Conditions

The equations solved are elliptic and, consequently, require the specification of boundary conditions over the whole perimeter of the solution domain. On the symmetry plane, symmetric quantities have zero normal gradients and anti-symmetric quantities are zero: the location of the outlet plane is chosen to be sufficiently far downstream for the boundary-layer approximations to hold which, in essence, precludes the need of the specification of boundary conditions there. The values of dependent variables at the inlet plane depend upon the nature of flow upstream: for simplicity, uniform profiles of velocity, k and ε are imposed with $k = 0.001\, U^2$ and $\varepsilon = (C_\mu{}^{1/2}\, k)^{3/2}/(.2D)$ corresponding to the plug flow in a smooth contraction.

Although the no-slip condition at the wall leads to sufficient boundary conditions for U, k and ε, their direct imposition is not appropriate since the turbulence model does not contain low Reynolds number terms which are important in this region. One possibility would be to incorporate these terms (as was done by Jones and Launder (12)) but the large variations of the dependent variables near the wall requires so fine a finite-difference grid as to be prohibitive for elliptic flows. Instead, wall-functions are used. These are based on Couette flow solutions in the near-wall region which, clearly, assume equilibrium. However, the functions are constructed in such a manner as to retain plausible results in non-equilibrium situations although their direct validation has not been achieved. The wall shear stress, τ_w, forms the boundary condition for the velocity parallel to the wall and the normal velocity is zero:

$$\tau_w = \frac{U_p}{y_p}\ \frac{\mu y_p^+}{\ln(E y_p^+)} \quad \text{where} \quad y_p^+ = \rho\,(k_p\, C_\mu^{1/2})^{1/2}\ \frac{y_p}{\mu} \tag{8}$$

The equation is not solved for ε at the near-wall grid node, but its value is specified through

$$\varepsilon_p = \frac{(C_\mu^{1/2}\, k_p)^{3/2}}{\kappa y_p} \tag{9}$$

In the kinetic energy equation, the diffusion to the wall is set to zero and the integral of dissipation over the near-wall region (which is a source term) is given by,

$$\int_0^{y_p} \varepsilon\, dy = (C_\mu^{1/2}\, k_p)^{3/2}\, \frac{1}{\kappa}\, \ln\,(E y_p^+) \tag{10}$$

In these relations, μ is the laminar viscosity; the subscript p refers to the grid node next to the wall and y_p and U_p are the normal distance and parallel velocity at that point. κ and E are the constants in the logarithmic law-of-the-wall and have values of 0.42 and 9.8.

RESULTS AND DISCUSSION

The procedure was used to calculate the flow properties in the curved diffuser, described above, in order to determine the flow patterns and to examine the influence of changes in geometric and turbulence model parameters. The standard case is for $L/D = 1.5$, $Re \equiv \rho UD/\mu = 10^5$ and the turbulence model constants taking the values quoted above.

Duct Shape

Figure 2 shows stream-function contours for four different duct shapes with L/D varying between 0.5 and 2.0. Stream-function is normalised to be zero at the wall and unity on the centre-line and, consequently, its minimum value, ψ_{min}, is a measure of the intensity of recirculation. It may be seen that for $L/D = 0.5$ there is a large separation region which extends some distance downstream before reattachment while, for $L/D = 2.0$, the recirculation zone is far smaller and is comparatively inextensive. These observations are confirmed by plotting the normalised distance to separation, ℓ_s/L (measured from the start of the curve), the distance to reattachment, ℓ_r/L, and ψ_{min} again L/D. This is done on figure 3. Several, possibly unexpected, points of interest emerge: the general trend of ℓ_s/L and ψ_{min} increasing and ℓ_r/L decreasing with L/D is to be expected, but the magnitude of some quantities is surprising. For the highest expansion rate, $L/D = 0.5$, $\psi_{min} = -0.019$ indicating that the flow rate in the recirculation zone is less than 2% of the main flow; and, as L/D increases, ℓ_s/L increases but slowly compared with the decrease in ℓ_r/L. That is, the normalised separation point is relatively insensitive to the rate of expansion.

By extrapolating the curves on figure 3, it may be seen that the singular point where $\psi_{min} = 0$, and $\ell_s = \ell_r$ occurs in the vicinity of $L/D = 2.5$: at this point, corresponding to incipient separation, $\ell_s/L = \ell_r/L \approx 3/4$. This value may be compared with $\ell/L = 1/4$, the location of maximum convex curvature, and $\ell/L = 1/2$, the location of the maximum rate of expansion: either of these points could be expected to be the location of incipient separation since, to first approximation, the former corresponds to maximum centrifugal force and the latter to maximum adverse pressure gradient. The fact that separation occurs further downstream indicates that the growth of the boundary-layer is a central factor either directly, or indirectly through its effect upon the pressure gradient.

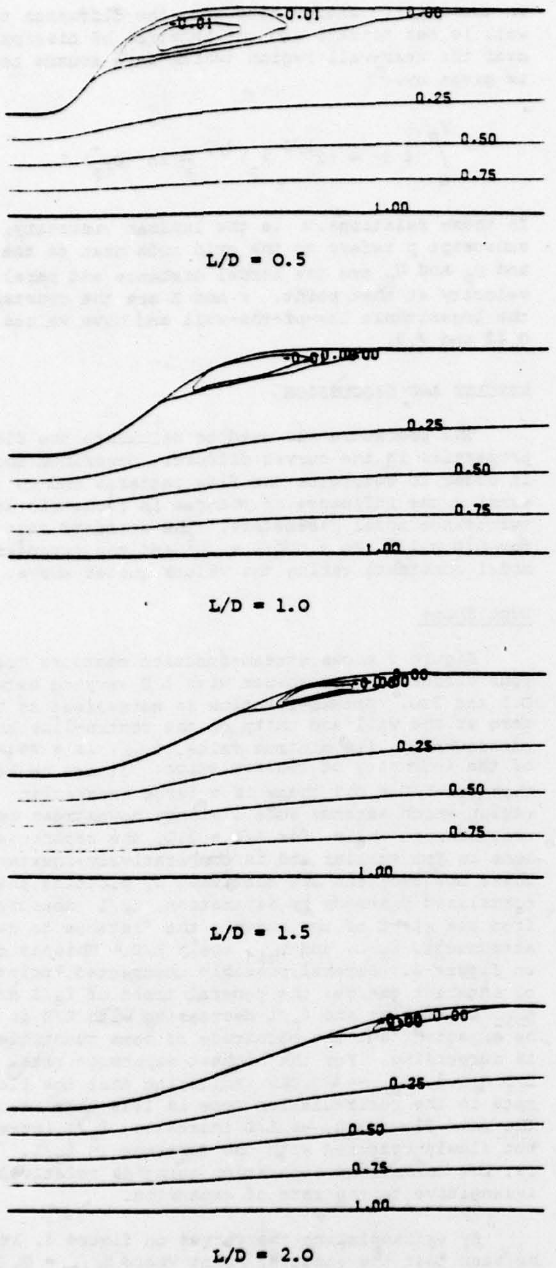

Fig. 2 Contours of stream-function in diffusers of different expansion rates

Modelling Parameters

If, as has been suggested, the growth of the boundary-layer is an important aspect of the flow, then the accurate representation of the flow as a whole can be expected to depend on the correct modelling of this process. Consequently it is informative to determine the sensitivity of calculated values to the modelling assuptions by altering the

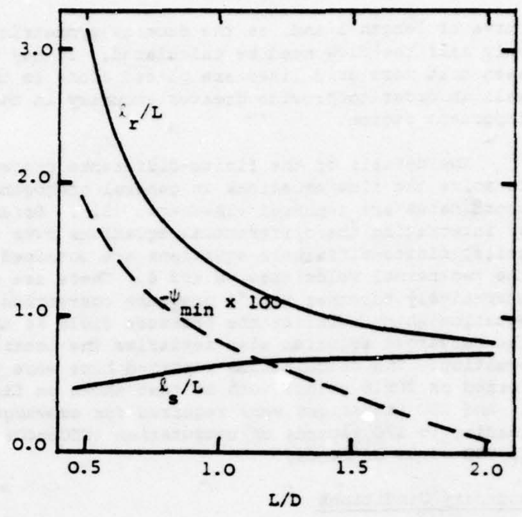

Fig. 3 ℓ_s/L, ℓ_r/L and ψ_{min} against L/D.

constants appearing in the models. Table 1 shows the percentage change in $(\ell_r-\ell_s)/L$ and ψ_{min} for a 10% decrease in C_μ and κ. C_μ is the dominant constant in the k-ε turbulence model and its decrease corresponds to decreasing the effective viscosity.

Table 1. Change in $(\ell_r-\ell_s)/L$ and ψ_{min} for a 10% decrease in C_μ and κ

	$(\ell_r-\ell_s)/L$	ψ_{min}
C_μ	9%	16%
κ	26%	14%

κ is the law-of-the-wall constant and its diminution causes a decrease in the effective viscosity close to the wall.

It may be seen from Table 1 that decreasing C_μ and κ results in the intensity of the recirculation, ψ_{min}, increasing by about 15%. confirming that this feature of the flow is sensitive both to the turbulence model and the wall functions. However, changing C_μ only causes a 9% change in the length of the recirculation zone whereas the same change in κ causes a 26% change. This indicates that not only is $(\ell_r-\ell_s)/L$ very sensitive to the wall functions but so also is the shape of the separation bubble: by decreasing κ, the back-flow is retarded less, promoting a longer separation bubble.

The observed sensitivity of the calculations to changes in C_μ and κ indicates that the accuracy of the predictions depends upon an accurate turbulence model and wall functions. Notwithstanding reservations about the dissipation equations, (4), the turbulence model can be expected to be as accurate in this as in other flows. The wall functions, on the other hand, are based on Couette flow solutions and have less physical foundation near separation and reattachment points. Consequently, before the procedure can be expected to produce reliable results, it is necessary to verify the performance of the wall functions and, if necessary, develop modifications.

CONCLUSION

The problem of calculating the flow properties of separated turbulent boundary layers has been considered and difficulties, not associated with other recirculating flows, have been identified. The task of providing an accurate model of the turbulence is at once more difficult and more important since the near-wall region is very influential. As these flows often occur on bodies with curved surfaces in a free-stream, there are practical difficulties connected with using a finite-difference method: the normally-used rectangular grids are ill-suited to curved surfaces and the potential flow and viscous flow solutions must be matched.

A calculation procedure has been outlined which solves the flow equations in general orthogonal coordinates, thus overcoming the difficulty of representing a boundary layer on a curved surface. The k-ε, two-equation, turbulence model is used to determine the Reynolds stresses and wall-functions are employed at solid boundaries. The procedure has been applied to the flow in a curved diffuser and the influence of the geometry has been demonstrated. It was found that the gross features of the calculated flow are sensitive to the assumptions incorporated in the turbulence model and the wall functions. Since the assumptions involved in the wall functions are suspect in some regions of the flow, it is necessary to validate their performance before the procedure can be expected to produce reliable results.

REFERENCES

1. Pope, S.B. and Whitelaw, J.H., "The calculation of near wake flows," J. Fluid Mech., Vol. 73, 1976, p.9.

2. Runchal, A.K. and Spalding, D.B., "Steady turbulent flow and heat transfer downstream of a sudden enlargement in a pipe of circular cross-section," HTS/71/15, 1971, Dept. of Mech. Engng., Imperial College, London.

3. Majumdar, A.K. and Bhaduri, D., "Mathematical modelling of flows in recessed wall flame holder," Appl. Math. Modelling, Vol. 1, 1976, p. 125.

4. Pope, S.B., "The limits of applicability of turbulent scale equations," 1977, Dept. of Mech. Engng., Imperial College, London.

5. Jones, W.P., "Laminarisation in strongly accelerated boundary layers," 1971, Ph.D. thesis, University of London.

6. Chou, P.Y., "On velocity correlations and the solution of the equations of turbulent fluctuation," Quart. Appl. Math., Vol. 3, 1945, p.38.

7. Harlow, F.H. and Nakayama, P.I., "Turbulent transport equations," Phys. Fluids, Vol. 10, 1967, p. 323.

8. Launder, B.E. and Spalding, D.B., "Mathematical Models of turbulence," Academic Press, London.

9. Pope, S.B., "A more general effective viscosity hypothesis," J. Fluid Mech., Vol. 72, 1975, p. 331.

10. Gosman, A.D. and Pun, W.M., "Calculation of recirculating flows." HTS/73/2, 1973, Dept. of Mech. Engng., Imperial College, London.

11. Pope, S.B., "The calculation of turbulent recirculating flows in general orthogonal coordinates," 1976, Dept. of Mech. Engng., Imperial College, London.

12. Jones, W.P. and Launder, B.E., "The prediction of laminarization with a two-equation model of turbulence," Int. J. Heat Mass Transfer, Vol. 15, 1972, p. 301.